JOURNAL OF GEOPHYSICAL RESEARCH, VOL. 96, NO. B10, PAGES 16,223–16,230, SEPTEMBER 10, 1991

Multifractal Analysis of the Microdistribution of Elements in Sedimentary Structures Using Images From Scanning Electron Microscopy and Energy Dispersive X Ray Spectrometry

A. BLOCK, W. VON BLOH, T. KLENKE, AND H. J. SCHELLNHUBER

Institute for the Chemistry and Biology of the Marine Environment and Physics Department, University of Oldenburg Oldenburg, Federal Republic of Germany

A novel method for the quantitative characterization of density distributions of elements in sedimentary geosystems is presented. This general technique is based on the multifractal analysis of image-processed elemental maps obtained by scanning electron microscopy combined with energy dispersive X ray spectrometry. Applications to microdistributions of Si, Fe, and Al in recent bioactive siliciclastic marine sediments are reported. Inhomogeneous scaling behavior of these elemental distributions is observed in all cases. Two main conclusions can be drawn: (1) The sedimentary matrix exhibits true fractal geometry and (2) the processes allocating and rearranging the elements are not of pure stochastic type. Therefore the identification of genetic processes may be possible on the basis of their "multifractal fingerprints".

1. INTRODUCTION

1.1. *Objectives*

The geometry of complex geosystems, like recent sediments or sedimentary rocks, is the spatial result of various interacting processes. These include genetic processes, like sedimentation, as well as intrinsic processes, like percolation of interstitial waters [*Thompson et al.*, 1987]. Distinct processes express themselves in specific structures, i.e., domains with chemical, biological, or physical properties different from those found in the immediate neighborhood [*Werner and Torrist*, 1990]. Such structures can be observed on many scales. Therefore answers on genetic and intrinsic questions can be gathered by the geometrical analysis of the component distribution/morphology. In addition, the geometry is a key for both the quantification of the components of a geosystem, and the description or, eventually, the modeling of its genetic and intrinsic mechanisms.

Direct spatial informations about local structures are mainly provided by photographs, maps, or other kinds of images, which are essential prerequisites for the determination of distribution and morphology of the components [*Smith*, 1986]. Usually, geometrical features are visualized by microscopical methods and analyzed by (automatic) measuring equipment, mainly based on television-type image analyzers or X-ray-type systems, applied to measurements in one, two, or even three dimensions [*Jones*, 1987]. The resulting images can be processed by a number of deterministic and statistical methods. The related stereological methods are used for the quantitative description of some features of interest like modal composition, particle size and texture, particle composition, particle distribution, arrangement, association, and pore volume [*Jones*, 1987; *Tucker*, 1988].

However, not only the geometrical analysis of components, such as minerals, biota, or pores, may yield data on the composition as well as the structure-forming processes and events: The distributions of elements, which can be regarded as subconstitutents of a mineralogical or biological support, provide essential and complementary structural information due to the specific occurrence of elements on the component support.

We present a method for the quantitative description of the geometry of elements, using the example of a sedimentary geosystem. It is based on recent developments in the physics of nonlinear dynamics and allows (1) the quantification and description of the distribution of elements and (2) the detection of genetic and intrinsic processes and properties via a geometrical analysis. It represents a novel tool to be combined with stereological methods, which are often limited and insufficient, especially as far as the genetic interpretation of the treated data is concerned. Our method is based on the concept of fractality and will therefore focus on scaling characteristics or self-similarities in the data at hand. A characterization of these features sheds light on the effective scales of the reigning genetic dynamical processes and also on the intrinsic structure-forming events.

We have employed scanning electron microscopy combined with energy dispersive X ray analysis (SEM/EDX) to obtain the local elemental distribution geometry and to produce elemental dot maps. These maps generate the distribution patterns of the more abundant elements; they are prepared by an image processing system in order to quantify numerically their scaling characteristics and to get information about the nonuniformity of the spatial element distribution function.

We have organized this paper as follows. First we will briefly review the basic definition of fractal dimension and its extension for characterizing nonuniform measures on fractals, the concept of multifractality. Then we will describe sampling and specimen preparation and our experimental settings. Finally, we present the results and discuss the method employed.

1.2. *Fractal Description of Self-Similar Objects*

Recently, novel and powerful methods for the quantitative analysis of structures and shapes in real geosystems have

Paper number 91JB01578.
0148-0227/91/91JB-01578$05.00

arisen from the application of the concept of fractals as introduced by *Mandelbrot* [1983]. At first sight, geometries of natural objects are bewildering in their complexity. They seem too complicated to be characterized and measured in a satisfying way. But quite often the spatial or temporal distribution of features exhibits a (statistical) symmetry with respect to magnification or reduction: the structures and characteristic forms at smaller scales look similar to the ones at larger scales. This scaling symmetry can be quantified by the fractal dimension. The latter has become an important tool for the characterization of exactly or approximately self-similar objects, which play a major role in many physical situations like nonlinear dynamics [*Schuster*, 1988; *Mayer-Kress*, 1986], critical phenomena [*Stinchcombe*, 1989], and growth processes [*Herrmann*, 1986]. However, nontrivial scaling behavior, i.e., invariance under contractions or dilations, seems to be also a crucial feature of many other natural structures and processes, although this invariance is often realized only in a subtle and statistical way.

Fractal analysis of natural systems has been performed in many realms, including material sciences [*Kaye*, 1989], chemistry [*Avnir*, 1989], and biology [*West and Goldberger*, 1987]. In the earth sciences, fractal analysis has been used to study, for instance, the topography of landscapes [*Huang and Turcotte*, 1989] and river networks [e.g., *Takayasu*, 1990] or the surface and bulk structure of minerals [*Krohn*, 1988*a*] and sedimentary bodies [*Thompson et al.*, 1987].

Careful investigation of the microstructure of sandstones indicates that their pore volume distribution can be divided into two domains: a short-length regime with fractal behavior and a long-length regime where fractal characteristics are negligible. The fractal part appears to be strongly governed by the growth of minerals and cements in the pore space [*Krohn*, 1988*b*].

Our present study extends to even smaller scales and focuses on the microdistribution of elements in real sedimentary bodies. Such a distribution defines a measure on the sedimentary microstructure, which is by itself a self-similar object, and therefore shows a more complicated behavior than a distribution on objects which are homogeneous and translational invariant. One single number, namely, the "ordinary" fractal dimension, may be sufficient for the geometrical characterization of the sedimentary matrix, but physical, chemical, or biological processes, or probability and weight distributions that take place on such a structure, have to be described by the more general concept of multifractality [*Halsey et al.*, 1986; *Coniglio et al.*, 1989; *Tel*, 1988]. The so-called generalized fractal dimensions yield detailed information regarding the nonuniformity of fractal measures. This information is very important in our case, as the nonuniformity of the distribution of elements within the sediment is assumed to be closely related to certain diagenetic processes and various system properties like permeability [*Thompson et al.*, 1987].

1.3. *Fractal Dimension and Multifractal Measures*

Self-similar or fractal structures embedded in Euclidean space E^d usually do not have a finite d-dimensional volume and cannot be described in terms of traditional geometry. They do not have any characteristic lengths. One consequence of this fact is that their boundary (surface; contour) is nowhere smooth and is therefore very difficult to measure. Famous examples are coastlines: their total length depends on the yardstick used [*Mandelbrot*, 1983]. In order to assign well-defined "contents" to such objects, D-dimensional Hausdorff measure has to be used [*Falconer*, 1985], where $D \in [0, d]$ is the Hausdorff dimension. While the rigorous determination of D is almost always impossible for a fractal structure represented by a point set $\mathbf{X} \subset E^d$ (for example, digitized photos, maps, or other experimental data, characterizing the geometrical features of the object under investigation), a very good estimate can be achieved, in general, by computing the so-called box-counting (or capacity) dimension D_B [e.g., *Grassberger and Procaccia*, 1983]:

It is defined as

$$D_B = \lim_{\varepsilon \to 0} \frac{\ln N(\varepsilon)}{\ln (1/\varepsilon)}, \tag{1}$$

where ε is the lattice constant of d cubic covers of $\mathbf{X}$ and $N(\varepsilon)$ is the number of cubes contained in the minimal cover. Numerically D_B is calculated by the following recipe: Count the number $N(\varepsilon)$ of boxes of edge length ε that are necessary to cover all points of the data set and calculate the slope of $\ln N(\varepsilon)$ versus $\ln \varepsilon$ for decreasing resolution parameter ε.

The single number D_B may be sufficient for a geometrical characterization of the fractal set considered, but, as mentioned before, processes or distributions that take place or are defined on such a structure have to be described by multifractal measures [*Tel*, 1988]. The formalism is based on generalized (box counting) fractal dimensions $D_B(q)$, $q \in \mathbf{R}$ [*Hentschel and Procaccia*, 1983], defined by

$$D_B(q) = \lim_{\varepsilon \to 0} \frac{1}{q-1} \frac{\ln \sum_{\nu=1}^{N(\varepsilon)} [p_\nu(\varepsilon)]^q}{\ln \varepsilon}. \tag{2}$$

Here the index ν labels the individual boxes of the ε cover and $p_\nu(\varepsilon)$ denotes the relative weight of the νth box. In practice, the measure under investigation is encoded in a finite ensemble of points in E^d (in our case it is given by the two-dimensional coordinates of the elemental dots representing the occurrence of the specified element in the sedimentary sample). Within this approximation, $p_\nu(\varepsilon)$ is given by

$$p_\nu(\varepsilon) = \frac{N_\nu(\varepsilon)}{N}, \tag{3}$$

where $N_\nu(\varepsilon)$ is the number of points falling into the νth box and N is the total number of dots. The definition of generalized box-counting dimensions obviously includes the ordinary one, i.e., $D_B = D_B(0)$. Note that $D_B(1)$ is the entropy dimension, $D_B(2)$ the correlation dimension of pairs of the points, $D_B(3)$ the correlation dimension of triples, etc. [*Schuster*, 1988].

Let us emphasize here that the spectrum of generalized fractal dimensions $D_B(q)$ quantifies the nonuniformity of the measure defined on the fractal set $\mathbf{X}$: If p were chosen as the $D_B(0)$-dimensional Hausdorff measure, then we would have $D_B(q) = D_B(0)$ for all $q \in \mathbf{R}$. In the following we will choose p as the two-dimensional measure. The occurrence of elements is supposed not to be restricted to just the self-similar sedimentary matrix. They may also be found in the pore space, and therefore the chosen "trivial" measure seems to be appropriate. If the generalized fractal dimen-

sions $D_B(q)$ depend on the "qth moment", then the density distribution of elements scales multifractally with respect to the two-dimensional measure, and the evaluated $D_B(q)$ quantify the nonuniformity.

2. METHODS

2.1. *Sampling and Specimen Preparation*

Samples were taken from lower supratidal sediments of the East-Frisian Waddensea region of the North Sea (German Bight). These recent bioactive siliciclastic marine sediments are highly porous and unconsolidated versicolored tidal flat substrates (subparallel laminated sandy sediments with thin microbial mat intercalations, Mellum Island/North Sea). The regional setting as well as the biological and petrographical conditions are described by *Gerdes et al.* [1985 and the references therein].

The samples were taken by inserting a box corer, which was immediately afterwords transferred to our laboratory facilities for further preparation. In the laboratory, small profiling columns of the upper layers (≈45 mm) were cut out and fixed in 1,5-pentanedial in seawater overnight. Before dehydration in a graded series of ethanol/aqua bidest mixtures (concentration series from 10 to 100% ethanol) the specimens were washed several times with degrading salt concentrations. The unconsolidated columns were embedded in epoxy resin prior to polishing. Special care was taken to achieve a polished surface plane. Finally, the specimens were sputtered with gold or graphite and examined by means of SEM/EDX equipment.

2.2. *SEM/EDX Imaging*

In general, SEM/EDX is a method of chemical as well as visual analysis of materials. The specimen is bombarded by a focused beam of high-energy electrons. The electron beam penetrates into the top of the specimen, and interaction with the different specimen-forming elements causes the emission of characteristic X rays. These rays are measured simultaneously by using solid-state, energy dispersive X ray detectors.

The geometrical information gained by this nondestructive method is not strictly confined to the two-dimensional surface plane. Due to the finite penetration of the incident beam there is a certain information depth, which increases with growing acceleration voltage of the incident electron beam. The spatial resolution of the dot maps is limited mainly by three factors: (1) X ray generation geometry, (2) magnification, and (3) optical equipment. Therefore the diameter of each dot may vary as a function of these operation parameters.

A Cambridge Instrument S 180 scanning electron microscope equipped with a Link Ortec 6230 EDX system was used in our investigations. Generally, the acceleration voltage was set to 20 keV and the integration time to 60 s. By means of this equipment, elemental dot maps are obtained, which document the spatial distribution of elements on the sedimentary body and are the basis of a numerical analysis via image processing as described below.

2.3. *Digital Image Processing*

The images are digitized for box-counting analysis, which is done by a CCD camera and an image processing unit. In the following step the coordinates of the elementary distribution are extracted from the digital picture in order to get a coordinate list, which is the appropriate data structure for the novel effective box-counting algorithm employed [*Block et al.*, 1990].

The digitizing of the image is done by a B/W-CCD (Pearpoint 800 pixel CCD) camera connected to an image processing unit (series 151 image processor by Imaging Technology, Incorporated) with a resolution of 512 × 512 pixels in 256 grayscales. The extraction of the point coordinates is quite simple to handle, because the SEM/EDX image consists of points of comparable intensity.

Without loss of information the image data can be reduced to binary (0/1) information by performing threshold filtering. Instead of storing the whole image, only the coordinates of the nonzero values in the digital image are retained.

The improved box-counting algorithm calculates directly the generalized fractal dimensions $D_B(q)$ by using the coordinate list created in the previous step. The algorithm is implemented on a parallel computer consisting of four INMOS limited transputers (T800 processor + 1 megabyte of random access memory), which are installed in an ordinary personal computer controlling the image processing unit and allowing fast processing of SEM/EDX images. The running time of the algorithm depends only on the number of points N, i.e., the computing time grows quasi-linearly with N ($O(N \log_2 N)$). Combination of this effective method with the powerful parallel hardware makes it possible to analyze even very large structures.

The accuracy of the D_B values is improved by applying a classwise linear regression method for minimizing the mean square deviation. This method gives also an estimate of the scaling region, which is always limited by finite size effects, i.e., by the limited resolution of the images.

TABLE 1. Effect of the Integration Time on the Observed Number of Points and the Fractal Dimensions $D_B(0)$ and $D_B(3)$

Integration Time	Points	$D_B(0)$	$D_B(3)$
30	6276	1.89	1.742
60	7514	1.89	1.746
125	7312	1.89	1.727

3. RESULTS

3.1. *Operational Conditions*

First of all, the influence of SEM/EDX operational conditions on the results for the fractal dimensions was tested for the equipment parameters integration time and acceleration voltage (Tables 1 and 2).

The variation of the integration time for sampling the

TABLE 2. Effect of the Acceleration Voltage on the Observed Number of Points and the Fractal Dimensions $D_B(0)$

Acceleration Voltage, keV	Points	$D_B(0)$
10	956	1.77
20	5341	1.88
40	682	1.76

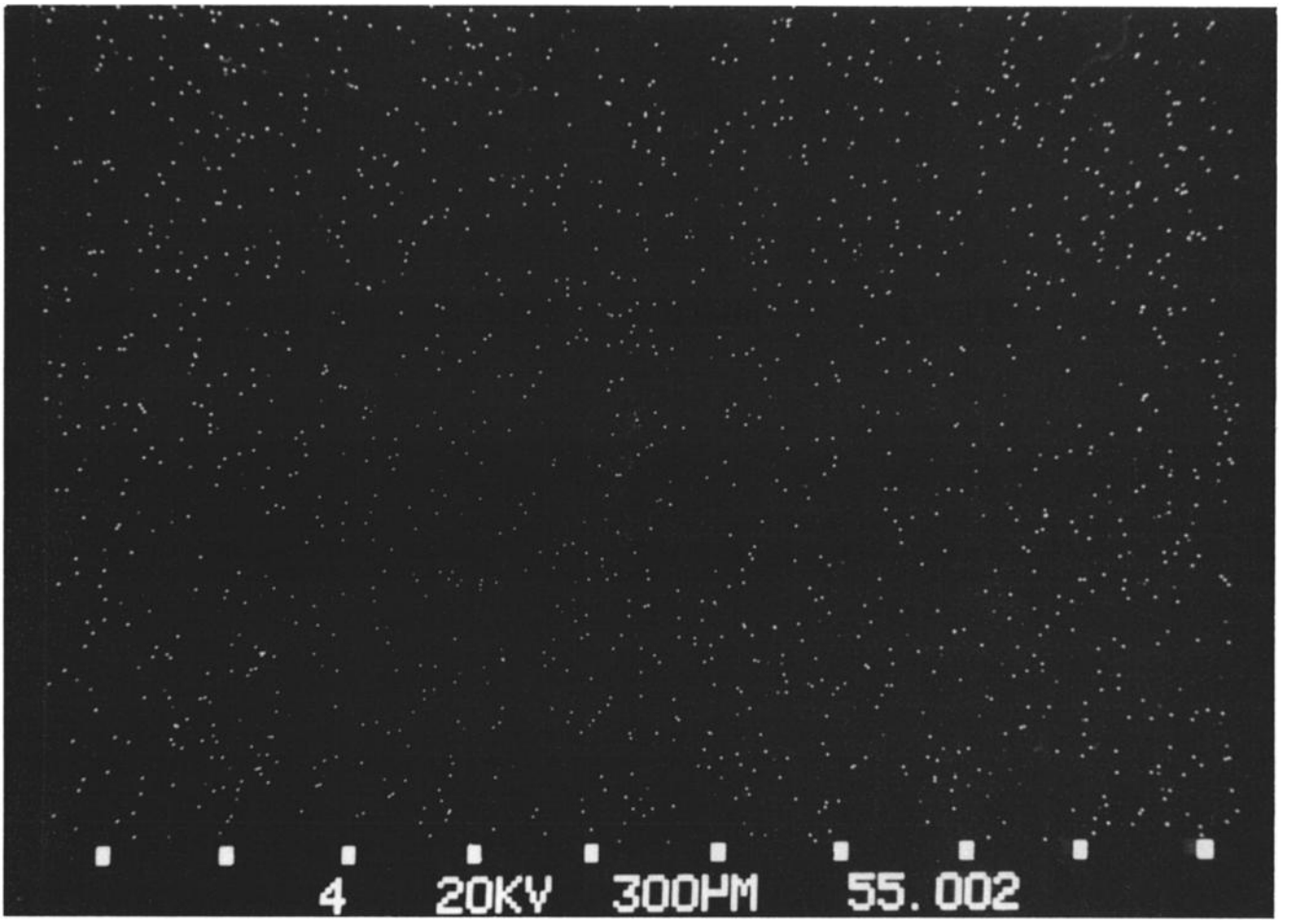

Fig. 1*a*. SEM/EDX Fe dot map: Fe distribution pattern of a sedimentary structure obtained from a profile (3 mm thickness) of the uppermost layers of a recent versicolored tidal flat sediment. The number of contributing points is 7514. The distance between two bars (white squares in the lower part of the operation display) is 300 μm. The diameter of each dot is about 8.6 μm, which defines the spatial resolution of the dot map and the lower limit of analysis in this specific case.

elemental dot maps from 30 to 125 s results in a unique fractal dimension $D_B(0) = 1.89$ in all cases (Table 1). The number of points differs slightly, probably due to lower excitation time (30 s) or the clustering of points to one larger point (125 s). Note that the $D_B(3)$ values found do not depend on the number of points. These values are significantly smaller than the corresponding $D_B(0)$ and prove the nonuniformity of the used two-dimensional measure!

The influence of the acceleration voltage on the elemental dot image (Table 2), however, is of greater importance. Both relatively low and high acceleration voltages gave insufficient dot map information. Possible reasons for this are deflection and the reduction of the effective energy of the incident low-energy electron beam (10 keV) or the reduction of the emitted X ray yield by the absorption of X rays generated in deeper specimen layers (40 keV). Evidently, the decrease in the number of points lowers the obtained fractal dimension.

3.2. *Operational Steps*

The different steps of the method employed can be well demonstrated by the sequence of Figures 1*a*–1*d*, which refer to the multifractal analysis of the Fe distribution in the sedimentary structure of a versicolored substrate:

The SEM/EDX Fe dot map (Figure 1*a*) does not exhibit the stratification features, which can be identified in the corresponding SEM picture. In the latter (not shown) an alternating layering of sandy laminae and microbial mats is the dominant petrographical feature. In the Fe dot map there are, however, domains of denser dotting indicating the nonrandom Fe distribution in the sediment.

The digitized image corresponds directly to the dot map, but the contrast of the image is enhanced, resulting in a visual "optimization" (Figure 1*b*).

The box-counting analysis of this Fe-distribution image yields a fractal dimension of $D_B(0) = 1.89 \pm 0.0129$ (Figure 1*c*).

Figure 1*d* shows the generalized fractal box-counting dimensions of Fe-distribution samples as a function of the moment parameter q. One observes a clear-cut multifractal scaling behavior of the Fe-distribution measure, which is largely independent of the amount of Fe contained in the sample! The occurrence of Fe in the sediment specimens under investigation is therefore highly inhomogeneous, i.e.,

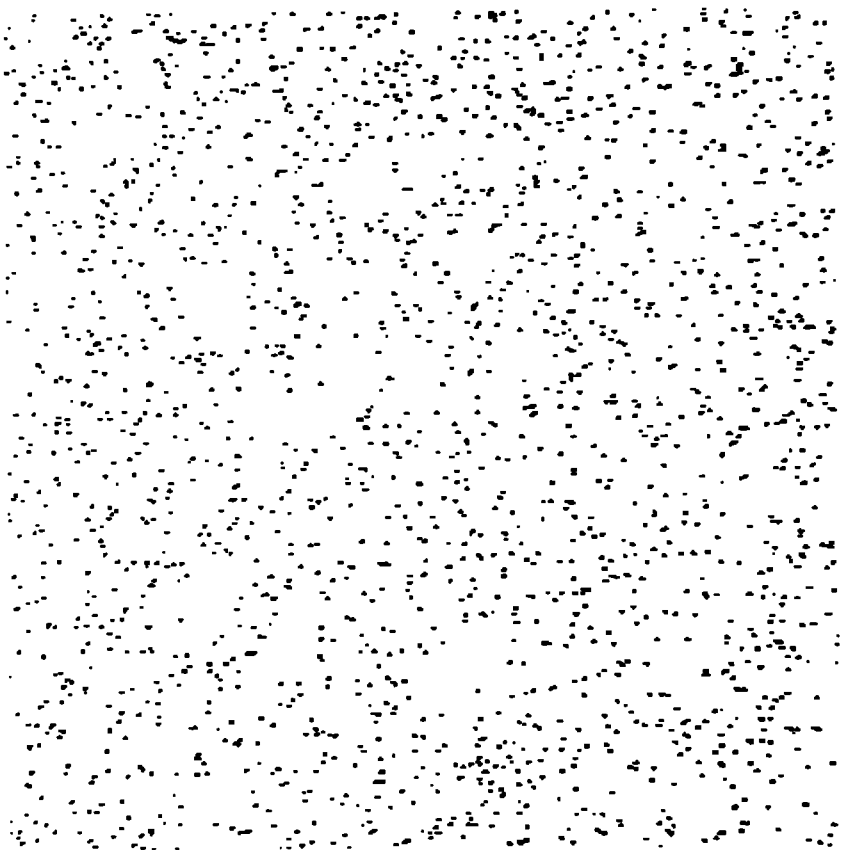

Fig. 1*b*. Digitized SEM/EDX elemental image. This is an operational "optimized" detail of the SEM/EDX Fe dot map of Figure 1*a*.

denser and sparser parts scale differently. Random disorder cannot give rise to such characteristics.

As a test, we have also analyzed the synthetic distribution measure of randomly placed dots for increasing point numbers on a two-dimensional grid of fixed size, namely, 512 × 512 lattice sites. Due to the finite size of the data set a spurious multifractal behavior of the random-sample dot map is observed, as shown in Figure 2*a*, but for all particle numbers up to $N = 7500$ this artifact can clearly be distinguished from the "true" multiscaling depicted in Figure 1*d*.

Further evidence for the multifractality of the real phenomena under investigation is provided by comparison with an artifical fractal, namely, a computer-generated Sierpinski carpet [see *Mandelbrot*, 1983] with almost the same Hausdorff dimension $D_B(0)$. This structure is obtained as follows: Divide the unit square into nine congruent subsquares and remove the central one. Apply the same operation to the remaining 8 subsquares and continue the process ad infin-

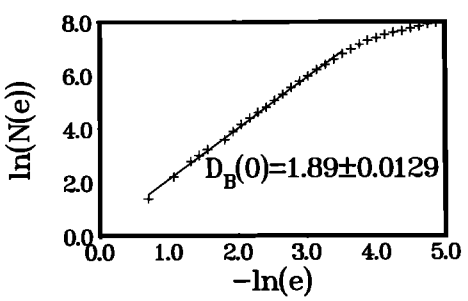

Fig. 1*c*. Box-counting analysis of the digitized elemental image of Figure 1*b*. The data for $-\ln(\varepsilon) > 3.5$ are excluded from the analysis because of finite size effects.

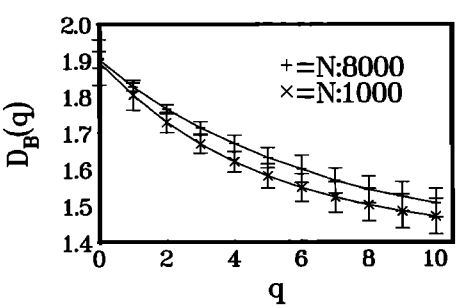

Fig. 1*d*. Numerical determination of the generalized fractal dimensions $D_B(q)$, $0 \leq q \leq 10$, for the abundance measure of Fe in different samples of the same uppermost layers of a recent versicolored tidal flat sediment. Two groups of samples are analyzed: one contains five specimens, which provide between 7073 and 8211 points; the other group consists of six specimens with a smaller amount of Fe, containing between 842 and 1320 dots. The error bars denote the mean square deviations.

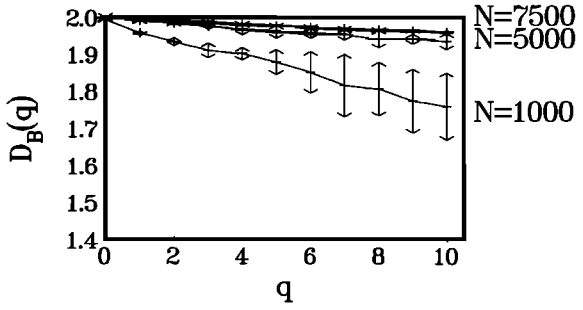

Fig. 2*a*. Generalized fractal dimensions $D_B(q)$, $0 \le q \le 10$, of computer-generated dot maps comprising up to 7500 points. The error bars denote the mean square deviations calculated by averaging over 20 dot maps for each fixed number of points.

itum. The result is a self-similar point set of fractal dimension $D_B(0) = \ln 8/\ln 3 \approx 1.89$.

A crucial fact here is that the emerging mass distribution scales homogeneously, i.e., $D_B(q) = D_B(0)$ for all $q \in \mathbf{R}$, if equal normalized weights are assigned to all subsquares belonging to the same generation. This illustrates a general theorem stating that monofractal measures necessarily arise whenever subsets are endowed with weights proportional to their $D_B(0)$-dimensional volume [*Block et al.*, 1990]. We expect therefore the spectrum of generalized dimensions of the Sierpinski carpet to differ markedly from the Fe spectrum even in the presence of finite-size effects.

This is indeed the case as Figure 2*b* demonstrates: The artificial fractal measure is encoded by approximately 2000, 4000, and 8000 points, respectively, chosen randomly from the exact set, and the associated $D_B(q)$ functions are plotted. Note that the finiteness of the data sets introduces some synthetic inhomogeneity, which decays rapidly, however, with increasing number of points. This is similar to the behavior of the random sample and clearly contrasts with the genuine multifractal characteristics depicted in Figure 1*d*.

The results for $D_B(q)$ as determined for random point sets ($N \approx 7500$), Fe dot maps ($N \approx 8000$), and the Sierpinski carpet ($N \approx 8000$) are summarized and compared in Table 3.

All samples were defined on identical quadratic grids. The inhomogeneity of the fractal scaling behavior, which may be measured by the difference $D_B(0) - D_B(q)$ is evident for the

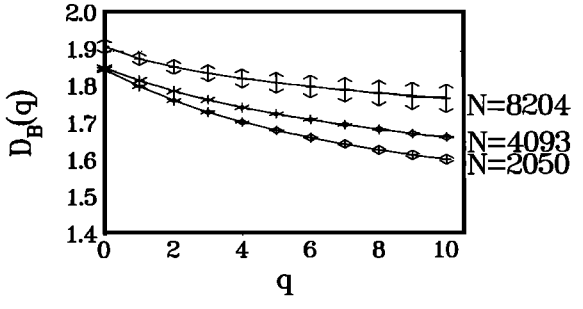

Fig. 2*b*. Generalized fractal dimensions $D_B(q)$, $0 \le q \le 10$, of a computer-generated homogeneous fractal measure as described in the text. Finite data sets of different length N have been produced by random sampling from the exact fractal set. The range of the error bars denotes the mean square deviations calculated by averaging over 10 samples for each fixed number of points. The dotted line indicates the exact fractal dimension $D_B(0)$.

TABLE 3. Generalized Fractal Dimensions $D_B(q)$

	$D_B(q)$		
q	Random Dot Map	Sierpinski Carpet	Fe Dot Map
0	2.00	1.90	1.90
1	1.99	1.87	1.83
2	1.99	1.85	1.77
3	1.98	1.83	1.71
4	1.98	1.82	1.67
5	1.98	1.81	1.63
6	1.97	1.80	1.60
7	1.97	1.79	1.57
8	1.96	1.78	1.54
9	1.96	1.77	1.52
10	1.96	1.77	1.51

$D_B(q)$ are calculated for random dot maps ($N = 7500$) (Figure 2*a*), for a numerically generated homogeneous fractal ($N \approx 8000$) (Figure 2*b*), and for Fe dot maps ($N \approx 8000$) (Figure 1*d*).

Fe data, whereas the variation is definitely smaller in the other cases.

3.3. *Multifractal Analysis and Interpretation*

All the spatial distribution measures of the three elements Si, Fe, and Al in the sedimentary structure investigated show a clear multifractal scaling behavior (Figure 3). The elemental spectra differ slightly, probably as a consequence of different genetic and intrinsic processes in certain modes and rates.

These processes determining the elemental distributions are phenomena of growth, aggregation, percolation, dissolution, etc. as part of the following general scenario for structure-forming events on clastic sedimentary geosystems:

The genesis of such a geosystem starts with the predepositional steps of crystallization, weathering, and transport of each detrital mineral. During the succession but also in combination of these steps the primary mineral is substantially and morphologically altered by physical, chemical, and biological processes. These steps are specific to each individual detrital component (minerals, biota, and organomineral associations). The sedimentary system is formed by the deposition of these detrital components under certain conditions and the postdepositional diagenetic steps. During the diagenesis the original assemblage of detrital components as well as the complementary pore space can be again substan-

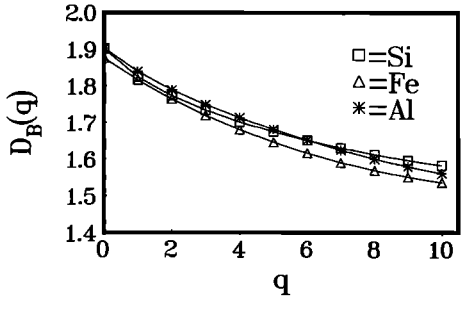

Fig. 3. Generalized fractal dimensions $D_B(q)$, $0 \le q \le 10$, characterizing the scaling properties of the microdistribution of Si, Fe, and Al, respectively, in a representative sample of the recent versicolored tidal flat sediment investigated. Number of points: Si: $N = 40{,}259$, Fe: $N = 22{,}132$, Al: $N = 26{,}970$.

tially and morphologically altered by the dissolution of minerals, by the breakdown and consumption of organic material, and by the growth of authigenic minerals and new microbial communities.

One relevant factor that controls the sediment-intrinsic percolation of reactive interstitial water through the pore space is of course the geometry of the structure: the modes and rates of processes, like the active hydrodynamic and the passive diffusive transport of fluids, depend on the sizes and shapes of the pores and their connectivity. In addition, there is an interaction between solid-matrix components and components transported by the percolating fluids. Again, modes and rates of the interaction during the passage of fluids through the reactive sedimentary system (dominantly sorption, molecular sieving, or biogenic geochemical transfer of element species) are controlled by the structural features of the anorganic/organic mineral/biota limited surface area and the total porosity.

Keeping this scenario in mind, it is not very surprising to find that the natural systems in question exhibit a variety of scaling characteristics in the arrangement of their components [*Avnir*, 1989; *Thompson et al.*, 1987]. In particular, the observed multifractality of certain elemental distributions is quite plausible: Some of the genetic and intrinsic processes just sketched, such as growth or dissolution, may be modeled in terms of diffusion-limited aggregation (DLA) or diffusion-limited deposition/precipitation on the self-similar sedimentary matrix, or by equivalent schemes of degradation of the latter [*Witten and Sander*, 1981]. Many variants of these models, emphasizing different aspects of the microscopic mechanisms, have been developed in the last years [*Jullien and Kolb*, 1984]. Extensive computer simulations of aggregation processes described within this framework have revealed that the resulting mass distributions have to be described by multifractal measures [*Feder*, 1988; *Avnir*, 1989; *Tel*, 1988]. We conjecture that the growth of biofilms and authigenic minerals as well as the sorption or reaction of particles transported by percolating waters cause similar phenomena in the distributions of elements in the fractal porous sediments investigated here.

The different elements and their distributions may serve to resolve the web of processes structuring the sediment geometry into specific components and mechanisms,like DLA-type precipitation: For instance, in the case of the bioactive siliciclastic sediments investigated, Si is an indicator of detrital mineral components (quartz). Al is an indicator for different minor mineral components (feldspars and terrigenous/authigenic clay minerals). Fe, however, as a partly geochemical and biological transferable element, can be used to identify a couple of components (terrigenous clay minerals and biota) as well as biofilms on the mineral surfaces and bioinduced authigenic minerals (sulphides and clay minerals).

In synopsis, a bouquet of different processes act together to produce the inhomogeneous distributions of Si, Fe, and Al, which can be analyzed in terms of multifractal calculus. We have not yet tried to assign individual traits of the multifractal spectrum to special actions and interactions. This is certainly a formidable but attractive task for future work.

The elemental overall fractal dimension on the structure was also determined (Figure 4). To that end an analysis was carried out for all elements detectable by the applied SEM/EDX technique, thus excluding the light elements with atomic mass ≤ 12 and the dominant elements of the organic components (C, N, O).

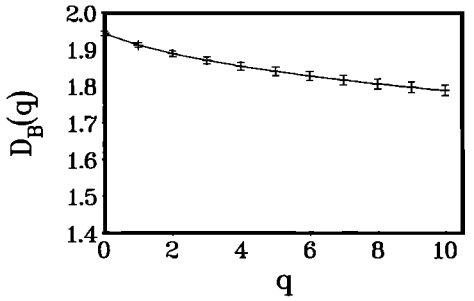

Fig. 4. Generalized fractal dimensions $D_B(q)$, $0 \leq q \leq 10$, characterizing the scaling properties of the union of the microdistributions of all detectable elements in the specimen. The number of points in the sample under investigation is $N = 64{,}848$. The error bars denote the mean square deviation of the point distance resulting from a classwise hierarchical regression analysis [*Späth*, 1983].

Our investigation yields an overall fractal dimension of $D_B(0) = 1.94 \pm 0.01$ for a typical sample. The observed variation in $D_B(q)$ characterized by the difference $D_B(0) - D_B(10)$ is nearly 0.155, whereas the corresponding value resulting from the analysis of a random dot map with the same number of points ($N = 62{,}000$) is smaller than 0.04! This finding supports again the multifractality of the phenomena under investigation and also indicates that the distribution of each element with atomic mass > 12 is affected by the fractal properties of the sedimentary matrix.

4. CONCLUSION

The multifractal analysis of elemental distributions in geosystems is a method that allows quantitative insights into the geometrical organization of these systems. We have demonstrated that certain elemental distributions in a recent sedimentary matrix reflect the fractal behavior of their mineralogical and biological support. This observation and the first results presented here indicate that both genetic processes and intrinsic properties can be detected and measured by the analysis of self-similarity of element density distributions by generating valuable information about the effective scales of the governing dynamical processes.

Future work will include other geosystems, such as carbonates or magmatites, in order to establish discrimination criteria on the basis of the $D_B(0)$ values and the multifractal spectra of the elemental distributions. We plan, in particular, the integration of advanced image analysis techniques, which allow the superposition of certain elemental dot maps and maps of the mineralogical/biological support. Besides specific genetic problems we intend to study intrinsic processes, especially sorption and reaction of substances in the fractal pore space of unconsolidated porous sediments. The distributions produced by these processes will be geometrically analyzed by the presented technique and simulated by cellular automata methods [*Wolfram*, 1983].

Acknowledgments. Financial support by the Federal Minister for Science and Technology (BMFT grant MFU 05798) is gratefully acknowledged.

REFERENCES

Avnir, D. (Ed.), *The Fractal Approach to Heterogeneous Chemistry*, 441 pp., John Wiley, New York, 1989.

Block, A., W. von Bloh, and H. J. Schellnhuber, Efficient box-counting determination of generalized fractal dimensions, *Phys. Rev. A*, *42*, 1869–1874, 1990.

Coniglio, A., L. De Arcangelis, H. J. Herrmann, Fractals and multifractals: Applications in physics, *Physica A*, *157*, 21–30, 1989.

Falconer, K. J., *The Geometry of Fractal Sets* 162 pp., Cambridge University Press, New York, 1985.

Feder, J., *Fractals*, p. 283, Plenum, New York, 1988.

Gerdes, G., W. E., Krumbein, and H. E. Reineck, The depositional record of sandy, versicolored tidal flats (Mellum Island, Southern North Sea), *J. Sediment. Petrol.*, *55*, 265–278, 1985.

Grassberger, P., and I. Procaccia, Measuring the strangeness of strange attractors, *Physica D*, *9*, 189–208, 1983.

Halsey, T. C., M. H. Jensen, L. P. Kadanoff, I. Procaccia, and B. I. Shraiman, Fractal measures and their singularities: The characterization of strange sets, *Phys. Rev. A*, *33*, 1141–1151, 1986.

Hentschel, H. G. E., and I. Procaccia, The infinite number of generalized dimensions of fractals and strange attractors, *Physica D*, *8*, 435–444, 1983.

Herrmann, H. J., Geometrical cluster growth models and kinetic gelation, *Phys. Rep.*, *136*, 153–227, 1986.

Huang, J., and D. L. Turcotte, Fractal mapping of digitized images: Application to the topography of Arizona and comparisons with synthetic images, *J. Geophys. Res.*, *94*, 7491–7497, 1989.

Jones, M. P., *Applied Mineralogy—A Quantitative Approach*, 259 pp., Graham and Trotman, London, 1987.

Jullien, R., and M. Kolb, Hierarchical model for chemically limited cluster-cluster aggregation, *J. Phys. A*, *17*, L639–L643, 1984.

Kaye, B. H., *A Random Walk Through Fractal Dimensions*, 421 pp., Verlag Chemie, Weinheim, Federal Republic of Germany, 1989.

Krohn, C. E., Sandstone fractal and Euclidean pore volume distributions, *J. Geophys. Res.*, *93*, 3286–3296, 1988*a*.

Krohn, C. E., Fractal measurements of sandstones, shales, and carbonates, *J. Geophys. Res.*, *93*, 3297–3305, 1988*b*.

Mandelbrot, B. B., *The Fractal Geometry of Nature*, 468 pp., W. H. Freeman, New York, 1983.

Mayer-Kress, G., (Ed.), *Dimensions and Entropies in Chaotic Systems*, 257 pp., Springer, Berlin, 1986.

Schuster, H. G., *Deterministic Chaos*, 270 pp., Verlag Chemie, Weinheim, Federal Republic of Germany, 1988.

Smith, D. J., High-resolution electron microscopy in surface science, in Chemistry and Physics on Solid Surfaces, edited by R. Vanselow, and R. Howe, *Springer Ser. Surf. Sci.*, *6*, 413–433, 1986.

Späth, H., *Cluster-Formation und Analyse*, 236 pp., Oldenbourg, München, 1983.

Stinchcombe, R. B., Fractals, phase transitions and criticality, *Proc. R. Soc. London, Ser. A*, *423*, 17–33, 1989.

Takayasu, H., *Fractals in the Physical Sciences*, 170 pp., Manchester University Press, Manchester, United Kingdom, 1990.

Tel, T., Fractals, multifractals and thermodynamics, *Z. Naturforsch. A*, *43*, 1154–1174, 1988.

Thompson, A. H., A. J. Katz, and C. E. Krohn, The microgeometry and transport properties of sedimentary rock, *Adv. Phys.*, *36*, 625–694, 1987.

Tucker, M., *Techniques in Sedimentology*, 394 pp., Blackwell, Oxford, 1988.

Werner, H. W., and A. Torrist, Interface and thin film analysis: Comparison of methods, trends, *Fresenius Z. Anal. Chem.*, *337*, 594–613, 1990.

West, B. J., and A. L. Goldberger, Physiology in fractal dimensions, *Am. Sci.*, *75*, 354, 1987.

Witten, T. A., and L. M. Sander, Diffusion-limited aggregation, a kinetic critical phenomenon, *Phys. Rev. Lett.*, *47*, 1400–1403, 1981.

Wolfram, S., Statistical mechanics of cellular automata, *Rev. Mod. Phys.*, *55*, 601–644, 1983.

A. Block, W. von Bloh, T. Klenke, and H. J. Schellnhuber, Institute for the Chemistry and Biology of the Marine Environment and Physics Department, University of Oldenburg, Postfach 2503, W-2900 Oldenburg, Federal Republic of Germany.

(Received January 2, 1991;
revised May 20, 1991;
accepted June 10, 1991.)

JOURNAL OF GEOPHYSICAL RESEARCH, VOL. 96, NO. B10, PAGES 16,161–16,168, SEPTEMBER 10, 1991

Magsat Magnetic Anomaly Contrast Across Labrador Sea Passive Margins

LAUREN M. BRADLEY

Astronomy Program, University of Maryland, College Park

HERBERT FREY

Geodynamics Branch, NASA Goddard Space Flight Center, Greenbelt, Maryland

Many passive margins not complicated by nearby anomalous crustal structure have satellite elevation crustal magnetic anomaly contrasts across them that are recognizable in reduced-to-pole versions of the Magsat and POGO data. In the Labrador Sea region this contrast is particularly well developed with strong positive anomalies overlying the continental crust of Greenland and eastern Canada and prominent negative anomalies situated over the Labrador Sea and Baffin Bay. We use forward modeling of the large-scale crustal bodies in this region (continental, oceanic, passive margin, several anomalous structures) to show that the Magsat anomaly contrast is due simply to the change in crustal susceptibility and thickness at the continental/oceanic crustal transition. Because the thickness varies more than the average susceptibility from continental to oceanic crust, the strong anomaly contrast is essentially an edge effect due mostly to the change in crustal structure.

INTRODUCTION

It has been said that the difference between continents and ocean basins is not obvious in the Magsat crustal anomaly data; that is, there is no strong signature of the continent-ocean transition that might be expected at passive margins due to the very different structure and composition of continental and oceanic crust [e.g., *Harrison et al.*, 1986; *Arkani-Hamed*, 1990]. *Meyer et al.* [1983] showed that the strongest continent/ocean crustal magnetic anomaly contrast would come from low-order terms normally removed when the main field is subtracted from Magsat data. *Harrison et al.* [1986] suggested that incomplete removal of the core field from the Magsat data has left a long-wavelength residual which swamps the passive margin signature or, alternatively, that the thickness-magnetization product for continental crust is the same as for oceanic crust, so no signature would be expected. We show below that these conclusions are incorrect for at least the Labrador Sea (and possibly other) passive margins.

Prominent signatures across some passive margins do occur in the Magsat and earlier POGO data. The most obvious examples are the Labrador Sea, around most of the periphery of Australia, and some parts of North America (especially across the Gulf of Mexico and the eastern seaboard) [*Frey*, 1982*a*; *Schnetzler et al.*, 1984; *Bradley and Frey*, 1986*a*]. These all lie at relatively high geomagnetic latitude, and the anomalies (generally positive over the continents negative over the oceanic crust) are closely situated over their likely source bodies and directly related to the magnetization contrast. At lower geomagnetic latitudes the relation between source body and location (and sign) of the associated magnetic anomaly is less direct. In order to obtain a realistic view of whether or not low-latitude passive margins have recognizable Magsat anomaly signatures, it is important to use a reduced-to-pole (RTP) version of the data and to look for anomaly contrasts (i.e., a change to a relative low or high across the margin). *Schnetzler et al.* [1984] described a number of examples. *Bradley and Frey* [1986*a*] reported that a survey of the world's passive margins which were not complicated by the presence of nearby submarine plateaus or other anomalous crust showed a large fraction have a recognizable anomaly contrast of 4 nT or greater. For most of these contrasts there was a relative positive over the continent and a relative negative over the oceanic crust. The magnitude of such a crustal contrast could depend on a number of factors, including the width, thickness, and intrusive history of the margin; the angle between the strike of the margin and the Magsat orbital track (along which filtering is done); and the strength and orientation of the geomagnetic field [*Schnetzler et al.*, 1984].

In order to determine whether or not the observed signatures are due to the structure and magnetization contrast between continental and oceanic crust, we modeled the most obvious example of a passive margin magnetic anomaly contrast, the Labrador Sea anomaly. This strong negative signature (versus positive anomalies over the adjacent continents of Canada and Greenland) is obvious in all versions of the Magsat and even POGO data, no matter how derived [*Frey*, 1982*a*; *Langel et al.*, 1982; *Langel and Thorning*, 1982; *Coles*, 1985; *Haines*, 1985; *Arkani-Hamid and Strangway*, 1985]. We use available geologic and geophysical data to produce a model for the crustal structure and magnetization of the Labrador Sea and the adjacent continents of Greenland and eastern Canada. From the crustal model we compute the expected satellite elevation magnetic anomaly and compare this with the observed anomaly pattern in Magsat RTP data for the area.

LABRADOR SEA MAGSAT DATA

The Labrador Sea region is one in which conditions for the expression of a satellite elevation magnetic anomaly contrast associated with the passive margin are close to optimum. The area is at high geomagnetic latitudes, so induced scalar anomalies can be strong and will be situated nearly over their source bodies. The continental margins strike at high angles

Paper number 91JB01500.
0148-0227/91/91JB-01500$05.00

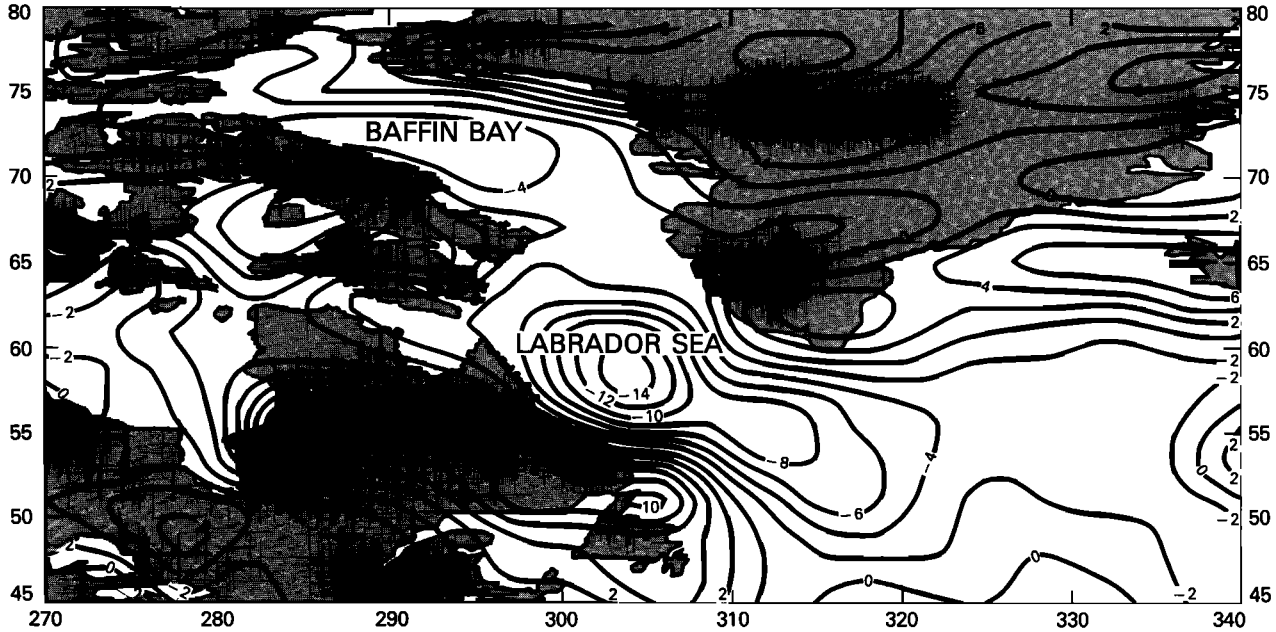

Fig. 1. Reduced-to-pole Magsat dawn data for the Labrador Sea region at 400 km elevation. Contour interval is 2 nT. Note the generally strong positive anomalies over the continents and negative anomalies over the oceans. Also note the relative positive over the Davis Strait separating Baffin Bay from the Labrador Sea and the relative negative running west-to-east across southern Greenland. See text for details.

to the Magsat orbit, so the anomaly amplitude is not likely to be much attenuated by along-track filtering which is used to remove external current noise. The width of the Labrador Sea is about twice the "resolution" element for Magsat data (about 400 km) and is bounded on both sides by continental crust. Thus if the passive margin anomaly signature is manifested as an edge effect due to the change from continental to oceanic magnetization and thickness, a change from positive to negative and back to positive would be expected.

In RTP dawn Magsat data (Figure 1) there is a strong negative anomaly over the Labrador Sea (−14 nT) flanked by strong positive anomalies over the adjacent continental crust of eastern Canada (+12 nT) and western Greenland (+4 to +10 nT). The Greenland positive is split by an east-west relative negative (see below). This negative feature appears in all versions of Magsat and POGO scalar anomaly maps which have been published [e.g., *Langel and Thorning*, 1982] and may represent an unrecognized major crustal structure [*Bradley and Frey*, 1986*b*]. In Figure 1 a 4-nT negative overlying Baffin Bay is flanked by 8- to 10-nT positive anomalies over the Canadian Arctic Islands and Greenland. The Davis Strait, which separates the Labrador Sea from Baffin Bay, has a relative positive anomaly overlying it (relative to Baffin Bay and the Labrador Sea) where the seafloor becomes elevated. By contrast, the Hudson Strait (a topographic low) has a relative negative anomaly overlying it compared to the positive anomalies over the adjacent Baffin Island and Labrador. There is excellent general correlation between topography and satellite elevation magnetic anomaly contrasts in this region, with negatives dominant in the low-lying areas and positives generally associated with the more elevated terrain.

Arkani-Hamed [1990] has suggested that the strong negative anomaly over the Labrador Sea is due to reversed thermoviscous remanent magnetization and may be peculiar to this region and its spreading history. He suggests that the location of the Labrador Sea between two continental cratons may also contribute to the Magsat elevation magnetic low but will contribute less than 4 nT of the observed contrast. This simply stated and unsupported conclusion depends on the assumed susceptibility and thickness contrasts between the continental and oceanic blocks. We show below that reasonable values for the crustal susceptibilities and thicknesses of the continental and oceanic bodies in the Labrador Sea region can account for the total observed contrast (about 20 nT), assuming only induced plus viscous (but not thermal) remanent magnetization. That is, passive margin anomalies might be expected at many continent-ocean boundaries (although not always with such a strong signature) and are not dependent on individual remanent magnetization patterns peculiar to some localities.

MODELING PROCEDURE

In order to calculate the magnetic signature expected at satellite elevation due to induced plus viscous magnetization, it is necessary to divide the region shown in Figure 1 into separate crustal bodies (Figure 2) and to determine the average susceptibility of each of these bodies. Most of Greenland, Labrador, and the Canadian Arctic Islands are treated as continental bodies. The Labrador Sea and Baffin Bay are modeled as oceanic crust (see below). Between these "continental" and "oceanic" bodies are placed blocks which represent the passive margins (see Figure 2). The Davis Strait, Hudson Strait, and a Greenland "rift" body are treated separately, as discussed below. The volumes of these bodies are defined using topographic or bathymetric data and seismic refraction data (where available) to define the crustal thickness. Susceptibilities for continental blocks are based

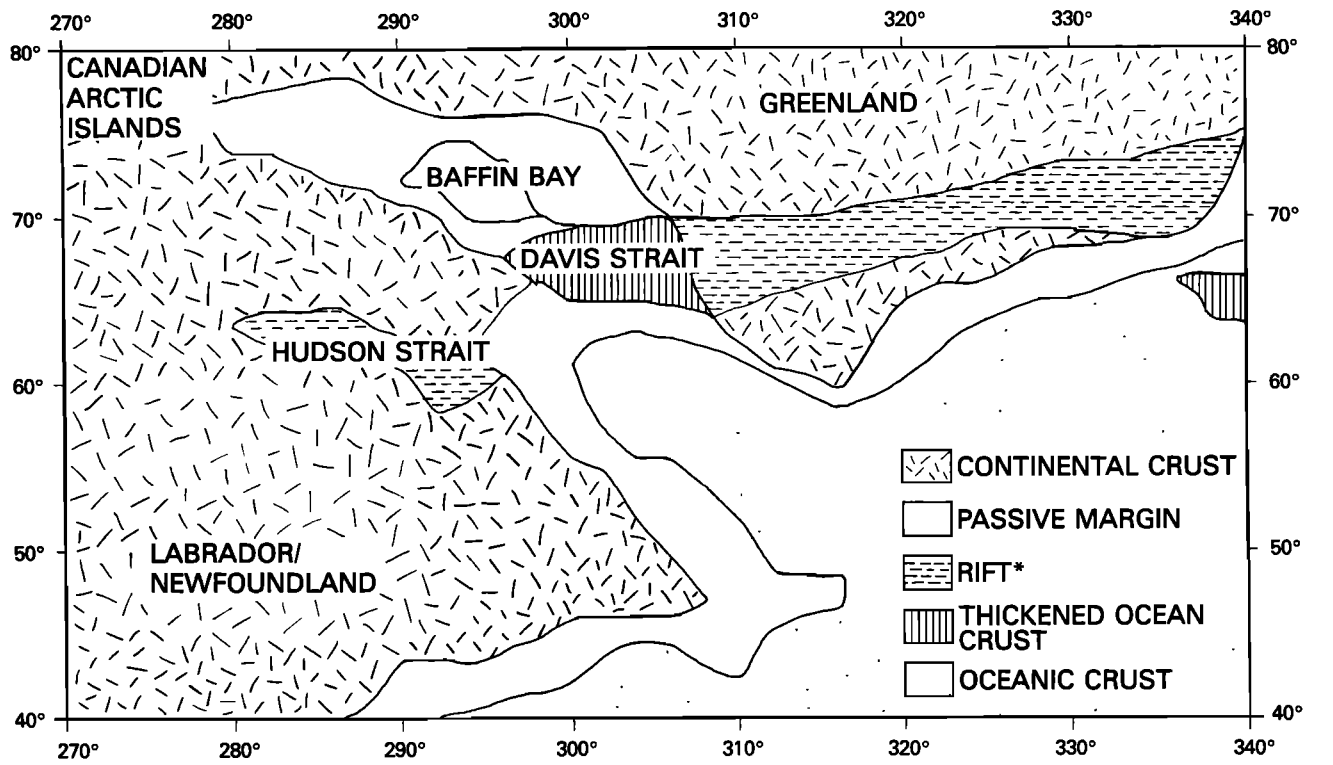

Fig. 2. Representation of the different types of crustal bodies used in calculating the model anomaly pattern for the Labrador Sea region. See text for details.

on the lower crustal value given by *Schnetzler* [1985]. Upper continental crustal susceptibilities are assumed to be negligible. Oceanic susceptibilities are from the model of *Thomas* [1987] which separately assigns the susceptibility appropriate for each crustal layer (2A, 2B, 3A, 3B). Oceanic sediments and continental and oceanic mantle are treated as nonmagnetic. Figure 3 shows the procedure for deriving a bulk or average susceptibility over the entire crustal column by adding up the (susceptibility) × (thickness) products for each layer and dividing by the total thickness. Table 1 summarizes the resulting average susceptibilities. Below we briefly describe the constraints on each of the model bodies.

Eastern Canada and the Canadian Arctic Islands

Seismic refraction studies by *Berry and Fuchs* [1973] suggest that the average crustal thicknesses in eastern Canada is 37 km, ranging from 34 km in the Superior to 45 km in the Grenville Province. For Labrador we adopt the value 42 km. In this study we model the Hudson Strait as a failed rift with crustal thickness 27.5 km based on the analysis of

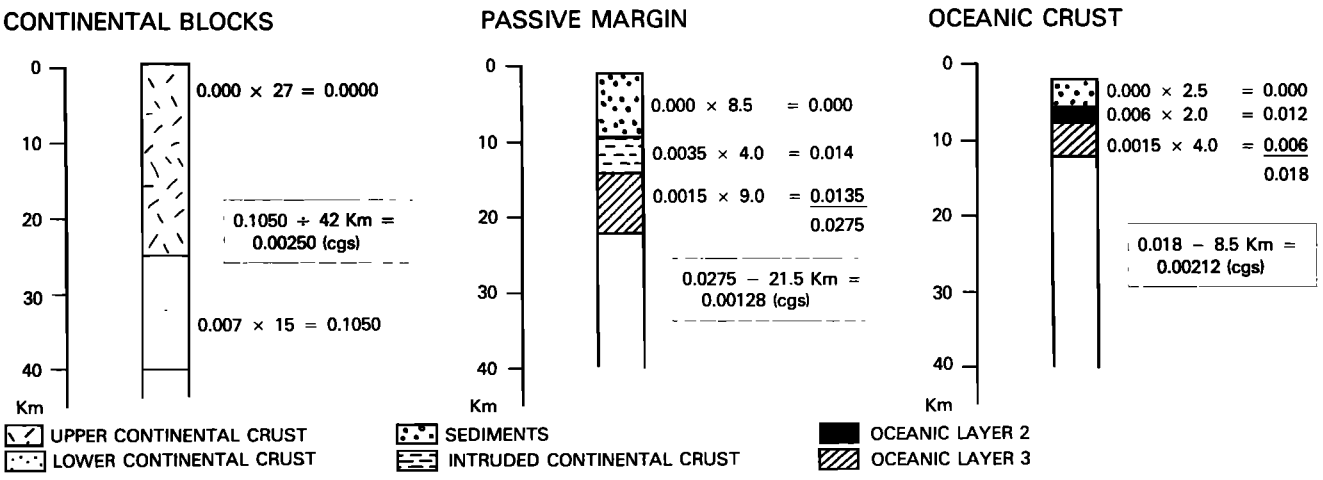

Fig. 3. Schematic representation of method used to calculate the average susceptibility for a crustal body. Magnetic susceptibilities based on *Thomas* [1987] and *Schnetzler* [1985] are separately assigned to each crustal layer, multiplied by the thickness of the layer, added to similar products for all the layers, then divided by the overall thickness (including nonmagnetic sediment thickness for ocean bodies) to produce an average for the entire crustal column.

TABLE 1. Magnetic Susceptibilities, Crustal Thicknesses, and Their Products for Model Bodies

Crustal Body	Average Susceptibility SI	Average Susceptibility cgs	Average Thickness, km	Average Susceptibility × Thickness SI	Average Susceptibility × Thickness cgs
Greenland	0.0314	0.0025	42.0	1.319	0.105
Labrador	0.0314	0.0025	42.0	1.319	0.105
Labrador Sea Baffin Bay*	0.0264	0.0021	8.5	0.224	0.018
Passive margins	0.0161	0.00128	10–30	0.322	0.026
Davis Strait	0.0276	0.0022	12.0	0.331	0.026
Hudson Strait	0.0289	0.0023	27.5	0.795	0.063
Greenland "rift"	0.0289	0.0023	27.5	0.795	0.063

Nonmagnetic sediments included in thickness of ocean bodies.
*Uncertain; see text for discussion.

seismic refraction, gravity, and aeromagnetic data by *Grant and Manchester* [1970]. The average crustal susceptibilities derived are nearly the same for these bodies: 0.0314 SI (0.0025 cgs) for Labrador and 0.0289 SI (0.0023 cgs) for the presumed thinner crust in the Hudson Strait.

Greenland

On the basis of sparse earthquake data, *Gregerson* [1970] estimated the crustal thickness to be 42 km in Greenland, roughly similar in crustal section to eastern Canada. The Magsat pattern over Greenland consists of two distinct positive lobes (10 and 4 nT in the north and south, respectively) separated by a relative negative which runs roughly east-west across the continent (see Figure 1). This is strongly suggestive of a major crustal feature or change in crustal structure. The anomaly signature has strong similarities to the Magsat pattern over the failed Viluy aulacogen which divides the Siberian Platform into two distinct blocks with distinct positive anomalies overlying them [*Frey*, 1982*b*; *Bradley and Frey*, 1986*b*]. As shown below, we find very good agreement between the calculated and observed magnetic anomaly pattern over Greenland when a 100-km-wide, 27.5-km-intermediate-thickness "riftlike" body in included in the Greenland model, stretching between Disco Island and Scoresby Sund (Figure 2). As shown in Table 1, the average susceptibility for the 42-km-thick portions of Greenland is calculated to be 0.0314 SI (0.0025 cgs), close to the 0.0289 SI (0.0023 cgs) value for the thinner Greenland "rift."

Passive Margins

There exists in the literature reasonable data to constrain the structure of the passive margin crustal bodies. For eastern Canada [*Hinze et al.*, 1979; *Keen and Barrett*, 1972; *Mayhew et al.*, 1970; *Ewing et al.*, 1966], western Greenland [*Featherstone et al.*, 1977; *Mayhew et al.*, 1970], and the northern portion of Baffin Bay [*Jackson et al.*, 1977] the passive margins were modeled as wedge-shaped bodies decreasing in thickness from 30 km at the edge of the continent to 10 km thickness at the 2000-m isobath, assumed to be the continental-oceanic crust transition. An average profile was adopted for all these margins based primarily on seismic refraction studies in the Labrador Sea [*Hinze et al.*, 1979; *C. E. Keen et al.*, 1972; *M. J. Keen et al.*, 1972; R. T. Haworth et al., preprint, 1984]. The upper portion of the crystalline crust was assumed to have a susceptibility about one-half that used for lower continental crust in Canada and Greenland. The lower portion of the passive margin crust was given a susceptibility similar to that of layer 3 for oceanic crust. The resulting average susceptibility was 0.0161 SI (0.00128 cgs) (see Table 1).

Deep Ocean Basins

The Labrador Sea, Baffin Bay and part of the Atlantic Ocean from the east coast of North America to south of Iceland east to 340° longitude were modeled as oceanic crustal bodies. There is an abundance of geophysical data for estimating the crustal structure and thickness of the Labrador Sea [*Hinze et al.*, 1979; *Mayhew et al.*, 1970]. Seafloor spreading magnetic anomalies in the Labrador Sea testify to its oceanic character [*Hyndman*, 1973; *Srivastava*, 1978]. The average crustal susceptibility for the Labrador Sea body is 0.0264 SI (0.0021 cgs) as shown in Figure 3, assuming 2.5 km of non-magnetic sediments overlying oceanic crust with a 2 km thick layer 2 and a 4 km thick layer 3 [*Thomas*, 1987].

Unlike the Labrador Sea, the opening history and physical characteristics of Baffin Bay are still not well understood [*Keen et al.*, 1990; *Keen and Pierce*, 1982; *Srivastava et al.*, 1981]. Interpretations range from a small oceanic basin [*Menzies*, 1982; *Westmiller*, 1974; *Barrett et al.*, 1971] to stretched continental crust [*Kerr*, 1967]. Refraction data show that the crust may be only 4 km thick with perhaps an equal thickness of overlying sediments [*Balkwill et al.*, 1990; *Srivastava et al.*, 1981; *C. E. Keen et al.*, 1972; *Keen and Barrett*, 1972; *Barrett et al.*, 1971]. Seafloor spreading anomalies are found in the region but are very irregular and hard to interpret [*Jackson et al.*, 1979]. If we assume that Baffin Bay is underlain by oceanic crust in this study but with an extremely thin layer 3 by comparison with other oceanic crust [*M. J. Keen et al.*, 1972], the average susceptibility derived for this body is mostly from layer 2 and would be somewhat higher than for the Labrador Sea (for comparable thicknesses of overlying sediments). In the model below a very high average susceptibility contrast of 0.0565 SI (0.0045 cgs) is used, based on a crystalline thickness of only 3 km.

We show that even with this high average susceptibility the Baffin Bay anomaly is not well reproduced, perhaps because the true volume of thinned ocean crust is underestimated by choosing the 2000-m isobath as the ocean/continent boundary.

Davis Strait

The Davis Strait (also called the Davis Strait Sill) is a bathymetric high which separates the Labrador Sea from Baffin Bay. A relative magnetic high lies over this elevated crust in the Magsat data (Figure 1). There is some controversy regarding the nature of the Davis Strait crust [*Srivastava et al.*, 1981; *van der Linden*, 1975; *Hyndman*, 1973; *Keen and Barrett*, 1972; *Clarke and Upton*, 1971]. Seismic refraction data are available but are ambiguous. We modeled this body as a region of thickened oceanic crust, following the interpretation of *Keen and Barrett* [1972]. Based on their model, the average susceptibility of the body would be 0.0276 SI (0.0022 cgs).

The average susceptibility derived above for each body was used for the entire crustal body in a three-dimensional, spherical Earth modeling program based on Gauss-Legendre quadrature integration (*von Frese et al.* [1981], as modified by Johnson (unpublished notes, 1984)) which calculated the magnetic anomaly at 400 km altitude in RTP inducing field of 50,000 nT. These calculated anomalies were then compared with the observed Magsat RTP anomalies. The results are described below.

Results and Discussion

Figure 4*b* shows the result of this modeling effort. Because the Magsat data have an arbitrary zero level which is determined by the data reduction procedures (removal of a degree and order 13 main or core field, along-track filtering with a long-wavelength cutoff filter to remove the external field effects), there is no reason to expect the calculated peak values (positive or negative) would equal those of the observed anomalies. But the peak-to-peak anomaly contrasts should be the same if we have used the right susceptibilities and volumes for the source bodies. In Figure 4*a* we have scaled the Magsat data from Figure 1 (adjusted the zero level) so that both observed and calculated anomalies agree in the center of the Labrador Sea. This is for convenience only; the comparisons described below can just as easily be made between Figure 1 (Magsat data without adjusted zero) and Figure 4*b*.

The anomalies calculated at satellite elevation from the model bodies describe above are overall in excellent agreement with the observed Magsat RTP anomalies. In particular, the contrast between the positive anomaly over Labrador (20–22 nT) and the negative over the Labrador Sea (−4 nT) is the same in the observed and calculated anomaly maps. Between southern Greenland and the Labrador Sea the contrast is 20 nT in the calculated map and 18–19 nT in the observed data. The comparisons with Baffin Bay are not quite this good, probably because of the uncertainty in the average susceptibility based on a poorly constrained crustal model. The Baffin Bay contrast with Greenland and eastern Canada is too great, implying that the Baffin Bay source body has too low an average susceptibility or too small a total volume. Given that we used an unusually high susceptibility, we suggest that our volume for the oceanic portion of Baffin Bay may be too small, reflecting the uncertainty in the ocean/continent transition in this area [*Keen et al.*, 1990]. Elsewhere the overall agreement in anomaly pattern is quite good, especially in the relative high over the Davis Strait between Baffin Bay and the Labrador Sea, the relative low over Hudson Strait, and the relative low running east-west across southern Greenland. This model incorporates the thinned ("riftlike") crustal body described above and shown in Figure 2. Without this proposed structure the overall contrast for Greenland with respect to both the Labrador Sea and eastern Canada is much poorer, with Greenland being too strong a positive anomaly.

The generally good agreement seen in Figure 4 suggests several things. First, the choice of susceptibilities used in the model must be nearly correct for the particular volumes of crustal bodies chosen here. That is, the Labrador Sea is best modeled as ordinary oceanic crust, the Davis Strait as thickened oceanic crust, and the Hudson Strait (and Greenland "rift") as thinned continental crust. Likewise, the average crustal susceptibilities for Greenland and eastern Canada must be nearly the same and close to 0.0314 SI (0.0025 cgs) for an average crustal thickness of 42 km. It is of course possible to find other susceptibility-thickness combinations that would match the observed Magsat anomalies. The point is that if Greenland and eastern Canada have about the same average crustal thickness, the Magsat data indicate that they both have about the same overall susceptibility structure as well (as might be expected if they were both once part of the same larger continent). Finally, the susceptibility model we have chosen for the passive margins (see Figure 3) cannot depart too far from reality (in terms of average crustal susceptibility) or the calculated anomaly pattern in Figure 4*b* would not agree so well with the observed data.

Second, for the Labrador Sea region the observed Magsat anomaly pattern across the passive margin can be explained simply by the transition from continental to oceanic crust and the change in thickness that accompanies that transition. There is no need to invoke local peculiarities of thermoviscous magnetization patterns to explain the Labrador Sea negative anomaly [cf. *Arkani-Hamed*, 1990]. It is also clear from our model that the product of thickness times susceptibility for continental crust is not equal to that for oceanic crust [cf. *Harrison et al.*, 1986]. From Table 1 and Figure 3 the average crustal susceptibility of the continental bodies and ordinary oceanic body (Labrador Sea) are nearly the same. However, they differ by almost a factor 5 in thickness, and the resulting difference between the thickness-susceptibility products causes the strong positive anomaly over the continents and the prominent negative over the oceans. For at least this passive margin, crustal structure is the source of the anomaly pattern.

An equally strong anomaly contrast occurs off southern Australia in the vicinity of the Australian Bight where a strong negative anomaly (−10 nT) over the ocean changes to a prominent positive (+12 nT) over the continent. The contrasts across other passive margins, where seen, are generally not so strong. Oceanic crust is probably less variable in structure and in susceptibility than is continental crust; the weaker contrasts observed for some passive margins may provide insight into how the deep continents

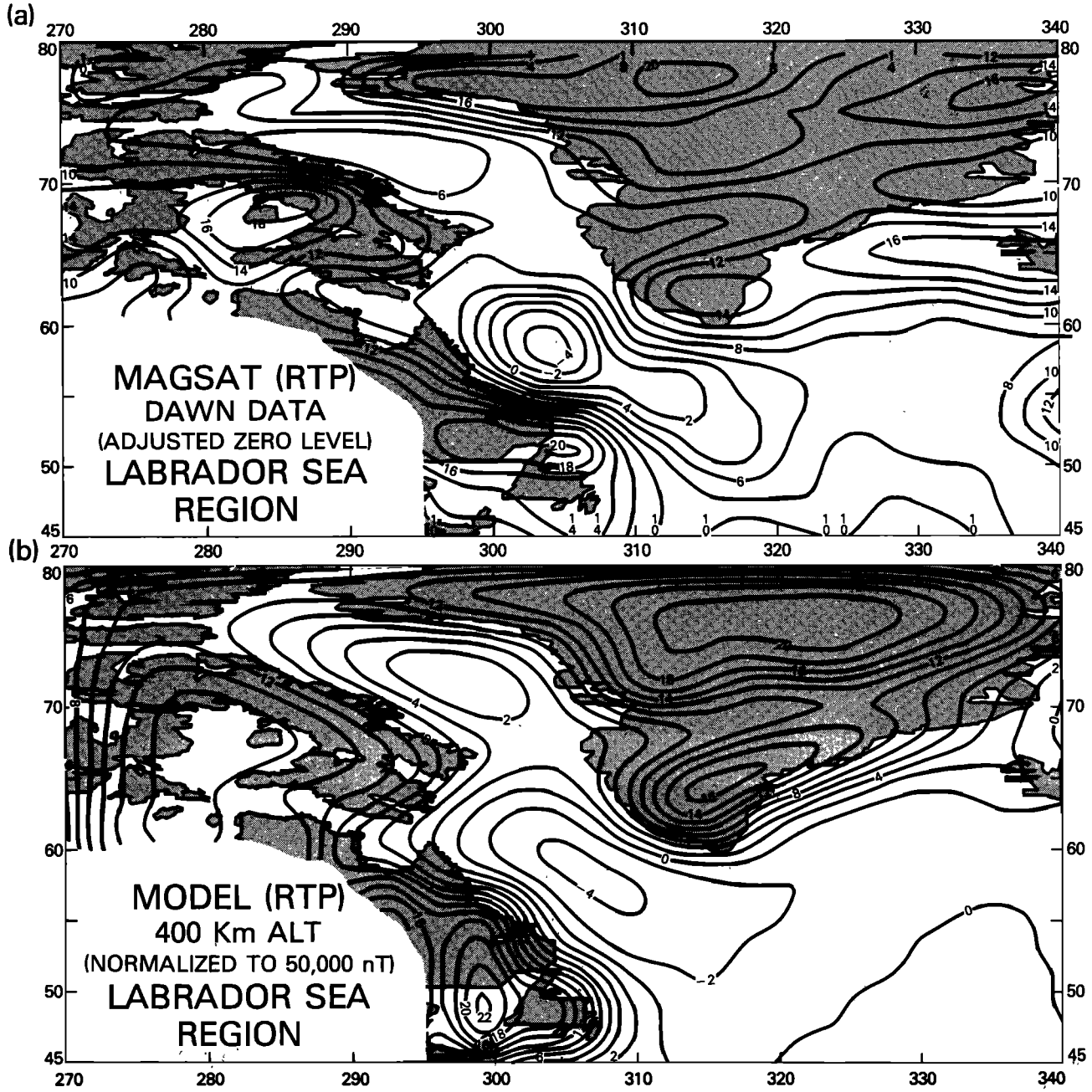

Fig. 4. Comparison of Magsat reduced-to-pole dawn data with calculated anomalies due to model bodies. (*a*) Magsat RTP dawn data with zero level adjusted to match model anomaly at center of Labrador Sea only (see text). (*b*) Anomaly pattern due to model bodies. Note the excellent agreement not only for the continent-oceanic crust contrast (eastern Canada-Labrador Sea-Greenland) but also for the relative high over the Davis Strait and the relative lows over the Hudson Strait and the Greenland "rift." See text for discussion.

differ (in magnetization) at different locations around the globe.

Third, a by-product of the more general modeling is that the east-west Greenland low can be represented by a wide region of thinned crust but with otherwise continental susceptibilities as used elsewhere in Greenland. This does not prove the existence of a "Greenland rift" but does strongly suggest that a major discontinuity in the crustal structure does exist and is manifested in the relative negative anomaly seen in the Magsat data. The character of this relative negative is very similar to that which overlies the Viluy aulacogen, which divides the Siberian Platform into two distinct blocks over which lie two distinct positive lobes in the Magsat data pattern [*Frey*, 1982*b*; *Bradley and Frey*, 1986*b*]. In the case of the Viluy aulacogen it is a significant thinning of the crust that gives rise to the relative anomaly (R. Baldwin and H. Frey, manuscript in preparation, 1991), similar to the situation modeled for Greenland above. One of the major uses of a RTP crustal anomaly map based on Magsat data may be the recognition of large-scale crustal structures in remote areas to which conventional geophysical studies could be directed.

Finally, more work is clearly needed to determine to what extent a continental-oceanic crustal signature is present in the Magsat data for other of the world's passive margins and what may be the source of those contrasts. The strength of such anomaly contrasts will depend on the properties of the margin, especially the width and change in crustal thickness across the margin and the details of the susceptibility structure of the continent, transition region, and adjacent oceanic crust. We cannot generalize from this one example without further investigation and modeling of additional passive margin anomalies.

CONCLUSIONS

A recognizable continental-oceanic crustal transition signature occurs in the Magsat crustal magnetic anomaly data for many passive margins, if reduced-to-pole versions of the data are used and if anomaly contrasts are examined. Forward modeling of the strongest of these passive margin anomalies, the Labrador Sea anomaly, shows that the average crustal susceptibilities for continental (eastern Canada, Greenland) and oceanic (Labrador Sea) blocks are about the same and that the strong contrast seen (20–26 nT) is due principally to the change in thickness from continental (42 km) to oceanic (8.5 km) crust. The Labrador Sea signature is essentially an edge effect caused by the change in crustal properties (composition and especially thickness) at the continent/ocean transition. It seems likely that such a signature may be present (though with generally lower amplitude) for many of the world's passive margins.

In the Magsat anomaly pattern we find evidence for a major crustal structure in south central Greenland, best modeled as a region of thinned continental crust ("rift") similar to the Viluy aulacogen in Siberia. The overall anomaly pattern for the area suggests that Greenland and northeastern Canada have similar crustal structure, the Labrador Sea is ordinary oceanic crust, the Davis Strait is thickened oceanic crust, and the Hudson Strait is thinned, rift-like continental crust.

Acknowledgments. The authors would like to thank C. C. Schnetzler and H. H. Thomas for helpful reviews of an earlier version of this manuscript and for discussions about the appropriate choice of crustal susceptibilities. We also gratefully acknowledge the constructive suggestions of W. Hinze, C. Raymond and two anonymous reviewers. L.M.B. was supported by the Geology Program of NASA HQ through University of Maryland grant NAG5-245.

REFERENCES

Arkani-Hamed, J., Magnetization of the oceanic crust beneath the Labrador Sea, *J. Geophys. Res.*, *95*, 7107–7110, 1990.

Arkani-Hamed, J., and D. W. Strangway, Intermediate-scale magnetic anomalies of the Earth, *Geophysics*, *50*, 2817–2830, 1985.

Balkwill, H. R., N. J. McMillan, B. MacLean, G. L. Williams, and S. P. Srivastava, Geology of the Labrador Shelf, Baffin Bay, and Davis Strait, in *Geology of the Continental Margin of Eastern Canada*, *Geol. Can.*, no. 2, edited by M. J. Keen and G. L. Williams, pp. 239–348, Geological Survey of Canada, Ottawa, Ont., 1990.

Barrett, D. L., C. E. Keen, K. S. Manchester, and D. I. Ross, Baffin Bay—An ocean, *Nature*, *229*, 551–553, 1971.

Berry, J. J., and K. Fuchs, Crustal structure of the Superior and Grenville provinces of the northeastern Canadian Shield, *Bull. Seismol. Soc. Am.*, *63*, 1193–1432, 1973.

Bradley, L. M., and H. Frey, Magsat magnetic anomalies associated with the continental oceanic crustal transition in the Labrador Sea (abstract), *Eos Trans. AGU*, *67*, 264, 1986*a*.

Bradley, L. M., and H. Frey, Magsat crustal anomalies and crustal structure in Greenland (abstract), *Eos Trans. AGU*, *67*, 920, 1986*b*.

Clarke, D. B., and B. G. J. Upton, Tertiary basalts of Baffin Island: Field relations and tectonic setting, *Can. J. Earth Sci.*, *8*, 248–258, 1971.

Coles, R. L., Magsat scalar magnetic anomalies at northern high latitudes, *J. Geophys. Res.*, *90*, 2576–2582, 1985.

Ewing, G. N., A. M. Dainty, J. E. Blanchard, and M. J. Keen, Seismic studies of the eastern seaboard of Canada: The Appalachian system, I, *Can J. Earth Sci.*, *3*, 89–109, 1966.

Featherstone, P. S., M. H. P. Bott, and J. H. Peacock, Structure of the continental margin of southeastern Greenland, *Geophys. J. R. Astron. Soc.*, *48*, 15–27, 1977.

Frey, H., Magsat scalar anomaly distribution: The global perspective, *Geophys. Res. Lett.*, *9*, 277–280, 1982*a*.

Frey, H., Magsat scalar anomalies and tectonic boundaries in Asia, *Geophys. Res. Lett.*, *9*, 299–302, 1982*b*.

Grant, A. C., and K. S. Manchester, Geophysical investigations in the Ungava Bay–Hudson Strait region of northern Canada, *Can. J. Earth Sci.*, *7*, 1062–1076, 1970.

Gregerson, S., Surface wave disperson and crustal structure in Greenland, *Geophys. J. R. Astron. Soc.*, *22*, 29–39, 1970.

Haines, G. V., Spherical cap harmonic analysis, *J. Geophys. Res.*, *90*, 2583–2591, 1985.

Harrison, C. G. A., H. M. Carle, and K. L. Hayling, Interpretation of satellite-elevation magnetic anomalies, *J. Geophys. Res.*, *91*, 3633–3650, 1986.

Hinze, K., H.-U. Schluter, A. C. Grant, S. P. Srivastava, D. Umpleby, and J. Woodside, Geophysical transects of the Labrador Sea: Labrador to southwest Greenland, *Tectonophysics*, *59*, 151–183, 1979.

Hyndman, R. D., Evolution of the Labrador Sea, *Can. J. Earth Sci.*, *10*, 637–644, 1973.

Jackson, H. R., C. E. Keen, and D. L. Barrett, Geophysical studies on the eastern continental margin of Baffin Bay and in Lancaster Sound, *Can. J. Earth Sci.*, *14*, 1991–2001, 1977.

Jackson, H. R., C. E. Keen, and R. K. H. Falconer, New geophysical evidence for seafloor spreading in central Baffin Bay, *Can J. Earth Sci.*, *16*, 2122–2135, 1979.

Keen, C. E., and D. L. Barrett, Seismic refraction studies in Baffin Bay: An example of a developing ocean basin, *Geophys. J. R. Astron. Soc.*, *30*, 253–271, 1972.

Keen, C. E., and J. W. Pierce, The geophysical implications of minimal Tertiary motion along Nares Strait and the Drift of Greenland, *Medd. Groenl. Geosci.*, *8*, 327–337, 1982.

Keen, C. E., D. L. Barrett, K. S. Manchester, and D. I. Ross, Geophysical studies in Baffin Bay and some tectonic implications, *Can. J. Earth Sci.*, *9*, 239–256, 1972.

Keen, C. E., B. D. Loncarevic, I. Reid, J. Woodside, R. T. Haworth, and H. Williams, Tectonic and geophysical overview, in *Geology of the Continental Margin of Eastern Canada*, Geological Survey of Canada, *Geol. Can.*, no. 2, edited by M. J. Keen and G. L. Williams, pp. 31–85, Ottawa, Ont., 1990.

Keen, M. J., J. Johnson, and I. Park, Geophysical and geological studies in eastern and northern Baffin Bay and Lancaster Sound, *Can. J. Earth Sci.*, *9*, 689–708, 1972.

Kerr, J. W., A submerged continental remnant beneath the Labrador Sea, *Earth Planet. Sci. Lett.*, *2*, 283–289, 1967.

Langel, R. A., and L. Thorning, A magnetic map of Greenland, *Geophys. J. R. Astron. Soc.*, *71*, 599–612, 1982.

Langel, R. A., J. D. Phillips, and R. J. Horner, Initial scalar magnetic anomaly map from Magsat, *Geophys. Res. Lett.*, *9*, 269–272, 1982.

Mayhew, M. A., C. L. Drake, and J. E. Nafe, Marine geophysical measurements on the continental margins of the Labrador Sea, *Can. J. Earth Sci.*, *7*, 199–214, 1970.

Menzies, A. W., Crustal history and basin development in Baffin Bay, *Medd. Groenl. Geosci.*, *8*, 295–312, 1982.

Meyer, J., J. H. Hufen, Siebert, and A. Hahn, Investigations of the internal geomagnetic field by means of a global model of the Earth's crust, *J. Geophys.*, *52*, 71–84, 1983.

Schnetzler, C. C., An estimation of the continental crust magneti-

zation and susceptibility from Magsat data for the conterminous United States, *J. Geophys. Res.*, *90*, 2617–2620, 1985.

Schnetzler, C. C., H. V. Frey, and H. H. Thomas, Satellite elevation magnetic anomalies over continent/ocean boundaries (abstract), *Eos Trans. AGU*, *65*, 202, 1984.

Srivastava, S. P., Evolution of the Labrador Sea and its bearing on the early evolution of the North Atlantic, *Geophys. J. R. Astron. Soc.*, *52*, 313–357, 1978.

Srivastava, S. P., R. K. H. Flaconer, and B. MacLean, Labrador Sea, Davis Strait, Baffin Bay: Geology and geophysics-a review, in Geology of North Atlantic Borderlands, edited by J. W. Kerr, and A. J. Fergusson, *Mem. Can. Soc. Pet. Geol.*, *7*, 337–398, 1981.

Thomas, H. H., A model of ocean basin crustal magnetization appropriate for satellite elevation anomalies, *J. Geophys. Res.*, *92*, 11,609–11,613, 1987.

van der Linden, W. J. M., Crustal attenuation and seafloor spreading in the Labrador Sea, *Earth Planet. Sci. Lett.*, *27*, 409–423, 1975.

von Frese, R. R. B., W. J. Hinze, L. W. Braile, and A. J. Luca, Spherical Earth gravity and magnetic anomaly modeling by Gauss-Legendre quadrature integration, *J. Geophys. Res.*, *86*, 234–242, 1981.

Westmiller, R. J., Crustal structure of Baffin Bay from the earthquake-generated *Lg* phase, *Can. J. Earth Sci.*, *11*, 123–130, 1974.

L. M. Bradley, Astronomy Program, University of Maryland, College Park, MD 20742.

H. Frey, Geodynamics Branch, NASA Goddard Space Flight Center, Code 921, Greenbelt, MD 20771.

(Received August 3, 1990;
revised May 16, 1991;
accepted June 5, 1991.)

JOURNAL OF GEOPHYSICAL RESEARCH, VOL. 96, NO. B10, PAGES 16,151–16,160, SEPTEMBER 10, 1991

Seafloor Compliance Observed by Long-Period Pressure and Displacement Measurements

WAYNE C. CRAWFORD, SPAHR C. WEBB, AND JOHN A. HILDEBRAND

Scripps Institution of Oceanography, University of California, San Diego La Jolla

Ocean surface waves with periods longer than 30 s create periodic, horizontally propagating pressure fields at the deep seafloor. Seafloor displacements resulting from these pressure fields depend on the density and elastic parameters of the oceanic crust. The displacement to pressure transfer function, the seafloor compliance, provides information about ocean crustal density and elasticity, and we outline a linearized inversion method to determine ocean crustal shear velocity from the compliance. By computing compliance partial differences with respect to changes in ocean crust shear velocity, we provide estimates of inversion stability and of the compliance sensitivity to crustal properties. Seafloor compliance, measured from pressure and acceleration spectra, is presented for two different sites: Axial Seamount on the Juan de Fuca Ridge and the West Cortez Basin in the California continental borderlands. The compliances and inverted structure for these two sites show significant differences; in particular, a zone of low shear strength is observed at depth within Axial Seamount, suggesting the presence of at least 3% partial melt within the upper 2500 meters of the ediface. These results suggest that the method provides a useful new geophysical prospecting tool.

INTRODUCTION

Knowledge of oceanic crustal structure provides important insights into crustal formation and hydrothermal circulation. Seismic methods are a practical approach to determining crustal structure; however, compressional and shear properties must be measured to provide a complete seismic picture of the oceanic crust. Shear velocities are particularly difficult to measure with conventional seismic techniques and are essential to determining oceanic crustal porosity [*Fryer et al.*, 1991]. Crustal porosity constrains hydrothermal circulation and seafloor acoustic reflectance, as well as providing information about oceanic crustal formation. A geophysical prospecting method sensitive to shear velocity structure could sense crustal magma chambers, which have low shear velocity.

We present a method for profiling ocean crustal elastic parameters using the ocean bottom pressure field as the driving source. This method is a development of a technique pioneered in shallow water by Yamamoto and others [*Yamamoto and Torii*, 1986; *Trevorrow et al.*, 1988; *Yamamoto et al.*, 1989]. A low-frequency pressure field is created on the ocean bottom by ocean surface gravity waves. The horizontal scale of the pressure field is set by the wavelength of the surface gravity waves. This pressure field causes deformation of the seafloor, resulting in seafloor pressure and vertical acceleration which show significant coherence below 0.03 Hz (Figures 1 and 2). The amplitude of seafloor deformation below 0.03 Hz depends on oceanic crustal elastic parameters, especially shear properties; low crustal rigidity leads to large seafloor displacements. Seafloor compliance is the transfer function between seafloor deformation and seafloor pressure as a function of frequency. We present measurements of seafloor compliance from two sites: Axial Seamount on the Juan de Fuca Ridge and the West Cortez Basin in the California continental borderlands. Seafloor compliance is significantly different at the two sites. West Cortez Basin has a thick sediment layer and is more compliant at high frequencies corresponding to shallow levels. Axial Seamount, an active volcano, has relatively high compliance at low frequencies corresponding to deep levels, suggesting reduced shear strength at depth within the volcano.

Coherence between seafloor pressure and vertical acceleration is also high in the microseism band, above 0.1 Hz. Energy in the microseism band is primarily associated with propagating elastic waves along the seabed and in the water. The compliance function in this band depends on phase velocities of the many modes of the oceanic waveguide. *Bradner* [1963] and others have suggested that ratios of vertical displacement to pressure associated with microseisms could be used to determine crustal structure, but in practice the various modes interfere to provide an ambiguous result.

Relating oceanic crustal structure to compliance has roots in work on Earth tides. *Beaumont and Lambert* [1972] determined that Earth tide measurements were contaminated by ocean tidal loading dependent on the structure of the Earth's upper layers. Measurements of ocean tidal loading from stations on land have proven useless for studying the elastic structure of the Earth because of the complicated tidal structure in coastal regions and the large wavelength of the effect. Measurements at the deep seafloor at tidal frequencies may be of more use for determining deep elastic structure. Recently, Yamamoto and others [*Yamamoto and Torii*, 1986; *Trevorrow et al.*, 1988; *Yamamoto et al.*, 1989] found the compliance of sediments forced by gravity water waves in shallow water (10-50 m) could be inverted to determine the shear modulus in the sediment. We invert compliance data for Earth structure using a technique applicable to hard rock as well as sediments. The inversion constrains shear velocities at sites where compressional velocities are constrained by other techniques, such as seismic refraction.

This paper differs from previous work in three areas: instrumentation, forward modeling of compliance, and inversion methods. The differences in instrumentation and forward modeling are necessary because our measurements are made at lower frequencies corresponding to the long wavelengths of ocean penetrating water waves in the deep ocean (more than 1000 m deep). We will briefly outline the theory of infragravity waves and seafloor compliance, then explain the method we use to invert

Paper number 91JB1577.
0148-0227/91/91JB-01577$05.00

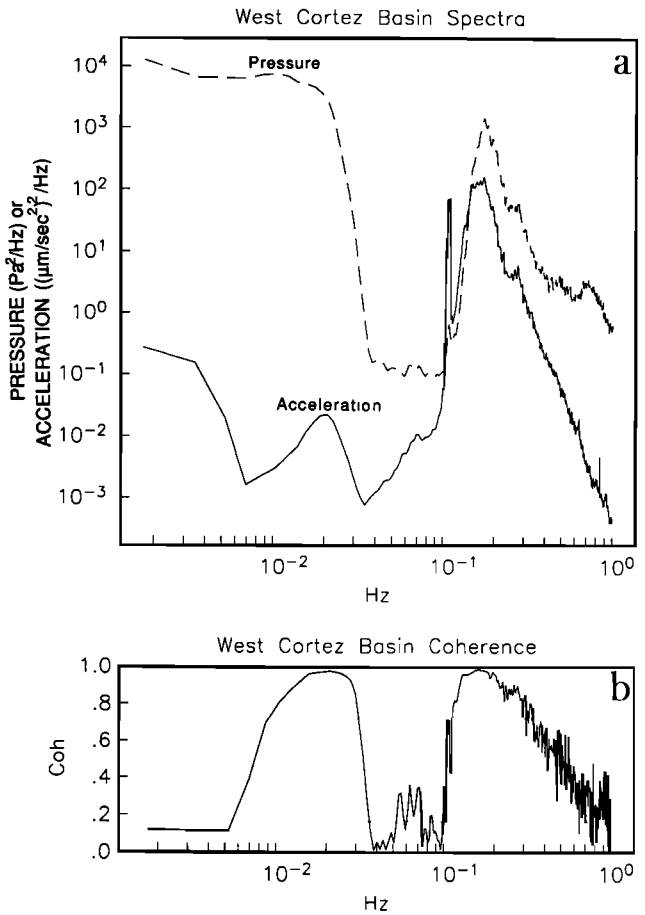

Fig. 1. West Cortez Basin (32°16'N, 119°14'W): (*a*) pressure and acceleration spectra; (*b*) coherence (solid curve) and 95% significance level (dotted line).

compliance data for shear velocity. Finally, we will show and invert compliance measurements at two oceanic sites.

THEORY

The term "infragravity wave" is used to describe long-period ocean surface gravity waves. Infragravity waves are differentiated from shorter period surface gravity waves because they are not directly generated by the action of wind on the water surface. Recent work has shown most of the long-period energy is generated at coastlines and propagates into deep water as free surface waves. The pressure field on the deep seafloor at periods greater than 20 s is generated by these waves [*Webb et al.*, 1991]. The waves have small amplitude, linear displacements, a simple frequency-to-wavenumber relation and wavelengths comparable to or greater than the ocean depth (shallow-water waves). The dispersion relation for a surface gravity wave is:

$$\omega^2 = gk \tanh(kH), \qquad (1)$$

where ω is the angular frequency of the waves, k is the wavenumber, g is acceleration due to gravity, and H is water depth [*Apel*, 1987]. Depending on the amplitude of the infragravity waves at the ocean surface, the highest frequency waves that can exert pressure on the bottom are those with wavelengths between ½ and 2 times the water depth ($k = 2\pi/nH$, $0.5<n<2$). The maximum frequency of infragravity wave seafloor pressure is therefore,

$$f_c = \left[\frac{g}{2\pi nH}\right]^{1/2}, \quad 0.5<n<2, \qquad (2)$$

using $\tanh(2\pi/n) \approx 1$, $n \leq 2$. For H = 1600 m, the maximum frequency of infragravity wave signals is between 0.022 and 0.044 Hz.

Vertical stress from infragravity waves displaces the seafloor. The transfer function between seafloor displacement and stress, the seafloor compliance, depends on the crustal density and elastic properties. Two compliances can be calculated: the transfer function between vertical displacement and vertical stress (vertical compliance), and the transfer function between horizontal displacement and vertical stress (horizontal compliance). Horizontal stress at the ocean-crust interface is zero; this provides a boundary condition for the compliance derivation. All discussion of compliance in this paper refers to vertical compliance. If both pressure and acceleration measurements were noise-free (and if infragravity waves are the only processes to displace the ocean floor at frequencies below f_c), the compliance would be the ratio of displacement to pressure. We have collected vertical compliance data using a gravimeter (long- period seismometer) and a differential pressure gauge. The gravimeter measures acceleration rather than displacement, but acceleration is $-\omega^2$ times displacement in the frequency domain. The acceleration spectrum has noise in the infragravity wave range; noise in the pressure spectrum is small by comparison as shown by correlation between adjacent sensors. Assuming all random noise is in the

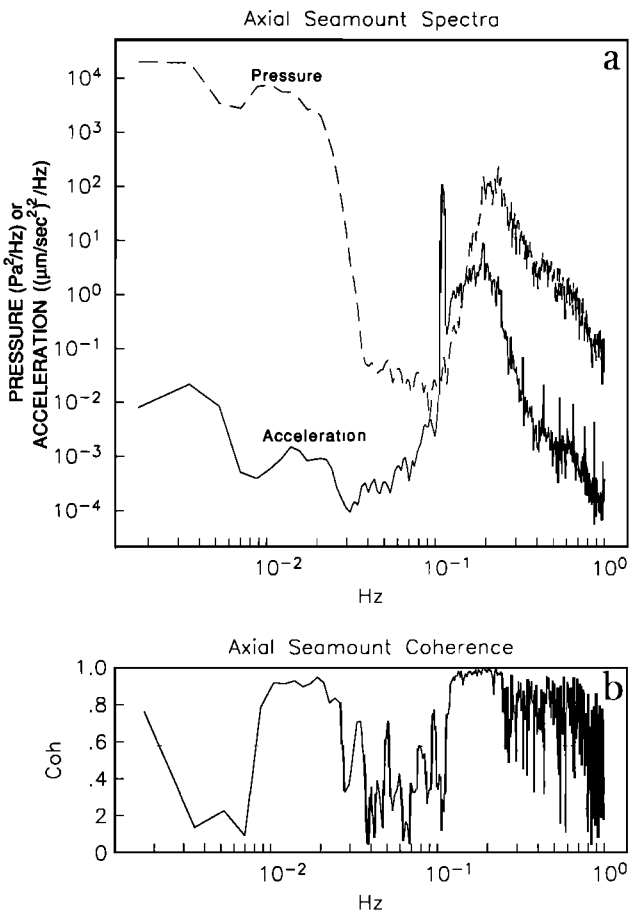

Fig. 2. Axial Seamount (45°57'N, 130°03'W): (*a*) pressure and acceleration spectra; (*b*) coherence (solid curve) and 95% significance level (dotted line).

acceleration/displacement spectrum, the square of the vertical compliance ($\hat{\xi}$) is obtained from the vertical displacement spectrum ($\hat{S}_d$), the pressure spectrum ($\hat{S}_p$), and the coherence between the two ($\hat{\gamma}_{pd}$) using the following equation:

$$\hat{\xi}^2(\omega) = \hat{\gamma}_{pd}{}^2(\omega)\,\frac{|\hat{S}_d(\omega)|}{|\hat{S}_p(\omega)|}. \tag{3}$$

Multiplying the ratio of displacement to pressure by the coherence squared accounts for both random noise in the displacement spectrum and the possibility that the low-frequency displacements have sources other than infragravity waves. An estimate of the compliance uncertainty is given by

$$\varepsilon\left[|\hat{\xi}(\omega)|\right] = \frac{\left[1-\hat{\gamma}_{pd}{}^2(\omega)\right]^{1/2}}{|\hat{\gamma}_{pd}(\omega)|\,\sqrt{2n_d}}\,|\hat{\xi}(\omega)|, \tag{4}$$

with n_d the number of data windows used to calculate the spectra and coherences [*Bendat and Piersol*, 1980].

The equation of motion in an elastic medium is:

$$\rho\frac{\partial^2 u_i}{\partial t^2} = (\lambda+\mu)\frac{\partial^2 u_j}{\partial x_j \partial x_i} + \mu\frac{\partial^2 u_i}{\partial x_j{}^2}; \tag{5}$$

u_i is the displacement of a particle in the x_i direction, ρ is the density of the material, μ is a Lamé parameter known as the rigidity or the shear modulus, and λ is the second Lamé parameter. We solve for the vertical compliance:

$$\xi(\omega) = \frac{u_z}{\tau_{zz}} = \frac{u_z}{\lambda(u_{x,x}+u_{z,z})+2\mu u_{z,z}}, \tag{6}$$

where $u_{i,j} = \partial u_i/\partial x_j$. Compressional velocity α and shear velocity β are related to the Lamé parameters λ and μ by $\rho\alpha^2 = (\lambda+2\mu)$ and $\rho\beta^2 = \mu$. Plane waves forcing the seafloor excite compressional (*P*) and vertical shear (*SV*) evanescent waves in the Earth. Equation (6) has not been solved analytically, but we can use a computational propagator matrix method to determine seafloor compliance, where the oceanic crust is modeled as a finite number of discrete flat layers overlying an infinite uniform half-space.

To relate the crustal elastic parameters and the compliance, we first model the Earth as a uniform half-space. *Sorrels and Goforth* [1973] derived the compliance of a uniform half-space when forced by a plane pressure wave traveling on the free surface at a much slower velocity than the *P* and *SV* wave velocities in the Earth. This situation is called quasi-static because the inertial terms are small, and applies to our study because infragravity waves have velocities less than 200 m s^{-1} in water up to 4000 m deep, while *P* and *SV* waves in the Earth typically travel at velocities greater than 2000 m s^{-1}. Under the quasi-static assumption,

$$\begin{aligned}\xi(\omega) &= \frac{u_z}{\tau_{zz}}(\omega) \\ &= -\frac{1}{k(\omega)}\left[\frac{\lambda+2\mu}{2\mu(\mu+\lambda)}\right] \\ &= -\frac{1}{k(\omega)}\left[\frac{\alpha^2}{2\rho\beta^2(\alpha^2-\beta^2)}\right]\end{aligned} \tag{7}$$

which leads to:

$$\frac{\partial|\xi|}{\partial\lambda} = -\frac{\mu^2}{2k\mu^2(\mu+\lambda)^2}, \tag{8A}$$

$$\frac{\partial|\xi|}{\partial\mu} = -\frac{2\mu^2+2\mu\lambda+\lambda^2}{2k\mu^2(\mu+\lambda)^2}. \tag{8B}$$

Since ρ, λ, and μ are always positive, all of the partial derivatives are negative; an increase in either of the Lamé parameters will result in a decrease in the magnitude of vertical compliance. The partial derivatives of $|\xi|$ with respect to seismic velocities α and β are also negative. This agrees with intuition that the less rigid or more compressible a material is, the farther it will be displaced by a given force. Assuming that different frequencies are tuned to structure at different depths in the crust, we speculate that a decrease in shear velocity at some depth will result in an increase of compliance at the corresponding frequency. From the equations (8A and 8B), $\partial|\xi|/\partial\mu$ must be at least twice the magnitude of $\partial|\xi|/\partial\lambda$ and typically is more than 5 times as great, meaning that vertical compliance is more sensitive to changes in rigidity μ than to changes in λ. Similarly, compliance is typically twice as sensitive to changes in shear velocity β than to changes in compressional velocity α. Equation (7) shows that compliance of a uniform half-space is less sensitive to changes in density ρ than to changes in compressional velocity α.

The problem of determining compliance for a laterally homogenous Earth with *P* and *SV* waves can be solved numerically. One of the most common numerical solutions is the propagator matrix method [*Aki and Richards*, 1980, pp. 273-283] combined with the method of minor vectors [*Woodhouse*, 1980]. For calculation of compliance of a known layered Earth model, we use an implementation of the minor vector propagator written by *Gomberg and Masters* [1988]. Two boundary conditions are (1) horizontal stress (τ_{zx}) vanishes at the seafloor; and (2) a uniform half-space of material underlies the layered model.

To understand the effect of crustal structure on the compliance function, we constructed five oceanic crustal models and computed their compliance, assuming a water depth of 1600 m. We

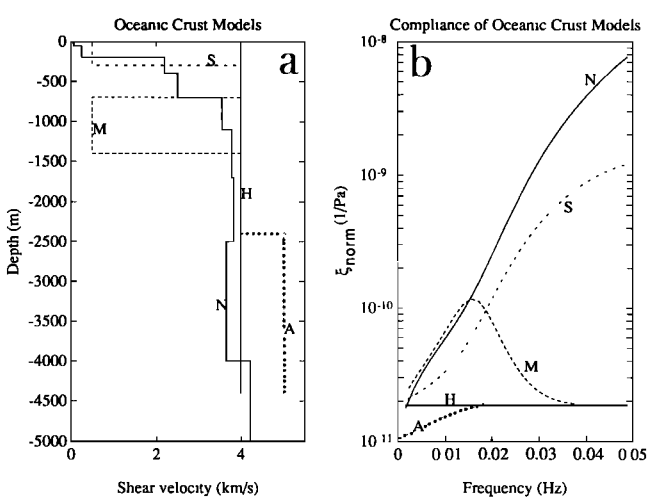

Fig. 3. Earth models and resulting compliances, H = uniform half-space, S = ideal sediment-covered model, M = ideal magma chamber model, A = ideal asthenosphere model, N = normal [*Spudich and Orcutt*, 1980] model: (*a*) shear velocities of the models: each assumes density = 2.5 g/cm^3, compressional velocity = 7 km/s; (*b*) compliances calculated from the models, assuming water depth = 1600 m, normalized by dividing by the wavenumber $k(\omega)$ of infragravity water waves.

calculate normalized compliance, the compliance after the filtering effect of the ocean is removed, by multiplying compliance by the wavenumber $k(\omega)$ of the water waves. The normalized compliance of a uniform half-space is constant (see equation (7)). Figure 3 shows the models and compliances of (1) a uniform half-space (model H); (2) a sedimentary basin model (model S); (3) a magma chamber model (model M); (4) a shallow asthenosphere model (model A); (5) normal oceanic crust [*Spudich and Orcutt*, 1980] (model N). All of the models have compressional velocity α=7 km/s, and density ρ=2.5 g/cm^3. Figure 3*b* shows that low-velocity zones correspond to regions of high compliance, in agreement with the partial derivatives of equation (8). Furthermore, it appears that shallow structure is sensed at higher frequencies than deep structure, in agreement with the intuitive argument that longer wavelength water waves penetrate deeper into the crust.

To test the properties of the compliance function inferred from Figure 3, we computed the partial differences of the compliance

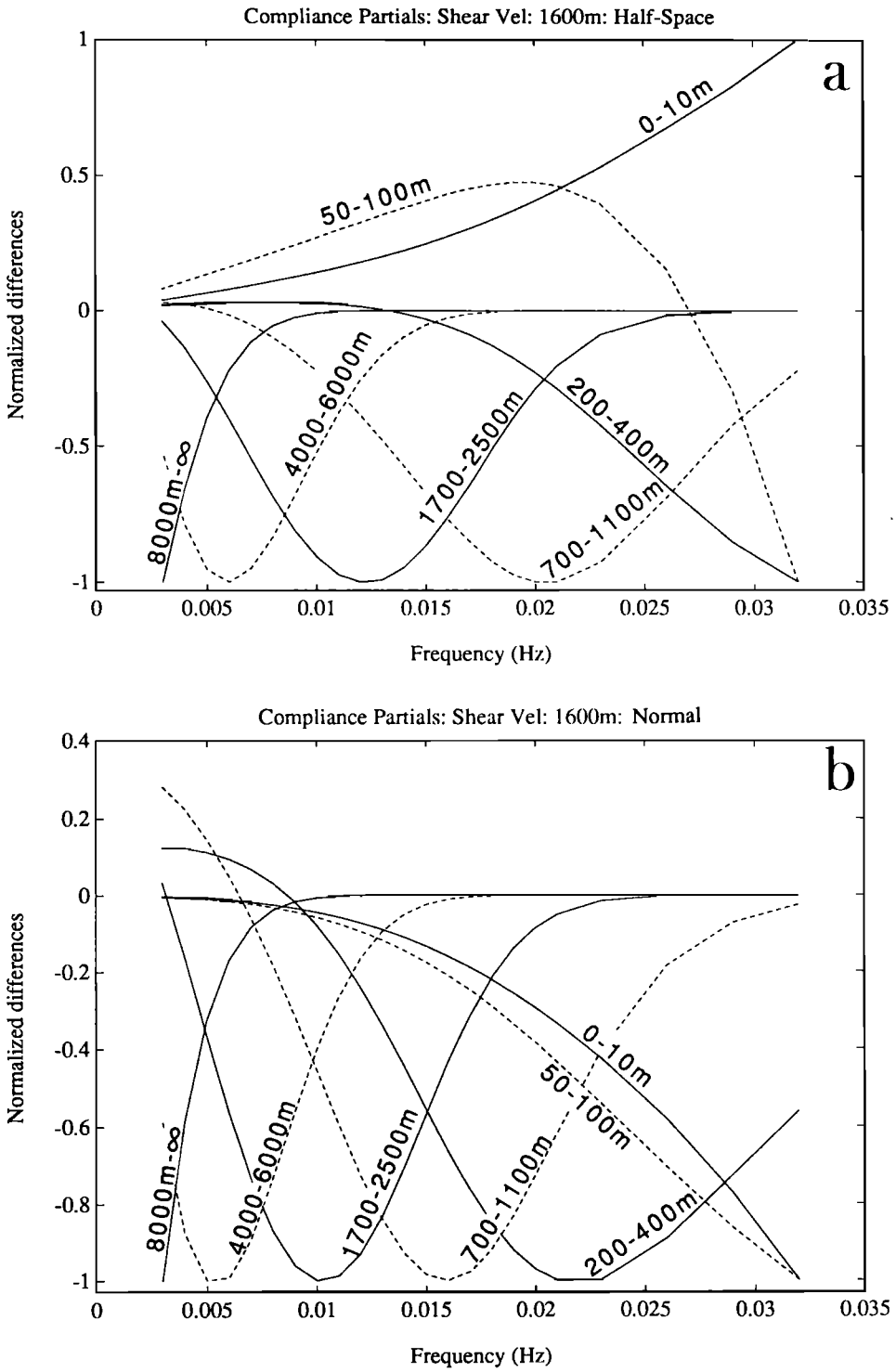

Fig. 4. Compliance sensitivity to changes in shear velocity of one layer of models H and N of figure 3. (*a*) half-space model (H) with depth of modified layer indicated, (*b*) normal oceanic crust model (N) with depth of modified layer indicated.

function for changes in shear velocity. We used the uniform half-space (model H) and the normal seafloor (model N) of Figure 3 to calculate these partial differences. To calculate each curve in Figure 4*a*, we increased the shear velocity of one layer of model H by 5% and calculated the compliance, then decreased the shear velocity of the same layer to 5% below its original value and calculated the compliance. We subtracted the second compliance from the first, and normalized the resulting vector by dividing by a positive constant so that the maximum absolute value of the vector was 1. The curves of Figure 4*b* were calculated using the same procedure, starting with the normal seafloor (model N). Normalization over emphasizes curves whose peaks are outside the frequency band of Figure 4 (the layers down to 400 m in Figure 4*a*; the layers down to 200 m in Figure 4*b*). It is apparent that different frequencies "tune" to structure at different depths, and that the tuning frequencies decrease with increasing depth. Figure 4*b*, the partials of the oceanic crust model, shows a shift of partial difference peaks to lower frequencies compared to Figure 4*a*. The low rigidity zone near the oceanic crust model surface amplifies the contribution of the shallow layers, masking the higher frequency contribution of changes in the deeper layers. If the compliance function were linear, Figures 4*a* and 4*b* would look the same. The danger of the nonlinearity is that it may allow more than one domain of attraction for the linearized compliance function. If there is more than one domain of attraction, the inversion result will not be unique. Unlike the partials calculated in equations (7) and (8), the partials of Figure 4 are not all negative. An increase in shear velocity β requires λ to decrease for the compressional velocity α to remain fixed. Therefore the effect of an increase in μ is countered by the effect of a decrease in λ. Since $\partial|\xi|/\partial\mu$ is typically greater magnitude than $\partial|\xi|/\partial\lambda$, the partial differences of compliance with respect to shear velocity are usually negative; however, $\partial|\xi|/\partial\beta(z)$ is positive at some frequencies and depths. Calculations of compliance function partial differences with respect to α and ρ suggest that compliance is typically twice as sensitive to changes in shear velocity β than to changes in compressional velocity α, and over 10 times as sensitive to changes in β than to changes in density ρ.

INVERSION

The goal of inverse theory is to calculate a model (in our case, shear velocity of the oceanic crust) from some data (in our case, seafloor compliance), when we know how to calculate the data as a function of the model. For discrete data, a discrete model, and a linear relation between the model and the data, we calculate the data vector $\mathbf{d}$ from the model vector $\mathbf{m}$ by multiplying the model by a matrix of representors $\mathbf{G}$:

$$\mathbf{Gm} = \mathbf{d}. \tag{9}$$

Our goal is to find $\mathbf{G}^{-g}$ such that

$$\mathbf{G}^{-g}\mathbf{d} = \mathbf{m}^{est}, \tag{10}$$

and

$$\mathbf{Gm}^{est} = \mathbf{GG}^{-g}\mathbf{d} = \mathbf{d} + \mathbf{T}, \tag{11}$$

where $\mathbf{T}$ represents uncertainty in the data. If the dimension of $\mathbf{m}^{est}$ equals the dimension of $\mathbf{d}$ and $\mathbf{d}$ is exact, then $\mathbf{G}^{-g} = \mathbf{G}^{-1}$. We don't know the number and thickness of layers in the earth, however, so this calculation is unreasonable, as it will usually result in a model with more structure than is necessary to explain the data. We construct a model with many more layers than there are data points so that we will not introduce unnecessary structure into the model. Furthermore, the data are never exact. As a result, there exist an infinite number of possible $\mathbf{G}^{-g}$ and an infinite number of $\mathbf{m}^{est}$ that will fit the data equally well. To select one $\mathbf{G}^{-g}$, we must have some preconception of what a good model looks like. To force the model toward this preconception, we choose a model norm for minimization. The construction of $\mathbf{G}^{-g}$ in order to minimize the chosen norm is discussed by *Parker* [1977] and *Menke* [1984]. The most common construction methods for $\mathbf{G}^{-g}$ are to minimize the L_2 norm of the first difference or the second difference of the model (hereafter referred to as C^1L_2 and C^2L_2 inversions). These constraints are used because they attempt to make the model as featureless as possible by minimizing the slope (C^1L_2) or the curvature (C^2L_2) of the model. With the C^2L_2 constraint, structure in $\mathbf{m}^{est}$ is due to structure in the true model and not an artifact of the inversion process. Another method of construction of $\mathbf{G}^{-g}$ is the "singular value decomposition" (SVD) technique [*Menke*, 1984], which minimizes the L_2 norm of the model with the empirical property that the second difference of the model is also decreased. *Yamamoto and Torii* [1986] have successfully used the SVD method on shallow-water compliance data. We do not use the SVD method because it does not explicitly minimize the second difference of the model and therefore allows extraneous structure. Discussion and illustration of the very different models that can be obtained by different methods of inversion of discrete, inexact data are found in *Constable et al.*, [1987] and *Smith and Booker* [1988].

Linear inverse theory has developed to the point where its application is straightforward. Unfortunately, the compliance problem is nonlinear. We must write $\mathbf{G}(\cdot)$ as a function of $\mathbf{m}$, and the linear algebra techniques of linear inverse theory are no longer applicable. A common method for solving nonlinear inverse problems is to treat them as linear inverse problems locally and to iterate to obtain a solution. This approach has the pitfall that there may be more than one "basin of attraction" for the function. The answer may not be unique, since $\mathbf{G}(\cdot)$ is dependent upon the starting model. When the problem is only weakly nonlinear (more specifically, when the functional to be minimized is convex) the linearization approach will be successful. *Yamamoto and Torii's* [1986] use of linear techniques is justified because their functional is only weakly nonlinear. We have not been able to prove that our functional is convex, so we must be more cautious in linearization of the inversion and use of techniques developed for linear inverse theory to characterize inversion quality.

We use Occam's inversion [*Constable et al.*, 1987] to obtain shear velocity structure from compliance data, using either C^1L_2 or C^2L_2 inversion. Forward problem solutions are calculated using the implementation of the minor vector propagator mentioned earlier. Models of compressional velocity ($\alpha(z)$) and density ($\rho(z)$) of the oceanic crust at the study site are assumed, and we invert compliance data for shear velocity. We use $\alpha(z)$ estimates from refraction and reflection seismology studies and estimate $\rho(z)$ based on the compressional velocities and facies analyses. Inversion accuracy is not as dependent on $\alpha(z)$ and $\rho(z)$ models as might be suspected, because of the much greater sensitivity of the compliance function to shear velocity than to these parameters.

A model with a thin layer of very low shear velocity results in a compliance function with a narrow, high compliance, peak. Relating the location of this peak to the depth of the low-velocity layer provides an estimate of the depth sensitivity of the compliance function. We calculated compliance of 28 models, each a

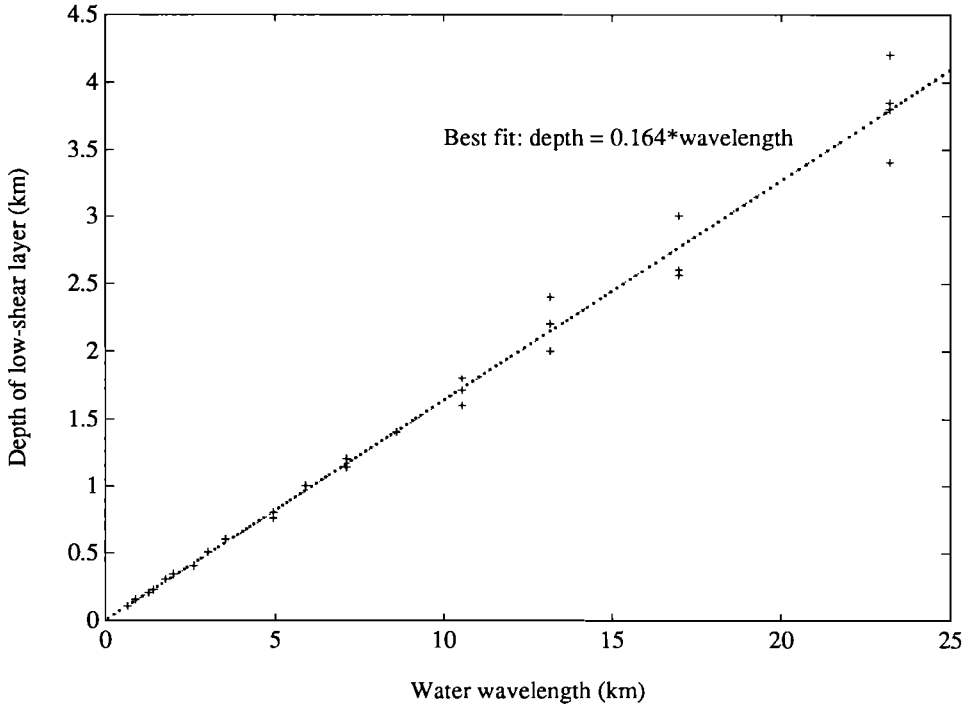

Fig. 5. Wavelength-depth relationship of a half-space with one thin layer of low shear velocity.

copy of model H with a 1 m thick low shear velocity layer inserted at a depth between 100 and 4200 m below the seafloor. We plot compliance peaks against water wavelength because the depth of penetration of water waves should depend on their wavelength. Equation (1) gives the relation between frequency and water wavelength. Figure 5 shows that the wavelength-depth relationship is linear for the uniform half-space model containing one, thin, low shear velocity layer. The water wavelengths are clustered at discrete values because they were derived from discrete frequencies. Figure 5 suggests that for the half-space model H, structural features are observed down to a depth approximately 1/6 the wavelength of the longest water wave coherent with seafloor acceleration. Because the surface waves excited in the seafloor decay exponentially with depth, the effect of seafloor structure on the compliance function decays exponentially with depth. We account for this by increasing layer thickness exponentially with depth, so that each layer has approximately equal effect on the compliance data. For the inversions in this paper we created a 50-m-thick top layer, then made every successive layer 1.1 times as thick as the layer above. The minor vector propagator program treats the bottom layer as an infinite half-space.

A standard test of linear inversion quality is calculation of a resolution matrix $\mathbf{R}=\mathbf{G}^{-g}\mathbf{G}$ [*Menke*, 1984]. For nonlinear inversion a linearized approximation of the resolution matrix is sometimes calculated from the $\mathbf{G}$ and $\mathbf{G}^{-g}$ of the last iteration of the inversion. The resulting resolution matrix often has very little to do with the actual resolution of the inversion because of the inadequacy of linearization [*Parker*, 1984]. We do not calculate resolution matrices in this paper. Instead, we computed C^2L_2 inversions of the models of Figure 3. We restricted compliance frequencies to the range obtained from our deep-ocean experimental sites. The thickness of the estimated model layers are independent of those used to generate the model, since we assumed no previous knowledge about the model. We added 5% noise to the compliances (from Figure 3*b*) before inverting.

The model inversions (Figure 6) show structure where their generating models had structure and, more importantly, no extraneous structure. Inversion of the half-space model (H) resulted in a half-space model. There is a slight error in shear velocity of the inverted half-space that is due to the 5% random noise we added to the compliances. We could easily calculate error bars for the inverted model, but only because we know that the starting model was also a half-space. Inversion of the normal oceanic crust model (N) resulted in a model very similar to model N. The negative slope below 2500 m of the N model inversion reflects a decrease in shear velocity that we put in model N at 2500 m depth. Inverted shear velocity does not increase at greater depths, suggesting that compliance in the frequency band of our experimental data cannot sense structure below approximately 2500 m depth. Inversion of the magma chamber model (M) generates a model with a low shear velocity zone, but the zone is at a greater depth than the model M magma chamber. The partial difference curves of Figure 4*b* suggest that a region of low shear velocity dominates the compliance function at lower than typical frequencies, which could be modeled as a region of slightly higher shear velocity at greater depths. The inverted model of the asthenosphere model (A) compliance data has much less structure than the original model, although it does show increasing shear velocity with depth. The inverted model's lack of structure is probably due to decreasing resolution with increasing depth, and because the structure in the asthenosphere model is near the empirical depth limit (2500 m) of the compliance frequency band. Inversion of the sediment-filled basin model (S) results in a model with more gradual velocity change than the sharp sediment-basement interface of model S. C^2L_2 inversion smooths the structure of model S over 2500 m of the inverted model. We speculate that the low shear velocity of the sediments dominate the compliance function, so that the effect of the basement rocks is not sensed until very low frequencies. We do not expect these methods will be able to discern much structure in rocks beneath a thick layer of sediments.

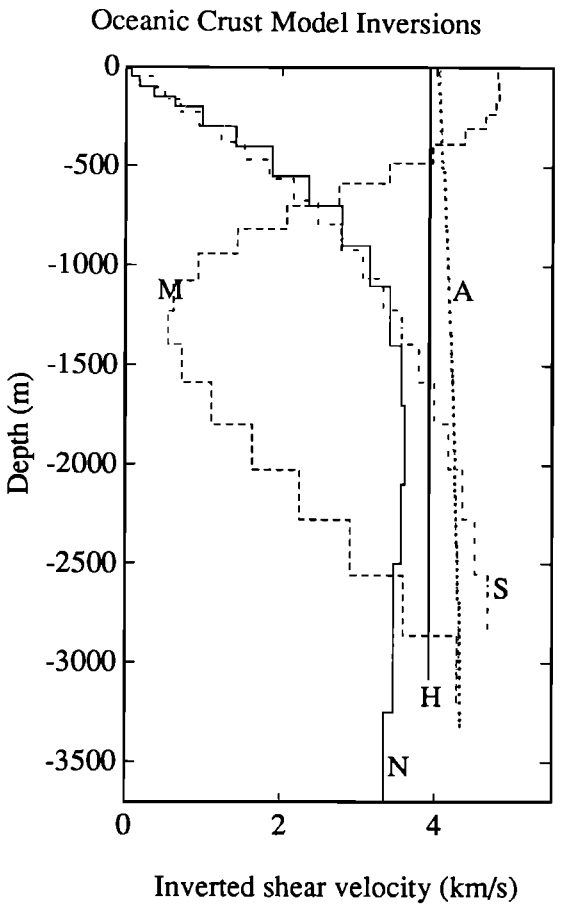

Fig. 6. Shear velocity C^2L_2 inversions of Figure 3B compliances plus 5% noise. H = uniform half-space, S = ideal sediment-covered model, M = ideal magma chamber model, A = ideal asthenosphere model, N = normal [*Spudich and Orcutt*, 1980] model.

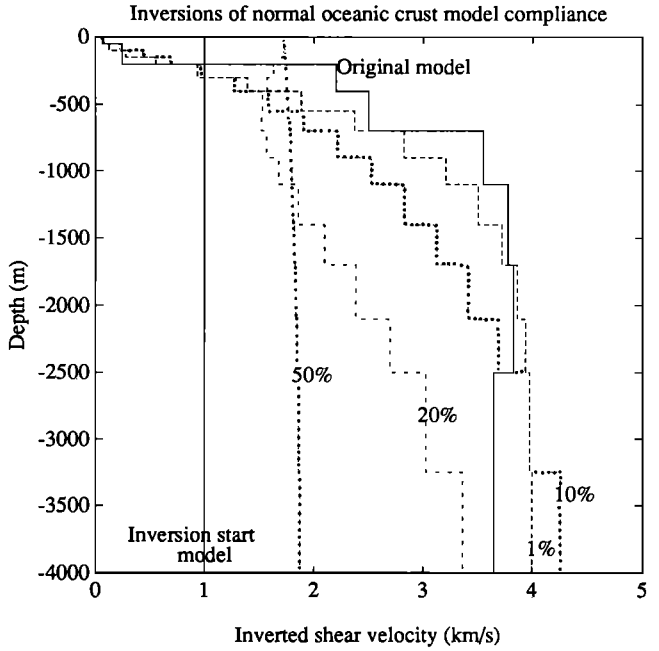

Fig. 7. Shear velocity C^2L_2 inversions of normal (model N) oceanic crust compliance plus different noise levels. Each curve is labeled with the amount of noise added to the compliance values as a percentage of the initial compliance values. Model N and the inversion starting model are displayed for comparison.

Inversion quality depends on the amount of noise in the data. Figure 7 shows inverted models of normal oceanic crust (Figure 3*a*, model N) with different noise levels added to the model's compliance. It appears that 10% noise is the most that we can accept and expect to obtain well-constrained inversions. When noise levels are high, there may be temptation to overfit the data in the model inversion. Even the slightest amount of overfitting, however, results in unwarranted and often extreme structure in the model [*Constable et al.*, 1987; *Smith and Booker*, 1988].

None of the inversions in this paper include error bars on the inverted models. When the model is an exact function of the data, it is reasonable to map uncertainty from the data onto the model. We use inverse theory because there exist an infinite number of models that fit the data equally well. The locus of these model solutions is impossible to determine, and uncertainty estimates derived from this locus would be very pessimistic estimates of the quality of our inversion, since the value of each model element is not explicitly constrained by C^2L_2 inversion. We do not ask the reader to trust the values of the model elements; instead, we state that the Earth's crust has more structure than the inverted models (compare, for example, Figures 3*a* and 5). Any structure in the inverted model reflects at least as much structure in the oceanic crust. The inference of inversion quality drawn from Figure 7 is the best quantitative error estimate we can make, and this applies only for oceanic crust models similar to model N.

INSTRUMENTATION

We use a LaCoste-Romberg underwater gravimeter to measure seafloor acceleration [*Lacoste*, 1967; *Hildebrand et al.*, 1990]. This sensor is used as a long-period seismometer on land [*Agnew and Berger*, 1978] and its useful frequency range is two decades lower than typical ocean bottom seismometers. LaCoste-Romberg underwater gravimeters are similar to conventional land gravimeters, except that the operation of underwater gravimeters is actuated by motors for leveling and for adjustment of the measurement micrometer. The sensor consists of a zero-length spring and a 0.1-kg mass. The position of the mass is sensed by capacitive plates. An analog feedback system is used to stabilize the mass position by applying a voltage to the capacitive plates. Tests of coherence between two of the land seismometers on the same pier suggest the instrument noise is flat at frequencies above 0.003 Hz, and may be as low as -181 dB relative to 1 $m^2 s^{-3}$ [*Agnew and Berger*, 1978]. The underwater gravimeter uses different electronics than these devices, however, and was limited by noise in the A/D converter at frequencies below 0.01 Hz. The gravimeter has recently been modified to reduce electronic noise; these modifications may extend the frequency range of coherence measurements and increase coherence in the infragravity wave band.

The pressure signal associated with the infragravity waves is measured using a differential gauge [*Cox et al.*, 1984]. The principle behind a differential gauge is to measure the difference of pressure between the ocean and a fluid within a rigid reference chamber. At short time scales the differences reflect pressure fluctuations in the ocean; at long time scales (greater than 1000 s) a capillary leak allows the reference chamber to equilibrate with ocean pressures. The differential mode permits the use of a very sensitive strain gauge to measure ocean pressure fluctuations while withstanding the enormous pressures of the deep ocean. Over-pressure relief valves protect the strain gauge during deployment and recovery. The gauge outperforms standard low-

frequency crystal hydrophones at frequencies below 0.1 Hz. There is high coherence in the infragravity wave frequency band when the pressure gauges are placed within a few meters of each other on the seafloor, and no coherence at frequencies above the cutoff frequency f_c derived in equation (2).

The gravimeter and pressure gauge are deployed together on a deep-ocean cable from a research vessel. Data comes up the cable at 2400 baud. Each data clump contains 42 bytes, resulting in a sampling rate of 7.143 Hz. Because of the sensitivity of the spring to changes in temperature, the gravimeter is temperature stabilized by a heater coil with thermostatic feedback. Electronic coupling with the heater current created the 0.1-Hz spike evident in Figures 1*a* and 2*a*. This coupling has since been removed from the gravimeter circuitry.

MEASUREMENTS

We calculated the vertical compliance of the seafloor between 0.01 and 0.025 Hz at Axial Seamount and between 0.008 Hz and 0.034 Hz at West Cortez Basin. Coherences in these bands are significant, although the useful bandwidth is limited by noise in the acceleration spectra. We only use data for which coherences are above the 95% significance level (the dotted line in Figures 1*b* and 2*b*). Both sites are at approximately 1600 m depth. The longest water wave coherent with our seafloor acceleration data is approximately 12.5 km long (=125m/s x 100 s), corresponding to a maximum depth sensitivity of about 2.5 km.

Axial Seamount is an active submarine volcano on the Juan de Fuca Ridge. The volcanic edifice marks the intersection of the Cobb-Eikleberg hot spot trace with the Juan de Fuca Ridge. Hot spots are believed to overlie deep-seated magma sources, and oceanic ridges may contain relatively shallow magma chambers, therefore Axial Seamount is an especially promising site for location of a magma chamber. An active seismic survey of Axial Seamount by *van Heeswijk* [1986] revealed very slow shallow compressional velocities, suggesting porous shallow structure within the volcano. Van Heeswijk's survey also disclosed a possible reflector within the caldera of Axial Seamount which could be the roof of a magma chamber. The presence of a caldera at the volcano's summit further suggests that a magma chamber may exist within the edifice [*Embley et al.*, 1990]. Absolute pressure measurements by *Fox* [1990] suggest that the caldera is undergoing deflation, also consistent with the presence of a magma chamber. Our measurement site (45°57'N, 130°03'W) was in the volcano's caldera, which has no appreciable sediment cover over young volcanic flows. Compliance data were collected for 45 min at the Axial Seamount site. The 0.1-Hz heater spike in the acceleration data was removed by subtracting a least squares fit sine wave. Spectra, coherences and compliances were calculated using six segments of data, each one 4096 samples long. Each segment was multiplied by a 4π prolate-spheroidal window [*Thomson*, 1977] before application of the Fourier transform.

West Cortez Basin is a California continental borderland basin filled with up to 750 m of turbidites and hemipelagic sediments. The basin is floored by deformed Mesozoic to lower Tertiary Franciscan-type basement [*Teng and Gorsline*, 1989]. At our measurement site (32°16'N, 119°14'W) 350 m of sediments cover the basement rock, as determined by reflection seismic profiling. Compliance data were collected for 8 hours at the West Cortez Basin site. Spectra, coherences and compliances were calculated using 71 segments of data, each one 4096 samples long. Each segment was multiplied by a 4π prolate-spheroidal window before application of the Fourier transform. The West Cortez Basin data set is much longer than the data set from Axial Seamount because the instruments at the former site were deployed from a moored research platform (R/P *FLIP*) rather than a ship.

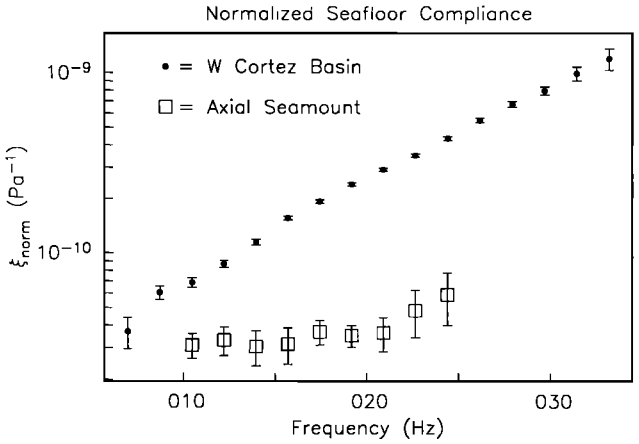

Fig. 8. Normalized compliances of Axial Seamount and West Cortez Basin calculated as in equation (3) over the infragravity wave frequency band where there is significant coherence between the two signals. Error estimates (equation (4)) are designated by vertical bars.

Figure 8 shows compliances calculated from the spectra and coherences of Figures 1 and 2. The effect of data series length on compliance uncertainty is evident; West Cortez Basin compliance is much better constrained than Axial Seamount compliance. C^2L_2 inversion of Axial Seamount compliance should allow less structure than C^2L_2 inversion of West Cortez Basin compliance. The West Cortez Basin compliance is significantly different than compliance at Axial Seamount. Compliances from the two sites appear to be nearly the same at the lowest frequencies but diverge at higher frequencies. Our half-space model (equations (7) and (8)) and the negative partial differences of Figure 4 predict that the low velocities of the West Cortez Basin sediments result in higher compliance at the higher-frequency end of the coherent band. Lower-frequency waves are affected by deeper structure than higher-frequency waves; waves below 0.02 Hz at West Cortez Basin are dominated by the rigid basement beneath the sediments. Error in calibration of the acceleration measurements is less than 1%. We estimate frequency-independent uncertainties in calibration of the pressure gauge to be 10%. The uncertainties are associated with the laboratory calibration, changes in electronic performance at seafloor temperatures, and compliance of pressure gauge seals. Uncertainty in the viscosity of the oil at seafloor pressures and temperatures [*Cox et al.*, 1984] affects the capillary leak time constant, creating frequency-dependent uncertainty. The time constant only affects the calibration at very low frequency; we estimate the uncertainty at 0.01 Hz to be less then 3%. The frequency-independent uncertainty of the pressure gauge calibration is relatively unimportant, because a frequency-independent change in compliance will not increase the structure of the inverted model.

Both data sets lose coherence at frequencies below 0.008 Hz (see Figures 1 and 2) due to electronic noise in the gravimeter A/D converter and decreasing acceleration signals. Gravimeter noise sources have been reduced by over 20 dB after these data were collected. The acceleration signal of a uniform half-space is proportional to ω in the infragravity wave band; we expect coherence between the gravimeter and pressure sensor will extend down to 0.002 Hz in subsequent deployments. At full ocean depth (5000 m), infragravity water waves at 0.002 Hz frequency are approximately 110 km long. Using the wavelength-depth rela-

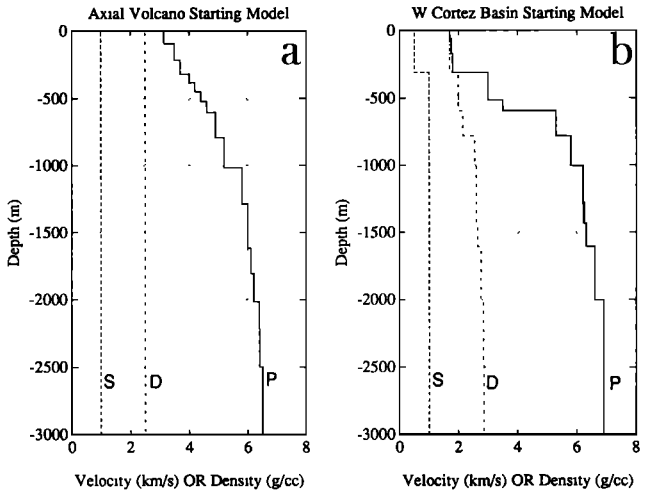

Fig. 9. Starting models for inversion of experimental data, S = shear velocity, P = compressional velocity, D = density: (*a*) Axial Seamount starting model, and (*b*) West Cortez Basin starting model.

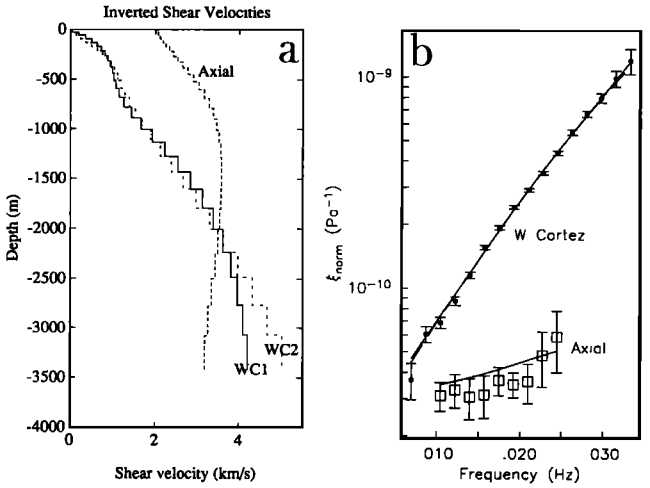

Fig. 10. Inversion of Axial Seamount and West Cortez Basin data: *a*) inverted shear velocities (WC1 = West Cortez Basin, C^1L_2 inversion; WC2 = West Cortez Basin, C^2L_2 inversion), and *b*) comparison of compliances of inverted models to data.

tion of Figure 5, compliance values taken in water of 5000 m depth may be sensitive to structure to a depth of 18 km below the seafloor. Compliance inversion is useful at ridge crests because of a lack of masking effects from sediments and because changes in shear velocity are probably more distinct near ridge crests. A typical ocean depth over a ridge crest is 2000 m; 0.002-Hz water waves have wavelengths of 70 km, and may be able to sense to 11 km depth. Deep structure is determined with lower resolution than shallow structure. Inversion of the magma chamber model (M) in Figure 6 suggests that a zone of low shear velocity shifts the effect of structure at depth to lower frequencies; a conservative prediction for inversion penetration is 6-7 km at a ridge crest.

Figure 9 shows the starting models for inversions at Axial Seamount and West Cortez Basin data. Our models of density ($\rho(z)$) and compressional velocity ($\alpha(z)$) at Axial Seamount (Figure 9*a*) are based on seismic refraction and reflection studies by *van Heeswijk* [1986]. The West Cortez Basin $\rho(z)$ and $\alpha(z)$ models (Figure 9*b*) are based on seismic reflection data (Scripps Institution of Oceanography, Geological Data Center; also Calvin Lee, personal communication, 1991), California continental borderland studies by *Teng and Gorsline* [1989], and sediment elastic parameter derivations by *Hamilton* [1980]. Figure 10 shows the results of the inversions. The West Cortez Basin data are well constrained, but inversion reveals no compelling structure. We first used C^2L_2 inversion to generate a West Cortez Basin model, (WC2 in Figure 10*a*) but because the inverted model had a low second difference we also generated a C^1L_2 inversion of the data (WC1 in Figure 10*a*). This inversion is similar to the WC2 inversion and provides confidence in the quality of the inversion. It appears that structure above 2500 m is well constrained for the West Cortez basin data. The inverted Axial Seamount model (Figure 10*a*) shows shear velocity that decreases with depth at depths greater than 1500 m beneath the seafloor. The decrease in shear velocity increases the L_2 norm of the second difference of the model. C^2L_2 inversion minimizes this value to the greatest degree allowed by the data; the region of low shear velocity is required to fit the data. At 2200 m depth, shear velocity has decreased by 8% from its maximum value. Assuming that the decrease in shear velocity is due to temperature effects, we calculate β(observed)/β(normal) $\leq$ 0.92. Studies of temperature effects on peridotites [*Sato et al.*, 1989] reveal this velocity variation is out of the range of temperature effects on solids and suggest partial melt. Applying relations for β(partial melt)/β(solid) from an experimental study of peridotite under 10+ kBar pressure [*Murase and Fukuyama*, 1980] and numerical models of rock independent of pressure [*Schmeling*, 1985], a region of at least 3% partial melt is required between 1500 and 2500 m depth within the edifice. This result is consistent with other suggestions of a magma chamber beneath Axial Seamount based on petrologic [*Rhodes et al.*, 1990], magnetic [*Tivey and Johnson*, 1990], gravimetric [*Hildebrand et al.*, 1990], hydrothermal [*Embley et al.*, 1990] and deformational [*Fox*, 1990] studies.

CONCLUSIONS

We have described an approach to profiling Earth structure, using pressure and displacement spectra to measure vertical compliance of the oceanic crust. Displacement information is measured using a low-frequency seismometer different from those found in conventional OBSs. We measured compliance at two sites, Axial Seamount and West Cortez Basin, and the compliance data agree with our knowledge of these sites. In particular, the difference between compliance of rocks and of thick sediments is apparent. The compliance data were inverted for a model of shear velocities. The data provide evidence for a region of partial melt beneath 1500 m depth below the caldera of Axial Seamount. The inversion accuracy is presently limited by the hardware-constrained coherence bandwidth between pressure and acceleration spectra. We believe that by decreasing electronic noise in the acceleration measurements we will improve the compliance measurements, providing good coherences to frequencies as low as 0.002 Hz.

There are many unanswered questions about the oceanic crust which could be better constrained through compliance inversions. With the ability to sense shear velocity structure to 6-7 km beneath a 2000-m-deep seabed, compliance inversion should constrain shear velocities to the bottom of young oceanic crust. The compressional information obtained from active seismic source experiments is complemented by shear information from the relatively simple process of compliance inversion.

Acknowledgments. We are indebted to V. Pavlicek, T. Deaton, and P. Hammer for development, construction and maintenance of the underwater gravimeter and differential pressure gauge. R. Parker and T. Yamamoto provided critical and insightful review of the paper. We thank S. Constable for the use of the Occam's inversion subroutines, and C. Lee for providing seismic reflection data and stacking velocities from West Cortez Basin. C. Fox and the NOAA Vents program supplied valuable ship time and encouragement. Research support was provided by the ONR Marine Geology and Geophysics program and the ONR MPL/ARL Program; we thank J. Kravitz and R. Jacobson for their encouragement and support.

REFERENCES

Agnew, D. C. and J. Berger, Vertical seismic noise at very low frequencies, *J. Geophys. Res.*, *83*, 5420-5424, 1978.

Aki, K., A. Christofferson, and E. S. Husebye, Determination of the three-dimensional seismic structure of the lithosphere, *J. Geophys. Res.*, *82*, 277-296, 1977.

Aki, K. and P. G. Richards, *Quantitative Seismology: Theory and Methods*, vol. I and II,W. H. Freeman, New York, 1980.

Apel, J. R., *Principles of Ocean Physics*, Academic, San Diego, California, 1987.

Beaumont, C. and A. Lambert, Crustal structure from surface load tilts using a finite element model, *Geophys. J.*, *39*, 203-226, 1972.

Bendat, J. S. and A. G. Piersol, *Engineering Applications of Correlation and Spectral Analysis*, John Wiley, New York, 1980.

Bradner, H., Probing sea-bottom sediments with microseismic noise, *J. Geophys. Res.*, *68*, 1788-1791, 1963.

Constable, S. C., R. L. Parker, and C. G. Constable, Occam's inversion: A practical algorithm for generating smooth models from electromagnetic sounding data, *Geophysics*, *52*, 289-300, 1987.

Cox, C. S., T. Deaton, and S. C. Webb, A deep sea differential pressure gauge, *J. Atmos. Oceanic Technol.*, *1*, 237-246, 1984.

Embley, R. W., K. M. Murphy, and C. G. Fox, High-resolution studies of the summit of axial volcano, *J. Geophys. Res.*, *95*, 12785-12872, 1990.

Fox, C. G., Evidence of active ground deformation on the mid-ocean ridge: Axial Seamount, Juan de Fuca Ridge, April-June 1988, *J. Geophys. Res.*, *95*, 12813-12822, 1990.

Fryer, G. J., D. J. Miller, and P. A. Miller, Seismic anisotropy and age-dependent structure of the upper oceanic crust, in *The Evolution of Mid-Oceanic Ridges*, edited by J. M. Sinton, pp. 1-8, AGU, Washington, D. C., 1991.

Gomberg, J. S. and T. G. Masters, Waveform modeling using locked-mode synthetic and differential seismograms: application to determination of the structure of Mexico, *Geophys. J.*, *94*, 193-218, 1988.

Hamilton, E. L., Geoacoustic modeling of the sea floor, *J. Acoust. Soc. Am.*, *68*, 1313-1340, 1980.

Hildebrand, J. A., J. M. Stevenson, P. T. C. Hammer, M. A. Zumberge, R. L. Parker, C. G. Fox, and P. J. Meis, A seafloor and sea surface gravity survey of Axial Volcano, *J. Geophys. Res.*, *95*, 12751-12763, 1990.

Lacoste, L. J. B., Measurement of gravity at sea and in the air, *Rev. Geophys.*, *5*, 477-526, 1967.

Menke, W., *Geophysical Data Analysis: Discrete Inverse Theory*, Academic , San Diego, California , 1984.

Murase, T. and H. Fukuyama, Structure and properties of liquids and glasses, *Year Book, Carnegie Inst. Wash.*, *79*, 307-310, 1980.

Parker, R. L., Understanding inverse theory, *Ann. Rev. Earth Planet. Sci.*, *5*, 35-64, 1977.

Parker, R. L., The inverse problem of resistivity sounding, *Geophysics*, *49*, 2143-2158, 1984.

Rhodes, J. M., C. Morgan, and R. A. Liias, Geochemistry of Axial Seamount lavas: Magmatic relation between the Cobb hotspot and the Juan de Fuca Ridge, *J. Geophys. Res.*, *95*, 12713-12733, 1990.

Sato, H., I. S. Sacks, and T. Murase, The use of laboratory velocity data for estimating temperature and partial melt fraction in the low-velocity zone: Comparison with heat flow and electrical conductivity studies, *J. Geophys. Res.*, *94*, 5689-5704, 1989.

Schmeling, H., Numerical models on the influence of partial melt on elastic, anelastic, and electric properties of rocks. Part I: elasticity and anelasticity, *Phys. Earth. Planet. Inter.*, *41*, 34-57, 1985.

Smith, J. T. and J. R. Booker, Magnetotelluric inversion for minimum structure, *Geophysics*, *53*, 1565-1576, 1988.

Sorrels, G. G. and T. T. Goforth, Low frequency Earth motion generated by slowly propagating, partially organized pressure fields, *Bull. Seismol. Soc. Am.*, *63*, 1583-1601, 1973.

Spudich, P. and J. Orcutt, A new look at the seismic velocity structure of the oceanic crust, *Rev. Geophys.*, *18*, 627-645, 1980.

Teng, L. S. and D. S. Gorsline, Late Cenozoic sedimentation in California continental borderland basins as revealed by seismic facies analysis, *Geol. Soc. Am. Bull.*, *101*, 27-41, 1989.

Thomson, D. J., Spectrum estimation techniques for characterization and development of WT4 waveguide I, *Bell Syst. Tech. J.*, *56*, 1769-1813, 1977.

Tivey, M. and H. P. Johnson, The magnetic structure of Axial Seamount, Juan de Fuca Ridge, *J. Geophys. Res.*, *95*, 12735-12750, 1990.

van Heeswijk, M., Shallow crustal structure of the caldera of Axial Seamount, Juan de Fuca Ridge, M.Sc. thesis, Oregon State Univ., 1986.

Webb, S. C., X. Zhang, and W. C. Crawford, Infragravity waves in the deep ocean, *J. Geophys. Res.*, *96*, 2723-2736, 1991.

Woodhouse, J. H., Efficient and stable methods for performing seismic calculations in stratified media, *Proc. Int. Sch. Phys. Enrico Fermi*, *78*, 127-151, 1980.

Yamamoto, T. and T. Torii, Seabed shear modulus profile inversions using surface gravity (water) wave-induced bottom waves, *Geophys. J. R. Astron. Soc.*, *85*, 413-431, 1986.

Yamamoto, T., M. V. Trevorrow, M. Badiey, and A. Turgut, Determination of the seabed porosity and shear modulus profiles using a gravity wave inversion, *Geophys. J. Int.*, *98*, 173-182, 1989.

W.C. Crawford, J.A. Hildebrand and S.C. Webb, Scripps Institution of Oceanography, 0205, University of California, San Diego, La Jolla, CA 92093-0205.

(Received October 10, 1990;
revised April 25, 1991;
accepted June 12, 1991.)

JOURNAL OF GEOPHYSICAL RESEARCH, VOL. 96, NO. B10, PAGES 16,231–16,240, SEPTEMBER 10, 1991

Visible and Near-Infrared (0.4–2.5 μm) Reflectance Spectra of Playa Evaporite Minerals

JAMES K. CROWLEY

U.S. Geological Survey, Reston, Virginia

Visible and near-infrared (VNIR; 0.4–2.4 μm) reflectance spectra were recorded for 35 saline minerals that represent the wide range of mineral and brine chemical compositions found in playa evaporite settings. The spectra show that many of the saline minerals exhibit diagnostic near-infrared absorption bands, chiefly attributable to vibrations of hydrogen-bonded structural water molecules. VNIR reflectance spectra can be used to detect minor hydrate phases present in mixtures dominated by anhydrous halite or thenardite, and therefore will be useful in combination with X ray diffraction data for characterizing natural saline mineral assemblages. In addition, VNIR reflectance spectra are sensitive to differences in sample hydration state and should facilitate in situ studies of minerals that occur as fragile, transitory dehydration products in natural salt crusts. The use of spectral reflectance measurements in playa studies should aid in mapping evaporite mineral distributions and may provide insight into the geochemical and hydrological controls on playa mineral and brine development.

INTRODUCTION

Playas, i.e., dry lake beds or salt pans, are widely distributed landforms in modern desert basins having restricted interior drainage systems and high evaporation rates. Perhaps the most striking features of many playas are crusts of efflorescent salt minerals that form by the evaporation of ground waters at playa surfaces. These crusts commonly are very extensive. For example, the Salar de Atacama in Chile, one of the world's largest salt pans, covers an area of roughly 2000 km^2, including vast expanses of efflorescent crusts [*Ericksen and Salas*, 1989]. Even relatively small playas, such as Teels Marsh, Nevada, can have efflorescent crusts that extend over several square kilometers. In addition to the efflorescent salt crusts, many playas contain large deposits of saline minerals formed by precipitation from standing brine or by displacive growth within brine-saturated clastic sediments [*Eugster and Hardie*, 1978]. Such deposits are major sources of industrial minerals, including halite, gypsum, sodium and magnesium sulfates, borax, lithium concentrates, and others [*Reeves*, 1978]. Because of their large size, and despite their geologic and economic importance, relatively few playas have been studied in detail. The enormous amount of sampling and laboratory work needed to characterize the playa brines and associated evaporite minerals is a significant problem.

This paper examines visible and near-infrared (VNIR; 0.4–2.5 μm) reflectance spectra of 35 playa evaporite mineral specimens and represents the initial phase of a project to explore the use VNIR reflectance measurements for investigating the mineralogy of playa efflorescent crusts. Reflectance measurements may be able to provide a rapid, qualitative estimate of sample mineralogy and thus permit more time-consuming analytical techniques, such as X ray powder diffraction, to be applied selectively. VNIR measurements can also be obtained with remote sensing instruments, which in principle, could greatly enhance the ability to study large playa surfaces. There is an extensive body of literature on the theory and use of VNIR spectral measurements, particularly as they have been applied in remote sensing studies of the Earth and planets [*Hunt*, 1977; *Clark and Roush*, 1984; *Vane and Goetz*, 1988].

What types of VNIR spectral features do playa evaporite minerals exhibit? Surprisingly few evaporite minerals have previously been examined in the VNIR wavelength range. *Hunt et al.* [1971, 1972] recorded VNIR reflectance spectra of gypsum, bassanite, halite, thenardite, and several borate minerals. *Hunt and Salisbury* [1971] and *Gaffey* [1987] also discussed the VNIR spectra of anhydrous carbonate minerals, such as calcite, dolomite, and magnesite. Numerous workers have presented midinfrared (MIR; 2.5–25 μm) transmission spectra of salt minerals, including most of the mineral species dealt with in this paper (see especially *Huang and Kerr* [1960], *Omori and Kerr* [1963], and *Schubert* [1967]). For playa investigations, however, VNIR reflectance spectra offer several important advantages over MIR transmission spectra. First, reflectance spectra can be recorded rapidly in the field, permitting in situ measurements of fragile mineral species that may not be sufficiently stable for transport to a laboratory. Reflectance measurements also require little sample preparation and in particular do not require grinding to obtain the extremely fine (<2 μm) particles normally used in MIR transmission work. Such grinding can cause dehydration and other structural changes in the saline minerals typical of playa settings. Another consideration involves the greater amount of material measured in reflectance versus transmission methods. Natural salt crusts may contain several minerals, making it difficult to ensure that the small quantity of sample examined in a MIR transmission spectrum is representative of the bulk material.

Several criteria were followed in selecting the 35 minerals included in this paper from the hundreds of saline mineral species that exist. First, all of the minerals chosen occur as efflorescent salts characteristic of continental evaporite settings at surface temperature and pressure conditions. Minerals known only from marine evaporite deposits, or resulting from subsurface diagenetic or metamorphic alteration of buried surface minerals, were not included. Also, rare accessory minerals that contain essential minor elements, such as fluorine, phosphorus, strontium, and barium, as well as many of the less common borate minerals were not exam-

Paper number 91JB01714.

ined. Relatively few anhydrous minerals were measured spectrally, as most would not be expected to exhibit absorption bands in the VNIR. Subject to these constraints, virtually all of the other important playa evaporite mineral species are included in this study.

Two questions that the current work does not attempt to address are the possible effects of element substitutions and structural disorder on saline mineral spectral features. Although both of these questions merit further study, spectral variations related to substitutions and/or structural disorder are likely to be difficult to discern. Substitutions involving major elements are limited in saline minerals [*Stewart*, 1963] and so would not be expected to produce major spectral changes. The limited substitution apparently reflects the ease with which many saline minerals transform into new phases given small changes in brine composition and temperature. Studies of disorder in saline minerals must address an especially difficult problem—that of identifying precise hydrogen atom locations for the structural water molecules that most of the minerals contain. A few reports have considered the possibility of structural disorder in the saline hydrate minerals examined here [*Baur*, 1964; *Levy and Lisensky*, 1978; *Choi and Mighell*, 1982]; however, structural data for additional samples are required before an assessment of spectral changes related to disorder can be made. Such data should eventually become available as more hydrate minerals are analyzed by neutron diffraction methods.

ANALYTICAL PROCEDURES

Thirteen of the mineral samples used in this study were synthesized either by evaporating aqueous solutions of suitable reagent materials or by dehydrating a related mineral or compound. Table 1 summarizes the procedures followed to prepare each of the synthetic specimens and gives other sample information. Additional comments on sample synthesis are given by *Crowley* [1991]. All of the samples listed in Table 1 were analyzed by X ray powder diffraction (Cu Kα source) to determine each specimen's identity and purity. The spectra and the X ray diffraction (XRD) patterns were recorded under dry laboratory conditions (relative humidity 25–30 %).

VNIR spectra were recorded on a Beckman Instruments model UV 5240 spectrophotometer equipped with an integration sphere. The data were obtained digitally and corrected for errors in the 100% line caused by the instrument and the white halon reference material [*Crowley et al.*, 1986]. Wavelength positions of absorption features measured with this system are periodically checked with a holmium oxide reference filter and are reproducible within ±4 nm (one digitization step). Other spectral quality considerations for dual-beam spectrometers similar to the one used in this study have been discussed at length by *Hunt* [1979]. Scan speed and spectral bandwidth, i.e., effective resolving power, are the chief parameters affecting spectral quality, and choosing these parameters represents a compromise between throughput and the need for maximum precision and spectral detail. The spectra in this study were produced using a scan speed of 2 nm/s and a spectral bandwidth of 8 nm or less over most of the VNIR wavelength range. Spectral bandwidth was slightly greater between 800–900 nm and 2400–2500 nm; these are the extremes of the energy range covered by the PbS detector.

All of the samples measured were moderately coarse powders (particle size approximately 250 μm) produced by crushing the mineral specimens with a silica mortar and pestle. In some cases, crushing the samples resulted in powders that were slightly damp, probably due to moisture liberated from fluid inclusions by the crushing process. VNIR spectra are very sensitive for detecting both adsorbed and structural water molecules [*Hunt*, 1977; *Aines and Rossman*, 1984]. Therefore, in order to minimize any spectral effects of adsorbed water, damp powders were dried in an oven for 2–4 min at 60°C prior to recording the spectra. Such samples were subsequently X rayed to ascertain that the mineralogy was not changed by this rapid drying procedure. Because many samples were only available in small amounts, and because of the need to avoid intense grinding, which might have caused the destruction of some mineral phases, spectra for different particle size ranges were not obtained.

Several of the minerals examined in this study are unstable and either dehydrate or deliquesce under dry laboratory humidity conditions. Minerals in this category include mirabilite, epsomite, bischofite, and the extremely hygroscopic calcium chloride hydrates. To characterize these minerals, spectra were recorded immediately before and after running each sample XRD pattern. Absent any spectral changes, the XRD data and the spectra were assumed to represent the sample mineralogy correctly.

SALINE MINERAL SPECTRA

VNIR absorption features result from two distinct processes, electronic transitions involving an atom's valence shell electrons and molecular vibrations involving quantized, but less energetic, distortions of interatomic bonds [*Hunt*, 1977]. Although electronic transitions are observed in some saline mineral spectra (e.g., absorption due to color centers in halide minerals), most of the VNIR features seen in saline minerals are vibrational in origin. The features generally can be attributed to internal vibration modes of certain molecular groups, particularly the carbonate, borate, and hydroxyl anion groups, and neutral water molecules. The principal or fundamental vibration modes of these groups generate absorption features in the MIR wavelength region, whereas VNIR features result from combinations and overtones of the MIR fundamentals [*Hunt*, 1977]. Other molecular groups, such as the phosphate, silicate, and sulfate anion groups, produce analogous MIR absorption bands but do not exhibit associated VNIR overtone features due to the lower frequencies of their MIR fundamentals [*Hunt*, 1977].

Spectra for the samples measured in this study are shown in Figures 1–8, which generally group the data according to the anions present in each mineral. The mineral burkeite, a sodium sulfocarbonate, is included with other carbonate species in Figure 4. Kainite, a potassium magnesium sulfochloride, is included with other chlorides in Figure 1. Teepleite, a sodium boron hydroxychloride, is shown with other borate minerals in Figure 8. Table 2 lists the wavelength positions of major absorption bands for each mineral and gives reflectance values at 2.5 μm for each spectrum. In Figures 1–8 the spectra are shown in a stacked format to portray the spectral features more clearly. The absolute reflectance values at 2.5 μm permit reconstruction of the "y" axis reflectance range for individual spectra. All of the

TABLE 1. Mineral Sample Information

Mineral	Formula	Source/Method of Preparation
		Borates
Borax	$Na_2B_4O_5(OH)_4 \cdot 8H_2O$	"Twenty Mule Team" commercial borax
Colemanite	$Ca_2B_6O_{11} \cdot 5H_2O$	Boron, California
Inderite	$MgB_3O_3(OH)_5 \cdot 5H_2O$	NMNH 137833, Kern County, California[a]
Meyerhofferite	$Ca_2B_6O_6(OH)_{10} \cdot H_2O$	NMNH 96075-3, Inyo County, California
Probertite	$NaCaB_5O_7(OH)_4 \cdot 3H_2O$	NMNH 165227, Boron, California
Teepleite[b]	$Na_2B(OH)_4Cl$	NMNH 102798, Borax Lake, California
Tincalconite	$Na_2B_4O_5(OH)_4 \cdot 3H_2O$	dehydration of borax at 60°C
Ulexite	$NaCaB_5O_6(OH)_6 \cdot 5H_2O$	Boron, California
		Carbonates
Calcite	$CaCO_3$	Joanna Limestone, Confusion Range, Utah
Burkeite[b]	$Na_6(CO_3)(SO_4)_2$	NMNH 105598, Searles Lake, California
Gaylussite	$Na_2Ca(CO_3)_2 \cdot 5H_2O$	NMNH 102876-2, Searles Lake, California
Nahcolite	$NaHCO_3$	"Arm and Hammer" commercial baking soda
Natron[c]	$Na_2CO_3 \cdot 10H_2O$	evaporation of $NaHCO_3$ solution at 5°C
Pirssonite	$Na_2Ca(CO_3)_2 \cdot 2H_2O$	NMNH 102781, Searles Lake, California
Trona	$Na_3(CO_3)(HCO_3) \cdot 2H_2O$	Green River Formation, Wyoming
		Chlorides
Antarcticite	$CaCl_2 \cdot 6H_2O$	evaporation of $CaCl_2$ solution at room temperature, r.h. <25%[d]
Bischofite	$MgCl_2 \cdot 6H_2O$	Fischer Scientific $MgCl_2 \cdot 6H_2O$ reagent
Carnallite	$KMgCl_3 \cdot 6H_2O$	NMNH 98011, Barcelona, Spain
Halite	NaCl	Bristol Dry Lake, California
Kainite	$MgSO_4 \cdot KCl \cdot 3H_2O$	NMNH 83904, Stassfurt, Germany
Sinjarite	$CaCl_2 \cdot 2H_2O$	dehydration of $CaCl_2 \cdot 4H_2O$ at 40°C
—[e]	$CaCl_2 \cdot 4H_2O$	dehydration of antarcticite at 40°C
		Sulfates
Bassanite	$2CaSO_4 \cdot H_2O$	dehydration of gypsum at 60°C
Bloedite	$Na_2Mg(SO_4)_2 \cdot 4H_2O$	Soda Lake, California
Epsomite	$MgSO_4 \cdot 7H_2O$	"Epsom salts" commercial product
Eugsterite[f]	$Na_4Ca(SO_4)_3 \cdot 2H_2O$	evaporation of $Na_2SO_4 + CaSO_4$ solution at 70°C
Gypsum	$CaSO_4 \cdot 2H_2O$	Mesquite playa, California
Hexahydrite	$MgSO_4 \cdot 6H_2O$	dehydration of epsomite at room temperature, r.h. <30%
Leonite	$K_2Mg(SO_4)_2 \cdot 4H_2O$	dehydration of picromerite at 40°C
Mirabilite	$Na_2SO_4 \cdot 10H_2O$	evaporation of Na_2SO_4 solution at room temperature, r.h. <30%
Pentahydrite	$MgSO_4 \cdot 5H_2O$	NMNH R-6091 "kieserite"
Picromerite	$K_2Mg(SO_4)_2 \cdot 6H_2O$	evaporation of $K_2SO_4 + MgSO_4$ solution at room temperature, r.h. <30%
Polyhalite	$K_2Ca_2Mg(SO_4)_4 \cdot 2H_2O$	NMNH 92669-4, Carlsbad, New Mexico
Starkeyite	$MgSO_4 \cdot 4H_2O$	dehydration of hexahydrite at 60°C
Syngenite	$K_2Ca(SO_4)_2 \cdot H_2O$	evaporation of $K_2SO_4 + CaSO_4$ solution at room temperature, r.h. <30%
Thenardite	Na_2SO_4	Saline Valley, California

[a]NMNH samples are from the Smithsonian Institute, National Museum of Natural History, Washington, D. C.
[b]Samples contain moderate amounts of trona.
[c]Sample contained a moderate amount of nahcolite.
[d]r.h. is relative humidity.
[e]Sample contained a small amount of antarcticite. There is no mineral name for this inorganic compound.
[f]Sample contained a small amount of gypsum.

values shown in Table 2 were measured directly from the digital spectra without removing the background "continuum" or applying other arbitrary processing procedures.

In most cases, the absorption features seen in the evaporite mineral spectra are caused by water molecules that are essential components in each mineral structure. Two exceptions to this general statement include the minerals halite (NaCl) and thenardite (Na_2SO_4), which are anhydrous but still exhibit broad water bands near 1.4 and 1.9 μm related to the presence of fluid inclusions and/or adsorbed water (Figures 1 and 3). Further exceptions include the anhydrous sulfocarbonate mineral burkeite (Figure 4), which exhibits a band near 2.36 μm, probably associated with vibration modes of the carbonate anion group [see *Hunt and Salisbury*, 1971; *Gaffey*, 1987]. Also, the hydrous borate minerals (Figures 7 and 8) exhibit absorptions in the 2.0- to 2.5-μm range that may be related to vibrations of borate anion groups [*Hunt et al.*, 1972].

The VNIR spectrum of gypsum (Figure 2) has been discussed previously by *Hunt et al.* [1971] and provides a useful framework for examining the other hydrate mineral spectra shown in Figures 1–8. According to *Hunt et al.* [1971], band assignments for gypsum in the VNIR may be made as follows: The relatively weak band seen near 1.0 μm probably represents a combination of the first overtone of the O-H stretching and the first overtone of the H-O-H bending fundamentals. The slightly more intense feature near 1.2 μm is assigned to a combination of the H-O-H bending fundamental and the first overtone of the O-H stretch. Absorption bands in the wavelength region between about 1.4 and 1.6 μm are due mainly to the first overtone(s) of the O-H stretching fundamental(s). Another group of

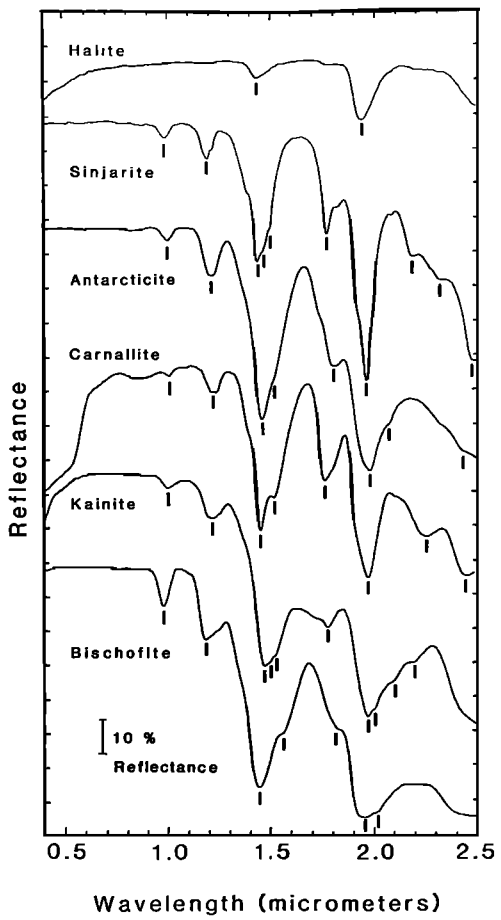

Fig. 1. Diffuse reflectance spectra of chloride and chloride hydrate minerals. Spectra are offset vertically for viewing purposes, and bars mark positions of absorption bands listed in Table 2. Vertical tick marks indicate reflectance intervals of 10%.

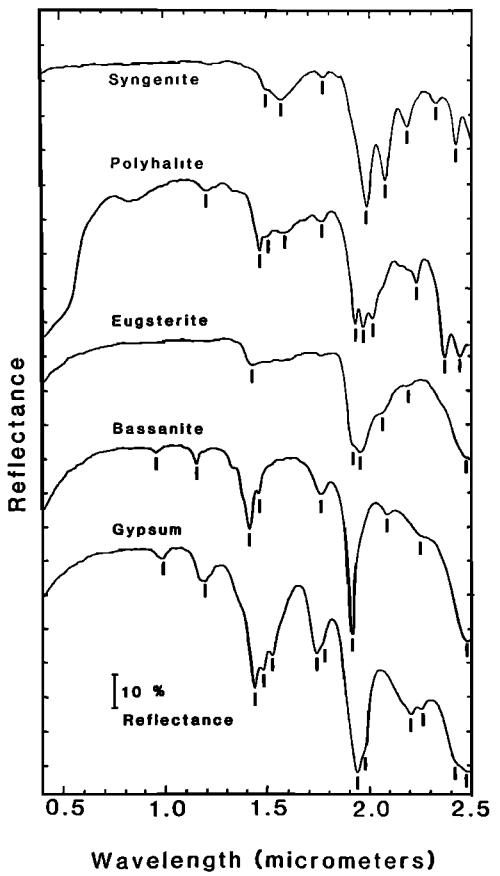

Fig. 2. Diffuse reflectance spectra of sulfate hydrate minerals. Spectra are offset vertically for viewing purposes, and bars mark positions of absorption bands listed in Table 2. Vertical tick marks indicate reflectance intervals of 10%.

bands positioned near 1.74 μm are assigned to combinations involving the fundamental H-O-H bend, the fundamental O-H stretch, and low frequency libration modes of the structural water molecules. The strong bands near 1.9 μm are assigned to a combination of the O-H stretching and the H-O-H bending fundamentals. Finally, the series of bands near 2.2 μm have been attributed to a combination of the fundamental O-H stretch plus the first overtone of the water libration modes.

Examination of the Figures 1–8 indicates that many of the hydrate mineral spectra resemble the gypsum spectrum, with some qualifications. First, the more strongly hydrated minerals, such as antarcticite (Figure 1), bischofite (Figure 1), mirabilite (Figure 3), natron (Figure 4), epsomite (Figure 5), and hexahydrite (Figure 5) show relatively broad absorption features, probably caused by the overlapping bands of water molecules in numerous slightly different bonding configurations. Less hydrated species, such as bassanite, polyhalite, and syngenite (Figure 2), generally show narrower absorption features, indicative of fewer water molecules per formula unit and less absorption band overlap. Many of the borate minerals, particularly probertite (Figure 7), and meyerhofferite, inderite, and teepleite (Figure 8), show one or more very narrow bands near 1.4 μm produced by structural hydroxyl groups that are not associated with water molecules. These narrow hydroxyl O-H stretching features are superimposed on the broader O-H stretching bands characteristic of the structural water molecules.

The hydrous carbonate minerals shown in Figure 4 present an interesting case, as CO_3^{-2} absorption bands occur between 2.0–2.5 μm in the anhydrous carbonates and may also be expected to occur here [*Hunt and Salisbury*, 1971; *Gaffey*, 1987]. For example, CO_3^{-2} bands occur near 2.33 and 2.53 μm in the spectrum of calcite, which is shown at the top of Figure 4 for comparison to the other mineral spectra. However, no such bands are clearly identifiable in the hydrous carbonates. Possible carbonate features include the minor gaylussite features near 2.32 and 2.44 μm, and the faint trona features near 2.21 and 2.39 μm. Because water molecules can also produce absorption bands in the 2.0- to 2.5-μm wavelength region, the assignment of the trona and gaylussite features is uncertain. Note that the burkeite sample is contaminated with a small amount of trona, which accounts for the water-related features near 1.51, 1.74, 1.94, and 2.04 μm in the burkeite spectrum. The CO_3^{-2} anion group is known to be somewhat distorted in most of the hydrous carbonates shown in Figure 4, so that the midinfrared fundamentals are split into multiple bands [*White*, 1974]. This splitting may serve to lower the intensity of any VNIR overtone features and may result in their being masked by the strong water absorption. Nahcolite lacks molecular water; however, its structure contains a network of strong hydrogen "bridges" (symmetrical H bonds) between the

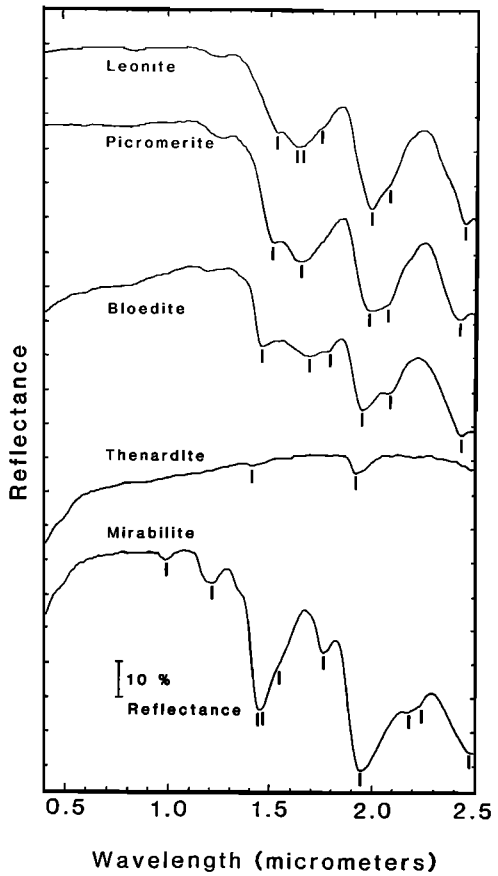

Fig. 3. Diffuse reflectance spectra of additional sulfate and sulfate hydrate minerals. Spectra are offset vertically for viewing purposes, and bars mark positions of absorption bands listed in Table 2. Vertical tick marks indicate reflectance intervals of 10%.

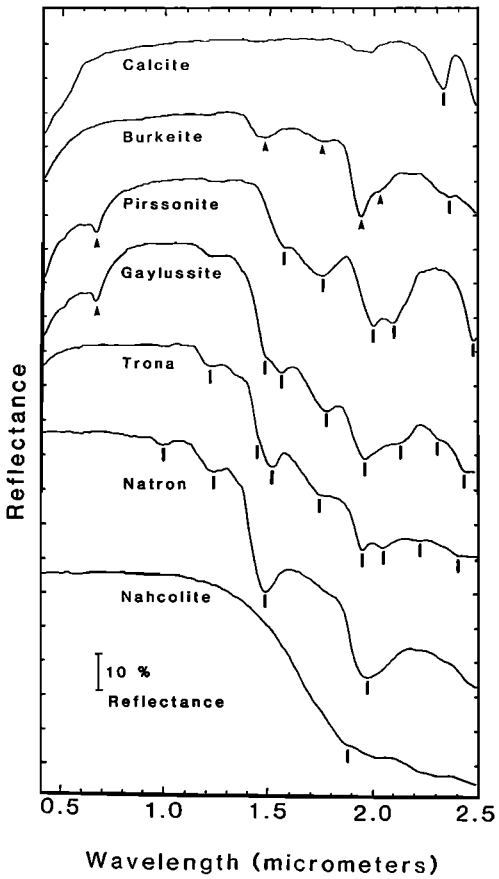

Fig. 4. Diffuse reflectance spectra of carbonate and carbonate hydrate minerals. Spectra are offset vertically for viewing purposes, and bars mark positions of absorption bands listed in Table 2. Arrows shown on the burkeite spectrum mark features due to trona, which is present as a contaminant. Arrows shown on the pirssonite and gaylussite spectra mark chlorophyll features probably due to small amounts of algae [*Gates*, 1980].

carbonate anions [*White*, 1974]. Nahcolite's midinfrared O-H stretching fundamentals are greatly broadened and displaced to lower frequencies [*Huang and Kerr*, 1960], and the VNIR spectrum exhibits a strong falloff between 1.4 and 1.8 μm associated with the first O-H stretching overtone (Figure 4). Trona contains similar hydrogen bridges, as well as hydrogen-bonded water molecules [*Choi and Mighell*, 1982]. A more definitive assignment of the hydrous carbonate mineral absorption features should be possible by using deuterium substitution techniques to help identify the water bands [*Falk and Knop*, 1973]. However, this was not undertaken in the present study.

Some of the minerals examined were produced by dehydrating other species (Table 1), and in several cases the spectra have been organized to show progressive changes associated with steps in the dehydration process. For example, Figure 5 shows spectra for epsomite, hexahydrite, pentahydrite, and starkeyite, i.e., magnesium sulfate in four different hydration states. The monohydrate kieserite, which was not included in this study, is stable under surface pressure and temperature conditions but evidently requires elevated temperatures or extended periods of time for formation [*Hardie*, 1984]. Figure 6 shows a similar dehydration series involving the two calcium chloride hydrate minerals, antarcticite and sinjarite, and the intermediate compound $CaCl_2 \cdot 4H_2$). In both Figure 5 and Figure 6 the more hydrated minerals generally show broader absorption features than their less hydrated derivatives. For example, notice the much broader band near 1.95 μm in antarcticite ($CaCl_2 \cdot 6H_2O$) compared with the same band in sinjarite ($CaCl_2 \cdot 2H_2O$). Progressive dehydration does cause come absorption features to disappear, (e.g., the 2.058-μm band in antarcticite); however, there is an opposing tendency for the less hydrated minerals to show additional band structure within the major absorption features. This tendency is well illustrated by the complex band structure within the broad 1.4-μm features of starkeyite (Figure 5) and sinjarite (Figure 6). Presumably, this complex band structure was masked by numerous overlapping water bands in the more strongly hydrated members of each series.

Mixtures Involving Hydrous and Anhydrous Minerals

Efflorescent salt crusts on playa surfaces are formed by the complete evaporation of brine [*Hardie*, 1968]; therefore fresh crusts should include mineral phases that account for all of the brine chemical components. However, most efflorescent crusts are dominantly composed of one or two minerals, notably thenardite (Na_2SO_4), halite (NaCl), or trona ($Na_3(CO_3)(HCO_3) \cdot 2H_2O$). Thus it is important to determine whether VNIR spectral data will permit the de-

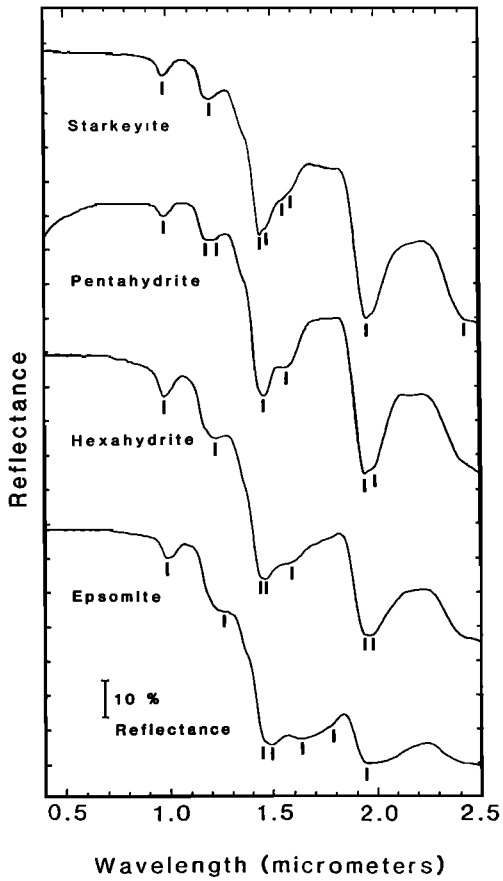

Fig. 5. Diffuse reflectance spectra of magnesium sulfate hydrate minerals. Spectra are offset vertically for viewing purposes, and bars mark positions of absorption bands listed in Table 2. Vertical tick marks indicate reflectance intervals of 10%.

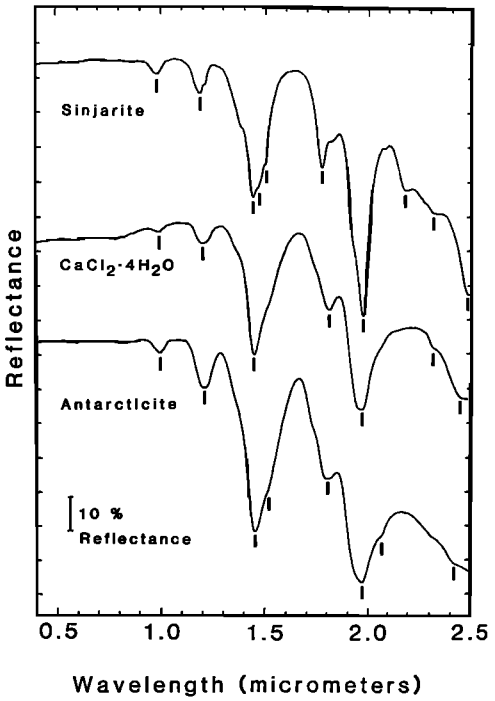

Fig. 6. Diffuse reflectance spectra of calcium chloride hydrate minerals. Spectra are offset vertically for viewing purposes, and bars mark positions of absorption bands listed in Table 2. Vertical tick arks indicate reflectance intervals of 10%.

tection of minor mineral constituents present in samples composed chiefly of these three minerals.

This question is explored in Figure 9, which shows an artificial mixture of 1.8 g halite with 0.2 g borax. Because of the large difference in formula weight between halite (58 g/mol) and borax (382 g/mol) the 10 wt % mixture actually represents a less than 2 mol % mixture of borax in halite. The minerals were ground together by using a mortar and pestle to ensure that their particle sizes (about 100 μm) were approximately equal. As discussed below, VNIR spectra of mixtures are strongly affected by particle size differences between the mixture components, and thus the use of equal particle sizes does not illustrate the full range of possible spectral variation. However, equigranular powders are believed to represent the natural occurrence of saline minerals in efflorescent crusts reasonably.

Shown to the right in Figure 9 is a small segment of the XRD pattern for the same mixture. It is evident from the figure that borax is discernable spectrally when mixed with relatively large amounts of halite. Borax is much less apparent in the XRD data, where the strongest borax peak located near 35° 2θ is only slightly above the noise level. The spectral sensitivity to borax in Figure 9 reflects strong absorption by water molecules in the borax structure, coupled with the nearly transparent character of the anhydrous halite. This same high degree of sensitivity to the presence of hydrate species is also to be expected in mixtures involving thenardite as a major anhydrous component. Mixtures involving trona will be less favorable for detecting other minor hydrate phases because the strong trona water absorption features (Figure 4) will tend to mask or distort the other hydrate mineral features. On the other hand, the presence of other hydrate phases in a trona-rich mixture would change trona's spectral appearance and indicate the need for further analysis of the sample.

DISCUSSION

The suite of saline hydrate minerals examined in this study is unusual as virtually all of the species produce distinctive VNIR spectral features. In contrast, many other minerals known to contain molecular water, for example, most zeolite minerals and the smectite clay minerals, do not exhibit the VNIR spectral diversity seen here [*Ehmann and Vergo*, 1986; *Clark et al.*, 1990]. This diversity reflects the importance of hydrogen bonds in the saline hydrates, minerals in which water is an essential component of the structural framework, not merely an occupant of structural cavities or interlayer spaces. The individual saline mineral structures involve hydrogen bonds of slightly different strengths, with stronger bonds generally resulting in O-H stretching absorption features that are displaced to lower frequencies and longer wavelengths [*Pimental and McClellan*, 1960]. Qualitatively, the frequency shifts reflect a lowering of the O-H bond force constants related to the redistribution of electron density between the oxygen, hydrogen, and other atoms involved in the hydrogen bond [*Falk and Knop*, 1973]. In this study, such frequency displacements are especially evident in the VNIR spectra of bloedite and the hydrous carbonates and borates, where the broadening and displacement of the first O-H overtone feature to longer wavelengths has sup-

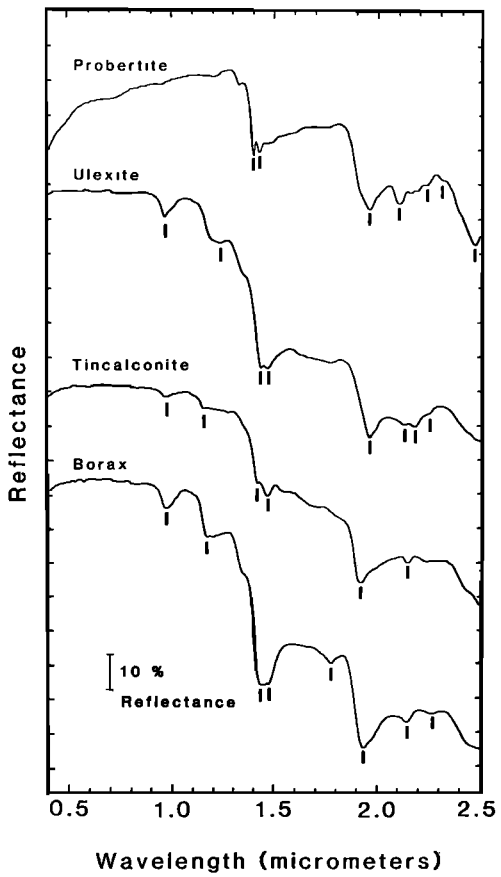

Fig. 7. Diffuse reflectance spectra of hydrous borate minerals. Spectra are offset vertically for viewing purposes, and bars mark positions of absorption bands listed in Table 2. Vertical tick marks indicate reflectance intervals of 10%.

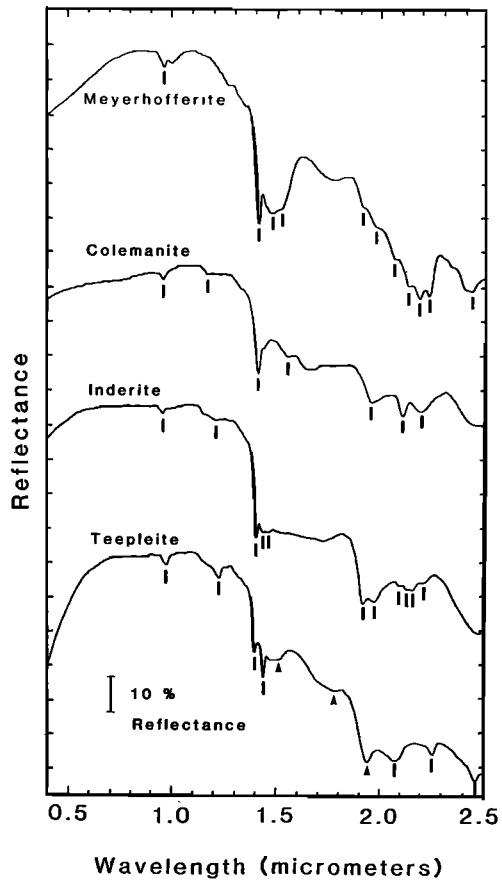

Fig. 8. Diffuse reflectance spectra of additional hydrous borate minerals. Spectra are offset vertically for viewing purposes, and bars mark positions of absorption bands listed in Table 2. Arrows shown on the teepleite spectrum mark features due to trona, which is present as a contaminant. Vertical tick marks indicate reflectance intervals of 10%.

pressed the reflectance between 1.4 and 1.9 μm. (For example, contrast the spectral appearance of bloedite with mirabilite in Figure 3).

The spectral variety seen in pure saline minerals points to the possibility of using VNIR spectra to study efflorescent salt crusts and the mineral-brine systems that the crusts represent. However, before proceeding to such a study, it is necessary to consider other variables that could complicate the interpretation of spectra recorded for natural crust samples.

Generally speaking, VNIR spectra recorded for different specimens of a single mineral may exhibit variations due to differences in sample particle size, minor compositional substitutions, and differences in structural order/disorder. Spectral effects related to minor substitutions and structural disorder have been reported to cause subtle band displacements and changes in relative band intensity [*Crowley and Vergo*, 1988; *Clark et al.*, 1990]. However, as stated earlier, element substitutions are not believed to be an important factor in the saline minerals of interest here. Spectral variations related to structural order/disorder in saline hydrate minerals might be significant but cannot presently be determined from the available structural data.

Particle size effects on VNIR spectra are relatively well understood. Particle size variations in pure minerals cause differences in the overall brightness of spectra, as well as differences in the depth, or "contrast" of the spectral absorption bands [*Hunt and Salisbury*, 1970]. Absorption band wavelengths are not affected by particle size variations; however, reduced spectral contrast in extremely fine-grained samples can cause weak absorption features to disappear [*Hunt and Salisbury*, 1970].

A much more complex problem is presented by mixtures of absorbing minerals in different particle size combinations. Such mixtures involve complicated scattering interactions among the mineral grains and generally show nonlinear spectral mixing relations [*Clark*, 1983]. Radiative transfer models have been developed that permit the spectra of mineral mixtures to be "deconvolved" into individual component abundances, provided that optical constants (absorption coefficients and indices of refraction) are available for all components over the wavelength range of interest [*Clark and Roush*, 1984]. Optical constants are currently being measured for some rock-forming minerals; however, as a practical matter, quantitative VNIR spectral analysis of most natural mixtures cannot yet routinely be performed (R. N. Clark, personal communication, 1991).

Despite the potential mixture problems just outlined, the use of VNIR spectra in conjunction with XRD and other data should facilitate the mineralogical analysis of natural salt crusts. Rapidity of measurement is one important advantage that spectra offer; dozens of VNIR spectra can be recorded

TABLE 2. Wavelength Positions of Major Visible and Near-Infrared Absorption Bands in Playa Evaporite Minerals

Mineral	Absorption Band Positions, μm	Percent Reflectance at 2.5 μm
	Borates	
Borax	0.976, 1.172, 1.428, 1.476, 1.774, 1.926, 2.140, 2.264	6
Colemanite	0.960, 1.168, 1.412, 1.556, 1,956, 2.104, 2.196	27
Inderite	0.960, 1.212, 1.408, 1.440, 1.464, 1.916, 1.976, 2.096, 2.136, 2.160, 2.212	18
Meyerhofferite	0.964, 1.412, 1.476, 1.520, 1.908, 1.976, 2.068, 2.136, 2.188, 2.232, 2.432	27
Probertite	1.400, 1.428, 1.960, 2.104, 2.240, 2.320, 2.460	25
Teepleite	0.988, 1.236, 1.404, 1.444, 2.074, 2.260, 2.456	22
Tincalconite	0.972, 1.156, 1.420, 1.470, 1.924, 2.148	22
Ulexite	0.968, 1.238, 1.428, 1.464, 1.948, 2.120, 2.168, 2.236	11
	Carbonates	
Calcite	2.335	48
Burkeite	2.364	51
Gaylussite	1.488, 1.564, 1.778, 1.964, 2.126, 2.316, 2.440	19
Nahcolite	1.850	11
Natron	0.996, 1.236, 1.486, 1.970	18
Pirssonite	1.576, 1.752, 1.994, 2.090, 2.476	32
Trona	1.220, 1.446, 1.518, 1.734, 1.940, 2.038, 2.214, 2.388	13
	Chlorides	
Antarcticite	1.000, 1.204, 1.454, 1.512, 1.808, 1.972, 2.058, 2.420	8
Bischofite	0.974, 1.182, 1.444, 1.556, 1.824, 1.952, 2.012	3
Carnallite	0.996, 1.216, 1.456, 1.520, 1.760, 1.976, 2.260, 2.454	11
Halite	1.432, 1.936	61
Kainite	1.000, 1.224, 1.470, 1.492, 1.518, 1.772, 1.964, 1.992, 2.084, 2.192	9
Sinjarite	0.984, 1.192, 1.432, 1.456, 1.492, 1.768, 1.952, 2.184, 2.308, 2.464	24
$CaCl_2 \cdot 4H_2O$	0.996, 1.204, 1.452, 1.812, 1.970, 2.320, 2.452	28
	Sulfates	
Bassanite	0.964, 1.160, 1.420, 1.468, 1.768, 1.912, 2.094, 2.252, 2.474	32
Bloedite	1.464, 1.698, 1.790, 1.948, 2.074, 2.428	20
Epsomite	0.990, 1.260, 1.460, 1.486, 1.634, 1.760, 1.956	3
Eugsterite	1.436, 1.928, 1.962, 2.068, 2.192, 2.480	48
Gypsum	0.992, 1.196, 1.440, 1.484, 1.530, 1.740, 1.768, 1.936, 1.964, 2.208, 2.262, 2.416, 2.474	18
Hexahydrite	0.976, 1.232, 1.436, 1.462, 1.572, 1.932, 1.960	6
Leonite	1.532, 1.624, 1.656, 1.752, 1.988, 2.068, 2.442	44
Mirabilite	0.992, 1.224, 1.448, 1.464, 1.548, 1.768, 1.946, 2.180, 2.236, 2.484	19
Pentahydrite	0.984, 1.188, 1.224, 1.458, 1.556, 1.932, 1.976	6
Picromerite	1.524, 1.654, 1.992, 2.072, 2.422	23
Polyhalite	1.216, 1.476, 1.512, 1.588, 1.776, 1.940, 1.976, 2.024, 2.240, 2.374, 2.446	40
Starkeyite	0.972, 1.202, 1.436, 1.460, 1.548, 1.596, 1.938, 2.412	9
Syngenite	1.496, 1.574, 1.772, 1.988, 2.076, 2.184, 2.326, 2.420	62
Thernardite	1.410, 1.922	63

Refer to Figures 1–8 for band locations. Reflectance values given at 2.5 μm.

in a single day of data collection. Furthermore, spectral data can be obtained and analyzed in the field, so that initial observations can be used to guide subsequent sampling efforts. VNIR spectra should be effective for identifying minor hydrate mineral phases in simple mixtures with halite and/or thenardite. More complex mixtures are likely to require XRD analysis, but spectra may still be useful for quickly recognizing that a mixture is present in a particular sample. Spectra may also help to narrow the choice of possible mixture constituents, thereby aiding in the interpretation of XRD data.

The spectral sensitivity to hydrate minerals could be important because minor chemical constituents in brines, such as potassium, boron, magnesium, and fluorine, frequently have significant geochemical implications. For example, an abundance of potassium-bearing minerals would signal an unusual brine composition, because potassium is normally depleted by adsorption on clays as ground waters slowly move through the subsurface towards a playa [*Eugster and Jones*, 1979]. Relatively little is known about spatial variations in efflorescent crust mineralogy or about compositional relations between surface minerals and the underlying brines. By providing data on the distribution of minor hydrate phases, VNIR spectra may help to answer both of these questions.

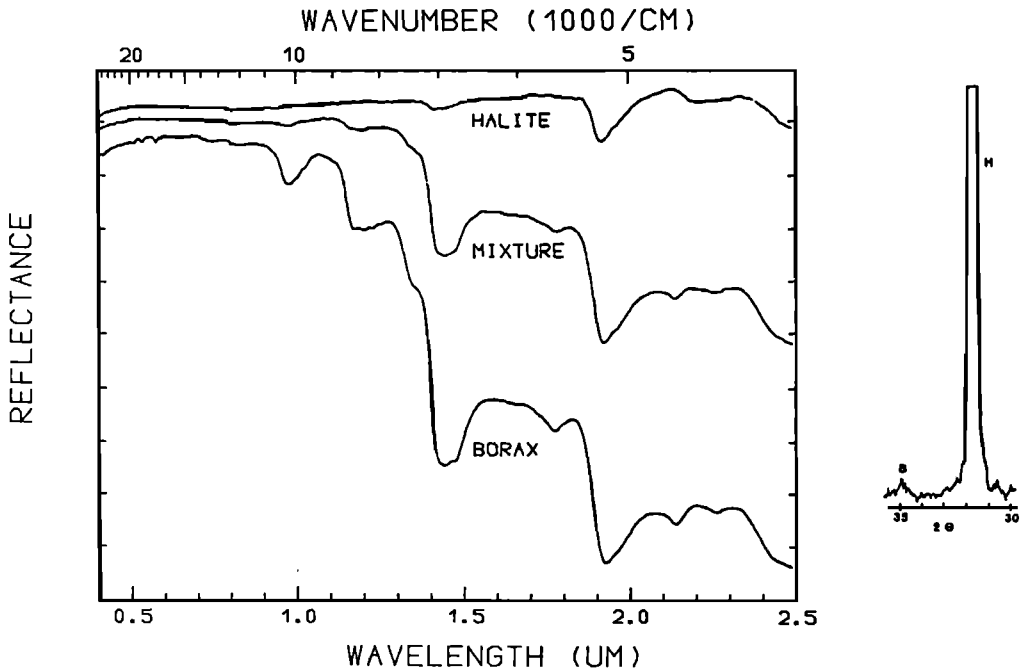

Fig. 9. Diffuse reflectance spectra of halite, borax, and a 10 wt % mixture of borax in halite. Because halite is anhydrous and relatively transparent in the VNIR, small amounts of strongly absorbing hydrate minerals are discernable in mixtures with halite. At right a portion of the XRD pattern for the same 10 wt % mixture illustrates the difficulty in detecting borax (B) in halite (H) (or other minor components in mixtures) by using XRD techniques alone. See text for additional discussion.

CONCLUSIONS

Visible and near-infrared reflectance spectra may be useful in field and laboratory studies of playa evaporite minerals. Many saline hydrate minerals found in playas exhibit characteristic, and potentially diagnostic, VNIR spectral features. Furthermore, VNIR spectra are highly sensitive to the presence of minor hydrate mineral species commonly present in efflorescent crusts composed mainly of halite and thenardite. Because it is relatively easy to measure large numbers of VNIR spectra, their use should facilitate mapping of efflorescent minerals and may lead to a better understanding of hydrological and geochemical controls affecting playa mineral and brine development. The next phase of this project will explore these matters by examining VNIR spectral measurements of natural saline mineral samples collected from several different field areas.

Acknowledgments. This research was conducted in partial fulfillment of the requirements for the Ph.D. degree at the University of Maryland, College Park. I would like to especially thank Ann G. Wylie (thesis director) as well as other faculty members of the Geology Department who provided valuable guidance in the course of this study. The work was also funded in part by the U.S. Geological Survey, Reston, Virginia. In this connection, I would particularly like to acknowledge the thoughtful advice and support of Lawrence C. Rowan of the Branch of Geophysics. Thanks are also due to manuscript reviewers Marguerite J. Kingston and David M. Sherman, and to the anonymous JGR reviewers.

REFERENCES

Aines, R. D., and G. R. Rossman, Water in minerals? A peak in the infrared, *J. Geophys. Res.*, *89*, 4059–4071, 1984.

Baur, W. H., On the crystal chemistry of salt hydrates, II, A neutron diffraction study of $MgSO_4 \cdot 4H_2O$, *Acta Crystallogr.*, *17*, 863–869, 1964.

Choi, C. S., and A. D. Mighell, Neutron diffraction study of sodium sesquicarbonate dihydrate, *Acta Crystallogr. Sect. B: Struct. Crystall. Cryst. Chem.*, *B38*, 2874–2876, 1982.

Clark, R. N., Spectral properties of mixtures of montmorillonite and dark carbon grains: Implications for remote sensing minerals containing chemically and physically adsorbed water, *J. Geophys. Res.*, *88*, 10,635–10,644, 1983.

Clark, R. N., and T. L. Roush, Reflectance spectroscopy: Quantitative analysis techniques for remote sensing applications, *J. Geophys. Res.*, *89*, 6329–6340, 1984.

Clark, R. N., T. V. V. King, M. Klejwa, G. A. Swayze, and N. Vergo, High spectral resolution reflectance spectroscopy of minerals, *J. Geophys. Res.*, *95*, 12,653–12,680, 1990.

Crowley, J. K., Geochemical study of playa efflorescent salt crusts and associated brines by using spectral reflectance, X-ray diffraction, and brine chemical data, Ph.D. dissertation, 168 pp., Univ. of Md., College Park, 1991.

Crowley, J. K., and N. Vergo, Near-infrared reflectance spectra of mixtures of Kaolin Group minerals: Use in clay mineral studies, *Clays Clay Min.*, *36*, 310–316, 1988.

Crowley, J. K., D. M. Sherman, and I. J. Bennett, A low-cost digital recording and display system for Beckman UV 5200 series spectrophotometers, *U.S. Geol. Surv. Open File Rep.*, *86-27*, 23 pp., 1986.

Ehmann, W. J., and N. Vergo, Spectral discrimination of zeolites and dioctahedral clays in the near-infrared, *Proceedings of the Fifth Thematic Conference on Remote Sensing for Exploration Geology*, Reno, Nevada, Sept. 29-October 2, 1986, pp. 417–425, Environmental Research Institute of Michigan, Ann Arbor, 1986.

Ericksen, G. E., and R. O. Salas, Geology and resources of salars in the Central Andes, *Geology of the Andes and Its Relation to Hydrocarbon and Mineral Resources*, *Earth Sci. Ser.*, v. 11, edited by G. E. Ericksen, pp. 151–164, Circum-Pacific Council for Energy and Mineral Resources, Houston, Tex., 1989.

Eugster, H. P., and L. A. Hardie, Saline Lakes, in *Lakes—Chemistry, Geology, Physics*, edited by A. Lerman, pp. 238–293, Springer-Verlag, New York, 1978.

Eugster, H. P., and B. F. Jones, Behavior of major solutes during closed-basin brine evolution, *Am. J. Sci.*, *279*, 609–631, 1979.

Falk, M., and O. Knop, Water in stoichiometric hydrates, in *Water, A Comprehensive Treatise*, vol. 2, edited by F. Franks, pp. 55–112, Plenum, New York, 1973.

Gaffey, S. J., Spectral reflectance of carbonate minerals in the visible and near-infrared (0.35–2.55 μm): Anhydrous carbonate minerals, *J. Geophys. Res.*, *92*, 1428–1440, 1987.

Gates, D. M., Biophysical Ecology, 469 pp., Springer-Verlag, New York, 1980.

Hardie, L. A., The origin of the Recent non-marine evaporite deposit of Saline Valley, Inyo County, California, *Geochim. Cosmochim. Acta*, *32*, 1279–1301, 1968.

Hardie, L. A., Evaporites: Marine or non-marine?, *Am. J. Sci.*, *284*, 193–240, 1984.

Huang, C. K., and P. F. Kerr, Infrared study of the carbonate minerals, *Am. Mineral.*, *45*, 311–324, 1960.

Hunt, G. R., Spectral signatures of particulate minerals in the visible and near-infrared, *Geophysics*, *42*, 501–513, 1977.

Hunt, G. R., Near-infrared (1.3–2.4 μm) spectra of alteration minerals—Potential for use in remote sensing, *Geophysics*, *44*, 1974–1986, 1979.

Hunt, G. R., and J. W. Salisbury, Visible and near-infrared spectra of minerals and rocks, I, Silicate minerals, *Mod. Geol.*, *1*, 283–300, 1970.

Hunt, G. R., and J. W. Salisbury, Visible and near-infrared spectra of minerals and rocks, II, Carbonates, *Mod. Geol.*, *2*, 23–30, 1971.

Hunt, G. R., J. W. Salisbury, and C. J. Lenhoff, Visible and near-infrared spectra of minerals and rocks, IV, Sulphides and sulphates, *Mod. Geol.*, *3*, 1–14, 1971.

Hunt, G. R., J. W. Salisbury, and J. C. Lenhoff, Visible and near-infrared spectra of minerals and rocks, V, Halides, phosphates, arsenates, vanadates and borates, *Mod. Geol.*, *3*, 121–132, 1972.

Levy, H. A., and G. C. Lisensky, Crystal structures of sodium sulfate decahydrate (Glauber's Salt) and sodium tetraborate decahydrate (Borax); Redetermination by neutron diffraction, *Acta Crystallogr. Sect. B: Struct. Crystall. Cryst. Chem.*, *B34*, 3502–3510, 1978.

Omori, K., and P. F. Kerr, Infrared studies of saline sulfate minerals, *Geol. Soc. Am. Bull.*, *74*, 709–734, 1963.

Pimental, G. C., and A. L. McClellan, *The Hydrogen Bond*, 475 pp., W. H. Freeman, New York, 1960.

Reeves, C. C., Jr., Economic significance of playa lake deposits, *Spec. Publ. Int. Assoc. Sedimentol.*, *2*, 279–290, 1978.

Schubert, K. D., Ultrarotspektrometrische Untersuchungen an Mineralsalzen, in *Kali-Bucher*, vol. 4, pp. 433–447, Verlag Grundstoffindustrie, Federal Republic of Germany, 1967.

Stewart, F. H., Marine evaporites, in Data of Geochemistry, 6th ed., edited by M. Fleischer, *U.S. Geol. Surv. Prof. Pap.*, 440-Y, 52 pp., 1963.

Vane, G., and A. F. H. Goetz, Terrestrial imaging spectroscopy, *Remote Sens. Environ.*, *24*, 1–29, 1988.

White, W. B., The carbonate minerals, in *The Infrared Spectra of Minerals*, *Monogr. Ser.*, vol. 4, edited by V. C. Farmer, pp. 227–284, Mineralogical Society, London, 1974.

J. K. Crowley, U.S. Geological Survey, Mail Stop 927, Reston, VA 22092.

(Received March 7, 1990;
revised June 3, 1991;
accepted June 11, 1991.)

JOURNAL OF GEOPHYSICAL RESEARCH, VOL. 96, NO. B10, PAGES 16,061–16,067, SEPTEMBER 10, 1991

The Patagonian Orocline: New Paleomagnetic Data From the Andean Magmatic Arc in Tierra del Fuego, Chile

W. DICKSON CUNNINGHAM, KEITH A. KLEPEIS, WULF A. GOSE, AND IAN W. D. DALZIEL

Institute for Geophysics and Department of Geological Sciences, University of Texas at Austin

The Hardy Formation is a 1300-m-thick succession of Upper Jurassic-Lower Cretaceous volcaniclastic sedimentary rocks interbedded with lava flows on Hoste Island at the southernmost tip of South America (55.5°S, 291.8°E). The strata are gently folded and metamorphosed to the prehnite-pumpellyite grade. A well-defined characteristic direction of magnetization, carried by magnetite, was readily identified in 95 samples from seven sites. At a given site, the directions group slightly better without structural correction. However, the means of the seven sites cluster better without tilt correction at the 99% significance level, implying that the magnetization postdates the folding event. It is most likely that the magnetization was acquired during the mid- to Late Cretaceous Andean orogeny that involved the folding and emplacement of the Patagonian Batholith. The fact that all samples are normally magnetized supports this age assignment. The pole position of 42.9°N, 156.6°E, α_{95}=3.3° implies that the sampling area has rotated counterclockwise relative to cratonic South America by 90.1 ± 11.9° with no significant flattening of inclination (F=1.9 ± 3.7°). Geologic considerations indicate that the rotation involved the entire Andean magmatic arc in Tierra Del Fuego. The results support interpretation of the Hardy Formation as part of the Andean magmatic arc deposited on the Pacific side of the Late Jurassic-Early Cretaceous Rocas Verdes marginal basin. Oroclinal bending of the arc in southernmost South America accompanied inversion of the marginal basin and the development of a Late Cretaceous-Cenozoic left-lateral transform system (South America-Antarctica) that later developed into the North Scotia Ridge.

INTRODUCTION

Between latitudes 50°S and 56°S the trend of the Andean Cordillera changes abruptly from a southerly direction to an easterly direction. This bend connects the main Andean belt in southern Chile and Argentina to the submarine ridges and emergent continental fragments of the North Scotia Ridge (Figure 1) and was named the Patagonian orocline by *Carey* [1955]. A longstanding problem that has confronted workers trying to resolve the tectonic evolution of the southernmost Andes and its relation to the Antarctic Peninsula-Scotia arc region has been determining whether the Patagonian orocline formed as a curved orogen, is a nonrotational arc that contains offset domains bounded by parallel, left-lateral strike-slip faults, or whether the bend is the product of orogenic rotation [*Marshak*, 1988].

Previous studies of bends in orogenic belts have demonstrated the utility of paleomagnetic analyses to determine the sense, magnitude, and timing of oroclinal bending [*Eldredge et al.*, 1985, and references therein; *Beck*, 1988]. These studies are based on the assumption that bending of an orogen results in progressive variations in paleomagnetic declinations around the bend. Comparison of paleomagnetic declinations from rocks collected around the bend with declinations obtained from stable cratonic rocks of the same age can provide sense and magnitude of rotation. Studies by *Dalziel et al.* [1973] and *Burns et al.* [1980] utilized paleomagnetism to address the problem of oroclinal bending in the southernmost Andes. Both studies concluded that some counterclockwise rotation of the southern tip of the South American continent has occurred since the Late Cretaceous, although the studies differed on the amount of rotation. Unfortunately, neither study presented data that pass modern confidence "filters" for data reliability [*Beck*, 1988].

In this study we present new paleomagnetic data from rocks of the Lower Cretaceous Andean magmatic arc on Peninsula Hardy in extreme southern Chile (Figure 1). Our results strongly indicate that the Patagonian orocline is the product of approximately 90° of counterclockwise crustal rotation since the mid-Cretaceous.

Paper number 91JB01498.
0148-0227/91/91JB-01498$05.00

GENERAL GEOLOGY

Southernmost Andes

Southernmost South America can be subdivided into four broad lithotectonic provinces from southwest to northeast: (1) the Patagonian batholith, a Late Jurassic to mid-Tertiary magmatic arc province, (2) the Rocas Verdes basin, a collapsed marginal basin of Late Jurassic to Early Cretaceous age, (3) the metamorphic hinterland, a multiply deformed uplifted metamorphic belt that was formerly the continental margin of the Rocas Verdes basin, and (4) the Late Cretaceous to Tertiary foreland fold and thrust belt of the Magallanes basin foredeep (Figure 1).

With the onset of Gondwana breakup in the Middle to Late Jurassic, southernmost South America has experienced a complex sequence of Mesozoic and Cenozoic tectonic events that is the focus of ongoing study and will only be briefly summarized here. (For a more thorough review of the structural and tectonic evolution of the region, see *Dalziel* [1989].) The oldest rocks in the region consist of Paleozoic to lower Mesozoic metasediments and metavolcanics that are interpreted as an ancient accretionary prism complex formed along Gondwana's Pacific margin [*Forsythe and Mpodozis*, 1979; *Dalziel*, 1982; *Dalziel and Forsythe*, 1986]. Initial Gondwana breakup resulted in the extrusion of large volumes of Kimmeridgian to Tithonian silicic volcanics and contemporaneous intrusion of anatectic granites associated

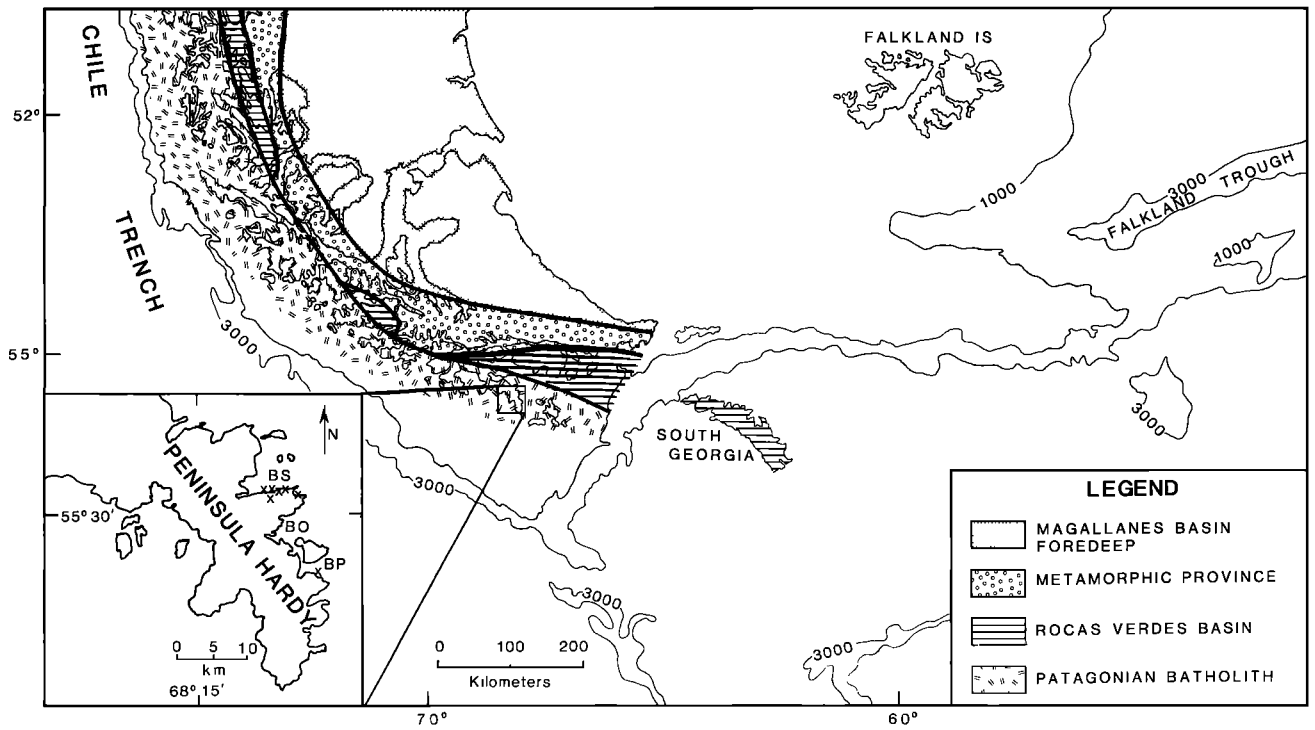

Fig. 1. Map of southernmost South America showing the four principal lithotectonic provinces and the location of Peninsula Hardy. Crosses are site locations: BS, Bahia Scotchwel; BP, Bahia Schapenham. The South Georgia platform is shown in its approximate predrift position with respect to South America [*Dalziel et al.*, 1975].

with regional extension [*Dalziel et al.*, 1974, 1987; *Mukasa et al.*, 1988]. During Late Jurassic-Early Cretaceous time the Rocas Verdes marginal basin lay inboard of a young volcanic arc [*Katz*, 1973; *Dalziel et al.*, 1974; *Bruhn and Dalziel*, 1977; *de Wit*, 1977; *Bruhn et al.*, 1978; *Dalziel*, 1981; *Mukasa et al.*, 1988]. This basin was floored in part by quasi-oceanic crust and received up to 6 km of sedimentary and volcanic infill [*Dalziel et al.*, 1974; *Dott et al.*, 1977; *Winn and Dott*, 1978]. During the mid-Cretaceous the marginal basin was closed and inverted as the arc collided or was "rewelded" to the continent. This event, the main phase of the Andean orogeny [*Dalziel and Palmer*, 1979], resulted in intense shortening, regional metamorphism, uplift of the southernmost Andes, and development of a downwarped foreland basin [*Halpern*, 1973; *Nelson et al.*, 1980; *Dalziel*, 1989]. Following marginal basin inversion, shortening propagated into the foreland resulting in the development of a foreland fold and thrust belt during Late Cretaceous to Early to mid-Tertiary time [*Winslow*, 1982]. Recent work [*Dalziel and Brown*, 1989] also suggests that during latest Cretaceous-Paleogene time, part of the metamorphic core zone of the cordillera experienced tectonic denudation. Finally, a throughgoing, strike-slip fault system that now cuts across the southernmost Andes may have initiated during the mid- to Late Cretaceous and evolved during the Tertiary, and been associated with the development of the Scotia plate and the final separation of South America from Antarctica [*Barker and Burrell*, 1977; *Winslow*, 1982].

Peninsula Hardy

Peninsula Hardy is principally composed of volcanic and intrusive igneous rocks, pyroclastic deposits, and thick turbidite sequences. Except for a series of Miocene extrusive rocks, most of the dated rocks on Peninsula Hardy are Upper Jurassic to Lower Cretaceous based on fossil evidence and are interpreted as a magmatic arc assemblage [*Suarez and Pettigrew*, 1976; *Suarez et al.*, 1985]. The Hardy Formation is the name given to a 1300 m thick succession of Upper Jurassic-Lower Cretaceous volcaniclastic rocks and interbedded lava flows found on Peninsula Hardy [*Suarez and Pettigrew*, 1976]. The rocks are gently folded and metamorphosed to zeolite or prehnite-pumpellyite grade. Both intensity of deformation and metamorphism increase northward toward the continent [*Bruhn and Dalziel*, 1977].

Data from five different sites from the south coast of Bahia Scotchwel, one from the coast southeast of Bahia Scotchwel and one from the coastline south of Bahia Schapenham (Figure 1), are presented here. Sample lithologies from these sites consist of thinly laminated mudstones, tuffaceous siltstones, graywackes, and a massive pyroclastic unit. Examination of thin sections of these units reveals that quartz, plagioclase, lithic fragments, calcite, metamorphic chlorite, fossil fragments, clays, pyroxene, and various opaques are the principal constituents for these rock types.

METHODS AND PRODEDURES

Two of us (W.D. Cunningham and K.A. Klepeis) spent 4 weeks on Peninsula Hardy in May 1988 collecting samples for a paleomagnetic study. Peninsula Hardy was chosen because of the low metamorphic grade of the fossiliferous rocks found there and because it is located on the less deformed outer arc of the Patagonian orocline oceanward of the ophiolitic complexes of the Rocas Verdes back-arc basin. A variety of rock types was sampled including fine- and coarse-grained sedimentary rocks, a mafic sill, volcaniclastic breccias, debris flow deposits, and a massive pyroclastic unit. Only those rocks that could provide an indication of paleohorizontal attitude were

sampled. Almost all sampling sites were located along coastal areas where access and good rock exposure were available. Most paleomagnetic samples were drilled in the field, but owing to difficulties with the drilling equipment, some oriented hand samples were also taken.

The remanent magnetization was measured with a cryogenic magnetometer. All samples were progressively thermally demagnetized in five to eight steps. The field in the cooling region following thermal demagnetization was less than 3 gammas. Throughout the experimental procedure the samples were kept in a magnetically shielded room where the magnetic field was approximately 100 gammas. The data were analyzed by calculating linear trends in orthogonal vector projections. Of the 94 samples, only two samples from site 593 were rejected from the analysis because their directions differed from the site mean by more than 2 angular standard deviations.

EXPERIMENTAL RESULTS

The natural remanent magnetization (NRM) directions of all samples point westerly with steep negative inclinations. The NRM intensities are of the order of 10^{-6} to 10^{-8} A m^2/kg. Upon progressive thermal demagnetization, most samples retained 60% or more of their NRM intensity up to about 400°C. Above this temperature, the intensities of most samples decreased markedly upon approaching the magnetite Curie point (Figure 2, sample 5162-3). Some samples contain a distinctive hematite component (Figure 2, sample 593-10). The directions changed very little during demagnetization up to 570°C. At higher temperatures, the directions started to scatter. Vector component diagrams confirm the predominance of only one component of magnetization with an occasional minor overprint which is readily removed by heating to 150° or 200°C. This holds true for both the finer grained sediments sampled at sites 5161, 5162, and 5181 and the coarser grained sediments at sites 5191, 551, 593, and 5182 (Figure 3).

The directions of characteristic remanent magnetization (ChRM) were calculated with the aid of vector component diagrams, typically encompassing the temperature range from 150° to 570° or 600°C. However, because most samples contain one dominant component of magnetization, it makes little difference for the statistical analysis whether one uses the directions at a particular demagnetization step or the ChRMs. Figure 4 illustrates this point for the data from site 593. It compares the mean directions and two statistical parameters for each demagnetization step with the corresponding values obtained using the ChRM. Only minor variations are observed

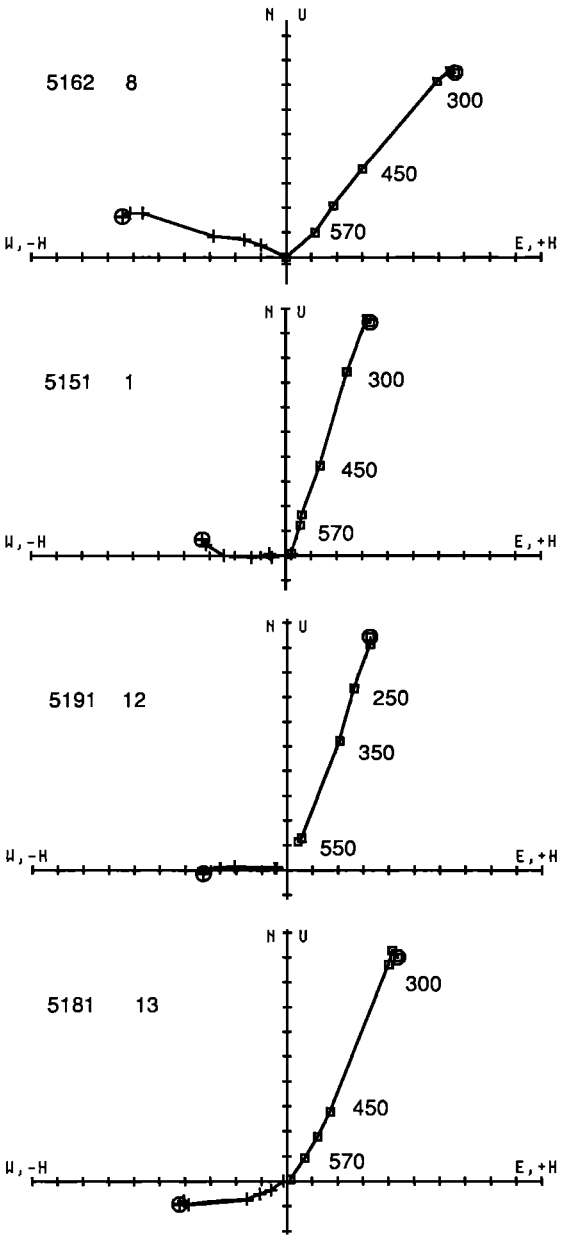

Fig. 3. Vector component diagrams. Squares are the projection onto the northeast plane; crosses are in the up-horizontal plane. Numbers indicate the demagnetization temperature in degrees Celsius. Data are uncorrected for bedding tilt.

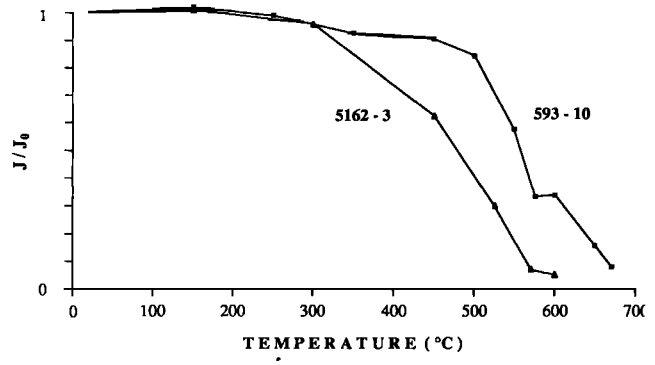

Fig. 2. Relative change in intensity during thermal demagnetization. Sample 5162-3 is dominated by magnetite, and sample 593-10 contains both magnetite and hematite.

in the temperature range from 250° to 600°C. The other sites show a similar behavior.

The site means, based on the characteristic remanent magnetization, and the statistical parameters are listed in Table 1. All sites yield good results as evidenced by the small circles of confidence (α_{95}) and the large values for Fisher's precision parameter k. For all but one site the ChRM directions cluster better without structural correction. The variations in bedding attitudes at a given site are too small to make the improvement statistically significant at the 90% confidence level with the exception of site 593 where the improvement is significant at the 95% level. The F test can also be applied to the means of the site means because the tilt corrections for the sites are different. The test shows that the in situ site means group better at the 99% significance level. Thus the observed

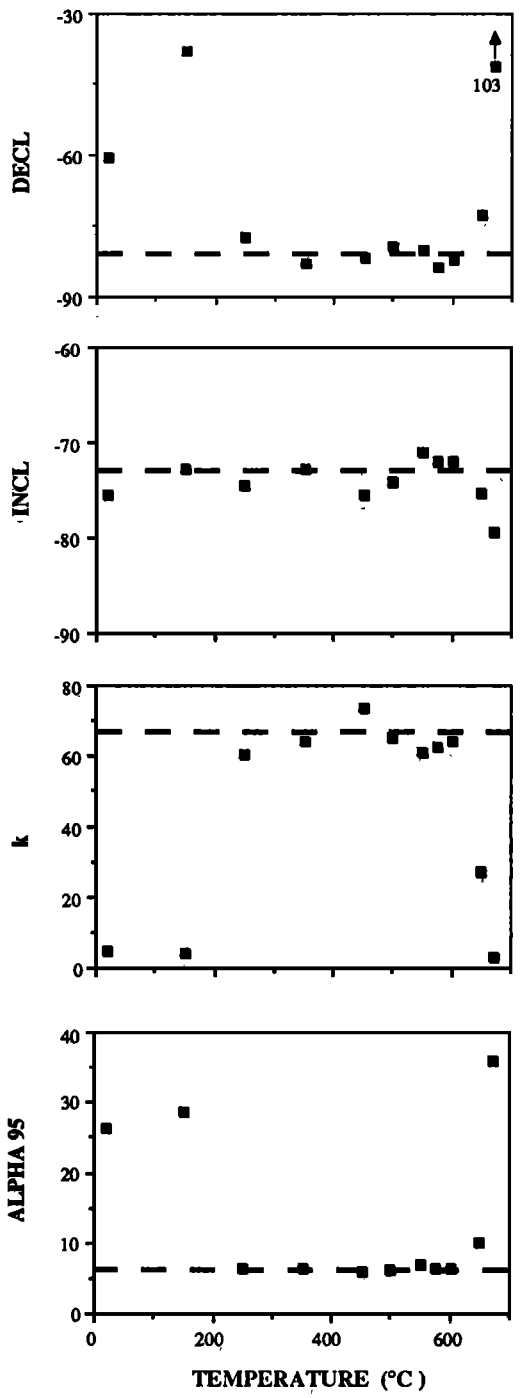

Fig. 4. Comparison of the mean direction and two statistical parameters from site 593 for each demagnetization step with the corresponding values based on the characteristic remanent magnetization (heavy dashed lines).

magnetization was acquired after the folding event. The in situ directions of the characteristic remanent magnetization of all sites are shown in Figure 5.

AGE OF MAGNETIZATION

On the basis of paleontological evidence, the age of the Hardy Formation ranges from Late Jurassic through Early Cretaceous [*Suarez and Pettigrew*, 1976], a time span characterized by frequent geomagnetic reversals [*Harland et al.*, 1982]. Because the sampling sites cover over 300 m of stratigraphic section (probably representing a large span of time), one would expect both normal and reversed polarity directions of magnetization if samples carried a primary depositional remanence. However, all samples are normally magnetized, suggesting remagnetization as was indicated by the fold test. Because of the consistent normal polarity, we consider it likely that the Hardy Formation was remagnetized during the Cretaceous normal polarity superchron (118-83 Ma). This is also the time of the Andean orogeny with associated regional metamorphism, deformation, and batholith emplacement that is interpreted to have occurred between 105 and 90 Ma [*Halpern*, 1973; *Dalziel and Palmer*, 1979; *Hervé et al.*, 1984; *Biddle et al.*, 1986; *Mukasa et al.*, 1988; *Dalziel*, 1989]. Thus we interpret the magnetization of the Hardy Formation as a thermoremanent magnetization acquired by heating and cooling during the middle part of the Cretaceous.

DISCUSSION

The mean direction of our seven sampling sites, uncorrected for bedding tilt, has a declination of 265.8°, an inclination of -72.6°, and a circle of confidence of $\alpha_{95} = 4.2°$. As a reference pole for cratonic South America we use the Cretaceous pole calculated by *Castillo et al.* [1991] which is based on 11 determinations (87.6°S, 31.0°E, $\alpha_{95} = 3.3°$). The reference pole yields an expected direction for Peninsula Hardy of D= 355.9° and I=-70.7°. Comparison of the observed and expected directions implies a counterclockwise rotation of the sampling area of R = 90.1°±11.9° using the method of *Beck* [1980] and *Demarest* [1983] (Figure 6). The flattening of the inclination which corresponds to a change in latitude is F = 1.9°±3.7° and is not statistically significant.

Although our sampling area is limited to Peninsula Hardy, we believe that the counterclockwise rotation of Peninsula Hardy was not an isolated block rotation but part of a regional rotation involving at least the magmatic arc and perhaps the entire orogen. Previous tests for oroclinal bending from other parts of the southernmost Andes [*Dalziel et al.*,1973; *Burns et al.*, 1980] do suggest, at least qualitatively, counterclockwise rotation of the southernmost Andes since the mid-Cretaceous. We believe that the overall 90° change in physiographic and structural trend in the southernmost Andes and the 90° counterclockwise rotation of Peninsula Hardy are not coincidental.

The large counterclockwise rotation suggested by the paleomagnetic data has important implications for Scotia arc evolution and Gondwana reconstructions between South America and Antarctica. Removal of the rotation from the southernmost Andes creates an approximately rectilinear trend for the magmatic arc prior to the Late Cretaceous. This disagrees with some previous workers' interpretations that there was an original cusp or indentation along the active margin in the area that later marked the zone of separation between the South America and Scotia plates [*Griffiths and Barker*, 1972]. If southernmost South America was not bent originally, then Gondwana reconstructions must allow for lateral overlap or adjacency between the northern Antarctic Peninsula and southernmost South America or somehow fit the Antarctic Peninsula so that it lines up at the southern end of the Andean Cordillera (Figure 7) [*Norton and Sclater*, 1979; *Lawver and Scotese*, 1987; *Grunow et al.*, 1987]. It is possible, however, that an originally curved magmatic arc was tectonically straightened during opening of the Rocas Verdes basin during the Middle to Late Jurassic and subsequently

TABLE 1. Summary of Paleomagnetic Data From Peninsula Hardy (55.5°S, 291.8°E)

Site	Lithology	N	R	D, deg	I, deg	k	α_{95}	Latitude	Longitude
5161	Mudstone/Siltstone	18/0	17.82	246.6	-71.9	97.0	3.5	-34.5	329.4
			17.82	264.3	-67.0	93.5	3.6		
5162	Mudstone/Siltstone	12/0	11.67	290.5	-69.5	33.1	7.7	-51.1	355.2
			11.63	344.1	-70.9	30.0	8.1		
5181	Mudstone/Siltstone	13/0	12.90	251.4	-70.8	115.1	3.9	-35.0	333.1
			12.88	279.4	-63.4	99.6	4.2		
5191	Siltstone/Sandstone	14/0	13.88	271.8	-73.2	105.6	3.9	-45.7	339.4
			13.85	288.4	-56.1	86.2	4.3		
551	Sand/Silt/Mudstone	18/0	17.36	256.1	-69.1	26.7	6.8	-34.9	337.8
			17.08	257.5	-84.0	18.4	8.3		
593	Sand/Silt/Mudstone	9/2	8.88	278.9	-73.0	66.7	6.4	-48.5	342.9
			8.65	337.5	-63.1	23.1	10.9		
5182	Pyroclastic Deposit	8/0	7.74	266.3	-76.4	26.7	10.9	-46.5	331.1
			7.74	235.4	-59.8	26.7	10.9		
Mean		7/0	6.97	265.8	-72.6	212.1	4.2	-42.5	337.8
			6.72	286.5	-70.6	21.5	13.3		

N is the number of samples used/rejected; R is the resultant vector; D is declination; I is inclination; k is Fisher's precision parameter; α_{95} is the radius of the circle of 95% confidence; Latitude and Longitude are the latitude and east longtiude of the corresponding virtual geomagnetic pole. For each site, the data in the first line are without structural correction, the data in the second line are with structural correction applied.

oroclinally bent after magnetization during basin closure. This is in keeping with the obvious reentrant in the Pacific margin of the Gondwana craton noted by *Dalziel* [1982].

An important question that cannot be answered at this time is whether oroclinal bending was the product of marginal basin closure during the mid-Late Cretaceous Andean orogeny or of Cretaceous-Tertiary strike-slip tectonics and Scotia plate development or both. We believe that the bending probably started sometime during or after the Andean orogeny or post-100 Ma (following regional metamorphism on Peninsula Hardy and acquisition of secondary magnetization) and probably ceased prior to the development of the Scotia Plate at approximately 35 Ma. This minimum age for rotation is based on the following considerations. The northeast trending continental margin southeast of Cape Horn is today approximately parallel to the northeast trending extinct spreading center in the middle of the Scotia Sea, from which it presumably rifted [*British Antarctic Survey*, 1985]. It seems likely that if the southern Andes had continued to rotate in a counterclockwise sense while the Scotia plate spreading center was active (35 -10 Ma [*Barker and Burrell*, 1977]), then the continental margin and spreading center axis would have lost

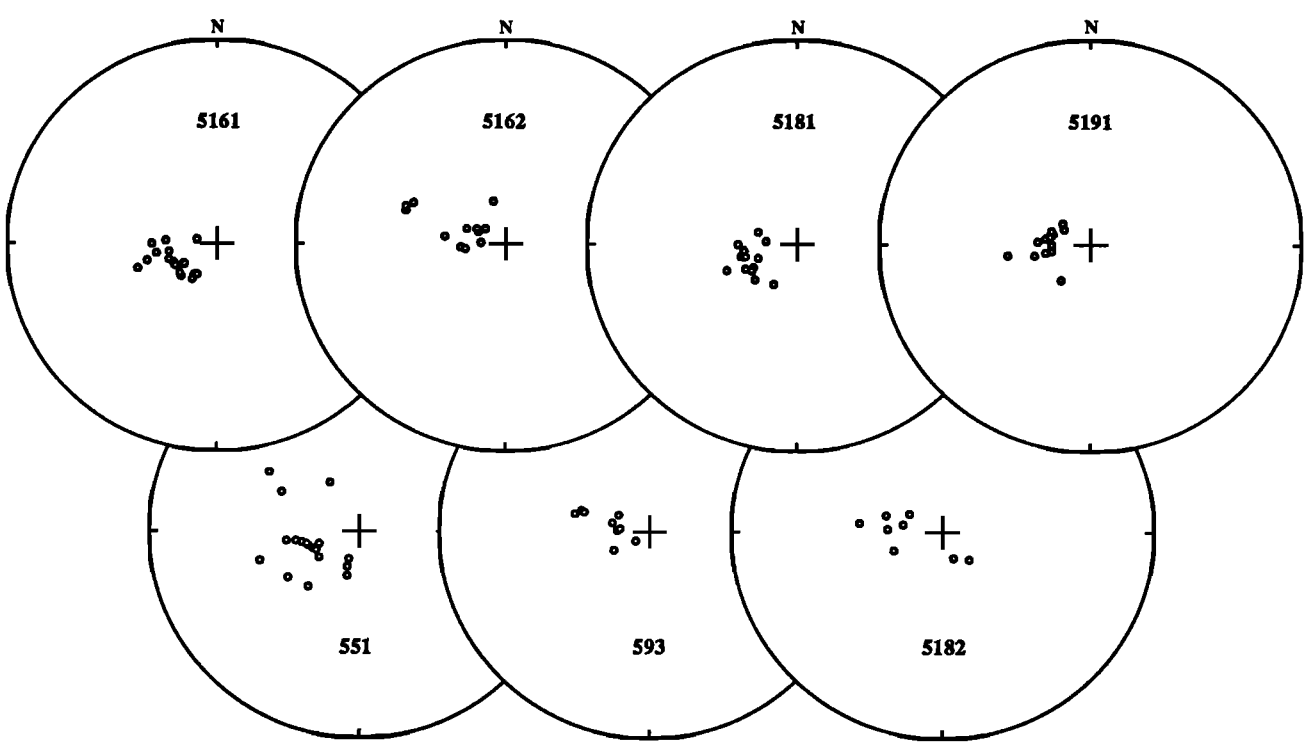

Fig. 5. Equal-area projections of the directions of the characteristic remanent magnetization without structural correction. Circles are in the upper hemisphere.

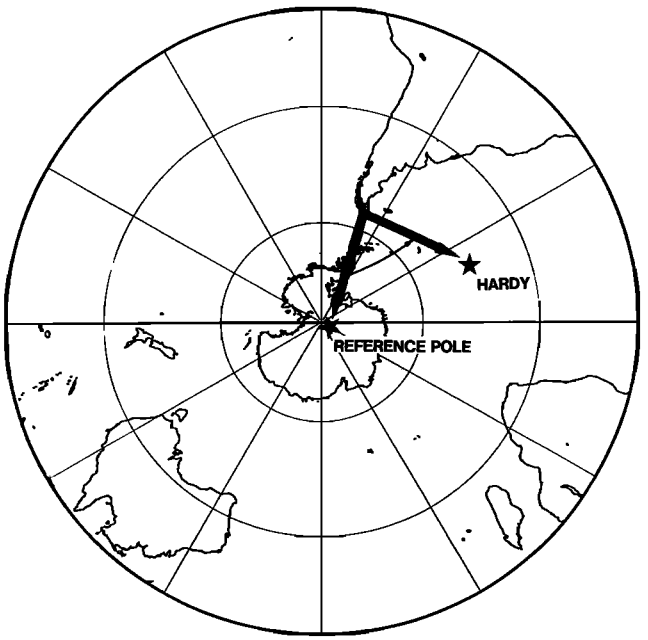

Fig. 6. Comparison of Hardy pole with mean Cretaceous reference pole for South America [*Castillo et al.*, 1991].

their parallelism. Likewise, we feel that it is unlikely that the oceanic crust of the Scotia plate was coupled to the southern tip of South America and might have rotated with it.

The opening of the South Atlantic along the South Atlantic ridge began at approximately 130 Ma and led to the westward transport of South America relative to Africa [*Lawver et al.*, 1985]. This time marked the onset of the closure of the Rocas Verdes basin and the Andean orogeny, and it is believed that Mid-Atlantic spreading resulted in forward motion of the South American plate in a mantle reference frame, as well as increased convergence rates along the Pacific margin which were accommodated by collapse of the basin [*Dalziel*, 1986]. The separation of East Antarctica from Africa along the Southwest Indian Ridge began in the Late Jurassic and led to the southwestward transport of Antarctica relative to Africa and ultimately to the southward transport of Antarctica relative to South America [*Lawver et al.*, 1985; L.A. Lawver, personal communication, 1991]. Thus since the time of the initial development of the America-Antarctic ridge, South America and Antarctica have diverged obliquely with a left-lateral component of separation (left-lateral because their westerly vector components of motion relative to Africa have different magnitudes; South America has been moving more directly westward and far faster than Antarctica's westward motion). We feel that this left-lateral oblique continental separation ultimately led to the opening of the Scotia Sea but must have been preceded by a transpressional continental wrenching system that later became transtensional before actual seafloor spreading began.

Thus we conclude that the Patagonian orocline probably formed during a time of complex regional tectonics during and/or after the Andean orogeny and preceding the opening of Drake Passage and represents a passive response to marginal basin closure and the development of a transpressional regional left-lateral shear system. It is interesting to note that similar tectonic conditions that led to the development of the Patagonian orocline may exist today east of southernmost South America where Burdwood Bank is under transpression [*Ludwig and Rabinowitz*, 1982] and the Falkland Trough is "zippering shut" from west to east. The tectonic processes occurring today in Burdwood Bank and the Falkland Trough may be a continuation of the tectonic processes that led to the closure of the Rocas Verdes basin and the counterclockwise rotation of the southernmost Andean magmatic arc.

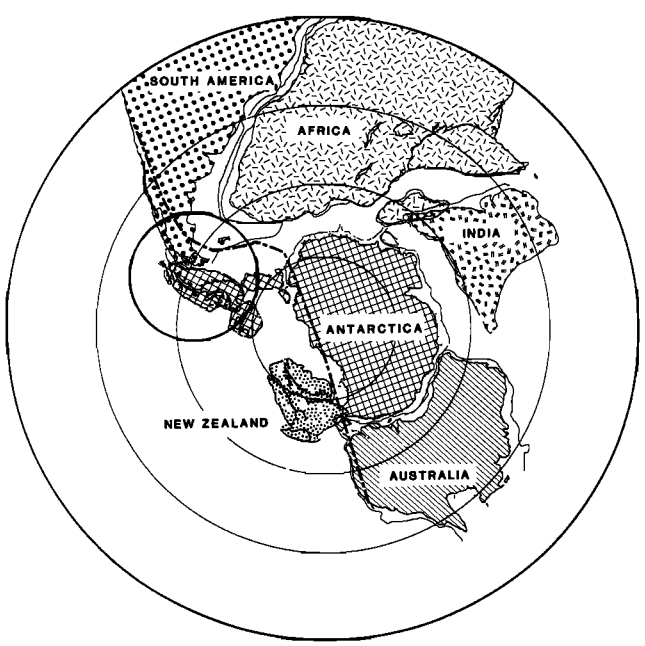

Fig. 7. Late Jurassic Gondwana reconstruction [*Grunow et al.*, 1987]. Dashed line shows approximate position of Gondwana cratonic margin. Results from this study raise questions regarding the correct fit between Antarctica and South America (circled area).

Acknowledgments. The authors thank Rich Hanson and Kip Miller for their help while in the field and the captain and crew of the R/V *Polar Duke* for transport in and out of the field. Funding was provided by the National Science Foundation Division of Polar Programs grant 86-43441 and Division of Ocean Sciences grant 87-16557. Special thanks are given to the Chilean Navy for permission to work on Peninsula Hardy and for nightly radio communication. Reviews by Robert Butler and Myrl Beck led to clarification of portions of the manuscript. This paper benefitted from discussions with Larry Lawver.

References

Barker, P. F., and J. Burrell, The opening of Drake Passage, *Mar. Geol., 25*, 15-34, 1977.

Beck, M. E., Jr., Paleomagnetic record of plate margin tectonic processes along the western margin of North America, *J. Geophys. Res.* 84, 7115-7131, 1980.

Beck, M. E., Jr., Analysis of Late Jurassic-Recent paleomagnetic data from active plate margins of South America, *J. S. Am. Earth Sci., 1*, (1), 39-52, 1988.

Biddle, K. T., M. A. Uliana, R. M. Mitchum, Jr., M. G. Fitzgerald, and R. C. Wright, The stratigraphic and structural evolution of the central and eastern Magallanes Basin, southern South America, *Spec. Publ. Int. Assoc. Sedimentol.*, 8, 41-61, 1986.

British Antarctic Survey, Tectonic Map of the Scotia Arc, scale 1:3,000,000, *BAS (Misc.) 3*, Cambridge, 1985.

Bruhn, R. L., and I. W. D. Dalziel, Destruction of the Early Cretaceous marginal basin in the Andes of Tierra del Fuego, in *Island Arcs, Deep Sea Trenches and Back-arc Basins, Maurice Ewing Ser.*, vol. 1, edited by M. Talwani and W. C. Pitman III, pp. 395-405, AGU, Washington, D. C., 1977.

Bruhn, R. L., C. R. Stern, and M. J. de Wit, Field and geochemical data bearing on the development of a Mesozoic volcano-tectonic rift zone and back-arc basin in southernmost South America, *Earth Planet. Sci. Lett., 41*, 32-46, 1978.

Burns, K. L., M. J. Rickard, L. Belbia, and F. Channelawn, Further paleomagnetic confirmation of the Patagonian orocline, *Tectonophysics, 63*, 75-90, 1980.

Castillo, J., W. A. Gose, and A. Peramau, Paleomagnetic results from Mesozoic strata in the Merida Andes, Venezuela, *J. Geophys. Res., 96*, 6011-6022, 1991.

Carey, S. W., The orocline concept in geotectonics. *Proc. R. Soc. Tasmania, 89*, 255-288, 1955.

Dalziel, I. W. D., Back-arc extension in the southern Andes, a review and critical reappraisal, Philos. *Trans. R. Soc. London, Ser. A 300*, 319-335, 1981.

Dalziel, I. W. D., Pre-Jurassic history of the Scotia Arc region, in *Antarctic Geoscience*, edited by C. Craddock, pp. 111-126, University of Wisconsin Press, Madison, 1982.

Dalziel, I. W. D., Collision and Cordilleran orogenesis: An Andean perspective, in Collision Tectonics, edited by A. P. Coward and A. C. Ries, *Geol. Soc. Spec. Publ. London, 19*, 389-404, 1986.

Dalziel, I. W. D., Tectonics of the Scotia Arc, Antarctica, *Field Trip Guideb.*, vol. T180, AGU, Washington, D. C., 1989.

Dalziel, I. W. D., and R. L. Brown, Tectonic denudation of the Darwin metamorphic core complex in the Andes of Tierra Del Fuego, Southernmost Chile: Implications for cordilleran orogenesis, *Geology, 17*, 699-703, 1989.

Dalziel, I. W. D., M. F. de Wit, and K. F. Palmer, Fossil marginal basin in the southern Andes, *Nature, 250*, 291-294, 1974.

Dalziel, I. W. D., R. H. Dott, R. D. Winn, and R. L. Bruhn, Tectonic relationships of South Georgia Island to the southernmost Andes, *Geol. Soc. Am. Bull., 86*, 1034-1040, 1975.

Dalziel, I. W. D., and R. F. Forsythe, Andean evolution and the terrane concept, in Tectonostratigraphic *Terranes of the Circum-Pacific Region*, edited by D. G. Howell, pp. 565-581, American Association of Petroleum Geologists, Houston, Tex., 1986.

Dalziel, I. W. D., R. Kligfield, W. Lowrie, and N. D. Opdyke, Paleomagnetic data from the southernmost Andes and the Antarctandes, in Implica*tions of Continental Drift to the Earth Sciences, Vol. 1*, edited by D. H. Tarling, and S. K. Runcorn, pp. 87-101, Academic, San Diego, Calif., 1973.

Dalziel, I. W. D., and K. F. Palmer, Progressive deformation and orogenic uplift at the southern extremity of the Andes, *Geol. Soc. Am. Bull., 90*, 259-280, 1979.

Dalziel, I. W. D., B. C. Storey. S. W. Garrett, A. M. Grunow, L. D. B. Herrod, and R. J. Pankhurst, Extensional tectonics and the fragmentation of Gondwanaland, in Continental Extensional Tectonics, edited by M. P. Coward, J. F. Dewey, and P. L. Hancock, *Geol. Soc. Spec. Publ. London, 28*, 433-441, 1987.

Demarest, H. H., Jr., Error analysis for the determination of tectonic rotation from paleomagnetic data. *J. Geophys. Res., 88*, 4321-4328, 1983.

de Wit, M. J., The evolution of the Scotia Arc as a key to the reconstruction of southwestern Gondwanaland, *Tectonophysics, 37*, 53-81, 1977.

Dott, R. H., Jr., R. D. Winn, Jr., M. J. de Wit, and R. L. Bruhn, Tectonic and sedimentary significance of Cretaceous Tekenika Beds of Tierra del Fuego, *Nature, 266*, 620-622, 1977.

Eldredge, S., V. Bachtadse, and R. Van Der Voo, Paleomagnetism and the orocline hypothesis, *Tectonophysics, 119*, 153-179, 1985.

Forsythe, R. D., and C. Mpodozis, El Archipiélago Madre de Dios, Patagonia occidental, Magallanes: Aspectos generales de la estratigrafia y estructura del 'basamento' pre-Jurassico Superior, *Rev. Geol. Chile, 7*, 13-29, 1979.

Griffiths, D. H., and P. F. Barker, Review of marine geophysical investigations in the Scotia Sea, in *Antarctic Geology and Geophysics*, pp. 3-11, edited by R. J. Adie, Oslo, Universitetsforlaget, 1972.

Grunow, A. M., D. V. Kent, and I. W. D. Dalziel, Mesozoic evolution of West Antarctica and the Weddell Sea Basin: New paleomagnetic constraints, *Earth Planet. Sci. Lett., 86*, 16-26, 1987.

Halpern, M., Regional geochronology of Chile south of 50° latitude, *Geol. Soc. Am. Bull., 84*, 2407-2422, 1973.

Harland, W. B., A. V. Cox, P. G. LLewellyn, C. A. G. Pickton, A. G. Smith, and R. Walters, *A Geologic Time Scale*, pp. 63-84, Cambridge University Press, New York, 1982.

Hervé, M., M. Suárez, and A. Puig, The Patagonian batholith S of Tierra del Fuego, Chile: Timing and tectonic implications, J. Geol. *Soc. London, 141*, 909-917, 1984.

Katz, H. R., and W. A. Watters, Geological investigation of the Yaghan Formation (upper Mesozoic) and associated igneous rocks of Navarino Island, southern Chile, *N. Z. J. Geol. Geophys., 9, 323*-359, 1966.

Lawver, L. A., and C. R. Scotese, A revised reconstruction of Gondwanaland, in *Gondwana Six: Structure, Tectonics, and Geophysics*, Geophys. Monogr. Ser., Vol. 40, edited by G. D. MacKenzie, AGU pp. 17-23, Washington, D. C., 1987.

Lawver, L. A., J. G. Sclater, and L. Meinke, Mesozoic and Cenozoic reconstructions of the south Atlantic, *Tectonophysics, 114*, 233-255, 1985.

Ludwig, W. J., and P. D. Rabinowitz, The collision complex of the North Scotia Ridge. *J. Geophys. Res. 87*, 3731-3740, 1982.

Marshak, S., Kinematics of orocline and arc formation in thin-skinned orogens, Tectonics, 7, (1), 73-86, 1988.

Mukasa, S. B., I. W. D. Dalziel, and M. Kunk, 40Ar/39Ar and U-Pb age constraints on kinematic evolution of the northern Scotia Arc, in *28th International Geological Congress Abstracts*, Washington, D. C., Vol. 2, 2-476, 1988.

Nelson, E. P., I. W. D. Dalziel, and A. G. Milnes, Structural geology of the Cordillera Darwin—collision style orogenesis in the southernmost Andes, *Eclogae Geol. Helv., 73*, 727-751, 1980.

Norton, I. O., and J. G. Sclater, A model for the evolution of the Indian Ocean and the breakup of Gondwanaland, *J. Geophys. Res., 84*, 6803-6830, 1979.

Suárez, M., and T. H. Pettigrew, An upper Mesozoic island-arc-back-arc system in the southern Andes and South Georgia, *Geol. Mag., 113*, 305-328, 1976.

Suárez, M., M. Hervé, and A. Puig, Hoja Isla Hoste e islas adyacentes, XII Región, *Carta Geol. Chile 65, 113 pp.*, Serv. Nac. de Geol. y Miner. de Chile, Santiago, 1985.

Tanner, P. W. G., Geological evolution of South Georgia, in An*tarctic Geoscience*, edited by C. Craddock, pp. 167-176, University of Wisconsin Press, Madison, 1982.

Winn, R. D., Jr., and R. H. Dott, Jr., Submarine-fan turbidities and resedimented conglomerates in a Mesozoic arc-rear marginal basin in southern south America, in Sedimen*tation in Submarine Canyons, Fans and Trenches*, edited by D. J. Stanley and G. Kelling, pp. 362-373, Dowden, Hutchinson, and Ross, Stroudsberg, Pa., 1978.

Winslow, M. A., The structural evolution of the Magallanes Basin and neotectonics in the southernmost Andes, in Antar*ctic Geoscience*, edited by C. Craddock, pp. 143-154, University of Wisconsin, Madison, 1982.

W. D. Cunningham, I. W. D. Dalziel, W. A. Gose, and K. A. Klepeis, Institute for Geophysics and Department of Geological Sciences, University of Texas at Austin, 8701 Mopac Boulevard, Austin, TX 78759-8345.

(Received November 28, 1990;
revised May 28, 1991;
accepted June 5, 1991.)

JOURNAL OF GEOPHYSICAL RESEARCH, VOL. 96, NO. B10, PAGES 16,335–16,348, SEPTEMBER 10, 1991

THE GRENVILLE FRONT TECTONIC ZONE: RESULTS FROM THE 1986 GREAT LAKES ONSHORE SEISMIC WIDE-ANGLE REFLECTION AND REFRACTION EXPERIMENT

Duryodhan Epili and Robert F. Mereu

Department of Geophysics, University of Western Ontario, London, Ontario, Canada

Abstract. The Grenville Front, which marks the orogenic boundary between the Archean Superior Structural Province and the much younger Grenville Province to the southeast, is one of the major tectonic features of the Canadian Shield. Within Canada, it is approximately 1900 km in length extending from the north shore of Lake Huron across Ontario and Quebec to Labrador. In 1986, a major coincident onship near-vertical reflection and onshore wide-angle reflection/ refraction experiment (GLIMPCE-Great Lakes International Multidisciplinary Program on Crustal Evolution) was conducted along a series of lines across the Great lakes. One of the lines, line J, ran across Georgian Bay and Lake Huron for a distance of 350 km and crossed the Grenville Front Tectonic Zone (GFTZ). The seismic signals from the air gun array source were well recorded by the onshore stations up to distances of 250 km with a seismic trace spacing of 50-62.5 m. The GFTZ had a profound effect on the nature of the reflector patterns observed on the onshore seismic sections. Data recorded by the stations on the east end of the line indicate that the crustal P phases are very complex and form a "shinglelike" pattern of reflected waves. Data recorded by stations at the center and at the western end of the line show that the Pg phases are normal and lack the shinglelike appearance. This character of arrivals was also observed on the corresponding S wave sections. A combined P and S wave forward modeling analysis shows that the GFTZ is composed of bands of reflectors dipping at angles of 20^0- 35^0 extending to the lower crust. These reflectors were also well imaged on the coincident near-vertical reflection data. Reflectors under the Britt domain to the east of the GFTZ have a shallower dip than those along the zone. The structure of the crust under the Manitoulin terrane to the west of the GFTZ is laterally homogeneous with a major intracrustal reflector at a depth of 17-20 km below the surface. Poisson's ratio is slightly higher to the east of the Grenville Front compared to the region to the west. The travel times of the PmP signals indicate that the Moho may be deeper under the GFTZ than under the surrounding regions. Our results give added support to tectonic theories that the Grenville Front owes its origin to a continental collision process.

Introduction

The Great Lakes International Multidisciplinary Program on Crustal Evolution (GLIMPCE) was formed during the fall of 1985 by a consortium of more than 60 scientists to investigate a number of Proterozoic structures on the North American continent including the Midcontinent Rift System (MRS), the Michipicoten Greenstone Belts, the Grenville Front (GF), the Grenville Front Tectonic Zone (GFTZ), and the Penokean and Huronian fold belts. Under this program, Geophoto Service Ltd. (GSI, Calgary, Alberta) collected marine multichannel near-vertical seismic reflection data along the profiles shown in Figure 1. The work was done during the months of August and September 1986. The equipment used consisted of a 3000-m-long 120-channel hydrophone streamer and a wide tuned air gun array of 128-L capacity. The array was composed of 60 active air guns which were fired at 20-to 25-s time intervals providing a trace spacing of 50-to 62.5-m on the record sections. At the same time that the near-vertical reflection experiment was carried out, a number of research groups recorded the air gun signals with sets of onshore stations to obtain coincident wide-angle reflection and refraction data sets. The 50-to 62.5-m refraction trace spacing is the first such data in North America and enabled us to see in minute detail the signal variation which one can get on a wide-angle reflection and refraction record section. In the past decade the average trace spacing for long-range seismic refraction experiments in Canada had been several kilometers mainly due to the inaccessibility of the area and lack of sufficient number of instruments. The details of the data acquisition parameters for this experiment are given in internal reports by the United States Geological Survey [Hutchinson et al., 1988] and the Geological Survey of Canada [Morel-a-l'Huissier et al., 1990]. A series of papers on the results from the near-vertical reflection experiments were presented by Behrendt et al. [1988, 1989, 1990], Green et al. [1988, 1989, 1990], Milkereit et al. [1988, 1990b], and Cannon et al. [1989]. Information on the onshore experiment and some preliminary results from the Lake Superior data were given by the GLIMPCE Seismic Refraction Working Group [1989], Epili and Mereu [1989], Milkereit et al. [1990a], and A. Trehu et al. [1991]. In this paper we present the results of our analysis of the onshore data from line J which crossed the Grenville Front near the boundary between the Georgian Bay and Lake Huron.

Paper number 91JB01258.
0148-0227/91/91JB-01258$05.00

Regional Tectonics

The 1986 GLIMPCE line J crossed the Britt Domain and the Grenville Front Tectonic Zone in the Grenville Province and the Manitoulin terrane in the Southern Province (Figure 2). The Grenville Front (GF), one of the primary targets of the GLIMPCE experiment, defines the

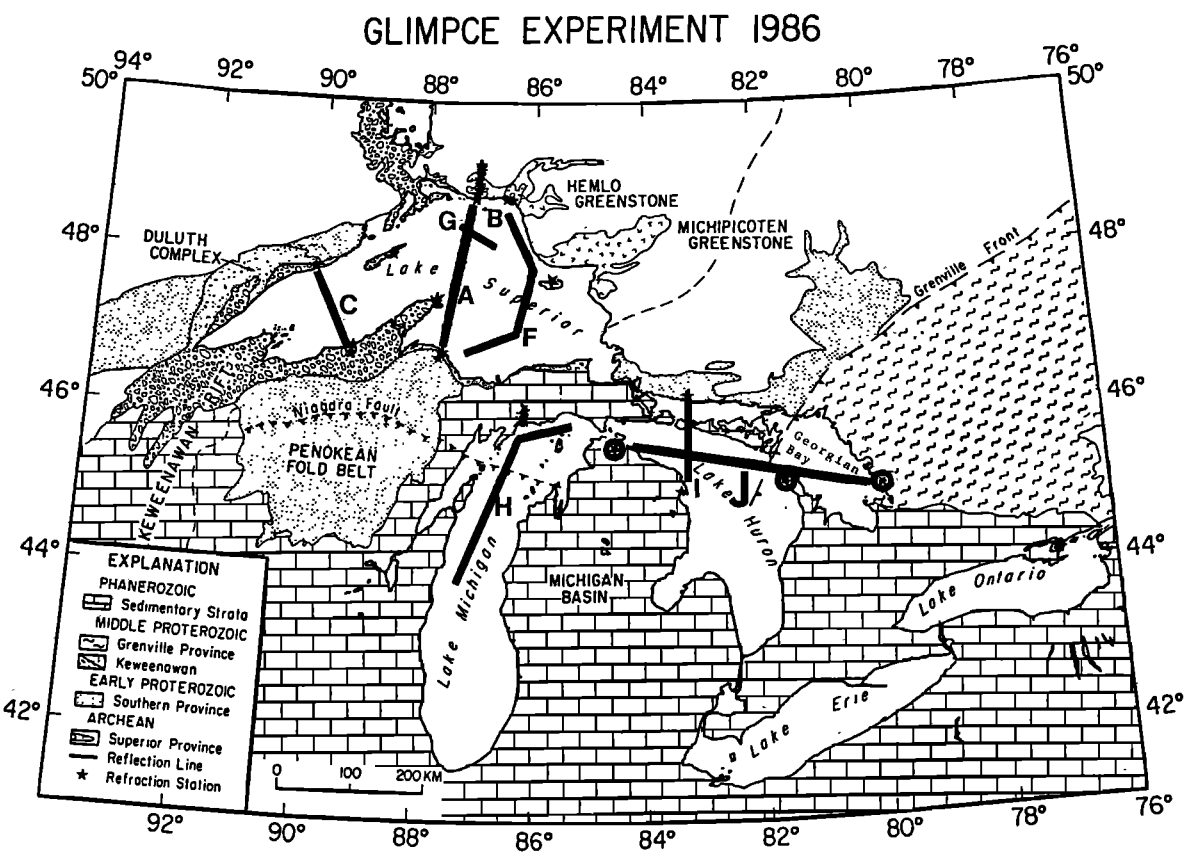

Fig. 1. Location of the 1986 GLIMPCE reflection and refraction seismic experiment. The analysis of line J is presented in this paper. Lines C, A, G, B, F, and H are over the Midcontinent Rift System and line J is over the Grenville Front Tectonic Zone. Line I is in the Manitoulin terrane crossing perpendicular to line J.

northwestern tectonic boundary of the Grenville Province. It separates the high-grade metamorphic rocks of the Grenville Province from low-grade metamorphic rocks of the Superior Province to the northwest and the Southern Province to the southwest and is the northwest limit of a large-scale northwest directed ductile thrusting associated with the Grenville Orogeny. Along thousands of kilometers of its length it is marked by a fault mylonite or cataclastic zone, a marked change in structural trend or metamorphic grade or a combination of these features [Wynne-Edwards, 1972]. On the southern half of Lake Huron, the front is not readily observed from surface exposures as it is hidden under Paleozoic cover. Its boundary here can only be delineated from magnetic and gravity anomalies [O'Hara and Hinze, 1980; Sharpton et al., 1987]. Both anomalies are positive over Lake Huron, indicating that the basement may be mafic. This is in contrast to the boundary in central Quebec where it is marked by a major gravity low [Grant, 1968; Tanner, 1969; Thomas and Tanner, 1975].

The GFTZ is approximately 30 km across superimposed upon earlier structures such as the Southern, Superior, and Nain provinces [Lumbers, 1978]. The region is characterized by ductile deformation and mylonite zones with foliation and layering aligned parallel to the GF. In simple terms, it is represented by a series of southeast dipping stacked crustal sheets [Gibb et al., 1983]. Seismic data from other lines crossing the Grenville Front to the east in Quebec provided evidence for a 5-to 10-km depression on the Moho along the GFTZ [Mereu and Jobidon, 1971; Berry and Fuchs, 1973; Mereu et al., 1986].

To the east of the GFTZ, line J crossed the Britt domain and the Parry Sound domain of the Central Gneiss Belt of the Grenville Province [Davidson and Morgan, 1980; Davidson, 1984]. The Britt domain is characterized by quartz feldspathic gneisses of both supracrustal and plutonic origin, deformed together and metamorphosed to middle to upper amphibolite facies along with local magmatite formation. The Parry Sound domain is a terrane of dark rocks consisting predominantly of mafic and intermediate rocks, layered pyroxene-bearing gneisses, with minor marble and other metasedimentary types. The metamorphic grade in this area is granulite facies. Unlike the Britt domain, potassic rocks in this area are rare.

The area to the west of the GF is divided into two Precambrian terranes: one north of the Manitoulin Island Discontinuity (MID) and the other south of the MID [Van Schumus et al., 1975; Green et al., 1988]. The northern part is underlain by Huronian metasedimentary rocks. The Precambrian rocks south of the discontinuity belong to the Manitoulin terrane [Green et al., 1988] and are covered by Paleozoic sediments. Granitic gneissic rocks were found in both terranes.

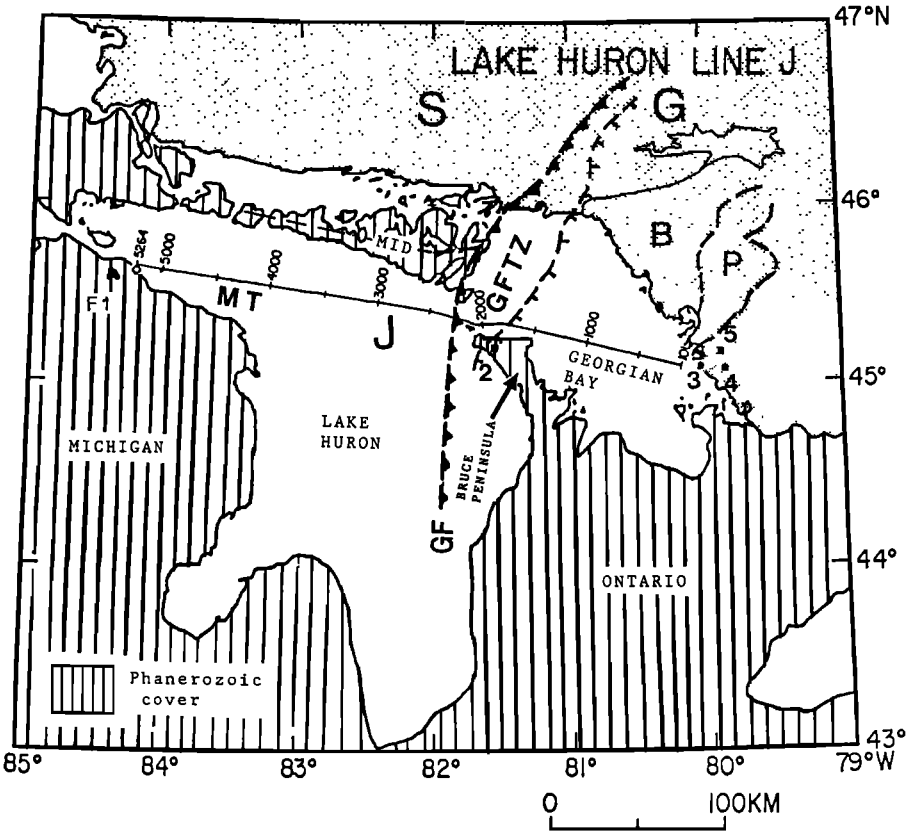

Fig. 2. Map showing the location of seismic line J across Georgian Bay and Lake Huron. The data recorded from the 2, 3, 4, 5, and F1 vertical component stations are used in this analysis. P, Parry Sound domain, B, Britt domain; GFTZ, Grenville Front Tectonic Zone; MT, Manitoulin Terrane; S, Superior Province; G, Grenville Province; MID, Manitoulin Island Discontinuity. Figure is modified from Davidson and Morgan[1980] and Hutchinson et al. [1988].

Recent geologic reviews of the region under study are given by Moore et al. [1986] and Green et al. [1988]. The Grenville Province, the youngest structural division of the Canadian Precambrian Shield, occupies approximately one million square kilometers at the southwest of the shield. It underwent several phases of restructuring during successive orogenies between 1700 Ma and 1000 Ma. Most model hypotheses of the geological evolution of the Grenville Province can be categorized into two groups; the continental collision model [Donaldson and Irving, 1972; Dewey and Burke, 1973; Baer, 1976; Young, 1980; Windley, 1986], where an ocean closure was involved in bringing two plates together, or the ensialic orogen model [Wynne-Edwards, 1972, 1976; Baer, 1981; Woussen et al., 1986], where no ocean is involved in the process and the features are formed in place due to major shear or thrust.

Line J Seismic Near-Vertical Reflection Results

The results of GLIMPCE line J multichannel seismic reflection data (Figure 3) over the GFTZ were given by Green et al. [1988, 1989, 1990]. Figure 3 shows that the structure below Lake Huron can be divided into three distinct units depending upon their reflection characteristics: (1) Manitoulin terrane in the west where the complex and highly reflective lower crustal layers are separated from less reflective upper crustal layers, (2) the GFTZ in the center, identified by a 30-km-wide zone of east dipping reflections, and (3) the structure to the east of the GFTZ in the central Gneiss belt characterized by shallow dipping reflections. Green et al. [1989] attributed the east dipping reflectors east of the Grenville Front to highly reflective mylonite shear zones and refer to the major intracrustal discontinuity west of the Grenville Front as the Penokean Decollement. They interpreted the data with a two-stage evolutionary model such that a northwest collision of the Grenville cratonic margin took place during the Penokean Orogeny. This was followed by the formation of a broad zone of east dipping ductile shear zones during the Grenville Orogeny.

Field Techniques, Trace Display, and Record Sections

Line J is approximately 323 km long and is the longest of the GLIMPCE lines. Figure 2 shows the location of the onshore stations and the shot numbers in the lake. Over 5000 air gun shots were fired over a 36-hour continuous period at a time interval of 20-25 s to provide an average trace spacing coverage of 50-62.5 m. The University of Western Ontario recorded the onshore data using vertical component stations (stations 3, 4, and 5

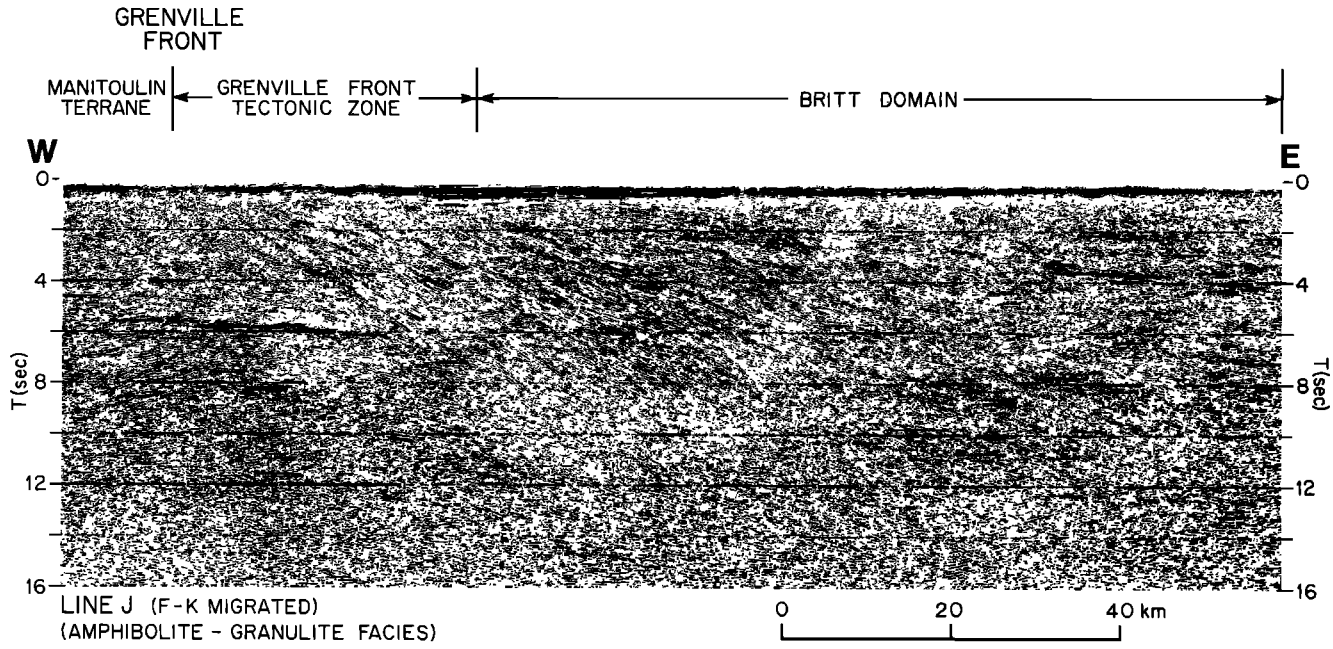

Fig. 3. F-K migrated seismic reflection data of eastern part of GLIMPCE marine profile J across the Grenville Front Tectonic Zone (GFTZ) and interior of the Grenville Orogen in Lake Huron/Georgian Bay. From from Green et al. [1990]. Note the steep dipping reflectors in the GFTZ and the major intracrustal reflector at about 6 s (two-way time) under the Manitoulin terrane.

in a triangular array over the Britt domain at the eastern end of the line and station 2 over the GFTZ on the Bruce Peninsula of Southern Ontario). The University of Wisconsin (using a 13-station array of three-component instruments) and the University of Illinois (using an industry-type multichannel recording system) recorded the data in Michigan at the western end of the line. In this paper we present mainly the processing and interpretation of the University of Western Ontario data set. Some of the U.S. data recorded at the western end of the line by the University of Wisconsin, Madison, is used to help interpret the reversed profile across Lake Huron.

The recording instruments employed by the University of Western Ontario were the portable frequency modulation systems which had been designed and built at the university in 1979. These have been used for various long-range refraction experiments which were carried out in Canada from 1979 to 1985. The seismometers were placed on rock outcrops and were vertical Mark Product LC4 with a natural frequency of 1 Hz. This limited our analysis to a study of only the vertical components of the P and S waves. The raw signals were recorded using a 35-Hz antialiasing filter and with five different gain settings to provide a large dynamic range of 85 dB. After completion of the field work, the 25,000 analog seismic traces were digitized with a sampling rate of 125 samples per second and organized into a computer usable form in the laboratory.

Data Processing Steps

The original data traces were contaminated with various types of noise. In order to interpret the observations effectively, a series of processing steps were applied to improve the signal-to-noise ratios. Many of the steps are similar to those used in reflection seismology and exploit the high coherencies available in the closely spaced traces. The effectiveness of each of the processing methods can best be seen by examining the individual seismic traces, as is illustrated in the selected examples shown in Figures 4 and 5. The following processing steps were carried out in order to create the final record sections for interpretation.

Trace Editing

Trace editing was first performed on the data using a simple technique which combines the root mean square (RMS) trace amplitudes and median filtering. An RMS amplitude was first obtained from the data in the first 10 s (reduced time -2 to 8 s). The trace was rejected if its RMS value was greater than 150% or smaller than 50% of the median RMS value of the adjacent 20 traces. If the trace had noise bursts, it appeared as a spike with high RMS value which was much larger than the median. If it was a dead trace with some instrument generated noise, its RMS value would be extremely small compared to the median. In both cases it was easy to recognize and reject the trace. The test procedure was repeated for all traces by shifting one trace each time.

Median Filtering

During a few hours of the recording period, there was an electrical storm which generated high-amplitude glitches on some of our records. A portion of this raw data and the despiked data for line J recorded at station 3 is shown in Figures 4a and 4b, respectively. The spikes were

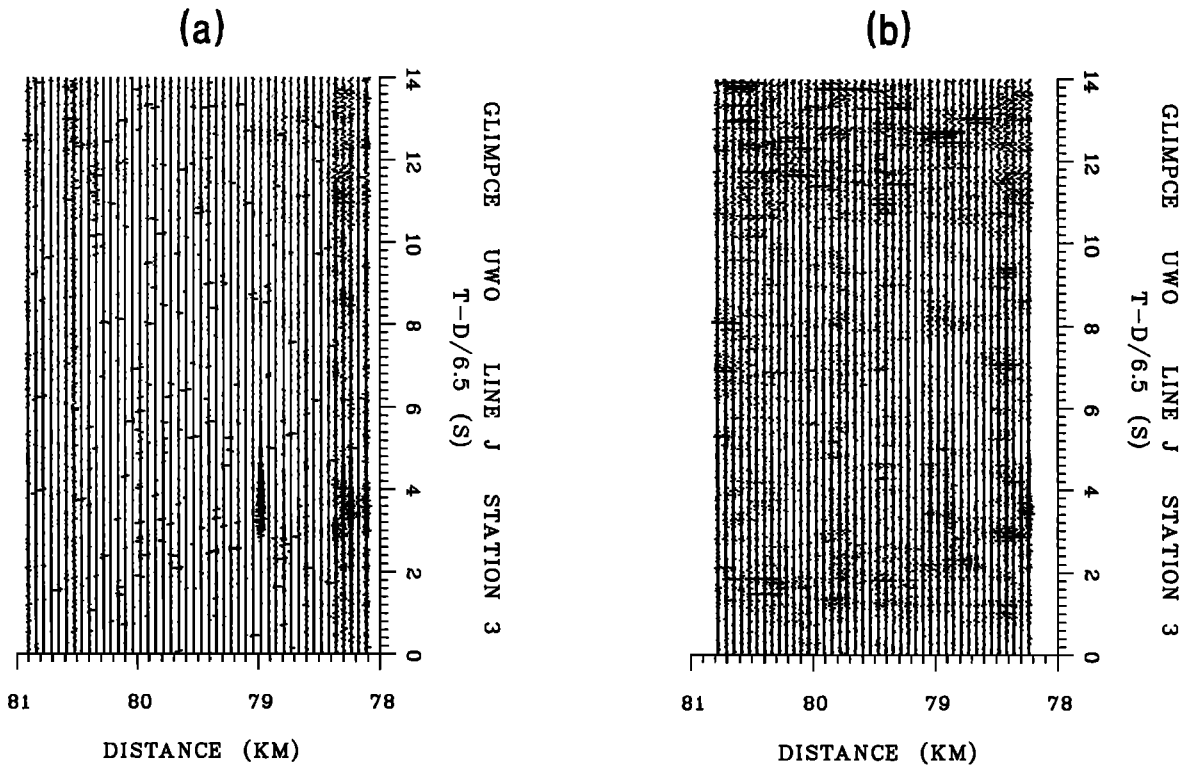

Fig. 4. Portion of the data for line J recorded at the Parry Sound station 3 for an offset distance of 78-81 km to show the effect of median filtering. (a) Field data. (b) Median filtered (a group of five adjacent traces is compared). The noise spikes on the field data which are due to an electrical storm are removed by the median filter. Note also the elimination of a noise burst for a trace offset of 78.97 km.

removed using a despiking method which was based on a median filter technique [Evans, 1982; Bednar, 1983; Naess and Bruland, 1985; Stewart, 1985]. The median filter is the one which extracts the middle value of an ascending sequence of numbers called the "median". In our method a multichannel median filtering technique was employed to discriminate the spikes and to substitute them by median amplitudes. First the median and absolute maximum value of n (n=5 in our case) samples from adjacent traces were compared. If the median was less than 60% of the absolute maximum amplitude of the group, then the reference sample amplitude was compared against the absolute maximum amplitude. If the reference amplitude was greater than the 60% of absolute maximum amplitude, then the reference value was replaced by the median. If the above condition was not met, the sample amplitude was untouched. This method is also effective for suppressing occasional noise bursts in the data (see, for example, the record for the offset distance 78.97 km in Figures 4a and 4b).

Band Pass Filtering

Because of periods of bad weather, some of the raw data were contaminated with wind and water wave noise. In Lake Superior, the wave noise was confined to the 1-to 3-Hz range and could easily be removed with a simple high pass filter. In Lake Huron and Georgian Bay, noise in a 1-to 35-Hz range was present. Some suppression of this noise was achieved with a 4-to 25-Hz Butterworth band pass filter, as most of the usable seismic energy was less than 20 Hz. The effectiveness of the band-pass filter can be seen by comparing Figures 5a and 5b.

Nth Root Stacking

Since the shots were fired every 20-25 s, much of the noise on the record sections was originated from the coda of the previous shot. Since this noise was in the same frequency range as the desired seismic signal, it could not be removed with a band-pass filter. Stacking or summing together of adjacent traces to produce another trace is found to be extremely useful in enhancing the signal-to-noise ratio. The inherent assumption for the straight stack is that the noise is uncorrelated, and the amplitudes and the signal-to-noise ratios are the same on all traces. The Nth root stack [Muirhead, 1968; Kanasewich et al., 1973, McFadden et al., 1986] is performed by taking the average of the Nth root of all the samples at a particular time for a group of channels and raising the results to Nth power with the sign of the observation preserved. The Nth root stacking of multichannel data is very useful when the noise is random. By increasing the root N from 2 to 4, or 8, the seismograms are improved remarkably, but strong signal distortion is observed because of the nonlinear nature of the Nth root stack technique. Therefore, no more than N=4 is recommended to

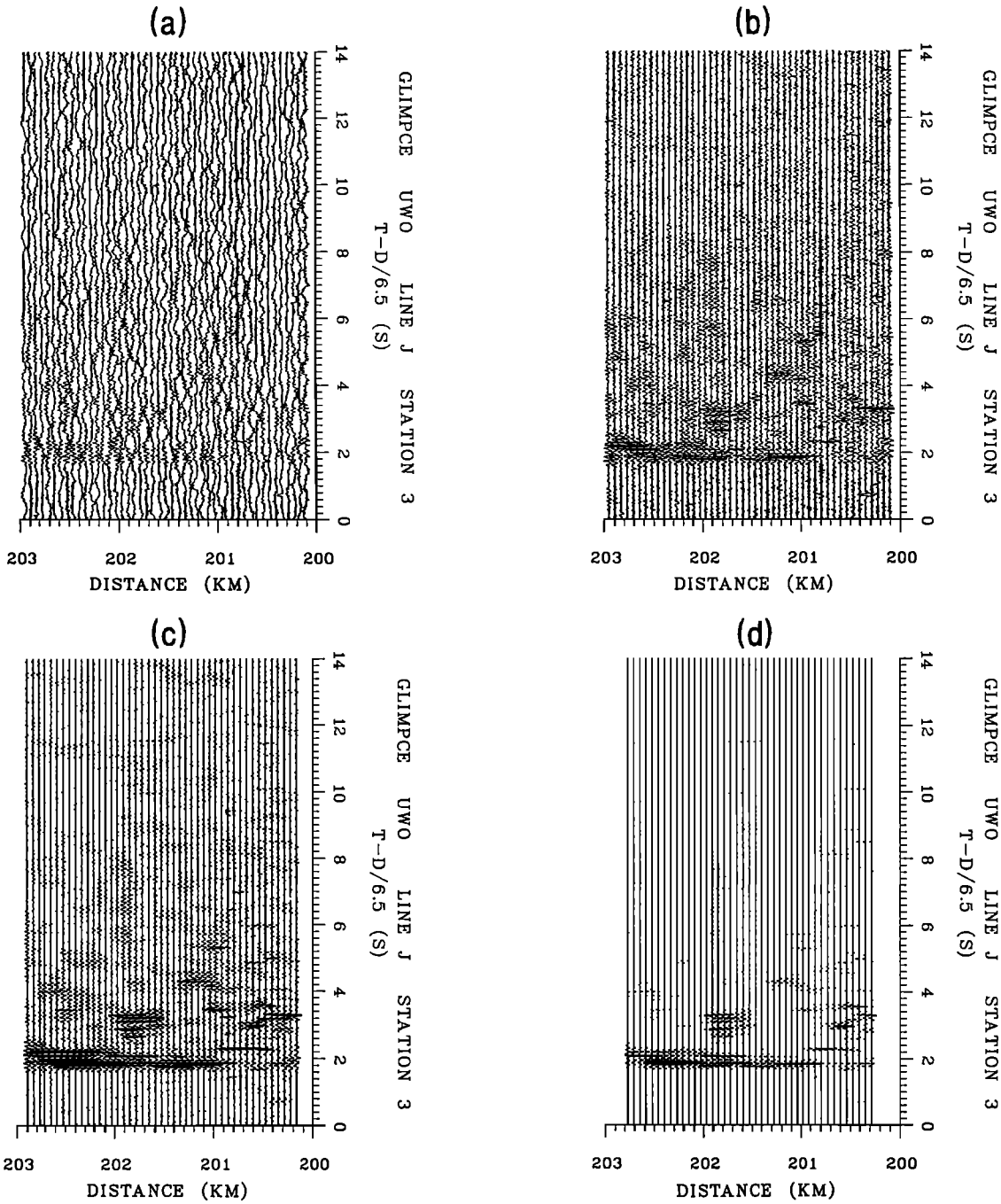

Fig. 5. Portion of the data for line J recorded at the Parry Sound station 3 for large offset distance of 200-203 km after different processing steps. (a) Field data. (b) Band-pass (4-25 Hz) filtered data. (c) Nth root stacked (N=2, three trace average) data. (d) Coherency filtered (coherency was scanned for five adjacent traces between 6 and 9 km/s). Note the improvement in signal to noise ratio after each processing step which enables one to identify the events clearly.

avoid the problem. The effectiveness of the Nth root stack filter can be seen by comparing Figures 5b and 5c.

Coherency Filtering

The common signal in a multichannel environment can be measured, enhanced, extracted, or shaped using operations which require some form of coherency measurement of signals. The coherency method used in this paper is similar to that of Milkereit et al. [1990a] and Z. Hajnal (personal communication, 1989). Here the observed data are weighted with a number which is computed from the maximum velocity stack. This maximum is determined by stacking the traces using a set of stacking velocities within a reasonable range. The effectiveness of the coherency filter can be seen by comparing Figures 5c and 5d. The filter in effect turns down the gains on amplitudes

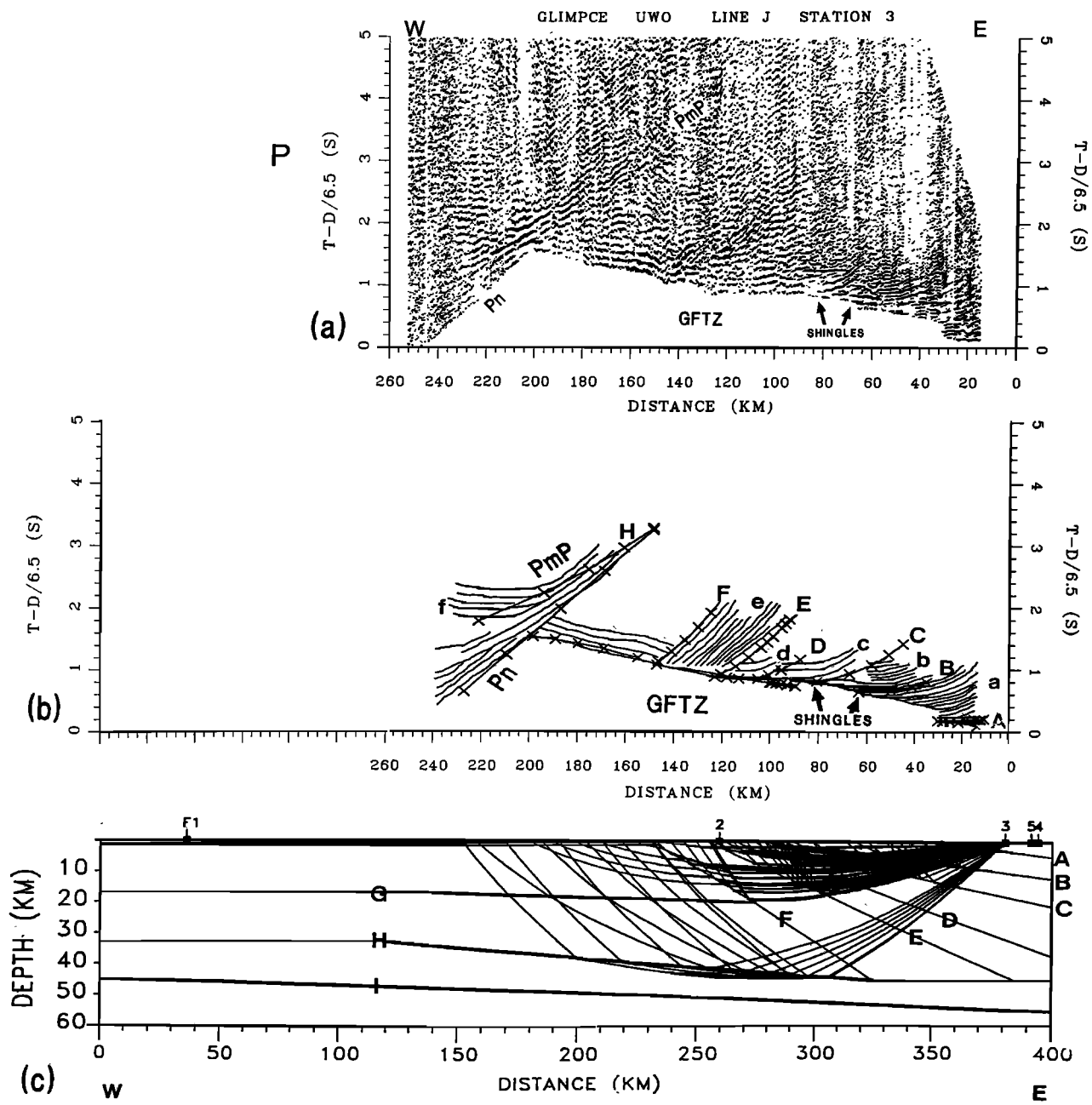

Fig. 6. (a) P wave record section for line J recorded at the Parry Sound station 3. (b) Comparison of theory and observation. Continuous lines grouped into a, b, c, d, e, and f are observed reflection hyperbolae. A, B, C, D, E, F, and H are theoretical ray trace-travel time branches associated with the corresponding model interfaces. (c) Ray trace diagram.

which have low-coherency weights. The data used in these examples come from a set of traces observed near the crossover point between Pg and PmP phases (see Figure 6a).

Data Display

In order to display the huge GLIMPCE refraction data sets into record sections in a practical manner, a special printer-plotter program developed by Mereu et al. [1990] was used. This enables one to transmit and plot a large data set from a mainframe computer to a personal computer (PC) and high-quality dot matrix printer. Since it is not possible to display the individual wiggles of a 5000-trace seismic section in a publishable diagram, we also adapted a technique which is commonly used in reflection processing. The amplitudes are trace normalized and plotted with only their positive amplitudes in a variable area format and with the small and negative amplitudes suppressed. This type of representation not only enables one to compress a large record section into an easy to see line diagram format, but it also enables one to see large-scale signal patterns in the sections which cannot be seen on the individual trace sections. Further improvements were made in

the appearance of the final record sections by correcting each of the traces for variations in water depth. Coda noise from previous shots which appeared before the onset of the first arrivals was also muted out of these sections in order that the first arrival patterns be enhanced.

Analysis and Interpretation

The main P wave vertical component processed record sections and analysis for stations 3, 2, and F1 are shown in Figures 6, 7, and 8, and S wave record sections for stations 3 and 2 are presented in Figure 9. The P wave sections were plotted using a reducing velocity of 6.5 km/s. The S wave sections were plotted with a reducing velocity of 3.75 km/s and time scale equal to $\sqrt{3}$ times that of the P time scale. This choice of reducing velocity and time scale means that the S wave record section should overlap the P section if the subsurface values of Poisson's ratio are 0.25 [El-Isa et al., 1987]. Any difference in arrival times in the P and S wave sections can be interpreted as resulting from a deviation in Poisson's ratio from 0.25 at depth.

Significant patterns of first and second arrival signals were first identified and plotted

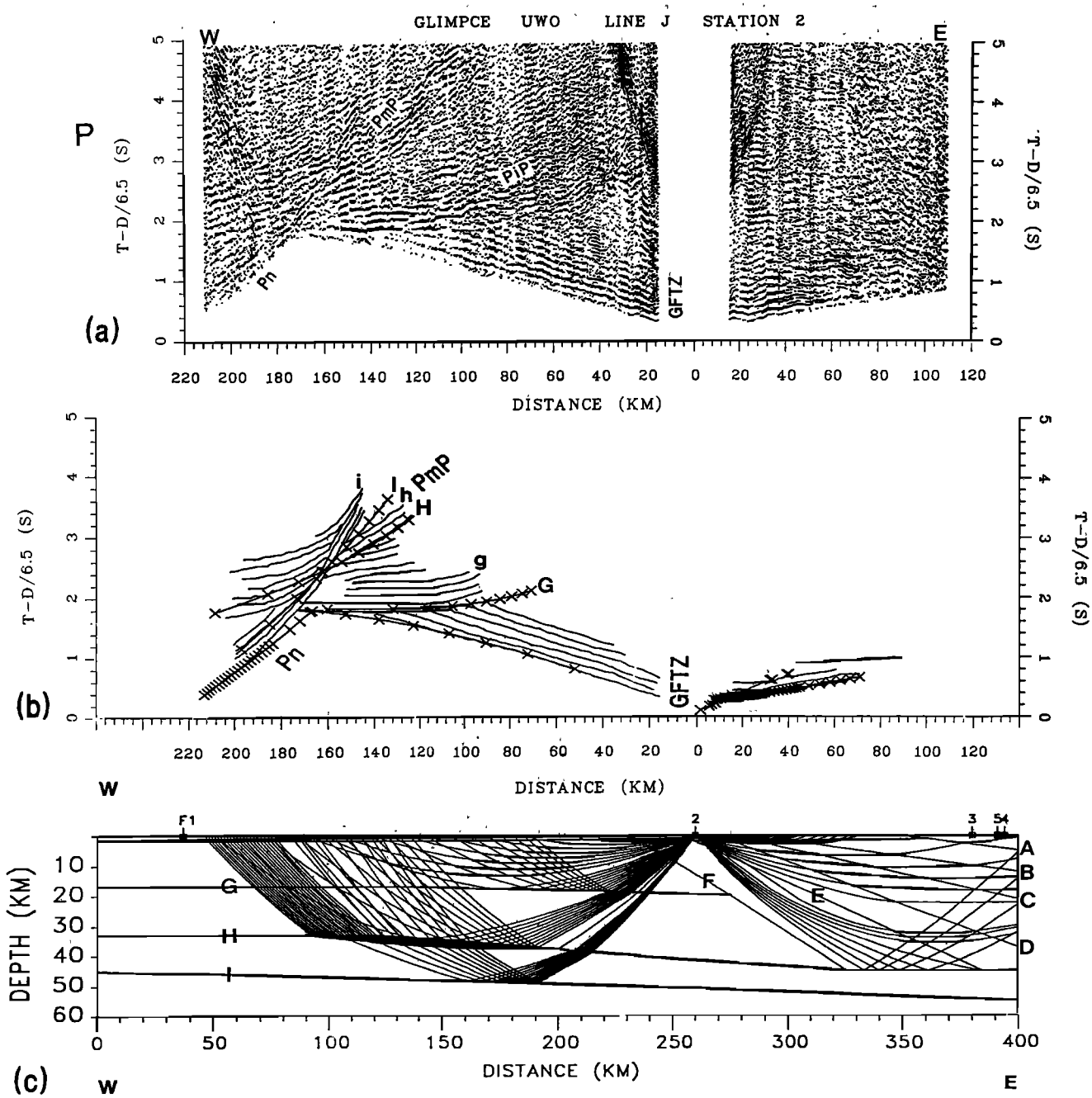

Fig. 7. (a) P wave record sections for line J recorded at the Bruce Peninsula station 2. (b) Comparison of theory and observation. Continuous lines g, h, and i are observed reflection hyperbolae. G, H, and I are the theoretical ray trace-travel time branches associated with the corresponding model interfaces. (c) Ray trace diagram.

in line diagrams for an easier comparison with the results obtained from the modeling experiments. These are shown in Figures 6b, 7b, and 8b. To invert the data, a starting model consistent with the geology of the area was first determined by combining the results of a least squares analysis of first arrival data and the results of the near vertical reflection data shown in Figure 3. Both the first arrival and later arrival travel time data were then inverted into a laterally heterogeneous subsurface depth model using an iterative interactive two-dimensional ray trace forward modeling method. The software, developed by Mereu [1990], uses the concept of dividing the model into triangular blocks each with its own constant velocity gradient. The linear form of the velocity function ensures that all ray paths within each triangle are arcs of circles thus enabling one to trace rays through the model efficiently.

For a given modeling iteration, rays were traced from the source location in the model to the free surface, and a comparison was made between the computed and observed travel times. Small adjustments were then made to the velocity

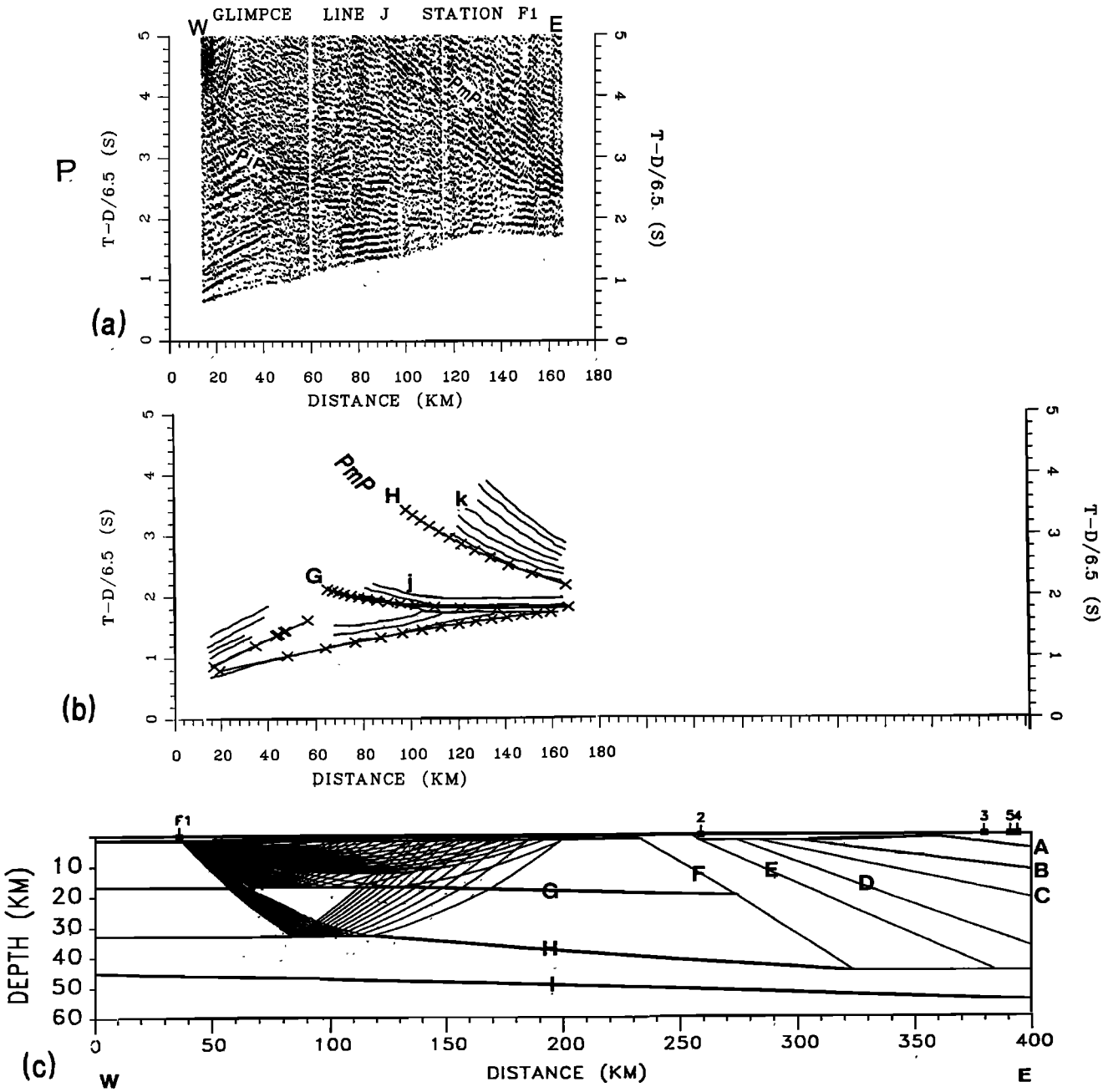

Fig. 8. (a) P wave record section for line J recorded at the University of Wisconsin, Madison, station F1 at the western end of the line. (b) Comparison of theory and observation. Continuous lines j and k are observed reflection hyperbolae. G and H are the theoretical ray trace-travel time branches associated with the corresponding model interfaces. (c) Ray trace diagram.

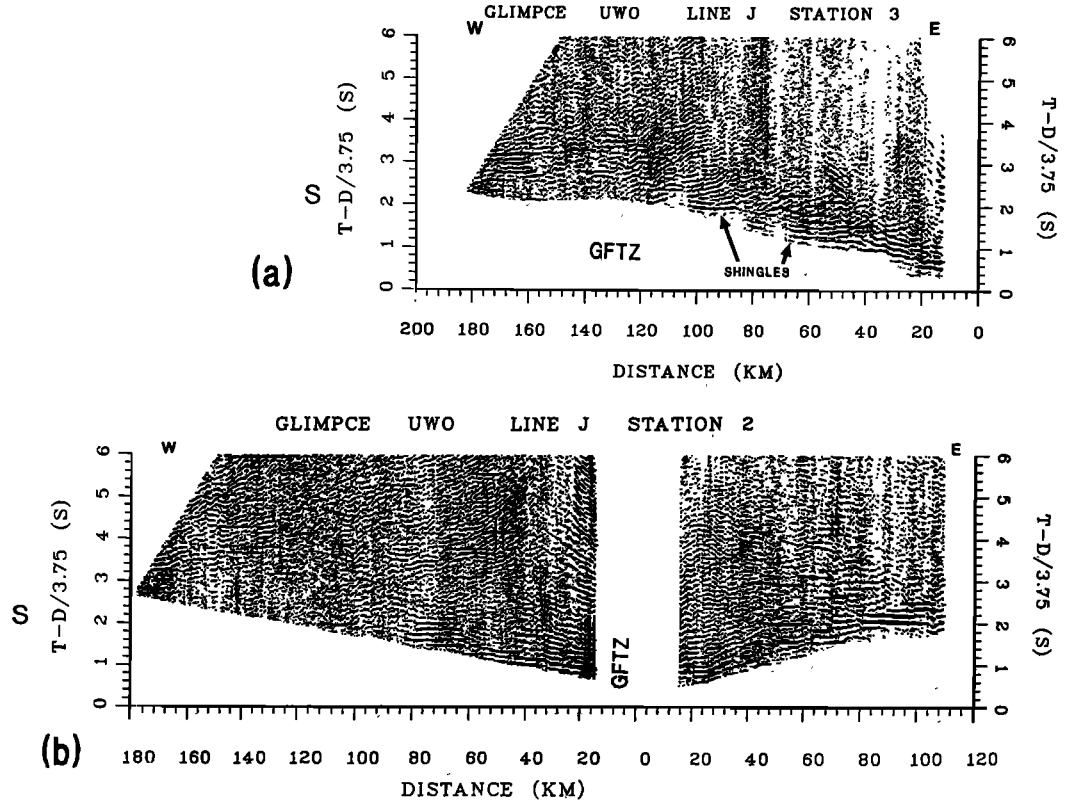

Fig. 9. S wave record sections for line J (a) recorded at the Parry Sound station 3 and (b) recorded at the Bruce Peninsula station 2. Note the similarities between these record sections and P wave record sections shown in Figures 6a and 7a.

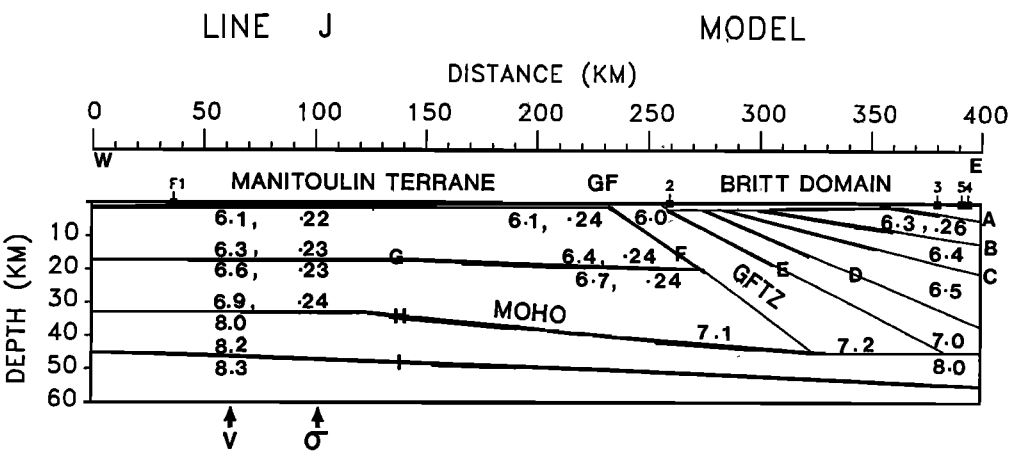

Fig. 10. Final two-dimensional seismic P wave velocity model showing the structure below line J. A, B, C, D, E, F, G, H, and I are the velocity discontinuities. Seismic P velocities and Poisson's ratio are marked on the model. Only deviations of Poisson's ratio from 0.25 are shown. The bold lines are the places where the structure is sampled by ray paths.

gradients and boundary positions until a good fit was obtained between all theoretical and observed amplitude data. The procedure of iterating to a good model started at the top, fitting the near-source observations, and then gradually working to greater depths in the model with the more distant observations. Figures 6c, 7c, and 8c illustrate the ray trace diagrams for stations 3, 2, and F1, respectively (see Figure 2 for their locations). These stations are on opposite sides of the Georgian Bay and Lake Huron. The theoretical travel times for the corresponding model superimposed on the line diagrams obtained from the record sections are represented in the the Figures 6b, 7b, and 8b. The observed and computed travel times are in good agreement. The ray trace diagrams not shown here for stations 4 and 5 and for the S waves are similar to that of station 3.

The final two-dimensional velocity and depth model obtained from the analysis of the data sets is given in Figure 10. An estimate of the

precision of this model was obtained by making small variations to the velocities and coordinates of the vertices of the triangular blocks of the model and then determine the effects this would have on the theoretical travel times. The studies showed that the velocities were determined to a precision 0.05 km/s and the depths to about 0.5 km for upper crustal layers. The precision of velocities decreases to 0.1 km/s and depths to nearly 1 km for the lower crustal layers. The dominant wavelength in the data lies between 300 m and 1 km.

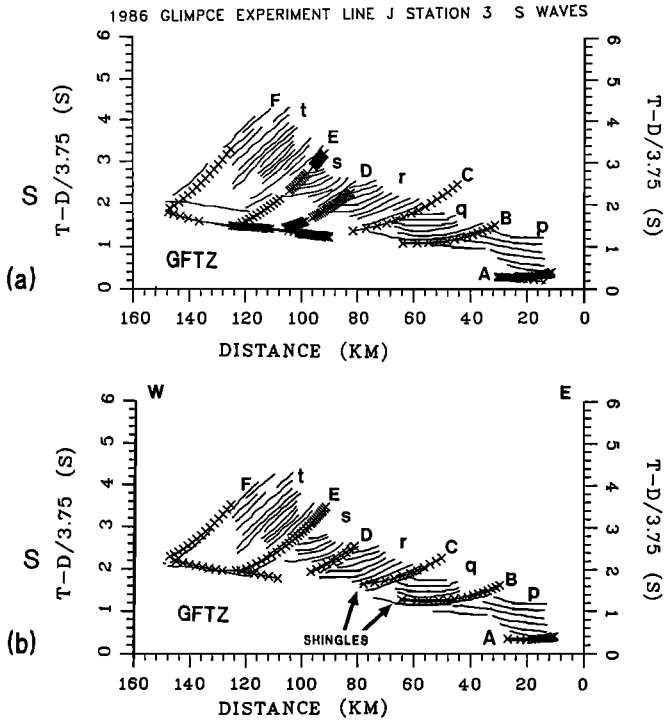

Fig. 11. (a) S wave theoretical travel times (assumed Poisson's ratio = 0.25) superimposed on the observed S wave line diagram obtained from the Parry Sound station 3 record section of Figure 9a. The mismatch of observations and theory clearly shows that Poisson's ratio must differ from 0.25. (b) S wave theoretical travel times superimposed on the observed S wave line diagram for a model with variable Poisson's ratio (the variation of Poisson's ratio from 0.25 is shown in Figure 10). Compare Figures 11a and 11b. p, q, r, s, and t are major groups of reflection hyperbolae. A, B, C, D, E, and F are the reflection travel time branches associated with corresponding interfaces shown in Figure 10.

Figure 11a shows the theoretical S wave travel times for the case where Poisson's ratio is assumed to be 0.25. Clearly, this is a serious mismatch. Figure 11b shows the S wave theoretical travel times after Poisson's ratio has been adjusted. The match with the observations is much better. The final values of Poisson's ratio shown in Figure 10 are, in general, greater than 0.25 at the eastern side of the GFTZ profile and less than 0.25 at the western side. The Poisson's ratios are obtained with the precision of 0.005.

Discussion and Conclusions

Examination of the patterns of arrivals on the record sections of Figures 6-9 reveals a number of interesting features. The Pg phases as observed by stations on the east end of the line J (see Figure 6a) are very complex and appear to have a "shinglelike" pattern up to a distance of 140 km to the west. The Sg phases as shown in Figure 9b also show a similar pattern. The large number of hyperbolalike curves in the record sections show that wide-angle reflections dominate these sections. Six major groups of reflection hyperbolae are seen. These are indicated as groups a, b, c, d, e, and f and are marked on the corresponding line diagrams shown in Figure 6b. The initial four groups are interpreted as arising from dipping subsurface reflectors under the Britt domain. The GFTZ appears as a separate group (group e) which was interpreted as arising from a band of reflectors dipping at angles of 20^{0}-35^{0} extending to the lower crust. These reflectors are also seen in the near vertical reflection section in Figure 3. Milkereit et al. [1990a] mapped these reflectors using a wide-angle migration technique. The image they obtained is reproduced in Figure 12. The energy from this group of dipping reflectors appears to diminish at a depth of 25-30 km below the surface. The width of the zone is 30-35 km with the Grenville Front marking its western boundary. This occurs at the surface a few

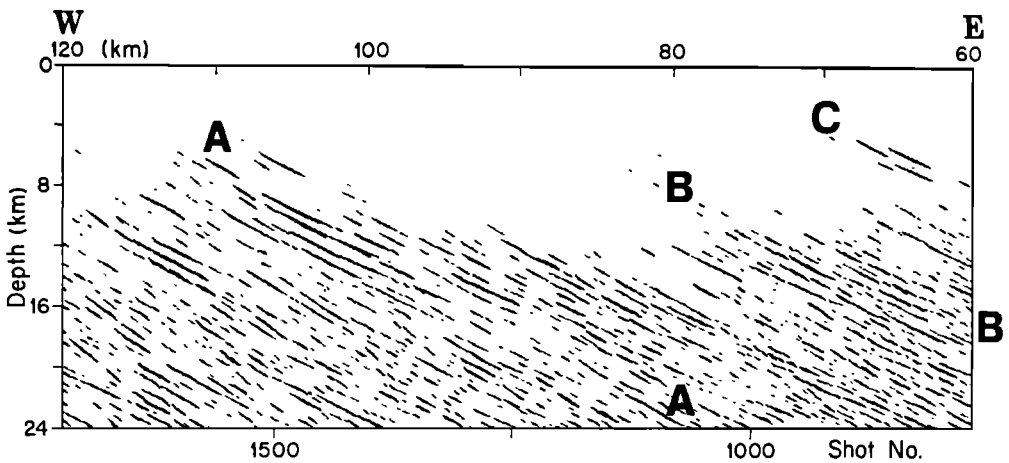

Fig. 12. A wide-angle migrated record section of line J across the GFTZ recorded at station 3. Note the series of steep (AA, BB, and C) reflectors in Grenville Front Tectonic Zone and Britt Domain. This figure is taken from Milkereit et al. [1990a].

kilometers to the east of the Bruce Peninsula. The sixth group of reflectors marked as "f" is interpreted as PmP reflected signals from the Moho.

The complex shingling patterns observed by the easternmost stations were absent from the record sections obtained on the Bruce Peninsula (Figures 7a and 9b). The section for station 2 looking toward the east does not have the shingling pattern, as in this case the waves are back-scattered from the reverse side of the reflectors as is seen on the ray tracing diagram of Figure 7c.

The sets of sloping reflectors which gave rise to the shingling effects on the eastern side of the Georgian Bay are absent under the Manitoulin terrane to the west of the GFTZ. A major intracrustal PiP travel time branch is seen on both the section from the Bruce Peninsula looking to the west and the reversed profile section obtained by the the F1 station in Michigan. This branch was interpreted as arising from a seismic boundary at a depth of 17-20 km. This boundary is also seen on the near-vertical section of Figure 3 and was described by Green et al. [1989] as the Penokean Decollement. This discontinuity separates a low reflective upper crust from a high reflective lower crust. The model shows a velocity jump of 6.4 to 6.7 km/s at this discontinuity. This reflector as well as other minor reflectors are truncated by the Grenville Front.

Both the near-surface velocity and Poisson's ratio were found to be lower under the Southern Province to the west of the front in comparison to the region under the Grenville Province to the east (Figure 10). The higher values of Poisson's ratio at the Britt domain (greater than 0.25) may indicate that rocks in that region have a more mafic content or may have a higher grade of metamorphism, whereas the rocks under the Manitoulin terrane may be related to quartz rich granites which intruded at 1.4-1.7 Ga into the Archean granites. These rock properties are similar to those hypothesized by O'Hara and Hinze [1980] based on the potential field data.

The data indicate that the seismic velocities increase to about 7 km/s at the base of the crust. Observations of the Pn signal are very weak but are discernible on the Figure 6a record section. Analyses of these signals as well as that of the complex PmP indicate that the Moho deepens from about 33 km at the western end of the line to approximately 41 km below the Manitoulin terrane. The control on the depth of the Moho below the GFTZ and the Britt Domain is limited by a lack of appropriate ray paths. The Moho itself is poorly defined in the reflection section of Figure 3. Indications of its presence occurs between 10 and 13 s two-way time of the profile. The PmP reflector patterns obtained from the Bruce Peninsula provide evidence for the presence of an upper mantle boundary at a depth of about 10 km below the Moho. The thickening of the GFTZ is in agreement with the results of previous seismic studies across the Grenville Front [Mereu and Jobidon, 1971; Mereu et al., 1986].

Two competing models are present in the literature as to the evolution of the Grenville Province (see above section on geology of the area). Our wide-angle reflection and refraction analysis can not resolve the controversy between these two hypotheses but can bring new insights to the problem and confirm an uplift environment under ductile conditions. The dipping reflectors from approximately 30° at the Grenville Front to 5-10° at the Britt Domain toward the eastern end of the profile indicate an uplift of the lower crust due to an enormous thrust. This is possibly the result of a tectonic collision process similar to the Himalayan type of environment as suggested by Windley [1986]. Similar zones of deeply penetrating dipping reflectors were obtained in Consortium for Continental Reflection Profiling (COCORP) seismic lines in the southeastern United States within the interiors of Phanerozoic orogenic belts which Nelson et al. [1985] interpreted as thrust ramps and suture zones. Thus the rocks to the east of the front were highly deformed due to intense strain forming a steeply dipping layered character with high reflectivity. A geologic factor contributing to the layered character is ductile strain, caused by stress in a thermally weakened middle crust [McCarthy and Thompson, 1988]. This process yields mylonite shear zones and intrusive mafic sheets which have prominent reflectivity. Green et al. [1990] and Milkereit et al. [1990a] mentioned that the reflections may be caused by mylonite zones which vary from tens to hundreds of meters and/or by anisotropic zones of mylonite and cataclasite.

The Moho is depressed to 45 km near the GFTZ compared to 35 km at the western end of the profile. The relatively thin crust (35 km) in the Archean Superior province is consistent with the global pattern of Archean crustal thickness [Durrheim and Mooney, 1991]. This crustal thickening is possibly due to a crustal plate being thrust upon the Superior craton. In an analysis of a COCORP line across the Grenville Front 500 km to the south in western Ohio, Pratt et al. [1989] found a broad zone of east dipping basement reflectors associated with the Grenville Front similar to the one that we observed in the GLIMPCE data. This is an indication that the Grenville Front is a major structural discontinuity that divides the midcontinent. They also have observed a set of west dipping reflectors on their section which they related to an ocean closure event during the Grenville orogeny.

Acknowledgments. We would like to thank the organizers of the GLIMPCE seismic experiment for giving us the opportunity to participate with them in this study. Special thanks is extended to A. Green of the GSC, who was the chief coordinator of the project, for his advice and assistance. The data from the western side of Lake Huron used in this work were provided by R. P. Meyer and the late H. M. Meyer of the University of Wisconsin, Madison. We are also indebted to all the members of the GLIMPCE refraction group for the helpful discussion concerning this research during various GLIMPCE symposia. We would also like to thank the University of Western Ontario technical staff J. Brunet, B. Price, B. Dunn, and C. Faust and the students T. P. Cox, J. Wu, T. Shortt, R. Secco, C. Spindler, P. J. Lenson, and P. F. Lenson for their help with the instrumentation and data collection in the field and subsequent laboratory

work in getting the data organized. Reviews by W. D. Mooney, J. Luetgert, and an annonomous reviewer have contributed substantially to this manuscript. This research project was supported by the following financial resources (1) NSERC grant A-1793, (2) EMR research grant 133, 348, 131, (3) DSS contract 2322-6-0771/01st, and (4) a Canadian Commonwealth Scholarship. One of us (D.E.) is on study leave from Oil and Natural Gas Commission, Dehradun, India.

References

Baer, A. J., The Grenville Province in Helikian times: A possible model of evolution, *Philos. Trans. R. Soc. London, Ser. A, 280*, 499-515, 1976.

Baer, A. J., A Grenvillian model of Proterozoic plate tectonics, in *Precambrian Plate Tectonics*, edited by A. Kroner, pp. 351-385, Elsevier, New York, 1981.

Bednar, J. B., Applications of median filtering to deconvolution, pulse estimation, and statistical editing of seismic data, *Geophysics, 48*, 1598-1610, 1983.

Behrendt, J. C., A. G. Green, W. F. Cannon, D. R. Hutchinson, M. W. Lee, B. Milkereit, W. F. Agena, and C. Spencer, Crustal structure of the Midcontinent Rift System: Result from GLIMPCE deep seismic reflection profiles, *Geology, 16*, 81-85, 1988.

Behrendt, J. C., A. G. Green, M. W. Lee, D. R. Hutchinson, W. F. Cannon, B. Milkereit, W. F. Agena, and C. Spencer, Crustal extension in the Midcontinent Rift System: Results from GLIMPCE deep seismic reflection profiles over Lakes Superior and Michigan, in *Properties and Processes of Earth's Lower Crust, Geophys. Monogr. Ser.*, 51, edited by R. F. Mereu, S. Mueller, and D. M. Fountain, pp. 81-89, AGU, Washington, D. C., 1989.

Behrendt, J. C., D. R. Hutchinson, M. Lee, C. R. Thornber, A. Trehu, W. Cannon, and A. Green, GLIMPCE seismic reflection evidence of deep-crustal and upper-mantle intrusions and magmatic underplating associated with the Midcontinent Rift System of North America, *Tectonophysics, 173*, 595-615, 1990.

Berry, M. J., and K. Fuchs, Crustal structure of the Superior and Grenville Provinces of the Northeastern Canadian Shield, *Bull. Seismol. Soc. Am., 63*, 1393-1432, 1973.

Cannon, W. F., et al., The North American Midcontinent Rift beneath Lake Superior from GLIMPCE seismic reflection profiling, *Tectonics, 8*, 305-332, 1989.

Davidson, A., Tectonic boundaries within the Grenville province of the Canadian Shield, *J. Geodyn., 1*, 433-444, 1984.

Davidson, A., and W. C. Morgan, Preliminary notes on the geology east of Georgian Bay, Grenville Structural Province, Ontario, Current Research Part A, *Pap. Geol. Surv. of Can., 81-1A*, 291-298, 1980.

Dewey, J. F., and K. C. A. Burke, Tibetan, Variscan, and Precambrian basement reactivation: Products of continental collision, *J. Geol., 81*, 683-692, 1973.

Donaldson, J. A., and E. Irving, Grenville Front and rifting of the Canadian Shield, *Nature, 237*, 139-140, 1972.

Durrheim, R. J., and W. D. Mooney, Archean and Proterozoic crustal evolution: Evidence from crustal seismology, *Geology, 19,* 606-609, 1991.

El-Isa, Z., J. Mechie, and C. Prodehl, Shear velocity structure of Jordan from explosion seismic data, *Geophys. J. R. Astron. Soc., 90*, 265-281, 1987.

Epili, D., and R. F. Mereu, The GLIMPCE seismic experiment: Onshore refraction and wide-angle reflection observations from a fan profile over the Lake Superior Midcontinent Rift System, in *Properties and Processes of Earth's Lower Crust, Geophys. Monogr. Ser.*, 51, edited by R. F. Mereu, S. Mueller, and D. M. Fountain, pp. 93-101, AGU, Washington, D. C., 1989.

Evans, J. R., Running median filters and a general despiker, *Bull. Seismol. Soc. Am., 72*, 331-338, 1982.

Gibb, R. A, M. D. Thomas, P. L. Lapointe, and M. Mukhopadhyay, Geophysics of proposed Proterozoic sutures in Canada, *Precambrian Res., 19*, 349-384, 1983.

GLIMPCE Seismic Refraction Working Group, GLIMPCE seismic experiments: Long-offset recordings, *Eos, Trans. AGU., 70*, 841, 852-. 853, 1989.

Grant, F. S., Two gravity profiles in the Manicouagan-Wabash area of west central Quebec, *Can. J. Earth Sci., 5*, 895-906, 1968.

Green, A. G., et al., Crustal structure of the Grenville Front and adjacent terranes, *Geology, 16,* 788-792, 1988.

Green, A. G., W. F. Cannon, B. Milkereit, D. R. Hutchinson, A. Davidson, J. C. Behrendt, C. Spencer, M. W. Lee, P. Morel-a-l'Huissier, and W. F. Agena, A "GLIMPCE" of the deep crust beneath the Great Lakes, in *Properties and Processes of Earth's Lower Crust, Geophys. Monogr. Ser.*, 51, edited by R. F. Mereu, S. Mueller, and D. M Fountain, pp. 65-80, AGU, Washington D. C., 1989.

Green, A., et al., Origin of deep crustal. reflections: seismic profiling across high-grade metamorphic Terranes in Canada, *Tectonophysics, 173,* 627-638, 1990.

Hutchinson, D. R., et al., A description of GLIMPCE, 1986, Large offset seismic data from the Great Lakes, *U.S. Geol. Surv. Open File Rep., 88-431*, 91 pp., 1988.

Kanasewich, E. R., C. D. Hemmings, and T. Alpaslan, Nth-root stack nonlinear multichannel filter, *Geophysics, 38*, 327-338, 1973.

Lumbers, S. B., Geology of the Grenville Front Tectonic Zone in Ontario, in *Toronto '78, Field Trips Guide Book*, edited by A. L. Currie, and W. O. Mackasey, Geological Association of Canada, pp 347-361, St. John's Newfoundland, 1978.

McCarthy, J., and G. A. Thompson, Seismic imaging of extended crust with emphasis on the western United States, *Geol. Soc. Am. Bull., 100,* 1361-1374, 1988.

McFadden, P. L., B. J. Drummond, and S. Kravis, The Nth-root stack: Theory, applications, and examples, *Geophysics, 51*, 1879-1892, 1986.

Mereu, R. F., An interpretation of data set I using the triangular block model method, in Studies of Laterally Heterogeneous Structures using Seismic Refraction and Reflection Data, edited by A. G. Green, Geol. Surv. Can. Pap., 89-13, 53-63, 1990.

Mereu, R. F., and G. Jobidon, A seismic investigation of the crust and Moho on a line perpendicular to the Grenville Front, *Can. J. Earth Sci., 8*, 1553-1583, 1971.

Mereu, R. F., D. Wang, O. Kuhn, D. A. Forsyth, A. G. Green, P. Morel, G. G. R. Buchbinder, D. Crossley, E. Schwarz, R. duBerger, C. Brooks, and R. Clowes, The 1982 COCRUST seismic experiment across the Ottawa-Bonnechere graben and Grenville Front in Ontario and Quebec, *Geophys. J. R. Astron. Soc., 84*, 491-514, 1986.

Mereu, R. F., B. Dunn, and J. Brunet, An efficient method for sending a large seismic section from a main frame computer to a dot matrix printer located at a remote site, *Tectonophysics, 173*, 155-161, 1990.

Milkereit, B., A. G. Green, P. Morel-a-l'Huissier, M. W. Lee, and W. F. Agena, 1986 Great Lakes seismic reflection survey migrated data, *Geol. Surv. of Can., Open File Rep. 1592*, 33 pp., Ottawa, Ont., 1988.

Milkereit, B., D. Epili, A. G. Green, R. F. Mereu, and P. Morel-a-l' Huissier, Migration of wide-angle reflection data from the Grenville Front in Lake Huron, *J. Geophys. Res., 93,* 10987-10998, 1990a.

Milkereit, B., A. G. Green, M. W. Lee, W. F. Agena, and C. Spencer, Pre- and poststack migration of GLIMPCE reflection data, *Tectonophysics, 173,* 1-13, 1990b.

Moore, J. M., The Introduction: 'Grenville Problem' then and now, in The Grenville Province, edited by J. M. Moore, A. Davidson, and A. J. Baer, Geol. Assoc. Can. Spec. Pap., 31, 1-11, 1986.

Morel-a-l-Huissier, P., J. H. Karl, A. Trehu, Z. Hajnal, R. F. Mereu, R. P. Meyer, J. L. Sexton, C. P. Ervin, A. G. Green, and D. Hutchinson, 1986 Great Lakes seismic refraction survey (GLIMPCE): Line A-Refraction mode, *Open File Rep. 2283,* 33 pp., Geol. Surv. of Can. Ottawa, Ont., 1990.

Muirhead, K. J., Eliminating false alarms when detecting seismic events automatically, *Nature, 217*, 533-534, 1968.

Naess, O. E., and L. Bruland, Stacking methods other than simple summation, in *Developments in Geophysical Exploration Methods-Vol.6* , edited by A. A. Fitch, pp. 189-223, Elsevier Applied Science , New York, 1985.

Nelson, K. D., J. A. Arnow, J. H. McBride, J. H. Willemin, J. Huang, L. Zheng, J. E. Oliver, L. D. Brown, and S. Kaufman, New COCORP profiling in the southeastern united states. part I: Late Paleozoic suture and Mesozoic rift basin, *Geology, 13*, 714-718, 1985.

O'Hara, N. W., and W. J. Hinze, Regional basement geology of Lake Huron, *Geol. Soc. Am. Bull., Part 1, 91*, 348-358, 1980.

Pratt, T., R. Culotta, E. Hauser, D. Nelson, L. Brown, S. Kaufman, and J. Oliver, Major Proterozoic basement features of the eastern midcontinent of North America revealed by recent COCORP profiling, *Geology, 17,* 505-509, 1989.

Sharpton, V. L., R. A. F. Grieve, M. D. Thomas, and J. F. Halpenny, Horizontal gravity gradient: an aid to the definition of crustal structure in North America, *Geophys. Res. Lett., 14*, 808-811, 1987.

Stewart, R. R., Median filtering: Review and a new F/K analogue design, *J. Can. Soc. Explor. Geophys., 21*, 54-63, 1985.

Tanner, J. G., A geophysical interpretation of structural boundaries in the eastern Canadian Shield, Ph.D. thesis, 194 pp., Univ. of Durham, England, 1969.

Thomas M. D., and J. G. Tanner, Cryptic suture in the eastern Grenville Province, *Nature, 256*, 392-394, 1975.

Trehu et al., Imaging the Midcontinent rift beneath Lake Superior using large aperture seismic data, *Geophysical Research Letters, 18*, 625-628, 1991.

Van Schmus, W. R., K. D. Card, and K. L. Harrower, Geology and ages of buried Precambrian basement rocks, Manitoulin Island, Ontario, *Can. J. Earth, Sci., 12*, 1175-1189, 1975.

Windley, B. F., Comparative tectonics of the western Grenville and the western Himalaya, in The Grenville Province, edited by J. M. Moore, A. Davidson, and A. J. Baer, Geol. Assoc. Can. Spec. Pap., 31, 341-348, 1986.

Woussen, G., D. W. Roy, E. Dimroth, and E. H. Chown, Mid-Proterozoic extensional tectonics in the core zone of the Grenville Province, in The Grenville Province, edited by J. M. Moore, A. Davidson, and A. J. Baer, Geol. Surv. Can. Spec. Pap., 31, 297-311, 1986.

Wynne-Edwards, H. R., The Grenville Province, in Variations in Tectonic Styles in Canada, edited by R. A. Price, and R. J. W. Douglas, Geol. Assoc. Can. Spec. Pap. 11, 263-334, 1972.

Wynne-Edwards, H. R., Proterozoic ensialic orogenesis: The millipede model of ductile plate tectonics, *Am. J. Sci., 276*, 927-953, 1976.

Young, G. M., The Grenville Orogenic Belt in the North Atlantic Continents, *Earth Sci. Rev., 16*, 277-288, 1980.

D. Epili and R. F. Mereu, Department of Geophysics, University of Western Ontario, London, Ontario N6A 5B7, Canada.

(Received May 3 1990;
revised February 28, 1991;
accepted April 10, 1991.)

JOURNAL OF GEOPHYSICAL RESEARCH, VOL. 96, NO. B10, PAGES 16,349–16,367, SEPTEMBER 10, 1991

Investigation of Deep Slab Structure Using Long-Period *S* Waves

JAMES B. GAHERTY[1]

Department of Geological Sciences, University of Michigan, Ann Arbor

THORNE LAY AND JOHN E. VIDALE[2]

Institute of Tectonics, Earth Sciences Board, University of California, Santa Cruz

Travel times and amplitudes of long-period *SH*, *ScSH*, *sSH*, and *sScSH* phases from several deep focus earthquakes in the northwest Pacific are analyzed for evidence of lithospheric slab penetration into the lower mantle. Inclusion of amplitude observations in the analysis provides constraints on lateral velocity gradients present in the deep slabs which are not resolvable using travel times alone. Travel time and amplitude residual spheres are presented for two deep focus events with good azimuthal coverage, but while interesting patterns are present, quantitative analysis is precluded by the lack of accurate methods for calculating synthetic long-period seismograms for three-dimensional slab models. Therefore, we focus our analysis on a two-dimensional approximation to the downdip geometry of the Kurile and Japan slabs, which allows comparison of a much larger data set with accurate two-dimensional synthetics, as well as the use of *sS* and *sScS* travel time and amplitude patterns as empirical corrections for deep mantle structure. While the limited azimuth range required for this approximation reduces the diagnostic capability of the data, it also increases our confidence that the corrected data are most sensitive to the near-source region. The *sS* and *sScS* observations indicate that the downdip shear wave travel time pattern previously attributed to a deep slab extension is primarily caused by broad-scale lower mantle heterogeneity. Once corrected for this structure, the *S* wave observations do not support a simple, undeformed slab steepening in dip and penetrating deep into the lower mantle beneath the Kurile and Japan Islands, as proposed by Jordan (1977) and Creager and Jordan (1984, 1986). Rather, the observations support shorter and/or broader slab models than those previously hypothesized: models which can probably be reconciled with *P* wave data. Further analysis of the complete three-dimensional patterns will be required for more precise resolution of the penetration depths of these slabs, if, indeed, any deep slab heterogeneity is actually seismically detectable.

Introduction

Determination of the structure and dynamics of subducting lithosphere is one of the foremost problems in Earth science. *Isacks et al.* [1968] first hypothesized that Wadati-Benioff zone earthquakes delineate cold lithospheric "slabs" that are sinking into the mantle at subduction zones. The magnitude of the thermally induced high seismic velocity anomalies associated with these slabs, the depth to which they penetrate, and the degree of deformation that they undergo en route, can potentially be determined by seismological analysis and used to place strong constraints on the nature of the upper mantle/lower mantle boundary and the style of convection present in the Earth's mantle. While some progress has been made in determining the properties of subducted lithosphere, proposed models of slab structure remain highly controversial, and thus the dynamic interpretations remain unresolved.

Perhaps the most fundamental question regarding slab structure is whether subducting lithospheric material penetrates into the lower mantle. Until the 1980s, seismological and geochemical observations were often interpreted as indicating that the subducted material is confined to the upper 650-700 km of the Earth. Seismicity in all Wadati-Benioff zones is observed to terminate at or above this depth range [*Isacks et al.*, 1968; *Isacks and Molnar*, 1971; *Stark and Frohlich*, 1985; *Rees and Okal*, 1987; *Frohlich*, 1989], and the deepest earthquakes in these zones have source mechanisms which generally indicate that the lithospheric slabs are in downdip compression at depths greater than 400 km [*Isacks and Molnar*, 1971; *Giardini and Woodhouse*, 1984; *Vassiliou*, 1984; *Apperson and Frohlich*, 1987]. When combined with the presence of a global 5-6% discontinuity in compressional and shear wave velocities at 650-700 km depth, these observations imply that subducting lithosphere encounters a contrast in material properties that resists deeper penetration.

The hypothesis that the change in material properties across the 670-km boundary is associated with, or accompanied by, a change in chemistry with sufficient density contrast to prevent the slabs from penetrating into the lower mantle is based on less direct evidence. One line of evidence is experimental work which indicates that the seismologically determined increase in density across the boundary is greater than that predicted for the expected phase changes to perovskite structure which take place near this depth for all of the common mantle minerals [e.g., *Jeanloz and Knittle*, 1989]. The notion of such a compositionally layered mantle is often invoked to provide multiple isolated reservoirs to account for chemical heterogeneity in mid-ocean ridge and ocean island basalts. Many researchers view the mineral physics experiments or seismological data as inconclusive, however, and favor interpretation of the 670-km discontinuity as entirely due to a phase change, perhaps associated with a viscosity increase that may cause mechanical resistance but will not prevent whole mantle convection (see *Silver et al.* [1988] for a review).

In the past few years, seismologists have been developing methods to image the velocity structure of the lower mantle

[1]Now at Department of Earth, Atmospheric, and Planetary Sciences, Massachusetts Institute of Technology, Cambridge.

[2]Now at U.S. Geological Survey, Menlo Park, California.

Paper number 91JB01483.
0148-0227/91/91JB-01483$05.00

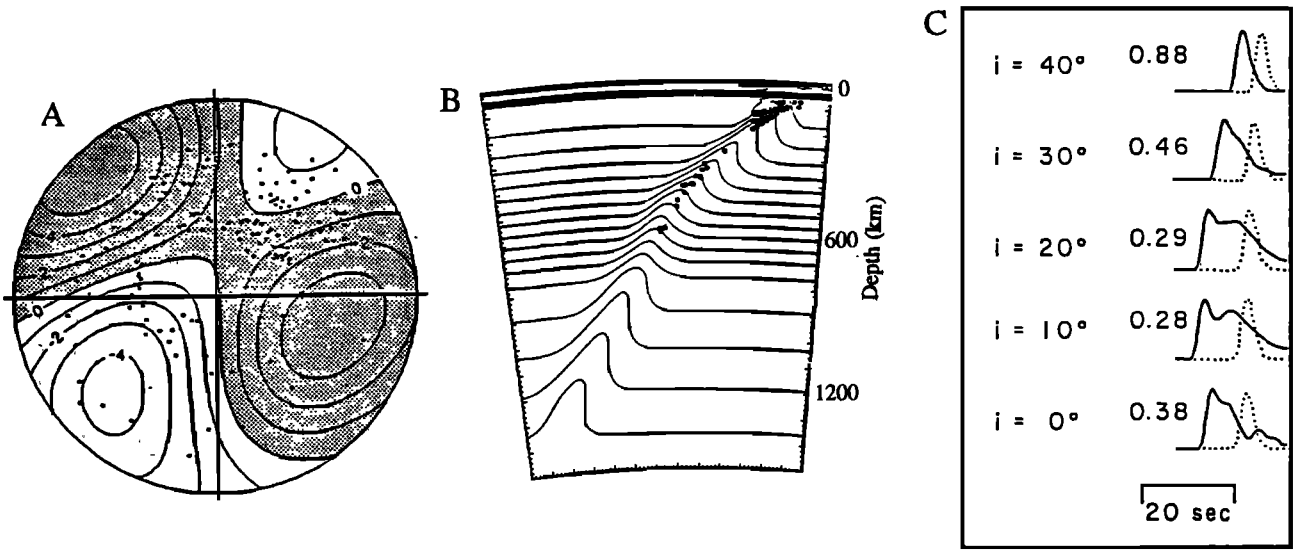

Fig. 1. (*a*) The smoothed *S* wave travel time residual sphere for event 8 analyzed by *Jordan* [1977]. Shaded areas are relatively slow arrivals, open areas are relatively fast arrivals, with contours in 1-s intervals. The strong NE-SW azimuthal trend, as well as travel time gradient in the NW quadrant, led to interpretation supporting deep slab structure. Figure is from *Creager and Jordan* [1984]. (*b*) Example slab model derived from *P* wave residual sphere analysis by *Fischer et al.* [1988], showing a high-velocity slab structure extending into the lower mantle with a steepening of dip below approximately 550 km. Velocity is contoured at 0.25 km/s intervals. (*c*) Synthetic *S* wave displacement pulses calculated for a model similar to to that shown in Figure 1*b* for a range of takeoff angles (*i*). Angle *i*=20° corresponds to the along slab-dip direction in the model. Numbers to the left of the pulse indicate the peak amplitude relative to PREM displacement (dotted pulses), and the extent of offset of the waveform relative to the PREM pulse corresponds to the travel time anomaly [*Vidale*, 1987].

beneath the deepest earthquakes. In general, the presence of a tabular high-velocity zone extending into the lower mantle can be used to argue (albeit not uniquely) for deep penetration of the slab, while lack of any such structure can be used to argue (also not uniquely) for deflection and containment of the slab in the upper mantle. Perhaps the strongest evidence favoring slab penetration below 700 km depth has been provided by several analyses of residual spheres for deep earthquakes [*Jordan*, 1977; *Creager and Jordan*, 1984, 1986; *Fischer et al.*, 1988, 1991]. The residual sphere [*Davies and McKenzie*, 1969] is a projection of travel time anomalies for a single event, corrected to the fullest degree possible for receiver and deep mantle anomalies, on a source focal sphere (Figure 1*a*). By comparing smoothed travel time residual patterns observed for individual deep focus earthquakes with synthetic residuals calculated for slab models with a variety of maximum penetration depths, these studies conclude that lithospheric material must penetrate with little distortion (other than steepening of dip and perhaps some advective thickening) to depths of at least 1000 km (Figure 1*b*) in many of the subduction zones in the western Pacific, including the Kurile and Japan slabs. However, several researchers [*Anderson*, 1987*a*; *Grand and Ding*, 1989; *Zhou and Anderson*, 1989; *Zhou et al.*, 1990] have recently argued that the residual sphere studies favoring deep slab penetration have failed to adequately account for the strength of near-source and/or deep mantle velocity anomalies. The latter studies assert that travel time residuals appropriately corrected for these anomalies cannot resolve or do not require lithospheric penetration into the lower mantle. This debate hinges on our knowledge of lower and upper mantle structure, which is very imprecise. Only when there is a much better understanding of the heterogeneous structure of the mantle as a whole will the complex residual sphere patterns be unambiguously explained.

In an alternate approach to this problem, several workers have directly inverted *P* and *S* wave travel time residuals from large sets of earthquakes for the velocity structure around and beneath Wadati-Benioff zone earthquakes. Tomographic images of the velocity structure of subduction zones in the northwest Pacific have been generated, with ambiguous results [*Kamiya et al.*, 1988, 1989; *Zhou and Clayton*, 1990]. While all of the studies resolve some features with intermittent high-velocity slab anomalies in the upper mantle, details of the structure in the uppermost lower mantle are poorly resolved. *Zhou and Clayton* [1990] conclude from these images that lithospheric slabs flatten to a subhorizontal orientation (beneath Japan) or spread outward at or near the 670-km discontinuity (beneath the Kuriles). *Kamiya et al.* [1988, 1989] conclude that the Japan slab steepens and penetrates into the lower mantle with a geometry similar to that preferred by *Creager and Jordan* [1986], while the northern Izu slab appears to bend horizontally westward near the upper mantle/lower mantle boundary. Attempts at resolution analysis [e.g. *Zhou*, 1988; *Zhou and Clayton*, 1990; *Spakman et al.*, 1989] are approximate and do not give great confidence in the noisy tomographic images. All of these studies utilize International Seismological Centre (ISC) travel time data, which have been shown to potentially be subject to systematic bias [e.g., *Grand*, 1990]; the conflicting conclusions drawn from similar data sets indicate that higher quality data will be required for resolution of this issue by tomographic methods.

Additional information on slab structure is contained within the waveforms and amplitudes of seismic body waves from deep earthquakes (Figure 1*c*). *Vidale* [1987] demonstrates that slablike velocity anomalies can defocus and severely distort synthetic waveforms with trajectories down the dip of the slab, and *Cormier and Kim* [1990] show that similar effects can be expected for ray paths within or at low angles to the slab, particularly along strike or obliquely downdip. *Sueisugu* [1989] analyzes short-period *P* wave travel time and amplitude observations from deep Kurile events and concludes that they are most consistent with a high-velocity slab penetrating below the 670-km discontinuity. In contrast, *Weber* [1990] compares amplitude (m_b) observations from the ISC catalogue with synthetic amplitude predictions and

concludes that the same Kurile slab does not penetrate beyond the 670-km discontinuity. *Silver and Chan* [1986] present complex waveforms recorded along the strike of the Kurile slab that they interpret to be due to multipathing along a lower mantle extension of the slab, although the multipathing interpretation has been questioned [*Cormier*, 1989; *Cormier and Kim*, 1990]. *Beck and Lay* [1986] analyze a similar, but more extensive, suite of data and conclude that the complexity observed by *Silver and Chan* [1986] is part of a broader pattern that may involve a deep slab extension but requires deep mantle heterogeneity as well.

In this paper, we attempt to constrain the deep structure of subducted slabs by jointly analyzing the travel time and amplitude behavior of a variety of horizontally polarized shear wave (*SH*) phases emanating from deep-focus earthquakes. Our primary sensitivity to deep slab structure is in the systematic behavior of *S* phases with respect to the slab. As mentioned above, *Grand and Ding* [1989], *Zhou and Anderson* [1989], and *Zhou et al.* [1990] contend that a substantial portion of the travel time variation observed by *Creager and Jordan* [1984, 1986] and *Fischer et al.* [1988] is due to long-wavelength lower mantle heterogeneity rather than slab extension into the upper part of the lower mantle. While the residual spheres analyzed by Creager and Jordan and Fischer et al. are corrected for lower mantle structure using model L02.56 of *Dziewonski* [1984] and smoothed to emphasize near-source variations, there is a strong concern that the heavily smoothed L02.56 model underestimates the strength of actual lower mantle anomalies, with the uncorrected lower mantle anomalies fortuitously projecting onto the residual sphere with a slablike pattern [*Zhou et al.*, 1990].

Given that existing lower mantle shear velocity heterogeneity models are of very low resolution, we use the upgoing ray paths, *sS* and *sScS*, to empirically correct for the deep mantle contribution to downgoing *S* and *ScS* paths. With these corrections, the resulting downgoing travel time residuals provide constraints on the velocity anomaly present immediately beneath the deep earthquakes, while the amplitude observations provide constraints on the deep velocity gradients. In this paper we primarily seek to understand the joint travel time and amplitude behavior of the seismic wave field in the downdip direction of the slab structure, making use of synthetic waveforms generated for this approximately two-dimensional geometry using the hybrid finite difference-Kirchhoff algorithm of *Stead and Helmberger* [1988]. We do not attempt to determine a single preferred structure for the Kurile and Japan slabs but instead evaluate the suite of slab models proposed by *Creager and Jordan* [1984, 1986] and *Fischer et al.* [1988] in terms of agreement with the *S* wave observations.

DATA ANALYSIS

We analyze over 760 seismograms from 25 intermediate and deep focus earthquakes from several northwest Pacific subduction zones (Figure 2 and Table 1); the seven best events are used for the evaluation of deep slab models, while all 25 are used to generate station statics. The data consist of long-period shear waves recorded globally on the World-Wide Standard Seismograph Network (WWSSN) and Canadian Seismograph Network (CSN), which we hand-digitized and rotated to obtain tangential and radial components. The events occurred between 1964 and 1984 and were selected on the basis of the following criteria: moderate size (m_b 5.5-6.1) with simple *SH* waveforms (indicative of minimal source complexity); favorable *SH* radiation to Europe and/or North America; and source locations resulting in

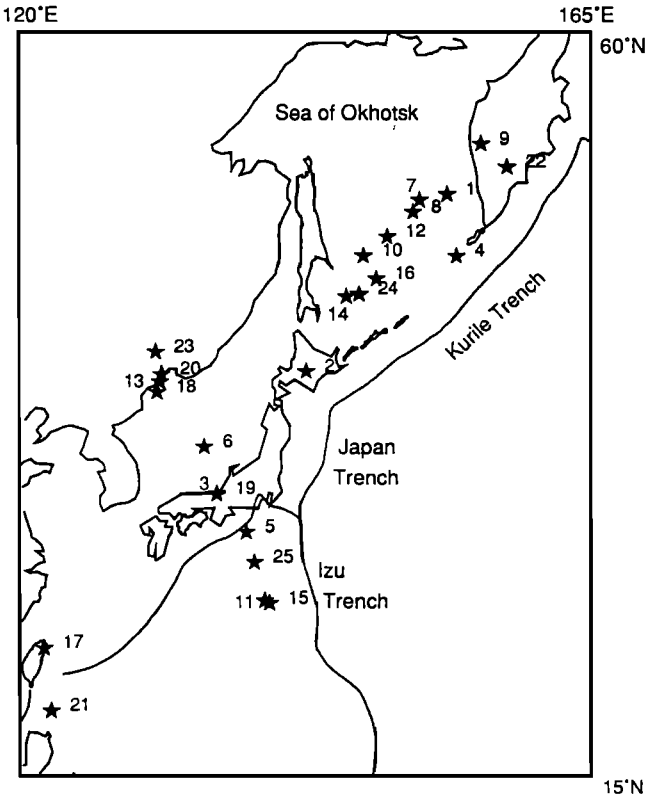

Fig. 2. Epicenters of events listed in Table 1 (stars) plotted on a Mercator projection of the northwest Pacific subduction zones. The majority of events are used to determine station correction factors.

dense station coverage at epicentral distances from 35° to 90° (thereby avoiding complexity in the waveforms due to upper mantle triplications or core diffraction).

Wherever possible, the long-period *SH* waveforms are analyzed over a time window that includes the phases *S*, *ScS*, *sS*, and *sScS*. We choose this suite of phases for a number of reasons. While the long-period waveforms are less sensitive than short-period energy to the narrow slab structures in which we are interested [*Weber*, 1990], they are also less vulnerable to rapid variations in attenuation and receiver structure known to complicate short-period amplitude observations [e.g., *Butler and Ruff*, 1980]. *SH* signals have relatively simple propagation effects away from the heterogeneous source region, including strong surface and core reflections and minimal receiver interactions, which facilitates the measurement of arrival times and amplitudes. Inclusion of the surface and core reflections ensures that the near-source region is sampled at a wide range of takeoff angles, which is critical for constraining the structure beneath the source.

For each arrival with sufficient signal-to-noise ratio, we measure a baseline-to-peak amplitude and a first-break arrival time, the latter having a conservative estimate of ±0.5 s relative accuracy. Travel time residuals are calculated using the predicted times for the ISC event location and origin time and the equivalent isotropic PREM 1-s shear velocity structure [*Dziewonski and Anderson*, 1981]; negative residuals correspond to early arrivals. Azimuth-independent *S* wave station corrections of *Toy* [1989] and *Wickens and Buchbinder* [1980] were applied. As discussed below, events are not relocated, as we ultimately restrict our attention to only a limited portion of the residual sphere. Amplitudes are equalized to an isotropic source by correcting for geometric spreading (calculated for the PREM model), the PREM attenuation structure, and double-couple focal mechanisms

TABLE 1. Event Information

Event	Date	ISC Location				Focal Mechanism			
		Origin Time, UT	latitude,°N	longitude,°E	depth,km	φ	δ	λ	References*
1	March 18, 1964	0437:25.7	52.56	153.67	424	48	84	-76	L83
2	July 4, 1967	2342:12.9	43.10	142.58	157	94	79	89	IM71
3	Aug. 13, 1967	2006:52.3	35.43	135.49	367	238	68	-84	ts
4	Dec. 1, 1967	1357:03.4	49.45	154.40	144	50	87	109	L83
5	Feb. 28, 1968	1208:01.8	32.95	137.85	348	180	86	97	M71
6	March 31, 1969	1925:27.0	38.49	134.52	397	38	75	230	ts
7	Sept. 5, 1970	0752:27.2	52.28	151.49	560	3	72	-90	ts
8	Jan. 29, 1971	2158:03.2	51.69	150.97	515	34	72	-110	ts
9	May 27, 1972	0406:49.6	54.97	156.33	397	24	85	-94	ts
10	Aug. 21, 1972	0623:48.6	49.47	147.08	573	15	17	47	ts
11	Jan. 31, 1973	2055:54.2	28.22	139.30	508	317	72	-74	ts
12	July 28, 1973	2006:35.4	50.45	148.92	585	51	76	-107	L83
13	Sept. 10, 1973	0743:32.3	42.48	131.05	552	24	17	107	ts
14	July 10, 1976	1137:14.0	47.31	145.75	402	41	89	-87	ts
15	Dec. 12, 1976	0108:51.1	28.04	139.67	503	328	72	-74	ts
16	June 21, 1978	1110:38.7	48.27	148.66	380	288	32	32	ts
17	Sept. 2, 1978	0157:34.2	24.81	121.87	115	34	28	138	ts
18	Aug. 16, 1979	2131:24.9	41.85	130.86	566	56	24	133	ts
19	March 31, 1980	0732:32.4	35.49	135.52	362	214	44	-149	ts
20	Nov. 27, 1981	1721:44.3	42.93	131.19	525	66	25	175	CMT
21	July 3, 1983	0249:28.2	20.19	122.41	221	332	37	-83	CMT
22	July 24, 1983	2307:31.8	53.91	158.36	190	319	1	4	ts
23	Oct. 8, 1983	0745:26.3	44.21	130.74	551	349	29	88	ts
24	April 23, 1984	2140:34.2	47.44	146.73	399	18	40	110	ts
25	April 24, 1984	0411:28.5	30.89	138.48	398	86	36	-150	ts

Focal mechanism is defined by the strike, dip, and rake of one of the nodal planes, in degrees, with the conventions described by *Aki and Richards* [1980].

*Focal mechanism references: L83, *Lay* [1983]; IM71, *Isacks and Molnar* [1971]; M71, *Mikumo* [1971]; CMT, Harvard CMT catalogue; ts, this study.

determined using the methodology described below. Amplitude station corrections are also calculated (as described below) and applied to the observations. The corrected travel time residuals and the logarithm (base 10) of the corrected amplitudes comprise the data set for the analysis.

Focal Mechanism Determination

To optimize the radiation pattern corrections, we employ a damped iterative least squares inversion technique to find the double-couple focal mechanism most consistent with the long-period *S* wave energy. *SH* and *ScSH* amplitude observations (corrected for attenuation and geometric spreading) are combined with *SH/SV* amplitude ratios and iteratively inverted for perturbations to the strike, dip, and rake of published *P* wave first motion or other starting mechanisms. Inversions resulting in a deviation from the initial mechanism of greater than 10° in any of the fault parameters are considered unstable, and the initial mechanism was retained. This only occurs for a few relatively sparsely recorded events. For a few well-sampled events, one of the three fault parameters is tightly constrained by polarity reversals, so that parameter is held fixed while the remaining parameters are determined. Our final double-couple mechanisms are included in Table 1.

As an example, Figure 3*a* depicts the lower hemisphere projection of the final solution for event 7, which had an initial mechanism with strike = 9°, dip = 74°, and rake = -85° [*Strelitz*, 1975], and a final mechanism of strike = 3°, dip = 72°, and rake = -90°. The corresponding reduction in variance of the amplitudes is 17%. For all 25 events, all of the observed *S*, *ScS*, *sS*, and *sScS* polarities are in agreement with the final mechanisms, justifying the use of double couple rather than more general moment tensor representations of these deep sources. We avoid using observations near radiation nodes since these have large correction factors.

Station Corrections

Prior to examining travel time and amplitude observations for near-source structure, effects of near-station crustal and upper mantle structure must be removed. Although station statics for S wave travel times have been calculated and interpreted by many researchers [e.g., *Sengupta*, 1975; *Wickens and Buchbinder*, 1980; *Romanowicz and Cara*, 1980; *Toy*, 1989], *S* wave amplitude statics have not been extensively studied for global data sets. Therefore, we apply a least squares inversion procedure to empirically determine the station statics for our amplitude data. In this procedure, for each of the 25 events, the *S*, *ScS*, *sS*, and *sScS* subsets (each corrected for *Q*, geometric spreading, and radiation pattern) are each considered as a separate "pseudoevent"; that is, the different phases for the 25 events give a total of 87 "pseudoevents" (some events lack *sS* and/or *sScS* observations). Event amplification factors are then calculated and removed from each pseudoevent using a least squares inversion that minimizes the scatter in the relative amplitude observations at each station. The mean value at each station is used as a station factor, with the overall set of station anomalies being normalized.

The results of this procedure are plotted in a lower hemisphere projection in Figure 3b. All 105 station anomalies are plotted at the direct *S* ray path position for the event 7 source location. In this projection, North American stations are in the northeast quadrant, European and Middle Eastern stations are to the northwest and west, and Asian, Australian, and Pacific island stations are to the south. Note the strong azimuthal pattern shifting from small arrivals at approximately N60°E to larger arrivals at N45°E. This pattern was previously observed by *Lay*

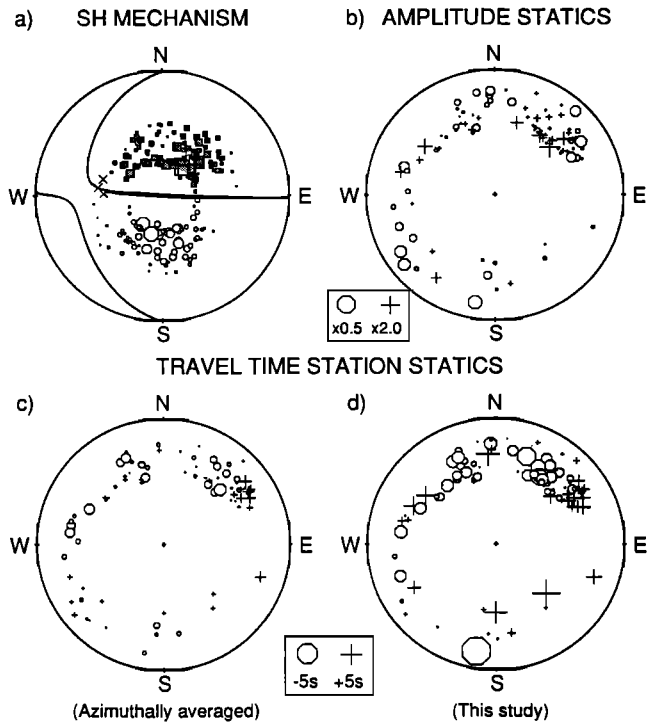

Fig. 3. Lower hemisphere projections of amplitude and travel time data using the hypocenter of event 7: (*a*) *SH* (*S*, *ScS*, *sS*, and *sScS*) amplitude observations from event 7, corrected only for geometric spreading and PREM attenuation structure, plotted with the final *SH* mechanism for the event. *sS* and *sScS* observations are projected to the lower hemisphere by correcting azimuth and takeoff angle by 180°. The azimuthal amplitude variation due to focal mechanism is clear. Crosses indicate nodal observations, and outer circumference corresponds to takeoff angle of 90°. (*b*) Empirical amplitude statics for all 105 stations, calculated as described in the text, and plotted at the *S* takeoff angle. Crosses are larger than average, and circles are smaller than average, with the size of the symbol indicating relative scale. Outer circumference corresponds to 60° takeoff angle. (*c*) Azimuthally averaged travel time statics for all stations (plotted at the *S* takeoff angle) from *Wickens and Buchbinder* [1980] and *Toy* [1989]. Crosses are relatively slow stations, and circles are relatively fast, with size variation indicating the relative scale. (*d*) Travel time statics for all stations determined empirically as described in text. Symbols are the same as those used in Figure 3*c*, and the circumferences of both Figures 3*c* and 3*d* correspond to takeoff angle of 60°.

and Helmberger [1983*a*], and is most simply interpreted as a change in the attenuation structure of the upper mantle, from low Q beneath the western United States to high Q beneath the eastern United States and Canada. Across Europe, the station statics vary rapidly, probably influenced by both attenuation and focusing variations, while the Australia and Pacific stations appear to have lower amplitudes on average.

An obvious hazard in empirically determining the station statics from this data set is the possibility of mapping systematic near-source structure to the receivers due to the similarity of the source locations within a group of westward dipping subducting slabs. We have attempted to minimize this by including sources from a variety of subduction zones with varying strike and dip (see Figure 2). In addition, by including observations spanning the full range of takeoff angles covered by *S*, *ScS*, *sS*, and *sScS*, we have ensured that a large subset of the data samples the near-source region at large angles to the strike and dip of the subducting slabs, and the greatest consistency in the amplitude anomalies should be due to the portions of the paths common to all phases, i.e., the near-station crust and upper mantle.

For the travel time station corrections, we have applied the azimuthally averaged statics of *Toy* [1989] and *Wickens and Buchbinder* [1980] (Figure 3*c*). These statics provide extensive coverage of the WWSSN and CSN networks, and the worldwide distribution of sources used in their determination ensures that the resultant statics are truly due to localized receiver mantle and crustal origins. However, it is known that receivers can exhibit strong azimuthal patterns [e.g., *Dziewonski and Anderson*, 1983]. To establish the influence of any azimuthal stations terms affecting our data, we also calculated travel time station statics from our data set in a manner identical to the procedure described above for the amplitude anomalies (Figure 3*d*). The empirically calculated residuals appear to be stronger (i.e., larger absolute value) than Toy's and Wickens and Buchbinder's, perhaps due to the lack of averaging over a variety of source locations. Overall, however, the correlation is reasonably high, with a linear correlation coefficient of 0.61, and the signal from the upper mantle structural variation across North America is again obvious, with the region beneath the western United States being slower than that beneath the eastern United States and Canada. The largest discrepancy between the azimuthally averaged residuals and ours appears to be at stations in the eastern United States and Canada, where our residuals are faster than the averaged values. This is consistent with the fact that South American sources give late arrivals for these stations [*Lay*, 1983], resulting in slower azimuthally averaged values relative to statics calculated for sources in the northwest Pacific. It is enticing to interpret our faster station residuals as due to long paths in a fast, deep root beneath cratonic North America [e.g., *Grand*, 1987] and therefore appropriate for correcting northwest Pacific-to-North America paths for receiver mantle structure. These paths roughly coincide with the strikes of the slabs being investigated, however, and we are concerned that all four phases (*S*, *ScS*, *sS*, and *sScS*) used to determine the station residuals may contain substantial near-source signal due to this geometry. Correction for these residuals could remove evidence of the near-source structure in which we are investigating, and we therefore take a conservative approach and use the published azimuthally averaged statics for our corrections. *Schwartz et al.* [1991] explore the observations in North America in greater detail. Note that our station residuals are very similar to Toy's at downdip azimuths where most of our analysis takes place, so the choice of station corrections does not critically influence our results.

RESIDUAL SPHERE ANALYSIS

The corrected travel time and amplitude observations can now be analyzed for patterns attributable to near-source and deep mantle structure. The residual sphere methodology allows for examination of both azimuthal and ray parameter patterns in the travel time and amplitude residuals. Note, however, that we have not attempted to remove bias in the travel time residuals due to potential source mislocation. While *Creager and Jordan* [1984, 1986] discuss the necessity of relocating the events used to analyze the *P* wave residual spheres, *Jordan* [1977] points out that any significant bias due to epicentral mislocation should be apparent on the residual sphere as a systematic variation in residual with the cosine of the azimuth (i.e., with a degree 1 pattern). In all well-sampled travel time residual spheres presented here, no such variation is observed. Errors in source depth primarily cause ray parameter-dependent trends; for example, if steeper rays are systematically relatively fast (as they consistently are in the data presented below), the source depth

may be underestimated. A vertically dipping fast slab may produce a similar ray parameter trend (accompanied by a degree 2 pattern), and thus this trend taken alone is fundamentally ambiguous. In every case that we observe a strong ray parameter trend in the downgoing phases, however, we observe a similar trend in the upgoing surface-reflected data that is opposite to that expected due to underestimation of the source depth. Thus, any attempt to eliminate the ray parameter trend in the downgoing data by shifting the source to a deeper depth will only enhance the upgoing trend, and vice versa. The balanced behavior between the upgoing and downgoing trends argues strongly against a significant depth mislocation in either direction. In addition, depth errors of over 80 km are required to account for the 2-3 s ray parameter trends observed in both the upgoing and downgoing data, which is much larger than the depth shifts found by relocating *P* waves. We conclude that an error in source depth is not responsible for the ray parameter trend, and any mislocation error that is present leads to travel time errors that are very small relative to our observed ray parameter trends, typically well under 0.5 s. While, in general, quantitatively relocating well-sampled events to remove systematic bias is not a difficult problem, such a procedure is unstable for uneven or sparse coverage of the focal sphere. Since most of our events have restricted or unbalanced azimuthal station distribution, we forego the relocation procedure and proceed with the requirement that azimuthal and ray parameter variations be interpreted cautiously.

Figure 4 presents travel time and log(amplitude) residual spheres for two deep Kurile events. The residuals are plotted on a lower hemisphere projection, with the center corresponding to a vertical takeoff angle, and the circumference corresponding to a takeoff angle of 60°. The travel time residual sphere for the January 29, 1971, event (event 8) is directly comparable to the residual sphere that *Jordan* [1977] determined for the same event using short-period *S* waves. *Creager and Jordan* [1984] show that source relocation has a very minor effect on the *S* wave residual sphere for this event, due to the lack of a degree 1 pattern (see Figure 1). Both travel time projections can also be compared with *P* wave residual spheres for these events determined by *Creager and Jordan* [1984, 1986]. The travel time patterns are dominated by the early arrival times at azimuths northeast and southwest from the source, which is along the slab strike direction (marked by arrows in Figure 4). *Jordan* [1977] shows that a high-velocity slab extending vertically beneath the event(s) can explain much of the pattern. In addition, the northwest quadrants of the travel time residual spheres are dominated by a strong trend with takeoff angle, with the *S* observations (outer band of observations on the figures) being 2-3 s slower than the *ScS* observations to the same stations. This is also consistent with the observations of *Jordan* [1977] for event 8, and can be explained by the same vertically extending high-velocity slab. The agreement between our travel time residuals and those determined from short-period data is encouraging, for it indicates that the decreased time resolution for long-period waveforms is offset by the stability of the waveforms, allowing for compensating consistency in the travel time picks.

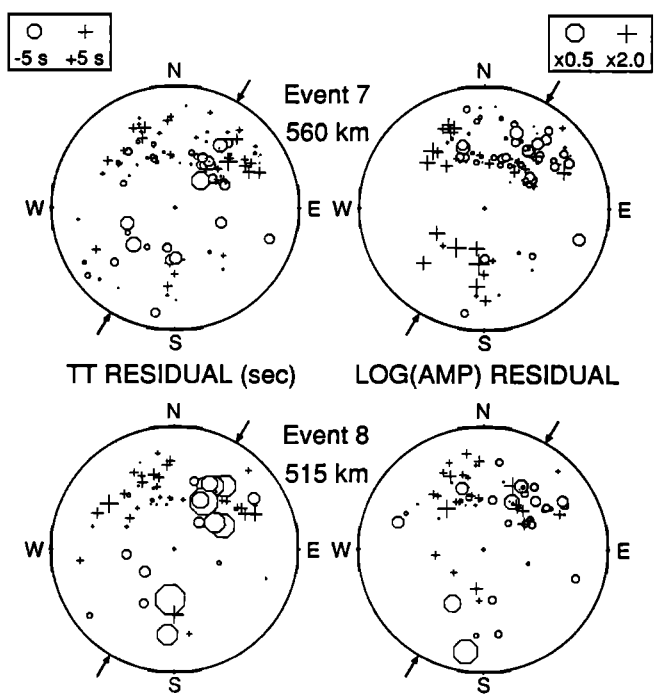

Fig. 4. Travel time and logarithmic amplitude residual spheres for events 7 (top) and 8 (bottom). Travel time residual spheres are on the left, and amplitudes are on the right. Data include *S* and *ScS* observations, with *S* plotting closest to the circumference and *ScS* plotting closer to the center. Symbols are as in Figure 3, with the symbol sizes linearly scaled relative to the key. Note that both the travel time and log (amplitude) residuals are demeaned prior to plotting and that the number of travel time observations is generally greater than the number of amplitude residuals, due to the bounds on the radiation pattern correction described in the text. Arrows on the perimeter of each sphere delineate the approximate strike of the Kurile slab.

The right side of Figure 4 shows the log(amplitude) residual spheres for events 7 and 8. Note that several stations for which travel times are measured are not included in the amplitude sphere. This is because proximity to the nodal planes make their corrected amplitudes unreliable. These are the first long-period *S* wave amplitude residual spheres of which we are aware, and potentially these can be used to place new constraints on slab structure. A major obstacle to quantitatively analyzing amplitude variations for complex three-dimensional structures is the difficulty of calculating reliable synthetic seismograms for such structures. Accurate numerical procedures (e.g., the finite difference method used here) can be used for two-dimensional structures, but three-dimensional techniques are still under development [*Cormier*, 1989; *Witte*, 1989]. *Cormier and Kim* [1990] have used simple geometric optics to compute travel time and amplitude patterns for several three-dimensional slab models, which can be used as a qualitative guide for slab effects. The geometric amplitude calculations are dominated by slowly varying patterns with minimum amplitudes at azimuths obliquely down the dip of the slab structure. This feature correlates well with early arrival times in the synthetic travel time patterns [*Cormier and Kim*, 1990] and is therefore consistent with defocusing by the high-velocity slab structure. At shorter spatial scales, the amplitude patterns show rapid variations, with regions of focusing near the strike of the slab, caused by caustics and multipathing along the gradients at the top and bottom of the structure. *Silver and Chan* [1986] suggested that such effects cause the waveform anomalies that they observe along the strike of the Kurile slab. These small-scale patterns are not well correlated with the travel time anomalies [*Cormier and Kim*, 1990]. The complexity of the amplitude patterns makes it extremely difficult to assess the amplitude residual spheres for coherent structure. In addition, *Cormier and Kim* [1990] show that while slowly varying patterns are robust, the rapid amplitude fluctuations near caustics are highly sensitive not only to the velocity gradients in the slab but also to the precise lateral location of the source within the slab.

This increase in the number of model parameters makes it difficult to model observations from an imperfectly known location.

We can make the qualitative assessment that the observed amplitude patterns (Figure 4) are not dominated by the degree 2 azimuthal trend that is present in the travel times and that there is greater variability between events. There does appear to be a region of consistently low-amplitude arrivals in the north, weakly correlated with the early arrivals in this direction. This may be consistent with defocusing, but the pattern is not mirrored in the south as it is in the travel times. These two events are located at the northeastern end of the Kurile slab, so any slab signature to the south should be as strong or stronger than the pattern to the north, as has been suggested on the basis of travel times [*Jordan*, 1977; *Creager and Jordan*, 1984]. There is a suggestion of a ray parameter trend apparent in the northwest quadrant of the spheres that we will analyze in depth in the next section. In general, however, the scatter in the data makes it difficult to assess the long-wavelength characteristics of the amplitude spheres.

Complete discussion of the full residual spheres for many other events will be presented in a future paper. We will concentrate here on a limited portion of the residual spheres that presently can be quantitatively modeled with reliable techniques.

DOWNDIP ANALYSIS

Jordan [1977] observed that the *S* wave travel time residual sphere for event 8 has a strong ray parameter (takeoff angle) trend in the northwest quadrant (see Figure 1, this paper, and Figures 6 and 8 of *Jordan* [1977]), with the *ScS* arrivals being fast relative to the *S* arrivals at azimuths in the downdip direction. This is manifested as a *ScS-S* differential travel time anomaly at the stations to the northwest, so it is clearly not due to receiver structure. This trend, which is apparent in our residual spheres as well (Figure 4), was interpreted by Jordan to be due to the *ScS* ray paths preferentially sampling a near-vertical slab extension in the lower mantle beneath the event. A large portion of the European and Middle Eastern WWSSN stations providing these observations falls within 45° of the downdip direction of the Kurile and Japan slabs, an azimuth range in which most proposed deep slab models (e.g., Figure 1*b*) predict simple, observable trends in both amplitude and travel time. The three-dimensional calculations of *Cormier* [1989] and *Cormier and Kim* [1990] predict smooth amplitude and travel time variation with distance (ray parameter) throughout these azimuths, and the two-dimensional calculations of *Vidale* [1987] (Figure 1c) and *Weber* [1990], which are appropriate for this downdip geometry, predict very similar patterns. This is, of course, partly the result of the very smooth slab structures that have been investigated, and more complex structures may produce less regular amplitude patterns. Unlike the along-strike azimuthal patterns, the amplitudes in this portion of the residual sphere appear to be fairly stable for variations in the lateral source location within the subducting slab (for long-period energy), allowing us to investigate structural aspects of the slab, such as strength of the anomaly, the velocity gradients present, and the depth of slab penetration.

Constraining our present study to the near slab-dip azimuth range simplifies our data processing, as bias in the travel time residuals due to epicentral location error should be relatively constant over the data subset and thus may be ignored. Large depth errors are required to cause significant trends with takeoff angle. For example, a 20-km depth error gives rise to only an average *ScS-S* anomaly of less than 0.5 s at these distances, and as discussed above, we believe that the potential errors in the depths

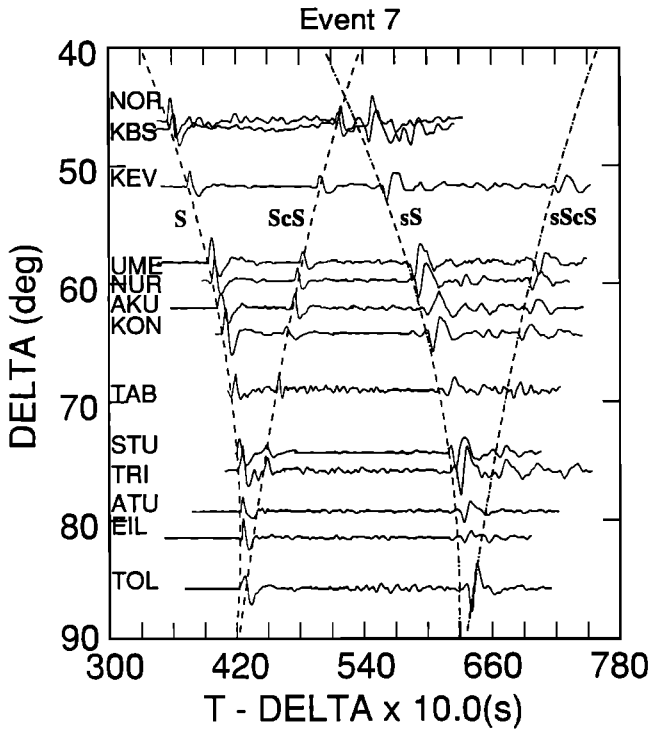

Fig. 5. Example profile of seismograms from European WWSSN stations for event 7. Travel time curves calculated for the PREM 1-s structure are displayed for *S*, *ScS*, *sS*, and *sScS*, and the seismograms are arranged so that each *S* arrival lines up with the *S* travel time curve.

of our sources is typically much less than 20 km. Source relocation of the magnitude reported by *Creager and Jordan* [1986] have almost no effect on the differential travel times *ScS-S* and *sScS-sS* in the range of interest. This is because relocation can remove only slowly varying trends from the residual sphere. Vertical variations do result in large baseline shifts in travel times between downgoing (*S*, *ScS*) paths and upgoing (*sS*, *sScS*) paths, but errors in upper mantle velocity structure may as well; therefore, we do not attempt to analyze absolute differences in travel time between these two groups.

A representative event profile of *SH* seismograms recorded in the near slab dip direction (European and Middle Eastern WWSSN stations) is presented in Figure 5. The traces are aligned such that the *S* first break coincides with the arrival time predicted for Preliminary Reference Earth Model (PREM). Even at this scale, the relatively early arrival of *ScS* phases is striking. The relatively accurate alignment of *sS* indicates that this is not due to a substantial error in source depth; improving the timing of the *sS* branch requires a slightly deeper source but would reduce the *ScS-S* anomalies by less than 0.2 s. Note that the *sS* and *sScS* observations for this event are very clear, allowing travel time and amplitude measurements to be made with good precision.

The advantage of including both upgoing and downgoing phases for this analysis is shown schematically in Figure 6. Ray paths for the *S*, *ScS*, *sS*, and *sScS* phases from a 515 km deep source are traced through the PREM structure to distances of 55° to 85°. The approximate geometry of the Kurile slab proposed by *Creager and Jordan* [1984] (Figure 1b) is superimposed. Figure 6 clarifies *Jordan's* [1977] interpretation of the strong travel time gradient from *S* to *ScS* observed for the Kurile events in Figure 4. The *ScS* rays have longer paths than the *S* rays within the proposed slab extension and therefore would be faster, as observed. This does require that the slab steepen in dip.

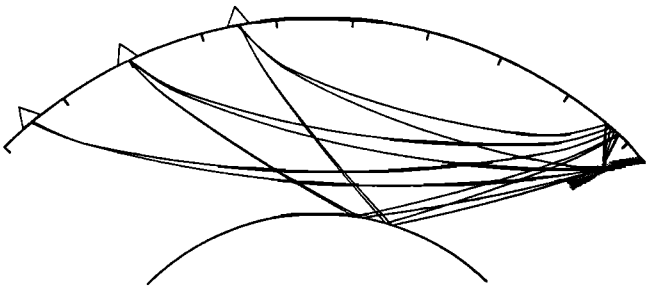

Fig. 6. Ray path diagram depicting preferential sampling of various mantle regions by the phases employed in this study. Rays are traced from a 515-km-deep source to receivers (triangles) at epicentral distances of 55°, 70°, and 85°. Beyond 79°, we cannot measure core reflected phases on the long-period records. Hatched region schematically outlines a slab structure with the approximate geometry proposed for the Kurile slab by *Creager and Jordan* [1984].

Alternatively, note that the *S* wave ray paths in this distance range have turning points several hundred kilometers above the core-mantle boundary, allowing for the possibility that the ray parameter dependence of the travel times is produced by large-scale heterogeneity in the lower mantle sampled by *ScS* but not *S*, or vice versa.

Figure 6 also demonstrates that the *sS* and *sScS* rays leave the slab at an upward angle, exiting the slab quickly and never sampling the proposed deep slab extension, so the travel times and amplitudes of these phases should be free of slab induced anomalies. In addition, note that once *sScS* and *ScS* are far from the near-source region, they have very similar paths in the deep mantle and near the receiver. The same is true for the *sS* and *S* paths. These simple relationships lead to the hypothesis that any relative patterns in the *sS* and *sScS* travel times and amplitudes may be used to correct the *S* and *ScS* patterns for deep and receiver mantle structure, thereby isolating any near-source signature in the *S* and *ScS* patterns. This applies only for the azimuth range near the down slab-dip direction, since the upgoing phases may encounter the slab at other azimuths. An obvious potential problem is the possibility of misinterpreting heterogeneous or anisotropic [*Ribe*, 1989] structure in the mantle wedge above the slab sampled by the *sS* and *sScS* phases as deep mantle structure and erroneously correcting for it. Because of this possibility, we analyze the data both with and without applying empirical deep mantle corrections based on the upgoing phases. However, as discussed below, the observations indicate that the gradational effect of the mantle wedge on the *sS* and *sScS* differential travel time and amplitude patterns is minimal, as might be expected given the tightly bundled *sS* and *sScS* ray paths in the region (Figure 6).

One of our primary methods of data presentation and model comparison will be on a "rose"-type diagram (Figure 7) that is essentially a two-dimensional cross section through a residual sphere. The plane of the cross section is along the down slab-dip direction: 301° for the Kurile slab [*Fischer et al.*, 1988] and 275° for the Japan slab [*Creager and Jordan*, 1984; *Fischer et al.*, 1988]. Observations with azimuths within ±45° of the downdip direction are included in the projection. Residuals are plotted at an angle corresponding to their takeoff angle and a radius corresponding to the relative size of the anomaly. Takeoff angle varies from 0° vertically down to 180° vertically up. On the travel time diagrams, the outer and inner circumferences correspond to a travel time residuals of +5 s and -5 s, respectively, and the circle between them represents the mean of the observations, i.e., a travel time residual of 0 s. On the amplitude diagrams, the residuals range from x2 at the outer circumference to x0.5 at the inner circumference, with a mean of x1 marked by the intermediate semicircle. The *S* and *ScS* observations are demeaned as a group so that variations within the group can be examined. The anomalies are plotted at takeoff angles that are corrected to preserve the angle between the ray and the plane of the proposed slab model. This procedure is just a mapping onto a two-dimensional geometry that minimizes distortion in the observed travel time and amplitude patterns that would result from inclusion of observations recorded at azimuths away from the purely downdip geometry. This projection should maximize any slab signature but may slightly distort any deep mantle trends. Of course, actual takeoff angles in a heterogeneous Earth may differ from these reference model calculations, but this model dependence is part of the problem. The *sS* and *sScS* observations are also demeaned as a group to emphasize their relative

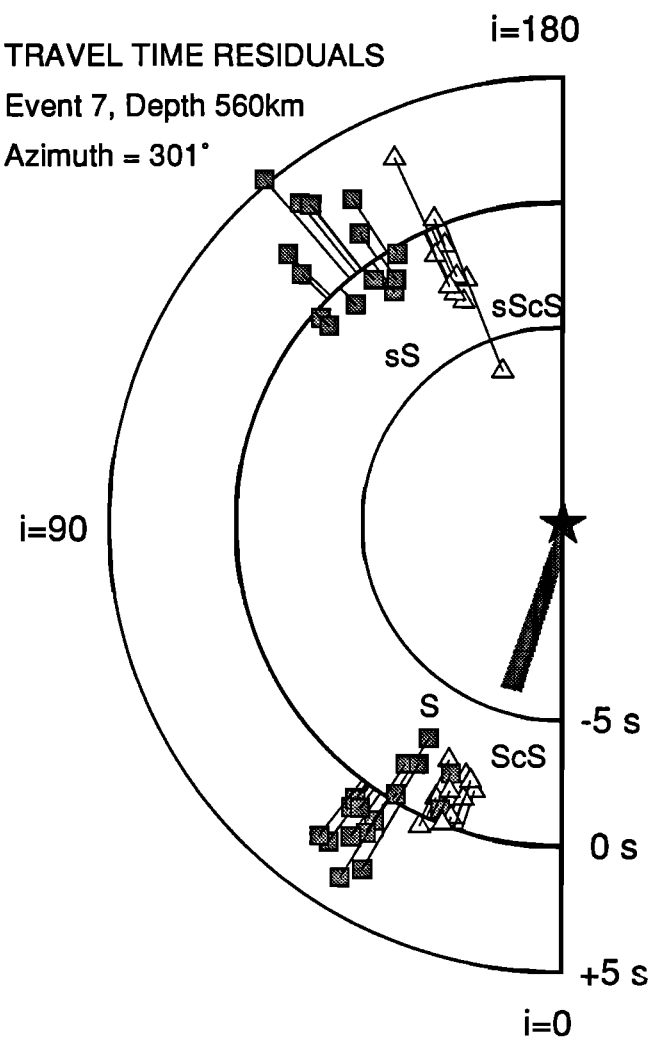

Fig. 7. Travel time observations in the azimuth range 45° on either side of the Kurile slab-dip direction, plotted on a residual rose diagram. Diagram represents a cross section through the residual sphere in Figure 4, at an azimuth of 301°. Takeoff angle (*i*) ranges from 0° to 180°, thereby including *sS* and *sScS* observations in addition to *S* and *ScS*. The takeoff angles for *S* and *ScS* (calculated for PREM) have been corrected to account for the projection into the plane of the cross section. The downgoing and upgoing data are demeaned separately, with relative variations ranging from 5 s slow (outer circumference) to 5 s fast (inner circumference). *S* and *sS* residuals are plotted as squares, and *ScS* and *sScS* residuals are plotted as triangles. Hatched region approximates the lower mantle slab dip preferred by *Fischer et al.* [1988], and tie lines connect each data point to the mean circle at the corrected takeoff angle.

variations, and are plotted at their true takeoff angles (calculated using PREM). All observations are connected to the mean circumference by a tie line that defines the corrected takeoff angle of the observation. The hatched region projecting radially from the source schematically represents the dip of potential deep slab structures extending below the source: for 515-570 km deep events, this geometry is as proposed for the corresponding slab model from *Fischer et al.* [1988]; for 380-400 km deep sources, the geometry is that of the Wadati-Benioff zone between the source and 600 km depth.

The travel time residuals plotted in Figure 7 clearly show the *S* to *ScS* gradient, with steeper (*ScS*) rays being faster, that was apparent in the northwest quadrant of the residual sphere in Figure 4. This trend appears to be geometrically consistent with a deep slab structure similar to that proposed by *Creager and Jordan* [1984] and *Fischer et al.* [1988]. However, note the similar trend in the surface reflected phases, with *sScS* being fast relative to *sS*. The data in Figure 5 indicate the correspondence of relatively early *ScS* and *sScS* phases at a common station. The simplest interpretation for the similarity between the two trends is that some portion of it is due to the common paths shared by *S* and *sS* and by *ScS* and *sScS* in the deep and near-receiver mantle (see Figure 6).

Slab Models

With these preliminary observations in mind, we now consider a suite of slab models (Figure 8) for which we calculate synthetic seismograms in the two-dimensional downdip geometry. These models provide travel time and amplitude calculations which we can compare with our observations. Figures 8*a*-8*c* represent variations of the Kurile slab models proposed by *Creager and Jordan* [1984, 1986] and *Fischer et al.* [1988]. These slabs have the general properties of a 52° dip above 500 km, steepening to 72° below 500 km. Figure 8*a* represents the *S* wave version of the simple, undeformed Kurile slab preferred by *Creager and Jordan* [1986] and refined by *Fischer et al.* [1988], which remains the most widely discussed model for deep slab structure. For this reason, all of our observations will initially be compared with predictions from this model. For brevity, this slab model will be designated as the "long, thin" slab.

Figure 8*b* represents a slab that thickens by a factor of 3 over a range of 150 km as it passes through the 670-km discontinuity. *Fischer et al.* [1988] found that modeling *P* wave travel time residual spheres alone could not resolve variations in slab thickness of this type, and this model therefore fits the *P* wave travel time observations nearly as well as the model in Figure 8*a*. We term these models the "fat" slab models. *Gurnis and Hager* [1988] showed that an increase in viscosity at the 670-km discontinuity could produce slab deformation and thickening in excess of a factor of 3, so it is important to determine if the travel time and amplitude observations prefer this type of model over a thin, undeformed slab. As pointed out by *Vidale* [1987] and *Cormier and Kim* [1990], the reduced lateral velocity gradients present in the thickened slab defocus the wave front less

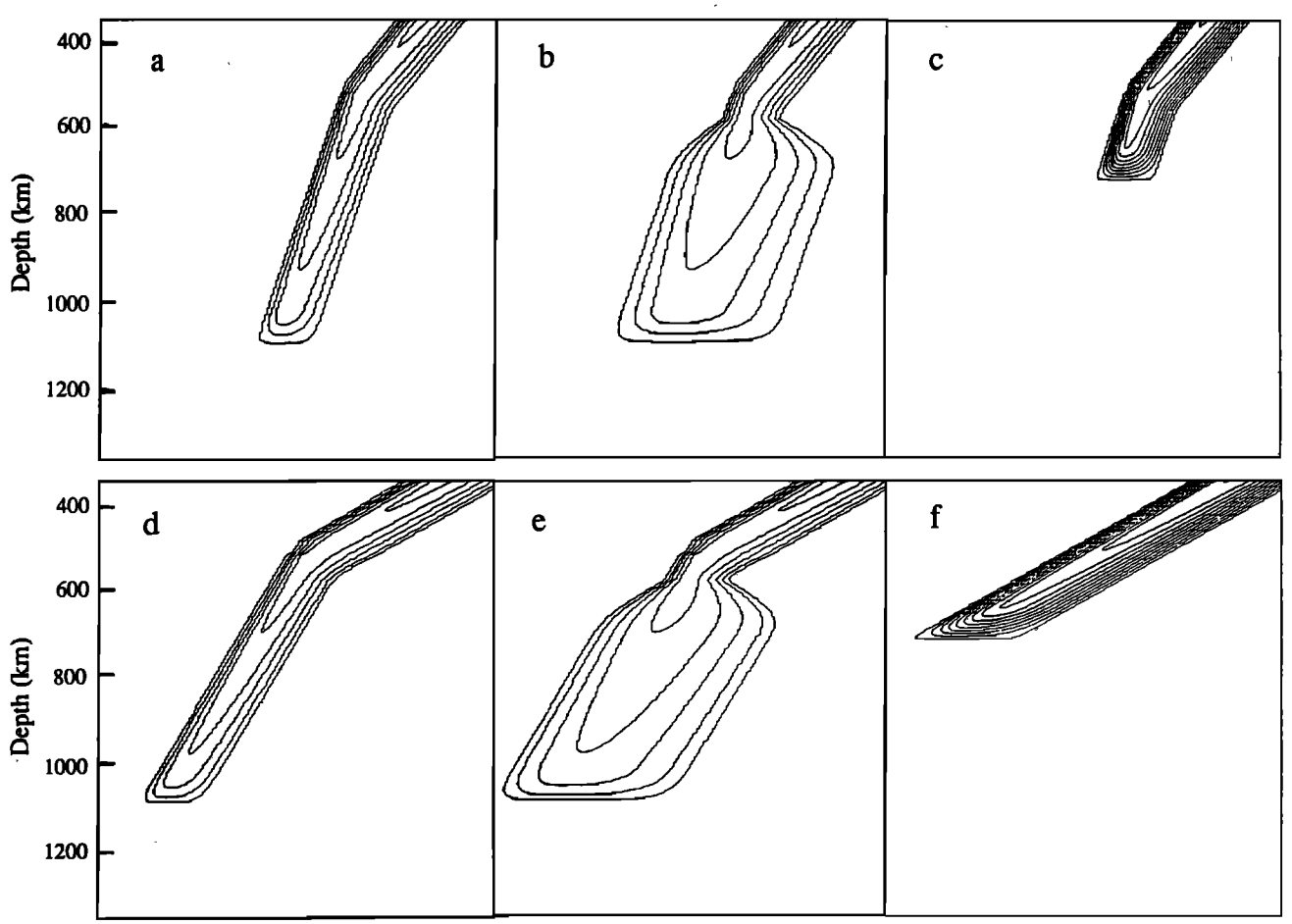

Fig. 8. Slab velocity structures (expressed as perturbations to PREM) for which synthetic travel time and amplitude residuals are computed by a finite difference method. These models are based on the models proposed by *Creager and Jordan* [1984, 1986] and *Fischer et al.* [1988]. (*a*) Long, thin, (*b*) fat, and (*c*) short Kurile slab models. (*d*) Long, thin, (*e*) fat, and (*f*) short Japan slab models. Contours represent percentage variation, ranging from 0% to 10% at 2% intervals for the long, thin and fat models and from 0% to 20% at 2% intervals for the short models.

efficiently than the thinner slab models, while the integrated travel time anomaly remains approximately the same, and therefore amplitude observations may be more diagnostic of slab thickness than travel times for simple slab geometries.

The third type of model that we explore is shown in Figure 8*c*. Given the possibility that we may be able to explain much of the travel time patterns with deep and near-receiver mantle structure, we explore models which terminate near the 670-km discontinuity, referred to as the "short" slab models. Presumably the slab would deflect horizontally near 670 km depth if it cannot penetrate into the lower mantle, but our ray paths cannot resolve such structure. Even if we cannot explain the travel time anomalies by deep mantle or receiver effects, the short slab model may be relevant. *Anderson* [1987*a*] has argued that anisotropy or isobaric phase changes within the cold slab structure may substantially increase the slab's velocity anomaly beyond that produced by the thermal anomaly alone, and therefore a short, very fast slab may be appropriate. In our short models, the strength of the anomaly is set at twice that of the deep penetrating slabs, so that the azimuthal travel time observations of *Creager and Jordan* [1984] and *Fischer et al.* [1988] are approximately preserved. Note that the short slab model for the Kuriles retains the increase in dip between 500 and 550 km, as this feature is consistent not only with the modeling of *Creager and Jordan* [1986] but also with the trend of Wadati-Benioff zone earthquakes in the central Kurile arc [*Veith*, 1974].

Figures 8*d*-8*f* depict the same categories of slab models adjusted to match the geometry of the Japan slab proposed by *Creager and Jordan* [1984, 1986]. These models have a dip of 30° above 550 km and a dip of 60° below 550 km. Note that the "short" Japan slab model does not incorporate this change in dip, as the hypocenters of 550-600 km depth events beneath the Sea of Japan do not indicate such a change.

A fundamental ambiguity in modeling deep slab structure is in estimating the strength of the velocity anomaly. *Creager and Jordan* [1986] modeled the travel time residuals from intermediate depth events to empirically determine the appropriate value of dV_P/dT to map their thermal models into velocity structures. For the Kurile slab, the resulting models have slab velocities ranging from approximately 5.7% faster than surrounding mantle at 350 km depth to 2.8% fast at 1150 km depth. For the Japan slab, the range is from 5.1% fast at 350 km depth to 3.2% fast at 1000 km depth. *Anderson* [1987*a*] has argued that these values are low due to unmodeled isobaric phase changes, and cites a variety of slab anomaly estimates that vary substantially with depth, but in general indicate a V_P anomaly of approximately 5% at intermediate depth [e.g., *Engdahl and Gubbins*, 1987] increasing to approximately 10% for the 600-700 km depth range [*Fitch*, 1975]. In addition, even assuming that the strength of the *P* wave anomaly is well determined, *Vidale* [1987] argues that the appropriate lower mantle anomaly for S waves is approximately twice as strong as that for *P* waves, based on comparisons of lateral velocity variations in the lower mantle [*Anderson*, 1987*b*] that indicate $\partial \ln V_s / \partial \ln V_p > 2$; recent thermodynamic calculations [*Agnon and Bukowinski*, 1990] support this conclusion.

The modeling presented here adopts an intermediate position within these estimates. Our deep models have a peak velocity anomaly of 10% at 350 km depth, which decreases linearly to approximately 5% at 1100 km depth. Note that these values represent the largest anomaly within the slab; the slab models are constructed with an asymmetric sine cross section, thus the average anomaly at each depth within the slab will be $2/\pi$ (0.64) times these values. The strength of the anomalies are similar to shear wave models studied by *Jordan* [1977], *Vidale* [1987], and *Cormier and Kim* [1990].

To generate amplitude and travel time calculations for these models, we impose the velocity anomaly models in Figure 8 onto an Earth-flattened PREM structure and calculate long-period synthetic seismograms at a suite of takeoff angles. The frequency content of the synthetics is comparable to that of the observations. Travel time and amplitude residuals are then measured relative to synthetics calculated for the PREM structure. These residuals are demeaned; that is, they include only relative variations, so they can be directly compared to the downdip data residuals. Travel time baselines are, in general, on the order of 6 s fast relative to PREM, and the amplitude baselines are on average approximately 0.6 times the PREM amplitude.

Synthetics are calculated for two source depths for each slab model: 380 km and 515 km in the Kurile slab models and 400 km and 560 km in the Japan slab models. Sources are located in the fastest (coldest) portion of the slab. To test the dependence of our results on this choice of source location, we have calculated seismograms for source locations laterally removed up to 20 km from the center of the slab in each direction. We find that over the range of takeoff angles presented here, the amplitude (or travel time) versus takeoff angle behavior is essentially constant with the variation in source location. Baseline shifts occur for the entire range of takeoff angle, but no differential behavior is observed. This is a major benefit of using long-period data for this study, as *Weber* [1990] has demonstrated that short-period amplitude calculations for simple slab models are highly dependent on the precise location of the source within the slab, thereby adding a poorly constrained model parameter to analyses using short-period data.

As mentioned above, the short models analyzed here have a peak velocity anomaly of 20%. Due to the rapid termination of these slab models beneath the deep focus sources, even this extreme anomaly produces very limited amplitude and travel time variation with takeoff angle, and numerical tests indicate that the differential patterns are similar for weaker slabs. Therefore, the choice of such a strong velocity anomaly will not significantly bias our results for these models.

Finally, we note that event 7, which has an ISC focal depth of 560 km, is compared to synthetics calculated for a source depth of 515 km. Synthetics calculated for a source depth of 560 km show essentially no differences in relative amplitude or travel time variation with takeoff angle relative to the 515-km synthetics, so for simplicity the latter calculations are used. Likewise, observations for event 14 (source depth of 402 km) are compared to synthetics calculated for a 380 km source depth.

Travel Time and Amplitude Observations

Figures 9*a-d* show travel time and amplitude residual rose diagrams for the four deep events that have the most complete upgoing and downgoing ray coverage from the Kurile slab. These diagrams are similar to the example in Figure 7, except that synthetic travel time and amplitude anomalies calculated for the long, thin slab are plotted along with the downgoing data. For each event, travel time residuals are plotted on the left, and amplitude residuals are on the right.

Several observations are apparent in these figures. First, note that the travel time residuals from all four events show a strong takeoff angle dependence, with the more steeply diving *ScS* observations being fast relative to *S*. The strength of this trend does not vary much with depth of the event; the trends for the events at 515 and 560 km depth (Figures 9*a* and 9*b*) are about the

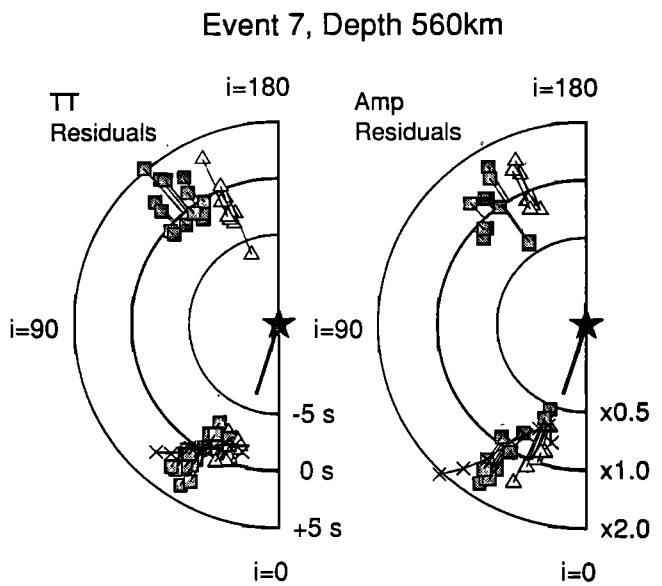

Fig. 9*a*. Travel time and amplitude residual rose diagrams for event 7, using the same plotting conventions outlined in Figure 7. The travel time diagram is on the left, the amplitude diagram is on the right. The synthetic travel time and amplitude residuals calculated for the long, thin slab model are now included as crosses with the *S* and *ScS* data.

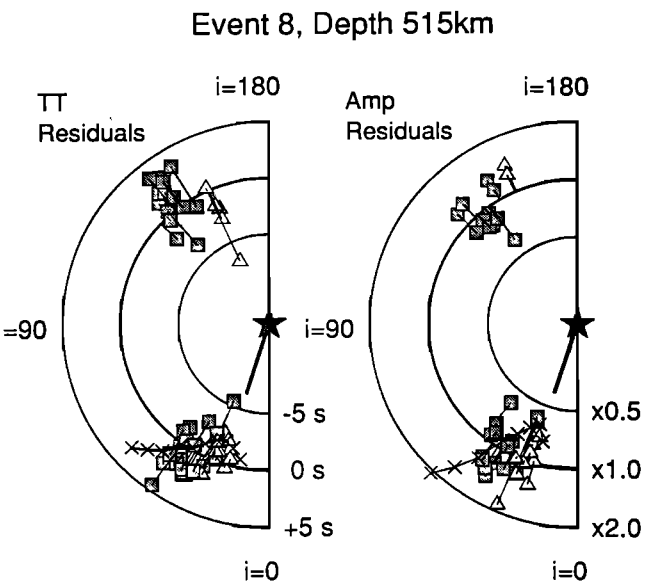

Fig. 9*b*. Same as Figure 9*a*, but for event 8.

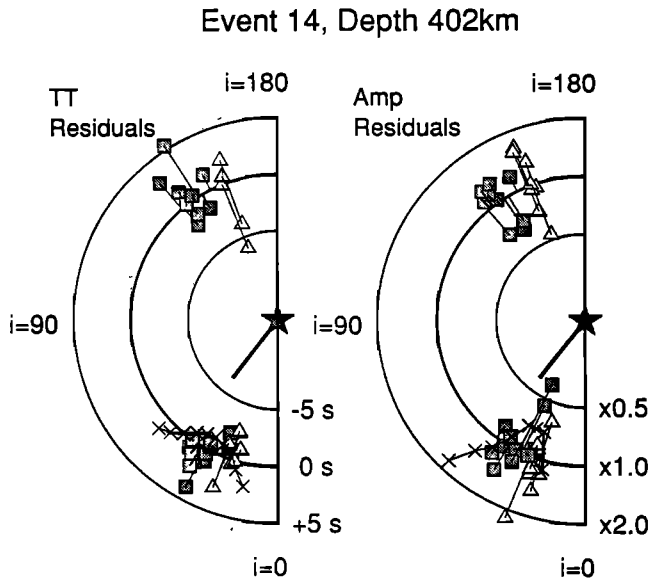

Fig. 9*c*. Same as Figure 9*a*, but for event 14.

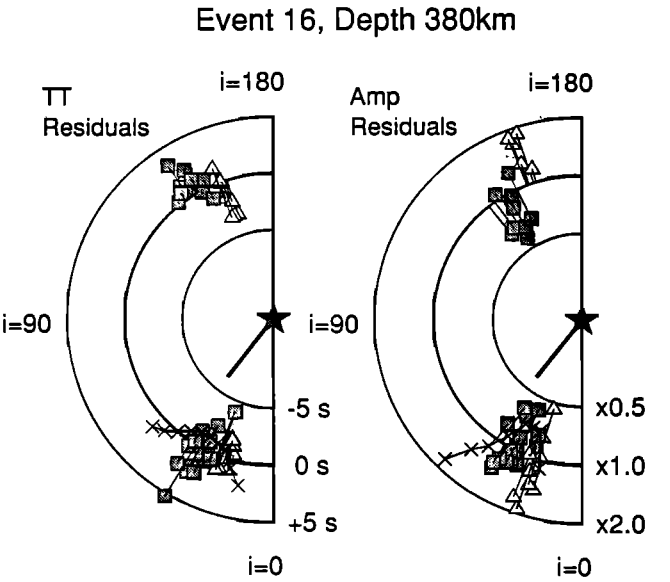

Fig. 9*d*. Same as Figure 9*a*, but for event 16.

same as those for the 380- and 402-km-deep events (Figures 9*c* and 9*d*). This is significant in evaluating these trends for slab structure, as the travel time residuals calculated for the long, thin slab model predict a weakening of the *S* to *ScS* trend as source depth decreases due to the change in slab dip (contrast the crosses in Figure 9*a* against those in Figure 9*c*, for example). This lack of depth dependence of the observed travel time residuals is consistent with observations made along strike of the Kurile slab by *Lay* [1983] and *Schwartz et al.* [1991] and is at odds not only with the calculations presented here, but also with the *P* wave residual sphere observations of *Creager and Jordan* [1984] for events in this region.

The travel time residuals for the upgoing phases *sS* and *sScS* also show consistent behavior for all four events, with the takeoff angle trend in residuals from *sS* to *sScS* mirroring the trend in the *S* and *ScS* residuals. However, the correlation between *S* and *sS* residuals and between *ScS* and *sScS* residuals is poor for these events (R=0.23), indicating that the scatter in the data is fairly high. As we see below, if the varying path behavior is further accounted for, much of the scatter is removed, and more coherent relative behavior becomes apparent.

The amplitude residuals in Figure 9 show greater scatter and less coherent structure than the travel times. The *S* and *ScS* amplitudes for event 7 (Figure 9*a*) show a strong trend similar to that observed in the travel times that is fairly consistent with the defocusing of *ScS* predicted for the long, thin slab model. Event 8 (Figure 9*b*) also shows a slight defocusing of *ScS* relative to *S*, but the trend is weaker than that calculated for the deep slab. Events 14 and 16 (Figures 9*c* and 9*d*) have more scatter and are difficult to evaluate, but the observations appear to lack any strong trend. This does not appear compatible with the predictions of the long, thin slab model.

The upgoing amplitude patterns are even more difficult to assess than the downgoing amplitudes. Events 7, 8, and 14 are all similar in that *sS* and *sScS* lack a well-developed trend. Event 16 shows a strong trend, with *sS* observations substantially smaller than *sScS* observations, which does not have a counterpart in the downgoing phases. Potential explanations for this trend include a strongly focusing/defocusing effect or heterogeneous anelastic structure in the mantle wedge. Alternatively, the isolated occurrence of this trend among a group of events that show fairly good coherence in other travel time and amplitude patterns perhaps indicates a source anomaly rather than a structural effect. Due to uncertainties in the amplitude baselines between the upgoing and downgoing observations, the *sS* and *sScS* amplitudes were not included in the focal mechanism determinations. Thus, this isolated trend may be indicative of an incorrect radiation pattern correction that preferentially affects the upgoing phases.

The travel time and amplitude residual rose diagrams for the three best recorded Japan slab events are shown in Figure 10. These diagrams only show the anomalies for downgoing paths because of poor *sS* and *sScS* radiation for all of these events. Due to the change in strike of the Japan slab relative to the Kurile slab, many of the European stations are no longer in the downdip direction, and thus even the *S* and *ScS* data are relatively sparse. Despite this sparsity, the observations still cover a range of takeoff angles that should be diagnostic of slab structure (note the calculated trends projected on the diagrams), so we include them for completeness. Event 6 is an event at approximately 400 km depth, in a portion of the slab with a very shallow (approximately 30°) dip. Thus, as indicated by the calculations for the long, thin slab model, this event should have very distinct travel time and amplitude patterns relative to the other (deeper) events. The travel times do not seem to support this prediction, although the scatter and sparse data distribution make it difficult to assess the observations. The amplitudes for event 6 do show a strong trend, with the *S* observations at the largest takeoff angles being substantially smaller than the other observations, as predicted by the long, thin slab model. The amplitudes for events 13 and 18 are quite sparse and scattered, but they clearly show a change in pattern from the shallower event that is in qualitative agreement with the long, thin slab model.

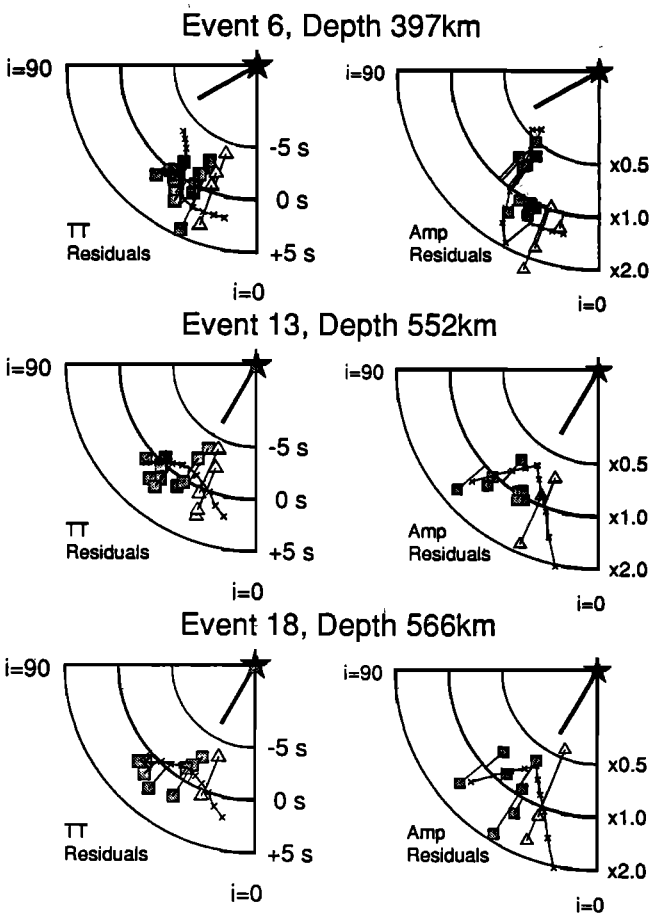

Fig. 10. Travel time and amplitude residual rose diagrams for three deep Japan events. *sS* and *sScS* data for these events is very poor, so the diagrams only include a downgoing takeoff angle range of 0° to 90°. Again, the crosses indicate the predicted patterns for the long, thin slab model.

While the diagrams in Figures 9 and 10 indicate that some significant trends exist in the downdip travel time and amplitude observations, it is clear that the scatter in the data limits our ability to constrain the slab models. However, for our two-dimensional geometry, much of the observed and predicted variation in the travel time and amplitude residuals involves relative behavior between *S* and *ScS* (or *sS* and *sScS*), and we thus can make a final correction to the data.

As depicted in Figure 6, the *S* and *ScS* observations at a given station have similar paths in the receiver mantle and crust, which may result in a common shift in the travel time or amplitude residuals of the two phases. The same is true for the *sS* and *sScS* observations. This common shift can be corrected for by removing the mean of the two upgoing or downgoing observations at each station. This preserves any takeoff angle trends in the data while reducing the variation due to heterogeneity that effects both *S* and *ScS*, or *sS* and *sScS*, recorded at a given station. This procedure is essentially a variant on differential time analysis, which has been used in many studies to isolate lower mantle structure [e.g., *Jordan and Lynn*, 1974; *Lay*, 1983]. In addition, we can stack observations from sources with similar depths.

Figure 11 shows the travel time residuals for the four deep Kurile events. In Figure 11*a*, the demeaned pairs of *sS* and *sScS* observations are plotted against ray parameter. Parameterization by ray parameter inherently accounts for variation in focal depth of the four events, allowing us to stack all of the *sS* and *sScS* observations to obtain a single trend. It is clear from the common slopes of the *sS* to *sScS* tie lines that much of the scatter apparent in the upgoing travel time residuals in Figure 9 is due to common path variations, and the data now display a very strong trend. The coherence of the trend over the four events is striking, and it is clear that all of the *sScS* travel times in the downdip direction are fast relative to the *sS* travel times to the same station. Similarly, the *ScS* to *S* behavior displays a clear trend (Figure 11*b*), and it appears quite similar to the *sScS* to *sS* trend. The linear correlation coefficient between the station demeaned *sS* and *S* observations, and *sScS* and *ScS*, has improved from 0.23 prior to demeaning to 0.80 after demeaning. The simplest interpretation of this trend is that it is a result of a laterally extensive region of high velocity near the core-mantle boundary or a region of anomalously slow velocity in the middle-lower mantle. In fact, *Tanimoto* [1990] found that the long wavelength velocity structure just above the core-mantle boundary beneath Eurasia is fast relative to PREM, and a laterally discontinuous high-velocity layer in *D*" has been proposed for this region [*Lay and Helmberger*, 1983b; *Baumgardt*, 1989; *Weber and Davis*, 1990].

Despite the strong correlation between the upgoing and downgoing phases, we explore the possibility that mantle wedge or crustal structure near the surface reflection points of the

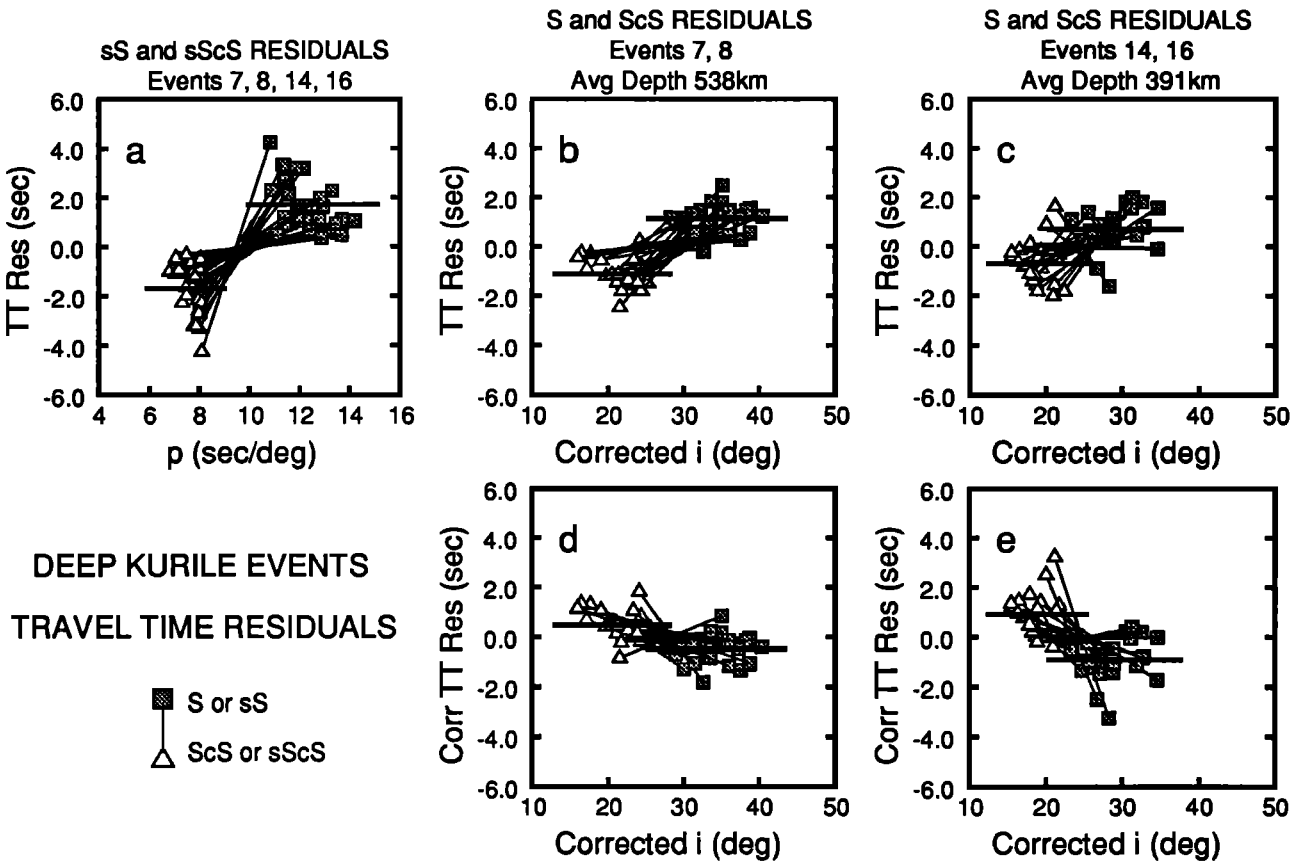

Fig. 11. Downdip travel time observations from deep Kurile events corrected for station behavior observed in each *S* and *ScS* (or *sS* and *sScS*) pair. Tie lines connect each *S* and *ScS* (or *sS* and *sScS*) pair. Solid horizontal lines delineate the mean of each of the *S* (*sS*) and *ScS* (*sScS*) populations. (*a*) Stack of pair-demeaned *sS* and *sScS* travel time residuals versus ray parameter for events 7, 8, 14, and 16. (*b*) Stack of *S* and *ScS* travel time residuals versus takeoff angle (corrected for projection into downdip azimuth) for events 7 and 8. (*c*) Same as Figure 11*b*, but for events 14 and 16. (*d*) Data from Figure 11*b* corrected for the deep mantle trend observed in Figure 11*a*. (*e*) Data from Figure 11*c* corrected for the trend observed in Figure 11*a*.

upgoing observations could be responsible for the *sS* to *sScS* trend. Figure 12 is a map of the Sea of Okhotsk with the *sS* and *sScS* travel time residuals for the four Kurile events plotted at their surface bounce points. It is clear that the observations do not span an ocean-to-continent transition or any other major structural feature. In addition, the close proximity of the *sS* and *sScS* bounce points (often within 200 km distance) and the spatial distribution of the four events would require extremely strong gradients or anisotropy with a complex, contorted geometry in the upper mantle to explain the rapid variation from *sS* to *sScS*. When this required complexity is contrasted with the simplicity of a laterally extensive anomalous velocity region in the lower mantle, and when the high correlation between the upgoing and downgoing travel time residuals is considered, it is apparent that the deep mantle is the most reasonable interpretation of the travel time anomaly. We will therefore apply the *sS* and *sScS* observations as an empirical correction for the deep mantle structure.

The demeaned *S* and *ScS* travel time residuals for events 7 and 8 are stacked in Figure 11*b* versus takeoff angle corrected for azimuth variation. The observations for the shallower events 14 and 16 are plotted in Figure 11*c*. Again, the station demeaning procedure has substantially reduced the scatter in the observations, and the *ScS* to *S* shift is well defined. Interestingly, the *ScS* to *S* gradient for events 14 and 16 is slightly reduced relative to the trend for events 7 and 8. This depth dependence was not apparent in the data prior to the station pair-demeaning procedure. Although the change in trend is small, such a depth dependence in

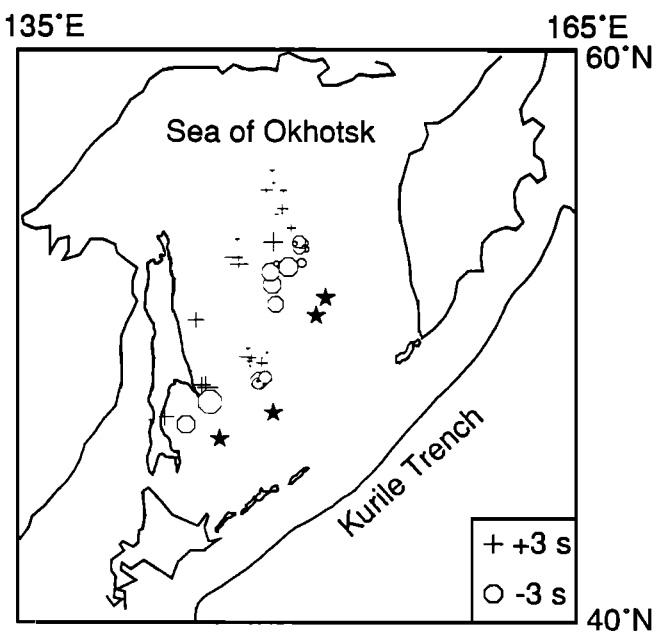

Fig. 12. Mercator projection of the Sea of Okhotsk region, with the *sS* and *sScS* travel time residuals observed in Figure 9 projected to the surface bounce point corresponding to each observation. Crosses and circles represent slow and fast, respectively, linearly scaled to the size of the residuals, and the stars indicate the epicenters of the events. Residuals from each event have been demeaned to highlight relative variations.

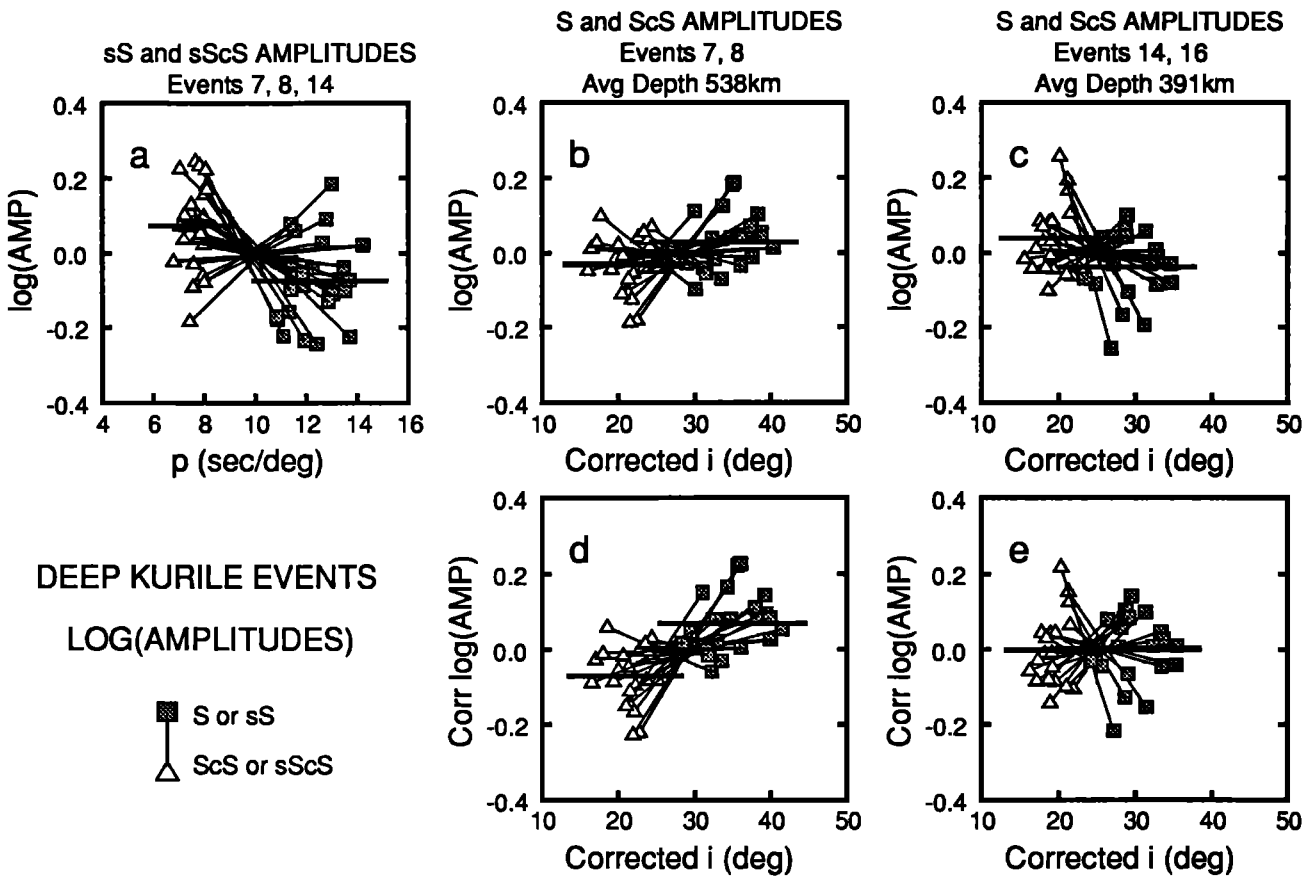

Fig. 13. Same as Figure 11, except for amplitude residuals instead of travel time residuals. (*a*) *sS* and *sScS* amplitudes versus ray parameter for events 7, 8, and 14. (*b*) *S* and *ScS* amplitudes versus corrected takeoff angle for events 7 and 8. (*c*) *S* and *ScS* amplitudes for events 14 and 16. (*d*) Data from Figure 13*b* corrected for deep mantle trend in Figure 13*a*. (*e*) Data from Figure 13*c* corrected for trend in Figure 13*a*.

the travel time patterns is predicted for the steepening long, thin slab models, as discussed earlier.

Figures 11*d* and 11*e* show the *S* and *ScS* travel time observations for the same event groupings, now corrected for deep mantle structure using the *sS* and *sScS* observations. Since the *sS* and *sScS* observations separate with significantly different means (1.6±0.4 s and -1.6±0.4 s, respectively, at a 99% confidence level) but considered separately, neither *sS* nor *sScS* show a ray parameter trend, we simply use the mean of the *sS* residuals as corrections for the *S* observations, and likewise correct *ScS* residuals with the *sScS* mean. For events 7 and 8 (Figure 11*d*), the resulting trend in travel time residuals with takeoff angle has a reversed polarity, with the *S* observations now fast relative to the *ScS* observations, although the strength of the trend is substantially reduced, with a mean offset of less than 1 s total. Events 14 and 16 also show a reversed trend (Figure 11*e*), somewhat stronger than that observed for the deeper events (mean offset of 1.4 s total). These results have profound implications for the proposed models of deep slab structure. The fact that the *sS* to *sScS* travel time residual variation is larger than that observed for the *S* and *ScS* paths indicates that the deep mantle structure thoroughly masks the travel time signature of the slab structure and was entirely responsible for the *S* to *ScS* gradient that can otherwise be explained by slab models that steepen in dip at 500 km depth. Once this deep mantle signature is removed, the resulting travel time residuals of the 380 to 402-km-deep events have patterns that would be expected for a slab with the known dip of the Wadati-Benioff zone in this region. Farther down the slab by approximately 150 km, the deeper events show a similar trend with takeoff angle, and the magnitude of the trend is reduced by 33%. This is clearly incompatible with the strong trend predicted in Figure 9*a* for the long, thin slab model, which calls for much more negative *ScS* residuals (relatively) than *S* residuals. We will compare the resultant trends to the other slab models after we have presented the amplitude observations.

Figure 13 presents the station demeaned amplitude observations from the four deep Kurile events. Whereas the station demeaning procedure removed much of the scatter from the travel time observations, the wide variation in slopes of the *S* to *ScS* tie lines within each data grouping indicate that much of the amplitude scatter is due to sources far from the receiver. Despite the observed scatter, however, there are subtle *S* to *ScS* trends which are worth considering.

The *sS* and *sScS* amplitude observations from events 7, 8, and 14 are shown in Figure 13*a*. As discussed above, the upgoing observations from event 16 have a strong trend which is not consistent with the observations from the other three events and were not included in this grouping. The data indicate a slight trend, with the *sScS* observations (mean value of 0.04) slightly larger than the *sS* observations (mean value of -0.04). When combined with the travel time trend of *sScS* being fast relative to *sS*, the amplitude groupings are perhaps indicative of a more attenuating structure along the *sS* paths relative to the *sScS* paths. If the arguments for a deep mantle origin of the upgoing travel time trend hold as well for amplitudes, we can isolate the attenuation structure in the deep mantle and correct the *S* and *ScS* amplitudes for its effect. However, since many of the individual *sScS* observations are in fact smaller than the corresponding *sS*

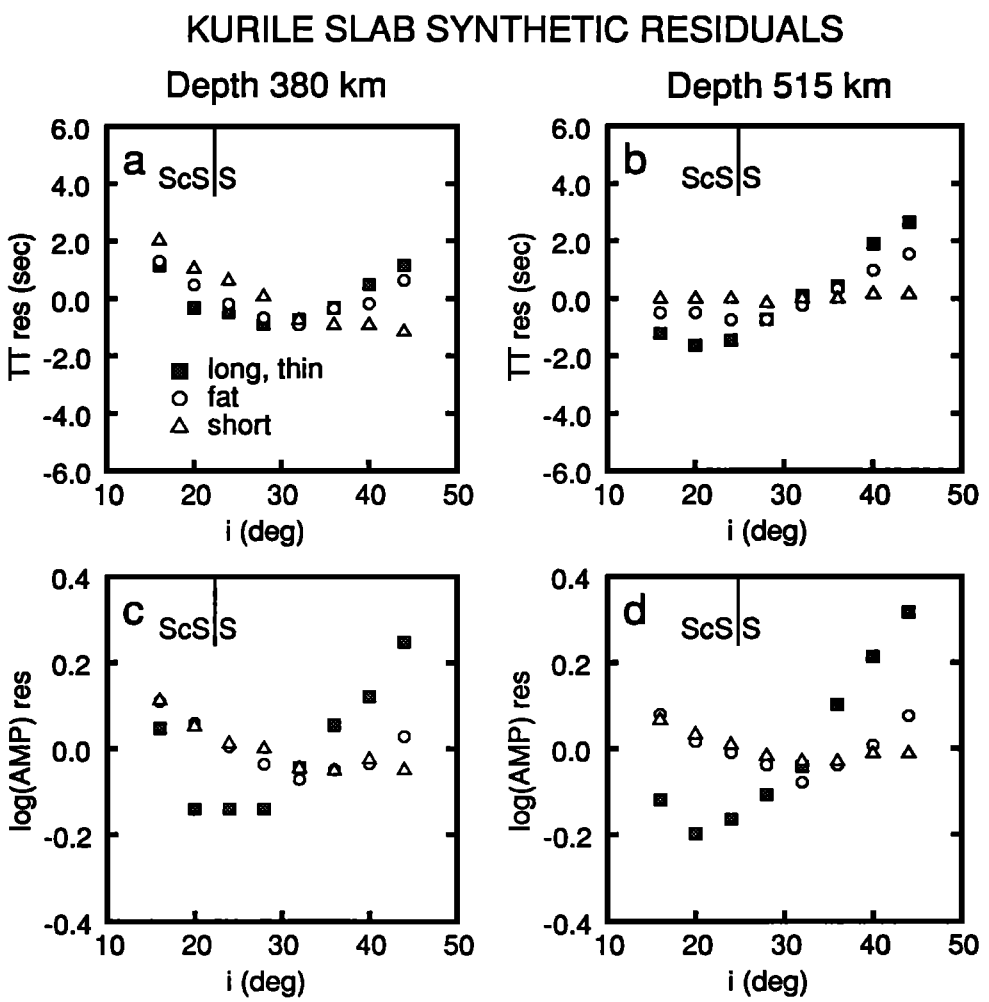

Fig. 14. Synthetic residuals versus takeoff angle for the three Kurile slab models presented in Figures 8*a*-8*c*. (*a*) Travel time residuals from 380-km source depth. (*b*) Travel time residuals from 515 km source depth. (*c*) Amplitude residuals from 380-km source depth. (*d*) Amplitude residuals from 515-km source depth. Approximate *S* and *ScS* takeoff angle ranges are indicated.

observations, the upgoing amplitude trend lacks the strong consistency of the travel time trend, and we are much less confident of this interpretation. The corrections for the lower mantle amplitude trend is fairly small (<20%) but still significant, so we explore the ramifications of pursuing this interpretation.

Figure 13*b* displays the amplitude observations from events 7 and 8. The *ScS* observations appear to be slightly small relative to *S*, the trend expected for the thin, deep slab model, although the mean values of the *S* and *ScS* residuals are less than +8% and -8% (relative to PREM), respectively, much less than that predicted for the long, thin slab. The trend of the offset for events 14 and 16 (Figure 13*c*), with *S* being smaller than *ScS*, is not consistent with the long, thin model, which predicts *ScS* defocusing even for events at source depths of 400 km (see calculated trends in Figure 9).

The amplitude residuals after the deep mantle corrections have been applied are presented in Figures 13*d* and 13*e*. Events 7 and 8 now display a stronger (±17%) offset between *S* and *ScS*, closer to that predicted for the thin, deep slab model. In contrast, the residuals for events 14 and 16 are now flat, clearly inconsistent with the strong defocusing expected for the deep, thin model. These trends will be combined with the travel time observations and compared with other slab model calculations in the next section.

Because of the sparse station distribution for the Japan slab events, the *S-ScS* pairing operation leaves too little data for detailed analysis. Therefore, we must rely on the patterns present in the residual rose diagrams (Figure 10) for our interpretation of deep Japan slab structure.

INTERPRETATION

By comparing the coupled travel time and amplitude behavior observed for the deep Kurile and Japan events with predictions for the suite of models presented in Figure 8, we will place constraints on the velocity structure beneath these events. Figure 14 presents the synthetic amplitude and travel time residuals for the three basic geometries hypothesized for the Kurile slab. As discussed previously, these residuals are demeaned; that is, they include only relative variations, so they can be directly compared to the downdip data residuals.

Travel Time Comparison

Figures 14*a* and 14*c* are the predictions calculated for a source depth of 380 km. It is interesting to note that at this source depth none of the slabs predict travel time residuals such that the *ScS* calculations are fast relative to *S*, as is observed in the travel time residuals that have not been corrected for the deep mantle (Figure

11*c*). This indicates that the fast *ScS* observations are indeed critically affected by deep mantle heterogeneity, and our preference for the travel time data that have been corrected for this deep mantle signal is reinforced. The corrected travel time observations (Figure 11*e*) are characterized by *S* residuals that are nearly 2 s fast relative to the *ScS* residuals. This is most consistent with the short, fast slab (*S* approximately 1.4 s fast); the long, fat slab predicts *S* observations 1 s fast relative to ScS, and the *S* residuals for the long, thin slab are only 0.7 s fast relative to *ScS*.

The travel time calculations for a source depth of 515 km are presented in Figure 14*b*. The predicted trends are smoother than those for the 380-km source because the slab extension is essentially straight below 515 km. The deep mantle corrected observations (Figure 11*d*) show *S* slightly fast (0.9 s) on average relative to *ScS*, most consistent with the short slab, which predicts no variation, or the fat slab, which predicts *ScS* to be fast by an average of only 0.2 s. If the deep mantle corrections are not applied, the data are consistent with the long, thin model, emphasizing the importance of the corrections.

Amplitude Comparison

The amplitude calculations in Figure 14*c* indicate that a 380-km-deep source in the long, thin slab will severely defocus both the *S* and *ScS* arrivals, while defocusing caused by the fat and short slabs will be less severe and will preferentially affect the *S* observations, so the *S* to *ScS* differential behavior over the limited range spanned by the data will be greater for these models than for the long, thin slab. Therefore, the uncorrected amplitude observations displayed in Figure 13*c* (*ScS* 20% larger than *S*) are very consistent with either the short or fat slabs but are slightly larger than the variation predicted for the long, thin slab (7%). If the deep mantle corrections to the amplitudes are taken into account, the observations show no *S* to *ScS* gradient in amplitude, consistent with the long, thin slab calculations by virtue of spanning a limited range of takeoff angle, but this comparison is not convincingly diagnostic.

Finally, the amplitude calculations for the 515-km-deep source are presented in Figure 14*d*. The calculations for the long, thin slab predict *S* amplitudes 40% larger than *ScS*, while the fat and short slabs predict *S* amplitudes 23% and 15% smaller than *ScS*, respectively. The defocusing of *S* relative to *ScS* in the fat and short slab models is not well correlated with the travel time calculations and seems to be controlled by the fact that the *S* energy encounters the strong lateral velocity gradients at the top edge of the slab, while the *ScS* energy exits the slab without encountering these strong gradients. While the strength of the *S* defocusing may be somewhat dependent upon our parameterization of the model structure, the relative lack of *ScS* defocusing is qualitatively robust. The amplitude observations without deep mantle corrections (Figure 13b) are characterized by *ScS* being 15% small relative to *S*. This falls between our predictions and favors a deep slab structure, but one wider or shorter than the long, thin model. The fat slab appears to be too broad, however, and the short slab too short. If the deep mantle corrections are applied to the amplitude observations (Figure 13*d*), the observed residuals are most consistent with the calculations for the long, thin model.

Interpretation of Kurile Data

A fundamental ambiguity in this analysis rests in the assessment of the deep mantle corrections. As discussed above, the consistency of the travel time behavior of the *sS* and *sScS* arrivals argues strongly for a deep mantle origin of the differential *sS* and *sScS* behavior, and the application of the resulting corrections to the *S* and *ScS* travel time data appears to be well founded. The major uncertainty is in how well the upgoing phases constrain the magnitude of the lower mantle contribution to the travel times. The amplitude behavior of the *sS* and *sScS* arrivals is not as stable, however, which argues against the application of a poorly resolved *sS* to *sScS* amplitude trend as a deep mantle correction.

In addition, we must make an effort to evaluate our relative confidence in the travel time and amplitude observations. In general, travel times have been much more extensively analyzed, and they have a relatively simple and predictable response to variations in Earth structure. This simplicity is apparent in the relative behavior between *S* and *ScS* residuals for the four Kurile events studied here. Of the 46 *S-ScS* pairs of residuals for these events, 42 (for the data without deep mantle corrections) display similar *S* to *ScS* differential behavior; that is, *ScS* is fast relative to *S*. This consistency elicits a high degree of confidence in the data. In contrast, the amplitude behavior of the seismic wave field is complex and poorly understood, an assessment borne out by the highly scattered differential behavior of the amplitude observations.

An argument can be made for placing high confidence in the interpretation of the amplitude observations from the deep Kurile events (events 7 and 8). In principal, the large waveform and amplitude distortions predicted for slab structure [*Vidale*, 1987; *Cormier and Kim*, 1990; *Weber*, 1990] should overwhelm the typical scatter in amplitude observations; the factor of 4 defocusing (relative to PREM) predicted by *Vidale* [1987] is in fact larger than the scatter observed here. Due to the distribution of stations and the geometry of the Kurile slab in the real Earth, actual observations only sample a limited portion of the ideal takeoff angle range that would constrain the slab structure. The predicted variation for the reduced range of takeoff angles is smaller, as is the case for the 380 km source depths in this study. However, for a 515-km or 560-km source depth, a slab dipping at an angle of 72° is well sampled by the *S* and *ScS* wavefield recorded at European stations, and thus the amplitude residuals from these events should be diagnostic of slab structure.

Therefore, if we rely primarily on the deep-mantle-corrected travel times, supported by the uncorrected amplitudes from the deepest events, we conclude that the *S* wave observations from the four deep Kurile events are inconsistent with a thin slab penetrating to great depths in the lower mantle, as proposed by *Jordan* [1977]. We cannot resolve between a short, thin slab and a longer, fat one, although the amplitude observations from events 7 and 8 do not strongly support a slab that has been thickened by a factor of 3, as modeled here. The travel times do not require a change in dip near 550 km, as proposed by *Jordan* [1977], but the amplitudes do show a small amount (15%) of systematic defocusing that is consistent with a slightly steeper dip, although this defocusing is not well predicted by any of the models examined here. The lack of evidence of a change in dip is also reported by *Suetsugu* [1989], who combines travel time tomography with forward modeling of amplitudes to argue for penetration of the Kurile slab straight into the lower mantle. Due to the small number of models that could be evaluated here, these conclusions should not be viewed as inconsistent, pending further exploration of slab geometries that will satisfy these observations.

Interpretation of Japan Data

The travel time and amplitude residual variations calculated for two source depths in the Japan slab models are presented in Figure

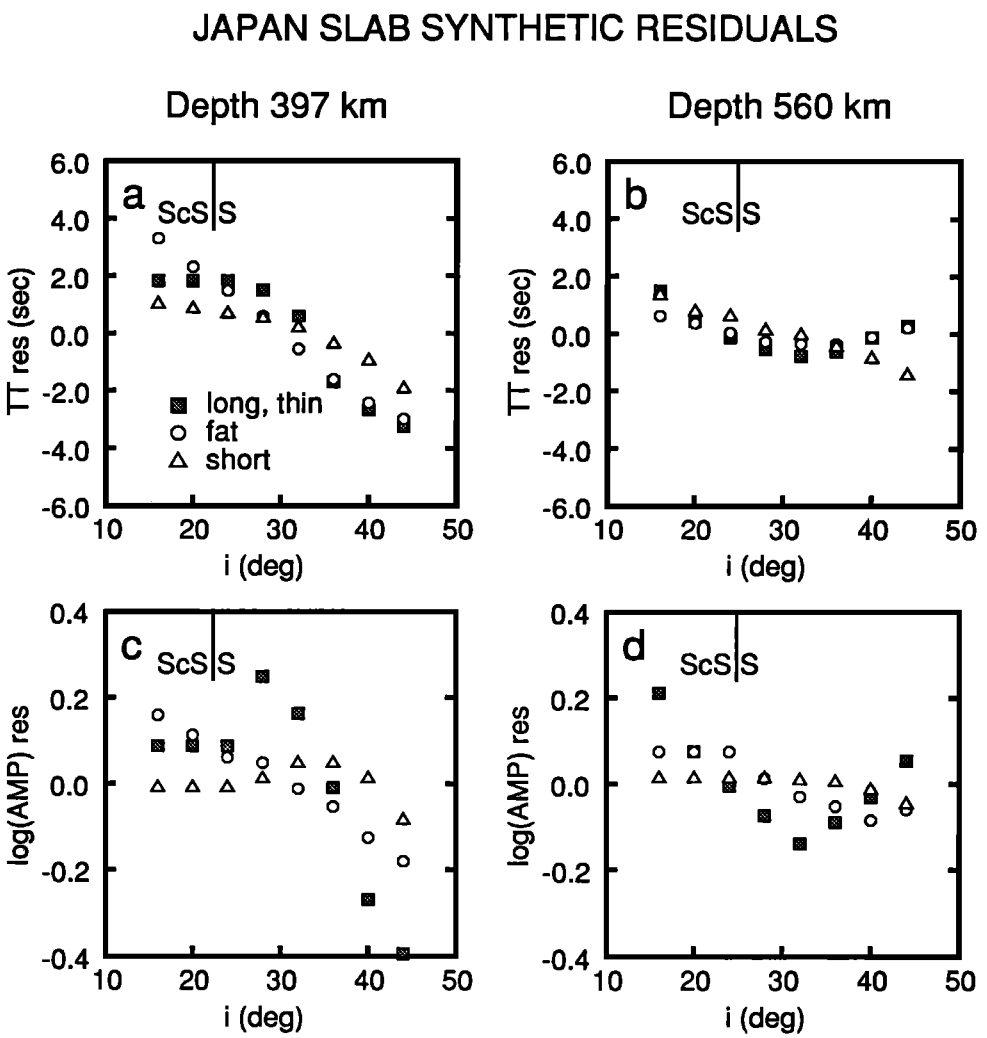

Fig. 15. Synthetic residuals vs. takeoff angle for the three Japan slab models presented in Figures 8*d*-8*e*. (*a*) Travel time residuals from 397-km source depth. (*b*) Travel time residuals from 560-km source depth. (*c*) Amplitude residuals from 397-km source depth. (*d*) Amplitude residuals from 560-km source depth. Approximate *S* and *ScS* takeoff angle ranges are indicated.

15. As discussed above, the limited data in the correct distance and azimuth range from these events makes it difficult to identify diagnostic trends; in particular, we must rely on the data as presented in Figure 10, due to the lack of *ScS* data needed for analyzing the *S-ScS* differential time patterns. We can use the predictions for the various slab models to draw some general conclusions regarding acceptable Japan slab structures given the limited data. First, note that the amplitude observations for event 6 (see Figure 10) show a strong trend, with the *S* phases with the largest takeoff angles having low amplitudes. This is consistent with defocusing in the shallow dipping slab beneath the (400 km deep) source in the upper mantle. While it was stated previously that this trend is consistent with a long, thin slab, it is now clear from Figure 15*c* that this trend is also expected for the other two slab models that we explored. Note that the deep, thin slab predicts strong focusing of the *S* arrivals near 30° takeoff angle, coinciding with the takeoff angles of several of the arrivals plotted in Figure 10. These arrivals show no sign of the expected focusing, and we tentatively conclude that a short or fat slab is more consistent with the amplitude data from this event. The scatter in the amplitude data from the two deeper events is too large to allow comparison to the strong trend calculated for the long, thin slab for these events. In addition, the calculated travel time residuals predict very similar behavior over the range of takeoff angles being examined, and therefore are not diagnostic of variation in slab structure, considering the noise level of the data.

Finally, an aspect of the data not extensively explored here is the structure of the deep mantle responsible for the strong trend in *S* to *ScS* (and *sS* to *sScS*) travel time residuals. Previous studies utilizing *ScS-S* differential times have mapped out a high-velocity zone at midlevels of the lower mantle beneath the Caribbean [*Jordan and Lynn*, 1974; *Lay*, 1983; *Grand*, 1987], a low-velocity region in the mid-lower mantle beneath Brazil [*Lay*, 1983], and low-velocity zones at the base of the mantle beneath the eastern Atlantic and India [*Lavely et al.*, 1986]. The data from events 7, 8, 14, and 16 sample the deep mantle beneath north central Siberia, and a fairly strong negative correlation found between the *S* travel time residuals and the differential times *ScS-S* (R=-0.61) may indicate the presence of an anomalously slow region at 1000-2000 km depth in the mantle. The spatial distribution of this heterogeneity and its relationship to a laterally varying discontinuity structure in *D*" is explored further by J.B. Gaherty and T. Lay [Investigation of laterally heterogeneous shear velocity structure in *D*" beneath Eurasia, submitted to *Journal of Geophysical Research*, 1991]. We do note that all recent attempts to develop empirical receiver and deep mantle corrections for *P* waves [*Grand and Ding*, 1989; *Suetsugu*, 1989; *Zhou and Anderson*, 1989; *Zhou et al.*, 1990] are coming to the compatible

conclusion that much of the power in the residual sphere travel time patterns is in fact caused by deep mantle structure.

CONCLUSIONS

We place further constraints on the deep velocity structure of the Kurile and Japan slabs by analyzing a large data set consisting of *S* wave travel time and amplitude residuals from deep focus earthquakes. We have empirically evaluated the systematic patterns present in the data due to heterogeneous lower mantle structure and compare the corrected observations with synthetic residuals calculated for models based on the deep slab structures proposed by *Creager and Jordan* [1984, 1986] and *Fischer et al.* [1988]. We find the following:

1. *sS* and *sScS* travel time residuals indicate that there is a large-scale velocity heterogeneity in the lower mantle beneath northern Siberia that fortuitously imitates a slab-like signature in the *S* and *ScS* travel time observations from deep Kurile events recorded at European WWSSN stations. Once this pattern is removed, the resulting travel time residuals are not compatible with the steeply dipping slab structure preferred by *Jordan* [1977]. Furthermore, although we hesitate to claim that the presence of a lower mantle shear velocity structure implies a similar *P* velocity structure, we point out that possibility that the *P* wave residual spheres are also biased by such a structure. *Creager and Jordan* [1984] note that the travel time residual versus takeoff angle gradient that we have investigated in detail here is in fact stronger for the *P* wave residual spheres from the deepest Kurile events than for the *S* wave residual sphere investigated by *Jordan* [1977], so it seems reasonable that similar deep mantle structure could be responsible for both patterns. *Zhou and Anderson* [1989], *Grand and Ding* [1989], and *Zhou et al.* [1990] have argued that other portions of the *P* wave residual sphere patterns are dominated by lower mantle and receiver structure in other regions. Overall, it seems clear that both the *P* and *S* lower mantle structure must be well determined before the travel time residual spheres can be unambiguously interpreted in terms of near-source structure.

2. Once lower mantle corrections are applied to the travel time residuals from the deep Kurile events, a substantially shorter and/or broader slab than that preferred by *Creager and Jordan* [1984, 1986] appears to be most consistent with the *S* wave travel time and amplitude observations in the downdip direction. Slabs with extreme broadening also appear to be inconsistent with the observations, limiting the extent of deformation of the slab near the 670-km discontinuity to less than a factor of 3 thickening.

Differentiating between a slab that terminates near 670-km and one that broadens and penetrates into the lower mantle is very difficult using data constrained to the downdip direction. However, this analysis, which emphasizes differential behavior between similar phases, eliminates many of the unknown quantities that complicate interpretations of azimuthal patterns in travel times and amplitudes (i.e., location errors, deep mantle structure, rapid station variations). This increases our confidence that we are, in fact, isolating and modeling the near-source structure. Down-dip sampling at a larger range of takeoff angles than that provided by European WWSSN stations would remove much of the ambiguity from the analysis. Alternatively, a dense network providing broadband data with full three-dimensional coverage would allow a more detailed evaluation of slab diffraction waveform effects beyond those manifested in simple travel time and amplitude observations.

Acknowledgments. J.B.G. received a Turner Fund grant from the Department of Geological Sciences at the University of Michigan. Special thanks to C. Young for the North American data used in this analysis, a thorough review of the manuscript, and many helpful discussions. K. Toy provided a tabulation of his travel time station statics; J. Edwards assisted with the digitizing; M. Weber, V. Cormier, and an anonymous reviewer provided helpful reviews of the manuscript. J.B.G. thanks T. Jordan for financial support, and B. Hager and T. Herring for computer time, during completion of this work at MIT. This research was supported by grants EAR 8451715 (T.L.) and EAR 8707578 (J.E.V.) from the National Science Foundation and by the W.M. Keck Foundation. Contribution 112, Institute of Tectonics and C.F. Richter Seismological Laboratory, U.C. Santa Cruz.

REFERENCES

Agnon, A., and M.S.T. Bukowinski, ∂s at high pressure and *d*ln*Vs*/*d*ln*Vp* in the lower mantle, *Geophys. Res. Lett.*, *17*, 1149-1152, 1990.

Aki, K., and P.G. Richards, *Quantitative Seismology*, 932 pp., W.H. Freeman, New York, 1980.

Anderson, D.L., Thermally induced phase changes, lateral heterogeneity of the mantle, continental roots and deep slab anomalies, *J. Geophys. Res.*, *92*, 13,968-13,980, 1987*a*.

Anderson, D.L., A seismic equation of state, II, Shear properties and thermodynamics of the lower mantle, *Phys. Earth Planet. Inter.*, *45*, 307-323, 1987*b*.

Apperson, K.D., and C. Frohlich, The relationship between Wadati-Benioff zone geometry and *P*, *T*, and *B* axes of intermediate and deep focus earthquakes, *J. Geophys. Res.*, *92*, 13,821-13,831, 1987.

Baumgardt, D.R., Evidence for a *P*-wave velocity anomaly in *D"*, *Geophys. Res. Lett.*, *16*, 657-660, 1989.

Beck, S.L., and T. Lay, Test of the lower mantle slab penetration hypothesis using broadband *S* waves, *Geophys. Res. Lett.*, *13*, 1007-1010, 1986.

Butler, R., and L.J. Ruff, Teleseismic short-period amplitudes: Source and receiver variations, *Bull. Seismol. Soc. Am.*, *70*, 831-850, 1980.

Cormier, V.F., Slab diffraction of *S* waves, *J. Geophys. Res.*, *94*, 3006-3024, 1989.

Cormier, V.F., and W. Kim, Three-dimensional modeling of subducted lithospheric slabs from the amplitudes and waveforms of *S* waves, *Sci. Rep. 2*, pp. 9-52, Geophys. Lab., Hanscom Air Force Base, Mass., 1990.

Creager, K.C., and T.H. Jordan, Slab penetration into the lower mantle, *J. Geophys. Res.*, *89*, 3031-3049, 1984.

Creager, K.C., and T.H. Jordan, Slab penetration into the lower mantle beneath the Mariana and other island arcs of the northwest Pacific, *J. Geophys. Res.*, *91*, 3573-3589, 1986.

Davies, D., and D.P. McKenzie, Seismic travel-time residuals and plates, *Geophys. J. R. Astron. Soc.*, *18*, 51-63, 1969.

Dziewonski, A.M., Mapping the lower mantle: Determination of lateral heterogeneity in *P* velocity up to degree and order 6, *J. Geophys. Res.*, *89*, 5929-5952, 1984.

Dziewonski, A.M., and D.L. Anderson, Preliminary reference earth model, *Phys. Earth Planet. Inter.*, *25*, 297-356, 1981.

Dziewonski, A.M., and D.L Anderson, Travel times and station corrections for *P* waves at teleseismic distances, *J. Geophys. Res.*, *88*, 3295-3314, 1983.

Engdahl, E.R., and D. Gubbins, Simultaneous travel time inversion for earthquake locations and subduction zone structure in the central Aluetian Islands, *J. Geophys. Res.*, *92*, 13,855-13,862, 1987.

Fischer, K.M., T.H. Jordan, and K.C. Creager, Seismic constraints on the morphology of deep slabs, *J. Geophys. Res.*, *93*, 4773-4783, 1988.

Fischer, K.M., K.C. Creager, and T.H. Jordan, Mapping the Tonga slab, *J. Geophys. Res., in press*, 1991.

Fitch, T.J., Compressional velocity in source regions of deep earthquakes, *Earth Planet. Sci. Lett.*, *26*, 156-166, 1975.

Frohlich, C., The nature of deep focus earthquakes, *Annu. Rev. Earth Planet. Sci.*, *17*, 227-254, 1989.

Giardini, D., and J.H. Woodhouse, Deep seismicity and modes of deformation in Tonga subduction zone, *Nature*, *307*, 505-509, 1984.

Grand, S.P., Tomographic inversion for shear velocity structure beneath the North American Plate, *J. Geophys. Res.*, *92*, 14,065-14,090, 1987.

Grand, S.P., A possible station bias in travel time measurements reported to ISC, *Geophys. Res. Lett.*, *17*, 17-20, 1990.

Grand, S.P., and X.-Y. Ding, Residual spheres and slab penetration into the lower mantle (abstract), *Eos Trans. AGU*, *70*, 1322, 1989.

Gurnis, M., and B.H. Hager, Controls on the structure of subducted slabs, *Nature, 335*, 317-321, 1988.

Isacks, B., and P. Molnar, Distribution of stresses in the descending lithospere from a global survey of focal-mechanism solutions of mantle earthquakes, *Rev. Geophys., 9*, 103-172, 1971.

Isacks, B., J. Oliver, and L.R. Sykes, Seismology and the new global tectonics, *J. Geophys. Res., 73*, 5855-5899, 1968.

Jeanloz, R., and E. Knittle, Density and composition of the lower mantle, *Philos. Trans. R. Soc. London, Ser. A, 328*, 377-389, 1989.

Jordan, T.H., Lithospheric slab penetration into the lower mantle beneath the Sea of Okhotsk, *J. Geophys., 43*, 473-496, 1977.

Jordan, T.H., and W.S. Lynn, A velocity anomaly in the lower mantle, *J. Geophys. Res., 79*, 2679-2685, 1974.

Kamiya, S., T. Miyatake, and K. Hirahara, How deep can we see the high velocity anomalies beneath the Japan Islands?, *Geophys. Res. Lett., 15*, 828-831, 1988.

Kamiya, S., T. Miyatake, and K. Hirahara, Three dimensional P wave velocity structure beneath the Japanese Islands, *Bull. Earthquake. Res. Inst. Univ. Tokyo, 64*, 457-485, 1989.

Lavely, E.M., D.W. Forsyth, and P. Friedemann, Scales of heterogeneity near the core-mantle-boundary, *Geophys. Res. Lett., 13*, 1505-1508, 1986.

Lay, T., Localized velocity anomalies in the lower mantle, *Geophys. J. R. Astron. Soc., 72*, 483-516, 1983.

Lay, T., and D.V. Helmberger, Body wave amplitude and travel time correlations across North America, *Bull. Seismol. Soc. Am., 73*, 1063-1076, 1983*a*.

Lay, T., and D.V. Helmberger, A lower mantle S wave triplication and the shear velocity structure of *D"*, *Geophys. J. R. Astron. Soc., 75*, 799-838, 1983*b*.

Mikumo, T., Source process of deep and intermediate earthquakes as inferred from long-period *P* and *S* waveforms, 2. Deep focus and intermediate depth earthquakes around Japan, *J. Phys. Earth, 19*, 303-320, 1971.

Rees, B.A., and E.A. Okal, The depth of the deepest historical earthquakes, *Pure Appl. Geophys., 125*, 699-715, 1987.

Ribe, N.M., Seismic anisotropy and mantle flow, *J. Geophys. Res., 94*, 4213-4223, 1989.

Romanowicz, B.A., and M. Cara, Reconsideration of the relations between *S* and *P* station anomalies in North America, *Geophys. Res. Lett., 7*, 417-420, 1980.

Schwartz, S.Y., T. Lay, and S.L. Beck, Shear wave travel time, amplitude, and waveform analysis: Constraints on deep slab structure and mantle heterogeneity, for earthquakes in the Kurile slab, *J. Geophys. Res., in press*, 1991.

Sengupta, M.K., The structure of the Earth's mantle from body wave observations, Sc.D. thesis, 578 pp., Mass. Inst. of Technol., Cambridge, 1975.

Silver, P.G., and W.W. Chan, Observations of body wave multipathing from broadband seismograms: Evidence for lower mantle slab penetration beneath the Sea of Okhotsk, *J. Geophys. Res., 91*, 13,787-13,802, 1986.

Silver, P.G., R.W. Carlson, and P. Olson, Deep slabs, geochemical heterogeneity, and large-scale structure of mantle convection: Investigation of an enduring paradox, *Annu. Rev. Earth Planet. Sci., 16*, 477-541, 1988.

Spakman, W., S. Stein, R. van der Hilst, and R. Wortel, Resolution experiments for NE Pacific subduction zone tomography, *Geophys. Res. Lett., 16*, 1097-1100, 1989.

Stark, P.B., and C. Frohlich, The depths of the deepest deep earthquakes, *J. Geophys. Res., 90*, 1859-1869, 1985.

Stead, R.J., and D.V. Helmberger, Numerical-analytical interfacing in two dimensions with applications to modeling NTS seismograms, *Pure Appl. Geophys., 128*, 157-193, 1988.

Strelitz, R., The September 5, 1970 Sea of Okhotsk earthquake: A multiple event with evidence of triggering, *Geophys. Res. Lett., 2*, 124-127, 1975.

Suetsugu, D., Lower mantle high velocity zone beneath the Kurils as inferred from *P* wave travel time and amplitude data, *J. Phys. Earth, 37*, 265-295, 1989.

Tanimoto, T., Long-wavelength *S*-wave velocity structure throughout the mantle, *Geophys. J. Int., 100*, 327-336, 1990.

Toy, K.M., Tomographic analysis of ISC travel time data for earth structure, Ph.D. thesis, Univ of Calif, San Diego, 1989.

Vassiliou, M.S., The state of stress in subducting slabs as revealed by earthquakes analyzed by moment tensor inversion, *Earth Planet. Sci. Lett., 69*, 195-202, 1984.

Veith, K.F. The relationship of island arc seismicity to plate tectonics, Ph.D. thesis, South. Methodist Univ., Dallas, Tex, 1974.

Vidale, J.E., Waveform effects of a high velocity, subducted slab, *Geophys. Res. Lett., 14*, 542-545, 1987.

Weber, M., Subduction zones--Their influence on traveltimes and amplitudes of *P* waves, *Geophys. J. Int., 101*, 529-544, 1990.

Weber, M., and J.P. Davis, Evidence of a laterally inhomogeneous lower mantle structure from *P*- and *S*-waves, *Geophys. J. Inter., 102*, 231-255, 1990.

Wickens, A.J., and G.G.R. Buchbinder, *S*-wave residuals in Canada, *Bull. Seismol. Soc. Am., 70*, 809-822, 1980.

Witte, D., The pseudospectral method for simulating wave propagation, Ph.D. thesis, Columbia Univ., New York, 1989.

Zhou, H.-W., How well can we resolve the deep seismic slab with seismic tomography?, *Geophys. Res. Lett, 15*, 1425-1428, 1988.

Zhou, H.-W., and D.L. Anderson, Teleseismic contributions to focal residual spheres and Tangshen earthquake sequence (abstract), *Eos Trans. AGU, 70*, 1322, 1989.

Zhou, H.-W., and R.W. Clayton, *P* and *S* wave travel time inversions for subducting slabs under the island arcs of the northwest Pacific, *J. Geophys. Res., 95*, 6829-6851, 1990.

Zhou, H.-W., D.L. Anderson, and R.W. Clayton, Modeling of residual spheres for subduction zone earthquakes, 1., Apparent slab penetration signatures in the NW Pacific caused by deep diffuse mantle anomalies, *J. Geophys. Res., 95*, 6799-6827, 1990.

J.B. Gaherty, Rm. 54-526, Department of Earth, Atmospheric, and Planetary Sciences, Massachusetts Institute of Technology, Cambridge, MA 02139.

T. Lay, Institute of Tectonics, Earth Sciences Board, Applied Sciences Bldg., University of California, Santa Cruz, CA 95060.

J.E. Vidale, U.S. Geological Survey, 345 Middlefield Road, MS 977, Menlo Park, CA 94025.

(Received October 19, 1990;
revised March 4, 1991;
accepted May 28, 1991.)

JOURNAL OF GEOPHYSICAL RESEARCH, VOL. 96, NO. B10, PAGES 16,401–16,414, SEPTEMBER 10, 1991

Seismicity and Detection/Location Threshold in the Southern Great Basin Seismic Network

JOAN GOMBERG

U.S. Geological Survey, Denver Federal Center, Denver, Colorado

A spatially varying model of the detection/location capabilities of the Southern Great Basin seismic network (SGBSN) has been derived that is based on simple empirical relations and statistics. This permits use of almost all the catalog data gathered; instead of ignoring data that are below the threshold of completeness, a spatially varying threshold model is developed so that subregions having lower completeness levels than the network as a whole can be outlined and the completeness level of each sub-region determined. Such a model is required to unambiguously identify regions that are aseismic due to natural processes rather than to limited detection and/or location capabilities. Accounting for spatial variations in detection/location threshold is also important for studies in which magnitude-frequency distributions are interpreted in terms of source scaling properties. The characteristics of the spatial distribution of earthquakes, where earthquake clusters and aseismic regions locate, appear to be stable at all magnitude levels so that inferences about where strain is being accommodated will be the same whether numbers of earthquakes or strain estimated from seismic moments are examined. For the southern Great Basin region these principal characteristics include clusters at the northern end of the Furnace Creek fault and in the Pahranagat Shear Zone, and a relatively large number of earthquakes in the northern and southeastern portions of the Nevada Test Site. These clusters cover regions much larger than the surface projections of any of the mapped faults. The extent to which seismicity is induced by nuclear testing is unclear. The predominantly aseismic regions include the area west of the Death Valley/Furnace Creek fault system and an almost complete absence of events at Yucca Mountain. Finally, a considerable number of isolated events in the SGBSN catalog cannot be correlated with mapped faults.

INTRODUCTION

The principal goal of this study is the development of a spatially variable detection/location threshold model for the Southern Great Basin Seismic Network (SGBSN). It is common practice when interpreting seismicity patterns to ignore data below the "magnitude of completeness" in order to avoid bias arising from non-uniform detection/location capabilities. Earthquakes with magnitudes below the completeness level may be missing from a catalog because the seismic waves they generate are too small to be adequately recorded at a sufficient number of seismic stations to be reliably located. One method of determining the magnitude of completeness is based on the Gutenberg-Richter relationship [*Gutenberg and Richter*, 1941, 1954]

$$\log N(m) = a - b\,m \qquad (1)$$

where $N(m)$ is the number of earthquakes with magnitude m and a and b are empirically derived constants. The magnitude of completeness is defined as the magnitude where the magnitude-frequency data begin to deviate from a linear relationship (see *Evernden* [1969], *Kelly and Lacoss* [1969], *Ringdal* [1975] *von Seggern and Blandford* [1976] or *Taylor et al.* [1990] for a summary). The observed magnitude-frequency distribution from the SGBSN are shown in Figure 1 and indicate that the magnitude of completeness is approximately 1.6. This means that if common practice were followed, approximately 2/3's of the catalog would have to be ignored and thus potentially some of the interesting signal.

Instead of ignoring data, a spatially varying threshold model is developed so that sub-regions having lower completeness levels than the network as a whole can be outlined and the completeness level of each sub-region determined. In this study the primary motivation for developing such a model is to be able to unambiguously identify regions that are aseismic due to natural processes rather than to limited detection and/or location capabilities. This is required for the identification of seismicity patterns within the SGBSN. The analysis of these patterns is described in a companion paper, [*Gomberg*, this issue] that is herein referred to as Paper II.

Calculation of the threshold model described in this paper is simple to implement and the validity of the results are easily verified. The derivation of threshold model does not require the statistical assumption that earthquakes are uniformly distributed spatially which is clearly inappropriate for the SGBSN (Figure 2) and for many other regions [*Reasenberg*, 1985]. The model is based on the assumption that the spatial change in detection threshold is related to amplitude decay due to attenuation and spreading since amplitudes below some signal-to-noise limit will not be detectable. The requirements for reliable earthquake location can also be accounted for since these also determine whether an event is included in a network seismicity catalog. Two independent methods of testing the validity of derived threshold models are also described. One method does assume a spatially uniform distribution of seismicity but it will be demonstrated that this is not necessarily problematic.

Most threshold studies have been done for the purpose of improving earthquake/explosion discrimination potential [e.g., *Ringdal*, 1986; *Evernden et al.*, 1986; *Sereno and Bratt*, 1989] although many of these are not published in easily accessed documents (D. Taylor, personal communication, 1991). While the number of publications describing local seismicity is great, few exist pertaining to local earthquake network detection/location capabilities. A literature search yields one report by the Nuclear Regulatory Commission [*Mauk and Christensen*, 1980] describing a complex method for determining a spatially variable

Paper number 91JB01593.

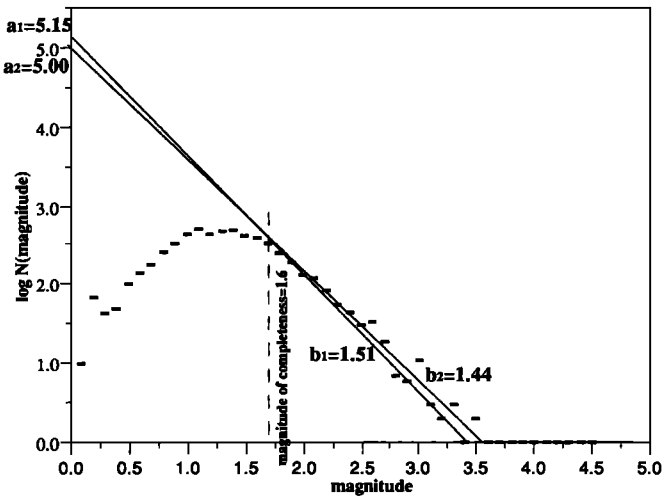

Fig. 1. (*a*) Magnitude-frequency data (solid rectangles) from the Southern Great Basin Seismic Network catalog for the years 1983 to 1989. The magnitude of completeness and *y*-intercepts (*a* 's) are estimated visually. The slopes are one standard deviation bounds on the maximum likelihood estimates of *b*. (*b*) Same as Figure 1*a* except that the slopes (*b* values) are estimated visually.

detection/location model and a paper by *Rydelek and Sacks* [1989] describing a method for determining a single threshold magnitude for the entire network. Application of methods developed for discrimination studies to local earthquake networks are not straightforward since they are based largely on use of regional or teleseismic data. Furthermore such models can only be validated by comparing them with other models [*Sereno and Bratt*, 1989] since actual data is generally not available (e.g., only recently have data become available from the USSR which is the principal focus of discrimination studies). This model development and verification approach ignores temporal and spatial variations in individual station noise and/or response characteristics and uses a single attenuation model for the entire region. Although the approach described in this paper is not as quantitatively rigorous as some of these others, it is adequate for the analysis described in Paper II. Furthermore, the approach has the advantage over others that the models developed are tested for consistency with real data.

Accounting for spatial variations in detection/location threshold may also be important for studies in which magnitude-frequency distributions are interpreted in terms of source properties [*Taylor et al.*, 1987, 1990; *Rydelek and Sacks*, 1989;*Trifu and Radulian*, 1991]. For example, several recent studies use a magnitude of completeness that is defined by *Rydelek and Sacks* [1989] as the lowest magnitude which is not preferentially reported during the night when the signal-to-noise ratio is greater. Observations that the *Rydelek and Sacks*' [1989] magnitude of completeness does not coincide with the magnitude at which a Gutenberg-Richter relationship no longer holds may be interpreted as evidence for non-self similar behavior of earthquake sources [*Taylor et al.*, 1987, 1990; *Rydelek and Sacks*, 1989]. When certain conditions are met (see Appendix A), spatial variations in threshold can introduce features in the magnitude-frequency distributions that might be interpreted to be consequences of physical processes. (Note that this is only a caution for future studies and does not imply that the aforementioned studies are incorrect.) Therefore, in order for such interpretations to be useful, the spatial variability in threshold must either be accounted for or shown to be unimportant.

DERIVATION OF A DETECTION/LOCATION THRESHOLD MODEL

The threshold model is based on the formula for local magnitude [*Richter*, 1958]

$$m = \log A(r_j)_{obs} + \log A(r_j) \tag{2}$$

where $A(r_j)_{obs}$ is the amplitude (corrected for instrument response) observed at the jth station located at a distance r_j from the source. $A(r_j)$ is a distance correction that accounts for amplitude decay. (Note that the sign convention of the correction term has been changed from the original definition for convenience.) The minimum magnitude earthquake that can be detected, $m=T_{min}$, is that event which produces the minimum amplitude that can be reliably recorded at the closest source-receiver distance r_{min}. This minimum amplitude is derived from a rearrangement of equation (2) yielding

$$\log A(r_{min})_{obs} = T_{min} - \log A(r_{min}) \tag{3}$$

To be detected an event must have a magnitude, m, that is sufficiently large that the associated amplitudes are at least equal to this minimum. This means that

$$\log A(r_j)_{obs} \geq \log A(r_{min})_{obs} \tag{4a}$$

Substituting from equation (3) results in the expression

$$\log A(r_j)_{obs} \geq T_{min} - \log A(r_{min}) \tag{4b}$$

and substituting from equation (2) and rearranging yields

$$m \geq T_{min} - \log A(r_{min}) + \log A(r_j) \tag{4c}$$

Finally the detection criterion is obtained assuming

$$\log A(r_{min}) = 0 \tag{5}$$

which physically is reasonable since it implies that at some distance attenuation and spreading are negligible. Equation (4c) becomes

$$m \geq T_{min} + \log A(r_j) \tag{6}$$

The potential for an event to be detected and located by the network is evaluated using equation (6) and substituting $A(r_j)$ with

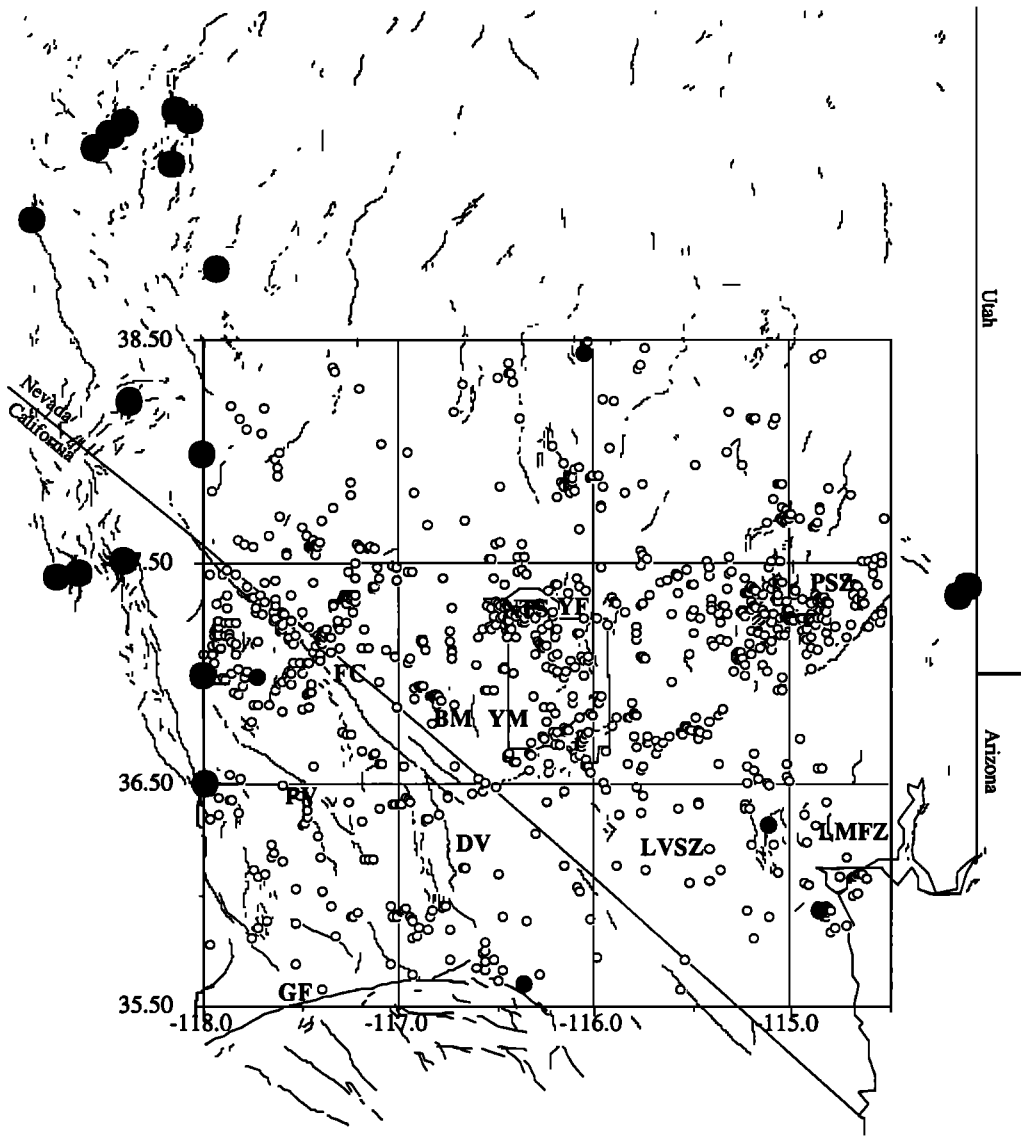

Fig. 2. Map of the area covered by the Southern Great Basin Seismic Network. Curved line segments are Quaternary fault scarps and lineaments inferred from geologic information [*Nakata et al.*, 1982]. Large solid circles are historic earthquake epicenters with magnitudes greater than approximately 6.0 [*Gawthrop and Carr*, 1988]. Epicenters of events recorded on the SGBSN between 1983 and 1989 are shown by the smaller solid circles for events recorded with local magnitude greater than 3.4 (the largest is 4.3), and open ovals are for events with magnitude greater than or equal to 1.6. Abbreviations are FC, Furnace Creek Fault; DV, Death Valley Fault Zone; LVSZ, Las Vegas Shear Zone; PSZ, Pahranagat Shear Zone; PV, Panamint Valley Fault Zone; GF, Garlock Fault; LMFZ, Lake Mead Fault Zone; YF, Yucca Fault; BM, Bear Mountain Fault; NTS, Nevada Test Site ; and YM, Yucca Mountain.

a weighted average amplitude, $\overline{A}$. The average is taken from the amplitudes calculated at all the stations in the network and a weighting can be used to account for criteria required to make an event locatable as well as detectable. Thus, an event located at the ith spatial point has to satisfy the equation

$$m_i \geq T_{\min} + \log \overline{A}_i \tag{7}$$

and the threshold magnitude (the minimum detectable/locatable magnitude), T_i, at this point is that which makes equation (7) an equality or

$$T_i = T_{min} + \log \overline{A}_i \tag{8}$$

The average amplitude at the ith point is calculated according to

$$\overline{A}_i = \left(\sum_{j=1}^{J} w_{ij}\right)^{-1} \sum_{j=1}^{J} w_{ij} A(r_{ij}) \tag{9}$$

where J is the number of stations in the network, $A(r_{ij})$ is the amplitude that would be observed at the jth station located at a distance r_{ij} from the ith point and w_{ij} is a weight. The weights can be designed so that phase arrivals from stations that provide greater constraint on the location have greater influence in the threshold estimate. For example, for one of the threshold models of the SGBSN discussed below, weights of the form

$$w_{ij} = 1/(0.01 r_{ij} + 0.88) \tag{10}$$

are used since this has the effect of giving greater weight to arrivals

from stations within 12 km of an event. This weighting is sensible because arrivals at stations closer than approximately 1.5 times the focal depth provide greater constraint on hypocenter estimates [*Gomberg et al.*, 1990] and most of the events within the SGBSN are probably shallower than 8 km depth [*Rogers et al.*, 1987a].

Finally, a spatially varying map of a threshold model is derived by calculating T_i (equation (8)) for points on a finely spaced grid covering the region of interest. This grid can be displayed in a shaded format or contoured. The first term in equation (8), $T_{\min}$, may be set equal to the smallest magnitude found in the network catalog. The second term, the average amplitude, can be calculated from empirically derived decay functions.

VALIDATION OF A DETECTION/LOCATION THRESHOLD MODEL

Two approaches to testing the validity of a threshold model are presented. The first test requires that the spatial distribution of earthquakes in different magnitude bins do not violate the predictions of the threshold model. For example, if the threshold model predicts a threshold contour for T=2.0, then no earthquakes with $m \leq 2.0$ should be observed outside this contour. Earthquakes with $m \leq 2.0$ should also be distributed within this contour with some events located at the edges of the bounded area. The validity of the entire contoured area cannot be checked since seismicity is often not spatially uniformly distributed [*Reasenberg*, 1985] resulting in regions inside the bounded area with no earthquakes at all.

The second validation test compares a theoretical magnitude-frequency curve with the observed data. The expected number of earthquakes at each magnitude predicted by the grid of threshold values, using an assumed value of T_{min} and the Gutenberg-Richter relationship (equation (1)) is

$$N(m)_{\text{total}} = \sum_{i=1}^{I} N_i(m) \tag{11}$$

where $N_i(m)$ is the number of earthquakes with magnitude m in the area corresponding to the ith grid point and I is the total number of grid points. $N_i(m)$ is derived according to

$$\begin{aligned} N_i(m) &= \frac{\Delta S_i}{S} 10^{a} 10^{-b m} && m \geq T_i \\ &= 0 && m < T_i \end{aligned} \tag{12}$$

ΔS_i is the area represented by each grid point, S is the total area, and a and b are the empirically determined values in the Gutenberg-Richter relationship.

The values of a and b may be estimated by linear regression, maximum likelihood, or visually. The maximum likelihood estimate of b is

$$b = \frac{1}{\bar{m} - m_o} \qquad \bar{m} = \frac{1}{n} \sum_{k=1}^{n} m_k \tag{13}$$

[*Aki*, 1965] where m_o is the minimum magnitude to be used in the estimate and n is the number of magnitudes. The most conservative statistical estimate of the uncertainty in b accounts for spatial and/or temporal variations in $\bar{m}$ and is calculated according to

$$\sigma(b) = \frac{b^2}{\log_{10} e} \sigma(\bar{m}) \qquad \sigma(\bar{m})^2 = [n(n-1)]^{-1} \sum_{k=1}^{n} (m_k - \bar{m})^2 \tag{14}$$

[*Shi and Bolt*, 1982].

The assumption that seismicity is uniformly distributed in space is implicit in this test which is clearly not true for the SGBSN region (Figure 2). This nonuniformity implies that the values of a and b vary for subregions. If certain conditions are met, the values of a and b estimated from all the data will be nearly identical to those that would be derived from estimating a and b (as in Figure 1) for subregions and averaging them. As long as the average is correctly predicted, it does not matter how the seismicity is distributed spatially and thus, the assumption of uniformly distributed seismicity implicit in equation (12) is justified.

A simple example illustrates this point. Suppose that the entire region of interest is divided in half with each half having a different magnitude-frequency distribution characterized by a_1, b_1, and a_2, b_2. The Gutenberg-Richter relationship for the entire region is

$$\begin{aligned} \log(N/2) &= (a - \log 2) - b m \\ &\approx \bar{a} - \bar{b} m + \log[1 + (\gamma \ln 10)^2] \end{aligned} \tag{15}$$

where

$$\bar{a} = \frac{a_1 + a_2}{2}, \quad \bar{b} = \frac{b_1 + b_2}{2}, \quad \gamma = \Delta a - \Delta b\, m$$

$$\Delta a = \frac{a_1 - a_2}{2}, \quad \Delta b = \frac{b_1 - b_2}{2}$$

provided that

$$\gamma \ln 10 < 1 \tag{16}$$

is satisfied. See Appendix B for the derivation of these equations. The requirement on the size of the parameter γ (a measure of the differences in the values of a and b) limits the size of the right-most term in equation (15) to be less than 0.3, which is smaller than the uncertainty in the value of a estimated from the SGBSN data (Figure 1*b*). Thus, when equation (16) is true, the b value for the entire region is nearly equal to the average b value of the two halves and the a value is nearly equal to the average plus a constant or

$$\log N(m) \approx \bar{a} + \log 2 - \bar{b} m \tag{17}$$

Physically a represents the total production of earthquakes during the time interval examined. The constant, log2, corrects for the fact that $\bar{a}$ corresponds to half the area and thus the total number of events is effectively halved.

To illustrate that this is may be true for real data, the SGBSN is divided into four quadrants of equal area and the average values are compared with the values estimated from the entire dataset (applying equation (15) twice). The b values are estimated using equation (13) and the a values are estimated visually. The results are summarized in Table 1 and show that the average of the b values for each quadrant differs from the b value for the entire dataset by only 0.03 and the average a differs from that for the entire dataset by only 0.10. Also note that the a and b values obtained by averaging values estimated for the northern and southern halves are distinctly different from those values obtained if the network data are divided instead from eastern and western halves. However, the average of either the north/south values or the east/west values are nearly identical. Similarly, the same average value would be obtained if the data were distributed uniformly so that the a and b values are the same for two halves. This further justifies the assumption implicit in equation (12).

TABLE 1. Values of a and b Derived from Magnitude-Frequency Data for Different Parts of the SGBSN

Area of Network	Location	$a - b\,m$
Entire Network	35.5 N to 38.5 N 118.0 W to 114.5 W	5.09 - 1.48 m
Northern Half	37.0 N to 38.5 N 118.0 W to 114.5 W	5.09 - 1.52 m
Southern Half	35.5 N to 37.0 N 118.0 W to 114.5 W	4.50 - 1.40 m
Average (Entire Network)		5.10 - 1.46 m
Eastern Half	35.5 N to 38.5 N 116.25 W to 114.5 W	4.77 - 1.44 m
Western Half	35.5 N to 38.5 N 118.0 W to 116.25 W	4.92 - 1.52 m
Average (Entire Network)		5.15 - 1.48 m
SE Quadrant	35.5 N to 37.0 N 116.25 W to 114.5 W	3.67 - 1.29 m
NE Quadrant	37.0 N to 38.5 N 116.25 W to 114.5 W	4.80 - 1.49 m
SW Quadrant	35.5 N to 37.0 N 118.0 W to 116.25 W	4.40 - 1.46 m
NW Quadrant	37.0 N to 38.5 N 118.0 W to 116.25 W	4.65 - 1.56 m
Average (Western Half)		4.83 - 1.51 m
Average (Eastern Half)		4.54 - 1.39 m
Average (Entire Network)		4.99 - 1.45 m

Averages are calculated according to equations (B4) and (B7).

A reasonable acceptable fit between the predicted and observed magnitude-frequency distributions is one in which the difference is no larger than the difference in theoretical distributions derived for bounding measured values of a and b. Since it is possible that source or propagation processes also (in addition to threshold variations) may cause magnitude-frequency distributions to deviate from a linear relationship [*Hanks and Boore*, 1984; *Taylor et al.*, 1987, 1990; *Rydelek and Sacks*, 1989;*Trifu and Radulian*, 1991; A. Snoke, personal communication, 1991], only a qualitative evaluation of the goodness of fit between the predicted and observed distributions is considered warranted. The extent to which source or propagation effects are important can only be determined with independent data and analyses that are beyond the scope of this study.

DETECTION/LOCATION THRESHOLD MODELS OF THE SOUTHERN GREAT BASIN SEISMIC NETWORK

The 55 stations of the SGBSN have been operating in essentially the same configuration since the beginning of 1983. The distribution of stations is shown in Figure 3 and details about the network are found in *Rogers et al.* [1987a]. For the purposes of this study it is assumed that all stations have identical dynamic ranges (e.g., they are all able to reliably record earthquakes of local magnitude $m=M_L=0.0$ to $M_L=4.3$). Only earthquakes in the geographic box with southwest corner 35.5°N, 118.0°W and northeast corner 38.5°N, 114.5°W are included in the SGBSN catalog. A local magnitude (5511 events) or a duration magnitude (296 events; duration magnitudes are calibrated against the local magnitudes) is assigned to all events used in the study. No attempt is made to account for radiation patterns or depth effects; the former are generally unknown and the station spacing and instrumentation

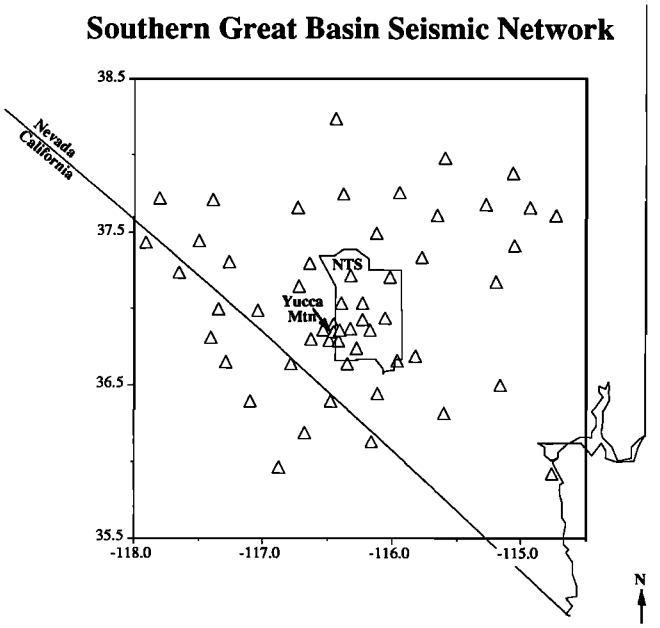

Fig. 3. Station map of SGBSN; station locations are indicated by triangles; the NTS (polygon in the center), location of Yucca Mountain and Nevada state boundary are shown for reference.

of the SGBSN are inadequate to estimate earthquake depths routinely with sufficient confidence to draw meaningful conclusions [*Gomberg*, 1991; *Gomberg et al.*, 1990]. The epicentral uncertainties are probably no more than a few kilometers which are insignificant with respect to this analysis [*Gomberg*, 1991]. It is simply assumed that the catalog magnitudes are sufficiently accurate for the purposes of this study.

In order to apply the second validation test to any models developed it is necessary to estimate the values of a and b in equation (1). Two lines for bounding values, $b \pm \sigma(b)$ calculated using equations (13) and (14) are plotted with the data on Figure 1*a*. These statistical estimates (even if two standard deviations are used) do not fully span the range of b values that one would estimate visually (Figure 1*b*). Furthermore, statistical uncertainties cannot account for deviations from a Gutenberg-Richter relation arising from physical processes as discussed above. Thus, the larger uncertainties (the visual estimates) are deemed more appropriate representations of the true uncertainty in b and are used in the analysis.

The first attempt to develop a threshold model for the SGBSN uses the empirically derived amplitude decay function developed for estimation of magnitudes using SGBSN data [*Rogers, et al.*, 1987b]. The decay function is

$$\begin{aligned} \log A(r) &= 0.833 \log(r) + 0.00164\, r + 0.88 \qquad r > 0.088 \\ &= 0 \qquad\qquad\qquad\qquad\qquad\qquad\quad r \le 0.088 \end{aligned} \tag{18}$$

Although this function as derived by *Rogers et al.* [1987b] is actually only zero at $r=0.088$ km, it is physically unreasonable to allow it to become negative at shorter distances since seismic waves are not amplified as they propagate (unless there are site amplification effects which are not meant to be represented by this function). This also is consistent with the requirements of the threshold model (equation (8)). No weights are used ($w_{ij}=1$ for all J) and $T_{\min}$ is set equal to the smallest magnitude found in the SGBSN catalog, $M_L \approx 0.1$.

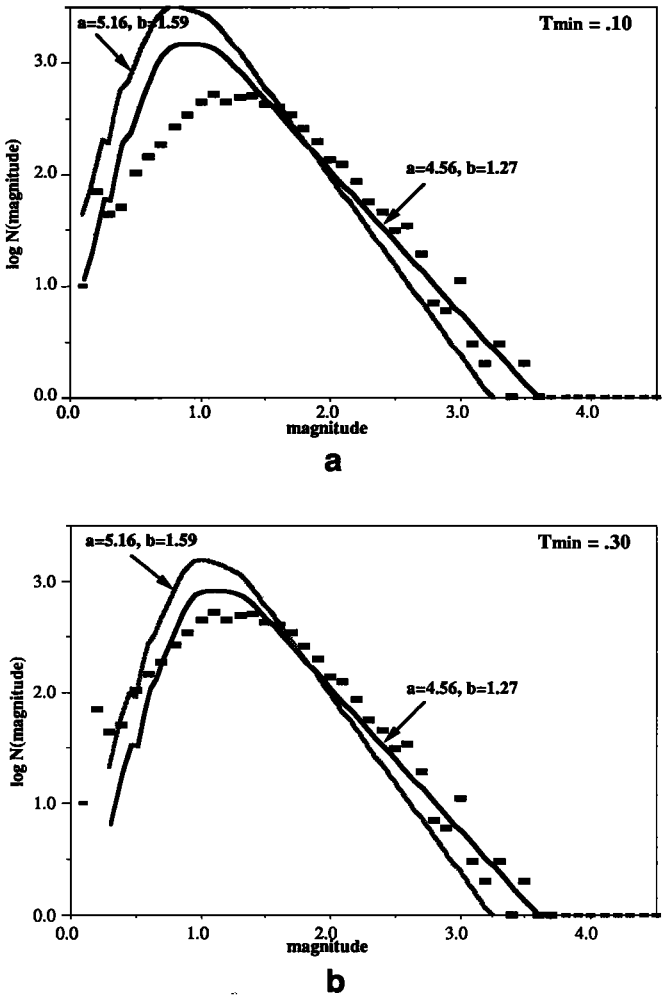

Fig. 4. Theoretical magnitude-frequency curves for the amplitude decay function of *Rogers et al.* [1987b] and minimum thresholds of (*a*) 0.1 and (*b*) 0.3 are shown by the solid lines. Two relations are shown in each plot corresponding to the bounding values of a and b determined from the data (Figure 1). The data are indicated by the solid rectangles.

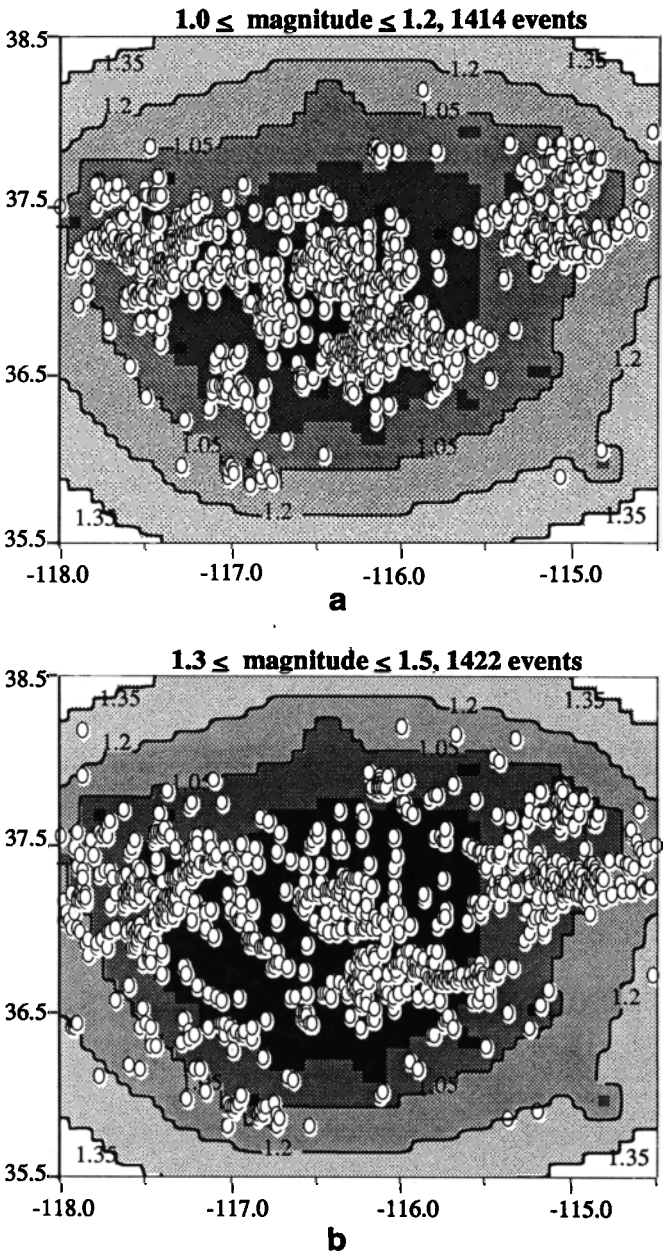

Fig. 5. Epicenter maps for events in the magnitude bins 1.0-1.2, 1.3-1.5, 1.6-1.8 and 1.9-2.1 superimposed on the threshold map calculated for the same parameters used to derive the curves shown in Figure 3*b*. Epicenters are indicated by the white ovals. The shading changes for each increment of 0.15 magnitude units and gets lighter as the threshold magnitude increases. The black areas correspond to the only regions in which events with magnitude less than 0.60 will be recorded.

This threshold model predicts a theoretical magnitude-frequency distribution [equations (11) and (12)] that does a poor job of fitting the observed data (Figure 4*a*); the difference between the predicted curves and the observations is greater than the difference between the two curves which are estimated from the bounding values of a and b. The simplest way to improve the fit is to increase T_{min} to a value of 0.3 (Figure 4*b*). There is little need to try to justify this since the model also fails the second validation test using either value of T_{min}. The spatial variations in the threshold model are shown in a shaded map view in Figure 5 for a value of T_{min}= 0.3 and are compared with the distribution of epicenters of events in increasing magnitude ranges. This threshold model predicts that earthquakes with magnitude greater than $M_L \approx 1.4$ will be detected and located everywhere. However, the observed spatial distribution as it varies with magnitude spreads out much more slowly and events are not observed at the perimeters of the network until they have magnitudes of approximately 1.6 and above.

The second validation test results suggest that the threshold increases more rapidly with distance from the center of the SGBSN than predicted by the first modeling attempt. Two alternatives are investigated although they are by no means the only possibilities. In the first case the SGBSN decay function (equation (18)) is still used but the calculated amplitudes are weighted according to equation (10). In the second case a decay function, $A(r)$, that decays more rapidly with distance is used (no weighting). In order to explore the effect of increasing the amplitude decay on the threshold model the amplitude decay function developed by *Bakun and Joyner* [1984] for central California is used. It is

$$\log A(r) = \log(r) + 0.00301\, r + 0.70 \quad r \geq 0.199 \text{ km}$$
$$= 0 \quad r < 0.199 \text{ km} \qquad (19)$$

(modified so that it does not become negative). An empirically constrained function is chosen rather than a purely hypothetical one

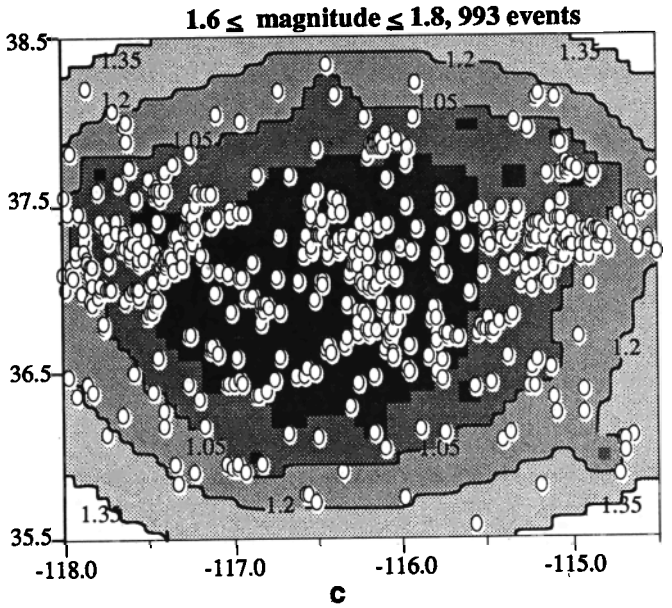

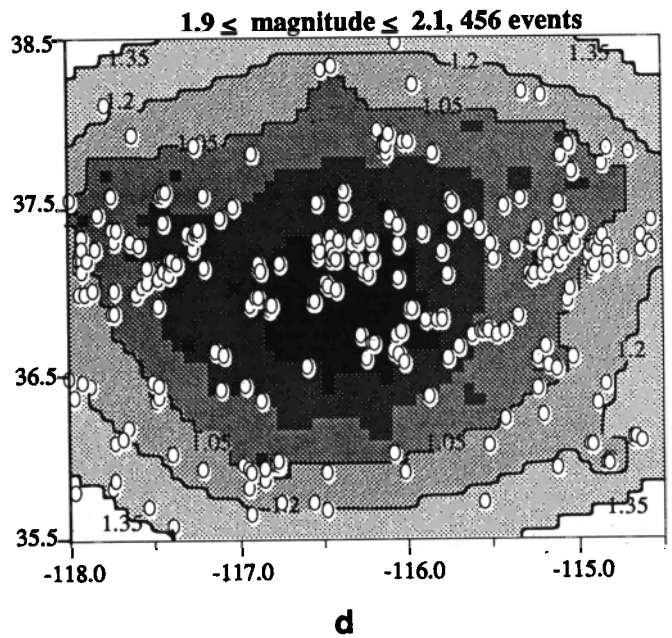

Fig. 5. (continued)

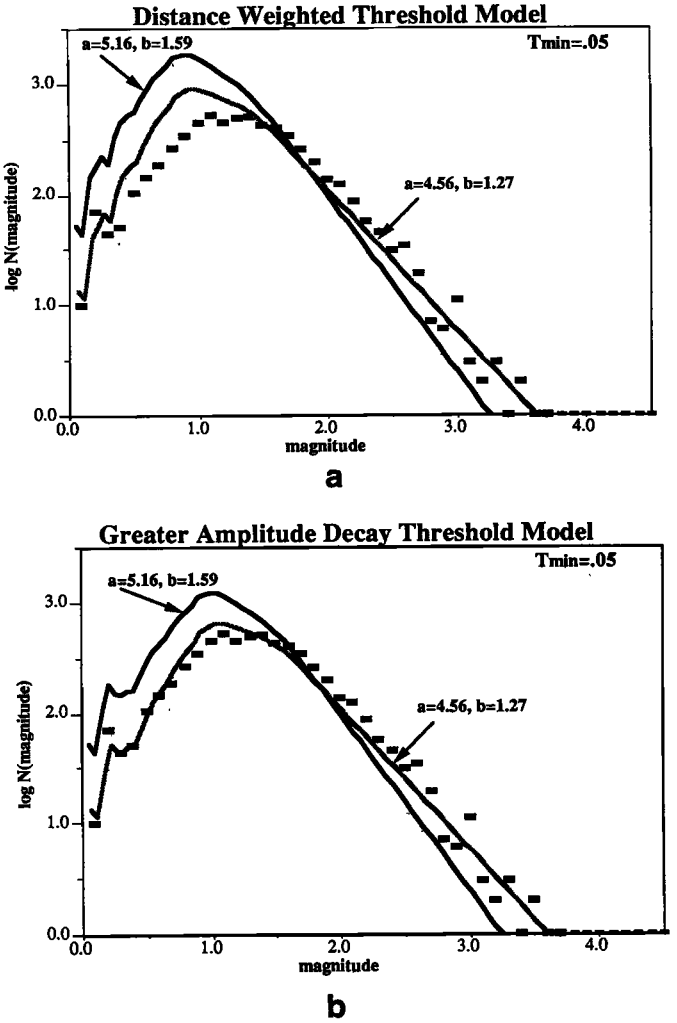

Fig. 6. Theoretical magnitude-frequency relations for two threshold models (see text and Figure 7) and T_{min}=0.05. Two relations are shown in each plot corresponding to the bounding values of a and b determined from the data. The data are indicated by the rectangles.

to ensure that it is realistic. A value of T_{min} = 0.05 is used for both cases.

The validity of these two models is tested by comparing the associated theoretical magnitude-frequency distribution with the observations (Figure 6). The difference in fits to the data is not considered sufficient to distinguish one threshold model as better than the other. Maps of these two threshold models (Figure 7) show that the first is essentially just a smoother version of the second. The smoother model is deemed most appropriate for subsequent interpretations because the data cannot resolve the variability of the second model and because the first explicitly accounts for earthquake location criteria (by using distance dependent weights).

The validity of this smoother threshold model is further verified by comparing it with the spatial distribution of earthquakes in different magnitude bins. Figure 8 shows a series of maps in which the threshold map is plotted with the epicenters in non-overlapping magnitude bins. These plots demonstrate that on average, the threshold map accurately predicts the observed distribution of epicenters. For example, earthquakes in the magnitude range 0.7 to 0.9 shown in Figure 8*c* extend to the limits of the region inside the 0.9 threshold contour and almost none are found outside. The same correspondence between the predicted and observed distributions is seen for all magnitude bins.

AVERAGE FEATURES OF THE SEISMICITY OF THE SOUTHERN GREAT BASIN

It is now possible to observe, with some rigor, several features of the spatial distribution of seismicity and to associate these with tectonic features. The threshold model serves as a series of magnitude dependent masks that can be placed over seismicity, tectonic, and/or geologic maps; this enables attention to be focused only on the regions where bias due to detection/location capabilities should be minimized. The seismicity in various magnitude bins, Quaternary faults identified by *Nakata et al.* [1982], and the appropriate threshold masks are shown in Figure 9. The most striking (visually) features of the seismicity are now described. In the remainder of this paper and in Paper II, the seismicity is

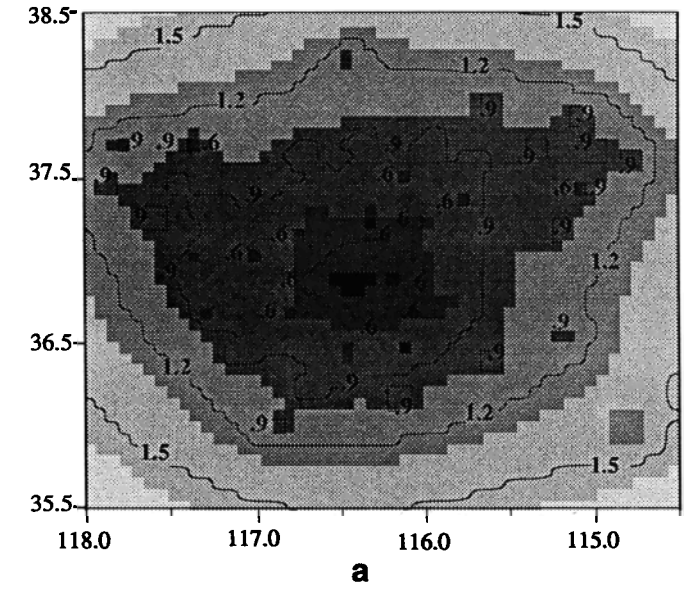

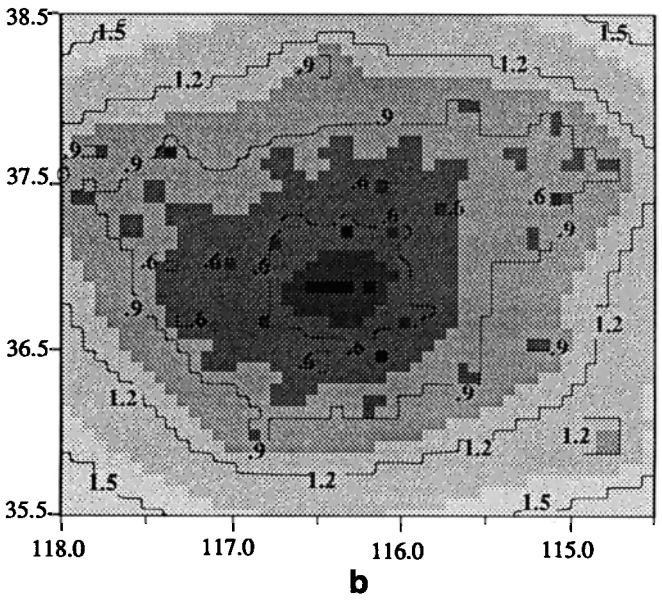

Fig. 7. (a) Shaded threshold map calculated assuming the amplitude decay function derived for the southern Great Basin [*Rogers et al.*, 1987b] with distance weights (see text). The black areas corresponds to the only regions in which events with magnitude less than 0.30 will be recorded. Each shading change indicates an increase of 0.3 magnitude units in the threshold. The contours correspond to the threshold map of Figure 7*b*. (*b*) Threshold map calculated assuming the amplitude decay relationship derived for central California [*Bakun and Joyner*, 1984]. The contours correspond to the threshold map of Figure 7*a*. The shading scale is the same as in Figure 7*a*.

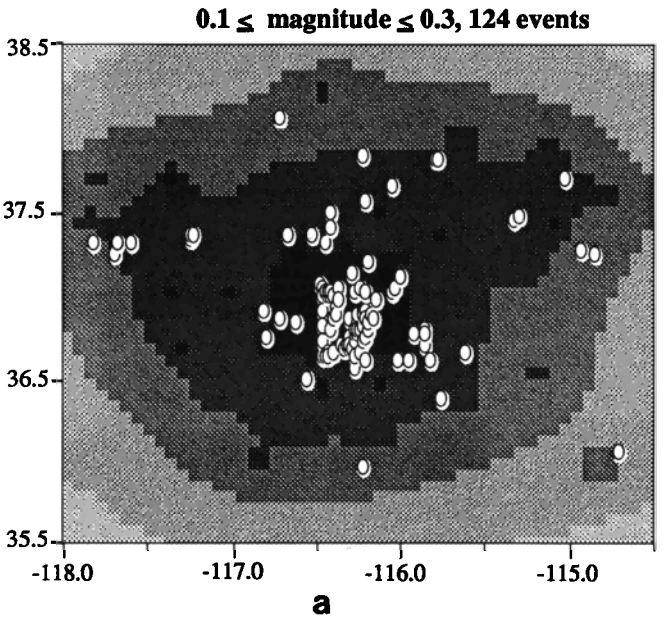

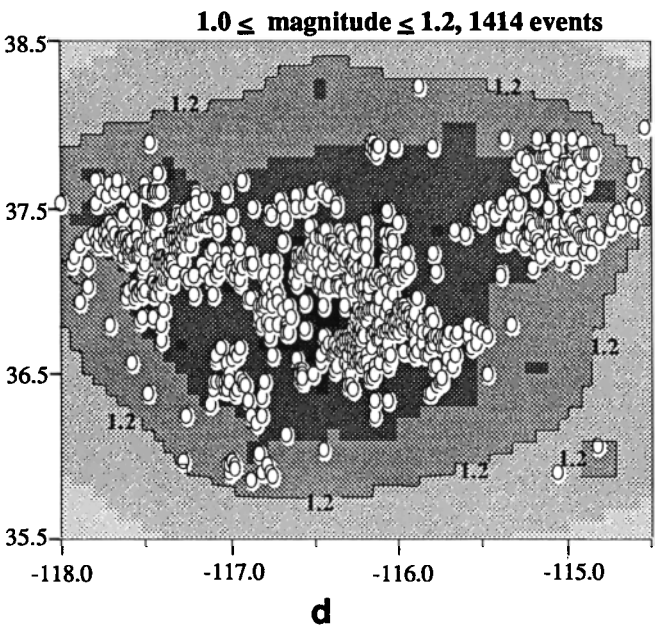

Fig. 8. (*a*) Epicenters (open ovals) from the SGBSN catalog for the period 1983 through 1989 in the magnitude bin 0.1-0.3 superimposed on the threshold map of Figure 7*a*. (*b*) As in Figure 8*a* but for the magnitude bin 0.4 to 0.6. (*c*) As in Figure 8*a* but for the magnitude bin 0.7 to 0.9. (*d*) As in Figure 8*a* but for the magnitude bin 1.0 to 1.2. (e) As in Figure 8*a* but for the magnitude bin 1.3 to 1.5. (*f*) As in Figure 8*a* but for magnitudes greater than or equal to 1.6.

discussed in terms of numbers of earthquakes. However, the patterns described are apparent for all magnitude bins implying that nearly the same patterns exist for the distribution of seismic moment or energy release as for numbers of earthquakes.

The most active areas (the greatest number of events at all magnitudes) are at the northern end of the Furnace Creek fault, in the Pahranagat Shear Zone, and around the northern and southeastern portions of the Nevada Test Site (NTS). Hypotheses relating these first two active zones to the strain field are discussed in Paper II. Understanding the nature of the activity in the NTS is more difficult due the potential for seismicity induced by nuclear testing [*McKeown and Dickey*, 1969; *US Atomic Energy Commission*, 1971; *Hamilton et al.*, 1972; *McKeown*, 1975]. Simple tests designed to elucidate temporal/spatial relationships between nuclear explosions and increased numbers of earthquakes yield ambiguous results. In the first test performed, all events within the NTS region (Figure 10*a*) that occur within 10 days following a nuclear explosion are removed from the catalog. If the process of inducing seismicity occurs on a scale of less than 10 days, then events should be preferentially removed in the area surrounding the northern NTS where all the nuclear explosions in the same time period occur (Figure 10*b*). The data from this

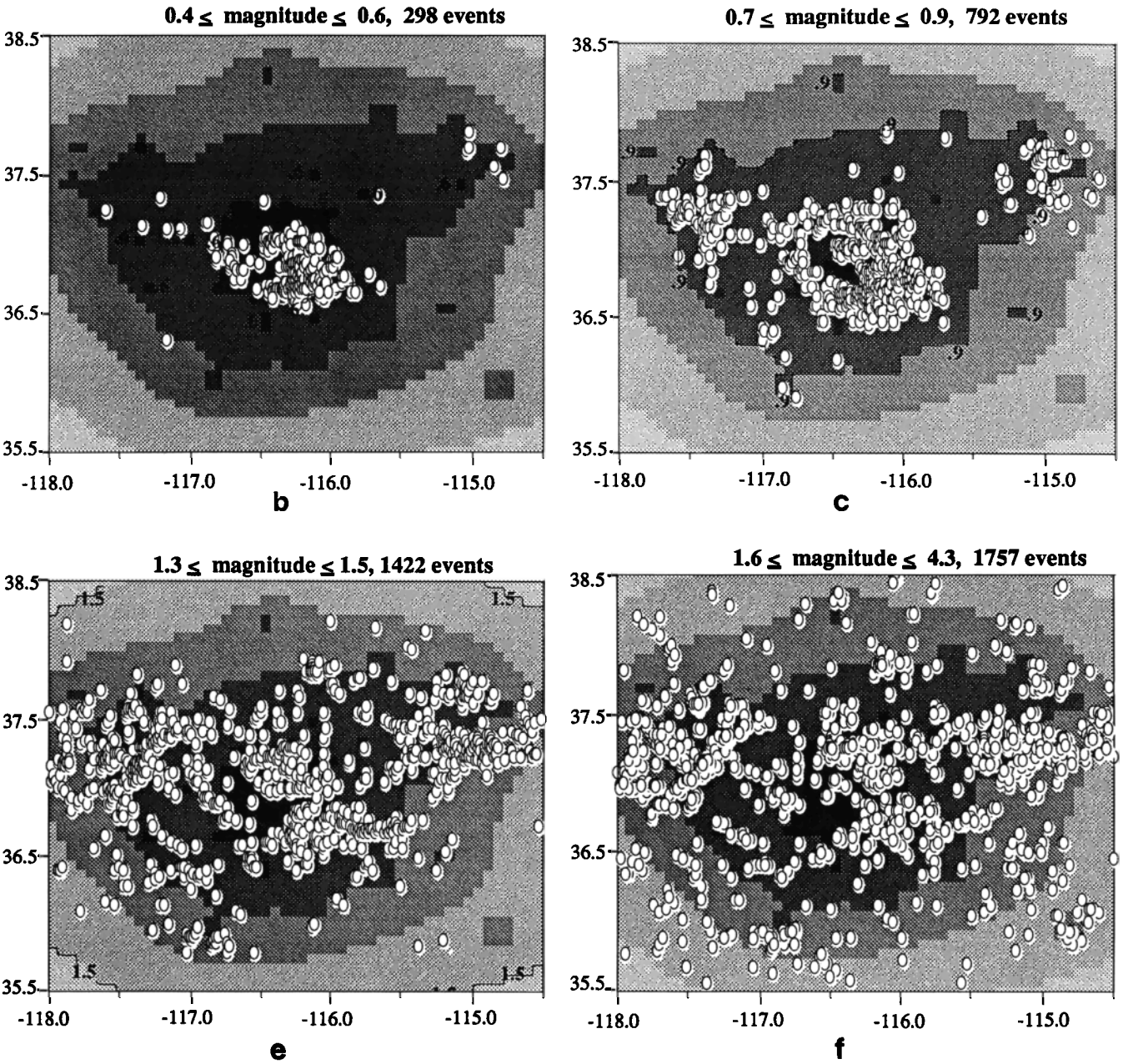

Fig. 8. (continued)

filtered catalog are shown in Figure 10*c* and the effects of increasing the period of inducement to 30 days are shown in Figure 10*d*. Visual examination of these filtered data do not indicate any obvious reduction of events in the vicinity of the nuclear explosions relative to the rest of the area. Another simple test compares seismicity prior to 1964 when most nuclear explosions occurred above ground and after 1963 when all explosions occurred below ground [*Griggs and Press*, 1961; *Springer and Kinnamann*, 1971]. While this comparison (Figure 11) strongly suggests that increased seismicity was induced in the NTS by nuclear explosions, extrapolating from these results to more recent times may not be valid. Many of the explosions during the time period around 1963 were several orders of magnitude larger than any since 1983. This and differences between the two time periods in station coverage and in magnitude scales used (note that there are many events with magnitude greater than 4.0 in the dataset shown in Figure 11 and only three in the SGBSN catalog between 1983 and 1989) make a meaningful extrapolation from the earlier period to the later one dubious.

Of relevance to the issue of site characterization of Yucca Mountain is the almost complete lack of seismicity at Yucca Mountain (Figures 2 and 9). The implications of this 'hole' in the relatively high seismicity levels of the NTS region and slightly lower levels just west of the Bear Mountain fault west of Yucca Mountain are of obvious importance in assessing the seismic hazard at Yucca Mountain. Is there a seismic gap ready to be filled by a large event, is it simply a region where shear strain does not accumulate and thus has a negligible potential for a large earthquake, or is this a temporary quiescence that will fill in if data are gathered for a longer duration?

Other more general features that are focussed on in the analysis described in Paper II are the relatively low levels of seismicity to the

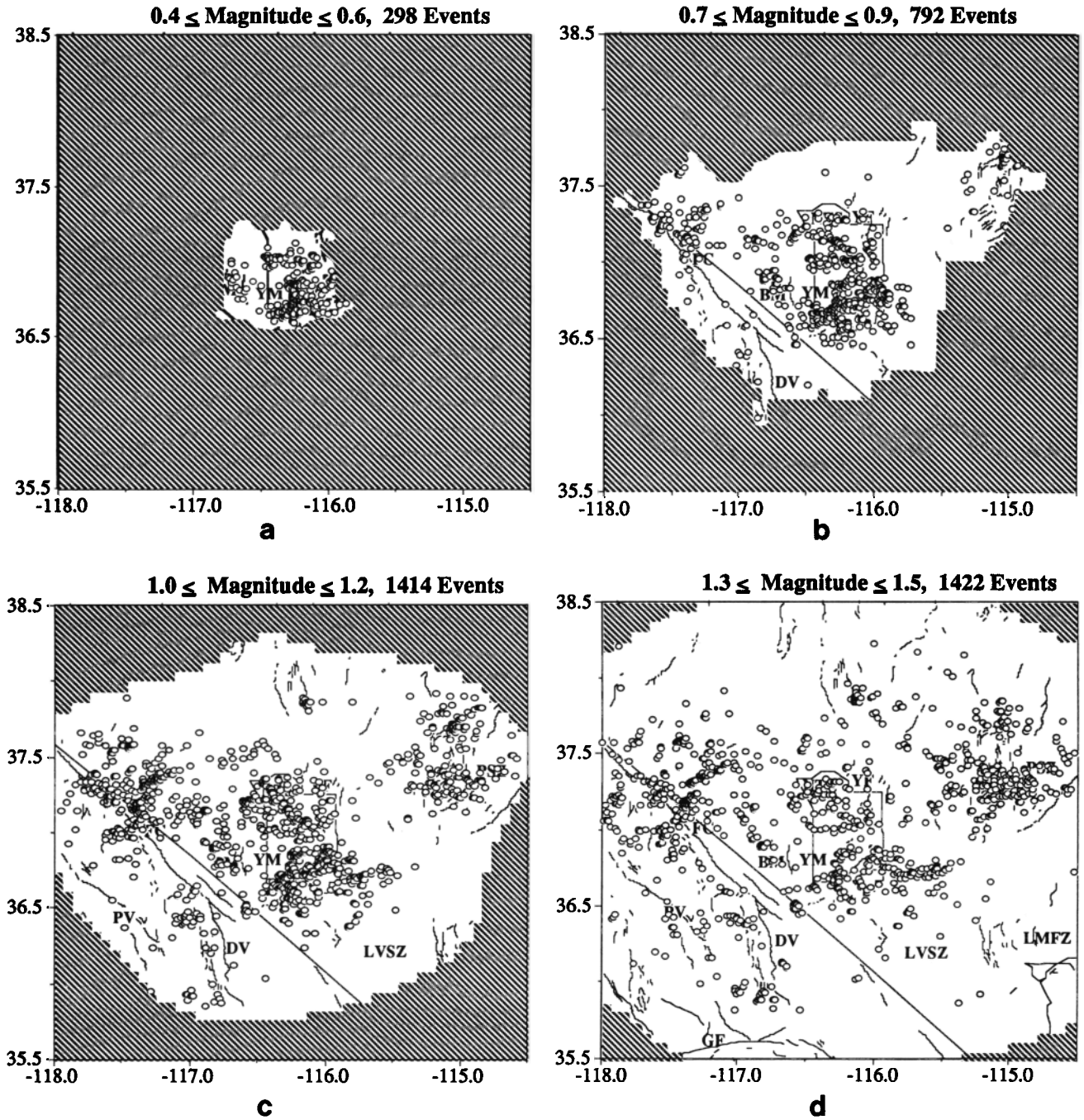

Fig. 9. (*a.*) Epicenters (open ovals) from the Southern Great Basin Seismic Network catalog for the period 1983 through 1989 in magnitude bin 0.4-0.6 superimposed on the same map shown in Figure 2. The shaded areas are those areas in which the detection threshold is higher than the largest magnitude in the bin as predicted by the threshold map shown in Figure 7*a*. Abbreviations are FC - Furnace Creek Fault; DV, Death Valley Fault Zone; LVSZ, Las Vegas Shear Zone; PSZ, Pahranagat Shear Zone; PV, Panamint Valley Fault Zone; GF, Garlock Fault; LMFZ, Lake Mead Fault Zone; YF, Yucca Fault; BM, Bear Mountain Fault; NTS, Nevada Test Site; and YM, Yucca Mountain. (*b*) As in Figure 9*a* but for the magnitude bin 0.7 to 0.9. (*c*) As in Figure 9*a* but for the magnitude bin 1.0 to 1.2. (*d*) As in Figure 9*a* but for the magnitude bin 1.3 to 1.5. Magnitudes greater than or equal to 1.6 (the magnitude of completeness) are shown in Figure 2.

west of the Death Valley/Furnace Creek fault system, and the significant number of events that cannot readily be correlated with mapped faults. The fresh fault scarp morphology of Death Valley and presence of hot springs are certainly suggestive of the existence of recent energetic tectonics [*Zhang et al.*, 1990] relative to the age of deformation suggested by the more subdued morphology of the rest of the study region. Recent deformation is also inferred from the results of detailed geologic studies done in the Panamint Valley [*Burchfiel et al.*, 1987; *Zhang et al.*, 1990]. *Wernicke et al.* [1988] estimate that tens of kilometers of displacement have occurred on the Death Valley fault system within the past four million years. Geologic data from regions to the east of Death Valley indicate that the rate and magnitude of deformation peaked much earlier; tectonic activity peaked more that 11 million years ago in the Las Vegas Shear Zone [*Wernicke et al.*, 1988], and about five million years ago in the Lake Mead Fault Zone [*Anderson*, 1973]. Thus, it is

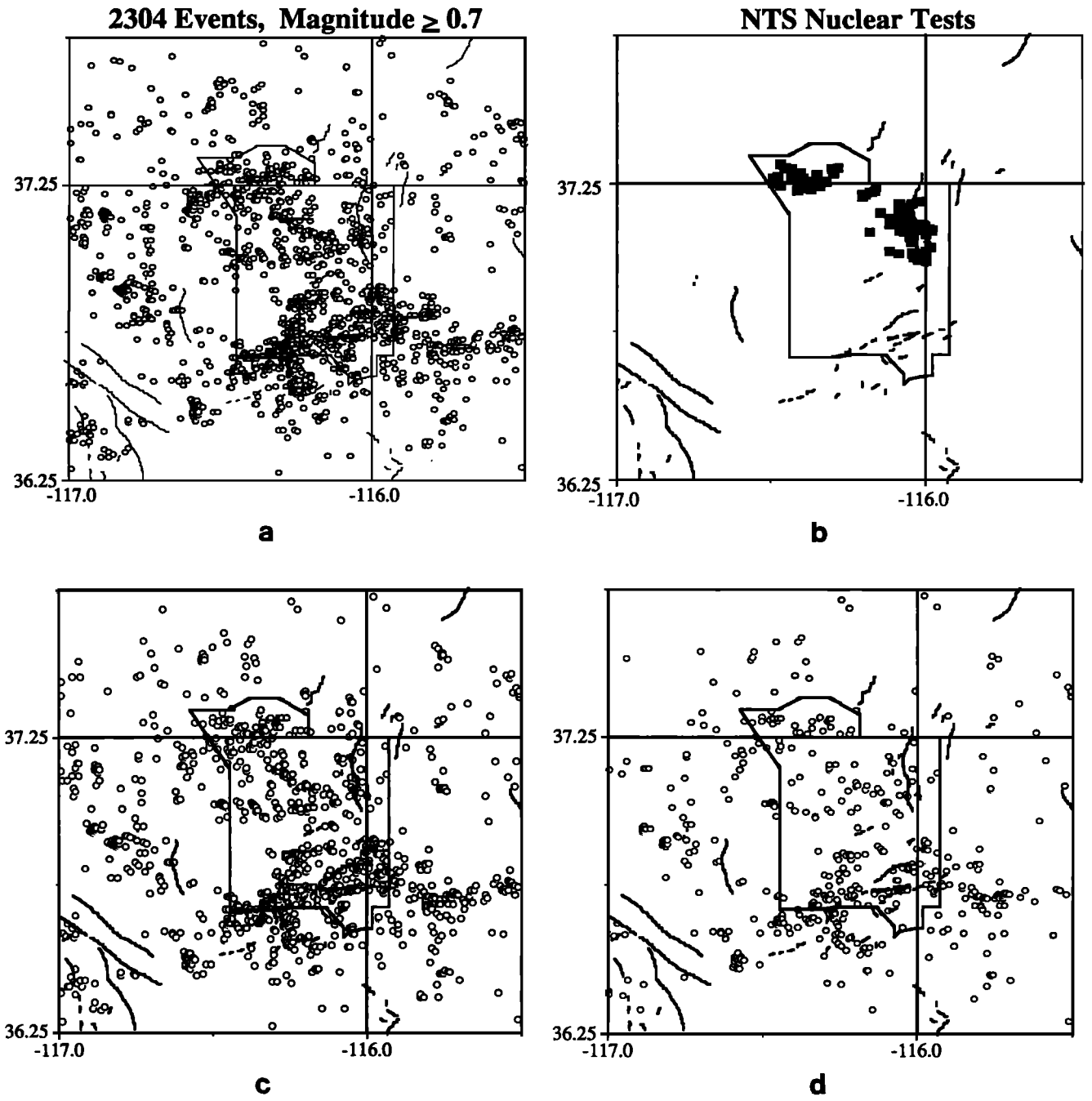

Fig. 10. (*a*) Earthquakes (open ovals) in the NTS region from the SGBSN catalog from 1983-1989 with $M_L \geq 0.7$ (catalog is complete over this area at this magnitude). Faults are from *Nakata et al.* [1982] and the outline of the NTS is shown for reference. (*b*) The same region as Figure 9*a* but with the locations of the nuclear tests done between 1983 and 1989 shown as solid rectangles. (*c*) All events shown in Figure 9*a* that occurred within 10 days of a nuclear test have been removed in this figure. Preferential removal of events in the region where the nuclear tests were done is not apparent. (*d*) As in Figure 9*c* except that all events with 30 days of a nuclear test have been removed. There is still no obvious preferential removal of events in the testing region.

somewhat surprising that although the most recent and greatest deformation in the southern Great Basin is occurring to the west of the Death Valley/Furnace Creek fault system, it has fewer small earthquakes.

CONCLUSIONS

A spatially varying model of the detection/location capabilities of the Southern Great Basin seismic network has been derived that is based on simple empirical relations and statistics. This permits use of almost all the catalog data gathered, rather than ignoring the two-thirds of the data that are below the threshold of completeness. The characteristics of the spatial distribution of earthquakes, where earthquake clusters and aseismic regions locate, appear to be stable at all magnitude levels so that inferences about where strain is being accommodated will be the same whether numbers of earthquakes or strain estimated from seismic moments are examined. These principal characteristics include clusters at the northern end of the Furnace Creek fault and in the Pahranagat Shear Zone, and a relatively large number of earthquakes in the northern and southeastern portions of the NTS. These clusters cover regions much

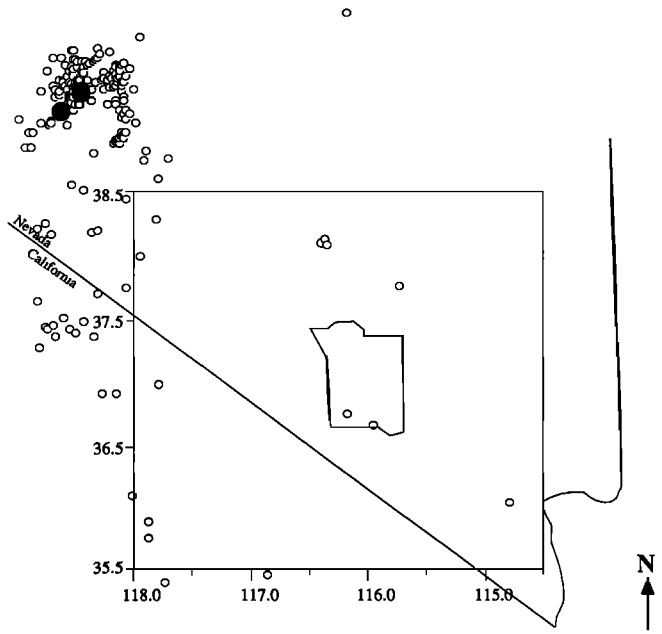

1954-1963 Epicenters, Magnitude ≥ 4.0

Fig. 11*a*. Epicenters (open circles) from the catalog of *Gawthrop and Carr* [1988] during the 10 years prior to the international agreement that all nuclear tests be done below ground. The cluster of events in the northwest are aftershocks of the 1954 Rainbow Mountain and Fairview Peak/Dixie Valley earthquakes (large solid circles). Note the small number of events in the NTS region.

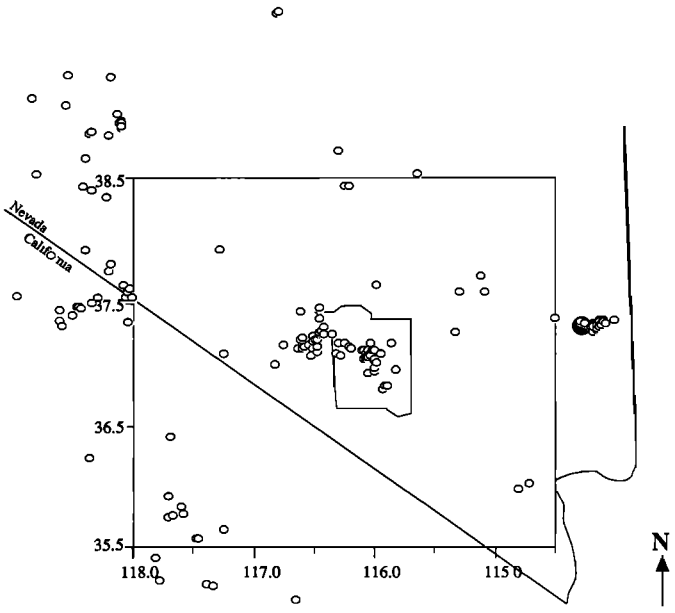

1964-1973 Epicenters, Magnitude ≥ 4.0

Fig. 11*b*. Epicenters (open circles) from the catalog of *Gawthrop and Carr* [1988] during the 10 years following the institution of the agreement that all nuclear tests be done below ground. The cluster of events in the east are aftershocks of the 1966 Clover Mountain earthquake (large solid circles). Note the increased number of events in the NTS region relative to the previous 10 years when testing was done above ground.

larger than the surface projections of any of the mapped faults. The extent to seismicity is induced by nuclear testing is unclear. The predominantly aseismic regions include the area west of the Death Valley/Furnace Creek fault system and an almost complete absence of events at Yucca Mountain. Finally, a considerable number of isolated events in the SGBSN catalog cannot be correlated with mapped faults.

APPENDIX A

A simple example is presented in this Appendix to illustrate why it is necessary to assess the importance of spatial variations in detection/location thresholds before determining a magnitude of completion using the method of *Rydelek and Sacks* [1989]. The method of estimating a magnitude of completion suggested by *Rydelek and Sacks* [1989] assumes that earthquakes are randomly distributed (with aftershocks removed) and that a day-night modulation in seismicity is due to reduced detection capabilities during the day when noise levels are greater. However, spatially variable detection/location thresholds will result in seismicity patterns that are not uniformly distributed and thus, since this violates one of the method's assumptions it may result in biased estimates of the magnitude of completion.

The method of estimating the Rydelek and Sacks' magnitude of completion is first summarized. For a given magnitude level, each event is plotted on a phasor diagram (a 24 hour clock) as a unit vector oriented at an angle determined by the origin time hour. A phasor sum for all events is compared with that expected for a random process and the catalog is deemed incomplete at the particular magnitude level being examined if the phasor sum exceeds some confidence level represented by a critical radius.

For illustrative purposes, suppose the 95% confidence limit is chosen corresponding to a critical radius of $R = 1.73\sqrt{N}$, where N is the total number of events in the catalog. Suppose also that the detection capability for one half of the network is greater than it is for the other half (e.g., there are more stations on one side of the network) and that N_1 events are detected in the former and N_2 in the latter. The phasor sum for the half with poorer detection capabilities could be such that it exceeds the 95% confidence limit ($R_1 > 1.73\sqrt{N_1}$) for the half alone. However, it is possible that the detection capability of the other half is sufficiently great such that it is complete ($R_2 < 1.73\sqrt{N_2}$) and "masks" the fact that catalog is incomplete for events in the other half of the network ($R < 1.73\sqrt{N_1+N_2}$). Thus, the magnitude of completion for the entire network will be underestimated. Similar examples can be designed to illustrate how, due to a spatially variable threshold, the magnitude of completion can also be overestimated.

APPENDIX B

The Gutenberg-Richter relationship [*Gutenberg and Richter*, 1941, 1954] describes the magnitude-frequency distribution

$$\log N(m) = a - b\,m \qquad \text{(B1)}$$

where $N(m)$ is the number of earthquakes with magnitude m and a and b are empirically derived constants. The following analysis shows that this relationship, under certain circumstances, represents an average of magnitude-frequency distributions for a number of subregions which may be characterized by differing values of a and b (Table 1). The fact that such variation is likely to exist is apparent from simple visual examination of regional seismicity patterns (e.g., Figure 2) and from theoretical studies which show that for small earthquakes these values depend on frictional properties of faults which are undoubtedly variable [*Carlson*, 1991].

Rewriting equation (B1) and letting a_1, b_1 and a_2, b_2 be representative of two nonoverlapping regions of the network that encompass all events ($N = N_1 + N_2$), then

$$N = N_1 + N_2 = 10^{a-bm} = 10^{a_1 - b_1 m} + 10^{a_2 - b_2 m} \quad \text{(B2)}$$

This can be simplified by rewriting the right-hand side according to

$$\begin{aligned} 10^{a-bm} &= 10^{\bar{a}-\bar{b}m}[10^{\gamma} + 10^{-\gamma}] \\ &= 10^{\bar{a}-\bar{b}m}[e^{\gamma \ln 10} + e^{-\gamma \ln 10}] \\ &= 10^{\bar{a}-\bar{b}m}[2\cosh(\gamma \ln 10)] \end{aligned} \quad \text{(B3)}$$

where

$$\bar{a} = \frac{a_1 + a_2}{2}, \quad \bar{b} = \frac{b_1 + b_2}{2}, \quad \text{(B4)}$$

$$\gamma = \Delta a - \Delta b\, m,$$

$$\Delta a = \frac{a_1 - a_2}{2}, \quad \Delta b = \frac{b_1 - b_2}{2}$$

If it is true that

$$\gamma \ln 10 < 1 \quad \text{(B5)}$$

then using a Taylor's series expansion equation (B3) can be written as

$$10^{a-bm} \approx 10^{\bar{a}-\bar{b}m} \times 2[1 + (\gamma \ln 10)^2]$$

or taking the logarithm

$$\begin{aligned} \log N(m) &= a - b\, m \\ &\approx (\bar{a} + \log 2) - \bar{b}\, m + \log[1 + (\gamma \ln 10)^2] \\ &\approx (\bar{a} + \log 2) - \bar{b}\, m \end{aligned} \quad \text{(B6)}$$

Because of the requirement described by equation (B5), neglecting the third term in equation (B6) will result in an error of no more than 0.3 in the value of $\log N(m)$. Thus, this demonstrates that a and b are related to the average values of the two subregions according to

$$a \approx (\bar{a} + \log 2) \quad \text{and} \quad b \approx \bar{b} \quad \text{(B7)}$$

The same logic can be applied to demonstrate that a and b represent approximate averages of a and b values for a greater number of smaller subregions.

Acknowledgments. This work was performed in accord with the U.S. Geological Survey/Department of Energy Interagency agreement DE-AIO8-78ET44802. The author would like to thank R. Herrmann, an anonymous reviewer, R. Bilham, J. Dewey, P. Bodin, S. Hartzell, K. Shedlock and G. Shideler, for thoughtful reviews, discussions, criticisms, and suggestions. The author is also grateful to P. Rydelek, D. Taylor, and A. Snoke for engaging in useful discussion. D. Overturf is responsible for maintaining the SGBSN and S. Harmsen for compiling the catalogue used in this study.

REFERENCES

Aki, K., Maximum likelihood estimate of b in the formula $\log N = a - bM$ and its confidence limits, *Bull. Earthquake Res. Inst. Tokyo Univ., 43*, 237-238, 1965.

Anderson, R.E., Large-magnitude late Tertiary strike-slip faulting north of Lake Mead, Nevada, *U.S. Geol. Surv. Prof. Pap., 794*, 18 pp., 1973.

Bakun, W.H. and W.B. Joyner, The ML scale in central California, *Bull. Seismol. Soc. Am., 74*, 1827-1843, 1984.

Burchfiel, B.C., K.V. Hodges, and L.H. Royden, Geology of the Panamint Valley-Saline Valley pull-apart system, California: Palinspastic evidence for low-angle geometry of a Neogene range-bounding fault, *J. Geophys. Res., 92*, 10,422-10,426, 1987.

Carlson, J.M., Time intervals between characteristic earthquakes and correlations with smaller events: An analysis based on a mechanical model of a fault, *J. Geophys. Res., 96*, 4255-4268, 1991.

Evernden, J.F., Precision of epicenters obtained by small numbers of worldwide stations, *Bull. Seismol. Soc. Am., 59*, 1365-1398, 1969.

Evernden, J.F., C.B. Archambeau, and E. Cranswick, An evaluation of seismic decoupling and underground nuclear test monitoring using high frequency seismic data, *Rev. Geophys., 24*, 143-215, 1986.

Gawthrop, W.H., and W.J. Carr, Location refinement of earthquakes in the southwestern Great Basin, 1931-1974, and seismotectonic characteristics of some of the important events, *U.S. Geol. Surv. Open File Rep., 88-560*, 64 pp., 1988.

Gomberg, J., Seismicity and shear strain in the southern Great Basin of Nevada and California, *J. Geophys. Res.*, this issue.

Gomberg, J., Seismic network configuration, earthquake hypocenter estimation: a re-evaluation and a new approach to an old problem, *U.S. Geol. Surv. Bull.*, in press, 1991.

Gomberg, J., K. Shedlock, and S. Roecker, The effect of *S*-wave arrival times on hypocenter determination, *Bull. Seismol. Soc. Am., 80*, 1605-1628, 1990.

Griggs, D.T., and F. Press, Probing the Earth with nuclear explosions, *J. Geophys. Res., 66*, 237-258, 1961.

Gutenberg, B., and C.F. Richter, Seismicity of the Earth, *Geol. Soc. Am. Spec. Pap., 34*, 1-133, 1941.

Gutenberg, B., and C.F. Richter, *Seismicity of the Earth and Associated Phenomena*, 2nd ed., 310 pp., Princeton University Press, Princeton, N. J., 1954.

Hamilton, R.M., B.E. Smith, F.G. Fischer, and P.J. Papanek, Earthquakes caused by underground nuclear explosions on Pahute Mesa, Nevada Test Site, *Bull. Seismol. Soc. Am., 62*, 1319-1341, 1972.

Hanks, T.C., and D.M. Boore, Moment-magnitude relations in theory and practice, *J. Geophys. Res., 89*, 6229-6235, 1984.

Kelly, E.J., and R.T. Lacoss, Estimation of seismicity and network detection capability, *Tech. Note 1969-41*, Lincoln Lab, Mass. Inst. of Tehnol., Cambridge, 1969.

Mauk, F.J., and D.H. Christensen, A probabilistic evaluation of earthquake detection and location capability for Illinois, Indiana, Kentucky, Ohio, and West Virginia, Div. of Reactor Safety Res., Office of Nuclear Reg. Res., USNRC, Rep. NUREG/CR-1648, R6,RA, 207 pp., Washinton, D.C., 1980.

McKeown, F.A., Relation of geological structure to seismicity at Pahute Mesa, Nevada Test Site, *Bull. Seismol. Soc. Am., 65*, 747-764, 1975.

McKeown, F.A., and D.D. Dickey, Fault displacements and motion related to nuclear explosions, *Bull. Seismol. Soc. Am., 59*, 2253-2269, 1969.

Nakata, J.K., C.M. Wentworth, and M.N. Machette, Quaternary fault map of the Basin and Range and Rio Grande Rift Provinces, western United States,scale 1:2.5M, *U.S. Geol. Surv. Open File Rep. 82-579*, 1982.

Reasenberg, P., Second-order moment of central California seismicity, . *Geophys. Res., 90*, 5479-5495, 1985.

Richter, C.F., *Elementary Seismology*, Chap. 22, W.H. Freeman, San Francisco, Calif., and London, 1958.

Ringdal, F., On the estimation of seismic detection thresholds, *Bull. Seismol. Soc. Am., 65*, 1631-1642, 1975.

Ringdal, F., Study of magnitude, seismicity, and earthquake detectability using a global network, *Bull. Seismol. Soc. Am., 76*, 1641-1659, 1986.

Rogers, A.M., S.C. Harmsen, and M.E. Meremonte, Evaluation of the seismicity of the southern Great Basin and its relationship to the tectonic framework of the region, *U.S. Geol. Surv. Open File Rep., 87-408*, 196 pp., 1987a.

Rogers, A.M., S.C. Harmsen, R.B. Hermann, and M.E. Meremonte, A study of ground motion attenuation in the southern Great Basin, Nevada-California, using several techniques for estimates of Q_s, $\log A_o$, and coda Q, *J. Geophys. Res., 92*, 3527-3540, 1987b.

Rydelek, P.A., and I.S. Sacks, Testing the completeness of earthquake catalogues and the hypothesis of self-similarity, *Nature, 337*, 251-253, 1989.

Sereno, T.J., and S.R. Bratt, Seismic detection capability at NORESS and implications for detection threshold of a hypothetical network in the Soviet Union, *J. Geophys. Res.*, *94*, 10397-10414, 1989.

Shi, Y., and B.A. Bolt, The standard error of the magnitude-frequency *b* value, *Bull. Seismol. Soc. Am.*, *72*, 1677-1687, 1982.

Springer, D.L. and R.L. Kinnamann, Seismic source summary for U.S. underground nuclear explosions, 1961-1970, *Bull. Seismol. Soc. Am.*, *61*, 1073-1098, 1971.

Taylor, D.W.A, J.A. Snoke, I.S. Sacks, and T. Takanami, Frequency and energy comparisons between shallow and subduction earthquakes near the Hokkaido corner, Japan: preliminary results, *Seismol. Res. Lett.*, *58*, 105, 1987.

Taylor, D.W.A., J.A. Snoke, I.S. Sacks, and T. Takanami, Nonlinear frequency-magnitude relationships in the Hokkaido Corner, Japan, *Bull. Seismol. Soc. Am.*, *80*, 340-353, 1990.

Trifu, C. and M. Radulian, Frequency-magnitude distribution of earthquakes in Vrancea: relevance for a discrete model, *J. Geophys. Res.*, *96*, 4301-4312, 1991.

U.S. Atomic Energy Commission, Seismology, aftershocks, and related phenomena associated with underground nuclear explosions, in *A Bibliography of Selected Papers with Abstracts*, 36 pp., Nevada Operations Office, Washington, D.C., 1971.

von Seggern, D., and R. Blandford, Seismic threshold determination, *Bull. Seismol. Soc. Am.*, *66*, 753-788, 1976.

Wernicke, B., G.J. Axen, and J.K. Snow, Basin and Range extensional tectonics at the latitude of Las Vegas, Nevada, *Geol. Soc. Am. Bull.*, *100*, 1738-1757, 1988.

Zhang, P., M. Ellis, D.B. Slemmons, and F. Mao, Right lateral displacements and the Holocene slip rate associated with pre-historic earthquakes along the southern Panamint Valley fault zone: Implications for southern Basin and Range tectonics, *J. Geophys. Res.*, *95*, 4857-4872, 1990.

J. Gomberg, U.S. Geological Survey, MS 966, Box 25046, DFC, Denver, CO 80225.

(Received January 24, 1991;
revised May 15, 1991;
accepted May 15, 1991.)

JOURNAL OF GEOPHYSICAL RESEARCH, VOL. 96, NO. B10, PAGES 16,069–16,081, SEPTEMBER 10, 1991

Late Cretaceous Paleomagnetism of the Tucson Mountains: Implications for Vertical Axis Rotations in South Central Arizona

JONATHAN T. HAGSTRUM AND PETER W. LIPMAN

U.S. Geological Survey, Menlo Park, California

The Tucson Mountains of southern Arizona are the site of an Upper Cretaceous caldera from which the rhyolitic Cat Mountain Tuff was erupted at about 72 Ma. Two magnetic units within the Cat Mountain Tuff are distinguished by paleomagnetic data in both the northern and southern Tucson Mountains. The resurgent Amole pluton (≈72 Ma) in the northern Tucson Mountains was emplaced soon after eruption of the Cat Mountain Tuff but cooled and was magnetized after northeastward tilting (50°–85°) of the adjacent caldera-fill sequence. Petrologic and paleomagnetic data indicate that the lower magnetic unit of the Cat Mountain Tuff caps the Silver Bell Mountains to the northwest. A previous paleomagnetic investigation (N = 34) indicates that the Silver Bell Mountains have been rotated clockwise 30° ± 16° (95% confidence level) about a vertical axis relative to cratonic North America. A similar paleomagnetic study of Upper Cretaceous volcanic, volcaniclastic, and intrusive units in the Tucson Mountains (N = 26) indicates that these rocks have been rotated 7° ± 14° clockwise relative to stable North America. A direct comparison of paleomagnetic directions for the lower unit of the Cat Mountain Tuff shows a 17° ± 10° clockwise rotation between the Silver Bell Mountains and the Tucson Mountains which supports the relative accuracy of the absolute rotations determined for these two mountain ranges. Preliminary paleomagnetic directions for middle Tertiary units from the Silver Bell and Tucson Mountains are consistent with clockwise rotation having occurred prior to deposition of these rocks. Clockwise rotation of crustal blocks in southern Arizona likely was associated with strike-slip movement on major northwest trending faults in the region, and this movement may have been related to oblique subduction of oceanic plates along the western continental margin in Late Cretaceous and early Tertiary time. The available paleomagnetic data indicate that rocks in southern Arizona have not remained unrotated with respect to North America since Late Cretaceous time and that vertical axis rotations may have played an important role in the region during Laramide deformation.

INTRODUCTION

This study of the Tucson Mountains supplements a previous study of the Silver Bell Mountains [*Hagstrum and Sawyer*, 1989] to the northwest (Figure 1) and is part of an ongoing paleomagnetic investigation of vertical axis rotations associated with Late Cretaceous to early Tertiary (Laramide) deformation in the Basin and Range province of southern Arizona. Other paleomagnetic studies in the region have concentrated on refining the Mesozoic and early Cenozoic North American apparent polar wander path (APWP) [*Vugteveen et al.*, 1981; *Kluth et al.*, 1982; *May and Butler*, 1986; *May et al.*, 1986] but are based on the assumption that rocks within the Basin and Range province of southern Arizona have remained unrotated with respect to cratonic North America since Jurassic time. In addition to the general consistency of these paleomagnetic data with the North American APWP, the assumption that Mesozoic rocks in southern Arizona have not undergone vertical axis rotations is also thought to be supported by the apparent internal consistency of fracture and dike trends within Laramide and Tertiary rocks in the region [*Rehrig and Heidrick*, 1976; *Heidrick and Titley*, 1982], by the overall similarity of middle Tertiary core complex transport directions [e.g., *Rehrig and Reynolds*, 1980], and by the lack of vertical axis rotations associated with late Cenozoic high-angle Basin and Range-type faulting [*Coney*, 1978]. More recent paleomagnetic investigations of Late Cretaceous and early Tertiary rocks in southern Arizona, however, have shown significant clockwise vertical axis rotations in the Silver Bell Mountains [*Hagstrum and Sawyer*, 1989] and in the Canelo Hills region [*Hagstrum and Lipman*, 1991] with respect to stable North America.

Clockwise rotation (≈30°) of the Silver Bell Mountains is inferred by *Hagstrum and Sawyer* [1989] to have been related to regional Late Cretaceous and early Tertiary northwest trending strike-slip faulting. The Silver Bell Mountains are bounded to the north and south by subvertical faults, and the N75°–80°W Ragged Top fault to the north shows evidence of major strike-slip displacement between ≈70 Ma and ≈26 Ma, although significant dip-slip displacement is also required. In addition, preliminary paleomagnetic data for middle Tertiary rocks in the vicinity of the Silver Bell Mountains imply that clockwise rotation occurred prior to ≈26 Ma [*Hagstrum and Sawyer*, 1989]. Northwest trending subvertical faults with probable strike-slip displacement are a major element of late Mesozoic tectonics in southeastern Arizona [*Titley*, 1976; *Drewes*, 1981], but movement along them is difficult to interpret because it has been recurrent and of diverse sense. *Heidrick and Titley* [1982] suggested that these faults would have been subjected to left-lateral shear during Laramide deformation based on a tectonic stress field for southern Arizona (σ_1 = N75°E) inferred from regional dike and fracture patterns. *Keith and Wilt* [1986] restrict left-lateral movement on these faults to a medial phase (65–55 Ma) of the Laramide orogeny that is also characterized by epizonal plutonism and porphyry copper mineralization. Recently, Mesozoic porphyry copper deposits across southern Arizona have been interpreted to be widely associated with eruptive centers of arc-related silicic volcanism [*Lipman and Sawyer*, 1985].

Paper number 91JB01618.

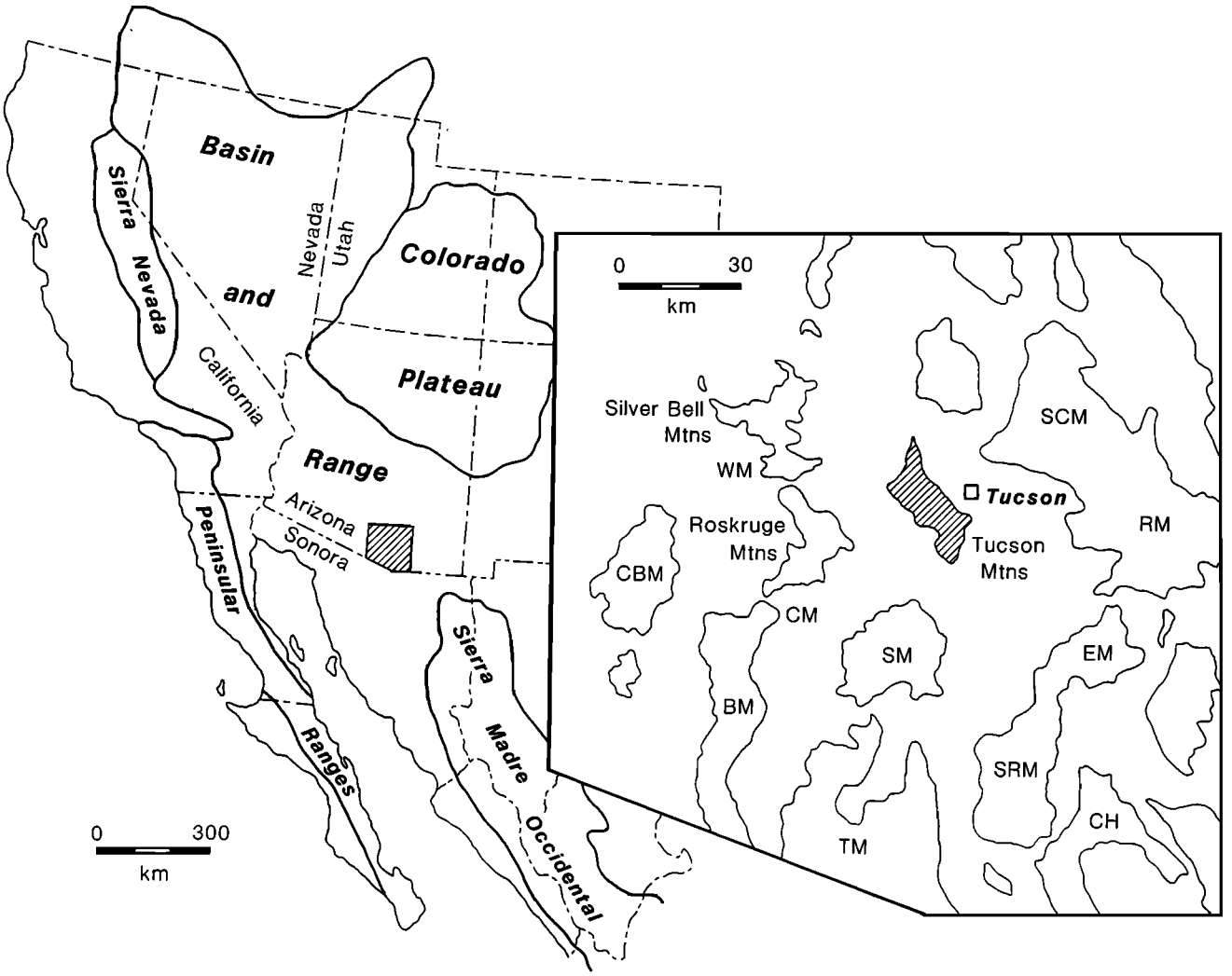

Fig. 1. Regional map (left) showing physiographic provinces in southwestern North America [after *Stewart*, 1978], and index map (right) showing location of the Tucson Mountains (32.2°N, 248.9°E) in south central Arizona. Mountain range abbreviations are BM, Baboquivari Mountains; CBM, Comobabi Mountains; CH, Canelo Hills; CM, Coyote Mountains; EM, Empire Mountains; RM, Rincon Mountains; SCM, Santa Catalina Mountains; SM, Sierrita Mountains; SRM, Santa Rita Mountains; TM, Tumacacari Mountains; and WM, Waterman Mountains.

Late Cretaceous ash flow volcanism and caldera formation in the Silver Bell Mountains [*Sawyer*, 1987] and in the Tucson Mountains [*Lipman*, 1989] produced locally thick sequences of volcanic and volcaniclastic rocks and regionally extensive ash flow sheets. The tuff of Confidence Peak was erupted from the Silver Bell caldera shortly before the Cat Mountain Tuff was erupted from the Tucson Mountains caldera. Paleomagnetic study of Upper Cretaceous rocks in the Silver Bell Mountains shows a 30° ± 16° clockwise rotation of this site relative to North America (*Hagstrum and Sawyer* [1989]; recalculated, see Table 3), and petrologic and age data [*Lipman*, 1991] indicate that the upper tuff unit capping the Silver Bell Mountains correlates with the Cat Mountain Tuff in the Tucson Mountains. This paleomagnetic study of the Tucson Mountains therefore was undertaken to determine a time-averaged paleomagnetic direction for the Tucson Mountains that could be compared with a reference direction for stable North America, and to evaluate the correlation of the Cat Mountain Tuff between the Silver Bell and Tucson Mountains.

Single cooling units of ash flow tuffs are usually magnetized over short periods of time relative to paleosecular variation (PSV) of the ancient geomagnetic field and have been correlated over large areas based on their uniform paleomagnetic directions [e.g., *Gromme et al.*, 1972; *Wells and Hillhouse*, 1989]. Thick intracaldera tuff units can have more variable paleomagnetic directions due to PSV and polarity reversals occurring during longer periods of cooling and magnetization [*Hagstrum and Lipman*, 1986; *R. L. Reynolds et al.*, 1986]. The eutaxitic structure of welded tuffs generally indicate the paleohorizontal [see *Hagstrum and Gans*, 1989], and between-site vertical axis rotations often can be determined from site mean directions after correction for structural tilt. In regions of crustal deformation characterized by rotations of fault blocks about near-vertical axes, however, correlations of tuff units can be supported only by site mean inclinations, because variations in declination are a direct measure of between-site vertical axis rotations. Thus the absolute rotations of the Silver Bell and Tucson Mountains, with respect to North America, can be tested by

comparing them with the relative rotation between the two mountain ranges shown by the paleomagnetic declinations for a correlated Cat Mountain Tuff.

GEOLOGIC SETTING

Predominantly Upper Cretaceous volcanic rocks are exposed in the Tucson Mountains to the west of the city of Tucson in south central Arizona (Figure 2). These rocks are considered to be parts of the fill of a large ash flow caldera [*Lipman*, 1989] from which the rhyolitic Cat Mountain Tuff was erupted at about 72 Ma [*Bikerman and Damon*, 1966]; (recalculated ages from *S. J. Reynolds et al.*, [1986]). Previously called the Cat Mountain Rhyolite, the Cat Mountain Tuff was initially mapped as overlying a widespread breccia unit, the Tucson Mountain Chaos [*Brown*, 1939]. This unit has been the subject of much debate and has been variously interpreted as the sole of an imbricate thrust sheet [*Brown*, 1939], as a volcanically erupted intrusive breccia related to a regional "volcanic orogeny" [*Mayo*, 1963; 1971*a*], as stoped fragments rafted from deeper levels by rising pyroclastic magma which later erupted the Cat Mountain Tuff [*Bikerman*, 1963; *Mayo*, 1971*b*], and as part of a regional andesitic unit extending from at least the Silver Bell Mountains to the north to the Santa Rita and Sierrita Mountains to the south [*Drewes*, 1981].

Lipman [1976] compared the Tucson Mountain Chaos with caldera collapse breccias in the San Juan Mountains, southwestern Colorado, and inferred that the Tucson Mountain Chaos was also landslide breccia associated with collapse of a large ash flow caldera within which the Cat Mountain Tuff had ponded. The slide breccias in the Tucson Mountains have a matrix of nonwelded tuff, and rather than underlying the Cat Mountain Tuff, they interfinger with welded tuff at multiple horizons. These relations imply that the exposed thickness of the caldera-filling Cat Mountain Tuff is as much as 3 to 4 km [*Lipman*, 1989]. The breccias contain blocks up to 0.5 km across, vary in clast composition between caldera sectors, and consist of Paleozoic sedimentary rocks, Jurassic silicic volcanic rocks, and Cretaceous sedimentary and volcanic rocks [*Lipman*, 1989]. Included with the Cretaceous volcanic rocks are clasts of tuff of Confidence Peak which was erupted earlier from the Silver Bell caldera. Zones of decreased welding in the Cat Mountain Tuff are locally associated with horizons of slide breccias and also occur high in the unit, probably reflecting eruptive pauses or decreased thermal efficiency during emplacement of ash flows; reworked sediments or other depositional units that might indicate sizable time breaks have not been found along such zones of decreased welding. Thus the Cat Mountain Tuff appears to be a single thick intracaldera ash flow sheet with complex welding zonations. A small segment of the structural boundary of the Tucson Mountain caldera may be represented by an arcuate fault along the northwest flank of the mountain range which downdrops Cretaceous sedimentary rocks against Jurassic rocks (Figure 2).

Along the northeast and southeast flanks of the Tucson Mountains, the Cat Mountain Tuff is conformably overlain by a thick caldera-fill sequence of andesitic to rhyolitic lavas, with interbedded volcaniclastic sediments, deposited soon after caldera collapse [*Lipman*, 1989]. These rocks have shallow northeasterly dip angles (5°–25°) along the southeast flank of the range and steep northeasterly dip angles (50°–85°) along the northeast flank. The large zoned Amole pluton exposed in the northern Tucson Mountains (Figure 2) is a resurgent ring intrusion which cuts and arches the steeply dipping caldera fill upward to the east and north [*Lipman*, 1989]. K-Ar biotite ages of about 73 Ma for this intrusion [*Bikerman and Damon*, 1966] indicate that it was emplaced soon after eruption of the Cat Mountain Tuff, within analytical uncertainties of the isotopic ages. The volume of slide breccia is greater than the volume of ash flow tuff within the northern parts of the caldera fill, implying catastrophic subsidence in this sector. In contrast, megabreccia is virtually absent along the inferred southern caldera margin, and the thickness of the tuff decreases to about 100 m. These relations imply a hinged southern margin of the caldera and an overall trapdoor geometry of subsidence [*Lipman*, 1989]. A gridwork of northwest and northeast trending normal faults disrupts the caldera fill volcanic rocks in several parts of the mountain range; displacements along these faults are generally small (25–100 m), but are difficult to determine in the field due to the scarcity of stratigraphic markers. Some of these faults may be related to middle Tertiary extension, but others appear to have been associated with caldera subsidence in Late Cretaceous time [*Lipman*, 1989].

Overlying the caldera-related Cretaceous rocks of the Tucson Mountains are middle Tertiary volcanic rocks exposed on Tumamoc Hill and "A" Mountain at the southeastern side of the range, and in the vicinity of Safford Peak at the northern end of the range (Figure 2). The oldest unit of the Tumamoc Hill-"A" Mountain sequence is a distinctive plagioclase-phyric flow which has a K-Ar plagioclase age of about 29 Ma [*Bikerman and Damon*, 1966]. K-Ar whole rock and mineral ages for the overlying basaltic andesites and tuffs range from 28 Ma to 24 Ma for the uppermost lava flow of Tumamoc Hill [*Bikerman and Damon*, 1966; *Shafiqullah et al.*, 1980]. The sequence of dacitic flows and tuffs near Safford Peak, including the dacitic neck which forms Safford Peak itself, have similar K-Ar biotite ages spanning about 28 Ma to 25 Ma [*Bikerman and Damon*, 1966]. The middle Tertiary volcanic rocks generally dip gently to the northeast (≃10°–20°) and in the southeastern Tucson Mountains are basically conformable with the underlying Cretaceous rocks. This implies that most of the eastward tilting of the mountain range was associated with Tertiary faulting that may have been related to formation of the Santa Catalina core complex to the east [*Lipman*, 1989].

METHODS

Upper Cretaceous rocks in the Tucson Mountains were sampled for paleomagnetic analysis at 44 sites (Table 1). The sampling objectives were (1) to collect enough rock units, deposited over a sufficient span of time, to average PSV of the ancient geomagnetic field, (2) the Cat Mountain Tuff for correlation purposes, and (3) the Amole pluton to determine its attitude at the time of magnetization. Samples were collected with a portable gasoline-powered drill and were oriented in the field with both magnetic and solar compasses and a clinometer. Structural attitudes for the volcanic units are based on interbedded sedimentary rocks, local flow contacts, or eutaxitic structures for pyroclastic rocks. Data for the Amole pluton were corrected for the shallow northeasterly dip angles (≃13°) of nearby middle Tertiary lava

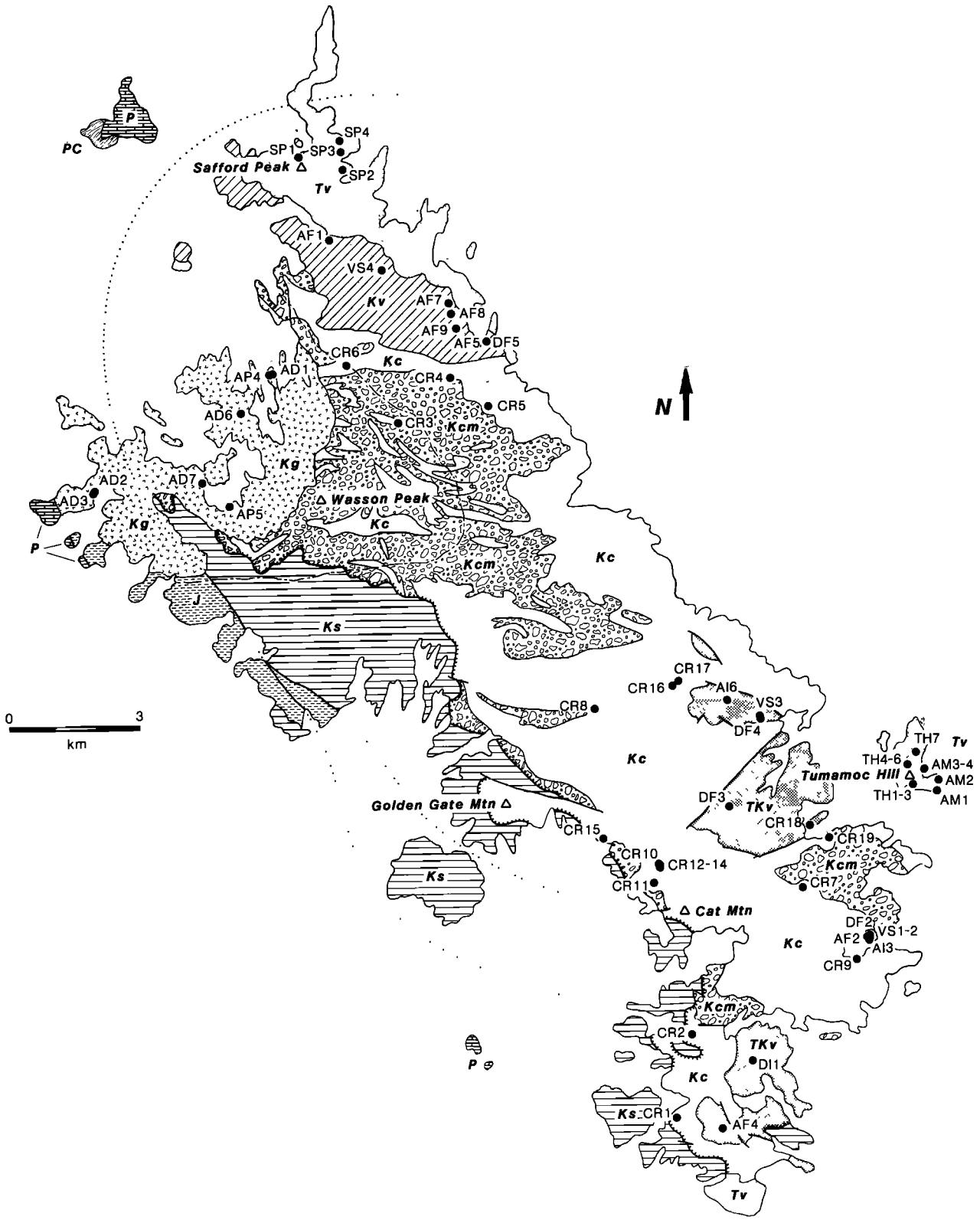

Fig. 2. Geologic map of the Tucson Mountains showing paleomagnetic sampling sites (see Tables 1 and 2). Map symbols are PC, Precambrian rocks; P, Paleozoic sedimentary rocks; J, Jurassic sedimentary and volcanic rocks; Ks, Cretaceous sedimentary rocks; Kc, Cretaceous Cat Mountain Tuff; Kcm, Cretaceous caldera collapse megabreccia; Kg, Cretaceous Amole pluton; Kv and TKv, Cretaceous and Tertiary caldera fill volcanic rocks; and Tv, Tertiary volcanic rocks. Fine lines indicate contacts; heavy lines indicate faults, dotted where concealed; hachured lines indicate floor of Tucson Mountains caldera; and broken line indicates outer limit of hornfels facies rocks surrounding the Amole pluton.

TABLE 1. Site Mean Directions and Poles for Upper Cretaceous Units in the Tucson Mountains, Arizona

Site	Uncorrected		Strike/Dip	Corrected		N	R	k	α_{95}	Pole	
	I	D		I	D					Latitude	Longitude
					Amole Pluton						
AD1	77.7	302.6	315/13	74.2	355.1	5	4.8527	27	15.0	61.6	243.8
AD2	60.9	1.1	315/13	50.6	12.9	5	4.9693	130	6.7	79.0	340.3
AD3	65.9	8.8	315/13	54.6	20.4	6	5.8794	41	10.5	72.8	323.7
AP4	77.1	320.7	315/13	70.9	2.3	7	6.9713	209	4.2	67.0	252.2
AP5	82.5	350.1	315/13	71.7	25.2	8	7.9935	1082	1.7	60.2	277.0
AD6	65.5	302.0	315/13	65.2	330.7	8	7.8483	46	8.2	63.2	201.4
AD7	58.8	339.8	315/13	51.7	355.7	10	9.8535	61	6.2	86.4	160.9
Average				63.7	4.1	(7)	6.8468	39	9.8	76.6	261.3
					Dacitic Rocks						
DI1	−72.5	171.4	359/10	−71.1	202.0	8	7.9566	161	4.4	62.0	275.7
DF2	−57.6	216.3	267/25	−36.1	201.9	7	6.9551	134	5.2	67.0	5.4
DF3*	−12.5	141.3	300/20	−4.7	144.1	8	7.9797	345	3.0	45.0	124.8
DF4	−88.1	263.7	280/33	−56.4	193.3	9	8.9372	127	4.6	78.1	311.8
DF5	−81.6	339.4	300/25	−69.4	228.7	4	3.9919	371	4.8	49.7	293.2
					Volcaniclastic Sedimentary Rocks						
VS1	46.7	337.7	275/20	28.4	344.0	5	4.9041	42	12.0	67.6	113.2
VS2	51.0	328.4	267/25	28.1	337.0	5	4.8922	37	12.7	62.9	124.9
VS3	−78.8	90.8	280/33	−57.1	169.3	9	8.9543	175	3.9	79.9	194.0
VS4	58.2	202.8	278/72	48.4	356.3	7	6.7735	26	12.0	85.7	116.5
					Andesitic Rocks						
AF1	−54.4	320.6	260/60	−57.7	202.4	8	7.9695	229	3.7	70.8	314.2
AF2	62.6	47.9	267/25	43.0	26.2	4	3.9269	41	14.5	66.0	349.7
AI3	76.2	338.0	275/18	59.0	352.8	7	6.8488	40	9.7	80.4	213.8
AF4	61.5	348.6	359/10	61.7	7.2	7	6.9370	95	6.2	77.9	274.8
AF5	−79.1	7.6	300/25	−74.6	225.8	8	7.9652	201	3.9	48.8	280.7
AI6	−71.2	113.1	300/25	−61.0	168.7	5	4.9765	171	5.9	76.7	209.5
AF7	−76.0	79.2	282/60	−34.5	176.3	6	5.9660	147	5.6	76.2	83.8
AF8	−63.3	55.5	282/60	−46.8	165.1	8	7.9013	71	6.6	76.5	324.4
AF9	−54.6	67.1	282/60	−44.0	150.7	8	7.9497	139	4.7	63.6	152.2
					Cat Mountain Tuff						
CR1	−30.8	167.3	110/05	−35.0	165.5	8	7.9899	692	2.1	71.7	117.9
CR2	−31.4	160.7	360/05	−32.9	163.7	7	6.9917	721	2.3	69.5	118.8
CR3	−63.7	83.6	268/62	−26.8	148.4	5	4.9547	88	8.2	56.0	134.2
CR4	−31.5	78.5	283/75	−28.5	131.1	7	6.9706	204	4.2	42.5	149.7
CR5	−73.5	134.6	293/51	−31.5	185.0	8	7.9617	183	4.1	74.1	51.3
CR6†	−41.7	27.0	278/70	−63.0	155.6	5	4.9825	228	5.1	67.5	198.6
CR7†	−61.2	152.5	338/20	−57.1	186.2	8	7.9578	166	4.3	82.5	289.9
CR8	−52.5	146.2	288/30	−30.0	164.5	8	7.9893	655	2.2	68.6	113.6
CR9	−60.5	168.7	267/25	−35.6	172.0	8	7.9846	453	2.6	75.6	101.0
CR10†	−76.0	133.7	308/30	−55.9	192.6	8	7.9651	200	3.9	78.7	313.1
CR11	−54.5	146.3	308/30	−37.8	173.7	8	7.9837	429	2.7	77.7	97.7
CR12†	−71.3	149.2	308/30	−49.6	190.4	6	5.9933	750	2.5	80.9	347.2
CR13†	−71.9	127.0	308/30	−55.7	184.5	6	5.9959	1211	1.9	84.5	290.4
CR14†	−72.7	135.0	308/30	−54.0	187.8	6	5.9958	1194	1.9	83.1	317.3
CR15	−58.4	153.1	290/25	−38.4	170.8	8	7.9734	263	3.4	76.6	108.9
CR16†	−63.7	94.5	285/25	−57.9	140.0	6	5.9303	72	8.0	57.1	181.3
CR17†	−71.2	73.5	285/25	−68.3	147.1	6	5.9956	1146	2.0	59.3	207.5
CR18	−43.0	162.4	300/20	−28.2	172.2	8	7.9540	152	4.5	71.4	93.3
CR19	−51.4	170.4	300/20	−34.7	181.0	7	6.9736	228	4.0	76.9	64.7
Average of the lower unit				−34.2	170.4	(8)	7.9622	185	4.1	74.0	104.0
Average of the upper unit†				−54.5	188.4	(5)	4.9927	544	3.3	82.5	314.6
					All Units						
Average				55.6	1.2	(26)	24.7784	20	6.4	86.0	262.2

I and D are inclination and declination of paleomagnetic directions in degrees, uncorrected/corrected for structural tilt; Strike/Dip is strike and dip of unit (dip 90° clockwise of strike) at or near site in degrees; N, number of samples (sites) analyzed; R is vector sum of N unit vectors; k is precision parameter [*Fisher*, 1953]; α_{95} is radius of 95% confidence in degrees; Latitude and Longitude are latitude and east longitude of northern hemisphere virtual geomagnetic pole corrected for tilt in degrees; Average is mean of paleomagnetic directions (see text).

*Not included in overall mean.

†Upper magnetic unit of the Cat Mountain Tuff.

TABLE 2. Site Mean Directions and Poles for Tertiary Units in the Tucson Mountains, Arizona

Site	Uncorrected		Strike/Dip	Corrected		N	R	k	α_{95}	Pole	
	I	D		I	D					Latitude	Longitude
					Tumamoc Hill						
TH1	59.9	294.5	301/15	58.3	319.7	5		[−112,−1]	[5.2,7.1]	56.9	182.2
TH2	57.6	253.2	301/15	66.7	276.4	7	6.9770	261	3.8	27.8	201.9
TH3	64.8	249.7	301/15	73.7	282.9	5	4.9656	116	7.1	33.8	212.7
TH4	70.8	246.7	301/15	78.9	297.0	8	7.9846	455	2.6	39.6	224.0
TH5	66.5	263.3	301/15	71.6	301.3	8	7.9702	235	3.6	43.5	208.3
TH6	73.9	287.3	301/15	70.9	335.5	6	5.9499	100	6.7	61.3	219.5
TH7	60.6	262.4	301/15	67.0	290.6	6	5.8780	41	10.6	36.9	199.8
Average				70.7	301.5	7	6.9135	69	7.3	43.7	206.4
					"A" Mountain						
AM1	64.7	321.8	301/15	56.5	344.6	6	5.8405	31	12.2	76.5	183.9
AM2	−47.8	162.1	301/15	−37.0	171.7	8	7.9865	517	2.4	76.2	103.5
AM3	−48.8	155.6	301/15	−39.1	166.7	7	6.9110	67	7.4	74.4	121.5
AM4	−44.5	182.8	301/15	−31.0	187.9	7	6.9573	140	5.1	72.9	42.5
Average				41.2	353.7	4	3.9158	36	15.6	79.7	103.3
					Safford Peak						
SP1*	23.6	173.1	315/13	31.2	167.6	7	6.9716	211	4.2	39.4	84.3
SP2	−41.1	176.1	315/13	−32.0	183.0	9	8.9077	87	5.6	74.7	57.9
SP3	−45.3	170.3	315/13	−36.9	179.0	7	6.9723	216	4.1	78.2	73.4
SP4	−60.0	167.4	315/13	−51.5	182.1	7	6.9458	111	5.8	88.2	342.8
Average				40.1	1.3	3	2.9679	62	15.8	80.5	61.3

See Table 1 notes. Bingham statistics [*Onstott*, 1980] for site TH1: R is not calculated, $[-k_1, -k_2]$ are the two Bingham concentration parameters, and $[\alpha_1, \alpha_2]$ are the two Bingham 95% confidence limits.
*Not included in overall mean.

flows, and available local or regional corrections were used for the other intrusive units. Structural corrections were made by a simple rotation of the inferred paleohorizontal to the present horizontal about the strike axis.

The Cat Mountain Tuff was initially sampled at sites in the southern Tucson Mountains to avoid potential structural complications associated with the more intensely deformed rocks to the north and to avoid thick sections that might have cooled more slowly and recorded significant PSV. Site CR6 was collected near the eastern margin of the Amole pluton (Figure 2) to see if these rocks had been remagnetized by the resurgent intrusion. Preliminary results implied the presence of two distinct magnetic units within the Cat Mountain Tuff, so further sampling was undertaken in nonwelded to densely welded portions of the tuff to refine the paleomagnetic directions and local stratigraphy of these two units. Postcaldera andesitic and dacitic lava flows were sampled at 11 geographically dispersed sites in order to sample the largest possible number of individual units representing the broadest possible range of time. In addition, intrusive bodies of similar composition were sampled at sites AI3, AI6, and DI1, and intercalated volcaniclastic units were sampled at sites VS1-4 (Table 1). The finer-grained granodioritic border phase (AP4-5) and late-stage aplite dikes (AD1-3 and AD6-7) of the Amole pluton were sampled at seven sites. The middle Tertiary volcanic rocks were samples at 11 sites in the vicinity of Tumamoc Hill and at five sites in the vicinity of Safford Peak (Table 2).

The remanent magnetization of individual specimens cut from the core samples was measured with a cryogenic magnetometer. Specimens from all samples were subject to progressive alternating field (af) demagnetization, and lines representing the characteristic magnetization directions were fitted to the demagnetization data using a least squares method based on principal component analysis [*Kirschvink*, 1980]. The statistical methods of *Fisher* [1953] were used in analyzing most within-site and unit means. Bingham statistics [*Onstott*, 1980] were calculated for the site mean direction (TH1, Table 2) determined using remagnetization circle analysis [*Halls*, 1978]. Estimates of inclination flattening and clockwise rotation of the paleomagnetic directions for sites in southern Arizona, with respect to North American reference or correlated tuff unit directions, and their 95% confidence limits (Table 3) were calculated after the methods of *Beck* [1980], as modified by *Demarest* [1983].

RESULTS

Natural remanent magnetization (NRM) directions and intensities for all samples from the Tucson Mountains were measured prior to af demagnetization treatments. Within-site NRM directions for samples of the Cat Mountain Tuff were typically well grouped but were moderately to strongly dispersed for samples from sites CR2–CR5 and CR19. The dispersed directions, in association with intensities 1–3 orders of magnitude higher than those for other samples of the tuff, indicate that samples from these five sites may have been affected by surface currents caused by direct or nearby lightning strikes. Excepting these five sites, the NRM intensities for sites in the Cat Mountain Tuff form two distinct populations: one with an estimated average intensity of 2.09×10^{-2} A m^{-1} and corresponding standard deviation (s) of 9.76×10^{-3} A m^{-1}, and another with an estimated average intensity of 2.28×10^{-1} A m^{-1} ($s = 1.75 \times 10^{-1}$ A m^{-1}). Af demagnetization was successful in removing presumed lightning-induced magnetizations from samples of the Cat Mountain Tuff and in isolating their reversed-polarity characteris-

TABLE 3. Vertical Axis Rotations of Upper Cretaceous and Tertiary Rocks in South Central Arizona

	I	D	N	R	k	α_{95}	d	r	Reference
				Tucson Mountains					
Upper Cretaceous rocks									
North America	57.5	353.8	(26)	24.5310	18	7.1			1
All units	55.6	1.2	(26)	24.7784	20	6.4	1.9 ± 7.5	7.4 ± 13.7	4
North America	57.5	353.8	(26)	24.5310	18	7.1			1
Amole pluton	63.7	4.1	(7)	6.8468	39	9.8	−6.2 ± 9.4	10.3 ± 20.4	4
Middle Tertiary rocks									
North America	49.9	352.2	(102)	94.6429	14	3.9			3
All units	40.8	357.0	(7)	6.8747	48	8.8	9.1 ± 7.5	4.8 ± 10.2	4
				Silver Bell Mountains					
Upper Cretaceous rocks									
North America	57.6	353.8	(26)	24.5310	18	7.1			1
All units	61.2	24.0	(34)	31.1472	12	7.6	−3.6 ± 8.1	30.2 ± 16.2	2
Middle Tertiary rocks									
North America	50.2	352.2	(102)	94.6429	14	3.9			3
All units	43.8	357.3	(10)	9.0541	10	16.5	6.4 ± 13.3	5.1 ± 18.5	2
				Cat Mountain Tuff					
Tucson Mountains	−34.2	170.4	(8)	7.9622	185	4.1			4
Silver Bell Mountains	−38.7	187.3	(4)	3.9705	102	9.2	−4.5 ± 7.8	17.0 ± 10.0	2

Abbreviations as in Table 1. Parameters d and r are inclination flattening and clockwise rotation at site with respect to expected field direction, in degrees, with 95% confidence limits after *Beck* [1980], as modified by *Demarest* [1983]. References are 1, expected direction at site calculated from pole at 82°N, 210°E, *Gunderson and Sheriff* [1991]; 2, *Hagstrum and Sawyer* [1989]; 3, calculated from pole at 83°N, 148°E, *Diehl et al.* [1983]; and 4, this study.

tic magnetizations (Figure 3*a*). Site mean directions for the tuff are listed in Table 1 and are shown both before and after application of structural corrections in Figure 4. The dispersion of uncorrected directions in Figure 4*a* generally reflect the increasing dip angles of the Upper Cretaceous units to the north in the Tucson Mountains, and the corrected directions (Figure 4*b*) show the presence of two populations, indicating that the Cat Mountain Tuff can be subdivided into two distinct magnetic units. Furthermore, the two populations of sites with different directions coincide with those of

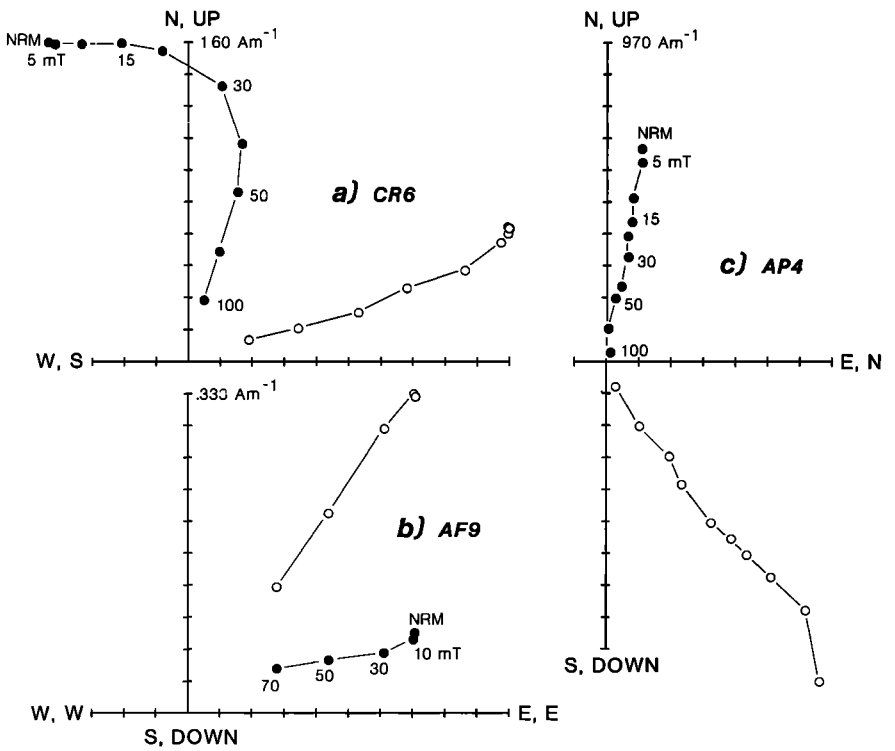

Fig. 3. Orthogonal projections of uncorrected alternating field demagnetization vector endpoints for samples of (*a*) Cat Mountain Tuff from site CR6, (*b*) caldera fill andesitic lava flow from site AF9, and (*c*) granodioritic border phase of the Amole pluton from site AP4. Solid symbols indicate projections of vector endpoints onto the horizontal plane and open symbols onto the vertical plane.

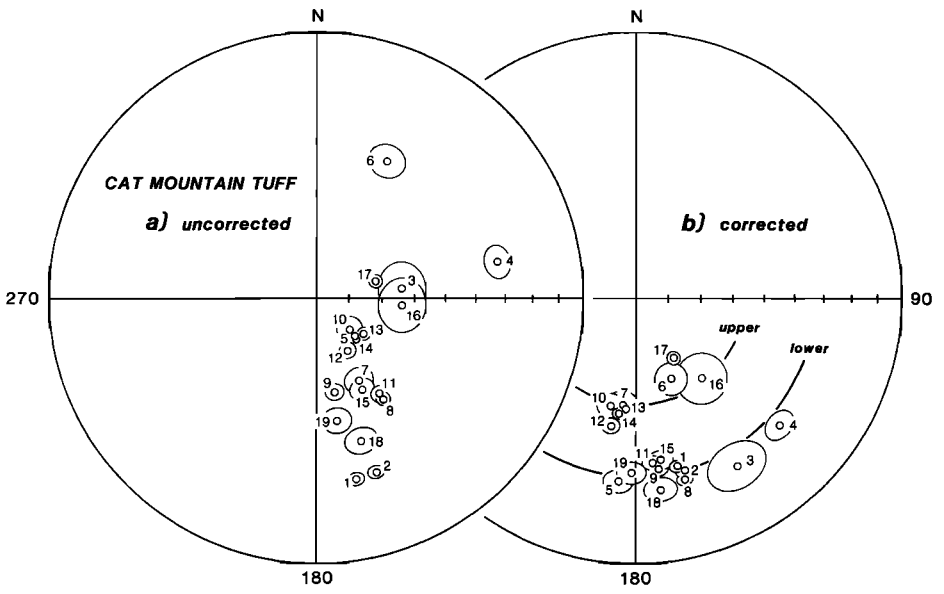

Fig. 4. Mean directions of sites with 95% confidence limits (*a*) uncorrected and (*b*) corrected for structural tilt for the Cat Mountain Tuff (Table 1). Small-circle arcs represent the average inclination values for the lower and upper magnetic units. Diagram is an equal-area plot in which open symbols indicate projection from the upper hemisphere.

NRM intensity, implying slight differences in quantity or size of the magnetic minerals between the two units of the tuff. The dispersion of the site mean inclinations [*McFadden and Reid*, 1982] decreases significantly (99% confidence level [*McElhinny*, 1964]) after correction for each unit, demonstrating that the remanent magnetizations predate tilting of the Cat Mountain Tuff. Because dispersion of the corrected site mean declinations along small-circle arcs (Figure 4*b*) most likely depends on the magnitude of inclined-axis rotation during deformation and therefore on the present dip angle [see *Chan*, 1988], sites with dip angles >45° are deemed unreliable. At less deformed sites this dispersion also could have resulted from local vertical axis rotations (e.g., CR16 and CR17). Samples from sites CR3–CR5 (lower unit) and sites CR6, CR16, and CR17 (upper unit) thus were omitted from unit mean calculations for the two magnetic units (Table 1).

The andesitic, dacitic, and volcaniclastic rocks of the caldera fill sequence also showed the probable effects of lightning-induced magnetizations, but af demagnetization was successful in determining the characteristic directions of magnetization for these rock units as well (e.g., Figure 3*b*). The caldera fill rocks have both normal- and reversed-polarity magnetizations (Figure 5), indicating that they were deposited over a significant period of time relative to PSV. Site DF3 is in a massive structureless flow(?), and a regional attitude was used for the structural correction. The inconsistency of the corrected direction for site DF3 with the other corrected directions (Table 1), however, implies that either the regional attitude is locally incorrect or the unit was magnetized in an anomalous geomagnetic field (i.e., excursion or reversal); this site therefore was omitted from the overall mean calculation.

Upon af demagnetization (Figure 3*c*), samples from the Amole pluton show consistent normal-polarity characteristic directions of magnetization (Table 1). The angular standard deviation value for the unit mean pole of the Amole pluton (S = 17.6°) is similar to the expected value (S = 15.5° ± 1°) for the latitude of the Tucson Mountains, based on models of recent PSV [*McFadden et al.*, 1988], and we infer that the pluton cooled and was magnetized over a sufficient period of time to average PSV. Normal- and reversed-polarity characteristic magnetizations for the middle Tertiary units, although limited in number, also indicate that these rocks were emplaced over a significant time interval with respect to PSV (Figure 5). Lightning-induced magnetizations also appear prevalent in these rocks, and one site in a lava flow near Safford Peak was completely overprinted and therefore discarded; the mean direction for the uppermost site on Tumamoc Hill (TH1) could only be determined using remagnetization circle analysis (Table 2 and Figure 6).

Dispersion of the site mean directions for Upper Cretaceous units in the Tucson Mountains (not including those for the Cat Mountain Tuff) is significantly decreased at the 95% confidence level [*McElhinny*, 1964] after structural correction, indicating that the remanent magnetizations predate deformation represented by these corrections (Table 1 and Figure 5). The angular standard deviation for the overall Late Cretaceous paleomagnetic pole for the Tucson Mountains (S = 20.8°) is larger than the expected model value based on PSV alone. The excessive dispersion is probably due to errors associated with the structural corrections; these errors are assumed to be nonsystematic and not to have significantly affected the overall mean paleomagnetic direction. The averaging of PSV by the paleomagnetic data for the Tucson Mountains is also supported by antipodal means for the normal-polarity (I = +55.7°, D = 359.2°, α_{95} = 9.5°, N = 13) and reversed-polarity (I = −55.6°, D = 182.9°, α_{95} = 9.7°, N = 13) site mean directions (Figure 5).

Discussion

Tucson Mountains

Mauger et al. [1965] suggested a regional correlation of the Cat Mountain Tuff in the Tucson Mountains with the tuff unit

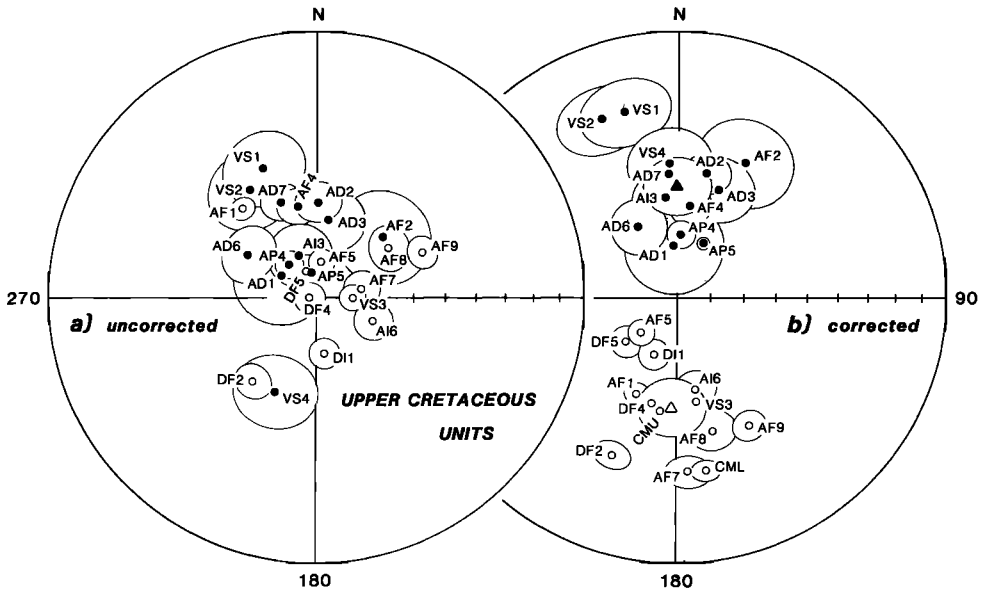

Fig. 5. Mean directions of sites with 95% confidence limits (*a*) uncorrected and (*b*) corrected for structural tilt for Upper Cretaceous units in the Tucson Mountains (Table 1). CMU and CML indicate means for the upper and lower magnetic units of the Cat Mountain Tuff, respectively. Triangular symbols indicate mean directions of the normal (N = 13) and reversed polarity (N = 13) site mean directions. Diagrams are equal-area plots in which solid symbols indicate projection from the lower hemisphere and open symbols from the upper hemisphere.

of the Mount Lord Volcanics, which caps the Silver Bell Mountains to the northwest (Figure 1). Although *Mauger et al.* [1965] reported a K-Ar sanidine age of 60.9 ± 1.8 Ma for the tuff unit of the Mount Lord Volcanics, which is significantly younger than that for the Cat Mountain Tuff in the Tucson Mountains (71.9 ± 2.1 Ma [*Bikerman and Damon*, 1966]), thin section observations showed that the apparent age of the sample from the Silver Bell Mountains most likely was reduced by argon diffusion related to a younger episode of alteration and mineralization [*Mauger et al.*, 1965]. Recently acquired petrologic data also support the correlation of the Cat Mountain Tuff between the Silver Bell and Tucson Mountains; in particular, the Cat Mountain Tuff has distinctively high zirconium contents (100–400 ppm [*Lipman*, 1991]). In addition, the paleomagnetic data for the Cat Mountain Tuff presented here and by *Hagstrum and Sawyer* [1989] support this correlation. A mean inclination calculated from the data for samples least affected by deformation or probable lightning strikes (sites CM1–CM4) for the tuff unit in the Mount Lord Volcanics of the Silver Bell Moun-

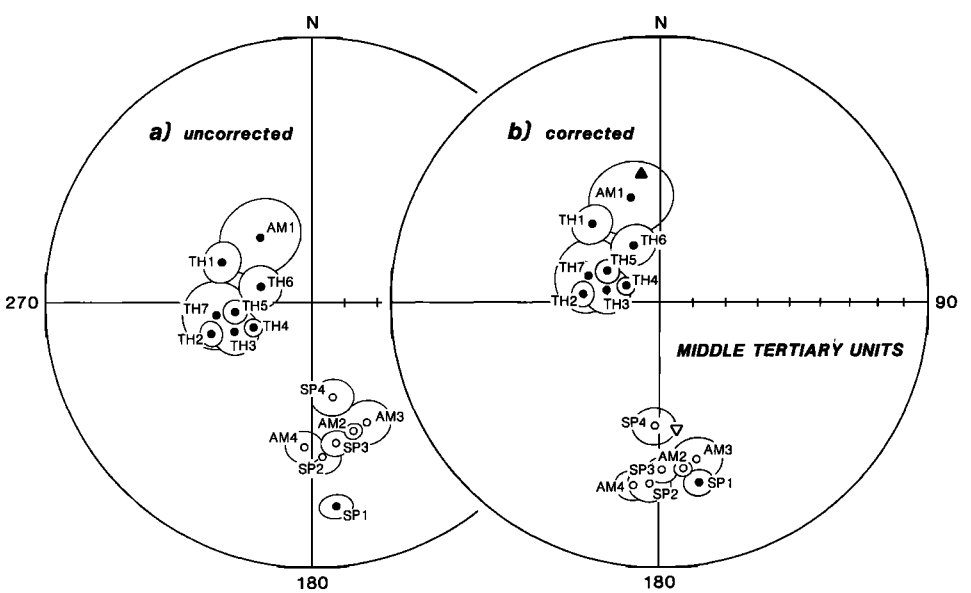

Fig. 6. Mean directions of sites with 95% confidence limits (*a*) uncorrected and (*b*) corrected for structural tilt for middle Tertiary units (Table 2). Triangular symbols indicate expected middle Tertiary directions for the Tucson Mountains. Diagram is an equal area plot in which solid symbols indicate projection from the lower hemisphere and open symbols from the upper hemisphere.

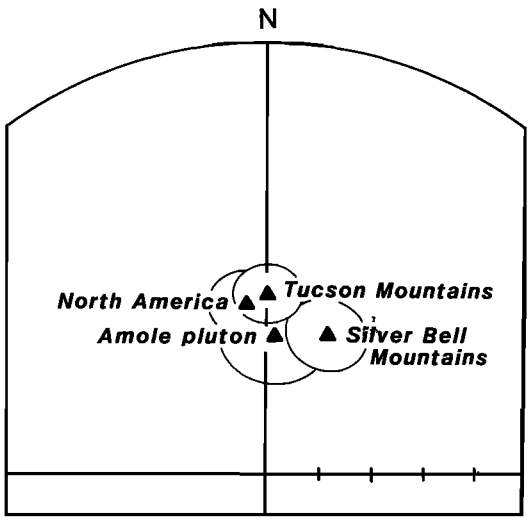

Fig. 7. Mean directions with 95% confidence limits for Upper Cretaceous units in the Tucson and Silver Bell Mountains and for the Amole pluton. Late Cretaceous reference direction for North America calculated from *Gunderson and Sheriff* [1991] (see Table 3). Diagram is an equal-area plot in which solid symbols indicate projection from the lower hemisphere.

tains (I = −38.7° ± 9.2°) is similar to that of the lower magnetic unit of the Cat Mountain Tuff (I = 34.2° ± 4.1°) in the Tucson Mountains (Table 3), and these inclinations are quite different than the average expected inclination for the region in Upper Cretaceous time (±58°). Furthermore, the mean declinations indicate a 17° ± 10° clockwise rotation of the Silver Bell Mountains relative to the Tucson Mountains (Table 3 and Figure 7). The 13° ± 19° difference between this 17° relative rotation between mountain ranges and the absolute clockwise rotation of the Silver Bell Mountains relative to North America (30°), although insignificant at the 95% confidence level, implies some clockwise rotation of the Tucson Mountains as well.

Comparison of the overall mean direction for Upper Cretaceous units in the Tucson Mountains (I = +55.6°, D = 1.2°, α_{95} = 6.4°, N = 26) to a reference direction calculated for contemporaneous units from stable North America (I = +57.5°, D = 353.8°, α_{95} = 7.1°, N = 26) indicates a slight northward shift (2° ± 8°) and clockwise rotation (7° ± 14°) of the site since Late Cretaceous time, although both these values are insignificant with 95% confidence (Table 3 and Figure 7). The magnitudes of the absolute rotations for the Tucson and Silver Bell Mountains strongly depend on the position of the North American reference pole, and because of rapid apparent wander in the Late Cretaceous, an accurate pole for this time has been difficult to determine. The best available estimate of a Late Cretaceous reference pole for North America is that recently published by *Gunderson and Sheriff* [1991] based on volcanic rocks in Montana (Table 3). No significant latitudinal shift relative to stable North America is expected for the Tucson Mountains since this time, and we attribute the observed inclination flattening value to error. The 7° ± 14° clockwise rotation of the Tucson Mountains, however, is of the same sense as the rotation (30° ± 16°) reported for the Silver Bell Mountains [*Hagstrum and Sawyer*, 1989] and is consistent with the 17° ± 10° relative rotation between mountain ranges indicated by paleomagnetic directions for the Cat Mountain Tuff. Thus we infer that the Tucson Mountains have probably undergone a clockwise vertical axis rotation of about 10°.

Similarity of the mean direction for the 73-Ma-old Amole pluton with the overall mean direction for the Tucson Mountains (Table 3), after correction for the tilt of the overlying volcanic units (≈13° NE, Table 2), indicates that most of the tilting of the northern Tucson Mountain block since Late Cretaceous time occurred after deposition of the middle Tertiary volcanic rocks. Steep tilting to the north and northeast of the caldera fill adjacent to the Amole pluton, however, occurred before the pluton cooled and acquired its characteristic magnetization in Late Cretaceous time. Thus these data support the interpretation that the caldera fill sequence was deformed by emplacement of the Amole pluton and that the pluton represents the solidified remnants of the magma chamber which underlay the Tucson Mountains caldera at the time of collapse and resurgent uplift. Although site CR6 in the Cat Mountain Tuff is within ≈600 m of the contact with the Amole pluton (Figure 2), samples from this site have not been significantly overprinted by a thermoremanent magnetization related to the nearby emplacement of the pluton; hornfels alteration of the country rock appears to be concentrated along the southeastern margin of the pluton in the vicinity of Wasson Peak.

The mean direction for site CR6 is among the group of mean directions with steeper inclinations (Table 1 and Figure 4*b*), indicating that this site is within the upper magnetic unit of the Cat Mountain Tuff. The identification of two distinct magnetic units within the intracaldera Cat Mountain Tuff is unusual because thick caldera-fill sequences of tuff usually cool over longer periods of time and record greater amounts of PSV [e.g., *Hagstrum and Lipman*, 1986; *R. L. Reynolds et al.*, 1986]. Rapid cooling of the thick (3 km) intracaldera Cat Mountain Tuff, composed predominantly of the lower magnetic unit, however, probably resulted from the introduction of large quantities of cold landslide-related megabreccia during its emplacement. This rapid cooling is corraborated by the nonwelded matrix of the intracaldera megabreccia. The ≈20° difference in inclination between the mean directions for the two magnetic units, however, may indicate that a significant amount of time (10^2–10^3 years) passed between magnetization of these units based on estimates of recent rates of secular variation [e.g., *Merrill and McElhinny*, 1983].

The two magnetic units in the upper part of the Cat Mountain Tuff could alternatively represent (1) the presence of two discrete depositional units for which the contact is concealed or (2) rapid PSV during laterally variable cooling of a single tuff unit. The first interpretation is favored by the bimodal distribution of inclinations and NRM intensities and by the observation of high and low inclinations in nonwelded to densely welded tuff. If this interpretation is correct, the paleomagnetic data for the intracaldera Cat Mountain Tuff provide criteria for inferring a concealed stratigraphic break and the presence of fault displacements sufficient to juxtapose the two units in a complicated pattern throughout the Tucson Mountains. The second interpretation of variable cooling within the upper part of a single depositional unit is favored by the observation of high (CR12–CR14, CR16, and CR17) and low (CR9 and CR18) inclinations in the upper nonwelded to partly welded zone of the tuff, where mapped

as immediately overlain by sedimentary rocks. Because no zoned of nonwelded to partly welded tuff is exposed at lower stratigraphic levels, it is difficult to account for the juxtaposition of two similar-appearing units at the paleomagnetic sampling sites by sizeable faults. Resolution of these alternatives, however, is not critical to the major interpretations of this study concerning regional vertical axis rotations.

Although the middle Tertiary volcanic units in the Tucson Mountains were deposited and magnetized over a time span including both normal- and reversed-polarity fields (Table 2 and Figure 6), the eruptive rates over this time span apparently were irregular. All lava flows sampled near Safford Peak show reversed-polarity magnetizations and were likely deposited within a single polarity chron, even though ash flow tuffs and volcanic sediments between dacite flows indicate some eruptive pauses between the lavas. The volcanic sequence, exposed on Tumamoc Hill and "A" Mountain, consists of lower and upper packets of basaltic andesite lavas separated by sediments and a weakly welded rhyolitic ash flow sheet. A polarity reversal is recorded within the lower packet, between eruption of the basal "turkey track" porphyritic andesite (AM1) and overlying flows of aphyric andesite (AM2 and AM3). The ash flow tuff (AM4) is similarly of reversed polarity, but seven flows of the upper lava packet (TM1–TM7) all have distinctive normal-polarity magnetizations (Figure 6*b*) that likely indicate rapid eruption during an interval of high-amplitude PSV; a $\simeq$70° counterclockwise rotation of these rocks is inconsistent with data for either "A" Mountain or Upper Cretaceous units in the southern Tucson Mountains. The mean direction for the dacite neck forming Safford Peak also probably reflects extreme PSV and was omitted, along with site means for Tumamoc Hill, from calculation of the overall middle Tertiary mean direction for the Tucson Mountains (Table 3). Although the remaining data (N = 7) are too few to completely average PSV, the general agreement of these data with those for the Silver Bell Mountains and with the expected North American direction (Table 3) is consistent with no significant vertical axis rotation of the Tucson Mountains after middle Tertiary time.

Regional Deformation

The clockwise vertical axis rotations inferred for the Silver Bell Mountains [*Hagstrum and Sawyer*, 1989], Tucson Mountains, and Canelo Hills region [*Hagstrum and Lipman*, 1991] imply that regional rotational deformation has occurred in southern Arizona since Late Cretaceous time. Although insufficient in number to convincingly average PSV, the paleomagnetic data for middle Tertiary units in the Silver Bell and Tucson Mountains imply that clockwise rotation of these mountain ranges preceded deposition of the Tertiary units. The clockwise rotations of the Silver Bell and Tucson Mountains, thus interpreted to be of Late Cretaceous to early Tertiary age, could be part of a larger pattern of clockwise rotations which have occurred since middle Cretaceous time along the western margin of the North American Cordillera [*Beck*, 1988]. Although no one mechanism can explain all of these rotations [*Cox*, 1980], most are clockwise [*Beck*, 1980] and therefore are possibly linked to regional dextral shear along the western margin of ancestral North America caused by northward oblique subduction of the Kula and Farallon plates [*Cox*, 1980; *Beck*, 1983; *Engebretson et al.*, 1984]. Paleomagnetic data for the Baja California Peninsula to the southwest [e.g., *Hagstrum and Filmer*, 1990] and for the Colorado Plateau to the north [*Steiner*, 1988; *Bryan and Gordon*, 1990; see also *Hamilton*, 1988] also indicate that clockwise rotations have occurred in southwestern North America since middle Cretaceous time, supporting the evidence for similar deformation in southern Arizona during Late Cretaceous and early Tertiary time. The shallow angle of subduction [e.g., *Dickinson and Snyder*, 1978; *Bird*, 1988] and rapid convergence rate [*Engebretson et al.*, 1984] inferred for the Farallon plate during this time would also contribute to the likelihood of rotational deformation in southern Arizona.

Mechanisms of vertical axis rotation considered by *Nelson and Jones* [1987] for the Las Vegas Valley shear zone also potentially apply to the rotations observed in southern Arizona and include (1) pervasive, continuous simple shear, (2) block rotation between conjugate shear faults, and (3) rotation of individual blocks in response to distributed shear in the ductile lower crust and mantle. Pervasive simple shear can be quickly eliminated for southern Arizona because the Upper Cretaceous rocks there do not show any evidence of extensive internal deformation or recrystallization that would be associated with this mechanism. Furthermore, the available paleomagnetic data for southern Arizona imply that the Silver Bell and Tucson Mountains each rotated as a rigid block. In models of rotation of conjugate shear faults, domains of rigid crustal blocks bounded by parallel strike-slip faults rotate along with the faults [e.g., *Ron et al.*, 1984; *McKenzie and Jackson*, 1986]. Paleomagnetic results for the lower unit of the Cat Mountain Tuff show that the individual rotations of the Silver Bell and Tucson Mountains are significantly different (17° $\pm$ 10°), implying that either the conjugate shear fault model is incorrect for southern Arizona or that the two mountain ranges were in different rotational domains [e.g., *Garfunkel and Ron*, 1985]. Vertical axis rotations of individual crustal blocks, driven by ductile shear below, depend upon the shape and orientation of the individual blocks [*Lamb*, 1987] and could explain the variable amount and sense of rotation observed in south central Arizona. Much more data is needed, however, before a well-constrained model of vertical axis rotations associated with Laramide deformation in south central Arizona can be constructed.

CONCLUSIONS

Comparisons of paleomagnetic data for Upper Cretaceous rocks in the Silver Bell [*Hagstrum and Sawyer*, 1989], Tucson Mountains, and Canelo Hills region [*Hagstrum and Lipman*, 1991] imply that all of these localities in south central Arizona have been rotated about vertical axes with respect to cratonic North America. The inference that rocks within the Basin and Range province of southern Arizona have all remained unrotated with respect to stable North America since Jurassic time thus is unfounded. Apparently concordant middle Tertiary paleomagnetic data for the Silver Bell Mountains [*Hagstrum and Sawyer*, 1989] and the Tucson Mountains (this study) imply that these clockwise rotations, at least, occurred during latest Cretaceous to early Tertiary time. *Hagstrum and Sawyer* [1989] suggested that the clockwise rotation of the Silver Bell Mountains was related to right lateral strike-slip displacement on northwest

trending faults bounding the Silver Bell block. Strike-slip faults most likely played an important role in the Laramide deformation of southern Arizona [*Keith and Wilt*, 1986], although evidence pertaining to their role has been difficult to obtain because of poor exposures in the region and the lack of local features indicating the sense and amount of displacement. The Silver Bell and Tucson blocks have been rotated clockwise different amounts, apparently in response to continuous ductile deformation in the lower crust and mantle associated with oblique subduction along the continental margin, although much more data is needed to determine the exact mechanism(s) of deformation. This rotational deformation is coincident with rapid plate convergence and Laramide compressional stresses and also could be related in part to inhomogeneous shortening of the crust in southern Arizona [*Davis*, 1979, 1981].

Acknowledgments. We thank the staffs of Saguaro National Monument and of Tucson Mountain County Park for permission to sample within the monument and park, and the University of Arizona for allowing us access to Tumamoc Hill. We are grateful to G. J. Calderone and R. F. Butler for contributing data for two sites (TH2 and TH3) on Tumamoc Hill. Discussions with D. A. Sawyer and R. M. Tosdal, and reviews by S. D. Sheriff, M. R. Hudson, S. L. Halgedahl, G. J. Calderone, and an anonymous reviewer helped to significantly improve the manuscript.

REFERENCES

Beck, M. E., Jr., Paleomagnetic record of plate-margin processes along the western edge of North America, *J. Geophys. Res.*, *85*, 7115–7131, 1980.

Beck, M. E., Jr., On the mechanism of tectonic transport in zones of oblique subduction, *Tectonophysics*, *93*, 1–11, 1983.

Beck, M. E., Jr., Block rotations in continental crust: Examples from western North America, in *Paleomagnetic Rotations and Continental Deformation*, edited by C. Laj, and C. Kissel, pp. 1–16, Kluwer Academic, Boston, Mass., 1988.

Bikerman, M., Origin of the Cat Mountain Rhyolite, *Ariz. Geol. Soc. Dig.*, *6*, 83–89, 1963.

Bikerman, M., and P. E. Damon, K/Ar chronology of the Tucson Mountains, Pima County, Arizona, *Geol. Soc. Am. Bull.*, *77*, 1225–1234, 1966.

Bird, P., Formation of the Rocky Mountains, western United States: a continuum computer model, *Science*, *239*, 1501–1507, 1988.

Brown, W. H., Tucson Mountains, an Arizona Basin Range type, *Geol. Soc. Am. Bull.*, *50*, 697–760, 1939.

Bryan, P., and R. G. Gordon, Rotation of the Colorado Plateau: An updated analysis of paleomagnetic poles, *Geophys. Res. Lett.*, *17*, 1501–1504, 1990.

Chan, L. S., Apparent tectonic rotations, declination anomaly equations, and declination anomaly charts, *J. Geophys. Res.*, *93*, 12,151–12,158, 1988.

Coney, P. J., The plate tectonic setting of southeastern Arizona, in Land of Cochise, edited by J. F. Callender et al., *Field Conf. Guideb. N. M. Geol. Soc.*, *29*, 285–290, 1978.

Cox, A., Rotation of microplates in western North America, in The Continental Crust and Its Mineral Deposits, edited by D. W. Strangway, *Geol. Assoc. Can. Spec. Pap.*, *20*, 305–322, 1980.

Davis, G. H., Laramide folding and faulting in southeastern Arizona, *Am. J. Sci.*, *279*, 543–569, 1979.

Davis, G. H., Regional strain analysis of the superposed deformations in southeastern Arizona and the eastern Great Basin, in Relations of Tectonics to Ore Deposits in the Southern Cordillera, edited by W. R. Dickinson, and W. D. Payne, *Ariz. Geol. Soc. Dig.*, *14*, 155–172, 1981.

Demarest, H. H., Jr., Error analysis for the determination of tectonic rotation from paleomagnetic data, *J. Geophys. Res.*, *88*, 4321–4328, 1983.

Dickinson, W. R., and W. S. Snyder, Plate tectonics of the Laramide orogeny, *Mem. Geol. Soc. Am.*, *151*, 355–366, 1978.

Diehl, J. F., M. E. Beck, Jr., S. Beske-Diehl, D. Jacobson, and B. C. Hearn, Jr., Paleomagnetism of the Late Cretaceous-early Tertiary north-central Montana alkalic province, *J. Geophys. Res.*, *88*, 10,593–10,609, 1983.

Drewes, H. D., Tectonics of southeastern Arizona, *U.S. Geol. Surv. Prof. Pap.*, *1144*, 96 pp., 1981.

Engebretson, D. C., A. Cox, and G. A. Thompson, Correlation of plate motions with continental tectonics: Laramide to Basin-Range, *Tectonics*, *3*, 115–119, 1984.

Fisher, R. A., Dispersion on a sphere, *Proc. R. Soc. London, Ser. A*, *217*, 295–305, 1953.

Garfunkel, Z., and H. Ron, Block rotation and deformation by strike-slip faults, 2, The properties of a type of discontinuous deformation, *J. Geophys. Res.*, *90*, 8589–8602, 1985.

Gromme, C. S., E. H. McKee, and M. C. Blake, Paleomagnetic correlations and potassium-argon dating of middle Tertiary ash-flow sheets in the eastern Great Basin, Nevada and Utah, *Geol. Soc. Am. Bull.*, *83*, 1619–1638, 1972.

Gunderson, J. A., and S. D. Sheriff, A new Late Cretaceous paleomagnetic pole from the Adel Mountains, west-central Montana, *J. Geophys. Res.*, *96*, 317–326, 1991.

Hagstrum, J. T., and P. E. Filmer, Paleomagnetic and tectonic constraints on the Late Cretaceous to early Tertiary northward translation of the Baja California peninsula, *Geofis. Int.*, *29*, 175–184, 1990.

Hagstrum, J. T., and P. B. Gans, Paleomagnetism of the Oligocene Kalamazoo tuff: Implications for middle Tertiary extension in east central Nevada, *J. Geophys. Res.*, *94*, 1827–1842, 1989.

Hagstrum, J. T., and P. W. Lipman, Paleomagnetism of the structurally deformed Latir volcanic field, northern New Mexico: relations to formation of the Questa caldera and development of the Rio Grande rift, *J. Geophys. Res.*, *91*, 7383–7402, 1986.

Hagstrum, J. T., and P. W. Lipman, Paleomagnetism of three Upper Jurassic ash-flow sheets in southeastern Arizona: Implications for regional deformation, *Geophys. Res. Lett.*, *18*, 1413–1416, 1991.

Hagstrum, J. T., and D. A. Sawyer, Late Cretaceous paleomagnetism and clockwise rotation of the Silver Bell Mountains, south central Arizona, *J. Geophys. Res.*, *94*, 17,847–17,860, 1989.

Halls, H. C., The use of converging remagnetization circles in paleomagnetism, *Phys. Earth Planet. Inter.*, *16*, 1–11, 1978.

Hamilton, W., Tectonic setting and variations with depth of some Cretaceous and Cenozoic structural and magmatic systems of the western United States, in *Metamorphism and Crustal Evolution of the Western United States, Rubey Volume 7*, edited by W. G. Ernst, pp. 2–40, Prentice-Hall, Englewood Cliffs, N. J., 1988.

Heidrick, T. L., and S. R. Titley, Fracture and dike patterns in Laramide plutons and their structural and tectonic implications, in *Advances in Geology of the Porphyry Copper Deposits*, edited by S. R. Titley, pp. 73–91, University of Arizona Press, Tucson, 1982.

Keith, S. B., and J. C. Wilt, Laramide orogeny in Arizona and adjacent regions: A strato-tectonic synthesis, *Ariz. Geol. Soc. Dig.*, *16*, 502–554, 1986.

Kirschvink, J. L., The least-squares line and plane and analysis of paleomagnetic data, *Geophys. J. R. Astron. Soc.*, *62*, 699–718, 1980.

Kluth, C. F., R. F. Butler, L. E. Harding, M. Shafiqullah, and P. E. Damon, Paleomagnetism of Late Jurassic rocks in the northern Canelo Hills, southeastern Arizona, *J. Geophys. Res.*, *87*, 7079–7086, 1982.

Lamb, S. H., A model for tectonic rotations about a vertical axis, *Earth Planet. Sci. Lett.*, *84*, 75–86, 1987.

Lipman, P. W., Caldera-collapse breccias in the western San Juan Mountains, Colorado, *Geol. Soc. Am. Bull.*, *87*, 1397–1410, 1976.

Lipman, P. W., Field guide to the Tucson Mountains caldera, in Field Excursions to Volcanic Terranes in the Western United States, vol. I, Southern Rocky Mountain Region, edited by C. E. Chapin and J. Zidek, *Mem. N. M. Bur. Mines Miner. Resour.*, *46*, 133–138, 1989.

Lipman, P. W., Geologic map of the Tucson Mountains caldera, *U.S. Geol. Surv. Misc. Invest. Map*, *I2205*, in press, 1991.

Lipman, P. W., and D. A. Sawyer, Mesozoic ash-flow caldera fragments in southeastern Arizona and their relation to porphyry copper deposits, *Geology*, *13*, 652–656, 1985.

Mauger, R. L., P. E. Damon, and B. J. Giletti, Isotopic dating of

Arizona ore deposits, *Trans. Am. Inst. Min. Metall. Pet. Eng.*, *232*, 81–87, 1965.

May, S. R., and R. F. Butler, North American Jurassic apparent polar wander: Implications for plate motion, paleogeography, and Cordilleran tectonics, *J. Geophys. Res.*, *91*, 11,519–11,544, 1986.

May, S. R., R. F. Butler, M. Shafiqullah, and P. E. Damon, Paleomagnetism of Jurassic rocks in the Patagonia Mountains, southeastern Arizona: Implications for the North American 170 Ma reference pole, *J. Geophys. Res.*, *91*, 11,545–11,555, 1986.

Mayo, E. B., Volcanic orogeny of the Tucson Mountains (a preliminary report), *Ariz. Geol. Soc. Dig.*, *6*, 61–82, 1963.

Mayo, E. B., Defense of "volcanic orogeny", *Ariz. Geol. Soc. Dig.*, *9*, 39–60, 1971*a*.

Mayo, E. B., Feeders of an ash flow sequence on Bren Mountain, Tucson Mountain Park, Arizona, *Ariz. Geol. Soc. Dig.*, *9*, 137–170, 1971*b*.

McElhinny, M. W., Statistical significance of the fold test in paleomagnetism, *Geophys. J. R. Astron. Soc.*, *8*, 338–340, 1964.

McFadden, P. L., and A. B. Reid, Analysis of paleomagnetic inclination data, *Geophys. J. R. Astron. Soc.*, *69*, 307–319, 1982.

McFadden, P. L., R. T. Merrill, and M. W. McElhinny, Dipole/quadrupole family modeling of paleosecular variation, *J. Geophys. Res.*, *93*, 11,583–11,588, 1988.

McKenzie, D., and J. Jackson, A block model of distributed deformation by faulting, *J. Geol. Soc. London*, *143*, 349–353, 1986.

Merrill, R. T., and M. W. McElhinny, *The Earth's Magnetic Field, Its History, Origin, and Planetary Perspective*, *Int. Geophys. Ser.*, *vol. 32*, 401 pp., San Diego, Calif., 1983.

Nelson, M. R., and C. H. Jones, Paleomagnetism and crustal rotations along a shear zone, Las Vegas Range, southern Nevada, *Tectonics*, *6*, 13–33, 1987.

Onstott, T. C., Application of the Bingham distribution function in paleomagnetic studies, *J. Geophys. Res.*, *85*, 1500–1510, 1980.

Rehrig, W. A., and T. L. Heidrick, Regional tectonic stress during the Laramide and late Tertiary intrusive periods, Basin and Range province, Arizona, *Ariz. Geol. Soc. Dig.*, *10*, 205–228, 1976.

Rehrig, W. A., and S. J. Reynolds, Geologic and geochronologic reconnaissance of a northwest-trending zone of metamorphic core complexes in southern and western Arizona, in Cordilleran Metamorphic Core Complexes, edited by M. D. Crittenden et al., *Mem. Geol. Soc. Am.*, *153*, 131–157, 1980.

Reynolds, R. L., M. R. Hudson, and K. Hon, Paleomagnetic evidence for the timing of collapse and resurgence of the Lake City caldera, San Juan Mountains, Colorado, *J. Geophys. Res.*, *91*, 9599–9613, 1986.

Reynolds, S. J., F. P. Florence, J. W. Welty, M. S. Roddy, D. A. Currier, A. V. Anderson, and S. B. Keith, Compilation of radiometric age determinations in Arizona, *Bull. Ariz. Bur. Geol. Miner. Technol.*, *197*, 258 pp., 1986.

Ron, H., R. Freund, Z. Garfunkel, and A. Nur, Block rotation by strike-slip faulting: Structural and paleomagnetic evidence, *J. Geophys. Res.*, *89*, 6256–6270, 1984.

Sawyer, D. A., Late Cretaceous caldera volcanism and porphyry copper mineralization at Silver Bell, Pima County, Arizona: Geology, petrology, and geochemistry, Ph.D. thesis, 400 pp., Univ. of Calif., Santa Barbara, 1987.

Shafiqullah, M., P. E. Damon, D. J. Lynch, S. J. Reynolds, W. A. Rehrig, and R. H. Raymond, K-Ar geochronology and geologic history of southwestern Arizona and adjacent areas, in Studies in Western Arizona, edited by J. P. Jenney and C. Stone, *Ariz. Geol. Soc. Dig.*, *12*, 201–260, 1980.

Steiner, M. B., Paleomagnetism of the Late Pennsylvanian and Permain: A test of the rotation of the Colorado Plateau, *J. Geophys. Res.*, *93*, 2201–2215, 1988.

Stewart, J. H., Basin-range structure in western North America: A review, *Mem. Geol. Soc. Am.*, *152*, 1–31, 1978.

Titley, S. R., Evidence for a Mesozoic linear tectonic pattern in southeastern Arizona, *Ariz. Geol. Soc. Dig.*, *10*, 71–101, 1976.

Vugteveen, R. W., A. E. Barnes, and R. F. Butler, Paleomagnetism of the Roskruge and Gringo Gulch Volcanics, southeast Arizona, *J. Geophys. Res.*, *86*, 4021–4028, 1981.

Wells, R. E., and J. W. Hillhouse, Paleomagnetism and tectonic rotation of the lower Miocene Peach Springs Tuff: Colorado Plateau, Arizona, to Barstow, California, *Geol. Soc. Am. Bull.*, *101*, 846–863, 1989.

J. T. Hagstrum, U.S. Geological Survey, Branch of Isotope Geology, MS 937, 345 Middlefield Road, Menlo Park, CA 94025.

P. W. Lipman, U.S. Geological Survey, Branch of Igneous and Geothermal Processes, MS 910, 345 Middlefield Road, Menlo Park, CA 94025.

(Received December 3, 1990;
revised May 24, 1991;
accepted June 14, 1991.)

JOURNAL OF GEOPHYSICAL RESEARCH, VOL. 96, NO. B10, PAGES 16,181–16,203, SEPTEMBER 10, 1991

Calculation of Bulk Modulus and Its Pressure Derivatives From Vibrational Frequencies and Mode Grüneisen Parameters: Solids With Cubic Symmetry or One Nearest-Neighbor Distance

ANNE M. HOFMEISTER

Department of Geology, University of California, Davis

The bulk modulus K_T can be related to structural parameters and to the sum of the squares of the vibrational frequencies, $\Sigma\nu_i^2$, for N-atom crystals of cubic symmetry or for any symmetry that contains only one nearest-neighbor distance. Required assumptions are the existence of (1) electrostatic forces exclusively between atoms at equivalent positions in the primitive unit cell, (2) pair-wise central repulsive potentials between all other atoms, and (3) rigid ions. Including pressure in the derivation requires a more stringent version of point 2, namely, (4) that the structure scales isotropically upon compression. This leads to structurally independent formulas for the pressure derivatives of bulk modulus at 1 atm: the only variables are K_T and sums involving ν_i^2 and the first or second pressurderivative of ν_i, i.e., the mode Grüneisen parameters. Implicit in all equations is the independence of the sums on wave vector. Thus, knowledge of zone center phonons (mostly infrared and Raman bands) is sufficient to calculate elastic properties. Investigating these relationships for 45 minerals with 10 different structures shows that $K_T(0)$ is predicted within 7% of experiment for 21 solids, all of which should lack strong interactions between atoms at equivalent sites in the Bravais unit cell (i.e., rutile, corundum, ilmenite, and spinel structures). The accuracy of the model strongly depends on the accuracy of the sum $\Sigma\nu_i^2$. Agreement for B1, B2, fluorite, and wurtzite structures is moderate to poor, as expected, because these structures place like atoms as second nearest neighbors and can thus violate assumption 1. For rocksalt, agreement varies, depends on the size of the cation, not on the polarizability (i.e. the ionic rigidity) as inferred earlier. Calculated K_T for the garnets is 1.367 time experimental K_T, instead of unity, which is related to the structure not scaling perfectly with pressure. Agreement is variable (3-20%) for the perovskite structure with large discrepancies associated with ill-constrained sums. However, for all structures, the relative size of K_T is predicted, so that the theory can be used for systematics for all minerals with the proper symmetry, reguardless of whether the assumptions are satisified. For all of the above mentioned structures, K'_0 and K''_0 are predicted within the experimental uncertainties from the available spectroscopic measurements of 13 solids for K'_0 and 6 solids for K''_0 at pressure. Based on this, the good agreement for ilmenite, which does not meet the symmetry requirements, and the structural independence of the formulas, the relations involving K'_0 and K''_0 are inferred to hold for structures more complex than cubic or A_XB_Y.

INTRODUCTION

The utility of calculating thermodynamic variables such as heat capacity or entropy from vibrational spectra has been demonstrated with the development of a semiempirical model based on lattice dynamics by *Kieffer* [1979]. This model has been applied successfully to a wide variety of minerals [*Kieffer* 1979, 1980; *Akaogi et al.*, 1984; *Ross et al.*, 1986; *Hofmeister et al.*, 1987; *Hofmeister*, 1987*a*; *Hofmeister and Chopelas*, 1991*a*; *Hofmeister and Ito*, 1991] and, moreover, can be used to calculate the pressure dependence of thermodynamic variables from spectra taken at high pressure [*Hofmeister et al.*, 1986*a*, *b*; *Chopelas* 1990*a*, *b*; *Chopelas and Hofmeister*, 1991], In contrast, calculation of elastic properties from vibrational spectra has been limited to a few substances: specifically, diatomic solids [*Blackman*, 1942; *Brout*, 1959; *Rosenstock*, 1963; *Mitra and Marshall*, 1964], stishovite [*Striefler and Barsch*, 1976], and forsterite [*Iishi*, 1978]. (The study on forsterite concerned force constants; all others involved modelling of interatomic potentials.) No attempt has been made to predict the pressure dependence of elastic constants from vibrational spectra, although it is now feasible to calculate elastic properties of relatively simple minerals from models of interatomic potentials. In this paper, a useful alternative approach will be developed for complex minerals that circumvents modelling of potentials and relates directly two properties (elasticity and vibrational characteristics) that depend on these unknown potentials. The theory presented here is a generalization of *Brout's* [1959] formulation for diatomic cubic solids. The utility and motivation for this attempt are (1) prediction of the pressure derivatives of the bulk modulus which are difficult to measure accurately for the relatively incompressible silicates yet are essential for determining the equation of state and relating mineral properties to seismological constraints on the Earth's interior, (2) prediction of K_T for structures that are too complex for direct modelling of the interatomic potentials, and (3) furthering our understanding of the relationships between microscopic and macroscopic properties of minerals. All minerals of appropriate structure having both compressional and vibrational data were tested in order to define the limits of applicability of the theory and to explore the nature of the chemical bond in complex minerals.

By assuming that ions are rigid and have Coulombic attractive forces and that repulsive forces are limited to nearest neighbors, *Blackman* [1942] and *Brout* [1959] related vibrational frequencies ν_i to the bulk modulus K_T for diatomic solids in the rock salt structure:

$$\sum_{i=1}^{6} \nu_i^2(\vec{k}) = 18\, r_0\, K_T / \mu \qquad (1)$$

where r_0 is the interatomic nearest-neighbor distance and μ is the reduced mass. For diatomic crystals with diamond or zinc-

Paper number 91JB01381.
0148-0227/91/91JB-01381$05.00

blend structures, the geometrical factor is $16\sqrt{3}$ rather than 18 [*Mitra and Marshall*, 1964]. Equation (1) implicitly shows that the Brout sum $\Sigma\nu_i^2(\vec{k})$ is independent of wave vector $\vec{k}$ for all $\vec{k}$ (under the stated assumptions) insofar as the right hand side of (1) is a constant and implies that zone center frequencies (e.g., Raman and infrared modes) are sufficient to calculate the bulk modulus, even though other (acoustic) modes exist. Any value of $\vec{k}$ can be chosen for the sum, but zone center frequencies are the most convenient and well determined. *Rosenstock* [1963] pointed out that the Brout sum will be independent of wave vector $\vec{k}$ for any solid with forces either being exclusively electrostatic (i.e., dipole or multipole interactions are allowed in addition to point coulombic) or only occurring between unlike atoms (atoms at nonequivalent positions in the primitive unit cell), given the assumption of rigid, nonoverlapping ions. In other words, forces between nearest neighbors are constrained only to be pair-wise central, whereas forces between second nearest neighbors must be electrostatic if the atoms are of the same type and lie in the same primitive unit cell.

Although (1) was originally derived for the highly ionic solids, agreement is generally best for purely covalent crystals (e.g., C, Si, and Ge) and becomes progressively worse as ionicity increases [*Mitra and Marshall*, 1964]. For alkali halides in particular, the difference between calculated and measured K_T ranges from 1% for NaF to 46% for LiCl, the average difference being 16% [*Mitra and Marshall*, 1964]. *Mitra and Marshall* [1964] attribute the discrepancy to the polarizability of atoms in ionic solids not being accounted for by *Brout's* [1959] derivation (i.e., the ions are not rigid). The size of the primitive unit cell seems to be more important, as follows.

The sum rule is least likely to be valid for crystals with small primitive unit cells, like B1, where like atoms (those at equivalent positions in the primitive unit cell) are second-nearest neighbors. For large primitive unit cells, the limitation of forces between like atoms to electrostatic interactions becomes almost trivial since these atoms are widely separated. Problems with ionic solids are expected because these generally have small primitive unit cells, strong interactions between second-nearest neighbors, and deformable ions, whereas covalent atoms have weaker interactions and fairly rigid ions. For many classes of minerals, the primitive unit cells are large, and bonding is partially covalent (e.g., the Si-O bond is 50% ionic-50% covalent), suggesting that it is worth testing formulas like Brout's (1) to see if the bulk modulus could be accurately predicted from vibrational spectra for substances of geologic interest.

This paper revises *Brout's* [1959] formula to include pressure terms in order to relate pressure derivatives of the bulk modulus to pressure derivatives of the vibrational frequencies. Previous derivations either did not account for the pressure terms [*Maradudin et al.*, 1971] or did not correctly account for the pressure dependence [*Wallace*, 1972] or are valid only for monatomic crystals and polyatomics with one interatomic distance and with atomic masses that follow $1/m_i \sim n/\Sigma m_i$ [*Wolf and Jeanloz*, 1985]. The derivation is extended to (1) cubic N-atom crystals, and to (2) A_XB_Y crystals of lower symmetry with one cation-anion nearest neighbor distance. Values predicted for K_T, $\partial K/\partial P$, and $\partial^2 K/\partial P^2$ are shown to compare reasonably well with experimental values for 45 minerals with rocksalt, CsCl, fluorite, wurtzite, perovskite, rutile, corundum, ilmenite, spinel, and garnet structures. Agreement is best for those structures that have small longitudinal optic-transverse optic (LO-TO) splittings, and have relatively weak like atom interactions, as well as inactive frequencies that can either be predicted reliably, or that constitute a small fraction of the total modes. In a future paper (*A. M. Hofmeister*, Pressure derivative of the bulk modulus, submitted to Journal of Geophysical Research, 1991), a simple approximation for the pressure derivative of the frequencies leads to the free volume equation [*Liebfreid and Ludwig*, 1961; *Vashchenko and Zubarev*, 1963; *Irvine and Stacey*, 1975; see also *Barton and Stacey*, 1985] and gives a method for bracketing K''_0.

CALCULATIONS

Extension of Brout's Formula to N-Atom Substances of Any Symmetry With One Nearest-Neighbor Distance

Crystals with formulas A_XB_Y can be described approximately by one unique nearest-neighbor distance, r_o. These include simple and complex structures: corundum, rutile, wurtzite, flourite, CsCl, and of course, rock salt. Actually, the corundum and rutile structures each have several slightly different interatomic distances. The few percent deviation among the r_o will not measurably affect the theory because the error in K_T introduced by ignoring the differences among the r_o is small compared to the experimental uncertainties in $\Sigma\nu_i^2(\vec{k})$ and K_T, even for the best constrained minerals.

The assumptions behind this derivation are (1) that the ions are rigid, (2) that the repulsive potentials (i.e., short range forces) can be approximated as being pair-wise spherically symmetric, and (3) that, as *Rosenstock* [1963] stated, the atomic interactions are unconstrained between unlike atoms (i.e., the potential can assume any form between atoms at nonequivalent positions in the primitive unit cell) but can only be electrostatic in nature between like atoms (those at equivalent positions in the primitive unit cell). (For further discussion see the paragraph following (1).) Requirement 3 is obviously fullfilled for minerals with large primitive unit cells but is problematic for those with small primitive unit cells, wherein like atoms are second-nearest neighbors. For a few of the structures (spinel, garnet, and ilmenite) the potential about the anions deviates slightly from spherical symmetry (Figure 1), which may lead to violation of requirement 2. This discrepancy is dealt with by representing the "spherical" potential as an average of the true potential of the anions (Figure 1) over the various directions (see later discussion and the appendix). Although this "averaging" out of the asymmetry conflicts with assumption (2), the exercise is worthwhile in that it provides one test of the limitations of the theory, that is, to what extent can directional bonding be present in a mineral, and Brout's sum rule still be valid? However, extension to these solids also requires that their compression must be nearly isotropic (within about 4%) because marked anisotropy during compression (e.g., via bond bending as in quartz) precludes use of a radially symmetric interatomic potential. In short, strongly directional bonding in a mineral means means that it is unlikely to be adequately modelled by the approach taken here. Rigidity of the ions (assumption 1) is strictly not fullfilled, but this will be shown to be a relatively minor factor. Moreover, this assumption is made in a large number of calculations of interatomic potentials in minerals, as is use of pair-wise additive central potentials (assumption 2) [e.g., *Wolf and Bukowinski*, 1987;

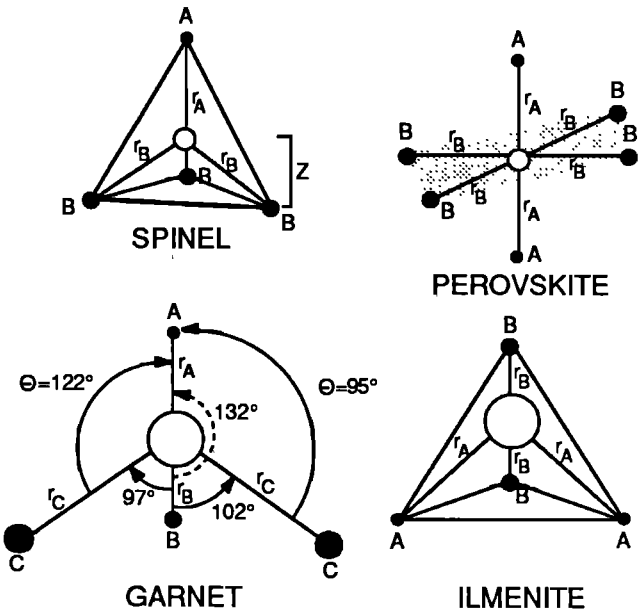

Fig. 1. Idealized oxygen geometries of spinel, cubic perovskite, garnet and ilmenite. Oxygen atoms are labeled large open circles. Cations are smaller solid circles labeled A, B, or C. Oxygen cation distances are label r_A, r_B, or r_C. For spinel, garnet, and ilmenite, the oxygens are enclosed by irregular tetrahedrons. The oxygen in perovskite is octahedrally coordinated. Values for the angles defined by cation-oxygen-cation positions are labeled for the garnet structure.

Hemley and Gordon, 1985; *Prossner and Graham*, 1984; *Hemley et al.*, 1987]. More recent models [*Wolf and Bukowinski*, 1988; *Isaak et al.*, 1990, and references therein] allow for overlapping ionic charge densities; however, the accuracy of predicting K_T from these PIB and VSMEG models is +10%, which is not better than that achieved for the rigid ion models. In contrast, the requirement that interactions between like atoms be limited to electrostatic forces (assumption 3) is slightly more restrictive than is used in calculations of interatomic potentials.

Brout's [1959] derivation is best understood by dividing it into two parts: the first involves relating vibrational frequencies to the interatomic potentials, and the second involves relating the bulk modulus to the same potentials. Generalizing *Brout's* [1959] derivation is simply a matter of proper enumeration of vibrational modes and elements of the $\underline{G}$ matrix. Vibrational frequencies for a given wave vector $\vec{k}$ are given by the secular equation

$$4\pi^2 \nu^2(\vec{k})\, e(\vec{k}) = \underline{G}(\vec{k})\, e(\vec{k}) \tag{2}$$

where $e(\vec{k})$ are the eigenvectors of the dynamical matrix $\underline{G}(\vec{k})$. For an N-atom solid, symmetry mandates that the number of vibrational frequencies is 3NF/Q (where Q is the number of Bravais cells contained in the crystallographic unit cell, F is the number of formula units in the crystallographic unit cell, and N is the number of atoms per formula unit) and also that 3NF/Q x 3NF/Q terms exits for the $\underline{G}$ matrix. Each term is labled by the three orthogonal directions $\alpha\beta$ = 1,2,3 and the index j for the each ion in the primitive cell. $\underline{G}$ can be divided into two parts; the first arising from electrostatic attractive forces ($^C\underline{G}$), and the second from repulsive forces ($^R\underline{G}$). By invariance of the trace in orthogonal transformations,

$$4\pi^2 \sum_{i=1}^{3NF/Q} \nu_i^2(\vec{k}) = \text{trace}\, \underline{G}(\vec{k}). \tag{3}$$

Note that a weighing function for the frequencies is not needed for this derivation. Thus, it is immaterial whether the frequencies result from atomic oscillations that are completely independent, or from vibrational modes that are mixed.

The electrostatic contribution (i.e. Coulombic, dipole, or multipole potentials) to the trace is removed by Laplace's theorem [*Rosenstock*, 1963], leaving

$$4\pi^2 \sum_{i=1}^{3NF/Q} \nu_i^2(\vec{k}) = \sum_{j=1}^{NF/Q} \sum_{\alpha=1}^{3} {}^R G_{\alpha\alpha}^{jj}(\vec{k}) \tag{4}$$

If the ions are rigid and the repulsive forces are restricted to nearest-neighbor interactions, then each component of the tensor is given by [*Born and Huang*, 1954]

$${}^R G_{\alpha\alpha}^{jj}(\vec{k}) = \frac{Z_j}{3m_j} \nabla^2 \Phi_j(r)\big|_{r_0}, \tag{5}$$

where Z_i, m_i, and Φ_i are the coordination, atomic mass and pair potential of the ith atom. For each atom, three equal terms are produced by the three equivalent directions; central forces are assumed to occur between each pair of atoms. Because there are only two types of atom for the case of solids with one interatomic distance (e.g., A_XB_Y compounds), there are only two types of repulsive pair potentials Φ_{+} and Φ_{-}. Their magnitudes must be the same or the crystal is unstable, so that (4) becomes

$$4\pi^2 \sum_{i=1}^{3NF/Q} \nu_i^2(\vec{k}) = \frac{3F}{Q} \sum_{i=1}^{NF/Q} G_i(\vec{k}) = \frac{F}{Q} \sum_{i=1}^{N} \frac{Z_i}{m_i} \nabla^2 \Phi(r)\big|_{r_0}. \tag{6}$$

The bulk modulus is defined as

$$\frac{1}{K_T} = -\frac{1}{V} \frac{\partial V}{\partial P}\bigg|_T. \tag{7}$$

Volume V is related to the internal energy U by

$$\partial U = -P \partial V. \tag{8}$$

By substituting (8) into (7), converting to derivatives in terms of r through the relationship

$$\frac{\partial V}{\partial r} = \frac{3V}{r}, \tag{9}$$

and using the definition of the Laplacian, (7) becomes

$$K_T(P) = V\left(\frac{\partial r}{\partial V}\right)^2 \nabla^2 U(r) + \frac{4}{3} P. \tag{10}$$

Note that this requires pair-wise central potentials. The second term is zero for ambient pressure. The internal energy can be separated into electrostatic and repulsive parts [*Born and Huang*, 1954; *Kittel*, 1971]:

$$\begin{aligned} U(r) &= \frac{F}{2} \sum_{i=1}^{N} u(r_i) = \frac{F}{2} \sum_{i=1}^{N} -\frac{A_i}{r_i} + Z_i \Phi_i(r_i) \\ &= \frac{F}{2} \sum_{i=1}^{N} -\frac{A_i}{r_i} + \frac{F}{2} \Phi(r) \sum_{i=1}^{N} Z_i, \end{aligned} \tag{11}$$

where A is a constant. Substitution of (11) into (10) gives

$$K_T(P) = \frac{FV}{2}\left(\frac{\partial r}{\partial V}\right)^2 \sum_{i=1}^{N} Z_i \nabla^2 \Phi(r)\big|_{r_0} + \frac{4}{3} P. \tag{12}$$

Taking the Laplacian of U by definition cancels out all electrostatic potentials. As *Rosenstock* [1963] pointed out, replacing the Coulombic potential of a point charge (-A/r) by any other multipole potential (A/r^m) or any linear combination thereof still results in (12). Combining (6), (9), and (12) results in

$$K_T(P) = \frac{4}{3}P + 4\pi^2 \frac{Q r_0^2}{18V} \sum_{i=1}^{N} Z_i \sum_{i=1}^{3NF/Q} \nu_i^2\left(P,\vec{k}\right) \Big/ \sum_{i=1}^{N} \frac{Z_i}{m_i} . \quad (13)$$

As in *Brout's* [1959] formula, the independence of the sum on wave vector is implicit in (13). Again, the sum can be calculated at any $\vec{k}$. Inclusion of $\vec{k}$ in (13) implies that a particular value will be used. The zone center ($\vec{k}$ is zero) is used because data are plentiful for this value (IR and Raman data are measures of zone center frequencies: inelastic neutron scattering (INS) data, which map the dependence of frequency on wave vector, are scant). Solids like rocksalt have large amounts of dispersion, but the Brout sum appears to be constant for the few substances with INS determinations [see *Rosenstock*, 1963].

For solids with a large number of modes, dispersion is low (e.g., Al_2O_3 data by *Bialas and Stolz* [1975]). The amount of overall dispersion is less for noncubic structures, than for cubic, for two reasons. First, the proportion of LO component is 1/2 rather than 1/3 of the optic modes. Second, LO modes are fairly independent of wave vector (e.g., TiO_2 data by *Traylor et al.* [1971]) in agreement with theory [*Burns*, 1985], which indicates that LO modes should be dispersionless because they are not coupled directly. Moreover, as the number of modes increases, the behavior of any individual mode is of little consequence.

Finite Temperature and Zero Point Corrections to the Bulk Modulus

The elastic constants have been calculated as strain derivatives of the static crystal potential. Thus, the bulk modulus calculated is K_0 at 298°, which should differ slightly than K_T(298°). (The calculated value is not K(0°) because room temperature values are used for V, r_i, and ν_i.) The correction is obtained from the free energy

$$F = U - TS + \frac{1}{2}\sum_i h\nu_i, \quad (14a)$$

where the last term is the zero point energy [*Wallace*, 1972]. By definition, the bulk modulus is

$$K_T = V\left(\frac{\partial^2 F}{\partial V^2}\right)_T = V\left(\frac{\partial^2 U}{\partial V^2}\right)_T - TV\left(\frac{\partial(\alpha K_T)}{\partial V}\right)_T + \frac{V}{2}\sum_i h\left(\frac{\partial^2 \nu_i}{\partial V^2}\right)_T, \quad (14b)$$

where α is the thermal expansivity. The first term in (14b) is calculated from the vibrational frequencies (13). The middle term is the finite temperature correction. The last term is the zero point correction. This is converted to a more tractable form using thermodynamic identities, which yields

$$K_T = V\left(\frac{\partial^2 U}{\partial V^2}\right)_T + T\left(\frac{\partial K_T}{\partial T}\right)_P + T\alpha K_T\left(\frac{\partial K_T}{\partial P}\right)_T + \frac{h}{2}\frac{K_T^2}{V}\sum_i \left(\frac{\partial^2 \nu_i}{\partial P^2}\right)_T + \frac{h}{2}\frac{K_T}{V}\left(K' + 1\right)\sum_i \left(\frac{\partial \nu_i}{\partial P}\right)_T . \quad (14c)$$

The magnitude of the correction to K_T can be calculated exactly for MgO and estimated for the remaining solids. The fourth term is zero for MgO in particular [*Chopelas*, 1990a], very close to zero for all solids, and equal to zero at ambient pressure for all dense solids measured so far [*Ferraro et al.*, 1971; *Nicol et al.*, 1972; *Shawyer and Sherman*, 1982; *Ferraro*, 1984; *Hofmeister et al.*, 1986*a*, *b*; *Hemley*, 1987; *Hofmeister*, 1987b; *Jephcoat et al.*, 1988; *Hofmeister et al.*, 1989; *Chopelas*, 1990b; *Chopelas and Hofmeister*, 1991]. Thus the zero point correction is given by the fifth term in (14c). For MgO, this is calculated as 0.7% of K_T from the vibrational data of *Chopelas* [1990a] and elasticity measurements of *Jackson and Neisler* [1982].

The second term in (14c) is negative and 4.5% for MgO, according to recent thermal measurements [*Isaak et al.*, 1989]. The third perm is positive and 2% using the above data sources. Thus for MgO, the thermal correction to the calculated bulk modulus is negative and less than 3%.

The total correction is then negative and about 2% for MgO. This inherent uncertainty is nearly the same as the difference

$$K_S - K_T = TV(\alpha K_T)^2 / C_V. \quad (14d)$$

where C_V is the heat capacity, and V in this case is per mole rather than per unit cell. For silicates and most other compounds, K_S-K_T is also about -2%. Thus, the calculated values should set a maximum for the bulk modulus. The uncertainties involving the zero point and thermal corrections will be smaller than the uncertainties in the Brout sum for almost all substances, and can thus be neglected in our calculations.

Connection With Brout's formula

The Bravais cell volume V_B for the rocksalt structure is

$$V_B = 2r_0^3 = \frac{V}{4}. \quad (15)$$

Taking the derivative of the above equation gives (9) which holds for any substance with one unique nearest neighbor distance. Combining (13) with Q = 4, $Z_1 = Z_2$, P = 0, and the definition of the reduced mass gives *Brout's* [1959] formula (1). Note that because Q=1 for the CsCl structure, and the dependence of V on r_0 differs from (15), Brout's formula must be modified by a numerical factor to be valid for any diatomic structure other than B1.

Relationship of Pressure Derivatives of Elastic Constants to Those of Vibrational Frequencies for Substances With One Interatomic Potential

Equations for the pressure derivatives for the elastic constants can be approached by two methods. The first is to take the pressure derivative of (13), resulting in

$$K'(P) = \frac{4}{3} + 4\pi^2 \sum_{i=1}^{N} Z_i \Big[\frac{2Qr_0^2}{9V}\sum_{i=1}^{3NF/Q} \nu_i\left(P,\vec{k}\right)\frac{\partial \nu_i\left(P,\vec{k}\right)}{\partial P} - \frac{Qr_0^2}{9V^2}\left(\frac{\partial V}{\partial P}\right)\sum_{i=1}^{3NF/Q} \nu_i^2\left(P,\vec{k}\right) + \frac{2Qr_0}{9V}\left(\frac{\partial r}{\partial P}\right)\sum_{i=1}^{3NF/Q} \nu_i^2\left(P,\vec{k}\right)\Big] \Big/ \sum_{i=1}^{N}\frac{Z_i}{m_i}. \quad (16)$$

Equations (7), (9), and (13) can be used to combine the last two terms into the result 1/3. The first term is simplified by (13) and by the definition of the mode Grüneisen parameter γ_i

$$\gamma_i = \frac{K_T}{\nu_i}\frac{\partial \nu_i}{\partial P} \quad (17)$$

to the following straightforward equation:

$$K'_0 = \frac{5}{3} + 2 \sum_{i=1}^{3NF/Q} \nu_{i0}^2(\vec{k})\,\gamma_{i0}(\vec{k}) \Big/ \sum_{i=1}^{3NF/Q} \nu_{i0}^2(\vec{k}). \quad (18)$$

This formula holds for any structure wherein the volume can be calculated closely by a single interatomic distance r_0 and wherin the structure scales approximately the same with pressure. For example, if the c axis decreases to half its 1 atm value at pressure P, then the a axis should also decrease to about $a_0/2$. A consequence of the required scaling is that the potentials must be pair-wise central. Thus, requiring the structure to scale is a more stringent version of Brout's original assumption. Substances such as quartz which compress via bond angle bending are thereby excluded. For anisotropic compression mechanisms, (1) to (8) would need to be modified to include the angular dependence of the interatomic potential.

Alternatively, the mode Grüneisen parameters can be obtained to second order from *Wallace's* [1972] equation

$$-2\gamma_i(P,\vec{k})\,4\pi^2\nu_i^2(P,\vec{k}) = e^{\dagger}(P,\vec{k})\frac{\partial \underline{G}(P,\vec{k})}{\partial \ln V}e(P,\vec{k}). \quad (19)$$

Summing over the vibrational modes i converts (19) to

$$-2\sum_{i=1}^{3NF/Q}\gamma_i(P,\vec{k})\,4\pi^2\nu_i^2(P,\vec{k}) = \text{trace}\frac{\partial \underline{G}(P,\vec{k})}{\partial \ln V} = \frac{3FV}{Q}\frac{\partial}{\partial V}\sum_{i=1}^{N} G_i(P,\vec{k}). \quad (20)$$

The electrostatic contribution to the trace is removed by Laplace's theorem. Therefore, applying equations that are analogous to (4) and (5) to (20) gives

$$-8\pi^2\sum_{i=1}^{3NF/Q}\gamma_i(P,\vec{k})\,\nu_i^2(P,\vec{k}) = \frac{FV}{Q}\frac{\partial}{\partial V}\sum_{i=1}^{N}\frac{Z_i}{m_i}\nabla^2\Phi(P,r)\Big|_{r0}. \quad (21)$$

Rearranging (12) and substituting it into (21) results in

$$-2\sum_{i=1}^{3NF/Q}\gamma_i\nu_i^2 \Big/ \sum_{i=1}^{3NF/Q}\nu_i^2 = \frac{r}{\left(K_T-\frac{4}{3}P\right)}\frac{\partial}{\partial V}\left[\frac{V\left(K_T-\frac{4}{3}P\right)}{r^2}\right] = \frac{r^2}{\left(K_T-\frac{4}{3}P\right)}\left[\frac{K_T-\frac{4}{3}P}{r^2} + \frac{V}{r^2}\left(\frac{\partial K_T}{\partial V} - \frac{4}{3}\frac{\partial P}{\partial V}\right) - 2\frac{V}{r^3}\left(K_T-\frac{4}{3}P\right)\frac{\partial r}{\partial V}\right]. \quad (22)$$

Equation (9) and the following definition

$$K'_T = \frac{\partial K_T}{\partial P} = -\frac{V}{K_T}\frac{\partial K_T}{\partial V}, \quad (23)$$

convert (22) to

$$-2\sum_{i=1}^{3NF/Q}\gamma_i(P,\vec{k})\,\nu_i^2(P,\vec{k}) \Big/ \sum_{i=1}^{3NF/Q}\nu_i^2(P,\vec{k}) = \frac{1}{3} + \frac{\left(\frac{4}{3}-K'\right)}{\left(K_T-\frac{4}{3}P\right)}K_T. \quad (24)$$

For zero pressure, this reduces to (18). Note that (24) was derived directly from (13), so that the two approaches are equivalent. This allows us to obtain all higher-order derivatives, if desired.

The higher-order derivative $K'' = \partial^2 K/\partial P^2$ can be obtained as a function of pressure by taking the derivative of (24) and using the definition of the second mode Grüneisen parameter

$$q_i = \frac{\partial \ln \gamma_i}{\partial \ln V}. \quad (25)$$

The result is

$$KK'' = K'\left(\tfrac{4}{3}-K'\right) + \left(1-\frac{4P}{3K}\right)\left[\frac{4\sum \nu_{i0}^2(P,\vec{k})\gamma_{i0}^2(P,\vec{k})}{\sum \nu_{i0}^2(P,\vec{k})} - \frac{2\sum \nu_{i0}^2(P,\vec{k})\gamma_{i0}(P,\vec{k})q_{i0}(P,\vec{k})}{\sum \nu_{i0}^2(P,\vec{k})}\right] + \left(\frac{1}{1-4P/3K_T}\right)\left[-1+\frac{2}{3}K' - \frac{8PK'}{K_T} - \frac{40P}{27K_T} - \frac{16P^2}{81K_T^2}\right]. \quad (26)$$

The zero pressure limit is therefore

$$K_0K''_0 = 4\frac{\sum \nu_{i0}^2(\vec{k})\gamma_{i0}^2(\vec{k})}{\sum \nu_{i0}^2(\vec{k})} - 2\frac{\sum \nu_{i0}^2(\vec{k})\gamma_{i0}(\vec{k})q_{i0}(\vec{k})}{\sum \nu_{i0}^2(\vec{k})} - (K'_0-1)^2, \quad (27)$$

where all summations are from 1 to 3 NF/Q in both (26) and (27). Implicit in (27) and (28) is the independence of the sums involving the vibrational frequencies and Grüneisen parameters on the wave vector.

Relationship of bulk moduli and pressure derivatives to vibrational frequencies and their pressure derivatives for N-atom cubic solids.

An equation analogous to *Brout's* [1959] formula can be derived for any cubic solid, regardless of the number of atoms or multiple interatomic distances, as long as the structure scales with pressure (i.e., compression is isotropic). In other words, the geometrical factors relating the different interatomic radii r_i to the volume and to each other must all depend on pressure in the same manner so that (9) holds for each r_i. A general formula will be derived and the geometrical factors will be presented for several mineral structures that are important to geophysics and materials science: garnet, spinel, cubic perovskite, and ilmenite. Although ilmenite is not cubic, it is included here because it is a derivative of the corundum structure which was covered in the previous two sections.

Equation 6 can be generalized to

$$4\pi^2\sum_{i=1}^{3NF/Q}\nu_i^2(\vec{k}) = \frac{F}{Q}\left[\sum_{i=1}^{cations}\frac{Z_i}{m_i}\nabla^2\Phi_i\Big|_{r_i} + \sum_{j=1}^{anions}\frac{N_j}{m_j}\left(\sum_{i=1}^{cations} a_i\nabla^2\Phi_i\Big|_{r_i}\right)\right] \quad (28)$$

where a_i is the number of each kind of cation coordinated to the specific anion, N_i is the number of each type of anion, and ϕ_i is the repulsive potential of the ith ion. The sum over cations refers to the different types, not the actual numbers. Our approach is to relate all of the potentials in the cubic structure to one radius and one potential through the geometry of the oxygen sites in the crystal (Figure 1; appendix), which has been idealized in order to allow for slight variation in geometry among different chemistries. Thus, we have assumed pair-wise central forces, with the result that the potentials about the anions does not appear to be spherically symmetric. For all cases, (28) reduces to

$$4\pi^2\sum_{i=1}^{3NF/Q}\nu_i^2(\vec{k}) = \frac{F}{Q}\left[\sum_{i=1}^{cations}\left(b_i+\frac{d_ir_1}{r_i}\right)\left(\frac{1}{m_i}+\frac{1}{m_-}\right)\right]\nabla^2\Phi_1\Big|_{r_1} \quad (29)$$

when r_1 is one particular metal-oxygen distance (for convenience, the shortest distance was selected, which in most

TABLE 1. Geometrical Factors.

Structure	Formula	Index	Atom	b_i	c_i	d_i
Perovskite (cubic)	BAO_3	1	A	6	12	0
		2	B	0	24	12
Ilmenite	ABO_3	1	A	6	12	0
		2	B	0	12	6
Spinel	AB_2O_4	1	A	4	8	0
		2	B	0	24	12
Garnet (cubic)	$C_3B_2A_3O_{12}$	1	A	12	24	0
		2	B	0	24 x 0.89	12 x 0.89
		3	C	0	48 x 0.65	24 x 0.65
Garnet (tetragonal)	$C_2DBA_3O_{12}$	1	A	12	24	0
		2	B	0	12 x 0.89	6 x 0.89
		3	C	0	48 x 0.65	24x 0.65
		4	D	0	12 x 0.89	6 x 0.89

cases is the tetrahedral Si-O distance, but any of the M-O distances will do), Φ_1 is the interatomic potential of that particular cation, m_- is the mass of the anion, and b_i and d_i are numerical constants related to a_i, N_i, Z_i, and the interatomic angles. Table 1 lists the constants b_i and d_i for pertinent cubic structures (plus ilmenite) which compress nearly isotropically and thus may be suitable for this analysis. Substitution of equations equivalent to (9) and use of the definitions of the Laplacian and the bulk modulus results in

$$K_T = \frac{4}{3} + \frac{FV}{2}\left[\frac{\sum_{i=1}^{\text{cations}} Z_i\left(\frac{\partial r_i}{\partial V}\right)^2 \nabla^2\Phi_i(r)\big|_{r_i}}{+\sum_{j=1}^{\text{anions}} N_j\left(\sum_{i=1}^{\text{cations}} a_i\left(\frac{\partial r_i}{\partial V}\right)^2 \nabla^2\Phi_i(r)\big|_{r_i}\right)}\right]. \quad (30)$$

As shown in the appendix, this equation simplifies to

$$K_T = \frac{4}{3}P + \frac{FV}{2}\left(\frac{\partial r_1}{\partial V}\right)^2\left[\sum_{i=1}^{\text{cations}} \frac{c_i r_i}{r_1}\right]\nabla^2\Phi_1(r)\big|_{r_1}. \quad (31)$$

The constants c_i, which are related to the geometry of the anion sites, are given in Table 1 for the pertinent mineral structures. Combining (9), (29) and (31) results in

$$K_T(P) = \frac{4}{3}P + 4\pi^2\frac{Q r_1^2}{18V}\frac{\sum_{i=1}^{\text{cations}} \frac{c_i r_i}{r_1}\sum_{i=1}^{3NF/Q} \nu_i^2(P,\vec{k})}{\sum_{i=1}^{\text{cations}}\left(b_i + \frac{d_i r_1}{r_i}\right)\left(\frac{1}{m_i}+\frac{1}{m_-}\right)}. \quad (32)$$

For rock salt, $a_i = Z_i = Z$, $N_i = 1$, and $\Phi_+ = \Phi_-$. Substituting these relations into (28) to (32) gives Brout's equation.

Calculation of Pressure Derivatives of Bulk Modulus for N-Atom Cubic Solids

Relationships for the pressure derivatives of the bulk modulus can be obtained as in the previous section. Taking the pressure derivative of equation (32) leads to an equation for K_0 that is identical to (18) if and only if the cubic symmetry is maintained. The pressure dependence of K' is obtained from *Wallace's* [1972] equation for γ_i (19). Equation (21) can be generalized to

$$-8\pi^2\sum_{i=1}^{3NF/Q}\gamma_i(P,\vec{k})\,\nu_i^2(P,\vec{k}) = \left(\frac{FV}{Q}\right)\frac{\partial}{\partial V}\left[\sum_{i=1}^{\text{cations}}\left(b_i+\frac{d_i r_1}{r_i}\right)\left(\frac{1}{m_i}+\frac{1}{m_-}\right)\nabla^2\Phi\big|_{r_1}\right]. \quad (33)$$

Use of (31) converts the left hand side of (33) to

$$\frac{18V}{Q}\frac{\partial}{\partial V}\left[\frac{V}{r_1^2}\left(K_T - \frac{4}{3}P\right)\frac{\sum_{i=1}^{\text{cations}}\left(b_i+\frac{d_i r_1}{r_i}\right)\left(\frac{1}{m_i}+\frac{1}{m_-}\right)}{\sum_{i=1}^{\text{cations}}\frac{c_i r_i}{r_1}}\right]. \quad (34)$$

Equation (34) can be simplified through comparison to (22) to

$$-2\sum_{i=1}^{3NF/Q}\gamma_i(P,\vec{k})\nu_i^2(P,\vec{k}) = \sum_{i=1}^{3NF/Q}\nu_i^2(P,\vec{k})\left[\frac{1}{3}+\frac{\left(\frac{4}{3}-K'\right)K_T}{\left(K_T-\frac{4}{3}P\right)}\right] + \frac{1}{4\pi^2}\frac{V^2}{18Qr_1^2}\left(K_T-\frac{4}{3}P\right)\frac{\partial}{\partial V}\left[\frac{\sum_{i=1}^{\text{cations}}\left(b_i+\frac{d_i r_1}{r_i}\right)\left(\frac{1}{m_i}+\frac{1}{m_-}\right)}{\sum_{i=1}^{\text{cations}}\frac{c_i r_i}{r_1}}\right]. \quad (35)$$

Because (9) holds for each r_i, the last term in (35) is identically zero. Thus for any cubic solid, regardless of the specific geometry, or for any solid described by one nearest neighbor distance, equations (24) and (18) hold for K' and K'_0, and equations (26) and (27) hold for K'' and K''_0.

RESULTS AND DISCUSSION

Comparison of experimental with calculated bulk modulus is limited to 39 minerals (other than alkali halides) that adhere to the symmetry requirements, and which have reasonably well-determined vibrational spectra and bulk moduli. In addition, data on the mode Grüneisen parameters are available for eight of these minerals and allow comparison of calculated and experimental derivatives of the bulk modulus. For completeness, five alkali halides for which vibrational frequencies have been measured as a function of pressure are also included in the compilation. The comparisons will be limited to the 1 atm limits, K_o, K'_o, and K''_0, because of the large experimental uncertainty in bulk modulus and its derivatives at elevated pressures.

The structural data needed for (13) and (32) are compiled in Tables 1 and 2. Vibrational data are complete only for corundum, $KMnF_3$, $KZnF_3$, and for compounds with the B1, B2, and fluorite structures (Table 3). Except for corundum and perovskite, these solids lack inactive modes. Only three other minerals ($MgSiO_3$ and $MgGeO_3$ ilmenite and TiO_2) have more than 90% of their modes been measured at zone center. The other rutile structure compounds may be included in the well-determined category, because the values of their inactive modes (16% of the total) are constrained from relationships with structural parameters for 11 compounds [*Hofmeister et al.*, 1990*a*]. For the noncubic structures, the Brout sum $\Sigma\nu_i^2$ was computed by assuming that the longitudinal and transverse branches (if present) each count as 1/2 of a mode for A_u and B_u symmetries or as 1 mode each for E_u, whereas for cubic structures, with T_u symmetry, the division is 2 TO and 1 LO. This should be valid as long as the LO-TO splitting is not extremely large. The frequencies in the dynamical matrix lie in between the LO and TO branches [*Turrell*, 1972]: if the splitting is large, then the values needed for the equations may

TABLE 2. Structural Data Used to Calculate Bulk Moduli

Structure	Formula	F	Q	V(Å)^3	r_1(Å)	r_2(Å)	r_3(Å)	r_4(Å)	Z_1	Z_2	Z_3	Z_4	Z.	References
B1	NaF	4	4	99.51	2.32				6				6	a
	NaCl			179.41	2.82				6				6	a
	MgO			74.78	2.107				6				6	a
	MnO			87.82	2.223				6				6	a
	CoO			77.31	2.13				6				6	a
	NiO			72.0	2.08				6				6	a
B2	CsCl	1	1	70.09	3.57				8				8	a
	CsBr			79.25	3.71				8				8	a
	CsI			95.31	3.95				8				8	a
Fluorite	CaF_2	4	4	163.004	2.36				8				4	a
	SrF_2			195.012	2.51				8				4	a
	BaF_2			238.34	2.69				8				4	a
Wurtzite	BeO	2	1	27.60	1.65				4				4	b
	ZnO			47.60	1.98				4				4	c
Perovskite	$SrTiO_3$	1	1	59.552	1.952	2.76			6	12			6	a
	$KMgF_3$			62.71	1.9865	2.809			6	12			6	a
	$KMnF_3$			73.56	2.095	2.963			6	12			6	a
	$KNiF_3$			64.58	2.006	2.837			6	12			6	a
	$KZnF_3$			66.68	2.027	2.867			6	12			6	a
	$KCoF_3$			67.37	2.0345	2.877			6	12			6	a
	$RbMnF_3$			66.67	2.0475	2.896			6	12			6	a
Rutile	SiO_2	2	1	46.512	1.774				6				3	d
	TiO_2			62.423	1.983				6				3	a
	SnO_2			71.508	2.057				6				3	a
	GeO_2			55.225	1.908				6				3	a
	MgF_2			65.2282	1.975				6				3	a
	ZnF_2			69.315	2.015				6				3	a
	FeF_2			72.999	2.032				6				3	a
Corundum	Al_2O_3	2	1	85.150	1.915				6				4	a
	Cr_2O_3			96.240	1.995				6				4	a
	Fe_2O_3			100.40	1.985				6				4	a
Ilmenite	$MgSiO_3$	2	1	87.51	1.799	2.077			6	6			4	e
	$MgGeO_3$			96.80	1.906	2.096			6	6			4	f
	$CdTiO_3$			118.52	1.89	2.24			6	6			4	g
	$LiNbO_3$			106.03	2.01	2.153			6	6			4	a
Spinel	Al_2MgO_4	8	4	529.4	1.937	1.921			4	6			4	h
	γ-Mg_2GeO_4			560.38	1.776	2.067			4	6			4	i
	γ-Mg_2SiO_4			524.56	1.655	2.070			4	6			4	j
	γ-Fe_2SiO_4			558.25	1.652	2.137			4	6			4	k
	γ-Ni_2SiO_4			520.5	1.654	2.063			4	6			4	k
Garnet	$Mg_3Al_2Si_3O_{12}$	8	2	1504.7	1.634	1.886	2.27		4	6	8		4	l
	$Mn_3Al_2Si_3O_{12}$			1565.7	1.637	1.902	2.33		4	6	8		4	l
	$Fe_3Al_2Si_3O_{12}$			1533.2	1.628	1.896	2.30		4	6	8		4	l
	$Ca_3Al_2Si_3O_{12}$			1661.9	1.645	1.924	2.40		4	6	8		4	l
	$Ca_3Fe_2Si_3O_{12}$			1753.2	1.643	2.024	2.43		4	6	8		4	l
Garnet'	$CaGeO_3$	32	2	1935.26	1.79	1.92	2.47	2.26	4	6	8	6	4	m

References: a, Wyckoff [1965]; b, Hazen and Finger [1986]; c, Abrahams and Bernstein [1969]; d, Hill et al. [1983]; e, Horiuchi et al. [1982]; f, Kirfel et al. [1978]; g, Liebermann [1976]; h, Finger et al. [1986]; i, Reichlin [1978]; i, Sasaki et al. [1982]; k, Yagi et al. [1974]; l, Novak and Gibbs [1971]; m, Prewitt and Sleight [1969]

differ significantly than those used here. The discrepancy is compounded by the square in the summation. For small splittings, the uncertainty is small compared to that incurred in estimated inactive modes for all structures. Also, for solids with a large number of modes, the value of a particular mode is decreases in importance, so the degree of LO-TO splitting affecting the sum similarly decreases as the number of modes increase.

Large LO-TO splittings are related to large effective charges on the ions, and large oscillator strengths. This, in turn, is related directly to bond strengths. The relationship of oscillator strength to peak width, and that of peak width to polarizability requires that large LO-TO splittings also be associated with large polarizability [see *Wooten*, 1972; *Burns*, 1985]. Thus, large LO-TO splittings will be associated with predominantly ionic bonds.

The calculations are limited to zone center phonons because inelastic scattering measurements, which give frequency as a function of wavenumber, are scant. Only for Al_2O_3 are INS data complete. These data show generally flat laying modes [*Bialas*

TABLE 3. Vibrational Data Used to Calculate K, K', and K"

Formula	Infrared Modes*			Raman Modes*			Inactive Modes			$\Sigma\nu_{io}^2$,	Mode Gruneisen Parameters			$\Sigma\nu_{io}^2\gamma_{io}$,
	Expected	Observed	References	Expected	Observed	References	Expected	Observed	References	cm^{-2}	Number	Type	References	cm^{-2}
NaF	3	3	a							293,000†	3(TO only)	IR	b	470,000
NaCl	3	3	a							123,488†	3	IR	c	212,000
MgO	3	3	d,e							837,126†	6	Raman	e	1,225,760
MnO	3	3	d							441,992†				
CoO	3	3	d							541,718†				
NiO	3	3	d							658,002†				
CsCl	3	3	a							46,827†	3 (TO only)	IR	a	106,000
CsBr	3	3	a							24,114†	3 (TO only)	IR	f	65,000
CsI	3	3	a							14,913†	3 (TO only)	IR	f	35,000
CaF_2	3	3	g	3	3	h				659,454†	3(TO) + 3	IR + Raman	i,j	907,300
SrF_2	3	3	g	3	3	k,l				477,729†	3(TO) + 3	IR + Raman	i,k	704,500
BaF_2	3	3	g	3	3	g				348,231†	3(TO) + 3	IR + Raman	i,k	489,900
BeO	3[b]	3[b]	m	7‡	7‡	m	2	0		4,995,000	7	Raman	n	6,876,000
ZnO	3[b]	3[b]	d	7‡	7‡	m	2	0		1,621,500				
$SrTiO_3$	9	9	o				3	calculated	p	1,602,000				
$KMgF_3$	9	9	q,r				3	systematics	r	1,210,995				
$KMnF_3$	9	9	s				3	3	s	827,617				
$KNiF_3$	9	9	q				3	systematics	r	1,090,995				
$KZnF_3$	9	9	s				3	3	s	868,368				
$KCoF_3$	9	9	tt				3	systematics	r	973,556				
$RbMnF_3$	9	9	q				3	systematics	r	755,902				
SiO_2	7	7	t	5	5	u	3	see text	v	6,919,000	7 + 4	IR + Raman	t,w	7,700,000
TiO_2	7	7	x,y	5	5	x,z	3	2	x,aa	3,777,691§				
SnO_2	7	7	bb	5	5	cc	3	calculated	dd,v	3,672,300				
GeO_2	7	7	v	5	5	ee	3	see text	v	4,272,600				
MgF_2	7	7	ff	5	5	gg	3	see text	v	2,286,500				
ZnF_2	7	7	ff	5	5	gg	3	see text	v	1,485,800				
FeF_2	7	7	ff	5	5	gg	3	see text	v	1,681,000				
Al_2O_3	8	8	hh	12	12	ii	5	5	jj,kk	8,757,633†				
Cr_2O_3	8	8	ll	12	10	mm	5	0		6,668,000				
Fe_2O_3	8	8	ll	12	12	mm	5	0		5,104,000				
$MgSiO_3$	12	12	nn	15	13	oo				8,938,000§				
$MgGeO_3$	12	10?	nn,pp	15	13	pp				6,428,000§				
$CdTiO_3$	12	12	rr	15	11	rr				5,563,000				
$LiNbO_3$	12	12	ss	15	11	ss				6,109,000				
Al_2MgO_4	12	12	uu	12	12	uu	15	6¶	uu,vv	11,630,000	12	IR,R,fluores	uu	16,200,000
γ-Mg_2GeO_4	12	12	pp,ww	12	12	pp,xx	15	0		9,034,000				
γ-Mg_2SiO_4	12	12	b	12	12	yy	15	0		11,228,000				
γ-Fe_2SiO_4	12	12	b,zz	12	0		15	0		9,235,000	12	IR	zz	11,062,000

γ-Ni_2SiO_4	12	9	g	12	12	aaa	15	0		10,320,000
$Mg_3Al_2Si_3O_{12}$	51	51	bbb	61	61	bbb	95	0		73,925,000
$Mn_3Al_2Si_3O_{12}$	51	51	bbb	61	61	bbb	95	0		69,650,000
$Fe_3Al_2Si_3O_{12}$	51	51	bbb	61	61	bbb	95	0		68,678,000
$Ca_3Al_2Si_3O_{12}$	51	51	bbb	61	61	bbb	95	0		67,633,000
$Ca_3Fe_2Si_3O_{12}$	51	51	bbb	61	61	bbb	95	0		61,573,000
$CaGeO_3$	98	40?	ccc	108	40?	ccc	31	0		50,000,000

References: a, *Ferraro* [1984]; b, unpublished data by A. M. Hofmeister, 1990; c, *Hofmeister* [1987*b*]; d, *Mitra* [1969]; e, *Chopelas* [1990*a*] MgO:Cr^{3+} was studied/ Zone edge $\Sigma\nu_i^2$ is 969,325.; f, *Shawyer and Sherman* [1982]; g, *Kaiser et al.* [1962]; h, *Srivanstan et al.* [1971]; i, *Ferraro et al.* [1971]; j, *Nicol et al.* [1972]; k, unpublished data by S.S. Mitra, cited by *Ferraro* [1984]; l, *Axe* [1965]; m, *Loh* [1968] and *Arguello et al.* [1969]; n, *Jephcoat et al.* [1988]; o, *Spitzer et al.* [1962]; p, *Rajagopol and Srinivasan* [1962]; q, *Nakagawa* [1973]; r, *Hofmeister and Billips* [1991]; s, *Lehner et al.* [1982]; t, *Hofmeister et al.* [1986*b*, 1990*b*]; u, *Hemley et al.* [1986]; v, *Hofmeister et al.* [1990*a*]; w, *Hemley* [1987]; x, *Traylor et al.* [1971]; y, *Eagles* [1964]; z, *Porto et al.* [1967]; aa, *Kaiyar and Krishnan* [1967]; bb, *Summit* [1968]; cc, *Scott* [1970]; dd, *Kaiyar et al.* [1971]; ee, *Sharma et al.* [1979]; ff, *Barker* [1963]; gg, *Porto et al.* [1967]; hh, *Barker* [1963]; ii, *Porto and Krishnan* [1967]; jj, *Bialas and Stolz* [1975]; kk, *Kappus* [1975]; ll, *Serna et al.* [1982]; mm, *Beattie and Gilson* [1970]; nn, *Hofmeister and Ito* [1991]; oo, *McMillan and Ross* [1987]; pp, *Ross and Navrotsky* [1988]; qq, *Baran and Botto* [1978]; rr, *Baran et al.* [1986]; ss, *Baran and Young* [1967]; tt, *Perry and Young* [1967]; uu, *Chopelas and Hofmeister* [1991]; vv, *Wood et al.*, [1968] and *Thompson and Grimes* [1978]; ww, *Preudhome and Tarte* [1972]; xx, *Guyot et al.* [1986]; yy, *McMillan and Akaogi* [1987]; zz, *Hofmeister et al.* [1986*a*]; aaa, *Yamanaka and Iishi* [1986]; bbb, *Hofmeister and Chopelas* [1991*b*]; ccc, *Ross et al.* [1986].

* These numbers reflect the degeneracy of the bands

† All zone-center frequencies are established

‡ Some of the IR and Raman modes are of the same symmetry.

§ The sum is well-constrained from knowledge of >92% of the modes

¶ Symmetry and number of bands is uncertain.

and Stolz, 1975], as is also seen for incomplete data on rutile [*Traylor et al.*, 1971] and on BeO wurtzite [*Ostheller et al.*, 1968]. Compounds with large number of modes are expected to have little dispersion. LO frequencies should be dispersionless unless they are coupled with TO modes [*Burns*, 1985], so that structures with a large proportion of IR modes are expected to have overall low dispersion. Thus, dispersion should not significantly influence the sum in all the large primitive unit cell structures (perovskite, rutile, corundum, ilmenite, spinel, and garnet; see Table 3). For the rocksalt structure, the sum appears to be a constant over wave vector, given the available data [*Rosenstock*, 1963]. The only structures where dispersion could possibly affect the sum are fluorite and B2, for which no INS data are available.

For the majority of the cases in which a small proportion (≤ 17%) of the modes were not observed (wurzite, rutile, corundum, and ilmenite structures), the missing frequencies were estimated with varying degrees of accuracy, as follows: (1) through comparison to known frequencies of chemically substituted minerals (i.e., Cr_2O_3 frequencies were derived from Al_2O_3 data), (2) from dependences of frequencies of rutile or ilmenite minerals on structural parameters such as lattice constant [*Hofmeister et al.*, 1990*a*; *Hofmeister and Ito*, 1991], and (3) by applying factor group analysis (FGA) and the correlation method [*Fateley et al.*, 1971] to the mineral structure. For example, stretching modes like ν_3 in the inactive symmetry of wurzites were estimated by the average ν_3 bands observed through infrared or Raman spectroscopy. By comparing the three estimates, uncertainties in the missing frequencies and hence in the Brout sum $\Sigma\nu_i^2$ could be estimated accurately.

For perovskite, INS data are available on $KMnF_3$ and $KZnF_3$ [*Lehner et al.*, 1982]. Relationships of fluorite perovskite frequencies to structural variables and cation masses allow prediction of the missing inactive mode within +10% [*Hofmeister and Billips*, 1991]. However, this contributes considerable uncertainty to the sum because the one inactive peak consitutes 25% of the optic modes. For $SrTiO_3$, the one inactive peak (three modes) was taken from calculations.

Large proportions (≥ 20%) of inactive modes have not been measured for the spinel and garnet structures. The five inactive frequencies of spinel (representing 15 modes) were estimated from through factor group analysis and the three methods described above. For $MgAl_2O_4$, side band fluorescence data provide information on at least one triple degenerate peak [*Chopelas and Hofmeister*, 1991]. The 55 inactive frequencies of garnet (95 modes) contribution was estimated by assuming that the bands could be described through FGA [*Fateley et al.*, 1971] by two methods: (1) that the missing frequencies equal the average of the observed bands in each category of motion or (2) that the sum of similar kinds of modes can be proportioned according to the number of modes. For example, in method 2 the sum of the observed ν_3^2 times the number expected over the number observed gives the Brout sum $\Sigma\nu_i^2$ for the asymmetric stretching modes. The Brout sums calculated by these two approaches differ by ~1%. The average value is reported in Table 3. Problems arising from the large number of inactive modes in silicate garnet are offset by this mineral's demonstrable lack of mode mixing and adherence to representation in terms of internal SiO_4 tetrahedral vibrations, translations, and rotations [*Hofmeister and Chopelas*, 1991b].

The experimental values for the bulk modulus (Table 4) were taken from measurements made at 1 atm (e.g.. by Brillouin

TABLE 4. Results on K_T and K'_0

Structure	Total Modes	Formula	K_T(expt),* GPa	References	K_T(calc), GPa	K'_0(expt)*	References	K'_0(calc)
Rock salt	6	NaF	46.2±0.2	a,b	43±2	5.5±0.4	a,b	4.9±0.4
		NaCl	23.8±0.03	c,d	20±1	5.5±0.25	c,d	5.1±0.5
		MgO	160.3±0.2	e	126±7	4.1±0.1	e	4.2±0.1
		MnO	154±2	f	80±5	4.7±0.2	g	
		CoO	179±2	f	105±6			
		NiO	196±10	h	131±7			
CsCl	6	CsCl	16.74±0.09	i	15.4±0.5	5.98±0.09	i	6.2±0.5
		CsBr	14.34±0.08	i	13.7±0.5	5.95±0.08	i	7.1±0.5
		CsI	11.89±0.05	i	10.3±0.5	5.93±0.08	i	6.3±0.5
Fluorite	9	CaF_2	82.0±0.5	j,k	76±3	4.7±0.2	j,k	4.4±0.5
		SrF_2	70.0±0.5	l	64±2.5	4.8±0.2	l	4.6±0.4
		BaF_2	56±1	k,m	47±2	5.1±0.2	m	4.5±0.4
Wurtzite	12	BeO	220±10	n,o	186±20	4.5±1.5	n	4.4±0.3
		ZnO	140±10	p	113±10			
Perovskite	15	$SrTiO_3$	172.0	q	137±10	5.5±0.3	r	
		$KMgF_3$	73.5±0.5	s	93±10	5.0±0.5	s	
		$KMnF_3$	63.2±1	t	68±1			
		$KNiF_3$	83.4	u	95±10			
		$KZnF_3$	77.6	v	76±1			
		$KCoF_3$	75.2	iii	80±5			
		$RbMnF_3$	65.6	jjj	74±5	4.9	jjj	
Rutile	18	SiO_2	306±4	w	312±4	3.3±1	x	3.9±0.4
		TiO_2	210±1	y,z	187±2	7±1	y,aa	
		SnO_2	212±2	bb	201±5	5.5±0.5	bb	
		GeO_2	258±3	cc	240±5	6.2±0.3	cc	
		MgF_2	100.0±0.5	dd,ee	96±4	5.1±0.1	ee,ff	
		ZnF_2	107±2.5	gg,hh	84±5	4.5±0.5	ii	
		FeF_2	100±5	ff	89±5	4.6±0.2	ff	
Corundum	30	Al_2O_3	251.5±1.5	jj,kk	248±5	4.3±0.2	jj,ll	
		Cr_2O_3	227±5	mm	220±20	2±1†	mm	
		Fe_2O_3	203±2	nn	165±15	4.5	oo	
Ilmenite	30	$MgSiO_3$	210±10[d]	pp	240±5			
		$MgGeO_3$	197±8	oo	195±6	2±1.5†	aa,qq	
		$CdTiO_3$	165±5	rr	167±3			
		$LiNbO_3$	114.3±1.2	ss	119±4			
Spinel	42	Al_2MgO_4	195±1	tt,uu	210±5	4.5±0.6	tt,uu	4.4±0.1
		γ-Mg_2GeO_4	179±1‡	vv	174±10	4±2	ww	
		γ-Mg_2SiO_4	184±1‡	xx	210±10			
		γ-Fe_2SiO_4	192±4	ww	203±20	4±2	aa,yy	4.1±0.5
		γ-Ni_2SiO_4	226±2	zz	233±10	16±2	zz	
Garnet	237	$Mg_3Al_2Si_3O_{12}$	171.7±0.5	aaa	242.5±0.5	4.5±1	bbb¶	
		$Mn_3Al_2Si_3O_{12}$	178±1	ccc	245.5±0.5	5±1	ddd¶	
		$Fe_3Al_2Si_3O_{12}$	176±3§	eee	240.3±0.6	5.4±1	eee¶	
		$Ca_3Al_2Si_3O_{12}$	167±7	ccc	225.8±0.7	4.3	fff	
		$Ca_3Fe_2Si_3O_{12}$	157±2	ggg	214.3±0.5	4±1	hhh	
Garnet'	237	$CaGeO_3$	124	oo	185±15	4†	oo	

References; a, *Bensch* [1972]; b, *Jones* [1976]; c, *Chbabildas and Ruoff* [1976]; d, *Spetzler et al.* [1972]; e, *Jackson and Niesler* [1982]; f, *Sumino et al.* [1976]; g, *Pacalo and Graham* [1986]; h, *Clendenen and Drickamer* [1966]; i, *Barsch and Chang* [1971]; j, *Briells and Vidal* [1975]; k, *Jones* [1977]; l, *Alterovittz and Gerlich* [1970]; m, *Wong and Schule* [1968]; n, *Hazen and Finger* [1986]; o, *Cline et al.* [1967]; p, *Tokarev et al.* [1975]; q, *Bell and Rupprecht* [1963]; r, *Beattie and Samara* [1971]; s, *Jones* [1979]; t, *Aleksandrov et al.* [1966]; u, *Nouet* [1973]; v, *Gesland et al.* [1972]; w, *Weidner et al.* [1982]; x, *Kuzio* [1977]; y, *Manghnani* [1969]; z, *Grimsditch and Ramdas* [1976]; aa, *Bass et al.* [1981]; bb, *Chang and Graham* [1975]; cc, *Wang and Simmons* [1973]; dd, *Jones* [1971]; ee. *Aleksandrov et al.* [1969]; ff. *Nakagiri et al.* [1987]; gg. *Hart* [1978]; hh. *Ramai* [1977]; ii. *Rai and Manghnani* [1976]; j, *Gieske and Barsch* [1968]; kk, *Hankey and Schuele* [1970]; ll, *d'Amour et al.* [1978]; mm, *Sato and Akimoto* [1979]; nn, *Lieberman and Schreiber* [1968]; oo,*Liebermann* [1974]; pp, *Weidner and Ito* [1985]; qq, *Sato et al.* [1977]; rr, *Liebermann* [1976], K_S stated; ss, *Cnkalova et al.* [1971] and *Smith and Welsh* [1971]; tt, *Finger et al.* [1986]; uu, *Chang and Barsch* [1973]; vv, *Weidner and Hamaya* [1983]; ww, *Liebermann* [1975]; xx, *Weidner et al.* [1984]; yy, *Finger et al.* [1979]; zz, *Nelson et al.* [1986]; aaa, *O'Neill et al.* [1989]; bbb, *Bonzcar et al.* [1979] and *Leitner et al.* [1977]; ccc, *Bass* [1989]; ddd, *Isack and Graham* [1976] ; eee, *Soga* [1967]; fff, *Halleck* [1973]; ggg, *Bass* [1986]; hhh, estimated from *Angel et al.* [1989]; iii, *Aleksiejuk and Kraska* [1975]; jjj, *Naimon and Granato* [1973].

* Uncertainties were estimated by comparing data of Sumino and Anderson [1984]

† Value of K' may be incorrect due to use of NaF scale.

‡ Estimated from K_S.

§ End-member values were extrapolated from intermediate compositions.

¶ Values of intermediates were used.

spectroscopy or ultrasonic or resonance techniques) if available. Compression measurements are less reliable, in that the K_0 and K'_0 values are related, as is indicated by the uncertainties in Table 4 (eg., $MgAl_2O_4$ [*Finger et al.*, 1986; *Chang and Barsch*, 1973] and BeO [*Hazen and Finger*, 1986; *Cline et al.*, 1967]). Accurate values for the pressure derivative K'_0 in lieu of high pressure ultrasonic, dilatometry, or Brillouin scattering measurements, are obtained from a combination of K_0 values measured at 1 atm and compression experiments [*Bass et al.*, 1981]. If the only measurements are volume-compressibility studies, then the uncertainty in K'_0 is roughly ±1 as indicated in Table 4. Uncertainties in ultrasonic studies are commonly 1% unless phases shifts are corrected for (in this case 0.1% is attainable) [*Jackson et al.*, 1981]. Uncertainties in Brillouin scattering are also about 1% [*Weidner and Vaughan*, 1977].

Evaluation of the validity of the model is not straightforward, not only because the inactive modes are often undetermined, but also because IR and Raman data are incomplete for some substances (Cr_2O_3, ilmenites, tetragonal garnet, Fe and Ni spinel: Table 3). Other factors anticipated to affect the usefulness of the model are (1) whether the assumptions concerning the interatomic potentials holds for each structure, (2) the effect of the chemistry on the potentials within each structure, (3) the effect of polarizability (i.e., nonrigid ions), and (4) the difference between LO and TO modes and the dynamical frequencies as discussed above. Therefore, the applicability of the theory will be assessed individually for each structure. This will separate out the effect that the proportion of inactive modes has on the calculation, and the effect that the structure has on the adherence of the interatomic potentials to the assumptions. Because of the small number of "true" tests (i.e., minerals with completely determined vibrational spectra and accurately determined elastic properties), statistics will not be applied. Instead, the theory will be evaluated according to the difference between the calculated and experimental bulk modulus and as to whether these two values overlap within experimental uncertainty. The categories are excellent (<3% difference), good (3-9%), moderate (10-15%), poor (16-25%), and very poor (>25%). Within each structural group, the different compounds will be compared with due consideration to the completeness of the data and points 1-4 above in an attempt to evaluate the effect of chemistry on the applicability of the theory.

Probably the most important factor affecting the validity of the theory is whether the interactions between like atoms can be modelled as entirely electrostatic. The form cannot be determined, but the relative importance of the interactions can be assessed by comparing the separation of the like atoms to that of the nearest and second-nearest neighbors. As shown in Table 5, the theory should be valid for the structures with large primitive unit cells in which like atoms are third-nearest neighbors or further: perovskite, rutile, corundum, ilmenite, spinel, and garnet. The theory is likely to fail for B1, B2, fluorite, and wurtzite structures in which like atoms are second nearest neighbors. The actual separation of the like atoms will have a secondary effect. Note that the values for the separation are only slightly larger for structures with large primitive unit cells. Considering both factors together suggests that it is unlikely that the theory will adequately represent wurtzite or the B1 structures, that agreement for fluorite and B2 will be only slightly better, that the theory is likely to be applicable to rutile, that good results should be attained for perovskite, ilmenite, and spinel, and that corundum and garnet should show excellent agreement. Ilmenite is more likely to fall in the good category than in the excellent, because it departs from the symmetry requirements.

Bulk Modulus at 1 atm

Overall, the values of the bulk modulus predicted from 13 and 32 correlate directly with experiment with a slope of unity, except for the garnets (Figure 2). Most of the scatter on Figure 2 is related to each mineral structure having a different slope, most of which are close to unity (Figures. 3a-3j). For 17 of the 45 minerals investigated, the predicted K_T is equal to the experimental, given the uncertainties in both determinations (Table 4). The discrepancy between experiment and theory depends on several factors: primarily, on the mineral structure which determines not only the proportion of the inactive modes but also the departure from pair-wise central forces, and most importantly, the magnitude of like-like atom interactions (as gauged by comparing them with second- and first-nearest neighbor characteristics). Second, the discrepancy depends on the chemistry which affects the bonding (i.e., the existence of magnetic interactions, or ions of considerably difference polyhedral compressibility). Polarizability appears to have a small effect. The variation in numbers of bands observed within each structural group has a minor effect on the accuracy of the theory. On the other hand, the range of the measured vibrational frequencies has a considerable effect, because compounds with many frequencies close together have better constrained Brout sums. In order to clarify these points, and to emphasize which minerals provide stringent tests (i.e., which have both well-constrained vibrational and elastic data), each structure is discussed in turn.

TABLE 5. Structural Relationships for Like Atoms

Structure	Distance Between Pairs of Like Atoms			r(like-like)/r(NN)	r(2NN)/r(NN)
	r(like-like)	2nn?	Value and Composition		
Rock salt (B1)	$a_o/\sqrt{2}$	yes	3.3 Å for NaCl	1.41	1.41
CsCl (B2)	a_o	yes	4.1 Å for CsCl	1.15	1.15
Fluorite	$a_o/\sqrt{2}$	yes	3.9 Å for CaF_2	1.63	1.63
Wurtzite	a_o	yes	2.6 Å for BeO	1.63	1.63
Perovskite	a_o	no	3.9 Å for $SrTiO_3$	2.0	1.4
Rutile	c_o	no	2.7 Å for SiO_2	1.5	1.3
Corundum	a_o(rhomb)	no	4.8 Å for Al_2O_3	2.7	1.3
Ilmenite	a_o(rhomb)	no	4.0 Å for $MgSiO_3$	2.7	1.3
Spinel	$a_o/2$	no	4.0 Å for γ-Mg_2SiO_4	2.1	1.4
Garnet	$a_o/2$	no	5.7 Å for $Mg_3Al_2Si_3O_{12}$	3.0-3.6	1.4-1.6

References for these data are found in Table 2.

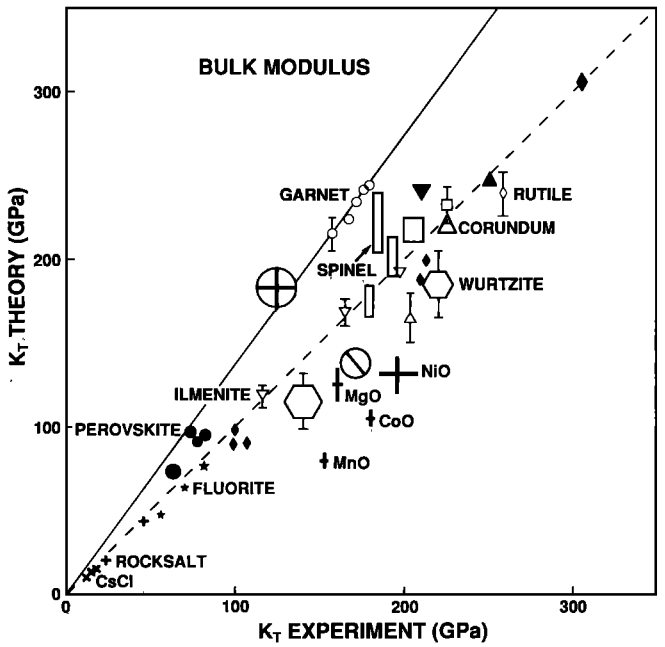

Fig. 2. Correlation of bulk modulus predicted from spectroscopy of (13) and (32) with measured bulk modulus for all substances in Table 4. Solid symbols, pluses, and crosses represent crystals with essentially complete spectral data. The uncertainty is reflected by size of symbol or by error bars. Different symbols represent the various structures. Plus, rocksalt; cross, CsCl; star, fluorite; hexagon, wurtzite; diamond, rutile; triangle, corundum; inverted triangle, ilmenite; shaded square or rectangle, spinel; slashed circle, perovskite; circle, garnet, circled plus, tetragonal garnet.

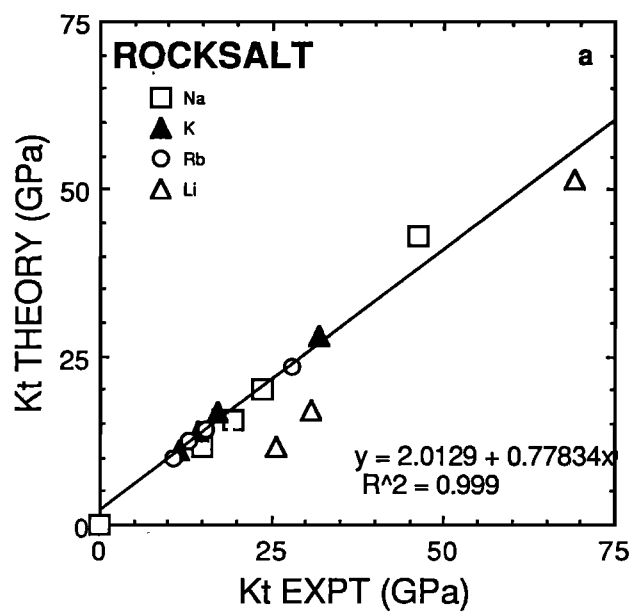

Fig. 3a-j. Relationships of calculated bulk modulus to experimental for each of the ten structural types. The lines are the least squares fit to the data and a point at the origin. Symbols are as in Figure 2. solid symbols indicate minerals where >92% of the modes are known. All modes are known for B1, B2, and fluorite. All structures except perovskite and rocksalt have well-constrained linear trends. This exceptions have distinct trends for each chemical series. In Figure 3a, only data on alkali halides are shown. For the oxides, see Figure 2. RbX data were used in fitting the curve.

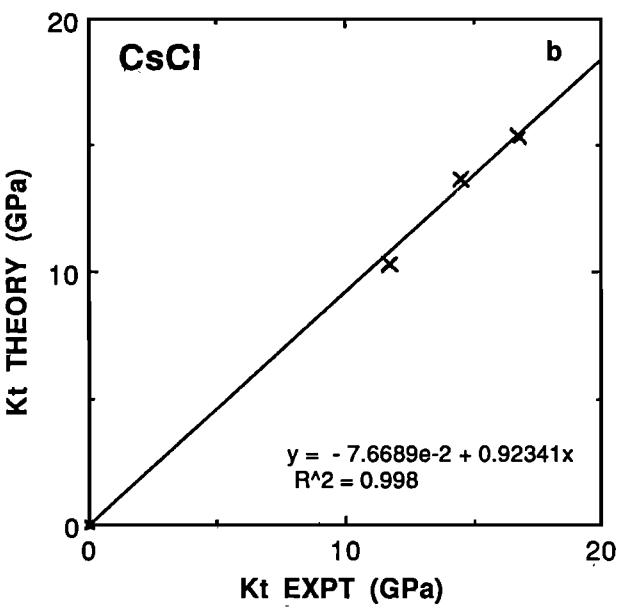

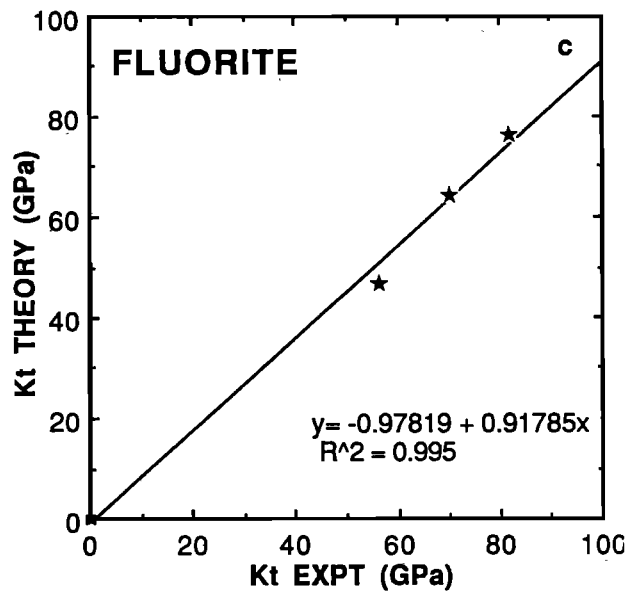

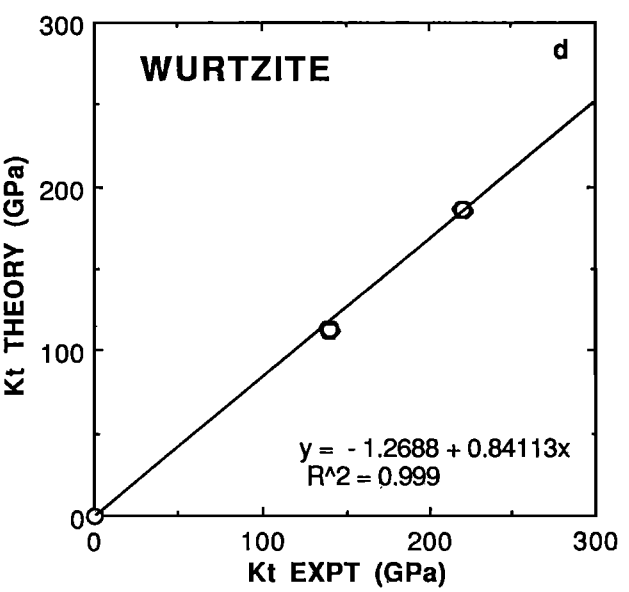

Fig. 3. (continued)

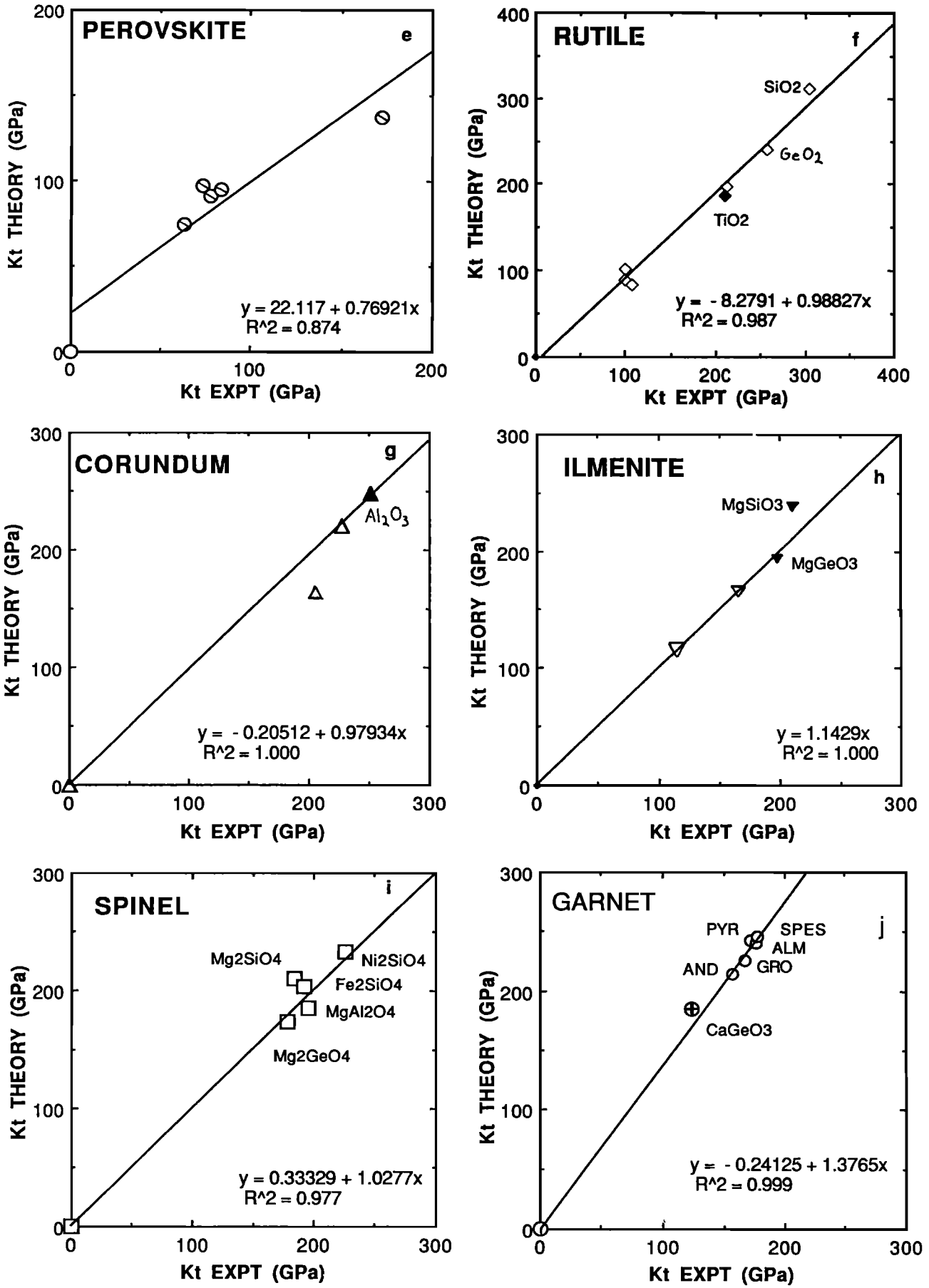

Fig. 3. (continued)

Structures with completely determined vibrational spectra. For the three structures that have completely determined vibrational spectra (B1, B2, and fluorite), the theory appears to generally underestimate bulk modulus, although systematic linear trends do exist for each structure. These minerals provide stringent tests of the theory, but problems are expected because like atoms in these structures are second-nearest neighbors (Table 5). For alkali halides in the rocksalt structure, agreement appears to depend on radius of the cation (Figure 3a), in that excellent agreement occurs for Rb and K halides, good agreement for Na, and the worst agreement occurs for Li halides. The variability can be connected with the nonelectrostatic interactions between like anions, in that the larger cations keep the anions further apart. On the other hand, the variability could also be related to the relative compressibility of the two sites: if the cations are too small to hold the anions apart, then the bulk modulus is solely related to the compressibility of the anion. For this extreme case (the Li halides), Brout's formula cannot be correct because anion and cation are assumed to play equivalent roles in the derivation.

Polarizability cannot account for the differences within the B1 structure, in that the molecular polarizabilities vary more within the cation series for which calculated K_T depends linearly on experiment (e.g., a_m of NaF = 1.2, NaCl = 3.3, NaBr = 4.4, NaI = 6.3 in units of 10^{-24} cm^3 [*Tessman et al.*, 1953]) than a_m within the anion series (LiCl=2.9, NaCl=3.3, KCl = 4.1, RbCl = 4.7 in units of 10^{-24} cm^3 [*Tessman et al.*, 1953]) for which linear relationships are not seen between theory and experiment (Figure 3a). In fact, agreement is best for the most polarizable Rb-halides. For oxides in the rocksalt structure, agreement is poor (Table 4 and Figure 2). The failure is likely a combination of the large LO-TO splitting adding uncertainty to the sum because the frequencies in the dynamical matrix lie in between the LO and TO branches [*Turrell*, 1972] and the small number of modes in the sum. Polarizability does not appear to be the cause because a_m values of MgO, CoO, and MnO are all small, about 2.0 x 10^{-24} cm^3 [*Tessman et al.*, 1953], as expected for a significantly covalent bond. Polarizability for these oxides is considerably lower than that for other compounds modelled well by the theory. Thus, assuming rigid ions does not limit the applicability of the theory. For the ionically bonded rock salt structure, the crucial assumption appears to be the degree of like-like atom interactions.

The Brout sum for MgO is 837,126 cm^{-2} for zone center frequencies [*Mitra*, 1969], but 969,325 cm^{-2} at the zone edge [*Chopelas*, 1990*a*]. The difference is significant, and suggests that one of the assumptions is not met for oxides in the B1 structure.

The good to moderate discrepancy for the CsCl structure (8-13% difference; Figure 3b) is surprising considering that strong like-like interactions are expected with such a small primitive unit cell (Table 5). However, the actual second nearest neighbor distances are large (because the eight-fold coordination places more atoms in a given space), so that better agreement was expected for B2 than for B1. Note also, that these compounds are more polarizable (a_m= 5.8 to 9.1 x 10^{-24} cm^3) than the B1 phases [*Tessman et al.*, 1953], suggesting once again that polarizability is a secondary factor, in contrast to that previously proposed [*Mitra and Marshall*, 1964]. Although the theory clearly cannot be used predictively for B2 compounds, a useable linear relationship exists between calculated and experimental K_T (Figure 3b).

Good to moderate agreement occurs for the fluorite structure (7-16% difference; Figure 3c). These compounds have weaker like-like atom interactions due to relatively larger distances. Fluorites are low to moderately polarizable (a_m= 2.5 to 4.0 x 10^{-24} cm^3 [*Tessman et al.*, 1953]), indicating that this factor is of minor importance. Note that the series XF_2, CsX, RbX, and KX show a linear relationship of calculated with experimental bulk modulus, whereas and NaX and LiX lie parallel to the slope of unity (Figs. 3a-c). Overall it appears that the B1 structure is the least well described by the theory, as suggested in Table 5. The theory cannot be used predictively with such small primitive unit cell compounds, yet the linear trends suggest that it may be useful for systematics for compounds that have small primitive unit cells and thus a high probability of strong like-like atom interactions.

Of the remaining structures, only three compounds have complete vibrational data, the mineral Al_2O_3, and the perovskites $KZnF_3$ and $KMnF_3$. The agreement for the first two compounds is excellent (1 and 3% difference with experiment, respectively). The higher accuracy is expected for corundum in that the Brout sum involves 25 modes established from about 20 peaks, whereas the Brout sum for perovskite involves 12 modes established from seven peaks. Prediction of K_T for $KMnF_3$ is less accurate, 8%. A likely reason for this lies in its unusual IR spectra: an extra band is present in the fundamental range [*Perry and Young*, 1967] which is due to resonance of the middle frequency IR mode with a combination/overtone of the lowest frequency IR mode with the inactive mode [*Hofmeister and Billips*, 1991]. Resonance in the system is likely to perturb the measured frequencies from those expected in the dynamical matrix.

Structures with incomplete spectral data. For the wurtzite structure, the agreement is generally poor (15-19% difference; Figure 3d), as suggested by the fact that like atoms constitute second nearest neighbors. A definative evaluation awaits more accurate determination of K_T and experimental or theoretical determination of the inactive modes which constitute 22% of the optical modes. INS measurements have been made for BeO, but the data are incomplete [*Ostheller et al.*, 1968]. The frequencies estimated through factor group analysis for the inactive modes of BeO are reasonable but probably not sufficiently accurate, because these same values result in ≈2% difference between predicted and measured heat capacity whereas accurate values of the zone center vibrational spectra yield less than 0.5% difference [*Hofmeister et al.*, 1987; *Hofmeister*, 1987b; *Hofmeister and Chopelas*, 1991*a*]. The uncertainty in the estimated Brout sum $\Sigma\nu_i^2$ for ZnO is unknown, but is probably smaller than that of BeO because the range of the measured ZnO frequencies is small [*Arguello et al.*, 1969]. Note that the wurtzite series is linear with a slope smaller than unity (Figure 3d), as was seen for the other small primitive unit cell structures.

For the perovskites, agreement between predicted and experimental K_T (Figure 3e) is variable but usually poor (3-25% difference), although three of the perovskites have predicted bulk moduli within the uncertainties of the experimental values. The like-like atom interactions are probably not strong (Table 5). However, the fluoride perovskites with the worst agreement are those with the smallest cations, suggesting that the mechanism of compression could differ from the isotropic mechanism assumed in the derivation. It is also likely that the inactive frequencies, which constitute 25% of the optional modes, cannot be predicted sufficiently

accurately from systematics due to complex dependencies of the IR and inactive modes on structure and cation mass [*Hofmeister and Billips*, 1991]. Because all IR modes are of one symmetry, mode mixing is a strong possibility, which would prohibit description in terms of internal motions of the octahedra and simple translations. For $SrTiO_3$, the values for the calculated inactive modes may be high because the rigid ion approximation was used [*Rajagopol and Srinivasan*, 1962; *Nakagawa et al.*, 1967] and this approach overestimates inactive modes for rutiles, which have similarly coordinated cations [*Hofmeister et al.*, 1990*a*]. Lastly, the Brout sum is not well constrained because these compounds exhibit moderately large LO-TO splittings [*Turrell*, 1972] and have only three measured bands over a moderately large range (80-600 cm^{-1}). It is clear that the theory is inadequate to predict properties of perovskites from Raman and IR frequencies. Note, however, that the sequence in experimental K_T for the KXF_3 series (Ni>Zn>~Co>Mg>Mn) is similar to the predicted results (Mg=Ni>Co>~Zn>Mn). This suggests that the theory may aid in systematic prediction of elasticity of perovskites but is insufficient to predict K_T from IR and Raman data.

Within the rutile family (Figure 3f), agreement is variable for bulk modulus (2-20% difference). However, the theory appears to be valid because the correlation is linear with a slope of 0.98 and because the experimental and theoretical values of K_T are equal given the uncertainties, except for TiO_2. Weak secondary features in the spectra of TiO_2 may indicate distortion from the rutile structure [*Hara and Nicol*, 1979]. If this is the case, the sum of the vibrational frequencies is inaccurate, and use of one interatomic distance is inappropriate. Furthermore, TiO_2 has very large LO-TO splittings, which decreases the accuracy of the Brout sum. Although the like atoms in rutile-types are close, they are not second-nearest neighbors (Table 5), so it is unlikely that the assumptions concerning the form of the potentials is violated. The best agreement occurs for oxides other than TiO_2 (Table 4) in accord with these having well constrained inactive modes [*Hofmeister et al.*, 1990*a*] based on correlations of frequencies with volume. Rutile-type fluorite frequencies are less well constrained because none of the inactive modes for any of these compounds have been established. The sum for FeF_2 is the least accurate, because the IR data were taken from a powder, rather than from a single crystal.

The corundum structure has overlapping experimental and theoretical values that are in excellent agreement ($\leq$ 3 % discrepancy) for K_T, except for Fe_2O_3. This compound is a poor test because the IR and Raman data were from polycrystals, so that the Brout sum may not be well contrained; moreover, it is likely that magnetic interactions affect the interatomic potentials for this compound. Thus, the model appears to be valid for corundum, in accord with its like atoms being widely separated, in terms of both distance and atoms intervening. The best agreement (1%) occurs for Al_2O_3, for which vibrational data are completely determined [*Barker*, 1963; *Porto and Krishnan*, 1967; *Bialas and Stolz*, 1975; *Kappus*, 1975].

For compounds in the ilmenite structure, which is a derivative of corundum and thus is strictly not appropriate, the theory appears to describe the bulk modulus well. Except for $MgSiO_3$, which is overestimated by 14%, theory for K_T matches experiment within the stated uncertainies and with a small difference (1-4%). A least squares fit of calculated K_T with experiment was linear with a slope of unity (Figure 3h). The lack of correspondence for $MgSiO_3$ does not appear to be related to uncertainties in the sum, because the only mode that was not observed (the highest-frequency E_g peak) was missing for all 15 compounds for which vibrational spectra are available [*Hofmeister and Ito*, 1991]. Its value was deduced to be degenerate with the highest-frequency A_g mode from the lack of any features at high energy that could be associated with E_g. This assumption is in line with atomistic calculations [*Wall and Price*, 1988] and is corroborated by accurate calculation of heat capacity based on this assignment [*Hofmeister and Ito*, 1991]. Thus, all the sums for the ilmenite compounds will be off by the same amount. The Brout sum is fairly well constrained, because of the the occurence of large number of absorption bands (18) within a narrow range of frequencies (800-350 cm^{-1}) [*Hofmeister and Ito*, 1991; *McMillian and Ross*, 1987; *Ross and Navrotsky*, 1988]. One plausible explanation for K_T of $MgSiO_3$ being overestimated is that polyhedral compressibilities of its cations vary considerably, whereas that of the other pairs of cations show smaller differences [*Hazen and Finger*, 1979]. In this manner, Mg sites could be taking up more than its share of the compression as alotted by the theory. In other words, the anisotropy of the structure for $MgSiO_3$ is too large to be ignored, as assumed in the calculations.

$LiNbO_3$ is included in the ilmenites, because the type and number of its vibrational modes are most similar to this structure. It is actually a hexagonal derivative of the perovskite structure. The bulk modulus for this compound is accurately predicted, which suggests that a variety of derivative structures may be amenable to the theory.

The spinel group, except for γ-Mg_2SiO_4, has good agreement (3-6% difference between experimental K_T and theory (Figure 3i) despite the large proportion of missing modes (roughly 1/3). For Al_2MgO_4, only 9 modes are missing [*Chopelas and Hofmeister*, 1991], but these are not readily estimated from factor group analysis because the strong bonding occurs within the edge-sharing octahedra, not within the isolated tetrahedra, as is the case for the silicates. All except γ-Mg_2SiO_4 have predicted values that match the experiment within the uncertainties, indicating that the theory is applicable for spinel. The overall good agreement is due to (1) the distribution of all the frequencies over a narrow range, lending to a constrained Brout sum, (2) spinel having a large primitive unit cell so that like atoms are not second nearest neighbors, and (3) silicate spinels are accurately described in terms of internal vs. external vibrations for the following reasons. The relative bond strengths in the silicate spinel structure are such that the SiO_4 tetrahedral group is highly covalent, and thus a stronger bond, compared to the ionic bonding of metal ions in the octahedral sites. Spinel's SiO_4 tetrahedra are isolated from one another. Chemically similar lower pressure olivine polymorphs are adequately described in terms of internal SiO_4 motions and cation translations [*Hofmeister*, 1987b; *Chopelas*, manuscript in preparation, 1991]. In addition, the similarity of the sites in the silicate spinels to those of the olivine polymorphs, which have nearly completely determined vibrational spectra, aids in estimation of the inactive frequencies. The poor correlation for γ-Mg_2SiO_4 (20% difference) may be related to the switchover in energy between the ν_4 and translational modes [*A. M. Hofmeister*, unpublished data, 1990; *Preudhome and Tarte*, 1972] which makes it more difficult to estimate the inactive modes. A more important factor may be the small size of the Mg cation compared to that

of its site, which results in a low polyhedral bulk modulus, contributes to lowering K_T, and violates the scaling assumption. Although scaling is not needed to derive (32), the assumption regarding pair-wise central forces is a consequence of the structure scaling with pressure. Thus, anisotropic expansion can be taken as an indication of noncentral forces in a solid.

Most of the largest discrepancies between theory and experiment for K_T occur for the garnet family (≥ 25% difference), although the trend is a well constrained line with a slope of 1.367 (Figure 3j). The failure may be related to the large portion of inactive modes (roughly 1/3). The similarity of Raman T_{2g} modes to IR TO components indicates that factor group analysis is appropriate for predicting the missing modes [*Hofmeister and Chopelas*, 1991*b*]. It is possible that the Brout sum (and hence K_T could be off (Figure 3j) because the observed IR frequencies are, for example, at the high end of the range of all bands. But it is unlikely that the inactive frequencies would be sufficiently lower than Raman and IR bands to place K_T on the 1:1 line. Thus, the slope exceeding unity for the garnet structure must result from its variance from the stated assumptions. One suggestion is that the garnets, like $MgSiO_3$ and γ-Mg_2SiO_4, have one site (i.e., the dodecahedron) that is more compressible than the others. For this case, the crystal structure does not scale as it is compressed, in violation of the assumptions. Obviously, the theory cannot be used predictively for garnets. However, the well-constrained line relating calculations to experiment indicates that the garnet structure is amenable to systematic calculation of K_T from spectroscopy.

K_T of $CaGeO_3$ tetragonal garnet falls on the same line as the cubic silicate garnets. The tetragonal structure has only 18% inactive modes, but the incomplete powder data result in a Brout sum that is less well constrained than that of cubic garnets with a larger number of inactive modes. The similar behavior of the cubic and tetragonal garnets and the good agreement obtained for the ilmenite structure suggests that elastic properties of other N-atom noncubic solids with volume depending on more than one interatomic distance can be modelled by Brout sums, although relation between experimental and calculated bulk modulus may be linear with a slope differing from unity.

The First Pressure Derivative of the Bulk Modulus at 1 atm

Agreement between experimentally determined K'_0 and those calculated from the pressure derivatives of the vibrational frequencies (18) is generally good. Evaluation of (18) at this time is limited because a large data base on frequencies as a function of pressure does not now exist and because the studies made in the 1970s are suspect due to early pressure calibrations being less reliable than today's ruby fluorescence technique. In addition, it is an experimental fact that almost all K'_0 experimental values cluster near 4 (Figure 4), so that a wide range of values is not available to test (18). Nevertheless, for 11 of the 12 substances having measured γ_i, the experimental and predicted K'_0 are equivalent, considering the experimental uncertainty (Figure 4). The average difference is 8%, such that the largest discrepancies occur for the close packed CsBr and BaF_2. Pressures in spectroscopic studies of these solids were not determined with the ruby fluorescence technique.

The ability of the theory to reproduce experimental K'_0 does not appear to depend strongly on the number of modes

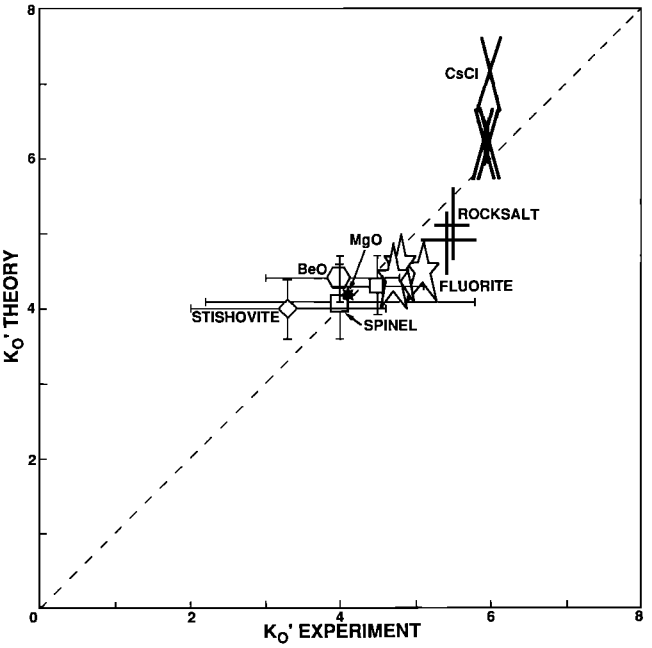

Fig. 4. Correlation of the first pressure derivative of the bulk modulus predicted from measured mode Grüneisen parameters with that determined compression experiments (18). Symbols are described in Figure 2, except that MgO is indicated by a solid, eight-point star. The theoretical K'_0 for the fluorite and CsCl structures is uncertain because pressure calibrations have been revised since these early diamond anvil cell studies.

observed under pressure, in that equally good agreement is obtained for γ-Fe_2SiO_4 for which 25% of the modes were measured, as compared to Al_2MgO_4 and to the B1, B2, fluorite, wurtzite, and rutile structures for which more than 75% of the modes were measured at pressure. The sparcity of data has a minor effect because, in general, the values of the mode Grüneisen parameters for a given structure commonly usually do not vary widely [*Ferraro et al.*, 1971; *Nicol et al.*, 1972; *Shawyer and Sherman*, 1982; *Ferraro*, 1984; *Hofmeister et al.*, 1986*a,b*; *Hemley*, 1987; *Hofmeister*, 1987*b*; *Jephcoat et al.*, 1988; *Hofmeister et al.*, 1989; *Chopelas*, 1990*a,b*; *Chopelas and Hofmeister*, 1991; *Hofmeister*, unpublished data, 1990]. Generally, data are available on the highest-frequency modes. Because of the square of the frequency in the sum, these are much more important in calculating K'_0 than the low-frequency modes. The mode Grüneisen parameters for the highest-energy bands vary the least in magnitude, because these bands are typically associated with the most tightly bonded and least compressible unit in the structure. The lower energy bands have more variable mode gammas, in line with their assignments as translations and rotations, but their contribution to the sum is small. For example, the B_{1g} mode in compounds with the rutile structure has a negative γ_i, but because this is one of the two lowest energy modes in the structure, its affect on the sum is slight. For the spinels in particular, the good agreement of theory with experimental K'_0 is due to the fact that the IR bands have a high or low mode Grüneisen parameter depending on whether the band is due to the tetrahedral or octahedral cation [*Hofmeister et al.*, 1986a, *A. M. Hofmeister*, unpublished data, 1990]. Hence the band assignments and FGA [*Fateley et al.*, 1971] allow accurate extrapolation of the IR pressure derivatives to the unmeasured modes.

For the CsCl and fluorite structures, the spectroscopic measurements were limited to 50 kbar, and the pressure calibration has been improved since these studies were made. Therefore, it is possible that the discrepancy between experiment and (18) for K'_0 will decrease from 8% current difference, once vibrational spectra are taken over a wider range of pressure using the ruby calibration.

For MgO, agreement is excellent between experiment and calculation. Note that both K'_0 and γ_i are well constrained by ultrasonic [*Jackson and Neisler*, 1982] and Raman [*Chopelas*, 1990*a*] measurements at high pressure. The same holds for the spinel Al_2MgO_4. For both of these compounds, the pressure derivatives are predicted with higher precision that K_T.

Rutile structures tend to have large values for K'_0 (5.5-7.0, Table 4). Stishovite (SiO_2) is apparently an exception, in that Brillouin scattering [*Weidner et al.*, 1982] along with volume measurements [*Ross et al.*, 1990] yield a low value of ~2.8. The large error is due to the relative incompressibility of this substance (K_T is 306 GPa). The relatively low experimental value [see also *Kuzio*, 1977; *Sato*, 1977] is corroborated by the prediction of 4.0 for K'_0 from vibrational spectroscopy as a function of pressure. Data on compounds with the rutile structure other than stishovite are not included because only their Raman bands were measured under pressure, the pressure range was small, and its calibrations may not be accurate.

For the remaining oxide, hexagonal BeO, almost all the active modes have been measured as a function of pressure [*Jephcoat et al.*, 1988]. The higher-energy modes all have γ_{io} of about 1.6, despite a large range in frequency. One inactive modes is expected to behave as the higher energy stretching ν_3 mode, whereas the other should act as the bending ν_4 mode. Hence, γ_{io} of the inactive modes are well-constrained, whereas their frequencies are not, leading to close correspondence for K'_0 but with a larger uncertainty in K_T.

The overall good correspondence between experiment and theory suggests that spectroscopy at pressure is a valid means to determine K'_0 in lieu of ultrasonic measurements under pressure or a combination of compression experiments and 1 atm elasticity measurements.

The Second Pressure Derivative of the Bulk Modulus at 1 atm

Experimental determinations of K''_0 are scarce because this quantity is related to the third pressure derivative of the volume, and because most minerals are relatively incompressible. Reliable data exist for a few soft substances: NaCl [*Chbabildas and Ruoff*, 1976; *Spetzler et al.*, 1972], MgO [*Jackson and Niesler*, 1982], and CsX [*Barsch and Chang*, 1971]. All compounds have small primitive unit cells. Within the experimental uncertainty (except for CsI), the spectroscopic value equals that derived from compression experiments (Table 6). The correct sign is predicted for all substances. For MgO, both experimental and calculated K''_0 bracket zero, so its sign is indeterminant. Use of the different equations of state in the comparison have a very minor effect on K''_0, compared to the experimental uncertainties, for $4 < K'_0 < 6$, as is the case here [see *Jeanloz*, 1988; *Hofmeister*, in press]. As shown in Table 6, K''_0 is subject to large uncertainties. However, these values are needed to obtain the correct curvature of volume with pressure at large compressions.

All solids with measured K''_0 have values that correlate inversely with K_0 as implicated by (27).

Comparison of Accuracy With Other Models for Bulk Modulus and Its Pressure Derivatives

Bulk moduli have also been predicted from models of interatomic potentials. Recent calculations for the structures investigated in this paper, on average, are accurate within 10% for both K_T and K' (Table 6). Insufficient calculations exist to infer accuracies for K''. The accuracy does not differ significantly between models which assume rigid ions and those which do not. The average accuracy for the current model is 10% for K_T and 7% for K'. For K'', predictions lie within the experimental uncertainties of measured quantities. Thus, the accuracy of predicting bulk modulus and its pressure derivatives from vibrational spectroscopy is as good or better than that achieved through modelling the interatomic potentials, for the cubic structures or stuctures with one interatomic distance. The current model is significantly better at predicting bulk modulus and its pressure derivatives for structures with large unit cells and well-constrained vibrational frequencies than are computations involving interatomic potentials. For any given structure, the current model is highly accurate (within a few percent), if analogues are available to constrain the slope of calculated versus experimental K_T. The greatest advantage of the current model is its ease of use, whereas the complicated computational models of interatomic potentials have the distinct advantage of predicting important quantities such as the temperature dependence of the volume, which the current extension of Brout's theory cannot.

CONCLUSIONS

From four assumptions: the existence of (1) only electrostatic forces between like atoms, (2) pair-wise central repulsive potentials, (3) rigid ions, and (4) scaling of the crystal structure during compression, formulas were derived relating the bulk modulus to vibrational frequencies and structural quantities for both N-atom cubic solids and solids that can be approximately modeled by one nearest-neighbor distance (13) and (32). For the same solids, the first and second pressure derivatives of the bulk modulus were shown to relate to those of vibrational frequencies and moreover to be independent of the mineral structure (18) and (27).

Agreement for K_T is structually dependent, and is good to excellent for structures with large primitive unit cells (rutile, corundum, ilmenite, and spinel). This correlation is associated with adherence to assumption 1 above: short-range repulsive forces are negligible for like atoms separated by space and by other atoms. For these minerals, the theoretical values are generally within a few percent of K_T, which is the magnitude of the sum of the zero point and thermal corrections. Large primitive unit cells are correlated with large number of modes. Consequently, (1) for minerals with many modes, dependence of frequency on wave vector (a symptom of violation of the assumptions) should average out, similar to results with *Kieffer's* [1979] thermodynamic theory, (2) as the number of modes increases, the contribution of the acoustic branches to the sum at nonzero **k** becomes vanishingly small so that the optic modes essentially contain all information (i.e. $\Sigma\nu_i^2(\mathbf{k}) = \Sigma\nu_i^2(0)$), (3) the uncertainty in each individual frequency becomes smaller and smaller in proportion to the sum, and (4) the LO-TO splittings are relatively small. The accuracy is further improved for minerals having a large number of modes within a relatively small frequency range.

The linear relationship between calculated and experimental

TABLE 6. Second Pressure Derivative of the Bulk Modulus

	Experiment				Theory			
Formula	K''_0*	K_T*	K'_0	References	K''_0	K_T*	K'_0	Reference
NaCl	-0.35±0.005	23.81	5.68	a	-0.26±0.27	20	5.1	this work
"	-0.24±0.005	23.81	5.65	b		32	5	j (SSMEG)
"	-1.5 ±1.5	23.78	5.98	c		24.6		j (rigid ion)
CsCl	-0.42±0.40	16.74	5.98	d	-0.26±0.3	15.4	6.2	this work
CsBr	-0.50±0.04	14.34	5.95	d	-0.32±0.3	13.7	7.1	this work
CsI	-0.73±0.08	11.89	5.93	d	-0.18±0.3	10.3	6.3	this work
MgO	-0.03±0.03	160.3	4.1	e	0.00±0.02	126	4.2	this work
					-0.026	180	4.15	k (PIB)
						139	4.18	l (PIB)
						177		m (VSMEG)
						185		m (CSMEG)
Al_2MgO_4	<-0.009	195	4.5	f	-0.01±0.02	210	4.4	this work
BeO		220	4	g	-0.02±0.02	186	4.4	this work
						186	3.86	n (PIB)
Al_2O_3		252	4.3	h		248		this work
						262	3.79	o (PIB)
SiO_2		306	3.3	i	-0.004±0.01	312	3.9	this work
						411	3.73	o (PIB)

*K''_0 in $kbar^{-1}$; K_T in kbar. All values were measured at room temperature. a, Chbabildas and Ruoff [1976], Birch-Murnghan equation of state; b, *Chbabildas and Ruoff* [1976], Grover-Getting-Kennedy equations of state; c, *Chbabildas and Ruoff* [1976], Keane equation of state; d,*Barsch and Chang* [1971], Keane's equation of state; e, *Jackson and Nieiser* [1982], second-order Murnaghan equation of state; f, *Hilbert and Graham* [1989]; g, *Hazen and Finger* [1986] and *Cline et al.* [1967]; h, *Gieske and Barsch* [1968] and *d'Amour et al.* [1978]; i, *Weidner et al.* [1982] and *Kuzio* [1977]; j, *Hemley and Gordon* [1985]; k, *Isaak et al.* [1990];, l, *Mehl et al.* [1986]; m, *Wolf and Bukowinski* [1988]; n, *Jephcoat et al.* [1988]; o, *Cohen* [1987].

$K_T(0)$ for the compounds that the theory does not predict well (B1, B2, fluorite, wurtzite, perovskite, and garnet) suggests that the theory is useable for systematics for a wide range of minerals that do not rigorously fit the requirements. The first four structures have small primitive unit cells which place like atoms as second-nearest neighbors, which is highly likely to violate assumption 1, above. Both garnet and perovskite have a large proportion (>20%) of inactive modes and modes distributed over a large range of frequency. Perovskite also has broad LO-TO splittings and a small number of peaks. These factors make precise determination of the Brout sum difficult, although the relative values for a given structure should be correct.

The existence of linear relationships between K_T and vibrational properties can be used to explain why correlations of elastic properties with volume or mean atomic mass are weak. Dependence of vibrations on atomic masses, interatomic distances, and volume is complicated. Direct relationships exist for the simplest structures, but, on average, the frequencies follow the mass or volume. Hence the correlation of bulk modulus with the sum of the frequencies for some substances can be reduced to more tenuous relationships with structure and mass.

Most silicates and germates were found to be highly amenable to this treatment, in accord with their vibrational spectra being reasonably well approximated by internal motions of SiO_4 and cation translations, or being constrained by trends of frequency with lattice parameters. Exceptions are the phases in Mg-Si-O, which are overestimated by the theory. The difference is ascribed to the variation in polyhedral compressibility, which leads to violation of assumption 4, above.

The degree to which assumption 3 is met (rigid ions) seems to be unimportant, as gauged by the slight effect polarizability has the accuracy of the calculations. The magnitude of like atom interactions (assumption 1), as determined by the structure and the degree of ionic bonding, is the most important factor affecting the accuracy of the calculations. Of slightly lesser importance is whether the structure scales with pressure. This assumption 4 is more stringent version of assumption 2: these appear to be identical, within the degree of accuracy achievable in the theory. The assumptions behind the theory are not identical but are no more restrictive than those required for calculations of atomic potentials currently used to model minerals of geophysical interest.

The limitations of the theory for predicting the derivatives appear to be less restrictive than those needed to predict K_T. The utility of the model is limited by mainly by the availability of accurate and complete spectroscopic data, both at 1 atm and at pressure.

For 12 of the 13 substances having measured γ_i, the experimental and predicted K'_0 are equivalent, considering the experimental uncertainty. The average difference for all 13 is 8%, such that the largest discrepancies occur for compounds with poorly established mode Grüneisen parameters. No difference was observed in the accuracy of the calculation between the large and small primitive unit cell structures. Agreement between experimental K'_0 and those predicted from vibrational spectra at high pressure (32) is good for all five solids with the proper symmetry for which data are available. All substances had the B1 or B2 structure.

The independence of the equations for the derivatives of the bulk modulus from structural factors suggest that equations (18)

and (32) may be pertinent to other minerals. This inference is supported by the accuracy of the ilmenite result and that the tetragonal garnet falls on the same trend as the cubic garnet. Neither of these structures adhere to the symmetry requirements, although both are derivatives of those that do. It is highly likely that the symmetry limitations can be removed for K'_0 and K''_0. Likely candidates are noncubic perovskites, which universally are slightly distorted from cubic symmetry, and which have all bands active, unlike cubic perovskites, and the modified spinel structure.

APPENDIX: DERIVATION OF GEOMETRICAL FACTORS RELATING INTERATOMIC POTENTIALS FOR SELECT SOLIDS

Solids containing more than one type of atom must be described by multiple interatomic potentials. Stability of the solid requires that the net force on a given atom be zero; thus, the potentials are related by the balance of the forces about the anions (oxygen in all cases considered here). This assumption of pair-wise additive potentials is commonly used in theoretical modelling of minerals [e.g. *Wall and Price*, 1988; *Wolf and Bukowinski*, 1987; *Hemley and Gordon*, 1985; *Prossner and Graham*, 1984; *Hemley et al.*, 1987]. The geometries of the oxygens in the structures considered here are idealized in order to derive formulas generally valid for structural types, rather than for individual mineral chemistries. The slight departures of the actual structures from the ideal of a few percent adds insignificant errors to the calculation, considering that Brout sum $\Sigma\nu_i^2(k)$ often contains uncertainties of about 5%. It is the uncertainty in the sum that limits the useful prediction of K_T from vibrational spectra.

Spinel AB_2O_4

The oxygen in the spinel structure is tetrahedrally coordinated (Figure 1). The height from the base defined by the three B atoms to the oxygen is ideally

$$z = \frac{1}{3} r_B = r_B \cos\theta \tag{A1}$$

where X is the oxygen to B-cation distance. Balancing the forces in the z direction requires

$$-\left.\frac{\partial\Phi_A}{\partial r}\right|_{r_A} = -3\left.\frac{\partial\Phi_B}{\partial r}\right|_{r_B}\cos\theta = \left.\frac{\partial\Phi_B}{\partial r}\right|_{r_B}. \tag{A2}$$

If the repulsive potentials are of the commonly assumed form

$$\Phi = \frac{C}{r^x}, \tag{A3}$$

where C and X can vary for the different types of atom, then

$$r_A\left.\frac{\partial^2\Phi_A}{\partial r^2}\right|_{r_A} = r_B\left.\frac{\partial^2\Phi_B}{\partial r^2}\right|_{r_B}. \tag{A4}$$

Substitution of (A-4) into equations (29) and (32) leads to equations (30) and (33) with the coefficients listed in Table 1.

Cubic Perovskite BAO_3

The idealized octahedral coordination of the oxygen (Figure 1) does not suggest a unique way to balance the forces. Therefore, as a first approximation we assume the simplest case possible, a spherical potential about the oxygen atom, i.e.,

$$\left.\frac{\partial\Phi_1}{\partial r}\right|_{r_1} = \left.\frac{\partial\Phi_2}{\partial r}\right|_{r_2} = \Phi'_2. \tag{A5}$$

This and (A-3) lead to the coefficient in Table 1 for use in (34). This oversimplification is likely to be incorrect for perovskite, but more realistic constraints are not called for until vibrational data for the triply degenerate inactive band is available.

Garnet $C_3B_2A_3O_{12}$

For this example, the departure of the oxygen tetrahedron from the ideal is sufficient to warrant accounting for. From Figure 1, balancing forces requires that

$$\Phi_1' = \Phi_2'\cos(180\text{-}132) + \Phi_3'\cos(180\text{-}95) + \Phi_3'\cos(180\text{-}122), \tag{A6}$$

Algebraic manipulations and use of (A3) result in

$$\Phi_2'' = 0.89\,\frac{r_1}{r_2}\Phi_1'' \tag{A7}$$

and

$$\Phi_3'' = 0.65\,\frac{r_1}{r_3}\Phi_1''. \tag{A8}$$

Substitution of (A7) and (A8) into equations (29) and (32) leads to the coefficients listed in Table 1. For garnets like $CaGeO_3$, the B site contains equal amounts of the Ca and Ge atoms, which leads to the modification given in Table 1.

Ilmenite BAO_3

Although ilmenite is not cubic, it is included in this analysis because its structure is derived from corundum structure, which contains one interatomic distance. The oxygen in ilmenite is tetrahedrally coordinated (Figure 1). Balancing the forces requires that

$$\left.\frac{\partial\Phi_1}{\partial r}\right|_{r_1} = \left.\frac{\partial\Phi_2}{\partial r}\right|_{r_2}. \tag{A9}$$

Substitution of (A-3) and (A-9) into (29) and (32) gives the coefficients listed in Table 1.

Acknowledgments. Support was provided by the Carnegie Institution of Washington, NSF grants EAR-8419984 and 8816531, and a Fellowship in Science and Engineering from the David and Lucile Packard Foundation. I thank A. Chopelas, R. J. Hemley, A. P. Jephcoat, and N. L. Ross for providing data in advance of publication; B. McAloon for computer programing; O. L. Andersen and R. E. Criss for advice; L. W. Finger, R. M. Hazen, R. J. Hemley, C. W. Prewitt, G. H. Wolf, and two anonymous reviewers for critical reviews or discussions. This paper is dedicated to my mother, Dee Hofmeister. Geophysical Laboratory, Carnegie Institution of Washington contribution 2117.

REFERENCES

Abrahams, S. C., and J. L. Bernstein, Remeasurement of the structure of hexagonal ZnO, *Acta Crystallogr., Sect. B, 25*, 1233-1236, 1969.

Akaogi, M., N. L. Ross, P. McMillan, and A. Navrotsky, The Mg_2SiO_4 polymorphs (olivine, modified spinel and spinel)-thermodynamic properties from oxide melt solution calorimetry, phase relations, and models of lattice vibrations, *Am. Mineral., 69*, 499-512, 1984.

Aleksandrov, K. S., L. M. Reshchikova, and B. V. Beznosikov, Behavior of the elastic constants of $KMnF_3$ single crystals near athe transtion of puckering, *Phys. Status. Solidi A, 15*, K177-K179, 1966.

Aleksandrov, K. S., L. A. Shabanova, and V. I. Zineko, Elastic constants of MgF_2 single crystals, *Phys. Stat. Solidi, 33*, K1-K11, 1969.

Aleksiejuk, M. and D. Kraska, Elastic properties of potassium cobalt (II) trifluoride ($KCoF_3$). *Phys. Status Solidi, 31*, K65, 1975.

Alterovitz, S., and D. Gerlich, Third order elastic moduli of strontium fluoride, *Phys. Rev. B Solid State, 1*, 2718-2723, 1970.

Angel, R. J., L. W. Finger, R. M. Hazen, M. Kanzaki, D. J. Weidner, R. C. Liebermann, and D. R. Veblen, Structure and twinning of single-crystal $MgSiO_3$ garnet synthesized at 17 GPa and 1800°C, *Am. Mineral., 74*, 509-512, 1989.

Arguello, C. A., D. L. Rousseau, and S. P. S. Porto, First-order Raman effect in wurtzite-type crystals, *Phys. Rev., 181*, 1351-1363, 1969.

Axe, J. D., Longwave latttice dynamics of the fluorite structure, *Phys. Rev. A Gen. Phys., 139*, 1215-1220, 1965.

Baran, E. J., and I. L. Botto, Die ir-spektren einiger doppeloxide mit ilmenite-struktur, *Z. Anorg. Allg. Chem., 444*, 282-288, 1978.

Baran, E. J., and I. L. Botto, Die Raman spektren von $ZnTiO_3$ und $CdTiO_3$, *Z. Anorg. Allg. Chem., 448*, 188-192, 1979.

Baran, E. J., I. L. Botto, F. Muto, N. Kumada, and N. Kinomura, Vibrational spectra of the ilmenite modifications of $LiNbO_3$ and $NaNbO_3$, *J. Mater. Sci. Lett., 5*, 671-672, 1986.

Barker, A. S., Infrared lattice vibrations and dielectric dispersion in corundum, *Phys. Rev., 132*, 1474-1481, 1963.

Barsch, G. R., and Z. P. Chang, Ultrasonic and static equation of state for Cesium halides, in *Accurate Characterization of the High Pressure Environment*, edited by E. C. Lloyd, NBS Spec. Pub. 326, 173-187, 1971.

Bass, J. D., Elasticity of uvarovite and andradite garnets, *J. Geophys. Res., 91*, 7505-7516, 1986.

Bass, J. D., Elasticity of grossular and spessartite garnets by Brillouin spectroscopy, *J. Geophys. Res. 94*, 7621-7628, 1989.

Bass, J. D., R. C. Liebermann, D. J. Weidner, and S. J. Finch, Elastic properties from acoustic and volume compression experiments, *Phys. Earth Planet. Inter., 25*, 140-158, 1981.

Barker, A. S., Transverse and longitudinal optic mode study in MgF_2 and ZnF_2, *Phys. Rev, 136*, 1290-1291, 1964

Beattie, A. G., and G. A. Samara, Pressure dependence of the elastic constants of $SrTiO_3$, *J. Appl. Phys., 42*, 2376, 1971.

Beattie, I. R., and T. R. Gilson, The single-crystal Raman spectra of nearly opaque materials. Iron (III) oxide and chromium (III) oxide, *J. Chem. Soc. Ser. A, 1970*, 980-986, 1970.

Bell, R. O., and G. Rupprecht, Elastic constants of strontuim titanate, *Phys. Rev., 129*, 90-94, 1963.

Bensch, W. A., Third order elastic constants of NaF, *Phys. Rev. B Solid State, 6*, 1504, 1972.

Bialas, H., and H. J. Stolz, Lattice dynamics of corundum, *Z. Phys. B, 21*, 319-324, 1975.

Blackman, M., Sum rule for lattice vibrations in diatomic solids, *Proc. R. Soc., London, Ser. A, 181*, 58, 1942.

Bonzcar, L. J., E. K. Graham, and H. Wang, The pressure and temperature dependence of the elastic constants of pyrope garnet, *J. Geophys. Res., 10*, 6360, 1972.

Born, M., and K. Huang, *Dynamical Theory of Crystal Lattices*, Oxford University Press, New York, 1954.

Briells, J., and D. Vidal, Variation des constantes elastiques de la fluorine CaF_2 avec la pression jusqu'a 12 kbar., *High Temp.High Pressures., 7*, 29-33, 1975.

Brout, R., Sum rule for lattice vibrations in ionic crystals, *Phys. Rev., 113*, 43-44, 1959.

Burns, G., *Solid State Physics*, pp. 450-487, Academic Press, San Diego, Calif., 1985.

Chang, E., and E. K. Graham, The elastic constants of cassiterite SnO_2 and their pressure and temperature dependence, *J. Geophys. Res., 80*, 2595-2599, 1975.

Chang, Z. P., and G. R. Barsch, Pressure dependence of singel-crystal elastic constants and anharmonic properties of spinel, *J. Geophys. Res., 78*, 2418-2433, 1973.

Chbabildas, L. C., and A. L. Ruoff, Isothermal equation of state for sodium chloride by the length-change-measurement technique, *J. Appl. Phys., 47*, 4182-4187, 1976.

Chopelas, A., Thermal Expansion, Heat Capacity, and Entropy of MgO at Mantle Pressures, *Phys. Chem. Miner., 17*, 142-148, 1990*a*.

Chopelas, A., Thermal properties of forsterite at mantle pressures derived from vibrational spectroscopy, *Phys. Chem. Minerals, 17*, 149-156, 1990*b*.

Chopelas, A., and A. M. Hofmeister, Vibrational spectroscopy of $MgAl_2O_4$ as a function of pressure, *Phys. Chem. Miner.*, in press, 1991.

Clendenen, R. L., and H. G. Drickamer, Lattice parameters of nine oxides and sulfides as a function of pressure, *J. Chem. Phys., 44*, 4223-4228, 1966.

Cline, C. F., H. L. Dunegan, and G. W. Henderson, Elastic constants of hexagonal BeO, ZnS, and CdSe, *J. Appl. Phys., 38*, 1944-1948, 1967.

Cnkalova, V. V., V. S. Bondarenlo, G. O. Fobina, and F. S. Stazlevskaya, Temperature dependence of the dielectric, piezoelectric, and elastic properties of lithium niobate crystals, *Izv. Akad. Nauk. SSSR, Ser. Fiz., 35*, 1886-1889, 1971.

Cohen, R. E., Calculation of elasticity and high pressure instabilites in corundum and stishovite with the potential induced breathing model, *Geophys. Res. Lett., 14*, 37-40, 1987.

d'Amour, H., D. Schiferl, W. Denner, H. Schulz, and W. B. Holzapfel, High-pressure single-crystal structure determinations for ruby up to 90 kbar using an automatic diffractometer, *J. Appl. Phys., 49*, 4411-4416, 1978.

Eagles, D. M., Infrared spectrum of rutile TiO_2, *J. Phys. Chem. Solids, 25*, 1243, 1964.

Fateley, W. G., N. T. McDevitt , and F. F. Bently, Infrared and Raman selection rules for lattice vibrations: The correlation method, *Appl. Spectrosc., 25*, 155-174, 1971.

Ferraro, J. R., *Vibrational Spectroscopy at High Internal Pressures: The Diamond Anvil Cell*, Academic Press, Orlando, Florida, 1984.

Ferraro, J. R., H. Horan, and A. Quattrochi, Pressure dependence of the infrared-active optical phonon modes in alkaline-earth fluorides, *J. Chem. Phys., 55*, 664-666, 1971.

Finger, L. W., R. M. Hazen, and T. Yagi, Crystal structures and electron densities of nickel and iron silicate spinels at elevated temperature or pressure, *Am. Mineral., 64*, 1002-1009, 1979.

Finger, L. W., R. M. Hazen, and A. M. Hofmeister, High-pressure crystal chemistry of spinel ($MgAl_2O_4$) and magnetite (Fe_3O_4): Comparisons with silicate spinels, *Phys. Chem. Miner., 13*, 215-220., 1986.

Gesland, J. Y., M. Binois, and J. Nouet, Constantes elastiques de la fluoperovskite $KZnF_3$, *C. R. Acad. Sci., Ser. B, 275*, 551-559, 1972.

Gieske, J. H., and G. R. Barsch, Pressure dependence of the elastic constants of single-crystalline aluminum oxide, *Phys. Status Solidi, 29*, 121-131, 1968.

Grimsditch, M. H., and A. K. Ramdas, Elastic and elasto-optic constants rutile from a Brillouin scattering study, *Phys. Rev., 14*, 1670-1682, 1976.

Guyot, F., H. Boyer, M. Madon, B. Velde, and J. P. Poirier, Comparison of the Raman microprobe spectra of $(Mg,Fe)_2SiO_4$ and Mg_2GeO_4 with olivine and spinel structures, *Phys. Chem. Miner., 13*, 91-95, 1986.

Halleck, P. M., *The Compression and Compressibility of Grossular Garnet: a Comparison of X-ray and Ultrasonic Methods.*, University of Chicago, Chicago, Ill., 1973.

Hankey, R. E., and D. E. Schuele, Third order elastic constants of Al_2O_3, *J. Acoust. Soc. Am., 48*, 190-202, 1970.

Hara, Y., and M. Nicol, Raman spectra and structure of rutile at high pressure, *Phys. Stat. Solidi B, 94*, 317-322, 1979.

Hart, S., The elastic constants of rutile structure fluoride, *S. Afr. J. Phys., 1*, 65-69, 1978.

Hazen, R. M., and L. W. Finger, Bulk modulus-volume relationship for cation-anion polyhedra, *J. Geophys. Res., 84*, 6723-6728, 1979.

Hazen, R. M., and L. W. Finger, High-pressure and high-temperature crystal chemistry of beryllium oxide, *J. Appl. Phys., 59*, 3728-3733, 1986.

Hemley, R. J., Pressure dependence of Raman spectra of SiO_2 polymorphs: α-quartz, coesite, and stishovite, in *High Pressure Research in Mineral Physics*, edited by M. H. Manghani, and Y. Syono, pp. 347-360, Terra Scientific, Tokyo, 1987.

Hemley, R. J., and R. G. Gordon, Theoretical study of solid NaF and NaCl at high pressures and temperatures, *J. Geoph. Res., 90*, 7803-7813, 1985.

Hemley, R. J., H. K. Mao, and E. C. T. Chao, Raman spectrum of natural and synthetic stishovite, *Phys. Chem. Miner., 13*, 285-290, 1986.

Hemley, R. J., M. D. Jackson, and R. G. Gordon, Theoretical study of the structure, lattice dynamics, and equations of state of perovskite-type $MgSiO_3$ and $CaSiO_3$, *Phys. Chem. Miner., 14*, 2-12, 1987.

Hilbert, E. G., and E. K. Graham, Elastic properties of stoichiometric $MgAl_2O_4$ spinel, *EOS Trans AGU, 70*, 1368, 1989,

Hill, R. J., M. D. Newton, and G. V. Gibbs, A chemical study of stishovite, *J. Solid State Chem., 47*, 185-200, 1983.

Hofmeister, A. M., Thermodynamic properties of NaCl in the B1 and

B2 phases from far-infrared spectroscopy at high pressure., *EOS Trans. AGU 68*, 433, 1987*a*.

Hofmeister, A. M., Single-crystal absorption and reflection infrared spectroscopy of forsterite and fayalite, *Phys. Chem. Miner., 14*, 499-513, 1987b.

Hofmeister, A. M., and K. Billips, Comparison of Infrared Reflectance Spectra of Fluoride Perovskites, *Spectrochimica Acta Part A*, in press, 1991

Hofmeister, A. M., and A. Chopelas, Thermodynamic properties of pyrope and grossular from vibrational spectroscopy, *Am. Mineral.76*, 880-891, 1991*a*.

Hofmeister, A. M., and A. Chopelas, Vibrational spectroscopy of end-member silicate garnets., *Phys. Chem. Miner., 17*, 503-526, 1991*b*.

Hofmeister, A. M., and E. Ito, Thermodynamic Properties of $MgSiO_3$ Ilmenite from Vibrational Spectra, *Phys. Chem. Miner., 17*, in press, 1991

Hofmeister, A. M., H.-K. Mao, and P. M. Bell, Spectroscopic determination of thermodynamic properties of γ-Fe_2SiO_4 at mantle pressures., *EOS Trans. AGU, 67*, 395, 1986a.

Hofmeister, A. M., J. Xu, and S. Akimoto, Thermodynamic implications of infrared spectroscopy of stishovite at mantle pressures., *Abstracts and Programs*, p. 126, International Mineralogical Association, Stanford, Calif., 1986b.

Hofmeister, A. M., T. C. Hoering, and D. Virgo, Vibrational spectra of beryllium aluminosilicates: heat capacity calculations., *Phys. Chem. Miner., 14*, 205-224, 1987.

Hofmeister, A. M., J. Xu, H.-K. Mao, P. M. Bell, and T. C. Hoering, Thermodynamics of Fe-Mg olivines at mantle pressures: Mid- and far-infrared spectroscopy at high pressure., *Am. Miner., 74*, 281-306, 1989.

Hofmeister, A. M., J. Horigan, and J. A. Campbell, Infrared spectra of GeO_2 rutile: prediction of inactive modes and bulk moduli for rutile-types from vibrational spectra., *Am. Miner., 75*, 1238-1248, 1990a.

Hofmeister, A. M., J. Xu, and S. Akimoto, Infrared spectra of synthetic and natural stishovite, *Am. Miner., 75*, 951-955, 1990*b*.

Horiuchi, H., M. Hirano, E. Ito, and Y. Matsui, $MgSiO_3$ (ilmenite-type): Single crystal X-ray diffraction study, *Am. Mineral., 67*, 788-793, 1982.

Iishi, K., Lattice dynamics of forsterite, *Am. Mineral., 63*, 1198-1209, 1978.

Irvine, R. D., and F. D. Stacey, Pressure dependence of the thermal Grüneisen parameter, with application to the Earth's lower mantle and outer core, *Phys. Earth Planet. Inter., 11*, 157-165, 1975.

Isaak, D. G. and E. K. Graham, The elastic properties of an almandine-spessartine garnet and elasticity in garnet solid solutions series, *J. Geophys Res. 81*, 2483, 1976.

Isaak, D. G., O. L. Anderson, and T. Goto, Measured elastic moduli of single-crystal MgO up to 1800 K, *Phys. Chem. Miner., 16*, 704-713, 1989.

Isaak, D. G., R. E. Cohen, and M. J. Mehl, Calculated elastic and thermal properties of MgO at high pressures and temperatures, *J. Geophys. Res., 95*, 7055-7067, 1990.

Jackson, I., and H. Niesler, The elasticity of periclase to 3 GPa and some geophysical implications, in *High-Pressure Research: Applications in Geophysics*, edited by S. Akimoto and M. H. Manghani, pp. 93-113, Academic Press, San Diego, Calif., 1982.

Jackson, I., H. Niesler, and D. Weidner, Explicit correction of ultrasonically determined elastic wave velocities for transducer-bond phase shifts, *J. Geophys. Res., 86*, 3736-3748, 1981.

Jephcoat, A. P., R. J. Hemley, H.-K. Mao, R. E. Cohen, and M. J. Mehl, Raman spectroscopy and theoretical modeling of BeO at high pressure, *Phys. Rev. B Solid State,, 37*, 4727-4734, 1988.

Jones, L. E. A., High-temperature elasticity of rutile structure MgF_2, *Phys. Earth Planet. Inter., 13*, 105-118, 1971.

Jones, L. E. A., High temperature elastic behavior of the elastic moduli of LiF and NaF in comparison with MgO and CaO, *Phys. Chem. Mineral., 1*, 179-197, 1976.

Jones, L. E. A., high-temperature elasticity of the fluorite-structure compounds CaF_2, SrF_2, and BaF_2, *Phys. Earth Planet. Inter., 15*, 77-89, 1977.

Jones, L. E. A., Pressure and temperature dependence of the single-crystal elastic moduli of the cubic perovskite $KMgF_3$, *Phys. Chem. Miner., 4*, 23, 1979.

Kaiser, W., W. G. Spitzer, R. H. Kaiser, and L. E. Horworth, Infrared properties of CaF_2, SrF_2, and BaF_2., *Phys. Rev., 127*, 1950-1954, 1962.

Kappus, W., Lattice dynamics of sapphite (corundum), part 2, Calculations of phonon dispersion, *Z. Phys. B, 21*, 325-331, 1975.

Katiyar, R. S., P. Dawson, M. M. Hargreave, and G. R. Wilkinson, Dynamics of the rutile structure, III, Lattice dynamics, infrared and Raman spectra of SnO_2, *J. Phys. C Solid State Phys., 4*, 2421-2431, 1971.

Katiyar, R. S., and R. S. Krishnan, The vibrational spectrum of rutile, *Phys. Lett. A, 25*, 525-526, 1967.

Kieffer, S. W., Thermodynamics and lattice vibrations of minerals, 3, Lattice dynamics and an approximation for minerals with application to simple substances and framework silicates, *Rev. Geophys. Space Phys., 17*, 20-34, 1979.

Kieffer, S. W., Thermodynamics and lattice vibrations of minerals, 4, Application to chain and sheet silicates and orthosilicates, *Rev. Geophys. Space Phys., 18*, 862-886, 1980.

Kirfel, A., E. Hinze, and G. Will, The rhombohedral high pressure phase of $MgGeO_3$ (ilmenite): synthesis and single crystal analysis, *Z. Kristallogr., 148*, 305-317, 1978.

Kittel, C., *Introduction to Solid State Physics*, John Wiley and Sons, Inc., New York, 1971.

Kuzio, M. R., *A determination of the isothernal bulk moduli of stishovite and its first pressure derivative from static compression data*., Thesis, Penn. State Univ., University Park, Penn., 1977.

Lehner, N., H. Rauh, K. Strobel, R. Geick, G. Heger, J. Bouillot, B. Renker, M. Rousseau, and W. G. Sterling, Lattice dynamics, lattice instabilities, and phase transitions in fluoride perovskites. *J. Phys. C Solid State Phys.,15*, 6545-6564 (1982).

Leitner, B. J., D. J. Weidner, and R. C. Liebermann, Elasticity of single crystal pyrope and implication for garnet solid solutions series, *Phys. Earth Planet. Inter. 22*, 111, 1980.

Liebermann, R. C., Elasticity of the ilmenite-perovskite phase transformation in $CdTiO_3$, *Earth Planet. Sci. Lett., 29*, 326-332, 1976.

Liebermann, R. C., Elasticity of pyroxene-garnet and pyroxene-ilmenite phase transformations in germanates., *Phys. Earth Planet Inter., 8*, 361-374, 1974.

Liebermann, R. C., Elasticity of olivine, beta, and spinel polymorphs of germanates and silicates, *Geophys. J. R. Astron. Soc., 42*, 889-929, 1975.

Liebermann, R. C., and E. Schreiber, Elastic constants of polycrystalline hematite as a fuction of pressure to 3 kilobars, *J. Geophys. Res., 73*, 6585-6590, 1968.

Loh, E., Optical phonons in BeO crystals, *Phys. Rev., 166*, 673-678, 1967.

Manghnani, M. H., Elastic constants of single-crystal rutile under pressures to 7.5 kilobars, *J. Geophys. Res., 74*, 4317-4328, 1969.

Maradudin, A. A., E. W. Montroll, G. H. Weiss, and I. P. Patova, Theory of lattice dynamics in the harmonic approximation, in *Solid State Physics: Advances in Research and Applications*, edited by H. Ehrenreich et al., pp. 1-708, Academic Press, San Diego, Calif., 1971.

McMillan, P., and M. Akaogi, Raman spectra of β-Mg_2SiO_4 (modified spinel) and γ-Mg_2SiO_4 (spinel), *Am. Mineral., 72*, 361-364, 1987.

McMillan, P. F., and N. L. Ross, Heat capacity calculations for Al_2O_3 corundum and $MgSiO_3$ ilmenite, *Phys. Chem. Miner., 14*, 225-234, 1987.

Mehl, M. J., R. J. Hemley, and L. L. Boyer, Potential-induced breathing model for the leastic moduli and hihg-pressure behaviou of the cubic alkaline-earth oxides, *Phys. Rev. B Solid State, 23*, 900-923, 1986.

Mitra, S. S., Infrared and Raman spectra due to lattice vibrations, in *Optical Properites of Solids*, edited by S. Nudelman, and S. S. Mitra, p. 333-451, Plenum, New York, 1969.

Mitra, S. S., and R. Marshall, Trends in the characteristic phonon frequencies of the NaCl-, diamond-, zinc-blende-, and wurtzite-type crystals, *J. Chem. Phys., 41*, 3158-3164, 1964.

Naimon, E. R., and A. V. Granato, Third-order elastic constants of $RbMnF_3$, *Phys. Rev., B Solid State, 7*, 20912094, 1973.

Nakagawa, I., A. Tsuchida, and T. Shimanouchi, Infrared transmission spectrum and lattice vibrational analysis of some perovskite fluorides, *J. Chem. Phys, 44*, 982-989, 1967.

Nakagawa, I., Transverse and longitudinal lattice frequencies and interionic potential in some AMF_3 perovskite fluoride crystals, *Spectrochim. Acta Part A, 29*, 1451-1461,1973.

Nakagiri, N., H. Manghnani, Y. H. Kim, and L. G. Ming, Crystal Structure of MgF_2 and FeF_2 under high pressure, in *High-Pressure*

Research in Mineral Physics, edited by M. H. Manghnani and Y. Syono, pp. 281-287, Terra Scientific, Tokyo, 1987.

Nelson, C. J., J. M. Brown, and Y. Sato-Sorensen, Compression of γ-Ni_2SiO_4 nickle silicate spinel, *EOS Trans. AGU, 67*, 1239, 1986.

Nicol, M., J. R. Kessler, Y. Ebisuzaki, W. D. Ellenson, M. Fong, and C. S. Gratch, Raman spectra of high pressure phases of solids, *Dev. Appl. Spectrosc., 10*, 79-105, 1972.

Nouet, J., *Elasticity of Fluorite Perovskites*, Ph. D. Thesis, Paris IV Univ., 1973.

Novak, G. A., and G. V. Gibbs, The crystal chemistry of the silicate garnets, *Am. Miner., 56*, 791-825, 1971.

O'Neill, B., J. Bass, J. R. Smyth, and M. T. Vaughan, Elasticity of a grossular-pyrope-almandine garnet, *J. Geophys. Res., 94*, 17,819-17,824, 1989.

Ostheller, G. L., R. E. Schmunk, R. M. Brugger, and R. J. Kearny, Phonon dispersion relation of beryllium oxide, *Neutron Inelastic Scattering Proc. Symp., 1*, 315-324, 1968.

Pacalo, R. E., and E. K. Graham, Pressure and temperature dependence of the elastic properties of MnO, *EOS Trans. AGU, 67*, 1240, 1986.

Perry, C. H., Far infrared reflectance spectra and dieelectric dispersion of a variety of materials having the perovskite and related structures, *Jpn. J. Appl. Phys., 4, Suppl. 1*, 564-573, 1965.

Perry, C. H., and E. F. Young, Infrared studies of some perovskite fluorides, I, Fundamental lattice vibrations, *J. Appl. Phys., 38*, 4616-4628, 1967.

Porto, S. P. S., P. A. Fleury, and T. C. Damen, Raman spectra of TiO_2, MgF_2, ZnF_2, FeF_2, and MnF_2, *Phys. Rev., 154*, 522-526, 1967.

Porto, S. P. S., and R. S. Krishnan, Raman effect of corundum, *J. Chem. Phys., 47*, 1009-1012, 1967.

Preudhome, J., and P. Tarte, Infrared studies of spinels, IV, Normal spinels with a high-valency tetrahedral cation, *Spectrochim. Acta, Part A, 28*, 69-79, 1972.

Prewitt, C. T., and A. W. Sleight, Garnet-like structures of high-pressure cadmium germanate and calcium germanate., *Science, 163*, 386-387, 1969.

Prosser, R. M., and E. K. Graham, Elastic properties of the lower mantle inferred from rigid ion lattice models., *Phys. Earth Planet. Inter., 34*, 85-101, 1984.

Rai, C. S., and M. H. Manghani, Pressure and temperature dependence of elastic modulai of polycrystalline MgF_2, *J. Am. Ceram. Soc., 59*, 499-506, 1976.

Rajagopol, A. K., and Srinivasan, Lattice dynamics of perovskite-type $SrTiO_3$, *Phys. Chem. Solids, 23*, 633, 1962.

Reichlin, R. L., *The Crystal Chemistry of Orthogermanates*, M.Sc. Thesis, State Univ. N. Y. at Stony Brook, 1978.

Rimai, D. S., Elastic properties of ZnF_2 between 4.2 and 300 K, *Phys. Rev. B Solid State, 16*, 4069-4077, 1977.

Rosenstock, H. B., Sum rule for lattice vibrations: Application to forces in diamond structures, *Phys. Rev., 129*, 1959-1961, 1963.

Ross, N. L., M. Akaogi, A. Navrotsky, J.-I. Suzuki, and P. McMillan, Phase transitions amoung the $CaGeO_3$ polymorphs (wollastonite, garnet, and perovskite structures): studies by high-pressure synthesis, high-temperature calorimetry, and vibrational spectroscopy and calculation, *J. Geophys. Res., 91* , 4685-4696, 1986.

Ross, N. L., and A. Navrotsky, Study of the $MgGeO_3$ polymorphs (orthopyroxene, clinopyroxene and ilmenite structures) by calorimetry, spectroscopy and phase equilibria, *Am. Miner., 73*, 1355-1365, 1988.

Ross, N. L., and A. Navrotsky, The Mg_2GeO_4 olivine-spinel transition, *Phys. Chem. Mineral., 14*, 473-481, 1987.

Ross, N. L., J. F. Shu, R. M. Hazen, and T. Gasparik, High pressure crystal chemistry of stishovite, *Amer. Mineral., 75*, 739-747., 1990.

Sasaki, S., C. T. Prewitt, Y. Sato, and E. Ito, Singel-crystal x-ray study of γ-Mg_2SiO_4, *J. Geophys. Res., 87*, 7829-7832, 1982.

Sato, Y., Equation of state of mantle mineral determined through high-pressure x-ray study., in *High-Pressure Research: Applications in Geophysics*, edited by M. H. Manghani, and S. Akimoto, pp. 307-323, Academic Press, San Diego, Calif., 1977.

Sato, Y., and S. Akimoto, Hydrostatic compression of four corundum-type compounds: α-Al_2O_3, V_2O_3, Cr_2O_3, and α-Fe_2O_3, *J. Appl. Phys., 50*, 5285-5291, 1979.

Sato, Y., E. Ito, and S. Akimoto, Hydrostatic compression of ilmenite phase of $ZnSiO_3$ and $MgGeO_3$, *Phys. Chem. Miner., 2*, 171-176, 1977.

Scott, J. F., Raman spectrum of SnO_2, *J. Chem. Phys., 53*, 852-853, 1970.

Sema, C. J., J. L. Rendon, and J. E. Iglesias, Infrared surface modes in corundum-type microcrystalline oxides, *Spectrochim. Acta, 38*, 797-802, 1982.

Sharma, S. K., D. Virgo, and I. Kushiro, Relationship between density, viscosity and structure of GeO_2 melts at low and high pressures, *J. NonCrystall. Solids, 33*, 235-248, 1979.

Shawyer, M. S., and W. F. Sherman, The pressure dependence of alkali halide TO mode frequencies, *Mod. Phys., 22*, 23-29, 1982.

Smith, R. T., and F. S. Welsh, Temperature dependence of the elastic, piezoelectric, and dielectric constants of lithium tantalate and lithium niobale, *Appl. Phys., 12*, 2219, 1971.

Soga, N., Elastic constants of garnet under pressure and temperature, *J. Geophys. Res., 72*, 4227-4234, 1967.

Spetzler, H., C. G. Sammis, and R. J. O'Connell, Equation of state of NaCl: Ultrasonic measurements to 8 kbar and 800°C and static lattice theory, *J. Phys. Chem. Solids, 33*, 1727-1750, 1972.

Spitzer, W. G., R. C. Miller, A. Kleinman, and L. E. Howarth, Far infrared dielectric dispersion in $BaTiO_3$, $SrTiO_3$, and TiO_2, *Phys. Rev., 126*, 1710-1721, 1962.

Srivanstan, R., M. V. Leuer, L. L. Chase, and W. E. Bron, Raman frequencies of fluorite crystals, *Phys. Lett. A, 36*, 333-334, 1971.

Striefler, M. E., and G. R. Barsch, Elastic and optical properties of stishovite, *J. Geophys. Res., 81*, 2453-2466, 1976.

Sumino, Y., and O. L. Anderson, Elastic constants of minerals, in *CRC Handbook of the Physical Properties of Rocks*, edited by S. Carmichael, pp. 139-280, CRC Press, Boca Raton, Fl., 1984.

Sumino, Y., M. Kumazawa, O. Nishizawa , and W. Pluschkell, The elastic constants of single crystal $Fe_{1-x}O$, MnO and CoO and the elasticity of stoichiometric magnesiowustite, *J. Phys. Earth, 28*, 475-495, 1976.

Summit, R., Infrared absorption of single-crystal stannic oxide: Optical lattice-vibration modes, *J. Appl. Phys., 39*, 3762-3767, 1968.

Tessman, J. R., A. H. Kahn, and W. Shockley, Electronic polarizabilities of ions in crystals, *Phys. Rev., 92*, 890-895, 1953.

Thompson, P., and N. W. Grimes, Observation of low energy phonons in spinel, *Solid State Commun., 25*, 609-611, 1978.

Tokarev, E. F., I. B. Kobyakov, I. P. Kuzmina, A. N. Lobachev, and G. S. Pado, Elastic, dielectric, and piezoelectric properties of zincite in the 4.2-800 temperature range, *Sov. Phys. Solid State, 17*, 629, 1975.

Traylor, J. G., H. G. Smith, R. M. Nicklow, and M. W. Wilkinson, Lattice dynamics of rutile, *Phys. Rev. B, 10*, 3457-3472, 1971.

Turrell, G., *Infrared and Raman Spectra of Crystals*, 389 pp., Academic Press, New York 1972.

Vashchenko, V. Y., and V. N. Zubarev, Concerning the Grüneisen constant, *Sov. Phys. Sol. State, 5*, 653-655, 1963.

Wall, A., and G. D. Price, Computer simulation of the structure, lattice dynamics, and thermodynamics of ilmenite-type $MgSiO_3$, *Am. Mineral., 73*, 224-231, 1988.

Wallace, D. C., *Thermodynamics of Crystals*, John Wiley, New York, 1972.

Wang, H., and G. Simmons, Elasticity of some mantle crystal structures 2. Rutile GeO_2, *J. Geophys. Res., 78*, 1262-1273, 1973.

Weidner, D. J., and M. T. Vaughan, A technique for measuring the single crystal elastic properties of high pressure phases, in *High-Pressure Science and Technology*, edited by K. D. Timmerhaus, and M. S. Barber, pp. 85-90, Plenum, New York, 1977.

Weidner, D. J., and N. Hamaya, Elastic properties of the olivine and spinel polymorphs of Mg_2GeO_4, and evalulation of elastic analogues, *Phys. Earth Planet. Inter., 33*, 275-283, 1983.

Weidner, D. J., and E. Ito, Elasticity of $MgSiO_3$ in the ilmenite phase, *Phys. Earth Planet Inter., 40*, 65-70, 1985.

Weidner, D. J., J. D. Bass, A. Ringwood, and W. Sinclair, The single-crystal elastic moduli of stishovite, *J. Geophys. Res., 87*, 4740-4746, 1982.

Weidner, D. J., H. Sawamoto, S. Sasaki, and M. Kumazawa, Single-crystal elastic properties of the spinel phase of Mg_2SiO_4, *J. Geophys. Res., 89*, 7852-7860, 1984.

Wolf, G. H., and M. S. T. Bukowinski, Theoretical study of the structural properties and equasions of state of $MgSiO_3$ and $CaSiO_3$ perovskites: Implications for lower mantle composition, in *High-Pressure Research in Mineral Physics*, edited by M. H. Manghnani and Y. Syono, pp. 313-335, Terra Scientific, Tokyo, 1987.

Wolf, G. H., and M. S. T. Bukowinski, Variational stabilization of the ionic charge densities in the electron-gas theory of crystals: applications to MgO and CaO, *Phys. Chem. Miner., 15*, 209-220, 1988.

Wolf, G. H., and R. Jeanloz, Vibrational properties of model monatomic crystals under pressure, *Phys. Rev. B Conds. Matter, 32*, 7798-7810, 1985.

Wong, C., and D. E. Schule, Pressure and temperature derivatives of the elastic constants of CaF_2 and BaF_2, *J. Phys. Chem. Solids, 29*, 1309, 1968.

Wood, D. L., G. F. Imbusch, R. M. Macfarlane, P. Kisliuk, and D. M. Larkin, Optical spectrum of Cr^{3+} ions in spinels, *J. Chem. Phys. 48*, 5255-5263, 1968.

Wooten, F., *Optical Properties of Solids*, 260 pp., Academic Press, San Diego, Calif., 1972.

Wyckoff, R. W. G., *Crystal Structures*, John Wiley, New York, 1965.

Yagi, T., F. Marumo , and S. Akimoto, Crystal structures of spinel polymorphs of Fe_2SiO_4 and Ni_2SiO_4, *Am. Miner., 59*, 486-490, 1974.

Yamanaka, T., and M. Iishi, Raman scattering and lattice vibrations of Ni_2SiO_4 spinel at elevated temperature, *Phys. Chem. Miner., 13*, 156-160, 1986.

A. M. Hofmeister, Department of Geology, University of California, Davis, CA 95616.

(Received October 17, 1989;
revised April 30, 1991;
accepted May 20, 1991.)

JOURNAL OF GEOPHYSICAL RESEARCH, VOL. 96, NO. B10, PAGES 16,169–16,180, SEPTEMBER 10, 1991

The High-Pressure Phase Diagram of $Fe_{0.94}O$: A Possible Constituent of the Earth's Core

ELISE KNITTLE[1] AND RAYMOND JEANLOZ

Department of Geology and Geophysics, University of California, Berkeley

Electrical resistivity measurements to pressures of 83 GPa and temperatures ranging from 300 K to 4300 K confirm the presence of both crystalline and liquid metallic phases of FeO at pressures above 60 - 70 GPa and temperatures above 1000 K. By experimentally determining the melting temperature of FeO to 100 GPa and of a model core composition at 83 GPa, we find that the solid-melt equilibria can be described by complete solid solution across the Fe-FeO system at pressures above 70 GPa. Our results indicate that oxygen is a viable and likely candidate for the major light alloying element of the Earth's liquid outer core. The data suggest that the temperature at the core-mantle boundary is close to 4800 (± 500) K and that heat lost out of the core accounts for more than 20% of the heat flux observed at the surface.

INTRODUCTION

The composition of the Earth's core is one of the most important and elusive problems in geophysics. From seismic wave velocities, cosmic chemical abundances, and the geomagnetic requirement that the core is metallic, it is known that the outer core consists of liquid iron alloyed with a small amount of a lighter component [*Birch*, 1964; *Stevenson*, 1981; *Brown and McQueen*, 1982, 1986]. The processes by which the core formed and acquired its present composition are poorly understood, however. These processes are significant in the geochemical history of the Earth because the formation of the core could have generated enormous amounts of heat and determined the compositions of the major silicate and metallic regions of the interior. At present, heat within the Earth may originate largely in the core, providing the source of energy for mantle convection and ultimately for surface processes such as plate tectonics. Therefore, the composition and thermal state of the core must be known if the chemistry and dynamics of the Earth's interior are to be understood.

The detailed nature of the boundary between the Earth's silicate mantle and metallic core is known only from seismic studies. These show that the lowermost part of the mantle is heterogeneous and that it has anomalous seismic velocity gradients [*Young and Lay*, 1987; *Lay and Helmberger*, 1983; *Cleary*, 1974; *Ruff and Helmberger*, 1982]. In addition, there is mounting evidence from high pressure and temperature experiments that the crystalline silicates of the Earth's lower mantle react chemically with the liquid iron of the outer core [*Knittle and Jeanloz*, 1986*b*, 1989; *Williams et al.*, 1987]. Such reactions between the mantle and core would plausibly result in the lowermost mantle being heterogeneous, and they may provide the light elements that are alloyed into the outer core. In particular, oxygen, the most abundant element of the mantle, could be the primary light component that is incorporated into the core.

At low pressure, iron-oxygen alloys form immiscible melts consisting of iron-rich metallic and iron oxide nonmetallic components [*Darken and Gurry*, 1946]. Thus, if oxygen is an important alloying constituent of iron in the core, it must become miscible with liquid iron at high pressure. That is, the iron oxide component must form a metallic melt, implying that there is a fundamental change in the chemical bonding of oxygen at high pressure relative to low pressure. This is exactly what has been argued by *Ringwood* [1977, 1979], who favors oxygen as the primary light alloying constituent of the Earth's outer core based on cosmochemical and geochemical considerations.

To determine whether oxygen alloys with liquid iron under core conditions, we studied the properties of FeO at high pressure and temperature. By measuring the electrical resistivity of FeO to pressures of 155 GPa and temperatures of ~ 4500 K, we have discovered that both liquid and crystalline FeO do indeed become metallic at elevated pressures and temperatures [*Knittle et al.*, 1986*b*; *Knittle and Jeanloz*, 1986*b*]. In addition, by measuring the melting temperatures of FeO and an Fe-FeO mixture at pressures up to 100 GPa, we are able to evaluate current bounds on the temperature at the boundary between the liquid core and solid mantle.

Our study complements previous equation of state measurements by shock wave [*Jeanloz and Ahrens*, 1980] and static high-pressure techniques [*Yagi et al.*, 1985]. The resistivity, equation of state, and melting data are combined here to construct a phase diagram for FeO; however, only the electrical resistivity data confirm the existence of a metallic phase of FeO and delineate its phase boundaries. Finally, we note that this paper provides details of our techniques used to measure electrical resistivity in the laser-heated diamond cell; these have been referred to in previous papers [*Knittle and Jeanloz*, 1986*b*; *Li and Jeanloz*, 1987].

EXPERIMENTAL PROCEDURE

The $Fe_{0.94}O$ used in our experiments was synthesized in the laboratory of H. Harrison at Purdue University, and it is the same material used by *Knittle et al.* [1986*b*]. The samples are polycrystalline, with ~ 0.1 - 1 cm grain size, and contain trace amounts of magnetite as a separate phase. Examination of a polished thin section shows the magnetite to be confined largely to one region of the wüstite boule, and therefore

[1]Now at Board of Earth Sciences, University of California, Santa Cruz.

Paper number 90JB00653.
0148-0227/91/90JB-00653$05.00

samples for the experiments were not taken from this region (estimated magnetite contamination is less than 5% by volume). The FeO was characterized by X ray diffraction to determine its stoichiometry using an empirical relation between lattice parameter and composition [cf. *Hazen and Jeanloz*, 1984]. The zero-pressure lattice parameter is 430.3 (±0.5) pm, corresponding to a composition Fe/O = 0.94 (±0.01) and a sample density of 5.373 (±0.004) Mg/m^3.

The $Fe_{0.94}O$ was ground into a powder for the room temperature, high-pressure electrical resistivity experiments, and a Mao-Bell-type diamond cell was used to generate the pressure [*Mao et al.*, 1979]. Methods for measuring electrical resistivity in the diamond cell have been described previously [*Mao et al.*, 1977; *Reichlin*, 1984]. In most measurements, including our own, a pseudo-four-lead technique is used. That is, the sample resistance is measured between two leads, each of which consists of a wire going through the high-pressure cell. For our purposes, contact resistance in unimportant at high pressures, and two leads at the sample are adequate. Before each measurements, however, the resistance across the individual wires and between the leads and diamond cell can be checked to avoid collecting data after a lead has been broken (lost contact) or shorted out against the gasket (false contact).

Using two similar methods, we have been able to more than double the maximum pressure to which electrical resistivity measurements have previously been made (Figure 1). In the first method, the samples are confined in an Inconel or spring-steel gasket which is coated with an insulating material to prevent the leads from making electrical contact with the metal gasket. An oxide mixed with epoxy (MgO or Al_2O_3) in a proportion of roughly 3:1 by volume proves to be satisfactory. A hole is drilled in the coated gasket, and the sample material is precompressed in the gasket before leads are attached. In this way, it is possible to ensure that the insulating material surrounds the sample. Leads of 10-25 μm platinum or tungsten wire are placed across the sample and are connected to external leads in such a way that there is no electrical contact between the leads and the body of the diamond cell. A small amount of ruby powder is pressed onto the sample, and the pressure is measured using the ruby fluorescence technique [*Barnett et al.*, 1973; *Mao et al.*, 1978].

In the second method, a spring steel gasket is again prepared by coating it with a mixture of epoxy and MgO. The gasket is indented between the diamonds, and a hole nearly as large as the culet diameter is drilled in the indented region. That is, nearly the entire indentation is drilled out. MgO is packed into this large gasket hole and compressed between the diamonds. Thus, the MgO serves as an insulating coating on the spring steel and as a supporting gasket between the diamonds. FeO and ruby are then laid on top of the MgO and 25 μm wires are placed on top of the sample as leads. With this second technique, the leads are less likely to be cut off at the sharp corner around the edge of the diamond culet than with the first technique. However, it is not clear that pressures as high as the maximum values obtained with the first technique can be achieved with the second [see *Li and Jeanloz*, 1987].

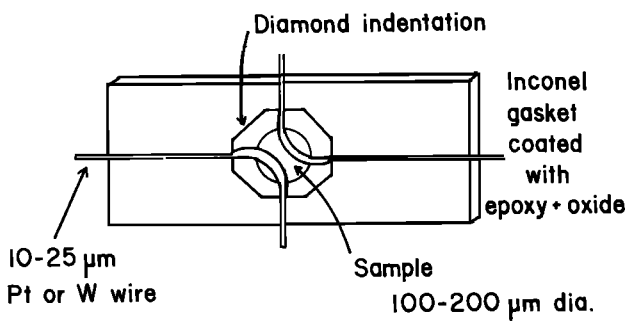

Fig. 1. Schematic experimental design for measuring resistivity at high pressures and room temperature in the diamond cell. The gasket is coated with epoxy mixed with either MgO or Al_2O_3 to insulate it from the electrical leads. The FeO sample is pressed into a hole drilled in the gasket and 25 μm Pt or W wires are placed over the sample. Electrical resistivity has been measured to 83 GPa with this method.

Resistivities are calculated from the measured resistances based on measuring the geometry of the sample and lead configuration at high pressure in the diamond cell. The sample dimensions and resistance (R) are substituted into the expression $\rho = (R \times W \times t)/L$ to obtain the sample resistivity (ρ). Here, W is the length of overlap of the leads (typically 100-200 μm), t is the sample thickness (~10-15 μm) and L is the distance between the leads (~100-200 μm). Reproducible resistance values for the powdered samples are usually not obtained until ~5 GPa, at which point porosity of the sample and bad contact between the sample and leads disappears. The resistance values for the diamond cell experiments are measured using a Keithley model 195A digital multimeter which records between 10^{-3} and 10^{6} ohms: they are highly reproducible and considered accurate to 0.5%. However, the conversion to resistivity is less certain due to the difficulty of precisely measuring the sample dimensions and thickness between the electrical leads. The final uncertainties in resistivity are typically 10-20%.

The experimental procedure for the high-temperature diamond cell experiments is basically that described above as the second method, and it is shown schematically in Figure 2. Instead of using powdered samples, a small chip of polycrystalline (precompressed) FeO is placed on top of the MgO, 25-μm platinum wires are laid over the sample and finely powdered ruby is placed over all. The ruby serves three purposes: (1) to insulate thermally the sample from the diamonds, which act as heat sinks due to their high thermal

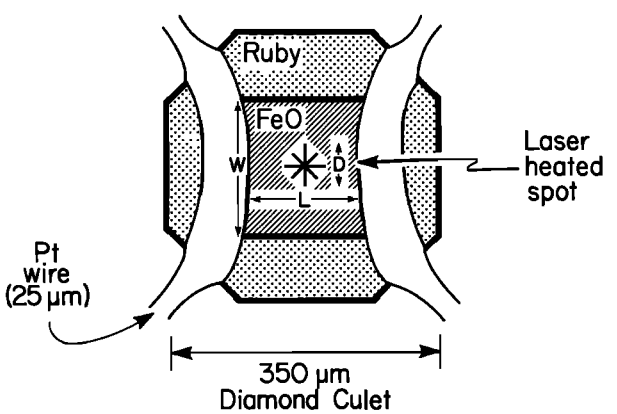

Fig. 2. Schematic experimental design for high pressure and high temperature electrical resistivity measurements in the diamond cell. A small chip of FeO is embedded in ruby and 25-μm Pt leads are pressed into the sample. The sample is heated with a cw Nd:YAG laser. The dimensions of the sample between the electrical leads are shown: the overlap of the leads is W (typically ~100-150 μm), the distance between the leads is L (~100-150 μm) and the diameter of the laser beam is D (~35 μm). The sample thickness is ~10 μm.

conductivity; (2) to prevent the FeO from chemically reacting with the diamond; and (3) to measure accurately the pressure across the entire FeO surface. The high-pressure, high-temperature experiments are carried out by simultaneously heating the FeO sample with a 25 Watt cw Nd:YAG laser and monitoring the change in resistance from the room temperature value. The temperature of the laser-heated spot in the FeO sample is measured spectroradiometrically using the system described by *Heinz and Jeanloz* [1987]. Since the laser-heated spot in the sample is small (~35 μm in diameter) in comparison with the distance between the electrical leads (L ~ 100-150 μm), different regions of the sample can be heated and measured at the various pressures generated by the pressure gradients across the sample. Care is taken to monitor the resistance when the electrical leads or the steel gasket are directly heated, but we do not report these spurious resistance values.

The high-pressure melting experiments on FeO are also carried out with the laser-heated diamond cell. In each of the experiments, small FeO chips (25-50 μm in diameter) are embedded in ruby powder placed in the hole that is drilled in a spring-steel gasket. Surrounding the sample with ruby serves the same three purposes as in the resistivity experiments. Melting is observed directly at high pressure and temperature: either a change in texture of the sample surface is observed after quenching in temperature or there is movement of the FeO-ruby interface due to chemical reaction with the surrounding medium. Here again, the temperatures are measured spectroradiometrically. In the melting experiments, but not in the resistivity experiments, the temperature gradients across the laser-heated spot are also measured [*Heinz and Jeanloz*, 1987]. Measurements of these temperature gradients are necessary in order not to underestimate the correct melting temperatures.

Finally, a melting point has been obtained for an Fe-FeO sample having a bulk composition that is in accord with the observed density of the outer core [*Jeanloz and Ahrens*, 1980]. The sample is a mechanical mixture of Fe and FeO powders (1-5 μm in size) mixed in equal proportions by weight, and thus corresponding to ~10 wt. % oxygen in Fe. The mixture was pressed together to form chips about 10 μm in thickness. Small chips, about 50 μm across, are embedded in ruby in a gasket, and the experimental procedure is the same as that described for the melting of FeO.

Resistivity data on FeO were obtained from four separate samples at room temperature, both on increasing and decreasing pressure and up to a maximum pressure of 83 GPa. In the high-temperature experiments, resistivity values were obtained from two samples at pressures between 64 and 74 GPa. The melting curve of FeO measured in this study is the compilation of results from 350 experiments on eleven different samples at pressures up to 100 GPa. For the Fe-FeO mixture, melting data were obtained at 85 (± 5) GPa on one sample.

RESULTS

High-Pressure Electrical Resistivity

The electrical resistivity of FeO at high pressure and room temperature is plotted in Figure 3. Over the entire pressure range, 0-83 GPa, the resistivity of FeO decreases by only a factor of two from the initial value of 1.7 (± 0.3) X 10^{-3} ohm m, and the change is reversible when the pressure is released. The absolute value of the high-pressure resistivity shows that FeO remains a semiconductor under these conditions. These results are qualitatively consistent with *Endo and Ito*'s [1982] measurement of the relative change in electrical resistance of FeO with pressure. FeO is known to undergo a phase transition from a paramagnetic semiconductor to an antiferromagnetic semiconductor at 180 K at zero pressure and at 300 K at 18 GPa [*Yagi et al.*, 1985; *Okamoto et al.*, 1967]. This transition is manifested by a slight distortion of the B1 (NaCl-type) structure in the antiferromagnetic state. Within the resolution of our data, however, there is no evidence for any change in the electrical resistivity of FeO across the transition.

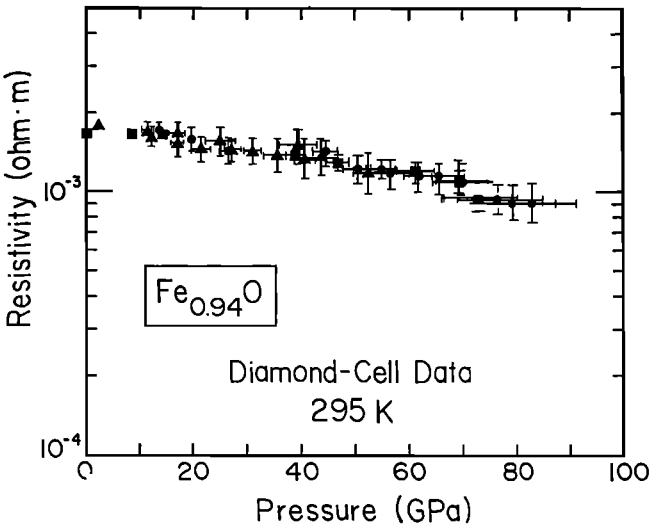

Fig. 3. Resistivity of $Fe_{0.94}O$ measured in the diamond cell at room temperature. Over the entire range of compression, the resistivity of FeO decreases only by a factor of 2.

In an earlier study, we reported the existence of a high-pressure metallic phase of FeO based upon measurements of resistivity under shock loading [*Knittle et al.*, 1986*b*]. In these experiments, FeO was shown to exhibit a resistivity of ~1 X 10^{-6} ohm m between pressures of 72 and 155 GPa, with temperatures ranging from 1200 K to 4000 K based on the calculated Hugoniot temperatures of *Jeanloz and Ahrens* [1980]. These values are comparable to the resistivity of iron measured under shock loading at similar pressures and temperatures (Figure 4). Additionally, the resistivities of both FeO and Fe increase slightly with increasing shock pressure and temperature. This is characteristic of metallic behavior, for which an increase in temperature creates increased electron-phonon scattering. Therefore, both the absolute magnitude and the trend of the resistivity with increasing temperature and pressure demonstrate that FeO is metallic above 70 GPa under shock condition.

The validity of comparing shock wave and diamond cell electrical resistivity data has been demonstrated previously for Fe_2O_3 [*Knittle and Jeanloz*, 1986*a*]. In the study of Fe_2O_3, the resistivity could be quantitatively compared between the two types of measurements in part because the temperature dependence of electrical resistivity is small [*Kondo et al.*, 1979; 1980]. Since the temperature dependence of resistivity is also small for FeO [*Bowen et al.*, 1975], it should similarly be

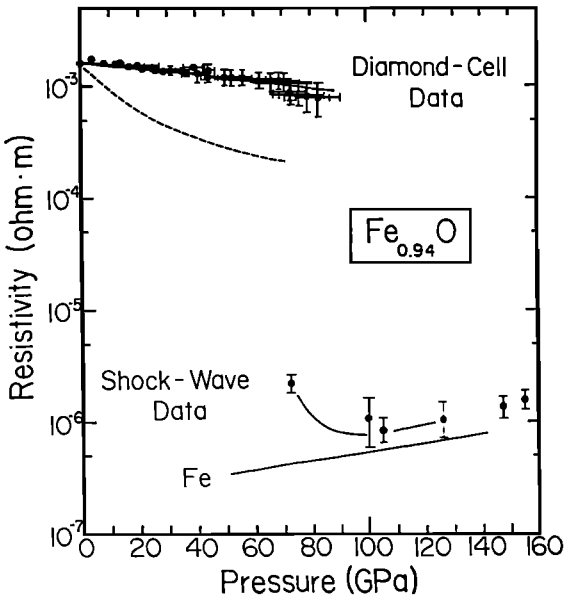

Fig. 4. Comparison of the static compression and shock wave resistivity measurements on $Fe_{0.94}O$ (from *Knittle and Jeanloz* [1986b]). The resistivity of iron under shock loading (*Keeler and Mitchell* [1969]) is plotted for comparison with the FeO. The diamond cell and shock wave data are not coincident, even though they overlap in pressure. The difference between the high-pressure, room temperature data (diamond cell) and the high-pressure, high-temperature (shock wave) data reflects the transition from semiconducting to metallic behavior with increasing temperature at pressures above ~70 GPa.

possible to compare resistivities measured in the diamond cell with those determined in shock wave experiments.

An explanation for the difference in the high-pressure resistivity of FeO between room temperature and high temperature (Figure 4) is that two different phases of FeO are sampled: and antiferromagnetic semiconducting phase at room temperature and a metallic phase at high temperature and pressures above 70 GPa [*Knittle and Jeanloz*, 1986b]. The presence of these two phases at high pressures also explains the difference between the equation of state measured under shock loading and that measured in the diamond cell. Whereas *Yagi et al.* [1985] observed no evidence for any phase transition in room temperature diamond cell experiments to 120 GPa, a volume decrease of 4% is evident at 70 GPa in the shock wave data of *Jeanloz and Ahrens* [1980]. They interpreted the volume decrease as being due to a transition from the B1 (NaCl-type) to a B2 (CsCl-type) structure. Although our electrical resistivity measurements confirm that a phase transition occurs at 70 GPa and high temperature to a metallic phase of FeO, they do not prove that a structural transition is involved. This is because a volume decrease is expected for most insulator-metal transitions in solids, either due to an associated structural transition or due to an isostructural collapse of the lattice at the metallization transition [*Adler*, 1968; *Goodenough*, 1971; *Brandow*, 1977].

High-temperature resistivity measurements were carried out in the diamond cell to complement the shock wave measurements, the purpose being to reproduce statically both the temperatures and pressures achieved along the Hugoniot. Because temperature can be varied at a given pressure in the laser-heated diamond cell, such experiments can confirm if FeO is behaving as a semiconductor both through the absolute value of the observed resistivity and through its change with temperature. In a semiconductor, the decrease in resistivity with increasing temperature (T) is due to the thermally activated process by which electrons are promoted from the valence to the conduction band. The resistivity is given by

$$\rho = \rho_0 \exp(E_a/k_B T) \quad (1)$$

where ρ_0 is independent of temperature, k_B is Boltzmann's constant, T is temperature (kelvin), and E_a is the activation energy for conduction.

From our interpretation of Figure 4, the expectation is that the absolute value of the measured resistance should decrease from its initial value for all laser-heated samples in the diamond cell. Specifically, semiconducting FeO should exhibit resistance decreasing exponentially as temperature increases above 300 K. At sufficiently high pressures and temperatures, however, we expect FeO to exhibit a low, metallic resistance that is only weakly dependent on temperature (trending toward higher resistance with increasing temperature). These two contrasting behaviors of electrical resistance are indeed found (see Figure 5 and Table 1). Qualitatively, this confirms that FeO behaves as a semiconductor below 70 GPa and a metal above this pressure.

The quantitative interpretation of our resistance measurements relies on assumptions about the electrical resistivity of FeO in the laser-heated spot. We use a model in which the total resistance measured across the sample by the electrical leads is a function of the resistances of the heated and cold regions of the FeO. In Figure 6, the resistances R_1, R_2, R_4, and R_5 are assumed to be given by the room temperature resistivity (ρ_{300K}) and the geometries of regions 1, 2, 4, and 5 in the sample. The values of the high-pressure, room temperature resistivities are obtained from our measurements as

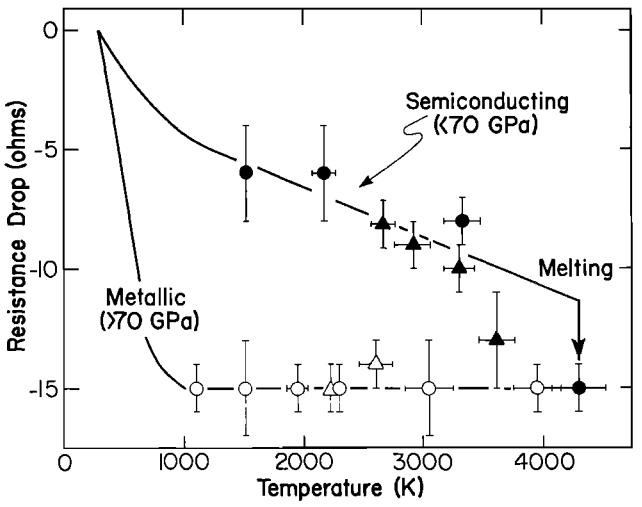

Fig. 5. Absolute change in resistance of the high-pressure, laser-heated FeO samples as a function of temperature. The triangles and circles represent two different samples, with points above (open symbols) and below (solid symbols) the metallization pressure of 70 GPa. The data below 70 GPa have a temperature dependence in accord with our prediction for semiconducting behavior. The data above 70 GPa and 1000 K exhibit no temperature dependence within the resolution of our measurements. This is consistent with our expectations for metallic FeO.

TABLE 1. Electrical Resistance Measurement in the Laser-Heated Diamond Cell

Sample[a]	Pressure,[b] GPa	Temperature, K	ρ_{300K}, ohm m	$\rho_{High\ Temp}$, ohm m	L, μm	W, μm	Resistance Drop, ohms	
							Measured	Calculated
FeO3as	72 (2)	1370 (61)	9.0×10^{-4} (1)	1.0×10^{-4} (1)	150 (30)	100 (20)	-15 (2)	-16 (2)
FeO4as	73 (2)	3360 (198)	9.0×10^{-4} (1)	1.0×10^{-4} (1)	150 (30)	100 (20)	-15 (1)	16 (2)
FeO5as	72 (2)	1080 (32)	9.0×10^{-4} (1)	1.0×10^{-4} (1)	150 (30)	100 (20)	-15 (1)	-16 (2)
FeO6as	72 (2)	1770 (73)	9.0×10^{-4} (1)	1.0×10^{-4} (1)	150 (30)	100 (20)	-15 (1)	-16 (2)
FeO7as	72 (2)	2640 (195)	9.0×10^{-4} (1)	1.0×10^{-4} (1)	150 (30)	100 (20)	-15 (2)	-16 (2)
FeO8as	64 (2)	1410 (66)	9.0×10^{-4} (1)	3.0×10^{-4} (1)	150 (30)	100 (20)	-6 (2)	-6 (2)
FeO9as	64 (2)	1850 (130)	9.0×10^{-4} (1)	1.5×10^{-4} (1)	150 (30)	100 (20)	-8 (1)	-8 (2)
FeO11am	64 (2)	3630 (265)	9.0×10^{-4} (1)	1.2×10^{-4} (1)	150 (30)	100 (20)	-15 (1)	-12 (2)
FeO12as	64 (2)	1940 (99)	9.0×10^{-4} (1)	2.0×10^{-4} (1)	150 (30)	100 (20)	-6 (2)	-6 (2)
FeO13as	73 (2)	2040 (49)	9.0×10^{-4} (1)	1.0×10^{-4} (1)	150 (30)	100 (20)	-15 (1)	-16 (2)
FeO14as	68 (2)	3070 (251)	9.0×10^{-4} (1)	1.4×10^{-4} (1)	120 (30)	80 (20)	-13 (2)	-11 (2)
FeO15as	68 (2)	2840 (124)	9.0×10^{-4} (1)	1.5×10^{-4} (1)	120 (30)	80 (20)	-10 (1)	-10 (2)
FeO16as	68 (2)	2530 (160)	9.0×10^{-4} (1)	1.7×10^{-4} (1)	120 (30)	80 (20)	-9 (1)	-8 (2)
FeO17as	68 (2)	2280 (100)	9.0×10^{-4} (1)	1.8×10^{-4} (1)	120 (30)	80 (20)	-8 (1)	-8 (2)
FeO18as	74 (2)	2260 (150)	9.0×10^{-4} (1)	1.0×10^{-4} (1)	120 (30)	80 (20)	-14 (1)	-15 (2)
FeO19as	74 (2)	2010 (65)	9.0×10^{-4} (1)	1.0×10^{-4} (1)	120 (30)	80 (20)	-15 (1)	-15 (2)

[a]a and b designate two different samples, s or m indicates if the sample is solid or melted.
[b]Pressure is measured before heating. Values in parentheses indicate the error in the last significant digit.

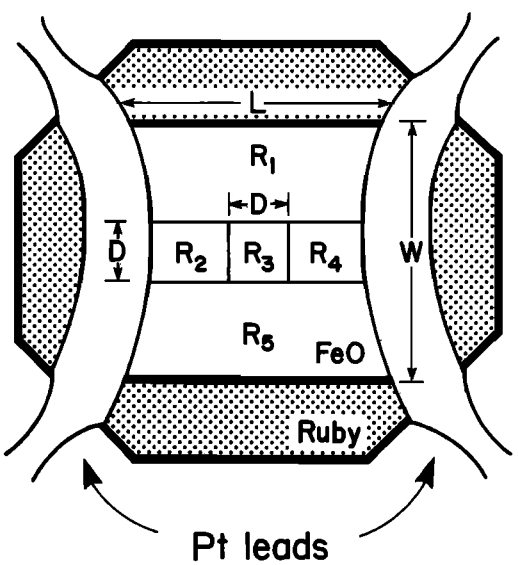

Fig. 6. Geometry used to calculate the total resistance across the laser-heated diamond cell. Region 3 (with resistance R_3) is the laser-heated area with lateral dimensions given by the diameter of the laser beam (D ~ 35 μm). Regions 1, 2, 4, and 5 are at room temperature. W and L are the same as the dimensions shown in Figure 2. The resistance for each region is calculated by assuming a resistivity value as summarized in Table 1. The total resistance is calculated by considering R_2, R_3 and R_4 to be in series and then considering R_1, R_{2+3+4}, and R_5 to be in parallel.

given in Figure 3. Region 3 represents the laser-heated spot. Its resistance (R_3) is given by the high temperature resistivity ($\rho_{High\ Temp}$) across a rectangular volume with sides approximated by the diameter of the laser beam and the thickness of the sample ($D \times D \times t$). D is ~ 35 μm in all of the calculations described here; this is based upon direct observations of the laser-heated regions and on the typical sizes for quenched laser-melted regions in our diamond cell samples. For heated sample regions below 70 GPa, the resistivities are calculated using the semiconductor expression for the temperature-dependence of the resistivity (equation (1)). The values for ρ_0 and Ea have been determined previously for FeO at zero pressure by *Bowen et al.* [1975]. We assume that ρ_0 and Ea do not change significantly with pressure, which is in accord with the results shown in Figure 5. For heated sample spots above 70 GPa, an initial estimate of the high-temperature resistivity can be taken as ~ 1×10^{-6}, as determined for metallic FeO under shock loading (Figure 4). In fact, our measurements in the laser-heated diamond cell are exactly reproduced with this value of $\rho_{High\ Temp}$, so we are justified in retaining it as our final estimate (Table 1).

The total predicted resistance for each sample is calculated in the following way. The individual resistance values for all five regions in the sample are determined from the geometries measured in the sample, as shown schematically in Figure 6, and the appropriate resistivities for the 300 K and high temperature regions as given in Table 1. Regions R_2, R_3, and R_4 are in series, so that $R_{2+3+4} = R_2 + R_3 + R_4$. The total sample resistance is given by R_1, R_{2+3+4}, and R_5, which are in parallel: $1/Rt_{otal} = 1/R_1 + R_{2+3+4} + 1/R_5$. This method reproduces the room temperature resistance observed in the samples before laser heating if the resistivity in R_3 is assumed to be the same as for the other regions.

The predicted total resistances for the sample are listed in Table 1 and shown by the curves in Figure 5. The good agreement between the predicted and measured resistances, in particular for different values of L and W, validates our conclusion that above 70 GPa our sample is metallic and below it is semiconducting. The ability of this model to describe the measurements indicates that the activation energy for resistivity is similar at zero pressure and high pressure: from our data we derive $E_a = 0.06$ (± 0.02) eV at 65 (± 5) GPa, which compares favorably with *Bowen et al.*'s [1975] zero-pressure value of $E_a = 0.07$ eV.

One implication of our measurements for the phase diagram of FeO is that the metallization pressure (70 ± 2 GPa) is independent of temperature between 1000 and 4000 K. Additionally, we measured a metallic resistance for a laser-heated spot of FeO that was observed to be molten at a

temperature of 4250 K and a pressure of 64 GPa. We interpret this result to indicate that liquid FeO is metallic at pressures of ~65 GPa and higher; that is, below and above the metallization pressure of the solid the liquid is metallic.

Melting Experiments and the FeO Phase Diagram

The melting curve of FeO measured to 100 GPa is shown in Figure 7 and the measured temperature bounds plotted are listed in Table 2. Below 70 GPa, the melting curve is well bracketed by the lowest temperature measured in the liquid and the highest temperature measured in the solid at a given pressure. The zero-pressure melting point is taken from the phase diagram of *Darken and Gurry* [1946] as 1650 K, and below 5 GPa our melting curve is in good agreement with the piston-cylinder results of *Lindsley* [1966]. Above 70 GPa, the melting temperature of FeO appears to rise rapidly as indicated by our inability to melt the sample at 102 (± 5) GPa. We are able to bracket the melting temperature to be above 5000 K at 100 GPa, however, from two measurements of temperature in the solid phase. Our interpretation of the melting slope at this pressure is conservation (dashed line in Figure 7) in that a more rapid increase of melting temperature with pressure would not violate our data. We note the coincidence of the change in the melting slope of FeO with the pressure of the metallization transition. This change in slope is consistent with the metallic high pressure phase being denser that the nonmetallic low-pressure phase of FeO, as shown by the Hugoniot measurements [*Jeanloz and Ahrens*, 1980]. Also, it is consistent with the entropy of fusion decreasing across the 70 GPa, metallization transition due to a decreased electronic entropy change: below 70 GPa, nonmetallic solid melts to a metallic liquid (large electronic entropy change on fusion), whereas above 70 GPa, metallic solid melts to metallic liquid (small electronic entropy change).

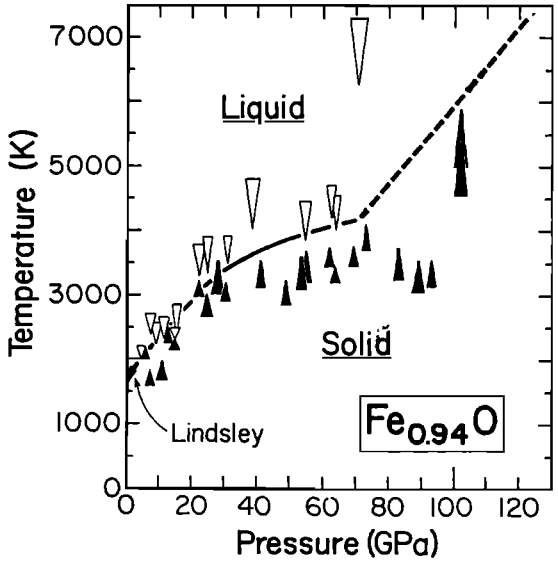

Fig. 7. Melting curve of FeO to 100 GPa. The open, downward pointing triangles represent the lowest temperature measured in liquid FeO at a given pressure. The solid upward pointing triangles represent the highest temperature measured in solid FeO. The size of the symbols indicates the formal error on the temperature measurements based on the quality of the spectral fit to a greybody function. Above 70 GPa, it becomes difficult to melt the sample, and the melting temperature can only be bracketed from below based upon points measured in the solid at 100 GPa.

TABLE 2. High Pressure Bounds on the Melting of $Fe_{0.94}O$

Pressure, GPa	Temperature, K	Phase
4.7	2075±112	Liquid
6.3	2100±105	Solid
7.3	2560±160	Liquid
8.0	1740±85	Solid
9.1	2410±130	Liquid
11.5	2450±180	Liquid
11.5	2340±70	Solid
14.8	2225±95	Solid
14.8	2440±190	Liquid
21.8	3140±150	Solid
21.8	3490±270	Liquid
25.1	2860±175	Solid
25.1	3640±230	Liquid
31.0	2940±105	Solid
31.0	3700±190	Liquid
38.4	4390±370	Liquid
40.8	3300±180	Solid
44.7	3210±200	Solid
49.5	4400±350	Liquid
53.8	3430±250	Solid
53.8	4150±280	Liquid
61.3	3590±140	Solid
61.8	4450±260	Liquid
68.6	3615±160	Solid
70.5	6615±485	Liquid
73.0	3920±200	Solid
89.1	3325±210	Solid
101.9	5413±500	Solid

All of the experimental data for FeO, electrical resistivity, melting, and equation of state, can be consolidated into the high-pressure, high-temperature phase diagram that is illustrated in Figure 8. Three solid phases of FeO are observed: an antiferromagnetic semiconductor at low temperatures, a paramagnetic semiconductor at lower pressures and high temperatures, and a metal at high pressures and high temperatures. The phase boundary between the paramagnetic semiconductor and the antiferromagnetic semiconductor is determined by connecting the zero pressure Neel temperature of FeO (180 K [*Okamoto et al.*, 1967]) to the pressure at which the Neel temperature is 300 K 18 GPa [*Yagi et al.*, 1985]. From the shock wave measurements, the paramagnetic to metallic phase boundary is at ~ 70 GPa in accord with the high-temperature electrical resistivity measurements in the diamond cell. Finally, the boundary between the antiferromagnetic phase and the metal is currently uncertain, so it is indicated by the shaded region in Figure 8.

The qualitative features of the phase diagram of FeO are similar to phase diagrams for a variety of other transition metal oxides and sulfides. In particular, V_2O_3, NiS, and VO_2 exhibit paramagnetic semiconductor (or insulator) to antiferromagnetic semiconductor (or insulator) transitions with increasing

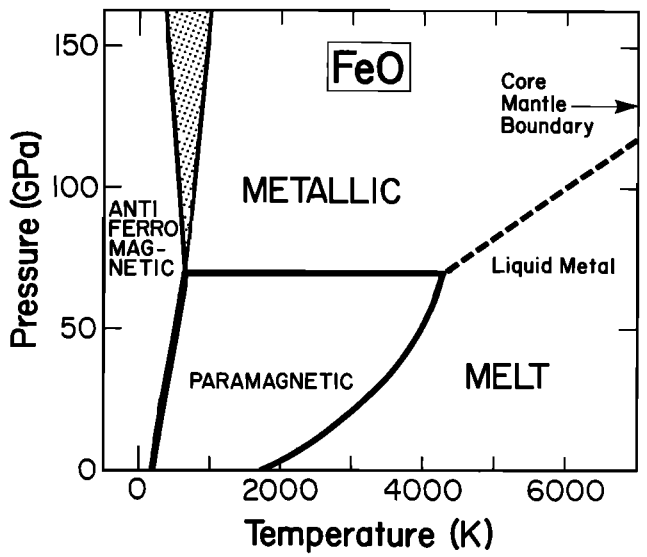

Fig. 8. Phase diagram for FeO at high pressures and temperatures. The diagram is a compilation of our resistivity and melting results, combined with previous equation of state and magnetic measurements [*Knittle and Jeanloz*, 1986b; *Jeanloz and Ahrens*, 1980; *Yagi et al.*, 1985; *Okamoto et al.*, 1967].

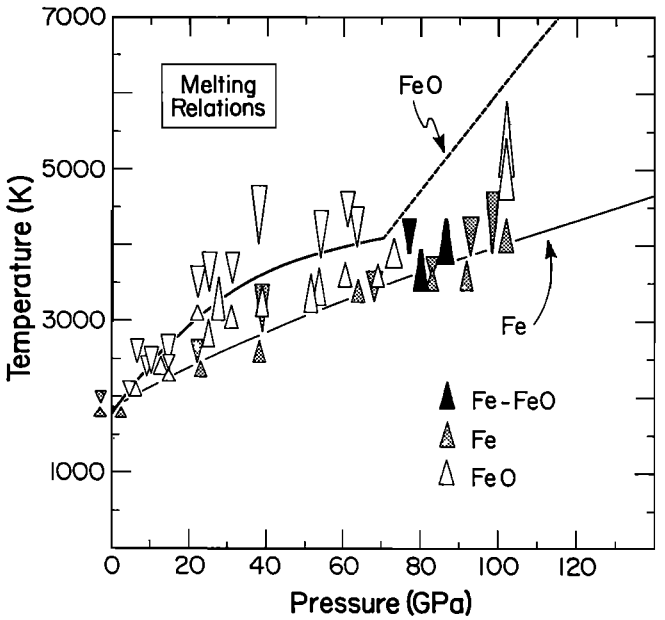

Fig. 9. The melting data for FeO and for a model core composition containing oxygen are plotted along with the previously determined melting temperatures for iron [*Williams et al.*, 1987]. The size and orientation of the symbols have the same meaning as in Figure 7. At all pressures above 5 GPa, the melting temperature of FeO exceeds that of Fe. The Fe-FeO model core composition contains 10 wt. % oxygen (corresponds to $Fe_{0.69}O_{0.31}$), and its melting temperature lies between that of Fe and FeO at 83 (± 5) GPa.

pressure, and insulator to metal transitions with increasing temperature and pressure. These have been extensively discussed in terms of the theory of Mott transitions [*Adler*, 1968; *Alascio et al.*, 1971; *Falicov et al.*, 1972; *Goodenough*, 1971; *Brandow*, 1977].

The System Fe-FeO

We have investigated the nature of the Fe-FeO system as a possible model for the dominant constituent of the Earth's core. According to the present results and the data of *Williams et al.* [1987], the melting temperature of FeO is higher than the melting temperature of metallic iron at all pressures above 5 GPa (Figure 9). Due to the change in the melting slope of FeO at the metallization transitions, the melting temperature of FeO exceeds that of Fe by at least 1000-2000 K at the pressure of the Earth's core-mantle boundary (136 GPa). Extrapolation of the melting curve of FeO beyond 100 GPa is difficult, but it seems improbable that the melting temperature continues to increase linearly to pressures of several hundred GPa.

Although the idea that the liquid outer core represents a eutectic composition has been widely discussed over the years [*Birch*, 1972, 1964; *Ringwood*, 1977, 1979; *Stevenson*, 1981; *McCammon et al.*, 1983], there are two end-member possibilities for the phase diagram of the core alloy composition: (1) the system has a eutectic composition (complete solid immiscibility); and (2) the system exhibits complete solid solution. Of the Fe-FeO system contains a eutectic, then the melting temperature of an intermediate composition that could make up the outer core should be lower than the melting temperatures of both Fe and FeO. However, if there is solid solution across the Fe-FeO system, the melting temperature of a core composition (Fe/FeO = 1.23 on a molar basis, with oxygen as the only alloying constituent) should be intermediate between the melting points of Fe and FeO.

Our results for the melting of a model core composition ($Fe_{0.69}O_{0.31}$) at 83 (± 5) GPa is 4000 (± 100) K (Figure 9). This corresponds to the second alternative, thus indicating that Fe-FeO behaves like a solid solution rather than as a eutectic system along the solidus at high pressure. Additionally, we note that we could not distinguish a difference between solidus (initiation of melting) and liquidus (initiation of crystallization) temperatures in this experiment.

Assuming ideal solid solution, we calculate the solidus and liquidus curves across the Fe-FeO system at 80 GPa for comparison with our measurement of the melting point for $Fe_{0.69}O_{0.31}$. In our calculations, we use the thermodynamic data that are summarized in Table 3 to determine values for the volume changes (ΔV_m) and entropy changes (ΔS_m) upon melting of Fe and FeO. The ratio ($\Delta V_m/\Delta S_m$) is given by the Clapeyron equation ($\Delta V_m/\Delta S_m$) = (dT_m/dP), where dT_m/dP is the measured melting slope of either Fe or FeO. From our data for FeO, dT_m/dP = 50 (± 15) K/GPa at 80 GPa, whereas for iron dT_m/dP = 20 (± 5) K/GPa [*Williams et al.*, 1987]. The volume change upon melting for iron has been estimated from shock wave experiments to be ~ 2 (± 1)% at 250 GPa [*Brown and McQueen*, 1982, 1986]. Although we are interested in ΔV_m for Fe at 80 GPa, we adopt a value of 2 ± 1% for our calculation (at zero pressure the volume change on melting is 3.5% [*Ubbelhode*, 1978]. When substituted into the Clapeyron equation, ΔS_m = 5 (± 3) J K^{-1} mol^{-1}. There is no direct information of ΔV_m or ΔS_m for FeO, which is treated here as $Fe_{0.5}O_{0.5}$ [*Kerrick and Darken*, 1975]. Therefore, we use the observed dT_m/dP for FeO and the results for ΔV_m and ΔS_m of iron as bounds for FeO ($Fe_{0.5}O_{0.5}$): as one bound we assume that the entropy change on melting is the same as for Fe and as another bound we assume that the volume changes are identical. The solidus and liquidus for the Fe-$Fe_{0.5}O_{0.5}$ join are then

TABLE 3*a*. Thermodynamic Data for γ - Fe and FeO for Calculation of Phase Diagram at 80 GPa

	γ - Fe	FeO
$\rho_{P=0,T=300K}$, Mg/m^3	8.0 ± 0.3[a]	6.05 ± 0.15[b]
K_{0T}, GPa	180 ± 10[c]	195 ± 10[b]
K'_{0T} ($\delta K/\delta P$)	4 ± 1[d]	4 ± 1[d]
$\langle\alpha\rangle_{high\ P,\ high\ T}$, $\times 10^{-5}K^{-1}$	1.0 ± 1.0[e]	1.0 ± 1.0
$T_{m,\ 80\ GPa}$, K	3600 ± 200[f]	4600 ± 200
$\rho_{80\ GPa,\ Tm}$, Mg/m^3	10.05 ± 0.47	7.44 ± 0.32
$MolarVolume_{80GPa,Tm}$, cm^3/mole	5.56 ± 0.34	9.56 ± 0.33
$\Delta T_m/\Delta P$, K/GPa	20 ± 5[f]	50 ± 5
ΔV_m	2 ± 1%[g]	2 ± 1%[ha] 5.6 ± 3.4%[hb]
ΔS_m, $JK^{-1}mole^{-1}$	5 ± 3	4 ± 2[ha] 10 ± 6[hb]

[a] Estimated based on $\rho_{P=0,T=300K}$ for α and ε-iron see *Anderson* [1987] for summary.

[b] From *Jeanloz and Ahrens* [1980].

[c] Estimated to fall between K_{0T} for ε-iron (K_{0T} = 193 ± 9 GPa: *Jephcoat et al.* [1986] and α-Fe (K_{0T} = 167 ± 2 GPa: *Guinan and Beshers* [1968].

[d] Estimated values for K'_{0T}. Although *Jeanloz and Ahrens* [1980] found a value of K'_{0T} for FeO from their study it is extremely uncertain (K'_{0T}= 3.4±5). The value K_{0T} = 4 (±1) is empirically justified for a wide range of materials [e.g., *Birch*, 1952].

[e] From *Jeanloz* [1979]. We assume that the estimated high pressure, temperature thermal expansion for iron under core conditions is also appropriate for FeO.

[f] Measured by *Williams et al.* [1987].

[g] Estimated volume change for the melting of iron at high pressure from *Brown and McQueen* [1982, 1986].

[h] Bounds on the volume change and entropy of melting for FeO were obtained by: *ha)* constraining ΔV_m for FeO to be equivalent to that of Fe and calculating ΔS_m; *hb)* constraining ΔS_m to be equivalent for Fe and FeO and calculating ΔV_m.

TABLE 3*b*. Calculation of Phase Diagram at 136 GPa

	γ - Fe	FeO
$T_{m,136\ GPa}$, K	4800 ± 200[f]	7300 ± 1000
$\rho_{136\ GPa,\ Tm}$, Mg/m^3	11.03 ± 0.57[a]	7.98 ± 0.60
$Molar\ Volume_{136\ GPa,\ Tm}$, cm^3/mole	5.06 ± 0.25	9.01 ± 0.48
$\Delta T_m/\Delta P$, K/GPa	20 ± 5[f]	35 ± 20
ΔV_m	2 ± 1%[g]	2 ± 1%[ha] 4.5 ± 3.3%[hb]
ΔS_m, $JK^{-1}mole^{-1}$	5 ± 3	5 ± 4[ha] 10 ± 6[hb]

calculated using the equations of *Seltz* [1934], with the results illustrated in Figure 10.

The phase loop in the $Fe\text{-}Fe_{0.5}O_{0.5}$ system at high pressures is extremely narrow according to our calculation. The main reason for this is that the temperatures involved are very high. The error envelope represents the formal error on the liquidus and solidus. However, this is a correlated error indication the amount by which the entire phase loop may shift; in general, the width of the loop remains constant and small. As can be seen from the diagram, our measurement of the melting temperature of $Fe_{0.69}O_{0.31}$ (61 mol % $Fe_{0.5}O_{0.5}$ and 39 mol % Fe) is remarkably consistent with the calculation, both in the absolute value of the melting temperature and in the narrowness of the phase loop between the liquidus and solidus. This agreement supports our conclusion that the system Fe-FeO behaves as a solid solution at high temperatures and pressures.

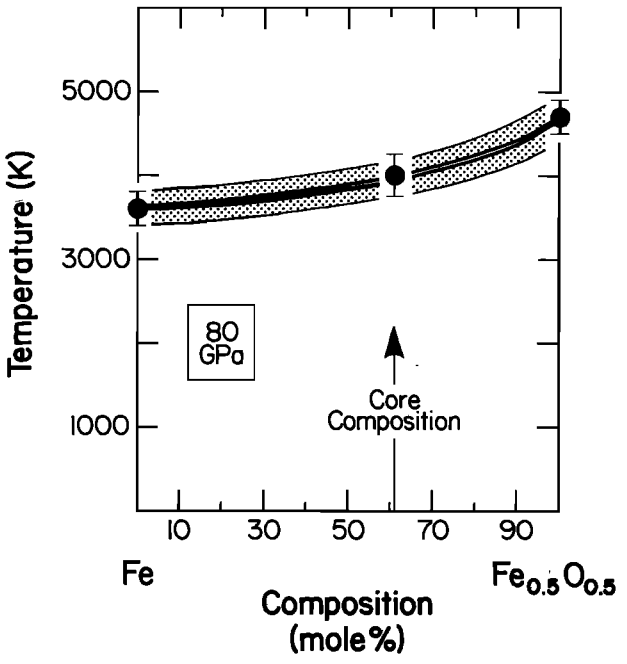

Fig. 10. Phase diagram calculated for the solid solution of Fe-FeO at 80 GPa. The thermodynamic data used to derive the liquidus and solidus are listed in Table 3*a*.

DISCUSSION

Crystal Structural Model of Fe-FeO Solid Solution

The observation that solid Fe and FeO behave like a solid solution implies that these components exist in the same crystal structure at high pressures and at temperatures just below melting [*Darken and Gurry*, 1953]. Although the high-temperature, high-pressure crystal structure of FeO is unknown from any direct experimental evidence, the observation of solid solution suggests a structure of FeO based upon the structure of the coexisting Fe. At the pressures and temperatures of the Earth's core-mantle boundary (136 GPa, ≥ 3600 K), iron is most likely in the face-centered cubic (γ) structure at the melting point, as illustrated in Figure 11 [*Liu*, 1975; *Birch*, 1972; *Brown and McQueen*, 1986]. Therefore, if it forms a solid solution with iron, metallic FeO must also be in a structure related to the face-centered cubic structure. This type of structure is not unprecedented, and it can be derived from the B2 (CsCl-type) structure which has been observed in a wide variety of alkali halides and monoxides under pressure. Specifically, it is known experimentally that the B2 structure can distort under pressure to form a body-centered tetragonal (CuAu I-type) structure, such that when the c/a ratio is $\sqrt{2}$ it is equivalent to the face-centered cubic structure as illustrated in Figure 12 [*Knittle and Jeanloz*, 1984, 1985; *Knittle et al.*, 1985]. An important question is whether or not the corresponding bond lengths in γ-Fe and the hypothetical body-centered tetragonal structure of metallic FeO are compatible with the formation of a solid solution.

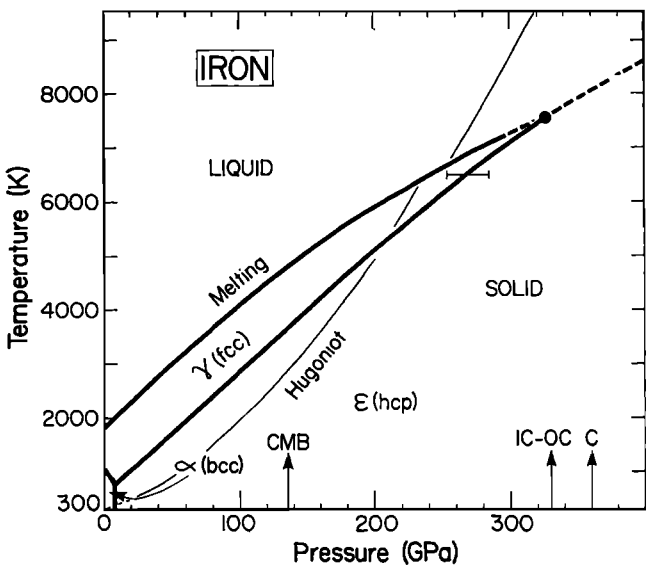

Fig. 11. Phase diagram of iron over the pressure and temperature range of the Earth's interior (pressures at the core-mantle boundary, CMB, inner core-outer core, IC-OC, and center, C, are indicated for reference). The melting curve and the Hugoniot (shock-compression curve) are from *Williams et al.* [1987]. The Hugoniot intersects the melting curve at 243 GPa and crossed from the ε (hcp) to γ (fcc) phase of solid iron at about 200 GPa [*Brown and McQueen*, 1980, 1982, 1986]. At low pressures and temperatures, the α (bcc) to ε transitions has been measured by *Manghnani et al.* [1987] and *Akimoto et al.* [1987]. The initial slope of the γ to ε transition has been determined by *Liu and Bassett* [1975], and the phase boundary between γ and ε iron is constrained by *Liu and Bassett*'s [1975] data and the Hugoniot at 200 GPa. Extrapolation of this boundary indicates that the γ-ε–liquid triple point occurs between 290 and 370 GPa.

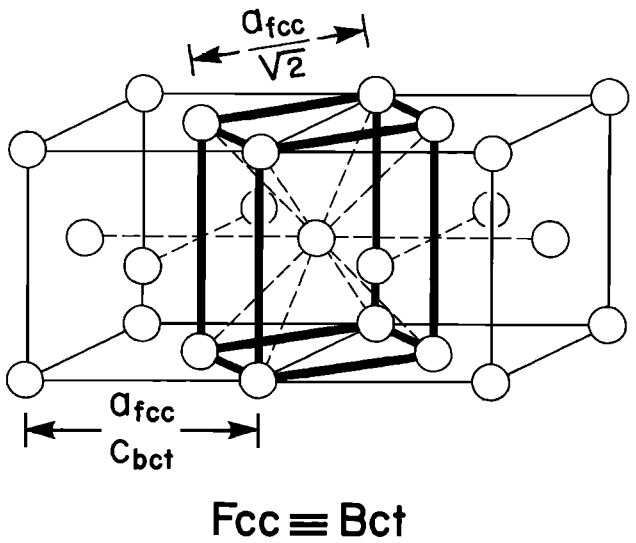

Fig. 12. Equivalence of the face-centered cubic (fcc) lattice (thin lines) and the body-centered tetragonal (bct) lattice (bold lines) when the ratio of bct lattice parameters $c_{bct}/a_{bct} = \sqrt{2}$. The lattice parameter, $a_{fcc} = c_{bct}$, of the fcc lattice gives the second neighbor distance for both the fcc and bct structures. The first neighbor distance in both structures is given by $a_{bct} = a_{fcc}/2$.

We compare the bond lengths within the Fe and FeO unit cells at 80 GPa, the pressure at which we infer solid solution between Fe and FeO from our melting data. The densities, and hence the unit cell volumes and bond lengths, for the solids at 80 GPa and 3600 (± 200) K are determined from the density, elastic, and thermal properties given in Table 3. We note that the equation of state measurements of *Jeanloz and Ahrens* [1980] and *Jephcoat et al.* [1986] give the volumes and hence the interatomic bond lengths for Fe and FeO at 80 GPa with only a relatively small thermal correction being required. In our analysis, we use the Birch-Murnaghan equation of state [*Birch*, 1978] and make the correction for thermal expansion to 3600 K using an estimate of the average high-pressure thermal expansion coefficient of 1.0 (±1.0) X 10^{-5} K^{-1} [*Jeanloz*, 1979]. For γ-iron the first-neighbor (Fe-Fe) and second neighbor (Fe-Fe) bond distances are found in this way to be 229 (± 4) pm and 325 (±4) pm respectively, whereas for FeO the first neighbor (Fe-O) and second neighbor (Fe-Fe or O-O) distances are 219 (± 5) pm and 309 (± 4) pm. As the bond lengths in the unit cells of Fe and FeO are the same to within 5%, we conclude that solid solution across the Fe-FeO system is quite plausible.

We have not proven that the Fe-FeO system exhibits ideal solid solution at high pressures, but our data are most simply interpreted in this way. If correct, this interpretation can only hold along the melting curve at pressures between 70 GPa and 330 (± 40) GPa, however, because it is over this interval that the high pressure metallic phase of FeO (inferred here to be in the distorted B2 or CuAu I structure) and the fcc γ-Fe phase are both stable (Figures 8 and 11). According to our analysis, there is no reason to expect that Fe and FeO form a solid solution above 330 GPa when we expect ε-iron to become the liquidus phase of iron; thus, it is likely that eutectic melting occurs at these pressures.

Core Composition and Temperature

From seismological constraints, the outer core is thought to contain about 8-10% by weight of a light component alloyed with the iron. Criteria for candidate light components include the ability to alloy with iron at high pressure and sufficient cosmochemical abundance to be present in the amount required seismologically. Based on these criteria, a number of elements have been proposed for the major light core constituent, most prominently H, C, N, Mg, O, Si, and S [cf. *Birch*, 1964, 1972; *Stevenson*, 1981; *Murthy and Hall*, 1970; *Ringwood*, 1977; *Brett*, 1976]. In addition, the outer core is thought to contain a small amount (about 4 wt %) of nickel by analogy with the composition of Fe meteorites [*Birch*, 1952]. However, since nickel does not significantly change the density of iron, it is not considered among the light alloying components [*McQueen and Marsh*, 1966]. Discriminating between the various candidates for the most abundant light element(s) relies on a consideration of their geochemistry. Hydrogen is extensively soluble in iron at high pressures [*Fukai and Suzuki*, 1986; *Fukai*, 1984; *Fukai and Akimoto*, 1983], and it may indeed be present in the outer core unless it is too volatile to be incorporated into the initial iron-rich core-forming liquid during the accretion of the Earth. Carbon, nitrogen, and silicon all form alloys with iron at low pressure and presumably do so at high pressures as well. In general, these elements have all been dismissed as important core constituents; carbon and nitrogen have been considered to be too volatile to partition into iron during core formation, and silicon has been ruled out due to its presumed insignificant

partitioning into liquid iron from silicates. Using similar arguments, Mg and MgO have also been dismissed [*Brett*, 1976; *Ringwood*, 1977; *Stevenson*, 1981].

The presence of sulfur in the Earth's core has remained a subject of debate. Sulfur readily alloys with iron at low pressures and has sufficient cosmochemical abundance to be present as the major light alloying element of the core. Additionally, it has been argued that the presence of sulfur in the core could account for the observed depletion of sulfur in the bulk Earth relative to chondrites [*Murthy and Hall*, 1970; *Brett*, 1976; *Stevenson*, 1981]. However, sulfur would also have been a volatile element in the accreting Earth, and it is for this reason that its presence in core-forming liquid has been questioned [*Ringwood*, 1977; *Hall and Murthy*, 1971; *Brown et al.*, 1984].

The presence of oxygen in the core has centered around the question of whether or not oxygen can alloy with iron under core conditions. Our results have shown that iron and oxygen do form a metallic liquid and a metallic solid solution at high pressures and temperature, thus removing the primary objection to the presence of oxygen in the core. The abundance of oxygen in the Earth, nearly 65 mol % of the crust and mantle, provides a ready source region for oxygen ingress and migration into the core. Also, experimental evidence shows that chemical reactions occur between liquid iron and crystalline silicates at high pressures and temperatures, with oxide clearly dissolving into the metallic alloy [*Knittle and Jeanloz*, 1989; *Williams et al.*, 1987; *Alder*, 1966]. In fact, these experiments make it appear inevitable that oxygen is present in the outer core because of the occurrence of chemical reactions at the core-mantle boundary. It is quite plausible that small amount of other major components of silicates, silicon and magnesium, are present in the Earth's core as well.

The presence of oxygen in the core has profound implications for the temperature at depth. Figure 10 shows that at high pressure (80 GPa) the Fe-FeO system is a solid solution. This behavior is strongly contrasted with that of the Fe-FeS system which maintains a eutectic to at least 80 GPa (*Williams and Jeanloz*, 1990). Therefore, if the core contained primarily sulfur, the melting temperature of the core composition would be expected to be lower than that of iron by as much as 1000 K. However, if oxygen is the sole light alloying component, then the melting temperature of the core composition would be higher than that of iron. To demonstrate the effect of oxygen, we have calculated the phase diagram of the Fe-FeO system at the pressure of the core-mantle boundary maintaining the assumption that the system is still a solid solution at these pressures.

The Fe-FeO phase diagram at 136 GPa, shown in Figure 13, is less constrained than that at 80 GPa. Although the properties of Fe are still well determined under these conditions, now the melting temperature of solid FeO, in addition to ΔV_m and ΔS_m, is uncertain. We know from our measurements that the melting temperature of FeO at 100 GPa is ~ 6000 K. Therefore, if the melting slope remains at 50 (± 15) K/GPa, then T_m ~ 7800 K at 136 GPa. Another estimate can be obtained by assuming that the melting slope becomes more like that of iron: 20 (± 5) K/GPa. In this case, the melting temperature of FeO is ~ 6720 K at 136 GPa. For the phase diagram calculation, averages of the melting slope and melting temperature bounds are considered and are summarized in Table 3*b*. Although somewhat uncertain, Figure 13 illustrates the effect that oxygen has on the melting temperature of pure iron at pressures above 70 GPa. With regard to the core, the effect

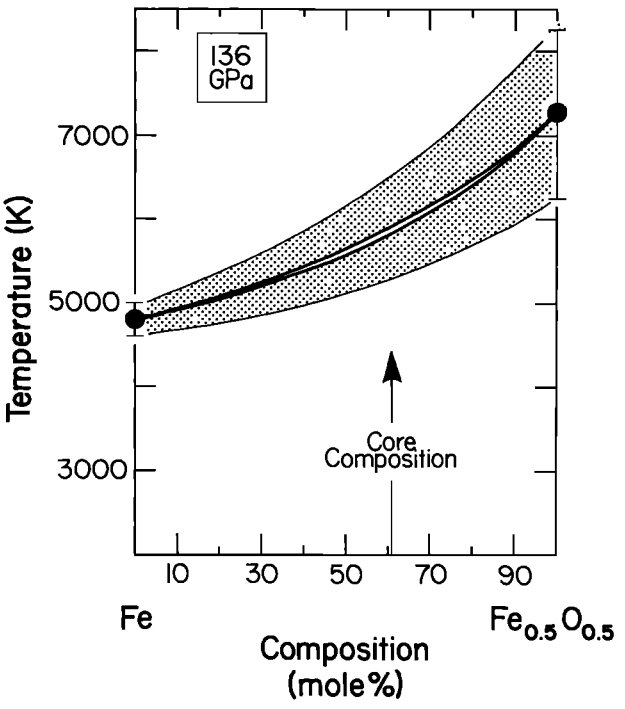

Fig. 13. Phase diagram for Fe-FeO extrapolated to 136 GPa, the pressure at the core-mantle boundary (see Table 3*b*).

of oxygen as the sole light alloying component is to make the melting temperature of the outer core higher than that of pure iron, perhaps a high as 6000 K, at the base of the mantle.

Williams et al. [1987] estimate the temperature at the core-mantle boundary to be 3800 (± 300) K. This is considered to be a lower bound on the temperature and is obtained by subtracting 1000 K from the melting temperature of pure iron to account for the effect of an unspecified light core component in depressing the melting point of iron [see *Brown and McQueen*, 1982]. As stated previously, this depression of the melting point is probably a reasonable estimate if the light alloying component is, for instance, sulfur. In fact, a melting point depression of 1000 K would also be appropriate if the light alloying component were silicon or magnesium. However, our experiments with FeO demonstrate that oxygen is not likely to behave in the same way at the conditions of the core-mantle boundary, and it does not depress the melting point of iron. One implication of our results is that melting point depression in the outer core to a small amount (1-3 % by weight in the core) of light contaminating component such as silicon or sulfur may be superimposed on the melting temperature of the iron-oxygen system. That is, the effect of oxygen in the core is to counteract the melting point depression of iron that may be caused by other components. As a result, the melting temperature of an oxygen-rich core composition could be depressed by only a few hundred degrees below that of pure iron, rather than by 1000 K. This expectation is supported by experimental observations: when iron is melted in the presence of oxides (Al_2O_3) or silicates ($(Mg,Fe)SiO_3$). the melting temperature of the metal-oxide reacted zone that is produced is typically 100 to 300 K lower than that of pure iron [cf. *Knittle and Jeanloz*, 1986*b*; *Williams et al.*, 1987].

Therefore our results on melting in the Fe-FeO system at high pressure are consistent with temperatures at the core-mantle boundary in excess of 3800 K and perhaps close to the 4800 K value that *Williams et al.* [1987] regarded as an upper

limit to the temperature at the core-mantle boundary. Such extreme temperatures are ~1000-2000 K higher than have been inferred for the base of the convecting mantle [cf. *Jeanloz and Richter*, 1979; *Jeanloz and Morris*, 1986; *Spiliopoulos and Stacy*, 1984]. If present, the large difference between the temperatures estimated for the base of the mantle and the top of the core would implies that a major thermal boundary layer occurs at the core-mantle boundary. A high temperature for the core would also be consistent with, and perhaps require, thermal models involving a second thermal boundary layer within the mantle, most likely at the 670 km discontinuity. However, the nature of this seismic discontinuity, whether it reflects a change in the bulk composition of the mantle or not, remains controversial [*Knittle et al.*, 1986*a*].

The inferred thermal boundary layer between mantle and core, with a temperature difference of 1000-2000 K, allow us to estimate the heat flux out of the *D"* layer into the lower mantle. For our estimate we assume that the *D"* layer is 200 km thick, the temperature gradient across the region is conductive and the thermal conductivity of the layer is 4 W $-m^{-1}$ K^{-1}. We regard this estimate of the thermal conductivity to be a lower bound based on the region being composed completely of silicate material with negligible radiative heat transfer. It is plausible that the chemically heterogeneous *D"* layer has regions anomalously enriched in metallic FeO; this would locally contribute to a higher thermal conductivity. Also, it may be necessary for *D"* to be stabilized by the presence of dense heterogeneities in order to sustain a 200-km-thick thermal boundary layer.

With these assumptions, our estimate of the heat flux of *D"* is 40 (± 20) mW m^{-2}. This value implies that the total heat emanating form the top of the *D"* layer into the lower mantle is 7 (± 4) X 10^{12} W. Therefore a minimum of 20 (± 10) % of the total heat that is lost through the Earth's surface may originate from *D"*.

CONCLUSIONS

The metallization of FeO under conditions of the Earth's deep interior provides a mechanism for incorporating oxygen into the core. Our experiments show that oxygen forms a metallic alloy with both liquid and solid iron at high pressure and temperatures. Considered together with the likelihood of chemical reactions occurring at the core-mantle boundary, this strongly suggests that the Earth's core contains oxygen regardless of whatever other elements may be present. The alloying of oxygen with iron under core conditions increases the melting point of pure iron rather than depressing it. Therefore, the presence of oxygen in the outer core is likely to counterbalance the melting-point depression of iron caused by other contaminants in the outer core (e.g., nickel, silicon, or sulfur). Our results suggest that temperatures at the core-mantle boundary are relatively high, near 4800 K, and therefore that a significant amount of the energy driving mantle convection is generated in the core.

Acknowledgments. We thank T.J. Ahrens, D.L. Anderson, D.L. Heinz, H.-K. Mao, A.E. Ringwood, D.J. Stevenson, Q. Williams, and T. Yagi for helpful comments. This work was supported by NASA.

REFERENCES

Adler, D., Mechanism for metal-nonmetal transitions in transition-metal oxides and sulfides, *Rev. Mod. Phys., 40*, 714-736, 1968.

Akimoto, S., T. Yagi, T. Suzuki, and O. Shimomura, Phase diagram of iron determined by high pressure x-ray diffraction using synchrotron radiation, in *High Pressure Research in Geophysics and Geochemistry*, edited by M.H. Manghnani and Y. Syono, pp. 149-154, AGU, Washington, D.C., 1987.

Alascio, B., A. Lopez, and V. Grünfeld, A model for the phase diagram of $(V_{1-x}Cr_x)_2O_3$, *Solid State Commun., 9*, 1711-1713, 1971.

Alder, B.J., Is the mangle soluble in the core?, *J. Geophys. Res., 71*, 4973-4979, 1966.

Anderson, O.L., Properties of iron at the Earth's core conditions, *Geophys. J.R. Astron. Soc., 84*, 561-579, 1987.

Barnett, J.D., S. Block and G.J. Piermarini, An optical fluorescence system for quantitative pressure measurement in the diamond-anvil cell, *Rev. Sci. Instrum., 44*, 1-9, 1973.

Birch, F., Elasticity and constitution of the Earth's interior, *J. Geophys. Res., 57*, 227-288, 1952.

Birch, F., The density and composition of the mantle and core, *J. Geophys. Res., 69*, 4377-43881964.

Birch, F., The melting relations of iron and temperatures in the Earth's core, *Geophys. J.R. Astron. Soc., 29*, 373-387, 1972.

Birch, F., Finite strain isotherm and velocities for single-crystal and polychrystalline NaCl at high pressures and 300 K, *J. Geophys. Res., 83*, 1257-1267, 1978.

Bowen, H.K., D. Adler, and B.H. Auker, Electrical and optical properties of FeO, *J. Solid State Chem., 12*, 355-359, 1975.

Brandow, B.H., Electronic structure of Mott insulators, *Adv. Phys., 26*, 651-808, 1977.

Brett, R., The Earth's core: Speculations on the composition of the core of the Earth, *Rev. Geophys., 14*, 375-383, 1976.

Brown, J.M., and R.G. McQueen, The melting of iron under core conditions, *Geophys. Res. Lett., 7*, 533-536, 1980.

Brown, J.M. ,and R.G. McQueen, The equation of state for iron and the Earth's core, in *High Pressure Research in Geophysics*, edited by S. Akimoto and M.H. Manghnani, pp. 611-623, Center for Academic Publishing, Tokyo, 1982.

Brown, J.M., and R.G. McQueen, Phase transitions, Gruneisen parameter, and elasticity for shocked iron between 77 GPa and 400 GPa, *J. Geophys. Res., 91*, 7485-7494, 1986.

Brown, J.M., T.J. Ahrens, and D.L. Shampine, Hugoniot data for pyrrhotite and the Earth's core, *J. Geophys. Res. 89*, 6041-6048, 1984.

Cleary, J.R., The *D"* region, *Phys. Earth Planet. Inter., 9*, 13-27, 1974.

Darken, L.S., and R.W. Gurry, The system iron-oxygen, II, Equilibrium and thermodynamics of liquid oxides and other phases, *J. Am. Chem. Soc., 68*, 798, 1946.

Darken, L.S., and R.W. Gurry, *Physical Chemistry of Metals*, 535 pp., McGraw-Hill, New York, 1953.

Endo, S., and K. Ito, Triple-state high pressure apparatus using sintered diamond anvils, in *High-Pressure Research in Geophysics*, edited by edited by S. Akimoto and M.H. Manghnani, pp. 3-12, Center for Academic Publishing, Tokyo, 1982.

Falicov, C.M., C.E.T. Goncalves da Silva, and B.A. Huberman, Metal-insulator and magnetic phase transitions: a thermodynamic model, *Solid State Commun., 10*, 455-458, 1972.

Fukai, Y., The iron-water reaction and the evolution of the Earth, *Nature, 308*, 174-175, 1984.

Fukai, Y. and S. Akimoto, Hydrogen in the Earth's core: experimental approach, *Proc. Jpn. Acad. Ser. B, 59*, 158-162, 1983.

Fukai, Y., and T. Suzuki, Iron-water reaction under high pressure and its implication in the evolution on the Earth, *J. Geophys. Res., 91*, 9222-9230, 1986.

Goodenough, J.B., Metallic oxides, in *Progress in Solid State Chemistry*, vol. 5, edited by H. Reiss, pp. 145-400, Pergamon Press, New York, 1971.

Guinan, M.W. and D.N. Beshers, Pressure derivatives of the elastic constants of α-iron to 10kbs, *J. Phys. Chem. Solids, 29*, 541-549, 1968.

Hall, H.T., and V. Rama Murthy, The early history of the Earth: Some critical element fractionations, *Earth Planet. Sci. Lett., 11*, 239-244, 1971.

Hazen, R.M. and R. Jeanloz, Wüstite ($Fe_{1-x}O$): A review of its defect structure and physical properties, *Rev. Geophys., 22*, 37-46, 1984.

Heinz, D.L., and R. Jeanloz, Temperature measurements in the laser-heated diamond cell, in *High Pressure Research in Geophysics and Geochemistry, Geophys. Monogr. Ser.*, vol. 39, edited by M.H.

Manghnani and Y. Syono, AGU, Washington, D.C., pp. 113-128, 1987.

Jeanloz, R., Properties of iron at high pressure and the state of the core, *J. Geophys. Res., 84*, 6059-6069, 1979.

Jeanloz, R., and T.J. Ahrens, Equations of state of FeO and CaO, *Geophys. J.R. Astron. Soc., 62*, 505-528, 1980.

Jeanloz, R., and S. Morris, Temperature distribution in the crust and mantle, *Annu. Rev. Earth Planet. Sci., 14*, 377-415, 1986.

Jeanloz, R., and F.M. Richter, Convection, composition and thermal state of the lower mantle, *J. Geophys. Res., 84*, 5497-5504, 1979.

Jephcoat, A., H.K. Mao, and P.M. Bell, Static compression of iron to 78 GPa with rare gas solids as pressure transmitting media, *J. Geophys. Res., 91*, 4677-4684, 1986.

Keeler, R.N., and A.C. Mitchell, Electrical conductivity demagnetization and the high pressure phase transitions in shock compressed iron, *Solid State Commun., 7*, 271-274, 1969.

Kerrick, D.M., and L.S. Darken, Statistical thermodynamic models for ideal oxide and silicate solid solutions, with application to plagioclase, *Geochim. Cosmochim. Acta, 39*, 1431-1442, 1975.

Knittle, E., and R. Jeanloz, Structural and bonding changes in cesium iodide at high pressures, *Science, 223*, 54-57, 1984.

Knittle, E., and R. Jeanloz, High-pressure x-ray diffraction and optical absorption studies of CsI, *J. Phys. Chem. Solids, 46*, 1179-1184, 1985.

Knittle, E., and R. Jeanloz, High-pressure electrical resistivity measurements of Fe_2O_3: Comparison of static compression and shock-wave experiements to 61 GPa, *Solid State Commun., 58*, 129-131, 1986*a*.

Knittle, E., and R. Jeanloz, High-pressure metallization of FeO and implications for the Earth's core, *Geophys. Res. Lett., 13*, 1541-1544, 1986*b*.

Knitle, E., A. Rudy, and R. Jeanloz, High-pressure phase transition in CsBr, *Phys. Rev. B., 31*, 588-590, 1985.

Knittle, E., R. Jeanloz, and G.L. Smith, The thermal expansion of silicate perovskite and stratification of the Earth's mantle, *Nature, 319*, 214-216, 1986a.

Knittle, E., R. Jeanloz, A.C. Mitchell, and W.J. Nellis, Metallization of $Fe_{0.94}O$ at elevated pressures and temperatures observed by shock-wave electrical resistivity measurements, *Solid State Commun., 59*, 513-515, 1986*b*.

Knittle, E. and R. Jeanloz, Simulating the core-mantle boundary: An experimental study of high-pressure reactions between silicates and liquid iron, *Geophys. Res. Lett., 16*, 609-612, 1989.

Kondo, K., T. Sunakawa, and A. Sawaoka, Pressure dependence on electrical resistivity and contacts of hematite crystal, *Jpn. J. Appl. Phys., 18*, 851-852, 1979.

Kondo, K., T. Mashimo, and A. Sawaoka, Electrical resistivity and phase transformation of hematite under shock compressions, *J. Geophys. Res., 85*, 977-982, 1980.

Lay, T. and D.L. Helmberger, A lower mantle *S*-wave triplication and the shear velocity structure of *D"*, *Geophys. J.R. Astron. Soc., 75*, 799-837, 1983.

Li, X., and R. Jeanloz, Measurement of the electrical conductivity of (Mg, Fe)SiO_3 perovskite and a perovskite-dominated assemblage at lower mantle conditions, *Geophys. Res. Lett., 14*, 1975-1078, 1987.

Lindsley, D.H., Pressure-Temperature Relations in the system FeO-SiO_2, *Year Book Carnegie Insti. Washington., 65*, 226-230, 1966.

Liu, L.G., On the (γ,ε,l) triple point of iron and the Earth's core, *Geophys. J.R. Astron. Soc., 43*, 697-705, 1975.

Liu, L.G., and W.A. Bassett, The melting of iron up to 200 kbar, *J. Geophys. Res., 80*, 3777-3782, 1975.

Manghnani, M.H., L.C. Ming, and N. Nakagiri, Investigation of the α-Fe to ε-Fe phase transition by synchrotron radiation, in *High Pressure Research in Geophysics and Geochemistry*, Geophys. Monogr. Ser., vol. 39, edited by M.H. Manghnani and Y. Syono, pp. 155-164, AGU, Washington, D.C., 1987.

Mao, H.-K., and P.M. Bell, Techniques of electrical conductivity measurement to 300 kbar, in *High Pressure Research Applications in Geophysics*, edited by M.H. Manghnani and S. Akimoto, pp. 493, Academic, San Diego, Calif., 1977.

Mao, H.-K., P.M. Bell, J.W. Shaner, and D.J. Steinberg, Specific volume measurements of Cu, Mo, Pd and Ag and calibration of the ruby R, fluorescence pressure gauge for 0.06 to 1 Mbar, *J. Appl. Phys., 49*, 3276-3283, 1978.

Mao, H.-K., P.M. Bell, K.J. Dunn, R.M. Chrenko, and R.C. DeVries, Absolute pressure measurements and analysis of diamonds subjected to maximum static pressures of 1.3-1.7 Mbar, *Rev. Sci. Instrum., 50*, 1002-1009, 1979.

McCammon, C.A., A.E. Ringwood, and I. Jackson, Thermodynamics of the system Fe-FeO-MgO at high pressure and temperature and a model for formation of the Earth's core, *Geophys. J.R. Astron. Soc., 72*, 577-595, 1983.

McQueen, R.M., and S.P. Marsh, Shock-wave compression of iron-nickel alloys and the Earth's core, *J. Geophys. Res., 71*, 1751-1756, 1966.

Murthy, V. Rama, and H.T. Hall, The chemical composition of the Earth's core: Possibility of sulfur in the core, *Phys. Earth Planet. Inter., 2*, 276-282, 1970.

Okamoto, T., H. Fujii, Y. Hidaka, and E. Tatsumoto, Effect of hydrostatic pressure on the Néel temperature in FeO and CoO, *J. Phys. Soc. Jpn., 23*, 1174, 1967.

Reichlin, R., Electrical resistance measurements of metals to 40 GPa in the diamond cell, *J. Physi., C Solid State Phys., 45*, 399-402, 1984.

Ringwood, A.E., Composition of the core and implications for the origin of the Earth, *Geochem. J., 11*, 111-136, 1977.

Ruff, L.J., and D.V. Helmberger, The structure of the lowermost mantle determined by short-period *P*-wave amplitudes, *Geophys. J.R. Astron. Soc., 68*, 95-119, 1982.

Seltz, H., Thermodynamics of solid solutions, I, Perfect solutions, *J. Am. Chem. Soc., 56*, 307, 1934.

Spiliopoulos, S., and F.D. Stacey, The Earth's thermal profile: Is there a mid-mantle thermal boundary layer?, *J. Geodyn., 1*, 61-77, 1984.

Stevenson, D.J., Models of the Earth's core, *Science, 241*, 611-619, 1981.

Ubbelohde, A.R., *The Molten State of Matter*, 241 pp., JohnWiley, New York, 1978.

Williams, Q. and R. Jeanloz, Melting relations in the iron-sulfur systam at ultrahigh pressures: Implications for the thermal state of the Earth, *J. Geophys. Res.*, 1990.

Williams, Q., R. Jeanloz, J. Bass, B. Svendsen, and T.J. Ahrens, The melting curve of iron to 250 gigapascals: A constraint on the temperature at the Earth's center, *Science, 236*, 181-183, 1987.

Yagi, T., T. Suzuki, and S. Akimoto, Static compression of wüstite ($Fe_{0.98}O$) to 120 GPa, *J. Geophys. Res., 90*, 8784-8788, 1985.

Young, C.J., and T. Lay, The core-mantle boundary, *Annu. Rev. Earth Planet. Sci., 15*, 25-46, 1987.

R. Jeanloz, Department of Geology and Geophysics, University of California, Berkeley, CA 94720.

E. Knittle, Board of Earth Sciences, University of California, Santa Cruz, CA 95064.

(Received April 7, 1988;
revised January 4, 1990;
accepted March 12, 1990.)

JOURNAL OF GEOPHYSICAL RESEARCH, VOL. 96, NO. B10, PAGES 16,131–16,150, SEPTEMBER 10, 1991

Variations in Heat Flow Across the Goban Spur and Galicia Bank Continental Margins

K. E. LOUDEN

Department of Oceanography, Dalhousie University, Halifax, Nova Scotia, Canada

J.-C. SIBUET, AND J.-P. FOUCHER

Ifremer, Centre de Brest, Plouzané, France

We present the results of 44 new heat flow stations which were taken in 1984 and 1989 in profiles across the Goban Spur and Galicia Bank continental margins (NW Atlantic Ocean). Simple extensional models indicate that the heat flow across both these Early Cretaceous rifted margins should increase from values of 45—50 mW/m^2 over oceanic crust to 65—80 mW/m^2 on the continents. The rate of this increase should help to constrain the mechanism (simple versus pure shear) by which the upper, more radiogenic continental crust is thinned. Measurements across Goban Spur increase from values of 40—45 mW/m^2 over oceanic crust to 50—55 mW/m^2 near the continental shelf. They follow the predicted trend for pure-shear rifting, but only if the value of upper crustal radiogenic heating is low (1—2 μW/m^3). Otherwise, they would require the upper crust to thin more rapidly than the total crustal thickness, as with a lower plate, simple-shear margin. Measurements across Galicia Bank show a very different pattern, with similar values over oceanic crust but much lower values (30—35 mW/m^2) nearer land. This is difficult to reconcile with any simple, single rifting event but is more compatible with an origin as a pure-shear or lower plate rather than upper plate margin. We also note that oceanic values of heat flow require asthenospheric temperatures 100°C lower than normal for both margins. This indicates that the triple junction in existance between these margin segments during the breakup of Iberia, Europe, and North America was not the site of a major mantle plume.

INTRODUCTION

Two simple models have been commonly presented as prototypes to describe the fundamental extensional characteristics of nonvolcanic continental margins: (1) the pure-shear model [*McKenzie*, 1978] and its variants and (2) the simple-shear model [*Wernicke*, 1985]. In pure-shear models, extension is produced by a series of seaward dipping faults in the brittle upper layer and ductal deformation in the lower layer. If the amount of extension differs between these two layers (as discussed by *Royden and Keen* [1980]), the detachment surface is horizontal. This results in a pattern of crustal and lithospheric thinning that is symmetric for each conjugate margin pair. In the simple-shear model, extension occurs along a single, low-angle detachment fault which penetrates through the crust and possibly into the lithosphere. This nonhorizontal detachment offsets the thinning of the upper region (including the crust) from that of the lower lithospheric region, resulting in an asymmetric conjugate pair of "upper plate" (hanging wall) and "lower plate" (footwall) margins.

Application of these models has been made in a number of detailed case studies in the North Atlantic region. Since these margins are known to have formed in the Mesozoic, the initial patterns of lithospheric thinning, which existed at the time of their creation, have been largely destroyed by a long subsequent period of conductive cooling. Thus observational evidence for characterizing the rifting process largely consists of seismic images of crustal structures from reflection and refraction profiles. Of these, the greatest definition has come from multichannel reflection profiles across the sediment-starved margins off western Europe [e.g., *Montadert et al.*, 1979a; *Le Pichon and Barbier*, 1987; *Peddy et al.*, 1989] or the moderately sedimented margins off eastern Canada [e.g., *Keen and de Voogd*, 1988; *Keen et al.*, 1989], where a clear image of the faulted, transitional crust has not been obscured by a thick sediment cover.

Other data, such as subsidence histories and thermal anomalies, should also show patterns that are model dependent [*Voorhoeve and Houseman*, 1988; *Buck et al.*, 1988; *Issler et al.*, 1989]; however, such data have not as yet been very definitive. For example, synrift and postrift subsidence for the pure-shear model should be symmetric on each conjugate margin and directly related to the stretching factor (i.e., areas with large synrift subsidence caused by the thinning of the crust should also be those with large postrift subsidence caused by the cooling of the lithosphere). For a simple-shear margin, the thermal history of the upper plate margin should be dominated by postrift, thermal subsidence; that of the lower plate margin should be dominated by initial, synrift subsidence. Unfortunately, such subsidence histories as determined from borehole samples on sediment-starved margins can suffer large uncertainties in microfaunal estimates of paleobathymetry [e.g., *Moullade et al.*, 1988]. On the other hand, for sediment-filled margins where the shallow paleobathymetry is better controlled, the thick sedimentary layer prevents a full sampling of synrift sequences, particularly on those sections of highly thinned crust that would best determine characteristic patterns of initial subsidence.

The thermal structure across old margins (i.e. older than a characteristic lithospheric time constant of 50—70

Paper number 91JB01453.
0148-0227/91/91JB-01453$05.00

Ma) should also be model specific. While the degree of lithospheric thinning at the time of rifting is no longer well constrained, heat flow measurements should still record the degree of asymmetry in attenuation of the more radiogenic continental crust. In pure-shear extension, we would expect this to be uniformly related to the stretching factor; for simple-shear, we would expect either a more rapid or a more gradual increase, depending on whether the crustal thickening is dominated by the less radiogenic, lower continental crust or more radiogenic, upper continental crust. However, data across old margins, from either boreholes or surface penetrations, suffer from a lack of adequate coverage and only two profiles have been able to be constructed from continent to ocean. One of these profiles, on thick sediments across the Nova Scotian margin off eastern Canada, is disturbed by salt diapirs and made uncertain by poorly constrained borehole conductivities [see *Louden and Wright*, 1989]. On the other profile across the Biscay margin off western France, *Foucher and Sibuet* [1980] could show only a very general, qualitative agreement between the pure-shear model and heat flow measurements.

The purpose of this paper is to help supplement these meager data by adding new measurements of surface heat flow across two margins in the northeastern Atlantic. One of these, Goban Spur, shows patterns of crustal thinning that have been associated with a pure-shear process, while the other, Galicia Bank, has different characteristics which have been attributed to either pure-shear or upper plate, simple-shear extension. Based on the previous discussion, we would expect for Goban Spur a uniform increase in heat flow with increasing continental crustal thickness, while for Galicia Bank, the increase should be either similar or more abrupt. Our observations, however, require only a gradual increase across Goban Spur and a decrease across Galicia Bank. This suggests that, in both cases, the radiogenic continental crust thins more rapidly than the total crustal thickness or the original rate of radiogenic heat production was low. The former implies formation by lower plate, simple-shear rifting; the latter by pure-shear rifting. Consistency with observed changes in crustal structure justifies the pure-shear origin for Goban Spur. There is, however, no indication from heat flow measurements for earlier suggestions of a simple-shear, upper plate model for Galicia Bank. Further clarification will require additional data, particularly including measurements of radiogenic heat production from the transitional basement of the Goban Spur and Galicia Bank margins and heat flow observations from their conjugate margins off Newfoundland.

REGIONAL SETTING

The Atlantic margins off western Europe offer an excellent location in which to observe possible variations in heat flow caused by differing processes of crustal thinning. Most importantly, the general tectonics of the region has already been intensively studied and densely sampled with gravity, magnetic, seismic, and borehole data. As previously mentioned, the margins are sediment starved, which means that complications caused by effects of thermal blanketing [*Hutchison*, 1985; *Lucazeau and Le Douaran*, 1985] are minimal. Numerous heat flow measurements have also been taken on land [*Lucazeau and Vasseur*, 1989]. Values of radiogenic heat production in the Paleozoic metamorphosed cratons which border these margins are generally high [e.g., *Jolivet et al.*, 1989], due to the presence of numerous granitic batholiths. Thus the gross difference in heat flow between ocean basin and continent is relatively large, as can readily be seen in Figure 1.

Three margin sections have been particularly well studied: the Celtic margin of the northern Bay of Biscay, the Goban Spur margin southwest of Ireland, and the western Galicia Bank margin off the northwestern Iberian peninsula. On the Celtic margin, a number of heat flow measurements have already been taken [*Erickson et al.*, 1979; *Foucher and Sibuet*, 1980; *Watremez*, 1980; J.-P. Foucher, unpublished data, 1988; D. Abbott, personal commun., 1990]. Deep reflection [*Montadert et al.*, 1979a], and refraction profiles [*Avedik et al.*, 1982] define the amount of crustal thinning across the complete continental transition. Recent profiles show evidence for simple shear along a decollement zone that dips toward the continent and cuts across the upper continental crust [*Le Pichon and Barbier*, 1987]. However, the direction of opening is slightly oblique to the strike of the margin, and the conjugate margin off northern Galicia Bank and the north coast of Spain [*Srivastava et al.*, 1990; *Sibuet and Collette*, 1991] cannot offer a comparison because it has been affected by subsequent compression during the Eocene Pyrenean orogeny [*Le Pichon and Sibuet*, 1971]. Therefore, in this study, we will concentrate on the later two margins, Goban Spur and western Galicia Bank, where shallow-penetration heat flow measurements had not previously been taken.

Goban Spur

The Goban Spur continental margin segment lies to the south of the Porcupine Seabight and to the north of the Jean Charcot escarpment (Figures 1 and 2). It is a relatively wide and shallow margin compared with those margins to the southeast, with an extensive region less than 2000 m deep (Figure 2). It formed during the Early Cretaceous by separation of the European and North American continents. Immediately to its south, a triple junction was active until chron 33 (80 Ma), during rotation of the Iberian peninsula to form the Bay of Biscay [*Olivet et al.*, 1984; *Srivastava and Tapscott*, 1986; *Sibuet and Collette*, 1991]. The absence of magnetic chron M0 in oceanic crust to the west of the margin (Figure 1) [*Guennoc et al.*, 1978; *Verhoef et al.*, 1986] and the dating of the synrift sedimentary sequences on the margin [*Montadert et al.*, 1979a; *Roberts et al.*, 1981; *Masson et al.*, 1985] indicate the beginning of oceanic crustal accretion within late early Albian time (about 105 Ma).

Reflection profiles across the margin (cf. Figure 13) show a series of rotated fault blocks which probably sole at the lower continental crust [*Peddy et al.*, 1989], in a manner similar to those recognized in the southeast across the Celtic margin [*Montadert et al.*, 1979a]. The tops of these blocks consist of limestones which probably formed in Jurassic shallow seas as part of earlier, aborted phases of rifting. Significant erosion of the upper blocks suggests that they were later uplifted as they were tilted. Within the half-grabens bounded by the rotated blocks, synrift sequences that were deposited as the margin subsided date from the Early Cretaceous to lower Albian.

Using the method of *Withjack and Jamison* [1986], *Sibuet* [1987] has shown from the orientation of basement faults

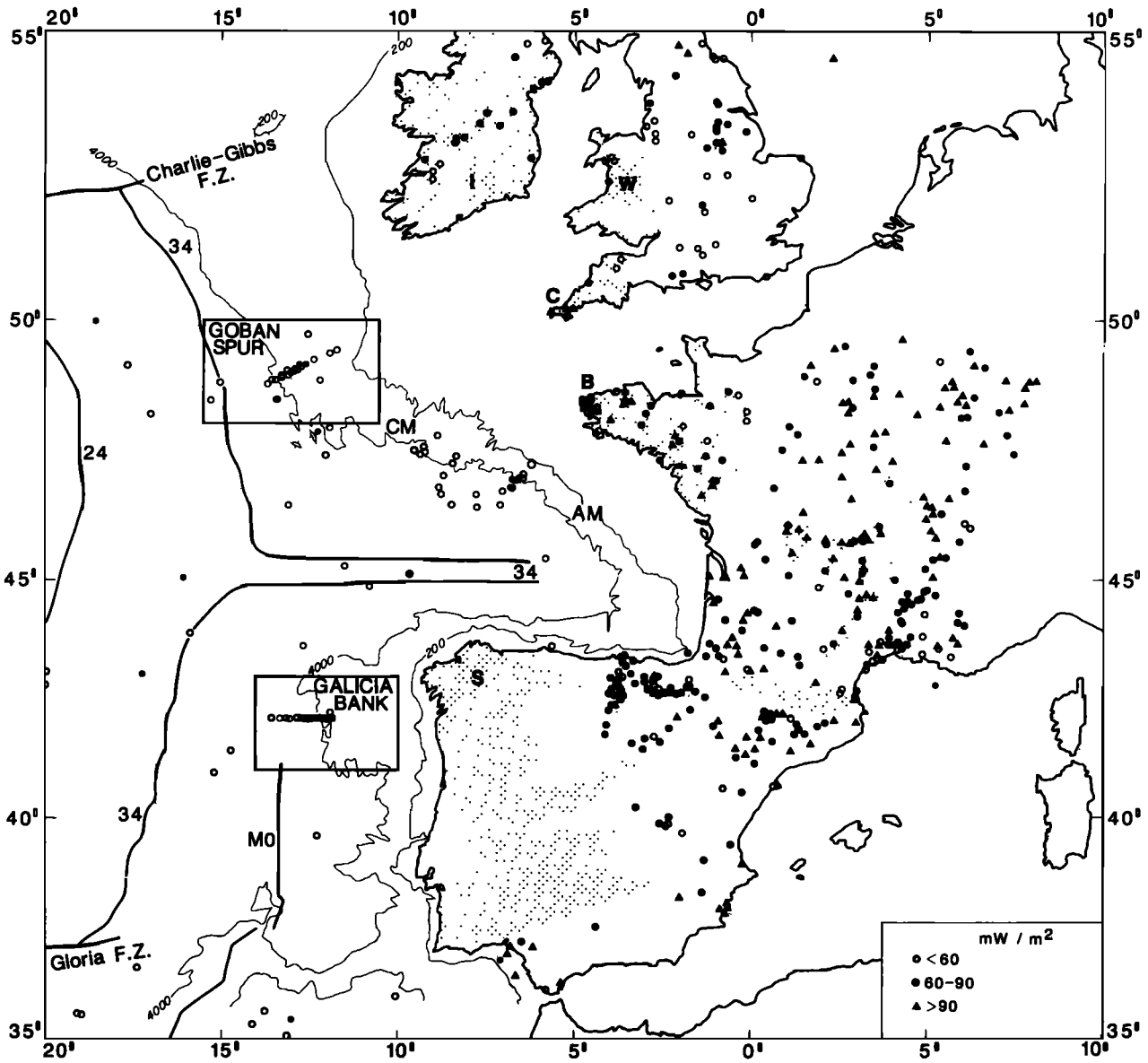

Fig. 1. Generalized, uncorrected heat flow values from the northwestern Atlantic Ocean and adjacent regions of western Europe. Sources of data are: seafloor heat flow [*Louden and Wright*, 1989; *Foucher et al.*, 1985; *Watremez*, 1980; Foucher, unpublished data, 1988; D. Abbott, personal communication, 1990]; Spain [*Albert-Beltran*, 1979]; France [*Lucazeau and Vasseur*, 1989]; Great Britain [*Bloomer et al.*, 1979]; and Ireland [*Brock*, 1989]. Boxes locate regions of Goban Spur (Figure 2) and Galicia Bank (Figure 4) surveys. Abbreviations are CM, Celtic margin; and AM, Armorican margin. Letters and shaded areas denote general regions of Paleozoic basement adjacent to the Mesozoic margins [after *Montadert et al.*, 1979b]. Bathymetry and location of magnetic anomaly chrons M0, 34, and 24 are from *Lallemand et al.* [1985], *Guennoc et al.* [1978], and *Verhoef et al.* [1986].

and the rift axis that this margin segment underwent pure extension. *Peddy et al.* [1989] have suggested that this extension was produced by a pure-shear mechanism. Their primary evidence is that thinning of the reflective zone within the lower crust on the WAM profile across Goban Spur is observed in the same proportion as the upper crust. Since pure-shear margins should form symmetrically, this conclusion apparently conflicts with the much narrower shape of its conjugate, the northeastern flank of Flemish Cap. However, comparison of deep seismic profiles across these two margins, once they have been placed in a reconstructed position [*Srivastava et al.*, 1988], show overall symmetry between continental crustal blocks about a zone of thinned crust, 65 km wide [*Keen et al.*, 1989]. It was therefore the location of breakup, offset toward the Flemish Cap side of the rift, that led to the asymmetric shape. The prebreakup symmetry of the Moho is more compatible with thinning by pure-shear as opposed to simple-shear extension. This would also explain the absence in the WAM profile of a major low-angle detachment fault within the thinned continental crust across Goban Spur [*Peddy et al.*, 1989], in contrast to the Celtic margin where a strong *S* reflector is observed dipping landward [*Le Pichon and Barbier*, 1987]. Note, however, that this interpretation is disputed by *Tankard and Welsink* [1988]. They represent Goban Spur as the upper plate half of a simple-shear boundary, with Orphan Basin as its lower plate conjugate, using the previous reconstructions of *Masson and Miles*

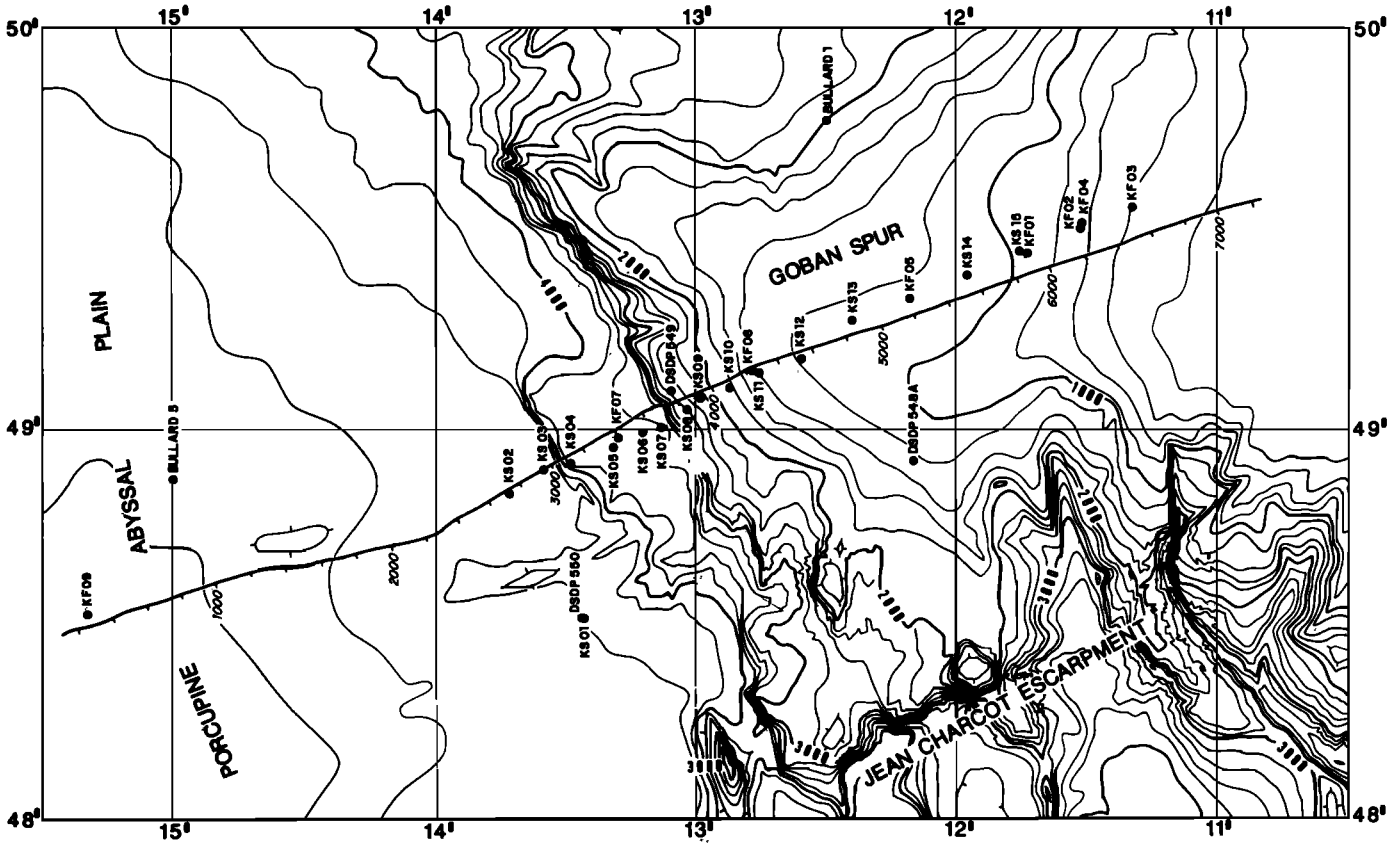

Fig. 2. Bathymetry of Goban Spur margin [*Sibuet et al.*, 1985] with locations of heat flow stations and shot points along the WAM reflection profile [*Peddy et al.*, 1989].

[1984]. No evidence is presented, however, for the existence of the appropriate intracrustal detachment fault.

Galicia Bank

The West Iberian margin is located to the south of Galicia Bank and northwest of the Vigo and Vasco Da Gama seamounts (Figures 1 and 5). Its gross bathymetric structure is quite similar to Goban Spur (cf. Figures 2 and 5), except that it lies approximately 1 km deeper and is separated from the Portuguese continental mainland to the east by the thickly sedimented Interior basin. The West Iberian margin was created between Iberia and North America to the south of the Biscay triple junction during two phases of rifting [*Mauffret and Montadert*, 1987]: the first beginning in the Late Jurassic (Oxfordian-Kimmeridgian), during which the Interior basin was formed [*Murillas et al.*, 1990], and the second in the Early Cretaceous (Valanginian-Hauterivian), during which the final morphology of the margin was acquired. Oceanic crust began to form at the end of this second phase (about 114 Ma), consistent with the identification of chron M0 (118 Ma) to the south (Figure 1) [*Guennoc et al.*, 1978; *Verhoef et al.*, 1986] and somewhat in advance of accretion westward of Goban Spur as the spreading center propagated to the north.

Reflection profiles across the margin show a series of rotated fault blocks (cf. Figure 13) similar to those observed across Goban Spur and the Celtic margins. Results from ODP Leg 103 drilling [*Boillot et al.*, 1988] show that these blocks were tilted during the later phase of extension (Hauterivian to Aptian), which postdated the subsidence and conformable deposition of synrift sediments from the previous period of rifting (Late Jurassic to Valanginian). The result was far less surface erosion of the upper parts of the tilted fault blocks than occurred at Goban Spur.

Similar to the Goban Spur margin, the Galicia Bank margin underwent pure extension [*Sibuet*, 1987]. In this case, however, there is evidence of serpentinized peridotite [*Boillot et al.*, 1980; 1986] near the ocean-continent boundary, which was either emplaced by diapirism through the veil of thinned continental crust [*Sibuet et al.*, 1987] or formed in association with the distal end of a crustal (*S*?) reflector [*Boillot et al.*, 1987, 1988]. These last authors have suggested that this extension was produced by simple shear along a fault which has cut the entire crust, producing an upper plate margin dominated by upper crustal rocks [*Boillot et al.*, 1986] with low seismic velocity [*Sibuet et al.*, 1987]. This conclusion, however, can be questioned by the fact that the *S* reflector in this case can only be observed for a very limited extent and, unlike the reflector under the Celtic margin, it dips slightly seaward and thus could not cut through the thickening continental crust. *Tankard and Welsink* [1988] have proposed an alternate interpretation, which considers Galicia Bank as the lower plate half of a simple shear boundary with the middle Grand Banks as its conjugate upper plate. However, this interpretation also suffers from the lack of clear evidence for a suitable detachment fault, in that no landward dipping intracrustal reflector can be observed under the Grand Bank basins.

HEAT FLOW OBSERVATIONS

Marine heat flow observations were taken using a trigger-release piston corer during two cruises, NORESTLANTE II

and III: the first to Goban Spur on the N/O *Le Suroit* in 1984 and the second to Goban Spur and Galicia Bank on the N/O *Jean Charcot* in 1989. Values of mean conductivity, thermal gradient, and heat flow with their associated standard deviations are reported in Table 1 for all stations, together with water depth, bottom water temperature, geographical position, depth of maximum penetration and correction due to basement topography. We also report data from DSDP sites 548A, 549, and 550 on Goban Spur, which have been recalculated from the original values [*Foucher et al.*, 1985; *Hyndman et al.*, 1987] using a linearly increasing conductivity with depth.

Temperatures

Sediment temperatures were digitally recorded every 10 s, during single penetrations lasting from 5 to 8 min of the 4.5- to 9-m-long corer outrigged with a maximum of 7 equally spaced thermistor sensors. Absolute temperatures are calibrated only to within approximately 50 mK accuracy, while relative temperature differences are accurate to 2 mK. Bottom water temperatures (BWT) are averages of absolute temperatures, recorded either by all stable thermistors immediately prior to penetration or, in the case of partial penetration, by those thermistors which remained in the water column. The effects of frictional heating upon

TABLE 1. Goban Spur and Galicia Bank Heat Flow

Station	Depth, m	BMT, °C	Latitude,N	Longitude,W	PEN m	N_k	k, $Wm^{-1}K^{-1}$	σ_k	N_G	G, mK/m	σ_G	Q, mW/m^2	σ_Q	%C	Q_c, mW/m^2
N2KS01	4400	2.66	48°30.9′	13°26.1′	4.5	5	0.86	0.06	6	46	3	39.6	5.3	-0.7	39.8
N2KS02	4485	2.69	48°49.9′	13°43.1′	3.6	5	0.86	0.05	6	52	3	44.7	5.2	-0.5	44.9
N2KS03	4480	2.66	48°53.5′	13°35.5′	4.5	5	0.78	0.02	6	53	4	41.3	4.2	-8.7	45.3
N2KS04	3870	2.63	48°54.5′	13°29.0′	5.3	2	0.91	0.05	7	45	2	41.0	4.1	-4.6	42.9
N2KS05	3710	2.61	48°56.9′	13°19.1′	4.5	11	0.82	0.03	6	54	2	44.3	3.3	-2.2	45.3
N2KS06	3647	2.77	48°59.2′	13°12.4′	9.0	26	0.84	0.05	6	63	2	52.9	4.8	-1.7	53.8
N2KS07	3520	2.82	49° 0.0′	13° 8.2′	4.8	12	0.84	0.03	6	53	2	44.5	3.3	-4.9	46.8
N2KS08	2600	3.19	49° 2.6′	13° 2.3′	4.5	4	0.95	0.05	6	58	6	55.1	8.6	-6.5	58.9
N2KS09	2346	3.39	49° 4.4′	12°59.3′	4.9	7	0.93	0.09	6	45	3	41.9	6.8	-4.4	43.8
N2KS10	1860	3.85	49° 5.9′	12°52.6′	4.8	*	0.97	0.04	6	66	2	64.0	4.6	-7.4	69.1
N2KS11	1445	5.44	49° 8.0′	12°45.8′	4.9	*	0.97	0.04	4	108	7	104.8	11.1	-3.5	108.6
N2KS12	1190	7.71	49°10.3′	12°35.7′	9.0	22	1.01	0.10	6	63	5	63.6	11.4	-3.2	65.7
N2KS13	950	8.10	49°16.2′	12°24.2′	9.0	10	1.01	0.09	6	55	2	55.6	7.0	-0.2	55.7
N2KS14	1125	8.27	49°23.0′	11°57.5′	4.9	11	0.94	0.07	6	50	3	47.0	6.3	0.6	46.7
N2KS15	950	8.96	49°26.5′	11°45.2′	4.8	*	0.89	0.06	6	57	3	50.7	6.1	-1.2	51.3
N3KF01	940	9.32	49°26.2′	11°43.8′	6.5	39	0.89	0.06							
N3KF02	639	10.00	49°30.0′	11°31.6′	5.7	15	0.90	0.05							
N3KF03	381	10.95	49°33.1′	11°19.5′	3.9	15	0.90	0.02	7	NL					
N3KF04	630	10.15	49°30.5′	11°31.4′	3.9	13	0.89	0.02	7	NL					
N3KF05	1119	8.28	49°19.3′	12°10.8′	4.2	15	0.98	0.08	5	NL					
N3KF06	1464	5.25	49° 8.5′	12°46.9′	3.9	14	0.97	0.07	4	64	6	62.1	10.3	-1.6	63.1
N3KF07	3672	2.51	48°58.3′	13°18.1′	3.9	*	0.82	0.03	7	54	2	44.3	3.3	-3.2	45.7
N3KF09	4800	2.64	48°31.5′	15°19.6′	3.9	11	0.77	0.03	6	50	3	38.5	3.8	-5.3	40.7
DSDP548A	1256	7.1-7.6	48°55.0′	12° 9.9′	282	*	1.40+.0011d		3	35	6	55.0+	8.0	1.4	54.2+
DSDP549	2533	3.4	49° 5.3′	13° 5.9′	417	24	1.38+.0011d		3	24	1	37.5+	0.4	-12.9	43.1+
DSDP550	4432	2.65	48°30.9′	13°26.4′	157	25	1.30+.0011d		3	44	4	61.0+	6.0	-0.7	61.4+
N3KF10	5277	2.58	42° 8.5′	13°18.7′	4.7	20	0.85	0.07	5	45	1	8.3	4.0	-3.9	39.8
N3KF11	5273	2.58	42° 8.7′	13° 8.7′	4.7	15	0.88	0.11	7	56	2	49.3	7.9	2.9	47.9
N3KF12	5272	2.58	42° 7.7′	13° 2.1′	4.7	14	0.86	0.05	6	55	2	47.3	4.5	2.9	46.0
N3KF15	5255	2.58	42° 9.7′	12°50.2′	2.7	*	0.88	0.10	3	45	2	39.6	6.3	-1.8	40.3
N3KF16	5238	2.57	42° 8.8′	12°42.8′	3.9	28	0.94	0.11	5	45	2	4.3	6.8	0.2	42.2
N3KF17	5233	2.57	42° 8.7′	12°37.8′	2.0	10	0.89	0.04	4	NL					
N3KF18	4990	2.55	42° 8.1′	12°31.2′	3.9	15	0.88	0.08	4	48	5	42.2	8.2	-6.5	45.2
N3KF19	4865	2.53	42° 8.8′	12°24.1′	3.9	*	0.84	0.06	5	40	4	33.6	5.8	-7.1	36.2
N3KF20	4765	2.52	42° 8.9′	12°18.0′	3.9	12	0.80	0.05	6	40	2	32.0	3.6	-8.4	34.9
N3KF21	4427	2.48	42° 8.7′	12°10.2′	3.9	18	0.87	0.04	4	74	4	64.4	6.4	-11.1	72.4
N3KF22	4205	2.48	42° 8.9′	12° 8.2′	3.9	*	0.86	0.03	6	52	2	44.7	3.3	-6.3	47.7
N3KF23	3950	2.50	42° 8.7′	12° 4.9′	3.9	5	0.86	0.03	6	46	2	39.6	3.1	0.4	39.4
N3KF24	3482	2.55	42° 7.9′	11°58.0′	3.9	13	0.81	0.03	7	32	2	25.9	2.6	-14.9	30.5
N3KF25	3570	2.47	42° 8.4′	11°55.5′	3.9	*	0.81	0.03	7	35	2	28.4	2.7	-11.3	32.0
N3KF26	2850	2.77	42° 8.4′	11°49.1′	1.8	8	1.08	0.05	4	NL					
N3KF27	2420	3.42	42° 8.2′	11°42.2′	2.4	9	0.98	0.03	5	NL					
N3KF28	2268	3.59	42° 7.9′	11°35.5′	3.0				7	NL					
N3KF29	2220	3.62	42° 8.5′	11°28.5′	3.6	15	0.93	0.07	7	NL					
N3KF30	3935	2.42	42°10.2′	12° 5.6′	3.9	13	0.80	0.05	6	42	3	33.6	4.5	-9.5	37.1
N3KF31	5214	2.49	42° 9.6′	12°39.0′	3.9	26	0.93	0.08	4	39	9	36.3	11.5	-3.4	37.5
N3KF32	5277	2.52	42° 9.0′	13°33.0′	3.9	15	0.81	0.04	6	54	3	43.7	4.6	2.0	42.9

Depth is water depth; BWT is bottom water temperature; PEN is approximate depth of penetration; σ_Q is $\sigma_k G + \sigma_G k$, where σ_k is standard deviation of thermal conductivity k and σ_G is standard deviation of temperature gradient G; %C is topographic correction; Q and Q_c are the uncorrected and corrected heat flow. N3KS designates a Norestlante III station; N2KS a Norestlante II station. NL indicates nonlinear temperature gradient.

*Conductivity k assumed from neighboring sites.

+For DSDP measurements, conductivities are determined assuming a linear increase with depth d (in meters) and heat flow Q is calculated from slope of temperature versus thermal resistance.

penetration were removed by linear extrapolation of each sensor's sediment temperatures relative to its own BWT as a function of reciprocal time, for postpenetration times exceeding 1—2 min. Values of background temperature calculated from linear fits with poor correlation coefficients (generally resulting in uncertainties in excess of 5 mK) were discarded.

Goban Spur. Figure 2 shows station locations across Goban Spur and into the Porcupine abyssal plain together with shot points along the WAM reflection profile [*Peddy et al.*, 1989]. Background sediment temperature versus depth relative to the uppermost thermistor penetrating the sediment at each station are plotted in Figure 3 with least squares fits to the mean linear temperature gradient. Some scatter beyond the resolution of the individual temperature determinations exists for several deepwater stations (e.g., N2KS03 and N2KS08). These we assume are due to disturbances during the penetration of the probe.

Other, more systematic departures from linearity are observed in the shallower water stations and are particularly severe for those taken during NORESTLANTE III (e.g., N3KF03—05). A plot of sediment temperature versus depth of penetration relative to the average BWT is given in Figure 4 for stations shallower than 1150 m. This suggests that significant variations in bottom water temperature (BTVs) must have occurred immediately prior to the NORESTLANTE III measurements, while BTVs previous to the earlier measurements are negligible. The duration and magnitude of the BTVs previous to the NORESTLANTE III observations are approximated using a series of simple step changes (Figure 4 and Table 2). Modeling of the deeper station, N3KF05 (1120 m), using the linear gradient and similar BWT at the neighboring station, N2KS14 (1125 m), indicates a period of temperatures elevated by 0.38°C from the present value of 8.28°C, between 5 and 85 days prior to observation in March 1989. Successively smaller increases during roughly the same period are suggested for the shallower stations, N3KF04 (0.28°C at 630 m) and N3KF03 (0.08°C at 381 m), assuming that the geothermal gradient remains relatively unchanged. In addition, station N3KF03 requires a temperature decrease of -0.15°C during the period previous to 150 days.

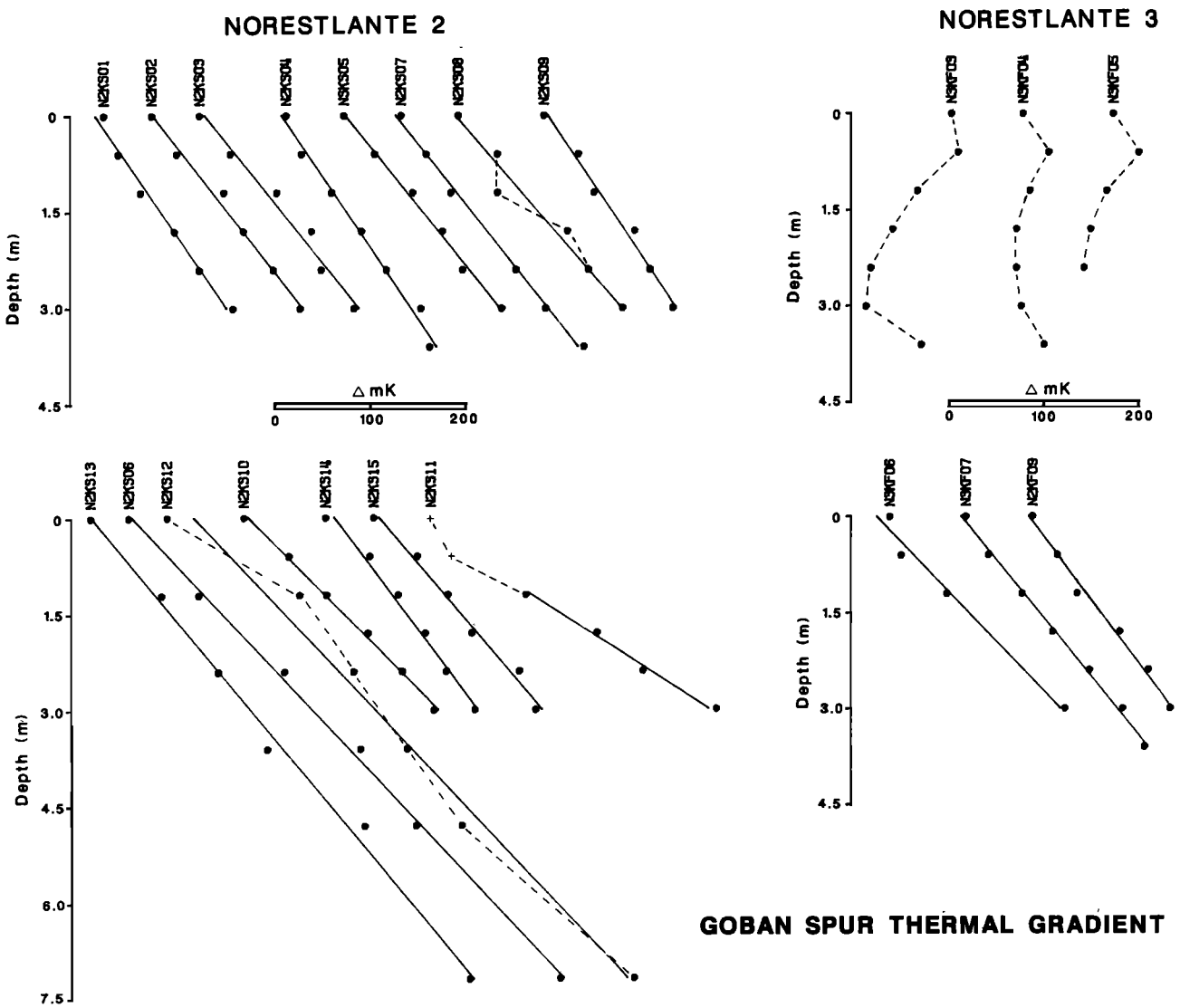

Fig. 3. Sediment temperature versus depth relative to the uppermost thermistor penetrating the sediment at each station on Goban Spur. Solid lines give least squares fits to the linear thermal gradients reported in Table 1. Large deviations from linearity are shown by dashed lines. Values indicated by crosses are not used in the linear fits.

The 2—3 month period and increased amplitude toward depths of 1000 m suggest that these temperature fluctuations are caused by an interaction between short-term, randomly occurring mesoscale eddies and the long-term northward motion of Mediterranean outflow. Measurements at 47°N, 14°50'W from the Tourbillon experiment, during the period September 1979 to May 1980 [*Le Groupe Tourbillon*, 1983], show temperature variations from two eddies, each of 2 months duration separated by a 4-month quiet period. Amplitudes increase from 0.4°C

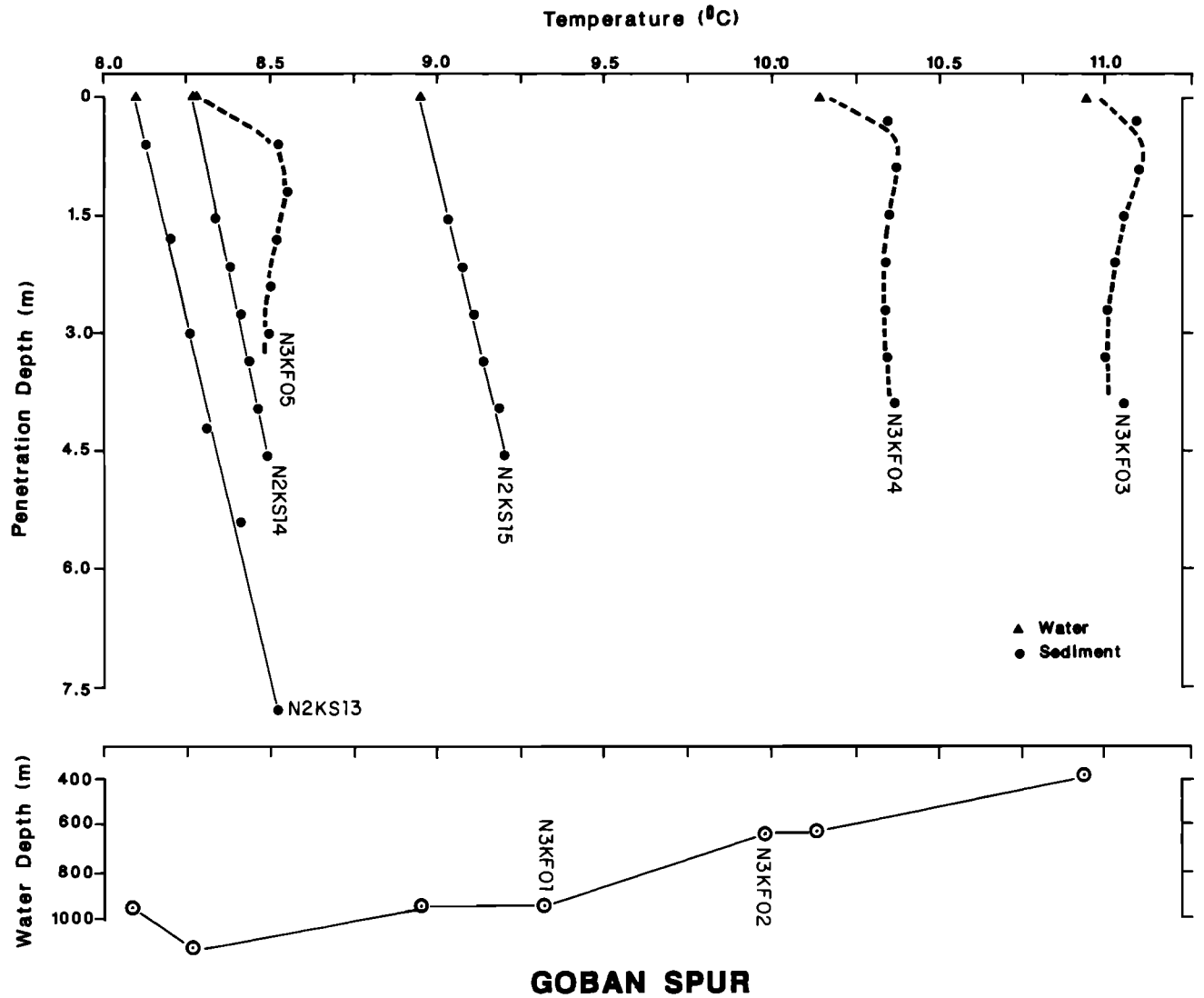

Fig. 4. Sediment temperature versus depth (solid circles) relative to each station's average bottom water temperature (solid triangles) for Goban Spur stations from the upper margin (water depths less than 1150 m). Solid lines show least squares fits to the linear thermal gradients reported in Table 1; dashed lines show non linear fits from thermal models with variations in bottom water temperature given in Table 2. Open circles show BWTs versus water depth.

TABLE 2. Square-Wave Models of Bottom Water Temperature Variations

Station	Depth, m	BTV, °C	Period, days	Grad, mK/m	BWT, °C	k, $Wm^{-1}K^{-1}$
			Goban Spur			
N3KF05	1119	+0.38	5-85	50	8.28	0.95
N3KF04	630	+0.28	2-75	53	10.15	0.90
N3KF03	381	+0.08	2-80	50	10.80	0.90
		-0.15	>150			
			Galicia Bank			
N3KF28-29	2245	+0.25	<80	35	3.39	0.95
N3KF26	2850	-0.12	<30	35	2.77	1.00
N3KF25	3570	-0.04	<2	35	2.47	0.80

Period is days before measurement of sediment temperatures; BTV is change in bottom water temperature relative to BWT; Grad is geothermal gradient; BWT is bottom water temperature; k is thermal conductivity.

at 400—600 m to >1.0°C between 850 and 1500 m, and subsequently decrease to <0.1°C for depths greater than 2000 m. The middle region of high temperature variability with time also shows a relatively rapid decrease in water temperature with depth, from 10°C at 600 m to 5°C at 1400 m [this study; *Fuglister*, 1960]. This zone is thought to be governed by a northward movement of the warm, saline Mediterranean outflow that mixes with the colder, fresher middepth water from the Labrador Sea [*Reid*, 1978]. Variations in this regional flow created by eddies are thought to produce the large temperature fluctuations centered at 1000 m.

Large, randomly occurring BTVs with typical periods of 30—90 days in water depths between 600 and 1500 m may explain other nonlinearities in the gradients observed on stations N2KS11—12 and N3KF06. They may also degrade the accuracy of geothermal gradients determined in this range of water depths from linear fits to selected sediment temperatures, particularly if they are limited to the upper 3 m such as at stations N2KS11 and N3KF06. To measure within 10% error an assumed geothermal gradient of 50 mK/m from linear fits to sediment temperatures, given random changes in bottom temperature of ±1°C with a period of 90 days, requires penetrations of at least 8—10 m or a detailed monitoring (or assumed stability) of the BWT for 1—2 years preceding the measurement. It is possible for geothermal gradients to be determined from shallower sediment temperatures, but this would require at least two coincident observations separated in time by a period less than those of the BTVs themselves [*Wang and Beck*, 1987]. Otherwise, it is possible to have relatively constant gradients as high as 80—100 mK/m for measurement depths less than 3 m.

Galicia Bank. Figure 5 shows station locations across the Galicia Bank margin and into the Iberia abyssal plain, together with shot points for the GP-101 reflection profile [*Mauffret and Montadert*, 1987]. Sediment temperature versus depth relative to each station's uppermost thermistor are plotted in Figure 6 with mean linear gradients. Scattered values occasionally exist for individual thermistors, particularly those of the deepest sensors whose cables may have been disturbed during the penetration of the corer into or through hard substrata.

Other, more systematic departures from linearity are primarily observed in the shallowest stations, N2KF26—29. Sediment temperatures relative to the mean BWT are plotted in Figure 7 versus depth of penetration for stations between 3500 and 2200 m. This region shows an increase in bottom water temperature across the slope from values of 2.5°C at 3600 m to 3.6°C at 2200 m. These depths are below those influenced by the Mediterranean outflow. The vertical temperature gradient is much smaller than that observed in the shallower water depths near Goban Spur discussed in the preceding section. Thus we would not expect to find large BTVs. Instead, however, simple models of these profiles (Figure 7 and Table 2) suggest that (1) an increase of 0.25°C occurred roughly 80 days prior to measurement at the shallowest stations, N3KF28—29 and (2) a decrease of ≤0.12°C occurred several days to a month before measurement at the deeper stations, N2KF25—26.

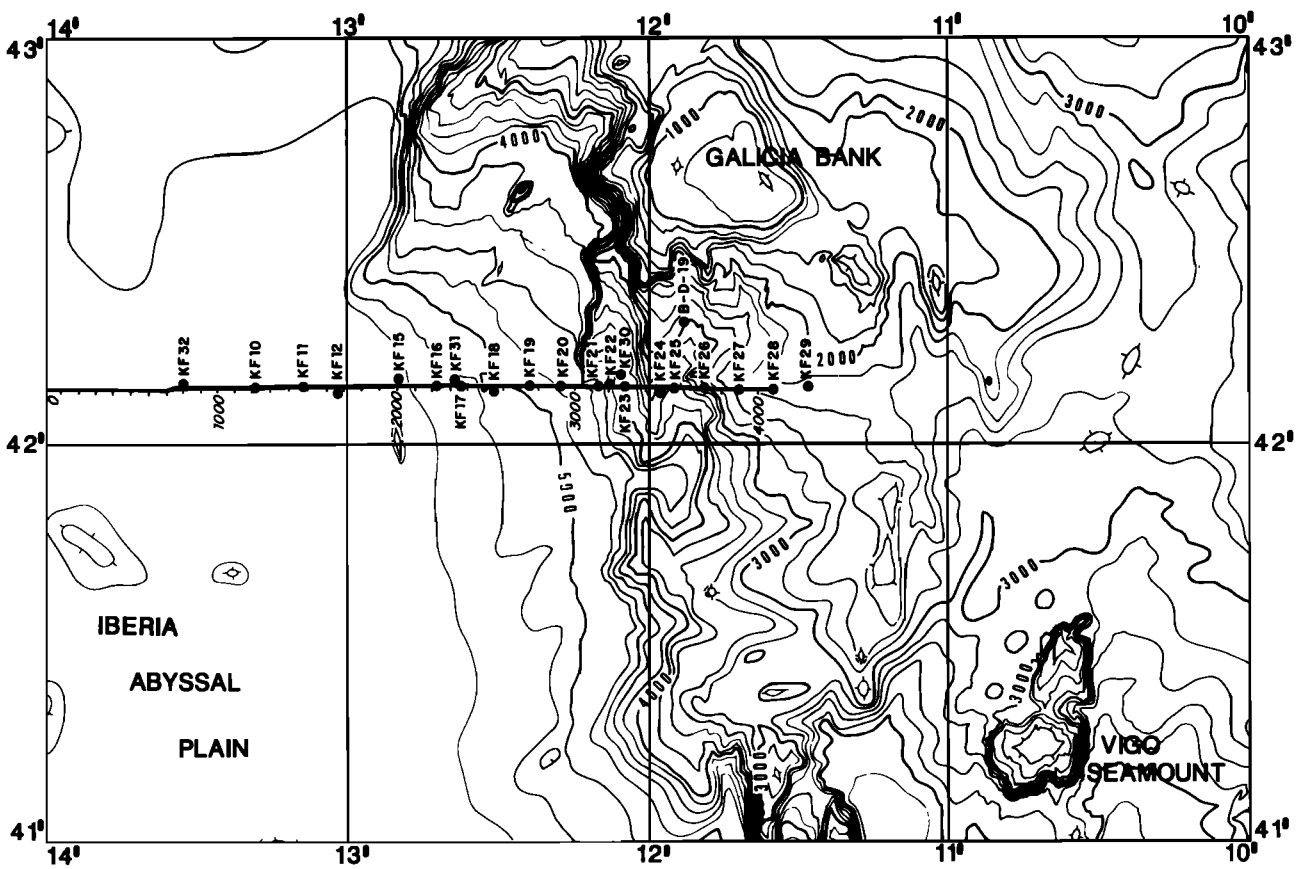

Fig. 5. Bathymetry of Galicia Bank margin [*Sibuet et al.*, 1987] with locations of heat flow stations and shot points along the GP-101 reflection profile [*Mauffret and Montadert*, 1987].

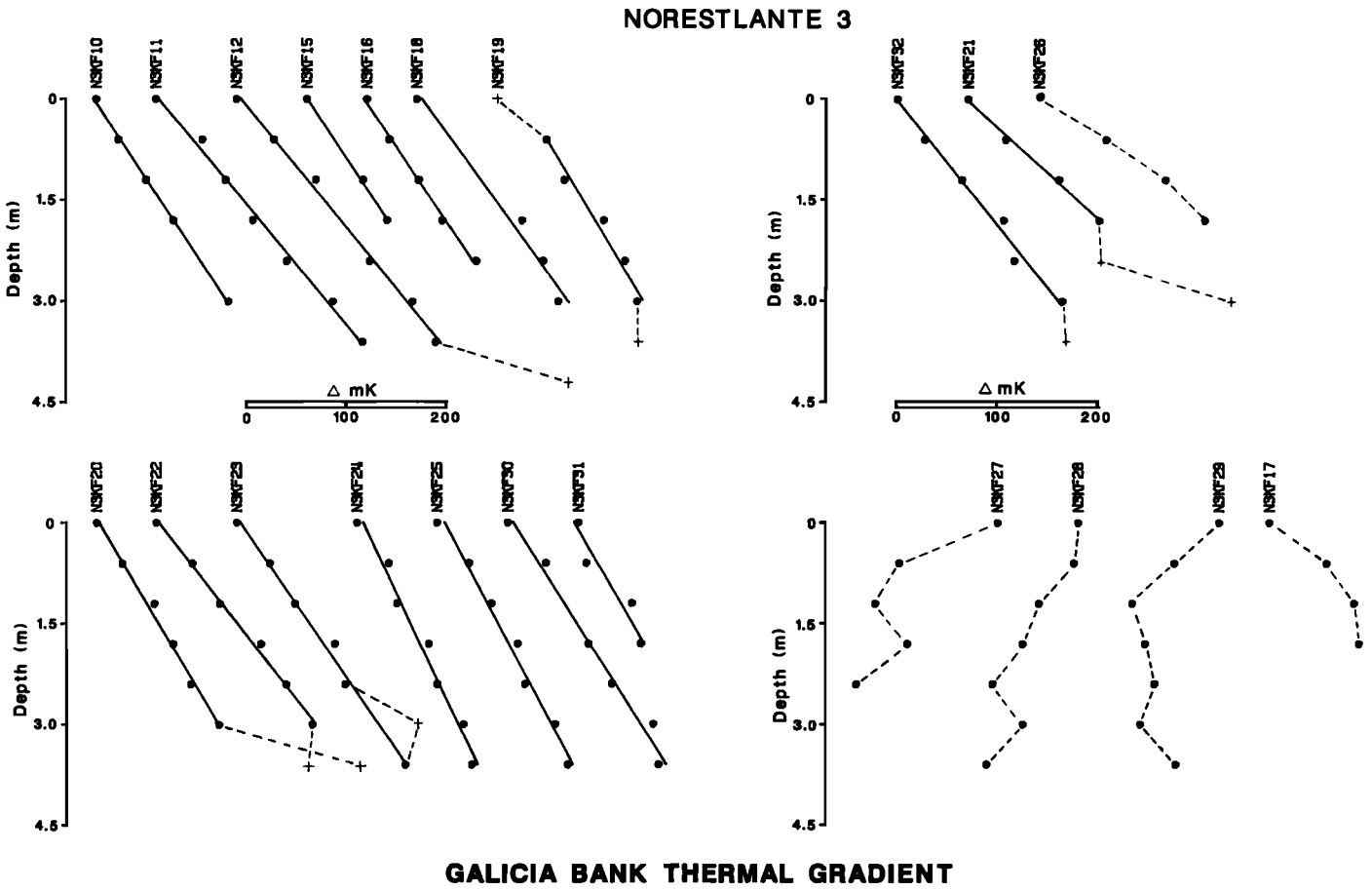

Fig. 6. Sediment temperature versus depth relative to the uppermost thermistor penetrating the sediment at each station on Galicia Bank. Other descriptions same as for Figure 3.

An association of these BTVs with mesoscale eddies is suggested by results from NEADS Site 3 at an adjacent westward location in the Iberia abyssal plain (42°N, 14°W). Water currents exhibit a kinetic energy peak at a typical mesoscale period (100 days) for all depths greater than 3000 m [*Gould*, 1983]. The stability of water temperatures, which vary less than 0.1°C over depths between 3500 and 5300 m [this paper; *Fuglister*, 1960], however, means that significant BTVs caused by these eddy motions are probably limited to water depths less than 3500 m. This is confirmed by the presence of consistent linear gradients determined from stations deeper than 3400 m.

Conductivities

Thermal conductivities were measured on core sections, immediately after thermal equilibration to shipboard laboratory temperature, using the continuous heating method [*Von Herzen and Maxwell*, 1959] over periods of 20 to 120 s with a digitally recording needle probe. Individual measurements using this technique have typical accuracies of 5% [*Goldberg*, 1981]. Correction to seafloor temperature and pressure was made using equations from *Ratcliffe* [1960].

Measurements of thermal conductivity for the Goban Spur sites are plotted in Figure 8. These show generally well defined means ($\sigma = 0.02$—$0.10\ \mathrm{Wm^{-1}K^{-1}}$) with magnitudes ranging from 0.77 to 1.01 $\mathrm{Wm^{-1}K^{-1}}$ (Table 1). The lower of these values come from the abyssal plain and fall within a normal range for oceanic sediments [*Louden and Wright*, 1989]. In a few cases (i.e., N2KS10, N2KS11, N2KS15, and N3KF07), we have calculated the heat flow using mean conductivities from adjacent stations which are better sampled. Except for station N3KF01, there is no clear trend of increasing conductivity with sediment depth. Note, however, that there is evidence for increasing conductivity within the greater depth intervals of the DSDP sites. Linear extrapolation of these data yields surface values of conductivity that are higher than those of our cores. This is consistent with conductivities that depend primarily on porosities which decrease in an exponential relationship with depth [*Hutchison*, 1985].

Conductivity measurements for the Galicia Bank stations are shown in Figure 9. Mean values of 0.80 to 1.08 $\mathrm{Wm^{-1}K^{-1}}$ are only slightly higher than observed along the Goban Spur transect, and standard deviations of 0.03 to 0.11 $\mathrm{Wm^{-1}K^{-1}}$ are similar. There is little evidence for systematic changes in conductivity with depth apart from the shallow measurements of stations N3KF18 and N3KF20. There is, however, some evidence for narrow, uncorrelated zones of high conductivity produced from sandy lens, suggestive of turbidite layers. The presence of coarse sediment flows may also explain the occasional difficulty that we experienced in penetrating the sediment at the eastern edge of the abyssal plain.

Heat Flow

Heat flow values in Table 1 are calculated using the product of the mean gradients and harmonic mean

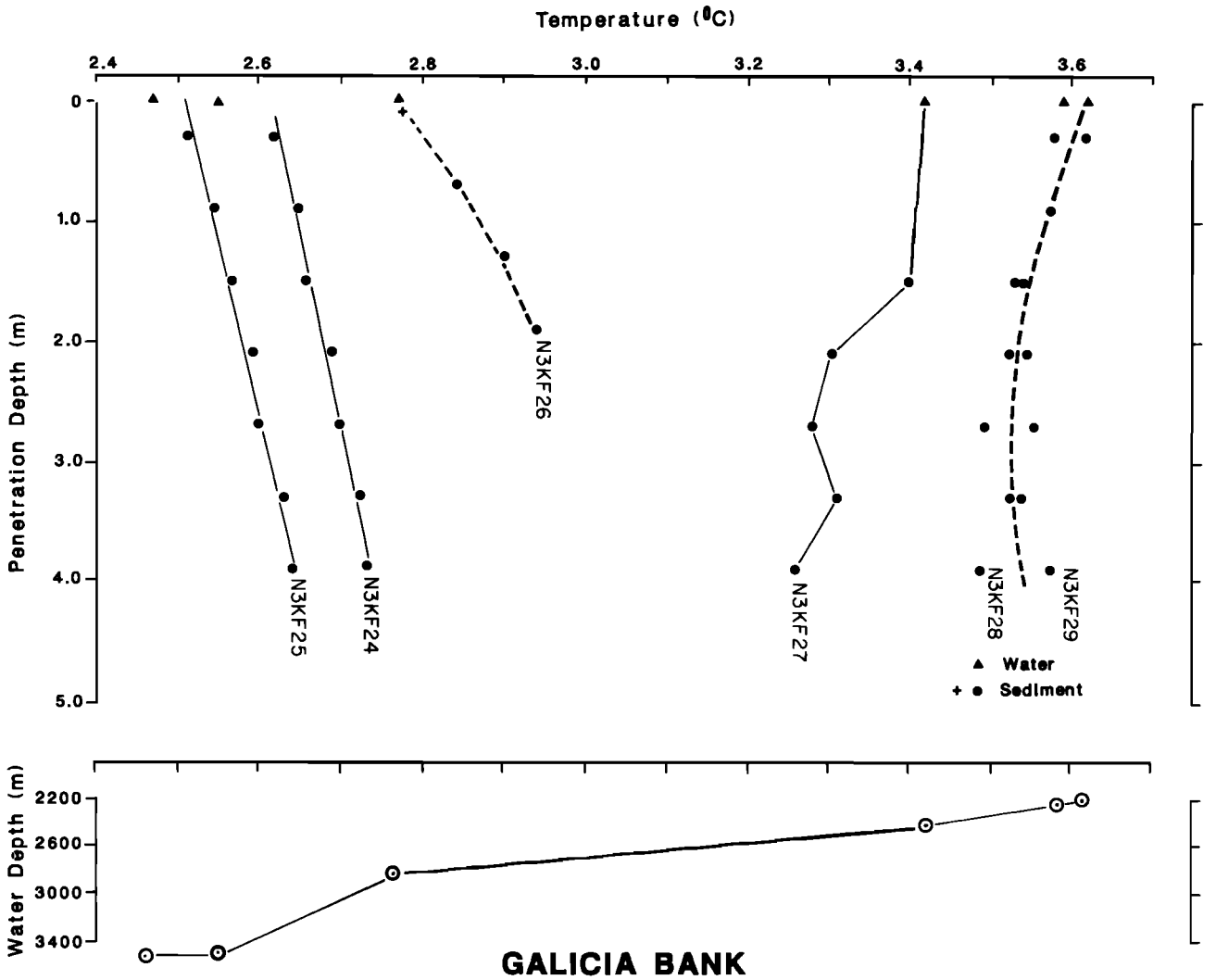

Fig. 7. Sediment temperature versus depth (solid circles) relative to each station's average bottom water temperature (solid triangles) for Galicia Bank stations from the upper margin (water depths less than 3600 m). Other descriptions same as for Figure 4.

conductivities. Standard deviations are calculated in the usual manner from $\sigma_Q = G\sigma_k + k\sigma_G$. Because of limitations in the sampling of the conductivity and temperature values, which differ significantly between stations, calculations of heat flow over smaller intervals are not particularly useful. Most stations, which are not obviously affected by BTVs as discussed above, yield similar values between the averaged and lowermost interval heat flow values. Exceptions are for stations KS10 (see below), KF18, and KF19, for which the heat flows calculated over the lowest interval are reduced by 22—59%.

Topographic corrections are calculated using a two-dimensional finite element method (C. Jaupart, personal communication, 1989), to simulate the effects produced by contrasts between the low-conductivity postrift sediment (k=1.0 $Wm^{-1}K^{-1}$) and higher-conductivity basement (k=2.5 $Wm^{-1}K^{-1}$). Subbottom topography for these layers is constrained by the two multichannel profiles, using assumed sediment and water velocities of 2.0 and 1.5 km/s, respectively. Corrected heat flow and topographic correction factors across the two margins (Table 1) are shown in Figures 10 and 11 as a function of distance along the reflection profiles. These results show that the topographic correction can be quite large but only very near the westward edges of those fault blocks which lie close to or break the seafloor. This is a region in which observations are rarely, if ever, possible. More typical values from areas of continuous sediment cover are ±10%. They are similar to the results of *Foucher and Sibuet* [1980] from the comparable environment of the Biscay margin.

Variations in corrected heat flow across the two margins, as observed in Figures 10 and 11, show two rather surprising features:

1. Goban Spur shows the expected increase in heat flow across the margin, from a value of 40 mW/m^2 on the oceanic crust at chron 34 to values of 47—56 mW/m^2 toward the continent at the eastern end of the profile. However, the increase does not start at the ocean continent boundary (OCB), as heat flow values between distances of 150 and 200 km along profile generally remain stable at 43—45 mW/m^2. DSDP Site 550 shows an isolated high value, which is inconsistent with our geographically coincident measurement at station N2KS01 as well as with other measurements over the oceanic crust. We have found no explanation for this large discrepancy. A region of high heat flow, with consistent measurements between 59 and

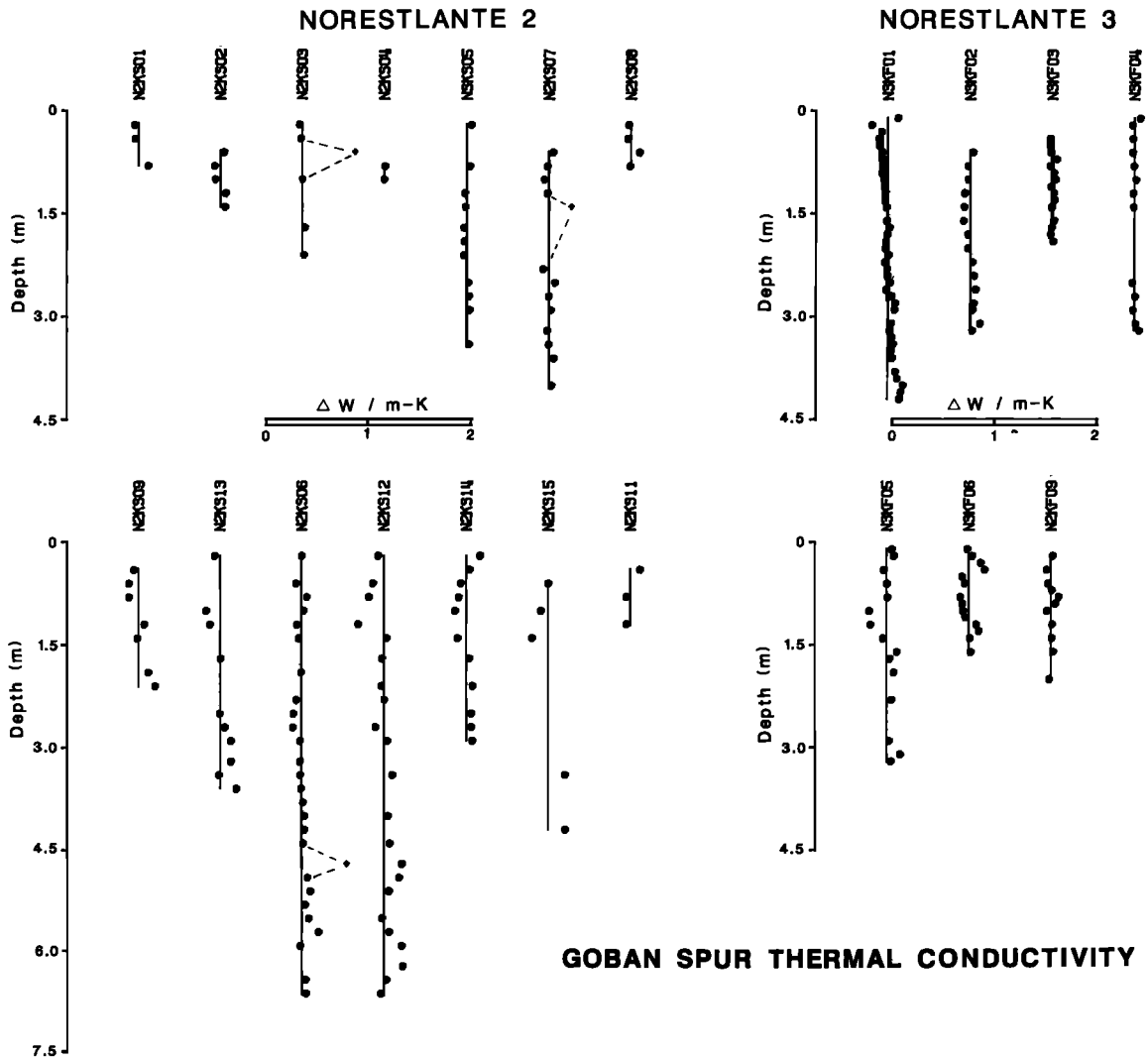

Fig. 8. Thermal conductivity versus sediment penetration depth for piston cores from Goban Spur stations. Values are corrected for water pressure and temperature and are plotted relative to each station's harmonic mean (shown by vertical solid lines). Mean values are calculated from data given by solid circles and reported in Table 1; dashed lines connect deviant data values (crosses) which are not used.

69 mW/m^2 from both cruises and one particularly high value of 109 mW/m^2 at station N2KS11, exists between approximately 200 and 250 km. As discussed before, most of these stations show nonlinearities which may indicate that they have been affected by BTVs. Even the most linear of these stations, N2KS10, exhibits gradients which change from 78 mK/m for its two uppermost thermistors to 55 mK/m between its two lowermost thermistors.

2. For Galicia Bank, there is a slow decrease in heat flow across the margin. Values over the ocean crust, west of the presumed OCB at the "lherzolite ridge", lie between 40 and 48 mW/m^2. These are similar to but somewhat less well constrained than oceanic values near Goban Spur. Values from the upper margin generally lie between 31 and 39 mW/m^2, although two values of 45 and 48 mW/m^2 and a single value of 72 mW/m^2 depart from the general trend.

INTERPRETATION

The surface heat flow data presented in the previous section are most readily interpreted in terms of the pure-shear, depth-independent model of continental extension [*McKenzie*, 1978]. In this model, heat flow and subsidence are parameterized as a function of a single variable β, which defines the fractional amount of initial, vertical thinning of both lithosphere and crust. Plotted as a function of β rather than distance, the heat flow across both margins can be compared directly even though the profiles across them have significantly different lengths (cf. distance scales in Figures 10 and 11). Following *Voorhoeve and Houseman* [1988], the effects of radiogenic heat production are included within the model, by addition of the quantity $H\,h\,[1 - h/2L]/\beta$, which linearly reduces as a function of β^{-1}. Here, H is the rate of radiogenic heating (μW/m^3), h is the thickness of radiogenic crust (in kilometers), and L is the lithospheric thickness (in kilometers).

Theoretical values of heat flow versus ln β, which result from this model, are shown in Figure 12 for a variety of ages. These show the competition between the increase in heat flow, due to the thinning of the oceanic lithosphere, versus the reduction, due to the thinning of the more radiogenic continental crust. By ages of 105 to 114 Ma,

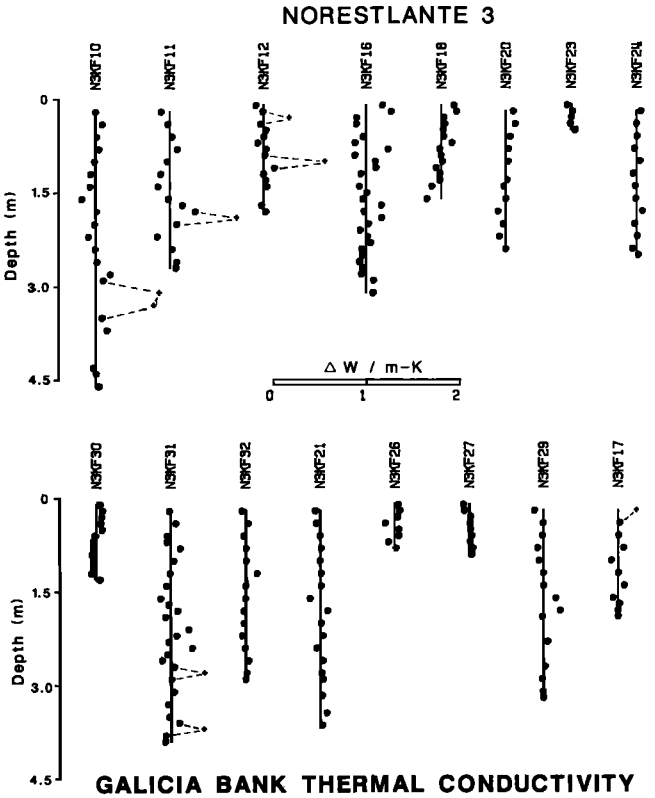

Fig. 9. Thermal conductivity versus sediment penetration depth for piston cores from Galicia Bank stations. Other descriptions same as for Figure 8.

representative of the Goban Spur and Galicia Bank margins, respectively, the expected variation in heat flow across the margin is controlled primarily by the crustal contribution. The residual mantle effect of approximately 10 mW/m^2 will not change greatly within the appropriate range of rifting ages for these margins.

Determination of β at our station locations must be made using both direct and indirect techniques. For Goban Spur, we use reflection data from the WAM profile [*Peddy et al.*, 1989] as illustrated in Figure 13*a*. β is determined directly, as the ratio of crustal thickness at each station (in seconds of two-way travel time) to crustal thickness over the unstretched continental section at the extreme eastern end of the profile. This assumes that the mean crustal seismic velocity remains the same across the margin and that no lower crust has been added by underplating during the rifting process. This latter assumption has recently been debated by *White and Peddy* [1990]. However, evidence from seismic velocities [*Peddy et al.*, 1989], basalt composition [*Maury et al.*, 1985], and our oceanic heat flow values (see below) suggests that asthenospheric temperatures were normal (or perhaps below average) during rifting, and therefore melt thicknesses would be less than 1—2 km for β values less than 4 [*McKenzie and Bickle*, 1988]. Unfortunately, it is not possible to confirm these estimates of β from indirect calculation using the geometry of the tilted fault blocks [*Le Pichon and Sibuet*, 1981], as erosion of the surface blocks is clearly present (Figure 13*a*). Similar complications for the Biscay margin have led to discrepancies between separate calculations of

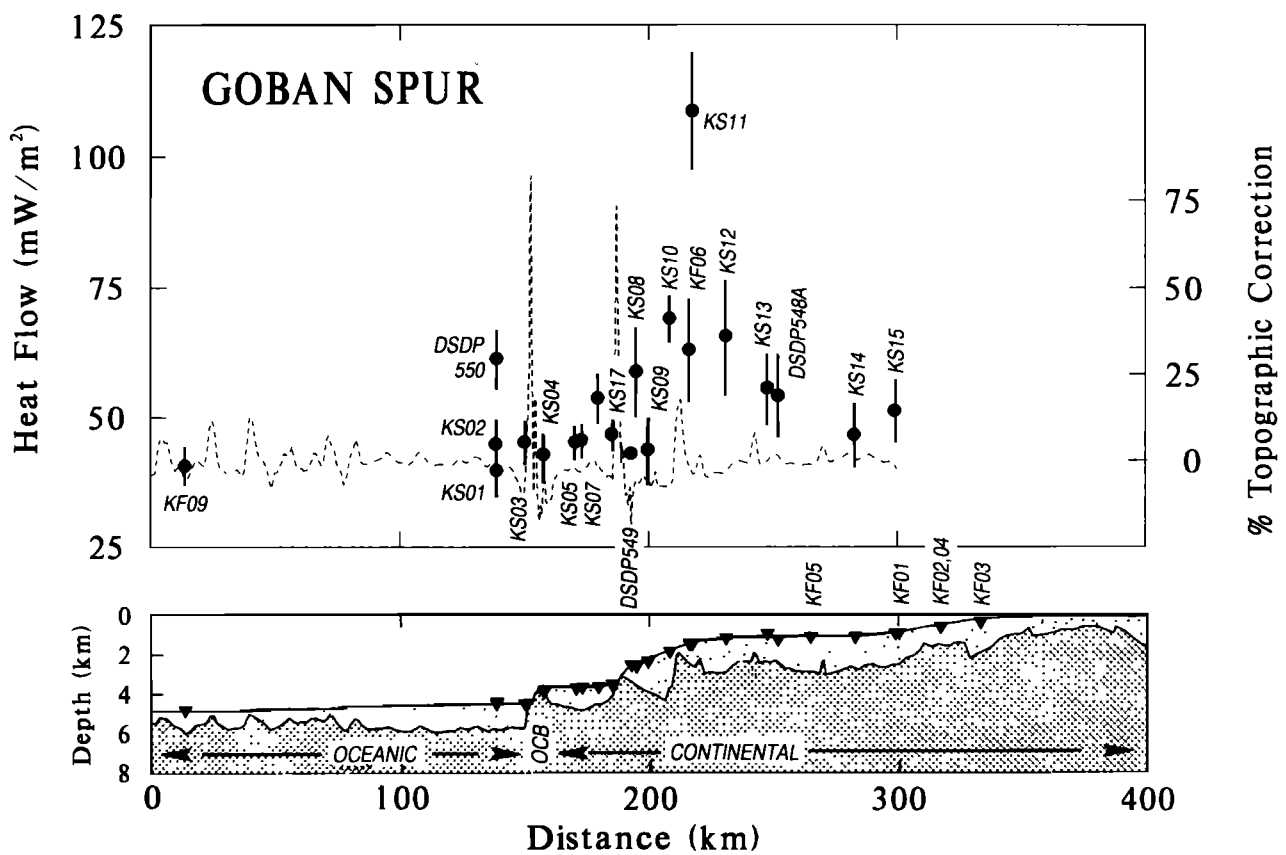

Fig. 10. Station locations, corrected heat flow (± 1σ), and topographic correction factor along the WAM reflecti profile. Corrections are calculated for simplified boundaries separating low-conductivity postrift sediments from high-conductivity basement as identified in the simplified reflection section. Note increase from oceanic to continental values. High values between 200 and 250 km may be affected by large BTVs.

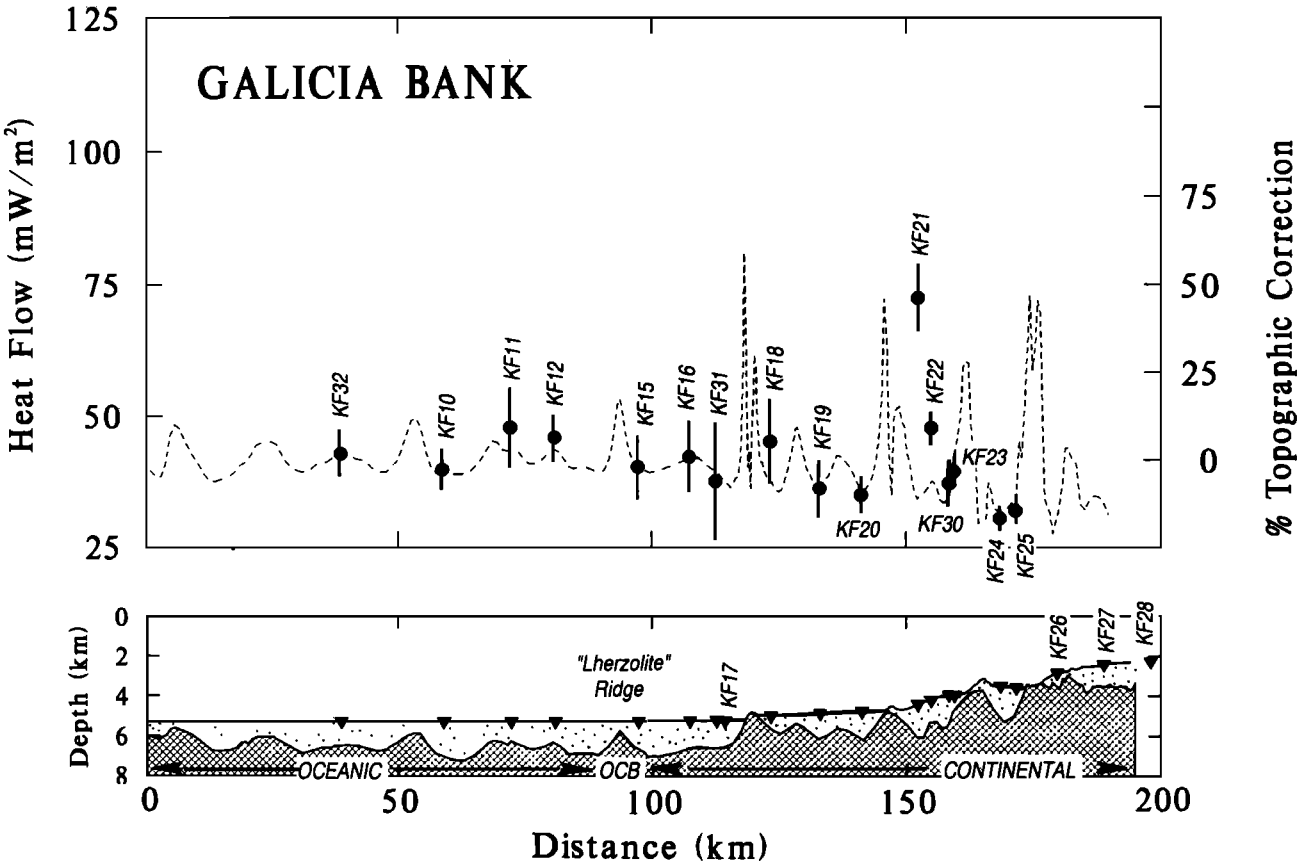

Fig. 11. Station locations, corrected heat flow (± 1σ) and topographic correction factor along the GP-101 reflection profile. Corrections are calculated for simplified boundaries separating low-conductivity postrift sediments from high-conductivity basement as identified in the simplified reflection section. Note decrease across margin from ocean to continent.

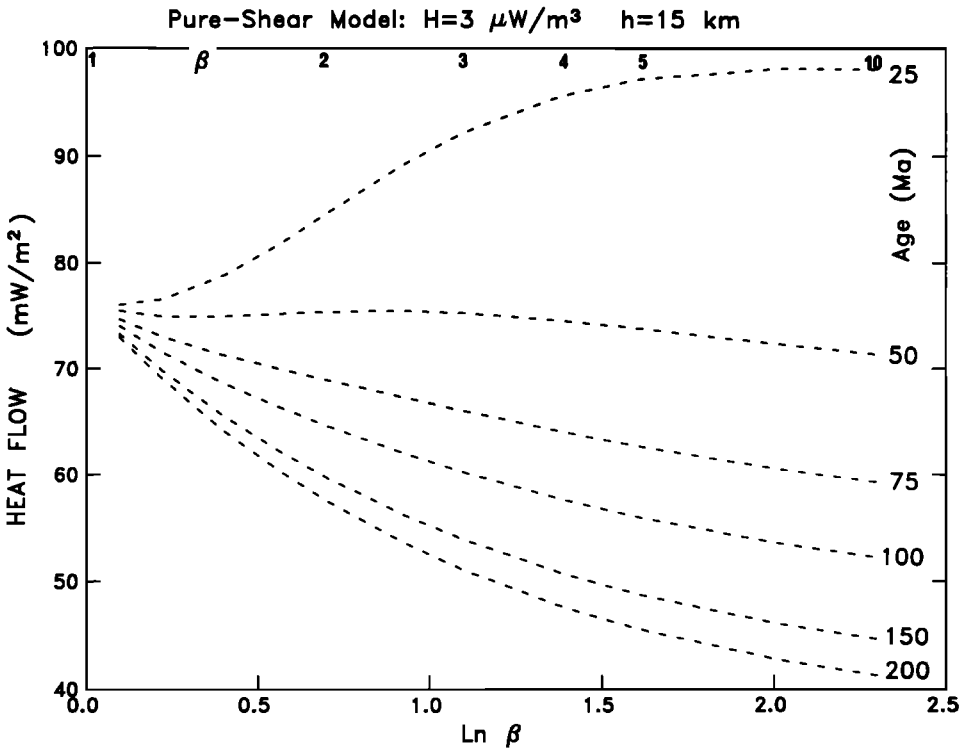

Fig. 12. Variations in heat flow with stretching factor (β) for the pure-shear model [*McKenzie*, 1978] including the effects of radiogenic heating [*Voorhoeve and Houseman*, 1988]. Separate curves are for separate lithospheric ages as indicated in millions of years; assumed values of radiogenic heat production (H) and thickness (h) are 3 μW/m^3 and 15 km, respectively.

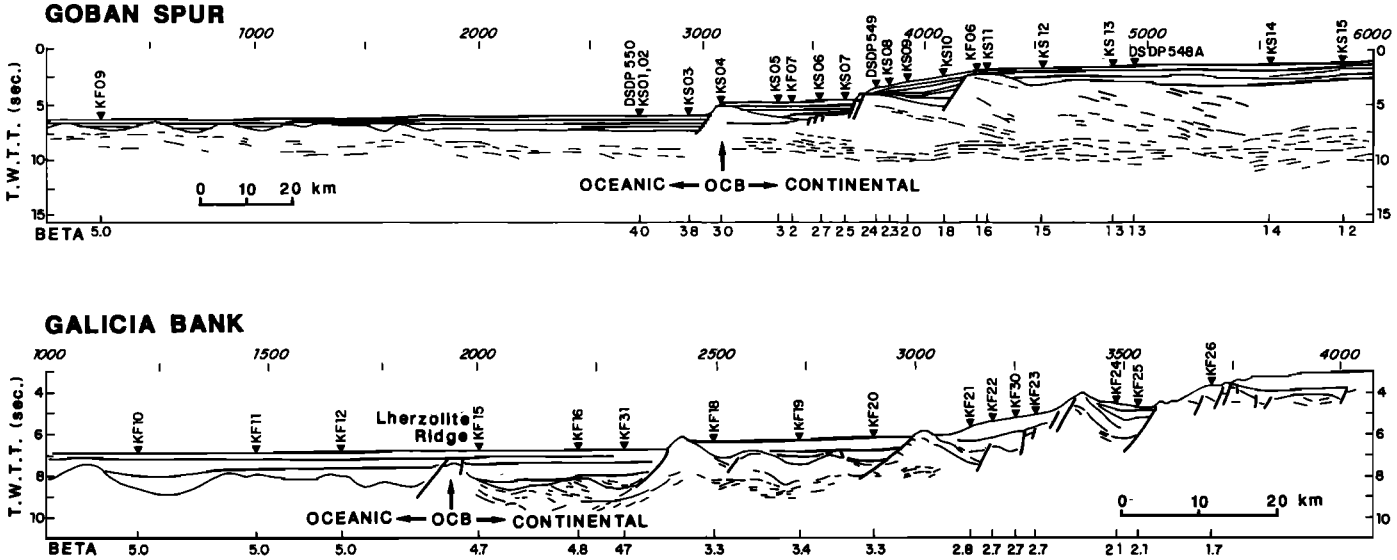

Fig. 13. Multichannel profiles WAM (Goban Spur) and GP101 (Galicia Bank) with locations of heat flow stations and calculated values of stretching parameter β. Reflections from tilted fault blocks, postrift sediments, and crustal reflectors and interpreted locations of ocean-continent boundary are identified in simplified line drawings.

stretching factors [e.g., *LePichon et al.*, 1983; *Chenet et al.*, 1983].

For Galicia Bank, the GP-101 profile (Figure 13*b*) does not exhibit a highly reflective lower crust terminating at the Moho as seen on the WAM profile; nor is there an isolated, identifiable Moho reflection. Thus we must use an indirect technique to calculate β. We have chosen to use the geometry of tilted fault blocks, which in this case are not seriously eroded (Figure 13*b*), following the relationship $Z = Z_t(1—1/\beta)$, as described by *Le Pichon and Sibuet* [1981], where Z is the sediment-corrected basement depth of the tilted blocks, β is the distance between two consecutive blocks divided by the width of the block, and Z_t is the oceanic depth for the appropriate crustal age t. In Figure 14, a value for Z_t of 7.5 km is estimated from observations across the Galacia margin (t=114 Ma) compared to a value of 6.4 km for Goban Spur (t=105 Ma). The larger slope chosen for Galicia Bank will influence our calculation for $\beta > 2.5$ (or $Z > 4$ km), to yield a smaller estimate for β than it would for the same subsidence, Z, at Goban Spur.

We also note in Figure 14 that values of β calculated from the tilting of the fault blocks do not follow a linear trend for the lower part of the margin, beginning approximately at the appearance of the intracrustal S reflector (shot point 3000 on Figure 13*b*). In addition, the average sediment-corrected basement depth for the oceanic crust west of Galicia Bank (6.30 ± 0.02 km) is 1 km greater than for oceanic crust west of Goban Spur (5.30 ± 0.16 km). These values are split by theoretical predictions of 5.8—5.9 km for oceanic crust of ages between 105 and 115 Ma [*Parsons and Sclater*, 1977]. The cause of these depth variations are unexplained but could cause us to overestimate β values over the outer margin of Galicia Bank relative to those for Goban Spur. The results of seismic refraction measurements across both Goban Spur and Galicia Bank will allow us eventually to compare techniques in refining the calculation of β; although we doubt that minor differences will alter the conclusions of this paper.

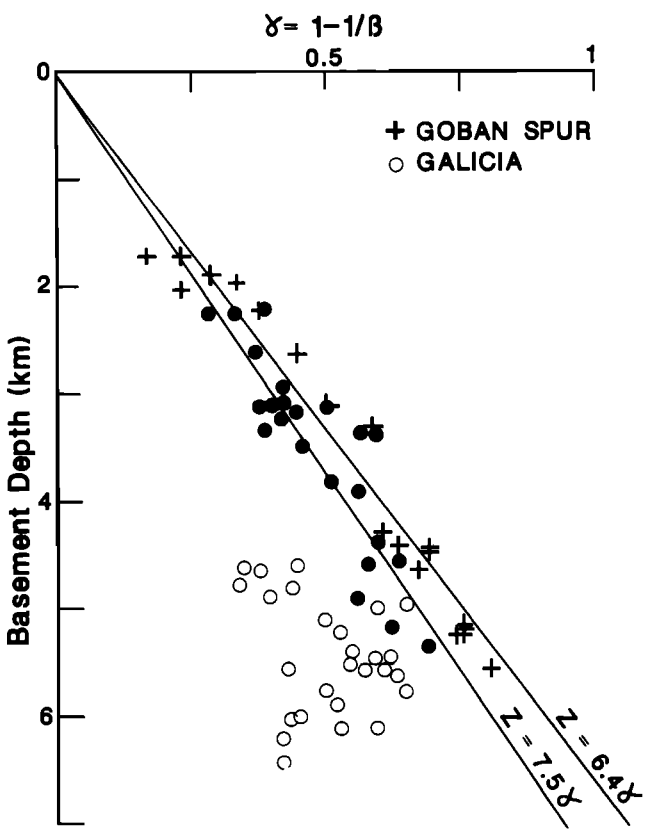

Fig. 14. Values of superficial extension as a function of sediment-corrected basement depth across the Galicia Bank continental margin (solid and open circles from *Sibuet* [1987]) compared to direct measurement of β versus subsidence across Goban Spur (crosses) derived from variations in crustal thickness along the WAM profile (Figure 13*a*). For Galicia Bank, solid symbols correspond to the upper part of the margin (shot points 3000-4000 in Figure 13*b*), while open symbols correspond to the lower part (shot points 2000-3000) above the location of the midcrustal *S* reflector.

In Figure 15, a comparison of heat flow observations across the two margins, including mean continental values from the shaded areas shown in Figure 1, to theoretical values from the pure-shear model for a variety of assumed initial contributions from radiogenic heating (Hh) shows that:

1. For Goban Spur, the majority of observations remain relatively constant for values of β larger than 1.5. This

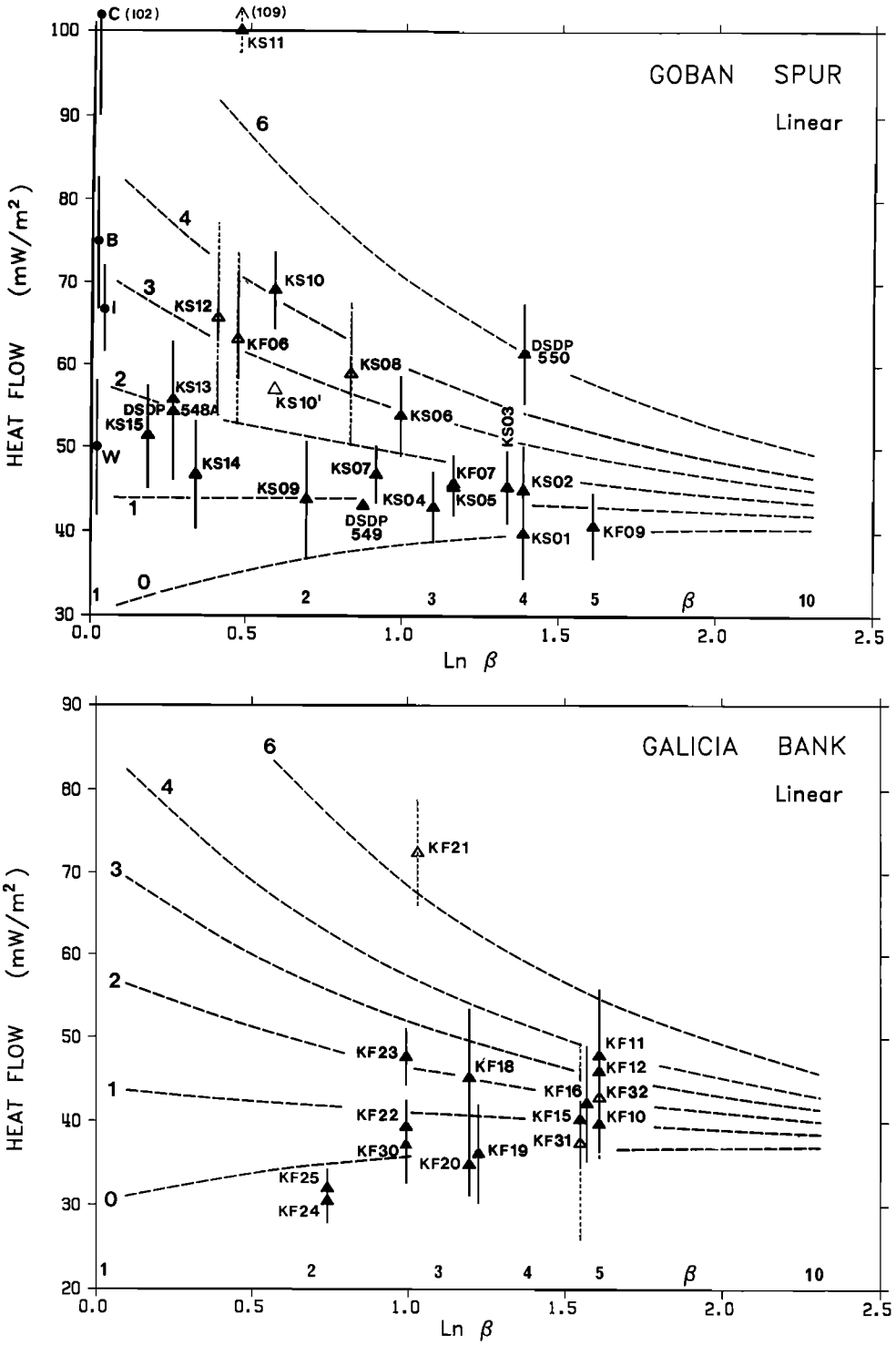

Fig. 15. Values of corrected heat flow (± 1σ) across Goban Spur and Galicia Bank as functions of stretching parameter β, compared to pure-shear models with linear relationship of radiogenic contribution to β. Open symbols and dotted error bars indicate values with significant nonlinearities in temperatures. Value for KS10′ (Goban Spur) uses gradient from deepest two temperatures only. Lithospheric ages for Goban Spur and Galicia Bank are 105 and 114 Ma, respectively. Values of radiogenic heat production (H) for separate curves are given in $\mu W/m^3$; thickness of radiogenic layer (h) is 15 km in all cases. Other parameters in the model are the same as used in Figure 12 except the in situ asthenospheric temperature (T_a), which is 1200°C.

would suggest only a small contribution from radiogenic heat production, with initial values between 1 and 2 $\mu W/m^3$ that would produce continental heat flow between 45 and 60 mW/m^2 similar to those observed in Wales (H=1.29 ± 0.66 $\mu W/m^3$, h=15 km) [*Richardson and Oxburgh*, 1978]. These fall below the observed mean values of heat flow from Brittany and Ireland of 70—80 mW/m^2, as well as the high mean radiogenic heat production (H=3.2 ± 1.2 $\mu W/m^3$, h=15.6 ± 0.6 km) from Brittany [*Jolivet et al.*, 1989]. There are some higher heat flow observations which fit models with initial radiogenic heating of 3—4 $\mu W/m^3$, but these come from shallow penetrations which may have been affected by BTVs, as discussed in the preceding section. The close agreement of the deeper, borehole measurements from DSDP sites 548A and 549 with low surface measurements gives added confidence that these lower values have not been significantly perturbed by environmental factors.

2. For Galicia Bank, apart from the one sporadically high value at N3KF21, the previously noted decrease in heat flow across the margin from ocean to continent can

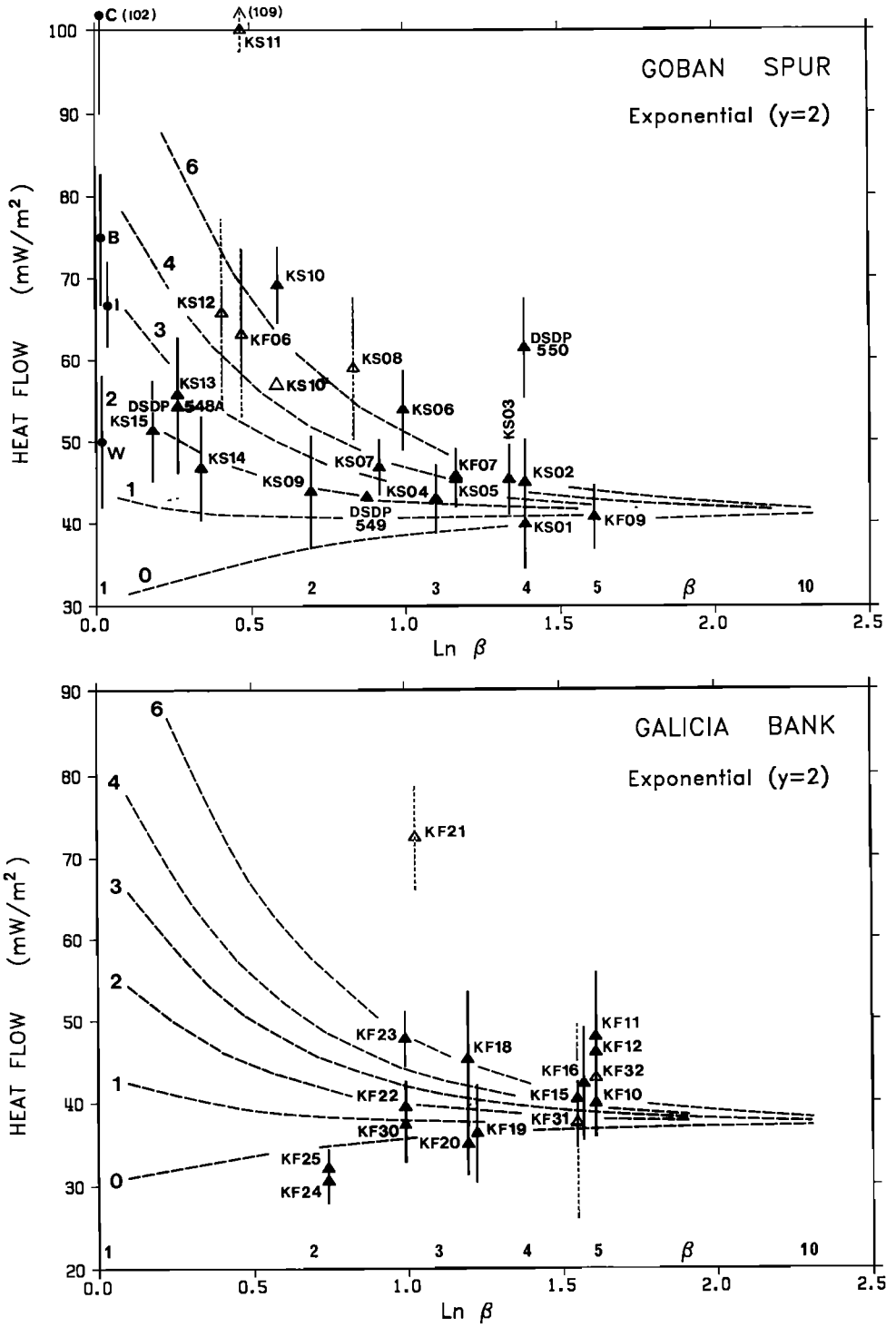

Fig. 16. Same as for Figure 15 except models use thermal contribution from radiogenic heating which decreases as β^{-2}.

only be matched by models with essentially zero radiogenic contribution.

Values of radiogenic heat production have not been reported for basement samples from DSDP cores or dredge hauls across Goban Spur. However, low values are compatible with the placement of the main Hercynian metamorphic belt to the south of our transect, as indicated by *Lefort et al.* [1980].

Alternatively, if high values of radiogenic heat production more typical of rocks from Ireland, SW Cornwall, and Brittany are considered, the constant level of heat flow to relatively small values of β across Goban Spur requires that radiogenic heat production decreases more rapidly than the thickness of the crust as a whole. This can be most simply modeled using a reduction in radiogenic heating as β^{-y} where $y > 1$. Qualitatively, this is what we would expect for a lower plate, simple shear model. More precise calculations [*Voorhoeve and Houseman*, 1988; *Issler et al.*, 1989] would require further knowledge of the geometry of the detachment fault and assumption of how the rate of crustal radiogenic heat production decreases with depth.

Figure 16 compares observations to a model with $y=2$. In this case, most of the low heat flow measurements can be fit by an unstretched radiogenic contribution of 2—3 $\mu W/m^3$, while the higher measurements fit models with 4—6 $\mu W/m^3$. If the higher measurements are representative of the true heat flow at depth, and not artifacts of particular BTVs, they may indicate real spatial variations in radiogenic heat production across the margin. Similar variations over distances of 50—100 km are clearly observed in the land heat flow data (see Figure 1), due primarily to the distribution of outcropping Hercynian granite batholiths. There is no reason to believe that similar heterogeneous geological continental structures do not also extend seaward across the margin [*Sibuet et al.*, 1990]. If, however, the high measurements result from BTVs, we could improve our fit to the low heat flow at small β by increasing y to values of 3—4. The same type of model could also explain previous data from the Biscay margin [*Foucher and Sibuet*, 1980], where heat flow values scatter between 36 and 47 mW/m^2 without significant increase, for β between 4 and 1.3.

For Galicia Bank (Figure 16), a similar model does not improve the fit, and one must still conclude that its continental crust has negligible radiogenic material. Although continental heat flow measurements are lacking within the Paleozoic section of northwestern Spain, the similarity in mean continental heat flow between most other Paleozoic sections (Wales excepted) suggests that this is not due to differences in the unstretched continental crust. Instead, it may be related to the Late Jurassic rifting episode that separated the outer bank from the continental mainland to create the Interior basin. We estimate a β value for this incipient rifting between 1.2 and 1.4 (Figure 14) from the 1—2 km of minimum subsidence for the Galicia Bank region (Figure 5). An attenuation of radiogenic heat production, in an exponential manner as modeled for Goban Spur, would predict a reduction of 30—50% in radiogenic heating for this value of β. Subsequent rifting during the Early Cretaceous would have commenced with a continental crust that might have already lost a significant fraction of its radiogenic material, in qualitative agreement with our observations. Confirmation of this suggestion must, however, await direct measurement of crustal radiogenic heat production.

CONCLUSIONS

The results of this study indicate the following:

1. The variation in heat flow across Goban Spur agrees with either pure-shear or lower plate, simple shear modes of rifting; there is no evidence for an upper plate origin. Given the consistency with changes in crustal structure shown by multichannel profiles, we prefer the pure-shear model. However, in that case the heat flow requires that the uppermost crust has relatively low concentrations of radiogenic material. To verify this, we need direct measurement of radiogenic heat production rates from borehole samples along the transect within the thinned continental crust.

2. The heat flow variation across the Galicia Bank is atypical, decreasing instead of increasing as the continental crust thickens. This result requires that its continental crust be totally depleted in radiogenic material, either from its beginning or as caused by a previous period of asymmetric rifting as a lower plate margin. There is no evidence which requires an upper plate origin for Galicia Bank. Unfortunately, microfaunal estimates of paleodepths at ODP sites 638, 639, and 641 [*Moullade et al.*, 1988] are too imprecise in these bathyal depths to add further constraints. Without such additional data, the existence of a previous rifting event which reduced the radiogenic upper crust is unproven.

We have also shown that significant nonlinearities in temperature gradients complicate our ability to measure the basement heat flow of both margins for low values of β. These perturbations are primarily caused by variations in bottom water temperature, most likely produced by deeply penetrating mesoscale eddies. These eddies can cause BTVs at depths where significant vertical gradients in the water temperature exist and are particularly evident across Goban Spur where they interact with the warm water outflow from the Mediterranean. Increased resolution will require subbottom penetrations of 8—10 m or geographically coincident observations separated by a period of approximately 1 month.

Two heat flow stations have very high values which cannot be explained by BTVs: DSDP 550 on oceanic crust immediately west of the Goban Spur margin and station KF21 on transitional crust west of Galicia Bank. The DSDP value does not agree with measurements from shallow penetrations in close proximity, but the reason for this large discrepancy is not obvious in the DSDP data. The high value at KF21 may indicate the presence of local erosional processes, of hydrothermal circulation, or of an abrupt local variation in crustal heat production. Disturbance of the lower two thermistors make this station too shallow to be conclusive.

We also show that there is a significant difference in the mean sediment-corrected basement depth of oceanic crust in the two regions. Values west of Galicia Bank are 1 km greater than values west of Goban Spur. The greater depths adjacent to Galicia Bank appear to be regional in extent rather than related to the formation of Galicia Bank per se, as sediment-corrected basement depths of between 6 and 7 km exist on oceanic crust south of Galicia Bank in the Iberia and Tagus abyssal plains [*Whitmarsh et al.*, 1990; *Mauffret et al.*, 1989]. The cause of these larger depths may partly be explained by crustal isostatic imbalances between

regions. The free-air gravity anomaly map of *Lalaut et al.* [1981] shows negative anomalies of -30 to -50 mGal in the Iberia and Tagus abyssal plains off western Galicia Bank and Portugal, compared to positive values of 10 to 20 mGal west of Goban Spur. However, to create an extra 1 km subsidence requires an original continental crust that is approximately 15% thicker (e.g., 35 versus 30 km) or less dense (2.8 versus 2.9 Mg/m^3). If totally uncompensated by thinner or more dense oceanic crust, this would create a free air anomaly of -100 mGal, or nearly twice that which is observed. Changes in oceanic crustal structure between basins could help to reduce the expected anomaly.

We finally note that low values of heat flow on oceanic crust, particularly those west of Goban Spur, are consistent with an in situ asthenospheric temperature of roughly 1200°C. This is roughly 100°C lower than suggested values of 1280°C for the creation of standard oceanic crust [*Foucher et al.*, 1982; *McKenzie and Bickle*, 1988]. A low asthenospheric temperature is consistent with the nonvolcanic nature of this margin but would imply, using the simplest petrologic model, the generation of unusually thin (about 2 km thick) oceanic crust. On the other hand, above normal basement depths and near zero free air anomalies west of Goban Spur suggest that this is probably not the case. Unusual crustal structure may, however, be indicated by the greater basement depths west and south of Galicia Bank as discussed above, but this suggestion requires further justification from refraction profiles.

Acknowledgements. We would like to thank the officers and crew of the N/O *Le Suroit* and the N/O *Jean Charcot*, and the technical support personnel (C. Toularastel, J.-P. Quéré, and J.-P. Le Formal) from the Département de Géosciences Marines (IFREMER, Centre de Brest), who helped take the heat flow measurements at sea. K.E.L. was supported while at IFREMER by a burse from the French government (Ministère des Affaires Étrangères) and while writing this paper at Dalhousie University by N.S.E.R.C. grant OGP0008459. C. Jaupart kindly supplied the computer code for making the two-dimensional topographic corrections, and S. Levesque supplied the code for calculating the effects of bottom water temperature variations. H. Pollack supplied a listing of continental heat flow values in France, Spain, and Great Britain. J.-P. Mazé helped draft the figures. G. Hammer helped prepare the text.

REFERENCES

Albert-Beltran, J.F., Heat flow and temperature gradient data from Spain, in *Terrestrial Heat Flow in Europe*, edited by V. Cermak and L. Rybach, pp. 261—266, Springer-Verlag, New York, 1979.

Avedik, F., A.L. Camus, A. Ginzburg, L. Montadert, D.G. Roberts, and R.B. Whitmarsh, A seismic refraction and reflection study of the continent-ocean transition beneath the North Biscay margin, *Philos. Trans. R. Soc. London, Ser. A, 305*, 5—25, 1982.

Bloomer, J.R., S.W. Richardson, and E.R. Oxburgh, Heat flow in Britain: an assessment of the values and their reliability, in *Terrestrial Heat Flow in Europe*, edited by V. Cermak and L. Rybach, pp. 293—300, Springer-Verlag, New York, 1979.

Boillot, G., S. Grimaud, A. Mauffret, D. Mougenot, J. Kornprobst, J. Mergoil-Daniel, and G. Torrent, Ocean-continent transition off the Iberian margin: a serpentinite diapir west of Galicia Bank, *Earth Planet. Sci. Lett., 48*, 23—34, 1980.

Boillot, G., M. Comas, J. Girardeau, J. Kornprobst, J.-P. Loreau, J. Malod, D. Mougenot, and M. Moullade, Fonds sous-marins basaltiques et ultramafiques au pied d'une marge stable. Résultats préliminaires de la campagne Galinaute (plongées du submersible Nautile à l'Ouest de l'Espagne), *C. R. Acad. Sci., Ser. 2, 303*, 1719—1724, 1986.

Boillot, G., *et al.*, Tectonic denudation of the upper mantle along passive margins: a model based on drilling results (ODP Leg 103, western Galicia margin, Spain), *Tectonophysics, 132*, 335—342, 1987.

Boillot, G., J. Girardeau, and J. Kornprobst, Rifting of the Galicia margin: crustal thinning and emplacement of mantle rocks on the seafloor, *Proc. Ocean Drill. Program, Sci. Results, 103*, 741—756, 1988.

Brock, A., Heat flow measurements in Ireland, *Tectonophysics, 164*, 231—236, 1989.

Buck, W.R., F. Martinez, M.S. Steckler, and J.R. Cochran, Thermal consequences of lithospheric extension: Pure and simple, *Tectonics, 7*, 213—234, 1988.

Chenet, P.-Y., L. Montadert, H. Gairaud, and D. Roberts, Extension ratio measurements on the Galicia, Portugal and northern Biscay continental margins: implications for evolutionary models of passive continental margins, in *Studies in Continental Margin Geology*, edited by J.S. Watkins and C.L. Drake, *AAPG Mem. 34*, 703—715, 1983.

Erickson, A.J., W.E. Avera, and R. Byrne, Heat flow results, DSDP Leg 48, *Initial. Rep. Deep Sea Drill. Prog., 48*, 277—288, 1979.

Foucher, J.-P. and J.-C. Sibuet, Thermal regime of the northern Bay of Biscay continental margin in the vicinity of the D.S.D.P. Sites 400—402, *Philos. Trans. R. Soc. London, Ser. A, 294*, 157—167, 1980.

Foucher, J.-P., X. Le Pichon, and J.-C. Sibuet, The ocean-continent transition in the uniform lithospheric stretching model: role of partial melting in the mantle, *Philos. Trans. R. Soc. London, Ser. A, 305*, 27—43, 1982.

Foucher, J.-P., P.-Y. Chenet, L. Montadert and J.-M. Roux, Geothermal measurements during Deep Sea Drilling Project Leg 80, *Initial Rep. Deep Sea Drill. Prog., 80*, 423—436, 1985.

Fuglister, F.C., Ocean Atlas of Temperature and Salinity Profiles and Data from the International Geophysical Year of 1957—1958, *Woods Hole Oceanogr. Inst. Atlas Ser.*, vol. 1, 209 pp., Woods Hole, Mass., 1960.

Goldberg, D.S., The Physical Properties of Deep Ocean Sediments from the Northern Atlantic: A Comparison of In-Situ and Laboratory Methods, M.Sc. thesis, Mass. Inst. of Technol., Cambridge, 1981.

Gould, W.J., The Northeast Atlantic Ocean, in *Eddies in Marine Science*, edited by A.R. Robinson, pp. 145—157, Springer-Verlag, New York, 1983.

Guennoc, P., H. Jonquet, and J.-C. Sibuet, Carte magnétique de l'Atlantique nord-est, anomalies du champ total; scale 1:2,400,000, Inst. Fr. de Rech. pour l'Exploit. de la Mer, Paris, 1978. (Available from BRGM, Serv. Promotion et Vente, Orléans, France).

Hutchison, I., The effects of sedimentation and compaction on oceanic heat flow, *Geophys. J. R. Astron. Soc., 82*, 439—460, 1985.

Hyndman, R.D., M.G. Langseth, and R.P. Von Herzen, Deep Sea Drilling Project geothermal measurements: a review, *Rev. Geophys., 25*, 1563—1582, 1987.

Issler, D., H. McQueen, and C. Beaumont, Thermal and isostatic consequences of simple shear extension of the continental lithosphere, *Earth Planet. Sci. Lett., 91*, 341—358, 1989.

Jolivet, J., G. Bienfait, J.-L. Vigneresse, and M. Cuney, Heat flow and heat production in Brittany (western France), *Tectonophysics, 159*, 61—72, 1989.

Keen, C.E., and B. de Voogd, The continent-ocean boundary at the rifted margin off eastern Canada: New results from deep seismic reflection studies, *Tectonics, 7*, 107—124, 1988.

Keen, C.E., C. Peddy, B. de Voogd, D. Matthews, Conjugate margins of Canada and Europe: results from deep reflection profiling, *Geology, 17*, 173—176, 1989.

Lalaut, P., J.-C. Sibuet, and C. Williams, Présentation d'une carte gravimétrique de l'Atlantique nort-est, *C. R. Acad. Sci., Ser. 2, 292*, 597—600, 1981.

Lallemand, S., J.-P. Mazé, S. Monti, and J.-C. Sibuet, Carte bathymétrique de l'Atlantique nord-est, scale 1:2,400,000, Ifremer, Paris, 1985. (Available from BRGM, Serv. Promotion et Vente, Orléans, France).

Lefort, J.-P., J.-J. Peucat, J. Deunff, and A. Le Herisse, The Goban Spur Paleozoic basement, *Initial Rep. Deep Sea Drill. Prog., 80*, 677—679, 1980.

Le Groupe Tourbillon, The Tourbillon experiment: a study of a mesoscale eddy in the eastern North Atlantic, *Deep Sea Res., 30*, 475—511, 1983.

Le Pichon, X., and F. Barbier, Passive margin formation by low-angle faulting within the upper crust: The northern Bay of Biscay margin, *Tectonics, 6*, 133—150, 1987.

Le Pichon, X., and J.-C. Sibuet, Comments on the evolution of the north-east Atlantic, *Nature, 233*, 257-258, 1971.

Le Pichon, X., and J.-C. Sibuet, Passive margins: A model of formation, *J. Geophys. Res., 86*, 3708—3720, 1981.

Le Pichon, X., J. Angelier, and J.-C. Sibuet, Subsidence and stretching, in *Studies in Continental Margin Geology*, edited by J.S. Watkins and C.L. Clarke, *AAPG Mem. 29*, 731—741, 1983.

Louden, K.E., and J.A. Wright, Marine heat flow data: a new compilation of observations and brief review of its analysis, in *Handbook of Seafloor Heat Flow*, edited by J.A. Wright and K.E. Louden, pp. 3—70, CRC Press, Boca Raton, Fla., 1989.

Lucazeau, F., and S. Le Douaran, The blanketing effect of sediments in basins formed by extension: a numerical model, application to the Gulf of Lion and Viking graben, *Earth Planet. Sci. Lett., 74*, 92—102, 1985.

Lucazeau, F., and G. Vasseur, Heat flow density data from France and surrounding margins, *Tectonophysics, 164*, 251—258, 1989.

Masson, D.G., and P.R. Miles, Mesozoic seafloor spreading between Iberia, Europe and North America, *Mar. Geol., 56*, 279—287, 1984.

Masson, D.G., L. Montadert, and R.A. Scrutton, Regional Geology of the Goban Spur continental margin, *Initial Rep. Deep Sea Drill. Prog., 80*, 1115—1140, 1985.

Mauffret, A. and L. Montadert, Rift tectonics on the passive continental margin off Galicia (Spain), *Mar. Pet. Geol., 4*, 49—69, 1987.

Mauffret, A., D. Mougenot, P.R. Miles, and J.A. Malod, Cenozoic deformation and Mesozoic abandoned spreading centre in the Tagus Abyssal Plain (west of Portugal): results of a multichannel seismic survey, *Can. J. Earth Sci., 26*, 1101—1123, 1989.

Maury, R.C., H. Gellon, H. Bougault, J.-L. Joron, M. Bohn, and P.-C. de Graciansky, Oceanic tholeiites from Leg 80 sites (Celtic Sea passive margin, Northeastern Atlantic): geochemistry and mineralogy, *Initial Rep. Deep Sea Drill. Prog., 80*, 939—946, 1985.

McKenzie, D., Some remarks on the development of sedimentary basins, *Earth Planet. Sci. Lett., 40*, 25—32, 1978.

McKenzie, D., and M.J. Bickle, The volume and composition of melt generated by extension of the lithosphere, *J. Petrol., 29*, 625—679, 1988.

Montadert, L., D.G. Roberts, O. de Charpel, and P. Guennoc, Rifting and subsidence of the northern continental margin of the Bay of Biscay, *Initial Rep. Deep Sea Drill. Prog., 48*, 1025—1060, 1979*a*.

Montadert, L., O. de Charpal, D. Roberts, P. Guennoc, and J.-C. Sibuet, Northeast Atlantic passive margins: rifting and subsidence processes, in *Deep Drilling Results in the Altantic Ocean: Continental Margins and Paleoenvironment, Maurice Ewing Ser.*, vol. 3, edited by M. Talwani, W.W. Hay, and W.B.F. Ryan, pp. 164—186, AGU, 1979*b*.

Moullade, M., M.-F. Brunet, and G. Boillot, Subsidence and deepening of the Galicia margin: the paleoenvironmental control, *Proc. Ocean Drill. Program Sci. Results, 103*, 733—740, 1988.

Murillas, J., D. Mougenot, G. Boillot, M.C. Comas, E. Banda, and A. Mauffret, Structure and evolution of the Galicia Interior basin (Atlantic western Iberian continental margin), *Tectonophysics, 184*, 297-319, 1990.

Olivet, J.-L., J. Bonnin, P. Beuzart, and J.-M. Auzende, *Cinématique de l'Atlantique Nord et Central*, 108 pp.. Centre National pour l'Exploitation des Océans, Paris, 1984.

Parsons, B., and J.G. Sclater, An analysis of the variation of ocean floor bathymetry and heat flow with age, *J. Geophys. Res., 82*, 803—827, 1977.

Peddy, C., B. Pinet, D. Masson, R. Scrutton, J.-C. Sibuet, M.R. Warner, J.-P. Lefort, and I.J. Shroeder, Crustal structure of the Goban Spur continental margin, Northeast Atlantic, from deep seismic reflection profiling, *J. Geol. Soc. London, 146*, 427—437, 1989.

Pinet, C., and C. Jaupart, The vertical distribution of radiogenic heat production in the Precambrian crust of Norway and Sweden: Geothermal implications, *Geophys. Res. Lett., 14*, 260—263, 1987.

Ratcliffe, E.H., The thermal conductivities of ocean sediments, *J. Geophys. Res., 65*, 1535—1541, 1960.

Reid, J.L., On the middepth circulation and salinity field in the North Atlantic Ocean, *J. Geophys. Res., 83*, 5063—5067, 1978.

Richardson, S.W., and E.R. Oxburgh, Heat flow, radiogenic heat production and crustal temperatures in England and Wales, *J. Geol. Soc. London, 135*, 323—337, 1978.

Roberts, D.G., D.G. Masson, and L. Montadert, Continental margin from the Porcupine Seabight to the Armorican marginal basin, in *Petroleum Geology of the Continental Shelf of Northwest Europe*, edited by L.V. Illing and G.D. Hobson, pp. 455—473, Institute of Petroleum, London, 1981.

Royden, L., and C.E. Keen, Rifting processes and thermal evolution of the continental maritn of eastern Canada determined from subsidence curves, *Earth Planet. Sci. Lett.*, 51, 343—361, 1980.

Sibuet, J.-C., Contribution à l'étude des mécanismes de formation des marges continentales passives, Thèse de doctorat d'état, 351 pp., Univ. de Bretagne Occidentale, Brest, France, 1987.

Sibuet, J.-C., and B. Collette, Triple junctions of Bay of Biscay and North Atlantic: new constraints on the kinematic evolution, *Geology*, in press, 1991.

Sibuet, J.-C., and X. Le Pichon, Structure gravimétrique du Golfe de Gascogne et le fossé marginal nord-espagnol, in *Histoire Structurale du Golfe de Gascogne*, vol. VI—9, edited by J. Debyser, X. Le Pichon, and L. Montadert, pp. 1—18, Technip, Paris, 1971.

Sibuet, J.-C., B. Mathis, L. Pastouret, J.-M. Auzende, J.-P. Foucher, P.M. Hunter, P. Guennoc, P.-C. de Graciansky, L. Montadert, and D.G. Masson, Morphology and basement structure of the Goban Spur continental margin (northeastern Atlantic) and the role of the Pyrenean orogeny, *Initial Rep. Deep Sea Drill. Prog., 80*, 1153—1165, 1985.

Sibuet, J.-C., J.-P. Mazé, P. Amortila, and X. Le Pichon, Physiography and structure of the western Iberian continental margin off Galicia from Sea-Beam and seismic data, *Proc. Ocean Drill. Prog. Initial Rep., 103*, 77—97, 1987.

Sibuet, J.-C., J. Dyment, C. Bois, B. Pinet, and H. Ondréas, Crustal structure of the Celtic Sea and western approches from gravity data and deep seismic profiles: Constraints on the formation of continental basins, *J. Geophys. Res., 95*, 10,999—11,020, 1990.

Srivastava, S.P., and C.R. Tapscott, Plate kinematics of the North Atlantic, in *The Geology of North America, Vol. M, The Western North Atlantic Region*, edited by P.R. Vogt and B.E. Tucholke, pp. 379—404, Geological Society of America, Boulder, Colo., 1986.

Srivastava, S.P., J. Verhoef, and R. Macnab, Results from a detailed aeromagneitc survey across the northeast Newfoundland margin, part 2, Early opening of the North Atlantic between the British Isles and Newfoundland, *Mar. Pet. Geol., 5*, 324—337, 1988.

Srivastava, S.P., H. Schouten, W.R. Roest, K.D. Klitgord, L.C. Kovacs, J. Verhoef, and R. Macnab, Iberian plate kinematics: a jumping plate boundary between Eurasia and Africa, *Nature, 334*, 756—759, 1990.

Tankard, A.J., and H.J. Welsink, Extensional tectonics, structural styles and stratigraphy of the Mesozoic Grand Banks of Newfoundland, in *Triassic-Jurassic Rifting and the Opening of the Atlantic Ocean*, edited by W. Manspeizer, pp. 129—165, Elsevier Science, New York, 1988.

Verhoef, J., B.J. Collette, P.R. Miles, R.C. Searle, J.-C. Sibuet, and C.A. Williams, Magnetic anomalies in the northeast Atlantic Ocean (35°-50° N), *Mar. Geophys. Res., 8*, 1—25, 1986.

Von Herzen, R.P., and A.E. Maxwell, The measurement of

thermal conductivity of deep-sea sediments by a needle probe method, *J. Geophys. Res., 64*, 1557—1563, 1959.
Voorhoeve, H., and G. Houseman, The thermal evolution of lithosphere extending on a low-angle detachment zone, *Basin Res., 1*, 1—9, 1988.
Wang, K. and A.E. Beck, Heat flow measurement in lacustrine or oceanic sediments without recording bottom temperature variations, *J. Geophys. Res., 92*, 12,837—12,845, 1987.
Watremez, P., Flux de chaleur sur le massif armoricain et sur la marge continentale: essai de modèlisation de l'évolution thermique de la marge armoricaine, Thèse de 3ème cycle, 108 pp., Univ. de Bretagne Occidentale, Brest, France, 1980.
Wernicke, B., Uniform-sense normal simple shear of the continental lithosphere, *Can. J. Earth Sci., 22*, 108—125, 1985.
White, R.S., and C. Peddy, Discussion on crustal structure of the Goban Spur continental margin, Northeast Atlantic, from deep seismic reflection profiling, *J. Geol. Soc. London, 147*, 892—894, 1990.
Whitmarsh, R.B., P.R. Miles, and A. Mauffret, The ocean-continent boundary off the western continental margin of Iberia, Part I, Crustal structure at 40°30'N, *Geophys. J. Int., 103*, 509-531, 1990.
Withjack, M.O., and W.R. Jamison, Deformation produced by oblique rifting, *Tectonophysics, 126*, 99—124, 1986.

J.-P. Foucher and J.-C. Sibuet, IFREMER Centre de Brest, BP 70, 29263 Plouzané, France.
K.E. Louden, Department of Oceanography, Dalhousie University, Halifax, N.S., Canada B3H 4J1.

(Received August 23, 1990;
revised April 15, 1991;
accepted June 4, 1991.)

JOURNAL OF GEOPHYSICAL RESEARCH, VOL. 96, NO. B10, PAGES 16,101–16,112, SEPTEMBER 10, 1991

A Theory of Ideal Bodies for Seamount Magnetism

ROBERT L. PARKER

Institute of Geophysics and Planetary Physics, Scripps Institution of Oceanography
University of California, San Diego, La Jolla

Recent studies of samples from seamounts indicate that the distribution of magnetic intensity is approximately lognormal, which implies that the commonly adopted models of interior magnetization based upon a constant vector with an isotropic perturbation are inappropriate. We develop a unidirectional model in which the direction of magnetization is fixed and the intensity is of one sign, with no upper limit on magnitude, which, if the seamount is built during a period of single magnetic polarity, is likely to be a better approximation. We show that models of this class fitting the data best in the two-norm sense conform to the ideal-body pattern comprising unidirectional, point dipoles in the surface of the seamount. Practical methods are developed for discovering the best data misfit associated with paleopole position. The methods are first tested on simple artificial magnetic anomalies and are found to be capable of recovering the true pole position with high accuracy when such a solution is possible; also when a mixed polarity artificial model is analyzed, it is found that there are no unidirectional solutions, just as would be hoped. The method is next applied to three seamount surveys. In the first it is found that every direction of magnetization is in accord with the data, so that apparently nothing useful can be learned from the survey without a stronger assumption; this result is in contrast with the results of an earlier solution based upon a statistical model, which yielded a high accuracy in the position of the paleopole. The second investigation provides a reasonably compact location of the paleopole of the seamount. The third magnetic anomaly is complex and earlier studies concluded this was necessarily the product of mixed polarity magnetization. We find that in fact unidirectional magnetizations can satisfy observation.

1. INTRODUCTION

A feature of all inverse problems of potential theory attempting to discover the distribution of the sources is a severe intrinsic nonuniqueness: completely known exterior magnetic and gravitational fields do not by themselves determine interior magnetizations or densities. The art of practical interpretation of such data is in choosing plausible restrictions that permit solutions to be found but which do not distort the information contained in the observations. From the pioneering work of *Vacquier* [1962] to the most recent methods [*Parker et al.*, 1987; *Parker*, 1988], geophysical techniques for the analysis of the magnetic anomalies of seamounts have depended in some way on the assumption that a uniform internal magnetization is a reasonably good first approximation and that nonuniformities would be either relatively small or at least reasonably symmetrically disposed about the mean vector. Yet the admittedly sparse evidence from drilling [*Kono*, 1977] and sampling of an uplifted marine volcano [*Gee et al.*, 1989] does not support this idealized picture. Rather, *Gee at al.* [1989] find the intensity of magnetization to be distributed according to a lognormal distribution caused mainly by the variations in lithology and cooling environment of the rock; intensity values range from less than $0.05\,\mathrm{A\,m^{-1}}$ to over $30\,\mathrm{A\,m^{-1}}$. Dredged samples of magnetic rocks from the seafloor also exhibit the lognormal distribution of natural remanent magnetism [*Kent et al.*, 1984]. Seamounts contain numerous pockets of highly magnetic material which means the uniform model is a poor approximation. On the other hand, unless the main field reverses during the formation of the seamount, the direction of magnetization does not vary widely. Fluctuations of secular variation contribute from 8° near the poles to 16° root-mean-square (RMS) at the equator, as deduced from the statistical model of secular variation of *Constable and Parker* [1988]; values of the same order come from paleomagnetic studies of virtual geomagnetic pole (VGP) dispersion [e.g., *McFadden and McElhinny*, 1984]. The magnetic field of the local magnetized material is likely to cause smaller perturbations. Hence large fluctuations are to be expected in magnetic intensity of the source material but not in the direction of magnetization. These facts suggest an idealization different from those considered up until now, one in which the model possesses a constant direction throughout but the magnitude of magnetization is allowed to vary within wide limits. In this paper we begin the study of models of this kind.

The first question to be asked is what can be learned in principle when the intensity is not strongly constrained. Suppose when we consider the complete set of models of constant direction we find only those with magnetizations lying within a certain cone to be capable of reproducing the observed magnetic anomaly pattern; this would constrain the permissible directions of the associated

Paper number 91JB01497.
0148-0227/91/91JB-01497$05.00

paleomagnetic pole. Since virtual geomagnetic pole positions are the principal product of seamount magnetism studies, this would be a valuable finding even if it were not accompanied by any information about the distribution of magnetization within the volume of the body. To the extent that constancy of direction is a valid condition, such a demonstration would be rigorous, an unusual quality in any geophysical investigation. (The calculations in this paper fall short of being completely rigorous because there is no bound on the possible error introduced by the approximation of discretization; we know, however, that the true cone of solutions is always larger than the one computed.) Alternatively, it might be discovered that none of the models in this class could provide an adequate fit to observation; then we could rigorously conclude that variable direction of magnetization was a necessity, with the possibility of the presence of both normal and reversed polarizations. To be able to reach such conclusions it is essential to demand a single polarity in the model magnetization for, as we shall note in the next section, the data are (to an excellent approximation) linear functionals of the magnetization distribution, and under these circumstances, every finite collection of data can be reproduced by a model of some kind if no nonlinear constraints are placed on the model. Another possibility is that every direction of magnetization is associated with an adequately fitting model; one would then be faced with a sobering conclusion: nothing useful could be learned about magnetic directions or paleopoles from the given set of observations without making further, and perhaps unwarranted, assumptions.

We shall see that the theory for this question has been provided in large part by the method of ideal bodies [*Parker*, 1974, 1975]. Two serious gaps exist in the original results: one concerns the ability of the method to handle imprecise data, the other is the lack of effective algorithms for handling the large number of observational constraints typical of a marine survey. Recent developments [*Ander and Huestis*, 1987; *Parker and Zumberge*, 1989] for the ideal body problem in gravity have settled the first question and gone a long way towards solving the second; an extension of these methods is, however, needed for our problem, and the necessary work will be done in the next section. We shall see that the ideal body solution in this case comprises a finite number of unidirectional dipoles located in the surface of the seamount. The numerical solution of the optimization problem whose solution gives the positions and moments of the dipoles is accomplished with quadratic programming. In practice the calculations require rather more computer time than those needed for the seminorm minimizations that form the basis of two earlier model techniques [*Parker et al.*, 1987; *Parker*, 1988].

In the third section of the paper we examine the performance of the method on several artificially generated data sets and compare the results with those of other methods. As might be expected, the newer analysis is always less restrictive in that it allows a wider range of permissible magnetization directions, but it is not unduly lenient. When an exact fit with data is demanded, the zone of uncertainty in pole position is found to be very small. We also attempt to recover a unidirectional model from an anomaly generated by a mixed polarity body; the attempt fails if exact matching of the anomaly is required. In the penultimate section we describe the application to three magnetic surveys of seamounts. These applications show that the unidirectional class of solution is remarkably powerful in its ability to match magnetic anomaly patterns. The anomaly of LR148.8W, a large young seamount on the Louisville Rise, can be matched by a unidirectional model with any magnetization direction. Thus additional assumptions are needed if the survey data are to provide conclusions about the paleopole of this seamount. In contrast, the set of paleopole positions consistent with the anomaly of Darwin seamount is confined mostly to the southern hemisphere, confirming the probable reversed polarity of this body deduced by earlier methods. The third survey, that of Jasper seamount, exhibits a central complex anomaly pattern which, according to previous studies, signifies the presence of normal and reversed magnetization. We find, however, no difficulty in fitting the anomaly with a variety of unidirectional models.

2. THEORY

The model magnetization inside the seamount V is a unidirectional vector field whose magnitude is an arbitrary function of position $\mathbf{s}$ within the body, with the condition that reversal of magnetization direction is prohibited: thus

$$\mathbf{M}(\mathbf{s}) = \hat{\mathbf{m}}\, m(\mathbf{s}), \qquad m(\mathbf{s}) \geq 0\,. \tag{1}$$

The observations are taken to be total field magnetic anomalies outside V, approximated in the familiar way by the field component along $\hat{\mathbf{B}}_0$, the direction of the main geomagnetic field in the vicinity. If N observations d_j are made at positions $\mathbf{r}_j$ relative to some fixed origin, it is readily shown [*Parker et al.*, 1987] that

$$d_j = \int_V g_j(\mathbf{s})\, m(\mathbf{s})\, d^3\mathbf{s}, \qquad j = 1, 2, \cdots N \tag{2}$$

where

$$g_j(\mathbf{s}) = \frac{\mu_0}{4\pi}\left[\frac{3\hat{\mathbf{m}}\cdot(\mathbf{r}_j - \mathbf{s})\,\hat{\mathbf{B}}_0\cdot(\mathbf{r}_j - \mathbf{s})}{|\mathbf{r}_j - \mathbf{s}|^5} - \frac{\hat{\mathbf{m}}\cdot\hat{\mathbf{B}}_0}{|\mathbf{r}_j - \mathbf{s}|^3}\right]. \tag{3}$$

Equation (2) is simply a statement that the magnetic anomaly seen at the observer position $\mathbf{r}_j$ is the combined effect of a set of unidirectional dipoles within V; (3) gives the contribution to the anomaly of a single point dipole of unit moment at $\mathbf{s}$.

Unless a condition like $m(\mathbf{s}) \geq 0$ is applied we can always find magnetization models in the form of (1) exactly satisfying the constraints (2), because these are linear functionals [see *Parker*, 1977] and because the representers g_j are linearly independent; the proof of linear independence given Appendix A of *Parker et al.*

[1987] can easily be modified for the present case of a fixed direction.

Since the representer g_j is obtained by differentiating $1/r$ twice and the observer is always outside the source region, it follows that

$$\nabla^2 g_j = 0 . \tag{4}$$

Suppose we temporarily impose an upper limit on the strength of magnetization, so that $0 \le m \le M_0$. Just for the moment we wish to satisfy the demands of the measurements (2) exactly, but we require the smallest possible M_0 that will do the job. Then the theory of ideal bodies [*Parker*, 1974, 1975] applies directly to this problem. According to this theory the magnetic intensity within V is either zero or M_0 and that the regions of positive magnetization are enclosed in smooth boundaries that always intersect the surface of the seamount. The boundaries of the magnetized zones are equipotential surfaces of multipole sources located at the observation sites. If we allow the maximum intensity to become arbitrarily large (in other words, we remove the magnitude constraint on intensity), we find the ideal-body solution degenerates into a set of point sources, in our case, point dipoles, in the boundary of V. All this was shown by *Parker* [1975]; the computational techniques given in that paper were severely limited in the number of observations that could be handled (no more than 15) and applied only to the case of exact fitting of the measurements. For practical application we will need some quite different techniques, which at first seem unrelated to the original ideal-body approach.

Looking for an exact solution with a certain optimal property, as the ideal-body theory does, presupposes a solution of some kind exists, but under the constraint of unidirectionality this may not always be the case; indeed, as we have already noted, finding those directions of magnetization incompatible with the observation will play an important part in the application of the theory. We proceed therefore by seeking the best fitting solution for fixed $\hat{\mathbf{m}}$ and $m \ge 0$; if the degree of misfit is unacceptably large, we must declare the direction $\hat{\mathbf{m}}$ inadmissible. As a misfit measure we shall use the familiar sum of squared discrepancies:

$$F[m] = \sum_{j=1}^{N} \left[d_j - \int_V g_j(\mathbf{s})\, m(\mathbf{s})\, d^3\mathbf{s} \right]^2 . \tag{5}$$

As discussed by *Parker et al.* [1987] one can estimate the expected size of this number from examination of the magnetic anomalies in the neighborhood of the seamount but far enough away from it to allow neglect of its magnetic influence. We shall show that the model magnetization minimizing (5) subject to nonnegativity of m consists of a set of no more than N dipoles situated in the surface of the seamount, an ideal-body configuration.

To come to grips with (5), we imagine solving an approximate, finite-dimensional version of the true semi-infinite optimization problem. The interior of the seamount is divided into K (a very large number) small cubes, V_k, each uniformly magnetized in the direction $\hat{\mathbf{m}}$ with nonnegative intensity m_k; the cubes fill V without overlapping, conforming to the boundary as well as possible. Then the integral in (5) can be replaced by a sum of the integrals taken over the cubes:

$$\int_V g_j(\mathbf{s})\, m(\mathbf{s})\, d^3\mathbf{s} = \sum_{k=1}^{K} G_{jk}\, m_k \tag{6}$$

where

$$G_{jk} = \int_{V_k} g_j(\mathbf{s})\, d^3\mathbf{s} . \tag{7}$$

Under this approximation the problem of finding the best fitting model becomes the following optimization:

$$\min_{m_k \ge 0} \sum_{j=1}^{N} \left(d_j - \sum_{k=1}^{K} G_{jk}\, m_k \right)^2 \tag{8}$$

or in the obvious vector and matrix notation

$$\min_{\mathbf{m} \ge 0} \| \mathbf{d} - G\,\mathbf{m} \|^2 . \tag{9}$$

This is an example of a quadratic program [*Lawson and Hanson*, 1974]. As shown by these authors, application of the Kuhn-Tucker conditions proves that no more than N of the K components of the vector $\mathbf{m}$ need be different from zero in an optimizing solution. Thus there are at most N magnetized cubes within the seamount, while the rest are unmagnetized, no matter how large K may be. If we imagine the number of cubes K tending towards infinity, we see the solution to the continuous problem becomes a set of at most N point dipoles inside V.

While this derivation of the form of the solution is simple and appeals directly to the numerical method which will be used for solving practical problems, it fails to bring out a most important property of the solution, that is, the fact that the dipoles are not distributed within V but are confined to the boundary, ∂V. To show this, we give a general result, which allows us to infer that the functional form of the ideal body solution is identical to that of the solution of the present problem. Specifically, we compare the nature of the solutions to two optimization problems: in the first an exact fit to the observations is required, and in the second the agreement with observation is specified by RMS misfit. Let the model m be in a normed vector space X and the N observations be calculated via linear functionals g_j: thus when we require the model predictions exactly to match the measurements, we have

$$d_j = g_j[m], \quad j = 1, 2, \cdots N \tag{10}$$

which is just an abstract form of (2). First we seek the element $m_0 \in X$ that minimizes a nonlinear penalty functional P; here we might mean the norm of m for example. An elementary way to set up the problem [see *Luenberger*, 1969] is by introducing N Lagrange multipliers μ_j, one for each member of (10), to construct an unconstrained functional on X:

$$U_1[m] = P[m] + \sum_{j=1}^{N} \mu_j (d_j - g_j[m]) \ . \qquad (11)$$

The desired minimum of P subject to (10) is found by discovering the stationary points of (11) with respect to variations in m. We take the Fréchet derivative [*Luenberger*, 1969] of (11) and set it to the zero element:

$$0 = D_P(m_0) + \sum_{j=1}^{N} \mu_j g_j \ . \qquad (12)$$

Strictly, D_P, the functional derivative of P, belongs to X^*, the space of all linear functionals on X, as does g_j. If (12) can be solved for m_0 and a suitable set of parameters can be found, we can construct the P minimizer. This is essentially the approach of *Parker* [1972].

Next we consider the second optimization problem in which we replace (10) with the condition

$$T^2 = \sum_{j=1}^{N} (d_j - g_j[m])^2 \qquad (13)$$

which is (5) written as a constraint. For statistical purposes, (13) should be an inequality, but in practice it is sufficient to solve the problem as written; see *Parker et al.* [1987]. To minimize P subject to (13) requires only one Lagrange multiplier λ in the unrestricted functional:

$$U_2 = P[m] + \lambda \{T^2 - \sum_{j=1}^{N} (d_j - g_j[m])^2\} \ . \qquad (14)$$

Differentiating as before gives

$$0 = D_P(m_0) + \sum_{j=1}^{N} 2\lambda (d_j - g_j[m_0]) g_j \ . \qquad (15)$$

This equation relates the element D_P to a linear combination of the elements g_j, since λ and the factors $(d_j - g_j[m])$ are just scalar constants. Hence in essential content (12) and (15) are the same. It follows that the same kinds of models solve the optimization problem whether an exact fit like (10), or a specified two-norm misfit like (13), is demanded.

With a few minor modifications this result shows that the nature of ideal bodies is unaltered if the data fitting criterion is relaxed to (13). One matter is the addition of a positivity constraint, which clearly affects both functionals U_1 and U_2 in the same way. Another technical point is that the minimized functional P would be the sup norm for the ideal body computations, and this is not strictly Fréchet differentiable; the same device as used by *Parker* [1972] of a sequence of p norms patches up the argument. Finally returning to the seamount problem, our desire is to minimize F in (5) rather than use it as a constraint. There is no difficulty in changing the role of the data misfit from a constraint to the objective functional and making the upper bound on m a constraint rather than the objective: the Lagrange multiplier formulation hardly looks any different.

The outcome of these considerations is as follows: when $F[m]$ is minimized subject to $0 \le m \le M_0$, the optimal solution is a magnetic ideal body as described earlier, comprising uniformly magnetized regions enclosed by smooth equipotential surfaces. A key result is that the magnetized zones can never be completely disconnected from the boundary of the seamount, a property derived from potential theory by *Parker* [1975]. Thus as M_0, the upper bound on magnetization intensity, is increased indefinitely, the dipole sources that develop must be in contact with the surface of the seamount. (If we wish to go directly to the result that the search for best unidirectional solutions need be performed only over the set of surface dipoles, without even mentioning the finite intensity solutions, there is an economical proof, provided by Gary Egbert in a review of this paper; it is given in the Appendix.) The surprising consequence is that, although the whole volume V of the seamount is available for sources, the optimal (that is, best fitting) model shuns the interior space and distributes magnetization only on the boundary. Elegance aside, the importance of this condition arises from the great saving in computation time. The numerical algorithm remains a quadratic program like (9), but the sources need not be distributed within V and so, to accomplish the same spatial resolution, the row dimension of G can be many times smaller, by as much as a factor of 20.

3. ARTIFICIAL EXAMPLES

To test the effectiveness of the process outlined in the previous section, I generated anomaly patterns associated with magnetization distributions inside a very simple shape, the cap of a sphere, with roughly the size and shape of a typical seamount; the details will be supplied shortly. The magnetic fields of the distribution can be computed very accurately [*Parker and Shure*, 1985], but for analysis of real measurements it is necessary to approximate the surface of the seamount by some flexible scheme involving finitely many elements. In order to retain compatibility with a large data base of surveys, I decided to retain the same model representation adopted by *Parker et al.* [1987] of a triangular tessellation; point dipoles are located only at the vertices of the polyhedral surface enclosing the model body. A particular dipole direction $\hat{\mathbf{m}}$ is selected and then the linear transformations mapping the dipole strengths at the vertices into anomaly values are computed by (3) and saved in the array G. The minimization (9) is performed by the nonnegative least squares algorithm, NNLS [*Lawson and Hanson*, 1974]. In so far as the number of dipole sites on the surface is dense enough, this single minimization gives the smallest possible misfit of all magnetizations possessing the particular direction. But we would like to know the minimum misfit over all directions. The only way to discover this is by means of a complete exploration of the unit sphere, since the variation of misfit with direction is a complicated function, often with many local minima. Then a systematic search process is carried out as follows. Because the chief interest in magnetization direction arises from the paleomagnetic context, it is instructive to plot the misfit between best model predic-

tion and observation on the sphere of VGP positions. This geographic sphere is scanned systematically, and the local vector $\hat{\mathbf{m}}$ is found for every selected pole location, then (9) is minimized and the RMS misfit assigned to the corresponding point on the VGP map. At the end of the complete calculation the values are contoured and plotted (Figure 2, for example).

We return to the artificial model: the body is a solid cap of a sphere (see Figure 1*b*). The radius of the sphere is 26 km; the cap has a base radius of 10 km and therefore stands 2 km above its base at the highest point; the body is located in water 4 km deep. In the first few experiments this body was given a uniform internal magnetization with an intensity of 2.32 $\mathrm{A\,m^{-1}}$ and a dip of 63.43°, which corresponds to a paleopole position 45° north of the seamount. Magnetic anomaly values were calculated on a 64-element rectangular array with spacing of 2.5 km. Computer runs were performed with the model in various geographic locations and with several declinations of the magnetization vector; for simplicity the ambient field direction $\hat{\mathbf{B}}_0$ was that of the axial dipole approximation and so always possessed vanishing declination. Figure 1*a* shows the magnetic anomaly when the seamount is sited on the equator on the Greenwich meridian and has been rotated and so the declination of the magnetization vector is 270°; this puts the true paleopole on the equator at 45° longitude. For the purposes of modeling, the surface of the body was represented as the altitudes at 305 points arranged in equilateral triangles, with sides 1.2 km. In each numerical experiment the artificial data were interpreted with the standard least squares approach and the seminorm minimizing method as well as with the new technique.

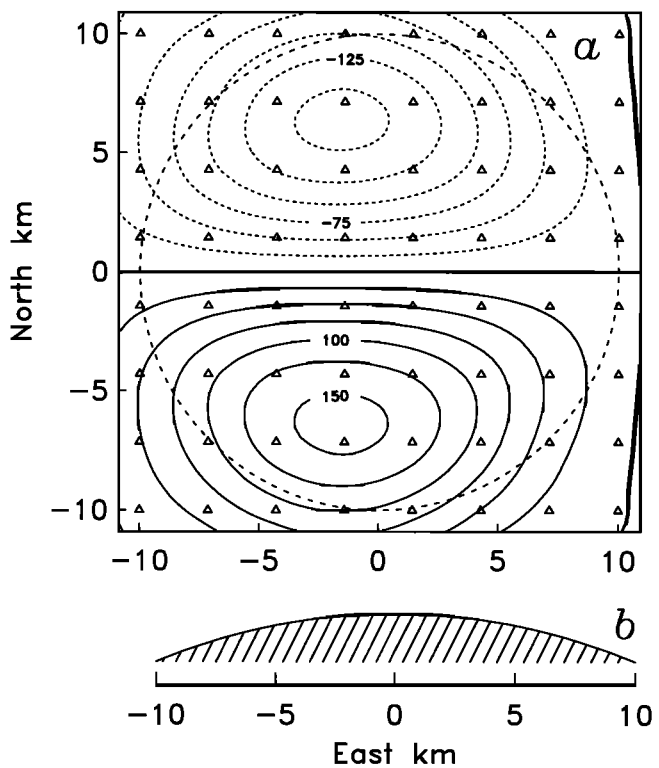

Fig. 1. (*a*) Total field anomaly map in nanotelsas of an artificial seamount in the shape of a spherical cap, uniformly magnetized with intensity 2.32 $\mathrm{A\,m^{-1}}$; the magnetic vector has inclination 63.43° and declination 270°. The ambient field is horizontal and points due north. The triangles mark the sites of the 64 magnetic observations used in the inversion. (*b*) Vertical section through the body drawn to true scale. The base of the body is 4 km below the level where the field is sampled.

The results of the new analysis of the survey depicted in Figure 1 are summarized in Figure 2, which shows the RMS misfit in nanoteslas plotted at the position of the corresponding VGP in Aitoff equal-area projection. This example is typical of all those in which the internal magnetization was uniform. Since this is an artificial problem based upon a uniform body, we expect to be able to fit the anomaly values exactly in the class of unidirectional magnetizations, and we can. The small oval on the equator labeled zero in Figure 2 encloses the region on the map of paleopole positions for which exact agreement with the 64 values can be obtained. The zone of perfect agreement is remarkably small, measuring about 4° across in latitude and 16° in longitude, and the area is centered right on the theoretical paleopole position. Recall that the exactly matching ideal-body models comprise point dipoles in the surface, while the original distribution is uniform throughout V. Naturally, there is no requirement that the model magnetization function should resemble the true one in order for us to be able to make valid inferences. If we consider the complete map, we must admit that the system is not very robust: when a small misfit is allowed, say, only 5 nT RMS (which is only 3% of the peak anomaly value), the size of the permitted oval of paleopole directions grows to become nearly 135° across at the equator. This suggests something discovered in practice: when the observations are inexact, constraints on paleopole location may be relatively weak. It hardly needs to be mentioned that the standard least squares method gave the exact pole position with insignificant errors; the confidence zones derived from the statistical heterogeneity model [*Parker*, 1988] were also tiny, but of course the model is quite inappropriate here because the misfit between model and anomaly value has its origin in small imperfections in the approximation of the shape of the seamount by triangles, not from any internal variability of magnetization.

A second artificial model was generated. In this one I attempted to mimic the magnetization of a complex body containing both polarities of magnetization, a body that should be very poorly modeled by the standard techniques and whose complexity should be made evident by the new method. Keeping the same location, orientation and external shape of the model, I added a central, reversely magnetized core as shown in Figure 3*b*. The intensity of magnetization was arranged so as exactly to cancel the dipole moment of the outer layer: this body has no net dipole moment. I increased the intensities of magnetization in the layers (which were equal and opposite vectors) to 6.7 $\mathrm{Am^{-1}}$ so that the RMS field value in this example and in the first one are approximately the

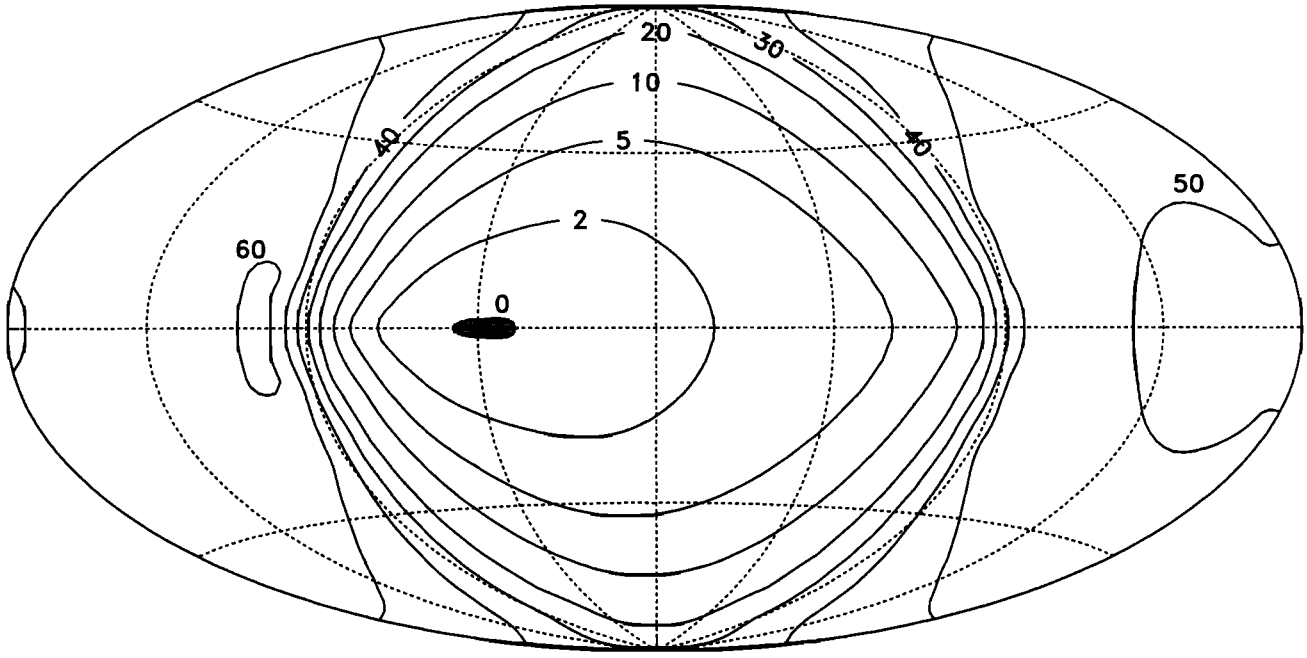

Fig. 2. RMS misfit of the best unidirectional magnetization matching the anomaly data shown in Figure 1*a*, plotted as a function of VGP location in Aitoff equal-area projection. Short dashed lines on this and other VGP maps are meridians and parallels spaced at 45°; the central vertical dashed line is the Greenwich meridian. Contour levels are marked in nanoteslas. Note the small size of the region designating exact fit.

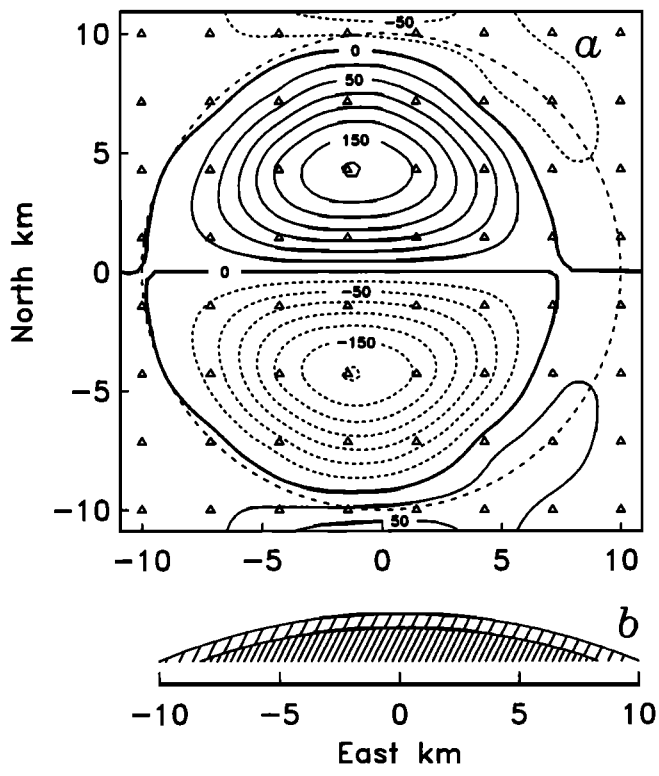

Fig. 3. (*a*) Total field anomaly map of the second artificial body; symbols and magnetic environment as in Figure 1. (*b*) Vertical section illustrating the makeup of the body in the form of a shell and a central core, each uniformly magnetized but in opposite directions. The volumes of the two zones are equal as are the intensities, 6.7 $A\,m^{-1}$.

same. The pattern of the anomaly is only slightly more complex than the field in Figure 1*a*; at first glance it resembles a smaller, reversed version of that anomaly. Figure 4 shows a plot of the same kind as Figure 2. Notice now that the misfit is never driven to zero, which means no unidirectional magnetization can exactly fit the anomaly data. This is of course exactly what we would wish for. The minimum attainable RMS misfit is 8.49 nT, so that, if the accuracy of the observed signal is high enough, the method can rule out the possibility of any unidirectional solution. The standard least squares solution gave a paleopole estimate within a degree of the one appropriate to the central core of the body, but the misfit was nearly 50 nT, and intensity of magnetization given to the body was only 1.05 $A\,m^{-1}$. When the most uniform solution was computed with RMS misfit of 1 nT, the nonuniform component of magnetization was 3.4 times larger in the norm than the uniform part. The 95% confidence error ovals computed by the statistical theory were about 140° across, indicating no reliance could be placed in the estimated pole position.

So far we have not mentioned the question of the error incurred by replacing the true minimization of (5) with the finite-dimensional approximation (8). A mathematically rigorous treatment of such errors has been recently developed by P. B. Stark (Inference in infinite-dimensional inverse problems: discretization and duality, submitted to Journal of Geophysical Research, 1990) but we shall be content with a fairly simple discussion. In effect we are restricting the possible location of the permissible dipole sources to just those points in a list, rather than allowing freedom of position anywhere in the

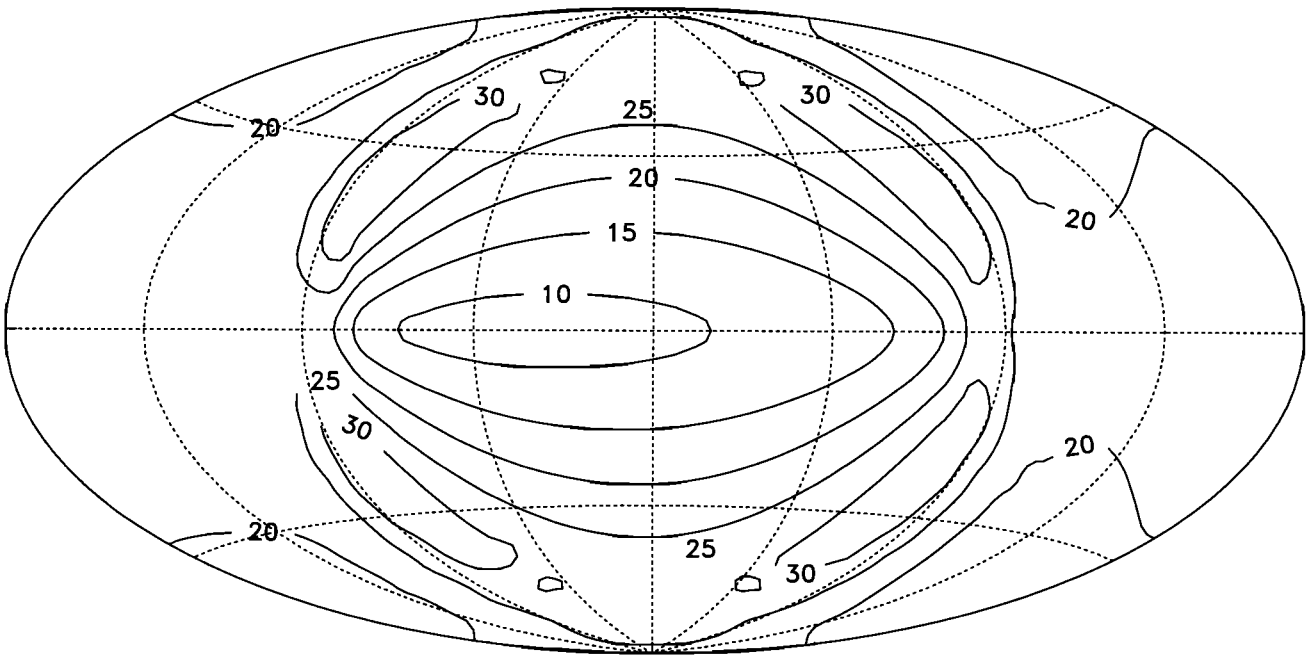

Fig. 4. Misfit map for second artificial problem. Note that no pole position is associated with an exact fit to the data.

surface. The error in the placement of a source dipole could be as large as one half the side of a triangular facet, and each side is about a half the local water depth, if we follow the rule of *Parker et al.* [1987]. But this relatively large location error is certainly not translated into a correspondingly large error in the minimum RMS misfit, the quantity of importance for the inverse problem. One obstacle to an empirical evaluation is the lack of exact solutions in closed form, against which the numerical solution might be tested. A series of numerical runs was performed using the artificial anomaly pattern of Figure 1, in which the number of points in the surface was increased from 87 to 428; the RMS misfit for a VGP on the equator at 100.4°E (the site of maximum misfit Figure 2), varied only between 62.9 and 61.3, less than 3%. The corresponding average separation between points in the surface varied from 2.8 km to 1.0 km, and the relation between misfit and separation was roughly linear. If the line is extrapolated to zero separation, we infer the true minimum misfit is 59.7, implying that even with the most coarse covering the error in misfit was less than 5%. As we shall see in the next section, inferences about the paleopole position depend directly upon the choice of allowed misfit, and this can rarely be estimated to 10 or even 20% accuracy. It seems safe to assume that the discretization error of the finite problem is insignificant compared with the uncertainties in the fitting criterion.

4. SEAMOUNT SURVEYS

The experienced gained with the tests described in the previous section supports the idea that magnetic surveys are capable of providing information about the direction of internal magnetization without the usual presumption of approximate uniformity. Some of the surveys discussed here have been analyzed by the standard least squares approach and by the newer seminorm minimization procedure; these results have been given by *Hildebrand and Parker* [1987]. In all the following examples with the ideal-body approach, it was found necessary to remove a local constant field and gradient before performing the minimizations; this is because when these are included as free parameters, they assume unrealistically large values. In principle, the local field can be estimated quite well from survey lines in the neighborhood of the seamount, but not so close to the seamount as to be within its anomalous field.

A natural choice for the first analysis of real data is the body LR148.8W, the large, very young seamount on the Louisville Rise that has figured in two earlier studies of new methodologies for seamounts [*Parker et al.*, 1987; *Parker*, 1988]. The results for this seamount were completely unexpected: every unidirectional magnetization gives an acceptable fit to the magnetic anomaly. For most VGP directions, exact matching of the magnetic observations was possible; the largest RMS misfit in the set of unidirectional models was only 8.0 nT, but it had been estimated in the earlier studies that 30 nT misfit would be adequate agreement. We must conclude that the survey data contain essentially no information about the magnetization direction within LR148.8W unless we are willing to assume the interior is approximately uniformly magnetized or make some other restrictive hypothesis. Of course, it has already been shown [*Parker*, 1988] that, if the interior magnetization is assumed to be uniform with only small-scale, isotropic fluctuations in the magnetization, the VGP location is

quite tightly constrained. Recall how attempts to limit the uncertainty by imposing an upper bound on the RMS magnetization were not successful [*Parker et al.*, 1987].

We consider next another large (volume 1196 km^3) seamount in the north Pacific ocean, Darwin seamount (22°N, 171°E), which has the distinction of being one of the few apparently reversely magnetized seamounts of the region. Darwin rests on seafloor about 150 m. y. old and is estimated to be between 106 and 109 m. y. old itself. Bathymetry data based on conventional echo sounding are shown in Figure 5. The base of the body is taken to be the 5100 m contour, which is shown dashed. The corresponding anomaly map appears in Figure 6; the 100 magnetic anomaly values used in the calculations were measured at the points indicated by triangles. Both of these maps are drawn to the same scale. Vacquier least squares analysis of the anomaly generates a southern hemisphere paleopole position, 43°S, 135°E; the RMS residual of 47 nT is unacceptably large in view of the fact that the magnetic anomaly itself is only 87 nT RMS, so that half the available signal remains unaccounted for. The upper surface of the polyhedral surface used to approximate the shape of the seamount contains 221 vertices and 405 triangular facets. The assumed plausible RMS residual for the Darwin survey is 20 nT. Somewhat surprisingly, when nonuniformity is allowed through seminorm minimization, the pole position remains almost unchanged (41°S, 131°E) if the misfit is reduced to 20 nT. A relatively large proportion of the magnetization must be nonuniform to achieve this level of agreement: the uniform component of magnetization in this solution has an intensity of 2.96 A m^{-1}, the RMS intensity of the nonuniform part is 1.36 A m^{-1}. The model of isotropic statistical heterogeneity yields a 95% uncertainty oval with axes measuring 33° by 11°.

Figure 7 is a contour diagram of the RMS misfit of the best unidirectional model as a function of assumed VGP position. The maximally uniform model at 20 nT misfit gives a pole position shown by the star, which, as mentioned earlier, is virtually identical to the least squares pole; the heavy oval surrounding the star is the 95% confidence region for the pole under the assumption of a short-scale, isotropic Gaussian model for the statistics of the nonuniform magnetization [*Parker*, 1988]. Notice the two minima of the misfit function within dashed 7 nT contours, both at about 30°S latitude with longitudes of 130°W and 110°E. The smallest value of misfit is 5.2 nT achieved at 29.9°S, 111.1°E. Unfortunately, any conclusions depend strongly on the level of misfit selected as acceptable. If one believes that 30 nT is adequate agreement, the map shows a small excluded region surrounding the north pole, but this does not rule out a large area of normal polarity. On the other hand, 10 nT misfit confines the allowed VGP locations almost entirely to the southern hemisphere in a crescent-shaped zone. This tolerance is almost certainly too small, given the amplitude of the diurnal variation (about 10 nT) and the normal crustal fields in the region of similar magnitude. We conclude that the survey data provide modest constraints on the paleopole of Darwin seamount: (1) Darwin seamount certainly could have been formed within a single polarity period because the anomaly is easily matched by a wide range of unidirectional magnetizations and (2) there is some evidence for its reversed state, although, depending on the assigned accuracy of fit, the paleopole could be in the northern hemisphere not far from the equator.

Our last example is Jasper seamount, a smaller body (volume 649 km^3) also in the North Pacific built on crust

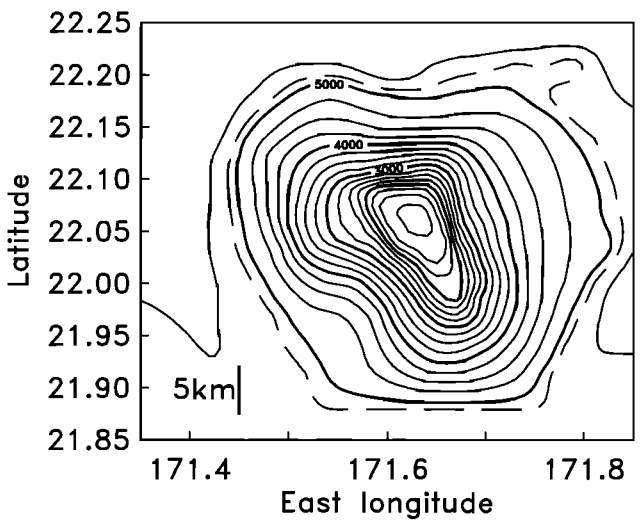

Fig. 5. Bathymetric contours of Darwin seamount with interval 250 m. The base of the model is the 5100 m level, shown dashed here and in Figure 6.

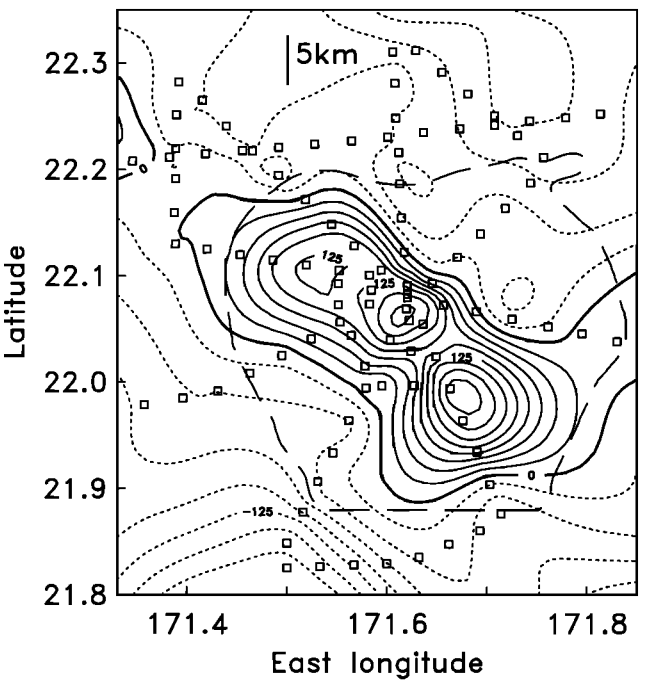

Fig. 6. Total field magnetic anomaly map for Darwin seamount, contour interval 25 nT. The triangles give the locations of the 100 magnetic observations used in the inversion. This map and Figure 5 are drawn to the same scale.

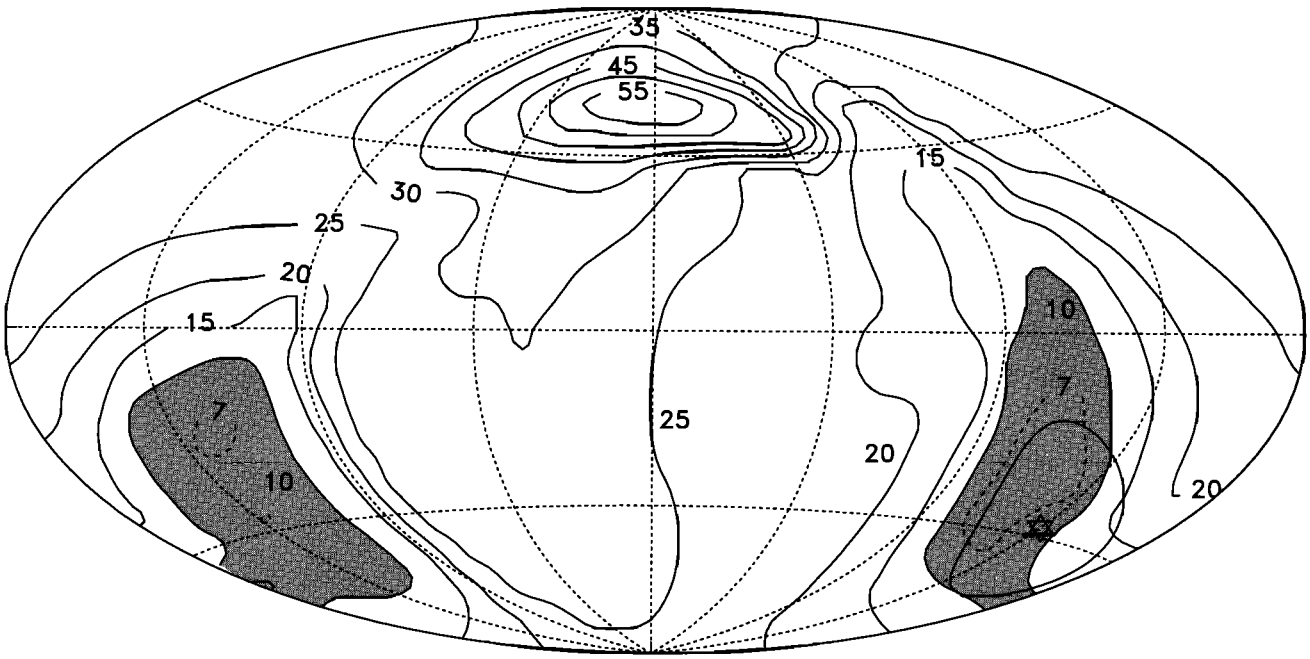

Fig. 7. Misfit map of RMS discrepancy between the best fitting unidirectional model and observation over Darwin seamount as a function of VGP location shown on Aitoff's equal-area projection. The star shows the paleopole position of the most uniform solution with a 20 nT misfit, and the surrounding curve is the 95% confidence boundary according to a statistical theory.

of about 24 Ma age; the age of Jasper seamount itself cannot be stated simply, since studies of dredged samples [*Gee et al.*, 1991] indicate an extended period of construction from 4 to 10 million years B. P. The magnetism of this seamount has been the subject of an intensive study [*Gee et al.*, 1988], which concluded on the basis of seminorm minimization and other evidence that reversed and normal magnetic material was present. Figure 8 shows the bathymetry of the body and the assumed base level of 3900 m. Figure 9 gives the magnetic anomaly contours. Notice the unusually complex central feature comprising two positive and two negative zones. It has been assumed that such a complex pattern could not be produced by magnetization of a single polarity. Unlike Darwin, which stands on Cretaceous crust where Vine-Mathews stripes are essentially absent, Jasper is situated in a region with a prominent crustal pattern. This is evident from the 100 nT, north-south striking, positive magnetic stripe (anomaly 6C) on the east of the seamount and its somewhat weaker negative companion 10 km to the west. Application of the theory has required that the magnetic field due the seamount could be easily isolated from the weaker fields of the crust, but clearly in this case that would be a dubious assumption. One solution would be to increase the permitted misfit (to 100 nT, say) and thereby include the magnetic stripes in the "noise." This could lead to only feeble constraints on the magnetic properties of the seamount. Another idea would be to attempt to subtract a model crustal field; we shall return to this approach later. When seminorm minimization and the new method were applied to a data set covering the whole survey, it was found that even in cases where the overall RMS misfit was acceptably low, the poorly fitted observations are highly concentrated on the edges of the survey, at points furthest from the seamount.

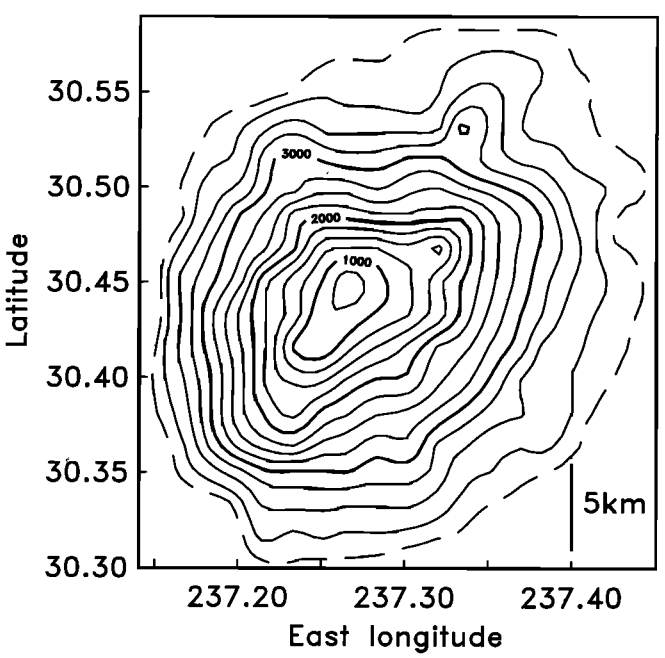

Fig. 8. Bathymetry of Jasper seamount, contour interval 250 m. The base of the model seamount is at 3900 m and is shown as dashed curve here and in Figure 9.

In other words, the model could not fit the purely crustal parts of the signal but managed to accommodate the anomaly over the seamount, even if this was contaminated with a crustal component. In this experiment we are testing the hypothesis that the complex anomaly pattern over the peak of Jasper seamount is incompatible with a unidirectional magnetization; we can do this without removing the magnetic stripe, provided we focus on the ano-

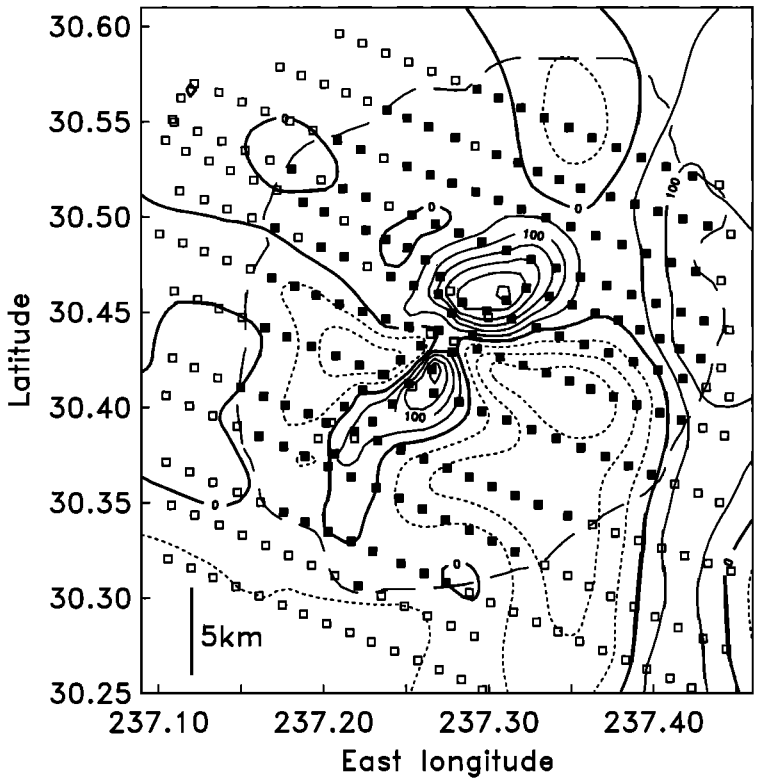

Fig. 9. Total field magnetic anomaly map for Jasper seamount, contour interval 50 nT. The squares give the sites of magnetic observations; the solid squares indicate the 170 sites used in the inversion. Note the unusual anomaly pattern directly over the peak of the seamount; also notice the strong N-S striking crustal anomaly at the east of the map.

maly over the seamount and exclude the peripheral field. In Figure 9 the solid squares indicate the location of the magnetic observations used in one run of the various inversion programs; all of them lie above Jasper seamount; there are 170 such magnetic data. The model body contains 227 surface points arranged into 513 triangular facets. A local field model in the form of a plane fitting the regional trend by least squares was subtracted from the anomaly. In the most uniform magnetization based on these data with a misfit of 20 nT, the nonuniform part is stronger than the uniform component: RMS intensity 0.84 $A\,m^{-1}$ and 0.77 $A\,m^{-1}$, respectively. Reversed magnetization (measured against the direction of the uniform vector) of high intensity is found in the model magnetization. This finding parallels the result of *Gee et al.* [1988] which was obtained from a slightly different subset of the data with a different misfit level. It suggests Jasper comprises rocks of both magnetic polarities, in accord with the intuitive interpretation of the magnetic anomaly map. But consider next the results summarized in Figure 10, which is a misfit map on the VGP sphere. We find that unidirectional magnetizations are capable of matching the complex anomaly to an accuracy of 20 nT over a large area of the sphere; in fact, the minimum misfit is only 6.50 nT for a VGP at 55.4° S, 168.4° E. This position is somewhat different from the paleopole position of the uniform component found by seminorm minimization by *Gee et al.* [1988], which was very near the south pole. Another set of minimizations was performed on an anomaly set corrected as far as possible for the effects of the crustal stripes. Of course the corrections can not be performed with any great confidence and are just interpolations through the seamount region of the stripes found north and south of it. Nonetheless, the results are very similar to those just reported: the zones of good agreement on the VGP sphere are located similarly, but as might be expected, the misfits are smaller (by about 30%). The minimum misfit level is 3.56 nT.

These remarkably good fits demonstrate that we are not entitled to conclude that both normal and reversed materials are present in Jasper solely on the basis of the sea surface magnetic anomaly. It has ready been mentioned that dating of dredged samples [*Gee et al.*, 1991] shows convincingly that Jasper's period of construction was very long and must cover a time when the geomagnetic field reversed; nonetheless, the magnetic anomaly survey does not provide independent support for this inference.

5. DISCUSSION

Gordon [1990] in a comparison of marine paleomagnetic poles derived from sedimentary cores and from analysis of seamount magnetic anomalies asserted that the results of seamount calculations were superior. He did not include in his survey any of the pole positions derived by more modern methods, unaccountably relying on poles obtained by ordinary least squares analysis in the style of Vacquier. As *Parker* [1988] has already pointed out, the Vacquier method is based upon an erroneous statistical model, namely, that the deviations

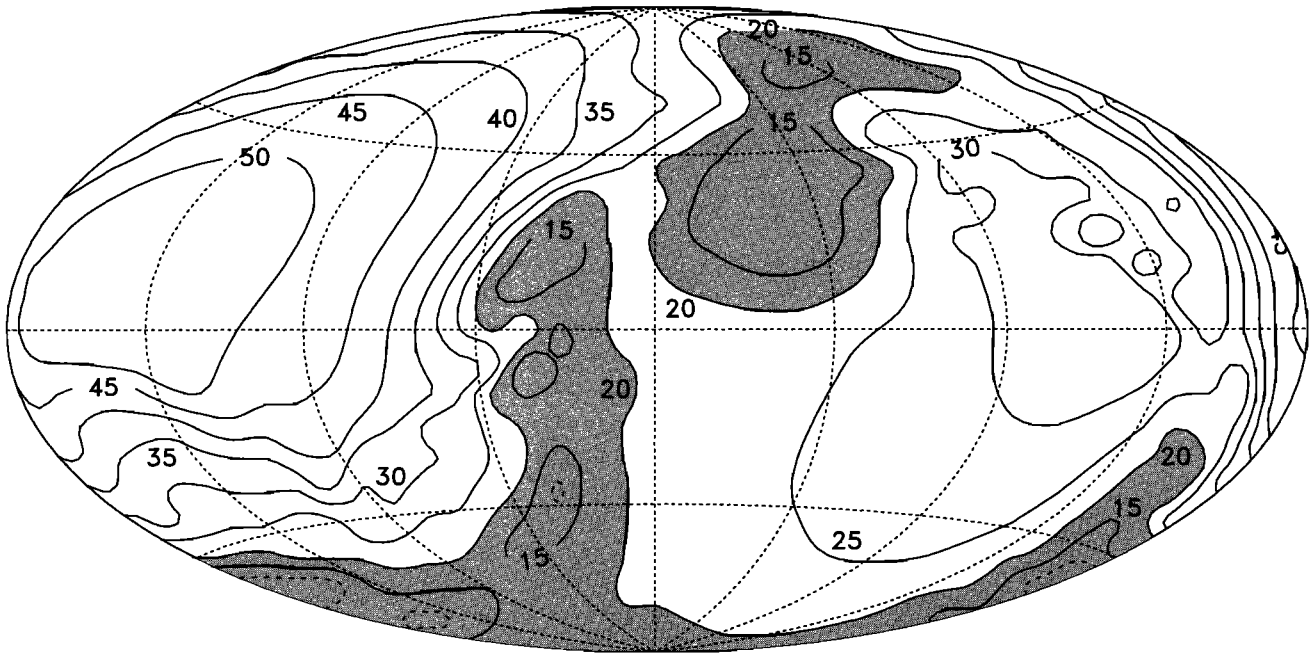

Fig. 10. Misfit map for unidirectional models of Jasper seamount plotted on the VGP sphere. Contour interval is 5 nT. The dashed contour is at 10 nT, and the smallest misfit of 6.5 nT has a paleopole location of −55.4°S, 168.4°W.

observed between the anomaly and the predictions of the uniform model must be statistically independent. The lognormal statistics of the source magnetism noted earlier by *Gee at al.* [1991] also make the uniform or uniform-plus-isotropic-perturbation models suspect as a basis of sound parameter estimation. The computations in this paper, performed with a theory that is more conservative in its assumptions regarding intensity distribution, exhibit poor localization of the paleopole, even (as in the case of LR148.8W) allowing the pole to lie anywhere on the globe, when the alternative methods claim gratifyingly small zones of uncertainty. Among the cases studied so far, when the new method does concentrate the position of the VGP, the zone of localization remains considerably larger than that predicted by earlier theories. A proper conclusion from the studies carried out here is that paleopole location based on seamount surveys is probably much less reliable than has been assumed in the literature.

Although we have shown that when the strength of the magnetized material is not limited, conclusions about directional properties of the magnetization can be drawn, these conclusions are likely to be somewhat disappointing in their scope. The next step is to ask how the inferences may be strengthened. Obviously it is reasonable to apply a bound to the intensity of magnetization at each point instead of permitting dipoles (equivalent to infinite intensity) as in the present scheme. It is conceivable that geologically correct upper bounds will have a negligible effect on the solution. We can check this by examining the ideal-body solutions themselves, something we have carefully avoided doing up until now; specifically, we compute the mean intensity of the ideal-body solution, if the dipoles are averaged over the whole volume. In the case of Darwin, with the VGP at its optimum position, the average intensity is 15.6 $A\,m^{-1}$, much larger than 3.34 $A\,m^{-1}$, the RMS value in the most uniform solution. Since 47% of the total dipole moment in the solution is concentrated in just four dipoles, it is highly probable that the application of an upper bound on the intensity will strongly modify the optimal answer. In the case of Jasper seamount the mean intensity averaged over the whole body of the optimal ideal-body model is smaller, only 5.5 $A\,m^{-1}$, and half of the moment is accounted for by 17 point sources. Here we might expect the imposition of an upper bound to have less drastic effects. From a computational perspective, the full ideal-body calculation with $0 \le m \le M_0$ represents a much greater challenge than the present calculations, mainly because the minimization must be carried out over a set of elements distributed throughout the seamount, rather than condensed in the surface. To do an adequate job the number of elements, K in equation (8), will be very large. For Darwin, K was 221 and for Jasper, 227, and a single solution of (8) required from 20 s to 1 min on a Sun Microsystems SPARC-1 workstation. Increasing K by a factor of 10 or 20 (by building this many layers under each surface point) will increase computer time by about the same factor, which at first glance seems to result in only a modest demand in computer resources. But maps like Figures 7 and 10 require the solution of many hundreds of optimization problems, and systematic searches like these are unavoidable because of the complexity of the misfit functions. These rough estimates indicate the computational load will be heavy, but not intolerable. Further work along these lines is planned.

APPENDIX

A reviewer, Gary Egbert, provided the following concise alternative proof of the main result of section 2, which the author gratefully acknowledges. We wish to show that the search for optimal solutions can be confined to the set of models comprising unidirectional dipoles in the surface of the seamount, a set we shall call $D(\partial V)$. It was shown by *Parker* [1975] that if there is an exact solution corresponding to a given collection of data d_j (that is a function m with $T=0$ in (13)), there is also a model in $D(\partial V)$ that satisfies the same data exactly. Suppose now that there is no exactly fitting model but there is one with squared misfit T^2 and this magnetization distribution generates magnetic anomaly data d_j'. It follows that there is a solution m' in $D(\partial V)$ with same magnetic anomaly values and hence with squared misfit T^2. Therefore we need only search over $D(\partial V)$ to find a model of some specified misfit, including the best fitting model.

Acknowledgments. The author wishes to thank John Hildebrand for his positive criticism and access to his data base of seamount magnetic surveys. He is also grateful to Lisa Tauxe and Cathy Constable for encouragement in difficult times. Finally, ONR grant N00014-90-J-1039 supported this work and paid for the computer workstation on which all the calculations were done; the author wishes to express his sincere thanks to ONR for their support.

REFERENCES

Ander, M. E., and S. P. Huestis, Gravity ideal bodies, *Geophysics, 52*, 1265–1278, 1987.

Constable, C. G., and R. L. Parker, Statistics of the geomagnetic secular variation for the past 5 m.y., *J. Geophys. Res., 93*, 11569–11581, 1988.

Gee, J., L. Tauxe, J. A. Hildebrand, H. Staudigel, and P. Lonsdale, Nonuniform magnetization of Jasper seamount, *J. Geophys. Res., 93*, 12159–12175, 1988.

Gee, J., H. Staudigel, and L. Tauxe, Contribution of induced magnetization to magnetization of seamounts, *Nature, 342*, 170–173, 1989.

Gee, J., H. Staudigel, and J. H. Natland, Geology and petrology of Jasper seamount, *J. Geophys. Res., 96*, 4083–4105, 1991.

Gordan, R. G., Test for bias in paleomagnetically determined paleolatitudes from Pacific plate Deep Sea Drilling Project sediments, *J. Geophys. Res., 95*, 8397–8404, 1990.

Hildebrand, J. A., and R. L. Parker, Paleomagnetism of the Cretaceous Pacific seamounts revisited, *J. Geophys. Res., 92*, 12695–12712, 1987.

Kent, D. V., B. M. Honnerez, N. B. Opdyke, and P. J. Fox, Magnetic properties of dredged ocean gabbros and the source of marine magnetic anomalies, *Geophys. J. R. Astron. Soc., 55*, 513–537, 1978.

Kono, M., Paleomagnetism of DSDP Leg 55 basalts and implications for the tectonics of the Pacific plate, *Initial Rep. Deep Sea Drill. Proj., 55*, 737–758, 1977.

Lawson, C. L., and R. J. Hanson, *Solving Least Squares Problems*, Prentice–Hall, Englewood Cliffs, N. J., 1974.

Luenberger, D. G, *Optimization by Vector Space Methods*, John Wiley, New York, 1969.

McFadden, P. L., and M. W. McElhinny, A physical model for paleosecular variation, *Geophys. J. R. Astron. Soc., 78*, 809–830, 1984.

Parker, R. L., Inverse theory with grossly inadequate data, *Geophys. J. R. Astron. Soc., 29*, 123–138, 1972.

Parker, R. L., Best bounds on density and depth from gravity data, *Geophysics, 39*, 644–649, 1974.

Parker, R. L., The theory of ideal bodies for gravity interpretation, *Geophys. J. R. Astron. Soc., 42*, 315–334, 1975.

Parker, R. L., Linear inference and the under-parameterized models, *Rev. Geophys. Space Phys., 15*, 446–456, 1977.

Parker, R. L., A statistical theory of seamount magnetism, *J. Geophys. Res., 93*, 3105–3115, 1988.

Parker, R. L., and L. Shure, Gravitational and magnetic fields of some simple solids of revolution, *Geophys. J. R. Astron. Soc., 80*, 631–647, 1985.

Parker, R. L., and M. A. Zumberge, An analysis of geophysical experiments to test Newton's law of gravity, *Nature, 342*, 29–31, 1989.

Parker, R. L., L. Shure, and J. Hildebrand, The application of inverse theory to seamount magnetism, *Rev. Geophys., 25*, 17–40, 1987.

Vacquier, V., A machine method for computing the magnetization of a uniformly magnetized body from its shape and a magnetic survey, in *Benedum Earth Magnetism Symposium*, pp 123–137, University of Pittsburgh Press, Pittsburgh, Pa., 1962.

R. L. Parker, Institute of Geophysics and Planetary Physics, Scripps Institution of Oceanography, University of California, San Diego, La Jolla, CA 92093-0225.

(Received January 16, 1991;
revised April 4, 1991;
accepted June 5, 1991.)

JOURNAL OF GEOPHYSICAL RESEARCH, VOL. 96, NO. B10, PAGES 16,529–16,533, SEPTEMBER 10, 1991

Microcrack-Induced Seismic Anisotropy of Sedimentary Rocks

C. M. SAYERS[1] AND J. G. VAN MUNSTER

Koninklijke/Shell Exploratie en Produktie Laboratorium, Rijswijk, Netherlands

The seismic anisotropy often detected in the Earth's crust has been attributed in large part to the presence of open microcracks showing some degree of alignment. This alignment is believed to result from the anisotropic state of in situ stress, since any cracks remaining open at depth will tend to be oriented normal to the direction of the minimum in situ stress. Previous workers have calculated the change in elastic wave velocities due to either randomly oriented or perfectly aligned cracks. In this paper the P and S wave anisotropy in the long-wavelength limit is calculated for an arbitrary orientation distribution of cracks. For the case of an orthotropic distribution of circular cracks it is found that a simple relation exists between the P and S wave anisotropy. To test this prediction, ultrasonic P and S wave velocities were measured for propagation in three orthogonal directions through three samples of Berea sandstone as a function of maximum compressive stress applied perpendicular to the bedding plane. The samples were 50-mm cubes and were stressed to peak in a true triaxial loading frame, while the principal stress components parallel to the bedding plane were held constant at 4 MPa.

1. INTRODUCTION

It has been suggested that the seismic anisotropy observed in the upper 10–20 km of the Earth's crust is often due to the presence of open microcracks showing some degree of alignment [*Crampin et al.*, 1984; *Crampin*, 1987]. Any cracks remaining open at depth will tend to be oriented normal to the direction of the minimum in situ stress. Observations of seismic anisotropy therefore have the potential of providing the orientation of the in situ stress field. For example, recent modeling of shear waveforms in three component shear wave vertical seismic profiles in the Paris Basin [*Crampin et al.*, 1986] is consistent with a distribution of vertical fluid-filled cracks aligned with strikes along N30°W, corresponding to the direction of maximum horizontal in situ stress in this area.

In the presence of oriented cracks the elastic wave velocities in the crust depend on the propagation direction and polarization of the wave. Previous workers have assumed either randomly orientated or perfectly aligned cracks. In this paper the P and S wave anisotropy is evaluated for rocks containing an arbitrary orthotropic orientation distribution of cracks. This includes the important case of axial symmetry, for which simplified equations are given. The theory is tested by comparing the predictions with measurements of the P and S wave anisotropy that develops in Berea sandstone as it is stressed to failure. Central to this comparison is the observation that the failure of brittle rocks during compression is preceded by the formation, growth, and coalescence of microcracks [*Paterson*, 1978; *Kranz*, 1983]. Tensile stress necessary for microcrack growth include shear along preexisting microcracks and stress concentrations around inhomogeneities.

The measurements reported are taken in the ultrasonic frequency range. Since the measurement is done on dry samples, dispersive effects resulting from elastic-wave-induced fluid flow are absent, and the velocities should be representative of those that would be obtained in the seismic frequency range provided that the size of any inhomogeneities and cracks is small compared to the wavelength. In the experiments reported here the maximum frequency transmitted through the samples is of the order of 1 MHz, corresponding to a wavelength greater than 10 times the grain diameter of the sandstone used. Since the length of cracks when first formed is of the order of the grain diameter, the measurements are expected to correspond to the long-wavelength limit except close to failure. Previous studies of microcrack-induced anisotropy in rocks using ultrasound include those of *Bonner* [1974], *Lockner et al.* [1977], and *Granryd et al.* [1983] on Westerly granite, *Gupta* [1973] on Indiana limestone, *Nur and Simmons* [1969] on Barre granite, *Hadley* [1975] on Westerly granite and San Marcos gabbro, and *Holt and Fjaer* [1987] on weakly consolidated sandstones. The present work, however, presents for the first time a quantitative relationship between the microcrack-induced P and S wave anisotropy valid for an arbitrary orthotropic orientation distribution of microcracks and tests this relationship using experimental results.

2. THEORY

It is assumed that the mechanical behavior of rock in the brittle field is determined by the formation, growth, and coalescence of microcracks. As a result of the anisotropy of the stress field, these microcracks show some degree of preferred orientation. To model the effect of this on ultrasonic velocities, these cracks are approximated by ellipsoids embedded in an isotropic background medium. For an ellipsoidal crack with principal axes $2a$, $2b$, $2c$ ($a \geq b \geq c$) it is convenient to introduce a set of axes $OX_1X_2X_3$ with origin at the center of the ellipsoid and OX_1, OX_2, and OX_3 along the a, b, and c axes, respectively (see Figure 1). The fourth order elastic stiffness tensor of the microcracked rock, C_{ijkl}, will be written in the form $C_{ijkl} = C^0_{ijkl} + \gamma_{ijkl}$, where γ_{ijkl} is the difference between C_{ijkl} and the elastic stiffness tensor C^0_{ijkl} of the uncracked rock, which will be assumed to be isotropic. If the axes $OX_1X_2X_3$ for all cracks are aligned, the rock will exhibit orthotropic symmetry with three orthogonal planes of mirror symmetry having plane

[1]Now at Shell Research Arnhem, Arnhem, Netherlands.

Paper number 91JB01232.
0148-0227/91/91JB-01232$05.00

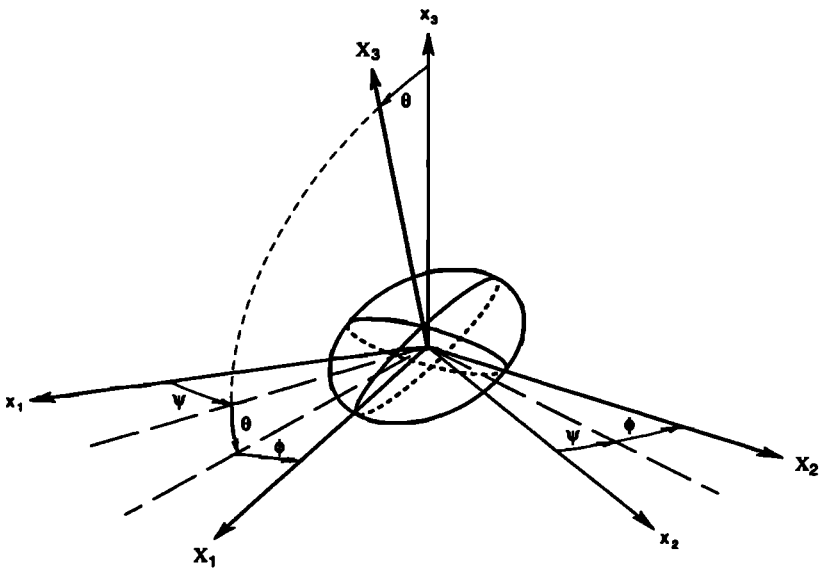

Fig. 1. The orientation of coordinate system $OX_1X_2X_3$ with origin at the center of an ellipsoidal crack with respect to the material coordinate system $Ox_1x_2x_3$ specified by Euler angles ψ, θ, and ϕ.

normals in the OX_1, OX_2, and OX_3 directions. If the γ_{ijkl} in this case are denoted by Γ_{ijkl}, then in the crack reference frame $OX_1X_2X_3$ the nonzero Γ_{ijkl} are Γ_{11}, Γ_{22}, Γ_{33}, $\Gamma_{12} = \Gamma_{21}$, $\Gamma_{23} = \Gamma_{32}$, $\Gamma_{31} = \Gamma_{13}$, Γ_{44}, Γ_{55}, and Γ_{66} in the Voigt (two-index) notation. For circular cracks with $a = b \gg c$, $\Gamma_{11} = \Gamma_{22}$, $\Gamma_{23} = \Gamma_{31}$, $\Gamma_{44} = \Gamma_{55}$ and $\Gamma_{66} = (\Gamma_{11} - \Gamma_{12})/2$. The anisotropy of Γ_{ijkl} in this case may be completely specified by three anisotropy parameters a_1, a_2, and a_3 [*Sayers*, 1988*a*, *b*], which are defined by

$$a_1 = \Gamma_{11} + \Gamma_{33} - 2\Gamma_{13} - 4\Gamma_{44} \quad (1)$$

$$a_2 = \Gamma_{11} - 3\Gamma_{12} + 2\Gamma_{13} - 2\Gamma_{44} \quad (2)$$

$$a_3 = 4\Gamma_{11} - 3\Gamma_{33} - \Gamma_{13} - 2\Gamma_{44}. \quad (3)$$

In general, the cracks will not be perfectly aligned, and a quantitative description of the elastic wave anisotropy requires a knowledge of the orientation distribution of cracks. The orientation of an ellipsoidal crack with principal axes $OX_1X_2X_3$ with respect to a set of axes $Ox_1x_2x_3$ fixed in the rock may be specified be three Euler angles ψ, θ, and ϕ, as shown in Figure 1. The orientation distribution of cracks is then given by the crack orientation distribution function $W(\xi, \psi, \phi)$ where $\xi = \cos\theta$, θ being the angle between OX_3 and Ox_3. $W(\xi, \psi, \phi)d\xi d\psi d\phi$ gives the fraction of cracks between ξ and $\xi + d\xi$, ψ and $\psi + d\psi$, and ϕ and $\phi + d\phi$. The elastic stiffnesses of the rock may be calculated in terms of the coefficients W_{lmn} in an expansion of the crack orientation distribution function in generalized Legendre functions [*Sayers*, 1988*a*, *b*]. Since the elastic stiffness tensor is of fourth rank, it depends only on the coefficients W_{lmn} of the expansion of $W(\xi, \psi, \phi)$ for $l \leq 4$. If the cracks are ellipsoidal and their orientation distribution is orthotropic with symmetry axes coincident with the reference axes $Ox_1x_2x_3$, the nonzero W_{lmn} are all real and are restricted to even values of l, m, and n. For circular cracks with $a = b \gg c$, $W_{lmn} = 0$ unless $n = 0$. The elastic stiffnesses are therefore determined in this case by W_{200}, W_{220}, W_{400}, W_{420}, and W_{440}, and the three anisotropy factors a_1, a_2, and a_3 defined above [*Sayers*, 1988*a*, *b*]. The ultrasonic wave velocities in the rock may then be obtained as solutions of the Christoffel equations [*Musgrave*, 1970]. For dry penny-shaped cracks the a_i may be calculated from the work of *Hudson* [1981]. The factor a_1 is found to be much smaller than a_2 and a_3 [*Sayers*, 1988*a*, *b*]. As a result, the coefficients W_{4m0} make only a small contribution to the measured ultrasonic wave velocities and may be ignored, the resultant equations for the velocities being

$$\rho v_{11}^2 = \rho \bar{v}_P^2 + 8\sqrt{10}\pi^2 a_3(W_{200} - \sqrt{6}W_{220})/105 \quad (4)$$

$$\rho v_{22}^2 = \rho \bar{v}_P^2 + 8\sqrt{10}\pi^2 a_3(W_{200} + \sqrt{6}W_{220})/105 \quad (5)$$

$$\rho v_{33}^2 = \rho \bar{v}_P^2 - 16\sqrt{10}\pi^2 a_3 W_{200}/105 \quad (6)$$

$$\rho v_{12}^2 = \rho v_{21}^2 = \rho \bar{v}_S^2 + 4\sqrt{10}\pi^2(7a_2 + 2a_3)W_{200}/315 \quad (7)$$

$$\rho v_{23}^2 = \rho v_{32}^2 = \rho \bar{v}_S^2 - 2\sqrt{10}\pi^2(7a_2 + 2a_3)(W_{200} - \sqrt{6}W_{220})/315 \quad (8)$$

$$\rho v_{31}^2 = \rho v_{13}^2 = \rho \bar{v}_S^2 - 2\sqrt{10}\pi^2(7a_2 + 2a_3)(W_{200} + \sqrt{6}W_{220})/315. \quad (9)$$

Here ρ is the density or the rock and $\bar{v}_P$ and $\bar{v}_S$ are the P and S wave velocities for a rock with the same density of cracks but with random crack orientations. The values $\bar{v}_P$ and $\bar{v}_S$ may be obtained from (4)–(9):

$$\bar{v}_P^2 = (v_{11}^2 + v_{22}^2 + v_{33}^2)/3 \quad (10)$$

$$\bar{v}_S^2 = (v_{12}^2 + v_{23}^2 + v_{31}^2)/3. \quad (11)$$

It is seen from (4)–(9) that the P and S wave anisotropies are not independent but are related by the following equations:

TABLE 1. Mineralogical Analysis of the Berea Sandstone Samples Studied in This Work

Sample	Quartz, % by Weight	K Feldspar, % by Weight	Kaolinite, % by Weight	Illite + Smectite, % by Weight
I	94	4	1	1
II	94	4	1	1
III	85	5	4	6

$$(v_{11}^2 - v_{22}^2) = A(v_{31}^2 - v_{23}^2) \quad (12)$$

$$(v_{11}^2 + v_{22}^2 - 2v_{33}^2) = A(2v_{12}^2 - v_{23}^2 - v_{31}^2) \quad (13)$$

where

$$A = 12a_3/(7a_2 + 2a_3). \quad (14)$$

For the small anisotropy observed in most rocks, (12) and (13) reduce to

$$(v_{11} - v_{22})/\bar{v}_P = B(v_{31} - v_{23})/\bar{v}_S \quad (15)$$

$$(v_{11} + v_{22} - 2v_{33})/\bar{v}_P = B(2v_{12} - v_{23} - v_{31})/\bar{v}_S \quad (16)$$

where $B = A(\bar{v}_S/\bar{v}_P)^2$. For transverse isotropy, with symmetry axis along Ox_3, $v_{11} = v_{22}$, $v_{23} = v_{31}$, and (13) reduces to $(v_{11}^2 - v_{33}^2) - A(v_{12}^2 - v_{31}^2)$.

3. Measurement of Stress-Induced Anisotropy

To test these predictions, ultrasonic velocities were measured in three 50-mm cubes of Berea sandstone cut parallel to the bedding plane. Berea is a light brown, fine-grained, well-sorted sandstone. Its mineralogy is mainly quartz, with small amounts of feldspar and clay minerals. A mineralogical description of the samples is given in Table 1. Ultrasonic velocities were measured with the samples in an air-dry condition using the true triaxial loading frame described by *Sayers et al.* [1990]. This apparatus is illustrated in Figure 2. The initial velocity was measured at a hydrostatic compressive stress of 4 MPa, after which the stress perpendicular to the bedding plane was raised in steps of 4 MPa to peak, keeping the other two stress components fixed. This loading configuration was chosen in order to investigate the magni-

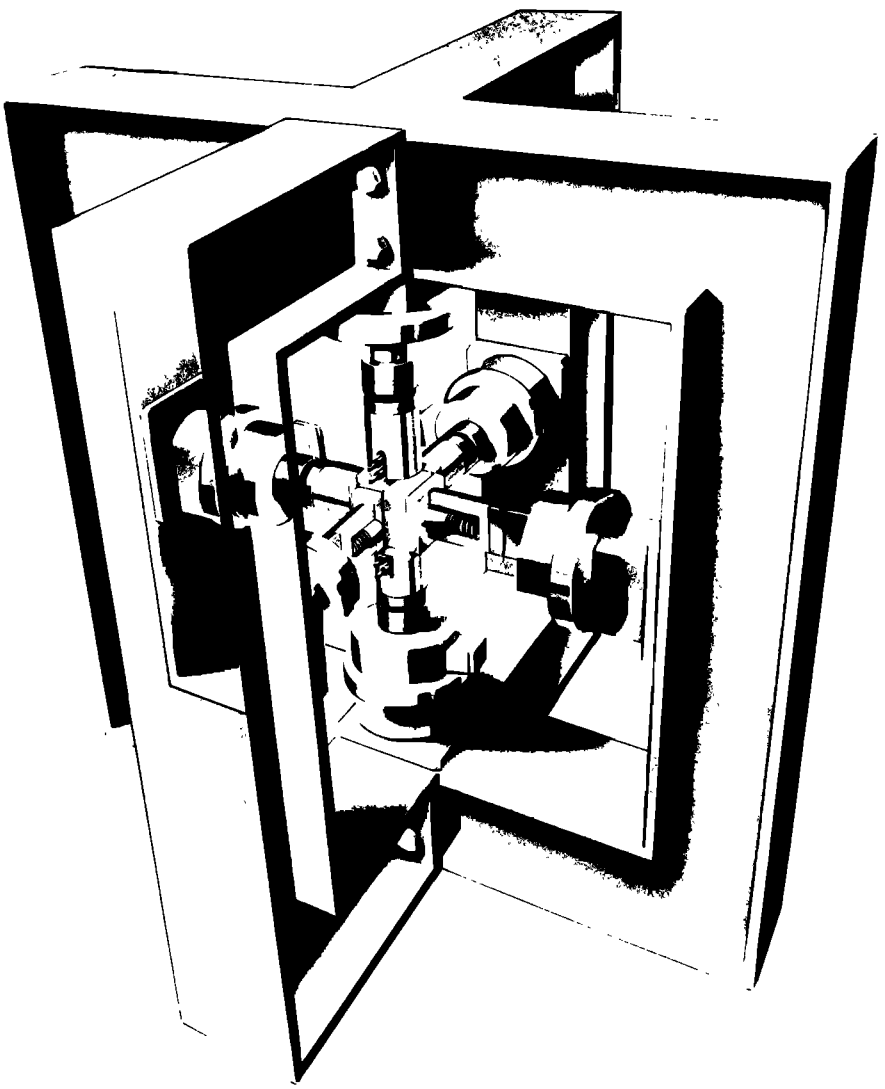

Fig. 2. Overview of experimental test setup.

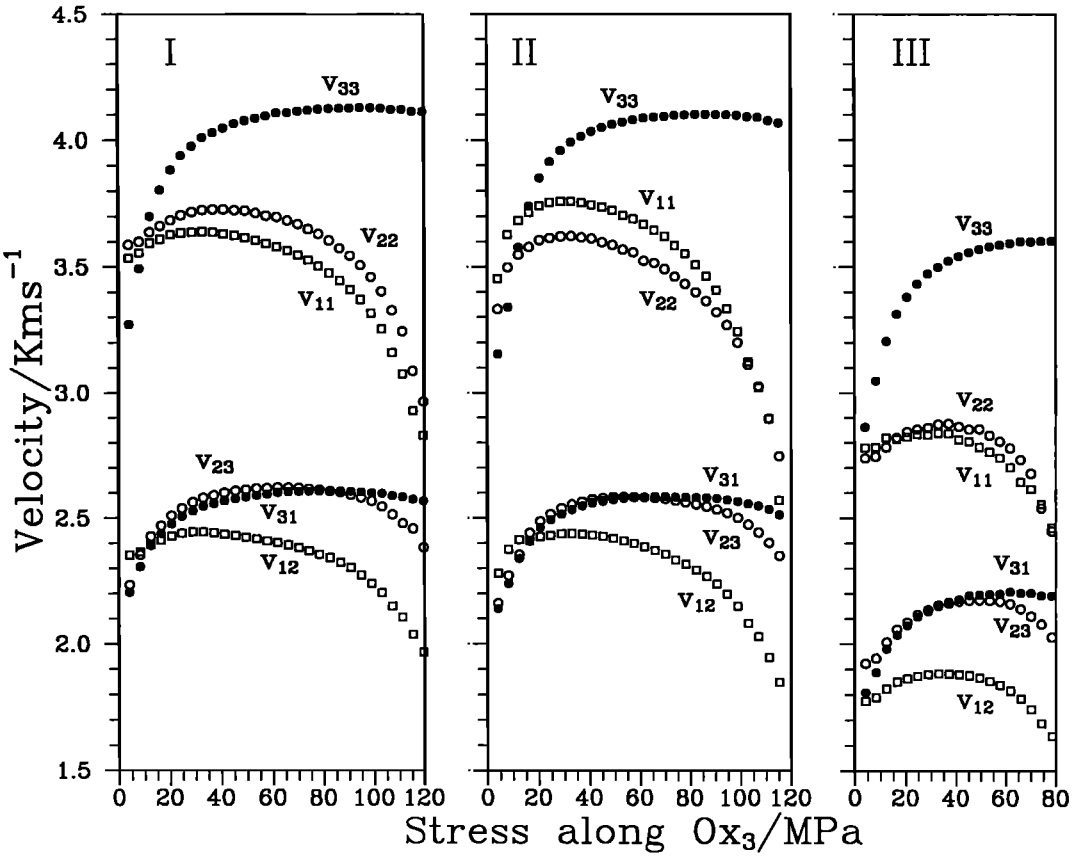

Fig. 3. *P* and *S* wave velocities in dry Berea sandstone as a function of major principal stress for Berea samples I, II, and III described in Table 1.

tude of any deviations from transverse anisotropy of the sample when a transversely anisotropic stress field is applied. The velocities are plotted in Figure 3 as a function of the major principal stress component using a reference set of axes chosen with Ox_3 perpendicular to the bedding plane and parallel to the direction of maximum stress and Ox_1 and Ox_2 parallel to the remaining cube edges. The velocities measured were v_{11}, v_{22}, and v_{33} (*P* waves) and v_{12}, v_{23}, and v_{31} (*S* waves).

4. Discussion

It is seen in Figure 3 that v_{33}, v_{23}, and v_{31} rise monotonically throughout most of the test but with a small drop immediately prior to failure; v_{11}, v_{22}, and v_{12} rise at first, but then drop after the first third of the test. The measurements for the two samples with low clay content are in agreement, but the sample with higher clay content is seen to have substantially lower velocities and to fail at a significantly lower value of the maximum compressive stress. At low stress the observed increase in wave velocity can be explained by the closure of preexisting microcracks and grain boundaries in the rock and, as the stress increases still further, by the formation of new microcracks and the growth and coalescence of preexisting cracks. The measurements may therefore by analyzed using the theory presented in section 2. It is seen in Figure 3 that for the loading configuration used in this work $v_{11} \approx v_{22}$ and $v_{31} \approx v_{23}$, so that (12) is approximately satisfied. Figures 4*a* and 4*b* show plots of $(v_{11}^2 + v_{22}^2 - 2v_{33}^2)$ against $(2v_{12}^2 - v_{23}^2 - v_{31}^2)$ and $(v_{11} + v_{22} - 2v_{33})/\bar{v}_P$ against $(2v_{12} - v_{23} - v_{31})/\bar{v}_S$ for the samples studied. Although these quantities are individually nonlinear functions of stress, they are found to be linearly related and in good agreement with the predictions of (13) and (16). A fit of these equations to the measurements gives $A = 3.628$ and $B = 1.583$, and therefore $\bar{v}_P/\bar{v}_S = (A/B)^{1/2} = 1.51$. This compares with the value $\bar{v}_P/\bar{v}_S = 1.5$ obtained by *Castagna et al.* [1985] for dry sandstones and corresponds to a Poisson's ratio $\nu = 0.11$. This is the same value as obtained by *Lo et al.* [1986] for Berea sandstone. The value $A = 3.628$ should be compared with the value $A = 5.036$ obtained using the theory of *Hudson* [1981] for dry, noncontacting cracks and a value of Poisson's ratio $\nu = 0.11$. This disagreement may be the result of grain boundary closure, since this is not included in the theory.

5. Conclusions

In this article, measurements have been reported of *P* and *S* wave velocities in three orthogonal directions in three cubic samples of Berea sandstone stressed to peak. Two of the samples had a low clay content and exhibited similar behavior, but the third sample with higher clay content had substantially lower ultrasonic velocities and failed at a significantly lower value of the maximum compressive stress. Theoretical expressions for the ultrasonic wave velocities in terms of the coefficients W_{lmn} in an expansion of the crack orientation distribution in generalized Legendre

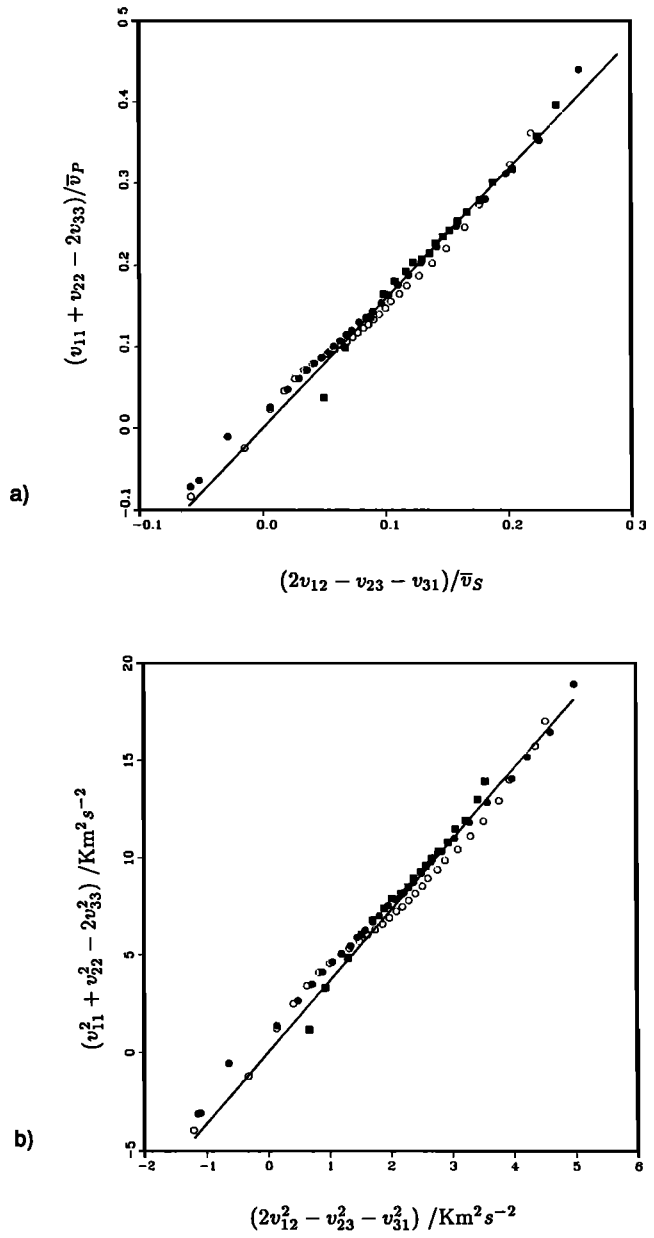

Fig. 4. Plot of (*a*) $(v_{11}^2 + v_{22}^2 - 2v_{33}^2)$ versus $(2v_{12}^2 - v_{23}^2 - v_{31}^2)$, and (*b*) $(v_{11} + v_{22} - 2v_{33})/\bar{v}_P$ versus $(2v_{12} - v_{23} - v_{31})/\bar{v}_S$, for the Berea samples I (open circles), II (solid circles), and III (solid squares). The lines are fits of equations (13) and (16) to the data.

functions give a linear relation between the *P* and *S* wave anisotropy for small-crack density. This prediction is confirmed by the experiment. The constant of proportionality here, however, is smaller than the value predicted by the theory of *Hudson* [1981] for dry, noncontacting cracks. This difference could result from the closure of grain boundaries during the experiment, since this is not included in the theory.

Acknowledgment. This paper is published by permission of Shell Internationale Research Maatschappij.

REFERENCES

Bonner, B. P., Shear wave birefringence in dilating granite, *Geophys. Res. Lett.*, *1*, 217–220, 1974.

Castagna, J. P., M. L. Batzle, and R. L. Eastwood, Relationships between compressional-wave and shear-wave velocities in clastic silicate rocks, *Geophysics*, *50*, 571–581, 1985.

Crampin, S., Geological and industrial implications of extensive-dilatancy anisotropy, *Nature*, *328*, 491–496, 1987.

Crampin, S., E. M. Chesnokov, and R. G. Hipkin, Seismic anisotropy—The state of the art II, *Geophys. J. R. Astron. Soc.*, *76*, 1–16, 1984.

Crampin, S., I. Bush, C. Naville, and D. B. Taylor, Estimating the internal structure of reservoirs with shear-wave VSPs, *The Leading Edge*, *5*, 35–39, 1986.

Granryd, L., I. C. Getting, and H. Spetzler, Path independence of acoustic velocity and attentuation in experimentally deformed Westerly granite, *Geophys. Res. Lett.*, *10*, 71–74, 1983.

Gupta, I. N., Seismic velocities in rock subjected to axial loading up to shear fracture, *J. Geophys. Res.*, *78*, 6936–6942, 1973.

Hadley, K., V_p/V_s anomalies in dilatant rock samples, *Pure Appl Geophys.*, *113*, 1–23, 1975.

Holt, R. M., and E. Fjaer, Acoustic behaviour of sedimentary rocks during failure, in *North Sea Oil and Gas Reservoirs*, edited by J. Kleppe, pp. 311–316, Graham and Trotman, London, 1987.

Hudson, J. A., Wave speeds and attentuation of elastic waves in material containing cracks, *Geophys. J. R. Astron. Soc.*, *64*, 133–150, 1981.

Kranz, R. L., Microcracks in rock: A review, *Tectonophysics*, *100*, 449–480, 1983.

Lo, T., K. B. Coyner, and M. N. Toksoz, Experimental determination of elastic anisotropy of Berea sandstone, *Geophysics*, *51*, 164–171, 1986.

Lockner, D. A., J. B. Walsh, and J. D. Byerlee, Changes in seismic velocity and attenuation during deformation of granite, *J. Geophys. Res.*, *82*, 5374–5378, 1977.

Musgrave, M. J. P., *Crystal Acoustics*, Holden-Day, Oakland, Calif., 1970.

Nur, A., and G. Simmons, Stress-induced velocity anisotropy in rock: An experimental study, *J. Geophys. Res.*, *74*, 6667–6674, 1969.

Paterson, M. S., *Experimental Rock Deformation—The Brittle Field*, 254 pp., Springer, New York, 1978.

Sayers, C. M., Inversion of ultrasonic wave velocity measurements to obtain the microcrack orientation distribution function in rocks, *Ultrasonics*, *26*, 73–77, 1988*a*.

Sayers, C. M., Stress-induced elastic wave anisotropy in fractured rock, *Ultrasonics*, *26*, 311–317, 1988*b*.

Sayers, C. M., J. G. van Munster, and M. S. King, Stress-induced ultrasonic anisotropy in Berea sandstone, *Int. J. Rock Mech. Min. Sci.*, *27*, 429–436, 1990.

C. M. Sayers, Shell Research Arnhem, P.O. Box 40 (Westervoortsedijk 67d), 6800 AA Arnhem, Netherlands.

J. G. van Munster, Koninlijke/Shell Exploratie en Produktie Laboratorium, 2288 CD Rijkswijk ZH, Netherlands.

(Received September 21, 1990;
revised April 8, 1991;
accepted April 27, 1991.)

JOURNAL OF GEOPHYSICAL RESEARCH, VOL. 96, NO. B10, PAGES 16,083–16,099, SEPTEMBER 10, 1991

Heat Flow Constraints on the South Pacific Superswell

CAROL A. STEIN

Department of Geological Sciences, University of Illinois at Chicago

DALLAS H. ABBOTT

Lamont-Doherty Geological Observatory, Palisades, New York

The South Pacific superswell has been defined as a large region of anomalously shallow bathymetry, low Love wave velocities, and low effective elastic thicknesses relative to those predicted for its age. These phenomena have been interpreted as reflecting a combination of lithospheric reheating and thinning, and dynamic uplift due to mantle flow. We use heat flow data to better constrain the thermal structure of this region and examine the predictions of various possible models. The average heat flow for the superswell region does not differ significantly from that for lithosphere of similar ages elsewhere on the Pacific plate. Given their uncertainties, the heat flow data imply that thermal lithospheric thickness exceeds 60 km, but cannot discriminate between greater thicknesses. The lack of observed high heat flow appears not to be explained by biases due to water circulation in the thin sediment cover, since the superswell heat flow is not higher than for sites elsewhere with similar sedimentary environments. The Darwin Rise has been proposed as a fossil superswell in the Cretaceous, on the basis of the many similar characteristics to the South Pacific superswell. We find that the Darwin Rise heat flow values do not exceed those for similar ages elsewhere in the Pacific and Atlantic. This observation suggests that any thermal effects associated with the formation of the Darwin Rise are no longer present, and it is consistent with the idea of a fossil superswell. The surface heat flow data thus provide no evidence that the temperatures in the uppermost portion of the lithosphere are significantly higher in the entire superswell region than in other areas of comparable age. This observation is intriguing given the suggestion that the thin effective elastic thicknesses inferred from seamount loading may reflect reheating of the lithosphere. Models in which the plate thicknesses and/or the basal temperatures are increased to yield temperatures high enough to explain the low effective elastic thicknesses predict surface heat flow much higher than observed. Reheating the lithosphere, as is proposed for hot spots, yields temperatures adequate to explain the effective elastic thicknesses only if reheating occurs at very shallow depths, and again implies a surface heat flow much greater than observed. Hence, unless shallow reheating is somehow localized beneath the seamounts, the thinner elastic thicknesses may reflect mechanical, rather than thermal, weakening of the lithosphere.

INTRODUCTION

Heat flow and bathymetric data provide constraints for thermal models of the formation and cooling of oceanic lithosphere and hence on its thermal structure [e.g., *Sclater and Francheteau*, 1970; *Parsons and Sclater*, 1977]. The depth of most oceanic seafloor is well fit by such models. However, a large region of the Pacific Ocean (west of the East Pacific Rise to ~160°W, ~9° – ~30°S) is substantially shallower than might be expected for its age, which ranges from 20 to 90 Ma. This area (Figure 1), termed the South Pacific superswell by *McNutt and Fisher* [1987], contains the Cook-Austral, Marquesas, Pitcairn, and Society seamount chains (Figure 2), which have been interpreted as hot spot tracks with volcanic edifices formed in the last 18 m.y. [*Morgan*, 1972; *Duncan and Clague*, 1985; Gordon and Henderson, unpublished manuscript, 1985]. Holocene volcanism occurs at several sites on the chains, such as Mehetia and MacDonald seamount. The NW-SE trend of the plateaus and island chains is at a high angle to both the isochrons and fracture zones, and is similar to that of the Hawaiian hot spot track.

The effective elastic thicknesses of the lithosphere calculated from the loading of these volcanoes and seamounts are substantially less than can be expected for the age of loading [*McNutt and Menard*, 1978; *Calmant and Cazenave*, 1987; *Calmant et al.*, 1990]. In addition, this area is associated with the Dupal geochemical anomaly [*Hart*, 1984, 1988], a geoid low [*McNutt and Judge*, 1990], a low-velocity zone for Love waves [*Nishimura and Forsyth*, 1985], and a correlation between the maximum Dupal anomaly location and low seismic velocities in the lower mantle [*Castillo*, 1988].

McNutt and Fisher [1987] inferred, from an analysis of bathymetric depth anomalies, that the superswell region was bounded by the Marquesas fracture zone to the north. The largest depth and negative geoid anomalies are between the Marquesas and the Austral fracture zones, but the superswell probably continues south of the Austral fracture zone (M. McNutt, personal communication, 1989). McNutt and Fisher proposed that the shallow bathymetry can be modeled if the lithosphere in the area has on average the temperature structure of a 75-km plate with a 1385°C basal temperature, in contrast to the standard oceanic thermal model of a 125-km-thick plate with basal temperature of ~1350°C. *McNutt and Judge* [1990] further suggest that the surface wave velocities and flexural strength data can be explained by a thermal plate 75 km thick and that the observed geoid low arises from a deeper low-density "superplume." In their model the thinned lithosphere is a consequence of enhanced heat flux from the convecting mantle and low viscosity beneath the plate, both of which prevent the growth of a stable lithospheric thermal boundary layer to thicknesses greater than 75 km. They suggest that small-scale convective instabilities in the low-viscosity zone may be an important mechanism responsible for maintaining a thinner plate. Such a mechanism was proposed for the origin of lineations, observed in altimetry data over a large region west of the East Pacific Rise including

Paper number 91JB00774.
0148-0227/91/91JB-00774$05.00

the superswell, with a trend approximately parallel to the absolute plate motion [*Haxby and Weissel*, 1986]. *McAdoo and Sandwell* [1989] suggest that although the lineations may be produced by small-scale convection very near the East Pacific Rise, they prefer an origin on older, anomalously weak lithosphere perhaps resulting primarily from shallow lithospheric loads, in the crust or near the Moho. One possible load might result from tension in the north-south direction [*Dunbar and Sandwell*, 1988].

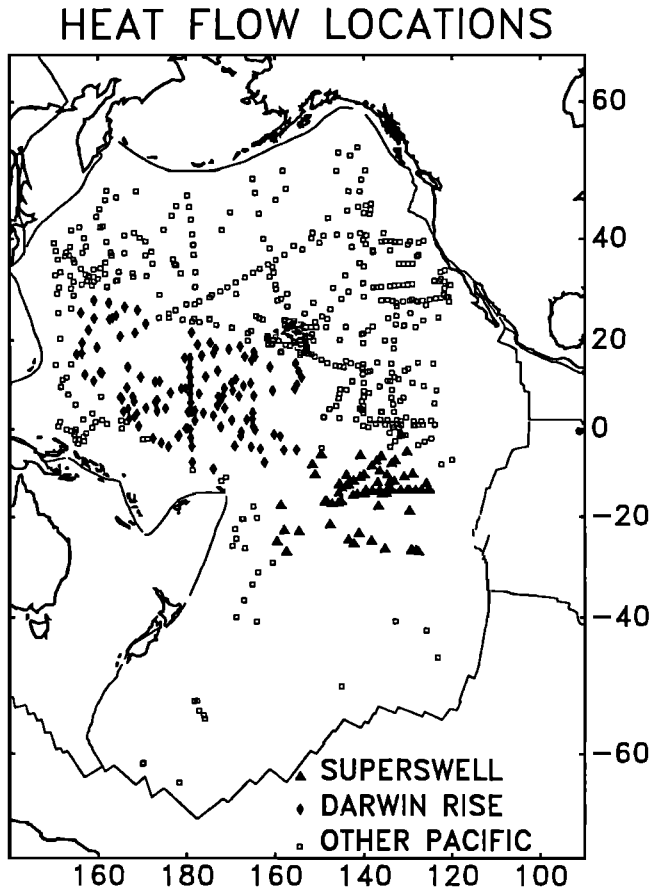

Fig. 1. Location of heat flow measurements used in this study on the Pacific plate, showing the superswell and Darwin Rise regions.

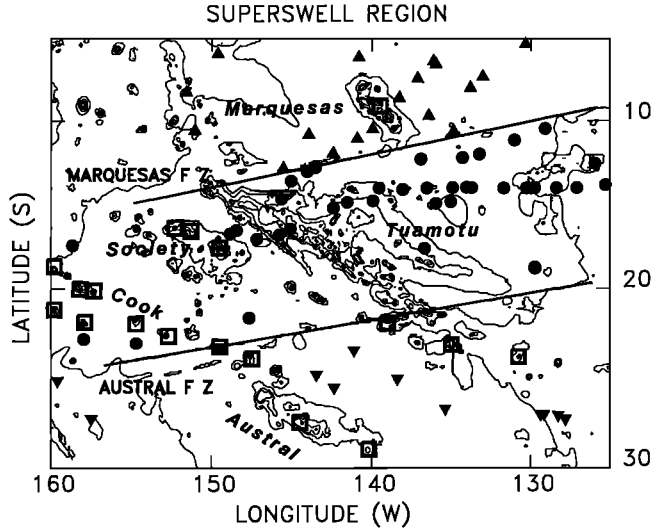

Fig. 2. South Pacific superswell bathymetry and heat flow sites. Heat flow sites north of the Marquesas fracture zone are represented by solid upward-pointing triangles, south of the Austral fracture zone by solid downward-pointing triangles, and between the two fracture zones by solid circles. Open squares indicate the locations of effective elastic thickness measurements [*Calmant and Cazenave*, 1986; *Calmant*, 1987]. Contour interval is 1000 m.

McNutt and Fisher [1987] also suggested that the Darwin Rise [*Menard*, 1964, 1984], a large region of rough relief in the western Pacific (Figure 1) including the Mid-Pacific Mountains, the Marshall Islands, the Magellan Seamounts, and the Wake Guyots, has similar characteristics to the present superswell and is a fossil superswell from the Cretaceous. Many of the hot spot tracks within the present-day South Pacific superswell can be traced back to the Darwin Rise [*Duncan and Clague*, 1985; Gordon and Henderson, unpublished manuscript, 1985]. The depths for the Darwin Rise are shallower than can be expected for its age [*Renkin and Sclater*, 1988], and the petrologic anomalies are similar to those in the superswell [e.g., *Hart*, 1984; *Natland and Wright*, 1984; *Staudigel et al.*, 1991]. The effective elastic thicknesses for this region are lower than can be expected for the age of loading [*Smith et al.*, 1989; *Wolfe and McNutt*, 1991]. *McNutt et al.* [1990] suggested that the Darwin Rise was dynamically uplifted about 113 ± 8 Ma and "superswell conditions" were present until about 70–80 Ma, implying that a superswell is a transient feature. The lack of velocity anomalies for Love waves beneath the Darwin Rise, unlike the present South Pacific superswell [*Nishimura and Forsyth*, 1985], also suggests that there is no present thermal anomaly in this region [*McNutt et al.*, 1990].

In these models, a superswell incorporates several aspects previously proposed in discussions of the origin of intraplate hot spots and swells. Thus, a superwell may be considered as a larger version of hot spots and swells. Models for the origin of such features generally rely on two primary effects, reheating mechanisms which elevate temperatures in the lower part of the lithosphere to asthenospheric temperatures [*Crough*, 1978; *Detrick and Crough*, 1978] or dynamic support due to mantle flow [*Parsons and Daly*, 1983; *Courtney and White*, 1986; *Robinson and Parsons*, 1988; *Liu and Chase*, 1989]. Heat flow data have been used to try and distinguish between these two end-member models for the Cape Verde Rise [*Courtney and White*, 1986], the Bermuda Rise [*Detrick et al.*, 1986], and the Hawaiian chain [*Von Herzen et al.*, 1982, 1989]. The presence of large heat flow anomalies would argue for the existence of large-scale reheating.

Determination of the relative contributions of lithospheric thinning and dynamic support to the superswell is complicated by two additional effects. First, the bathymetry reflects the emplacement of the seamounts [*McNutt and Fisher*, 1987; *McNutt and Judge*, 1990]. In addition, the bathymetry may reflect anomalous conditions at the time when the lithosphere formed, prior to passage over the mantle region that gives rise to superswell phenomena. This possibility is suggested by the observation that 0 to 12-Ma seafloor on the western flank of the East Pacific Rise is shallower and subsides more slowly than that on the eastern flank [*Mammerickx et al.*, 1975; *Cochran*, 1986]. *Marty and Cazenave* [1989] determined similar slow subsidence rates for this area (region 27 in their study) extending from young lithosphere to 100-Ma lithosphere. Hence *Calmant et al.* [1990] suggest that the regional depth anomalies may, in part, be remnants of the ridge processes, unrelated to midplate hot spot volcanism. Alternatively, the difference in subsidence rates between the two sides of the East Pacific Rise may reflect mantle processes and flow (M. McNutt, personal communication, 1990).

In this paper we examine the heat flow data for the South Pacific superswell region to determine if there is any evidence for higher than expected lithospheric temperatures. We then investigate whether a thinned lithosphere or reheating model can both explain the observed heat flow data and produce sufficiently high upper lithospheric temperatures to account for the lower lithospheric strength implied by the flexural data. In addition, we examine the heat flow for the Darwin Rise to determine if there is any detectable present temperature anomaly associated either with the mid-Cretaceous volcanic events or indicating if superswell conditions might still be present.

HEAT FLOW DATA SET

We have compiled heat flow data for the Pacific plate using the data from *Louden* [1989] and published and unpublished data from Lamont-Doherty Geological Observatory (LDGO) (Figure 1). The youngest lithosphere included is 20 Ma, the age of the youngest available heat flow measurement site for the South Pacific superswell region. We excluded data within a few hundred kilometers of trenches, where bending of the lithosphere may cause fracturing and hence reintroduce water circulation in the crust [*Abbott and Fisk*, 1986]. Our data set contains 853 measurements, of which 124 are for the Darwin Rise and 76 are for the South Pacific superswell region. Of these, the unpublished LDGO data account for 21 from the superswell and 32 for the Darwin Rise. The heat flow data for the superswell and Darwin Rise are listed in Tables 1 and 2. In assembling the heat flow data, we considered a number of factors including the site sedimentary environment, thermal conductivity, and instrument evaluation.

Sedimentary Environment

Heat flow measurements can be biased in conditions where a significant portion of the heat transfer occurs via water circulation, rather than conduction in the rock and sediment [*Lister*, 1972; *Williams et al.*, 1974]. As the sediment cover increases to a thickness of 100–200 m and insulates the convecting system, the average measured heat flow increases and approaches that theoretically expected by plate cooling models, which assume conductive heat transfer [*Anderson and Hobart*, 1976; *Sclater et al.*, 1976; *Davis and Lister*, 1977]. Heat flow sites are thus characterized by the sedimentary cover to indicate whether water circulation may be affecting the heat flow.

We examined seismic reflection records for the LDGO heat flow sites to determine the sedimentary environment, using categories proposed by *Sclater et al.* [1976]. A site classified "A" has flat or rolling hills with more than 150–200 m of continuous sediment cover within 18 km. A "B" site has flat or rolling hills with generally continuous sediment cover, with either an outcropping basement high or thin sedimentary cover. A "C" site is an area of rolling hills or rough topography with a thin or variable sediment cover, and "D" denotes a site with sediment in ponds next to outcropping basement highs.

Conductivity

The heat flow is the product of the measured thermal gradient and the thermal conductivity. Although ideally the conductivity should be measured either in situ or from a piston core taken at the measurement site, approximately 28% of the heat flow measurements for the superswell and Darwin Rise and 41% of those for the rest of the Pacific plate have estimated conductivities. Often in earlier studies, the estimates were based on the nearest available conductivity measurement, at times 500 km or more away, or global average values.

Stein and Abbott [1991] examined methods to best estimate the thermal conductivity. They found that the variation between the closest adjacent sites with measured conductivity increases with increasing separation, such that sites within 200 km are on average significantly closer in conductivity than sites further apart. Two factors may contribute to this effect. Conductivity generally varies with lithology [e.g., *Langseth and Von Herzen*, 1970], with mean conductivity highest for carbonate oozes, intermediate for deep-sea clays, and least for siliceous oozes. Also, there is a suggestion that conductivity decreases with increasing seafloor depth. Tests with the measured data suggest that of several methods, the best predictor of conductivity is the mean value measured within 200 km. Using the mean within a geographic region is a somewhat poorer estimate, and the ocean-wide mean and value at the nearest site are poorer still.

Following *Stein and Abbott* [1991], we reassigned the heat flow values with estimated conductivity in the superswell and Darwin Rise. Fourteen of the superswell and eight of the Darwin Rise values had measured conductivity within 200 km. Nine of the superswell and 23 of the Darwin Rise values did not have measured conductivity within 200 km and new values were estimated from regional averages. The mean of the absolute difference between the old and new conductivity values was about 10% (0.073 W m^{-1} K^{-1}), with 35 of the 54 new values higher than the original estimate.

Instrument Evaluations

The quality of heat flow measurements are evaluated from the number of temperature measurements, the errors of the measurements at each depth, the tilt of the instrument, and whether or not conductivity was measured or estimated. The evaluation scale for LDGO data is from 10 (excellent) to 0 (poor) [*Langseth and Taylor*, 1967]. *Louden* [1989] uses a different scale, in which measurements are evaluated as A, B, C or E. For comparison, LDGO evaluations 9 and 10 would be A, 6–8 would be B, and 5–1 would be C. An E evaluation means that no information is available on the quality.

Heat flow measurements with evaluations less than or equal to 5 have generally been considered unreliable. To test this, we grouped the Pacific plate data set by the evaluations, and examined its variation with age (Figure 3a). The lithospheric ages of the heat flow sites were determined by interpolating the isochrons of *McNutt and Fisher* [1987] for the superswell, *Renkin and Sclater* [1988] for the North Pacific, and S. Cande (personal communication, 1989) for the rest of the Pacific plate. The age bins used were those from the global compilation of *Sclater et al.* [1980]. The means, medians, and standard deviations for the data are plotted in Figure 3b. Except for the measurements with the poorest evaluations, the standard deviations for the data from older (>100 Ma) lithosphere are significantly less than for the younger lithosphere. The standard deviations for the poorest group (≤5, or categories C and E) generally exceed those in either the 9–10 (category A) or 6–8 (category B) group. This generalization fails only for three age bins (65–80 Ma, 125–140 Ma, and 160–200 Ma) with only a small number of measurements (5, 4, and 3 respectively) in the poorest group. Hence for our analysis of the superswell and Darwin Rise regions, we used only stations with evaluations in categories A and B (10–6).

For the measurements with the best evaluations (category A; 9–10) the median in each age bin is almost the same as the mean. In general, the difference between the mean and the

Table 1. Superswell Region

Cruise/No.	Area[a]	Latitude, deg	Longitude, deg	Heat Flow, mW m^{-2}	Evaluation[b]	Environment[c]	Depth, m	Reference[d]	Notes[e]
				Unpublished Data					
C11-114	NF	-6.13	-140.85	58.6	9	A	4343	1	
C11-116	NF	-10.83	-143.97	57.4	9	D	4749	1	
C11-117	NF	-12.87	-145.55	57.4	8	C	4662	1	
C11-119	SS	-14.82	-139.97	55.3	10	C	2950	1	
C11-120	SS	-12.32	-136.95	42.3	7	D	4103	1	
C11-121	NF	-10.63	-134.87	28.1	7	C	3860	1	
C15-4	SF	-26.78	-135.40	745.	3	D	4248	1	
C15-6	SF	-27.08	-129.40	14.2	6	C	3871	1	
C17-130	SF	-25.22	-159.60	23.2	10	D	5231	1	
C17-132	SS	-22.88	-157.97	64.6	10	D	4759	1	
C17-133	SS	-23.12	-154.70	67.5	10	D	4869	1	
V21-49	SS	-14.88	-135.05	38.7	4	C	4431	1	
ARIAD-2	SS	-18.76	-129.77	63.7	7	B	4130	2	A,G
ARIAD-4A	SS	-18.81	-129.77	127.	8	B	4150	2	A,G
ARIAD-4B	SS	-18.81	-129.77	88.5	8	B	4130	2	A,G
ARIAD-4C	SS	-18.81	-129.76	83.1	8	B	4130	2	A,G
ARIAD-4E	SS	-18.81	-129.76	63.7	8	B	4150	2	A,G
ARIAD-4F	SS	-18.81	-129.75	76.6	8	B	4170	2	A,G
ARIAD-4G	SS	-18.80	-129.74	56.1	8	B	4170	2	A,G
ARIAD-4H	SS	-18.80	-129.74	61.5	8	B	4170	2	A,G
ARIAD-4I	SS	-18.80	-129.74	52.9	8	B	4170	2	A,G

Cruise/No.	Area[a]	Latitude, deg	Longitude, deg	Heat Flow, mW m^{-2}	Evaluation[b]	Environment[c]	Depth, m	Reference[d]	Notes[e]
				Published Data					
CAP-31B	SS	-17.47	-158.67	66.2	A	U	4880	3	
CAP-33B	SS	-12.80	-143.55	15.1	A	U	4300	3	
D-2	SS	-14.98	-136.02	27.2	E	U	4510	4	
D-3	SS	-21.67	-147.68	40.6	A	U	4760	4	
MSN-64	NF	-10.57	-151.08	49.4	A	U	5070	5	
MSN-65	NF	-8.28	-151.60	60.3	A	U	5190	5	
MSN-66	NF	-5.92	-149.65	31.4	A	U	5160	5	
MSN6-62	SF	-27.32	-157.50	44.4	A	A	4960	6	
RIS-120	SS	-13.87	-125.33	43.5	A	U	3680	5	
RIS-121	SS	-14.03	-127.12	7.5	B	U	3930	5	L
RIS-122	SS	-14.03	-128.42	42.7	A	U	3995	5	
RIS-123	SS	-14.03	-129.80	119.	B	U	4120	5	L
RIS-124	SS	-14.05	-130.30	34.3	B	U	4090	5	L
RIS-125	SS	-14.05	-131.73	20.1	A	U	4010	5	
RIS-127	SS	-14.03	-133.75	41.6	B	U	4290	5	L
RIS-128	SS	-14.03	-134.92	49.0	A	U	4220	5	
RIS-129	SS	-14.05	-136.57	29.3	B	U	4290	5	L
RIS-130	SS	-14.15	-138.10	71.2	A	U	4040	5	
RIS-131	SS	-14.05	-139.58	69.9	A	U	3925	5	
RIS-132	SS	-14.92	-141.57	78.9	B	U	2610	5	L
RIS-133	SS	-15.25	-142.43	46.9	A	U	3725	5	
RIS-134	SS	-16.50	-145.12	71.2	E	U	1440	5	
RIS-135	SS	-16.87	-145.82	56.5	A	U	2750	5	
RIS-136	SS	-17.08	-147.22	8.8	A	U	4190	5	
RIS-137	SS	-16.77	-148.87	6.6	B	U	4200	5	L
RIS-138	SS	-16.57	-148.50	47.3	A	U	4250	5	
RIS-140	SS	-14.72	-145.67	50.2	A	U	2770	5	
RIS-141	SS	-13.62	-145.05	12.1	B	U	4390	5	
RIS-142	SS	-13.05	-144.05	54.0	A	U	4960	5	
RIS-143	SS	-12.77	-143.57	49.1	B	U	4480	5	L
RIS-144	NF	-11.97	-142.45	49.8	A	U	4520	5	
RIS-145	NF	-11.08	-140.95	17.0	B	U	4270	5	L
RIS-146	NF	-10.50	-139.98	15.5	A	U	4140	5	
RIS-147	NF	-8.63	-138.30	69.9	A	U	4080	5	
RIS-148	NF	-7.45	-137.18	32.7	E	U	4400	5	L
RIS-149	NF	-6.38	-136.18	54.9	A	U	4350	5	
SCAN8-H1	NF	-6.56	-136.01	108.	A	U	4440	7	L
SCAN8-H2	SS	-12.24	-134.31	86.7	A	U	4225	7	
SCAN8-H4	SF	-24.89	-143.49	56.4	A	U	4624	7	L
ST8HF48	SS	-12.58	-125.99	23.0	E	C	4015	8	L
ST8HF49	SS	-14.01	-134.06	59.2	E	B	4469	8	L
C15-2	SF	-23.50	-141.15	107.	7	D	4546	8	
C15-3	SF	-25.12	-138.43	189.	4	D	4212	8	
C15-5	SF	-27.07	-129.20	18.0	6	C	3860	8	
C15-7	SF	-27.13	-128.30	62.0	8	C	3977	8	
C15-8	SF	-27.33	-127.85	84.6	6	D	3720	8	
V18-100	NF	-9.70	-136.47	69.3	10	B	4329	9	
V18-101	NF	-8.00	-133.83	80.9	10	B	4565	9	

TABLE 1. (continued)

Cruise No.	Area[a]	Latitude, deg	Longitude, deg	Heat Flow, mW m^{-2}	Evaluation[b]	Environment[c]	Depth, m	References[d]	
Published Data (continued)									
V18-102	NF	-7.33	-133.05	63.0	10	B	4491	9	
V18-105	NF	-5.32	-130.37	39.2	8	C	4640	9	
V21-46	SS	-10.48	-129.13	14.2	7	B	4160	8	B
V21-47	SS	-11.17	-131.08	36.0	10	B	4268	8	B
V21-48	SS	-12.03	-133.25	11.7	7	C	3718	8	B,C
V21-50	SS	-17.65	-136.72	15.5	7	B	3391	8	
V21-54	SF	-25.60	-142.38	55.7	7	C	4343	8	

[a]Areas are as follows: NF, north of Marquesas fracture zone; SF, south of Austral fracture zone; SS, between Marquesas and Austral fracture zones.

[b]Measurement evaluation. Scales are 0–10 from *Langseth and Taylor* [1967] and A–E from *Louden* [1989].

[c]Sedimentary environment from *Sclater et al.* [1976]. "U" denotes sites with undetermined environments.

[d]References are as follows: 1, unpublished LDGO data; 2, M. A. Hobart et al., manuscript in preparation, 1991; 3, *Maxwell* [1958]; 4, *Von Herzen* [1959]; 5, *Von Herzen and Uyeda* [1963]; 6, *Anderson and Von Herzen* [1978]; 7, *Sclater et al.* [1972]; 8, *Anderson et al.* [1978]; 9, *Langseth et al.* [1965].

[e]Notes are as follows: A, M. A. Hobart determined a thermal conductivity of 0.77 W m^{-1} K^{-1} for ARIAD data using the water content method. Following *Stein and Abbott* [1991], we reestimate the thermal conductivity at 0.831 W m^{-1} K^{-1}. B, reevaluated environment. C, typographical error in published heat flow value. G, conductivity reestimated using regional method. L, conductivity reestimated using local method.

Table 2. Darwin Rise

Cruise/No.	Latitude, deg	Longitude, deg	Heat Flow, mW m^{-2}	Evaluation[a]	Environment[b]	Depth, m	Reference[c]	Note[d]
Unpublished Data								
C10-36	2.05	-169.85	50.2	10	B	5365	1	
C10-37	4.90	-171.42	86.4	4	B	5411	1	G
C10-38	7.52	-172.83	54.5	8	C	5865	1	G
C10-41	-1.65	178.18	54.0	10	C	5440	1	
C10-42	-3.97	176.05	34.2	6	C	5026	1	G
C10-67	16.90	155.13	60.7	10	A	5775	1	
C10-68	19.45	156.42	32.5	4	B	5447	1	G
C10-69	22.35	157.82	58.2	8	A	5402	1	
C10-70	24.78	159.13	48.2	4	B	5682	1	G
C12-40	3.68	-165.05	59.3	10	A	5351	1	
C12-41	2.33	-165.20	59.8	10	B	5365	1	
C12-42	0.65	-164.87	49.4	10	B	5106	1	
C12-43	-0.18	-164.50	53.8	8	D	5336	1	
C12-44	-4.55	-163.28	48.4	9	C	4839	1	
C12-45	-7.73	-162.38	9.6	6	A	4266	1	
C12-66	12.48	157.00	51.5	8	B	5883	1	
C17-118	4.10	165.73	50.3	10	A	4574	1	
C17-119	6.80	165.40	55.0	10	A	5158	1	
C17-120	4.63	166.83	52.3	10	A	4729	1	
C17-121	3.50	168.83	58.0	10	A	4376	1	
C17-122	4.18	173.50	95.6	8	A	4900	1	
V21-63	26.43	169.03	53.6	10	B	5982	1	
V21-64	27.08	166.07	51.5	10	A	5954	1	
V21-65	27.90	162.52	50.2	10	B	5954	1	
V24-64	11.85	169.68	47.7	4	A	5137	1	
V28-110	15.68	-165.22	24.0	6	B	5320	1	
V28-112	10.65	-169.80	17.6	9	C	2439	1	
V28-113	7.67	-171.75	42.3	10	B	5404	1	
V32-40	28.42	159.13	47.8	10	B	6030	1	
V32-41	25.93	156.17	52.2	10	A	5961	1	
V32-70	17.20	156.37	53.2	8	A	5809	1	
V32-71	2.30	167.10	49.9	10	A	4287	1	

Cruise/No.	Latitude, deg	Longitude, deg	Heat Flow, mW m^{-2}	Evaluation[a]	Environment[b]	Depth, m	Reference[c]	Note[d]
Published Data								
V24-51	9.30	-155.52	43.5	7	A	5234	10	
V24-52	10.22	-155.02	138.	4	A	5302	10	
V24-53	11.77	-154.03	53.2	6	A	5209	10	
V24-54	13.13	-154.53	44.0	10	B	5451	10	
V24-55	14.95	-155.30	58.2	8	A	5539	10	
V24-57	17.52	-164.68	48.6	8	A	5473	10	
V24-58	16.48	-166.78	54.8	10	A	5234	10	
V24-59	13.30	-172.92	58.6	8	B	5680	10	
V24-60	12.02	-175.62	67.4	8	B	5280	10	
V24-62	9.28	178.95	72.4	10	C	5704	10	
V24-63	10.88	173.00	57.8	10	A	5374	10	

Table 2. (continued)

Cruise No.	Latitude, deg	Longitude, deg	Heat Flow, mW m^{-2}	Evaluation[a]	Environment[b]	Depth, m	References[c]	Note[d]
			Published Data (continued)					
V24-65	14.13	166.80	64.9	8	A	5587	10	
V24-67	20.87	165.12	49.8	8	A	5544	10	
V24-69	23.65	170.87	51.9	8	A	5936	10	
V24-76	21.78	-178.78	65.1	8	B	5444	10	G
V24-77	16.13	179.73	55.3	10	A	5330	10	
V24-79	8.32	176.42	52.2	4	C	5097	10	
V24-80	6.57	173.50	73.4	8	B	4991	10	
V24-81	4.85	170.92	47.4	10	A	4501	10	
V24-82	2.82	168.18	61.3	8	A	4409	10	L
CAP-2B	0.67	169.28	78.7	A	U	4310	3	
CIRCE-6H	21.62	168.48	42.5	A	U	5698	7	L
CIRCE-7H	18.45	159.82	46.2	A	U	5668	7	G
DSDP462A	7.24	165.03	49.0	A	A	5181	14	
LSDH-60	6.28	168.18	41.0	A	U	4840	11	
LSDH-61	7.42	167.92	44.8	A	U	4950	11	
LSDH-62	10.92	174.02	58.2	A	U	5535	11	
LSDH-63	8.15	-177.13	50.7	A	U	5310	11	
LSDH-64	9.40	-171.40	31.7	B	U	4210	11	G
LSDH-66	10.65	-169.75	27.4	B	U	2500	11	L
LSDH-67	11.45	-168.83	47.7	A	U	5290	11	
MAHI-47	-9.20	-173.98	81.2	A	U	5227	11	
MAHI-49	-3.83	-169.07	69.5	B	U	5020	11	
MAHI-50	-0.57	-167.60	45.6	A	U	5355	11	
MAHI-51	-1.57	-167.72	52.3	A	U	5683	11	
MP-32	18.30	-173.38	30.2	A	U	3900	3	
MP-35-2	19.47	-174.58	54.0	A	U	4900	3	
MP-36	16.75	-176.40	49.8	A	U	5040	3	
MP-38	19.03	-177.32	45.6	A	U	4750	3	
MSN-5	14.18	-161.13	46.5	A	U	5685	11	
MSN-6	7.63	-168.12	54.0	A	U	5000	11	
MSN-7	3.10	-173.97	51.5	A	U	5250	11	
MSN-8	0.10	179.95	56.9	A	U	5290	11	
NOVA-A3	18.72	-167.78	57.3	A	U	5021	7	G
NOVA-A4	18.15	-170.43	74.5	B	U	5198	7	
NOVA-A5	17.25	-173.85	46.3	B	U	5059	7	L
NOVA-A6	16.58	-176.52	54.3	A	U	5199	7	L
NOVA-A7	16.00	-179.10	46.8	A	U	5094	7	L
NOVA-A8	14.03	-179.23	48.2	A	U	5639	7	G
NOVA-A9	11.82	-179.10	44.4	A	U	5540	7	G
NOVA-A10	9.90	-179.00	55.3	A	U	6148	7	
NOVA-A11	8.12	-179.12	54.3	A	U	5740	7	L
NOVA-A12	6.00	-179.00	45.8	A	U	5778	7	G
NOVA-A13	3.93	-178.78	49.0	A	U	5384	7	
NOVA-A15	-0.02	-179.13	56.5	A	U	5404	7	
NOVA-A16	-1.98	-179.02	54.0	A	U	5584	7	
NOVA-A17	-4.02	-178.75	62.2	A	U	5989	7	G
NOVA-A18	-7.67	-178.60	67.6	A	U	6018	7	G
PROA-40	-3.12	174.42	40.6	A	U	4950	11	
PROA-41	-2.07	172.48	33.5	A	U	4270	11	
PROA-44	3.67	-176.25	18.4	B	U	4995	11	
PROA-45	1.95	-178.02	56.3	B	U	5330	11	G
PROA-46	0.25	-179.70	58.6	B	U	5400	11	
PROA-47	-1.38	178.40	53.2	A	U	5400	11	
PROA-54	-4.05	-165.42	22.6	A	U	4020	11	
PROA-55	6.38	-172.53	49.8	B	U	5840	11	G
PROA-56	8.87	-169.53	54.4	A	U	5300	11	
PROA-57	9.98	-167.08	47.3	A	U	5250	11	
PROA-58	10.55	-165.53	47.3	A	U	4340	11	
SCAN3-H1	16.40	-164.41	54.0	A	U	5582	7	
SCAN5-H3	9.49	166.54	49.4	A	U	4592	7	
SCAN5-H4	9.34	179.90	38.9	A	U	6152	7	
SOLIS-22	-4.78	-157.95	25.9	C	U	1695	11	G
SOLIS-28	-1.28	-160.17	57.4	B	U	2532	11	
SOLIS-29	-1.62	-158.78	83.7	B	U	2015	11	
SOLIS-31	-4.73	-155.13	33.2	E	U	2538	11	G
SOLIS-41	0.60	-172.22	46.5	A	U	5658	11	
SOLIS-43	2.22	-166.45	50.7	B	U	5548	11	
SOLIS-44	8.75	-160.53	18.0	B	U	4816	11	
SOLIS-45	7.68	-164.80	46.9	A	U	4960	11	
SOLIS-47	5.43	-173.10	47.7	A	U	5797	11	
SOLIS-48	4.20	-178.07	46.8	E	U	5209	11	G
SOLIS-49	3.92	-179.55	44.0	A	U	5684	11	
SOLIS-50	4.75	175.28	45.6	A	U	5122	11	

Table 2. (continued)

Cruise No.	Latitude, deg	Longitude, deg	Heat Flow, mW m^{-2}	Evaluation[a]	Environment[b]	Depth, m	References[c]	Note[d]
Published Data (continued)								
SOLIS-51	6.17	173.00	9.6	C	U	4912	11	
V6334	11.10	159.00	58.8	B	U	5300	12	G
V6333-22	12.99	160.55	71.3	B	U	5140	12	G
V6333-25	12.89	160.71	186.	B	U	4680	12	G
V6333-27	12.78	160.91	147.	B	U	4640	12	G
ZETES-71	25.25	164.13	50.7	A	U	4943	13	
ZETES-72	24.89	163.35	47.3	A	U	4970	13	
ZETES-73	24.53	162.61	45.0	B	U	4930	13	L

[a]Measurement evaluation. Scales are 0–10 from *Langseth and Taylor* [1967] and A–E from *Louden* [1989].
[b]Sedimentary environment from *Sclater et al.* [1976]. "U" denotes sites with undetermined environments.
[c]References are as follows: 1, unpublished LDGO data; 3, *Maxwell* [1958]; 7, *Sclater et al.* [1972]; 10, *Langseth et al.* [1971]; 11, *Halunen and Von Herzen* [1973]; 12, *Kuzmin et al.* [1972]; 13, *Vacquier et al.* [1966]; 14, *Boyce* [1981].
[d]Notes are as follows: G, conductivity reestimated using regional method. L. Conductivity reestimated using local method.

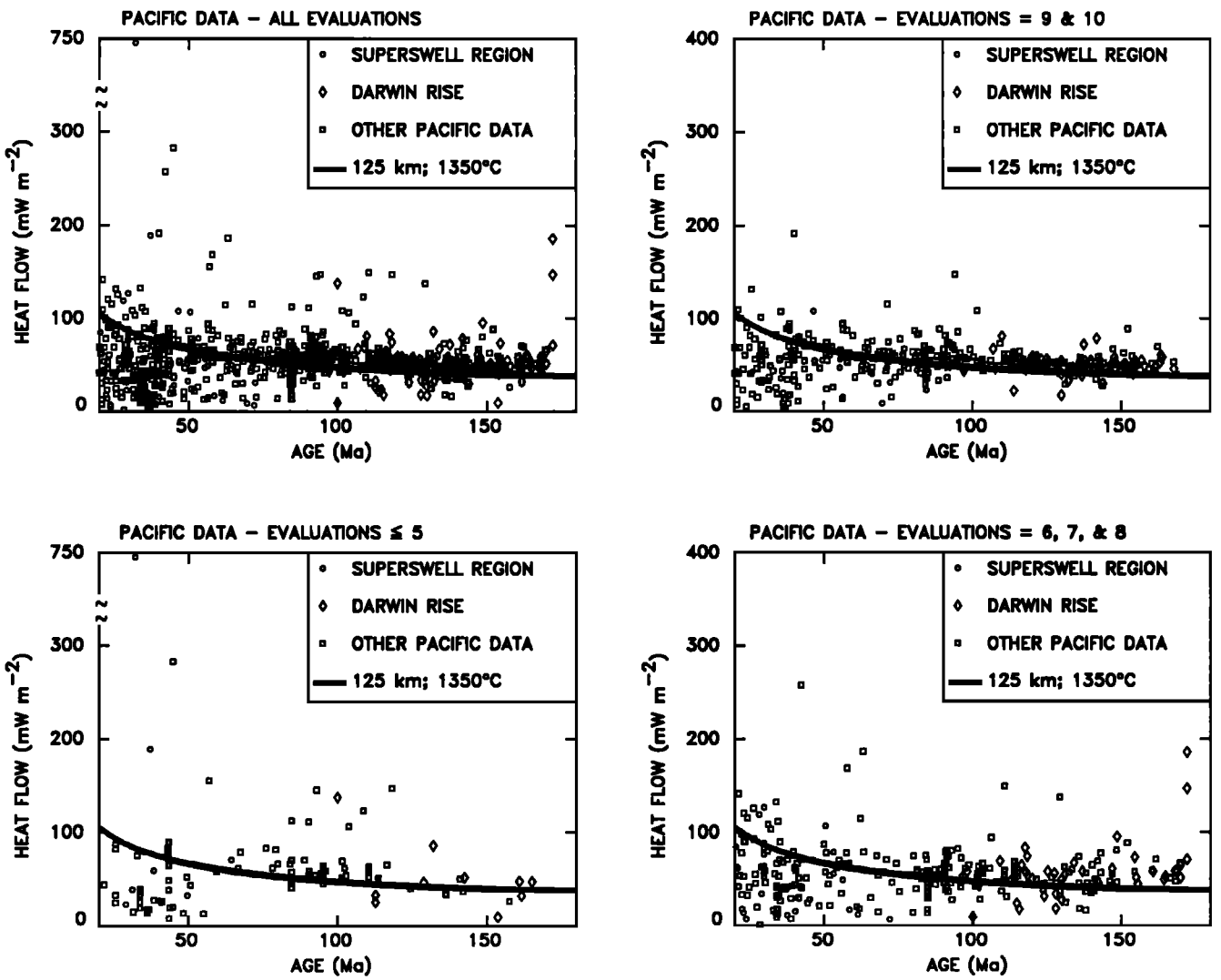

Fig. 3*a*. Heat flow data for the Pacific plate (Figure 1) as a function of age, sorted by instrument evaluations. LDGO data are evaluated from 10 (excellent) to 0. The measurements with the poorest evaluations (≤ 5; bottom left) have considerably more scatter than those with the better (6-8) and best (9-10) evaluations plotted on the right side. The thick solid lines show the heat flow predicted for a 125-km-thick plate with a 1350°C basal temperature.

median decreases with increasing age and is most noticeable for the poorest evaluation category. Presumably, this variation reflects the trend of lower standard deviations with both increasing age and instrument evaluations.

We compared the variation in heat flow with age to that predicted by a standard thermal model of a 125-km-thick plate with a basal temperature of 1350°C [*Parsons and Sclater*, 1977]. Over the 20- to 180-Ma age range, neither the entire heat flow data nor those with only the best (9–10) evaluations show convincing evidence for a decrease in heat flow with age. For ages younger than about 50 Ma the measured heat flow is less than predicted, presumably because much of the heat

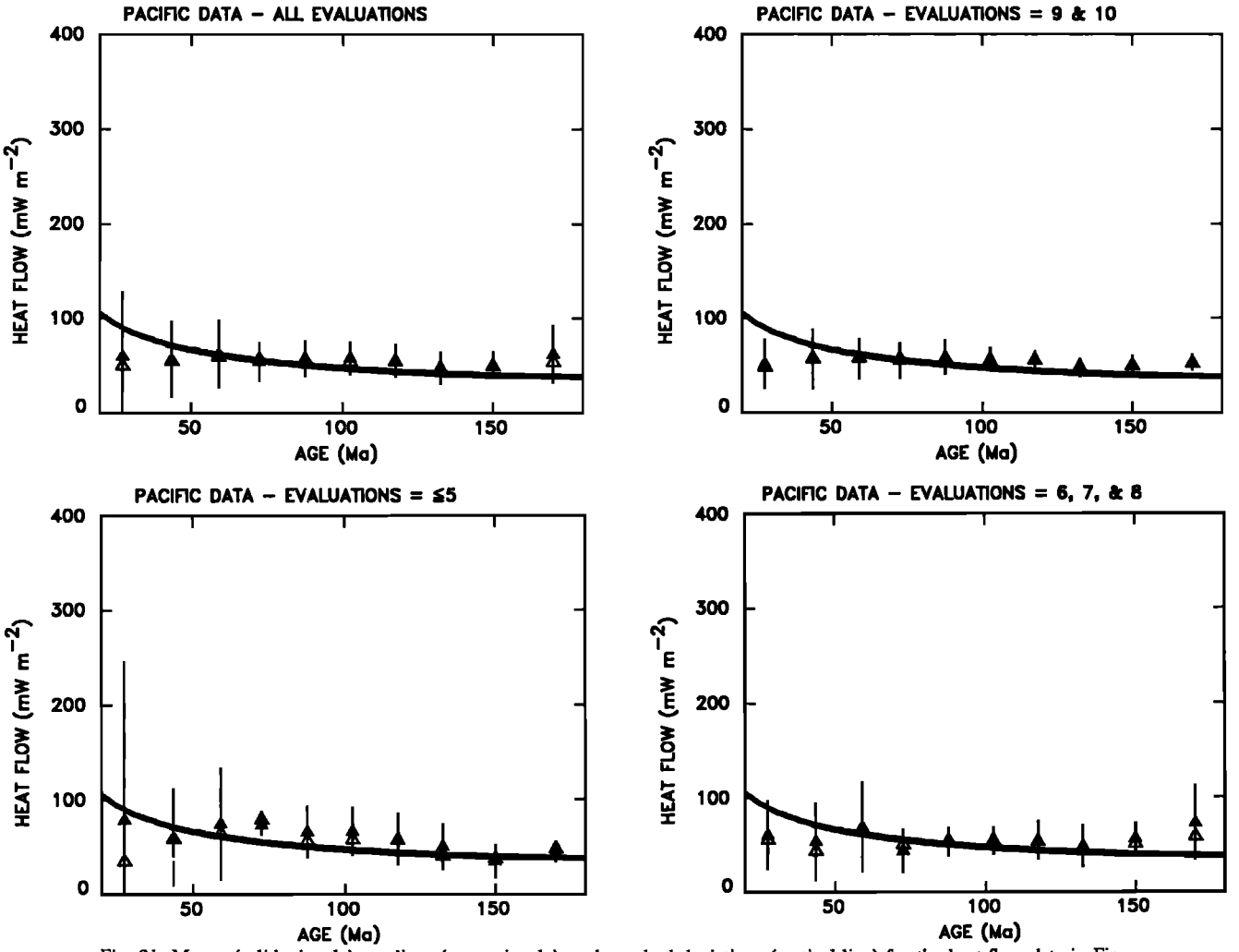

Fig. 3*b*. Means (solid triangle), medians (open triangle), and standard deviations (vertical line) for the heat flow data in Figure 3*a*. When the median and mean values are comparable, the median symbols are sometimes not visible. The thick solid lines show the heat flow expected for a 125-km-thick plate and a 1350°C basal temperature. The standard deviations for the poorest category (lower left) generally exceed those for the others.

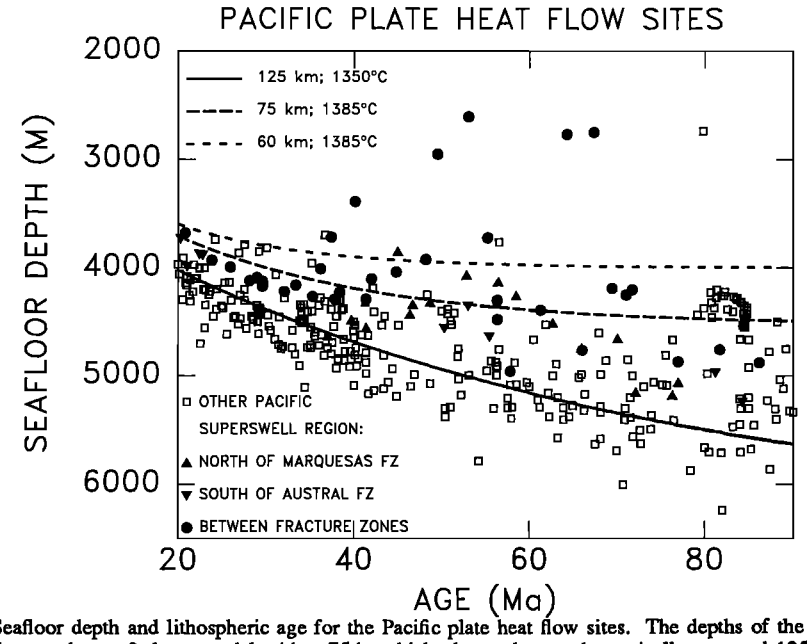

Fig. 4. Seafloor depth and lithospheric age for the Pacific plate heat flow sites. The depths of the heat flow sites in superswell region are better fit by a model with a 75-km-thick plate, whereas the typically assumed 125-km-thick plate better fits the depths of the other Pacific plate sites.

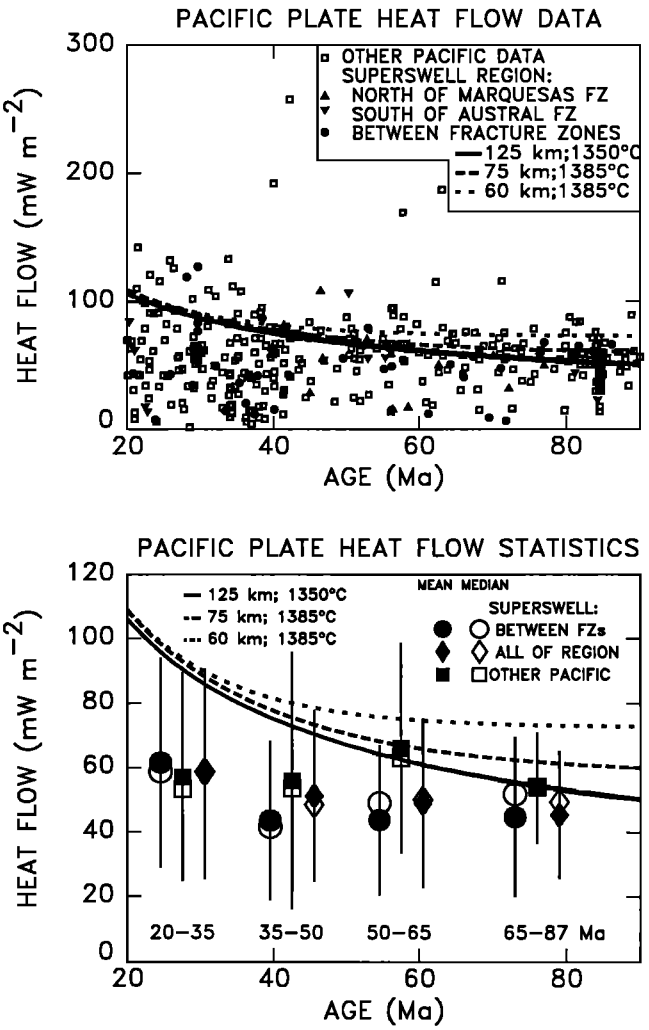

Fig. 5. *(top)* Heat flow and lithospheric age for sites in the superswell region and elsewhere on the Pacific plate. The heat flow values for the superswell are not generally greater than other Pacific plate values. The heat flow values between the Marquesas and Austral fracture zones, the area of greatest depth anomalies, are not on average greater than those for the whole superswell region. *(bottom)* Means, medians, and standard deviations of heat flow values in the superswell region, the area between the Marquesas and Austral fracture zones, and elsewhere on the Pacific plate. Given the large standard deviations, the superswell heat flow data suggest that lithospheric thicknesses exceeds 60 km, but cannot discriminate between greater thicknesses.

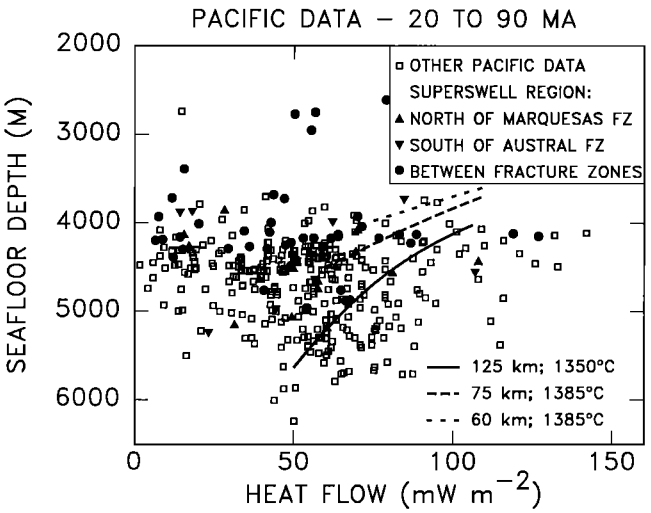

Fig. 6. Seafloor depths and heat flow for the heat flow sites. There does not appear to be any obvious relationship between depth and heat flow for sites either on the superswell or elsewhere on the Pacific plate. The solid and dashed lines, none of which fit the data well, represent the expected relationship between heat flow and depth for models with different plate thicknesses and basal temperatures for lithospheric ages between 20 and 90 Ma. Five Pacific values are excluded, one at a depth less than 1000 m and four with heat flow values greater than 150 mW m^{-2}.

transfer occurs by water circulation. For ages greater than about 100 Ma the observed heat flow exceeds that predicted. We discuss this further in the section on the Darwin Rise.

SUPERSWELL REGION

The heat flow sites provide good regional coverage of the superswell and, for comparison, the region surrounding it (Figure 2). Of the 76 heat flow data, 68 have good (6–10) evaluations and are used in the analysis. The data are divided into three groups: 17 from north of the Marquesas fracture zone, 9 from south of the Austral fracture zone, and 42 between these fracture zones, the region presumably most affected by the formation of the superswell.

The heat flow sites sample the region of shallower bathymetry described by *McNutt and Fisher* [1987]. Figure 4 shows that the superswell heat flow sites are consistently shallower than the sites with the same age elsewhere on the Pacific plate. As can be expected, the depths for the superswell sites are better fit by a model with a 75 km plate, whereas a 125-km plate better fits the depth of the other Pacific plate heat flow sites.

Figure 5 shows the heat flow data versus age for the superswell region and elsewhere on the Pacific plate. The means, medians and standard deviations are shown in Figure 5 (bottom). In this plot, the data are divided into four age bins, each containing an approximately equal number of data for the superswell. Several important points emerge:

1. The heat flow values for the superswell are not significantly higher than for the corresponding ages elsewhere on the Pacific plate.

2. The data show no significant difference between the heat flow for the area of greatest depth anomalies (between the Marquesas and Austral fracture zones) compared with the entire superswell region.

3. The heat flow data neither require nor exclude the possibility of a thinner thermal lithosphere: 125- and 75-km-thick plates are admissible for both the superswell and the remainder of the Pacific.

4. The superswell heat flow data exclude the possibility of a plate thinner than 60 km, which would also produce depth anomalies greater than those observed (Figure 4).

Since the superswell was defined by shallow seafloor, we tested whether the heat flow values correlate with depth for the superswell region and the other Pacific sites with similar lithospheric age. No obvious relationship between depth and heat flow appears for either data set (Figure 6). We did not correct for sediment loading, but given the large scatter in the data, such a small correction (probably less than 100 m for the superswell and generally less than 300 m for the other Pacific values) would have little effect. Comparison with the trends predicted by plate models for 20- to 90-Ma lithosphere shows that the sites with shallower depths do not exhibit the higher

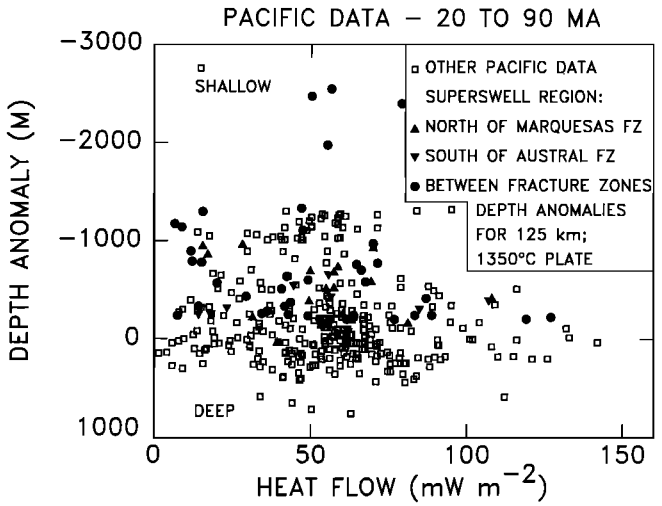

Fig. 7. Depth anomalies with respect to a 125-km-thick plate with 1350°C basal temperature versus heat flow for the heat flow sites in the superswell region and elsewhere in the Pacific (Figure 6). Although the superswell is defined by shallow bathymetry, there is no obvious correlation between the depth anomaly and the heat flow values.

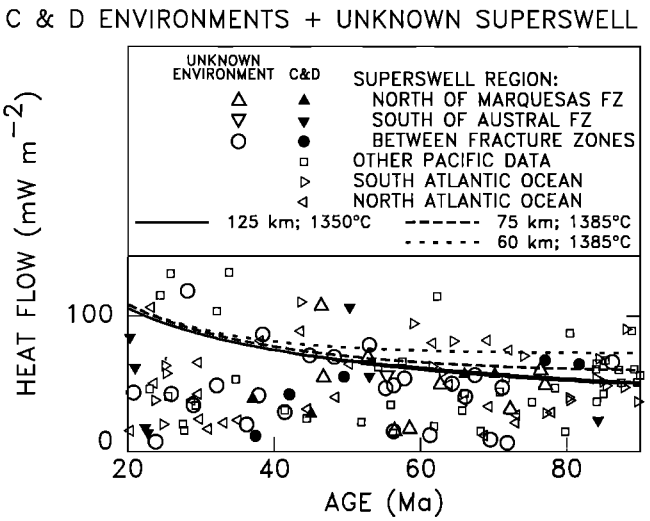

Fig. 8. Heat flow at superswell sites with C and D environments elsewhere in the Pacific and the Atlantic versus age. Superswell sites with insufficient data to determine the sedimentary environments are also included, since most of the sites with determined environments are in the C or D categories. Heat flow values for the superswell region are not high compared to those at the other sites.

heat flow expected if the elevation were controlled by lithospheric temperatures. Comparison of the heat flow values to the depth anomalies relative to those for a 125-km plate (Figure 7) also shows no obvious correlation for either the superswell or the rest of the Pacific. Moreover, the depth anomalies show no correlation with the heat flow anomalies relative to a 125-km-thick plate (not plotted).

Possible Biases Due to Water Circulation

One possible explanation for the absence of measured high heat flow is the removal of heat due to water circulation in the poorly sedimented superswell region. Throughout most of the superswell region there is a very thin sedimentary cover, less than 100 m (0.1 s two-way travel time) [*Ludwig and Houtz*, 1979]. The sedimentary environment category for 38 of the 76 heat flow measurements are known. Two are in category A, 16 are in B, 12 are in C, and 8 are in D. Nine of the sixteen B sites are from the detailed survey at 18°S, 130°W. Hence most of the superswell heat flow measurements are at sites with C and D environments.

To test if the observed superswell heat flux is abnormal, we compared the data from superswell sites with C and D environments, and those for which we had insufficient data to determine the environment, with 39 measurements at C and D sites elsewhere in the Pacific and 45 from such sites in the Atlantic [*Herman*, 1987] (Figure 8). Again, we find no significant differences between the average values for the superswell and the other oceans, nor between the Marquesas and Austral fracture zones and the areas directly to the north and south. In some cases, the superswell data are somewhat lower than the other regions.

We have other reasons for doubting that water circulation seriously biases our results. At sites where heat flow was determined from three or more temperature measurements with depth, the possible effect of water flow and the flow velocity can often be measured. Vertical water flow results in temperature gradients that are nonlinear [*Bredehoeft and Papadopulos*, 1965]. Of the 24 sites at which three or more temperatures were measured, only one (C11-116) shows a nonlinear gradient. Given this observation and the comparison with the C and D sites elsewhere, we consider it unlikely that the absence of a large observed heat flow anomaly for the superswell region results from a bias due to water circulation near the sea floor.

Darwin Rise

We also examined heat flow data for the Darwin Rise, the region of rough relief in the western Pacific that *McNutt and Fisher* [1987] suggested was a fossil superswell in the Cretaceous on the basis of the many characteristics similar to those of the South Pacific superswell. *Halunen and Von Herzen* [1973] noted that the heat flow across some of this region was relatively constant and proposed that any additional heat flow associated with the Darwin Rise had been dissipated. We analyzed additional heat flow data gathered since that study and used subsequent studies that determined lithospheric ages for the region.

The precise boundaries of the Darwin Rise region are difficult to define, since a large area of the present western Pacific plate was affected by a diffuse pattern of volcanic activity during the Cretaceous [*Schlanger et al.*, 1981]. We chose the study area to include a region surrounding the continuation of hot spot tracks from the present-day superswell, an area roughly south and east of Hawaii and north of the Samoan hot spot track. Heat flow data are available at 124 sites in the region (Figure 9) of which 114 have evaluations between 6 and 10 (categories A and B). The depths for the Pacific plate heat flow sites (Figure 10) are about 700 m deeper than might expected for a 75-km-thick plate. They are, however, shallower than might be expected for a 125-km- thick plate. *McNutt et al.* [1990] suggest that the depth anomaly is consistent with their proposed tectonic history of the region, including the termination of superswell conditions about 70–80 Ma.

The heat flow values for the Darwin Rise, with lithospheric ages of about 95–173 Ma, are similar to the rest of the Pacific plate (Figure 11, top). In each of the four age bins (Figure 11, bottom) the difference of the means between the Darwin Rise data and that elsewhere in the Pacific is less than 10 mW m^{-2} and the maximum difference in median value is 7 mW m^{-2}.

A potential difficulty with comparison of the Darwin Rise data with data of comparable age elsewhere in the Pacific is that a large region of the Pacific plate outside of the Darwin Rise

was also affected by Mesozoic volcanism. We thus also compared the Darwin Rise heat flow data with data for similar age lithosphere in the Atlantic. For this comparison, we used only the best data, stations with known A sedimentary environments. Again, the Darwin Rise values are no higher than for the other areas (Figure 12).

We regard the observation that the Darwin Rise heat flow does not exceed that for lithosphere of comparable age elsewhere in the Pacific and Atlantic as significant and as illustrating that whatever thermal changes may have been associated with the formation of the Darwin Rise are no longer present. This would be consistent with the idea of a fossil superswell. We do not, however, ascribe great significance to the fact that the Darwin Rise data heat flow values exceed those predicted for a 125-km-thick plate. This discrepancy occurs elsewhere for ages exceeding about 100 Ma, an effect previously noted whose cause remains obscure [*Sclater et al.*, 1980; *Davis et al.*, 1984; *Detrick et al.*, 1986; *Courtney and White*, 1986; *Louden et al.*, 1987; *Davis*, 1989; *Lister et al.*, 1990]. An additional complexity for the Darwin Rise, and quite possibly elsewhere, is that volcanic edifices formed far from the ridge crests contribute

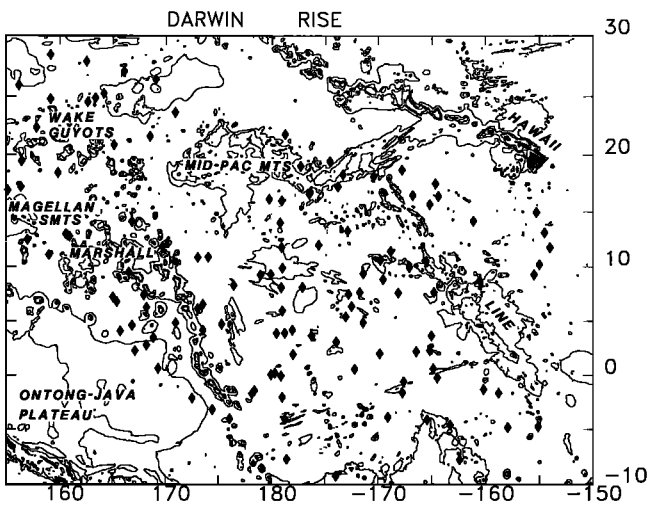

Fig. 9. Darwin Rise bathymetry (1500-m contours) and heat flow locations (solid diamonds).

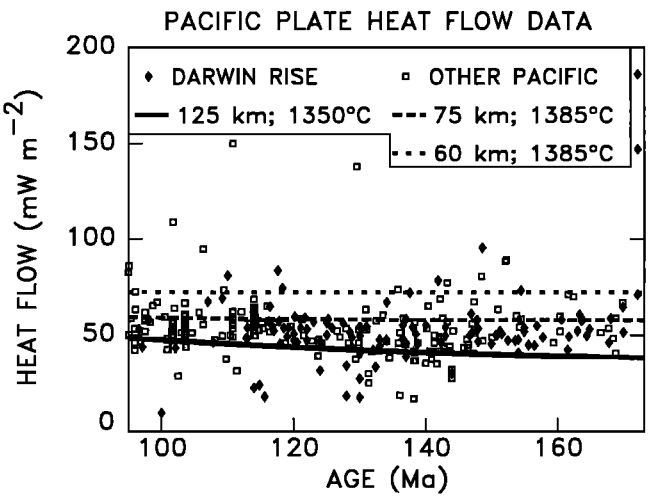

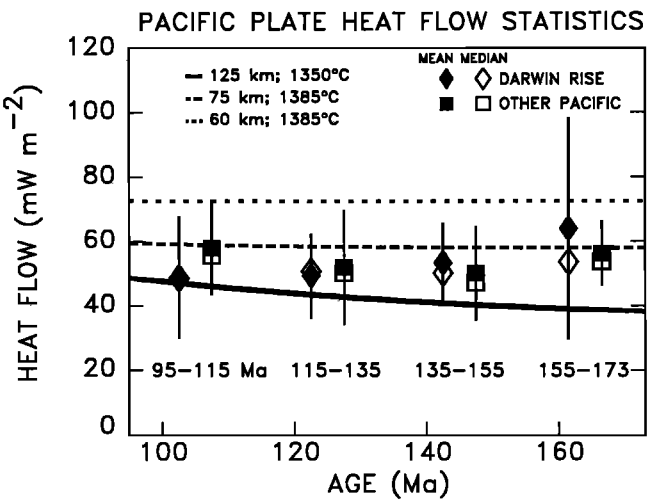

Fig. 11. *(top)* Heat flow versus age for sites on the Darwin Rise and Pacific plate. On average the values from the Darwin Rise are similar to those for the rest of the Pacific plate. The average heat flow exceeds that expected for a 125-km-thick plate model but is typical of data for similar ages on other plates. *(bottom)* Means, medians, and standard deviations for the Darwin Rise and other Pacific plate heat flow measurements. The relatively large difference between the median and mean values for the 155–173 Ma age bin results from the high heat flow of stations V6333-25 and V6333-27 (Table 2).

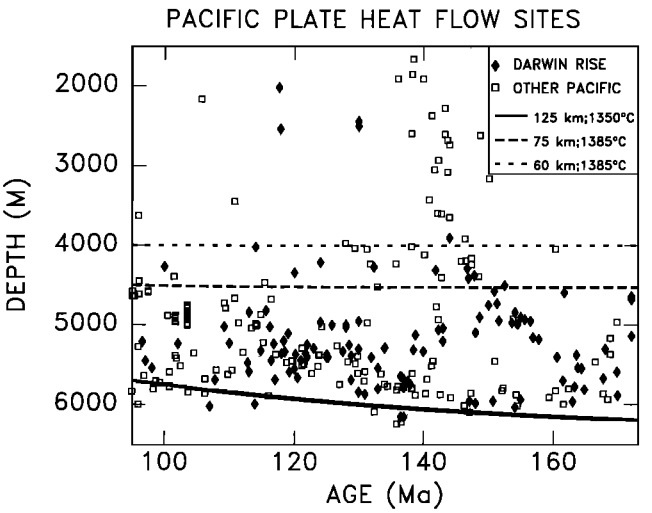

Fig. 10. Depth versus age for the Darwin Rise and other Pacific plate heat flow sites. The depths for both areas are shallower than might be expected for their age, assuming a 125-km-thick plate, but deeper than might be expected for a 75-km-thick plate.

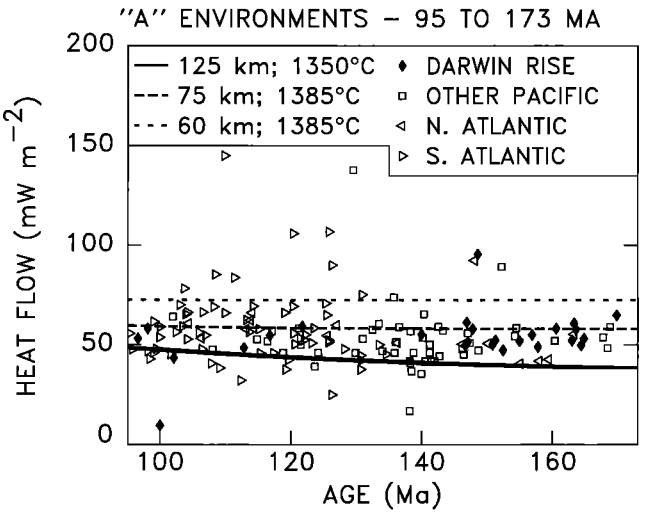

Fig. 12. Heat flow versus age for sites with known A environments on Darwin Rise, elsewhere on the Pacific plate, and the Atlantic. The Darwin Rise heat flow is not anomalously high compared with the other regions.

significantly to the topography, further obscuring the relation between heat flow and depth.

THERMAL MODELS

We next consider the implications of the heat flow data and other observations for the thermal structure and evolution of the superswell region. For this purpose, we investigated which thermal structures might reconcile two basic constraints. First, the heat flux for the superswell and the Darwin Rise is no higher than for lithosphere of comparable age elsewhere in the Pacific. Second, the effective elastic thickness of the lithosphere in the superswell region is significantly less than that for lithosphere of comparable age elsewhere.

Effective Elastic Thickness

The effective elastic thickness T_e of the lithosphere, as inferred from the deflections due to loads such as seamounts, generally increases with the square root of the age of the lithosphere at the time of loading [*Watts et al.*, 1980]. This effect is thought to reflect the decrease in lithospheric strength with depth due to increasing temperature, such that the effective elastic thickness as a function of age can be approximated as controlled by the depth to an isotherm [*Bodine et al., 1981*]. A global compilation derived using the Seasat gravity and SYNBAPS bathymetric data bases shows that the effective elastic thicknesses beneath 18 islands and seamounts in the superswell region are anomalously low for their age of loading (Figure 13) compared with 20 other Pacific sites [*Calmant* 1987; *Calmant and Cazenave*, 1987], 11 Atlantic, and 6 Indian Ocean sites [*Calmant et al.*, 1990]. The calculation of effective elastic thickness from an observed deflection depends, of course, on a variety of model parameters. *McNutt and Judge* [1990] also note, using somewhat different values, that the effective elastic thicknesses in the superswell are significantly lower than for hot spots elsewhere. For our modeling, we use the larger *Calmant et al.* [1990] data set.

The low effective elastic thicknesses have been used to support the suggestion of higher than normal temperatures associated with either multiple rejuvenation due to hot spots or the more recently proposed superswell model for the South Pacific and the Darwin Rise. *Menard and McNutt* [1982] suggested that multiple rejuvenation events due to the passage of the young lithosphere over numerous hot spots might explain the shallow depths, high density of volcanoes, and low effective elastic thicknesses. *Calmant and Cazenave* [1987] suggested that multiple rejuvenation events might explain their data. *McNutt and Fisher* [1987], however, proposed that multiple rejuvenation had to affect a very large region and would presumably not give rise to a systematic variation in the depth anomalies with age. They thus hypothesized that the superswell mantle anomaly is a transient feature, whereas the hot spots are longer duration phenomena which give rise to surface volcanism more easily when the lithosphere is thinned under superswell conditions.

We explored a range of steady state and time dependent (reheating) thermal models to see whether the thin effective elastic thicknesses can be reconciled with the absence of a heat flow anomaly. Our starting point was the constraint that the effective elastic thicknesses inferred for sites outside the superswell correspond to depths between the 300° and 600°C isotherms predicted for a 125-km-thick plate thermal model. We used the simple assumption that if the low effective elastic thicknesses for the superswell reflect thermal structure, these

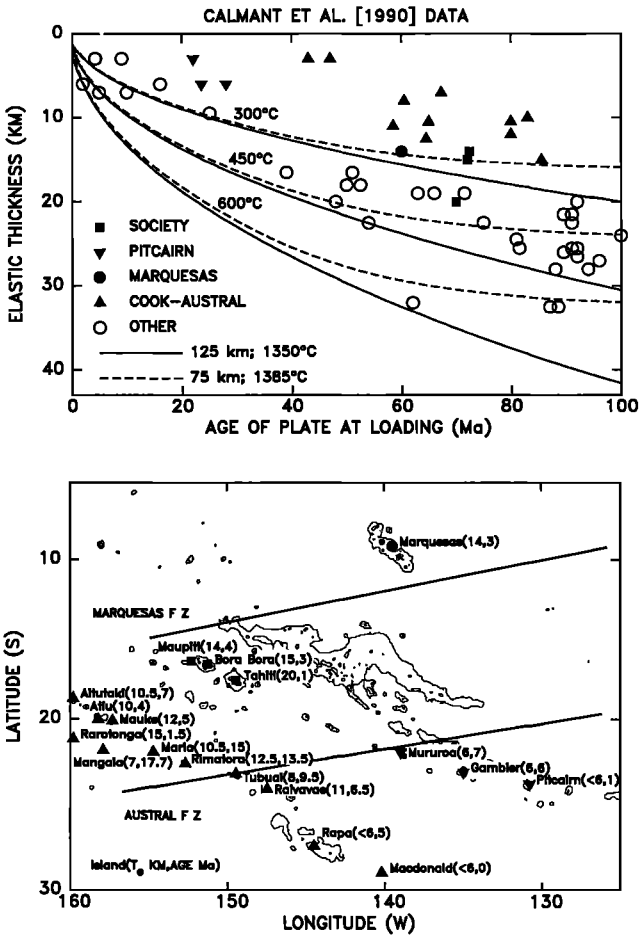

Fig. 13. *(top)* Effective elastic thickness (T_e) versus age of the plate at loading, and isotherms predicted for 125-km and 75-km-thick plates. A 75-km-thick plate does not have sufficiently higher temperatures at upper lithospheric depths compared with the 125-km-thick plate to account for the lower T_e. *(bottom)* Location of T_e measurements in the superswell region. The different seamount chains are indicated by the symbols from the upper panel. The numbers in parentheses are the T_e in km and age of volcanism in Ma [*Calmant et al.*, 1990]. The 1000- and 3500-m contours are shown.

thicknesses should be between the elevated 300° and 600°C isotherms. We examined models that achieve this weakening to see whether the predicted heat flow exceeded that observed.

Steady State Models

The simplest model that can give rise to different elevations and surface heat flow is one in which the plate evolves with different thickness and/or basal temperatures than those normally assumed (125 km; ~1350°C). For example, thinner plate thicknesses and higher basal temperatures will result in higher surface heat flow and shallower bathymetry. Such a mechanism for the observed heat flow anomalies in the central Indian Ocean was considered and then rejected given the lack of regional depth anomalies [*Stein and Weissel*, 1990].

We compared the predicted depths of the isotherms (Figure 13, top) for a 125-km-thick plate and the 75-km-thick plate proposed by *McNutt and Fisher* [1987]. The depths to the isotherms in the upper lithosphere for a 75-km-thick plate are only slightly shallower than for "normal" lithosphere with the age range at the time of loading for the South Pacific superswell. This result is not unexpected, as conductive heat transfer

requires a finite time for the location of the bottom boundary to significantly affect the cooling process. Hence a 75-km-thick plate alone is insufficient to explain the low effective elastic thickness data. A 40-km-thick plate with a 1350°C basal temperature or a 75-km-thick plate with a 2000°C basal temperature can raise the isotherms sufficiently to fit the effective elastic thickness data (Figure 14, top). Such models, however, predict heat flow substantially greater than observed (Figure 14, middle) and seafloor depths much shallower than observed (Figure 14, bottom). In addition, such lithospheric thicknesses or basal temperatures seem geologically unreasonable.

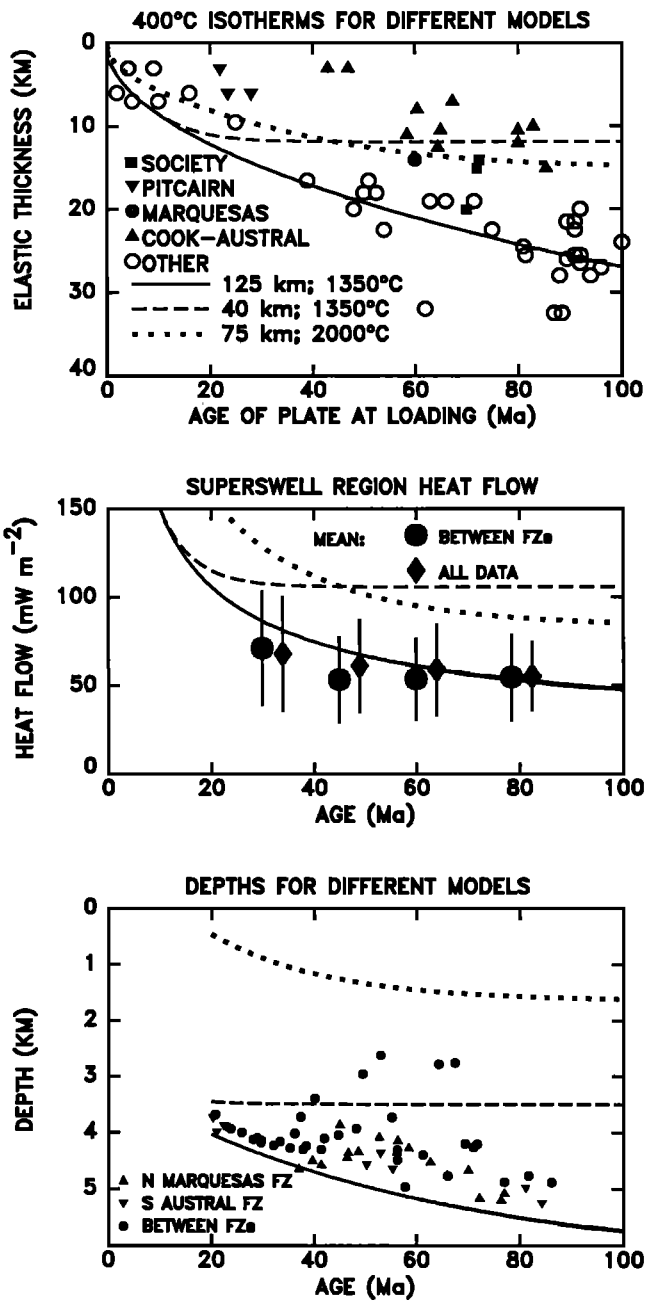

Fig. 14. *(top)* Measured effective elastic thicknesses and depths to the 400°C isotherm for three different models of basal temperature and plate thicknesses. *(middle)* Heat flow expected for the different models. *(bottom)* Depths and ages of the heat flow measurement sites in the superswell and those expected for the different models. Models having sufficiently high upper lithospheric temperatures to fit the T_e data have too high heat flow and elevations compared with the data.

Time Dependent Models

An alternative class of models are those in which the thermal structure of the lithosphere is perturbed at some time and then evolves. The effect on surface heat flow from changes in the temperature with depth depends on the depth of the perturbation and the time since its initiation [*Carslaw and Jaeger*, 1959].

Unfortunately, it is difficult to date the formation of the superswell. We can estimate a minimum age provided that the thin effective elastic thicknesses beneath seamounts in the superswell area imply that these loads were emplaced by hot spots subsequent to the formation of the superswell. Since the oldest seamount in the superswell with thin T_e, Mangaia, in the Cook-Austral Islands, is dated at 17.7 Ma [*Calmant*, 1987], anomalous conditions must predate its formation. Even under this assumption, of course, the superswell might be significantly older.

For a hot spot reheating model, in which the bottom portion of the lithosphere is reset to asthenospheric temperatures [*Crough*, 1978; *Detrick and Crough*, 1978], the depth to reheating determines the anomalous bathymetry and heat flow with time. The shallower the reheating depth, the greater the depth anomaly, the sooner the maximum surface heat flow anomaly occurs, and the greater its magnitude. The depth for reheating is estimated largely from bathymetry. *Crough* [1978] proposed that hot spots reset the temperature structure to that of a 25-Ma lithosphere, and *McNutt* [1987] proposed that reheating occurred up to the initial location of the 900°C isotherm.

To approximate the conditions for the superswell, we calculated the temperature structure and heat flow predicted by the half-space reheating model of *Von Herzen et al.* [1982]. Reheating to the depth of the 900°C isotherm for lithosphere in the range of ages for the superswell results in very little shallowing of the 400°C isotherm. For example, Figure 15 shows unperturbed (solid line) and perturbed (dashed line) isotherms and surface heat flow with time expected for the reheating of 45-Ma lithosphere to the depth of the 900°C isotherm, 45 km. Although the heat flow anomaly predicted is small enough to not violate our heat flow data constraint, the increase in temperature in the upper lithosphere is insufficient to explain the effective elastic thickness data. Much shallower reheating depths are required to elevate the temperatures sufficiently to fit the T_e data. For example, 45-Ma lithosphere must be thinned to 15 km depth (Figure 16) to place the largest effective elastic thicknesses in the expected temperature range. Such thinning would give rise to predicted heat flow much larger than observed. Moreover, such a shallow reheating depth would be substantially shallower than that previously proposed for other hot spots. The same difficulties occur for reheating at the other lithospheric ages in the superswell.

DISCUSSION

The heat flow data and our modeling demonstrate the difficulties in interpreting the low effective elastic thicknesses for the South Pacific and the fossil Darwin Rise superswells in terms of thermal weakening due to high upper lithospheric temperatures. Since the T_e values are about half those for lithosphere outside the superswells, the isotherms should be at about half the normal depths, and the surface heat flow should be about twice that expected. Since such high heat flow is not observed, we feel that regional reheating sufficient to explain the effective elastic thickness data is unlikely.

In addition, a regional reheating model has other difficulties. The sites in the region of maximum depth anomalies (between

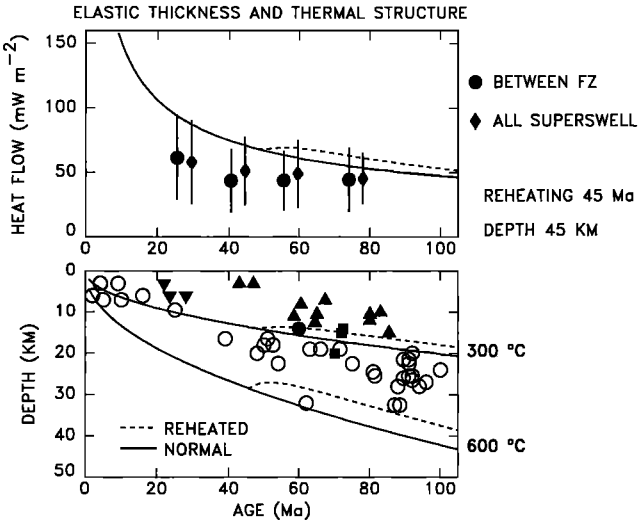

Fig. 15. Model for reheating 45-Ma lithosphere to a depth of 45 km. Although the calculated heat flow anomaly *(top)* is plausible given the observed heat flow, such a model does not give sufficient reheating of the upper lithosphere *(bottom)* to account for the low T_e. In the bottom panel, the seamount chains are indicated by symbols used in Figure 13.

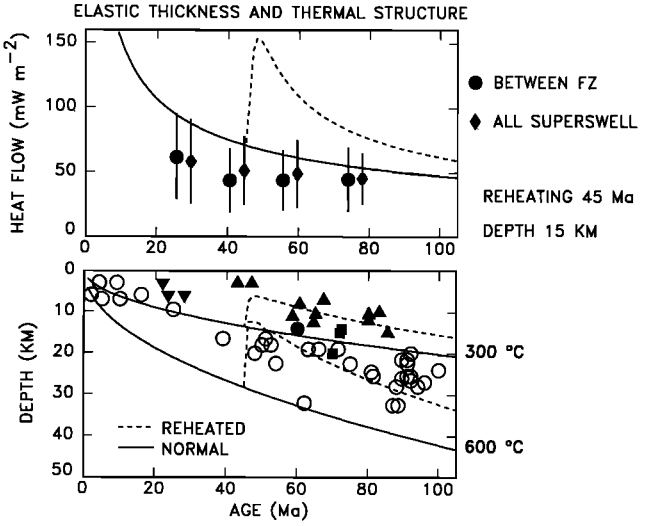

Fig. 16. Model for reheating 45-Ma lithosphere to a depth of 15 km. Although this model produces sufficient reheating in the upper lithosphere to account for the largest T_e of the superswell sites, it predicts a heat flow anomaly significantly larger than that observed. In the bottom panel, the seamount chains are indicated by symbols used in Figure 13.

the Marquesas and Austral fracture zones), which should be the most affected by the superswell, do not have the lowest effective elastic thicknesses. The Society Islands (near the center of the superswell) and the Marquesas have about the same T_e (Figure 13), although the latter is not in the superswell since the only depth anomalies north of the Marquesas fracture zone are those associated with this volcanic chain [*McNutt and Fisher*, 1987]. Of the three measurements in the Society Islands, Tahiti has the highest T_e for all the 18 superswell region sites, but this large value may result from the site not being in equilibrium thickness yet [*Calmant and Cazenave*, 1986]. However, this does not explain the relatively high values for Bora-Bora and Maupiti. Conversely, the five sites with the thinest effective elastic thicknesses (Pitcairn, Gambier, Mururoa, MacDonald, and Rapa) are south of the Austral fracture zone and hence outside the region of maximum depth anomalies. Finally, if regional reheating occurred then sites with the larger depth anomalies should be associated with higher heat flow, but this is not observed (Figure 7).

Our observation of a lack of a heat flow anomaly for the superswell and inference that significant shallow regional reheating has not occurred is consistent with new results for the Hawaiian hot spot chain. *Von Herzen et al.* [1989] suggest, from detailed heat flow data and comparison with other old lithosphere, that little reheating has occurred. They suggest that their data are compatible with at most about 100°–200°C increase at the base of the plate and hence that a model assuming a significant dynamic component to explain the elevation of hot spots is required. In addition, recent results show that surface wave velocities along the Hawaiian-Emperor chain from Midway to Oahu are similar to those expected for unperturbed 100-Ma lithosphere, and significantly faster than those expected if the Hawaiian swell originates primarily by large-scale reheating [*Woods et al.*, 1991].

What alternatives are there to a regional reheating model? We can see three possibilities that might reconcile the lack of high heat flow and the thin effective elastic thicknesses.

First, the heat flow and T_e observations could be consistent if the high temperatures occur only below the seamounts rather than throughout the region. Unfortunately, since the heat flow measurements were not taken to address this issue, only a few are within 200 km of the seamounts beneath which T_e has been determined (Figure 2). The few measurements close to these seamounts do not show dramatically high heat flow. The heat flow values for the Marquesas (RIS 145, 146, and 147) and for the Society (RIS 136, 137, and 138) sites are not anomalous relative to the means and standard deviations for the age group. For the Austral-Cook chain, C13-132 and 133 and CAP-31B are a few mW m^{-2} greater than the mean plus 1 standard deviation, but less than would be expected if the plate were thermally weakened. Nonetheless, given the limited data and their location, we cannot exclude local reheating to very shallow depths.

A natural question posed by the possibility of local reheating is why such a phenomenon would occur for the superswell hot spots but not others, since the effective elastic thicknesses observed near other hot spots (Figure 13) are significantly greater. The hotspots of the superswell region are not thought to be exceptional ones; each of the four hot spots (Pitcairn, Marquesas, MacDonald, and Tahiti) has about 3/8 the buoyancy flux of Hawaii [*Sleep*, 1990]. Similarly, *McNutt and Judge* [1990] proposed that the concentration of hot spots in the superswell occurs because the thinned lithosphere is easily penetrated by numerous, but relatively weak, thermal plumes that might be incapable of producing midplate volcanoes on normal lithosphere. Hence these hot spots often produce volcanoes only intermittently as a result of preexisting weaknesses in a plate and/or the thinner plate associated with the formation of the superswell [*McNutt and Fisher*, 1987; *McNutt et al.*, 1989]. Inferred geotherms from analyses of mantle xenoliths would be useful, but few data are available for the superswell region. A study of ultramafic xenoliths, consisting of mainly spinel lherzolites, near Papeete (Tahiti), suggests temperatures of ~1100°C at pressures less than about 15–20 kbar [*Tracy*, 1980] (about 45–60 km) and thus suggests that very shallow reheating is not occurring.

Second, the low effective elastic thicknesses might result from mechanical rather than thermal weakening of the lithosphere. The presence of a significant amount of volatiles, such

as water, might result in a weaker rheology. Alternatively, weakening might be due to successive intrusion events resulting in cracking, flexing and reheating the lithosphere. This hypothesis has the same difficulty as that of local reheating under the seamounts, in that it is unclear why the superswell hot spots should show this effect whereas others do not. Perhaps the explanation lies in the complex tectonic history of the region. The Cook-Austral island chain has many anomalous features and is less linear and more segmented than the Hawaiian chain [*Okal and Batiza*, 1987]. *Turner and Jarrard* [1982] proposed that the Cook-Austral chain violated the age-distance relationship predicted for a single hot spot and suggested that a hot spot model for the chain would require three hot spots. Also, an area through part of the chain may have been affected by hot spot activity sometimes between the Late Cretaceous and Eocene [*Diament and Baudry*, 1987]. The Pitcairn chain was emplaced on lithosphere previously affected by the Easter hot spot (Gordon and Henderson, unpublished manuscript, 1985) and may have a complicated pattern of volcanism due to the complex interaction of the hot spot with fracture zones [*Okal and Cazenave*, 1985]. Although such effects might explain the unusual low T_e for the Cook-Austral and Pitcairn chain, it is more difficult to explain the low values for the Society and Marquesas.

Third, the low effective elastic thicknesses could reflect regional intraplate stresses resulting from plate boundary forces, such as suggested for the Indian Ocean [*Cloetingh and Wortel*, 1985, 1986; *Stein et al.*, 1989], or from the mantle upwelling associated with the superswell. The flexural response of the lithosphere to an applied load depends on both the mechanical properties and the regional stress [*Turcotte and Schubert*, 1982]. This possibility is suggested by the presence in the superswell area of widespread seismicity, some of whose epicenters seem unrelated to volcanic events, in contrast to Hawaii where most of the epicenters appear related to active volcanoes [*Wysession et al.*, 1991]. However, a simple line load model assuming elastic behavior [*Hetenyi*, 1974] suggests that to reduce the effective elastic thicknesses by even 20%, ~400 MPa (4 kbar) of compressional stress would be required. It seems unlikely that intraplate stresses would be so large given that the level of Pacific intraplate seismicity is not as high as that in the Indian Ocean.

CONCLUSIONS

The absence of a regional heat flow anomaly for the superswell argues against a regional reheating of the upper lithosphere sufficient to explain the thin effective elastic thicknesses as a consequence of thermal weakening. The heat flow and effective elastic thickness data might perhaps be reconciled if beneath seamounts in the superswell area either major shallow reheating or mechanical weakening occurs. Additional data on the effective elastic thicknesses of superswell seamounts and their ages, and additional heat flow data near these seamounts, would be useful for better understanding the dynamics and evolution of the South Pacific superswell and the Darwin Rise.

Acknowledgments. This research was supported by grants 21625-G2 and 19134-AC2-C from the Petroleum Research Fund, administered by the American Chemical Society and ONR N00014-87-K-204. We thank Richard Gordon, David McAdoo, Marcia McNutt, Emile Okal, David Sandwell, Sy Schlanger, Seth Stein, and Mark Woods for useful discussions and advice. We thank Mark Hobart for permission to use the ARIAD heat flow data. We thank C. R. B. Lister for a preprint of his manuscript. Lamont-Doherty Geological Observatory contribution 4784.

REFERENCES

Abbott, D., and M. Fisk, Tectonically controlled origin of three unusual rock suites in the Woodlark Basin, *Tectonics, 5*, 1145–1160, 1986.

Anderson, R. N., and M. A. Hobart, The relation between heat flow, sediment thickness, and age in the eastern Pacific, *J. Geophys. Res., 81*, 2968–2989, 1976.

Anderson, R. N., and R. P. Von Herzen, Heat flow on the Pacific-Antarctic Ridge, *Earth Planet. Sci. Lett., 41*, 451–460, 1978.

Anderson, R. N., M. A. Hobart, R. P. Von Herzen, and D. J. Fornari, Geophysical surveys on the East Pacific Rise–Galapagos Rise system, *Geophys. J. R. Astron. Soc., 54*, 141-166, 1978.

Bodine, J. H., M. S. Steckler, and A. B. Watts, Observations of flexure and the rheology of the oceanic lithosphere, *J. Geophys. Res., 86*, 3695–3707, 1981.

Boyce, R. E., Electrical resistivity, sound velocity, thermal conductivity, density-porosity and temperature, obtained by laboratory techniques and well logs: Site 462 in the Nauru Basin of the Pacific Ocean, *Initial Rep. Deep Sea Drill. Proj., 61*, 743–761, 1981.

Bredehoeft, J. D., and I. S. Papadopulos, Rates of vertical groundwater movement estimated from the Earth's thermal profile, *Water Resour. Res., 2*, 325–328, 1965.

Calmant, S., The elastic thickness of the lithosphere in the Pacific Ocean, *Earth Planet. Sci. Lett., 85*, 277–288, 1987.

Calmant, S., and A. Cazenave, The effective elastic lithosphere under the Cook-Austral and Society Islands, *Earth Planet. Sci. Lett., 77*, 187–202, 1986.

Calmant, S., and A. Cazenave, Anomalous elastic thickness of the oceanic lithosphere in the south-central Pacific, *Nature, 328*, 236–238, 1987.

Calmant, S., J. Francheteau, and A. Cazenave, Elastic layer thickening with age of the oceanic lithosphere: A tool for prediction of age of volcanoes or oceanic crust, *Geophys. J. Int., 100*, 59–67, 1990.

Carslaw, H. S., and J. C. Jaeger, *Conduction of Heat in Solids*, pp., 510 *Oxford University Press*, New York, 1959.

Castillo, P., The Dupal anomaly as a trace of the upwelling lower mantle, *Nature, 336*, 667–670, 1988.

Cloetingh, S., and R. Wortel, Regional stress field of the Indian plate, *Geophys. Res., Lett., 12*, 77–80, 1985.

Cloetingh, S., and R. Wortel, Stress in the Indo-Australian plate, *Tectonophysics, 132*, 49–67, 1986.

Cochran, J. R., Variations in subsidence rates along intermediate and fast spreading mid-ocean ridges, *Geophys. J. R. Astron. Soc., 87*, 421–454, 1986.

Courtney, R. C., and R. S. White, Anomalous heat flow and geoid across the Cape Verde Rise: Evidence for dynamic support from a thermal plume in the mantle, *Geophys. J. R. Astron. Soc., 87*, 815–867, 1986.

Crough, S. T., Thermal origin of mid-plate hot-spot swells, *Geophy. J. R. Astron. Soc., 55*, 451–469, 1978.

Davis, E. E., Thermal aging of oceanic lithosphere, *in Handbook of Seafloor Heat Flow*, edited by J. A. Wright and K. E. Louden, pp. 145–167, CRC Press, Boca Raton, Fla., 1989.

Davis, E. E., and C. R. B. Lister, Heat flow measured over the Juan de Fuca Ridge: Evidence for widespread hydrothermal circulation in a highly heat transportive crust, *J. Geophys. Res., 82*, 4845–4860, 1977.

Davis, E. E., C. R. B. Lister, and J. G. Sclater, Towards determining the thermal state of old ocean lithosphere: Heat-flow measurements from the Blake-Bahama outer ridge, north-western Atlantic, *Geophys. J. R. Astron. Soc, 78* , 507–545, 1984.

Detrick, R. S., and S. T. Crough, Island subsidence, hot spots, and lithosphere thinning, *J. Geophys. Res., 83*, 1236–1244, 1978.

Detrick, R. S., R. P. Von Herzen, B. Parsons, D. Sandwell, and M. Dougherty, Heat flow observations on the Bermuda Rise and thermal models of midplate swells, *J. Geophys. Res., 91*, 3701–3723, 1986.

Diament, D., and N. Baudry, Structural trends in the Southern Cook and Austral archipelagoes (south central Pacific) based on an analysis of Seasat data: Geodynamic implications, *Earth Planet Sci. Lett., 85*, 427–438, 1987.

Dunbar, J. A., and D. T. Sandwell, A boudinage model for crossgrain lineations, *Eos Trans. AGU, 69*, 1429, 1988.

Duncan, R. A., and D. A. Clague, Pacific plate motion recorded by linear volcanic chains, *The Ocean Basins and Margins 7A: The*

Pacific Ocean, edited by A. E. Nairn, F. G. Stehli, and S. Uyeda, pp. 89–121, Plenum, New York, 1985.

Halunen, A. J., and R. P. Von Herzen, Heat flow in the western equatorial Pacific Ocean, *J. Geophys. Res., 78*, 5195–5208, 1973.

Hart, S. R., A large-scale isotope anomaly in the southern hemisphere mantle, *Nature, 309*, 753–757, 1984.

Hart, S. R., Heterogeneous mantle domains: Signatures, genesis and mixing chronologies, *Earth Planet. Sci. Lett., 90*, 273–296, 1988.

Haxby, W. F., and J. K. Weissel, Evidence for small-scale mantle convection from Seasat altimeter data, *J. Geophys. Res., 91*, 3507–3520, 1986.

Herman, B. M., The thermal evolution of oceanic lithosphere in the South Atlantic, Ph.D. thesis, 347 pp., Columbia Univ., New York, 1987.

Hetenyi, M., *Beams on Elastic Foundation*, 255 pp., University of Michigan Press, Ann Arbor, 1974.

Kuzmin, V. A., A. E., Suzyumov, and A. V., Bezludov, Geothermic soundings on the Manihiki Plateau and the Marcus-Necker Rise (the Pacific Ocean), (in Russian), *Okeanologiya, 12*, 1044–1046, 1972.

Langseth, M. G., and P. T. Taylor, Recent heat flow measurements in the Indian Ocean, *J. Geophys. Res., 72*, 6249–6260, 1967.

Langseth, M. G., and R. P. Von Herzen, Heat flow through the floor of the world oceans, in *The Sea*, vol. 4, edited by A. E. Maxwell, pp. 299–352, Interscience, New York, 1970.

Langseth, M. G., P. J. Grim, and M. Ewing, Heat-flow measurements in the east Pacific Ocean, *J. Geophys. Res., 70*, 367–380, 1965.

Langseth, M. G., I. Malone, and D. Berger, Sea floor geothermal measurements from Vema cruise 24, 452 pp., Columbia Univ., *Tech. Rept. 3-CU-3-71*, New York, 1971. (Available as *NTIS A0729682* from Natl. Tech. Inf. Serv., Springfield, Va.)

Lister, C. R. B., On the thermal balance of a mid-ocean ridge, *Geophys. J. R. Astron. Soc., 26*, 515–535, 1972.

Lister, C. R. B., J. G. Sclater, E. E. Davis, H. Villinger, and S. Nagihara, Heat flow maintained in oceanic basins of great age: Investigations in the north-equatorial west Pacific, *Geophys. J. Int., 102*, 603–630, 1990.

Liu, M., and C. G. Chase, Evolution of midplate hotspot swells: Numerical solutions, *J. Geophys. Res., 94*, 5571–5584, 1989.

Louden, K. E., Marine heat flow data listing, Appendix B, *in Handbook of Seafloor Heat Flow*, pp. 325–485, edited by J. A. Wright and K. E. Louden, CRC Press, Boca Raton, Fla., 1989.

Louden, K. E., D. O. Wallace, and R. C. Courtney, Heat flow and depth versus age for the Mesozoic northwest Atlantic Ocean: Results from the Sohm abyssal plain and implications for the Bermuda Rise, *Earth Planet. Sci. Lett., 83*, 109–122, 1987.

Ludwig, W. J. and R. E. Houtz, Isopach map of sediments in the Pacific Ocean basin and marginal sea basins, Am. Assoc. Pet. Geol., Tulsa, Okla., 1979.

Mammerickx, J., R. N. Anderson, H. W. Menard, and S. M. Smith, Morphology and tectonic evolution of the east-central Pacific, *Geol. Soc. Am. Bull., 86*, 111–118, 1975.

Marty, J. C., and A. Cazenave, Regional variations in subsidence rate of oceanic plates: A global analysis, *Earth Planet. Sci. Let., 94*, 301–315, 1989.

Maxwell, A., The outflow of heat under the Pacific Ocean, Ph.D. thesis, Univ. of Calif., Los Angeles, 1958.

McAdoo, D. C., and D. T. Sandwell, On the source of cross-grained lineations in the central Pacific gravity field, *J. Geophys. Res., 94*, 9341–9352, 1989.

McNutt, M. K., Temperature beneath midplate swells: The inverse problem, in *Seamounts, Islands, and Atolls, Geophys. Monogr. Ser.*, vol. 43, edited by B. H. Keating, P. Fryer, R. Batiza, and G. W. Boehlert, 123–132, AGU, Washington, D.C., 1987.

McNutt, M. K., and K. M. Fisher, The South Pacific superswell, in *Seamounts, Islands, and Atolls, Geophys. Monogr. Ser.*, vol. 43, edited by B.H. Keating, P. Fryer, R. Batiza, and G. W. Boehlert, pp. 25–34, AGU, Washington, D.C., 1987.

McNutt, M. K., and A. V. Judge, The superswell and mantle dynamics beneath the South Pacific, *Science, 248*, 969–975, 1990.

McNutt, M., and H. W. Menard, Lithospheric flexure and uplifted atolls, *J. Geophys. Res., 83*, 1206–1212, 1978.

McNutt, M. K., K. M. Fisher, S. Kruse, and J. Natland, The origin of the Marquesas fracture zone ridge and its implications for the nature of hot spots, *Earth Planet. Sci. Lett., 91*, 381–393, 1989.

McNutt, M. K., E. L. Winterer, W. W. Sager, J. H. Natland, G. Ito, The Darwin Rise: A Cretaceous superswell?, *Geophys. Res. Lett., 17*, 1101–1104, 1990.

Menard, H. W., *Marine Geology of the Pacific*, 271 pp., McGraw-Hill, New York, 1964.

Menard, H. W., Darwin reprise, *J. Geophys. Res., 89*, 9960–9968, 1984.

Menard, H. W., and M. McNutt, Evidence for and consequences of thermal rejuvenation, *J. Geophys. Res., 87*, 8570–8580, 1982.

Morgan, W. J., Plate motions and deep mantle convection, *Geol. Soc. Am. Bull., 132*, 7–22, 1972.

Natland, J. H., and E. Wright, Magmatic lineages and mantle sources of Cretaceous seamount in the central Pacific, *Eos Trans. AGU, 65*, 1075–1076, 1984.

Nishimura, C. E., and D. W. Forsyth, Anomalous Love-wave phase velocities in the Pacific: Sequential pure-path and spherical harmonic inversion, *Geophys. J. R. Astron. Soc., 81*, 389–407, 1985.

Okal, E. A., and R. Batiza, Hotspots: The first 25 years, in *Seamounts, Islands, and Atolls, Geophys. Monogr. Ser.*, vol. 43, edited by B.H. Keating, P. Fryer, R. Batiza, and G.W. Boehlert, pp. 1–11, AGU, Washington, D.C., 1987.

Okal, E. A., and A. Cazenave, A model for the plate tectonic evolution of the east-central Pacific based on Seasat investigations, *Earth Planet. Sci. Lett., 72*, 99–116, 1985.

Parsons, B., and S. Daly, The relationship between surface topography, gravity anomalies, and temperature structure of convection, *J. Geophys. Res., 88*, 1129–1144, 1983.

Parsons, B., and J. G. Sclater, An analysis of the variation of ocean floor bathymetry and heat flow with age, *J. Geophys. Res., 82*, 803–827, 1977.

Renkin, M. L., and J. G. Sclater, Depth and age in the North Pacific, *J. Geophys. Res., 93*, 2919–2935, 1988.

Robinson, E. M., and B. Parsons, Effect of a shallow low-viscosity zone on the formation of midplate swells, *J. Geophys. Res., 93*, 3144–3156, 1988.

Schlanger, S. O., H. C. Jenkyns, and I. Premoli-Silva, Volcanism and vertical tectonics in the Pacific basin related to global Cretaceous transgressions, *Earth Planet. Sci. Lett., 52*, 435–449, 1981.

Sclater, J. G. and J. Francheteau, The implications of terrestrial heat flow observations on current tectonic and geochemical models of the crust and upper mantle of the Earth, *Geophys. J. R. Astron. Soc., 20*, 509–542, 1970.

Sclater, J. G., U. G. Ritter, and F. S. Dixon, Heat flow in the southwestern Pacific, *J. Geophys. Res., 77*, 5697–5708, 1972.

Sclater, J. G., J. Crowe, and R. N. Anderson, On the reliability of oceanic heat flow averages, *J. Geophys. Res., 81*, 2997–3006, 1976.

Sclater, J. G., C. Jaupart, and D. Galson, The heat flow through oceanic and continental crust and the heat loss of the Earth, *Rev. Geophys., 18*, 269–311, 1980.

Sleep, N. H., Hotspots and mantle plumes: Some phenomenology, *J. Geophys. Res., 95*, 6715–6736, 1990.

Smith, W. H. F., H. Staudigel, A. B. Watts, and M. S. Pringle, The Magellan Seamounts: Early Cretaceous record of the South Pacific isotopic and thermal anomaly, *J. Geophys. Res., 94*, 10,501–10,523, 1989.

Staudigel, H., K. H. Park, M. Pringle, J. L. Rubenstone, W. S. F. Smith, and A. Zindler, The longevity of the South Pacific isotopic and thermal anomaly, *Earth Planet. Sci. Lett., 102*, 24–44, 1991.

Stein, C. A., and D. H. Abbott, Implications of estimated and measured thermal conductivity for oceanic heat flow studies, *Mar. Geophys. Res.*, in press, 1991.

Stein, C. A., and J. K. Weissel, Constraints on the central Indian basin thermal structure from heat flow, seismicity and bathymetry, *Tectonophysics., 176*, 315–332, 1990.

Stein, C. A., S. Cloetingh, and R. Wortel, Seasat-derived gravity constraints on stress and deformation in the northeastern Indian Ocean. *Geophys. Res. Lett., 16*, 823–826, 1989.

Tracy, R. J., Petrology and genetic significance of an ultramafic xenolith suite from Tahiti, *Earth Planet. Sci. Lett., 48*, 80–96, 1980.

Turcotte, D. L., and G. Schubert, *Geodynamics: Applications of Continuum Physics to Geological Problem*, John Wiley, New York, 1982.

Turner, D. L., and R. D. Jarrard, K-Ar dating of the Cook-Austral island chain: A test of the hotspot hypothesis, *J. Volcanol. Geotherm. Res., 12*, 187–220, 1982.

Vacquier, V., S. Uyeda, M. Yasui, J. Sclater, C. Corry, and T. Watanabe, Studies of the thermal state of the Earth., The 19th paper: Heat-flow measurements in the northwestern Pacific, *Bull. Earthquake Res. Inst., Univ. Tokyo, 44*, 1519–1535, 1966.

Von Herzen, R., Heat-flow values from the southeastern Pacific, *Nature, 183*, 882–883, 1959.

Von Herzen, R., and S. Uyeda, Heat flow through the eastern Pacific Ocean floor, *J. Geophys. Res., 68*, 4219–4250, 1963.

Von Herzen, R. P., R. S. Detrick, S. T. Crough, D. Epp and U. Fehn, Thermal origin of the Hawaiian swell: Heat flow evidence and thermal models, *J. Geophys. Res., 87*, 6711–6723, 1982.

Von Herzen, R. P., J. J. Cordery, R. S. Detrick, and C. Fang, Heat flow and the thermal origin of the hot spot swells: The Hawaiian swell revisited, *J. Geophys. Res., 94*, 13,783–13,799, 1989.

Watts, A. B., J. H. Bodine and M. S. Steckler, Observations of flexure and the state of stress in the oceanic lithosphere, *J. Geophys. Res., 85*, 6369–6376, 1980.

Williams, D. L., R. P. Von Herzen, J. G. Sclater, and R. N. Anderson, The Galapagos spreading centre: Lithospheric cooling and hydrothermal circulation, *Geophys. J. R. Astron. Soc., 38*, 587–608, 1974.

Wolfe, C. J. and M. K. McNutt, Compensation of Cretaceous seamounts of the Darwin Rise, Northwest Pacific Ocean, *J. Geophys. Res., 96*, 2363–2374, 1991.

Woods, M. T., J. J. Leveque, E. A. Okal, and M. Cara, Two-station measurements of Rayleigh wave group velocity along the Hawai'ian Swell, *Geophys. Res. Lett, 18*, 105–108, 1991.

Wysession, M. E., E. A. Okal, and K. L. Miller, Intraplate seismicity of the Pacific basin, 1913–1988, *Pure Appl. Geophys., 135*, 261–359, 1991.

D. H. Abbott, Lamont-Doherty Geological Observatory, Columbia University, Palisades, NY 10964.

C. A. Stein, Department of Geological Sciences, University of Illinois at Chicago, Box 4348, m/c 186, Chicago, IL 60680.

(Received July 16, 1990;
revised March 5, 1991;
accepted March 11, 1991.)

JOURNAL OF GEOPHYSICAL RESEARCH, VOL. 96, NO. B10, PAGES 16,113–16,129, SEPTEMBER 10, 1991

Structural Development of Sumisu Rift, Izu-Bonin Arc

BRIAN TAYLOR, ADAM KLAUS[1], GLENN R. BROWN [2], AND GREGORY F. MOORE

School of Ocean and Earth Science and Technology, University of Hawaii, Honolulu

YUKINOBU OKAMURA AND FUMITOSHI MURAKAMI

Geological Survey of Japan, Tsukuba, Japan

Geophysical swath mapping, multichannel seismic profiling, and ocean drilling data are used to document the structural evolution of Sumisu Rift and to analyze the pattern of strain resulting from extension of an intraoceanic island arc. The ~120-km-long, 30-50-km-wide Sumisu Rift is bounded to the north and south by structural and volcanic highs west of the Sumisu and Torishima calderas and longitudinally by curvilinear border fault zones with both convex and concave dip slopes. The zig-zag pattern of normal faults (average strikes 337° and 355°) indicates extension oriented 076° ± 10°, orthogonal to the volcanic arc. Three oblique transfer zones divide the rift along strike into four segments with different fault trends and uplift/subsidence patterns. Differential strain across the transfer zones is accommodated by interdigitating, rift-parallel faults and sometimes by cross-rift volcanism, rather than by strike- or oblique-slip faults. From estimates of extension (2-5 km), the age of the rift (~2 Ma), and the accelerating subsidence, we infer that Sumisu Rift is in the early synrift stage of back arc basin formation. Following an early sag phase, half graben formed with synthetically faulted, structural rollovers facing large-offset (2-2.5 km throw) border fault zones. In the three northern rift segments the largest faults are on the arc side and dip 60°-75°W, whereas in the southern segment they are on the west side and dip 25°-50°E. The present "full graben" stage is dominated by hanging wall antithetic faulting, basin widening by footwall collapse, and a concentration of subsidence in an inner rift. The hanging wall collapses, but not necessarily as a result of border fault propagation from adjacent rift segments. Whereas the border faults may penetrate the rheologically weak lithosphere ($T_e \approx 3$ km), many of the hanging wall and footwall collapse structures are detached only a few kilometers below the seafloor. Back arc volcanism, usually erupted along faults, occurs in the rift and along the protoremnant arc during both stages. Where drilled, the arc margin has been uplifted 1.1 ± 0.5 km concurrently with ~1.1 km of rift basin subsidence. Extremely high sedimentation rates, up to 6 m/kyr in the inner rift, have kept pace with synrift faulting, created a smooth basin floor, and resulted in sediment thicknesses that mimic the differential basin subsidence. A linear zone of weakness caused by the greater temperatures and crustal thickness along the arc volcanic line controls the initial locus of rifting. Rifts are better developed between the arc edifices; intrusions may be accommodating extensional strain adjacent to the arc volcanoes. No obvious correlations are observed between the rift structures and preexisting cross-arc trends.

INTRODUCTION AND PREVIOUS WORK

Although active rifting of intraoceanic island arcs was first proposed about 20 years ago [*Karig*, 1971; *Packham and Falvey*, 1971], the extensional mechanisms associated with stretching arc lithosphere remain poorly known. Investigations using swath-mapping sonar, seismic, sedimentologic, petrologic, and heat flow techniques have begun to reveal the surficial pattern of extensional strain and the nature and structural control of rift volcanism, sedimentation, and hydrothermal circulation, as well as the influence of the line of active arc volcanoes on rifting processes [*Sibuet et al.*, 1987; *Taylor et al.*, 1990*a*; *Wright et al.*, 1990].

One of the better studied active arc rift systems occurs south of Honshu, Japan (Figure 1). Bathymetric depressions west of the Izu-Bonin island arc were first observed by *Mogi* [1968] and *Hotta* [1970]. Investigations using reconnaissance seismic and bathymetric data [*Karig and Moore*, 1975; *Honza and Tamaki*, 1985] were sufficient to identify the presence and gross morphology of these fault-bounded basins and allowed the hypothesis that they were extensional in origin.

Sumisu Rift (Figure 1), in the Izu-Bonin island arc, has been the focus of recent investigations by the Hawaii Institute of Geophysics and the Geological Survey of Japan. Densely spaced single-channel seismic data have been collected to define shallow rift structures [*Murakami*, 1988; *Brown and Taylor*, 1988]. SeaMARC II side scan sonar imagery and bathymetry [*Brown and Taylor*, 1988; *Taylor et al.*, 1988*a*, *b*] and Sea Beam bathymetry [*Taylor et al.*, 1990*a*] investigations mapped the surficial distribution of faults, volcanoes, and sediments. Additional sedimentologic [*Nishimura and Murakami*, 1988], volcanic [*Fryer et al.*, 1990; *Hochstaedter et al.*, 1990], and heat flow [*Yamazaki*, 1988; *Taylor et al.*, 1990*a*] studies have begun to document the sediment and

[1]Now at Ocean Research Institute, University of Tokyo, Japan.
[2]Now at Department of Geology, University of Toronto, Canada.

Paper number 91JB01900.
0148-0227/91/91JB-01900$05.00

volcanic rock types, processes, and distribution, as well as the nature of hydrothermal circulation.

Extension of the Izu-Bonin arc has resulted in the formation of asymmetric rift basins located adjacent to the active volcanic arc that are 20-60 km wide by 20-120 km long. The rifts are bounded by normal fault zones and are separated along strike by structural highs and chains of submarine volcanoes [*Honza and Tamaki*, 1985; *Taylor et al.*, 1984; *Brown and Taylor*, 1988; *Murakami*, 1988]. Individual rift basins are segmented along strike by cross-trending transfer zones that link opposing border fault zones [*Taylor et al.*, 1990*a*; *Taylor and Shipboard Scientific Party*, 1990].

Structural control of volcanism is commonly observed in these back arc rift basins where extrusive volcanics (1) are concentrated along cross-trending accommodation zones, (2) are elongate parallel to rift faulting, (3) form clusters of aligned vents along rift faults, and (4) extend outward onto the rift margins [*Brown and Taylor*, 1988; *Taylor et al.*, 1990*a*]. Within the rift basins, the presence of geochemically "back arc basin basalts" indicates that a magma source little influenced by arc components is present even at the earliest stages of arc rifting [*Fryer et al.*, 1990; *Hochstaedter et al.*, 1990; *Gill et al.*, 1991]. Active back arc rift basin hydrothermal circulation, evidenced by high and variable heat flow, may occur along rift faults and/or through permeable rift basin sediments [*Yamazaki*, 1988; *Taylor et al.*, 1990*a*].

Sediment input to the Izu-Bonin rift basins is dominated by volcaniclastic sediments, erupted from the adjacent volcanic arc, that are distributed throughout the region by eruptive events and redeposited in the rift basin by submarine mass flows [*Nishimura and Murakami*, 1988; *Brown and Taylor*, 1988]. Sediment deposition is modulated by variable subsidence of rift blocks, as well as by volcanic ridges that can influence sediment transport pathways.

Prior to the collection of multichannel seismic (MCS) data (*Taylor et al.* [1990*b*] and this study) and Ocean Drilling Program (ODP) leg 126 drilling of Sumisu Rift [*Taylor et al.*, 1990*c*], little was known about (1) the nature and structure of the prerift section beneath the rift basin, (2) the age of initiation of rift formation, (3) the facies and processes of synrift sedimentary fill, and (4) the rate of synrift sedimentation and basin subsidence.

In June-August 1987 as part of the ODP leg 126 site survey, we conducted a 96-channel seismic survey of the Sumisu Rift (Figure 2). Data acquisition and processing parameters are described by *Taylor et al.* [1990b]. We sought to constrain the mechanisms of rifting arc lithosphere by determining the deep crustal structure of this back arc rift. In this paper we present the results of the MCS survey and the detailed tectonic interpretation permitted by integrating this data (Figures 3 and 4) with leg 126 ocean drilling data, as well as previously collected seismic and swath mapping data (Figure 5).

TECTONIC SETTING

Subduction of the Pacific plate beneath the west Philippine Sea plate (Figure 1) began in the early Eocene [*Karig*, 1975] and by the end of the early Oligocene an intraoceanic volcanic arc massif had formed a 200-km-wide forearc [*Taylor and Shipboard Scientific Party*, 1990] composed of tholeiitic and boninitic volcanic rocks [*Natland and Tarney*, 1981]. The Izu-Bonin forearc basin is a product of mid-Oligocene rifting of this Eocene and early Oligocene arc massif [*Leg 126 Shipboard Scientific Party*, 1989; *Taylor et al.*, 1990*c*]. Rifting of the Izu-Bonin-Mariana island arc, followed by late Oligocene to early Miocene seafloor spreading in the Shikoku (25-15 Ma [*Chamot-Rooke*, 1989]) and Parece Vela basins (30-17 Ma [*Mrozowski and Hayes*, 1979]), formed back arc basins that separated the remnant arc (Palau-Kyushu Ridge) from the Izu-Bonin-Mariana Arc.

A second stage of Mariana arc rifting and latest Miocene (6 Ma) to Recent back arc spreading in the Mariana Trough has separated the Mariana arc from its second remnant arc, the west Mariana Ridge [*Hussong and Uyeda*, 1982]. In contrast, the Izu-Bonin arc is still in the second stage of back arc rift formation; the rifts are forming along most of its length adjacent to the active volcanic arc (Figure 1) [*Karig and Moore*, 1975; *Honza and Tamaki*, 1985; *Tamaki*, 1985]. These back arc rift basins are semicontinuous along strike, segmented by structural highs and chains of submarine volcanoes, and have not yet developed into the back arc spreading stage [*Taylor et al.*, 1984, 1990*a*, *b*].

SUMISU RIFT ARCHITECTURE

Sumisu Rift is located west of the frontal arc Sumisu, South Sumisu, and Torishima, submarine calderas (Figures 1 and 2). It extends 120 km from approximately 30.5° to 31.5°N and is 30-50 km wide. It is the longest of the Izu-Bonin rifts; some structural depressions are nearly equidimensional and only 20-30 km across (Figure 1). Sumisu Rift is bounded to the north and south by structural and volcanic highs west of Sumisu and Torishima calderas and longitudinally by large-offset normal fault zones that are 2-10 km wide (Figures 3 and 6). Two to three faults accommodate the majority of the ~1 km of surficial throw, and >1 km of additional throw beneath the sedimented rift basin floor, across the border faults. The MCS data show that these faults dip steeply (60°-75°), except in the southwest where dips are 25°-50°. Previous interpretations based on bathymetry and unmigrated single-channel seismic data significantly underestimated the fault dips (20°-50° [*Taylor et al.*, 1990*a*]).

Sumisu Rift has two sediment depocenters that are separated at a sill depth of 2080 m by an en echelon ridge of extrusive volcanics (Figures 2, 4, and 6). The North (Kita) Sumisu Basin (NSB) and South (Minami) Sumisu Basin (SSB) exhibit fairly smooth sedimented basin floors that are 2100-2150 m and 2200-2275 m deep, respectively, with gently sloping rises up to 2000 m depth in the north and south.

The border, and other rift-parallel, faults delineate four structural provinces across strike from east to west (Figures 3 and 6): (1) the arc margin; (2) the inner rift, the locus of maximum subsidence and sediment thickness; (3) the outer rift; and (4) the protoremnant arc. Oblique transfer zones also divide Sumisu Rift along strike into four segments with differing fault trends and uplift/subsidence patterns (Figures 6 and 7). The shallowest rift segment is in the north, adjacent Sumisu caldera, where faults have an average trend of 336° (region D, Figure 6). An east trending transfer zone at 31°16'-20'N separates this area from the north central segment, where fault strikes average 355° (regions C and E, Figure 6) and the inner rift basement is about 1 km deeper (Figures 2 and 4). In the south central segment, south of the NE trending central transfer zone marked by volcanics, fault strikes

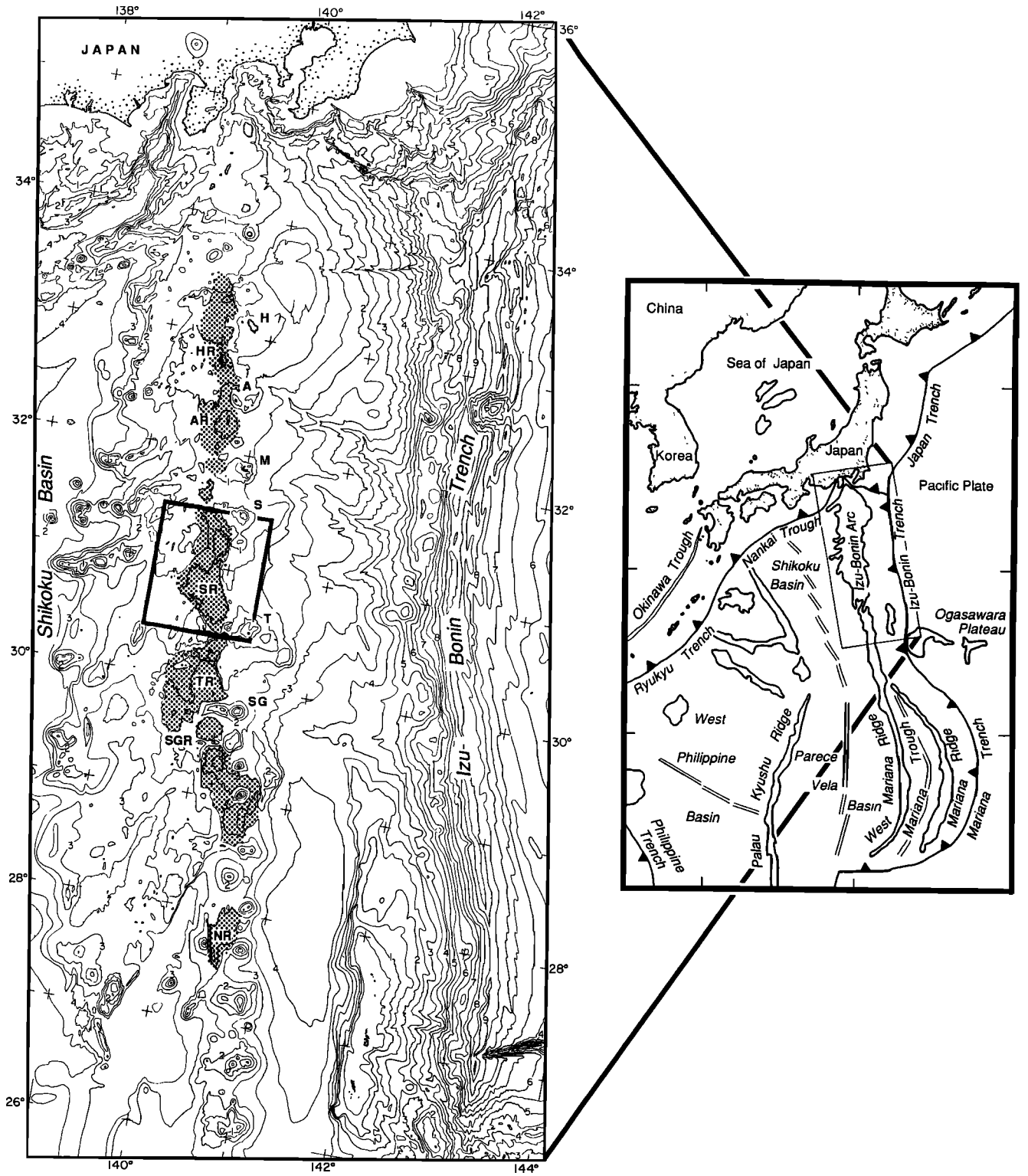

Fig. 1. (Right) Generalized tectonic map of the western Pacific. The box outlines the area of the Izu-Bonin arc-trench system shown on the left. (Left) Bathymetric map of the Izu-Bonin arc-trench system [*Taylor et al.*, 1990*b*]. Arc rifts (HR, Hachijo Rift; AR, Aoga Shima Rift; SR, Sumisu Rift; TR, Torishima Rift; SGR, Sofu Gan Rift; NR, Nishinoshima Rift) are stippled and the nearby island arc volcanos are labeled (H, Hachijo Jima; A, Aoga Shima; M, Myojin Sho; S, Sumisu Jima; T, Torishima; SG, Sofu Gan). Box locates Sumisu Rift study area shown in Figure 2. The contour interval is 500 m, labeled in kilometers.

average 339° (regions B and F, Figure 6). This is the widest segment of Sumisu Rift and differs from the two northern segments in having a second half graben in the outer rift that has subsided to nearly the same level as the inner rift. The three northern rift segments have larger-throw border fault zones on the east than on the west (Figures 3 and 6). In contrast, the southern segment, south of an east trending transfer zone at 30°40'-43'N and adjacent to Torishima caldera

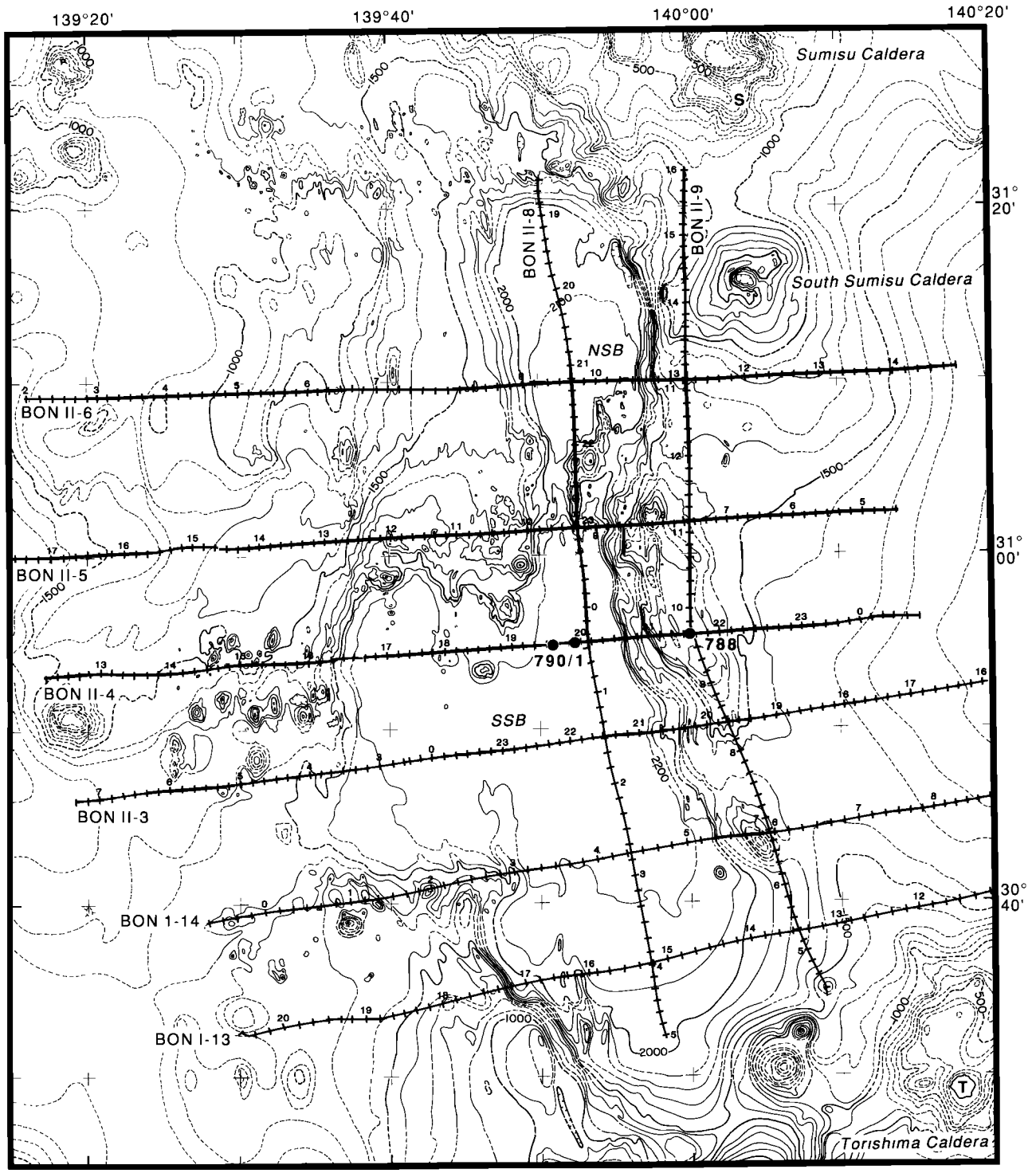

Fig. 2. Bathymetric map of Sumisu Rift showing the location of multichannel seismic profiles (Figures 3 and 4; R/V *Fred Moore* 3505/07). The bathymetry is based on SeaMARC II data [*Taylor et al.*, 1988*b*] augmented by ship track data and bathymetric charts 6526 and 6527 of the Hydrographic Department of the Japanese Maritime Safety Agency. Tick marks along the ships tracks are at ten minute intervals, labeled in hours. The contour interval is 100 m, except for the 2250-m contour, which is dotted. Dashed contours are either interpolated or not based on SeaMARC II data. The island arc volcanoes Sumisu Jima and Torishima are labeled S and T. NSB, North Sumisu Basin; SSB, South Sumisu Basin. Open circles locate ODP sites 788, 790, and 791 on line 4.

and Kotori submarine volcano, has a large-offset border fault zone on the west and a gentle rollover out of the basin on the east. The faults in this segment strike 333° on average (region A, Figure 6). The footwalls of the border faults, particularly those of the southern two rift segments, are uplifted and rotated away from the rift axis.

ARC MARGIN

The active frontal arc volcanos, Sumisu Jima and Torishima, lie on the southern rim of much larger submarine

calderas (Figure 2). South Sumisu caldera, 20 km south of Sumisu Jima, has a horseshoe-shaped rim 300-400 m below sea level (bsl). Kotori submarine volcano, west of Torishima, lies at the southern end of Sumisu Rift on the basement high separating Sumisu and Torishima rifts (Figure 2). The arc margin is bounded on the west by large-offset border fault zones north of 30°41'N and by a monocline, cut by small-offset normal faults, farther south (Figures 2, 3, 6, and 7). To the east, the arc margin gently slopes into the forearc basin. Its undulations along strike are a function of the degree of footwall uplift (profile 9, Figure 4).

South of 30°41'N, the arc margin forms the monoclinal side of a half graben and is characterized by three principle seismic units (profile 13, Figure 3). The middle unit has high-amplitude, conformable, and mainly continuous reflectors up to 1 km (0.9 s) thick. To the west this unit is pervasively faulted down into the rift basin. This unit unconformably overlies a sequence characterized by more chaotic (faulted) and larger amplitude reflectors; it is erosionally truncated and draped by ~200-250 m (0.35 s) of more transparent and discontinuous reflections. The uppermost seismic unit is continuous, with only minor normal fault offsets, with the uppermost rift basin sequence. It laps onto the arc margin rift flank uplift to the north (profile 9, Figure 4).

North of 30°41'N, the uplifted footwall of the border faults forms an arc margin typically 1 km above the sedimented rift basin floor. Three types of rift flank uplifts are observed: (1) large rotated fault blocks bounded by west-dipping faults (profiles 5 and 14, Figure 3); (2) broad, little tilted uplifts cut by closer-spaced normal faults dipping both to the east and west (profiles 3 and 4, Figure 3); and (3) relatively flat uplifts (profile 6, Figure 3).

The first type occurs in two regions of the arc margin, 30°41'-46'N (seismic profile 14, Figure 3) and 31°00'-05'N (profile 5, Figure 3). These rift flank uplifts have two to three fault blocks that dip east at up to 16°, between 60° and 70° west dipping normal faults spaced about 3 km apart.

Between these two regions of tilted blocks, the arc margin is cut by active, closely spaced, normal faults that dip 65°-75° to both the east and west and result in only minor block tilting (profiles 3 and 4, Figure 3; profile 9, Figure 4). In this region, the faults exhibit an anastomozing and relay pattern (Figure 6; see also Figure 7 of *Taylor et al.* [1990*a*]). Although this region is cut by numerous small-offset (20-150 m) faults, two to three large-offset (300-400 m) faults account for the majority of the total throw down into the rift basin.

The north central rift segment is bounded by a narrow border fault zone composed of two 400-500-m-offset fault zones (Figures 3 and 5). The arc margin appears quite flat on profile 6 (Figure 3), in part because of the volcaniclastic apron from South Sumisu caldera just to the north and also because of the intrusion near 1400 hours.

The centers of the footwall uplifts exhibit continuous, parallel, high-amplitude reflections similar to those on the ramping arc margin south of 30°41'N (profiles 3 and 4, Figure 3; profile 9, Figure 4). The reflection sequences within the steeper tilted blocks are less well imaged (profiles 5, 9, and 14). All reflections become increasingly disrupted in the border fault zone by the pervasive faulting and possibly by volcanic intrusions similar to those observed during submersible investigations along the eastern rift wall [*Taylor et al.*, 1990*a*]. Well-stratified upper forearc sequences lap onto the eastern side of the footwall uplifts (Figure 3).

ODP leg 126 site 788 [*Taylor et al.*, 1990*c*] drilled 374 m into the arc margin at the intersection of MCS profiles 4 and 9 and recovered dominantly Pliocene pumiceous gravels and conglomerates (Figures 2 and 8). An unconformity (30 m below seafloor (bsf)) dates the rift flank uplift and presumably the onset of rifting as >275 ka and <2.35 Ma. The distinctive stratified prerift volcaniclastics are observed on MCS records to >1200 mbsf. Benthic foraminifers from ~270 mbsf indicate water depths of 2-3 km at ~4 Ma, which constrains the amount of rift flank uplift at this 1113-mbsl site to 0.6-1.6 km [*Kaiho*, 1991].

Except for the region where the central transfer zone and NE volcanic trend intersect the arc margin (31°05'N to 31°12'N; Figure 6), there is a striking lack of evidence of extrusive volcanism along the volcanic front between the major arc calderas.

PROTOREMNANT ARC

The rift basin is bounded to the west by the protoremnant arc, which rises 300-1500 m above the sedimented basin floor. It includes a large rotated block in the south and a multiply-faulted high in the north. The margin is lowest (1700-2000 mbsl) between 30°40' and 48'N, adjacent to the wide south central rift segment. The margin is characterized by a reflective sequence of presumed prerift volcaniclastic sediments beneath a thin Quaternary cover (Figure 3).

The normal-faulted rift flank uplift south of 30°42'N exhibits rotated and tilted fault blocks (Figure 9) similar in form to those observed in the Bay of Biscay and on other passive margins [*de Charpal et al.*, 1978; *Montadert et al.*, 1979]. The MCS data image fault-plane reflections bounding some of these well-stratified blocks. The faults have low near-surface dips (25°-50°) and some flatten with depth to ~25°. They do not appear to pass through a region of horizontal reflections at ~4.5 s (~2 km bsf, Figure 9), which may be a zone of detachment. Faults bounding rotated blocks beneath the rift basin are detached at even shallower levels. Small-offset west dipping normal faults occur to the west of the border faults (Figure 9).

North of 30°48'N, the protoremnant arc margin is flat to gently west dipping (Figures 3 and 7). The deeper stratified sections are cut by numerous, variably but often west dipping, small-offset normal faults, whereas the surface-breaking faults dominantly dip east (Figures 3 and 10).

Volcanism on the protoremnant arc margin is concentrated along extensions of the transfer zones and in the north (Figure 6). Individual flows and vents are rift elongate and often are aligned either along or parallel to faults. Regions interpreted as extrusive volcanism based on side scan sonar imagery have incoherent reflections on MCS sections [e.g., Figure 9).

RIFT BASIN

The locus of maximum sediment thickness (>1 km) and basin subsidence occurs along an inner rift adjacent to the arc margin (Figures 3 and 7). Typical basin floor depths along the inner rift change from 1600 mbsl in the northern segment to 2100 mbsl in the NSB and 2250 mbsl in the SSB (Figure 2). In the two northern rift segments, a multiply-faulted but less subsided (1300-1900 mbsl) and thinly sedimented outer rift lies between the inner rift and the border faults to the west (profiles 5 and 6, Figure 3). In the south central rift segment, the outer rift has subsided below 2200 mbsl. Below the

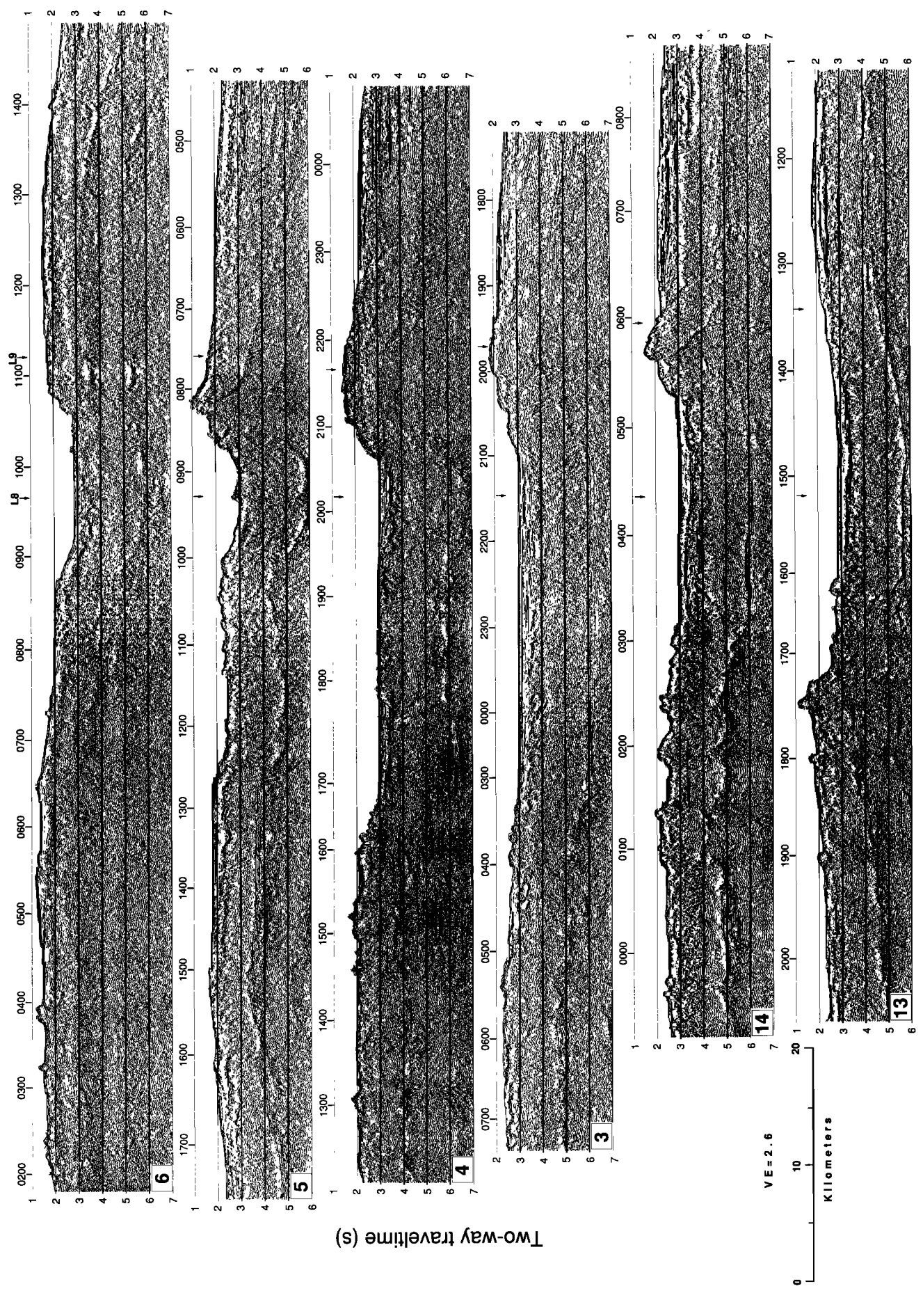

Fig. 3a. Cross-rift, migrated, 96-channel, seismic profiles. Large-scale versions of these profiles are published by *Taylor et al.* [1990*b*].

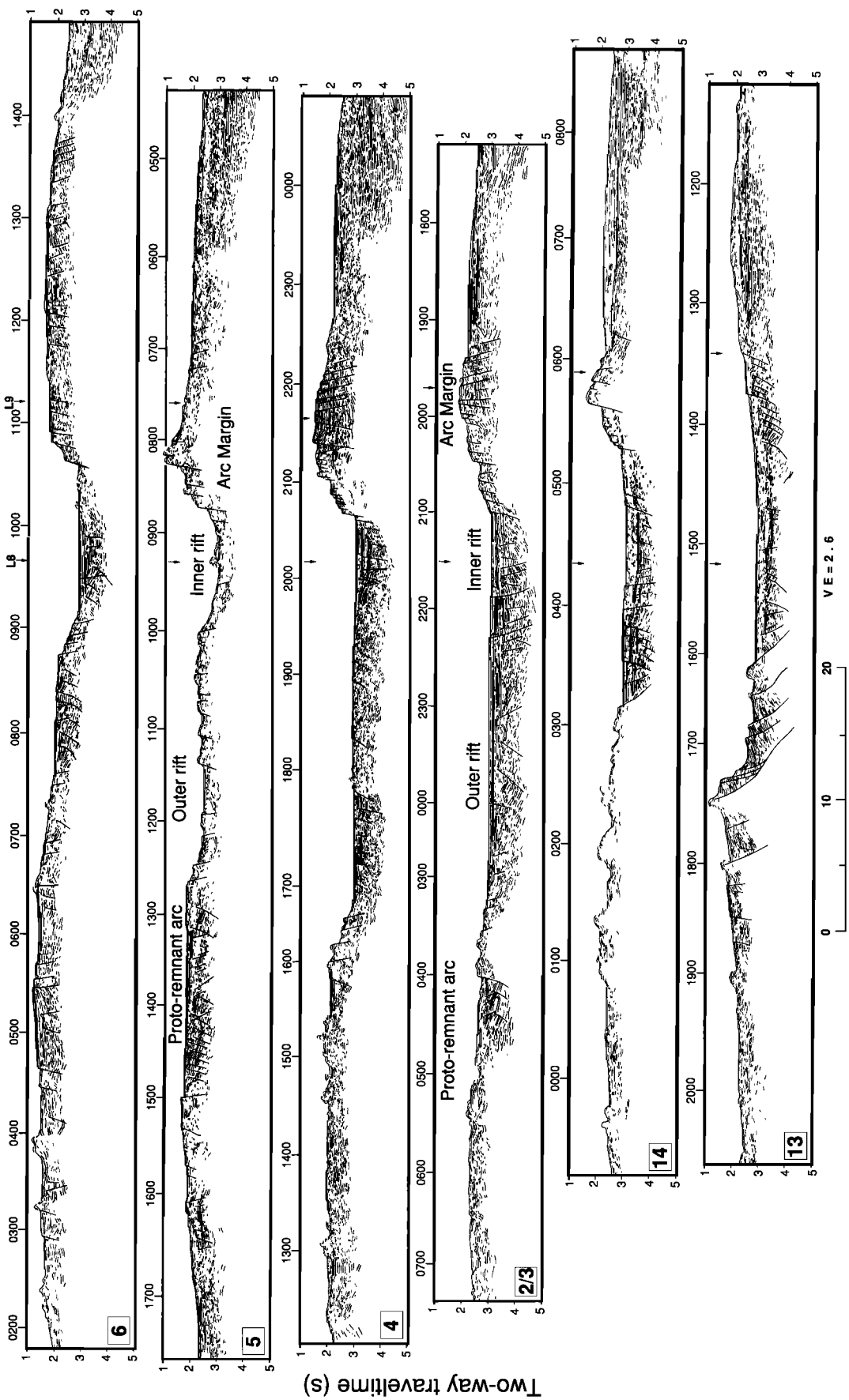

Fig. 3b. Line drawings of multichannel seismic profiles. The location of profiles is shown in Figure 2.

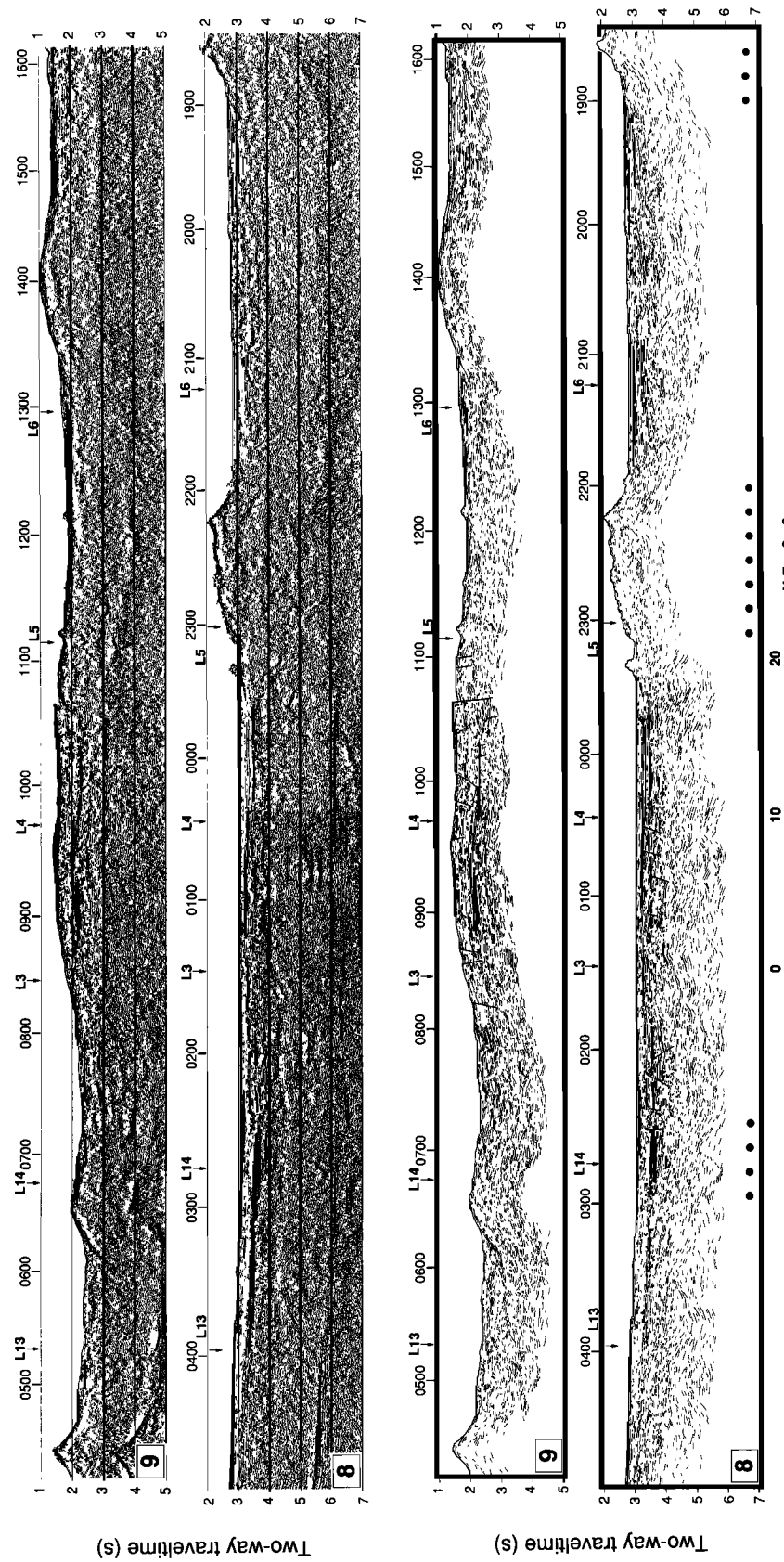

Fig. 4. Longitudinal, migrated, 96-channel, seismic profiles (top) and line drawings of same (bottom). The location of profiles is shown in Figure 2. The dots at the base of profile 8 show where transfer zones intersect the profile.

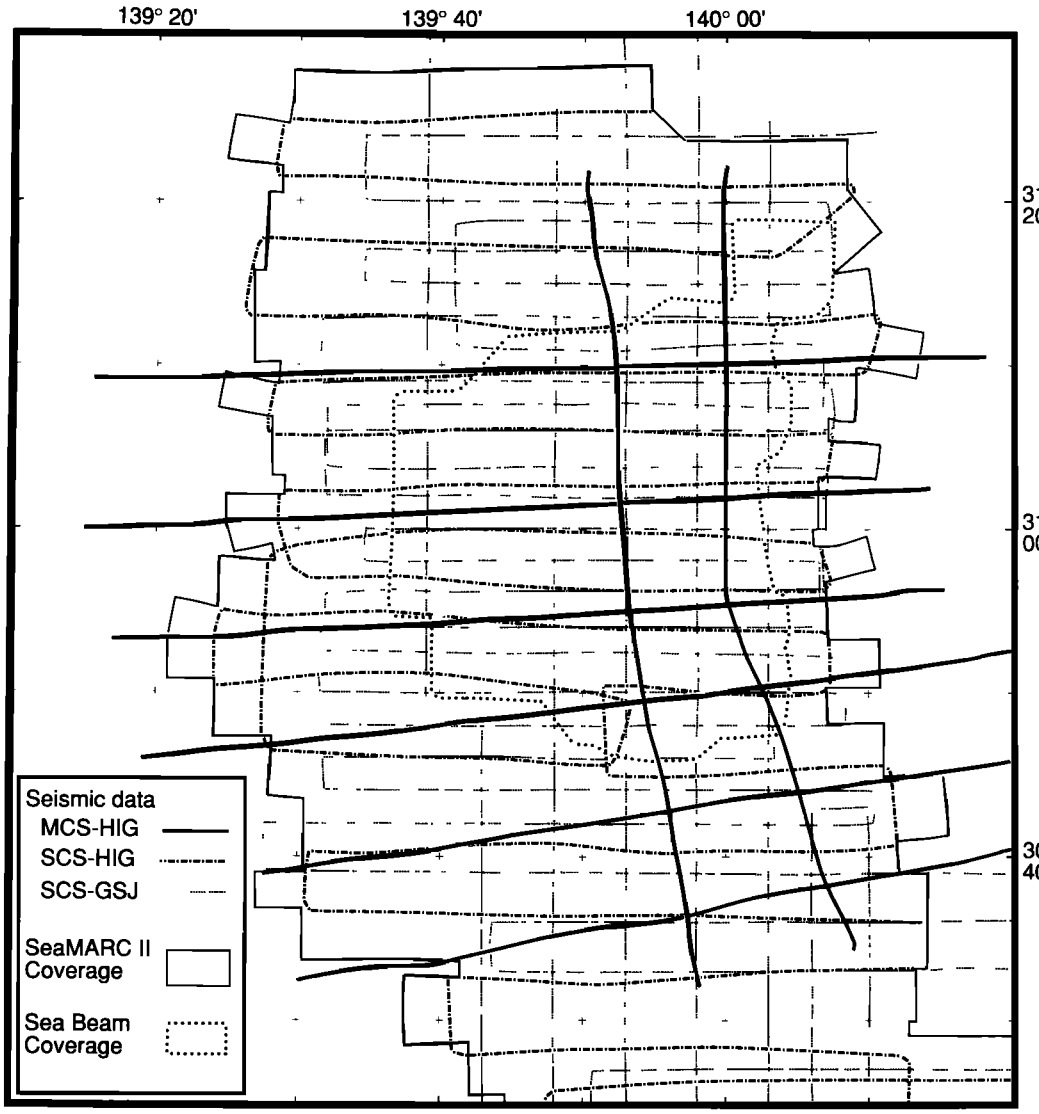

Fig. 5. Data location map: multichannel (R/V *Fred Moore*, FM3505 and FM3507: solid lines) and single-channel seismic profiles (R/V *Kana Keoki* cruise KK840428 leg 02: dash-dot; R/V *Hakurei Maru* cruises in 1979, 1980, 1984, and 1985: dotted line), SeaMARC II side scan sonar imagery and bathymetry (*Taylor et al.* [1988*a*, *b*], solid outline), and Sea Beam bathymetry (*Taylor et al.* [1990*a*], dotted outline].

sediment plain there is a half graben separated from the inner rift by a structural high (profiles 3 and 4, Figure 3).

ODP sites 790 and 791 were drilled on the western margin of the inner-rift half graben in the SSB (Figure 8). Both sites bottomed in vesicular basalt interpreted as a synrift deep submarine eruption [*Gill et al.*, 1990; *Taylor et al.*, 1990*c*], which was underlain at site 791 by tuffs interpreted as a sequence of island arc pyroclastic flows. Definite prerift sequences were not penetrated. At site 791, the volcanic horizons correspond to a high-amplitude reflector that is difficult to trace for even a kilometer away from the drill site. The thick, well-stratified prerift sequences imaged on the arc margin are obscured beneath the rift basin.

Although the lithostratigraphies are similar at both basin sites, differential subsidence has resulted in a thickening of basin fill toward the eastern margin of the half graben; site 791 recovered an expanded section from that at site 790 (Figure 8). Nannofossil-rich clays and claystones (unit II) overlie the volcanics. The oldest sediments are ~1.1 Ma [*Taylor et al.*, 1990*c*]. Correlation of unit II throughout the rift basin is difficult because of the lack of strong continuous reflectors, complex faulting, and local deposition in small fault-block-bounded depocenters.

Unit II is overlain by thick pumiceous and vitric gravels, sands, and silts (unit I). The seismic character of unit I is highly variable throughout the SSB, ranging from transparent or discontinuous to high-amplitude, parallel reflections. In addition, there is a gradual transition from discontinuous, low-amplitude reflections in the southern SSB toward the north where higher-amplitude, continuous reflections are observed (profile 8, Figure 4).

Sedimentation rates (not corrected for compaction) increase from 90 and 300 mm/kyr between 0.5 and 1 Ma to 150 and 800 mm/kyr from 0.1 to 0.4 Ma to 1.5 and 4 m/kyr since 0.1 Ma (unit I) at sites 790 and 791, respectively (Figure 8) [*Firth and Isiminger-Kelso*, 1991; *Nishimura et al.*, 1991]. Benthic

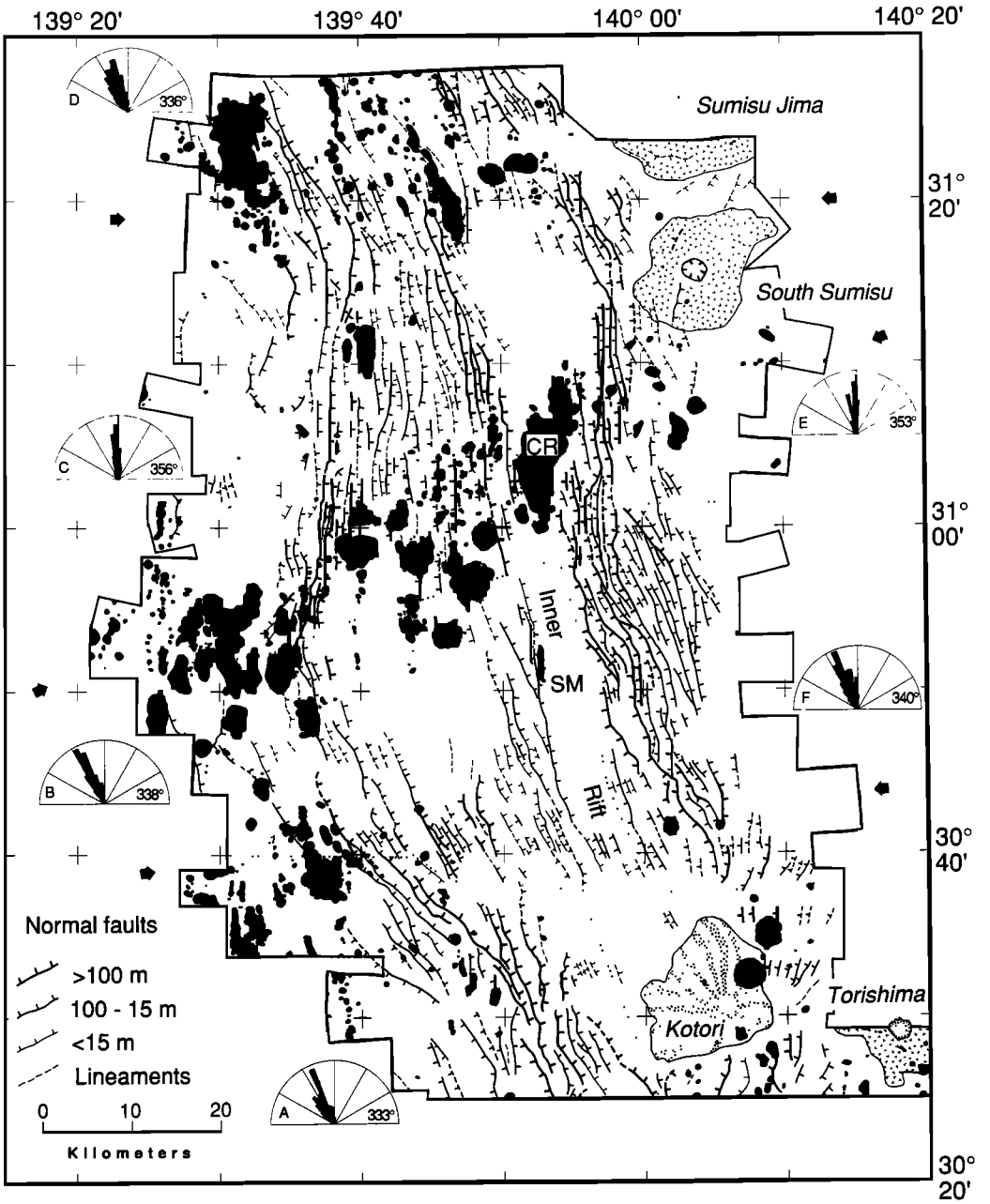

Fig. 6. Structural map of the Sumisu Rift. The location of data used to constrain interpretations is shown in Figure 5. Extrusive volcanic rocks are shown as solid areas [from *Taylor et al.*, 1990*a*]. The active arc calderas are Sumisu, South Sumisu, and Torishima; Kotori is a pyroclastic cone. CR and SM stand for Central Ridge and Shadow Mountain. Polar histograms (cumulative fault length versus azimuth) and average fault strike are shown for various regions outlined by dots. Arrows point to the three transfer zones.

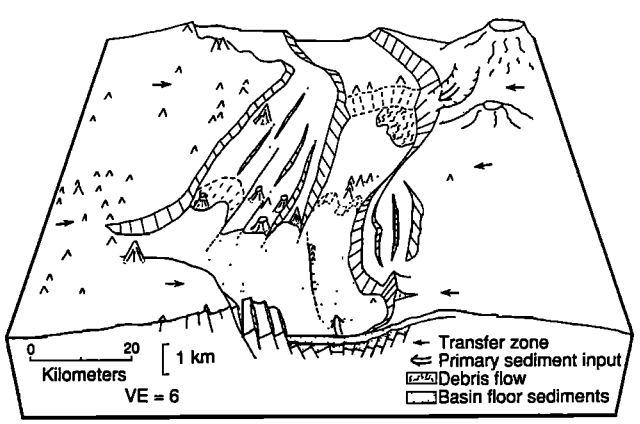

Fig. 7. Perspective block diagram of Sumisu Rift, viewed from an elevation of 65°, looking 345°, and with a vertical exaggeration of 6.

foraminifers indicate that all the sediments were deposited in similar water depths to the present [*Kaiho*, 1991]; we infer that sedimentation is approximately matching subsidence.

Syndepositional faulting and subsidence has created reflector sequences that exhibit progressive tilting with depth and often onlap earlier synrift reflectors or prerift blocks. For example, the bedding is subhorizontal at site 790, but at site 791 the dip gradually increases to 15°-20° near 600 mbsf and 45° by 800 mbsf [*Taylor et al.*, 1990*c*]. *Taylor* [1991] infers that the west dipping normal fault just east of site 791 is

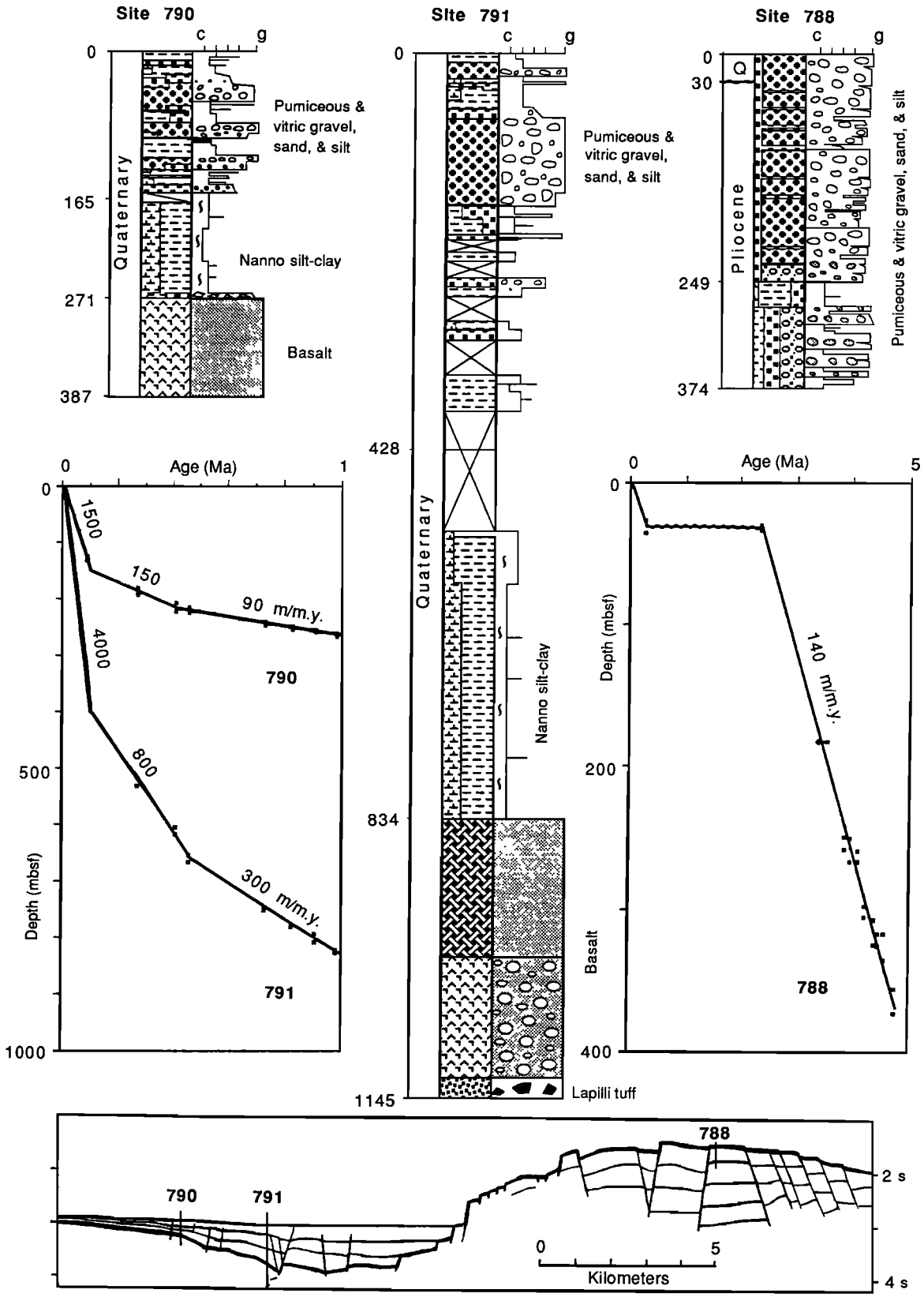

Fig. 8. Stratigraphy of ODP leg 126 sites 788, 790, and 791 including lithologic columns, age versus depth diagrams, and a simplified cross section [*Taylor et al.*, 1990*c*]. The age versus depth diagrams are modified using data from *Firth and Isiminger-Kelso* [1991] and *Nishimura et al.* [1991]. The average sedimentation rate for each age-depth segment is labeled in meters per million years.

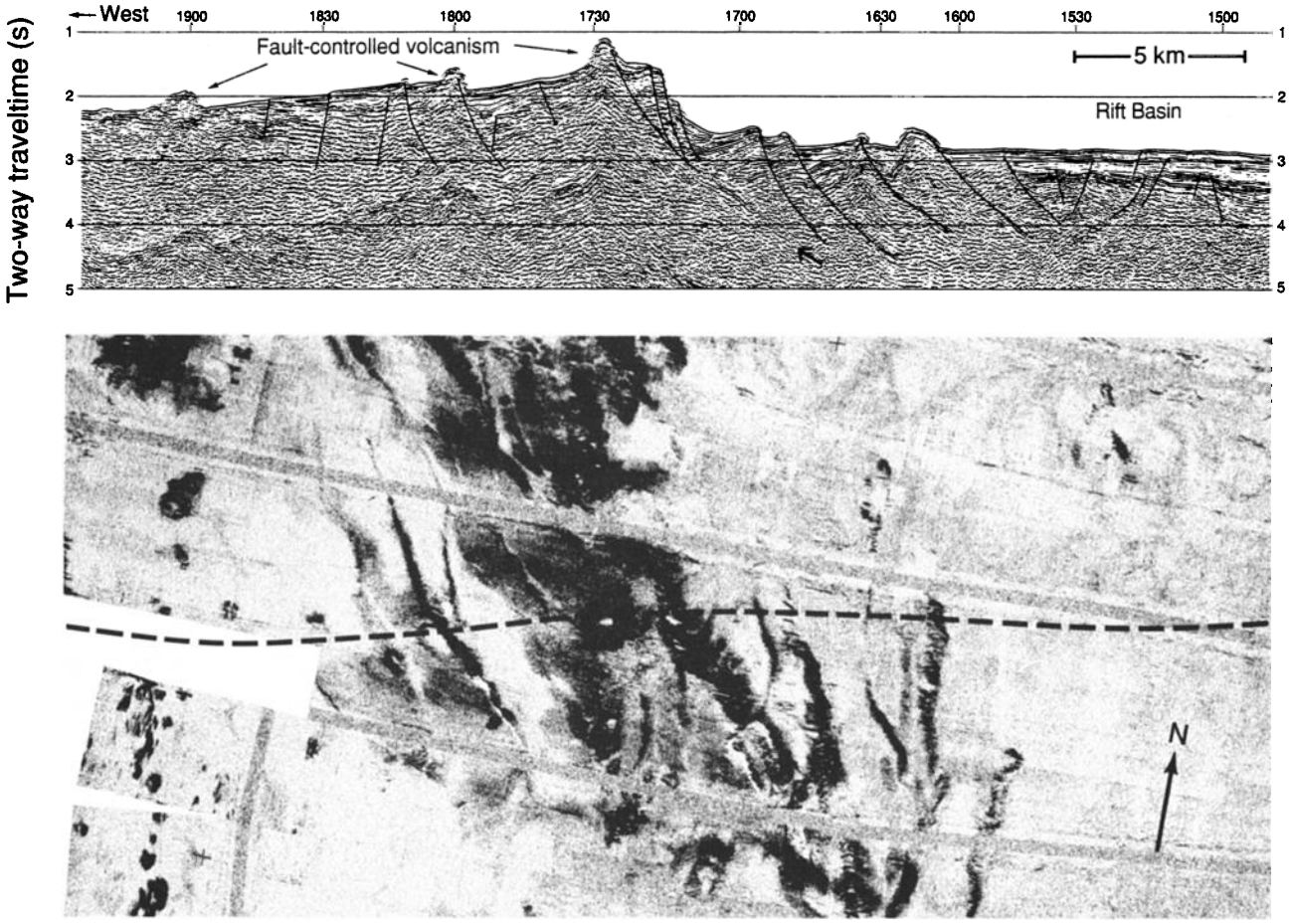

Fig. 9. (top) Multichannel seismic profile 13 and (bottom) SeaMARC II side scan sonar imagery across the southwestern border fault zone. The dashed line on the side scan data locates the seismic profile. The side scan data display strong acoustic returns (e.g., fault scarps or extrusive volcanics) as dark and weak acoustic returns (e.g., sediments) as light. In addition to routine processing (through migration) the seismic profile has been corrected for the effects of dip using prestack dip moveout and is displayed at a seafloor vertical exaggeration of 2.6. The border fault dips range from 25°-50°, with apparent dips as low as 20°. Fault plane reflections are observed from several of the shallow-dip faults, as pointed to by the thick arrow.

listric. Figure 11 shows an example where the variably tilted and faulted deeper horizons are cut by active east dipping faults, thereby reversing the direction of tilting of the western two thirds of the section. The two to three east dipping faults that bound the western side of the inner rift in the SSB are extremely fast slipping, as they offset, with a cumulative throw of 55-70 m, the rapidly sedimented (4 m/kyr) basin floor.

The pattern of sediment accumulation, basin subsidence and volcanic intrusions since 67 ka in SSB is shown in Figure 12. This isopach map was constructed by correlating our MCS data with recovered core material from ODP sites 790 and 791 using shipboard physical properties velocities to convert depths (mbsf) into two-way travel times. Next, a distinctive reflector that corresponds to 67 ka was mapped throughout the SSB. Correlation of deeper reflectors throughout the basin is problematic because of pervasive faulting. Although the prerift sequences observed on the rift margins presumably underlie the rift basin, their similar facies to the synrift fill (Figure 8), together with overprinting by faulting and volcanism (Figure 6), prevents clear distinction of the two sequences and the preparation of depth to "basement" (prerift) maps. In the late Quaternary, the maximum sediment thickness, and basin subsidence, is located within the inner rift where the 67 ka isopach is more than 0.5 s of two-way travel time (~400 m). This implies that sedimentation rates within the inner rift are as high as 6 m/kyr. Another rift-elongate, fault-controlled depocenter is observed in the outer rift and is outlined by the 0.2-s isopach (Figure 12).

Synrift sediments are disrupted by volcanic intrusions that occur along rift faults and rift parallel trends (Figures 6 and 12). Shadow Mountain, a 50 to 75-m-high, 3-km-long fissure ridge (near 30°51'N, 139°53'E) was emplaced along the fault that bounds the western side of the inner rift. A linear series of small intrusions that penetrate the seafloor, near 139°40' E between 30°50'N and 30°57'N, parallel the local rift fault trends (Figures 6 and 12). The synrift volcanics are dominantly basalts of back-arc basin composition, little influenced by arc components [*Fryer et al.*, 1990; *Gill et al.*, 1990, 1991; *Hochstaedter et al.*, 1990].

PRERIFT STRUCTURES

Unlike continents, where cratons or thrust-thickened crust can provide complex structural anisotropy, island arcs may

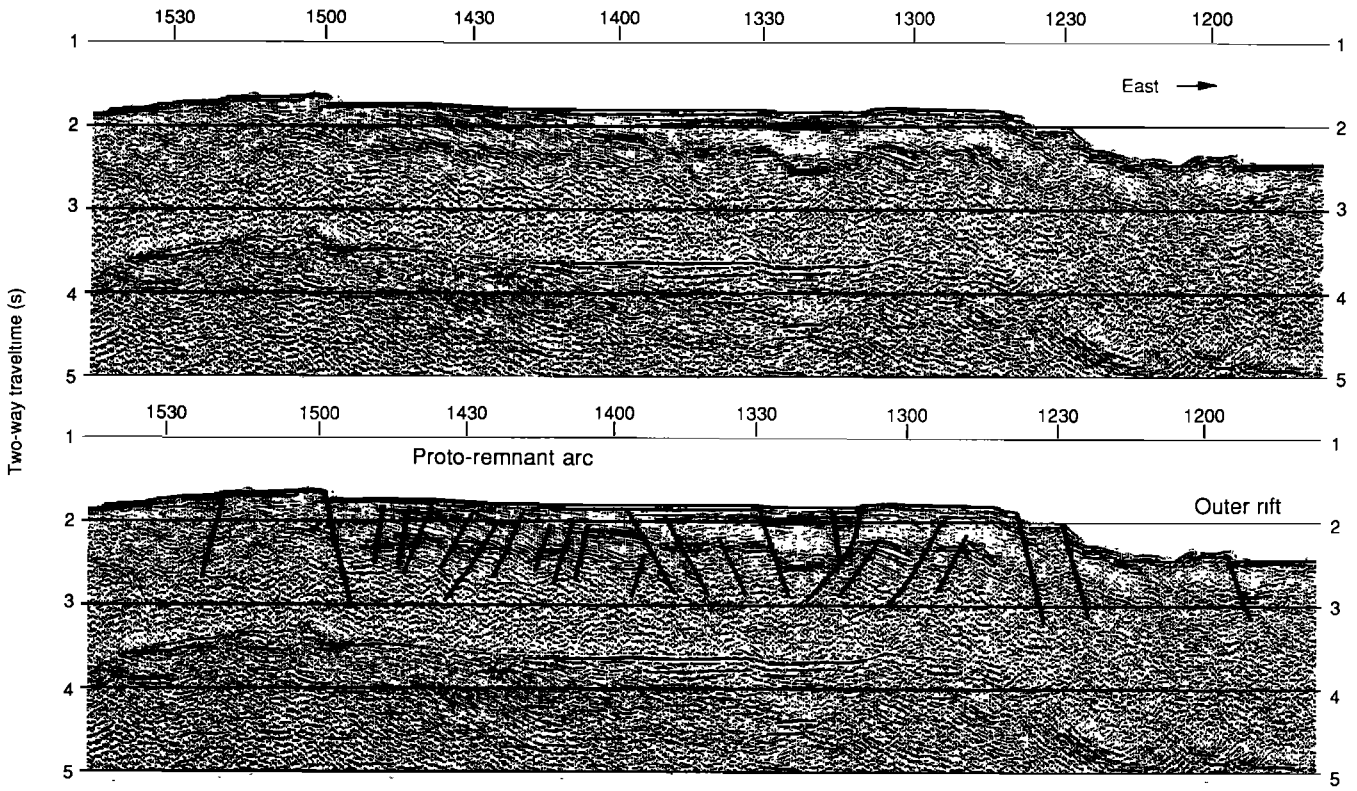

Fig. 10. A section of seismic profile 5 (VE=2.6) illustrating fault superposition on the protoremnant arc margin. The majority of the later faults dip east whereas many of the early faults dip west, synthetic to the border faults bounding the rift to the east (see Figure 3).

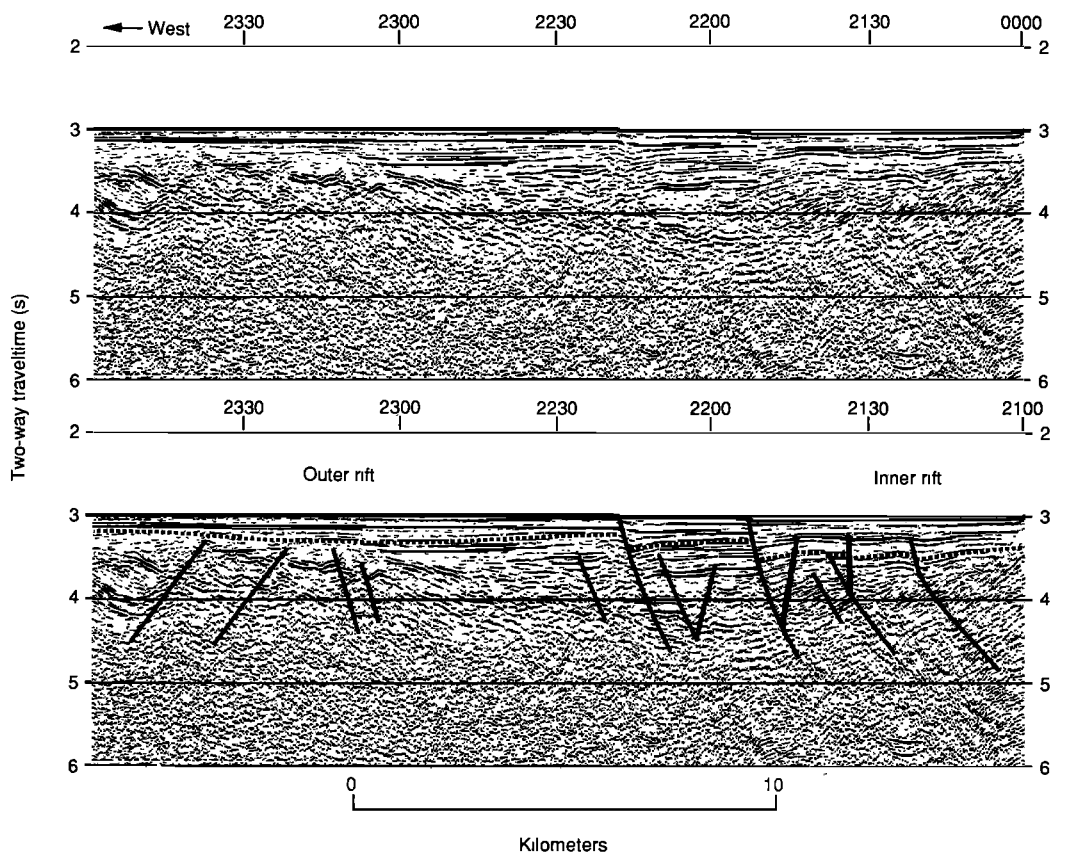

Fig. 11. Section of seismic profile 3 (VE=2.6) in the rift basin illustrating the reversal of stratigraphic tilting by the late stage, inner-rift-bounding faults. The thin dotted line locates the reflector isopached in Figure 12.

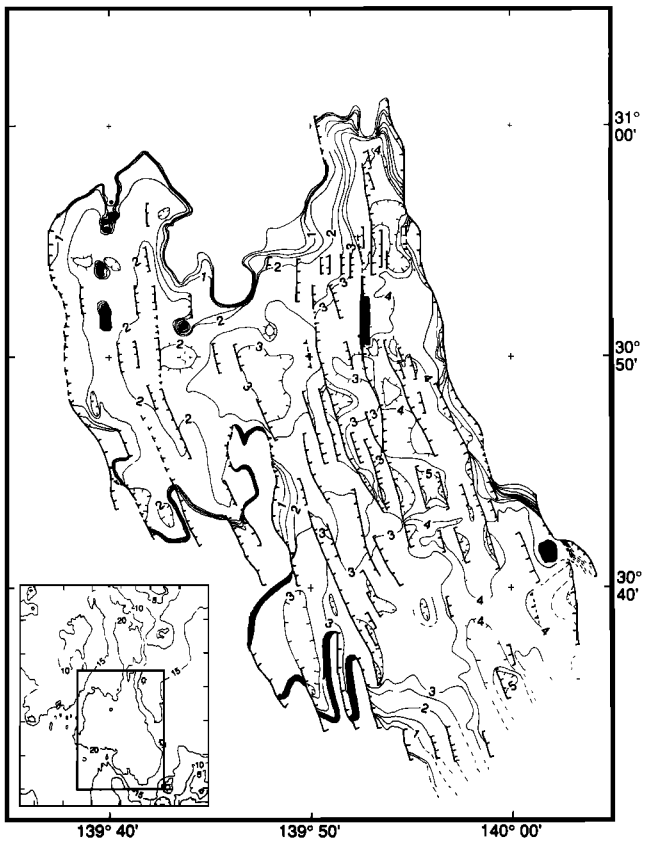

Fig. 12. South Sumisu Basin isopach map of a reflector (see Figure 11) corresponding to 67 ka. Contours are labelled in tenths of seconds of two-way travel time. The contour interval is 0.05 s; volcanic extrusions are solid. The stipple pattern identifies regions with sediment thicknesses >0.35 s, primarily within the inner rift. The box within the inset bathymetric map shows the location of the isopach map.

have a more two-dimensional rheology. As in other arcs, elevated heat flow and thicker crust are associated with the Izu-Bonin volcanic line [*Hotta*, 1970; *Honza and Tamaki*, 1985]. Two-ship refraction profiles suggest that the depth to Moho is about 20 km beneath the volcanic front at 28°-32°N, compared to 15 km beneath the outer forearc high and 12 km beneath the Shikoku Basin [*Hotta*, 1970; *Honza and Tamaki*, 1985; *Japanese DELP Research Group on Back-arc Basins*, 1989]. Thicker crust and higher heat flow have been shown to weaken the lithosphere [*Vink et al.*, 1984; *Steckler and ten Brink*, 1986; *Kuznir and Park*, 1987]. We therefore infer that the line of arc volcanoes creates a linear zone of lithospheric weakness that controls the location of rifting. This implies that rifting can occur on either side of the active arc, as is observed globally [*Taylor and Karner*, 1983]. In the Izu-Bonin arc, the majority of the rifts are back arc, but at 29°N one of the rifts is on the forearc side of the volcanic front (Figure 1).

The arguments above would suggest that arc rifting should initiate adjacent to the volcanoes. In fact, just the opposite is observed (Figure 1). For example, structural highs and volcanoes adjacent to Sumisu Jima, Torishima, and Sofu Gan bound the ends of the Sumisu and Torishima rifts. Likewise the rifts farther north narrow adjacent to Myojin Sho and Aoga Shima (Figure 1). The rifts are better developed between, rather than adjacent to, the arc volcanoes. We suggest that this may result from arc magmatism accommodating some of the extension, intrusions rather than faulting taking up the strain adjacent to the arc volcanoes. The large submarine shield volcano at 28.3°N may have suppressed or overprinted rift basin development between the Sofu Gan and Nishinoshima rifts (Figure 1).

As outlined previously, the Izu-Bonin arc was stretched in the Oligocene, prior to 25-15-Ma back arc spreading in the Shikoku Basin. There are major relict NNE and NNW trending half graben in the forearc and the back arc, many of which are still recognizable in the bathymetry (Figure 1). NE to E trending chains of seamounts are prominent to the west of the arc; some may have been erupted along Shikoku Basin fracture zones. Whether any of these cross-arc features have influenced the present rift structures, such as the similarly trending transfer zones, is equivocal. In the case of Sumisu Rift, however, there are no obvious correlations of synrift and prerift structures.

FAULT PATTERN

Normal faulting in the Sumisu Rift exhibits a zig-zag pattern in plan view [*Murakami*, 1988; *Brown and Taylor*, 1988; *Taylor et al.*, 1990*a*], with dominant 337° ± 10° and 355° ± 10° strikes (Figure 6). Transfer zones occur where the rift segments change trend (~31°18'N and ~31°N) or change asymmetry (~30°40'N). The differential stretching and uplift/subsidence across the transfer zones is accommodated by relay zones of interdigitating, rift-parallel normal faults, and sometimes by cross-rift volcanism, rather than by rift-oblique strike-slip faults (Figures 4 and 6) [*Taylor et al.*, 1990*a*]. The zig-zag fault pattern is evidenced at all scales, along individual faults as well as between rift segments (Figure 6). Faults with both trends dip both east and west, forming a geometry with orthorhombic symmetry. This fault style is consistent with recent theoretical [*Reches*, 1983; *Krantz*, 1988] and empirical [*Oertel*, 1965; *Reches and Dieterich*, 1983] models of fault formation in three-dimensional strain fields. These models predict that the maximum strain direction is perpendicular to the bisector of the acute angle between the two fault trends. In the Sumisu case, this analysis suggests an extension direction 076° ± 10°E, orthogonal to the trend of the volcanic arc (170°).

Note that although the border fault zones are curvilinear, they have convex as well as concave dip slopes (Figures 6 and 7). *Rosendahl* [1987], although acknowledging evidence for an orthorhombic fault geometry in the east African rifts, has argued that the fundamental unit of rift architecture is a concave half graben, several of which may be linked along strike by oblique transfer zones. Convex, as well as concave, zig-zag border fault systems are well documented for the east African rifts, however (e.g., between the Moba and Marungu basins of the Tanganyika Rift [*Ebinger*, 1989*b*]) and we do not see evidence for Rosendahl's preferred pattern in the Izu-Bonin rifts.

STRUCTURAL EVOLUTION

Our minimum estimates of extension across Sumisu Rift using measurements of fault offsets on MCS sections range from 2 to 5 km, with the higher values for the southern rift segment where fault dips are shallower. Cumulative throws across the border fault zones range from 2 to 2.5 km. Together with the young age of the system (~2 Ma) and the

accelerating subsidence rates (both documented by leg 126 drilling), these data indicate that Sumisu Rift is still in the early synrift stage of its development. Nevertheless, an evolution in structural style is already apparent from the seismic stratigraphy (Figures 3, 9, 10, and 11).

Figure 13 shows our schematic interpretation of the structural development of Sumisu Rift, including some of the along-strike variations. Sections 1a and 1b (Figure 13) show a two-stage development of the northern Sumisu Rift segments, based on our interpretation of seismic profiles 5 and 6 (Figures 3 and 10). Sections 2 and 3 (Figure 13) show the structural variations seen in the south central (profiles 3 and 4), and southern (profile 13), rift segments (Figures 3, 9, and 11). The first rift stage, which follows an even earlier sag phase, is a half graben with a structural rollover facing a large-offset border fault zone. The hanging wall faults are typically synthetic to the border faults (Figure 13, sections 1a and 2) though not always (note the sag and the antithetic faults in Figures 9 and 13, section 3). The zig-zag fault pattern and the alternating rift asymmetry (Figures 6 and 7) would already exist at this stage. This fault geometry is similar to that observed early in the development of continental rifts such as in east Africa [e.g., *Rosendahl*, 1987; *Ebinger*, 1989*b*].

The present "full graben" stage is heralded by the initiation of dominantly antithetic faulting in the hanging wall as well as by a concentration of subsidence in an inner rift along the arc side (Figure 13, section 1b). Similar focusing of rift subsidence is seen in continental rifts [*Ebinger*, 1989*b*], but in contrast to inferences from east African rifts [*Ebinger*, 1989*a*], the hanging wall collapse is not necessarily the result of the propagation of border faults from the adjacent rift segments. Rather, the border faults and hanging wall faults of adjacent rift segments may be discontinuous across transfer zones, as is the case across the central and southern Sumisu Rift transfer zones (Figures 6 and 7). Backarc magmatism occurs in the rift and on the protoremnant arc margin during both stages (Figure 13). Jostling (see-saw motion) of rift basin fault blocks, the development of an outer-rift graben, and basin widening by footwall collapse, may accompany the second stage (Figure 13, section 2).

The rift flanks are flexurally uplifted as the hanging walls subside; the footwall rebounds isostatically to compensate for the mechanical unloading [*Weissel and Karner*, 1989]. Benthic foraminifer data indicate 1.1 ± .5 km of flank uplift at site 788 during the ~1.1 km of basin subsidence (volcanic and sedimentary filling at near-constant water depths) at site 791 [*Kaiho*, 1991; *Taylor*, 1991]. Unpublished isostatic modeling by B.Taylor in Weissel and Karner's lab showed that bathymetry and gravity profiles across Sumisu and Torishima rifts can be fit well by models with small amounts of extension (~5 km) on low-angle (~25°) normal faults offsetting a rheologically weak lithosphere (effective elastic thickness $T_e \approx 3$ km) of arc crustal thickness (15-20 km). *Weissel and Karner* [1989] published a similar result for the Coriolis Trough, the active back arc rift of the New Hebrides arc. Such modeling fits particularly well the data for the gently sloping footwall flanks, such as observed on profiles 5 and 13 (Figure 3), but does not attempt to match the shorter-wavelength structures resulting from footwall and hanging wall collapse. Many of the latter structures, such as the rotated block at 0600 on profile 14 (Figure 3), the rotated blocks beneath the rift basin on profile 13 (Figure 9), and the region of site 791 (discussed previously), are detached only a few kilometers below the seafloor.

Whether or not the border faults offset the entire crust and lithosphere remains speculative as the MCS data do not image the faults for more than a few kilometers subseafloor. The heave and the dips of the border faults as well as the rollover geometry of the rift basin are substantially different in Figure 13, sections 1b and 3, which approximately correspond to seismic profiles 6 and 13 (Figure 3). Area balance depth-to-detachment estimates [*Gibbs*, 1984] indicate 10-15 km versus 5-10 km detachment depths, respectively, but such estimates make several unconstrained assumptions. Thus, although the geometry of the northern rift segments is consistent with high-angle faults substantially cutting through the crust, whereas in the southern rift segment the faults may be detached at midcrustal to upper-crustal levels, these are speculations not conclusions.

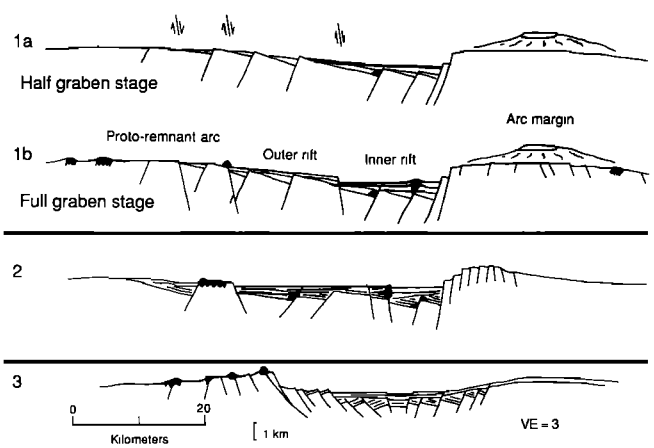

Fig. 13. Schematic interpretation of the structural evolution of Sumisu Rift (1a and 1b), with two along-strike variations (2 and 3). Solid regions represent volcanics. See text for discussion.

CONCLUSIONS

The data presented herein document the structural evolution of Sumisu Rift and allow a detailed analysis of the pattern of strain resulting from extension of an intraoceanic island arc. The ~120-km-long, 30-50-km-wide rift basin is bounded by normal fault zones dipping 60°-75° in the north and 25°-50° in the south. The rift is asymmetric and the largest offset border faults (2-2.5 km throw) alternate sides along the length of the rift, being on the arc side in the north but on the west side in the south.

Normal faults divide the region into four structural provinces across strike, from east to west (1) the arc margin, (2) the inner rift, the locus of maximum subsidence, (3) the outer rift, and (4) the protoremnant arc. Oblique transfer zones segment the rift along strike into four segments that exhibit different fault trends and uplift/subsidence patterns. Differential strain across the transfer zones is accommodated by interdigitating, rift-parallel faults and sometimes by cross-rift volcanism, rather than by oblique- or strike-slip faults. No obvious correlations are observed between the border faults or transfer zones and preexisting cross-arc trends to either side of the rift. The zig-zag pattern of normal faults (average strikes 337° and 355°) result from fault formation in orthorhombic

symmetry in response to 076° ± 10° extension, orthogonal to the volcanic arc. The curvilinear border fault zones exhibit both convex and concave dip slopes.

From estimates of extension (2-5 km), the age of the rift (~2 Ma) and the accelerating subsidence, we infer that Sumisu Rift is in the early synrift stage of back arc basin formation. Following an early sag phase, half graben formed with synthetically faulted, structural rollovers facing large-offset border fault zones. The present "full graben" stage is dominated by hanging wall antithetic faulting, basin widening by footwall collapse, and a concentration of subsidence in the inner rift. The hanging wall collapses but not necessarily as a result of border fault propagation from adjacent rift segments.

Whereas the border faults may penetrate the rheologically weak lithosphere ($T_e \approx 3$ km), many of the hanging wall and footwall collapse structures are detached only a few kilometers below the seafloor. Backarc volcanism, usually erupted along faults, occurs in the rift and along the protoremnant arc margin during both stages. Where drilled, the arc margin has been uplifted 1.1 ± 0.5 km concurrently with ~1.1 km of rift basin subsidence. Extremely high sedimentation rates (up to 6 m/kyr in the inner rift) have kept pace with synrift faulting, create a smooth basin floor, and result in sediment thicknesses that mimic the variable basin subsidence.

A linear zone of weakness caused by the greater temperatures and crustal thickness along the arc volcanic line controls the initial locus of rifting. Rifts are better developed between the arc edifices; intrusions may be accommodating extensional strain adjacent to the arc volcanoes.

Acknowledgments. This work was supported by NSF grants OCE86-14687 to B. Taylor, and OCE-8700826 and OCE-8996141 to G. Moore, and an NSF/JOI postcruise grant to B. Taylor, G. Moore, P. Cooper, and A. Klaus. We would like to thank the Ocean Drilling Program for drilling in the Sumisu Rift, G. Karner, F. Martinez, and J. Weissel for extensive and insightful discussions regarding rifting, the Geological Survey of Japan for their scientific collaboration and hospitality, the officers, crew and technicians of the R/V *Fred Moore* and R/V *Hakurei-maru* as well as W. Barrens, P. Cooper, R. Horine, M. MacKay, Y. Nakamura, and Y. Nogi for their help in acquiring the seismic data at sea, R. Horine and M. Mackay for assistance in seismic data processing, J. and P. Wessel for fault azimuth and rose diagram programs, and N. Hulbirt and B. Bays for drafting. We thank Roger Buck and Leigh Royden for their constructive reviews. This is University of Hawaii SOEST contribution 2611.

REFERENCES

Brown, G., and B. Taylor, Sea-floor mapping of the Sumisu Rift, Izu-Ogasawara (Bonin) island arc, *Bull. Geol. Surv. Jpn., 39*, 1-38, 1988.

Chamot-Rooke, N., Le Bassin de Shikoku de sa formation a l'ecaillage intra-oceanique: evolution tectonique et mechanique, Ph.D. thesis, 295 pp., Univ. Pierre et Marie Curie, Paris, 1989.

de Charpal, O., P. Guennoc, L. Montadert, and D. G. Roberts, Rifting, crustal attenuation and subsidence in the Bay of Biscay, *Nature, 275*, 706-711, 1978.

Ebinger, C. J., Geometric and kinematic development of border faults and accommodation zones, Kivu-Rusizi Rift, Africa, *Tectonics, 8*, 117-133, 1989*a*.

Ebinger, C. J., Tectonic development of the western branch of the East African rift system, *Geol. Soc. Am. Bull., 101*, 885-903, 1989*b*.

Firth, J., and M. Isiminger-Kelso, Pleistocene and Oligocene-Miocene calcareous nannofossils from the Sumisu Rift and Izu-Bonin forearc basin, leg 126, *Proc. Ocean Drill. Program Sci. Results, 126*, in press, 1991.

Fryer, P., B. Taylor, C. H. Langmuir, and A. G. Hochstaedter, Petrology and geochemistry of lavas from the Sumisu and Torishima backarc rifts, *Earth Planet. Sci. Lett, 100*, 161-178, 1990.

Gibbs, A. D., Balanced cross-section construction from seismic sections in areas of extensional tectonics, *J. Struct. Geol., 5*, 153-160, 1984.

Gill, J., et al., Explosive deep water basalt in the Sumisu backarc rift, *Science, 248*, 1214-1217, 1990.

Gill, J., C. Seales, P. Thompson, A. Hochsteadter, and C. Dunlap, Petrology and geochemistry of Plio-Pleistocene volcanic rocks from the Izu Arc and Sumisu Rift, leg 126, *Proc. Ocean Drill. Program Sci. Results, 126*, in press, 1991.

Hochstaedter, A. G., J. B. Gill, M. Kusakabe, S. Newman, M. Pringle, B. Taylor and P. Fryer, Volcanism in the Sumisu Rift, I, The effect of distinctive volatiles on fractionation, *Earth Planet. Sci. Lett., 100*, 179-194, 1990.

Honza, E., and K. Tamaki, The Bonin Arc, in *The Ocean Basins and Margins*, vol. 7, *The Pacific Ocean*, edited by A. E. M. Nairn and S. Uyeda, pp. 459-502, Plenum, New York, 1985.

Hotta, H., A crustal section across the Izu-Ogasawara Arc and Trench, *J. Phys. Earth., 18*, 125-141, 1970.

Hussong, D. M., and S. Uyeda, Tectonic processes and the history of the Mariana Arc: A synthesis of the results of Deep Sea Drilling Project leg 60, *Initial Rep. Deep Sea Drill. Proj., 60*, 909-929, 1982.

Japanese DELP Research Group On Back-arc Basins, Report on DELP 1987 cruises in the Ogasawara area, parts I-VII, *Bull. Earthquake Res. Inst. Univ. Tokyo, 64*, 119-254, 1989.

Kaiho, K., Oligocene to Quaternary benthic foraminifers and paleobathymetry of the Izu-Bonin Arc, ODP leg 126, *Proc. Ocean Drill. Program Sci. Results, 126*, in press, 1991.

Karig, D. E., Origin and development of marginal basins in the western Pacific, *J. Geophys. Res., 76*, 2542-256, 1971.

Karig, D. E., Basin genesis in the Philippine Sea, *Initial Rep. Deep Sea Drill. Proj., 31*, 857-879, 1975.

Karig, D. E., and G. F. Moore, Tectonic complexities in the Bonin Arc system, *Tectonophysics, 27*, 97-118, 1975.

Krantz, R. W, Multiple fault sets and three-dimensional strain: Theory and application, *J. Struct. Geol., 10*, 225-237, 1988.

Kuznir, N. J., and R. G. Park, The extensional strength of the continental lithosphere: Its dependence on geothermal gradient, and crustal composition and thickness, in Continental Extensional Tectonics, edited by M. P. Coward, J. G. Dewey, and P. L. Hancock, *Geol. Soc. Spec. Publ. (London) 28*, 35-52, 1987.

Leg 126 Shipboard Scientific Party, Arc Volcanism and Rifting, *Nature, 342*, 18, 1989.

Mogi, A., The Izu Ridge (in Japanese), in *Fossa Magna*, edited by M. Hoshino, pp. 217-221, Geological Society of Japan, Tokyo, 1968.

Montadert, L, O. de Charpal, D. Roberts, P. Guennoc, and J-C Sibuet, Northeast Atlantic passive continental margins: Rifting and subsidence processes, in *Deep Drilling Results in the Atlantic Ocean: Continental Margins and Paleoenvironment, Maurice Ewing Ser.*, vol. 3, edited by M. Talwani, W. Hay, and W.B.F. Ryan, pp. 154-186, AGU, Washington, D.C., 1979.

Mrozowski, C. L., and D. E. Hayes, The evolution of the Parece Vela Basin, eastern Philippine Sea, *Earth Planet. Sci. Lett., 46*, 49-67, 1979.

Murakami, F., Structural framework of the Sumisu Rift, Izu-Ogasawara Arc, *Bull. Geol. Surv. Jpn., 39* , 1-21, 1988.

Natland, J. H., and J. Tarney, Petrologic evolution of the Mariana arc and backarc basin system — a synthesis of drilling results in the South Philippine Sea, *Initial Rep. Deep Sea Drill. Proj., 60*, 877-908, 1981.

Nishimura, A., and F. Murakami, Sedimentation of the Sumisu Rift, Izu-Ogasawara Arc, *Bull. Geol. Surv. Jpn., 39*, 39-61, 1988.

Nishimura, A., K. Rodolfo, A. Koizumi, J. Gill, and K. Fujioka, Episodic deposition of Pliocene-Recent pumice deposits of the Izu-Bonin Arc, leg 126, *Proc. Ocean Drill. Program Sci. Results, 126*, in press, 1991.

Oertel, G., The mechanism of faulting in clay experiments, *Tectonophysics, 2*, 343-393, 1965.

Packham, G. H., and D. A. Falvey, An hypothesis for the formation

of marginal seas in the western Pacific, *Tectonophysics, 11*, 79-109, 1971.

Reches, Z., Faulting of rocks in three-dimensional strain fields, II, Theoretical analysis, *Tectonophysics, 95*, 133-156, 1983.

Reches, Z., and J. H. Dieterich, Faulting of rocks in three-dimensional strain fields, I, Failure of rocks in polyaxial, servo-control experiments, *Tectonophysics, 95*, 111-132, 1983.

Rosendahl, B. R., Architecture of continental rifts with special reference to East Africa, *Annu. Rev. Earth Planet. Sci., 15*, 445-503, 1987.

Sibuet, J.-C., et al., Back arc extension in the Okinawa Trough, *J. Geophys. Res., 92*, 14,041-14,063, 1987.

Steckler, M. S., and U. S. ten Brink, Lithospheric strength variations as a control on new plate boundaries: examples from the northern Red Sea, *Earth Planet. Sci. Lett, 79*, 120-132, 1986.

Tamaki, K., Two modes of back-arc spreading, *Geology, 13*, 475-478, 1985.

Taylor, B., Rifting and the volcanic-tectonic evolution of the Izu-Bonin-Mariana arc, *Proc. Ocean Drill. Program Sci. Results, 126*, in press, 1991.

Taylor, B., and G. D. Karner, On the evolution of marginal basins, *Rev. Geophys., 21*, 1727-1747, 1983.

Taylor, B., and Shipboard Scientific Party, Introduction, *Proc. Ocean Drill. Program Initial Rep., 126*, 5-11, 1990.

Taylor, B., D. Hussong, and P. Fryer, Rifting of the Bonin Arc, *Eos Trans. AGU, 65*, 1006, 1984.

Taylor, B., G. Brown, D. Hussong, and P. Fryer, SeaMARC II sidescan acoustic imagery of Sumisu and Torishima Rifts, Izu-Ogasawara Island Arc, scale 1:200,000, *Mar. Geol. Map Ser. 31*, Geol. Surv. Jpn., Tsukuba, 1988*a*.

Taylor, B., G. Brown, D. Hussong, and P. Fryer, Bathymetry of Sumisu and Torishima Rifts, Izu-Ogasawara Island Arc, 1:200,000, *Mar. Geol. Map Ser. 31*, Geol. Surv. Jpn., Tsukuba, 1988*b*.

Taylor, B., G. Brown, P. Fryer, J. Gill, F. Hochstaedter, H. Hotta, C. Langmuir, M. Leinen, A. Nishimura, and T. Urabe, Alvin-SeaBeam studies of the Sumisu Rift, Izu-Bonin arc, *Earth Planet. Sci. Lett, 100*, 127-147, 1990a.

Taylor, B., G. Moore, A. Klaus, M. Systrom, P. Cooper, and M. MacKay, Multichannel seismic survey of the central Izu-Bonin Arc, *Proc. Ocean Drill. Program Initial Rep., 126*, 51-60, 1990*b*.

Taylor, B, et al., *Proceedings of the Ocean Drilling Program, Initial Reports*, vol. 126, 1002 pp, Ocean Drilling Program, College Station, Tex., 1990*c*.

Vink, G. E., W. J. Morgan and W.-L. Zhao, Preferential rifting of continents: A source of displaced terranes, *J. Geophys. Res., 89*, 10,072-10,076, 1984.

Weissel, J. K., and G. D. Karner, Flexural uplift of rift flanks due to mechanical unloading of the lithosphere during extension, *J. Geophys. Res., 94*, 13,919-13,950, 1989.

Wright, I., L. Carter, and K. Lewis, Gloria survey of the oceanic-continental transition of the Havre-Taupo back-arc basin, *Geo Mar. Lett., 10*, 59-67, 1990.

Yamazaki, T., Heat flow in the Sumisu Rift, Izu-Ogasawara (Bonin) Arc, *Bull. Geol. Surv. Jpn., 39*, 63-70, 1988.

G. R. Brown, Department of Geology, University of Toronto, 170 College St., Toronto, Ontario, Canada, M5S 1A1.

A. Klaus, Ocean Research Institute, University of Tokyo, 1-15-1, Minamidai, Nakano-ku, Tokyo 164, Japan.

G. F. Moore and B. Taylor, Department of Geology and Geophysics, SOEST, University of Hawaii at Manoa, 2525 Correa Rd., Honolulu, HI 96822.

F. Murakami and Y. Okamura, Geological Survey of Japan, 1-1-3 Higashi, Tsukaba, Ibaraki 305, Japan.

(Received January 14, 1991;
revised June 17, 1991;
accepted July 18, 1991.)

JOURNAL OF GEOPHYSICAL RESEARCH, VOL. 96, NO. B10, PAGES 16,223–16,230, SEPTEMBER 10, 1991

Multifractal Analysis of the Microdistribution of Elements in Sedimentary Structures Using Images From Scanning Electron Microscopy and Energy Dispersive X Ray Spectrometry

A. BLOCK, W. VON BLOH, T. KLENKE, AND H. J. SCHELLNHUBER

Institute for the Chemistry and Biology of the Marine Environment and Physics Department, University of Oldenburg Oldenburg, Federal Republic of Germany

A novel method for the quantitative characterization of density distributions of elements in sedimentary geosystems is presented. This general technique is based on the multifractal analysis of image-processed elemental maps obtained by scanning electron microscopy combined with energy dispersive X ray spectrometry. Applications to microdistributions of Si, Fe, and Al in recent bioactive siliciclastic marine sediments are reported. Inhomogeneous scaling behavior of these elemental distributions is observed in all cases. Two main conclusions can be drawn: (1) The sedimentary matrix exhibits true fractal geometry and (2) the processes allocating and rearranging the elements are not of pure stochastic type. Therefore the identification of genetic processes may be possible on the basis of their "multifractal fingerprints".

1. INTRODUCTION

1.1. *Objectives*

The geometry of complex geosystems, like recent sediments or sedimentary rocks, is the spatial result of various interacting processes. These include genetic processes, like sedimentation, as well as intrinsic processes, like percolation of interstitial waters [*Thompson et al.*, 1987]. Distinct processes express themselves in specific structures, i.e., domains with chemical, biological, or physical properties different from those found in the immediate neighborhood [*Werner and Torrist*, 1990]. Such structures can be observed on many scales. Therefore answers on genetic and intrinsic questions can be gathered by the geometrical analysis of the component distribution/morphology. In addition, the geometry is a key for both the quantification of the components of a geosystem, and the description or, eventually, the modeling of its genetic and intrinsic mechanisms.

Direct spatial informations about local structures are mainly provided by photographs, maps, or other kinds of images, which are essential prerequisites for the determination of distribution and morphology of the components [*Smith*, 1986]. Usually, geometrical features are visualized by microscopical methods and analyzed by (automatic) measuring equipment, mainly based on television-type image analyzers or X-ray-type systems, applied to measurements in one, two, or even three dimensions [*Jones*, 1987]. The resulting images can be processed by a number of deterministic and statistical methods. The related stereological methods are used for the quantitative description of some features of interest like modal composition, particle size and texture, particle composition, particle distribution, arrangement, association, and pore volume [*Jones*, 1987; *Tucker*, 1988].

However, not only the geometrical analysis of components, such as minerals, biota, or pores, may yield data on the composition as well as the structure-forming processes and events: The distributions of elements, which can be regarded as subconstitutents of a mineralogical or biological support, provide essential and complementary structural information due to the specific occurrence of elements on the component support.

We present a method for the quantitative description of the geometry of elements, using the example of a sedimentary geosystem. It is based on recent developments in the physics of nonlinear dynamics and allows (1) the quantification and description of the distribution of elements and (2) the detection of genetic and intrinsic processes and properties via a geometrical analysis. It represents a novel tool to be combined with stereological methods, which are often limited and insufficient, especially as far as the genetic interpretation of the treated data is concerned. Our method is based on the concept of fractality and will therefore focus on scaling characteristics or self-similarities in the data at hand. A characterization of these features sheds light on the effective scales of the reigning genetic dynamical processes and also on the intrinsic structure-forming events.

We have employed scanning electron microscopy combined with energy dispersive X ray analysis (SEM/EDX) to obtain the local elemental distribution geometry and to produce elemental dot maps. These maps generate the distribution patterns of the more abundant elements; they are prepared by an image processing system in order to quantify numerically their scaling characteristics and to get information about the nonuniformity of the spatial element distribution function.

We have organized this paper as follows. First we will briefly review the basic definition of fractal dimension and its extension for characterizing nonuniform measures on fractals, the concept of multifractality. Then we will describe sampling and specimen preparation and our experimental settings. Finally, we present the results and discuss the method employed.

1.2. *Fractal Description of Self-Similar Objects*

Recently, novel and powerful methods for the quantitative analysis of structures and shapes in real geosystems have

Paper number 91JB01578.
0148-0227/91/91JB-01578$05.00

arisen from the application of the concept of fractals as introduced by *Mandelbrot* [1983]. At first sight, geometries of natural objects are bewildering in their complexity. They seem too complicated to be characterized and measured in a satisfying way. But quite often the spatial or temporal distribution of features exhibits a (statistical) symmetry with respect to magnification or reduction: the structures and characteristic forms at smaller scales look similar to the ones at larger scales. This scaling symmetry can be quantified by the fractal dimension. The latter has become an important tool for the characterization of exactly or approximately self-similar objects, which play a major role in many physical situations like nonlinear dynamics [*Schuster*, 1988; *Mayer-Kress*, 1986], critical phenomena [*Stinchcombe*, 1989], and growth processes [*Herrmann*, 1986]. However, nontrivial scaling behavior, i.e., invariance under contractions or dilations, seems to be also a crucial feature of many other natural structures and processes, although this invariance is often realized only in a subtle and statistical way.

Fractal analysis of natural systems has been performed in many realms, including material sciences [*Kaye*, 1989], chemistry [*Avnir*, 1989], and biology [*West and Goldberger*, 1987]. In the earth sciences, fractal analysis has been used to study, for instance, the topography of landscapes [*Huang and Turcotte*, 1989] and river networks [e.g., *Takayasu*, 1990] or the surface and bulk structure of minerals [*Krohn*, 1988*a*] and sedimentary bodies [*Thompson et al.*, 1987].

Careful investigation of the microstructure of sandstones indicates that their pore volume distribution can be divided into two domains: a short-length regime with fractal behavior and a long-length regime where fractal characteristics are negligible. The fractal part appears to be strongly governed by the growth of minerals and cements in the pore space [*Krohn*, 1988*b*].

Our present study extends to even smaller scales and focuses on the microdistribution of elements in real sedimentary bodies. Such a distribution defines a measure on the sedimentary microstructure, which is by itself a self-similar object, and therefore shows a more complicated behavior than a distribution on objects which are homogeneous and translational invariant. One single number, namely, the "ordinary" fractal dimension, may be sufficient for the geometrical characterization of the sedimentary matrix, but physical, chemical, or biological processes, or probability and weight distributions that take place on such a structure, have to be described by the more general concept of multifractality [*Halsey et al.*, 1986; *Coniglio et al.*, 1989; *Tel*, 1988]. The so-called generalized fractal dimensions yield detailed information regarding the nonuniformity of fractal measures. This information is very important in our case, as the nonuniformity of the distribution of elements within the sediment is assumed to be closely related to certain diagenetic processes and various system properties like permeability [*Thompson et al.*, 1987].

1.3. *Fractal Dimension and Multifractal Measures*

Self-similar or fractal structures embedded in Euclidean space E^d usually do not have a finite d-dimensional volume and cannot be described in terms of traditional geometry. They do not have any characteristic lengths. One consequence of this fact is that their boundary (surface; contour) is nowhere smooth and is therefore very difficult to measure. Famous examples are coastlines: their total length depends on the yardstick used [*Mandelbrot*, 1983]. In order to assign well-defined "contents" to such objects, D-dimensional Hausdorff measure has to be used [*Falconer*, 1985], where $D \in [0, d]$ is the Hausdorff dimension. While the rigorous determination of D is almost always impossible for a fractal structure represented by a point set $\mathbf{X} \subset E^d$ (for example, digitized photos, maps, or other experimental data, characterizing the geometrical features of the object under investigation), a very good estimate can be achieved, in general, by computing the so-called box-counting (or capacity) dimension D_B [e.g., *Grassberger and Procaccia*, 1983]:

It is defined as

$$D_B = \lim_{\varepsilon \to 0} \frac{\ln N(\varepsilon)}{\ln (1/\varepsilon)}, \tag{1}$$

where ε is the lattice constant of d cubic covers of $\mathbf{X}$ and $N(\varepsilon)$ is the number of cubes contained in the minimal cover. Numerically D_B is calculated by the following recipe: Count the number $N(\varepsilon)$ of boxes of edge length ε that are necessary to cover all points of the data set and calculate the slope of $\ln N(\varepsilon)$ versus $\ln \varepsilon$ for decreasing resolution parameter ε.

The single number D_B may be sufficient for a geometrical characterization of the fractal set considered, but, as mentioned before, processes or distributions that take place or are defined on such a structure have to be described by multifractal measures [*Tel*, 1988]. The formalism is based on generalized (box counting) fractal dimensions $D_B(q)$, $q \in \mathbf{R}$ [*Hentschel and Procaccia*, 1983], defined by

$$D_B(q) = \lim_{\varepsilon \to 0} \frac{1}{q-1} \frac{\ln \sum_{\nu=1}^{N(\varepsilon)} [p_\nu(\varepsilon)]^q}{\ln \varepsilon}. \tag{2}$$

Here the index ν labels the individual boxes of the ε cover and $p_\nu(\varepsilon)$ denotes the relative weight of the νth box. In practice, the measure under investigation is encoded in a finite ensemble of points in E^d (in our case it is given by the two-dimensional coordinates of the elemental dots representing the occurrence of the specified element in the sedimentary sample). Within this approximation, $p_\nu(\varepsilon)$ is given by

$$p_\nu(\varepsilon) = \frac{N_\nu(\varepsilon)}{N}, \tag{3}$$

where $N_\nu(\varepsilon)$ is the number of points falling into the νth box and N is the total number of dots. The definition of generalized box-counting dimensions obviously includes the ordinary one, i.e., $D_B = D_B(0)$. Note that $D_B(1)$ is the entropy dimension, $D_B(2)$ the correlation dimension of pairs of the points, $D_B(3)$ the correlation dimension of triples, etc. [*Schuster*, 1988].

Let us emphasize here that the spectrum of generalized fractal dimensions $D_B(q)$ quantifies the nonuniformity of the measure defined on the fractal set $\mathbf{X}$: If p were chosen as the $D_B(0)$-dimensional Hausdorff measure, then we would have $D_B(q) = D_B(0)$ for all $q \in \mathbf{R}$. In the following we will choose p as the two-dimensional measure. The occurrence of elements is supposed not to be restricted to just the self-similar sedimentary matrix. They may also be found in the pore space, and therefore the chosen "trivial" measure seems to be appropriate. If the generalized fractal dimen-

sions $D_B(q)$ depend on the "qth moment", then the density distribution of elements scales multifractally with respect to the two-dimensional measure, and the evaluated $D_B(q)$ quantify the nonuniformity.

2. METHODS

2.1. *Sampling and Specimen Preparation*

Samples were taken from lower supratidal sediments of the East-Frisian Waddensea region of the North Sea (German Bight). These recent bioactive siliciclastic marine sediments are highly porous and unconsolidated versicolored tidal flat substrates (subparallel laminated sandy sediments with thin microbial mat intercalations, Mellum Island/North Sea). The regional setting as well as the biological and petrographical conditions are described by *Gerdes et al.* [1985 and the references therein].

The samples were taken by inserting a box corer, which was immediately afterwords transferred to our laboratory facilities for further preparation. In the laboratory, small profiling columns of the upper layers (≈45 mm) were cut out and fixed in 1,5-pentanedial in seawater overnight. Before dehydration in a graded series of ethanol/aqua bidest mixtures (concentration series from 10 to 100% ethanol) the specimens were washed several times with degrading salt concentrations. The unconsolidated columns were embedded in epoxy resin prior to polishing. Special care was taken to achieve a polished surface plane. Finally, the specimens were sputtered with gold or graphite and examined by means of SEM/EDX equipment.

2.2. *SEM/EDX Imaging*

In general, SEM/EDX is a method of chemical as well as visual analysis of materials. The specimen is bombarded by a focused beam of high-energy electrons. The electron beam penetrates into the top of the specimen, and interaction with the different specimen-forming elements causes the emission of characteristic X rays. These rays are measured simultaneously by using solid-state, energy dispersive X ray detectors.

The geometrical information gained by this nondestructive method is not strictly confined to the two-dimensional surface plane. Due to the finite penetration of the incident beam there is a certain information depth, which increases with growing acceleration voltage of the incident electron beam. The spatial resolution of the dot maps is limited mainly by three factors: (1) X ray generation geometry, (2) magnification, and (3) optical equipment. Therefore the diameter of each dot may vary as a function of these operation parameters.

A Cambridge Instrument S 180 scanning electron microscope equipped with a Link Ortec 6230 EDX system was used in our investigations. Generally, the acceleration voltage was set to 20 keV and the integration time to 60 s. By means of this equipment, elemental dot maps are obtained, which document the spatial distribution of elements on the sedimentary body and are the basis of a numerical analysis via image processing as described below.

2.3. *Digital Image Processing*

The images are digitized for box-counting analysis, which is done by a CCD camera and an image processing unit. In the following step the coordinates of the elementary distribution are extracted from the digital picture in order to get a coordinate list, which is the appropriate data structure for the novel effective box-counting algorithm employed [*Block et al.*, 1990].

The digitizing of the image is done by a B/W-CCD (Pearpoint 800 pixel CCD) camera connected to an image processing unit (series 151 image processor by Imaging Technology, Incorporated) with a resolution of 512 × 512 pixels in 256 grayscales. The extraction of the point coordinates is quite simple to handle, because the SEM/EDX image consists of points of comparable intensity.

Without loss of information the image data can be reduced to binary (0/1) information by performing threshold filtering. Instead of storing the whole image, only the coordinates of the nonzero values in the digital image are retained.

The improved box-counting algorithm calculates directly the generalized fractal dimensions $D_B(q)$ by using the coordinate list created in the previous step. The algorithm is implemented on a parallel computer consisting of four INMOS limited transputers (T800 processor + 1 megabyte of random access memory), which are installed in an ordinary personal computer controlling the image processing unit and allowing fast processing of SEM/EDX images. The running time of the algorithm depends only on the number of points N, i.e., the computing time grows quasi-linearly with N ($O(N \log_2 N)$). Combination of this effective method with the powerful parallel hardware makes it possible to analyze even very large structures.

The accuracy of the D_B values is improved by applying a classwise linear regression method for minimizing the mean square deviation. This method gives also an estimate of the scaling region, which is always limited by finite size effects, i.e., by the limited resolution of the images.

TABLE 1. Effect of the Integration Time on the Observed Number of Points and the Fractal Dimensions $D_B(0)$ and $D_B(3)$

Integration Time	Points	$D_B(0)$	$D_B(3)$
30	6276	1.89	1.742
60	7514	1.89	1.746
125	7312	1.89	1.727

3. RESULTS

3.1. *Operational Conditions*

First of all, the influence of SEM/EDX operational conditions on the results for the fractal dimensions was tested for the equipment parameters integration time and acceleration voltage (Tables 1 and 2).

The variation of the integration time for sampling the

TABLE 2. Effect of the Acceleration Voltage on the Observed Number of Points and the Fractal Dimensions $D_B(0)$

Acceleration Voltage, keV	Points	$D_B(0)$
10	956	1.77
20	5341	1.88
40	682	1.76

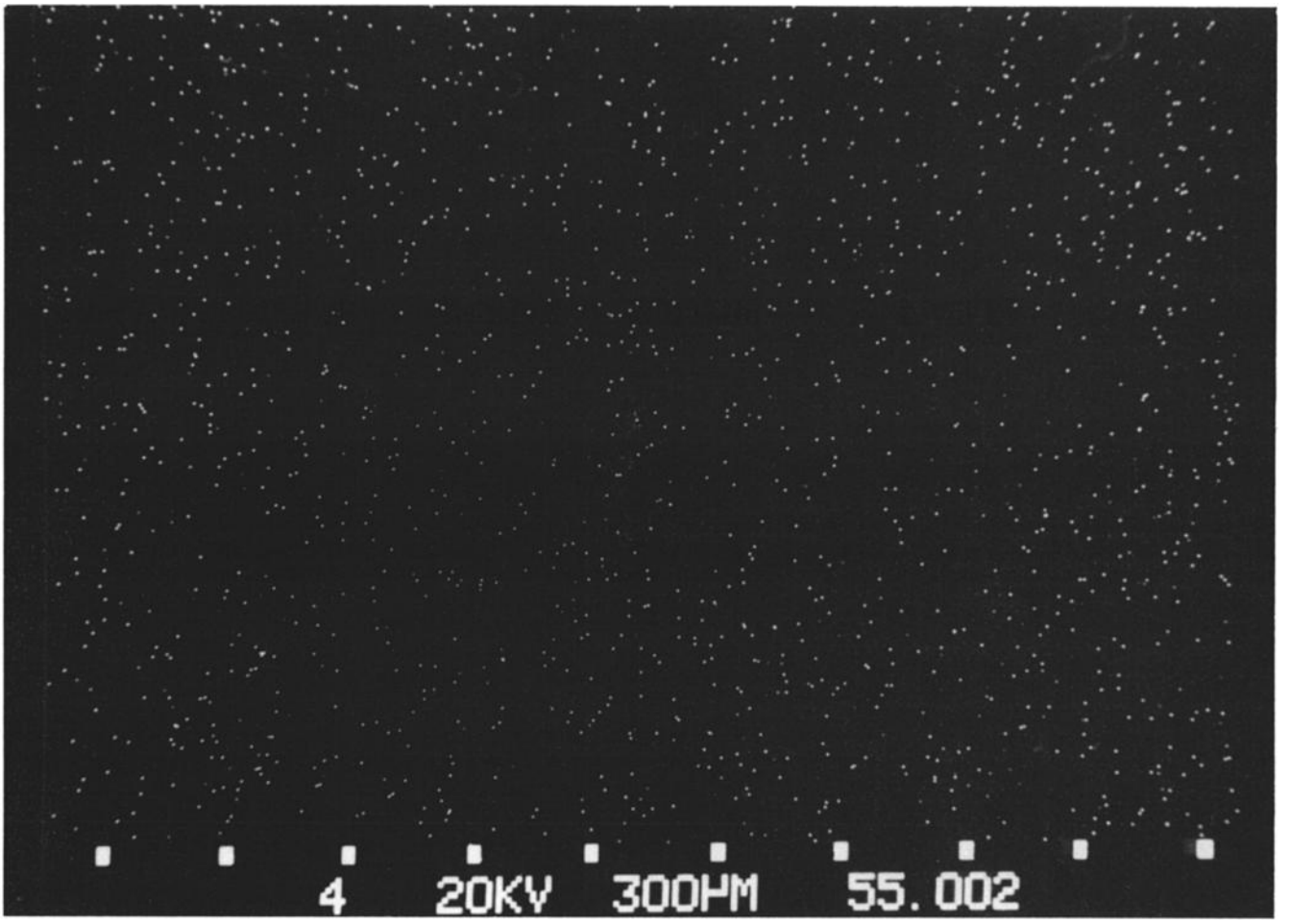

Fig. 1*a*. SEM/EDX Fe dot map: Fe distribution pattern of a sedimentary structure obtained from a profile (3 mm thickness) of the uppermost layers of a recent versicolored tidal flat sediment. The number of contributing points is 7514. The distance between two bars (white squares in the lower part of the operation display) is 300 μm. The diameter of each dot is about 8.6 μm, which defines the spatial resolution of the dot map and the lower limit of analysis in this specific case.

elemental dot maps from 30 to 125 s results in a unique fractal dimension $D_B(0) = 1.89$ in all cases (Table 1). The number of points differs slightly, probably due to lower excitation time (30 s) or the clustering of points to one larger point (125 s). Note that the $D_B(3)$ values found do not depend on the number of points. These values are significantly smaller than the corresponding $D_B(0)$ and prove the nonuniformity of the used two-dimensional measure!

The influence of the acceleration voltage on the elemental dot image (Table 2), however, is of greater importance. Both relatively low and high acceleration voltages gave insufficient dot map information. Possible reasons for this are deflection and the reduction of the effective energy of the incident low-energy electron beam (10 keV) or the reduction of the emitted X ray yield by the absorption of X rays generated in deeper specimen layers (40 keV). Evidently, the decrease in the number of points lowers the obtained fractal dimension.

3.2. *Operational Steps*

The different steps of the method employed can be well demonstrated by the sequence of Figures 1*a*–1*d*, which refer to the multifractal analysis of the Fe distribution in the sedimentary structure of a versicolored substrate:

The SEM/EDX Fe dot map (Figure 1*a*) does not exhibit the stratification features, which can be identified in the corresponding SEM picture. In the latter (not shown) an alternating layering of sandy laminae and microbial mats is the dominant petrographical feature. In the Fe dot map there are, however, domains of denser dotting indicating the nonrandom Fe distribution in the sediment.

The digitized image corresponds directly to the dot map, but the contrast of the image is enhanced, resulting in a visual "optimization" (Figure 1*b*).

The box-counting analysis of this Fe-distribution image yields a fractal dimension of $D_B(0) = 1.89 \pm 0.0129$ (Figure 1*c*).

Figure 1*d* shows the generalized fractal box-counting dimensions of Fe-distribution samples as a function of the moment parameter q. One observes a clear-cut multifractal scaling behavior of the Fe-distribution measure, which is largely independent of the amount of Fe contained in the sample! The occurrence of Fe in the sediment specimens under investigation is therefore highly inhomogeneous, i.e.,

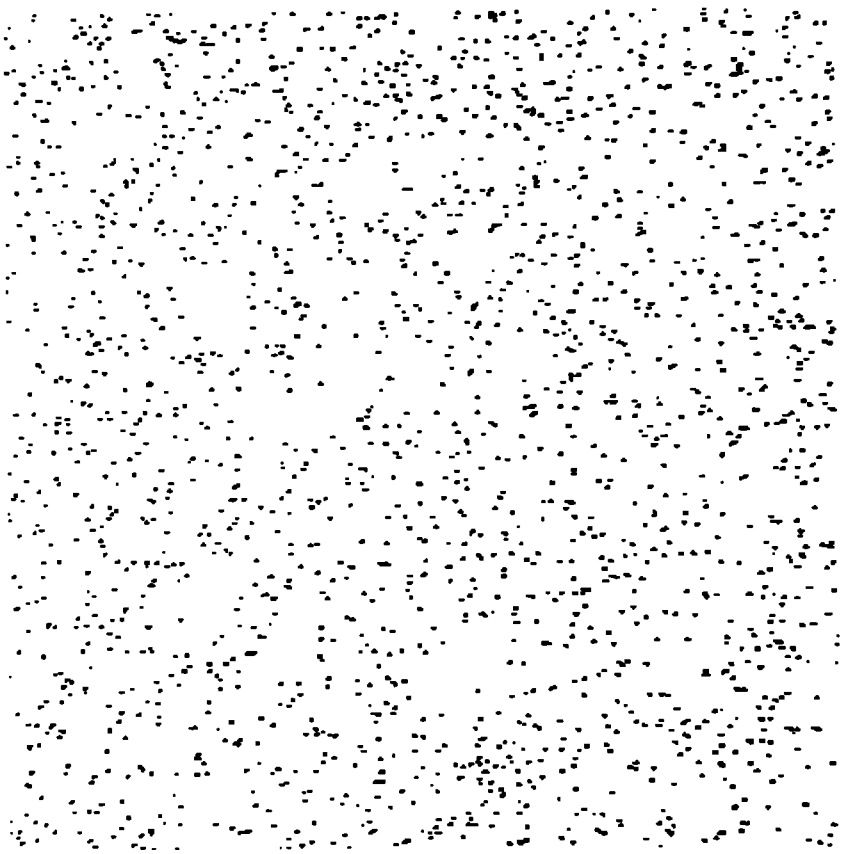

Fig. 1*b*. Digitized SEM/EDX elemental image. This is an operational "optimized" detail of the SEM/EDX Fe dot map of Figure 1*a*.

denser and sparser parts scale differently. Random disorder cannot give rise to such characteristics.

As a test, we have also analyzed the synthetic distribution measure of randomly placed dots for increasing point numbers on a two-dimensional grid of fixed size, namely, 512 × 512 lattice sites. Due to the finite size of the data set a spurious multifractal behavior of the random-sample dot map is observed, as shown in Figure 2*a*, but for all particle numbers up to $N = 7500$ this artifact can clearly be distinguished from the "true" multiscaling depicted in Figure 1*d*.

Further evidence for the multifractality of the real phenomena under investigation is provided by comparison with an artifical fractal, namely, a computer-generated Sierpinski carpet [see *Mandelbrot*, 1983] with almost the same Hausdorff dimension $D_B(0)$. This structure is obtained as follows: Divide the unit square into nine congruent subsquares and remove the central one. Apply the same operation to the remaining 8 subsquares and continue the process ad infin-

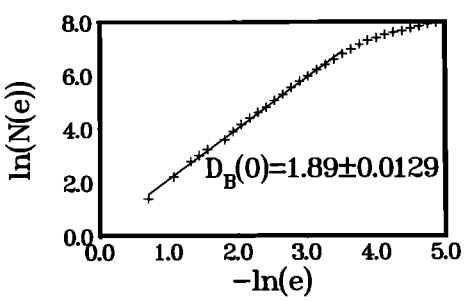

Fig. 1*c*. Box-counting analysis of the digitized elemental image of Figure 1*b*. The data for $-\ln(\varepsilon) > 3.5$ are excluded from the analysis because of finite size effects.

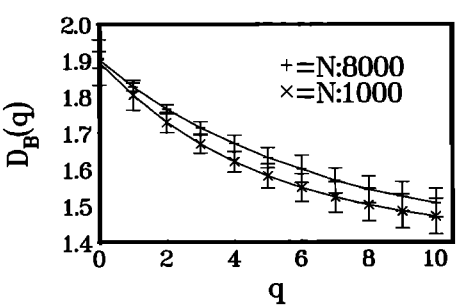

Fig. 1*d*. Numerical determination of the generalized fractal dimensions $D_B(q)$, $0 \leq q \leq 10$, for the abundance measure of Fe in different samples of the same uppermost layers of a recent versicolored tidal flat sediment. Two groups of samples are analyzed: one contains five specimens, which provide between 7073 and 8211 points; the other group consists of six specimens with a smaller amount of Fe, containing between 842 and 1320 dots. The error bars denote the mean square deviations.

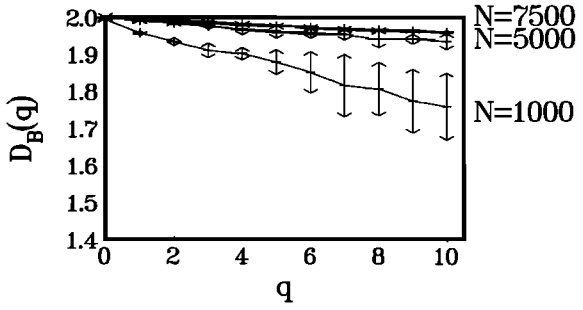

Fig. 2*a*. Generalized fractal dimensions $D_B(q)$, $0 \le q \le 10$, of computer-generated dot maps comprising up to 7500 points. The error bars denote the mean square deviations calculated by averaging over 20 dot maps for each fixed number of points.

itum. The result is a self-similar point set of fractal dimension $D_B(0) = \ln 8/\ln 3 \approx 1.89$.

A crucial fact here is that the emerging mass distribution scales homogeneously, i.e., $D_B(q) = D_B(0)$ for all $q \in \mathbf{R}$, if equal normalized weights are assigned to all subsquares belonging to the same generation. This illustrates a general theorem stating that monofractal measures necessarily arise whenever subsets are endowed with weights proportional to their $D_B(0)$-dimensional volume [*Block et al.*, 1990]. We expect therefore the spectrum of generalized dimensions of the Sierpinski carpet to differ markedly from the Fe spectrum even in the presence of finite-size effects.

This is indeed the case as Figure 2*b* demonstrates: The artificial fractal measure is encoded by approximately 2000, 4000, and 8000 points, respectively, chosen randomly from the exact set, and the associated $D_B(q)$ functions are plotted. Note that the finiteness of the data sets introduces some synthetic inhomogeneity, which decays rapidly, however, with increasing number of points. This is similar to the behavior of the random sample and clearly contrasts with the genuine multifractal characteristics depicted in Figure 1*d*.

The results for $D_B(q)$ as determined for random point sets ($N \approx 7500$), Fe dot maps ($N \approx 8000$), and the Sierpinski carpet ($N \approx 8000$) are summarized and compared in Table 3.

All samples were defined on identical quadratic grids. The inhomogeneity of the fractal scaling behavior, which may be measured by the difference $D_B(0) - D_B(q)$ is evident for the

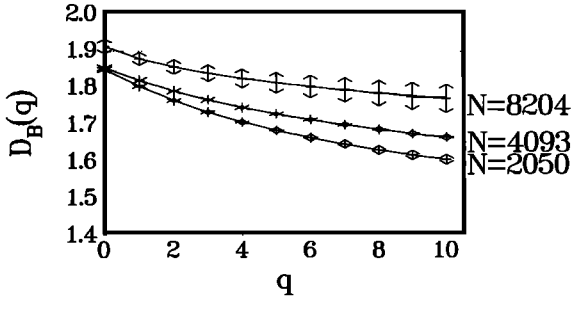

Fig. 2*b*. Generalized fractal dimensions $D_B(q)$, $0 \le q \le 10$, of a computer-generated homogeneous fractal measure as described in the text. Finite data sets of different length N have been produced by random sampling from the exact fractal set. The range of the error bars denotes the mean square deviations calculated by averaging over 10 samples for each fixed number of points. The dotted line indicates the exact fractal dimension $D_B(0)$.

TABLE 3. Generalized Fractal Dimensions $D_B(q)$

	$D_B(q)$		
q	Random Dot Map	Sierpinski Carpet	Fe Dot Map
0	2.00	1.90	1.90
1	1.99	1.87	1.83
2	1.99	1.85	1.77
3	1.98	1.83	1.71
4	1.98	1.82	1.67
5	1.98	1.81	1.63
6	1.97	1.80	1.60
7	1.97	1.79	1.57
8	1.96	1.78	1.54
9	1.96	1.77	1.52
10	1.96	1.77	1.51

$D_B(q)$ are calculated for random dot maps ($N = 7500$) (Figure 2*a*), for a numerically generated homogeneous fractal ($N \approx 8000$) (Figure 2*b*), and for Fe dot maps ($N \approx 8000$) (Figure 1*d*).

Fe data, whereas the variation is definitely smaller in the other cases.

3.3. *Multifractal Analysis and Interpretation*

All the spatial distribution measures of the three elements Si, Fe, and Al in the sedimentary structure investigated show a clear multifractal scaling behavior (Figure 3). The elemental spectra differ slightly, probably as a consequence of different genetic and intrinsic processes in certain modes and rates.

These processes determining the elemental distributions are phenomena of growth, aggregation, percolation, dissolution, etc. as part of the following general scenario for structure-forming events on clastic sedimentary geosystems:

The genesis of such a geosystem starts with the predepositional steps of crystallization, weathering, and transport of each detrital mineral. During the succession but also in combination of these steps the primary mineral is substantially and morphologically altered by physical, chemical, and biological processes. These steps are specific to each individual detrital component (minerals, biota, and organomineral associations). The sedimentary system is formed by the deposition of these detrital components under certain conditions and the postdepositional diagenetic steps. During the diagenesis the original assemblage of detrital components as well as the complementary pore space can be again substan-

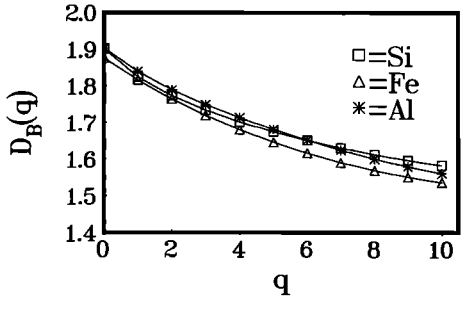

Fig. 3. Generalized fractal dimensions $D_B(q)$, $0 \le q \le 10$, characterizing the scaling properties of the microdistribution of Si, Fe, and Al, respectively, in a representative sample of the recent versicolored tidal flat sediment investigated. Number of points: Si: $N = 40{,}259$, Fe: $N = 22{,}132$, Al: $N = 26{,}970$.

tially and morphologically altered by the dissolution of minerals, by the breakdown and consumption of organic material, and by the growth of authigenic minerals and new microbial communities.

One relevant factor that controls the sediment-intrinsic percolation of reactive interstitial water through the pore space is of course the geometry of the structure: the modes and rates of processes, like the active hydrodynamic and the passive diffusive transport of fluids, depend on the sizes and shapes of the pores and their connectivity. In addition, there is an interaction between solid-matrix components and components transported by the percolating fluids. Again, modes and rates of the interaction during the passage of fluids through the reactive sedimentary system (dominantly sorption, molecular sieving, or biogenic geochemical transfer of element species) are controlled by the structural features of the anorganic/organic mineral/biota limited surface area and the total porosity.

Keeping this scenario in mind, it is not very surprising to find that the natural systems in question exhibit a variety of scaling characteristics in the arrangement of their components [*Avnir*, 1989; *Thompson et al.*, 1987]. In particular, the observed multifractality of certain elemental distributions is quite plausible: Some of the genetic and intrinsic processes just sketched, such as growth or dissolution, may be modeled in terms of diffusion-limited aggregation (DLA) or diffusion-limited deposition/precipitation on the self-similar sedimentary matrix, or by equivalent schemes of degradation of the latter [*Witten and Sander*, 1981]. Many variants of these models, emphasizing different aspects of the microscopic mechanisms, have been developed in the last years [*Jullien and Kolb*, 1984]. Extensive computer simulations of aggregation processes described within this framework have revealed that the resulting mass distributions have to be described by multifractal measures [*Feder*, 1988; *Avnir*, 1989; *Tel*, 1988]. We conjecture that the growth of biofilms and authigenic minerals as well as the sorption or reaction of particles transported by percolating waters cause similar phenomena in the distributions of elements in the fractal porous sediments investigated here.

The different elements and their distributions may serve to resolve the web of processes structuring the sediment geometry into specific components and mechanisms,like DLA-type precipitation: For instance, in the case of the bioactive siliciclastic sediments investigated, Si is an indicator of detrital mineral components (quartz). Al is an indicator for different minor mineral components (feldspars and terrigenous/authigenic clay minerals). Fe, however, as a partly geochemical and biological transferable element, can be used to identify a couple of components (terrigenous clay minerals and biota) as well as biofilms on the mineral surfaces and bioinduced authigenic minerals (sulphides and clay minerals).

In synopsis, a bouquet of different processes act together to produce the inhomogeneous distributions of Si, Fe, and Al, which can be analyzed in terms of multifractal calculus. We have not yet tried to assign individual traits of the multifractal spectrum to special actions and interactions. This is certainly a formidable but attractive task for future work.

The elemental overall fractal dimension on the structure was also determined (Figure 4). To that end an analysis was carried out for all elements detectable by the applied SEM/EDX technique, thus excluding the light elements with atomic mass ≤ 12 and the dominant elements of the organic components (C, N, O).

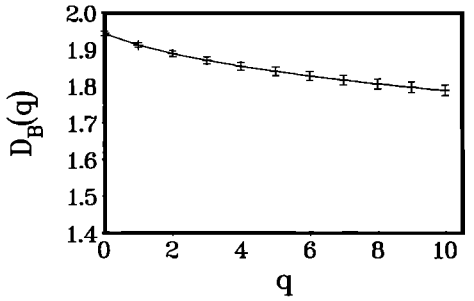

Fig. 4. Generalized fractal dimensions $D_B(q)$, $0 \leq q \leq 10$, characterizing the scaling properties of the union of the microdistributions of all detectable elements in the specimen. The number of points in the sample under investigation is $N = 64{,}848$. The error bars denote the mean square deviation of the point distance resulting from a classwise hierarchical regression analysis [*Späth*, 1983].

Our investigation yields an overall fractal dimension of $D_B(0) = 1.94 \pm 0.01$ for a typical sample. The observed variation in $D_B(q)$ characterized by the difference $D_B(0) - D_B(10)$ is nearly 0.155, whereas the corresponding value resulting from the analysis of a random dot map with the same number of points ($N = 62{,}000$) is smaller than 0.04! This finding supports again the multifractality of the phenomena under investigation and also indicates that the distribution of each element with atomic mass > 12 is affected by the fractal properties of the sedimentary matrix.

4. CONCLUSION

The multifractal analysis of elemental distributions in geosystems is a method that allows quantitative insights into the geometrical organization of these systems. We have demonstrated that certain elemental distributions in a recent sedimentary matrix reflect the fractal behavior of their mineralogical and biological support. This observation and the first results presented here indicate that both genetic processes and intrinsic properties can be detected and measured by the analysis of self-similarity of element density distributions by generating valuable information about the effective scales of the governing dynamical processes.

Future work will include other geosystems, such as carbonates or magmatites, in order to establish discrimination criteria on the basis of the $D_B(0)$ values and the multifractal spectra of the elemental distributions. We plan, in particular, the integration of advanced image analysis techniques, which allow the superposition of certain elemental dot maps and maps of the mineralogical/biological support. Besides specific genetic problems we intend to study intrinsic processes, especially sorption and reaction of substances in the fractal pore space of unconsolidated porous sediments. The distributions produced by these processes will be geometrically analyzed by the presented technique and simulated by cellular automata methods [*Wolfram*, 1983].

Acknowledgments. Financial support by the Federal Minister for Science and Technology (BMFT grant MFU 05798) is gratefully acknowledged.

REFERENCES

Avnir, D. (Ed.), *The Fractal Approach to Heterogeneous Chemistry*, 441 pp., John Wiley, New York, 1989.

Block, A., W. von Bloh, and H. J. Schellnhuber, Efficient box-counting determination of generalized fractal dimensions, *Phys. Rev. A*, *42*, 1869–1874, 1990.

Coniglio, A., L. De Arcangelis, H. J. Herrmann, Fractals and multifractals: Applications in physics, *Physica A*, *157*, 21–30, 1989.

Falconer, K. J., *The Geometry of Fractal Sets* 162 pp., Cambridge University Press, New York, 1985.

Feder, J., *Fractals*, p. 283, Plenum, New York, 1988.

Gerdes, G., W. E., Krumbein, and H. E. Reineck, The depositional record of sandy, versicolored tidal flats (Mellum Island, Southern North Sea), *J. Sediment. Petrol.*, *55*, 265–278, 1985.

Grassberger, P., and I. Procaccia, Measuring the strangeness of strange attractors, *Physica D*, *9*, 189–208, 1983.

Halsey, T. C., M. H. Jensen, L. P. Kadanoff, I. Procaccia, and B. I. Shraiman, Fractal measures and their singularities: The characterization of strange sets, *Phys. Rev. A*, *33*, 1141–1151, 1986.

Hentschel, H. G. E., and I. Procaccia, The infinite number of generalized dimensions of fractals and strange attractors, *Physica D*, *8*, 435–444, 1983.

Herrmann, H. J., Geometrical cluster growth models and kinetic gelation, *Phys. Rep.*, *136*, 153–227, 1986.

Huang, J., and D. L. Turcotte, Fractal mapping of digitized images: Application to the topography of Arizona and comparisons with synthetic images, *J. Geophys. Res.*, *94*, 7491–7497, 1989.

Jones, M. P., *Applied Mineralogy—A Quantitative Approach*, 259 pp., Graham and Trotman, London, 1987.

Jullien, R., and M. Kolb, Hierarchical model for chemically limited cluster-cluster aggregation, *J. Phys. A*, *17*, L639–L643, 1984.

Kaye, B. H., *A Random Walk Through Fractal Dimensions*, 421 pp., Verlag Chemie, Weinheim, Federal Republic of Germany, 1989.

Krohn, C. E., Sandstone fractal and Euclidean pore volume distributions, *J. Geophys. Res.*, *93*, 3286–3296, 1988*a*.

Krohn, C. E., Fractal measurements of sandstones, shales, and carbonates, *J. Geophys. Res.*, *93*, 3297–3305, 1988*b*.

Mandelbrot, B. B., *The Fractal Geometry of Nature*, 468 pp., W. H. Freeman, New York, 1983.

Mayer-Kress, G., (Ed.), *Dimensions and Entropies in Chaotic Systems*, 257 pp., Springer, Berlin, 1986.

Schuster, H. G., *Deterministic Chaos*, 270 pp., Verlag Chemie, Weinheim, Federal Republic of Germany, 1988.

Smith, D. J., High-resolution electron microscopy in surface science, in Chemistry and Physics on Solid Surfaces, edited by R. Vanselow, and R. Howe, *Springer Ser. Surf. Sci.*, *6*, 413–433, 1986.

Späth, H., *Cluster-Formation und Analyse*, 236 pp., Oldenbourg, München, 1983.

Stinchcombe, R. B., Fractals, phase transitions and criticality, *Proc. R. Soc. London, Ser. A*, *423*, 17–33, 1989.

Takayasu, H., *Fractals in the Physical Sciences*, 170 pp., Manchester University Press, Manchester, United Kingdom, 1990.

Tel, T., Fractals, multifractals and thermodynamics, *Z. Naturforsch. A*, *43*, 1154–1174, 1988.

Thompson, A. H., A. J. Katz, and C. E. Krohn, The microgeometry and transport properties of sedimentary rock, *Adv. Phys.*, *36*, 625–694, 1987.

Tucker, M., *Techniques in Sedimentology*, 394 pp., Blackwell, Oxford, 1988.

Werner, H. W., and A. Torrist, Interface and thin film analysis: Comparison of methods, trends, *Fresenius Z. Anal. Chem.*, *337*, 594–613, 1990.

West, B. J., and A. L. Goldberger, Physiology in fractal dimensions, *Am. Sci.*, *75*, 354, 1987.

Witten, T. A., and L. M. Sander, Diffusion-limited aggregation, a kinetic critical phenomenon, *Phys. Rev. Lett.*, *47*, 1400–1403, 1981.

Wolfram, S., Statistical mechanics of cellular automata, *Rev. Mod. Phys.*, *55*, 601–644, 1983.

A. Block, W. von Bloh, T. Klenke, and H. J. Schellnhuber, Institute for the Chemistry and Biology of the Marine Environment and Physics Department, University of Oldenburg, Postfach 2503, W-2900 Oldenburg, Federal Republic of Germany.

(Received January 2, 1991;
revised May 20, 1991;
accepted June 10, 1991.)

JOURNAL OF GEOPHYSICAL RESEARCH, VOL. 96, NO. B10, PAGES 16,319–16,333, SEPTEMBER 10, 1991

Crustal Subsidence, Seismicity, and Structure Near Medicine Lake Volcano, California

DANIEL DZURISIN

David A. Johnston Cascades Volcano Observatory, U.S. Geological Survey, Vancouver, Washington

JULIE M. DONNELLY-NOLAN, JOHN R. EVANS, AND STEPHEN R. WALTER

U.S. Geological Survey, Menlo Park, California

The pattern of historical ground deformation, seismicity, and crustal structure near Medicine Lake volcano illustrates a close relation between magmatism and tectonism near the margin of the Cascade volcanic chain and the Basin and Range tectonic province. Between leveling surveys in 1954 and 1989 the summit of Medicine Lake volcano subsided 389 ± 43 mm with respect to a reference bench mark 40 km to the southwest (average rate = 11.1 ± 1.2 mm/yr). A smaller survey across the summit caldera in 1988 suggests that the subsidence rate was 15–28 mm/yr during 1988–1989. Swarms of shallow earthquakes ($M \leq 4.6$) occurred in the region during August 1978, January–February 1981, and September 1988. Except for the 1988 swarm, which occurred beneath Medicine Lake caldera, most historical earthquakes were located at least 25 km from the summit. The spatial relation between subsidence and seismicity indicates (1) radially symmetric downwarping of the volcano's summit and flanks centered near the caldera and (2) downfaulting of the entire edifice along regional faults located 25–30 km from the summit. We propose that contemporary subsidence, seismicity, and faulting are caused by (1) loading of the crust by more than 600 km^3 of erupted products plus a large volume of mafic intrusives; (2) east-west extension in the western Basin and Range province; and, to a lesser extent, (3) crystallization or withdrawal of magma beneath the volcano. Thermal weakening of the subvolcanic crust by mafic intrusions facilitates subsidence and influences the distribution of earthquakes. Subsidence occurs mainly by aseismic creep within 25 km of the summit, where the crust has been heated and weakened by intrusions, and by normal faulting during episodic earthquake swarms in surrounding, cooler terrain.

INTRODUCTION AND SCOPE

The Medicine Lake region in northeastern California, located near the margin of the Cascades volcanic chain and the Basin and Range tectonic province, provides an excellent opportunity to study the relation between tectonism and magmatism near a convergent plate margin. The region is seismically active, and earthquakes have been monitored for several decades. Extensive leveling surveys were conducted throughout the region in 1954, and they can be repeated to determine vertical strain rates. In addition, Medicine Lake volcano's recent eruptive history is well known, and the regional crustal structure has been studied using various geophysical techniques. Our study combines results from repeat leveling surveys, earthquake monitoring, and measurements of crustal structure to develop a model that explains most aspects of contemporary ground deformation and seismicity.

GEOLOGIC SETTING AND ERUPTIVE HISTORY

Medicine Lake volcano is a Pleistocene-Holocene shield volcano located about 50 km east-northeast of Mount Shasta, between the crest of the Cascade Range to the west and the Basin and Range tectonic province to the east (Figure 1). The Medicine Lake shield rises about 1200 m above the Modoc Plateau to an elevation of 2376 m. Lavas from Medicine Lake volcano cover nearly 2000 km^2, and their volume is estimated to be at least 600 km^3, making it the largest volcano by volume in the Cascade Range. Medicine Lake volcano began to grow about 1 m.y. ago, following eruption of a large volume of tholeiitic high-alumina basalt. Similar high-alumina basalt has continued to erupt around the volcano throughout its history. Although mafic lavas predominate on the volcano's flanks, all lava compositions from basalt to rhyolite have erupted during Pleistocene time. The lower flanks consist of mostly basaltic and some andesitic lavas. Basalt is mostly absent at higher elevations, where andesite dominates and rhyolite and small volumes of dacite are present [*Donnelly-Nolan*, 1988].

During the past 11,000 years, eruptive activity at Medicine Lake volcano has been episodic. Eight eruptions produced about 5.3 km^3 of basaltic lava during a time interval of a few hundred years about 10,500 years ago. That eruptive episode was followed by a hiatus that ended with a small andesitic eruption about 4300 years ago. During the most recent eruptive episode between 3000 and 900 years ago, eight eruptions produced approximately 2.5 km^3 of lava ranging in composition from basalt to rhyolite. Late Holocene lava compositions include basalt and andesite, but silicic lavas dominate [*Donnelly-Nolan et al.*, 1989].

Medicine Lake caldera is a 7 × 12 km depression in the summit area of the volcano. *Anderson* [1941] suggested that the caldera formed by collapse after a large volume of andesite was erupted from vents along the caldera rim. However, the distribution of late Pleistocene vents, mostly concentrated along the rim, suggests that ring faults already existed when most of the andesite erupted [*Donnelly-Nolan*, 1988]. No single large eruption has been related to caldera

Paper number 91JB01452.

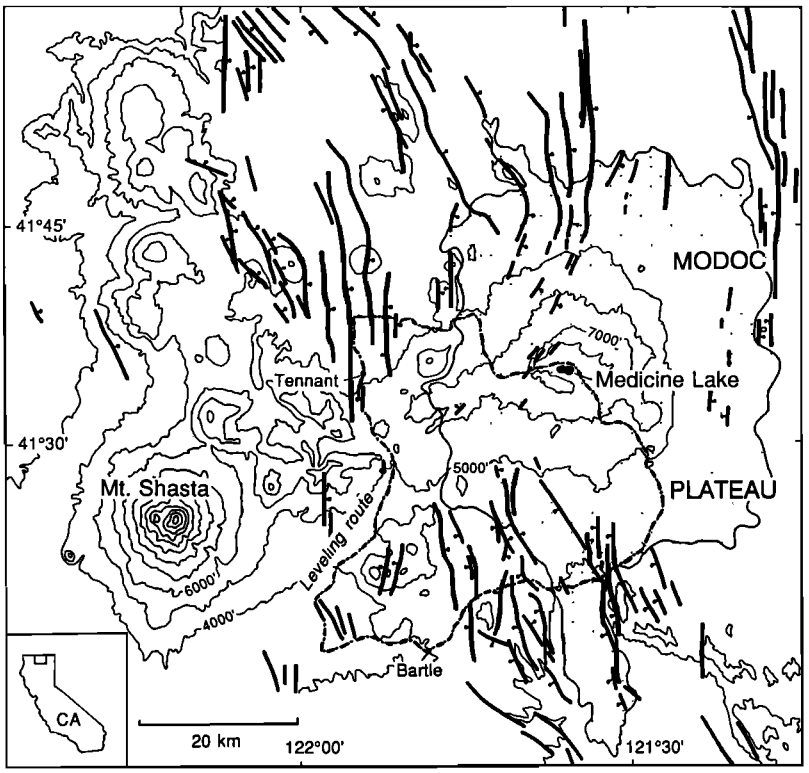

Fig. 1. Location map showing the Medicine Lake volcano–Mount Shasta area of the southern Cascade Range, northern California. Pattern indicates extent of lavas of Medicine Lake volcano. Heavy lines are faults, with bar and ball on downthrown side (*Gay and Aune* [1958] and air photograph interpretation). Heavy dotted-dashed line represents the 1954–1989 leveling route. Contour interval is 1000 feet (305 m).

formation. The only eruption recognized to have produced ash flow tuff occurred in late Pleistocene time, and this eruption was too small to account for formation of the caldera [*Donnelly-Nolan and Nolan*, 1986]. *Donnelly-Nolan* [1988] concluded that Medicine Lake caldera formed by collapse in response to repeated extrusions of mostly mafic lava beginning early in the history of the volcano (perhaps in a manner similar to the formation of Kilauea caldera, Hawaii). She hypothesized several small differentiated magma bodies fed by and interspersed among a plexus of dikes and sills. In her model, late Holocene andesitic to rhyolitic lavas were derived by fractionation, assimilation, and mixing from high-alumina basalt parental magma.

CRUSTAL STRUCTURE

The crustal structure beneath Medicine Lake volcano is dominated by a roughly columnar region, approximately 40 km thick and 50 km in diameter, consisting of mostly high-velocity material superposed on what has been interpreted as either (1) a transition zone from Klamath terrain to basement equivalent to Sierran batholith [*Fuis et al.*, 1987] or (2) an underplated Basin and Range structure in a back arc setting [*McKee et al.*, 1983; *Catchings*, 1987]. Seismic refraction measurements indicate that a high-velocity basement underlies 3–5 km of low-velocity material, which presumably consists of lava flows from Medicine Lake volcano plus interbedded lava flows and sediment of the Modoc Plateau. Schlumberger soundings in the area detected a "geoelectric basement" with a resistivity greater than 200 ohm m at a depth of 1.5 km beneath Medicine Lake caldera [*Zohdy and Bisdorf*, 1990], near the contact between the base of the volcano and the underlying Modoc Plateau.

Various lines of evidence suggest that virtually the entire crustal column beneath Medicine Lake volcano has been intruded by mafic dikes, is still hot, and may be locally molten. The low-velocity layer near the surface is underlain at the volcano by a high-velocity, high-density lens that extends from about 1 km to at least 3 km below the caldera (from about 1 km above to 1 km below sea level; Figure 9*a*). This feature has been interpreted as a complex of mafic-to-silicic material intruded into Modoc Plateau materials [*Finn and Williams*, 1982; *Zucca et al.*, 1986; *Evans and Zucca*, 1988]. An active source seismic tomography experiment indicated that seismic wave fronts are steepened by a radially symmetric, high-velocity anomaly 5–10 km beneath the volcano [*Evans and Zucca*, 1988]. This high-velocity root extends to even greater depths, as shown by inversion of teleseismic travel time data. The inversion indicates that the lower crust, upper mantle, and possibly the middle crust are 2–4% faster than surrounding material. In addition, the upper and middle crust beneath the volcano may be seismically attenuating, on the basis of interpretation of a seismic refraction study [*Catchings*, 1983].

At Newberry volcano, a shield volcano in central Oregon that is geologically similar to Medicine Lake volcano, *Stauber et al.* [1988] used teleseismic data to image a columnar high-velocity feature that extends from within 10 km of the surface to about 25 km depth. They interpreted this feature as a largely subsolidus mafic intrusive complex. On the basis of the surface geology and seismic data from

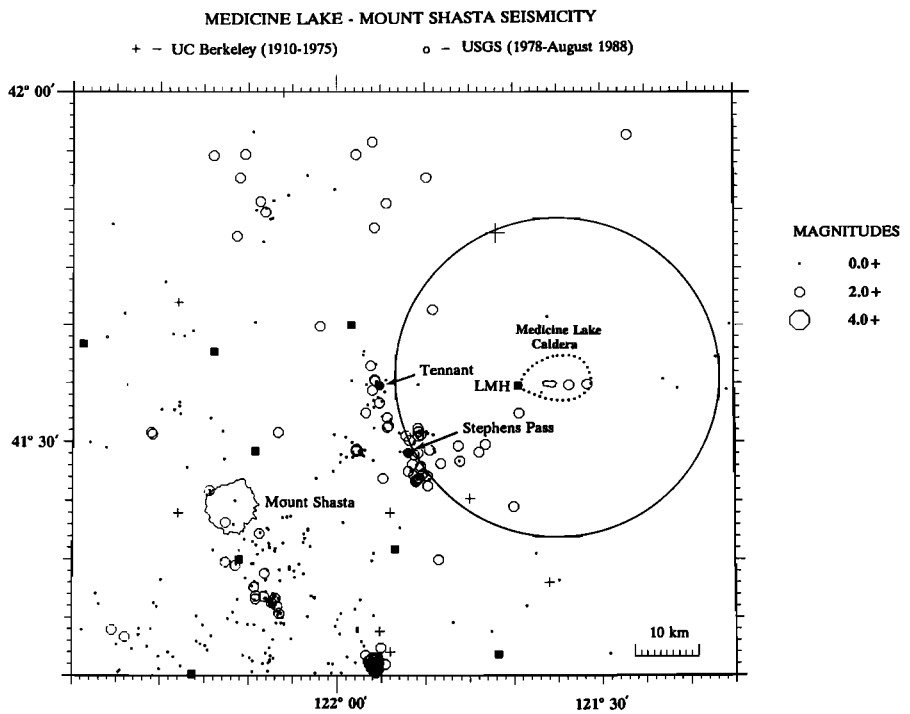

Fig. 2. Seismicity in the Medicine Lake–Mount Shasta region for the period from 1910 to August 1988. Solid squares represent seismographs of the USGS Mount Shasta network, including Little Mount Hoffman (LMH) on the west rim of Medicine Lake caldera. Large circle encloses a relatively aseismic area within 25 km of the summit of Medicine Lake volcano. Clusters of earthquakes near Tennant and Stephens Pass occurred during swarms in 1981 and 1978, respectively [from *Bolt and Miller*, 1975; USGS, unpublished data, 1991].

Medicine Lake volcano, and by analogy to Newberry volcano, we conclude that the lower and possibly middle crusts beneath Medicine Lake volcano consist of silicic rocks intruded by numerous dikes and sills that contain gabbro and diabase (slowly cooled equivalents of mafic melts), perhaps with variable amounts of basalt melt. In the upper mantle the high-velocity anomaly may represent ultramafic residuum left by removal of this basalt. This conclusion is consistent with (1) geochemical evidence suggesting that generation of intermediate and silicic melts from basaltic melts by fractionation and assimilation occurs in the upper crust [*Grove and Baker*, 1984; *Grove and Donnelly-Nolan*, 1986; *Grove et al.*, 1988] and (2) the eruption of primitive mantle-derived basalt throughout the history of Medicine Lake volcano [*Donnelly-Nolan*, 1988].

The high-resolution active seismic tomography experiment mentioned above detected a low-velocity, low-Q region in the upper crust beneath Medicine Lake caldera [*Evans and Zucca*, 1988]. The anomalous feature, which extends from about 1 to 3 km below sea level (i.e., 3–5 km beneath the caldera), has a diameter of about 3 km and a volume of the order of 10 km^3. It is interpreted as a small silicic magma body, on the basis of its distinctive seismic signature, its association with an active magmatic system, and various geologic, geochemical, and geophysical considerations [*Evans and Zucca*, 1988; *Evans and Walter*, 1989]. No other magma bodies were suggested by the experiment, which had a spatial resolution of 1–2 km in the upper 5–7 km of the crust beneath the caldera and most of the shield.

SEISMICITY

Prior to the first seismograph records in 1909, there were various reports of seismic activity in the Medicine Lake region. G. W. Courtright, a local rancher and trapper, felt numerous earthquakes and saw "flames" and ground cracks near Glass Mountain in January and February 1910 [*Finch*, 1928]. Finch also reported that "earthquakes originating in the mountain and accompanied by rattling noises have been noted by Forest Service officials for at least 15 years." He added, "Similar noises and shakes have been observed by Mr. Courtright for a much longer period."

Seismic records collected by the University of California Berkeley Seismographic Stations starting in 1909 show no earthquakes in the Medicine Lake–Mount Shasta region prior to 1950 [*Bolt and Miller*, 1975]. However, instrumental coverage during that interval was such that events smaller than M 4 probably would not have been located. As additional stations were added in the 1950s, earthquakes as small as M 3.0 began to be located in the Mount Shasta area. Still, no events were detected near Medicine Lake volcano through 1975 (Figure 2).

In 1980 the U.S. Geological Survey (USGS) extended its northern California seismic network by installing nine short-period, vertical seismometers around Mount Shasta. The new stations included one on the western edge of Medicine Lake caldera at Little Mount Hoffman (LMH, Figure 3*a*). Seismic signals are telemetered by a combination of radio and telephone lines to the USGS office in Menlo Park,

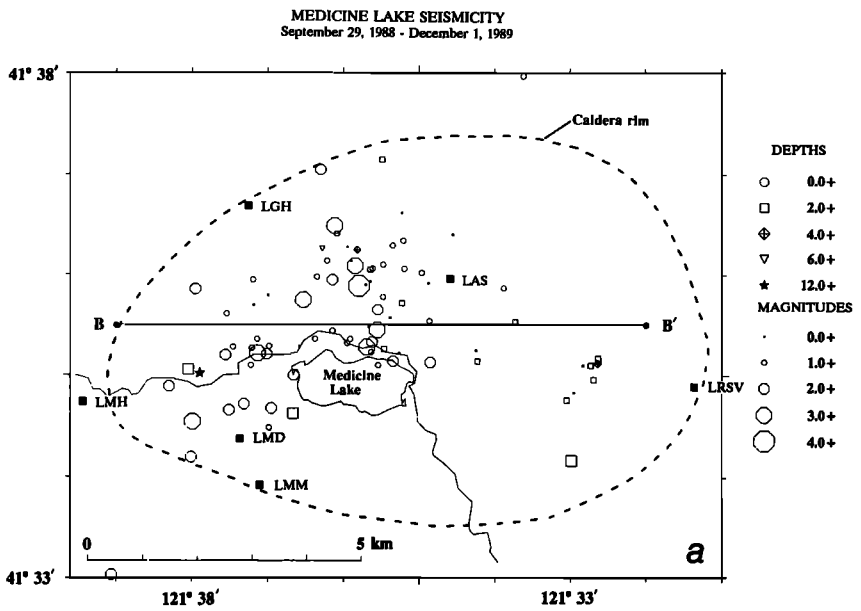

Fig. 3*a*. Located earthquakes of the 1988 Medicine Lake swarm and its aftershocks. Epicenters are shown as open symbols, and seismographs of the USGS Medicine Lake network, installed in October 1988, are shown as solid squares. Solid line at lower left represents the main road across the caldera that was leveled in 1954, 1988, and 1989; dashed line represents the caldera rim. The star about 2 km west of the west end of Medicine Lake marks the location of a long-period earthquake that occurred at 15 km depth on December 1, 1989. Line B-B′ shows the orientation of the cross section shown in Figure 3*b*.

California, where they are recorded and earthquakes are identified, timed, and located. Earthquakes are located with HYPOINVERSE [*Klein*, 1989] using a homogeneous layered crustal model determined from refraction studies [*Catchings*, 1983, 1987]. For a full discussion of instrumentation and data processing, see *Lester and Meagher* [1978] and *Stewart and O'Neill* [1980].

Between 1980 and the September 1988 swarm (see below), only three earthquakes were located in the vicinity of Medicine Lake caldera. Two of these events occurred in the eastern part of the caldera, in an area active after the 1988 swarm. The third event was a long-period earthquake that occurred on October 14, 1986. An approximate location for this event places it about 13 km beneath the western edge of the caldera, close to the hypocenter of a well-located long-period earthquake that occurred on December 1, 1989 (see the 1988 Medicine Lake swarm, Figure 3).

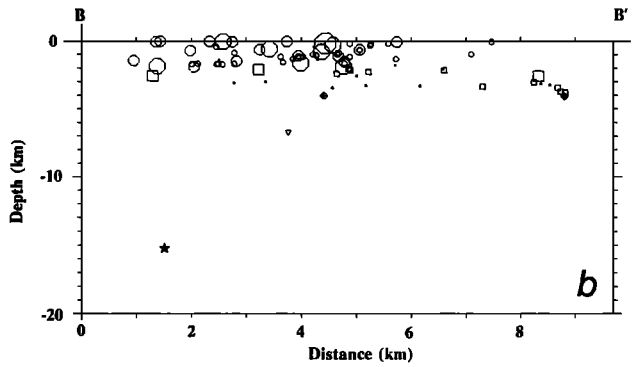

Fig. 3*b*. Cross section shows depths of the earthquakes that occurred during the 1988 swarm. All epicenters shown in Figure 3*a* were projected onto a vertical plane through B-B′. Star at about 15 km depth represents the same long-period earthquake as in Figure 3*a*.

1978 Stephens Pass Swarm

The apparent seismic quiescence near Medicine Lake volcano was broken by an intense swarm of shallow earthquakes that began with a M 4.6 event on August 1, 1978. The initial shock was followed within the next 90 min by six events of M 3.5–4.5 and within 24 hours by 100–200 events of $M \geq 2$ [*Cramer*, 1978; *Bennett et al.*, 1979]. The epicentral area was centered 15 km south of the town of Tennant and 5 km south of Stephens Pass, approximately midway between Medicine Lake volcano and Mount Shasta (Figure 2). A second flurry of activity began with a M 4.3 event on August 12. On August 14, U.S. Forest Service personnel reported large fissures across Stephens Pass Road 5 km south of Stephens Pass.

Subsequent field observations documented a 2-km-long, 75-m-wide zone of tensional fractures, grabens, and circular depressions ("sink holes") within the grabens. The zone trended north-south through the epicentral area (Figure 4). Vertical displacements were as large as 1 m in the grabens and 1.5 m in the circular depressions [*Cramer*, 1978; *Bennett et al.*, 1979]. An 8-km-long aftershock zone dips eastward away from the ground breakage; focal depths increase eastward to a maximum of about 4 km. Focal mechanisms suggest east-west extension on a north striking fault dipping 35°–45° east [*Cramer*, 1978], consistent with the pattern of north striking normal faults in the region.

1981 Tennant Swarm

Another swarm of shallow earthquakes occurred during January–February 1981, in this case almost directly beneath

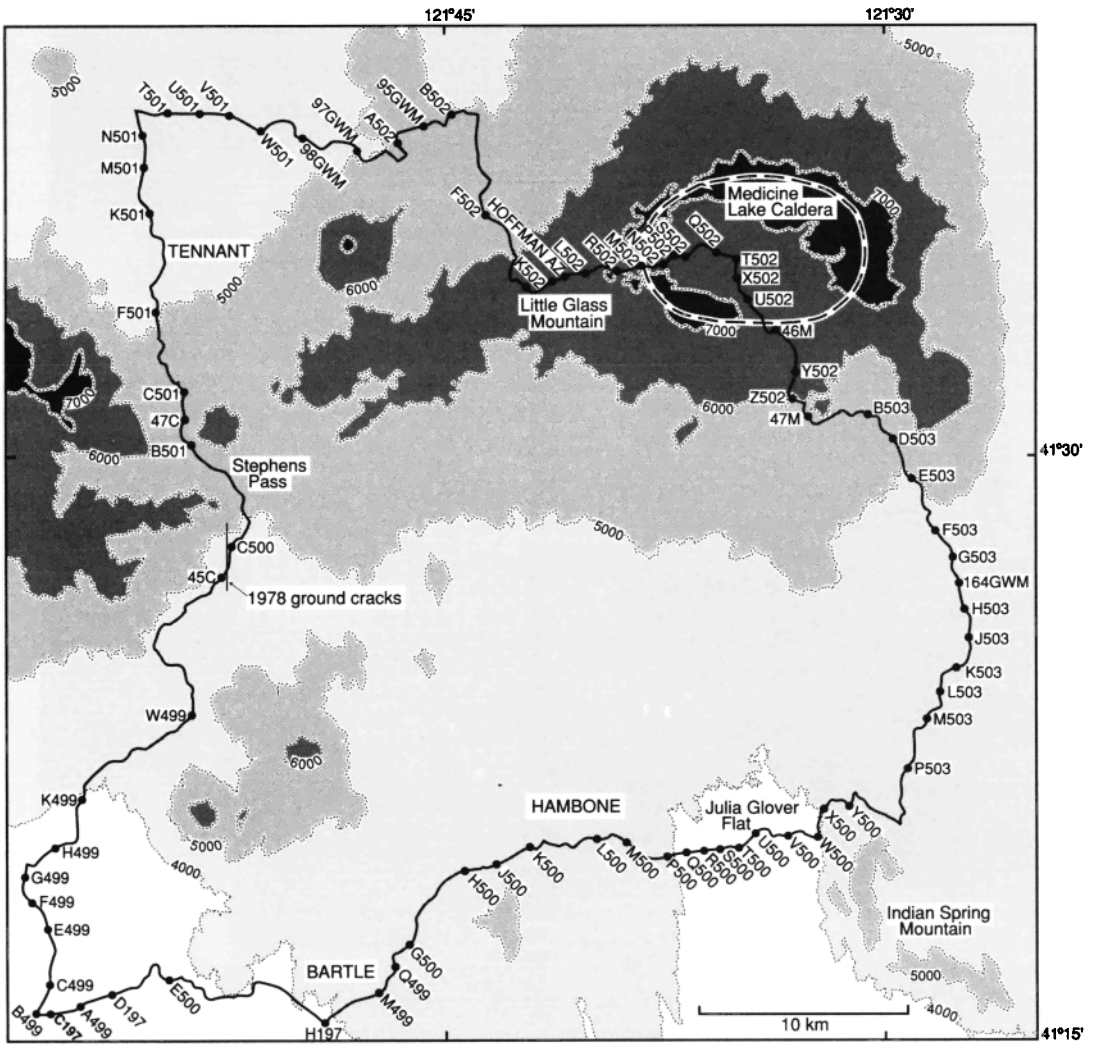

Fig. 4. Locations of bench marks along the 193-m leveling circuit across Medicine Lake volcano and Stephens Pass. Also shown are the locations of Bartle, Hambone, Tennant, and several features mentioned in the text. Stippling indicates five elevation ranges, from less than 4000 feet (1220 m) above sea level (no stippling) to more than 7000 feet above sea level (2130 m) (the heaviest stippling); contour interval is 1000 feet (305 m). Throughout the text, stadia distances are measured counterclockwise from H197, the southernmost mark in the circuit, near Bartle. Dashed line marks the boundary of Medicine Lake caldera; solid line between bench marks C500 and 45C near Stephens Pass indicates the area of ground breakage associated with the 1978 Stephens Pass earthquake swarm [from *Bennett et al.*, 1979].

the small town of Tennant, about 10 km north of Stephens Pass. The activity began on January 1, 1981, with an earthquake that was felt by residents of Tennant (A. M. Allison, personal communication, 1981). Several dozen additional events, all of $M < 3.0$, were recorded on seismographs of the Mount Shasta network from January 5 to January 8. Activity increased abruptly early on January 9 with a M 4.1 earthquake, the largest of the sequence, followed by 26 events of $M \geq 2.0$ within the next 24 hours, including 11 events of $M \geq 3.0$. Seismicity declined markedly over the next several weeks, with several flurries of small events ($2.0 \leq M \leq 3.0$) on January 12 and again in early February.

Temporary seismic stations were installed by January 15, after the main part of the sequence had ended. Well-determined focal depths for aftershocks recorded by the temporary stations all are very shallow, generally less than 2 km. The aftershock zone is about 10 km long and elongate in a north-south direction, suggesting movement on a north striking fault aligned with the regional structural pattern (Figures 1 and 2). Despite the large extent of the aftershock zone and the shallowness of the seismicity, no ground breakage was reported. However, minor ground breakage could have been obscured by a thin layer of snow covering the ground at the time (J. Coakley, personal communication, 1990).

1988 Medicine Lake Swarm

The Medicine Lake swarm began on the morning of September 29, 1988, with a flurry of some 20 small events, the largest of M 3.3. The swarm peaked in the late afternoon with more than 80 earthquakes recorded in 1 hour, including two M 3.5 events and one M 4.1 event, the largest of the

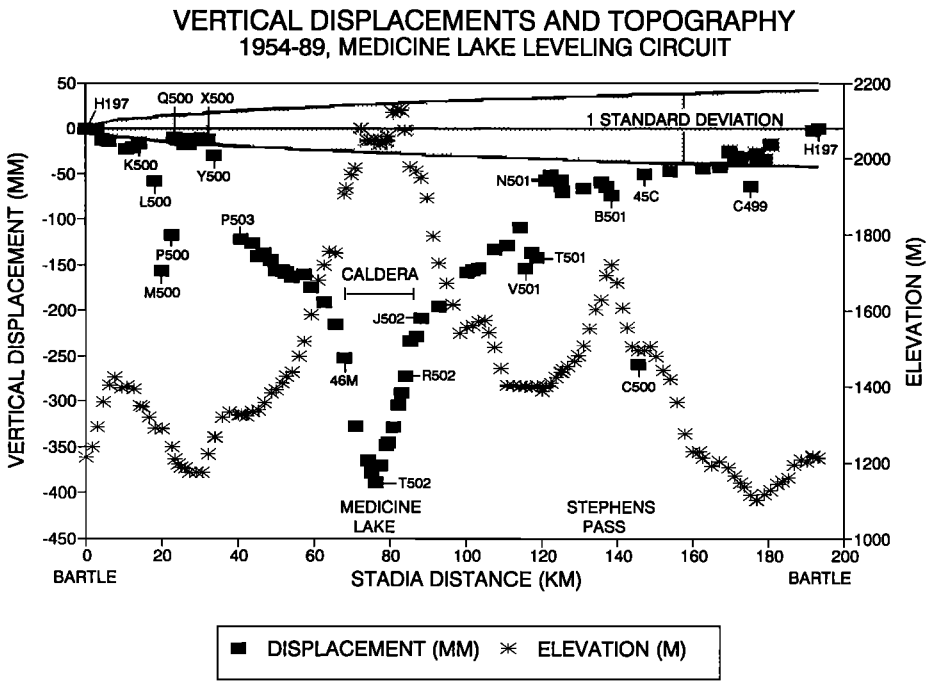

Fig. 5. Topographic profile (asterisks) and 1954–1989 vertical displacements (squares) along the Medicine Lake–Stephens Pass leveling circuit. Stadia distance is measured counterclockwise from H197 near Bartle, which is held fixed (see Figure 4). Stippled area indicates 1 standard deviation in the vertical displacements, based on published standards for second-order, class II leveling surveys (1954) and first-order, class II surveys (1989) [*Vanicek et al.*, 1980]. At any stadia distance the vertical dimension of the stippled area indicates the height of the 1-sigma error bar at that distance.

sequence. Activity declined rapidly with 90 earthquakes recorded in the next 24 hours, several events per day during October 1988, and several events per week during the remainder of 1988. Several additional seismographs were installed around Medicine Lake caldera in late October 1988 (Figure 3). Sporadic flurries of small events ($M \leq 3.1$) occurred beneath Medicine Lake caldera throughout 1989 [*Walter and Dzurisin*, 1989].

All 1988–1989 earthquakes occurred beneath Medicine Lake caldera, primarily north or west of Medicine Lake (Figure 3*a*) and within about 2 km of the surface (Figure 3*b*). A small cluster of events occurred in April 1989 at depths of 3–4 km beneath the eastern part of the caldera. With one exception, all 1988–1989 earthquakes were short-period, tectonic-type events. A long-period event of M 2.7 occurred about 15 km beneath the western part of the caldera on December 1, 1989. Similar long-period events have been recorded (1) beneath Kilauea and Mauna Loa volcanoes in Hawaii; (2) beneath Long Valley caldera, the Lassen volcanic center, and near the Geysers/Clear Lake area, all in California; and (3) at Yellowstone caldera in Wyoming. The significance of such long-period events may not be the same at every volcano, but their association with young magmatic systems suggests that they record movement of mafic magma or other fluids within the crust [e.g., *Koyanagi et al.*, 1987; *Chouet et al.*, 1987].

Leveling Results

A 193-km leveling circuit across Medicine Lake volcano and Stephens Pass via the towns of Tennant and Bartle (Figure 4) was first measured in 1954 by the National Geodetic Survey (NGS) using second-order, class II procedures. The circuit was remeasured in 1989 by the USGS Cascades Volcano Observatory (CVO), using first-order, class II procedures. CVO also measured a 20-km segment of the same circuit, from bench mark J502 near Little Glass Mountain eastward across Medicine Lake caldera via T502 to 46 M, in August 1988 and October 1988. All appropriate corrections specified by NGS [*Schomaker and Berry*, 1981; *Balazs and Young*, 1982] were applied to the measurements, including rod scale corrections based on calibrations performed at the National Bureau of Standards and refraction corrections based on measured temperatures. Misclosures for the 193-km circuit were 5.4 mm in 1954 and 19.7 mm in 1989, compared to NGS specifications of 111 mm (8 mm/km$^{1/2}$ $L^{1/2}$ for second-order, class II surveys) and 69 mm (5 mm/km$^{1/2}$ $L^{1/2}$ for first-order, class II surveys [*Vanicek et al.*, 1980]), respectively. An analysis of random and systematic errors in the surveys is given in the Appendix.

Vertical Displacements, 1954–1989

Figures 4–6 show bench mark locations, topography, and vertical displacements during 1954–1989 along the Medicine Lake leveling circuit. Displacements are relative to bench mark H197 near Bartle, which was held fixed as a reference. A broad area of subsidence centered at Medicine Lake caldera and extending across the entire volcano is evident in Figures 5 and 6. The maximum measured subsidence was 389 ± 43 mm at T502, which corresponds to an average annual rate of 11.1 ± 1.2 mm/yr during the 35-year interval spanned by the surveys. T502 is the bench mark nearest to the center of the caldera.

Between 1954 and 1989, large local displacements occurred south of Medicine Lake caldera near M500 (east of

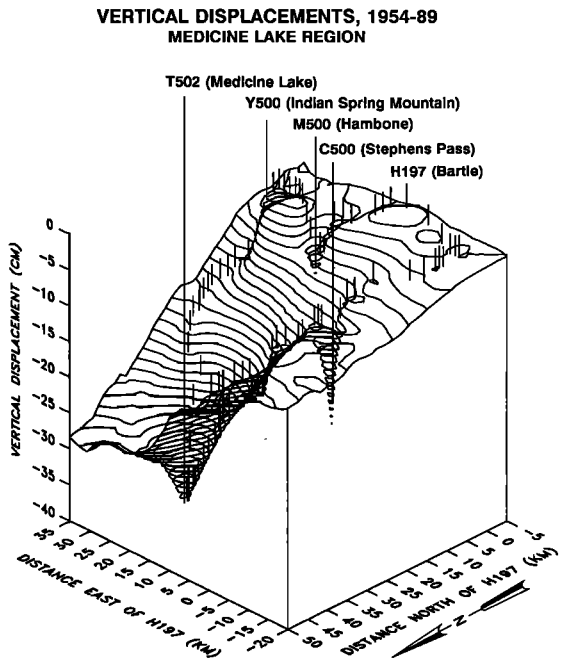

Fig. 6. Three-dimensional representation of the 1954–1989 vertical displacements in the Medicine Lake region. Curved lines represent contours of relative vertical displacement (contour interval = 10 mm). Locations of bench marks along the leveling route are indicated by small vertical lines. View is from the northwest. Displacements are known accurately only at the marks; elsewhere they were extrapolated using a gridding program with an inverse square weighting scheme. Fault displacements near M500 (Hambone), Y500 (Julia Glover Flat), and C500 (Stephens Pass) are not portrayed accurately because the leveling traverse did not sample those areas in detail.

Hambone) and Y500 (northeast end of Indian Spring Mountain), and also west of the caldera near V501 and N501 (north of Tennant) and C500 (Stephens Pass) (Figures 4–6). C500 is located within the epicentral area of the 1978 Stephens Pass earthquake swarm, near the southern end of a zone of ground cracks that formed during the swarm [*Bennett et al.*, 1979]. C500 is on the east (downthrown) side of the surface cracks, while nearby marks are on the west side. We attribute the anomalous movement of C500 to the effects of the 1978 swarm. V501 and N501 are located near the northern margin of the epicentral area associated with the 1981 Tennant earthquake swarm, near a prominent north striking regional fault (Figures 1 and 4). We suspect that the anomalous movements of V501, N501, and two intervening marks occurred during the 1981 swarm. M500 and Y500 are located near prominent, young-looking normal faults that bound Indian Spring Mountain and Julia Glover Flat in horst-and-graben terrain about 30 km south of Medicine Lake caldera (Figure 4). One fault forms the eastern boundary of Julia Glover Flat and offsets by about 10 m a basalt flow dated 10,600 years B.P. [*Donnelly-Nolan et al.*, 1989]. The large displacements of marks near M500 and Y500 indicate that some of these faults have been active since 1954. A search of regional seismic records for the period from 1911 to 1989 turned up only one earthquake larger than M 2.0 in the area; a M 3.2 event on February 16, 1959, located about 10 km east-southeast of Hambone, beneath Julia Glover Flat. However, the records are incomplete for events of $M \leq 4.5$ prior to about 1950 and of $M \leq 3.5$ during 1950–1980. Therefore a swarm of smaller earthquakes could have gone undetected, as evidenced by the absence of recorded earthquakes near Glass Mountain associated with the 1910 swarm reported by *Finch* [1928].

Inspection of Figures 4 and 5 suggests that historical faulting has downdropped Medicine Lake volcano by 5–10 cm with respect to the surrounding plateau (i.e., P503 relative to Y500 and T501 relative N501; Figure 5). Owing to the configuration of the leveling route, it is unclear whether this subsidence is bounded by a north striking graben or a basin centered at Medicine Lake caldera. The existence of a circular subsidence feature nested within a major north striking graben encompassing both Medicine Lake volcano and Mount Shasta has been proposed on the basis of regional magnetic and gravity anomalies [*Blakely et al.*, 1985; *Blakely and Jachens*, 1990], but those anomalies are considerably larger than the area of subsidence surrounding Medicine Lake caldera.

It is surprising that Julia Glover Flat, a young-looking graben that the leveling route crosses between Q500 and X500, was stable during 1954–1989 while adjacent areas to the west and northeast subsided 10–15 cm (Figure 5). This sense of movement is opposite to what has prevailed over longer time scales, as indicated by the current topography and by large Holocene movements on faults that bound the graben. Thus Julia Glover Flat seems particularly prone to faulting and subsidence in the future.

Vertical Displacements, 1988–1989

Any relation between the subsidence during 1988–1989 and the September 1988 earthquake swarm is difficult to demonstrate, because movements were barely larger than measurement error. Vertical displacements within Medicine Lake caldera from August 1988 to August 1989 are mostly less than 2 standard deviations of the measurements and therefore of marginal significance. However, the measured displacements suggest that the intracaldera subsidence rate was at least as high during 1988–1989 as during 1954–1989. The average subsidence rate at T502 with respect to J502 was 13.8 ± 3.5 mm during 1988–1989 compared to 5.2 ± 0.2 mm/yr during 1954–1989. The amount of movement at T502 during 1988–1989 seems anomalous relative to nearby bench marks (Figure 7), but even at adjacent marks the 1988–1989 subsidence rates were higher than the 1954–1989 rates (e.g., at X502, 7.6 ± 4.0 mm/yr during 1988–1989 compared to 4.8 ± 0.3 mm/yr during 1954–1989). The 1988 and 1989 surveys did not include H197, so subsidence rates with respect to H197 can only be estimated by comparison with the 1954–1989 results. From 1954 to 1989 the amount of subsidence at T502 with respect to J502 was about half the amount at T502 with respect to H197 (Figure 5). Assuming the subsidence pattern did not change, we doubled the 1988–1989 subsidence rates with respect to J502 to estimate the rates with respect to H197. Thus we estimate that the center of Medicine Lake caldera subsided 15 mm/yr (X502) to 28 mm/yr (T502) with respect to H197 during 1988–1989, compared to 11.1 ± 1.2 mm/yr at T502 during 1954–1989.

SUBSIDENCE MECHANISMS

Mechanisms that might cause subsidence of Medicine Lake volcano and sporadic earthquake swarms in the sur-

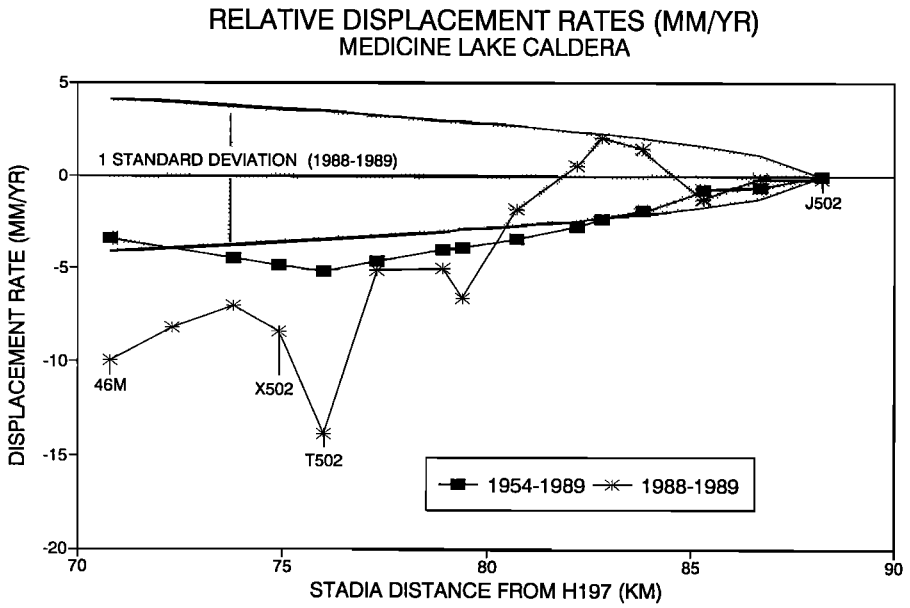

Fig. 7. Annual vertical displacement rates relative to J502 for the periods 1954–1989 (squares) and August 1988 to August 1989 (asterisks) along a 20-km leveling traverse across Medicine Lake caldera. Stippled area indicates 1 standard deviation in the 1988–1989 displacement rates. At any stadia distance the vertical dimension of the stippled area indicates the height of the 1-sigma error bar for the 1988–1989 measurements at that distance. See Figure 4 for locations of bench marks.

rounding area include (1) crustal thinning caused by extension in the western Basin and Range province, (2) loading of the crust by the weight of the volcano and its subvolcanic intrusive complex, (3) densification during cooling and crystallization of magma, and (4) deflation caused by magma withdrawal. We propose that mechanisms 1 and 2 are primarily responsible for historical subsidence and that mechanisms 3 and 4 may contribute over longer time scales.

Crustal Extension

Several lines of evidence indicate that an important mechanism for historical subsidence at Medicine Lake volcano is thinning and bending of the crust in response to regional tectonic extension. Although the contemporary extension rate has yet to be measured, structural and geologic evidence indicates that Medicine Lake volcano lies in a region of east-west extension that has been active at least through late Holocene time. Seismic and leveling data show that extension and faulting have continued to the present. The Medicine Lake area is cut by numerous north striking normal faults with up to a few hundred meters of displacement. Others may be partially or completely buried by young lava flows. Open ground cracks, common on and around Medicine Lake volcano, have N30°W to N30°E orientations and east-west opening directions consistent with the extensional direction indicated by regional faults [*Donnelly-Nolan*, 1988]. The same is true for cracks that formed during the 1978 Stephens Pass earthquakes, which had focal mechanisms indicating east-west extension on a north striking fault [*Cramer*, 1978].

If the mechanical response of the crust in the Medicine Lake region were laterally homogeneous, east-west extension would cause grabens and fissures to form along a north striking axis, creating a north trending trough. That is not the pattern observed at Medicine Lake volcano, where the known subsidence is more or less symmetric about the center of Medicine Lake caldera. However, could such a pattern result from east-west extension if the crust beneath the volcano is mechanically weaker than its surroundings? Using a finite element model of the crust and upper mantle beneath the Yellowstone region, *Meertens* [1987] demonstrated the reverse process, i.e., that regional compressive strain can cause doming of mechanically weak crust. He proposed that such weakness is a consequence of elevated temperatures and fracturing associated with the Yellowstone magmatic and hydrothermal systems. If similar conditions prevail beneath Medicine Lake volcano (as indicated by interpretation of seismic data), then subsidence of weak subvolcanic crust could be a result of Basin and Range extension.

Crustal Loading

Another mechanism that may contribute to subsidence at Medicine Lake volcano is crustal loading by the volcanic edifice and dense mafic intrusions. A similar mechanism has been proposed to account for subsidence of the Hawaiian Islands [*Moore*, 1970]. The dimension over which the crust is loaded, which determines the response depth, is an order of magnitude larger in Hawaii (400 km) than at Medicine Lake volcano (40 km). Therefore a classical isostatic response of the asthenosphere is unlikely at Medicine Lake volcano. However, a similar response might occur within the upper lithosphere, because is has been heated and weakened by numerous mafic intrusions.

Studies of samples from eight drill holes located on the upper flanks of Medicine Lake volcano indicate that five of the holes penetrated the entire volcanic pile. In drill cores from each of those holes, fresh aphyric lavas of Medicine Lake volcano abruptly give way to altered flows, sediments,

and/or porphyritic lavas, some of which are petrographically unlike Medicine Lake lavas [*Donnelly-Nolan*, 1990]. One hole on the west flank reached a highland of pre–Medicine Lake volcano vents and flows (at 4600 feet, 1402 m elevation) that connects westward to Mount Shasta. The other four holes penetrated the base of Medicine Lake volcano at elevations of 2487–3365 feet (758–1026 m), well below the level of the surrounding Modoc Plateau (1250 m). The possibility that a circular basin 0.5 km deep may have existed at the location where Medicine Lake volcano was built is thought to be unlikely. No thick sequences of sediment are present in any of the drill holes, nor do the underlying basalt flows show signs of eruption into water. We conclude that the crust under the volcano has been downwarped approximately 0.5 km relative to the surrounding plateau, at least partly as a result of crustal loading.

The downwarped part of the volcanic edifice does not contribute significantly to the isostatic load, because it displaces rocks of similar density [*Zucca et al.*, 1986]. However, the drill core observations indicate the large magnitude of subsidence that has occurred over geologic time scales, and it is likely that at least part of the historical subsidence is caused by this mechanism. More subsidence may have occurred deeper in the crustal column if magmatic intrusion caused unrecorded uplift, which seems likely on the basis of seismic evidence for dense intrusive material throughout the crustal column. One consequence of the downwarping is that the volume of the volcano may be significantly greater than the previous estimate of 600 km^3. The volume of Medicine Lake volcano that has been downwarped below 1250 m elevation is approximately 150 km^3, so the total volume of the volcanic pile is estimated to be 750 km^3.

The long-term subsidence rate calculated from the amount of downwarping can be compared to the historical subsidence rate determined from measured displacements. Geologic mapping shows that Medicine Lake volcano had attained essentially its current configuration by about 150,000 years B.P., so the current subsidence rate can be estimated as 0.5 km/1.5 $\times$ 10^5 years = 3 mm/yr (assuming that the entire load was emplaced 150,000 years ago). This estimate is of the same order as, but almost a factor of 4 less than, the subsidence rate during 1954–1989 measured by leveling (11.1 $\pm$ 1.2 mm/yr). The implication is that the effect of crustal loading has increased through time to account for the current subsidence rate or, more likely, that crustal loading is not the dominant cause of contemporary subsidence.

Cooling and Crystallization of Magma

Subsidence may also result from densification in response to fluid loss during cooling and crystallization of magma. Even for a large rhyolitic system with a vigorous hydrothermal system such as Yellowstone, the thermal contraction caused by cooling of crystalline rock is negligible. However, if heat is extracted from the crustal column by cooling and crystallization of magma, the amount of contraction is appreciable. At Yellowstone, crystallization of rhyolite initially containing 2 wt % water results in a 7% decrease in volume, assuming that all of the released aqueous fluid escapes to the shallow, hydrostatically pressured part of the hydrothermal system [*Fournier*, 1989; *Dzurisin et al.*, 1990]. The amount of contraction would be somewhat less for silicic magmas, which typically contain less water. Note that this mechanism causes both horizontal contraction and subsidence, owing to the net decrease in volume.

Although there is scant surface evidence for a significant hydrothermal system beneath Medicine lake volcano, high vertical temperature gradients in three drill holes suggest that a considerable amount of heat may be available in the shallow subsurface [*Donnelly-Nolan et al.*, 1989]. The most likely heat sources are the low-velocity, low-Q zone beneath the caldera or an underlying zone of mafic intrusions. If the heat is derived from crystallizing magma in either of these zones, resulting fluid loss may account for part of the historical subsidence. If so, the thermal and chemical signature of the magma is greatly attenuated at the surface, possibly by flushing through the shallow groundwater system.

Magma Withdrawal

Evans and Walter [1989] proposed that deflation of the shallow magma chamber identified by a seismic tomography experiment [*Evans and Zucca*, 1988] caused the floor of Medicine Lake caldera to bow downward and eventually fail under bending stresses during the September 1988 earthquake swarm (Figure 9*a*). Although deflation of this chamber might contribute to subsidence, the leveling observations and modeling results (see the section on source models) show that the chamber is too small and shallow to account for the full extent of the 1954–1989 subsidence. Two long-period earthquakes have occurred recently in the depth range 13–15 km beneath Medicine Lake caldera, but their relation to the 1954–1989 subsidence is uncertain. Perhaps intruding mafic magma accumulates temporarily at 10–15 km depth, cools, densifies, and then sinks while still fluid to cause subsidence. Withdrawal of silicic magma from shallower depth seems less likely, owing to its lower density and greater effective viscosity. In either case, magma withdrawal probably is of secondary importance except during eruptive or intrusive episodes, when large volumes of magma move rapidly to the surface or into the rift zones.

SOURCE MODELS

A realistic model of the 1954–1989 subsidence would include both viscoelastic and brittle deformation (i.e., downsagging and faulting) and would be constrained by both horizontal and vertical displacement data. Lacking horizontal data, we used a simple point source elastic model [*Mogi*, 1958] to estimate the depth of the deformation source (i.e., volume decrease) from the measured vertical displacements. Although the model assumes that the crust is homogeneous and elastic, the effects of faulting and tectonic strain can be factored in qualitatively to explore the range of likely source depths. First, we consider all of the observations except for several marks obviously affected by faulting. Then we consider only those marks within 25 km of T502, where the subsidence profile is smooth and no faulting is indicated. In each case the volume change in the source region is adjusted to match the observed subsidence at T502.

Using a single deformation source, the best fit is obtained for a source depth of 15 km and a volume decrease of 550 $\times$ 10^6 m^3 (Figure 8*a*). A slightly better fit results from including two sources: one at 15 km depth (volume decrease of 450 $\times$

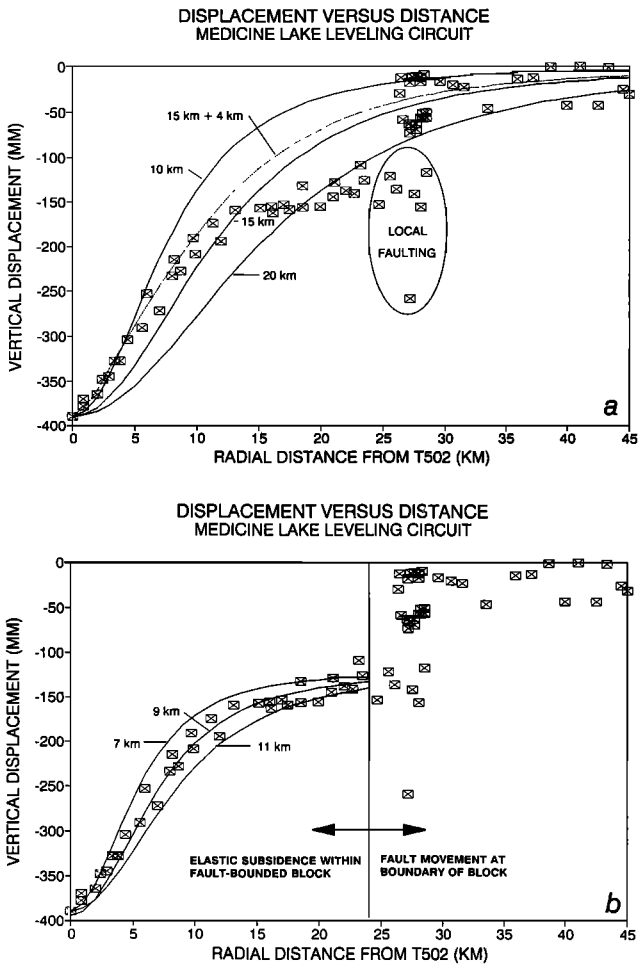

Fig. 8. Vertical displacement during 1954–1989 versus radial distance from bench mark T502 (near the center of Medicine Lake caldera) from leveling (squares) and from point source elastic models of bodies at the indicated depths (curved lines). (*a*) Attempt to fit all of the observations except those obviously affected by faulting. Solid lines represent effects of single sources centered at depths of 10, 15, and 20 km; dashed line represents the combined effect of two sources, one at 4 km depth and one at 15 km depth. The source volume decreases required to produce the indicated subsidence for sources at various depths are (in units of 10^6 m^3) 980 (depth = 20 km), 550 (15 km), 245 (10 km), and 450 + 7 (15 + 4 km). Each model was fit to the data by inspection; other combinations of depth and source volume change are possible. Ellipse encloses seven marks affected by local faulting (V501, U501, T501, C500, P503, M500, and P500) which were ignored when fitting the curves to the data. (*b*) Attempt to fit only those observations within 25 km of T502, assuming that more distant points are affected by faulting. The required source volume changes are (in units of 10^6 m^3) 205 (11 km), 140 (9 km), and 83 (7 km). Vertical line separates marks within 25 km of T502, where the subsidence profile is smooth, from those farther away and subject to faulting. Only marks to the left of the line were considered for the model.

10^6 m^3) and another at 4 km depth (volume decrease of 7 × 10^6 m^3). The deeper source corresponds to the approximate locations of two long-period earthquakes that might indicate a magma storage zone, and the upper source corresponds to the low-velocity, low-Q anomaly interpreted by *Evans and Zucca* [1988] as a silicic magma body beneath Medicine Lake caldera. The addition of a second source improves the fit slightly, but the improvement may simply reflect the increased degrees of freedom in the model.

An alternative model is illustrated in Figure 8*b*. The shape of the subsidence profile in Figure 5 and the offset near a radial distance of 25 km in Figure 8*a* suggest that the entire volcano, including the downwarped area centered at T502, has been downfaulted 5–10 cm relative to the surrounding plateau. This is illustrated in Figure 5 by the relative displacements of X500 and P503 near a stadia distance of 40 km and of N501 and T501 near a stadia distance of 120 km. To exclude the effect of faulting from the second model, we considered only those marks located within 25 km of T502. A volume decrease of 140 × 10^6 m^3 centered at 9 km depth yields the best fit. This model probably underestimates the true source depth by ignoring the far-field deformation, while the previous model may overestimate the depth slightly by ignoring the effect of faulting. A possible advantage of the second model, in view of the lack of a single large magma body beneath Medicine Lake caldera, is that smaller subsurface volume changes are needed to explain the amount of historical subsidence.

We suspect that the source is actually a vertically extended plexus of dikes with subsidiary magma storage zones at depths of 10–15 km and 3–5 km. This interpretation is based on (1) regional geophysical measurements that suggest the presence of mafic intrusions throughout the crust; (2) the occurrence of long-period earthquakes, suggesting magma movement, at 10–15 km depth; (3) seismic tomography measurements that indicate a small magma chamber at 3–5 km depth; and (4) the geodetic modeling results described above.

Conceptual Model

Our preferred model of the Medicine Lake magmatic system is illustrated in Figure 9. The dominant causes of subsidence are (1) crustal loading by the volcano plus dense subvolcanic intrusions and (2) crustal thinning due to Basin and Range extension. Both processes are facilitated by heat-induced crustal weakening; indeed, without such weakening, the load probably would be supported by an elastic upper lithosphere. A roughly columnar region beneath the edifice has been intruded extensively by basalt, most of which has solidified, thereby heating and weakening the crustal column (Figure 9*c*). An unknown fraction of this melt has differentiated to more silicic material that has intruded the upper crust and erupted at the surface, as has some of the parental basalt. Addition of mass and heat causes the volcano and underlying crust to subside. At the same time, Basin and Range extension thins the weakened crust, causing it to subside further. Possible subsidiary causes of surface subsidence include fluid loss during crystallization of magma and withdrawal of magma as a result of cooling or eruptions.

Earthquakes are largely absent from the heated crustal column but occur around its periphery. Historical earthquake swarms and faulting episodes mark the transition from relatively warm crust near the volcano to cooler crust 25 km or more from the summit. The inner zone deforms more steadily and mostly aseismically, while the outer zone deforms episodically by brittle failure. The pattern of subsidence is roughly symmetric about Medicine Lake caldera, except possibly for north-south elongation caused by east-west tectonic extension.

In the summit area, most tectonic strain is released by

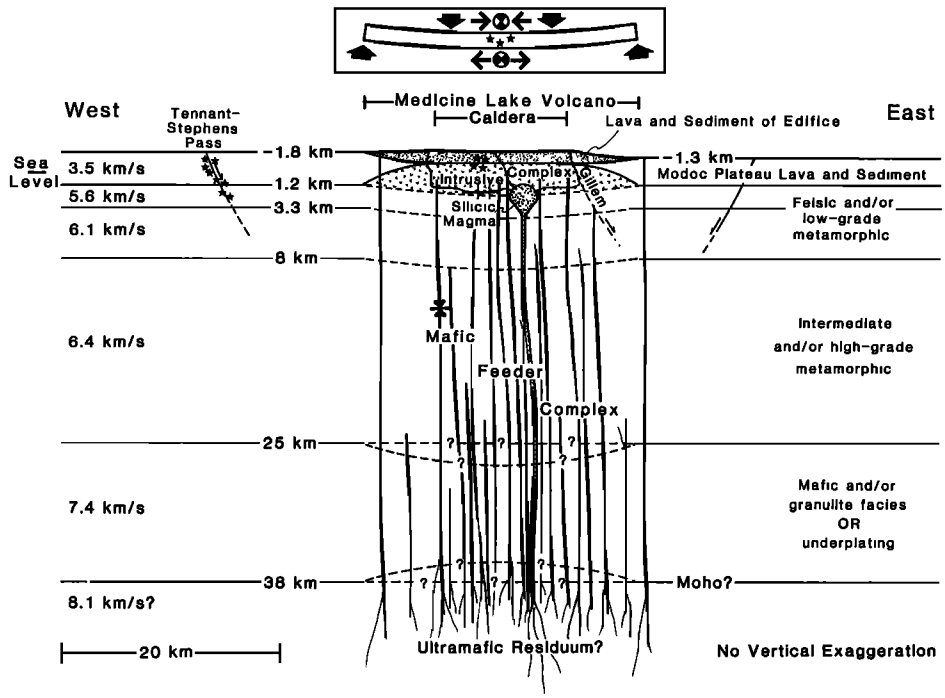

Fig. 9*a*. Conceptual model for Medicine Lake volcano. Many details are abstracted or rendered in schematic. East-west cross section through the volcano, showing major volcano-tectonic features plus the bending moment mechanism believed to be responsible for a shallow earthquake swarm in the summit region. Large arrows indicate load; small arrows, stars, and "focal spheres" indicate response. Velocity structure and rock types are abstracted from a seismic refraction study by *Zucca et al.* [1986]. Asterisk represents a relatively deep, long-period earthquake like those which occurred beneath the volcano on October 14, 1986, and December 12, 1989.

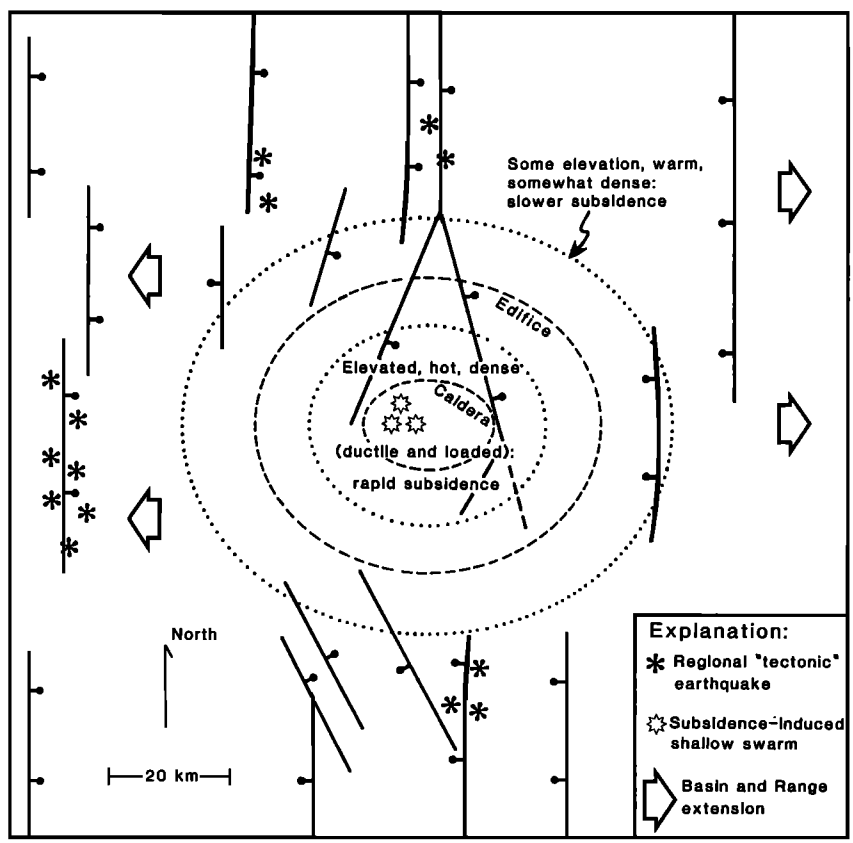

Fig. 9*b*. Plan view schematic of regional structure and loading stresses. "Tectonic" earthquakes (stars) are rare or absent in the heated crust beneath the volcano, except for shallow earthquake swarms that occur in the relatively cool, brittle lavas and sediment of the volcanic edifice.

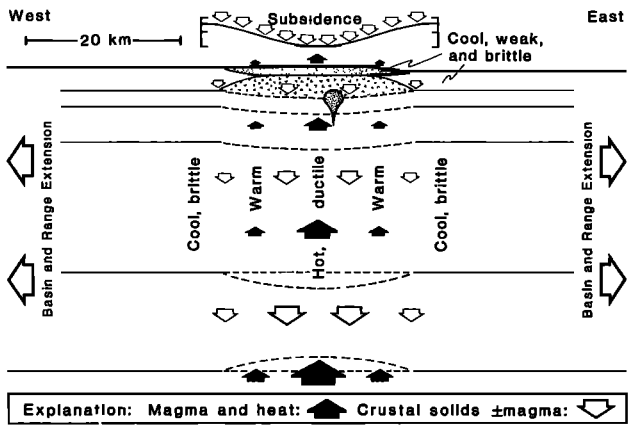

Fig. 9c. Cross section showing mass and heat transfer in the crustal column beneath the volcano. Both the edifice and a column of relatively dense, mafic intrusive material load the column. Heating by intrusions weakens the column, so it subsides in response to the load and to Basin and Range extension. It is unclear whether deeper boundaries would suffer net upward or downward deflections (dashed lines). Episodic withdrawal of magma and fluid loss during crystallization also may also contribute to subsidence.

thermally augmented creep and subsidence. Episodic swarms of shallow earthquakes are caused by subsidence-induced bending of a weak, brittle surface layer consisting of lava flows and related sediment, i.e., the volcanic edifice and possibly some underlying Modoc Plateau rocks (Figure 9a). In theory this layer fails under compression near the surface and under extension near its base. At Medicine Lake caldera, there is weak evidence from earthquake focal mechanisms for compression near the surface and extension a few kilometers deeper. Most earthquakes in the 1988–1989 swarm occurred near the center of bending, i.e., at the center of the caldera near T502.

The dominant control on the pattern of seismicity in the Medicine Lake region is the system of north striking normal faults formed by crustal extension at the western edge of the Basin and Range province. For this reason, seismic activity over geologic time scales presumably reflects the pervasive north-south structural grain in the region. The historical record is too short for this pattern to assert itself fully, but the character of earthquake swarms such as those near Stephens Pass in 1978 and Tennant in 1981 is consistent with normal faulting along north striking faults. An important secondary control on regional seismicity is the transition from warm to cool crust about 25 km from the summit of Medicine Lake caldera.

Tectonism and volcanism appear to be linked at Medicine Lake volcano to the extent that ground breakage in the context of regional crustal extension sometimes is accompanied by eruption of lava to the surface. A set of northeast striking, east-west opening ground cracks formed during the Little Glass Mountain eruption about 1000 years ago on the upper west flank of the volcano [*Fink and Pollard*, 1983]. This fracturing was accompanied by emplacement of rhyolite domes at about 10 sites along a 7.5-km-long N30°E alignment. Other vents also are located along inferred faults and fissures, and most vents form alignments oriented between N30°W and N30°E (similar to regional fault trends). Magma movement probably occurs more commonly along north striking dikes than central conduits, although the latter may occur under Medicine Lake caldera where small differentiated magma bodies may be present [*Donnelly-Nolan*, 1988; *Evans and Zucca*, 1988].

This model can be tested by repeated geodetic measurements across the inferred transition from aseismic subsidence to episodic normal faulting. The Global Positioning System (GPS) of satellite geodesy is capable of measuring vertical and horizontal displacements to an accuracy of about 1 cm over horizontal distances of at least 200 km [*Davis et al.*, 1989; *Prescott et al.*, 1989] and thus is well suited to this task. USGS established a regional network of GPS stations in the Mount Shasta–Medicine Lake region during July 1990. The network will be remeasured in 3–5 years to determine the contemporary strain rate and to characterize further the relation between tectonism and magmatism in this transitional zone between the Cascades and the Basin and Range.

APPENDIX: ANALYSIS OF LEVELING ERRORS

Random Error

The magnitude of random error in leveling surveys can be estimated by closing a circuit, double running all or part of a traverse or assuming that the error is typical of other surveys of the same order and class. On the basis of several decades of NGS experience the standard deviation σ of an observed elevation difference h measured by leveling is given by

$$\sigma(h) = \beta(L)^{1/2}$$

where β, in units of mm/km$^{1/2}$, is a constant for each order and class of leveling and L is the distance along the traverse. The standard deviation of a vertical displacement (i.e., change in an observed elevation difference between surveys) is given by

$$\sigma(\Delta h) = [\sigma_1(h)^2 + \sigma_2(h)^2]^{1/2}$$

where σ_1 and σ_2 are the standard deviations of the observed elevation differences from the first and second surveys, respectively. The contemporary value of β is 0.7 mm/km$^{1/2}$ for first-order, class II surveys and 1.3 mm/km$^{1/2}$ for second-order, class II surveys. However, NGS experience indicates that the value of β for second-order surveys during 1917–1955 (including the 1954 survey at Medicine Lake) was about 3 mm/km$^{1/2}$ [*Vanicek et al.*, 1980]. Thus the standard deviation of vertical displacements measured between the 1988 and the 1989 surveys is taken as 1 mm/km$^{1/2}$ $L^{1/2}$, and the standard deviation of vertical displacements measured between the 1954 and the 1989 surveys is taken as 3.1 mm/km$^{1/2}$ $L^{1/2}$. This corresponds to an accumulated 1-σ uncertainty of ±4.5 mm along the 1988–1989 traverse and ±43 mm around the 1954–1989 circuit.

Systematic Error

Inspection of the 1954–1989 leveling results suggests an inverse correlation between elevation and vertical displacement or, in other words, between slope and tilt (Figure 5). Such a correlation could be a consequence of (1) volcanotectonic processes responsible for subsidence or (2) systematic leveling errors that accumulate with elevation (e.g., rod scale or refraction error) and are not completely removed by corrections. The mean slope along the leveling circuit varies

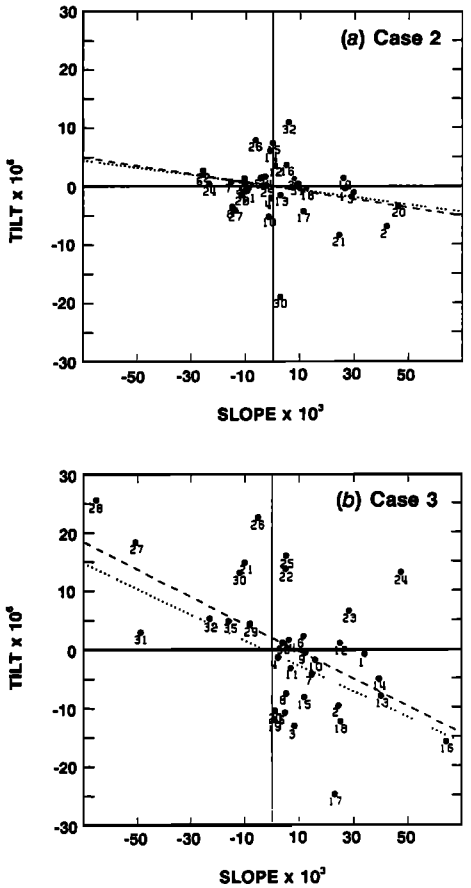

Fig. A1. Tilt versus slope plots and regression lines (*a*) for sections of the leveling circuit located off Medicine Lake volcano (case 2) and (*b*) for sections located on the volcano (case 3). Dashed regression lines are for the unweighted case; dotted lines are for the weighted case. Numbers denote bench mark pairs (i.e., sections) that differ in the two plots. See the Appendix for details.

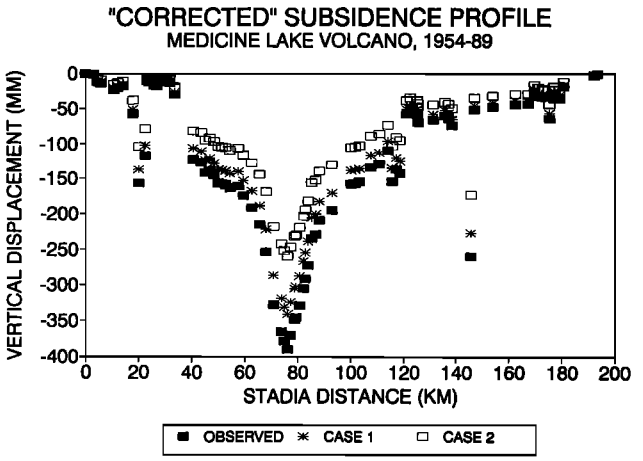

Fig. A2. Observed and "corrected" subsidence profiles showing the effect of removing the tilt-slope correlation determined in cases 1 and 2. In each case the linear regression coefficient m was used to adjust the observed values to $m = 0$.

from almost zero near Tennant to about 2% on the flanks of Medicine Lake volcano and near Stephens Pass (Figure 5). Accumulation of systematic error is possible in such terrain, but the largest cumulative correction applied to either the 1954 or the 1989 data was only 43 mm (K. Koepsell, personal communication, 1990; CVO, unpublished data, 1991). Therefore barring a serious flaw in the corrections, any residual error is likely to be much smaller than the maximum subsidence during 1954–1989 (389 ± 43 mm). We verified that conclusion in two ways. First, we applied linear regression analysis to the 1954–1989 results to determine the magnitude of any slope-dependent error [*Stein*, 1981]. Next, we analyzed a 1958 leveling survey in Virginia for evidence of slope-dependent error. The same rods were used for the 1958 Virginia survey and the 1954 Medicine Lake survey, so any rod calibration error should be common to both surveys.

To assess the significance of the apparent correlation between tilt and slope, we calculated regression coefficients m, Y intercepts b, and correlation coefficients r for the equation $\tau = m\theta + b$, where τ and θ represent tilt and slope, respectively, for each section along the leveling circuit. Two weighting functions were used: (1) equal weight for all data points (hereafter referred to as "unweighted") and (2) $1/\sigma^2$, where σ is the standard deviation from random leveling error for each section ("weighted"). The latter approach takes account of the fact that tilt is better determined for long sections than for short sections.

Three cases were evaluated in detail. Case 1 included 70 of the 81 sections measured in 1989. Twelve benchmarks were excluded for the following reasons: (1) their displacements were anomalous relative to adjacent marks, and they are judged to be unstable (Z502, C499); (2) their displacements were large and probably caused by faulting (L500, M500, P500, V501, U501, T501, C500); or (3) they formed unusually short sections ($L \leq 0.3$ km) for which tilt was poorly determined (TENNANT, TENNANT AZ). Inclusion of these marks in the regression analysis yielded ambiguous results (i.e., the unweighted and weighted fits were much different), because sections involving these marks were conspicuous outliers on plots of tilt versus slope. Such outliers strongly influence the least squares fit if data points are unweighted. Case 2 included only those sections from case 3 that are located off Medicine Lake volcano (i.e., zero to 30 km or 110–193 km from H197, measured counterclockwise along the leveling circuit; $N = 35$). Conversely, case 3 included only those sections from case 1 that are located on the volcano (30–110 km from H197; $N = 35$). Results of the regression analysis are given in Figures A1 and A2 and Table A1, along with the critical values of r for various levels of significance α (i.e., $\pm r_c(\alpha)$). Two variables are correlated at the 1-α confidence level if $r \leq -r_c(\alpha)$ (inverse correlation) or $r \geq +r_c(\alpha)$ (direct correlation).

For case 1, both unweighted and weighted values of r indicate that tilt and slope are linearly correlated at the >99% confidence level, consistent with the inference drawn earlier from inspection of Figure 5. However, when only marks located off Medicine Lake volcano are included in the regression analysis (case 2), the correlation between tilt and slope is either not significant (unweighted) or barely significant (weighted) at the 92% confidence level. Conversely, if only marks located on the volcano are included (case 3), the correlation is significant even at the 99% level (Table A1). These results can be verified by closer inspection of Figure 5: tilt and slope are inversely related on Medicine Lake volcano, but not near Stephens Pass, where steep topogra-

TABLE A1. Linear Regression Statistics

	Case 1	Case 2	Case 3
Number of sections N	70	35	35
Regression coefficient, m*	$-1.771 \pm 0.415 \times 10^{-4}$	$-0.727 \pm 0.488 \times 10^{-4}$	$-2.348 \pm 0.621 \times 10^{-4}$
	$(-1.594 \pm 0.350 \times 10^{-4})$	$(-0.640 \pm 0.369 \times 10^{-4})$	$(-2.200 \pm 0.549 \times 10^{-4})$
Y intercept b*	$+8.075 \pm 9.482 \times 10^{-4}$	$-8.645 \pm 85.284 \times 10^{-5}$	$+1.988 \pm 1.688 \times 10^{-3}$
	(0)	(0)	$(-6.311 \pm 14.895 \times 10^{-4})$
Correlation coefficient r*	−0.455	−0.247	−0.539
	(−0.478)	(−0.285)	(−0.561)
Critical values of r, $\pm r_c(\alpha = 0.10)$	±0.195	±0.279	±0.275
Critical values of r, $\pm r_c(\alpha = 0.05)$	±0.232	±0.330	±0.325
Critical values of r, $\pm r_c(\alpha = 0.02)$	±0.274	±0.387	±0.381
Critical values of r, $\pm r_c(\alpha = 0.01)$	±0.302	±0.424	±0.418

*Values that are not in parentheses are unweighted. Values that are in parentheses are weighted.

phy similar to that at the volcano is not reflected in the subsidence profile. We conclude that the strong correlation between tilt and slope is spatially associated with the volcano, presumably because the subsidence mechanism is volcanogenic. A corollary of this interpretation is that cases 1 and 3 overestimate the importance of slope-dependent error, while case 2 may be representative.

To calculate an upper bound for the magnitude of slope-dependent error in the Medicine Lake data, we "corrected" the 1954–1989 subsidence profile using the regression coefficients determined for cases 1 and 2 (Figure A2). Removal of the case 2 regression line reduces the maximum subsidence during 1954–1989 by about 13% to 340 mm. The corresponding values are 33%, to 260 mm, if the case 1 regression line is used. The possibility of nonlinear errors cannot be excluded, but lacking evidence to the contrary, we conclude that slope-dependent error accounts for less than one third of the 1954–1989 subsidence at Medicine Lake volcano.

This conclusion is supported by analysis of leveling observations in 1958 and 1985 along a 40-km traverse from Talcott, West Virginia, to Glenlyn, Virginia. First-order, class II procedures were followed for both surveys. The 1958 survey used the same pair of rods that was used for the 1954 survey at Medicine Lake; the 1985 survey used NGS rods 121176, 132181, 270711, and 277921 (K. Koepsell, personal communication, 1990). Assuming that the rods used in 1985 and 1989 were properly calibrated, any rod scale error associated with the rods used in 1954 and 1958 should be present in both the 1958–1985 (Virginia) and the 1954–1989 (Medicine Lake) data sets.

Vertical displacements and topography are apparently correlated in the Virginia data set (Figure A3), but the magnitude of the correlation is smaller than for the Medicine Lake case and is of opposite sign. In the Virginia case, approximately 20 mm of apparent uplift accumulates over 200 m of vertical relief, suggesting the possibility of a rod scale error of about 100 parts per million (ppm). At Medicine Lake, 389 mm of subsidence accumulates over 1000 m of relief, which would require a rod scale error of almost 400 ppm in the opposite sense. Clearly, both cases cannot be explained by the same rod scale error in the 1954/1958 rods; a combination of errors in at least two rod pairs would be required. Errors of such magnitude would be unprecedented for calibrated USGS or NGS rods. *Strange* [1980] showed that the largest apparent scale difference between any two sets of rods used for 64 repeat surveys over 17 profiles in southern California with topographic relief ranging from about 600 m to 2200 m was less than 160 ppm. Therefore we conclude that any rod scale error in the 1954–1989 results is small compared to the amount of real subsidence: less than 33% and probably less than 13%.

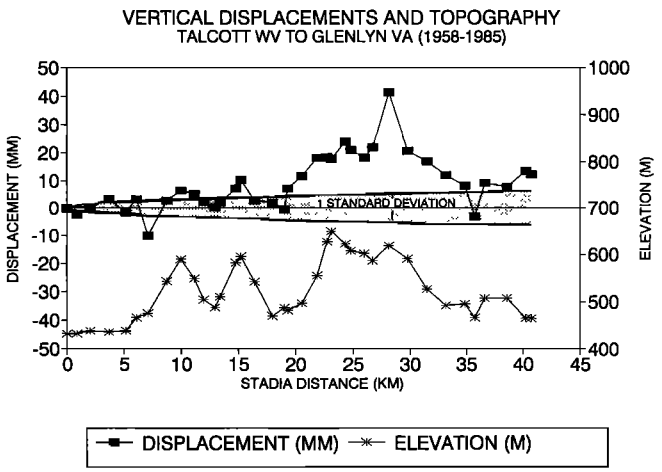

Fig. A3. Vertical displacements (1958–1985) and topography along a 40-km leveling traverse from Talcott, West Virginia, to Glenlyn, Virginia. Procedures for first-order, class II leveling were followed for both surveys. NGS data were provided by K. Koepsell (personal communication, 1990). Stippled area indicates 1 standard deviation in the leveling measurements. At any stadia distance the vertical dimension of the stippled area indicates the height of the 1-sigma error bar at that distance.

Acknowledgments. Special thanks to members of CVO's 1989 Medicine Lake leveling crews: Erika Anderson, Stuart Ashbaugh, Marvin Couchman, Steve Hoffine, Gene Iwatsubo, Gordon Keating, Jack Kleinman, Dave Schneider, Jim Sproull, Don Swanson, Mary Turner, Dave Wieprecht, Ed Wolfe, and Ken Yamashita. Kathy Koepsell of the National Geodetic Survey provided helpful information concerning the 1954 leveling survey, including additional data discussed in the Appendix. U.S. Forest Service personnel from the Klamath, Modoc, and Shasta national forests provided essential logistical support. Marianne Guffanti, Patrick Muffler, and James Smith shared their knowledge of the regional geology and contributed to the development of ideas presented in the manuscript. Ross Stein provided software and guidance for the evaluation of systematic error in the leveling surveys; John Ewert, Jeff Marso, and Arnold Okamura did the same for point source modeling of the subsidence data. Marianne Guffanti, Paul Delaney, Ross Stein, Roger Denlinger, and an anonymous colleague provided helpful reviews. Ellen Longee greatly improved one of the figures using a computer graphics software package.

REFERENCES

Anderson, C. A., Volcanoes of the Medicine Lake Highland, California, *Univ. Calif. Publ. Geol. Sci.*, *25*, 347–422, 1941.

Balazs, E. I., and G. M. Young, Corrections applied by the National Geodetic Survey to precise leveling observations, *Tech. Memo. NOS NGS 34*, 12 pp., Natl. Oceanic and Atmos. Admin., Boulder, Colo., 1982.

Bennett, J. H., R. W. Sherburne, C. H. Cramer, C. W. Chesterman, and R. H. Chapman, Stephens Pass earthquakes, Mount Shasta—August 1978, *Calif. Geol.*, *32*(2), 27–34, 1979.

Blakely, R. J., and R. C. Jachens, Volcanism, isostatic residual gravity, and regional tectonic setting of the Cascade volcanic province, *J. Geophys. Res.*, *95*, 19,439–19,451, 1990.

Blakely, R. J., R. C. Jachens, R. W. Simpson, and R. W. Couch, Tectonic setting of the southern Cascade Range as interpreted from its magnetic and gravity fields, *Geol. Soc. Am. Bull.*, *96*, 43–48, 1985.

Bolt, B. A., and R. D. Miller, Catalogue of earthquakes in northern California and adjoining areas, 1 January 1910–31 December 1972, Seismographic stations, report, Univ. of Calif., Berkeley, 1975.

Catchings, R. D., Crustal structure from seismic refraction in the Medicine Lake area of the Cascade Range and Modoc Plateau, northern California, Master's thesis, 97 pp., Univ. of Wis., Madison, 1983.

Catchings, R. D., Crustal structure of the northwestern United States, Ph.D. thesis, 182 pp., Stanford Univ., Stanford, Calif., 1987.

Chouet, B., R. Y. Koyanagi, and K. Aki, Origin of volcanic tremor in Hawaii, II, Theory and discussion, in Volcanism in Hawaii, vol. 2, edited by R. W. Decker, T. L. Wright, and P. H. Stauffer, *U.S. Geol. Surv. Prof. Pap.*, *1350*, 1259–1280, 1987.

Cramer, C. H., The Stephen's Pass earthquake swarm of August 1978, east of Mt. Shasta, California (abstract), *Eos Trans. AGU*, *59*(12), 1130, 1978.

Davis, J. L., W. H. Prescott, J. L. Svarc, and K. J. Wendt, Assessment of global positioning system measurements for studies of crustal deformation, *J. Geophys. Res.*, *94*, 13,635–13,650, 1989.

Donnelly-Nolan, J. M., A magmatic model of Medicine Lake volcano, California, *J. Geophys. Res.*, *93*, 4412–4420, 1988.

Donnelly-Nolan, J. M., Geology of Medicine Lake volcano, Northern California Cascade Range, *Trans. Geotherm. Resour. Counc.*, *Part II*, *14*, 1395–1396, 1990.

Donnelly-Nolan, J. M., and K. M. Nolan, Catastrophic flooding and eruption of ash-flow tuff at Medicine Lake volcano, California, *Geology*, *14*, 875–878, 1986.

Donnelly-Nolan, J. M., D. E. Champion, C. D. Miller, and D. A. Trimble, Implications of post-11,000-year volcanism at Medicine Lake volcano, northern California Cascade Range, in Proceedings of Workshop XLIV, Geological, Geophysical, and Tectonic Setting of the Cascade Range, *U.S. Geol. Surv. Open File Rep.*, *89-178*, 556–590, 1989.

Dzurisin, D., J. C. Savage, and R. O. Fournier, Recent crustal subsidence at Yellowstone Caldera, Wyoming, *Bull. Volcanol.*, *52*, 247–270, 1990.

Evans, J. R., and S. R. Walter, Relation of recent seismicity to tomographic structure at Medicine Lake volcano, northern California (abstract), *Seismol. Res. Lett.*, *60*, 31, 1989.

Evans, J. R., and J. J. Zucca, Active high-resolution seismic tomography of compressional wave velocity and attenuation structure at Medicine Lake volcano, northern California Cascade Range, *J. Geophys. Res.*, *93*, 15,016–15,036, 1988.

Finch, R. H., Lassen report no. 14, *Volcano Lett.*, *161*, 1928. (Reprinted in *The Volcano Letters*, edited by R. S. Fiske, T. Simkin, and E. A. Nielsen, p. 161, Smithsonsian Institution, Washington, D.C., 1987.)

Fink, J. H., and D. D. Pollard, Structural evidence for dikes beneath silicic domes, Medicine Lake Highland volcano, California, *Geology*, *11*, 458–461, 1983.

Finn, C., and D. L. Williams, Gravity evidence for a shallow intrusion under Medicine Lake volcano, California, *Geology*, *10*, 503–507, 1982.

Fournier, R. O., Geochemistry and dynamics of the Yellowstone National Park hydrothermal system, *Annu. Rev. Earth Planet. Sci.*, *17*, 13–53, 1989.

Fuis, G. S., J. J. Zucca, W. D. Mooney, and B. Milkereit, A geologic interpretation of seismic-refraction results in northeastern California, *Geol. Soc. Am. Bull.*, *98*, 53–65, 1987.

Gay, T. E., Jr., and Q. A. Aune, Alturas sheet, geologic map of California, scale 1:250,000, Calif. Div. of Mines and Geol., Sacramento, 1958.

Grove, T. L., and M. B. Baker, Phase equilibrium controls on the tholeiitic versus calc-alkaline differentiation trends, *J. Geophys. Res.*, *89*, 3253–3274, 1984.

Grove, T. L., and J. M. Donnelly-Nolan, The evolution of young silicic lavas at Medicine Lake volcano, California: Implications for the origin of compositional gaps in calc-alkaline series lavas, *Contrib. Mineral. Petrol.*, *92*, 281–302, 1986.

Grove, T. L., R. J. Kinzler, M. B. Baker, J. M. Donnelly-Nolan, and C. E. Lesher, Assimilation of granite by basaltic magma at Burnt Lava Flow, Medicine Lake volcano, northern California, *Contrib. Mineral. Petrol.*, *99*, 320–343, 1988.

Klein, F. W., User's guide to HYPOINVERSE, a program for VAX computers to solve for earthquake locations and magnitudes, *U.S. Geol. Surv. Open File Rep.*, *89-314*, 49 pp., 1989.

Koyanagi, R. Y., B. Chouet, and K. Aki, Origin of volcanic tremor in Hawaii, I, Data from the Hawaiian Volcano Observatory, 1969–1985, in Hawaiian Volcanism, edited by R. W. Decker, and T. L. Wright, *U.S. Geol. Surv. Prof. Pap.*, *1350*, 1221–1258, 1987.

Lester, R. W., and K. L. Meagher, Catalog of earthquakes along the San Andreas fault system in central California for the year 1984, *U.S. Geol. Surv. Open File Rep.*, *78-1010*, 89 pp., 1978.

McKee, E. H., W. A. Duffield, and R. J. Stern, Late Miocene and early Pliocene basaltic rocks and their implications for crustal structure, northeastern California and south-central Oregon, *Geol. Soc. Am. Bull.*, *94*, 292–304, 1983.

Meertens, C. M., Tilt tides and tectonics at Yellowstone National Park, Ph.D. thesis, 236 pp., Univ. of Colo., Boulder, 1987.

Mogi, K., Relation between the eruptions of various volcanoes and the deformation of the ground surfaces around them, *Bull. Earthquake Res. Inst. Univ. Tokyo*, *36*, 99–134, 1958.

Moore, J. G., Relationship between subsidence and volcanic load, Hawaii, *Bull. Volcanol.*, *34*, 562–576, 1970.

Prescott, W. H., J. L. Davis, and J. L. Svarc, Global positioning system measurements for crustal deformation: Precision and accuracy, *Science*, *244*, 1337–1340, 1989.

Schomaker, M. C., and R. M. Berry, Geodetic leveling, *Manual NOS NGS 3*, Natl. Geod. Surv., Natl. Oceanic and Atmos. Admin., Rockville, Md., 1981.

Stauber, D. A., S. M. Green, and H. M. Iyer, Three-dimensional *P* velocity structure of the crust below Newberry volcano, Oregon, *J. Geophys. Res.*, *93*, 10,095–10,107, 1988.

Stein, R. S., Discrimination of tectonic displacement from slope-dependent errors in geodetic leveling from southern California, 1953–1977, in *Earthquake Prediction: An International Review*, *Maurice Ewing Ser.*, vol. 4, edited by D. W. Simpson and P. G. Richards, pp. 441–456, AGU, Washington, D. C., 1981.

Stewart, S. W., and M. E. O'Neill, Calculation of the frequency response of the USGS telemetered short-period seismic system, *U.S Geol. Surv. Open File Rep.*, *80-143*, 83 pp., 1980.

Strange, W. E., The effect of systematic errors on geodynamic analysis, in *Second International Symposium on Problems Related to the Redefinition of North American Vertical Geodetic Networks*, pp. 705–729, Canadian Institute of Surveying, Surveys and Mapping Branch, Ottawa, 1980.

Vanicek, P., R. O. Castle, and E. I. Balazs, Geodetic leveling and its applications, *Rev. Geophys.*, *18*, 505–524, 1980.

Walter, S., and D. Dzurisin, The September 1988 earthquake swarm at Medicine Lake volcano, northern California (abstract), *Eos Trans. AGU*, *70*(43), 1189–1190, 1989.

Zohdy, A. A. R., and R. J. Bisdorf, Schlumberger soundings near Medicine Lake, California, *Geophysics*, *55*, 956–964, 1990.

Zucca, J. J., G. S. Fuis, B. Milkereit, W. D. Mooney, and R. D. Catchings, Crustal structure of northeastern California, *J. Geophys. Res.*, *91*, 7359–7382, 1986.

J. M. Donnelly-Nolan, J. R. Evans, and S. R. Walter, U.S. Geological Survey, 345 Middlefield Road, Menlo Park, CA 94025.

D. Dzurisin, David A. Johnston Volcano Observatory, U.S. Geological Survey, 5400 MacArthur Boulevard, Vancouver, WA 98661.

(Received October 6, 1990;
revised May 13, 1991;
accepted June 4, 1991.)

JOURNAL OF GEOPHYSICAL RESEARCH, VOL. 96, NO. B10, PAGES 16,251–16,262, SEPTEMBER 10, 1991

Geochemical Complexities Preserved in the Volcanic Rocks of the Zambales Ophiolite, Philippines

CYNTHIA A. EVANS[1]

Lamont-Doherty Geological Observatory, Columbia University, Palisades, New York

GERRY CASTENEDA AND HELEN FRANCO

Philippine Bureau of Mines and Geosciences, Quezon City

The geochemical characteristics of the volcanic rocks from the Zambales Ophiolite, Luzon, Philippines, indicate that the oceanic crust now preserved in the ophiolite must have been generated in an oceanic subduction zone environment. The volcanic rocks and dikes range in composition from magnesian basalt (including mid-ocean ridge basalt (MORB), island arc tholeiite, and boninite-like lavas) to andesite and dacite and have trace element abundances which suggest derivation from a mantle source which was heterogeneous on both regional and local scales. The sources are mixtures of components variably depleted with respect to a MORB source. Differences exist between respective exposures of the ophiolite. From north to south the following geochemical patterns in the basaltic rocks emerge: Sm/Nd decreases with corresponding decreases in $^{143}Nd/^{144}Nd$. Rare earth element (REE) patterns range from extremely light REE (LREE) depleted with generally low abundances of all REE (1-5X chondritic) to patterns which are slightly LREE depleted, similar to MORB patterns. Throughout the range, Sr isotopic abundances are relatively high ($^{87}Sr/^{86}Sr$ = 0.7035-0.7040). Perhaps more significant than the regional geochemical trends, however, is that all volcanic provinces display ranges of rock compositions, and the spatial distribution of basalts with such variable geochemical affinities indicate superposition, interfingering, and possible mixing of different lavas. We suggest that the array of geochemical data from the Zambales ophiolite can be explained in terms of processes observed in present-day convergent plate margins, such as the Marianas or Lau Basin in the western Pacific. Complicated plate boundaries which have existed for long periods of time, including closely opposing and changing subduction systems, the rifting of arcs, and the formation of backarc basins may result in the superposition of one lava type on another or may produce many small domains in the upper mantle sources for subduction-related lavas, some of which become extremely depleted or secondarily enriched. Magmas derived from such a heterogeneous mantle will display ranges in geochemical characteristics, possibly similar to those observed in the Zambales ophiolite. Indeed, recent studies from present-day backarc systems suggest that young arc volcanism is superimposed on MORB-like crust and that basalt compositions of certain backarc basins are zoned inward from arc-like to MORB-like. These studies indicate that relationships between arc and MORB-like crust in young subduction complexes is extremely complex (Hawkins and Melchior, 1985; Volpe et al. 1987, 1990). We extrapolate arguments from studies of zoned backarc systems to the Zambales Ophiolite and, in turn, use data from the Zambales Ophiolite as a ruler for defining the scale of variation in these complex supra-subduction zone systems.

INTRODUCTION

Many ophiolite complexes are now recognized to have been generated in supra-subduction zone environments which include backarc, forearc, and arc or incipient arc settings. Modern forearc, arc, and backarc systems have complicated structural and geochemical relationships which may be unique to each subduction system considered [e.g., *Stern et al.*,1989; *Bloomer et al.*,1989; *Lin et al.*, 1989; *Hawkins and Melchior*, 1985; *Sinton and Fryer*, 1987]. Ophiolites that formed as part of a convergent margin may preserve such structural and compositional complexities. The identification of such ophiolites as simple arc or backarc terranes will be difficult.

The Zambales Ophiolite in western Luzon, Philippine Islands, preserves a section of oceanic crust and upper mantle which was generated in a supra-subduction zone environment. Large-scale, along-strike heterogeneities in the ophiolite have been observed and discussed by several authors [*Bacuta*, 1978; *Evans*, 1983; *Hawkins and Evans*, 1983; *Evans and Hawkins*, 1989; *Rossman et al.*, 1989; *Geary et al.*, 1989]. The northern sections of the range (Barlo-Acoje areas, Figure 1) have volcanic rocks that range from boninite to island arc tholeiite compositions and occur with an unusual plutonic section dominated by great thicknesses of layered dunite, wehrlite, pyroxenite, and gabbronorite with some harzburgite and lherzolite. The central part of the range includes MORB-like basalts as well as some arc tholeiites that occur with more "normal" olivine gabbro and gabbroic rocks. Very little work has been done on the rocks from the southern part of the range.

The thrust of this study was to better constrain the compositional differences observed within the various volcanic sections of the Zambales Ophiolite and to compare these findings to modern young, intra-oceanic volcanic arc-backarc systems. In this context, geochemical data from the different volcanic sections of the Zambales Range Ophiolite are presented. These data suggest that:

1. The ophiolite was generated in a supra-subduction zone environment because many of the volcanic and hypabyssal rocks have the geochemical signatures of arc volcanics.

2. The mantle source for the ophiolite was heterogeneous. Both regional trends and small-scale source heterogeneities are reflected in the compositions and spatial distributions of the volcanic rocks.

[1]Now at Lockheed Engineering and Sciences Company, Houston, Texas.

Paper number 91JB01488.
0148-0227/91/91JB-01488$05.00

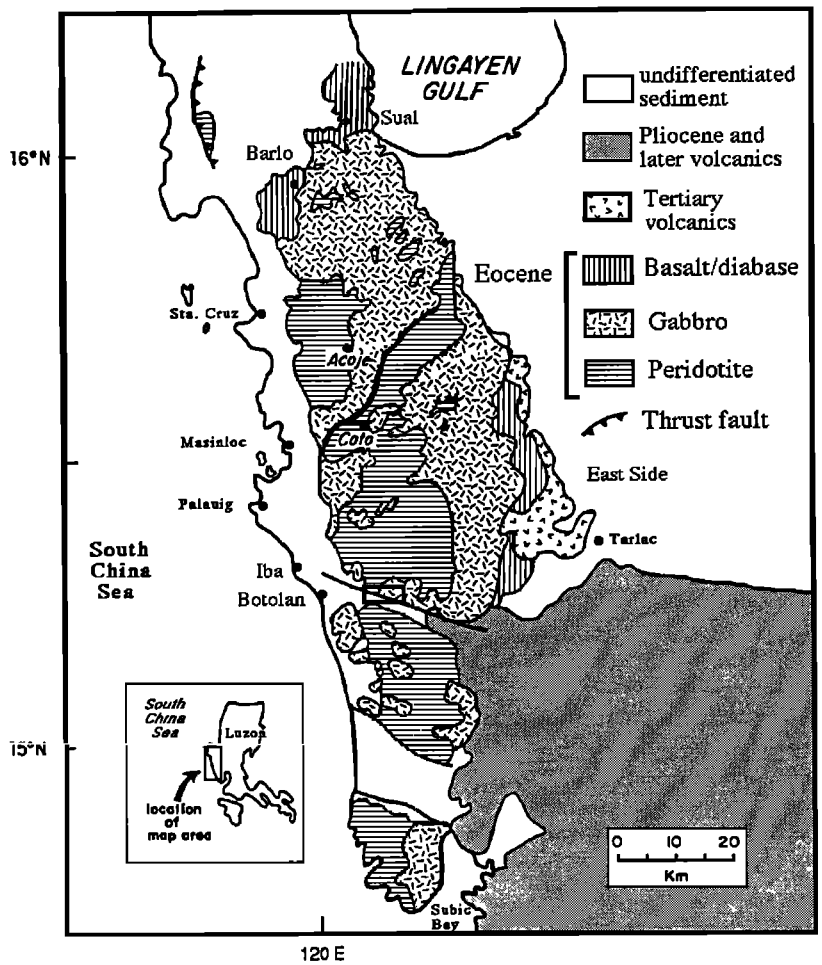

Fig. 1. Geologic map of the Zambales Range. The volcanic sections discussed in text are labeled. The Lawis fault, also referred to in the text, is the NE-SW trending fault (heavy line) between Acoje and Coto in the northern ophiolite massif. The "East Side" basalts come from the basalt section just west and northwest of Tarlac; the boxed region east of Botolan is where the Botolan dikes were collected.

3. The ophiolite serves as an analog to presently active oceanic subduction systems which have experienced long periods of subduction.

Regional Geology

The island of Luzon in the northern Philippines is sandwiched between two subduction zones of opposite polarity (the Manila and Philippine trenches) and is dissected by a large, north trending left-lateral strike slip fault, the Philippine fault [*Gervasio*, 1971; *Hamilton*, 1979; *Hashimoto*, 1980; *de Boer et al.*, 1980]. Several geologic provinces, including fragments of ophiolites, continental blocks, and island arcs comprise the Philippine archipelago [e.g., *de Boer et al.*, 1980; *Karig*, 1983; *Fuller et al.*, 1983]. The Zambales Ophiolite is one of the major components of Luzon. It is a relatively intact section of oceanic crust with no large dismemberments or evidence of major structural disruptions like repetitions of units. It strikes northerly for over 130 km and is tilted to the east. Because of the eastward tilting, the west and central exposures are composed mainly of tectonized harzburgite and dunite, with some ultramafic and mafic cumulates. The upper sections of the ophiolite (gabbros, diabase dikes/sills, pillow basalts, silicic rocks) are exposed along the eastern and northern part of the range (Figure 1). Hemipelagic and pelagic sediments (Aksitero Formation) overlie the upper pillow lavas and basaltic breccias along the eastern margin of the ophiolite [*Garrison et al.*, 1979; *Schweller and Karig*, 1979; *Schweller et al.*, 1983].

The oceanic crust preserved in the Zambales Ophiolite was formed in the Eocene-early Oligocene, based on nannofossil age determinations from basal limestones of the Aksitero formation [*Garrison et al.*, 1979; *Schweller and Karig*, 1979; *Schweller et al.*, 1983; 1984]. K-Ar dates on diabase basalts and dikes in the Barlo and Coto Mine regions are 44-46 MYBP [*Fuller et al.*, 1989]. Ophiolitic debris in the Moriones formation, which overlies the Aksitero formation, indicates that the ophiolite was uplifted and being eroded by late Oligocene-early Miocene [*Schweller et al.*, 1983; 1984; *Bachman et al.*, 1983].

Zambales Range Ophiolite

The following summary of the geology of the Zambales Range is based on previous regional studies by several workers [e.g., *Stoll*, 1958; *Rossman*, 1964; *Bryner*, 1969; *Philippine Bureau of Mines*, 1963; *Bacuta*, 1978; *Hawkins and Batiza*, 1977; *Hawkins*, 1980; *Abrajano*, 1984; *Rossman et al.*, 1989].

The Zambales Ophiolite comprises three major sections of mafic-ultramafic rocks (Figure 1). The northern section is the largest and the best studied. It is further subdivided into the

Acoje and Coto blocks, as described below. The three ophiolite sections are separated from each other by grabens filled with recent sediments (Figure 1).

The two ophiolite sequences exposed in the northern Zambales Range are typified by sections in the vicinities of the Acoje-Barlo area and Coto Mines (Figure 1). For the sake of simplicity, these two sections will be referred to as the Acoje and Coto blocks. A major fault (Lawis fault) separates parts of the Acoje and Coto blocks, but the contact is not well defined for the entire length of the presumed boundary. The structural relationships between the two blocks are not definitive; no accessible outcrops occur along key sections of the contact. The occurrence of ranges of volcanic compositions in both blocks together with complicated intrusive relations obscure "boundaries" between the two sections [*Geary et al.*, 1989; C. A. Evans, work in progress].

Major differences between the Acoje and Coto sequences include: (1) The average compositions of the volcanic rocks are different. The Acoje block includes island arc tholeiites and some boninites, the Coto block has more rocks with N-MORB compositions. (2) There are large variations in the lithology and composition of the cumulate sequences. The Acoje block cumulates include a 1000 m thick sequence of olivine-pyroxene rocks, including orthopyroxene-bearing assemblages. The overlying gabbros are olivine-plagioclase (An90-95)-orthopyroxene and clinopyroxene rocks. The Coto block cumulates lack the thick cumulate ultramafic section and the gabbros are plagioclase-clinopyroxene (+/- olivine) assemblages. (3) The thicknesses of the crustal sections of the two blocks are quite different primarily due to the thickness of the respective plutonic sections. The gabbroic section is greater than 7 km for the Acoje block and less than 5 km for the Coto block. (4) There are differences in the structures and compositions within the tectonized peridotites, including chromite bodies. The Acoje peridotite comprises more dunite and orthopyroxene-poor harzburgite than the Coto peridotite, and the rocks have extremely deformed fabrics. The chromite bodies at Acoje are rich in Cr and poor in Al compared with those within the Coto peridotite.

The field, petrological and geochemical data were interpreted by *Hawkins and Evans* [1983] and *Evans* [1983] to indicate that both an incipient island arc (Acoje) and possible backarc basin section (Coto) of oceanic crust were in early stages of construction and preserved in the Zambales Ophiolite. *Geary et al.* [1989] conclude that the Zambales ophiolite was constructed in a supra-subduction zone environment by multistage crustal formation.

Separate from the ophiolite are the arc volcanic rocks associated with subduction along the Manila Trench. Plio-Pleistocene volcanic centers occur along the eastern margin of the Zambales Range, and lavas from the Bataan peninsula overlap (and possibly intrude) the ophiolite in the Subic Bay region [e.g., *Wolfe and Selfe*, 1983]. Pillow basalts, andesites and dikes from the Plio-Pleistocene volcanic centers are not included in this study.

DATA

Field Work

Field work and sample collection included mapping and sampling along the perimeter of the Zambales Range. This work complemented earlier field studies by the authors and other geologists. The areas (Figure 1) we targeted for the most detailed studies included drainages through the basaltic section along the east side of the range (hereafter referred to as East Side), the Sual coast in the northeast corner of the range along the Lingayen Gulf (Sual), dikes in the Coto Mines region (Coto), and volcanic and dike outcrops along the graben margin east of Botolan (Botolan). "Security" reasons prevented us from working in the Barlo region, but we had mapped and sampled there in previous field seasons.

Dikes and sills were generally fresher than the extrusive rocks and were sampled preferentially when pillows and flows were too altered. Lack of exposure and structural complications do not allow reconstruction of temporal sequences in any volcanic section, except relative timing of pillows, flows, or dikes within individual outcrops.

Rock Descriptions

A brief description of field relationships and petrographic data are given for each section. In general, phenocrysts are uncommon in the volcanic rocks of the Zambales Ophiolite. Olivine is rare and clinopyroxene is the most abundant phenocryst. Where present, phenocryst and xenocryst assemblages (especially clinopyroxene) exhibit wide ranges of compositions and very complex zoning, as well as resorption. Some orthopyroxene and large crystals of resorbed and very calcic (An90) plagioclase occur in samples from the Barlo area (Figure 1). Smaller plagioclase crystals are common in all volcanic sections. Together, the mineral data suggest that magma mixing may have been common.

East Side. The volcanic and dike sections from the eastern drainages of the Zambales Range are well described by *Geary and Kay* [1983] and *Geary et al.* [1989]. Most of our samples are from the same sections. The drainages cut through the pillow-dike sections and into gabbros, but we do not feel that our samples can be reconstructed into any stratigraphic sequence.

The volcanic rocks are very fine grained. Original textures were ophitic and phenocrysts rare. Primary igneous minerals include plagioclase and clinopyroxene, and olivine pseudomorphs are sometimes present. The basalts are altered to chlorite and clays, some epidote, and ubiquitous actinolite. Some calcite vugs and quartz veins are also present. The upper basaltic breccias are extremely altered.

Coto and Botolan. Individual dikes and swarms of dikes occur in these two regions. The dikes, ranging between 0.5 and 3 m in thickness, cut through the peridotite and lower cumulate sections of the ophiolite. They occur every few meters to several tens of meters. The dikes are generally fine grained and aphyric, with various alteration assemblages ranging from low greenschist to amphibolite. Although dike trends occur in any compass direction, they are generally at a high angle to the peridotite-gabbro boundary. The dikes in the Coto Mines strike generally NE; several swarms of dikes east of Botolan also trend northeasterly, but a significant number also strike NW.

Sual. Similar rock types and alterations to those described in the East Side volcanics are observed in the volcanic and dike sections in the Sual area (Figure 1). Swarms of dikes striking NW are predominant. Flows and pillows are rare and are extremely altered where they occur (primarily as screens caught between dike swarms, e.g., samples from Luz 634). The dikes have ranges of textures which are independent of the size of the dike, suggesting that the dikes were intruded under variable

thermal regimes. Their mineralogy is dominated by plagioclase and clinopyroxene altered to actinolite. The abundance of gabbroic screens between the dike swarms suggests the section outcropping along the Lingayen Gulf preserves the base of oceanic layer 2, near the gabbro-dike boundary.

Barlo. Volcanic rocks from the Barlo area include altered vitrophyres, some with large phenocrysts, glomerocrysts, and xenocrysts. The phenocryst assemblage is dominated by clinopyroxene which is 0.3-1.5 cm in size, with compositions of En 50-55 Wo 36-43 Fs 6-9. Zoned grains often have less calcic and more Mg-rich rims. However, both cores and rims have variable compositions and display complex zoning, suggesting that magma mixing was important. Rare orthopyroxene grains (En 73-80) also occur. Olivine pseudomorphs are present as rounded crystals (now serpentinized) with occasional chromite inclusions. Plagioclase phenocrysts are rare and are extremely resorbed when they occur. They have very calcic compositions (An 90). The groundmass is variolitic with clinopyroxene (En 54 Wo 30 Fs 14-17) and plagioclase (An 77-82) laths.

Alteration of these volcanic rocks includes the formation of clays and chlorite, actinolite and epidote, the serpentinization of olivine, and the formation of calcite and quartz vugs. The high degree of alteration and association with massive sulfide deposits suggest that these rocks were in the vicinity of extensive hydrothermal systems.

Geochemistry

Methods. Whole rock geochemistry (major and trace element) and Nd and Sr isotopic studies have been done on suites of samples from all volcanic localities in the Zambales Range. Whole rock major and trace element compositions were determined by direct current plasma emission spectrometer (DCP), except where noted, and Nd and Sr isotopes by mass spectrometry using the facilities at Lamont-Doherty Geological Observatory (L-DGO). REE concentrations were obtained by DCP, neutron activation, and isotope dilution. Duplicate samples measured by both DCP and neutron activation yielded concentration differences less than 15%, and generally less than 10%. Electron microprobe facilities at L-DGO were used for individual mineral compositions.

All samples were screened petrographically, and alteration rinds, veins, and vugs were removed. Approximately 25-50 g of rock/sample was powdered, and 100 mg of sample was used for the DCP analyses. Powders were baked at 950°C for 45 min. 100-200 mg of sample was leached in 2.5N HCl until the leachate ran clear for the Nd and Sr isotopic analyses. Isotopic techniques are similar to those described by *Hart and Brooks* [1974] (Sr) and *Richard et al.* [1976] and *Zindler et al.* [1979] (Nd). Standard values used for isotopic determinations were $^{87}Sr/^{86}Sr$ (E and A $SrCO_3$) = 0.70800; $^{143}Nd/^{144}Nd$ (La Jolla Nd standard) = 0.511860.

Results. Whole rock major and trace element data and isotopic compositions are given in Tables 1 and 2. Several plots summarize the geochemical data and display the geochemical distinctions between the different volcanic sections.

Figure 2 shows TiO_2 abundance plotted against FeO*/MgO for the Zambales ophiolite volcanics (FeO*= total iron reported as FeO). The rocks from the East Side follow a trend similar to the MORB field (higher TiO_2 for a given FeO*/MgO). Rocks from the northern part of the ophiolite (Barlo and Sual) follow an arc-tholeiitic trend, defined by western Pacific arc tholeiites (lower TiO_2 for a given FeO*/MgO). The dikes from Coto and Botolan also have generally lower TiO_2 abundances but are more transitional between the MORB and island arc tholeiite (IAT) trends.

Element ratio plots of the high field strength (HFS) elements also display separate arrays for the rocks from the different volcanic sections in the Zambales ophiolite. Figure 3 plots Zr against Zr/Y [after *Pearce and Cann,* 1973]. The

TABLE 1*a*. Whole Rock Analyses for Barlo Area Rocks

	Luz 28D	Luz 160C	Luz 354A	Luz 160A	Luz 163A	Luz 159	Average*
Rock type	pillow	pillow	pillow	dike	dike	pillow	
SiO2	53.91	56.07	50.88	52.81	54.02	53.49	54.33
TiO2	0.26	0.28	0.36	0.24	0.44	0.22	0.31
Al2O3	13.74	16.31	16.03	13.94	16.37	13.67	15.29
Fe2O3	8.32	8.75	8.21	8.74	9.32	8.74	8.21
MnO	0.12	0.16	0.22	0.22	0.21	0.23	0.18
MgO	9.94	8.79	9.96	14	7.94	13.08	9.77
CaO	10.22	4.06	10.76	7.76	8.11	7.76	8.00
Na2O	1.16	5.67	0.64	1.44	1.63	2.01	2.40
K2O	2.17	0.03	0.47	0.37	0.6	0.7	0.38
P2O5	0.03	0.1	0.18	0.05	0.04	0.02	0.07
Sum	100.32	100.22	97.71	99.57	98.68	99.92	98.96
Ba		25	31	36	27	22	31
Sr	35	41	33		62	50	51
Cr	800	216	314		211	495	233
Ni	278	105	103	200	89	251	117
V	235	234	280	232	269	239	240
Zr	10	20	19		19	16	20
Y	10	13	14	8	16	11	12
Ce/Sm	0.71	0.35			0.21		
Ce/Yb	0.34	0.17			0.10		

Major element analyses are in weight percent; trace element analyses are in parts per million. Blanks indicate that data are not available.

* Average of 9 samples.

northern volcanic units (Sual and Barlo) have lower abundances of the HFS elements and much lower Zr/Y, similar to IAT. The East Side basalts have MORB-like abundances of these elements. Data from the Coto and Botolan dikes fall in the overlap field between MORB and IAT. However, all volcanic sections show geochemical scatter, and this is especially notable in the rocks from Sual.

Similar compositional distributions between the volcanic sections can be seen in other compositional plots. For example, Figures 4 and 5 show Ti-Zr and Ti-V for the basaltic

TABLE 1*b*. Whole Rock Analyses for Sual Volcanic Rocks and Dikes

	Luz 634N	Luz 634G	Luz 632D	Luz 516E	Luz 516B	Luz 516H	Luz 516J	Luz 516D	Luz 627C	Luz 660A	Luz 123A	Average*
Rock type	lower pillow	dike	dike	dike	flow	upper pillow	dike	dike	dike	dike	micro-gabbro	
SiO2	54.19	52.59	55.65	62.00	54.71	55.56	54.02	52.90	55.24	58.23	51.99	55.35
TiO2	0.63	0.91	1.01	0.91	0.99	0.99	0.45	0.40	0.81	0.44	0.21	0.73
Al2O3	13.72	16.97	15.73	13.30	14.67	14.93	15.89	16.08	15.81	16.14	13.46	15.44
Fe2O3	7.74	12.52	13.53	10.83	12.03	12.00	9.45	8.00	10.33	8.33	9.90	10.13
MnO	0.28	0.20	0.18	0.12	0.19	0.17	0.18	0.18	0.12	0.17	0.23	0.18
MgO	11.35	5.50	5.02	2.86	3.95	4.48	7.51	9.41	4.76	5.58	12.98	6.05
CaO	6.73	4.77	6.82	3.56	6.10	3.67	5.06	7.34	9.94	9.11	11.21	6.32
Na2O	4.97	6.01	2.45	5.40	4.45	5.37	4.02	4.15	2.42	1.61	0.86	4.33
K2O	0.03	0.02	0.12	1.90	1.12	2.69	3.45	1.28	0.27	0.13	0.04	0.70
P2O5	0.08	0.08	0.07	0.09	0.11	0.09	0.05	0.06	0.08	0.05	0.02	0.09
Sum	99.71	99.56	100.58	100.97	98.32	99.95	100.08	99.80	99.78	99.78	100.90	99.29
Ba	4	20	5	219		59	257	95	4	10	31	48
Sr	32	41	90	44	80	131	124	173	48	89	80	71
Cr	506	12	26	12	76	18	54	165	27	156	118	102
Ni	184	19	22	14	11	19	44	71	28	43	93	48
V	195	388	375	316	440	349	261	233	389	197	165	301
Zr	48	57	50	51	40	61	34	37	60	41	20	46
Y	13	22	22	19	20	23	14	13	22	20	13	18
Zn	156	236	110	92	91	55	70	66	54	79		92
Cu	7	136	100	16	48	7	107	72	8	17		52
Sc	32	34	31	24	43	26	21	33	35	31		30
Ce/Sm				0.51	0.73	1.01	1.32	1.09				
Ce/Yb				0.46	0.65	0.77	0.86	0.79				

Major element analyses are in weight percent; trace element analyses are in parts per million. Blanks indicate that data are not available.
*Average of 35 samples.

TABLE 1*c*. Whole Rock Analyses for East Side Rocks

Sample	Luz 116D	Luz 116F	Luz 118C	Luz 423F	Luz 616A	Luz 119B	Average*
Rock type	dike	dike	dike	dike	dike	micro-gabbro	
SiO2	50.87	50.15	52.90	50.98	50.89	49.74	50.92
TiO2	0.91	0.98	1.47	1.01	1.57	0.37	1.05
Al2O3	15.93	16.47	15.97	19.88	14.69	15.95	16.48
FeO*	8.94	8.58	10.87	7.44	11.51	9.40	9.46
MnO	0.21	0.19	0.26	0.17	0.21	0.09	0.19
MgO	8.15	9.12	5.48	6.44	7.60	9.74	7.76
CaO	11.91	12.19	9.41	12.34	9.53	13.50	11.48
Na2O	1.83	1.94	3.09	1.97	3.63	1.18	2.27
K2O	0.01	0.22	0.05	0.31	0.16	0.11	0.14
P2O5	0.09	0.09	0.17	0.20	0.16	0.24	0.16
Sum	98.85	99.93	99.67	100.74	99.94	100.32	99.91
Ba	13			18	10	24	16
Sr	120	107	157	136	163	90	129
Cr	70			138	221		143
Ni	56	153	18	62	70		72
V	240	219	340	249	284	285	270
Zr	62	61	131	71	111	285	120
Y	25	15	0	23	32	14	18
Zn					5	16	10
Cu					14		
Sc					38		
Ce/Sm	0.70						
Ce/Yb	0.74						

Major element analyses are in weight percent; trace element analyses are in parts per million. Blanks indicate that data are not available.
*Average of six samples.

rocks from the Zambales Ophiolite. The diagonal lines represent Ti/Zr and Ti/V ratios, respectively. Chondritic values for Ti/Zr are about 110 [*Sun and Nesbitt*, 1978]. The volcanic rocks loosely cluster about this ratio, but large ranges in Ti and Zr concentrations are displayed, and some provinces also display a large range in Ti/Zr ratio. *Sun and Nesbitt* [1978] suggest highly variable Ti/Zr may be due to variable secondary LREE enrichment of an already depleted mantle source.

The fields in Figure 5 (Ti versus V) have been defined by *Shervais* [1982]. The "arc-like" lavas have low Ti/V (corresponding to both lower Ti and higher V abundances), whereas the East Side basalts have higher Ti, lower V, and higher Ti/V ratios. The Botolan dikes have the widest range of Ti/V. *Shervais* [1982] suggests that Ti/V reflects the oxidation state of the magma. Again, these data are consistent with other data indicating heterogeneity of Zambales lavas, with mixed characteristics including both MORB and arc affinities.

The relatively unfractionated volcanics rocks and dikes from the Zambales Ophiolite have highly variable Ni and Cr

TABLE 1*d*. Whole Rock Analyses for Coto Area Dikes

	C-2	C-8	C-12	Luz 209A	Luz 209Y	Luz 209ZH	Luz 215M	Luz 399A	Average*
Rock type	dike	dike	dike	dike	dike	dike	dike	dike	
SiO2	55.69	53.54	53.50	54.89	53.10	49.49	54.12	52.37	52.76
TiO2	0.78	0.73	1.09	1.17	0.60	0.47	0.94	0.86	0.79
Al2O3	15.63	16.34	15.20	15.83	16.41	15.39	17.02	16.27	16.01
Fe2O3	11.45	11.53	12.32	11.93	8.34	7.54	11.36	11.00	10.37
MnO	0.18	0.19	0.19	0.15	0.19	0.21	0.13	0.18	0.17
MgO	4.22	4.72	4.19	4.10	7.37	10.66	4.23	5.31	6.44
CaO	8.84	9.46	8.60	8.39	10.42	14.31	9.42	7.28	10.37
Na2O	2.65	2.53	2.68	2.49	3.21	1.44	3.23	3.97	2.56
K2O	0.03	0.12	0.13	0.12	0.28	0.05	0.15	0.21	0.11
P2O5	0.08	0.07	0.07	0.09	0.21	0.04	0.08	0.14	0.10
Sum	99.55	99.23	97.97	99.16	100.13	99.39	100.68	97.59	99.60
Ba	9	12	11	18	26	23	21	21	15
Sr	101	105	110	115	106	197	118	130	117
Cr	34	26	31	9	158	382	8	9	131
Ni	30	24	35	6	63	162	10	33	64
V	337	365	356	424	282	229	386	370	368
Zr	70	56	60	39	39	26	36	45	49
Y	23	19	21	18	16	12	18	19	19
Zn	66	81	85						64
Cu	28	14	52						60
Sc	30	31	31						32
Ce/Sm	0.47							0.49	
Ce/Yb	0.38							0.37	

Major element analyses are in weight percent; trace element analyses are in parts per million. Blanks indicate that data are not available.
* Average of 16 samples.

TABLE 1*e*. Whole Rock Analyses for Botolan Dikes

	Luz 252	Luz 254	Luz 256B	Luz 259D	Luz 666F	Luz 666K	Luz 670C	Luz 675	Average*
Rock type	dike	dike	dike	dike	dike	dike	dike	dike	
SiO2	52.86	52.97	52.53	50.74	55.87	56.52	50.28	51.38	53.24
TiO2	0.98	0.95	0.70	1.62	0.34	0.71	0.75	0.82	0.84
Al2O3	17.52	16.25	15.97	15.21	15.23	14.50	14.80	16.70	15.82
Fe2O3	9.38	11.18	8.42	9.85	8.19	6.49	9.80	10.07	9.37
MnO	0.10	0.14	0.16	0.18	0.14	0.14	0.16	0.17	0.16
MgO	5.19	6.32	6.77	6.65	7.93	7.44	10.48	6.73	6.64
CaO	10.04	9.71	9.97	9.58	11.32	8.75	11.14	10.67	9.43
Na2O	4.41	2.55	3.06	4.39	2.27	4.91	2.61	3.46	3.64
K2O	0.05	0.67	0.36	0.10	0.02	0.17	0.06	0.11	0.21
P2O5	0.12	0.13	0.20	0.20	0.04	0.07	0.07	0.08	0.11
Sum	100.55	100.73	97.98	98.34	101.36	99.70	100.15	100.19	99.46
Ba	25	18	46	0	64	11	9	11	
Sr	178	149	144	88	121	98	121	121	126
Cr	40	8	20	192	326	46	520	53	111
Ni	67	19	19	74	74	40	197	53	54
V	367	423	306	287	219	220	272	274	290
Zr	57	51	63	130	38	51	40	51	57
Y	24	25		42	12	17	21	21	21
Zn					56	36	36	43	69
Cu					188	73	26	34	56
Sc					29	39	34	38	29

Major element data are in weight percent; trace element analyses are in parts per million. Blanks indicate that data are not available.
*Average of 15 samples.

TABLE 2. Isotope Analyses for Selected Samples From the Zambales Ophiolite

	Nd, ppm	Sm, ppm	$^{143}Nd/^{144}Nd$	Error	Sm/Nd	$^{87}Sr/^{86}Sr$	Error
Luz 160C	1.61	0.79	0.513203	0.000024	0.49	N/A	
Luz 163A	2.32	1.01	0.513512	0.000051	0.44	N/A	
514A CPX	0.16	0.12	0.513041	0.000135	0.76	0.704029	0.000018
Luz 627C	1.02	0.43	0.513227	0.000029	0.42	N/A	
Luz 632D	2.83	1.25	0.513150	0.000021	0.44	N/A	
Luz 634N	0.90	0.35	0.513232	0.000135	0.38	N/A	
Luz 123A	1.17	0.54	0.513241	0.000028	0.46	0.704993	0.000030
Luz 116D	4.75	1.99	0.513250	0.000078	0.40	0.704213	0.000031
Luz 119B	3.22	1.32	0.513145	0.000028	0.41	N/A	
Luz 256B	3.85	1.54	0.513120	0.000029	0.40	0.704325	0.000025
Luz 259 di.	5.25	2.25	0.513205	0.000020	0.43	N/A	
Luz 666K	1.26	0.48	0.513064	0.000031	0.38	N/A	

The samples with poor $^{143}Nd/^{144}Nd$ measurements (errors greater than 30) were not used in the arguments in the text and are not plotted in Figure 8. N/A means not available.

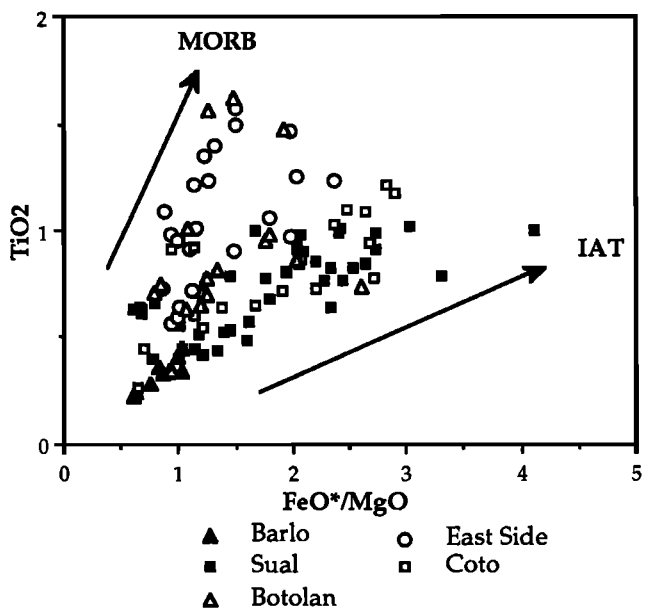

Fig. 2. Plot of FeO*/MgO versus TiO_2 for Zambales volcanics. The symbols correspond to the different volcanic sections. Previously defined trends for MORB and island arc tholeiites (IAT) are shown by arrows.

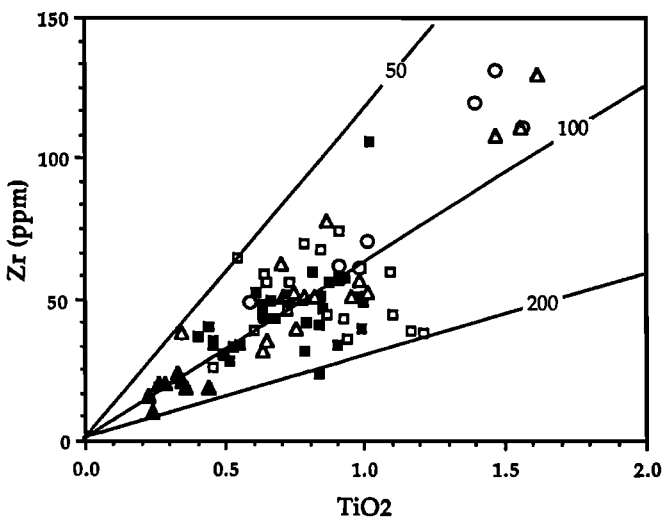

Fig. 4. TiO_2 versus Zr abundance for Zambales volcanic rocks. Symbols are the same as in Figure 2. The diagonal lines correspond to Ti/Zr ratios.

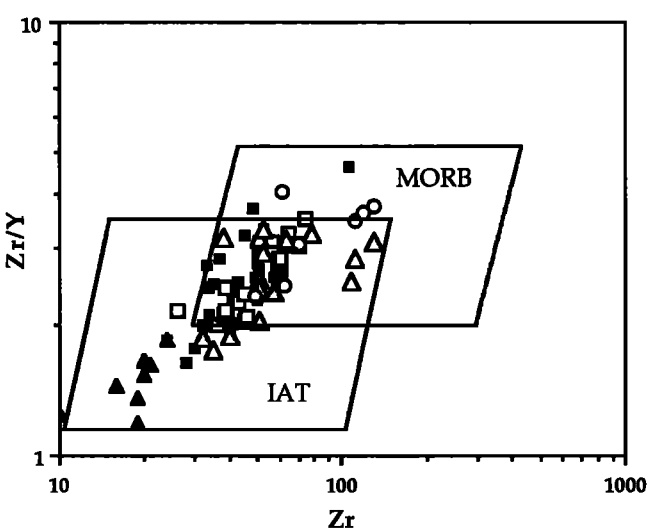

Fig. 3. Zr (in parts per million) versus Zr/Y for Zambales volcanics, with IAT and MORB fields taken from *Pearce and Cann* [1973]. Symbols are the same as in Figure 2.

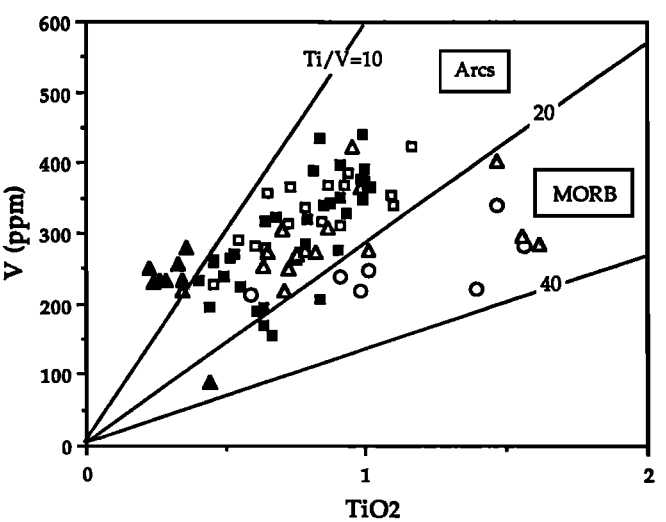

Fig. 5. TiO_2 versus V abundance for Zambales volcanic rocks. Symbols are the same as in Figure 2. The diagonal lines correspond to Ti/V, after *Shervais* [1982].

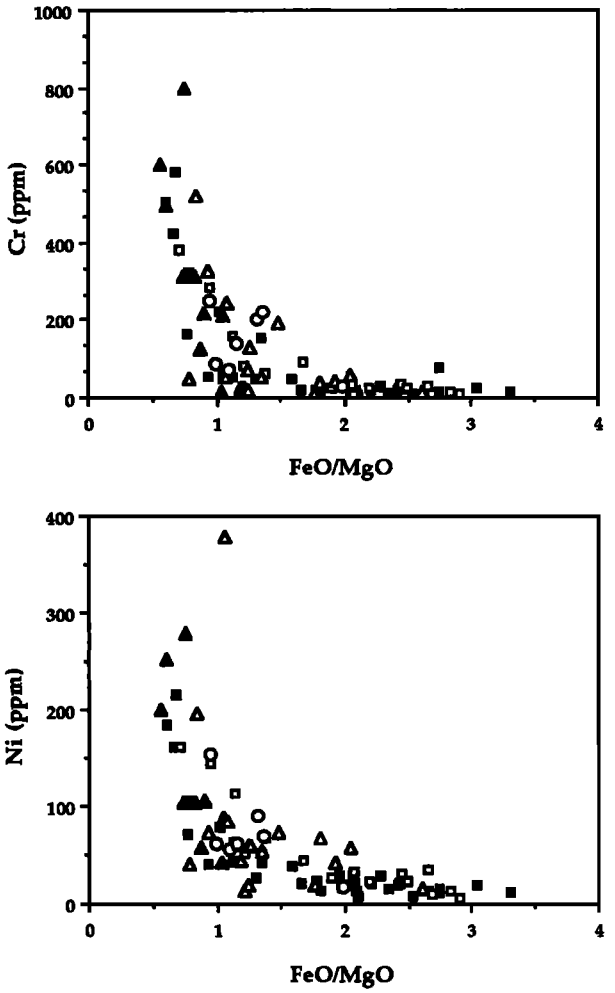

Fig. 6. Cr and Ni versus FeO*/MgO for Zambales volcanics. A range of abundances is displayed for both Ni and Cr. Symbols are the same as in Figure 2.

abundances (Figure 6). For a given FeO*/MgO, rocks from Sual and Barlo have lower Ni and Cr abundances (similar to IAT), although very primitive rocks have very high concentrations of these two compatible elements. Pillows and dikes from the other volcanic sections have much greater ranges of Ni and Cr for a given FeO/MgO, especially the Coto and Botolan dikes. *Geary et al.* [1989] also noted a bimodal distribution of Ni and Cr abundances in the rocks from the east side of the range.

Figure 7 presents chondrite-normalized REE values from representative volcanic and doleritic rocks from different parts of the ophiolite. Again, these data underscore the differences in geochemistry between volcanic provinces. Some volcanic sections, specifically Barlo (Figure 7*a*), are noteworthy because of the extreme REE depletion, especially LREE, of these rocks. This is consistent with their very low abundances of other HFS elements. The Sual rocks in Figure 7*b* include samples with both patterns which are depleted with respect to MORB abundances and MORB-like patterns (slightly LREE-depleted, and abundances roughly 10X chondritic values). The range of REE abundances for Sual rocks is similar to the ranges of abundances of other diagnostic trace elements and ratios.

We report only one pattern from the East Side of the range (Luz 116D, Figure 7*c*). The sample shows a REE pattern which is very similar to MORB patterns. More data, demonstrating a broader range of values, are given by *Geary et al.* [1989]. However, the point we make is that the number of volcanic rocks with MORB-like REE patterns is greater on the East Side than other volcanic sections. The other patterns in Figure 7*c* (Luz 209ZH and 399A) are dikes in the peridotite from the central part of the range (Coto and Botolan).

Some radiogenic isotope data from the Zambales Ophiolite have also been collected. (Table 2, Figure 8). Data from both leached CPX separates and leached whole rocks indicate that the mantle source for these volcanics was slightly enriched in Rb but not in LREE. The whole rock samples have high $^{87}Sr/^{86}Sr$ and fall well off the mantle array, strongly suggesting that seawater alteration was pervasive in these rocks.

Figure 8 shows the $^{143}Nd/^{144}Nd$ versus Sm/Nd for selected samples from different volcanic provinces in the Zambales range. Three different features in this plot can be noted. First, a crude trend is displayed from the northern to southern exposures of the range. Within the ophiolite, rocks from the north (Barlo and Sual) have generally higher $^{143}Nd/^{144}Nd$ and Sm/Nd values, and samples from the south (Botolan) have the lowest values for these ratios.

Second, the ophiolite data data display a roughly linear correlation. The variations in both Nd isotopic ratio and Sm/Nd ratio suggest that the volcanic rocks tapped a heterogeneous source and that either mixing occurred in the source region or different melts were mixed prior to their eruption. The linear array is similar to data from Mariana Trough basalts [*Volpe et al.*, 1987, 1990], which have been interpreted to indicate very small scale source heterogeneities.

Third, $^{143}Nd/^{144}Nd$ and Sm/Nd values are as high or higher than values for normal MORB, indicating the derivation of volcanic rocks from a very depleted mantle source. The very high (or depleted) $^{143}Nd/^{144}Nd$ values of some of these samples are consistent with their extremely LREE-depleted patterns. This is quite different from the Nd isotopic composition of lavas from the Troodos ophiolite, which indicate a LREE enrichment [*McCulloch and Cameron*, 1983; *Taylor and Nesbitt*, 1988].

DISCUSSION

We have used concentrations and ratios of HFS elements, REE, and Nd isotopes to document compositional ranges between different volcanic sections of the ophiolite. The separate compositional trends from different volcanic sections displayed in Figures 2-8, and particularly the REE and $^{143}Nd/^{144}Nd$ data from the different volcanic sections suggest that the ophiolitic lavas make up at least two compositional end members (IAT and MORB) that cannot be related simply by differential partial melting or fractional crystallization. We make special note of the range of compositions found in each volcanic locality. In some cases, the range of compositional variability is sampled in a single outcrop, with compositions changing within meters (e.g., Sual samples 634 and 632, and 516). Also, the relative abundances of IAT and MORB lavas change between the respective volcanic sections [this work and *Geary et al.*, 1989].

The northernmost volcanic and doleritic rocks in the Zambales ophiolite, those in the Barlo and Sual regions (Figure 1), have definitive volcanic arc geochemistry including rocks with boninitic affinities (Barlo, Table 1*a*); no such rocks occur elsewhere in the range. The occurrence of boninites strongly suggests a forearc environment for the

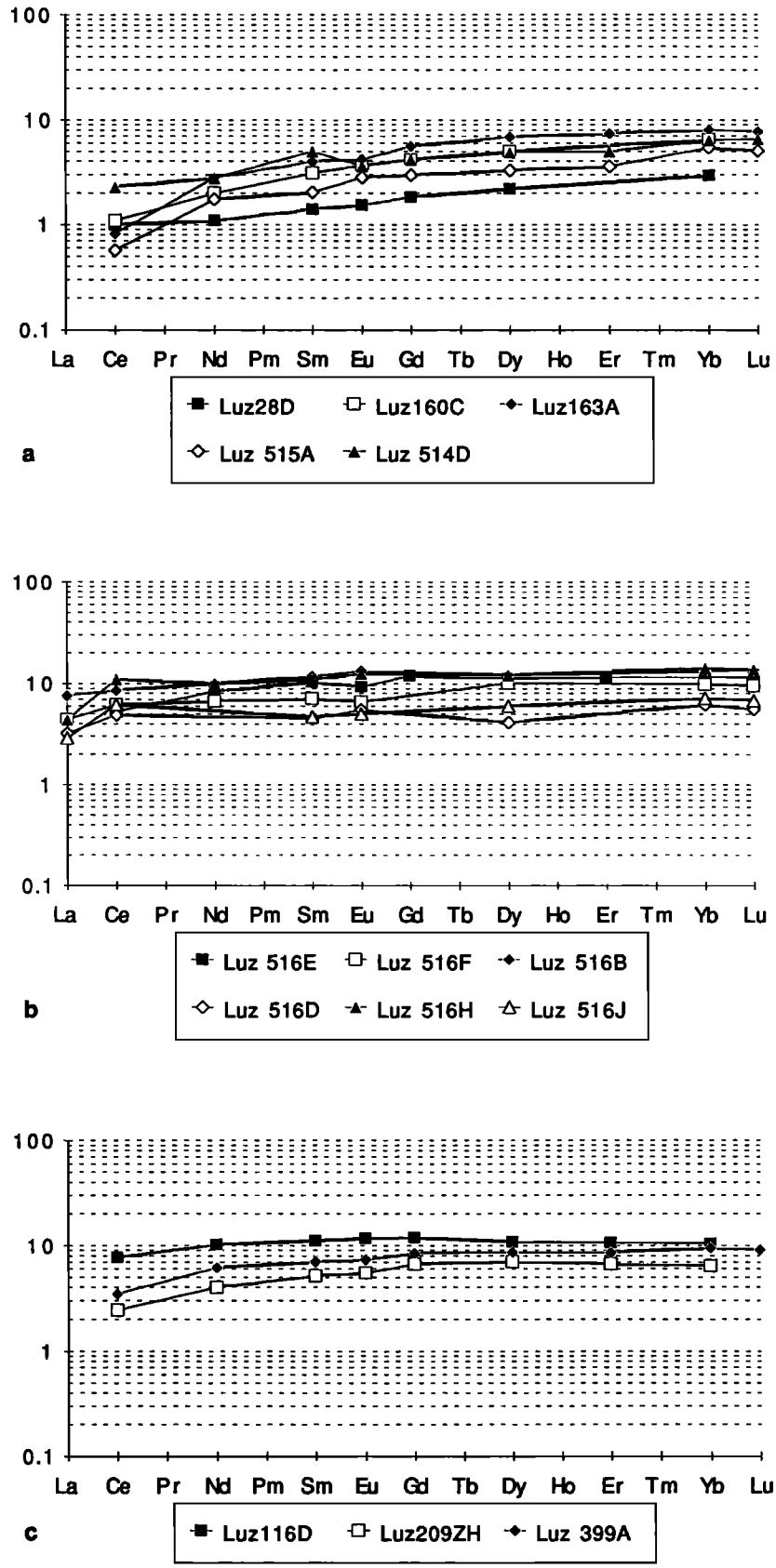

Fig. 7. REE patterns for selected volcanic rocks from (*a*) Barlo, including boninitic rocks (Luz 28D), (*b*) Sual, and (*c*) Coto and East Side. The data were obtained by isotope dilution (previously reported in *Hawkins and Evans*, [1983]), neutron activation (Luz 516B, 516D, 516F, 516H, 516J) and DCP techniques. Note that all Barlo rocks (Figure 7*a*) show extreme LREE depletion.

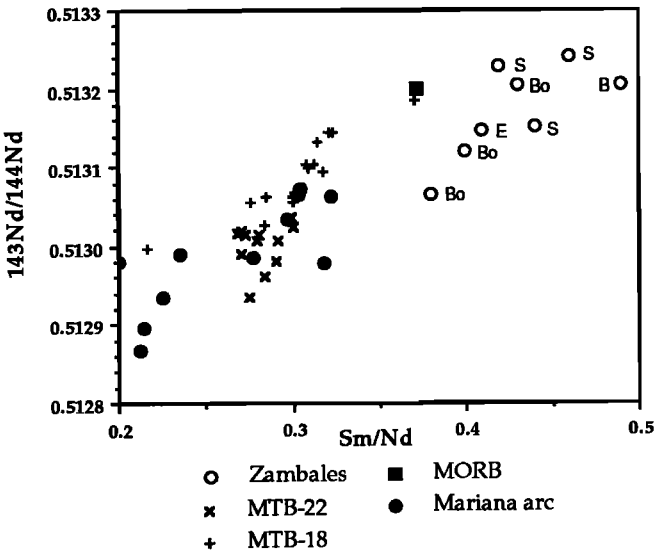

Fig. 8. $^{143}Nd/^{144}Nd$ versus Sm/Nd for Zambales ophiolite. Data from respective volcanic localities in the Zambales Ophiolite display a regional trend with higher ratios from the northern sections of the ophiolite and lower ratios from the central and southern Zambales. Notations are B, Barlo; S, Sual; C, Coto; Bo, Botolan; and E, East Side. Comparative data from the Mariana arc and Mariana Trough are from *Stern and Bibee* [1984], *Stern et al.* [1990], *Lin et al.* [1990], *Volpe et al.* [1987, 1990]. MTB-18 and MTB-22 are samples from the Mariana Trough from 18°N and 22°N, respectively.

Zambales ophiolite. Greater abundances of MORB-like volcanic rocks occur on the East Side of the range, although the East Side also includes rocks with compositions transitional with arc tholeiites (Table 1*c*) and [*Geary et al.*, 1989]. Data from the dikes in Coto and Botolan have compositions which are IAT to transitional between arc tholeiite and MORB compositions.

We do not fully understand the significance of the geochemical variations displayed in the Zambales ophiolite, but we suggest that the ophiolite preserves an evolving oceanic crustal section from a supra-subduction zone environment, probably on the backarc or forearc edge of a young volcanic arc. Because all volcanic sections in the ophiolite include data with mixed affinities to IAT and MORB, we cannot definitively ascribe a backarc, nascent arc, or forearc setting for the ophiolite. Furthermore, recent studies on backarc basins [e.g., *Volpe et al.*, 1987; *Hawkins and Melchior*, 1985] indicate that volcanic arcs from present-day backarc basins show mixed chemical characteristics between IAT and MORB. Also, arc systems like the Mariana island arc are built on backarc or thinned forearc crust. Uncertainties regarding extrusive and intrusive relationships of young arcs to their substrate (backarc, forearc, or MORB) indicate that the spatial distribution of MORB-like and arc-like lavas in young arcs will be complex (see discussion of *Stern et al.* [1989]).

The geochemical data from the Zambales suggest the existence of variably depleted upper mantle sources for the ophiolitic lavas. Due to the large ranges of compositions that occur over a limited regional extent (less than 130 km) within the ophiolite, and even within each volcanic section, we infer that mantle heterogeneity occurs on a relatively small regional scale. As such, the ophiolite serves as a valuable ruler by which to measure compositional and spatial variation of volcanic rocks in supra-subduction zone environments.

The local and regional compositional heterogeneities documented in the Zambales ophiolite complex clearly indicate that the generation of the crust now preserved as ophiolite was quite complicated. Possible explanations for the field and compositional data from the Zambales Ophiolite volcanics are (1) the inception of an arc on normal ocean crust or on back-arc basin crust, (2) modification of the source for backarc basin crust by a piece of subducted slab, or (3) early volcanic activity in a forearc. *Geary et al.* [1989] discuss the first and third explanations; the second is similar to that proposed by *Sinton and Fryer* [1987]. Although we are not suggesting that the ophiolite was necessarily generated in a back-arc basin environment, we do note similar ranges of IAT and MORB-like rocks from zoned backarc basins like the Mariana Trough. For a comparative discussion, we examine some of the data from recent studies of the Mariana Trough. *Hawkins and Melchior* [1985], *Volpe et al.* [1987, 1990], *Sinton and Fryer* [1987], *Hawkins et al.* [1990], and *Stern et al.* [1990] all report the recovery of lavas from the Mariana Trough with variably mixed geochemical characteristics between N-MORB and Mariana island arc basalts. *Volpe et al.* [1990] report compositional changes in as little as 10 m and conclude that mantle heterogeneities must be on the scale of individual melt batches. Furthermore, the Mariana Trough is concentrically zoned from the outside in, with more island arc basalts found along the margins and more MORB-like lavas in the center of the basin [*Hawkins and Melchior*, 1985; *Stern et al.*, 1990]. The arguments to explain the compositional diversity in the Mariana Trough include (1) modification of the source for Mariana Trough basalts by earlier episodes of melting; (2) assimilation of components (melts or fluids) from a subducted slab, either an earlier episode of subduction or the present system; (3) physical mixing of subarc and MORB-like mantle sources; and (4) physical mixing of melts derived from separate mantle sources.

Regardless of the specific explanation or combination of the above explanations, it is apparent that the mantle beneath the Mariana Trough is heterogeneous on a very local scale as well as a regional scale in order to account for both the heterogeneity of lavas from the center of the basin and the compositional zonation of the basin. The mantle heterogeneity in the Mariana Trough system must be related to the extended history of subduction in the region, including multiple episodes of island arc volcanism. Although they are not quantified to the same extent as the Mariana Trough, we predict there were ranges of compositions reflecting similar scales of mantle heterogeneities in the nascent arc and forearc settings of the Mariana arc.

Like the Mariana Trough, the Zambales ophiolite has lavas with trace element compositions intermediate between N-MORB and IAT. There is compositional diversity observed with individual volcanic sections as well as on a regional scale. Unlike the Mariana Trough, the Zambales lavas are more depleted in incompatible elements (Figure 8) and include boninites which are generally associated with forearc settings. The trends and ranges of lava compositions and specifically the trace element data indicate that the mantle source for the Zambales ophiolite must have been extremely depleted but then variably enriched with LREE and other incompatible elements in order to explain the various ratios and isotopic

abundances. Furthermore, the secondary enrichment of the mantle source (or the mixing of lavas from different sources) must occur on a very small scale in order to account for compositional variations within individual volcanic sections. Given this, the Zambales is a very good analog to the spatial-temporal-compositional variation observed in present-day arc-backarc systems.

Many western Pacific subduction systems have experienced long histories of subduction occurring over tens of millions of years. Such complicated plate boundaries which have existed through several episodes of changing subduction systems including subduction jumps, subduction zone reversals, arc splitting, and backarc and or forearc volcanism, must produce many small domains in the upper mantle, some of which become extremely depleted or variably enriched. Subsequent magma production may result in the interfingering and superposition of very different lavas. The magmas will be products of the partial melting of a heterogeneous mantle which varies on a small scale and in three dimensions, and will carry the mixed geochemical signatures from the complex mantle source.

Paleomagnetic studies suggest that the Zambales Ophiolite was formed as oceanic crust in the vicinity of the present-day Celebes Sea [*Fuller et al.*, 1983; *Karig*, 1983]. Furthermore, the Indonesian-Philippine convergent margin has been the site of changing subduction systems throughout the Cenozoic [e.g., *Karig*, 1973; *Hamilton*, 1977, 1979]. The complicated geochemistry preserved in the Zambales Ophiolite volcanic rocks is consistent with the regional history of the area where it was generated. To this end, the ophiolite is a valuable field locale for defining the scale of compositional variation in supra-subduction zone setting, and further detailed geochemical studies of the lavas may yield insight into the long-term compositional evolution of the upper mantle associated with convergent plate margins.

Acknowledgments. This work built on much previous work by Philippino investigators including G. Bacuta, A. Apostle, and R. Villones, all under the direction of Guillermo Balce, the former director of the Bureau of Mines and Geosciences, as well as independent efforts by geologists at Acoje and Benguet Corporation Mines. J. Rubenstone provided invaluable help in the collection and interpretation of the isotopic data, and D. Christie did likewise for data collected by DCP. T. Plank assisted in sample collection and field interpretation. Critical reviews by S. Bloomer and R. Stern greatly improved the manuscript. This work was supported by NSF grant RII860085.

REFERENCES

Abrajano, J.A., Jr., The petrology and low-temperature geochemistry of the sulfide-bearing mafic-ultramafic units of the Acoje massif, Zambales Ophiolite, Philippines: characterization of mineral and fluid equilibria, Ph.D. dissertation, 474 pp. Washington Univ. St. Louis, Mo. 1984.

Bachman, S.B., S.D. Lewis, and W.J. Schweller, Evolution of a forearc basin, Luzon Central Valley, Philippines, *AAPG Bull., 67*, 1143-1162, 1983.

Bacuta, G.C., Jr., Geology of some alpine-type chromite deposits in the Philippines, report, 22pp., Bur. of Mines, Manila, Philippines, 1978.

Bloomer, S.H., R.J. Stern, E. Fisk, and C.H. Geschwind, Shoshonitic volcanism in the northern Mariana arc, 1, Mineralogic and major trace element characteristics, *J. Geophys. Res., 94*, 4469-4496, 1989.

Bryner, L., Ore deposits of the Philippines: an introduction to their geology, *Econ. Geol., 64*, 644-666, 1969.

de Boer, J., L.A. Odom, P.C. Ragland, F.C. Snider, and N.R. Tilford, The Bataan orogene: eastward subduction, tectonic rotations and volcanism in the western Pacific (Philippines), *Tectonophysics, 67*, 252-282, 1980.

Evans, C.A., Petrology and geochemistry of the transition from mantle to crust beneath an island arc-backarc basin pair: Zambales Range ophiolite, Luzon, Philippines, Ph.D. thesis, 299 pp., Univ. Calif., San Diego, 1983.

Evans, C.A., and J.W. Hawkins, Compositional heterogeneities in upper mantle peridotites from the Zambales Range Ophiolite, Luzon, R.P., *Tectonophysics, 168*, 23-41, 1989.

Fuller, M., R. McCabe, I.S. Williams, J. Almasco, R.Y. Encina, A.S. Zanoria, and J.A. Wolfe, Paleomagnetism in Luzon, in *The Tectonic and Geologic Evolution of Southeast Asian Seas and Islands, part 2, Geophys. Monogr. Ser.*, vol. 27, edited by D. E. Hayes, pp. 79-94, AGU, Washington, D.C., 1983.

Fuller, M., R. Haston, and J. Almasco, Paleomagnetism of the Zambales ophiolite, Luzon, northern Philippines, *Tectonophysics, 168*, 171-204, 1989.

Garrison, R.E., E. Espiritu, L.J. Horan, and L.E. Mack, Petrology, sedimentology and diagenesis of hemipelagic limestone and tuffaceous turbidites in the Aksitero formation, central Luzon, Philippines, *U.S. Geol. Surv. Prof. Pap. 1112*, 16 pp., 1979.

Geary, E., and R. Kay, Petrological and geochemical documentation of ocean floor metamorphism in the Zambales ophiolite, Philippines, in *The Tectonic and Geologic Evolution of Southeast Asian Seas and Islands, part 2, Geophys. Monogr. Ser.*, vol. 27, edited by D. E. Hayes, pp. 139-156, AGU, Washington, D.C., 1983.

Geary, E. E. , R.W. Kay, J.C. Reynolds, and S.M. Kay, Geochemistry of mafic rocks from the Coto Block, Zambales Ophiolite, Philippines: trace element evidence for two stages of crustal growth, *Tectonophysics, 168*, 43-63, 1989.

Gervasio, F.C., Geotectonic development of the Philippines, *J. Geol. Soc. Philipp., 25*, 18-38, 1971.

Hamilton, W., Subduction in the Indonesian region, in *Island Arcs, Deep Sea Trenches, and Backarc Basins, Maurice Ewing Ser.*, vol. 1, edited by M. Talwani and W. Pitman, pp. 15-31., AGU, Washington, D.C., 1977.

Hamilton, W., Tectonics of the Indonesian region. *U. S. Geol. Surv. Prof. Pap., 1078*, 345 pp., 1979.

Hart, S., and C. Brooks, Clinopyroxene partitioning of K, Rb, Cs, Sr, and Ba, *Geochim. Cosmochim. Acta, 38*, 1799-1806, 1974.

Hashimoto, W., Geologic development of the Philippines, *Contrib. Geol. Paleontol. Southeast Asia*, CCXVII, 83-190, 1980.

Hawkins, J.W., Petrology of backarc basins and island arcs: their possible role in the origin of ophiolites, in *Proceedings of the International Ophiolite Symposium, Cyprus, 1979*, edited by A. Panayiotou, pp. 244-254, Cyprus Geol. Survey Department, Nicosia, Cyprus, 1980.

Hawkins, J.W. and R. Batiza, Petrology and geochemistry of an ophiolite complex: Zambales Range, Luzon, R.P. (abstract), *Eos Trans. AGU, 58*, 1244, 1977.

Hawkins, J.W. and C.A. Evans, Geology of the Zambales Range Luzon, Philippine Islands: ophiolite derived from an island arc-backarc pair, in *The Tectonic and Geologic Evolution of Southeast Asian Seas and Islands, part 2, Geophys. Monogr. Ser.*, vol. 27, edited by D. E. Hayes, pp. 95-123, AGU, Washington, D.C., 1983.

Hawkins, J.W. and J.T. Melchior, Petrology of Mariana Trough and Lau Basin basalts, *J. Geophys. Res., 90*, 11431-11468, 1985.

Hawkins, J.W., P.F. Lonsdale, J.D. MacDougall, and A.M. Volpe, Petrology of the axial ridge of the Mariana Trough backarc spreading center, *Earth Planet. Sci. Lett., 100*, 226-250, 1990.

Karig, D.E., Plate convergence between the Philippines and the Ryukyu Islands, *Mar. Geol., 14*, 153-168, 1973.

Karig, D.E., Accreted terranes in the northern part of the Philippine archipelago, *Tectonics, 2*, 211-236, 1983.

Lin, P.-N., R.J. Stern, and S.H. Bloomer, Shoshonitic volcanism in the northern Mariana arc, 2, Large-ion lithophile and rare earth element abundances: Evidence for the source of incompatible element enrichments in intraoceanic arcs, *J. Geophys. Res., 94*, 4497-4514, 1989.

Lin, P.-N., R.J. Stern, J. Morris, and S. H. Bloomer, Nd- and Sr-isotopic composition of lavas from the northern Mariana and southern Volcano arcs: Implications for the origin of island arc melts, *Contrib. Mineral. Petrol., 105*, 381-392, 1990.

McCulloch, M ., and W. Cameron, Nd-Sr study of primitive lavas from the Troodos ophiolite, Cyprus: Evidence of a subduction related setting, *Geology, 11*, 727-731, 1983.

Pearce, J., and J. Cann. Tectonic setting of basic volcanic rocks determined using trace element analyses, *Earth Planet. Sci. Lett., 19*, 290-300, 1973.

Philippine Bureau of Mines, Geologic map of the Philippines, scale 1:1,000,000, Manila, 1963.

Richard, P., N. Schmizu, and C. Allegre, 143Nd/144Nd, a natural tracer: an application to oceanic basalts, *Earth Planet. Sci Lett., 31*, 269-278, 1976.

Rossman, D.L., Chromite deposits of the north-central Zambales Range, Luzon, Philippines. *U.S. Geol. Surv. Open File Rep.*, 65 pp. 1964.

Rossman, D.L., G.C. Casteneda, and G.C. Bacuta, Geology of the Zambales ophiliolite, Luzon, Philippines, *Tectonophysics, 168*, 1-23, 1989.

Schweller, W.J., and D.E. Karig, Constraints on the origin and emplacement of the Zambales ophilite, Luzon, Philippines, *Geol. Soc. Am. Abstr. Programs, 11*, 152-153, 1979.

Schweller, W.J., D.E. Karig, and S.B. Bachman, Original setting and emplacement history of the Zambales ophiolite, Luzon, Philippines, from stratigraphic evidence, in *The Tectonic and Geologic Evolution of Southeast Asian Seas and Islands, part 2, Geophys. Monogr. Ser.*, vol. 27, edited by D. E. Hayes, pp. 124-138, AGU, Washington, D.C., 1983.

Schweller, W.J., P.H. Roth, D.E. Karig, and S.B. Bachman, Sedimentation history and biostratigraphy of ophiolite-related Tertiary sediments, Luzon, Philippines, *Geol. Soc. Am. Bull., 95*, 1333-1342, 1984.

Shervais, J., T-V plots and the petrogenesis of modern and ophiolitic lavas, *Earth Planet. Sci. Lett., 59*, 101-118, 1982.

Sinton, J. H. and P. Fryer, Mariana Trough lavas from 18°N: Implications for the origin of back-arc basin basalts. *J. Geophys. Res., 92*, 12782-12802, 1987.

Stern, R.J. and L.D. Bibee, Esmeralda Bank: Geochemistry of an active submarine volcano in the Mariana Island Arc, *Contrib. Mineral. Petrol., 86*, 159-169, 1984.

Stern, R.J., S.H. Bloomer, P.-N. Lin, and N.C. Smoot, Submarine arc volcanism in the southern Mariana Arc as an ophiolite analogue, *Tectonphysics, 168*, 151-170, 1989.

Stern, R.J., P.-N. Lin, J.D. Morris, M.C. Jackson, P. Fryer, S.H. Bloomer, and E. Ito, Enriched back-arc basin basalts from the northern Maraina Trough: implications for the magmatic evolution of back-arc basins, *Earth Planet. Sci. Lett., 100*, 210-225, 1990.

Stoll, W.C., Geology and petrology of the Masinloc chromite deposit, Zambales, Luzon, Philippine Islands, *Geol. Soc. Am. Bull. , 69*, 419-448, 1958.

Sun, S., and R.W. Nesbitt, Geochemical regularities and genetic significance of ophiolitic basalts, *Geology, 6*, 689-693, 1978.

Taylor, R. N., and R.W. Nesbitt, Light rare-earth enrichment of supra-subduction zone mantle: Evidence from the Troodos ophiolite, Cyprus, *Geology, 16*, 448-451, 1988.

Volpe, A.M., J. D. MacDougall, and J. W. Hawkins, Mariana Trough basalts (MTB): trace element and Sr-Nd isotopic evidence for mixing between MORB-like and arc-like melts, *Earth Planet. Sci. Lett., 82*, 241-254, 1987.

Volpe, A.M., J.D. MacDougall, G.W. Lugmair, J.W. Hawkins, and P. Lonsdale, Fine-scale isotopic variation in Mariana Trough basalts: evidence for heterogeneity and a recycled component in backarc basin mantle, *Earth Planet. Sci. Lett., 100*, 251-264, 1990.

Wolfe , J. A., and S. Selfe, Structural lineaments and neogene volcanism in southwestern Luzon, in *The Tectonic and Geologic Evolution of Southeast Asian Seas and Islands, part 2, Geophys. Monogr. Ser.*, vol. 27, edited by D. E. Hayes, pp.157-172, AGU, Washington, D.C., 1983.

Zindler, A., S. Hart, F. Frey, and S. Jakobsson, Nd and Sr isotope ratios and rare earth element abundances in Reykjanes Peninsula basalts: evidence for mantle heterogeneity beneath Iceland, *Earth Planet. Sci. Lett, 45*, 249-262, 1979.

G.C. Casteneda and H. Franco, Philippine Bureau of Mines and Geosciences, North Avenue, Diliman, Quezon City, Philippines.

C.A. Evans, MC C102, Lockheed Engineering and Sciences Company, P.O. Box 58561, Houston, TX 77258-8561.

(Received May 10, 1989;
revised March 1, 1991;
accepted May 28, 1991.)

JOURNAL OF GEOPHYSICAL RESEARCH, VOL. 96, NO. B10, PAGES 16,383–16,399, SEPTEMBER 10, 1991

Seismicity and Shear Strain in the Southern Great Basin of Nevada and California

JOAN GOMBERG

U.S. Geological Survey, Denver Federal Center, Denver, Colorado

This study examines the relationship between the distribution of small earthquakes ($M_L \leq 4.3$) and mechanisms of strain accumulation and relaxation in an area with long repeat times between large events, the Southern Great Basin Seismic Network (SGBSN) region. The Great Basin is a unique continental extensional province characterized by normal and strike-slip faulting, high heat flow, crust of thin to normal thickness, and high elevations. The SGBSN is operated to provide data to address suitability issues pertaining to Yucca Mountain, Nevada which is being evaluated as a potential site for a national mined geologic nuclear waste repository. Suitability issues include estimation of the probability of occurrence of future damaging earthquakes, the characterization of the mechanisms that drive hydrologic flow, and the identification of fractures (faults) that might act as flow conduits or barriers. This study attempts to explain the distribution of small earthquakes in terms of spatial variations in the shear strain field; where strain concentrates there should be a greater number of small earthquakes. Strain field models are constructed under the assumption that long term fault behavior perturbs an otherwise uniform strain field. These strain field models are then interpreted with regard to the regional tectonics and site suitability issues. Modeling results provide one possible explanation of why earthquake clusters cover regions much larger than the surface projections of any of mapped major faults; clusters in a wide band along and extending northeast of the northern half of the Furnace Creek fault may correspond to elevated shear strains along the fault and a broad cluster in the Pahranagat Shear Zone may be associated with shear strain arising from a distribution of smaller localized faults. The relatively large number of small earthquakes in the southern and eastern portions of the Nevada Test Site is consistent with the strain field models. A minimum in shear strain at Yucca Mountain is predicted by all models consistent with an almost total lack of earthquakes observed there. The region to the west of the Death Valley/Furnace Creek fault system, the portion of the study area with the most active deformation but few small earthquakes, is an area of low shear strain. A possible reason for this is that the fault configuration in the area is optimal for accommodating regional deformation via large earthquakes or creep. While there is also a relative lack of earthquakes at Yucca Mountain, this may be indicative of a lack of accumulating strain energy and thus, a lower potential for a large earthquake.

INTRODUCTION

It is apparent that the temporal and spatial distribution of small earthquakes may contain important clues to understanding the distribution of stress and strain prior to and following large earthquakes (approximately $M_s \geq 6.0$) in regions with short recurrence times and high levels of background seismicity (small earthquakes not associated with a large event) [*Stein and Lisowski*, 1983; *Mendoza and Hartzell*, 1988; *USGS Staff*, 1990]. However, in regions such as the southern Great Basin, which have long recurrence intervals (thousands of years) between large earthquakes the value of seismic monitoring is less clear. The principal goals of this study are to gain an understanding of why spatially variable distributions of small earthquakes recorded on the Southern Great Basin Seismic Network (SGBSN) exist, what they reveal about the strain field, and how faults accommodate regional deformation. This understanding may then be used to estimate the potential for the occurrence of large earthquakes on major faults in the southern Great Basin. The identification of seismicity patterns in the study area is described in a companion paper, [*Gomberg*, this issue] which herein will be referred to as Paper I.

The Great Basin is a continental extensional province characterized by normal and strike-slip faulting, high heat flow, crust of thin to normal thickness, and high elevations [*Zoback et al.*, 1981]. An understanding of the tectonics that give rise to these characteristics (e.g., brittle and ductile deformation, magmatism) in the vicinity of the SGBSN may also provide insight into processes outside the study area; e.g., the greater extensional deformation of the Basin and Range to the north, the relatively stable Colorado Plateau to the east, and associated with the transform plate boundary in California to the west. In order to understand the driving mechanisms for tectonism in these regions it is necessary to characterize the strain rates and the nature of the strain field. This is especially challenging in the SGBSN region because of the paucity of historic and Holocene large (ground rupturing) earthquakes, and the fact that regional displacement (e.g., relative motion between tectonic provinces or subplates; *Smith and Sbar* [1974]) is accommodated by a complex system of faults.

In addition to providing data useful in addressing the above scientific issues, the SGBSN is operated to provide data to assess the suitability of Yucca Mountain, Nevada as a potential site for a national mined geologic nuclear waste repository. One objective of the Yucca Mountain Site Characterization Project is to estimate the likelihood of occurrence and characteristics of future damaging earthquakes. Another fundamental objective is to characterize the mechanisms that drive hydrologic flow and the distribution of fractures (microfractures to faults) that might act as flow conduits or barriers [*Fox et al.*, 1991]. Achievement of the first objective is difficult because of the lack of local modern instrumental recordings of any earthquakes with magnitude greater than M_L=4.3. The locations of all earthquakes in the vicinity of the SGBSN with $M_s \geq 6.0$ and earthquakes with $M_L \geq 3.5$ recorded by the SGBSN are shown in Figure 1.

The approach taken to identify the most striking features of the

Paper number 91JB01576.

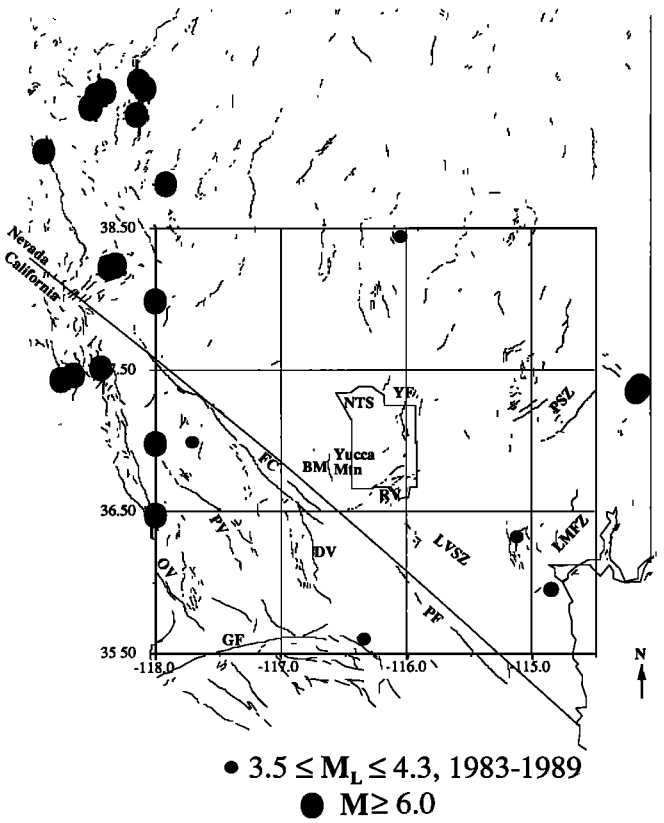

Fig. 1. Map of the area covered by the Southern Great Basin Seismic Network. Curved line segments are Quaternary fault scarps and lineaments inferred from geologic information [*Nakata et al.*, 1982]. Large solid circles are epicenters of earthquakes with magnitudes greater than approximately 6.0, and smaller solid circles are epicenters of events recorded on the SGBSN with local magnitude greater than 3.4 (the largest is 4.3) between 1983 and 1989. Abbreviations are FC, Furnace Creek Fault; DV, Death Valley Fault Zone; LVSZ, Las Vegas Shear Zone; PSZ, Pahranagat Shear Zone; PV, Panamint Valley Fault Zone; GF, Garlock Fault; LMFZ, Lake Mead Fault Zone; YF, Yucca Fault; BM, Bear Mountain Fault; RV, Rock Valley Faults; OV, Owens Valley Faults; PF, Pahrump Fault; NTS, Nevada Test Site.

seismicity of the southern Great Basin is described in Paper I. In summary, the features identified in that study include the following.

1. Clusters of earthquakes exist at all magnitudes at the northern end of the Furnace Creek fault and in the Pahranagat Shear Zone. These clusters cover areas much larger than the surface projections of any of the mapped faults.
2. A relatively large number of earthquakes (with respect to the rest of the SGBSN region) occur in the southern and eastern portions of the Nevada Test Site (NTS), and to a lesser extent west of the Bear Mountain fault (Figure 1). The northern NTS also has numerous small earthquakes but these may be caused by non-tectonic processes related to the frequent nuclear testing done in this part of the NTS.
3. A "hole" (lack of earthquakes) in the relatively high seismicity levels of the NTS region is centered on Yucca Mountain.
4. A considerable number of events in the SGBSN catalog cannot readily be correlated with mapped faults.
5. The region where recent deformation appears to be greatest, to the west of the Death Valley/Furnace Creek fault system, has few small earthquakes.
6. Seismicity patterns are nearly identical for all magnitude bins. This means that the same view of where regional deformation is occurring can be obtained by examining numbers of earthquakes or by summing slip estimated from seismic moments.

This study attempts to explain the distribution of small earthquakes in terms of spatial variations in the shear strain field. A uniform strain field is modified by long term fault behavior resulting in regions of strain concentration or reduction. Where there are strain concentrations, it is proposed that there should be a greater number of small earthquakes. A series of strain field models are constructed using the two-dimensional boundary element technique of *Crouch and Starfield* [1983]. This approach is used to model shear strain near Hollister, California [*Mavko*, 1982] and more recently in a number of studies that model the morphology in terms of dilational strains [*Bilham and King*, 1989; *Hackman et al.*, 1990; *King and Ellis*, 1990]. Unlike California where most of the seismicity is discussed with reference to larger ($M_S > 5.0$) earthquakes [*Stein and Lisowski*, 1983; *Mendoza and Hartzell*, 1988; *USGS Staff*, 1990; *Seeber and Armbruster*, 1990; *Michael et al.*, 1990; *King et al.*, 1990] there have been no such earthquakes in the SGBSN region since its installation in 1978. The absence of large historical events within the SGBSN vicinity means that the observed seismicity is probably not due to postseismic phenomena (assuming Omori's Law [*Omori*, 1984] in which the aftershock rate is inversely proportional to the time since the main event). Thus, the current seismicity probably represents the response to steady state deformation. This may be an important distinction if inferred strain fields are to be used as inputs for hydrologic models in which large excursions of the water table are attributed to rapid, large magnitude changes in the stress field [*Fox et al.*, 1991].

BOUNDARY ELEMENT MODEL CONSTRUCTION

A summary of the general displacement discontinuity boundary element algorithm used to calculate shear strain fields is now presented; the specific application to studies of elastic deformation in the crust of the southern Great Basin is described following this section. The strain fields calculated in this study arise from slip on faults in an otherwise uniform deformation field. Faults are represented as vertical slits in a thin plate and variable slip and strike may be included by discretizing each fault into segments (fault boundary elements) for which stress and/or displacement boundary conditions are specified (top of Figure 2*a*). Those fault boundary elements that do not have specified fixed displacement discontinuities (relative slip equivalent to Burgers vectors for an elastic dislocation; elements 1-4 of Figure 2*a*) can slip in response to fixed relative slip specified on other elements (elements 7-8 of Figure 2*a*) and to a regional deformation field that is otherwise uniform over the entire area of interest. Pure shear slip faulting is modeled using fault element boundary conditions of zero shear stress and zero normal displacement. Normal or thrust faulting may be approximated by allowing the fault elements to open or close which requires specifying zero shear normal stress boundary conditions.

The effect of uniform regional deformation is investigated by placing two parallel, straight boundaries (regional boundary elements) with fixed shear and normal displacements of opposite sense on either side of the region of interest (elements 5-6, bottom of Figure 2*a*). These regional boundary elements are sufficiently long so that end effects are negligible in the region of interest [*Bilham and King*, 1989]. Regional deformation fields consistent with both regional displacement directions (e.g., known from geodetic information) and principal strain axes (e.g., known from earthquake focal mechanisms) can be modeled. Since infinitesimal

strain is assumed, the regional strain field can be considered as the superposition of simple shear arising from the specified shear displacements and of extension due to both the normal and shear displacements on the regional boundary elements.

The following discussion summarizes how to model strain fields consistent with a specified regional extension direction, θ_e, and a regional displacement direction, θ_d, (both measured with respect to north) by appropriately specifying the orientation and the shear and normal displacements, u_s and u_n respectively, on the regional boundary elements. This is illustrated in Figure 2*b*. Let Ψ be the angle between east and the regional boundary elements. The direction of maximum shear is parallel to the boundary elements and the maximum extension direction associated with the simple shear is oriented at $\Psi + 45°$ [*Jaeger and Cook*, 1977]. The magnitude of the extension, $|\varepsilon_e|$, arising from the simple shear is equal to the magnitude of the shear strain, $|\varepsilon_s|$, which is equal to the ratio of the shear displacement and the distance between the two regional boundary elements ($|\varepsilon_e| = |\varepsilon_s| = |u_s| W^{-1}$). This extension adds vectorally to the extension arising from the normal displacements which is described by the formula $\varepsilon_n = 2u_n W^{-1}$.

When $\theta_e > \theta_d$ the extension direction (the orientation of ε_{total} in Figure 2*b*) is determined by the relation

$$\theta_e = \psi + \sin^{-1}\left(\frac{\nu}{\sqrt{2(\nu^2 + \sqrt{2}\nu + 1)}}\right) - 45 \qquad (1a)$$

where $\nu = 2|u_n||u_s|^{-1}$ and the regional displacement direction (the orientation of u_{total} in Figure 2*b*) is

$$\theta_d = \psi + \tan^{-1}(\nu/2) - 90 \qquad (1b)$$

(top of Figure 2*b*). When $\theta_e < \theta_d$ the equivalent relations are

$$\theta_e = \psi - \sin^{-1}\left(\frac{\nu}{\sqrt{2(\nu^2 + \sqrt{2}\nu + 1)}}\right) - 135 \qquad (2a)$$

and

$$\theta_d = \psi - \tan^{-1}(\nu/2) - 90 \qquad (2b)$$

(bottom of Figure 2*b*). A table of directions, θ_e and θ_d, is easily calculated for a suite of values of ψ and ν and appropriate values selected for the desired extension and displacement directions.

The stress and strain conditions on the fault and regional boundary elements are linearly related to shear and normal displacement discontinuities across each element. The Greens functions relating stress and strain to the discontinuities are exact and the displacement discontinuities can be solved for using any standard matrix inversion. Having found the displacement discontinuities on all elements it is then possible to analytically calculate stresses, strains, and displacements anywhere in the medium [see *Crouch and Starfield*, 1983].

BOUNDARY ELEMENT MODELS: APPLICATION TO CRUSTAL DEFORMATION

Introduction

The first step in applying the boundary element algorithm to study deformation in the brittle portion of the Earth's crust is to specify boundary conditions on faults. One boundary condition on fault elements is the requirement that all major faults have zero shear strength (stress). If it assumed that most regional strain is taken up by motion on faults, then this boundary condition should be true when averaged over many thousands of years or equivalently many earthquake cycles [*Zhang et al.*, 1990; *Fox and Carr*, 1989]. The same boundary condition may be appropriate on shorter time scales (years) if faults creep or if a large earthquake has recently occurred. This may be justified because the time required for a fault to become strong (heal) following rupture is unknown and thus, may be many years. Fault healing times are thought to be variable as evidenced by seismicity rates which surely reflect fault properties; seismicity rates are known to be highly variable during inter-seismic periods and are not well understood [*Ambraseys*, 1989]. Recent in situ stress data bearing on fault strength come from a major strike-slip fault, the San Andreas fault in California. These data suggest that the San Andreas is an extremely weak boundary in an otherwise strong crust [*Zoback et al.*, 1987]; unfortunately, no similar data exist for normal faults anywhere or from strike-slip faults within the Great Basin province.

A second boundary condition on fault boundary elements is required to fully determine the two-dimensional deformation field. Although the degree to which the southern Great Basin is extending is uncertain, identification of active normal faults from geologic and morphologic data and from earthquake focal mechanisms indicates that extensional deformation is presently occurring [*Zoback et al.*, 1981; *Harmsen and Rogers*, 1986; *Minster and Jordan*, 1987; *Wernicke et al.*, 1988; *Hodges et al.*, 1989]. This extension is included in the modeling by allowing faults to open (specifying zero normal stress on fault boundaries). A comparison of the strain field for a normal fault with fixed shear displacement and a vertical fault with a fixed amount of displacement normal to the fault is shown in Figure 3 to illustrate that except for distances within approximately the width of the surface projection of the dipping fault, the strain fields are very similar. Thus, this approximation should be adequate to explain general features of the regional strain field.

A word about the shading scheme used in this figure and all subsequent figures showing shear strain models is warranted. The magnitude of the shear strain is illustrated only in a relative sense such that darker shading indicates greater shear strain. The shading scale for each figure is qualitatively set for each figure to emphasize the variability in the strain field. The absolute shear strain values are not considered significant since the real values are not known nor are the strains associated with earthquakes in these magnitude ranges.

The limitations and assumptions inherent in this approach are now summarized. While the modeling does not account for effects of material heterogeneity, this may be considered a benefit by allowing the extent to which fault configuration (strike orientation and variability, and length) alone effects the strain field. It is also assumed that the same boundary conditions are valid for all faults; although this may not be correct, the data are insufficient to prove otherwise. The plane strain assumptions made in the modeling make it equivalent to modeling deformation in a thin plate and thus, only the contribution of faults that have length comparable to the elastic thickness of the crust, or approximately 4-8 km [*King et al.*, 1988], may be studied. The fault maps shown in Figure 1 have many faults shorter than this and their contribution is ignored. The assumption of plain strain conditions in models of the Basin and Range is not new [e.g., see *Shawe*, 1965; *Hill and Troxel*, 1966; *Hill*, 1982].

Finally, it is assumed that the seven years of seismicity data used are not anomalous. It is undoubtedly true that future earthquake

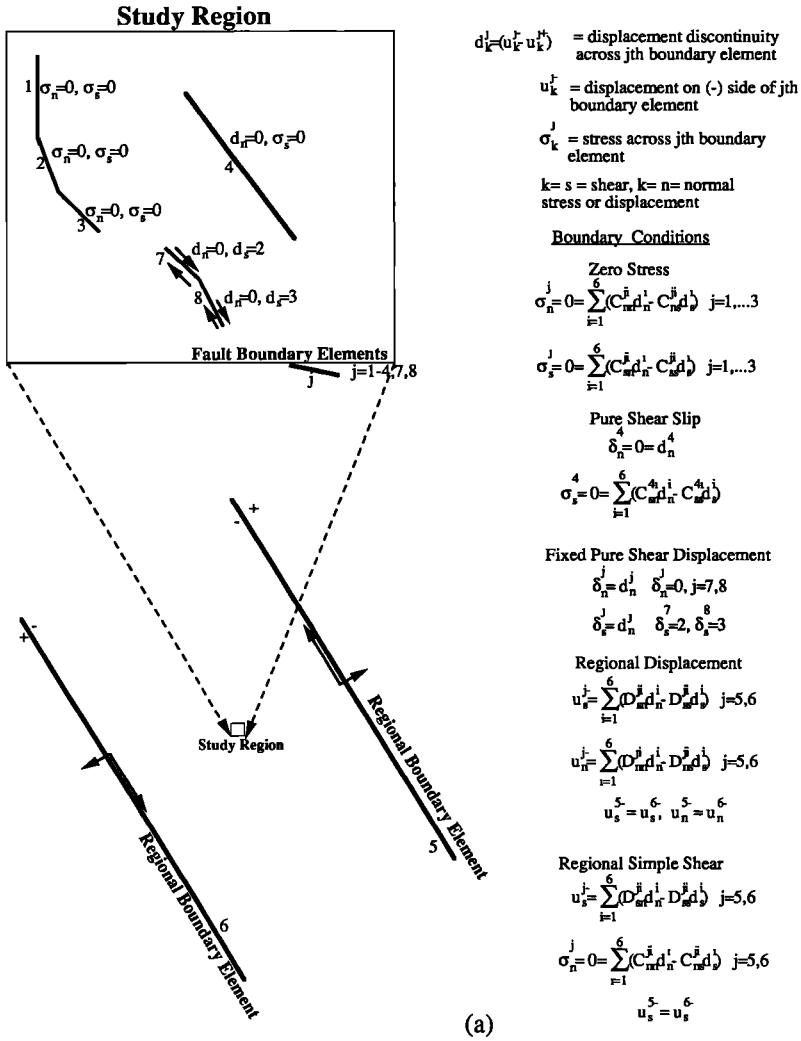

Fig. 2*a*. Schematic diagram of the the information specified when generating a boundary element model. The study region (top left) containing faults that are free to slip in directions normal and parallel to to the fault (elements 1-3), a shear fault (no normal displacement) that slips freely (element 4), and a shear fault with fixed relative displacement across it (elements 7 and 8). Regional boundary elements (bottom left; elements 5 and 6) are used to simulate a uniform regional deformation field. When the normal displacement on the regional elements is zero and the shear displacements are equal, a simple shear regional deformation field is generated between the two elements far away from their ends. When the normal and shear displacements are nonzero, the orientation of the elements and ratio of shear and normal displacements can be specified in a manner consistent with specific directions of displacement of the study area relative to a region on one side and with principal strain axes (see text).

clusters will develop in presently aseismic areas and presently active areas will become quiescent. Thus, models with areas of high shear strain having few earthquakes are not necessarily invalid since future seismicity may occur in such areas. The coincidence of a zone of active seismicity with a zone of low shear strain may also be reconciled by resorting to arguments about temporal changes in seismicity patterns. However, the changes required imply that the patterns presently apparent are anomalous; the seismicity would have to increase everywhere outside this zone such that what presently is considered a high concentration of earthquakes becomes a relatively low one. Unfortunately this assumption cannot be tested due to the short duration of seismic monitoring in the region. Recognizing this and the aforementioned assumptions, the objective of the modeling is to investigate to what extent simple models can explain the general features of the seismicity.

Simple Fault Models

A set of theoretical shear strain fields associated with very simple fault configurations illustrate some basic characteristics of the shear strain field (Figure 4) and lead one to conclude that a complex distribution of seismicity should be observed and that off-fault earthquakes are to be expected. The examples in Figures 4*a*-4*c* illustrate that (1) the simplest shear strain field resulting from a straight fault with fixed shear displacement (no displacements normal to the fault surfaces are allowed for Figures 4*a*-4*e*) is complex and is symmetric about the fault, (2) shear strain concentrates around fault ends and bends, and (3) shear strain can concentrate around bends in faults even when the displacement occurs elsewhere on the fault (e.g., analogous to rupture on one part of a fault and creep elsewhere). Thus, we might expect to find the greatest number of small events around fault ends and bends. Since there is a complex network of fault configurations in the southern Great Basin, a complex distribution of earthquakes is anticipated at scales comparable to fault dimensions.

The examples shown in Figures 4*d*-4*f* illustrate the effects of superimposing the shear strain fields from a uniform regional simple shear strain field and that due to a fault that responds (slips freely) to the regional strain. These indicate that (1) an asymmetric shear

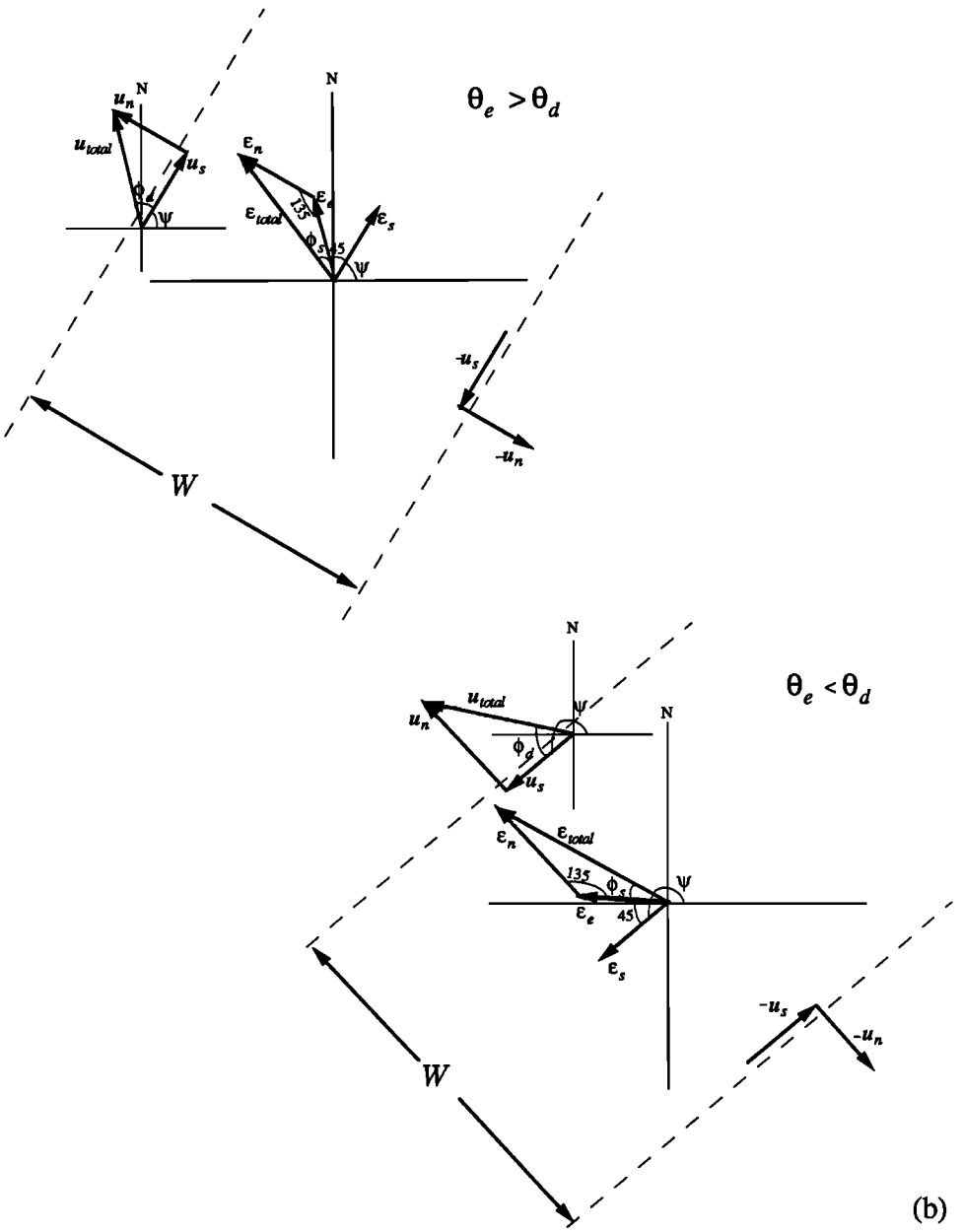

Fig. 2*b*. Schematic example of regional boundary elements (dashed lines) and specified shear and normal displacement boundary conditions, u_s and u_n, resulting in a particular orientation of the principal axis of extension, ε_{total}, and a regional displacement vector, u_{total}. See the text for greater explanation.

strain field with adjacent concentrations of high and low strain may result, (2) the regions of highest shear strain extend beyond the fault trace, (3) the shear strain field appears to be insensitive to the orientation of the regional boundary elements at least for a simple shear regional deformation field, and (4) allowing normal displacements broadens the region of strain relaxation (there are more degrees of freedom to relieve the strain). These results suggest that seismicity data might provide some constraint on the orientation of the regional strain field and that regions of high and low seismicity should be expected both on and off fault traces. Thus, it may be possible to explain the degree and pattern of off-fault seismicity in the Southern Great Basin by invoking simple physical models similar to those just described. *Fox et al.* [1991] suggest that opening of fractures in fault zones may explain the characteristics of hydrologic flow patterns. These results suggest that faulting may cause smaller scale fracturing over a larger area than the immediate vicinity of the fault and therefore may have an even greater affect on flow than previously anticipated.

BOUNDARY ELEMENT MODELS: APPLICATION TO THE SOUTHERN GREAT BASIN

Shear Strain Field Models

The faults that are included in the modeling are chosen based on the recency of displacement on them as inferred from geologic data. Faults with evidence of Holocene and/or historic displacements [*Nakata et al.*, 1982; *Carr*, 1984; *Reheis*, 1988; *Zhang et al.* 1990; P. Thenhaus, M. Ellis, and R.E. Anderson, personal communications, 1990] are digitized and visually smoothed for

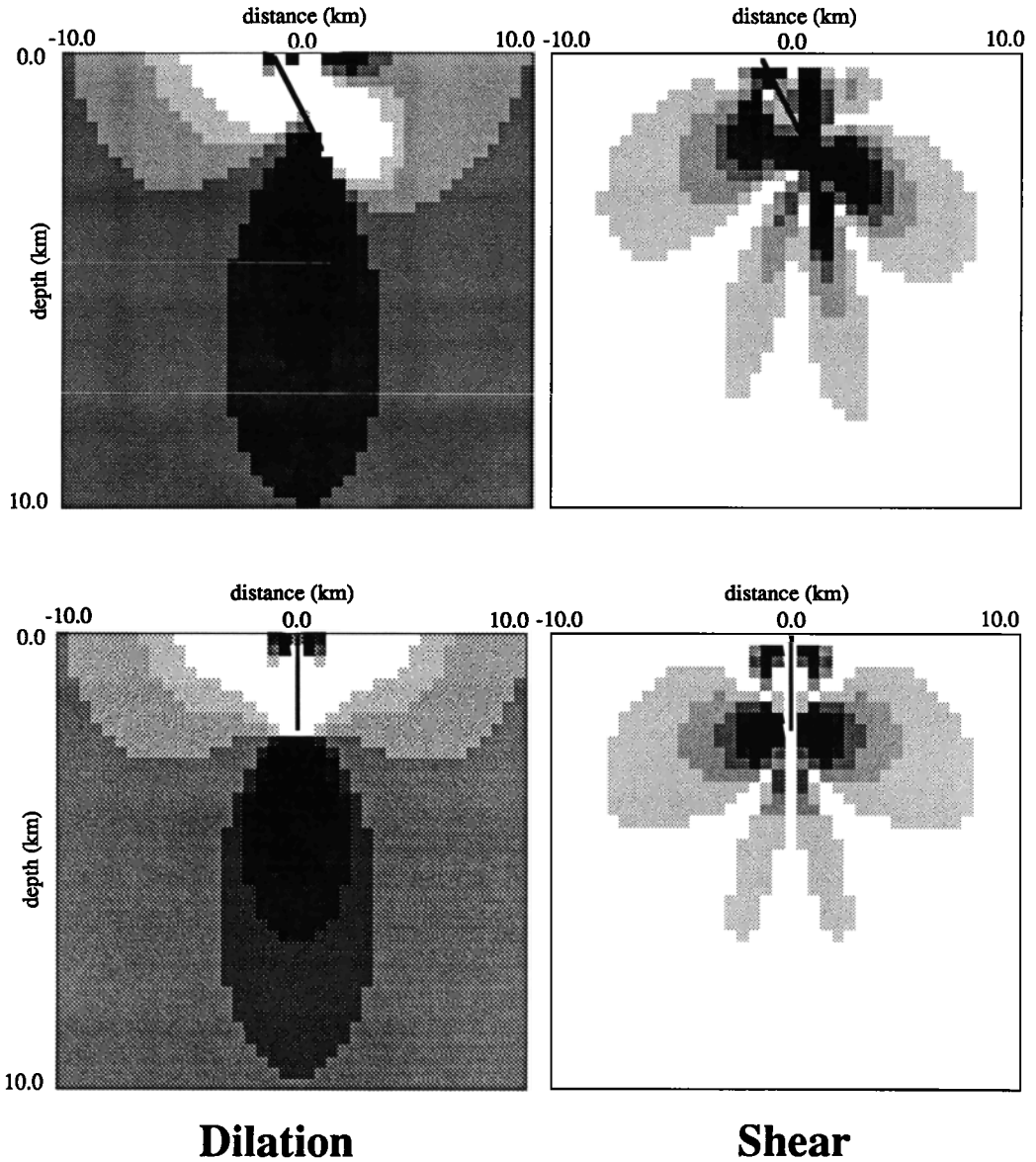

Fig. 3. Cross sections of shear and dilational strain fields due to fixed, uniform slip on single faults (boundary elements) in a half-space. The top two figures are the dilatational (left) and shear (right) strain fields for a fault that is 2.2 km long in cross-section dipping at 45° with shear slip of 10 m and no normal displacement. The bottom two figures are for a 2.0 km long, vertically dipping fault that has 0.71 km of normal opening motion and no shear displacement. The slip on the vertical fault is meant to represent the normal component of motion on the dipping fault. Note that the strain fields are similar beyond distances approximately equal to the surface projection of the dipping fault, especially for the shear strain which is what is being modeled in this study. In the dilational fields, gray (the background color) indicates no dilational strain or area change, lighter shading is compressional, and darker shading is dilational. Only the absolute value of the shear strain is plotted, with the regions of greatest shear strains being black, and the least white.

input as fault boundary elements in the boundary element algorithm (Figure 5a). Only the longest faults are included to be consistent with the plain strain approximation. No faults are included in the Pahranagat Shear Zone because little is known about which faults are/were active, or when and how much slip occurred on them; several alternative models for this region are discussed below.

The first set of models illustrates the sensitivity of the shear strain field to the orientation of and displacements specified on the regional boundary elements which determine the nature of the uniform regional deformation field. Estimates of the orientations of principal strain axes in the southern Great Basin and of the direction of regional displacement are used to constrain a uniform regional deformation field. Focal mechanisms of large earthquakes indicate that the extension direction in the Great Basin is dominantly westward with respect to stable North America [*Smith and Sbar*, 1974] and the axes of maximum extension inferred from several dozen focal mechanisms from the SGBSN are generally oriented N60°W ± 10° (S. Harmsen, personal communication 1990). *Zoback* [1989] analyzes faults slip data, in situ stress measurements, and focal mechanisms from central Nevada and the NTS and concludes that the axis of maximum tension is oriented between N45°W and N60°W. This consistency from a variety of data suggests that the principal extension direction is approximately uniform on a regional scale [*Zoback et al.*, 1981; *Zoback*, 1989].

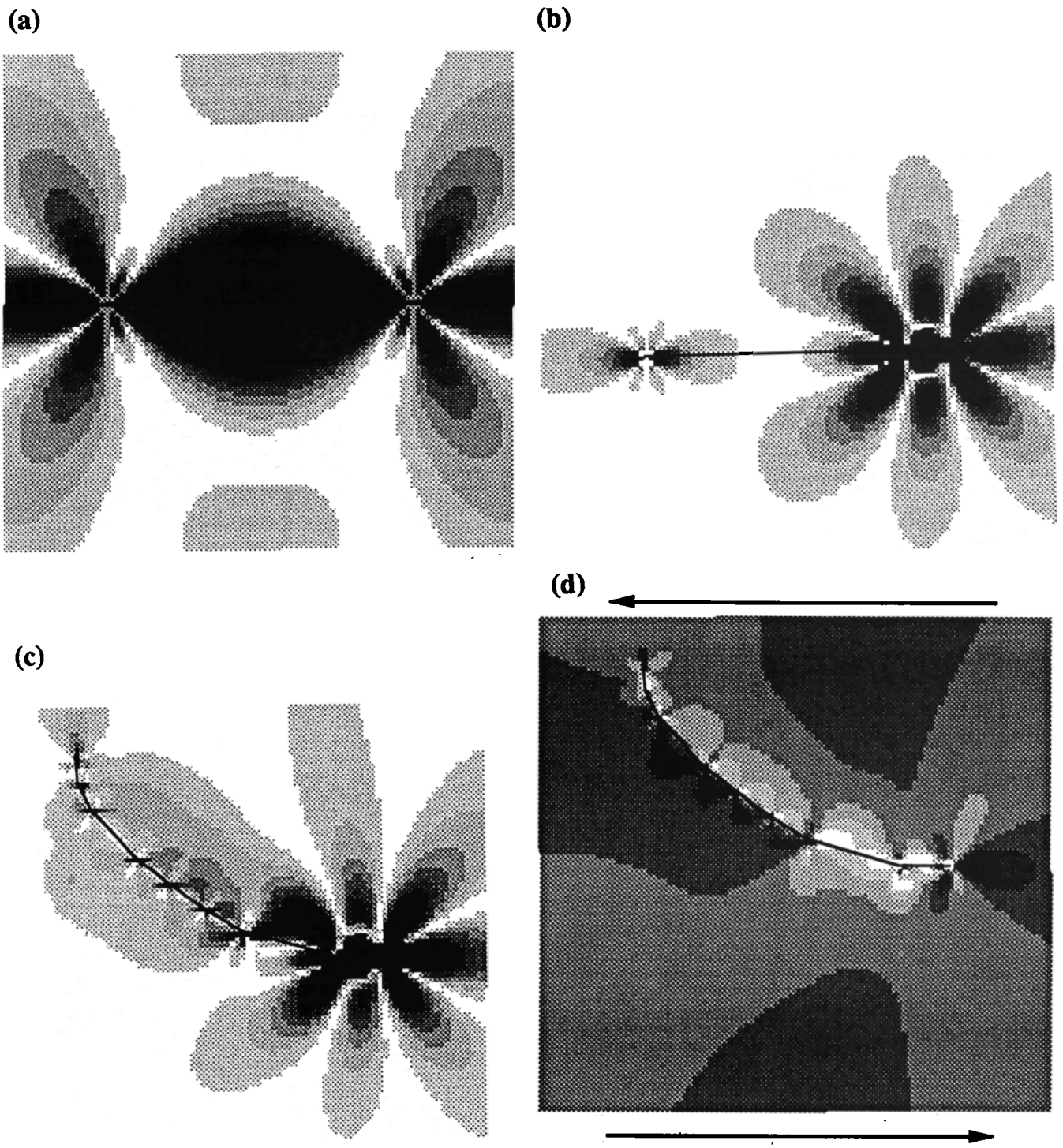

Fig. 4. (*a*) Map views of the absolute value of the shear strain field for a 300 km long straight fault with 1 m of fixed, uniform shear slip specified. The fault ends are located where the strain lobes meet on either end. The regions of greatest shear strain are black, and the shading is lighter for regions of lesser strain. The shading scaling is arbitrary, as it is meant to emphasize the variation in the shear strains, not the absolute values. Note that although the units are specified in kilometers, the problem is scale independent. (*b*) The shear strain field due to a 300 km straight fault (solid line) with fixed, uniform shear slip of 1 m along a 50 km segment on the right side of the fault. The remaining 250 km of the fault is freely slipping (no normal displacements are allowed). Note that there is a small amount of strain at the left end where no fixed slip was specified. (*c*) The same as in Figure 4*b* , but now the fault bends. Note that the shear strain now spreads along the entire length of the fault, even where no fixed slip was specified and that small "knots" of higher strain concentrate where oblique fault segments are joined. (*d*) Same fault configuration as in Figure 4*c* except that there is no fixed slip specified. Instead, a uniform regional simple shear strain field is applied using distant boundary faults (see text) such that the direction of maximum shear is indicated by the arrows. Zero shear stress and zero normal displacement boundary conditions are specified on the fault, so that it can slip freely but cannot open or close. Note that along the right side the fault bisects a region of minimum shear but as it begins to bend more sharply, the fault separates regions of high and low shear strain. (*e*) Same parameters as in Figure 4*d* except that the orientation of the regional strain field is oriented at 90° with respect to the case in Figure 4*d*. The strain field near the fault has not changed very much but there seems to be a reduction in the shear strain away from the fault. (*f*) Same parameters are specified as in Figure 4*e* except that normal displacements on the fault are now allowed. This causes the region of low shear stress to broaden over a larger area and a greater concentration of shear strain results at the left end of the fault.

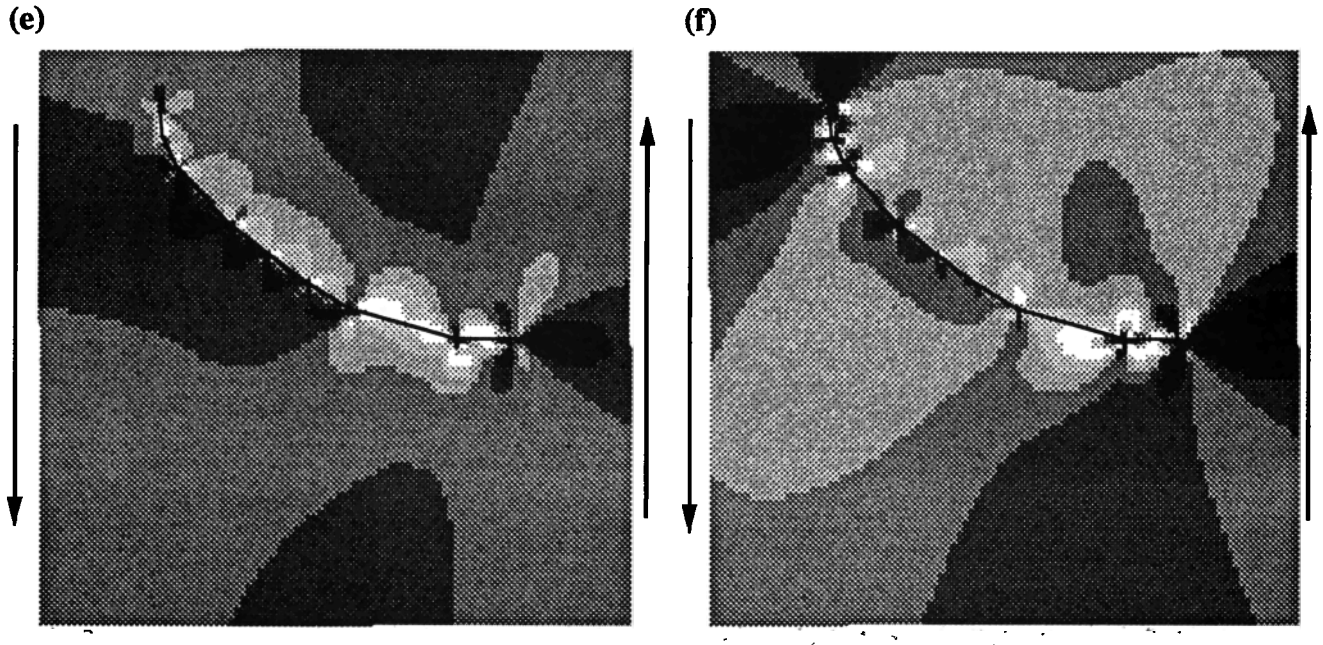

Fig. 4. (continued)

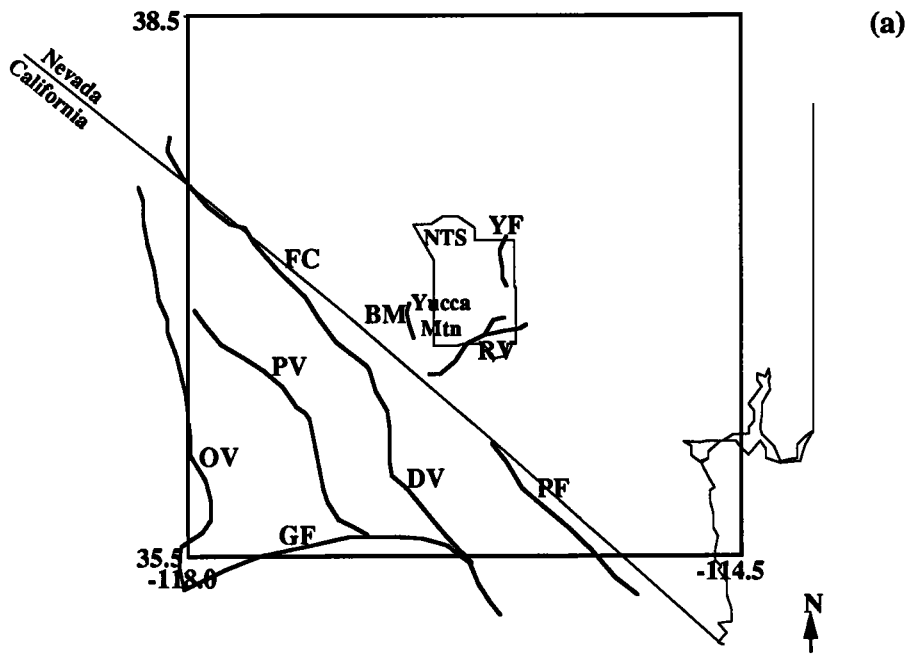

Fig. 5*a*. Boundary element representation of faults with historic or Holocene displacement used as input to the shear strain field models. Zero shear and normal stress boundary conditions are specified on all faults. Abbreviations are FC - Furnace Creek Fault; DV, Death Valley Fault Zone; PV, Panamint Valley Fault Zone; GF, Garlock Fault; YF, Yucca Fault; BM, Bear Mountain Fault; RV, Rock Valley Faults; OV, Owens Valley Faults; PF, Pahrump Fault; NTS, Nevada Test Site. (*b*) The resultant shear strain field when the direction of maximum extension direction of N46°W and regional displacement is N34°W. The ratio of normal displacement to shear displacement on the regional boundary faults is indicated as the opening/shear ratio, and the positive value of this ratio indicates that the shear displacement is left-lateral (top of Figure 2*b*). The regions of greatest shear strain are black, and the shading is lighter for regions of lesser strain. The shading scheme here and in all subsequent figures is the same as in Figure 3. (*c*) The resultant shear strain field when the direction of maximum extension direction of N60°W and regional displacement is N34°W. (*d*) The resultant shear strain field when the direction of maximum extension direction of N46°W and regional displacement is N64°W. The negative value of the opening/shear ratio indicates that the shear displacement is right-lateral (bottom of Figure 2*b*) (*e*) The resultant shear strain field when the direction of maximum extension direction of N60°W and regional displacement is N64°W.

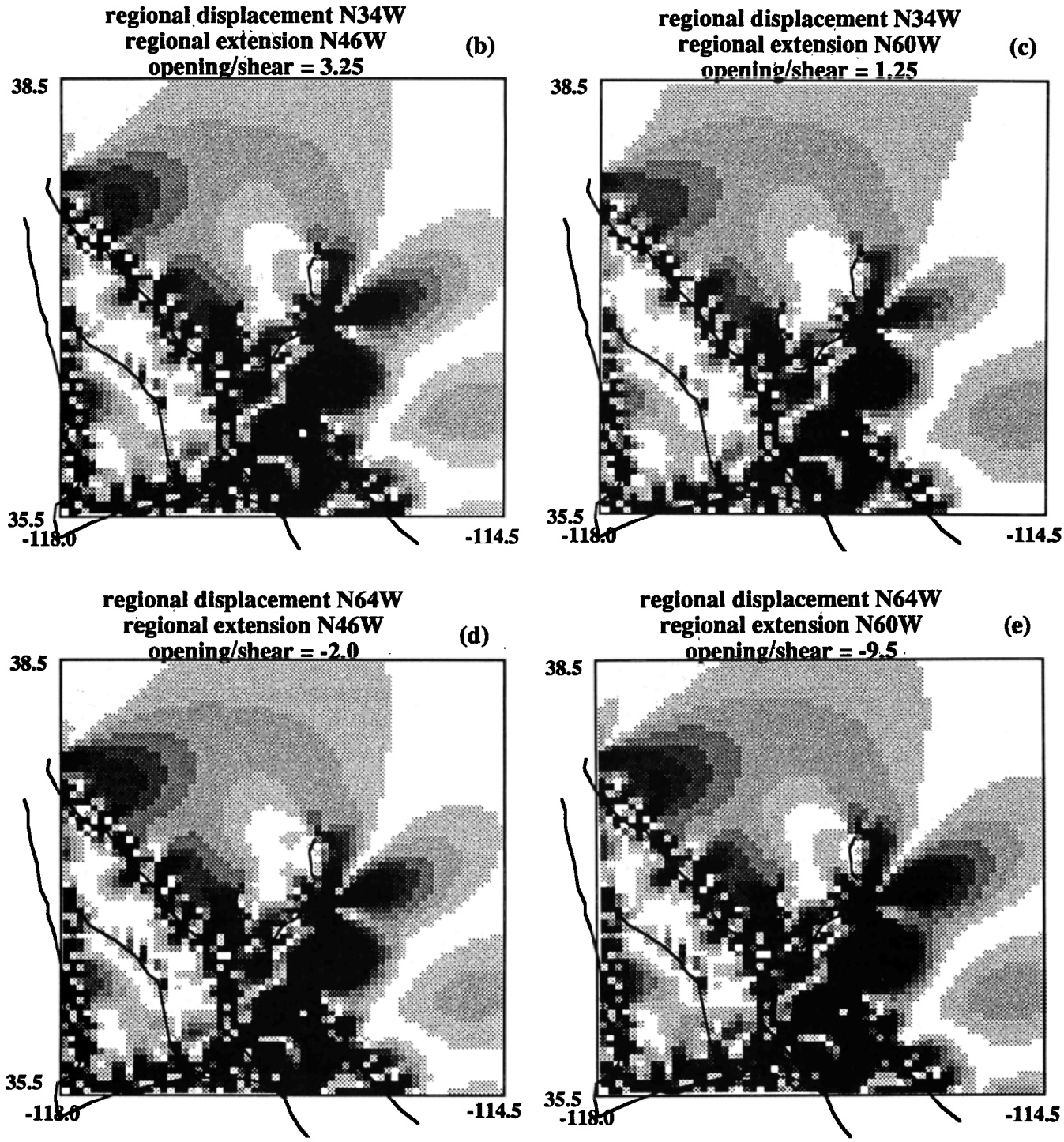

Fig. 5. (continued)

Estimates of a regional displacement vector vary depending on the amount of geologic data used in combination with geodetic data. *Minster and Jordan* [1987] determine directions of motion of the Sierra Nevada with respect to the Colorado Plateau (assumed stationary) that range from N48°W±17° when only geodetic data (VLBI) are used to N64°W±10° for solutions based only on geologic data. Other analyses of VLBI data only yield estimates generally consistent with the *Minster and Jordan* [1987] purely geodetic solution; a direction of N45°W is determined by *Argus and Gordon* [1990] and N34°W±7° [*Ward*, 1990]. One might argue that solutions derived from geodetic data should be more accurate than those based on less precise geologic data [*Ward*, 1990] or alternatively, that models based on geologic data may be more indicative of the long term processes being modeled in this study. Fortunately, as illustrated in Figures 5*b* -5*e*, for the purpose of this study it does not matter which alternative is selected. Four models are derived using bounding directions such that the regional boundary element conditions are consistent with axes of maximum extension oriented at N46°W and N60°W with corresponding regional displacement vector orientations of N34°W and N64°W.

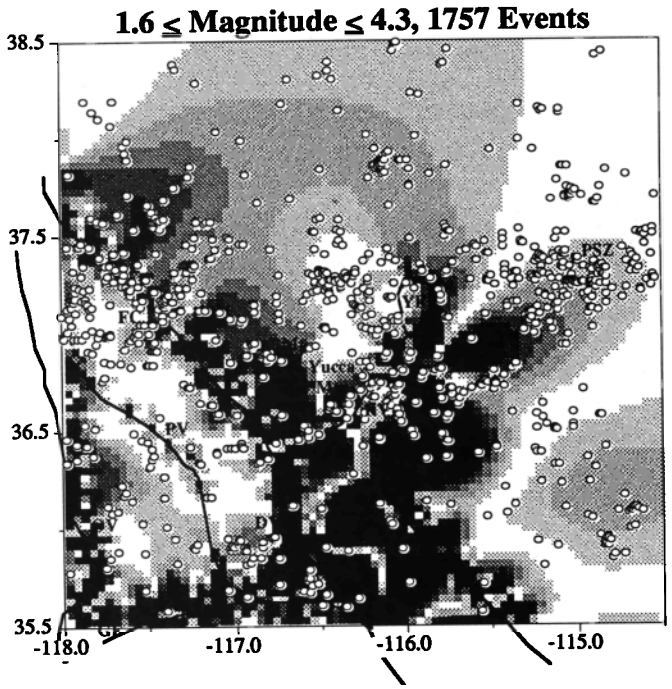

Fig. 6. The shear strain field when the direction of maximum extension direction of N52°W and regional displacement direction is N34°W with seismicity above the magnitude of completeness. Earthquake locations are indicated by the open circles. See the text for discussion of the relationship between the shear strain model and features of the seismicity.

The resultant shear strain fields shown in Figures 5*b*-5*e* are essentially identical implying that the modeling is robust with respect to the uncertainty in the regional deformation field.

The shear strain field compatible with a maximum extension direction of N52°W and regional displacement vector orientation of N34°W is consistent with the general characteristics of the seismicity at and above the magnitude of completeness (Paper I) as shown in Figure 6. As will be discussed and shown latter, seismicity patterns are similar for all magnitude ranges although clearer at smaller magnitudes owing to the greater concentration of smaller events. Areas of the highest shear strain to the south and east of Yucca Mountain are also regions of high seismicity. The relatively high seismicity in the northern NTS may be induced by nuclear testing so that the lack of shear strain in the region need not represent a failure of the modeling. The "hole" in the seismicity at Yucca Mountain (see Paper I) is coincident with a region of lowest shear strain in the NTS region. The region of low seismicity west of the Death Valley/Furnace Creek faults is also a region of least shear strain. Shear strains are high along and within a band approximately 25 km wide just to the northeast of the Death Valley/Furnace Creek faults. This is generally coincident with clusters of earthquakes distributed along the northern half of the fault system.

It is interesting to note that there is a rotational component associated with the simple shear component of the regional deformation field (Figure 7). If these models are meaningful then vertical axis rotations should be observed on a regional scale. *Hudson and Geissman* [1991] document rotation in Dixie Valley just northwest of this study area. They conclude that Tertiary rotations occurred on local and regional scales and although not definitive, probably not on the scale of the entire Basin and Range province. *Rosenbaum et al.* [1991] suggest that vertical axis rotations of Yucca Mountain are a consequence of processes that may affect a region the size of the SGBSN area. They propose that rotations of Yucca Mountain are a consequence of either motion on a right lateral strike-slip fault responding to regional east-west extension/north-south compression or of strain gradients originating in the most highly extended Death Valley. Block rotation in the southern Great Basin is also inferred from paleomagnetic data in the Lake Mead fault zone [*Ron et al.*, 1986] and in the Las Vegas Shear Zone [*Nelson and Jones*, 1987]. Apparent rotations of stress axes determined from geologic fault slip data in the Rock Valley fault system (Figure 1) in the southern part of the NTS and from near Lake Mead may be due to rotations of the structures rather than the stress field [*Frizzell and Zoback*, 1987; *Angelier et al.*, 1985].

The relatively low shear strain in the Pahranagat Shear Zone shown in Figure 6 is inconsistent with the large number of earthquakes there suggesting that there are faults missing from the model that might result in a greater concentration of shear strain in the zone. *Shawe* [1965] describes the Pahranagat Shear Zone as a 'major structural zone' with geologic evidence of left-lateral strike slip deformation, *Tschanz and Pampeyan* [1970] estimate that approximately 14 km of left-lateral displacement has occurred on the northeast trending Pahranagat fault system, and *Carr* [1984] describes both right-lateral and later left-lateral displacements on structures in the Pahranagat region. The effect of a single Pahranagat fault on the strain field model is illustrated in Figure 8a; the fault nearest the 1966 Clover Mountain earthquake ($M_s \approx 6.0$; [*Gawthrop and Carr*, 1988]; see Figure 1) is added to the set of faults used to derive the model shown in Figure 6. An alternative model, shown in Figure 8*b*, explores the possibility that the Pahranagat system is actually a continuation of the Rock Valley fault system. This possibility has been suggested by *Shawe* [1965] and by *Fox et al.* [1991], although *Carr* [1984] states that there is little geologic evidence of continuity. These two models differ significantly in the eastern third of the study region and little has changed elsewhere. The effect of extending the end of the Rock Valley fault into the Pahranagat area reduces the shear strain in the region where the seismicity is greatest. This negative result suggests that faults in the Pahranagat and Rock Valley regions are not part of a single continuous system. Inclusion of the postulated Pahranagat fault in Figure 8*a* does elevate the shear strain in an area coincident with the observed cluster of earthquakes. This suggests that other faults in the Pahranagat region also may contribute to elevating the shear strain similarly, thereby resulting in the significant seismicity observed.

Fault Slip and Earthquake Potential

An absence of shear strain in a locality can imply that either the regional deformation is efficiently accommodated by the faults in the vicinity or that strain simply does not concentrate in the region. In the former case strain accumulates and is then relaxed during large earthquakes or creep. In the latter case, strain does not accumulate and few moderate or only small earthquakes would be expected. These two possibilities can be discriminated by examining the resultant slip that occurs on each fault in response to the regional deformation field. The magnitudes of the total slip (normal and shear) along each fault for the model shown in Figure 8*a* are plotted in Figure 9. Interpretation of this slip distribution may not be meaningful since the sense of slip (relative opening or closing normal displacement, right- or left-lateral relative shear displacement) is not always consistent with the sense of fault displacements inferred from geologic observations. For example, most of the Death Valley/Furnace Creek faults close (e.g., representing thrust faulting) and are left-lateral which is inconsistent

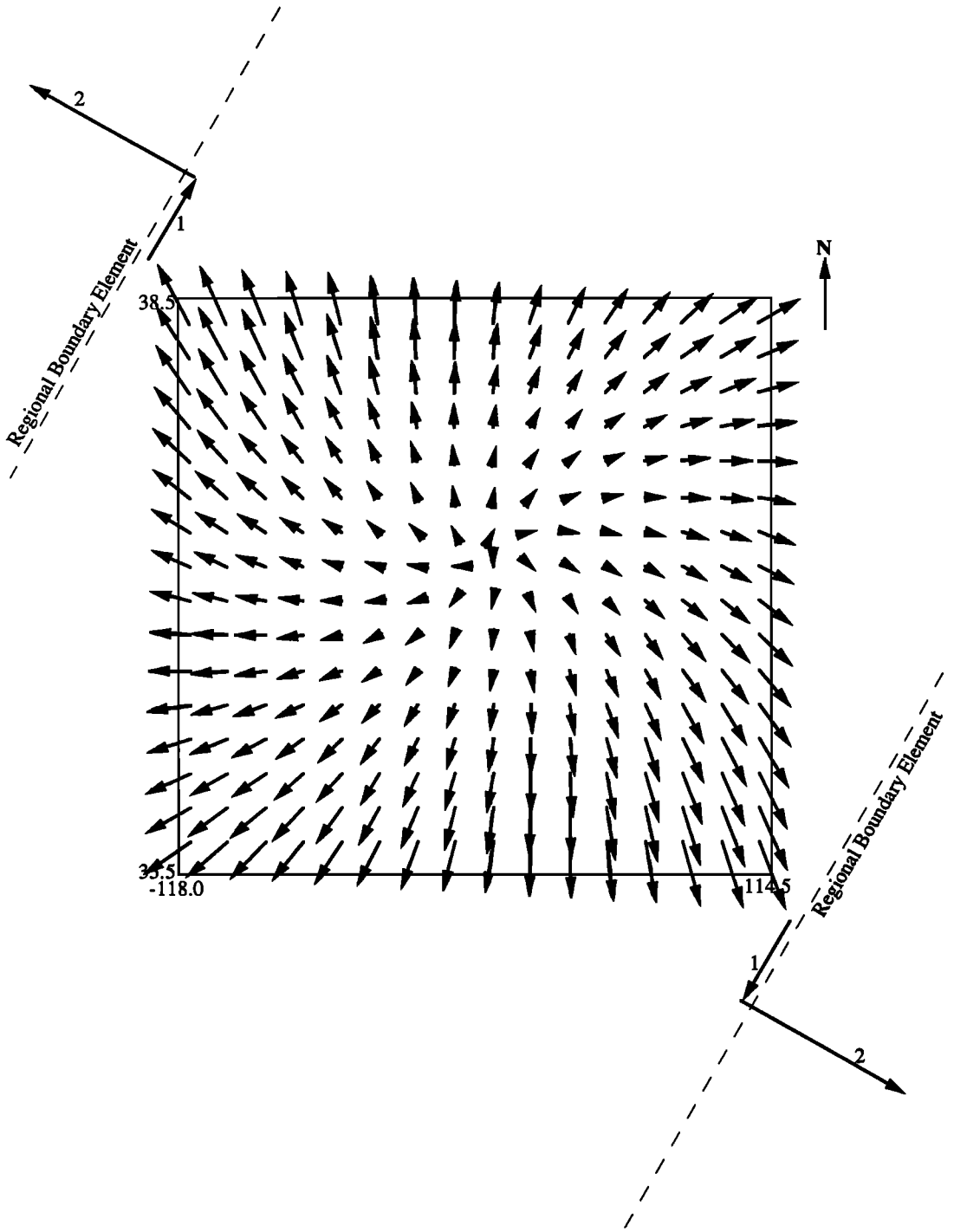

Fig. 7. Displacement vectors indicating the displacement of points relative to their initial positions for a uniform regional deformation field in which the direction of maximum extension direction is N52°W and regional displacement is N34°W. The vector lengths are proportional to the displacement, and the shear/normal displacement ratio for the regional element (dashed lines) boundary conditions is equal to 1/2. This illustrates the rigid body rotation associated with the component of simple shear in the strain field.

with geologic information [*Burchfiel et al.*, 1987; *Zhang et al.*, 1990]. This is because the models are the "best" only in a mathematical sense and not with regard to any geological information other than the fault configuration and boundary conditions.

Models are constructed that are consistent with several simple requirements on the sense of slip by following the strategy described below. The morphology (e.g. ranges bounded by large normal faults) and geology of the Great Basin clearly indicate that the dip-slip component of displacement is dominantly normal on most faults. Thus, acceptable models are those in which all normal fault slip (relative displacement) must be equivalent to normal faulting (opening) with the exception of the southern segment of the Death Valley fault and the Pahrump fault (R.E. Anderson, personal communication, 1990). Although less stringently enforced since the morphologic signature is not as obvious, the requirements on the

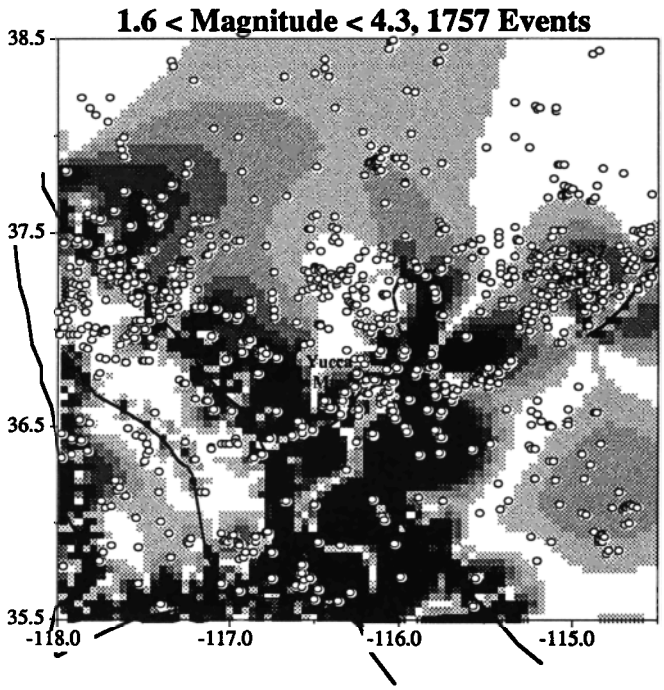

Fig. 8*a*. Shear strain field for a regional deformation field in which the direction of maximum extension direction is N52°W and regional displacement is N34° (as in Figure 6) showing the effect of introducing a fault in the Pahranagat Shear Zone. Epicenters of earthquakes with $M_L \geq 1.6$ are shown by the open circles.

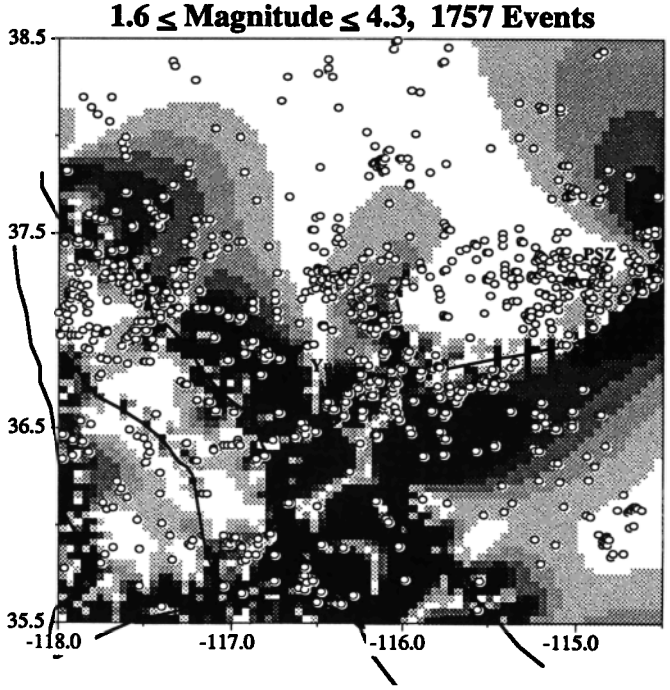

Fig. 8*b*. Same as Figure 8*a* except that the fault in the Pahranagat Shear Zone is now connected to the Rock Valley fault system.

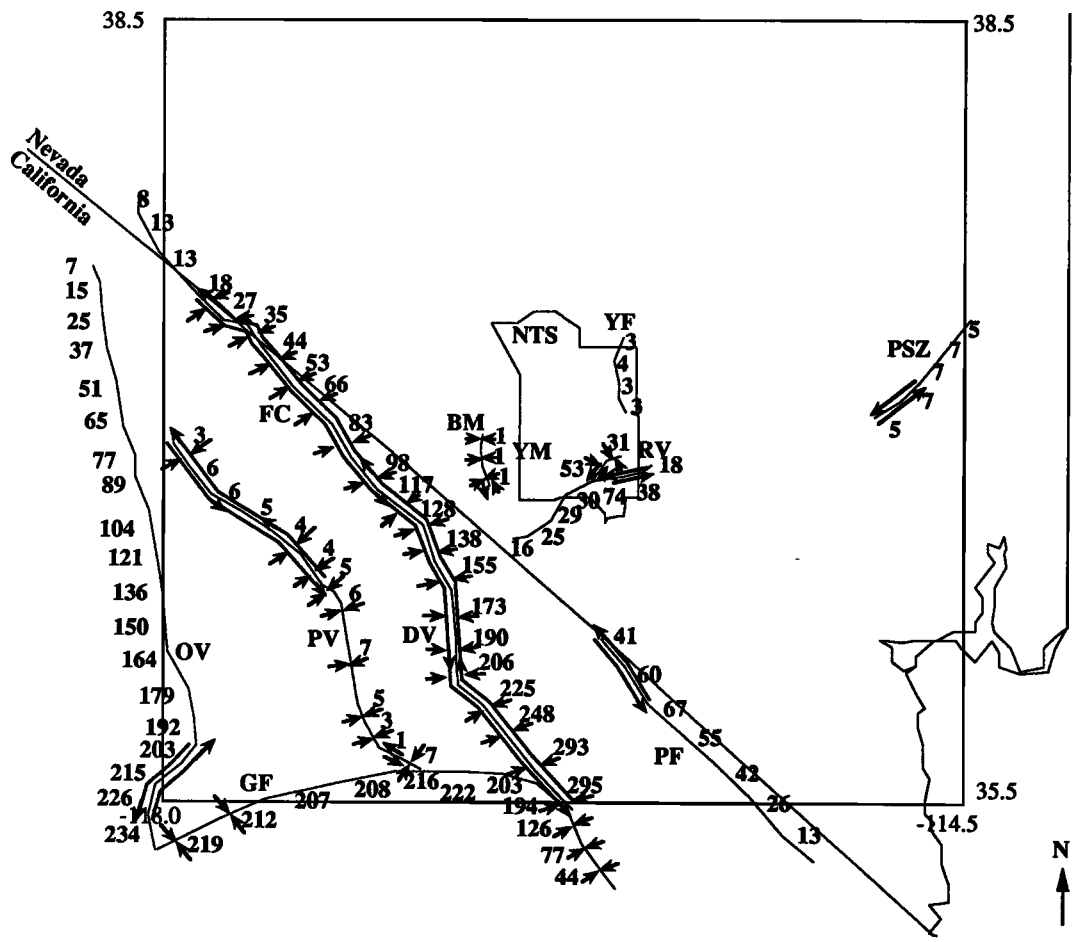

Fig. 9. Values of the total Euclidean slip (square-root of the squared shear plus squared normal slip magnitudes) on each fault or boundary element for the model shown in Figure 8*a*. Note that the scaling is arbitrary, as the figure is meant to illustrate only relative slip. Similar results are obtained for all other models generated. The fault segments with arrows perpendicular to the faults indicate closing normal slip (thrust faulting), and parallel arrows indicate left-lateral slip. Fault segments without perpendicular or parallel arrows have opening (normal) and right-lateral slip, respectively.

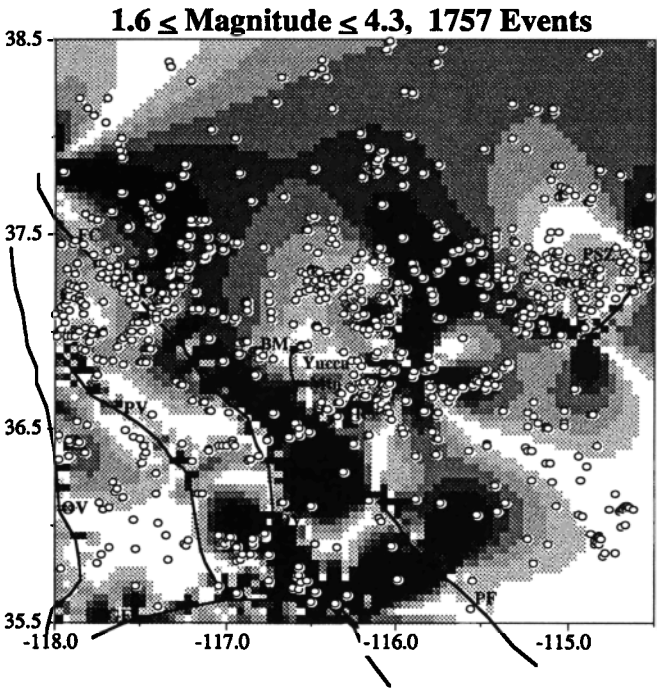

Fig. 10*a*. Shear strain field for a regional deformation field in which the direction of maximum extension direction is N52°W and regional displacement is N34° and one fault in the Pahranagat Shear Zone (as in Figure 8*a*). Epicenters of earthquakes with $M_L \geq 1.6$ are shown by the open circles. Slip magnitudes and directions are constrained on specified fault segments, as indicated in Figure 11.

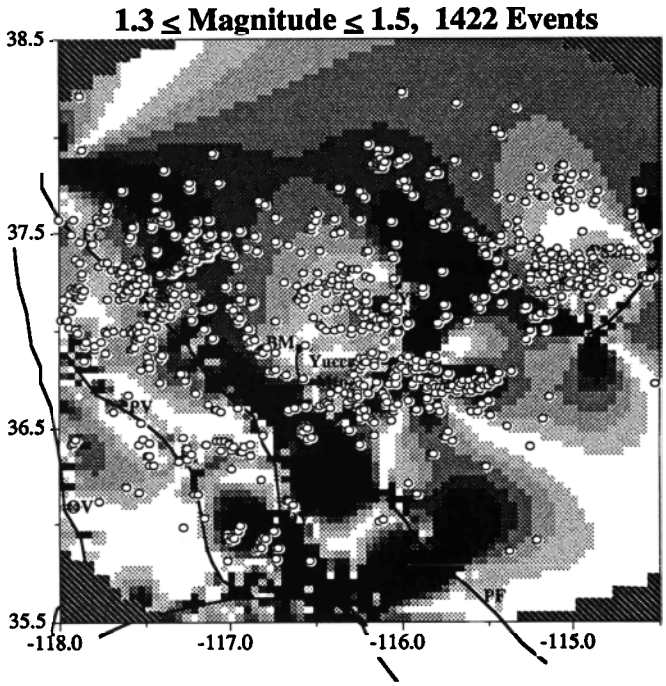

Fig. 10*b*. Same as Figure 10*a* but with epicenters of earthquakes with $1.3 \geq M_L \geq 1.5$. Regions with diagonal stripes cover areas for which the SGBSN catalog is incomplete in this magnitude range (Paper I).

strike-slip (shear) component of slip for acceptable models are that the Death Valley, Furnace Creek, and Owens Valley fault systems must be predominantly right lateral and the western half of the Garlock fault be left-lateral [*Burchfiel et al.*, 1987; *Zhang et al.*, 1990]. The magnitude, orientation, and timing of slip on faults east of these are not well known [*Zhang et al.*, 1990]. Some deviation from these requirements on the senses of normal and shear slip is considered acceptable since the models represent a highly simplified version of the true distribution of faults and thus, the partitioning of slip among them should also only be accurate in an average sense.

The first step in determining models of the slip distribution consistent with the above requirements on the sense of slip is to solve for models in which the normal and shear slip directions on each fault element are fixed a priori using a nonnegative least squares (NNLS) algorithm [*Lawson and Hanson*, 1974]. All fault elements are required to open with the exception of the southern end of the Death Valley and Pahrump faults (which must close). Faults trending northwesterly are only allowed to slip in a right-ateral sense and those trending northeasterly in a left-lateral sense [*Wright*, 1976; *Hill*, 1982]. In order to ensure that the specified regional deformation field is maintained, the constraint equations for the regional boundary elements are weighted higher when finding the solution. A solution is found using the NNLS algorithm with these slip constraints and the boundary elements and conditions used to generate the model shown in Figure 8. Adding sign constraints on all elements makes the problem over-determined and it is not be possible to find solutions that satisfy all of the boundary conditions specified on the fault boundary elements (zero shear and normal stresses). The NNLS algorithm does not allow for specification of slip directions on only a subset of faults so that the constraints imposed are far more stringent than the requirements for acceptable models described above. However, since the NNLS solutions represent best fits and satisfy the model slip sense requirements it is reasonable to use portions of them to find solutions which also satisfy all the boundary conditions.

The second step is to fix a minimum number of fault slip magnitudes and directions to ensure that the final model is consistent with the aforementioned sense of slip requirements. The slip magnitudes that result from the NNLS solutions are used as fixed

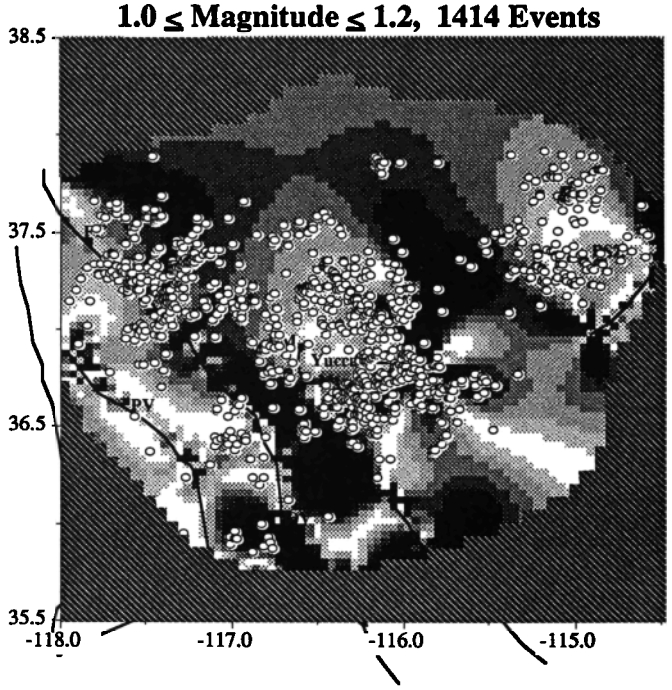

Fig. 10*c*. Same as Figure 10*a* but with epicenters of earthquakes with $1.0 \geq M_L \geq 1.2$; striped regions mask areas for which the SGBSN catalog is incomplete in this magnitude range.

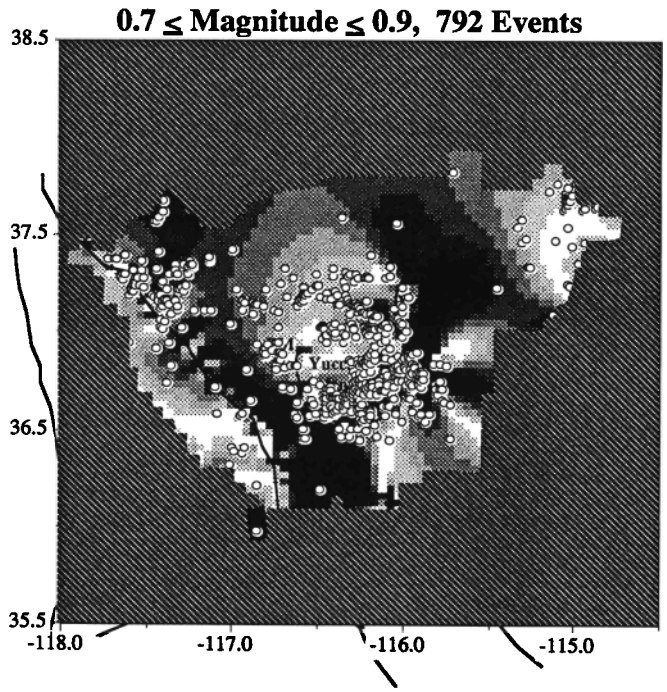

Fig. 10*d*. Same as Figure 10*a* but with epicenters of earthquakes with $0.7 \geq M_L \geq 0.9$; striped regions mask areas for which the SGBSN catalog is incomplete in this magnitude range.

relative displacement boundary conditions. For example, to derive the shear strain field shown in Figure 10*a* , the relative normal displacements on the Owen's Valley, Death Valley, Furnace Creek, and Pahrump fault systems and the shear displacements on the Garlock fault are fixed at values equal to those obtained from the NNLS solution. As before, the normal component of slip on the Garlock, the shear component on the Owen's Valley, Death Valley, Furnace Creek, and Pahrump fault systems, and both shear and normal components of all other faults are free to slip in response to the applied regional deformation field thereby resulting in a model solution that satisfies all the boundary conditions and in general, all the slip sense requirements. The resultant distribution of slip is shown in Figure 11; before discussing the implication of this slip distribution the model is validated by comparing the associated shear strain field with the seismicity data for all magnitude ranges (Figure 10).

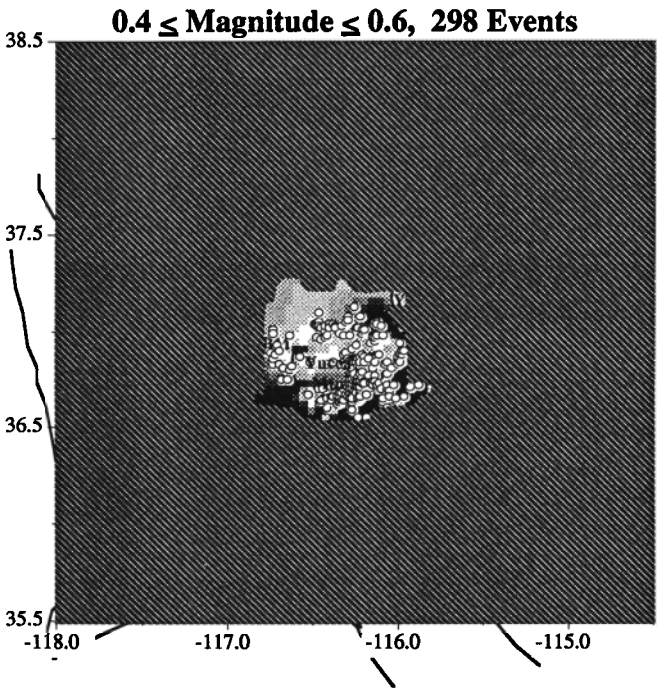

Fig. 10*e*. Same as Figure 10*a* but with epicenters of earthquakes with $0.4 \geq M_L \geq 0.6$; striped regions mask areas for which the SGBSN catalog is incomplete in this magnitude range.

The basic characteristics of the shear strain field observed in the unconstrained model (Figure 8*a*) are also apparent in this model (Figure 10). The nonuniformity and stability of the of seismicity patterns becomes even clearer at smaller magnitudes. As before, high shear strain to the south and east of Yucca Mountain corresponds to a strong concentration of earthquakes and the 'hole' in seismicity over Yucca Mountain is coincident with a shear strain minimum. High shear strain is found along the northern side of the Death Valley/Furnace Creek faults with a broad lobe of high strain extending northward from the Furnace Creek fault in the general vicinity of a broad cluster of earthquakes. The region to the west of these faults still shows relatively low shear strain, consistent with the relatively low level of seismicity. In order to verify that conclusions drawn from unconstrained models about the nature of faulting in the Pahranagat Shear Zone are still valid, a constrained model is constructed following the above steps and using the fault configuration of Figure 8*b* (connecting the Rock Valley fault to one in the Pahranagat). As before, the effect of this alternative fault geometry is to lower the shear strain in the Pahranagat region contrary to the observation of a significant number of earthquakes there (Figure 12).

Other models constructed using slightly different slip constraints show that all the characteristics of the strain field just discussed are stable and several generalizations about the distribution of slip can be made. The examples of the later shown in Figure 11 illustrates that the greatest amount of slip occurs on the fault systems including and west of the Death Valley/Furnace Creek faults. The distribution of slip calculated for the unconstrained model (Figure 9) shows this more clearly. (Although the slip on the fault system referenced as the Panamint Valley fault is low, the average slip for all the faults including and west of the Death Valley/Furnace Creek faults is still relatively high.) Even though the direction of slip is not correct, the unconstrained model results also support the interpretation that on average, the fault systems including and west of the Death Valley/Furnace Creek faults are most efficient at relaxing the regional strain as evidenced by the larger magnitude slip and low shear strain in the region. Thus, accumulated regional strain may be relaxed during large earthquakes having large magnitude slip over a substantial fault length rather than via many small earthquakes. (Although it is scant, geologic evidence suggests that creep is not a significant process in this area [*Zhang et al.*, 1990].) The relatively small amplitude slip on the Bear Mountain and Yucca faults and the relative absence of seismicity in the vicinity of Yucca Mountain may be indicative of a lack of strain accumulation. It is important to note that the aseismic nature of Yucca Mountain has been noted elsewhere (J.N. Brune et al., Microearthquakes at Yucca Mountain, Nevada submitted to *Bulletin of the Seismological Society of America*, 1991) and that it has also been interpreted as a consequence of magmatic processes [*Parsons and Thompson*, 1991] or may simply represent a quiescent period. However, if it is assumed that the above interpretation of the strain field models is correct, then inferences about the relative seismic hazard can be

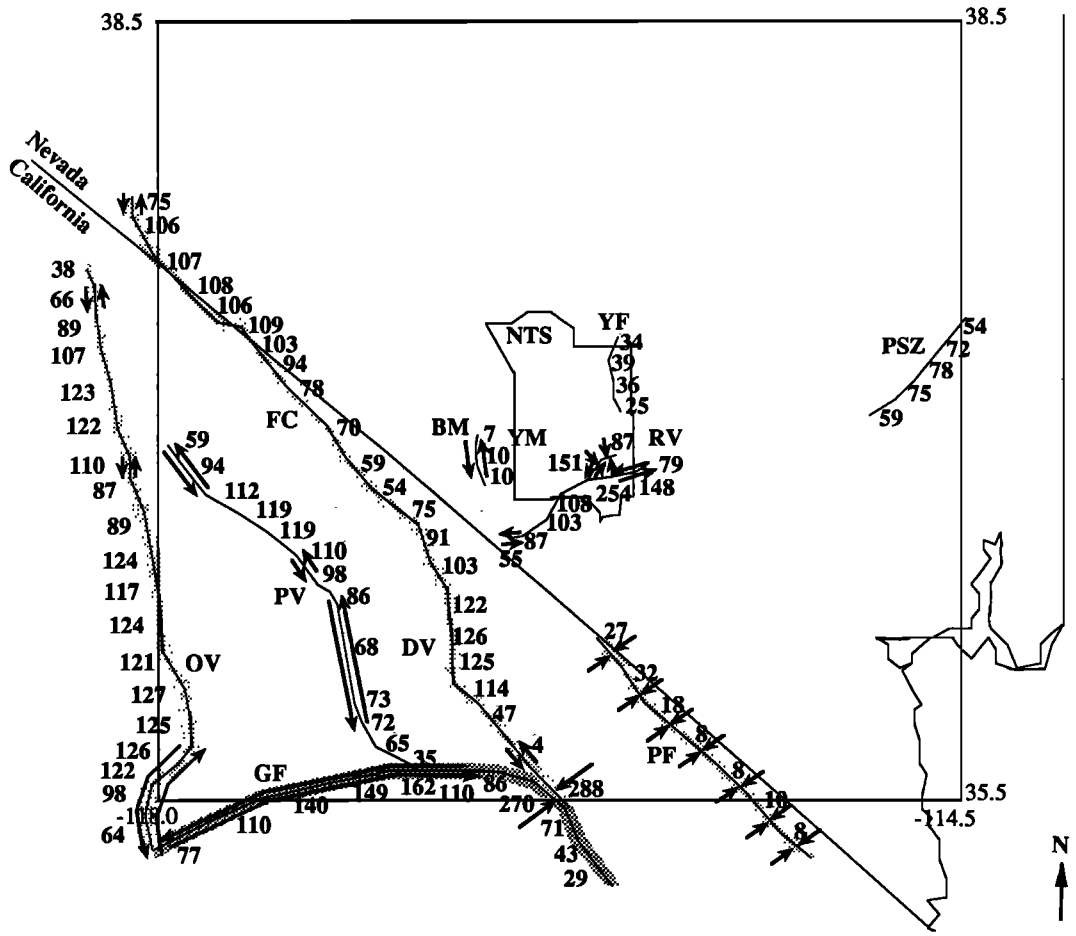

Fig. 11. Values of the total Euclidean slip on each fault for a model in which slip magnitude and direction are fixed for a subset of fault segments, consistent with geologic information. The corresponding shear strain field is shown in Figure 10. Scaling is arbitrary, illustrating only relative slip. The convention for the arrows (or lack of arrows) is identical to that in Figure 9. The fault segments for which the normal slip is fixed a priori are indicated by the lighter shading, and those with fixed shear slip are indicated by the darker shading.

made. In summary, although both regions are relatively lacking in small earthquakes, the potential for large earthquakes may be much greater in the Death Valley/Furnace Creek region than in the vicinity of Yucca Mountain.

CONCLUSIONS

The possibility that the general features of the seismicity are associated with concentrations of high and low shear strain that are generated by faults in an otherwise uniform deformation field is explored through a series of boundary element modeling experiments. The model parameters include fault configurations (strike orientation and variation, and length) and zero shear and normal stress boundary conditions, and uniform regional deformation fields. The results of these modeling experiments suggest that the distribution of shear strain magnitude is very sensitive to fault configuration and very stable with respect to different regional deformation fields. Even the simplest fault models predict complex patterns of shear strain with highs and lows that do not necessarily lie on the fault traces. The same is true for models of the SGBSN region indicating that off-fault seismicity should actually be expected and that the relationship of small earthquakes with a distribution of faults is not necessarily obvious.

Lobes of high shear strain are associated with fault ends, bends, and intersections and may span broad areas. This may explain why earthquake clusters cover regions much larger than the surface projections of any of the mapped faults. The area covered by the clusters at the northern half of the Furnace Creek fault is generally coincident with a zone of high shear strain in the models. The cluster in the Pahranagat Shear Zone may be associated with shear strain arising from a distribution of small localized faults. While highly speculative, the preferred fault configuration in the Pahranagat Shear Zone derived from the modeling are contrary to the suggestion of *Fox et al.* [1991] that the large ground water transmissivity between the Pahranagat and the Death Valley groundwater basin is a consequence of continuous Quaternary faulting between the two areas. The relatively large numbers of earthquakes in the southern and eastern portions of the NTS are consistent with the strain field models. Low shear strain in the northern NTS is coincident with active seismicity; however, these earthquakes may be induced by nuclear testing. A minimum in shear strain centered on Yucca Mountain is predicted by all models, consistent with the almost total lack of earthquakes there.

The region to the west of the Death Valley/Furnace Creek fault system has the broadest area of low shear strain which is consistent with the low number of small earthquakes observed in the region. This seismicity is somewhat counter-intuitive since it is also the portion of the study area with most recent deformation. The modeling results suggest that the reason for this is that the fault

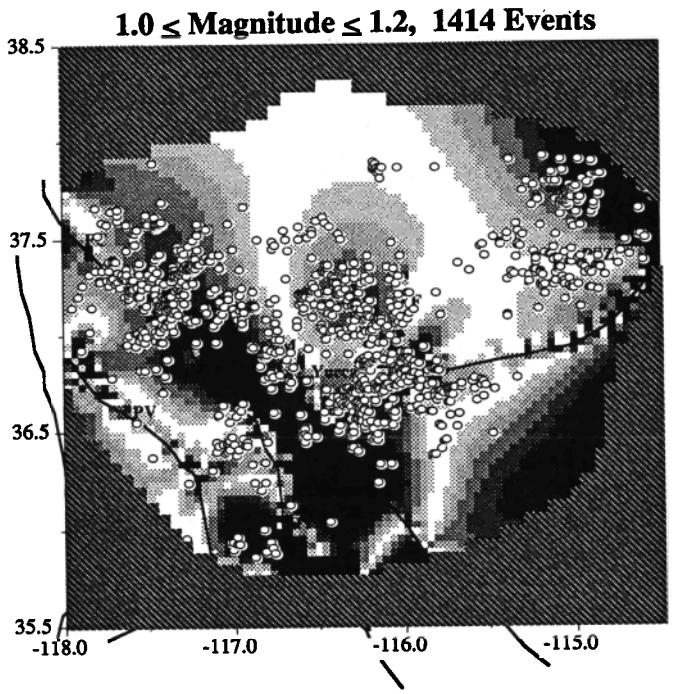

Fig. 12. Shear strain field for a regional deformation field in which the direction of maximum extension direction is N52°W and regional displacement is N34°, and instead of an isolated fault in the Pahranagat Shear Zone, there is now a single continuous fault extending into the Pahranagat region from the Rock Valley fault (as in Figure 8*b*). Epicenters of earthquakes with $1.0 \geq M_L \geq 1.2$ are shown by the open circles; striped regions mask areas for which the SGBSN catalog is incomplete in this magnitude range. Slip magnitudes and directions are constrained on specified fault segments, as indicated in Figure 11.

configuration in the area is optimal for relaxing regional deformation via the occurrence of large earthquakes. Although there is also a relative lack of earthquakes at Yucca Mountain, the lack of seismicity there may be indicative of a lack of accumulating strain and thus, a lower potential for a large earthquake.

Acknowledgments. This work was performed in accord with the U.S. Geological Survey/Department of Energy Interagency agreement DE-AIO8-78ET44802. The author would like to thank R. Bilham, J. Dewey, R.E. Anderson, S. Hartzell, K. Shedlock, Jim Savage, and an anonymous reviewer for thoughtful reviews, discussions, criticisms, and suggestions. Special thanks to P. Bodin for his review and many hours spent listening and debating. G.C.P. King provided the original boundary element code used to calculate the shear strain models.

REFERENCES

Ambraseys, N.N, Temporary seismic quiescence: SE Turkey, *Geophys. J. R. Astron. Soc., 96*, 1989.

Angelier, J., B. Colletta, and R.E. Anderson, Neogene paleostress changes in the Basin and Range: A case study at Hoover Dam, Nevada-Arizona, *Geol. Soc. Am. Bull., 96*, 347-361, 1985.

Argus, D.F., and R.G. Gordon, Constraints from VLBI on Pacific-North America motion and deformation, *Eos Trans. AGU, 71*, 860, 1990.

Bilham, R.G., and G.C.P. King, The morphology of strike-slip faults: Examples from the San Andreas fault, California, *J. Geophys. Res., 94*, 10,204-10,216, 1989.

Burchfiel, B.C., K.V. Hodges, and L.H. Royden, Geology of Panamint Valley--Saline Valley pull-apart system, California: Palinspastic evidence for low-angle geometry of a neogene range-bounding fault, *J. Geophys. Res., 92*, 10422-10426, 1987.

Carr, W., Regional structural setting of Yucca Mountain, southwestern Nevada, and late Cenozoic rates of tectonic activity in part of the southwestern Great Basin, Nevada and California, U.S. Geol. Surv. Open File Rep., 84-854, 109 pp., 1984

Crouch, S.L., and A.M. Starfield, *Boundary Element Methods in Solid Mechanics*, Chap.s 5 and 7, George Allen and Unwin, London, 1983.

Fox, K.F., Jr., and M.D. Carr, Neotectonics and volcanism at Yucca Mountain and vicinity, Nevada, in *Radioact.Waste Manage. Nucl. Fuel Cycle, 13*, 37-50, 1989.

Fox. K.F., Jr., R.W. Spengler, M.D. Carr, and W.B. Byers, Potential effects of Quaternary tectonism on the hydrology of Yucca Mountain, in *Selected USGS Studies of the Yucca Mountain, Nevada and California Area through 1989, USGS Bull.*, in press, 1991.

Frizzell, V.A., and M.L. Zoback, Stress orientation determined from fault slip data in the Hampel Wash area, Nevada and its relation to the contemporary stress field, *Tectonics, 2*, 89-98, 1987.

Gawthrop, W.H., and W.J. Carr, Location refinement of earthquakes in the southwestern Great Basin, 1931-1974, and seismotectonic characteristics of some of the important events, *U.S. Geol. Surv. Open File Rep., 88-560*, 64 pp., 1988.

Gomberg, J., Seismicity and detection/location threshold in the Southern Great Basin Seismic Network, *J. Geophys. Res.*, this issue.

Harmsen, S.C. and A.M. Rogers, Inferences about the local stress field from focal mechanisms: applications to earthquakes in the southern Great Basin of Nevada, *Bull. Seismol. Soc. Am., 76*, 1560-1572, 1986.

Hackman, M.C., G.C.P. King, and R. Bilham, The mechanics of the south Iceland seismic zone, *J. Geophys. Res., 95*, 17,339-17,352, 1990.

Hill, D., Contemporary block tectonics: California and Nevada, *J. Geophys. Res., 87*, 5433-5450, 1982.

Hill, M.L., and B.W. Troxel, Tectonics of the Death Valley region, California, *Geol. Soc. Am. Bull., 77*, 435-438, 1966.

Hodges, K.V., L.W. McKenna, J. Stock, J. Knapp, L. Page, K. Sternlof, D. Silverberg, G. Wust, and J.D. Walker, Evolution of extensional basins and Basin and Range topography of Death Valley, *Tectonics, 8*, 453-467, 1989.

Hudson, M.R., and J.W. Geissman, Paleomagnetic evidence for the age and extent of middle Tertiary counterclockwise rotation, Dixie Valley region, west central Nevada, *J. Geophys. Res., 96*, 3979-4006, 1991.

Jaeger, J.C. and N.G.W. Cook, *Fundamentals of Rock Mechanics*, Chap. 2, John Wiley, New York, 1977.

King, G.C.P., J. Rundle, and R. Stein, The growth of geologic structures by repeated earthquakes, 1., Conceptual framework, *J. Geophys. Res., 93*, 13,307-13,318, 1988.

King, G.C.P. and M. Ellis, The origin of large local uplift in extensional regions, *Nature, 348*, 689-692, 1990.

King, G.C.P., A.G. Lindh, and D.H. Oppenheimer, Seismic slip, segmentation, and the Loma Prieta earthquake, *Geophys. Res. Lett., 17*, 1449-1452, 1990.

Lawson, C.L., and R.J. Hanson, *Solving Least Squares Problems*, Chap. 23 and Appendix C, Prentice-Hall, Englewood Cliffs, New Jersey, 1974.

Mavko, G.M., Fault interaction near Hollister, California, *U.S. Geol. Surv. Open File Rep., 82-180*, 115-138, 1982.

Mendoza, C., and S.H. Hartzell, Aftershock patterns and main shock faulting, *Bull. Seismol. Soc. Am., 78*, 1438-1449, 1988.

Michael, A.J., W.L. Ellsworth, and D.H. Oppenheimer, Coseismic stress change during the 1989 Loma Prieta, California earthquake, *Geophys. Res. Lett., 17*, 1441-1445, 1990.

Minster, B., and T. Jordan, Vector constraints on western United States deformation from space geodesy, neotectonics, and plate tectonics, *J. Geophys. Res., 92*, 4798-4804, 1987.

Nakata, J.K., C.M. Wentworth, and M.N. Machette, Quaternary fault map of the Basin and Range and Rio Grande Rift Provinces, western United States,scale 1:2.5M, *U.S. Geol. Surv. Open File Rep., 82-579*, 1982.

Nelson, M.R., and C.H. Jones, Paleomagnetism and crustal rotations along a shear zone, Las Vegas range, southern Nevada, *Tectonics, 6*, 13-33, 1987.

Omori, F., On the aftershocks of earthquakes, *J. Coll. Sci., Tokyo Imp. Univ., 7*, 111-200, 1984.

Parsons, T., and G.A. Thompson, Coupled processes of normal faulting and dike intrusion in tectonically extended regions, *Seismol. Res. Lett., 62*, 26, 1991.

Reheis, M. C., Preliminary study of Quaternary faulting on the east side of Bare Mountain, Nye County, Nevada, *U.S. Geol. Surv. Bull., 1790*, 103-112, 1988.

Ron, H., A. Aydin, and A. Nur, Strike-slip faulting and block rotation in the Lake Mead fault system, *Geology, 4*, 1020-1023, 1986.

Rosenbaum, J.G., M.R. Hudson, and R.B. Scott, Paleomagnetic constraints on the geometry and timing of deformation at Yucca Mountain, Nevada, *J. Geophys. Res., 96*, 1963-1980, 1991.

Seeber, L., and J.G. Armbruster, Fault kinematics in the 1989 Loma Prieta rupture area during 20 years before that event, *Geophys. Res. Lett., 17*, 1425-1428, 1990.

Shawe, D.R., Strike-slip control of Basin-Range structure indicated by historical faults in western Nevada, *Geol. Soc. Am. Bull., 76*, 1361-1378, 1965.

Smith, R.B., and M.L. Sbar, Contemporary tectonics and seismicity of the western United States with emphasis on the Intermountain Seismic Belt, *Geol. Soc. Am. Bull., 85*, 1205-1218, 1974.

Stein, R.S., and M. Lisowski, The Homestead Valley earthquake sequence, California: Control of aftershocks and postseismic deformation, *J. Geophys. Res., 88*, 6477-6490, 1983.

Tschanz, C.M. and E.H. Pampeyan, Geology and mineral deposits of Lincoln County, Nevada, *Bull. Nev. Bur. Mines Geol., 73*, 83-84, 1970.

U.S. Geological Survey Staff, The Loma Prieta, California, Earthquake: An anticipated event, *Science, 247*, 286-293, 1990.

Ward, S. N., Pacific-North America plate motions: new results from Very Long Baseline Interferometry, *J. Geophys. Res., 95*, 21965-21982, 1990.

Wernicke, B., G.J. Axen, and J.K. Snow, Basin and Range extensional tectonics at the latitude of Las Vegas, Nevada, *Geol. Soc. Am. Bull., 100*, 1738-1757, 1988.

Wright, L., Late Cenozoic fault parameters and stress fields in the Great Basin and westward displacement of the Sierra Nevada block, *Geology, 4*, 489-494, 1976.

Zhang, P., M. Ellis, D.B. Slemmons, and F. Mao, Right lateral displacements and the Holocene slip rate associated with pre-historic earthquakes along the southern Panamint Valley fault zone: Implications for southern Basin and Range tectonics, *J. Geophys. Res., 95*, 4857-4872, 1990.

Zoback, M. D., M.L. Zoback, V.S. Mount, J. Suppe, J.P. Eaton, J.H. Healy, D. Oppenheimer, P. Reasenberg, L. Jones, C.B. Raleigh, I.G. Wong, O. Scotti, C. Wentworth, New evidence on the state of stress of the San Andreas Fault system, *Science, 238*, 1105-1111, 1987.

Zoback, M.L., State of stress and modern deformation in the northern Basin and Range province, *J. Geophys. Res., 94*, 7105-7128, 1989.

Zoback, M.L., R.E. Anderson, and G.A. Thompson, Cainozoic evolution of the state of stress and style of tectonism of the Basin and Range province of the western United States, *Philos. Trans. R. Soc. London, Ser. A*, 407-434, 1981.

J. Gomberg, U.S. Geological Survey, MS 966, Box 25046, DFC, Denver, CO 80225.

(Received January 24, 1991;
revised June 10, 1991;
accepted June 14, 1991.)

JOURNAL OF GEOPHYSICAL RESEARCH, VOL. 96, NO. B10, PAGES 16,369–16,381, SEPTEMBER 10, 1991

Tomography of the Western United States From Regional Arrival Times

THOMAS HEARN,[1] NOUREDDINE BEGHOUL,[2] AND MUAWIA BARAZANGI

Institute for the Study of the Continents, Cornell University, Ithaca, New York

First arrival times from regional distances (200-1200 km) in the western United States extracted from the International Seismological Centre (ISC) data set were inverted in a tomographic study to map the laterally varying *Pn* velocity structure of the uppermost mantle (i.e., the mantle lid) and to estimate the crustal static delay at each seismograph station. Synthetic data were used to evaluate resolution. Results correlate well with major tectonic features. We find low uppermost mantle velocities (V < 7.9 km/s) centered in the Basin and Range Province surrounded by uppermost mantle of higher, more normal *Pn* velocities (V > 7.9 km/s). These low apparent *Pn* velocities are primarily due to the effects of isostasy, hotspot volcanism, and crustal extension. We interpret the low apparent *Pn* velocities beneath the Sierra Nevada (7.6-7.7 km/s) to be the result of time delays introduced by ray paths tunneling through the deep crustal root. The Yellowstone hotspot, migrating along the Snake River Plain, has left low velocity (<7.6-7.8 km/s), hot upper mantle in its wake. Lower *Pn* velocities (~7.8 km/s) beneath the extensional Basin and Range are also presumably due to hotter uppermost mantle. Based on station static delays for the Basin and Range, we infer that Moho depths there do not vary significantly from 30 km. Normal continental *Pn* velocities (~8.0 km/s) as well as thicker crust (40-50 km) underlying the Rocky Mountains, Wyoming Basin Province, Colorado Plateau, and the northern Columbia Plateau indicate the presence of relatively cool uppermost mantle beneath these regions.

INTRODUCTION

Pn velocity and crustal thickness are fundamental parameters that are used to infer the thermal and tectonic history of the lithosphere. Lateral variations in *Pn* velocity have been associated with variations in upper mantle temperature, compositional differences, and pressure effects. Generally, temperature differences have the dominant effect [e.g., *Black and Braile*, 1982]. Crustal thickness variations result from many different tectonic factors including crustal extension or compression, isostatic forces, and magmatic underplating and intrusion. Thus, mapping *Pn* velocity and crustal thickness can yield valuable constraints on the styles of tectonic deformation that are responsible for the evolution of the continental crust. Both *Pn* velocity and crustal thickness have been primary targets of many large-scale refraction and reflection profiles in the United States [e.g., *Braile et al.*, 1989]. While some regions, such as the central Basin and Range Province, have had crustal structure mapped on the scale of a few kilometers, other regions, such as the Colorado Plateau and the Rocky Mountains, have only had a few measurements taken.

To better map regional variations in crustal and uppermost mantle structure, we selected first arrival times from regional events (distances < 11°) and inverted them to investigate both the crust and uppermost mantle structure in the western United States. These regional first arrivals are affected by both lateral variations in crustal structure and by velocity variations in the mantle part of the lithosphere that is often referred to as the mantle lid. Our results show direct correlation between velocities on the surface of the upper mantle and inferred crustal thicknesses and the major geological provinces of the western United States. These regional variations in uppermost mantle velocity and crustal thickness most likely reflect the effects of magmatism, uplift, extension, and compression on the crust and upper mantle.

In our analysis of the travel time data we first examine the important issues of data quality and data selection. Next, the travel time data are modeled as a refracted *Pn* phase traveling through the mantle lid, and previously developed tomographic inversion techniques are applied to the selected data set to find a solution which consists of station static delays and the lateral variations in slowness within the mantle lid. Resolution is evaluated by the use of synthetic data structures. Finally, we interpret our results in terms of the regional geology and active tectonics of the western United States.

DATA

The data set used in this study are travel times from the International Seismological Centre (ISC). This data set has formed the basis for tomography of the whole Earth as well as regional studies [e.g., *Dziewonski and Anderson*, 1983; *Dziewonski*, 1984; *Zhou and Clayton*, 1990]. The ISC data set is primarily meant for earthquake location, not tomography. Travel time picks are made by individuals at different institutions with varying instruments, and hence the first arrivals we use are subject to misidentification and both random and systematic measurement errors. Substantial systematic errors towards late picks are known to be introduced at low-gain stations [*Grand*, 1990]. We find that long-period instruments can also introduce such bias. Many other factors such as station site and event focal mechanism can also influence the signal to noise ratio and hence cause late travel time picks. It is the massive quantity of observations in this data set that makes reliable solutions possible. Although strict data selection criteria are imposed, we must rely primarily on the large number of observations in this data set to average out statistical errors.

We selected a total of 14,077 rays traveling between 200 km and 1223 km in the western United States recorded from 1964 through 1987 from an original data base of almost 50,000

[1]Now at Physics Department, New Mexico State University, Las Cruces.

[2]Now at Department of Geophysics, University of Western Ontario, London, Ontario, Canada.

Paper number 91JB01509.
0148-0227/91/91JB-01509$05.00

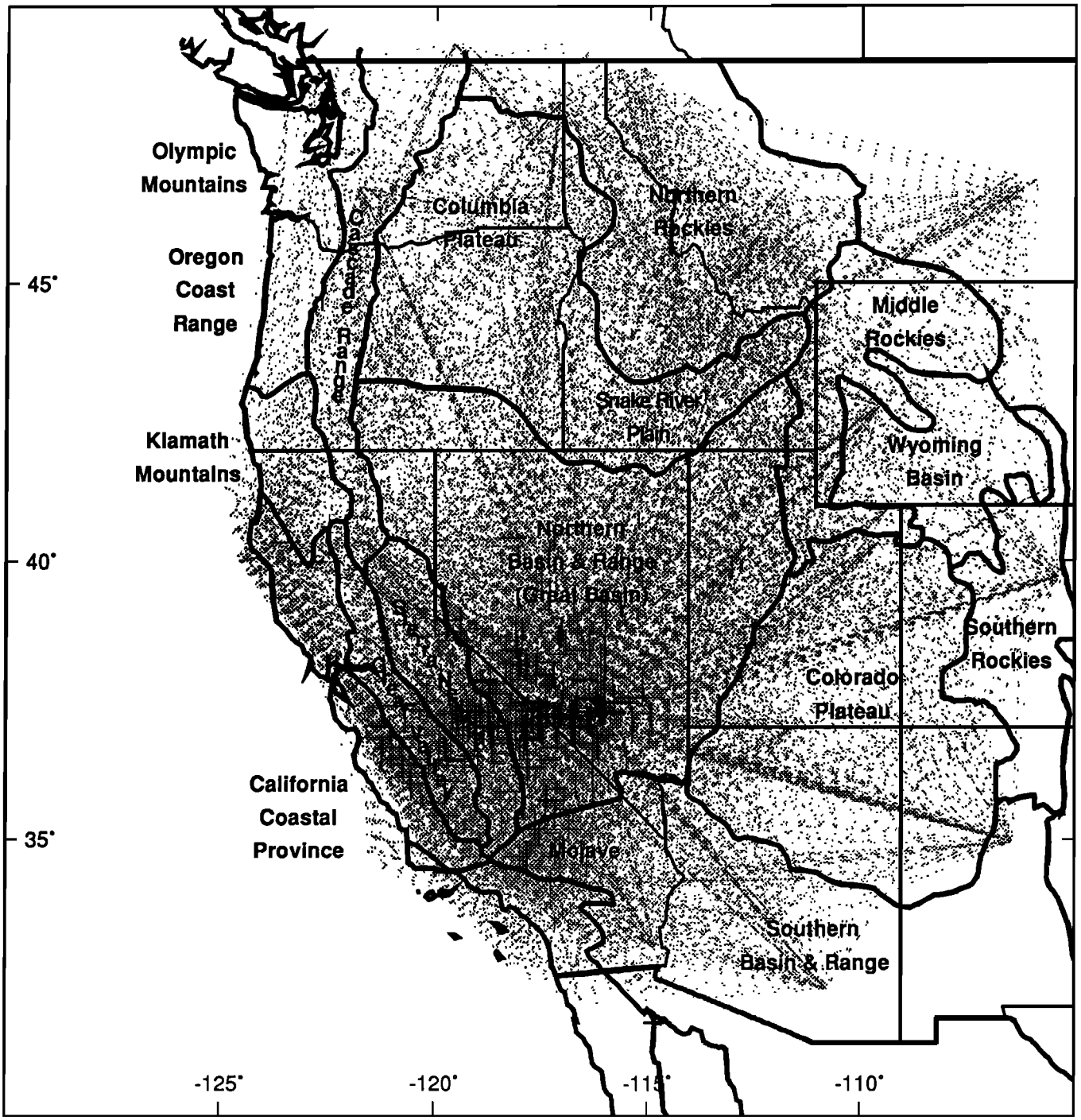

Fig. 1. All *Pn* ray paths used are plotted on a base map of the western United States. Coverage is greatest in California and the Great Basin. Canada, Mexico, the Rio Grande Rift, and the Pacific Ocean are not covered. The geographical provinces are from *Fenneman* [1946].

arrivals (Figure 1). The distance range was selected based on results from *Beghoul and Barazangi* [1990], who plot travel times between on-azimuth station pairs as a function of distance for the Basin and Range Province. From 2° to about 12° the apparent *Pn* velocity is constant indicating a negligible velocity gradient within the mantle lid. Hence all ray paths in that distance range can be modeled as refracted ray paths that travel through the uppermost mantle. We limited our final residual to be a maximum of 6 s; this is roughly the maximum residual one would expect from events at the 12° if the *Pn* velocity perturbation is 0.25 km/s and the crustal thickness varies by 6 km.

An iterative data selection procedure was used to help ensure a quality solution. All travel times are first corrected for receiver topography assuming a velocity of 5.5 km/s for the surface layer. The following criteria are used in selecting data:

1. Only first arrivals are used.
2. Only arrivals recorded with a precision of 0.1 s or better were used.
3. Only events located with a precision better than 0.1° in both latitude and longitude were used.
4. Sources and receivers are between 32° and 49° north latitude and 105° to 125° west longitude.

5. Source to receiver distance is between 200 km and 1223 km.

6. Each arrival within the station array has an ISC assigned travel time residual of 12 s maximum.

7. Each event is recorded worldwide by at least 20 stations (i.e., effectively a minimum event size criterion).

8. Each event is recorded within the western United States by at least 15 stations.

9. Each station within the area records at least 20 events.

10. Each arrival has a maximum residual of 6 s relative to a straight line fit of travel times to distance for the entire data set.

Because the last three selection criteria influence each other, the data are winnowed using an iterative procedure that results in a least squares straight line fit to the data. The slope of the travel time versus offset line gives the mean inverse velocity of the ray paths, the intercept gives an estimate of mean crustal delay. We use these initial estimates of *Pn* velocity and mean crustal delay as the starting model for the subsequent iterative tomography.

Ray paths used are shown in Figure 1. The number of arrivals per station ranges from the imposed minimum of 20 arrivals to a maximum of 603 arrivals. As one might expect, station and source densities are highest in California.

METHOD

The regional travel times are all modeled as refracted *Pn* ray paths. Earth curvature alone will make the most distant (i.e., 1223 km) of these rays bottom at about 30 km beneath the Moho, thus reaching well into the mantle lid. The tomographic method used fits perturbations from the simple linear refraction travel time curve that was found during the data selection process. There are three portions to *Pn* a refracted ray path travel times: the source to mantle ray path, the ray path through the mantle, and the ray path from the mantle to the receiver (Figure 2). This is described by the time term equation as

$$t = a + b + Ds$$

where a is the event static delay, b is the station static delay, D is source receiver distance, and s is mantle slowness (1/velocity).

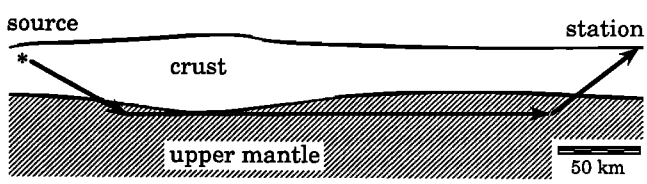

Fig. 2. Schematic cross section of the ray path of a regional *Pn* arrival (approximately 1:1 scale). Such ray paths have three portions, associated with the source, the receiver, and the mantle. Our tomographic method solves for the static delays associated with sources and receivers and for the lateral upper mantle velocity variations encountered by the mantle portion of the ray path.

Both station and event delays are expressed in terms of crustal thickness and crustal velocity:

$$\text{delay} = \int (s_c^2 - s^2)^{1/2} dz$$

where s_c is the crustal slowness profile as a function of depth. The integral is evaluated from sea level to the Moho depth or from the hypocenter depth to the Moho depth. Event delays reflect not only crustal thickness and velocity variations but also errors in the source depth and the origin time. Because of these many unknowns they cannot be interpreted.

The station delays represent the combined effect of crustal thickness, crustal velocity and mantle velocity. The effect of laterally varying mantle velocity on the station delays can be implicitly removed in the inversion process by replacing D, the total source to receiver distance, by the distance the ray actually travels within the mantle [*Hearn*, 1984]. Trade-off between the crustal velocity and the crustal thickness can only be resolved by independent knowledge of the near-station velocity structure; however, crustal thickness changes have the most effect. One second of relative delay time indicates about 10.4 km of crustal thickening (assuming a 6.3 km/s constant velocity for the crust). Observed variations in mean crustal velocity (e.g., 6.2-6.6 km/s [*Braile et al.*, 1989]) could account for a total of 0.5 s of relative delay time at most. Since the computed delays span over 2 s, our interpretation of the station delays is primarily in terms of crustal thickness.

For estimating slowness variations within the uppermost mantle, it is gridded in a single layer and the slowness within each grid cell is determined. The travel time equation then becomes [*Hearn*, 1984]

$$t = a + b + \sum d_i s_i$$

where d_i is the distance the ray travels in cell i and s_i is the slowness for cell i and the sum is over all cells through which the ray travels.

The tomographic method used here is that of *Hearn and Clayton* [1986*a*, *b*] with a few modifications. For backprojection of the data the following steps are then taken:

1. Source delays are estimated by the mean residual for each event and new residuals calculated.

2. Station delays are estimated by the mean residual at each station and new residuals are calculated.

3. Slownesses (inverse velocities) are determined by the weighted mean of the apparent slownesses, t/D, of all rays traversing each cell and new residuals are calculated.

4. The process is repeated to convergence.

This is a Simultaneous Iterative Reconstruction Technique (SIRT) [*Van der Sluis and Van der Vorst*, 1987] that starts with the residuals relative to the least squares line found during the selection procedure of the data. The particular weight for the estimation of cell slownesses used here, Dd, the product of the total ray path distance with the ray distance traversed within a cell, is chosen so that a constant velocity field will be reconstructed in one pass. Convergence of SIRT processes to a least squares solution is shown by *Van der Sluis and Van der Vorst* [1987]. With SIRT techniques only a few iterations are required to reconstruct the main features of the image. By stopping the iteration early, the higher-order, more poorly resolved features of the image are suppressed. In practice, we stopped the iterations when the change in the rms residual became less than 1%.

The results of six iterations are plotted in Figures 3*a* and 3*b*. Figure 3*a* is the *Pn* velocity for the western United States. This figure was median filtered to eliminate extreme points that are caused by poorly sampled cells. Figure 3*b* shows the static delays for all stations used and Table 1 lists the stations and their static delays. Our final standard error is 0.88 s, considerably reduced from 1.52 s standard error relative to the starting model. This is a large amount of error, although perhaps not too surprising, considering the nature of the data base. To see the effect of such errors on our inversion, we turn to the analysis of noise and resolution.

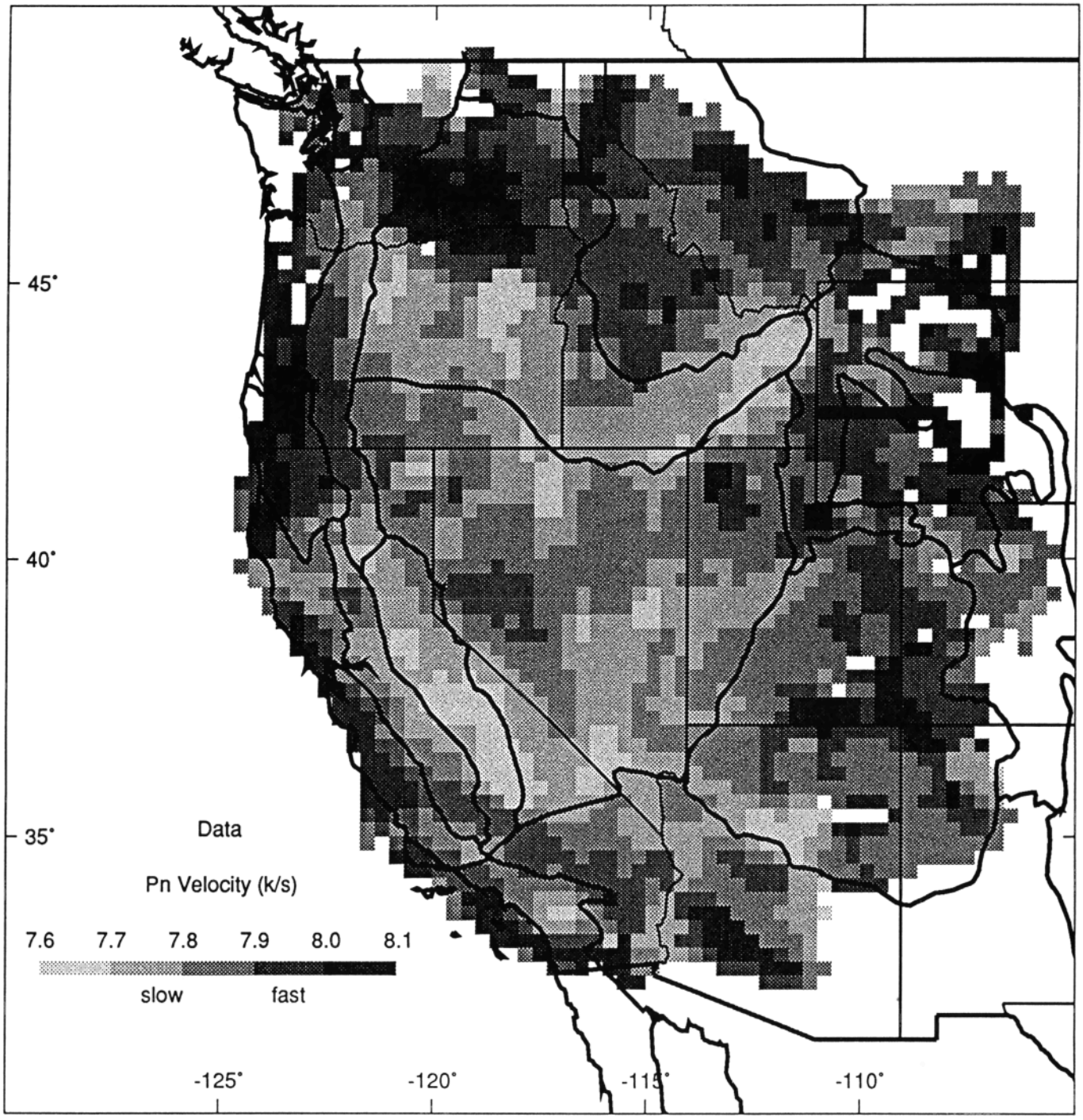

Fig. 3*a*. Upper mantle *Pn* velocity in the western United States. The lowest velocities are found under the Sierra Nevada and are likely to be due to its crustal root. The Great Basin and the Snake River Plain also have lower velocities, while the Colorado Plateau, the Mojave, the Rockies, and the Pacific Northwest have higher velocities. Only cells with 10 or more ray paths are shown.

RESOLUTION

Resolution in tomography problems is best investigated with the use of synthetic test models. A test model that includes both velocity and delay variations as well as random noise is used to create a synthetic data set using the same ray paths as in the actual data. This data set is then inverted in the same manner as the real data set. By comparing inversion results the quality of the tomographic solution can be assessed for different regions.

Synthetic anomalies were defined in regions roughly corresponding to the Sierra Nevada, the northern Basin and Range, the Snake River Plain, the Colorado Plateau, the Cascades, and Idaho with various different velocities and station delays. This test model is displayed in Figures 4*a* and 4*b*. Input event statics were randomly assigned values of +1.0 s, 0.0 s, and -1.0 s. We used the root-mean-square residual from our actual results to set the standard deviation of the added noise to

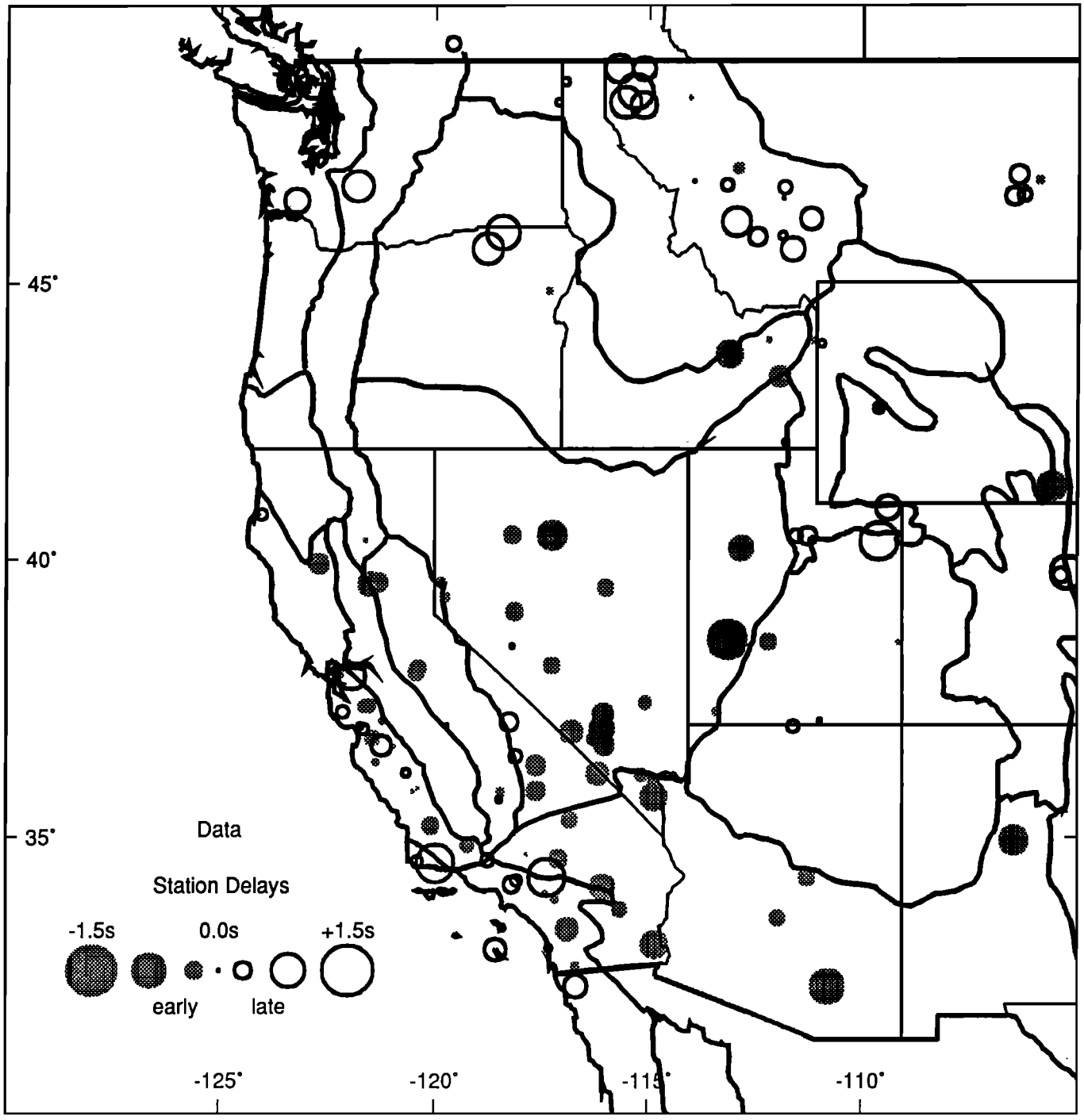

Fig. 3*b*. Crustal station delays in the western United States. Negative delays indicate thin or fast crust. Positive delays primarily represent the effect of thick crust but may also be caused by a slower crust.

0.88 s. This is a large amount of noise; nonetheless, we are still able to reconstruct all of the principle features of the model.

The results of the synthetic inversion are shown in Figures 5*a* and 5*b*. The anomalies are well located although slightly subdued in magnitude. Regional velocity is determined to about 0.1 km/s. Station delay errors are usually correct within 0.3 s, but stations with limited coverage can show much larger errors. A test model that did not include added noise demonstrated that much of the error in the reconstruction is due to the large amount of noise. The noise-free tests yielded well-defined velocity anomalies but showed that the station delays can be sensitive to trade-off with the velocity field. For example, stations east of the Colorado Plateau show early static delays. These early static delay estimates are attributable to a narrow range of ray azimuth at stations near the edge of the covered area. The nearby fast velocity anomaly has affected all the ray paths going to these stations. Similar delay errors can be found at stations in northwest Montana. This is a fundamental problem with the data set: Without full azimuth coverage at each station the trade-off between the crustal delay and mantle velocity anomaly cannot

TABLE 1. Listing of Station Locations, Computed Station Delays, and the Number of Arrivals per Station

Station	Latitude	Longitude	Elevation, m	Static Delay, s	Count
ABL	34.86	-119.22	1981	-0.41	44
ABQ	34.94	-106.46	1849	-0.39	25
ALQ	34.94	-106.46	1849	-0.81	411
AMM	46.09	-112.95	2051	0.84	30
ARN	37.35	-121.53	628	-0.37	280
BAR	32.68	-116.67	520	-0.18	33
BCH	35.20	-120.09	1140	-0.46	54
BCN	35.98	-114.84	776	-0.31	79
BDW	42.78	-109.58	2190	0.05	260
BEI	42.12	-111.78	1859	0.17	85
BFW	46.49	-123.21	902	0.72	29
BKU	38.55	-113.13	1859	-1.14	26
BLP	34.56	-120.40	134	0.32	30
BMN	40.43	-117.22	1500	-0.86	432
BMO	44.85	-117.31	1189	-0.15	163
BOZ	45.60	-111.63	1575	0.70	37
BTY	36.88	-116.77	1183	-0.64	23
BW0	42.78	-109.56	2200	0.18	30
CBC	36.93	-121.66	219	0.33	30
CBX	32.31	-116.66	0	0.68	32
CED	34.28	-117.34	1067	1.08	21
CIS	33.41	-118.40	485	0.07	25
CKM	47.07	-112.91	1353	-0.28	20
CLC	35.82	-117.60	766	-0.52	136
CLX	48.21	-115.13	1975	0.77	40
CMB	38.03	-120.39	719	-0.42	23
CPX	36.93	-116.06	1285	-0.72	31
CRC	37.24	-122.13	607	0.33	31
CWC	36.44	-118.08	1620	0.37	26
DAC	36.28	-117.59	1433	-0.54	40
DAU	40.41	-111.26	2771	0.52	38
DCI	43.96	-111.10	2020	-0.21	30
DCU	40.41	-111.53	1829	0.38	30
DUG	40.19	-112.81	1477	-0.68	441
EUR	39.48	-115.97	2178	-0.43	603
FGU	40.93	-109.39	1982	0.69	88
FHC	40.82	-124.00	610	0.32	76
FRI	36.99	-119.71	119	0.08	308
GCA	36.97	-111.59	1339	0.35	284
GLA	33.08	-114.83	627	-0.79	283
GLD	39.75	-105.22	1762	0.96	75
GLR	37.20	-116.03	1435	-0.60	44
GMW	47.55	-122.79	506	0.74	40
GOL	39.70	-105.37	2359	0.42	250
GSC	35.30	-116.81	990	-0.43	144
HAY	33.71	-115.64	439	-0.40	23
HCC	36.98	-121.72	159	0.16	45
HHM	48.35	-114.03	1100	-0.09	29
HID	43.96	-112.16	1527	-0.12	36
HPI	43.71	-113.10	2597	-0.76	69
HRY	46.71	-111.83	1341	0.36	43
IMW	43.90	-110.94	2646	0.18	50
ISA	35.66	-118.47	835	0.15	156
JAS	37.95	-120.44	457	-0.42	477
KPK	39.59	-121.31	897	-0.53	93
KVN	39.06	-118.10	1829	-0.48	20
LAO	46.69	-106.22	744	0.06	37
LAR	41.31	-105.58	2400	-0.83	36
LBM	46.51	-111.85	1524	0.06	21
LC3	46.57	-106.25	682	0.38	23
LC4	46.74	-106.37	764	-0.00	26
LCC	45.84	-111.88	1669	0.23	35
LD1	46.84	-105.89	759	-0.21	27
LD3	46.55	-106.48	800	0.51	40
LD4	46.94	-106.38	713	0.54	26
LDM	48.45	-115.32	838	1.01	90
LEE	37.24	-113.38	1097	-0.23	24
LHD	48.26	-115.56	1134	0.90	39
LLA	36.62	-120.94	475	-0.03	262
LON	46.75	-121.81	854	0.90	196
LRM	45.82	-112.46	2326	0.51	157
LSM	36.74	-116.27	1140	-0.29	55
LVN	36.11	-115.14	610	-0.35	22
MCV	36.63	-116.00	1158	-0.54	29

TABLE 1. (continued)

Station	Latitude	Longitude	Elevation, m	Static Delay, s	Count
MCW	48.68	-122.83	693	1.11	20
MDC	37.88	-121.91	1173	0.79	22
MFW	45.90	-118.41	384	1.00	55
MHC	37.34	-121.64	1282	-0.30	529
MIN	40.35	-121.61	1495	-0.06	387
MMA	33.55	-111.96	426	-0.42	72
MNA	38.43	-118.16	1525	0.09	120
MNV	38.43	-118.15	1507	-0.12	199
MSO	46.83	-113.94	1264	0.02	194
MSU	38.51	-112.17	2141	-0.42	99
MWC	34.22	-118.06	1730	0.31	46
NEL	35.71	-114.84	1061	-0.75	33
NEW	48.26	-117.12	760	0.20	246
NOP	36.13	-116.15	970	-0.65	73
NRR	39.57	-119.85	1634	-0.26	33
NTI	48.63	-116.96	823	0.23	29
ORV	39.56	-121.50	362	-0.66	351
PAS	34.15	-118.17	295	0.47	241
PEC	33.89	-117.16	616	-0.19	77
PGC	48.65	-123.45	5	0.58	35
PHA	35.86	-120.40	455	-0.00	125
PI6	42.73	-109.61	2225	0.27	22
PLM	33.35	-116.86	1692	-0.64	61
PNO	45.61	-118.76	402	0.91	53
PNT	49.32	-119.62	550	0.41	112
PRI	36.14	-120.67	1187	0.22	543
PRN	37.41	-115.05	1470	-0.35	44
PRS	36.33	-121.37	363	-0.16	258
PV0	38.50	-109.14	2652	-0.09	23
PYR	34.58	-118.74	1247	0.38	44
RMT	39.92	-122.67	0	-0.54	23
RMU	37.08	-110.97	1536	0.10	57
RVR	33.99	-117.38	260	-0.13	34
RXF	48.87	-115.12	1231	0.66	69
SAO	36.76	-121.44	350	-0.39	467
SBB	34.69	-117.82	832	-0.04	57
SCI	32.98	-118.55	219	0.62	22
SDW	34.61	-117.07	1184	-0.50	109
SLB	33.01	-117.29	38	0.19	27
SLD	37.08	-121.22	443	-0.14	168
STC	36.63	-121.23	259	0.59	57
SXM	46.15	-111.21	1993	0.65	34
SYP	34.53	-119.98	1305	1.12	39
TFO	34.28	-111.27	1492	-0.43	75
TIN	37.06	-118.23	1195	0.52	31
TMI	43.31	-111.92	2179	-0.57	69
TNP	38.08	-117.23	1932	-0.43	107
TPC	34.11	-116.05	720	-0.70	55
TPH	38.08	-117.22	1890	-0.29	30
TUC	32.31	-110.78	985	-0.98	293
UBO	40.32	-109.59	1600	1.12	109
UVN	40.44	-118.16	1926	-0.48	46
WCN	39.31	-119.76	1709	-0.25	240
WHM	46.76	-113.18	1792	0.34	20
WKR	35.81	-120.51	503	-0.04	107
WKT	35.79	-118.44	890	-0.21	66
YKM	48.86	-115.71	1509	0.82	54
ZSP	37.94	-122.26	119	-0.35	80

be fully resolved. Thus, caution must be used in interpreting both station delays and velocity anomalies in regions with incomplete azimuth coverage, particularly near the edge of the sampled region. Unfortunately, the number of arrivals alone is not necessarily a good measure of error in the station delays nor is the number of ray paths per cell a good indicator of the quality of the estimated velocity. One indicator to solution quality is the azimuthal ray path distribution in a region; this is partially provided by the ray paths drawn in Figure 1. It is this criterion and the resolution results that we use to guide our interpretations. In view of our results we have avoided interpreting regions along the edge of the model, particularly those along the western and northern margins where ray path coverage is particularly thin.

Other factors that affect the resolution are not accounted for by this synthetic model. For example, the ray paths may deviate laterally from the simple refraction model we assume here due to lateral velocity variations. However, we feel that errors due to ray path distortion are probably overshadowed by the much more serious errors introduced by earthquake mislocations. The events are located not only on the basis of the *Pn* arrivals used here but also use data collected at local distances (less than 200•

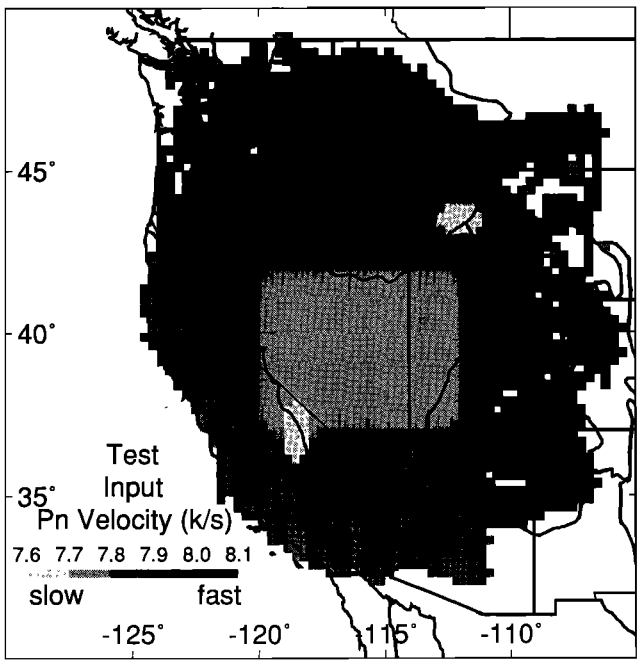

Fig. 4a. Input model of *Pn* velocity anomalies used to investigate resolution. These anomalies, along with the station delays of Figure 4b and random noise, are used to create a set of synthetic travel times for the ray path set.

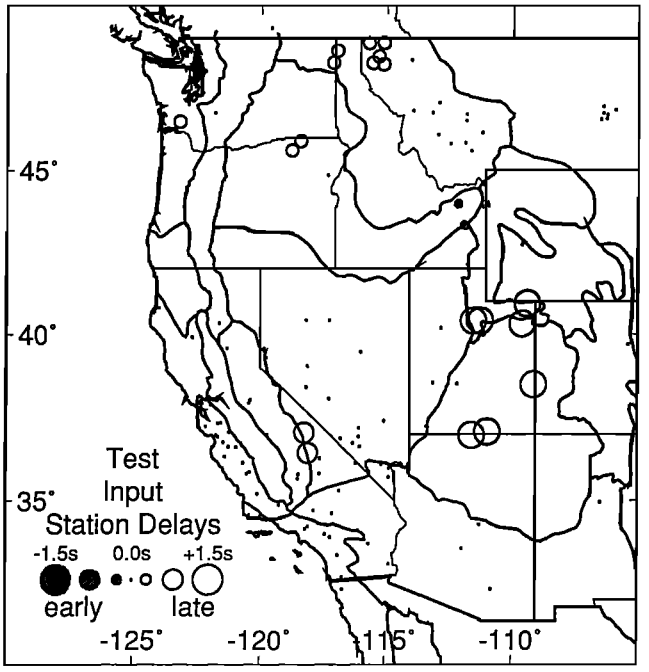

Fig. 4b. Input model of crustal station delays used to investigate resolution. These anomalies, along with the *Pn* velocities of Figure 4a and random noise, are used to create a set of synthetic travel times for the ray path set.

km) and teleseismic distances (greater than 1223 km). Thus, without including those extra arrivals in the inversion there is little we can do to address the mislocation problem. Because of this we are very cautious in interpreting the details in our results, but only address the regional differences.

Finally, substantial (2-4%) anisotropy has been reported for numerous studies in the region [*Bamford et al.*, 1979; *Vetter and Minster*, 1981; *Hearn*, 1984; *Zervas and Crosson*, 1986; *Beghoul and Barazangi*, 1990], and hence anisotropy must affect the travel time data used here. However, when ray paths are well distributed with azimuth, such anisotropic variations in apparent velocity should cancel. When synthetic models which included substantial anisotropy (4%) were tested, slowness variations and station delays were still resolvable. Thus, we believe anisotropy does not appreciably affect our estimation of lateral velocity variations. However, since our results represent the azimuthal averaged velocity, while refraction results yield the velocity along specific azimuths, some discrepancy between the two methods may result.

Regional Results

The original straight-line fit to the data set indicates a mean *Pn* velocity of 7.85 km/s and a mean Moho depth of around 36±5 km with respect to sea level. This crustal thickness was based on the intercept time of 5.8 s assuming a crustal velocity of 6.3 km/s and a mean source depth of 10 km. The lateral velocity variations and the station delays found in the tomography are perturbations from these values.

Unfortunately, the depth estimate calculated from the intercept time is too crude to calibrate the relative station delays to an absolute Moho depth. Instead we calibrate the absolute Moho depth by using some widely recorded stations (>200 *Pn* arrivals) that lie near regional reflection and refraction lines. *Mooney and Brocher* [1987] have shown that Moho depths from reflection and refraction profiles agree to within the error of the measurements (commonly 10% of the depths). Station BMN (432 recorded *Pn* arrivals and -0.9 s station static) is near COCORP (Consortium for Continental Reflection Profiling) Nevada line 3 [*Klemperer et al.*, 1986] which has a two-way reflection travel time depth of 9.6 s relative to 1065 m above sea level. Using a 6.3 km/s crustal velocity, we then estimate a depth of about 29 km for this station, which is 1-4 km less than the thickness estimated from a refraction profile located about 40 km west of station BMN [*Holbrook*, 1990; *Benz et al.*, 1990; *Catchings and Mooney*, 1991]. Station EUR (603 recorded *Pn* arrivals and -0.4 s station static) is at the end of a regional refraction line which indicates a depth of 33 km [*Prodehl*, 1979; *Thompson et al.*, 1989]. Using a 7.85 km/s *Pn* velocity and a 6.3 km/s crust, these two stations indicate that a 0.0 s static delay corresponds to about 38 km. All depths we infer in this paper are relative to that value.

We find uppermost mantle velocity variations that range from about 7.6 km/s to 8.1 km/s (Figure 3a). The low velocities found under the Sierra Nevada are probably related to crustal root structure. The extensional Great Basin in the center of the map shows consistently low velocities as does the southern Columbia Plateau-Snake River volcanic province. These regions with low *Pn* velocity are surrounded by higher *Pn* velocities of the Pacific Coast, the Colorado Plateau, Wyoming Basin Province, and the Rocky Mountains which have normal continental *Pn* velocities of 8.0 km/s and above. Our map of *Pn* velocity shows many differences compared with maps based on compiled refraction profiling results [e.g., *Braile et al.*, 1989]. However, regions with the major discrepancies (the Sierra Nevada, Snake River Plain, Colorado Plateau, Rocky Mountains, and Columbia Plateau) are also the regions with the fewest seismic refraction profiles, and we believe our results of the uppermost mantle velocities in those regions are better constrained.

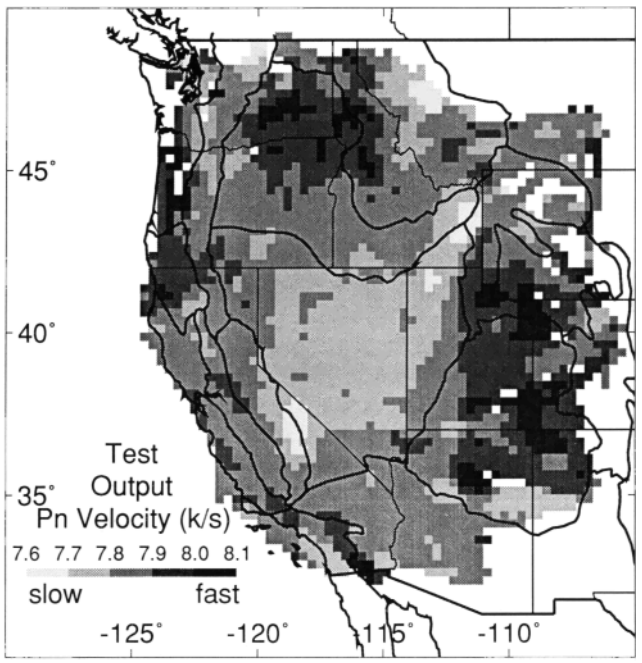

Fig. 5a. Output *Pn* velocity model from synthetic travel times created from Figures 4a and 4b. The major velocity anomalies input are reasonably well defined.

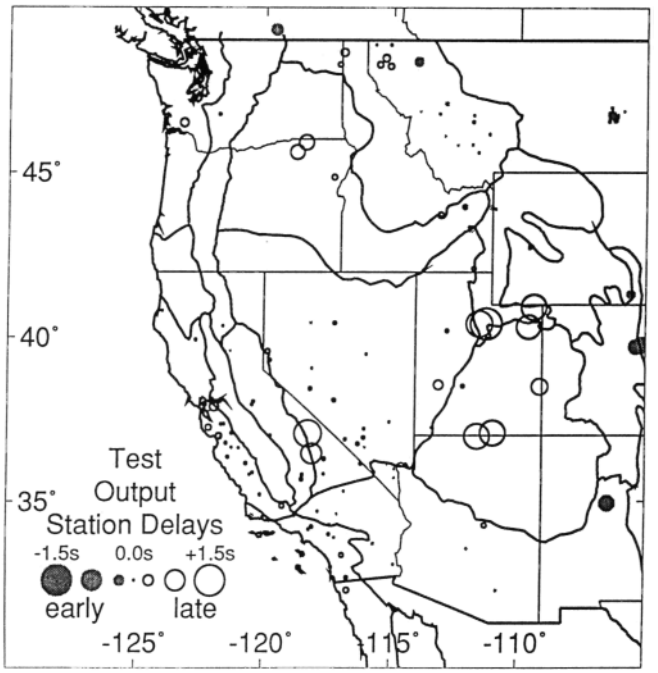

Fig. 5b. Output station delays from synthetic travel times created from Figures 4a and 4b. Stations on the edge of the data coverage have considerable errors. This is due to the poor azimuthal coverage at such stations.

In several places, neighboring stations have contrasting delays. These may be caused by systematic errors in the arrival picks for low signal to noise stations. Instrument type, period and gain, cultural, agricultural, and surf noise as well as site conditions all affect the signal detectability and hence can introduce a station dependent bias. *Grand* [1990] reported that station gain also introduces substantial bias. We identified all the low-gain stations (listed as less than 60,000 gain), long-period stations and broadband stations in our final data set for which data were listed [*Poppe*, 1979]. We found that almost all of the long-period (FLG, UKI, SEA, SPO, FER, LAC) and broadband (ELK, KNB, KN-, WDC) stations gave systematically late readings relative to neighboring short-period stations, many by over 1 s, and so we eliminated all long-period and broadband stations from our final inversion. We also found that many of the low-gain stations (BKS, BRK, BUT, COR, FRE, GCC, KFC, PCC, SHW, SLC) seemed to be relatively late, and so we also eliminated those arrivals. Unfortunately, most stations are not listed fully enough to evaluate, and station gains are changed frequently. Thus we must rely on the spatial consistency of the delays as the primary quality check. The main purpose of this study, however, is to view the major variations in delays and velocity; it is not to do a station by station comparison. Since these systematic errors are station dependent, and not path dependent, they directly affect mainly the station delay estimates. We found that our elimination of long-period, broadband stations, and low-gain stations did not significantly change our slowness image.

The station static delays shown in Figure 3b span over 2 s and represent predominately the effect of crustal thickness variations. Compared to current maps of crustal thickness [e.g., *Braile et al.*, 1989; *Smith et al.*, 1989], we have relatively few stations. Because of this, as well as the high probability of systematically late station delays, we did not produce a map of crustal thickness. Instead we will interpret the station delays on a regional basis. The gross pattern of the delays has positive delays in the north and along the coast and early negative delays within the Basin and Range Province. The delays found here correlate well with current maps of crustal thickness in the western United States which show the relatively thin extensional interior of the western United States [e.g., *Mooney and Braile*, 1989; *Braile et al.*, 1989; *Mooney and Weaver*, 1989].

Sierra Nevada

The Sierra Nevada, and the White Mountains to the east, are considered to be compensated mountain chains with crustal thicknesses up to 55 km [e.g., *Pakiser and Brune*, 1980; *Chase and Wallace*, 1988]. Mountain roots cause rays to be delayed and this leads to a low apparent *Pn* velocity. Some authors, however, have recently suggested that the mountains are underlain by partial melt and that no root exists [*Jones et al.*, 1990]. Objectively, our results cannot differentiate between these two models but only show the presence of very low velocity material under the mountain crest. We believe that regional *Pn* ray paths tunnel through the root and are partially imaging velocities in the lower crust; and, hence, the 7.6 km/s low velocity underneath the high crest of the Sierra Nevada (maximum elevation 4300 m) is a result of this ray path geometry (Figure 3a). Such ray paths are not "classical" *Pn* rays but probably do not deviate substantially from true *Pn* ray paths. Stations wholly within the Sierra Nevada should show appreciable delays if a root is present. Station TIN (elevation 1195 m, on the eastern side of the Sierra) has a delay of 0.5 s (about 43 km crustal thickness) that may be root related. Station ISA (elevation 835 m, in the southern tip of the Sierra) shows a delay of 0.2 s indicating a 40 km crust there. Unfortunately, there are no stations in the highest part of the mountain range with which to investigate the root.

Another low velocity anomaly (7.6 km/s) occurs along the northwest Sierra foothills and the northeast Central Valley (Fig-

ure 3*a*). Elevations are not extremely high in the region so it is doubtful much of a crustal root exists. A profile in the Sierran foothills from an earthquake in Oroville was shown by *Oppenheimer and Eaton* [1984] to have a velocity of 7.4 km/s and may be related to the same feature. The cause of this anomalous zone is difficult to ascertain.

California

The plate boundary in southernmost California juxtaposes the low *Pn* velocities associated with the Peninsular Ranges against the North American plate of normal *Pn* velocity. The central and northern California coasts show normal continental *Pn* velocities (~8.0 km/s) that probably reflect the oceanic origin of the upper mantle there. These results compare well with the major features found in seismic array studies of *Pn* in southern California and central California but clearly lack the resolution that could be obtained with those data sets [e.g., *Hearn*, 1984; *Hearn and Clayton*, 1986*b*; *Oppenheimer and Eaton*, 1984]. Direct comparison with the station delays of *Hearn* [1984] shows that most of the stations with positive delays in southern California may be due to systematically late picks. The rest of the delays indicate crustal thicknesses of 30-33 km, which is about 4 km thicker than *Hearn* [1984] and 2 km thicker than *Mooney and Weaver* [1989]; however, again we must caution that inferred delays have a possible late bias.

Basin and Range

Crustal delays within the northern Basin and Range Province show median values of about -0.5 s (~32 km Moho depth). The COCORP reflection lines that traverse the central Great Basin show a flat Moho at a depth of 30 km [*Klemperer et al.*, 1986]. The general delay trends indicate crustal thickening by almost 5 km from northern to southern Nevada.

Velocities in the northern Basin and Range are around 7.8 km/s, which is consistent with prior estimates [e.g., *Thompson et al.*, 1989; *Beghoul and Barazangi*, 1990; *Pakiser*, 1985]. High quality refraction lines recently recorded by the PASSCAL (Program for Array Seismic Studies of the Continental Lithosphere) group in the western Basin and Range [*Benz et al.*, 1990; *Holbrook*, 1990]. Despite the high quality *Pn* arrivals observed, these authors disagree on the *Pn* velocity. While *Holbrook* [1990] reports *Pn* velocities of 7.7-7.9 km/s, *Benz et al.* [1990] and *Catchings and Mooney* [1991] report velocities of 7.9-8.0 km/s. The difference probably represents the inherent ambiguity of using the explosion refraction method to determine mantle velocity. Our results support the lower velocities. Teleseismic results show that this low *Pn* velocity of the Basin and Range extends well into the uppermost mantle [e.g., *Dueker and Humphreys*, 1990; *Grand*, 1987]. The high heat flow of the region as well as its thin crust imply a high Moho temperature that is almost near solidus [*Morgan and Gosnold*, 1989]. Therefore, the low uppermost mantle velocity in the Basin and Range Province is probably due to the effect of high temperature.

The Moho in the southern Basin and Range appears to be different than the Moho in the northern Basin and Range. Upper mantle velocities are clearly higher (7.8-8.0 km/s) in the southern Basin and Range, and average elevations are lower. In addition, reflection and refraction profiling shows possibly faulted Moho of variable depths ranging from 36 km to less than 26 km and finds a less distinct reflection Moho than was found in the northern Basin and Range [*Hauser et al.*, 1987; *Goodwin and Thompson*, 1988; *Hauser and Lundy*, 1989; *Hearn*, 1984; *Warren*, 1969]; this may possibly indicate that less extensive magmatic underplating has occurred in the south. A cooler mantle in the southern Basin and Range than in the north could explain all these observations of higher *Pn* velocity, lower average elevation, more variation in crustal thickness, Moho faulting, and a less distinct reflection Moho.

Colorado Plateau

Early refraction work to investigate *Pn* in the Colorado Plateau estimated *Pn* velocities of around 7.8-8.0 km/s and a crust of about 40 km thick [*Ryall and Stuart*, 1963; *Roller*, 1965; *Bucher and Smith*, 1971; *Keller et al.*, 1979]. Recently, however, *Beghoul and Barazangi* [1989] argued that these data are of poor quality and estimated a *Pn* velocity of 8.1 km/s based upon reported earthquake travel times. They use this result to argue for a delamination model as a cause for the uplift of the Colorado Plateau. Our results show velocities of 7.8-8.1 km/s in the plateau. Velocities seem to be higher in the eastern plateau. Unfortunately, our data thin dramatically in the eastern plateau and are due almost entirely to the three stations located east of the plateau. The test resolution model shows that such lateral variations in the plateau should be resolvable. Thus, we feel that our results suggest that there is more lateral variation in mantle velocities under the plateau than has been previously assumed.

Crustal thickness in the Colorado Plateau has also been the subject of much inquiry and debate. Estimates of crustal thickness are available from COCORP reflection results. Those reflection lines, in Arizona and Utah, show a reflection Moho consistently at about 15-17 s, indicating crustal depths greater than 50 km [*Hauser and Lundy*, 1989; *Allmendinger et al.*, 1986]. There are two stations on the Arizona-Utah border that lie between these reflection lines which indicate a crustal thickness of about 40 km. Our resolution test model had no difficulty in determining the correct delays, and we expect any systematic errors in picking to be late, not early. Thus, we find it difficult to reconcile the delays with the reflection results except to suggest that, as with the *Pn* velocity in the plateau, there may exist considerable structural variation within the Colorado Plateau that has not been fully appreciated in past work.

Rocky Mountains

To the north of the Colorado Plateau, in the Wyoming Basin Province, the Rocky Mountains, and even extending into the northern Columbia Plateau, *Pn* velocities are the highest in the western United States, varying between 7.9 and 8.1 km/s. Station delays are also systematically higher indicating a thick crust of 40-45 km. However, these regions are on the edge of our study area where ray paths are thinnest, and our resolution test shows that trade-offs between station delays and the estimated velocities may occur. Thus, we refrain from interpreting any specific features. These regions represent cratonic crust underlying the western cordillera. The higher *Pn* velocity and the greater crustal thickness of the region are characteristic of stable crustal areas [e.g., *Mooney and Braile*, 1989]. Although considerable tectonic upheaval has obviously occurred during the Cenozoic in the Rocky Mountains, it was primarily compressional tectonism, and upper mantle velocities were not thermally affected.

Snake River Plain

The Snake River Plain is the most dramatic example of uppermost mantle velocity variation found in this study. The Snake River Plain slow velocity anomaly shows the thermal

track of the Yellowstone hotspot extending to Yellowstone Caldera. The lowest *Pn* velocity values are around 7.6 km/s (see Figure 3*a*). Our resolution test model, which included a low velocity anomaly in the eastern Snake River Plain, underestimated the magnitude of the velocity anomaly there. Thus, our estimate of an uppermost mantle velocity of 7.6 km/s there probably represents an upper bound to the true uppermost mantle velocity. Crustal delays indicate thicknesses near Yellowstone that are only slightly greater than those found in the Basin and Range province. Results from field experiments in the eastern Snake River Plain indicate a crustal thickness based on the *PmP* phase of 42 km and a *Pn* velocity of 7.9 km/s [*Smith et al.*, 1982; *Braile et al.*, 1982]. Data from Nevada Test Site recorded in the western Snake River Plain indicates velocities of 7.9 km/s [*Hill and Pakiser*, 1966]. The results from the eastern Snake River Plain are based on very weak *Pn* arrivals, and we feel that the magnitude of the eastern Snake River Plain velocity anomaly is simply too large to be compatible with those prior measurements of *Pn* velocity.

The extremely low uppermost mantle velocity beneath the Snake River Plain is almost certainly related to thermal heating, probably partial melt. Teleseismic tomography indicates that this low velocity anomaly extends nearly 200 km into the mantle [e.g., *Dueker and Humphreys*, 1990; *Iyer et al.*, 1981; *Evans*, 1982]. Our results show the major anomaly is under the eastern Snake River Plain, not Yellowstone Caldera. *Dueker and Humphreys* [1990] also site the main velocity anomaly under the Eastern Snake River Plain. These combined results document the existence of a deep mantle heat source, possibly a hotspot, driving the Snake River-Yellowstone volcanic system.

Columbia Plateau

The Columbia Plateau appears to be divided into two parts. The northern part, in Washington, shows normal (8.0 km/s) *Pn* velocity, while the southern part, often refered to as the High Lava Plains in eastern Oregon, shows lower velocities (7.8 km/s) that may be due to the effects of Basin and Range extension or Columbia Plateau volcanism. The boundary between high and low *Pn* velocities within the Columbia Plateau roughly coincides with the Klamath-Blue Mountain Lineament which runs along the north side of the Klamath Mountains northeast to the Oregon-Washington-Idaho corner [*Riddihough et al.*, 1986]. This lineament is thought to be the southern margin of the Columbia Embayment, the Proterozoic plate margin, and thus may separate oceanic and continental mantle. However, our test model, as well as the thin ray path coverage, shows that we should expect difficulties in resolving any distinct boundaries within the Columbia Plateau but should only expect to image the general velocity trend.

Estimates of *Pn* refraction velocities under the Columbia Plateau in Washington and Oregon [*Catchings and Mooney*, 1988*a*, *b*] obtained a 40-km-thick crust and a high *Pn* velocity of 8.4 km/s in Washington and a 37 km Moho and a 8.1 km/s velocity in Oregon; however, these *Pn* velocities were based on unreversed *Pn* segments that consisted of mostly secondary arrivals. Indeed, earlier work by *Hill* [1972] proposed two alternate crustal models, one of which had a thin (25 km) crust. *Zervas and Crosson* [1986] found an 8.2 km/s *Pn* velocity in west Washington. Our results agree with higher *Pn* velocities (>8.0 km/s) in Washington but indicate that lower *Pn* velocities prevail in Oregon and southern Idaho. Few stations are available in these regions, but those present indicate crustal thicknesses of 40+ km in the central Columbia Plateau region.

Pacific Northwest and the Cascade Range

Ray path coverage in the Pacific Northwest, particularly western Washington, is particularly poor. Most of the paths are north-south in direction, and this will cause poor north-south resolution. Caution is therefore required when interpreting results in those regions.

The high *Pn* velocities (8.0-8.1 km/s) of the Pacific northwest coast are probably related to the underthrust oceanic mantle of the subducting Juan de Fuca plate. The few delays in western Oregon and Washington are positive, indicating a thick crust (40+ km). Some of the larger delays might be due to sediments affecting crustal velocities in the Puget Sound region such as found by *Zervas and Crosson* [1986].

Refraction and gravity work in the region shows that the Moho thickens from about 25 km along the coast to over 40 km in the Cascades [*Mooney and Weaver*, 1989]. The change from subducted oceanic lithosphere (high *Pn* velocity, thin crust, landward dipping Moho, accreted terrain) to continental lithosphere (lower *Pn* velocity, thick crust, volcanic arc) occurs along the western boundary of the Cascade Range.

Work in the Cascade Range has indicated a 44-km crustal thickness and a low 7.7 km/s *Pn* velocity [*Leaver et al.*, 1984]. Our results show slightly higher *Pn* velocities of about 7.9 km/s along the Cascade Range. If a crustal root exists within the Cascades, it is not significant enough to seriously disturb the apparent velocity of regional ray paths in the same manner as the Sierra Nevada. This indicates a root of less than 20 km.

DISCUSSION AND CONCLUSIONS

Worldwide *Pn* velocities beneath continents average about 8.1 km/s [e.g., *Mooney and Braile*, 1989], yet the western United States has an average velocity around 7.9 km/s. This low average velocity probably reflects the dominance of thermal processes in the western United States throughout the Cenozoic. Our map of upper mantle velocities (see Figure 3*a*) shows a relatively large window of low apparent *Pn* velocity surrounded by normal apparent *Pn* velocities (see also *Hearn et al.* [1990] for a color version of the velocity map). We infer that the tectonics of three regions dominate this low velocity window: Isostasy in the Sierra Nevada, hotspot volcanism in the Snake River Plain, and crustal extension in the Basin and Range. Normal *Pn* velocities are observed in the surrounding regions, including the Colorado Plateau, Wyoming Basin Province, Rocky Mountains, northern Columbia Plateau, and the Pacific Coast. The processes of compression and uplift that have affected some of these regions during the Cenozoic apparently did not radically affect the *Pn* velocity.

Regions of low uppermost mantle velocity, the Snake River Plain and the Basin and Range Province, are also regions of Cenozoic volcanism, magmatic intrusion, and high heat flow. This leads to the inference of *Black and Braile* [1982], among others, that *Pn* velocity is controlled by upper mantle temperature. However, the same thermal processes that serve to lower *Pn* velocity, volcanism and extension, may also cause compositional variations through magmatic differentiation and intrusion. Also, the origin of uppermost mantle material in the western United States varies dramatically from oceanic to cratonic and compositional variations might be expected between upper mantle of vastly different origins. Finally, pressure differences resulting from different crustal thicknesses will also have an effect on rock velocities. Nonetheless, the correspondence we find between low upper mantle velocity and areas of high heat

flow, extension, and volcanism is very striking and leads us to conclude that temperature is the primary factor explaining observed *Pn* velocity variations.

Low upper mantle velocity in the western United States is also a dominant feature of teleseismic tomography [e.g., *Grand*, 1987; *Dueker and Humphreys*, 1990; *Iyer and Hitchcock*, 1989] indicating that upper mantle temperature differences can extend up to several hundred kilometers in depth, and hence substantial upwelling and thermal uplift must result from thermal density contrasts. This inferred upwelling and the accompanying processes of extension, uplift, and plate motion are what now dominate the present-day tectonics of the western United States.

Acknowledgments. We thank E. Hauser and B. Isacks for useful discussions and comments and E. Fielding for help with the printing. We also thank associate editor W. Mooney for his very helpful review. This work was performed under NSF grant EAR-8904534. Institute for the Study of the Continents contribution 146.

REFERENCES

Allmendinger, R.W., H. Farmer, E.C. Hauser, J. Sharp, D. Von Tish, J.E. Oliver, and S. Kaufman, Phanerozoic tectonics of the Basin and Range-Colorado Plateau transition from COCORP data and geologic data: A review, in *Reflection Seismology: The Continental Crust, Geodyn. Ser.*, vol. 14, edited by M. Barazangi and L. Brown, pp. 257-267, AGU, Washington, D. C., 1986.

Bamford, D., M. Jentsch, and C. Prodehl, *Pn* anisotropy studies in norther Britain and the eastern and western United States, *Geophys. J. R. Astron. Soc., 57*, 397-429, 1979.

Beghoul, N., and M. Barazangi, Mapping high *Pn* velocity beneath the Colorado Plateau constrains uplift models, *J. Geophys. Res., 94*, 7083-7104, 1989.

Beghoul, N., and M. Barazangi, Azimuthal anisotropy of velocity in the mantle lid beneath the Basin and Range Province, *Nature, 348*, 536-538, 1990.

Benz, H.R., R.B. Smith, and W.D. Mooney, Crustal structure of the northwestern Basin and Range Province from the 1986 program for array seismic studies of the Continental lithosphere seismic experiment, *J. Geophys. Res., 95*, 21,823-21,842, 1990.

Black, P.R., and L.W. Braile, *Pn* velocity and cooling of the continental lithosphere, *J. Geophys. Res., 87*, 10,557-10,568, 1982.

Braile, L.W., R.B. Smith, J. Ansorge, M.R. Baker, M.A. Sparlin, C. Prodehl, M.M. Schilly, J.H. Healy, St. Mueller, and K.H. Olsen, The Yellowstone-Snake River Plain seismic profiling experiment: Crustal structure of the eastern Snake River Plain, *J. Geophys. Res., 87*, 2597-2609, 1982.

Braile, L.W., W.J. Hinze, R.R.B. von Frese, and G.R. Keller, Seismic properties of the crust and uppermost mantle of the conterminous United States and adjacent Canada, in Geophysical Framework of the United States, edited by L.C. Pakiser, and W.D. Mooney, *Geol. Soc. Am. Mem. 172*, 655-680, 1989.

Bucher, R.L., and R.B. Smith, Crustal structure of the eastern Basin and Range Province and the northern Colorado Plateau from phase velocities of Rayleigh waves, in, *Structure and Physical Properties of the Earth's Crust, Geophys. Monogr. Ser.*, vol. 14, edited by J.G. Heacock, pp. 57-70, AGU, Washington, D.C., 1971.

Catchings, R.C., and W.D. Mooney, Basin and Range crustal and upper mantle structure, northwest to central Nevada, *J. Geophys. Res., 96*, 6247-6267, 1991.

Catchings, R.D., and W.D. Mooney, Crustal structure of east central Oregon: Relation between Newberry Volcano and regional crustal structure, *J. Geophys. Res., 93*, 10,081-10,094, 1988*a*.

Catchings, R.D., and W.D. Mooney, Crustal structure of the Columbia Plateau: Evidence for continental rifting, *J. Geophys. Res., 93*, 459-474, 1988*b*.

Chase, C.G., and T.C. Wallace, Flexural isostasy and the uplift of the Sierra Nevada of California, *J. Geophys. Res., 93*, 2795-2802, 1988.

Dueker, K., and E. Humphreys, Upper mantle velocity structure of the eastern Great Basin: Evidence for small scale convection, *Geophys. Res. Lett., 17*, 1327-1330, 1990.

Dziewonski, A.M., Mapping the lower mantle: Determination of lateral heterogeneity in *P* velocity up to degree and order 6, *J. Geophys. Res., 89*, 5929-5952, 1984.

Dziewonski, A.M. and D.L. Anderson, Travel times and station corrections for *P* waves at teleseismic distances, *J. Geophys. Res., 88*, 3295-3314, 1983.

Evans, J.R., Compressional wave velocity structure of the upper 350 km under the eastern Snake River Plain near Rexburg, Idaho, *J. Geophys. Res., 87*, 2654-2670, 1982.

Fenneman, N.M., Physical divisions of the United States, U.S. Geol. Surv. map, Reston, Va., 1946.

Goodwin, E.B., and G.A. Thompson, The seismically reflective crust beneath highly extended terrains: Evidence for its origin in extension, *Geol. Soc. Am. Bull., 100*, 1616-1626, 1988.

Grand, S.P., Tomographic inversion for shear velocity beneath the North American plate, *J. Geophys. Res., 92*, 14,065-14,090, 1987.

Grand, S.P., A possible station bias in travel time measurements reported to ISC, *Geophys. Res. Lett., 17*, 17-20, 1990.

Hauser, E., and J. Lundy, COCORP deep reflections: Moho at 50 km (16 s) beneath the Colorado Plateau, *J. Geophys. Res., 94*, 7071-7082, 1989.

Hauser, E.C., J. Gephart, T. Latham, J. Oliver, S. Kaufman, and L. Brown, COCORP Arizona transect: Strong crustal reflections and offset Moho beneath the transition zone, *Geology, 15*, 1103-1106, 1987.

Hearn, T.M., *Pn* travel times in southern California, *J. Geophys. Res., 89*, 1843-1855, 1984.

Hearn, T.M., and R.W. Clayton, Lateral velocity variations in southern California, I, Results for the upper crust from *Pg* waves, *Bull. Seismol. Soc. Am., 76*, 495-509, 1986*a*.

Hearn, T.M., and R.W. Clayton, Lateral velocity variations in southern California, II, Results for the lower crust from *Pn* waves, *Bull. Seismol. Soc. Am., 76*, 511-520, 1986*b*.

Hearn, T.M., N. Beghoul, and M. Barazangi, First tomographic study of western U.S. completed, *Eos Trans. AGU, 71*, 1083, 1990.

Hill, D.P., Crustal and upper mantle structure of the Columbia Plateau from long range seismic refraction measurements, *Geol. Soc. Am. Bull., 83*, 1639-1648, 1972.

Hill, D. and L.C. Pakiser, Crustal structure between the Nevada Test Site and Boise, Idaho from seismic-refraction measurements, in *The Earth Beneath the Continents, Geophys. Monogr. Ser.*, vol. 10, edited by J.S. Steinhart and T.J. Smith, pp. 391-419, AGU, Washington, D. C., 1966.

Holbrook, W.S., The crustal structure of the northwestern Basin and Range Province, Nevada, from wide-angle seismic data, *J. Geophys. Res., 95*, 21,843-21,870, 1990.

Iyer, H.M., and T. Hitchcock, Upper-mantle velocity structure in the continental U.S. and Canada, in Geophysical Framework of the United States, edited by L.C. Pakiser and W.D. Mooney, *Mem. Geol. Soc. Am. 172*, 681-710, 1989.

Iyer, H.M., J.R. Evans, G. Zandt, R.M. Stewart, J.M. Coakley, and J.N. Roloff, A deep low-velocity body under the Yellowstone caldera, Wyoming: Delineation using teleseismic *P*-wave residuals and tectonic interpretation, *Geol. Soc. Am. Bull., 92*, 792-798, 1981.

Jones, C.H., H. Kanamori, and S.W. Roecker, The missing root: Teleseismic and regional *Pn* arrivals observed in the southern Sierra Nevada, California (abstract), *Eos Trans. AGU, 71*, 1558, 1990.

Keller, G.R., L.W. Braile, and P. Morgan, Crustal structure, geophysical models and contemporary tectonism of the Colorado plateau, *Tectonophysics, 61*, 131-147, 1979.

Klemperer, S.L., T.A. Hauge, E.C. Hauser, J.E. Oliver, and C.J. Potter, The Moho in the northern Basin and Range province, Nevada, along the COCORP 40N seismic-reflection transect, *Geol. Soc. Am. Bull., 97*, 603-618, 1986.

Leaver, D.S., W.D. Mooney, and W.M. Kohler, A seismic refraction study of the Oregon Cascades, *J. Geophys. Res., 89*, 3121-3134, 1984.

Mooney, W.D., and L.W. Braile, The seismic structure of the continental crust and upper mantle of North America, in *The Geology of North America–An Overview*, edited by A.W. Bally and A.R. Palmer, pp. 39-52, Geological Society of America, Boulder, Colo., 1989.

Mooney, W.D., and T.M. Brocher, Coincident seismic reflection/refraction studies of the continental lithosphere: A global review, *Rev. Geophys., 25*, 723-742, 1987.

Mooney, W.D., and C.S. Weaver, Regional crustal structure and tectonics of the Pacific Coastal States; California, Oregon, and Washington, in Geophysical Framework of the United States, edited by L.C. Pakiser, and W.D. Mooney, *Mem. Geol. Soc. Am. 172*, 129-162, 1989.

Morgan, P., and W.D. Gosnold, Heat flow and thermal regimes in the continental United States, in Geophysical Framework of the United

States, edited by L.C. Pakiser, and W.D. Mooney, *Mem. Geol. Soc. Am. 172*, 493-522, 1989.

Oppenheimer, D.H., and J.P. Eaton, Moho orientation beneath central California from regional earthquake travel times, *J. Geophys. Res., 89*, 10,267-10,282, 1984.

Pakiser, L.C., Seismic exploration of the crust and upper mantle of the Basin and Range province, in *Geologists and Ideas; A History of North American Geology, Centennial Special Volume 1*, edited by E.T. Drake and W.M. Jordan, pp. 453-469, Geological Society of America, Boulder, Colo., 1985.

Pakiser, L.C. and J.N. Brune, Seismic models of the root of the Sierra Nevada, *Science, 210*, 1088-1094, 1980.

Poppe, B.B., Historical survey of U.S. seismograph stations, *U.S. Geol. Surv. Prof. Pap. 1096*, 1979.

Prodehl, C., Crustal structure of the western United States, *U.S. Geol. Surv. Prof. Pap., 1034*, 1-74, 1979.

Riddihough, R., C. Finn, and R. Couch, Klamath-Blue Mountain Lineament, Oregon, *Geology, 14*, 528-531, 1986.

Roller, J.C., Crustal structure in the eastern Colorado Plateaus province from seismic refraction measurements, *Bull. Seismol. Soc. Am., 55*, 107-119, 1965.

Ryall, A., and D.J. Stuart, Travel times and amplitudes form nuclear explosions, Nevada Test Site to Ordway, Colorado, *J. Geophys. Res., 68*, 5821-5835, 1963.

Smith, R.B., M.M. Schilly, L.W. Braile, J. Ansorge, J.L. Lehman, M.R. Baker, C. Prodehl, J.H. Healy, S. Mueller, and R.W. Greensfelder, The 1978 Yellowstone-Eastern Snake River Plain seismic profiling experiment: Crustal structure of the Yellowstone region and experiment design, *J. Geophys. Res., 87*, 2583-2589, 1982.

Smith, R.B., W.C. Nagy, K.A. Julander, J.J. Viveiros, C.A. Barker, and D.G. Gants, Geophysical and tectonic framework of the eastern Basin and Range-Colorado Plateau-Rocky Mountain transition, in Geophysical Framework of the United States, edited by L.C. Pakiser and W.D. Mooney, *Mem. Geol. Soc. Am. 172*, 205-233, 1989.

Thompson, G.A., R. Catchings, E. Goodwin, S. Holbrook, C. Jarchow, C. Mann, J. McCarthy, and D. Okaya, Geophysics of the western Basin and Range province, in Geophysical Framework of the United States, edited by L.C. Pakiser and W.D. Mooney, *Mem. Geol. Soc. Am. 172*, 177-204, 1989.

Van der Sluis, A., and H.A. van der Vorst, Numerical solution of large, sparse linear algebraic systems arising from tomographic problems, in *Seismic Tomography*, edited by G. Nolet, pp. 49-83, D. Ridel, Hingham, Mass., 1987.

Vetter, U., and J.B. Minster, *Pn* velocity anisotropy in southern California, *Bull. Seismol. Soc. Am., 71*, 1511-1530, 1981.

Warren, D.H., A seismic refraction survey of crustal structure in central Arizona, *Geol. Soc. Am. Bull., 80*, 257-282, 1969.

Zervas, C.E., and R.S. Crosson, *Pn* observation and interpretation in Washington, *Bull. Seismol. Soc. Am., 76*, 521-546, 1986.

Zhou, H. and R.W. Clayton, *P* and *S* wave travel time inversions for subducting slab under the island arcs of the northwest Pacific, *J. Geophys. Res., 95*, 6829-6851, 1990.

M. Barazangi, Institute for the Study of the Continents, Cornell University, Ithaca, NY 14853.

M. N. Beghoul, Department of Geophysics, University of Western Ontario, London, Ontario, Canada, N6A 5B7.

T. M. Hearn, Physics Department, New Mexico State University, Las Cruces, NM 88003.

(Received July 9, 1990;
revised April 8, 1991;
accepted May 29, 1991)

JOURNAL OF GEOPHYSICAL RESEARCH, VOL. 96, NO. B10, PAGES 16,263–16,274, SEPTEMBER 10, 1991

Garnet and Pyroxenes in the Mantle: A Test of the Majorite Fractionation Hypothesis

CLAUDE HERZBERG

Department of Geological Sciences, Rutgers University, New Brunswick, New Jersey

TIBOR GASPARIK

Mineral Physics Institute, Department of Earth and Space Sciences
State University of New York, Stony Brook

Experimental data are reported for the compositions of garnets and pyroxenes that coexist with liquid in the system CaO-MgO-Al_2O_3-SiO_2 (CMAS) at 80-160 kbar. All experiments were run using the uniaxial split sphere apparatus at Stony Brook. Our data have permitted a refinement of Gasparik's (1990a) thermodynamic analysis of garnets and pyroxenes that occur at and below the solidus; our results should provide precise estimates of the temperature-pressure conditions at which peridotite and garnet xenoliths equilibrated in the mantle. An examination is also made of the composition of garnet that crystallizes as a liquidus phase; it is demonstrated to be a function of both composition and pressure. Pressure has the effect of changing the composition of garnet from pyropic at around 80 kilobars to pyroxene-like (majorite) at pressures in excess of 140 kbar, changes that mirror those seen for garnets in the subsolidus. Failure to consider the effects of pressure on the composition of liquidus garnet can result in an erroneous test of the hypothesis that garnet fractionation occurred in early Earth history. It is shown that primitive mantle peridotite could have formed as a liquid by 35% majorite garnet fractionation from a CV chondrite like Allende at 200-260 kbar. These results support the hypothesis that extensive or possibly total melting occurred during the growth of the Earth by accretion of planetesimals (e.g., Davies, 1985; Abe and Matsui, 1985; Stevenson, 1987; Wetherill, 1990) and that majorite fractionation could have occurred during this time (Ohtani and Sawamoto, 1987). Removal of majorite to the lower mantle during the crystallization of a magma ocean is a successful way of explaining differences in MgO/SiO_2 and CaO/Al_2O_3 between mantle peridotite and chondrite.

INTRODUCTION

Garnets and pyroxenes exhibit considerable chemical variability in response to changes in temperature and pressure. From these changes, it has been possible to position where in the mantle garnet peridotite xenoliths resided prior to excavation, and they yielded the first geological constraints on the geotherm [e.g., *Boyd*, 1973; *Carswell and Gibb*, 1980; *Lane and Ganguly*, 1980; *Finnerty and Boyd*, 1984). Xenoliths of garnet peridotite appear to have equilibrated at pressures in the 30-60 kbar range.

At pressures above 100 kbar, a great deal of pyroxene becomes dissolved into the garnet phase [*Ringwood*, 1967; *Akaogi and Akimoto*, 1977; *Kanzaki*, 1987; *Gasparik*, 1989, 1990a]. The effect of pressure is to expand the stability field of garnet, and garnet becomes majoritic when its chemistry approximates that of pyroxene itself. This was determined experimentally, and the phase relations were reasonably well understood before the first naturally occurring samples were reported as inclusions in diamond [*Moore and Gurney*, 1985] and as xenoliths in kimberlite [*Haggerty and Sautter*, 1990]. It is now generally agreed that garnet is everywhere present in the transition zone of the Earth, although estimates of its abundance vary with opinions on the chemistry of the Earth at that depth.

Paper number 91JB01481.
0148-0227/91/91JB-01481$05.00

Garnet is also the liquidus phase for chondrite, peridotite, and komatiite compositions at high pressures [*Herzberg*, 1983; *Herzberg and O'Hara*, 1985; *Ohtani et al.* 1986; *Takahashi*, 1986; *Herzberg et al.*, 1990]. From this observation emerged the hypothesis that majorite garnet may have fractionated during an early melting and differentiation event [*Herzberg and O'Hara*, 1985; *Ohtani et al.*, 1986; *Ohtani and Sawamoto*, 1987]. The idea is that this process may have yielded upper mantle peridotite formed as a partial melt or a residual liquid from an initially chondritic Earth. This, however, was disputed by *Kato et al.* [1988] and *Agee and Walker* [1988]. From experimental work on the compositions of coexisting garnet and liquid at high pressures, they argued that majorite garnet fractionation was not important because it predicts a geochemistry of upper mantle peridotite that is not observed.

It is clear that a whole range of important geological problems depend on an comprehensive understanding of how the geochemistry of garnet, in addition to its coexisting pyroxenes, varies at high pressures. In this paper we report the results of experimental work on the compositions of garnets and pyroxenes that coexist with liquid in the system CMAS (CaO-MgO-Al_2O_3-SiO_2) between the liquidus and the solidus in the 80-160 kbar range. There is a plethora of experimental data in the subsolidus, and a thermodynamic analysis of these results has been provided by *Gasparik* [1990a]. The compositions of garnets and pyroxenes along the solidus predicted by *Gasparik*'s [1990a] analysis are in excellent agreement with our experimental observations reported below. However, small

differences do exist, and these have permitted a refinement to be made of *Gasparik*'s [1990a] thermodynamic analysis. We now have a fairly complete understanding of how garnet and pyroxenes behave geochemically at all temperatures throughout the upper mantle and transition zone. Although the applications are many, we focus our attention on a test of the majorite fractionation hypothesis.

EXPERIMENTAL METHOD

All experiments were carried out using the 2000 ton split sphere anvil apparatus at Stony Brook. A detailed description of the press, the sample assembly, and the techniques has been given in numerous papers [*Gasparik*, 1989; 1990*a*; *Herzberg et al.*, 1990] and will not be repeated here.

The compositions of the starting materials were restricted to the system CaO-MgO-Al_2O_3-SiO_2, and they are listed in Table 1. These were prepared by mixing together oxide and carbonate reagents and sintering the material at 1200°C for 5 days prior to running. Starting materials were loaded into rhenium containers, and 10 mm size assemblies were used. These were then fired at 1000°C for 1 hour prior to running in order to expel all water.

Run conditions ranged from 80 to 160 kbar, and from 2000 to 2240°C nominal. Run durations were typically 3-5 min at temperature. Thin sections were made of the run products, and the compositions of the garnets and pyroxenes were determined by electron microprobe. The results are listed in Tables 2, 3, and 4. Solidus temperatures are somewhat lower than the nominal temperatures of the experiments, and the values given were estimated from the thermal gradients in the charges; these are about 50°C within 0.7 mm of the hot spot, steepening to around 250°C at the cold end [*Herzberg et al.*, 1990; *Presnall and Gasparik*, 1990]. The error in estimating the solidus from the nominal thermocouple emf and temperature gradient is likely to be about +/- 75°C.

GARNETS AND PYROXENES ON AND BELOW THE SOLIDUS

Experimental Results

The compositions of garnet and pyroxenes that coexist with liquid on the solidus are given in Table 2. The pyroxenes are remarkably homogenous. However, some heterogeneity exists for garnet, particularly in CaO and Al_2O_3. We have observed the greatest variability and the highest alumina contents for garnets immediately below the solidus, and the range of values seen in each experiment is given by one standard deviation about the mean. The high alumina contents of garnets below the solidus are likely to be disequilibrium growth features. In contrast, pyroxene compositions below the solidus are essentially the same as those found elsewhere, demonstrating that reaction

TABLE 1. Compositions of Starting Materials

	Starting Materials			
	1	2	3	4
SiO_2	50.25	53.14	54.58	58.92
Al_2O_3	5.06	3.37	2.53	-
MgO	40.88	39.12	38.23	35.58
CaO	3.81	4.37	4.66	5.50
Total	100.00	100.00	100.00	100.00

Starting materials are 1, chondrite (C); 2, $C_{67}Px_{33}$; 3, $C_{50}Px_{50}$; and 4, Pyroxene (Px). Values are in weight percent.

TABLE 2. Experimental Results

	Chondrite			$C_{67}Px_{33}$			$C_{67}Px_{33}$			$C_{67}Px_{33}$		
	Gt	Cpx	Opx	Gt	Cpx	Opx	Gt	Cpx	Opx	Gt	Cpx	Opx
SiO_2	46.61 (0.41)	57.38 (0.21)	58.61 (0.51)	46.80 (0.46)	57.58 (0.26)	58.78 (0.32)	47.56 (0.29)	57.59 (0.28)	58.75 (0.25)	48.46 (0.85)	58.34 (0.33)	59.81 (0.21)
Al_2O_3	21.81 (0.75)	1.77 (0.17)	2.00 (0.15)	21.69 (0.41)	1.78 (0.06)	1.58 (0.22)	20.53 (0.26)	1.40 (0.19)	1.40 (0.08)	19.17 (1.24)	1.06 (0.13)	1.13 (0.16)
MgO	28.46 (0.57)	31.33 (0.52)	36.84 (0.36)	28.52 (0.19)	32.55 (0.34)	37.58 (0.58)	29.63 (0.33)	32.27 (0.59)	37.42 (0.38)	29.95 (0.55)	32.82 (0.59)	37.89 (0.73)
CaO	3.12 (0.62)	9.02 (0.54)	2.37 (0.39)	3.49 (0.08)	7.89 (0.32)	2.02 (0.64)	3.13 (0.14)	8.39) (0.87)	2.35 (0.32)	3.24 (0.34)	8.18 (0.67)	1.95 (0.54)
Total	100.03	99.52	99.82	100.50	99.80	99.94	100.67	99.65	99.92	100.82	100.40	100.78
O	6.000	6.000	6.000	6.000	6.000	6.000	6.000	6.000	6.000	6.000	6.000	6.000
Si	1.575	1.976	1.973	1.576	1.971	1.975	1.598	1.977	1.977	1.625	1.986	1.992
Al	0.869	0.072	0.079	0.861	0.072	0.063	0.806	0.057	0.056	0.758	0.043	0.044
Mg	1.434	1.608	1.849	1.431	1.661	1.883	1.484	1.652	1.877	1.497	1.665	1.881
Ca	0.113	0.333	0.085	0.126	0.289	0.073	0.113	0.309	0.085	0.116	0.298	0.070
T nominal (°C)		2000			2050			2070			2140	
T solidus (°C)		1950			2000			2035			2065	
P (kbar)		80			90			100			110	
Time (min)		4.0			4.0			3.0			4.0	

Abbreviations are Gt, garnet; Cpx, clinopyroxene; Opx, orthopyroxene; Cpx1, high Ca clinopyroxene; Cpx2, low Ca clinopyroxene. Numbers in parentheses are 1 standard deviation of multiple analyses.

TABLE 2. (continued)

	Chondrite			$C_{50}Px_{50}$			$C_{50}Px_{50}$			Pyroxene	
	Gt	Cpx1	Cpx2	Gt	Cpx1	Cpx2	Gt	Cpx1	Cpx2	Cpx1	Cpx2
SiO_2	49.34 (0.66)	58.02 (0.32)	59.04 (0.45)	52.38 (1.10)	58.13 (0.61)	60.06 (0.73)	55.64 (0.71)	57.60 (0.26)	59.39 (0.38)	57.17 (0.80)	58.80 (0.90)
Al_2O_3	16.94 (1.05)	0.80 (.08)	0.78 (.08)	13.02 (1.55)	0.57 (.06)	0.36 (.06)	6.20 (0.73)	0.28 (0.05)	0.17 (0.04)	0.00	0.00
MgO	31.11 (.71)	32.70 (1.14)	37.45 (.34)	31.78 (.89)	30.70 (.55)	37.39 (.41)	34.98 (0.61)	29.40 (0.49)	38.25 (0.64)	29.10 (0.90)	39.62 (0.46)
CaO	2.85 (.95)	7.91 (1.33)	2.34 (.24)	3.18 (.47)	9.95 (.67)	1.72 (.41)	2.89 (0.92)	12.21 (0.50)	1.92 (0.73)	13.06 ((0.79)	1.27 (0.40)
Total	100.24	99.43	99.61	100.36	99.35	99.53	99.71	99.50	99.73	99.33	99.69
O	6.000	6.000	6.000	6.000	6.000	6.000	6.000	6.000	6.000	6.000	6.000
Si	1.663	1.993	1.992	1.760	2.008	2.021	1.881	2.002	2.000	1.998	1.982
Al	0.673	0.032	0.031	0.516	0.023	0.014	0.247	0.011	0.007	0.000	0.000
Mg	1.563	1.674	1.884	1.592	1.581	1.875	1.763	1.523	1.920	1.516	1.990
Ca	0.103	0.291	0.085	0.114	0.368	0.062	0.105	0.454	0.069	0.489	0.046
T nominal(°C)		2150			2220			2240			2200
Solidus (°C)		2100			2150			2180			2200
P (kbar)		120			130			140			150
Time (min)		4.0			5.0			4.0			4.0

rates involving garnet are somewhat slower than those for pyroxene. High alumina garnets are also seen on the liquidus, but these are unrelated to those for garnets below the solidus. In the presence of a melt phase, the garnets tend to become much more uniform in composition, and the increase in alumina content from the solidus to the liquidus is an equilibrium feature that has been well documented in other experiments [*Herzberg et al.*, 1990].

The raw data from Table 2 are shown in Figure 1. The effect of pressure is most evident in garnet, which changes from being pyropic to majoritic throughout the 80-140 kbar range. The trend is similar to that observed by *Gasparik* [1989] at lower temperatures, except that it is displaced to lower contents of CaO. This is consistent with a temperature dependence to the grossular content of garnet, first reported by *Yamada and Takahashi* [1984]. Pressure also affects the mutual solubility of coexisting pyroxenes. Although the amount of enstatite dissolved in high Ca clinopyroxene is extremely high at all pressures, pressure tends to strongly reduce it in the 130-140 kbar range. This was predicted to occur by *Gasparik* [1990a], and arises when orthopyroxene (Pbca) transforms to a high-pressure clinoenstatite structure (C2/c) [*Pacalo and Gasparik*, 1990] at around 116 kbar.

Another look at our solidus garnet data is provided in Figure 2. The important observation is that there is extremely good agreement between our experimentally observed garnets and those predicted by the thermodynamic model of *Gasparik* [1990a]. This prediction is based on an extrapolation to solidus temperatures of reversed data in the 1250-1750°C range and run at times of 5.8 to 7.1 hours [*Gasparik*, 1989; 1990a]. These long duration experiments compare with run times of about 4 min at 2000-2240°C in the experiments reported here and demonstrate once again that equilibrium is reached within minutes in the presence of a silicate melt phase [*Herzberg et al.*, 1990]. There is, however, some disagreement between our results and those predicted by *Gasparik* [1990a]. The discrepancy at 140 kbar arises from the simplified thermodynamic treatment of the garnet, the simplification being the assumption that it behaves as an ideal pseudobinary system. The present model, shown as "this work" and discussed below, introduces some nonideality and results in a greatly improved description of even the low-temperature data.

A detailed look at our low calcium pyroxene compositions is given in Figure 3. As expected, the Al_2O_3 content is extremely low, and we draw attention to the high level of precision that has never been achieved before. These improved data yield contents of alumina that are signficantly higher than those predicted by *Gasparik* [1990a]. This is important because these contents are typical of those seen in orthopyroxenes from garnet peridotite xenoliths, indicating that our data hold considerable promise for improved thermobarometry of mantle rocks.

Thermodynamic Evaluation of the Results

The approach is identical to the one used by *Gasparik* [1990a]. The main emphasis is on calculating the isopleths which indicate the compositions of coexisting orthopyroxene, clinopyroxene, and garnet, an assemblage that is a thermobarometer for garnet peridotites in the mantle.

The CMAS system is fairly complex. To make the calculation of the phase relations possible, the simplifications discussed by *Gasparik* [1987] were adopted. For the assemblage orthopyroxene + clinopyroxene + garnet, the calcium content

TABLE 3. Liquidus Garnet Compositions

	Starting Material						
	1	2	2	2	1	3	3
P kbar	80	90	100	110	120	130	140
SiO_2	46.75	46.81	47.56	48.13	49.14	52.21	54.55
Al_2O_3	22.24	22.15	20.35	18.60	17.36	12.28	7.84
MgO	29.08	28.27	29.63	30.34	31.94	32.39	35.42
CaO	2.14	3.47	3.13	2.49	1.66	3.36	1.89
Total	100.21	100.70	100.67	99.56	100.10	100.24	99.70
O	6.000	6.000	6.000	6.000	6.000	6.000	6.000
Si	1.572	1.572	1.598	1.631	1.653	1.760	1.841
Al	0.881	0.877	0.806	0.743	0.688	0.488	0.312
Mg	1.457	1.415	1.484	1.533	1.602	1.627	1.782
Ca	0.077	0.125	0.113	0.090	0.060	0.121	0.068

See Table 1 for starting materials.

of orthopyroxene and garnet is low. By avoiding a rigorous treatment of the calcium solubility in these, the task is simplified and similar to the calculation of phase relations on the enstatite-pyrope join. In clinopyroxene, mixing in the two octahedral sites is mutually independent [*Gasparik*, 1984], indicating that a two-pyroxene thermometer from data on the enstatite-diopside join can be used in alumina-bearing systems without modification.

The procedure of fitting the new data to derive improved thermodynamic parameters involved three steps:

1. Modification of the model for the enstatite-diopside join [*Gasparik*, 1990b].
2. Modification of the model for the enstatite-pyrope join [*Gasparik*, 1990a].
3. Extension of the phase relations in the enstatite-pyrope system to the system CMAS.

Enstatite-diopside join. The phase relations on the enstatite-diopside join ($Mg_2Si_2O_6$-$CaMgSi_2O_6$) considered here include three pyroxene solid solutions with six end-members; these are orthopyroxene (OEn-ODi), high clinopyroxene (CEn-CDi), and high-pressure clinopyroxene (PCEn-PCDi). Experimental data used are the large data set at 1 bar to 60 kbar summarized by *Carlson and Lindsley* [1988; Table 1], the data of *Gasparik* [1989] at 100 kbar, and the data presented here (Table 2). The new data were fitted to the equations of *Gasparik* [1990a]:

$$RT \ln a_{En} = RT \ln X_{En} + A_G X^2_{Di} + B_G(4X^3_{Di} - 3X^2_{Di})$$
$$RT \ln a_{Di} = RT \ln X_{Di} + A_G X^2_{En} + B_G(3X^2_{En} - 4X^3_{En})$$

yielding the following parameters (J, bar, K):

$$A_G(\text{Cpx}) = 29{,}270 - 0.01P$$
$$B_G(\text{Cpx}) = -2{,}800 + 0.03P$$
$$A_G(\text{Opx}) = A_G(\text{PCpx}) = 20{,}000$$

For the equilibria

$$\text{OEn} = \text{CEn} \quad (1)$$
$$\text{ODi} = \text{CDi} \quad (2)$$
$$\text{OEn} = \text{PCEn} \quad (3)$$
$$\text{ODi} = \text{PCDi} \quad (4)$$

the Gibbs energy equations are

$$\Delta G(1) = 3{,}457 - 1.95T + 0.048P - 10^{-7}P^2$$
$$\Delta G(2) = -32{,}845 + 12T - 0.16P$$
$$\Delta G(3) = 5{,}000 + 3.72T - 0.12P$$
$$\Delta G(4) = -15{,}000 + 0.15P$$

An important new contribution of this study is the observation that the content of calcium in the M2 site of clinopyroxene is fairly constant along the solidus, close to 30% in the pressure range of 80-120 kbar. Thus the corresponding isopleth in our new model coincides with the solidus. The calcium contents at 130 and 140 kbar place direct constraints on the volume change of the orthopyroxene to high-pressure clinopyroxene transition [*Pacalo and Gasparik*, 1990]. The resulting value of 1.2 cm^3/mol is less than the value of 2 cm^3/mol predicted by *Gasparik* [1989]; this early estimate was based on the assumption that the transformation in the $Mg_2Si_2O_6$ pyroxene is analogous to the orthopyroxene-clinopyroxene transformation in $Mg_2Ge_2O_6$ [*Ross and Navrotsky*, 1988], for which the volume change is 2.34 cm^3/mol. However, the volume change in $Mg_2Si_2O_6$ is still substantial, and the analogy is still likely to be valid.

All parameters which are not pressure dependent are identical to the model of *Gasparik* [1990b]. Thus the 1 bar data of *Carlson* [1988] are fitted equally well. The fit to the high-pressure data is not as good as in the model of *Gasparik* [1990b]. However, the discrepancies are mostly limited to the orthopyroxene compositions and thus will not affect two-pyroxene thermometry which is based on the clinopyroxene compositions. At 15 kbar, the equilibrium amongst orthopyroxene, clinopyroxene, and pigeonite is at 1430°C, slightly lower than 1465°C reported by *Schweitzer* [1982] but close to 1436°C estimated by *Carlson and Lindsley* [1988].

TABLE 4. Experimental Results for Pyroxene Starting Composition

	P, kbar	
	150	160
T nominal °C	2200	2240
T solidus °C	2200	2200
Time, min	4.0	4.0
Crystallization Sequence	L	L
	L + Cpx2	L + Gt
	L + Cpx2 + Cpx1	Gt
	Cpx2 + Cpx1	Gt + Cpx1

Abbreviations are L, liquid; Gt, garnet; Cpx1, high Ca clinopyroxene; and Cpx2, low Ca clinopyroxene.

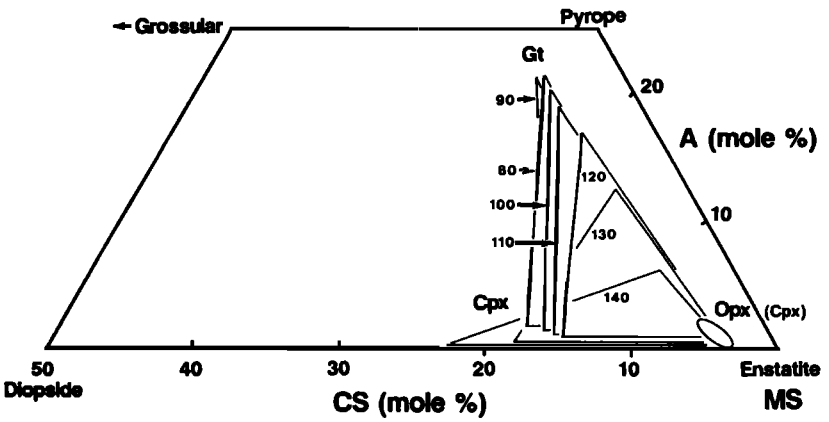

Fig. 1. Raw experimental data of garnet and pyroxene compositions on the solidus at the pressures indicated (in kilobars), from Table 2.

Enstatite-pyrope join. The phase relations on the enstatite-pyrope join include assemblages which are close analogues of spinel (Sp) and garnet (Gt) peridotites. Experimental constraints have until now been limited to pressures below 40 kbar [*MacGregor*, 1974; *Danckwerth and Newton*, 1978; *Perkins et al.*, 1981; *Gasparik and Newton*, 1984]. Our new data are important because they largely remove uncertainties associated with the potentially model-dependent extrapolation of the low pressure data to higher pressures, far beyond the experimental range, and they have resulted in substantial improvement in thermobarometry of mantle-derived garnet peridotites. In parameterizing our data, we used the mixing properties for the solid solution pyrope (Py; $Mg_3Al_2Si_3O_{12}$)-majorite (Mj; $Mg_4Si_4O_{12}$) from *Gasparik* [1990a] and assumed ideal mixing between enstatite (OEn; $Mg_2Si_2O_6$) and Mg-Tschermak (MgTs; $MgAl_2SiO_6$). The equations of interest and their parameters (J, bar, K) are

$$\text{OEn} + \text{Sp} = \text{MgTs} + \text{Fo} \qquad (5)$$

$$RT \ln X_{\text{MgTs}} - RT \ln X_{\text{OEn}} + \Delta G(5) = 0$$

$$\Delta G(5) = 23{,}000 - 2.3T + 0.04P$$

$$\text{OEn} + \text{MgTs} = \text{Py} \qquad (6)$$

$$RT \ln a_{\text{Py}} - RT \ln X_{\text{MgTs}} - RT \ln X_{\text{OEn}} + \Delta G(6) = 0$$

$$RT \ln a_{\text{Py}} = 2RT \ln X_{\text{Py}} - 4TX^2_{\text{Mj}} - 20T(3X^2_{\text{Mj}} - 4X^3_{\text{Mj}})$$

$$\Delta G(6) = 8{,}700 - 93T + 19T^{1.2} - (0.83 - 28 \times 10^{-7}P)P$$

$$2\text{OEn} = \text{Mj} \qquad (7)$$

$$RT \ln a_{\text{Mj}} - 2RT \ln X_{\text{OEn}} + \Delta G(7) = 0$$

$$RT \ln a_{\text{Mj}} = 2RT \ln X_{\text{Mj}} - 4TX^2_{\text{Py}} - 20T(4X^3_{\text{Py}} - 3X^2_{\text{Py}})$$

$$\Delta G(7) = 184{,}700 + 3.44T - 1.24P$$

The system CMAS. The calcium content of orthopyroxene is very low at all pressures. To simplify the calculation of the orthopyroxene isopleths, the calcium content of orthopyroxene was neglected. However, the alumina content of orthopyroxene had to be adjusted to compensate for the effect of calcium [*Gasparik*, 1987], so that X^{M1}_{Al} (Opx in model MAS) = $1.04X^{M1}_{Al}$ (Opx in CMAS). Orthopyroxene is then treated as an ideal binary solution with the components enstatite and Mg-Tschermak.

Garnet in the CMAS system is a reciprocal solution of pyrope (Py), grossular (Gr), Mg-majorite (Mj; $Mg_4Si_4O_{12}$), and Ca-

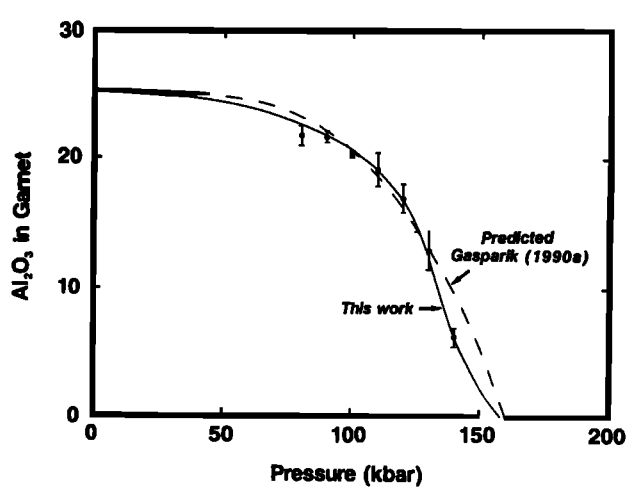

Fig. 2. Experimentally observed alumina contents (weight %) of garnets coexisting with pyroxenes on the solidus (Table 2) and a thermodynamic evaluation (this work), compared with contents predicted by *Gasparik* [1990a].

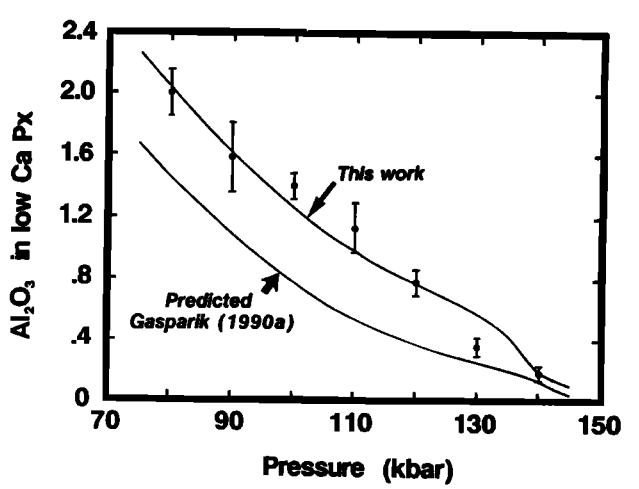

Fig. 3. Experimentally observed alumina contents (weight %) of orthopyroxene and low calcium clinopyroxene coexisting with clinopyroxene and garnet on the solidus (Table 2) and a thermodynamic evaluation (this work), compared with contents predicted by *Gasparik* [1990a].

majorite (CaMj; $Ca_3MgSi_4O_{12}$). To simplify the calculation of the garnet isopleths, garnet is treated as a pseudobinary solution of (Py, Gr)-(Mj, CaMj). The first appearance of garnet on the enstatite-diopside join is controlled by the mixing properties of Mj-CaMj garnet and by the high-pressure clinoenstatite (PCEn) to majorite reaction [*Gasparik*, 1990a]. To simplify the approach, the mixing of calcium and magnesium in the octahedral site of garnet was neglected; it is unlikely that calcium would enter the octahedral site. The excess parameters for the mixing of calcium and magnesium on the dodecahedral site were estimated from the displacements of two reactions. One of these, at lower pressures, is the displacement of the spinel to garnet reaction caused by the grossular content of garnet in CMAS with respect to pure pyrope in MAS [*Gasparik*, 1984]. The second of these, at higher pressures, arises from the displacement of the high-pressure clinoenstatite to majorite reaction, caused by the calcium content of garnet (X_{Ca}) with respect to the same reaction in the $MgSiO_3$ system. The results are (J, bar, K)

$$2\text{PCEn} = \text{Mj} \qquad (8)$$

$$RT \ln a_{Mj} - 2RT \ln X_{PCEn} + \Delta G(8) = 0$$

$$RT \ln a_{Mj} = 3RT \ln (1 - X_{Ca}) + (93T - 0.3P)X^2_{Ca}$$

$$\Delta G(8) = 174{,}700 - 4.0T - 1.0P$$

In the system CMAS, the mole fraction of calcium in the dodecahedral site of garnet is almost independent of temperature and pressure. It is 0.13-0.15 at 15-30 kbar [*Howells and O'Hara*, 1978; *Jenkins and Newton*, 1979; *Perkins and Newton*, 1980], and at 157 kbar and 1650°C on the enstatite-diopside join [*Gasparik*, 1989]. In this model, a constant value of 0.14 was adopted for all temperatures and pressures. Because of this simiplified treatment, the model value underestimates the calcium content of garnet at lower temperatures [*Gasparik*, 1989], and overestimates them at solidus temperatures (this study).

The mixing properties of the garnet pseudobinary join (Py, Gr) - (Mj, CaMj) were derived from the data of *Gasparik* [1989] and the data in this study, yielding (J, bar, K)

$$RT \ln a_{Mj} = 3RT \ln 0.86 + 2RT \ln (1 - X_{Al}) + 0.14^2(93T - 0.3P) - (86{,}000 - 60T + 0.4P)(4X^3_{Al} - 3X^2_{Al}) - 20T(12X^4_{Al} - 16X^3_{Al} + 5X^2_{Al})$$

$$RT \ln a_{Py} = 3RT \ln 0.86 + 2RT \ln X_{Al} + 0.14^2(93T - 0.3P) - (86{,}000 - 60T + 0.4P)[3(1 - X_{Al})^2 - 4(1 - X_{Al})^3] - 20T[12(1 - X_{Al})^4 - 16(1 - X_{Al})^3 + 5(1 - X_{Al})^2]$$

where X_{Al} is the mole fraction of aluminum in the octahedral site of garnet.

The orthoenstatite to high-pressure clinoenstatite transition in the system MAS is displaced to slightly higher pressures with addition of calcium. To account for this displacement, slightly different parameters were used for this reaction. For the equilibrium

$$\text{OEn} = \text{PCEn (in CMAS)} \qquad (9)$$

$$\Delta G(9) = 4{,}900 + 3.8T - 0.12P$$

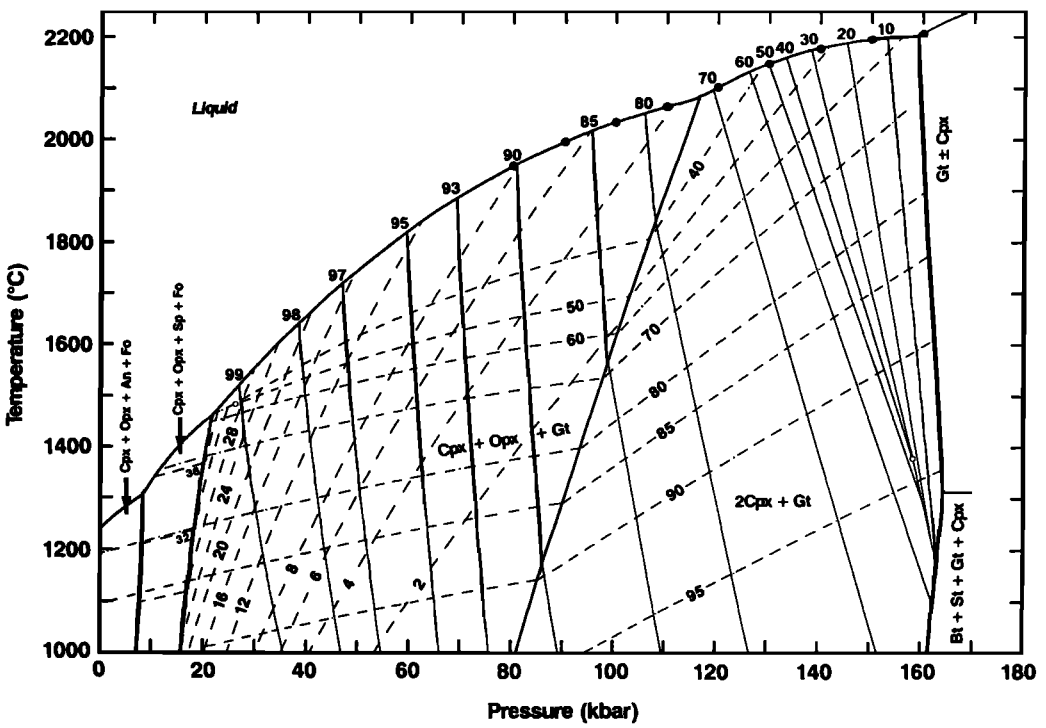

Fig. 4. Phase diagram for the system CaO-MgO-Al_2O_3-SiO_2. Heavy solid lines are univariant boundaries and the solidus. Light solid lines are isopleths indicating the mole percent of aluminum (100Al/6 oxygens) in the octahedral site of garnet. Light dashed lines are the pyrope content (100Al/6 oxygens) of orthopyroxene. Light dot-dashed are the mole percent of calcium (100Ca/6 oxygens) in the M2 site of diopsidic clinopyroxene; the 30% isopleth coincides with the solidus. Small open circles are singular points terminating miscibility gaps. Large solid circles position the solidus in these experiments (Tables 2 and 4); the solidus is slightly elevated in the 2Cpx + Gt field compared to that given by *Herzberg et al.* [1990] owing to the stabilization of high-pressure clinoenstatite. The solidus at low pressures is from *Presnall et al.* [1979].

Analytical solutions to the above equations are summarized in Figure 4, a phase diagram for peridotite compositions. Although this diagram is similar to its progenitor [*Gasparik*, 1990a, Figure 7], the improvements should yield improved estimates of the temperatures and pressures at which samples from the mantle equilibrated prior to excavation.

GARNETS ON THE LIQUIDUS

An examination is now made of the effect of pressure on the composition of garnet that crystallizes as a liquidus phase. The liquidus garnets listed in Table 3 have been plotted in Figures 5 and 6 together with data reported by *Ohtani et al.* [1986], *Ohtani and Sawamoto* [1987], *Ohtani et al.* [1989], *Kato et al.* [1987], *Kato et al.* [1988], *Ito and Takahashi* [1987], *Wei et al.* [1990], *Agee* [1990], and *Herzberg et al.* [1990]. In all cases, these are liquidus garnets that crystallized from highly magnesian peridotite, komatiite, and chondrite compositions. It should be noted that with one exception the liquid compositions used were the bulk compositions in the experiments. Many investigators have attempted to determine directly the composition of the liquid phase adjacent to their liquidus garnets by defocused electron microprobe analysis [e.g., *Ohtani et al.*, 1986; *Kato et al.*, 1988]. The problem with this approach is that the liquid phase quenches to a dense matt of quench crystals, and this material is difficult to analyse with precision. An example is given in Table 5. This is the result of defocused beam analyses of the quench liquid portion adjacent to liquidus garnets for an experiment at 140 kbar reported by *Herzberg et al.* [1990; P-12], a result that is fairly close to the actual liquid composition. Use of liquid compositions determined in this way also yields diagrams similar to Figures 5 and 6. However, the error is large and propagates to huge uncertainties in such parameters as CaO/Al_2O_3 (Table 5). Use of a well-measured bulk composition will minimize these uncertainties and should be a good approximation of the liquid composition for experiments that contain only a small number of garnet crystals immediately on the liquidus. The liquid and bulk compositions will become increasingly disparate and the error increasingly magnified for experiments in which the abundance of garnet is large or for garnets that are located somewhere between the liquidus and the solidus; examples of these problems are discussed below.

TABLE 5. Defocussed Beam Analysis of Quench Liquid

	Quench[1] Liquid	Sample[2]
SiO_2	47.66 (2.59)	47.16 (0.94)
Al_2O_3	5.39 (2.92)	6.36 (0.13)
MgO	40.54 (8.03)	41.93 (0.84)
CaO	5.70 (2.99)	5.59 (0.11)
Total	99.29 (9.42)	101.04 (1.27)
CaO/Al_2O_3	1.06 (0.80)	0.88 (0.02)
Al_2O_3/SiO_2	0.11 (0.06)	0.13 (0.00)

1 Analyst C. T. Herzberg
2 Analyst M. J. Carr [*Herzberg et al.*, 1990].
Numbers in parentheses are one standard deviation.

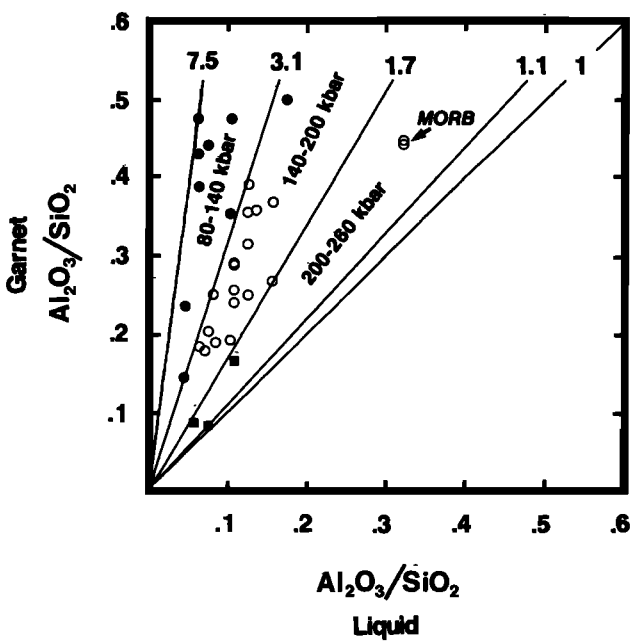

Fig. 5. Compositions of liquidus garnets as a function of composition and pressure (weight ratios). Solid circles are all data in the 80-140 kbar range. Open circles are all data in the 140-200 kbar range. Solid squares are all data in the 200-260 kbar range. Numbered slopes are values of K_{10}. Data base is given in the text. Liquid compositions are the bulk compositions, except the 260 kbar data of *Agee* [1990] which is a defocussed beam analysis; use of Agee's Allende bulk composition from either *McCarthy and Ahrens* [1972] or from *Clarke et al.* [1970] yields $K_{10} < 1.0$ (unlikely), indicating that the bulk composition is not a good indicator of the liquid composition for this experiment (see text). MORB data is at 200 kbar nominal [Kato et al., 1988].

Alumina partitions preferentially into the garnet phase, but this varies considerably with pressure. For example, the partitioning changes from strong at around 80 kbar where the Al_2O_3 content of garnet is around 22% (Table 3) to very weak at 250 kbar where Al_2O_3 in garnet is typically 4% [*Ohtani and Sawamoto*, 1987; *Agee*, 1990]. For the exchange reaction

$$Al_2O_{3,L} + SiO_{2,G} = Al_2O_{3,G} + SiO_{2,L} \quad (10)$$

the partition coefficient can be written:

$$K_{10} = \frac{(Al_2O_3/SiO_2)_G}{(Al_2O_3/SiO_2)_L}$$

Figure 5 shows that the effect of pressure is large, resulting in a reduction of K_{10} from around 7.5 at about 80 kbar to nearly 1 at around 260 kbar. This is another way of showing that garnets which crystallize from ultrabasic liquids change from being highly aluminous at low pressures to majoritic, or pyroxene-like, in the 200-260 kbar range. These compositional changes for liquidus garnets mirror the changes observed for garnets at and below the solidus (Figure 4).

Pressure also has an important effect on how Ca and Al partition between garnet and liquid, and this is shown in Figure 6. For the exchange reaction

$$CaO_L + Al_2O_{3,G} = CaO_G + Al_2O_{3,L} \quad (11)$$

the partition coefficient is

$$K_{11} = \frac{(CaO/Al_2O_3)_G}{(CaO/Al_2O_3)_L}$$

It can be seen that the effect of pressure is to increase K_{11} substantially from around 0.1 at around 80 kbar to around 0.71 at around 260 kbar. Again this occurs because garnets that crystallize from ultrabasic liquids change from pyropic to majoritic with increasing pressure.

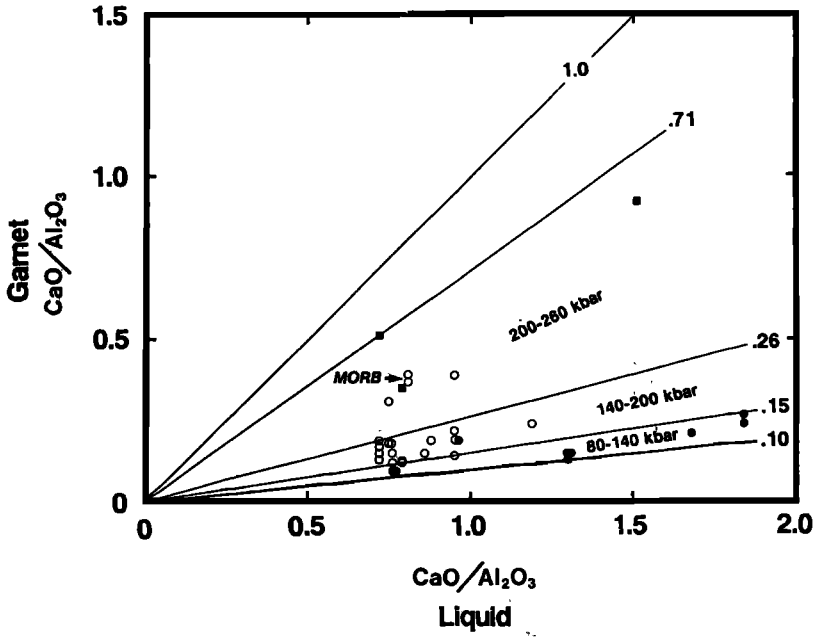

Fig. 6. Compositions of liquidus garnets as a function of composition and pressure (weight ratios). Symbols are same as Figure 5. Numbered slopes are values of K_{11}. Liquid compositions are the bulk compositions, except the 260 kbar data of *Agee* [1990] which is a defocussed beam analysis; use of Agee's bulk composition yields $K_{11} > 1.0$ (unlikely). [MORB data is at 200 kbar nominal [*Kato et al.*, 1988].]

A close inspection of Figure 6 shows that a few garnets do not plot in their proper fields. It is likely that most of these are not actually liquidus garnets but instead are garnets that crystallized somewhere between the liquidus and the solidus. This is based on the observation that CaO/Al_2O_3 for garnet increases substantially with a reduction in temperature from the liquidus to the solidus [*Herzberg et al.*, 1990, Figure 12], and use of the bulk composition instead of an actual liquid composition will give rise to an error (see also discussion above). Additionally, three garnets crystallized from a mid ocean ridge basalt (MORB) composition in the experiments of *Kato et al.* [1988; BA 271, 272, 273; 10.5% MgO] do not plot in their proper fields, indicating that K_{10} and K_{11} may be somewhat affected by bulk composition. Although this is of thermodynamic interest, it is not geologically important because liquids in the range of hundreds of kilobars are not basaltic. Instead, they are invariably ultrabasic in composition [*Herzberg et al.*, 1990]. The content of MgO ranges from 25% to 42% for the komatiite, chondrite, and peridotite compositions which were used to construct Figures 5 and 6. For this spectrum of ultrabasic compositions the experimental data show no systematic variations in K_{10} and K_{11} with MgO, so that Figures 5 and 6 should be appropriate for all high pressure possibilities involving ultrabasic magmas.

A TEST OF THE MAJORITE FRACTIONATION HYPOTHESIS

The hypothesis that upper mantle peridotite is a solidified liquid that was derived from chondrite by fractionation of garnet is reasonable because garnet is the liquidus phase for chondrite compositions in the 100-250 kbar range [*Ohtani et al.*, 1986; *Ohtani and Sawamoto*, 1987; *Herzberg et al.*, 1990]. However, *Kato et al.* [1988] and Agee and Walker [1988] rejected this idea on the grounds that garnet fractionation would have yielded liquids that do not have the geochemical properties of mantle peridotite. We are now in the position to reevaluate the conclusions of *Kato et al.* [1988] and *Agee and Walker* [1988] from our understanding of the geochemistry of majorite garnet as a liquidus phase (Figures 5 and 6).

Figures 7, 8, and 9 show the compositions of liquids which are produced by the fractionation of garnet from a bulk Earth having the composition of Allende, a CV carbonaceous chondrite. We have selected Allende rather arbitrarily because

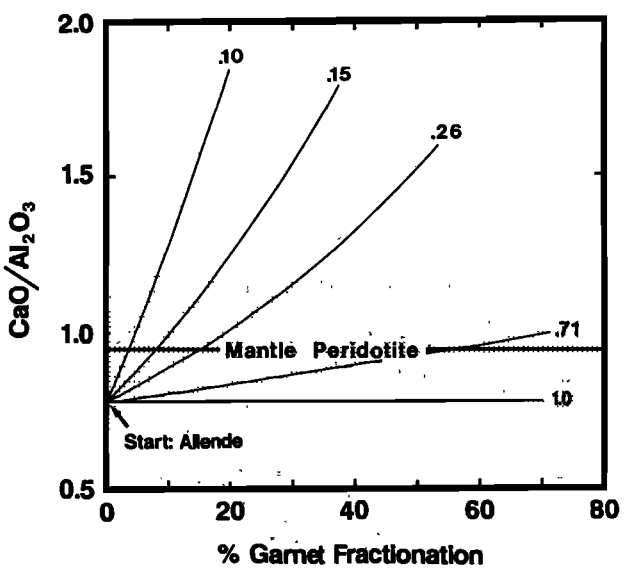

Fig. 7. Lime/alumina weight percent ratios of liquids formed by fractional crystallization of garnet from an Allende carbonaceous chondrite composition. Data for Allende is from *McCarthy and Ahrens* [1972]. CaO/Al_2O_3 for average mantle peridotite is from *Herzberg et al.* [1990], and the range shown is one standard deviation. Numbered lines are the partition coefficient K_{11}.

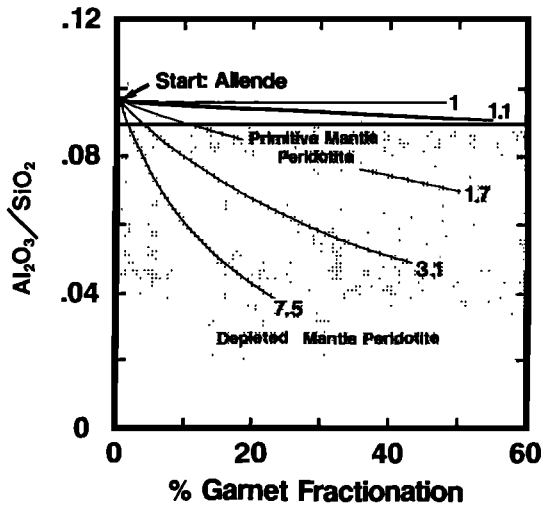

Fig. 8. Alumina/silica weight percent ratios of liquids formed by fractional crystallization of garnet from an Allende starting material. Peridotite data base is from *Herzberg et al.* [1990]. Numbered lines are the partition coefficient K_{10}.

all CV meteorites yield similar results. The compositions of garnets that crystallize from a liquid of a known composition were computed by parameterizing the geochemistry of the liquidus garnet data base to the following equations:

$$SiO_{2,G} = \frac{213}{[(K_{10}Al_2O_{3,L}/SiO_{2,L})(2 + K_{11}CaO_L/Al_2O_{3,L}) + 3.56]}$$

$$Al_2O_{3,G} = SiO_{2,G}K_{10}Al_2O_{3,L}/SiO_{2,L}$$
$$CaO_G = Al_2O_{3,G}K_{11}CaO_L/Al_2O_{3,L}$$
$$MgO_G = 100 - SiO_{2,G} - Al_2O_{3,G} - CaO_G$$

where the oxides are in weight percent.

Inspection of Figure 7 shows that the amount of garnet fractionation that is necessary to yield CaO/Al_2O_3 for a liquid having the composition of average mantle peridotite varies considerably, depending on the value of the partition coefficient. For fractionation in the 80-140 kbar pressure range, K_{11} = 0.10 to 0.15 (Figure 6), and only 4-8% garnet removal can be accomodated. At pressures in the 160-200 kbar range, K_{11} = 0.15 to 0.26, and 8-15% garnet fractionation is possible. In the 200-260 kbar range, the garnets are more majoritic in chemistry, and 15-60% can be removed. At pressures greater than this amount, no solution is possible because perovskite is likely to become the liquidus phase [*Ohtani and Sawamoto*, 1987; *Agee*, 1990].

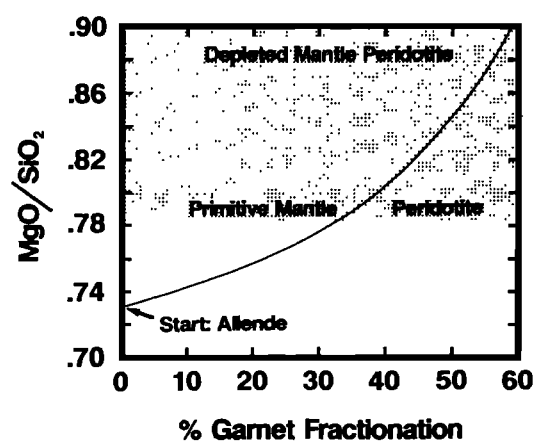

Fig. 9. Magnesia/silica weight percent ratios of liquids formed by fractional crystallization of garnet from an Allende starting material.

A wide range of Al_2O_3/SiO_2 exists for mantle peridotite, and the range is shown in Figure 8. Those compositions exhibiting the lowest values are likely to be depleted mantle peridotite, formed as residues during partial melting of primitive mantle peridotite [e.g., *Palme et al.*, 1978]; we are therefore primarily concerned with the formation of primitive mantle peridotite. Figure 8 shows once again that it could have formed as a liquid by the removal of around 2% garnet at 80 kbar (K_{10} = 7.5) to about 60% garnet at 260 kbar (K_{10} = 1.1).

Garnet fractionation provides a simple mechanism for deriving mantle peridotite from a chondritic source that is enriched in silica. Figure 9 shows that approximately 35% majorite garnet fractionation is necessary to form a liquid with the composition of primitive mantle peridotite. Although only 2-8% pyropic garnet fractionation at low pressures can yield mantle-like CaO/Al_2O_3 and Al_2O_3/SiO_2, this small amount is insufficient to increase MgO/SiO_2 to values that characterize primitive mantle peridotite. This point illustrates the need to consider all elements and elemental ratios simultaneously, with a unique solution possible only by approximately 35% majorite fractionation at pressures in the 200-260 kbar range. Removal of moderate amounts of majorite to the lower mantle during the crystallization of a magma ocean is clearly a very successful way of explaining differences in MgO/SiO_2 and CaO/Al_2O_3 between mantle peridotite and chondrite.

Before any experimental data were available, *Herzberg and O'Hara* [1985] proposed that mantle peridotite could have been derived from chondrite by melting and removal of garnet or pyroxene in the 100-150 kbar range; specifically, it was suggested that mantle peridotite has the composition of a liquid that was uniquely determined by a eutectic at 100-150 kbar. Since that time, a great deal of experimental data have been obtained, and it is now known that the melting of chondrites at 100-150 kbar occurs at peritectic points, and these have compositions that are higher in SiO_2 and CaO/Al_2O_3 than primitive mantle peridotite [*Herzberg et al.*, 1990; C.T. Herzberg, Depth and drgree of melting of komatiites, submitted to *Journal of Geophysical Research*, 1991). The work presented here also demonstrates that a significant amount of majorite fractionation could not have occurred at 100-150 kbar; much higher pressures, the 200-260 kbar range, would have been needed. The question that then emerges is how peridotite liquids could have formed at these pressures. One possibility is that they are compositionally coincident with liquids at a very high pressure invariant point involving liquid + majorite + perovskite + magnesiowustite, a phase assemblage that has been observed in the experiments of *Ohtani and Sawamoto* [1987] and *Agee* [1990]. Another possibility is that these liquids are not coincident with an invariant point and that majorite fractionation in the 200 kbar range was the result of some kind of a stochastic event, caused possibly by the operation of imperfect fractional crystallization in a turbulently convecting and rapidly cooling magma ocean. The testing of these important possibilities must await the acquisition of additional experimental data in the 200-250 kbar range.

The C1 carbonaceous chondrites are another possible composition for the Earth, material that most closely resembles the composition of the photosphere of the Sun [*Anders and Grevesse*, 1989]. Compared to the CV chondrites, they are

enriched in silica and depleted in alumina [e.g., *Jagoutz et al.*, 1979]. However, the difficulty with a C1 chondrite such as Orgueil is that primitive mantle peridotite cannot be derived from it by the removal of garnet, and this is illustrated in Figure 10. The problem is that C1 chondrites are depleted in alumina compared to primitive mantle peridotite, as is manifest in lower Al_2O_3/SiO_2, and removal of garnet lowers Al_2O_3/SiO_2 even more. This suggests that if the Earth was formed from planetesimals with a C1-type chondrite composition, some other differentiation mechanism was involved.

Kato et al. [1988] suggested that large amounts of garnet fractionation (50%) would have been necessary in order to generate the MgO/SiO_2 of mantle peridotite, and they rejected this hypothesis because it would have been accompanied by fractionations of Ca/Al etc. that are not observed. This conclusion, however, is erroneous for the following important reasons: (1). Kato et al. did not consider the effect of pressure on changing the composition of garnet, (2). the analysis of Kato et al. was restricted to an assumed C1 chondritic Earth, which is demonstrably a problem (Figure 10), but they did not consider the CV chondrites that work so well (Figures 7, 8, and 9) (3). Kato et al. assumed that mantle peridotite is the same as pyrolite, and pyrolite is generally assumed to be chondritic in all elements except Mg/Si. But inspection of actual peridotite samples demonstrates that mantle peridotite is not chondritic in the major elements (for example, see Figure 7 and *Herzberg et al.*, [1990]).

Kato et al. [1988] also argued that majorite garnet fractionation would also yield concentrations of the incompatible lithophile trace elements (e.g., Sm/Yb, Sc/Sm) that are not observed. This is the strongest argument in their favor, but one that is well beyond the scope of this paper. We only wish to point out that this conclusion is based on yet another assumption; that is, samples of primitive mantle peridotite are assumed to be material that is truly primordial and unmodified by magmatic reprocessing throughout the last 4.5 billion years of geological time. However, there is now a growing body of evidence that challenges this view because of the importance of subsequent stages of partial melting with garnet as a residual phase [eg., *Salters and Hart*, 1989]. It is likely that even primitive mantle peridotite is residual to a certain extent, and any second stage reprocessing with garnet in the residue will render ambiguous any test of majorite fractionation. We will show in another paper that chondritic-looking ratios of lithophile trace elements can be produced in mantle peridotite that has suffered subsequent stages of partial melting.

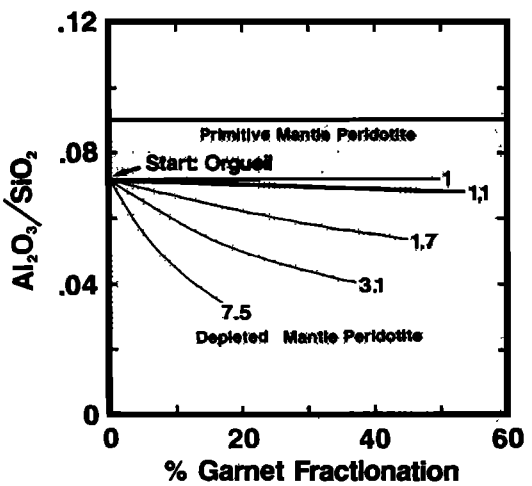

Fig. 10. Alumina/silica weight percent ratios of liquids formed by fractional crystallization of garnet from a C1 chondrite starting material (Orgueil [*Anders and Grevesse*, 1989]). Numbered lines are the partition coefficient K_{10}.

CONCLUSIONS

The major element geochemical behavior of garnet and pyroxenes at all conditions throughout the mantle is now fairly well understood. This includes temperatures that range from the liquidus to the subsolidus. For temperatures at and below the solidus, a rigorous calibration has been made of the effect of pressure on changing the composition of garnet from pyropic at low pressures to pyroxene-like (majorite) at high pressures. A precise determination has also been made of the pyroxene compositions in equilibrium with these high pressure garnets. The results should yield an improved understanding of the temperature-pressure conditions at which peridotite and garnet xenoliths equilibrated in the mantle.

The geochemistry of garnet that crystallizes from ultrabasic liquids is a function of both the composition of the liquid and pressure. Pressure has the effect of changing garnet from pyropic at around 80 kbar to pyroxene-like (majorite) at pressures in excess of 140 kbar, mimicing the changes observed at and below the solidus. Failure to take these effects into account can yield erroneous results in numerical simulations of garnet fractionation at high pressures. It is demonstrated that primitive mantle peridotite could have formed as a liquid by 35% majorite garnet fractionation from a CV chondrite like Allende at 200-260 kbar. These results support the hypothesis that extensive melting occurred during the growth of the Earth by accretion of planetesimals [*Davies*, 1985; *Abe and Matsui*, 1985; *Stevenson*, 1987; *Wetherill*, 1990] and that majorite fractionation could have occurred during this time [*Ohtani and Sawamoto*, 1987]. Removal of moderate amounts of majorite to the lower mantle during the crystallization of a magma ocean is a successful way of explaining differences in MgO/SiO_2 and CaO/Al_2O_3 between mantle peridotite and chondrite.

Acknowledgments. This research was partially supported by National Science Foundation grants EAR 89-16836 to C. Herzberg and EAR 90-03748 to T. Gasparik. The high-pressure experiments reported in this paper were performed in the Stony Brook High Pressure Laboratory, which is jointly supported by the National Science Foundation Division of Earth Sciences (EAR 89-17563) and the State University of New York at Stony Brook. Thanks are extended to Carl Agee and an anonymous reviewer for their comments.

REFERENCES

Abe, Y., and T. Matsui, The formation of an impact-generated H_2O atmosphere and its implications for the early thermal history of the earth, Proc. Lunar Planet. Sci. Conf. 15th, Part 2, *J. Geophys. Res. 90*, suppl., C545-C559, 1985.

Agee, C.B., A new look at differentiation of the Earth from melting experiments on the Allende meteorite, *Nature*, *346*, 834-837, 1990.

Agee, C.B., and D. Walker, Mass balance and phase density constraints on early differentiation of chondritic mantle, *Earth Planet. Sci. Lett.*, *90*, 144-156, 1988.

Akaogi, M., and S. Akimoto, Pyroxene-garnet solid-solution equilibria in the systems $Mg_4Si_4O_{12}$ - $Mg_3Al_2Si_3O_{12}$ and $Fe_4Si_4O_{12}$ - $Fe_3Al_2Si_3O_{12}$

at high pressures and temperatures, *Phys. Earth Planet. Inter.*, *15*, 90-106, 1977.

Anders, E., and N. Grevesse, Abundances of the elements: Meteoritic and solar, *Geochim. Cosmochim. Acta*, *53*, 197-214, 1989.

Boyd, F.R., A pyroxene geotherm, *Geochim. Cosmochim. Acta*, *37*, 2533-2546, 1973.

Carlson, W.D., Subsolidus phase equilibria on the forsterite-saturated join $Mg_2Si_2O_6$-$CaMgSi_2O_6$ at atmospheric pressure, *Am. Mineral.*, *73*, 232-241, 1988.

Carlson, W.D., and D.H. Lindsley, Thermochemistry of pyroxenes on the join $Mg_2Si_2O_6$-$CaMgSi_2O_6$, *Am. Mineral.*, *73*, 242-252, 1988.

Carswell, D.A., and F.G.F. Gibb, Geothermometry of garnet lherzolite nodules with special reference to those from kimberlites of northern Lesotho, *Contrib. Mineral. Petrol.*, *74*, 403-416, 1980.

Clarke, R.S. Jr., E. Jarosewich, B. Mason, J. Nelen, M. Gomez, and J.R. Hyde, The Allende, Mexico, Meteorite Shower, *Smithsonian Contrib. Earth Sci.*, *5*, 53 pp., 1970.

Danckwerth, P.A., and R.C. Newton, Experimental determination of the spinel peridotite to garnet peridotite reaction in the system MgO-Al_2O_3-SiO_2 in the range 900°-1,100°C and Al_2O_3 isopleths of enstatite in the spinel field, *Contrib. Mineral. Petrol.*, *66*, 189-201, 1978.

Davies, G.F., Heat deposition and retention in a solid planet growing by impacts, *Icarus*, *63*, 45-68, 1985.

Finnerty, A.A., and F.R. Boyd, Evaluation of thermobarometers for garnet peridotites, *Geochim. Cosmochim. Acta*, *48*, 15-28, 1984.

Gasparik, T., Two-pyroxene thermobarometry with new experimental data in the system CaO-MgO-Al_2O_3-SiO_2, *Contrib. Mineral. Petrol.*, *87*, 87-97, 1984.

Gasparik, T., Orthopyroxene thermobarometry in simple and complex systems, *Contrib. Mineral. Petrol.*, *96*, 357-370, 1987.

Gasparik, T., Transformation of enstatite-diopside-jadeite pyroxenes to garnet, *Contrib. Mineral. Petrol.*, *102*, 389-405, 1989.

Gasparik, T., Phase relations in the transition zone, *J. Geophys. Res.*, *95*, 15,751-15,769, 1990*a*.

Gasparik, T., A thermodynamic model for the enstatite-diopside join, *Am. Mineral.*, *75*, 1080-1091, 1990*b*.

Gasparik, T., and R.C. Newton, The reversed alumina contents of orthopyroxene in equilibrium with spinel and forsterite in the system MgO-Al_2O_3-SiO_2, *Contrib. Mineral. Petrol.*, *85*, 186-196, 1984.

Haggerty, S.E., and V. Sautter, Ultradeep (greater than 300 kilometers), ultramafic upper mantle xenoliths, *Science*, *248*, 993-996, 1990.

Herzberg, C.T., Solidus and liquidus temperatures and mineralogies for anhydrous garnet-lherzolite to 15 GPa, *Phys. Earth Planet. Inter.*, *32*, 193-202, 1983.

Herzberg, C.T., and M.J. O'Hara, Origin of mantle peridotite and komatiite by partial melting, *Geophys. Res. Lett.*, *12*, 541-544, 1985.

Herzberg, C., T. Gasparik, and H. Sawamoto, Origin of mantle peridotite: Constraints from melting experiments to 16.5 GPa, *J. Geophys. Res.*, *95*, 15,779-15,803, 1990.

Howells, S., and M.J. O'Hara, Low solubility of alumina in enstatite and uncertainties in estimated paleogeotherms, *Philas. Trans. R. Soc. London, Ser. A*, 288, 471-486, 1978.

Ito, E., and E. Takahashi, Melting of peridotite under the lower mantle condition, *Nature*, *328*, 514-517, 1987.

Jagoutz, E., H. Palme, H. Baddenhausen, K. Blum, M. Cendales, G. Driebus, B. Spettel, V. Lorenz, and H. Wanke, The abundance of major, minor, and trace elements in the Earth's mantle as derived from primitive ultramafic nodules, *Proc. Lunar Planet. Sci. Conf.*, *10th*, 2031-2050, 1979.

Jenkins, D.M., and R.C. Newton, Experimental determination of the spinel peridotite to garnet peridotite inversion at 900°C and 1,000°C in the system CaO-MgO-Al_2O_3-SiO_2, and at 900°C with natural garnet and olivine, *Contrib. Mineral. Petrol.*, *68*, 407-419, 1979.

Kanzaki, M., Ultrahigh-pressure phase relations in the system $Mg_4Si_4O_{12}$-$Mg_3Al_2Si_3O_{12}$, *Phys. Earth Planet. Inter.*, *49*, 168-175, 1987.

Kato, T., T. Irifune, and A.E. Ringwood, Majorite partition behavior and petrogenesis of the earth's upper mantle, *Geophys. Res. Lett.*, *14*, 546-549, 1987.

Kato, T., A.E. Ringwood, and T. Irifune, Experimental determination of element partitioning between silicate perovskites, garnets and liquids: constraints on early differentiation of the mantle, *Earth Planet. Sci. Lett.*, *89*, 123-145, 1988.

Lane, D.L., and J. Ganguly, Al_2O_3 solubility of orthopyroxene in the system MgO-Al_2O_3-Si_2: A reevaluation, and mantle geotherm, *J. Geophys. Res.*, *85*, 6963-6972, 1980.

MacGregor, I.D., The system MgO-Al_2O_3-SiO_2: Solubility of Al_2O_3 in enstatite for spinel and garnet peridotite compositions, *Am. Mineral.*, *59*, 110-119, 1974.

McCarthy, T.S., and L.H. Ahrens, Chemical sub-groups amongst HL chondrites, *Earth Planet. Sci. Lett.*, *14*, 97-102, 1972.

Moore, R.O., and J.J. Gurney, Pyroxene solid solution in garnets included in diamond, *Nature*, *318*, 553-555, 1985.

Ohtani, E., and H. Sawamoto, Melting experiment on a model chondritic mantle composition at 25 GPa, *Geophys. Res. Lett.*, *14*, 733-736, 1987.

Ohtani, E., T. Kato, and H. Sawamoto, Melting of a model chondritic mantle to 20 GPa, *Nature*, *322*, 352-353, 1986.

Ohtani, E., I. Kawabe, J. Moriyama, and Y. Nagata, Partitioning of elements between majorite garnet and melt and implications for petrogenesis of komatiite, *Contrib. Mineral. Petrol.*, *103*, 263-269, 1989.

Pacalo, R.E.G., and T. Gasparik, Reversals of the orthoenstatite-clinoenstatite transtition at high pressures and high temperatures, *J. Geophys. Res.*, *95*, 15,853-15,858, 1990.

Palme, H., H. Baddenhausen, K. Blum, M. Cendales, G. Dreibus, H. Hofmeister, H. Kruse, C. Palme, B. Spettel, E. Vilcsek, and H. Wanke, New data on lunar samples and achondrites and a comparison of the least fractionated samples from the earth, the moon and the eucrite parent body, *Proc. Lunar Planet. Sci. Conf.*, *9th*, 25-57, 1978.

Perkins, D., and R.C. Newton, The compositions of coexisting pyroxenes and garnet in the system CaO-MgO-Al_2O_3-SiO_2 at 900°-1,100°C and high pressures, *Contrib. Mineral. Petrol.*, *75*, 291-300, 1980.

Perkins, D., T.J.B. Holland, and R.C. Newton, The Al_2O_3 contents of enstatite in equilibrium with garnet in the system MgO-Al_2O_3-SiO_2 at 15-40 kbar and 900°-1,600°C, *Contrib. Mineral. Petrol.*, *78*, 99-109, 1981.

Presnall, D.C., and T. Gasparik, Melting of enstatite from 10 to 16.5 GPa and the forsterite (Mg_2SiO_4)-majorite ($MgSiO_3$) eutectic at 16.5 GPa: Implications for the origin of the mantle, *J. Geophys. Res.*, *95*, 15,771-15,777, 1990.

Presnall, D.C., J.R. Dixon, T.H. O'Donnell, and S.A. Dixon, Generation of mid-ocean ridge tholeiites, *J. Petrol.*, *20*, 3-35, 1979.

Ross, N.L., and A. Navrotsky, Study of the $MgGeO_3$ polymorphs (orthopyroxene, clinopyroxene, and ilmenite structures) by calorimetry, spectroscopy, and phase equilibria, *Am. Mineral.*, *73*, 1355-1365, 1988.

Ringwood, A.E., The pyroxene-garnet transformation in the Earth's mantle, *Earth Planet. Sci. Lett.*, *2*, 255-263, 1967.

Salters, V.J.M., and S.R. Hart, The hafnium paradox and the role of garnet in the source of mid-ocean-ridge basalts, *Nature*, *342*, 420-422, 1989.

Schweitzer, E., The reaction pigeonite = $diopside_{ss}$ + $enstatite_{ss}$ at 15 kbars, *Am. Mineral.*, *67*, 54-58, 1982.

Stevenson, D.J., Origin of the moon - the collision hypothesis, *Annu. Rev. Earth Planet. Sci.*, *15*, 271-315, 1987.

Takahashi, E., Melting of a dry peridotite KLB-1 up to 14 GPa: Implications on the origin of peridotitic upper mantle, *J. Geophys. Res.*, *91*, 9367-9382, 1986.

Wei, K., R.G. Tronnes, and C.M. Scarfe, Phase relations of aluminum-undepleted and aluminum-depleted komatiites at pressures of 4-12 GPa, *J. Geophys. Res.*, *95*, 15,817-15,827, 1990.

Wetherill, G., Formation of the Earth, *Annu. Rev. Earth Planet. Sci.*, *18*, 205-256, 1990.

Yamada, H., and E. Takahashi, Subsolidus phase relations between coexisting garnet and two pyroxenes at 50 to 100 kbar in the system CaO-MgO-Al_2O_3-SiO_2, in *Kimberlites II: the mantle and crust-mantle*

relationships, edited by J. Kornprobst, pp. 247-255, Elsevier, Amsterdam, 1984.

T. Gasparik, Mineral Physics Institute, Department of Earth and Space Sciences, State University of New York, Stony Brook, NY 11794.

C. Herzberg, Rutgers University, Department of Geological Sciences, Wright Geological Laboratory, Busch Campus, New Brunswick, NJ 08903.

(Received November 19, 1990;
revised April 15, 1991;
accepted May 28, 1991.)

JOURNAL OF GEOPHYSICAL RESEARCH, VOL. 96, NO. B10, PAGES 16,471–16,494, SEPTEMBER 10, 1991

Crustal Structure of the Western New England Appalachians and the Adirondack Mountains

STEPHEN HUGHES AND JAMES H. LUETGERT

U.S. Geological Survey, Menlo Park, California

We present an interpretation of the crustal velocity structure of the New England Appalachians and the Adirondack Mountains based on a seismic refraction/wide-angle reflection experiment in eastern North America extending from the Adirondacks in New York State through the northern Appalachians in Vermont and New Hampshire to central Maine. Modeling of the eastern portion of the profile within the New England Appalachians shows a subhorizontal layered crust with upper crustal velocities ranging from 5.5 to 6.2 km/s, a midcrustal velocity of 6.4 km/s, and a lower crustal velocity of approximately 6.8 km/s. Crustal thickness increases from 36 km beneath Maine to 40 km in Vermont. Little evidence is seen for structures at depth directly related to the White Mountains or the Green Mountains. A major lateral velocity change in the upper and mid crust occurs between the Appalachians and the Adirondacks. This boundary, projecting to the surface beneath the Champlain Valley, dips to the east beneath the Green Mountains and extends to a depth of ~25 km below the eastern edge of the Connecticut Valley Synclinorium in Vermont. The Tahawus Complex, a series of strong horizontal reflections at 18–24 km depth beneath the Adirondack Highlands, is seen to dip eastward beneath Vermont. Upper crustal rocks in the Adirondack Mountains have Poisson's ratios of 0.28 ± 0.01 that can be correlated with the Marcy Anorthosite. Poisson's ratios of 0.24 ± 0.01 calculated for rocks of the Connecticut Valley Synclinorium indicate a siliceous upper crust in Vermont. The lower crust is considered to be best represented by intermediate to mafic granulites; a high Poisson's ratio (0.26–0.27) tends to support a mafic lower crust in the New England Appalachians. This seismic refraction/wide-angle reflection experiment provides further evidence for the obduction of the allochthonous western Appalachian units onto Grenvillian crust above a zone of detachment that penetrates at least to midcrustal depths and was the locus of successive Paleozoic thrusting.

INTRODUCTION

The New England Appalachians are characterized by a series of tectonostratigraphic terranes accreted to North America during multiple Paleozoic orogenic events. Three major terranes are identified across the northern Appalachians: (1) a western terrane underlain by Grenvillian crust and overthrust by allochthons that contain Grenvillian basement with lower Paleozoic shelf sediments, (2) a central terrane typified by island arc volcanics of the Bronson Hill Anticlinorium and miogeoclinal lithologies of the Merrimack Synclinorium, and (3) an Avalonian terrane with distinctive Precambrian and mid-Paleozoic faunas. It is increasingly recognized that such terranes are in fact a complex composite collage of smaller (suspect) terranes.

The deeply eroded Appalachian Orogen is the center of numerous controversies relating to the mechanisms and extent of terrane accretion during the lower Paleozoic. Seismic refraction/wide-angle reflection experiments are capable of resolving deep continental structures and provide a means of inferring relationships between the surface geology and the underlying crust. This paper reports on recently acquired seismic refraction/wide-angle reflection data collected across the northern New England Appalachians and attempts to answer the following questions: (1) What is the velocity structure of the New England crust? (2) What is the structural relationship between the Grenville Province and the allochthonous New England Appalachians? (3) What constraints can be applied to the inference of lower crustal composition from compressional and shear wave data? We begin with an overview of the regional geology observed along the profile and present a summary of the interpreted crustal structure from previous geophysical studies in New England before moving on to a description of the two-dimensional seismic velocity model. Finally, an interpretation of the crustal velocity structure and the inferred crustal composition is presented.

Paper number 91JB01657.

PROFILE GEOLOGY

The refraction/wide-angle reflection profile discussed here extends from the Grenville Province exposed in northern New York State, across the central New England Appalachians and on into central Maine (Figure 1). The profile crosses six tectonostratigraphic units, which are from west to east: (1) the middle Proterozoic Grenville basement exposed in the Adirondack Mountains (northern New York), (2) autochthonous platformal sediments and allochthonous slope rise sediments of the Taconic sequence, (3) imbricated and metamorphosed lower Paleozoic flysch deposits and underlying Grenvillian basement of the Green Mountains (central Vermont), (4) Silurian to Lower Devonian metapelites of the Connecticut Valley Synclinorium (eastern Vermont), (5) Ordovician forearc sediments and volcanics of the Bronson Hill Anticlinorium (New Hampshire), and (6) metamorphosed and deformed Silurian to Devonian turbidites of the Merrimack Synclinorium. Numerous articles have been written discussing the tectonic evolution of the northern New England region [*Osberg*, 1978; *Robinson and Hall*, 1979; *Williams and Hatcher*, 1982; *Bradley*, 1983; *Zen*, 1983; *Taylor*, 1989]. However, for the purpose of our study we present a generalized overview of the lithotectonic units traversed by the profile and describe the nature of the contacts between these units.

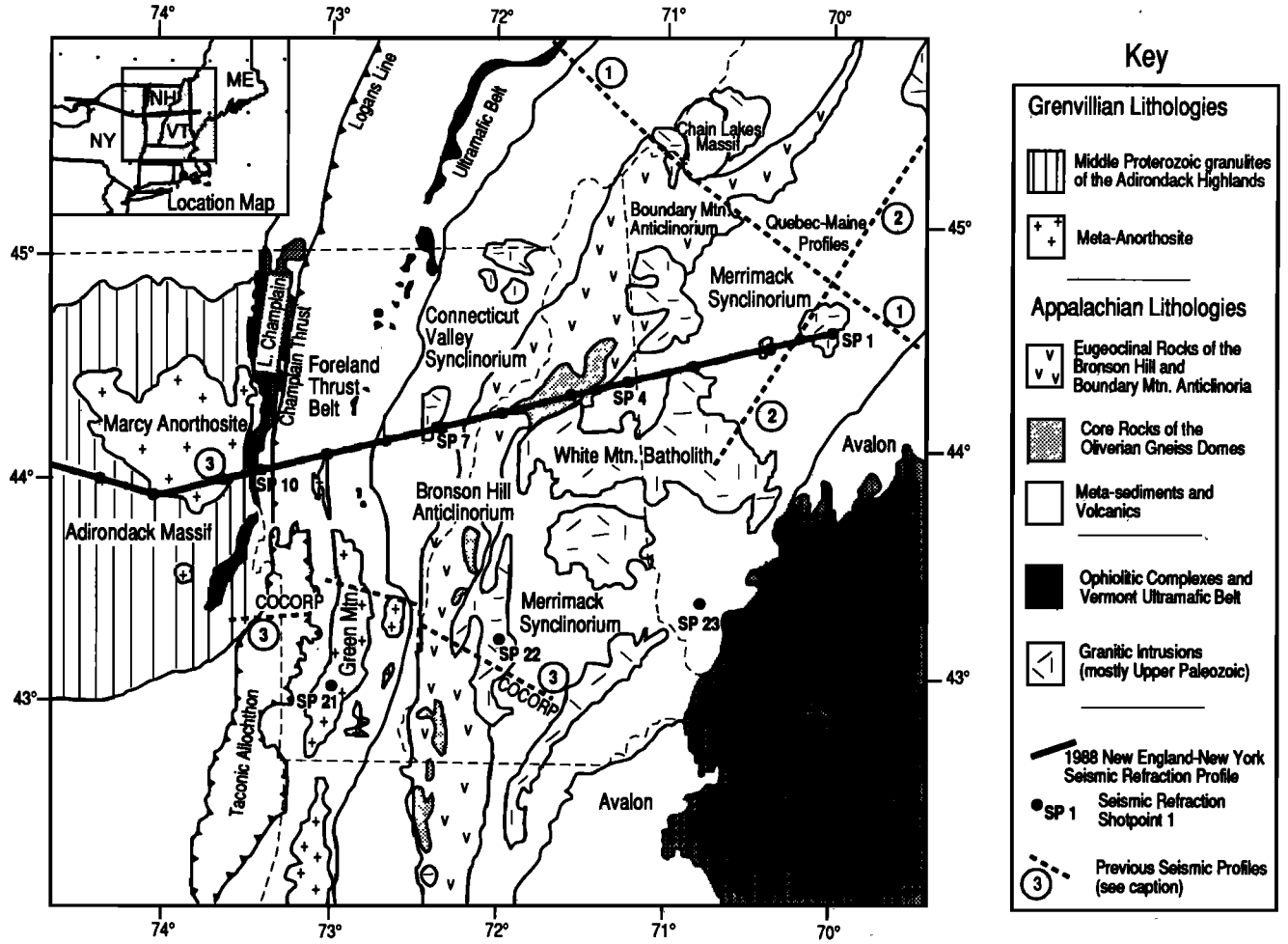

Fig. 1. Simplified geologic map showing the location of the 1988 New England seismic refraction/wide-angle reflection profile. Inset map shows regional location of the entire profile. Inline shot points are marked by dots along the profile, and fan shots are shown offset to the south. Previous seismic profiles are shown by the dashed lines: (1) the Quebec-Maine seismic reflection and refraction profiles [*Spencer et al.*, 1989], (2) the USGS refraction profile along the axis of the Merrimack Synclinorium [*Hennet et al.*, 1991], and (3) the southern Vermont and Adirondack deep seismic reflection profile collected by COCORP [*Ando et al.*, 1984]. Geology simplified after *Williams* [1978] and *McLelland and Isachsen* [1986].

Our transect begins in the Proterozoic domal massif of the Adirondack Mountains, which forms an anomalous topographic feature extending southward from the Grenville Province of eastern Canada. The Adirondack Highlands expose an oblique section through the Proterozoic mid to lower crust [*Selleck*, 1980; *McLelland and Isachsen*, 1986]. A complex assemblage of ductily deformed and interleaved granulite facies metapelites, marbles, and quartzites are exposed in the Adirondack Highlands [*Weiner et al.*, 1984; *McLelland and Isachsen*, 1986]. Intruding the gneisses are meta-anorthosite bodies, the largest of which is the Marcy Anorthosite (Figure 1). The Adirondack dome is surrounded by Cambrian platformal carbonates and quartzites which lie unconformably upon the Grenvillian basement. This autochthonous wedge of Cambrian sediments lies in situ between Grenvillian basement and the allochthonous Taconic (Mid-Upper Ordovician) units of the western Appalachians.

The contact between the Appalachian and Grenville provinces lies beneath the Champlain Valley. In the Champlain Valley Cambrian to Early Ordovician continental shelf sediments and deep marine clastics (Foreland Thrust Belt) lie unconformably on the Grenvillian autochthon. These sediments have been interpreted as an accretionary complex developed above the eastward subducting Grenvillian margin during he Mid-Ordovician Taconic Orogeny [*Rowley and Kidd*, 1980; *Stanley and Ratcliffe*, 1985]. Subsequent closure of the Taconic subduction system resulted in the obduction of allochthonous slices of Grenvillian "basement" which now form the core of the Green Mountain massif exposed in central Vermont. To the east of the Green Mountains, the Taconic "suture" is traced by the Vermont Ultramafic Belt which is interpreted as altered slivers of oceanic crust and upper mantle imbricated with accretionary prism sediments [*Osberg*, 1978; *Bradley*, 1983; *Stanley and Ratcliffe*, 1985].

From the eastern edge of the Green Mountains the profile proceeds eastward across the Connecticut Valley Synclinorium. Silurian to Lower Devonian metapelites and carbonates attain chlorite grade metamorphism [*Rodgers*, 1970]. These post-Taconic sediments are interpreted to be a shallow thrust sheet juxtaposed against the Bronson Hill Anticlinorium by the Ammonoosuc fault. The Bronson Hill island arc complex accreted in the Taconic Orogeny is

exposed as a linear belt of volcanics stretching through eastern Vermont and western New Hampshire. The Bronson Hill Anticlinorium can be traced through the central New England Appalachians as an aligned chain of elliptical gneissic domes (Oliverian Plutonic Series) mantled by a series of Mid-Ordovician metavolcanics and metasediments. Metamorphic grades vary from greenschist facies to upper amphibolite facies at the cores of the Oliverian Domes [*Rodgers*, 1970]. Overlying these eugeoclinal lithologies is a series of Silurian to Lower Devonian metapelites and carbonates belonging to the Connecticut Valley Synclinorium to the west and the Merrimack Synclinorium to the east.

The Merrimack Synclinorium lies to the east of the Bronson Hill Anticlinorium. This broad structural low contains a thick sequence of Silurian to Devonian deep marine clastics and, locally, calc-silicates and metavolcanics typically attaining upper amphibolite grade metamorphism. At least three phases of nappe emplacement and associated regional metamorphism in the Acadian (Mid-Devonian) orogenic events have resulted in widespread ductile deformation of these midcrustal rocks now exposed at the present erosion surface [*Chamberlain and England*, 1985; *Eusden et al.*, 1987]. The Merrimack Synclinorium has been extensively intruded by Acadian granites of the New Hampshire Plutonic Series and by the Jurassic White Mountain Magma Series which forms a north-south elongate batholith composed predominantly of syenite, granite, and monzonite [*McHone and Butler*, 1984].

Crustal Structure and Geophysical Framework

A recent synthesis of geophysical data collected through the Appalachian Orogen indicates that significant differences exist in the deep crust between the northern Appalachians and the adjacent Grenville Province [*Taylor*, 1989]. The New England Appalachians are characterized by a relatively thick crust (~40 km) with an average seismic velocity of 6.4 km/s, whereas the Adirondacks have a somewhat thinner curst (36 km), and high velocities (≥6.6 km/s) are observed throughout the crust in this region [*Taylor and Töksoz*, 1982; *Taylor*, 1989]. Previous deep crustal studies in the New England Orogen have included seismic refraction/wide-angle reflection profiles collected in northern Maine and Quebec and seismic reflection profiles collected across southern Vermont and northern New York State. Interpretation of these data sets suggest that the autochthonous Grenville basement extends beneath at least the western portion of the allochthonous Appalachian Orogen.

Seismic reflection and refraction profiles were obtained in 1984 by the U.S. Geological Survey and the Geological Survey of Canada across and along strike to the northern Appalachians in Maine and Quebec (Figure 1, line 1). Analysis of the seismic data from the Quebec-Maine transect provides evidence for the eastward extension of the Grenville beneath the northern Appalachians. A major zone of reflections can be traced over some 200 km from shallow depths beneath the Saint Lawrence Lowlands to approximately 25 km below the Chain Lakes Massif [*Stewart et al.*, 1986; *Spencer et al.*, 1987; *Spencer et al.*, 1989]. These reflections have been interpreted as a "décollement" separating the Grenvillian basement from the allochthonous Appalachians [*Spencer et al.*, 1989].

In central Maine a 180-km-long cross profile shot along the axis of the Merrimack Synclinorium reveals a 38-km-thick crust (Figure 1, line 2). In the region where line 2 crosses the seismic refraction/wide-angle reflection profile discussed herein the upper crust has velocity between 6.0 and 6.3 km/s and is characterized by strong lateral and vertical seismic velocity variations. The base of the Merrimack Synclinorium at 15 km depth is marked by an increase in velocity to 6.4 km/s. The lower crust has a velocity of 6.8 km/s [*Hennet et al.*, 1991]. Normal moveout corrections applied to Moho reflections in the vicinity of our profile (shot point 2) indicate that the crust is 37–38 km thick in eastern Maine [*Luetgert et al.*, 1987].

Deep seismic reflection profiles in southern Vermont (Figure 1, line 3) display the seismically transparent Grenville basement extending eastward beneath the "thin skin" of the Taconic sequence to approximately 25 km beneath the Connecticut Valley Synclinorium [*Brown et al.*, 1983; *Ando et al.*, 1984]. The buried edge of the Grenville Province was interpreted to be a highly deformed thrust-imbricated zone passing eastward into a transitional lower crust of undetermined basement type. The Green Mountains were identified as an imbricated thrust slice obducted above the lower crustal penetrating ramp. Reflection profiling across the southern Adirondacks revealed a striking band of high reflectivity between 6 and 8 two-way travel time, or approximately 18–26 km in depth [*Brown et al.*, 1983; *Klemperer et al.*, 1985]. These authors applied the name Tahawus Complex to this set of reflections, and this name is retained here.

Experiment

Seismic refraction/wide-angle reflection data were acquired by the U.S. Geological Survey (USGS), the U.S. Air Force Geophysical Laboratory (AFGL), and the Geological Survey of Canada (GSC) during the fall of 1988. This profile is 650 km long and traverses the central New England Appalachians before extending west through the Adirondacks and into the Proterozoic craton of southern Ontario. The results of analysis of the easternmost 300 km of this profile are presented below. Exceptionally high quality seismic data were obtained at offsets ranging from 0 to 450 km along a continuous linear refraction profile recorded in three separate deployments. Data were recorded by 120 USGS portable FM cassette recorders [*Murphy*, 1989] and 150 GSC digital instruments (I. Asudeh, personal communication, 1988). In each case 2-Hz geophones were deployed. The seismometer spacing was nominally 800 m with an estimated survey location error of 25 m. In total, 32 shots, ranging in size from 900 kg to 2700 kg, were detonated along the entire profile length; three fan shots were also recorded. The shot point spacing was 30 to 40 km [*Luetgert et al.*, 1990].

Description of the Principal Seismic Phases

The data set gathered by this seismic experiment provides a unique opportunity to derive the seismic velocity structure of the New England Appalachians and adjacent Grenville terrane. We present a brief description of the principal phases observed in the seismic record sections. Emphasis will be placed on broad generalities, although it should be borne in mind that lateral variations do exist along the length of the profile. Subsequently, the major features of the derived two-dimensional model are highlighted, and a de-

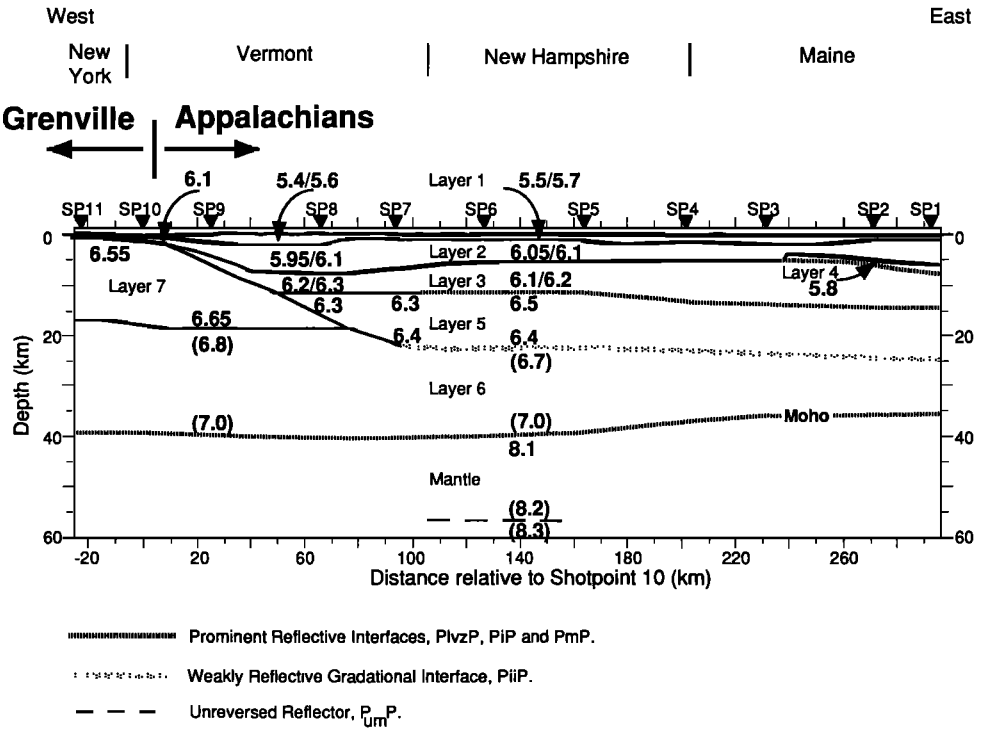

Fig. 2. Seismic velocity model derived from the 1988 New England seismic refraction/wide-angle reflection data. Velocity interfaces are consistent with the observed phases; well-constrained reversed control is achieved throughout the upper and midcrust. The model is a first-order representation of complex layered and gradational interfaces within the New England Appalachians and Adirondack Mountains. Topography is included in the model. Layer numbers are referenced in the text and in subsequent ray diagrams. All velocities are shown in kilometers per second. Distance is plotted relative to shot point 10 (Figure 1).

tailed description of the travel time and synthetic amplitude modeling used to derive the final model shown in Figure 2 is presented.

The record section for shot point 1 is representative of the seismic data gathered in New England; principally, it shows four characteristic phases labeled P_g, $P_{lvz}P$, P_iP, and P_mP on Figure 3. The upper crust in New England is characterized by a laterally extensive and impulsive first-arrival branch (P_g) with apparent velocity 6.0–6.1 km/s. Significantly, no crustal first-arrival phases are observed with apparent velocities exceeding 6.2 km/s. The relatively low amplitude of the first-arrival branch at offsets exceeding 50 km is a result of plotting normalized traces, where the amplitude of the first-arrival branch is relative to the amplitude of the secondary arrivals. In Maine, localized high-amplitude wide-angle reflections ($P_{lvz}P$) are observed at offsets from the source of 20–60 km. Prominent midcrustal wide-angle reflections (P_iP) are the most striking feature of this data set. In western Maine and New Hampshire, strongly coherent wide-angle reflections appear at postcritical offsets between 70 and 120 km. Evidence for phases refracted within the lower crust in New England are tenuous. The seismic velocity structure of the lower crust must be indirectly inferred from analysis of Moho reflections (P_mP) as they asymptotically approach the lower crustal refracted phase. In New England the upper mantle is characterized by emergent direct arrivals (P_n) at offsets exceeding 160 km and by segmented en echelon P_mP reflections, possibly indicative of complex lamination around the crust-mantle transition. The apparent velocity of the upper mantle is 8.0 ± 0.1 km/s.

The record section for shot point 10 west is characteristic of data collected across the Grenvillian Adirondack massif (Figure 4). Exceptionally high upper crustal velocities (6.6 km/s) are associated with the Grenvillian crust. Conspicuous high-amplitude, wide-angle reflections (P_tP) are observed at offsets between 50 and 90 km. Strongly coherent en echelon reflection segments (P_tP) suggest a laminated midcrustal body beneath the Adirondack massif, referred to previously as the Tahawus Complex.

Seismic Modeling

Two-dimensional ray-trace modeling, asymptotic ray-theory synthetics and full-waveform reflectivity synthetic seismograms were used to derive a seismic velocity model from this data set. The two-dimensional seismic velocity model is comprised of two discrete and independently derived "blocks" which are connected by a midcrustal penetrating ramp structure (Figure 2). The New England Appalachian crust is essentially composed of three subhorizontal planar layers: (1) an upper crust with apparent velocities in the range 6.0–6.2 km/s, (2) a 10-km-thick midcrustal layer modeled with a negative gradient between 6.5 and 6.4 km/s, and (3) a lower crustal layer with an estimated velocity of 6.7–7.0 km/s. In northern New York State the Grenvillian Adirondack Mountains are represented by a model consisting of a two-layer crust. High upper crustal velocities of 6.6

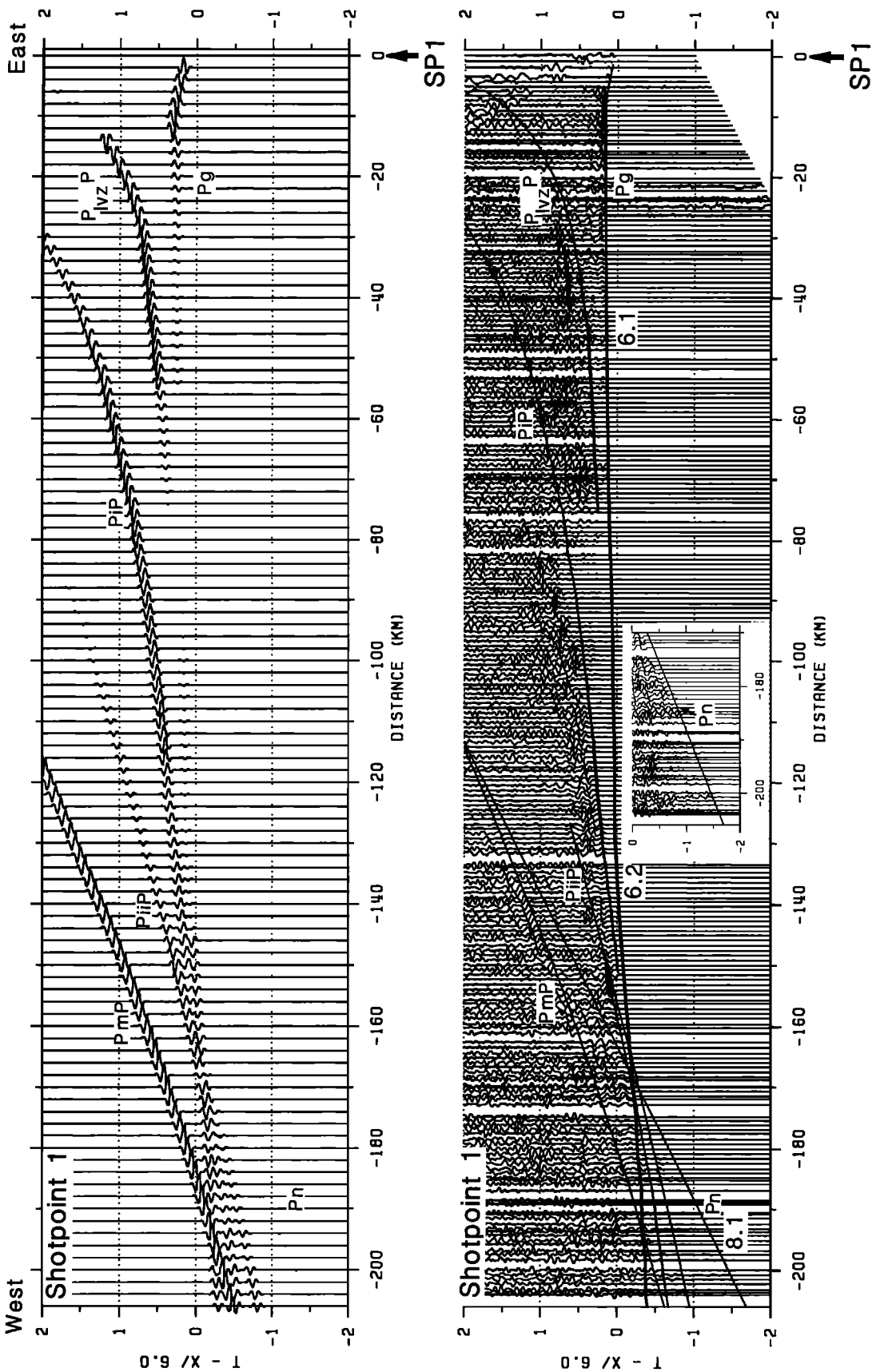

Fig. 3. Trace-normalized seismic refraction data from shot point 1 (SP1) and ray-synthetic seismogram (top) calculated for the eastern portion of the model in Figure 2. Shot point 1 is representative of data collected across the New England Appalachians and shows characteristic large-amplitude coherent midcrustal reflections (P_tP). The model predicts strongly coherent P_mP reflections, which are not observed in the data; the Moho may be laminated beneath the central New England Appalachians. Data are plotted using a reducing velocity of 6.0 km/s. No filtering has been applied to the data. Key to phase identification (used for all figures): P_g, the diving or continuously refracted P wave in the upper crustal layers, with an apparent velocity between 6.0 and 6.2 km/s; P_r, the refracted P wave through the Grenvillian ramp structure; P_7, the refracted P wave in the Grenville upper crust (layer 7), with an apparent velocity of 6.6 km/s; P_n, the uppermost mantle refracted phase, with an apparent velocity between 8.0 and 8.1 km/s; P_tP, the wide-angle reflection from the midcrustal interface (layers 3/5), no corresponding refracted first arrival is observed from layer 5; P_hP, the wide-angle reflection from the lower crustal interface (layers 5/6), no corresponding refracted first arrival is observed from layer 6; P_mP, the wide-angle reflection from the crust-mantle boundary; and P_tP, the wide-angle reflection from the top of the Tahawus Complex (layers 7/6).

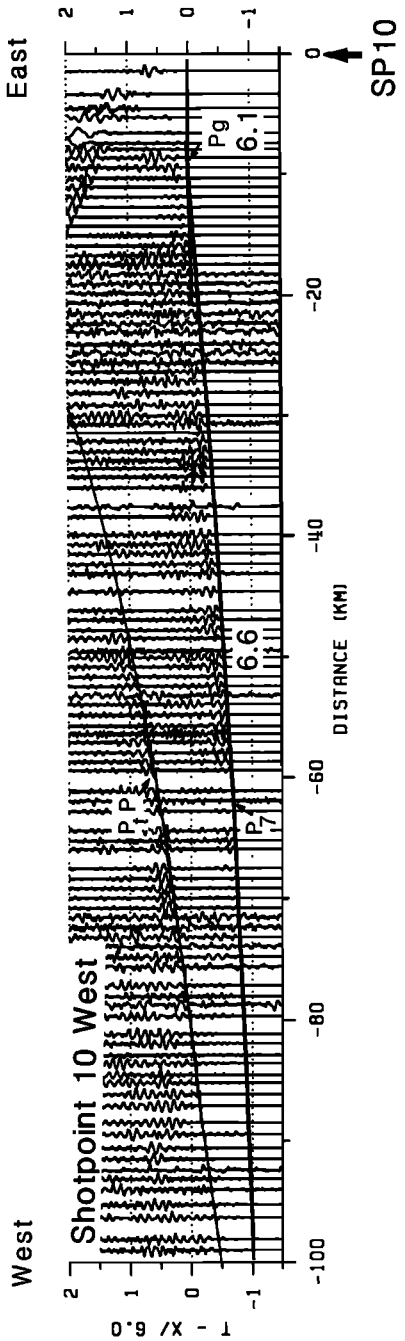

Fig. 4. Record section for shot point 10 west (SP10 west) plotted in trace-normalized format with distances plotted relative to the shot point. Seismic refraction data collected across the Adirondack Mountains characteristically show high upper crustal velocities (6.6 km/s) compared to those observed in the Appalachians. Large-amplitude coherent reflections (P_tP) observed at offsets between 50 and 90 km are related to a laminated midcrustal interface referred to by *Klemperer et al.* [1985] as the Tahawus Complex. See Figure 3 for key to phase identification.

km/s and a midcrustal reflecting interface are the most prominent features of the model in this region. Once modeling was completed for the Appalachian and Adirondack "blocks", the contact between these two terranes was analyzed. The high-velocity Adirondack "block" was imaged in the form of a ramp extending to midcrustal depths beneath the Appalachian upper crust in Vermont (Figure 2). Crustal thickness varies from 36 km in western Main to 40 km in Vermont.

Modeling of this Appalachian data set was completed in successive phases, each used to constrain subsequent iterations and so to improve the resolution of the final model. Initially, seismic velocity functions for each shot point were calculated using one-dimensional ray-trace modeling assuming a plane homogeneous layered Earth [*Luetgert*, 1988*b*, *c*]. Reference was made to reciprocal travel times to aid in the identification and correlation of phases. The shot point spacing is insufficient to resolve individual igneous bodies, and consequently minor travel-time perturbations associated with localized variations in the surface geology have not been modeled. The one-dimensional models were extensively used to minimize the number of iterations required in successive two-dimensional ray-trace modeling described in the following section.

An initial composite two-dimensional seismic velocity model was constructed by contouring one-dimensional homogeneous layer solutions computed at each shot point. Iterative two-dimensional ray-tracing was used to constrain the velocity boundaries [*Cerveny et al.*, 1977; *Luetgert*, 1988*a*]. Topography was included in the model. Incorporation of wide-angle and near-vertical reflections for each shot point significantly increased the resolution of the model. Identification of critical points for the major reflected phases (P_mP, P_tP) allowed velocity contrasts across interfaces to be estimated. Seismic velocity gradients and velocity contrasts were estimated by means of amplitude modeling. In the eastern part of the profile the model is approximately one-dimensional, and full-waveform reflectivity modeling was used to determine the relative amplitude characteristics of the observed phases.

Generally, observed and calculated travel times for the model presented in Figure 2 match to 0.1 s or less, with no mismatches greater than 0.2 s. The sensitivity of the model is greatest in the uppermost 10 km where the ray density is greatest. Within the upper crust (layers 2/3) the error in depth to interfaces is probably no greater than several hundred meters, and the corresponding precision in the derived velocity is 6.05 ± 0.05 km/s. The velocity gradient in the upper crust is 0.01 s^{-1}; this value is tightly constrained by the lateral persistence of the first-arrival phase (P_g). The magnitude of the midcrustal velocity discontinuity (layers 3/5) is inferred from amplitude modeling to be precise to ±0.1 km/s. Considerably more uncertainty exists for the velocity structure of the lower crust as this has largely been indirectly inferred from secondary arrivals. The precision of the modeled lower crustal velocity is probably no better than 6.8 ± 0.2 km/s; beyond these limits acceptable travel time and amplitude constraints are exceeded. In view of the poorly constrained lower crustal velocity structure, a 2-km uncertainty in the Moho depth may be expected, although the dipping geometry is unlikely to be affected by this. Uncertainties introduced by the interpretive step of phase

correlation are usually much larger than the quantifiable uncertainties listed above [*Mooney*, 1989].

Description of the New England model: A detailed description of the compressional wave velocity model shown in Figure 2 is presented below. Justification of each layer in terms of its apparent velocity and structure is related to the key phases identified on the record sections. The upper crust is represented by a model consisting of three layers. The near surface (layer 1) has seismic velocities in the range 5.5–5.7 km/s. An additional "cover" layer is modeled along the eastern portion of the profile, with a seismic velocity of 5.0 km/s. The upper crust (layer 2) is characterized by a seismic velocity of 6.05 km/s increasing to 6.1 km/s at the base of the layer. The 6.05 km/s refracted phase is observed extending to offsets of 120 km, requiring a vertical seismic velocity gradient in layer 2 of 0.01 s^{-1} (P_g in Figure 3). Throughout New England the first-arrival phase (P_g) is laterally continuous, indicating that near-surface velocity variations (statics) do not affect the data. Between shot points 7 and 10, layer 2 thickens, and somewhat lower velocities are included in the model in this region (5.95–6.1 km/s). The incorporation of slower velocities into the model provides a travel time delay observed in the first-arrival refracted branch from shot point 4. Immediately east of shot point 10 a 6.1 km/s near-surface velocity is incorporated within layer 2.

Layer 3, with a seismic velocity of 6.1–6.2 km/s, varies laterally in thickness and occurs between depths of 5 and 15 km. First arrivals from layer 3 are observed at offsets exceeding 120 km and signify a continuous increase in velocity with depth in the uppermost crust rather than a first-order velocity discontinuity (Figure 5). Between shot points 7 and 9 the velocity of layer 3 is increased to 6.2–6.3 km/s. A first-order velocity discontinuity in this region of the model satisfies near-offset reflections from shot point 7 east (Figure 5) and additionally allows refracted arrivals from shot point 7 west to successfully turn through the ramp structure. The velocity structure of the ramp is discussed more fully in the following sections.

Large-amplitude reflections ($P_{lvz}P$) are observed on shot points 1, 2, and 3 at offsets of 20–60 km. These reflections are delayed in arrival time by as much as 0.5 s and are best modeled by a low-velocity zone with a velocity of 5.8 km/s as shown by layer 4 in Figure 2. One-dimensional travel time modeling enabled the geometry of this upper crustal reflector to be determined. Integration of the one-dimensional models into the two-dimensional model produced a 1-km-thick low-velocity zone with a velocity of 5.8 km/s (Figure 6). The velocity of the low-velocity zone (5.8 km/s) is determined by amplitude modeling and by the abrupt termination of this set of reflections from shot point 1 at an offset of ~80 km ($P_{lvz}P$ in Figure 3). Amplitude modeling of this discontinuous low-velocity body produces a good match with the observed reflected phases, although it is hard to determine the magnitude of the seismic gradient within this layer. One-dimensional full-waveform reflectivity solutions were calculated for shot point 1 and produced an exceptionally close correlation to the relative amplitudes observed along the profile.

The midcrust has been modeled with a negative gradient; the vertical seismic velocity gradient decreases from 6.5 km/s to 6.4 km/s over a 10-km depth interval in layer 5 (Figure 2). The top of layer 5 rises from 14.5 km in the east to 11.5 km in the west before merging with the ramp beneath shot point 9. Large-amplitude postcritical reflected arrivals observed at 70–120 km offsets define this midcrustal interface (P_iP in Figure 5). Full-waveform reflectivity modeling indicated that a seismic velocity step from 6.2 km/s to 6.5 km/s at the top of layer 5 would satisfy critical point and amplitude constraints. Reflections originating from the top of layer 5 are not all equally as coherent or large in amplitude, yet the model predicts laterally continuous high-amplitude reflections. Clearly, two-dimensional ray-tracing can only produce an approximate first-order representation of complex layered and laterally varying interfaces within the Earth. No refracted first arrivals are observed from layer 5. Two possible models were considered to fulfill the above described midcrustal reflections without a corresponding refracted phase: (1) a thin high-velocity layer and (2) a negative gradient layer. First, a thin positive gradient high-velocity layer, where refractions are terminated and limited refracted energy returns to the surface, was rejected because of the added complexity of determining the velocity between such a thin layer and the top of the lower crust. The second option of a negative gradient layer was chosen in preference as it produced the simplest solution to the observed phases. Since negative gradients cannot be resolved by amplitude modeling, this is an inferred structure. It is not necessary to have a negative gradient through the entire thickness of layer 5; an intermediate layer of, say, 6.45 km/s with a positive gradient is not ruled out although arrivals from such a layer would have to be "hidden". Immediately east of the Grenville ramp, layer 5 has a positive velocity gradient; this is an essential feature of the model, as without it rays originating from within the Adirondacks and propagating to midcrustal depths would never be refracted toward the surface (Figure 2).

The lower crust is modeled as a "hidden" layer and lies below 25 km depth (layer 6 in Figure 2). Refracted first arrivals are not observed from the lower crust because of longer travel times for direct arrivals from the lower crust than for the upper crustal refractions. Estimates of the lower crustal velocity must be indirectly inferred. We have three principal constraints on the velocity of the lower crust: (1) an estimate of 6.8 km/s for the lower crustal velocity was obtained from P_mP reflections as they asymptotically approached the lower crustal refracted phase, (2) travel time modeling of critical P_mP reflection hyperbolae indicates a high-velocity, high-gradient lower crust, and (3) estimates of crustal thickness in the vicinity of our profile of around 38 km support a high velocity (6.8 km/s) in the lower crust [*Luetgert et al.*, 1987; *Hennet et al.*, 1991]. The lower crust has been modeled with a velocity of 6.7 km/s increasing to 7.0 km/s at the base of the crust. The velocity gradient modeled in the lower crust is constrained by the curvature of the P_mP hyperbola. Reflectivity modeling necessitates a minimum velocity discontinuity between layers 5 and 6. Perturbations in the modeled lower crustal velocities exceeding ±0.2 km/s significantly degrade travel time fits for Moho reflections. P_mP does not bottom any further east than shot point 3. Between shot points 1 and 3 the model is constrained by the USGS refraction profile along the axis of the Merrimack Synclinorium [*Hennet et al.*, 1991].

The top of the lower crust is represented in the model by a first-order velocity discontinuity. A first-order velocity discontinuity is presented as the simplest possible model

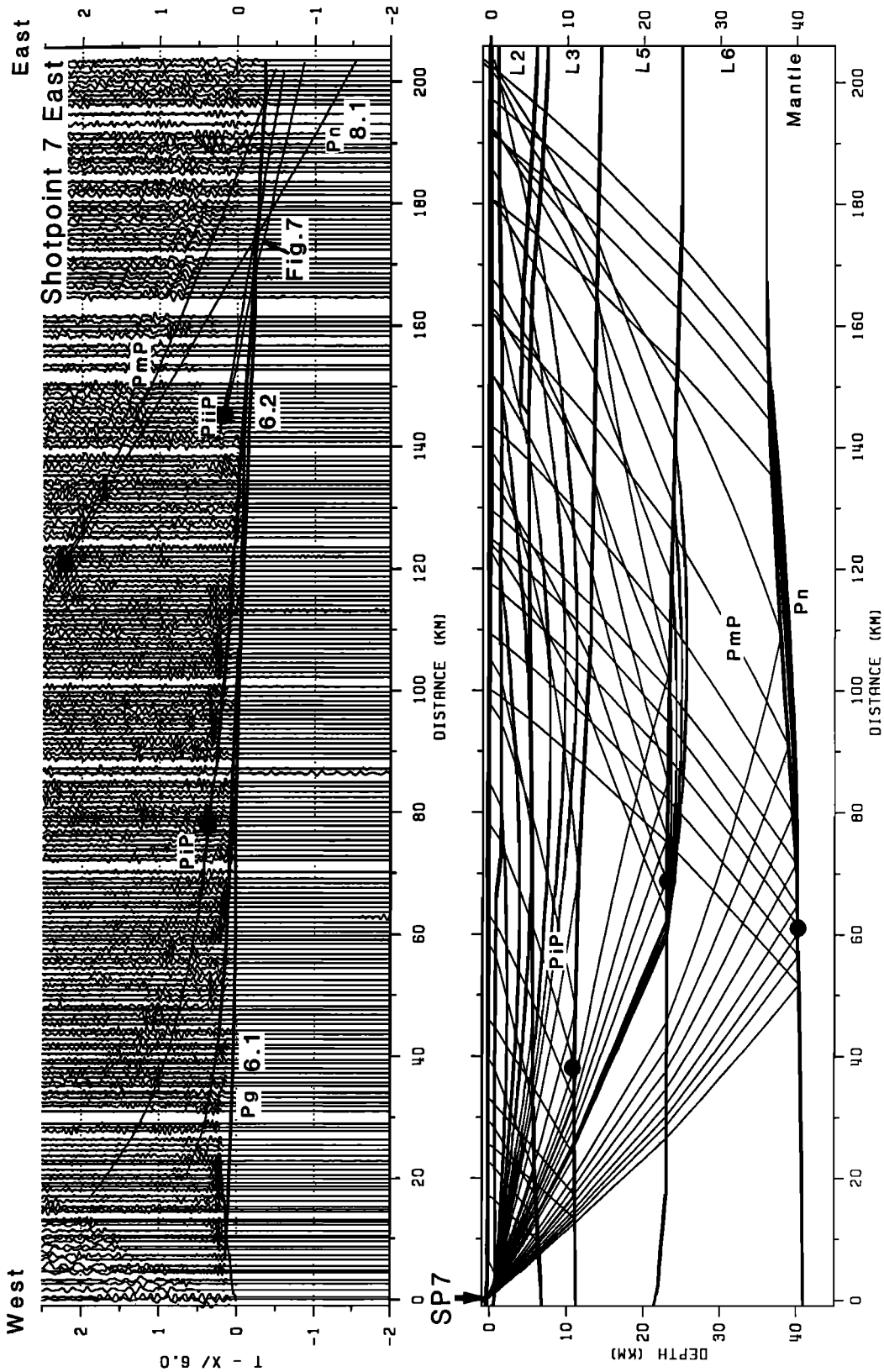

Fig. 5. Trace-normalized seismic refraction data from shot point 7 east (SP7 east) and ray diagram (bottom) for the eastern portion of the model shown in Figure 2. The New England seismic velocity structure is fully reversed by SP7 east. Midcrustal reflections (P_iP) show an advanced travel time relative to that observed for shot point 1. Critical points are marked on the data by the solid dots, and the corresponding critical distances are marked on the model. Distances are plotted relative to shot point 7. See Figure 3 for key to phase identification.

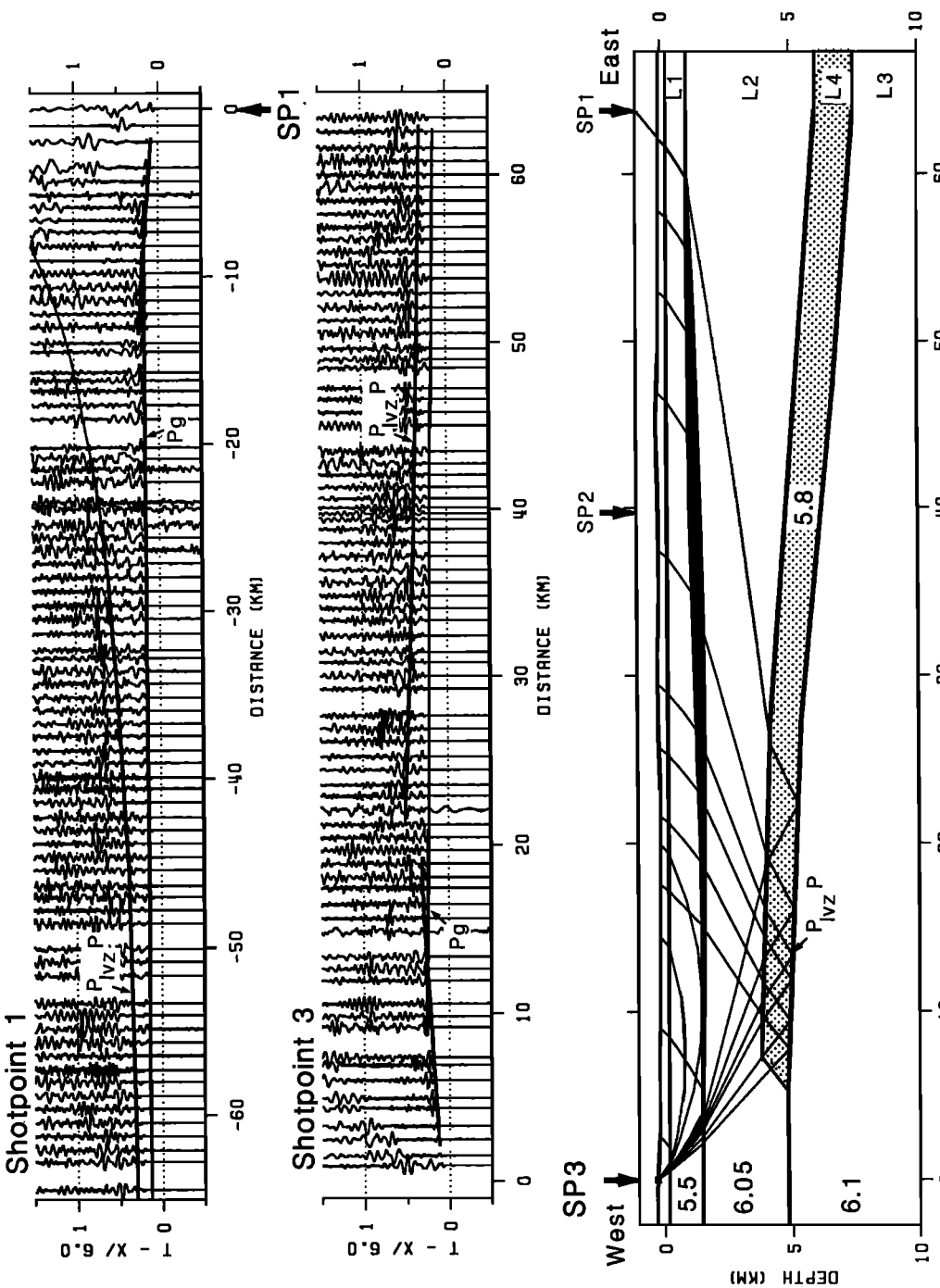

Fig. 6. Near-offset trace-normalized seismic refraction data from shot point 1 (top) and shot point 3 (middle). Large-amplitude upper crustal reflections ($P_{lvz}P$) observed from shot points in western Maine are best modeled by a thin low-velocity layer. Ray diagram for shot point 3 (bottom) shows precritical reflections from the base of the low-velocity layer. Distances are plotted relative to the shot point. See Figure 3 for key to phase identification.

which fits the observed travel time constraints. The shallowest possible depths to the top of the lower crust is given by modeling lower crustal refractions so that they are coincident with the picked first arrivals (Figure 7*a*). The geometry of the lower crustal interface is poorly constrained because reflections from the top of the lower crust are indistinct (Figure 7*b*). The modeled $P_{ii}P$ reflection shown on Figure 5 is an artifact of modeling a hidden lower crust rather than a correlatable reflected phase. The top of the lower crust is modeled with a 6.7 km/s seismic velocity. Velocities as low as 6.5 km/s at the top of the lower crust are incompatible with prior estimates of crustal thickness in Maine and New Hampshire [*Luetgert et al.*, 1987; *Hennet et al.*, 1991], while velocities as high as 6.9 km/s for the top of the lower crust would produce large-amplitude lower crustal reflections relative to P_mP and P_iP which are not observed. Ray theory synthetic models of the lower crustal reflection ($P_{ii}P$) are inconsistent with observed lower crustal reflectivity (Figure 3), suggesting that this interface is more complex than the first-order velocity discontinuity used for travel time modeling. The primary observation of crustal thickness obtained from critical P_mP reflections is satisfied in preference to information obtained from synthetic models necessitating a high velocity in the lower crust. The top of the lower crust is considered to be best represented by a gradational velocity interface, incapable of generating coherent reflections.

The geometry of the crust-mantle transition is constrained by Moho reflections (P_mP) and direct arrivals from the upper mantle (P_n). Together these indicate that the crust thickens from 36 km beneath western Maine to 40 km beneath Vermont. In the eastern portion of our model between shot points 1 and 7, a tightly constrained crust-mantle geometry is determined from complementary and reciprocal crust/mantle phases (Figure 7*a*). Greater emphasis was placed on modeling critical Moho reflections than on modeling low-amplitude emergent direct arrivals from the mantle. Although lower crustal velocities are relatively poorly constrained, thinning of the crust toward the east is a primary feature of the data set as indicated by the relative P_n crossover distances on shot points 1 and 7.

Exceptionally coherent large-amplitude Moho reflections (P_mP) observed from shot point 10 east, provide information on the crust-mantle transition beneath Vermont and New Hampshire. Compelling evidence for a 40-km-thick crust beneath Vermont is provided by strongly coherent postcritical P_mP reflections observed at offsets between 90 and 140 km on shot point 10 (Figure 8). At wider angles, delayed en echelon P_mP reflection segments are observed (Figure 8, arrows a and b). Three possible explanations are considered for this feature: (1) a step in the Moho, (2) complex lamination at the base of the crust, and (3) out of plane reflections. First, the delay observed at an offset of 150 km from shot point 10 in the P_mP arrivals can be modeled by a step in the Moho (Figure 9*b*). High upper mantle gradients are required to avoid a shadow zone in the P_n arrivals. Although such a model adequately satisfies travel time constraints, it is rejected on the basis that it is thought to be geologically less likely. The later two suggestions cannot be readily qualified. However, compositional lamination at the base of the crust may be invoked on the basis that estimates of crustal thickness obtained from postcritical P_mP reflections are compatible with those obtained from P_n arrivals from shot point 10. The delayed large-amplitude reflections on shot point 10 may be caused by out of phase effects (Figure 8, arrow b).

Reflections observed on shot point 10 at offsets greater than 240 km with an apparent velocity exceeding 8.1 km/s are interpreted as an upper mantle reflection (Figure 8, $P_{um}P$). These upper mantle reflections tend to dominate the low-amplitude emergent P_n arrivals on shot point 10, adding further complexity to the determination of crustal thickness in New England. These upper mantle reflections ($P_{um}P$) are unreversed and are tentatively modeled by a small velocity step in the upper mantle.

Description of the Grenville model: The easternmost edge of the Adirondack massif is incorporated within the model as shown in Figure 2. The Grenvillian upper crust is characterized by exceptionally high upper crustal velocities (6.55–6.65 km/s). A thin surface layer is modeled with a velocity of 6.1 km/s. The top of a midcrustal interface is sharply defined by prominent midcrustal reflections at offsets of 50–90 km (Figure 4). This midcrustal body is referred to by *Klemperer et al.* [1985] as the Tahawus Complex, and it has been modeled by a planar midcrustal velocity discontinuity dipping to the east within the Grenvillian crust. Precritical reflections from the eastern extent of the Tahawus Complex observed on shot point 7 west provide important new evidence for the continuation of the Tahawus Complex beneath Vermont (P_tP in Figure 10). Amplitude modeling of shot point 7 west is severely restricted due to the combination of upper crustal reflections resulting in a complex summation of phases. Shot point 10 west lacks any upper crustal reflections, and this facilitates amplitude modeling of this midcrustal feature. A velocity contrast of 6.65 km/s to 6.8 km/s at 17 km depth adequately satisfies the observed travel time constraints. Improved amplitude matching may be obtained by a somewhat higher velocity contrast at the top of the Tahawus Complex, although the velocity at the top of the lower crust may not exceed 6.8 km/s, because higher apparent velocities will result in an advanced arrival time relative to the observed first-arrival phase in the Adirondacks. The lower crust beneath the Adirondack Massif is modeled with a velocity of 6.8–7.0 km/s; this adequately satisfies the previously discussed constraints imposed by critical P_mP reflections from shot point 10.

Description of the ramp structure: The contact between the Appalachian and Grenvillian provinces is marked by a lateral change in apparent velocity. This lateral transition in apparent velocity is observed at the same receiver position for all shot points traversing the Appalachian-Grenville boundary (Figure 11). Because this lateral change in apparent velocity occurs at a fixed receiver position, it marks a steeply dipping interface in the seismic velocity model. Constraints on the geometry of the Appalachian-Grenville contact are imposed by the apparent velocity and travel time paths of phases traversing the boundary. Shot points 9 and 10 situated immediately adjacent to the seismic velocity boundary provide critical reverse control on the discontinuity in the uppermost crust. The upper edge of the seismological boundary is located ~10 km east of shot point 10; this point is marked "hinge" in Figure 11. The boundary separating the low-velocity Appalachian crust from the high-velocity Grenvillian crust is therefore defined by the position of lateral transition in apparent velocity and by travel time modeling of upper and mid crustal phases traversing the boundary.

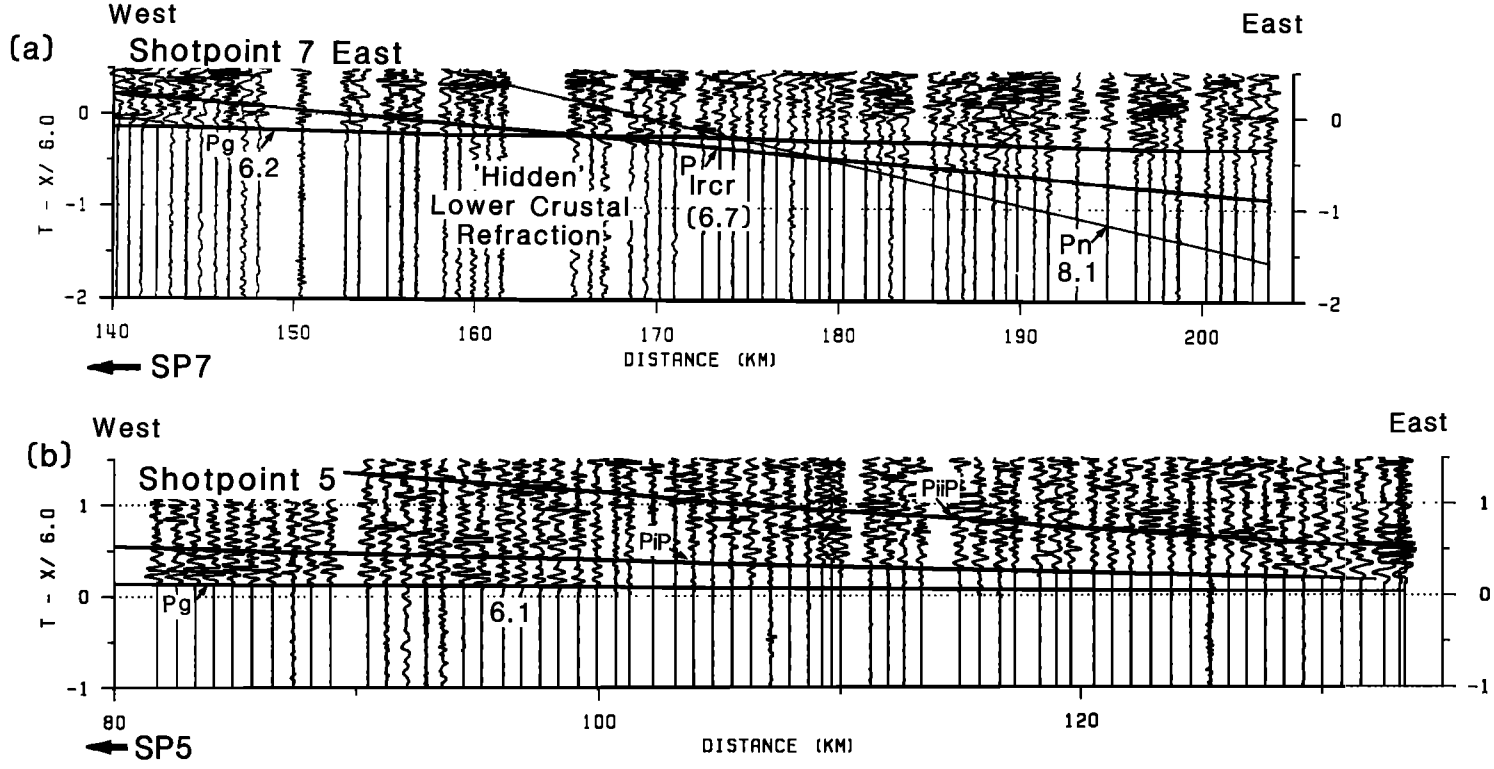

Fig. 7. Trace-normalized record sections from (*a*) shot point 7 east showing refracted direct arrivals from the lower crust (P_{lrcr}) modeled so that they are coincident with the first arrival around the P_n crossover and (*b*) shot point 5 showing weakly coherent critical reflections from the top of the lower crust ($P_{ll}P$) that are observed only in the absence of strong midcrustal reflections (P_lP). Note that the first-arrival branch is observed at offsets of 120 km with an apparent velocity of 6.1 km/s. Distances are plotted relative to shot point in each case. See Figure 3 for key to phase identification.

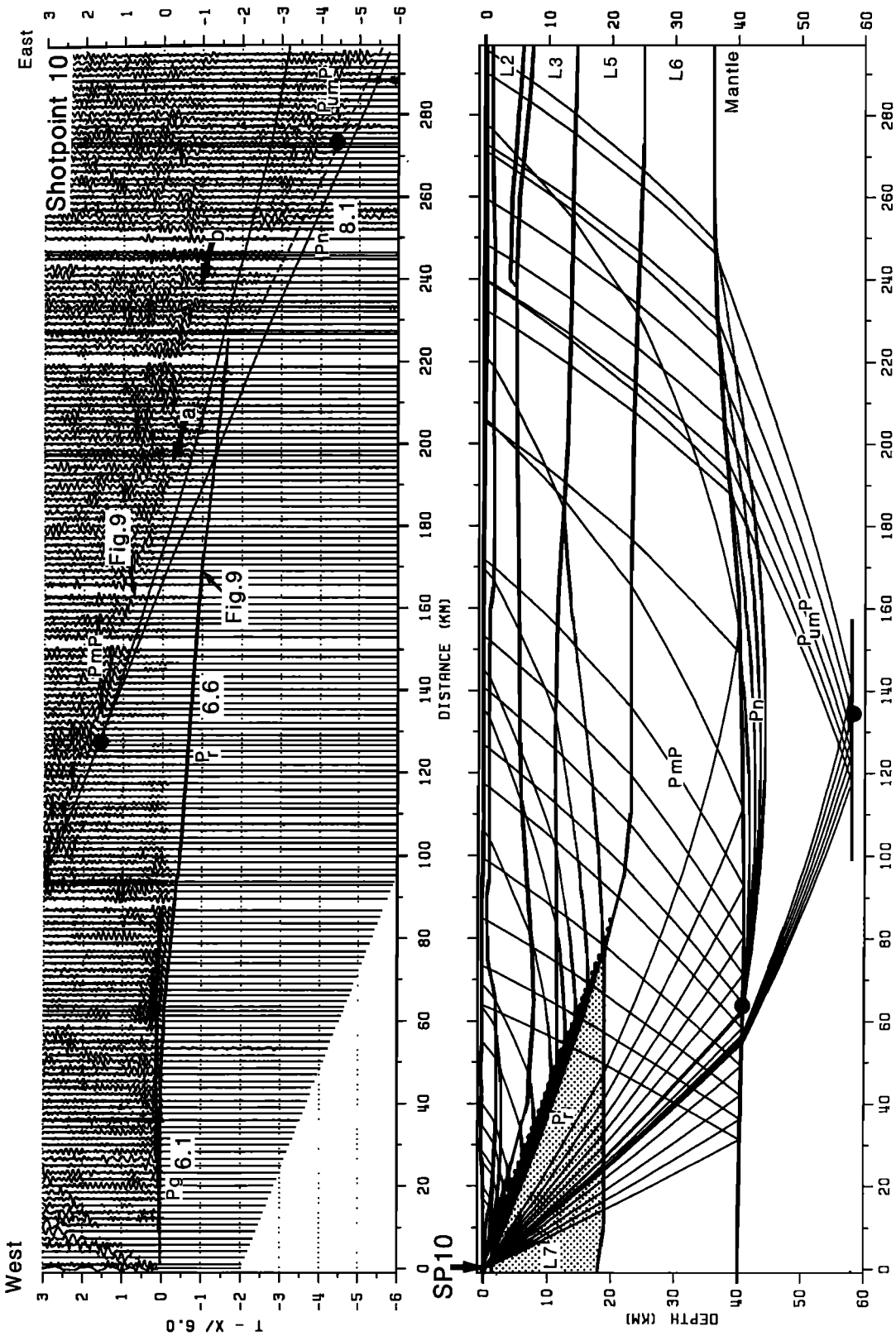

Fig. 8. Trace-normalized seismic refraction data from shot point 10 east (SP10 east) and ray diagram (bottom) for the model shown in Figure 2. Large-amplitude P_mP reflections dominate the record section. Offset and segmented *PmP* reflections (arrows a and b) may be the result of compositional lamination at the base of the crust or out of plane effects. The Grenville ramp structure is highlighted by the dotted line. For clarity, only every second seismic trace is plotted. Distances are plotted relative to shot point 10. See Figure 3 for key to phase identification.

A steeply dipping interface which extends to midcrustal depths beneath Vermont separates the high-velocity Grenville "block" from the lower velocities observed in the Appalachian upper crust. This velocity interface, referred to as the Grenville ramp, is reversed at all depths. Progressively deeper portions of the ramp are sampled by shot points at successively greater offsets from the Appalachian-Grenville contact. Rays originating from the west are refracted through the ramp structure and are transmitted through the lower-velocity Appalachian crust. Shot points west of the ramp therefore characteristically show high apparent Grenville velocities, followed by a rapid transition to a lower apparent velocity at offsets beyond the hinge (shot point 11 in Figure 11). East of the ramp the mirror image of this effect is observed; low Appalachian velocities give way to high Grenvillian velocities at offsets beyond the hinge (shot point 8 in Figure 11). The dipping structure of the ramp is determined by the modeling of apparent velocity and travel times for ray paths from several different shot points which traverse the ramp. The travel times of ray paths originating from shot points east of the ramp in Vermont can be integrated together to provide information on the dipping geometry of the ramp (Figure 11). If the boundary is too steeply dipping, then modeled arrivals will be too early and have too high an apparent velocity (and vice versa).

Constraints on the modeled geometry are imposed by reversing shot points in the Adirondacks. The deep geometry of the ramp structure is controlled by refracted first arrivals that have sampled Grenvillian velocities at their refracting horizon. Rays that are refracted through the deepest portions of the Grenvillian ramp are attenuated; on shot point 10 for example, the first-arrival branch is emergent at offsets exceeding 100 km. The apparent velocity of refracted first arrivals that have been transmitted down the ramp to midcrustal depths is characteristic of the high-velocity (6.6 km/s) Grenvillian crust. Because high-velocity "Grenvillian" first arrivals are observed extending into the Appalachians at offsets of 200 km from the Appalachian-Grenvillian contact, the ramp must continue to midcrustal depths. This effect can be seen on shot point 10, which lies almost directly above the ramp and whose refracted arrivals have a phase velocity of 6.6 km/s (P_r in Figure 9*a*). High apparent velocity discontinuous reflections are observed from the top of the ramp. Although these reflections cannot be satisfactorily resolved by two-dimensional ray-trace modeling, they indicate that the ramp is likely to be a complex laminated/imbricated structure.

Shear Wave Analysis

Shear wave velocities used in conjunction with compressional wave velocities provide important constraints on estimates of crustal composition. In this section, shear wave arrival times are qualitatively compared with those of compressional waves, and Poisson's ratios are calculated for phases traversing the upper and lower crust. Extended length travel time plots were produced to determine the strength of the recorded shear waves. Qualitative analysis was first carried out by overlaying shear wave data reduced at 3.46 km/s and plotted on a time axis compressed by $3^{1/2}$ to allow compressional and shear wave sections to be overlain and compared one to one. Such comparisons are in effect a measure of the relative compressional and shear wave velocities of the crust, and for a "normal" crustal Vp/Vs ratio of 1.732, shear wave arrivals should align exactly with those of the compressional waves. A delayed shear wave arrival indicates a high Vp/Vs ratio (and vice versa).

Prominent shear wave arrivals produced by shot point 10 enable Vp/Vs ratios to be determined for the rocks of the Appalachian and Grenville crustal blocks. An estimate of the average crustal shear wave velocity can be obtained by inspection of crust/mantle reflections. Large-amplitude wide-angle reflections from the base of the crust show delayed S_mS compared to that which would be expected for a "normal" Vp/Vs ratio, indicating that the New England Appalachians have a high average crustal Vp/Vs ratio (Figure 9*b*). In the Appalachian upper crust, shear waves are advanced by up to 0.3 s compared to that which would be expected for a "normal" Vp/Vs ratio (S_r in Figure 12*a*). In comparison, the upper crustal shear wave phase in the Adirondacks is delayed by at least 0.5 (S_7 in Figure 12*a*). Reflections from the Tahawus Complex are delayed by almost a second (S_tS in Figure 12*a*). These qualitative observations show relatively slow shear wave velocities in the Adirondacks (high Vp/Vs ratio) and somewhat higher shear wave velocities in the Appalachians (low Vp/Vs ratio).

A useful criterion for determining crustal compositions is the calculation of Poisson's ratio. Arrival times of compressional and shear wave phases at a given receiver location were picked, enabling Poisson's ratio to be calculated for any particular travel time path [*Luetgert*, 1990]. For a given ray set (arrival branch), multiple calculations of Poisson's ratio may be made, which when averaged together provide information on the region of the crust through which the ray set has penetrated. For ray paths originating from shot point 10 and traversing the Appalachian upper crust, normal Poisson's ratios of 0.24 ± 0.01 were obtained, while higher ratios of 0.28 ± 0.01 were obtained for the upper crust in the Adirondacks (Figure 12*b*). Somewhat more coherent results were obtained for the upper crust than for Moho reflections, where lower signal to noise ratios hampered precise shear wave arrival time picks. A Poisson's ratio of 0.26 ± 0.01 was obtained by picking travel times for P_mP and S_mS arrivals on shot point 10. The derived Poisson's ratios are discussed more fully in terms of their relation to crustal composition in the following sections.

Discussion

The compressional wave velocity model derived for the western New England Appalachians and the Adirondack Mountains provides important new constraints on the deep crustal structure of juxtaposed Proterozoic/lower Paleozoic terranes in eastern North America. In the present study, seismic refraction/wide-angle reflection data are interpreted to show a steeply dipping ramp structure that separates the Proterozoic craton of North America from the obducted Appalachian allochthons. Recent compilations of geologic and geophysical data collected in the northern Appalachians include studies by *Taylor* [1989], *Hatcher et al.* [1990], *Costain* [1990], and *Stewart et al.* [1991]. We present a synthesis of the most recent seismic experiments traversing the Appalachian-Grenville boundary in New England. The integration of compressional and shear wave velocity information obtained in this study with geologic and physical property data is used to infer the deep crustal composition of these juxtaposed terranes.

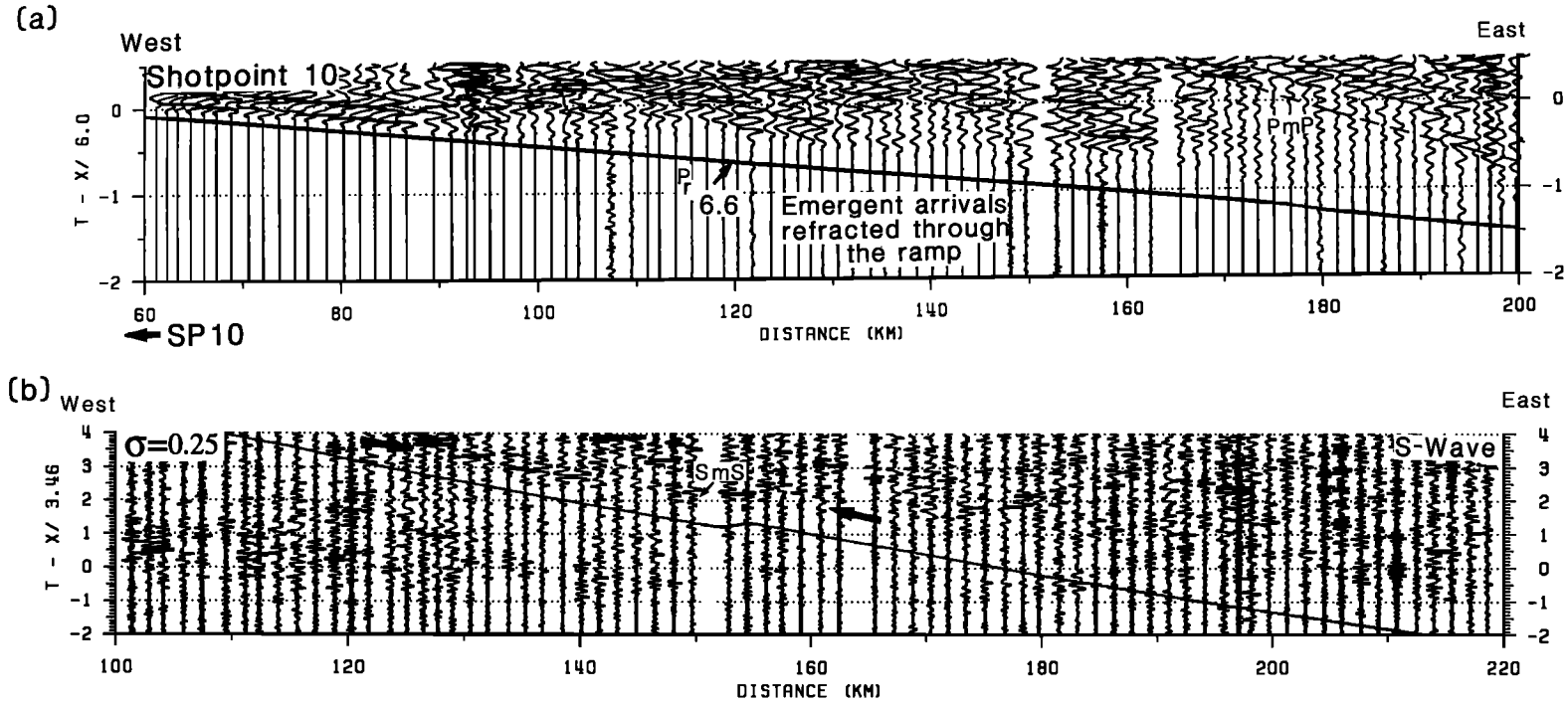

Fig. 9. Enlarged portions of the record section for shot point 10 east (Figure 8) showing (*a*) the refracted phase through the Grenville ramp *Pr* and (*b*) segmented and en echelon Moho reflections. The delayed P_mP arrivals at 150 km can be modeled by a small step in the Moho although this geometry is regarded as geologically less likely. Predicted travel times (solid lines) are plotted on the *S* wave section, assuming a Poisson's ratio of 0.25. The delayed S_mS phase provides evidence for a mafic lower crust beneath the New England Appalachians. On the *S* wave section the reduction velocity is 3.46 km/s, and the time axis is compressed by $3^{1/2}$ relative to the *P* wave time axis. See Figure 3 for key to phase identification.

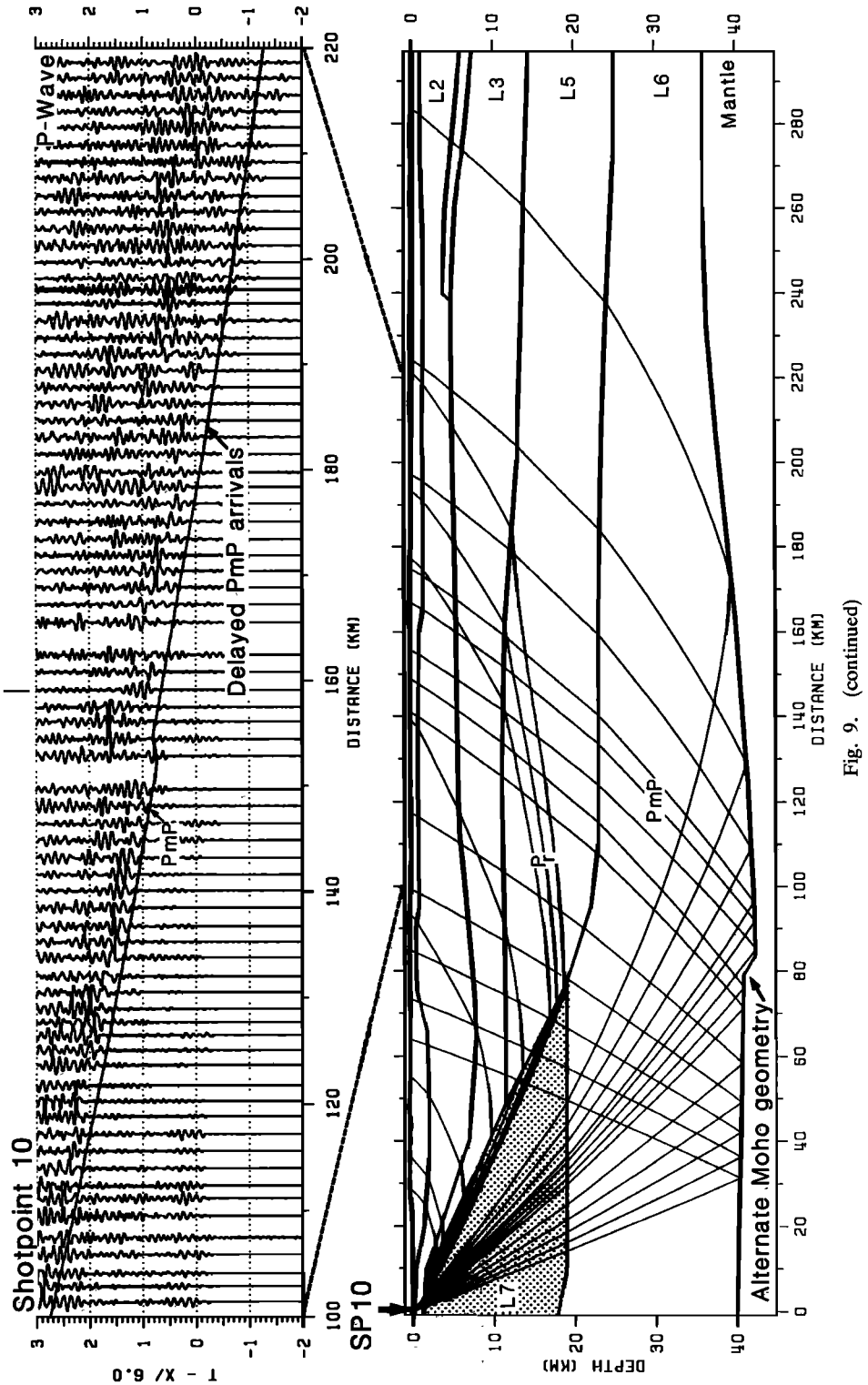

Fig. 9. (continued)

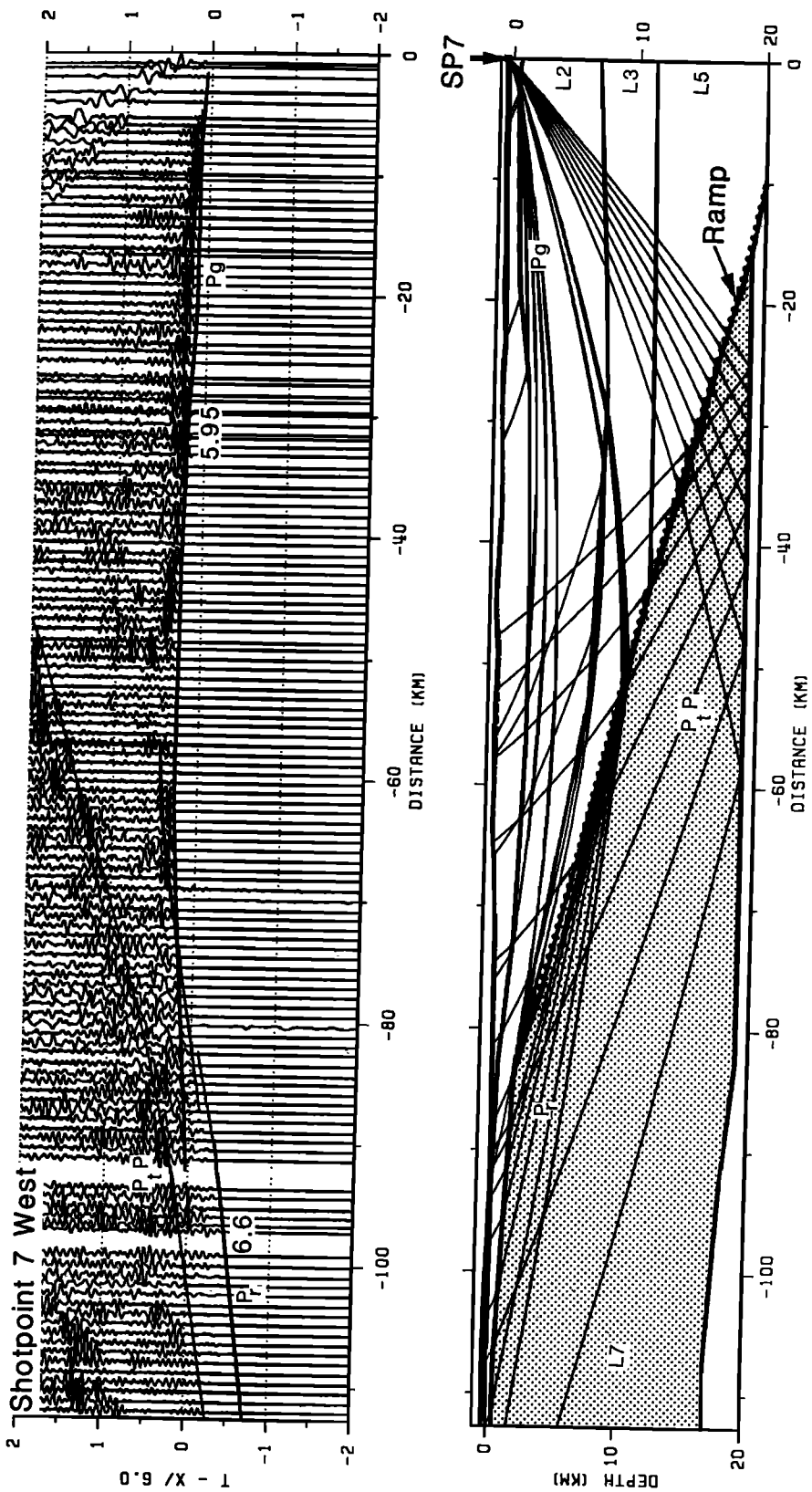

Fig. 10. Trace-normalized seismic refraction data from shot point 7 west (SP7 west) and ray diagram (bottom) for the western portion of the model shown in Figure 2. A lateral velocity transition is marked by the abrupt increase in apparent velocity at −80 km. Precritical reflections (P_rP) from SP7 west provide important new evidence for the continuation of the Tahawus Complex beneath western Vermont. Distances are plotted relative to shot point 7. The Grenvillian crust is shown stippled, and the ramp structure is highlighted by the dotted line. See Figure 3 for key to phase identification.

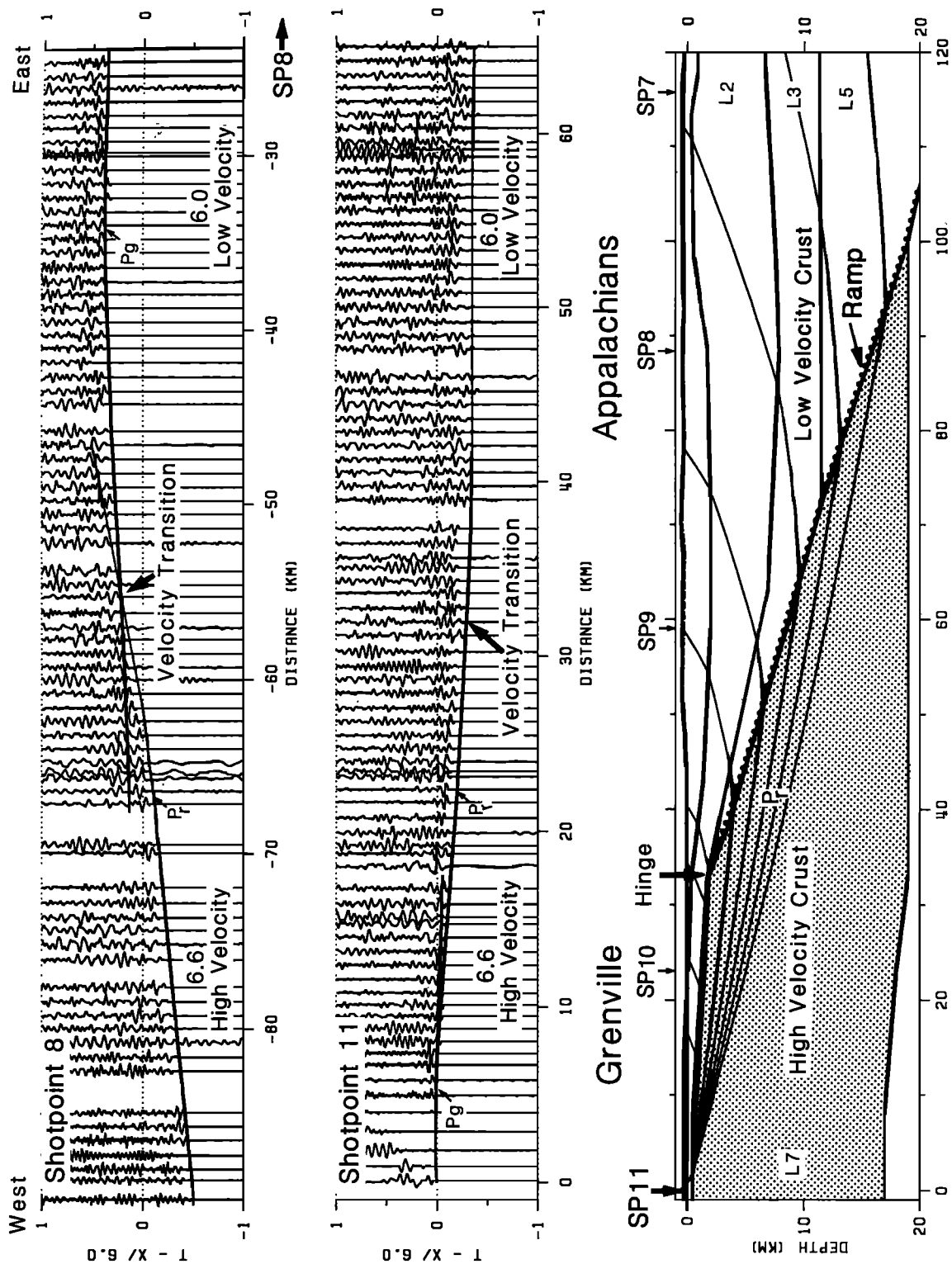

Fig. 11. The Appalachian-Grenville contact is characterized by a lateral velocity transition. This velocity transition is located at the same receiver position for all shot points traversing the boundary and is labeled "hinge". East of the hinge in the Adirondack upper crust, high velocities are observed, while west of the hinge, low Appalachian velocities are observed. The record section for shot point 8 (top) shows an increase in apparent velocity at offsets beyond the hinge. Shot point 11 (middle) shows a decrease in apparent velocity beyond the hinge. See Figure 3 for key to phase identification.

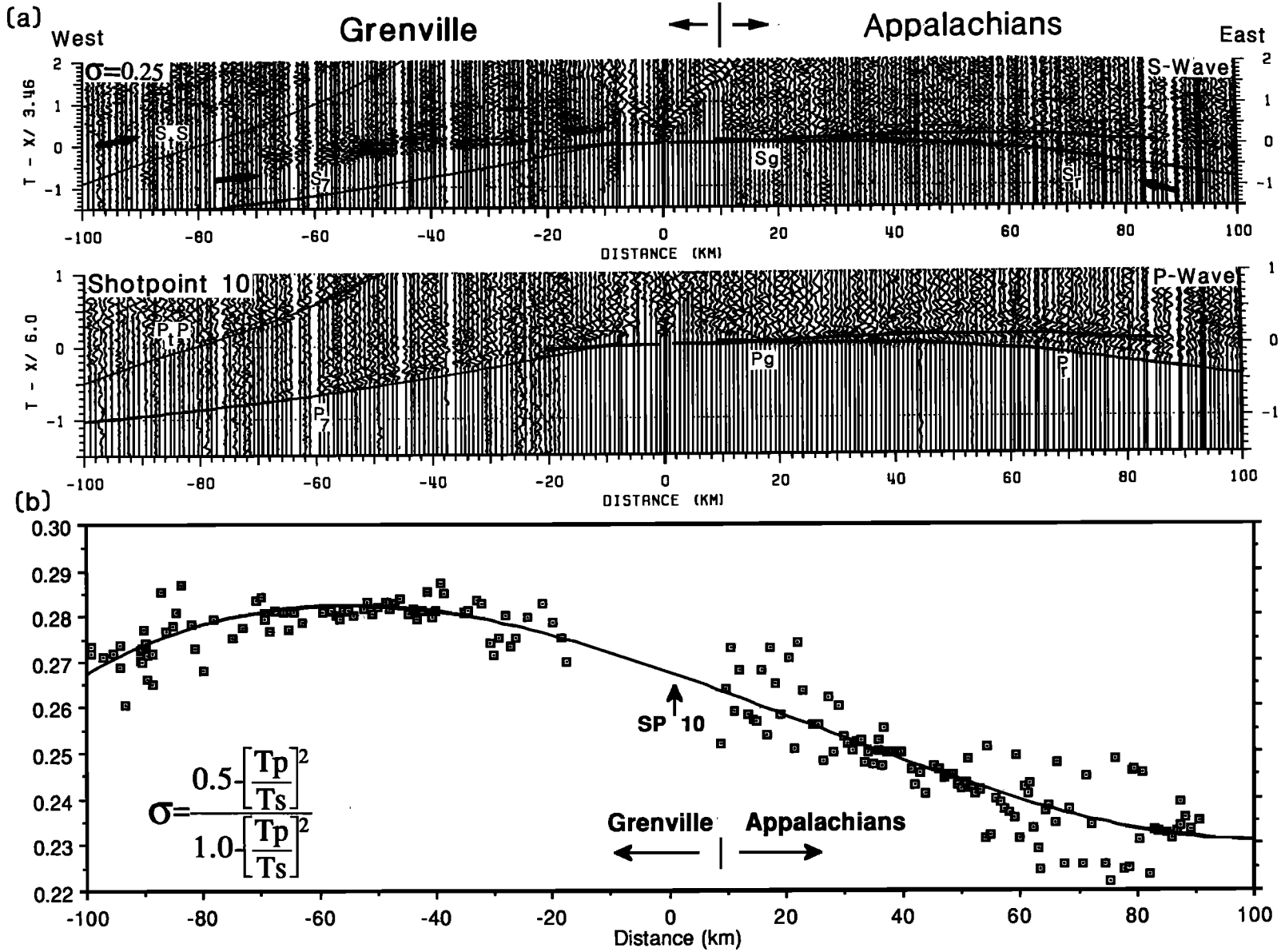

$$\sigma = \frac{0.5 - \left[\frac{Tp}{Ts}\right]^2}{1.0 - \left[\frac{Tp}{Ts}\right]^2}$$

Fig. 12. Variations in Poisson's ratio in upper crustal rocks near the edge of the Adirondack Mountains. (*a*) Record sections for shot point 10 show delayed *S* wave arrivals for ray paths through the Grenvillian crust and advanced *S* wave arrivals in the Appalachians. Predicted travel times (solid lines) for the model shown in Figure 2 are plotted on the *S* wave section, assuming a Poisson's ratio of 0.25. (*b*) Upper crustal P_g and S_g arrival times at each receiver station have been used to calculate Poisson's ratio from shot point 10. High Poisson's ratios observed in the Adirondack Highlands can be correlated with the Marcy Anorthosite, and normal Poisson's ratios observed for the upper crust in Vermont indicate the predominance of quartz-rich lithologies. See Figure 3 for key to phase identification.

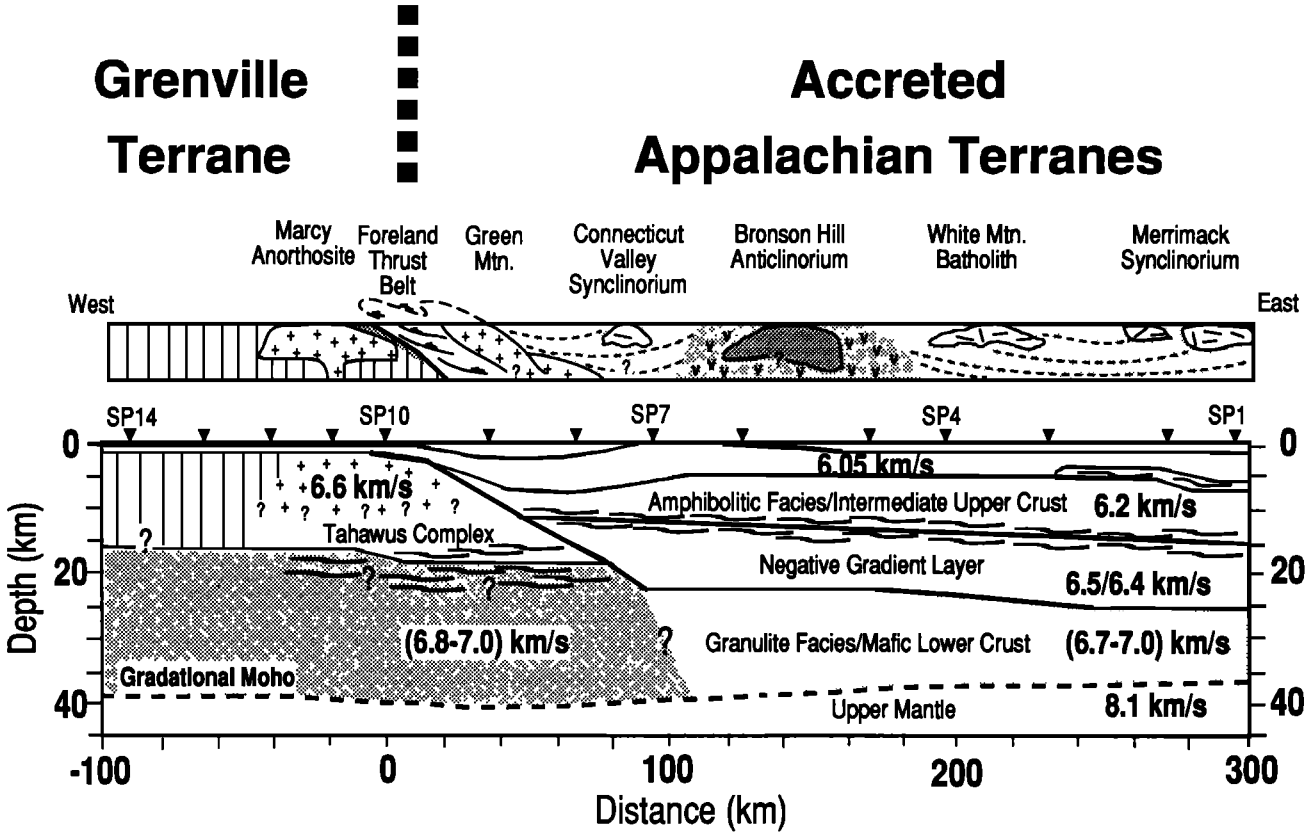

Fig. 13. Geologic interpretation of the first-order velocity model shown in Figure 2. A midcrustal penetrating ramp separates the Grenvillian crustal block from the accreted Appalachian terranes. A ramp structure divides the high-velocity Grenville terrane from the lower-velocity subhorizontally layered Appalachian crust. The lower crust is shown as a continuous layer, but it may be divided into discrete Appalachian/Grenville units. Solid lines indicate first-order velocity discontinuities; dashed lines indicate complex laminated gradational interfaces. Prominent midcrustal reflective interfaces are highlighted by the wavy lines.

Structure of the Grenvillian ramp: The Grenvillian ramp imaged by forward modeling of this seismic data set separates the autochthonous Grenville rocks and their "cover" sequence of the Adirondack region from the allochthonous Appalachian terranes. The relatively low resolution of the New England-New York seismic refraction profile means that only broad features of the seismic velocity structure of the crust are resolved. In short, we can trace a velocity interface that separates high seismic velocities characteristic of the Grenvillian upper crust from those of the lower-velocity rocks of the western Appalachians (Figure 13). The simplicity of this velocity interface belies the geological complexity of the basement-cover relationship of the Grenville crustal block. In the Champlain Valley, autochthonous platformal carbonates and quartzites lie in situ above the Grenvillian basement. These platformal rocks are imbricated with allochthonous slope rise lithologies of the Foreland Thrust Belt. Further east the Green Mountain Anticlinorium exposes obducted slices of Grenvillian basement interposed between the allochthonous "cover" sequence in the Taconic Orogeny. This imbricated wedge of allochthonous and autochthonous rocks is at its narrowest, and most structurally complex, at the point were the New England–New York seismic profile crosses into the Grenvillian crust. We interpret the Grenvillian ramp as the basal detachment of the allochthonous thrusted rocks of the Appalachians. The Grenville ramp is likely to be a highly complex thrust-imbricated and mylonitized remnant of the pre-Taconic (Ordovician) margin of proto–North America, upon which the accreted Bronson Hill island arc complex was obducted in Mid-Upper Ordovician times. Subsequent reactivation of the ramp in the Acadian Orogeny (Devonian) is strongly suggested by tectonic syntheses in the New England region [*Rowley and Kidd*, 1980; *Stanley and Ratcliffe*, 1985].

In the vicinity of our profile the transition from autochthonous Grenvillian lithologies to the accreted allochthons of the western Appalachians is delineated by the Champlain thrust (Logans Line). Comparison of results obtained from recent seismic experiments traversing the Appalachian-Grenville boundary may be usefully illustrated by aligning the models obtained from these experiments with respect to Logans Line (Figure 14). In northern Maine a major zone of reflections extends from shallow depths beneath the Foreland Thrust Belt to 25 km depth beneath the Chain Lakes Massif [*Stewart et al.*, 1986; *Spencer et al.*, 1987, 1989]. This reflection package has been interpreted as a "décollement" surface separating the allochthonous upper crustal units of the Appalachians from the autochthonous Grenvillian crust which underlies much of the western Appalachians (Figure 14*a*). Comparison of the Quebec-Maine "décollement" surface with the ramp model presented herein suggests that a remarkable degree of similarity exists along strike between these two models (Figure 14*b*). In the New England–New York seismic experiment the subcrop of the ramp structure

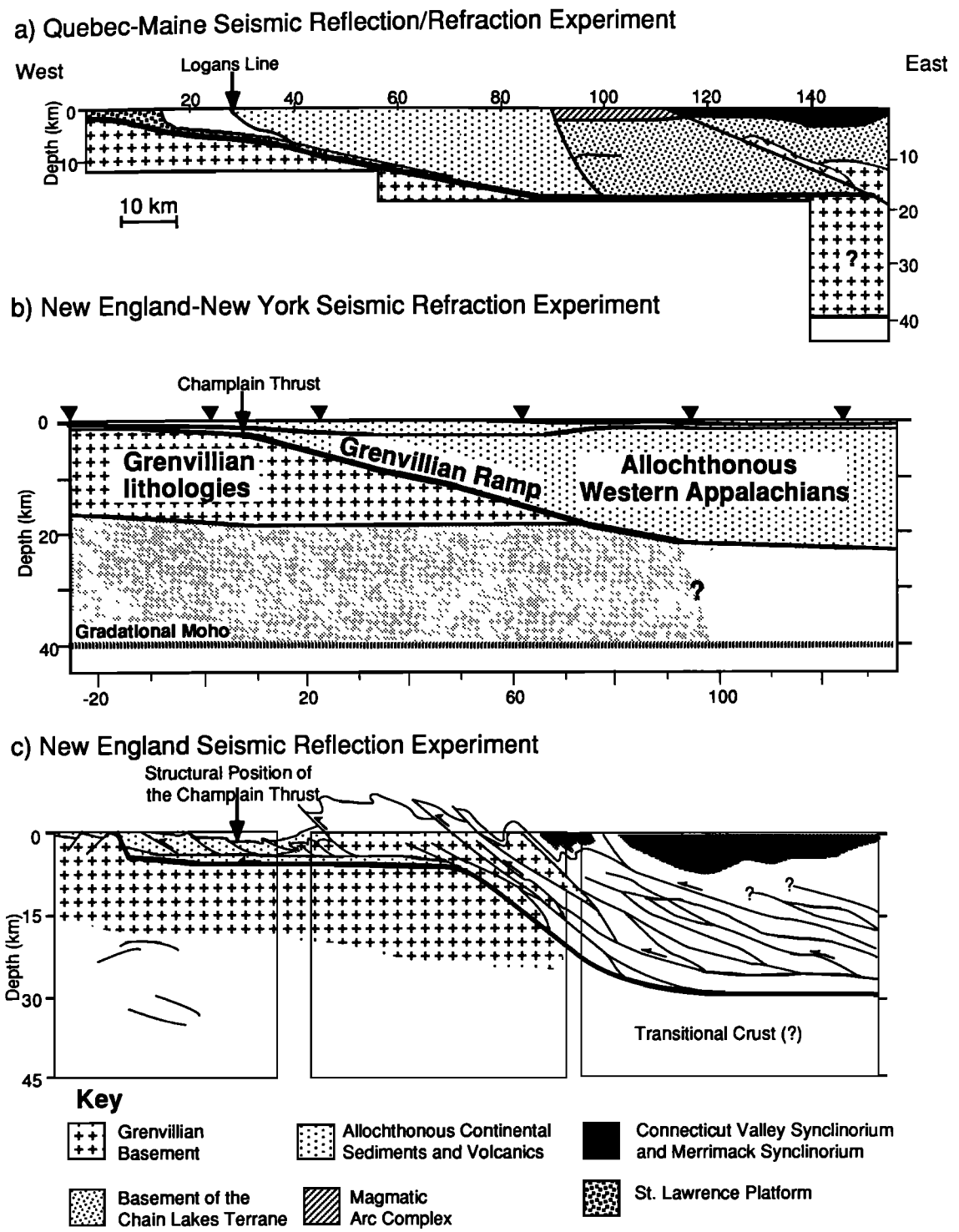

Fig. 14. Comparison of recent seismic experiments across the Appalachian-Grenville terrane boundary in New England. From north to south the results obtained from these seismic experiments are (*a*) the Quebec-Maine reflection/refraction experiment in southern Quebec [*Stewart et al.*, 1986; *Spencer et al.*, 1987, 1989], (*b*) the New England seismic refraction profile discussed herein, and (*c*) deep reflection profiling across the Taconic Allochthon in southern Vermont [*Brown et al.*, 1983; *Ando et al.*, 1984]. The boundary between the Grenvillian Province and the accreted Appalachians is characterized by noticeably similar planar ramp structures extending to midcrustal depths beneath the thrusted allochthons of the western Appalachians.

lies approximately at the position of the Champlain thrust. The resolution of the data does not allow us to definitively link these two features. Deep seismic reflection profiling in southern Vermont images a "thin skin" detachment beneath the Taconic allochthon which extends in the form of a steep "steplike" thrust imbricated structure beneath the Bronson Hill Anticlinorium to a depth of 30 km as shown in Figure 14*c* [*Brown et al.*, 1983; *Ando et al.*, 1984; *Phinney and*

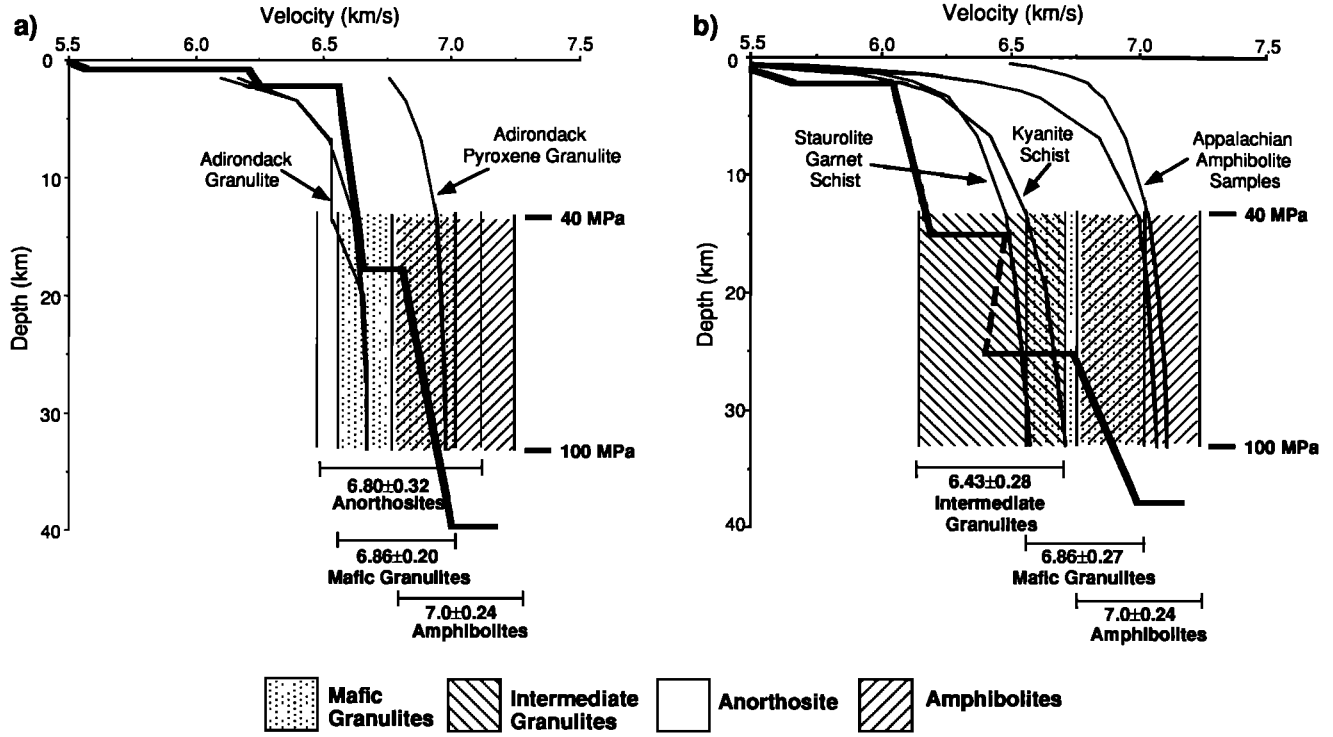

Fig. 15. Comparison of one-dimensional velocity functions (heavy line) for (*a*) the Appalachians (shot point 4) and (*b*) Adirondacks (shot point 11) with laboratory velocity measurements of samples at elevated pressures. Average seismic velocities are presented for possible constituents of the lower crust; ranges shown are one standard deviation [*Holbrook et al.*, 1991]. The lower crustal velocities beneath the central Appalachians are inferred to be best represented by mafic granulites (anhydrous feldspar, pyroxene, and garnet assemblages). Laboratory data have been corrected for temperature using a geotherm of 15°C/km [*Blackwell*, 1971] and an average thermal coefficient of 2.0×10^{-4} km/(s °C^{-1}) [*Christensen*, 1979; *Kern and Richter*, 1981]. Samples referenced are from *Christensen* [1965] and *Holbrook et al.* [1991].

Roy-Chowdhury, 1989]. Recent reprocessing of the southern Vermont profiles has resulted in a reinterpretation which suggests that the Appalachian/Grenville boundary is delineated by a series of steep planar imbricated fault zones extending into the lower crust [*Thigpen*, 1989]. Despite the relatively low resolution of seismic refraction profiling a consistent image of the buried edge of the Grenville Province emerges from comparison of the Quebec-Maine transect, the Vermont profiles, and the present study. The variations observed in the near-surface geometry of the ramp structure most likely owe their origin to lateral geologic discontinuities in the allochthonous Appalachian units. In the light of these results we tentatively suggest that the buried edge of the Grenville Province may be mapped extending beneath the Appalachians to a depth of around 25 km, at least as far as the eastern boundary of the Connecticut Valley Synclinorium.

Composition of the Grenvillian crust: In the present study the Grenvillian upper crust is characterized by high compressional wave velocities (6.6 km/s) and high Poisson's ratios (0.28 ± 0.01). Laboratory measurements of compressional wave velocities and Poisson's ratios for samples of Adirondack granulites and meta-anorthosites at elevated pressures are consistent with the derived velocity model shown in Figure 15*a* [*Birch*, 1960; *Christensen and Fountain*, 1975]. The Marcy Anorthosite is exposed at the western end of our profile as it crosses the metaigneous Adirondack massif. Gravity modeling of the Marcy Anorthosite indicates that it is tabular in shape and extends to a depth of 4 km, possibly with roots extending to 10–15 km [*Simmons*, 1964]. A suitable seismological analogue of the gravity model would be a 4-km-thick anorthosite layer with a velocity of 6.6 km/s, underlain by a layer composed of granulitic gneisses (exposed in the Adirondacks). Samples of granulitic gneisses in the high-pressure laboratory generally have upper crustal velocities less than those of anorthosite [*Birch*, 1960; *Christensen*, 1965; *Christensen and Fountain*, 1975]. Thus, if the Marcy Anorthosite were a shallow sheetlike intrusion as suggested by gravity modeling, a decrease in signal amplitude and a simultaneous delay in the arrival time branch from the lower-velocity gneissic crust would be observed. The absence of such features indicates that at the base of the Marcy Anorthosite, similar compressional wave velocities are observed for both the anorthosite and the underlying gneisses. At depths exceeding 10 km, meta-anorthosite and granulitic gneisses have similar compressional wave velocities and as such are seismically indistinguishable. The Marcy Anorthosite is likely to be around 10 km thick (Figure 13).

Composition of the Appalachian crust: The New England Appalachian upper crust is composed of upper greenschist to middle amphibolite facies sediments/volcanics and numerous intermediate to acidic metaigneous bodies. No identifiable reflections or travel time anomalies were observed from such major bodies as the Green Mountains, the Bronson Hill Anticlinorium, or the White Mountain Batholith. High-

amplitude upper crustal reflections observed beneath the easternmost extent of our profile may be explained by the presence of gneissic layering or by the subcrop of the New Hampshire Series granites exposed along the profile, and this would certainly fit with extrapolations of gravity models derived for the New Hampshire granites [*Nielson et al.*, 1976; *Hodge et al.*, 1982]. The modeled upper crustal velocities of around 6.1–6.2 km/s are consistent with laboratory measurements for a compositionally diverse set of gneisses, schists, metagabbros, and granodiorites [*Birch*, 1960; *Christensen*, 1965; *Christensen and Fountain*, 1975] (W. S. Holbrook et al., The seismic velocity structure of the deep continental crust, submitted to *Journal of Geophysical Research*, 1991).

The two-dimensional seismic velocity model for the New England Appalachian crust significantly lacks lateral velocity variations which might be correlated with terrane boundaries (Figure 13). This must, in part, be a consequence of the extensive obduction that formed the western Appalachians, where terrane boundaries are interpreted as highly imbricated structures [*Rowley and Kidd*, 1980; *Stanley and Ratcliffe*, 1985]. We envisage successive high-grade thermal "pulses" associated with at least three orogenic episodes resulting in regional amphibolite metamorphism, widespread plutonic intrusion, migmatization and, at deep levels, wholescale melting and mixing resulting in a largely homogenized Appalachian crustal block. Removal of the upper crust through successive periods of unroofing/isostatic uplift [*Eusden et al.*, 1987; *Chamberlain et al.*, 1985; *Harrison et al.*, 1989] reveals a window into highly deformed and altered midcrustal rocks which appear seismically homogeneous. The apparent seismic homogeneity of the New England upper crust is thus a possible indication of the overall mineralogical similarity of the constituents of the present-day upper crust. It is thus the case that although widely differing lithologies are observed at outcrop throughout the New England Appalachians, we are unable to resolve their seismological heterogeneity in the present study.

In this study, the midcrust (layer 5) is represented by a 10-km-thick layer which has been modeled with a negative seismic velocity gradient (Figure 13). This feature of the model may be related to compositional and thermal properties of the midcrust. Zones of velocity reversal can be produced by the anisotropic thermal expansion of the individual mineral constituents of the crust [*Christensen*, 1979; *Kern and Richter*, 1981]. In the eastern United States the geothermal gradient is ~15°C/km [*Blackwell*, 1971]. High thermal coefficients for likely constituents of the midcrust (amphibolitic granitic gneisses) mean that critical thermal gradients will be exceeded, and a velocity reversal will result [*Christensen*, 1979; *Kern and Richter*, 1981]. The magnitude of the velocity reversal produced by high temperatures is dependent on the the thermal gradient and the mineralogy of the crust, but it is unlikely to exceed 0.01 s^{-1} [*Christensen*, 1979]. At the top of the midcrust a planar reflecting horizon marks an abrupt increase in seismic velocity. The appearance of prominent midcrustal reflections over regional dimensions is a noticeable feature of this data set and of others collected in the vicinity [*Klemperer and Luetgert*, 1987; *Luetgert and Mann*, 1990; *Hennet et al.*, 1991]. Midcrustal reflectivity may be related to gneissic lamination, igneous "ponding", fluid rich zones in the midcrust, or bulk compositional changes. While all of the above may be considered as suitable proponents, the associated increase in seismic velocity observed in this study is most likely representative of bulk compositional change across the midcrustal interface. We consider that the midcrustal reflector delineates an increase in the mafic content of the crust.

Uncertainties in the derived velocity structure of the lower crust mean that lower crustal compositions cannot be unequivocally determined. In this study, shear wave velocity information is used to reduce the uncertainty in inferring the composition of the lower crust from compressional wave velocities alone, since shear wave velocities are sensitive to the felsic content of the crust. The incorporation of shear wave velocities into models of crustal composition enables the calculation of Poisson's ratio, a parameter which may be most usefully thought of as an indication of the relative quartz/feldspar content of the crust. Regions which exhibit low Poisson's ratios (low Vp/Vs) are typically quartz rich, since quartz has high shear wave velocities [*Christensen and Fountain*, 1975]. An estimate of Poisson's ratio for the lower crust may be obtained by removing the observed upper crustal Poisson's ratios from values obtained from phases traversing the whole crust. The delayed S_mS phase relative to a "normal" Vp/Vs ratio of 1.732 indicates an average crustal Poisson's ratio of 0.26 ± 0.01 (Figure 9*b*). Upper crustal rocks in New England have "normal" Poisson's ratios (0.24 ± 0.01). The travel time delay observed for phases traversing the entire crust must be restricted to the lower crust. Poisson's ratios for lower crustal rocks beneath the New England Appalachian are then likely to exceed 0.26.

A recent compilation of laboratory-measured rock velocities enables both compressional and shear wave velocities to be calculated for a particular rock type [*Holbrook et al.*, 1991]. Although the assignment of seismic velocity to rock type is highly dependent on the samples chosen to represent a particular compositional range, this data set provides a useful means of specifying end-members of a compositional series beyond which constraints imposed by in situ seismic velocities can not be satisfied. The high compressional wave velocities (6.7–7.0 km/s) and high Poisson's ratios (0.26–0.27) observed for rocks of the lower crust tend to favor an intermediate-mafic composition. Possible constituents of the lower crust include anorthosite, intermediate-mafic granulites, and amphibolitic assemblages. Laboratory determinations of Poisson's ratios for samples of anorthosites of around 0.29 [*Holbrook et al.*, 1991] suggest that anorthosite is an unlikely constituent of the lower crust in New England. Amphibolitic assemblages (metagabbro/hornblende, feldspar, pyroxene) at elevated pressures generally have compressional wave velocities exceeding those derived herein, while felsic granulites generally have compressional wave velocities much less than those observed beneath the New England Appalachians [*Birch*, 1960; *Christensen*, 1965; *Holbrook et al.*, 1991]. The most favorable composition for the lower crust is a mafic granulite facies assemblage containing feldspar, pyroxene, and garnet (Figure 15*b*).

Xenoliths provide direct evidence of lower crustal composition and can be used to reduce the nonuniqueness inherent in inferring composition from seismic velocities alone. Lamprophyre dike suites at Ayres Cliff, Quebec, and North Hartland, Vermont, contain granulite facies xenoliths [*Williams and McHone*, 1984; *Trzcienski and Marchildon*, 1989]. The xenoliths from Ayres Cliff are relatively unaltered and are commonly of two types: (1) metapelitic assemblages

originating from midcrustal depths, which are interpreted as Cambrian metasediments and (2) mafic assemblages and anorthosite fragments which are readily correlated to Grenville exposures in the Adirondacks. The North Hartland xenoliths are relatively unaltered lower crustal/upper mantle ultramafics and quartz-plagioclase granulites. These xenoliths support the existence of Grenville crust extending beneath the Appalachians at least as far as the western edge of the Connecticut Valley Synclinorium.

The obduction of the western Appalachians against the Grenvillian crustal block in the Taconic Orogeny has resulted in the juxtaposition of allochthonous lower Paleozoic continental sediments and volcanics against the Proterozoic protolith of North America. The seismic refraction date set obtained in this study allows us to characterize the seismic velocity structure of the accreted terranes in the New England Orogen. We can trace a steeply dipping ramp structure that divides the Grenvillian crust from the allochthonous Appalachian units emplaced during the Taconic Orogeny. The Grenvillian ramp extends to midcrustal depths at least as far as the western portion of the New England Appalachians. The Grenvillian lower crust appears seismically indistinguishable from the lower crust beneath the accreted Appalachian allochthons in spite of profound differences in the upper crustal structures and lithologies. This suggests that the lower crust may have been largely reformed, homogenized, and annealed during successive lower Paleozoic orogenic events and subsequent Mesozoic extension.

Acknowledgments. The data presented in this paper were collected by the U.S. Geological Survey, the Geological Survey of Canada, and the U.S. Air Force Geophysics Laboratory. We thank Walter Mooney (USGS), Jill McCarthy (USGS), and Bruce Beaudoin (Stanford University) for constructive reviews of earlier drafts of this manuscript. S.H. gratefully acknowledges financial support provided by the National Environmental Research Council, United Kingdom, (GT4/88/GS/64) and thanks his colleagues at the USGS, Menlo Park, California, for their assistance and encouragement. Reviews by Dave Stewart (USGS) and two anonymous reviewers greatly enhanced this manuscript.

REFERENCES

Ando, C. J., et al., Crustal profile of a mountain belt: COCORP deep seismic reflection profile in New England and implications for architecture of convergent mountain chains, *AAPG Bull.*, *68*, 819–837, 1984.

Birch, F., The velocity of compressional waves in rocks at 10 kbar, 1, *J. Geophys. Res.*, *65*, 1083–1102, 1960.

Blackwell, D. D., The thermal structure of the continental crust, in *The Structure and Physical Properties of the Earth's Crust*, *Geophys. Monogr. Ser.*, vol. 14, edited by J. G. Heacock, AGU, Washington, D. C., 1971.

Bradley, D. C., Tectonics of the Acadian Orogeny in New England and adjacent Canada, *J. Geol.*, *91*, 381–400, 1983.

Brown, L., C. Ando, S. Klemperer, J. Oliver, S. Kaufman, B. Czuchra, T. Walsh, and Y. W. Isachsen, Adirondack-Appalachian crustal structure: The COCORP northeast traverse, *Geol. Soc. Am. Bull.*, *94*, 1173–1184, 1983.

Cerveny, V., I. A. Molotkov, and I. Psencik, *Ray Method in Seismology*, 214 pp., Karolva University Press, Prague, 1977.

Chamberlain, C. P., and P. C. England, The Acadian thermal history of the Merrimack Synclinorium in New Hampshire, *J. Geol.*, *93*, 593–602, 1985.

Christensen, N. I., Compressional wave velocities in metamorphic rocks at pressures to 10 kbar, *J. Geophys. Res.*, *70*, 6147–6164, 1965.

Christensen, N. I., Compressional-wave velocities in rocks at high temperatures and pressures, critical thermal gradients, and crustal low velocity zones, *J. Geophys. Res.*, *84*, 6849–6857, 1979.

Christensen, N. I., and D. M. Fountain, Constitution of the lower continental crust based on experimental studies of seismic velocities in granulite, *Geol. Soc. Am. Bull.*, *86*, 227–236, 1975.

Costain, J. K., R. D. Hatcher, Jr., C. Coruh, T. J. Pratt, S. R. Taylor, J. J. Litehiser, and I. Zietz, Geophysical characteristics of the Appalachian crust, in *The Appalachian-Ouachita Orogen in the United States*, *The Geology of North America*, vol. F-2, edited by R. D. Hatcher, Jr., pp. 385–416, Geological Society of America, Boulder, Colo., 1990.

Eusden, J., W. A. Bothner, and A. M. Hussey, The Kearsarge-Central Maine synclinorium of southeast New Hampshire and southwestern Maine: Stratigraphic and structural relations of an inverted section, *Am. J. Sci.*, *287*, 246–264, 1987.

Harrison, M. T., F. S. Spear, and M. T. Heilzer, Geochronologic studies in central New England II: Post-Acadian hinged and differential uplift, *Geology*, *17*, 185–189, 1989.

Hatcher, R. D., Jr., P. H. Osberg, A. A. Drake, Jr., P. Robinson, and W. A. Thomas, Tectonic map of the U.S. Appalachians, in *The Appalachian-Ouachita Orogen in the United States*, *The Geology of North America*, vol. F-2, plate 1, edited by R. D. Hatcher, Jr., et al., Geological Society of America, Boulder, Colo., 1990.

Hennet, C. G., J. H. Luetgert, and R. A. Phinney, The crustal structure in central Maine from coherency processed refraction data, *J. Geophys. Res.*, *96*, 12,023–12,037, 1991.

Hodge, D. S., D. A. Abbey, M. A. Harbin, J. L. Patterson, M. J. Ring, and J. F. Sweeney, Gravity studies of subsurface mass distributions of granitic rocks in Maine and New Hampshire, *Am. J. Sci.*, *282*, 1289–1324, 1982.

Kern, H., and A. Richter, Temperature derivatives of compressional and shear wave velocities in crustal and mantle rocks at 6 Kbar confining pressure, *J. Geophys.*, *49*, 47–56, 1981.

Klemperer, S. L., and J. H. Luetgert, A comparison of reflection and refraction processing and interpretation methods applied to conventional refraction data from coastal Maine, *Bull. Seismol. Soc. Am.*, *77*, 614–630, 1987.

Klemperer, S. L., L. D. Brown, J. E. Oliver, C. J. Ando, B. L. Czuchra, and S. Kaufman, Some results of COCORP seismic reflection profiling in the Grenville-age Adirondack Mountains, New York State, *Can. J. Earth Sci.*, *22*, 141–153, 1985.

Luetgert, J. H., Users manual for RAY83/R83PLT: Interactive two-dimensional raytracing/synthetic seismogram package, *U.S. Geol. Surv. Open File Rep.*, *88-238*, 1988*a*.

Luetgert, J. H., Users manual for RSEC88: Interactive computer program for plotting seismic refraction record sections, *U.S. Geol. Surv. Open File Rep.*, *88-262*, 1988*b*.

Luetgert, J. H., Users manual for R1D84: Interactive modeling of one-dimensional velocity depth functions, *U.S. Geol. Surv. Open File Rep.*, *88-262*, 1988*c*.

Luetgert, J. H., and C. E. Mann, Avalon terrane in eastern coastal Maine: Seismic refraction-wide-angle reflection data, *Geology*, *18*, 878–881, 1990.

Luetgert, J. H., C. E. Mann, and S. L. Klemperer, Wide-angle crustal reflections in the northern Appalachians, *Geophys. J. R. Astron. Soc.*, *89*, 183–188, 1987.

Luetgert, J. H., S. Hughes, J. Cipar, S. Mangino, D. Forsyth, and I. Asudeh, Data report for O-NYNEX, the 1988 Grenville-Appalachian seismic refraction experiment in Ontario, New York and New England, *U.S. Geol. Surv. Open File Rep.*, *90-426*, 1990.

McHone, J. G., and J. R. Butler, Mesozoic igneous provinces of New England and the opening of the North Atlantic Ocean, *Geol. Soc. Am. Bull.*, *95*, 757–765, 1984.

McLelland, J. M., and Y. W. Isachsen, Synthesis of geology of the Adirondack Mountains, New York, and their tectonic setting within the southwestern Grenville Province, in The Grenville Province, edited by J. M. Moore, A. Davidson, and A. J. Baer, *Geol. Assoc. Can. Spec. Pap.*, *31*, 75–94, 1986.

Mooney, W. D., Seismic methods for determining earthquake source parameters and lithospheric structure, in Geophysical Framework of the Continental United States, edited by L. C. Pakiser and W. D. Mooney, *Mem. Geol. Soc. Am.*, *172*, 11–34, 1989.

Murphy, J. M., USGS FM cassette seismic-refraction recording system, *U.S. Geol. Surv. Open File Rep.*, *89-570*, 1989.

Nielson, D. L., R. G. Clark, J. B. Lyons, E. J. Englund, and D. J. Boris, Gravity models and mode of emplacement of the New Hampshire Plutonic Series, *Mem. Geol. Soc. Am., 146*, 301–318, 1976.

Osberg, P. H., Synthesis of the geology of the Northeastern Appalachians, U.S.A., in I.G.C.P. Project 27, Caledonian-Appalachian Orogen of the North Atlantic Region, edited by E. T. Tozer et al., *Pap. Geol. Surv. Can., 78-13*, 137–147, 1978.

Phinney, R. A., and K. Roy-Chowdhury, Reflection seismic studies in the eastern United States, in Geophysical Framework of the Continental United States, edited by L. C. Pakiser, and W. D. Mooney, *Mem. Geol. Soc. Am., 172*, 613–653, 1989.

Robinson, P., and L. M. Hall, Tectonic synthesis of southern New England, in *The Caledonides in the U.S.A., I.G.C.P. Project 27*, edited by D. R. Wones, pp. 73–81, Virginia Polytechnic Institute Press, Blacksburg, Va., 1979.

Rogers, J., *The Tectonics of the Appalachians, Reg. Geol. Ser.*, edited by L. U. De Sitter, pp. 91–115, Wiley-Interscience, New York, 1970.

Rowley, D. B., and W. S. F. Kidd, Stratigraphic relationships and detrital composition of the medial Ordovician flysch of western New England: Implications for the tectonic evolution of the Taconic Orogeny, *J. Geol., 89*, 199–218, 1980.

Selleck, B. W., Post orogenic history of the Adirondack region; a review, *Geol. Soc. Am. Bull., 91*, 120–124, 1980.

Simmons, G., Gravity survey and geological interpretation, northern New York, *Geol. Soc. Am. Bull., 75*, 81–98, 1964.

Spencer, C., A. Green, and J. H. Luetgert, More seismic evidence on the location of the Grenville basement beneath the Appalachians of Quebec-Maine, *Geophys. J. R. Astron. Soc., 89*, 177–182, 1987.

Spencer, C., A. Green, P. Morel-a-l'Huissier, B. Milkereit, J. H. Luetgert, D. B. Steward, J. D. Unger, and J. D. Phillips, Allochthonous units in the Northern Appalachians: Results from the Quebec-Maine seismic reflection and refraction surveys, *Tectonics, 8*, 667–696, 1989.

Stanley, R. S., and M. N. Ratcliffe, Tectonic synthesis of the Taconic Orogeny in western New England, *Geol. Soc. Am. Bull., 96*, 1227–1250, 1985.

Stewart, D. B., J. D. Unger, J. D. Phillips, R. Goldsmith, W. H. Poole, C. P. Spencer, A. G. Green, M. C. Loiselle, and P. St-Julien, The Quebec-Western Maine seismic reflection profile: Setting and first year results, in *Reflection Seismology: The Continental Crust, Geodyn. Ser.*, vol. 14, edited by M. Barazangi and L. Brown, pp. 189–199, AGU, Washington, D. C., 1986.

Stewart, D. B., B. E. Wright, J. D. Unger, J. D. Phillips, D. R. Hutchinson, J. H. Luetgert, W. A. Bothner, K. D. Klitgord, L. M. Liberty and C. Spencer, The Quebec-Maine-Gulf of Maine Transect, Southeastern Canada, Northeastern United States of America; Global Geoscience Transect 8, *U.S. Geol. Surv. Open File Rep., 91-353*, 1991.

Taylor, S. R., Geophysical framework of the Appalachians, in Geophysical Framework of the Continental United States, edited by L. C. Pakiser and W. D. Mooney, *Geol. Soc. Am. Mem., 172*, 317–348, 1989.

Taylor, S. R., and M. N. Töksoz, Crust and upper-mantle velocity structure in the Appalachian orogenic belt: Implications for tectonic evolution, *Geol. Soc. Am. Bull., 93*, 315–329, 1982.

Thigpen, J. T., Seismic reflection evidence for imbricate basement slices in central New England, Msc. thesis, 95 pp., Cornell Univ., Ithaca, N. Y., 1989.

Trzcienski, W. E., and N. Marchildon, Kyanite-garnet bearing Cambrian rocks and Grenville granulites from the Ayer's Cliff, Quebec, Canada, lamprophyre dike suite: Deep crustal fragments from the northern Appalachians, *Geology, 17*, 637–640, 1989.

Wiener, R. W., J. M. McLelland, W. I. Isachsen, and L. M. Hall, Stratigraphy and structural geology of the Adirondack Mountains, New York: Review and synthesis, in The Grenville Event in the Appalachians and Related Topics, edited by M. J. Bartholomew, *Spec. Pap. Geol. Soc. Am., 194*, 1–55, 1984.

Williams, H., Tectonic lithofacies map of the Appalachian Orogen, Map 1a, Canadian contribution, 5, I.G.C.P. project 27, the Appalachian-Caledonides Orogen, Memorial University of Newfoundland, 1978.

Williams, H., and R. D. Hatcher, Suspect terrains and the accretionary history of the Appalachian Orogen, *Geology, 10*, 530–536, 1982.

Williams, N. A., and J. G. McHone, Mantle and crustal xenoliths from the North Hartland dyke, Vermont, *Geol. Soc. Am. Abstr. Programs, 16*, 71, 1984.

Zen, E-an, Exotic terranes in the New England Appalachians-limits, candidates, and ages: A speculative essay, *Mem. Geol. Soc. Am., 158*, 55–81, 1983.

S. Hughes and J. H. Luetgert, U.S. Geological Survey, Branch of Seismology, MS 977, 345 Middlefield Road, Menlo Park, CA 94025.

(Received November 13, 1990;
revised April 10, 1991;
accepted May 29, 1991.)

JOURNAL OF GEOPHYSICAL RESEARCH, VOL. 96, NO. B10, PAGES 16,275–16,293, SEPTEMBER 10, 1991

Heck and Heckle Seamounts, Northeast Pacific Ocean: High Extrusion Rates of Primitive and Highly Depleted Mid-ocean Ridge Basalt on Off-Ridge Seamounts

M. I. LEYBOURNE AND N. A. VAN WAGONER

Department of Geology, Acadia University, Wolfville, Nova Scotia, Canada

We analyzed, petrographically and chemically, basalt from eight dredge hauls from the Heck and Heckle seamounts, northeast Pacific Ocean. Major elements were determined for mineral, glass, and whole rock samples, and trace and rare earth elements were determined for glass and whole rock samples. The dredge hauls included hyaloclastites and fragments from sheet flows and pillows. The clinkery fragments are interpreted to be deformed sheet flow tops, characteristic of high effusion rates. The hyaloclastites recovered are reworked deposits, as indicated by the wide compositional range of the glass shards, abundance of clay and calcite matrix, and bedding. Most rocks are aphyric, but the analyzed plagioclase and olivine phenocrysts and microcrysts are equilibrium compositions and show minor compositional zonation (up to 7.5% An, <1% Fo). Calculated quenching temperatures range from 1228° to 1216°C, decrease with decreasing Mg #, and are consistent with phase equilibria. The seamount lavas are primitive (Mg # 68.7-59.5) and restricted in compositional range ($[La/Ce]_n$ = 0.65-0.77). The basalts are equivalent to highly depleted mid-ocean ridge basalt ($[La/Sm]_n$ = 0.29-0.41) and are at the depleted end of the range in composition of basalts from East Pacific seamounts. They are more depleted than basalts from the adjacent West Valley spreading axis. The lavas can be produced by partial melting of a depleted source. Mineralogical and geochemical evidence is consistent with rapid ascent of the Heck and Heckle lavas through oceanic crust with little residence time in magma chambers. Lavas of the Heck and Heckle Seamount chains have a limited range of incompatible element ratios, whereas the adjacent West Valley Segment of the Juan de Fuca Ridge is highly heterogeneous. In contrast, lavas from the East Pacific near-ridge seamounts exhibit a wider range of incompatible element ratios than do the adjacent East Pacific Rise basalts. On the West Valley Segment, magma supply is less robust associated with lower spreading rates compared to the East Pacific Rise at 10°N. In contrast, at fast spreading centers robust melting produces a mixed mantle signature in axial lavas, while suppressed melting at the seamounts reveals the heterogeneities. We suggest that at some spreading ridges, more fertile portions of the mantle are preferentially melted such that the outwelled portions of the mantle tapped by the seamounts are more depleted.

INTRODUCTION

Seamounts are ubiquitous features of the seafloor. The majority of small off-axis seamounts apparently originate at ridge-transform intersections, fracture zones [*Batiza and Vanko*, 1983], overlapping spreading centers and elevated portions of ridge crests [*Fornari et al.*, 1987; *Batiza et al.*, 1988] and are associated with fast, medium, and slow spreading centers [*Fornari et al.*, 1987; *Batiza et al.*, 1989]. The occurrence of small off-axis seamounts poses several interesting questions related to mid-ocean ridge basalt (MORB) petrogenesis. For example, why is there excess volcanism at the seamounts, what is the nature of the source, and how do seamount plumbing systems differ from the adjacent spreading axis? Small off-axis seamount chains are not believed to be the manifestation of classical thermochemical "hot spots" of the type that produced the Hawaiian Islands but instead are envisaged to be the result of (1) small thermal anomalies ("minihotspots") that preferentially melt in front of a ridge system [*Desonie and Duncan*, 1990; *Barone and Ryan*, 1990], (2) melting of low-temperature heterogeneities in advance of a migrating ridge crest [*Davis and Karsten*, 1986], or (3) off-axis diking through fractures [*Sleep*, 1984].

Previous studies of small off-axis seamount chains in the East Pacific Ocean have provided some of the most conclusive evidence for small-scale mantle heterogeneities, with at least four end-member domains [*Batiza and Vanko*, 1984; *Zindler et al.*, 1984; *Fornari et al.*, 1988*a*, *b*; *Graham et al.*, 1988; *Hart*, 1988]. The most significant indications that the mantle is heterogeneous on a small scale are the wide range in incompatible element ratios (e.g., $[La/Sm]_n$, $[Ce/Yb]_n$, Zr/Y) and in isotopic signatures of basalt samples recovered from a single seamount [*Batiza and Vanko*, 1984; *Zindler et al.*, 1984; *Fornari et al.*, 1988*a*, *b*; *Allan et al.*, 1988; *Graham et al.*, 1988; *Prinzhofer et al.*, 1989; *Hart*, 1988]. In addition, on some seamounts, a broad compositional spectrum of basalts are produced ranging from depleted mid-ocean ridge basalt (N-type MORB) to alkalic lavas (P-type MORB) [*Batiza and Vanko*, 1984]. The production of alkalic lavas on small off-axis seamounts may be a function of the seamount moving to the flank of the melting anomaly and thus tapping mantle with lower amounts of partial melting beneath thicker lithosphere [*Fornari et al.*, 1988*b*]. The large compositional diversity from depleted to enriched lavas has been interpreted to indicate that the small-scale mantle heterogeneities are ineffectively mixed during partial melting and ascent of mantle material [*Batiza and Vanko*, 1984; *Zindler et al.*, 1984]. Other seamount chains, such as the Lamont Seamount Chain, have restricted chemical and incompatible element compositions, although span a wide range of isotopic ratios [*Allan et al.*, 1989; *Fornari et al.*, 1988*a*, *b*].

Basalts erupted at mid-ocean ridges also require a heterogeneous mantle source [*Batiza and Vanko*, 1984; *Holness and Richter*, 1989; *Prinzhofer et al.*, 1989; *Graham et al.*, 1988; *Hart*, 1988], but the range of isotopic and incompatible element ratios may be obscured by magma mixing in magma chambers, with the degree of homogenization of magma related to spreading rate [*Cohen and O'Nions*, 1982; *Holness and Richter*, 1989]. Magma mixing beneath seamounts may be impeded by the apparent lack of long-lived magma chambers, a situation analogous to slow spreading ridges [*Le Roex et al.*, 1983; *Dosso et al.*, 1988]. For example, there is a greater range of isotopic and incompatible element ratios on East Pacific seamounts than on the adjacent ridge segments of the East Pacific Rise [*Batiza and Vanko*, 1984; *Fornari et al.*, 1988*b*].

Paper number 91JB00595.
0148-0227/91/91JB-00595$05.00

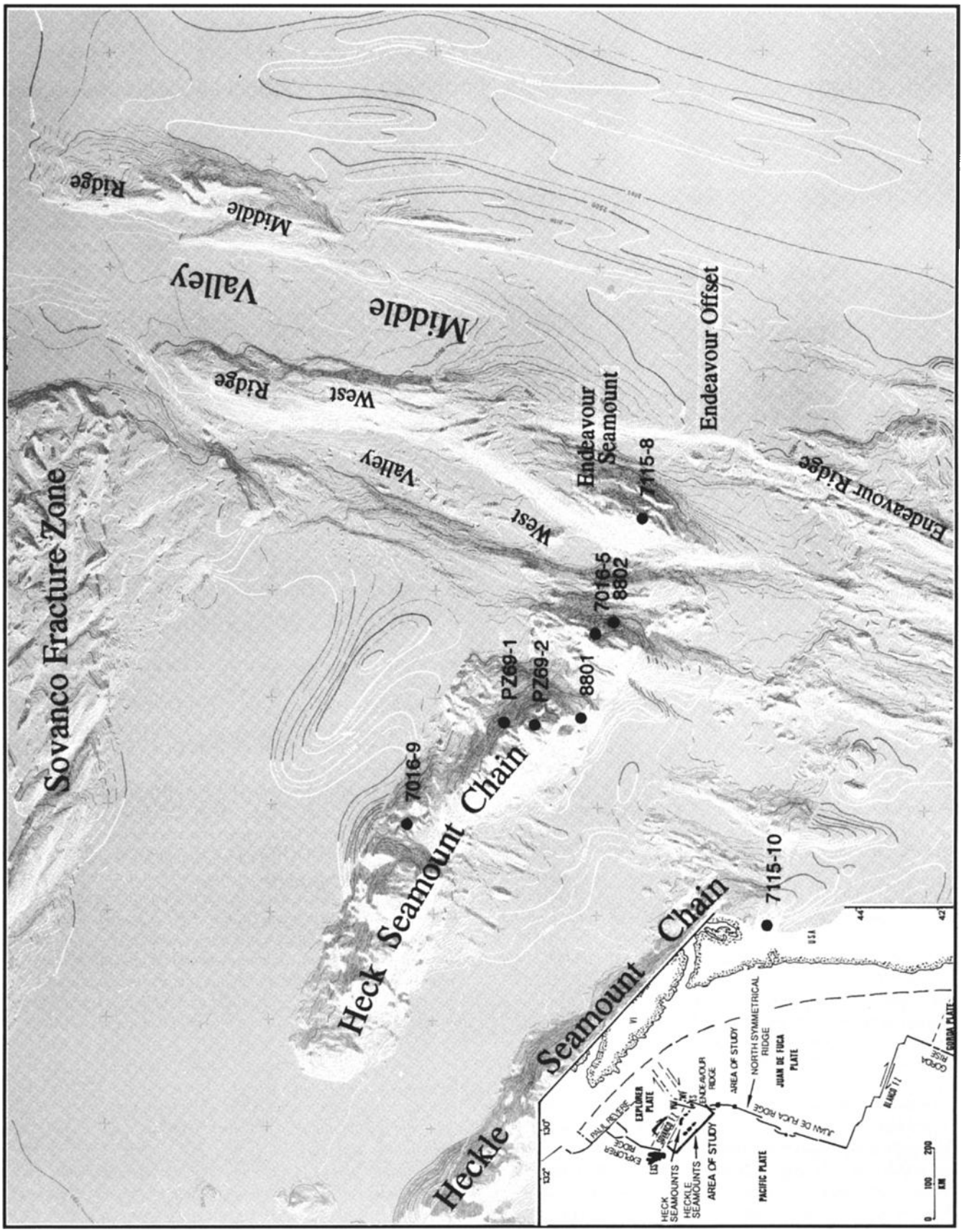

Fig. 1. Sea Beam bathymetric map of the study area [after *Davis et al.*, 1987*a*] showing the dredge haul locations. Endeavour Seamount (7115-8), East Peak (7016-5, C = 8802), Heck Seamount (PZ69-1, PZ69-2, 8801), West Peak (7016-9), Heckle Seamount (7115-10). Inset shows regional setting of the study area. WV, West Valley; MV, Middle Valley; ES, Endeavour Seamount; EXS, Explorer Seamount.

Previous studies of the Heck and Heckle Seamount chains, relying on major element whole rock geochemistry, suggested that they are restricted in compositional range [*Barr*, 1972, 1974]. We conducted a detailed study of these seamounts for the purpose of interpreting the volcanic and petrogenetic processes that produced their lavas and comparing these processes to other seamounts and to the adjacent ridge crest.

The Heck and Heckle Seamount chains are in the northeast Pacific Ocean, adjacent to the Endeavour Ridge and West Valley at the northern end of the Juan de Fuca Ridge. Endeavour Ridge and West Valley form an overlapping spreading center (Figure 1). The offset region is dominated by the Endeavour Seamount (Figure 1) which has been interpreted to be either the western extension of the Heck Seamount Chain [*Barr*, 1972; *Karsten et al.*, 1986], an isolated portion of West Ridge [*Scott et al.*, 1988], the east bounding axial ridge of West Valley, or an High Inside Corner [*Macdonald*, 1989]. Interpretation of the origin of Endeavour Seamount is complicated by the fact that it is apparently reversely magnetized [M. Tivey, personal communication, 1988] and highly faulted in response to the overlapping ridge tips.

Both the Heck and Heckle Seamount chains are parallel to the absolute motion of the Pacific plate [*Lee and Hammond*, 1985]. The Heck Seamount Chain consists of eight coalesced volcanic cones on three plateaux (Figure 1) [*Davis et al.*, 1987*a*]. The shallowest cone on the Heck Seamount Chain is <1100 m depth. The Heckle Seamount Chain is located south of Heck seamounts. The Heckle seamounts consist of seven coalesced volcanic cones along its 80 km length [*Davis et al.*, 1987*a*], the shallowest edifice rises to <1600 m depth.

SAMPLING AND ANALYTICAL METHODS

Basalt samples from eight dredge hauls (Figure 1 and Table 1) were analyzed for their petrography, mineral chemistry, and whole rock and glass major and trace element geochemistry, including the rare earth elements (REE). The ship location was determined using Loran A (1969 and 1971 cruises), Loran C, and Global Positioning Satellite (GPS) navigation systems (Table 1).

Both whole rock and glass separates were prepared for chemical analysis. The analytical methods utilized are described by *Van Wagoner and Leybourne* [this issue]. Briefly, major and minor element analyses for the glasses were determined by a JEOL 733 four wavelength spectrometer electron microprobe on standard polished thin sections. Glass analyses are an average of 5-8 points for pillow and sheet flows, or three points for hyaloclastite, using a defocussed beam (10 μm). Mineral analyses used a focused electron beam (1 μm) under the same operating conditions. Whole rock major and trace elements were determined by X ray fluorescence (XRF) spectrometry at St. Mary's University, Halifax, Nova Scotia, and REE and additional trace elements by inductively coupled plasma mass spectrometry (ICP-MS) at Memorial University, St. Johns, Newfoundland. The errors associated with the different analytical methods are given in Table 2. Gd analyses are consistently low and are probably related to Gd analytical difficulties [S. Jackson, personal communication, 1989].

TABLE 1. Dredge Site Locations and Descriptions

Dredge and Location	Site Descriptions	Latitude °N	Longitude °W	Depth, m	Navigation Method	Physiographic Location
7115-8[a] Endeavour Smt	One pillow recovered of plagioclase-phyric glass covered basalt with palagonite up to 5 mm in thickness. Minor Fe oxide stains occur on exposed surfaces.	48° 18.5'	129° 04'	2377-1829	Loran A	southwest flank
7016-5[a] East Peak	50 kg of small clinkery basalt and glass fragments, which are Mn coated, and one holocrystalline fragment. Many fragments entirely glassy with palagonized oute surfaces. Tubular vesicles give a contorted appearance to these samples.	48° 20'	129° 15'	1463-1426	Loran A	northwset flank
8802 East Peak	50 kg of basalt fragments, both pillow and sheet flow fragments, with rare clinkery fragments. Samples show variable degrees of Mn coatings from nonexistent to a few millimeters thick. Many fragments have glassy selvages.	48° 19'	129° 12.7'	1900-1850	Loran C/GPS	east flank
PZ69-1[a] Heck Smt	200 kg of clinkery and ropey basalt fragments with Mn crust and palagonized glass. Fresh glass is preserved. Tubular vesicles give a contorted appearance to these samples.	48° 26'	129° 22.5'	1445-1335	Loran A	north flank
PZ69-2[a] Heck Smt	Few small basalt and glass fragments. The outer surface of the glass is palagonized. Hyaloclastites were also recovered.	48° 24'	129° 23'	1150-1135	Loran A	south flank
8801 Heck Smt	Two large pillow fragments with very thick Mn/palagonite crust but with thick glass selvages beneath. Also recovered was a large block of volcaniclastic lithic arenite, presumably a glacial eratic. Hyaloclastites and various pebbles also recovered.	48° 21.2'	129° 21.8	2100-2060	Loran C/GPS	southeast flank
7016-9[a] West Peak	25 kg of small fragments of clinkery basalt that are Mn oxide coated and glassy beneath palagonite alteration. Tubular vesicles are common. Many fragments are altered in the groundmass to smectite and chlorophaeite.	48° 32'	129° 32'	1830-1740	Loran A	east flank
7115-10[a] Heckle Smt	45 kg of massive pillow fragments coated with Mn crusts. Glassy rims are altered to palagonite.	48° 09'	129° 42'	2660-2325	Loran A	east end

[a]Descriptions from *Barr* [1972] and this study

RESULTS

Flow Morphology

Three main basalt forms were recovered from the seamounts: pillow basalt fragments, sheet flow fragments, and highly contorted clinkery and ropey basalt fragments (Table 1). The pillow basalts are marginally more common than sheet flow and clinker fragments. They have morphologies and textures typical of normal mid-ocean ridge basalts [e.g., *Bryan*, 1972]. The sheet flow fragments are tabular blocks commonly with ropey surfaces.

Two samples from East Peak contain subangular rock fragments that are more crystalline than the host rock (Figure 2). The rock

TABLE 2. Geochemical Results

	Sample											
	7115-8-1	7115-8-1	7016-5-A	7016-5-B	7016-5-D	8802-02	8802-03	8802-04	8802-05	8802-10	PZ69-1-A	PZ69-1-A
Location	ES	ES	EP	EP	EP	EP	EP	EP	EP	EP	HS	HS
Sample type	glass	whole rock	glass	glass	glass	glass	glass	glass	glass	glass	glass	whole rock
SiO_2	50.79	49.35	49.90	50.19	50.40	50.76	50.89	50.55	50.67	50.37	50.28	50.02
TiO_2	1.18	1.05	0.93	0.87	0.89	1.11	1.17	1.06	1.08	1.11	1.08	1.01
Al_2O_3	14.54	15.56	15.51	16.39	15.74	14.81	14.67	15.11	15.07	14.91	14.56	14.77
Cr_2O_3	0.10	-	0.07	0.01	0.10	0.01	0.01	0.01	0.01	0.01	0.08	-
FeO^T	9.18	9.03*	8.36	8.02	8.33	9.33	9.26	8.87	8.89	9.17	8.99	9.16*
MnO	0.21	0.15	0.27	0.05	0.17	0.10	0.05	0.07	0.07	0.06	0.27	0.15
MgO	8.46	7.96	9.03	8.72	9.25	8.12	7.86	8.36	8.28	8.16	8.43	7.50
CaO	12.96	12.96	13.19	13.09	11.59	12.44	12.76	12.73	12.89	12.98	13.34	13.03
Na_2O	2.62	2.06	2.59	2.40	2.41	2.48	2.48	2.50	2.42	2.53	2.43	2.58
K_2O	0.06	0.04	0.05	0.02	0.03	0.03	0.02	0.02	0.02	0.03	0.06	0.10
LOI	-	0.20	-	-	-	-	-	-	-	-	-	0.30
Total	100.10	98.43	99.90	99.75	98.91	99.19	99.18	99.27	99.40	99.31	99.52	98.62
Mg #	64.6	65.9	68.1	68.3	68.7	63.3	62.7	65.1	64.8	63.8	65.0	64.3
Cr		[354]										[421]
Ni		[74]										[80]
Sc	38	34		36				44			34	36
Ba	5.9	5.5 [17]		2				2.7			2.5	3
Li	4.1	3.7		4.1				5.6			4	4.1
Rb	0.43	0.4		0.14				0.2			0.1	2
Sr	77	81 [79]		67				80			71	77 [75]
Th	0.1	0.1		0.04				0.06			0.05	0.06
Hf	1.8	1.6		1.3				1.9			1.5	1.6
Nb	0.93	6.7		0.36				0.40			4.3	0.5
Ta	0.066			0.044				0.051			0.262	
Y	22	20 [24]		18				23			21	21 [25]
Zr	50	44 [57]		35				53			42	43 [54]
La	1.48	1.44		0.83				1.30			1.11	1.15
Ce	5.18	4.91		3.21				5.19			4.09	4.18
Pr	1.00	0.94		0.67				1.03			0.83	0.84
Nd	5.90	5.45		4.12				5.68			4.94	4.99
Sm	2.31	2.21		1.78				2.37			2.09	2.16
Eu	0.94	0.99		0.75				0.95			0.82	0.83
Gd	3.10	2.91		2.49				3.12			2.86	2.81
Tb	0.63	0.57		0.51				0.65			0.59	0.58
Dy	4.41	3.88		3.47				4.53			4.00	3.99
Ho	0.98	0.87		0.73				0.99			0.87	0.88
Er	2.77	2.53		2.28				3.01			2.68	2.67
Tm	0.40	0.36		0.32				0.44			0.39	0.38
Yb	2.57	2.32		2.18				2.82			2.60	2.58
Lu	0.39	0.35		0.33				0.41			0.39	0.40
$[La/Ce]_n$	0.75	0.76		0.67				0.65			0.71	0.72
$[La/Sm]_n$	0.40	0.41		0.29				0.35			0.33	0.34

	Sample											
	PZ69-1-16	PZ69-2-A	8801-01	8801-02	7016-9-A	7016-9-A	7016-9-B	7016-9-C	7115-10-3	7115-10-3	Chondrite	Errors
Location	HS	HS	HS	HS	WP	WP	WP	WP	HcS	HcS		
Sample type	glass	glass	glass	glass	glass	whole rock	glass	glass	glass	whole rock		
SiO_2	50.96	50.73	50.44	50.62	50.62	50.13	50.87	50.91	50.82	50.85		Weight % 0.26
TiO_2	1.07	1.19	1.01	0.98	1.08	0.96	1.08	1.09	1.43	1.28		0.04
Al_2O_3	14.79	14.49	15.15	15.42	14.89	15.06	14.74	14.64	13.91	14.49		0.15
Cr_2O_3	0.11	0.04	0.02	0.01	0.08	-	0.10	0.10	0.05	-		0.02
FeO[T]	8.91	9.37	8.27	8.23	8.89	8.80*	9.00	9.07	10.14	9.78*		0.14
MnO	0.18	0.31	0.07	0.12	0.32	0.13	0.19	0.19	0.39	0.17		0.03
MgO	8.44	7.99	8.54	8.20	8.49	7.21	8.91	8.94	7.53	7.10		0.11
CaO	13.00	13.01	13.01	12.96	13.23	13.05	13.04	13.03	12.23	12.45		0.13
Na_2O	2.45	2.71	2.41	2.49	2.47	2.64	2.41	2.47	2.74	2.30		0.10
K_2O	0.05	0.07	0.03	0.03	0.06	0.26	0.03	0.04		0.18		0.02
LOI	-	-	-	-	-	0.40	-	-	-	0.30		
Total	99.96	99.91	98.96	99.05	100.13	98.64	100.37	100.48	99.24	98.90		
Mg #	65.2	62.8	67.2	66.4	65.4	64.3	66.2	66.1	59.5	61.4		
Cr						[400]				[236]		Relative % [4.1]
Ni						[45]				[69]		[2.0]
Sc	37		41			34	37	26		32		4.5
Ba	1.8		2.1			4.3 [5]	1.9	1.6		9.6 [1]		3.8 [4.3]
Li	4.4		5.3			4.5	4.5	3.0		3.6		2.4
Rb	0.16		0.2			6 [7]	0.13	0.09		2.9 [1]		6.7 [2.5]
Sr	74		90			84 [88]	71	51		80 [94]		2.5 [2.5]
Th	0.05		0.06			0.06	0.04	0.04		0.07		19.0
Hf	1.7		1.7			1.6	1.6	1.1		1.8		4.2
Nb	0.47		0.6			0.6	1.0	0.29		0.6		18.2
Ta	0.045		0.066				0.077	0.033				18.6
Y	21		21			19 [22]	21	15		21 [27]		2.2 [6.6]
Zr	43		49			41 [56]	42	30		50 [75]		2.4 [1.0]
La	1.12		1.36			1.34	1.11	0.84		1.60	0.367	1.9
Ce	4.24		5.05			4.56	4.20	3.01		5.60	0.957	2.1
Pr	0.83		0.93			0.89	0.86	0.60		1.09	0.137	1.7
Nd	4.93		5.11			5.16	5.15	3.58		6.23	0.711	2.0
Sm	2.17		2.14			2.12	2.17	1.46		2.37	0.231	2.4
Eu	0.84		0.91			0.82	0.86	0.62		0.92	0.087	2.8
Gd	2.74		2.87			2.58	2.91	1.96		3.10	0.306	1.6
Tb	0.56		0.59			0.56	0.59	0.44		0.62	0.058	2.2
Dy	4.06		3.94			3.86	4.06	2.89		4.14	0.381	1.5
Ho	0.90		0.85			0.81	0.90	0.62		0.92	0.0851	1.4
Er	2.73		2.57			2.51	2.78	2.03		2.88	0.249	2.4
Tm	0.38		0.36			0.36	0.39	0.29		0.42	0.0356	3.3
Yb	2.52		2.37			2.34	2.49	1.80		2.67	0.248	1.6
Lu	0.41		0.36			0.37	0.39	0.28		0.40	0.0381	2.4
$[La/Ce]_n$	0.69		0.70			0.77	0.69	0.73		0.75		
$[La/Sm]_n$	0.32		0.40			0.40	0.32	0.36		0.42		

Location abbreviations: ES, Endeavour Seamount; WP, West Peak; HS, Heck Seamount; EP, East Peak; HcS, Heckle Seamount. Chondrite values after *Evensen et al.* [1978]. Brackets indicate XRF data.

*Total Fe as Fe_2O_3 (XRF).

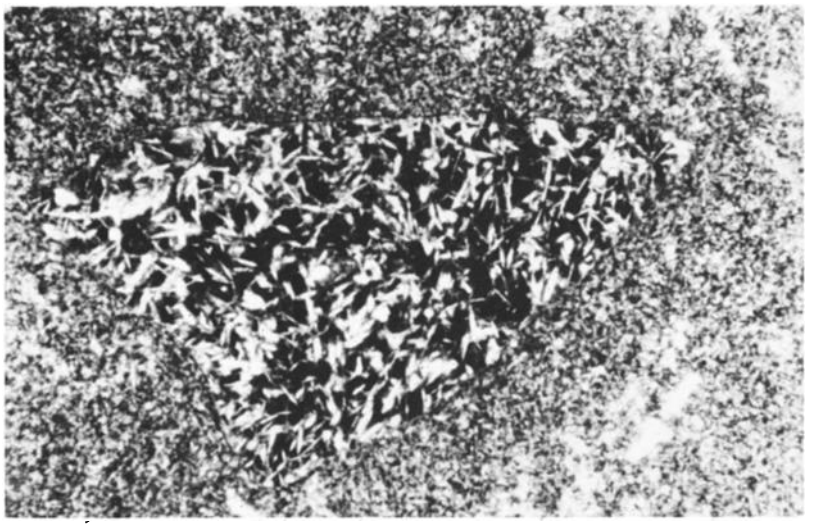

Fig. 2. Photomicrograph of a subangular rock fragment from East Peak sample 7016-5-A. Olivine and plagioclase microphenocrysts are the crystalline phases in the rock fragment. The rock fragment is probably a rip-up clast from a previous flow. The olivine in the rock fragment is more mafic than olivine in the host rock (Figure 7). Note also the altered mesostasis of the host rock. Field of view is 4.7 mm. Plane polarized light.

TABLE 3. Petrographic Data

Sample	Plagioclase	Olivine	Clino-pyroxene	Spinel	Vesicles	Matrix	Glass	Texture[a]	Ground-mass[b]	Alteration[c]	Analyzed By[d]	Sample Source[e]
					Endeavour Seamount							
7115-8-1	9.0	0.8	tr	-	0.4	90.1	√	1-4	plag,ol,cpx	1	1-5	C
					Heck Seamount Chain							
East Peak												
7016-5-A	0.4	tr	-	tr	1.1	99.6	√	1-3, 5	plag	2	4, 5	C
7016-5-B	Glass fragments only						√	1		2	3	C
7016-5-D	1.1	tr	-	tr	0.2	98.9	√	1, 5	-	2	4, 5	C
8802-02	1.8	tr	-	-	1.4	98.2	√			2 - 4	4, 5	A
8802-03	1.4	0.8	-	-	0.7	97.8	√			2 - 4	3, 4, 5	A
8802-04							√				4, 5	A
8802-05							√				4, 5	A
8802-10	8.7	0.8	-	-	0.4	90.5	√				4, 5	A
Heck Seamount												
PZ69-1-A	1.5	0.3	-	-	?	98.2	√	1-3, 5	plag	2	1-5	B
PZ69-1-16	0.6	-	-	-	0.4	99.4	√	1-2, 5		2	3-5	B
PZ69-2-A	0.1	-	-	-	0.9	99.9	√	1-3, 5		2	4, 5	B
8801-01							√		plag, ol		3, 4, 5	A
8801-02							√		plag, ol		4, 5	A
West Peak												
7016-9-A	1.8	tr	-	-	0.3	98.2	√	1-3, 5	plag	2	1, 2, 4, 5	C
7016-9-B	Glass fragments only						√	1, 5		2	3-5	C
7016-9-C	Glass fragments only						√	1, 5		2	3, 4	C
					Heckle Seamount Chain							
7115-10-3	3.2	0.8	0.4	-	0.5	95.6	√	1-4	plag	4	1, 2, 4, 5	C

Check is glass present; dash is not present. Samples with three numbers, e.g., PZ69-1-A, are identified as PZ69, year and cruise number; 1, dredge number; A, sample. Samples with two numbers, e.g., 8802-05, are identified as 8802, year and dredge number; 05, sample.

[a]1, glass; 2, variolitic; 3, plumose intergrowths; 4, hyalopilitic; 5, flow banding.

[b]plag, plagioclase; ol, olivine; cpx, clinopyroxene.

[c]1, fresh; 2, fractures with Fe and palagonite stains; 3, as 2 but also vesicle linings; 4, alteration of mesostasis at edge of sample.

[d]1, XRF; 2, ICP (whole rock); 3, ICP (glass); 4, microprobe glass; 5, microprobe mineral phases.

[e]Sample source: A, GSC cruise of *J. P. Tully* in 1988; collected by M. Leybourne; J. M. Franklin Chief Scientist. B, UBC cruise of CSS *Parizeau* in 1969; provided by S. M. Barr and R. L. Chase; R. L. Chase Chief Scientist. C, UBC cruises of CFAV *Endeavour* in 1970 and 1971; provided by S. M. Barr and R. L. Chase; S. M. Barr Chief Scientist.

fragments are probably rip-up clasts from previous flows as they are too fine grained to be intrusive fragments.

Clinkery fragments were recovered from the Heck Seamount Chain (Table 1). The clinkery fragments are highly contorted and very glassy, and many fragments contain glass rims on all surfaces. They commonly exhibit complex flow-banding textures (Table 3) defined by differences in the proportions of glass and varioles/plumose intergrowths and/or by glass color variations (Figure 3). Microprobe analyses of different colored bands in Heck Seamount sample PZ69-1-A show no systematic differences in major element chemistry that might account

Fig. 3. Photomicrograph showing highly contorted flow banding texture in East Peak sample 7016-5-D. Note the flow alignment of plagioclase laths and the variations in glass color which may be due to variations in fO_2. Field of view is 12 mm. Plane polarized light.

for the color variation. The glass color variations may be related to variations in the fO_2 [*Bender et al.*, 1978]. In some bands, plagioclase microlites are flow aligned as are some vesicles (Figure 3). The clinkery fragments are similar in morphology to those interpreted to form by deformation of sheet flow tops [e.g., *Ballard et al.*, 1979] or by lava fountaining at seamounts [e.g., *Batiza et al.*, 1984; *Smith and Batiza*, 1989]. Submarine sheet flows are characteristic of high extrusion rates [e.g., *Ballard et al.*, 1979].

Hyaloclastites

Hyaloclastites are deposits of blocky and cuspate nonvesicular glass shards [*Fisher and Schmincke*, 1984; *Smith and Batiza*, 1989]. Hyaloclastite deposits are common on young off-axis seamounts [*Lonsdale and Spiess*, 1979; *Batiza et al.*, 1984; *Bonatti and Harrison*, 1988; *Smith and Batiza*, 1989], and ancient seamount deposits [*Staudigel and Schmincke*, 1984]. Recent observations by deep-tow camera and submersible indicate that hyaloclastite deposits are intimately associated with sheet flows and spatter deposits [*Smith and Batiza*, 1989].

Hyaloclastites were dredged from Heck Seamount at two localities (PZ69-2 and 8801, Figure 1 and Tables 1 and 4). The hyaloclastites from the two sites differ in petrography and geochemistry (Table 4). Both blocks and fluidal glass shards occur in sample PZ69-2-B (Figure 4). The sample is bedded with parallel alignment of shards and crystals. In contrast, the hyaloclastite samples from site 8801 (samples 8801-03 and 8801-04) comprise glass shards which are predominantly blocky (Figure 5) and show no preferential orientation. These samples are massive to very crudely bedded. Hyaloclastites from both sites contain glass shards with flow banding textures similar to those described for the clinkery basalt fragments. The hyaloclastites from site 8801 are probably younger than PZ69-2-B as the samples do not have Mn coatings and are not indurated, and the carbonate matrix has not been completely replaced by clays and Fe-Mn oxides.

Individual glass shards of hyaloclastites from both areas were analyzed by electron microprobe to determine the major element composition and compositional spectrum of each sample. Site 8801, which is characterized by blocky shards, exhibits the largest compositional range of the two sites, although the compositional range is significant for both sites (Table 5 and Figure 6). The compositional range of the shards for the 8801-04 sample is greater than all the rock samples from the Heck Seamount Chain in this study (Figure 6).

Petrography and Mineral Chemistry

The seamount rocks are aphyric to very sparsely phyric with only a few samples containing more than 2% phenocrysts (Table 3). The mineral assemblages are plag, plag + ol and, in two samples, plag + ol + cpx. Magnesiochromite spinel is a rare accessory phase of some samples from East Peak (Table 3). The high Cr and low Al content of the spinel is indicative of low-pressure crystallization [*Fisk and Bence*, 1979] and is typical of off-axis seamounts [*Allan et al.*, 1988]. Clinopyroxene occurs only in the samples from Endeavour and Heckle seamounts, both of which contain rare (trace to 0.4%; Table 3) clinopyroxene microphenocrysts. In the Heckle Seamount sample, clinopyroxene also occurs in glomerocrysts with plagioclase microphenocrysts and as groundmass granules in the flow interior. East Peak sample 7016-5-A also contains very rare well-rounded clinopyroxene fragments that appear out of equilibrium.

Plagioclase is the dominant mineral in all the rocks (Table 3) and occurs predominantly as megacrysts and phenocrysts (terminology from *Bryan* [1979]). Microphenocrysts are common in the pillow basalts but rare to absent in the glassy clinkery basalt fragments. The plagioclase megacrysts and phenocrysts are generally tabular to bladed, euhedral to subhedral, commonly occur in glomerocrysts, and are generally normally zoned (Figures 7*a* and 7*b* and Table 6). The largest core to rim variation is 7.5% anorthite and the largest variation between rim and microphenocryst composition is 10% anorthite (Figures 7*a* and 7*b* and Table 6). Plagioclase usually shows little marginal reaction with the host melt in the glassy fragments. The plagioclase megacrysts and phenocrysts generally plot above the *Drake* [1976] equilibrium plagioclase line but are within the error envelope, whereas microphenocrysts are close to Drake equilibrium compositions (Figure 8).

Some of the plagioclase megacrysts are host to glass inclusions. As Fe/Mg ratios are not affected by post entrapment crystallization [*Stakes et al.*, 1984], these glass inclusions indicate equilibrium with more primitive melts than the host rock. For example, an inclusion in a plagioclase megacryst from the Endeavour Seamount sample has Mg # = 73.3, whereas the host glass has Mg # = 64.6. Similarly, for West Peak sample 7016-9-A, the inclusion (Mg # = 69) is more mafic than the host glass (Mg # = 64). In contrast, a glass inclusion from a plagioclase megacryst in East Peak sample 7016-5-A is more evolved (Mg # = 64.4) than the host glass (Mg # = 68).

TABLE 4. Hyaloclastite Data

Sample	Glass Shards	Rock Fragments	Crysal Fragments	Matrix	Comments
PZ69-2-B	35%; Blocky shards dominant, especially in upper section. Fluidal and cuspate fragments increase toward the bottom. Shards show parallel alignment. Crystal fragments rarely in glass. Glass is variably altered from fresh to palagonite altered. Rare shards show flow banding.	2%; mafic rock fragments up to 8mm.	8%; plagioclase dominant with rare cpx and ol fragments. Fragments typically have broken edges, crystal faces rare.	55%; matrix material consists of clays, palagonite and Fe-Mn oxides.	Graded bedding. Hand sample is Mn coated and indurated.
8801-03, 8801-04	30%; mostly blocky shards with very rare fluidal and cuspate forms. Shards are nonvesicular. Some shards are flow banded. Shards are rarely rounded and rarely show alteration. Typically, glass contains no crystals.	trace; basaltic fragments	0.5%; plagioclase with rare cpx and ol. Crystal fragments are typically rounded or with broken surfaces.	69.5%; matrix consists of very fine grained clays and lesser amounts of carbonate (micrite). Radiolaria and more rare foraminifera.	In hand sample, unbedded to very crudely bedded. In thin section, shards tend to be concentrated in layers. When recovered, samples were pliable.

Olivine is less common than plagioclase (Table 3). It occurs mainly as phenocrysts in the clinkery basalts and as microphenocrysts in the pillow basalts. The phenocrysts are commonly subhedral to anhedral but rarely skeletal. Olivine commonly forms glomerocrysts with plagioclase. The olivine crystals analyzed are virtually all equilibrium compositions and there is little within-sample variation in forsterite (Fo) content (Figure 9 and Table 7). The core to rim and the phenocryst-microphenocryst variation in forsterite content never exceeds 1% Fo (Figure 9 and Table 7). Some olivine crystals are reversely zoned indicating either magma mixing, with the core forming in a less primitive melt, or polybaric crystallization, with increasing pressure producing a higher K_D for the partitioning of Fe and Mg between olivine and a melt [*Bender et al.*, 1978; *Ulmer*, 1989]. An olivine crystal in Heck Seamount sample PZ69-2-A is too fayalitic to be in equilibrium with the host melt. It is highly resorbed and obviously a xenocryst (Figure 9). A rock fragment incorporated in a flow from East Peak (sample 8802-02) contains olivine microphenocrysts that are more Fo-rich than the olivine phenocrysts in the host rock, suggesting that the fragment come from a more primitive basalt (Figure 9 and Table 7).

Geothermometry

Estimates of quenching temperature of the glass using various olivine-glass geothermometers [*Roeder and Emslie*, 1970; *Bender et al.*, 1978] show a good correlation with Mg # (Figure 10a). The highest calculated temperatures are for the East Peak 7016-5 samples which are the most mafic samples in the study. The temperatures for these rocks are 1228°-1233°C based on the *Roeder and Emslie* [1970] geothermometer and 1216°-1223°C using the *Bender et al.* [1978] geothermometer. There is a systematic decrease in temperature and Mg # to the most evolved sample (Heckle Seamount 7115-10-3) with the lowest calculated temperature (1196°C [*Roeder and Emslie*, 1970] and 1178°C [*Bender et al.*, 1978]).

Several experimental studies indicate that under most conditions, olivine is the first phase to crystallize from a basaltic melt, followed by plagioclase and finally by clinopyroxene [*Bender et al.*, 1978; *Walker et al.*, 1979; *Grove and Bryan*, 1983; *Tormey et al.*, 1987]. The temperature of first appearance of a phase is partly dependent on the chemistry of the melt but the temperature ranges are 1210°-1260°C (olivine), 1195°-1235°C (plagioclase), and 1160°-1195°C (clinopyroxene) [*Bender et al.*, 1978; *Walker et al.*, 1979; *Grove and Bryan*, 1983; *Tormey et al.*, 1987]. The study lavas show a general decrease in calculated temperatures along olivine and plagioclase extraction lines toward the ol-plag-cpx cotectic (Figure 10*b*). The Heckle Seamount sample is the only sample with significant clinopyroxene, and its calculated temperature is consistent with the temperature of onset of clinopyroxene fractionation and plots near the cotectic in ALFE space (Figure 10*b*).

Geochemistry

The seamount lavas are very primitive and relatively restricted in compositional range (Figure 6 and Table 2). The most primitive lavas are from East Peak (7016-5 rocks) with Mg # 68.1-68.7 and are near the upper limit of MORB sampled to date [*Basaltic Volcanism Study Project*, 1981]. The most evolved sample is from Heckle Seamount with a glass Mg # of 59.5, although compared to MORB sampled at ridge crests, this is only moderately evolved [*Basaltic Volcanism Study Project*, 1981]. The glass analyses indicate that the rocks are olivine-hypersthene normative with normative olivine ranging from 3% to 13%. The whole rock analysis for Heckle Seamount sample 7115-10-3 is quartz normative (1.39%).

Although rocks from a single dredge haul do not always fall on a single line of liquid descent, overall, the samples show little scatter in

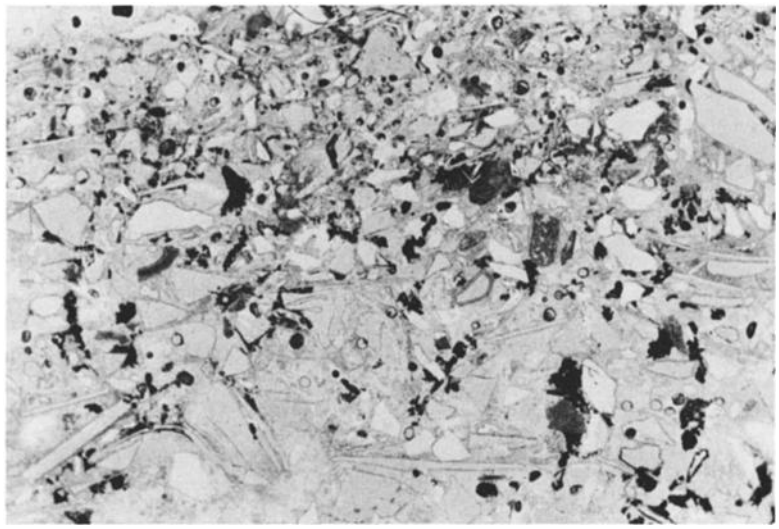

Fig. 4. Photomicrograph of Heck Seamount hyaloclastite sample PZ69-2-B, showing blocky and fluidal glass shards and crystal fragments. Field of view is 6.5 mm. Plane polarized light.

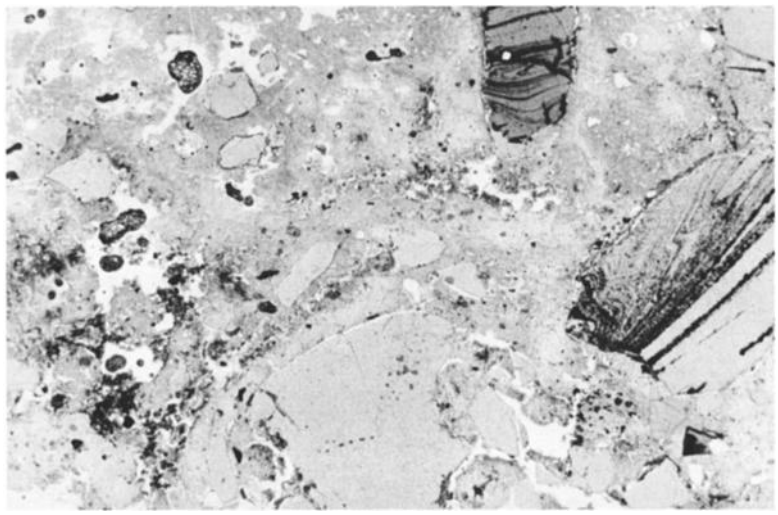

Fig. 5. Photomicrograph of Heck Seamount hyaloclastite sample 8801-03 showing blocky glass shards an a clay and carbonate matrix. Field of view is 13 mm. Plane polarized light.

variation diagrams (Figure 6). Mg # correlates negatively with the incompatible elements TiO_2, FeO^T, and Na_2O, and positively with the compatible elements Al_2O_3 and CaO (Figure 6 and Table 2). Na_2O shows a negative correlation with Mg #, except for two whole rock analyses. K_2O is poorly correlated with Mg #, but the K_2O content in these rocks is very low and near the detection limit of the electron microprobe (Table 2). The TiO_2 versus Mg # plot exhibits the least amount of scatter due to the incompatibility of TiO_2 in the main fractionating phases (olivine and plagioclase) over the range of Mg # of the study lavas. Two of the whole rock analyses are moderately plagioclase-phyric (Table 3) and are therefore more depleted in TiO_2 than the other analyses as a result of phenocryst dilution. The constant CaO/Al_2O_3 ratio (Figure 2) indicates the importance of olivine fractionation over plagioclase and clinopyroxene fractionation, consistent with the high calculated solidus temperatures (Figure 10*a*).

The incompatible element ratios of the seamount lavas are even more uniform than the major elements, showing very linear trends on covariation plots such as Zr versus Y and La versus Ce (Figure 11). These ratios indicate highly depleted (D-type MORB) compositions (e.g., Zr/Nb = 54 - 133, Zr/Y = 1.9 - 2.4). Incompatible element concentration of the seamount lavas are at the most depleted end of the MORB spectrum [*Basaltic Volcanism Study Project*, 1981] e.g., Zr = 30-75 ppm, Y = 15-27 ppm, Rb = 0.09-0.43 ppm for glass analyses, Sr = 51-94 ppm and Nb = 0.29-0.93 ppm (Figure 12 and Table 2) The Nb concentrations in these seamount lavas are extremely low and were only detectable because of the very low detection limits of the ICP-MS method (0.003-0.017 ppm, depending on analytical run). Nb was not reliably detected in the seamount samples analyzed by XRF (detection limit is generally around 5 ppm for XRF).

Chondrite normalized REE patterns are LREE depleted, at the lower limit for MORB, and essentially subparallel with minor crossing profiles (Figure 12). There is great similarity in the $[La/Ce]_n$, $[La/Sm]_n$, and $[Ce/Yb]_n$ ratios (Figures 13 and 14). Sample 7016-9-C from West Peak is the most depleted sample in the study and has the lowest REE

TABLE 5. Chemical Analyses of Glass Shards in Hyaloclastites

	Sample									
	PZ69-2-B	PZ69-2-B	PZ69-2-B	PZ69-2-B	PZ69-2-B	PZ69-2-B	PZ69-2-B	PZ69-2-B	PZ69-2-B	PZ69-2-B
Shard type	blocky	blocky	blocky	elongate	fluidal	fluidal	elongate	blocky	blocky	blocky
SiO_2	50.28	50.20	50.34	49.99	50.46	50.30	50.37	50.14	50.14	50.20
TiO_2	1.47	1.39	1.40	1.38	1.43	1.35	1.17	1.45	1.45	1.16
Al_2O_3	14.65	14.55	14.61	14.60	14.52	14.64	14.62	14.74	14.70	14.88
Cr_2O_3	0.10	0.09	0.09	0.09	0.09	0.09	0.10	0.12	0.10	0.10
FeO^T	10.31	10.08	10.20	9.79	10.43	10.23	9.68	10.27	10.39	9.15
MnO	0.20	0.21	0.18	0.20	0.20	0.20	0.20	0.21	0.21	0.17
MgO	7.53	7.52	7.54	7.61	7.37	7.68	7.98	7.59	7.60	8.04
CaO	11.70	12.03	12.02	12.08	11.97	12.06	12.39	11.95	11.78	12.67
Na_2O	2.83	2.78	2.69	2.76	2.83	2.89	2.54	2.81	2.78	2.51
K_2O	nd	nd	nd	nd	nd	nd	nd	nd	nd	nd
Total	99.06	98.85	99.05	98.48	99.30	99.44	99.04	99.29	99.15	98.88
Mg #	59.1	59.6	59.4	60.6	58.3	59.8	62.0	59.4	59.2	63.5
	Sample									
	8801-04	8801-04	8801-04	8801-04	8801-04	8801-04	8801-04	8801-04	8801-04	8801-04
Shard type	blocky	blocky	blocky	blocky	blocky	blocky	blocky	blocky	blocky	blocky
SiO_2	50.67	50.61	50.55	50.59	50.45	50.44	50.33	50.30	50.18	50.27
TiO_2	1.18	1.29	1.33	1.28	1.17	1.29	1.37	1.02	1.35	1.32
Al_2O_3	14.88	14.73	14.80	14.69	14.71	14.53	14.50	15.18	14.51	14.47
Cr_2O_3	0.09	0.08	0.09	0.08	0.10	0.09	0.10	0.11	0.09	0.09
FeO^T	9.57	10.02	9.86	10.21	9.54	10.06	10.39	8.39	10.50	10.68
MnO	0.19	0.20	0.20	0.20	0.17	0.21	0.22	0.16	0.21	0.21
MgO	8.02	7.56	7.72	7.62	7.83	7.66	7.59	8.62	7.62	7.42
CaO	12.40	12.13	12.18	11.94	12.38	12.02	11.98	13.14	11.85	11.70
Na_2O	2.67	2.70	2.84	2.78	2.62	2.70	2.73	2.38	2.87	2.89
K_2O	nd	nd	nd	nd	nd	nd	nd	nd	nd	nd
Total	99.67	99.33	99.55	99.37	98.97	99.00	99.20	99.31	99.18	99.04
Mg #	62.4	59.9	60.8	59.6	61.9	60.1	59.1	67.1	59.0	57.9

nd, not determined.

concentrations of 2.28-8.14 times chondrite. Heckle Seamount sample 7115-10-3 is the most evolved sample and has the highest REE concentrations of 4.35-11.80 times chondrite (Figure 12 and Table 2). The PZ69-1 samples from Heck Seamount all have identical REE patterns, whereas the 7016-9 REE patterns are essentially parallel, but there is a large variation in REE abundance. The whole rock sample, 7115-8-1 from the Endeavour Seamount, has slightly lower total REE, a greater positive Eu anomaly and lower HREE than LREE compared to the glass sample, due to dilution by the plagioclase which constitutes 9 modal percent (Table 3 and Figure 12) [*Hanson*, 1980].

The apparent positive Eu anomalies, may be the result of analytical problems with Gd resulting in low Gd values [*Van Wagoner and Leybourne*, this issue]. However, positive Eu anomalies have been observed in primitive lavas from seamounts adjacent to the East Pacific Rise [*Batiza and Vanko*, 1984] so that the Heck Seamount Chain Eu anomalies may be a real feature of the lavas.

DISCUSSION

Formation of Hyaloclastites

Several models have been postulated for the formation of hyaloclastite deposits on off-axis seamounts. *Bonatti and Harrison* [1988] argued for formation of hyaloclastites by contraction granulation of lavas which are very viscous, are low in temperature, have high crystal/liquid ratio, occur at ridges with low spreading rate, and undergo high stress from steep thermal gradients. The Heck Seamount hyaloclastites are inconsistent with this mode of formation because (1) the glass shards are aphyric, (2) some shards show flow banding and fluid textures, and (3) the shards span a spectrum of mafic compositions.

Other proposed mechanisms for the formation of hyaloclastite are (1) spalling of glass from flow margins [*Fisher and Schmincke*, 1984; *Batiza et al.*, 1984], and (2) hydrovolcanic eruptions involving contraction granulation and perhaps steam explosions of high volume, low viscosity lavas, possibly as a result of lava fountaining [*Batiza et al.*, 1984; *Smith and Batiza*, 1989]. In this case the lava fountaining hypothesis would require hyaloclastite formation at depths greater than the volatile fragmentation depth [*Kokelaar*, 1986]. Typically, hyaloclastite shards are nonvesicular [this study; *Fisher and Schmincke*, 1984; *Batiza et al.*, 1984; *Smith and Batiza*, 1989], indicating fragmentation by granulation or steam explosions involving superheating of water in contact with hot lava [*Kokelaar*, 1986], although extrusion due to caldera collapse or rapid magma injection into a high level magma chamber has been suggested as physical mechanisms of generating lava fountaining without vesiculation [*Smith and Batiza*, 1989]. Hyaloclastites believed to be formed by hydrovolcanic processes are distinguished by (1) restricted chemical diversity, (2) fluidal textures of shards, (3) crystal-poor shards, (4) bedding due to mass transport of the voluminous deposit, and (5) deposits are commonly associated with spatter at a vent site.

The hyaloclastites from the Heck Seamounts have a high percentage of matrix material (clay and/or calcite) (Figure 5), and the glass shards show chemical diversity that cannot be accounted for by fractionation during a single eruption (Figure 6). These factors suggest that the

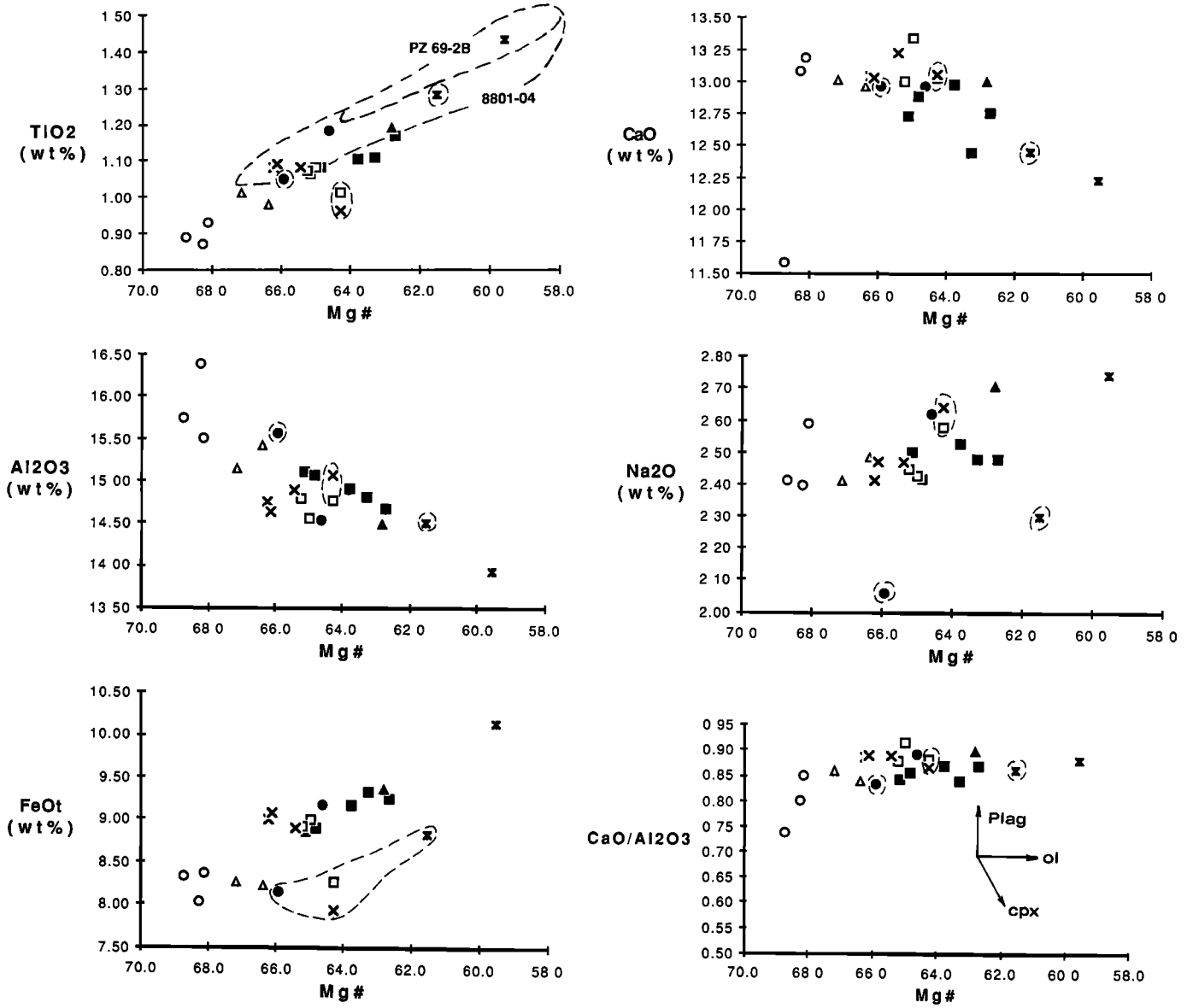

Fig. 6. Major elements plotted against Mg #. Symbols enclosed by dashed lined are whole rock analyses. Note the strong correlations of all the major elements with Mg #. The TiO_2 versus Mg # plot includes fields for the glasses from the hyaloclastite samples. Indicated on the CaO/Al_2O_3 versus Mg # plot are vectors indicating the effects of olivine, plagioclase and clinopyroxene fractionation. Symbols as in Figure 10*b*. Data are from Table 2 and Table 5.

hyaloclastites sampled were produced from spalling of pillow and ropey sheet flows. The lack of crystal fragments in the glass shards reflects the aphyric seamount lavas from which they are derived. Reworking and mixing of shards from different flows can be accomplished by ocean bottom currents [e.g., *Heezen and Rawson*, 1977; *Marks*, 1981]. The crystal fragments in sample PZ69-2-B are difficult to explain but may be due to either minor reworking which has removed any adhered glass or some form of hydrovolcanic eruption.

Significance of Magma Chambers

The importance of magma chambers can be indicated by evidence for magma chamber processes such as extensive fractionation or magma mixing. The covariation of major and trace elements with Mg # (Figures 6 and 15), the general increase in REE concentration with decreasing Mg # (Figure 12), and the chemical variation of melt inclusions in plagioclase megacrysts are consistent with relatively restricted olivine and plagioclase fractionation. This fractionation could occur either during magma ascent through the suboceanic lithosphere and/or within ephemeral magma chambers. The Cr and Ni contents of the Heck and Heckle Seamount lavas are consistent with limited crystal fractionation of primary magmas [*Basaltic Volcanism Study Project*, 1981]. The Heck and Heckle Seamount lavas sampled cluster at the primitive end of the MORB spectrum (Mg # = 68.7-59.5) and lack extreme fractionates. Although our sampling was restricted, other studies of off-axis seamounts have revealed similarly primitive compositions [*Batiza and Vanko*, 1984; *Fornari et al.*, 1988*b*; *Allan et al.*, 1989]. We found little mineralogical evidence for significant magma mixing (Figures 7,8, and 9), most rocks are aphyric, but minor reverse zoning of the olivine phenocrysts and megacrysts is consistent with either magma mixing or polybaric crystallization.

The chemical and mineralogical evidence is consistent with rapid ascent of the Heck and Heckle magmas through the oceanic crust with

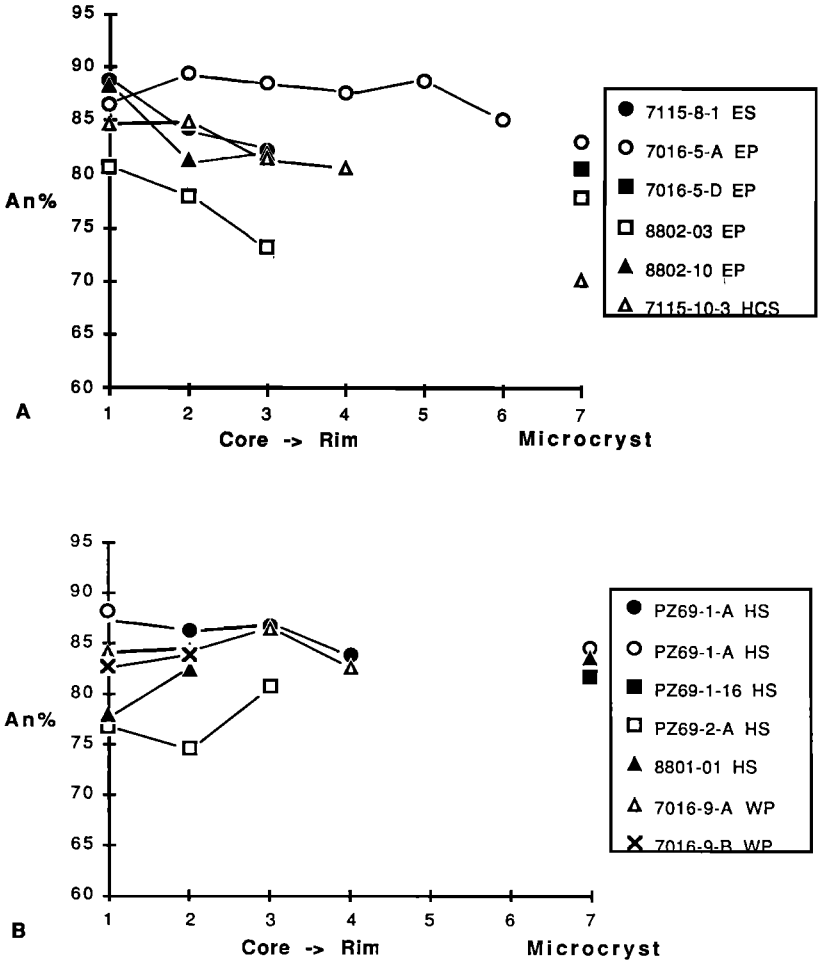

Fig. 7. Core to rim variations in anorthite content of plagioclase megacrysts and phenocrysts. At the right are the compositions of the coexisting microphenocrysts. (*a*) Endeavour Seamount, East Peak, Heckle Seamount. (*b*) Heck Seamount, West Peak. Data are from Table 6.

little residence time in magma chambers, similar to lava generation processes at other off-axis seamounts [*Batiza and Vanko*, 1984; *Fornari et al.*, 1988*b*]. The lack of long-lived magma chambers allows eruption of melts that may be considered near primary, such as the most mafic lavas from East Peak (MgO = 8.7-9.3; Mg # 68.7), consistent with high pressure experimental work [*Fujii and Bougault*, 1983; *Takahashi and Kushiro*, 1983; *Presnall and Hoover*, 1984; *Fujii and Scarfe*, 1985].

Source

All of the rocks sampled and analyzed from eight different dredge hauls are highly depleted in incompatible elements. Element ratios that characterize relative homogeneity of the source show little variation (e.g., $[La/Ce]_n$ = 0.65-0.77, $[La/Sm]_n$ = 0.29-0.41, $[Ce/Yb]_n$ = 0.38-0.55, Zr/Y = 1.94-2.30) and there is a strong correlation between Mg # and incompatible elements (e.g., Mg # versus TiO_2 (Figure 6)). It is possible to model our data by 15-20% batch partial melting of a depleted lherzolite (Figure 14). Obviously, if the source were more depleted than the modelled lherzolite, smaller amounts of partial melting would be required. Limited isotopic data from the Heckle Seamount Chain also indicate derivation from a highly depleted source ($^{87}Sr/^{86}Sr$=0.70237-0.70246, $^{143}Nd/^{144}Nd$=0.513212-0.513239) [*Hegner and Tatsumoto*, 1989].

It is difficult to obtain stratigraphic representation of a seamount sampling by dredge. Although our sampling was relatively restricted, preliminary major element data of a subsequent survey of these seamounts [*Karsten et al.*, 1990] have not revealed any significant differences.

Comparison With Other Off-Axis Seamounts

The Heck and Heckle seamounts have a similar range of incompatible element ratios as the Lamont Seamount, but do not show the variation in incompatible elements that is more typical of other small off-axis seamounts of the East Pacific Ocean (Figure 15). *Batiza and Vanko* [1984] and *Fornari et al.* [1988*a*,*b*] studied several such chains adjacent to the East Pacific Rise and found large variations in the incompatible element ratios along the seamounts chains and even on a single seamount (Figure 15). On some seamounts, the entire range from N-type MORB to P-type MORB has been found [*Batiza and Vanko*, 1984; *Zindler et al.*, 1984].

The Heck and Heckle Seamount lavas are very primitive, restricted, and depleted in composition and compositional range compared with the active portions of the adjacent ridge (West Valley and Endeavour Ridge (Figures 12 and 13)). The great heterogeneity of the lavas from West Valley requires a currently heterogeneous mantle source in order to account for the incompatible element rations, particularly $[La/Ce]_n$ (Figure 13). The Lamont seamounts are also more primitive and more depleted than the adjacent East Pacific Rise at 10° N. In contrast to the Heck and Heckle seamounts, however, the Lamont seamounts span a broader range of incompatible element and isotopic ratios than the adjacent ridge segment [*Fornari et al.*, 1988*b*].

TABLE 6. Plagioclase Microprobe Analyses

	7115-8-1			7016-5-A						
	Core M	z M	Rim M	Core M	z M	z M	z M	z M	Rim M	m	m
SiO_2	46.56	47.69	48.18	46.56	45.79	45.61	46.05	46.14	46.93	47.65	45.70
TiO2	0.07	0.09	0.08	0.06	0.04	0.04	0.06	0.00	0.05	0.00	0.00
Al_2O_3	33.81	32.76	32.49	33.19	33.52	33.65	33.23	33.29	32.55	32.79	33.00
FeO^T	0.36	0.42	0.53	0.38	0.35	0.35	0.36	0.33	0.42	0.43	0.42
MnO	0.04	0.00	0.00	0.16	0.12	0.13	0.09	0.16	0.15	0.01	0.03
MgO	0.21	0.24	0.28	0.21	0.18	0.19	0.15	0.17	0.20	0.26	0.21
CaO	18.17	17.47	17.14	18.39	19.28	19.15	18.55	18.99	18.42	17.65	17.73
Na_2O	1.29	1.79	2.06	1.60	1.28	1.39	1.45	1.35	1.79	1.98	1.87
K_2O	0.02	0.05	0.02	0.00	0.00	0.00	0.00	0.00	0.00	0.00	0.00
Total	100.53	100.51	100.78	100.55	100.56	100.51	99.94	100.43	100.51	100.77	98.96
An	88.6	84.4	82.1	86.4	89.3	88.4	87.6	88.6	85.0	83.1	84.0

	7016-5-D	8802-03				8802-10			PZ69-1-A		
	p	m	Core M	z M	Rim M	Core M	z M	Rim M	Core p	z p	z p
SiO_2	48.14	48.78	48.04	48.17	50.41	46.07	47.88	47.72	46.21	46.63	46.37
TiO_2	0.08	0.00	0.00	0.00	0.00	0.00	0.00	0.02	0.02	0.03	0.00
Al_2O_3	32.01	32.46	32.88	32.19	31.04	34.44	32.86	33.35	33.70	32.74	32.59
FeO^T	0.50	0.60	0.48	0.44	0.65	0.33	0.40	0.51	0.43	0.47	0.45
MnO	0.03	0.00	0.00	0.00	0.00	0.00	0.00	0.00	0.08	0.09	0.13
MgO	0.30	0.26	0.24	0.28	0.36	0.23	0.23	0.25	0.19	0.16	0.16
CaO	15.49	16.71	16.60	16.19	15.05	18.35	17.01	17.36	18.27	18.19	18.37
Na_2O	2.07	2.60	2.21	2.52	3.06	1.35	2.16	2.12	1.39	1.61	1.55
K_2O	0.03	0.00	0.00	0.00	0.00	0.00	0.00	0.00	0.00	0.00	0.00
Total	98.65	101.41	100.45	99.79	100.57	100.77	100.54	101.33	100.29	99.92	99.62
An	80.5	78.0	80.6	78.0	73.1	88.3	81.3	81.9	87.9	86.2	86.8

	PZ69-1-A			PZ69-1-16	PZ69-2-A			8801-01		
	Rim p	Core p	Rim p	ml	m	Core p	z p	Rim p	Core p	Rim p	m
SiO_2	47.68	46.20	47.48	46.47	48.86	49.09	47.44	47.82	48.67	46.74	46.78
TiO_2	0.04	0.07	0.06	0.01	0.08	0.08	0.06	0.06	0.01	0.00	0.03
Al_2O_3	32.35	33.50	32.48	33.50	32.26	30.16	32.47	31.59	31.91	33.14	33.42
FeO^T	0.50	0.34	0.50	0.65	0.59	0.53	0.59	0.70	0.43	0.48	0.44
MnO	0.07	0.08	0.08	0.00	0.04	0.14	0.16	0.15	0.00	0.00	0.00
MgO	0.19	0.16	0.17	0.21	0.29	0.26	0.24	0.24	0.31	0.29	0.24
CaO	17.42	18.67	17.77	17.94	16.48	16.41	15.16	17.31	16.10	16.63	17.59
Na_2O	1.86	1.39	1.89	1.82	2.02	2.75	2.85	2.29	2.51	1.96	1.89
K_2O	0.00	0.00	0.00	0.00	0.01	0.00	0.00	0.00	0.00	0.00	0.00
Total	100.11	100.41	100.43	100.60	100.63	99.42	98.97	100.16	99.94	99.24	100.39
An	83.8	88.1	83.9	84.5	81.8	76.7	74.6	80.7	78.0	82.4	83.7

	7016-9-A				7016-9-B		7115-10-3				
	Core M	z M	z M	Rim M	Core p	Rim p	Core M	z M	z M	Rim M	m
SiO_2	47.37	47.03	46.30	47.62	47.79	45.21	46.11	46.52	47.63	47.39	50.88
TiO_2	0.08	0.06	0.08	0.05	0.05	0.05	0.07	0.07	0.06	0.08	0.05
Al_2O_3	32.29	32.33	32.75	32.49	32.46	33.48	32.49	33.32	31.41	32.93	30.20
FeO^T	0.48	0.45	0.57	0.60	0.48	0.49	0.50	0.67	0.54	0.64	0.86
MnO	0.15	0.16	0.23	0.18	0.01	0.01	0.16	0.20	0.16	0.19	0.00
MgO	0.23	0.20	0.19	0.19	0.28	0.26	0.17	0.17	0.19	0.21	0.27
CaO	17.32	17.61	18.06	17.05	17.39	16.87	17.58	17.57	17.27	16.77	15.49
Na_2O	1.82	1.80	1.55	1.98	2.00	1.78	1.77	1.73	2.18	2.23	3.62
K_2O	0.00	0.00	0.00	0.00	0.02	0.01	0.00	0.00	0.00	0.00	0.00
Total	99.74	99.64	99.73	100.16	100.48	98.16	98.85	100.25	99.44	100.44	101.37
An	84.0	84.4	86.6	82.6	82.8	84.0	84.6	84.9	81.4	80.6	70.3

M, megacryst; p, phenocryst; m, microphenocryst; z, zone between core and rim.

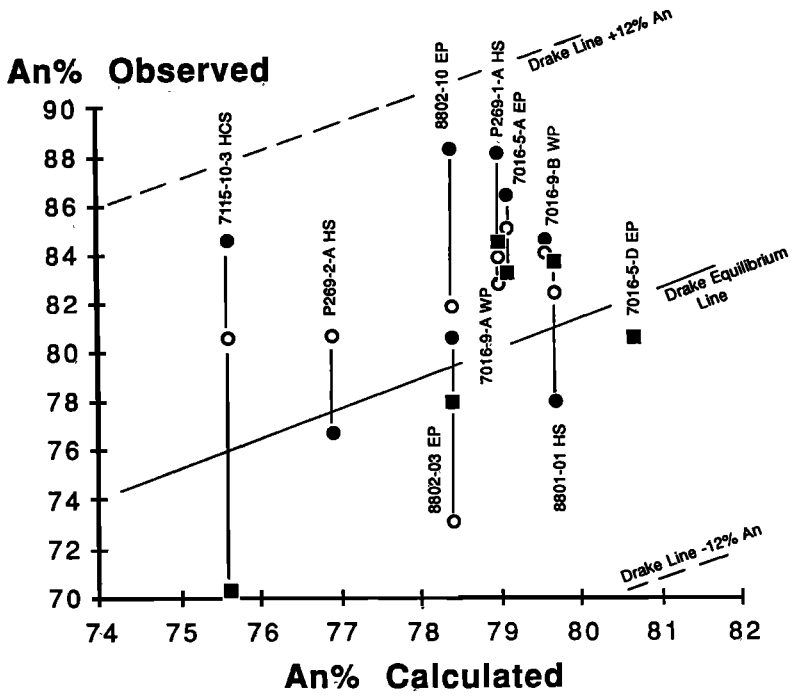

Fig. 8. Analyzed plagioclase compositions plotted against calculated equilibrium plagioclase compositions using the equation of *Drake* [1976]. Also shown are the equilibrium line and error envelope (±12 mol % An [*Drake*, 1976]). Data are from Table 6. Solid circles, core compositions; open circles, rim compositions; squares, microphenocryst compositions.

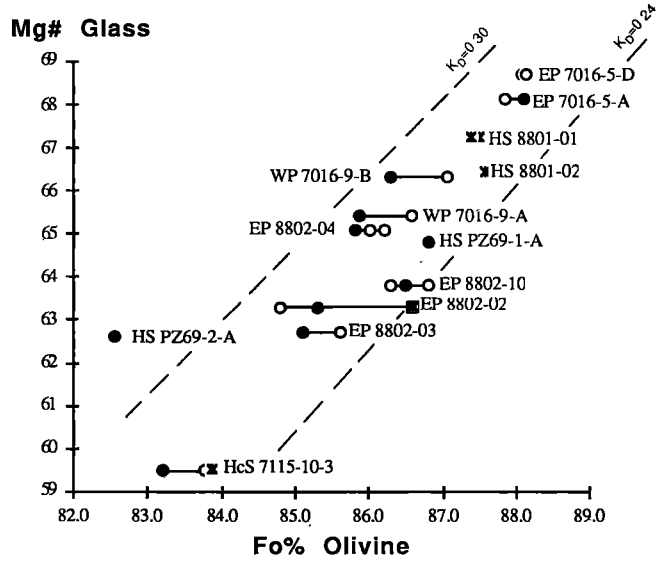

Fig. 9. Mg # of the host glass plotted against the forsterite content of olivine. Equilibrium lines indicate the partitioning of Fe and Mg between the glass and olivine assuming K_D = 0.24-0.30 [after *Stakes et al.*, 1984]. Solid circles, core phenocryst; open circles, rim; asterisks, microphenocryst; asterisks in box, microphenocryst from a rock fragment. Data are from Table 7.

The predominance of primitive lavas associated with the other small off-axis seamount chains [*Batiza and Vanko*, 1984; *Fornari et al.*, 1988*b*; *Batiza et al.*, 1989] has been interpreted to be a function of the greater importance of subaxial magma chamber in the ridge environment compared to off-axis seamounts [*Batiza and Vanko*, 1984; *Fornari et al.*, 1988*a,b*; *Allan et al.*, 1989]. As previously discussed, our mineralogical and glass geochemistry support this interpretation.

The difference in the degree of heterogeneity of the adjacent ridge segments is a function not only the mantle characteristics but also magma supply. The ridge system adjacent to the Heck and Heckle seamounts is very heterogeneous, and the heterogeneities are not mixed because there is a less robust magma supply associated with lower spreading rates compared to the East Pacific Rise at 10°N [*Leybourne and Van Wagoner*, 1989; *Van Wagoner and Leybourne*, this issue; *Karsten et al.*, 1990; *Allan et al.*, 1989].

Of significance is why small off-axis seamount chains with typically depleted compositions are erupted in close proximity to ridge segments with more enriched compositions. Seamounts formed near the East Pacific Rise have been interpreted to be derived by partial melting of small-scale mantle heterogeneities which are ineffectively mixed before eruption, resulting in the range of rock types [*Batiza and Vanko*, 1984; *Fornari et al.*, 1988*a,b*] (Figure 15).

Davis and Karsten [1986] postulated that small off-axis seamount chains could be produced by melting of low-temperature mantle heterogeneities in advance of a migrating ridge crest, which should produce a progression along the chain from enriched to depleted compositions toward the ridge as the enriched mantle components are consumed. The chemistry of the Heck, Heckle, and Lamont seamounts does not support this model [*Allan et al.*, 1989; *Karsten et al.*, 1990]. More recently, *Karsten et al.* [1990] suggested that the Heck and Heckle Seamounts tapped the same mantle source as the adjacent ridge lavas with the compositional differences between the seamounts, abyssal ridges, and ridge crest reflecting temporal changes in the melting regime of the subaxial mantle. Alternatively, the mantle source may have been more depleted at the time the Heck and Heckle seamounts formed [B. Cousens, personal communication, 1990]. *Michael et al.* [1989] argued that enrichment of the ridge segments north of the Cobb Offset is a recent phenomena. Additional evidence from the West Valley Segment of the Juan de Fuca Ridge supports this hypothesis [*Van Wagoner and Leybourne*, this issue]. In this case, at

TABLE 7: Olivine Microprobe Analyses

	7016-5-A		7016-5-D		8801-01		8802-02			
	Core p	Rim p	Core p	Rim p	m	m	m	Core p	Rim p	rock frag
SiO_2	40.36	40.61	40.00	39.81	40.02	39.45	40.23	39.56	39.83	39.79
TiO_2	0.03	0.00	0.00	0.06	0.06	0.00	0.03	0.03	0.04	0.00
Al_2O_3	0.04	0.03	0.03	0.04	0.06	0.07	0.06	0.04	0.04	0.03
Cr_2O_3	0.00	0.00	0.00	0.00	0.00	0.12	0.00	0.07	0.06	0.11
FeO^T	11.41	11.72	11.58	11.54	11.73	11.90	11.64	13.76	13.77	12.73
NiO	0.14	0.14	0.34	0.40	0.14	0.00	0.22	0.07	0.06	0.09
MnO	0.23	0.20	0.00	0.00	0.27	0.18	0.23	0.29	0.25	0.20
MgO	47.34	47.46	47.91	48.11	46.05	46.43	45.95	44.68	43.26	46.10
CaO	0.32	0.40	0.33	0.37	0.36	0.41	0.34	0.30	0.32	0.31
Total	99.87	100.56	100.19	100.33	98.69	98.56	98.70	98.80	97.63	99.36
Fo	88.1	87.8	88.1	88.1	87.5	87.4	87.6	85.3	84.8	86.6

	8802-03		8802-04				8802-10			PZ69-1-A
	Core p	Rim p	Core M	Rim M	Core p	Rim p	Core p	Rim p	p	Core p
SiO_2	39.54	39.44	39.60	39.66	39.26	39.47	40.31	40.41	40.41	39.82
TiO_2	0.01	0.04	0.00	0.01	0.04	0.04	0.00	0.02	0.04	0.00
Al_2O_3	0.07	0.00	0.05	0.04	0.03	0.06	0.00	0.03	0.07	0.04
Cr_2O_3	0.06	0.06	0.02	0.04	0.07	0.04	0.02	0.00	0.13	0.03
FeO^T	13.80	13.35	13.36	12.98	13.13	13.12	12.90	12.48	13.12	12.61
NiO	0.07	0.09	0.13	0.08	0.00	0.00	0.00	0.12	0.07	0.17
MnO	0.30	0.29	0.21	0.20	0.24	0.22	0.21	0.23	0.22	0.30
MgO	44.13	44.61	45.22	45.43	46.01	45.18	46.19	46.07	46.33	46.55
CaO	0.30	0.32	0.27	0.30	0.30	0.34	0.28	0.32	0.32	0.32
Total	98.28	98.20	98.86	98.74	99.08	98.47	99.91	99.68	100.71	99.84
Fo	85.1	85.6	85.8	86.2	86.2	86.0	86.5	86.8	86.3	86.8

	PZ69-2-A	7016-9-A		7016-9-B		7115-10-3		
	m	Core p	Rim p	Core p	Rim p	m	Core p	Rim p
SiO_2	39.44	39.70	39.55	39.26	39.51	39.49	39.33	39.43
TiO_2	0.04	0.01	0.04	0.05	0.05	0.03	0.00	0.00
Al_2O_3	0.03	0.00	0.03	0.03	0.02	0.00	0.00	0.03
Cr_2O_3	0.00	0.00	0.06	0.00	0.00	0.02	0.00	0.04
FeO^T	16.59	13.54	12.83	13.43	12.59	15.24	15.64	15.32
NiO	0.07	0.00	0.14	0.34	0.41	0.10	0.11	0.08
MnO	0.38	0.30	0.22	0.00	0.00	0.28	0.25	0.21
MgO	44.08	46.08	46.37	47.42	47.40	44.44	43.49	44.32
CaO	0.17	0.33	0.38	0.32	0.36	0.38	0.34	0.34
Total	100.80	99.96	99.62	100.85	100.34	99.98	99.16	99.77
Fo	82.6	85.8	86.6	86.3	87.0	83.9	83.2	83.8

M, megacryst; p, phenocryst; m, microphenocryst; frag, fragment.

the time the seamounts formed, the mantle may have resembled the mantle source for the Juan de Fuca Ridge south of the Cobb Offset (Figure 13). However, the Heck and Heckle seamounts are still at the depleted end of the lavas south of the Cobb Offset (Figure 13).

Seamount petrogenesis is a poorly constrained problem. If at medium to slow spreading ridges more fertile portions of the mantle are preferentially melted, the mantle material that outwells will be depleted of enriched mantle components. Subsequent melting at the seamount would then produce consistently depleted lavas compared to the adjacent ridge. The small variations in incompatible element ratios that do exist on the Heck and Heckle seamounts ($[La/Ce]_n$=0.65-0.77) may then be the result of mixing of small amounts of enriched mantle material, thus accounting for the deviation of data points from the partial melting curve in Figure 14. The Heck and Heckle seamounts represent approximately 2 m.y. of volcanism, based on magnetic lineations [*Lee and Hammond*, 1985; *Barr*, 1974], indicating a continuous supply of a depleted source.

This interpretation does not require remelting of previously melted portions of mantle [e.g., *Allan et al.*, 1989] but does require melting of the more depleted and refractory portions of the mantle that were not melted beneath the ridge crest. In contrast, at fast spreading centers, robust melting produces a mixed mantle signature in axial lavas, while suppressed melting at the seamounts reveals the heterogeneities [*Batiza and Vanko*, 1984; *Allan et al.*, 1989]. For seamount chains that are depleted, such as the Heck and Heckle seamounts and the Lamont seamounts, the melting anomaly is envisaged to be relatively shallow [*Desonie and Duncan*, 1990] so that it only the outwelled mantle will undergo partial melting. Other seamount chains in the eastern Pacific Ocean, e.g., the Cobb-Eickleberg Seamount chain, are longer lived and contain more enriched components, possibly reflecting deeper melting anomalies [*Desonie and Duncan*, 1990].

Alternatively, enriched lavas may be the early products of seamount volcanism subsequently covered by later lavas that are difficult to sample by dredge. We have positive evidence for the first hypothesis

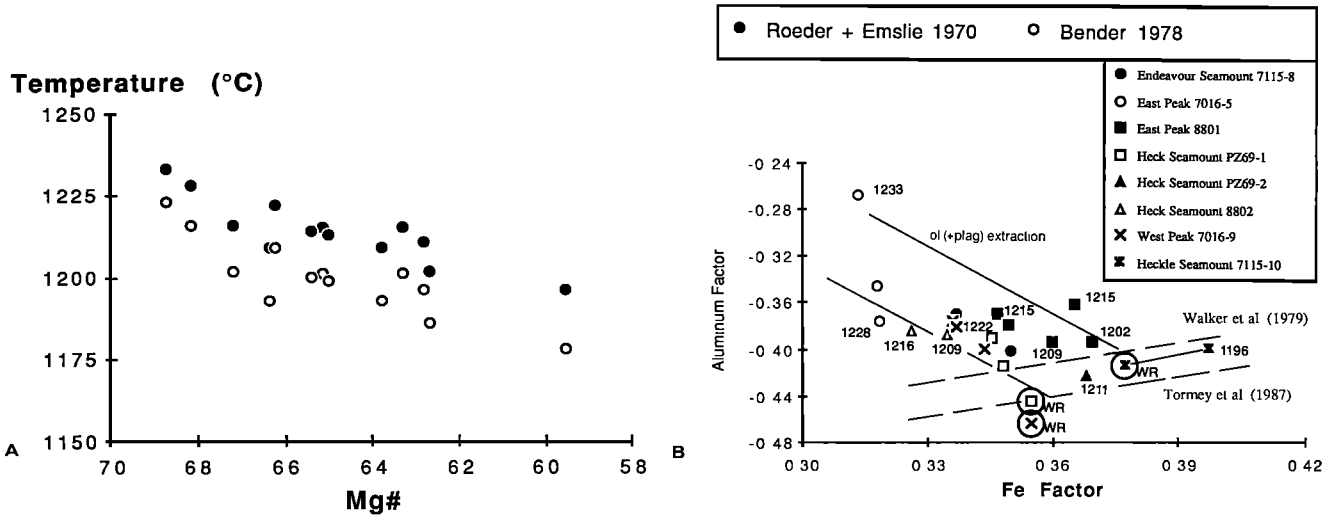

Fig. 10. (*a*) Calculated crystallization temperature plotted against Mg #. Temperatures were calculated using the Mg partition between olivine and glass equations from *Roeder and Emslie* [1970] and *Bender et al.* [1978]. (*b*) Al factor plotted against Fe factor after *Reid et al.* [1989]. Cotectics are after *Walker et al.* [1979] and *Tormey et al.* [1987] are shown. Symbols are keyed to calculated temperature [*Roeder and Emslie*, 1970].

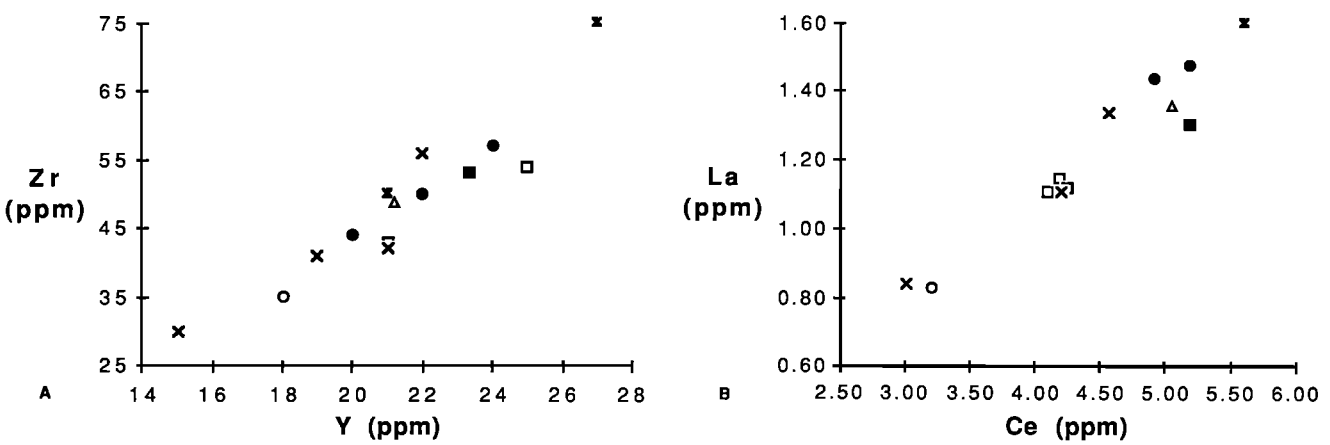

Fig. 11. Incompatible element variation diagrams, showing that samples all plot on a single line with very little scatter. (*a*) Zr versus Y. (*b*) Ce versus La. Symbols are as in Figure 10*b*. Data are from Table 2.

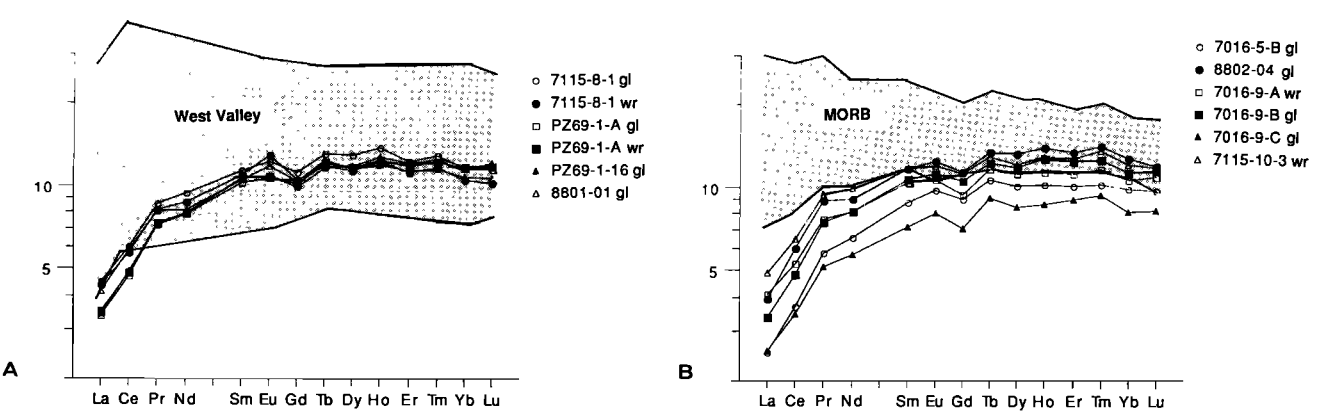

Fig. 12. Chondrite normalized REE plots. Note the parallel REE patterns of all the samples and similar La/Sm and Ce/Yb ratios. The samples appear to have positive Eu anomalies but this may be an analytical problem with Gd (see text). Diagrams plotted using spider program [*Wheatley and Rock*, 1988]. Also shown are fields for MORB [after *Basaltic Volcanism Study Project*, 1981] and West Valley [*Van Wagoner and Leybourne*, this issue].

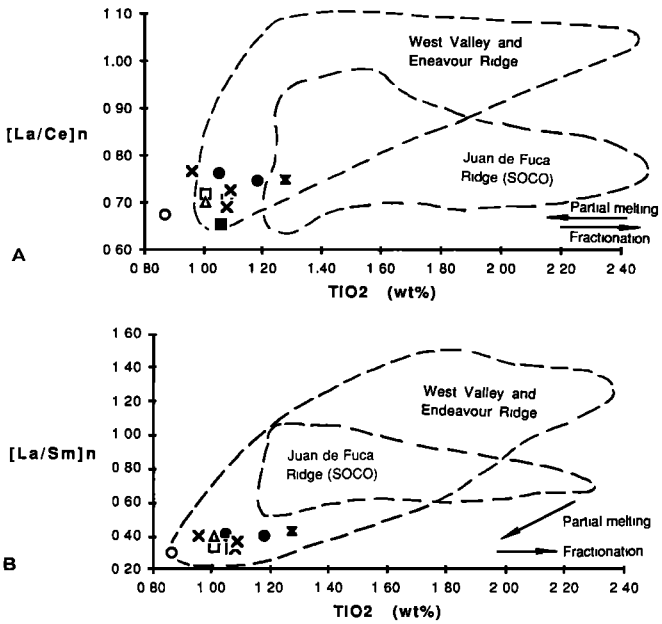

Fig. 13. Incompatible element ratio plotted against incompatible element. (*a*) $[La/Ce]_n$ versus TiO_2. (*b*) $[La/Sm]_n$ versus TiO_2. Both plots show the depletion of the Heck and Heckle Seamount lavas in the LREE and TiO_2 and the far more restricted range of LREE compared to rocks of the adjacent West Valley and Endeavour Ridge Segments of the Juan de Fuca Ridge. West Valley and Endeavour Ridge data from *Van Wagoner and Leybourne* [this issue]. Also shown is the field for axial lavas on the Juan de Fuca Ridge south of the Cobb Offset (SOCO). Data are from *Rhodes et al.* [1990]. On the $[La/Ce]_n$ versus TiO_2 plot both partial melting and fractional crystallization do not alter the $[La/Ce]_n$ ratio, whereas in the $[La/Sm]_n$ plot, the extent of partial melting affects the $[La/Sm]_n$ ratio. Symbols are as in Figure 10*b*. Data are from Table 2.

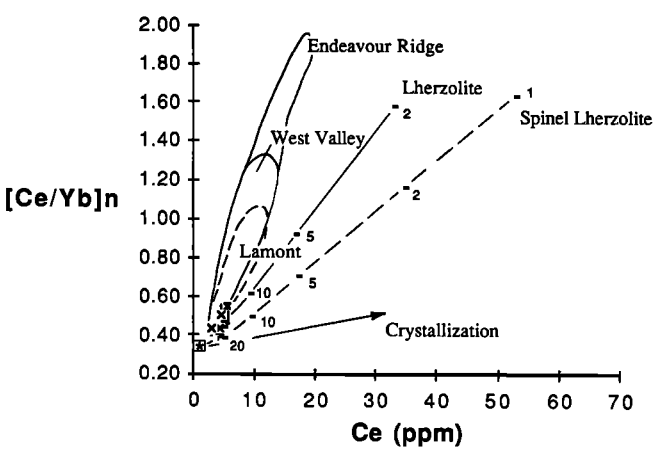

Fig.14. $[Ce/Yb]_n$ plotted against Ce. The Heck and Heckle Seamount lavas show a similar trend to melting of depleted lherzolite (source indicated by large enclosed asterisk). The lherzolite was modelled as 50% olivine, 30% orthopyroxene, 20% clinopyroxene (melting fraction 15:35:50). The spinel lherzolite was modelled as 60% ol, 20% opx, 10% cpx, 10% spinel (melting fraction 5:5:45:45). Crystal fractionation is clearly not responsible for the variation in Ce/Yb. Also shown are fields for the Lamont Seamounts [*Fornari et al.*, 1988] and the West Valley and Endeavour Ridge Segments [*Van Wagoner and Leybourne*, this issue] showing the more restricted range of the Heck and Heckle seamount lavas. The melting lines also indicate the percentage partial melting. Symbols are as in Figure 10*b*. Data are from Table 2.

in the heterogeneity of the West Valley and Endeavour Ridge lavas (Figures 13 and 14). Increased and deeper sampling of seamounts and study of other seamounts associated with medium to slow spreading ridges may further constrain lava petrogenesis.

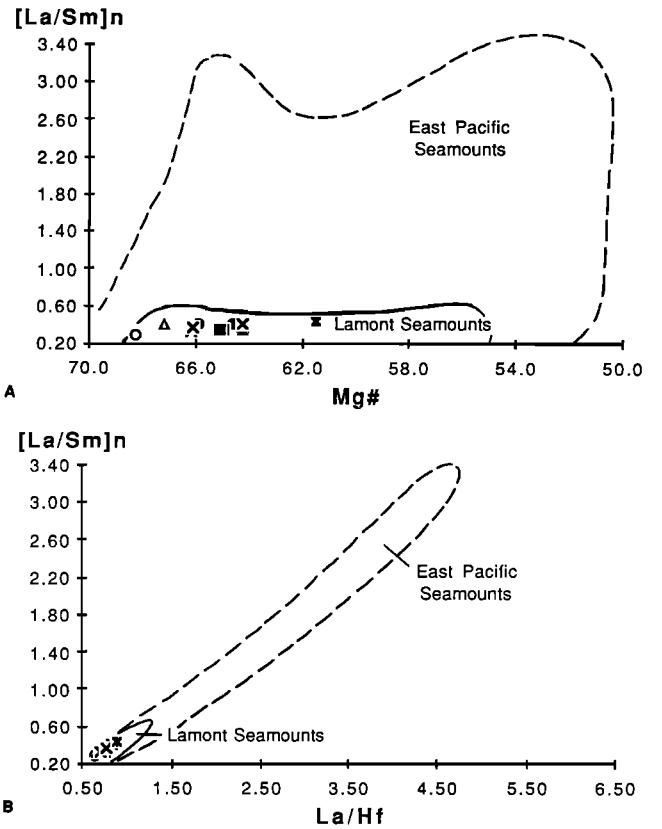

Fig. 15. Incompatible element plots showing the very depleted and primitive nature of the Heck and Heckle Seamount lavas compared to East Pacific seamounts (data from *Batiza and Vanko* [1984]). The Heck and Heckle Seamount lavas are similar to the Lamont Seamount lavas but are more restricted in compositional range. Lamont Seamount data are from *Fornari et al.* [1988]. (*a*) $[La/Sm]_n$ versus Mg #. (*b*) $[La/Sm]_n$ versus La/Hf. Symbols are as in Figure 10*b*. Data are from Table 2.

Endeavour Seamount

Endeavour Seamount is an enigmatic feature because it is unclear whether it is a seamount of the Heck Seamount Chain [*Karsten et al.*, 1986] or a portion of West Ridge isolated due to the overlap of West Valley and Endeavour Ridge at the Endeavour Offset [*Scott et al.*, 1988]. West Ridge represents uplifted oceanic crust [*Davis and Lister*, 1977] but recovery of relatively fresh pillow basalts [*Barr*, 1972; *Leybourne*, 1988] and regions of high back-scatter in Sea MARC II imagery [*Davis et al.*, 1987*b*] indicates relatively recent volcanism. Evidence that Endeavour Seamount is part of West Ridge is that it is roughly continuous with West Ridge, and it is highly faulted [*Scott et al.*, 1988]. Evidence that Endeavour Seamount is a seamount is its shape, high elevation, and that it is on strike with the Heck Seamount Chain [*Karsten et al.*, 1986].

Endeavour Seamount is chemically similar to the other Heck seamounts. However, rocks recovered from West Ridge at 48°31'N are also highly depleted N-type MORB [*Van Wagoner and Leybourne*, this issue] with REE patterns similar to Endeavour Seamount (Figure 12). Although it is difficult to conclusively identify Endeavour Seamount as a seamount, we prefer this interpretation due to its chemical similarity to the Heck Seamounts coupled with its physiographic characteristics. It is possible that the lavas recovered from West Ridge are tapping the same off-axis, depleted source as the seamount lavas given their similarity to the Heck Seamount lavas (Mg # = 67.8, $[La/Ce]_n$ = 0.62, $[La/Sm]_n$ = 0.25) [*Leybourne and Van Wagoner*, this issue].

CONCLUSIONS

1. The flow banding textures in some of the Heck and Heckle Seamount lavas are indicative of high effusion rates associated with either contorted sheet flows or lava fountaining. The clinkery lavas may be associated with hyaloclastites. Hyaloclastites are reworked deposits of spalled glassy flow margins with lesser evidence for hydrovolcanic eruptions.

2. The Heck and Heckle Seamount lavas are aphyric to sparsely phyric. Plagioclase megacrysts are rare compared to rocks from the adjacent West Valley Segment. Phenocrysts of plagioclase and olivine show little zonation (up to 7.5% An, <1% Fo). Phenocrysts are equilibrium phases; reversely zoned olivine may be indicative of polybaric crystallization.

3. That magma chambers are subordinate features beneath these seamounts such that magmas have minimal residence time at upper crustal levels is supported by the fact that the seamount lavas are very primitive, have high crystallization temperatures, are restricted in compositional range and lack xenocrysts or complex zoning of phenocrysts, and phenocrysts are equilibrium compositions.

4. The Heck and Heckle Seamount lavas are consistently highly depleted MORB, are at the most depleted range of East Pacific seamount lavas, and exhibit a relatively restricted range in incompatible element ratios. The Heck and Heckle seamounts are morphologically and geochemically similar to the Lamont Seamount Chain adjacent to the East Pacific Rise at 10°N but do not show the same variation of incompatible elements that is more typical of other small off-axis seamounts of the East Pacific Ocean. The Lamont, Heck, and Heckle seamounts are more primitive and depleted than active portions of the adjacent ridge segment, but in contrast to the Heck and Heckle seamounts, the Lamont seamounts span a broader range of incompatible element and isotopic ratios than the adjacent ridge segment. The difference in the heterogeneity of the adjacent ridge segment is a function of mantle characteristics and magma supply. On the ridge segment adjacent to the Heck and Heckle seamounts the magma supply is less robust than that associated with lower spreading rates than the East Pacific Rise at 10°N such that heterogeneities in the source are less effectively mixed.

5. Formation of the Heck and Heckle seamount lavas is consistent with off-axis tapping of a mantle source that has had enriched mantle components removed by partial melting beneath the adjacent mid-ocean ridge.

Acknowledgments. We would like to thank the Captain, crew, and scientists on board the CSS *John P. Tully* for their assistance in collection of the samples from West Valley. The field work was facilitated greatly by the support of Jim Franklin. We would also like to thank Sandra Barr and Dick Chase for providing additional samples. We are grateful for discussions with Sandra Barr, Scott Swinden, and Jim Franklin. Thorough reviews by Jill Karsten, Rodey Batiza, Brian Cousens, and an anonymous reviewer greatly improved the manuscript. This research was funded by a Natural Science and Engineering Research Council of Canada operating grant and an Energy, Mines and Resources of Canada Research Agreement awarded to N. Van Wagoner.

REFERENCES

Allan, J. F., R. O. Sack, and R. Batiza, Cr-rich spinels as petrogenetic indicators: MORB-type lavas from the Lamont seamount chain, eastern Pacific, *Am. Mineral., 73*, 741-753, 1988.

Allan, J. F., R. Batiza, M. R. Perfit, D. J. Fornari, and R. O. Sack, Petrology of lavas from the Lamont Seamount Chain and adjacent East Pacific Rise, 10° N, *J. Petrol., 30*, 1245-1298, 1989.

Ballard, R. D., R. T. Holcomb, and T. H. van Andel, The Galapagos Rift at 86°W, 3, Sheet flows, collapse pits, and lava lakes of the rift valley, *J. Geophys. Res., 84*, 5407-5422, 1979.

Barone, A. M., and W. B. F. Ryan, Single plume model for asynchronous formation of the Lamont Seamounts and adjacent East Pacific Rise terrains, *J. Geophys. Res., 95*, 10,801-10,827, 1990.

Barr, S. M., Geology of the northern end of the Juan de Fuca Ridge and adjacent continental slope, Ph.D. thesis, 287 pp., Univ. of British Columbia, Vancouver, 1972.

Barr, S. M., Seamount chains formed near the crest of the Juan de Fuca Ridge, northeast Pacific Ocean, *Mar. Geol., 17*, 1-19, 1974.

Basaltic Volcanism Study Project, *Basaltic Volcanism on the Terrestrial Planets*, 1286 pp.., Pergamon, New York, 1981.

Batiza, R., and D. Vanko, Volcanic development of small oceanic central volcanoes on the flanks of the East Pacific Rise inferred from narrow beam echo sounder surveys, *Mar. Geol., 54*, 53-90, 1983.

Batiza, R., and D. Vanko, Petrology of young Pacific seamounts, *J. Geophys. Res., 89*, 11,235-11,260, 1984.

Batiza, R., D. J. Fornari, D. A. Vanko, and P. Lonsdale, Craters, calderas, and hyaloclastites on young Pacific seamounts, *J. Geophys. Res., 89*, 8371-8390, 1984.

Batiza, R., J. Brodholt, J. Karsten, D. Vanko, and R. O. Sack, Petrogenesis of young seamounts near transforms and OSC's of the EPR 5°-15°N, *Eos Trans. AGU, 69*, 1475, 1988.

Batiza, R., P. J. Fox, P. R. Vogt, S. C. Cande, N. R. Grindlay, W. G. Melson, and T. O'Hearn, Morphology abundance, and chemistry of near-ridge seamounts in the vicinity of the Mid-Atlantic Ridge ≈ 26°S, *J. Geol., 97*, 209-220, 1989.

Bender, J. F., F. N. Hodges, and A. E. Bence, Petrogenesis of basalts from the project FAMOUS area: Experimental study from 0-15 kbars, *Earth Planet. Sci. Lett., 41*, 277-302, 1978.

Bonatti, E., and C. G. A. Harrison, Eruption styles of basalt in oceanic spreading ridges and seamounts: Effects of magma temperature and viscosity, *J. Geophys. Res., 93*, 2967-2980, 1988.

Bryan, W. B., Morphology of quench crystals in submarine basalts, *J. Geophys. Res., 77*, 5812-5817, 1972.

Bryan, W. B., Regional variation and petrogenesis of basalt glasses from the FAMOUS area, Mid-Atlantic Ridge, *J. Petrol., 20*, 293-325, 1979.

Cohen, R. S., and R. K. O'Nions, The Pb, Nd, and Sr isotopic structure of ocean ridge basalts, *J. Petrol., 23*, 299-324, 1982.

Davis, E. E., and J. L. Karsten, On the cause of the asymmetric distribution of seamounts about the Juan de Fuca Ridge: Ridge crest migration over a heterogeneous asthenosphere, *Earth Planet. Sci. Lett., 79*, 385-396, 1986.

Davis E. E., and C. R. B. Lister, Tectonic structures on the Juan de Fuca Ridge, *Geol. Soc. Am. Bull., 88*, 346-363, 1977.

Davis, E., R. Currie, and B Sawyer, Bathymetry map 6-1987, northern Juan de Fuca Ridge, Geol. Surv. of Can., Energy Mines and Resour., Ottawa, 1987*a*.

Davis, E., R. Currie, and B Sawyer, Acoustic imagery map 14-1987, northern Juan de Fuca Ridge, Geol. Surv. of Can., Energy Mines and Resour., Ottawa, 1987*b*.

Desonie, D. L., and R. A. Duncan, The Cobb-Eickelberg Seamount Chain: Hotspot volcanism with mid-ocean ridge basalt affinity, *J. Geophys. Res., 95*, 12,697-12,711, 1990.

Dosso, L., H. Bougault, P. Beuzart, J.-Y. Calvez, and J.-L. Joron, The geochemical structure of the South-East Indian Ridge, *Earth Planet. Sci. Lett., 88*, 47-59, 1988.

Drake, M. J., Plagioclase-melt equilibria, *Geochim. Cosmochim. Acta, 40*, 457-465, 1976.

Evensen, N. M., P. J. Hamilton, and R. K. O'Nions, Rare earth abundances in chondritic meteorites, *Geochim. Cosmochim. Acta, 42*, 1199-1212, 1978.

Fisher, R. V., and H.-U. Schmincke, *Pyroclastic Rocks*, 472 pp., Springer-Verlag, New York, 1984.

Fisk, M. R., and A. E. Bence, Experimental studies of spinel crystallization in FAMOUS basalt 527-1-1 (abstract), *Eos Trans. AGU 60*, 420, 1979.

Fornari, D. J., R. Batiza, and M. A. Luckman, Seamount abundances and distribution near the East Pacific Rise 0°-24°N based on Seabeam data, in *Seamounts, Islands, and Atolls, Geophys. Monogr. Ser.*, vol. 43, edited by B. H. Keating et al., pp. 13-21, AGU, Washington, D.C., 1987.

Fornari, D. J., M. R. Perfitt, J. F. Allan, and R. Batiza, Small-scale heterogeneities in depleted mantle sources: Near-ridge seamount lava geochemistry and implications for mid-ocean ridge magmatic processes, *Nature, 331*, 511-513, 1988*a*.

Fornari, D. J., M. R. Perfitt, J. F. Allan, R. Batiza, R. Haymon, A. Barone, W. B. F. Ryan, T. Smith, T. Simkin, and M. A. Luckman, Geochemical and structural studies of the Lamont seamounts: Seamounts as indicators of mantle processes, *Earth Planet. Sci. Lett., 89*, 63-83, 1988*b*.

Fujii, T., and H. Bougault, Melting relations of a magnesian abyssal tholeiite and the origin of MORB's, *Earth Planet. Sci. Lett., 62*, 283-295, 1983.

Fujii, T., and C. M. Scarfe, Composition of liquids coexisting with spinel lherzolite at 10 kbars and the genesis of MORB's, *Contrib. Mineral. Petrol., 90*, 18-28, 1985.

Graham, D. W., A. Zindler, M. D. Kurz, W. J. Jenkins, R. Batiza, and H. Staudigel, He, Pb, Sr, and Nd isotope constraints on magma genesis and mantle heterogeneity beneath young Pacific seamounts, *Contrib. Mineral. Petrol., 99*, 446-463, 1988.

Grove, T. L., and W. B. Bryan, Fractionation of pyroxene-phyric MORB at low pressure: An experimental study, *Contrib. Mineral. Petrol., 84*, 293-309, 1983.

Hanson, G. N., Rare earth elements in petrogenetic studies of igneous systems, *Annu. Rev. Earth Planet. Sci., 8*, 371-406, 1980.

Hart, S. R., Heterogeneous mantle domains: Signatures, genesis and mixing chronologies, *Earth Planet. Sci. Lett., 90*, 273-296, 1988.

Heezen, B. C., and M. Rawson, Visual observations of contemporary erosion and tectonic deformation on the Cocos Ridge crest, *Mar. Geol., 23*, 173-196, 1977.

Hegner, E., and M. Tatsumoto, Pb, Sr, and Nd isotopes in seamount basalts from the Juan de Fuca Ridge and Kodiak-Bowie Seamount Chain, northeast Pacific, *J. Geophys. Res., 94*, 17,839-17,846, 1989.

Holness, M. B., and F. M. Richter, Possible effects of spreading rate on MORB isotopic and rare earth composition arising from melting of a heterogeneous source, *J. Geol., 97*, 247-260, 1989.

Karsten, J. L., and J. R. Delaney, Hot spot-ridge crest convergence in the Northeast Pacific, *J. Geophys. Res., 94*, 700-712, 1989.

Karsten, J. L., S. R. Hammond, E. E. Davis, and R. G. Currie, Detailed geomorphology and neotectonics of the Endeavour Segment, Juan de Fuca Ridge: New results from Sea Beam swath mapping, *Geol. Soc. Am. Bull., 97*, 213-221, 1986.

Karsten, J. L., et al., Petrology of Heck, Heckle and Springfield seamounts, *Eos Trans. AGU, 71*, 259, 1990.

Kokelaar, P., Magma-water interactions in subaqueous and emergent basaltic volcanism, *Bull. Volcanol., 48*, 275-289, 1986.

Lee, J. S., and S. R. Hammond, Origin of Heck and Heckle seamount chains, Juan de Fuca Ridge, *Eos Trans. AGU, 66*, 403, 1985.

Le Roex, A. P., H. J. B. Dick, A. J. Erlank, A. M. Reid, F. A. Frey, and S. R. Hart, Geochemistry, mineralogy and petrogenesis of lavas erupted along the Southwest Indian Ridge between the Bouvet Triple Junction and 11°E, *J. Petrol., 24*, 267-318, 1983.

Leybourne, M. I., Volcanism and geochemistry of parts of the Endeavour Segment of the Juan de Fuca Ridge system and associated seamounts, M.Sc. thesis, 177 pp., Acadia Univ., Wolfville, Nova Scotia, Canada, 1988.

Leybourne, M. I., and N. A. Van Wagoner, Volcanism and geochemistry of parts of the Endeavour Segment of the Juan de Fuca Ridge and associated seamounts, paper presented at 28th International Geological Congress, Washington, D. C., 1989.

Lonsdale, P., and F. N. Spiess, A pair of young cratered volcanoes on the East Pacific Rise, *J. Geol., 87*, 157-173, 1979.

Macdonald, K. C., Endeavour Seamount, De Steiguer Ridge and Magic Mt.: Examples of migrating High Inside Corners caused by coupled uplift at the intersections of rifted spreading centres and ridge axis discontinuities, *Eos Trans. AGU, 70*, 1302, 1989.

Marks, N. S., Sedimentation on new ocean crust: The Mid-Atlantic Ridge at 37°N, *Mar. Geol., 43*, 65-82, 1981.

Michael, P. J., R. L. Chase, and J. F. Allan, Petrologic and geologic variations along the southern Explorer Ridge, northeast Pacific Ocean, *J. Geophys. Res., 94*, 13,895-13,918, 1989.

Presnall, D. C., and J. D. Hoover, Composition and depth of primary mid-ocean ridge basalts, *Contrib. Mineral. Petrol., 87*, 170-178, 1984.

Prinzhofer, A., E. Lewin, and C. J. Allegre, Stochastic melting of the marble cake mantle: evidence from local study of the East Pacific Rise at 12°50' N, *Earth Planet. Sci. Lett., 92*, 189-206, 1989.

Reid, J. B., jr., E. Steig, and W. B. Bryan, Major element evolution of basaltic magmas: A comparison of the information in CMAS and ALFE projections, *Contrib. Mineral. Petrol., 101*, 318-325, 1989.

Rhodes, J. M., C. Morgan, and R. A. Liias, Geochemistry of Axial Seamount lavas: Magmatic relationship between the Cobb Hotspot and the Juan de Fuca Ridge, *J. Geophys. Res., 95*, 12,713-12,733, 1990.

Roeder, P. L., and R. F. Emslie, Olivine-liquid equilibrium, *Contrib. Mineral. Petrol., 29*, 275-289, 1970.

Scott, S. D., R. L. Chase, J. F. Allan, and P. M. Herzig, Hydrothermal deposits and recent volcanism at the southern end of West Valley, Juan de Fuca Ridge, *Eos Trans. AGU, 69*, 1497, 1988.

Sleep, N. H., Tapping of magmas from ubiquitous mantle heterogeneities: An alternative to mantle plumes?, *J. Geophys. Res., 89*, 10,029-10,041, 1984.

Smith, T. L., and R. Batiza, New field and laboratory evidence for the origin of hyaloclastite flows on seamount summits, *Bull. Volcanol., 51*, 96-114, 1989.

Stakes, D. S., J. W. Shervais, and C. A. Clifford, The volcanic-tectonic cycle of the FAMOUS and AMAR valleys, Mid-Atlantic Ridge (36°47'N): Evidence from basalt glass and phenocryst compositional variations for a steady state magma chamber beneath the valley midsections, AMAR 3, *J. Geophys. Res., 89*, 6995-7028, 1984.

Staudigel, H., and H.-U. Schmincke, The Pliocene seamount series of La Palma/Canary Islands, *J. Geophys. Res., 89*, 11,195-11,215, 1984.

Takahashi, E., and I. Kushiro, Melting of a dry peridotite at high pressures and basalt magma genesis, *Am. Mineral., 68*, 859-879, 1983.

Tormey, D. R., T. L. Grove, and W. B. Bryan, Experimental petrology of normal MORB near the Kane Fracture Zone: 22°-25° N, Mid-Atlantic Ridge, *Contrib. Mineral. Petrol., 96*, 121-139, 1987.

Ulmer, P., The dependence of the Fe^{2+} - Mg cation-partitioning between olivine and basaltic liquid on pressure, temperature and composition, *Contrib. Mineral. Petrol., 101*, 261-273, 1989.

Van Wagoner, N. A., and M. I. Leybourne, Evidence for magma mixing and a heterogeneous mantle on the West Valley Segment of the Juan de Fuca Ridge, *J. Geophys. Res., this issue.*

Walker, D., T. Shibata, and S. E. DeLong, Abyssal tholeiites from the Oceanographer Fracture Zone, II, Phase equilibria and mixing, *Contrib. Mineral. Petrol., 70*, 111-125, 1979.

Wheatley, M. R., and N. M. S. Rock, Spider: A Macintosh program to generate normalised multi-element spidergrams, *Am. Mineral., 73*, 919-921, 1988.

Zindler, A., H. Staudigel, and R. Batiza, Isotope and trace element geochemistry of young Pacific seamounts: Implications for the scale of upper mantle heterogeneity, *Earth Planet. Sci. Lett., 70*, 175-195, 1984.

M. I. Leybourne and N. A. Van Wagoner, Department of Geology, Acadia University, Wolfville, Nova Scotia, Canada B0P 1X0.

(Received May 2, 1990;
revised February 6, 1991;
accepted February 22, 1991.)

JOURNAL OF GEOPHYSICAL RESEARCH, VOL. 96, NO. B10, PAGES 16,047–16,060, SEPTEMBER 10, 1991

Late Paleozoic Paleomagnetic Results From the Junggar block, Northwestern China

YIANPING LI, ROBERT SHARPS, AND MICHAEL MCWILLIAMS

Department of Geophysics, Stanford University, Stanford, California

YONGAN LI, QIANG LI, AND WEI ZHANG

Xinjiang Geology Research Institute, Urumqi, Xinjiang, People's Republic of China

We have obtained middle Carboniferous to Permian paleomagnetic results from the Junggar block in order to test its tectonic coherence and to reconstruct its late Paleozoic position. From Hoboksar, on the northwestern margin of Junggar, a paleomagnetic pole from basic/silicic flows yields ϕ_p = 299°E, λ_p = 70°N (N = 15 sites, K/A_{95} = 36/ 6.4°). In the same general area, a pole from lava flows, plutons and as well as from remagnetized limestones/sandstones, is at ϕ_p = 350°E, λ_p = 69°N (N = 26 site, K/A_{95} =15/7.5°). Farther to the southwest in Keramayi, a pole from late Paleozoic dike swarms lies at ϕ_p = 230°E , λ_p = 80°N (N = 23 sites, K/A_{95} = 16/ 7.8°). In the southern margin near Urumqi, from sedimentary rocks and volcaniclastics of the Middle to Upper Carboniferous Qijiagou and Aoertu formations, a pole is produced at ϕ_p = 7°E, λ_p = 72°N (N = 15 sites, K/A_{95} = 28/7.4°). From the Middle Carboniferous Liushugou Formation and dike swarms intruding into the formation, two poles are located at ϕ_p = 231°E, λ_p = 69°N (N = 4 sites, K/A_{95} = 46/ 13.7°) and ϕ_p = 172°E, λ_p = 55°N (N = 7 sites, K/A_{95} = 17/ 15.1°), respectively, though reliabilities of these two poles are in question. Magnetic polarities of all the poles in our study are exclusively reversed. Based on positive fold tests and a baked contact test, we believe that these magnetizations were acquired during the Kiaman reversed interval (250-320 Ma). More accurate ages of the magnetizations cannot be resolved at present. Despite widely separate locations, the pole positions are roughly located on a small circle segment around the Junggar block. Similar inclinations suggest a coherent Junggar block since Permian time. Based on the results of this study and other published paleomagnetic data, a mean middle Carboniferous to Permian paleomagnetic pole is calculated at ϕ_p = 329°E, λ_p = 82°N (N = 6 poles, K/A_{95} = 26/13.4°). Recognition of late Paleozoic apparent polar wander for Junggar is obscured by a lack of detailed geochronologic data and possible relative horizontal rotations around vertical axis. The paleolatitude for the southern Junggar predicted by this pole is only 4° south of the present latitude. Difference exists between the mean pole from Junggar and Permian poles from other tectonic units in Asia (Tarim, Siberia, Kazakhstan, and North and South China), indicating post-Permian relative motions. At the boundary between Tarim and Junggar, this motion is likely to have a left-lateral sense.

INTRODUCTION

Central Asia is a complex mosaic of continental blocks, island arcs, and oceanic basins which are believed to have been assembled since late Paleozoic time. The Junggar block (physiographically, the Junggar basin) is located in northwestern China, covering an area of nearly 130,000 km^2 (Figure 1). The triangularly shaped Junggar basin is bounded by high ridges of the eastern Tian Shan on the south ("Shan" means mountain in Chinese). The Borohoro Shan, Tian Shan and Bogda Shan separate the Junggar basin from the Yili, Tarim, and Turpan basins. On the northwest, the basin is bounded by relatively low uplands of the West Junggar mountain system which are formed by folded Lower, Middle, and some Upper Paleozoic rocks. On the northeast, the basin is bounded by the Altai mountain system and the Kelameili uplift.

The origin and nature of the Junggar block have been controversial. In one hypothesis, the Junggar block is floored by Precambrian continental crust [*Zhang et al.*, 1984]. The main argument to support this hypothesis is that the depth of Moho ranges from 42 to 44 km [*Huang et al.*, 1987; *Ma*, 1987] as derived from gravity data. However, if the post-Devonian sediments are stripped away, the Junggar block is actually thinner than other continental blocks in central Asia such as Siberia [*Coleman*, 1989]. A second hypothesis suggests that the Junggar basin is underlain by early to middle Paleozoic oceanic crust trapped during the late Paleozoic consolidation of central Asia [*Feng et al.*, 1989; *Coleman*, 1989; *Carroll et al.*, 1990]. Highly deformed and dismembered ophiolites ranging in age from Cambrian to Devonian occur in fold belts on all sides of the Junggar block. Lead isotope studies on mid-Carboniferous (321 ± 7 Ma) anorogenic granitic plutons in the West Junggar Mountains suggest that they were derived from partial melting of oceanic crust with no contribution from Precambrian basement [*Feng et al.*, 1989; *Kwon et al.*, 1989]. Upper Paleozoic sandstones deposited in the eastern and southern Junggar basin are indicative of a magmatic arc provenance, further supporting the oceanic crust origin hypothesis [*Carroll et al.*, 1990]. *Hsu* [1988] proposed that the Junggar block is a Carboniferous back arc basin separated from Paleo-Tethys to the south by a late Paleozoic frontal arc. *Carroll et al.* [1990] concluded that extension of the Junggar Ocean, if it existed, must have ceased prior to the Permian based on sedimentary history records in the southern Junggar. *Watson et al.* [1987] and *Carroll et al.* [1990] interpreted Junggar as a flexurally subsiding foreland basin filled with non-marine clastics during the late Permian-early Triassic.

The southern margin of Eurasia in the late Paleozoic is believed to be marked by the Tian Shan-Hegen Suture near the northern boundary of China [*Zhang et al.*, 1984; *Huang et al.*, 1987]. This view is supported by the analysis of the Visean coral faunas and the Cathaysian, Angara, and Kuznetsk floras, which suggests that the discontinuity between the Cathaysian and the Middle Asian coral faunas and as well as the boundary between the Cathaysian and Angara/Kuznetsk floras coincide with the Tian Shan fold belt [*Hu*, 1985; *Smith*, 1988]. If so, the Junggar block must have occupied a higher latitude region than the Tarim, North China, and South China blocks during Carboniferous and Permian.

Paleomagnetic data can help to measure displacement histories of individual terranes which make up the Junggar block. Prior to our study, there were few published paleomagnetic results from the Junggar block [*Li et al.*, 1989; *Chen et al.*, 1991]. In 1988, we collected late Paleozoic rocks

Paper number 91JB01619.
0148-0227/91/91JB-01619 $05.00

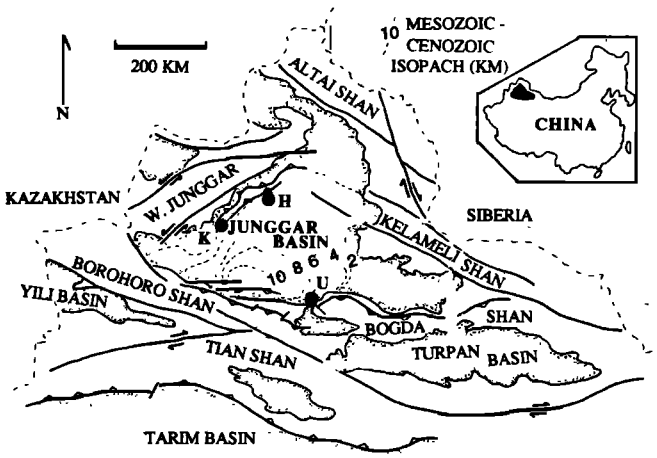

Fig. 1. Generalized tectonic map of northwestern China. Circles indicate the paleomagnetic sampling region: H, Hoboksar; K, Keramayi; and U, Urumqi (modified from *Carroll et al.* [1990]).

in three regions along the margins of Junggar under a cooperative paleomagnetic research project between the Geophysics Department at Stanford University and the Xinjiang Geology Institute in Urumqi. The areas sampled for paleomagnetic study are Hoboksar and Keramayi on the northwestern margin and Urumqi on the southern margin of Junggar (Figure 1). The results from Late Paleozoic dike swarms from the Keramayi region have been published elsewhere [*Li et al.*, 1989].

GEOLOGY

The stratigraphy of the Junggar block can be divided into pre-Carboniferous, Carboniferous, Permian volcanic and sedimentary rocks, and Mesozoic and Cenozoic nonmarine sedimentary rocks [*Xinjiang Stratigraphic Compiling Group*, 1981; *Feng et al.*, 1989; *Coleman*, 1989; *Lee*, 1985; *Ulmishek*, 1986]. The pre-Carboniferous basement of the basin is composed of Ordovician, Silurian, and Devonian sedimentary and metamorphic complexes, which are well exposed in the eastern and western margins of the basin. The Lower Carboniferous rocks are dominantly volcanic, overlain by Upper Carboniferous marine flysch with only a few scattered volcanic rocks including ash layers. Marine sedimentation continued in the central and southwestern parts of the basin. But by late Permian time, the marine seaway was completely closed, giving way to continental intermontane-sedimentary deposition. Mesozoic and Cenozoic continental fluvial and lacustrine deposits of coarse to fine clastics are very thick in the southern parts of the basin (Figure 1).

The Upper Paleozoic Qijiagou section is located 20 km southeast of Urumqi (Figure 1), near Qijiagou village. The section is on the southern edge of the Junggar basin and the northern foothills of the Bogda Shan. Structurally, it is on the north limb of a large east-west trending Neogene faulted anticlinorium. The oldest rocks in the Bogda Shan are a 2-3 km thick section of Lower to Middle Carboniferous andesitic volcaniclastics. The basinal deposits are overlain by an 800-m regressive marine sequence, which at its base consists of carbonate and volcaniclastic turbidites. Productid brachiopods from the Qijiagou Formation have been dated as Middle to Upper Carboniferous [*Carroll et al.*, 1990]. The turbidite section grades upward into Upper Carboniferous slope and shelf shales and volcaniclastic sandstones. Stromatolites deposited in the early Permian record the final stages of withdrawal of the Junggar ocean.

We have sampled three Middle-Upper Carboniferous formations: Liushugou (C_{2l}), Qijiagou ($C_{2\text{-}3q}$), and Aoertu (C_{3a}). The Liushugou Formation is the oldest and composed mainly of andesitic volcanic breccia, tuffaceous breccia, tuff intercalated with andesite porphyrite and minor siltstone and limestone lenses, bearing abundant fusulinids [*Liao et al.*, 1987]. We collected oriented samples at 13 sites (8uc3 to 8uc15) from the upper part of the formation, seven of which were from dike swarms intruding into the section. The Qijiagou Formation has a total thickness of 281 m and is divided into three members according to lithological character. It mainly consists of volcaniclastics, sandstones interbedded with sandy limestone and biocalcilutite. The contact between the Qijiagou and Liushugou formations is conformable. The upper member of the Qijiagou Formation from which our seven sites (8uc1,2, 24-28) were collected is 189 m thick, containing more thickly bedded limestone than the other members. The lower part of this member is yellow-green, thin-bedded siltstone and fine-grained sandstone interbedded with sandy limestone. Abundant fossils, including fusulinids, foraminifera, corals, brachiopods, are found in the formation, yielding a middle to late Carboniferous age [*Liao et al.*, 1987]. The Upper Carboniferous Aoertu Formation is 175 m thick and is mainly composed of dark green, yellow-green, and gray-black siltstone and sandstone. In the lower part, it is intercalated with a small amount of thin-bedded and lensoid sandy limestone, decreasing gradually upward. The upper part is dominated by gray to black siltstone intercalated with pebble-bearing sandstone and conglomerate. Eight sites (8uc16-21) were collected from grayish black siltstone of the upper part of the Aoertu Formation.

Hoboksar is located in the northwest part of the Junggar basin (Figure 1). The oldest rocks exposed are Middle-Upper Ordovician, in turn overlain by Silurian, Devonian, and Carboniferous marine deposits.

The Upper Devonian Honggulerun Formation (D_{3h}) consists of a 595-m section of siliceous siltstone, sandstone, and muddy limestone, containing corals *Nalivkinella* sp., *Dictyoclostus* sp., *Cyrtospirifer* sp., *Athyris sulcifer Nalivkin*, *Platyrachella* sp., *Camarotoechia* sp., *Plicatifera* sp., *Productella* sp., and trilobite *Phacops* sp. (Xinjiang Bureau of Geology, unpublished report, 1973). It is conformable with both underlying and overlying strata. Three sites (8hp5-7) were collected from a 20-m overturned section of thin bedding limestones in Bulungou. The Heshantou Formation (C_{1h}) consists of gray siliceous mudstone, siltstone, calcareous sandstone, and calcareous limestone. Brachiopods in the limestones indicate a Visean age (C_1). The upper part of the formation grades into conglomerate layers and contains thin coal beds. The Heshantou Formation is 1500 m thick and is conformable with both the overlying Carboniferous Sarlebulake Formation and underlying Upper Devonian Talebahatai Formation. Three sites (8hc8-10) were collected from the Heshantou Formation in a thin limestone section in Heshantou. The Sarlebulake Formation (C_{1s}) consists of 592 m of gray-black, yellowish sandstone, conglomerate, and siltstone, interbedded with extrusive and volcaniclastic rocks. Fossils found in the formation are *Angaropteridium cardiopteroides* (*Sehmal.*) *Zalessky*, *Calamites* sp., and *Neoggerathiopsis* sp. There is a hiatus between the Sarlebulake and overlying Harlegiawu formations. Three sites (8hp16-19), in addition to one from a pluton intruding into the Sarlebulake Formation, were collected from the Sarlebulake Formation.

The Harlegiawu Formation (C_{2h}) is a 234-m suite of continental silicic volcanic and volcaniclastic rocks, containing plant fossils: *Calamites* sp. and *Noeggerathiopsis* sp. The Karlargang Formation (C_{2k}) consists of 1436 m rhyolitic flows, tuff, and interbedded sandstone and shale layers. The lower part of formation contains coal layers with plant fossils *Angaropteridium cardiopteroides (Schmal) Zalessky*, *Cardioneura sp.*, *Sphenophyllum* sp., *Pursongia* sp., *Noeggerathiopsis* sp., etc. The Karlargang Formation lies conformably upon the Harlegiawu Formation but is overlain unconformably by Upper Jurassic sandstone. The ages of the Harlegiawu and Karlargang formations are assigned to the middle Carboniferous (Xinjiang Bureau of Geology, unpublished report, 1973), based on regional lithologic comparison. A total of 18 sites were collected from the Karlargang and Harlegiawu formations.

U-Pb, Rb-Sr and ^{40}Ar-^{39}Ar isotopic ages on plutons and volcanic rocks in western Junggar cluster around 325 Ma [*Bureau of Geology and Mineral Resources of Xinjiang*, 1987].

However, isotopic age data are sparse in the region we have studied. Two K-Ar ages from granitic plutons in the Hoboksar region are 278 and 267 Ma; one age from volcanic rocks is 243 Ma.

PALEOMAGNETIC STUDY

General Procedure

Generally, we collected six to eight field-drilled samples at each site using a portable drill. Samples were oriented in situ using a Brunton Compass and in many cases were checked by a Sun shadow angle reading. No significant difference was found between magnetic and solar azimuths.

Most samples were measured and demagnetized in the paleomagnetic laboratory at Stanford University using an automated cryogenic magnetometer with integrated, alternating field (AF) demagnetization coils and a Schonsted (TSD-1) oven. For specimens subjected to thermal demagnetization, bulk magnetic susceptibility as a function of heating step was monitored using a Bartington magnetic susceptibility meter, model M.S.2. A few samples were measured and demagnetized by thermal and AF methods in the paleomagnetic laboratory of the University of New Mexico.

AF demagnetization treatments consisted of 8-15 steps in progressively higher fields up to a peak field of 80 mT. In thermal demagnetization treatments, samples were heated in 50°C or 100°C steps from 50°C to a maximum of 690°C depending upon the rock type. After each thermal demagnetization step, a 5-mT AF demagnetization was performed just before measurement inside the magnetometer to eliminate viscous components acquired while the sample was transferred from the oven to the magnetometer. AF or thermal demagnetization results are plotted on orthogonal vector diagrams [*Zijderveld*, 1967]. Principal component analysis [*Kirschvink*, 1980] was used to obtain a characteristic direction and in some cases a lower H_C/T_{lub} (H_C: coercive force; T_{lub}: laboratory unblocking temperature) component for each specimen.

Urumqi Region

Liushugou Formation (C_{2l}) and associated dikes. Thirteen sites from the Liushugou Formation were collected from a continuous section in Liushugou (the Liushu Valley, "gou" means valley in Chinese). Six sites come from andesitic flows, tuffs, and interbedded clastics. Seven sites come from mafic dikes intruding into the bedded rocks. In many cases, the dikes were intruded into the section along existing fractures or faults. The age of the dikes is not known, although we have not seen any dike intruding into the overlying Qijiagou and Aoertu formations. Samples in most sites show well-grouped and stable magnetizations after AF or thermal demagnetization, although a presumably viscous magnetization is usually removed during the low range of AF or thermal demagnetization. Typical orthogonal demagnetization diagrams are shown in Figure 2. The directions of magnetization of individual specimens from site 8uc15 are not well defined and are inconsistent within the site. The mean direction from site 8uc11 is not consistent with the overall population (Table 1). Thus data from sites 8uc11 and 8uc15 are not used for the final calculation.

The mean direction from the Liushugou Formation is significantly different from that of the dikes which intruded it, and therefore they are not combined (Figure 3 and Table 1). The difference suggests that the magnetizations were acquired at different times. The mean inclination from the dikes is not significantly different from the mean inclination of the Qijiagou and Aoertu formations (described below). The difference in declination is significant, which could indicate that the Junggar block experienced a significant orientation shift (some 70°) between the middle Carboniferous and late Permian. Since only seven dikes were sampled and tilt correction is made on the assumption that the dikes intruded flat beddings, the difference may reflect insufficient averaging of geomagnetic secular variation and inaccurate tilt corrections.

Tilt-corrected directions of the dikes are better grouped than those in situ, while for the lava flows/volcaniclastics of the Liushugou Formation, the situation is reversed (Figure 3). In both cases, the change of grouping is not statistically significant. Because of the small number of sites and the divergence of the directions after tilt correction, we have chosen not to use the results from the Liushugou Formation for tectonic interpretation.

Qijiagou (C_{2-3q}) and Aoertu (C_{3a}) formations. Samples of the Middle to Upper Carboniferous Qijiagou Formation were collected from Qijiagou and Serenzhigou. Sites 8uc24 to 8uc26 were collected from a coherent section dipping to the northwest. Sites 8uc24 and 8uc25 come from basaltic flows below and above a 15-m-thick limestone lens. Site 8uc26 is from pillow basalts, about 20 m stratigraphically above site 8uc25. The pillows are not widely exposed and probably reflect a small, isolated fissure eruption. Sites 8uc27 and 8uc28 were collected from thickly bedded dark gray sandstones.

The Upper Carboniferous Aoertu Formation has been sampled at two localities. Sites 8uc16-17 were collected from a roadcut in Gejiagou, and sites 8uc18-23 were collected from a 100-m coherent section in Jinjinzhigou. At Jinjinzhigou, the samples were collected from a monocline with a large variation in bedding attitudes so that a fold test can be attempted. The demagnetization behavior of samples from the Qijiagou and Aoertu formations is straightforward (Figure 2). Except for site 8uc2, well-grouped directions at each site are readily isolated. Site 8uc2 is located in volcaniclastic rocks, and only two samples from black tuffaceous siltstone show a direction of magnetization consistent with that of site 8uc1, a few meters below stratigraphically. Other samples from gray coarse-grained sandstone exhibit directions scattered around the present Earth field (PEF) direction. Only two specimens from site 8uc26 are measurable; others have been damaged before arrival at the laboratory. AF demagnetization was most effective in removing viscous components parallel to the PEF direction (Figure 2).

The mean direction of the Qijiagou Formation is indistinguishable from that of the Aoertu Formation, suggesting either that the polar wander of the Junggar block was negligible from late middle Carboniferous to late Carboniferous times, the Qijiagou Formation was remagnetized at about the same time the Aoertu Formation acquired a primary magnetization, or both the Qijiagou and Aoertu formations were remagnetized at some later time. Because of their similarity, the two groups of directions were combined together to yield a mean direction.

Variable bedding attitudes allowed us to conduct a fold test on the Qijiagou and Aoertu formations. Tilt-corrected directions are statistically better grouped than the in situ directions at the 99% confidence level, establishing a prefolding age of the magnetization (Figure 3 and Table 1), though the last major phase of tectonic activity in the region occurred in the Neogene. The positive fold test, together with exclusively reversed polarity, is consistent with the hypothesis that the magnetization was acquired during the Kiaman reversed polarity interval (320-250 Ma)[*Harland et al.*, 1982].

Hoboksar Region

Samples from Hoboksar were collected from two locations: Heshantou (47°11'N, 86°41'E) and Bulungou (46°42'N, 86° 01'E).

The Harlegiawu and Karlargang formations (C_{2h} and C_{2k}). We collected samples of silicic volcanic rocks from the Harlegiawu and Karlargang formations, near Bulungou village, in both limbs of a syncline which trends in approximately NNW-SSE. From the western limb which dips to the northeast, sites 9hp37-45 were collected; sites 8hp46-54 were collected from the eastern limb dipping to the northwest. The 18 sites are distributed along directions perpendicular to the strikes of bedding. Bedding attitudes were measured from interbedded sedimentary beds or tuff layers. The dips in the western limb of the syncline range from 11° to 17° and 20° to 40° in the

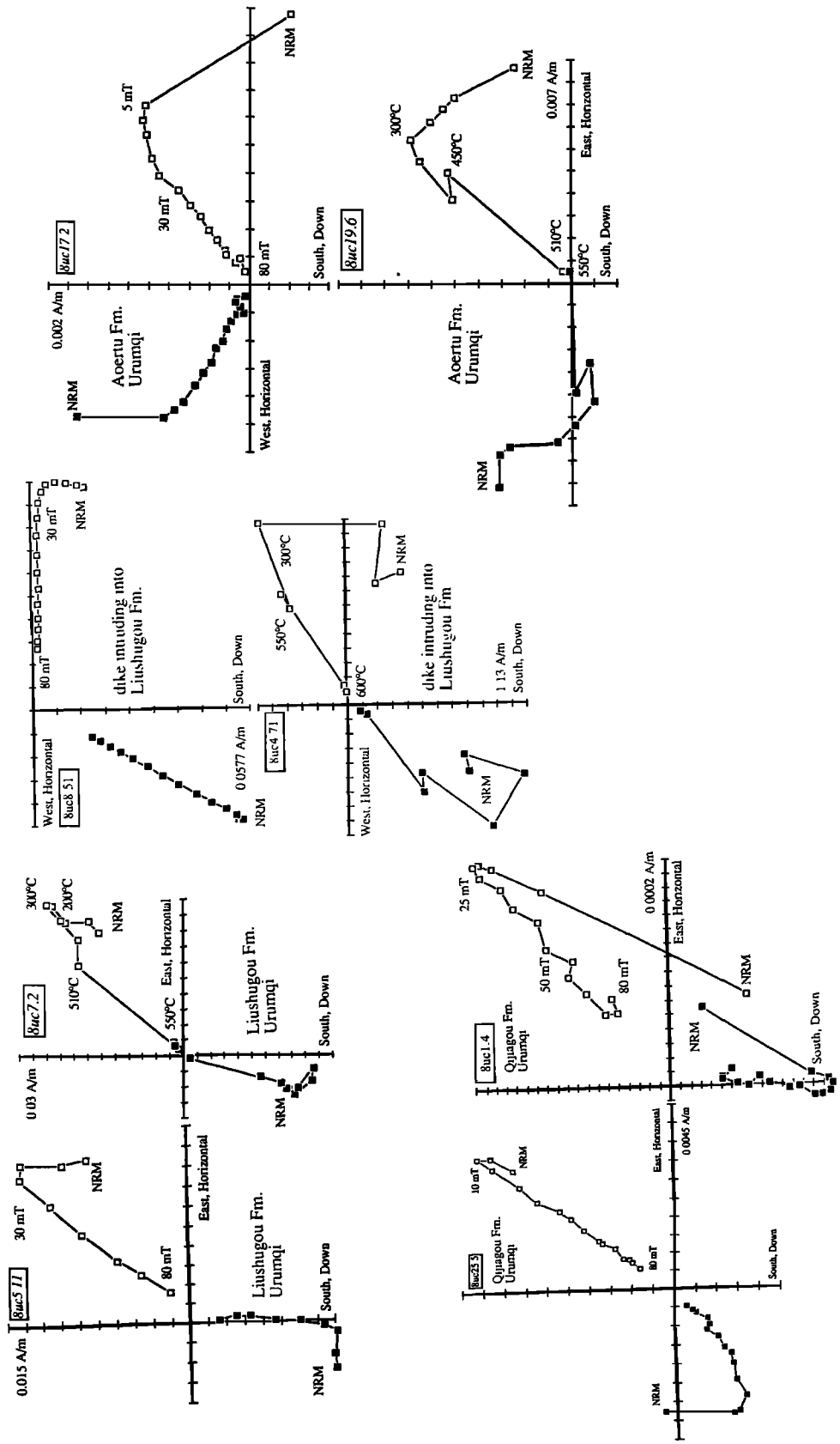

Fig. 2. Orthogonal vector thermal and AF demagnetization diagrams of specimens from the Urumqi region. Solid symbols refer to the projection on the horizontal plane; Open symbols refer to the projection of inclination (geographic coordinates).

TABLE 1. Urumqi C_{2-3} (Latitude 43°47'N, Longitude 87°45'E)

Site*	Age	N(M)	D	I	D_c	I_c	k	a_{95}	L	S(D)
Aoertu Formation (Late Carboniferous, C_{3a}) and Qijiagou Formation (Middle Carboniferous, C2q)										
8uc16	C_{3a}	6(6)	291	-51	175	-56	29	12.6	SS	231(64W)
8uc17	C_{3a}	5(5)	297	-50	163	-63	74	7.8	SS	226(63W)
8uc18	C_{3a}	6(6)	282	-43	152	-65	62	8.6	SS	210(67W)
8uc19	C_{3a}	6(6)	280	-44	153	-63	51	9.5	SS	210(67W)
8uc23	C_{3a}	6(6)	240	-59	174	-60	110	6.4	SS	206(35W)
8uc22	C_{3a}	6(6)	244	-65	157	-62	67	8.2	SS	204(38W)
8uc20	C_{3a}	6(6)	251	-67	148	-63	299	3.9	SS	203(40W)
8uc21	C_{3a}	6(6)	267	-69	137	-67	655	2.6	SS	203(40W)
8uc28	C2q	6(6)	214	-64	147	-49	55	9.1	SS	197(42W)
8uc27	C2q	6(6)	230	-63	150	-56	47	8.9	SS	197(42W)
8uc26	C2q	2(2)	196	-67	139	-43	-	-	BS	197(42W)
8uc25	C2q	6(6)	233	-59	157	-57	46	9.9	BS	197(42W)
8uc24	C2q	5(6)	256	-46	191	-69	15	20.0	BS	197(42W)
8uc2	C2q	2(5)	213	-40	165	-64	-	-	VC	158(41W)
8uc1	C2q	5(5)	209	-53	113	-76	31	14	LS	140(42W)
$A+Q_b$	C_{2-3}	15	250	-60	-	-	17	9.6		
$A+Q_a$	C_{2-3}	15	-	-	155	-62	52	9.7		
Liushugou Formation (Middle Carboniferous)										
8uc5	C_{21}	6(6)	182	-48	186	-67	53	9.2	VC	86(19S)
8uc9	C_{21}	6(6)	203	-27	222	-65	23	14.0	VC	97(41S)
8uc7	C_{21}	6(6)	188	-45	188	-79	118	6.2	VC	98(34S)
8uc11†	C_{21}	6(6)	193	-78	64	-58	25	13.7	FL	140(41S)
8uc12	C_{21}	4(5)	202	-51	123	-72	41	14.6	VC	140(41S)
8uc15†	C_{21}	3(4)	228	30	228	-18	23	26.6	VC	118(50S)
L_b	C_2	4(6)	194	-43	-	-	38	15	-	-
L_a	C_2	4(6)	-	-	185	-74	32	16	-	-
Dikes Intruding Into Liushugou Formation										
8uc3	C_{21}	6(6)	200	-21	209	-56	568	2.8	DK	97(36S)
8uc4	C_{21}	7(7)	227	-7	247	-42	31	10.9	DK	97(52S)
8uc6	C_{21}	6(6)	195	-37	203	-55	24	13.8	DK	86(19S)
8uc10	C_{21}	6(6)	213	-9	224	-44	50	9.6	DK	97(41S)
8uc8	C_{21}	5(6)	207	-3	221	-51	150	6.3	DK	97(53S)
8uc13	C_{21}	7(7)	215	-34	266	-74	19	14.0	DK	107(49S)
8uc14	C_{21}	4(4)	213	-12	227	-58	36	15.5	DK	107(49S)
$Dikes_b$	C_2-P	7(7)	210	-18	-	-	23.8	12.6	-	-
$Dikes_a$	C_2-P	7(7)	-	-	226	-56	28.7	11.5	-	-

N(M), number of samples used (measured) or number of sites in the grand mean; *D*, *I* and D_c, I_c are declination and inclination in geographic and stratigraphic coordinates. *k* and a_{95}, precision parameter estimate and radius of the 95% confidence limit in degrees. C_2, C_3, and C_{2-3} indicate middle Carboniferous, late Carboniferous and middle-late Carboniferous. L, lithological description, LS, limestone; SS, sandstone; VC, volcaniclastic; DK, dike; FL, flow. S(D): strike and dip directions.

*, $A + Q_b$ and $A + Q_a$ are the in situ and tilt-corrected grand mean directions of the Qijiagou and Aoertu formations. L_b and L_a are the in situ and tilt-corrected grand mean directions of the Liushugou Formation. $Dikes_b$ and $Dikes_a$ are the in situ and tilt-corrected grand mean directions of the dikes intruding into the Liushugou Formation.

†, Excluded from the grand mean. The grand mean direction is a Fisherian average of site mean directions.

eastern limb. As discussed below, the syncline probably formed in late Paleozoic time and certainly was not formed later than the Jurassic because the Karlargang Formation is overlain unconformably by Jurassic sandstones. Most of samples are silicic volcanics, but sites 8hp44-47 come from andesitic basaltic flows which lie close to a fault along the foothill. As a result, bedding attitudes of sites 8hp44-46 are obscured.

The samples can be split into two groups based upon their behavior during AF and thermal demagnetizations. Samples from the first group have moderate coercivities, and the characteristic component of magnetization can be isolated after AF treatments of 60-80 mT. Thermal demagnetization is as effective as AF demagnetization in removing occasional viscous components. Magnetic components of the first group can be selected according to end-points or linear segments to the origin. The first group includes sites 8hp37-39, 8hp43-44, 8hp46-50, and 8hp52-54 (Figure 4). The mean direction of these sites after tilt correction is D/I =166°/-49°, N = 11 sites, R =10.75, k = 40 and a_{95} = 7.3°, with no correction for plunge. This mean direction is not significantly different from the mean direction of all sites and thus in our analysis we have used the overall mean direction (Table 2).

The samples from the second group cannot be demagnetized by AF treatment since they have coercivities higher than 80 mT, which is the highest peak AF field we can attain with our instruments. During thermal demagnetization, characteristic components similar to these isolated from the first group are found. But the directions are not well defined as linear segments. One noticeable difference between these two groups is different magnetic phases as shown by unblocking temperature. For the first group, magnetite is the main magnetic phase for the characteristic components, whereas hematite is the dominant magnetic phase for the samples in the second group. Results of sites 8hp44-46 are not included in calculating the grand mean direction as bedding attitudes are not clear for these sites.

Based upon measurements of bedding attitude from the west and east limbs of the syncline, a hinge line of azimuth (43°)

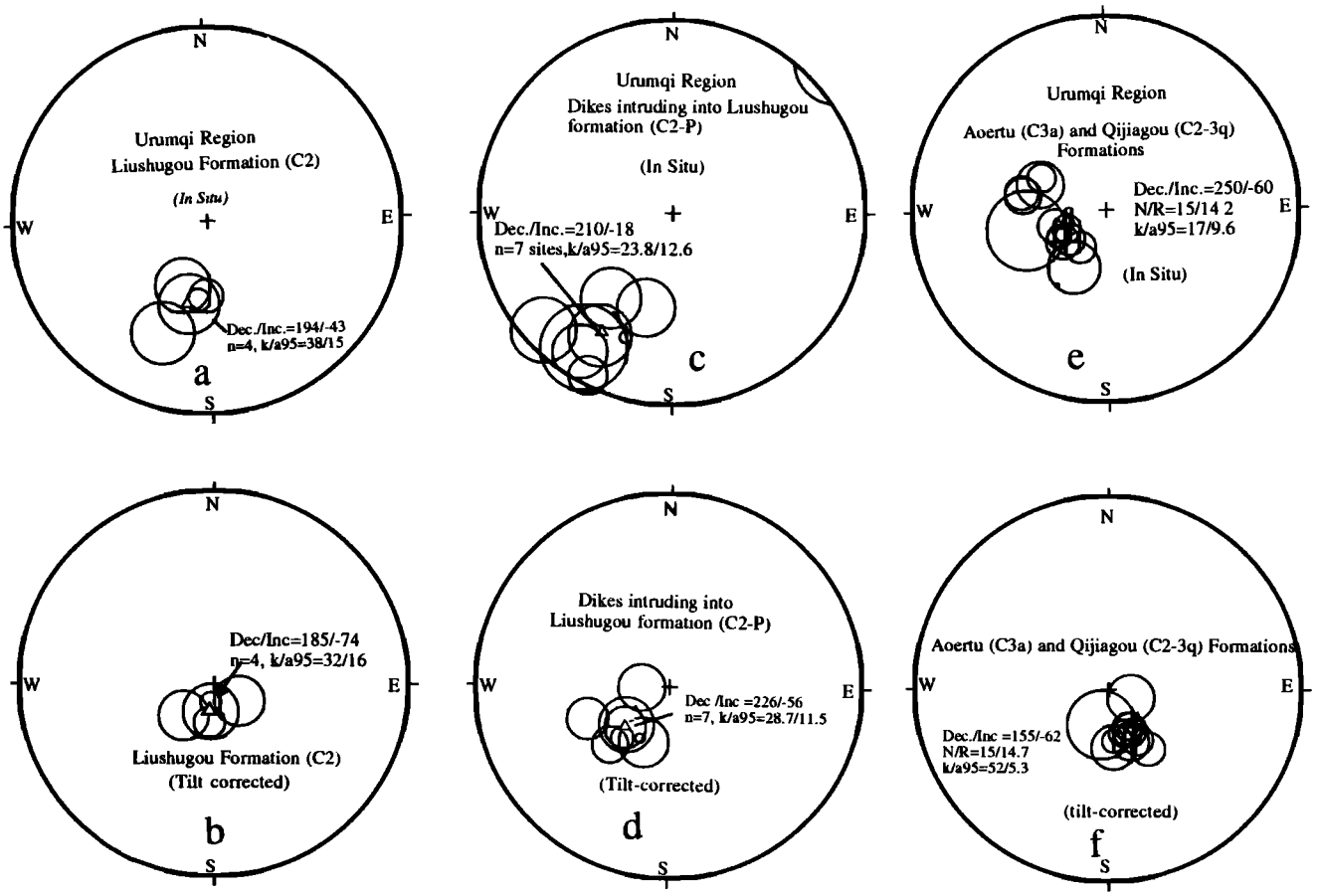

Fig. 3. Equal-angle stereographic projections of site-mean directions of the Liushugou Formation (C_{2l}, Figures 3*a* and 3*b*), dikes intruding into the Liushugou Formation (Figures 3*c* and 3*d*), and the Qijiagou and Aoertu formations ($C_{2\text{-}3q}$ and C_{3a}, Figures 3*e* and 3*f*). Circles are the 95% confidence limits around the site-mean directions (centers). Average of site-mean direction is plotted as open triangle with the 95% confidence limit. All projections are on upper hemispheres.

and plunge (13°) is established by a great circle fit of poles to bedding planes. Site mean directions of magnetization were first rotated (along with poles to bedding plane) to correct for plunge, then rotated to correct for tilt to yield a grand mean direction (Table 2). For comparison, site-mean directions and grand mean direction based on convention tilt correction (one-step) are also listed in Table 2. The net difference between two means calculated by different correction procedures is only 2° in declination because of the shallow 13° plunge.

The tilt-corrected directions are better grouped than those before tilt corrections at p =0.01 (Figure 5) [*McElhinny*, 1964; *McFadden and Jones*, 1981], establishing a pre-Jurassic magnetization age. The exclusively reversed polarity constrains the age of the magnetization to be middle-late Carboniferous to Permian, corresponding to the Kiaman reversed polarity interval.

A low H_c/T_{lub} normal polarity component usually removed in the range of less than 20 mT or 200° can be isolated from almost all sites. The mean direction of this component for a total of 18 sites is D/I =4°/63°, k = 58 and a_{95} = 4.6° in geographic coordinates, indistinguishable from the present Earth field direction at the sampling location. Scatter of this component increases when corrected for tilt, giving a mean direction at D/I =1°/46°, k =18 and a_{95}=8.5°. We believe it to be a Quaternary viscous component.

Honggulerun Formation (D_{3h}). Small viscous components removed during demagnetization are roughly aligned along the PEF direction. Both AF and thermal demagnetizations reveal a characteristic component with a southeast declination and a moderate positive inclination. Demagnetization trajectories in the high thermal or AF demagnetization ranges converge toward the origin (Figure 4). The mean of the tilt-corrected characteristic components is not statistically different from the mean directions of the younger Heshantou and Sarlebulake formations, as described below.

Because late Paleozoic plutons and volcanic rocks are exposed in the vicinity of the sampling locality, we believe that the characteristic magnetization isolated from the Devonian Honggulerun Formation may represent an overprint caused by plutons or volcanic rocks during late Paleozoic but before the tilting. This view is supported by (1) the observation that the mean direction in stratigraphic coordinates is not significantly different from those of the Carboniferous Heshantou Formation (C_{1h}) and Sarlebulake Formation (C_{1s}) (Table 3) and (2) the magnetic polarity is exclusively reversed.

The Heshantou Formation (C_{1h}). The magnetic behavior of samples from the Heshantou Formation (C_{1h}) becomes univectorial to the origin after demagnetization to 20 mT or 200° C (Figure 4). These characteristic components have northwest declinations and negative inclinations, far removed from the in situ present Earth field direction. However, after tilt correction, the characteristic components become aligned with the stable magnetic directions isolated from other the Upper Paleozoic formations.

The Sarlebulake Formation (C_{1s}) and baked contact test. Similar in situ directions from sandstones of the Lower Carboniferous Sarlebulake Formation and a pluton intruding into the sandstones (sites 16-18) suggest that the sandstones near the contact carry a secondary magnetization (Figure 6). Tilt-corrected directions of magnetization of site 8hc19 from the same formation but some 2 km away from the pluton are indistinguishable from the in situ direction of sites 8hp16-18 (Figure 6 and Table 3) and the tilt-corrected directions of the

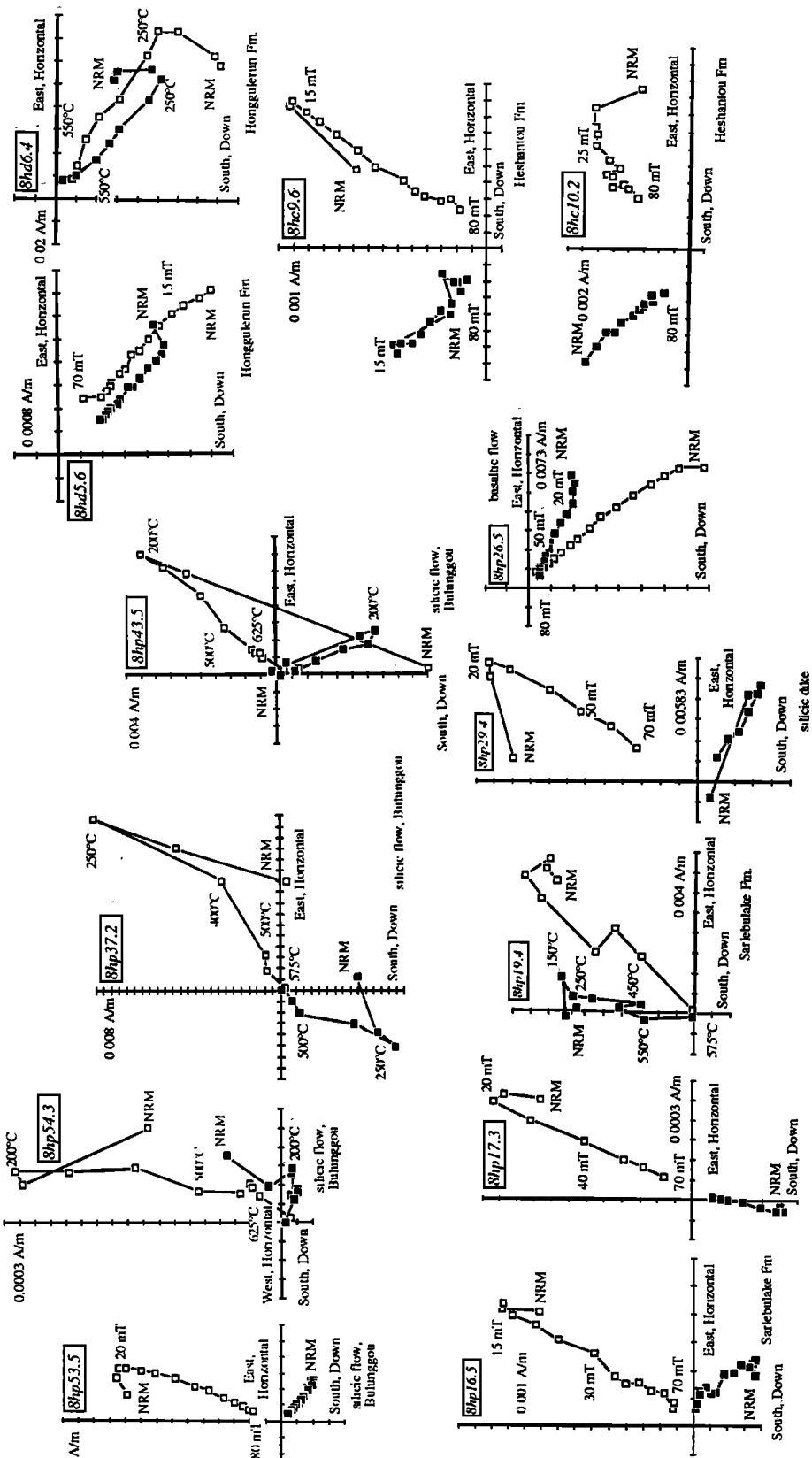

Fig. 4. Orthogonal vector thermal and AF demagnetization diagrams of specimens from the Hoboksar region. Solid symbols refer to the projection on the horizontal plane; Open symbols refer to the projection of inclination (geographic coordinates).

TABLE 2. Hoboksar, Silicic Flows C_{2-3}-P_1 (Latitude 46°42'N, Longitude 86°03'E)

Site	Age	N(M)	D	I	D_c	I_c	k	a_{95}	L	S(D)
					West Limb					
8hp37	C_{2k}	5(5)	202	-54	188	-46	50	10.9	RF	224(15W)
8hp38	C_{2k}	4(5)	181	-57	193	-50	55	12.5	RF	330(11E)
8hp39	C_{2k}	5(6)	164	-66	190	-57	63	9.7	RF	325(17E)
8hp40	C_{2k}	3(6)	148	-47	165	-45	52	17.2	RF	331(17E)
8hp41	C_{2k}	6(6)	156	-43	168	-37	97	6.8	RF	320(15E)
8hp42	C_{2k}	6(6)	157	-42	170	-41	59	12	RF	340(15E)
8hp43	C_{2k}	6(6)	168	-47	181	-45	47	9.9	SS	348(13E)
M37-43b	C_2	7(7)	167	-52	-	-	33	10.7	-	-
M37-43a	C_2	7(7)	-	-	178	-46	67	7.4	-	-
M37-43ap	C_2	7(7)	-	-	178	-46	63	7.6	-	-
					East Limb					
8hp47	C_{2h}	6(6)	150	-61	161	-42	112	6.3	AF	267(20W)
8hp48	C_{2h}	6(6)	190	-81	163	-53	188	4.9	AF	240(30W)
8hp49	C_{2k}	5(6)	137	-85	139	-51	154	6.2	AF	225(34W)
8hp50	C_{2k}	6(6)	201	-88	160	-49	287	3.9	RF	244(39W)
8hp51	C_{2k}	6(6)	313	-85	161	-56	27	13.2	RF	244(39W)
8hp52	C_{2k}	6(6)	210	-84	167	-51	367	3 5	RF	245(35W)
8hp53	C_{2k}	6(6)	140	-72	161	-39	134	5.8	RF	258(35W)
8hp54	C_{2k}	6(6)	111	-77	153	-49	149	5.5	RF	256(33W)
M47-54b	C_2	8(8)	151	-82	-	-	50	7.9	-	-
M47-54a	C_2	8(8)	-	-	155	-49	104	5.5	-	-
M47-54ap	C_2	8(8)	-	-	158	-49	105	5.4	-	-
					Mean of Both West and East Limbs					
Tb	C_2	15(15)	163	-68	-	-	17	9.5	-	-
Ta	C_2	15(15)	-	-	166	-48	46	5.7	-	-
Tap	C_2	15(15)	-	-	168	-48	52	5.3	-	-
Ib	C_2	15(15)	-	-66	-	-	12	13	-	-
Ia	C_2	15(15)	-	-	-	-47	99	4.4	-	-
					Sites Excluded From the Mean					
8hp44	C_{2k}	4(6)	186	-52	-	-	72	10.9	BF	-
8hp45	C_{2k}	7(7)	174	-47	-	-	138	5.0	BF	-
8hp46	C_{2k}	5(5)	205	-47	-	-	115	7.2	AF	-

Abbreviations are the same as in Table 1. For lithology, RF, rhyolitic flow; SS, sandstones; BF, basaltic flow; AF, andesitic flow. M37-43b and M37-43a, and M47-54b and M47-54a are in situ and tilt-corrected grand mean directions of sites 37-43 (west limb), and sites 47-54 (east limb). Tb and Ta are in situ and tilt-corrected grand mean directions of sites 37-43 and sites 47-54 all together. M37-43ap, M47-54ap and Tap are the final grand mean directions corrected for plunge (dip vector: 43°, dip: 13°NE). Ib and Ia are mean inclinations before and after tilt correction based on inclination-only average.

other sedimentary units. Assuming that both localities were tilted at the same time, this observation suggests that (1) the characteristic magnetization of the site far removed from the pluton has not been overprinted by the pluton; (2) tilting of the formation occurred before the intrusion of the plutons; and (3) the age of the pluton is younger than early Carboniferous but within the Kiaman interval (250-320 Ma).

Sites in plutons, dikes, and lava flows and tilt test. Sites 8hd1 and 2 were collected in a roadcut just south of the Hoboksar township. Sites 8hd3-4, and 8hp35-36 are from intrusions intruding into the Honggulerun (D_{3h}) Formation near Bulungou. Sites 8hc11-13 are located in plutons at Heshantou. Sites 8hp14 and 15 were collected from a dike and a lava flow in roadcuts near Heshantou. Bedding attitudes of sites 8hp20-26 were determined by averaging several readings of lava flow surfaces. Sites 8hp27-30 and sites 8hp32-34 were collected from silicic dikes in the vicinity of site 8hp31, which is collected from sandstones of the Sarlebulake Formation(?). Stable, consistent magnetizations could not be obtained from sites 8hc12-13, 8hp25, and 8hp34. Sites 8hp33 and 8hp35 are badly weathered and give directions which are not consistent with directions isolated from the other sites at the same localities. Site 8hp28 probably records a portion of transitional behavior of the geomagnetic field. The paleohorizontal control on sites 8hd1-2, and 8hc11 are uncertain. Thus results from sites 8hc12-13, 8hp25, 8hp33-35, 8hd1-2, and 8hc11 bear no tectonic significance and will not be discussed further. All samples in other sites demonstrate stable magnetic directions (Figure 4 and Table 3). These sites are either plutons/lava flows in contact with sedimentary rocks, or dikes intruded vertically.

The grand mean direction of the sites in plutons, lava flows and dikes is similar to the mean directions of the Honggulerun (D_{3h}), Heshantou (C_{1h}), and Sarlebulake (C_{1s}) formations, indicating that either (1) magnetizations in different formations and different types of rock were acquired essentially at about the same time or (2) there is little apparent polar wander (APW) during the Carboniferous for the Junggar block. Because all the sites are reversely magnetized, we believe that age of magnetization may be constrained within the Kiaman reversed polarity interval (250-360 Ma). Because of the secondary nature of magnetizations in the sedimentary units we have combined all data from the plutons, lava flows, dikes, and sedimentary units together to produce a mean direction from Hoboksar.

Remagnetization of the sedimentary units (D_{3h}, C_{1h}, and C_{1s}) must have occurred before folding because the tilt-corrected directions are significantly better grouped than the in situ directions (Table 3). Similarly, if we perform a tilt test on the tilted lava flows, plutons, and sedimentary rocks, a

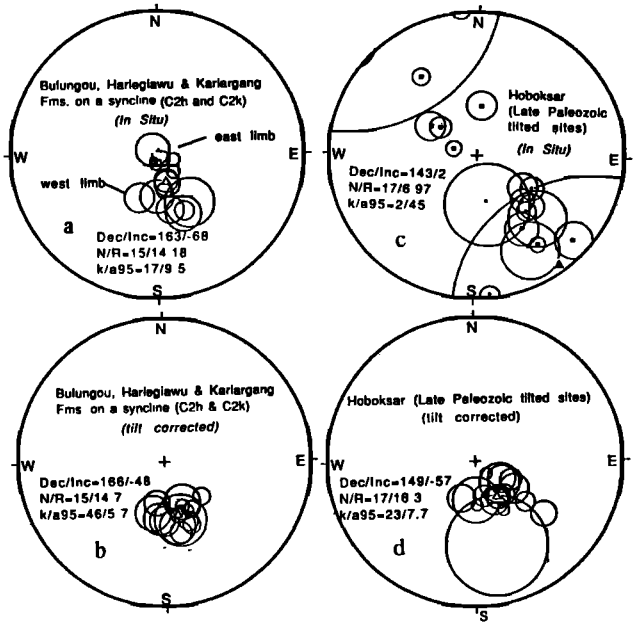

Fig. 5. Equal-angle stereographic projections of site-mean directions of the Harlegiawu and Karlargang formations (C_{2l} and C_{2k}, Figures 5*a* and 5*b*, all projected on upper hemispheres); remagnetized sedimentary units, tilted plutons and lava flows (Figures 5*c* and 5*d*, solid dots are projected on lower hemispheres, open squares are projected on upper hemispheres). Circles are the 95% confidence limit around the site-mean directions (centers). Average of site-mean direction is plotted as open or solid triangle (upper or lower hemisphere projection) with the 95% confidence limit.

positive tilt test is obtained at $p = 0.01$ (Figure 5 and Table 3). The in situ directions of some dikes and pluton (sites 8hp14, 8hp18, 8hp27, and 8hp29-32) in Hoboksar are indistinguishable from the tilt-corrected directions of the sedimentary units (Figure 5 and Table 3). This fact indicates that igneous activity and folding in the Hoboksar region were concurrent. This observation leads us to believe that the syncline within the Harlegiawu and Karlargang formations formed shortly after the eruptions of silicic flows and hence conclude that the magnetizations of these formations (C_{2h} and C_{2k}) are primary.

Isothermal Remanent Magnetization Acquisition Experiments

Isothermal remanent magnetization (IRM) acquisition experiments on some representative samples are shown in Figure 7. Results of all samples, except 8hp54.4 from a rhyolitic flow and 8hp29.6 from a pluton which are not saturated before 1 T, indicate the absence of appreciable high coercivity magnetic phases.

Discussion and Tectonic Interpretation

Each site-mean direction was converted into a virtual geomagnetic pole (VGP). Then, paleomagnetic pole positions for formations/locations were calculated assuming the VGPs belong to a Fisherian statistical distribution [*Fisher*, 1953]. Late Paleozoic paleomagnetic poles reported from different regions of Junggar are listed in Table 4, and some of them have been plotted in Figure 8. In addition to the poles obtained from this study, they also include a middle-late Permian pole from the Urumqi region (JG6 of Table 4 [*Sharps*, 1990]), a late Permian pole from the Heavenly Lake region, southern Junggar (JG5 of Table 4 [*Nie et al.*, 1989]), a remagnetized Permian pole from the Keramayi region, western Junggar (JG 9 of Table 4 [*Zhao et al.*, 1990]), and a late Paleozoic pole from the dike swarms in the Keramayi region (JG 3 of Table 4 [*Li et al.*, 1989]).

The pole JG6 was calculated from a synfold magnetization [*Zhao et al.*, 1990]. This pole differs in declination only from the pole JG3, which was obtained from the same region [*Li et al.*, 1989]. Although apparent polar wander may have produced this difference, local block rotation or incorrect tilt correction or a combination of the both probably caused the difference. The pole JG 5 is reported to be from Permian turbidites [*Nie et al.*, 1989]. A primary magnetization is supported by a fold test. Four specimens at one site (out of seven site) show normal polarity, suggesting that the age of the magnetization is near the upper boundary of the Kiaman reversed interval at 250 Ma (S. Nie, personal communication, 1989). If the magnetization of the four normal polarity specimens is indeed primary, then the pole JG5 is probably the youngest among all poles plotted in Figure 8. The inclination predicted from the pole JG5 is consistent with that from the pole JG6 from the Urumqi region, which passes a fold test [*Sharps*, 1990], despite the difference in declination. The pole JG6 is indistinguishable from the pole JG4 of the underlying Qijiagou and Aoertu formations [*Sharps*, 1990], although the samples were collected from separate sections.

The important observation from our study is that despite the wide separation between the sampling localities, there is a good general agreement between inclinations from the southern and northwestern margins of the Junggar block, suggestive of coherence since Permian. In addition, the similarity between Permian inclination and present inclination indicates that the Junggar block has experienced little net latitude shift since Permian time. Unfortunately, concordant and exclusively negative inclinations also allow the possibility of remagnetization during the Kiaman reversed polarity interval. A post-Permian remagnetization, however, is unlikely because the magnetization age is constrained by a baked contact test, fold tests, and the data come from widely distributed regions and from different lithologies with an exclusively reversed magnetic polarity. In addition, the directions of magnetization from the late Paleozoic units are not resemble to any known younger magnetizations [*Y. A. Li et al.*, 1990; *Chen et al.*, 1991]. Second-order differences between results from the three regions are mainly in declination and are not readily explainable. The following are five potential explanations.

Apparent polar wander (APW). Magnetization ages from this study are constrained to be from early Carboniferous to late Permian. The relative ages of the magnetizations from different regions are not known. Within the same general sampling region, poles from different stratigraphic units are not consistent, indicating possible polar wander. For example, poles PG4 from the Qijiagou and Aoertu formations and the Permian strata are different from the pole from the late Permian pole PG5 of the Heavenly Lake area. In the Hoboksar region, the difference between the two pole positions could reflect apparent polar wander. In general, late Paleozoic APW for Junggar is reflected by a change of declination, from NNW to NNE (Figure 8).

Relative block rotation. At least part of difference in declination between results from different regions could be due to relative horizontal rotations about the vertical axis. This is suggested by the fact that the colatitudes predicted by these poles are very close to each other. Post-Permian thrusting which can cause local rotation has been well documented in the southern and northwestern margins of the Junggar block [*Avouac et al.*, 1990; *Feng et al.*, 1989; *Ulmishek*, 1986; *Lee*, 1985].

Uncertainty in tilt correction. The pole JP9 is based on a synfolding magnetization and thus paleo-horizontal reference may have been lost. Another pole (JP8) from the dikes intruding into the Liushugou Formation is based on an assumption that the dikes intruded into flat sedimentary beds. Any initial tilting of the sedimentary rocks could have produced a directional bias in the magnetization. For the Hoboksar region, results from plutons, dikes, and lava flows and remagnetized sedimentary units could be synfolding because volcanism, magmatism, and folding appear to be concurrent.

Secular variation (SV) of the geomagnetic field. It is difficult

TABLE 3. Hoboksar, Sedimentary, Lava Flow, Dike, Pluton (C_{2-3}-P_1, Latitude 47°10'N, Longitude 86°35'E)

Site	Age	N(M)	D	I	D_c	I_c	k	a_{95}	L	S(D)
Sedimentary Units (Honggulerun, Heshantou, and Sarlebulake Formations)										
8hd5*	D_{3h}	6(6)	138	35	154	-60	115	6.2	LS	25(103W)
8hd6*	D_{3h}	6(6)	125	48	126	-54	41	10.6	LS	25(103W)
8hd7*	D_{3h}	6(6)	134	42	141	-56	72	8	LS	25(103W)
8hc8*	C_{1h}	6(6)	286	-72	130	-42	109	6.4	LS	213(65W)
8hc9*	C_{1h}	6(6)	302	-50	125	-65	42	10.5	LS	213(65W)
8hc10*	C_{1h}	6(6)	308	-56	118	-59	71	8	LS	213(65W)
8hp16	C_{1s}	6(6)	160	-65	-	-	279	4	SS	70(75S)
8hp17	C_{1s}	6(6)	194	-69	-	-	242	4.3	SS	70(75S)
8hc19*	C_{1s}	6(6)	5	-52	154	-56	43	10.3	SS	260(70N)
8hp31	?	8(8)	184	-37	-	-	79	6.3	SS	223(80N)
Sites in Lava Flow, Dike, and Pluton										
8hd3*	?	6(6)	136	29	178	-60	17	16.7	PT	13(115W)
8hd4*	?	6(6)	133	35	166	-62	70	8.1	PT	13(115W)
8hp14	?	6(6)	181	-57	-	-	171	5.1	DK	-
8hp15*	?	5(5)	173	1	150	-47	349	4	FL	118(65S)
8hp18	?	6(6)	129	-57	-	-	20	28.6	PT	-
8hp20*	?	7(7)	148	-28	200	-60	37	10	PT	23(55E)
8hp21*	?	7(7)	131	-7	148	-57	53	8.4	FL	23(55E)
8hp22*	?	5(6)	145	-16	178	-56	334	4.2	FL	23(55E)
8hp23*g	?	6(6)	167	53	166	-32	-	2.5	FL	73(85S)
8hp24*	?	5(6)	150	17	133	-65	21	14.9	FL	73(85S)
8hp26*	?	7(7)	121	42	128	-29	63	7.7	FL	73(85S)
8hp27	?	6(6)	137	-52	-	-	173	5.1	DK	-
8hp29	?	7(7)	123	-64	-	-	201	4.3	DK	-
8hp30	?	5(5)	144	-63	-	-	322	4.3	DK	-
8hp32	?	3(6)	157	-61	-	-	49	17.9	DK	-
8hp36*	?	7(7)	325	-23	140	-77	-	5.1	PT	234(80N)
$Mean_b$	C_1-P	26(32)	148	-33	-	-	2	28.4	-	-
$Mean_a$	C_1-P	26(32)	-	-	151	-58	24	5.9	-	-
$Mean_b$*	C_1-P	17(17)	143	2	-	-	2	45	-	-
$Mean_a$*	C_1-P	17(17)	-	-	149	-57	23	7.7	-	-

Abbreviations are the same as in Table 1. For lithology, PT, pluton; LS, limestone; DK, dike; FL, lava flow; SS, sandstone. Mean direction of site 8hp23 is obtained from analysis of remagnetization circles. $Mean_b$* and $Mean_a$* are in situ and tilt-corrected mean directions of tilted sites only. $Mean_b$ and $Mean_a$ are in situ and tilt-corrected mean directions of all sites accepted.

*, Corrected for tilting.

to assess whether SV has been averaged in late Paleozoic paleomagnetic studies because of the presence of only a single magnetic polarity. However, for each pole in our study, the between-site k value is much smaller than the within-site k, suggesting that at least some secular variation has been averaged. The expected dispersion value (S) of Carboniferous-Permian is 17° at the equator [*Merrill and McElhinny*, 1983]. The mean S and its 95% confidence level for poles from Junggar is 17° ± 10°.

Permian back arc spreading. If Permian spreading occurred in the Junggar block as suggested by *Hsu* [1988], there may be a difference between the results from the northwestern (Hoboksar and Keramayi) and southern parts (Urumqi) of the Junggar block. Lack of precise age determination of magnetizations in each formation/unit does not allow us to test the back arc spreading hypothesis conclusively, although the hypothesis is permissible using the available data.

Because the discordance of the poles listed in Table 4 can be caused by different factors such as APW, SV, relative block rotation, and back arc spreading, we believe that a mean of the poles produces a conservative middle Carboniferous to late Permian paleomagnetic pole for Junggar. A Fisherian average of the six poles yields a pole at λ = 82°N, φ = 329°E, K =26 and A_{95} = 13.4°. The poles of JP8 and JP9 are excluded from the mean because of uncertainty in paleohorizontal control. Although the mean pole surely underestimates the APW during Carboniferous and Permian times, it reduces potential local effects and experimental errors associated with each individual pole and provides a general tectonic description for the whole Junggar block in late Carboniferous and Permian times.

In Figure 9, we compare late Paleozoic results from Junggar with late Paleozoic poles from Siberia, Kazakhstan, Tarim, and North China blocks. For Tarim, only three Carboniferous poles have been reported [*Bai et al.*, 1987; *Zhai et al.*, 1988; *Sharps*, 1990]. One is from the combined Lower and Middle Carboniferous Bashisuogong (C_{1b}), Bijingtawu (C_{2b}), and Suogedangtawa (C_{2s}) formations in the Wushi region of northwestern Tarim and is believed to represent a Permian overprint [*Sharps*, 1990]. The other two were both from the Upper Carboniferous Kangkeling Formation (Chinese system) in the Aksu region of northwestern margin of Tarim. The pole given by *Bai et al.* [1987] is also thought to represent a secondary magnetization, since the pole position is indistinguishable from those of the Permian. The pole given by *Zhai et al.* [1988] passes a fold test at p = 0.01. However, the latest folding phase in this region is Tertiary. The paleolatitude predicted by this pole is higher than that predicted by the Permian poles, whereas the general trend for Tarim during late Paleozoic (Devonian-Permian) is a northward motion [*Y. P. Li et al.*, 1990].

The Permian pole from the Tarim block is a mean of four independent studies from different rock types (limestone, sandstone, basalts and dikes) and widely separate locations [*Sharps et al.*, 1989] which has been confirmed by two recent studies [*Fang et al.*, 1989; Z. Meng, personal communication, 1989]. We have used this Permian pole for our comparison with Junggar.

It is clear from Figure 9 that the mean pole from the Junggar block is distinct from its surrounding blocks, suggesting substantial post-Permian relative motion. However, the late

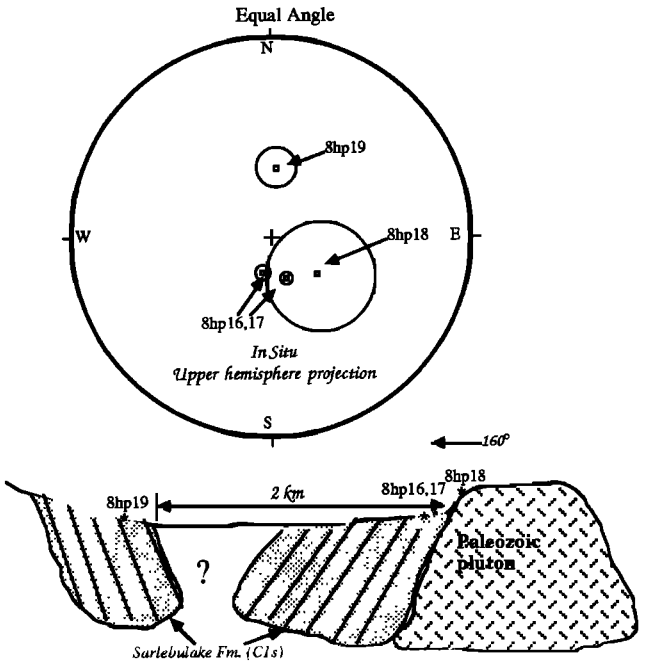

Fig. 6. Sketch of a baked contact test on the Sarlebulake Formation (C_{1s}) and the pluton intruding into the Formation. (Top): Equal-angle stereographic projections of site-mean directions plotted on upper hemispheres; (Bottom): Sketch of contact between the sandstones of the Sarlebulake Formation and the pluton intruding into the formation; asterisks are locations of sampling sites.

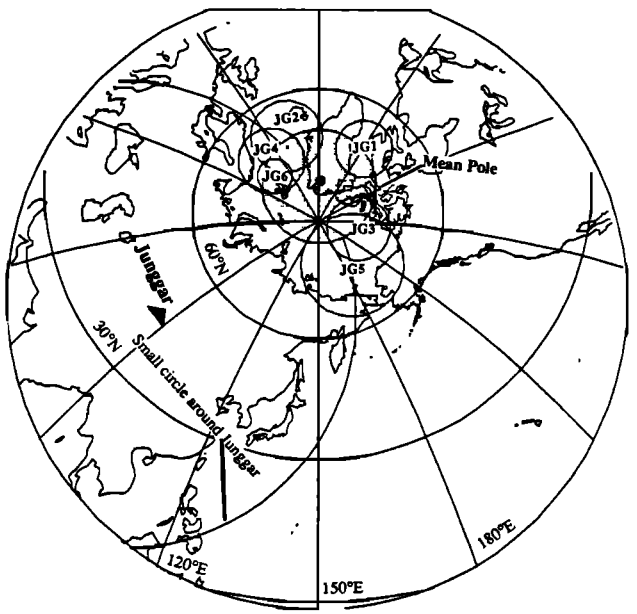

Fig. 8. Oblique polar projection of late Paleozoic paleomagnetic poles from the Junggar Block (Table 4). The mean pole is a shaded circle centered around a solid dot.

Carboniferous to Permian paleolatitude of the Junggar block predicted by our paleomagnetic results fit well with other geologic information.

Comparison of paleomagnetic poles also indicates late Carboniferous/Permian latitudinal proximity of Junggar, Tarim, Siberia, and Kazakhstan, supporting the hypothesis that (1) Junggar has been associated with Laurasia since at least middle Carboniferous [*Sharps*, 1990] and (2) Tarim arrived at the southern margin of Laurasia by Permian times. Middle-late Carboniferous flora in Junggar clearly belong to Angara, suggesting that Junggar had been attached or close to the south margin of the Siberia or Kazakhstan blocks since the middle Carboniferous times [*Hu*, 1985]. According to previous paleogeographic reconstructions based on flora/fauna and field geologic information, Junggar block was located between 35° and 50° latitudes during late Carboniferous [*Ziegler*, 1981; *Scotese*, 1984; *Watson et al.*, 1987; *Nie et al.*, 1990] . Our paleomagnetic results are in good agreement with those reconstructions.

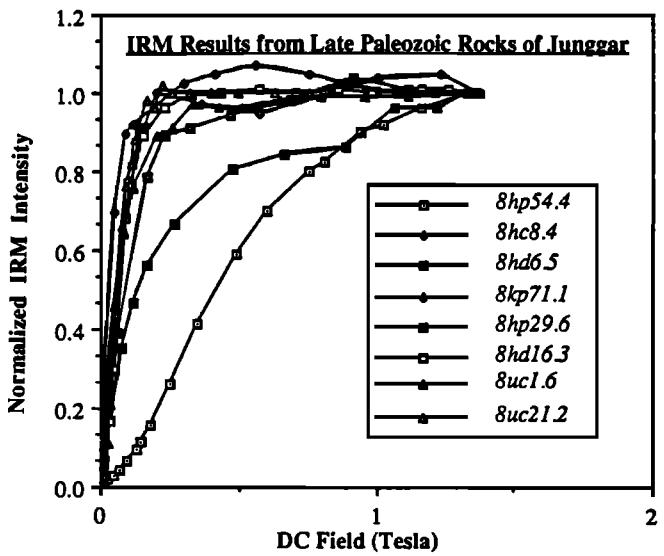

Fig. 7. Normalized isothermal remanent magnetization of specimens studied. Hoboksar region: 8hp54.4 is from a rhyolitic flow of the Karlargang Formation; 8hc8.4 is from limestone of the Heshantou Formation; 8hd6.5 is from limestone of the Honggulerun Formation; 8hp29.6 is from a dike; 8hd16.3 is from sandstone of the Sarlebulake Formation. Urumqi region: 8uc1.6 is from limestone of the Qijiagou Formation; 8uc21.2 is from sandstone of the Aoertu Formation. 8kp71.1 is from a late Paleozoic mafic dike in Keramayi [*Li et al.*, 1989].

There is a consensus among geologic community that the Tarim block accreted to the southern margin of Laurasia in late Carboniferous to early Permian [*Wang and Liu*, 1981; *Zhang et al.*, 1984; *Watson et al.*, 1987; *Li*, 1988; *Sharps*, 1990]. However, there has been a relative motion between the Junggar and Tarim blocks since then. For an example, the net latitudinal shift of Junggar since the Permian times is 4° (for a reference point at 45°N and 86.5°E, the change is from 41°N in the Permian to 45°N at present), whereas for the Tarim block the shift is 9° (31°N during the Permian to 40° at present for a reference point at 40°N, 80°E). The 5° difference or approximately 550 km probably represents post-collision continental shortening in the Tian Shan region (Figure 10). Continental shortening during the Cenozoic is evident in the Tian Shan Ranges [*Molnar and Tapponier*, 1975; *Avouac et al.*, 1990], and is estimated to be ~100 km across the Tian Shan near Urumqi based on a surface geology study [*Avouac et al.*, 1990]. We should emphasize that amount of the continental shortening based on paleomagnetic data is most likely. Given the nature of paleomagnetic data, any conclusion on this order (5°) is probably not statistically significant. Paleomagnetic data presented here also reveal the post-Paleozoic motion between Junggar and Kazakhstan, Siberia, and Tarim as evidenced by significantly different declinations predicted by the late Carboniferous/Permian paleomagnetic poles from Junggar, Siberian, Kazakhstan, and Tarim. The mean paleomagnetic directions from Junggar point basically to the north to northwest, whereas the expected directions of Tarim, Kazakhstan and Siberia point to from N40°E to even E10°S (Figures 9 and 11). Although this difference in declination could be accounted for by local structures, the results from three different, widely separate localities are so consistent that a relative rotation between the Junggar block and its adjacent units is most likely.

TABLE 4. Late Paleozoic Paleomagnetic Poles From Junggar, Western China

Location	Pole	Age	N	Long^P	Lat^P	Long^S	Lat^S	K	A_{95}	Reference
Bulungou	JG1	C_2	15	299	70	86.1	46.7	36	6 4	this study
Hoboksar	JG2	C_{2-3}-P	26	350	69	86.6	47 2	15	7 5	this study
Keramayi	JG3	C_3-P	23	230	80	84.7	45.4	16	7.8	*Li et al* [1989]
Qijiagou+Aocrtou	JG4	C_{2-3}	15	7	72	87.6	43.8	28	7.4	this study
Heavenly Lake	JG5	P_2	7	188	76	88.0	43.8	24	13	*Nie et al.* [1989]
Urumqi	JG6	P	78*	13	75	87.8	43.8	17	4	*Sharps* [1990]
Final Mean		C_{2-3}-P	6	329	82	-	-	26	13.4	this study
Liushugou†	JG7	C_2-P	4	231	69	87.8	43.8	46	13.7	this study
Dikes in Liushugou†	JG8	C_2-P	7	172	55	87.8	43.8	17	15.1	this study
West Junggar†	JG9	P(?)	11	178	51	84.2	45.5	58	6	*Zhao et al.* [1990]

N, Long^P, Lat^P, Long^S, Lat^S, K, A_{95} are number of site, pole position (longitude and latitude), sampling location (longitude and latitude), Fisher's precision parameter, and radius of the 95% confidence circle.
*, Number of sample.
†, Excluded from the final mean.

Post-Permian relative motion can be interpreted as clockwise rotations of Tarim, Kazakhstan, and Siberia relative to an arbitrarily fixed Junggar block. One possible consequence of the clockwise rotations is a left-lateral strike-slip motion between the Junggar block and its adjacent tectonic units, depending on locations of the Euler rotation poles. Paleomagnetic data from Tarim, when compared with the data from Siberia, suggest a significant eastward motion of Tarim relative to Siberia since Paleozoic [*Li*, 1988; *Zhao et al.*, 1990]. To accomplish this motion, a series of left-lateral strike-slip faults must exist between Tarim and Siberia. The left-lateral strike-slip motion along the boundary between the Junggar and Tarim blocks as suggested by paleomagnetic data from the Junggar block, is in good agreement with what is predicted from other independent paleomagnetic studies. It has been suggested that because of the penetration of India into the Asian continent, most parts of China have been pushed southeastward and rotated clockwise [*Tapponnier et al.*, 1982]. Limited Mesozoic paleomagnetic data from Tarim and Junggar indicate some 10° clockwise rotation of Tarim relative to Junggar since Jurassic [*Y. A. Li et al.*, 1990; *Chen et al.*, 1991]. Whether the left-lateral strike-slip motion is related to the collision of India and Asia remains to be confirmed by further late Mesozoic and Cenozoic paleomagnetic data from the Tarim and Junggar blocks.

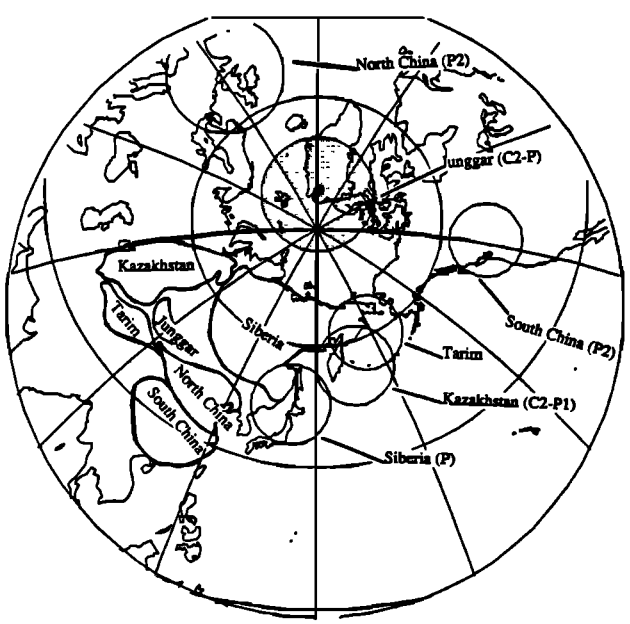

Fig. 9. Oblique polar projection (the same projection as Figure 8) of middle Carboniferous to Permian poles from Junggar (this paper), Tarim [*Sharps et al.*, 1989], Siberia [*Khramov et al.*, 1985], Kazakhstan [*Khramov et al.*, 1981], North and South China blocks [*Zhao and Coe*, 1987].

CONCLUSION

Carboniferous and Permian paleolatitudes obtained from widely separate localities around the Junggar block argue for its coherence since Permian time. Consistently steep inclinations, similar to the present one, indicate an affinity of the Junggar block with Laurasia during Permian [*Sharps*, 1990] and possibly Carboniferous as well, and little net shift in the north-south direction for the Junggar block since Permian. Prefolding magnetizations with an exclusively reversed magnetic polarity constrain the magnetizations to be between 250 and 320 Ma (the Kiaman reversed polarity interval). Whether concordant Carboniferous and Permian directions of magnetization suggest little APW or denote a remagnetization in the Kiaman reversed polarity interval (250-320 Ma) cannot be distinguished. In contrast, the Tarim block was located 10° south of the Junggar block during the Carboniferous and Permian [*Zhai et al.*, 1988; *Sharps et al.*, 1989] and was dominated by the Cathaysian flora, suggesting that Tarim was separated from Junggar by the ancestral Tian Shan. Since Permian times, some 550 km of continental shortening has occurred between the Tarim and Junggar blocks, presumably in

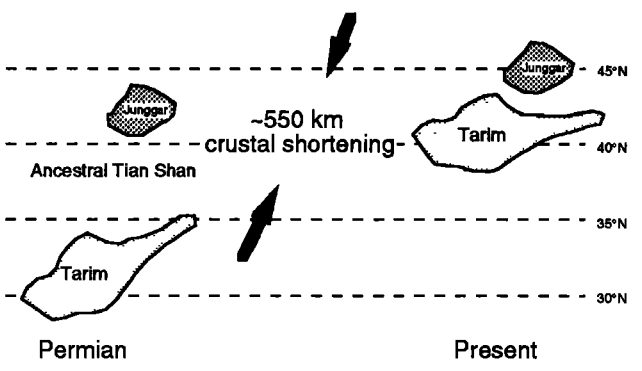

Fig. 10. Sketch of Permian reconstructions (constrained in latitude only) for the Tarim and Junggar blocks. Crustal shortening across the Tian Shan since the accretion of Tarim to the southern margin of Laurasia is estimated to be about 550 km based on paleomagnetic data (*Sharps et al* [1989] and this study).

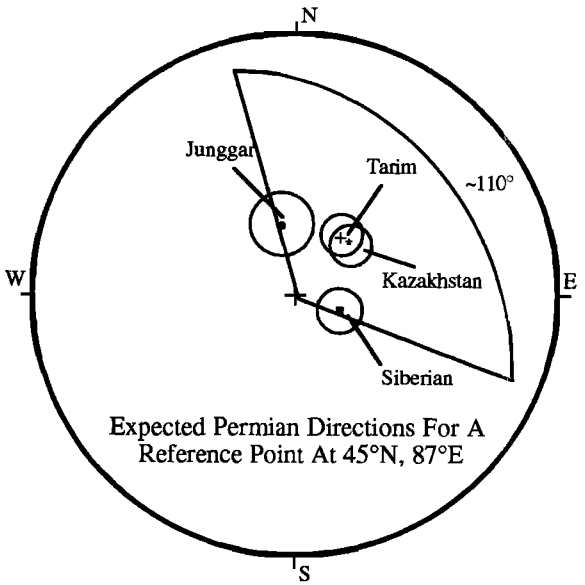

Fig. 11. Expected Permian directions from paleomagnetic poles of Junggar, Tarim, Kazakhstan, and Siberian for a reference point at 45°N, 87°E, plotted on equal-angle stereographic projection (lower hemisphere projection).

the Tian Shan region. Both North China and South China blocks are located in low latitudes during the Permian [*Zhao et al.*, 1987], and thus the collision between the North China and Junggar blocks must be post-Permian.

Finally, the discrepancy in declinations from Junggar, Tarim, Kazakhstan, and Siberian suggests post-Permian relative motions between Junggar and its adjacent blocks. A net result is that motion between Junggar and Tarim is likely to have a left-lateral strike-slip sense, consistent with other geological and paleomagnetic evidence.

Acknowledgments. This work is a part of a collaborative paleomagnetic research project between the Department of Geophysics at Stanford University and Xinjiang National 305 Project Office of China, Urumqi, China. We thank the staff of the Xinjiang Geology Institute (Urumqi) for help with sample collection. Y. Li is greatly indebted to John Geissman of University of New Mexico for using paleomagnetic laboratory facility at UNM. We thank A. Carroll, C. McKnight, J. Lin, and N. Opdyke for helpful reviews. Financial support was provided in part by National Science Foundation (EAR-8618562, EAR-8718562, and EAR-8817774); the Stanford-China Geosciences Industrial Affiliates Program whose sponsors include Amoco, Anschutz, Chevron, ELF Aquitaine, Exxon, Mobil, Occidental, Pecten, Texaco, and Unocal; Geophysics Department of Stanford University; and the National 305 Project Office, Urumqi, Xinjiang, China.

REFERENCES

Avouac, J. P., P. Tapponnier, M. Bai, H. You, and G. Wang, Field evidence for active faulting and folding along the northern piedmont of the Tien Shan (Xinjiang, China) (abstract), *Eos Trans. AGU, 71*, 1561, 1990.

Bai, Y., G. Chen, Q. Sun, Y. Sun, Y. Li, Y. Dong, and D. Sun, Late Paleozoic polar wander path for the Tarim Block and tectonic significance, *Tectonophysics, 139*, 145-153, 1987.

Bureau of Geology and Mineral Resources of Xinjiang , No.1 Regional Geological Surveying Party, List of geologic isotopic data from Xinjiang (in Chinese with English abstract), *Xinjiang Geol. 5*, 16-106, 1987.

Carroll, A., Y. Liang, S. Graham, X. Xiao, M. Hendrix, J. Chu, and C. McKnight, Junggar basin, northwest China: Trapped late Paleozoic ocean, *Tectonophysics, 181*, 1-14, 1990.

Chen, Y., et al., Paleomagnetic study of Mesozoic continental sediments along the northern Tien Shan (China) and heterogeneous strain in central Asia, *J. Geophys. Res., 96*, 4065-4082, 1991.

Coleman, R., Continental growth of northwest China, *Tectonics, 8*, 621-635, 1989.

Fang, D., G. Jin, H. Chen, Y. Guo, Z. Wang, S. Ying, and X. Tan, Discussion on paleomagnetism and tectonic evolution of Tarim plate (China) from late Paleozoic to Mesozoic, paper presented at the 4th National Conference on Paleomagnetism, Paleomagn. Comm. of Chin. Geol. Assoc. and Aerophys. Comm. of China, Hangzhou, 1989.

Feng, R. Coleman, G. Tilton, and X. Xiao, Tectonic evolution of the West Junggar Mountains, Xinjiang, China, *Tectonics, 8*, 1-22, 1989.

Fisher, R. A., Dispersion on a sphere, *Proc. R. Soc. London Ser. A, 217*, 295-305, 1953.

Harland, W. B., A. V. Cox, P. G. Llewelyn, A. G. Pickton, A. G. Smith, and R. Walter, *A Geologic Time Scale*, 131 pp., Cambridge University Press, New York, 1982.

Hsu, K. J., Relict back-arc basins: Principles of recognition and possible new examples from China, in *New Perspectives in Basin Analysis* edited by K.L. Kleinpell and C. Paola, pp. 245-263, Springer-Verlag, New York, 1988.

Hu, Y., Characteristics of the Permian floras in the western part of China (in Chinese), *Reg. Geol. China, 12*, 100-108, 1985.

Huang, T. K., J. Ren, C. Jiang, Z. Zhang, and D. Qin, *Geotectonic Evolution of China*, 203 pp., Springer-Verlag, New York, 1987.

Khramov, A. N., G. N. Petrova, and D. M. Pechersky, Paleomagnetism of the Soviet Union, in *Paleoreconstruction of the Continents, Geodyn. Ser.*, vol. 2, edited by M. W. McElhinny and D. A. Valencio, pp. 159-194, AGU, Washington, D. C., 1981.

Khramov, A. N., E. L. Gurevich, R. A. Komissarova, E. P. Osipova, S. A. Pisarevsky, V. P. Rodionov, and I. P. Slautsitais, Paleomagnetism, microplates and Siberian plate consolidation, *J. Geodyn., 2*, 127-139, 1985.

Kirschvink, J. L., The least-squares line and plane and the analysis of paleomagnetic data, *Geophys. J. R. Astron. Soc., 62*, 699-718, 1980.

Kwon, S.-T., G. R. Tilton, R. G. Coleman, and Y. Feng, Isotopic studies bearing on the tectonics of the West Junggar Region, Xinjiang, China, *Tectonics, 8*, 719-727, 1989.

Lee, K. Y., Geology of the petroleum and coal deposits in the Junggar basin, Xinjiang Uygur Zizhiqu, northwest China, *US Geol. Surv. Open File Rep, 85-230*, 53 pp., 1985.

Li, Y. A. Li, Y., R. Sharps, M. McWilliams, Q. Li, W. Zhang, Mesozoic paleomagnetic results from the Junggar block, Xinjiang Province, northwest China (abstract), *Eos Trans. AGU, 71*, 1292, 1990.

Li, Y. P., Paleomagnetism of western China and the southern Sierra Nevada, Ph.D. dissertation, 234 pp., Stanford Univ., Stanford, Calif., 1988.

Li, Y., R. Sharps, M. McWilliams, N. Amos, Y. A. Li, Q. Li, and W. Zhang, Paleomagnetic results from late Paleozoic dikes from northwestern Junggar block, northwestern China, *Earth Planet. Sci. Lett., 94*, 123-130, 1989.

Li, Y. P., M. McWilliams, R. Sharps, A. Cox, Y. A. Li, Q. Li, Z. Gao, Z. Zhang, and Y. Zhai, A Devonian paleomagnetic pole from red beds of the Tarim block China, *J. Geophys. Res., 95*, 19,185-19,198, 1990.

Liao, Z., L. Lu, N. Jiang, F. Xia, F. Sun, Y. Zhou, S. Li, and Z. Zhang, Carboniferous and Permian in the western part of the east Tianshan Mountains, *Guide Book Excursion 4*, 39 pp., 11th Int. Congr. of Carboniferous Stratigraphy and Geol., Beijing, 1987.

Ma, X., Lithospheric dynamics map of China and adjacent seas, scale 1:4,000,000, Geol. Publ. House, Beijing, China, 1987.

McElhinny, M., Statistical significance of the fold test in paleomagnetism, *Geophys. J. R. Astron. Soc., 8*, 338-340, 1964.

McFadden, P., and D. Jones, The fold test in paleomagnetism, *Geophys. J. R. Astron. Soc., 67*, 53-58, 1981.

Merrill, R., and M. McElhinny, *The Earth's Magnetic Field: Its History, Origin and Planetary Perspective*, 401 pp., Academic, San Diego, Calif., 1983.

Molnar, P., and P. Tapponnier, Cenozoic tectonics of Asia: Effects of a continental collision, *Science, 189*, 419-425, 1975.

Nie, S., D. B. Rowley, R. Van Der Voo, and M. Li, Late Paleozoic Paleomagnetic results from Northwest China and Permian Asian Plate Reconstructions (abstract), *Eos Trans. AGU, 70*, 1071, 1989.

Nie, S., D. B. Rowley, and A. Ziegler, Constraints on the locations of Asian microcontinents in Palaeo-Tethys during the Late Paleozoic,

in *Paleozoic Palaeogeography and Biogeography*, vol. 12, edited by W. S. McKerrow and C. R. Scotese, pp. 397-408, *Mem. Geol. Soc. London* , 1990.

Scotese, C. R., An Introduction to this volume: Paleozoic paleomagnetism and assembly of Pangea, in *Plate Reconstruction From Paleozoic Paleomagnetism, Geodyn. Ser.* vol. 12, edited by R. Van der Voo, C. R. Scotese, and N. Bonhommet, pp.1-10, AGU, Washington, D. C., 1984.

Sharps, R., Paleomagnetism and tectonics of northwest China, Ph. D. dissertation, 225 pp., Stanford Univ., Stanford, Calif., 1990.

Sharps, R., M. McWilliams, Y. P. Li, A. Cox, Z. Zhang, Y. Zhai, Z. Gao, Y. A. Li, and Q. Li, Lower Permian paleomagnetism of the Tarim Block, northwestern China, *Earth Planet. Sci. Lett., 92*, 275-291, 1989.

Smith, A. B., Late Paleozoic biogeography of East Asia and palaeontological constraints on plate tectonic reconstructions, *Philos. Trans. R. Soc. London, Ser. A 326*, 189-227, 1988.

Tapponnier, P., A. Peltzer, A. Dain, R. Armijo, and P. Cobbold, Propagating extrusion tectonics in Asia: New insights from simple experiments with plasticine, *Geology, 10*, 611-616, 1982.

Ulmishek, G., Geology and petroleum resources of basins in western China, *Argonne Natl. Lab. Rep., ANL/ES-146*, 131 pp., 1986.

Wang, H., and B. Liu, Paleogeographic frame of China since Middle Proterozoic (in Chinese), *J. Stratigr., 5*, 77-89, 1981.

Watson, M. P., A. B. Hayward, D. N. Parkinson, and Z. M. Zhang, Plate tectonic history, basin development and petroleum source rock deposition onshore China, *Mar. Pet. Geol., 4*, 205-225, 1987.

Xinjiang Stratigraphic Compiling Group, *Regional Stratigraphic Tables of Northwest China, Volume on Xinjiang* (in Chinese), 496 pp., Geol. Publ. House, Beijing, 1981.

Zhai, Y., Z. Zhang, Y. A. Li, Q. Li, Y. P. Li, M. McWilliams, A. Cox, and R. Sharps, A study of Upper Carboniferous paleomagnetism for the Tarim Block (in Chinese with English abstract), *Geoscience, 2*, 43-56, 1988.

Zhang, Z. M., J. G. Liou, and R. G. Coleman, An outline of the plate tectonics of China, *Geol. Soc. Am. Bull., 95*, 295-312, 1984.

Zhao, X., and R. S. Coe, Paleomagnetic constraints on the collision and rotation of north and south China, *Nature, 327*, 141-144, 1987.

Zhao, X., R. Coe, Y. Zhou, H. Wu, and J. Wang, New paleomagnetic results from northern China: collision and suturing with Siberia and Kazakhstan, *Tectonophysics, 181*, 43-81, 1990.

Ziegler, A. M., Paleozoic paleogeography, in *Paleoreconstruction of the continents, Geodyn. Ser.*, vol. 2, edited by M. W. McElhinny and D. A. Valencio, pp. 31-37, AGU, Washington, D. C., 1981.

Zijderveld, J. D. A., AC demagnetization of rocks: Analysis of results, in *Methods in Paleomagnetism*, edited by D. W. Collinson, K. M. Creer, and S. K. Runcorn, pp. 254-286, Elsevier, New York, 1967.

Q. Li, Y. A. Li, and W. Zhang, Xinjiang Geology Research Institute, Urumqi, Xinjiang, People's Republic of China.

Y. P. Li, M. McWilliams, and R. Sharps, Department of Geophysics, Stanford University, Stanford, CA 94305.

(Received December 19, 1990;
revised April 26, 1991;
accepted June 14, 1991.)

Correction to "The GEM-T2 Gravitational Model" by J.G. Marsh et al.

In the paper "The GEM-T2 Gravitational Model" by J.G. Marsh et al. (*Journal of Geophysical Research, 95* (B13), 22,043-22,071, 1990) there was a mistake made in the computation of Table 7. The corrected table is shown below. These values are also corrections for those of *Christodoulidis et al.*, [1988] where the GEM-T1 results were shown. When taking into account the effect of the secular change in the second degree zonal harmonic as given by *Yoder et al.* [1983] of $1.29 \pm 0.28 \times 10^{-22}$ rad s^{-2} when mapped into the braking of the Earth's rotation rate [see *Christodoulidis et al.*, 1988], the GEM-T2 values correspond to 1.64 ms/century, which are considerably closer (than reported in our text) to astronomic studies of *Stephenson and Morrison* [1984] who find a value of 1.4 ms/century for telescopic data since 1620. The authors apologize for any inconveniences caused by these errors and acknowledge Steven R. Dickman of the State University of New York at Binghamton for bringing to our attention problems in our computer code.

Table 7. Comparison of GEM–T1 and GEM–T2 Dynamic Tide Models for Secular Change in the Mean Motion of the Moon ($\dot{n}$) and in the Rotational Velocity of the Earth ($\dot{\Omega}$)

Tide	GEM–T1		GEM–T2		GEM–T1		GEM–T2	
	$\dot{n}$	$\sigma_{\dot{n}}$	$\dot{n}$	$\sigma_{\dot{n}}$	$\dot{\Omega}$	$\sigma_{\dot{\Omega}}$	$\dot{\Omega}$	$\sigma_{\dot{\Omega}}$
056.554 Sa	0.00	0.00	0.00	0.00	0.00	0.00	0.00	0.00
057.555 Ssa	0.00	0.00	0.00	0.00	0.02	0.03	0.01	0.07
058.554	0.00	0.00	0.00	0.00	0.00	0.00	0.00	0.00
065.455 Mm	0.01	0.31	0.01	0.12	-0.00	0.12	-0.00	0.05
075.555 Mf	0.13	0.18	0.19	0.16	0.03	0.07	0.04	0.06
075.565	0.01	0.06	0.01	0.06	0.00	0.02	0.00	0.02
135.655 Q1	-0.17	0.04	-0.17	0.04	-0.02	0.01	-0.02	0.01
145.545 O1f	-0.10	0.02	-0.10	0.02	-0.01	0.01	-0.01	0.01
145.555 O1	-3.28	0.25	-3.15	0.21	-0.71	0.07	-0.68	0.06
155.455 M1f	-0.00	0.00	-0.00	0.00	-0.00	0.00	-0.00	0.00
155.655 M1	-0.01	0.00	-0.01	0.00	-0.00	0.00	-0.00	0.00
162.556 π1	0.00	0.00	0.00	0.00	-0.00	0.00	-0.00	0.00
163.555 P1	0.00	0.00	0.00	0.00	-0.06	0.10	-0.13	0.04
164.556 S1	0.00	0.00	0.00	0.00	-0.00	0.00	-0.00	0.00
165.545 K1f	--	--	--	--	-0.00	0.00	-0.00	0.00
165.555 $K1_{mn}$	--	--	--	--	--	--	--	--
165.555 $K1_{m}$	--	--	--	--	--	--	--	--
165.565 K1s	--	--	--	--	-0.01	0.00	-0.01	0.00
166.554 Ψ1	0.00	0.00	0.00	0.00	-0.00	0.00	-0.00	0.00
167.555 ϕ1	0.00	0.00	0.00	0.00	-0.00	0.00	-0.00	0.00
175.455 J1	-0.01	0.00	-0.01	0.00	-0.00	0.00	-0.00	0.00
185.555 OO1	-0.00	0.00	-0.00	0.00	-0.00	0.00	-0.00	0.00
245.655 N2	-1.42	0.16	-1.38	0.14	-0.21	0.04	-0.20	0.04
255.545 M2s	-0.02	0.01	-0.02	0.01	-0.00	0.00	-0.00	0.00
255.555 M2	-19.87	0.40	-20.30	0.39	-4.31	0.09	-4.40	0.09
265.455 L2	0.01	0.00	0.01	0.00	-0.00	0.00	-0.00	0.00
271.557	0.00	0.00	0.00	0.00	-0.00	0.00	-0.00	0.00
272.556 T2	0.00	0.00	0.00	0.00	-0.00	0.05	-0.00	0.04
273.555 S2	0.00	0.00	0.00	0.00	-0.34	0.04	-0.34	0.03
274.554 R2	0.00	0.00	0.00	0.00	-0.00	0.00	-0.00	0.00
275.555 $K2_{mn}$	--	--	--	--	--	--	--	--
275.555 $K2_{m}$	--	--	--	--	--	--	--	--
285.455	-0.00	0.00	-0.00	0.00	-0.00	0.00	-0.00	0.00
295.555	0.00	0.00	0.00	0.00	-0.00	0.00	-0.00	0.00
Total	-24.75	0.61	-24.94	0.51	-5.64	0.22	-5.75	0.16

$\dot{n}$ and $\sigma_{\dot{n}}$ are in arc sec century^{-2}. $\dot{\Omega}$ and $\sigma_{\dot{\Omega}}$ are in 10^{-22} rad s^{-2}.

(Received May 27, 1991.)

Paper number 91JB01757.
0148-0227/91/91JB-01757$02.00

JOURNAL OF GEOPHYSICAL RESEARCH, VOL. 96, NO. B10, PAGES 16,241–16,250, SEPTEMBER 10, 1991

The Hechiceros Caldera: a Recently Identified Mid-Tertiary Caldera in Eastern Chihuahua, Mexico

STEVEN P. RITTER AND JOSEPH C. CEPEDA

Department of Biology and Geosciences and Killgore Research Center, West Texas State University, Canyon

Geologic mapping of Tertiary volcanic rocks in the Sierra Hechiceros, 50 to 80 km south of Big Bend National Park has delineated a 20 by 25 km Mid-Tertiary caldera, herein named the Hechiceros Caldera. This caldera was formed by the eruption of the Palomas tuff which has a minimum volume of approximately 170 km³, and is distributed radially around the caldera. The caldera was filled with more than 500 meters of postcaldera rhyolitic lavas which overflowed the caldera margin and caused additional subsidence. The rocks of the Sierra Hechiceros are subalkalic and include rhyolites and dacites. The chemistry of these rocks is transitional between the calc-alkalic province of the Sierra Madre Occidental and the alkalic rocks of the eastern Trans-Pecos magmatic province. The potassium argon ages both the Palomas tuff and the postcaldera El Jobero rhyolite are about 29 ±0.6 Ma.

INTRODUCTION

The wide belt of volcanic and plutonic rocks emplaced along the western edge of North America during Cretaceous and Tertiary time formed as a result of the subduction of an oceanic plate beneath the western margin of the North American continent[*Atwater*, 1970; *Lipman et al.*, 1972; *Christiansen and Lipman*, 1972; *McDowell and Clabaugh*, 1979]. This magmatism resulted in the emplacement of shallow plutons, lava flows of varying composition, and voluminous intermediate to silicic ash flow tuffs.

The volcanic rocks of northern Mexico and west Texas can be subdivided into three parts, from west to east: (1) the Sierra Madre Occidental of western Mexico, which consists of a thick sequence of rhyolitic ash flow tuffs resting on a volcanic-plutonic complex of intermediate composition, and is the most extensive remnant of volcanism, (2) the transition zone of eastern Chihuahua containing isolated outcrops of volcanic rocks; and (3) the predominantly alkalic Trans-Pecos Texas volcanic field, and its southern extension into northern Coahuila.

Several calderas have been identified in western Chihuahua and Durango [*Swanson and McDowell*, 1984], as well as in the Trans-Pecos region of west Texas and adjacent eastern Chihuahua.

The calderas of Trans-Pecos Texas and adjacent Mexico range in size from 4 to 30 km in diameter[*Henry and Price*, 1984]. Two calderas, the San Carlos and Santana, are present in northeastern Chihuahua, near the town of Manuel Benevides(Figure 1). The Sierra Hechiceros is located southeast of these two calderas, spanning the border between the states of Chihuahua and Coahuila, Mexico.

This paper describes the stratigraphic sequence of the Sierra Hechiceros and presents evidence for a large collapse caldera, the vent area from which some of the described units were erupted.

Paper number 91JB01425
0148-0227/91/91JB-01425 $05.00

STRATIGRAPHY OF THE SIERRA HECHICEROS VOLCANIC SEQUENCE

A composite stratigraphic section of the Sierra Hechiceros includes approximately 1600 m of Tertiary volcanic and volcaniclastic rocks(Figure 2). It includes basalts, dacitic and rhyolitic lava flows, volcaniclastic sedimentary rocks, rhyolitic ash flow tuffs and air fall tuffs, which unconformably overlie Cretaceous sedimentary rocks. Within the map area (Figure 3), six stratigraphic units have been delineated. These units are, in ascending order, The El Matadero formation, the San Antonio dacite, the La Mota dacite, the Agua Dulce formation, the Palomas tuff, and the El Jobero rhyolite. The latter four units originated from vent areas within the range, although the vent areas have been subsequently covered by the younger Palomas tuff and El Jobero rhyolite. All of the stratigraphic names used in this report are to be considered informal names.

Cretaceous rocks crop out at the north end of the range and probably underlie the entire range. Rare cobbles of Cretaceous limestone are found in arroyos on the crest of the range and were probably incorporated as xenoliths within rising magma, and subsequently released by erosion.

The La Mota dacite is named for exposures near La Mota in the vicinity of Palomas. It crops out on the northwest side of the Sierra Hechiceros. The thickest exposures occur in the northern part of the range where the dacite overlies the 29.8 Ma La Cuesta tuff [*Gunderson*,1983] which does not crop out in the map area. The La Mota dacite consists of several lava flows, and attains a maximim exposed thickness of 20 m in the vicinity of Palomas. The vent area for this unit is probably near Palomas.

The Agua Dulce formation is composed of a sequence of tuffaceous rocks, conglomerates, and air fall tuffs. This volcaniclastic unit is named for outcrops exposed at Ranchito Agua Dulce on the western edge of the range. The unit has a maximum thickness of approximately 65 m, and thins northward due to pre-existing topography on the La Mota dacite and post-depositional erosion. Small, cliff-forming conglomerates and reworked tuff beds are exposed in the drainage at Ranchito Agua Dulce and along the slope of the range below the Palomas tuff, but elsewhere, the tuffaceous beds are usually weathered and easily eroded.

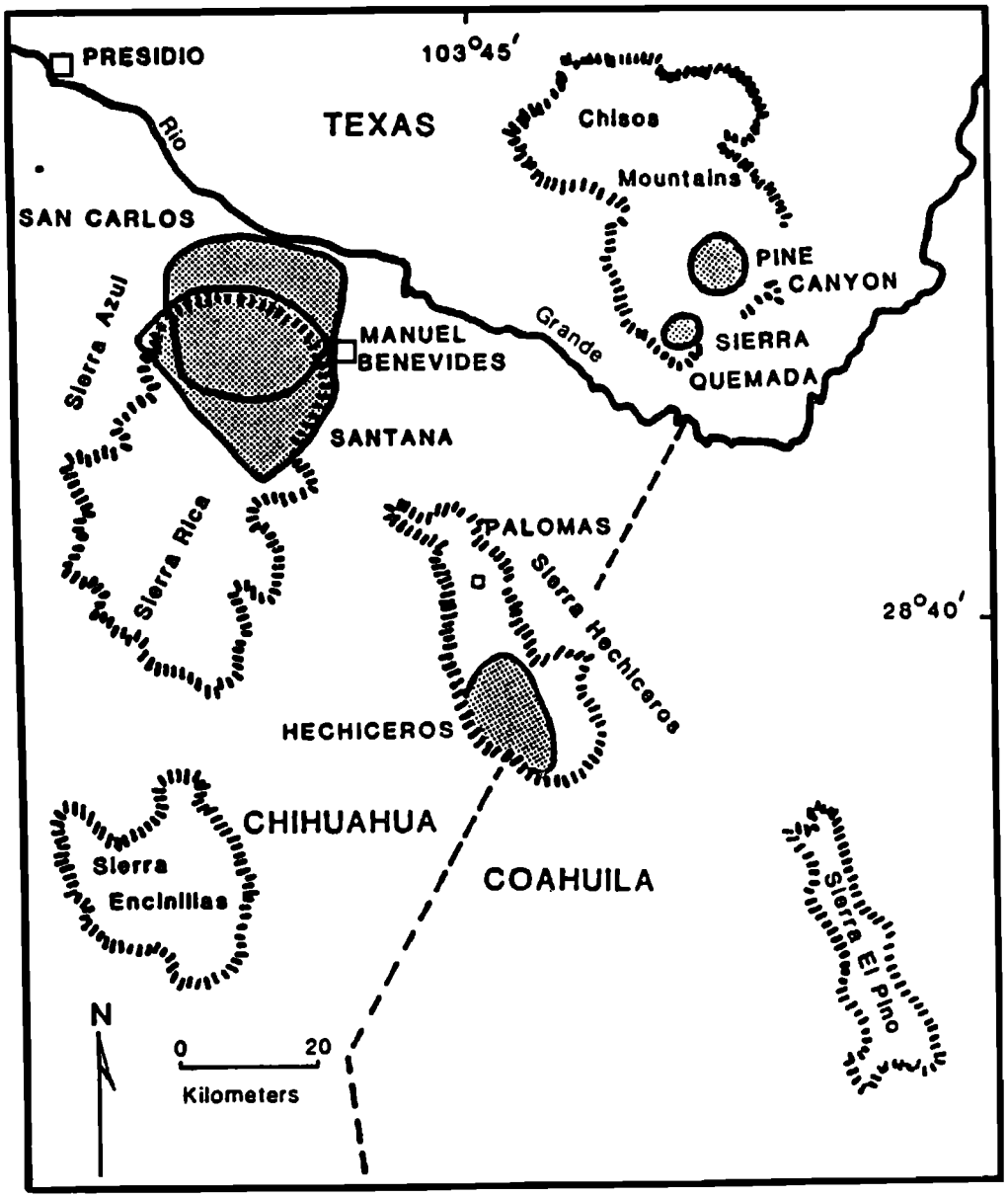

Fig. 1 Mountain ranges and Tertiary calderas in the Big Bend area of Texas and adjacent Mexico. Location and outline of caldera boundaries, other than for Hechiceros Caldera, are from Henry and McDowell[1986].

Palomas Tuff

The Palomas tuff overlies the Agua Dulce formation and consists of two rhyolitic welded tuffs and an associated underlying unwelded or partiallly welded tuff. Welded portions of the ash flow tuffs form prominent cliffs that cap mesas along the western margin of the mountain range. The welded tuffs also cap mesas around the Ejido Palomas. Erosion has produced a small bench between the two welded zones, each a distinct cooling unit in this area.

Unwelded PalomasTuff. Unconformably overlying the Agua Dulce formation at Agua Dulce is a 34-m thick grayish-orange pink unbedded tuff. Dacite xenoliths up to 7 cm in diameter make up less than 1% of the rock. Crystals of feldspar and quartz are rare. Yellow pumice fragments up to 33 cm in diameter are found throughout the member but most of the pumice ranges in size from 4 to 10 cm in diameter. No evidence for rafting or inverse sorting of the pumice fragments was observed.

In thin section, the tuff consists mainly of vitric ash, with crystals of sanidine and quartz ranging in size from 0.3 to 2 millimeters. The massive nature and thickness of the unit suggests close proximity to the source area. The lack of distinctive bedding and abundance of vitric ash suggests that this unit is a nonwelded pyroclastic flow.

Lower Welded Tuff. The lower welded member of the Palomas tuff is 95 m thick at Agua Dulce and appears to conformably overlie the unwelded ash flow member below it. The contact is horizontal at Agua Dulce and is marked by the darker color of the ash flow tuff above relative to the unwelded tuff. An increase in lithic inclusions is also observed at the contact. The base of the ash flow tuff is poorly welded and pumice fragments are not collapsed. The degree of welding increases upward, accompanied by increasing compaction of pumice fragments.

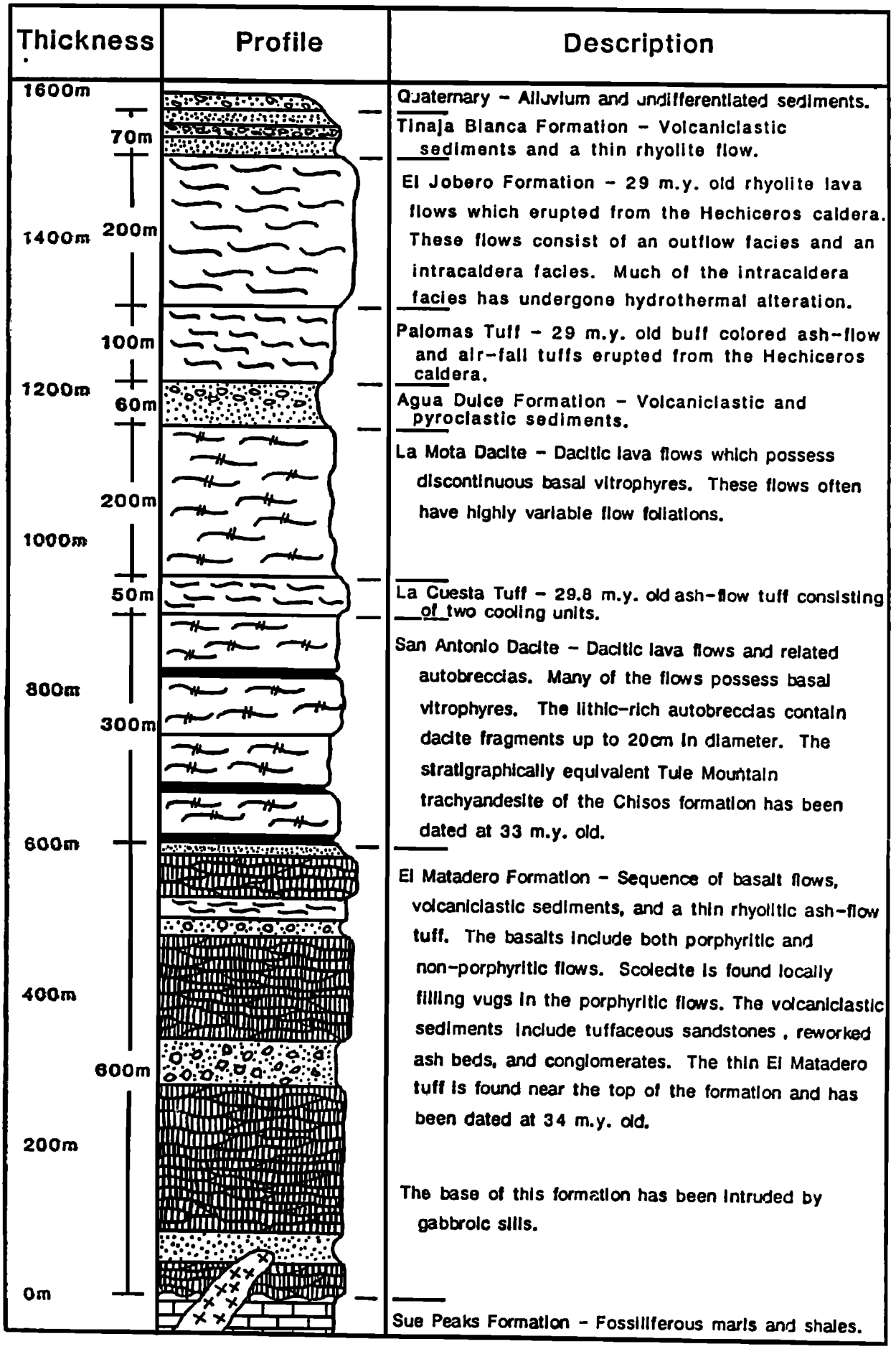

Fig. 2 Composite stratigraphic section of the Tertiary volcanic units in the Sierra Hechiceros(from Hardy, 1987). Only Cretaceous unit exposed in the Sierra Hechiceros is the Sue Peaks Formation.

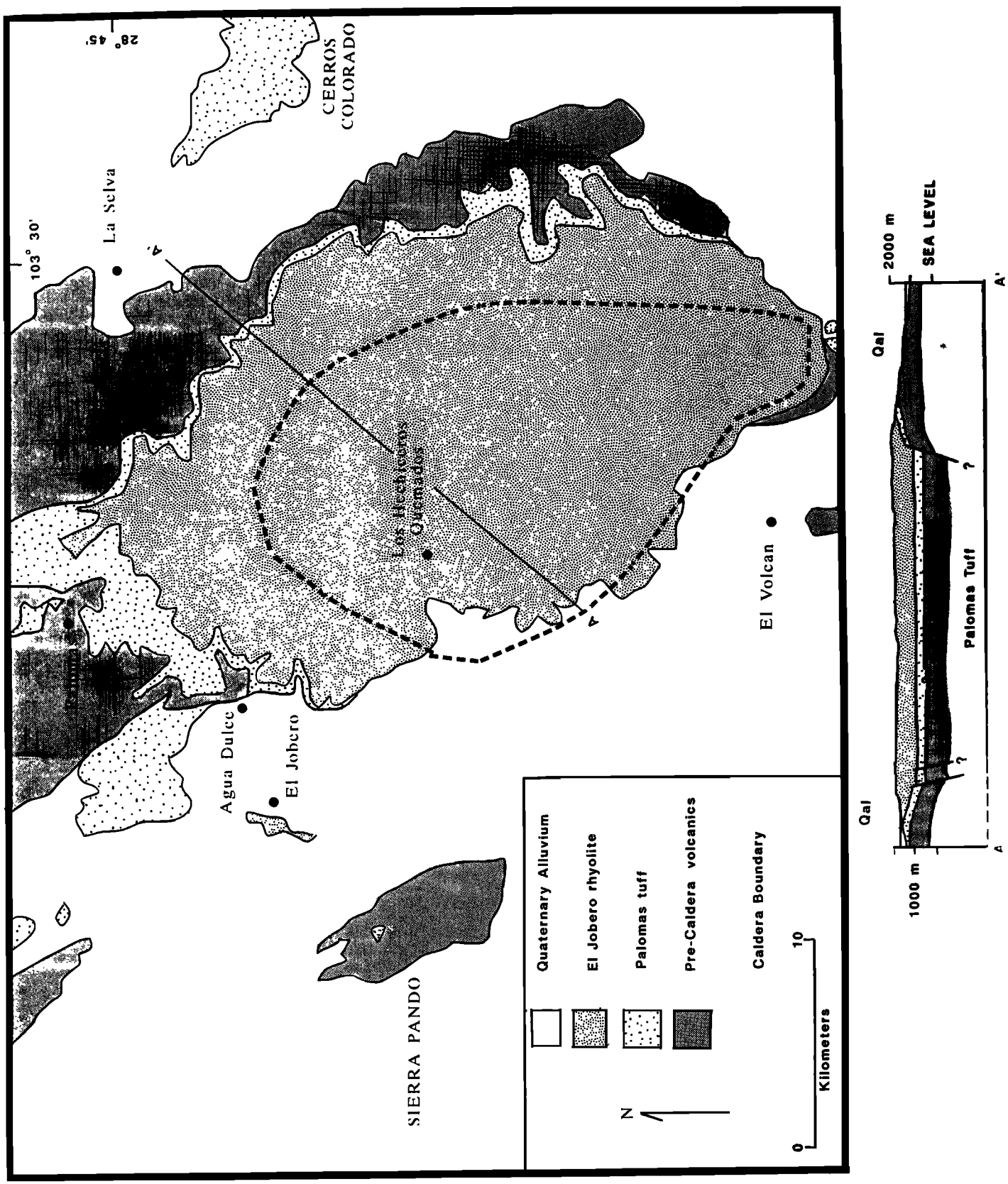

Fig. 3. Idealized geologic map and cross section of the Hechiceros Caldera in the southern half of the Sierra Hechiceros, Chihuahua and Coahuila, Mexico.

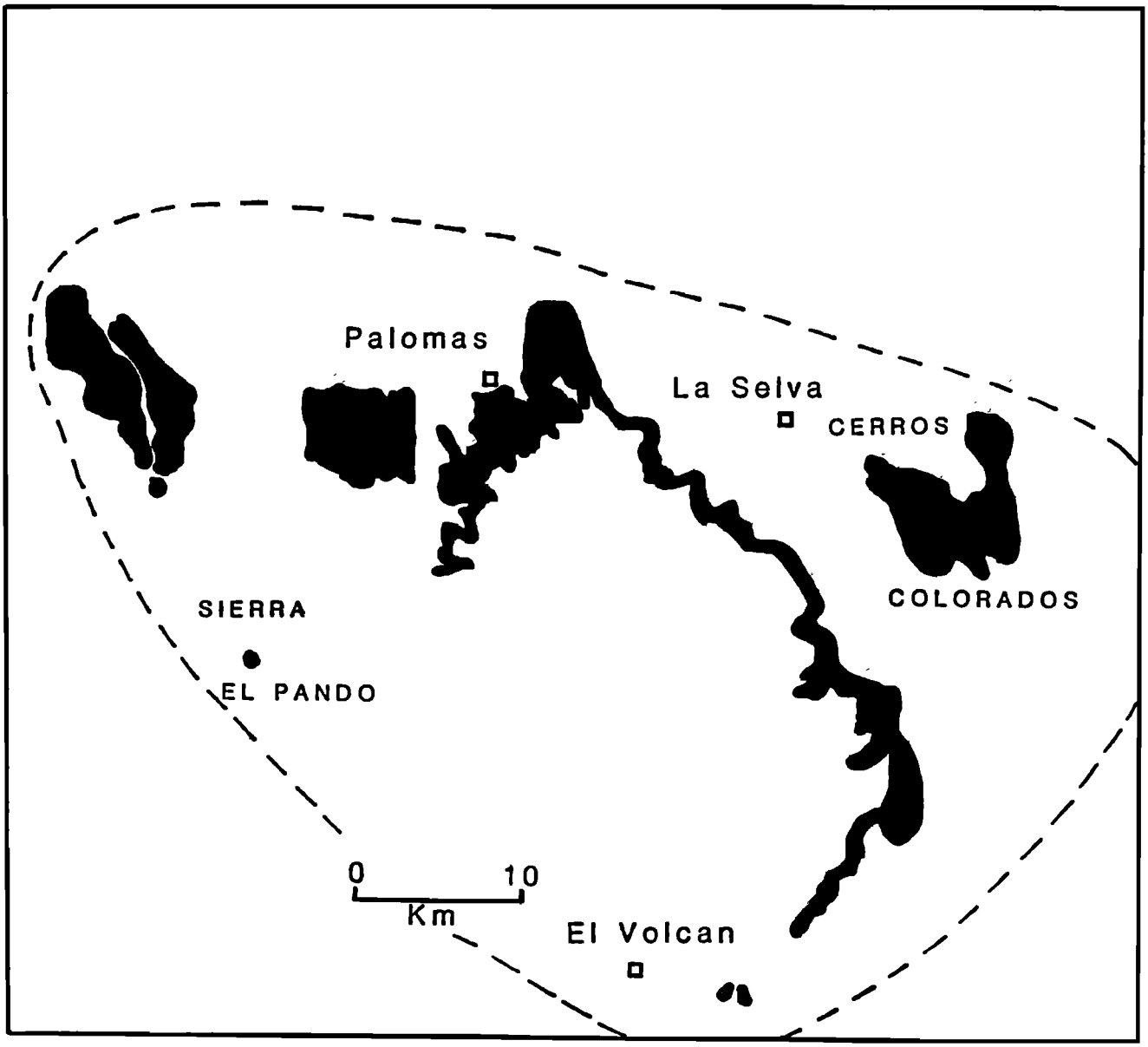

Fig. 4. Map showing present outcrop area of Palomas tuff(solid) and inferred former distribution delineated by long- dashed line.

The unwelded to partially welded portion is anomalously thick(>60 m). The most likely explanation for this thickness of partially welded ash-flow is that the eruption temperature increased as more of the pyroclastic material was vented or that the mixing with air decreased as the eruption progressed. The lower partially welded to nonwelded portion has a vitric ash matrix and abundant vapor phase crystallization in open spaces within the rock. The upper, densely welded cliff-forming portion of this ash flow has a devitrified groundmass. This devitrification is present only where dense welding has occurred. There is a complete gradation in welding from the basal nonwelded or partially welded ash flow(60+m) upward into a densely welded, cliff-forming(20 m thick) ash flow tuff.

Upper Welded Tuff. The upper welded member of the Palomas tuff overlies a thin, weathered zone on the lower welded tuff. At Agua Dulce, the two welded units form separate cliffs. The thickness of the upper member is 20 m, whereas at Cerros Colorados, east of the range, it is 41 m. The upper ash flow is a hard,densely welded tuff. There is an upward decrease in welding in this member, and xenoliths are rare and commonly less than 1 cm in diameter.

Phenocrysts, averaging 2 mm in diameter, represent 4 to 10 % of the upper ash flow tuff member in thin section. They consist of sanidine, quartz, and minor amounts of plagioclase in a devitrified eutaxitic matrix. Crystals of sanidine and quartz are occasionally seen within the devitrified pumice lenses and may be vapor phase in origin. The groundmass is also completely devitrified. No fresh vitrophyre of either ash flow tuff member has been found.

El Jobero Rhyolite

The El Jobero rhyolite is a thick sequence of rhyolitic lava flows that covers a large portion of the crest of the Sierra

Hechiceros. The unit is named for Rancho El Jobero on the west side of the range. It can be subdivided into an out-flow and intracaldera facies, but because of the gradational nature of the change, distinction between the two facies is not readily evident in all outcrops near the presumed caldera boundary. Much of the intracaldera lava is hydrothermally altered. Flow banding and ramp structures are observed outside the caldera and slabby, vertical sheeting is widespread within the caldera.

Outside the caldera, the El Jobero consists of at least two flows with a combined maximum thickness of 50 m. Flowage features are probably of both primary flow origin and due to secondary adjustments to underlying topography.

In contrast to the underlying phenocryst-poor Palomas tuff, the El Jobero rhyolite contains up to 20% phenocrysts; 10-15% sanidine, up to 5 mm in diameter, 3-5% quartz and minor plagioclase and clinopyroxene.

Within the caldera, the El Jobero rhyolite is made up of a basal sheeted unit, an autobrecciated unit, and additional flow units. The base of the formation is not exposed within the caldera but has a minimum thickness of 500 m.

The sheeting is in the form of a vertical or subvertical slabby jointing that has been observed in intracaldera flows at several other Tertiary calderas, as, for example, in the San Juan volcanic field of southwestern Colorado [*Dungan et al., 1989*].

Differences between intracaldera and extracaldera El Jobero rhyolite include a coarse-grained groundmass within the caldera in contrast to a fine-grained, devitrified groundmass outside the caldera. There is also a prevalence of slabby vertical jointing and hydrothermal alteration within the caldera. The result is an intracaldera facies characterized by intense vertical or subvertical sheeting and liesegang banding.

CALDERA FORMATION AND ASSOCIATED VOLCANIC ACTIVITY

Structural and stratigraphic evidence for a Tertiary caldera in the Sierra Hechiceros is summarized below. The three units which erupted from the vicinity of the Hechiceros caldera are the La Mota dacite, the Palomas tuff and the El Jobero rhyolite. These units crop out only within the Sierra Hechiceros although remnants of the Palomas tuff have been found in the Cerros Colorados to the east and the Sierra El Pando to the west [Figure 4]. The La Mota dacite crops out in an areally restricted area around the village of Palomas northeast and outside of the caldera boundary and is overlapped to the west by the younger Palomas tuff and El Jobero rhyolite.

The Palomas tuff was erupted from the Sierra Hechiceros as it thickens toward the southern Hechiceros from areas to the north, east and west. In the western flank of the Cerros Colorados 8 km southeast of La Selva it attains a thickness of 135 m, and all three members are represented. At Rancho Pena Blanca, recent reconnaissance work indicates almost 200 m of Palomas tuff exposed in the canyon walls. Twenty kilometers west of the Sierra Hechiceros, Palomas tuff is exposed in a small paleovalley in the Sierra El Pando. On the south end of the range only small, scattered outcrops of Palomas tuff of indeterminate thickness have been located.

The outcrop area for the El Jobero rhyolite is even more restricted, confined only to the Sierra Hechiceros and the narrow plain west of the Sierra Hechiceros to Rancho El Jobero. Within the range, outcrops of El Jobero extend as far north as the latitude of Palomas. El Jobero lavas are not found in the Sierra El Pando, where the Palomas is overlain by a dacite lava, or in the Cerros Colorados where the Palomas is the youngest volcanic unit exposed. Maximum thickness of the El Jobero rhyolite occurs in the central part of the range in the vicinity of El Encampanado where approximately 500 m of rhyolite lava flows are exposed. It thins away from this location in all directions. Based on the evidence presented, we propose that the Palomas tuff represents the initial caldera-forming eruptive unit and the younger El Jobero rhyolite represents lava flows that filled and overflowed this caldera. The two units are approximately the same age, 29 Ma (Table 1).

TABLE 1. K-Ar Age Data

Unit/Sample	%K	$\%^{40}Ar$	$\%^{40}Ar, x10^{-6}s/g$	Age, Ma+1
Palomas tuff (lower ash flow) LT-101	7.93 7.92	93.3	8.749	28.2±0.6
Palomas tuff (upper ash flow) UBC-AD-1	7.50 7.28	93.3	8.463	29.2±0.6
El Jobero formation (outflow) ELJ-101	6.79 6.68	91.7	7.816	29.6±0.6

All data based on alkali feldspar.

Eruption of the lava flows of the El Jobero rhyolite modified the area around the caldera by causing additional subsidence and tilting of units within and outside of the caldera.

Assuming an average thickness of 80 m and initial continuous distribution of the Palomas tuff (to compensate for unwelded ignimbrite and variable thickness) within the Sierra Hechiceros and between the proximal and distal outcrops, the tuff covered an area of approximately 2100 km^2 and had a volume (dense rock equivalent) of 170 km^3. This is a minimum estimate which does not include any air fall material carried outside the area or any anomalous thickness of Palomas tuff buried within the caldera beneath the caldera-filling El Jobero lavas.

Based upon an estimated 25-km-diameter caldera, a collapse of 400-500 m of a cylindrical, piston-like slab is hypothesized, as a result of the eruption of the Palomas tuff alone (Figure 5).

NATURE OF THE CALDERA BOUNDARY

The structural caldera boundary is exposed in only a few places, but can be inferred within 100-200 m in most instances. For example, northwest of Los Hechiceros de Quemado, the El Jobero rhyolite changes from a vertically sheeted and hydrothermally altered unit with a coarsely crystalline interlocking groundmass that is suggestive of an intrusive rock to a more finely crystalline devitrified interlocking groundmass which is neither sheeted nor hydrothermally altered. This transition occurs over a distance of 200 m. The position of the northern caldera boundary can be inferred by the increasing southerly dip of Palomas tuff toward the center of the caldera. The overlying El Jobero increases in thickness toward the caldera from north to south and obscures the position of the caldera boundary.

The caldera boundary is best exposed in the southern end of the range. At a point approximately 2 km southwest of Los Hechiceros de Quemados where the boundary trends northeast typical intracaldera El Jobero is ponded against bedded,

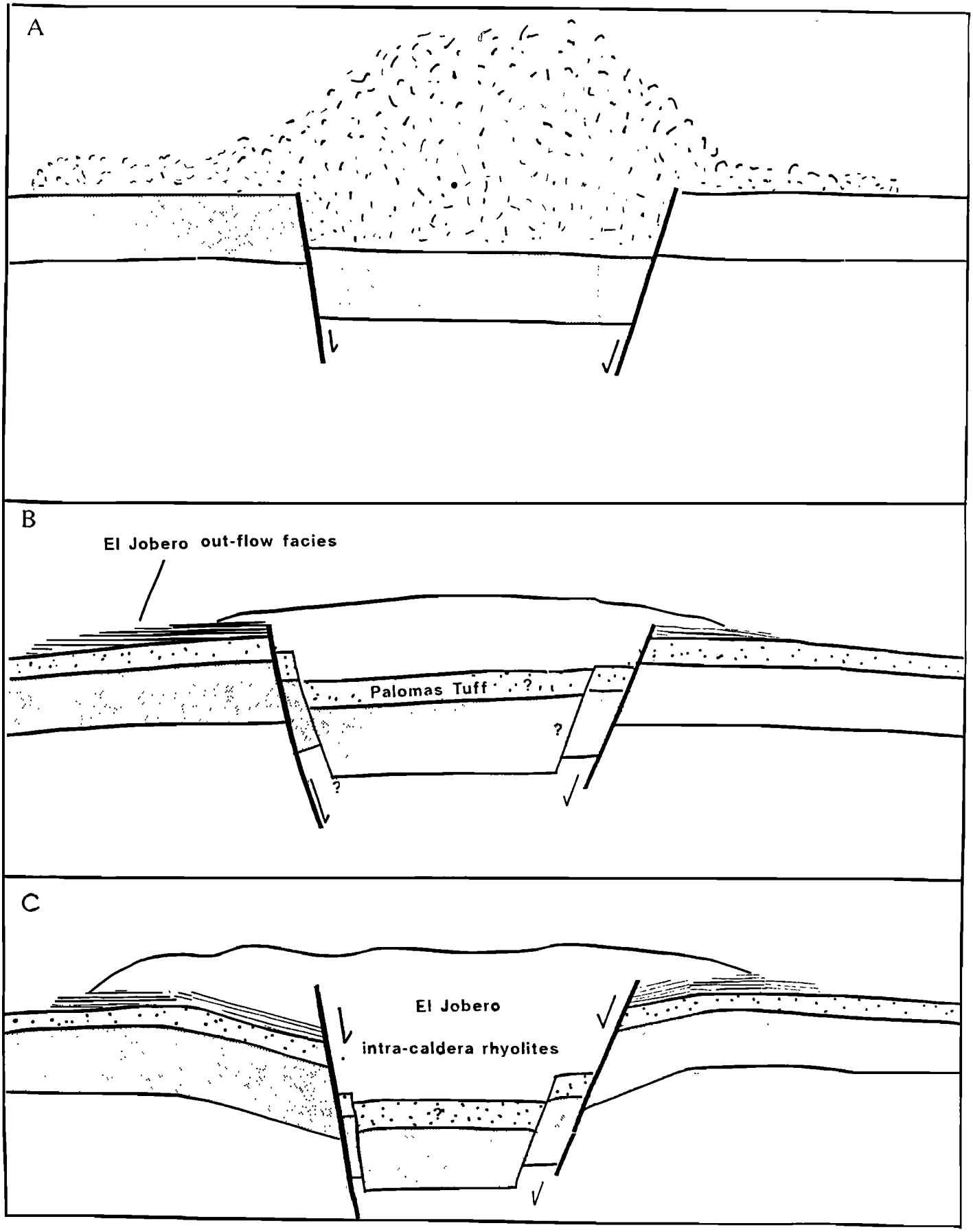

Fig. 5. Idealized diagram showing (a) eruption of the Palomas ash-flow tuff and caldera formation, (b) eruption of El Jobero rhyolite formation which overflows the caldera margin, and (c) continued subsidence of the caldera which modified the caldera margin and tilted the Palomas tuff and pre-caldera units outside the caldera toward the caldera.

biotite-bearing tuffs that dip away from the caldera boundary. Biotite is not found in either the El Jobero rhyolite or the Palomas tuff but occurs in some tuffs of the precaldera Aqua Dulce formation and tuffs of the older El Matadero formation. Overlying the bedded biotite bearing tuffs at this locality is typical El Jobero outflow facies. This boundary can be traced from this locality to the southeast, where, at the low hills which mark the southern end of the Sierra Hechiceros, Palomas tuff forms outcrops just outside the apparent caldera boundary. The caldera boundary here is also marked by numerous, generally equidimensional or elongated (parallel to the caldera boundary) silicified zones developed in the vertically sheeted intracaldera El Jobero rhyolite. The rock retains the sheeted structure typical of the intracaldera facies but has been replaced by silica. These zones probably represent the subsurface expression of hot springs localized at the caldera boundary.

K-AR GEOCHRONOLOGY

K-Ar age determinations were made on alkali feldspar mineral separates from all major rhyolitic units. The K-Ar ages obtained are in good agreement with ages of other units that interfinger with the rocks of the Sierra Hechiceros, except for one anomalous date of 41.9 Ma for the intracaldera El Jobero rhyolite; this date is not included in Table 1.

The tuff of the El Matadero formation has been dated at 34 Ma and is near the top of the El Matadero basalt sequence. An interval of erosion of considerable duration is suggested by a thick sequence of boulder to pebble conglomerates in the basal El Matadero formation.

The La Cuesta tuff which crops out in the northern part of the range has been dated at 29.8 + 0.6 Ma [*Gunderson, 1983*]. It overlies the San Antonio dacite, derived primarily from sources to the north of the Sierra Hechiceros, and underlies the La Mota dacite which crops out in the vicinity of Palomas. This dacite lava is the earliest recognized volcanism within the Sierra Hechiceros.

The El Jobero formation followed soon after the eruption of the Palomas tuff as they are virtually the same age, 29 Ma, and only slightly younger than the La Cuesta tuff. Although of similar age as the Palomas, the La Cuesta tuff, we believe, did not originate within the Sierra Hechiceros area.

ROCK CHEMISTRY

Whole-rock chemical analyses (Table 2) of the El Jobero rhyolite, lower and upper welded ash flow tuff members of the Palomas tuff and the La Mota and San Antonio dacites, were used for classification and comparisons with rocks from adjacent areas.

The rocks of the Sierra Hechiceros plot within the subalkalic field of Irvine and Baragar [*1971*] and include rhyolites and dacites. Basalts of the El Matadero formation were analyzed by Gunderson [*1983*] and have silica contents of 47-54 wt %.

The chemistry of these rocks is transitional between the calc-alkalic province of the Sierra Madre Occidental and the alkalic rocks of the eastern Trans-Pecos magmatic province. This transitional character and the greater similarity to the rocks of the Sierra Madre Occidental is evident in Figure 6. Detailed knowledge of trace element chemistry is needed to refine the relationship of these rocks to the adjacent Trans-Pecos alkalic and metaluminous provinces.

SUMMARY

The volcanic rocks of the Sierra Hechiceros span an age range from 34 Ma, the age of the tuff of the El Matadero formation, to 29 Ma, the age of the volcanism associated with the formation of the Hechiceros Caldera. Because there are no demonstrable vent areas for the San Antonio dacite or the La Cuesta tuff (dated at 29.8 Ma) in the Sierra Hechiceros, the timing of volcanism within the range can be further constrained to between 30 and 29 Ma. Initial volcanism within the Sierra Hechiceros began with eruption of the La Mota Dacite lavas in the northern part of the range, from vents now buried by the younger Palomas and El Jobero rhyolites.

The Hechiceros Caldera, which formed during the same time period as the San Carlos and Santana calderas (Figure 1), is similar to other northeastern Chihuahua calderas in that it erupted exclusively rhyolitic rocks. However, it differs from them in that it experienced continued voluminous eruptions of magma after ash flow deposition and initial caldera formation. Accordingly, it has a much greater volume to diameter ratio, although the caldera forming ash flow tuff (the Palomas tuff) has a volume similar to that erupted from the San Carlos and Santana calderas.

TABLE 2. Whole Rock Chemical Analyses

	Palomas Tuff Upper Ash Flow Tuff		Palomas Tuff Lower Ash Flow Tuff			El Jobero Formation		La Mota Dacite	San Antonio Dacite
	UB-101	EM-100	LT-101	P1-25	P3-81	STR	ELJ-101	Pa-101	G1
SiO_2	74.49	75.27	72.17	73.11	74.19	73.05	74.78	64.33	65.59
Al_2O_3	12.99	12.93	14.89	12.61	12.37	13.30	12.49	15.87	15.56
Fe_2O_3	2.01	1.93	2.24	1.90	1.93	1.86	2.12	2.63	2.90
FeO	0.12	0.12	<0.05	0.12	0.09	0.89	0.29	1.49	2.17
MnO	0.05	0.03	0.04	0.04	0.04	0.05	0.04	0.10	0.11
MgO	0.37	0.07	0.21	0.05	0.06	<0.04	0.11	1.03	0.84
CaO	1.08	0.64	1.69	2.11	1.77	1.00	0.76	3.24	2.76
Na_2O	2.57	3.21	2.88	3.2	3.31	3.32	3.27	4.67	4.08
K_2O	5.21	5.68	5.29	5.54	5.36	5.06	5.25	3.18	4.44
TiO_2	0.15	0.14	0.21	0.15	0.16	0.22	0.17	0.90	0.91
P_2O_5	<0.25	0.73	0.99	0.19	0.22	0.33	0.50	2.18	1.37
CO_2	0.31	<0.01	0.06	0.9	0.64	<0.01	<0.01	<0.01	<0.01
Total	100.18	100.75	100.67	100.08	100.13	99.08	99.78	99.62	100.74

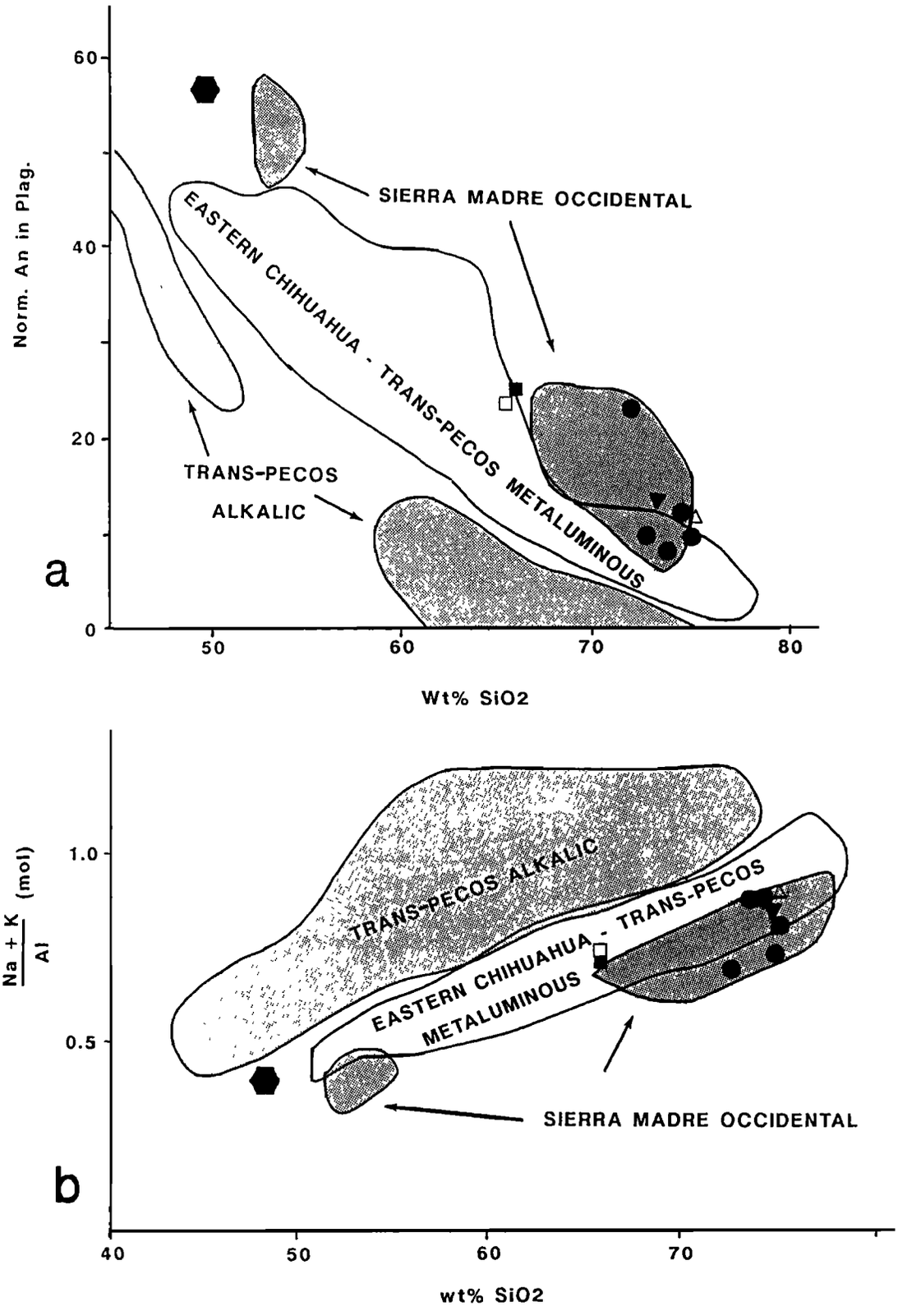

Fig. 6. (a)Normative anorthite content of plagioclase versus silica and (b)(Na+K)/Al versus silica plots for the eastern Chihuahua , Trans-Pecos and Sierra Madre Occidental provinces(from McDowell and Clabaugh, 1979). Hexagon is average El Matadero basalt; solid square represents La Mota dacite; open square is San Antonio dacite; circles represent lower Palomas welded tuff; solid triangle is intracaldera El Jobero rhyolite and open triangle is outflow facies of El Jobero rhyolite.

Acknowledgments. Field work and laboratory work was supported, in part, by the Killgore Research Center, West Texas State University. The K-Ar age dating and whole-rock chemical analyses were carried out by Chris Henry at the Texas Bureau of Economic Geology, Austin, Texas. Mineral separation was done at Killgore Research Center, West Texas State University and potassium and argon analyses were run by Chris Henry at the Bureau of Economic Geology. Ing. Fernando de la Fuente, Consejo de Recursos Minerales, in Chihuahua, was helpful in obtaining aerial photographs and topographic maps of the area. The authors would like to express their appreciation to W. A. Duffield, Tom Stevens, Bob Varga and R. J. Tilling who reviewed earlier versions of this paper.

REFERENCES

Atwater, T. , Implications of Plate Tectonics for the Cenozoic Tectonic Evolution of Western North America: *Geol. Soc. America Bull., 81*, 3513-3536, 1970.

Christiansen, R. L. and P. W. Lipman, Cenozoic volcanism and plate-tectonic evolution of the Western United States II: Late Cenozoic, *Philos. Trans. R. Soc. London, ser. A*, 271, 249-284, 1972.

Dungan, M. A. , P. W. Lipman, M. Colucci, K. Ferguson, and S. Balsley, Southeastern Platoro Caldera Complex, in *Field Excursions to Volcanic Terranes in the western U.S.*, vol. 1, edited by C. E. Chapin and J. Zidek, pp. 305-329, New Mexico Bur. Mines Memoir 47, 1989.

Gunderson, R. P., Geology and geochemistry of the Benevides-Pozos Area, Eastern Chihuahua, Mexico, M. S. thesis, 135 pp., Univ. of Calif. at Santa Cruz, 1983.

Hardy, H. The igneous geology of the San Antonio area, northeastern Chihuahua, Mexico, M.S. thesis, 135 pp. West Texas State Univ., Canyon, 1987.

Henry, C. D., and F. W. McDowell, Geochronology of magmatism in the Tertiary volcanic field, Trans-Pecos Texas, *Texas Bur. Econ. Geol. Guidebook 23*, pp. 99-122, 1986.

Henry, C. D. and J. G. Price, Variations in caldera development in the Tertiary volcanic field of Trans-Pecos Texas, *J. Geophys. Res.* 89(B10),8765-8786, 1984.

Irvine, T. N. and W. R. A. Baragar, A guide to the chemical classification of the common volcanic rocks, *Can. J. Earth Sci., 8*, 523-548, 1971.

Lipman, P. W., H. J. Prostka, and R. L. Christiansen, Cenozoic volcanism and plate-tectonic evolution of the western United States I: Early and Middle Cenozoic, *Philos. Trans. R. Soc. London, ser. A, 271*, 217-248, 1972.

McDowell, F. W., and S. E. Clabaugh, Ignimbrites of the Sierra Madre Occidental and their relation to the tectonic history of western Mexico, in *Ash Flow Tuffs*, Geol. Soc. America Special Paper 180,pp. 113-124, 1979.

Swanson, E. R., and F. W. McDowell, Calderas of the Sierra Madre Occidental volcanic field, western Mexico, *J. Geophys. Res.,89(B10)*, 8787-8799,1984.

S. Ritter and J. C Cepeda, Killgore Research Center and Department of Biology and Geosciences, West Texas State University, Canyon, TX 79016

(Received May 9, 1989;
revised November 19, 1990;
accepted January 10, 1991)

JOURNAL OF GEOPHYSICAL RESEARCH, VOL. 96, NO. B10, PAGES 16,205–16,222, SEPTEMBER 10, 1991

Frequency Dependent Electrical Properties of Polycrystalline Olivine Compacts

JEFFERY J. ROBERTS AND JAMES A. TYBURCZY

Department of Geology, Arizona State University, Tempe, Arizona

The complex electrical properties of polycrystalline San Carlos olivine compacts were measured over the range of frequency 10^{-4}-10^{4} Hz from 800° to 1400°C under controlled oxygen fugacity. The impedance data display a strong frequency dependence that is evidenced most clearly when the results are displayed in the complex impedance plane. A parameterized model of the frequency dependent electrical response using equivalent electrical circuits is presented. Two distinct conduction mechanisms of the sample are observed: grain interior and grain boundary conduction. Each occurs over a different range of frequency. The resistance of each mechanism adds in series resulting in a lower total DC conductivity for polycrystalline olivine than for either mechanism separately. The total DC conductivity is dominated by the grain interior conductivity above 1200°C, whereas the grain boundary conductivity has the strongest influence below 1000°C. Impedance spectra of natural dunite samples exhibit a similar type of frequency dependence. The grain interior conductivity displays a change in slope at 1344°C and has activation energies of 1.45 eV (800°-1344°C) and 4.87 eV (>1344°C). The grain boundary conductivity has an activation energy of 2.47 eV. In these cases, the f_{O_2} for each experimental run was controlled at that of the wustite-magnetite oxygen buffer. Experiments on samples with different grain sizes reveal no dependence of DC conductivity on grain size for either mechanism, although the relaxation time and real relative permittivity of the grain boundary mechanism are dependent on grain size. Because of the electrical response observed at low frequencies, care must be taken in the inversion of electromagnetic field observations using laboratory measurements made in the kilohertz range since they may not be the same as DC measurements. Impedance measurements must be performed over a range of relatively low frequencies to assess the role of grain boundaries on the overall electrical response of polycrystalline materials.

INTRODUCTION

The electrical properties of Earth materials are strongly dependent on frequency, temperature, and point defect chemistry. Results from laboratory studies of the electrical properties of relevant Earth materials such as olivine are used to interpret upper mantle and lower crustal profiles of conductivity versus depth derived from field observations. Grain boundaries are known to play an important role in the diffusive and electrical properties of polycrystalline materials. It is the purpose of this study to investigate the electrical properties of polycrystalline geologic materials by taking advantage of information gained through the use of AC electrical measurements. We have investigated the electrical impedance of polycrystalline olivine compacts as a function of frequency to determine the processes contributing to the electrical response at low frequencies. Impedance is the total opposition to current flow in response to an AC signal and is a complex quantity, generally expressed as a magnitude and a phase ($|Z|$, ϕ), or as a real component and an imaginary component (Z', Z''), or as a resistance and a capacitance (R, C). In rocks, impedance normally contains both resistive and capacitive components.

Many studies have demonstrated that rocks other than olivine that exist in the crust (wet, dry, and partially molten rocks) display frequency dependent electrical behavior [e.g., *Knight*, 1984; *Lockner and Byerlee*, 1985; *Will and Nover*, 1986; *Sato et al.*, 1986]. While there has been much study of the electrical properties of olivine [e.g., *Hughes*, 1955; *Duba*, 1972; Duba *et al.*, 1974; *Cemic et al.*, 1980; *Lacam*, 1983; *Schock et al.*, 1989], few experiments have been performed investigating the frequency dependence of electrical properties. The earliest study of this nature regarding olivine is that by *Abelard and Baumard* [1980], who investigated the AC properties of sintered polycrystalline forsterite between 400° and 900°C. They observed a strong frequency dependence over the range 10^{-1} to 10^{5} Hz. They suggest that the electrical response they observe at frequencies under 1 Hz may be caused by microstructure or electrode processes. *Sato* [1986] measured the high-temperature (1000°-1400°C) AC electrical properties of San Carlos olivine single crystals between 10^{4} and 10^{-1} Hz to find conductivities and dielectric constants as a function of oxygen partial pressure. Sato concluded that between 1200° and 1400°C and at relatively high oxygen partial pressures ($f_{O_2} \geq 10^{-5}$ Pa), dielectric constants are proportional to $P_{O_2}{}^{1/6}$ and the major defect species contributing to conduction are Mg vacancies and electron holes. At lower oxygen partial pressures, Sato observed a weaker P_{O_2} dependence and suggested that Mg interstitials and electrons contribute to the electrical conductivity in addition to Mg vacancies and electron holes.

Cygan and Lasaga [1986] determined the dielectric and polarization behavior of synthetic single-crystal forsterite over the frequency range 20 kHz to 1 MHz from 25° to 1000°C. The dielectric constant was dependent on frequency, temperature, and orientation. Their study also verified the polarizability additivity rule at high temperature; that is, polarization of oxide components can be summed to give the polarization of forsterite. A detailed comparison with the results of this study is difficult because of the different range of frequency and the important influence of iron on the electrical properties of olivine.

Most work involving grain boundary transport of geologic materials has come from studies of intergranular diffusion [*Naughton and Fujikawa*, 1959; *Brady*, 1983; *Watson*, 1986], rather than electrical measurements. The electrical conductivity of a natural polycrystalline dunite has been studied in a recent paper by *Constable and Duba* [1990]. Constable and Duba observe little or no difference in the electrical properties of the polycrystalline

Paper number 91JB01574.
0148-0227/91/91JB-01574$05.00

material compared to their studies of single crystal olivine. It is important to note, however, that their study does not fully consider the effects of frequency on the electrical measurements.

We have measured the frequency dependent electrical behavior of polycrystalline olivine over the frequency range 10^{-4} to 10^4 Hz. It is important to measure the electrical response of Earth materials over this frequency range because field measurements are made in this range of frequencies, and in this low-frequency range we observe an electrical response that may be due to the presence of grain boundaries. We studied ground, pressed compacts for several reasons: (1) fine-grained materials are less likely to undergo thermal stress initiated grain boundary microfracturing than more coarse-grained natural materials [*Evans*, 1978]; (2) grinding creates fresh grain boundaries that are unaltered by secondary processes, a frequent problem in natural rocks; (3) material with a range of grain sizes at identical composition can be studied; and (4) examination of polycrystalline materials of a fine grain size yields an electrical response that is averaged over all crystallographic orientations. We recognize at least two drawbacks to this approach: (1) any naturally occurring grain boundary materials or phases may be diluted or destroyed by grinding and creating more grain surface area than exists in the rock originally; and (2) grain growth during sintering creates new grain surfaces that may not be truly representative of the naturally occurring case.

In this work we report (1) a set of measurements on ground-and-pressed polycrystalline olivine samples of grain size 75-180 μm over the temperature range 800°-1400°C; (2) the electrical response of ground-and-pressed polycrystalline olivines at 1200°C as a function of grain size; and (3) measurements performed on a natural polycrystalline olivine sample at 900° and 1200°C. A preliminary report of some of these results, with a much simplified analysis, has been published [*Tyburczy and Roberts*, 1990].

EXPERIMENTAL PROCEDURES

Sample preparation. The ground-and-pressed polycrystalline samples were prepared from San Carlos olivine (Fo_{91}) single crystals that were free of alteration and inclusions to a magnification of 40x. These crystals were crushed and ground to a fine powder in an agate ball mill and sieved to a specific size fraction. Pellets were prepared in two ways: by hot pressing in a piston cylinder apparatus and by cold pressing followed by heating at 1 atm total pressure. The samples prepared in the piston cylinder apparatus were sintered at 1314°C and 24 kbar for 36 hours using Fe-soaked Pt capsules. Microprobe analysis verified that iron gain or loss was negligible in these samples. This method of sample preparation was used to prepare the largest grain size samples (75-180 μm grain size fraction) and produced pellets with final bulk densities 98% of theoretical density. The second method of sample preparation, cold press/anneal, worked well for the smaller grain size fractions. Powder of a specific grain size fraction was pressed into "green" pellets at room temperature between 18 and 25 kbar. The pellets were sintered in a 1-atm gas mixing furnace at a temperature of 1430°C for periods of 5-12 hours at an $f_{O_2} \approx 2.5 \times 10^{-3}$ Pa. Sintering resulted in densification and a 10-20% increase in grain size. The final bulk densities of the pellets were 92-96% of theoretical density. In general, longer sintering times increased the final bulk density of a sample by a very small amount; most of the densification took place in the first few hours. No difference in electrical response due to sample preparation method was observed.

The natural sample is a dunite from the San Quintin volcanic field in Baja California, Mexico [*Basu and Murthy*, 1977]. The dunite contains approximately 95% olivine ($Fo_{90.5}$), 3% clinopyroxene, and 2% spinel. It is relatively fine-grained with an average grain size of 0.2-0.4 mm. The particular sample employed has no serpentine or chlorite alteration and is an excellent rock for comparison with the ground-and-pressed samples (Figure 1).

Electrical measurements were made on disks that were polished on both sides using diamond paste with a final grit of 0.25 μm. The samples were cleansed and rinsed ultrasonically in ethanol prior to applying electrodes. The two-electrode technique was generally used for the electrical measurements, except for specific cases (discussed below) in which three- and four-electrode methods were used. Electrodes were either sputtered Pt followed by Pt paint and a thin Pt sheet or Pt paint and Pt sheet. No difference in electrical response was observed with these two methods of electrode preparation. At temperatures greater than 1250°C, lengthy experiments resulted in Fe loss to the Pt electrodes. This loss of Fe was confined to the outermost 25 μm of the sample and the loss in this outer zone was generally less than 2 wt % Fe. One effect of Fe loss is the increase of Z' over the entire frequency range. Iron loss was checked for by making measurements at a specific frequency at different times during the course of an experiment. Surface conduction was kept to a minimum by preparing samples with a large diameter to thickness ratio (8-12). Sample thicknesses were 0.5-1 mm. Additional experiments using a three-electrode technique (two electrodes and driven guard ring) verified that surface conduction was negligible. A four-electrode experiment (separate current and voltage electrodes) was performed on the natural sample to aid in the interpretation of the experimental results. Post run optical and scanning electron microscope analysis showed some porosity, both intergranular and intragranular, and minor cracking (presumably caused by differential stress upon cooling; Figure 2). These features were minor and not interconnected and therefore had little or no effect upon the overall electrical properties of the sample [*Beekmans and Heyne*, 1976]. Grain boundary microcracking and the effects of porosity are treated further in the appendix.

Samples were placed into the furnace and allowed to equilibrate to experimental conditions for a period of 4-20 hours. The length of time required for the sample to equilibrate is related to the sample dimensions, the grain size, and the mobility of point defects. During equilibration the resistance of the sample was

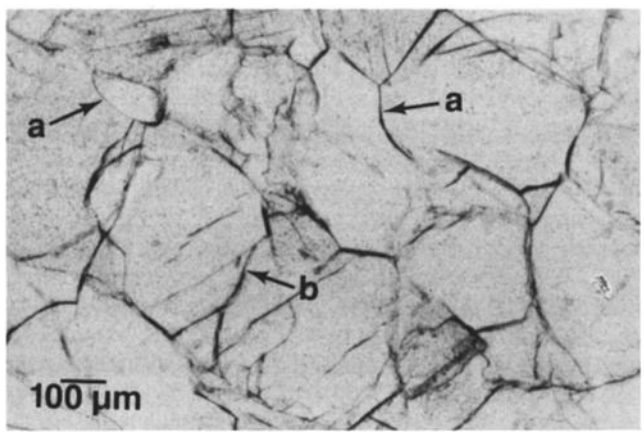

Fig. 1. Optical micrograph of San Quintin dunite, plane polarized light. The field of view consists entirely of olivine grains and shows little or no alteration along grain boundaries a. The area indicated by b is a fracture across the large grain.

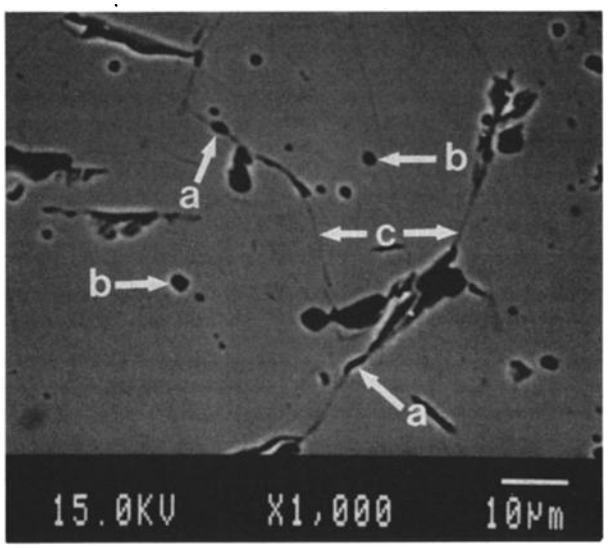

Fig. 2. Backscatter SEM image of sample PC6. Sample was prepared by cold pressing followed by high temperature anneal. Pores occur both intergranularly (a) and isolated within grains (b). Fractures and plucked areas resulting from post-experiment specimen preparation can be seen along grain boundaries (c). See appendix for discussion of microfracturing and effects of porosity on electrical measurements.

monitored at specific frequencies and gradually reached a steady value. Subsequent temperature changes were gradual, typically 50° or 100°C over a period of 1 hour. The oxygen fugacity was controlled with a CO/CO_2 mixture and was accurate to within ±0.15 log units. The experiments were performed at the f_{O_2} of the wustite-magnetite buffer [*Myers and Eugster*, 1983], and vary between ~10^{-14} Pa at 800°C and ~10^{-1} Pa at 1400°C. Temperatures were controlled and monitored to ±3°C with type B Pt 70-Rh 30/Pt 94-Rh 6 thermocouples. The temperature gradient between the top and bottom of the sample was less than 1°C.

Impedance measurements. Electrical measurements were made over the frequency range 5 x 10^{-5} to 10^4 Hz using the data collection system shown in Figure 3 and described in detail by *Olhoeft* [1979, 1985]. A sinusoidal signal from channel A of the frequency synthesizer was passed through a precision decade resistor and then the sample. The potential drops across the precision resistor and across the sample that corresponded to current and voltage, respectively, were measured with high input impedance differential amplifiers (input impedance > 13 GΩ). The resistance of the precision resistor was varied to approximately that of the sample so that the voltage drop across the sample was between 0.3 and 0.8 V. The current and voltage measurements were made at discrete time intervals determined by the frequency of channel B that was phase locked to channel A. These measurements were digitized by analog to digital converters and stored in computer memory. The data stored, $J(t)$ (current) and $E(t)$ (potential difference), comprise the Lissajous figure and were converted to impedance magnitude $|Z|$ and phase angle ϕ for each frequency using a matrix inversion technique [*Olhoeft*, 1979, 1985]. Driven shields were used to help reduce capacitive coupling that occurred between the measurement leads when measuring high impedance samples at relatively high frequencies. Examination of RC circuits of precision resistors and capacitors having impedances and time constants approximately those of the samples indicated that the accuracy of the measuring system was within 1.5% for $|Z|$ and ±30 mrad for ϕ. Below 100 Hz the accuracy of the phase measurement improved to ±12 mrad.

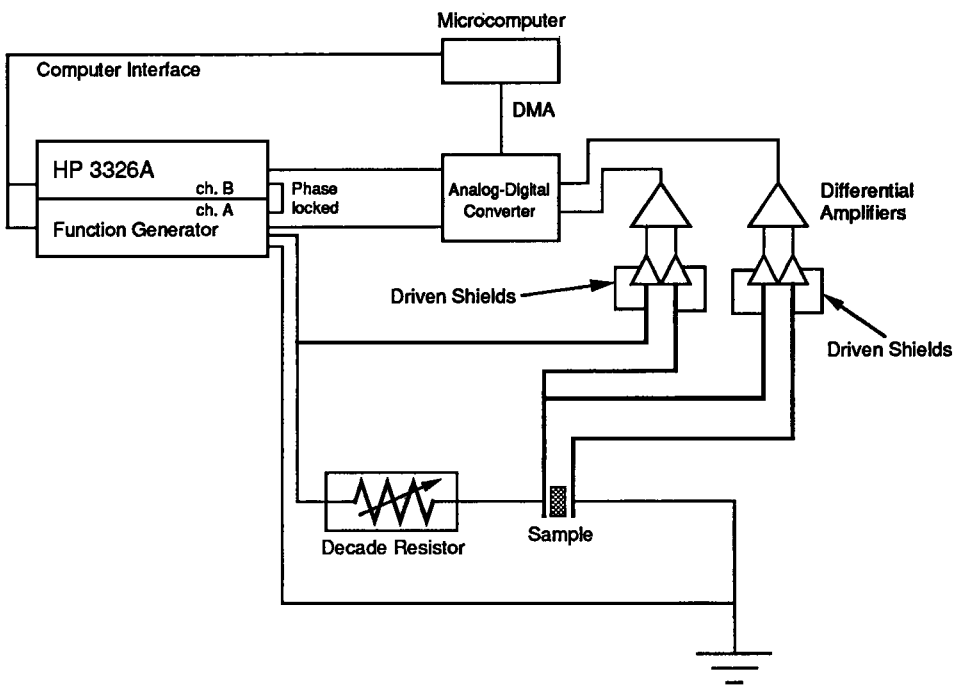

Fig. 3. Schematic diagram of the experimental apparatus. A sine wave from channel A of the function generator (HP 3326A) is passed through the decade resistor and then the sample. The potential drops through the decade resistor and the sample, corresponding to current and voltage, respectively, are measured at discrete time intervals using the differential amplifiers and analog-to-digital converter and stored in computer memory through the direct memory access (DMA). See text for further discussion.

The electrical measurements were made in a 1-atm total pressure gas mixing furnace powered by either an AC or DC power supply. Because of the high impedance of the samples, possible pickup of extraneous electrical signals by the electrical leads extending from the measuring device to the sample required additional precautions. A DC power supply (Hewlett-Packard 6475C) was employed to eliminate electrical noise from furnace elements at high temperatures ($T \geq 1300$°C). The outside of the furnace tube was wrapped with a grounded Pt sheet to further shield the samples and eliminate noise from the heating elements. Below 1300°C the Pt shield effectively eliminated electrical noise caused by the AC power supply. In an additional effort to reduce electrical noise, the alumina tube containing the electrical leads inside the furnace was coated with Pt and connected to ground. During the electrical measurements the monitoring thermocouple was disconnected because it was found to be an additional source of electrical noise.

As mentioned in the introduction, impedance is a complex quantity that includes an ohmic resistance (the real component) and a reactance (the imaginary component). The complex impedance Z^* is given by

$$Z^* = Z' - jZ'' \quad (1)$$

where the asterisk denotes a complex quantity, a single prime indicates a real quantity, the double prime indicates an imaginary quantity, and j is $\sqrt{-1}$. The real and imaginary parts of the impedance are obtained from the measured quantities $|Z|$ and ϕ determined at a given frequency by

$$Z' = |Z| \cos\phi, \quad (2)$$

$$Z'' = |Z| \sin\phi. \quad (3)$$

The choice of measuring and displaying the data in the complex impedance plane is one of practical convenience. The complex impedance, along with the sample dimensions, contains all the information needed to describe the AC response in the other commonly employed formalisms: complex admittance, complex permittivity, and complex modulus [e.g., *Cole and Cole*, 1941; *Bauerle*, 1969; *Hodge et al.*, 1976]. The relationships between the different formalisms may be summarized as [*Macdonald and Johnson*, 1987]

$$Y^* = (Z^*)^{-1}, \quad (4)$$

$$M^* = j\,\omega C_O Z^*, \quad (5)$$

$$\kappa^* = (j\,\omega C_O Z^*)^{-1}, \quad (6)$$

where Y^* is the admittance, M^* the modulus, κ^* the relative permittivity ($= \varepsilon^*/\varepsilon_O$), ω the angular frequency, and C_O the capacitance of the empty electrical cell in vacuum, given by $C_O = \varepsilon_O A/l$. ε^* is the permittivity of the sample, ε_O is the permittivity of free space and has a value of 8.854×10^{-12} F/m, and A/l is the area/length ratio of the sample. Each formalism emphasizes different aspects of the AC response, and we find that plots in the complex impedance plane are the most illustrative and useful in terms of modeling the data. The permittivity and modulus formalisms refer to properties of the material, while the impedance and admittance formalisms involve the measured response of the sample with dimensions A and l. All the formalisms (including resistivity and conductivity) can be expressed as a combination of real and imaginary components as in equation (1).

RESULTS

Experimental data. A typical set of impedance measurements is shown in Figure 4. The data shown in Figure 4 are the results of an experiment on a ground-and-pressed polycrystalline olivine sample at 1200°C and an f_{O_2} of 10^{-5} Pa with a grain size of 35-45 μm. Figure 4*a* is a graph of the measured parameters $|Z|$ and ϕ plotted against frequency. The phase angle displays a strong

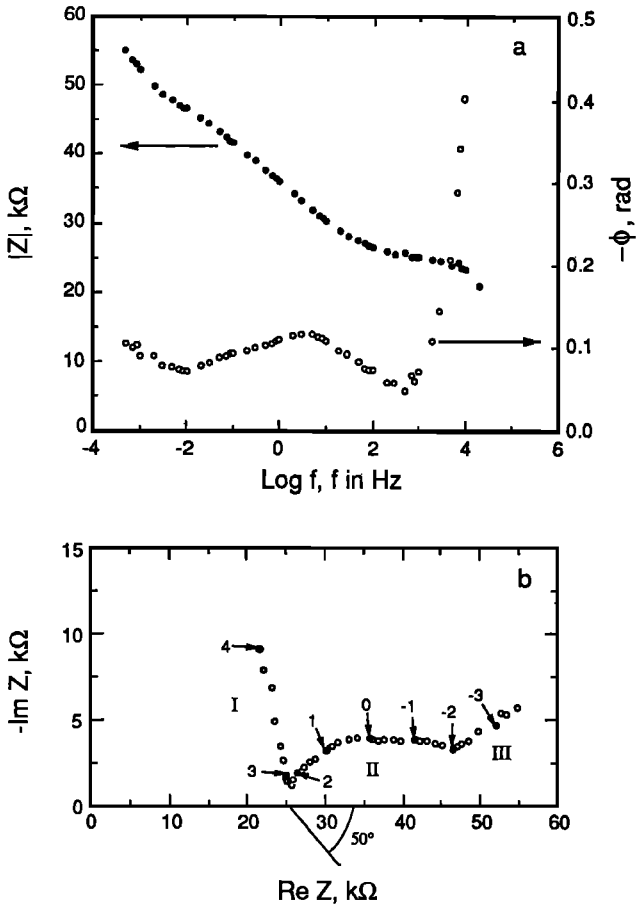

Fig. 4. Impedance spectrum of a sintered compact (grain size 35-45 μm) of San Carlos olivine at 1200°C, $f_{O_2} = 10^{-5}$ Pa. (*a*) Impedance magnitude $|Z|$ (solid circles) and phase angle ϕ (open circles) versus log frequency. (*b*) Complex plane plot, -Im Z versus Re Z. Small numerals are log frequency of the corresponding solid symbol; note that frequency increases toward the origin. The origin of the center impedance arc (the arc occurring from 10^{-2} to $10^{2.5}$ Hz) lies below the real axis, inclined at an angle of 50° with respect to the real axis (see text for discussion).

dependence on frequency, and two minima are clearly seen. The impedance magnitude increases across the entire frequency spectrum. In Figure 4*b*, the imaginary part of the complex impedance Z'' is plotted against the real part Z', in what is referred to as a "complex plane" plot. The complex impedance plane plot displays parts of three impedance arcs, which are circular arcs approximately centered on the real axis. Each arc corresponds to a separate conduction process or mechanism that is dominant at a different range of frequency and has a different relaxation time τ relative to the other arcs. Experiments on samples with different thicknesses show that the widths of each of the first two highest-frequency impedance arcs vary directly with sample thickness, indicating that these high-frequency impedance arcs represent bulk electrical properties of the sample rather than those of the measurement system or electrodes.

Complex impedance plots of the experiments performed over the temperature range 800°-1400°C at 50° or 100°C intervals on the 75-180 μm grain size sample at the f_{O_2} corresponding to the wustite-magnetite (W-M) solid buffer are shown in Figure 5. With increasing temperature, both the real and imaginary impedances decrease. In general, each experiment displays three impedance arcs occurring at high-, intermediate-, and low-frequency ranges (referred to as arcs I, II, and III, respectively, Figure 4). An arc

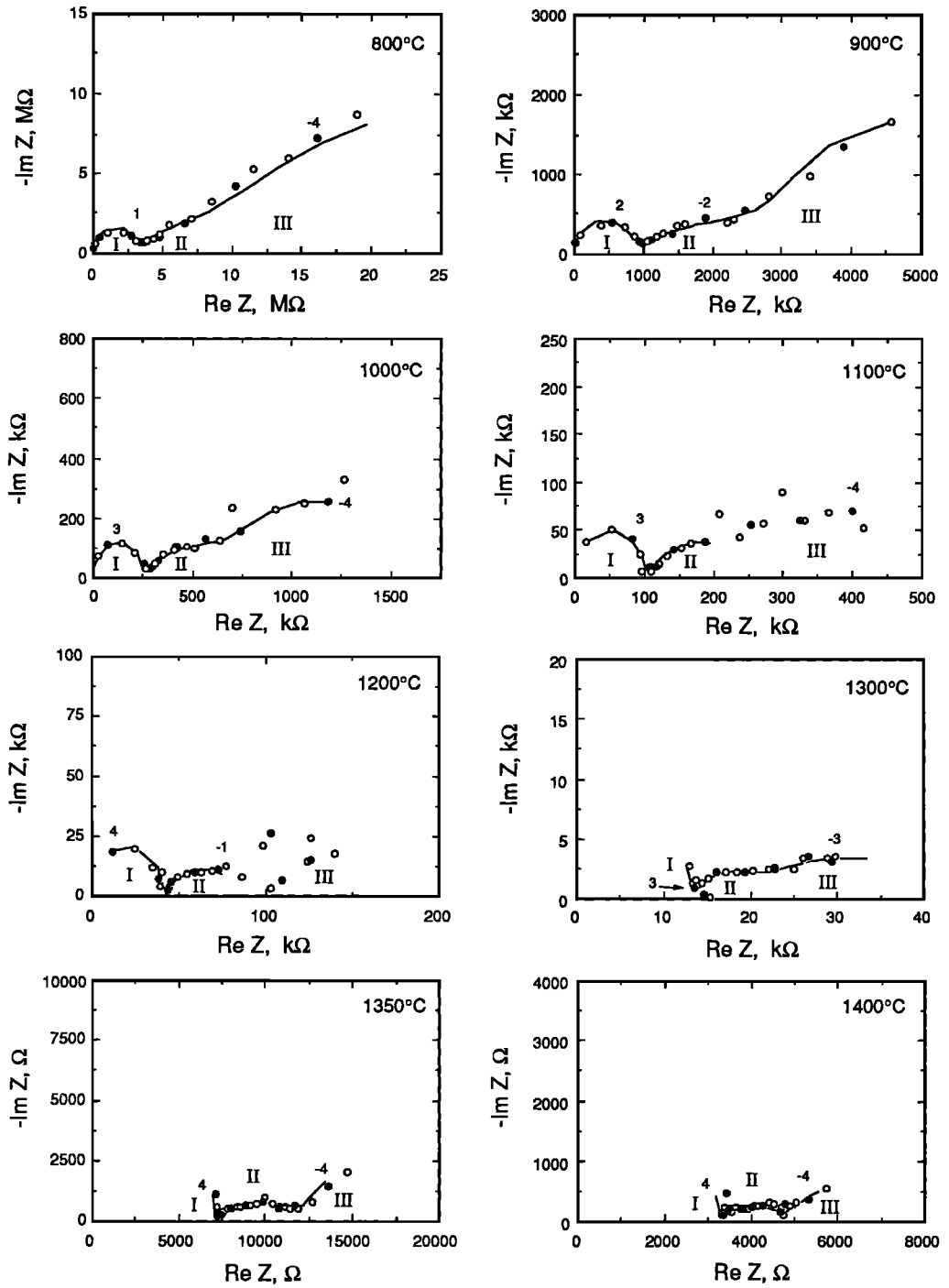

Fig. 5. Complex plane plots of impedance for pressed San Carlos olivine compacts of grain size 75-180 μm at temperatures between 800° and 1400°C. At each temperature, the f_{O_2} is that of the W-M oxygen buffer. Note different scales for each plot. The frequency increases toward the origin and each solid data point occurs once per decade of frequency. Small numerals are log frequency of the corresponding solid symbol, and open symbols are at intermediate frequencies. The line through each data set is a model obtained by analysis using equivalent electrical circuits (see text).

can be partial or incomplete if it extends past the range of measurement and adjacent impedance arcs can overlap. Arc I, the highest-frequency arc, is evident at all temperatures, and the range of frequency over which this arc occurs increases with increasing temperature (~10^1-10^3 Hz at 800°C; >10^3 Hz at 1400°C). Arc II, the intermediate-frequency arc, overlaps arc III, the low-frequency arc; this effect lessens with increasing temperature.

Figure 6 shows the experimental results of a set of experiments performed at 1200°C and an f_{O_2} of 10^{-5} Pa on ground-and-pressed San Carlos olivine for two different grain size ranges: 7-15 and 35-45 μm. The largest grain size 75-180 μm experimental data are shown in Figure 5. The data display features similar to those of the data in Figures 4 and 5, three impedance arcs occurring in series, although for the smallest grain size experiment the high-frequency impedance arc is not well resolved due to the limited range of measurement frequency.

Experiments were performed on the natural dunite from San Quintin at 900°C (f_{O_2} = $10^{-10.4}$ Pa) and 1200°C (f_{O_2} = 10^{-5} Pa;

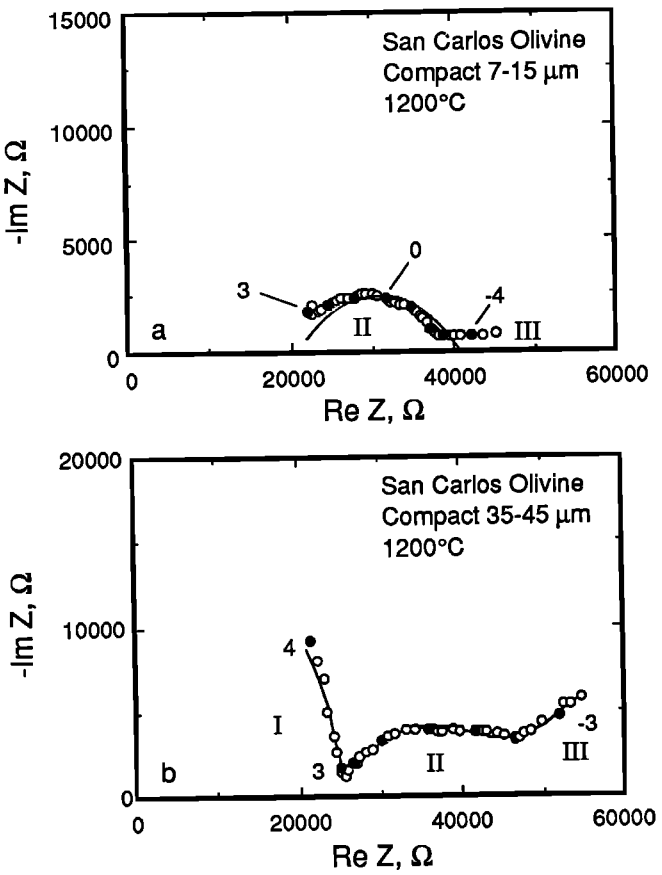

Fig. 6. Complex plane plots of impedance for San Carlos olivine compacts with different grain sizes. T = 1200°C, $f_{O_2} = 10^{-5}$ Pa. Solid lines are fits to experimental data using equivalent circuits (see text). (*a*) 7-15 μm; (*b*) 35-45 μm.

Figure 7). Once again we observe the high-frequency arc shifting to a higher frequency range at higher temperatures, as noted in the ground-and-pressed compacts. At ~1200°C both two- and four-electrode experiments were performed. Experiments performed using the four-electrode technique remove the effects of electrodes from the measurements [*Lockner and Byerlee*, 1985; *Olhoeft*, 1985]. Comparison of experiments using two- and four-electrode configurations (Figures 7*a* and 7*b*) shows differences in both the real and imaginary parts of the impedance, particularly at low frequencies. Below 10^{-2} Hz the two-electrode data show a more steeply increasing impedance than the four-electrode data. The four-electrode configuration experiment shows that arcs I and II are related to properties of the sample. In the two-electrode configuration experiment the three impedance arcs are not well resolved; arc II, the low-frequency impedance arc that relates to sample properties, is partially obscured by electrode effects that occur at the lowest frequencies.

In the complex impedance plane an electrode response can appear as a separate or overlapping impedance arc or as a straight line [*Archer and Armstrong*, 1980]. A straight line is characteristic of diffusional processes at the sample-electrode interface [*Macdonald and Franceschetti*, 1987]. In Figures 4*b*, 5, and 6 it is difficult to judge if the response at the lowest frequencies (<10^{-2} Hz) is really a straight line or the high-frequency portion of a large impedance arc. The type of response observed is dependent on the number of mobile charged species and whether or not they are blocked at the electrodes. Because of high capacitance associated

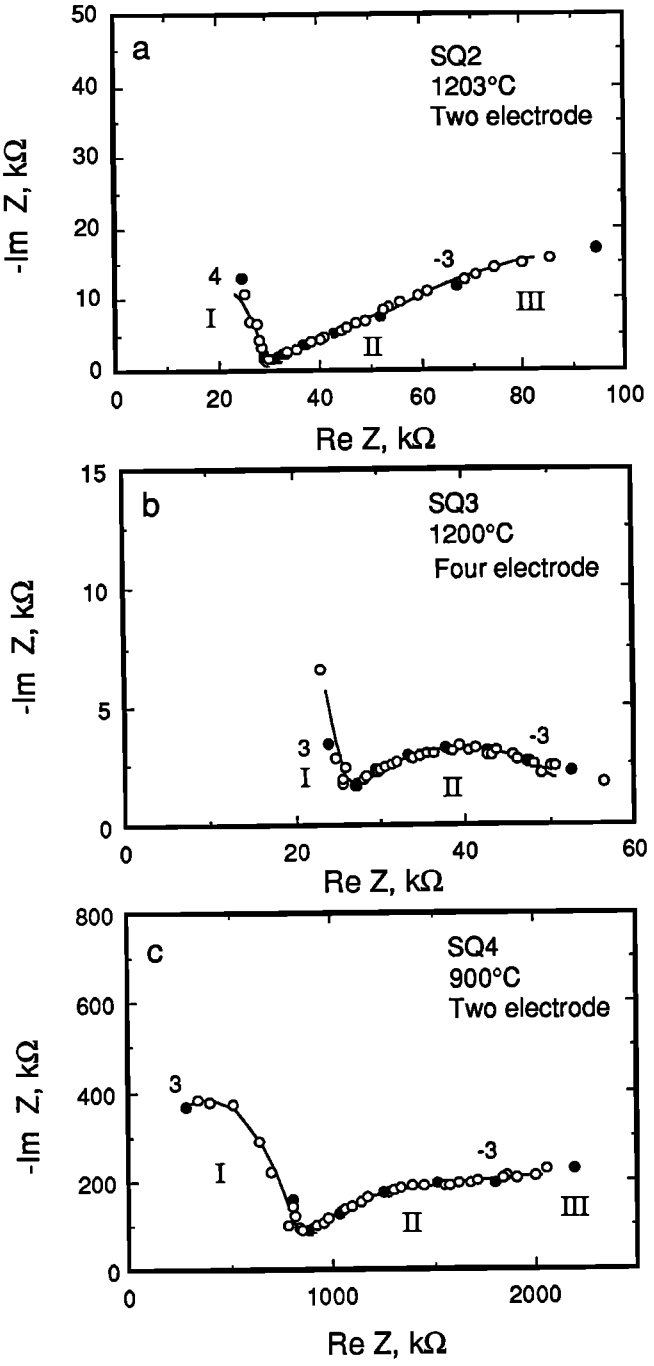

Fig. 7. Complex plane plots of impedance for San Quintin dunite using two- and four-electrode methods. Solid lines are fits to experimental data using equivalent circuits (see text). (*a*) 1203°C, two-electrode, $f_{O_2} = 10^{-5}$ Pa. (*b*) 1200°C, four-electrode, $f_{O_2} = 10^{-5}$ Pa. (*c*) 900°C two-electrode, $f_{O_2} = 10^{-10.4}$ Pa. Two-electrode results show low-frequency, high-impedance behavior characteristic of electrode effects. Four-electrode method eliminates electrode effects from the measurement and reveals low-frequency behavior of the sample. In this particular case, the low-frequency response of the sample is obscured by the electrode effects in the two-electrode measurement. Compare with Figure 4.

with blocking at electrodes, the electrode response occurs at the lowest frequencies of measurement, consistent with our results. Thus we conclude that the third (lowest frequency) arc represents electrical processes at the sample-electrode interface and is not related to the electrical properties of the sample and the two highest-frequency arcs represent bulk properties of the sample.

The real and imaginary relative permittivities κ' and κ'' as a function of frequency for the ground-and-pressed San Carlos olivine compact (75-180 μm grain size range) are presented in Figure 8 for 800°, 1000°, 1200°, and 1400°C. The real and imaginary relative permittivities are also referred to as the relative dielectric constant and relative loss factor, respectively [*von Hippel*, 1954]. Both the real and imaginary relative permittivities increase with increasing temperature. The real relative permittivity decreases with increasing frequency from 10^{-4} to 10^{1} Hz and has a slope of about -1 (log-log plot). At high frequencies (>10^{2}-10^{3} Hz) the real permittivity flattens out to a nearly constant value. This value is related to the internal capacitance of the measuring system (see discussion section). The imaginary relative permittivity is higher in value than the real permittivity and also decreases with increasing frequency over the entire frequency range of measurement (slope ≈ -1).

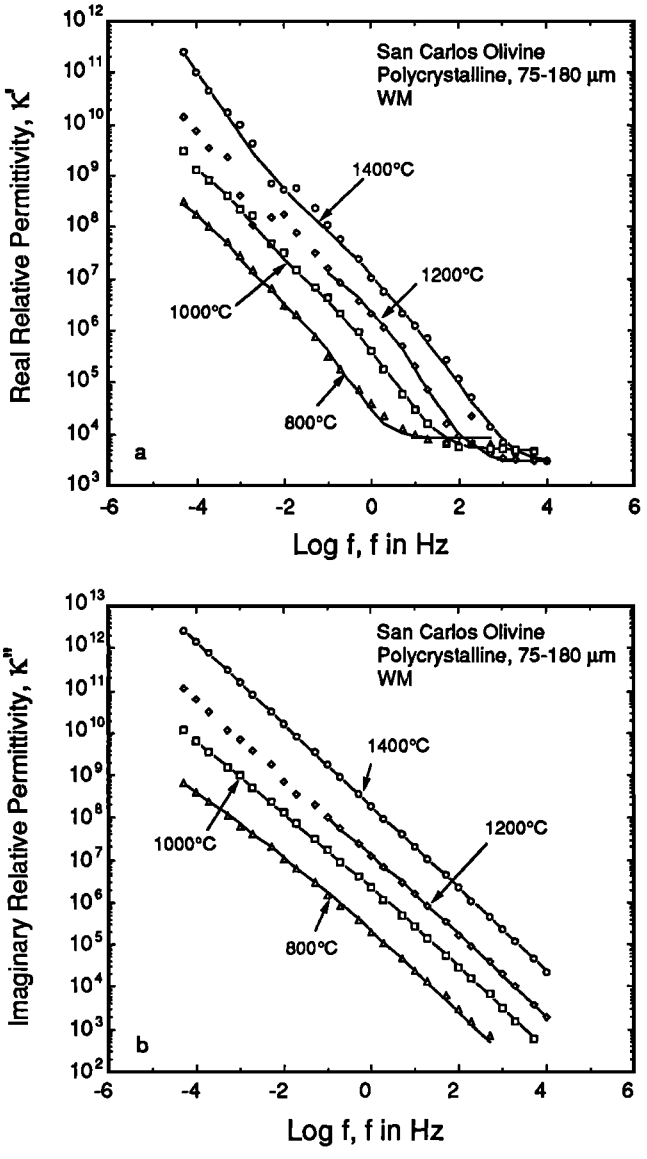

Fig. 8. (*a*) Log of real relative permittivity κ' versus log frequency for San Carlos olivine compacts, grain size 75-180 μm. (*b*) Log of imaginary relative permittivity κ'' versus log frequency. Triangles, 800°C; squares, 1000°C; diamonds, 1200°C; circles, 1400°C. Solid lines are fits to experimental data using equivalent circuits (see text).

DISCUSSION

Equivalent circuit modeling of experimental data. Several types of models have been used in the description, modeling, and interpretation of impedance data. These models include equivalent electrical circuits, geometric models such as the bricklayer model, and effective medium models (such as the Maxwell and Fricke models). Each of these models and the relationships between them will be discussed in some detail. We begin the analysis of our experimental data by using equivalent circuits. Equivalent circuits are electrical circuits made of resistors and capacitors in arrangements that respond with frequency in the same manner as the sample. Portions of the equivalent circuit represent different processes occurring in the sample and at the sample-electrode interface. The equivalent circuit approach is perhaps the most basic of the various models, but non unique interpretations arise because many circuits can give identical responses. The more complex the equivalent circuit the harder it is to relate specific elements within the circuit to the physical or chemical processes of the sample responsible for the observed electrical behavior. An advantage to using the equivalent circuit approach to modeling is that it is relatively easy to accurately describe the electrical response of the sample over a large range of frequency.

The simplest equivalent RC circuit that approximately corresponds to the experimental observations is a circuit consisting of three parallel RC elements that add in series. This circuit was originally used by *Bauerle* [1969] to describe the electrical behavior of polycrystalline $ZrO_2 \cdot Y_2O_3$. The circuit and its schematic response plotted in the complex plane are shown in Figure 9. Each resistor-capacitor pair corresponds to an arc in the complex impedance plane that is identified with a specific transport mechanism. The capacitor C_{sys} is in parallel with the entire circuit because it includes the system capacitance as well as the high-frequency capacitance of the sample. The system capacitance and the capacitance of mechanism 1 are observed at high frequencies (>100 Hz). Because the system capacitance and the capacitance of mechanism 1 act in parallel, they add linearly. The system capacitance for the current experimental set up has been determined to be about 270 pF and masks the smaller mechanism 1 capacitance.

The complex impedance of a parallel RC circuit element is given by

$$Z^* = \frac{R - j\omega C R^2}{1 + \omega^2 C^2 R^2}. \quad (7)$$

From this equation we see that as $\omega \rightarrow 0$ (i.e., DC) the impedance has no imaginary component and is equal to the resistor value R. This is the point on the real axis intersected by an impedance arc. Thus the width of each arc on the real axis is equal to the value of the corresponding resistor of the parallel RC circuit element. This width on the real axis is extremely important because no assumptions are required to obtain the resistance value. The lowest-frequency point on the real axis corresponding to the electrical properties of the sample results from arc I and arc II and is the total DC resistance of the sample. This resistance value is converted to a DC resistivity ρ by correcting for sample geometry,

$$\rho = R\,A/l \quad (8)$$

where A/l, the geometric factor, is the facial area to thickness ratio of the disk-shaped sample. The conductivity σ is the reciprocal of the resistivity, $1/\rho$.

In the simplest case, the point at the top of an impedance arc is the point at which

$$\omega \tau_c = 1 \quad (9)$$

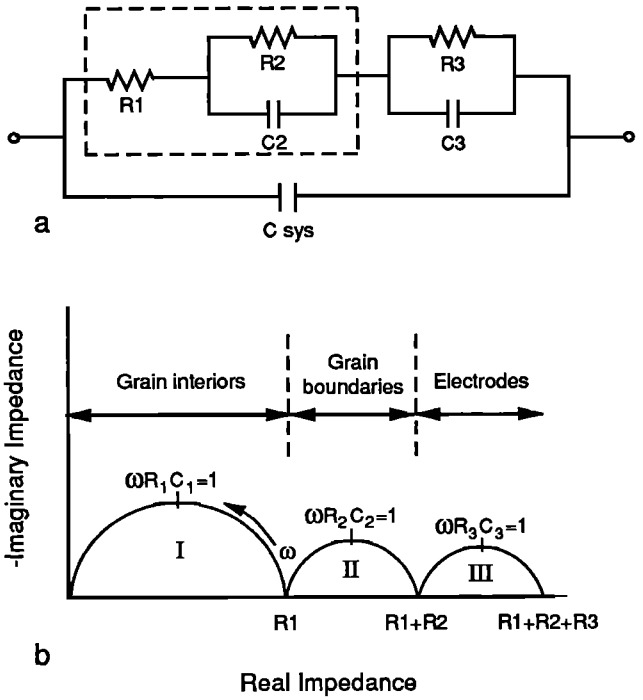

Fig. 9. (*a*) Simplified equivalent circuit employed to model electrical response of polycrystalline olivine compacts. See text for discussion. Dashed box encloses elements intrinsic to material response. (*b*) Schematic response of equivalent circuit in the complex plane, illustrating characteristic impedance arcs associated with each element of equivalent circuit. Note that form of the schematic response requires $R_1C_1 << R_2C_2 << R_3C_3$ (see text).

where ω is the angular frequency and τ_C is the characteristic time constant (or relaxation time) and is equal to $R \cdot C$, where R is the characteristic DC resistance and C is the capacitance. Impedance arcs will be separate and distinct in the complex plane if τ_C for each arc differs by a factor of 10 or more. The highest frequency has the lowest relaxation time. In the series case the total impedance is given by the linear addition of Z^* (equation (7)) for each parallel RC element.

Modeling the data with distributed circuit elements. Impedance arcs can have centers that fall below the real axis in complex plane diagrams (e.g., Figure 4*b*). This occurrence indicates a deviation from ideality in the frequency dispersion of real materials and is often termed anomalous dispersion [*Jonscher*, 1975; *Knight*, 1984]. Anomalous low-frequency dispersion is attributed to a distribution of relaxation times; that is, the frequency at which $\omega\tau$ equals one is not a single value but is distributed over a range of frequencies. One possible explanation for this behavior is nonuniformity of material such as variable grain boundary thickness [*van Dijk and Burggraaf*, 1981]. We observe that the depressed impedance arc behavior occurs primarily in the lower-frequency arcs. The first, highest-frequency impedance arc does not exhibit this behavior.

Real circuit components such as resistors and capacitors approximate ideal behavior over a limited frequency range [*Hurt and Macdonald*, 1986]. Circuit components that do not behave ideally are said to have "distributed" rather than "lumped-constant" properties because their responses are distributed over a range of frequency. Real materials also behave in this manner and distributed circuit elements (and their empirical formulations) are needed to describe the material behavior. In order to accurately model and describe the experimental data, we need to modify the equivalent circuit shown in Figure 9 by introducing a constant phase element as a device to be incorporated in the equivalent circuit.

The constant phase element CPE has an empirical electrical response of the form

$$Z^*_{CPE} = (Y^*_{CPE})^{-1} = (j\omega\tau)^{-\alpha} \qquad (10)$$

where α is a frequency independent parameter. Distributed elements and circuits, including the CPE, are discussed at length by several authors [e.g., *Macdonald*, 1985; *Raistrick*, 1987]. A CPE in series with a resistor (Figure 10*a*) produces a straight line in the complex impedance plane inclined at an angle with respect to the real axis that intercepts the real axis at R as $\omega \to \infty$.

The CPE was introduced to the Debye circuit (a circuit consisting of a resistor and capacitor in series, in parallel with an additional capacitor) by *Cole and Cole* [1941] to model non-Debye behavior of liquids and solids (i.e., depressed arcs) in the complex dielectric plane. The distributed circuit that describes a depressed arc in the complex impedance plane is a CPE in parallel with a resistor (Figure 10*b*). The impedance of this circuit is given by

$$Z^*_{ZARC} = \frac{R}{1 + (j\omega\tau)^{\alpha}} \qquad (11)$$

where Z^*_{ZARC} indicates the complex impedance of an arc depressed in the impedance plane. The exponent α relates to θ the angle of depression of the impedance arc ($\alpha = 1 - 2\theta/\pi$) and varies between 0 and 1. For $\alpha = 1$ the CPE is an ideal capacitor (no depression, center of impedance arc falls on the real axis), and there is a single time constant τ equal to $R \cdot C$. For $\alpha = 0$ the CPE is an ideal resistor, and there is no imaginary (capacitive) component. The total circuit that describes the experimentally measured electrical response of our samples (modified from Figure 9) is shown in Figure 11 and consists of a resistor in series with two distributed elements also in series. The capacitor C_{sys} is in parallel with the entire circuit. The circuit components relating to properties of the sample are enclosed in the dashed box.

Using the circuit in Figure 11 and a complex nonlinear least squares (CNLS) fitting routine [*Macdonald et al.*, 1982; *Hurt and Macdonald*, 1986], we were able to fit the data and obtain values for each of the specific components and parameters. Models of the data obtained in this manner are shown as solid lines through the experimental data for each experiment in Figures 5, 6, and 7. The circuit parameters obtained from the CNLS fits are listed in Table

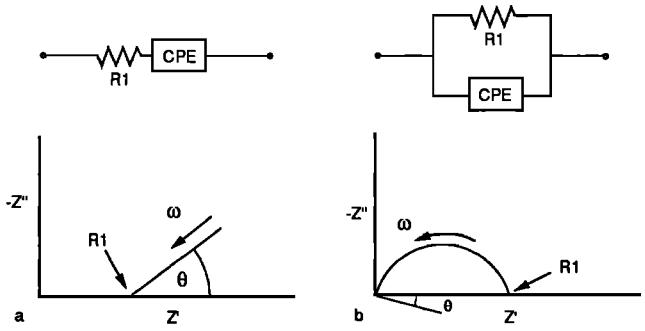

Fig. 10. (*a*) Schematics of circuit and response in the complex impedance plane for a constant phase element (CPE) in series with a resistor. (*b*) A CPE in parallel with a resistor produces a semicircular arc with the center located below the real axis in the complex impedance plane. This type of response is observed in the second, intermediate-frequency, impedance arc of the polycrystalline olivine samples of this study.

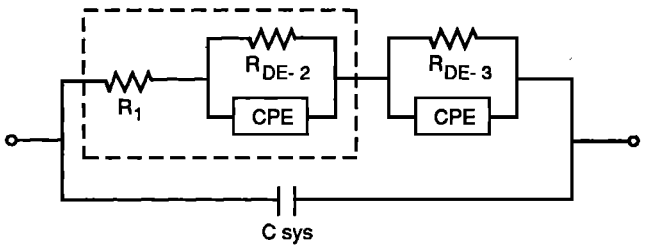

Fig. 11. The modified equivalent circuit that describes the overall response observed in the polycrystalline olivines of this study. This circuit produces three impedance arcs in the complex plane, two of which have centers below the real axis.

1, along with the estimated standard deviations for each parameter. Certain sets of the impedance data cannot be fit with good fit statistics (e.g., PA 800°C, Table 1). Despite the statistical shortcomings of the fit to this particular data set, the determined parameters adequately describe the data in the complex impedance plane (Figure 5), as the real and imaginary impedances as a function of log frequency (Figure 12), and in the relative permittivity representation (Figure 8). In some of the experiments the data at the lowest frequencies exhibit considerable scatter (e.g., Figure 5, 1100°, 1200°C) for reasons that are unknown. The fits performed on these data sets do not include the lowest frequency points. For each plotted experiment, the model curves extend over the range of frequency used in the fit.

Interpretation of conductivity mechanisms. We have already determined that the third, lowest-frequency impedance arc is caused by processes occurring at the sample electrode interface. To identify the processes causing the two impedance arcs representing bulk material properties, we compare our results with those of similar experiments on oxide and ceramic systems [e.g., *Chu and Seitz*, 1978; *van Dijk and Burggraaf*, 1981; *Verkerk, et al.*, 1982*a*; *Tuller*, 1985]. When portions of three arcs are observed in these studies, they have been attributed to (1) grain interiors (highest-frequency, lowest impedance arc), (2) grain boundaries (intermediate-frequency, impedance arc), and (3) electrode processes (lowest-frequency, highest-impedance arc). Impedance arcs separated in the complex plane have time constants $\tau_1 << \tau_2 << \tau_3$, and the same trend is observed in capacitance values ($C_1 << C_2 << C_3$). If grain boundaries are a barrier to the conducting defect species and are areas where polarization occurs [*Kingery et al.*, 1976], then it is reasonable to assume that grain boundaries have a higher capacitance (and higher κ') than the interior of a crystal grain. Thus a grain boundary impedance arc would occur at lower frequencies than a grain interior impedance arc.

A study of the electrical conductivity of diopside single crystals from 800° to 1300°C over the frequency range 10^{-3} to 10^5 Hz revealed frequency dependent behavior of impedance magnitude and phase angle [*Huebner and Voight*, 1988]. An impedance arc was observed over the highest frequency range (10^2 to 10^5 Hz). The impedance (and conductivity) values of the crystal interiors were taken at the frequencies where the phase angle was closest to zero, usually between 10 and 100 Hz, corresponding to the width of the impedance arc. Our measurements show a similar electrical response over the frequency range 10^2 to 10^4 Hz (Figure 4); the highest-frequency impedance arc in our work is attributed to a grain interior conduction mechanism.

Comparison of the frequency response in the complex plane of our polycrystalline experiment to the single crystal results of *Sato* [1986] also supports the grain interior/grain boundary

TABLE 1. Experimental Conditions and Parameters Derived From Fits to the Data Using the Equivalent Circuit of Figure 11

Sample	Temperature, °C	Grain Size, μm	Geometric Factor, m	R_1, Ω	C_1, pF	R_{DE2}, Ω	τ_{DE2}, s	Ψ_{DE2}	R_{DE3}, Ω	τ_{DE3}, s	Ψ_{DE3}
PA	800			$3.20 \pm 0.25 \times 10^6$	$1.71 \pm 0.14 \times 10^{-9}$	$4.28 \pm 9.65 \times 10^6$	$1.18 \pm 3.34 \times 10^1$	0.57 ± 0.28	$4.05 \pm 9.45 \times 10^7$	$1.15 \pm 6.89 \times 10^4$	0.54 ± 0.60
	900			$7.53 \pm 0.05 \times 10^5$	$1.14 \pm 0.01 \times 10^{-10}$	$3.26 \pm 0.08 \times 10^6$	$7.84 \pm 0.95 \times 10^1$	0.32 ± 0.00	$2.89 \pm 0.11 \times 10^6$	$3.59 \pm 0.11 \times 10^3$	0.97 ± 0.02
	1000			$2.38 \pm 0.01 \times 10^5$	$1.03 \pm 0.01 \times 10^{-9}$	$5.13 \pm 0.05 \times 10^5$	$3.66 \pm 0.13 \times 10^0$	0.44 ± 0.00	$7.97 \pm 0.09 \times 10^5$	$1.17 \pm 0.01 \times 10^3$	0.68 ± 0.01
	1100	75-180	0.0231	$9.98 \pm 0.01 \times 10^4$	$7.08 \pm 0.03 \times 10^{-10}$	$1.58 \pm 0.07 \times 10^5$	$9.27 \pm 1.06 \times 10^{-1}$	0.56 ± 0.01	n.d.	n.d.	n.d.
	1200			$4.08 \pm 0.01 \times 10^4$	$6.23 \pm 0.01 \times 10^{-10}$	$4.78 \pm 0.02 \times 10^4$	$4.10 \pm 0.21 \times 10^{-1}$	0.55 ± 0.01	n.d.	n.d.	n.d.
	1300			$1.31 \pm 0.01 \times 10^4$	$5.10 \pm 0.01 \times 10^{-10}$	$6.03 \pm 0.65 \times 10^3$	$3.22 \pm 0.17 \times 10^{-2}$	0.62 ± 0.02	$2.47 \pm 0.28 \times 10^4$	$1.28 \pm 0.44 \times 10^2$	0.35 ± 0.03
	1350			$6.96 \pm 0.20 \times 10^3$	$3.26 \pm 0.32 \times 10^{-10}$	$5.66 \pm 0.38 \times 10^3$	$9.75 \pm 3.60 \times 10^{-1}$	0.33 ± 0.02	$5.41 \pm 1.35 \times 10^3$	$9.64 \pm 2.65 \times 10^3$	0.79 ± 0.20
	1400			$3.18 \pm 0.07 \times 10^3$	$5.86 \pm 1.38 \times 10^{-10}$	$1.76 \pm 0.25 \times 10^3$	$1.29 \pm 0.81 \times 10^{-1}$	0.36 ± 0.06	$1.93 \pm 2.34 \times 10^3$	$7.39 \pm 21.48 \times$	0.61 ± 0.31
PC10	1200	7-15	0.0424	$2.05 \pm 0.01 \times 10^4$	*	$2.01 \pm 0.01 \times 10^4$	$8.66 \pm 0.12 \times 10^{-2}$	0.30 ± 0.00	n.d.	n.d.	n.d.
PC6F	1200	35-45	0.0392	$2.42 \pm 0.03 \times 10^4$	$2.59 \pm 0.07 \times 10^{-10}$	$1.97 \pm 0.52 \times 10^4$	$1.14 \pm 0.30 \times 10^{-1}$	0.44 ± 0.04	$2.54 \pm 77.9 \times 10^5$	$6.26 \pm 270 \times 10^6$	0.30 ± 0.26
SQ2	1203		0.0215	$2.75 \pm 0.01 \times 10^4$	$2.52 \pm 0.02 \times 10^{-10}$	$4.47 \pm 0.78 \times 10^4$	$2.96 \pm 2.41 \times 10^1$	0.26 ± 0.01	$6.18 \pm 1.01 \times 10^4$	$1.99 \pm 0.33 \times 10^3$	0.49 ± 0.03
SQ3	1200	200-400	0.0227	$2.28 \pm 0.02 \times 10^4$	$6.83 \pm 0.22 \times 10^{-10}$	$3.36 \pm 0.04 \times 10^4$	$3.84 \pm 0.25 \times 10^0$	0.24 ± 0.00	*	*	*
SQ4	900		0.0267	$7.24 \pm 0.52 \times 10^5$	$2.68 \pm 0.07 \times 10^{-10}$	$5.19 \pm 7.85 \times 10^5$	$9.08 \pm 9.71 \times 10^{-1}$	0.40 ± 0.16	$1.97 \pm 1.27 \times 10^6$	$2.98 \pm 6.55 \times 10^3$	0.25 ± 0.12

Method of sample preparation: PA, hot press (piston cylinder); PC, cold press/ one atmosphere sinter; SQ, natural rock sample. Geometric factor is the area/length ratio of the experimental cell. n.d., not determined.

* No impedance arc.

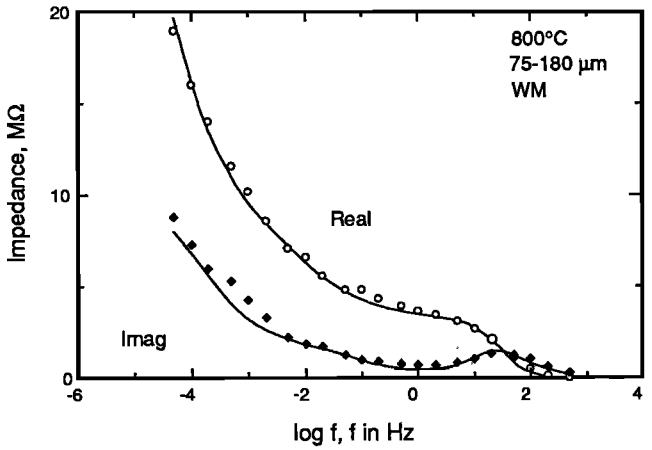

Fig. 12. Model fit of real and imaginary impedances versus log frequency for San Carlos olivine compact (800°C, 75-180 μm, W-M oxygen buffer) demonstrating applicability of equivalent circuit analysis in the description of the total electrical response in several different representations. Compare to Figures 5, 8*a*, and 8*b*.

interpretation. Sato reports values of κ' and σ' for single-crystal San Carlos olivine over the frequency range 0.1-1000 Hz. We compare the experimental results at 1200° and 1400°C for both the [001] and [010] directions obtained at the oxygen fugacities closest to those of our experiments. To compare Sato's results with our findings, we have converted Sato's data to real and imaginary resistivities. Because Sato reports κ' at 0.1, 1.0, 10, 92, and 1000 Hz and the conductivity σ' at only the two extremes of frequency, we have assumed that ρ' ($1/\sigma'$) varies linearly with log frequency over the range of frequency he studied, roughly consistent with our observations (Figures 4 and 12). The conclusions below are not strongly dependent on this assumption. Since the complex impedance is

$$Z^* = \frac{1}{j\omega C_o \kappa^*}, \tag{12}$$

and

$$\kappa^* = \kappa' - j\kappa'', \tag{13}$$

we find that

$$Z^* = \frac{\kappa'' - j\kappa'}{\omega C_o\{(\kappa')^2 + (\kappa'')^2\}}. \tag{14}$$

The imaginary relative permittivity is

$$\kappa'' = \frac{\sigma'}{\omega \varepsilon_o}. \tag{15}$$

After taking into account sample geometry, ρ' and ρ'' are given by

$$\rho' = \frac{\kappa''}{\omega \varepsilon_o\{(\kappa')^2 + (\kappa'')^2\}} \tag{16}$$

$$\rho'' = \frac{\kappa'}{\omega \varepsilon_o\{(\kappa')^2 + (\kappa'')^2\}}. \tag{17}$$

The data obtained in this manner are plotted in the complex resistivity plane in Figure 13, along with our experimental data. At 1200°C (Figure 13*a*), Sato's values of the real resistivities of single-crystal olivine in the [001] and [010] directions are about 3 and 5 times, respectively, the grain interior resistivity in our experiments. The discrepancy in impedance magnitude is unexplained; however, we note that the grain interior DC resistivities of San Carlos olivine obtained in the present work are within a factor of 2 of the kilohertz resistivities determined by *Schock et al.* [1989]. Sato's measurements appear to display portions of two impedance arcs. The frequency of the cusp (the

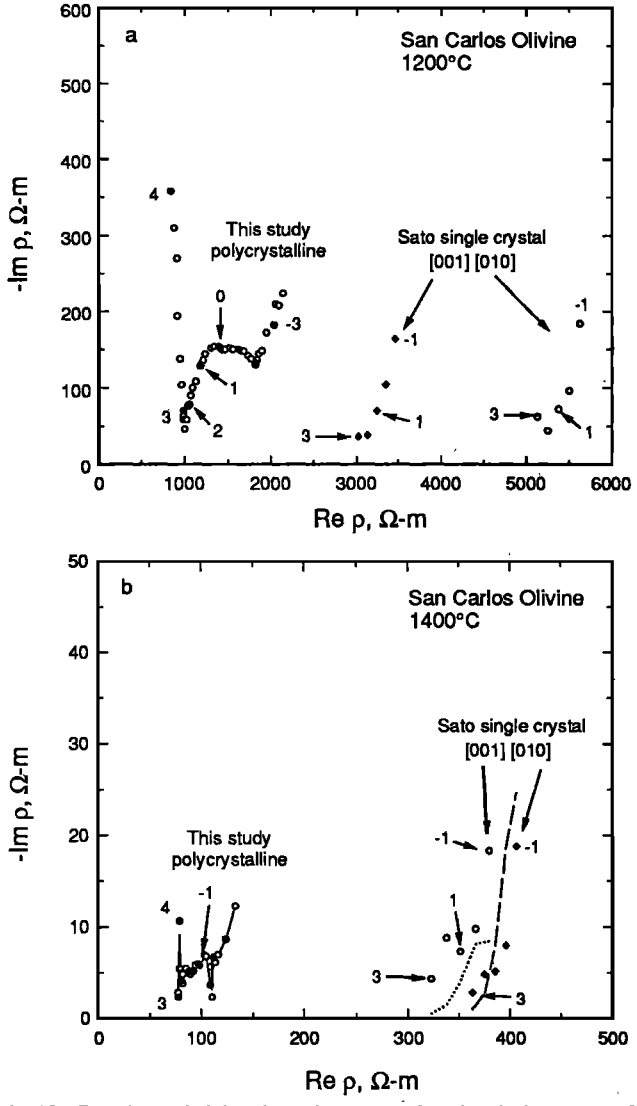

Fig. 13. Complex resistivity plane plots comparing electrical response of polycrystalline San Carlos olivine compacts with the San Carlos single crystal results of *Sato* [1986]. (*a*) Comparison at 1200°C for the [001] and [010] directions. The f_{O_2} of Sato's experiments is $10^{-5.3}$ Pa. Sato's measurements were performed at 1000, 92, 10, 1, and 0.1 Hz. (*b*) A similar comparison at 1400°C. The f_{O_2} of Sato's 1400°C experiments is ~$10^{-1.2}$ Pa Included are Sato's models for frequency dependent dielectric response converted to impedances: dotted line, [001]; dashed line, [010]. See text for further discussion.

point where the impedance arc meets the real axis) is about the same as in our measurements, between 100 and 1000 Hz. The differences in the shapes of the second lower-frequency arcs are important in their interpretation. Our measurements at 0.1-1 Hz occur near the peak of the second impedance arc, while those same frequencies in Sato's single-crystal experiment do not appear to occur near a peak. Sato's lowest-frequency data are very nearly a straight line, suggesting diffusional processes occurring at the sample-electrode interface. Sato has interpreted the low-frequency response as being caused by the partial blocking of Mg vacancies at the electrodes. The comparison of the two experiments at 1200°C suggests that the polycrystalline impedance spectrum has an additional impedance arc, attributable to the presence of grain boundaries.

A similar situation is observed in the comparison at 1400°C (Figure 13*b*). The single-crystal real resistivity is about 4.5-5

times larger than that of the polycrystalline sample, with the [001] and [010] directions closer in value than at 1200°C. Again, the reasons for the significantly higher values of resistivity of Sato's single-crystal study than for our polycrystalline samples are not clear. For both orientations the data point at 92 Hz has a relatively high imaginary resistivity, which could possibly be interpreted as evidence of an impedance arc. Interpreted as such, the impedance arc would span 2 decades of frequency (10-1000 Hz), while the second impedance arc of the polycrystalline experiment covers a much larger 5 decade range of frequency. The model of the frequency dependence of κ' put forth by Sato is plotted as a dotted line and does not show the increase in ρ'' at 92 Hz. The model fits the [010] data well but in the [001] case deviates from the experimental data at low frequencies.

By analogy with the studies of ceramic systems and by comparison with the single-crystal experiments of *Huebner and Voight* [1988] and *Sato* [1986], we suggest that the highest-frequency arc (> 200 Hz) corresponds to the bulk conduction properties of the material (grain interiors, modified by the measurement system capacitance), the arc at intermediate frequencies (10^{-2} to 200 Hz) is attributable to grain boundary transport, and the low frequency arc (< 10^{-2} Hz) is due to electrode processes. We continue this discussion by examining the results in view of the grain interior/grain boundary interpretation.

Bricklayer model. A simple geometric model used to describe and model conduction in ceramic systems that applies to the results of this study is the "bricklayer" model [*van Dijk and Burggraaf*, 1981; *Verkerk et al.*, 1982*b*]. The bricklayer model helps us to use impedance spectra to further analyze microstructural properties of polycrystalline olivine and provides a qualitative justification to the equivalent circuit we have chosen to model the experimental results. In this model (Figure 14*a*), cubic grains are everywhere surrounded by a thin grain boundary. There are two end-member paths of conduction that are represented by equivalent circuits. A conduction path through a grain, across a grain boundary, and through a grain repeatedly (path 1) results in a series equivalent circuit. Path 2 is the grain boundary only path, along which a mobile charge would completely bypass grain interiors. The two possible paths act in parallel; for a given material, one or the other may dominate allowing simplification of the entire equivalent circuit (Figure 14*b*). If the grain boundary only path is very resistive, then the parallel grain boundary element will be bypassed and the schematic reduces to the series equivalent circuit (Figure 14*c*). The ground-and-pressed samples of this study exhibit this type of response. In terms of an effective medium model (appendix), equation (A2) yields series-type behavior when $\tau'_2 >> \tau'_1$. For example, if the two paths are approximately equal in impedance, it is necessary that the grain boundary segment of path 1, being very thin, has a negligibly small impedance in path 1. In path 2, however, the grain boundary segment will be measurable and the grain boundary and grain interior impedances add in a parallel manner. The schematic shown in Figure 14*b* would then reduce to a circuit having the grain boundary element in parallel with the grain interior element. This simplified equivalent circuit produces only a single impedance arc in the complex plane (excluding the one due to electrode processes), whose parameters are governed by the parallel combination of grain boundary and grain interior properties. We have not observed this type of parallel behavior in the natural samples we have studied thus far.

Effect of grain size. The complex electrical response as a function of grain size was separated into grain interior and grain

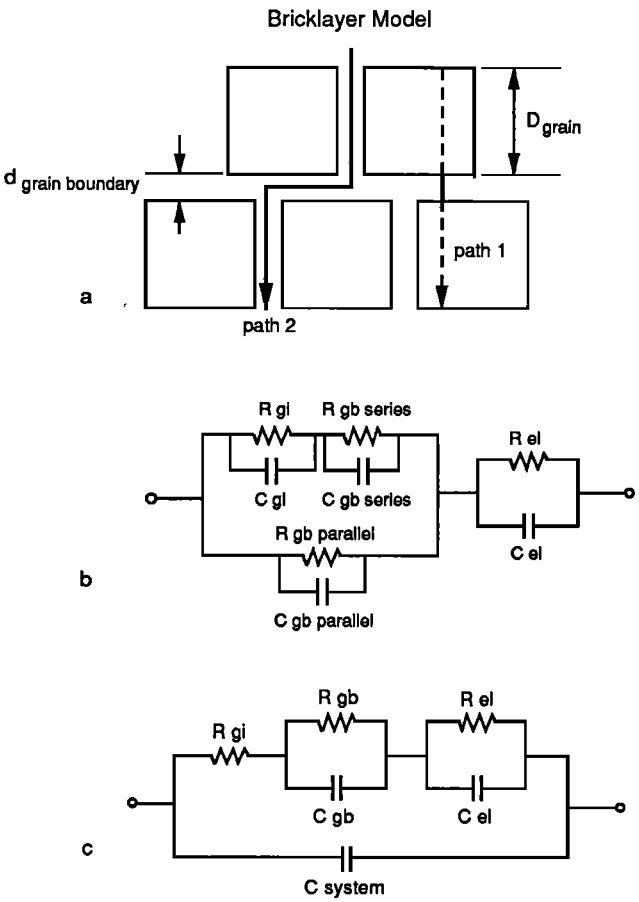

Fig. 14. Bricklayer model for electrical transport through a polycrystalline medium and equivalent circuit response. (*a*) Schematic diagram illustrating the two end-member paths. Path 1 goes through a grain interior (gi) and then across a grain boundary (gb), repeatedly. Path 2 is the grain boundary only path. (*b*) Complete equivalent circuit that includes both path 1 and path 2 acting in parallel (el stands for electrode). (*c*) Simplified equivalent circuit that corresponds to experimental results, showing grain interiors and grain boundaries acting in series (path 1). C_{system} includes the relatively small grain interior capacitance term.

boundary contributions and is shown in Table 2. The effect of f_{O_2} variation between 10^{-5} and 10^{-4} Pa on grain boundary conductivity is expected to be minor if the f_{O_2} dependence is similar to that of single-crystal olivine. It is important to note that the grain boundary conductivity determined from $\sigma_{gb,\,DC} = (R_2 \cdot A/l)^{-1} = \sigma_{gb\text{-}bulk}$ (where R_2 is defined in Figure 11) is the macroscopic grain boundary conductivity. It is a bulk property of the polycrystalline olivine sample (and is not specific to the grain boundary material itself). The microscopic grain boundary conductivity $\sigma_{gb\text{-}micro}$ is the conductance per unit length of grain boundary material and can be calculated using

$$\sigma_{gb\text{-}micro} = \sigma_{gb\text{-}bulk}\,(d/D) \qquad (18)$$

where d is the grain boundary width and D is the grain size (bricklayer model, see Figure 14 and *van Dijk and Burggraaf* [1981]). Figure 15 is a graph of $\sigma_{gb\text{-}bulk}$ versus grain size. No macroscopic grain boundary DC conductivity dependence on grain size is observed in this system. Assuming a constant grain boundary width, constant $\sigma_{gb\text{-}bulk}$ requires that $\sigma_{gb\text{-}micro}$ decrease with increasing grain size, varying as $1/D$.

The grain size independence of $\sigma_{gb\text{-}bulk}$ is an interesting result that has been observed in other systems. In the Y_2O_3-ZrO_2 system a linear dependence of $\sigma_{gb\text{-}bulk}$ on grain size is observed

TABLE 2. DC Electrical Conductivity of Polycrystalline Olivine Compacts at 1200°C

Sample	Grain Size, μm	$\log_{10} f_{O_2}$, Pa	Bulk Density, g/cm^3	Percent Theoretical Density	Grain Interior Conductivity, S/m	Bulk Grain Boundary Conductivity, S/m
PC10	7-15	-5.0	3.06	92	$1.15 \pm 0.05 \times 10^{-3}$	$1.17 \pm 0.05 \times 10^{-3}$
PC6F	35-45	-5.0	n.d.	n.d.	$1.05 \pm 0.06 \times 10^{-3}$	$1.29 \pm 0.35 \times 10^{-3}$
PA	75-180	-4.0	3.27	98	$1.06 \pm 0.05 \times 10^{-3}$	$9.06 \pm 0.04 \times 10^{-4}$

Grain interior conductivity is $(R_1 * GF)^{-1}$; grain boundary conductiviy is $(R_{DE2} * GF)^{-1}$. GF (geometric factor) listed in Table 1. n.d., not determined.

for grain sizes up to 3 μm [*Verkerk et al.*, 1982*b*], with no grain size dependence observed for grain sizes between 3 and 100 μm. In samples such as high purity polycrystalline alumina, the effects of grain boundary conduction are found to be small unless the grain size is very small (<0.1 μm) or there is the formation of a separate phase at the grain boundaries [*Kingery et al.*, 1976]. Our results are consistent with these observations; however, we have not experimented on samples with sufficiently small grain sizes to observe any dependence of $\sigma_{gb\text{-}bulk}$ on grain size, if it exists. If the bulk grain boundary conductivity is independent of grain size as in this study, the DC conductivity results of laboratory experiments on samples with grain sizes of 10-100 μm can be extrapolated to grain sizes thought to exist in the mantle.

One possible explanation for the independence of $\sigma_{gb\text{-}bulk}$ on grain size is that there exists a finite amount of grain boundary "phase" or material that is responsible for conduction along grain boundaries in the natural rock. By taking large grains of olivine and crushing and grinding them to a fine powder, we have greatly increased the surface area. In the final product, a hot-pressed compact, we may have grain boundaries that are barren; a consequence of diluting the original grain boundary material. This would mean that the diluted grain boundaries are more conductive than undisturbed grain boundaries with original material. Examination of grain boundary electrical properties of natural rocks and further investigation on the nature of grain boundary conduction are needed. More experiments as a function of grain size need to be performed to properly address the effect of grain size on the electrical properties of polycrystalline olivine.

Two parameters that vary with grain size are the real relative permittivity κ'_2 ($\kappa'_2 = \tau_{DE\text{-}2}/R_{DE\text{-}2}\,\varepsilon_O\,A/l$) and the time constant $\tau_{DE\text{-}2}$ (Figures 16 and 17). Both these parameters pertain to the grain boundary impedance arc and are obtained from the model results listed in Table 1. In Figure 16 we see a linear variation of

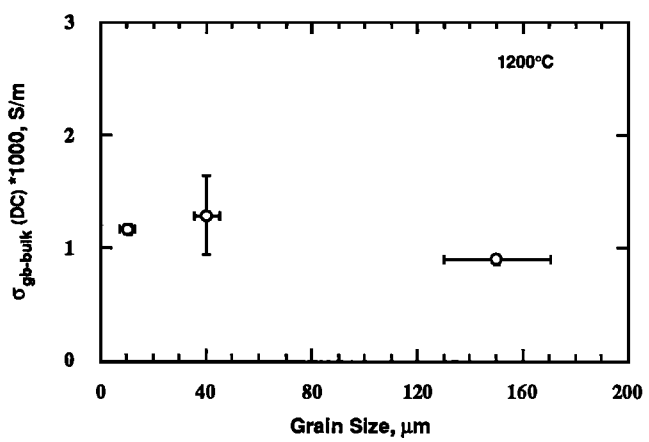

Fig. 15. Grain boundary conductivities $\sigma_{gb\text{-}bulk}$ versus grain size for San Carlos olivine compacts at 1200°C, $f_{O_2} = 10^{-5}$ Pa (75-180 μm sample $f_{O_2} = 10^{-4}$ Pa). X direction error bars represent the range of grain size for each sample.

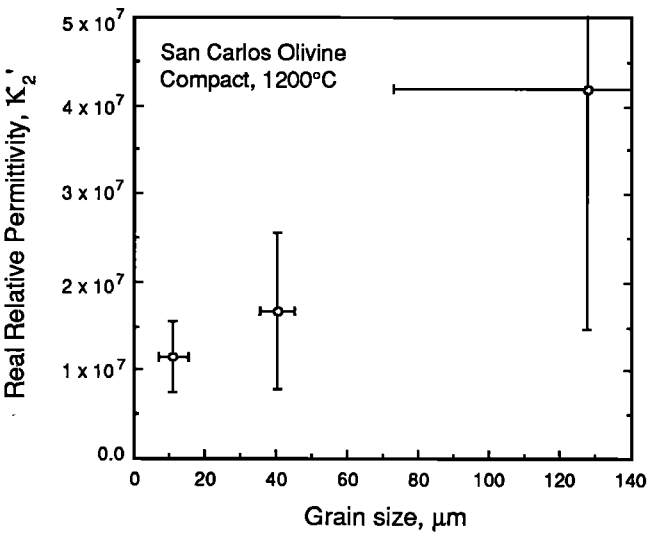

Fig. 16. The real relative permittivity of the grain boundaries κ'_2 plotted against grain size for the experiments at 1200°C. X direction error bars represent the range of grain size for each sample.

κ'_2 with grain size. The time constant is independent of sample dimensions and varies linearly with grain size. Similar observations have been made in the Y_2O_3-ZrO_2 system which displays a linear relation between capacity (capacitance per unit length) and grain size in the grain size range 0.1 to 100 μm [*Verkerk et al.*, 1982*b*].

Temperature dependence. The capacitances and relaxation times obtained from 800° to 1400°C (Table 1) are plotted against

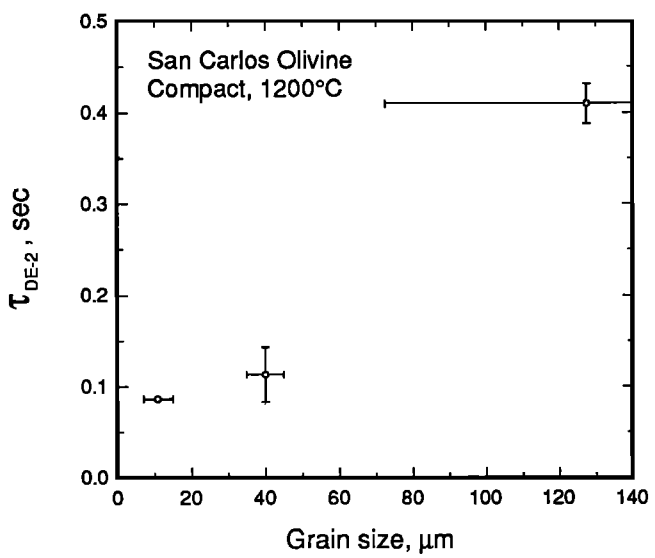

Fig. 17. The time constant of the grain boundary impedance arc τ_2 versus grain size. X direction error bars represent the range of grain size for each sample.

reciprocal temperature in Figure 18. Only the parameters pertaining to the material response (the two highest-frequency mechanisms) are plotted. The capacitance of mechanism 1 decreases with increasing temperature (Figure 18*a*). This parameter contains the system capacitance, but since C_{system} is independent of temperature (confirmed by comparison with room temperature measurements), this trend relates to the capacitance of the grain interiors. The capacitance of the grain boundaries has been calculated from the relaxation time $\tau_{DE\text{-}2}$. The value of C_{gb} (C_2) is approximately constant with increasing temperature and is about 10^4 times C_1. The time constant τ_1 was calculated from R_1 and C_1. For both grain interiors and grain boundaries τ decreases with increasing temperature (Figure 18*b*).

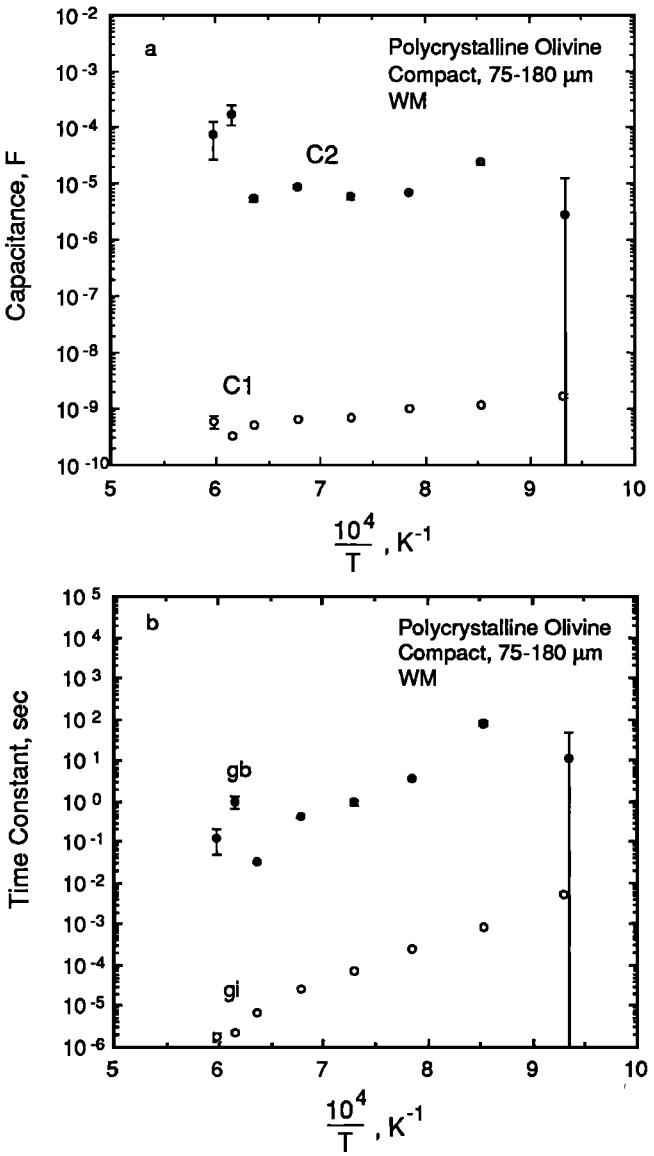

Fig. 18. Temperature dependence of equivalent circuit fitting parameters obtained from complex nonlinear least squares analysis (Table 1). Error bars represent uncertainty in the fit parameters, symbols are larger than error where no error bar is visible. (*a*) Capacitances C_1 and C_2 plotted against reciprocal temperature. The capacitance C_1 contains the system capacitance and masks the relatively small grain interior capacitance (see text). The capacitance C_2 represents the grain boundary capacitance and is approximately constant from 800° to 1400°C. (*b*) Time constants for grain interiors (gi) and grain boundaries (gb) versus reciprocal temperature. Both time constants decrease with increasing temperature, primarily because of decreased resistance.

Figure 19 displays $\sigma_{gi\text{-}DC}$ and $\sigma_{gb\text{-}bulk\text{-}DC}$ for the 75-180 μm grain size fraction versus reciprocal temperature. The conductivities plotted are derived from the parameters R_1 and $R_{DE\text{-}2}$ listed in Table 1. At temperatures below 1200°C σ_{gi} is greater than $\sigma_{gb\text{-}bulk}$; above 1200°C $\sigma_{gb\text{-}bulk}$ is greater than σ_{gi}. Fits to the data are shown as lines, and each of the two conductivity mechanisms is fit differently. The grain interior conductivity displays a break in slope between 1200° and 1250°C and is fit with two straight lines, a four-parameter fit of the form

$$\sigma = \sigma_{o,1} \exp(-E_{act,1}/kT) + \sigma_{o,2} \exp(-E_{act,2}/kT), \quad (19)$$

where the subscripts 1 and 2 refer to the two different lines.

The grain boundary conductivity from 900° to 1400°C is fit with a single line (two-parameter fit):

$$\sigma = \sigma_o \exp(-E_{act}/kT). \quad (20)$$

The 800°C grain boundary conductivity value is excluded from the fit because of the high uncertainty in this data point. The decision to fit the data as a single line as opposed to two lines is based on F test statistics [*Draper and Smith*, 1981; *Bowerman et al.*, 1986]. In the grain interior case, fitting the data with a double straight line is significant at the 99.9% confidence level and therefore justified. This type of fit is consistent with the commonly observed change from extrinsic to intrinsic conduction with increasing temperature. Measurement of the Seebeck coefficient [*Schock et al.*, 1989] indicates that the sign of the charge carrier in olivine changes from positive to negative above 1390°C. This change is interpreted as a change in the conducting defect species from electron holes to Mg vacancies. In this study the two grain interior lines cross at 1344°C and may relate to the change in charge carrier observed by Schock et al.

A double line fit to the grain boundary data is significant at about the 85% confidence level. This confidence interval is not high enough to justify the double line fit without prior evidence of a

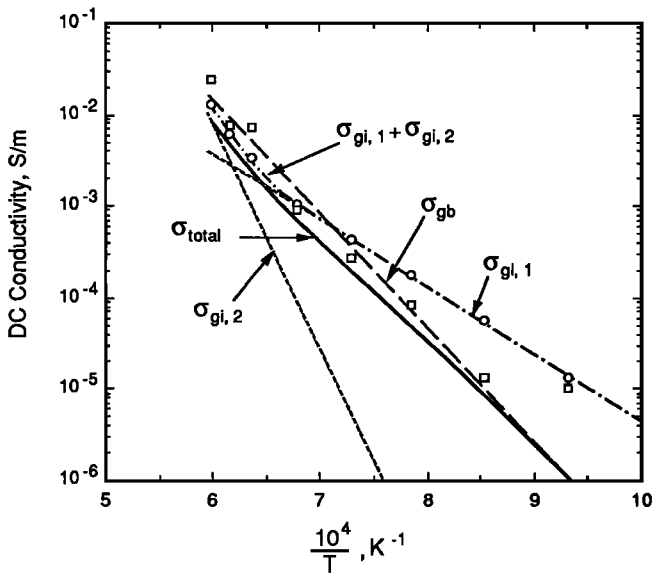

Fig. 19. Log DC conductivity versus reciprocal temperature for the results of this study. Oxygen fugacity was held to that of the W-M buffer. The grain interior conductivity, open circles, is fit with double straight lines (dotted lines). The sum of these two lines is labeled $\sigma_{gi,1} + \sigma_{gi,2}$ (dash-dotted line). The grain boundary conductivity, open squares, is fit with a single long dashed line. The heavy solid line labeled σ_{total} is the series sum of grain interior and grain boundary conductivity.

change in slope of the grain boundary conductivity [*Bowerman et al.*, 1986]. We are unaware of such evidence for olivine from conductivity or diffusion studies, although at least one study has observed two line behavior of grain boundary conductivity (β"-alumina from -130° to 400°C [*Lilley and Strutt*, 1979]). The fit parameters (activation energies and preexponential terms) are summarized in Table 3. The activation energies include the effect of f_{O_2} variation along the W-M oxygen buffer [*Constable and Duba*, 1990]. For the grain boundaries $E_{act,gb\text{-}bulk}$ is between the $E_{act,gi}$ determined for the two different grain interior lines. Because the resistivities of the two mechanisms act in series,

$$\frac{1}{\sigma_T} = \frac{1}{\sigma_{gi}} + \frac{1}{\sigma_{gb\text{-}bulk}}, \qquad (21)$$

and the total DC conductivity is approximately 2-5 times lower than the grain interior conductivity. The ratio of $\sigma_{gb\text{-}bulk}$ to σ_{gi} increases with increasing temperature (Figure 20). At 1400°C, $\sigma_{gb\text{-}bulk}$ is more than twice that of σ_{gi}. At high temperatures (above 1200°C) the total DC conductivity is controlled by σ_{gi}, a direct result of the series behavior of the electrical response. Similar conductivity behavior is observed in polycrystalline ceramic systems [*Kingery et al.*, 1976].

Comparison with other experimental conductivity studies. The total DC conductivity derived through the use of equation (21) is plotted as a function of reciprocal temperature in Figure 21. Also shown in Figure 21 is the effective medium model conductivity of San Carlos olivine as calculated by *Shankland and Duba* [1990] from the single crystal conductivity data of *Schock et al.* [1989]. The experiments by Schock et al. were performed at a constant gas ratio (CO_2/CO) of 10:1, while our experiments were performed at f_{O_2} corresponding to the W-M oxygen buffer curve. At 1200°C the f_{O_2} are nearly the same ($\approx 10^{-4}$ Pa), and between 1100° and 1400°C they differ by less than an order of magnitude. Since the experimentally observed conductivity of olivine varies according to $f_{O_2}^{1/11\text{-}1/5.5}$ [*Constable and Duba*, 1990], the variation in conductivity caused by the different f_{O_2} in the temperature range 1100°-1400°C is small and the data are suitable for comparison. Shankland and Duba's model calculates a conductivity averaged equally over the three crystallographic directions. For temperatures up to 1250°C our results for grain interiors are in good agreement with this calculation. At higher temperatures the two results begin to diverge but are within 1/2 order of magnitude.

The experimentally determined conductivity of a polycrystalline dunite rock from Jackson County, North Carolina (JC dunite; Fo_{93}) is also shown in Figure 21 [*Constable and Duba*, 1990]. The experiment was performed at a constant gas mix of 10:1 CO_2/CO, and data were collected at three frequencies, 10^2, 10^3, and 10^4 Hz. No frequency dependence of conductivity was reported in this frequency range. The JC dunite displays a lower conductivity than both the grain interior conductivity and the effective medium average and is roughly 1/2 order of magnitude lower than the effective medium average of San Carlos olivine.

TABLE 3. Activation Energies and Preexponential Terms for DC Electrical Conductivity of San Carlos Olivine Compacts

Conduction Mechanism	E_{act}, eV	log σ_o, S/m
Grain boundary (bulk)	2.47 ± 0.15	5.64 ± 0.52
Grain interior (1)	1.45 ± 0.01	1.99 ± 0.02
Grain interior (2)	4.87 ± 0.08	12.65 ± 0.26

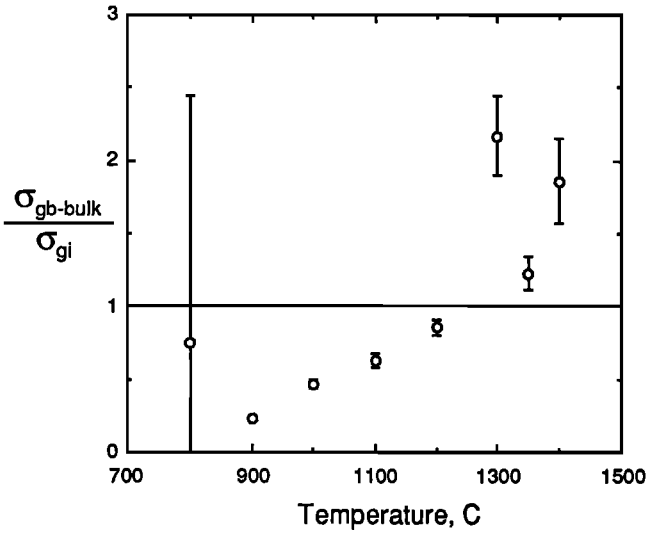

Fig. 20. Grain boundary/grain interior conductivity ratio σ_{gb}/σ_{gi} versus temperature for San Carlos olivine compacts.

The JC dunite and grain interior conductivities at low temperature have nearly the same slope (1.60 and 1.45 eV, respectively). Constable and Duba conclude that grain boundary conduction plays a negligible role in the total conductivity of this polycrystalline material because the conductivity they measure is close to that of single crystals of similar composition. The lower iron content of the Jackson County Dunite, compared to San Carlos olivine, is at least partly responsible for the lower measured conductivity. Assuming JC Dunite behaves electrically similar to our specimens, Constable and Duba do not measure the conductivity at frequencies sufficiently low to observe a grain boundary response in series with the grain interiors, and thus we expect the total conductivity for the JC Dunite to be as much as 2-3 times lower than the values

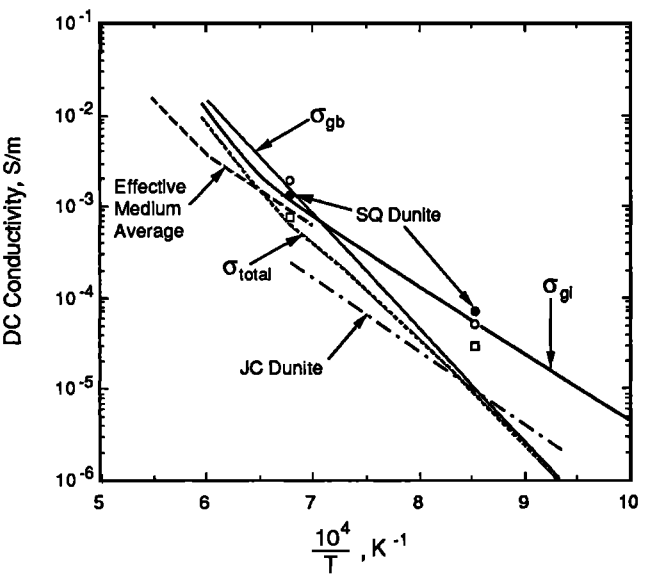

Fig. 21. Log DC conductivity versus reciprocal temperature for this and other studies. Grain interior and grain boundary conductivity, solid lines; series sum, dotted line (this study). Effective medium orientational average of olivine single crystal conductivity, dashed line [*Shankland and Duba*, 1990]; dunite conductivity, dash-dot line (Jackson County, North Carolina [*Constable and Duba*, 1990]). Symbols are the conductivity of San Quintin dunite (this study); σ_{gi}, open circles; $\sigma_{gb\text{-}bulk}$, solid circles; series sum of σ_{gi} and σ_{gb} ($1/\sigma_{tot} = 1/\sigma_{gi} + 1/\sigma_{gb}$), open squares.

reported. In our own preliminary measurements on a natural dunite at 900° and 1200°C (San Quintin dunite, Figure 21), we do observe that grain boundary and grain interior conductivities act in series, just as for the pressed compacts, indicating basic agreement with the results of Constable and Duba in terms of grain interior conductivity and suggesting that resistive, charge blocking grain boundaries are common in natural dunites.

The factors that cause the polycrystalline olivine materials of this study to exhibit resistive grain boundaries are not certain. The studies that report conductivities for natural dunites an order of magnitude or more greater than for single crystal olivine do not cover sufficiently broad frequency ranges to observe series grain boundary behavior if it existed [*Rai and Manghnani*, 1978; *Haak*, 1982]. Sato and coworkers observed frequency dependent response of partially molten gabbro that they attributed to physical constriction of the interconnections between melt pockets, but did not find grain boundaries to be resistive at temperatures below $T_{solidus}$ [*Sato and Ida*, 1984; *Sato et al.*, 1986]. Proposed causes of low grain boundary conductivity that have been discussed in the literature include impurity or phase segregation along grain boundaries and static space-charge polarized regions that exist at equilibrium on grain boundaries [*Kingery et al.*, 1976; *Chu and Seitz*, 1978]. Identification and characterization of the grain boundary structures and processes that control grain boundary conductivity are important problems that remain for future work. It is likely that in natural materials there exists extreme variability in the composition of grain boundaries and in their transport properties.

CONCLUSIONS

The frequency dependent electrical properties of polycrystalline San Carlos olivine display two impedance arcs in the complex plane. These two impedance arcs are representative of two different conduction mechanisms with different time constants. Only by making complex impedance measurements at frequencies as low as 10^{-3} to 10^{-4} Hz are we able to distinguish these two conduction mechanisms. Our interpretation of these mechanisms is that the highest-frequency impedance arc is caused by conduction through grain interiors and the low-frequency impedance arc is attributable to conduction through grain boundaries. By modeling the electrical response with equivalent circuits of resistors and capacitors we are able to determine the separate conductivities of both grain interiors and grain boundaries. The grain interior and grain boundary resistances add in series; the resulting total conductivity is 2-5 times lower than that of the grain interior measurements from this study. Our electrical measurements of a natural dunite also show series behavior of grain boundaries and grain interiors. Through comparison with the natural dunite we have shown that our synthetic rocks (with the problems associated with them) behave in a manner similar to natural rocks and therefore are representative of some mantle and crustal rocks. The grain boundaries do not enhance the conductivity of these samples. We do not observe a dependence of the bulk grain boundary conductivity on grain size; however, other parameters such as τ and κ' do demonstrate a dependence on grain size. Such behavior has been observed in other ceramic systems. Electrical measurements made on a natural dunite over a more limited range of frequency than our study [*Constable and Duba*, 1990] are not in conflict with our conclusion that grain boundary resistivity adds in series with grain interior resistivity.

It is important to measure the electrical properties of polycrystalline materials in the frequency range of 10^2 to 10^{-5} Hz, because it is in this low-frequency region that the effects of grain boundaries are observed. Geophysical methods used to construct electrical conductivity versus depth profiles employ measurements in this low-frequency range and laboratory measurements made in the kilohertz range may be less appropriate for use in the inversions of the field measurements. We observe a phase angle as high as 75-90 mrad at frequencies as low as 10^{-2} Hz that is not a result of processes occurring at the electrodes. This may be important in the inversion of field electromagnetic measurements if it is assumed that at these low frequencies there is no imaginary impedance component in the response of the material.

The electrical conductivity of olivine displays a strong dependence on temperature and has been used to infer temperatures in the upper mantle and lower crust from conductivity versus depth profiles. Our results indicate two distinct regions for the temperature dependence of the electrical conductivity of polycrystalline olivine; from 800° to 1250°C the grain interior conductivity is higher than the bulk grain boundary conductivity and from 1250° to 1400°C the bulk grain boundary conductivity is higher than the grain interior conductivity. Above 1250°C the DC conductivity of polycrystalline olivine (including grain boundaries in series) yields temperature estimates 30°-50°C higher than estimates based on grain interior conductivities alone. The potential for underestimating temperature is greater in the lower temperature range of 800°-1250°C. In this range of temperature, assuming the conductivity to be that of polycrystalline olivine, temperatures 50°-130°C higher than the temperatures based on the higher-frequency grain interior conductivity values result. Temperature estimates based on single-crystal conductivity values or measurements of polycrystalline samples that do not consider grain boundary transport can be lower than temperatures calculated from rocks that display series behavior of grain interiors and grain boundaries. These differences are important to our understanding and interpretation of the conditions and processes occurring in the lower crust and upper mantle.

APPENDIX

Thermal expansion anisotropy and microcracking. Thermal expansion anisotropy of olivine may lead to microfracture formation during the heating and cooling of the samples. Theoretical treatment of microfracture from thermal expansion anisotropy is given by *Evans* [1978]. The critical grain size for the onset of microfracture l_{co} is estimated by

$$l_{co} \approx \frac{5.2\,(1+\nu)^2\,\gamma_{gb}}{E\,(\Delta\alpha\Delta T)^2} \qquad \text{(A1)}$$

where ν is Poisson's ratio, γ_{gb} is the grain boundary fracture energy, E is Young's modulus, $\Delta\alpha$ is one-half of the difference between the maximum and minimum directions of the thermal expansion coefficient, and ΔT is the change in temperature. These parameters are not known exactly, but reasonable estimates may be made from the literature. Poisson's ratio is calculated from the elastic moduli of *Kumazawa and Anderson* [1969] at 1000°C for an olivine of composition $Fo_{92.72}Fa_{7.24}Te_{0.04}$ (Te is tephroite, Mn_2SiO_4) and is equal to 0.256. The grain boundary fracture energy γ_{gb} is estimated from the single-crystal fracture energy data of olivine. It is assumed that the grain boundaries will fracture more easily than the single crystal and that γ_{gb} will be less than the single crystal fracture energy. *Swain and Atkinson* [1978] report both calculated fracture energies (8.63 J/m^2, [010] and 12.06 J/m^2, [001]) and experimentally determined fracture energies (0.98 J/m^2,

[010] and 1.26 J/m^2, [001]) for single-crystal olivine. For the present calculation we employ a range of γ_{gb} of 1-2 J/m^2. An appropriate value for E is 170 GPa, a value between the data for a single crystal ($Fo_{92.7}$) in the [010] and [001] directions [*Kumazawa and Anderson*, 1969] and close to the value given for Balsam Gap dunite [*Skinner*, 1966]. The thermal expansion data of Skinner (1966) indicate that the maximum difference in thermal expansion coefficient α for different crystallographic directions in olivine is approximately 6x10^{-6} C^{-1} ($Fo_{89.9}$) at 1000°C. This difference is nearly constant over the temperature range 20°-1000°C. Based on this information, $\Delta\alpha$ is estimated to be 3x10^{-6} °C^{-1} for any temperature range [*Evans*, 1978].

Using the above parameter estimates the range of critical grain size for the onset of cracking from equation (A1) for the cooling of a sample from 1200°C to room temperature (ΔT = 1175°C) is about 3.9-7.8 μm. The sample with the smallest grain size studied, 7-15 μm (Table 1), was cooled from 1200°C to room temperature in less than 1 hour and shows no microfractures upon postrun examination. The samples with larger grain sizes cooled from 1200°C do show cracks upon postrun examination, suggesting that equation (A1) and the above approximations are reasonable.

For a ΔT of 100°C the range of l_{co} is 534-1072 μm, a much larger grain size than any of the samples with the exception of the natural dunite. Since samples are recovered that have no microfractures, we assume that the amount of time required for the equilibration of a sample to the experimental conditions is also sufficient to heal most microfractures and that changing the temperature in small increments during an experiment induces no microfractures that will affect on our measurements.

Effect of porosity on impedance measurements. As discussed above, the samples studied contain 2-8 vol % porosity. The amount of porosity was determined by direct density measurements prior to impedance measurements. Microscopic examination indicates that most of the porosity occurs as isolated intergranular and intragranular pores. We consider the effects of intragranular and intergranular porosity on AC impedance measurements separately. We first employ the Maxwell model for a two phase dispersion to examine the influence of intragranular porosity [*Maxwell*, 1881]. The Maxwell model treats a material as a continuous matrix (phase 1) interspersed with a second phase (phase 2) of different electrical properties, that is, a suspension of spherical particles. The Maxwell model is particularly useful because it takes into account the effects of conductivity, dielectric permittivity, and volume fraction on the complex conductivity. The total complex conductivity of the system is given by

$$\psi_t = \psi_2 + \frac{(\psi_1 - \psi_2)(1 - x_2)}{1 + \frac{x_2(\psi_1 - \psi_2)}{2(\psi_1 + \psi_2)}} \qquad \text{(A2)}$$

where ψ_t is the total complex conductivity, ψ_1 and ψ_2 are the complex conductivities of the matrix and dispersed phase, X_2 is the volume fraction of the dispersed phase. The complex conductivity is defined as

$$\psi_i = \sigma_i + j\omega\varepsilon'_i \qquad \text{(A3)}$$

where σ_i is the DC conductivity and ε'_i is the real part of the dielectric permittivity (dielectric constant) of phase i and j is $\sqrt{-1}$. In the present analysis the second (dispersed) phase consists of pores, assumed to be spherical. Equation (A2) assumes that distortion of the electric field by a dispersed particle does not influence the electric field of other particles, limiting its use to situations where X_2 is less than 0.3 [*Bonanos et al.*, 1987]. To estimate the effect of porosity on our measurements, we have used equations (A2) and (A3) to generate simulated conductivity spectra and have converted these to complex resistivity spectra through

$$\rho^* = \psi^{-1} \qquad \text{(A4)}$$

(ρ^* and ψ are complex quantities). Two simulated impedance spectra are shown in Figure A1. The parameters used to generate these plots closely correspond to our experiments at 1200°C. We employed a value for σ_{DC} of 1.0 x 10^{-3} S/m for the matrix material and a very low conductivity of 1.0 x 10^{-9} S/m for the empty pore space. The permittivities employed were ε_1' = 8.854 x 10^{-10} F/m (a typical value for many solids at elevated temperatures) and ε_2' = 8.854 x 10^{-12} F/m (the value for vacuum). The simulated spectra display one impedance arc. For the ε' values chosen a dispersed second phase of lower conductivity in a surrounding matrix produces no additional impedance arcs. The DC resistivity of a material with no porosity is seen in Figure A1 to be 1000 Ω m, and a sample with 2% porosity has a DC resistivity of 1031 Ω m. Varying the conductivity of the pore spaces does not result in two impedance arcs as long as $\sigma_1/\sigma_2 \geq 10$. The only effect is to widen the impedance arc which results in a higher value of apparent DC resistivity. Thus the two impedance arc behavior of the experimental results is not caused by the minor amount of porosity in the samples. *Brailsford and Hohnke* [1983] similarly concluded that small amounts of isolated porosity do not add additional impedance arcs in ceramic oxides. The two impedance arc behavior reflects the bulk electrical properties of the system.

For DC conditions (ω=0), equation (A2) reduces to

$$\sigma_t = \sigma_2 + \frac{2x_1(\sigma_1+\sigma_2)(\sigma_1-\sigma_2)}{(2+x_2)\sigma_1+(1+x_1)\sigma_2} \qquad \text{(A5)}$$

where x_1, x_2 and σ_1, σ_2 are the volume fractions and DC conductivities (or relative DC resistivities) of the matrix and dispersed phase, respectively. The conductivities calculated according to equation (A5) are the same as those calculated using

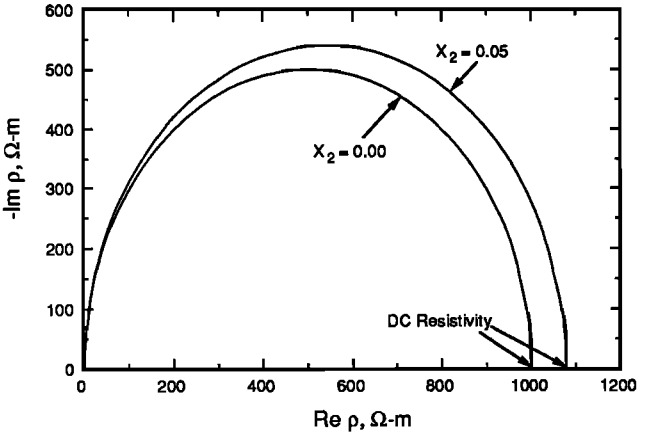

Fig. A1. Complex plane plot calculated using equation (A4) showing effect of dispersed porosity on bulk impedance. Matrix material has σ_{DC} = 10^{-3} S/m and ε' = 8.854 x 10^{-10} F/m. Pores (medium 2) have σ_{DC} = 10^{-9} S/m and ε' = 8.85 x 10^{-12} F/m (the value for a vacuum). X_2 is volume fraction of porosity.

the Hashin-Shtrikman upper bound for effective bulk DC conductivity of a two phase mixture as outlined by *Waff* [1974]. For the range of porosities in our samples, we estimate that the resistivities we measure are 3-11% higher than the actual resistivities of pore-free material.

An analysis by *Brailsford and Hohnke* [1983] evaluates the effects of both intergranular and intragranular porosity on resistivity measurements. They conclude that a small amount of intragranular porosity has little or no effect on the value of bulk (grain interior) resistivity, similar to the analysis above. Intergranular porosity has a potentially large effect on the measured values of grain boundary resistivity. The observed grain boundary resistivity of *Brailsford and Hohnke* [1983] is given by

$$\rho_{gb\text{-}obs} = \frac{\phi_{gb} + \frac{3}{2}\phi_p}{3\sigma_{gb\text{-}micro}} \qquad \text{(A6)}$$

where ϕ_{gb} and ϕ_p are the volume fractions of grain boundaries and pores, respectively. Equation (A6) is derived by assuming a pore conductivity of zero. The effect of porosity on $\rho_{gb\text{-}obs}$ of PC10, the sample with the greatest amount of porosity, has been evaluated using equation (A6). Assuming a grain boundary thickness of 10 nm, the grain boundary volume fraction is 3×10^{-3}, and also assuming that half of the pores occur between grains (ϕ_p=0.04), we see that in terms of resistivity, $\rho_{gb\text{-}obs} \approx 20\ (\rho_{gb\text{-}macro})$. This result represents an extreme upper bound of the effects of intergranular porosity. There are several factors to consider. The conductivity of the pore spaces is not necessarily zero, some surface conduction probably occurs. A pore between grains does not displace only grain boundary material but both grain boundary and surrounding crystalline material. Most of the volume of the pore displaces surrounding crystal material, and a much lower fraction of the total pore volume displaces grain boundary material. The model by Brailsford and Hohnke does not account for these factors. Assuming a grain boundary width of 10 nm, and a pore diameter of 1 μm, only 1.5×10^{-4} % of the volume of the pore displaces grain boundary material. Reanalysis of equation (A6) with $\phi_{p,gb}=6 \times 10^{-8}$ yields $\rho_{gb\text{-}obs} = \rho_{gb\text{-}macro}$; that is, 4% porosity on grain boundaries does not affect the measured values of ρ_{gb}. The similarity of the electrical response of the natural samples we have examined that have no visible porosity to the response of the ground-and-pressed samples seems to bear this out.

In this paper we do not correct for the effect of porosity due to the uncertain nature of the correction and report the actual measured values. However, we caution that porosity can affect measured values of resistivity. The presence of porosity does not introduce any additional impedance arcs. The homogeneous model of porosity (equation (A5)) gives a reasonable maximum estimate of the error introduced by porosity in the ground-and-pressed samples of this study.

Acknowledgments. We thank Bob Norton and Chris Skiba for technical assistance and Sue Selkirk for help drafting the figures. Jack Lowell (Helicon Designs) and Mark Rovetta (ASU) donated sample materials. The Materials Preparation Facility at ASU assisted in the preparation of some of the samples . Electron microprobe analyses were performed at ASU with the assistance of James Clark. The computer program used in fitting the data (LOMFP) was obtained from J. R. Macdonald. We also thank Tom Shankland for providing the nonlinear curve fit routine for the conductivity versus reciprocal temperature fits. The critical reviews of Al Duba and an anonymous reviewer were beneficial to this work. This work was supported by the National Science Foundation, Division of Earth Sciences, under grants EAR-8916796 and EAR-8657357.

REFERENCES

Abelard, P., and J. F. Baumard, Electric and dielectric properties of forsterite between 400 and 900°C, Phys. Earth Planet. Inter., 23, 98-102, 1980.

Archer, W. I., and R. D. Armstrong, The application of A. C. impedance methods to solid electrolytes, in Electrochemistry, vol. 7, edited by H. R. Thirsk, pp. 157-202, The Chemical Society, London, 1980.

Basu, A. R., and V. R. Murthy, Ancient lithospheric lherzolitic xenolith in alkali basalt from Baja California, Earth Planet. Sci. Lett., 35, 239-246, 1977.

Bauerle, J. E., Study of solid electrolyte polarization by a complex admittance method, J. Phys. Chem. Solids, 30, 2657-2670, 1969.

Beekmans, N. M., and L. Heyne, Correlation between impedance, microstructure and composition of calcia-stabilized zirconia, Electrochim. Acta, 21, 303-310, 1976.

Bonanos, N., B. C. H. Steele, and E. P. Butler, Characterization of materials, in *Impedance Spectroscopy*, edited by J. R. Macdonald, pp. 191-237, John Wiley, New York, 1987.

Bowerman, B. L., R. T. O'Connell, and D. A. Dicvkey, *Linear Statistical Models, an Applied Approach*, 690 pp., Duxbury Press, Boston, Mass., 1986.

Brady, J. B., Intergranular diffusion in metamorphic rocks, *Am. J. Sci., 283-A*, 181-200, 1983.

Brailsford, A. D., and D. K. Hohnke, The electrical characterization of ceramic oxides, *Solid State Ionics, 11*, 133-142, 1983.

Cemic, L., G. Will, and E. Hinze, Electrical conductivity measurements on olivines Mg_2SiO_4-Fe_2SiO_4 under defined thermodynamic conditions, *Phys. Chem. Miner., 6*, 95-107, 1980.

Chu, S. H., and M. A. Seitz, The ac electrical behavior of polycrystalline ZrO2-CaO, *J. Solid State Chem., 23*, 297-314, 1978.

Cole, K. S., and R. H. Cole, Dispersion and absorption in dielectrics, I, Alternating current characteristics, *J. Chem. Phys., 9*, 341-351, 1941.

Constable, S. C., and A. G. Duba, The electrical conductivity of olivine, a dunite and the mantle, *J. Geophys. Res., 95*, 6967-6978, 1990.

Cygan, R. T., and A. C. Lasaga, Dielectric polarization behavior of forsterite at elevated temperatures, *Am. Min., 71*, 758-766, 1986.

Draper, N. R., and H. Smith, *Applied Regression Analysis*, 709 pp., John Wiley, New York, 1981.

Duba, A., Electrical conductivity of olivine, *J. Geophys. Res., 77*, 2483-2495, 1972.

Duba, A., H. C. Heard, and R. N. Schock, Electrical conductivity of olivine at high pressure and under controlled oxygen fugacity, *J. Geophys. Res., 79*, 1667-1673, 1974.

Evans, A. G., Microfracture from thermal expansion anisotropy, I, Single phase systems, *Acta Metall., 26*, 1845-1853, 1978.

Fricke, H., The Maxwell-Wagner dispersion in a suspension of ellipsoids, *J. Phys. Chem., 57*, 934-937, 1953.

Haak, V., A comparison of the electrical conductivity of natural mono- and polycrystalline olivines—A case to decide, in High-Pressure Researches in Geoscience, edited by W. Schreyer, pp. 407-417, E. Schweizerbart'sche, Stuttgart, 1982.

Hodge, I. M., M. D. Ingram, and A. R. West, Impedance and modulus spectroscopy of polycrystalline solid electrolytes, *J. Electroanal. Chem., 74*, 125-143, 1976.

Huebner, J. S., and D. E. Voight, Electrical conductivity of diopside: Evidence for oxygen vacancies, *Am. Mineral., 73*, 1235-1254, 1988.

Hughes, H., The pressure effect on the electrical conductivity of peridot, *J. Geophys. Res., 60*, 187-191, 1955.

Hurt, R. L., and J. R. Macdonald, Distributed circuit elements in impedance spectroscopy: A unified treatment of conductive and dielectric systems, *Solid State Ionics, 20*, 111-124, 1986.

Jonscher, A. K., The interpretation of non-ideal dielectric admittance and impedance diagrams, *Phys. Status. Solidi, 32*, 665-676, 1975.

Kingery, W. D., H. K. Bowen, and D. R. Uhlmann, *Introduction to Ceramics*, 2nd ed., John Wiley, 1032 pp., New York, 1976.

Knight, R. J., The Dielectric Constant of Sandstones, 5 Hz to 13 MHz, Ph.D. dissertation, Stanford Univ., Stanford, Calif., 1984.

Kumazawa, M., and O. L. Anderson, Elastic moduli, pressure derivatives, and temperature derivatives of single-crystal olivine and single crystal forsterite, *J. Geophys. Res., 74*, 5961-5972, 1969.

Lacam, A., Pressure and composition dependence of the electrical conductivity of iron-rich synthetic olivines to 200 kbar, *Phys. Chem. Miner., 9*, 127-132, 1983.

Lilley, E., and J. E. Strutt, Bulk and grain boundary ionic conductivity in polycrystalline β"-alumina, *Phys. Status. Solidi., 54*, 639-650, 1979.

Lockner, D. A., and J. D. Byerlee, Complex resistivity measurements of confined rock, *J. Geophys. Res., 90*, 7837-7847, 1985.

Macdonald, J. R., Generalizations of "universal dielectric response" and a general distribution-of-activation-energies model for dielectric and conducting systems, *J. Appl. Phys., 58*, 1971-1978, 1985.

Macdonald, J. R., and D. R. Franceschetti, Physical and electrochemical models, in *Impedance Spectroscopy*, edited by J.R. Macdonald, pp. 84-132, John Wiley, New York, 1987.

Macdonald, J. R., and W. B. Johnson, Fundamentals of impedance spectroscopy, in *Impedance Spectroscopy*, edited by J.R. Macdonald, pp. 1-20, John Wiley, New York, 1987.

Macdonald, J. R., J. Schoonman, and A. P. Lehnen, The applicability and power of complex nonlinear least squares for the analyses of impedance and admittance data, *J. Electroanal. Chem., 131*, 77-95, 1982.

Maxwell, J. C., *A Treatise on Electricity and Magnetism*, 2nd ed., Clarendon, Oxford, 1881.

Myers, J., and H. P. Eugster, The system Fe-Si-O: Oxygen buffer calibrations to 1,500K, *Contrib. Mineral. Petrol., 82*, 75-90, 1983.

Naughton, J. J., and U. Fujikawa, Measurement of intergranular diffusion in a silicate system: Iron in forsterite, *Nature, 184*, 54-56, 1959.

Olhoeft, G. R., Electrical properties, in Initial Report of the Petrophysics Laboratory, *U.S. Geol. Surv. Circ., 789*, 1-26., 1979.

Olhoeft, G. R., Low frequency electrical properties, *Geophysics, 50*, 2492-2503, 1985.

Rai, C. S., and M. H. Manghnani, Electrical conductivity of ultramafic rocks to 1820 Kelvin, *Phys. Earth Planet. Inter., 17*, 6-13, 1978.

Raistrick, I. D., The electrical analogs of physical and chemical processes, in *Impedance Spectroscopy*, edited by J.R. Macdonald, pp. 27-84, John Wiley, New York, 1987.

Sato, H., High temperature a.c. electrical properties of olivine single crystal with varying oxygen partial pressure: Implications for the point defect chemistry, *Phys. Earth Planet. Inter., 41*, 269-282, 1986.

Sato, H., and Y. Ida, Low frequency electrical impedance of partially molten gabbro: The effect of melt geometry on electrical properties, *Tectonophysics, 107*, 105-134, 1984.

Sato, H., M. H. Manghnani, B. R. Lienert, and A. T. Weiner, Effects of electrode polarization on the electrical properties of partially molten rock, *J. Geophys. Res., 91*, 9325-9332, 1986.

Schock, R. N., A. G. Duba, and T. J. Shankland, Electrical conduction in olivine, *J. Geophys. Res., 94*, 5829-5839, 1989.

Shankland, T. J., and A. G. Duba, Standard electrical conductivity of isotropic, homogeneous olivine in the temperature range 1100-1500°C, *Geophys. J. Int., 103*, 25-31, 1990.

Skinner, B. J., Thermal expansion, in Handbook of Physical Constants, *Mem. Geol. Soc. Am., 97*, 75-96, 1966.

Swain, M. V., and B. K. Atkinson, Fracture surface energy of olivine, *Pure Appl. Geophys., 116*, 866-872, 1978.

Tuller, H. L., Electrical conduction in ceramics: Toward improved defect interpretation, in *Point Defects in Minerals, Geophys. Monogr. Ser.*, vol. 31, edited by R. N. Schock, pp. 47-68, AGU, Washington, D. C., 1985.

Tyburczy, J. A., and J. J. Roberts, Low frequency electrical response of polycrystalline olivine compacts: Grain boundary transport, *Geophys. Res. Lett., 17*, 1985-1988, 1990.

van Dijk, T., and A. J. Burggraaf, Grain boundary effects on ionic conductivity in ceramic GdxZr1-xO2-(x/2) solid solutions, *Phys. Status Solidi, 63*, 229-240, 1981.

Verkerk, M. J., A. J. A. Winnubst, and A. J. Burggraaf, Effect of impurities on sintering and conductivity of yttria-stabilized zirconia, *J. Mater. Sci., 17*, 3113-3122, 1982*a*.

Verkerk, M. J., B. J. Middelhuis, and A.J. Burgraaf, Effect of grain boundaries on the conductivity of high-purity ZrO2-Y2O3 ceramics, *Solid State Ionics, 6*, 159-170, 1982*b*.

von Hippel, A. R., *Dielectric Materials and Applications*, 438 pp. MIT Press, Cambridge, Mass., 1954.

Waff, H. S., Theoretical considerations of electrical conductivity in a partially molten mantle and implications for geothermometry, *J. Geophys. Res., 79*, 4003-4010, 1974.

Watson, E. B., An experimental study of oxygen transport in dry rocks and related kinetic phenomena, *J. Geophys. Res., 91*, 14,117-14,131, 1986.

Will, G., and G. Nover, Measurement of the frequency dependence of the electrical conductivity and some other petro-physical parameters of core samples from the Konzen (west Germany) drill hole, *Ann. Geophys. Ser., B, 2*, 173-182, 1986.

Wimmer, J. M., H. C. Graham, and N. M. Tallan, Microstructural and polyphase effects, in *Electrical Conductivity in Ceramics and Glass, Part B*, edited by N. M. Tallan, pp. 619-652, Marcel Dekker , New York, 1974.

J. J. Roberts and J. A. Tyburczy, Department of Geology, Arizona State University, Tempe, AZ 85287-1404.

(Received December 27, 1990;
revised May 30, 1991;
accepted June 11, 1991.)

JOURNAL OF GEOPHYSICAL RESEARCH, VOL. 96, NO. B10, PAGES 16,529–16,533, SEPTEMBER 10, 1991

Microcrack-Induced Seismic Anisotropy of Sedimentary Rocks

C. M. SAYERS[1] AND J. G. VAN MUNSTER

Koninklijke/Shell Exploratie en Produktie Laboratorium, Rijswijk, Netherlands

The seismic anisotropy often detected in the Earth's crust has been attributed in large part to the presence of open microcracks showing some degree of alignment. This alignment is believed to result from the anisotropic state of in situ stress, since any cracks remaining open at depth will tend to be oriented normal to the direction of the minimum in situ stress. Previous workers have calculated the change in elastic wave velocities due to either randomly oriented or perfectly aligned cracks. In this paper the P and S wave anisotropy in the long-wavelength limit is calculated for an arbitrary orientation distribution of cracks. For the case of an orthotropic distribution of circular cracks it is found that a simple relation exists between the P and S wave anisotropy. To test this prediction, ultrasonic P and S wave velocities were measured for propagation in three orthogonal directions through three samples of Berea sandstone as a function of maximum compressive stress applied perpendicular to the bedding plane. The samples were 50-mm cubes and were stressed to peak in a true triaxial loading frame, while the principal stress components parallel to the bedding plane were held constant at 4 MPa.

1. INTRODUCTION

It has been suggested that the seismic anisotropy observed in the upper 10–20 km of the Earth's crust is often due to the presence of open microcracks showing some degree of alignment [*Crampin et al.*, 1984; *Crampin*, 1987]. Any cracks remaining open at depth will tend to be oriented normal to the direction of the minimum in situ stress. Observations of seismic anisotropy therefore have the potential of providing the orientation of the in situ stress field. For example, recent modeling of shear waveforms in three component shear wave vertical seismic profiles in the Paris Basin [*Crampin et al.*, 1986] is consistent with a distribution of vertical fluid-filled cracks aligned with strikes along N30°W, corresponding to the direction of maximum horizontal in situ stress in this area.

In the presence of oriented cracks the elastic wave velocities in the crust depend on the propagation direction and polarization of the wave. Previous workers have assumed either randomly orientated or perfectly aligned cracks. In this paper the P and S wave anisotropy is evaluated for rocks containing an arbitrary orthotropic orientation distribution of cracks. This includes the important case of axial symmetry, for which simplified equations are given. The theory is tested by comparing the predictions with measurements of the P and S wave anisotropy that develops in Berea sandstone as it is stressed to failure. Central to this comparison is the observation that the failure of brittle rocks during compression is preceded by the formation, growth, and coalescence of microcracks [*Paterson*, 1978; *Kranz*, 1983]. Tensile stress necessary for microcrack growth include shear along preexisting microcracks and stress concentrations around inhomogeneities.

The measurements reported are taken in the ultrasonic frequency range. Since the measurement is done on dry samples, dispersive effects resulting from elastic-wave-induced fluid flow are absent, and the velocities should be representative of those that would be obtained in the seismic frequency range provided that the size of any inhomogeneities and cracks is small compared to the wavelength. In the experiments reported here the maximum frequency transmitted through the samples is of the order of 1 MHz, corresponding to a wavelength greater than 10 times the grain diameter of the sandstone used. Since the length of cracks when first formed is of the order of the grain diameter, the measurements are expected to correspond to the long-wavelength limit except close to failure. Previous studies of microcrack-induced anisotropy in rocks using ultrasound include those of *Bonner* [1974], *Lockner et al.* [1977], and *Granryd et al.* [1983] on Westerly granite, *Gupta* [1973] on Indiana limestone, *Nur and Simmons* [1969] on Barre granite, *Hadley* [1975] on Westerly granite and San Marcos gabbro, and *Holt and Fjaer* [1987] on weakly consolidated sandstones. The present work, however, presents for the first time a quantitative relationship between the microcrack-induced P and S wave anisotropy valid for an arbitrary orthotropic orientation distribution of microcracks and tests this relationship using experimental results.

2. THEORY

It is assumed that the mechanical behavior of rock in the brittle field is determined by the formation, growth, and coalescence of microcracks. As a result of the anisotropy of the stress field, these microcracks show some degree of preferred orientation. To model the effect of this on ultrasonic velocities, these cracks are approximated by ellipsoids embedded in an isotropic background medium. For an ellipsoidal crack with principal axes $2a$, $2b$, $2c$ ($a \geq b \geq c$) it is convenient to introduce a set of axes $OX_1X_2X_3$ with origin at the center of the ellipsoid and OX_1, OX_2, and OX_3 along the a, b, and c axes, respectively (see Figure 1). The fourth order elastic stiffness tensor of the microcracked rock, C_{ijkl}, will be written in the form $C_{ijkl} = C^0_{ijkl} + \gamma_{ijkl}$, where γ_{ijkl} is the difference between C_{ijkl} and the elastic stiffness tensor C^0_{ijkl} of the uncracked rock, which will be assumed to be isotropic. If the axes $OX_1X_2X_3$ for all cracks are aligned, the rock will exhibit orthotropic symmetry with three orthogonal planes of mirror symmetry having plane

[1]Now at Shell Research Arnhem, Arnhem, Netherlands.

Paper number 91JB01232.
0148-0227/91/91JB-01232$05.00

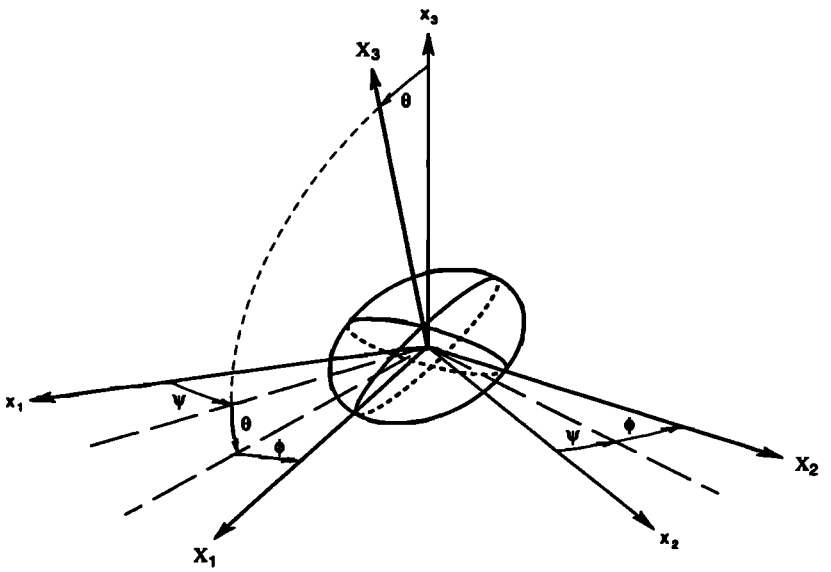

Fig. 1. The orientation of coordinate system $OX_1X_2X_3$ with origin at the center of an ellipsoidal crack with respect to the material coordinate system $Ox_1x_2x_3$ specified by Euler angles ψ, θ, and ϕ.

normals in the OX_1, OX_2, and OX_3 directions. If the γ_{ijkl} in this case are denoted by Γ_{ijkl}, then in the crack reference frame $OX_1X_2X_3$ the nonzero Γ_{ijkl} are Γ_{11}, Γ_{22}, Γ_{33}, $\Gamma_{12} = \Gamma_{21}$, $\Gamma_{23} = \Gamma_{32}$, $\Gamma_{31} = \Gamma_{13}$, Γ_{44}, Γ_{55}, and Γ_{66} in the Voigt (two-index) notation. For circular cracks with $a = b \gg c$, $\Gamma_{11} = \Gamma_{22}$, $\Gamma_{23} = \Gamma_{31}$, $\Gamma_{44} = \Gamma_{55}$ and $\Gamma_{66} = (\Gamma_{11} - \Gamma_{12})/2$. The anisotropy of Γ_{ijkl} in this case may be completely specified by three anisotropy parameters a_1, a_2, and a_3 [*Sayers*, 1988*a*, *b*], which are defined by

$$a_1 = \Gamma_{11} + \Gamma_{33} - 2\Gamma_{13} - 4\Gamma_{44} \quad (1)$$

$$a_2 = \Gamma_{11} - 3\Gamma_{12} + 2\Gamma_{13} - 2\Gamma_{44} \quad (2)$$

$$a_3 = 4\Gamma_{11} - 3\Gamma_{33} - \Gamma_{13} - 2\Gamma_{44}. \quad (3)$$

In general, the cracks will not be perfectly aligned, and a quantitative description of the elastic wave anisotropy requires a knowledge of the orientation distribution of cracks. The orientation of an ellipsoidal crack with principal axes $OX_1X_2X_3$ with respect to a set of axes $Ox_1x_2x_3$ fixed in the rock may be specified be three Euler angles ψ, θ, and ϕ, as shown in Figure 1. The orientation distribution of cracks is then given by the crack orientation distribution function $W(\xi, \psi, \phi)$ where $\xi = \cos\theta$, θ being the angle between OX_3 and Ox_3. $W(\xi, \psi, \phi)d\xi d\psi d\phi$ gives the fraction of cracks between ξ and $\xi + d\xi$, ψ and $\psi + d\psi$, and ϕ and $\phi + d\phi$. The elastic stiffnesses of the rock may be calculated in terms of the coefficients W_{lmn} in an expansion of the crack orientation distribution function in generalized Legendre functions [*Sayers*, 1988*a*, *b*]. Since the elastic stiffness tensor is of fourth rank, it depends only on the coefficients W_{lmn} of the expansion of $W(\xi, \psi, \phi)$ for $l \leq 4$. If the cracks are ellipsoidal and their orientation distribution is orthotropic with symmetry axes coincident with the reference axes $Ox_1x_2x_3$, the nonzero W_{lmn} are all real and are restricted to even values of l, m, and n. For circular cracks with $a = b \gg c$, $W_{lmn} = 0$ unless $n = 0$. The elastic stiffnesses are therefore determined in this case by W_{200}, W_{220}, W_{400}, W_{420}, and W_{440}, and the three anisotropy factors a_1, a_2, and a_3 defined above [*Sayers*, 1988*a*, *b*]. The ultrasonic wave velocities in the rock may then be obtained as solutions of the Christoffel equations [*Musgrave*, 1970]. For dry penny-shaped cracks the a_i may be calculated from the work of *Hudson* [1981]. The factor a_1 is found to be much smaller than a_2 and a_3 [*Sayers*, 1988*a*, *b*]. As a result, the coefficients W_{4m0} make only a small contribution to the measured ultrasonic wave velocities and may be ignored, the resultant equations for the velocities being

$$\rho v_{11}^2 = \rho \bar{v}_P^2 + 8\sqrt{10}\pi^2 a_3(W_{200} - \sqrt{6}W_{220})/105 \quad (4)$$

$$\rho v_{22}^2 = \rho \bar{v}_P^2 + 8\sqrt{10}\pi^2 a_3(W_{200} + \sqrt{6}W_{220})/105 \quad (5)$$

$$\rho v_{33}^2 = \rho \bar{v}_P^2 - 16\sqrt{10}\pi^2 a_3 W_{200}/105 \quad (6)$$

$$\rho v_{12}^2 = \rho v_{21}^2 = \rho \bar{v}_S^2 + 4\sqrt{10}\pi^2(7a_2 + 2a_3)W_{200}/315 \quad (7)$$

$$\rho v_{23}^2 = \rho v_{32}^2 = \rho \bar{v}_S^2 - 2\sqrt{10}\pi^2(7a_2 + 2a_3)(W_{200} - \sqrt{6}W_{220})/315 \quad (8)$$

$$\rho v_{31}^2 = \rho v_{13}^2 = \rho \bar{v}_S^2 - 2\sqrt{10}\pi^2(7a_2 + 2a_3)(W_{200} + \sqrt{6}W_{220})/315. \quad (9)$$

Here ρ is the density or the rock and $\bar{v}_P$ and $\bar{v}_S$ are the P and S wave velocities for a rock with the same density of cracks but with random crack orientations. The values $\bar{v}_P$ and $\bar{v}_S$ may be obtained from (4)–(9):

$$\bar{v}_P^2 = (v_{11}^2 + v_{22}^2 + v_{33}^2)/3 \quad (10)$$

$$\bar{v}_S^2 = (v_{12}^2 + v_{23}^2 + v_{31}^2)/3. \quad (11)$$

It is seen from (4)–(9) that the P and S wave anisotropies are not independent but are related by the following equations:

TABLE 1. Mineralogical Analysis of the Berea Sandstone Samples Studied in This Work

Sample	Quartz, % by Weight	K Feldspar, % by Weight	Kaolinite, % by Weight	Illite + Smectite, % by Weight
I	94	4	1	1
II	94	4	1	1
III	85	5	4	6

$$(v_{11}^2 - v_{22}^2) = A(v_{31}^2 - v_{23}^2) \quad (12)$$

$$(v_{11}^2 + v_{22}^2 - 2v_{33}^2) = A(2v_{12}^2 - v_{23}^2 - v_{31}^2) \quad (13)$$

where

$$A = 12a_3/(7a_2 + 2a_3). \quad (14)$$

For the small anisotropy observed in most rocks, (12) and (13) reduce to

$$(v_{11} - v_{22})/\bar{v}_P = B(v_{31} - v_{23})/\bar{v}_S \quad (15)$$

$$(v_{11} + v_{22} - 2v_{33})/\bar{v}_P = B(2v_{12} - v_{23} - v_{31})/\bar{v}_S \quad (16)$$

where $B = A(\bar{v}_S/\bar{v}_P)^2$. For transverse isotropy, with symmetry axis along Ox_3, $v_{11} = v_{22}$, $v_{23} = v_{31}$, and (13) reduces to $(v_{11}^2 - v_{33}^2) - A(v_{12}^2 - v_{31}^2)$.

3. Measurement of Stress-Induced Anisotropy

To test these predictions, ultrasonic velocities were measured in three 50-mm cubes of Berea sandstone cut parallel to the bedding plane. Berea is a light brown, fine-grained, well-sorted sandstone. Its mineralogy is mainly quartz, with small amounts of feldspar and clay minerals. A mineralogical description of the samples is given in Table 1. Ultrasonic velocities were measured with the samples in an air-dry condition using the true triaxial loading frame described by *Sayers et al.* [1990]. This apparatus is illustrated in Figure 2. The initial velocity was measured at a hydrostatic compressive stress of 4 MPa, after which the stress perpendicular to the bedding plane was raised in steps of 4 MPa to peak, keeping the other two stress components fixed. This loading configuration was chosen in order to investigate the magni-

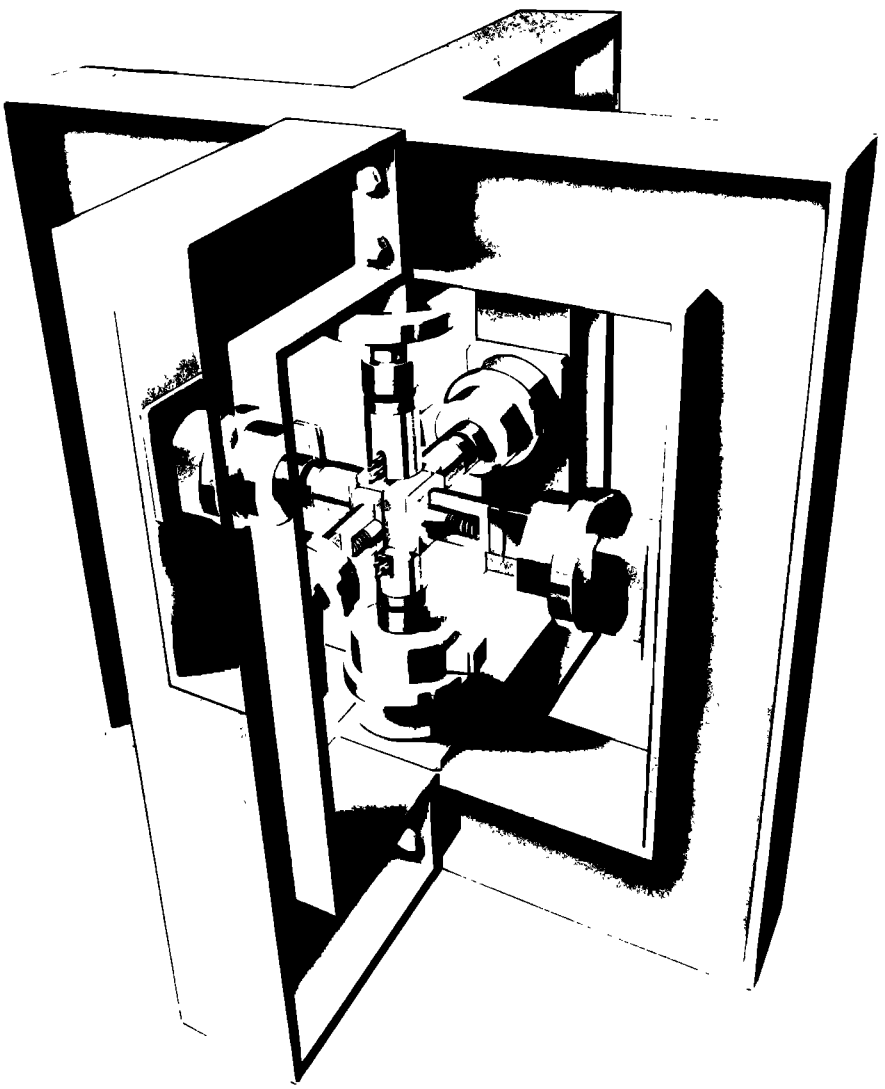

Fig. 2. Overview of experimental test setup.

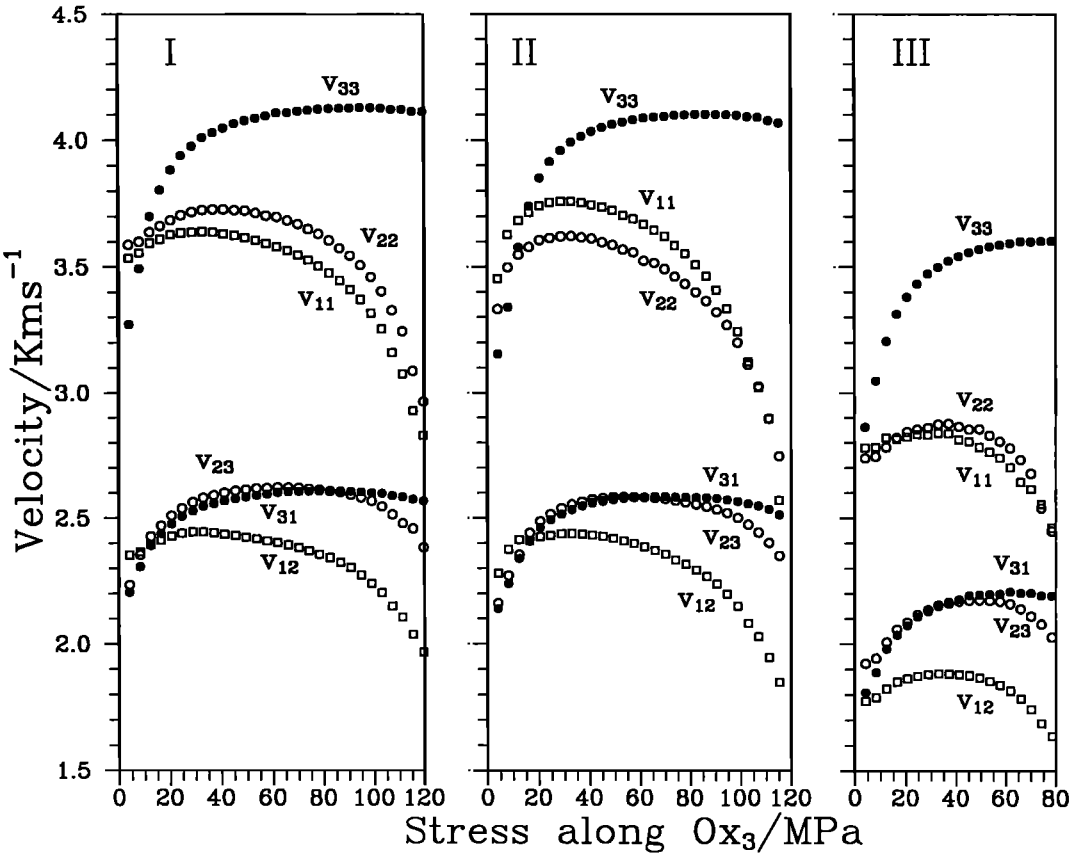

Fig. 3. *P* and *S* wave velocities in dry Berea sandstone as a function of major principal stress for Berea samples I, II, and III described in Table 1.

tude of any deviations from transverse anisotropy of the sample when a transversely anisotropic stress field is applied. The velocities are plotted in Figure 3 as a function of the major principal stress component using a reference set of axes chosen with Ox_3 perpendicular to the bedding plane and parallel to the direction of maximum stress and Ox_1 and Ox_2 parallel to the remaining cube edges. The velocities measured were v_{11}, v_{22}, and v_{33} (*P* waves) and v_{12}, v_{23}, and v_{31} (*S* waves).

4. Discussion

It is seen in Figure 3 that v_{33}, v_{23}, and v_{31} rise monotonically throughout most of the test but with a small drop immediately prior to failure; v_{11}, v_{22}, and v_{12} rise at first, but then drop after the first third of the test. The measurements for the two samples with low clay content are in agreement, but the sample with higher clay content is seen to have substantially lower velocities and to fail at a significantly lower value of the maximum compressive stress. At low stress the observed increase in wave velocity can be explained by the closure of preexisting microcracks and grain boundaries in the rock and, as the stress increases still further, by the formation of new microcracks and the growth and coalescence of preexisting cracks. The measurements may therefore by analyzed using the theory presented in section 2. It is seen in Figure 3 that for the loading configuration used in this work $v_{11} \approx v_{22}$ and $v_{31} \approx v_{23}$, so that (12) is approximately satisfied. Figures 4*a* and 4*b* show plots of $(v_{11}^2 + v_{22}^2 - 2v_{33}^2)$ against $(2v_{12}^2 - v_{23}^2 - v_{31}^2)$ and $(v_{11} + v_{22} - 2v_{33})/\bar{v}_P$ against $(2v_{12} - v_{23} - v_{31})/\bar{v}_S$ for the samples studied. Although these quantities are individually nonlinear functions of stress, they are found to be linearly related and in good agreement with the predictions of (13) and (16). A fit of these equations to the measurements gives $A = 3.628$ and $B = 1.583$, and therefore $\bar{v}_P/\bar{v}_S = (A/B)^{1/2} = 1.51$. This compares with the value $\bar{v}_P/\bar{v}_S = 1.5$ obtained by *Castagna et al.* [1985] for dry sandstones and corresponds to a Poisson's ratio $\nu = 0.11$. This is the same value as obtained by *Lo et al.* [1986] for Berea sandstone. The value $A = 3.628$ should be compared with the value $A = 5.036$ obtained using the theory of *Hudson* [1981] for dry, noncontacting cracks and a value of Poisson's ratio $\nu = 0.11$. This disagreement may be the result of grain boundary closure, since this is not included in the theory.

5. Conclusions

In this article, measurements have been reported of *P* and *S* wave velocities in three orthogonal directions in three cubic samples of Berea sandstone stressed to peak. Two of the samples had a low clay content and exhibited similar behavior, but the third sample with higher clay content had substantially lower ultrasonic velocities and failed at a significantly lower value of the maximum compressive stress. Theoretical expressions for the ultrasonic wave velocities in terms of the coefficients W_{lmn} in an expansion of the crack orientation distribution in generalized Legendre

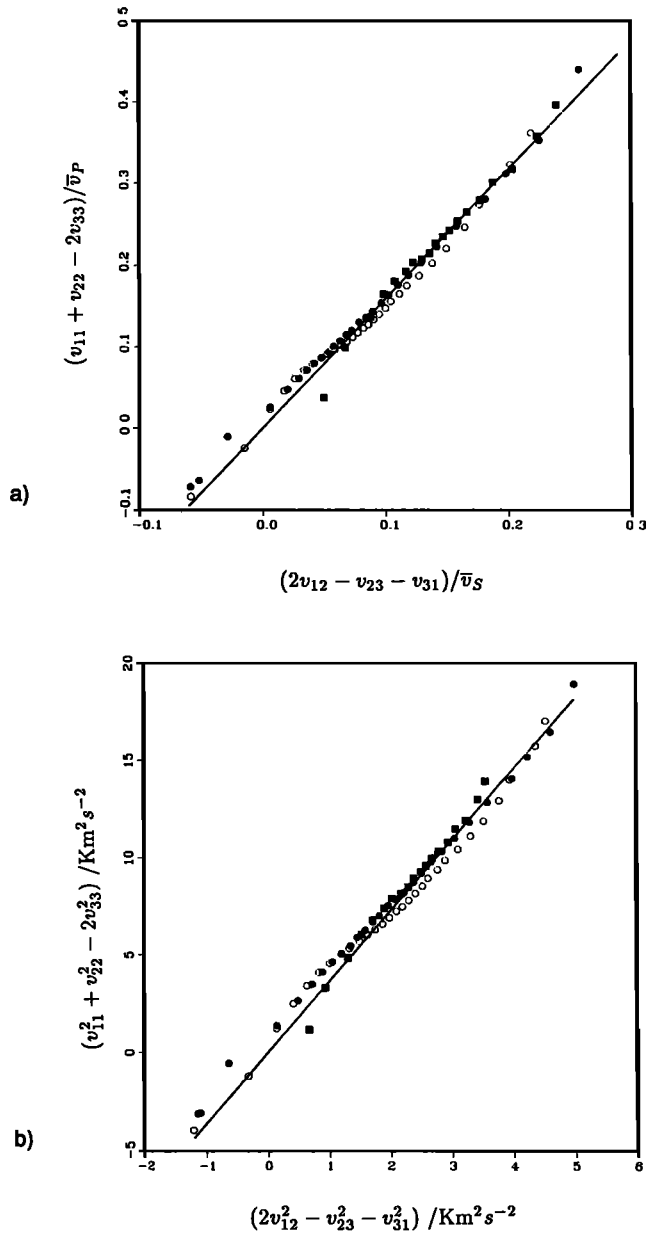

Fig. 4. Plot of (*a*) $(v_{11}^2 + v_{22}^2 - 2v_{33}^2)$ versus $(2v_{12}^2 - v_{23}^2 - v_{31}^2)$, and (*b*) $(v_{11} + v_{22} - 2v_{33})/\bar{v}_P$ versus $(2v_{12} - v_{23} - v_{31})/\bar{v}_S$, for the Berea samples I (open circles), II (solid circles), and III (solid squares). The lines are fits of equations (13) and (16) to the data.

functions give a linear relation between the *P* and *S* wave anisotropy for small-crack density. This prediction is confirmed by the experiment. The constant of proportionality here, however, is smaller than the value predicted by the theory of *Hudson* [1981] for dry, noncontacting cracks. This difference could result from the closure of grain boundaries during the experiment, since this is not included in the theory.

Acknowledgment. This paper is published by permission of Shell Internationale Research Maatschappij.

REFERENCES

Bonner, B. P., Shear wave birefringence in dilating granite, *Geophys. Res. Lett.*, *1*, 217–220, 1974.

Castagna, J. P., M. L. Batzle, and R. L. Eastwood, Relationships between compressional-wave and shear-wave velocities in clastic silicate rocks, *Geophysics*, *50*, 571–581, 1985.

Crampin, S., Geological and industrial implications of extensive-dilatancy anisotropy, *Nature*, *328*, 491–496, 1987.

Crampin, S., E. M. Chesnokov, and R. G. Hipkin, Seismic anisotropy—The state of the art II, *Geophys. J. R. Astron. Soc.*, *76*, 1–16, 1984.

Crampin, S., I. Bush, C. Naville, and D. B. Taylor, Estimating the internal structure of reservoirs with shear-wave VSPs, *The Leading Edge*, *5*, 35–39, 1986.

Granryd, L., I. C. Getting, and H. Spetzler, Path independence of acoustic velocity and attentuation in experimentally deformed Westerly granite, *Geophys. Res. Lett.*, *10*, 71–74, 1983.

Gupta, I. N., Seismic velocities in rock subjected to axial loading up to shear fracture, *J. Geophys. Res.*, *78*, 6936–6942, 1973.

Hadley, K., V_p/V_s anomalies in dilatant rock samples, *Pure Appl Geophys.*, *113*, 1–23, 1975.

Holt, R. M., and E. Fjaer, Acoustic behaviour of sedimentary rocks during failure, in *North Sea Oil and Gas Reservoirs*, edited by J. Kleppe, pp. 311–316, Graham and Trotman, London, 1987.

Hudson, J. A., Wave speeds and attentuation of elastic waves in material containing cracks, *Geophys. J. R. Astron. Soc.*, *64*, 133–150, 1981.

Kranz, R. L., Microcracks in rock: A review, *Tectonophysics*, *100*, 449–480, 1983.

Lo, T., K. B. Coyner, and M. N. Toksoz, Experimental determination of elastic anisotropy of Berea sandstone, *Geophysics*, *51*, 164–171, 1986.

Lockner, D. A., J. B. Walsh, and J. D. Byerlee, Changes in seismic velocity and attenuation during deformation of granite, *J. Geophys. Res.*, *82*, 5374–5378, 1977.

Musgrave, M. J. P., *Crystal Acoustics*, Holden-Day, Oakland, Calif., 1970.

Nur, A., and G. Simmons, Stress-induced velocity anisotropy in rock: An experimental study, *J. Geophys. Res.*, *74*, 6667–6674, 1969.

Paterson, M. S., *Experimental Rock Deformation—The Brittle Field*, 254 pp., Springer, New York, 1978.

Sayers, C. M., Inversion of ultrasonic wave velocity measurements to obtain the microcrack orientation distribution function in rocks, *Ultrasonics*, *26*, 73–77, 1988*a*.

Sayers, C. M., Stress-induced elastic wave anisotropy in fractured rock, *Ultrasonics*, *26*, 311–317, 1988*b*.

Sayers, C. M., J. G. van Munster, and M. S. King, Stress-induced ultrasonic anisotropy in Berea sandstone, *Int. J. Rock Mech. Min. Sci.*, *27*, 429–436, 1990.

C. M. Sayers, Shell Research Arnhem, P.O. Box 40 (Westervoortsedijk 67d), 6800 AA Arnhem, Netherlands.

J. G. van Munster, Koninlijke/Shell Exploratie en Produktie Laboratorium, 2288 CD Rijkswijk ZH, Netherlands.

(Received September 21, 1990;
revised April 8, 1991;
accepted April 27, 1991.)

JOURNAL OF GEOPHYSICAL RESEARCH, VOL. 96, NO. B10, PAGES 16,415–16,427, SEPTEMBER 10, 1991

Crustal Velocity and Moho Topography in Central New Hampshire

EYLON SHALEV AND JEFFREY PARK

Department of Geology and Geophysics, Yale University, New Haven, Connecticut

ARTHUR LERNER-LAM

Lamont-Doherty Geological Observatory, Columbia University, Palisades, New York

The White Mountain Batholith in central New Hampshire is a major plutonic, topographic and gravimetric feature, superimposed on the NE-SW trending regional pattern of accreted terranes in northeastern North America. Compressional and shear-wave arrival times from a two-dimensional seismic array experiment are used to constrain a one-dimensional crustal velocity model and Moho topography for central New Hampshire. Our deployment, a "piggyback" on the Ontario-New York-New England refraction experiment (ONYNEX), recorded 10 explosive sources using 20 three-component digital seismometers. The crust can be modeled as 34.5 km thick, and with three layers having linear gradients without midcrust discontinuities. For this model, P-velocities are 6.1-6.2 km/s in the upper crust, and 6.2-6.8 km/s in the lower crust. S-velocities are 3.5-3.7 km/s in the upper crust, and 3.7-3.9 km/s in the lower crust. Because Moho reflections comprise our principal constraints on lower-crustal velocities, there is a tradeoff between lower-crustal velocity and crustal thickness. In particular, an average crustal thickness of 39-40 km, reported elsewhere in New England, is not precluded by our data. The Poisson's ratio for the crust varies between 0.23-0.26, in the lower range of values reported for crustal minerals. Our dataset is consistent with $\lesssim$2% lateral variation in the upper crust underlying the New Hampshire and White Mountain Plutonic Series, but larger variations deeper than 15 km. If modeled in terms of Moho topography, PmP traveltime residuals and $PmP - P$ residuals suggest thicker crust (36-37 km) under the White Mountain batholith, with thinner crust (33-34 km) to the east and southwest of the White Mountains. Such topography of the Moho correlates well with both the surface elevation and the Bouguer gravity anomaly in the region. Gravity data do not favor the simplest alternative model: a thick low-velocity granitic lower crust beneath the batholith. Using a simplified density model, roughly 30–35% of the gravity anomaly in the White Mountain region can be modeled as the result of the inferred Moho depression, requiring only a 5 km low-density root for the White Mountain batholith. The short wavelength of the Moho topography is consistent with a very low flexural rigidity for the lithosphere ($\approx 10^{21}$ Nt-m), suggesting that the plutons were intruded into a weak lithosphere. A rapid transition from positive to negative PmP residuals falls along a line that parallels the onshore extension of the Kelvin Seamounts, and may correspond to the "line of weakness" hypothesized by Sykes (1978) to have been tectonically active during the opening of the North Atlantic Ocean at 100-200 Ma.

INTRODUCTION

In the last decade, a number of seismic refraction experiments have been performed in northern New England to investigate the structure and tectonic evolution of its crust [*Murphy and Luetgert*, 1987, 1986; *Luetgert et al.*, 1990]. The 1988 Ontario-New York-New England Refraction Experiment (ONYNEX) was undertaken principally by the U.S. Air Force, the U.S. Geological Survey, and the Geological Survey of Canada, using a linear refraction geometry. Refraction studies offer the resolution afforded by a linear array of closely-spaced receivers, with the shortcoming that crustal structure is modeled typically as one- or two-dimensional. The tectonics of New England and the adjacent maritime provinces of Canada is typically modelled as predominantly two-dimensional (2–D) in crustal seismic studies, consisting of NE-SW striking terranes accreted to the North American Craton during the Paleozoic. Superimposed on this geometry is more detailed geology, of which the plutonic suites of central New Hampshire are among the more salient expressions. These plutonic suites have been associated with a NW-SE trend of Mesozoic plutonism that extends from the Kelvin Seamounts offshore into southern Quebec [e.g. *Sykes*, 1978]. This plutonism, hypothetically associated with the opening of the Atlantic Ocean, cross-cuts the Paleozoic terranes in the region, adding a third dimension to the region's tectonics and, presumably, to its velocity structure. One needs to interpolate between two refraction lines, or extrapolate away from a single line, in order to infer three-dimensional (3–D) crustal velocity structure. Data from a 2–D seismic array offers more-direct constraints on 3–D crustal velocity structure, but typically with more limited resolution.

We report results of a "piggyback" deployment, obtained during the first phase of the ONYNEX experiment, of a 2–D array of 20 three-component seismometers on hard-rock sites in central New Hampshire. We use arrival-time data from a 2–D array to estimate, independently of the refraction data, the one-dimensional (1–D) velocity structure of central New Hampshire, and use reflected-wave arrivals to investigate Moho topography. One would like to address with this data several issues regarding the crustal structure of central New Hampshire: (1) the general velocity structure of an area characterized by granitic intrusions, (2) the vertical extent of the large granitic intrusion correspond-

Paper number 91JB01591.
0148-0227/91/91JB-01591$05.00

ing to the White Mountains, (3) the depth and the shape of the Moho discontinuity, which can constrain the mode of gravity compensation, (4) P and S-velocity structure, which can be used to estimate the Poisson's ratio and constrain the crustal mineralogy. Although the small size of our dataset enables only a preliminary assessment of these problems, our analysis reveals strong evidence for significant 3–D velocity structure below the upper crust, which appears to be related to the near-linear cross-cutting plutonic features previously noted in the surface geology of the northeast United States and eastern Canada.

Central New Hampshire is an area dominated by plutonic intrusion. The metamorphosed rocks of the Ordovician-Silurian Kearsarge-Central Maine synclinorium were intruded by the Devonian-Carboniferous New Hampshire plutonic suite 390-325 Ma. During the subsequent opening of the North Atlantic Ocean, the area was intruded by the White Mountain plutonic-volcanic suite between 220 and 100 Ma [*Lyons et al.*, 1982; *Zartman*, 1988; *Foland and Faul*, 1977; *Billings*, 1956]. The Ordovician-Silurian metasediments are part of the Gander terrane [*Williams and Hatcher*, 1983] that joined North America as part of the Devonian Acadian orogeny. The microstructure of the metamorphic rocks suggest three cycles of folding as the result of that orogeny [*Lyons et al.*, 1982; *Dykstra et al.*, 1987]. The now-metamorphosed New Hampshire plutonic suite outcrops in large areas, mainly in the western part of the state. Gravimetric data suggest that the Devonian-Carboniferous plutons are thin, no more than 2.5 km deep [*Nielson et al.*, 1976; *Hodge et al.*, 1982]. The intrusion of the younger, unmetamorphosed White Mountain plutonic-volcanic suite (see *Billings* [1956] for comprehensive description) occurred in three distinct stages over a period of 100-120 M.Y. [*Zartman*, 1988; *Foland and Faul*, 1977]. The two largest episodes of plutonism occurred at 160-195 Ma and 100-120 Ma. There are approximately 30 intrusive bodies ranging in size from small stocks to the 500 km^2 White Mountain batholith. Fission track ages and estimates of crystallization depth suggest a 5-8 km depth of emplacement for the White Mountain magma [*Chamberlain and England*, 1985]. Gravity data over the White Mountain pluton suggests that this large plutonic feature is thicker than the older intrusions.

Several ways for incorporating the White Mountain and New Hampshire intrusions into the framework of plate tectonics have been proposed. *Morgan* [1971] noted a near-linear arrangement of oceanic and continental magmatism from eastern Canada through to the Kelvin seamount chain in the Atlantic ocean, and proposed that the features are the result of heating by a mantle hot-spot. However, age determination of rock samples from the plutons [*Foland and Faul*, 1977] show that there is no progressive age change along the intrusive sequence, so that a hot-spot origin is unlikely. The collinear Mesozoic magmatism encouraged the search for a different causal relation. *Ballard and Uchupi* [1972] suggested the extension of a fracture zone, as part of the Atlantic ocean opening, as the origin of the intrusions. A similar model is that the New Hampshire plutons and the Kelvin seamounts chain are part of a Paleozoic zone of weakness that was reactivated as a transform fault during the opening of the Atlantic ocean [*Sykes*, 1978].

The plutonic history of central New Hampshire, coupled with the relatively large topographic relief of the area (maximum elevation 1911 m at Mount Washington), suggests a significant perturbation to the predominantly two-dimensional surface expression of tectonics in the Northeast United States. Crustal velocity models for the region are relatively simple. Although central New Hampshire has not been modeled in detail, the velocity structure of northern New England has been studied by several researchers (see *Taylor and Toksoz* [1982] and *Taylor* [1989] for a summary). *Taylor et al.* [1980] used P, S, and P_n travel-time data from 170 regional earthquakes with magnitudes $1.5 \leq M \leq 3.8$ and epicentral distances $\lesssim$600 km. Their crustal model consists of a two-layer 40 km thick crust; the upper 15 km has a P-velocity (V_p) of 6.1 km/s, and the lower part has a P-velocity of 7.0 km/s. *Taylor and Toksoz* [1982] also reported Rayleigh-wave dispersion measurements for the northeastern Appalachians for the station pair of St. Johns, Newfoundland, and Ogdensburg, New Jersey. The crustal S-velocity (V_s) structure derived by this study was characterized by 40 km thick crust, but the uncertainties of this inversion were ±5 km [*Taylor*, 1989], and the crustal structure is averaged over the path. In a study of the 1984 Maine refraction profile along the strike of the regional geology, *Hennet et al.* [1991] modeled the crust close to central New Hampshire with three main layers: a top layer, to 13-15 km depth, with velocities of 6.2-6.3 km/s, a middle layer between 13-15 and 24 km with velocity of 6.4 km/s, and a bottom layer between 24 and 40 km with velocity of 6.8 km/s. *Hughes and Luetgert* [1991], in a study of the ONYNEX seismic refraction experiment, argue that the crust in north-central New Hampshire consists of three main layers: an upper layer, to 13-15 km depth, with velocities of 6.05-6.2 km/s; a negative-gradient layer between 13-15 and 24 km with velocities of 6.5-6.4 km/s; and a lowermost crust between 24 and 37-40 km with velocities of 6.7-7.0 km/s.

EXPERIMENT GEOMETRY AND DATA DESCRIPTION

The ONYNEX seismic experiment was a joint refraction experiment undertaken by the United States Geological Survey, the U.S. Air Force Geophysics Laboratory (AFGL) and the Geological Survey of Canada, The refraction line ran from central Maine to eastern Ontario, Canada [*Mangino and Cipar*, 1990; *Luetgert et al.*, 1990], and was shot in September 1988. We used 20 three-component instruments from the National Center for Earthquake Engineering Research (NCEER) and Lamont-Doherty Geological Observatory for a piggyback experiment during the easternmost shot sequence in Maine and New Hampshire. Shot locations for the 10 explosions are given in Table 1. The 20 instruments were placed between the refraction line and two fan shots to the south of the line (Figure 1) in order to receive signals from a wide range of azimuths. The field hardware consisted of 2-Hz three-component L22 sensors with EDA PRS-4 digital recorders operating at 100 samples per seconds. Data were recorded in two-minute windows timed to coincide with the explosions. Sites for the instruments were chosen to cover evenly the survey area. Each recording site was tested with a drum seismograph to verify that the site was on hard-rock outcrops and not on erratic boulders. In general, the effort expended in the search for hard-rock sites was rewarded with excellent recorded waveforms. However, hardware at the site on Mount Kadigen, New Hampshire failed completely and station 18 had intermittent problems

TABLE 1. Shot List

Shot	Latitude (North)	Longitude (West)	Elevation (m)
1	44.5902	69.7461	95
2	44.5632	70.0445	122
3	44.4590	70.5227	277
4	44.4114	70.9696	317
5	44.3362	71.3850	519
6	44.2807	71.8313	329
7	44.1785	72.2365	460
10	44.0536	73.3865	35
22	43.2361	71.8589	325
23	43.4491	70.6718	79

TABLE 2. Station List

Site	Latitude (North)	Longitude (West)	Elevation (m)
1	43.1222	71.3639	243
2	43.4169	71.3125	213
3	43.5328	70.9136	231
4	43.6369	71.2050	295
5	43.8317	71.2731	149
6	43.7722	71.4314	216
7	43.8014	71.0078	164
8	44.1858	71.0122	149
9	43.9306	70.8819	134
10	44.0667	71.1658	182
11	44.2664	71.2447	569
12	44.2111	71.4058	578
13	44.1808	71.7028	626
14	44.0261	71.4922	869
15	44.0436	71.7939	565
16	43.8744	71.5533	486
17	43.7819	71.7958	176
18	43.5811	71.5919	359
19	43.4267	71.8083	304

with its horizontal components. Instrumental noise with $f = 1$ Hz was evident in data from a few instruments, and was removed with bandpass-filtering. As the sensitivity of the L22 sensor is weak at 1 Hz, the degradation of the recorded waveform in this process was judged minimal. We collected records from 190 source-receiver pairs that were usable for picking phase arrival times. Instrument sites, numbers and locations are in Table 2.

The response of the L22 sensors is known to be complicated near 25 Hz [*Menke et al.*, 1991], so we applied a causal lowpass filter to the data before picking phase arrival times. First-arrival P-phases on the seismograms were clearly identifiable, including several weak phases interpreted as P_n. First-arrival phase picks have an estimated accuracy of 0.05 s. In addition, we were able to identify the arrival time of SH and SV waveforms for all the records, PmP for 40% of the records and somewhat fewer SmS phases. The estimated accuracy of these later picks is 0.15 s. Most of the S-waveforms are complicated; in fact, for many phases identified as 'SH,' the vertical-component motion correlates with motion on the transverse component (Figure 2).

1-D VELOCITY STRUCTURE

The dataset acquired in our experiment has a 3-D raypath pattern that is sensitive to lateral crustal structure. To estimate a one-dimensional reference model, we treated the dataset as a single gather from a single source, plotting the traces against source-receiver distance. The correlation between adjacent traces in an ordinary record section cannot be expected in such a plot, as adjacent traces can have different sources and completely different propagation paths. A traveltime curve defined by first-arrival phases P and S is identifiable in the pseudo record section, but neither Moho reflections nor possible midcrustal phases are coherent trace-

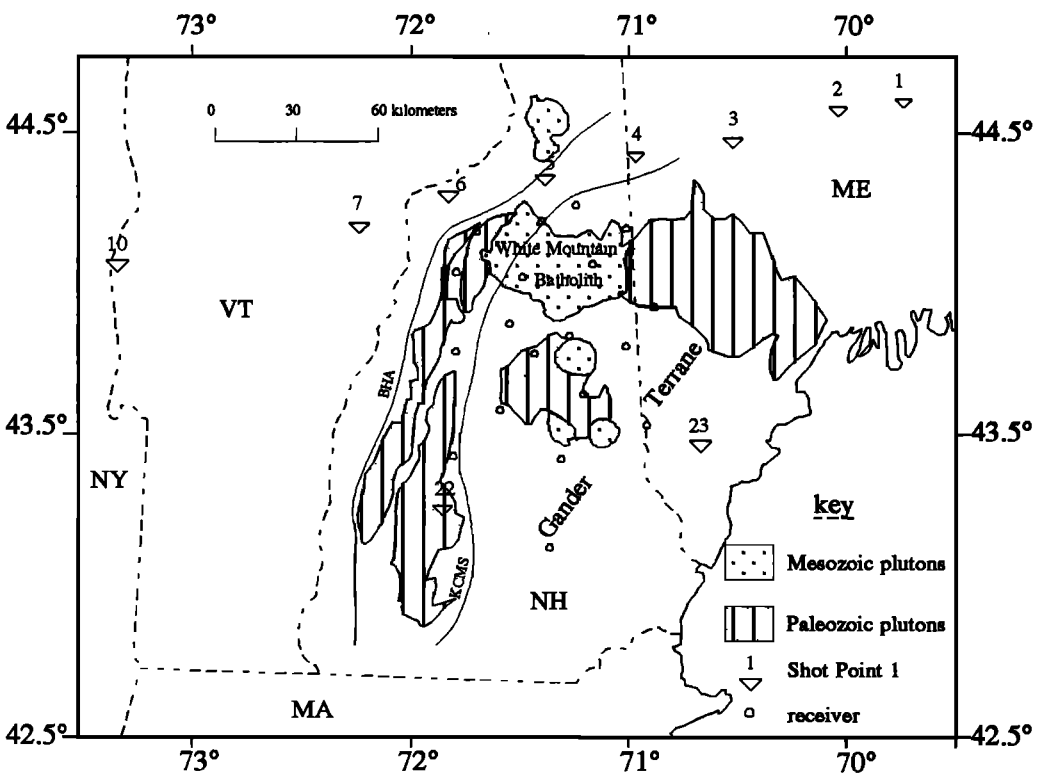

Fig. 1. Map of the experiment area. Triangles represent the explosion sites, circles the receivers. BHA stands for Bronson Hill Anticlinorium, KCMS stands for Kearsarge-Central Maine Synclinorium.

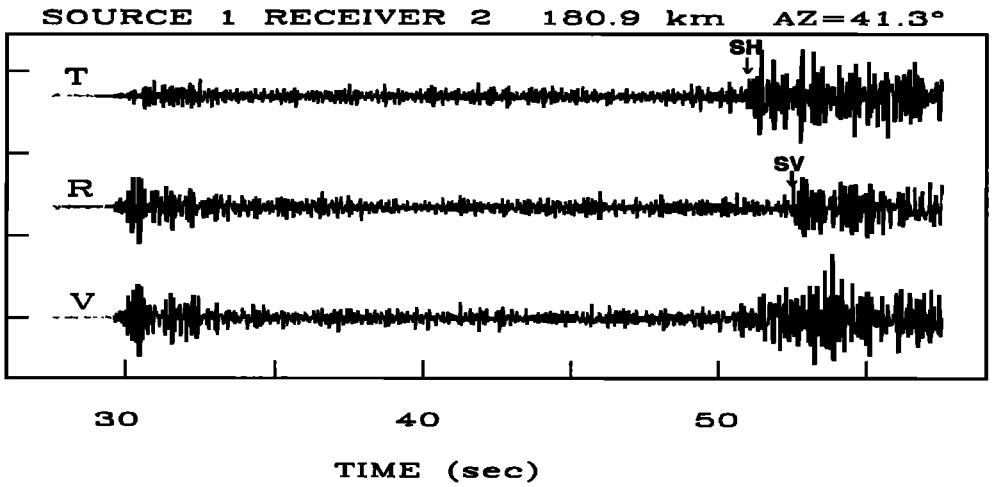

Fig. 2. Example of independent arrival times and waveforms for *SH* and *SV*. The bottom trace is the vertical component, the middle is the radial component, and the top is the transverse component. The *S* arrival in the vertical component correlates with the *SH* arrival in the transverse component.

to-trace, presumably as a result of lateral velocity variations in the crust.

Time picks of first-arrival *P* comprise the largest group of constraints for the 1–D reference velocity model, but are sensitive only to the velocity structure from the surface to approximately 15 km depth. The *PmP* arrivals are sensitive to the velocity structure of the whole crust and the Moho depth. The P_n arrivals constrain the velocity below the Moho discontinuity. We took the *S* arrival time as the average of the *SH* and *SV* arrival times, when both can be identified. Complications in the *S*-waveforms may be due to *S*-to-*P* conversions in the surface layers of the crust. *Sp* precursors, if identified as *S* arrivals, would bias the inferred velocity model toward higher velocities. Relatively few *SmS* phases can be identified with confidence, therefore the 1–D *S*-velocity structure is weakly constrained relative to the *P*-velocity structure. This degrades, but does not preclude, our ability to constrain Poisson's ratio in the lower crust.

The first-arrival data fall into two groups: the arrivals from Shot 10 in the west, and the arrivals from the other 9 shots (Figure 3). The earlier arrival time of the signals from Shot 10 can be explained by higher crustal velocity to the west of the array. Shot 10, located near the New-York-Vermont border, is the only shot in our dataset in the Grenville Province of the North American continent. Faster crustal velocities in this province are inferred by *Hughes and Luetgert* [1991] and *Taylor et al.* [1980]. The arrivals from Shot 10 also differ in the apparent velocity beneath the Moho. Rays traveling west and southwest have high apparent P_n-velocity (8.3 km/s), and rays traveling east from Shot 10 have low apparent P_n-velocity (7.6 km/s). This can be explained by (1) a dipping Moho that deepens from west to east, (2) a thickened crust with an intermediate-velocity lower crustal layer, (3) anomalously low compressional velocity in the upper mantle under the Grenville province. The third explanation is unlikely, as there is no other evidence of elevated temperatures. The boundary between the Grenville and Gander crustal blocks has been identified by *Ando et al.* [1984] and *Hughes and Luetgert* [1991] as a ramp structure dipping eastward from the approximate location of the New York-Vermont border under the Green Mountains of Vermont and terminating in the mid-crust under the Bronson Hill Anticlinorium near the Vermont-New Hampshire border. Such a ramp structure would complicate the interpretation, as ray paths from Shot 10 to our array would travel through the associated fossil thrust zone in the upper crust. The dip of the ramp, clearly evident as a midcrustal reflector packet in the COCORP line reported by *Ando et al.* [1984], is in the same sense as that expected from the sign of the P_n-velocity anomaly. Unfortunately, only this one shot from the Grenville province was recorded in our experiment, so we excluded data from Shot 10 from the 1–D velocity inversion and the estimation of Moho depth variations. The remaining distribution of *PmP* arrivals was poorly situated to discriminate whether the Moho dips east of our array.

The 1–D velocity model was constructed using the 171 source-receiver pairs from the 2–D array (excluding Shot 10) as one gather, and fitting the $X - T$ data using an iterative least squares algorithm. The traveltimes can be fit by a simple three-layer crustal model. A thin low-velocity layer in the shallow crust, presumably representing a shallow weathered layer, models an offset at about 20 km in the observed traveltimes. Our dataset is sensitive only to the integrated traveltime in this layer and can be modeled adequately using layer 1 in the ONYNEX crustal model of *Hughes and Luetgert* [1991]. One expects this surface "weathered" layer to be highly heterogeneous laterally, and to be largely responsible for the *P*-wave codas and complicated *S*-waveforms observed in our data, see also *menke et al.* [1990]. Another layer boundary was placed at 15 km depth (separating Layers 2 and 3) as this corresponds roughly to the deepest point sampled by first-arrival *Pg* in our experiment. The lower crustal velocities are constrained by the less-numerous *PmP* and *SmS* observations. As no coherent midcrustal reflector was evident in a record section made from all 190 source-receiver pairs, we assumed the velocity to be continuous at the 15 km boundary between Layers 2 and 3. This is in contrast to the midcrustal reflector at 15 km depth in many crustal models for northern New England, e.g., *Hennet et al.* [1991] for the 1984 Maine-Quebec transect. The shot gathers from Shots 1, 5 and 7 in the ONYNEX refraction line at the northern border of our array deployment, shown by *Hughes and Luetgert* [1991], show evidence of *P*-wave energy from a midcrustal reflector, especially for downrange distances of

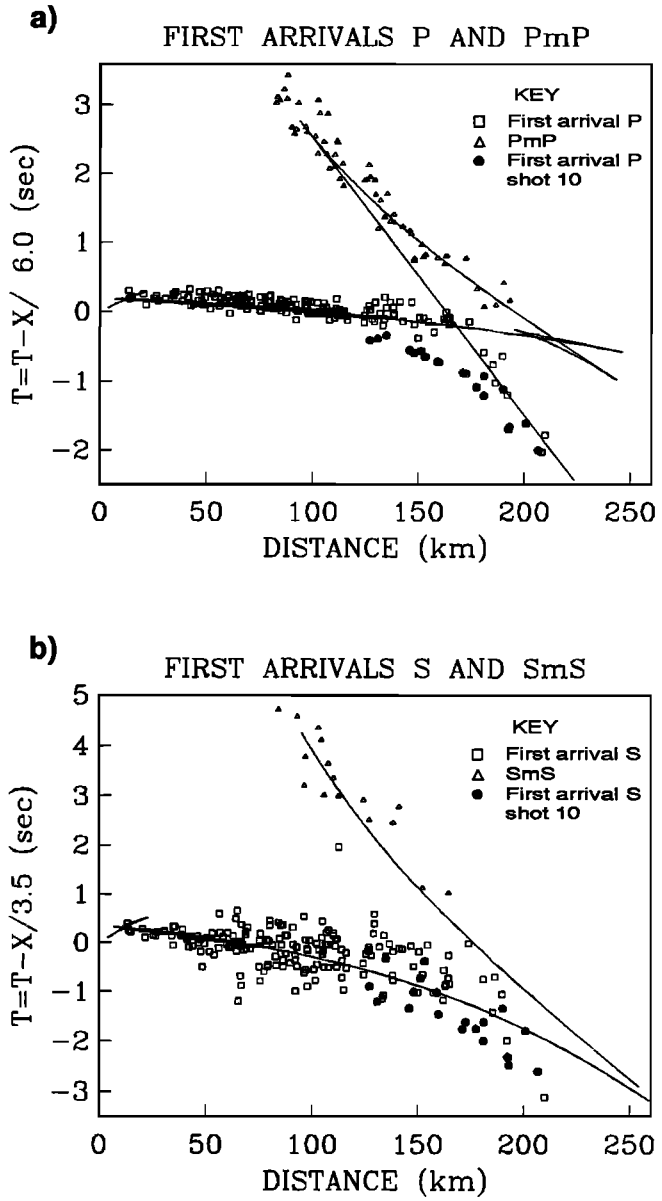

Fig. 3. (a) First arrival P, PmP, and the traveltime curve of the preferred P-velocity model. Squares represent P arrival times, triangles represent PmP arrival times, solid circles represent P arrivals from shot 10. The first arrivals P from shot 10 show a different structure and were excluded from the model computation. Estimated accuracy of the time picks: $P \pm 0.05$ s, $PmP \pm 0.15$ s. (b) First arrival S, SmS, and the travel time curve of the preferred S-velocity model. The first arrival S from shot 10 were excluded from the model computation. Accuracy of time picks: $S \pm 0.15$ s, $SmS \pm 0.15$ s.

75-115 km. In some cases visual inspection of individual traces collected in our 2–D deployment reveals waveforms consistent with these shot gathers, that is, with a "PiP" phase arrival caused by a mid-crustal velocity jump. We divided records in the 75-115 km distance range into two groups, according to whether they were consistent or not consistent with the existence of a prominent midcrustal reflector. Pseudo-record sections of vertical motion from each group are displayed in Figure 4. Roughly two thirds of the records do not show persuasive evidence of a reflector at 15 km depth. Inspection of the source-receiver midpoints of the two groups (Figure 5) reveals that the two types of records are intermingled spatially, but with large areas (e.g., most of the White Mountain Batholith) where evidence for a mid-crustal reflector is absent. It cannot be determined from this data whether the mid-crustal interface is also absent or is merely obscured by scattered energy.

We used the nonlinear least-square routine from *Press et al.* [1986] to invert the $X - T$ data for velocity structure in three steps. The first step was to find the velocity gradient in the top 15 km using the first arrival P (or S) waves. The second step was to find the velocity gradient of the lower crustal layer and the Moho depth. We used the PmP and SmS arrivals for the second step, using the upper crustal structure from the first step. The third step was to fit the P-velocity below the Moho using the P_n arrivals. There is a trade-off between lower-crustal velocity and crustal thickness, as the principal independent constraint offered by the PmP traveltimes is the two-way traveltime. Slower average lower-crustal velocity leads to thinner crust and faster velocity to thicker crust. Figure 6 contours the average PmP rms misfit residuals against Moho depth and the average velocity in the lower crust (layer 3). The best fitting model places the Moho at 34-35 km depth with an average velocity of 6.5 km/s in the lower crust. Other studies in Central New Hampshire and Western Maine [*Hughes and Luetgert*, 1991; *Hennet et al.*, 1991; *Taylor et al.*, 1980] infer a 38-40 km crust with 6.65-6.75 km/s average lower crustal velocity. Such a model is not excluded by our observations. A model with 39 km thick crust and 6.7 km/s average lower crust velocity fits the PmP data with an average misfit $> 2.5\sigma = 0.38$ s, while the best-fitting model achieves an average $< 1.6\sigma = 0.24$ s. The pattern of PmP residuals, discussed below, suggests significant Moho topography, so this misfit difference may have weak significance. The situation is not changed significantly if a mid-crust velocity jump from 6.2 to 6.5 km/s at 15 km depth, as favored by *Hughes and Luetgert* [1991], is fixed a priori in the inversion procedure. Figure 7 shows the results of the 1–D velocity inversion for the preferred 1–D model for all the shots excluding Shot 10.

We performed a tomographic inversion, using first arrival P-waves, to model the 3–D velocity structure in the top 14 km of the crust. Three problems hampered this inversion: source location geometry, small number of rays, and the small traveltime perturbations relative to the 1–D velocity model. The source-receiver pattern leads to a reasonable ray-crossing pattern at depths of 1.5 km to 7.5 km under the array, which encompasses most of the White Mountain Batholith. However, most of the rays that penetrate deeper then 7.5 km originate from Shot 1 and Shot 2 in the northeast. Therefore the results of the tomographic inversion for depths greater than 7.5 km are poorly constrained. The rms P traveltime residual, as can be seen in Figure 3, is fairly small (less than 0.1 s). The small number of rays (171 source receiver pairs) motivated us to use cubic B-spline as a basis function for the velocity parameterization. *Firbas* [1987] and *Michelini and McEvilly* [1991] use the same parameterization in 2–D and 3–D tomographic inversion. Using B-splines as basis functions enables us to use fewer velocity parameters [*Firbas*, 1987], and to obtain an overdetermined set of inversion equations. We obtained 50% variance reduction in a tomographic inversion using $6 * 6 * 4 = 144$ cubic B-spline functions. The deviation of the 3–D structure from the 1–D structure, between 1.5 and 7.5 km depth where ray

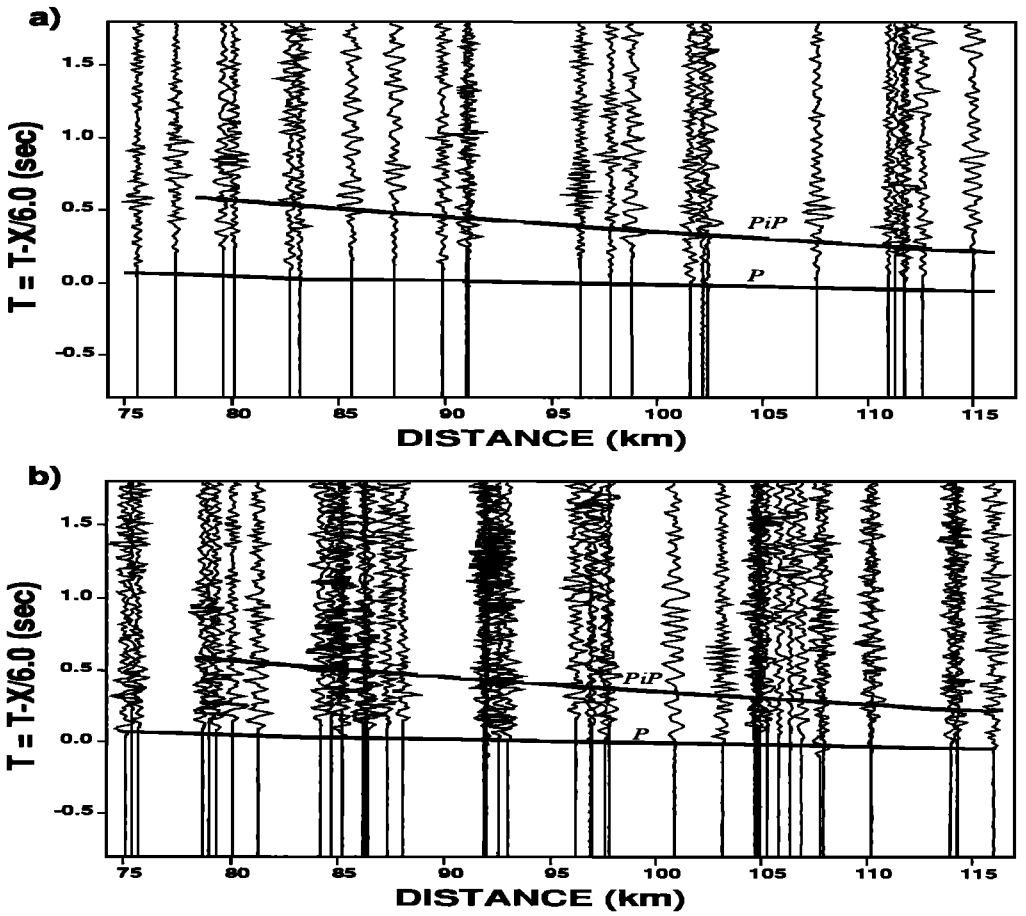

Fig. 4. Pseudo record sections of vertical component for source-receiver distance of 75–115 km. P is the predicted P-wave arrival time, PiP is the locus of predicted arrival times for a reflection from an interface at 15 km depth. (a) Traces consistent with a PiP phase from a midcrustal reflector. (b) Traces that do not appear consistent with a PiP phase from a midcrustal reflector.

coverage is adequate, reached roughly 2% at maximum, but was mostly $\lesssim$1%, with a spatial pattern that was not stable to changes in the smoothing parameter. These results suggest that our array did not detect significant medium-scale

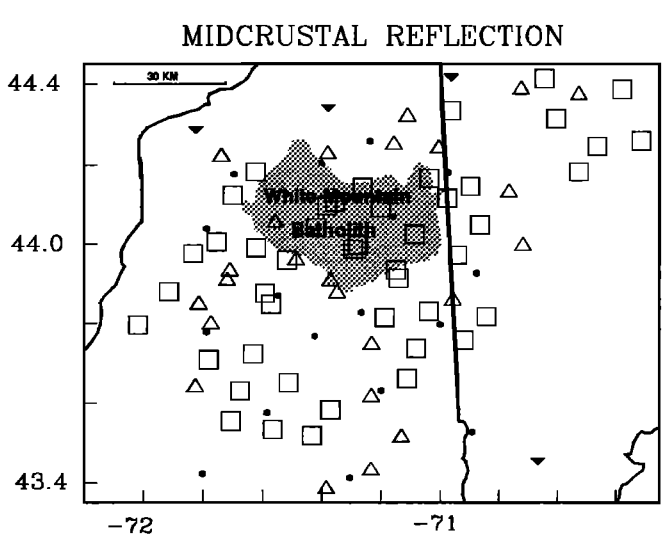

Fig. 5. Map of the source-receiver midpoints for distances in the range 75–115 km. Squares represent midpoints for traces with no apparent midcrustal reflection. Triangles represent midpoints for traces where a midcrustal reflection is apparent.

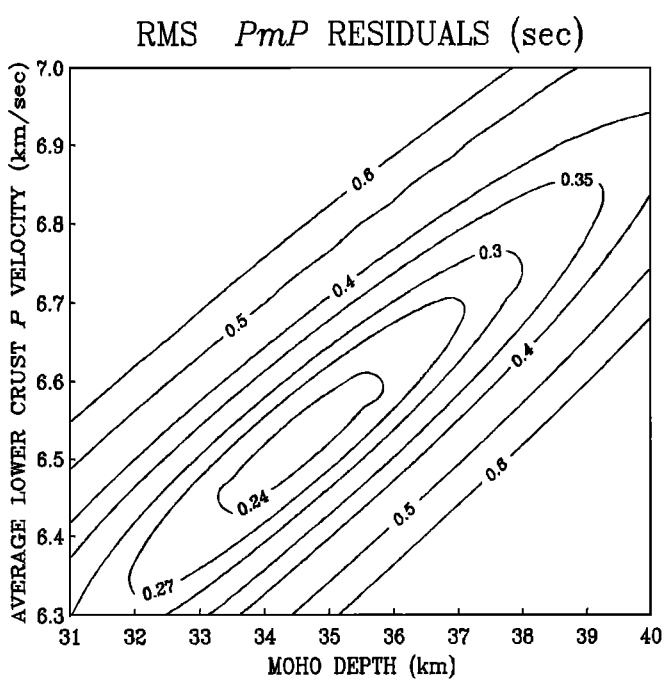

Fig. 6. Contour map of the rms traveltime residuals of the PmP observations, graphed against the average velocity in the lower crust (15 km to the Moho) and the depth of the Moho. Contour value is in seconds. The estimated accuracy of the time picks for the PmP is ±0.15 s.

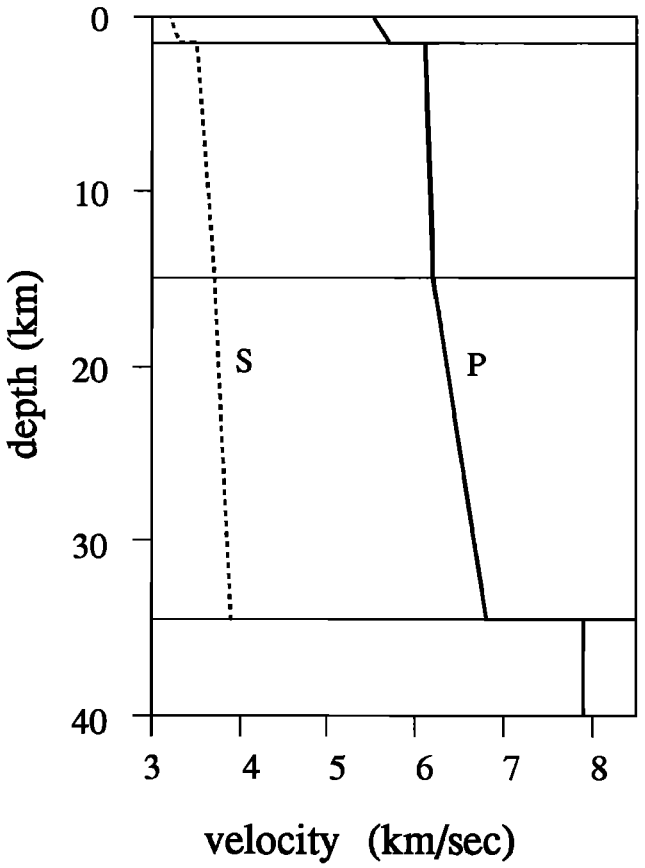

layer	depth	velocity top		velocity bottom	
		P	S	P	S
1	1.5	5.5	3.2	5.7	3.3
2	15.0	6.1	3.5	6.2	3.7
3	34.5	6.2	3.7	6.8	3.9
Moho	na	8.0	nd	na	na

Fig. 7. Reference 1-D P and S-velocity structures for the crust in central New Hampshire; na, not applicable, nd, no data.

(30-80 km) 3–D velocity structure in the upper crust of central New Hampshire. and are consistent with the hypothesis that the granite batholith lacks a strong "velocity signature" relative to the surrounding metamorphosed rocks.

PmP Residuals and Moho Topography

Unlike the first-arrival P-waves in our data set, the PmP traveltime residuals, relative to the simple three-layer 1–D reference model, have sizable amplitude and a clear spatial pattern. PmP traveltime residuals are due both to velocity perturbations in the crust and Moho topography. The energy of P and PmP phases travel in similar paths in the upper crust. Differential $PmP-P$ residuals are one measure of the influence of shallow lateral variations in velocity, particularly structure near the source and receiver. We found no significant correlation between the P residuals and the PmP residuals, suggesting that the cause of the observed PmP residuals (Figure 8*a*) is likely to lie deeper than 15 km. Another argument for a deeper origin of the PmP residuals is the failure of the tomographic inversion (described above) to detect large P-velocity variations in the uppermost crust. Positive PmP residuals in the area of the White Mountains suggest thick crust and/or slow velocity in the lower crust. To produce a negative 0.4 s PmP deviation, the crust should be 3 km thicker or the average P-velocity in the lower crust should be 4–5% slower than the 1–D reference model. Simple density models for the crust (see below) argue that the Bouguer gravity anomaly associated with the White Mountain pluton can be compensated at depths shallower than 15 km, so that a large, slow granitic lower-crustal root to the batholith seems unlikely. It is therefore reasonable to associate the large-scale pattern of the PmP residuals with changes in Moho depth.

The PmP traveltime residuals relative to the preferred 1–D model are plotted in Figure 8*a*. This pattern can be linked to crustal thickness variations or lateral change in crustal velocity, or both. In the middle of the map there are PmP reflections from several directions and sources, and the correlation of residuals among nearby bounce points argues for an explanation in terms of Moho depth variations. Toward the northeast and west there are few PmP crossings and it is less easy to distinguish if the early arrival times are the result of shallow Moho or of higher velocity in the lower crust. Figure 8*b* shows the depth of the Moho in km, calculated by perturbation theory, relative to the 1–D reference model, assuming that all the PmP residuals result from Moho depth variations. Referenced to the best-fit 1–D velocity model discussed above, the Moho is 36-37 km deep under the White Mountains, and 33-34 km deep to the east and to the southwest of the White Mountains. The association of late PmP arrivals with thick crust is only weakly dependent on the details of the reference 1–D velocity model. If we use a different velocity model that fits our data less well, but still adequately (e.g., that of *Hughes and Luetgert* [1991]), the baseline depth of the Moho will be different, but the pattern of PmP residuals is robust. In fact, Moho topography inferred using a 1–D model with the Moho at 39-40 km is roughly 50% greater in relief, both because the lower crust has larger P-velocity and the average PmP residuals are larger.

Fluctuations in PmP residuals and crustal thickness in northern New England have been reported by other authors, but a direct comparison with our inferred thickness variations must involve a correction for the different 1–D velocity models used. *Kafka and Ebel* [1988], using PmP arrival times, compute Moho a depth of 36-38 km in the northeastern corner of this study area, while Figure 8 shows a Moho depth of 34-35 km. Much of the discrepancy between the two studies arises because *Kafka and Ebel* [1988] use an average crustal P-velocity of 6.4 km/s, which is higher than the average velocity of the 1–D model in this paper. If we compute the Moho depth for the northeast corner with a normal moveout velocity of 6.4 km/s, the depth is 35-36 km, in closer agreement with the previous study. *Kafka and Ebel*

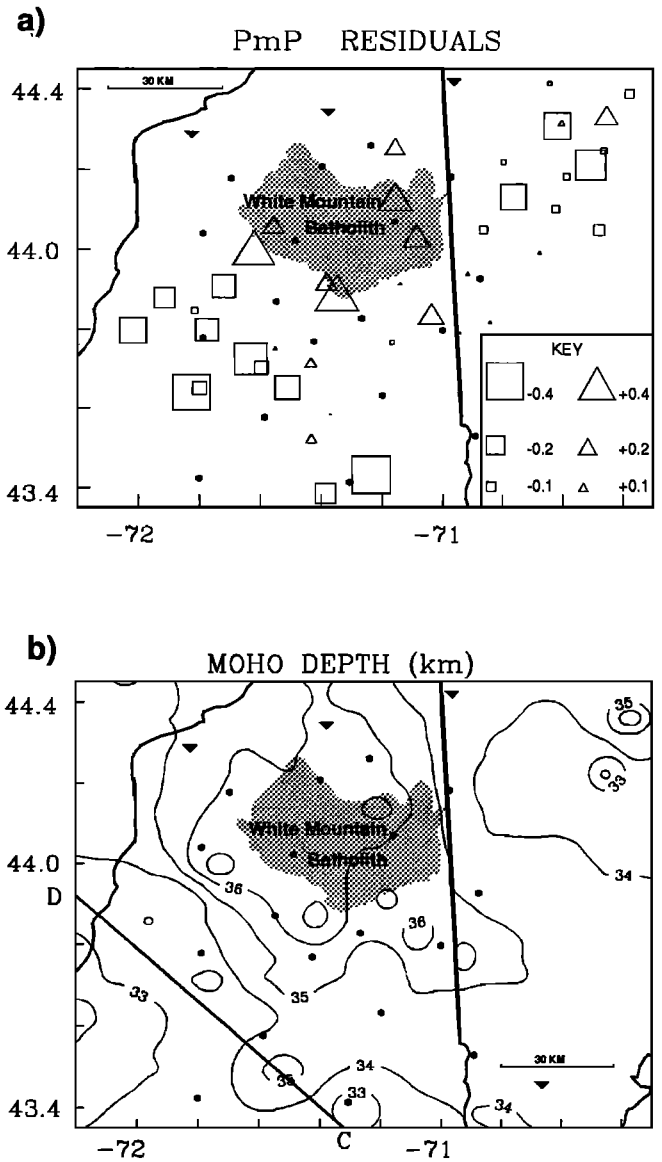

Fig. 8. (a) PmP traveltime residuals. Squares represent early arrivals, triangles late arrivals. The size of the symbol shows the size of the residual, the largest symbol representing 0.4 s. (b) Contour map of Moho depth as determined by PmP arrival times. Line $C - D$ is the line of weakness hypothesized by *Sykes* [1978].

[1988] also estimate Moho depth of 46 km using a single reflection point under the White Mountains. The relatively thicker estimate is qualitatively consistent with our results, but, even using the 40-km-thick 1–D crustal model preferred by *Hughes and Luetgert* [1991], exceeds our estimated depth-to-Moho by $\gtrsim$2 km. *Luetgert et al.* [1987] report traveltime residuals as large as 1 s for data from south-central Maine, 50-150 km northeast of our array in central New Hampshire. This would translate into 3.5-4.0 km of Moho topography, assuming that the traveltime residuals are the result of change in Moho depth. *Kafka and Ebel* [1988] argued for a 10 km change in Moho depth over 50 km distance in Maine.

Some features of our PmP residuals are consistent with data collected on the ONYNEX refraction line. The ONYNEX refraction model estimates a gradual 2-3 km increase of crustal thickness between Shots 3 and 5, corresponding to the western flank of the White Mountains and consistent with the trend of the PmP residuals in the northeast portion of our deployment. In addition, *Hughes and Luetgert* [1991] report, using data collected from Shot 10, a discontinuous shift in PmP traveltimes consistent with a "step" in the Moho 10 km west of the location of Shot 7. Examination of the reversed profile from Shot 4 across this feature reveals significant reflected energy from the lower crust, but no spatially coherent waveforms that can be taken for PmP arrivals. *Hughes and Luetgert* [1991] propose an explanation in terms of lower-crustal layering for the shift in PmP traveltimes observed from Shot 10, but the location of this feature is close to that predicted by a northwest extension of the sharp gradient in PmP residuals in our data. The spatial extent of the late PmP arrivals, as well as their observation on a variety of ray paths in our data set, leads us to favor an explanation in terms of Moho depth variations.

DISCUSSION

Poisson Ratio

From the P and S-velocities in Figure 7 we can compute the Poisson's ratio σ for the average crust, which appears to be fairly low, varying in the range $0.23 < \sigma < 0.26$. If S converts to P in the uppermost layer of the model, misidentification of Sp as S would bias S-wave velocity positively by less than 1%, and bias the Poisson's ratio negatively by less than 0.01. Unless large-scale S-to-P conversion occurs deeper in the crust, the average crustal Poisson's ratio would appear to be fairly low. Variations of σ with depth are poorly constrained. Although the relationship between Poisson's ratio and mineralogy is not simple [*Holbrook*, 1989; *Holbrook et al.*, 1988], the range of values indicates quartz-rich crust in central New Hampshire. The constraint on the Poisson ratio is strongest in the upper crust, where our results agree with those derived by *Hughes and Luetgert* [1991] for northern New Hampshire from the ONYNEX refraction line. The constraint is weaker in the lower crust, owing to the sparseness of identifiable SmS phases, and disagrees with the model of *Hughes and Luetgert* [1991], which proposes an extension of Grenvillian lower crust under New Hampshire with Poisson ratio 0.28-0.29. However, *Hughes and Luetgert* [1991] use Shot 10 for this estimate of Poisson's ratio, and most of the raypaths in the lower crust from this shot are outside our study area.

As with the elusive 15-km velocity interface, some records in our dataset favor the lower crust σ of the ONYNEX refraction model. Assuming identical raypaths and $\sigma = 0.25$, the S traveltime is $\sqrt{3}$ times the P traveltime. Rescaling the time axis of seismic traces by this factor allows visual assessment of the Poisson's ratio: if the ONYNEX refraction model is a good model for the lower crust, the rescaled SmS phase would lag PmP by roughly 1 s. Figure 9*a* shows data consistent with this prediction from a source-receiver pair (Shot 2, receiver 5) whose propagation path is roughly parallel to the ONYNEX refraction line. However most of the observations, especially raypaths in the central portion of the array, are more consistent with $\sigma \approx 0.25$ (Figure 9*b*), that is, PmP and SmS arrive at the same scaled time.

The Poisson's ratio in the lower crust is not well constrained due to sparse SmS observations. Also, the relationship between Poisson's ratio and rock composition is

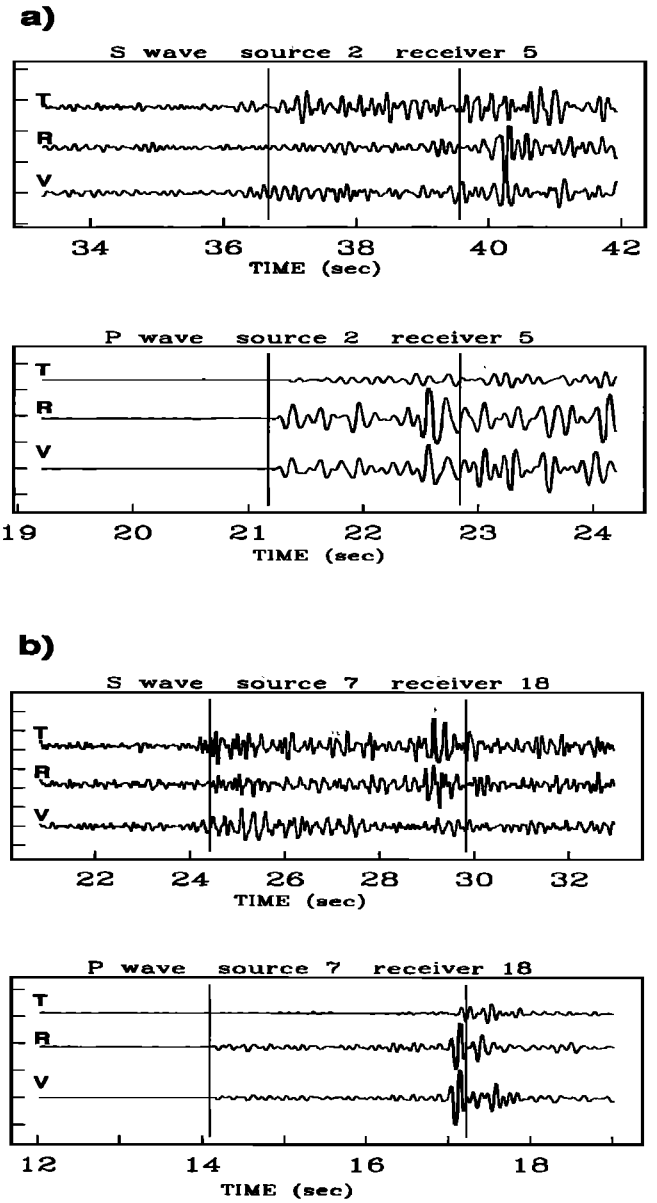

Fig. 9. Visual inspection of crustal-average Poisson's ratio σ. The bottom plot of each pair graphs the P-wave, the top plot graphs the S-wave with the time axis compressed by a factor of $\sqrt{3}$ relative to the P-wave time axis. For crustal-average $\sigma = 0.25$, the left vertical line is the predicted P/S arrival, the right vertical line is the predicted PmP/SmS arrival. Early arrival of the SmS relative to the PmP indicates lower average σ in the whole crust. Late arrival of the SmS relative to the PmP show higher average σ in the whole crust. (a) Example of record consistent with $\sigma = 0.27$. (b) Example of record consistent with $\sigma = 0.24$.

not simple [*Christensen and Fountain*, 1975; *Holbrook et al.*, 1988]. Therefore an estimate of the rock type in the lower crust beneath our array is highly uncertain. However, the data suggests spatial variation in lower crustal Poisson's ratio. If the source for the New Hampshire granites was in the lower crust, some difference in Poisson's ratio between this region and the lower crust of surrounding regions is not unexpected. Based on the published reports by *Christensen and Fountain* [1975] and *Manghnani et al.* [1974], the low σ value of 0.25-0.26 in the lower crust and the P-velocity of 6.8 km/s is consistent with rocks of the granulite facies in the lower crust of central New Hampshire.

Gravity Model

We compared the Moho depth as defined by PmP traveltime residuals with the topography (Figure 10*a*) and the Bouguer gravity anomaly (Figure 10*b*) obtained from the DNAG data distribution [*Hittelman et al.*, 1989]. Although the visual correlation is good, more PmP data from north of the White Mountains are needed to determine better the extent to which Moho topography correlates with the surface topography and gravity of central New Hampshire. However, it is instructive to examine the ability of highly simplified end-member models to account for the observations. Averaged locally in the DNAG dataset, the White Mountains rise 0.4 km above the surrounding area. Setting granite density at 2.67 g/cm^3, and density contrast across the Moho at 0.3 g/cm^3, the Moho deflection needed to compensate for the 0.4 km height is 3–3.5 km. Figure 8 shows that our data are consistent with a 3 km Moho depression under the White Mountains, consistent with full compensation. We tested an Airy model for crustal compensation by computing an assumed crustal thickness from the surface elevation, and comparing it with the Moho depth as com-

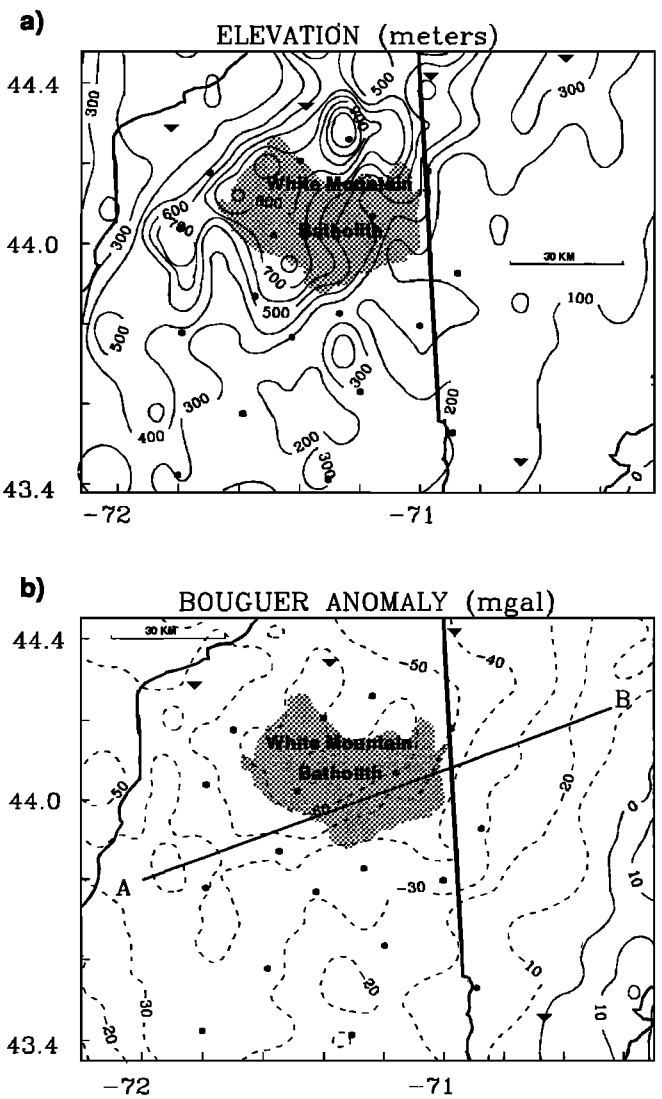

Fig. 10. (a) five-minute topography map for central New Hampshire. (b) Bouguer gravity anomaly for central New Hampshire.

puted by the *PmP*. The Airy model performed poorly for *PmP* bounce points that are southwest of the line of sharp gradient in the *PmP* residuals. However, we obtained 36% variance reduction in *PmP* residuals for bounce points that are northeast of that line, which we consider significant in light of the uncertainties in the *PmP* time picks.

We also tried to fit the Moho depth to the Bouguer anomaly along line A-B in Figure 10b using 2.67 g/cm^3 for the density of granite, 2.82 g/cm^3 for the density of adjacent crust [*Nielson et al.*, 1976], and a density jump of 0.3 g/cm^3 across the Moho (Figure 11). The shape of the granite body is poorly known, and we fit only for the depth of the granite body over the gravity low – extending the pluton under the surface to allow smooth blending of the gravity anomaly. The apparent thickening of the crust can explain roughly a third of the gravity anomaly under the White Mountain batholith. The other two thirds can be explained by a granite body 5 km thick. If a Moho with no depression under the White Mountains is assumed and the lower crust is laterally homogeneous, the granite batholith should extend to 8 km depth to effect Pratt compensation. Uncertainties in the depths of compensation are substantial owing to the highly simplified nature of the analysis. However, it appears unnecessary for the batholith to extend into the lower crust, and the gravity perturbation associated with the inferred Moho topography allows the batholith to be quite shallow. The depth of the bottom of the batholith would be different if we had chosen to model it as a number of thin fault-dependent horizontal granitic bodies, as suggested by *Hodge et al.* [1982] for the older New Hampshire plutonic suite. The White Mountain batholith is a younger granite body with a substantial gravity-low associated with it, therefore simple modeling of the batholith as one continuous granite body is assumed.

Flexural Rigidity Modeling

The spatial correlation of gravity, topography and *PmP* residuals over Central New Hampshire encourages the examination of simple geodynamic models for the crust. If Moho topography is the cause of the *PmP* residuals, we can treat the thickened crust as a positive mass anomaly supported by the underlying lithosphere, and test for the latter's flexural response. The halfwidth of the inferred Moho depression under the White Mountains, as measured from Figure 8, is roughly 50 km. The scale length of apparent deformation is too short to represent a perfect elastic response unless the flexural rigidity is very low. Its dependence on the flexural rigidity of the lithosphere, assuming no horizontal stress [*Turcotte and Schubert*, 1982],

$$\lambda = \frac{3}{4}\pi \left(\frac{4D}{g\Delta\rho}\right)^{1/4} \quad (1)$$

where λ is the halfwidth of the flexure, D the flexural rigidity, $\Delta\rho$ is the density contrast, and g is gravitational acceleration. For $\Delta\rho = 500$ kg m^{-3}, $D = 3 \times 10^{20}$ Nt-m. This very low estimate can be increased somewhat if we model the emplacement of the White Mountain Batholith on a line of weakness for the lithosphere, appropriate if the line from the Kelvin Seamounts through central New Hampshire (and perhaps to the Monteregian Hills in southern Quebec) was the extension of an oceanic fracture zone at the opening of the North Atlantic [*Ballard and Uchupi*, 1972; *Sykes*, 1978]. The flexure length for a "broken plate" model [*Turcotte and Schubert*, 1982] is two-thirds of the length for an unbroken plate, leading to an estimate $D = 1 \times 10^{21}$ Nt-m. This flexural rigidity value is lower by a factor of 50 relative to the lowest flexural rigidity found in other studies of continental lithosphere [*Walcott*, 1970; *Stephenson and Lambeck*, 1985; *Kusznir and Karner*, 1985; *McNutt et al.*, 1988; *Willett et al.*, 1985]. For reasonable choices of parameters the corresponding elastic thickness is only 5 km.

This thickness seems too thin for the lithosphere in New Hampshire, so a less simple model should be tried. The White Mountain plutonic suite was emplaced in the mid-Cretaceous and earlier and the present surface topography has developed over $\geq 10^8$ yr in response to erosion and differential (i.e., isostatic) uplift. It may be more reasonable to model the lithosphere as a viscoelastic plate, where the apparent flexural rigidity decreases with time after load emplacement. Examples discussed by *Walcott* [1970] suggest that 10^8 years of gravity loading can reduce the apparent flexural rigidity of "ordinary" continental lithosphere from 10^{25} Nt-m to roughly 2×10^{21} Nt-m, but only if the corresponding Maxwell viscosity of the lithosphere is an order of magnitude smaller than typical lithospheric values. The heat flow in central New Hampshire, for non-granitic sites, is 56 ± 12 mW m^{-2} [*Hittelman et al.*, 1989], consistent with relatively cold, high-viscosity lithosphere.

It is possible that the batholith and inferred Moho topography formed at a time when the lithosphere was regionally thin [*Phinney*, 1985]. This hypothesis is reasonable if the formation of the White Mountain granites is related to a "leaky" fracture zone or reactivated "zone-of-weakness" associated with the opening of the North Atlantic Ocean in the Mesozoic. In Figure 8*a*, a ridge of early *PmP* arrivals (interpreted as shallow Moho) is evident southwest of the White Mountains, and a zone of high gradient is evident between the ridge and the White Mountains. The strike and the location of this gradient are consistent with the line-of-weakness/transform-fault in *Sykes* [1978]. The extension of this "step" in the Moho crosses the ONYNEX refraction line

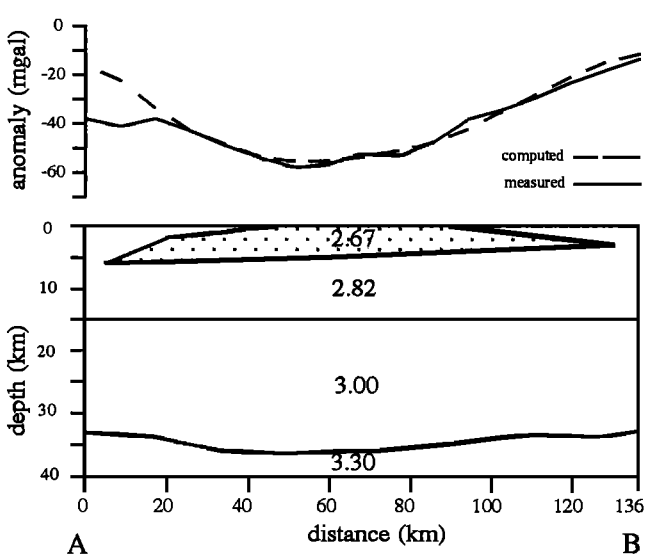

Fig. 11. Gravity model for line A-B in Figure 10b, showing the observed (solid line) and computed (dashed line) values of the Bouguer gravity anomaly. The crustal density model is simplified to test the effect of Moho fluctuation and the thickness of the White Mountain Batholith.

near the location of Shot 7, 10 km distant from where the ONYNEX record section from Shot 10 [*Hughes and Luetgert*, 1991] exhibits a step in PmP arrival times. Modeling the lithospheric response, with a fault or local shear zone serving as the southwestern wall of the depression under the White Mountains, changes the halfwidth of the broken plate model from 50 km to 85 km. The flexural rigidity implied by this halfwidth is 1×10^{22} Nt-m, and, for reasonable parameters, the apparent elastic thickness is 10 km. These are still very low values but closer to values reported in other studies, and support the hypothesis that the New Hampshire igneous bodies formed when the lithosphere was thin. Constraining the tectonic origin of such a feature is beyond the scope of this paper, but if it represents the pre-existing zone of weakness hypothesized by *Sykes* [1978], the absence of such a structural trend in the surface geology suggests an origin before the collision of the Gander Terrane against the North American continent.

Figure 12 shows three possible southwest-northeast cross-sections across the White Mountains and perpendicular to the assumed buried Moho relief. The first cross-section shows a deep granite body and flat Moho topography, which can satisfy the gravity data. The second cross-section shows a shallower granite body and a Moho depression under the White Mountains, which can satisfy the gravity data and the PmP residuals. The third cross-section shows a shallow granite body and deep Moho under the White Mountains, and the southwestern border of the Moho depression is a buried Moho-displacing fault or shear zone associated with the steep gradient of the PmP residuals. This third model satisfies the gravity data, fits the PmP residuals better than the second model, and leads to a flexural rigidity value that is closer to values reported in other studies. Because integrated traveltime is the principal seismic constraint on the lower crust, another possible model would prescribe a low-velocity lower crust (~ 4% negative P-velocity anomaly), with the gravity data satisfied by either a thicker granite pluton or lower density in the lower crust. Evidence discussed above for low lower-crustal Poisson's ratio under the central New Hampshire plutons would be consistent with the large lower crustal compositional variations implied by this model. However, (1) the short distance over which the PmP residuals change from positive to negative (seen also in the ONYNEX refraction profile from Shot 10), and (2) the gravity data do not require a thick low-velocity lower-crustal layer, lead us to favor an explanation in terms of Moho topography. However, the limitations of our dataset do not allow conclusive arguments for or against these models, and they are presented as working hypotheses for further studies in the area.

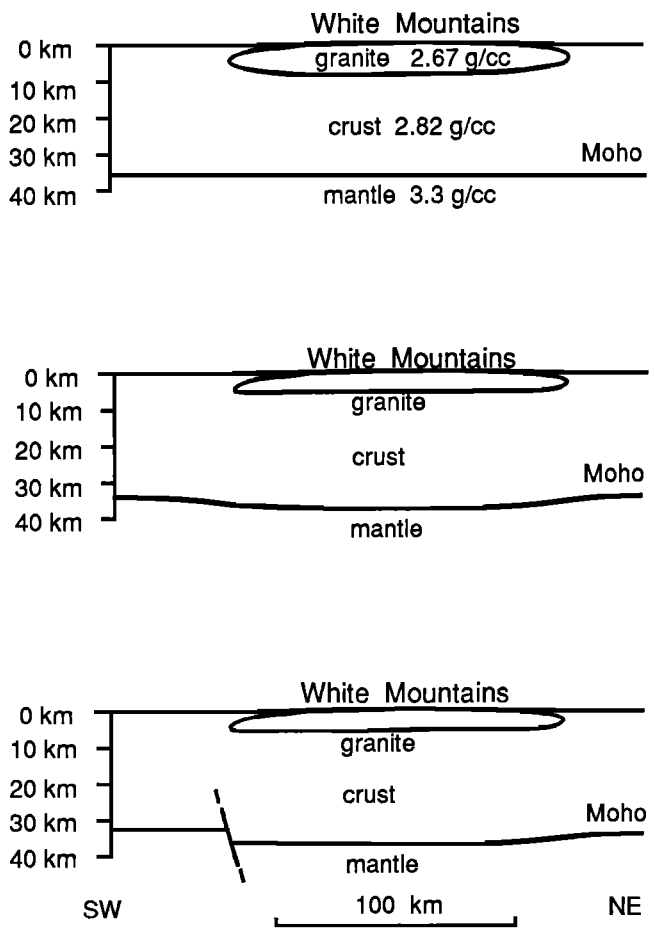

Fig. 12. Cartoons of hypothesized cross sections from southwest to northeast across the White Mountain Batholith. (Top) A thick granite batholith and no Moho fluctuation. (Middle) A shallow granite batholith with a Moho depression. (Bottom) A shallow granite batholith with a Moho depression, bounded on the southwestern border with a buried fault.

CONCLUSIONS

A principal conclusion of this study is that observations of P-waves that interact with the lower crust and Moho in central New Hampshire suggest significant 3–D velocity structure, so that straightforward extrapolation from 2–D refraction-line velocity models requires caution. PmP traveltime residuals from explosion-source data collected in a 2–D array in Central New Hampshire suggests fluctuation of the Moho depth with amplitude ≈ 3 km, with thicker crust under the White Mountain batholith and to its southwest, and thinner crust east and southwest of the White Mountains. The 1–D reference P-velocity model for this estimate, derived from our P traveltimes, has a crustal thickness of 34.5 km. If we use a 1–D reference P-velocity model favored by other studies of northern New England, with a faster lower crust and an average crustal thickness near 40 km, both the PmP residuals and the inferred topography are amplified, the latter by 50%. This depression in the Moho correlates well with the topography and gravity anomalies in the region. Comparison with gravity data suggests that 30–35% of the observed anomaly can be related to the inferred Moho topography, suggesting the low-density root of the White Mountains need only be 5 km deep. A very low flexural rigidity for the lithosphere is found when the Moho depression is modeled as the response of the lithosphere to the load of the White Mountains. A buried lithospheric fault or suture southwest of the White Mountains is hypothesized, to explain an apparent rapid change in the PmP residuals there, seen both in our observations and in the ONYNEX refraction profile from Shot 10. Modeled with this hypothesis, the flexural rigidity of the lithosphere increases to 1×10^{22} Nt-m, corresponding to an elastic thickness of 10 km. This is a low value, suggesting that the plutons were emplaced when the lithosphere was (at least locally) thinned, but it is within the range of values found elsewhere for continental lithosphere.

The average 1–D velocity model for central New Hampshire, as determined from 171 source-receiver pairs, can be modeled by a simple two-layer linear-gradient P-velocity model of 6.1 to 6.2 km/s in the upper crust, and 6.2 to 6.8 km/s in the lower crust. No extended midcrustal reflectors are observed, although a third of the records in the 75-115 km distance range show waveforms consistent with a prominent midcrustal reflector at 15 km depth, which was discerned in data from the ONYNEX refraction line to the north of our deployment. S arrival times are less certain due to waveform complexity, but can be modeled by a similar linear-gradient model with S-velocities 3.5 to 3.7 km/s in the upper crust, and 3.7 to 3.9 km/s in the lower crust. The average thickness of the crust as modeled by PmP is 34.5 km, but a model with higher lower-crust velocity and 39-40 km crustal thickness is not excluded by the PmP arrival times. Average Poisson's ratio σ is inferred to be 0.23 to 0.26 within the crust in central New Hampshire.

Acknowledgments. We thank Klaus Jacob and Ted Koczynski of the National Center for Earthquake Engineering Research (NCEER) for providing field support. We thank Dorothy Koch, Martin Olsen, and Chia Ya Chang for help in the deployment of the instruments, and the Naswa Resort of Laconia, New Hampshire, for serving as an agreeable base camp. Mark Brandon offered useful advice and helped us use his PC computer lab for various tasks. James Luetgert, Stephen Hughes, and Christel Hennet gave us preprints in advance of publication and offered useful comments. We thank the reviewers for many useful comments. This research was supported by NCEER grant 88-1302 and NSF grant EAR-8657206.

REFERENCES

Ando, C.J., B.L. Czuchra, S.L. Klemperer, L.D. Brown, M.J. Cheadle, F.A. Cook, J.E. Oliver, S. Kaufman, T. Walsh, J.B. Thompson, Jr., J.B. Lyons, and J.L. Rosenfeld, Crustal profile of mountain belt: COCORP deep seismic reflection profiling in New England Appalachians and implication for architecture of convergent mountain chains, *AAPG Bull., 68*, 819–837, 1984.

Ballard, R.D., and E. Uchupi, Carboniferous and Triassic rifting: A preliminary outline of the tectonic history of the Gulf of Maine, *Geol. Soc. Am. Bull., 83*, 2285–2302, 1972.

Billings, M.P., *The Geology of New Hampshire*, part II, *Bedrock geology*, 203 pp., New Hampshire State Planning and Development Commission, Concord, N.H., 1956.

Chamberlain, C.P., and P.C. England, The Acadian thermal history of the Merrimack synclinorium in New Hampshire, *J. Geol., 93*, 593–602, 1985.

Christensen, N.I., and D.M. Fountain, Constitution of the lower continental crust based on experimental studies of seismic velocities in granulite, *Geol. Soc. Am. Bull., 86*, 227–236, 1975.

Dykstra, J., W.A. Bothner, and A.M. Hussey, The Kearsarge-Central Maine Synclinorium of southeastern Maine: stratigraphic and structural relations of an inverted section, *Am. J. Sci., 287*, 242–264, 1987.

Firbas, P., Tomography from seismic profiles, in *Seismic Tomography*, edited by G. Nolet, pp. 189–202, D. Reidel, Hingham, Mass., 1987.

Foland, K.A., and H. Faul, Ages of the White Mountain intrusives New Hampshire, Vermont, and Maine, USA, *Am. J. Sci., 277*, 888–904, 1977.

Hennet, C.G., J.H. Luetgert, and R.A. Phinney, The crustal structure in central Maine from coherency processed refraction data, *J. Geophys. Res., 96*, 12,023–12,037, 1991.

Hittelman, A.M. J.O. Kinsfather, and H. Meyers, Geophysics of North America CD-ROM, U.S. Department of Commerce, Boulder, Colo., 1989.

Hodge, D., D.A. Abbey, M.A. Harbin, J.L. Patterson. M.J. Ring, and J.F. Sweeney, Gravity studies of subsurface mass distribution of granitic rocks in Maine and New Hampshire, *Am. J. Sci., 282*, 1289–1324, 1982.

Holbrook, W. S., A petrological model of the laminated lower crust in southwest Germany based on wide-angle P- and S-wave seismic data, in *Properties and Processes of the Earth's Lower Crust, Geophysical Monogr. Ser.*, vol 51, edited by R.F Mereu, S. Mueller and D.M. Fountain, pp. 121–126, AGU, Washington D.C., 1989.

Holbrook, W. S., D. Gajewski, A. Krammer and C. Prodehl, An interpretation of wide-angle shear and compressional wave data in southwest Germany: Poisson's ratio and petrologic implications, *J. Geophys. Res., 93*, 12,081–12,106, 1988.

Hughes, S., and J.H. Luetgert, Crustal structure of the western New England Appalachians and Adirondack Mountains, *J. Geophys. Res.*, in press, 1991.

Kafka, A.L., and J.E. Ebel, Seismic structure of the earth's crust underlying the state of Maine, in *Studies in Maine geology*, Vol 1, pp. 137–156, Maine Geological Survey, Augusta, Maine, 1988.

Kusznir, N., and G. Karner, Dependence of the flexural rigidity of the continental lithosphere on rheology and temperature, *Nature, 316*, 138–142, 1985.

Luetgert, J.H., S. Hughes, J.Cipar, S. Mangino, D. Forsyth, and I. Asudeh, Data report for ONYNEX, the 1988 Grenville- Appalachians seismic refraction experiment in Ontario, New York and New England, *U.S. Geol. Surv. Open File Rep., 90-426*, 1990.

Luetgert, J.L., C.E. Mann, and S.L. Klemperer, Wide-angle deep crustal reflection in the northern Appalachians, *Geophys. J. Roy. astron. Soc., 89*, 183–188, 1987.

Lyons, J.B., E.L. Boudette, and J.N. Aleinikoff, The Avalonian and Gander zones in central eastern New England, Major structural zones and faults of the northern Appalachian, edited by P. St. Julian, and J. Beland, *Geol. Assoc. Can. Spec. Pap., 24*, 43–66, 1982.

Manghnani, M.H., R. Ramananantoandro, and S.P. Clark, Compressional and shear wave velocities in granulite facies rocks and eclogites to 10 kbar, *J. Geophys. Res., 79*, 5427–5446, 1974.

Mangino, S., and J. Cipar, Data report for the 1988 Ontario-New York-New England seismic refraction experiment: three component profiles, *Environ. Res. Pap., No. 1054*, 1990.

McNutt, M.K., M. Diament, and M.G. Kogan, Variation of elastic plate thickness at continental thrust belt, *J. Geophys. Res., 93*, 8825–8838, 1988.

Menke, W., A.L. Lerner-Lam, B. Dubendorff, and J. Pacheco, Polarization and coherence of 5 to 30 Hz seismic wave fields at a hard-rock site and their relevance to velocity heterogeneities in the crust, *Bull. Seismol. Soc. Am., 80*, 430–449, 1990.

Menke, W., L. Shengold, G. Hongsheng, H. Ge, and A. Lerner-Lam, Performance of the short-period geophones of the IRIS/PASSCAL array, *Bull. Seismol. Soc. Am., 81*, 232–242, 1991.

Michelini, A., and T.V. McEvilly, Seismological studies in Parkfield, I, Simultaneous inversion for velocity structure and hypocenters using cubic B-spline parameterrization, *Bull. Seismol. Soc. Am., 81*, 524–552, 1991.

Morgan, W. J., Convection plumes in the lower mantle, *Nature, 230*, 42–43, 1971.

Murphy, J.M. and J.H.Luetgert, Data report for the 1984 Maine along-strike seismic-refraction profile, *U.S. Geol. Surv. Open File Rep., 87-133*, 1987.

Murphy, J.M. and J.H.Luetgert, Data report for the Maine-Quebec cross-strike seismic-refraction profile, *U.S. Geol. Surv. Open File Rep., 86-47*, 1986.

Nielson, D.L., R.G. Clark, J.B. Lyons, E.J. Englund, and D.J. Borns, Gravity models and mode of emplacement of the New Hampshire plutonic series, *Geol. Soc. Am. Mem., 146*, 301–318, 1976.

Phinney, R.A., A seismic cross section of the New England Appalachian: the orogen exposed, in *Reflection Seismology: The Continental Crust, Geodynamic Ser.*, vol. 14, edited by M. Barazangi and L. Brown, pp. 157–172, AGU, Washington, D.C., 1986.

Press, W.H., B.P. Flannery, S.A. Teukolsky, and W.T. Vetterling, *Numerical Recipes*, Cambridge University Press, New York, 1986.

Stephenson, R., and K. Lambeck, Isostatic response of the lithosphere with in-plate stress: Application to central Australia, *J. Geophys. Res.*, *90*, 8581–8588, 1985.

Sykes, L. R., Intraplate seismicity, reactivation of preexisting zones of weakness, alkaline magmatism, and other tectonism predating continental fragmentation, *Rev. Geophys. 16*, 621–688, 1978.

Taylor, S.R., Geophysical framework of the Appalachians and adjacent Grenville Province, *Geol. Soc. Am. Mem.*, *172*, 317–348, 1989.

Taylor, S.R., and M.N. Toksoz, Crust and upper-mantle velocity structure in the Appalachian orogenic belt: implication for tectonic evolution, *Geol. Soc. Am. Bull.*, *93*, 315–329, 1982.

Taylor, S.R., M.N. Toksoz, and M.P Chaplin, Crustal structure of the northeastern United States: contrasts between Grenville and Appalachian provinces, *Science, 208*, 595–597, 1980.

Turcotte, D.L., and G. Schubert, *Geodynamics Applications of Continuum Physics to Geological Problems*, John Wiley, New York, 1982.

Walcott, R.I., Flexural rigidity thickness and viscosity of the lithosphere, *J. Geophys. Res.*, *75*, 3941–3954, 1970.

Willett, S.D., D.S. Chapman, and H.J.Neugebauer, A thermomechanical model of continental lithosphere, *Nature, 314*, 520–523, 1985.

Williams, H., and R.D. Hatcher, Jr., Appalachian suspect terranes, *Geol. Soc. Am. Mem.*, *158*, 33–53 1983.

Zartman, R.E., Three decades of geochronologic studies in the New England Appalachians, *Geol. Soc. Am. Bull.*, *100*, 1168–1180, 1988.

A. Lerner-Lam, Lamont-Doherty Geological Observatory, Columbia University, Palisades, NY 10964.

J. Park and E. Shalev, Department of Geology and Geophysics, Yale University, P.O. Box 6666, New Haven, CT 06511.

(Received August 2, 1990;
revised April 10, 1991;
accepted June 10, 1991)

JOURNAL OF GEOPHYSICAL RESEARCH, VOL. 96, NO. B10, PAGES 16,429–16,454, SEPTEMBER 10, 1991

Shear Wave Splitting and Subcontinental Mantle Deformation

PAUL G. SILVER

Department of Terrestrial Magnetism, Carnegie Institution of Washington, Washington, D. C.

W. WINSTON CHAN

Teledyne Geotech, Alexandria Laboratories, Alexandria, Virginia

We have made measurements of shear wave splitting in the phases *SKS* and *SKKS* at 21 broadband stations in North America, South America, Europe, Asia, and Africa. Measurements are made using a retrieval scheme that yields the azimuth of the fast polarization direction ϕ and delay time δt of the split shear wave plus uncertainties. Detectable anisotropy was found at most stations, suggesting that it is a general feature of the subcontinental mantle. Delay times range from 0.65 s to 1.70 s and average about 1 s. Somewhat surprisingly, the largest delay time is found in the 2.7 b.y.-old Western Superior Province of the Canadian Shield. The splitting observations are interpreted in terms of the strain-induced lattice preferred orientation of mantle minerals, especially olivine. We consider three hypotheses concerning the origin of the continental anisotropy: (1) strain associated with absolute plate motion, as in the oceanic upper mantle, (2) crustal stress, and (3) the past and present internal deformation of the subcontinental upper mantle by tectonic episodes. It is found that the last hypothesis is the most successful, namely that the most recent significant episode of internal deformation appears to be the best predictor of ϕ. For stable continental regions, this is interpreted as "fossil" anisotropy, whereas for presently active regions, such as Alaska, the anisotropy reflects present-day tectonic activity. In the stable portion of North America there is a good correlation between delay time and lithospheric thickness; this is consistent with the anisotropy being localized in the subcontinental lithosphere and suggests that intrinsic anisotropy is approximately constant. The acceptance of this hypothesis has several implications for subcontinental mantle deformation. First, it argues for coherent deformation of the continental lithosphere (crust and mantle) during orogenies. This implies that the anisotropic portion of the lithosphere was present since the deformational episode and rules out the addition of undeformed material to this layer by subsequent "underplating" or conductive growth of the thermal boundary layer. One of the most important issues in the study of orogenies is the need to reconcile the formation of thickened lithosphere with the paradoxically high mantle temperatures often associated with orogenic episodes. Most efforts to date have focussed on modes of deformation whereby the cold lithospheric mantle is removed (by convective instability or delamination) and replaced by warm asthenosphere. These models, however, are incompatible with the evidence for preserved coherent lithospheric deformation; rather, the deformed mantle appears to have been heated in place. We suggest that the elevated mantle temperatures may be due to the strain heating accompanying the deformation.

INTRODUCTION

The steadily increasing evidence that mantle anisotropy is due to the strain induced lattice preferred orientation (LPO) of upper mantle minerals [see *Nicolas and Christensen*, 1987], an idea originally proposed by *Hess* [1964], has provided a means of inferring modes of mantle deformation from observations of seismic anisotropy. There have been numerous studies of upper mantle anisotropy below the ocean basins: measurements of P_n velocity from refraction surveys [e.g., *Raitt et al.*, 1969; *Shearer and Orcutt*, 1986], and both azimuthal and polarization anisotropy in long-period surface waves [e.g., *Forsyth*, 1975; *Nataf et al.*, 1984; *Tanimoto and Anderson*, 1985; *Montagner and Tanimoto*, 1990]. Nearly all of these studies can be successfully interpreted as due to the strain induced by plate-motion processes: seafloor spreading at the mid-ocean ridges, the differential motion of the lithosphere and asthenosphere, or more generally, the mantle flow induced by the motions of the plates.

An equally successful characterization of subcontinental mantle deformation from anisotropic observations has yet to fully emerge. Not only is plate tectonics less successful in describing the features of the continents and in predicting deformation in the subcontinental mantle, but the much shorter horizontal length scales of coherent continental deformation make the study of anisotropy more difficult using the techniques typically applied to the oceans. Notable exceptions are the few P_n observations on the continents [*Bamford*, 1977; *Bamford et al.*, 1979; *Vetter and Minster*, 1981; *Beghoul and Barazangi*, 1990]. The problem of smaller length scales can be addressed by the use of a particular manifestation of anisotropy, shear wave splitting [*Christensen*, 1966; *Keith and Crampin*, 1977]. Splitting in teleseismic shear waves such as *SKS*, *ScS*, and *S*, with steep arrival angles beneath the receiver, provides excellent lateral resolution in the upper mantle, and thus allows for the direct comparison of anisotropy with surface tectonic and geologic features possessing typical continental dimensions. Measurements of shear wave splitting in waves sampling the upper mantle began less than a decade ago with the pioneering work of Ando and coworkers using S-waves from nearby events in the descending slab [*Ando and Ishikawa*, 1982, *Ando et al.*, 1983; *Bowman and Ando*, 1987] and *ScS* [*Ando*, 1984; see also *Fukao*, 1984]. Because *ScS* is most easily used in the distance range of less than 30°, it provides information primarily about the anisotropy in tectonic areas along active continental margins. *ScS*, however,

Paper number 91JB00899.
0148–0227/91/91JB–00899$05.00

is less useful in studying stable continental interiors that are relatively devoid of seismic activity. One important advance in retrieving splitting information has been the utilization of SKS. First employed by *Vinnik et al.* [1984], this phase has begun to be exploited extensively in teleseismic splitting [*Kind et al.*, 1985; *Silver and Chan*, 1988; *Vinnik et al.*, 1989*a*; *Ansel and Nataf*, 1989; *Savage et al.*, 1990, hereafter called SSM], because it has many advantages for the study of the continents. First, the observed anisotropy can be localized to the receiver side of the path due to the P to S conversion at the core-mantle boundary (CMB). Second, the detection of anisotropy is much simpler; since SKS is radially polarized in an isotropic, spherically symmetric Earth, detectable energy on the transverse component, SKS_T, signifies deviations from these idealized properties. As the effects of anisotropy and lateral heterogeneity can be easily distinguished, SKS_T becomes an excellent diagnostic for the presence of anisotropy. Third, SKS is most easily observed beyond 85°, allowing the study of stable continental interiors. Finally, SKS represents a nearly vertical ray path through the mantle, so that the propagation direction is essentially constant; this allows for a somewhat simpler analysis.

Silver and Chan [1988, hereafter called SC] began a systematic study of continental anisotropy through SKS splitting, with the ultimate goal of obtaining a general characterization of subcontinental mantle deformation. They not only found anisotropy at all stations studied, but also proposed that the splitting is predominantly caused by "fossil" strain in the subcontinental mantle due to the last major episode of tectonic activity. The present report represents a continuation of that study. In particular it seeks to test the fossil strain hypothesis with an expanded data set, against two alternatives: plate-motion related strain, analogous to that found in the oceanic upper mantle, and present-day crustal stress. Each of these hypotheses carries implications. For example, if the plate-motion hypothesis is correct, it would argue that the strains associated with plate motion dominate subcontinental mantle deformation, so that oceanic and continental upper mantle may be treated similarly in this respect. But if the fossil strain hypothesis is true, it argues for something quite different: that the orogenic and rifting episodes responsible for producing the fabric of continental geology have also imparted this same fabric to the mantle. Anisotropy would then constitute the extension of structural geology to the mantle and help provide a geologic history of the entire continental lithosphere.

The evaluation of these hypotheses requires knowledge of three relationships: (1) between splitting and anisotropy; (2) between anisotropy and strain; and (3) between strain and geologic/tectonic processes. For a homogeneous medium, the relation between the splitting parameters, the fast polarization direction ϕ and delay time δt, and the elasticity tensor C_{ijkl} is straightforward even for the most general anisotropy. While it can become quite complicated for multiple regions of anisotropy, however, the assumption of a localized homogeneous anisotropic layer appears to be justified in most cases and will be utilized for the applications in the present report.

Assuming that anisotropy is caused by the lattice preferred orientation (LPO) of mantle minerals, the relation between anisotropy and strain requires knowledge of composition and mineralogy, along with the single-crystal elastic constants and dominant slip systems for these minerals. Since these properties are reasonably well known for the upper mantle above 400 km depth, the problem is reduced to finding an orientation distribution function (ODF) for the primary anisotropic minerals (such as olivine and orthopyroxene) as a function of finite strain. In fact, seismological applications only require a relationship between a suitably averaged macroscopic elasticity tensor $< C_{ijkl} >$ derived from the ODF, and finite strain. Obtaining an appropriate relationship has involved the interplay of theory [*McKenzie*, 1979; *Ribe*, 1989*a*; *Ribe and Yu*, 1991] laboratory measurements, and observations of mantle xenoliths [see *Nicolas and Poirier*, 1976; *Gueguen and Nicolas*, 1980; *Christensen*, 1984].

The third relation requires a kinematic or dynamic description of the relevant tectonic process, and a constitutive relation. This issue has been addressed for the strain associated with oceanic plate motion (spreading, subduction, absolute plate motion) and mantle convection [*McKenzie*, 1979; *Ribe*, 1989*a*, *b*] with emphasis on the resulting anisotropy. Continental strain has been examined by several studies [e.g., *England and McKenzie*, 1982, 1983; *England*, 1983; *Bird*, 1984, 1988; *Molnar*, 1988a; *England and Houseman*, 1989], although the implications for seismic anisotropy have not been discussed.

In this report we present shear wave splitting measurements from all presently available three-component broadband stations from the GDSN network, the NARS array, and the Chinese Digital Seismic Network (CDSN). This includes measurements from the continents of North America, South America, Eurasia, and Africa. We will also discuss two other related studies, one which examines splitting in the Basin and Range (SSM), and the other which examines IRIS/IDA stations [*Given and Silver*, 1990], which have used the same measurement scheme as the present study.

MEASUREMENT OF SHEAR WAVE SPLITTING PARAMETERS

In an isotropic, homogeneous medium a shear wave arriving at the surface at time T_o after traversing a path of length L can be written as a vector function

$$\mathbf{u}(\omega) = \mathbf{A}w(\omega)\exp[-i\omega T_o] \quad (1)$$

where $\mathbf{A}$ is the complex vector amplitude, and $w(\omega)$ is the wavelet function which is the product of the Fourier-transformed source time function, attenuation operator and instrument response. We assume that $\mathbf{A}$ can be approximated by $A\hat{\mathbf{p}}$, where A is a complex scalar and $\hat{\mathbf{p}}$ is a real unit vector pointing in the displacement direction and which is contained in the plane orthogonal to the propagation direction $\hat{\mathbf{b}}$. Incorporating A into the definition of $w(\omega)$, (1) is rewritten as

$$\mathbf{u}(\omega) = w(\omega)\exp[-i\omega T_o]\hat{\mathbf{p}} \quad (2)$$

In essence, we are ignoring phase shifts in the radial component due to the free surface. For the steep arrival angles used in the present report, this should be an excellent approximation.

We model the splitting due to anisotropy as the geometrical operations of projecting $\hat{\mathbf{p}}$ onto the fast and slow polarization directions $\hat{\mathbf{f}}$ and $\hat{\mathbf{s}}$ and then time-shifting these

two components by $\delta t/2$ (earlier) and $-\delta t/2$ (later), respectively. For an elasticity tensor C_{ijkl}, $\hat{\mathbf{f}}$ and $\hat{\mathbf{s}}$ are the two quasi-shear eigenvectors of the polarization matrix $\mathbf{V}$ defined by

$$\rho V_{il} \equiv C_{ijkl}\,\hat{b}_j\,\hat{b}_k \tag{3}$$

[*Backus*, 1965] with eigenvalues β_2^2 and β_1^2 corresponding to the two squared shear velocities. For small anisotropy, δt can be conveniently expressed in terms of a relative perturbation in shear velocity $\delta\hat{\beta} = \beta_o^{-1}(\delta\beta_1 - \delta\beta_2)$ as

$$\delta t = \beta_o^{-1} L \delta\hat{\beta} \tag{4}$$

where $\delta\beta_{1,2} = \beta_{1,2} - \beta_o$ and β_o is the isotropic shear velocity defined such that $\delta\beta_1 + \delta\beta_2 = 0$. The process of producing a split shear wave $\mathbf{u}_s(\omega)$ can be represented as the application of the splitting operator

$$\mathbf{\Gamma} \equiv \exp[i\omega\delta t/2]\hat{\mathbf{f}}\hat{\mathbf{f}} + \exp[-i\omega\delta t/2]\hat{\mathbf{s}}\hat{\mathbf{s}} \tag{5}$$

to a signal of the form (2) with the resulting split waveform

$$\mathbf{u}_s(\omega) = w(\omega)\exp[-i\omega T_o]\mathbf{\Gamma}(\phi, \delta t)\cdot\hat{\mathbf{p}} \tag{6}$$

where ϕ is the angle between $\hat{\mathbf{f}}$ and $\hat{\mathbf{p}}$. Defining the tensor

$$\delta\mathbf{T} = \delta t/2(\hat{\mathbf{f}}\hat{\mathbf{f}} - \hat{\mathbf{s}}\hat{\mathbf{s}}) \tag{7}$$

$\mathbf{\Gamma}$ may be more compactly written as

$$\mathbf{\Gamma} = \exp[i\omega\delta\mathbf{T}(\phi, \delta t)] \tag{8}$$

in analogy with the isotropic case (2).

The two parameters that may be estimated are δt and ϕ. A straightforward way of doing so is to try to correct for the anisotropy and choose the pair that most nearly returns (6) into the form (2) by reversing the geometrical operations: that is, search for the inverse operator $\mathbf{\Gamma}^{-1}$. From (5), we note that this operator is unitary so that the inverse is simply the complex conjugate $\mathbf{\Gamma}^*$. Assuming the polarization plane of the shear wave is known, $\mathbf{\Gamma}^{-1}$ may be found by computing the two dimensional time-domain covariance matrix of particle motion in that plane, as its eigenvalues may then be used as a measure of linearity [*Vidale*, 1986]. We define the covariance c_{ij} between any two orthogonal components of ground motion, making angles of ϕ and $\phi + \pi/2$ with $\hat{\mathbf{p}}$,

$$c_{ij}(\phi, \delta t) = \int_{-\infty}^{\infty} u_i(t)u_j(t - \delta t)dt \qquad i, j = 1, 2 \tag{9}$$

for lag δt.

In the absence of anisotropy, $\mathbf{c}$ will possess one nonzero eigenvalue $\lambda_1 = E_u = \int_{-\infty}^{\infty} w(t)^2 dt$ and corresponding eigenvector $\hat{\mathbf{p}}$ (see (2)). In the presence of anisotropy, $\mathbf{c}$ will have two nonzero eigenvalues, λ_1, λ_2 unless $\phi = n\pi/2$ ($n = 0, 1, 2, \ldots$) or δt is zero. Thus, one may search for $\mathbf{\Gamma}^{-1}$ such that the corrected seismogram $\tilde{\mathbf{u}}_s(\omega) = \mathbf{\Gamma}^{-1}\cdot\mathbf{u}_s(\omega)$ possesses a singular covariance matrix. For any candidate pair of values (ϕ, δt), the covariance matrix $\tilde{\mathbf{c}}(\phi, \delta t)$ for the rotated and shifted seismograms may be expressed in terms of the covariance $\mathbf{c}(\delta t)$ of a reference coordinate system (say north-south, east-west), and will have the components

$$\tilde{c}_{11}(\phi, \delta t) = \int_{-\infty}^{\infty} \tilde{u}_1^2(t + \delta t/2)dt = \tilde{c}_{11}(\phi, 0)$$
$$= R_{1i}(\phi)c_{ij}(0)R_{1j}(\phi) \tag{10}$$

$$\tilde{c}_{22}(\phi, \delta t) = \int_{-\infty}^{\infty} \tilde{u}_2^2(t - \delta t/2)dt = \tilde{c}_{22}(\phi, 0)$$
$$= R_{2i}(\phi)c_{ij}(0)R_{2j}(\phi) \tag{11}$$

$$\tilde{c}_{12}(\phi, \delta t) = \int_{-\infty}^{\infty} \tilde{u}_1(t + \delta t/2)\tilde{u}_2(t - \delta t/2)dt$$
$$= R_{1i}(\phi)c_{ij}(\delta t)R_{2j}(\phi) \tag{12}$$

$$\tilde{c}_{21}(\phi, \delta t) = \tilde{c}_{12}(\phi, \delta t) \tag{13}$$

where the rotation tensor $\mathbf{R}$ defines the change of coordinate system from the reference frame to that defined by the trial fast and slow polarization directions. Equations (10)–(13) demonstrate that $\tilde{\mathbf{c}}$ may be formed by taking linear combinations of the covariance and zero-lag autocovariance in the original reference frame, which allows for efficient evaluation of candidate operators. In the presence of noise $\eta(t)$, $\tilde{\mathbf{c}}$ will not be singular and one seeks instead the matrix that is most nearly singular. While there are apparently different eigenvalue-based measures of linearity such as maximizing λ_1, λ_1/λ_2, minimizing λ_2 or $\lambda_1\lambda_2$, they are in fact equivalent. This is because the two-dimensional trace $\Theta = \lambda_1 + \lambda_2$ of $\tilde{\mathbf{c}}$ is invariant with respect to changes in either ϕ or δt. Various methods of estimating splitting parameters may thus be put in this context. Maximizing the cross-correlation between components, a method used by *Bowman and Ando* [1987], is similar to minimizing the determinant, which can be seen from the relationship $\lambda_1\lambda_2 = c_{11}c_{22} - c_{12}^2$. Maximizing the ratio λ_1/λ_2 (aspect ratio) has been applied by *Shih et al.* [1989]. Finally, finding the minimum of λ_2, λ_2^{min}, is equivalent to the method of SC. The importance of λ_2^{min} is that it constitutes a measure of variance of the noise process. As such, it can provide the basis for calculating a confidence region for the two splitting parameters. Such a procedure has been applied by SC, SSM, and *Given and Silver* [1990] and is discussed below.

An important special case in splitting estimation is where the isotropic polarization vector $\hat{\mathbf{p}}$ is known, as with *SKS* and *SKKS*. If viewed on the radial and transverse components, one obtains for a noise free seismogram, the time-domain expressions

$$u_r(t) = w(t + \delta t/2)\cos^2\phi + w(t - \delta t/2)\sin^2\phi \tag{14}$$

$$u_t(t) = -\frac{1}{2}[w(t + \delta t/2) - w(t - \delta t/2)]\sin(2\phi) \tag{15}$$

In this case the energy $E_t = \int_{-\infty}^{\infty} \tilde{u}_t^2(t)dt$ on the corrected transverse component can be minimized instead of λ_2, as in SC. Equations (14) and (15) demonstrate an additional important diagnostic for these phases. For δt small compared to the characteristic period of study, u_r is only slightly broadened and distorted, while u_t, which is identically zero in an isotropic medium, is approximately proportional to the derivative of the radial component. Note that this relationship will hold for any pair of components in the directions parallel and orthogonal to $\hat{\mathbf{p}}$.

Error Estimation

Error estimation is an important part of the splitting measurement. In many cases, only a few records will be available and evaluating the uncertainty of each measurement is essential. This is especially true for portable experiments, where the observing time is necessarily short. For an n-point discrete time series, λ_2^{min} is the sum-of-squares of a noise process which, it is assumed, is approximately χ^2-distributed. For ν degrees of freedom and k parameters, we take the confidence region at the α confidence level to be defined by values of λ_2 satisfying

$$\frac{\lambda_2}{\lambda_2^{min}} \leq 1 + \frac{k}{\nu - k} f_{k,\nu-k}(1-\alpha) \qquad (16)$$

[*Jenkins and Watts*, 1968; *Bates and Watts*, 1988], where f is the inverse of the F-distribution. In our case $k = 2$, $\alpha = 0.05$, and ν, a quantity that depends both on the instrument response and noise spectrum, is usually much smaller than n. A discussion of expression (16) and the number of degrees of freedom is given in the appendix. Briefly, from each minimum obtained, an estimate of $\hat{\nu}_i = \nu_i/n_i$ for the ith record is calculated; then all estimates for one station are averaged to obtain $< \hat{\nu} >$. For the networks we have used, the product of $\hat{\nu}$ and the sampling rate is roughly constant and equal to one degree of freedom for each second of record. The confidence region is then defined for the ith record using $< \hat{\nu} > n_i$ degrees of freedom. If the confidence region is approximately Gaussian, then its bounding values along the parameter axes correspond to 2σ marginal uncertainties for ϕ and δt. In cases where this region is not symmetric but approximately ellipsoidal, we determine the largest symmetric region that includes the asymmetric region. In either case, we take one half of the bounding values of the confidence region (along the parameter axes) as the 1σ uncertainties. In cases of no observable splitting, there is a characteristic nonellipsoidal contour pattern that may be interpreted as allowing the three options $\delta t = 0$, $\hat{\mathbf{p}} = \hat{\mathbf{f}}$ or $\hat{\mathbf{p}} = \hat{\mathbf{s}}$. The second two possibilities can be evaluated by utilizing different values of $\hat{\mathbf{p}}$.

In order to test the statistical assumptions that have gone into the error estimation, we have performed two simple numerical experiments, taking a synthetic shear wave, adding Gaussian random noise with known variance, and finally obtaining splitting estimates. In both cases we have used the geometry of event 85253 (Table 1) to station RSON (Table 2) with a back azimuth ϕ_b of $-46°$ and have introduced the splitting parameters of $(\phi, \delta t) = (75.0°, 1.75\ s)$ in case one and $(-39.0°, 1.75\ s)$ in case two. (In discussing the observations, ϕ will be referenced to north instead of the polarization direction $\hat{\mathbf{p}}$.) We have convolved the noise with a box-car filter of length $1s$ (four samples). The filter is found to reduce the number of degrees of freedom by a factor of 2.5. The weighted (by standard deviation) mean for five realizations is $(\phi, \delta t) = (73 \pm 3°, 1.80 \pm 0.15\ s)$. Figure 1*a* shows one of the realizations. For case 2, ϕ_b and ϕ differ by only 7° . Note in Figure 1*b* the characteristic contour pattern for this case, signifying the absence of detectable splitting. A similar pattern is obtained for $\delta t \simeq 0$ or $\phi \simeq \phi_b + 90°$.

Resolution

In making the measurements, we have concentrated on broadband digital stations because of the greatly improved resolution. The average value of δt for teleseismic splitting is approximately 1 s. For long-period instruments with characteristic periods of 20 s, this is a subtle effect. The result is reduced detectability and increased uncertainty in the splitting parameters. For SKS, this is seen by writing E_t (using (15)) as

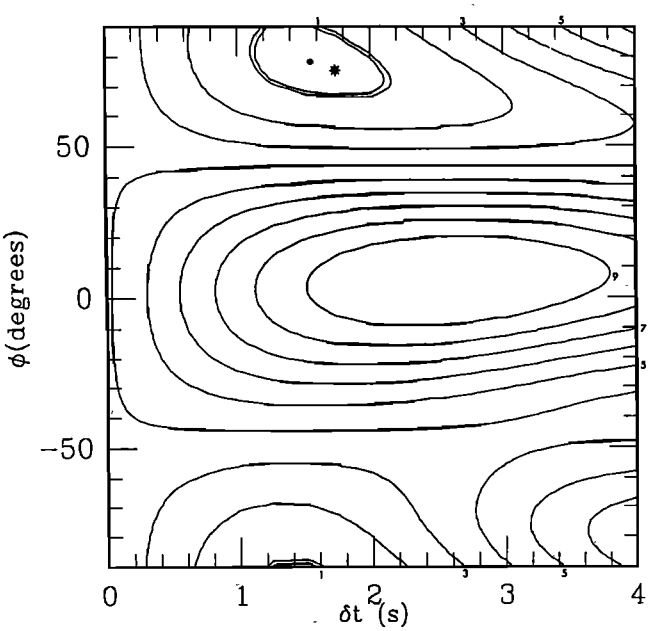

Fig. 1*a*. Contour plot of energy on E_t on corrected transverse component for synthetic example with $(\phi, \delta t)$=(75°, 1.75 s). Correlated Gaussian noise, produced by convolving uncorrelated noise with a box car of 1 *s* in length (four samples) has been added to synthetics before processing. The filter reduces the number of degrees of freedom by a factor of about 2.5. Geometry is for station RSON (Table 2) and event 85253 (see Table 1), which is at a back azimuth of −46. Double contour is 95% confidence interval. Solid circle is estimated minimum; star is actual value. Note that confidence interval successfully accounts for the uncertainty.

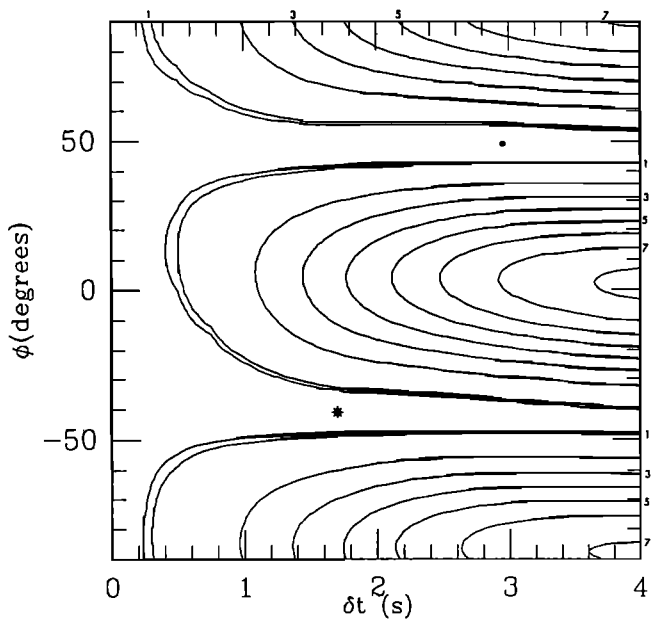

Fig. 1*b*: Same as Figure 1*a*, but for $(\phi, \delta t)$=(−39°, 1.75 s). Contour is typical for the absence of splitting and allows for the three possibilities: $\phi \sim \phi_b, \phi \sim \phi_b + 90°$, or $\delta t \sim 0$. In this case, $\phi \sim \phi_b$.

$$E_t = \sin^2(2\phi) \int_{\infty}^{\infty} |w(\omega)|^2 \sin^2(\omega \delta t/2) d\omega \qquad (17)$$

where we have utilized Parseval's theorem. The integrand is a product of $|w(\omega)|^2$ modulated by an oscillating function with maxima at $\omega = (2n+1)\pi/\delta t$ and zeros at $\omega = 2n\pi/\delta t$. For $\delta t = 1$ s, the maxima occur at 0.5 Hz, 1.5 Hz, 2.5 Hz, etc., with zeros at 0 Hz, 1 Hz, 2 Hz, etc. For a broadband instrument that is flat to velocity, a wavelet function with characteristic duration τ_c [*Silver and Jordan*, 1983] will have a maximum at about τ_c^{-1}. Thus, energetic intermediate and deep focus events with short durations close to $2\delta t$ are the most useful. The difficulty of using long-period data is that at the peak sensitivity of the instrument (about 0.05 Hz), the integrand is down by a factor of nearly 50 compared to the maximum. Broadband data are also preferred to narrow band short-period sensors, as cycle-skipping is minimized and several maxima, rather than one frequency maximum, can be utilized.

RESULTS

The data for this study consist of SKS and $SKKS$ phases in the distance range 85–140° from three-component broadband data compiled by the GDSN (including DWWSSN, RSTN), GRF, NARS array, and the CDSN. We have considered all events deeper than 80 km and m_b greater than 5.7 (Table 1). For each station listed in Table 2, we have made individual measurements on all available records with sufficiently excited and isolated SKS and $SKKS$ phases. Measurements are made in two ways: minimizing E_t and minimizing λ_2. We normally take the former procedure as the measurement and use the latter as a check for the influence of lateral heterogeneity. In this way, we can allow for the possibility that the presence of SKS_T can be explained by the rotation of $\hat{\mathbf{p}}$ away from the predicted direction ϕ_b (e.g., by a dipping layer) rather than splitting. In performing the minimization, we have chosen increments of 1° and 0.05 s for $(\phi, \delta t)$.

TABLE 1. List of Earthquakes Used in Study

Event	Year	Month	Day	Time, UT	Latitude	Longitude	Depth, km	m_b
79138	1979	05	18	2018:03.50	24.13	142.41	598.00	5.8
81247	1981	09	04	1115:13.90	9.95	124.00	651.00	5.6
83153	1983	06	02	2012:50.70	−9.51	−71.25	598.60	5.9
83237	1983	08	25	2023:33.30	33.51	131.48	126.40	6.1
83304	1983	10	31	1737:56.30	−9.02	119.18	83.40	6.0
83328	1983	11	24	0530:34.20	−7.48	128.17	178.50	6.4
83355	1983	12	21	1205:06.40	−28.19	−63.17	601.90	6.2
84032	1984	02	01	0728:28.70	49.06	146.59	573.40	5.9
84047	1984	02	16	1718:41.60	36.43	70.83	207.60	6.1
84065	1984	03	05	0333:51.00	8.15	123.76	649.10	6.5
84066	1984	03	06	0217:21.30	29.38	138.93	457.40	6.2
84115	1984	04	24	0411:29.10	30.91	138.43	403.10	6.1
84151	1984	05	30	0749:43.70	−4.84	151.58	174.40	6.2
84191	1984	07	09	2319:03.60	−5.79	111.30	533.50	5.8
84289	1984	10	15	1021:07.50	−15.86	−173.64	128.40	6.5
84304	1984	10	30	0105:49.90	−17.11	−174.08	141.00	6.0
84322	1984	11	17	1345:49.20	−18.78	−178.03	451.40	6.1
84325	1984	11	20	0815:16.20	5.17	125.12	202.20	6.4
84327	1984	11	22	1707:36.20	−17.78	−178.05	645.80	5.9
85011	1985	01	11	1441:58.60	0.20	123.58	189.10	5.9
85054	1985	02	23	1341:55.00	−10.25	161.13	84.80	6.0
85093	1985	04	03	2021:36.30	28.23	139.52	468.70	5.9
85100	1985	04	10	1626:20.60	29.96	138.93	420.00	5.8
85113	1985	04	23	1615:12.00	15.34	120.61	188.40	6.3
85121	1985	05	01	1327:56.10	−9.20	−71.23	599.90	6.0
85154	1985	06	03	1206:33.50	−15.23	−173.64	139.60	6.0
85161	1985	06	10	1537:01.00	−27.96	−67.00	151.40	5.8
85214	1985	08	02	0746:53.30	36.17	70.78	120.10	6.1
85240	1985	08	28	2050:48.30	−21.01	−178.98	624.60	6.1
85253	1985	09	10	0639:01.70	27.21	139.85	501.00	5.8
85282	1985	10	09	0115:04.70	−6.79	107.08	153.80	5.9
85285	1985	10	12	0212:57.90	−21.66	−176.38	155.00	5.9
85291	1985	10	18	0419:06.40	46.32	146.27	271.30	5.9
85304	1985	10	31	2149:20.20	−28.69	−63.17	596.00	5.8
86015	1986	01	15	2017:31.40	−21.37	170.33	146.30	6.0
86066	1986	03	07	0246:52.00	−4.99	151.71	115.90	6.0
86128	1986	05	08	1437:35.90	4.63	125.50	165.50	5.8
86146	1986	05	26	1906:16.00	−20.19	178.86	538.30	6.4
86175	1986	06	24	0311:30.90	−4.45	143.94	102.30	6.6
86179	1986	06	28	0503:47.50	−20.04	−176.06	211.20	6.1
86197	1986	07	16	1241:28.30	−19.51	169.16	111.10	6.2
87078	1987	03	19	1714:41.30	−14.90	167.23	149.60	5.5
87119	1987	04	29	1427:35.70	−19.01	−177.74	384.90	5.9
87184	1987	07	03	1010:43.80	31.20	130.32	168.20	5.8
88184	1988	07	02	1001:28.90	−14.28	167.18	142.70	5.9
88223	1988	08	10	1311:19.40	−14.88	167.29	124.80	6.2
89233	1989	08	21	1825:40.70	−4.09	154.45	487.10	6.0
89320	1989	11	16	0839:42.40	−17.69	−179.06	530.70	5.8
89333	1989	11	29	0549:03.50	−25.39	179.52	526.60	5.6

TABLE 2. Measurements

Station	N SKS_R	N SKS_T	N $SKKS_R$	N $SKKS_T$	ϕ, deg	σ_ϕ, deg	δt, s	$\sigma_{\delta t}$, s	Lat. deg	Long. deg	Location
RSSD	20	8	5	2	55	5	0.65	0.10	44.12	−104.04	Black Hills, WY
RSON	14	12	6	4	76	2	1.70	0.05	50.86	−93.70	Red Lake, ONT
RSNT	12	8	2	1	51	4	1.20	0.05	62.48	−114.59	Yellowknife, NWT
COL	8	7	0	0	−82	3	1.55	0.10	64.89	−147.79	College, AK
GRA1	6	3	0	0	77	4	1.05	0.15	49.69	11.22	Graefenberg, W. Germany
RSCP	5	2	2	0	59	6	0.75	0.15	35.59	−85.57	Cumberland Plateau, TN
SLR	5	3	3	0	81	8	1.10	0.10	−25.73	28.28	Silverton, S. Africa
RSNY	3	2	5	1	74	5	0.90	0.15	44.55	−74.53	Adirondack, NY
HIA	3	3	0	0	−20	5	0.70	0.15	49.26	119.74	Hila, China
LON	2	2	0	0	84	11	1.00	0.20	46.75	−121.81	Longmire, WA
TOL	2	2	0	0	84	4	1.00	0.15	39.88	−4.05	Toledo, Spain
WMQ	2	2	0	0	39	4	1.00	0.15	43.82	87.69	Wulumuqi, China
NRA0	2	0	3	0	00	–	–	–	60.74	11.54	NORESS, Norway
KEV	2	0	0	0	00	–	–	–	69.76	27.01	Kevo, Finland
NE04	2	0	1	0	00	–	–	–	52.81	6.67	Witteveen, NL
NE05	2	0	1	0	00	–	–	–	52.13	5.17	Utrecht, NL
SCP	3	0	4	0	60	–	–	–	40.79	−77.79	State College, PA
BDF	1	0	1	0	66	–	–	–	−15.66	−47.90	Brazilia, Brazil
KMI	2	0	0	0	−69	–	–	–	25.12	102.74	Kunming, China
NE15	0	0	1	0	13	–	–	–	50.81	5.83	Valkenburg, NL
NE16	2	0	0	0	54	–	–	–	45.76	3.10	Clermont-Ferrand, FR
ARU*					68	–	0.90	–	56.40	58.60	Arti, USSR
OBN*					5	–	0.50	–	55.10	36.36	Obninsk, USSR
NNA*					−54	–	1.10	–	−11.99	−76.84	Nana, Peru
MNV†					75	–	0.90	–	38.43	−118.15	Mina, NV
LAC†					−54	–	1.20	–	34.39	−116.41	Landers, CA

$SK(K)S_R$ refers to the number of isolated, well recorded $SK(K)S$ phases on the radial component. $SK(K)S_T$ refers to the number of isolated, well recorded $SK(K)S$ phases on the transverse that allowed for a well constrained measurement of splitting. Parameter ϕ is the fast polarization direction (clockwise with respect to north), δt is the delay time in seconds, and σ_ϕ and $\sigma_{\delta t}$ are the 1σ uncertainties. Stations with 00 and dashes for the next three columns do not exhibit splitting from at least two different nonorthogonal back azimuths and are interpreted as having splitting below the threshold of the data. Stations with a nonzero value for ϕ and dashes for the next three columns, do not exhibit splitting from at least one back azimuth or at least two orthogonal back azimuths and are interpreted as either having splitting below the threshold of the data or a fast polarization direction equal to ϕ or $\phi + 90^\circ$.

* Measurements taken from *Given and Silver* [1990].

† Measurements taken from SSM (value of ϕ for MNV represent average for the northern Basin and Range).

The resulting estimates of $(\phi, \delta t)$, given in Table 2, were formed from weighted averages of the individual measurements. Rather than relying solely on the uncertainties derived from the noise model, we have modified the error estimates to allow for other unknown sources of error. First, for individual measurements, we place lower allowable limits on the standard deviations of ϕ and δt; these are $\sigma_\phi \geq 5^\circ$, $\sigma_{\delta t} \geq 0.2$ s. Second, $2\sigma_\phi \geq 45^\circ$ is interpreted as a failure to detect splitting. Third, we estimate a reduced chi-square, $\tilde{\chi}^2$, for variation of the individual measurements about the mean, using the predicted values of σ_ϕ and $\sigma_{\delta t}$. This provides a measure of whether the predicted variation adequately reflects the observed variation. In cases where $\tilde{\chi}^2 > 1$ (predicted errors appear too small), the values of σ_ϕ and $\sigma_{\delta t}$ for the means are scaled up by $\sqrt{\tilde{\chi}^2}$ so that $\tilde{\chi}^2 = 1$. If $\tilde{\chi}^2 < 1$ (predicted errors too large), the estimated uncertainty is left unchanged. In a few cases, the formal uncertainties give reasonable error bars, but the estimated ϕ is close to ϕ_b or $\phi_b + 90^\circ$. These situations are characterized by an increased sensitivity of the size of the confidence region to the critical contour level. These are usually taken to be cases of undetectable splitting.

In Figures 2 through 4 we give some examples of measurements made. For each measurement we determine $(\phi, \delta t)$ and then display three diagnostics that each evaluate different aspects of the measurement. (1) Radial and transverse seismograms are displayed uncorrected and corrected using the estimated splitting parameters. This provides a measure of the success of the two-parameter model in removing the energy on the transverse component. (2) We superimpose the fast and slow components of the isolated SKS (or $SKKS$) phases, both uncorrected and corrected, and plot the particle motion for these two cases. This illustrates both the phase coherence of the two components and the degree to which the correction procedure produces linear particle motion. (3) In order to assess the uncertainty of each measurement and to check for multiple minima, a contour plot of $E_t(\phi, \delta t)$ is produced with the 95% contour level drawn plus multiples of this level. We present some examples that illustrate the range of splitting parameters that may be obtained: some that have well constrained anisotropy, and others that show marginally detectable splitting.

Finally, for each of the stations, we display the results of all of the measurements for which there is a good radial component phase. All measurements are plotted as a function of ϕ_b as in Figure 5. The closed symbols represent constrained measurements; the others signify null measurements (splitting not detected) and are plotted with ϕ corresponding to ϕ_b or $\phi_b + 90^\circ$, whichever is closer to the positive observations. This is illustrated in Figures 5 – 7 for stations RSON, RSSD, and COL, as we have the most number of records for each. Note that in the case of RSON, the results are very consistent as a function of ϕ_b over a range of about 120°. RSSD is at the limit of detectability for the RSTN inter-

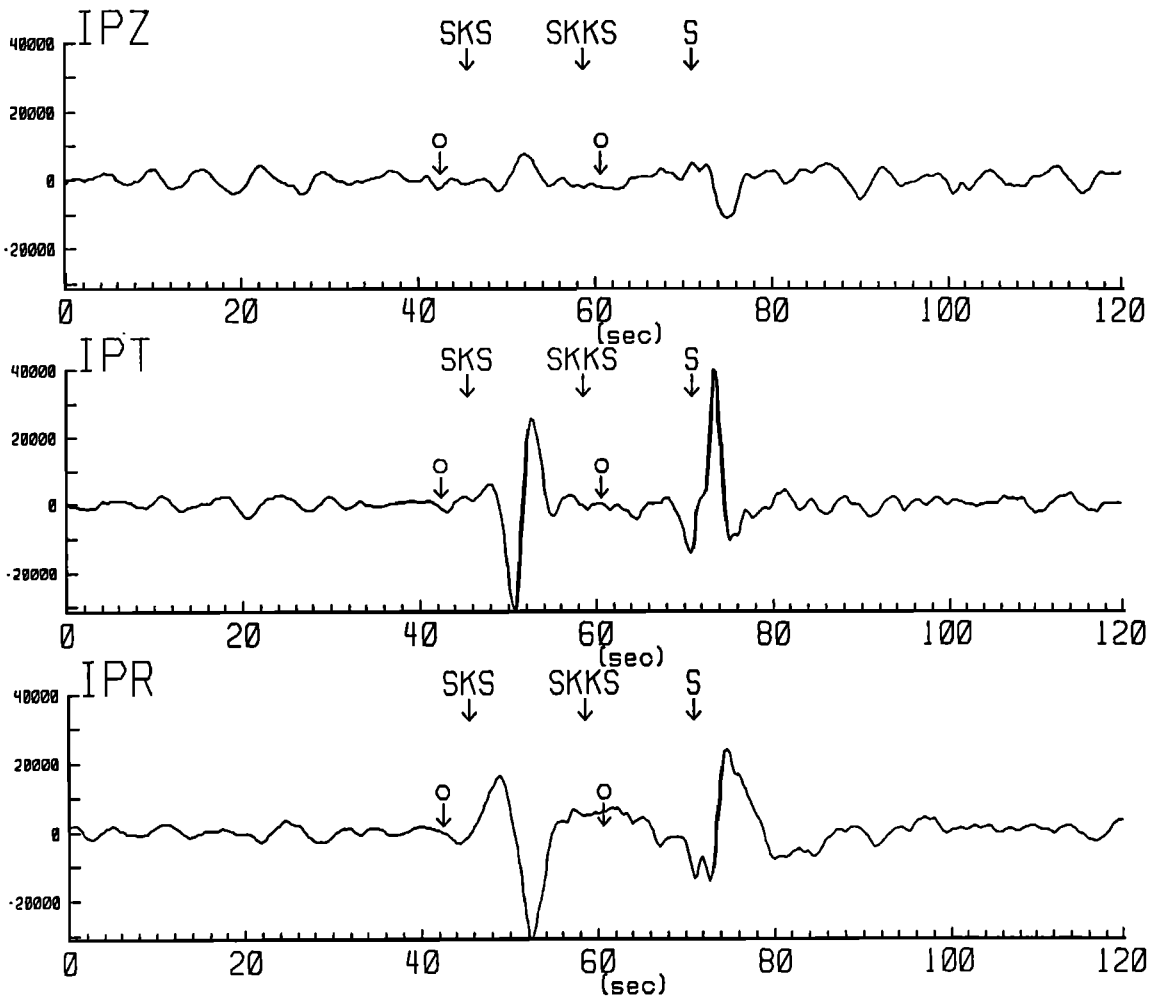

Fig. 2*a*. Three-component broadband seismogram of SKS for station RSON and event 85253. Predicted arrival time from PREM at 1 s [*Dziewonski and Anderson*, 1981] of SKS and related shear waves. Circles with arrows mark the interval used to make the measurement.

mediate period channel (δt=0.65 s), which is why there are so many more null measurements. Nevertheless, there are sufficient measurements over a range of ϕ_b to suggest that the results are well constrained. In only one case is there a suggestion of azimuthal dependence of the splitting. For COL (Figure 7*a*) several measurements of ϕ over the range ϕ_b=100–230° yield a consistent value. However, one record, for which ϕ_b=261° gives an answer that is clearly inconsistent with the rest; a greater sampling of this backazimuth range will be required to confirm this. In the average quoted in Table 2, we have not included this record although adding it does not change the average of ϕ by more than 10° .

The measurements for all stations are plotted in Figure 8. There are three categories of measurements, each denoted by a different symbol. First, those with well constrained observable anisotropy are given by a solid symbol proportional in size to δt and a line whose orientation gives ϕ. Second, there are open symbols where no anisotropy was detected. Given the resolution of our data, this constrains δt to be less than about 0.5 s. Third, there are stations that exhibit no splitting but which possess a limited range of ϕ_b, so that anisotropy is still possible but with only two allowable values of ϕ.

In all, we have analyzed 21 stations in this study. We have also plotted the results from SSM (LAC, MNV; MNV has been assigned the average value obtained in that study for the northern Basin and Range) and *Given and Silver* [1990] (NNA, OBN, ARU). While the stations are concentrated in North America and Eurasia, we do have results for all continents, with the exception of Australia and Antarctica. The largest value of δt is found for RSON, δt=1.70 s, followed by COL with δt=1.55 s, while the smallest detectible is δt=0.65 s for station RSSD; the average value is 1.0 s.

Characterization of the Anisotropy

While the phases SKS and $SKKS$, with nearly vertical ray paths through the mantle, provide excellent lateral resolution, the depth resolution is poor. One can regard the splitting parameters as representing the integrated effect along the entire mantle path on the receiver side. Information about source side anisotropy is lost through the S to P conversion at the core-mantle boundary (CMB). In certain cases, it is possible to obtain tighter depth constraints. For example, the stations RSON and RSSD are about 1000 km apart at the surface. While each station shows little dependence of $(\phi, \delta t)$ on ϕ_b as shown in Figures 5 and 6, their delay times represent the largest difference in the data set. The insensitivity to ϕ_b argues for homogeneous anisotropy within a cone whose vertex is at the station and whose base

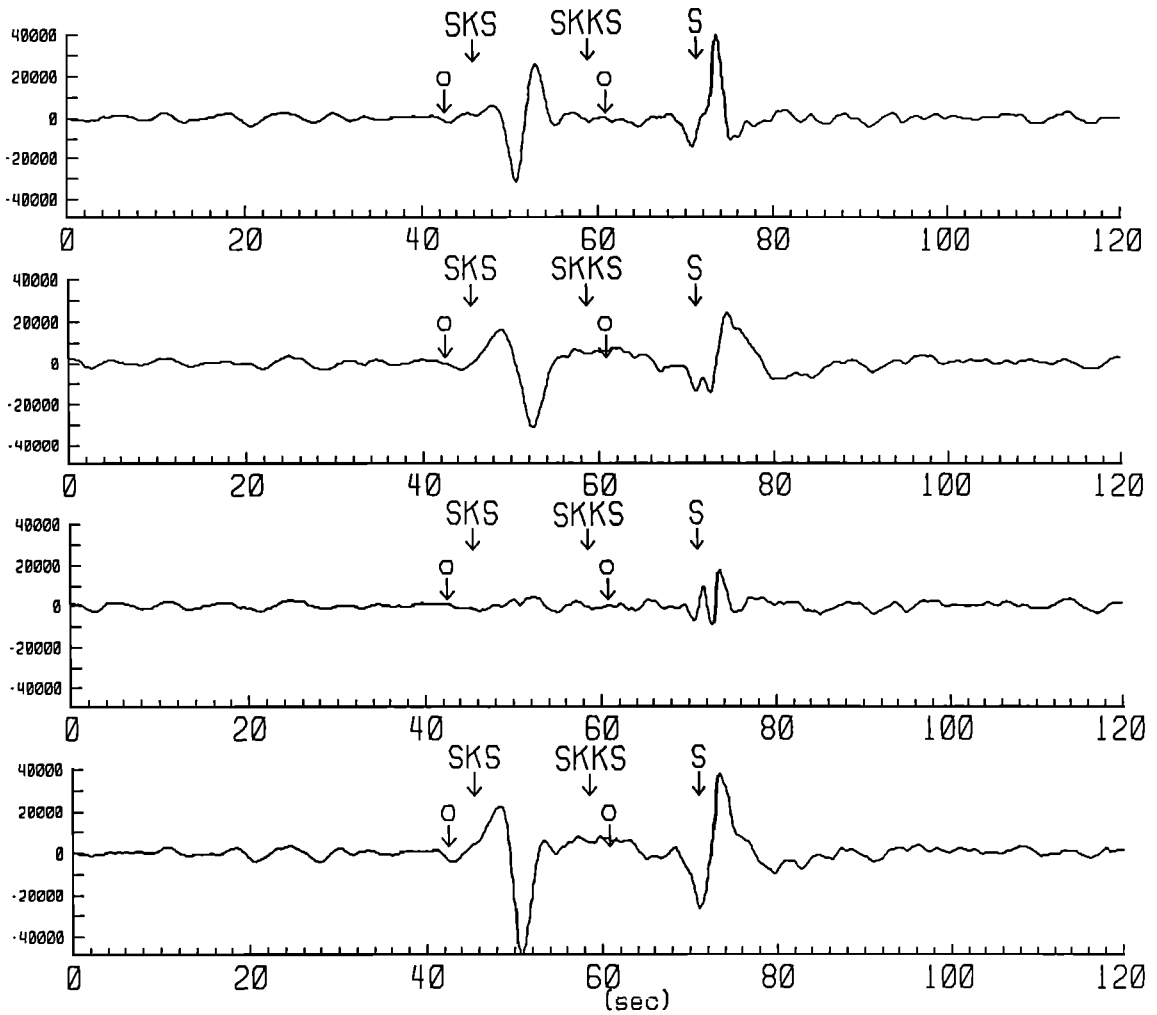

Fig. 2*b*. (Top two traces) Original transverse and radial components. (Bottom two traces) Corrected transverse and radial components. Note that in the corrected seismogram, transverse component SKS has been removed.

has a radius of about 1500 km at the CMB. The disparity between these stations means that the anisotropic regions lie outside the volume defined by the intersection of the two cones. This constrains the anisotropy to lie in the upper half of the mantle, above about 1000 km depth. While this is not a very tight constraint, it does rule out significant contributions from such regions as D'' as giving rise to the anisotropy. Support for an upper mantle source comes from a recent portable experiment which deployed 22 stations between RSON and RSSD [*Silver et al.*, 1989; P.G. Silver and S. Kaneshima, The APT89 seismic experiment: Shear-wave splitting results, submitted to Geophysical Research Letters, 1991]. Preliminary results for one event, well recorded by most of the stations, shows variations in splitting along the traverse with length scales of a few hundred kilometers. This would suggest that the anisotropy lies well within the upper mantle.

Contribution of the Crust

In order to determine the size of the mantle anisotropy we need to estimate the extent of crustal contribution to the splitting. The presently available evidence suggests that the crustal component is in fact small and can be effectively ignored in most cases. We first note that shear wave splitting measurements that exist for the upper crust [*Crampin and Booth*, 1985; *Savage et al.*, 1989] and entire crust [*Kaneshima et al.*, 1988; *Kaneshima and Ando*, 1989; *McNamara et al.*, 1989; *McNamara*, 1990] yield delay times in the range 0.1–0.3 s. On average this is about a factor of 5 smaller than what we observe. Second, confining the anisotropy entirely to the crust would require unreasonably high effective crustal anisotropy of about 5–16%. In order to produce the typically simple split waveforms we observe, any crustal contribution would have to be coherent with the mantle (i.e., same fast polarization direction) or else it could complicate or even diminish the mantle component.

As discussed by SC, a direct assessment of the total crustal component beneath some stations such as RSON, can be obtained by the use of the radially polarized phase, $Pm\acute{n}S$ [see *Clarke and Silver*, 1991] that converts from P to S at the Moho. This is because it is only sensitive to shear wave splitting in the crust. At RSON in particular, this phase is clearly observable and has been used previously to model the crustal structure under this station [*Owens et al.*, 1987]. We have searched for very impulsive events recorded at RSON, for which $Pm\acute{n}S$ is clearly observed, and the back-azimuth is within 5° of where we see the strongest SKS_T arrivals. Shown in Figure 9 are two such events that occurred beneath the Sea of Okhotsk. While $Pm\acute{n}S$ is observed on the radial components of both events, the transverse com-

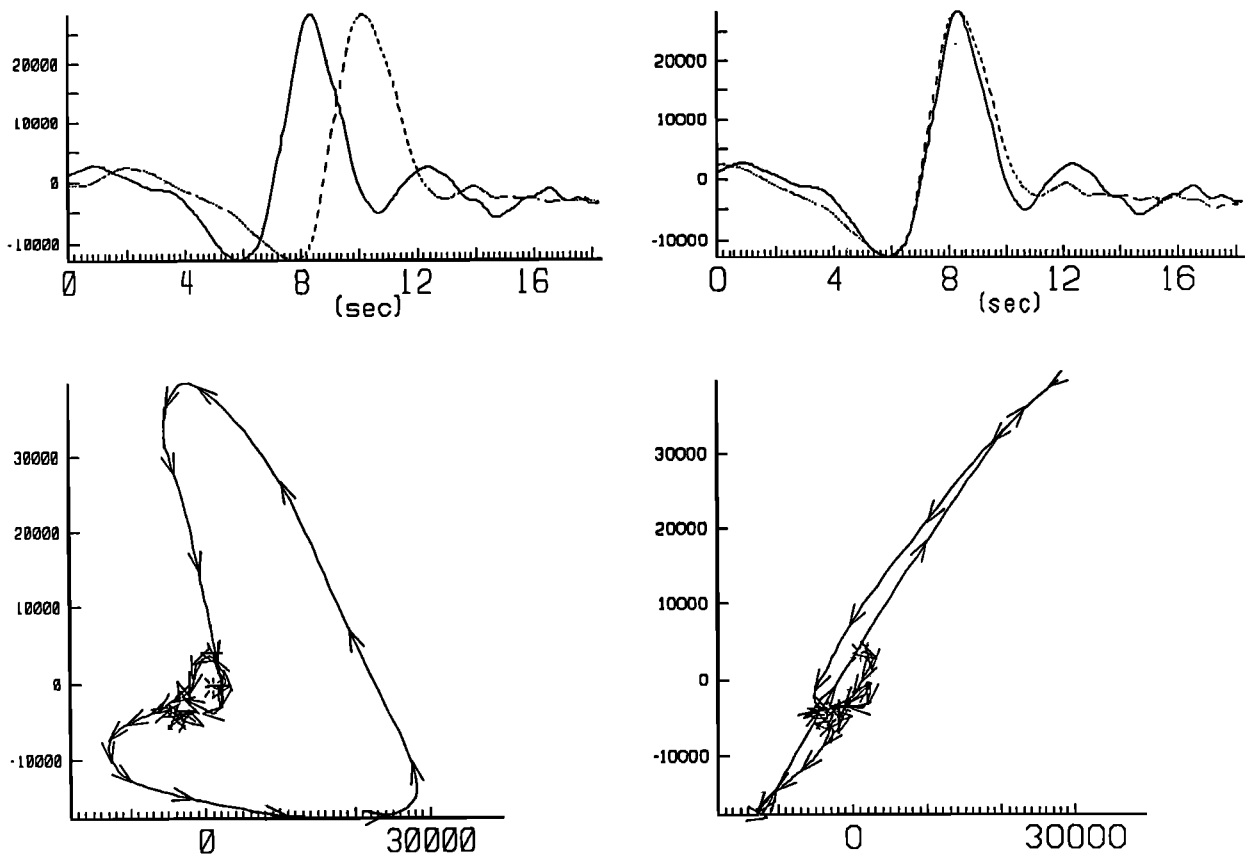

Fig. 2c. (Top two traces) Superposition of fast (ϕ direction) and slow components (ϕ +90°) uncorrected (left) and corrected (right). (Bottom) Particle motion for fast and slow components uncorrected (left) and corrected (right). Corrections made using estimated values of ($\phi, \delta t$).

ponents shows no detectable signal during the same time interval. This strongly suggests that the coherent crustal component is no more than about 0.5 s (corresponding to 4% anisotropy throughout the entire crust) and is probably closer to the 0.1–0.3 s range quoted above. Preliminary attempts to measure crustal anisotropy using *PmS* in the Basin and Range [*McNamara et al.*, 1989] appear to be successful and may lead to a general procedure for separating out the two components.

Relation of Splitting to Tectonic/Geologic Processes

As mentioned in the introduction, the interpretation of splitting observations in terms of tectonic/geologic processes involves a chain of relations: between splitting and anisotropy, between anisotropy and strain (through LPO), and between strain and tectonic processes. We briefly review the data relevant to these relationships and state the assumptions that will be used to interpret the data.

Splitting and Anisotropy

One of the essential parameters that is required to interpret anisotropic measurements is the parameter $\delta\hat{\beta}$ in equation (4), as it provides an estimate of the effective layer thickness L. The single-crystal elastic constants for olivine provide an absolute upper bound on the maximum allowable splitting $\delta\hat{\beta}_{max}$ of about 0.10 [*Verma*, 1960; *Kumazawa and*

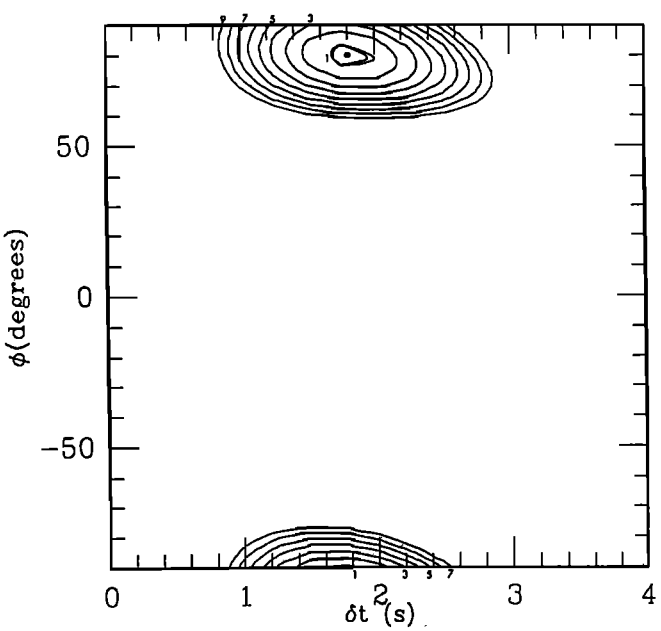

Fig. 2d. Contour plot of $E_t(\phi, \delta t)$. Minimum value shown along with 95% confidence region (double contour) and multiples of that contour level. For symmetric ellipsoidal regions, we take the 1σ confidence level to be half the bounding values of this region along the parameter axes. For asymmetric regions, we use the smallest symmetric region that includes the original confidence region.

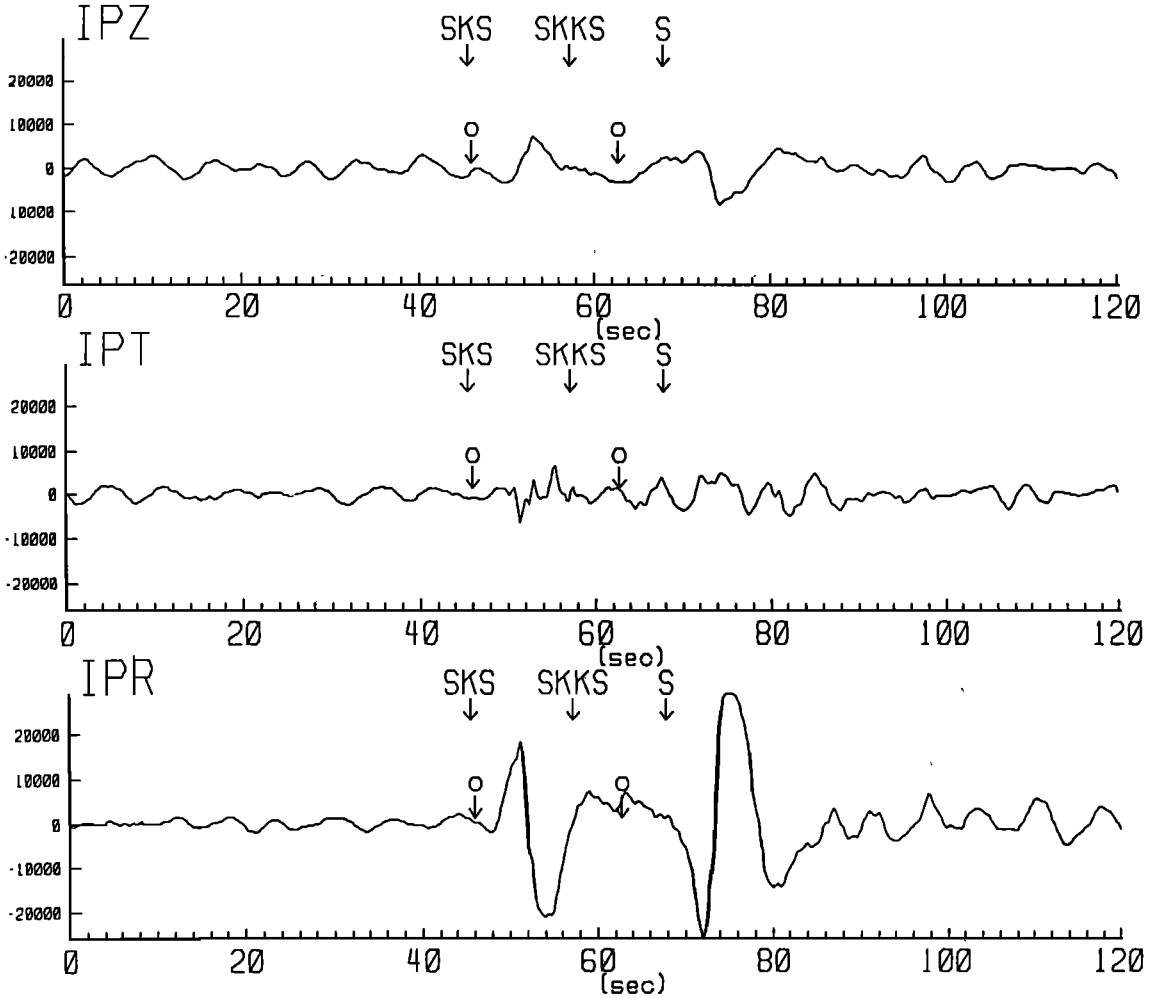

Fig. 3*a*

Fig. 3. Same as Figure 2 for station RSSD, event 85253.

Anderson, 1969] for propagation along the crystallographic axes. For certain intermediate propagation directions in the [010] plane, $\delta\hat{\beta}$ can get as high as 0.17, although the average value in this plane is close to 0.10. The upper mantle, however, is only 50–70% olivine with the rest primarily orthopyroxene (see SC for a discussion), a mineral that is much less anisotropic than olivine. In addition, crystals are far from being perfectly aligned so that the strain-induced LPO of mantle minerals produces an ODF and macroscopic $\delta\hat{\beta}_{max}$ that is somewhat below the single-crystal value. The most direct methods for estimating this parameter are by utilizing mantle samples derived from ophiolites, Alpine peridotites, or xenoliths from kimberlite pipes. The two most common methods are petrofabric analysis combined with estimates of the single-crystal elastic constants, and ultrasonic measurements. The most extensive data set is for ophiolites [*Christensen*, 1984], where $\delta\hat{\beta}_{max} \simeq 0.04$. This same value is also found for kimberlite xenoliths (D. Mainprice, personal communication, 1990) and will be adopted in the estimation of effective layer thickness. In this case, 1 s of delay time corresponds to 115 km. Thus the range for our data set is 75 km (RSSD) to nearly 200 km (RSON).

The single-crystal elastic constants for olivine show that propagation along [010] and [001] produces a large value of $\delta\hat{\beta}$ with ϕ parallel to [100]. Propagation along [100] would probably not produce observable splitting. That ϕ can usually be taken as the direction of [100] for observable splitting (a relation that also appears to hold for aggregates that possess strong [100] preferred orientation [*Christensen*, 1984]), is of central importance in the interpretation of splitting observations.

LPO-Induced Anisotropy and Finite Strain

It is generally accepted that the primary cause of LPO is finite strain, ϵ [*Nicolas and Poirier*, 1976; *McKenzie*, 1979; *Nicolas and Christensen*, 1987; *Ribe and Yu*, 1991], and as a result it is possible to regard splitting observations as functions of finite strain as well. There are two relations of interest: one of magnitude, $\delta t = \delta t(|\epsilon|)$, and one of orientation, $\phi = \phi(\hat{\epsilon}_i)$, where the $\hat{\epsilon}_i$ (i=1,2,3) are the three principal strain directions of ϵ corresponding to the shortening, intermediate, and extension directions, respectively. The most relevant relation involves the behavior of the [100] axis of olivine. Based on observations of naturally occurring peridotites, laboratory work and theoretical modeling [*Nicolas and Poirier*, 1976; *McKenzie*, 1979; *Christensen*, 1984; *Nicolas and Christensen*, 1987; *Ribe and Yu*, 1991], [100] is predicted to be parallel to $\hat{\epsilon}_3$ (extension direction) for nearly all kinds of finite strain: uniaxial extension (pure shear), uniaxial shortening (pure shear, [010] is parallel to

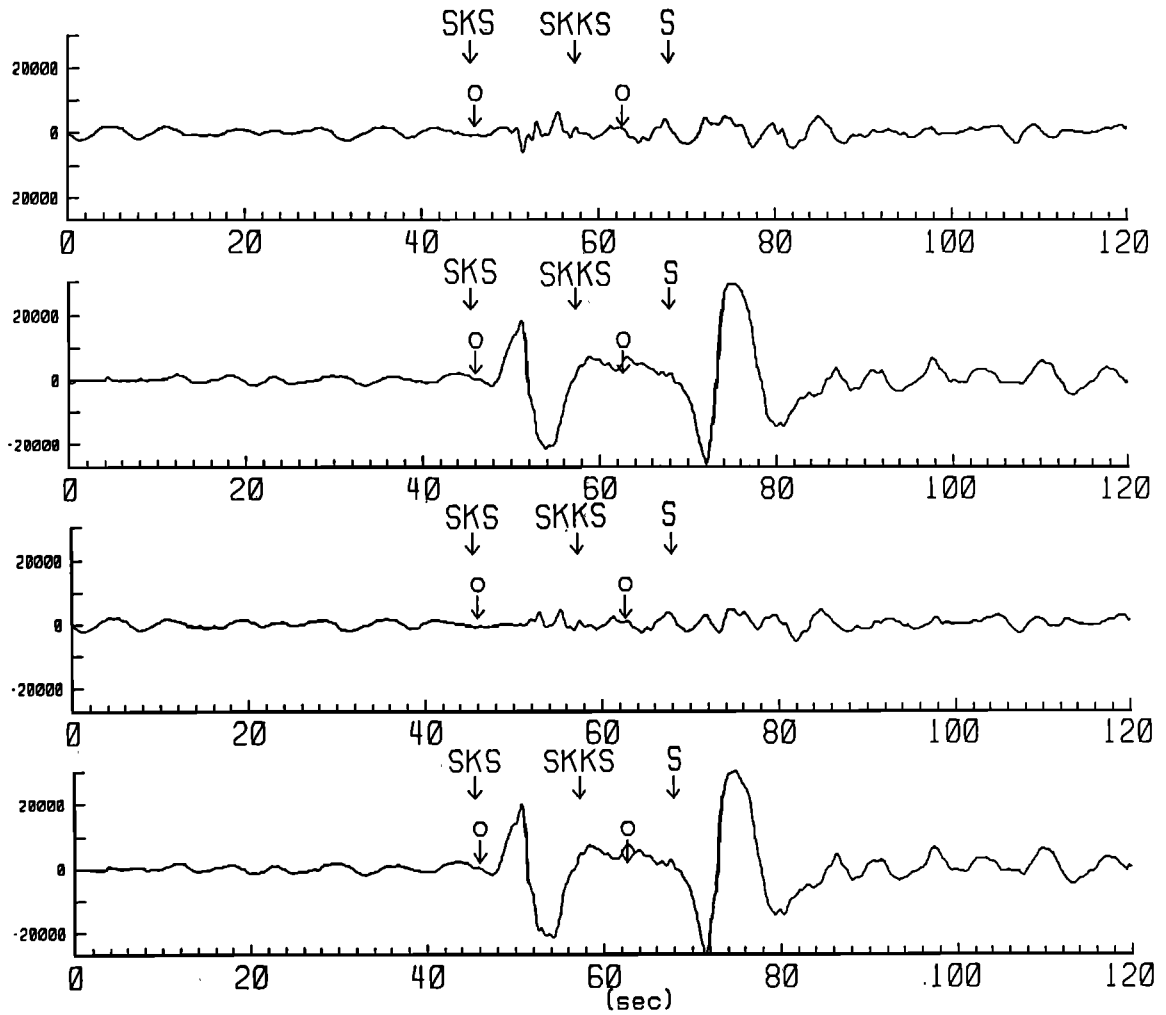

Fig. 3*b*

$\hat{\epsilon}_1$ while both [100] and [001] are in the extension plane containing $\hat{\epsilon}_2, \hat{\epsilon}_3$), and progressive simple shear [*Hobbs et al.*, 1976; *McKenzie*, 1979]. This last mode of deformation is appropriate for the differential motion between a plate and underlying mantle, or relative motion along plate boundaries (RPM); in this case [100] is contained within the flow plane, and is parallel to the flow direction [*Nicolas and Poirier*, 1976]. Since ϕ is generally parallel to [100], we expect ϕ to follow these same rules.

Mantle Strain and Tectonic Processes

How does the subcontinental mantle deform in response to various tectonic processes, such as orogenic episodes, extension, large-scale strike-slip faulting or plate motion? As with the case of olivine deformation, there are certain generalizations that may be made regarding continental deformation which we use in the subsequent analysis. (1) We treat collisional episodes as producing pure shear within the subcontinental mantle, with $\hat{\epsilon}_1$ parallel to the collision direction and both $\hat{\epsilon}_2$ and $\hat{\epsilon}_3$ in the plane perpendicular to it. (2) We regard extensional regimes such as the Basin and Range as exhibiting pure shear with $\hat{\epsilon}_3$ parallel to the extension direction. (3) We assume that both relative (RPM) and absolute plate motion (APM) produce progressive simple shear as a result of differential motion between the plates in the former case and between the plate and a presumed stationary mantle in the latter. Thus, for strike-slip plate boundaries such as the San Andreas Fault, $\hat{\epsilon}_3$ should be parallel to the fault strike (for large finite strain); for convergent margins, $\hat{\epsilon}_3$ should be parallel to the relative plate motion vector between the downgoing and overlying plate. Finally, for APM, $\hat{\epsilon}_3$ should be parallel to the APM direction.

It has been proposed that there is often a large strike-slip component associated with major continental orogenies such as the Hercynian, and that much of the deformation occurs by simple, rather than pure shear [*Vauchez and Nicolas*, 1991]. This mode of deformation has been referred to as transpression and has also been proposed for the Archean deformation in the Canadian Shield [see *Card*, 1990]. In this case, there will be strike-slip faulting that is parallel to orogenic structures. Thus, the strike-slip component will tend to align $\hat{\epsilon}_3$ perpendicular to the collision direction, as in the pure shear case, although $\hat{\epsilon}_3$ is restricted to be in the horizontal plane.

CANDIDATE PROCESSES

Putting together the above relationships, we are in a position to make predictions of ϕ (for vertical propagation of *SKS*) for various sources of mantle strain. This provides us with a means of distinguishing between modes of

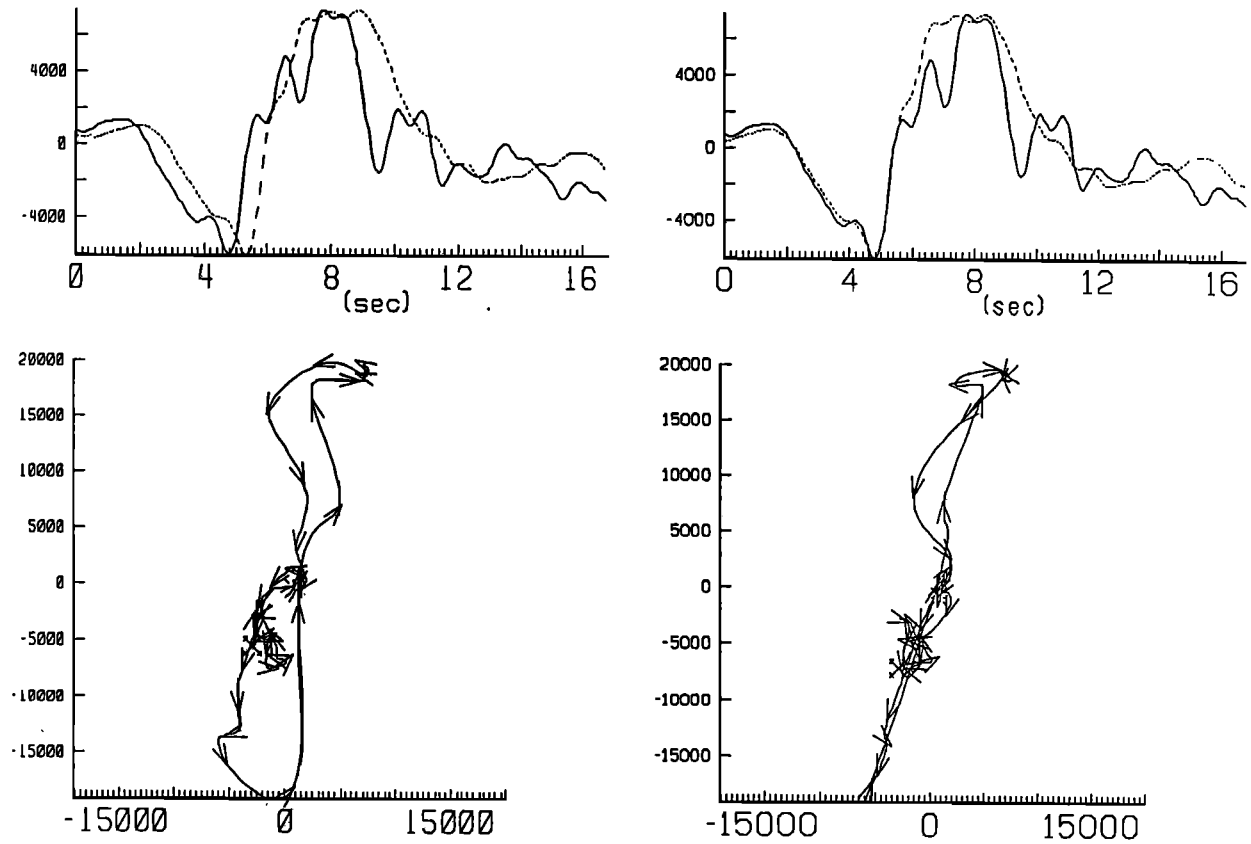

Fig. 3c

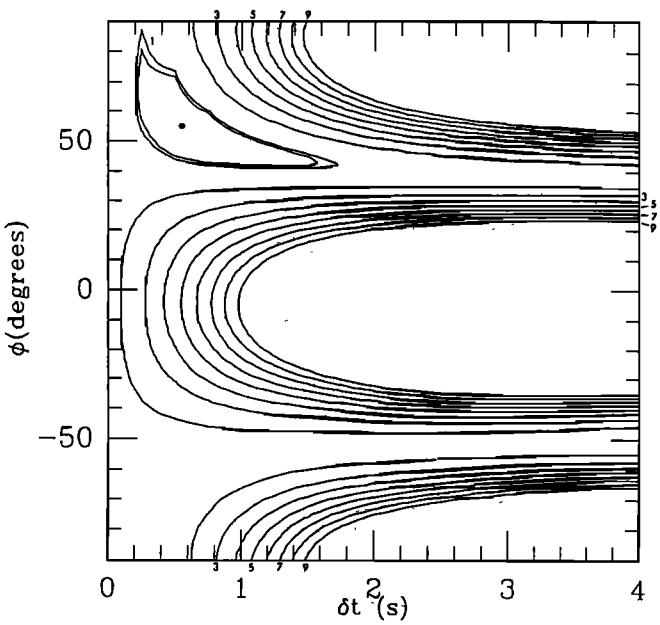

Fig. 3d

deformation, localizing the anisotropy and ultimately identifying the dominant processes. For this purpose, we consider three candidate hypotheses for producing the observed anisotropy. The first is inspired by what is believed to occur in the oceanic upper mantle: namely, that the anisotropy is the result of absolute plate motion, concentrating strain in the asthenosphere but possibly producing strain in the lithosphere as well. This will be referred to as the APM hypothesis. This model predicts that the fast polarization direction ϕ_{apm} is parallel to the APM direction for the plate. It furthermore predicts that ϕ should be smoothly varying over the plate; assuming δt is solely a function of plate speed, δt should be smoothly varying as well.

The second hypothesis is that the present-day stress measured in the continental crust reflects lithospheric-wide stress that ultimately produces strain-induced anisotropy. The global survey of crustal stress measurements by *Zoback et al.* [1989] provides a means of testing this possibility. The crustal stress (CS) hypothesis is conceptually different from APM in that it does not invoke a particular physical process. Rather, it states that the processes responsible for crustal stress (basal drag from APM, ridge push, mountain-building, rifting...), are also responsible for mantle anisotropy. This hypothesis is more difficult to evaluate than APM, however, because LPO-induced anisotropy is a function of finite strain [*Nicolas and Christensen*, 1987], not instantaneous stress. Thus one must assume a constitutive relation between the two and unfortunately there is no unique relationship. The most straightforward would be to equate the compression, intermediate, and tension stress axes with the shortening, intermediate, and extension finite strain axes respectively. This would be most appropriate for pure shear in tensional and collisional regimes as the result of membrane stresses (i.e., those derived from forces parallel to the plane of the plate). Using the maximum horizontal stress (maximum compression) direction $\hat{\sigma}_{hmax}$ provided by *Zoback et al.* [1989], the predicted fast polarization direction ϕ_c should then be orthogonal to $\hat{\sigma}_{hmax}$. Predictions are much more difficult to make in regions that are deforming by progressive simple shear (strike-slip fault-

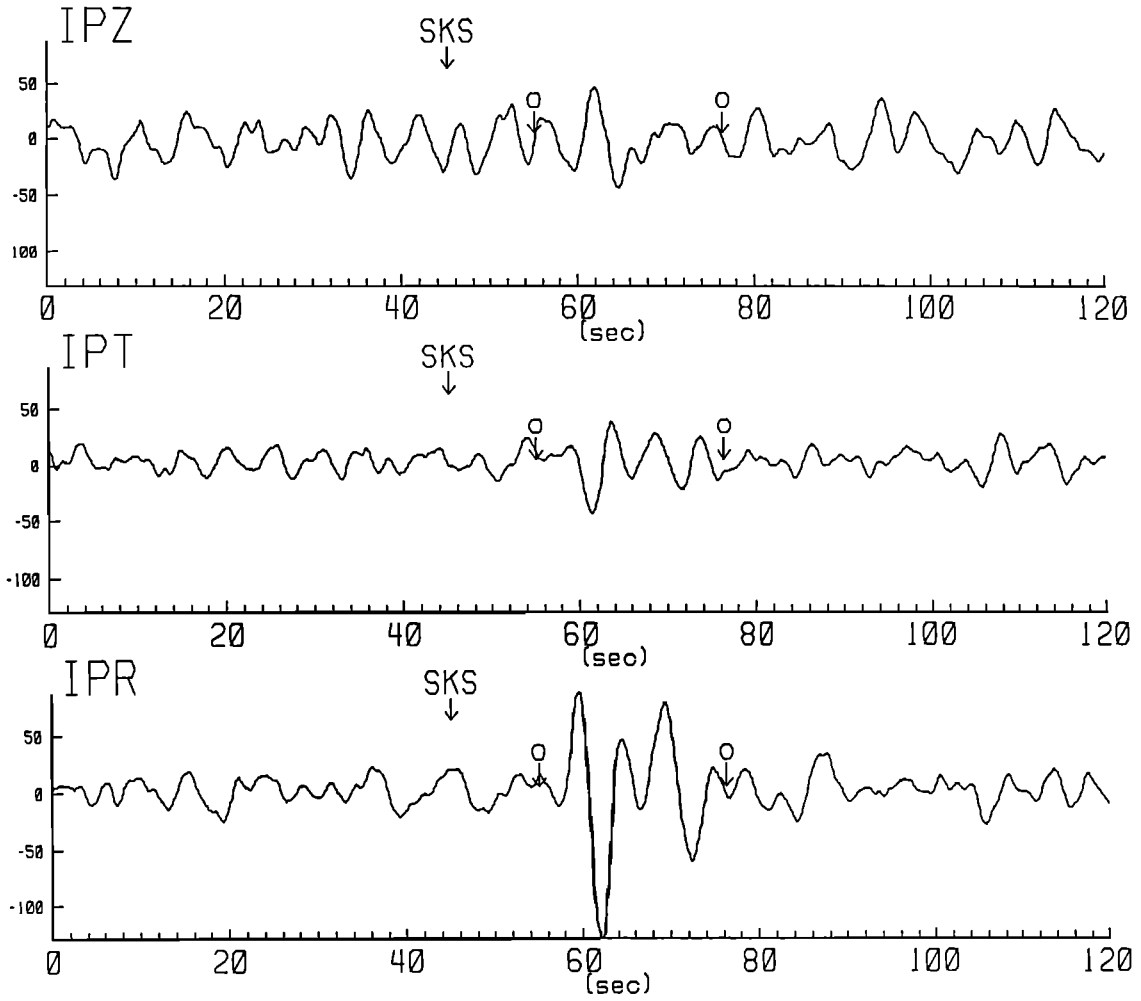

Fig. 4a

Fig. 4. Same as Figure 2 for station SLR, event 84151.

ing) and characterized by $\hat{\sigma}_{hmax}$ and minimum horizontal shear stress $\hat{\sigma}_{hmin}$ magnitudes that are comparable. The orientation of the finite strain principal axes would depend on which of the two planes of maximum shear stress has actually failed. An additional ambiguity is introduced if the strains are produced by a basal shear stress as would be the case with APM-related resistive drag forces on the plate. Assuming that this would cause $\hat{\sigma}_{hmax}$ to be in the direction of absolute plate motion, then ϕ_c should be parallel to the $\hat{\sigma}_{hmax}$ direction.

The third hypothesis is that mantle anisotropy is dominated by the last significant episode of internal coherent deformation (ICD) of the continental lithosphere by tectonic processes such as orogenies, rifting episodes, and strike-slip deformation. These strains are assumed to be the result of membrane stresses, in contrast to basal shear stresses. It is assumed that the anisotropy is preserved in the lithosphere unless there is subsequent deformation that overprints it. The coherence predicts that the strain field revealed in the structural geology of the Earth's surface constitutes a reliable measure of mantle strain and thus provides a geologically derived prediction, ϕ_g, based on the expected relation between ϕ and strain, as discussed above. In particular, we take ϕ_g to be perpendicular to the inferred collisional direction (or parallel to the structural trends) for orogenic episodes, and parallel to the extension direction for regions undergoing extension. Finally, for deformation near major strike-slip plate boundaries, ϕ_g is predicted to be parallel to the strike of the fault.

The three candidate processes can be grouped in the following way. Both the APM and CS hypotheses imply that anisotropy is due to present day processes, as does the ICD hypothesis in tectonically active areas. However, ICD predicts that "fossil" anisotropy is dominant in regions that are tectonically stable, with the important implication that the anisotropy would then provide a history of deformation in the mantle. APM would predict that anisotropy is localized in the asthenosphere with perhaps some anisotropy in the lithosphere as well. CS and ICD would both argue for lithospheric deformation. With regard to the lithosphere, APM implies that mantle strains are produced by basal shear stresses, whereas ICD predicts that they are caused by membrane stresses. The CS hypothesis would allow for either type of deformation.

Absolute Plate Motion

In order to test this possibility, we have computed the APM velocity vectors for the model AM1-2 [*Minster and Jordan*, 1978] at each of the stations for which anisotropy has been clearly observed. The predictions are shown in Figure 10 and may be compared to Figure 8. For many of the North American stations, the general ENE trend of the ob-

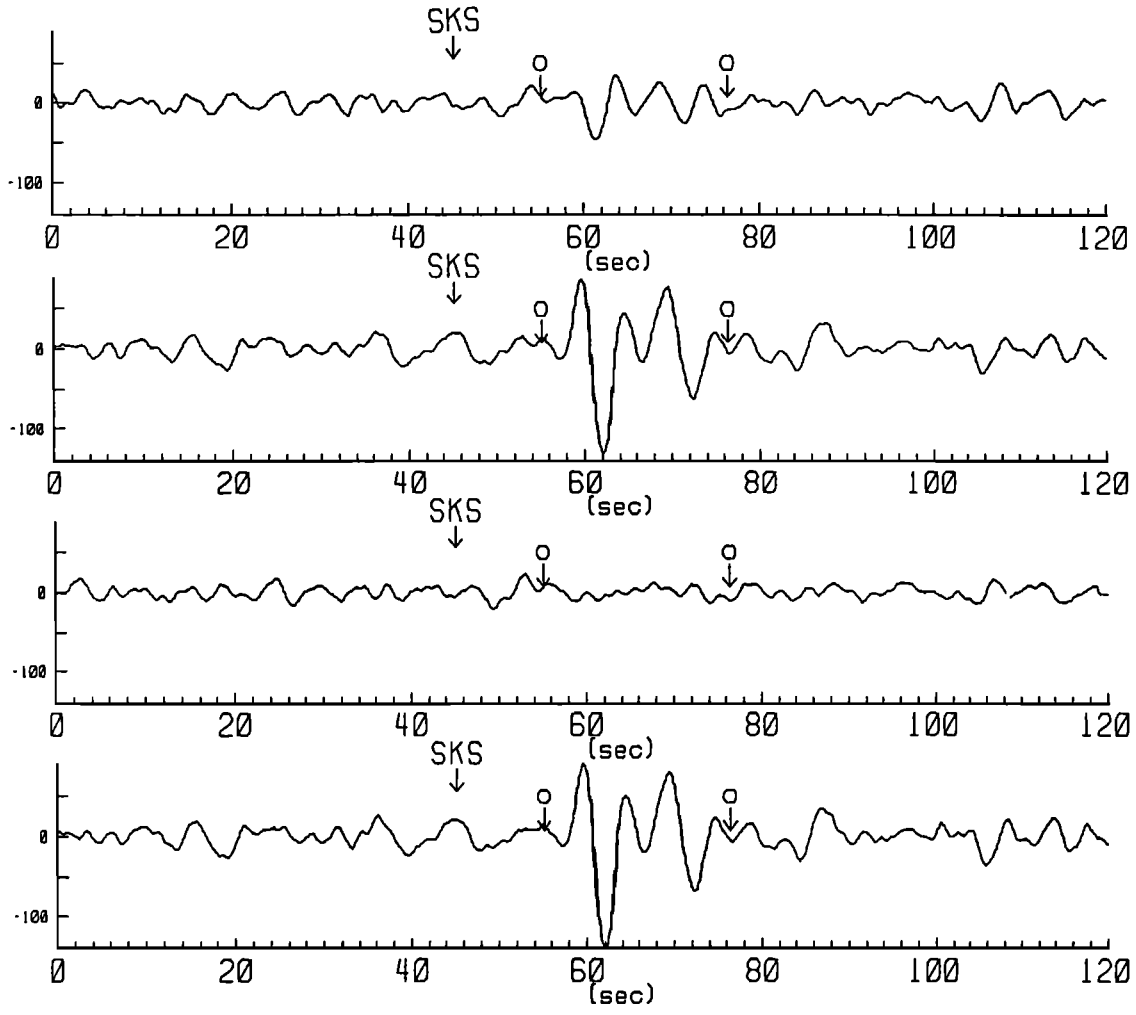

Fig. 4*b*

servations appears to correspond to ϕ_{apm}. The notable exceptions are COL and LAC (SSM). For the other continents, there are several stations that are at a high angle to ϕ_{apm}: NNA in South America, SLR in Africa, and TOL and GRA1 in Europe. In the case of active continental margins, such as NNA and COL, what is plotted is the ϕ_{apm} for the continental plate. One could rightfully argue that it would be more appropriate to consider either ϕ_{apm} for the descending plate or ϕ_{rpm}, corresponding to the relative motion vector between the continental and oceanic plates. If these directions are chosen, however, the discrepancy remains because for both stations, the three directions are roughly parallel. For COL, ϕ_{apm} for the Pacific plate is $-26°$ and ϕ_{rpm} is approximately NS. Similarly, in South America ϕ_{apm} for both the Nazca and South American plates are roughly EW as is ϕ_{rpm}. A histogram of the angle $\phi - \phi_{apm}$ is shown in Figure 11. As one can see, the agreement between predicted and observed directions is not good. The APM prediction of plate-wide coherence in ϕ meets with limited success as well. Of the two plates for which we have a significant amount of data, North America and Eurasia, North America appears to show platewide coherence; however, Eurasia does not. This is especially apparent for the stations in China (HIA, WMQ) and the Soviet Union (ARU, OBN).

The APM hypothesis would have to be substantially modified to reconcile these difficulties. First, it would have to be abandoned for tectonic areas, leaving stable areas as the possible domain of applicability. This would work for stable North America, but apparently not for Eurasia. It could be argued, however, that in the case of Eurasia, the APM velocity is so low that (1) the direction may be in error, and (2) APM-related strains may be too small to produce anisotropy. With regard to the first point, a recently proposed absolute plate motion model HS2-NUVEL1 [*Gripp and Gordon*, 1990], based on the relative plate motion model NUVEL-1 [*DeMets et al.*, 1990], predicts plate motions for Europe that differ in direction by 90° from AM1-2. The errors are so large, however, that the differences between models for the Eurasian plate are not statistically significant [*Gripp and Gordon*, 1990]. Thus, it appears that this issue may not be resolved for some time. Regardless of what the true APM velocities are for Eurasia, lack of coherence of ϕ values within this Eurasian plate suggest that APM strains are not dominant. This may be due to the second point, that APM velocities are low. This implies, however, that the only region left for the APM hypothesis is stable North America or other undeformed, fast-moving plates.

Even within stable North America, there are difficulties with this hypothesis. The large variation in δt between RSSD and RSON (which are only 1000 km apart) argues that plate speed could not be the only variable controlling δt. Lithospheric thickness might be proposed as another important parameter. If the anisotropy is localized in the asthenosphere, one would expect anisotropy to be strongest

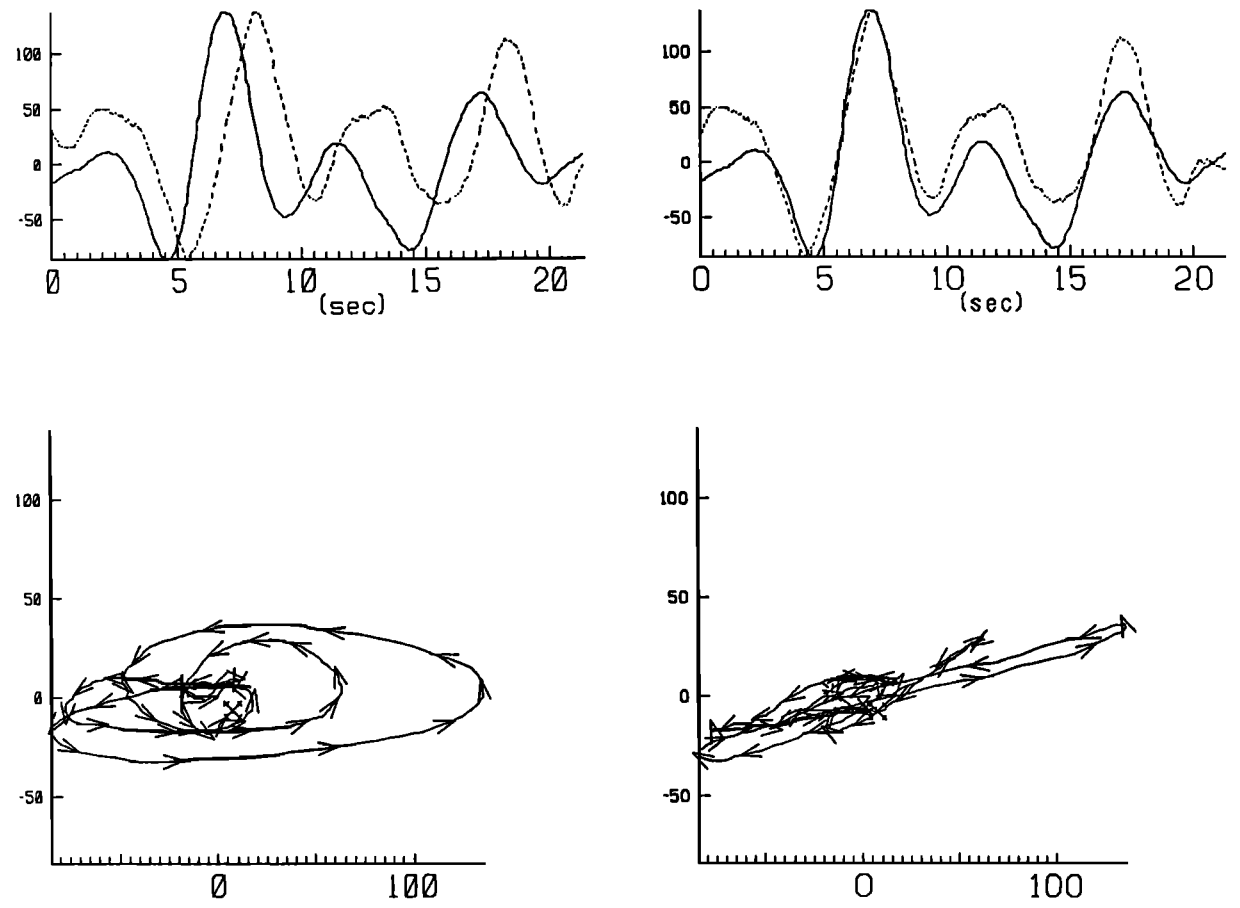

Fig. 4c

where the lithosphere is thinnest, as is apparently true in the ocean basins (the observations of anisotropy in the oceanic upper mantle from long period surface waves find the largest anisotropy in the youngest lithosphere near the mid-ocean ridges [*Montagner and Tanimoto*, 1990]). In contrast, if the anisotropy is the result of the uniform straining of the continental lithosphere, one would expect larger delay times to occur in regions with thicker lithosphere. Since RSON appears to have thicker lithosphere than RSSD [see *Grand*, 1987], the latter possibility would seem more reasonable.

Present-Day Crustal Stress

Since it is not possible to obtain crustal stress estimates at the locations of the stations analyzed, the comparison with the splitting observations must be done in a more qualitative manner. Such an evaluation can be made by concentrating on particularly coherent regions of crustal stress where interpolation is warranted. From *Zoback et al.* [1989], the two regions with the most data and most uniform horizontal stress orientations are North America and Western Europe. Assuming that $\phi_c \perp \hat{\sigma}_{hmax}$, the expected relationship for a pure shear response to membrane stresses, we find that ϕ_c is at a high angle to ϕ for all of the stations in stable North America, since $\hat{\sigma}_{hmax}$ ranges from NE to ENE; the CS hypothesis is more successful for tectonic areas to the west, especially COL and LON, where $\hat{\sigma}_{hmax}$ is nearly NS. For Western Europe, assuming a range of values of $\hat{\sigma}_{hmax}$ of NW to NNW, ϕ_c should range from NE to ENE. Both of our measurements are E to ENE, as are most of the ϕ measurements from *SKS* splitting obtained at other Western

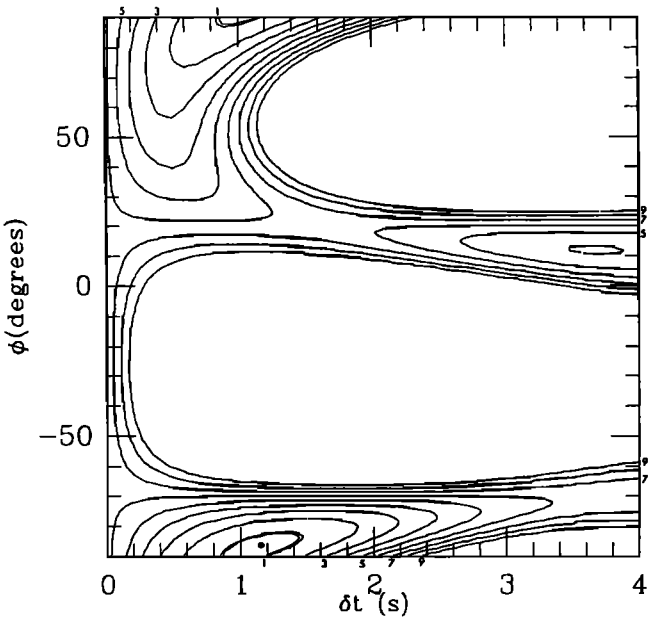

Fig. 4d

European stations [*Vinnik et al.*, 1989*b*], and would thus be marginally consistent with this prediction.

If instead we assume $\phi_c \parallel \hat{\sigma}_{hmax}$, appropriate for APM-related basal shear stresses, we again meet with mixed success. The CS hypothesis does reasonably well in stable North America as ϕ_c and ϕ both point in the direction NE to ENE, although it is inconsistent with the tectonic stations

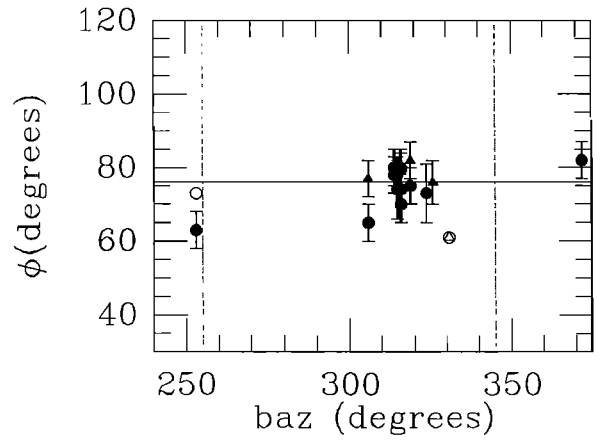

Fig. 5*a*. Fast polarization direction ϕ versus back azimuth ϕ_b for station RSON. Circles are SKS and triangles are $SKKS$. Solid symbols represent well constrained observations of splitting, while open symbols represent cases where splitting is not detectable. In this second case, point is plotted as polarization direction ϕ_b or $\phi_b + 90°$. Solid horizontal line gives weighted average value $< \phi >$ (see Table 3) of solid symbols. Dashed lines correspond to predicted "null" directions where no splitting should be observed, given $< \phi >$. For simplicity, range is given as $0° \leq \phi \leq 180°$ rather than $-90° \leq \phi \leq 90°$. Error bars are 1σ uncertainties.

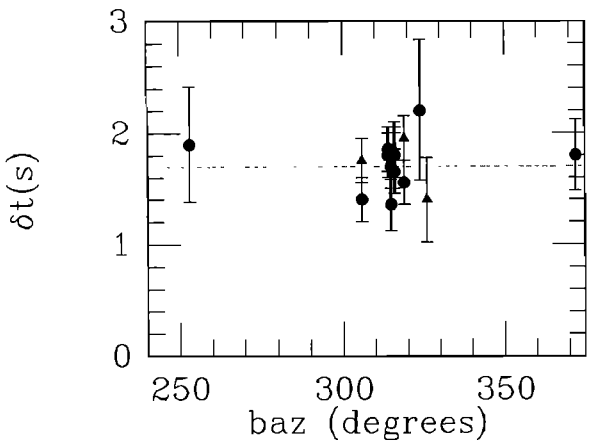

Fig. 5*b*. Estimates of delay time. Same symbol description as in Figure 5*a*. Dashed line gives weighted average $< \delta t >$. Error bars are 1σ uncertainties.

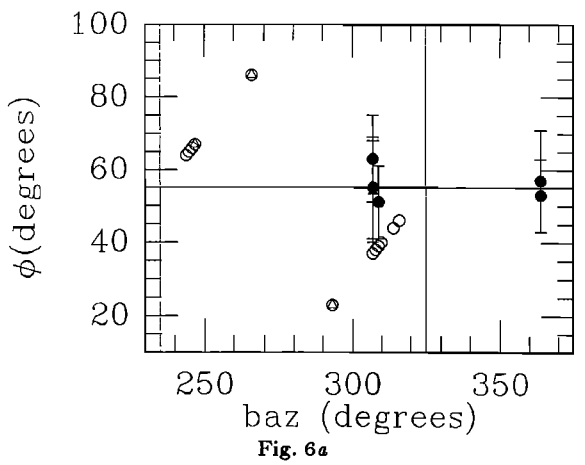

Fig. 6*a*

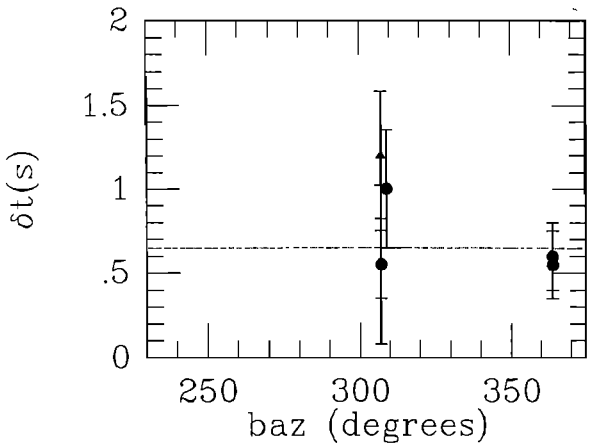

Fig. 6*b*

Fig. 6. Same as Figure 5 for station RSSD.

LON and COL. It is also inconsistent with the Western European stations, since ϕ_c would range from NW to NNW.

In order to more successfully reconcile ϕ_c and ϕ, it would be necessary to invoke different relationships between ϕ_c and $\hat{\sigma}_{hmax}$ for various regions. The most reasonable would be to assume the dominance of APM-related basal shear stress ($\phi_c \parallel \hat{\sigma}_{hmax}$) in presently stable areas and membrane stresses ($\phi_c \perp \hat{\sigma}_{hmax}$) for areas of active tectonism. This is successful for North America, but it is more difficult to explain the West European data. Although the Western European stations are situated in relatively stable areas, the only way to reconcile the crustal stress data would be to invoke $\phi_c \perp \hat{\sigma}_{hmax}$, which is the assumed relationship for tectonic areas.

Internal Coherent Deformation

To test the ICD hypothesis, we need to determine the strain field of the last major tectonic episode, as inferred from the surface geology. We have compiled geologic information for each of the stations for which splitting has been detected and for which fairly unambiguous geologic information can be obtained; a predicted fast polarization direction, ϕ_g, is determined as given in Table 3 using the relationships between modes of continental deformation and mantle strain. Where precise numerical values were not available, we have converted compass directions as follows: NS: 0° , EW: 90° , NE-SW: +45° ENE-WSW: +67.5° etc. There is ultimately some subjectivity in making such an estimate. However, in most of the areas where anisotropy is observed there is a relatively unambiguous fabric. There are some exceptions to this: first, there is presently insufficient geologic information available to determine ϕ_g for either the Soviet stations (OBN, ARU) or the Chinese stations (WMQ, HIA), and these stations have not been included. For RSSD there is both Archean and Proterozoic fabric of roughly equal strength whose strikes are at right angles to each other. We have reported both directions. For MNV in the Basin and Range we have reported the direction for the present day extension as well as for the somewhat stronger pre-Miocene extension (see SSM). In Figures 12*a* and 12*b* are displayed a histogram of $\phi - \phi_g$ for our data set. Figure 12*a* corresponds to the younger deformation, 12*b* to the older. We note that in most cases there is a striking agreement in the directions. The places where the APM and crustal stress hypotheses appeared to be good predictors of ϕ, namely eastern North America, are precisely the places in which ϕ_{apm}, ϕ_c and ϕ_g are nearly parallel. In addition, the

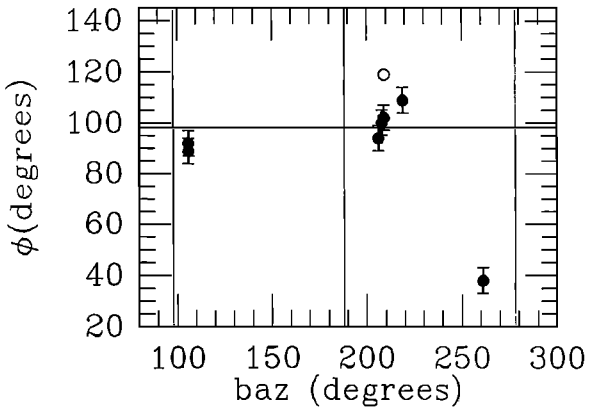

Fig. 7a

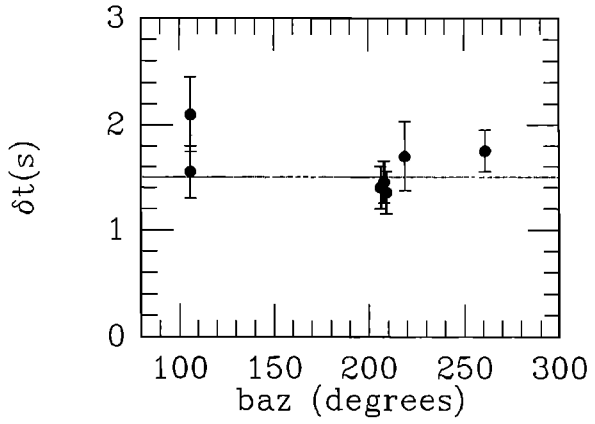

Fig. 7b

Fig. 7. Same as Figure 5 for station COL.

obvious discrepancies with ϕ_{apm}: COL, LAC, NNA, SLR, TOL, and GRA1 are reasonably well accounted for by this model.

The ICD hypothesis also explains some of the variations in δt in stable North America. Given equal values of $\delta\hat{\beta}$ and assuming the anisotropy is in the lithosphere, δt should correlate with lithospheric thickness. One plausible measure of thickness, at least in stable continental areas, is the lateral variation in shear wave vertical delay times. Such information is available in North America from the model of *Grand* [1987]. Plotted in Figure 13 is a contour map of the vertical delay times δT (integrated from 400 km depth to the surface) along with the locations of the the five stations in stable North America, as well as portable stations that were deployed along a traverse between RSSD and RSON [*Silver et al.*, 1989; P.G. Silver and S. Kaneshima, submitted manuscript, 1991]. In Figure 14 is a plot of δT versus δt for these stations. Note that there is indeed a good correlation both for the permanent and portable stations. The existence of such a correlation is consistent with the proposition that the anisotropy has a lithospheric rather than deeper mantle source and that $\delta\hat{\beta}$ is roughly constant.

Of the three hypotheses, the ICD appears to be the most successful in accounting for the entire data set. Ultimately, the only region where the APM hypothesis has any success is stable North America, a region where the ICD hypothesis is equally successful. The CS hypothesis was the most difficult to evaluate, due to the need to assume a constitutive relationship. No one relation, however, appears to satisfy the data, even for stable areas.

SPECIFIC STATIONS OF INTEREST

Some of the stations are of particular interest because of their location and because of their unusual splitting parameters. We therefore discuss RSON and RSSD, which possess the largest and smallest delay times in the data set, COL, which possesses the second largest delay time and is located in a region of large-scale tectonic activity, SLR, which is situated within the Archean Kaapvaal Craton, and GRA1, which shows evidence for two sources of anisotropy. Some of the other stations have been discussed previously by SC.

RSON: Red Lake, Ontario

This station, first discussed by SC, yields the largest delay time in our data set and thus warrants special attention. Paradoxically, it is situated in one of the most geologically stable regions in the world: an 800 km by 1000 km block of E-W trending gneiss and greenstone terrains in the Western Superior province of the Canadian Shield; it is also distinguished by unusually fast shear velocities [*Grand*, 1987]. It was noted in SC that there is an excellent correlation between ϕ and the dominant fabric present in both small-scale and large-scale features (see their Figure 4). This region experienced a large-scale episode of north-south compressional deformation at the end of the Archean, formerly referred to as the Kenoran Orogeny. The deformation, which has been extensively dated, took place from 2.73 to 2.70 b.y ago, with the older deformation occurring to the north of RSON and the younger deformation to the south [*Card*, 1990]. The portable data [*Silver et al.*, 1989] suggest that the large delay times persist about 300 km to the south of RSON.

RSSD: Black Hills, South Dakota

RSSD is distinguished by having the smallest delay time in the data set (0.65 s). It is also the closest station to RSON. RSSD sits on the eastern edge of the Wyoming Craton along the boundary between the Craton and the Trans-Hudson orogenic zone. While it took part in late Archean deformation, it has subsequently been exposed to the Proterozoic Trans-Hudson deformation as well as the Laramide Orogeny. The structural fabric in the Black Hills is fairly complex and is dominated by the NE-SW Archean and NW-SE Proterozoic events [*Gosselin et al.*, 1988; *Dewitt et al.*, 1986]. As these two directions are virtually perpendicular to each other, they would tend to cancel each other out. This may partially account for the small δt. The value of ϕ is closer to ϕ_g for the Archean direction and would suggest that, at least in the mantle, the Archean deformation is the stronger of the two.

COL: Fairbanks, Alaska

Outside of RSON, this station possesses the largest delay time in the data set, $(\phi, \delta t)$=(−82°,1.55 s); it is also situated in the most tectonically active region, the result of a convergent plate boundary. Crustal stress measurements indicate that the convergence produces roughly NS compression [*Nakamura et al.*, 1980; *Gedney*, 1985; *Zoback and Zoback*, 1980] and associated strain throughout most of Alaska [*Estabrook et al.*, 1988]. The combination of parallel strike-slip motion along major faults and orogenic features suggests a "transpressional" mode of deformation. The closest features to COL are the strike-slip Denali Fault and

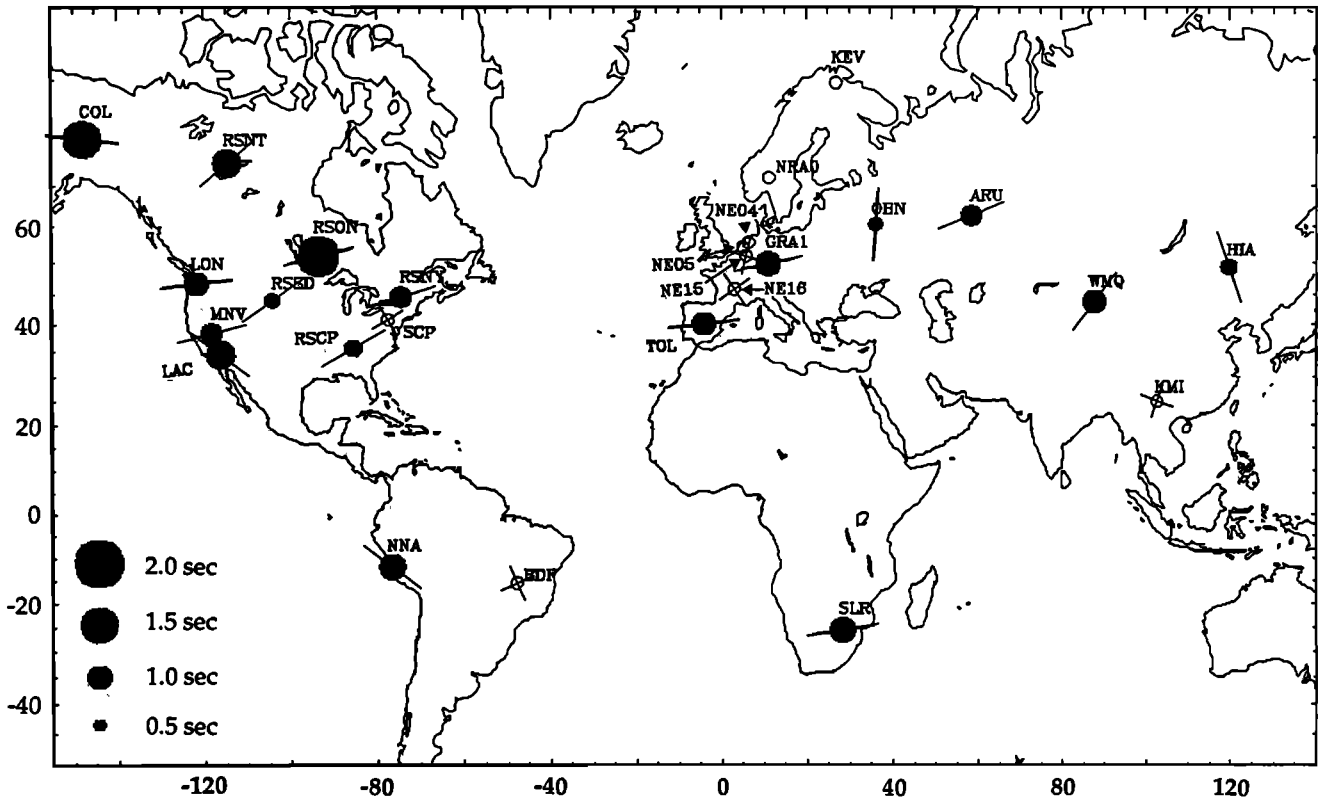

Fig. 8. World map of splitting results. All results are from this study except for MNV and LAC [*Savage et al.*, 1990] and OBN, ARU, NNA [*Given and Silver*, 1990]. Solid symbols give size of delay time δt according to the legend, and the orientation of the line gives the fast polarization direction ϕ. Open symbols (no line) denote the absence of detectable splitting from at least two nonorthogonal back azimuths. Stations with two orthogonal lines denote the absence of splitting for one back azimuth or two orthogonal back azimuths so that splitting is still allowed, but ϕ must lie along one of these two directions.

the Alaska Range to the south of COL and the strike-slip Tintina-Kaltag fault system to the north. At the longitude of the station, all features strike approximately EW. This direction is the same as ϕ, strongly suggesting that the subcontinental mantle is being deformed in the same way.

The thickness of subcontinental mantle is constrained by the presence of the subducting slab. The closest slab-related seismicity is about 50 km to the southwest, and approaches depths of 140 km [*Gedney and Davies*, 1986], so that the presumed aseismic extension of the slab under COL would have a depth of about 200 km. The delay time δt predicts a layer thickness of about 170 km of mantle material and is thus consistent with the deformation of the entire subcontinental mantle. Similar behavior is seen for other convergent plate margins. NNA, on the west coast of Peru (Figure 8) yields a value of ϕ that is parallel to the coastal mountains. This same result is seen in two other splitting studies in analogous areas. Using data from portable stations in Columbia, South America recording events within the Bucharamanga nest, *Savage et al.* [1989] found that estimates of $\phi(\sim 0°)$ were parallel to coastal mountains. Similarly, below Honshu, Japan estimates of ϕ from direct S waves coming up vertically from events in the downgoing slab yield values of ϕ parallel to the dominant mountain ranges in Honshu (S. Kaneshima, personal communication, 1990). These results are somewhat surprising. The two studies that have modeled flow-induced anisotropy associated with subduction, *McKenzie* [1979] and *Ribe* [1989*b*], both predict large strains and strong anisotropy above the slab, but with ϕ parallel to the direction of convergence. Our results suggest that the dominant effect is instead the shortening and deformation within the overlying subcontinental mantle.

SLR: Silverton, South Africa

SLR is situated within the Kaapvaal Craton just north of the Witwatersrand Basin. It is only about 20 km from the Premier mine, the oldest Kimberlite pipe in the world (1 b.y. old). This site then provides perhaps the best opportunity to compare the properties of mantle xenoliths with anisotropy. While the rocks from this mine have yet to be analyzed for anisotropy, some mines several hundred km to the south have been analyzed (D. Mainprice and X. Christensen, personal communications, 1990) with values of $\delta\tilde{\beta}_{max}$ that are consistent with those found elsewhere. The value of 1.1s for δt corresponds to a layer thickness of about 120 km. The last large-scale deformational episode to affect this part of the Kaapvaal Craton is related to the the 2.6–2.7 b.y.-old north-south collision between the Kaapvaal

Fig. 9. P waves from two deep-focus events. (Top) April 23, 1984, m_b=6.0, depth 415 km, ϕ_b= 321° . (Bottom) April 20, 1984, m_b=6.0, depth 581 km, ϕ_b= 321° . Events were recorded at station RSON with the same back-azimuths as events showing strong transverse component SKS phase (see Figure 2). Shown are the vertical, radial, and transverse components of the phase $P\acute{m}S$. Note clear $P\acute{m}S_R$ but absence of observable $P\acute{m}S_T$ for both events.

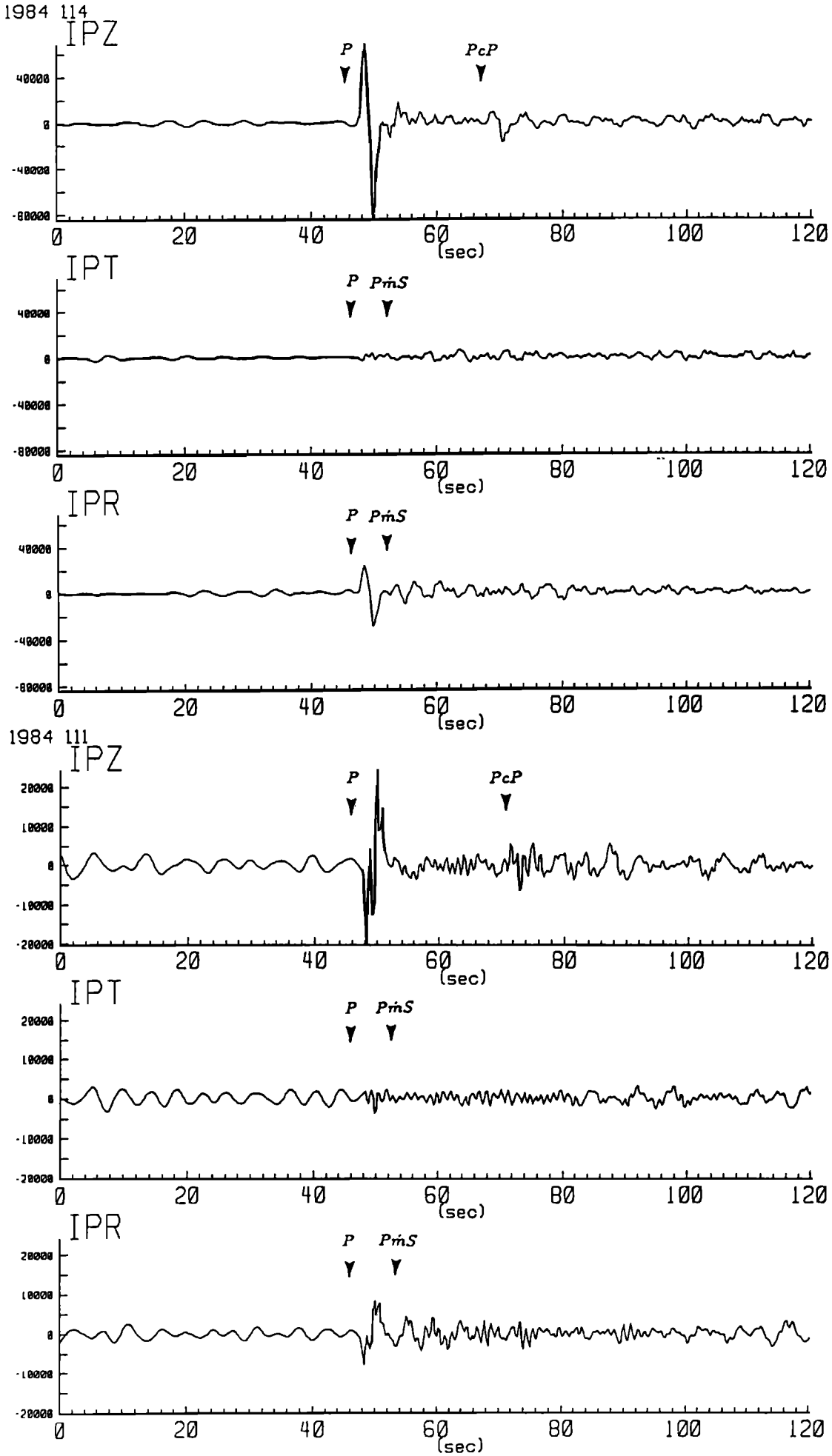

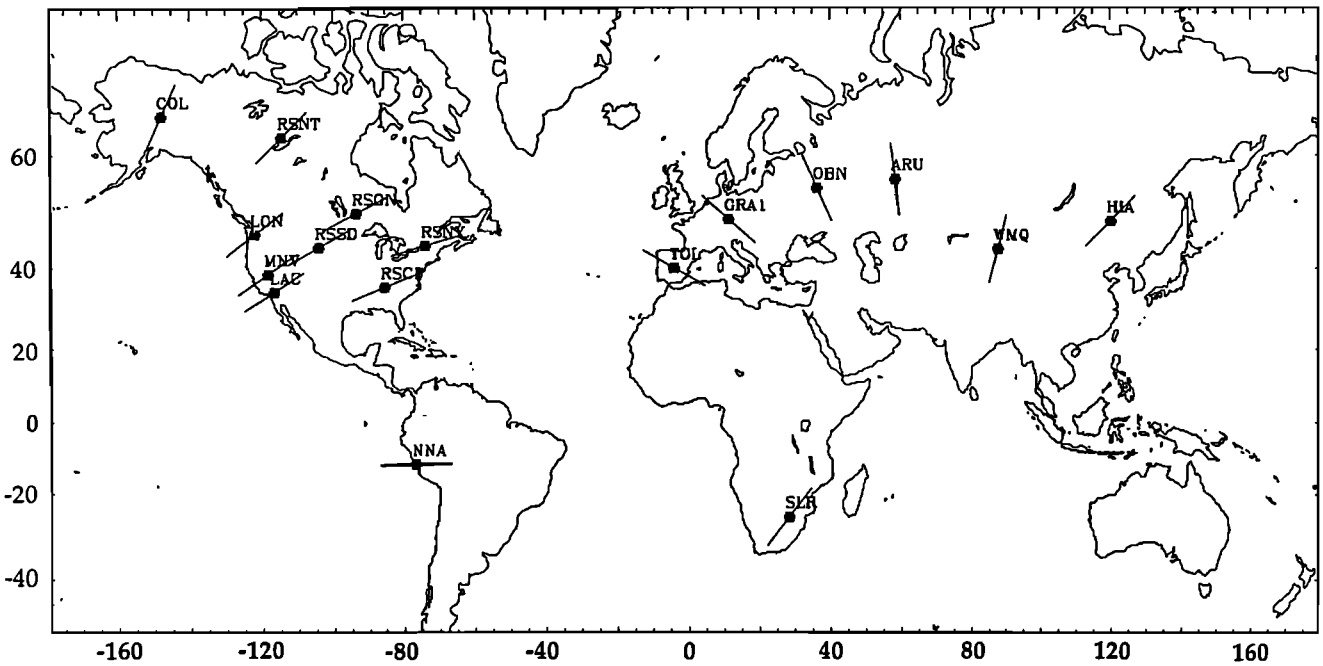

Fig. 10. The predicted values of the fast polarization directions ϕ_{apm}, based on the absolute plate motion (APM) velocity vectors from the model AM1-2 [*Minster and Jordan*, 1978] for all stations with detectable splitting. Here, ϕ_{apm} is taken to be parallel to the APM direction.

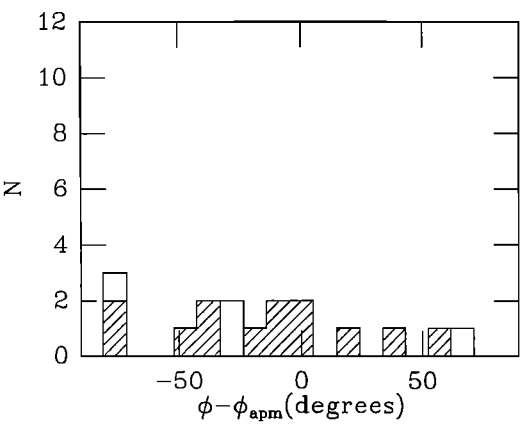

Fig. 11. Histogram of ϕ - ϕ_{apm} for all stations with splitting measurements. Shading denotes stations with available geologic information. Includes data from SSM and *Given and Silver* [1990].

and Zimbabwe cratons that gave rise to the Limpopo belt to the north. Volcanism and deformational features found within the Kaapvaal Craton have been interpreted by *Burke et al.* [1986] as an Andean-style arc, in which the Craton was shortened and thickened during the collision. The Witwatersrand basin has been interpreted as a foreland basin; its northern boundary marks the southward extent of the shortened block and is characterized by east-west trending thrust faults. The detailed zircon-based dating of sediments in the Witwatersrand basin are consistent with this picture [*Robb et al.*, 1990]. SLR is just at the southern edge of the collisional plateau and the fast polarization direction of 81° is virtually parallel to the trend of the Witwatersrand northern boundary, strongly suggesting that this event was the primary cause of the observed anisotropy.

GRA1: Grafenberg Array, West Germany

As first discussed in SC, ϕ for GRA1 is nearly east-west. The strongest deformation seen in these rocks are associated with Hercynian deformation [see *Behr et al.*, 1984]. GRA1 is situated on a ENE-WSW trending thrust fault separating the Saxothuringikum and Moldanubikum zones. The close correspondence between ϕ and ϕ_g suggests that this deformation is producing the anisotropy. This region is of special interest as there was a study in Germany of P wave anisotropy using P_n [*Bamford*, 1977], where the fast propagation direction was found to be ϕ=22.5°. Since this should also be the fast polarization direction for split shear waves, if caused by the a-axis of olivine, then there is a clear discrepancy between the two results. *Fuchs* [1983] noted that the direction of maximum shear stress, as inferred from the source mechanisms of crustal events, is essentially parallel to the P_n fast propagation direction and concluded that this relation would hold if the crustal stress pattern penetrated into the uppermost mantle and if the a-axis of olivine aligns itself in this direction. The SKS results, corroborated by *Vinnik et al.* [1989*b*], would suggest that the P_n results are sampling a superficial feature, while the SKS results are sampling lithospheric-wide, earlier deformation.

A discrepancy between SKS splitting and P_n anisotropy is also found in the Basin and Range. As discussed by SSM, measurements of shear wave splitting yield a value for ϕ that is about 75° and is more closely associated with the larger pre-Miocene extension ($\phi_g \simeq 68°$) rather than the present-day extension ($\phi_g \simeq -60°$). However, splitting results for the crust [*McNamara et al.*, 1989] and P_n observations [*Beghoul and Barazangi*, 1990] for the uppermost mantle are more consistent with the present extension being the cause. The discrepancy can again be explained by a superficial and relatively weak deformation superimposed upon a deeper stronger one.

DISCUSSION AND CONCLUSIONS

Characterizing Deformation in the Subcontinental Mantle

Shear wave splitting observations constitute an important way in which to characterize subcontinental mantle defor-

TABLE 3. Predicted Values of the Fast Polarization Direction, ϕ_g, Based on the Surface Geology

Station	ϕ_g	Ref.	Basis
COL	+90	1	Strike of Denali fault zone and Alaska range both of which strike almost exactly EW directly south of COL; maximum compressive stress direction
RSNT	+45	2	Foliation direction in Yellowknife greenstone belt and adjacent western Granodiorite
RSON	+83	3,4	Average foliation direction in Archean Granite-Greenstone terrains; strike of subprovince boundaries
RSSD	+45/−45	5	Dominant Archean/Proterozoic fabric. Both fabrics appear to be of equal strength in surface rocks
RSCP	+45		Strike of Grenville deformation
RSNY	+67.5	6	Local strike of Adirondaks
LAC	−45		Strike of San Andreas Fault system
MNV	−67.5 +67.5	7,8	Strike of present-day/ pre-Miocene extension
TOL	+90	9	Strike of fabric from Hercynian deformation
GRA1	+67.5	10	Strike of fabric from Hercynian deformation
MNA	−45		Approximate strike of coastal ranges in Peru
SLR	+80	11,12	Strike of fabric from 2.6-b.y.-old collision with Zimbabwe Craton
LON	+90	13	Perpendicular to present-day most compressive stress direction

Where precise numerical estimates are not available, compass directions are converted to numerical values: EW = 90; NS = 0; NE-SW = 45; NWSE = −45; ENE-WSW = +67.5; WNW-ESE = −67.5. Where two values are given (RSSD, MNV) there are two predominant directions.

References are 1, *Nakamura et al.* [1980]; 2, *Henderson* [1985]; 3, *Beakhouse* [1985]; 4, G. Stott (personal communication, 1988); 5, *Gosselin et al.* [1988]; 6, *Whitney et al.* [1989]; 7, *Zoback et al.* [1981]; 8, *Eaton* [1982]; 9, *Julivert et al.* [1972]; 10, *Behr et al.* [1984]; 11, *Burke et al.* [1986]; 12, *Robb et al.* [1990]; 13, *Zoback and Zoback* [1980].

mation and ultimately to examine the dynamics and evolution of continents. As we have shown, the measurements collected thus far are most successfully interpreted as due to strain-induced mantle anisotropy that is dominantly produced by the past and present internal coherent deformation of the continental lithosphere. In particular, the splitting parameters are best predicted by the last significant episode of continental activity (as seen in the structural geology of surface rocks). This appears to apply equally well to presently active areas (such as Alaska) and areas that were last active in the Archean (such as the Canadian Shield and Kaapvaal Craton).

This result is in marked contrast to the ocean basins, where mantle anisotropy appears to be caused by the progressive simple shear accompanying past and present-day plate motions. This is not to say that APM-related strains are completely absent beneath continents. Rather, it suggests that the internal deformation of the plate, a feature of continents but not of oceans, is a very strong source of upper mantle anisotropy. As more shear wave splitting results are obtained from the rapidly expanding number of portable and permanent broadband stations, the full extent of oceanic-style anisotropy in the subcontinental mantle can be more extensively evaluated.

The existence of coherent lithospheric deformation should not be very surprising. Continental breakup and collision, the essential components of the Wilson Cycle, are, after all, interactions between plates. Coherent deformation over the thickness of the continental lithosphere would be a most likely outcome. The long-term survival of this deformation in the form of "fossil anisotropy" [SC] requires, above all, the absence of subsequent deformation. This, in turn, is enhanced by temperatures that are below the critical temperature T_c where creep in mantle materials is expected to be unimportant over geologic time scales. Based on published data for creep in olivine, T_c is about 900°C [*Goetze and Kohlstedt*, 1973; *Nicolas*, 1989] . Thus, the depth to

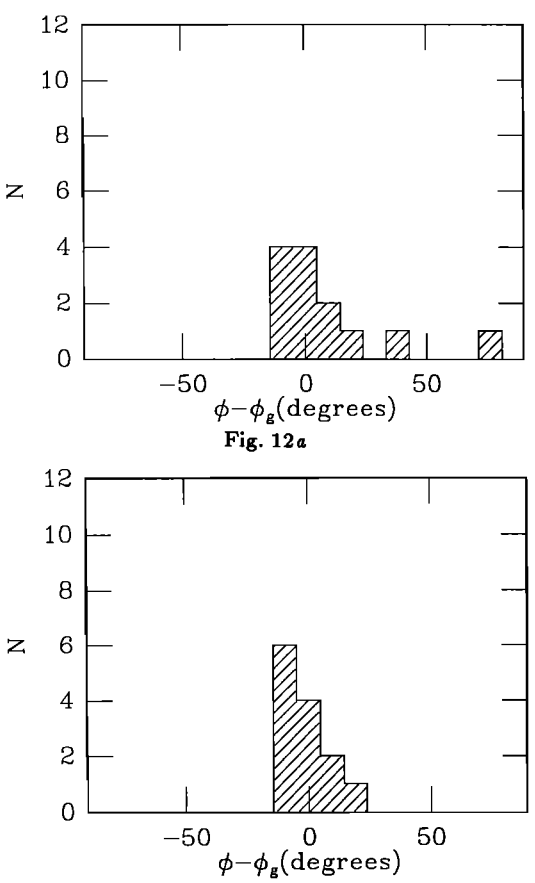

Fig. 12*a*

Fig. 12*b*

Fig. 12. Histogram of ϕ - ϕ_g (predicted ϕ based on surface geology/tectonics, Table 3). Includes data from SSM and *Given and Silver* [1990]. For RSSD and MNV, there are two prevalent directions in the data: Archean and Proterozoic for RSSD and pre-Miocene and present-day for MNV; (*a*) uses the younger deformation for both stations, and (*b*) uses the older deformation. Note that in either case, ϕ_g is a better predictor of ϕ than ϕ_{apm}.

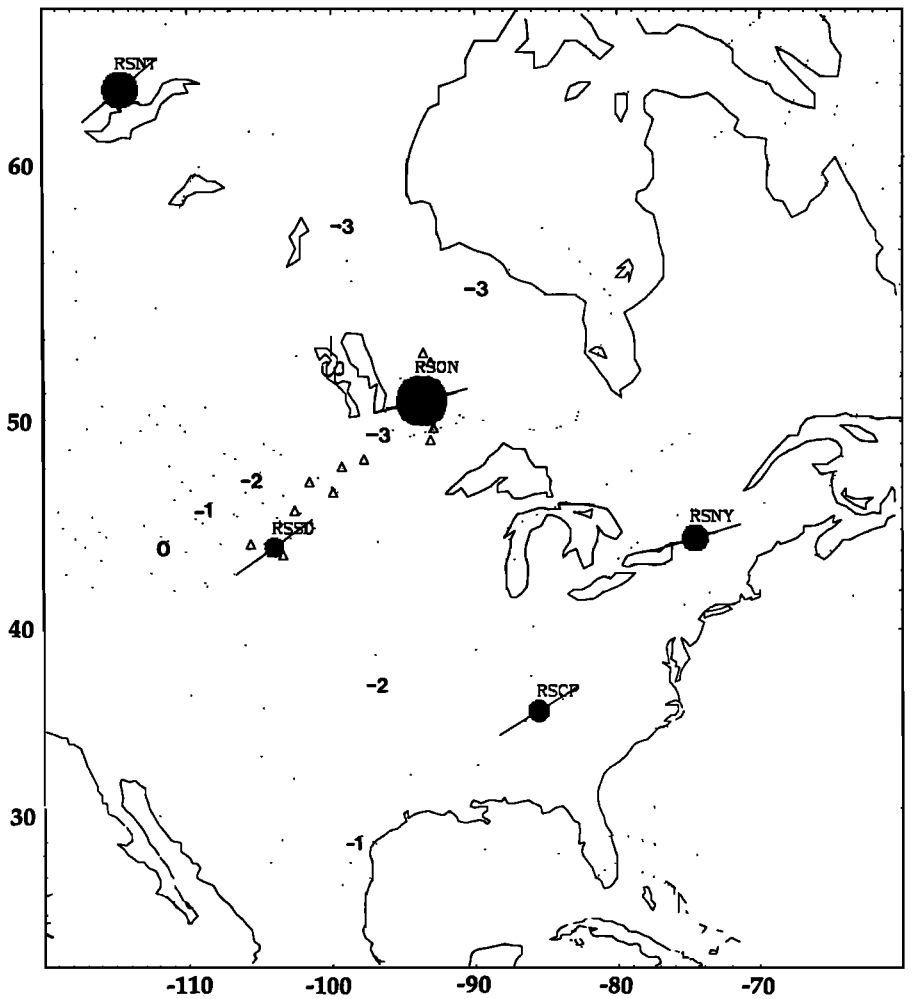

Fig. 13. Map of North America with coutours of shear-velocity delay time obtained by integrating the three-dimensional velocity model of *Grand* [1987] from 400 km to the surface. Contour interval is 0.5 s. More negative delay times correspond to higher velocities. Also shown are the locations of the five permanent stations in stable North America plus locations of the stations from a portable experiment [*Silver et al.*, 1989; P. G. Silver and S. Kaneshima, unpublished manuscript, 1991] between RSON and RSSD for which splitting has been detected.

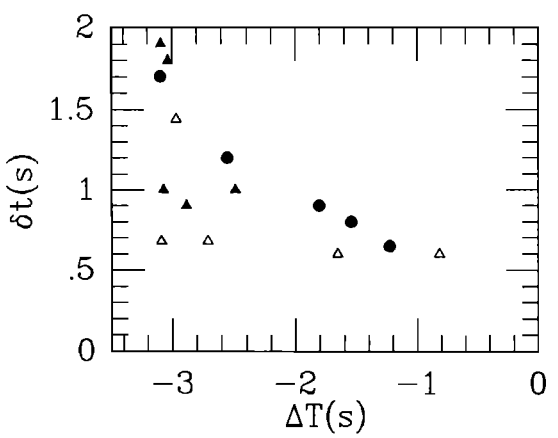

Fig. 14. Plot of δt versus ΔT for stations shown in Figure 13. Solid circles are the permanent stations. Triangles denote the results from the portable stations. Solid and open symbols represent broadband and short-period sensors, respectively. Note the good negative correlation between ΔT and δt.

the deepest preserved anisotropy, D_a, should correspond to a temperature near T_c. If the thickness of the lithosphere is defined by the 1300°C isotherm, D_a would represent about 2/3 of that thickness. As discussed above, such estimates are consistent with independent constraints on lithospheric thickness [see *Grand*, 1987].

The shear wave splitting measurements provide a means for evaluating the ways in which the subcontinental mantle evolves over time. For example, if the inferred mantle deformation can be associated with a dated surface deformation, this effectively dates the mantle material down to D_a, as having been present since the deformation. This constraint is similar to that obtained from diamond inclusion data [see *Richardson et al.*, 1984]. Specifically, the anisotropic portion of the subcontinental mantle had to have been present since the time of the deformational event. This rules out formation by subsequent "underplating." Also, the anisotropic layer could not have been formed merely by the conductive growth of the thermal boundary layer. The material added to the lithosphere by this process would have had to participate in the same deformational event and translate coherently with the surface since the event.

Another application of the splitting data is in assessing the relative strength and penetration depth of geologic episodes. For two stations, GRA1 in West Germany and MNV in the Basin and Range, the effect of present-day activity appears to be limited to the crust and uppermost mantle, while the previous episode has ostensibly deformed most of the lithosphere. This would imply that for both

stations, contemporary tectonic activity is not sufficiently strong to produce lithospheric-wide deformation.

The Orogeny Paradox

The simplest model for subcontinental mantle deformation based on the ICD hypothesis is that the continental plate is shortened and thickened by orogenies. The expected characteristics of this deformed plate would be a thickened crust and a low-temperature, high (seismic) velocity, thickened lithospheric mantle. Yet, this model raises a serious paradox. Present and recent orogenies do not fit this description. Instead, they commonly have thick crust associated with what appears to be thinned lithosphere: low mantle seismic velocities, high heat flow, and surface volcanism. The two best known examples are North Central Tibet [see *Molnar*, 1988*b* and references therein], formed by the collision between India and Eurasia, and the Altiplano [*Isacks*, 1988], formed by the convergence between the Nazca and South American plates. In fact orogenies appear to leave the mantle hotter, not cooler in general. *Sclater et al.* [1980] have shown that one of the important predictors of surface heat flow is the age since the last orogenic episode, suggesting that orogenies reheat the lithosphere. Where is the thickened subcontinental lithospheric mantle?

To date, efforts to resolve this paradox have focussed on more complex modes of orogenic deformation that serve to remove the cold subcontinental mantle. One way is by arguing that a thickened thermal boundary layer indeed forms, but is removed by the development of a convective instability and replaced by warm asthenosphere [e.g., *Houseman et al.*, 1981; *England and Houseman*, 1989]. The other is by asserting that the subcontinental mantle delaminates from the crust as a result of interactions with a subducted slab [*Bird*, 1978, 1988; *Isacks*, 1988].

Such models, however, are inconsistent with the preserved record of coherent lithospheric-wide deformation suggested by the shear wave splitting results given in the present report. These observations suggest that despite elevated temperatures, the original subcontinental mantle has not been removed and has instead been heated in place. How might we now resolve the paradox? One possibility is that we have misinterpreted the splitting observations. The most direct way of testing this possibility would be to obtain splitting parameters for regions that clearly show this paradoxical character, such as north-central Tibet and the Altiplano. The ICD hypothesis would predict a large value of δt with ϕ orthogonal to the collision direction. The "mantle removal" models would predict very little anisotropy.

Assuming the ICD hypothesis is correct, another means of resolving this paradox is required. One possibility is the strain heating that must accompany deformation. In order to satisfy the observed properties of the mantle, a temperature increase of several hundred degrees would be required. Assuming that the finite strain is of order unity (consistent with doubling crustal thickness), the orogeny is rapid (<<100 m.y.), and all mechanical work is converted to heat, then 100 MPa (1 Kbar) would produce a temperature increase of about 35°–40°C. Thus orogenic stresses of several hundred MPa would be required. The importance of this effect then hinges on the actual level of orogenic stresses. Although such stresses have been traditionally thought to be somewhat less than 100 MPa [e.g., *Molnar and Lyon-Caen*, 1988], we note that estimates of lithospheric stress in the literature range from tens of MPa to several hundred. There are several studies, in fact, that argue for NS compressional stresses of several hundred MPa in the Northeast Indian Ocean, that appear to be directly related to the collision between India and Eurasia. These are based on evidence for the lithospheric buckling of oceanic lithosphere [*McAdoo and Sandwell*, 1985; *Stein et al.*, 1989] and on the numerical modeling of the net forces on the Indo-Australian plate [*Cloetingh and Wortel*, 1986]. In addition, thin viscous sheet models of the formation of the Tibetan plateau [*England and Houseman*, 1986] appear to require stresses of several hundred MPa. This at least suggests that such stress levels are not implausible. If orogenic stresses are in fact low, then the orogeny paradox remains, and some other mechanism for heating the mantle in place will be required.

APPENDIX: CALCULATION OF CONFIDENCE REGION

The confidence region is determined from the sum-of-squares function $S(\phi, \delta t)$ for an n-point time series: $E_t(\phi, \delta t)$ in the case of SKS and $\lambda_2(\phi, \delta t)$ in the case of other S phases. If the minimum value of $S(\phi, \delta t)$, $S_{min}(\phi, \delta t)$ may be regarded as a χ^2 variable with n degrees of freedom, which would be true for a Gaussian white noise process, then the confidence region may be constructed for the α confidence level from the following expression

$$\frac{\lambda_2}{\lambda_2^{min}} \leq 1 + \frac{k}{n-k} f_{k,n-k}(1-\alpha)$$

[*Jenkins and Watts*, 1968; *Bates and Watts*, 1988], where f is the inverse of the F probability distribution, k is the number of parameters, two in our case, and $\alpha = 0.05$ corresponds to the 95% confidence level. If $S(\phi, \delta t)$ is not distributed χ^2_n, appropriate modifications must be made. We assume that $S(\phi, \delta t)$ is approximately χ^2_ν-distributed where ν, which depends both on the instrument response and noise spectrum, is usually much smaller than n. Parameter ν is found in the following way. We define

$$E = \frac{T}{2} \int_{-\infty}^{\infty} \eta^2(t) dt \qquad (A1)$$

where $\eta(t)$ is a finite-length sample of the noise process of length T. It is assumed that we can write $\eta(t)$ as the convolution of an uncorrelated Gaussian noise process $g(t)$, and a filter, $f(t)$. By Parseval's theorem, (A1) can then be written in the frequency domain as

$$E = \frac{T}{2} \int_{-\infty}^{\infty} |f(\omega)|^2 |g(\omega)|^2 d\omega \qquad (A2)$$

For digital data, (A2) may be approximated by a finite sum of terms up to the Nyquist frequency and with frequency spacing 1/T:

$$E \simeq \sum_{n=1}^{N-1} |f_n|^2 |g_n|^2 + \frac{1}{2}(|f_o|^2 |g_o|^2 + |f_N|^2 |g_N|^2) \qquad (A3)$$

If E is approximately χ^2 distributed then we may estimate the degrees of freedom from the expression

$$\nu = 2\frac{< E >^2}{\mathrm{Var}[E]} \qquad (A4)$$

[*Jenkins and Watts*, 1968]. From the definition of E, and assuming g_n has zero mean and variance σ^2, we can write

$$< E >= \sigma^2[\sum_{n=1}^{N-1} |f_n|^2 + \frac{1}{2}(|f_o|^2 + |f_N|^2)] \equiv \sigma^2 F_2 \quad (A5)$$

Since

$$< E^2 >= \sigma^4(F_2^2 + F_4), \quad (A6)$$

it follows that

$$\mathrm{Var}[E^2] = \sigma^4 F_4 \quad (A7)$$

where

$$F_4 = \sum_{n=1}^{N-1} |f_n|^4 + \frac{1}{2}(|f_o|^4 + |f_N|^4)] \quad (A8)$$

In (A6), the assumption that the real and imaginary parts of g_n are independent and normally distributed has been used in computing its fourth moment. Substituting these results into (A4),

$$\nu = 2\frac{F_2^2}{F_4} \quad (A9)$$

Finally, it is necessary to determine the quantities F_2^2 and F_4 in (A9). One could accomplish this by knowledge of the instrument response and assumptions about the noise process. We have chosen, however, to determine this directly from the data. In analogy with the definition of E, we define the freqency domain sum

$$E_4 = \sum_{n=1}^{N-1} |f_n|^4 |g_n|^4 + \frac{1}{3}(|f_o|^4 |g_o|^4 + |f_N|^4 |g_N|^4) \quad (A10)$$

whose expected value is

$$< E_4 >= 2\sigma^4 F_4 \quad (A11)$$

Consider the quantity

$$\tilde{\nu} \equiv 2(\frac{2E^2}{E_4} - 1) \quad (A12)$$

Writing $E^2 =< E^2 > +\delta E^2$ and $E_4 =< E_4 > +\delta E_4$ and using expressions (A6),(A9), and (A11), we find that to first order in $\delta E^2/< E^2 >$ and $\delta E_4/< E_4 >$, $\tilde{\nu}$ is an unbiased estimate of ν. Since both E^2 and E_4 can be determined from the data, we can estimate $\tilde{\nu}$ for each record and then take the average value of several records, assuming a stationary noise process. Expressed as the ratio $\hat{\nu} = \nu/n$, it is found that $\hat{\nu}$ is typically 0.3 for RSTN intermediate channel and about 0.12 for DWWSSN intermediate channel and for NARS. In general, this comes out to one degree of freedom per second for all of the networks, and thus appears to be independent of digitizing interval for the data we are using.

Acknowledgments. We thank S. Shirey, T. Kusky, M. Kingston, A. Riaza, and J. Boyd for help with the geology of various stations, N. Ribe, P. Tapponnier, and Ines Cifuentes for useful discussions, C. Bina for help with a contour plotting routine, and S. Grand for providing the vertical delay times for his model. Helpful reviews were provided by A. Nicolas, S. Kaneshima, M. Savage, N. Valette-Silver, G. Helffrich, D. Wiens, and an anonymous reviewer. We also thank M. Acierno for providing computer support and J. Dunlap for assistance with manuscript preparation. This research was sponsored by the National Science Foundation grant EAR87210001 and by the Carnegie Institution of Washington, Department of Terrestrial Magnetism.

REFERENCES

Ando, M., ScS polarization anisotropy around the Pacific Ocean, *J. Phys. Earth*, *32*, 179–196, 1984.

Ando, M., and Y. Ishikawa, Observations of shear-wave velocity polarization anisotropy beneath Honshu, Japan: two masses with different polarizations in the upper mantle, *J. Phys. Earth*, *30*, 191–199, 1982.

Ando, M., Y. Ishikawa, and F. Yamazaki, Shear wave polarization anisotropy in the upper mantle beneath Honshu, Japan, *J. Geophys. Res.*, *88*, 5850–5864, 1983.

Ansel, V., and H.-C. Nataf, Anisotropy beneath 9 stations of the GEOSCOPE broadband network as deduced from shear-wave splitting, *Geophys. Res. Lett.*, *16*, 409–412, 1989.

Backus, G.E., Possible forms of seismic anisotropy of the uppermost mantle under oceans, *J. Geophys. Res.*, *70*, 3429–3439, 1965.

Bamford, D., P_n velocity anisotropy in a continental upper mantle, *Geophys. J. R. Astron. Soc.*, *49*, 29–48, 1977.

Bamford, D., M. Jentsch, and C. Prodehl, P_n anisotropy studies in northern Britain and the eastern and western United States, *Geophys. J. R. Astron. Soc.*, *57*, 397–429, 1979.

Bates, D. M., and D. G. Watts, *Nonlinear Regression Analysis and Its Applications*, John Wiley, New York, 1988.

Beakhouse, G. P., The relationship of supracrustal sequences to a basement complex in the western English River subprovince, Evolution of Archean Supracrustal Sequences, Geol. Assoc. Can. Spec. Pap., 28, 169–178, 1985.

Beghoul, N., and M. Barazangi, Azimuthal anisotropy of velocity in the mantle lid beneath the Basin and Range Province, *Nature*, *348*, 536–538, 1990.

Behr, H.-J., W. Engel, W. Franke, P. Giese, and K. Weber, The Variscan Belt in central Europe: Main structures, geodynamic implications, open questions, *Tectonophysics*, *109*, 15–40, 1984.

Bird, P., Initiation of intracontinental subduction in the Himalaya, *J. Geophys. Res.*, *83*, 4975–4987, 1978.

Bird, P., Laramide crustal thickening event in the Rocky Mountain foreland and Great Plains, *Tectonics*, *3*, 741–758, 1984.

Bird, P., Formation of the Rocky Mountains, western United States; a continuum computer model, *Science*, *239*, 1501–1507, 1988.

Bowman, J. R., and M. Ando, Shear-wave splitting in the upper-mantle wedge above the Tonga subduction zone, *Geophys. J. R. Astron. Soc.*, *88*, 25–41, 1987.

Burke, K., W. S. F. Kidd, and T. Kusky, Is the Ventersdorp rift system of Southern Africa related to a continental collision between the Kaapvaal and Zimbabwe cratons at 2.64 Ga ago? *Tectonophysics*, *115*, 1–24, 1985.

Burke, K., W. S. F. Kidd, T. M. Kusky, Archean Foreland Basin Tectonics in the Witwatersrand, South Africa, *Tectonics*, *5*, 439–456, 1986.

Card, K. D., A review of the Superior Province of the Canadian Shield, a product of Archean accretion, *Precambrian Res.*, *48*, 99–156, 1990.

Christensen, N. I., Shear wave velocities in metamorphic rocks at pressures to 10 kilobars, *J. Geophys. Res.*, *71*, 3549–3556, 1966.

Christensen, N. I., The magnitude, symmetry and origin of upper mantle anisotropy based on fabric analyses of ultramafic tectonics, *Geophys. J. R. Astron. Soc.*, *76*, 89–112, 1984.

Clarke, T. J., and P. G. Silver, A procedure for the systematic interpretation of body wave seismograms, 1, Application to Moho depth and crustal properties, *Geophys. J. Int.*, *104*, 41–72, 1991.

Cloetingh, S., and R. Wortel, Stress in the Indo-Australian plate, *Tectonophysics*, *132*, 49–67, 1986.

Crampin, S., and D. C. Booth, Shear-wave polarizations near the North Anatolian Fault, II, Interpretation in terms of crack-induced anisotropy, *Geophys. J. R. Astron. Soc.*, *83*, 75–92, 1985.

DeMets, C., R. G. Gordon, D. F. Argus, and S. Stein, Current plate motions, *Geophys. J. Int.*, *101*, 425–478, 1990.

Dewitt, E., J. A. Redden, A. B. Wilson, and D. Buscher, Mineral resource potential and geology of the Black Hills National Forest, South Dakota and Wyoming, *U.S. Geol. Surv. Bull.*, *1580*, 1986.

Dziewonski, A. M., and D. L. Anderson, Preliminary reference Earth model, *Phys. Earth Planet. Inter.*, *25*, 297–356, 1981.

Eaton, G. P., The Basin and Range Province: Origin and tectonic significance, *Annu. Rev. Earth Planet. Sci.*, *10*, 409–440, 1982.

England, P., Constraints on extension of continental lithosphere, *J. Geophys. Res.*, *88*, 1145–1152, 1983.

England, P., and G. Houseman, Finite strain calculations of continental deformation 2. Comparison with the India-Asia collision zone, *J. Geophys. Res.*, *91*, 3664–3676, 1986.

England, P., and G. Houseman, Extension during continental convergence, with application to the Tibetan Plateau, *J. Geophys. Res.*, *94*, 17,561–17,579, 1989.

England, P., and D. McKenzie, A thin viscous sheet model for continental deformation, *Geophys. J. R. Astron. Soc.*, *70*, 295–321, 1982.

England, P., and D. McKenzie, Correction to "A thin viscous sheet model for continental deformation," *Geophys. J. R. Astron. Soc.*, *73*, 523–532, 1983.

Estabrook, C. H., D. B. Stone, and J. N. Davies, Seismotectonics of northern Alaska, *J. Geophys. Res.*, *93*, 12,026–12,040, 1988.

Forsyth, D. W., The early structural evolution and anisotropy of the oceanic upper-mantle, *Geophys. J. R. Astron. Soc.*, *43*, 103–162, 1975.

Fuchs, K., Recently formed elastic anisotropy and petrological models for the continental subcrustal lithosphere in southern Germany, *Phys. Earth Planet. Inter.*, *31*, 93–118, 1983.

Fukao, Y., Evidence from core-reflected shear waves for anisotropy in the Earth's mantle, *Nature*, *309*, 695–698, 1984.

Gedney, L., Stress trajectories across the northeast Alaska Range, *Bull. Seismol. Soc. Am.*, *75*, 1125–1134, 1985.

Gedney, L., and J. N. Davies, Additional evidence for down-dip tension in the Pacific plate beneath central Alaska, *Bull. Seismol. Soc. Am.*, *76*, 1207–1214, 1986.

Given, H., and P. G. Silver, Shear-wave splitting from the IRIS/IDA stations, *Eos Trans. AGU*, *71*, 555, 1990.

Goetze, C., and D. L. Kohlstedt, Laboratory study of dislocation climb and diffusion in olivine, *J. Geophys. Res.*, *78*, 5961–5971, 1973.

Gosselin, D. C., J. J. Papike, R. E. Zartman, and Z. E. Peterman, Archean rocks of the Black Hills, South Dakota: Reworked basement from the southern extension of the Trans-Hudson Orogen, *Geol. Soc. Am. Bull.*, *100*, 1244–1259, 1988.

Grand, S. P., Tomographic inversion for shear velocity beneath the North American plate, *J. Geophys. Res.*, *92*, 14,065–14,090, 1987.

Gripp, A. E., and R. G. Gordon, Current plate velocities relative to the hotspots incorporating the Nuvel-1 global plate motion model, *Geophys. Res. Lett.*, *17*, 1109–1112, 1990.

Gueguen, Y., and A. Nicolas, Deformation of mantle rocks, *Annu. Rev. Earth Planet Sci.*, *8*, 119–144, 1980.

Henderson, J. B., Geology of the Yellowknife-Hearne Lake area, district of MacKenzie: A segment across an archean basin, *Geol. Surv. Can. Mem.*, *414*, 1985.

Hess, H. H., Seismic anisotropy of the uppermost mantle under oceans, *Nature*, *203*, 629–631, 1964.

Hobbs, B. E., W. D. Means, and P. F. Williams, *An Outline of Structural Geology*, John Wiley, New York, 1976.

Hoffman, P. F., and G. Ranalli, Archean aseismic flake tectonics, *Geophys. Res. Lett.*, *15*, 1077–1080, 1988.

Houseman, G. A., D. P. McKenzie, and P. Molnar, Convective instability of a thickened boundary layer and its relevance for the thermal evolution of continental convergent belts, *J. Geophys. Res.*, *86*, 6115–6132, 1981.

Isacks, B. L., Uplift of the Central Andean Plateau and bending of the Bolivian orocline, *J. Geophys. Res.*, *93*, 3211–3231, 1988.

Jenkins, G. M., and D. G. Watts, *Spectral Analysis and Its Applications*, Holden-Day, San Francisco, Calif., 1968.

Julivert, M., J. M. Fontbote, A. Riveiro, and L. Conde, Mapa tectonico de la peninsula Iberica y Baleares, *Inst. Geol. Min.* (Madrid, Spain), 1972.

Kaneshima, S., and M. Ando, An analysis of split shear waves observed above crustal and uppermost mantle earthquakes beneath Shikoku, Japan: Implications in effective depth extent of seismic anisotropy, *J. Geophys. Res.*, *94*, 14,077–14,092, 1989.

Kaneshima, S., M. Ando, and S. Kimura, Evidence from shear-wave splitting for the restriction of seismic anisotropy to the upper crust, *Nature*, *335*, 627–629, 1988.

Keith, C. M., and S. Crampin, Seismic body waves in anisotropic media: Synthetic seismograms, *Geophys. J. R. Astron. Soc.*, *49*, 225–243, 1977.

Kind, R., G. L. Kosarev, L. I. Makeyeva, and L. P. Vinnik, Observations of laterally inhomogeneous anisotropy in the continental lithosphere, *Nature*, *318*, 358–361, 1985.

Kumazawa, M., and O. L. Anderson, Elastic moduli, pressure derivatives, and temperature derivatives of single-crystal olivine and single-crystal forsterite, *J. Geophys. Res.*, *74*, 5961–5972, 1969.

McAdoo, D. C., and D. T. Sandwell, Folding of oceanic lithosphere, *J. Geophys. Res.*, *90*, 8563–8569, 1985.

McKenzie, D., Finite deformation during fluid flow, *Geophys. J. R. Astron. Soc.*, *58*, 689–715, 1979.

McNamara, D. E., Evidence for azimuthal seismic anisotropy in the Basin and Range province: implications for middle to lower crustal tectonic processes, M.S. thesis, 125 pp., University of Missouri, Columbia, 1990.

McNamara, D. E., T. J. Owens, G. Zandt, and G. E. Randall, Evidence for azimuthal seismic anisotropy in the Basin and Range province: implications for lower crustal properties, *Geol. Soc. Am. Abstr. Program*, *21*, 321, 1989.

Minster, J. B., and T. H. Jordan, Present-day plate motions, *J. Geophys. Res.*, *83*, 5331–5354, 1978.

Molnar, P., Continental tectonics in the aftermath of plate tectonics, *Nature*, *335*, 131–137, 1988*a*.

Molnar, P., A review of geophysical constraints on the deep structure of the Tibetan Plateau, the Himalaya and the Karakoram, and their tectonic implications, *Philos. Trans. R. Soc. London*, *326*, 33–88, 1988*b*.

Molnar, P., and H. Lyon-Caen, Some simple physical aspects of the support, structure, and evolution of mountain belts, *Geol. Soc. Am.*, *218*, 179, 1988.

Montagner, J.-P., and T. Tanimoto, Global anisotropy in the upper mantle inferred from the regionalization of phase velocities, *J. Geophys. Res.*, *95*, 4797–4819, 1990.

Nakamura, K., G. Plafker, K. H. Jacob, and J. N. Davies, A tectonic stress trajectory map of Alaska using information from volcanoes and faults, *Bull. Earthquake Res. Inst.*, *55*, 89–100, 1980.

Nataf, H.-C., I. Nakanishi, and D. L. Anderson, Anisotropy and shear-velocity heterogeneities in the upper mantle, *Geophys. Res. Lett.*, *11*, 109–112, 1984.

Nicolas, A., *Structures of Ophiolites and Dynamics of Oceanic Lithosphere*, Kluwer Academic Publishers, Dordrecht, The Netherlands, 1989.

Nicolas, A., and N. I. Christensen, Formation of anisotropy in upper mantle peridotites — A review, in *Composition, Structure and Dynamics of the Lithosphere-Asthenosphere System* Vol. 16 (eds Fuchs, K. & Froidevaux, C.) 111–123 (Am. Geophys. Un., Washington D.C., 1987).

Nicolas, A., and J. P. Poirier, *Crystalline Plasticity and Solid State Flow in Metamorphic Rocks*, 444 pp., John Wiley, New York, 1976.

Nicolas, A., and F. Boudier, and A. M. Boullier, Mechanisms of flow in naturally and experimentally deformed peridotites, *Am. J. Sci.*, *273*, 853–876, 1973.

Owens, T. J., S. R. Taylor, and G. Zandt, Crustal structure at Regional Seismic Network stations determined from inversion of broadband teleseismic P waveforms, *Bull. Seismol. Soc. Am.*, *77*, 631–662, 1987.

Raitt, R. W., G. G. Shor, T. J. G. Francis, and G. B. Morris, Anisotropy of the Pacific upper mantle, *J. Geophys. Res.*, *74*, 3095–3109, 1969.

Ribe, N. M., A continuum theory for lattice preferred orientation, *Geophys. J.*, *97*, 199–207, 1989*a*.

Ribe, N. M., Seismic anisotropy and mantle flow, *J. Geophys. Res.*, *94*, 4213–4223, 1989*b*.

Ribe, N. M., and Y. Yu, A theory for plastic deformation and textural evolution of olivine polycrystals, *Geophys. J. Int.*, in press, 1991.

Richardson, S. H., J. J. Gurney, A. J. Erlank, and J. W. Harris,

Origins of diamonds in old enriched mantle, *Nature*, *310*, 198–202, 1984.

Robb, L. J., D. W. Davis, and S. L. Kamo, U-Pb ages on single detrital zircon grains from the Witwatersrand Basin, South Africa: Constraints on the age of sedimentation and on the evolution of granites adjacent to the basin, *J. Geology*, *98*, 311–328, 1990.

Savage, M. K., X. R. Shih, R. P. Meyer and R. C. Aster, Shear-wave anisotropy of active tectonic regions via automated S-wave polarization analysis, *Tectonophysics*, *165*, 279–292, 1989.

Savage, M. K., P. G. Silver and R. P. Meyer, Observations of teleseismic shear-wave splitting in the Basin and Range from portable and permanent stations, *Geophys. Res. Lett.*, *17*, 21–24, 1990.

Sclater, J. G., C. Jaupart, and D. Galson, The heat flow through oceanic and continental crust and the heat loss of the Earth, *Rev. Geophys. Space Phys.*, *18*, 269–311, 1980.

Shearer, P. M., and J. A. Orcutt, Compressional and shear wave anisotropy in the oceanic lithosphere - the Ngendei seismic refraction experiment, *Geophys. J. R. Astron. Soc.*, *87*, 967–1003, 1986.

Shih, X. R., R. P. Meyer, and J. F. Schneider, An automated, analytical method to determine shear-wave splitting, *Tectonophysics*, *165*, 271–278, 1989.

Silver, P. G., and W. W. Chan, Implications for continental structure and evolution from seismic anisotropy, *Nature*, *335*, 34–39, 1988.

Silver, P. G., and T. H. Jordan, Total-moment spectra of fourteen large earthquakes, *J. Geophys. Res.*, *88*, 3273–3293, 1983.

Silver, P. G., R. P. Meyer, D. E. James, and S. B. Shirey, A portable experiment to determine properties of the subcontinental mantle: Preliminary results, *Eos Trans. AGU*, *70*, 1227, 1989.

Stein, C. A., S. Cloetingh, and R. Wortel, Seasat-derived gravity constraints on stress and deformation in the northeastern Indian Ocean, *Geophys. Res. Lett.*, *16*, 823–826, 1989.

Tanimoto, T., and D. L. Anderson, Lateral heterogeneity and azimuthal anisotropy of the upper mantle: Love and Rayleigh waves 100–250 s, *J. Geophys. Res.*, *90*, 1842–1858, 1985.

Vauchez, A., and A. Nicolas, Mountain building: strike-parallel motion and mantle anisotropy, *Tectonophysics*, *186*, 183–201, 1991.

Verma, R. K., Elasticity of some high-density crystals, *J. Geophys. Res.*, *65*, 757–766, 1960.

Vetter, U., and J.-B. Minster, P_n velocity anisotropy in southern California, *Bull. Seismol. Soc. Am.*, *71*, 1511–1530, 1981.

Vidale, J. E., Complex polarization analysis of particle motion, *Bull. Seismol. Soc. Am.*, *76*, 1393–1405, 1986.

Vinnik, L. P., G. L. Kosarev, and L. I. Makeyeva, Anizotropiya litosfery po nablyudeniyam voln SKS and SKKS, *Dokl. Akad. Nauk USSR*, *278*, 1335–1339, 1984.

Vinnik, L. P., V. Farra, and B. Romanowicz, Azimuthal anisotropy in the Earth from observations of SKS at GEOSCOPE and NARS broadband stations, *Bull. Seismol. Soc. Am.*, *79*, 1542–1558, 1989*a*.

Vinnik, L. P., R. Kind, G. L. Kosarev, and L. I. Makeyeva, Azimuthal anisotropy in the lithosphere from observations of long-period *S*-waves, *Geophys. J. Int.*, *99*, 549–559, 1989*b*.

Whitney, P. R., S. R. Bohlen, J. D. Carl, W. deLorraine, Y. W. Isachsen, J. McLelland, J. F. Olmsted, and J. W. Valley, The Adirondack Mountains — A section of deep Proterozoic crust, *Field Trip Guidebook T164, Montreal, Canada to Albany, New York, June 30–July 8, 1989*, AGU, Washington D.C., 1989.

Zoback, M. L., and M. Zoback, State of stress in the conterminous United States, *J. Geophys. Res.*, *85*, 6113–6156, 1980.

Zoback, M. L., R. E. Anderson, and G. A. Thompson, Cainozoic evolution of the state of stress and style of tectonism of the Basin and Range province of the western United States, *Philos. Trans. R. Soc. London, Ser. A*, *A 300*, 407–434, 1981.

Zoback, M. L., M. D. Zoback, J. Adams, M. Assumpcão, S. Bell et al., Global patterns of tectonic stress, *Nature*, *341*, 291–298, 1989.

W. W. Chan, Teledyne Geotech Alexandria Laboratories, 314 Montgomery Street, Alexandria, VA 22314.

P. G. Silver, Department of Terrestrial Magnetism, Carnegie Institution of Washington, 5241 Broad Branch Road NW, Washington, DC 20015.

(Received August 2, 1990;
revised March 11, 1991;
accepted November 19, 1990.)

JOURNAL OF GEOPHYSICAL RESEARCH, VOL. 96, NO. B10, PAGES 16,295–16,318, SEPTEMBER 10, 1991

Evidence for Magma Mixing and a Heterogeneous Mantle on the West Valley Segment of the Juan de Fuca Ridge

N. A. VAN WAGONER AND M. I. LEYBOURNE

Department of Geology, Acadia University, Wolfville, Nova Scotia, Canada

We studied basaltic rocks of the northern end of the Juan de Fuca Ridge to compare the volcanology, geochemistry, and petrogenesis of spatially related rocks of an active spreading center (West Valley and West Ridge), the Sovanco Fracture Zone, the Middle Ridge, and the adjacent Endeavour and Northern Symmetrical ridges. Rocks were analyzed for mineral chemistry and major, trace, and rare earth elements (REE). Crystallization temperatures and equilibrium phase compositions were calculated. The complex zoning and disequilibrium compositions of plagioclase and olivine megacrysts and phenocrysts from all areas except West Ridge, Sovanco Fracture Zone (7123-7), and Endeavour Ridge indicate mixing in shallow level magma chambers. The rocks range from primitive (up to Mg # = 68) in the West Valley south and West Ridge areas to evolved ferrobasalts (Mg # as low as 52) at West Valley central, West Valley north, and Northern Symmetrical Ridge. The rocks from the West Valley axis span the range of Mg #. Rocks from West Valley are transitional to enriched (e.g., $[La/Ce]_n$ = 0.89-1.06), as are rocks from Endeavour Ridge (e.g., $[La/Ce]_n$ = 0.88-1.06). Rocks from West Valley wall, Middle Ridge, Sovanco Fracture Zone, and Northern Symmetrical Ridge are light REE depleted (e.g., $[La/Ce]_n$ = 0.76-0.88), and the most depleted rocks are from West Ridge (e.g., $[La/Ce]_n$ = 0.62). The chemically heterogeneous character of the lavas exists both within site and within a single dredge haul (West Valley north and Endeavour Ridge rocks) and between sites, indicating that the mantle source is heterogeneous on a variety of scales. The range in incompatible element ratios can be modelled as binary mixing between an enriched source and a depleted source. Further, trace element systematics require variations in the degree of partial melting. Lava chemistry and ridge morphology are consistent with southward propagation of spreading in West Valley to form an overlap with the Endeavour Segment. West Valley (West Valley north, central and south) is dominated by extension over volcanism and is thus thermally and magmatically depressed. Rocks from the West Valley Segment span a broader compositional range than ridge systems to the south, reflecting the heterogeneity of the source and the lack of robust volcanism to homogenize the chemistry. Zero age rocks from West Valley are similarly enriched in $[La/Ce]_n$ as zero age rocks from the Endeavour and Explorer ridges. Rocks from the West Valley wall, the Middle Ridge, and the older Sovanco Fracture Zone rocks are depleted similar to rocks of the Juan de Fuca Ridge south of the Cobb Offset. This difference suggests that enrichment of the mantle source north of the Cobb Offset has been a recent phenomena.

INTRODUCTION

The Juan de Fuca Ridge is a medium-rate spreading center situated in the northeast Pacific Ocean, approximately 300 km off the coast of North America. The ridge extends for a length of 500 km between the Blanco and Sovanco fracture zones and was subdivided into eight smaller ridge segments by *Karsten et al.* [1987] (Figure 1). The northern part, the Endeavour Segment, is further divided into the Endeavour Ridge and the West Valley Segment. Active seafloor spreading along the West Valley Segment now occurs in West Valley and was initiated during the Brunhes epoch when it is inferred to have "jumped" from Middle Valley, a parallel valley to the east (Figure 1) [*Barr and Chase*, 1974; *Nobes et al.*, 1986].

The southern Juan de Fuca Ridge has been extensively studied over the last two decades with respect to the geochemistry and petrogenesis of its basaltic rocks [*Kay et al.*, 1970; *Clague and Bunch*, 1976; *Eaby et al.*, 1984; *Liias*, 1986]. However, the West Valley Segment has been less extensively studied. Previous studies, based on major element geochemistry, indicated that the basaltic rocks of the West Valley Segment are normal, depleted mid-ocean ridge basalts [*Barr and Chase*, 1974; *Karsten et al.*, 1987], but the detailed chemical characteristics and petrogenetic processes of the West Valley Segment rocks and the relationships between the geochemical signature, ridge morphology and rift propagation were not previously assessed.

This study includes rocks collected from different settings within the West Valley Segment: (1) West Valley, an actively spreading mid-ocean ridge, (2) the walls of West Valley, (3) Middle Ridge, the axial ridge of the formerly active spreading centre to the east of West Valley [*Barr and Chase*, 1974; *Davis and Lister*, 1977; *Karsten et al.*, 1987], and (4) the Sovanco Fracture Zone (Figure 1). These rocks are compared with samples from the Endeavour Ridge and the Northern Symmetric Ridge of the Juan de Fuca Ridge, south of the Cobb Offset.

Paper number 91JB00592.
0148-0227/91/91JB-00592$05.00

REGIONAL GEOLOGY

The Juan de Fuca Ridge separates the Pacific plate from the Juan de Fuca and Explorer plates (remnants of the former Farallon plate) which are presently being subducted beneath the North American plate [*Atwater*, 1970; *Riddihough*, 1984]. The interpretation of the Juan de Fuca Ridge as an active spreading center [*Raff and Mason*, 1961], with a seafloor spreading rate of 5.8 cm/yr (full rate) [*Vine and Wilson*, 1965], and the interpretation of the last 20 m.y. history of the Juan de Fuca Ridge and surrounding ocean basin [e.g., *Hey*, 1977; *Hey and Wilson*, 1982; *Riddihough*, 1984; *Carlson*, 1981; *Karsten and Delaney*, 1989] are based primarily on magnetic lineations and bathymetry.

The structures of the Juan de Fuca Ridge and patterns of magnetic lineations are complex. This complexity has been attributed to changes in the azimuth of spreading as a result of (1) propagating rifts [*Hey*, 1977; *Hey and Wilson*, 1982], perhaps due to the hotspot that produced the Cobb-Eickleberg Seamount Chain [*Karsten and Delaney*, 1989], (2) asymmetric spreading and variable degrees of resistance to movement on transform faults [*Carlson*, 1981], and (3) changes in the poles of rotation of the Juan de Fuca plate [*Riddihough*, 1984].

The West Valley Segment comprises several deep valleys up to 15 km wide separated by ridges (Figure 1) [*Barr*, 1972]. Middle Valley is filled with turbidite sediments up to 1800 m in thickness due to its close proximity to the North American continental margin [*Davis et*

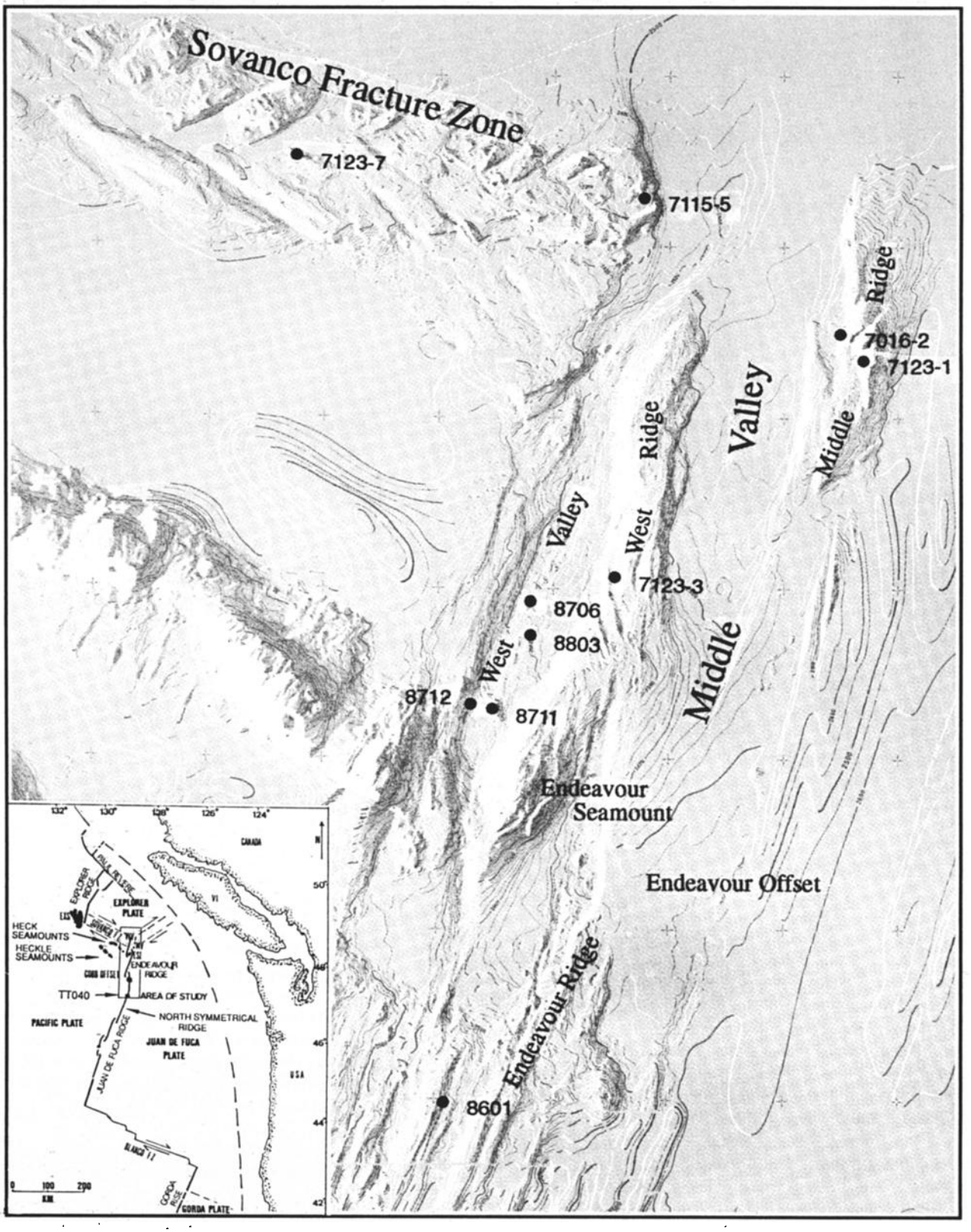

Fig. 1. Bathymetric map of the study area [from *Davis et al.*, 1987*a*] showing physiographic regions and dredge locations. The location of dredge TT040 from the Northern Symmetrical Ridge and the regional setting of the study area are indicated on the inset map. EXS, Explorer Seamount; WV, West Valley; MV, Middle Valley; and EX, Explorer Ridge.

al., 1976; *Nobes et al.*, 1986]. West Valley receives little turbidite sedimentation [*Barr and Chase*, 1974], and fresh pillow, lobate, and sheet flows are exposed on the seafloor (M.I. Leybourne and N.A. Van Wagoner, manuscript in preparation, 1991). The zone of active volcanism is in the southern portion of the inner rift and comprises small (60-250 m in height) volcanoes which are visible on Sea MARC II side scan sonar data [*Karsten et al.*, 1986]. The southern tip of West Valley forms an overlapping spreading centre with the Endeavour Ridge [*Karsten et al.*, 1986]. The overlap region is dominated by the enigmatic Endeavour Seamount.

TABLE 1. Description of Dredge Hauls, Locations and Megascopic Features

Dredge and Location	Site Descriptions	Relative Age	Physiographic Feature	Latitude °N	Longitude °W	Depth, m	Navigation
8706 WVn West Valley north	A large recovery, consisting of a large number of lobate basalt fragments ranging in size from a few centimeters to a large pillow 40 cm in diameter. The rocks are very uniform in appearance, very fresh although the glassy margin is not very thick. Phenocrysts of plagioclase, olivine, and clinopyroxene are visible. There are no Mn stainings, although many surfaces exhibit a red-brown stain. The inner surface of most of the samples consists of a cavity that is quite crystalline.	1	small volcano, West Valley	48° 29'	129° 02.5'	2955-2950	Loran C and GPS Sat Nav
8803 WVc West Valley Central	Small recovery, consisting of two fist-sized chunks and numerous pebble-sized fragments. The fragments are very glassy and very uniform in appearance. The upper surfaces of many of the fragments have microropy texture. Megacrysts of plagioclase and olivine are visible. Only minor palagonite.	1	floor of West Valley	48° 26.7'	129° 02'	2920-2900	Loran C and GPS Sat Nav
8711 WVs West Valley south	Only a few chips of porphyritic (plagioclase) basaltic glass were recovered from the large volcano at the southern end of West Valley. The glass is extremely fresh with no sign of palagonite alteration.	1	large volcano, West Valley	48° 23'	129° 07'	2880-2892	Loran C
8712 WVW West Valley wall	Only two fist-sized fragments and numerous centimeter-sized fragments were recovered. The rocks are uniformly highly plagioclase-phyric basalt with a surface coating Mn over fresh glass.	2.5	west wall, West Valley	48° 23.5'	129° 07.5'	2850-2711	Loran C and GPS Sat Nav
7123-3 WR West Ridge	90 kg of pillow fragments of olivine- and plagioclase-phyric basalt. Samples are very fresh though the upper surface of the glass is palagonized and mud coated with no Mn crust.	2	west flank, West Ridge	48° 31'	128° 55'	2652-2377	Loran A
7123-1 MR Middle Ridge	135 kg of blocky to pillow-shaped basalt fragments that are coated with Mn-oxide. Glassy breccia altered to palagonite covers the upper surface of some fragments. Both holocrystalline and porphyritic fragments with glassy rims were recovered.	4	west flank, Middle Ridge	48° 44'	128° 33'	2012-1865	Loran A
7016-2 MR Middle Ridge	100 kg recovery of blocky fragments with Mn and Fe oxide coatings. Samples are plagioclase-phyric and altered along fractures. Some fragments have a glassy margin, the upper surface of which is palagonized.	4	west flank, Middle Ridge	48° 45'	128° 34.5'	2377-2103	Loran A
7123-7 SFZ Sovanco Fracture Zone	Very large recovery (750 kg) of fresh pillow basalt and blocky fragments with minor Mn crust and palagonized glassy surfaces. Samples are essentially aphyric and unaltered and have thick glassy margins.	2	western peak, Sovanco Ridge	48° 55.5'	129° 23.5'	2286-2103	Loran A
7115-5 SFZ Sovanco Fracture Zone	Large recovery (150 kg) of blocky basalt fragments with Mn crust and palagonite in samples with a glass margin. Both holocrystalline basalt and plagioclase- and olivine-phyric basalts were recovered. Some fragments are quite altered to smectite and chlorophaeite; others are fairly fresh.	2 - 4	east fault scarp, Sovanco Ridge	48° 53'	128° 51.5'	2505-2377	Loran A
8601 ER Endeavour Ridge	A large recovery of essentially aphyric Mn and mud-coated, blocky and angular, basalt fragments. Many of the samples have an outer glassy margin. Alteration is minimal and occurs as an alteration rim of variable thickness parallel to the outer margin.	3	Endeavour Ridge	48° 00'	129° 10'	~ 2400	Loran C
TT040 NSR North Symmetrical Ridge	Similar to 8601. Blocky, angular basalt fragments with Mn and Fe oxide coatings with alteration slightly more pervasive, suggesting that the rocks are older. The rocks range from aphyric to sparsely phyric. Some samples retain a thin glassy margin.	3	Juan de Fuca Ridge	47° 00.5'	129° 18'	~ 2600	Loran A

The Sovanco Fracture Zone separates the West Valley Segment from the Explorer Ridge to the north. The Sovanco Fracture Zone is not physiographically or magnetically well defined [*Barr and Chase*, 1974; *Karsten et al.*, 1987], and sediment adjacent to the Sovanco Fracture Zone shows no sign of deformation [*Barr*, 1972]. The width and poor definition of the Sovanco Fracture Zone are a result of southward migration and rotation [*Botros and Johnson*, 1988]. *Barr* [1972] dredged pillow basalts from basement highs on the Sovanco Fracture Zone and interpreted these highs to be volcanic peaks.

SAMPLING AND ANALYTICAL METHODS

Samples from 11 dredge hauls (Table 1) were analyzed for their petrography, mineral chemistry, and major, trace, and rare earth element geochemistry. Three dredge sites (8706; 8803; 8711) are from the axis of West Valley where exposure of fresh basalt flows was indicated on Sea MARC II side scan sonar data [*Davis et al.*, 1987*b*]. Dredge sites are also located on the west wall of West Valley (8712), the east wall of West Ridge (7123-3), two sites along Middle Ridge (7123-1; 7016-2), and two locations from the Sovanco Fracture Zone (7123-7; 7115-5). For comparative purposes, rocks from two additional dredge hauls from the Endeavour Ridge (8601) and the Northern Symmetrical Ridge (TT040) (south of the Cobb Offset) were studied. The dredge locations are listed on Table 1 and plotted with respect to the Sea Beam bathymetry in Figure 1. The samples were collected during several expeditions to the area beginning with the 1970 and 1971 University of British Columbia cruises of the CFAV *Endeavour*, when samples were collected by S. Barr and R. Chase, and ending with the 1988 Geological Survey of Canada cruise of the *J. P. Tully*, when samples were collected by M. Leybourne (see Table 5).

Major and minor element geochemistry of the glasses and minerals were determined from standard polished thin sections using a JEOL 733 four wavelength spectrometer electron microprobe at the Dalhousie Regional microprobe facility. All analyses were carried out with a 15-kV electron acceleration potential and a 5-nA sample current. The published glass analyses are averages of 5-8 points from one thin section using a defocussed beam (10 μm) with counting times of 40 s for each element. Replicate analyses of glass standard USNM 111240-52 were used to determine accuracy. Mineral chemistry of olivine, plagioclase, clinopyroxene, and spinel was determined using a focused electron beam (1 μm) under the same operating conditions. Geologic standards were used for calibration and data were reduced using an on line Tracor Northern matrix correction program (ZAF). Errors for the major elements are give in Table 2.

Whole rock samples were crushed to <1 cm size fragments in a steel jaw crusher and hand picked to remove fragments exhibiting alteration. About 80 grams were then ground to less than 200 mesh in a ring mill using a tungsten-carbide head. The major elements were determined from fused glass discs and the trace elements (Cr, Ga, V, Zn, Ni, Zr, Y, Nb, Cu, Ba, Rb) from pressed powder pellets on a Philips PW1400 sequential X ray fluorescence (XRF) spectrometer utilizing

TABLE 2. Electron Microprobe Analyses

	Sample										
	8706-05	8706-07	8706-23	8711-02	8803-01	8803-03	8712-05	8712-06	7123-3-A	7123-1-C	7016-2-19
Location	WVn	WVn	WVn	WVs	WVc	WVc	WVW	WVW	WR	MR	MR
SiO_2	50.15	50.33	50.26	49.80	49.71	50.39	49.44	49.46	49.82	49.97	49.72
TiO_2	2.06	2.18	1.83	1.22	2.36	2.39	1.71	1.82	1.10	1.77	1.21
Al_2O_3	13.79	13.57	14.13	15.49	14.13	13.88	15.28	15.16	16.05	14.23	15.02
Cr_2O_3	0.11	0.11	0.01	0.13	0.03	0.02	0.11	0.12	0.07	0.06	0.09
FeO^T	10.99	11.39	10.87	8.32	11.50	11.40	10.25	9.97	8.31	10.79	9.25
MnO	0.26	0.27	0.14	0.20	0.18	0.20	0.21	0.22	0.30	0.31	0.33
MgO	6.91	6.66	6.83	8.93	6.39	6.32	8.36	8.26	8.83	7.43	8.78
CaO	11.43	11.41	11.56	12.73	10.95	10.58	11.62	11.67	12.66	12.02	12.67
Na_2O	3.09	3.12	2.91	2.43	3.18	3.17	2.51	2.63	2.86	2.52	2.35
K_2O	0.21	0.21	0.19	0.14	0.30	0.32	0.11	0.10	0.04	0.15	0.06
Total	98.99	99.24	98.73	99.39	98.73	98.67	99.60	99.42	100.04	99.25	99.47
Mg #	55.5	53.7	55.4	68.0	52.4	52.3	61.8	62.1	67.8	57.7	65.3

	Sample									
	7123-7-2	7123-7-124	7115-5-A	8601-01	8601-02	8601-04	8601-05	TT040/15	TT040/17	Error, wt %
Location	SFZ	SFZ	SFZ	ER	ER	ER	ER	NSR	NSR	
SiO_2	49.71	49.73	50.85	50.45	50.97	50.89	49.46	49.96	50.49	0.26
TiO_2	1.30	1.28	1.50	1.50	1.51	1.64	1.80	2.18	1.71	0.04
Al_2O_3	15.49	14.92	14.37	15.54	15.58	14.90	15.82	13.44	13.65	0.15
Cr_2O_3	0.04	0.11	0.06	0.09	0.10	0.13	0.12	0.07	0.05	0.02
FeO^T	9.08	8.95	10.00	8.43	8.46	9.13	8.66	12.43	11.59	0.14
MnO	0.20	0.18	0.26	0.18	0.18	0.19	0.19	0.25	0.22	0.03
MgO	9.29	9.60	7.34	8.07	7.99	7.84	7.79	6.87	7.45	0.11
CaO	12.15	11.69	12.32	11.77	11.80	12.16	11.68	11.24	11.76	0.13
Na_2O	2.68	2.47	2.88	3.03	3.03	3.06	3.22	2.80	2.48	0.10
K_2O	0.08	0.06	0.09	0.28	0.29	0.13	0.32	0.16	0.10	0.02
Total	100.02	98.99	99.68	99.35	99.91	100.06	99.07	99.39	99.51	
Mg #	67.0	68.0	59.3	65.5	65.1	63.0	64.0	52.2	56.0	

Locations are WVn, West Valley north; WVs, West Valley south; WVc, West Valley central; WVW, West Valley Wall; WR, West Ridge; MR, Middle Ridge; SFZ, Sovanco Fracture Zone; ER, Endeavour Ridge; NSR, North Symmetrical Ridge.

a Rh-anode tube at the St. Mary's Regional XRF facility. Loss on ignition (LOI) was determined by heating the sample for 1.5 hours at 1050°C in an electric furnace. All Fe is converted to Fe_2O_3 assuming total oxidation of iron after LOI. Relative errors are given in Table 3.

Glass chips were removed from the outer rims of the rocks and crushed to less than 35 mesh with a mortar and pestle. Approximately 100 mg of glass were then carefully hand-picked under a binocular microscope to remove any fragments containing phenocrysts or surface alteration. The picked glasses were ultrasonically washed in acetone and distilled water for 5 min.

Rare earth elements (REE) and additional trace elements (Sc, Ba, Li, Rb, Sr, Th, Hf, Nb, Y, Zr) were determined for 100-mg sample aliquots of selected whole rock and glass powders. The samples were digested in HF/HNO_3, and the resultant solutions were analyzed by inductively coupled plasma mass spectrometry (ICP-MS) using the method of standard addition to correct for matrix effects. Eight of the samples were analyzed in duplicate and the relative percent error for the rare earth elements is excellent (the greatest relative percent error is 3.3%) and generally very good for the trace elements (2-6% relative error) with the exception of Nb (18% relative error). Relative errors are given in Table 4. Gd is consistently low and this is probably related to analytical difficulties (S. Jackson, personal communication, 1989). The ICP-MS regional facility at Memorial University was used for these analyses.

Petrographic investigations were carried out on standard and polished thin sections cut perpendicular to the outer margins. In most cases, basalt fragments with a glassy margin were used so that phase relationships at the time of eruption could be determined. Modal percentages were determined by point counting 1500-2000 points using a 0.5 x 0.2 mm spacing from the glassy margin inward (Table 5). Microlites were counted with groundmass. Crystal texture terminology is after *Donaldson and Brown* [1977], *Bryan* [1979], *Stakes et al.* [1984], and *Hummler and Whitechurch* [1988].

RESULTS

Petrography and Mineral Chemistry

The petrography of each sample is indicated in Table 5. Petrography and mineral chemistry of each sample site are summarized in Table 6. In general, the samples are unaltered to moderately altered. The most severe alteration occurs in some of the samples from the Sovanco Fracture Zone and Middle Ridge. The greater resistance of glass to seawater alteration in the short term (<1 Ma [*Hekinian*, 1982]) is shown by these most severely altered samples where olivine has been altered in the crystalline interior but is fresh in the glassy margin (Table 5). Plagioclase phenocrysts or megacrysts occur in all the samples studied with the exception of the olivine tholeiites from the Sovanco Fracture Zone (dredge haul 7123-7) and is the most abundant phase in all the rocks except for those from West Ridge. Olivine occurs in all the rocks studied. Only some of the more evolved samples with Mg #<57 (Mg # = (molar MgO/(molar MgO + molar FeO^T * 0.90) *100)) contain clinopyroxene phenocrysts. Spinel was observed in five of the samples chosen for microprobe analysis, all with glass Mg #>64 (Table 6).

The textures of, and the relationships between, the crystals in glassy basaltic rocks have important implications for the interpretation of crystal-melt equilibria [*Bryan*, 1979]. Mineral chemistry, in particular the complexly zoned megacrysts, provides information of the preeruption history of the magma and the physical and chemical changes that occurred in the magma chamber [*Kuo and Kirkpatrick*, 1982].

West Valley north. The plagioclase crystals are typically euhedral, but many exhibit marginal reaction with the melt. Plagioclase phenocrysts and megacrysts are complexly zoned with cores ranging from An 79.6-64.3 (Table 7 and Figures 2*a* and 3). However, the rim compositions are remarkably similar in An content (An 67.1-69.2), and similar to the coexisting microphenocrysts (An 67.4-70.5) (Figure 2a). Core compositions are removed from the *Drake* [1976] equilibrium line but within the error envelope, whereas the rim and microphenocryst compositions are closer to equilibrium with the glass (Figure 3). The variation of plagioclase zonation within a single sample, but the similar and equilibrium rim and microphenocryst compositions, indicates that the phenocrysts and megacrysts had different crystallization histories yet equilibrated with the host melt prior to eruption and quenching.

Forsterite (Fo) content of the olivine phenocrysts ranges from Fo 83.8 to 81.7 for the cores to Fo 81.2 to 80.1 for the rims of phenocrysts (Table 8). Rim compositions of phenocrysts approach equilibrium. The microphenocrysts range from Fo 83.4 to 77.8 and in only one case fall in the equilibrium field according to the assumed K_D values (Figure 4a).

Clinopyroxene occurs as subhedral to anhedral endiopsides and augites, chemically similar to low-pressure clinopyroxenes from the AMAR and FAMOUS areas of the Mid-Atlantic Ridge [*Bryan*, 1979; *Stakes et al.*, 1984]. The clinopyroxene phenocrysts are higher in Al, Cr, Ti, and Ca and lower in Fe and Mg than the glomerocryst clinopyroxene (Table 9). The increase in Ca and decrease in Mg are consistent with the melt having fractionated between the time the two crystals formed. The increase in Ti and Al in clinopyroxene phenocrysts may be the result of an increase in the cooling rate of the magma during phenocryst formation [*Coish and Taylor*, 1979; *Shibata et al.*, 1979]. Both equilibrium and disequilibrium clinopyroxene phenocrysts occur in these rocks (Figure 4*b*).

West Valley Central. The plagioclase megacrysts are normally zoned with core compositions of An 88.2 to 85.3 and rim compositions of An 82.4-79.4 (Table 7 and Figure 2*a*) but are clearly out of equilibrium with the host glass (Figure 3). The microphenocryst is more evolved than the megacrysts (An 62.5) but is too albitic for the host glass (Figure 3).

The olivine megacrysts and phenocrysts are normally zoned and range in composition from Fo 86.7 to 80.0 for the cores and Fo 84.6 to 79.4 for the rims. The cores and most of the rims are out of equilibrium with the host glass, but the microphenocryst compositions (Fo 80.1-79.6) approach or are in equilibrium (Figure 4*a*). Despite the evolved chemistry of these very glassy rocks, no clinopyroxene was observed.

West Valley south. The analyzed plagioclase megacryst of the West Valley south is moderately zoned (oscillating), and the rim composition is only slightly less anorthitic (An 87.0) than the core composition (An 88.7) (Figure 2*a*). Both core and rim An compositions exceed the calculated equilibrium composition but are near the upper limit of the error envelope (Figure 3).

Olivine crystals are compositionally restricted (Fo 87.9 to 87.5) and in equilibrium with the host glass (Figure 4*a*). The spinel phenocrysts are magnesiochromites similar in composition to those from the FAMOUS area of the Mid-Atlantic Ridge [*Fisk et al.*, 1982].

West Valley Wall. The West Valley Wall rocks are plagioclase cumulates. The plagioclase megacrysts are very calcic (An 90.3 to 88.3) and exhibit very little core to rim variation. However, microphenocrysts have a much lower An content (An 74.2) (Figure 2*b*). The cores and rims of the megacrysts are clearly too anorthitic to be in equilibrium with the host melt, whereas the microphenocryst is close to the Drake equilibrium line (Figure 3). The glass inclusions in the plagioclase megacrysts reveal that the plagioclase crystallized from a considerably more primitive melt (Mg # 71-72) than the host melt (Mg # 62).

TABLE 3. X Ray Fluorescence Anlyses

	Sample											
	8706-05	8706-07	8706-08a	8706-18	8711-02	8712-01	7123-3-A	7123-1-A	7123-1-B	7016-2-19	7016-2-A	7123-7-2
Location	WVn	WVn	WVn	WVn	WVs	WVW	WR	MR	MR	MR	MR	SFZ
SiO_2	50.10	49.53	49.80	49.90	49.50	48.00	48.48	49.81	50.13	48.83	48.78	49.69
TiO_2	1.73	1.66	1.69	1.74	1.17	1.21	0.94	1.67	1.98	1.00	0.94	1.25
Al_2O_3	14.80	14.52	14.70	14.60	17.70	20.60	15.09	14.07	13.50	17.90	18.25	15.00
$Fe_2O_3^T$	11.90	10.80	11.80	11.70	9.10	8.40	8.81	11.13	11.65	7.92	7.86	9.50
MnO	0.19	0.17	0.19	0.19	0.17	0.13	0.15	0.17	0.19	0.13	0.13	0.15
MgO	7.43	7.27	7.47	7.47	7.28	6.02	11.46	6.66	6.35	6.12	6.19	8.26
CaO	11.52	11.82	11.52	11.45	12.93	13.26	11.59	11.81	11.14	13.80	13.68	11.75
Na_2O	2.70	2.29	2.70	2.70	2.30	2.00	2.16	2.54	2.41	2.33	1.96	2.42
K_2O	0.18	0.19	0.19	0.18	0.16	0.11	0.01	0.07	0.35	0.11	0.11	0.12
LOI	0.40	0.20	0.50	0.60	0.40	0.70	0.30	0.60	0.70	1.30	1.20	0.40
P_2O_5	0.17	0.16	0.16	0.16	0.11	0.10	0.06	0.15	0.20	0.08	0.08	0.12
Total	100.35	98.61	100.14	99.91	100.32	99.98	99.05	98.68	98.60	99.52	99.18	98.66
Mg #	57.8	59.6	58.1	58.4	63.7	61.1	74.1	56.8	54.5	62.9	63.4	65.6
Cr	241	248	224	228	260	206	844	163	83	384	354	470
Cu	58	74	59	61	85	35	66	71	68	78	70	64
Ga	18	19	19	20	nd	19	16	19	17	15	17	17
Ni	67	65	68	66	79	88	332	57	41	79	80	183
V	332	321	323	330	220	223	206	356	400	255	241	280
Zn	101	93	95	94	76	71	73	90	112	76	73	80
Ba	30	33	16	22	85	15	9	7	20	nd	nd	9
Rb	2	4	0	2	nd	2	nd	nd	4	nd	2	1
Sr	116	117	117	114	108	101	68	100	122	82	82	111
Nb	9.0	8.0	8.0	8.0	nd	4.0	1.0	4.0	3.0	2.0	4.0	2.0
Zr	115	113	111	113	59	77	49	111	142	58	58	85
Y	32	32	33	30	23	23	22	37	40	24	25	26
Zr/Y	3.59	3.53	3.36	3.77	2.57	3.35	2.23	3.00	3.55	2.42	2.32	3.27
Zr/Nb	12.78	14.13	13.88	14.13		19.25	49.00	27.75	47.33	29.00	14.50	42.50

	Sample										
	7123-7-124	7115-5-B	7115-5-C	7115-5-22	8601-01	8601-03	8601-04	8601-05	TT040/15	TT040/17	Errors, wt %
Location	SFZ	SFZ	SFZ	SFZ	ER	ER	ER	ER	NSR	NSR	
SiO_2	49.50	48.69	48.41	48.76	49.75	50.10	49.80	49.10	49.33	50.21	0.08
TiO_2	1.25	1.47	1.08	1.48	1.47	1.63	1.61	1.68	2.10	1.70	0.007
Al_2O_3	14.97	15.19	18.82	15.31	15.22	15.10	15.00	16.00	13.44	13.82	0.06
$Fe_2O_3^T$	9.53	9.70	7.88	9.89	8.97	10.00	9.90	9.90	12.68	11.51	0.13
MnO	0.15	0.15	0.12	0.16	0.15	0.17	0.17	0.16	0.20	0.19	0.004
MgO	9.13	7.29	6.04	7.30	7.80	7.61	7.39	7.80	6.43	6.91	0.13
CaO	11.71	11.80	13.08	11.93	11.77	11.77	11.99	11.43	11.23	11.97	0.04
Na_2O	2.51	2.90	2.32	2.78	2.57	2.80	2.90	2.90	2.51	2.06	0.14
K_2O	0.08	0.24	0.17	0.19	0.35	0.39	0.21	0.48	0.23	0.17	0.003
LOI	0.20	1.60	1.40	1.80	0.30	0.80	0.60	0.90	0.20	0.10	
P_2O_5	0.12	0.15	0.10	0.15	0.19	0.19	0.14	0.23	0.19	0.14	0.005
Total	99.15	99.18	99.42	99.75	98.54	99.97	99.10	100.04	98.54	98.78	
Mg #	67.8	62.3	62.7	61.8	65.6	62.6	62.1	63.4	52.7	56.9	
											Relative %
Cr	479	359	318	374	331	292	323	273	118	166	4.1
Cu	65	62	56	58	68	64	69	56	54	61	4.1
Ga	17	19	15	20	16	19	19	21	23	21	7.0
Ni	184	132	77	124	96	83	83	121	63	77	2.0
V	277	301	233	310	257	281	295	255	441	409	1.6
Zn	84	87	71	90	75	81	82	78	119	113	2.1
Ba	14	13	nd	9	74	54	36	51	5	17	4.3
Rb	nd	1	1	0	3	1	0	5	< 5	5	2.5
Sr	113	129	115	131	192	191	128	236	96	79	2.5
Nb	2.0	4.0	4.0	4.0	11.0	10.0	4.0	12.0	5.0	nd	12.4
Zr	84	105	75	105	119	127	105	147	139	111	1.0
Y	25	30	21	29	24	27	29	26	43	35	6.6
Zr/Y	3.36	3.50	3.57	3.62	4.96	4.70	3.62	5.65	3.23	3.17	
Zr/Nb	42.00	26.25	18.75	26.25	10.82	12.70	26.25	12.25	27.80		

See Table 2 footnote. LOI, loss on ignition.

TABLE 4. Inductively Coupled Plasma Mass Spectrometry Analyses

	Sample											
	8706-05	8706-23	8711-02	8803-01	8712-01	8712-05	7123-3-A	7123-3-A	7123-1-A	7016-2-A	7123-7-2	7123-7-2
Location	WVn	WVn	WVs	WVc	WVW	WVW	WR	WR	MR	MR	SFZ	SFZ
Rock Type	glass	glass	glass	glass	whole rock	glass	glass	whole rock	whole rock	whole rock	glass	whole rock
Sc	27	21	35	43	23	36	35	28	38	29	20	32
Ba	29.4	10	34	70	10.6	15	1.4	1.3	6.8	2.9	2.8	7.2
Li	4.4	3.6	4.6	8.4	4	5.9	4.4	3.8	6	6	2.6	4.5
Rb	2.2	0.9	3.1	6.7	1.4	1.5	0.12	0.2	0.8	2.1	0.21	1.9
Sr	96	64	128	154	96	96	80	68	95	78	72	112
Th	0.45	0.14	0.50	0.92	0.3	0.28	0.09	0.03	0.18	0.1	0.06	0.09
Hf	3.3	1.9	2.4	4.4	2	3	1.8	1.5	3	1.5	1.5	2.3
Nb	3.1	2.2	5.3	15.2	3.1	3.2	0.5	0.3	2.1	1.2	0.8	1.0
Zr	78	61	78	152	61	94	46	37	90	44	45	67
Y	24	21	24	39	20	31	23	18	31	19	15	22
La	5.03	2.41	5.03	10.35	2.52	3.68	0.99	0.83	3.34	1.52	1.40	1.44
Ce	13.42	7.05	12.49	25.52	7.65	11.09	4.14	3.47	10.70	4.90	4.69	4.91
Pr	2.15	1.21	1.92	3.63	1.29	1.87	0.90	0.73	1.89	0.91	0.89	0.94
Nd	11.07	6.59	9.48	16.19	6.88	10.18	5.45	4.64	9.85	5.06	4.78	5.45
Sm	3.71	2.39	2.96	5.13	2.49	3.62	2.49	1.95	3.56	1.98	1.77	2.21
Eu	1.30	0.83	1.09	1.81	0.89	1.25	0.95	0.85	1.31	0.80	0.67	0.90
Gd	4.36	3.06	3.66	5.92	3.05	4.24	2.92	2.67	4.46	2.66	2.11	2.91
Tb	0.88	0.59	0.70	1.15	0.62	0.90	0.61	0.54	0.89	0.56	0.43	0.57
Dy	5.92	3.94	4.63	7.53	4.05	5.97	4.25	3.68	5.96	3.73	2.79	3.88
Ho	1.26	0.85	0.98	1.60	0.88	1.24	0.90	0.78	1.28	0.82	0.59	0.87
Er	3.72	2.56	2.95	4.65	2.64	3.83	2.78	2.26	3.95	2.40	1.80	2.53
Tm	0.55	0.36	0.42	0.67	0.39	0.55	0.39	0.34	0.56	0.35	0.27	0.36
Yb	3.66	2.39	2.69	4.36	2.51	3.64	2.50	2.18	3.68	2.25	1.62	2.32
Lu	0.56	0.35	0.41	0.64	0.39	0.54	0.39	0.33	0.57	0.36	0.25	0.35
Zr/Y	3.25	2.90	3.25	3.90	3.05	3.03	2.00	2.06	2.90	2.32	3.00	3.05
Zr/Nb	25.16	27.73	14.72	10.02	19.68	29.38	97.87	123.33	42.86	36.67	60.00	67.00
$[La/Ce]_n$	0.98	0.89	1.05	1.06	0.86	0.86	0.62	0.62	0.81	0.81	0.78	0.76
$[La/Sm]_n$	0.85	0.63	1.07	1.27	0.64	0.64	0.25	0.27	0.59	0.49	0.50	0.41
$[Ce/Yb]_n$	0.95	0.77	1.20	1.52	0.79	0.79	0.43	0.41	0.75	0.56	0.75	0.55

	Sample										
	7123-7-124	7115-5-B	8601-04	8601-04	8601-05	8601-05	TT040/15	TT040/15	TT040/17	Chondrite Normalizing Values	Relative % Error
Location	SFZ	SFZ	ER	ER	ER	ER	NSR	NSR	NSR		
Rock Type	glass	whole rock	glass	whole rock	glass	whole rock	glass	whole rock	glass		
Sc	32	42	36	39	32	34	39	40	39		6.7
Ba	4.2	10.6	25	26.3	54	57.2	19	20.7	12.2		3.8
Li	4.1	8	5	4.3	4.2	3.4	6.8	6.5	5.6		2.4
Rb	0.29	5.1	2.1	2.4	4.7	6.6	1.9	3.8	2.5		6.7
Sr	115	157	134	133	230	246	97	101	80		2.5
Th	0.07	0.25	0.26	0.28	0.67	0.7	0.29	0.32	0.25		19
Hf	2.2	3.4	2.6	2.8	3.2	3.7	3.7	4	3.1		4.2
Nb	1.0	3.1	4.1	3.9	2.3	10.1	3.3	3.2	2.3		18
Zr	68	106	88	89	121	133	121	121	93		2.4
Y	22	21	27	27	24	25	40	41	33		2.2
La	2.22	4.20	4.02	4.03	8.74	9.35	4.79	5.03	3.55	0.367	1.9
Ce	7.66	13.11	11.62	11.88	21.40	22.93	14.21	14.95	10.81	0.957	2.1
Pr	1.44	2.23	2.04	2.02	3.11	3.25	2.44	2.58	1.89	0.137	1.7
Nd	7.96	11.69	9.89	10.39	14.12	14.92	13.23	13.60	10.29	0.711	2.0
Sm	2.90	4.04	3.45	3.54	3.94	3.97	4.52	4.77	3.70	0.231	2.4
Eu	1.07	1.46	1.28	1.29	1.34	1.47	1.56	1.70	1.28	0.087	2.8
Gd	3.43	4.68	4.07	4.17	4.10	4.44	5.48	5.99	4.60	0.306	1.6
Tb	0.69	0.94	0.80	0.81	0.77	0.80	1.14	1.23	0.91	0.058	2.2
Dy	4.48	6.33	5.34	5.54	4.80	5.33	7.70	8.06	6.28	0.381	1.5
Ho	0.95	1.36	1.14	1.17	1.00	1.09	1.67	1.75	1.37	0.0851	1.4
Er	2.88	4.04	3.41	3.42	3.07	3.28	4.90	5.20	4.34	0.249	2.4
Tm	0.41	0.57	0.49	0.50	0.42	0.49	0.72	0.76	0.63	0.0356	3.3
Yb	2.61	3.88	3.11	3.33	2.83	3.05	4.67	5.07	4.32	0.248	1.6
Lu	0.40	0.58	0.48	0.49	0.40	0.47	0.75	0.79	0.64	0.0381	2.4
Zr/Y	3.09	5.05	3.26	3.30	5.04	5.32	3.03	2.95	2.82		
Zr/Nb	68.00	34.19	21.46	22.82	52.61	13.17	36.67	37.81	40.43		
$[La/Ce]_n$	0.76	0.84	0.90	0.88	1.06	1.06	0.88	0.88	0.85		
$[La/Sm]_n$	0.48	0.65	0.73	0.72	1.40	1.48	0.67	0.66	0.60		
$[Ce/Yb]_n$	0.76	0.87	0.97	0.92	1.96	1.95	0.79	0.76	0.65		

See Table 2 footnote.

TABLE 5. Petrography and Modal Abundances

Sample	Plagioclase	Olivine	Pyroxene	Spinel	Vesicles	Matrix	Glass	Texture[a]	Ground Mass[b]	Alteration[c]	Analyzed By[d]	Sample Source[e]
						West Valley north						
8706-05	7.5	3.6	1.3	-	1.7	87.6	√	1-5	p,ol,c	1	1, 2, 4, 5	A
8706-07	13.0	6.7	1.9	-	0.1	78.4	√	1-5	p,ol,c	1	1, 4, 5	A
8706-08a	9.3	3.1	2.7	-	1.1	84.9	√	1-5	p,ol,c	1	1	A
8706-18	10.6	2.5	1.9	-	1.3	85.0	√	1-5	p,ol,c	1	1	A
8706-23	12.0	1.5	3.7	-	0.7	82.8	√	1-5	p,ol,c	1	3, 4	A
						West Valley central						
8803-01	8.3	1.8	-	-	0.1	89.9	√	1-4	p,ol	1	3, 4, 5	B
8803-03	9.0	1.9	-	-	0.2	89.1	√	1		1	4, 5	B
						West Valley south						
8711-02A	48.5	0.5	-	tr	?	51.0	√	1		2	1, 3-5	A
						West Valley Wall						
8712-01	21.6	0.9	-	-	1.0	77.5		2-3, 7	p,ol	2	1, 2	A
8712-03	29.0	0.5	-	-	0.5	70.5		2-3, 7	p,ol	2		A
8712-04	36.6	0.3	-	tr	3.6	63.1	√	1-2	p	2		A
8712-05	Glass fragments only						√	1		1	3-5	A
8712-06	40.5	1.5	-	0.1	0.5	58.0	√	1		2	4, 5	A
						West Ridge						
7123-3-A	7.5	9.2	-	tr	0.3	83.3	√	1-4	p	1	1-5	C
7123-3-B	6.3	9.1	-	0.1	0.1	84.5	√	1-4	p	1		C
						Middle Ridge						
7016-2-A[f]	X	?	X					2-4		7	1, 2	C
7016-2-19	25.7	0.7	-	tr	2.2	73.6	√	1-3	p	3, 5	1, 4, 5	C
7123-1-A[f]	X		X					6	p,c,op	3, 5	1, 2	C
7123-1-B	2.9	-	3.6	-	0.7	93.5	√	1-6	p,c	3, 5	1	C
7123-1-C	7.7	1.4	-	-	0.9	90.9	√	1-4	p	3, 5	4, 5	C
7123-1-D	Hyaloclastite											C
						Sovanco Fracture Zone						
7115-5-A	9.1	3.3	-	-	0.9	87.6	√	4, 6, 7	p	3, 6	4, 5	C
7115-5-B[f]	X	X						5-6	p	3, 5	1, 2	C
7115-5-C	34.7	2.1	-	-	0.1	63.2		3-5	p	3, 6	1	C
7115-5-22	6.6	2.8	-	-	0.8	90.6	√	1-3	p,ol	3, 5	1	C
7123-7-2	-	0.2	-	-	0.6	99.8	√	1-4	ol,p	1	1-4	C
7123-7-124	-	0.6	-	-	1.2	99.4	√	1-4	ol,p	1	1, 3-5	C
						North Symmetrical Ridge						
TT040/15	1.7	0.3	-	-	1.1	98.0	√	1-4	p,ol	4	1-5	E
TT040/17	2.3	-	0.2	-	0.1	97.5	√	1-3	p,c	4	1, 2, 4, 5	E
						Endeavour Ridge						
8601-01	0.3	tr	-	-	1.8	99.7	√	1-4, 7	p,ol	4	1, 4	D
8601-02	0.5	tr	-	-	0.9	99.5	√	1-4, 7	p,ol	4	1, 4, 5	D
8601-03[f]	X	X	X	-				5, 7	p,ol,c,op	4	1	D
8601-04	0.6	0.3	-	-	0.8	99.1	√	1-4, 7	p,ol	4	1-5	D
8601-05	1.0	1.1	-	-	1.1	97.9	√	1-4, 7	p,ol	4	1-5	D

Checks, glass present; dashes, not present; tr, trace. Samples with three numbers, e.g., 7115-5-A, are identified as 7115, year and cruise number; 5, dredge number; A, sample number. Samples with two numbers, e.g., 8706-05, are identified as 8706, year and dredge number and, 05, sample number.

[a]1, glass; 2, variolitic; 3, plumose intergrowths; 4, hyalopilitic; 5, intersertal; 6, intergranular; 7, pilotaxitic.

[b]p, plagioclase; ol, olivine; c, clinopyroxene; op, Fe-Ti oxides.

[c]1, fresh; 2, fractures with Fe and palagonite stains; 3, as 2 but also vesicle linings; 4, alteration of mesostasis at edge of sample; 5, as 4 with some olivine alteration; 6, general alteration of mesostasis and olivine; 7, as 6 but all olivine in crystalline interior altered.

[d]1, XRF; 2, ICP-MS (whole rock); 3, ICP-MS (glass); 4, microprobe glass; 5, microprobe mineral phases.

[e]Sample source: A, GSC cruise of *J. P. Tully* in 1988; collected by M. Leybourne; J. M. Franklin Chief Scientist. B, GSC cruise of *J. P. Tully* in 1987; collected by M. Leybourne; J. M. Franklin Chief Scientist. C, UBC cruises of CFAV *Endeavour* in 1970 and 1971; provided by S. M. Barr and R. L. Chase; S. M. Barr Chief Scientist. D, GSC cruise of CFAV *Endeavour* in 1986; J. M. Franklin Chief Scientist. E, Archive samples provided by S. M. Barr.

[f]Holocrystalline samples not point counted, X indicates presence of a phase.

The rare olivine crystals are compositionally variable. The megacrysts (Fo 89.0 to 87.7) are normally zoned and out of equilibrium, whereas the microphenocrysts (Fo 84.3) are equilibrium phases (Figure 4a). Spinel is similar in composition and content to those from West Valley south.

West Ridge. The analyzed plagioclase phenocryst is reversely zoned (An 75.2 to 75.8), but the microphenocryst composition is more anorthitic (An 79.8) than the phenocryst (Figure 2*b*). Both are in equilibrium (Figure 3). In contrast, a large olivine megacryst is normally zoned (Fo 89.0 to 87.9). However, the rim and microphenocryst (Fo 87.8) compositions are similar and are in equilibrium with the host glass (Figure 4*a*). The most Al-rich and Cr-poor spinels analyzed are from the West Ridge rocks which may be a function of the lack of cocrystallizing plagioclase and the large amount of olivine crystallization resulting in less competition for the Al and more for Cr (Table 10).

Middle Ridge (7123-1). Plagioclase megacrysts and phenocrysts are reversely and normally zoned (An 71.6 to 69.0 for the cores and An 74.0 to 65.5 for the rims) but have rim compositions that are within 5% An of the coexisting microphenocryst (69.8) (Figure 2*b*). All crystals analyzed are low in An for the chemistry of the host glass (Figure 3).

Olivine phenocrysts are slightly reversely zoned (Fo 82.8 to 83.1),

TABLE 6. Summary of Mineral Chemistry

Physiographic Region and Samples	Minerals Present[a]	Zoning[b]	Mineral Compositions[c]	Comments
West Valley north	plag p > M, m	R, N, O	An 80.7-67.5, m = 70.5-67.4	Complexly zoned megacrysts and phenocrysts of plag, ol, and cpx with variable core compositions. Plagioclase rims and microcrysts are similar. Ol and cpx show wide rim and microcryst variation.
8706-05/07	ol p >> M, m	N	Fo 83.8-80.1, m = 83.4-77.8	
	cpx p >> M, m	N	En 45.80-51.44	
West Valley central	plag M > p, m rare	N	An 86.6-79.4, m = 62.5	Large, normally zoned plag megacrysts, the cores of which are well outside the Drake equilibrium envelope. Ol megacrysts and phenocrysts are highly variable and out of disequilibrium; microcrysts are close to equilibrium.
8803-01/03	ol M > p, m	N	Fo 86.7-79.4, m = 80.1-79.6	
West Valley south	plag M	O	An 88.7-84.0	Large equant plag megacrysts, typically glomerophyric, within the Drake equilibrium envelope but well above the equilibrium line. The ol phenocrysts exhibit little variation and are equilibrium phases.
8711-02	ol p	-	Fo 87.9-87.5	
	sp		Cr# = 0.44, Mg# = 0.74	
West Valley wall	plag M, m	O	An 90.3-88.3, m = 74.2	Large equant plag megacrysts, typically glomerophyric, within the Drake equilibrium envelope but well above the equilibrium line. The plag megacrysts show little core to rim variation. Ol megacrysts are well out of equilibrium and very different from microcrysts.
8712-05/06	ol M, m	N	Fo 89.0-87.7, m = 84.3	
	sp		Cr# = 0.41, Mg# = 0.73	
West Ridge	plag p, m	R	An 75.2-75.8, m = 79.8	Plag are essentially equilibrium phases. The olivine megacrysts and phenocrysts are large, skeletal with disequilibrium cores.
7123-3-A	ol M = p, m	N	Fo 89.0-87.9, m = 87.8	
	sp		Cr# = 0.31-0.37, Mg# = 0.73-0.77	
Middle Ridge	plag p >> M, m	R, O	An 74.0-65.5, m = 69.8	Plag are below the equilibrium line but within the Drake equilibrium envelope. Ol shows little variation, and the ol are equilibrium phases.
7123-1-C	ol p, m	R	Fo 83.1-82.8, m = 83.0-82.8	
Middle Ridge	plag M >> p, m	N, O	An 90.2-76.3	Plag are within Drake equilibrium envelope, but the cores are near the upper limit. Ol show little variation and are in equilibrium.
7016-2-19	ol M, p, m	N	Fo 86.5-86.3, m = 86.3	
	sp		Cr# = 0.46, Mg# = 0.72	
Sovanco FZ	ol p, m	-	Fo 88.1, m = 86.5	Ol phenocrysts and microcrysts are equilibrium phases. No plag.
7123-7-2/124				
Sovanco FZ	plag M >> p, m	O, N	An 90.1-66.8, m = 72.6-66.0	Plag megacrysts cores are at the upper limit and above the Drake equilibrium envelope. Large core to rim variations in An content. Ol megacrysts and phenocrysts are out of equilibrium.
7115-5-A/C	ol M > p, m	N	Fo 86.2-85.5, m = 84.4-82.8	
Endeavour Ridge	plag p, m	O	An 79.8-75.2, m = 72.4-60.7	Most plag stradle the Drake equilibrium line. Plag microcrysts are variable in composition, some are very albitic and approach the lower limits of the equilibrium envelope. Ol are restricted in composition and are equilibrium phases.
8601-02/04/05	ol m		Fo m = 86.5-84.2	
North	plag M > p, m	N	An 92.0-79.8, m = 81.3	Large plag megacrysts are very out of equilibrium. Ol megacrysts and phenocrysts are also out of equilibrium. Cpx are in equilibrium.
Symmetrical Ridge	M > p, m	N	Fo 84.4-83.0, m = 78.2	
TT040/15/17	cpx p, m	N	En 43.47-51.07	

[a] plag, plagioclase; ol, olivine; cpx, clinopyroxene; sp, spinel; M, megacrysts; p, phenocryst; m, microcryst.
[b] N, normal; R, reverse; O, oscillatory.
[c] compositions from Tables 7, 8, 9, and 10. Cr # = Cr/(Cr+Al), Mg # = Mg/(Mg+Fe).

TABLE 7. Plagioclase Microprobe Analyses

	8706-05									8706-07					
	Core p	z p	Rim p	m	Core p	z p	Rim p	p	p	Core p	z p	z p	z p	Rim p	Core M
SiO_2	48.65	51.65	51.18	50.83	50.01	47.49	50.92	52.13	50.70	48.31	50.53	50.56	51.00	51.53	52.01
TiO_2	0.00	0.00	0.00	0.03	0.00	0.03	0.00	0.00	0.07	0.00	0.01	0.00	0.12	0.12	0.12
Al_2O_3	31.60	29.46	29.34	30.38	30.72	32.40	30.14	29.88	30.05	32.45	29.71	29.34	30.31	29.59	29.64
FeO^T	0.46	0.61	0.77	0.58	0.48	0.54	0.49	0.76	0.63	0.50	0.49	0.49	0.61	0.74	0.65
MnO	0.00	0.00	0.00	0.00	0.00	0.00	0.00	0.00	0.00	0.02	0.00	0.00	0.00	0.00	0.03
MgO	0.22	0.22	0.23	0.26	0.17	0.13	0.17	0.24	0.21	0.17	0.22	0.21	0.22	0.22	0.16
CaO	16.95	13.95	14.22	14.65	15.39	17.05	14.47	13.9	14.67	16.54	14.88	14.65	14.62	13.74	13.55
Na_2O	2.42	3.89	3.86	3.39	3.23	2.25	3.56	3.70	3.49	2.34	3.34	3.56	3.35	3.65	4.16
K_2O	0.00	0.00	0.00	0.00	0.00	0.00	0.00	0.00	0.00	0.00	0.00	0.00	0.03	0.00	0.08
Total	100.30	99.78	99.60	100.12	100.00	99.89	99.75	100.61	99.82	100.33	99.18	98.81	100.26	99.59	100.40
An%	79.5	66.5	67.1	70.5	72.5	80.7	69.2	67.5	69.9	79.6	71.1	69.5	70.7	67.5	64.3

	8706-07			8803-03						8711-02		
	z M	z M	m	Core M	Rim M	Core M	zM	Rim M	m	Core M	z M	Rim M
SiO_2	49.93	51.13	51.93	46.15	47.14	45.86	45.94	48.07	52.85	45.78	47.13	46.17
TiO_2	0.13	0.13	0.13	0.00	0.00	0.00	0.02	0.02	0.09	0.00	0.00	0.00
Al_2O_3	30.40	29.57	29.36	32.98	32.64	34.09	33.71	32.69	29.26	33.98	32.60	33.84
FeO^T	0.68	0.75	0.79	0.45	0.48	0.38	0.39	0.54	0.70	0.37	0.38	0.41
MnO	0.03	0.03	0.00	0.00	0.00	0.00	0.00	0.00	0.00	0.00	0.00	0.00
MgO	0.22	0.19	0.20	0.19	0.19	0.19	0.19	0.22	0.24	0.22	0.25	0.19
CaO	14.18	14.35	13.95	17.68	17.37	18.05	17.71	16.72	12.89	18.66	17.84	18.26
Na_2O	3.53	3.47	3.73	1.69	2.05	1.33	1.51	2.40	4.27	1.32	1.79	1.51
K_2O	0.05	0.00	0.03	0.00	0.00	0.00	0.00	0.00	0.00	0.00	0.00	0.00
Total	99.15	99.62	100.12	99.14	99.87	99.90	99.47	100.66	100.30	100.33	99.99	100.38
An%	68.9	69.6	67.4	85.3	82.4	88.2	86.6	79.4	62.5	88.7	84.6	87.0

	8712-05			8712-06											
	Core M	z M	z M	z M	Rim M	Core M	z M	z M	Rim M	Core M	z M	z M	z M	z M	Rim M	m
SiO_2	45.92	46.35	45.88	46.22	46.21	45.96	44.96	45.20	45.80	45.17	45.94	46.16	46.19	45.56	45.62	50.39
TiO_2	0.06	0.07	0.03	0.04	0.06	0.00	0.00	0.00	0.00	0.00	0.02	0.00	0.00	0.00	0.00	0.06
Al_2O_3	34.12	33.84	34.05	33.97	34.09	33.77	34.23	34.38	34.01	33.71	33.55	33.98	33.63	33.67	33.74	30.82
FeO^T	0.40	0.39	0.39	0.44	0.46	0.38	0.39	0.33	0.44	0.37	0.34	0.38	0.32	0.41	0.46	0.77
MnO	0.03	0.03	0.02	0.05	0.02	0.00	0.00	0.00	0.02	0.02	0.00	0.00	0.00	0.03	0.00	0.00
MgO	0.26	0.25	0.26	0.24	0.22	0.18	0.18	0.16	0.18	0.19	0.21	0.22	0.18	0.19	0.18	0.26
CaO	18.80	18.43	18.20	18.54	18.43	18.86	18.92	19.01	18.71	18.33	18.69	18.15	18.67	18.66	18.73	15.59
Na_2O	1.12	1.33	1.29	1.28	1.22	1.17	1.24	0.15	1.37	1.21	1.30	1.22	1.37	1.33	1.23	3.00
K_2O	0.00	0.00	0.02	0.01	0.01	0.00	0.00	0.00	0.00	0.00	0.00	0.00	0.00	0.00	0.00	0.00
Total	100.71	100.69	100.14	100.79	100.72	100.32	99.92	99.23	100.53	99.00	100.05	100.11	100.36	99.85	99.96	100.89
An%	90.3	88.4	88.6	88.9	89.3	89.9	89.4	98.6	88.3	89.3	88.8	89.2	88.3	88.6	89.4	74.2

	7123-3-A			7123-1-C						7016-2-19					
	Core p	Rim p	ml	ml	Core M	Rim M	Core p	z p	Rim p	Core M	z M	z M	Rim M	Core M	z M	Rim M
SiO_2	48.95	48.47	48.06	51.24	50.43	49.74	50.62	50.93	51.60	45.28	45.72	45.70	48.41	45.91	45.39	46.20
TiO_2	0.07	0.05	0.08	0.09	0.07	0.05	0.05	0.08	0.09	0.05	0.06	0.06	0.06	0.03	0.00	0.02
Al_2O_3	30.02	31.34	30.96	29.88	30.18	30.83	29.73	29.69	28.75	33.46	33.82	33.62	31.39	33.61	33.79	33.42
FeO^T	0.51	0.56	0.50	0.66	0.52	0.57	0.60	0.64	0.91	0.50	0.38	0.38	0.80	0.31	0.24	0.41
MnO	0.13	0.15	0.16	0.11	0.07	0.06	0.11	0.12	0.11	0.20	0.19	0.13	0.17	0.00	0.00	0.00
MgO	0.22	0.20	0.23	0.23	0.20	0.23	0.19	0.19	0.29	0.16	0.18	0.19	0.40	0.25	0.22	0.22
CaO	15.77	15.97	16.85	14.69	15.24	15.58	14.64	14.77	13.95	18.69	18.77	18.44	16.03	18.50	19.54	18.58
Na_2O	2.88	2.82	2.35	3.52	3.34	3.03	3.63	3.48	4.06	1.12	1.24	1.31	2.75	1.52	1.21	1.75
K_2O	0.00	0.00	0.00	0.00	0.00	0.00	0.00	0.00	0.00	0.00	0.00	0.00	0.00	0.00	0.00	0.00
Total	98.55	99.56	99.19	100.42	100.05	100.09	99.57	99.90	99.76	99.46	100.36	99.83	100.01	100.13	100.39	100.60
An%	75.2	75.8	79.8	69.8	71.6	74.0	69.0	70.1	65.5	90.2	89.3	88.6	76.3	87.1	89.9	85.4

	7115-5-A											8601-04			
	Core M	z M	z M	z M	Core M	z M	z M	Rim M	m	ml	ml	ml	ml	ml	ml
SiO_2	47.38	46.99	48.39	48.95	47.01	47.29	46.51	48.02	50.85	50.56	51.52	54.45	51.74	50.53	50.72
TiO_2	0.01	0.04	0.02	0.04	0.00	0.01	0.03	0.02	0.00	0.11	0.08	0.06	0.06	0.00	0.15
Al_2O_3	32.72	32.80	31.11	31.04	33.09	32.94	32.74	32.21	30.01	28.90	29.58	26.96	29.71	30.46	30.37
FeO^T	0.34	0.33	0.43	0.50	0.45	0.48	0.45	0.48	0.57	0.79	0.72	1.08	0.85	0.65	0.75
MnO	0.02	0.07	0.00	0.06	0.08	0.11	0.00	0.08	0.09	0.07	0.08	0.00	0.01	0.01	0.04
MgO	0.16	0.14	0.20	0.20	0.11	0.13	0.12	0.13	0.23	0.34	0.31	0.38	0.31	0.24	0.25

TABLE 7. (continued)

	7115-5-A											8601-04			
	Core M	z M	z M	z M	Core M	z M	z M	Rim M	m	ml	ml	ml	ml	ml	ml
CaO	17.68	18.04	16.92	16.30	17.82	17.85	18.20	17.25	14.93	13.82	14.73	12.98	14.09	15.20	14.67
Na_2O	2.03	1.89	2.56	2.87	1.69	1.68	1.54	2.18	3.12	3.89	3.60	4.65	3.85	3.20	3.27
K_2O	0.00	0.00	0.00	0.00	0.00	0.00	0.00	0.00	0.00	0.00	0.00	0.00	0.00	0.00	0.03
Total	100.34	100.30	99.63	99.96	100.25	100.49	99.59	100.37	99.80	98.48	100.62	100.56	100.62	100.29	100.25
An%	82.8	84.1	78.5	75.8	85.4	85.4	86.7	81.4	72.6	66.3	69.3	60.7	66.9	72.4	71.3

	8601-05					TT040/17				
	Core p	z p	z p	Rim p	ml	Core M	z M	z M	Rim M	m
SiO_2	48.94	49.19	49.28	48.43	52.02	45.43	46.91	48.49	48.78	48.19
TiO_2	0.12	0.07	0.11	0.11	0.15	0.05	0.07	0.05	0.05	0.06
Al_2O_3	31.23	31.82	31.28	31.88	29.23	34.32	32.72	31.89	31.72	32.51
FeO^T	0.54	0.52	0.45	0.60	0.78	0.36	0.55	0.52	0.62	0.68
MnO	0.00	0.05	0.04	0.00	0.03	0.01	0.00	0.03	0.00	0.05
MgO	0.19	0.16	0.17	0.21	0.31	0.24	0.28	0.31	0.24	0.30
CaO	16.23	16.14	14.96	16.79	14.06	19.10	17.61	16.38	16.47	16.89
Na_2O	2.40	2.54	2.73	2.35	3.74	0.92	1.59	2.25	2.30	2.14
K_2O	0.03	0.01	0.02	0.01	0.06	0.02	0.01	0.00	0.01	0.00
Total	99.68	100.50	99.04	100.38	100.38	100.43	99.73	99.92	100.18	100.82
An%	78.9	77.8	75.2	79.8	67.5	92.0	86.0	80.1	79.8	81.3

M, megacryst; p, phenocryst; m, microphenocryst; z, zone between core and rim.

similar to microphenocryst compositions (Fo 82.8 to 83.0), and equilibrium phases (Figure 4*a*). Clinopyroxene is an important phase in sample 7123-1-B where is occurs as anhedral to subhedral phenocrysts and as groundmass granules (Table 5).

Middle Ridge (7016-2). Plagioclase megacrysts have very anorthitic core and mantle regions (An 90.2 to 87.1) with more albite-rich rims (An 85.4 to 76.3) (Figure 2*b*). Most are disequilibrium compositions (Figure 3).

Olivine phenocrysts range from Fo 86.5 to 86.3, similar to the microphenocryst compositions (Fo 86.3), and both are equilibrium phases (Figure 4*a*). Sample 7016-2-19 contains trace amounts of spinel (Table 5) which are similar in composition to the West Valley south and West Valley wall magnesiochromites (Table 10).

Sovanco Fracture Zone (7123-7). Olivine is the only phenocryst phase in these rocks (Table 5). The phenocrysts are unzoned (Fo 88.1) and more Fo-rich than the microphenocrysts (Fo 86.5). Both are equilibrium phases (Figure 4*a*).

Sovanco Fracture Zone (7115-5). Plagioclase megacrysts are commonly in complex glomerocrysts and are host to numerous glass inclusions. A glass inclusion from a megacryst in sample 7115-5-A is more mafic than the host glass (inclusion Mg # 64). The megacrysts exhibit normal or oscillatory zonation but core compositions are more anorthitic (An 89.0 to 82.8) than rims (An 81.4 to 66.8) (Figure 2*c*). In both samples, one of the rim compositions approaches the co-existing microphenocryst compositions (An 72.6 to 66.0) (Figure 2*c*). The megacrysts plot above the *Drake* [1976] equilibrium line, whereas the microphenocrysts extend from equilibrium to more albitic compositions (Figure 3).

The olivine phenocryst from sample 7115-5-A is very slightly zoned and too forsteritic (Fo 86.2 to 86.0) for the host glass. The megacryst from 7115-5-C is not zoned (Fo 85.5). The microphenocrysts are less forsteritic (Fo 82.8 to 84.4) and approach equilibrium (Figure 4*a*).

Endeavour Ridge. The plagioclase phenocryst from sample 8601-05 exhibits oscillating zonation, with a progressive decrease in anorthite content outward from the core (An 78.9 to 75.2) but increase at the rim (An 79.8) (Figure 2*c*). Microphenocrysts range from An 72.4 to An 60.7. The phenocryst plots slightly above the *Drake* [1976] equilibrium line but well within the error envelope, whereas the microphenocrysts are equilibrium to more albitic compositions, plotting outside the error envelope (Figure 3).

Olivine shows small variation in forsterite content (Fo 86.5 to 84.2), with all crystals being close to equilibrium compositions (Figure 4*a*).

Northern Symmetrical Ridge. A plagioclase megacryst from Juan de Fuca Ridge sample TT040/17 has a very large core with the highest anorthite content analyzed in this study (An 92.0). The rim shows very fine zones (An 80.1 to 79.8), the outermost of which has a rim composition similar to the coexisting microphenocryst (An 81.3) (Figure 2*c*). The core is well out of equilibrium with the host melt. The rim and microphenocryst compositions also plot above the *Drake* [1976] equilibrium line but well within the error envelope (Figure 3). The olivine megacryst from TT040/17 is normally zoned (Fo 84.4 to 83.0), and both the core and rim compositions are out of equilibrium with the host glass (Figure 4*a*). Sample TT040/15 contains olivine microphenocrysts (Fo 78.2) which are equilibrium phases (Figure 4*a*).

Clinopyroxene is a rare phenocryst and microlite phase in sample TT040/17. The phenocrysts are endiopsides and are in equilibrium with the host glass (Figure 4*b*).

Geothermometry

Crystallization temperatures were calculated using olivine-glass [*Roeder and Emslie*, 1970; *Bender et al.*, 1978; *Glazner*, 1984] and plagioclase-glass [*Glazner*, 1984] geothermometers (Figure 5). In calculating crystallization temperatures, olivine and plagioclase microphenocryst compositions were used or, where not available, the rim compositions of phenocrysts were used.

Crystallization temperatures systematically decrease with decreasing Mg # (the rocks range from Mg # 68 to 52 and temperatures from 1250° to 1175°C). Exceptions are some of the temperatures calculated using the plagioclase geothermometer in which case the crystal used may not be in equilibrium due to variations in cooling rate and/or pressure differences [*Stakes et al.*, 1984]. There is a systematic

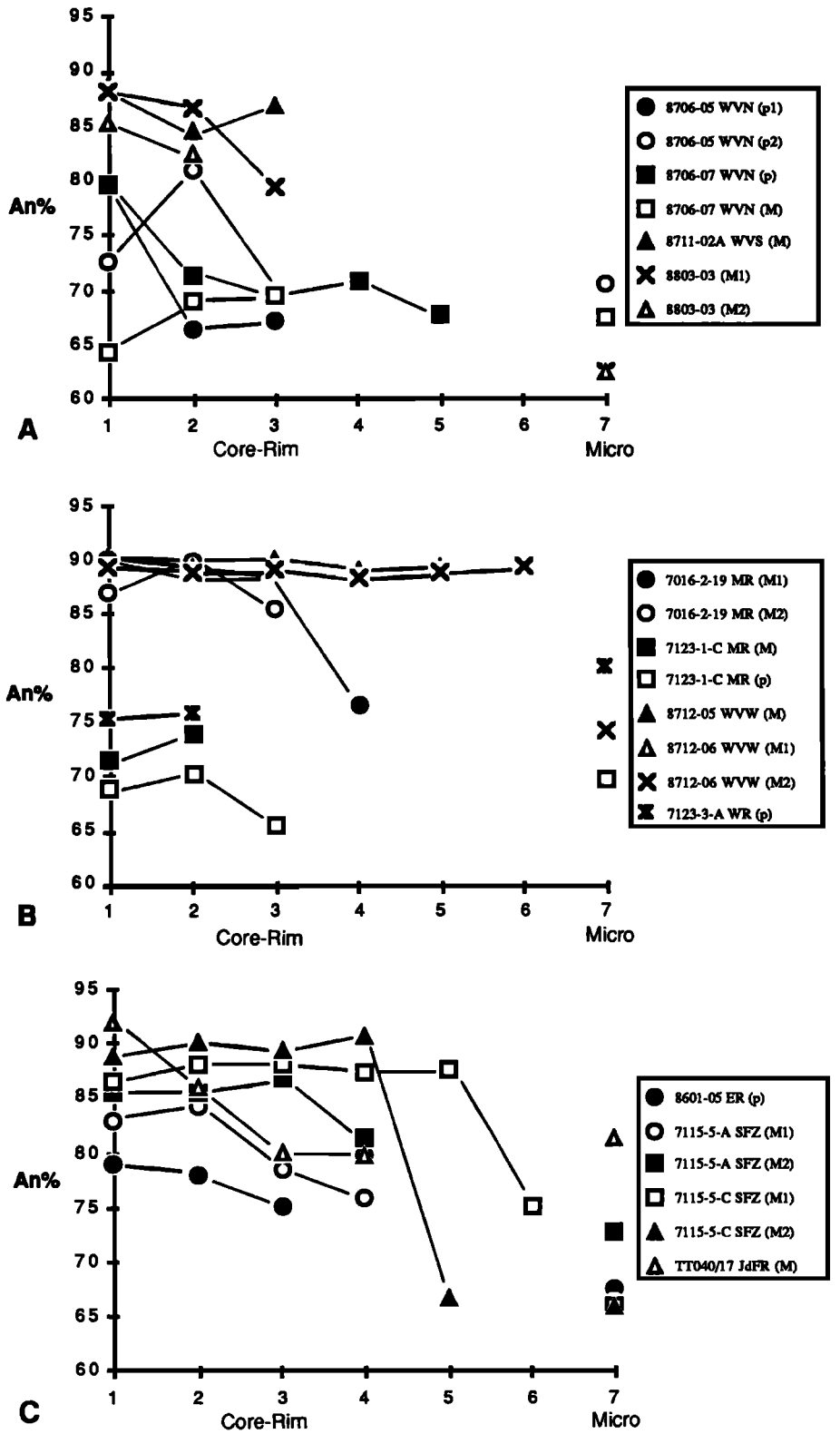

Fig. 2. Core to rim variation in anorthite compositions of plagioclase megacrysts and phenocrysts. At the right are the compositions of the coexisting microphenocrysts. (*a*) West Valley, (*b*) West Valley wall, West Ridge, and Middle Ridge, and (*c*) Endeavour Ridge, Sovanco Fracture Zone, and Northern Symmetrical Ridge. Location abbreviations are as in Table 1. Data are from Table 7.

difference in calculated temperatures using the olivine geothermometers such that for any one sample, T[*Roeder and Emslie*, 1970) > T[*Bender et al.*, 1978] > T[*Glazner*, 1984]. This difference is a result of differences in the partition coefficients of Fe and Mg between the olivine and the liquid used in the temperature calculations.

At low pressure, up to 8.5 kbar [*Bender et al.*, 1978], the general crystallization sequence is ol, ol + pl, ol + pl + cpx with decreasing temperature and increasing fractionation. The calculated temperatures and observed phases in the rocks generally fit this crystallization sequence. The olivine basalts from Sovanco Fracture Zone (7123-7)

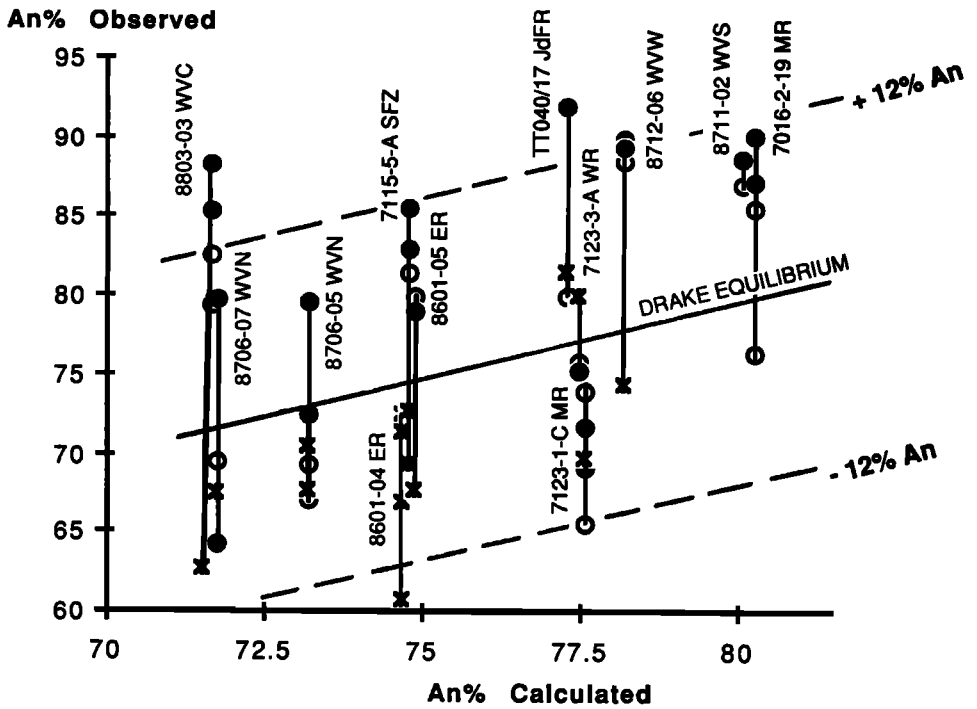

Fig. 3. Diagram of the measured anorthite (An) content of plagioclase cores (solid circle), rims (open circle), and microphenocrysts (asterisk) plotted against the calculated anorthite content using the method of *Drake* [1976]. The solid line is the equilibrium composition. The method has an error of ±12% An. Note the disequilibrium of the core compositions. Location abbreviations are as in Table 1. Data are from Table 7.

and the picrite from West Ridge (7123-3-A) have the highest calculated temperatures. The lowest calculated temperatures are for the more evolved clinopyroxene-bearing rocks.

Major Element Geochemistry

Glass analyses of the rocks range from very primitive lavas with Mg # up to 68.0 in the West Valley south and West Ridge areas to evolved ferrobasalts with glass Mg # as low as 52.2 at West Valley central, West Valley north and Northern Symmetrical Ridge (Table 2 and Figure 6). The rocks from the present axis of West Valley (WVn, WVc, WVs) span the range of Mg # (Table 2). All glasses analyzed are hypersthene and olivine normative with the exception of Endeavour Ridge sample 8601-05, which is slightly hypersthene normative. Whole rock Mg # ranges up to 74.1 at West Ridge, as a result of olivine accumulation. Whole rock analyses are also hypersthene and olivine normative, but some of the evolved samples from Middle Ridge, West Valley north, and the Northern Symmetrical Ridge are quartz normative.

Most of the major elements show good correlation with Mg # with the exception of the plagioclase-phyric whole rock samples, which are enriched in CaO and Al_2O_3 and depleted in the other elements (Figure 6). TiO_2, FeO, and to a lesser extent K_2O show good negative correlations with Mg #, whereas CaO and Al_2O_3 show good positive correlations with Mg # (Figure 6). The glass analyses for the rocks from the axis of West Valley (WVn, WVc, WVs) form a trend that approximates a liquid line of descent, as represented by the solid line in Figure 6. The glass analyses for the West Ridge rocks are more depleted in TiO_2 and K_2O and more enriched in Na_2O for the same Mg # than the West Valley rocks. The rocks from Middle Ridge, Sovanco Fracture Zone and Northern Symmetrical Ridge also tend to be more depleted TiO_2 and K_2O compared to the West Valley trend. The West Valley wall rocks are slightly enriched in TiO_2 and FeO compared to the West Valley rocks and the Endeavour Ridge rocks are enriched in TiO_2, Al_2O_3, Na_2O, and K_2O but depleted in CaO and FeO. Within dredge samples from West Valley north and Endeavour Ridge do not fall on a single line of liquid descent (Figure 6).

Trace Element Geochemistry

Mid-ocean ridge basalts (MORB) are generally classified on the basis of Zr/Y or La/Sm ratios as N-type, T-type and E-type [e.g., *Le Roex et al.*, 1983; *Karsten et al.*, 1990; *Michael et al.*, 1989]. However, the La/Ce ratio is less affected by partial melting processes and is a better indicator of source enrichment [*Langmuir et al.*, 1977; *Basaltic Volcanism Study Project*, 1981]. The rocks studied range from N-type MORB ($[La/Ce]_n < 0.9$) through T-type MORB ($[La/Ce]_n = 0.9$-1.0) to E-type MORB ($[La/Ce]_n > 1.0$) (Table 4 and Figures 7 and 8).

Rocks from the axis of West Valley (WVn, WVc, WVs) are transitional to enriched in LREE ($[La/Ce]_n = 0.89$-1.06, $[La/Sm]_n = 0.63$-1.27, $Zr/Y = 2.57$-3.90) (Figures 8 and 9) with REE abundances ranging from 10.8 to 28.2 times chondrite (Figure 7). Endeavour Ridge shows the same transitional to enriched characteristic ($[La/Ce]_n = 0.88$-1.06, $[La/Sm]_n = 0.72$-1.48, $Zr/Y = 3.26$-5.32) (Figures 8 and 9) and REE abundances from 10.6 to 23.8 times chondrite. The rocks from the Endeavour Ridge are similar in composition to other samples recovered from the present axis of the Endeavour Ridge [*Liias*, 1986; *Karsten et al.*, 1990] (Figure 13). Rocks from West Valley wall, Middle Ridge, and Sovanco Fracture Zone are LREE depleted ($[La/Ce]_n = 0.76$-0.86, $[La/Sm]_n = 0.48$-0.65, $Zr/Y = 2.32$-5.05) (Figures 8 and 9) and REE abundances from 3.8 to 16.8 times chondrite (Figure 7). The most depleted samples are clearly from West Ridge ($[La/Ce]_n = 0.62$, $[La/Sm]_n = 0.25$-0.27, $Zr/Y = 2.00$-2.27) (Figures 8 and 9) with REE abundances 2.3 to 11.1 times chondrite (Figure 7). The lavas from West Ridge may be considered as D-type lavas similar to some off-axis seamounts [e.g., *Barone and Ryan*, 1990]. The rocks from the Northern Symmetrical Ridge are also depleted in LREE ($[La/Ce]_n = 0.85$-0.88, $[La/Sm]_n = 0.60$-0.67, $Zr/Y = 2.82$-3.23) (Figures 8 and 9) with

TABLE 8. Olivine Microprobe Analyses

	8706-05				8706-07						
	m	Core p	Rim p	m	m	m	m	Core M	Rim M	Core p	Rim p
SiO_2	39.10	39.66	39.07	38.75	39.58	39.61	39.57	39.72	38.97	39.52	39.46
TiO_2	0.00	0.03	0.06	0.05	0.05	0.05	0.02	0.00	0.00	0.05	0.05
Al_2O_3	0.00	0.04	0.01	0.03	0.02	0.01	0.02	0.03	0.00	0.03	0.00
Cr_2O_3	0.04	0.00	0.03	0.02	0.05	0.00	0.02	0.02	0.00	0.06	0.05
FeO^T	17.80	15.57	18.26	20.04	16.38	17.42	15.66	16.98	17.62	14.97	18.30
NiO	0.15	0.15	0.00	0.11	0.15	0.14	0.06	0.15	0.16	0.12	0.07
MnO	0.22	0.00	0.00	0.22	0.32	0.30	0.24	0.19	0.24	0.13	0.11
MgO	43.00	44.58	41.31	39.30	43.75	42.88	44.23	42.48	42.65	43.53	41.87
CaO	0.27	0.32	0.34	0.27	0.32	0.33	0.31	0.29	0.30	0.30	0.42
Total	100.58	100.35	99.08	98.79	100.62	100.74	100.13	99.86	99.94	98.71	100.33
Fo	81.2	83.6	80.1	77.8	82.6	81.4	83.4	81.7	81.2	83.8	80.3

	8803-01							8803-03						
	Core m1	Rim m2	Rim m2	Core M	Rim M	Core p	Rim p	Core p	Rim p	Core p	Rim p	m	Core p	Rim p
SiO_2	38.53	38.51	38.42	38.66	38.81	39.88	39.59	40.15	39.70	39.63	39.72	39.52	39.32	39.00
TiO_2	0.07	0.05	0.08	0.03	0.03	0.04	0.04	0.03	0.05	0.01	0.03	0.01	0.04	0.08
Al_2O_3	0.05	0.03	0.05	0.13	0.11	0.03	0.00	0.08	0.04	0.01	0.06	0.08	0.12	0.00
Cr_2O_3	0.00	0.04	0.05	0.04	0.05	0.00	0.00	0.08	0.01	0.01	0.04	0.01	0.00	0.00
FeO^T	18.40	18.85	18.32	16.77	18.19	12.77	14.80	14.15	18.08	17.73	18.87	18.75	18.30	18.84
NiO	0.00	0.00	0.18	0.00	0.00	0.27	0.17	0.11	0.09	0.07	0.03	0.19	0.00	0.07
MnO	0.37	0.36	0.31	0.28	0.30	0.25	0.25	0.33	0.15	0.25	0.20	0.23	0.39	0.30
MgO	41.26	41.37	41.45	42.32	42.32	46.64	45.57	45.22	42.27	42.22	42.30	41.98	42.29	40.63
CaO	0.26	0.29	0.27	0.29	0.25	0.29	0.30	0.30	0.28	0.32	0.32	0.33	0.28	0.28
Total	98.94	99.50	99.13	98.52	100.06	100.17	100.72	100.45	100.67	100.25	101.57	101.10	100.74	99.20
Fo	80.0	79.6	80.1	81.8	80.6	86.7	84.6	85.1	80.6	80.9	80.0	80.0	80.5	79.4

	8711-02			8712-06			7123-3-A			7123-1-C				
	p	p	p	Core M	Rim M	m	Core M	Rim M	ml	m	ml	Core p	Rim p	Rim p
SiO_2	40.34	40.37	40.07	40.13	40.11	39.89	40.39	40.24	40.09	39.50	39.29	39.24	39.37	38.99
TiO_2	0.00	0.00	0.00	0.00	0.00	0.00	0.03	0.00	0.01	0.05	0.03	0.00	0.02	0.03
Al_2O_3	0.01	0.02	0.05	0.00	0.00	0.03	0.06	0.03	0.05	0.06	0.05	0.11	0.03	0.02
Cr_2O_3	0.00	0.04	0.03	0.02	0.03	0.04	0.02	0.03	0.04	0.06	0.04	0.05	0.06	0.03
FeO^T	11.48	11.81	12.08	10.65	11.76	14.90	10.67	11.45	11.71	16.23	15.95	16.16	16.05	16.13
NiO	0.16	0.11	0.20	0.24	0.28	0.24	0.22	0.19	0.12	0.08	0.04	0.14	0.17	0.19
MnO	0.10	0.17	0.11	0.16	0.00	0.19	0.18	0.21	0.18	0.35	0.38	0.37	0.33	0.32
MgO	46.70	47.18	47.36	48.22	47.15	44.86	48.53	46.81	47.45	43.84	43.82	43.66	44.20	44.20
CaO	0.30	0.31	0.29	0.27	0.28	0.27	0.31	0.33	0.38	0.35	0.35	0.30	0.31	0.31
Total	99.09	100.01	100.19	99.69	99.61	100.42	100.41	99.29	100.03	100.52	99.95	100.03	100.54	100.22
Fo	87.9	87.7	87.5	89.0	87.7	84.3	89.0	87.9	87.8	82.8	83.0	82.8	83.1	83.0

	7016-2-19			7123-7-2		7123-7-124	7115-5-A			7115-5-C			
	Core M	Rim M	m	Core p	Rim p	m	Core p	Rim p	ml	ml	ml	Core p	Rim p
SiO_2	40.06	39.59	39.48	39.97	40.14	39.42	40.20	39.76	39.27	39.90	39.27	39.89	39.71
TiO_2	0.00	0.00	0.00	0.01	0.00	0.08	0.05	0.01	0.01	0.06	0.04	0.06	0.01
Al_2O_3	0.05	0.04	0.05	0.06	0.04	0.39	0.06	0.01	0.03	0.06	0.03	0.01	0.06
Cr_2O_3	0.00	0.02	0.04	0.05	0.08	0.00	0.08	0.05	0.07	0.06	0.05	0.05	0.05
FeO^T	12.97	13.09	13.04	11.52	11.56	12.87	13.19	13.42	14.86	14.83	16.20	13.88	13.72
NiO	0.05	0.12	0.09	0.31	0.26	0.34	0.18	0.16	0.17	0.12	0.16	0.13	0.08
MnO	0.28	0.21	0.21	0.29	0.26	0.00	0.36	0.31	0.28	0.26	0.27	0.28	0.29
MgO	46.69	46.19	46.16	47.95	47.90	46.15	46.19	46.27	44.80	44.97	43.80	45.94	45.40
CaO	0.29	0.34	0.33	0.26	0.32	0.52	0.35	0.31	0.32	0.32	0.40	0.31	0.36
Total	100.39	99.60	99.40	100.42	100.56	99.77	100.66	100.30	99.84	100.58	100.22	100.55	99.68
Fo	86.5	86.3	86.3	88.1	88.1	86.5	86.2	86.0	84.3	84.4	82.8	85.5	85.5

	8601-02		8601-04			8601-05			TT040/15	TT040/17		
	m	gl m	m	m	m	ml	m	m	m	Core p	Rim p	Rim p
SiO_2	39.72	39.42	39.88	40.03	39.99	39.23	39.85	39.94	38.36	39.50	38.84	38.93
TiO_2	0.10	0.08	0.00	0.04	0.03	0.00	0.00	0.01	0.09	0.06	0.04	0.05
Al_2O_3	0.04	0.04	0.00	0.06	0.00	0.03	1.67	0.00	0.00	0.02	0.00	0.02
Cr_2O_3	0.00	0.00	0.04	0.00	0.05	0.05	0.05	0.04	0.00	0.00	0.00	0.00
FeO^T	13.52	13.73	14.02	14.82	14.70	13.22	13.33	12.97	21.00	14.96	16.43	15.28
NiO	0.38	0.34	0.15	0.19	0.21	0.23	0.17	0.22	0.34	0.40	0.44	0.39
MnO	0.00	0.00	0.18	0.00	0.13	0.19	0.12	0.17	0.00	0.00	0.00	0.00
MgO	46.87	46.68	45.26	44.31	44.64	46.34	43.39	46.61	42.14	45.46	44.94	44.23
CaO	0.36	0.40	0.36	0.38	0.34	0.30	0.80	0.33	0.35	0.27	0.37	0.36
Total	100.99	100.69	99.89	99.83	100.09	99.59	99.38	100.29	102.28	100.67	101.06	99.26
Fo	86.1	85.8	85.2	84.2	84.4	86.2	85.3	86.5	78.2	84.4	83.0	83.8

M, megacryst; p, phenocryst; m, microphenocryst; gl, glomerocryst.

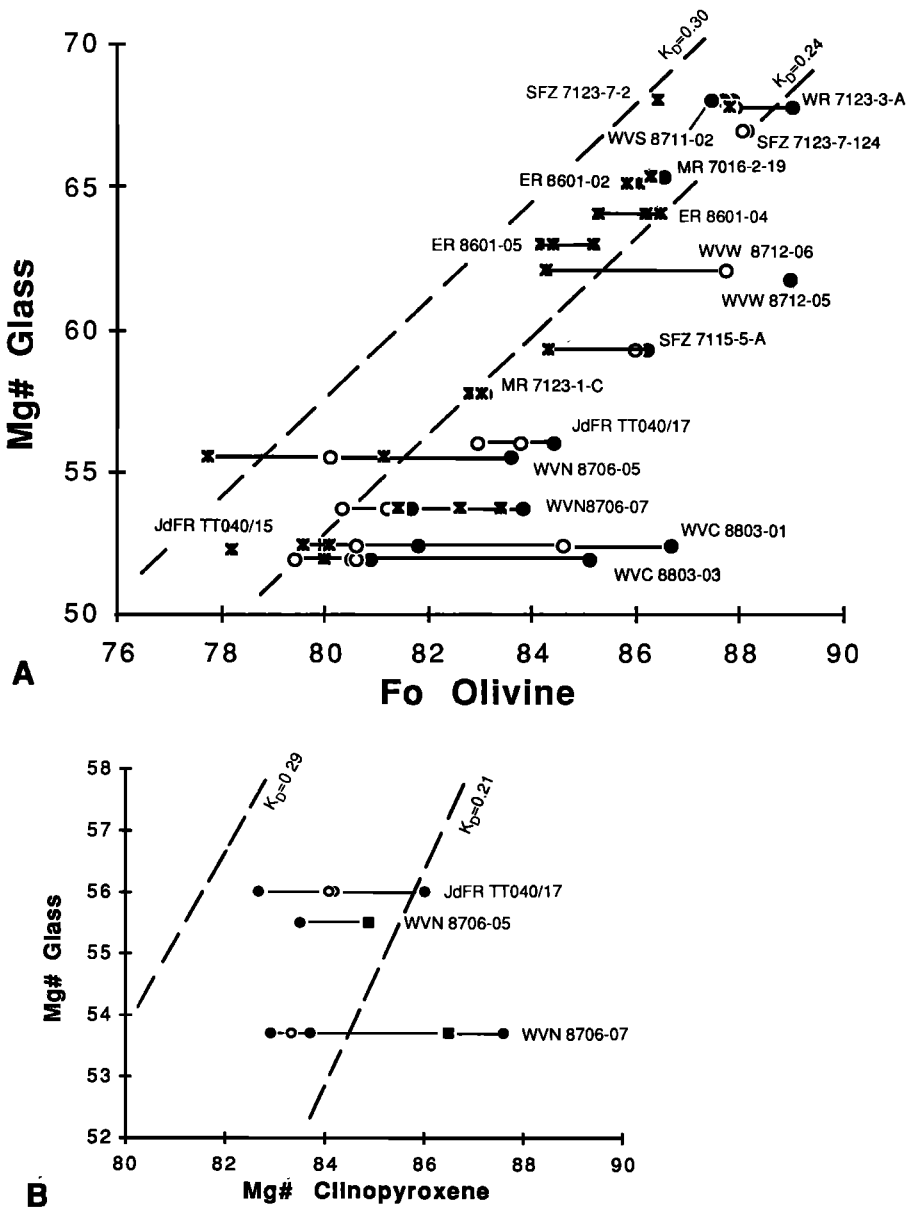

Fig. 4. (*a*) Plot of the Mg # of the host glass against forsterite (Fo) content of olivine. Equilibrium lines indicate the partitioning of Fe and Mg between the glass and olivine assuming K_D = 0.24 - 0.30 [after *Stakes et al.*, 1984]. (*b*) Plot of Mg # glass against the Mg # of clinopyroxene phenocrysts. Equilibrium lines are drawn assuming K_D =0.21 - 0.30 [after *Stakes et al.*, 1984]. Solid circle, core compositions of phenocrysts and megacrysts; open circle, rim compositions; asterisk, microphenocryst compositions; solid square, glomerocrysts. Location abbreviations are as in Table 1. Data are from Tables 8 and 9.

REE abundances from 9.7 to 17.7 times chondrite (Figure 7). The samples from the Northern Symmetrical Ridge dredge haul are fairly typical of rocks previously recovered on the Northern Symmetrical Ridge south of the Cobb Offset [*Liias*, 1986] (Figure 13).

Discussion

Magma Mixing

Magma mixing is an integral part of magma chamber systematics beneath mid-ocean ridges [*Donaldson and Brown*, 1977; *Walker et al.*, 1979; *Rhodes et al.*, 1979; *Kuo and Kirkpatrick*, 1982; *Nabelek and Langmuir*, 1986; *Hummler and Whitechurch*, 1988]. Petrographic and mineralogical evidence indicates that magma mixing has occurred in all areas from which samples described here originated except on the Endeavour Segment, the West Ridge, and the Sovanco Fracture Zone (7123-7).

One of the main lines of evidence for magma mixing is the occurrence of disequilibrium phenocrysts and megacrysts. Most of the cores of plagioclase phenocrysts and megacrysts are more anorthitic than coexisting microphenocrysts. Calculation of equilibrium plagioclase compositions using the method of *Drake* [1976] suggests that in many cases, phenocrysts and megacrysts are out of equilibrium with the host glass (Figure 3). In addition, many of the samples host disequilibrium olivine phenocrysts and megacrysts, and for the more evolved rocks, there is wide variation in olivine forsterite content (Figure 4). These features are characteristic of the rocks from West Valley north, West Valley central, West Valley Wall, Sovanco Fracture Zone (7115-5), and Northern Symmetrical Ridge. The West Valley north rocks also host equilibrium and disequilibrium clinopyroxene.

Although the West Valley central rocks are evolved ferrobasalts and should be at the three phase cotectic (Figure 6), they do not contain

TABLE 9. Clinopyroxene Microprobe Analyses

	T1040/17				8706-05			8706-07			
	p	Core p1	Rim p1	Core p2	Rim p2	p	glomero p	p	glomero p	Core p	Rim p	Core m
SiO_2	51.73	52.20	51.96	51.65	52.85	52.75	51.04	52.53	50.49	50.60	50.38	51.26
TiO_2	0.36	0.55	0.48	0.81	0.47	0.54	0.93	0.48	0.74	0.98	0.89	0.72
Al_2O_3	1.98	2.54	2.33	1.80	2.18	1.79	4.18	2.28	3.95	3.76	3.84	3.45
Cr_2O_3	0.00	0.41	0.50	0.06	0.37	0.31	0.38	0.79	1.19	0.36	0.52	0.65
FeO*	5.84	6.93	6.18	10.17	6.77	7.21	5.96	5.14	4.97	6.38	6.30	6.39
NiO	0.27	0.00	0.00	0.00	0.00	0.08	0.00	0.00	0.02	0.00	0.01	0.00
MnO	0.00	0.20	0.23	0.29	0.24	0.19	0.13	0.09	0.11	0.23	0.30	0.25
MgO	18.11	16.69	16.61	15.15	18.04	18.41	16.88	18.31	16.06	15.65	15.91	16.57
CaO	19.58	19.70	19.97	19.47	18.99	18.55	20.40	20.24	21.49	20.79	20.86	19.52
Na_2O	0.24	0.30	0.28	0.38	0.25	0.22	0.27	0.30	0.30	0.33	0.33	0.31
Total	98.11	99.52	98.54	99.78	100.16	100.05	100.17	100.16	99.32	99.08	99.34	99.12
En	51.07	48.05	48.24	43.47	50.83	51.44	48.38	51.23	46.83	45.80	46.20	48.47

M, megacryst; p, phenocryst; m, microphenocryst; glomero; glomerocryst.

clinopyroxene. MORB can show chemical evidence for clinopyroxene fractionation but not contain clinopyroxene due either to magma mixing [*Stakes et al.*, 1984; *Christie and Sinton*, 1986; *Davis and Clague*, 1987] or to three-phase crystallization at lower portions of a magma chamber followed by a period of resorption [*Stakes et al.*, 1984]. The low CaO/Al_2O_3 ratios for the West Valley central rocks may indicate that prior to mixing these rocks were experiencing clinopyroxene fractionation. In addition, the rocks lie along the three phase cotectic in aluminium-iron (ALFE) space (Figure 10), suggesting clinopyroxene fractionation. Glass inclusions in plagioclase from the West Valley wall and Sovanco Fracture Zone (7115-5) rocks do not plot on the same olivine (+plagioclase) fractionation lines on the ALFE diagram as the host glasses and thus are not related by crystal fractionation (Figure 10).

The rocks from West Valley south and Middle Ridge host disequilibrium plagioclase megacrysts that are complexly zoned (Figures 2*a* and 3), although olivine phenocrysts from these rocks are restricted in composition and in equilibrium with the host melt. These features are consistent with magma mixing given that olivine reequilibrates rapidly compared to plagioclase [*Fisk et al.*, 1982].

Plagioclase which is more calcic than predicted by the *Drake* [1976] equation has been crystallized experimentally [*Walker et al.*, 1979], so the equilibrium line in Figure 3 may be incorrectly positioned [*Stakes et al.*, 1984]. If the equilibrium line were moved to a more anorthitic position, the plagioclase microphenocrysts would then be too albitic for the host melt. This can occur as a result of undercooling and variations in the rate of cooling [*Kuo and Kirkpatrick*, 1982; *Stakes et al.*, 1984]. However, the crystallization temperatures calculated using the plagioclase-glass geothermometer of *Glazner* [1984] were calculated using the microphenocryst compositions (i.e., the most albitic compositions), and for the most part, these temperatures are similar to the temperatures calculated using the *Glazner* [1984] olivine-glass geothermometer (Figure 5). In addition, there is a somewhat better correlation between microcryst compositions and glass compositions than between megacryst/phenocryst compositions and glass compositions (Figure 3). Both features suggest that the plagioclase microphenocrysts have not been significantly undercooled with respect to the olivine microphenocrysts and that many of the calcic plagioclase megacrysts formed in a hotter, more mafic melt than the host glass and are disequilibrium phases. Some variation in cooling rate is suggested by the plagioclase microphenocrysts from the Sovanco Fracture Zone sample 7115-5-A and the Endeavour Ridge samples 8601-04 and 8601-05 which show wide ranges in An content (Figure 3). The range in anorthite content for these microphenocrysts may represent crystal growth at different times during transport from a magma chamber to the seafloor [e.g., *Stakes et al.*, 1984, *Kuo and Kirkpatrick* , 1982]. Alternatively, if the magmas are mixed, the microphenocrysts may represent different populations of plagioclase.

Fractional Crystallization

The overall major element trends toward evolved compositions are produced by fractionation. However, the sample sites are too widely separated in space and time to be related by fractional crystallization from a single magma chamber. Even where the sites were closer together, the variations in trace and major elements do not support fractional crystallization as a major process controlling chemical trends (Figures 6 and 8). On a local scale, poor residuals are obtained by least squares modelling (not shown), even down to the scale of a single dredge haul (e.g., Endeavour Ridge; Figure 6). In addition, the lavas do not fall on a single liquid line of descent in ALFE space (Figure 10).

TABLE 10. Spinel Microprobe Analyses

	8711-02	8712-06	7123-3-A		7016-2-19
	WVS	WVW	WR1	WR2	MR
TiO_2	0.73	0.43	0.37	0.55	0.75
Al_2O_3	29.89	32.95	39.93	34.65	28.28
Cr_2O_3	34.54	34.42	26.88	30.47	35.27
FeO^T	17.60	16.28	13.67	17.01	19.9
NiO	0.00	NA	0.38	0.30	NA
MnO	0.49	0.38	0.38	0.36	0.43
MgO	16.28	16.96	18.08	16.56	15.33
CaO	0.28	0.05	0.03	0.21	0.09
Na_2O	0.13	0.08	0.08	0.08	0.06
K_2O	0.01	0.05	0.00	0.00	0.03
Total	99.95	101.60	99.80	100.19	100.14
$Mg/Mg+Fe^{2+}$	0.74	0.73	0.77	0.73	0.72
Cr/Cr+Al	0.44	0.41	0.31	0.37	0.46

WVS, West Valley South; WVW, West Valley Wall; WR, West Ridge; MR, Middle Ridge.

Mantle Heterogeneity

Previous studies of the mantle source region for MORB show that it is heterogeneous on a variety of scales [*Cousens et al.*, 1984; *Batiza and Vanko*, 1984; *Langmuir et al.*, 1986; *Macdougall and Lugmair*, 1986; *Holness and Richter*, 1989]. Variations in incompatible element ratios provide evidence of source heterogeneity (e.g., $[La/Ce]_n$, $[La/Sm]_n$, $[Ce/Yb]_n$, Zr/Y) [*Langmuir et al.*, 1978; *Basaltic Volcanism Study Project*, 1981]. The ratio $[La/Ce]_n$ is the most insensitive to various petrogenetic processes including partial melting and disequilibrium melting [*Basaltic Volcanism Study Project*, 1981)].

We have documented a wide variation in all of the incompatible element ratios (Figures 8, 9, 11 and 12) from the depleted West Ridge lava ($[La/Ce]_n$ = 0.62, $[La/Sm]_n$ = 0.25 and $[Ce/Yb]_n$ = 0.41) to the enriched West Valley central, West Valley south and Endeavour Ridge lavas ($[La/Ce]_n$ = 1.05-1.07, $[La/Sm]_n$ = 1.07 - 1.48, and $[Ce/Yb]_n$ = 1.20 - 1.96). These variations occur even in the spatially and temporally related rocks of West Valley north, West Valley central, West Valley south, West Valley Wall, and West Ridge. Even within a single dredge haul there are heterogeneities in the incompatible element ratios. The West Valley north rocks range from $[La/Ce]_n$ =

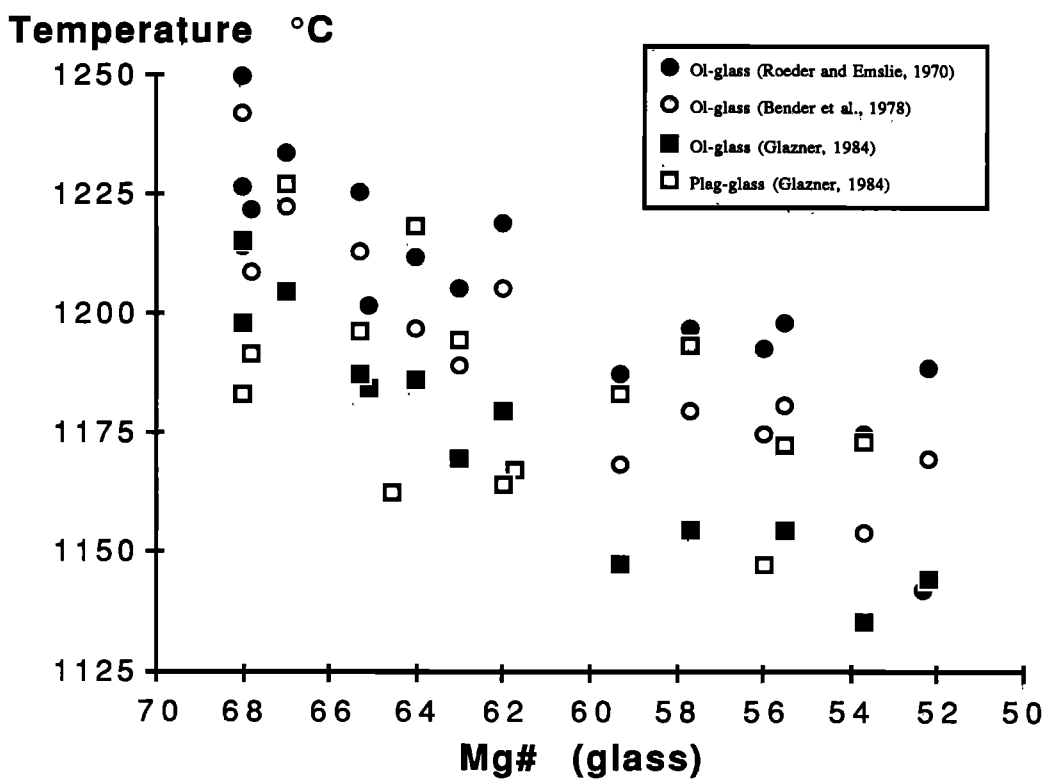

Fig. 5. Calculated crystallization temperatures plotted against Mg #. Solid circle is the olivine-glass geothermometer of *Roeder and Emslie* [1970]; open circle is the olivine-glass geothermometer of *Bender et al.* [1978]; squares are the olivine (solid) and plagioclase (open) geothermometers of *Glazner* [1984].

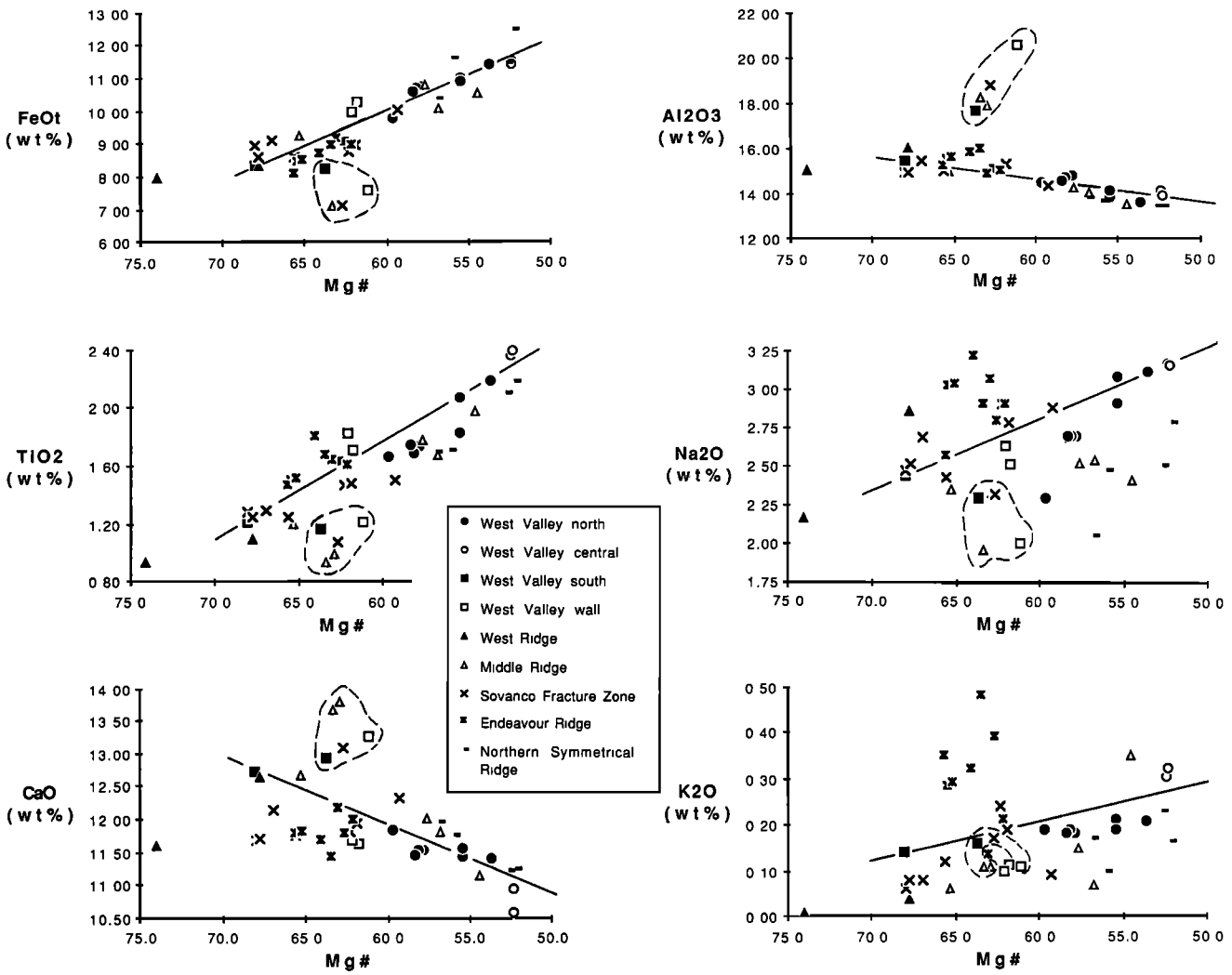

Fig. 6. Major element variation diagrams for both the glass and whole rock analyses plotted against Mg #. Dashed fields indicate highly plagioclase-phyric samples. Note also the very high Mg # (74) of the olivine-phyric West Ridge whole rock sample. Solid line indicates a West Valley trend based on glass samples. Data are from Tables 2 and 3.

0.89 to 0.98, $[La/Sm]_n$ = 0.63 to 0.85, $[Ce/Yb]_n$ = 0.77 to 0.95 and the Endeavour Ridge rocks vary from $[La/Ce]_n$ = 0.90 to 1.07, $[La/Sm]_n$ = 0.72 to 1.48, $[Ce/Yb]_n$ = 0.93 to 1.96 (Figures 8, 11 and 12). The large variation in the incompatible element ratios (Tables 3 and 4) is consistent with a heterogeneous mantle source on (1) a small scale, within sites (e.g., West Valley north, Endeavour Ridge) and (2) a larger scale, between sites (e.g., West Valley north, West Valley central, West Valley south, West Valley Wall, West Ridge).

The range in incompatible element ratios can be modelled by binary mixing of an enriched and depleted mantle source (Figure 11) [*Langmuir et al.*, 1977; *Hart*, 1988]. Such binary mixing was used to explain the range in incompatible element ratios for parts of the Mid-Atlantic Ridge [*Langmuir et al.*, 1977]. The samples of this study form a spectrum between an enriched source represented by the Endeavour Ridge 8601-05 samples and a highly depleted source represented by the West Ridge lava (Figure 11). The samples maintain the same relative positions in the companion plots, a requirement of the mixing model [*Langmuir et al.*, 1977].

Partial Melting

Partial melting was modelled as batch partial melting (equilibrium) because any disequilibrium that occurs during melting has the greatest influence on the residual and the first liquids, rather than the total melt fraction [*Prinzhofer et al.*, 1989]. An enriched and deleted spinel lherzolite and lherzolite were used in the modelling. It can be assumed that garnet was not a residual phase after partial melting of the source regions of the study lavas because of the low $[Ce/Yb]_n$ ratios (Table 4) [*Hanson*, 1980]. Similarly, the lack of Eu anomalies in the primitive lavas suggests that plagioclase was not an important residual phase [*Hanson*, 1980]. It is likely, therefore, that the lavas were derived from partial melting of mantle within the spinel stability field, as modelled in Figure 12.

Results of modelling show not only that the source is heterogeneous but also that variations in the amounts of partial melting within sites and between sites are required to produce the lavas. The West Ridge sample is highly depleted and is indicative of higher amounts of partial melting than the other samples (Figure 11). The enriched Endeavour Ridge sample (8601-05) was probably produced by much lower amounts of partial melting. The West Valley south and West Valley central lavas were derived from a mantle source similar to the Endeavour Ridge enriched (8601-05) lavas, based on the similar $[La/Ce]_n$ ratios (Table 4 and Figure 8*a*) but require higher amounts of partial melting to account for the other incompatible element ratios (Figure 8*b*). The lavas from the two Middle Ridge dredge hauls are from a similar source (Figure 8*a*) but were apparently produced by different amounts of partial melting (7123-1-A > 7016-2-A). Similarly, the

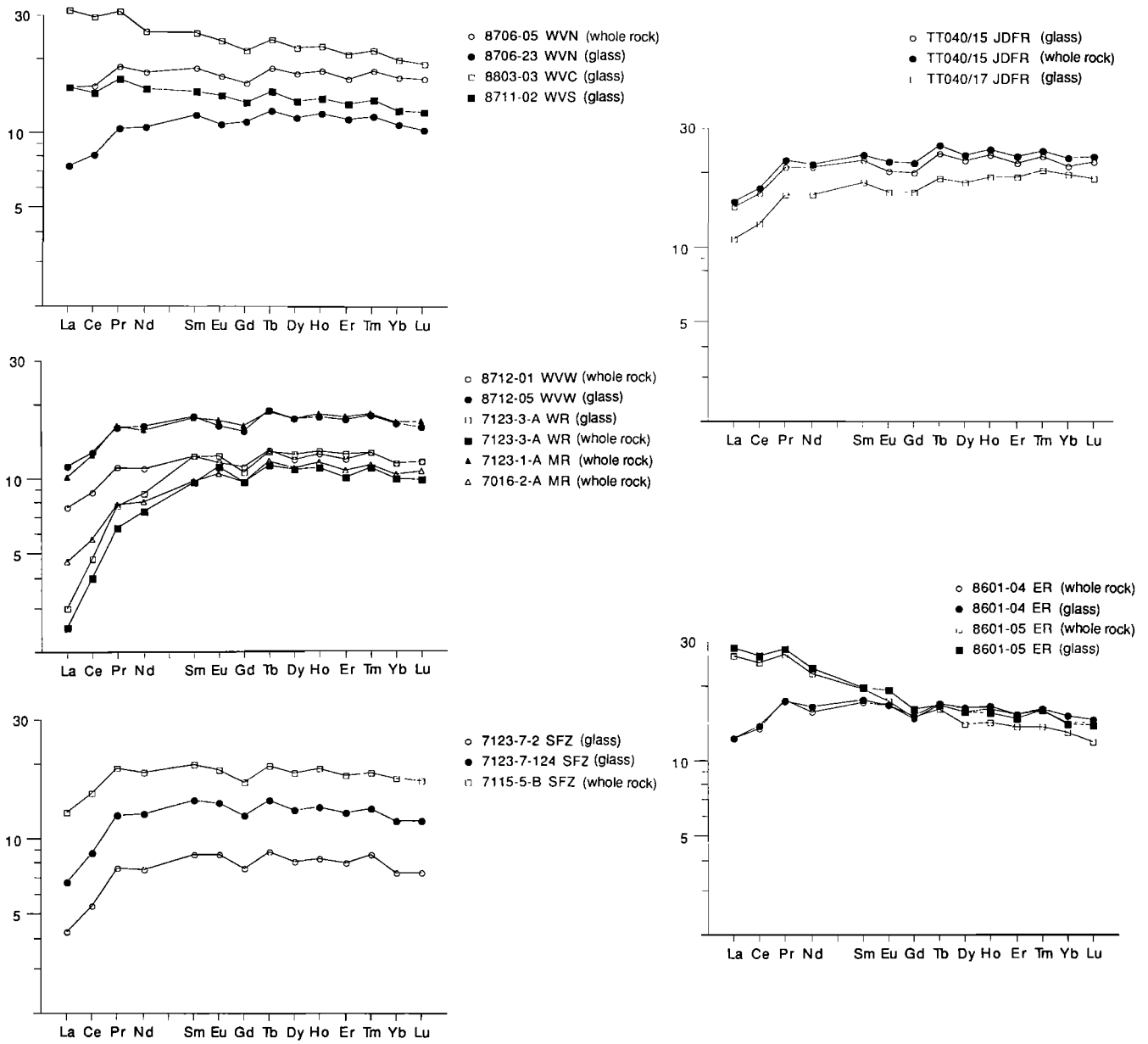

Fig. 7. Chondrite normalized rare earth element diagrams for both the whole rock and glass data. Note the wide variation in light rare earth element enrichment from the highly depleted West Ridge rocks to the enriched Endeavour Ridge rocks. Data were plotted using the Spider program for the Macintosh computer [*Wheatley and Rock*, 1988]. Data are from Table 4. Location abbreviations are as in Table 1.

parent magma for the Sovanco Fracture Zone 7123-7 samples probably was produced by greater amounts of partial melting compared to the Sovanco Fracture Zone 7115-5 samples (Figure 8*b*).

The type of model envisaged for the petrogenesis of the West Valley Segment lavas is similar to that of *Prinzhofer et al.* [1989] where a heterogeneous mantle is variably melted and variably mixed and the magma chemistry is overprinted by shallow level fractional crystallization. For the West Valley north, West Valley central, West Valley south, West Valley Wall, Sovanco Fracture Zone (7115-5), and Northern Symmetrical Ridge rocks, the magma chemistry is additionally overprinted by magma mixing in shallow level magma chambers.

Rift Propagation

Rift propagation has been shown to be an important tectonic process of ridge evolution [*Sinton et al.*, 1983; *Christie and Sinton*, 1986; *Johnson et al.*, 1983; *Liias*, 1986; *Karsten et al.*, 1987]. There is morphological and chemical evidence that is consistent with southward propagation of volcanism.

Sea Beam and Sea MARC II data from the Endeavour Offset region [*Karsten et al.*, 1986; *Davis et al.*, 1987*a*, *b*] indicate that West Valley extends south of Endeavour Seamount to form an overlapping spreading center with the northern end of the Endeavour Ridge [*Karsten et al.*, 1986]. Sea MARC II data also indicate recent volcanism in the southern portion of West Valley and near East Peak [*Davis et al.*, 1987*b*], the nearest edifice on the Heck Seamount Chain to the west of West Valley. Fresh lavas have been recovered from the southern tip of West Valley [*Scott et al.*, 1988]. If the ridge is propagating to the south, the West Valley south volcano would be located 20 km behind the tip of the propagator, and West Valley central and West Valley north would be located 30 and 35 km behind the tip of the propagator, respectively (Figure 1). Primitive lavas typically occur near the tip of the propagator with evolved ferrobasalts occurring behind the tip

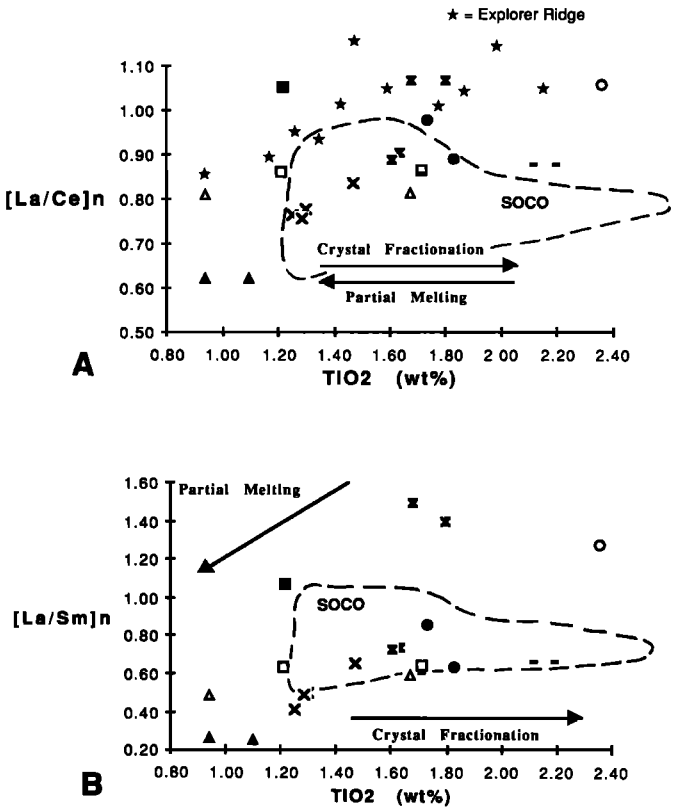

Fig. 8. Plots of incompatible element ratios against an incompatible element. (*a*) $[La/Ce]_n$ versus TiO_2. This diagram indicates the large variation in $[La/Ce]_n$ which cannot be produced by variations in the degree of partial melting or crystal fractionation. Also shown are data from the Explorer Ridge(stars) from *Michael et al.* [1989]. (*b*) $[La/Sm]_n$ versus TiO_2. The effects of varying the degree of partial melting are illustrated. Also included are data from the ridge axis of the Juan de Fuca Ridge south of the Cobb Offset (SOCO) (data from *Rhodes et al.* [1990]). Data are from Tables 2 and 4. Symbols are as in Figure 6.

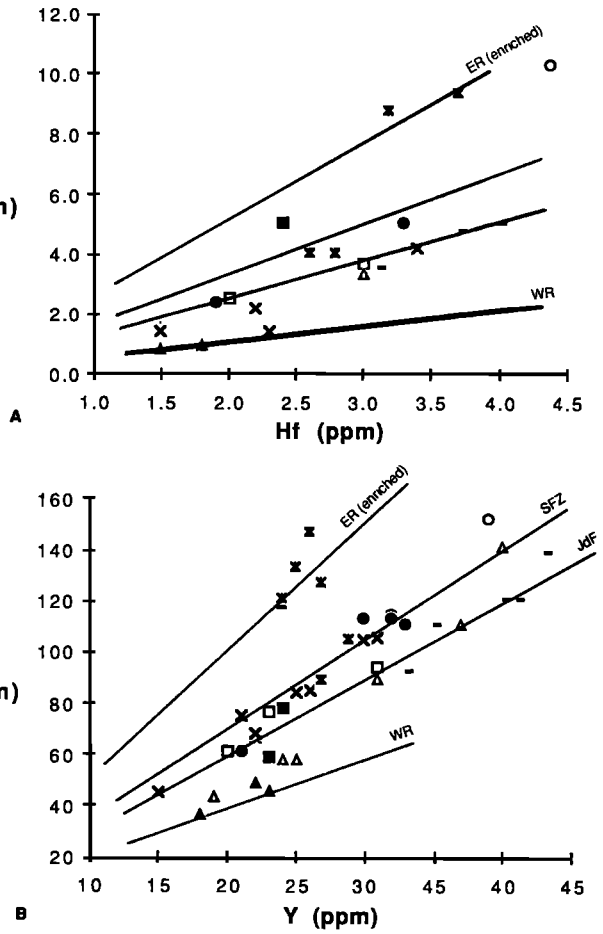

Fig. 9. Incompatible element variation diagrams illustrating the different degrees of incompatible element enrichment. Lines of equal slope are drawn from the origin, and trends are indicated for some areas. (*a*) La versus Hf. (*b*) Zr versus Y. Data are from Tables 3 and 4. Symbols are as in Figure 6.

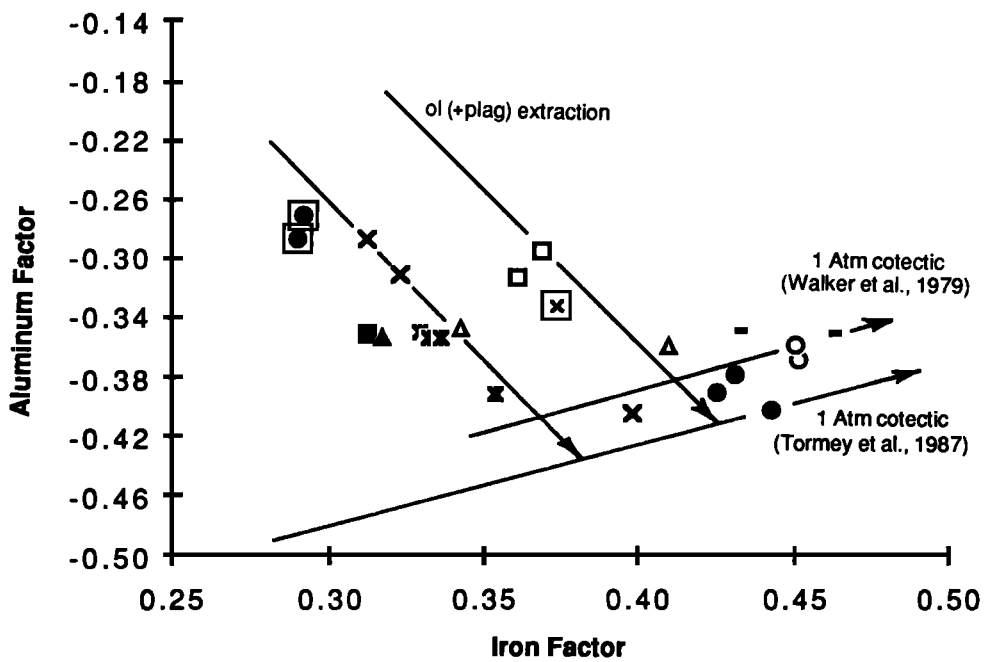

Fig. 10. Plot of Aluminium Factor against Iron Factor [*Reid et al.*, 1989] for the glass chemistry (from Table 2) and glass inclusion chemistry (boxed symbols). Shown on the diagram are olivine (+plagioclase) extraction lines and the 1 atmosphere cotectics of *Tormey et al.* [1987] and *Walker et al.* [1979]. The glass chemistry for the West Valley Segment span a wide range parallel to the cotectic indicating variations in the mineralogy of the mantle source of the parent magmas. Symbols are as in Figure 6.

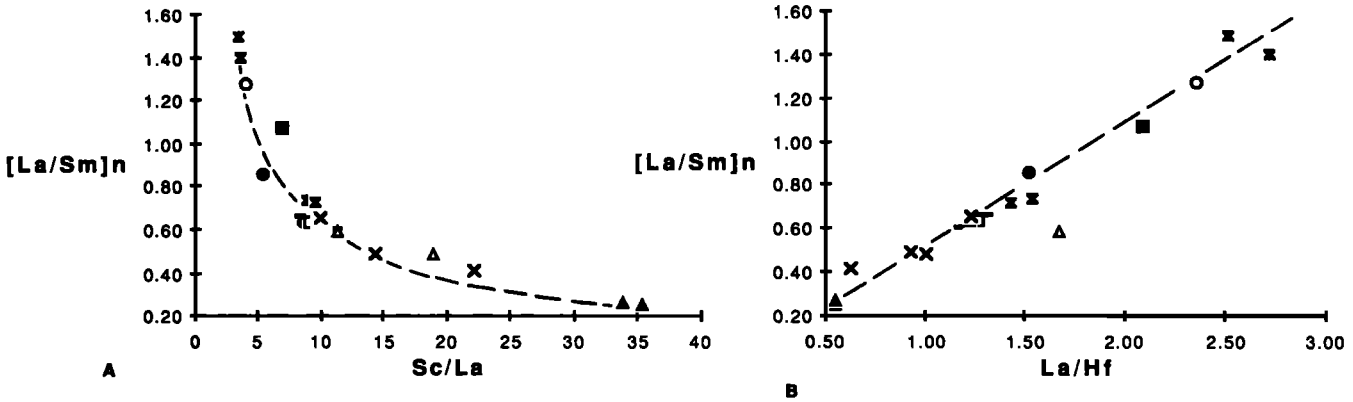

Fig. 11. Binary mixing companion plots of *Langmuir et al.* [1978]. Data points maintain their relative position on the plots as required by the binary mixing model [*Langmuir et al.*, 1978]. The Endeavour Ridge (8601-05) sample represents the enriched mantle end-member and the West Ridge lava, the depleted end-member. Data are from Table 4. Symbols are as in Figure 6.

[*Sinton et al.*, 1983; *Christie and Sinton*, 1986; *Johnson et al.*, 1983]. In addition, magma chambers tend to be less important near the tip of the propagator, while further behind the propagator, small magma chambers become important [e.g., *Christie and Sinton*, 1986]. The West Valley south lavas are primitive and low in FeO^T and TiO_2 (Figure 6). The West Valley central and West Valley north lavas are evolved FeTi basalts. West Valley central has the highest iron (FeO^T = 11.25-11.50 wt %) and TiO_2 (2.36-2.40 wt %) of the samples in the study area. The rocks from both West Valley north and West Valley central show good evidence for magma mixing, consistent with fractionation and repeated injection in small magma chambers. The primitive nature of the West Valley south rocks suggests minimal residence time in a magma chamber.

Temporal and Spatial Relationships

Many models have been proposed to explain overall chemical evolution at ridge crests. Most recently, *Karsten et al.* [1990] accounted for enriched lavas at the Endeavour Ridge by postulating a

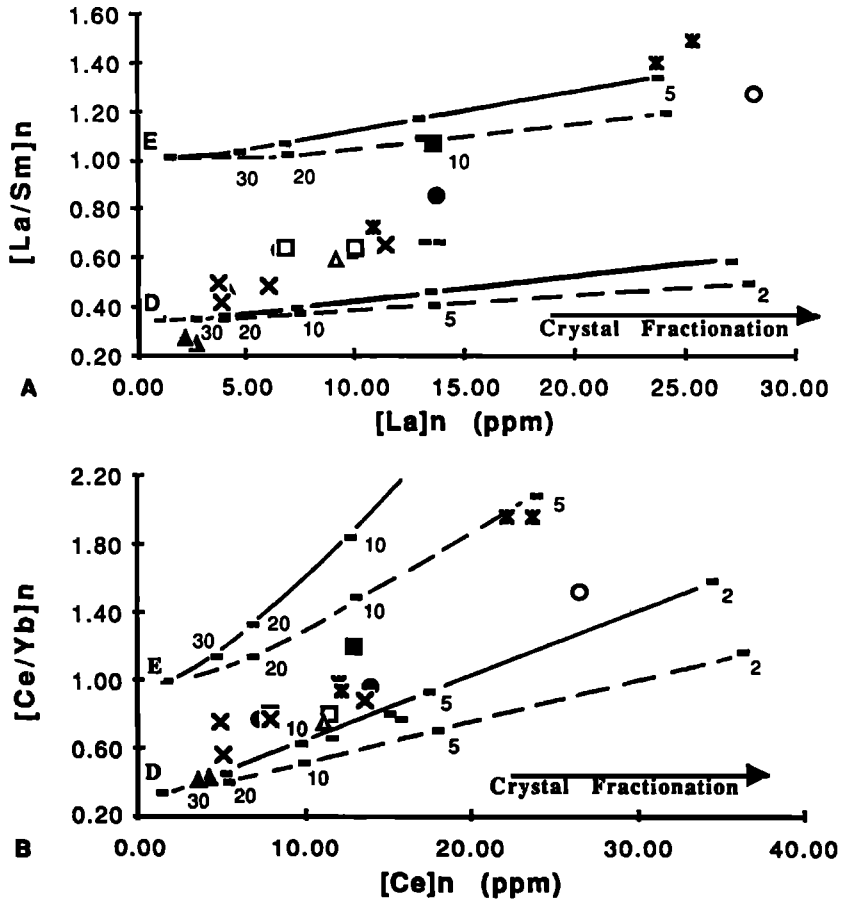

Fig. 12. Plots of (*a*)$[La/Sm]_n$ versus $[La]_n$, and (*b*) $[Ce/Yb]_n$ versus $[Ce]_n$ with partial melting curves for enriched (E) and depleted (D) model mantle compositions (dashed line = 60% olivine, 20% orthopyroxene, 10% clinopyroxene and 10% spinel; solid line = 50% olivine, 30% orthopyroxene, and 20% clinopyroxene). Numbers indicate percent melted. Note the range in relative degrees of partial melting suggested by the modelling. Partial melting modelled using the program Magma-86 [*Hughes*, 1987]. Data are from Table 4. Symbols are as in Figure 6.

temporal change in the thermal regime resulting in a decrease in the depth and extent of melting, with failing of the ridge segment. In contrast, *Michael et al.* [1989] argued that for the Juan de Fuca Ridge north of the Cobb Offset, enrichment of the subaxial mantle has been relatively recent and may be related to pulses of enriched material from the deep mantle which veins the more depleted upper mantle.

Our West Valley axis (WVn, WVc, WVs) rocks are the most enriched rocks of the West Valley Segment, similar in enrichment (based on $[La/Ce]_n$ ratios) to zero age lavas from both the Endeavour and Explorer ridges (Figure 8*a*). The West Valley north, central, and south lavas are all very young (Table 1) and represent some of the most recent volcanism on this ridge segment. The West Valley morphology is characteristic of a ridge dominated by extensional forces over volcanism. In terms of the *Kappel and Ryan* [1986] model of medium rate spreading ridge development, West Valley appears to be at the initial stages of volcanism. However, due to a possible cold edge effect because of the proximity of the Sovanco Fracture Zone [*Fox and Gallo*, 1984], it is possible that West Valley will remain thermally depressed. The West Valley wall rocks are interpreted to represent lavas erupted at the West Valley axis.

Both West Ridge and Middle Ridge were interpreted to have formed at the Middle Valley axis when it was the locus of spreading followed by rotation and uplift [*Davis and Lister*, 1977]. Both are LREE depleted (Figure 8), although the West Ridge lavas are more depleted than Middle Ridge. Their chemistry can be modelled by variations in partial melting of a variably depleted source (Figure 12). The samples we studied differ in apparent age (Table 1), however, with the West Ridge rocks being younger than the Middle Ridge rocks. Sea MARC II imagery [*Davis et al.*, 1987*b*] also indicates that there has been recent volcanic activity on West Ridge. Therefore, the West Ridge lavas may indicate more recent off-axis melting of a depleted source. If the Middle Ridge rocks do represent Middle Valley volcanism, then clearly either the source was more depleted than the source of the West Valley rocks or the thermal regime at that time was more robust.

A similar age variation was recognized for the Sovanco Fracture Zone samples (Table 1). The Sovanco Fracture Zone 7115-5 rocks are relatively old and were either formed at the Middle Valley axis or were erupted within the fracture zone itself (Figure 1). The 7115-5 lavas are geochemically similar to the Middle Ridge lavas (Figure 8*a*). The Sovanco Fracture Zone (7123-7) lavas used in this study are relatively young (Table 1) and have been interpreted to represent volcanism within the fracture zone [*Barr and Chase*, 1974].

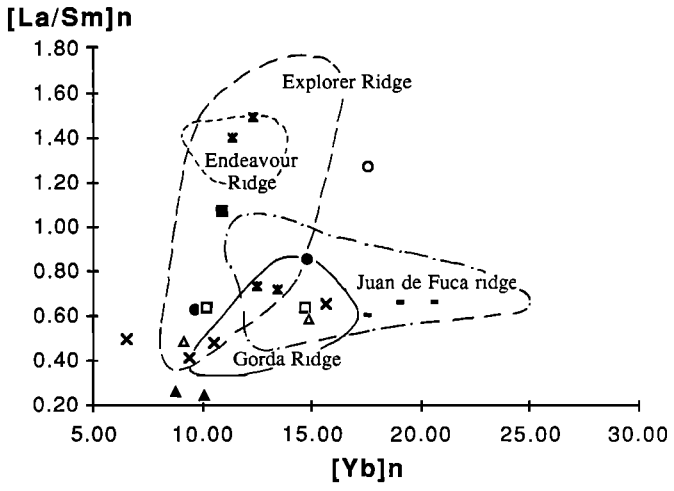

Fig. 13. A regional comparison of the rocks from this study with rocks from the Explorer Ridge [*Cousens*, 1982; *Cousens et al.*, 1984], the Endeavour and Juan de Fuca Ridges [*Liias*, 1986], and the Gorda Rift [*Davis and Clague*, 1987]. The study lavas extend to more depleted compositions and are not as enriched in $[La/Sm]_n$ as the Explorer and Endeavour Ridges but are similar to the Juan de Fuca and Gorda ridges. The West Valley south and central rocks are as enriched as the Explorer Ridge in $[La/Ce]_n$ (Figure 8*a*). Note that the Endeavour Ridge and Juan de Fuca Ridge samples used in this study plot within the fields of previous studies of those ridge systems. Data are from Table 4. Symbols are as in Figure 6.

We have evidence for temporal variations in the West Valley Segment volcanism by comparing the Middle Ridge and older Sovanco Fracture Zone rocks with the West Valley axis rocks. Rocks from both these areas more depleted than the rocks from the axis of West Valley (Figure 8*a*) and are comparable to rocks on the Juan de Fuca Ridge south of the Cobb Offset (SOCO) (Figures 8 and 13). The Juan de Fuca Ridge south of the Cobb Offset is in various stages of ridge evolution [e.g., *Kappel and Ryan*, 1986]. Yet, all SOCO rocks are transitional to depleted in LREE (Figure 8) [*Rhodes et al.*, 1990], suggesting a different mantle source, regardless of the stage of ridge evolution. The fact that the West Valley axis rocks are similar in enrichment to the active Endeavour and Explorer Segments, while the older Middle Ridge and Sovanco Fracture Zone rocks are similar to SOCO lavas, argues for the *Michael et al.* [1989] hypothesis that enrichment of lavas north of the Cobb Offset has been a recent phenomena.

Comparison With MORB From Adjacent Ridge Segments

Rocks from the West Valley Segment span a broader compositional range, over a smaller area, than rocks collected from the Juan de Fuca Ridge [*Eaby et al.*, 1984; *Liias*, 1986], Gorda Ridge [*Davis and Clague*, 1987], and Endeavour Ridge [*Liias*, 1986] (Figure 13). This likely not only reflects the heterogeneity of the source but also the fact that West Valley is thermally or magmatically depressed. However, zero age rocks from West Valley axis are as enriched in $[La/Ce]_n$ as rocks from the Endeavour and Explorer ridges (Figure 8*a*).

Rocks from the Explorer Ridge span a compositional range similar to our rocks (Figures 8*a* and 13). This is interesting because the two areas have many tectonic features in common. At the south of both the Explorer and West Valley systems is an elevated ridge (Southern Explorer Ridge and Endeavour Ridge) which bifurcates to the north into parallel axial valleys which abut against a fracture zone (West and Middle Valley abut the Sovanco Fracture Zone; Explorer Rift and Explorer Deep abut the Paul Revere Ridge). In both cases, seafloor spreading has jumped to the western axial valley in recent times [*Barr and Chase*, 1974; *Cousens et al.*, 1984; *Nobes et al.*, 1986].

CONCLUSIONS

1. There is textural and mineralogical evidence for magma mixing in shallow level magma chambers for all areas except West Ridge, Endeavour Ridge, and Sovanco Fracture Zone (7123-7).

2. The lavas range from very primitive compositions (WR, SFZ, WVs) to more evolved ferrobasalts (WVn, WVc). The Endeavour Ridge rocks are slightly depleted in FeO^T but enriched in TiO_2 with respect to the West Valley trend, whereas the Northern Symmetrical Ridge rocks are depleted in TiO_2 but enriched in FeO^T. There is within site major element variability for the West Valley north, the Endeavour Ridge, and the Northern Symmetrical Ridge rocks.

3. There is a wide range in incompatible element ratios from the highly depleted West Ridge lavas to the enriched West Valley central and Endeavour Ridge lavas. Within-site variability in incompatible element ratios occurs at West Valley north, Endeavour Ridge and North Symmetrical Ridge. The incompatible element ratios require a heterogeneous mantle source on a small (within site) and large (between site) scale. The range in incompatible element ratios can be modelled as binary mixing between an enriched and a depleted source.

4. The trace element systematics require some variations in the degree of partial melting with the highly depleted West Ridge lavas the

product of large amounts of partial melting and the West Valley central and Endeavour Ridge lavas the products of lower degrees of partial melting.

5. The petrogenetic model envisaged for the West Valley Segment lavas is derivation from a variably melted, heterogeneous mantle source, followed by mixing and/or fractionation in shallow level magma chambers.

6. The morphology of West Valley and the geochemistry of the rocks (WVn, WVc, WVs) are consistent with ridge propagation to the south.

7. West Valley (WVn, WVc, WVs) is dominated by extension over volcanism and thus thermally and magmatically depressed. Rocks from the West Valley Segment span a broader compositional range than ridge systems to the south, reflecting the heterogeneity of the source and the lack of robust volcanism to homogenize the chemistry.

8. Zero age rocks from West Valley are similarly enriched in $[La/Ce]_n$ as the zero age rocks from Endeavour and Explorer ridges. Rocks from West Valley wall and Middle Ridge and the older Sovanco Fracture Zone rocks are similarly depleted to rocks of the Juan de Fuca Ridge south of the Cobb Offset. This difference suggests that enrichment of the mantle source north of the Cobb Offset has been a recent phenomena.

Acknowledgments. We would like to thank the Captain, crew, and scientists on board the CSS *John P. Tully* for their assistance in collection of the samples from West Valley and Jim Franklin (Chief Scientist) for his support. We would also like to thank Sandra Barr and Dick Chase for providing additional samples. We are grateful for discussions with Sandra Barr, Scott Swinden, and Jim Franklin. Thorough reviews by Jill Karsten, Rodey Batiza, Brian Cousens, and an anonymous reviewer greatly improved the manuscript. This research was funded by a Natural Science and Engineering Research Council of Canada operating grant and an Energy, Mines and Resources research agreements to N. Van Wagoner.

REFERENCES

Allan, J. F., R. O. Sack, and R. Batiza, Cr-rich spinels as petrogenetic indicators: MORB-type lavas from the Lamont seamount chain, eastern Pacific, *Am. Mineral., 73,* 741-753, 1988.

Atwater, T., Implications of plate tectonics for the Cenozoic evolution of western North America, *Geo. Soc. Am. Bull., 81,* 3513-3536, 1970.

Barone, A. M., and W. B. F. Ryan, Single plume model for asynchronous formation of the Lamont Seamounts and adjacent East Pacific Rise terrains, *J. Geophys. Res., 95,* 10.801-10.827, 1990.

Barr, S. M., Geology of the northern end of the Juan de Fuca Ridge and adjacent continental slope, Ph.D. thesis, Univ. of British Columbia, Vancouver, 287 pp., 1972.

Basaltic Volcanism Study Project, *Basaltic Volcanism on the Terrestrial Planets*; 1286 pp., Pergamon Press, New York, 1981.

Barr, S. M., and R. L. Chase, Geology of the northern end of the Juan de Fuca Ridge and sea-floor spreading, *Can. J. Earth Sci., 11,* 1384-1406, 1974.

Batiza, R., and D. Vanko, Petrology of young Pacific seamounts, *J. Geophys. Res., 89,* 11,235-11,260, 1984.

Bender, J. F., F. N. Hodges, and A. E. Bence, Petrogenesis of basalts from the project FAMOUS area: Experimental study from 0-15 kbars, *Earth Planet. Sci. Lett., 41,* 277-302, 1978.

Botros, M., and H. P. Johnson, Tectonic evolution of the Explorer-northern Juan de Fuca region from 8 Ma to the present, *J. Geophys. Res., 93,* 10,421-10,437, 1988.

Bryan, W. B., Morphology of quench crystals in submarine basalts, *J. Geophys. Res., 77,* 5812-5817, 1972.

Bryan, W. B., Regional variation and petrogenesis of basalt glasses from the FAMOUS area, Mid-Atlantic Ridge, *J. Petrol., 20,* 293-325, 1979.

Carlson, R. L., Late Cenozoic rotations of the Juan de Fuca Ridge and the Gorda Rise: A case study, *Earth Planet. Sci. Lett., 77,* 171-188, 1981.

Christie, D. M., and J. M. Sinton, Major element constraints on melting, differentiatio]*n* and mixing of magmas from the Galapagos 95.5°W propagating rift system, *Contrib. Mineral. Petrol., 94,* 274-288, 1986.

Clague, D. A., and T. E. Bunch, Formation of ferrobasalt at east Pacific mid-ocean spreading centers, *J. Geophys. Res., 81,* 4247-4256, 1976.

Coish, R. A., and L. A. Taylor, The effects of cooling rate on texture and pyroxene chemistry in DSDP leg 34 basalt: A microprobe study, *Earth Planet. Sci. Lett., 42,* 389-398, 1979.

Cousens, B. L., Major and trace element geochemistry of basalts from the explorer area, northeast Pacific Ocean, M.Sc. thesis, Univ. of British Columbia, Vancouver, 98 pp., 1982.

Cousens, B. L., R. L. Chase, and J. G. Schilling, Basalt geochemistry of the Explorer Ridge, northeast Pacific Ocean, *Can. J. Earth Sci., 21,* 157-170, 1984.

Davis, A. S., and D. A. Clague, Geochemistry, mineralogy, and petrogenesis of basalt from the Gorda ridge, *J. Geophys. Res., 92,* 10467-10483, 1987.

Davis, E. E., and C. R. B. Lister, Tectonic structures on the Juan de Fuca Ridge, *Geol. Soc. Am. Bull., 88,* 346-363, 1977.

Davis E. E., C. R. B. Lister, and B. T. R. Lewis, Seismic structure of the Juan de Fuca Ridge: Ocean bottom seismometer results from the median valley, *J. Geophys. Res., 81,* 3541-3555, 1976.

Davis, E., R. Currie, and B. Sawyer, Bathymetry map 6-1987, northern Juan de Fuca Ridge, Geol. Surv. of Can., Energy Mines and Resour., Ottawa, 1987*a*.

Davis, E., R. Currie, and B. Sawyer, Acoustic imagery map 14-1987, northern Juan de Fuca Ridge, Geol. Surv. of Can., Energy Mines and Resour., Ottawa, 1987*b*.

Donaldson, C. H., and R. W. Brown, Refractory megacrysts and magnesian-rich melt inclusions within spinel in oceanic tholeiites: Indicators of magma mixing and parental magma composition, *Earth Planet. Sci. Lett., 37,* 81-89, 1977.

Drake, M. J., Plagioclase-melt equilibria, *Geochim. Cosmochim. Acta, 40,* 457-465, 1976.

Eaby, J., D. A. Clague, and J. R. Delaney, Sr isotope variations along the Juan de Fuca Ridge, *J. Geophys. Res., 89,* 7883-7890, 1984.

Evensen, N. M., P. J. Hamilton, and R. K. O'Nions, Rare earth abundances in chondritic meteorites, *Geochim. Cosmochim. Acta, 42,* 1199-1212, 1978.

Fisk, M. R., A. E. Bence, and J. G. Schilling, Major element chemistry of Galapagos Rift Zone magmas and their phenocrysts, *Earth Planet. Sci. Lett., 61,* 171-189, 1982.

Fox, P. J., and D. G. Gallo, A tectonic model for ridge-transform-ridge plate boundaries: Implications for the structure of oceanic lithosphere, *Tectonophys., 104,* 205-242, 1984.

Glazner, A. F., Activities of olivine and plagioclase components in silicate melts and their applications to geothermometry, *Contrib. Mineral. Petrol., 88,* 260-268, 1984.

Hanson, G. N., Rare earth elements in petrogenetic studies of igneous systems, *Annu. Rev. Earth Planet. Sci., 8,* 371-406, 1980.

Hart, S. R., Heterogeneous mantle domains: Signatures, genesis and mixing chronologies, *Earth Planet. Sci. Lett., 90,* 273-296, 1988.

Hekinian, R., *Petrology of the Ocean Floor,* 393pp., Elsevier Scientific, New York, 1982.

Hey, R., A new class of "pseudofaults" and their bearing on plate tectonics: A new propagating rift model, *Earth Planet. Sci. Lett., 37,* 321-325, 1977.

Hey, R. N., and D. S. Wilson, Propagating rift explanation for the tectonic evolution of the northeast Pacific—The pseudomovie, *Earth Planet. Sci. Lett., 58,* 157-168, 1982.

Holness, M. B., and F. M. Richter, Possible effects of spreading rate on MORB isotopic and rare earth composition arising from melting of a heterogeneous source, *J. Geol., 97,* 247-260, 1989.

Hughes, S. S., Magma-86; Computer program, Hughes Magmatics, Corvallis Oregon, 1987.

Hummler, E., and W. Whitechurch, Petrology of basalts from the Central Indian Ridge (lat. 25°23'S, long. 70°04'E): Estimates of frequencies and fractional volumes of magma injections in a two-layered reservoir, *Earth Planet. Sci. Lett., 88,* 169-181, 1988.

Johnson, H. P., J. L. Karsten, J. R. Delaney, E. E. Davis, R. G. Currie, and R. L. Chase, A detailed study of the Cobb offset of the Juan de Fuca Ridge: Evolution of a propagating rift, *J. Geophys. Res., 88,* 2297-2315, 1983.

Kappel, E. S., and B. F. Ryan, Volcanic episodicity and a non-steady state rift valley along northeast Pacific spreading centers: Evidence from Sea MARC I, *J. Geophys. Res., 91,* 13,925-13,940, 1986.

Karsten, J. L., and J. R. Delaney, Hot spot-ridge crest convergence in the northeast Pacific, *J. Geophys. Res., 94,* 700-712, 1989.

Karsten, J. L., J. R. Delaney, and E. E. Davis, An overview of tectonic, volcanic, and petrologic processes on northeast Pacific spreading centres (abstract), in *Recent Hydrothermal Mineralization at Seafloor Spreading Centres: Tectonic, Petrologic and Geochemical Constraints, Programs and Abstracts,* p. 00, Mineral Exploration Research Institute, McGill University, Montreal, February 5-6, *IREM-MERI Publ. 87-1,* Que., 1987.

Karsten, J. L., J. R. Delaney, J. M. Rhodes, and R. A. Liias, Spatial and temporal evolution of magmatic systems beneath the Endeavour Segment,

Juan de Fuca Ridge: Tectonic and petrologic constraints, *J. Geophys. Res., 95*, 19, 235-19, 256, 1990.

Karsten, J. L., S. R. Hammond, E. E. Davis, and R. G. Currie, Detailed geomorphology and neotectonics of the Endeavour Segment, Juan de Fuca Ridge: New results from Sea Beam swath mapping, *Geol. Soc. Am. Bull., 97*, 213-221, 1986.

Kay, R. W., N. J. Hubbard, and P. W. Gast, Chemical characteristics and origin of oceanic ridge volcanic rocks, *J. Geophys. Res., 75*, 1585-1613, 1970.

Kuo, L. C., and R. J. Kirkpatrick, Pre-eruptive history of phyric basalts from DSDP legs 45 and 46: Evidence from morphology and zoning patterns in plagioclase, *Contrib. Mineral. Petrol., 79*, 13-27, 1982.

Langmuir, C. H., J. F. Bender, A. E. Bence, G. N. Hanson, and S. R. Taylor, Petrogenesis of basalts from the FAMOUS area: Mid-Atlantic Ridge, *Earth Planet. Sci. Lett., 36*, 133-156, 1977.

Langmuir, C. H., R. D. Vocke, G. N. Hanson, and S. R. Hart, A general mixing equation with applications to Icelandic basalts, *Earth Planet. Sci. Lett., 37*, 380-392, 1978.

Langmuir, C. H., J. F. Bender, and R. Batiza, Petrological and tectonic segmentation of the East Pacific Rise, 5°30'-14°30'N, *Nature, 322*, 422-429, 1986.

Le Roex, A. P., H. J. B. Dick, A. J. Reid, A. M. Frey, and S. R. Hart, Geochemistry, mineralogy and petrogenesis of lavas erupted along the Southwest Indian Ridge between the Bouvet Triple Junction and 11°E, *J. Petrol., 24*, 267-318, 1983.

Liias, R. A., Geochemistry and petrogenesis of basalts erupted along the Juan de Fuca Ridge, Ph.D. thesis, 264 pp, Univ. of Mass., Cambridge, 1986.

Macdougall, J. D., and G. W. Lugmair, Sr and Nd isotopes in basalts from the East Pacific Rise: significance for mantle heterogeneity, *Earth Planet. Sci. Lett., 77*, 273-284, 1986.

Michael, P. J., R. L. Chase, and J. F. Allan, Petrologic and geologic variations along the Southern Explorer Ridge, northeast Pacific Ocean, *J. Geophys. Res., 94*, 13,895-13,918, 1989.

Nabelek, P. I., and C. H. Langmuir, The significance of unusual zoning in olivines from FAMOUS area basalt 527-1-1, *Contrib. Mineral. Petrol., 93*, 1-8, 1986.

Nobes, D. C., L. K. Law, and R. N. Edwards, The determination of resistivity and porosity of the sediments and fractured basalt layers near Juan de Fuca Ridge, *Geophys. J. R. Astro. Soc., 86*, 289-317, 1986.

Prinzhofer, A., E. Lewin, and C. J. Allegre, Stochastic melting of the marble cake mantle: evidence from local study of the East Pacific Rise at 12°50'N, *Earth Planet. Sci. Lett., 92*, 189-206, 1989.

Raff, A. D., and R. G. Mason, Magnetic survey off the west coast of North America, 40°N latitude to 50°N latitude, *Geo. Soc. Am. Bull., 72*, 1267-1270, 1961.

Reid, J. B., Jr., E. Steig, and W. B. Bryan, Major element evolution of basaltic magmas: A comparison of the information in CMAS and ALFE projections, *Contrib. Mineral. Petrol., 101*, 318-325, 1989.

Rhodes, J. M., M. A. Dungan, D. P. Blanchard, and P. E. Long, Magma mixing at mid-ocean ridges: Evidence from basalts drilled near 22°N on the Mid-Atlantic Ridge, *Tectonophysics, 55*, 35-61, 1979.

Rhodes, J. M., C. Morgan, and R. A. Liias, Geochemistry of Axial Seamount lavas: Magmatic relationship between the Cobb Hotspot and the Juan de Fuca Ridge, *J. Geophys. Res., 95*, 12,713-12,733, 1990.

Riddihough, R., Recent movements of the Juan de Fuca Plate system, *J. Geophys. Res., 89*, 6980-6994, 1984.

Roeder, P. L., and R. F. Emslie, Olivine-liquid equilibrium, *Contrib. Mineral. Petrol., 29*, 275-289, 1970.

Scott, S. D., R. L. Chase, J. F. Allan, and P. M. Herzig, Hydrothermal deposits and recent volcanism at the southern end of West Valley, Juan de Fuca Ridge, *Eos Trans. AGU, 69*, 1497, 1988.

Shibata, T., S. E. DeLong, and D. Walker, Abyssal tholeiites from the Oceanographer Fracture Zone 1: Petrology and Fractionation, *Contrib. Mineral. Petrol., 70*, 89-102, 1979.

Sinton, J. M., D. S. Wilson, D. M. Christie, R. N. Hey, and J. R. Delaney, Petrologic consequences of rift propagation on oceanic spreading ridges, *Earth Planet. Sci. Lett., 62*, 193-207, 1983.

Stakes, D. S., J. W. Shervais, and C. A. Clifford, The volcanic-tectonic cycle of the FAMOUS and AMAR valleys, Mid-Atlantic Ridge (36°47'N): Evidence from basalt glass and phenocryst compositional variations for a steady state magma chamber beneath the valley midsections, AMAR 3, *J. Geophys. Res., 89*, 6995-7028, 1984.

Tormey, D. R., T. L. Grove, and W. B. Bryan, Experimental petrology of normal MORB near the Kane Fracture Zone: 22°-25°N, Mid-Atlantic Ridge, *Contrib. Mineral. Petrol., 96*, 121-139, 1987.

Vine, F. J., and J. T. Wilson, Magnetic anomalies over a young oceanic ridge off Vancouver Island, *Science, 150*, 485-489, 1965.

Walker, D., T. Shibata, and S. E. DeLong, Abyssal tholeiites from the Oceanographer Fracture Zone, II, Phase equilibria and mixing, *Contrib. Mineral. Petrol., 70*, 111-125, 1979.

Wheatley, M. R., and N. M. S. Rock, Spider: A Macintosh program to generate normalised multi-element spidergrams, *Am. Mineral., 73*, 919-921, 1988.

M. I. Leybourne and N. A. Van Wagoner, Department of Geology, Acadia University, Wolfville, Nova Scotia, Canada B0P 1X0.

(Received May 11, 1990;
revised February 6, 1991;
accepted February 23, 1991.)

JOURNAL OF GEOPHYSICAL RESEARCH, VOL. 96, NO. B10, PAGES 16,597–16,623, SEPTEMBER 10, 1991

A Rheologically Layered Three-Dimensional Model of the San Andreas Fault in Central and Southern California

CHARLES A. WILLIAMS[1] AND RANDALL M. RICHARDSON

Department of Geosciences, University of Arizona, Tucson

Three-dimensional kinematic finite element models of the San Andreas fault in central and southern California have been used to estimate the effects of rheological parameters and fault slip distribution on the horizontal and vertical deformation in the vicinity of the fault. The models include the effects of vertically layered power law viscoelastic rheology, and isostatic forces are considered in calculations of vertical uplift. Several different rheological layering schemes are used, using laboratory results on rock rheology to define the properties of the various layers. The depth to which the fault remains locked between earthquakes (D) is held constant at 20 km for the entire locked portion of the fault between Cholame and the Salton Sea. Between Hollister and Cholame the entire fault is assumed to slip at a rate consistent with a relative plate velocity of 35 mm/yr along a direction striking N41°W. Steady aseismic slip corresponding to plate velocity is imposed below the fault locking depth to a depth H on the locked section of the fault. The depth to which aseismic slip occurs (H) is assigned a value of either 20 km or 40 km, resulting in two versions of each rheological model. Variations in the model parameters are found to produce distinctive deformation patterns, providing a means for differentiating between models. Specifically, lower effective viscosities near the surface result in increased strain rates and uplift rates at all times during the earthquake cycle. Lower effective viscosities also produce subsidence near the creeping portion of the fault. Models that do not include aseismic slip below the fault locking depth (H = 20 km) display greater time dependence in both horizontal and vertical deformation than those including aseismic slip below the locking depth (H = 40 km). These differences are due, in part, to the time-invariant nature of the imposed slip condition. The differences are more pronounced as the effective viscosity close to the surface is increased. The vertical uplift rate is particularly sensitive to the depth of aseismic slip (H) at the two bends in the fault, especially for models with high effective viscosities below the surface. For models in which the effective viscosity near the surface is relatively low, measurements of total uplift at the two bends in the fault could provide sufficient resolution to distinguish between models with and without aseismic slip over time periods of 10 to 20 years or more with current abilities to measure vertical uplift. Among our San Andreas fault models, the one most consistent with current strain rate data includes aseismic slip between 20 and 40 km (H = 40 km) and uses assumed rheological properties from the surface to 100 km depth consistent with laboratory results for wet rock samples. The rheological parameters for this model are based on laboratory results for the following rock types wet granite in the upper crust (0 to 20 km), wet diabase in the lower crust (20 to 40 km), wet dunite in the upper mantle (40 to 100 km), and dry olivine below 100 km. These modeling results are preliminary, however, and several additional factors should be considered prior to constructing a comprehensive model. Furthermore, it should be emphasized that the present models represent a small subset of possible rheological models, and numerous other models may provide similar or better fits to the data. The field of possible models will continue to narrow with further knowledge of the variations in Earth composition and temperature with depth, with more information on rock rheology, and with further observations of the earthquake cycle.

INTRODUCTION

One of the primary goals of modern geophysical investigations is an understanding of the processes related to repeated earthquake occurrence at major plate boundaries. These studies are important not only in estimating earthquake hazard potential but also for the information they yield on plate movements, plate driving stresses, and the structure and composition of the Earth. The San Andreas fault in California represents an ideal location for this type of research. The proximity of the fault to major population and industrial centers and its easy accessibility have resulted in large quantities of high-quality deformation data, providing the necessary means for constraining physical models of strain accumulation and release on the San Andreas fault.

Numerous models of the earthquake cycle have been proposed for the San Andreas fault. Many of these are based on the model initially proposed by *Nur and Mavko* [1974], consisting of a displacement dislocation in an elastic layer overlying a linear viscoelastic (Maxwell) half-space. Models of this sort include those of *Savage and Prescott* [1978], *Spence and Turcotte* [1979], and *Rundle* [1986]. The model of *Savage and Prescott* [1978] was used by *Thatcher* [1983] to calculate shear strain rates, providing a reasonable fit to observations along the San Andreas fault. It has also been used by *Williams and Richardson* [1988] in an inverse analysis attempting to place some constraints on fault parameters with available shear strain rate observations. In addition to these kinematic models, several models have been proposed that consider the dynamic aspects of the problem, including those of *Li and Rice* [1987], *Li and Lim* [1988], and *Rundle* [1988*a*, *b*]. Most of these models consider the case of an infinitely long rectangular fault and are therefore essentially two-dimensional. The work of *Rundle* [1986, 1988*b*], however, has emphasized the importance of considering variations in fault geometry.

There are two primary points which have not yet been addressed by San Andreas fault models. First, only linear viscoelastic rheologies have been considered. In most cases, a simple elastic layer-over-viscoelastic-half-space model has been assumed. A large volume of work exists, however, indicating that actual Earth structure is considerably more complex [e.g., *Meissner and Strehlau*, 1982; *Chen and Molnar*, 1983; *Strehlau and Meissner*, 1987]. Furthermore, laboratory measurements show that actual rock rheology is better represented by a power law rather than a linear viscoelastic relationship [*Kirby*, 1983;

[1]Now at Department of Geological and Geophysical Sciences, Princeton University, Princeton, New Jersey.

Paper number 91JB01484.
0148-0227/91/91JB-01484$05.00

Kirby and Kronenberg, 1987*a*, *b*]. It is important to estimate the possible effects of laboratory-inferred power law rheology on model results. Second, current models calculate only the horizontal components of deformation, neglecting vertical uplift. With increased accuracy in leveling surveys, and the addition of other types of information such as that from the global positioning system (GPS), vertical uplift data represent an additional means of constraining San Andreas fault models.

This study attempts to address these points by producing fully three-dimensional finite element models of the San Andreas fault in central and southern California, using laboratory results on rock rheology [*Kirby*, 1983; *Kirby and Kronenberg*, 1987*a*, *b*] to define the properties of various layers in the Earth. Although a number of present models are consistent with current horizontal geodetic observations, it is quite possible that predicted vertical uplift may vary considerably among these models. In our study, both horizontal and vertical deformation patterns for several different models are calculated to determine whether the models predict distinctive patterns at various times in the earthquake cycle. In cases where distinctive patterns coincide with existing observations, these data may be used to evaluate the models. In many cases, the distinctive patterns occur in regions or times where no data are currently available. These regions thus represent potentially useful observation sites for the future.

The parameters of interest in this analysis are the depth to which the fault remains locked between earthquakes, the depth to which aseismic slip occurs below the locking depth, and the variation in the viscous properties of the Earth with depth. Recent models have produced a wide range of values for these parameters [*Thatcher*, 1983; *Thatcher and Rundle*, 1984; *Rundle*, 1986, 1988*b*; *Li and Rice*, 1987; *Li and Lim*, 1988]. Estimates of the fault locking depth range from 9 to 20 km, while the depth to which aseismic slip occurs (which corresponds to the base of the elastic layer for these models) has been assigned values ranging from 10 to 40 km. Estimates of viscosity for the Earth below the elastic layer have varied from 2×10^{18} to 1×10^{20} Pa s. It is likely that the use of layered power law viscoelastic models could significantly affect these parameter estimates. If, for example, the behavior of the upper crust were not purely elastic, it would be expected to strain more rapidly in response to imposed stress. If this fact is not considered, estimates of the model parameters will be in error. A more likely possibility is an alternating effective viscosity with depth, as discussed in the next section. In this case, relatively low effective viscosities would be expected throughout the lithosphere except near the tops of the upper crust, lower crust, and upper mantle. It is important to compare the results of this type of model with those obtained from models consisting of an elastic layer overlying a linearly viscoelastic half-space.

The models presented here are loosely based on the layer-over-a-half-space model of *Savage and Prescott* [1978], which is in turn derived from the model of *Nur and Mavko* [1974]. The layer-over-a-half-space model is the most common type of rheological model currently being used to study the San Andreas fault [e.g., *Rundle*, 1986, 1988*b*; *Li and Rice*, 1987; *Li and Lim*, 1988]. Figure 1 demonstrates the differences between the Savage and Prescott model and our model. The Savage and Prescott model, which is shown in cross section in Figure 1*a*, is characterized by a fault locking depth (D) and an elastic layer thickness (H). Aseismic slip is assumed to occur below D to the base of the elastic layer, on the dashed portion of the fault in Figure 1*a*. In our model (Figure 1*b*), there is no elastic layer as such, and the parameter H instead represents the depth to which aseismic slip occurs. There are therefore two primary differences between our model and that of Savage and Prescott. First of all, Earth structure is represented as a number of rheological layers, rather than a single elastic layer overlying a viscoelastic half-space. Secondly, the depth to which aseismic slip occurs is independent of the rheological layering scheme.

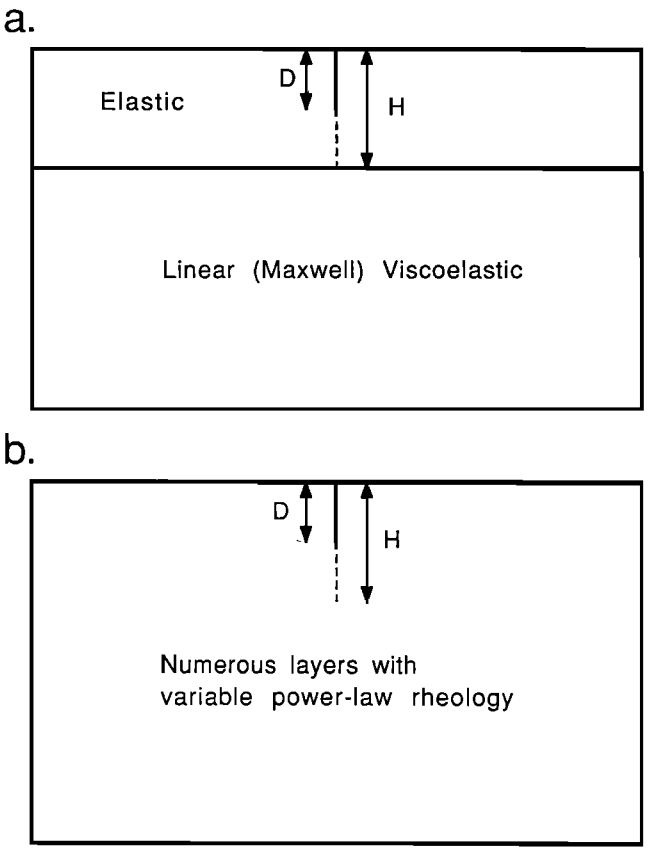

Fig. 1. Models used in the study. (*a*) *Savage and Prescott* [1978] model. (*b*) Nonlinear layered model.

Our models, like that of *Savage and Prescott* [1978], are purely kinematic, meaning that the slip on the fault is specified rather than being a result of the calculations. Several dynamic models have also been developed. One of these [*Li and Rice*, 1987; *Li and Lim*, 1988] is partially kinematic, as the amount of coseismic displacement and the earthquake recurrence interval are specified. Below the fault locking depth, however, we assume a constant resistive stress boundary condition rather than impose a constant slip rate. The assumption of aseismic slip below the locking depth is a common feature of current strike-slip fault models and is supported by the results of *Tse and Rice* [1986]. They found that steady state sliding is unstable above a certain depth within the Earth and is stable below this depth. Therefore stick-slip (seismic) behavior would be expected above this depth, with steady state sliding below. The results of *Tse and Rice* [1986] demonstrate that broadly distributed creep flow below the seismogenic zone is not the only possible mechanism of aseismic slip at depth. A final model is that of *Rundle* [1988*a*, *b*]. This is a three-dimensional model in which the fault displacements are completely determined as a result of the calculations.

Kinematic models are used in this study for the sake of simplicity. Our analysis focuses on the effects of rheological properties and the depth of aseismic slip on the observed deformation, and it does not consider other complexities of fault mechanics. In the Earth, it is likely that there is accelerated aseismic slip below the locking depth immediately following an earthquake, as in the model of *Savage* [1990]. The imposition of steady aseismic slip at depth in our models (for models with $H > D$) will probably result in an exaggerated difference between models including aseismic slip below the locking depth and those that do not. However, our results will serve to emphasize the differences between models in which slip at depth occurs on a discrete fault (aseismic slip at depth, i.e., $H > D$) and those in which slip at depth is accomplished by

viscous shear (no aseismic slip at depth, i.e., $H = D$). The exact values obtained from our models should be interpreted with some care, since the degree to which the results are influenced by imposed steady aseismic slip is not known.

Velocity boundary conditions corresponding to plate motion are applied along vertical planes at the extreme edges of the grid, far from the fault. An alternative method would be the application of these conditions along the base of the model. It is unlikely that our choice of boundary conditions will have a significant effect on the results, which are not calculated until steady flow has occurred at depth. Thus the entire "upper mantle" portion of the model is essentially moving at plate velocity at distances far from the fault. As described by *Li and Rice* [1987], the cyclically time-dependent displacement field of their solution depends only on the far-field plate velocity; it does not depend on the distance-varying velocity boundary conditions applied to the base of their model. Model results should therefore be insensitive to the method in which the time-independent velocity boundary conditions are applied.

Our boundary conditions are chosen to be consistent with geodetic determinations along the fault [*Minster and Jordan*, 1987; *DeMets et al.*, 1987] rather than with plate motion determinations, such as NUVEL1 [*DeMets et al.*, 1990]. One of the ramifications of this assumption is a reduction in the component of fault-normal stress, since NUVEL1 predicts a more northerly trending motion (N36°W as compared to N41°W) and a higher velocity (48 mm/yr as opposed to 35 mm/yr). Recent investigations have indicated that the primary stress component near the San Andreas fault is a compressive stress perpendicular to the fault [*Mount and Suppe*, 1987; *Zoback et al.*, 1987]. This can be explained if the San Andreas is a relatively weak fault, unable to support significant amounts of shear stress. This idea has strong observational support. The absence of a heat flow anomaly associated with the fault indicates that it cannot support shear stresses greater than about 10–20 MPa [*Brune et al.*, 1969; *Lachenbruch and Sass*, 1980]. More recently, *Jones* [1988] has used focal mechanisms for a number of small to intermediate earthquakes to determine the principal stress axes near the fault. These results show a nearly constant angle of about 65° between the maximum horizontal compressive stress and the local strike of the San Andreas, implying a weak fault.

Geodetic observations, on the other hand, are generally consistent with fault-parallel right-lateral shear [e.g., *Prescott and Savage*, 1976; *Prescott et al.*, 1979; *King and Savage*, 1983; *Savage*, 1983], such that the principal axes of strain rate are oriented at approximately 45° to the local strike of the fault. This observed discrepancy in direction between geodetic and stress determinations may be reconciled if the geodetic observations are considered to be the changes from a reference state induced by the earthquake cycle while the stress measurements represent the background value (J. Savage, personal communication, 1990). Thus our models more accurately reflect the short-term changes in deformation than the long-term stress state. For kinematic models, it is most reasonable to choose a framework defined by geodetic observations, particularly since these are the observations used to constrain the models. Since the effects of fault friction are effectively bypassed with kinematic models, the question of fault strength does not apply. Instead, slip on the fault is completely defined, regardless of the stresses acting on it.

POWER LAW VISCOELASTIC RHEOLOGY

The elastic rebound theory of *Reid* [1910, 1911] was based on the assumption that the Earth's behavior is perfectly elastic over extended periods of time. While elastic behavior is certainly a reasonable assumption over extremely short time periods, there is ample evidence of nonelastic behavior over longer periods. The first quantitative evidence of nonelastic behavior was the observed postglacial rebound in Scandinavia. This was explained by *Haskell* [1935, 1936] as the viscous response of the Earth's mantle to postglacial unloading. An analysis of viscosity variation with depth in the Earth's mantle was performed by *Gordon* [1965, 1967], who assumed that viscous deformation within the Earth occurred by Nabarro-Herring (diffusion) creep. This mechanism consists of the diffusion of lattice vacancies within crystal grains. A similar mechanism is grain boundary (Coble) creep, in which diffusion occurs along grain boundaries. Both of these mechanisms lead to a Newtonian fluid behavior, in which the steady state strain rate is linearly proportional to the applied stress.

An alternative mechanism, dislocation creep, was considered by *Weertman* [1970]. Dislocations contribute to creep primarily through dislocation climb or dislocation glide. Weertman's results indicated that dislocation creep should be the dominant mechanism except at very low stresses (less than 1000 Pa). A dislocation creep mechanism predicts that the steady state creep rate is proportional to a power of the stress. Dislocation creep deformation therefore leads to power law viscous behavior. Power law rheology has been examined by a number of authors, including *Weertman* [1970], *Melosh* [1980], *Turcotte and Schubert* [1982], *Kirby* [1983, 1985], and *Kirby and Kronenberg* [1987*a*, *b*].

Although more complicated formulations are possible (see, for example, *Kirby* [1985]), the creep law that represents dislocation processes may be described by the power law relationship

$$\dot{\varepsilon}_s = A\sigma^n \exp(-H^* / RT) \tag{1}$$

where $\dot{\varepsilon}_s$ is the steady state creep rate, $\sigma = (\sigma_1 - \sigma_3)$ is the differential stress, T is the absolute temperature, R is the ideal gas constant, A is a material constant, n is the power law exponent, and $H = E^* + PV^*$ is the activation enthalpy (E^* is the activation energy, V^* is the activation volume, and P is the mean normal stress). As discussed by *Strehlau and Meissner* [1987], the pressure factor PV^* is typically smaller than the uncertainties in E^* and is therefore neglected in this study.

A number of quantities may be defined in analogy to Newtonian (linear) viscosity [see *Melosh*, 1980]. Newtonian viscosity is defined in terms of the differential stress and the steady state creep rate as

$$\eta = \frac{\sigma}{2\dot{\varepsilon}_s} \tag{2}$$

An analogous quantity, the effective viscosity, may be defined for power-law behavior:

$$\eta_{eff} = \frac{\sigma}{2\dot{\varepsilon}_s} = \frac{\exp(H^*/RT)}{2A\sigma^{n-1}} \tag{3}$$

It can therefore be seen that the effective viscosity is dependent not only upon the type of rock under consideration but also upon the temperature and the applied differential stress. An increase in either the temperature or the differential stress results in a lower effective viscosity. The effective viscosity may also be described in terms of the strain rate, convenient for this study, where the emphasis is on deformation.

$$\eta_{eff} = \frac{1}{2}\dot{\varepsilon}_s^{\left(\frac{1-n}{n}\right)}\left[A\exp(-H^* / RT)\right]^{-\frac{1}{n}} \tag{4}$$

For all values of n greater than 1, the effective viscosity is inversely proportional to the strain rate. High strain rates may thus be expected to produce low effective viscosities. Since the stress and strain rate are generally not known beforehand, it is necessary to define a viscosity quantity that is independent of the applied stress or strain rate. A viscosity coefficient may be obtained from equation (3) by eliminating the stress term.

$$\eta_c = \frac{\exp(H^* / RT)}{2A} \tag{5}$$

The viscosity coefficient is the quantity used in the computa-

tions of this study and is incorporated into the finite element formulation [see *Melosh and Raefsky*, 1980].

Only viscous behavior has been considered to this point; however, the behavior of rocks in the Earth is more adequately described by viscoelastic behavior. The viscoelastic model used in this study is analogous to a Maxwell viscoelastic material. It may be represented by a linear elastic spring in series with a dashpot that has a power law viscous response. A useful measure of the time dependence of a viscoelastic material is the Maxwell time (τ_M), which is the amount of time necessary for the creep deformation to equal the elastic deformation. For a Maxwell viscoelastic material, in which the viscous behavior is Newtonian (linear), the Maxwell time is simply the viscosity of the material divided by its shear modulus. For a power law material, the effective viscosity may be substituted for the viscosity in the Maxwell model, yielding the following relationship:

$$\tau_M = \frac{\varepsilon_{elastic}}{\dot{\varepsilon}_s} = \frac{\eta_{eff}}{\mu} = \frac{\exp(H^*/RT)}{2\mu A \sigma^{(n-1)}} \quad (6)$$

The Maxwell time is a useful indicator of whether a material may be considered as an elastic solid or a viscous fluid over the time period of interest. The time period of interest in this study is of the order of 150 years (the earthquake recurrence interval). Any material with a Maxwell time considerably greater than this will thus behave elastically, while any material with a Maxwell time much less than this will behave as a viscous fluid.

A number of authors have addressed the problem of rheological layering within the Earth as it relates to laboratory results on power law flow [*Meissner and Strehlau*, 1982; *Chen and Molnar*, 1983; *Kusznir and Karner*, 1985; *Kusznir and Park*, 1986; *Ranalli and Murphy*, 1987; *Strehlau and Meissner*, 1987; *Bird*, 1989; *Melosh*, 1990]. One observation that has focused attention on this problem is the limited depth ranges over which earthquakes are observed [*Meissner and Strehlau*, 1982; *Chen and Molnar*, 1983]. *Chen and Molnar* [1983] found that in many areas, earthquakes were observed in the upper crust and upper mantle, but relatively few earthquakes were observed in the lower crust. This was attributed to a change in material types at the Moho combined with the increase of temperature with depth. As can be seen from (3) and (4), the effective viscosity decreases exponentially with increasing temperature and would thus decrease with depth. In the model of *Chen and Molnar* [1983], it was assumed that frictional failure (as described by *Byerlee* [1978]) was the dominant deformational mode in the upper crust. In the lower crust, deformation was assumed to be controlled by a quartz-diabase flow law, since the flow stress for geological strain rates (of the order of 10^{-15} s^{-1}) is less than the fracture stress at these depths. Mantle behavior was considered to be controlled by an olivine flow law. Since the flow stress for olivine is much greater than that for quartz or diabase at the same temperature and pressure, another region of high strength exists just below the Moho. The two regions of high yield stress (in the upper crust and upper mantle) are thus the only regions where seismic behavior is possible. By examining a large number of earthquakes and estimating the temperatures at the depths of the deepest events, *Chen and Molnar* [1983] found limiting temperatures of 250°–450°C for crustal materials and 600°–800°C for mantle materials. For the San Andreas fault, seismic behavior is generally absent below depths of 12 to 15 km, where the temperature is estimated to be about 350° ± 100°C [*Lachenbruch and Sass*, 1973, 1978]. A recent exception to this limit is the Loma Prieta earthquake of October 17, 1989, which occurred at a depth of approximately 18 km [*Ward and Page*, 1989].

Although much laboratory work has been done, caution must be used when applying laboratory results to actual geological situations. There is a fairly large uncertainty in the flow law parameters for any given rock type. As an example, the "best estimate" parameters given by *Kirby* [1983] for olivine in its natural state with no water added are: $\log_{10}A = 4.8 \pm 1.2$ (A in units of s^{-1} MPa^{-n}), $n = 3.5 \pm 0.6$, $E^* = 533 \pm 60$ kJ mol^{-1}, and $V^* = (17 \pm 4) \times 10^{-6}$ m^3 mol^{-1}. Additional uncertainties arise because of the effects of water and possible contributions of grain-size sensitive diffusional creep at fine grain sizes [*Kirby and Kronenberg*, 1987*a*]. A final problem is the exponential dependence of effective viscosity on temperature, as is seen in (3) and (4). As mentioned in the preceding paragraph, temperature estimates can vary by ±100°C. Later in this section it will be shown that if the assumed value of the surface heat flow varies by ±10 mW/m^2, the predicted effective viscosity can vary by 2 or more orders of magnitude. Despite the uncertainties in applying these laboratory results to the Earth, it is important to determine how incorporation of laboratory measurements into fault models influences the predicted deformation.

It is impossible to determine the composition and rheology of the Earth at every point in a fault model. A number of authors have found, however, that the creep rate within a polymineralic rock is controlled by the weakest phase if it composes at least 30% of the volume of the rock [*Carter et al.*, 1981; *Shelton and Tullis*, 1981]. The rheological behavior can then be estimated from the rheology of the principal constituents at the depth of interest. In the upper crust, the rheological properties are likely to be dominated by quartz. The lower crust, which probably has a lower quartz content, may be controlled by a feldspar or pyroxene rheology. Within the upper mantle, the flow rate is likely to be dominated by olivine.

For the finite element modeling, the materials chosen to represent the various rheological layers were granite, diabase, olivine, and dunite. The elastic and viscous properties of these materials are listed in Table 1. The viscosity parameters (power law exponent, A, and activation energy) were obtained from Table 1 of *Strehlau and Meissner* [1987]. The elastic parameters represent average values derived from several sources [*Birch*, 1966; *Turcotte and Schubert*, 1982], simplified for numerical

TABLE 1. Elastic and Viscoelastic Parameters Used in the Modeling for Various Material Types

Material Type	Young's Modulus, Pa	Poisson's Ratio	Shear Modulus, Pa	Density, kg/m^3	Power Law Exponent	$\log_{10}A$	Activation Energy, kJ/mol
"Elastic"	1.5×10^{11}	0.25	6.00×10^{10}	3000	1.0	–	–
"Viscoelastic"	1.5×10^{11}	0.25	6.00×10^{10}	*	1.0	–	–
Dry granite	5.0×10^{10}	0.25	2.00×10^{10}	3000	2.9	–0.2	106
Wet granite	5.0×10^{10}	0.25	2.00×10^{10}	3000	1.5	2.0	137
Dry diabase	8.0×10^{10}	0.25	3.20×10^{10}	3000	3.4	6.5	260
Wet diabase	8.0×10^{10}	0.25	3.20×10^{10}	3000	3.0	7.9	276
Dry olivine	1.6×10^{11}	0.28	6.25×10^{10}	3300	3.5	15.5	535
Wet dunite	1.6×10^{11}	0.28	6.25×10^{10}	3300	3.4	14.4	444

The logarithm base ten of A is given. The units of A are GPa^{-n} s^{-1}.

*Density is equal to 3000 kg/m^3 for all material above 40 km, and 3300 kg/m^3 for all material below 40 km.

convenience. This simplification seems justified due to the uncertainty in determining the actual composition of the region of interest. The densities were chosen to be 3000 kg/m^3 for all material above 40 km (the assumed Moho) and 3300 kg/m^3 for all material below this depth, to simplify the isostatic aspects of the problem. Also listed in Table 1 are materials labeled as "elastic" and "viscoelastic." These represent the properties used in a linear (Maxwell) viscoelastic model analogous to that of *Savage and Prescott* [1978], which is used for comparison to the nonlinear models.

Since effective viscosity decreases exponentially with increasing temperature (see equations (3) and (4)) it is necessary to construct a temperature profile for the region of interest. This is probably one of the major sources of uncertainty in the calculations. The rheological behavior is extremely sensitive to temperature, and the temperature at depth is difficult to determine accurately. A relatively simple profile was chosen for this study because of the difficulty in accurately determining the temperature and also because the temperature gradient represents an average over a large surface area (the grid covers an area approximately 700 km × 1300 km). The method chosen was that of *Chapman* [1986], which incorporates the mantle model of *Schatz and Simmons* [1972]. This method assumes steady state, one-dimensional conductive heat transfer, with observed heat flow as the principal constraint. Using this method, a geotherm consistent with a surface heat flow of 75 mW/m^2 was calculated. This value is consistent with the value of 78 mW/m^2 obtained by averaging the San Andreas heat flow values for regions 4, 5, 6, and 7 in Figure 8 and Table 2 of *Lachenbruch and Sass* [1980]. This profile is shown by the thin solid line in Figure 2. The discretization of the profile used in the finite element calculations is represented by the thick solid line in Figure 2. Also shown are the profiles that would be generated by assuming a heat flow of 65 mW/m^2 (thin dashed line) and 85 mW/m^2 (thin dotted line). The profiles for heat flows of 65 and 85 mW/m^2 are shown to demonstrate how uncertainties in the observed heat flow for the thermal model influence the predicted temperature. Further variations in the predicted temperature arise due to uncertainties in other model parameters (such as conductivity and heat generation) as well as the nature of the model itself. For the thermal models shown here, the slope changes dramatically at about 100 km depth, where the geotherm intercepts the mantle 1300°C adiabat. The assumed temperature below this depth is not particularly important, as the model results are relatively unaffected by viscosity changes below 100 km.

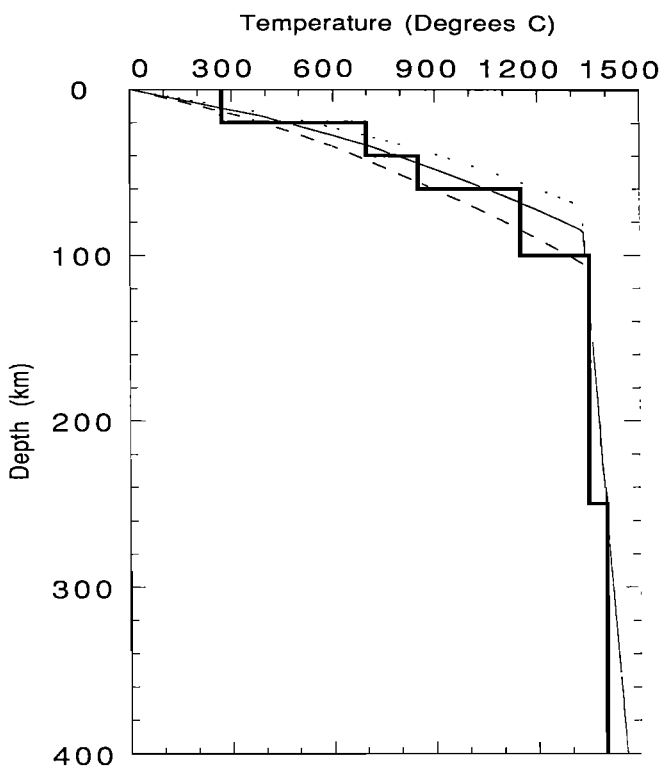

Fig. 2. Temperature profile used for the San Andreas modeling. The thin solid line represents the geotherm calculated for an assumed surface heat flow of 75 mW/m^2, and the thick solid line is the discretization of this profile used in the finite element calculations. The thin dashed line and the thin dotted line represent the geotherms calculated for assumed surface heat flows of 65 mW/m^2 and 85 mW/m^2, respectively.

The rheological properties of the various models are listed in Tables 2*a*–2*e*. The first model (Table 2*a*) is a linear (Maxwell) viscoelastic model that is used for comparison with the nonlinear models. The assumed temperature profile is not important in this case, as the model simply consists of an "elastic" layer overlying a "viscoelastic" layer. Since the grid extends to a depth of 400 km, a factor of 10 greater than the maximum depth of elastic behavior, the viscoelastic layer may be considered to be a half-space. For a Maxwell viscoelastic material, the viscosity coefficient (given by equation (5)) and the effective viscosity (given by equation (3)) are equivalent. For the nonlinear models, effective viscosity and Maxwell time were calculated for an assumed strain rate of 2×10^{-14} s^{-1}, a typical value for the strain rate close to the fault, as determined from the calculations. The Maxwell time may be calculated from (6). The properties of the linear model used in the finite element calculations are shown graphically in Figure 3, which shows the effective viscosity and Maxwell time as a function of depth. In Figure 3, and those that follow, effective viscosity will be shown with solid lines, and Maxwell time with dashed lines. There are two versions of the linear model in which aseismic slip occurs to different depths. The thick lines represent the model in which there is no aseismic slip below the locking depth (H = 20 km), while the thin lines represent a model that includes aseismic slip (H = 40 km). Throughout the rest of this paper, models that include aseismic slip at depth will be referred to as A models, while those that do not will be referred to as B models. The definitions of the fault locking depth (D) and elastic layer thickness (H) for the linear models are shown in Figure 1*a*. For the linear models, the A and B versions differ in both the depth of aseismic slip and in the thickness of the surface elastic layer. The viscosity chosen to simulate an elastic layer is sufficient to produce elastic behavior over any time period of geologic interest (1×10^{33} Pa s).

Although there are numerous possible rheological models, four were chosen for this study (in addition to the linear model described above). The viscoelastic properties are listed in Tables 2*b*–2*e*. The first of these models (Table 2*b*) is the simplest, but it is perhaps not geologically reasonable, as it assumes that the behavior of the entire crust is dominated by a granite rheology. Below the Moho, the rheological properties chosen are those for olivine. This is also true of models 2 and 3. In all models, the Moho depth is assumed to be 40 km. This is probably somewhat deep for southern California, but a shallower depth would have required elements with unacceptable aspect ratios near the surface. The effective viscosity and Maxwell time as a function of depth for model 1 are shown in Figure 4. Effective viscosity is shown with solid lines, and Maxwell time is shown with dashed lines. The thin lines represent the values determined from the temperature profile (75 mW/m^2) of Figure 2, while the thick lines represent the discrete values used in the finite element computations. Although this model contains only two different materials (granite and olivine), a number of layers occur in the finite element calculations due to the strong temperature dependence of rheological properties. Analysis of Figure 4 reveals that the upper crust and uppermost mantle would be expected to exhibit elastic behavior

TABLE 2*a*. Linear Model

Depth Range, km	Material Type	Temperature, °C	Viscosity Coefficient, Pa^n s	Effective Viscosity, Pa s	Maxwell Time, years
0-20	"elastic"	–	1×10^{33}	1×10^{33}	5.28×10^{14}
20-40*	"elastic"	–	1×10^{33}	1×10^{33}	5.28×10^{14}
20-40†	"viscoelastic"	–	2×10^{19}	2×10^{19}	10.6
40-400	"viscoelastic"	–	2×10^{19}	2×10^{19}	10.6

Tables 2*a*–2*e* list properties of the various models. Elastic and viscoelastic parameters used are listed in Table 1. Effective viscosity and Maxwell time were calculated assuming a strain rate of 2×10^{-14} s^{-1}.

*H = 40 km.

†H = 20 km.

TABLE 2*b*. Nonlinear Model 1

Depth Range, km	Material Type	Temperature, °C	Viscosity Coefficient, Pa^n s	Effective Viscosity, Pa s	Maxwell Time, years
0-20	dry granite	270	1.57×10^{36}	1.82×10^{21}	2880
20-40	dry granite	700	4.89×10^{31}	5.08×10^{19}	80.5
40-60	dry olivine	850	3.84×10^{40}	1.46×10^{21}	743
60-100	dry olivine	1150	2.18×10^{35}	4.64×10^{19}	23.5
100-250	dry olivine	1350	8.28×10^{32}	9.44×10^{18}	4.79
250-400	dry olivine	1400	2.53×10^{32}	6.73×10^{18}	3.42

TABLE 2*c*. Nonlinear Model 2

Depth Range, km	Material Type	Temperature, °C	Viscosity Coefficient, Pa^n s	Effective Viscosity, Pa s	Maxwell Time, years
0-20	dry granite	270	1.57×10^{36}	1.82×10^{21}	2880
20-40	dry diabase	700	5.72×10^{37}	3.65×10^{20}	362
40-60	dry olivine	850	3.84×10^{40}	1.46×10^{21}	743
60-100	dry olivine	1150	2.18×10^{35}	4.64×10^{19}	23.5
100-250	dry olivine	1350	8.28×10^{32}	9.44×10^{18}	4.79
250-400	dry olivine	1400	2.53×10^{32}	6.73×10^{18}	3.42

TABLE 2*d*. Nonlinear Model 3

Depth Range, km	Material Type	Temperature, °C	Viscosity Coefficient, Pa^n s	Effective Viscosity, Pa s	Maxwell Time, years
0-20	dry granite	270	1.57×10^{36}	1.82×10^{21}	2880
20-40	wet diabase	700	4.13×10^{33}	1.37×10^{20}	136
40-60	dry olivine	850	3.84×10^{40}	1.46×10^{21}	743
60-100	dry olivine	1150	2.18×10^{35}	4.64×10^{19}	23.5
100-250	dry olivine	1350	8.28×10^{32}	9.44×10^{18}	4.79
250-400	dry olivine	1400	2.53×10^{32}	6.73×10^{18}	3.42

TABLE 2*e*. Nonlinear Model 4

Depth Range, km	Material Type	Temperature, °C	Viscosity Coefficient, Pa^n s	Effective Viscosity, Pa s	Maxwell Time, years
0-20	wet granite	270	2.39×10^{24}	5.23×10^{20}	829
20-40	wet diabase	700	4.13×10^{33}	1.37×10^{20}	136
40-60	wet dunite	850	3.56×10^{36}	1.61×10^{20}	81.9
60-100	wet dunite	1150	1.58×10^{32}	8.46×10^{18}	4.29
100-250	dry olivine	1350	8.28×10^{32}	9.44×10^{18}	4.79
250-400	dry olivine	1400	2.53×10^{32}	6.73×10^{18}	3.42

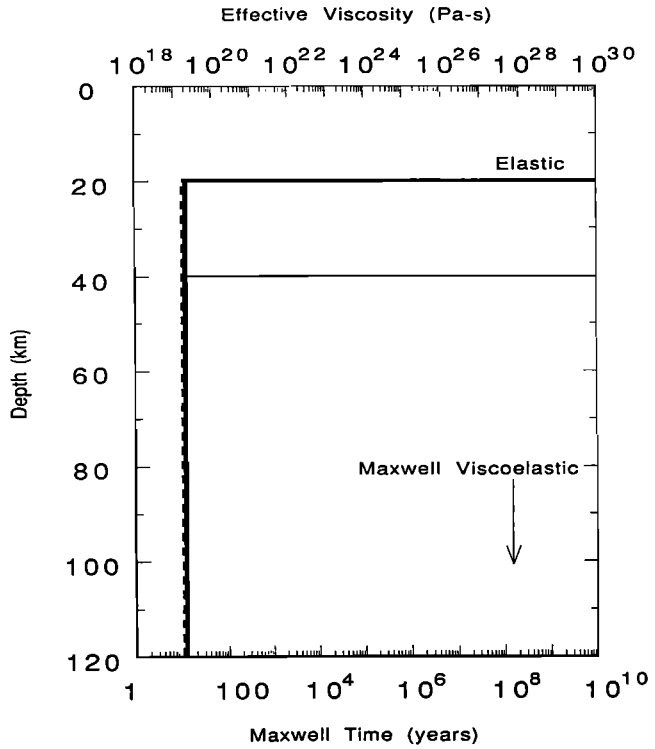

Fig. 3. Effective viscosity and Maxwell time for the linear models as a function of depth. Solid lines represent effective viscosities, and dashed lines represent Maxwell times. Thick lines are the profiles for models with H = 20 km (B models), and thin lines are the profiles for models with H = 40 km (A models).

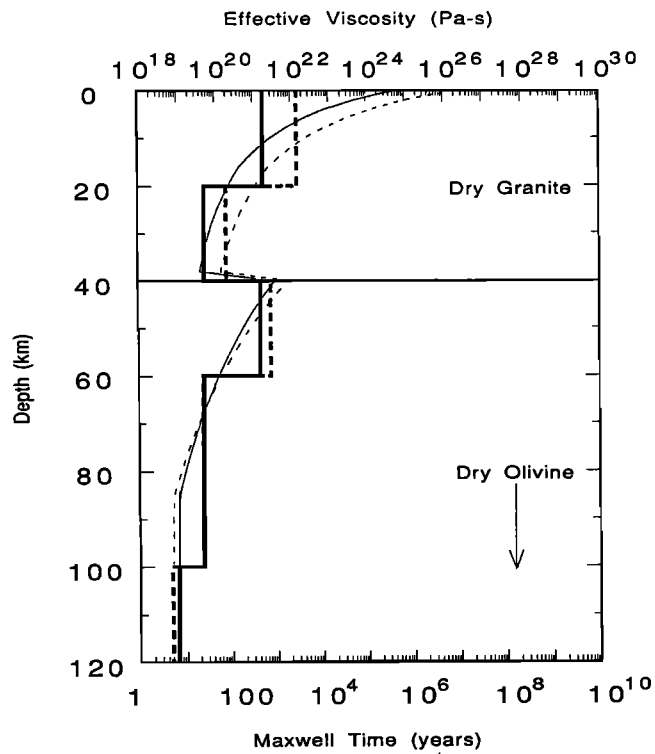

Fig. 4. Effective viscosity and Maxwell time for the nonlinear model 1 as a function of depth. Solid lines represent effective viscosities, and dashed lines represent Maxwell times. Thin lines represent the profiles calculated from the 75 mW/m^2 geotherm of Figure 2, and thick lines represent the discretized versions used in the finite element calculations.

over the time period of interest (150 years). The lower crust, on the other hand, has a Maxwell time of the order of the earthquake recurrence interval and would thus be expected to display some time-dependent behavior. Viscous behavior would also be expected from the mantle below 60 km depth.

The second nonlinear model (Table 2*c* and Figure 5) perhaps represents a more realistic view of actual Earth rheology. This model has rheological properties consistent with a granite upper crust and a diabase lower crust. The behavior of the mantle is consistent with laboratory results on dry olivine, as in model 1. The crustal layering results in two viscosity minima within the crust. Unfortunately, our finite element mesh is too coarse for this level of detail. For this model, time-dependent behavior would be restricted primarily to the mantle below 60 km (see Figure 5). Even ignoring the discretization effects, this model would display considerably less time dependence than model 1, since the Maxwell time at the base of the crust is considerably greater than model 1 (compare Figures 4 and 5).

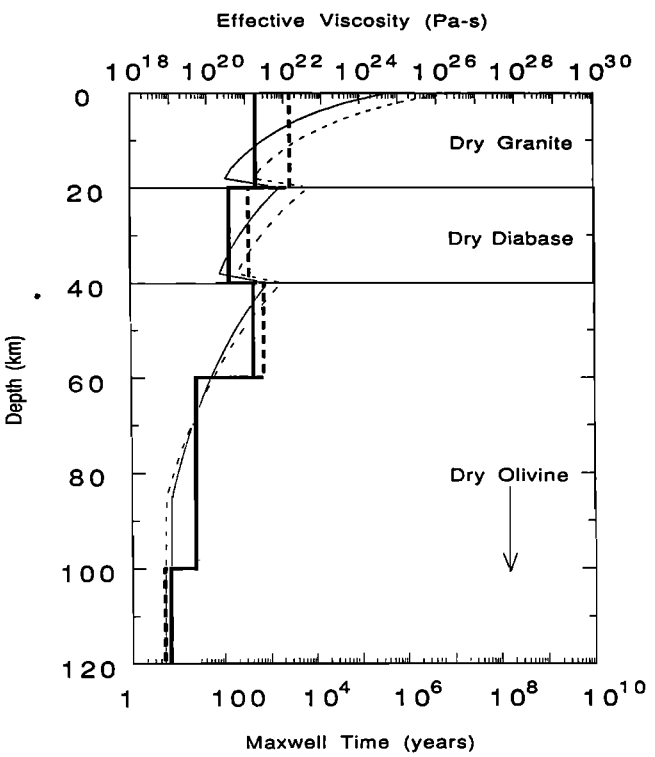

Fig. 5. Same results as Figure 4 for nonlinear model 2.

Models 1 and 2 describe completely dry rheologies; however, the presence of water can have a significant effect on viscous flow. This effect is included in model 3 (Table 2*d*), which includes laboratory results for wet diabase in the lower crust. The existence of water in the lower crust is somewhat debatable, but there is enough evidence for hydration at depth that it cannot be ruled out as a possibility (see *Strehlau and Meissner* [1987] for a summary). In this study, it is of interest to determine the effects of hydrated minerals on the model response. As may be seen from Figure 6, the presence of water has a significant effect on the rheological properties of diabase. The resulting profiles are similar to those of model 1, with a viscous layer in the lower crust sandwiched between the elastic layers in the upper crust and mantle. The time-dependent characteristics of models 1 and 3 should be similar.

The final model, model 4 (Table 2*e* and Figure 7), considers the entire crust and upper mantle to be hydrated to a depth of 100 km. The use of rheological properties for wet dunite in the

upper mantle results in a smaller difference between the behavior of the lower crust and upper mantle (compare Figure 7 with Figures 5 and 6). As a result, the discretized profile used in the finite element calculations does not include a low viscosity layer between the upper crust and lower mantle; instead it includes a fairly constant effective viscosity from 20 to 60 km depth. Below 100 km, the assumed rheology is that of dry olivine, as in the previous models. The relatively low effective viscosities down to 100 km depth should produce significant time-dependent effects. All of the models extend to a depth of 400 km, but only the first 120 km are shown in Figures 3–7. All of the models exhibit the same rheological behavior below 100 km depth, except for the linear models. Below 100 km, there is very little change in the effective viscosity because of the relatively shallow slope of the mantle adiabat (0.4°K/km) below this depth.

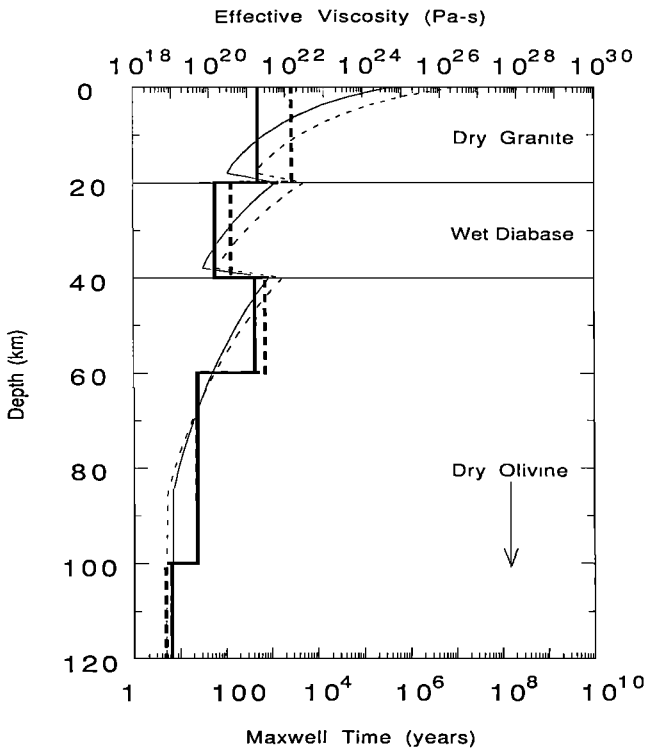

Fig. 6. Same results as Figure 4 for nonlinear model 3.

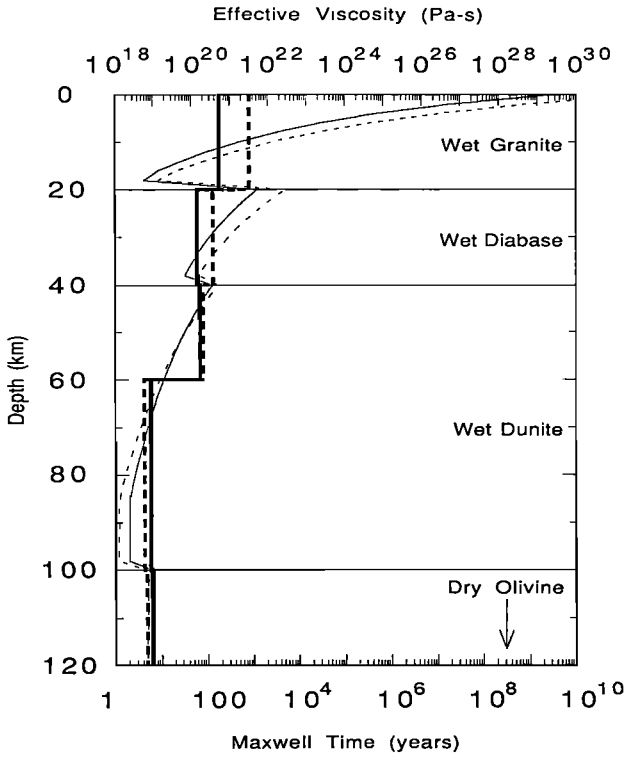

Fig. 7. Same results as Figure 4 for nonlinear model 4.

To evaluate the degree to which uncertainties in the temperature profile are propagated into the viscosity model, effective viscosities for model 4 were calculated for the two alternate temperature profiles shown in Figure 2. These results are shown in Figure 8. The results assuming a surface heat flow of 85 mW/m^2 (thin dotted line in Figure 2) are shown with a thin dotted line, and those for a surface heat flow of 65 mW/m^2 (thin dashed line in Figure 2) are shown with a thin dashed line. The viscosity profile representing the physical model upon which the finite element models are based (thin solid line) and the discrete representation of this profile used in the finite element models (thick solid line) are also shown. These results demonstrate that an uncertainty in the observed heat flow of 10 mW/m^2 can cause the effective viscosity to vary over almost 2 orders of magnitude for this particular model. This effect is most prominent near the base of the upper crust and gradually decreases with depth. Model results should therefore be interpreted very carefully, due to the large amount of uncertainty introduced by the strong temperature dependence of effective viscosity.

In all of the models, there are sharp boundaries between different material types, while in the Earth these boundaries are almost certainly gradational. This problem is always encountered when attempting to describe continuous phenomena in the real world with a discrete numerical technique. Our analysis should describe the first-order effects of a rheologically layered Earth. Higher-order effects may be evaluated by refining the finite element mesh used in the modeling.

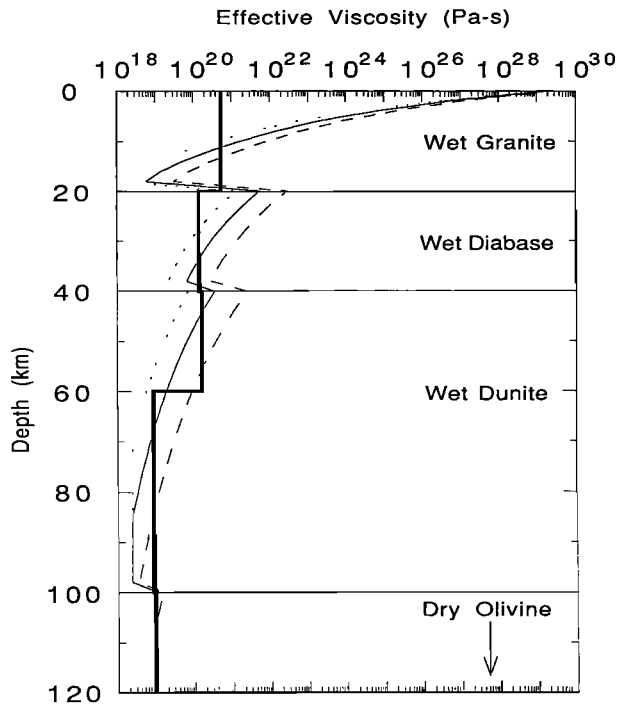

Fig. 8. Effective viscosity as a function of depth for nonlinear model 4 calculated for assumed surface heat flows of 65 mW/m^2 (thin dashed line), 75 mW/m^2 (thin solid line), and 85 mW/m^2 (thin dotted line). The thick solid line is the discretized profile used in the finite element calculations.

MODEL DESCRIPTION AND IMPLEMENTATION

Model Description

The models used in this study are derived from the infinite rectangular fault model described by *Savage and Prescott* [1978], as described previously and illustrated in Figure 1. The cross-sectional views shown in Figure 1 are understood to extend infinitely both into and out of the plane of the view. In practice, a half-space model may be adequately simulated by a numerical model with dimensions that are considerably greater than the thickness of the elastic layer. This procedure is followed in the present study, both in simulating the model of Figure 1*a* and in producing models of the type shown in Figure 1*b*. In both models, the fault is locked to a depth D between earthquakes. At time T (the earthquake recurrence time) coseismic displacement (U) occurs on the locked portion of the fault, with a magnitude determined by plate velocity. If plate motion is spatially uniform, occurring at a constant relative rate given by v_0 then $U = v_0T$. In the Savage and Prescott model, aseismic slip below the locking depth occurs to a depth H, which represents the thickness of the elastic layer. In the nonlinear models of this study, there is no elastic layer as such, and the parameter H instead represents the depth to which aseismic slip occurs. The aseismic slip rate between D and H is equal to the relative plate velocity.

The models in our study are completely three-dimensional, offering a number of advantages over two-dimensional models. First, our analysis is able to include the effects of both horizontally and vertically varying structures. In the present analysis, only horizontal variations (corresponding to changes in fault strike) are considered, as the variation of Earth structure with depth (i.e., changes in fault dip) is not well known. In any case, complex vertically varying geometries would not be warranted in this preliminary study. Another advantage of a three-dimensional analysis is the ability to calculate vertical as well as horizontal deformation. Although observations of vertical uplift along the San Andreas fault are presently restricted to a limited area and have large uncertainties, they could conceivably play an important role in resolving the differences between competing fault models (see *Stein* [1987], *Craymer and Vaníček* [1989], and *Stein et al.* [1989] for a discussion of the accuracy of vertical uplift measurements defining the "Palmdale uplift").

Calculation of Vertical Uplift

Although the calculation of vertical uplift with the finite element method is not difficult, it is important to consider a number of factors. Foremost among these are the effects of isostasy. Any uplift that occurs as a result of tectonic forces must be countered by isostatic forces proportional to the amount of uplift. If this were not true, tectonic uplift could continue indefinitely, resulting in infinite topography. Ordinarily, this would be the case in time-dependent finite element calculations, with or without the use of body forces. At each time step, uplift would proceed in a manner dictated by the present set of forces, regardless of the amount of uplift that had occurred in the previous time step. This is a result of the infinitesimal strain approximation used in most finite element calculations. All spatial quantities are referenced to the initial nodal positions, so that the entire grid geometry remains unchanged over the course of the calculations. Therefore, no matter how much vertical uplift has been induced by the applied boundary conditions, the system of body forces will be the same as it was initially.

A simple solution exists to remedy this problem that does not require major modifications to the finite element code. Isostasy in time-dependent problems may be simulated through the use of Winkler restoring forces (for an explanation, see Chapter 14 of *Desai* [1979]). This method has been incorporated into the finite element code by H. J. Melosh (unpublished computer program, 1988). These forces are essentially one-dimensional spring elements that are applied at the boundaries between density contrasts. The spring constant is chosen to be proportional to the magnitude of the density contrast. Therefore any vertical displacement increment away from the initial position results in a force in the opposite direction that is proportional to the density contrast and the amount of the displacement increment.

The situation is represented in Figure 9, which shows the case of a single layer with one-dimensional spring elements applied at the bottom and top of the layer. It is obvious that any vertical movement of the surface S_1 will be countered by a force increment k_1x, where k_1 is the spring constant for the upper set of springs and x is the vertical displacement increment. A similar situation exists for surface S_2. To simulate isostatic effects, it is only necessary to make the spring constants proportional to the corresponding density contrast. For the upper surface, this contrast would be $\Delta\rho_{10} = \rho_1 - \rho_0$. The contrast for the lower surface is $\Delta\rho_{21} = \rho_2 - \rho_1$. In the present finite element calculations, the surface S_1 represents the Earth's surface, and the surface S_2 represents the Moho; these are the two most prominent density contrasts in the lithosphere. For the sake of simplicity, these are the only density contrasts included in this analysis. The density contrast for surface S_1 would then be 3000 kg/m^3, while that for surface S_2 would be 300 kg/m^3 (see Table 1).

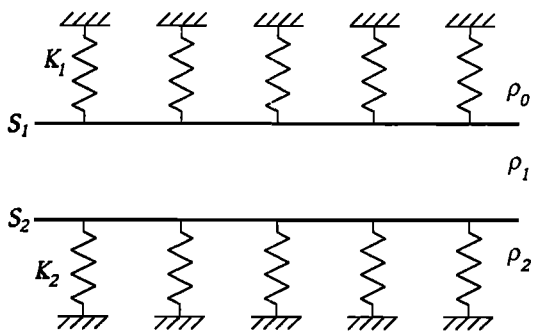

Fig. 9. Physical analogy of Winkler restoring forces. Springs with constants k_1 and k_2 are attached to surfaces S_1 and S_2.

In practice, the restoring forces are applied through a modification of the stiffness matrix. Assume, for the sake of simplicity, an element e with only two degrees of freedom. The local stiffness matrix for this simplified element is given by

$$K_{ij}^e = \begin{bmatrix} K_{11}^e & K_{12}^e \\ K_{21}^e & K_{22}^e \end{bmatrix} \tag{7}$$

Assume that K_{11}^e corresponds to the vertical degree of freedom for a node of element e that is contained in the surface S_1. Then the modified stiffness matrix including the restoring force is

$$K_{ij}^e = \begin{bmatrix} K_{11}^e + k_{11}^e & K_{12}^e \\ K_{21}^e & K_{22}^e \end{bmatrix} \tag{8}$$

The magnitude of k_{11}^e is given by

$$k_{11}^e = \frac{\Delta\rho_{10}\, g A_{S_1}^e}{n_{S_1}^e} \tag{9}$$

where $A_{S_1}^e$ is the area of element e contained in surface S_1, $n_{S_1}^e$ is the number of element nodal points in element e contained in S_1, and g is the gravitational acceleration (9.8 m/s^2). A similar situation exists for surface S_2.

The spring constant values are therefore added directly to the diagonal entries of the global stiffness matrix for the appropriate vertical degree of freedom. The sign of k^e_{11} is always positive, such that the restoring force acts in the direction opposite any displacement. Thus an upward displacement on surface S_1 (simulating the creation of new topographic highs) would result in a force directed downward, while a downward displacement of surface S_1 (resulting in a mass deficit) would produce an upward directed buoyancy force. For surface S_2 a downward displacement would simulate root formation, producing an upward directed buoyancy force, while an upward displacement would correspond to the production of a mass excess at depth, resulting in a downward directed force.

Body forces are not included in the calculations for several reasons. Foremost among these is the likelihood that the nontectonic (gravitationally induced) stresses in the crust and upper mantle approach a state of lithostatic stress [*McGarr*, 1988]. If this is true, the nontectonic deviatoric stress is zero everywhere in the Earth. Since the deformation is only affected by the deviatoric stress (recall that σ in (1)–(3) and (6) represents the differential stress), the gravitational body forces simply represent a depth-dependent pressure that can be removed from the calculations. Since this study is only concerned with deformation at the surface and not with stresses, body forces represent an unnecessary complication and are not included.

The present analysis does not include the effects of existing topography. The results are therefore valid for initially flat surfaces. In addition, the effects of erosion are not considered. Although both of these factors will influence the results, they were not included in the analysis for the sake of simplicity. Both of these effects may be included in more complex models.

Finite Element Modeling of the Problem

The finite element code used in this analysis is a three-dimensional adaptation of the two-dimensional code of *Melosh and Raefsky* [1980]. Fault slip is included by means of the split node technique [*Melosh and Raefsky*, 1981]. With this method, the fault displacement (or displacement increment) is specified. Using this technique, it is possible to apply either steady slip corresponding to plate velocity or abrupt slip at specified times. The split node method thus results in kinematic model behavior since the fault displacements are independent of the prevailing stress regime. A new method (the "slippery node" technique [*Melosh and Williams*, 1989]) allows fault slip to occur in response to stress and also allows fault friction to be specified. The use of this method would introduce an unnecessary degree of complexity to this preliminary investigation, however. At present, it is desirable to consider only rheological or geometrical parameters.

Two types of finite element calculations are performed. The first type of calculation assumes an infinitely long rectangular fault, analogous to the model of *Savage and Prescott* [1978]. This is done for two reasons. First, this allows a comparison of the numerical results with the analytical results of *Savage and Prescott* [1978] to test the accuracy of the numerical model. Second, this provides a simple means of examining the characteristics of the various models. The second type of calculation includes a more realistic representation of San Andreas fault geometry, with fault strike varying to match the observed strike of the fault. The grids used for the two types of calculations are similar, except for the assumed variation in fault strike. For the remainder of this paper, models that do not include variations in fault strike (infinitely long rectangular faults) will be referred to as "rectangular fault models," while those that include the effects of varying fault strike will be referred to as "San Andreas fault models."

The grid used for the rectangular fault models is shown in Figures 10*a* and 10*b*, and the grid incorporating San Andreas fault geometry is shown in Figures 11*a* and 11*b*. Figures 10*a* and 11*a* show map views of the grids and the imposed boundary conditions. The arrows represent velocity boundary conditions corresponding to the relative plate velocity and are applied to all nodes on the left- and right-hand sides of the grids

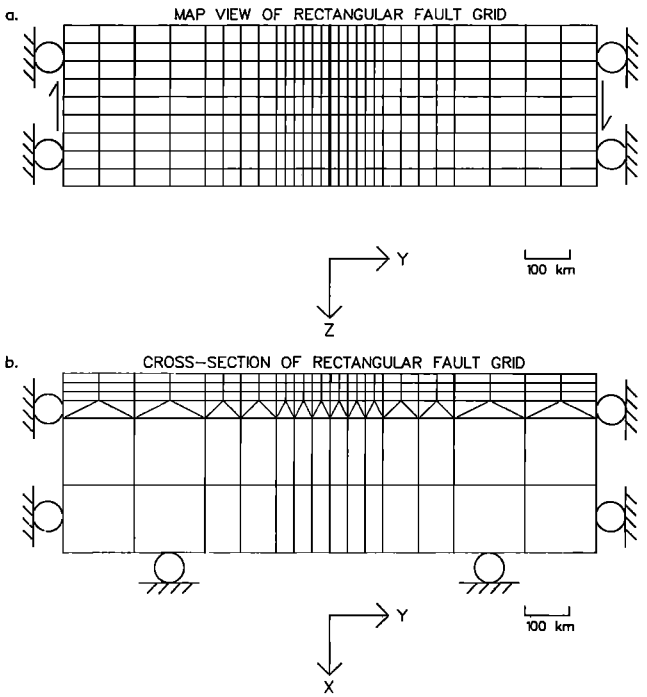

Fig. 10. Grid used in the rectangular fault modeling. The thick solid line represents the locked portion of the fault. (*a*) Map view. (*b*) Cross-sectional view.

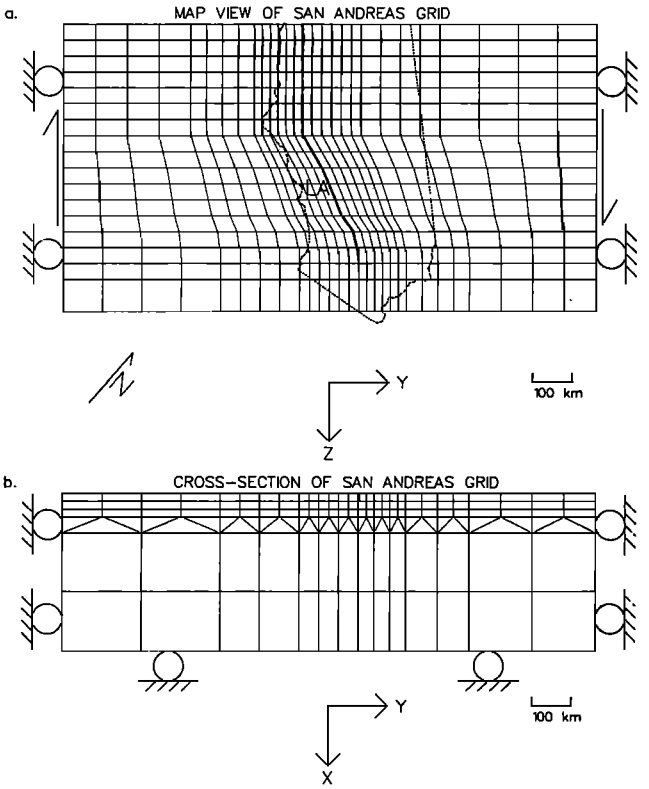

Fig. 11. Grid used in the models incorporating San Andreas fault geometry. The thick solid line represents the locked portion of the fault, and the dashed line represents the creeping section. (*a*) Map view. (*b*) Cross-sectional view of southern end of grid.

(corresponding to the minimum and maximum y values, respectively). The northern and southern boundaries of the grids (corresponding to the minimum and maximum z values, respectively) are left free. The thick, solid lines represent the portion of the fault that is locked between earthquakes. The dashed line on Figure 11*a* represents the creeping portion of the fault. Figures 10*b* and 11*b* are cross-sectional views of the grids. The thick, solid lines represent the locked portion of the fault. For B models, this line also represents the depth of aseismic slip, H (i.e., no aseismic slip). For A models, aseismic slip extends below this depth to the next layer of elements. The rheological properties are constant within each layer of elements (there are six layers). The San Andreas grid (Figure 11) is composed of 2618 three-dimensional elements containing 2898 nodal points. The x, y, and z dimensions are 400 km, 1350 km, and 720 km, respectively. The rectangular fault grid has x, y, and z dimensions of 400 km, 1200 km, and 360 km and contains 1386 elements and 1610 nodes. The smallest elements occur closest to the fault. These elements have dimensions of 20 km in the x and y directions and 40 km in the z direction.

The choice of element dimensions was dictated by three goals: keeping the elements as small as possible in the region of interest, making the elements as nearly equidimensional as possible, and using the minimum number of elements. The first goal arises from the desire to obtain maximum resolution in both the calculated deformation and the assigned material properties. The second goal is a result of the finite element formulation, in which the interpolations are performed for the idealized shape of a cube. The final goal reflects the limitations of the computer on which the calculations are performed. The present analysis was performed on a CONVEX C1, a vector processor with 32 megabytes of core memory. Although it was possible to use a finer mesh grid, the memory requirements of the resulting stiffness matrix exceeded the computer's capabilities. The memory swapping required to handle the stiffness matrix resulted in an excessively long calculation time. One solution to this problem is an alternate method of storing the stiffness matrix (sparse matrix techniques are presently being explored). The simplest method is to use a machine with a greater amount of core memory. The San Andreas fault models used in this study had run times of about 10 hours on a CONVEX C1.

The computer limitations place a number of constraints on the grid geometry. For instance, the maximum vertical resolution is 20 km, which occurs near the surface. For this reason, the fault locking depth (D) and the depth of aseismic slip (H) are constrained to values that are multiples of 20 km. In the calculations that follow, the locking depth will always be assumed to be equal to 20 km (except for the creeping portion of the fault, where $D = 0$), since earthquakes on the San Andreas are generally not observed below this depth. The depth of aseismic slip will be assumed to be either 20 km (no aseismic slip below the locking depth) or 40 km (aseismic slip between 20 and 40 km). On the creeping portion of the fault, aseismic slip occurs from the surface to the depth of aseismic slip, H. The changes in material properties are similarly constrained (see Tables 2*b*–2*e*). The horizontal resolution is also affected, which prevents the incorporation of adjacent faults into the present model. Although appreciable slip occurs on faults other than the San Andreas, it is presently not possible to include them in the analysis.

One assumption of this analysis is that the overall deformation field will be dominated by the largest magnitude earthquakes, with smaller earthquakes producing local perturbations in the overall pattern of deformation. For this reason, only the largest magnitude earthquakes which rupture a significant portion of the fault are included in the analysis. The last earthquake of such magnitude in southern California was the Fort Tejon earthquake of 1857, which had a magnitude greater than 8 and ruptured 360 to 400+ km of the fault [*Sieh*, 1978]. For simplicity, it is assumed that earthquakes with a relative coseismic displacement (U) of 5.25 m occur every 150 years, rupturing the entire fault from just south of Cholame to the southern end of the fault shown in Figure 11*a*, which is near the Salton Sea. This is the portion of the fault shown by the solid line in Figure 11*a*. The average recurrence time (T) of 150 years is consistent with the estimate of 132 years given by *Sieh et al.* [1989], determined by sediment analysis. The coseismic displacement in each earthquake is assumed to keep pace with the plate velocity. The assumed relative plate velocity ($v_0 = U/T$) is then 35 mm/year, which is applied parallel to the z axis (see Figures 9*a* and 10*a*). For the San Andreas calculations, the z axis is oriented N41°W, while for rectangular fault models the axis orientation has no particular meaning. These values are consistent with current geodetic and geologic determinations of motion on the San Andreas fault [*Minster and Jordan*, 1987; *DeMets et al.*, 1987]. Plate velocity is applied to a depth H below the locking depth on the fault, to simulate aseismic slip at depth. The results of *King et al.* [1987] indicate that shallow aseismic slip occurs near Cholame and increases with distance north of this location. To simulate this creeping portion of the fault, the locking depth is assumed to be zero for the fault segment between Hollister and Cholame (dashed section in Figure 11*a*). For this section, plate velocity is applied from the surface to a depth H.

Below the southern end of the San Andreas fault shown in Figure 11*a*, no slip is applied. The rectangular fault models, which use the grid shown in Figures 10*a* and 10*b*, do not include a creeping section or a permanently locked section. There are two extreme possibilities for the boundary conditions at the southern end of the San Andreas fault model: aseismic slip from the surface to a depth H, such that there is no accumulation of strain; or no slip at all, such that there is a secular buildup of strain. Although a number of arguments could be advanced for the first condition, we decided to apply the second condition to our models. The primary reason was the relative infrequency of large-magnitude earthquakes below the southern termination of the fault used in our model (Figure 11*a*). For example, *Wesnousky* [1986] indicates that no slip occurred along the Imperial fault for at least 700 years preceding the 1940 magnitude 6.9 earthquake. It is therefore clear that there is some strain accumulation in this region, although probably not as much as that used in our model. Over a sufficiently long time period, our boundary conditions would result in unreasonably large amounts of strain accumulation near the southern terminus of the fault; however, over the time period used in the modeling (1500 years), the strain accumulation is not excessive. When interpreting our model results, it should be recognized that the predicted strain magnitudes near the southern portion of the grid are probably greater than they should be. It is also important to realize that, because of the relatively coarse mesh of the finite element grid used for the calculations and because of the imposed slip boundary conditions, the deformation associated with the two bends in the fault is likely to be exaggerated as well. The coarse grid mesh results in relatively sharp fault bends. Thus, when slip is imposed, the sudden change in direction causes interference between material on either side of the fault. This effect would probably be reduced with a finer grid mesh and stress-dependent slip conditions.

In order to achieve steady state behavior, it is necessary to run the model through a number of earthquake cycles. After a sufficient number of cycles, the results for each cycle are identical. It was found that 10 earthquake cycles were generally sufficient to produce steady state model response. In the results that follow, all values are determined following the ninth earthquake in a sequence. For the nonlinear models, each earthquake cycle consists of 100 discrete time steps of 1.5 years each. For the linear models, it is possible to decrease the number of time steps without significantly affecting the accuracy of the results. Each earthquake cycle for these models is composed of 20 time steps. The size of the time steps ranges from 1.5 years near the beginning of the cycle (where the time dependence is greatest)

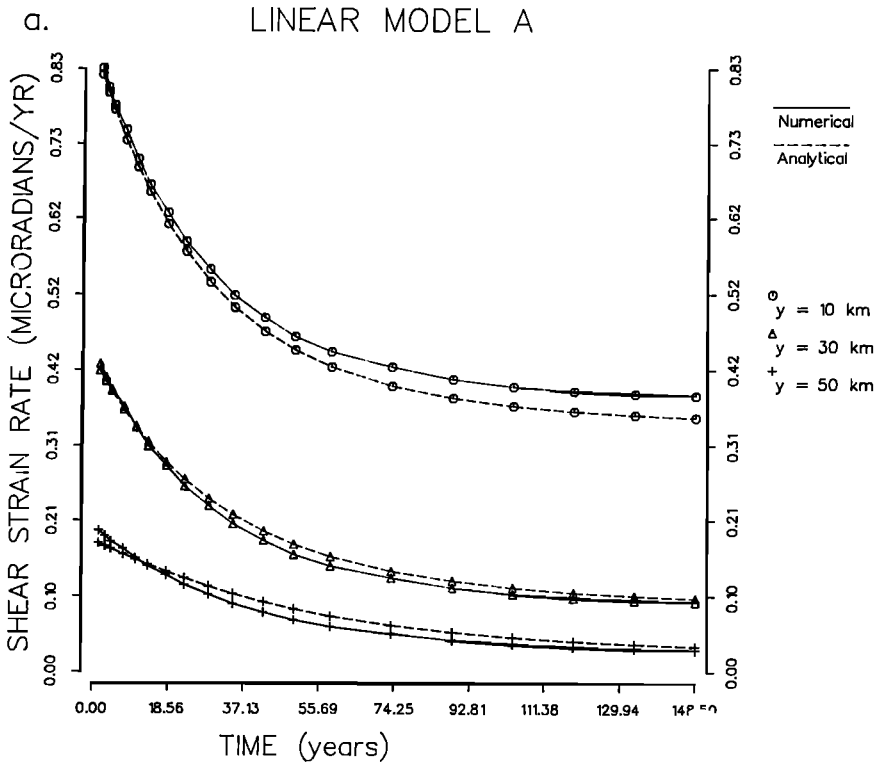

Fig. 12. Engineering shear strain rate as a function of time since the last earthquake for rectangular fault models at various distances from the fault. The finite element results are shown with solid lines, and the analytical solution is shown with dashed lines. The results are shown for (*a*) linear model A (H = 40 km) and (*b*) linear model B (H = 20 km).

to 15 years near the end of the cycle. It is not possible to substantially increase the size of the time steps for the nonlinear models because of numerical instabilities. This may be understood from an inspection of (1). Since the steady state strain rate is proportional to a power of the differential stress, a higher power law exponent means that the strain rate is more sensitive to the system of stresses. For materials with large power law exponents, it is therefore necessary to recalculate the stresses fairly frequently in order to accurately determine the strain rate. In other words, small time steps are necessary to successfully linearize a highly nonlinear problem.

RESULTS

Rectangular Fault Models

The quantities of interest for the rectangular fault models are values of horizontal shear strain rate parallel to the fault ($\dot{\gamma}_{yz}$ in Figure 10*a*). These values are calculated at various times since the last earthquake and various distances from the fault along a line perpendicular to the fault. Numerical results for a linear model are compared to an analytical solution to evaluate the accuracy of the finite element method. The analytical solution is obtained by taking spatial and time derivatives of the displacement equations given by *Savage and Prescott* [1978]. The results thus represent the out-of-plane strain rate for an infinitely long (into the plane) rectangular fault contained in an elastic layer overlying a Maxwell viscoelastic half-space. Figures 12*a* and 12*b* demonstrate how well the numerical results match the analytical solution. These are plots of shear strain rate ($\dot{\gamma}_{yz}$) versus time since the last earthquake at various distances from the fault. The units of shear strain rate in these plots are microradians per year, following the engineering convention. For the San Andreas results, all units will be in terms of microstrain per year, and shear strain rate ($\dot{\epsilon}_{yz}$) will thus be a tensor quantity (engineering shear strain rate, a scalar quantity, is twice the tensor shear strain rate). Both of these figures represent models with an elastic layer of thickness H containing a fault locked to a depth D = 20 km overlying a Maxwell viscoelastic half-space with a viscosity of 2×10^{19} Pa s. Figure 12*a* depicts the results for a model in which aseismic slip extends to a depth H = 40 km, while Figure 12*b* shows the results for a model in which there is no aseismic slip at depth (H = 20 km). Recall that for models of the type described by *Savage and Prescott* [1978] and *Thatcher* [1983], the parameter H, in addition to describing the depth to which aseismic slip occurs, also defines the thickness of the surface elastic layer. Thus the model described by Figure 12*a* (which will be referred to as linear model A) has an elastic layer with a thickness of 40 km, while that described by Figure 12*b* (linear model B) has an elastic layer thickness of 20 km.

The numerical results provide an excellent approximation to the analytical solution, as demonstrated by Figures 12*a* and 12*b*. The model with H = 40 km (Figure 12*a*) displays less time dependence close to the fault than does the model with H = 20 km (Figure 12*b*). This is consistent with the results of *Thatcher* [1983], who indicated that the influence of the viscoelastic half-space becomes greater as the thickness of the elastic layer is decreased.

To explore the effects of nonlinear rheologies on model results, four types of nonlinear models were used, with the rheological parameters given in Tables 2*b*–2*e* and Figures 4–7. There are two versions of each nonlinear model: those with H = 40 km (A models) and those with H = 20 km (B models). The engineering shear strain rate ($\dot{\gamma}_{yz}$) versus time since the last earthquake for model 1A (solid line) and model 1B (dashed line) is shown in Figure 13. These models, which assume a granite crust overlying an olivine mantle (see Figure 4), display less time dependence than the linear models. In addition, the effects of aseismic slip are much less noticeable than in the linear models, particularly close to the fault. Most available geodetic observations lie fairly close to the fault, and most of the

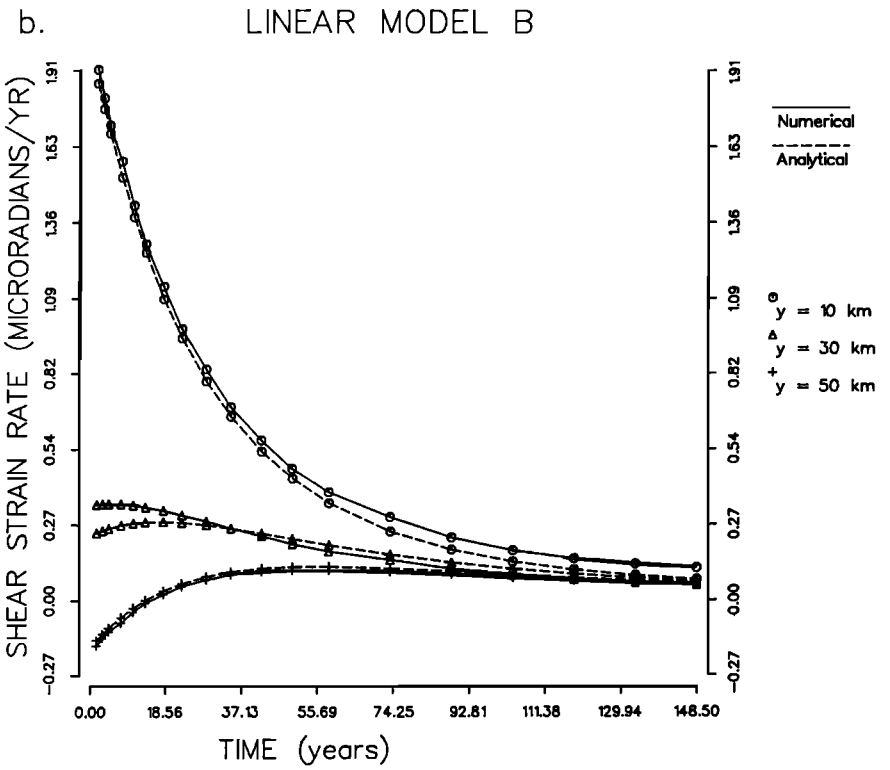

Fig. 12. (continued)

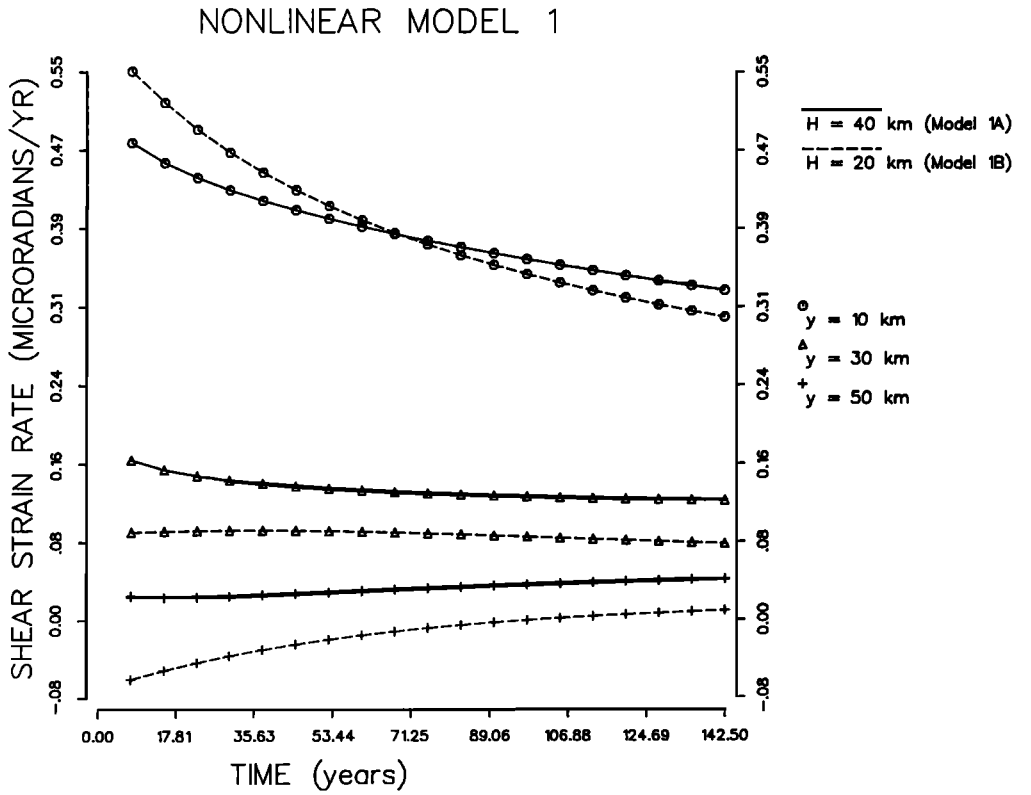

Fig. 13. Engineering shear strain rate as a function of time since the last earthquake for nonlinear model 1 (rectangular fault) at various distances from the fault. The solid lines represent the results for nonlinear model 1A (H = 40 km), and the dashed lines represent the results for nonlinear model 1B (H = 20 km).

accurate observations have been made relatively recently. If the 1857 earthquake is considered to be the time origin for this plot, then a time of 130 years would correspond to the year 1987, fairly close to the present. At a distance of 10 km from the fault and a time of about 130 years in Figure 13, there is very little difference in the predicted shear strain rate for models 1A and 1B. Therefore, although it might be possible to differentiate between these two models early in the earthquake cycle based

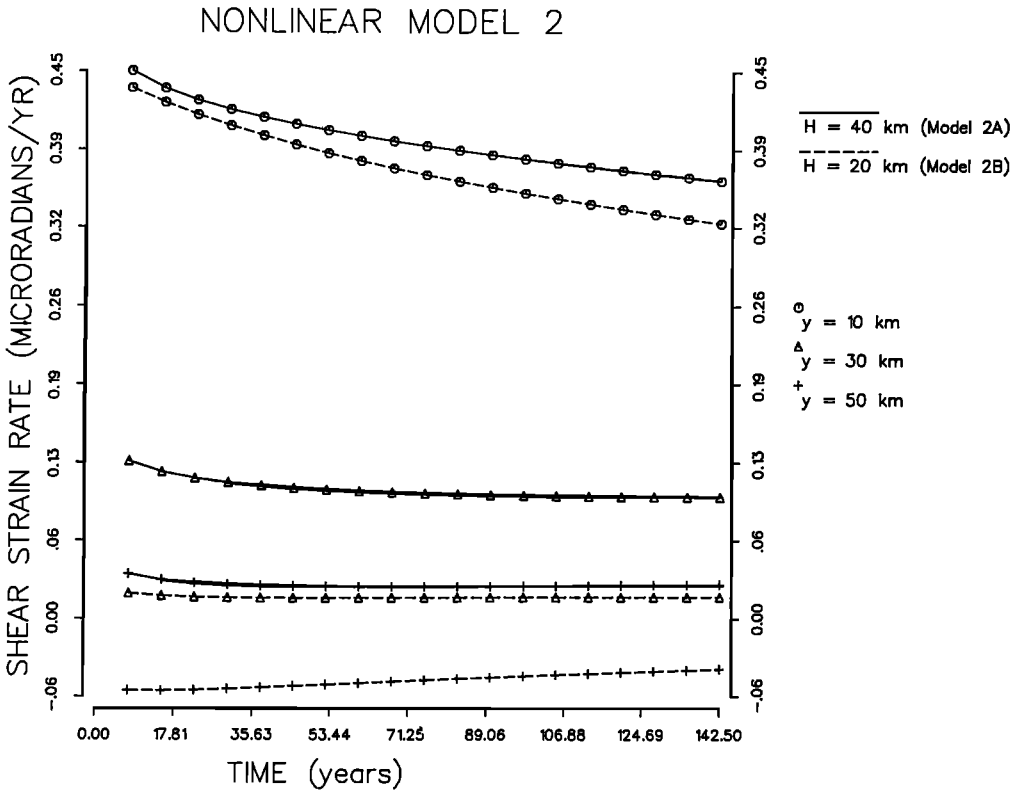

Fig. 14. Same results as Figure 13 for nonlinear model 2.

only on horizontal strain rate information, it would be difficult to do so at the present position within the earthquake cycle.

The characteristics of models 2A and 2B are demonstrated in Figure 14. As expected, these models display less time dependence than do models 1A and 1B (compare Figures 4 and 5). The presence of aseismic slip at depth (solid lines in Figure 14) appears to result in a higher shear strain rate, and this effect increases with distance from the fault. The same is generally true of models 1A and 1B (Figure 13), except for very close to the fault at times early in the earthquake cycle.

This same trend is observable for models 3A and 3B (Figure 15). In this case, aseismic slip at depth results in a higher shear strain rate at all times. Comparison of Figures 14 and 15 indicates that models 2A and 3A predict virtually identical shear strain rates at all times and distances from the fault. Model 1A (Figure 13) also predicts shear strain rates similar to models 2A and 3A, but the magnitude varies more with time. The corresponding models that do not include aseismic slip at depth (models 1B, 2B, and 3B) differ significantly, however. This seems to indicate that aseismic slip at depth may have a greater influence over the observed deformation than the rheological properties if the properties are not significantly different. The extent to which the results are influenced by aseismic slip at depth would probably be reduced if the slip were a calculated response rather than an imposed condition, however. These three model types are very similar in their viscoelastic properties, differing only in the lower crust.

Models 4A and 4B (Figure 16) provide ample evidence of the importance of rheological properties. The shear strain rate patterns predicted by these two models do not resemble those of any of the other models. In general, the predicted shear strain rates for models 4A and 4B are much higher than for the other models. Models 4A and 4B have significantly different properties in the upper crust and upper mantle than the other nonlinear models. Therefore, although the presence of aseismic slip at depth may control the observed deformation over a limited range of rheological properties, knowledge of the variation of rheological properties with depth is of primary importance in determining predicted deformation patterns.

The linear models (A and B) display a greater time dependence than do any of the nonlinear models. This is due to the fact that the linear models have a lower effective viscosity than the nonlinear models at depths less than 60 km (see Tables 2*a*–2*e*). Since time-dependent behavior is dominated by the viscosities at relatively shallow depths, the linear models are more affected by viscous behavior. The models that display the greatest time dependence (besides the linear models) are models 1A and 1B and models 4A and 4B. Models 1A and 1B have the shortest Maxwell time at depths from 20 to 40 km (see Figure 4 and Table 2*b*), while models 4A and 4B have the shortest Maxwell time from 0 to 20 km and 40 to 100 km depth (see Figure 7 and Table 2*e*). Results from other models (not shown here) indicate that changes in the Maxwell time below 100 km depth have no appreciable effect on the predicted deformation. With the temperature profile assumed for this analysis, the Maxwell time at depths greater than 100 km is less than 10 years, so the mantle below this depth should behave as a fluid over the time period of interest (150 years). The determination of the viscosity profile within 100 km of the Earth's surface is thus of primary importance in providing accurate models of the earthquake cycle on the San Andreas fault.

Through analysis of Figures 12–16, it should be possible to determine which models will be distinguishable on the basis of strain rate observations close to the fault at times close to the present. Linear model A and nonlinear models 1A, 1B, 2A, 2B, 3A, and 4B all predict similar strain rates at a distance of 10 km from the fault and a time of 130 years since the last earthquake in the area. Thus it is difficult to distinguish between these models based only on current strain rate observations that lie close to the fault. Linear model B and nonlinear model 3B predict significantly lower shear strain rates, while nonlinear model 4A predicts a higher shear strain rate. These models

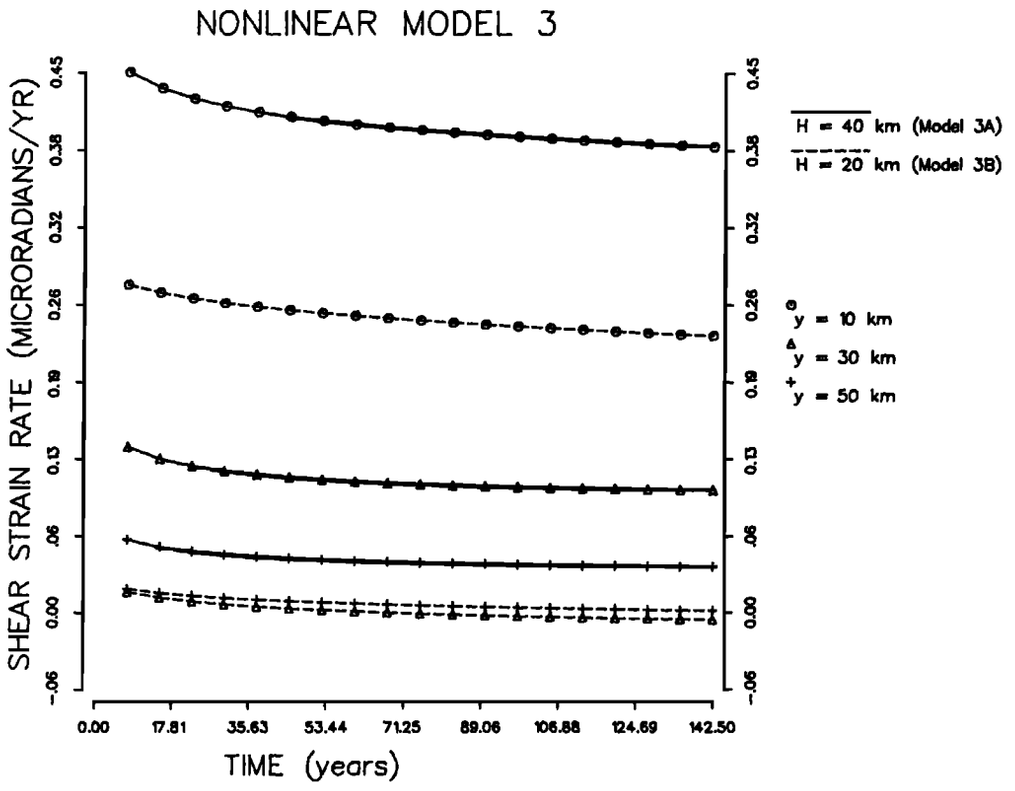

Fig. 15. Same results as Figure 13 for nonlinear model 3.

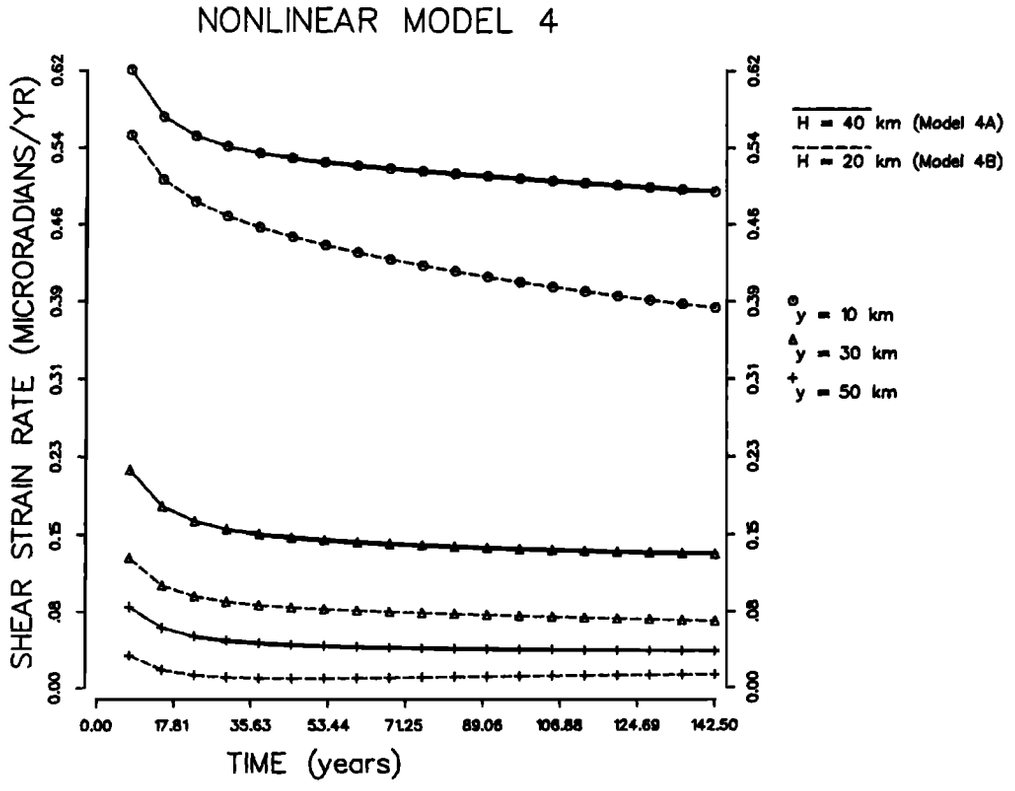

Fig. 16. Same results as Figure 13 for nonlinear model 4.

should thus be relatively simple to distinguish on the basis of strain rate observations. To test this hypothesis, it is useful to look at models which provide a better representation of actual San Andreas fault geometry.

Strain Rate Results for Models That Include Fault Geometry

For each of the models described in the previous section, results were calculated for a corresponding model that included

TABLE 3. Observed Values of Strain Rate Determined From Trilateration Results, and the Time Periods Over Which Measurements Were Taken

Network	$\dot{\varepsilon}_{11}$	$\dot{\varepsilon}_{22}$	$\dot{\varepsilon}_{12}$	Interval	Source
Salton	0.18 ± 0.01	−0.16 ± 0.01	−0.025 ± 0.005	1972–1984	*Savage et al.* [1986]
Anza	0.15 ± 0.01	−0.15 ± 0.01	0.005 ± 0.005	1973–1984	*Savage et al.* [1986]
Cajon	0.13 ± 0.03	−0.16 ± 0.02	0.095 ± 0.015	1974–1984	*Savage et al.* [1986]
Tehachapi	0.15 ± 0.01	−0.11 ± 0.01	0.060 ± 0.005	1973–1984	*Savage et al.* [1986]
Los Padres	0.12 ± 0.01	−0.14 ± 0.01	0.005 ± 0.005	1973–1984	*Savage et al.* [1986]
Carrizo	0.29 ± 0.06	−0.09 ± 0.06	−0.010 ± 0.030	1977–1981	*Savage* [1983]

The units of strain rate are in microstrain per year. The shear strain rate is thus a tensor quantity and does not follow engineering convention.

the variations in strike observed along the San Andreas fault. These computations were performed using the grid of Figures 11*a* and 11*b*, with the boundary conditions given in the section on finite element modeling of the problem. The observations of interest are determinations of horizontal strain rate. A number of such observations exist from a variety of sources. Most current observations are obtained from U.S. Geological Survey trilateration networks. These values are calculated by inverting a number of line-length changes within a network to obtain strain values. These calculations are performed at various times within an interval to provide an average strain rate for the interval. The methods used in determining strain rate are discussed by *Savage et al.* [1981, 1986]. The observations used in this study for comparison to predicted results are trilateration results determined from geodolite surveys of a number of networks [*Savage*, 1983; *Savage et al.*, 1986]. The values used in this analysis, the time period for which the results were obtained, and their corresponding standard deviations are listed in Table 3.

The results from six different networks are used in this analysis. The networks used are Salton, Anza, Cajon, Tehachapi, Los Padres, and Carrizo. In calculating the predicted values, it is necessary to take into account the area covered by each network. An approximate solution to this problem is as follows. First, the individual line locations for each network are obtained (those for this analysis were obtained from *Savage et al.* [1986] and W. Prescott (personal communication, 1990)). The strain rate is determined by averaging over the elements which contain any portion of a survey line. The weight assigned to each element is determined by the number of lines which pass through it. In addition, if a line passes through more than one element, the weight due to this line is divided equally between the elements through which it passes. This procedure provides a reasonable simulation of the method by which the strain rate observations are made; however, there will be some problems associated with the coarseness of the finite element grid. The strain rate magnitude falls off very quickly with distance from the fault, so any inaccuracies in the weighting of a particular element could have an appreciable effect on the predicted strain rate.

To determine how the predicted strain rate changes with time, it is necessary to observe the predicted values both early and late in the earthquake cycle. This is done in Figures 17–21. The first of each of these figures (Figures 17*a*, 18*a*, 19*a*, 20*a*, and 21*a*) represents the principal axes of strain rate at a time early in the earthquake cycle. For the linear models (Figure 17*a*), this time is 13.5 years since the last great earthquake in the area. Measuring from the 1857 earthquake, this corresponds to the year 1870.5. Figures 18*a*, 19*a*, 20*a*, and 21*a* depict the principal axes of strain rate at a time of 15 years since the last great earthquake (1872, as measured from the 1857 earthquake) for the nonlinear models. The lines with arrows on the end signify the principal axes of extension, while those with no arrows denote the principal axes of contraction. The axes with solid arrowheads (on the west side of the fault for each plot) represent models with no aseismic slip at depth (H = 20 km, or B models),

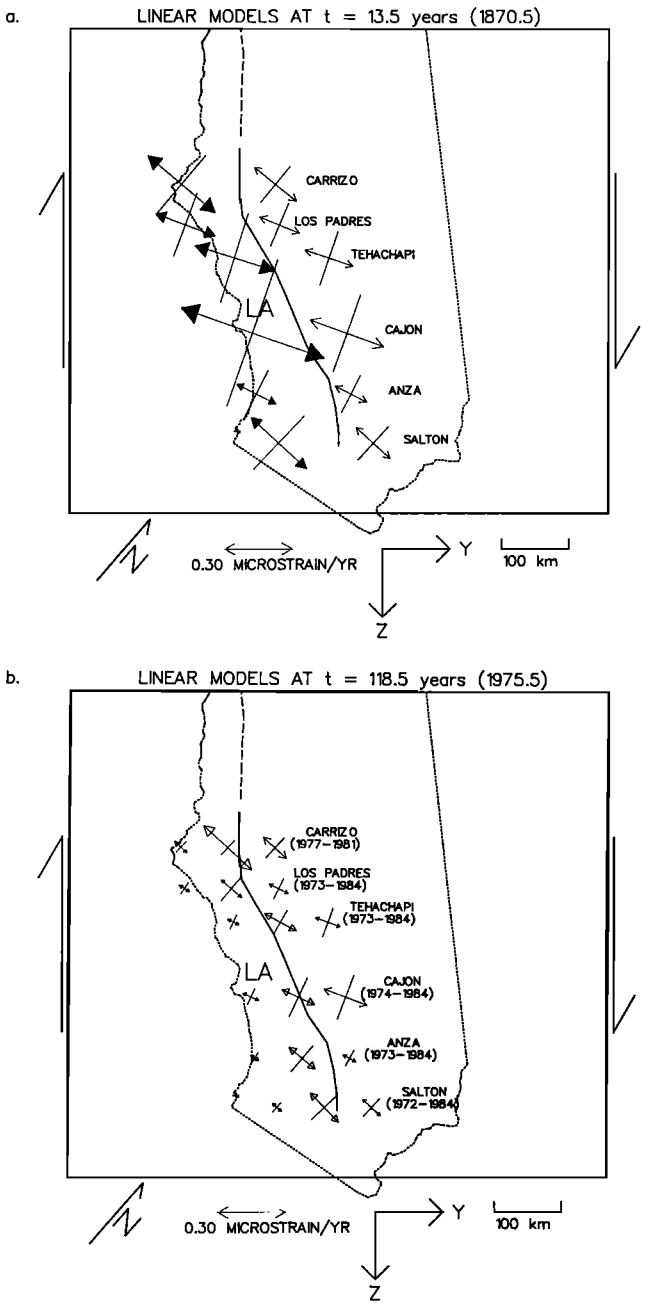

Fig. 17. Principal axes of strain rate for the linear models at (*a*) t = 13.5 years (1870.5) and (*b*) t = 118.5 years (1975.5). Arrows denote extension, and straight lines represent contraction. Axes with plain arrows (on the east side of the fault) are results for models with H = 40 km (A models). Axes with solid arrows (on the west side of the fault) are results for models with H = 20 km (B models). Axes with open arrows (in the center, shown only for t = 118.5 years) are trilateration results for the time periods listed in the legends to the right.

while those with plain arrowheads (on the east side of the fault) are the axes for models with $H = 40$ km (A models). To the right of the principal axes are the names of the corresponding trilateration networks.

The principal axes at a time close to the present are shown in Figures 17*b*, 18*b*, 19*b*, 20*b*, and 21*b*. For the linear models (Figure 17*b*), the axes are shown for a time of 118.5 years since the last great earthquake, corresponding to the year 1975.5. The results for the nonlinear models (Figures 18*b*, 19*b*, 20*b*, and 21*b*) show the principal axes at a time of 120 years since the last earthquake, which translates to the year 1977. Also shown in Figures 17*b*–21*b* are the observed values of strain rate determined from trilateration results (open arrowheads, between the two sets of predicted values). The locations of the principal axes denoting the observed values represent the approximate locations of the centroids of the networks. At the right are shown the network names and the time periods over which the observed values were calculated. It will be noted that the time periods for the observed and predicted results do not coincide exactly. This should not have a significant effect, however, since the strain rate does not change appreciably between adjacent time steps late in the earthquake cycle (see Figures 12–16).

Based on our previous analysis of the rectangular fault results shown in Figures 12–16, it should be possible to make some predictions about the model characteristics demonstrated in Figures 17–21. For example, the greatest time dependence should be displayed by the linear models and by nonlinear models 1 and 4. The linear models (Figures 17*a* and 17*b*) clearly display the greatest time dependence, with a dramatic decrease in the magnitude of the strain rate with time. This is particularly true for linear model B, which does not include aseismic slip at depth. This behavior could have been deduced from an analysis

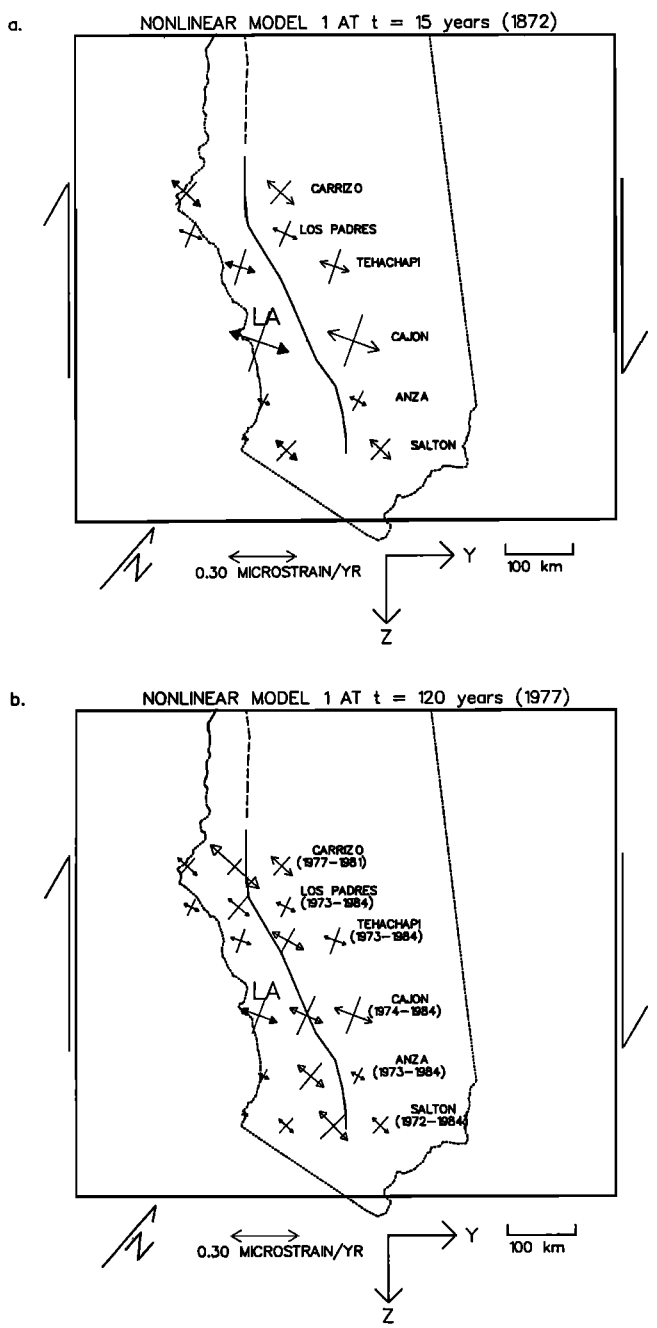

Fig. 18. Principal axes of strain rate for nonlinear model 1 at (*a*) $t = 15$ years (1872) and (*b*) $t = 120$ years (1977), using the same notation as Figure 17.

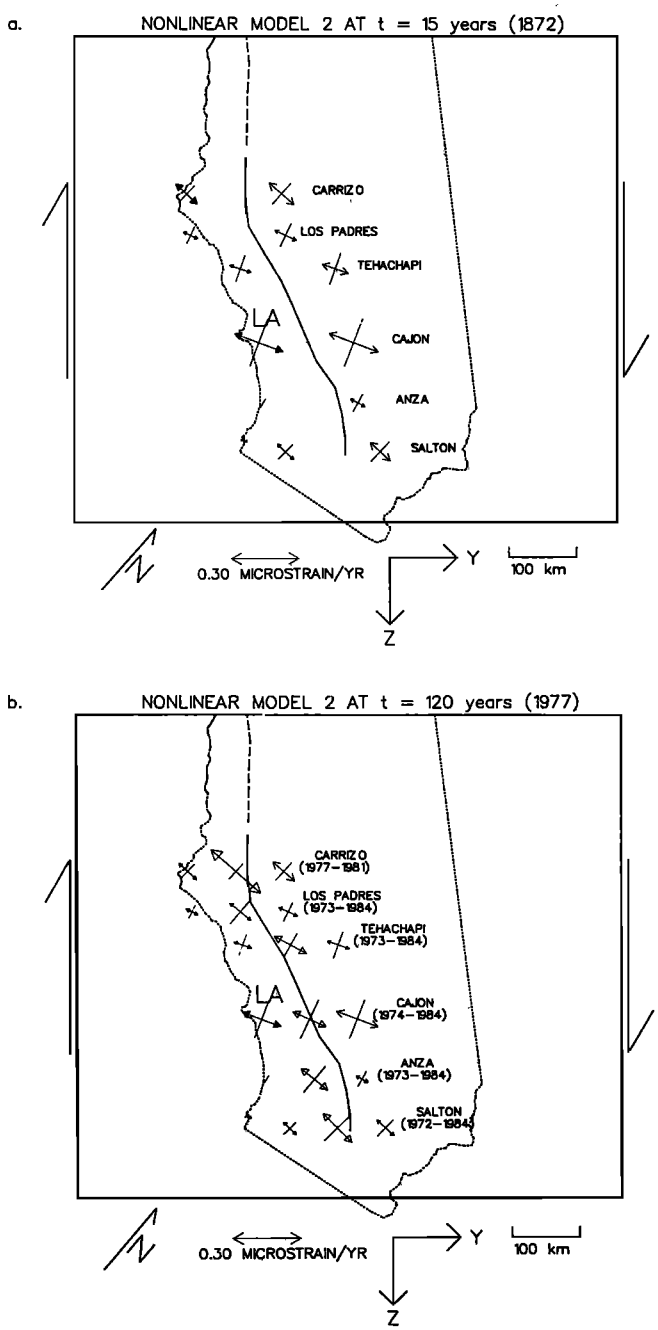

Fig. 19. Principal axes of strain rate for nonlinear model 2 at (*a*) $t = 15$ years (1872) and (*b*) $t = 120$ years (1977), using the same notation as Figure 17.

of Figures 12*a* and 12*b*. Inspection of Figures 18 and 21 reveals that nonlinear models 1 and 4 display a greater time dependence than the other nonlinear models, as anticipated from the analysis of rectangular fault models. Again, the effect is more pronounced for models which do not include aseismic slip at depth. Analysis of the rectangular fault models also indicates that nonlinear model 4 should produce strain rates that are greater in magnitude than the other models, which is again supported by the results of the San Andreas fault models (see Figures 16 and 21). The results of the rectangular fault models also suggested that linear model A and nonlinear models 1A, 1B, 2A, 2B, 3A, and 4B should all predict similar values for the strain rate at the present position within the earthquake cycle. This seems to be generally true, with the exception of model 2B, which predicts slightly smaller values than the other models. Linear model B and nonlinear model 3B produce lower strain rates, while nonlinear model 4A predicts a higher strain rate, in accordance with the rectangular fault models. All models are generally consistent with right-lateral shear, which results in a slight counterclockwise rotation (of the order of 15° to 20°) of the principal axes along the Big Bend portion of the fault.

Through an analysis of Figures 17–21 we can obtain a general impression of which models provide the closest fit to the data. For example, the predicted strain rates for linear model B and nonlinear model 3B are obviously much smaller than the observed values. However, it is difficult to truly evaluate the model results from this graphical representation. In order to quantify the differences in the model predictions, a more objective technique must be used. It should be emphasized that the uncertainties in the model parameters, and the possible range of

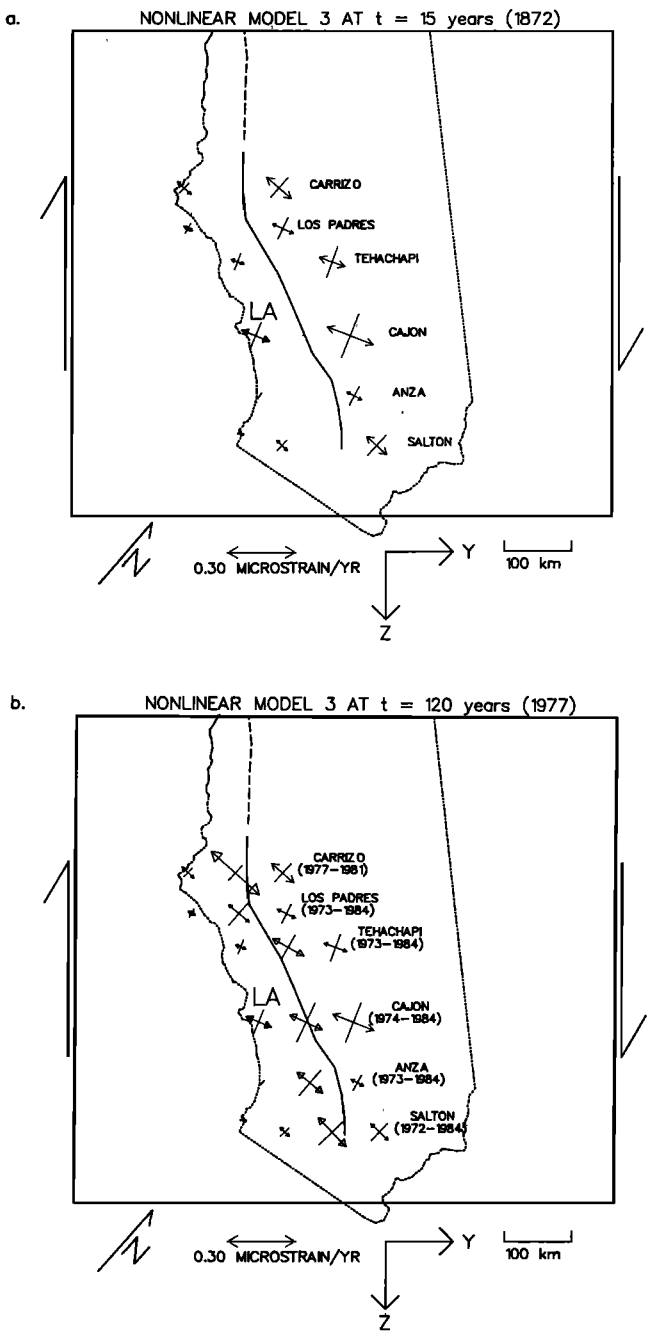

Fig. 20. Principal axes of strain rate for nonlinear model 3 at (*a*) $t = 15$ years (1872) and (*b*) $t = 120$ years (1977), using the same notation as Figure 17.

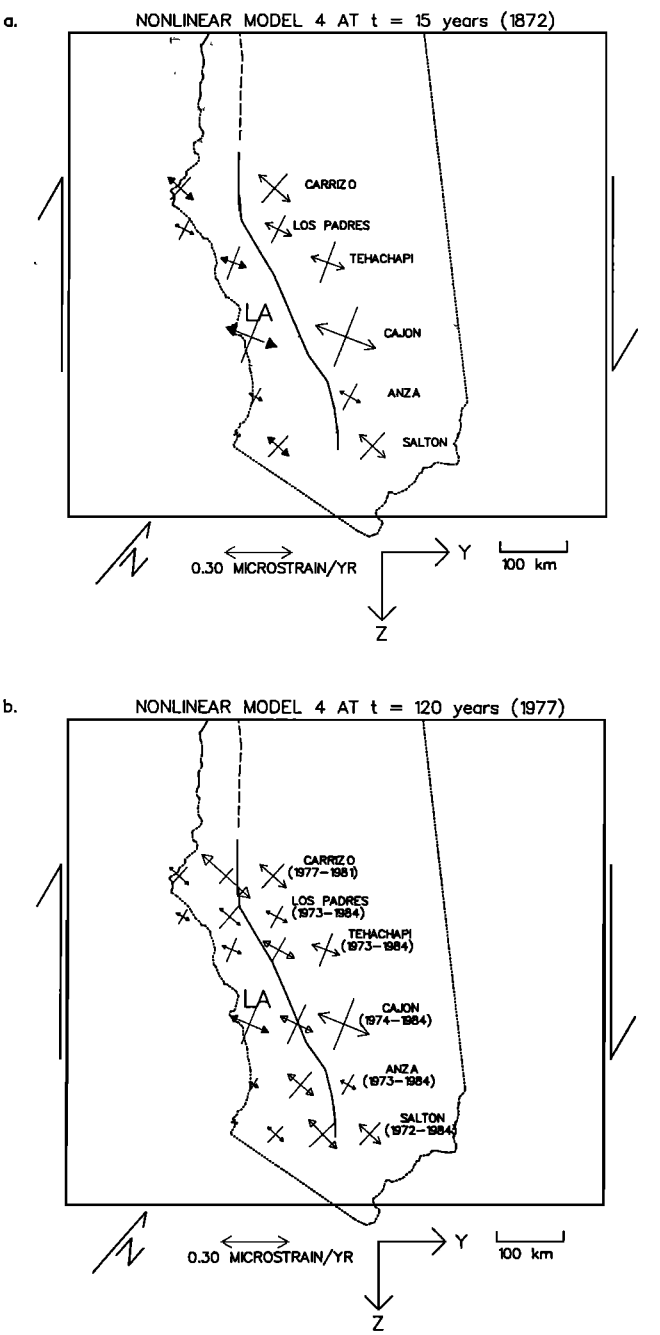

Fig. 21. Principal axes of strain rate for nonlinear model 4 at (*a*) $t = 15$ years (1872) and (*b*) $t = 120$ years (1977), using the same notation as Figure 17.

models, are much too large at this point to select one model over another on the basis of data misfit. The following analysis is simply a useful means of quantifying the differences between the models presented here. The method used follows that outlined by *Jackson* [1973]. First, all tensor components are rotated into a common coordinate system. The system chosen is that of *Savage et al.* [1986], in which the 1 axis is directed east and the 2 axis north. The data misfit for each network may then be determined. The data misfit may be defined as

$$b_i \equiv b_i^{obs} - b_i^{pre} \tag{10}$$

where the subscript i represents the particular observation under consideration and b_i^{obs} and b_i^{pre} denote observed and predicted values, respectively. The rms residual is then

$$r \equiv \sqrt{\frac{1}{n}\sum_{i=1}^{n} b_i^2} \tag{11}$$

where n represents the number of observations. For the present analysis, this would correspond to the number of tensor strain rate components under consideration.

Although the rms residual provides some idea of the fit to the data, it does not take into consideration the variations in the quality of the data. This may be accomplished by utilizing the data covariance matrix. For the case of statistically independent data errors, this reduces to a diagonal matrix of data variances. The weighted data misfit is then

$$\hat{b}_i \equiv \frac{b_i}{\sigma_i} \tag{12}$$

where σ_i is the standard deviation of the i^{th} observation. The weighted rms residual may be obtained by replacing b_i in (11) with the weighted data misfit from (12). This weighting scheme insures that misfits to observations that are not well known (i.e., those with large standard deviations) will contribute a smaller amount to the weighted rms residual than the misfits to well-known data. Note that the weighted rms residual is dimensionless, since the units of standard deviation are the same as those of the observation.

The predicted values for each model, along with the rms and weighted rms residuals, are given in Tables 4*a*–4*j*. The residuals are given for each network as well as for all six networks as a whole. Ideally, the total rms residual for a given model should be less than one. This would mean that, on average, the model is fitting the data to within the data uncertainties. This is not the case for the present models, however. The model that provides the closest fit to the data is model 4A (Table 4*i*), with a weighted rms residual of 4.53.

In almost all cases, the predicted values for $\dot{\varepsilon}_{11}$ and $\dot{\varepsilon}_{22}$ are substantially smaller than the observed values. This is true of all networks except Cajon, where the predicted values sometimes exceed the observed values. The small magnitudes for the normal components of strain rate represent, at least in part, a deficiency in the amount of fault-parallel shear strain rate. If $\dot{\varepsilon}_{11}$ were equal in magnitude to $\dot{\varepsilon}_{22}$, this would represent a case of pure right-lateral shear across a vertical plane striking N45°W, close to the average strike of the San Andreas fault. Although the observed values of $\dot{\varepsilon}_{11}$ and $\dot{\varepsilon}_{22}$ are generally not equal in magnitude, the predicted values could, in most cases, be increased (or decreased, in the case of $\dot{\varepsilon}_{22}$) by equal amounts to produce values closer to those of the data. The shear component $\dot{\varepsilon}_{12}$ represents right-lateral shear across a vertical plane striking N90°E, and the magnitudes should be expected to be relatively small. In general, the models which do not include aseismic slip at depth predict substantially smaller strain rate values. Therefore it seems reasonable that increasing the depth of aseismic slip should increase the magnitudes of the predicted strain rates and should thus provide a better fit to the data. Alternatively, the locking depth could be decreased. This should then result in an increase in the shear strain rate close to the fault and late in the earthquake cycle, in a manner similar to the results of *Thatcher* [1983]. A locking depth of 15 km is probably more appropriate than the value of 20 km assumed in this study, as earthquakes on the San Andreas fault are rarely observed below this depth [*Sibson*, 1982; *Jones*, 1988].

A better fit to the data could also be achieved by allowing the fault parameters to vary along the length of the fault. The simplest and most reasonable parameters to vary are, again, the fault locking depth and the depth of aseismic slip. The fault locking depth may be constrained by the maximum focal depths along different portions of the fault, and the depth of aseismic slip can then be adjusted to produce the proper amount of shear

TABLE 4*a*. Linear Model A

Network	$\dot{\varepsilon}_{11}$	$\dot{\varepsilon}_{22}$	$\dot{\varepsilon}_{12}$	RMS Residual	Weighted RMS Residual
Salton	0.109	−0.109	−0.00654	0.0517	5.49
Anza	0.0588	−0.0733	0.0304	0.0703	7.48
Cajon	0.156	−0.155	0.135	0.0275	1.61
Tehachapi	0.0844	−0.103	0.0860	0.0410	4.85
Los Padres	0.0799	−0.0858	0.0496	0.0467	6.45
Carrizo	0.138	−0.118	−0.00393	0.0893	1.49
Total	–	–	–	0.0580	5.10

Tables 4*a*–4*j* list predicted results and residuals (observed minus predicted values) for the various models. All values are in units of microstrain per year, except for the weighted rms residual, which is dimensionless.

TABLE 4*b*. Linear Model B

Network	$\dot{\varepsilon}_{11}$	$\dot{\varepsilon}_{22}$	$\dot{\varepsilon}_{12}$	RMS Residual	Weighted RMS Residual
Salton	0.0560	−0.0576	−0.000897	0.0939	9.69
Anza	0.0413	−0.0498	0.0163	0.0856	8.63
Cajon	0.0670	−0.0668	0.0433	0.0715	3.56
Tehachapi	0.0471	−0.0599	0.0353	0.0676	7.19
Los Padres	0.0533	−0.0569	0.0160	0.0618	6.28
Carrizo	0.0748	−0.0649	−0.00366	0.125	2.09
Total	–	–	–	0.0869	6.79

TABLE 4c. Nonlinear Model 1A

Network	$\dot{\varepsilon}_{11}$	$\dot{\varepsilon}_{22}$	$\dot{\varepsilon}_{12}$	RMS Residual	Weighted RMS Residual
Salton	0.0982	−0.0968	−0.00802	0.0605	6.28
Anza	0.0598	−0.0728	0.0299	0.0700	7.43
Cajon	0.138	−0.133	0.114	0.0197	1.08
Tehachapi	0.0741	−0.0923	0.0752	0.0458	4.83
Los Padres	0.0787	−0.0810	0.0477	0.0484	6.45
Carrizo	0.125	−0.105	−0.00342	0.0957	1.60
Total	–	–	–	0.0613	5.22

TABLE 4d. Nonlinear Model 1B

Network	$\dot{\varepsilon}_{11}$	$\dot{\varepsilon}_{22}$	$\dot{\varepsilon}_{12}$	RMS Residual	Weighted RMS Residual
Salton	0.0874	−0.0864	−0.00738	0.0691	7.13
Anza	0.0463	−0.0589	0.0243	0.0805	8.28
Cajon	0.129	−0.127	0.112	0.0216	1.17
Tehachapi	0.0659	−0.0811	0.0696	0.0516	5.25
Los Padres	0.0640	−0.0672	0.0390	0.0566	6.60
Carrizo	0.115	−0.0936	−0.00507	0.101	1.69
Total	–	–	–	0.0681	5.70

TABLE 4e. Nonlinear Model 2A

Network	$\dot{\varepsilon}_{11}$	$\dot{\varepsilon}_{22}$	$\dot{\varepsilon}_{12}$	RMS Residual	Weighted RMS Residual
Salton	0.102	−0.0996	−0.00812	0.0580	6.04
Anza	0.0548	−0.0693	0.0273	0.0732	7.65
Cajon	0.151	−0.142	0.120	0.0215	1.17
Tehachapi	0.0739	−0.0952	0.0761	0.0457	4.85
Los Padres	0.0774	−0.0797	0.0453	0.0486	6.31
Carrizo	0.127	−0.105	−0.00328	0.0947	1.58
Total	–	–	–	0.0614	5.20

TABLE 4f. Nonlinear Model 2B

Network	$\dot{\varepsilon}_{11}$	$\dot{\varepsilon}_{22}$	$\dot{\varepsilon}_{12}$	RMS Residual	Weighted RMS Residual
Salton	0.0794	−0.0756	−0.00906	0.0764	7.80
Anza	0.0255	−0.0363	0.0110	0.0974	9.76
Cajon	0.139	−0.132	0.115	0.0204	1.12
Tehachapi	0.0579	−0.0748	0.0603	0.0569	5.69
Los Padres	0.0514	−0.0555	0.0290	0.0643	6.87
Carrizo	0.107	−0.0842	−0.00844	0.106	1.77
Total	–	–	–	0.0756	6.32

TABLE 4g. Nonlinear Model 3A

Network	$\dot{\varepsilon}_{11}$	$\dot{\varepsilon}_{22}$	$\dot{\varepsilon}_{12}$	RMS Residual	Weighted RMS Residual
Salton	0.107	−0.106	−0.00776	0.0534	5.61
Anza	0.0563	−0.0724	0.0299	0.0717	7.59
Cajon	0.152	−0.144	0.121	0.0219	1.19
Tehachapi	0.0767	−0.0971	0.0788	0.0443	4.82
Los Padres	0.0783	−0.0799	0.0464	0.0485	6.38
Carrizo	0.132	−0.107	−0.00218	0.0920	1.54
Total	–	–	–	0.0595	5.11

TABLE 4*h*. Nonlinear Model 3B

Network	$\dot{\varepsilon}_{11}$	$\dot{\varepsilon}_{22}$	$\dot{\varepsilon}_{12}$	RMS Residual	Weighted RMS Residual
Salton	0.0574	−0.0534	−0.00722	0.0944	9.60
Anza	0.0155	−0.0230	0.00387	0.107	10.7
Cajon	0.0989	−0.0912	0.0718	0.0456	2.26
Tehachapi	0.0391	−0.0529	0.0372	0.0732	7.67
Los Padres	0.0342	−0.0387	0.0155	0.0769	7.56
Carrizo	0.0738	−0.0546	−0.00747	0.126	2.11
Total	–	–	–	0.0910	7.47

Table 4*i*. Nonlinear Model 4A.

Network	$\dot{\varepsilon}_{11}$	$\dot{\varepsilon}_{22}$	$\dot{\varepsilon}_{12}$	RMS Residual	Weighted RMS Residual
Salton	0.131	−0.134	−0.00684	0.0338	3.84
Anza	0.0714	−0.0951	0.0340	0.0578	6.47
Cajon	0.191	−0.188	0.152	0.0508	2.62
Tehachapi	0.0960	−0.124	0.0941	0.0377	5.08
Los Padres	0.0940	−0.0973	0.0473	0.0378	5.67
Carrizo	0.156	−0.143	−0.00448	0.0831	1.39
Total	–	–	–	0.0529	4.53

TABLE 4*j*. Nonlinear Model 4B

Network	$\dot{\varepsilon}_{11}$	$\dot{\varepsilon}_{22}$	$\dot{\varepsilon}_{12}$	RMS Residual	Weighted RMS Residual
Salton	0.0955	−0.0951	−0.00645	0.0624	6.51
Anza	0.0467	−0.0620	0.0187	0.0788	7.99
Cajon	0.148	−0.146	0.112	0.0166	0.85
Tehachapi	0.0709	−0.0921	0.0635	0.0469	4.70
Los Padres	0.0648	−0.0692	0.0251	0.0531	5.68
Carrizo	0.116	−0.105	−0.00455	0.101	1.68
Total	–	–	–	0.0653	5.23

strain rate. Other parameters that are likely to vary along the fault are earthquake recurrence time and coseismic displacement. As mentioned before, the kinematically imposed slip condition of our model is likely to exaggerate the effects of deep aseismic slip. Therefore, in order to achieve the same increase in shear strain rate for a dynamic model (in which deep aseismic slip is a calculated response), it would probably be necessary to extend the depth of aseismic slip by a greater amount than would be necessary in our model.

Among the models considered in this study, the best fit to the data is provided by linear model A and nonlinear models 1A, 2A, 3A, 4A, and 4B. The only models that seem to be completely ruled out on the basis of horizontal strain rate data are linear model B and nonlinear models 2B and 3B. In all cases, the models that include aseismic slip at depth (H = 40 km) provide a better fit to the data than the corresponding model which does not include aseismic slip (H = 20 km). Furthermore, the best fit is provided by models incorporating a wet rheology to a depth of 100 km. At present, however, it would be unwise to form a strong preference for any of these preliminary models based on the fit to horizontal strain rate data. Our models were not chosen to represent a detailed picture of earthquake occurrence on the San Andreas fault. They were selected to demonstrate the characteristics that should be expected from various fault models. Having investigated the horizontal deformation patterns produced by these models, it is instructive to consider the predicted vertical deformation.

Uplift Rate Results for Models That Include Fault Geometry

Comparison of model results to observed horizontal strain rate data provides useful constraints on the possible model types; however, stronger constraints may be imposed by also considering the vertical uplift predicted by the different models. Vertical uplift has historically been determined by leveling surveys, and the validity of these results is uncertain, particularly in relation to the so-called Palmdale uplift [*Stein*, 1987; *Craymer and Vaníček*, 1989; *Stein et al.*, 1989]. The basic debate stems from the question of whether the technique possesses sufficient resolution to determine an uplift of the stated magnitude. More recent procedures, however, have significantly increased the precision of leveling surveys (20 to 30 mm over a 100-km horizontal distance) (J. Savage, personal communication, 1990). Furthermore, with the advent of methods such as satellite laser ranging (SLR), very long baseline interferometry (VLBI), and GPS, the possibility of accurate vertical uplift measurements has become much more likely. For example, the U.S. Geological Survey has been using GPS measurements to survey several networks since 1986, with vertical resolutions of the order of 2 to 4 cm [*Davis et al.*, 1989]. It therefore appears that vertical uplift determinations may become an important consideration in constraining San Andreas fault models in the near future.

As mentioned in the previous section, all but three of the proposed models provide a similar fit to the horizontal strain

rate data. Among these models, however, many predict significantly different uplift rates at different points in the earthquake cycle. The predicted uplift rates for several models are contoured in Figures 22–26. Figures 22*a*, 23*a*, 24*a*, 25*a*, and 26*a* represent the predicted uplift rate at a time shortly after the last earthquake in the region. For linear model A (Figures 22*a* and 22*b*), this time is 13.5 years after the earthquake (corresponding to the year 1870.5), while for the nonlinear models (Figures 23–26) the results are shown for a time of 15 years after the last great earthquake in the region (corresponding to the year 1872). Figures 22*b*, 23*b*, 24*b*, 25*b*, and 26*b* show the predicted uplift rate at a time of 148.5 years (2005.5) for the linear model and 142.5 years (1999.5) for the nonlinear models. The values are given in millimeters per year, and the contour interval is 0.5 mm/yr. Uplift is indicated by solid contours, and subsidence is shown with dashed contours.

A common feature of these models is the relative absence of subsidence. Only in a few cases is a small region of negative uplift present along the creeping section of the fault. Subsidence is only prominent in the linear models (linear model A is shown in Figure 22). It is also present to a slight extent in nonlinear model 4A, shown in Figure 25. The regions of uplift associated with the two bends in the fault are prominent features. The maximum magnitude for this uplift occurs for nonlinear model 4A early in the earthquake cycle (Figure 25*a*), where it attains a value of 3.5 mm/yr at the northern bend.

Although there are some similarities between the uplift rates predicted by the various models, there are a number of important

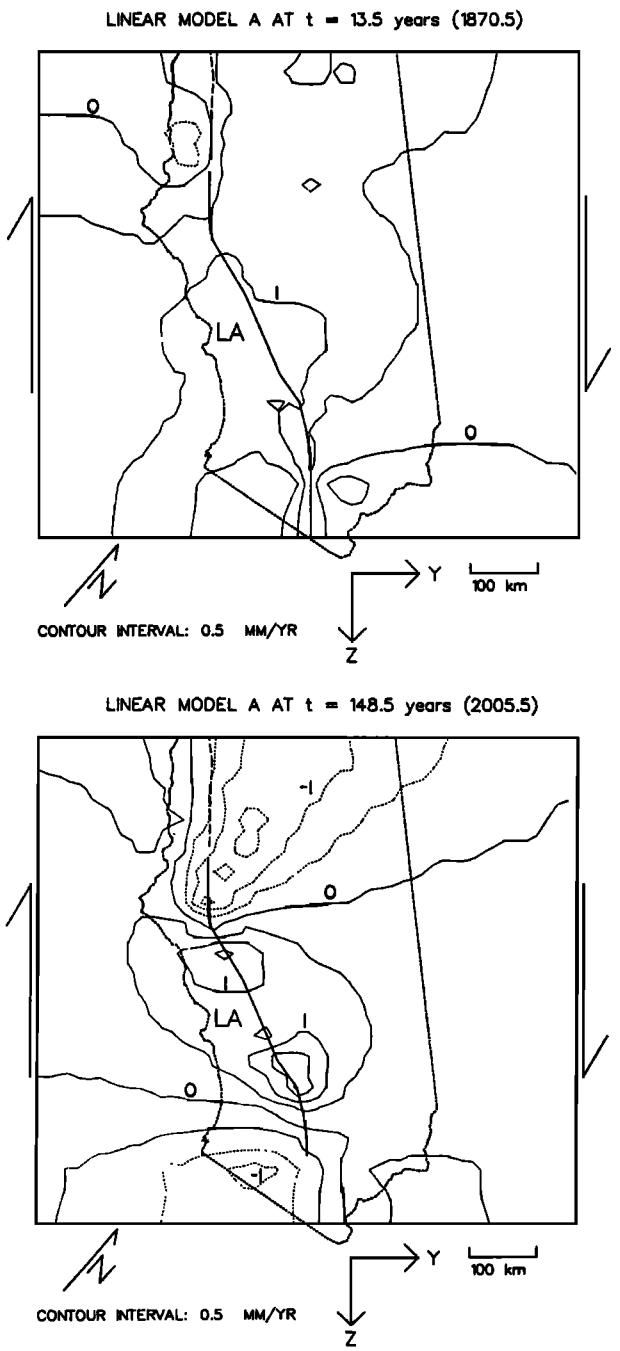

Fig. 22. Contours of uplift rate in millimeters per year for linear model A at (*a*) t = 13.5 years (1870.5) and (*b*) t = 148.5 years (2005.5). Solid contours represent uplift, and dashed lines represent subsidence.

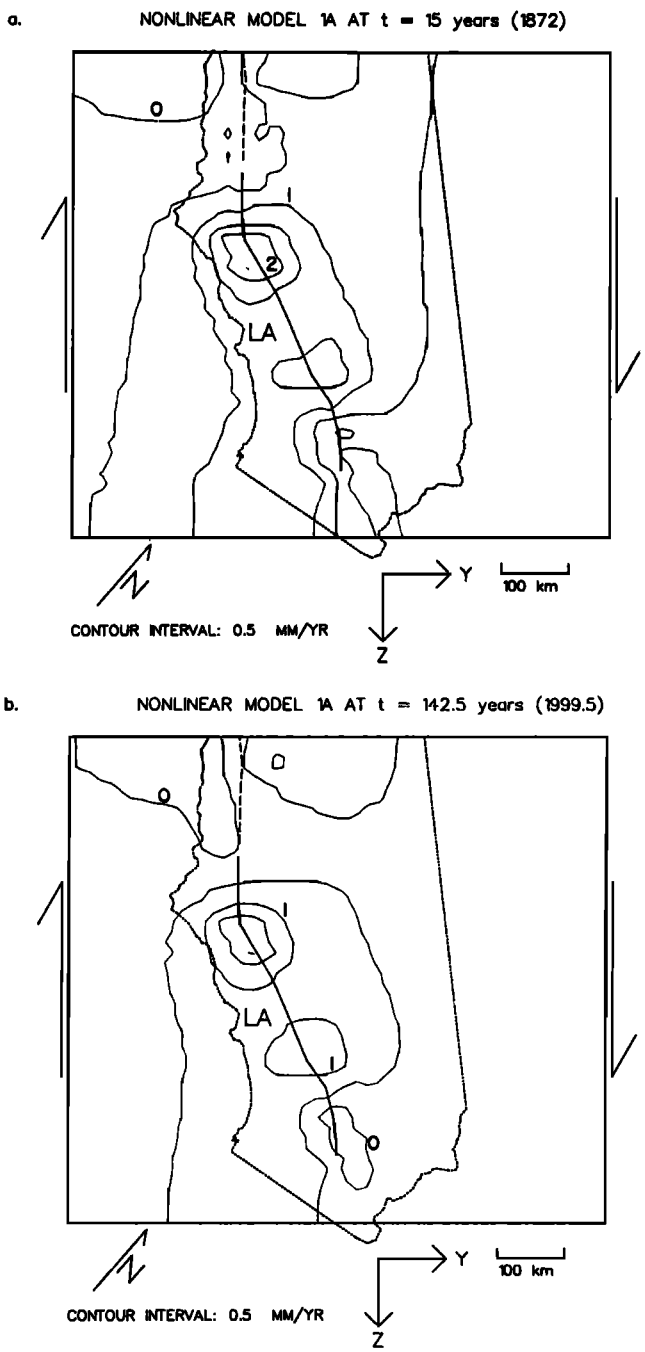

Fig. 23. Contours of uplift rate in millimeters per year for nonlinear model 1A at (*a*) t = 15 years (1872) and (*b*) t = 142.5 years (1999.5).

differences. The linear model (Figures 22*a* and 22*b*) displays a number of distinctive characteristics. For instance, the region of maximum uplift migrates with time, from near the southern termination of the fault to a position just north and east of the southern bend in the fault. In addition, the region of subsidence moves from the western to the eastern side of the creeping portion of the fault and increases in magnitude. The occurrence of subsidence appears to be correlated with a greater amount of time-dependent behavior, since models in which the effective viscosity near the surface is relatively high display virtually no subsidence at any point in the earthquake cycle.

Nonlinear model 1A (Figures 23*a* and 23*b*) predicts fairly constant uplift with time. The only perceptible change with time is a slight decrease in the magnitude of the uplift rate at times late in the earthquake cycle (compare Figures 23*a* and 23*b*). This provides a strong contrast to nonlinear model 1B (Figures 24*a* and 24*b*), which predicts essentially zero uplift at times late in the cycle. Initially, nonlinear models 1A and 1B (Figures 23*a* and 24*a*) predict fairly similar uplift patterns, although the predicted magnitudes are greater for model 1A. As time passes, however, the uplift rates for model 1A remain nearly constant, while those for model 1B decrease substantially. This is similar to the results for horizontal deformation. The presence of aseismic slip at depth tends to decrease the time dependence of the predicted deformation while increasing its magnitude. If current resolution of vertical uplift is of the order of 20 to 30 mm/yr, it should be possible to detect a difference in uplift rates of 2 mm/yr over a time period of 10–15 years, which

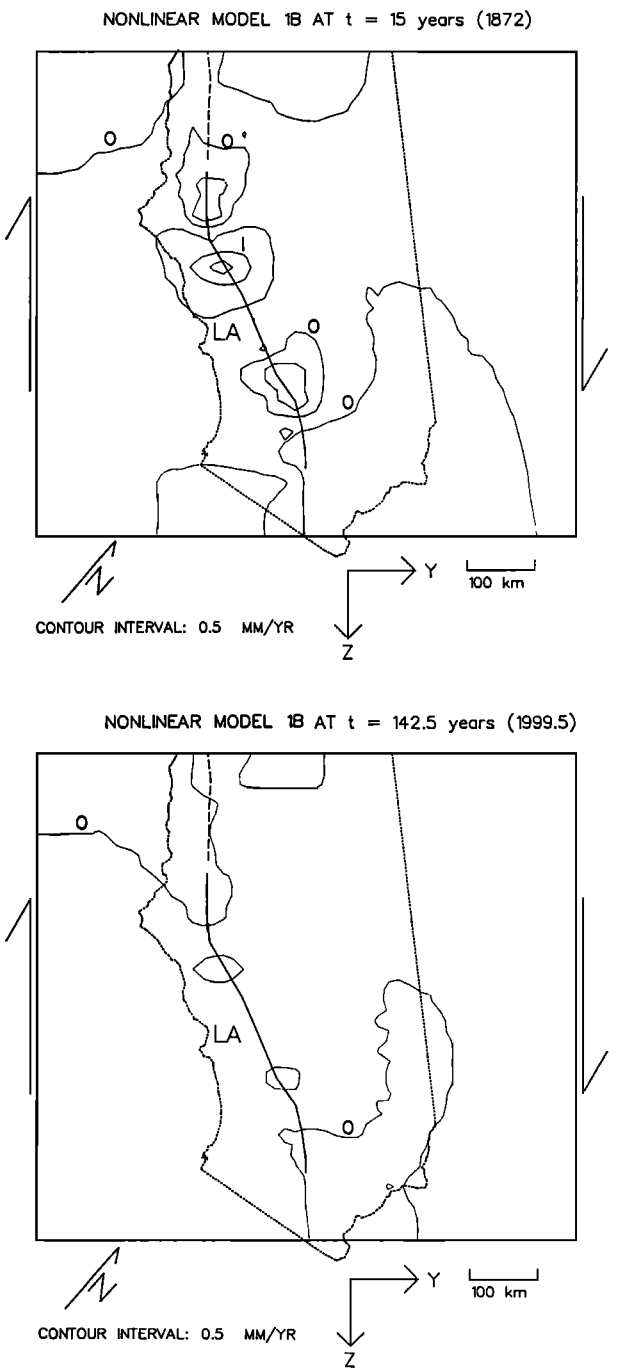

Fig. 24. Contours of uplift rate in millimeters per year for nonlinear model 1B at (*a*) t = 15 years (1872) and (*b*) t = 142.5 years (1999.5).

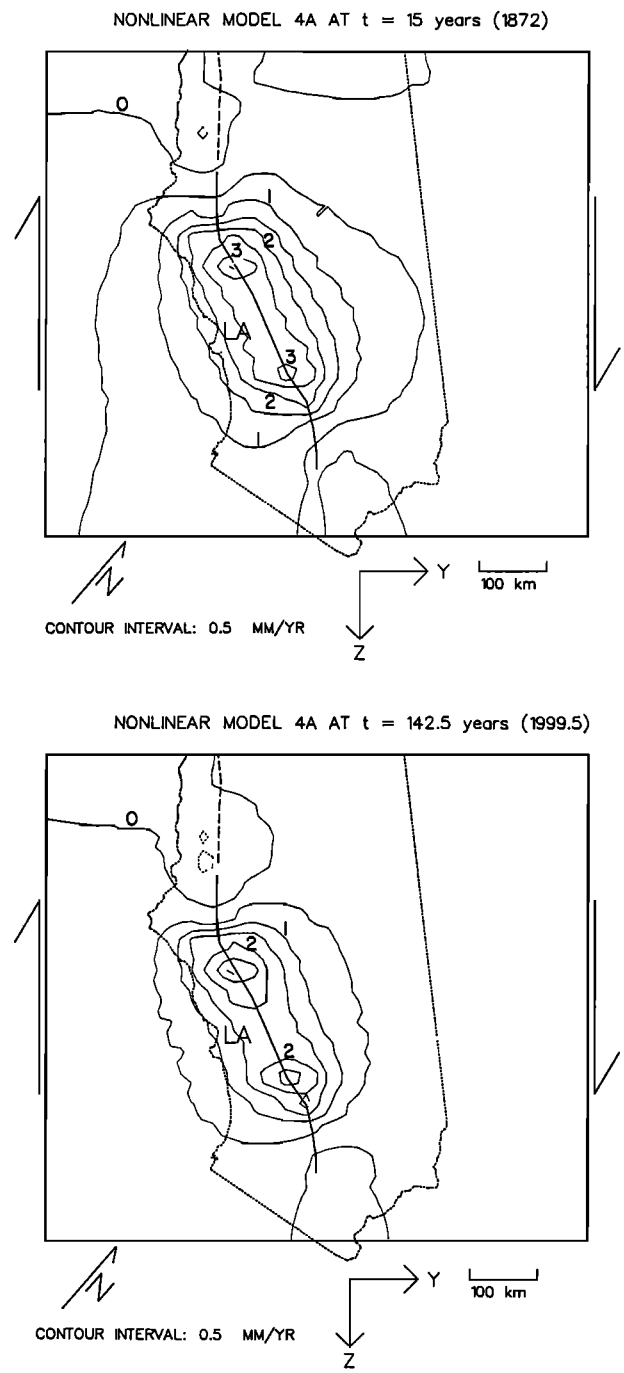

Fig. 25. Contours of uplift rate in millimeters per year for nonlinear model 4A at (*a*) t = 15 years (1872) and (*b*) t = 142.5 years (1999.5).

would be sufficient to differentiate between two models such as 1A and 1B.

Models 4A and 4B also display distinctive vertical uplift patterns. Model 4A (Figures 25*a* and 25*b*) predicts large uplift rates at all times during the cycle. The predicted uplift rates vary little with time, the primary differences being a decrease in the maximum magnitude (from 3.5 to 3.0 mm/yr) and a narrowing of the region of uplift around the Big Bend region at times late in the earthquake cycle. Model 4B (Figures 26*a* and 26*b*) again displays the reduction of uplift rate with time characteristic of models that do not include aseismic slip at depth, but the effect is not as dramatic as for the other models. In this case, the uplift rate decreases with time from a maximum of about 3.0 mm/yr to a value of 2.0 mm/yr, and the region of uplift narrows to include only the area immediately adjacent to the Big Bend.

It would be difficult to distinguish between models 4A and 4B based only on predicted vertical uplift rates, since the values differ by only about 1 mm/yr; however, the slight difference in predicted uplift rates could have a large effect on the cumulative uplift over an entire earthquake cycle, as demonstrated by Figures 27*a* and 27*b*. These show contours of total uplift since the last earthquake at a time of 142.5 years. Model 4A (Figure 27*a*) predicts a maximum uplift of 450 mm at the northern bend in the fault, while model 4B (Figure 27*b*) predicts an uplift of only 300 mm. Thus, although short-term measurements of uplift rate may not provide sufficient resolution to distinguish between models, determinations of vertical uplift over time scales of 10–20 years or more should provide useful constraints on possible fault models.

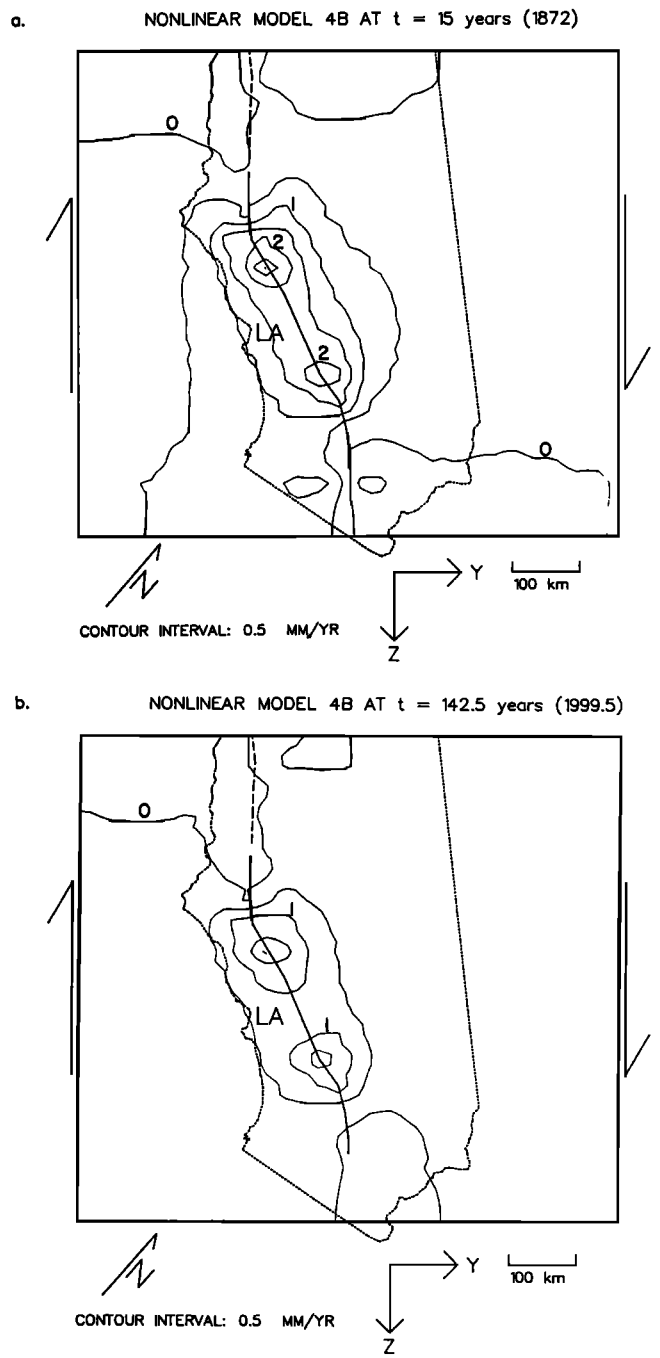

Fig. 26. Contours of uplift rate in millimeters per year for nonlinear model 4B at (*a*) t = 15 years (1872) and (*b*) t = 142.5 years (1999.5).

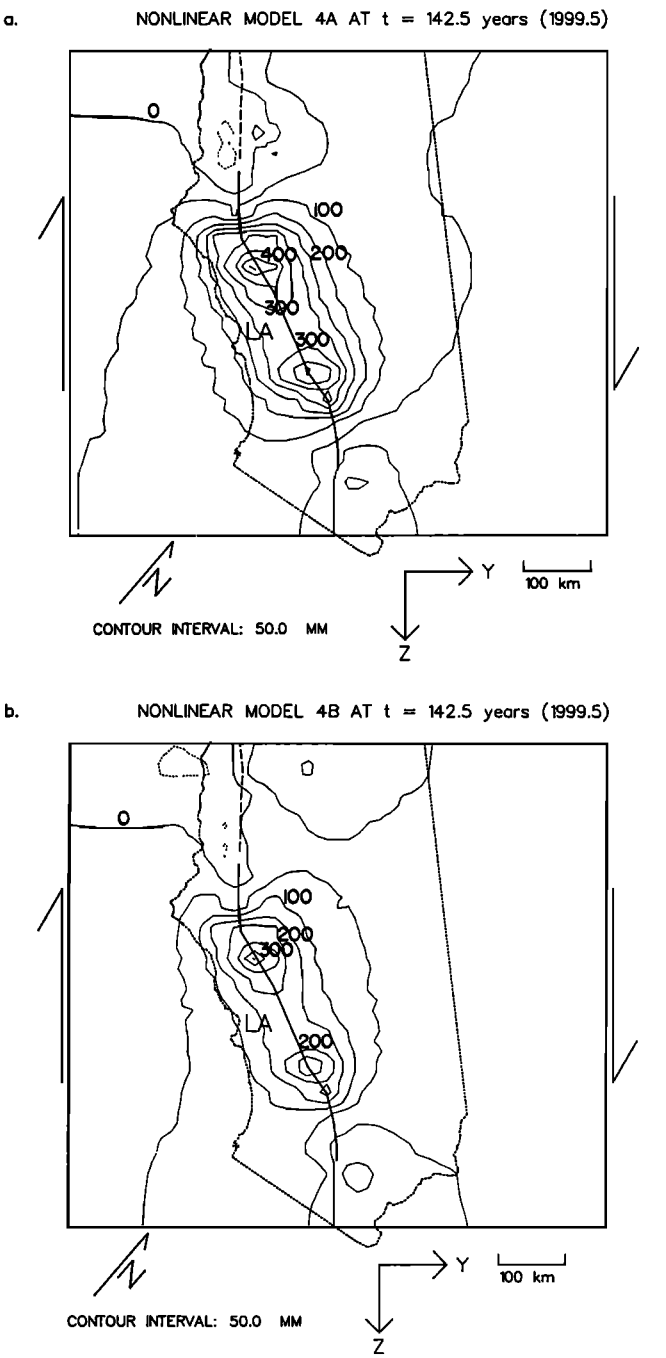

Fig. 27. Contours of total uplift in millimeters at t = 142.5 years (1999.5) for (*a*) nonlinear model 4A and (*b*) nonlinear model 4B.

DISCUSSION AND CONCLUSIONS

We have demonstrated that fault models with differing rheological stratification schemes and slip distributions predict distinctive deformation patterns, thus providing a means for distinguishing between various models. Models that do not include aseismic slip below the fault locking depth predict deformation patterns that are strongly dependent on time since the last earthquake. Both predicted strain rates and predicted uplift rates decrease dramatically in magnitude from the beginning to the end of the earthquake cycle. The results of *Thatcher* [1983] indicated that increasing the thickness of the elastic layer relative to the fault locking depth had the effect of damping the response of the underlying viscoelastic half-space, thus decreasing the time-dependent behavior of the model. The present results show that this effect could also be due, at least in part, to the depth to which aseismic slip occurs rather than simply the thickness of the surface elastic layer. All of the nonlinear models of this study have two versions: with and without aseismic slip below the fault locking depth. The rheological stratification for each model type was identical. For example, models 1A and 1B differed only in the depth to which aseismic slip occurred; they did not differ in their rheological properties. The only explanation for the enhanced time dependence of the B models is the absence of aseismic slip. Thus time-dependent behavior is influenced by the presence or absence of aseismic slip at depth as well as by the depth to which elastic behavior extends. The present models, as well as that of *Thatcher* [1983], specify steady aseismic slip at depth. If the aseismic slip instead occurred as a calculated response to stress conditions, it is likely that the differences between our A and B models would be substantially reduced.

The models incorporating aseismic slip below the locking depth display a lesser degree of time dependence. For the nonlinear models, the predicted strain rates near the beginning of the earthquake cycle are similar for models with and without aseismic slip; however, by the end of the cycle, the strain rates for models without slip have decreased substantially in magnitude relative to those with slip. The models without aseismic slip generally predict slightly smaller uplift rates at the beginning of the earthquake cycle and substantially smaller rates near the end of the cycle than do the corresponding models that include aseismic slip below the locking depth.

Modeling results indicate that the observed spatial and temporal pattern of surface deformation is controlled by the assumed rheological properties within 100 km of the Earth's surface. It is unlikely that changes in the properties below this depth would influence the results in any case, since the predicted rheology of olivine at this depth suggests a Maxwell time of the order of 10 years, which is considerably less than the earthquake recurrence interval of 150 years. The mantle below 100 km depth should behave essentially as an inviscid fluid on this time scale. The rheological properties above 100 km depth produce a number of observable characteristics. The first, and most obvious, is an enhanced time dependence of the predicted deformation for lower effective viscosities. For instance, the greatest time dependence among the nonlinear models is displayed by model 1, which has a relatively low effective viscosity from 20 to 40 km depth (dry granite rheology), and by model 4, which has relatively low viscosities from 0 to 20 km (wet granite rheology) and from 40 to 100 km depth (wet dunite rheology). The rheological properties of model 4 also result in higher overall values of strain rate and uplift rate. This is probably a result of the assumed wet granite rheology at the surface, which would be more readily deformed by applied stresses. Thus the commonly used assumption of a purely elastic layer at the surface may not be an accurate portrayal of actual Earth rheology, since viscoelastic effects may manifest themselves at depths as shallow as 10 km for a wet granite rheology (see Figure 7).

Among the present models, the best fit to the strain rate data is provided by nonlinear model 4A. This model assumes aseismic slip from 20 to 40 km depth and includes rheological properties corresponding to a wet granite upper crust, a wet diabase lower crust, and a wet dunite upper mantle from 40 to 100 km depth. This model fits the data best because it produces the largest fault-parallel shear strain rate. Even so, this model underestimates the magnitude of the strain rate for all networks except Cajon and Carrizo (compare Table 3 with Table 4*i*). The simplest method for achieving a better fit to the data would be to adjust the fault locking depth and the depth of aseismic slip along the length of the fault. For example, the depth of aseismic slip could be increased in regions where the strain rate is underestimated and decreased in areas where the strain rate is overestimated. Such a procedure, while it would result in a smaller rms residual, would not necessarily produce a realistic picture of San Andreas fault processes, since other parameters not yet considered may produce similar results.

From analysis of Figures 17–21 it is not obvious whether there are any particular regions where the horizontal strain rates would be more sensitive to changes in the locking depth, depth of aseismic slip, or rheological properties; however, the uplift rate (Figures 22–26) is very location specific. For example, the region adjacent to the creeping portion of the fault is sensitive to rheological changes. Models with relatively low effective viscosities near the surface predict subsidence in this area, while models with higher effective viscosities predict essentially zero uplift. Furthermore, some models, such as linear model A (Figure 22) and, to a much lesser extent, nonlinear model 4A (Figure 25), display a slight increase of subsidence in this area with time since the last earthquake. In the case of linear model A, the region of subsidence also moves with time.

The uplift rates at the two bends in the fault are sensitive to the depth of aseismic slip, particularly for models with relatively high effective viscosities at depth (compare nonlinear models 1A and 1B in Figures 23 and 24). In this case, models which do not include aseismic slip at depth show a dramatic decrease in uplift rates with time since the last earthquake. The total uplift over longer time scales in the Big Bend region may be a useful constraint for models with lower effective viscosities (see nonlinear models 4A and 4B in Figures 27*a* and 27*b*).

The observed strain rate data are best fit by model 4A, although the fit is not very good in a root mean square sense. There are a number of additional factors that could be included. One factor may be the discrepancy between the plate motions determined from plate models and those derived from geodetic observations along the fault, as discussed in the introduction. This may have some relation to the difference in orientations of the observed principal axes of stress and strain rate [*Mount and Suppe*, 1987; *Zoback et al.*, 1987]. To resolve problems of this nature it will be necessary to include adjacent faults in the model, since slip on these faults is likely to affect the stress regime of the San Andreas fault.

The two most important contributions of the present models are the incorporation of layered, power law viscoelastic rheologies and the calculation of vertical uplift. The use of power law viscoelastic behavior allows the direct application of laboratory results to actual Earth processes. The rheological properties of the present models are thus constrained not only by the fit of the model results to observed deformation data but also by current knowledge of variations in Earth composition and temperature with depth. Despite the uncertainties in laboratory measurements of rock rheology, it is obvious from our results that consideration of alternative rheologies can have a significant effect on predicted deformation patterns. The determination of vertical uplift provides another useful constraint on possible fault models. The present models show that the predicted uplift rate for different models can vary from essentially zero to as much as 3 mm/yr. The data necessary to resolve these small

values of uplift rate should be forthcoming in the near future. The addition of vertical uplift data to the existing horizontal deformation and stress orientation data sets should provide strong constraints on future San Andreas fault models.

Acknowledgments. We would like to thank William Prescott for providing us with a map of the Carrizo Geodolite network. This paper benefited greatly from reviews by J. C. Savage and an anonymous reviewer. This research was supported by NASA grant NAG-326.

REFERENCES

Birch, F., Compressibility; elastic constants, in Handbook of Physical Constants, edited by S. P. Clark, Jr., *Mem. Geol. Soc. Am.*, *97*, 97–173, 1966.

Bird, P., New finite element techniques for modeling deformation histories of continents with stratified temperature-dependent rheology, *J. Geophys. Res.*, *94*, 3967–3990, 1989.

Brune, J. N., T. L. Henyey, and R. F. Roy, Heat flow, stress, and rate of slip along the San Andreas fault, California, *J. Geophys. Res.*, *74*, 3821–3827, 1969.

Byerlee, J. D., Friction of rocks, *Pure Appl. Geophys.*, *116*, 615–626, 1978.

Carter, N. L., D. A. Anderson, F. D. Hansen, and R. L. Kranz, Creep and creep rupture of granitic rocks, in *Mechanical Behavior of Crustal Rocks, Geophys. Monogr. Ser.* , vol. 24, edited by N. L. Carter, M. Friedman, J. M. Logan, and D. W. Stearns, pp. 61–82, AGU, Washington, D. C., 1981.

Chapman, D. S., Thermal gradients in the continental crust, in The Nature of the Lower Continental Crust, edited by J. B. Dawson, D. A. Carswell, J. Hall, and K. H. Wedepohl, *Spec. Publ. Geol. Soc. Am.*, *24*, 63–70, 1986.

Chen, W.-P., and P. Molnar, Focal depths of intracontinental and intraplate earthquakes and their implications for the thermal and mechanical properties of the lithosphere, *J. Geophys. Res.*, *88*, 4183–4214, 1983.

Craymer, M. R., and P. Vaníček, Comment on "Saugus-Palmdale, California, field test for refraction error in historical leveling surveys" by R. S. Stein, C. T. Whalen, S. R. Holdahl, W. E. Strange, and W. Thatcher, and reply to "Comment on 'Further analysis of the 1981 southern California field test for levelling refraction by M. R. Craymer and P. Vaníček' by R. S. Stein, C. T. Whalen, S. R. Holdahl, W. E. Strange, and W. Thatcher," *J. Geophys. Res.*, *94*, 7667–7672, 1989.

Davis, J. L., W. H. Prescott, J. L. Svarc, and K. J. Wendt, Assessment of global positioning system measurements for studies of crustal deformation, *J. Geophys. Res.*, *94*, 13,635–13,650, 1989.

DeMets, C., R. G. Gordon, S. Stein, and D. F. Argus, A revised estimate of Pacific-North America motion and implications for western North America plate boundary zone tectonics, *Geophys. Res. Lett.*, *14*, 911–914, 1987.

DeMets, C., R. G. Gordon, D. F. Argus, and S. Stein, Current plate motions, *Geophys. J. Int.*, *101*, 425–478, 1990.

Desai, C. S., *Elementary Finite Element Method*, 434 pp., Prentice-Hall, Englewood Cliffs, N. J., 1979.

Gordon, R. B., Diffusion creep in the Earth's mantle, *J. Geophys. Res.*, *70*, 2413–2418, 1965.

Gordon, R. B., Thermally activated processes in the Earth: Creep and seismic attenuation, *Geophys. J.*, *14*, 33–43, 1967.

Haskell, N. A., The motion of a viscous fluid under a surface load, *Physics*, *6*, 265–269, 1935.

Haskell, N. A., The motion of a viscous fluid under a surface load, part II, *Physics*, *7*, 56–61, 1936.

Jackson, D. D., Marginal solutions to quasi-linear inverse problems in geophysics: the edgehog method, *Geophys. J. R. Astron. Soc.*, *35*, 121–136, 1973.

Jones, L. M., Focal mechanisms and the state of stress on the San Andreas fault in southern California, *J. Geophys. Res.*, *93*, 8869–8891, 1988.

King, N. E. and J. C. Savage, Strain-rate profile across the Elsinore, San Jacinto, and San Andreas faults near Palm Springs, California, 1973–81, *Geophys. Res. Lett.*, *10*, 55–57, 1983.

King, N. E., P. Segall, and W. Prescott, Geodetic measurements near Parkfield, California, 1959–1984, *J. Geophys. Res.*, *92*, 2747–2766, 1987.

Kirby, S. H., Rheology of the lithosphere, *Rev. Geophys. Space Phys.*, *21*, 1458–1487, 1983.

Kirby, S. H., Rock mechanics observations pertinent to the rheology of the continental lithosphere and the localization of strain along shear zones, *Tectonophysics*, *119*, 1–27, 1985.

Kirby, S. H., and A. K. Kronenberg, Rheology of the lithosphere: selected topics, *Rev. Geophys.*, *25*, 1219–1244, 1987*a*.

Kirby, S. H., and A. K. Kronenberg, Correction to "Rheology of the lithosphere: selected topics," *Rev. Geophys.*, *25*, 1680–1681, 1987*b*.

Kusznir, N. J., and G. Karner, Dependence of the flexural rigidity of the continental lithosphere on rheology and temperature, *Nature*, *316*, 138–142, 1985.

Kusznir, N. J., and R. G. Park, Continental lithosphere strength: the critical role of lower crustal deformation, in The Nature of the Lower Continental Crust, edited by J. B. Dawson, D. A. Carswell, J. Hall, and K. H. Wedepohl, *Spec. Pub. Geol. Soc. Am.*, *24*, 79–93, 1986.

Lachenbruch, A. H., and J. H. Sass, Thermo-mechanical aspects of the San Andreas fault system, in *Proceedings of the Conference on the Tectonic Problems of the San Andreas Fault System*, pp. 192–205, Stanford University Press, Palo Alto, Calif., 1973.

Lachenbruch, A. H., and J. H. Sass, Models of an extending lithosphere and heat flow in the Basin and Range province, *Mem. Geol. Soc. Am.*, *152*, 209–250, 1978.

Lachenbruch, A. H., and J. H. Sass, Heat flow and energetics of the San Andreas fault zone, *J. Geophys. Res.*, *85*, 6185–6222, 1980.

Li, V. C., and H. S. Lim, Modeling surface deformations at complex strike-slip plate boundaries, *J. Geophys. Res.*, *93*, 7943–7954, 1988.

Li, V. C., and J. R. Rice, Crustal deformation in great California earthquake cycles, *J. Geophys. Res.*, *92*, 11,533–11,551, 1987.

McGarr, A., On the state of lithospheric stress in the absence of applied tectonic forces, *J. Geophys. Res.*, *93*, 13,609–13,617, 1988.

Meissner, R., and J. Strehlau, Limits of stresses in continental crusts and their relation to the depth-frequency distribution of shallow earthquakes, *Tectonics*, *1*, 73–89, 1982.

Melosh, H. J., Rheology of the Earth: Theory and observation, in *Physics of the Earth's Interior*, edited by A. M. Dziewonski and E. Boschi, pp. 318–335, North-Holland, New York, 1980.

Melosh, H. J., Mechanical basis for low-angle normal faulting in the Basin and Range province, *Nature*, *343*, 331–335, 1990.

Melosh, H. J., and A. Raefsky, The dynamical origin of subduction zone topography, *Geophys. J. R. Astron. Soc.*, *60*, 333–354, 1980.

Melosh, H. J., and A. Raefsky, A simple and efficient method for introducing faults into finite element computations, *Bull. Seismol. Soc. Am.*, *71*, 1391–1400, 1981.

Melosh, H. J., and C. A. Williams, Mechanics of graben formation in crustal rocks: A finite element analysis, *J. Geophys. Res.*, *94*, 13,961–13,973, 1989.

Minster, J. B., and T. H. Jordan, Vector constraints on western U.S. deformation from space geodesy, neotectonics, and plate motions, *J. Geophys. Res.*, *92*, 4798–4804, 1987.

Mount, V. S., and J. Suppe, State of stress near the San Andreas fault: implications for wrench tectonics, *Geology*, *15*, 1143–1146, 1987.

Nur, A., and G. Mavko, Postseismic viscoelastic rebound, *Science*, *183*, 204–206, 1974.

Prescott, W. H., and J. C. Savage, Strain accumulation on the San Andreas fault near Palmdale, California, *J. Geophys. Res.*, *81*, 4901–4908, 1976.

Prescott, W. H., J. C. Savage, and W. T. Kinoshita, Strain accumulation rates in the western United States between 1970 and 1978, *J. Geophys. Res.*, *84*, 5423–5435, 1979.

Ranalli, G., and D. C. Murphy, Rheological stratification of the lithosphere, *Tectonophysics*, *132*, 281–295, 1987.

Reid, H. F., Permanent displacements of the ground, in *The California Earthquake of April 18, 1906, Report of the State Earthquake Investigation Commission, vol. 2*, pp. 16–28, Carnegie Institution of Washington, Washington, D. C., 1910.

Reid, H. F., The elastic-rebound theory of earthquakes, *Univ. Calif. Publ. Geol. Sci.*, *6*, 413–444, 1911.

Rundle, J. B., An approach to modeling present-day deformation in southern California, *J. Geophys. Res.*, *91*, 1947–1959, 1986.

Rundle, J. B., A physical model for earthquakes, 1, Fluctuations and interactions, *J. Geophys. Res.*, *93*, 6237–6254, 1988*a*.

Rundle, J. B., A physical model for earthquakes, 2, Application to southern California, *J. Geophys. Res.*, *93*, 6255–6274, 1988*b*.

Savage, J. C., Strain accumulation in the western United States, *Annu. Rev. Earth Planet. Sci.*, *11*, 11–43, 1983.

Savage, J. C., Equivalent strike-slip earthquake cycles in half-space and lithosphere-asthenosphere Earth models, *J. Geophys. Res.*, *95*, 4873–4879, 1990.

Savage, J. C., and W. H. Prescott, Asthenosphere readjustment and the earthquake cycle, *J. Geophys. Res.*, *83*, 3369–3376, 1978.

Savage, J. C., W. H. Prescott, M. Lisowski, and N. E. King, Strain accumulation in southern California, 1973-1980, *J. Geophys. Res.*, *86*, 6991–7001, 1981.

Savage, J. C., W. H. Prescott, and G. Gu, Strain accumulation in southern California, 1973–1984, *J. Geophys. Res.*, *91*, 7455–7473, 1986.

Schatz, J. F., and G. Simmons, Thermal conductivity of Earth materials at high temperatures, *J. Geophys. Res.*, *77*, 6966–6983, 1972.

Shelton, G. L., and J. Tullis, Experimental flow laws for crustal rocks (abstract), *Eos Trans. AGU*, *62*, 396, 1981.

Sibson, R. H., Fault zone models, heat flow, and the depth distribution of earthquakes in the continental crust of the United States, *Bull. Seismol. Soc. Am.*, *72*, 151–163, 1982.

Sieh, K. E., Slip along the San Andreas fault associated with the great 1857 earthquake, *Bull. Seismol. Soc. Am.*, *68*, 1421–1448, 1978.

Sieh, K., M. Stuiver, and D. Brillinger, A more precise chronology of earthquakes produced by the San Andreas fault in southern California, *J. Geophys. Res.*, *94*, 603–623, 1989.

Spence, D. A., and D. L. Turcotte, Viscoelastic relaxation of cyclic displacements on the San Andreas fault, *Proc. R. Soc. London Ser. A*, *365*, 121–149, 1979.

Stein, R. S., Contemporary plate motion and crustal deformation, *Rev. Geophys.*, *25*, 855–863, 1987.

Stein, R. S., C. T. Whalen, S. R. Holdahl, W. E. Strange, and W. Thatcher, Reply to "Comment on 'Saugus-Palmdale, California, field test for refraction error in historical leveling surveys' by R. S. Stein, C. T. Whalen, S. R. Holdahl, W. E. Strange, and W. Thatcher" by Michael R. Craymer and Peter Vaníček and comment on 'Further analysis of the 1981 southern California field test for levelling refraction' by M. R. Craymer and P. Vaníček," *J. Geophys. Res.*, *94*, 7673–7677, 1989.

Strehlau, J., and R. Meissner, Estimation of crustal viscosities and shear stresses from an extrapolation of experimental steady state flow data, in *Composition, Structure and Dynamics of the Lithosphere-Asthenosphere System, Geodyn. Ser.*, vol. 16, edited by K. Fuchs and C. Froidevaux, pp. 69–87, AGU, Washington, D. C., 1987.

Thatcher, W., Nonlinear strain buildup and the earthquake cycle on the San Andreas fault, *J. Geophys. Res.*, *88*, 5893–5902, 1983.

Thatcher, W., and J. B. Rundle, A viscoelastic coupling model for the cyclic deformation due to periodically repeated earthquakes at subduction zones, *J. Geophys. Res.*, *89*, 7631–7640, 1984.

Tse, S. T., and J. R. Rice, Crustal earthquake instability in relation to the depth variation of frictional slip properties, *J. Geophys. Res.*, *91*, 9452–9472, 1986.

Turcotte, D. L., and G. Schubert, *Geodynamics Applications of Continuum Physics to Geological Problems*, 450 pp., John Wiley, New York, 1982.

Ward, P. L., and R. A. Page, The Loma Prieta Earthquake of October 17, 1989, pamphlet, edited by L. D. Hodgen and J. A. Troll, 16 pp., U.S. Geol. Surv., Menlo Park, Calif., 1989.

Weertman, J., The creep strength of the Earth's mantle, *Rev. Geophys.*, *8*, 145–168, 1970.

Wesnousky, S. G., Earthquakes, Quaternary faults, and seismic hazard in California, *J. Geophys. Res.*, *91*, 12,587–12,631, 1986.

Williams, C. A., and R. M. Richardson, A nonlinear least-squares inverse analysis of strike-slip faulting with application to the San Andreas fault, *Geophys. Res. Lett.*, *15*, 1211–1214, 1988.

Zoback, M. D., M. L. Zoback, V. S. Mount, J. Suppe, J. P. Eaton, J. H. Healy, D. Oppenheimer, P. Reasenberg, L. Jones, C. B. Raleigh, I. G. Wong, O. Scotti, and C. Wentworth, New evidence on the state of stress of the San Andreas fault system, *Science*, *238*, 1105–1111, 1987.

R.M. Richardson, Department of Geosciences, University of Arizona, Tucson, AZ 85721.

C.A. Williams, Department of Geological and Geophysical Sciences, Princeton University, Princeton, NJ 08544.

(Received July 5, 1990;
revised April 10, 1991;
accepted May 28, 1991.)

JOURNAL OF GEOPHYSICAL RESEARCH, VOL. 96, NO. B10, PAGES 16,455–16,469, SEPTEMBER 10, 1991

Crustal Structure of the Active Margin, South Central Alaska: An Interpretation of Seismic Refraction Data From the Trans-Alaska Crustal Transect

LORRAINE W. WOLF

Phillips Laboratory, Earth Sciences Division, Hanscom Air Force Base, Massachusetts

DAVID B. STONE AND JOHN N. DAVIES

Geophysical Institute, University of Alaska, Fairbanks

Seismic refraction and wide-angle reflection data from the U.S. Geological Survey's Trans-Alaska Crustal Transect are used to investigate the upper crustal structure of southcentral Alaska and to develop a model using two-dimensional asymptotic ray theory. The data considered here are from the N-S 126-km Cordova Peak refraction profile, which was positioned to cross the Chugach and Prince William terranes. These two tectonostratigraphic terranes form part of a large accretionary complex related to the Alaska subduction zone. Interpretation of data from the Cordova Peak profile indicates systematically higher velocities in Chugach terrane rocks as compared with Prince William terrane rocks at comparable depths. Unconsolidated sediment and glacial ice overlie Chugach terrane rocks of unusually high compressional velocities (4.7–7.0 km/s) in the upper 10 km of crust. A northward thickening metasedimentary and metavolcanic flysch sequence, having an average velocity of 6.0 km/s, is underlain by metavolcanic mafic basement rocks having an average velocity of 6.6 km/s. The upper 10 km of the Prince William terrane have compressional velocities ranging from 3.7 to 6.2 km/s and are correlated with clastic sedimentary and volcanic rocks which are overlain by younger terrigenous sedimentary rocks and underlain by mafic to ultramafic Prince William terrane basement rocks. The upper crustal velocity structures of the Chugach and Prince William terranes are distinct to at least 10 km depth, which suggests that the Contact fault zone is a boundary which extends to at least 10 km. Midcrustal layers beneath the Chugach terrane contain two velocity reversals which may indicate the presence of off-scraped oceanic sediment, overpressurized zones, shear zones, or some combination of these possibilities. Data from energy sampling midcrustal layers beneath the Prince William terrane do not provide similar evidence for low-high velocity zones in that area.

INTRODUCTION

Southern Alaska is a geologically and tectonically complex area which offers a modern setting for the study of subduction environments and accretionary processes (Figure 1). It consists of a collection of tectonostratigraphic terranes which were accreted to North America along a convergent margin. A contribution to our understanding of the tectonic processes and geologic history of southern Alaska has come from the data collected as part of the Trans-Alaska Crustal Transect (TACT) project, an ongoing program of geological and crustal seismic investigations. The crustal model for south central Alaska presented here is based on an interpretation of the TACT Cordova Peak seismic refraction/wide-angle reflection profile. A model based on the intersecting Chugach profile was developed previously [*Wolf and Levander*, 1989] and is used to constrain the model developed in this paper.

The TACT corridor in southern Alaska is located in a transitional zone influenced by both convergent and transform tectonic margins (Figure 1). To the west, the Pacific plate is subducting beneath the North American plate, beginning along the Aleutian trench. To the east, transform motion is distributed along the Fairweather fault system. Relative motion between the Pacific and the North American plate was described by the RM1 model [*Minster et al.*, 1974] to be approximately NNW at a rate of 6 cm/yr, an estimate which is in agreement with more recent estimates for this region [*Engebretson et al.*, 1985; *Ma et al.*, 1989]. Estimates of convergence rates and paleolatitudes suggest that the terranes in southern Alaska contain accreted rocks originally formed south of their present latitudes [*Stone et al.*, 1982; *von Huene et al.*, 1985]. The Yakutat terrane, which is currently accreting to southern Alaska, appears to be moving with the Pacific plate, but at a slightly slower rate [*Perez and Jacob*, 1980; *Lahr and Plafker*, 1980; *Bruns*, 1983].

The 126-km Cordova Peak seismic refraction line is a N-S trending dip profile which crosses both the Chugach and Prince William terranes (Figure 2). At its midpoint, the Cordova Peak line intersects the Chugach line, a 135-km profile which parallels the regional E-W strike of the Chugach Mountains. The Chugach and Prince William terranes form an accretionary complex divided by the Contact Fault zone, a zone of steeply dipping faults along which rocks of the Prince William terrane have been thrust beneath older rocks of the Chugach terrane. In the western part of the Gulf of Alaska, the Aleutian trench forms the southern boundary of the Prince William terrane.

GEOLOGIC SETTING

The Chugach terrane consists of highly deformed, accreted and metamorphosed clastic sedimentary rock and oceanic crust [*Winkler et al.*, 1981]. It has been divided, from

Paper number 91JB01482.
0148-0227/91/91JB-01482$05.00

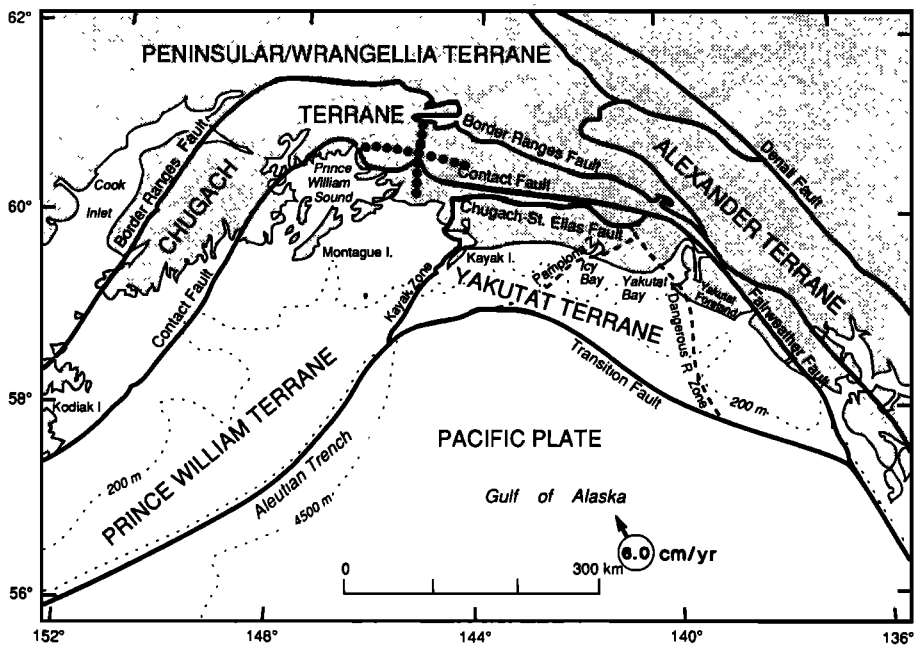

Fig. 1. Regional tectonic map of southern Alaska modified from *Jones et al.* [1981, 1987]. Arrow indicates relative motion between Pacific and North American plates [*Minster et al.*, 1974]. Small dots correspond to bathymetric contours. Large dots indicate location of TACT seismic refraction/wide-angle reflection lines discussed in this paper.

north to south, into three major fault-bounded sequences: the Upper Jurassic or older Liberty Creek schists, the Jurassic or older to Lower Cretaceous McHugh Complex, and the Upper Cretaceous Valdez Group [*Winkler et al.*, 1981; *Silberling and Jones*, 1984; *Plafker et al.*, 1989] (Figure 2).

The Valdez Group, which forms the bulk of the Chugach terrane, consists mainly of continentally derived sediments which were eroded from a magmatic arc and deposited in a deep-sea fan [*Winkler et al.*, 1981; *Plafker et al.*, 1989]. Beneath the deposited sedimentary rocks, mafic volcanic oceanic rocks form the terrane basement. The Chugach terrane moved northward to its present location, forming a thick accretionary prism which was later progressively metamorphosed in a low-pressure/high-temperature event beginning in latest Cretaceous and continuing in Paleogene time [*Hudson and Plafker*, 1982]. An observed metamorphic gradient in Valdez Group rocks increases from greenschist facies in the west to amphibolite facies east of the Copper River, in the Chugach Metamorphic Complex [*Hudson and Plafker*, 1982; *Sisson and Hollister*, 1988]. To the south, metavolcanic rocks exposed at the surface are juxtaposed with sedimentary rocks of the Prince William terrane along the Contact fault zone. The total stratigraphic thickness of the Chugach terrane is unknown.

The Prince William terrane contains accreted rocks of the Orca Group, a late Paleocene and early through middle Eocene deep-sea fan deposit interbedded with oceanic basalts, having an estimated thickness of 6–10 km [*Winkler and Plafker*, 1981; *Plafker*, 1987]. Overlying the Orca Group are late Eocene or older to Quaternary siliciclastic sedimentary rocks which were deposited in shelf or slope basins at their current locations. These younger sedimentary rocks constitute a relatively undeformed sequence estimated to be less than 4 km thick.

Similarity in lithology and depositional environment between the sandstones of the Chugach and Prince William terranes has raised some question as to whether the two terranes are geologically distinct entities [*Dumoulin*, 1988]. It has been argued that minor differences observed in rocks of the two terranes in central Prince William Sound may simply reflect a metamorphic gradient and that the Contact fault may be an out-of-sequence thrust fault, rather than a terrane boundary.

Felsic to intermediate Eocene hypabyssal and plutonic rocks were intruded into the Chugach and Prince William terranes at about 50 Ma, following the start of regional metamorphism [*Plafker et al.*, 1989]. The intrusions form dikes and dike swarms, as well as small stocks and sills, which crop out in the vicinity of the seismic transect. Crosscutting relationships indicate that the intrusions postdate deposition of Orca Group rocks and major motion along the Contact fault. Although rocks of the Yakutat terrane are not seen along the transect, subsurface boundaries of the terrane may well extend westward to the transect and beyond.

Data and Analysis

The N-S Cordova Peak profile extends from the Border Ranges fault zone to the Gulf of Alaska (Figure 2). It is a reversed profile consisting of five chemical explosions, rang-

Fig. 2. (Opposite) Generalized geologic map of southern Alaska showing location of TACT seismic refraction profiles (heavy lines). Other lines correspond to cross sections in Figure 12. Chugach refraction profile extends from SP 17 to SP 20; Cordova Peak profile extends from SP 11 to SP 37. SP 36 is the southern off-end shot for the Cordova Peak profile. Small dots indicate receiver positions. Crosses indicate shot points. Units Kvv, Kvg, and Kjm, metavolcanic rocks; Kvs, metamorphosed flysch; Kvg, rocks in Chugach Metamorphic Complex; Tg, igneous intrusive rocks; T0 and T1, sedimentary and volcanic rocks.

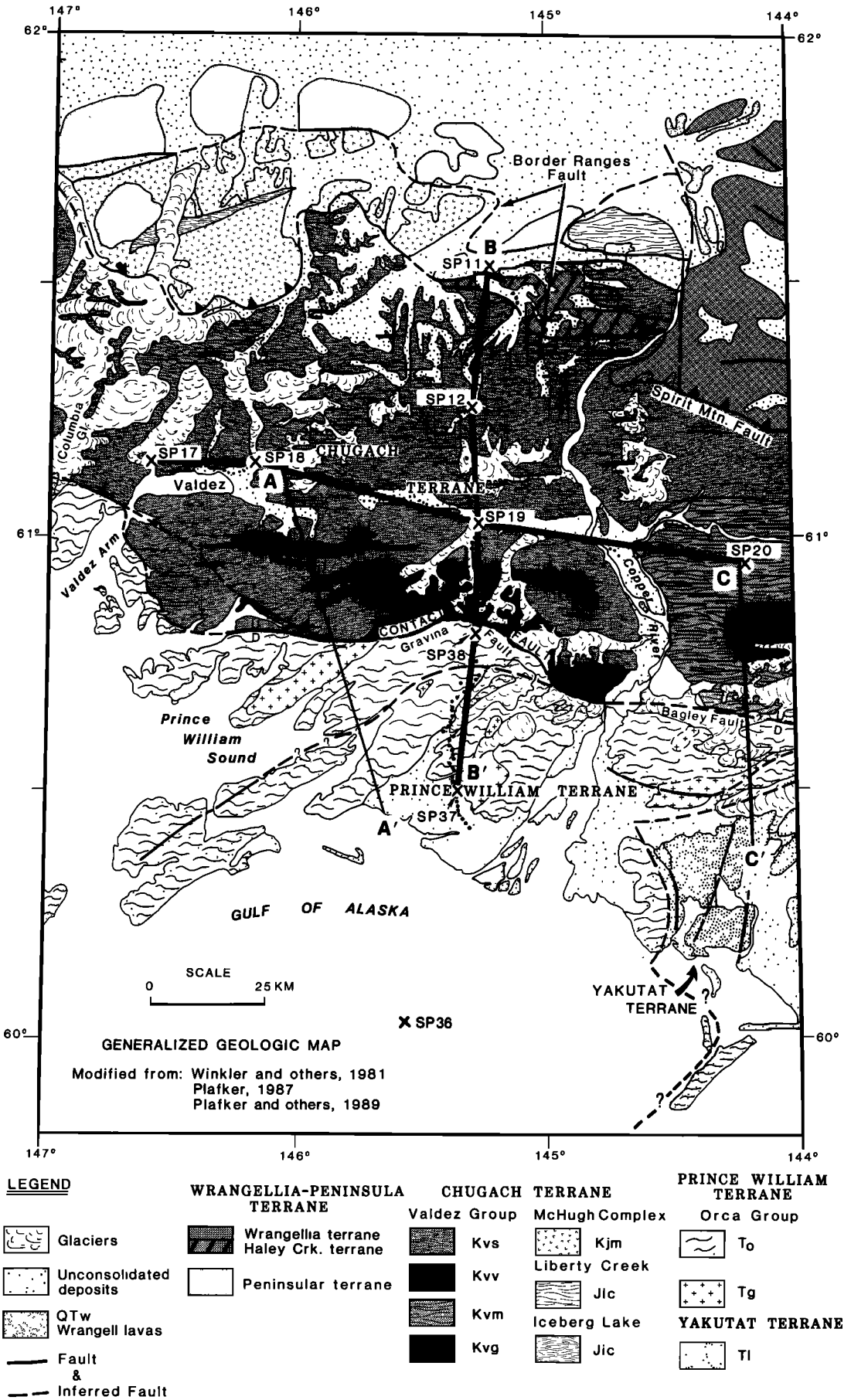

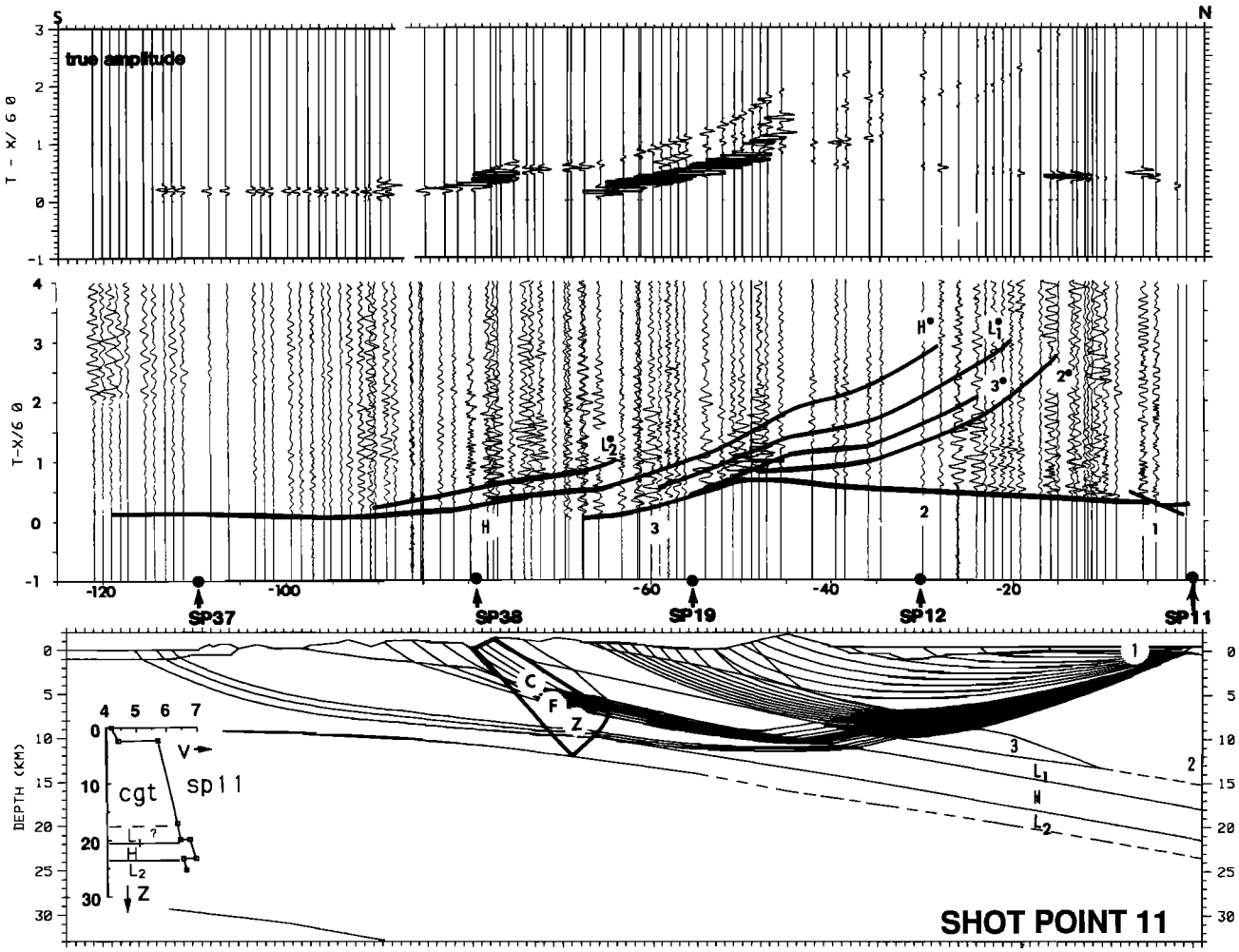

Fig. 3. Reduced-time true amplitude record section with calculated travel time curves, synthetic record section, and ray diagram for shot point 11 (SP 11). Calculated travel times from the same branch are connected and overlie observed data. Phases are correlated with layer numbers in the model (reflected branches marked with bullitts). Average velocities are shown in Figure 8. Ray diagram illustrates areas sampled by shot, but to avoid clutter, only some phases are shown. All phases are used to produce synthetic seismograms. Insert contains velocity-depth function for the model at the shot point. Dashed lines indicate no velocity discontinuity or lack of information. All subsequent data figures follow the same format (cgt, Chugach terrane; pwt, Prince William terrane; yak, Yakutat terrane; CFZ, Contact fault zone; L1, L2, H, low-/high-velocity zones).

ing in size from 926 to 1389 kg (2040–3060 lb) and spaced at approximately 40 km. Each shot was recorded by approximately 120 portable seismic cassette recorders spaced at 1-km intervals in a fixed array [*Wilson et al.*, 1987]. Shot points 11, 12, and 19 lie within the McHugh Complex and the Valdez Group rocks of the Chugach terrane. Shot points 38 and 37 lie south of the Contact fault zone, within rocks of the Prince William terrane. Shot point 19 marks the intersection of the Cordova Peak dip line with the Chugach strike line.

The five shots of the Cordova Peak profile have been interpreted using two-dimensional asymptotic ray methods [*Cerveny et al.*, 1977; *Luetgert*, 1987]. Field records indicate that the seismic data are of good quality except at long offsets, where signal to noise ratios make it difficult to pick first arrivals in some record sections. Calculated travel times were generally fit to within 0.10 s of observed arrivals. Synthetic seismograms produced using the program R86PLT [*Luetgert*, 1987] were used to analyze relative within-trace amplitudes and to refine the velocity structure within the model.

Results of the modeling are shown in Figures 3–7. Each figure contains a comparison of the field data from one shot point with the calculated travel times and synthetic seismograms from the preferred model. Record sections are plotted with a reduction velocity of 6 km/s and are trace normalized, except where indicated. Ray diagrams illustrate the subsurface areas sampled in different layers, but for simplification, only representative rays are shown. Simplified topography is drawn from local maxima and minima as determined from receiver elevations.

The starting model for the Cordova Peak interpretation was constructed from (1) a synthesis of one-dimensional models from each of the shot points, (2) a model based on surface geology and geologic cross sections, and (3) the previously derived model for the intersecting Chugach line [*Wolf and Levander*, 1989]. The starting model was then iteratively adjusted and revised. It was not possible to constrain rigorously the Cordova Peak dip model at shot point 19 (the intersecting point of the two lines) with the velocity-depth function from the Chugach model. Velocities

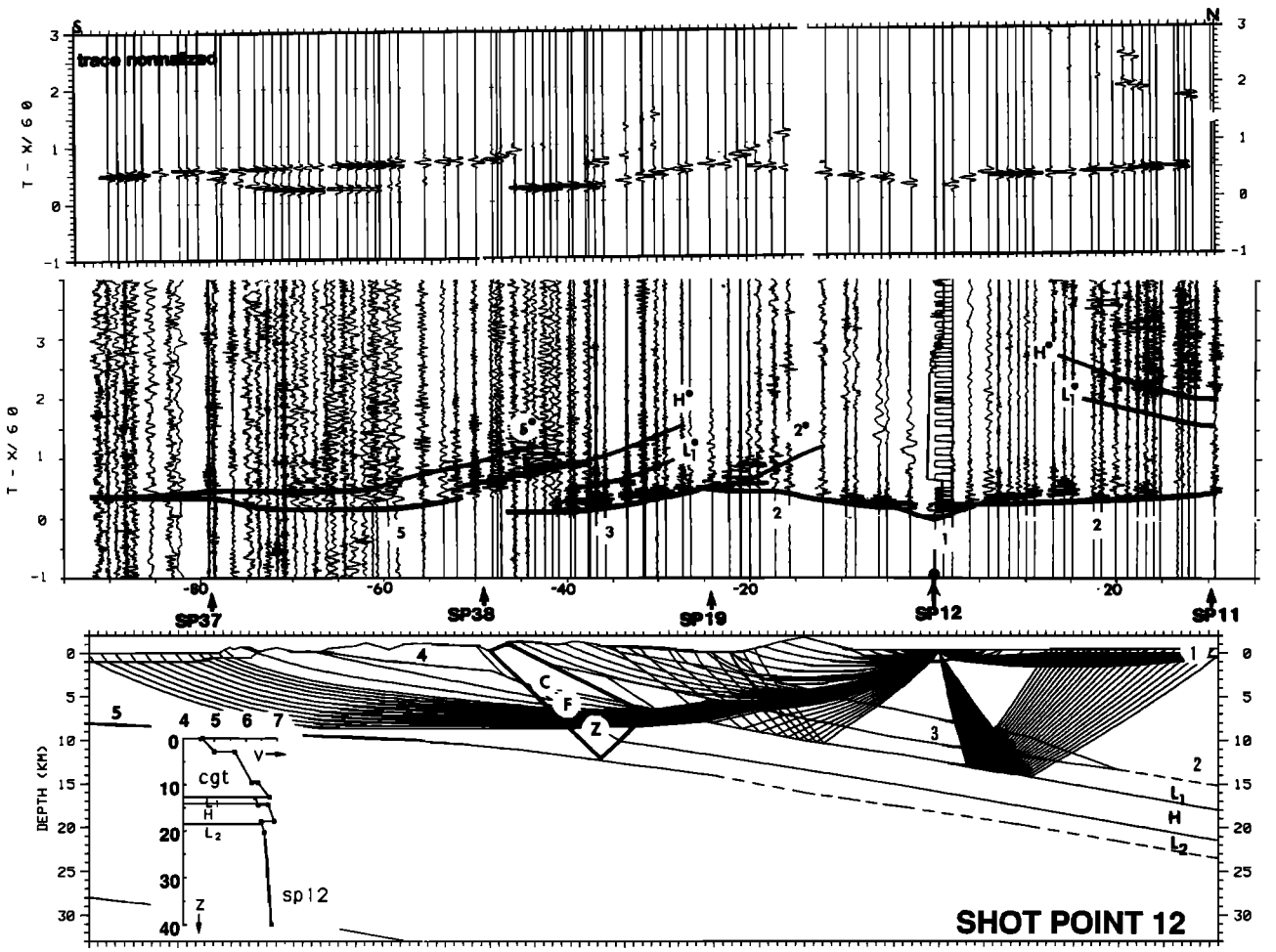

Fig. 4. Reduced-time record section with calculated travel times, synthetic record section, and simplified ray diagram for shot point 12 (SP 12). See Figure 3 caption for details.

of the strike line were systematically higher than those observed in the dip line. Possible explanations for velocity-depth function discrepancies between the strike and dip models in the upper crustal layers include out-of-plane reflections, nonuniqueness of solution, and anisotropy. The last possibility is discussed in more detail later.

Seismic Model

The seismic velocity model derived for the Cordova Peak profile is shown with a possible geologic model in Figure 8. Figure 8 displays average compressional velocities within each layer for specific areas of the model. Layers 1–3 represent rocks of the Chugach terrane, most of which have surface expression north of the Contact fault zone (Figure 2). Compressional velocities at the surface in the Chugach terrane range from a low of 4.0 km/s in sedimentary rocks to a high of 5.8 km/s in exposed bedrock. Clearly observed primary arrivals and prominent reflections generally provide good constraints on depths to interfaces of the first 3 layers (Figures 3–5). A comparison of primary arrivals at offsets within 20 km to the north and south in the record from shot point 19 shows slower apparent velocities to the north (Figure 5). To the north, no high-amplitude reflection occurs in the shot record until approximately 23 km offset and 0.75 s. To the south, wide-angle reflections from shallow dipping layers occur much closer to the shot point (18 km, 0.25 s). Similarly, the data from shot point 12 contain a strong high-amplitude phase to the south at 16 km offset and 1.0 s but lack a similar phase to the north (Figure 4). A true amplitude plot of the data from shot point 11 shows a decay of amplitudes with offset distance associated with the refracted phase within layer 2 and a lack of a strong, continuous reflected phase until about 45 km offset (Figure 3). The difference in observations of energy travelling northward from shot point 19 versus southward from shot point 11 is attributed to a northward thickening of the second layer related to the structural dip (Figure 8).

A strong refracted phase in the data from shot points 11, 12, and 19 provides justification for layer 3 in the model. Layer 3, exposed at the surface just north of the Contact fault zone, is 3–4 km thick and has a high average velocity (6.6 km/s). In the record from shot point 11, weak first-arriving energy at 30–45 km offset is followed at 47 km and 0.75 s by a strong phase, attributed to refracted energy within layer 3, having a high apparent velocity (Figure 3). In the record from shot point 12, a similar phase (labelled "3") occurs at 25 km offset to the south and 0.5 s but is absent in the data to the north, where offsets do not extend far enough to record refracted energy from this layer (Figure 4). Data from shot point 19 contain a strong arrival (labelled "3")

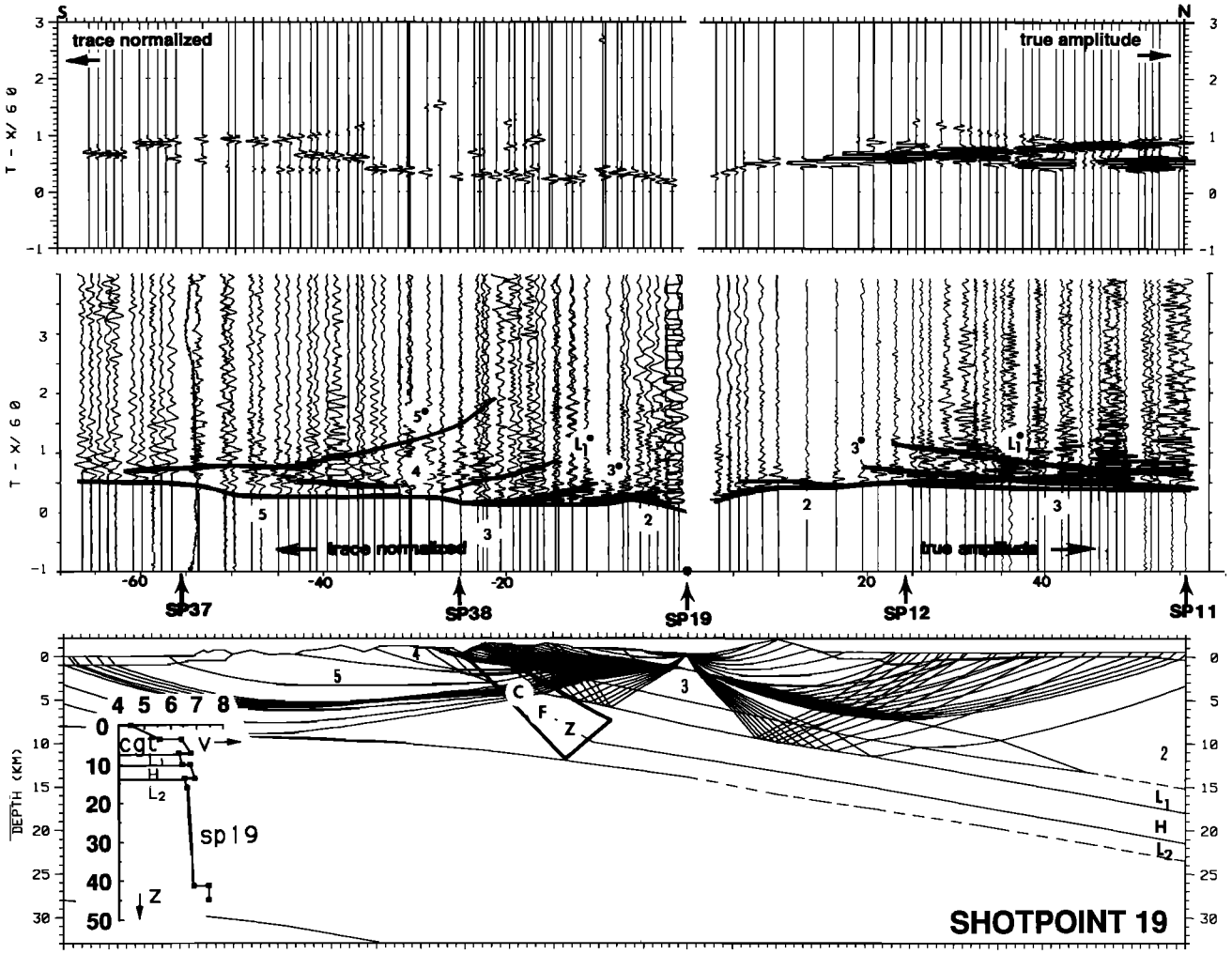

Fig. 5. Reduced-time record section with calculated travel times, synthetic record section, and simplied ray diagram for shot point 19 (SP 19). A true-amplitude plot is shown for data to the north, but data associated with energy travelling through the Contact fault zone are presented in trace-normalized format, since complexities of the structure here make amplitude modelling difficult. Shot point 19 marks the intersection of strike and dip profiles. See Figure 3 caption for details.

occurring within 10 km offset to the south; a counterpart is seen to the north at 26 km offset (Figure 5). The characteristic strength of this phase in the shot records and its association with faster apparent velocities to the south and slower apparent velocities to the north provide evidence for the northward dip of layer 3 in the model and a justification for its relatively steep vertical velocity gradient (6.4–6.75 km/s). Attempts to carry this layer northward over the entire length of the profile without invoking a substantial lateral velocity gradient resulted in travel times greater than 0.2 s faster than first arrivals observed in the record from shot point 11. As an alternative, layer 3 was modelled to pinch out and the thickness of layer 2 was increased to the north; this approach provided a more successful match to observed travel times in reversed shot records (Figures 3 and 5).

The velocity of surface rocks in the Prince William terrane range from a low of 3.7 km/s to a high of 5.6 km/s. The significantly lower velocities associated with Prince William terrane rocks as compared with those of the Chugach terrane at comparable depths are clearly evidenced in the shot records. Primary arrivals from shot point 38, which is located within the Contact fault zone, are fairly symmetric within 15 km of the shot point (Figure 6). Since the structure is assumed to be north dipping on the basis of geologic data, the similarity in apparent velocity of rocks to the north and south is attributed to the presence of higher velocity rocks north of the Contact fault zone. Beyond 15 km offset, slower apparent velocities are observed for energy arriving to the south than at similar offsets to the north, where rays penetrate the higher velocity Chugach terrane and midcrustal rocks. Reversed shots in the Prince William terrane indicate an average velocity of 6.1 km/s for rocks in the upper crust corresponding to layer 5 in the model (Figure 8). A high-amplitude secondary phase occurring in the record from shot point 37 at approximately 33 km offset to the north and 1.2 s is attributed to a reflection from the base of layer 5 in the model (Figure 7). In all shot records, travel time delays of approximately 0.17 s are observed in the vicinity of the Contact fault zone (Figures 3–7).

A group of midcrustal rocks containing low-/high-velocity pairs begins at approximately 6 km beneath shot point 19 in the model (Figure 8). The model contains two low-velocity

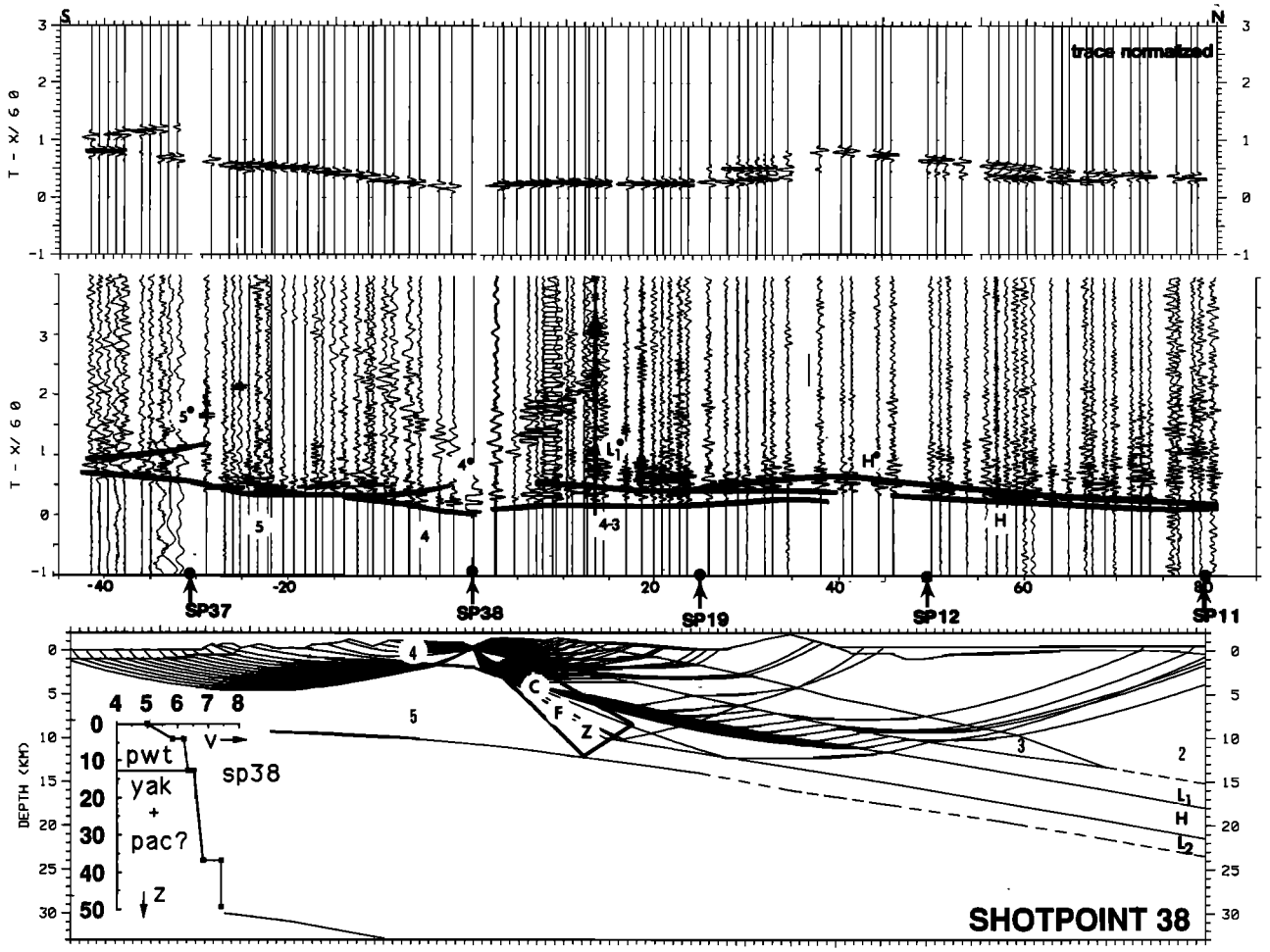

Fig. 6. Reduced-time record section with calculated travel times, synthetic record section, and simplied ray diagram for shot point 38 (SP 38). See Figure 3 caption for details.

zones: a 2.5-km-thick zone having an average velocity of 6.3 km/s (LVZ_1) and a 2- to 3-km-thick zone having an average velocity of 6.6 km/s (LVZ_2). Directly beneath the first velocity reversal is a sharp increase in average velocity to 6.8 km/s, corresponding to a high-velocity layer (HVZ). The low-velocity zones are indicated in the refraction data by (1) high-amplitude secondary arrivals (thought to result from energy reflecting from the base of the low-velocity layers), (2) complication in the record section associated with rays passing through midcrustal layers, and (3) delays or skips in the travel time curves. These travel time delays form en echelon arrivals that are best observed in the refraction data from the Chugach strike profile and are discussed in detail in that analysis [*Wolf and Levander*, 1989].

Preliminary models of the Chugach line used four low-/high-velocity pairs to match en echelon arrivals observed in the data [*Fuis and Ambos*, 1986; *Page et al.*, 1986]. This model resulted in primary arrivals from the higher-velocity layers occurring at distances not seen in the field data. A more successful approach used reflectivity methods to model en echelon arrivals in the data from the Chugach strike profile as multiple reflections within the second low-velocity zone [*Flueh et al.*, 1989]. Although the reflectivity method is more exact, it was not a suitable option for modelling the Cordova Peak line, where the crustal structure is complicated and interfaces are dipping. Offsets along the Cordova Peak dip profile are not adequate to constrain the depth or thickness of the second low-velocity zone, but it is included in the model based on interpretations of the Chugach line.

Evidence for the midcrustal low-velocity zones is best seen in the records from shot points 19 and 11. A secondary phase arriving at an offset of 25 km to the north and 1.2 s in the record from shot point 19 is correlated with energy reflecting off the base of LVZ_1 (Figure 5). A similar phase is observed to the south at 16 km offset and approximately 0.85 s. In the record from shot point 11, high-amplitude secondary arrivals as well as high apparent velocities at offsets of 45–85 km are attributed to rays passing through midcrustal areas containing the velocity reversals and high-velocity layer (Figure 3). An en echelon pattern, so predominant in data from the strike profile, is observed here.

Distinct horizons appearing in the Chugach seismic reflection data were used in the refraction model to provide some constraint on the depths to interfaces of these low-/high-velocity layers [*Fisher et al.*, 1989]. At least three bands of reflectors in the midcrust are imaged in the reflection data and are used here to provide information on the continuity of layers at the model's northern section, where reversed ray coverage is lacking. The absence of travel time delays and multiple high-amplitude secondary arrivals associated with

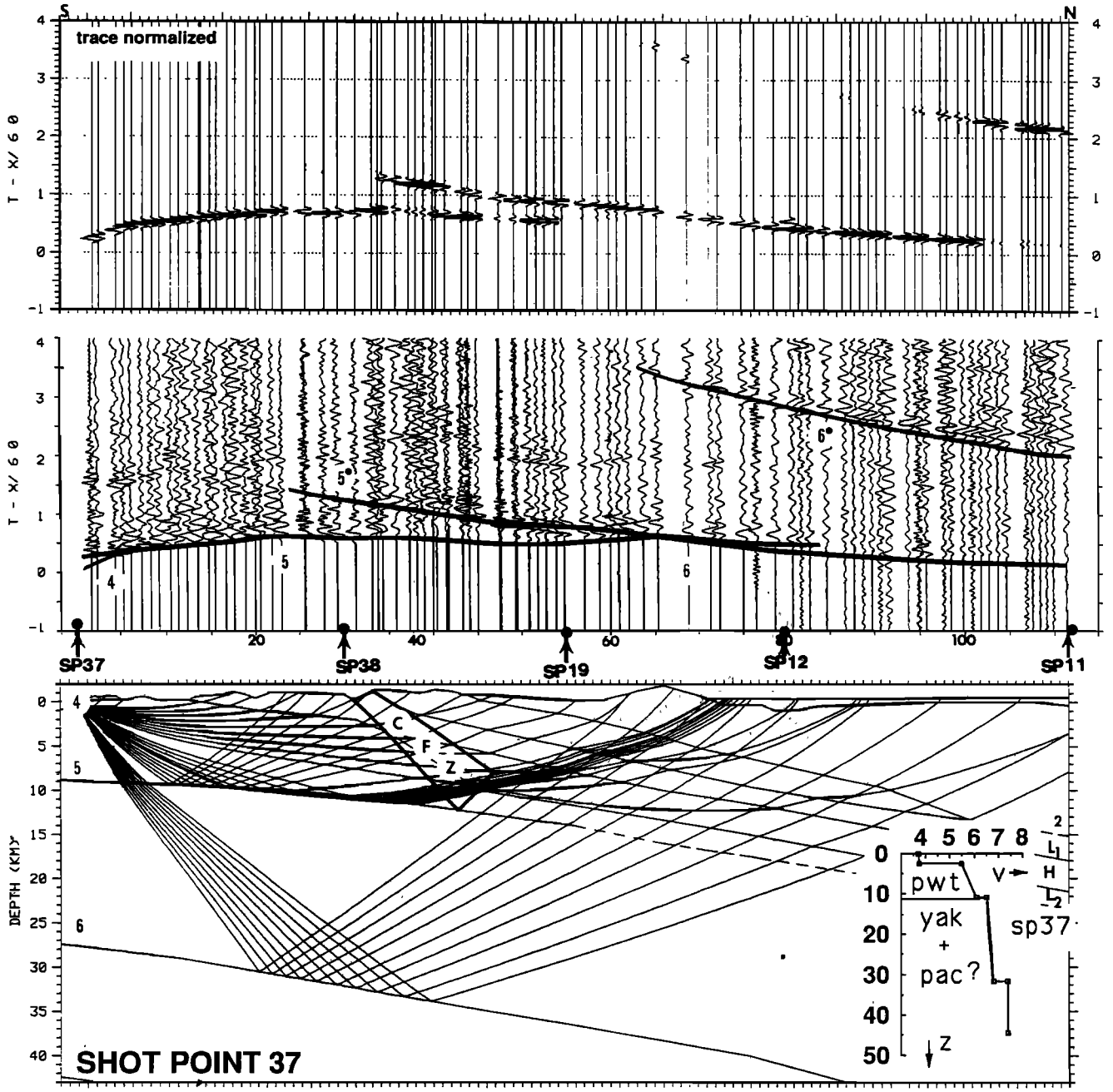

Fig. 7. Reduced-time record section with calculated travel times, synthetic record section, and simplied ray diagram for shot point 37 (SP 37). See Figure 3 caption for details.

energy sampling midcrustal regions beneath the Prince William terrane suggests that these low-/high-velocity zones are not present in that area. The midcrustal layers beneath the Chugach terrane are therefore not shown to extend southward beyond the Contact fault zone in the model.

The velocity structure of deeper layers beneath the Chugach and Prince William terranes is not well constrained by the Cordova Peak refraction data because offset coverage is insufficient. In the record from shot point 37, a late arriving phase is observed beginning at approximately 65 km offset and 3.5 s (Figure 7). This phase has an apparent velocity of 6.8 km/s and is modelled as a reflection from the lower crust (Figure 7). Without a refracted phase from the layer below, however, the depth and velocity of this layer are only weakly constrained. A late arriving phase also occurs in the record from shot point 11 at about 118 km offset and 2.1 s, but reliable identification of this phase or its apparent velocity is impossible without more data at longer offsets (Figure 3).

Earthquake hypocenters for events believed to be located within the subducting plate provide a lower limit for the overriding crust [*Davies*, 1975; *Lahr*, 1975; *Stephens et al.*, 1984; *Wolf and Levander*, 1989; *Page et al.*, 1989]. The upper limit of these hypocenters can be traced northward from the Aleutian trench to approximately a 22-km depth beneath shot point 19 (Figure 8). No corresponding high-

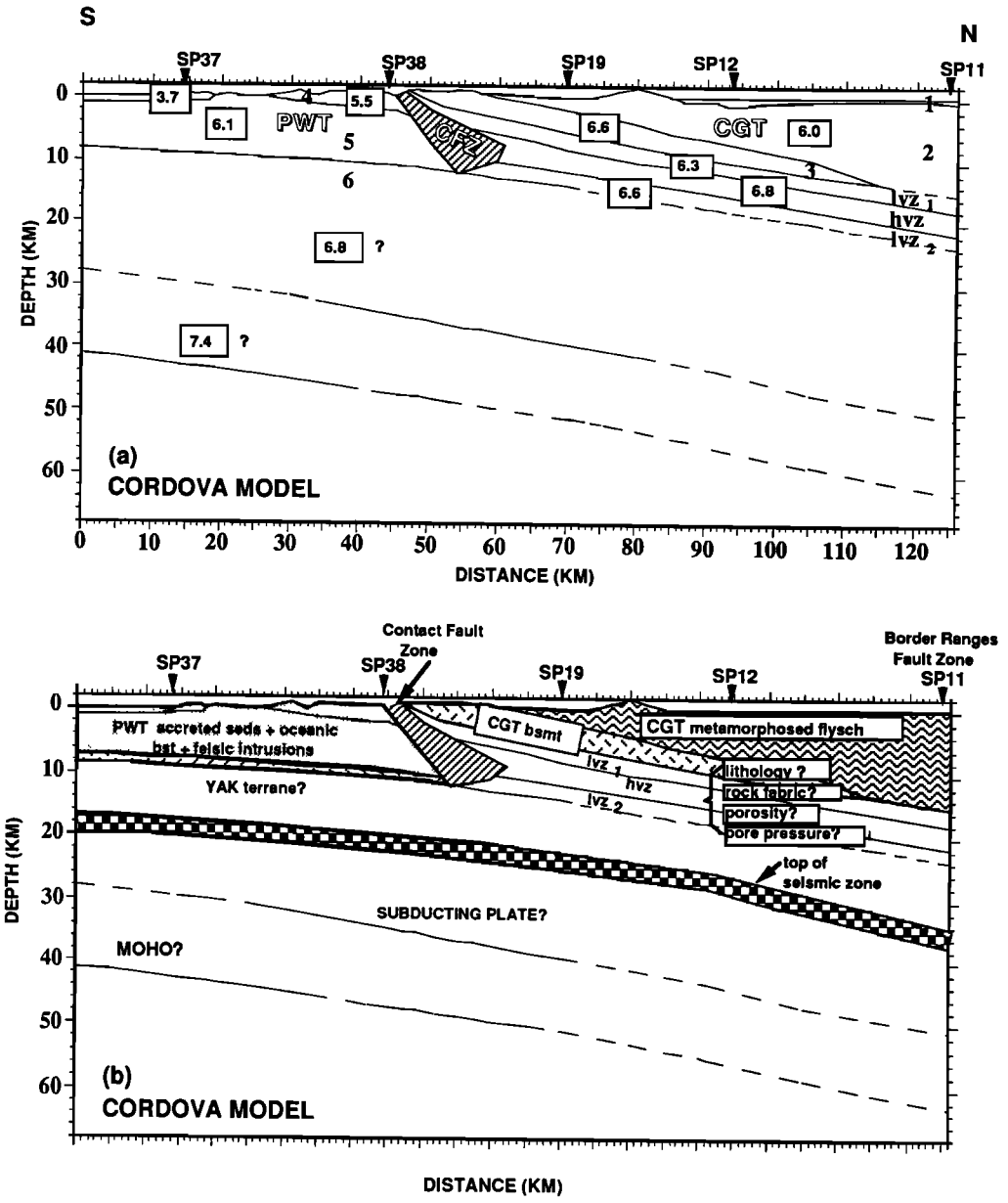

Fig. 8. Models showing average seismic velocities and possible geologic structure based on interpretation of U.S. Geological Survey Cordova Peak profile: (*a*) Seismic model showing average velocities (km/s) for model layers. Velocities and boundaries at model ends are not well constrained. (*b*) Possible geologic interpretation based on seismic model and cross section from *Plafker et al.* [1989]. Top of seismic zone constructed from *Page et al.* [1989].

amplitude phase is seen in the refraction data which can be correlated with a reflection from this depth, however. The lack of a prominent arrival could be the result of a low impedance contrast between the subducting and overriding plates or of high noise levels in the data at far offsets.

The data from shot point 36, an off-end shot to the south of the Cordova Peak profile, provide some information on deep structure. A high-amplitude late arriving phase is observed in the data beginning at approximately 80 km offset and 4 s, with an apparent velocity of 7.4 km/s (Figures 2 and 9). Since the subducting crust is presumed to be north dipping, the travel time of this phase indicates a reflector at greater depth (40–45 km) than that imaged in the data from shot points 37. It is postulated that the high-amplitude secondary phase observed in the off-end shot record is from energy sampling the crust/mantle boundary and that the phase beginning at 3.5 s in the data from shot point 37 indicates some intermediate reflector within the subducting crust.

Figure 10 is a composite rendition of information from earthquake and reflection data overlain on the seismic model proposed here. Figure 10 also contains a model based on refraction, reflection, and earthquake data acquired in the vicinity of Vancouver Island [*Hyndman et al.*, 1990]. Both diagrams are plotted at the same scale. Several similarities between the two areas are apparent. In both cases, a zone of prominent subhorizontal reflectors occurs in the midcrust, above earthquake hypocenters signifying the upper part of the subducting plate [*Page et al.*, 1989; *Hyndman et al.*, 1990]. *Clowes et al.* [1987] identified three bands of dipping reflectors which underlie a "lid" of accreted terranes (la-

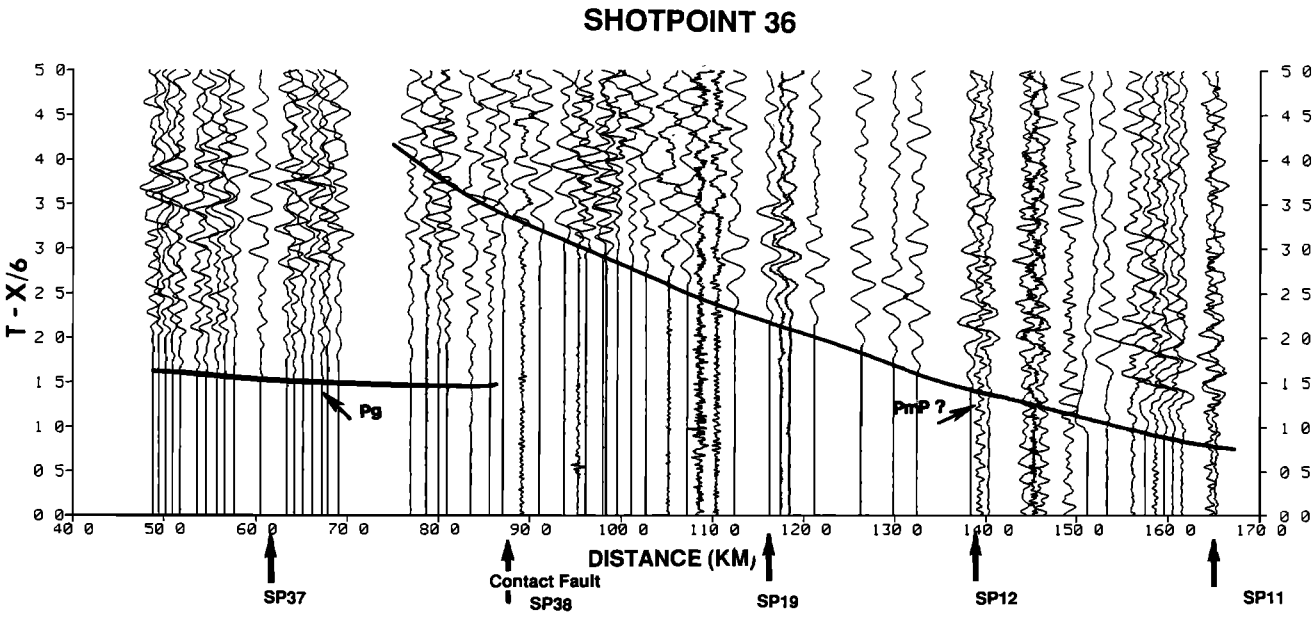

Fig. 9. Trace-normalized record section for shot point 36 (SP 36), an off-end shot for the Cordova Peak profile. The *Pg* phase dies out at approximately 90 km offset. A pronounced phase (*PmP*?) having an apparent velocity of 7.4 km/s appears at approximately 80 km and 4.0 s.

belled "C", "E" and "F" in Figure 10*a*). *Fisher et al.* [1989] imaged a similar set of reflecting zones beneath the accreted Chugach terrane (Figure 10*b*). In both cases, the midcrustal reflectors (forming a zone about 20 km thick) are approximately parallel to the inferred top of the subducting plate and occur at depths associated with velocity reversals in the refraction models. In both cases, the top of the seismic zone is nearly coincident with the deepest set of reflectors.

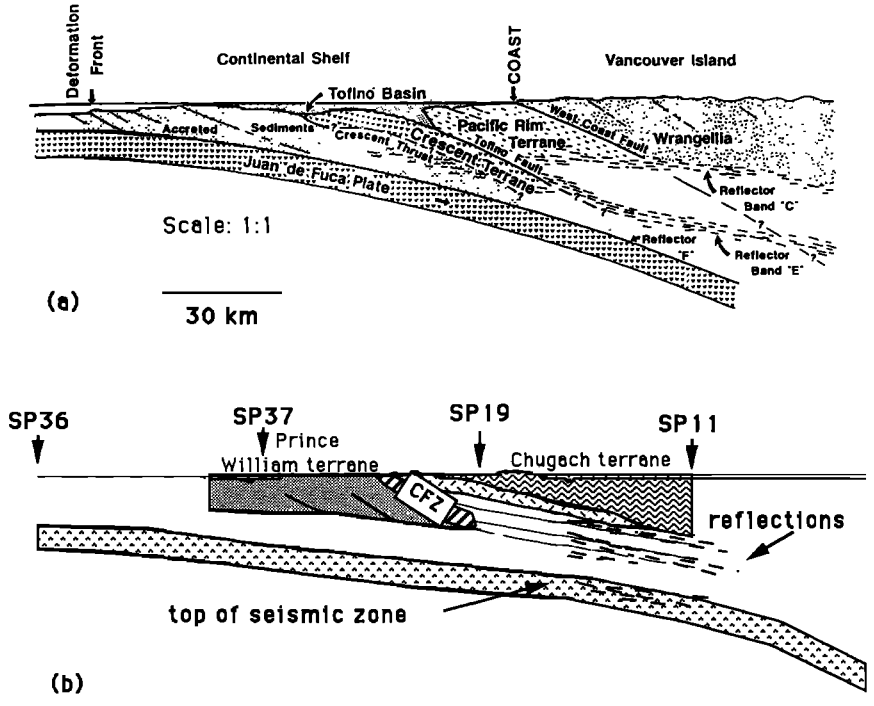

Fig. 10. Composite drawing showing similarities of crustal structure beneath southcentral Alaska and the Vancouver Island margin: (*a*) Interpretive crustal model from *Hyndman et al.* [1990, Figure 11] based on refraction, reflection and earthquake data [*Green et al.*, 1986; *Clowes et al.*, 1987; *Drew and Clowes*, 1990]. (*b*) Crustal model constructed from refraction interpretation (this paper), reflection data [*Fisher et al.*, 1989] and earthquake data [*Page et al.*, 1989]. In each case, a zone of prominent, subhorizontal midcrustal reflectors, about 20 km thick, occurs above the subducting plate and earthquake foci, where brittle failure is assumed. Reflections correlate well with positions of low-velocity zones in refraction interpretations from both areas.

GEOLOGIC INTERPRETATION

A possible geologic interpretation is shown with the detailed velocity model of the upper crustal structure along the Cordova Peak refraction profile in Figure 8. Layers 1–3 are correlated primarily with metamorphosed flysch and volcanic rocks of the Valdez Group. The northward thickening of layer 2 agrees with geologic models for the area and is in part due to thrust faulting and imbrication within the accretionary complex. Rocks of the McHugh Complex probably occur near the north end of the profile but are covered by surficial deposits. Complication in the record from shot point 11 close to the shot point may represent a subsurface contact between rocks of the Valdez Group and McHugh Complex or may be the result of diffracted or scattered energy from dikes which have intruded nearby areas of the transect. Although high-amplitude secondary arrivals are present in the record within 25 km offset from this shot point, they lack continuity between traces for any reasonable distance and do not form an identifiable phase (Figure 3). Another geologic feature which may contribute to the complicated arrival pattern and high near-surface velocities is the rootless Haley Creek terrane, a thin sliver of metasedimentary and metavolcanic rocks which has been thrust over Chugach terrane rocks in this area of the transect [*Wallace*, 1985; *Wolf and Wallace*, 1988; *Plafker et al.*, 1989; *Nokleberg et al.*, 1989] (Figure 2). Shot spacing and receiver density make detailed modelling of igneous intrusive rocks and the structural relationships between rocks of the Haley Creek terrane and those of the Chugach terrane difficult because the features are too small (<1–2 km).

Layer 3 of the model corresponds to an elongate outcrop belt of mafic volcanic rocks, just north of the Contact fault zone, which forms the oceanic basement of the terrane (Figures 2 and 8). High velocities associated with these rocks were also seen in the data from the Chugach seismic refraction profile [*Wolf and Levander*, 1989]. This volcanic unit makes a good marker for subsurface structure, because it produces prominent reflections and clear refracted arrivals in the seismic data. The change in the velocity-depth function between shot point 19 and shot points 11 and 12 indicates that layer 3, with its high velocities, probably pinches out to the north (Figure 8).

Layers 4 and 5 of the seismic model are correlated with Orca Group and overlying rocks of the Prince William terrane. Lateral variations in velocity within the upper 5 km of crust are associated with accreted sedimentary rocks which have been intruded by felsic igneous rocks, particularly near the fault zone, in the form of sills and plutons (Figure 2). Velocities in layer 5 (6.1 km/s) are consistent with those of sedimentary rocks which have been metamorphosed. A strong reflected phase from the base of layer 5 is attributed to a lithologic change at approximately 9 km depth. Mafic volcanic rocks, mainly oceanic basalts, have been observed in the Prince William terrane to the south of the transect and may project northward to occur at approximately this depth. These mafic rocks in contact with sedimentary rocks could provide an impedance contrast which would account for the high-amplitude secondary phase seen in the data (labelled 5* in Figure 7).

The seismic refraction data do not provide good constraints on the subsurface location of the Contact fault zone, which is better imaged by other geophysical techniques. The best fit model shown in Figure 8 is the result of iterative trials of over 15 different configurations of the Contact fault zone. Based on geologic investigations [*Winkler and Plafker*, 1981; *Plafker et al.*, 1986], potential field data (discussed below) and the best fit seismic model, the Contact fault system is shown as having moderate northward dips (approximately 45°). Layer 4 in the model appears to crosscut the fault zone and may represent a combination of intrusive igneous and sedimentary rocks. This crosscutting relationship has been observed at the surface (Figure 2). Although the precise geometry and location at depth of the boundary between the Prince William and Chugach terranes are not known, the seismic refraction data indicate very different velocity-depth functions for the two terranes to at least 10 km depth.

Midcrustal layers beneath the Chugach terrane are difficult to interpret because they are not seen in the mapped surface geology. Possible geologic interpretations have been discussed in the analysis of the Chugach strike profile [*Wolf and Levander*, 1989]. The dip profile through the Chugach terrane does not provide information which would clearly eliminate any of the possible models discussed in the earlier work. The preferred interpretation of the data is that there exist at least two low-velocity zones in the Chugach terrane: one which pinches out to the east in the strike direction [*Wolf and Levander*, 1989] and a deeper one which may be more laterally extensive (Figure 8). Low velocities could represent subducted oceanic or terrigenous clastic sediments in which variable porosity contributes to lateral and vertical velocity variations. High-velocity layers, which underlie the low-velocity zones, are thought to consist of mafic to ultramafic rocks, possibly comprising relict subducted oceanic crust. The low-/high-velocity zones could also indicate overpressurized areas or shear zones resulting from midcrustal decollements.

Geologic interpretation of the model with respect to deep structural relationships is speculative, since the area covered by rays from reversed shots is limited. Two reflecting horizons indicated by the refraction data appear to be located within the subducting Pacific plate (Figure 8). Only the phase velocities observed in the data from shot point 36, however, are high enough to be correlated with energy sampling the crust/mantle boundary within the subducting plate (Figure 9).

DISCUSSION OF OTHER GEOPHYSICAL DATA

Observed gravity and magnetic data provide restrictions on the crustal structure determined from seismic refraction data alone [*Andreason et al.*, 1964; *Barnes*, 1977; *U.S. Geological Survey*, 1979*a*, *b*; *Page et al.*, 1986]. Along the Cordova Peak line, complete Bouguer gravity values show a broad high located near shot point 19. Magnetic data along the transect show a relative high just to the north of the Contact fault zone which decreases gradually northward to the Border Ranges fault zone. Both high's correlate well with the high-velocity mafic oceanic basement rocks which crop out between the Contact fault zone and shot point 19 (Figures 2 and 8). Gravity values for the area near shot point 38 are interpreted to indicate an apparent dip of the Contact fault zone of approximately 45° to the north in the upper layers (D. Campbell, personal communication, 1988). Neither gravity nor seismic data, however, constrain the attitude of the fault in deeper layers. The decrease of gravity

and magnetic values northward in the dip direction corresponds to thickened sequences of flysch and steepened dip of the subducting plate beneath the Chugach terrane.

Rock samples collected along the transect for measurements of compressional velocities support the observation that Chugach terrane rocks are associated with unusually high velocities. Average velocities often attributed to mafic or ultramafic oceanic rocks (6.3–7.0 km/s at 300 MPa) are observed in metasedimentary rocks of the Valdez Group and average velocities at similar pressures for metavolcanic rocks, such as pillow basalts, are even higher (6.8–7.1 km/s) (N. Christensen, written communication, 1988). Although velocities observed in the seismic refraction data cannot be definitively correlated with rock type, the laboratory measurements provide guidelines for the geologic interpretation of the seismic model.

Studies of the Valdez Group rocks to determine anisotropy in the upper crust of the Chugach terrane show that energy travelling parallel to the foliation direction is significantly faster than that travelling perpendicular to foliation [*Brocher et al.*, 1989; *Brocher and Christensen*, 1990]. In addition, the studies show that the effects of anisotropy in the rocks can be seen to pressures of 600 MPa (6 kbar). A comparison of the velocity-depth functions and primary arrivals from shot point 19 in the Chugach profile with those from the Cordova Peak profile shows that velocities seen in data from the Cordova Peak line are slower than those observed at comparable depths along the Chugach line (Figure 11). Discrepancies between the strike and dip velocities in the Chugach terrane may be in part attributed to fracture or foliation orientations, out-of-plane reflections, changes in porosity and metamorphic grade, and the nonuniqueness of the model. This last factor is most pronounced for deeper layers.

Thermal studies of the Chugach terrane indicate that Valdez Group rocks have undergone high-temperature/low-pressure metamorphism not easily explained by mechanisms traditionally proposed for such regional events in subduction zone environments [*Hudson and Plafker*, 1982; *Sisson and Hollister*, 1988]. A regional event resulted in metamorphism of Chugach terrane rocks to greenschist facies. A second and more localized thermal event in early to middle Eocene time resulted in metamorphism to amphibolite facies in the core of the Chugach Metamorphic Complex. Studies of mineralogy and CO_2-rich fluid inclusions indicate that amphibolite facies metamorphism of the rocks occurred at approximately 10 km depth [*Sisson and Hollister*, 1988; *Sisson et al.*, 1989]. The significance of thermal history for the refraction interpretation is that it provides evidence that low-pressure/high-temperature metamorphosed rocks can occur at relatively shallow depths in subduction zone environments and that associated dewatering of underplated sediments can produce zones of high fluid pressures and high porosities at midcrustal depths. These, in turn, could account for low-velocity zones in midcrustal areas. In his interpretation of geophysical data from offshore British Columbia, *Hyndman* [1989] asserts that increased porosity in crustal layers can result in velocity reductions of up to 15%, a figure which would more than adequately account for the velocity reversals seen in the south central Alaska data.

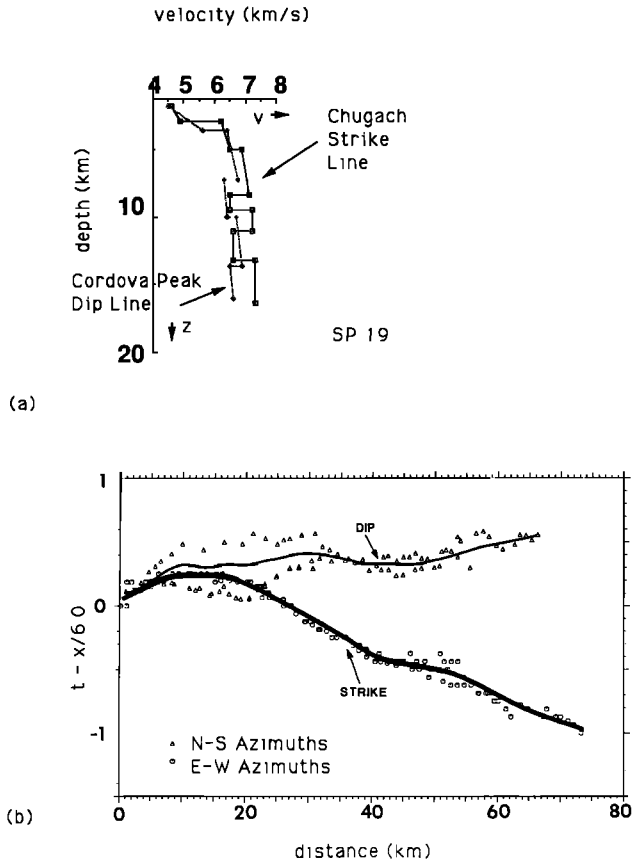

Fig. 11. A comparison of (*a*) velocity-depth functions at shot point 19 for the Cordova Peak and the Chugach seismic refraction profiles and (*b*) observed primary arrivals in records from shot point 19 for both profiles: triangles, Cordova Peak (N-S dip direction); circles, Chugach (E-W strike direction). Solid lines are averages between N-S directions (Cordova Peak line) and E-W directions (Chugach line), included to roughly account for the effect of dipping layers on travel times. Figures illustrate azimuthal variation of velocities and the corresponding discrepancies in seismic models for the Chugach and Cordova Peak profiles. Differences in velocities and interface locations for the upper crust can be explained in part by anisotropy, but differences for deeper layers probably reflect the nonuniqueness of the forward modelling method, limitations of the data due to receiver and shot spacing, and poor signal-to-noise ratios at long offsets.

Discussion and Summary

An attempt to tie the model for the Cordova Peak dip line with mapped surface geology and the previous interpretation of the Chugach strike line is illustrated by the fence diagram in Figure 12. This composite diagram shows the inferred structure beneath the Chugach profile as determined from the refraction data and projects it southward based on the mapped surface geology and refraction interpretation for the Cordova Peak line. The upper layers along each refraction line have been modelled to correspond with mapped contacts between surface rocks and to reflect observed structure as far as the ray-tracing algorithm would permit. Much lateral velocity variation exists within the upper 5 km of crust in both the Chugach and Prince William terranes. In both terranes, this variation is attributed to local areas of surficial deposits, to changes in metamorphic grade, and to laterally discontinuous igneous rocks which were intruded into country rock. Evidence for seismic anisotropy in the

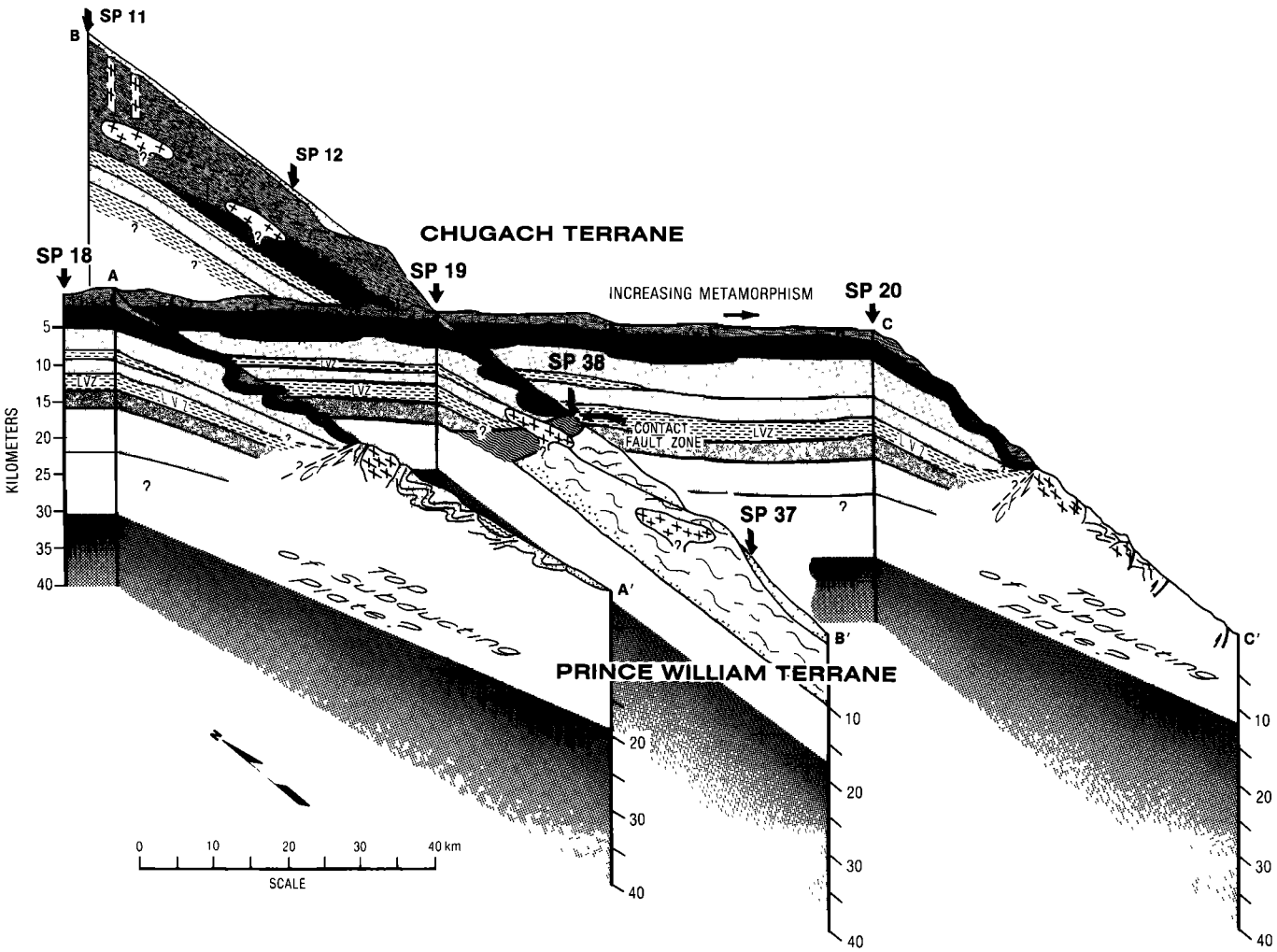

Fig. 12. Fence diagram illustrating possible geologic interpretation along lines shown in Figure 2. East-west cross section is based on interpretation of refraction data from the Chugach refraction profile [*Wolf and Levander*, 1989]. North-south cross section at SP 19 contains the model developed in this paper. Other cross sections are based on surface geology [*Winkler and Plafker*, 1981]. Both the Chugach and Prince William terranes are shown to extend to less than 10 km. The Chugach terrane is underlain by a region of midcrustal reflectors thought to contain two velocity reversals. A similar midcrustal package is not indicated by the data for the area beneath the Prince William terrane. Earthquake foci indicate approximate location of subducting plate and provide a lower limit to the overriding crustal package (western line from *Stephens et al.* [1984]; eastern line from *Wolf and Levander* [1986]). The Contact fault zone (CFZ) marks the boundary between the Chugach and Prince William terranes and is indicated by the data to extend to at least 10 km depth. Variation in shading pattern east of SP 19 marks the boundary of the Chugach Metamorphic Complex [*Hudson and Plafker*, 1982].

upper crust of the Chugach terrane from rock velocity studies is supported by the results of the refraction modelling presented here.

On the surface, the Contact fault zone appears to mark a major suture which separates two geologically different rock assemblages along the transect. The interpretation presented in Figures 8 and 12 is that rocks to the south have been accreted to and thrust under rocks of the Chugach terrane along the Contact fault zone. Although the Contact fault zone forms a boundary separating areas of the crust with differing velocity structures, it is uncertain from the seismic data whether the fault is a suture between geologically distinct assemblages or is simply an out-of-sequence thrust in an accretionary complex. A thrust of this sort could transport higher-velocity basement rocks closer to the surface, thus creating very different velocity-depth functions to either side of the fault plane.

Midcrustal layers beneath the Chugach terrane are assumed to be rocks which lack surface expression and do not extend southward beyond the Contact fault zone. These lower layers have velocities compatible with those of oceanic crust, and it is suggested that they comprise layered oceanic crust imbricated during large-scale subduction. Velocity reversals may represent subducted sedimentary rocks which have zones of high-porosity, overpressurized zones or shear zones associated with midcrustal decollements. Complication in the shot records, travel time delays, and high-amplitude secondary arrivals associated with energy passing through this region beneath the Chugach terrane are not observed in records of energy sampling midcrustal regions

beneath the Prince William terrane. The differences in velocity structure between northern and southern sections of the Cordova Peak profile indicate that the Contact fault zone is a boundary which extends to at least 10 km depth and either truncates or soles into midcrustal layers beneath the Chugach terrane. A coincident reflection survey along the profile through the Chugach terrane indicates strong midcrustal reflectors which approximately correspond to the positions of low-velocity zones in the refraction model. Similar midcrustal reflectors and associated low-velocity zones are imaged in seismic data from Vancouver Island.

Earthquake foci are believed to delineate the top of the subducting Pacific plate at approximately 22–30 km depth below the Chugach refraction profile and provide a lower limit for the upper crustal package (Figure 12). Although several models exist to describe the geometry of the Wadati-Benioff zone, the refraction data do not yield much information which would better define its shape. A lack of evidence in the refraction data for a sharp velocity contrast at the inferred location of the plate interface, however, suggests that the bottom of the overriding crust and the top of the subducting plate may have similar composition or physical properties. Although they are insufficient to determine uniquely the complex geometries and structural relationships of the accreted Chugach and Prince William terranes, particularly with respect to the lower crust, the refraction data from the Chugach and Cordova Peak profiles provide good constraints on upper crustal features which have dimensions of at least several kilometers.

Acknowledgments. The authors would like to thank the U.S. Geological Survey and Walter Mooney for providing the refraction data used in this study, J. Luetgert for gracious sharing of software, and B. Page for help with earthquake data. TACT workshops hosted by the USGS provided much valuable information and discussion. Reviews of the manuscript by G. Fuis, R. Clowes, and an anonymous reviewer greatly improved its quality. L.W. would also like to acknowledge support from the Air Force during manuscript preparation.

REFERENCES

Andreason, G. E., A. Grantz, I. Zietz, and D. F. Barnes, Geological interpretation of magnetic and gravity data in the Copper River Basin, Alaska, *U.S. Geol. Surv. Prof. Pap, 316-H*, 135–153, 1964.

Barnes, D. F., Bouguer gravity map of Alaska, scale 1:2,500,000, *U.S. Geol. Surv. Geophys. Invest. Map, GP-913*, 1977.

Brocher, T. M., and N. I. Christensen, Seismic anisotropy due to preferred mineral orientation in shallow crustal rocks in southern Alaska, *Geology*, *18*, 737–740, 1990.

Brocher, T. M., M. A. Fischer, E. L. Geist, and N. I. Christensen, High-resolution seismic reflection/refraction study of the Chugach-Peninsular terrane boundary, southern Alaska, *J. Geophys. Res.*, *94*, 4441–4455, 1989.

Bruns, T. R., Model for the origin of the Yakutat block, an accreting terrane in the northern Gulf of Alaska, *Geology*, *11*, 718–721, 1983.

Cerveny, V., A. Moltokov, and I. Psencik, *Ray Method in Seismology*, 214 pp., University of Karlova, Prague, Czechoslovakia, 1977.

Clowes, R. M., M. T. Brandon, A. G. Green, C. J. Yorath, A. Sutherland Brown, E. R. Kanasewich, and C. Spencer, LITHOPROBE—Southern Vancouver Island: Cenozoic subduction complex imaged by deep seismic reflections, *Can. J. Earth Sci.*, *24*, 31–51, 1987.

Davies, J. N., Seismological investigations of plate tectonics in south central Alaska, Ph.D. dissertation, 193 pp., Univ. of Alaska, Fairbanks, 1975.

Drew, J. J., and R. M. Clowes, A re-interpretation of the seismic structure across the active subduction of western Canada, in Studies of Laterally Heterogeneous Structures Using Seismic Refraction and Reflection Data, edited by A. G. Green, *Pap. Geol. Surv. Can.*, *89-13*, 115–132, 1990.

Dumoulin, J. A., Sandstone petrographic evidence and the Chugach-Prince William terrane boundary in southern Alaska, *Geology*, *16*, 456–460, 1988.

Engebretson, D., A. Cox, and R. G. Gordon, Relative motions between oceanic and continental plates in the Pacific Basin, *Spec. Pap. Geol. Soc. Am.*, *206*, 54 pp., 1985.

Fisher, M. A., T. M. Brocher, W. J. Nockleberg, G. Plafker, and G. L. Smith, Seismic reflection images of the crust of the northern part of the Chugach terrane, Alaska: Results of a survey for the Trans-Alaska Crustal Transect (TACT), *J. Geophys. Res.*, *94*, 4424–4440, 1989.

Flueh, E. R., W. D. Mooney, G. S. Fuis, and E. L. Ambos, Crustal structure of the Chugach Mountains, southern Alaska: A study of peg-leg multiples from a low-velocity zone, *J. Geophys. Res.*, *94*, 16,023–16,034, 1989.

Fuis, G. S., and E. L. Ambos, Deep structure of the Contact Fault and the Prince William terrane: Preliminary results of the 1985 TACT seismic-refraction survey, U.S. Geological Survey Accomplishments in Alaska, 1985, *U.S. Geol. Surv. Circ.*, *978*, 41–45, 1986.

Green, A. G., R. M. Clowes, C. J. Yorath, C. Spencer, E. R. Kanasewich, M. T. Brandon, and A. Sutherland Brown, Seismic reflection imaging of the subducting Juan de Fuca plate, *Nature*, *319*, 210–213, 1986.

Hudson, T., and G. Plafker, Paleogene metamorphism in an accretionary flysch terrane, eastern Gulf of Alaska, *Geol. Soc. Am. Bull.*, *92*, 1280–1290, 1982.

Hyndman, R. D., Dipping seismic reflectors, electrically conductive zones, and trapped water in the crust over a subducting plate, *J. Geophys. Res.*, *93*, 13,391–13,405, 1989.

Hyndman, R. D., C. J. Yorath, R. M. Clowes, and E. E. Davis, The northern Cascadia subduction zone at Vancouver Island: Seismic structure and tectonic history, *Can. J. Earth Sci.*, *27*, 313–329, 1990.

Jones, D. L., N. J. Silberling, H. C. Berg, and G. Plafker, Tectonostratigraphic terrane map of Alaska, *U.S. Geol. Surv. Open File Rep.*, *81-792*, 1981.

Jones, D. L., N. J. Silberling, P. J. Coney, and G. Plafker, Lithotectonic terrane map of Alaska (west of the 41st meridian), *U.S. Geol. Surv. Misc. Field Stud. Map, MF-1874-A*, 1987.

Lahr, J. C., Detailed seismic investigation of Pacific-North American plate interaction in southern Alaska, Ph.D. dissertation, 88 pp., Columbia Univ., New York, 1975.

Lahr, J. C., and G. Plafker, Holocene Pacific-North American plate interaction in southern Alaska: implications for the Yakataga seismic gap, *Geology*, *8*, 483–486, 1980.

Luetgert, J., Programs RAY86 and R86PLT: Interactive two-dimensional raytracing/synthetic seismogram package (VAX/VMS) version, *U.S. Geol. Surv.*, Menlo Park, Calif., 1987.

Ma, C., J. W. Ryan, and D. Caprette, Crustal dynamics project data analysis—1988, VLBI geodetic results 1979–87, *NASA Tech. Memo.*, *TM-100723*, 214 pp., 1989.

Minster, J. B., T. J. Jordan, P. Molnar, and E. Haines, Numerical modelling of instantaneous plate tectonics, *Geophys. J. R. Astron. Soc.*, *36*, 541–576, 1974.

Nokleberg, W. J., G. Plafker, J. S. Lull, W. K. Wallace, and G. R. Winkler, Structural analysis of the southern Peninsular, southern Wrangellia, and northern Chugach terranes along the Trans-Alaska Crustal Transect, northern Chugach Mountains, Alaska, *J. Geophys. Res.*, *94*, 4297–4320, 1989.

Page, R. A., G. Plafker, G. S. Fuis, W. J. Nokleberg, E. L. Ambos, W. E. Mooney, and D. L. Campbell, Accretion and subduction tectonics in the Chugach Mountains and Copper River Basin, Alaska: Initial results of the Trans-Alaska Crustal Transect, *Geology*, *14*, 501–505, 1986.

Page, R. A., C. D. Stephens, and J. C. Lahr, Seismicity of the Wrangell and Aleutian Wadati-Benioff zones and the North American plate along the Trans-Alaska Crustal Transect, Chugach Mountains and Copper River Basin, southern Alaska, *J. Geophys. Res.*, *94*, 16,059–16,082, 1989.

Perez, O. J., and K. H. Jacob, Tectonic model and seismic potential

of the eastern Gulf of Alaska and Yakataga seismic gap, *J. Geophys. Res.*, *85*, 7132–7150, 1980.

Plafker, G., Regional geology and petroleum potential of the northern Gulf of Alaska continental margin, in *Geology and Resource Potential of the Continental Margin of Western North America and Adjacent Ocean Basins, AAPG Circum-Pac. Earth Sci. Ser.*, vol. 6, edited by D. W. Scholl, A. Grantz, and J. G. Vedder, pp. 229–268, American Association of Petroleum Geologists, Houston, Tex., 1987.

Plafker, G., W. J. Nokleberg, J. S. Lull, S. M. Roeske, and G. R. Winkler, Nature and timing of deformation along the Contact Fault System in the Cordova, Bering Glacier and Valdez Quadrangle, U.S. Geological Survey Accomplishments in Alaska, 1985, *U.S. Geol. Surv. Circ.*, *978*, 74–77, 1986.

Plafker, G., W. J. Nokleberg, and J. S. Lull, Bedrock geology and tectonic evolution of the Wrangellia, Peninsular, and Chugach terranes along the Trans-Alaska Crustal Transect in the Chugach Mountains and southern Copper River Basin, *J. Geophys. Res.*, *94*, 4255–4295, 1989.

Silberling, N. J., and D. L. Jones, Lithotectonic terrane maps of the North American Cordillera, *U.S. Geol. Surv. Open File Rep.*, *84-523*, A1–A12, 1984.

Sisson, V. B., and L. S. Hollister, Low-pressure facies series metamorphism in an accretionary sedimentary prism, southern Alaska, *Geology*, *16*, 358–361, 1988.

Sisson, V. B., L. S. Hollister, and T. C. Onstott, Petrologic and age constraints on the origin of a low-pressure/high-temperature metamorphic complex, southern Alaska, *J. Geophys. Res.*, *94*, 4392–4410, 1989.

Stephens, C. D., K. A. Fogelman, J. C. Lahr, and R. A. Page, Wrangell Benioff zone, southern Alaska, *Geology*, *12*, 373–376, 1984.

Stone, D. B., B. C. Panuska, and D. R. Packer, Paleolatitudes versus time for southern Alaska, *J. Geophys. Res.*, *87*, 3697–3707, 1982.

U.S. Geological Survey, Aeromagnetic map of parts of the Cordova and Middleton Island 1 by 3 quadrangles, Alaska, scale 1:250,000, *U.S. Geol. Surv. Open File Rep.*, *79-223*, 1979*a*.

U.S. Geological Survey, Aeromagnetic map of part of the Valdez 1 by 3 quadrangle, Alaska, scale 1:250,000, *U.S. Geol. Surv. Open File Rep.*, *79-381*, 1979*b*.

von Huene, R., G. Keller, T. R. Bruns, and K. McDougall, Cenozoic migration of Alaskan terranes indicated by paleontologic study, in *Tectonostratigraphic Terranes of the Circum-Pacific Region, Earth Sci. Ser.*, vol. 1, edited by D. G. Howell, pp. 121–136, Circum-Pacific Council for Energy and Mineral Resources, Houston, Tex., 1985.

Wallace, W. K., Tectonic evolution of the Haley Creek terrane, a rootless thrust sheet in the Chugach Mountains, Alaska, *Geol. Soc. Am. Abstr. Programs*, *17*, 416, 1985.

Wilson, J. M., P. Meador, and G. Fuis, Data report for the 1985 TACT seismic refraction survey, south-central Alaska, *U.S. Geol. Surv. Open File Rep.*, *87-440*, 78 pp., 1987.

Winkler, G. R., and G. Plafker, Geologic map and cross sections of the Cordova and Middleton Island quadrangles, southern Alaska, scale 1:250,000, *U.S. Geol. Surv. Open File Rep.*, *81-1164*, 26 pp., 1 sheet, 1981.

Winkler, G. R., M. L. Silberman, A. Grantz, R. J. Miller, and E. M. MacKevett, Jr., Geologic map and summary geochronology of the Valdez quadrangle, southern Alaska, scale 1:250,000, *U.S. Geol. Surv. Open File Rep.*, *80-892A*, 2 sheets, 1981.

Wolf, L. W., and A. R. Levander, Upper crustal structure of the accreted Chugach terrane, Alaska, *J. Geophys. Res.*, *94*, 4457–4466, 1989.

Wolf, L. W., and W. K. Wallace, Upper crustal structure of the Chugach and Prince William terranes, Alaska, *Eos Trans. AGU*, *69*, 44, 1988.

J. N. Davies and D. B. Stone, Geophysical Institute, University of Alaska, Fairbanks, AK 99775.

L. W. Wolf, Air Force Geophysics Laboratory, LWH, Hanscom AFB, MA 01731-5000.

(Received July 17, 1989;
revised May 20, 1991;
accepted May 20, 1991.)

JOURNAL OF GEOPHYSICAL RESEARCH, VOL. 96, NO. B10, PAGES 16,509–16,524, SEPTEMBER 10, 1991

Surface Deformation and Energy Release Rates for Constant Stress Drop Slip Zones in an Elastic Half-Space

M. WU, J. W. RUDNICKI, C. H. KUO, AND L. M. KEER

Department of Civil Engineering, Northwestern University, Evanston, Illinois

Free surface displacements, stress intensity factors, and energy release rates are calculated for planar slip zones in an elastic half-space subjected to a prescribed shear stress drop. Although the method can treat arbitrarily shaped planar zones and distributed stress drops, for simplicity, results are presented only for circular and elliptic zones and uniform stress drops. Calculations of the stress intensity factors and energy release rates for various geometries indicate that solutions for the half-space differ by less than 10% from those in the full space if the distance from the slip zone center to the free surface is greater than the downdip width of the slip zone. In addition, the influence of the free surface is greater for decreasing dip angle. For slip zones that are near the free surface and, especially, those that break the surface there is a coupling between slip and normal relative displacement. That is, for a prescribed shear stress drop and zero normal stress change, slip induces relative normal displacement. As example applications, these solutions are used to reexamine the coseismic geodetic data from three earthquakes: 1966 Parkfield, 1983 Borah Peak, and 1987 Whittier Narrows. The geometries, moments, and stress drops are similar to those inferred in previous studies using dislocation methods. However, the stress drop inferred here may be more reliable because stress drop is one of the parameters adjusted to fit the observed surface deformations. In addition, the method makes it possible to estimate the critical energy release rate at the termination of rupture. Values for the Parkfield, Borah Peak, and Whittier Narrows earthquakes are 1.5×10^6 J/m^2, 1.2×10^6 J/m^2, and 2×10^8 J/m^2, respectively.

INTRODUCTION

Why do earthquake ruptures start and stop? In order to address this question we require a criterion for propagation. Although rupture criteria in the Earth's crust are not known with any certainty, a simple one that is widely used in fracture mechanics and is often adopted in faulting problems is that the energy released per unit area of slip advance is equal to a critical value [*Rudnicki*, 1980; *Rice*, 1980, 1983; *Li*, 1987]. This criterion is undoubtedly too simple to describe in detail the actual processes of rupture and slip propagation. Nevertheless, when these more complex processes occur in a zone near the fault rupture edge having a length scale much smaller than other relevant lengths, e.g., fault rupture length, distance to the free surface, etc., it is well known that the energy release criterion provides a good description of rupture [e.g., *Rudnicki*, 1980; Rice, 1980, 1983]. Furthermore, because the stress and displacement fields near the edge of a crack in a linear elastic body have a universal form characterized by the stress intensity factors (coefficients of the singular stresses), the energy release rate can be expressed in terms of these factors [*Rice*, 1968].

An impediment to the application of this criterion to slip in the Earth's crust has been the difficulty of calculating stress intensity factors for realistic geometries. Although many results are known for two-dimensional problems and for simple crack shapes in three-dimensional bodies [*Murakami*, 1987], there are few analytical results for cracks in an elastic half-space.

In this paper we present a numerical method for calculating the stresses and displacements in an elastic half-space due to embedded and surface-breaking zones of prescribed stress drop. For simplicity, we present results only for elliptical zones and constant stress drops, but the method is sufficiently general to treat arbitrary planar shapes and spatially varying stress drops. Because the method incorporates the exact asymptotic form of the slip near the edge of a crack in a linear elastic body, results for the stress intensity factors are accurate. Furthermore, the method is based upon integration of the exact form of the displacement due to a point force in a half-space and hence can treat accurately cases in which the slip zone intersects the surface of the half-space.

We present results for the effect of the free surface on the stress intensity factors, the moment, and the energy release rate. Two features are of particular interest: the distance from the free surface at which its effect is negligible and the effect of proximity of the free surface on the tendency of the rupture to propagate toward it.

As applications of this method, we reexamine the coseismic geodetic data for three earthquakes: 1966 Parkfield, 1983 Borah Peak, and 1987 Whittier Narrows. In this approach, the stress drop is a parameter of the model and hence is constrained by comparison of the calculated and observed surface displacements. Furthermore, if the slip zone is assumed to propagate according to the criterion that the energy release rate equals a critical value, then we are able to estimate the critical value at the termination of rupture.

The stress drop method which we use here can be contrasted with the more common dislocation approach. The dislocation approach models slip zones by approximating them as surfaces of prescribed displacement discontinuity. Comparison of the calculated surface deformations with observations is used to infer the geometry of the slip zones and the distribution of slip. An advantage of the dislocation approach is its simplicity: once the solution for an elemental point slip is determined, results for general distributions of slip and complex shapes can be obtained by quadrature. As a result, this approach has become a staple for inferring

Paper number 91JB01043.
0148-0227/91/91JB-01043$05.00

information about slip from surface deformation measurements.

A disadvantage of this dislocation approach is that it is purely kinematic: it relates surface deformation to slip at depth but does not directly yield information about the stresses that produced the slip. More specifically, when the distribution of slip is approximated by constant slip elements (as is usually the case), the average stress change is unbounded. Consequently, stress drop can be inferred only indirectly. For example, the typical method is to calculate the moment and infer the stress drop by using the relation between the moment and the stress drop for a circular crack in an infinite body. Thus the stress drop is determined from a slip distribution that is different from the one inferred from the observations and used to calculate the moment. Furthermore, because the stress near the edge of a zone modeled by constant slip elements is not only singular but nonintegrable, it is not possible to calculate an energy release rate. As a result, the information concerning rupture propagation obtained by this method is limited.

The next section of the paper briefly describes the formulation of the problem and the numerical method used. Succeeding sections present results for the effect of the free surface on slip zones of various geometries and depths and for application of the stress drop approach to reexamine the coseismic geodetic data for three earthquakes.

Method of Analysis

The goal is to obtain the stress and displacement fields in an elastic half-space caused by a prescribed stress drop on a planar surface of discontinuity S. To do this, we develop first an expression for the stress in the half-space due to a prescribed displacement discontinuity. When this expression is evaluated on the surface of discontinuity S, it becomes an integral equation for the unknown distribution of displacement discontinuities arising from the prescribed stress change on S. This equation is solved by using a numerical method that expresses it as a system of linear algebraic equations. Once the appropriate distribution of displacement discontinuities is determined, other quantities of interest, such as the free surface displacement and the stress intensity factors, can be determined.

Consider an elastic body in which the stresses σ_{ij} are related to the displacement gradients $u_{k,l}(=\partial u_k/\partial x_l)$ by

$$\sigma_{ij} = C_{ijkl}u_{k,l} \tag{1}$$

where C_{ijkl} is the tensor of elastic moduli. For the case of an isotropic material considered here C_{ijkl} has the following form:

$$C_{ijkl} = \frac{2\mu\nu}{(1-2\nu)}\,\delta_{ij}\delta_{kl} + \mu(\delta_{ik}\delta_{jl} + \delta_{il}\delta_{jk}) \tag{2}$$

where μ is the shear modulus, ν is Poisson's ratio, and δ_{ij} is the Kronecker delta. Let $B_1(\boldsymbol{\xi})$ be relative displacements

$$B_i(\boldsymbol{\xi}) = u_i^+ - u_i^- \tag{3}$$

on a planar surface of discontinuity S with a unit normal $\mathbf{n}$ directed from the (−) to the (+) side of S. The resulting displacements elsewhere in the body are given by [e.g., *Steketee*, 1958]

$$u_i(\mathbf{x}) = \int_S C_{klmn}n_m B_n(\boldsymbol{\xi})\,\frac{\partial G_{ik}}{\partial \xi_l}(\mathbf{x}, \boldsymbol{\xi})\,d\boldsymbol{\xi} \tag{4}$$

where $G_{ij}(\mathbf{x}, \boldsymbol{\xi})$ is the displacement in the ith direction at $\mathbf{x}$ due to a unit point force in the jth direction at $\boldsymbol{\xi}$. The corresponding stresses are obtained by substituting (4) into (1):

$$\sigma_{ij} = C_{ijkl}C_{pqmn}\int_S n_m B_n(\boldsymbol{\xi})\,\frac{\partial^2 G_{kp}}{\partial x_l\,\partial \xi_q}(\mathbf{x}, \boldsymbol{\xi})\,d\boldsymbol{\xi} \tag{5}$$

Although the displacement discontinuity is unknown, we require that it produce a prescribed stress (drop) p_j on S:

$$n_i\sigma_{ij} = -p_j \qquad \text{for } \mathbf{x} \text{ on } S \tag{6}$$

Substitution of (5) into (6) yields the following integral equation:

$$\int_S K_{mn}(\mathbf{x}, \boldsymbol{\xi})B_n(\boldsymbol{\xi})\,d\boldsymbol{\xi} = -p_m(\mathbf{x}) \qquad \text{for } \mathbf{x} \text{ on } S \tag{7}$$

where

$$K_{mn} = n_i C_{imkl}C_{pqrn}n_r\,\frac{\partial^2 G_{kp}}{\partial x_l\,\partial \xi_q} \tag{8}$$

Once the $B_n(\boldsymbol{\xi})$ are determined from (7), the displacements of any point in the half-space and, in particular, of the free surface can be obtained from (4).

In order to implement these results for elliptical slip zones in a half-space, we use the two coordinate systems shown in Figure 1. The origin of the y_1 system is at the center of the slip zone a distance h below the free surface. The y_1 and y_2 axes lie in the plane of the slip zone, and the y_3 axis is perpendicular to the slip surface. The y_1 axis is horizontal and points along one axis of the ellipse in the direction of the slip zone strike. The y_2 axis points along the other axis of the ellipse in the direction of slip zone dip and is inclined at an angle α from the vertical. Thus the slip zone dips at an angle $\pi/2 - \alpha$. The x_i system has its origin at the surface directly above the center of the slip zone. The x_1 axis is horizontal, parallel to the y_1 axis, and in the direction of slip zone strike. The x_2 axis is vertical and points down into the half-space. The x_3 axis is horizontal and in the same vertical plane as the x_2 axis.

The kernel (8) can be calculated from *Mindlin*'s [1936] solution for a point force in an elastic half-space (also see *Mindlin* [1955] and *Mindlin and Cheng* [1950]) or, alternatively, by specializing the results of *Lee and Keer* [1986] and of *Lee et al.* [1987] for a bimaterial interface. The appendix records expressions for these kernels in components relative to the slip zone coordinate system y_i. The kernels of the integral (4) are also listed there in components relative to the half-space coordinate system x_i.

The numerical solution of the integral equation (7) follows the method developed by *Lee and Keer* [1986] for a tensile crack near a bimaterial interface. A feature of the method is that the variation of the relative displacements near the edge of the slipping zone is constrained to have the form appropriate for a crack in an isotropic linear elastic body. More specifically, the relative displacements near the crack edge have the following asymptotic form [e.g., *Rice*, 1968]:

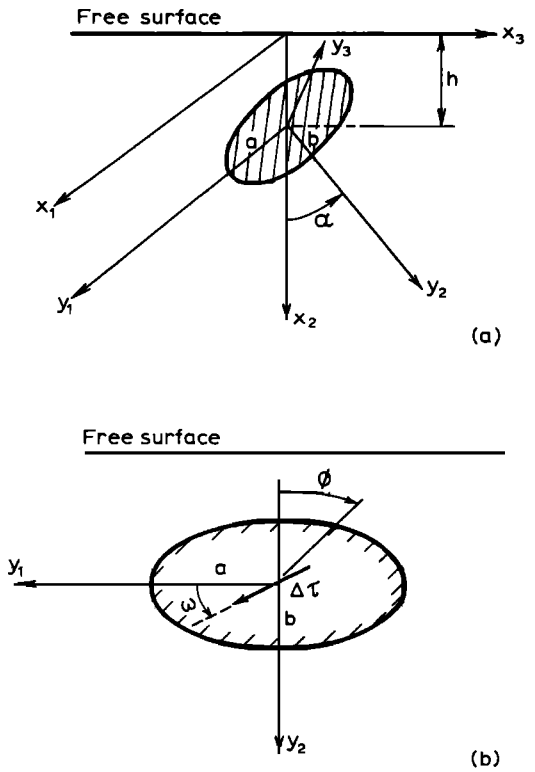

Fig. 1. (*a*) Geometry and coordinate systems for an inclined elliptical slip zone in the Earth's crust: The origin of the y_i system is at the center of the slip zone a distance h below the free surface. The y_1 and y_2 axes lie in the plane of the slip zone, and y_3 is perpendicular to the slip surface. The origin of the x_i system is on the half-space surface directly above the slip zone center. The x_1 axis is parallel to y_1 and in the direction of slip zone strike, and the x_2 axis is perpendicular to the half-space surface. The angle between the vertical (x_2 axis) and the y_2 axis is α. (*b*) View perpendicular to the plane of the slip zone (y_1y_2 plane). Polar angle ϕ is measured from the negative y_2 direction in the crack plane (y_1y_2). The orientation of the stress drop $\Delta\tau$ is defined by the angle ω measured from the y_1 (striking) direction.

$$(B_{\mathrm{I}}, B_{\mathrm{II}}, B_{\mathrm{III}}) = \frac{4(1-\nu)}{\mu}\left[\frac{\rho}{2\pi}\right]^{1/2}[K_{\mathrm{I}}, K_{\mathrm{II}}, K_{\mathrm{III}}/(1-\nu)] \tag{9}$$

as $\rho \rightarrow 0$, where ρ is distance from the crack edge, B_{I} is the relative opening (mode I), and B_{II} and B_{III} are relative displacements for shearing perpendicular to (mode II) and parallel to (mode III) the crack edge. The constants K_{I}, K_{II}, and K_{III} are the corresponding stress intensity factors. Because the relative displacements near the edge of any crack in a linear elastic isotropic body have this form (9), any differences in geometry or applied loading are reflected entirely in different values of the stress intensity factors. The result (9) is embedded in the numerical solution by choosing the $B_i(\xi)$ to have the following form:

$$B_i(\xi) = [2a\varepsilon - \varepsilon^2]^{1/2} f_i(\xi) \tag{10}$$

where ε is the shortest distance of the integration point ξ to the crack front, and a is the larger semiaxis of the elliptical slip zone [*Murakami and Nemat-Nasser*, 1983]. Hence resolving the B_i near the crack edge into components perpendicular and parallel to the edge and comparing with (9) yields results for the stress intensity factors. Once the stress intensity factors have been determined, the energy release rate, that is, the energy released per unit area of advance of the slip zone, is expressed in terms of these factors as follows:

$$\mathrm{G} = \frac{(1-\nu)}{2\mu}[K_{\mathrm{I}}^2 + K_{\mathrm{II}}^2 + K_{\mathrm{III}}^2/(1-\nu)] \tag{11}$$

The numerical solution of (7) proceeds by dividing the slip surface into triangular domains in which $f_i(\xi)$ are assumed to be constant over each triangle. Imposition of the stress drop values at the centers of the triangular elements reduces (7) to a set of algebraic equations. For all cases to be considered here, the loading and geometry are symmetric with respect to the y_2y_3 plane; hence only half of the crack surface is used in solving (7). More specifically, for the results to be presented, the half-crack is divided into 80 triangular elements. The regular portions of the integrals over the triangles are evaluated numerically, but a combination of exact and numerical integration is used to treat the singular part [*Lee and Keer*, 1986]. *Lee and Keer* [1986] have shown that for a circular crack subjected to uniform pressure in an infinite body the mode I stress intensity factor calculated by this method has 0.85% error in comparison with the exact solution.

Effect of the Free Surface

Although the solution for an elliptical shear crack in an infinite space can be obtained by specializing results of *Eshelby* [1957] and has been studied in detail by *Kostrov and Das* [1984], there exist no analytical results for shear cracks in an elastic half-space. In this section we present results for the energy release rate, stress intensity factors, and moment for slip zones in an elastic half-space. For simplicity, we consider only elliptical cracks and constant stress drops, but the solution method, as described in the previous section, can treat arbitrary planar configurations and distributed stress drops. In order to examine the effects of the free surface, we compare the results with those for a crack of the same geometry and stress drop in an infinite space.

As shown in Figure 1, the model contains six parameters: the depth of the slip center h; the lengths of the principal semiaxes (a and b); the inclination of the fault plane, defined by the angle α from the normal to half-space surface; the stress drop level $\Delta\tau$, and the stress drop direction, defined by the angle ω from the y_1 (striking) direction. The change in normal stress on the slip surface is specified to be zero. Two types of shear loading conditions are considered: the stress drop direction is parallel to the Earth's surface ($\omega = 0$), corresponding to strike-slip faulting; and the stress drop direction is along the dip direction of the fault ($\omega = +\pi/2$), corresponding to dip-slip (normal) faulting. For brevity, results for the stress intensity factors are presented only for an inclined ($\alpha = \pi/4$) circular slip zone with normal dip-slip loading ($\omega = \pi/2$). However, for the moment and energy release rates we consider both a circular crack and an elliptical crack with aspect ratio $a/b = 2$. For each crack shape we consider the following five possibilities: a deep vertical ($d/b = 3$; $\alpha = 0$), two moderately deep vertical ($d/b = 2$; $\alpha = 0$ and $d/b = 1$; $\alpha = 0$), a shallow vertical ($d/b = 0.1$; $\alpha = 0$), and a shallow inclined crack ($d/b = 0.1$; $\alpha = \pi/4$), where d is the depth of the crack top (See inset of

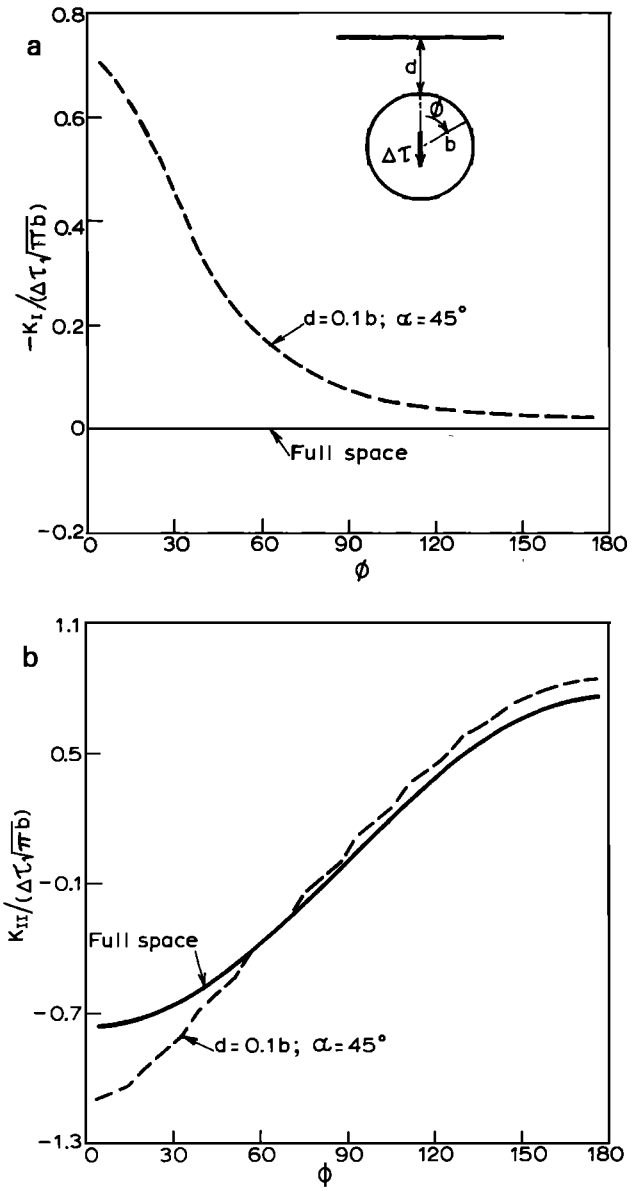

Fig. 2. Stress intensity factors (*a*) K_I, (*b*) K_{II}, and (*c*) K_{III}, divided by $\Delta\tau(\pi b)^{1/2}$, for a shallow inclined circular crack ($d = 0.1b$, $\alpha = 45°$; see inset in Figure 2*a*) against the polar angle ϕ. The solid line shows the result for a crack of the same geometry in a full space. (Because $K_I < 0$, the negative of the stress intensity factor is plotted in Figure 2*a*.)

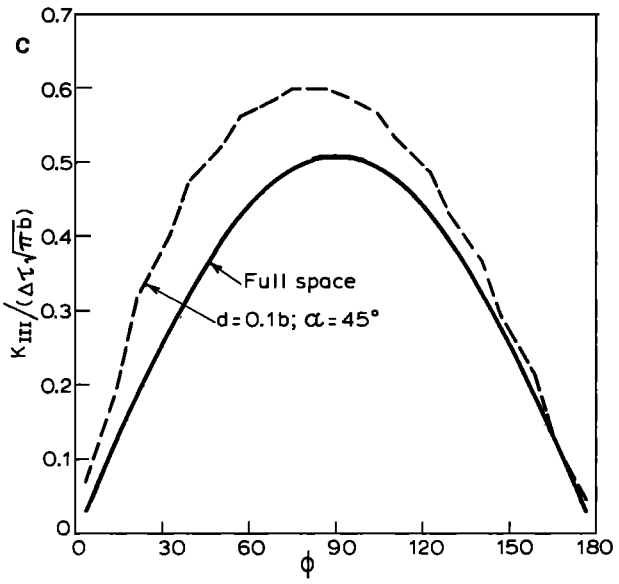

Fig. 2. (continued)

Figure 2*a*). In the calculations of the next two subsections, Poisson's ratio is taken to be 1/3, but $\nu = 1/4$ in the subsection on the moment.

Stress Intensity Factors

As an example of the effect of the free surface on the stress intensity factors K_I, K_{II}, and K_{III}, we examine the solution for an inclined circular crack ($d/b = 0.1$; $\alpha = \pi/4$) subjected to normal dip-slip ($\omega = \pi/2$) loading. The stress intensity factors, divided by $\Delta\tau(\pi b)^{1/2}$, are plotted against the polar angle ϕ (defined in Figure 1) and compared with the corresponding full space results in Figures 2*a*, 2*b*, and 2*c*. For a crack in an infinite isotropic elastic body there is no coupling between slip and normal relative displacement. Consequently, the mode I (opening) stress intensity factor K_I is identically zero, as shown in Figure 2*a*. However, the presence of the free surface causes a coupling between shear slip and normal relative displacement (in this case, interpenetration) and, as a result, K_I is nonzero. The corresponding effect in two-dimensional problems was noted by *Dmowska and Kostrov* [1973] and has been discussed by *Dmowska and Rice* [1986].

The magnitude of the effect diminishes with distance from the free surface and with the angle α. For vertical slip zones, symmetry rules out the possibility of relative normal displacement. However, for inclined slip zones near the free surface the effect can be substantial. For results shown in Figure 2 the magnitude of K_I at the shallowest point of the slip zone ($\phi = 0°$) is nearly 2/3 the maximum value of K_{II}, which also occurs at $\phi = 0°$.

In reality, interpenetration of the fault surfaces cannot occur and, except for slip zones very near the free surface, the ambient normal stress will presumably suppress any tendency for the slip to be accompanied by opening. The magnitude of normal stress changes can be estimated by solving (7) subject to the condition that $B_3 = 0$ (where B_3 is the relative displacement normal to the slip surface). Two of the equations (7) can then be solved for the slip components. Substituting these into the third yields the normal traction required to suppress any opening or interpenetration. In particular, for the crack shown in Figure 2 we found that the maximum compressive traction required to prevent interpenetration of the crack surfaces is about 87% of the applied shear stress drop. For this case, K_{II} and K_{III} differ from those shown in Figures 2*b* and 2*c* by less than 10% (K_I is zero).

As discussed by *Dmowska and Rice* [1986], the coupling of normal relative displacement and slip near the free surface means that the shear stress drop alone cannot be specified a priori; if slip is assumed to be governed by Coulomb friction, then only a linear combination of the changes in normal stress and the shear stress can be specified. Although, as noted above, this effect can be significant near the free surface, for simplicity, we do not consider it further here.

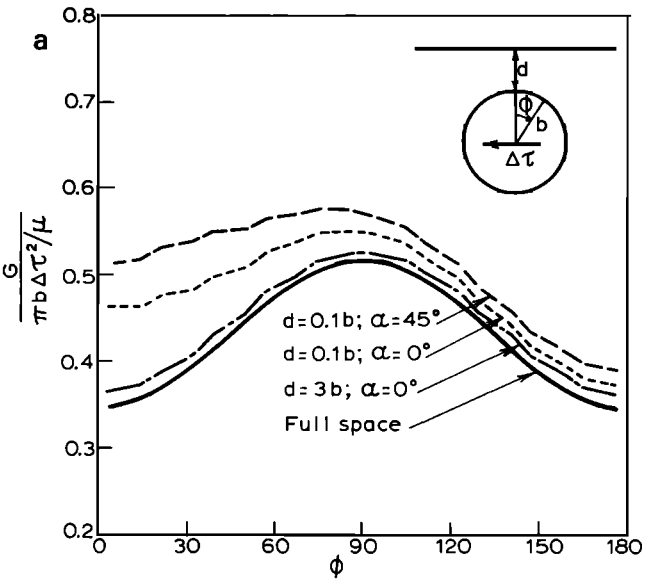

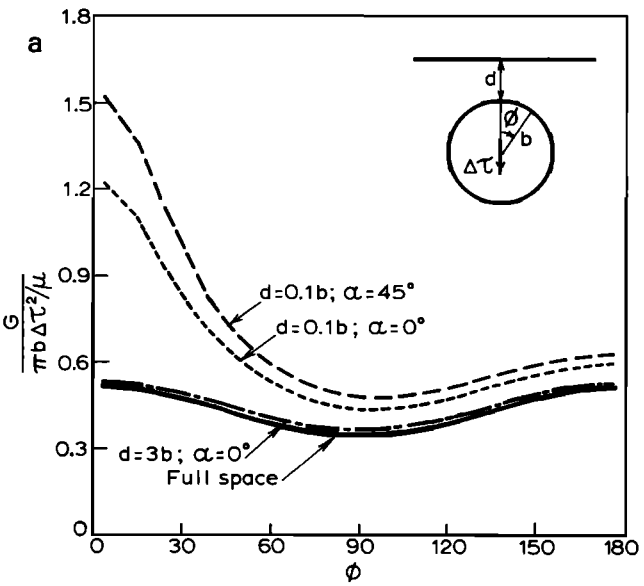

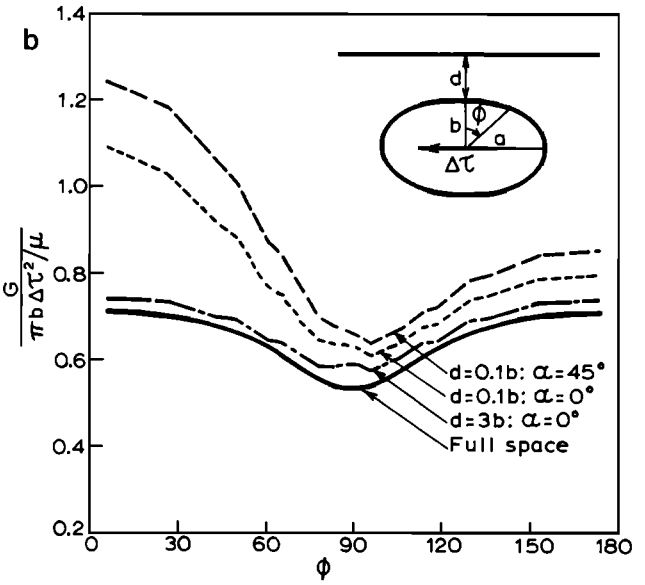

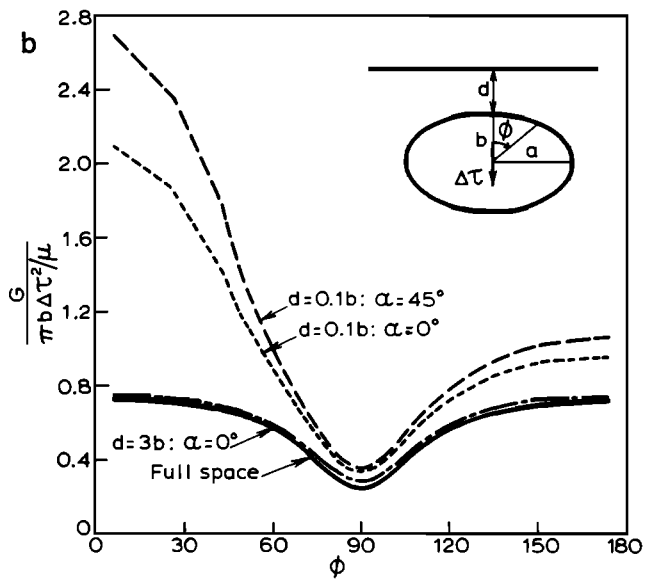

Fig. 3. Energy release rate G (11), divided by $\pi b\Delta\tau^2/\mu$, against ϕ for (*a*) circular and (*b*) elliptical (aspect ratio $a/b = 2$) slip zones subjected to strike-slip loading.

Fig. 4. Energy release rate G (11), divided by $\pi b\Delta\tau^2/\mu$, against ϕ for (*a*) circular and (*b*) elliptical (aspect ratio $a/b = 2$) slip zones subjected to dip-slip loading.

Energy Release Rate

Although it is instructive to consider the stress intensity factors individually, only the combination defined by (11) enters the expression for the energy release rate. Figures 3 and 4 plot the variation of the energy release rate G, divided by $\pi b\Delta\tau^2/\mu$, against the polar angle ϕ for different crack configurations for the cases of strike-slip and normal dip-slip motion. As indicated in these figures, the distributions of the normalized energy release rate for the deep slip zones ($d/b = 3$) are about the same as for the corresponding full-space sources, as expected. Only when the ratio $d/b = 1.0$ do the results differ by as much as 10% from those for the full space solutions. The energy release rates for the shallow slip zones, however, can differ significantly from the full space results, depending on the configuration and loading condition. Overall, the free-surface effect is greater for dip slip than for strike slip, given the same crack geometry.

For both the circular (Figure 3*a*) and the elliptical slip (Figure 3*b*) zones with strike-slip loading, the variation of the energy release rate with ϕ is similar to that for the same slip zone in an infinite body. For the circular zone the energy release rate is largest at the side ($\phi = 90°$) and decreases toward the top ($\phi = 0°$) and bottom ($\phi = 180°$). For the elliptical crack with aspect ratio $a/b = 2$, the energy release rate is greatest at the edge nearest the free surface and least at the side of the slip zone ($\phi = 90°$). The presence of the free surface causes G to increase for both the circular and elliptical zone with the greatest increase occurring nearest to the free surface. More specifically, for shallow dipping zones the energy release rate induced by the shallow vertical crack ($d/b = 0.1$; $\alpha = 0$) is greater than that for the full space source by about 33% near the top of the crack ($\phi \simeq 0$) and by less than 7% along the portion of the crack front away from the free surface of the Earth ($\phi > 90°$). When this shallow

source dips at 45° ($d/b = 0.1$; $\alpha = 45°$), the difference is increased about 15%. For the elliptical geometry (strike slip; $a/b = 2$), even larger differences (50% and 70%) occur for the shallow vertical ($d/b = 0.1$; $\alpha = 0$) and shallow inclined crack ($d/b = 0.1$; $\alpha = 45°$) (Figure 3*b*).

The difference in the variation of the energy release rates with ϕ for the circular and elliptic slip zones can be understood in terms of the behavior of the stress intensity factors for the full space solution [*Kostrov and Das*, 1984]. At $\phi = 0°$ (and 180°) the solution is pure mode III ($K_{II} = 0$), and at $\phi = 90°$ the solution is pure mode II ($K_{III} = 0$). As discussed in detail by *Kostrov and Das* [1984], the ratio of the mode II stress intensity factor at $\phi = 90°$ to the mode III stress intensity factor at $\phi = 0°$ (and 180°) is $(b/a)^{1/2}/(1 - \nu)$. Hence the corresponding ratio of the energy release rate at $\phi = 90°$ to that at $\phi = 0°$ is $(b/a)/(1 - \nu)$. Thus, for the circular slip zone, **G** at $\phi = 90°$ is 1.5 times that at $\phi = 0°$ (for $\nu = 1/3$). For the elliptical slip zone with aspect ratio $a/b = 2$, **G** at $\phi = 90°$ is 0.75 times that at $\phi = 0°$.

If the slip zone is assumed to spread in the direction of the greatest energy release rate, then the results of Figure 3*a* suggest that an initially circular zone propagates horizontally rather than toward the free surface. However, Figure 3*b* shows that an increase in the aspect ratio b/a increases the energy release rate both at the top and bottom of slip zone ($\phi = 0°$, 180°), but the increase is greater at the top near the free surface. Thus, for an initially circular slip zone, horizontal propagation would be followed by propagation toward the free surface before the aspect ratio reached $b/a = 2$. For an initially elliptical slip zone (with $b/a \geq 2$), propagation would occur first toward the free surface.

Figures 4*a* and 4*b* show the variation of the energy release rate with ϕ for dip-slip loading of circular (Figure 4*a*) and elliptical slip zones. As for the strike-slip loading, the variation is similar to that for the full space solutions. For both the circular and elliptical zones, **G** is least at $\phi = 90°$ and increases toward the top and bottom of the slip zone. For shallow zones the dip-slip loading causes a particularly large increase of **G** toward the free surface. Specifically, for a shallow ($d = 0.1b$) vertical ($\alpha = 0$), circular slip zone, the values exceed those for the full space solution by about 150% near the free surface and by 20% away from the free surface. For the inclined shallow circular crack ($d/b = 0.1$; $\alpha = 45°$) the difference is about 18% larger. Figure 4*b* shows that the energy release rates for the vertical ($\alpha = 0°$) elliptical crack at a depth of $d = 0.1$b exceed those for the full space by even larger amounts: 200% near the top of the crack and 38% near the bottom. For the inclined shallow elliptical crack ($d/b = 0.1$; $\alpha = 45°$) the difference can be as large as 250%. Because the maximum energy release rates all occur at the top of the slip zone for these two geometries, dip-slip rupture would tend to break to the surface rather than grow along strike.

Moment

The stress intensity factors and energy release rates arise naturally in considering crack models of slip zones. But a parameter more commonly used in interpreting observations is the seismic moment. Because the stress drop is specified in the approach used here, the slip distribution and hence the moment are calculated as part of the solution.

In this subsection we examine the effect of the free surface on the relation between the moment and the stress drop. In particular, consider the single component of the moment tensor given by

$$M = \mu \int_S B_\tau(\xi)\, d\xi \tag{12}$$

where B_τ is the relative slip in the direction of the applied stress drop (Figure 1). Hence M is the component M_{31} or M_{32} in the crack coordinate system (y_i), depending on whether the loading is strike slip or dip slip, respectively; similarly, B_τ is B_1 or B_2 depending on the loading. In general, the slip will also have a component orthogonal to the applied stress drop. For example, *Kostrov and Das* [1984] have shown that for an elliptical shear crack in an infinite body the slip is parallel to the applied shear stress only if the latter is applied in the direction of one of the principal axes of the ellipse. In the half-space problems considered here the slip will be in the direction of the applied shear stress only when the problem is symmetric with respect to the loading direction. The magnitude of the slip orthogonal to the applied stress is, however, much smaller than that in the direction of the shear stress. In addition, as noted previously, when the change in normal traction on the slip surface is taken as zero, there is a normal relative displacement, and hence M_{33} is nonzero. However, unless the slip surface is very near the free surface, this component is also small and, for simplicity, we ignore it.

For constant stress drop slip zones the moment M (equation (12)) is proportional to the stress drop $\Delta\tau$ and can be expressed as follows:

$$M = C\, \Delta\tau\, A^{3/2} \tag{13}$$

where A is the area of the slip surface and C is a nondimensional quantity that depends on Poisson's ratio and the geometry. For example, for a circular slip zone in an infinite space, C is

$$C = \frac{16(1 - \nu)}{3\pi^{3/2}(2 - \nu)} \tag{14}$$

For an elliptical slip zone in an infinite body with principal semiaxes a and $b < a$, C is given by

$$C = \frac{4}{3\pi^{1/2}}\, k_1^{1/2} k^2 [(k^2 - \nu)E(k) + \nu k_1^2 K(k)]^{-1} \tag{15}$$

if $\Delta\tau$ is applied parallel to the larger semiaxis, and by

$$C = \frac{4}{3\pi^{1/2}}\, k_1^{1/2} k^2 [(k^2 + \nu k_1^2)E(k) - \nu k_1^2 K(k)]^{-1} \tag{16}$$

if $\Delta\tau$ is applied parallel to the smaller semiaxis [*Dmowska and Rice*, 1986]. In (15) and (16), $k_1 = b/a$, $k = 1 - k_1^2$, and $E(k)$ and $K(k)$ are complete elliptic integrals of the first and second kinds, respectively.

The expression (13), with C given by (14), is often used to estimate the stress drop when the moment is determined by kinematic models. As noted earlier, for kinematic models using constant relative displacement elements, the actual average stress drop is unbounded. Furthermore, the value of C given by (14) is for an infinite space. Consequently, it is of interest to determine the effect of the free surface on the

TABLE 1. Values of $C = M/(\Delta\tau A^{3/2})$

	Strike Slip ($\omega = 0°$)		Dip Slip ($\omega = 90°$)	
	$a/b = 1$	$a/b = 2$	$a/b = 1$	$a/b = 2$
Full space	0.4105	0.4042	0.4105	0.3523
$d/b = 3$; $\alpha = 0°$	0.4169	0.4180	0.4177	0.3630
$d/b = 0.1$; $\alpha = 0°$	0.4327	0.4473	0.4823	0.4488
$d/b = 0.1$; $\alpha = 45°$	0.4481	0.4707	0.5117	0.4810

value of C and hence the effect on inference of the stress drop from the moment by (14).

Table 1 lists the values of C for the slip zones considered in Figures 3 and 4 and the corresponding values for a slip zone of the same geometry and loading in an infinite space. Poisson's ratio of $\nu = 0.25$ is used for these calculations. Values of C, using (12) and (13), for the deep cracks ($d/b = 3$) differ by less than 3% from those, using (14)–(16), for the full space cracks of the same geometries and stress drops. For the vertical shallow cracks, the half-space moments differ from the corresponding full space results by 6% for the circular and 11% for the elliptical crack for the case of strike slip and by 18% for the circular and 27% for the elliptical crack for the case of dip slip, respectively. For the inclined shallow cracks, additional differences up to 10% are observed. Because of the coupling between the shear slip and the normal relative displacement, the moment component M_{33} (along the normal direction of the crack surface) can be as large as about two thirds of the larger shear component.

INTERPRETATION OF COSEISMIC SURFACE DEFORMATIONS

As examples of the application of this method, we use it to reexamine the coseismic surface deformations of three earthquakes: 1987 Whittier Narrows, 1983 Borah Peak, and 1966 Parkfield. The coseismic deformations for these earthquakes have been studied previously using kinematic models. The present approach differs from those previous because the geometry and the stress drop, rather than the slip distribution, are inferred from the observations. The slip distribution is then calculated for the inferred stress drop and geometry.

For each earthquake a set of forward searches is performed to find the model parameters that give a best fit to the coseismic slip data subject to the constraint that the model geometry agrees roughly with the aftershock distribution. Then, by using the stress drop and crack geometry determined from a best model, the corresponding slip moment and energy release rate are calculated and compared, together with the model parameters, with those inferred from previous studies. The results are summarized in Table 2. For the calculations in this section, a Poisson's ratio $\nu = 0.25$ and a shear modulus $\mu = 3 \times 10^4$ MPa, an average value for the Earth's crust, are assumed.

1987 Whittier Narrows

The 1987 Whittier Narrows earthquake occurred within the Los Angeles basin in southern California. The geologic and tectonic setting have been described by *Davis et al.* [1989]. The coseismic surface elevation changes were detected by geodetic surveys [*Lin and Stein*, 1989]. A crosslike geodetic network, centered coincidentally on the epicenter, was surveyed 20 months before the earthquake and resurveyed immediately after. The surveys reveal that the ground surface was uplifted by 50 mm, but no surface rupture was observed. *Lin and Stein* [1989] used a model of an inclined rectangular dislocation of uniform dip slip in an elastic half-space [*Mansinha and Smylie*, 1971] to interpret the observed deformation as due to reverse dip slip of a deep thrust fault beneath the center of the network. Because the geodetic data alone cannot constrain the fault geometry and slip magnitude uniquely, *Lin and Stein* [1989] also considered the aftershocks which occupied a region extending from the depth of 12 km to 16 km. For their best model, the fault length along strike is 4.5 km, the downdip width is 6 km, the depth of the upper end of the fault plane is 12 km, the dip angle is 30°, and the coseismic slip is 1.1 m.

Here we employ an alternative approach to interpret coseismic deformation reported by *Lin and Stein* [1989]. Specifically, we model the event as reverse dip slip of an inclined elliptical slip zone in an elastic half-space and assume a stress drop along the negative dip direction (Figure 1: $\omega = -90°$). For the best model, which matches the deformation data well and is consistent with the aftershock locations, the slip zone is circular with a radius of 3.0 km, the depth of the fault center is 14.2 km, and the dip angle is 40°. The total rms misfit is 5.8 mm, slightly larger than the rms pure error, which is 4.9 mm. The surface projection of the fault plane of our preferred model is shown in Figure 5*a*; the

TABLE 2. Comparison Between Modeling Results

	Whittier Narrows ($M = 6.0$)		Parkfield ($M = 5.6$)		Borah Peak ($M = 6.9$)	
	Lin and Stein [1989]	This Study	*King et al.* [1987]	This Study	*Barrientos et al.* [1987]	This Study
Length (along strike), km	4.5	6.0	30	50	18 and 8	36
Width (downdip), km	6.0	6.0	5	14	18 and 8	18.5
Depth (to rupture top), km	12	12.3	3	1.75	0	0
Dip	30°N	40°N	90°	90°	49°SW	50°SW
Strike	N90°E	N90°E	···	N142°E	N152°E	N152°E
Slip, m	1.09	1.0/1.5 (ave/max)	0.91	0.5/0.76 (ave/max)	2.1 and 1.4	1.4/2.2 (ave/max)
Stress drop, MPa	17.5	16	···	1.43	3.0	1.8
Moment, dyn cm	1.0×10^{25}	0.96×10^{25}	4.5×10^{25}	7.2×10^{25}	2.9×10^{26}	2.4×10^{26}
G, J/m^2	···	2×10^8	···	1.5×10^6	···	1.2×10^6
rms/pure error	0.93	1.18	···	0.97	2.5	6

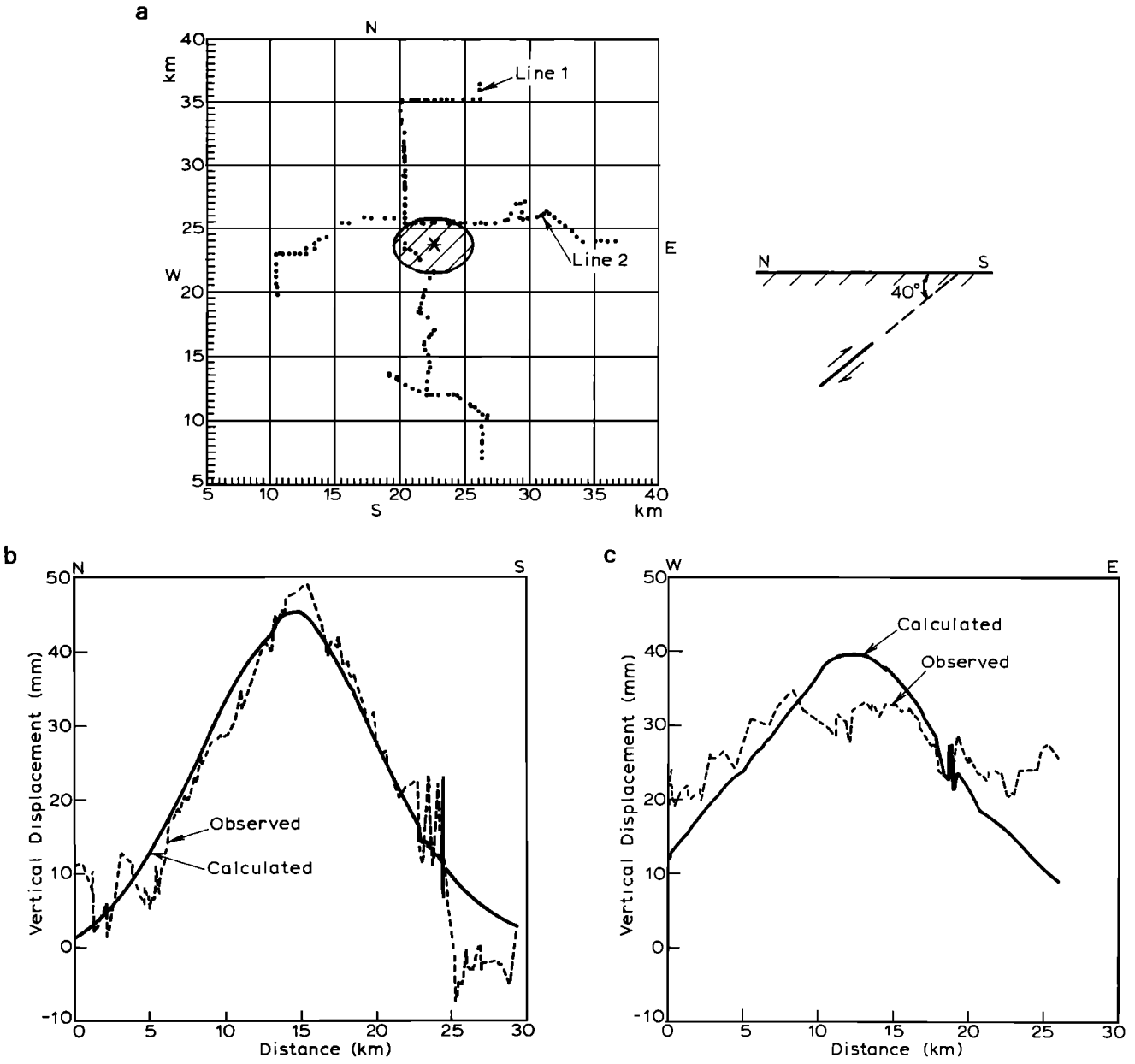

Fig. 5. Model fit to the coseismic surface deformation of the 1987 Whittier Narrows earthquake. (*a*) Leveling monuments and the surface projection of the model fault. Asterisk represents the epicenter of the earthquake. (*b*) Fit to data along leveling line 1. (*c*) Fit to data along leveling line 2.

model fits to data along two leveling routes, line 1 (N-S) and line 2 (E-W), are shown in Figures 5*b* and 5*c*, respectively.

As shown in Figure 5*b*, the predicted surface displacement agrees well with the observed data along line 1 except at the southern end. The fit to data is not as good along line 2 but is still satisfactory (Figure 5*c*). These results are similar to those of *Lin and Stein* [1989]. The stress drop and moment determined for the preferred model are 16 MPa and 0.96×10^{25} dyn cm, respectively, compared with the 17.5 MPa and the 1.0×10^{25} dyn cm determined by Lin and Stein. Because the ratio of the depth to slip zone radius is relatively large ($\simeq 4$), the energy release rate for this model is approximately constant along the fault front and is essentially identical to that for a slip zone of the same geometry and stress drop in an infinite body. The value is estimated to be about 2.0×10^8 J/m^2.

The dipping angle (40°) of our best model is about 10° larger than inferred by Lin and Stein using their dislocation method. If we use the same dip (30°) as theirs, the rms error is increased to 6.3 mm. The coseismic slip data are not critically sensitive to the radius of the slip region. More specifically, the area can be varied from moderately larger (radius 5 km) to much smaller (radius 1 km) than that defined by the aftershock distribution without affecting the rms error significantly. In addition, while keeping the width (along dip) of the fault to be 5 km, horizontal length of slip up to 16 km is permitted by the deformation data. Because the ratio of depth to slip region radius is large, the uplift data can be fit reasonably well by a point source. For the point dip-slip source having the same inclination, depth, and moment as the best crack model, the uplift data can be fitted with the

TABLE 3. Observed and Calculated Line Length Changes

Station-Station	Observed, mm	Calculated, mm	Residual, mm
Bench-Bonnie	−69 ± 24	−78.3	9.3
Bench-Cotton	42 ± 19	51.2	−9.2
Bench-Kenser	−137 ± 24	−163.4	26.4
Bench-Mason	30 ± 18	13.6	16.4
Bonnie-Cotton	27 ± 18	−16.3	43.3
Bonnie-Kenser	5 ± 16	−4.2	9.2
Bonnie-Mason	81 ± 24	85.5	−4.5
Castle-Shade	115 ± 38	88.8	26.2
Cotton-Kenser	−5 ± 24	−24.9	19.9
Cotton-Mason	167 ± 26	159.6	7.4
Kenser-Mason	−7 ± 20	−27.1	20.1
Mine Mountain-Shade	58 ± 18	65.4	−7.4
Park-Red Hill	−160 ± 24	−124.4	−35.6

Mean misfit (rms) = 21.4 mm.

rms error of 6.4 mm, only 10% larger than the crack model's misfit.

1966 Parkfield

Trilateration measurements made by several agencies since 1959 near Parkfield provide geodetic data that place constraints on the motion across the San Andreas fault [*King et al.*, 1987]. Line length changes observed shortly after the 1966 Parkfield earthquake in that area have been the focus of much effort. Several investigators modeled the 1966 shock as a vertical rectangular dislocation of uniform strike slip in an elastic half-space [e.g., *Chinnery*, 1961]. Distributed dislocation models were also considered by approximating the slip as uniform in small rectangular cells [*Stuart et al.*, 1985; *Segall and Harris*, 1987]. However, because there were only 13 lines near the 1966 rupture zone, the length, depth, and width of the slip region cannot be constrained strongly by the geodetic observations alone [*King et al.*, 1987; *Segall and Harris*, 1987].

Additional constraints come from the distribution of aftershocks, which were concentrated at depths of 2–4 and 8–10 km on a nearly vertical plane extending 30 km SE of the main shock epicenter [*Eaton et al.*, 1970]. The absence of surface offset immediately following the main shock [*Smith and Wyss*, 1968] indicates that the 1966 coseismic slip probably did not reach the Earth's surface. Therefore most coseismic slip models have used a rupture geometry that extends from a depth of 2–4 km to a depth of 8–10 km with the length ranging from 20 to 40 km [*Archuleta and Day*, 1980; *King et al.*, 1987; *Segall and Harris*, 1987].

We propose a model of a vertical elliptical crack embedded in an elastic half-space. The surface of the crack is subjected to a uniform shear stress drop along the strike direction (Figure 1; $\alpha = 0$ and $\omega = 0$). The fit of the preferred model to the line length changes [*King et al.*, 1987] is provided in Table 3. The trilateration net and the surface trace of the model slip zone are shown in Figure 6. The surface center of the model fault is located near the middle point of the line connecting Mason and Kenger stations, the strike direction is nearly parallel to that of the line of Mason and Bench stations, and the top, the bottom, and the horizontal length of the fault are 1.75, 15.75, and 50 km, respectively (Table 2 and Figure 6). Although the area of the model rupture plane is moderately larger than the region

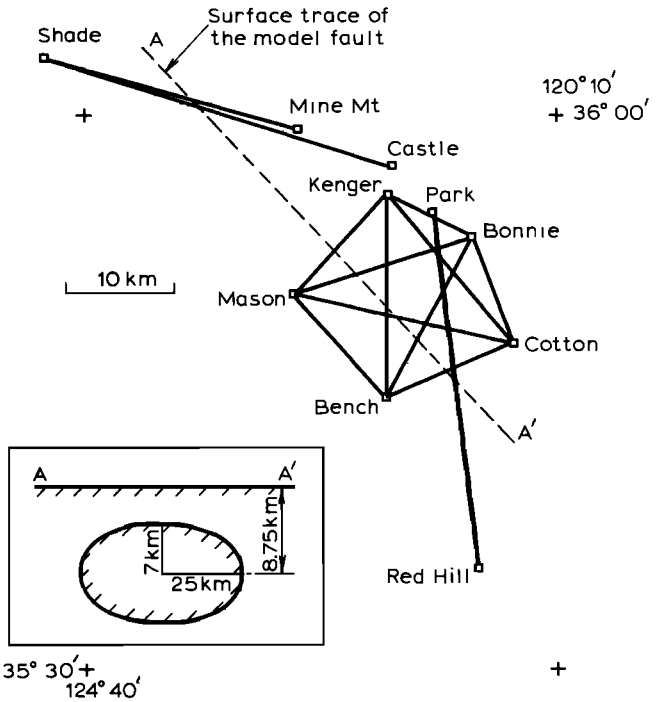

Fig. 6. Trilateration net and surface trace of the model slip zone inferred for the 1966 Parkfield earthquake.

defined by the aftershocks, the mean misfit to the data is significantly smaller (20% less) than models having slip areas much less than the aftershock region. The mean misfit of the preferred model to the data is 21.4 mm, lower that the average standard deviation of the data, which is 22.5 mm (Table 3). The only significant misfit occurs for the line connecting Bonnie and Cotton stations (Table 3). The observed line length change is 27 mm; the predicted value is −16 mm, close to the −10 mm predicted by *Segall and Harris* [1987] using a distributed dislocation model. The reason for this misfit is uncertain.

The stress drop and moment determined are about 1.43 MPa and 7.2×10^{25} dyn cm, respectively. Our estimated moment is larger than the 4.5×10^{25} dyn cm obtained by *King et al.* [1987] using the dislocation approach (Table 2) and the $(0.9–2.1) \times 10^{25}$ dyn cm inferred from surface waves by *Tsai and Aki* [1969] but falls within the range of $(3.7–8.1) \times 10^{25}$ dyn cm estimated by *Segall and Harris* [1987] using a distributed dislocation model. The maximum energy release rate occurs near the top of the slip zone and is estimated to be approximately 1.5×10^6 J/m^2. This value is consistent with the 0.8×10^6 J/m^2 estimated by *Aki* [1978] as corresponding to arrest of this earthquake but much greater than the estimate by *Husseini et al.* [1975] of 1.1×10^2 J/m^2.

If the area of the slip region is constrained so that its top, bottom, and horizontal length vary between 2–4, 8–10, and 20–40 km, where the aftershocks concentrated, then the model that fits the data best occupies the largest possible area. The mean misfit of this model to the data is 27 mm. Better fits are obtained when the rupture zone extends below the region of aftershocks to about 16 km depth. The coseismic line length changes permit slip extending even deeper than 16 km. The Park-Red Hill and Castle-Shade line length changes are much more sensitive to the horizontal length of

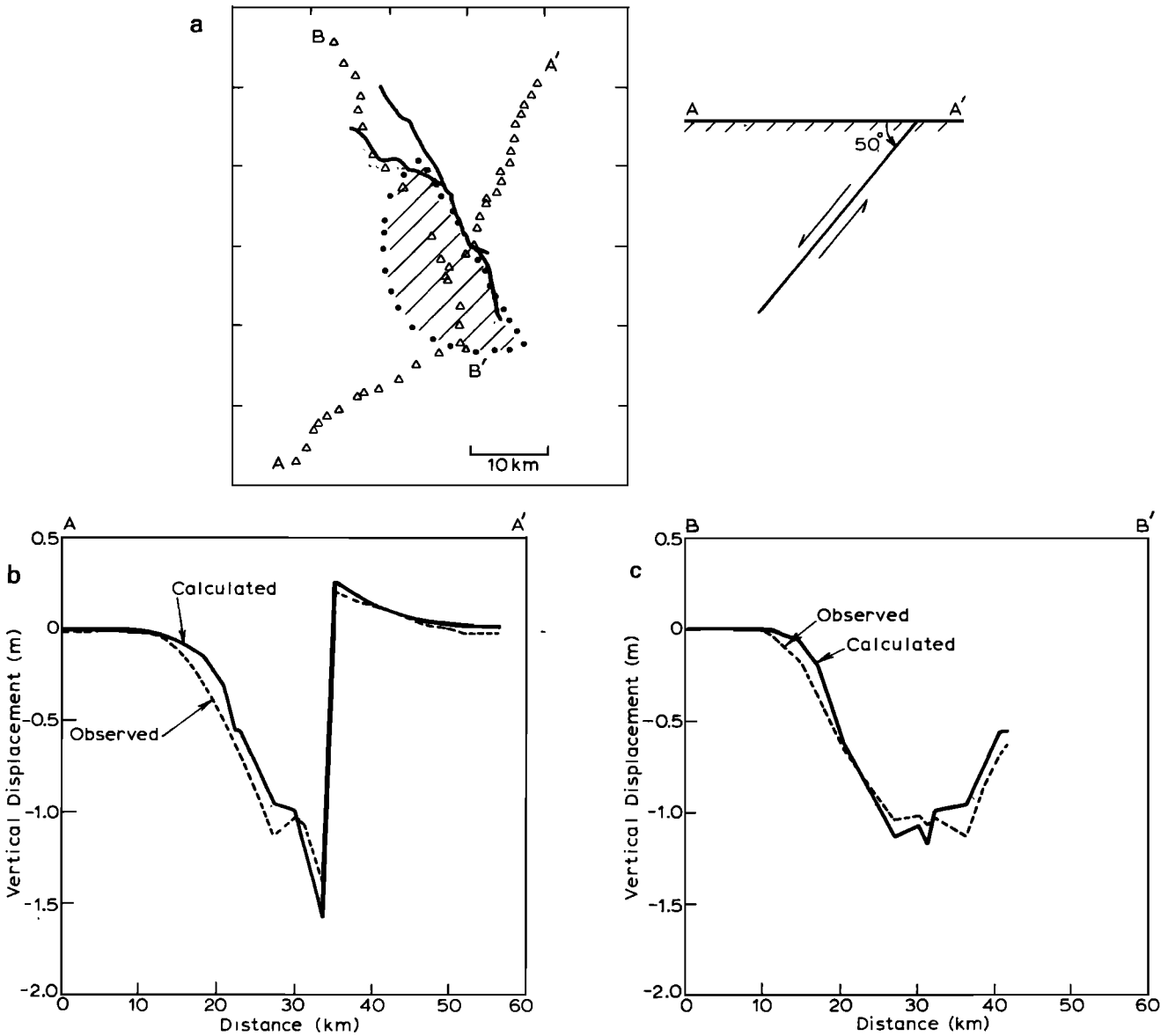

Fig. 7. Model fit to the coseismic surface deformation of the 1983 Borah Peak earthquake. (*a*) Leveling monuments and the surface projection of the model fault. (*b*) Fit to data along leveling line AA′ (pure error = 12 mm). (*c*) Fit to data along leveling line BB′ (pure error = 12 mm).

the slip region than other lines. Model fit can be degraded significantly for slip zones with horizontal lengths much shorter than 40 km, but longer length is permitted by the data. These results are in agreement with those of *King et al.* [1987].

1983 Borah Peak

The Borah Peak segment of the Lost River fault lies in the northern Basin and Range Province. The 1983 Borah Peak earthquake, a large normal-faulting event, presumably resulted from regional extension of the Basin and Range. The earthquake ruptured the central 35-km segment, the length of the surface rupture trace, of the 100-km-long Lost River fault [*Barrientos et al.*, 1987].

The surface deformation associated with this event was reported by *Stein and Barrientos* [1985]. Two leveling lines, with line AA′ nearly normal to the fault and line BB′ about parallel to the main fault trace, were surveyed in 1933 (Figure 7*a*). Line AA′ was surveyed again in 1948. Both lines were resurveyed in 1985. Thus the survey includes 20 months of deformation following the earthquake. *Stein and Barrientos* [1985] have shown that the 1983–1984 postseismic slip is about 2% of the coseismic slip. By using dislocation models, *Barrientos et al.* [1987] studied the 1933–1948 preseismic deformation and the 1985 postseismic data to invert for the subsurface fault geometry and slip magnitude at Borah Peak. In their inversion procedure the strike of rupture planes was fixed to be consistent with the fault trace. Their best model consists of two planes of the same dip and strike: an 18 × 18 km main plane with 2.1 m slip and an 8 × 8 km second plane with 1.4 m slip located along strike northwest of the main plane. The dip angle of the planes is 49°. The rms misfit is 30 mm, 2.5 times the data noise level. This geometry agrees well with the focal mechanism of the

main shock [*Doser and Smith*, 1985] and the aftershock distribution [*Richins et al.*, 1985].

We use a dip-slip crack model to reexamine the surface deformation associated with this 1983 earthquake. Because the fault ruptured to the surface in the Borah Peak event, the dip-slip zone is approximated by a semielliptical geometry. For the parameters shown in Figure 1 we take $\omega = 90°$ and $h = 0$. As shown in Table 2, the strike (150°) and dip (50°) of our best model are similar to those of *Barrientos et al.* [1987], but the surface center of the slip zone is 3 km SE of theirs. The horizontal length of 36 km and width along dip of 18.5 km for our model are larger than but close to those (26 km and 18 km) for their best model. Normal dip slip is required over the surface of the fault. Figure 7*a* shows the surface projection of the model fault plane; Figures 7*b* and 7*c* indicate the model fit to data along line AA′ and line BB′, respectively.

Overall, the predicted values roughly match the observations. However, the predicted displacement significantly overshoots the maximum elevation change and moderately underestimates the other large elevation changes for line AA′. For line BB′ the predicted displacement moderately overestimates about half of the data and underestimates the other half data. The rms error of the fit to data is large, about 70 mm, 6 times the rms pure error. The better fit obtained by *Barrientos et al.* [1987] using the distributed slip model and the pattern of the discrepancy between the predictions here and observations on line AA′ suggest that the constant stress drop assumption needs to be relaxed in order to improve the fit to the data: uniform stress drop constrains the slip to be distributed roughly elliptically, and therefore the slip is largest at the center and tapers to zero at the edge. However, because the purpose here is to illustrate the approach and to provide estimates for the slip-induced energy release rate rather than fit the data precisely, we have not pursued nonuniform stress drop models.

The stress drop and moment determined by our best model are 1.8 MPa and 2.4×10^{26} dyn cm, respectively, smaller than the 3.0 MPa and 2.9×10^{26} dyn cm inferred by Barrientos et al. using a single-plane model which is 18 km in width and 23 km in length (No stress drop and moment values were reported for their two-plane model). The maximum (calculated) energy release rate occurs at the ends of the surface trace of the rupture and is estimated to be 1.2×10^6 J/m^2.

Because this event breaks the surface, there is a strong coupling between slip and normal relative displacement. Because we have specified zero normal stress change on the slip surface in (6), the fault surfaces are predicted to interpenetrate. For the best fitting model the predicted interpenetration is about 1.6 m at the surface, 73% of the maximum relative displacement along dip, and decreases to zero at the deepest portion of the fault. Of course, in actuality, the fault will not interpenetrate because the normal stress will increase in compression. To estimate the magnitude of the normal stress change, we repeated the calculation but required that the normal relative displacement be zero. (This change has negligible effect on the fit of the leveling data.) The resulting normal traction is compressive (tending to open the crack) over most of the fault surface with a maximum value of about 110% of the applied shear stress drop occurring at the surface. Surprisingly, a small tensile stress (about 7% of the applied shear) is required on the deepest portions of the fault. Apparently, this occurs because preventing interpenetration of the crack faces near the surface tends to cause the deeper portions to open. A more complicated analysis that includes the effect of the change in normal stress on the resistance to slip is needed to determine more accurately the magnitude of the normal stress changes. However, these limiting cases suggest that the effect can be significant.

CONCLUDING DISCUSSION

In this paper we have described a numerical method for determining the displacements in an elastic half-space caused by slip on planar zones in response to a prescribed shear stress drop. Although, for simplicity, we have presented results only for uniform stress drops and elliptical slip zones, the method can be applied to arbitrarily shaped planar zones and distributed stress drops. By incorporating the appropriate asymptotic form of the displacement field near the edge of a crack in a linear elastic isotropic body, we are able to calculate accurately the stress intensity factors and hence the energy release rates. These quantities can be used in propagation criteria for determining the advance of the slip zone.

Because so few solutions exist for crack models of slip zones in a half-space, the magnitude and nature of the effect of the free surface have been uncertain. To examine this effect, we have presented results for the stress intensity factors and energy release rates for slip zones of various shapes, depths, and inclinations and compared them with solutions for slip zones of the same shape in an elastic full space. Although the details depend on the specific geometry, in general, when the distance of the slip zone center from the free surface (h) is greater than the downdip width of the slip zone ($2b$), the difference between the half-space and full space results is less than 10%. In addition, the influence of the free surface increases with decreasing dip angle.

We have also examined in detail the effect of the free surface on the relation between the seismic moment and the stress drop (see (13) and Table 1). The seismic moment is a relatively well-determined observational parameter, and the relation between the stress drop and the moment for a circular or elliptical crack in an infinite elastic body is often used to infer the stress drop. Again, the results indicate that the effect of the free surface is small (less than about 10%) unless the fault rupture is very near to the free surface (h less than the downdip width $2b$). The effect can, however, be significant for dipping faults that rupture to (or nearly to) the free surface.

Another effect of the free surface revealed by the calculations here is the coupling of slip with normal relative displacement which has been noted previously in two-dimensional problems by *Dmowska and Kostrov* [1973]. Because of this coupling, the shear resistance, which is proportional to the normal stress for a simple Coulomb condition, is coupled to the slip. Consequently, as remarked by *Dmowska and Rice* [1986], it is not possible to specify the shear stress drop a priori, and iteration is necessary to obtain the solution for a given shear stress drop. Although we have not pursued a full analysis of this coupling, some insight can be gained from consideration of the limiting cases in which either the normal stress change on the fault or the normal relative displacement is specified as zero.

When the change in normal stress is specified to be zero (as has been the case here, except where noted), the calculations indicate that the surfaces of reverse dip-slip faults tend to open and those of normal dip-slip faults tend to interpenetrate. (Actual interpenetration is prevented by an increase in normal compressive stress, and opening is opposed by the ambient compressive stress). Conversely, if the relative normal displacement is required to be zero, slip induces changes in normal stress. For reverse slip the change in normal stress is tensile (tending to prevent opening) over most of the rupture. For normal dip-slip motion the normal stress changes are compressive over most of the slip surface.

As example applications of the solutions, we have used them to reexamine surface deformation data from the 1987 Whittier Narrows, 1973 Borah Peak, and 1966 Parkfield earthquakes. In all three cases the geometries, stress drops, and moments inferred are similar to those obtained previously by others using kinematic models. The agreement lends additional confidence in the previous results, and the slight differences give an indication of the resolution. A significant difference between the approaches is the manner of determining the stress drop. In the solutions here the stress drop is one of the parameters adjusted to fit the observations. The slip distribution is then calculated for the inferred stress drop and geometry and used to determine the moment. In the kinematic models the slip magnitude and, possibly, distribution are chosen to fit the observations. The stress drop is then inferred from the moment, typically, by using the relation for a circular crack in an infinite body. As noted above, this relation is reasonably accurate, but significant loss in accuracy occurs if the slip zone is close to the free surface.

The additional information obtained by the present method is an estimate of the critical energy release rate (energy released per unit area advance of the slip zone). This estimate is obtained by assuming that the slip zone propagated according to the criterion that the energy release rate is equal to a critical value that reflects the resistance of the material. Although this criterion is simple, it is thought to be a good approximation when the actual inelastic processes associated with slip propagation occur in a zone near the slip zone edge that is small compared with other relevant length scales [*Rudnicki*, 1980; *Rice*, 1980, 1983; *Li*, 1987]. The slip zone stops advancing either because the available energy release decreases (perhaps due to a decrease in stress drop) or the slip zone has propagated into a region of higher critical energy release rate [*Husseini et al.*, 1975]. Thus the energy release rate inferred from the coseismic geodetic data is a lower bound on the critical energy release rate at the termination of rupture.

The critical energy release rates estimated for the three earthquakes considered here are 1.5×10^6 J/m^2 (Parkfield), 1.2×10^6 J/m^2 (Borah Peak), and 2×10^8 J/m^2 (Whittier Narrows). The value for Parkfield occurs at the top of the slip zone, and that for Borah Peak occurs at the ends of the surface trace of the slip zone. The Whittier Narrows event was deep enough that there was little variation around the edge. *Li* [1987] has tabulated values of the critical energy release rate inferred for crustal faulting (also see *Rudnicki* [1980]). These range from 10^0 to 10^8 J/m^2 with most of the values ranging from 10^5 to 10^8 J/m^2. The values inferred here are toward the upper end of this range, and that for the Whittier Narrows event is as large as any cited by *Li* [1987]. *Wong* [1982, 1986] has collected values of the critical energy release rate inferred from slip on sawcut laboratory specimens. These values are of the order of 10^4 J/m^2 and hence about 2 orders of magnitude less than typical for crustal faults. *Martel and Pollard* [1989] have estimated values of critical shear fracture energy release rates ranging from 5×10^2 to 2×10^4 J/m^2, of the order of laboratory values, from field observations of slip along small faults in granite rock.

As indicated by this short summary, currently available estimates of values of the critical energy release rate for crustal faulting are not numerous and exhibit considerable variation. Additional estimates and knowledge of their variation through the crust would contribute to a better understanding of the initiation and arrest of earthquake ruptures.

APPENDIX

The terms K_{mn} in (7) relative to the crack surface coordinate system y_i are given below:

$$K_{11} = \frac{\mu}{4\pi(\kappa+1)}\left\{\frac{2}{r_1^3}(\kappa-1) + \frac{3}{r_1^5}(3-\kappa)(y_1-\xi_1)^2 + \frac{2}{r_2^3}(\sin^2\alpha - \kappa + \kappa^2\cos^2\alpha) + \frac{3\bar{y}}{r_2^5}[-1 - 2\sin^2\alpha + \kappa(2\cos^2\alpha+1)] + \frac{12H}{r_2^5}(-5 + 7\cos^2\alpha + \kappa\sin^2\alpha) + \frac{120H}{r_2^7}[4H\sin^2\alpha + \bar{y}^2(3-4\cos^2\alpha)] - \frac{3360H^2\bar{y}^2\sin^2\alpha}{r_2^9} - 6\cos^2\alpha T_3\right\}$$

$$K_{12} = \frac{\mu}{4\pi(\kappa+1)}\left\{\frac{3}{r_1^5}(3-\kappa)(y_1-\xi_1)(y_2-\xi_2) + \frac{6\bar{y}\cos\alpha}{r_2^5}(h + y_2\cos\alpha) \cdot [-1 + 12\sin^2\alpha - \kappa(1+4\sin^2\alpha)] - \frac{3\bar{y}}{r_2^5}(y_2-\xi_2)[(1+4\sin^2\alpha - 2\sin^4\alpha) - \kappa(2\cos^2\alpha+1) - 2\kappa^2\sin^2\alpha\cos^2\alpha] + \frac{120H\bar{y}}{r_2^7}[2\cos\alpha(h + y_2\cos\alpha)(\kappa\sin^2\alpha + 7\cos\alpha - 6) + (y_2-\xi_2)(3-4\cos^2\alpha)] + \frac{3360H^2\sin^2\alpha\bar{y}}{r_2^9} \cdot [2\cos\alpha(h + y_2\cos\alpha) - (y_2-\xi_2)] - \frac{3}{2}\bar{y}\sin^2\alpha T_2\right\}$$

$$K_{13} = \frac{\mu\bar{y}\sin\alpha}{4\pi(\kappa+1)}\left\{\frac{24\cos^2\alpha}{r_2^5}(3-\kappa)(h+y_2\cos\alpha) - \frac{6\cos^3\alpha}{r_2^5}(1-\kappa^2)(y_2-\xi_2) + \frac{120H}{r_2^7}\cdot[(h+y_2\cos\alpha)(-1-7\cos 2\alpha+2\kappa\cos^2\alpha) - (y_2-\xi_2)(\kappa-1)\cos\alpha] - \frac{6720H^2\sin^2\alpha}{r_2^9}\cdot(h+y_2\cos\alpha) - 6\cos^3\alpha T_2\right\}$$

$$K_{22} = \frac{\mu}{4\pi(\kappa+1)}\left\{\frac{2}{r_1^3}(\kappa-1)+\frac{3}{r_1^5}(3-\kappa)(y_2-\xi_2)^2 + \frac{\cos 4\alpha}{r_2^3}(-7+\kappa)+\frac{48H}{r_2^5}(2+5\sin^2\alpha - 27\sin^2\alpha\cos^2\alpha+\kappa\sin^2\alpha\cos^2\alpha) + \frac{3\bar{y}^2}{r_2^5}[(3-22\sin^2\alpha\cos^2\alpha)-\kappa\cos 4\alpha - 2\kappa^2\sin^2\alpha\cos^2\alpha] + \frac{3\sin^2 2\alpha\sin^2\alpha}{2r_2^5}(\kappa^2-1)(y_2-\xi_2)^2 + \frac{60H}{r_2^7}[-8H\sin^2 2\alpha(9-16\cos^2\alpha) + \bar{y}^2(-2+7\sin^2 2\alpha-4\sin^2\alpha-\kappa\sin^2 2\alpha)] + \frac{3360H\sin^2\alpha}{r_2^9}(4H\sin^2\alpha-\bar{y}^2\cos 2\alpha) + \frac{3}{2}\sin^2 2\alpha T_1\right\}$$

$$K_{23} = \frac{\mu\sin\alpha}{4\pi(\kappa+1)}\left\{\frac{8\cos^3\alpha}{r_2^3}(4-\kappa) - \frac{24H\cos 2\alpha\cos\alpha}{r_2^5}(10-\kappa) + \frac{6\bar{y}^2\cos^3\alpha}{r_2^5}(-7+4\kappa-\kappa^2) + \frac{24\cos^2\alpha}{r_2^5}(y_2-\xi_2)[2h+(y_2+\xi_2)\cos\alpha] + \frac{3\sin^2 2\alpha\cos\alpha}{2r_2^5}(y_2-\xi_2)^2(\kappa^2-1) + \frac{120H\cos\alpha}{r_2^7}[-12H\sin^2\alpha+\bar{y}^2\cos 2\alpha(4-\kappa)] + \frac{1680H^2\bar{y}^2\sin 2\alpha\sin\alpha}{r_2^9} - \frac{120H}{r_2^7}\cdot(y_2-\xi_2)\left(3\cos 2\alpha+\frac{28H\sin^2\alpha}{r_2^7}\right)\cdot[2h+(y_2+\xi_2)\cos\alpha]+6\cos^3\alpha T_1\right\}$$

$$K_{33} = \frac{\mu}{4\pi(\kappa+1)}\left\{\frac{4}{r_1^3}-\frac{4}{r_2^3}(1-2\cos^4\alpha+2\kappa\cos^4\alpha) - \frac{12H}{r_2^5}[2(1+10\cos^2\alpha-14\cos^4\alpha)+\kappa\sin^2\alpha] + \frac{6\bar{y}^2\cos^4\alpha}{r_2^5}(-3+4\kappa-\kappa^2) + \frac{3\sin^2 2\alpha\cos^2\alpha}{2r_2^5}\cdot(\kappa^2-1)(y_2-\xi_2)^2 + \frac{240H\sin^2\alpha}{r_2^7}\cdot[4H(5\cos^2\alpha-2)+(\kappa-1)\bar{y}^2\cos^2\alpha] + \frac{13440H^3\sin^4\alpha}{r_2^9}+6\cos^4\alpha T_1\right\}$$

where

$$\kappa = 3-4\nu$$

$$T_1 = (\kappa^2-1)\left[\frac{1}{r_2r_4^2}-\frac{2\sin^2\alpha}{r_2^2r_4^2}\left(\frac{2}{r_4}+\frac{1}{r_2}\right)(y_2-\xi_2)^2 + \frac{\sin^4\alpha}{r_2^3r_4^2}\left(\frac{1}{r_2^2}+\frac{2}{r_2r_4}+\frac{2}{r_4^2}\right)(y_2-\xi_2)^4\right]$$

$$T_2 = (\kappa^2-1)(y_2-\xi_2)\left[\frac{1}{r_2^2r_4^2}\left(\frac{1}{r_2}+\frac{2}{r_4}\right) - \frac{\sin^2\alpha}{r_2^3r_4^2}\left(\frac{1}{r_2^2}+\frac{2}{r_2r_4}+\frac{2}{r_4^2}\right)(y_2-\xi_2)^2\right]$$

$$T_3 = (\kappa^2-1)\left[\frac{1}{r_2r_4^2}-\frac{\bar{y}^2\sin^2\alpha}{r_2^3r_4^2}\left(\frac{1}{r_2^2}+\frac{2}{r_2r_4}+\frac{2}{r_4^2}\right)(y_2-\xi_2)^2\right]$$

$$\bar{y} = y_1-\xi_1$$

$$r_1^2 = (y_1-\xi_1)^2+(y_2-\xi_2)^2$$

$$r_2^2 = \bar{y}^2+(y_2-\xi_2)^2+4H$$

$$r_4 = r_2+2h+(y_2+\xi_2)\cos\alpha$$

$$H = h^2+h(y_2+\xi_2)\cos\alpha+y_2\xi_2\cos^2\alpha$$

The reciprocal theorem requires that $K_{ij}(y, \xi) = K_{ji}(\xi, y)$, and this relation determines the remaining elements of K_{ij}.

The displacements in the elastic half-space are obtained by using (4), which can be written as follows:

$$u_i(\mathbf{x}) = \int_S \bar{K}_{in}(\mathbf{x}, \boldsymbol{\eta}) b_n(\boldsymbol{\eta})\, d\boldsymbol{\eta}$$

where

$$\bar{K}_{in}(\mathbf{x}, \boldsymbol{\eta}) = C_{jlmn} n_m \frac{\partial G_{ij}}{\partial \eta_l}(\mathbf{x}, \boldsymbol{\eta})$$

The terms $\bar{K}_{in}$ relative to the half-space coordinate system x_i are listed below:

$$\bar{K}_{i1}(\mathbf{x}, \boldsymbol{\eta}) = \mu\left[-\sin\alpha\left(\frac{\partial G_{i1}}{\partial \eta_2} + \frac{\partial G_{i2}}{\partial \eta_1}\right) + \cos\alpha\left(\frac{\partial G_{i1}}{\partial \eta_3} + \frac{\partial G_{i3}}{\partial \eta_1}\right)\right]$$

$$\bar{K}_{i2}(\mathbf{x}, \boldsymbol{\eta}) = \mu\left[-\sin 2\alpha\left(\frac{\partial G_{i2}}{\partial \eta_2} - \frac{\partial G_{i3}}{\partial \eta_3}\right) + \cos 2\alpha\left(\frac{\partial G_{i3}}{\partial \eta_2} + \frac{\partial G_{i2}}{\partial \eta_3}\right)\right]$$

$$\bar{K}_{i3}(\mathbf{x}, \boldsymbol{\eta}) = \lambda \frac{\partial G_{ij}}{\partial \eta_j} + 2\mu\left[\sin^2\alpha \frac{\partial G_{i2}}{\partial \eta_2} + \cos^2\alpha \frac{\partial G_{i3}}{\partial \eta_3} - \sin\alpha\cos\alpha\left(\frac{\partial G_{i2}}{\partial \eta_3} + \frac{\partial G_{i3}}{\partial \eta_2}\right)\right]$$

The derivatives of the Green's function are as follows:

$$\frac{\partial G_{ij}}{\partial \eta_n} = \frac{1}{16\pi\mu(1-\nu)}\left\{-(3-4\nu)\frac{\delta_{ij}}{R_1^2}\frac{\partial R_1}{\partial \eta_n} - \frac{\delta_{ij}}{R_2^2}\frac{\partial R_2}{\partial \eta_n} - \left[\frac{1}{R_1^3} + \frac{(3-4\nu)}{R_2^3}\right] \cdot [\delta_{in}(x_j - \eta_j) + \delta_{jn}(x_i - \eta_i)] - 3(x_i - \eta_i)(x_j - \eta_j)\left[\frac{1}{R_1^4}\frac{\partial R_1}{\partial \eta_n} + \frac{(3-4\nu)}{R_2^4}\frac{\partial R_2}{\partial \eta_n}\right] + \frac{2x_2\delta_{2n}\delta_{ij}}{R_2^3} - \frac{6x_2\eta_2\delta_{ij}}{R_2^4}\frac{\partial R_2}{\partial \eta_n} + \frac{6x_2}{R_2^5}[\delta_{in}\eta_2(x_j - \eta_j) + \delta_{jn}\eta_2(x_i - \eta_i) - \delta_{2n}(x_i - \eta_i)(x_j - \eta_j)] + \frac{30x_2\eta_2}{R_2^6}\frac{\partial R_2}{\partial \eta_n} \cdot (x_i - \eta_i)(x_j - \eta_j) - 4(1-\nu)(1-2\nu)\frac{\delta_{ij}}{\bar{R}_2^2}\frac{\partial \bar{R}_2}{\partial \eta_n} + \frac{4}{R_2\bar{R}_2^2}(1-\nu)(1-2\nu)[\delta_{in}(x_j - \eta_j) + \delta_{jn}(x_i - \eta_i)] + 4(1-\nu)(1-2\nu)(x_i - \eta_i)(x_j - \eta_j) \cdot \left[\frac{1}{R_2\bar{R}_2^2}\frac{\partial R_2}{\partial \eta_n} + \frac{1}{R_2\bar{R}_2^3}\frac{\partial \bar{R}_2}{\partial \eta_n}\right]\right\} \quad i, j = 1, 3$$

$$\frac{\partial G_{2j}}{\partial \eta_n} = \frac{1}{16\pi\mu(1-\nu)}\left\{-\left[\frac{1}{R_1^3} + \frac{(3-4\nu)}{R_2^3}\right] \cdot [\delta_{2n}(x_j - \eta_j) + \delta_{jn}(x_2 - \eta_2)] - \frac{3}{R_1^4}\frac{\partial R_1}{\partial \eta_n}(x_2 - \eta_2)(x_j - \eta_j) - \frac{3(3-4\nu)}{R_2^4}\frac{\partial R_2}{\partial \eta_n}(x_2 - \eta_2)(x_j - \eta_j) + \frac{6x_2}{R_2^5}[\delta_{jn}\eta_2(x_2 + \eta_2) - \delta_{2n}(x_j - \eta_j) \cdot (x_2 + \eta_2) - \delta_{2n}\eta_2(x_j - \eta_j)] + \frac{30x_2\eta_2}{R_2^6}\frac{\partial R_2}{\partial \eta_n}(x_2 + \eta_2)(x_j - \eta_j) - \frac{4\delta_{jn}}{R_2\bar{R}_2}(1-\nu)(1-2\nu) - 4(1-\nu) \cdot (1-2\nu)(x_j - \eta_j)\left(\frac{1}{R_2^2\bar{R}_2}\frac{\partial R_2}{\partial \eta_n} + \frac{1}{R_2\bar{R}_2^2}\frac{\partial \bar{R}_2}{\partial \eta_n}\right)\right\} \quad j = 1, 3$$

$$\frac{\partial G_{i2}}{\partial \eta_n} = \frac{1}{16\pi\mu(1-\nu)}\left\{-\left(\frac{1}{R_1^3} + \frac{(3-4\nu)}{R_2^3}\right) \cdot [\delta_{2n}(x_i - \eta_i) + \delta_{in}(x_2 - \eta_2)] - \frac{3}{R_1^4}\frac{\partial R_1}{\partial \eta_n}(x_2 - \eta_2)(x_i - \eta_i) - \frac{3(3-4\nu)}{R_2^4}\frac{\partial R_2}{\partial \eta_n}(x_2 - \eta_2)(x_i - \eta_i) + \frac{6x_2}{R_2^5}[\delta_{2n}(x_2 + \eta_2)(x_i - \eta_i) + \delta_{2n}\eta_2(x_i - \eta_i) - \delta_{in}\eta_2(x_2 + \eta_2)] - \frac{30x_2\eta_2}{R_2^6}\frac{\partial R_2}{\partial \eta_n}(x_2 + \eta_2)(x_i - \eta_i) + \frac{4\delta_{in}}{R_2\bar{R}_2}(1-\nu)(1-2\nu) + 4(1-\nu)(1-2\nu)(x_i - \eta_i) \cdot \left(\frac{1}{R_2^2\bar{R}_2}\frac{\partial R_2}{\partial \eta_n} + \frac{1}{R_2\bar{R}_2^2}\frac{\partial \bar{R}_2}{\partial \eta_n}\right)\right\} \quad i = 1, 3$$

$$\frac{\partial G_{22}}{\partial \eta_n} = \frac{1}{16\pi\mu(1-\nu)} \left\{ -\frac{(3-4\nu)}{R_1^2}\frac{\partial R_1}{\partial \eta_n} - \frac{2\delta_{2n}}{R_1^3}(x_2-\eta_2) - \frac{3}{R_1^4}\frac{\partial R_1}{\partial \eta_n}(x_2-\eta_2) - \frac{1}{R_2^2}\frac{\partial R_2}{\partial \eta_n}[8(1-\nu)^2-(3-4\nu)] + \frac{2\delta_{2n}}{R_2^3} \cdot [(3-4\nu)(x_2+\eta_2)-x_2] - \frac{3}{R_2^4}\frac{\partial R_2}{\partial \eta_n} \cdot [(3-4\nu)(x_2+\eta_2)^2 - 2x_2\eta_2] + \frac{6\delta_{2n}x_2}{R_2^5}(x_2+\eta_2)^2 + \frac{12\delta_{2n}x_2\eta_2}{R_2^5}(x_2+\eta_2) - \frac{30x_2\eta_2}{R_2^6}\frac{\partial R_2}{\partial \eta_n}(x_2+\eta_2)^2 \right\}$$

where

$$R_1 = [(x_1-\eta_1)^2 + (x_2-\eta_2)^2 + (x_3-\eta_3)^2]^{1/2}$$

$$R_2 = [(x_1-\eta_1)^2 + (x_2+\eta_2) + (x_3-\eta_3)^2]^{1/2}$$

$$\bar{R}_2 = R_2 + x_2 + \eta_2$$

Acknowledgments. This work has been supported jointly by the National Science Foundation and the U.S. Geological Survey through NSF grant EAR-8707392. Ross Stein provided the data for the Borah Peak and Whittier Narrows earthquakes. Paul Segall provided the data for the Parkfield earthquake. It is a pleasure to acknowledge their help. Thoughtful comments by reviewers Ruth Harris and Stephen Martel and by Associate Editor Jack Boatwright substantially improved the manuscript. In addition, we are grateful to Alan Rubin for pointing out an error in the sign of the normal relative displacement caused by slip.

REFERENCES

Aki, K., Origin of the seismic gap: What initiates and stops a rupture propagation along a plate boundary?, in Proceedings of Conference VI, Methodology for Identifying Seismic Gaps and Soon-to-Break Gaps, 1978, *U.S. Geol. Surv. Open File Rep., 78-943*, 3–46, 1978.

Archuleta, R. J., and S. M. Day, Dynamic rupture in a layered medium: The 1966 Parkfield earthquake, *Bull. Seismol. Soc. Am., 70*, 671–689, 1980.

Barrientos, S. E., R. S. Stein, and S. N. Ward, Comparison of the 1959 Hebgen Lake, Montana and the 1983 Borah Peak, Idaho, earthquakes from geodetic observations, *Bull. Seismol. Soc. Am., 77*, 784–808, 1987.

Chinnery, M. A., The deformation of the ground around surface faults, *Bull. Seismol. Soc. Am., 51*, 355–372, 1961.

Davis, T. L., J. Namson, and R. F. Yerkes, A cross section of Los Angeles basin: Seismically active fold and thrust belt, the Whittier Narrows earthquake and earthquake hazard along the northern edge of the Los Angeles basin, *J. Geophys. Res., 94*, 9644–9664, 1989.

Dmowska, R., and B. V. Kostrov, A shearing crack in a semi-space under plane strain conditions, *Arch. Mech., 25*, 421–440, 1973.

Dmowska, R., and J. R. Rice, Fracture theory and its seismological applications, in *Continuum Theories in Solid Earth Physics*, edited by R. Teisseyre, pp. 187–255, Polish Scientific, Warsaw, 1986.

Doser, D. I., and R. B. Smith, Source parameters of the October 28, 1983 Borah Peak, Idaho, earthquake from body wave analysis, *Bull. Seismol. Soc. Am., 75*, 1041–1051, 1985.

Eaton, J. P., M. E. O'Neill, and J. M. Murdock, Aftershocks of the 1966 Parkfield-Cholame, California earthquake: A detailed study, *Bull. Seismol. Soc. Am., 60*, 1151–1197, 1970.

Eshelby, J. D., The determination of the elastic field of an ellipsoidal inclusion, and related problems, *Proc. R. Soc. London, Ser. A, 241*, 276–396, 1957.

Husseini, M. I., D. B. Jovanovich, M. J. Randall, and L. B. Freund, The fracture energy of earthquakes, *Geophys. J. R. Astron. Soc., 43*, 367–385, 1975.

King, N. E., P. Segall, and W. Prescott, Geodetic measurements near Parkfield, California, 1959–1984, *J. Geophys. Res., 92*, 2474–2766, 1987.

Kostrov, B. V., and S. Das, Evaluation of stress and displacement fields due to an elliptical plane shear crack, *Geophys. J. R. Astron. Soc., 78*, 19–33, 1984.

Lee, J. C., and L. M. Keer, Study of a three-dimensional crack terminating at an interface, *J. Appl. Mech., 108*, 311–316, 1986.

Lee, J. C., T. N. Farris, and L. M. Keer, Stress intensity factors for cracks of arbitrary shape near an interfacial boundary, *Eng. Fract. Mech., 27*, 27–41, 1987.

Li, V., Mechanics of shear rupture applied to earthquake zones, in *Rock Fracture Mechanics and Geophysics*, edited by B. Atkinson, Academic, pp. 351–428, Academic, San Diego, Calif., 1987.

Lin, J., and R. S. Stein, Coseismic folding, earthquake recurrence, and the 1987 source mechanism at Whittier Narrows, Los Angeles basin, California, *J. Geophys. Res., 94*, 9614–9632, 1989.

Mansinha, L., and D. E. Smylie, The displacement fields on inclined faults, *Bull. Seismol. Soc. Am., 61*, 1433–1440, 1971.

Martel, S. J., and D. D. Pollard, Mechanics of slip and fracture along small faults and simple strike-slip fault zones in granite rock, *J. Geophys. Res., 94*, 9417–9428, 1989.

Mindlin, R. D., Force at a point in the interior of a semi-infinite solid, *Physics, 7*, 195–202, 1936.

Mindlin, R. D., Force at a point in the interior of a semi-infinite solid, *Proc. Midwest. Conf. Solid Mech., 1st*, 56–59, 1955.

Mindlin, R. D., and D. H. Cheng, Nuclei of strain in the semi-infinite solid, *J. Appl. Phys., 21*, 926–933, 1950.

Murakami, Y. (Ed.), *Stress Intensity Factors Handbook*, vol. 2, Pergamon, New York, 1987.

Murakami, Y., and S. Nemat-Nasser, Growth and stability of interacting surface flaws of arbitrary shape, *Eng. Fract. Mech., 17*, 193–210, 1983.

Rice, J. R., Mathematical analysis in the mechanics of fracture, in *Fracture: An Advanced Treatise*, vol. 2, edited by H. Liebowitz, pp. 191–311, Academic, San Diego, Calif., 1968.

Rice, J. R., The mechanics of earthquake rupture, in Physics of the Earth's Interior, edited by A. M. Dziewonski and E. Boschi, *Proc. Int. School Phys. Enrico Fermi, 78*, 555–649, 1980.

Rice, J. R., Constitutive relations for fault slip and earthquake instabilities, *Pure Appl. Geophys., 121*, 443–475, 1983.

Richins, W. D., R. B. Smith, C. J. Lanser, J. E. Zollweg, J. T. King, and J. C. Pechmann, The 1983 Borah Peak, Idaho, earthquake: Relationship of aftershocks to mainshock, surface faulting, and regional tectonics, in Workshop XXVIII on the Borah Peak Earthquake, *U.S. Geol. Surv., Open File Rep. 85-290*, 285–310, 1985.

Rudnicki, J. W., Fracture mechanics applied to the earth's crust, *Annu. Rev. Earth Planet. Sci., 8*, 489–525, 1980.

Segall, P., and R. Harris, Earthquake deformation cycle on the San Andreas fault near Parkfield, California, *J. Geophys. Res., 92*, 10,511–10,525, 1987.

Smith, S. W., and M. Wyss, Displacement on the San Andreas fault subsequent to the 1966 Parkfield earthquake, *Bull. Seismol. Soc. Am., 58*, 1955–1973, 1968.

Stein, R. S., and S. E. Barrientos, High-angle normal faulting in the intermountain seismic belt: Geodetic investigation of the 1983 Borah Peak, Idaho earthquakes, *J. Geophys. Res., 90*, 11,355–11,366, 1985.

Steketee, J. A., Some geophysical applications of the elasticity theory of dislocations, *Can. J. Phys., 36*, 1168–1198, 1958.

Stuart, W. D., R. J. Archuleta, and A. G. Lindh, Forecast model for moderate earthquakes near Parkfield, California, *J. Geophys. Res., 90*, 592–604, 1985.

Tsai, Y.-B., and K. Aki, Simultaneous determination of the seismic

moment and attenuation of seismic surface waves, *Bull. Seismol. Soc. Am.*, *59*, 275–287, 1969.
Wong, T.-F., Shear fracture energy of Westerly granite from post-failure behavior, *J. Geophys. Res.*, *87*, 990–1000, 1982.
Wong, T.-F., On the normal stress dependence of the shear fracture energy, in Earthquake Source Mechanics *Geophys. Monogr. Ser.*, vol. 37, edited by S. Das, J. Boatwright, and C. H. Scholz, pp. 1–11, AGU, Washington, D. C., 1986.

L. M. Keer, C. H. Kuo, J. W. Rudnicki, and M. Wu, Department of Civil Engineering, Northwestern University, Evanston, IL, 60208-3109.

(Received August 2, 1990;
revised February 27, 1991;
accepted April 8, 1991.)

JOURNAL OF GEOPHYSICAL RESEARCH, VOL. 96, NO. B10, PAGES 16,525–16,528, SEPTEMBER 10, 1991

On the Measurement of Body Wave Dispersion

ANTONI M. CORREIG[1]

Laboratori d'Estudis Geofísics "Eduard Fontseré", Institut d'Estudis Catalans, Facultat de Física, Barcelona, Spain

A method is devised to measure body wave dispersion in terms of the arrival time of a narrow band-pass filtered signal. The arrival time is defined as the expectation of the arrival time of the wave front minus half the duration of the first pulse. Body wave dispersion is related to an absorption band, and its transfer function is found. By interpreting the absorption band as a filter and identifying the dispersion as the (frequency dependent) group delay of the filter the measured dispersion is interpreted as due to a cascade of filters composed of the following elements: intrinsic attenuation, source time function, and finiteness of the fault.

INTRODUCTION

It has long been accepted (see *Jackson and Anderson* [1970] for a review) that the internal friction of the medium Q^{-1} is practically independent of frequency. However, once the analysis of coda waves for the retrieval of coda-Q was widely used [*Aki and Chouet*, 1975], it became apparent that, at least for high frequencies, coda-Q was strongly frequency dependent. This dependence was also found for short-period shear waves [*Orcutt*, 1987]. *Liu et al.* [1976] constructed a phenomenological model to explain the constancy of Q^{-1} by superposing a number of Debye absorption peaks. Q^{-1} is constant in the frequency interval defined by the low and high cutoff frequencies and varies asymptotically as f at the low-frequency limit and as f^{-1} at the high-frequency limit. This model is thus able to explain the constancy of Q^{-1} as obtained from body and surface waves and free oscillations as well as the frequency dependence of Q^{-1} obtained at short periods.

It is well known that for causality to be preserved in an attenuative medium, body waves must be dispersive, attenuation and dispersion being related through Kramers-Kröning relations. It is the aim of this study to present a method for the measurement of the body wave dispersion, based on the measurement of the arrival time of some selected frequencies that conform the signal. The first version of the method was applied to the measurement of body wave dispersion of local earthquakes. Because the signal was mainly composed of high frequencies, the arrival time was picked up by eye, but some ambiguities arose at the lower frequencies, and the need for a more objective criterion was apparent. In the present study a rigorous and objective method is presented, valid for all ranges of frequencies. Once the dispersion is obtained, it can be used as a new and independent set of observations.

Our study starts with the eikonal equation, which is recognized as a Hamilton-Jacoby equation. Following the formalism of quantum mechanics, the associated Hamiltonian and generalized momenta are interpreted as operators acting on a wave function, which in turn can be interpreted as a probability amplitude. We now have all the elements to define the arrival time of a pulse as an expectation value, thus solving the problem of the subjectivity of picking up the arrival time of a signal in presence of noise "by eye" or through a prediction from an Earth model [*Doornbos*, 1983]. Indeed, this is a crucial point because it is the basis of the method of measuring the body wave dispersion.

By interpreting the dispersion as the frequency-dependent group delay of a filter, the measured group delay can be modeled as being due to the contribution of the following four filters: attenuative operator, source time function, finiteness of fault, and crustal transfer function, although this effect can be neglected. As an application, the new set of data can be used, by itself or along with data from other sources, as input in an inversion process to retrieve the parameters of the three contributions simultaneously. For the case in which the attenuation operator is known, the measurement of body wave dispersion would provide a powerful method to retrieve the gross features of source parameters. Alternatively, if the source is known, the method provides a way to measure the attenuation from all seismic phases of interest.

KINEMATICS OF SEISMIC WAVES

The propagation of seismic waves is described by the eikonal equation

$$(\nabla S)^2 - u^2(\mathbf{r}) = 0, \tag{1}$$

where $S = S(\mathbf{r})$ is the wave front and $u(\mathbf{r})$ is the medium slowness. Equation (1) can be regarded as a Hamilton-Jacobi equation that can be rewritten as

$$\frac{\partial S}{\partial z} - \left[u^2(\mathbf{r}) - \left(\frac{\partial S}{\partial x}\right)^2 - \left(\frac{\partial S}{\partial y}\right)^2\right]^{1/2} = 0, \tag{2}$$

where the coordinate z acts as the parameter of motion. Equation (2) can formally be written as

$$\frac{\partial S}{\partial z} + H(x, y, p_x, p_y; z) = 0 \qquad p_x = \frac{\partial S}{\partial x}, p_y = \frac{\partial S}{\partial y}, \tag{3}$$

where the Hamiltonian H is given by

$$H(x, y, p_x, p_y; z) = -[u^2(x, y, z) - p_x^2 - p_y^2]^{1/2}. \tag{4}$$

p_x and p_y are the generalized momenta. Once the Hamiltonian is obtained, a Lagrangian can be defined through a Legendre transformation [*Goldstein*, 1963]

[1]Also at Departament de Geologia Dinàmica, Geofisica i Paleontologia, Facultat de Física, Barcelona, Spain.

Paper number 91JB01429.
0148-0227/91/91JB-01429$05.00

$$L(x, y, \dot{x}, \dot{y}; z) = u(x, y, z)(1 + \dot{x}^2 + \dot{y}^2)^{1/2}, \quad (5)$$

where $\dot{x} \equiv dx/dz$. The equations of motion will satisfy the Euler-Lagrange equations that will be obtained from a variational principle [*Courant and Hilbert*, 1962]

$$\delta \int u(x, y, z)\, ds = 0, \qquad ds = (\dot{x}^2 + \dot{y}^2 + 1)^{1/2} dz, \quad (6)$$

so that the travel-time integral along the ray path is stationary (Fermat's principle) and given by

$$T(x, y, z) = \int u(x, y, z)\, ds, \quad (7)$$

where the integral is taken along the ray path.

Propagation effects through an attenuative medium can be modeled by assuming a linear viscoelastic medium. In such a case in (7) the slowness u will be the inverse of a complex, dispersive velocity given by

$$\hat{c}(\omega) = [\hat{M}(\omega)/\rho]^{1/2}, \quad (8)$$

where $\hat{M}(\omega)$ is the complex elastic modulus and ρ the medium density. Consequently, the travel time will be a complex function of frequency, and (7) can be written as

$$\hat{T}(\omega) = \int \frac{ds}{\hat{c}(\omega)}. \quad (9)$$

It is assumed, at this stage, that there are no scattering loses. By imposing causality the following expression (a form of the Kramers-Kröning relation) is found [*Choy and Cormier*, 1986]

$$\text{Re } \hat{T}(\omega) = Re\ \hat{T}(\infty) + H[t^*(\omega)]/2, \quad (10)$$

where

$$\text{Re } \hat{T}(\infty) = t = \int \frac{ds}{Re\ \hat{c}(\infty)},$$

$$\text{Re } \hat{T}(\omega) = t(\omega) = \int \frac{ds}{Re\ \hat{c}(\omega)}, \quad (11)$$

$$t^*(\omega) = 2 \int \frac{ds}{\text{Im } \hat{c}(\omega)},$$

and H means Hilbert transform. Re $\hat{T}(\infty)$ represents the fastest arriving frequency component, the infinite frequency, and Re $\hat{T}(\omega)$ represents the arrival of frequency component ω.

Equation (10) suggests that the dispersion can be measured as the difference in arrival time of a frequency ω with respect to a reference frequency ω_r,

$$\Delta t = t(\omega) - t(\omega_r) = H[t^*(\omega) - t^*(\omega_r)]/2. \quad (12)$$

To relate the observations (Δt) to the model parameters (the right-hand side of (12)), a specific attenuative model must be assumed. Following *Liu et al.* [1976] a continuous relaxation model is assumed for which the (real) phase velocity is given by [*Ben-Menahem and Singh*, 1981]

$$\frac{C_\infty}{C(\omega)} = 1 + \frac{1}{\pi} Q_m^{-1} \left[\ln \frac{\tau_1}{\tau_2} + \frac{1}{2} \ln \left(\frac{1 + \omega^2 \tau_2^2}{1 + \omega^2 \tau_1^2} \right) \right], \quad (13)$$

where ω is the frequency, $\tau_1^{-1} = s_1$ and $\tau_2^{-1} = s_2$ are the high- and low-frequency cutoffs, respectively, of the frequency band, and Q_m is a constant which defines the flat part of the $Q(\omega)$ spectrum.

Because of the difficulty of computing the Hilbert transform of $t^*(\omega)$, the following approximation can be used. $C_\infty/C(\omega)$ can be rewritten as a function of travel time by substituting $C_\infty = s/t$ and $C(\omega) = s/t(\omega)$, with t, $t(\omega)$, and s with the same meaning as in (11). It can be argued that in dealing with travel time, group velocity should be used instead of phase velocity. However, in an absorbing medium the meaning of group velocity as the velocity of energy flow is not clear. In practical terms, this discrepancy is not a real problem, because for $\omega \to \infty$ and for $\omega \to 0$, $C(\omega) = U(\omega)$, and if Q^{-1} is not too large, $C^{-1}(\omega) \approx U^{-1}(\omega)$. Hence we can write

$$\frac{C_\infty}{C(\omega)} \simeq \frac{t(\omega)}{t}. \quad (14)$$

By substituting (13) into (14), $t(\omega)$ is obtained, and Δt is thus related to medium parameters. The result is

$$\Delta t = \frac{t}{2\pi} Q_m^{-1} \ln \left[\frac{(1 + \omega^2 \tau_2^2)(1 + \omega_r^2 \tau_1^2)}{(1 + \omega^2 \tau_1^2)(1 + \omega_r^2 \tau_2^2)} \right]. \quad (15)$$

Arrival Time of a Seismic Pulse

The use of (15) to relate observed dispersion Δt to medium parameters is based on the assumption that the arrival time of the signal can be picked up with very high precision and is independent of the noise contents and that the same criterion is used to analyze the distinct frequency contents of the signal. The Hamiltonian formalism offers us the theoretical basis for a definition of the arrival time with the above mentioned characteristics.

The Hamiltonian (4) has been obtained from the eikonal equation (1). Basically, the Hamiltonian formulation is a formulation in terms of rays, the analog in classical mechanics being the motion of a particle. By analogy to the transition from classical to quantum theory, a correspondence can be established for the transition of geometrical optics (geometrical ray theory) to wave optics. This correspondence can be achieved by interpreting the generalized momenta p_x and p_y of (3) and the Hamiltonian (4) as operators:

$$p_x = -\frac{i}{\omega} \frac{\partial}{\partial x}$$

$$p_y = -\frac{i}{\omega} \frac{\partial}{\partial y} \quad (16)$$

$$H = \frac{i}{\omega} \frac{\partial}{\partial z}$$

acting on a wave function $\bar{\Psi}$. The constant $1/\omega$ is formally introduced in place of Planck's constant. Such an interpretation has been previously made by *Gloge and Marcuse*

[1969]. By introducing the above defined operators into the Hamiltonian function (4) the Helmholtz equation is obtained

$$\nabla^2\bar{\Psi} + k^2\bar{\Psi} = 0, \qquad k = \omega u, \tag{17}$$

or in time domain the wave equation

$$\nabla^2\Psi - \frac{1}{v^2}\frac{\partial^2\Psi}{\partial t^2} = 0. \tag{18}$$

In (17) and (18) the wave functions $\bar{\Psi}(r, \omega)$ and $\Psi(r, t)$ may be identified with the amplitude of a scalar wave and k with its corresponding wave number.

Further following the formal analogy with quantum mechanics, the wave function can be interpreted as a probability amplitude. Consider the wave function $\Psi(r, t)$. For a fixed point $r = r_0$, the wave function will be a function only of the time, $\Psi = \Psi(t)$. If Ψ fulfills the normalization condition

$$\int_{-\infty}^{\infty} \Psi\Psi^* \, dt = 1, \tag{19}$$

then the function

$$I(t) = |\Psi|^2 \tag{20}$$

is the probability density of the arrival of a wave front at a time t. Hence the expectation value of the arrival time of a wave front is given by

$$\langle t \rangle = \int_{-\infty}^{\infty} \Psi^* t \Psi \, dt. \tag{21}$$

The duration D_t of a pulse is defined as [*Keilis-Borok*, 1989]

$$D_t^2 = 2\int_{-\infty}^{\infty} \Psi^*(t - \langle t \rangle)^2\Psi \, dt. \tag{22}$$

From (21) and (22) the arrival time of the P and S wave can be defined as

$$t_a = \langle t \rangle - D_t/2. \tag{23}$$

This is the criterion we propose for the computation of the arrival time.

GROUP DELAY OF A FILTER

An attenuation operator, such as the one described by the continuous relaxation model, can be interpreted as a filter with the body wave dispersion corresponding to the group delay of the filter, defined as

$$r(\omega) = -\frac{d\psi(\omega)}{d\omega}, \tag{24}$$

where $\psi(\omega)$ is the phase of the filter. If instead of only one filter the system consists of a cascade of filters, because of linearity the resulting group delay will be the sum of the group delay of each filter. Specifically, apart from the attenuation operator we can interpret as filters the source time function, the finiteness of the source, and the response of the layered crust.

Source Time Function

Consider, for simplicity, the exponential decay function

$$s(t) = H(t)e^{-t/\tau}, \qquad \tau > 0. \tag{25}$$

Its Fourier transform is

$$S(\omega) = \frac{\tau}{1 + i\omega\tau} \tag{26}$$

and its group delay

$$r(\omega) = \frac{\tau}{1 + (\omega\tau)^2}. \tag{27}$$

Depending on the value of the parameter τ this group delay can be significant.

Finiteness of the Source

The finiteness of the source can be modeled as [*Ben-Menahem and Singh*, 1981]

$$f(\omega) = \frac{\sin X}{X} e^{-ix} \tag{28}$$

$$X = \omega\frac{L}{2v}\left(1 - \frac{v}{c}\cos\Theta\right),$$

where L is the fault length, v the rupture velocity, c the wave velocity, and Θ the angle between the direction of rupture and the epicenter-receiver direction. Because the phase is linear with ω, the group delay will be a function of the azimuth only.

Response of a Layered Crust

The influence of a layered crust on the amplitude and phase on a body wave has long been recognized [*Phinney*, 1964]. By interpreting the crustal transfer function as a filter, (24) will provide us with the corresponding group delay. The crustal response has been computed by means of the Haskell matrix formalism [*Haskell*, 1953] for two extreme crustal models: (1) a continental crust 45 km thick composed of six layers over a half-space and (2) an oceanic crust 6 km thick composed of three layers. In neither case could the dispersion be obtained (however, dispersion is present for a stack of a few hundred layers).

MEASUREMENT OF THE BODY WAVE DISPERSION

As previously stated, (12) or its approximate solution (15), provides the method for the measurement of body wave dispersion as the difference in arrival time of a frequency component ω of the signal with respect to a frequency component of reference ω_r. To obtain Δt for the observed seismograms, we have first to isolate some frequency components of the signal and then measure the arrival time of the corresponding frequency component.

The frequency component of the signal can be obtained, following *Correig and Mitchell* [1989], through a band-pass filtering process at some selected frequencies. Butterworth filters are very suitable because of their stability. As this process of filtering by itself will introduce a group delay, the filtered signal has to be corrected for it. The correction to be

applied can easily be computed from the phase of the filter. In a similar way, a correction for the group delay of the seismograph response is needed.

Once a frequency component of the signal is isolated (strictly speaking, a narrow band of frequencies), the arrival time of the wave can be computed from (23). Note that because the recorded amplitude is real, the expectation value can be written

$$\langle t \rangle = \frac{\int_{-\infty}^{\infty} t\Psi^2 \, dt}{\int_{-\infty}^{\infty} \Psi^2 \, dt} \tag{29}$$

and similarly for D_t^2.

CONCLUSIONS

A method is presented for the measurement of the body wave dispersion, based on the measurement of the arrival time of several narrow frequency bands of the signal. The present study constitutes a generalization of a previous work of *Correig and Mitchell* [1989]: a rigorous method is actually provided for the determination of the arrival time of any seismic phase of interest and for any frequency band, i.e., suitable for use with broadband data.

In practical terms the expectation value can be computed from the recorded amplitudes of the pulse of the seismic phase, and because the expectation arrival time is obtained through an integration process of the full pulse, errors in the exact determination of the beginning of the pulse will not affect the expected arrival time, so we can consider the measurement of the dispersion to be quite precise, and much more precise than direct measurement of the attenuation.

Acknowledgments. This research was supported in part by the Dirección General para la Investigación Cientifica y Technológica under grant PB86-0431-C05-03.

REFERENCES

Aki, K., and B. Chouet, Origin of coda waves: Source, attenuation, and scattering effects, *J. Geophys. Res.*, *80*, 3322–3342, 1975.

Ben-Menahem, A., and J. S. Singh, *Seismic Waves and Sources*, Springer-Verlag, New York, 1981.

Choy, G. L., and V. F. Cormier, Direct measurements of the mantle attenuation operator from broadband *P* and *S* waveforms, *J. Geophys. Res.*, *91*, 7326–7342, 1986.

Correig, A. M., and B. J. Mitchell, Attenuative body wave dispersion at La Cerdanya, eastern Pyrenees, *Phys. Earth Planet. Inter.*, *57*, 304–310, 1989.

Courant, R., and D. Hilbert, *Methods of Mathematical Physics*, John Wiley, New York, 1962.

Doornbos, D. J., Observable effects of the seismic absorption band in the Earth, *Geophys. J. R. Astron. Soc.*, *75*, 693–711, 1983.

Gloge, D., and D. Marcuse, Formal quantum theory of light rays, *J. Opt. Soc. Am.*, *59*, 1629–1632, 1969.

Goldstein, H., *Mecánica clásica*, Aguilar, Barcelona, 1963.

Haskell, N. A., The dispersion of surface waves on a multilayered media, *Bull. Seismol. Soc. Am.*, *43*, 17–34, 1953.

Jackson, D. D., and D. L. Anderson, Physical mechanism of seismic wave attenuation, *Rev. Geophys. Space Phys.*, *8*, 1–63, 1970.

Keilis-Borok, V. I., (Ed.), *Seismic Surface Waves in a Laterally Inhomogeneous Earth*, Kluwer Academic, Boston, Mass., 1989.

Liu, H. P., D. L. Anderson, and H. Kanamori, Velocity dispersion due to anelasticity: Implications for seismology and mantle composition, *Geophys. J. R. Astron. Soc.*, *89*, 933–964, 1976.

Orcutt, J. A., Structure of the Earth's oceanic crust and uppermost mantle, *Rev. Geophys.*, *25*, 1177–1196, 1987.

Phinney, R. A., Structure of the Earth's crust from spectral behavior of long-period body waves, *J. Geophys. Res.*, *69*, 2997–3017, 1964.

A. M. Correig, Laboratori d'Estudis Geofísics "Eduard Fontseré", Institut d'Estudis Catalans, Facultat de Física, Martí Franquès 1, 08028 Barcelona, Spain.

(Received January 30, 1991;
revised May 21, 1991;
accepted May 28, 1991.)

JOURNAL OF GEOPHYSICAL RESEARCH, VOL. 96, NO. B10, PAGES 16,401–16,414, SEPTEMBER 10, 1991

Seismicity and Detection/Location Threshold in the Southern Great Basin Seismic Network

JOAN GOMBERG

U.S. Geological Survey, Denver Federal Center, Denver, Colorado

A spatially varying model of the detection/location capabilities of the Southern Great Basin seismic network (SGBSN) has been derived that is based on simple empirical relations and statistics. This permits use of almost all the catalog data gathered; instead of ignoring data that are below the threshold of completeness, a spatially varying threshold model is developed so that subregions having lower completeness levels than the network as a whole can be outlined and the completeness level of each sub-region determined. Such a model is required to unambiguously identify regions that are aseismic due to natural processes rather than to limited detection and/or location capabilities. Accounting for spatial variations in detection/location threshold is also important for studies in which magnitude-frequency distributions are interpreted in terms of source scaling properties. The characteristics of the spatial distribution of earthquakes, where earthquake clusters and aseismic regions locate, appear to be stable at all magnitude levels so that inferences about where strain is being accommodated will be the same whether numbers of earthquakes or strain estimated from seismic moments are examined. For the southern Great Basin region these principal characteristics include clusters at the northern end of the Furnace Creek fault and in the Pahranagat Shear Zone, and a relatively large number of earthquakes in the northern and southeastern portions of the Nevada Test Site. These clusters cover regions much larger than the surface projections of any of the mapped faults. The extent to which seismicity is induced by nuclear testing is unclear. The predominantly aseismic regions include the area west of the Death Valley/Furnace Creek fault system and an almost complete absence of events at Yucca Mountain. Finally, a considerable number of isolated events in the SGBSN catalog cannot be correlated with mapped faults.

INTRODUCTION

The principal goal of this study is the development of a spatially variable detection/location threshold model for the Southern Great Basin Seismic Network (SGBSN). It is common practice when interpreting seismicity patterns to ignore data below the "magnitude of completeness" in order to avoid bias arising from non-uniform detection/location capabilities. Earthquakes with magnitudes below the completeness level may be missing from a catalog because the seismic waves they generate are too small to be adequately recorded at a sufficient number of seismic stations to be reliably located. One method of determining the magnitude of completeness is based on the Gutenberg-Richter relationship [*Gutenberg and Richter*, 1941, 1954]

$$\log N(m) = a - b\,m \qquad (1)$$

where $N(m)$ is the number of earthquakes with magnitude m and a and b are empirically derived constants. The magnitude of completeness is defined as the magnitude where the magnitude-frequency data begin to deviate from a linear relationship (see *Evernden* [1969], *Kelly and Lacoss* [1969], *Ringdal* [1975] *von Seggern and Blandford* [1976] or *Taylor et al.* [1990] for a summary). The observed magnitude-frequency distribution from the SGBSN are shown in Figure 1 and indicate that the magnitude of completeness is approximately 1.6. This means that if common practice were followed, approximately 2/3's of the catalog would have to be ignored and thus potentially some of the interesting signal.

Instead of ignoring data, a spatially varying threshold model is developed so that sub-regions having lower completeness levels than the network as a whole can be outlined and the completeness level of each sub-region determined. In this study the primary motivation for developing such a model is to be able to unambiguously identify regions that are aseismic due to natural processes rather than to limited detection and/or location capabilities. This is required for the identification of seismicity patterns within the SGBSN. The analysis of these patterns is described in a companion paper, [*Gomberg*, this issue] that is herein referred to as Paper II.

Calculation of the threshold model described in this paper is simple to implement and the validity of the results are easily verified. The derivation of threshold model does not require the statistical assumption that earthquakes are uniformly distributed spatially which is clearly inappropriate for the SGBSN (Figure 2) and for many other regions [*Reasenberg*, 1985]. The model is based on the assumption that the spatial change in detection threshold is related to amplitude decay due to attenuation and spreading since amplitudes below some signal-to-noise limit will not be detectable. The requirements for reliable earthquake location can also be accounted for since these also determine whether an event is included in a network seismicity catalog. Two independent methods of testing the validity of derived threshold models are also described. One method does assume a spatially uniform distribution of seismicity but it will be demonstrated that this is not necessarily problematic.

Most threshold studies have been done for the purpose of improving earthquake/explosion discrimination potential [e.g., *Ringdal*, 1986; *Evernden et al.*, 1986; *Sereno and Bratt*, 1989] although many of these are not published in easily accessed documents (D. Taylor, personal communication, 1991). While the number of publications describing local seismicity is great, few exist pertaining to local earthquake network detection/location capabilities. A literature search yields one report by the Nuclear Regulatory Commission [*Mauk and Christensen*, 1980] describing a complex method for determining a spatially variable

Paper number 91JB01593.

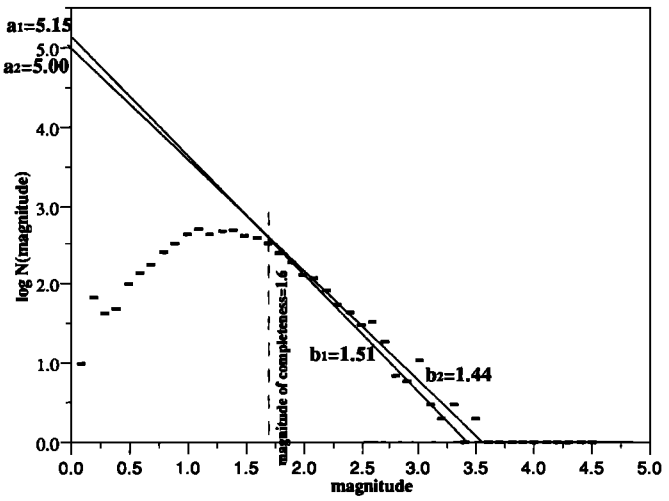

Fig. 1. (*a*) Magnitude-frequency data (solid rectangles) from the Southern Great Basin Seismic Network catalog for the years 1983 to 1989. The magnitude of completeness and *y*-intercepts (*a* 's) are estimated visually. The slopes are one standard deviation bounds on the maximum likelihood estimates of *b*. (*b*) Same as Figure 1*a* except that the slopes (*b* values) are estimated visually.

detection/location model and a paper by *Rydelek and Sacks* [1989] describing a method for determining a single threshold magnitude for the entire network. Application of methods developed for discrimination studies to local earthquake networks are not straightforward since they are based largely on use of regional or teleseismic data. Furthermore such models can only be validated by comparing them with other models [*Sereno and Bratt*, 1989] since actual data is generally not available (e.g., only recently have data become available from the USSR which is the principal focus of discrimination studies). This model development and verification approach ignores temporal and spatial variations in individual station noise and/or response characteristics and uses a single attenuation model for the entire region. Although the approach described in this paper is not as quantitatively rigorous as some of these others, it is adequate for the analysis described in Paper II. Furthermore, the approach has the advantage over others that the models developed are tested for consistency with real data.

Accounting for spatial variations in detection/location threshold may also be important for studies in which magnitude-frequency distributions are interpreted in terms of source properties [*Taylor et al.*, 1987, 1990; *Rydelek and Sacks*, 1989;*Trifu and Radulian*, 1991]. For example, several recent studies use a magnitude of completeness that is defined by *Rydelek and Sacks* [1989] as the lowest magnitude which is not preferentially reported during the night when the signal-to-noise ratio is greater. Observations that the *Rydelek and Sacks*' [1989] magnitude of completeness does not coincide with the magnitude at which a Gutenberg-Richter relationship no longer holds may be interpreted as evidence for non-self similar behavior of earthquake sources [*Taylor et al.*, 1987, 1990; *Rydelek and Sacks*, 1989]. When certain conditions are met (see Appendix A), spatial variations in threshold can introduce features in the magnitude-frequency distributions that might be interpreted to be consequences of physical processes. (Note that this is only a caution for future studies and does not imply that the aforementioned studies are incorrect.) Therefore, in order for such interpretations to be useful, the spatial variability in threshold must either be accounted for or shown to be unimportant.

DERIVATION OF A DETECTION/LOCATION THRESHOLD MODEL

The threshold model is based on the formula for local magnitude [*Richter*, 1958]

$$m = \log A(r_j)_{obs} + \log A(r_j) \tag{2}$$

where $A(r_j)_{obs}$ is the amplitude (corrected for instrument response) observed at the jth station located at a distance r_j from the source. $A(r_j)$ is a distance correction that accounts for amplitude decay. (Note that the sign convention of the correction term has been changed from the original definition for convenience.) The minimum magnitude earthquake that can be detected, $m=T_{min}$, is that event which produces the minimum amplitude that can be reliably recorded at the closest source-receiver distance r_{min}. This minimum amplitude is derived from a rearrangement of equation (2) yielding

$$\log A(r_{min})_{obs} = T_{min} - \log A(r_{min}) \tag{3}$$

To be detected an event must have a magnitude, m, that is sufficiently large that the associated amplitudes are at least equal to this minimum. This means that

$$\log A(r_j)_{obs} \geq \log A(r_{min})_{obs} \tag{4a}$$

Substituting from equation (3) results in the expression

$$\log A(r_j)_{obs} \geq T_{min} - \log A(r_{min}) \tag{4b}$$

and substituting from equation (2) and rearranging yields

$$m \geq T_{min} - \log A(r_{min}) + \log A(r_j) \tag{4c}$$

Finally the detection criterion is obtained assuming

$$\log A(r_{min}) = 0 \tag{5}$$

which physically is reasonable since it implies that at some distance attenuation and spreading are negligible. Equation (4c) becomes

$$m \geq T_{min} + \log A(r_j) \tag{6}$$

The potential for an event to be detected and located by the network is evaluated using equation (6) and substituting $A(r_j)$ with

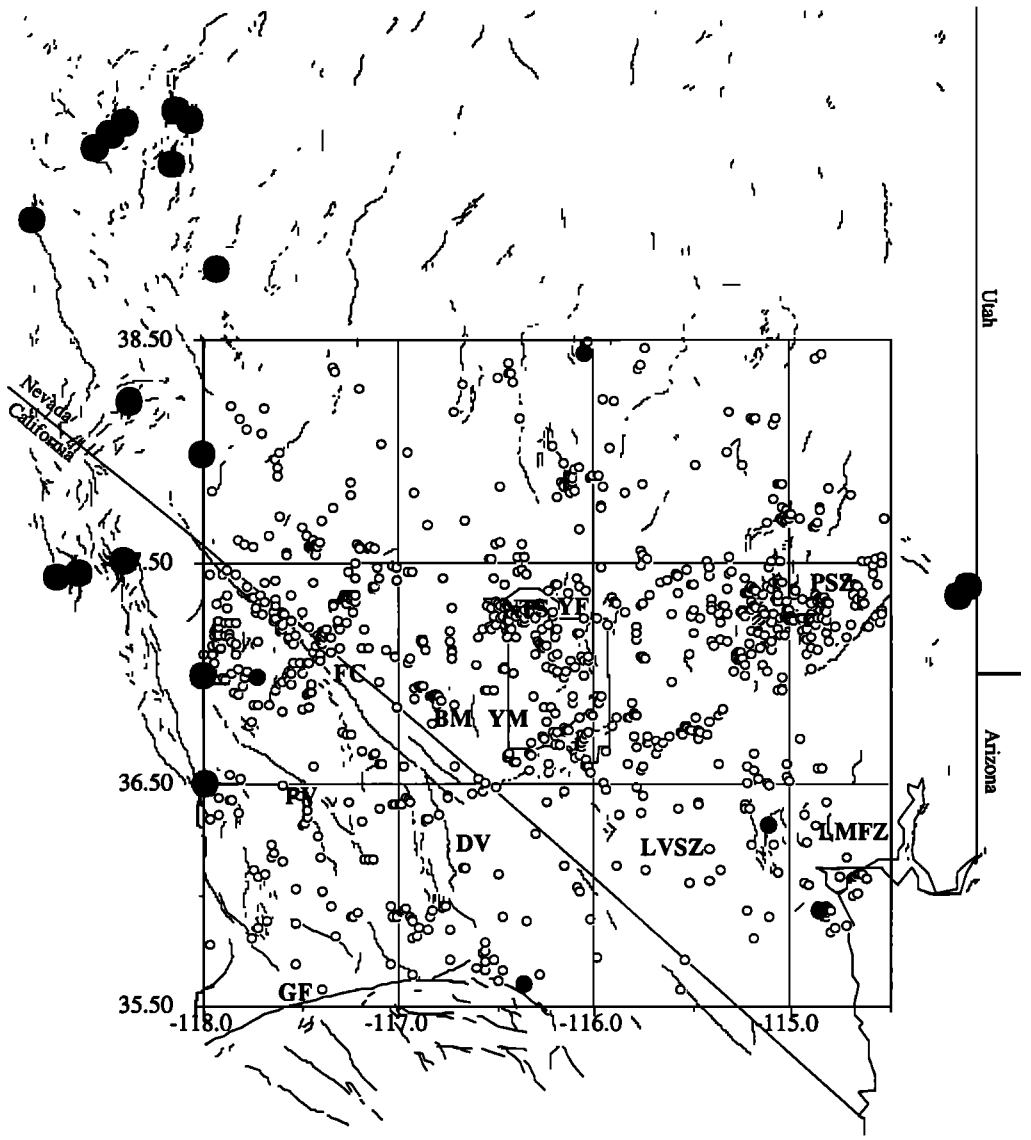

Fig. 2. Map of the area covered by the Southern Great Basin Seismic Network. Curved line segments are Quaternary fault scarps and lineaments inferred from geologic information [*Nakata et al.*, 1982]. Large solid circles are historic earthquake epicenters with magnitudes greater than approximately 6.0 [*Gawthrop and Carr*, 1988]. Epicenters of events recorded on the SGBSN between 1983 and 1989 are shown by the smaller solid circles for events recorded with local magnitude greater than 3.4 (the largest is 4.3), and open ovals are for events with magnitude greater than or equal to 1.6. Abbreviations are FC, Furnace Creek Fault; DV, Death Valley Fault Zone; LVSZ, Las Vegas Shear Zone; PSZ, Pahranagat Shear Zone; PV, Panamint Valley Fault Zone; GF, Garlock Fault; LMFZ, Lake Mead Fault Zone; YF, Yucca Fault; BM, Bear Mountain Fault; NTS, Nevada Test Site ; and YM, Yucca Mountain.

a weighted average amplitude, $\overline{A}$. The average is taken from the amplitudes calculated at all the stations in the network and a weighting can be used to account for criteria required to make an event locatable as well as detectable. Thus, an event located at the ith spatial point has to satisfy the equation

$$m_i \geq T_{\min} + \log \overline{A}_i \tag{7}$$

and the threshold magnitude (the minimum detectable/locatable magnitude), T_i, at this point is that which makes equation (7) an equality or

$$T_i = T_{min} + \log \overline{A}_i \tag{8}$$

The average amplitude at the ith point is calculated according to

$$\overline{A}_i = \left(\sum_{j=1}^{J} w_{ij}\right)^{-1} \sum_{j=1}^{J} w_{ij} A(r_{ij}) \tag{9}$$

where J is the number of stations in the network, $A(r_{ij})$ is the amplitude that would be observed at the jth station located at a distance r_{ij} from the ith point and w_{ij} is a weight. The weights can be designed so that phase arrivals from stations that provide greater constraint on the location have greater influence in the threshold estimate. For example, for one of the threshold models of the SGBSN discussed below, weights of the form

$$w_{ij} = 1/(0.01 r_{ij} + 0.88) \tag{10}$$

are used since this has the effect of giving greater weight to arrivals

from stations within 12 km of an event. This weighting is sensible because arrivals at stations closer than approximately 1.5 times the focal depth provide greater constraint on hypocenter estimates [*Gomberg et al.*, 1990] and most of the events within the SGBSN are probably shallower than 8 km depth [*Rogers et al.*, 1987a].

Finally, a spatially varying map of a threshold model is derived by calculating T_i (equation (8)) for points on a finely spaced grid covering the region of interest. This grid can be displayed in a shaded format or contoured. The first term in equation (8), $T_{\min}$, may be set equal to the smallest magnitude found in the network catalog. The second term, the average amplitude, can be calculated from empirically derived decay functions.

VALIDATION OF A DETECTION/LOCATION THRESHOLD MODEL

Two approaches to testing the validity of a threshold model are presented. The first test requires that the spatial distribution of earthquakes in different magnitude bins do not violate the predictions of the threshold model. For example, if the threshold model predicts a threshold contour for T=2.0, then no earthquakes with $m \leq 2.0$ should be observed outside this contour. Earthquakes with $m \leq 2.0$ should also be distributed within this contour with some events located at the edges of the bounded area. The validity of the entire contoured area cannot be checked since seismicity is often not spatially uniformly distributed [*Reasenberg*, 1985] resulting in regions inside the bounded area with no earthquakes at all.

The second validation test compares a theoretical magnitude-frequency curve with the observed data. The expected number of earthquakes at each magnitude predicted by the grid of threshold values, using an assumed value of T_{min} and the Gutenberg-Richter relationship (equation (1)) is

$$N(m)_{\text{total}} = \sum_{i=1}^{I} N_i(m) \tag{11}$$

where $N_i(m)$ is the number of earthquakes with magnitude m in the area corresponding to the ith grid point and I is the total number of grid points. $N_i(m)$ is derived according to

$$\begin{aligned} N_i(m) &= \frac{\Delta S_i}{S} 10^{a} 10^{-b m} && m \geq T_i \\ &= 0 && m < T_i \end{aligned} \tag{12}$$

ΔS_i is the area represented by each grid point, S is the total area, and a and b are the empirically determined values in the Gutenberg-Richter relationship.

The values of a and b may be estimated by linear regression, maximum likelihood, or visually. The maximum likelihood estimate of b is

$$b = \frac{1}{\bar{m} - m_o} \qquad \bar{m} = \frac{1}{n} \sum_{k=1}^{n} m_k \tag{13}$$

[*Aki*, 1965] where m_o is the minimum magnitude to be used in the estimate and n is the number of magnitudes. The most conservative statistical estimate of the uncertainty in b accounts for spatial and/or temporal variations in $\bar{m}$ and is calculated according to

$$\sigma(b) = \frac{b^2}{\log_{10} e} \sigma(\bar{m}) \qquad \sigma(\bar{m})^2 = [n(n-1)]^{-1} \sum_{k=1}^{n} (m_k - \bar{m})^2 \tag{14}$$

[*Shi and Bolt*, 1982].

The assumption that seismicity is uniformly distributed in space is implicit in this test which is clearly not true for the SGBSN region (Figure 2). This nonuniformity implies that the values of a and b vary for subregions. If certain conditions are met, the values of a and b estimated from all the data will be nearly identical to those that would be derived from estimating a and b (as in Figure 1) for subregions and averaging them. As long as the average is correctly predicted, it does not matter how the seismicity is distributed spatially and thus, the assumption of uniformly distributed seismicity implicit in equation (12) is justified.

A simple example illustrates this point. Suppose that the entire region of interest is divided in half with each half having a different magnitude-frequency distribution characterized by a_1, b_1, and a_2, b_2. The Gutenberg-Richter relationship for the entire region is

$$\begin{aligned} \log(N/2) &= (a - \log 2) - b m \\ &\approx \bar{a} - \bar{b} m + \log[1 + (\gamma \ln 10)^2] \end{aligned} \tag{15}$$

where

$$\bar{a} = \frac{a_1 + a_2}{2}, \quad \bar{b} = \frac{b_1 + b_2}{2}, \quad \gamma = \Delta a - \Delta b\, m$$

$$\Delta a = \frac{a_1 - a_2}{2}, \quad \Delta b = \frac{b_1 - b_2}{2}$$

provided that

$$\gamma \ln 10 < 1 \tag{16}$$

is satisfied. See Appendix B for the derivation of these equations. The requirement on the size of the parameter γ (a measure of the differences in the values of a and b) limits the size of the right-most term in equation (15) to be less than 0.3, which is smaller than the uncertainty in the value of a estimated from the SGBSN data (Figure 1*b*). Thus, when equation (16) is true, the b value for the entire region is nearly equal to the average b value of the two halves and the a value is nearly equal to the average plus a constant or

$$\log N(m) \approx \bar{a} + \log 2 - \bar{b} m \tag{17}$$

Physically a represents the total production of earthquakes during the time interval examined. The constant, log2, corrects for the fact that $\bar{a}$ corresponds to half the area and thus the total number of events is effectively halved.

To illustrate that this is may be true for real data, the SGBSN is divided into four quadrants of equal area and the average values are compared with the values estimated from the entire dataset (applying equation (15) twice). The b values are estimated using equation (13) and the a values are estimated visually. The results are summarized in Table 1 and show that the average of the b values for each quadrant differs from the b value for the entire dataset by only 0.03 and the average a differs from that for the entire dataset by only 0.10. Also note that the a and b values obtained by averaging values estimated for the northern and southern halves are distinctly different from those values obtained if the network data are divided instead from eastern and western halves. However, the average of either the north/south values or the east/west values are nearly identical. Similarly, the same average value would be obtained if the data were distributed uniformly so that the a and b values are the same for two halves. This further justifies the assumption implicit in equation (12).

TABLE 1. Values of a and b Derived from Magnitude-Frequency Data for Different Parts of the SGBSN

Area of Network	Location	$a - b\,m$
Entire Network	35.5 N to 38.5 N 118.0 W to 114.5 W	5.09 - 1.48 m
Northern Half	37.0 N to 38.5 N 118.0 W to 114.5 W	5.09 - 1.52 m
Southern Half	35.5 N to 37.0 N 118.0 W to 114.5 W	4.50 - 1.40 m
Average (Entire Network)		5.10 - 1.46 m
Eastern Half	35.5 N to 38.5 N 116.25 W to 114.5 W	4.77 - 1.44 m
Western Half	35.5 N to 38.5 N 118.0 W to 116.25 W	4.92 - 1.52 m
Average (Entire Network)		5.15 - 1.48 m
SE Quadrant	35.5 N to 37.0 N 116.25 W to 114.5 W	3.67 - 1.29 m
NE Quadrant	37.0 N to 38.5 N 116.25 W to 114.5 W	4.80 - 1.49 m
SW Quadrant	35.5 N to 37.0 N 118.0 W to 116.25 W	4.40 - 1.46 m
NW Quadrant	37.0 N to 38.5 N 118.0 W to 116.25 W	4.65 - 1.56 m
Average (Western Half)		4.83 - 1.51 m
Average (Eastern Half)		4.54 - 1.39 m
Average (Entire Network)		4.99 - 1.45 m

Averages are calculated according to equations (B4) and (B7).

A reasonable acceptable fit between the predicted and observed magnitude-frequency distributions is one in which the difference is no larger than the difference in theoretical distributions derived for bounding measured values of a and b. Since it is possible that source or propagation processes also (in addition to threshold variations) may cause magnitude-frequency distributions to deviate from a linear relationship [*Hanks and Boore*, 1984; *Taylor et al.*, 1987, 1990; *Rydelek and Sacks*, 1989;*Trifu and Radulian*, 1991; A. Snoke, personal communication, 1991], only a qualitative evaluation of the goodness of fit between the predicted and observed distributions is considered warranted. The extent to which source or propagation effects are important can only be determined with independent data and analyses that are beyond the scope of this study.

DETECTION/LOCATION THRESHOLD MODELS OF THE SOUTHERN GREAT BASIN SEISMIC NETWORK

The 55 stations of the SGBSN have been operating in essentially the same configuration since the beginning of 1983. The distribution of stations is shown in Figure 3 and details about the network are found in *Rogers et al.* [1987a]. For the purposes of this study it is assumed that all stations have identical dynamic ranges (e.g., they are all able to reliably record earthquakes of local magnitude $m=M_L=0.0$ to $M_L=4.3$). Only earthquakes in the geographic box with southwest corner 35.5°N, 118.0°W and northeast corner 38.5°N, 114.5°W are included in the SGBSN catalog. A local magnitude (5511 events) or a duration magnitude (296 events; duration magnitudes are calibrated against the local magnitudes) is assigned to all events used in the study. No attempt is made to account for radiation patterns or depth effects; the former are generally unknown and the station spacing and instrumentation

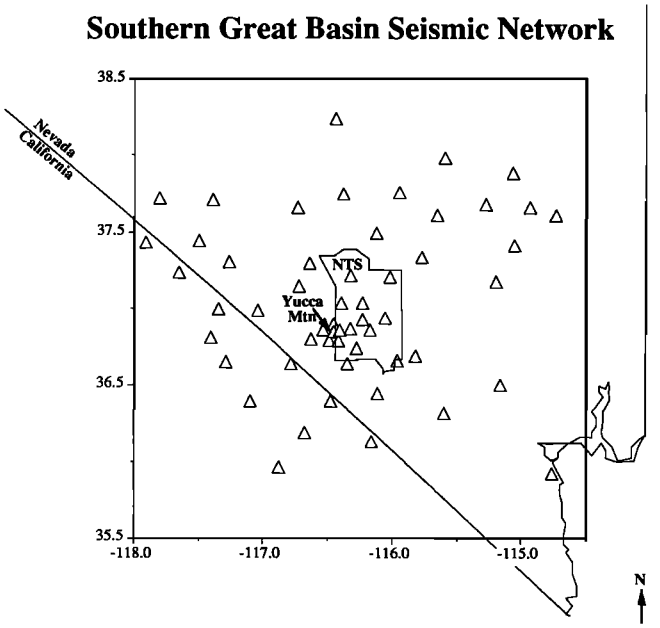

Fig. 3. Station map of SGBSN; station locations are indicated by triangles; the NTS (polygon in the center), location of Yucca Mountain and Nevada state boundary are shown for reference.

of the SGBSN are inadequate to estimate earthquake depths routinely with sufficient confidence to draw meaningful conclusions [*Gomberg*, 1991; *Gomberg et al.*, 1990]. The epicentral uncertainties are probably no more than a few kilometers which are insignificant with respect to this analysis [*Gomberg*, 1991]. It is simply assumed that the catalog magnitudes are sufficiently accurate for the purposes of this study.

In order to apply the second validation test to any models developed it is necessary to estimate the values of a and b in equation (1). Two lines for bounding values, $b \pm \sigma(b)$ calculated using equations (13) and (14) are plotted with the data on Figure 1*a*. These statistical estimates (even if two standard deviations are used) do not fully span the range of b values that one would estimate visually (Figure 1*b*). Furthermore, statistical uncertainties cannot account for deviations from a Gutenberg-Richter relation arising from physical processes as discussed above. Thus, the larger uncertainties (the visual estimates) are deemed more appropriate representations of the true uncertainty in b and are used in the analysis.

The first attempt to develop a threshold model for the SGBSN uses the empirically derived amplitude decay function developed for estimation of magnitudes using SGBSN data [*Rogers, et al.*, 1987b]. The decay function is

$$\begin{aligned} \log A(r) &= 0.833 \log(r) + 0.00164\, r + 0.88 \qquad r > 0.088 \\ &= 0 \qquad\qquad\qquad\qquad\qquad\qquad\quad r \le 0.088 \end{aligned} \tag{18}$$

Although this function as derived by *Rogers et al.* [1987b] is actually only zero at $r=0.088$ km, it is physically unreasonable to allow it to become negative at shorter distances since seismic waves are not amplified as they propagate (unless there are site amplification effects which are not meant to be represented by this function). This also is consistent with the requirements of the threshold model (equation (8)). No weights are used ($w_{ij}=1$ for all J) and $T_{\min}$ is set equal to the smallest magnitude found in the SGBSN catalog, $M_L \approx 0.1$.

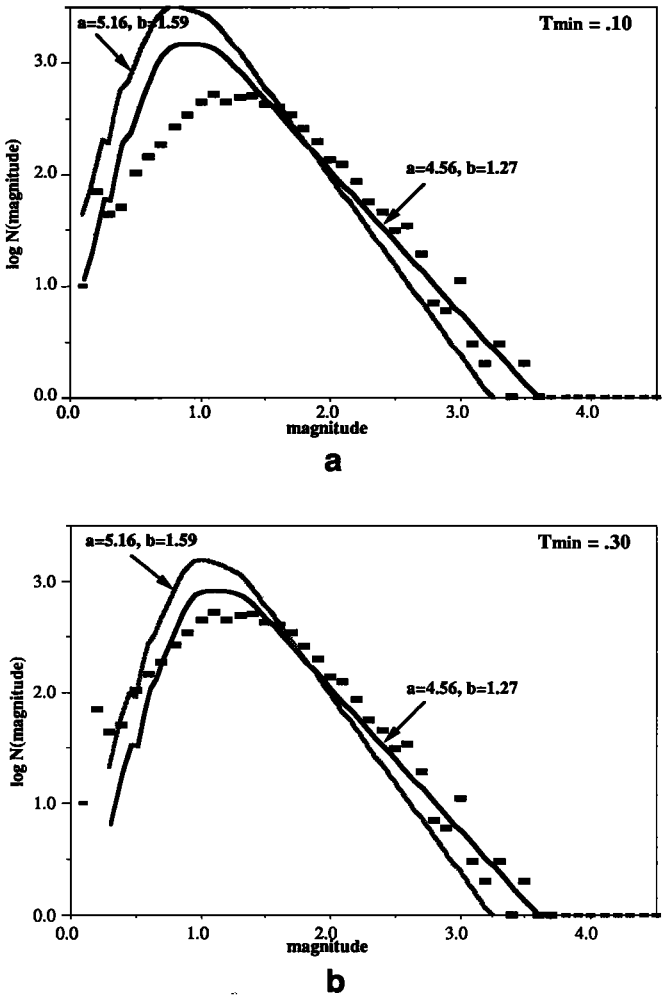

Fig. 4. Theoretical magnitude-frequency curves for the amplitude decay function of *Rogers et al.* [1987b] and minimum thresholds of (*a*) 0.1 and (*b*) 0.3 are shown by the solid lines. Two relations are shown in each plot corresponding to the bounding values of a and b determined from the data (Figure 1). The data are indicated by the solid rectangles.

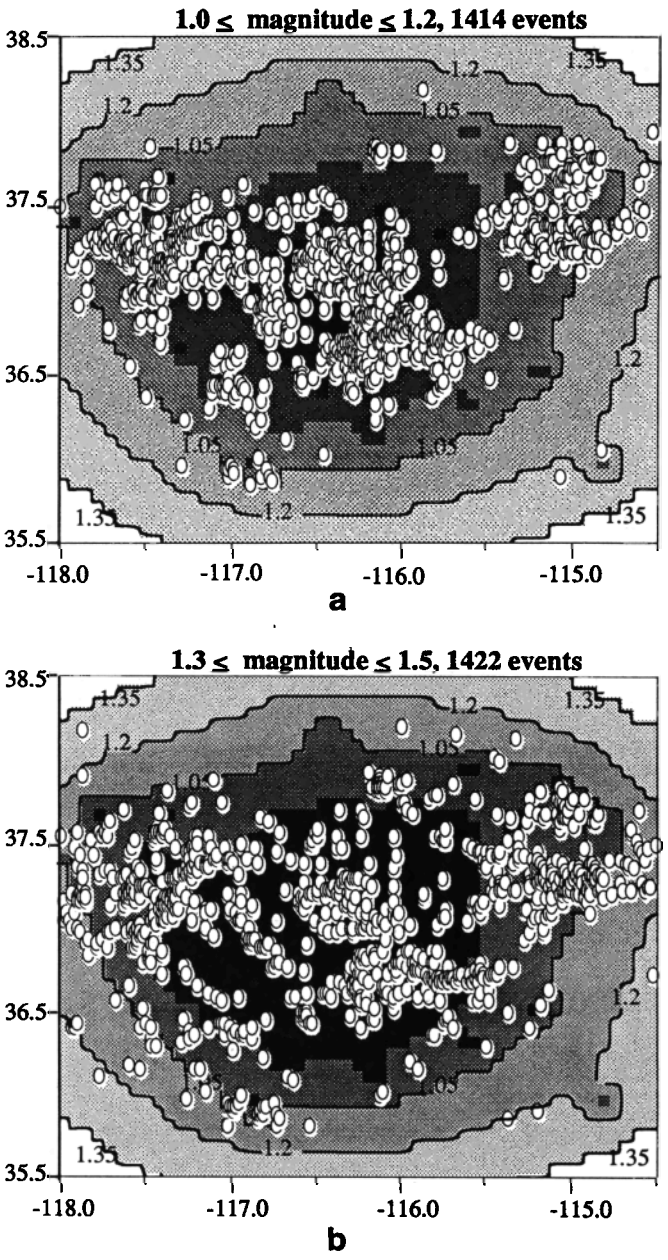

Fig. 5. Epicenter maps for events in the magnitude bins 1.0-1.2, 1.3-1.5, 1.6-1.8 and 1.9-2.1 superimposed on the threshold map calculated for the same parameters used to derive the curves shown in Figure 3*b*. Epicenters are indicated by the white ovals. The shading changes for each increment of 0.15 magnitude units and gets lighter as the threshold magnitude increases. The black areas correspond to the only regions in which events with magnitude less than 0.60 will be recorded.

This threshold model predicts a theoretical magnitude-frequency distribution [equations (11) and (12)] that does a poor job of fitting the observed data (Figure 4*a*); the difference between the predicted curves and the observations is greater than the difference between the two curves which are estimated from the bounding values of a and b. The simplest way to improve the fit is to increase T_{min} to a value of 0.3 (Figure 4*b*). There is little need to try to justify this since the model also fails the second validation test using either value of T_{min}. The spatial variations in the threshold model are shown in a shaded map view in Figure 5 for a value of T_{min}= 0.3 and are compared with the distribution of epicenters of events in increasing magnitude ranges. This threshold model predicts that earthquakes with magnitude greater than $M_L \approx 1.4$ will be detected and located everywhere. However, the observed spatial distribution as it varies with magnitude spreads out much more slowly and events are not observed at the perimeters of the network until they have magnitudes of approximately 1.6 and above.

The second validation test results suggest that the threshold increases more rapidly with distance from the center of the SGBSN than predicted by the first modeling attempt. Two alternatives are investigated although they are by no means the only possibilities. In the first case the SGBSN decay function (equation (18)) is still used but the calculated amplitudes are weighted according to equation (10). In the second case a decay function, $A(r)$, that decays more rapidly with distance is used (no weighting). In order to explore the effect of increasing the amplitude decay on the threshold model the amplitude decay function developed by *Bakun and Joyner* [1984] for central California is used. It is

$$\log A(r) = \log(r) + 0.00301\, r + 0.70 \quad r \geq 0.199 \text{ km}$$
$$= 0 \quad r < 0.199 \text{ km} \qquad (19)$$

(modified so that it does not become negative). An empirically constrained function is chosen rather than a purely hypothetical one

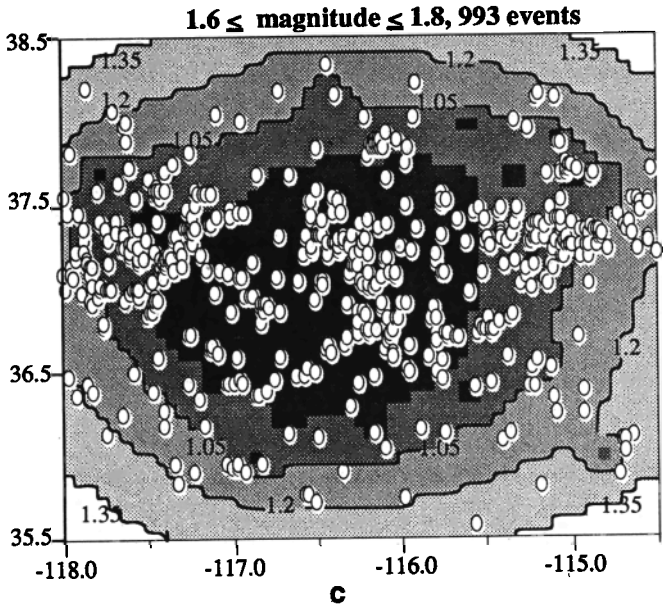

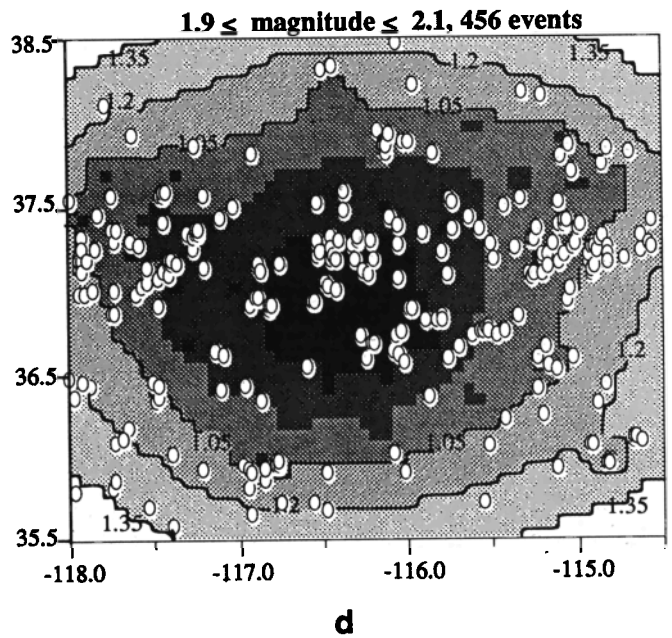

Fig. 5. (continued)

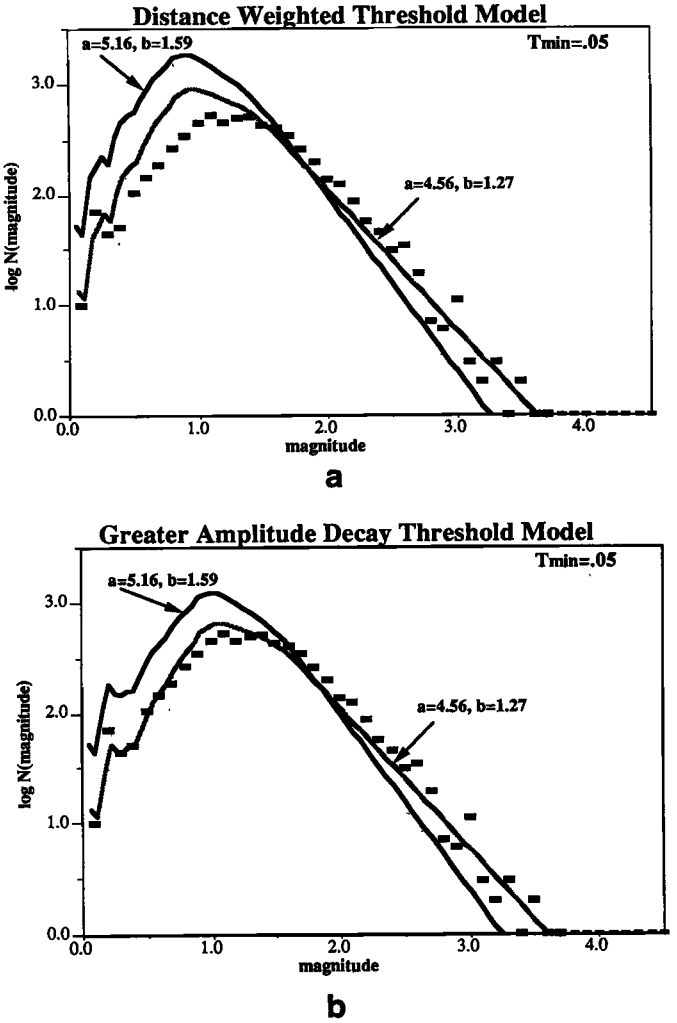

Fig. 6. Theoretical magnitude-frequency relations for two threshold models (see text and Figure 7) and T_{min}=0.05. Two relations are shown in each plot corresponding to the bounding values of a and b determined from the data. The data are indicated by the rectangles.

to ensure that it is realistic. A value of T_{min} = 0.05 is used for both cases.

The validity of these two models is tested by comparing the associated theoretical magnitude-frequency distribution with the observations (Figure 6). The difference in fits to the data is not considered sufficient to distinguish one threshold model as better than the other. Maps of these two threshold models (Figure 7) show that the first is essentially just a smoother version of the second. The smoother model is deemed most appropriate for subsequent interpretations because the data cannot resolve the variability of the second model and because the first explicitly accounts for earthquake location criteria (by using distance dependent weights).

The validity of this smoother threshold model is further verified by comparing it with the spatial distribution of earthquakes in different magnitude bins. Figure 8 shows a series of maps in which the threshold map is plotted with the epicenters in non-overlapping magnitude bins. These plots demonstrate that on average, the threshold map accurately predicts the observed distribution of epicenters. For example, earthquakes in the magnitude range 0.7 to 0.9 shown in Figure 8*c* extend to the limits of the region inside the 0.9 threshold contour and almost none are found outside. The same correspondence between the predicted and observed distributions is seen for all magnitude bins.

AVERAGE FEATURES OF THE SEISMICITY OF THE SOUTHERN GREAT BASIN

It is now possible to observe, with some rigor, several features of the spatial distribution of seismicity and to associate these with tectonic features. The threshold model serves as a series of magnitude dependent masks that can be placed over seismicity, tectonic, and/or geologic maps; this enables attention to be focused only on the regions where bias due to detection/location capabilities should be minimized. The seismicity in various magnitude bins, Quaternary faults identified by *Nakata et al.* [1982], and the appropriate threshold masks are shown in Figure 9. The most striking (visually) features of the seismicity are now described. In the remainder of this paper and in Paper II, the seismicity is

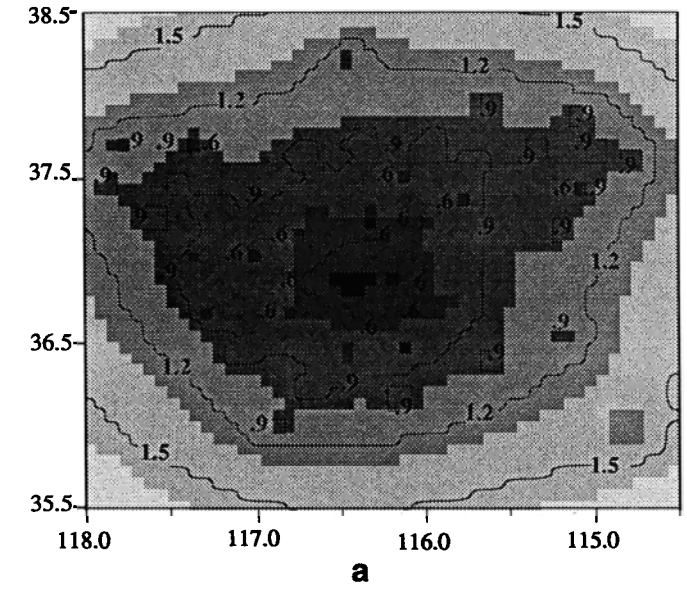

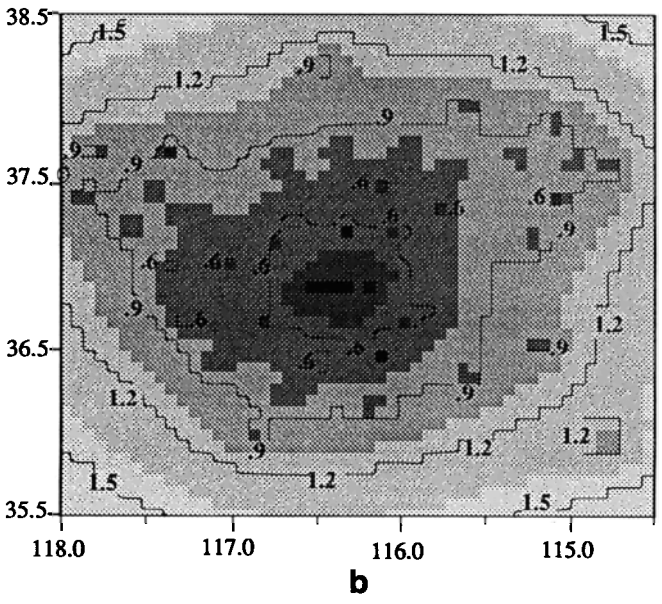

Fig. 7. (a) Shaded threshold map calculated assuming the amplitude decay function derived for the southern Great Basin [*Rogers et al.*, 1987b] with distance weights (see text). The black areas corresponds to the only regions in which events with magnitude less than 0.30 will be recorded. Each shading change indicates an increase of 0.3 magnitude units in the threshold. The contours correspond to the threshold map of Figure 7*b*. (*b*) Threshold map calculated assuming the amplitude decay relationship derived for central California [*Bakun and Joyner*, 1984]. The contours correspond to the threshold map of Figure 7*a*. The shading scale is the same as in Figure 7*a*.

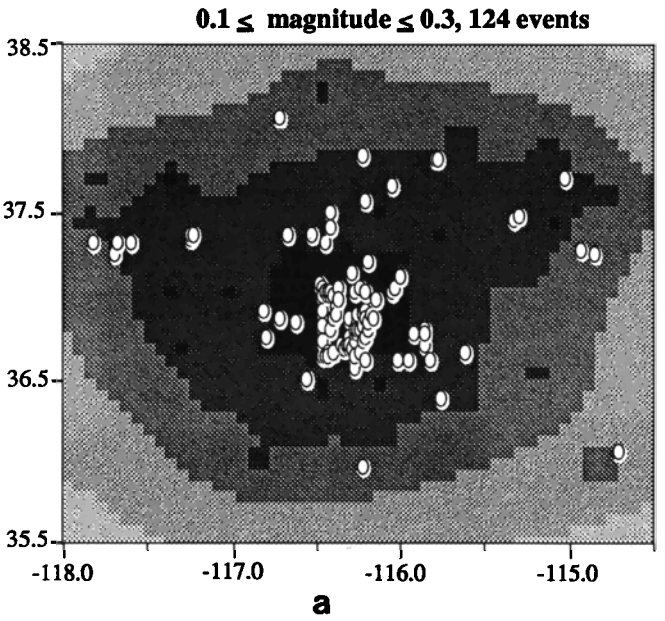

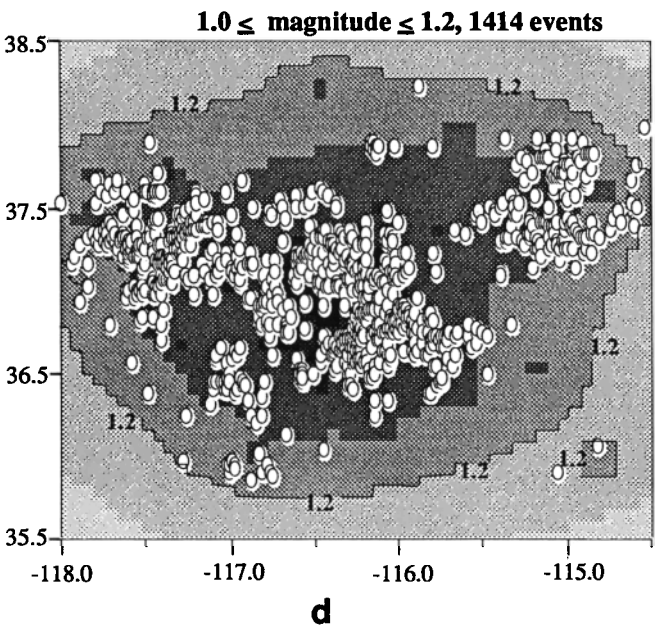

Fig. 8. (*a*) Epicenters (open ovals) from the SGBSN catalog for the period 1983 through 1989 in the magnitude bin 0.1-0.3 superimposed on the threshold map of Figure 7*a*. (*b*) As in Figure 8*a* but for the magnitude bin 0.4 to 0.6. (*c*) As in Figure 8*a* but for the magnitude bin 0.7 to 0.9. (*d*) As in Figure 8*a* but for the magnitude bin 1.0 to 1.2. (e) As in Figure 8*a* but for the magnitude bin 1.3 to 1.5. (*f*) As in Figure 8*a* but for magnitudes greater than or equal to 1.6.

discussed in terms of numbers of earthquakes. However, the patterns described are apparent for all magnitude bins implying that nearly the same patterns exist for the distribution of seismic moment or energy release as for numbers of earthquakes.

The most active areas (the greatest number of events at all magnitudes) are at the northern end of the Furnace Creek fault, in the Pahranagat Shear Zone, and around the northern and southeastern portions of the Nevada Test Site (NTS). Hypotheses relating these first two active zones to the strain field are discussed in Paper II. Understanding the nature of the activity in the NTS is more difficult due the potential for seismicity induced by nuclear testing [*McKeown and Dickey*, 1969; *US Atomic Energy Commission*, 1971; *Hamilton et al.*, 1972; *McKeown*, 1975]. Simple tests designed to elucidate temporal/spatial relationships between nuclear explosions and increased numbers of earthquakes yield ambiguous results. In the first test performed, all events within the NTS region (Figure 10*a*) that occur within 10 days following a nuclear explosion are removed from the catalog. If the process of inducing seismicity occurs on a scale of less than 10 days, then events should be preferentially removed in the area surrounding the northern NTS where all the nuclear explosions in the same time period occur (Figure 10*b*). The data from this

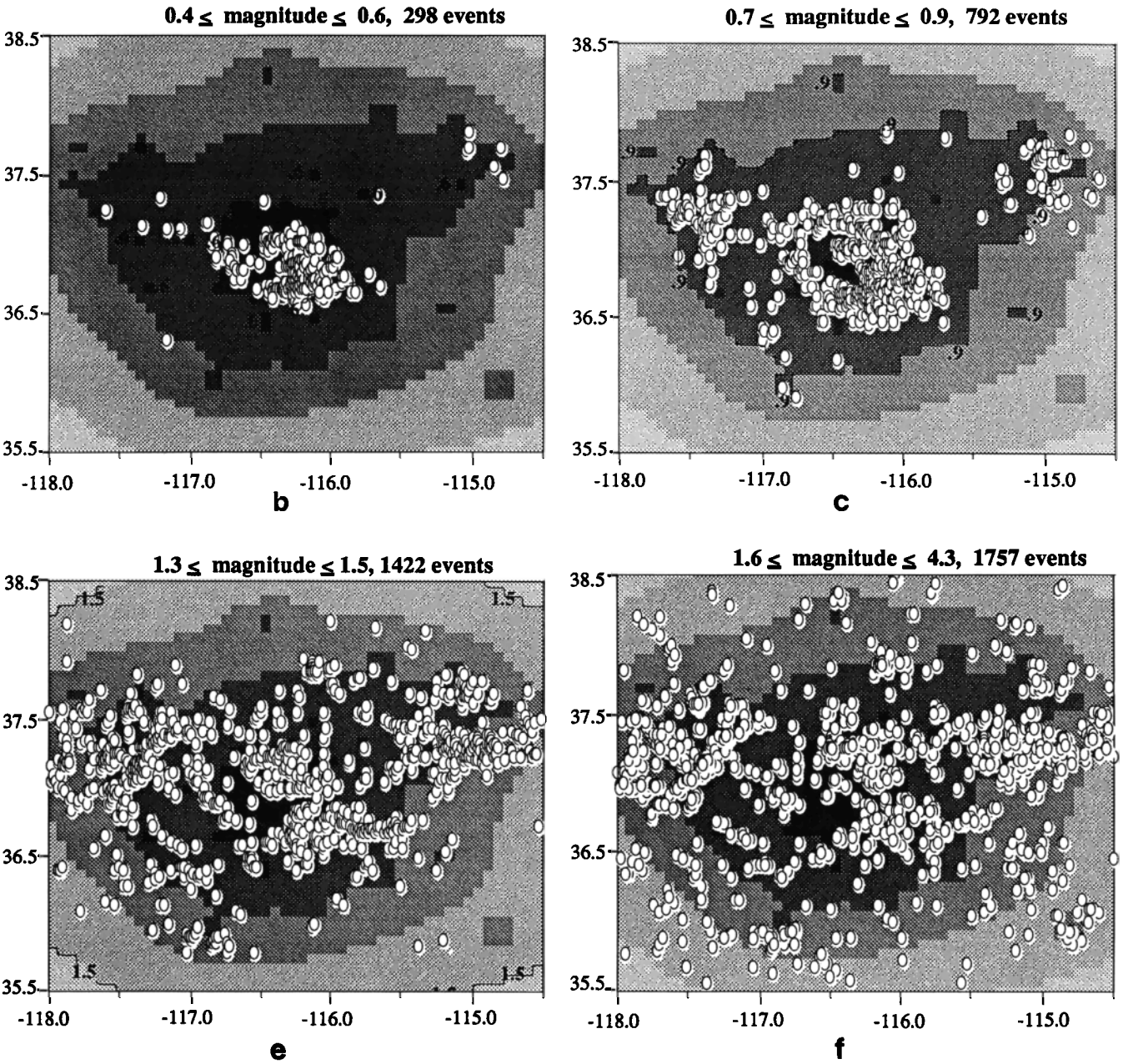

Fig. 8. (continued)

filtered catalog are shown in Figure 10*c* and the effects of increasing the period of inducement to 30 days are shown in Figure 10*d*. Visual examination of these filtered data do not indicate any obvious reduction of events in the vicinity of the nuclear explosions relative to the rest of the area. Another simple test compares seismicity prior to 1964 when most nuclear explosions occurred above ground and after 1963 when all explosions occurred below ground [*Griggs and Press*, 1961; *Springer and Kinnamann*, 1971]. While this comparison (Figure 11) strongly suggests that increased seismicity was induced in the NTS by nuclear explosions, extrapolating from these results to more recent times may not be valid. Many of the explosions during the time period around 1963 were several orders of magnitude larger than any since 1983. This and differences between the two time periods in station coverage and in magnitude scales used (note that there are many events with magnitude greater than 4.0 in the dataset shown in Figure 11 and only three in the SGBSN catalog between 1983 and 1989) make a meaningful extrapolation from the earlier period to the later one dubious.

Of relevance to the issue of site characterization of Yucca Mountain is the almost complete lack of seismicity at Yucca Mountain (Figures 2 and 9). The implications of this 'hole' in the relatively high seismicity levels of the NTS region and slightly lower levels just west of the Bear Mountain fault west of Yucca Mountain are of obvious importance in assessing the seismic hazard at Yucca Mountain. Is there a seismic gap ready to be filled by a large event, is it simply a region where shear strain does not accumulate and thus has a negligible potential for a large earthquake, or is this a temporary quiescence that will fill in if data are gathered for a longer duration?

Other more general features that are focussed on in the analysis described in Paper II are the relatively low levels of seismicity to the

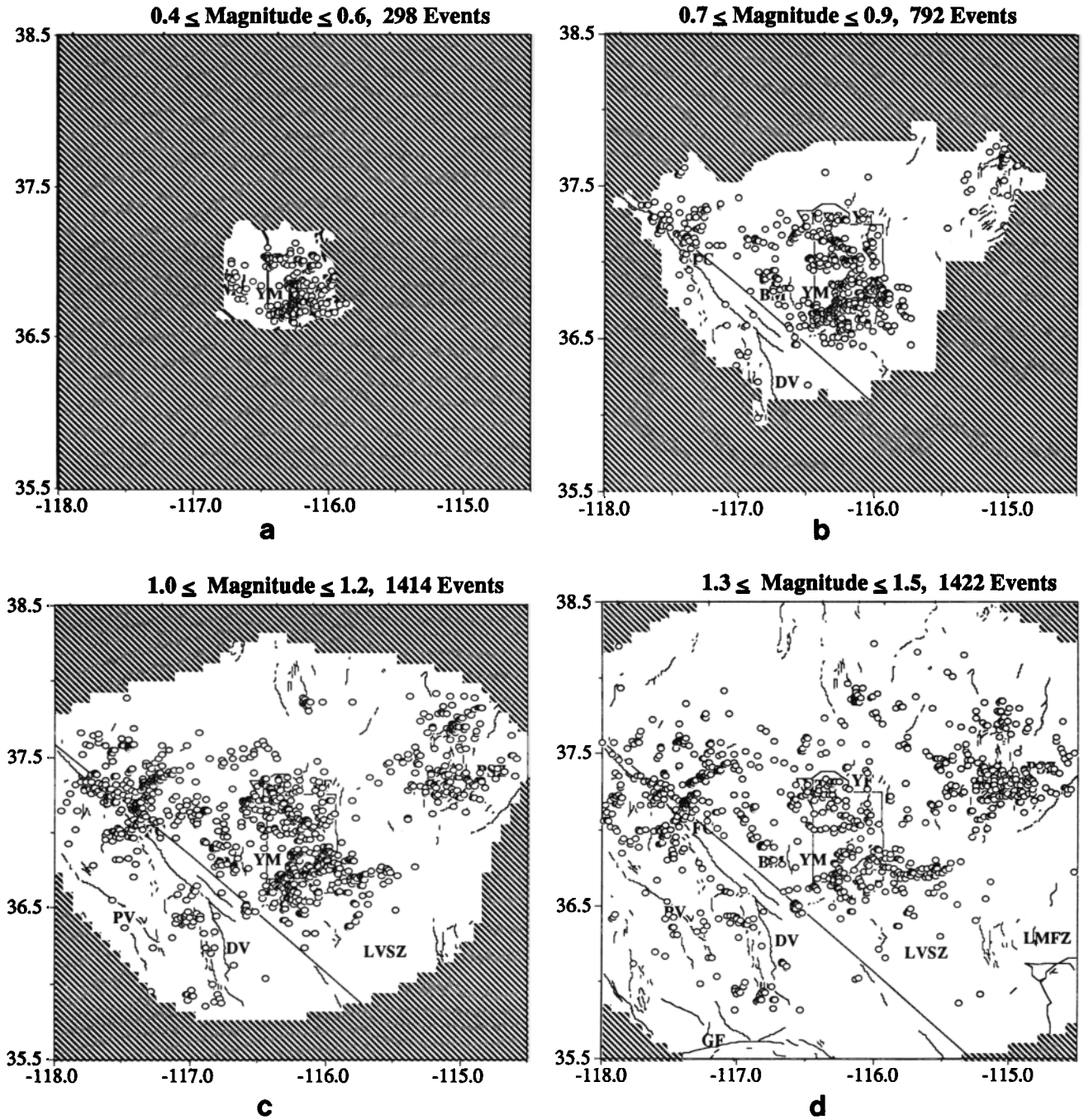

Fig. 9. (*a.*) Epicenters (open ovals) from the Southern Great Basin Seismic Network catalog for the period 1983 through 1989 in magnitude bin 0.4-0.6 superimposed on the same map shown in Figure 2. The shaded areas are those areas in which the detection threshold is higher than the largest magnitude in the bin as predicted by the threshold map shown in Figure 7*a*. Abbreviations are FC - Furnace Creek Fault; DV, Death Valley Fault Zone; LVSZ, Las Vegas Shear Zone; PSZ, Pahranagat Shear Zone; PV, Panamint Valley Fault Zone; GF, Garlock Fault; LMFZ, Lake Mead Fault Zone; YF, Yucca Fault; BM, Bear Mountain Fault; NTS, Nevada Test Site; and YM, Yucca Mountain. (*b*) As in Figure 9*a* but for the magnitude bin 0.7 to 0.9. (*c*) As in Figure 9*a* but for the magnitude bin 1.0 to 1.2. (*d*) As in Figure 9*a* but for the magnitude bin 1.3 to 1.5. Magnitudes greater than or equal to 1.6 (the magnitude of completeness) are shown in Figure 2.

west of the Death Valley/Furnace Creek fault system, and the significant number of events that cannot readily be correlated with mapped faults. The fresh fault scarp morphology of Death Valley and presence of hot springs are certainly suggestive of the existence of recent energetic tectonics [*Zhang et al.*, 1990] relative to the age of deformation suggested by the more subdued morphology of the rest of the study region. Recent deformation is also inferred from the results of detailed geologic studies done in the Panamint Valley [*Burchfiel et al.*, 1987; *Zhang et al.*, 1990]. *Wernicke et al.* [1988] estimate that tens of kilometers of displacement have occurred on the Death Valley fault system within the past four million years. Geologic data from regions to the east of Death Valley indicate that the rate and magnitude of deformation peaked much earlier; tectonic activity peaked more that 11 million years ago in the Las Vegas Shear Zone [*Wernicke et al.*, 1988], and about five million years ago in the Lake Mead Fault Zone [*Anderson*, 1973]. Thus, it is

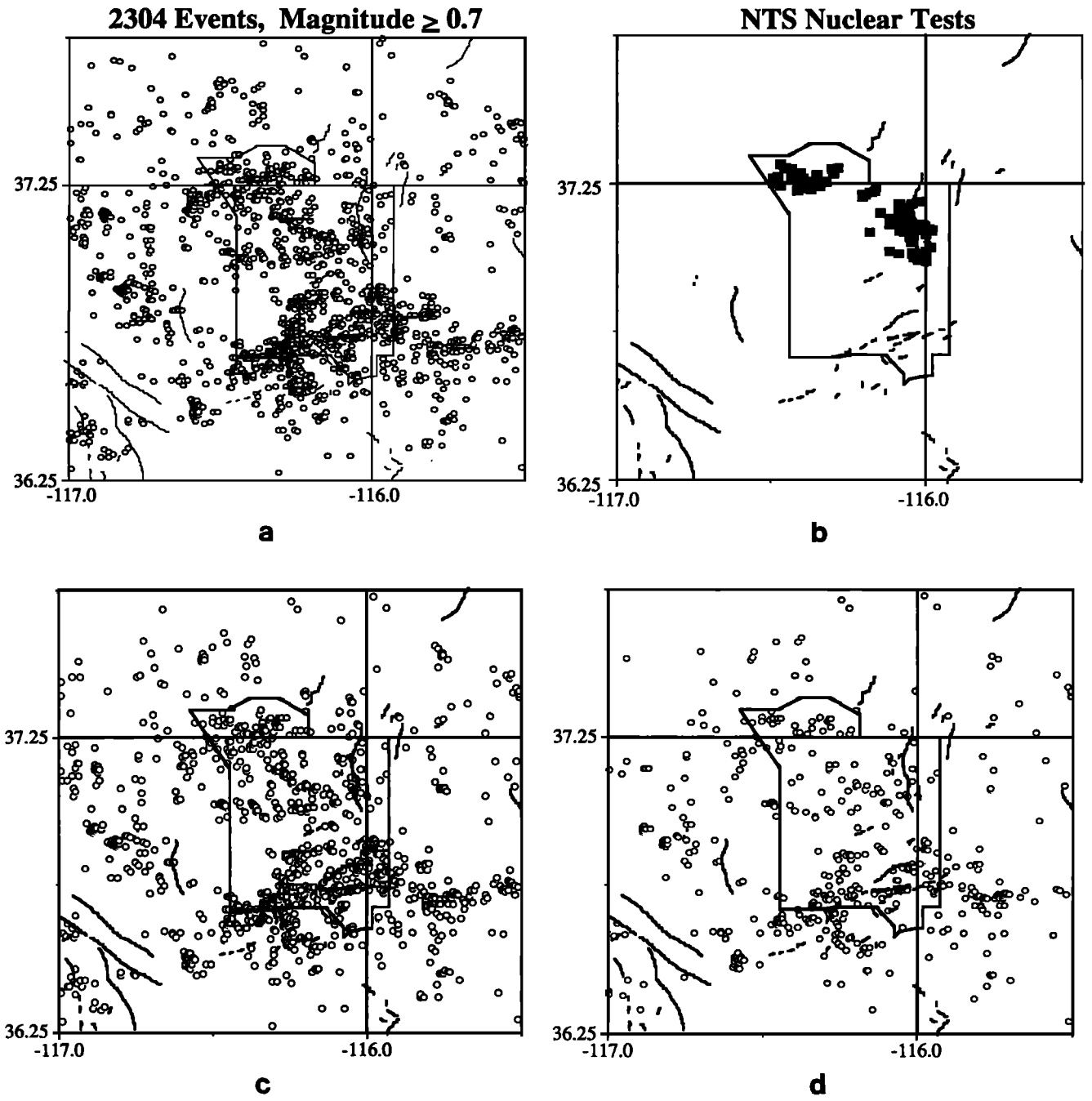

Fig. 10. (*a*) Earthquakes (open ovals) in the NTS region from the SGBSN catalog from 1983-1989 with $M_L \geq 0.7$ (catalog is complete over this area at this magnitude). Faults are from *Nakata et al.* [1982] and the outline of the NTS is shown for reference. (*b*) The same region as Figure 9*a* but with the locations of the nuclear tests done between 1983 and 1989 shown as solid rectangles. (*c*) All events shown in Figure 9*a* that occurred within 10 days of a nuclear test have been removed in this figure. Preferential removal of events in the region where the nuclear tests were done is not apparent. (*d*) As in Figure 9*c* except that all events with 30 days of a nuclear test have been removed. There is still no obvious preferential removal of events in the testing region.

somewhat surprising that although the most recent and greatest deformation in the southern Great Basin is occurring to the west of the Death Valley/Furnace Creek fault system, it has fewer small earthquakes.

CONCLUSIONS

A spatially varying model of the detection/location capabilities of the Southern Great Basin seismic network has been derived that is based on simple empirical relations and statistics. This permits use of almost all the catalog data gathered, rather than ignoring the two-thirds of the data that are below the threshold of completeness. The characteristics of the spatial distribution of earthquakes, where earthquake clusters and aseismic regions locate, appear to be stable at all magnitude levels so that inferences about where strain is being accommodated will be the same whether numbers of earthquakes or strain estimated from seismic moments are examined. These principal characteristics include clusters at the northern end of the Furnace Creek fault and in the Pahranagat Shear Zone, and a relatively large number of earthquakes in the northern and southeastern portions of the NTS. These clusters cover regions much

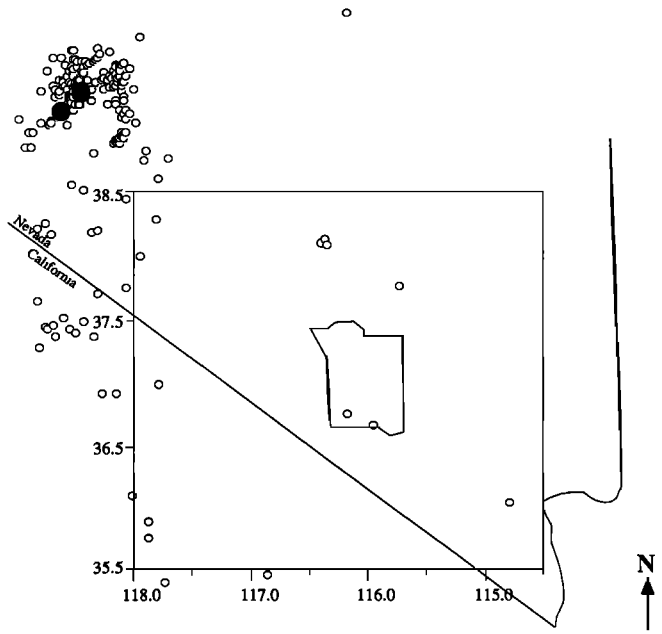

1954-1963 Epicenters, Magnitude ≥ 4.0

Fig. 11*a*. Epicenters (open circles) from the catalog of *Gawthrop and Carr* [1988] during the 10 years prior to the international agreement that all nuclear tests be done below ground. The cluster of events in the northwest are aftershocks of the 1954 Rainbow Mountain and Fairview Peak/Dixie Valley earthquakes (large solid circles). Note the small number of events in the NTS region.

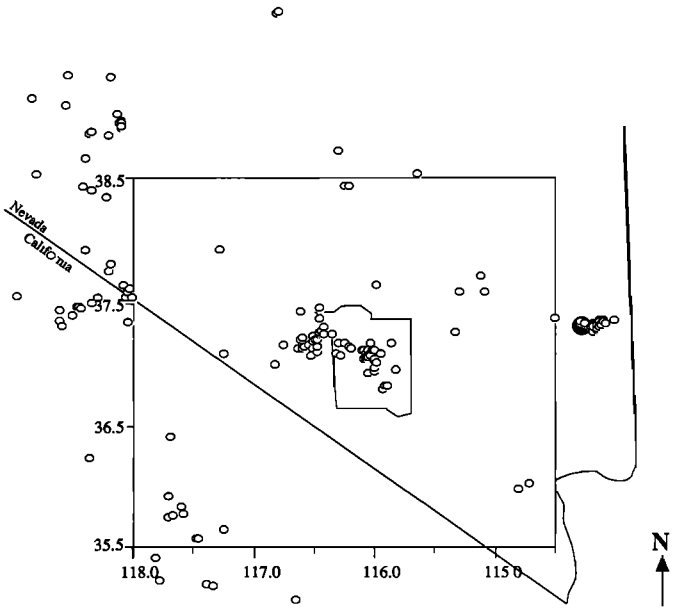

1964-1973 Epicenters, Magnitude ≥ 4.0

Fig. 11*b*. Epicenters (open circles) from the catalog of *Gawthrop and Carr* [1988] during the 10 years following the institution of the agreement that all nuclear tests be done below ground. The cluster of events in the east are aftershocks of the 1966 Clover Mountain earthquake (large solid circles). Note the increased number of events in the NTS region relative to the previous 10 years when testing was done above ground.

larger than the surface projections of any of the mapped faults. The extent to seismicity is induced by nuclear testing is unclear. The predominantly aseismic regions include the area west of the Death Valley/Furnace Creek fault system and an almost complete absence of events at Yucca Mountain. Finally, a considerable number of isolated events in the SGBSN catalog cannot be correlated with mapped faults.

APPENDIX A

A simple example is presented in this Appendix to illustrate why it is necessary to assess the importance of spatial variations in detection/location thresholds before determining a magnitude of completion using the method of *Rydelek and Sacks* [1989]. The method of estimating a magnitude of completion suggested by *Rydelek and Sacks* [1989] assumes that earthquakes are randomly distributed (with aftershocks removed) and that a day-night modulation in seismicity is due to reduced detection capabilities during the day when noise levels are greater. However, spatially variable detection/location thresholds will result in seismicity patterns that are not uniformly distributed and thus, since this violates one of the method's assumptions it may result in biased estimates of the magnitude of completion.

The method of estimating the Rydelek and Sacks' magnitude of completion is first summarized. For a given magnitude level, each event is plotted on a phasor diagram (a 24 hour clock) as a unit vector oriented at an angle determined by the origin time hour. A phasor sum for all events is compared with that expected for a random process and the catalog is deemed incomplete at the particular magnitude level being examined if the phasor sum exceeds some confidence level represented by a critical radius.

For illustrative purposes, suppose the 95% confidence limit is chosen corresponding to a critical radius of $R = 1.73\sqrt{N}$, where N is the total number of events in the catalog. Suppose also that the detection capability for one half of the network is greater than it is for the other half (e.g., there are more stations on one side of the network) and that N_1 events are detected in the former and N_2 in the latter. The phasor sum for the half with poorer detection capabilities could be such that it exceeds the 95% confidence limit ($R_1 > 1.73\sqrt{N_1}$) for the half alone. However, it is possible that the detection capability of the other half is sufficiently great such that it is complete ($R_2 < 1.73\sqrt{N_2}$) and "masks" the fact that catalog is incomplete for events in the other half of the network ($R < 1.73\sqrt{N_1+N_2}$). Thus, the magnitude of completion for the entire network will be underestimated. Similar examples can be designed to illustrate how, due to a spatially variable threshold, the magnitude of completion can also be overestimated.

APPENDIX B

The Gutenberg-Richter relationship [*Gutenberg and Richter*, 1941, 1954] describes the magnitude-frequency distribution

$$\log N(m) = a - b\,m \qquad \text{(B1)}$$

where $N(m)$ is the number of earthquakes with magnitude m and a and b are empirically derived constants. The following analysis shows that this relationship, under certain circumstances, represents an average of magnitude-frequency distributions for a number of subregions which may be characterized by differing values of a and b (Table 1). The fact that such variation is likely to exist is apparent from simple visual examination of regional seismicity patterns (e.g., Figure 2) and from theoretical studies which show that for small earthquakes these values depend on frictional properties of faults which are undoubtedly variable [*Carlson*, 1991].

Rewriting equation (B1) and letting a_1, b_1 and a_2, b_2 be representative of two nonoverlapping regions of the network that encompass all events ($N = N_1 + N_2$), then

$$N = N_1 + N_2 = 10^{a-bm} = 10^{a_1 - b_1 m} + 10^{a_2 - b_2 m} \quad \text{(B2)}$$

This can be simplified by rewriting the right-hand side according to

$$\begin{aligned} 10^{a-bm} &= 10^{\bar{a}-\bar{b}m}[10^{\gamma} + 10^{-\gamma}] \\ &= 10^{\bar{a}-\bar{b}m}[e^{\gamma \ln 10} + e^{-\gamma \ln 10}] \\ &= 10^{\bar{a}-\bar{b}m}[2\cosh(\gamma \ln 10)] \end{aligned} \quad \text{(B3)}$$

where

$$\bar{a} = \frac{a_1 + a_2}{2}, \quad \bar{b} = \frac{b_1 + b_2}{2}, \quad \text{(B4)}$$

$$\gamma = \Delta a - \Delta b\, m,$$

$$\Delta a = \frac{a_1 - a_2}{2}, \quad \Delta b = \frac{b_1 - b_2}{2}$$

If it is true that

$$\gamma \ln 10 < 1 \quad \text{(B5)}$$

then using a Taylor's series expansion equation (B3) can be written as

$$10^{a-bm} \approx 10^{\bar{a}-\bar{b}m} \times 2[1 + (\gamma \ln 10)^2]$$

or taking the logarithm

$$\begin{aligned} \log N(m) &= a - b\, m \\ &\approx (\bar{a} + \log 2) - \bar{b}\, m + \log[1 + (\gamma \ln 10)^2] \\ &\approx (\bar{a} + \log 2) - \bar{b}\, m \end{aligned} \quad \text{(B6)}$$

Because of the requirement described by equation (B5), neglecting the third term in equation (B6) will result in an error of no more than 0.3 in the value of $\log N(m)$. Thus, this demonstrates that a and b are related to the average values of the two subregions according to

$$a \approx (\bar{a} + \log 2) \quad \text{and} \quad b \approx \bar{b} \quad \text{(B7)}$$

The same logic can be applied to demonstrate that a and b represent approximate averages of a and b values for a greater number of smaller subregions.

Acknowledgments. This work was performed in accord with the U.S. Geological Survey/Department of Energy Interagency agreement DE-AIO8-78ET44802. The author would like to thank R. Herrmann, an anonymous reviewer, R. Bilham, J. Dewey, P. Bodin, S. Hartzell, K. Shedlock and G. Shideler, for thoughtful reviews, discussions, criticisms, and suggestions. The author is also grateful to P. Rydelek, D. Taylor, and A. Snoke for engaging in useful discussion. D. Overturf is responsible for maintaining the SGBSN and S. Harmsen for compiling the catalogue used in this study.

REFERENCES

Aki, K., Maximum likelihood estimate of b in the formula $\log N = a - bM$ and its confidence limits, *Bull. Earthquake Res. Inst. Tokyo Univ., 43*, 237-238, 1965.

Anderson, R.E., Large-magnitude late Tertiary strike-slip faulting north of Lake Mead, Nevada, *U.S. Geol. Surv. Prof. Pap., 794*, 18 pp., 1973.

Bakun, W.H. and W.B. Joyner, The ML scale in central California, *Bull. Seismol. Soc. Am., 74*, 1827-1843, 1984.

Burchfiel, B.C., K.V. Hodges, and L.H. Royden, Geology of the Panamint Valley-Saline Valley pull-apart system, California: Palinspastic evidence for low-angle geometry of a Neogene range-bounding fault, *J. Geophys. Res., 92*, 10,422-10,426, 1987.

Carlson, J.M., Time intervals between characteristic earthquakes and correlations with smaller events: An analysis based on a mechanical model of a fault, *J. Geophys. Res., 96*, 4255-4268, 1991.

Evernden, J.F., Precision of epicenters obtained by small numbers of worldwide stations, *Bull. Seismol. Soc. Am., 59*, 1365-1398, 1969.

Evernden, J.F., C.B. Archambeau, and E. Cranswick, An evaluation of seismic decoupling and underground nuclear test monitoring using high frequency seismic data, *Rev. Geophys., 24*, 143-215, 1986.

Gawthrop, W.H., and W.J. Carr, Location refinement of earthquakes in the southwestern Great Basin, 1931-1974, and seismotectonic characteristics of some of the important events, *U.S. Geol. Surv. Open File Rep., 88-560*, 64 pp., 1988.

Gomberg, J., Seismicity and shear strain in the southern Great Basin of Nevada and California, *J. Geophys. Res.*, this issue.

Gomberg, J., Seismic network configuration, earthquake hypocenter estimation: a re-evaluation and a new approach to an old problem, *U.S. Geol. Surv. Bull.*, in press, 1991.

Gomberg, J., K. Shedlock, and S. Roecker, The effect of *S*-wave arrival times on hypocenter determination, *Bull. Seismol. Soc. Am., 80*, 1605-1628, 1990.

Griggs, D.T., and F. Press, Probing the Earth with nuclear explosions, *J. Geophys. Res., 66*, 237-258, 1961.

Gutenberg, B., and C.F. Richter, Seismicity of the Earth, *Geol. Soc. Am. Spec. Pap., 34*, 1-133, 1941.

Gutenberg, B., and C.F. Richter, *Seismicity of the Earth and Associated Phenomena*, 2nd ed., 310 pp., Princeton University Press, Princeton, N. J., 1954.

Hamilton, R.M., B.E. Smith, F.G. Fischer, and P.J. Papanek, Earthquakes caused by underground nuclear explosions on Pahute Mesa, Nevada Test Site, *Bull. Seismol. Soc. Am., 62*, 1319-1341, 1972.

Hanks, T.C., and D.M. Boore, Moment-magnitude relations in theory and practice, *J. Geophys. Res., 89*, 6229-6235, 1984.

Kelly, E.J., and R.T. Lacoss, Estimation of seismicity and network detection capability, *Tech. Note 1969-41*, Lincoln Lab, Mass. Inst. of Tehnol., Cambridge, 1969.

Mauk, F.J., and D.H. Christensen, A probabilistic evaluation of earthquake detection and location capability for Illinois, Indiana, Kentucky, Ohio, and West Virginia, Div. of Reactor Safety Res., Office of Nuclear Reg. Res., USNRC, Rep. NUREG/CR-1648, R6,RA, 207 pp., Washinton, D.C., 1980.

McKeown, F.A., Relation of geological structure to seismicity at Pahute Mesa, Nevada Test Site, *Bull. Seismol. Soc. Am., 65*, 747-764, 1975.

McKeown, F.A., and D.D. Dickey, Fault displacements and motion related to nuclear explosions, *Bull. Seismol. Soc. Am., 59*, 2253-2269, 1969.

Nakata, J.K., C.M. Wentworth, and M.N. Machette, Quaternary fault map of the Basin and Range and Rio Grande Rift Provinces, western United States,scale 1:2.5M, *U.S. Geol. Surv. Open File Rep. 82-579*, 1982.

Reasenberg, P., Second-order moment of central California seismicity, . *Geophys. Res., 90*, 5479-5495, 1985.

Richter, C.F., *Elementary Seismology*, Chap. 22, W.H. Freeman, San Francisco, Calif., and London, 1958.

Ringdal, F., On the estimation of seismic detection thresholds, *Bull. Seismol. Soc. Am., 65*, 1631-1642, 1975.

Ringdal, F., Study of magnitude, seismicity, and earthquake detectability using a global network, *Bull. Seismol. Soc. Am., 76*, 1641-1659, 1986.

Rogers, A.M., S.C. Harmsen, and M.E. Meremonte, Evaluation of the seismicity of the southern Great Basin and its relationship to the tectonic framework of the region, *U.S. Geol. Surv. Open File Rep., 87-408*, 196 pp., 1987a.

Rogers, A.M., S.C. Harmsen, R.B. Hermann, and M.E. Meremonte, A study of ground motion attenuation in the southern Great Basin, Nevada-California, using several techniques for estimates of Q_s, $\log A_o$, and coda Q, *J. Geophys. Res., 92*, 3527-3540, 1987b.

Rydelek, P.A., and I.S. Sacks, Testing the completeness of earthquake catalogues and the hypothesis of self-similarity, *Nature, 337*, 251-253, 1989.

Sereno, T.J., and S.R. Bratt, Seismic detection capability at NORESS and implications for detection threshold of a hypothetical network in the Soviet Union, *J. Geophys. Res.*, *94*, 10397-10414, 1989.

Shi, Y., and B.A. Bolt, The standard error of the magnitude-frequency *b* value, *Bull. Seismol. Soc. Am.*, *72*, 1677-1687, 1982.

Springer, D.L. and R.L. Kinnamann, Seismic source summary for U.S. underground nuclear explosions, 1961-1970, *Bull. Seismol. Soc. Am.*, *61*, 1073-1098, 1971.

Taylor, D.W.A, J.A. Snoke, I.S. Sacks, and T. Takanami, Frequency and energy comparisons between shallow and subduction earthquakes near the Hokkaido corner, Japan: preliminary results, *Seismol. Res. Lett.*, *58*, 105, 1987.

Taylor, D.W.A., J.A. Snoke, I.S. Sacks, and T. Takanami, Nonlinear frequency-magnitude relationships in the Hokkaido Corner, Japan, *Bull. Seismol. Soc. Am.*, *80*, 340-353, 1990.

Trifu, C. and M. Radulian, Frequency-magnitude distribution of earthquakes in Vrancea: relevance for a discrete model, *J. Geophys. Res.*, *96*, 4301-4312, 1991.

U.S. Atomic Energy Commission, Seismology, aftershocks, and related phenomena associated with underground nuclear explosions, in *A Bibliography of Selected Papers with Abstracts*, 36 pp., Nevada Operations Office, Washington, D.C., 1971.

von Seggern, D., and R. Blandford, Seismic threshold determination, *Bull. Seismol. Soc. Am.*, *66*, 753-788, 1976.

Wernicke, B., G.J. Axen, and J.K. Snow, Basin and Range extensional tectonics at the latitude of Las Vegas, Nevada, *Geol. Soc. Am. Bull.*, *100*, 1738-1757, 1988.

Zhang, P., M. Ellis, D.B. Slemmons, and F. Mao, Right lateral displacements and the Holocene slip rate associated with pre-historic earthquakes along the southern Panamint Valley fault zone: Implications for southern Basin and Range tectonics, *J. Geophys. Res.*, *95*, 4857-4872, 1990.

J. Gomberg, U.S. Geological Survey, MS 966, Box 25046, DFC, Denver, CO 80225.

(Received January 24, 1991;
revised May 15, 1991;
accepted May 15, 1991.)

JOURNAL OF GEOPHYSICAL RESEARCH, VOL. 96, NO. B10, PAGES 16,471–16,494, SEPTEMBER 10, 1991

Crustal Structure of the Western New England Appalachians and the Adirondack Mountains

STEPHEN HUGHES AND JAMES H. LUETGERT

U.S. Geological Survey, Menlo Park, California

We present an interpretation of the crustal velocity structure of the New England Appalachians and the Adirondack Mountains based on a seismic refraction/wide-angle reflection experiment in eastern North America extending from the Adirondacks in New York State through the northern Appalachians in Vermont and New Hampshire to central Maine. Modeling of the eastern portion of the profile within the New England Appalachians shows a subhorizontal layered crust with upper crustal velocities ranging from 5.5 to 6.2 km/s, a midcrustal velocity of 6.4 km/s, and a lower crustal velocity of approximately 6.8 km/s. Crustal thickness increases from 36 km beneath Maine to 40 km in Vermont. Little evidence is seen for structures at depth directly related to the White Mountains or the Green Mountains. A major lateral velocity change in the upper and mid crust occurs between the Appalachians and the Adirondacks. This boundary, projecting to the surface beneath the Champlain Valley, dips to the east beneath the Green Mountains and extends to a depth of ~25 km below the eastern edge of the Connecticut Valley Synclinorium in Vermont. The Tahawus Complex, a series of strong horizontal reflections at 18–24 km depth beneath the Adirondack Highlands, is seen to dip eastward beneath Vermont. Upper crustal rocks in the Adirondack Mountains have Poisson's ratios of 0.28 ± 0.01 that can be correlated with the Marcy Anorthosite. Poisson's ratios of 0.24 ± 0.01 calculated for rocks of the Connecticut Valley Synclinorium indicate a siliceous upper crust in Vermont. The lower crust is considered to be best represented by intermediate to mafic granulites; a high Poisson's ratio (0.26–0.27) tends to support a mafic lower crust in the New England Appalachians. This seismic refraction/wide-angle reflection experiment provides further evidence for the obduction of the allochthonous western Appalachian units onto Grenvillian crust above a zone of detachment that penetrates at least to midcrustal depths and was the locus of successive Paleozoic thrusting.

INTRODUCTION

The New England Appalachians are characterized by a series of tectonostratigraphic terranes accreted to North America during multiple Paleozoic orogenic events. Three major terranes are identified across the northern Appalachians: (1) a western terrane underlain by Grenvillian crust and overthrust by allochthons that contain Grenvillian basement with lower Paleozoic shelf sediments, (2) a central terrane typified by island arc volcanics of the Bronson Hill Anticlinorium and miogeoclinal lithologies of the Merrimack Synclinorium, and (3) an Avalonian terrane with distinctive Precambrian and mid-Paleozoic faunas. It is increasingly recognized that such terranes are in fact a complex composite collage of smaller (suspect) terranes.

The deeply eroded Appalachian Orogen is the center of numerous controversies relating to the mechanisms and extent of terrane accretion during the lower Paleozoic. Seismic refraction/wide-angle reflection experiments are capable of resolving deep continental structures and provide a means of inferring relationships between the surface geology and the underlying crust. This paper reports on recently acquired seismic refraction/wide-angle reflection data collected across the northern New England Appalachians and attempts to answer the following questions: (1) What is the velocity structure of the New England crust? (2) What is the structural relationship between the Grenville Province and the allochthonous New England Appalachians? (3) What constraints can be applied to the inference of lower crustal composition from compressional and shear wave data? We begin with an overview of the regional geology observed along the profile and present a summary of the interpreted crustal structure from previous geophysical studies in New England before moving on to a description of the two-dimensional seismic velocity model. Finally, an interpretation of the crustal velocity structure and the inferred crustal composition is presented.

Paper number 91JB01657.

PROFILE GEOLOGY

The refraction/wide-angle reflection profile discussed here extends from the Grenville Province exposed in northern New York State, across the central New England Appalachians and on into central Maine (Figure 1). The profile crosses six tectonostratigraphic units, which are from west to east: (1) the middle Proterozoic Grenville basement exposed in the Adirondack Mountains (northern New York), (2) autochthonous platformal sediments and allochthonous slope rise sediments of the Taconic sequence, (3) imbricated and metamorphosed lower Paleozoic flysch deposits and underlying Grenvillian basement of the Green Mountains (central Vermont), (4) Silurian to Lower Devonian metapelites of the Connecticut Valley Synclinorium (eastern Vermont), (5) Ordovician forearc sediments and volcanics of the Bronson Hill Anticlinorium (New Hampshire), and (6) metamorphosed and deformed Silurian to Devonian turbidites of the Merrimack Synclinorium. Numerous articles have been written discussing the tectonic evolution of the northern New England region [*Osberg*, 1978; *Robinson and Hall*, 1979; *Williams and Hatcher*, 1982; *Bradley*, 1983; *Zen*, 1983; *Taylor*, 1989]. However, for the purpose of our study we present a generalized overview of the lithotectonic units traversed by the profile and describe the nature of the contacts between these units.

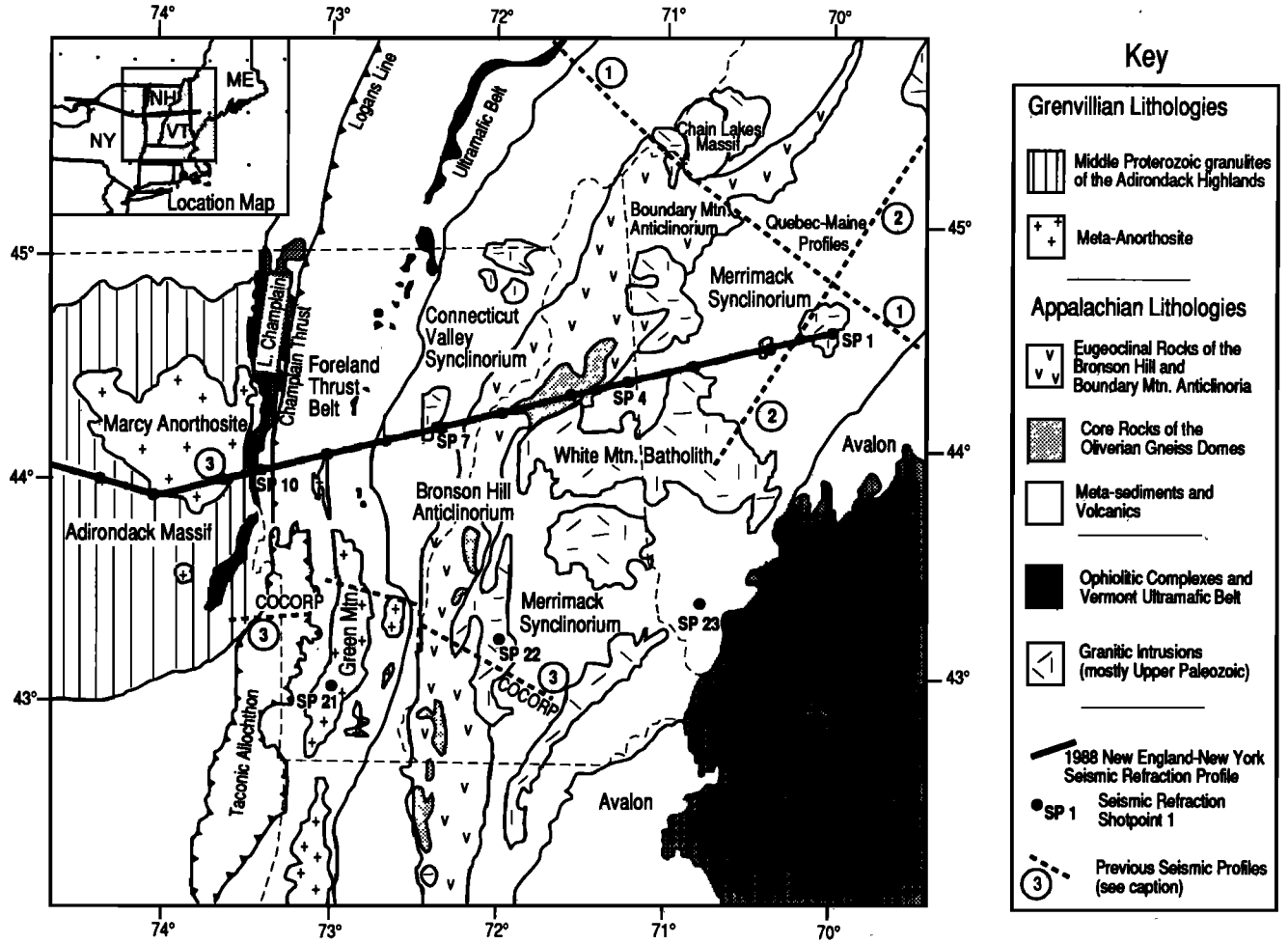

Fig. 1. Simplified geologic map showing the location of the 1988 New England seismic refraction/wide-angle reflection profile. Inset map shows regional location of the entire profile. Inline shot points are marked by dots along the profile, and fan shots are shown offset to the south. Previous seismic profiles are shown by the dashed lines: (1) the Quebec-Maine seismic reflection and refraction profiles [*Spencer et al.*, 1989], (2) the USGS refraction profile along the axis of the Merrimack Synclinorium [*Hennet et al.*, 1991], and (3) the southern Vermont and Adirondack deep seismic reflection profile collected by COCORP [*Ando et al.*, 1984]. Geology simplified after *Williams* [1978] and *McLelland and Isachsen* [1986].

Our transect begins in the Proterozoic domal massif of the Adirondack Mountains, which forms an anomalous topographic feature extending southward from the Grenville Province of eastern Canada. The Adirondack Highlands expose an oblique section through the Proterozoic mid to lower crust [*Selleck*, 1980; *McLelland and Isachsen*, 1986]. A complex assemblage of ductily deformed and interleaved granulite facies metapelites, marbles, and quartzites are exposed in the Adirondack Highlands [*Weiner et al.*, 1984; *McLelland and Isachsen*, 1986]. Intruding the gneisses are meta-anorthosite bodies, the largest of which is the Marcy Anorthosite (Figure 1). The Adirondack dome is surrounded by Cambrian platformal carbonates and quartzites which lie unconformably upon the Grenvillian basement. This autochthonous wedge of Cambrian sediments lies in situ between Grenvillian basement and the allochthonous Taconic (Mid-Upper Ordovician) units of the western Appalachians.

The contact between the Appalachian and Grenville provinces lies beneath the Champlain Valley. In the Champlain Valley Cambrian to Early Ordovician continental shelf sediments and deep marine clastics (Foreland Thrust Belt) lie unconformably on the Grenvillian autochthon. These sediments have been interpreted as an accretionary complex developed above the eastward subducting Grenvillian margin during he Mid-Ordovician Taconic Orogeny [*Rowley and Kidd*, 1980; *Stanley and Ratcliffe*, 1985]. Subsequent closure of the Taconic subduction system resulted in the obduction of allochthonous slices of Grenvillian "basement" which now form the core of the Green Mountain massif exposed in central Vermont. To the east of the Green Mountains, the Taconic "suture" is traced by the Vermont Ultramafic Belt which is interpreted as altered slivers of oceanic crust and upper mantle imbricated with accretionary prism sediments [*Osberg*, 1978; *Bradley*, 1983; *Stanley and Ratcliffe*, 1985].

From the eastern edge of the Green Mountains the profile proceeds eastward across the Connecticut Valley Synclinorium. Silurian to Lower Devonian metapelites and carbonates attain chlorite grade metamorphism [*Rodgers*, 1970]. These post-Taconic sediments are interpreted to be a shallow thrust sheet juxtaposed against the Bronson Hill Anticlinorium by the Ammonoosuc fault. The Bronson Hill island arc complex accreted in the Taconic Orogeny is

exposed as a linear belt of volcanics stretching through eastern Vermont and western New Hampshire. The Bronson Hill Anticlinorium can be traced through the central New England Appalachians as an aligned chain of elliptical gneissic domes (Oliverian Plutonic Series) mantled by a series of Mid-Ordovician metavolcanics and metasediments. Metamorphic grades vary from greenschist facies to upper amphibolite facies at the cores of the Oliverian Domes [*Rodgers*, 1970]. Overlying these eugeoclinal lithologies is a series of Silurian to Lower Devonian metapelites and carbonates belonging to the Connecticut Valley Synclinorium to the west and the Merrimack Synclinorium to the east.

The Merrimack Synclinorium lies to the east of the Bronson Hill Anticlinorium. This broad structural low contains a thick sequence of Silurian to Devonian deep marine clastics and, locally, calc-silicates and metavolcanics typically attaining upper amphibolite grade metamorphism. At least three phases of nappe emplacement and associated regional metamorphism in the Acadian (Mid-Devonian) orogenic events have resulted in widespread ductile deformation of these midcrustal rocks now exposed at the present erosion surface [*Chamberlain and England*, 1985; *Eusden et al.*, 1987]. The Merrimack Synclinorium has been extensively intruded by Acadian granites of the New Hampshire Plutonic Series and by the Jurassic White Mountain Magma Series which forms a north-south elongate batholith composed predominantly of syenite, granite, and monzonite [*McHone and Butler*, 1984].

Crustal Structure and Geophysical Framework

A recent synthesis of geophysical data collected through the Appalachian Orogen indicates that significant differences exist in the deep crust between the northern Appalachians and the adjacent Grenville Province [*Taylor*, 1989]. The New England Appalachians are characterized by a relatively thick crust (~40 km) with an average seismic velocity of 6.4 km/s, whereas the Adirondacks have a somewhat thinner curst (36 km), and high velocities (≥6.6 km/s) are observed throughout the crust in this region [*Taylor and Töksoz*, 1982; *Taylor*, 1989]. Previous deep crustal studies in the New England Orogen have included seismic refraction/wide-angle reflection profiles collected in northern Maine and Quebec and seismic reflection profiles collected across southern Vermont and northern New York State. Interpretation of these data sets suggest that the autochthonous Grenville basement extends beneath at least the western portion of the allochthonous Appalachian Orogen.

Seismic reflection and refraction profiles were obtained in 1984 by the U.S. Geological Survey and the Geological Survey of Canada across and along strike to the northern Appalachians in Maine and Quebec (Figure 1, line 1). Analysis of the seismic data from the Quebec-Maine transect provides evidence for the eastward extension of the Grenville beneath the northern Appalachians. A major zone of reflections can be traced over some 200 km from shallow depths beneath the Saint Lawrence Lowlands to approximately 25 km below the Chain Lakes Massif [*Stewart et al.*, 1986; *Spencer et al.*, 1987; *Spencer et al.*, 1989]. These reflections have been interpreted as a "décollement" separating the Grenvillian basement from the allochthonous Appalachians [*Spencer et al.*, 1989].

In central Maine a 180-km-long cross profile shot along the axis of the Merrimack Synclinorium reveals a 38-km-thick crust (Figure 1, line 2). In the region where line 2 crosses the seismic refraction/wide-angle reflection profile discussed herein the upper crust has velocity between 6.0 and 6.3 km/s and is characterized by strong lateral and vertical seismic velocity variations. The base of the Merrimack Synclinorium at 15 km depth is marked by an increase in velocity to 6.4 km/s. The lower crust has a velocity of 6.8 km/s [*Hennet et al.*, 1991]. Normal moveout corrections applied to Moho reflections in the vicinity of our profile (shot point 2) indicate that the crust is 37–38 km thick in eastern Maine [*Luetgert et al.*, 1987].

Deep seismic reflection profiles in southern Vermont (Figure 1, line 3) display the seismically transparent Grenville basement extending eastward beneath the "thin skin" of the Taconic sequence to approximately 25 km beneath the Connecticut Valley Synclinorium [*Brown et al.*, 1983; *Ando et al.*, 1984]. The buried edge of the Grenville Province was interpreted to be a highly deformed thrust-imbricated zone passing eastward into a transitional lower crust of undetermined basement type. The Green Mountains were identified as an imbricated thrust slice obducted above the lower crustal penetrating ramp. Reflection profiling across the southern Adirondacks revealed a striking band of high reflectivity between 6 and 8 two-way travel time, or approximately 18–26 km in depth [*Brown et al.*, 1983; *Klemperer et al.*, 1985]. These authors applied the name Tahawus Complex to this set of reflections, and this name is retained here.

Experiment

Seismic refraction/wide-angle reflection data were acquired by the U.S. Geological Survey (USGS), the U.S. Air Force Geophysical Laboratory (AFGL), and the Geological Survey of Canada (GSC) during the fall of 1988. This profile is 650 km long and traverses the central New England Appalachians before extending west through the Adirondacks and into the Proterozoic craton of southern Ontario. The results of analysis of the easternmost 300 km of this profile are presented below. Exceptionally high quality seismic data were obtained at offsets ranging from 0 to 450 km along a continuous linear refraction profile recorded in three separate deployments. Data were recorded by 120 USGS portable FM cassette recorders [*Murphy*, 1989] and 150 GSC digital instruments (I. Asudeh, personal communication, 1988). In each case 2-Hz geophones were deployed. The seismometer spacing was nominally 800 m with an estimated survey location error of 25 m. In total, 32 shots, ranging in size from 900 kg to 2700 kg, were detonated along the entire profile length; three fan shots were also recorded. The shot point spacing was 30 to 40 km [*Luetgert et al.*, 1990].

Description of the Principal Seismic Phases

The data set gathered by this seismic experiment provides a unique opportunity to derive the seismic velocity structure of the New England Appalachians and adjacent Grenville terrane. We present a brief description of the principal phases observed in the seismic record sections. Emphasis will be placed on broad generalities, although it should be borne in mind that lateral variations do exist along the length of the profile. Subsequently, the major features of the derived two-dimensional model are highlighted, and a de-

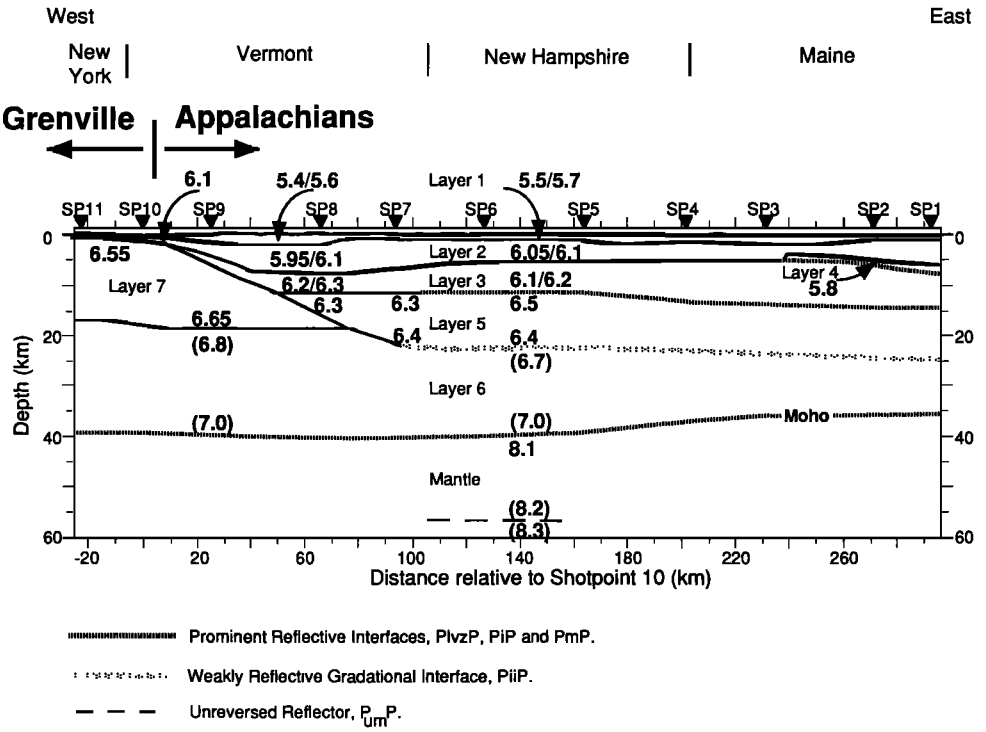

Fig. 2. Seismic velocity model derived from the 1988 New England seismic refraction/wide-angle reflection data. Velocity interfaces are consistent with the observed phases; well-constrained reversed control is achieved throughout the upper and midcrust. The model is a first-order representation of complex layered and gradational interfaces within the New England Appalachians and Adirondack Mountains. Topography is included in the model. Layer numbers are referenced in the text and in subsequent ray diagrams. All velocities are shown in kilometers per second. Distance is plotted relative to shot point 10 (Figure 1).

tailed description of the travel time and synthetic amplitude modeling used to derive the final model shown in Figure 2 is presented.

The record section for shot point 1 is representative of the seismic data gathered in New England; principally, it shows four characteristic phases labeled P_g, $P_{lvz}P$, P_iP, and P_mP on Figure 3. The upper crust in New England is characterized by a laterally extensive and impulsive first-arrival branch (P_g) with apparent velocity 6.0–6.1 km/s. Significantly, no crustal first-arrival phases are observed with apparent velocities exceeding 6.2 km/s. The relatively low amplitude of the first-arrival branch at offsets exceeding 50 km is a result of plotting normalized traces, where the amplitude of the first-arrival branch is relative to the amplitude of the secondary arrivals. In Maine, localized high-amplitude wide-angle reflections ($P_{lvz}P$) are observed at offsets from the source of 20–60 km. Prominent midcrustal wide-angle reflections (P_iP) are the most striking feature of this data set. In western Maine and New Hampshire, strongly coherent wide-angle reflections appear at postcritical offsets between 70 and 120 km. Evidence for phases refracted within the lower crust in New England are tenuous. The seismic velocity structure of the lower crust must be indirectly inferred from analysis of Moho reflections (P_mP) as they asymptotically approach the lower crustal refracted phase. In New England the upper mantle is characterized by emergent direct arrivals (P_n) at offsets exceeding 160 km and by segmented en echelon P_mP reflections, possibly indicative of complex lamination around the crust-mantle transition. The apparent velocity of the upper mantle is 8.0 ± 0.1 km/s.

The record section for shot point 10 west is characteristic of data collected across the Grenvillian Adirondack massif (Figure 4). Exceptionally high upper crustal velocities (6.6 km/s) are associated with the Grenvillian crust. Conspicuous high-amplitude, wide-angle reflections (P_tP) are observed at offsets between 50 and 90 km. Strongly coherent en echelon reflection segments (P_tP) suggest a laminated midcrustal body beneath the Adirondack massif, referred to previously as the Tahawus Complex.

Seismic Modeling

Two-dimensional ray-trace modeling, asymptotic ray-theory synthetics and full-waveform reflectivity synthetic seismograms were used to derive a seismic velocity model from this data set. The two-dimensional seismic velocity model is comprised of two discrete and independently derived "blocks" which are connected by a midcrustal penetrating ramp structure (Figure 2). The New England Appalachian crust is essentially composed of three subhorizontal planar layers: (1) an upper crust with apparent velocities in the range 6.0–6.2 km/s, (2) a 10-km-thick midcrustal layer modeled with a negative gradient between 6.5 and 6.4 km/s, and (3) a lower crustal layer with an estimated velocity of 6.7–7.0 km/s. In northern New York State the Grenvillian Adirondack Mountains are represented by a model consisting of a two-layer crust. High upper crustal velocities of 6.6

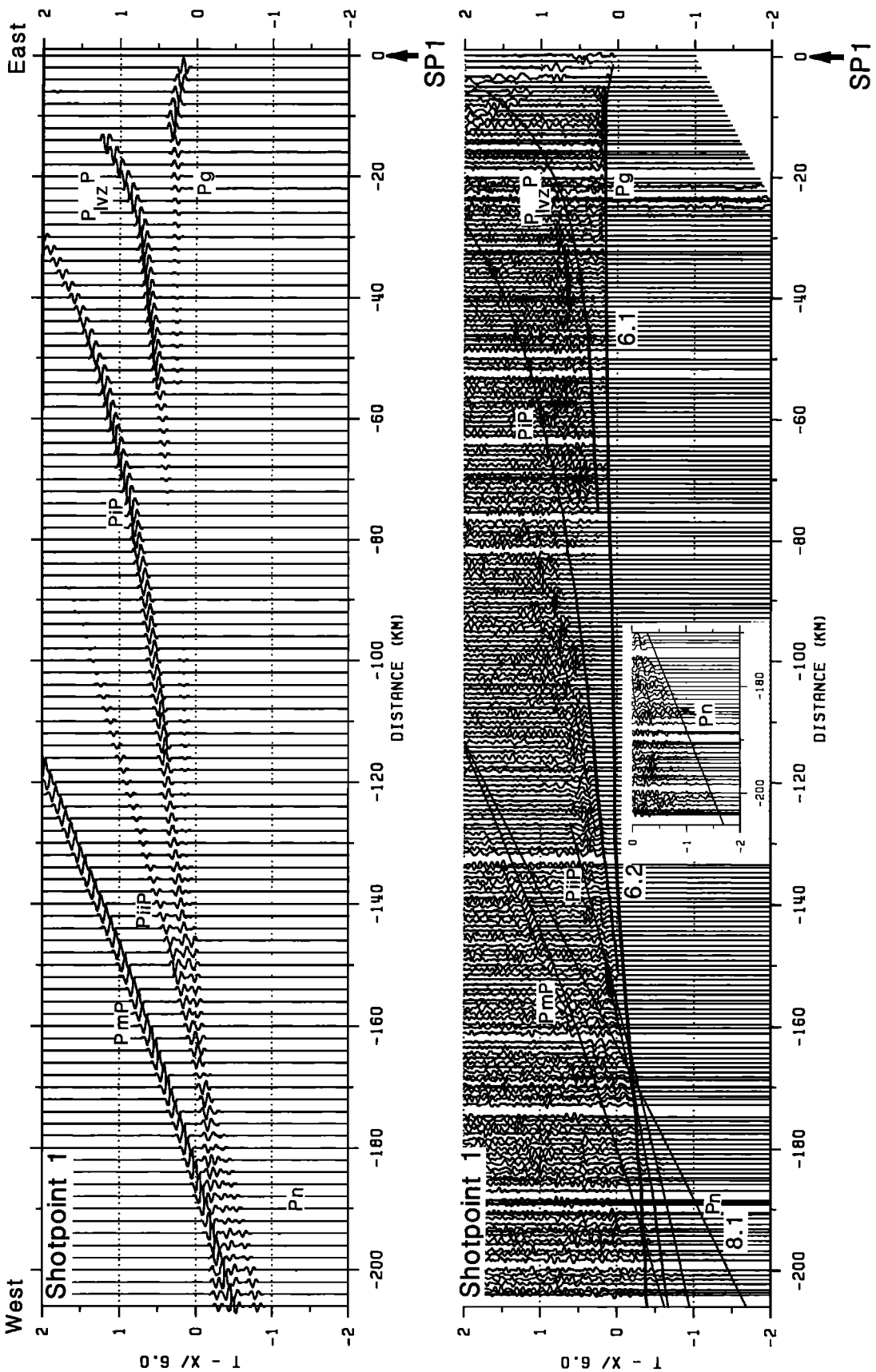

Fig. 3. Trace-normalized seismic refraction data from shot point 1 (SP1) and ray-synthetic seismogram (top) calculated for the eastern portion of the model in Figure 2. Shot point 1 is representative of data collected across the New England Appalachians and shows characteristic large-amplitude coherent midcrustal reflections (P_tP). The model predicts strongly coherent P_mP reflections, which are not observed in the data; the Moho may be laminated beneath the central New England Appalachians. Data are plotted using a reducing velocity of 6.0 km/s. No filtering has been applied to the data. Key to phase identification (used for all figures): P_g, the diving or continuously refracted P wave in the upper crustal layers, with an apparent velocity between 6.0 and 6.2 km/s; P_r, the refracted P wave through the Grenvillian ramp structure; P_7, the refracted P wave in the Grenville upper crust (layer 7), with an apparent velocity of 6.6 km/s; P_n, the uppermost mantle refracted phase, with an apparent velocity between 8.0 and 8.1 km/s; P_tP, the wide-angle reflection from the midcrustal interface (layers 3/5), no corresponding refracted first arrival is observed from layer 5; P_hP, the wide-angle reflection from the lower crustal interface (layers 5/6), no corresponding refracted first arrival is observed from layer 6; P_mP, the wide-angle reflection from the crust-mantle boundary; and P_tP, the wide-angle reflection from the top of the Tahawus Complex (layers 7/6).

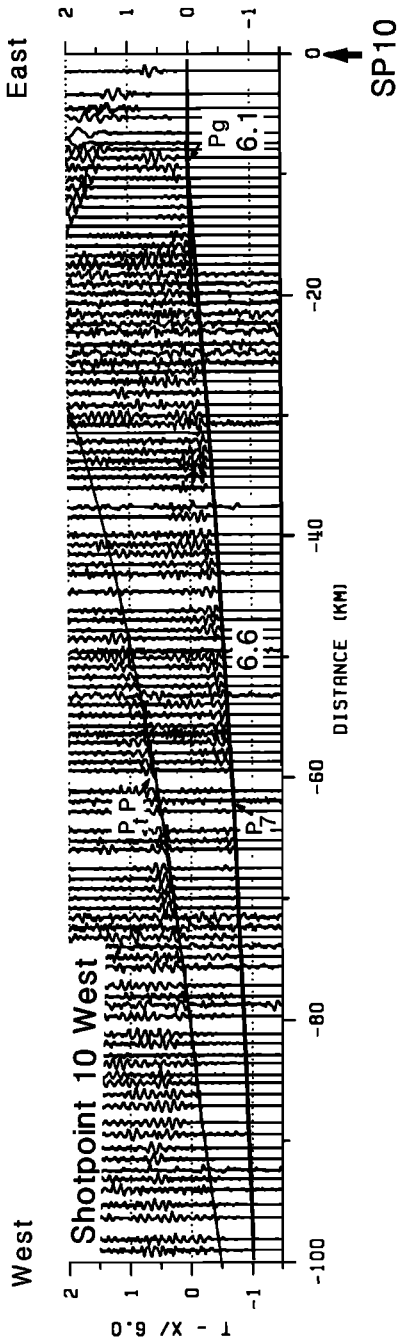

Fig. 4. Record section for shot point 10 west (SP10 west) plotted in trace-normalized format with distances plotted relative to the shot point. Seismic refraction data collected across the Adirondack Mountains characteristically show high upper crustal velocities (6.6 km/s) compared to those observed in the Appalachians. Large-amplitude coherent reflections (P_tP) observed at offsets between 50 and 90 km are related to a laminated midcrustal interface referred to by *Klemperer et al.* [1985] as the Tahawus Complex. See Figure 3 for key to phase identification.

km/s and a midcrustal reflecting interface are the most prominent features of the model in this region. Once modeling was completed for the Appalachian and Adirondack "blocks", the contact between these two terranes was analyzed. The high-velocity Adirondack "block" was imaged in the form of a ramp extending to midcrustal depths beneath the Appalachian upper crust in Vermont (Figure 2). Crustal thickness varies from 36 km in western Main to 40 km in Vermont.

Modeling of this Appalachian data set was completed in successive phases, each used to constrain subsequent iterations and so to improve the resolution of the final model. Initially, seismic velocity functions for each shot point were calculated using one-dimensional ray-trace modeling assuming a plane homogeneous layered Earth [*Luetgert*, 1988*b*, *c*]. Reference was made to reciprocal travel times to aid in the identification and correlation of phases. The shot point spacing is insufficient to resolve individual igneous bodies, and consequently minor travel-time perturbations associated with localized variations in the surface geology have not been modeled. The one-dimensional models were extensively used to minimize the number of iterations required in successive two-dimensional ray-trace modeling described in the following section.

An initial composite two-dimensional seismic velocity model was constructed by contouring one-dimensional homogeneous layer solutions computed at each shot point. Iterative two-dimensional ray-tracing was used to constrain the velocity boundaries [*Cerveny et al.*, 1977; *Luetgert*, 1988*a*]. Topography was included in the model. Incorporation of wide-angle and near-vertical reflections for each shot point significantly increased the resolution of the model. Identification of critical points for the major reflected phases (P_mP, P_tP) allowed velocity contrasts across interfaces to be estimated. Seismic velocity gradients and velocity contrasts were estimated by means of amplitude modeling. In the eastern part of the profile the model is approximately one-dimensional, and full-waveform reflectivity modeling was used to determine the relative amplitude characteristics of the observed phases.

Generally, observed and calculated travel times for the model presented in Figure 2 match to 0.1 s or less, with no mismatches greater than 0.2 s. The sensitivity of the model is greatest in the uppermost 10 km where the ray density is greatest. Within the upper crust (layers 2/3) the error in depth to interfaces is probably no greater than several hundred meters, and the corresponding precision in the derived velocity is 6.05 ± 0.05 km/s. The velocity gradient in the upper crust is 0.01 s^{-1}; this value is tightly constrained by the lateral persistence of the first-arrival phase (P_g). The magnitude of the midcrustal velocity discontinuity (layers 3/5) is inferred from amplitude modeling to be precise to ±0.1 km/s. Considerably more uncertainty exists for the velocity structure of the lower crust as this has largely been indirectly inferred from secondary arrivals. The precision of the modeled lower crustal velocity is probably no better than 6.8 ± 0.2 km/s; beyond these limits acceptable travel time and amplitude constraints are exceeded. In view of the poorly constrained lower crustal velocity structure, a 2-km uncertainty in the Moho depth may be expected, although the dipping geometry is unlikely to be affected by this. Uncertainties introduced by the interpretive step of phase

correlation are usually much larger than the quantifiable uncertainties listed above [*Mooney*, 1989].

Description of the New England model: A detailed description of the compressional wave velocity model shown in Figure 2 is presented below. Justification of each layer in terms of its apparent velocity and structure is related to the key phases identified on the record sections. The upper crust is represented by a model consisting of three layers. The near surface (layer 1) has seismic velocities in the range 5.5–5.7 km/s. An additional "cover" layer is modeled along the eastern portion of the profile, with a seismic velocity of 5.0 km/s. The upper crust (layer 2) is characterized by a seismic velocity of 6.05 km/s increasing to 6.1 km/s at the base of the layer. The 6.05 km/s refracted phase is observed extending to offsets of 120 km, requiring a vertical seismic velocity gradient in layer 2 of 0.01 s^{-1} (P_g in Figure 3). Throughout New England the first-arrival phase (P_g) is laterally continuous, indicating that near-surface velocity variations (statics) do not affect the data. Between shot points 7 and 10, layer 2 thickens, and somewhat lower velocities are included in the model in this region (5.95–6.1 km/s). The incorporation of slower velocities into the model provides a travel time delay observed in the first-arrival refracted branch from shot point 4. Immediately east of shot point 10 a 6.1 km/s near-surface velocity is incorporated within layer 2.

Layer 3, with a seismic velocity of 6.1–6.2 km/s, varies laterally in thickness and occurs between depths of 5 and 15 km. First arrivals from layer 3 are observed at offsets exceeding 120 km and signify a continuous increase in velocity with depth in the uppermost crust rather than a first-order velocity discontinuity (Figure 5). Between shot points 7 and 9 the velocity of layer 3 is increased to 6.2–6.3 km/s. A first-order velocity discontinuity in this region of the model satisfies near-offset reflections from shot point 7 east (Figure 5) and additionally allows refracted arrivals from shot point 7 west to successfully turn through the ramp structure. The velocity structure of the ramp is discussed more fully in the following sections.

Large-amplitude reflections ($P_{lvz}P$) are observed on shot points 1, 2, and 3 at offsets of 20–60 km. These reflections are delayed in arrival time by as much as 0.5 s and are best modeled by a low-velocity zone with a velocity of 5.8 km/s as shown by layer 4 in Figure 2. One-dimensional travel time modeling enabled the geometry of this upper crustal reflector to be determined. Integration of the one-dimensional models into the two-dimensional model produced a 1-km-thick low-velocity zone with a velocity of 5.8 km/s (Figure 6). The velocity of the low-velocity zone (5.8 km/s) is determined by amplitude modeling and by the abrupt termination of this set of reflections from shot point 1 at an offset of ~80 km ($P_{lvz}P$ in Figure 3). Amplitude modeling of this discontinuous low-velocity body produces a good match with the observed reflected phases, although it is hard to determine the magnitude of the seismic gradient within this layer. One-dimensional full-waveform reflectivity solutions were calculated for shot point 1 and produced an exceptionally close correlation to the relative amplitudes observed along the profile.

The midcrust has been modeled with a negative gradient; the vertical seismic velocity gradient decreases from 6.5 km/s to 6.4 km/s over a 10-km depth interval in layer 5 (Figure 2). The top of layer 5 rises from 14.5 km in the east to 11.5 km in the west before merging with the ramp beneath shot point 9. Large-amplitude postcritical reflected arrivals observed at 70–120 km offsets define this midcrustal interface (P_iP in Figure 5). Full-waveform reflectivity modeling indicated that a seismic velocity step from 6.2 km/s to 6.5 km/s at the top of layer 5 would satisfy critical point and amplitude constraints. Reflections originating from the top of layer 5 are not all equally as coherent or large in amplitude, yet the model predicts laterally continuous high-amplitude reflections. Clearly, two-dimensional ray-tracing can only produce an approximate first-order representation of complex layered and laterally varying interfaces within the Earth. No refracted first arrivals are observed from layer 5. Two possible models were considered to fulfill the above described midcrustal reflections without a corresponding refracted phase: (1) a thin high-velocity layer and (2) a negative gradient layer. First, a thin positive gradient high-velocity layer, where refractions are terminated and limited refracted energy returns to the surface, was rejected because of the added complexity of determining the velocity between such a thin layer and the top of the lower crust. The second option of a negative gradient layer was chosen in preference as it produced the simplest solution to the observed phases. Since negative gradients cannot be resolved by amplitude modeling, this is an inferred structure. It is not necessary to have a negative gradient through the entire thickness of layer 5; an intermediate layer of, say, 6.45 km/s with a positive gradient is not ruled out although arrivals from such a layer would have to be "hidden". Immediately east of the Grenville ramp, layer 5 has a positive velocity gradient; this is an essential feature of the model, as without it rays originating from within the Adirondacks and propagating to midcrustal depths would never be refracted toward the surface (Figure 2).

The lower crust is modeled as a "hidden" layer and lies below 25 km depth (layer 6 in Figure 2). Refracted first arrivals are not observed from the lower crust because of longer travel times for direct arrivals from the lower crust than for the upper crustal refractions. Estimates of the lower crustal velocity must be indirectly inferred. We have three principal constraints on the velocity of the lower crust: (1) an estimate of 6.8 km/s for the lower crustal velocity was obtained from P_mP reflections as they asymptotically approached the lower crustal refracted phase, (2) travel time modeling of critical P_mP reflection hyperbolae indicates a high-velocity, high-gradient lower crust, and (3) estimates of crustal thickness in the vicinity of our profile of around 38 km support a high velocity (6.8 km/s) in the lower crust [*Luetgert et al.*, 1987; *Hennet et al.*, 1991]. The lower crust has been modeled with a velocity of 6.7 km/s increasing to 7.0 km/s at the base of the crust. The velocity gradient modeled in the lower crust is constrained by the curvature of the P_mP hyperbola. Reflectivity modeling necessitates a minimum velocity discontinuity between layers 5 and 6. Perturbations in the modeled lower crustal velocities exceeding ±0.2 km/s significantly degrade travel time fits for Moho reflections. P_mP does not bottom any further east than shot point 3. Between shot points 1 and 3 the model is constrained by the USGS refraction profile along the axis of the Merrimack Synclinorium [*Hennet et al.*, 1991].

The top of the lower crust is represented in the model by a first-order velocity discontinuity. A first-order velocity discontinuity is presented as the simplest possible model

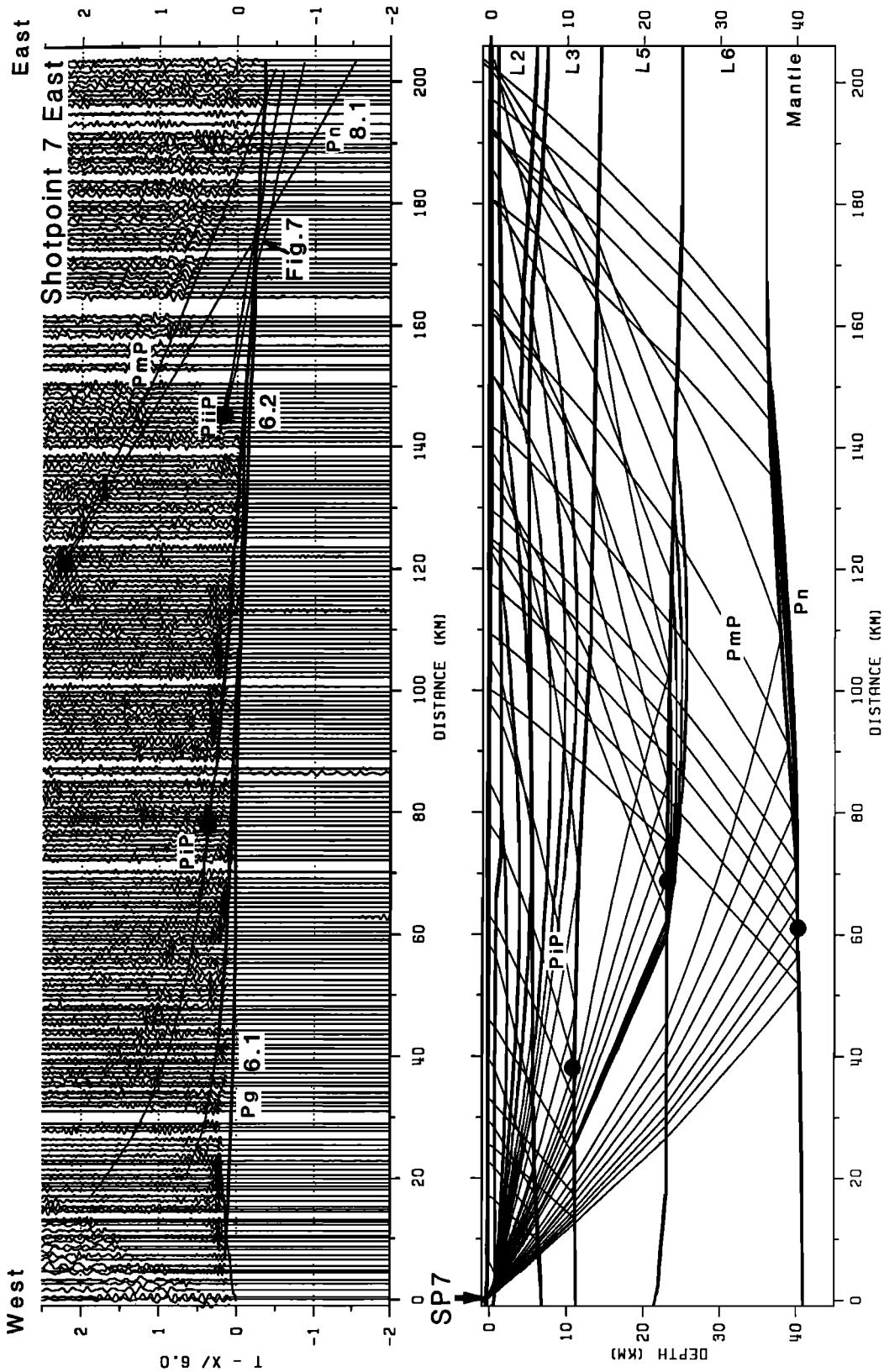

Fig. 5. Trace-normalized seismic refraction data from shot point 7 east (SP7 east) and ray diagram (bottom) for the eastern portion of the model shown in Figure 2. The New England seismic velocity structure is fully reversed by SP7 east. Midcrustal reflections (P_iP) show an advanced travel time relative to that observed for shot point 1. Critical points are marked on the data by the solid dots, and the corresponding critical distances are marked on the model. Distances are plotted relative to shot point 7. See Figure 3 for key to phase identification.

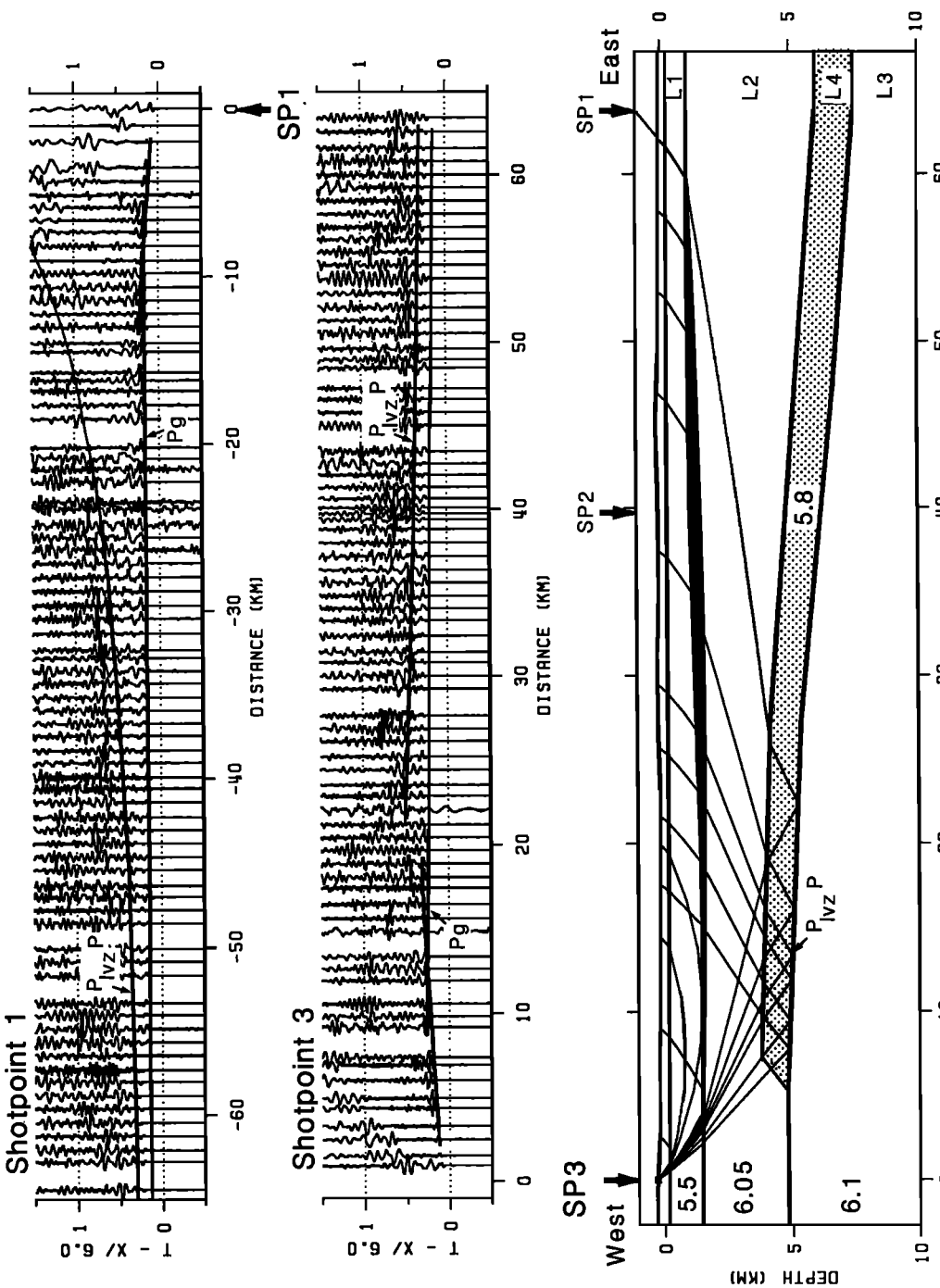

Fig. 6. Near-offset trace-normalized seismic refraction data from shot point 1 (top) and shot point 3 (middle). Large-amplitude upper crustal reflections ($P_{lvz}P$) observed from shot points in western Maine are best modeled by a thin low-velocity layer. Ray diagram for shot point 3 (bottom) shows precritical reflections from the base of the low-velocity layer. Distances are plotted relative to the shot point. See Figure 3 for key to phase identification.

which fits the observed travel time constraints. The shallowest possible depths to the top of the lower crust is given by modeling lower crustal refractions so that they are coincident with the picked first arrivals (Figure 7*a*). The geometry of the lower crustal interface is poorly constrained because reflections from the top of the lower crust are indistinct (Figure 7*b*). The modeled $P_{ii}P$ reflection shown on Figure 5 is an artifact of modeling a hidden lower crust rather than a correlatable reflected phase. The top of the lower crust is modeled with a 6.7 km/s seismic velocity. Velocities as low as 6.5 km/s at the top of the lower crust are incompatible with prior estimates of crustal thickness in Maine and New Hampshire [*Luetgert et al.*, 1987; *Hennet et al.*, 1991], while velocities as high as 6.9 km/s for the top of the lower crust would produce large-amplitude lower crustal reflections relative to P_mP and P_iP which are not observed. Ray theory synthetic models of the lower crustal reflection ($P_{ii}P$) are inconsistent with observed lower crustal reflectivity (Figure 3), suggesting that this interface is more complex than the first-order velocity discontinuity used for travel time modeling. The primary observation of crustal thickness obtained from critical P_mP reflections is satisfied in preference to information obtained from synthetic models necessitating a high velocity in the lower crust. The top of the lower crust is considered to be best represented by a gradational velocity interface, incapable of generating coherent reflections.

The geometry of the crust-mantle transition is constrained by Moho reflections (P_mP) and direct arrivals from the upper mantle (P_n). Together these indicate that the crust thickens from 36 km beneath western Maine to 40 km beneath Vermont. In the eastern portion of our model between shot points 1 and 7, a tightly constrained crust-mantle geometry is determined from complementary and reciprocal crust/mantle phases (Figure 7*a*). Greater emphasis was placed on modeling critical Moho reflections than on modeling low-amplitude emergent direct arrivals from the mantle. Although lower crustal velocities are relatively poorly constrained, thinning of the crust toward the east is a primary feature of the data set as indicated by the relative P_n crossover distances on shot points 1 and 7.

Exceptionally coherent large-amplitude Moho reflections (P_mP) observed from shot point 10 east, provide information on the crust-mantle transition beneath Vermont and New Hampshire. Compelling evidence for a 40-km-thick crust beneath Vermont is provided by strongly coherent postcritical P_mP reflections observed at offsets between 90 and 140 km on shot point 10 (Figure 8). At wider angles, delayed en echelon P_mP reflection segments are observed (Figure 8, arrows a and b). Three possible explanations are considered for this feature: (1) a step in the Moho, (2) complex lamination at the base of the crust, and (3) out of plane reflections. First, the delay observed at an offset of 150 km from shot point 10 in the P_mP arrivals can be modeled by a step in the Moho (Figure 9*b*). High upper mantle gradients are required to avoid a shadow zone in the P_n arrivals. Although such a model adequately satisfies travel time constraints, it is rejected on the basis that it is thought to be geologically less likely. The later two suggestions cannot be readily qualified. However, compositional lamination at the base of the crust may be invoked on the basis that estimates of crustal thickness obtained from postcritical P_mP reflections are compatible with those obtained from P_n arrivals from shot point 10. The delayed large-amplitude reflections on shot point 10 may be caused by out of phase effects (Figure 8, arrow b).

Reflections observed on shot point 10 at offsets greater than 240 km with an apparent velocity exceeding 8.1 km/s are interpreted as an upper mantle reflection (Figure 8, $P_{um}P$). These upper mantle reflections tend to dominate the low-amplitude emergent P_n arrivals on shot point 10, adding further complexity to the determination of crustal thickness in New England. These upper mantle reflections ($P_{um}P$) are unreversed and are tentatively modeled by a small velocity step in the upper mantle.

Description of the Grenville model: The easternmost edge of the Adirondack massif is incorporated within the model as shown in Figure 2. The Grenvillian upper crust is characterized by exceptionally high upper crustal velocities (6.55–6.65 km/s). A thin surface layer is modeled with a velocity of 6.1 km/s. The top of a midcrustal interface is sharply defined by prominent midcrustal reflections at offsets of 50–90 km (Figure 4). This midcrustal body is referred to by *Klemperer et al.* [1985] as the Tahawus Complex, and it has been modeled by a planar midcrustal velocity discontinuity dipping to the east within the Grenvillian crust. Precritical reflections from the eastern extent of the Tahawus Complex observed on shot point 7 west provide important new evidence for the continuation of the Tahawus Complex beneath Vermont (P_tP in Figure 10). Amplitude modeling of shot point 7 west is severely restricted due to the combination of upper crustal reflections resulting in a complex summation of phases. Shot point 10 west lacks any upper crustal reflections, and this facilitates amplitude modeling of this midcrustal feature. A velocity contrast of 6.65 km/s to 6.8 km/s at 17 km depth adequately satisfies the observed travel time constraints. Improved amplitude matching may be obtained by a somewhat higher velocity contrast at the top of the Tahawus Complex, although the velocity at the top of the lower crust may not exceed 6.8 km/s, because higher apparent velocities will result in an advanced arrival time relative to the observed first-arrival phase in the Adirondacks. The lower crust beneath the Adirondack Massif is modeled with a velocity of 6.8–7.0 km/s; this adequately satisfies the previously discussed constraints imposed by critical P_mP reflections from shot point 10.

Description of the ramp structure: The contact between the Appalachian and Grenvillian provinces is marked by a lateral change in apparent velocity. This lateral transition in apparent velocity is observed at the same receiver position for all shot points traversing the Appalachian-Grenville boundary (Figure 11). Because this lateral change in apparent velocity occurs at a fixed receiver position, it marks a steeply dipping interface in the seismic velocity model. Constraints on the geometry of the Appalachian-Grenville contact are imposed by the apparent velocity and travel time paths of phases traversing the boundary. Shot points 9 and 10 situated immediately adjacent to the seismic velocity boundary provide critical reverse control on the discontinuity in the uppermost crust. The upper edge of the seismological boundary is located ~10 km east of shot point 10; this point is marked "hinge" in Figure 11. The boundary separating the low-velocity Appalachian crust from the high-velocity Grenvillian crust is therefore defined by the position of lateral transition in apparent velocity and by travel time modeling of upper and mid crustal phases traversing the boundary.

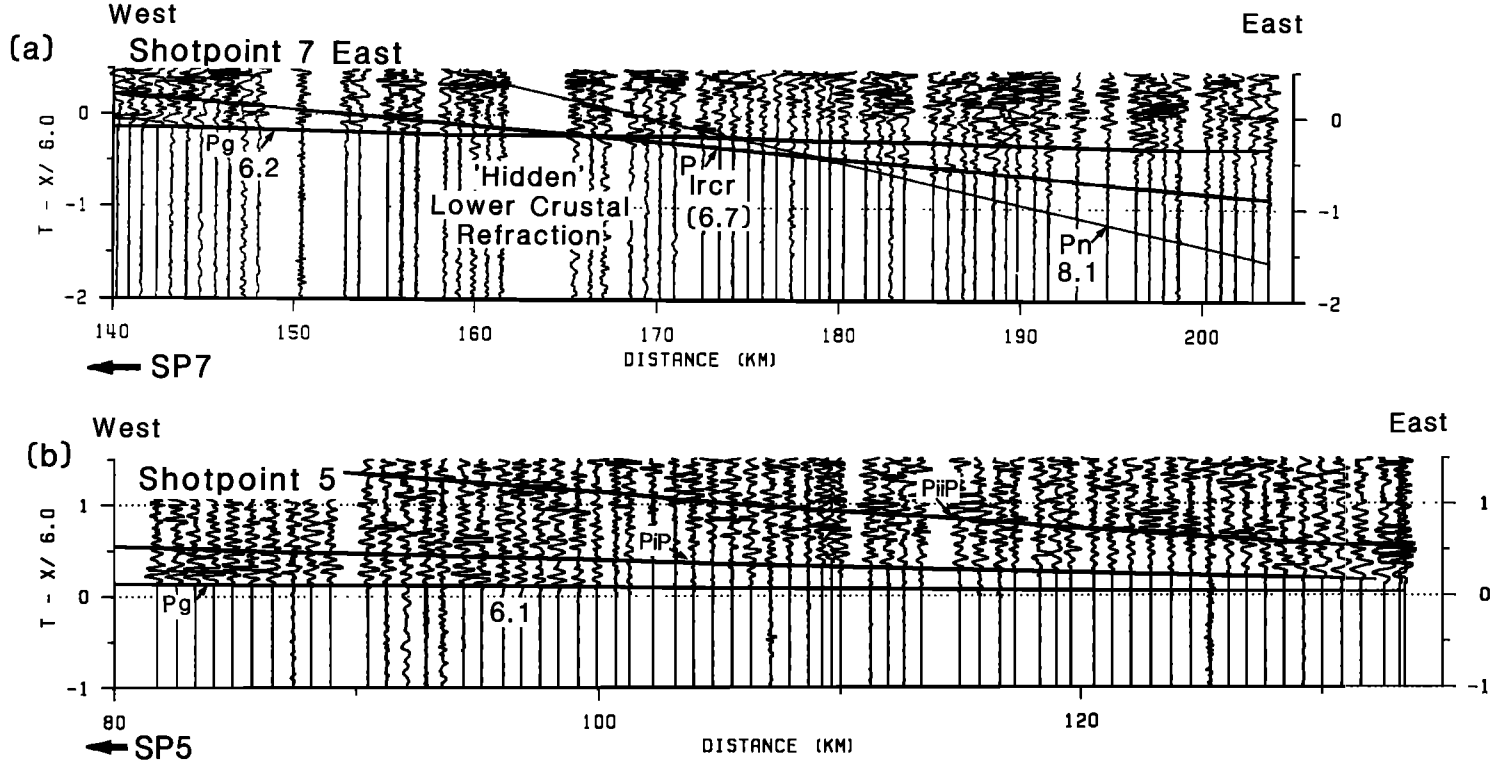

Fig. 7. Trace-normalized record sections from (*a*) shot point 7 east showing refracted direct arrivals from the lower crust (P_{lrcr}) modeled so that they are coincident with the first arrival around the P_n crossover and (*b*) shot point 5 showing weakly coherent critical reflections from the top of the lower crust ($P_{ll}P$) that are observed only in the absence of strong midcrustal reflections (P_lP). Note that the first-arrival branch is observed at offsets of 120 km with an apparent velocity of 6.1 km/s. Distances are plotted relative to shot point in each case. See Figure 3 for key to phase identification.

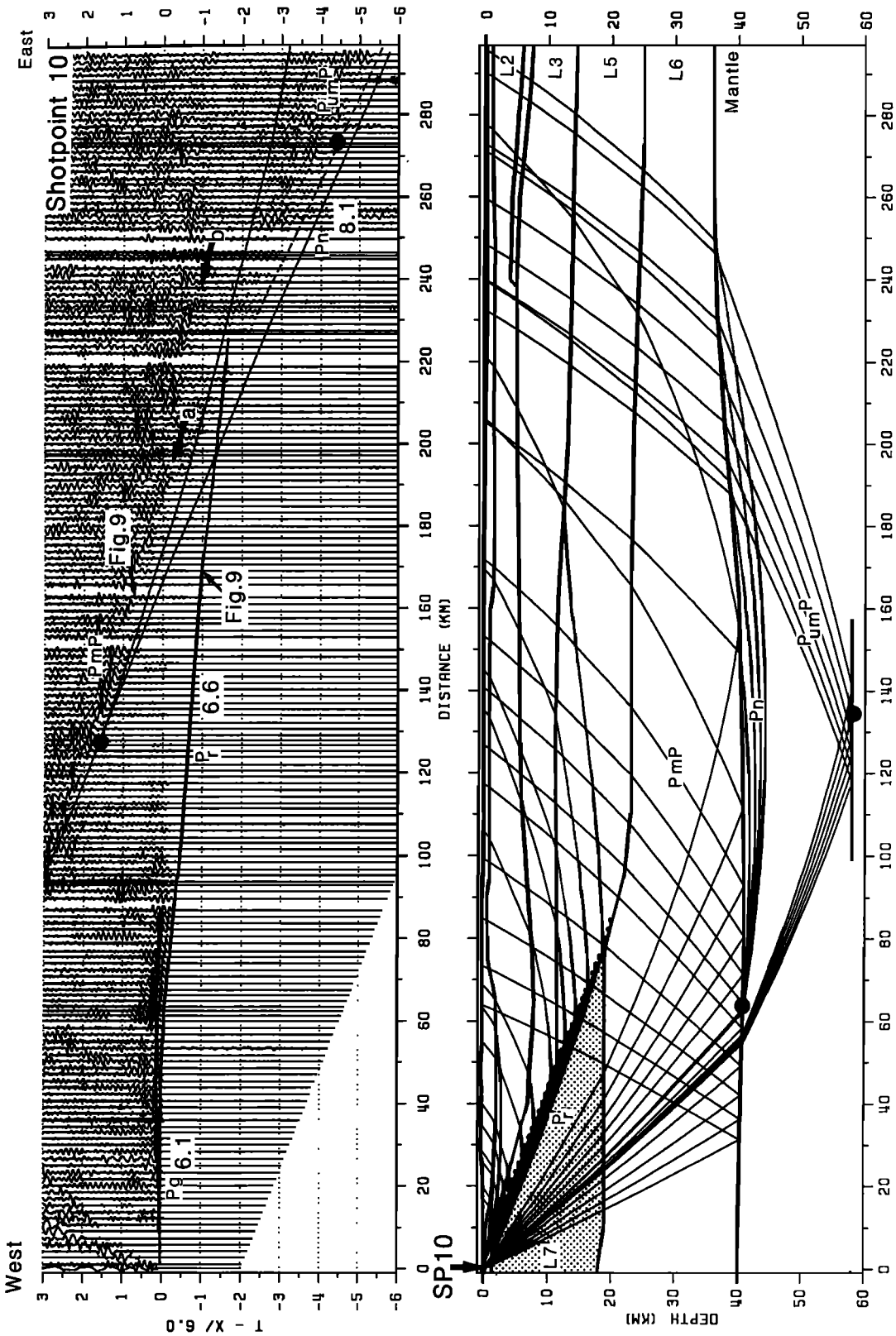

Fig. 8. Trace-normalized seismic refraction data from shot point 10 east (SP10 east) and ray diagram (bottom) for the model shown in Figure 2. Large-amplitude P_mP reflections dominate the record section. Offset and segmented *PmP* reflections (arrows a and b) may be the result of compositional lamination at the base of the crust or out of plane effects. The Grenville ramp structure is highlighted by the dotted line. For clarity, only every second seismic trace is plotted. Distances are plotted relative to shot point 10. See Figure 3 for key to phase identification.

A steeply dipping interface which extends to midcrustal depths beneath Vermont separates the high-velocity Grenville "block" from the lower velocities observed in the Appalachian upper crust. This velocity interface, referred to as the Grenville ramp, is reversed at all depths. Progressively deeper portions of the ramp are sampled by shot points at successively greater offsets from the Appalachian-Grenville contact. Rays originating from the west are refracted through the ramp structure and are transmitted through the lower-velocity Appalachian crust. Shot points west of the ramp therefore characteristically show high apparent Grenville velocities, followed by a rapid transition to a lower apparent velocity at offsets beyond the hinge (shot point 11 in Figure 11). East of the ramp the mirror image of this effect is observed; low Appalachian velocities give way to high Grenvillian velocities at offsets beyond the hinge (shot point 8 in Figure 11). The dipping structure of the ramp is determined by the modeling of apparent velocity and travel times for ray paths from several different shot points which traverse the ramp. The travel times of ray paths originating from shot points east of the ramp in Vermont can be integrated together to provide information on the dipping geometry of the ramp (Figure 11). If the boundary is too steeply dipping, then modeled arrivals will be too early and have too high an apparent velocity (and vice versa).

Constraints on the modeled geometry are imposed by reversing shot points in the Adirondacks. The deep geometry of the ramp structure is controlled by refracted first arrivals that have sampled Grenvillian velocities at their refracting horizon. Rays that are refracted through the deepest portions of the Grenvillian ramp are attenuated; on shot point 10 for example, the first-arrival branch is emergent at offsets exceeding 100 km. The apparent velocity of refracted first arrivals that have been transmitted down the ramp to midcrustal depths is characteristic of the high-velocity (6.6 km/s) Grenvillian crust. Because high-velocity "Grenvillian" first arrivals are observed extending into the Appalachians at offsets of 200 km from the Appalachian-Grenvillian contact, the ramp must continue to midcrustal depths. This effect can be seen on shot point 10, which lies almost directly above the ramp and whose refracted arrivals have a phase velocity of 6.6 km/s (P_r in Figure 9*a*). High apparent velocity discontinuous reflections are observed from the top of the ramp. Although these reflections cannot be satisfactorily resolved by two-dimensional ray-trace modeling, they indicate that the ramp is likely to be a complex laminated/imbricated structure.

Shear Wave Analysis

Shear wave velocities used in conjunction with compressional wave velocities provide important constraints on estimates of crustal composition. In this section, shear wave arrival times are qualitatively compared with those of compressional waves, and Poisson's ratios are calculated for phases traversing the upper and lower crust. Extended length travel time plots were produced to determine the strength of the recorded shear waves. Qualitative analysis was first carried out by overlaying shear wave data reduced at 3.46 km/s and plotted on a time axis compressed by $3^{1/2}$ to allow compressional and shear wave sections to be overlain and compared one to one. Such comparisons are in effect a measure of the relative compressional and shear wave velocities of the crust, and for a "normal" crustal Vp/Vs ratio of 1.732, shear wave arrivals should align exactly with those of the compressional waves. A delayed shear wave arrival indicates a high Vp/Vs ratio (and vice versa).

Prominent shear wave arrivals produced by shot point 10 enable Vp/Vs ratios to be determined for the rocks of the Appalachian and Grenville crustal blocks. An estimate of the average crustal shear wave velocity can be obtained by inspection of crust/mantle reflections. Large-amplitude wide-angle reflections from the base of the crust show delayed S_mS compared to that which would be expected for a "normal" Vp/Vs ratio, indicating that the New England Appalachians have a high average crustal Vp/Vs ratio (Figure 9*b*). In the Appalachian upper crust, shear waves are advanced by up to 0.3 s compared to that which would be expected for a "normal" Vp/Vs ratio (S_r in Figure 12*a*). In comparison, the upper crustal shear wave phase in the Adirondacks is delayed by at least 0.5 (S_7 in Figure 12*a*). Reflections from the Tahawus Complex are delayed by almost a second (S_tS in Figure 12*a*). These qualitative observations show relatively slow shear wave velocities in the Adirondacks (high Vp/Vs ratio) and somewhat higher shear wave velocities in the Appalachians (low Vp/Vs ratio).

A useful criterion for determining crustal compositions is the calculation of Poisson's ratio. Arrival times of compressional and shear wave phases at a given receiver location were picked, enabling Poisson's ratio to be calculated for any particular travel time path [*Luetgert*, 1990]. For a given ray set (arrival branch), multiple calculations of Poisson's ratio may be made, which when averaged together provide information on the region of the crust through which the ray set has penetrated. For ray paths originating from shot point 10 and traversing the Appalachian upper crust, normal Poisson's ratios of 0.24 ± 0.01 were obtained, while higher ratios of 0.28 ± 0.01 were obtained for the upper crust in the Adirondacks (Figure 12*b*). Somewhat more coherent results were obtained for the upper crust than for Moho reflections, where lower signal to noise ratios hampered precise shear wave arrival time picks. A Poisson's ratio of 0.26 ± 0.01 was obtained by picking travel times for P_mP and S_mS arrivals on shot point 10. The derived Poisson's ratios are discussed more fully in terms of their relation to crustal composition in the following sections.

Discussion

The compressional wave velocity model derived for the western New England Appalachians and the Adirondack Mountains provides important new constraints on the deep crustal structure of juxtaposed Proterozoic/lower Paleozoic terranes in eastern North America. In the present study, seismic refraction/wide-angle reflection data are interpreted to show a steeply dipping ramp structure that separates the Proterozoic craton of North America from the obducted Appalachian allochthons. Recent compilations of geologic and geophysical data collected in the northern Appalachians include studies by *Taylor* [1989], *Hatcher et al.* [1990], *Costain* [1990], and *Stewart et al.* [1991]. We present a synthesis of the most recent seismic experiments traversing the Appalachian-Grenville boundary in New England. The integration of compressional and shear wave velocity information obtained in this study with geologic and physical property data is used to infer the deep crustal composition of these juxtaposed terranes.

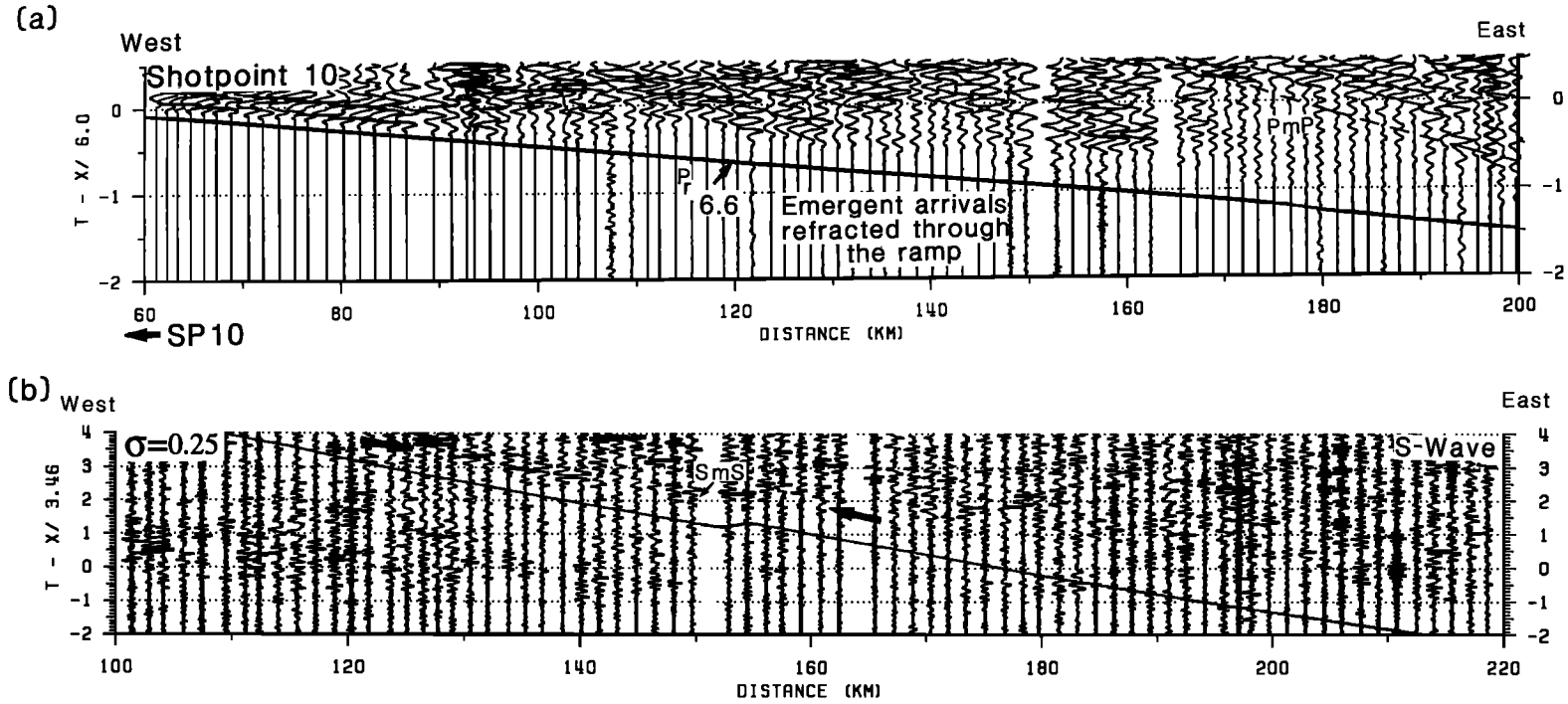

Fig. 9. Enlarged portions of the record section for shot point 10 east (Figure 8) showing (*a*) the refracted phase through the Grenville ramp *Pr* and (*b*) segmented and en echelon Moho reflections. The delayed P_mP arrivals at 150 km can be modeled by a small step in the Moho although this geometry is regarded as geologically less likely. Predicted travel times (solid lines) are plotted on the *S* wave section, assuming a Poisson's ratio of 0.25. The delayed S_mS phase provides evidence for a mafic lower crust beneath the New England Appalachians. On the *S* wave section the reduction velocity is 3.46 km/s, and the time axis is compressed by $3^{1/2}$ relative to the *P* wave time axis. See Figure 3 for key to phase identification.

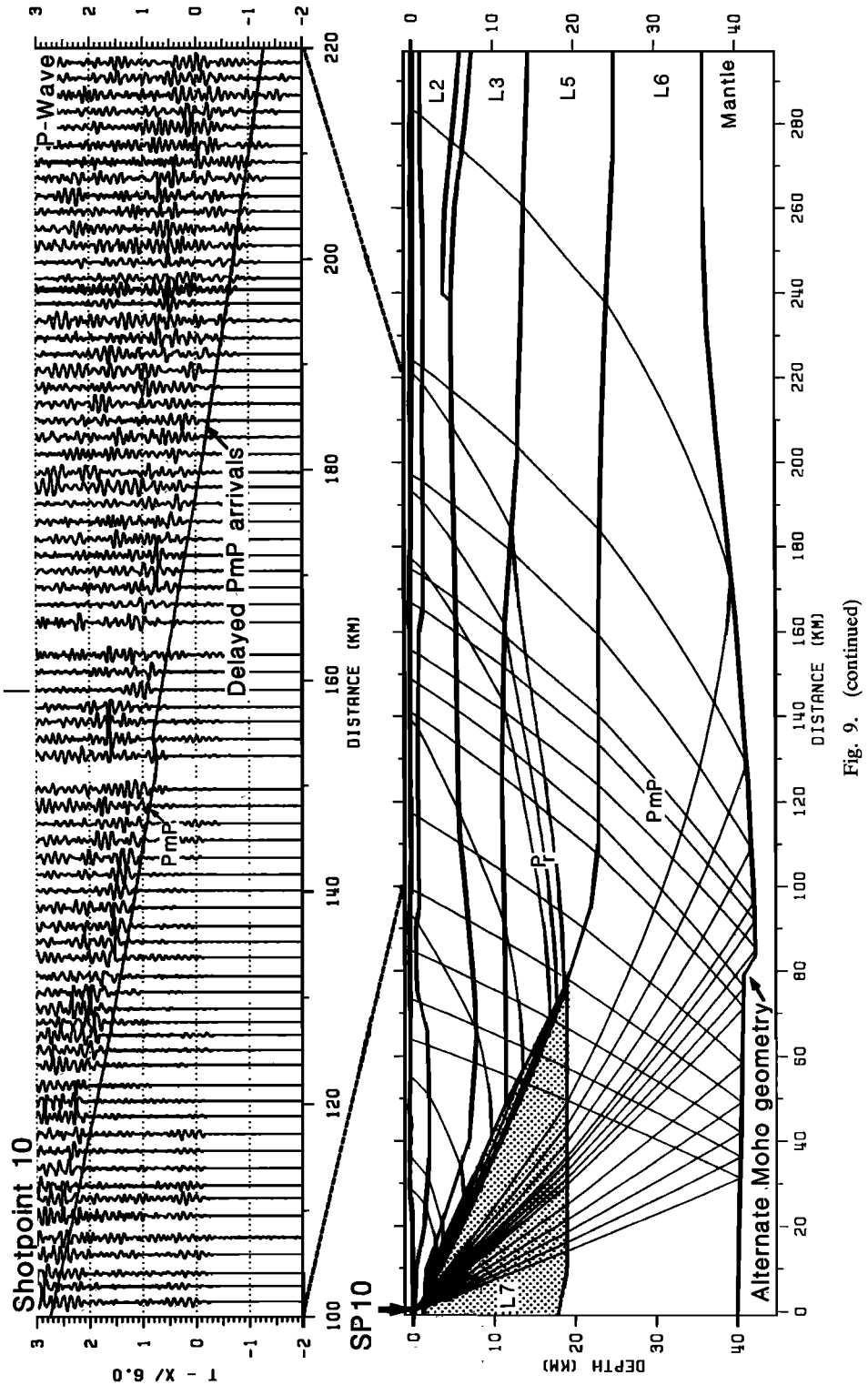

Fig. 9. (continued)

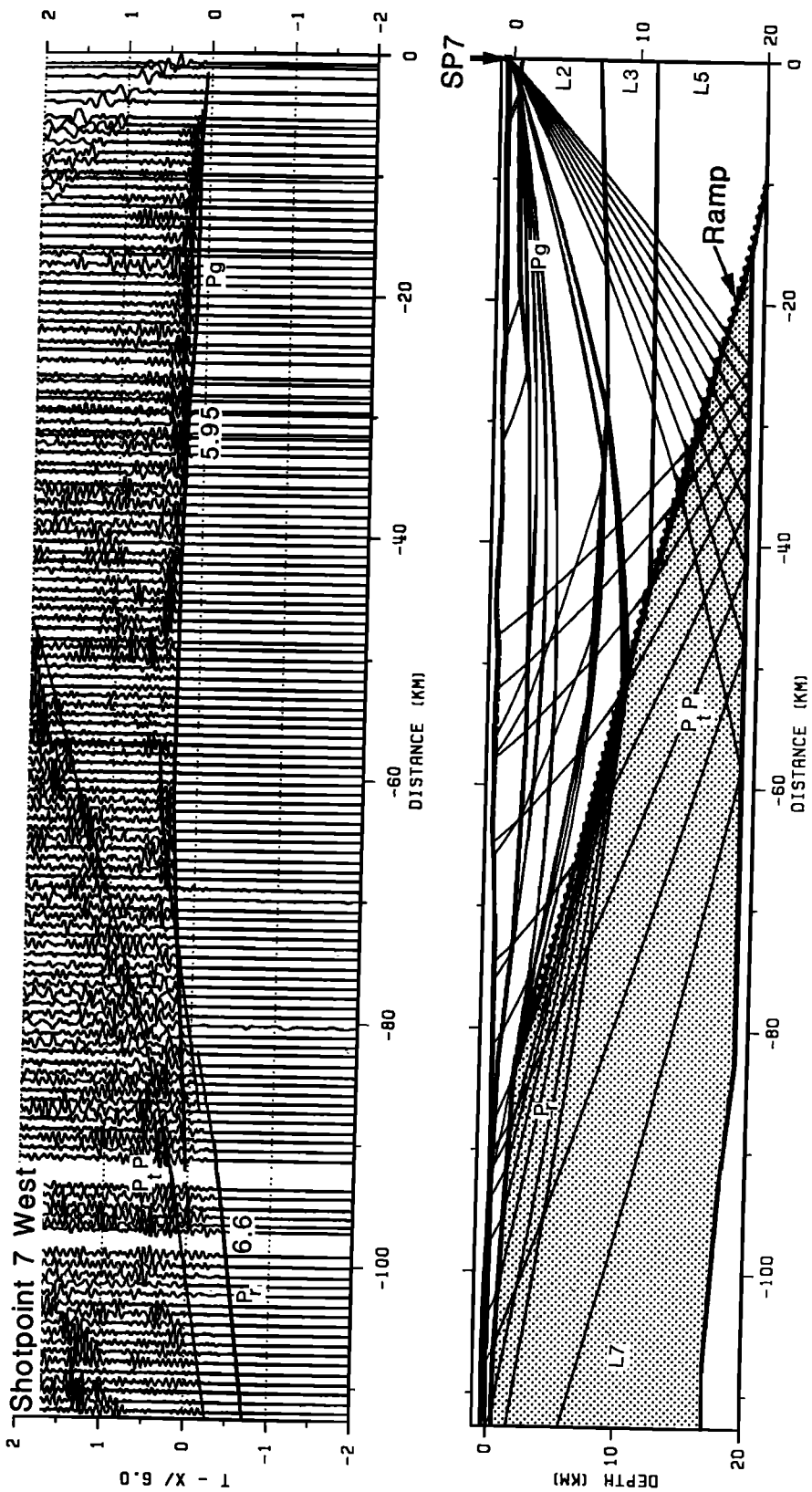

Fig. 10. Trace-normalized seismic refraction data from shot point 7 west (SP7 west) and ray diagram (bottom) for the western portion of the model shown in Figure 2. A lateral velocity transition is marked by the abrupt increase in apparent velocity at −80 km. Precritical reflections (P_rP) from SP7 west provide important new evidence for the continuation of the Tahawus Complex beneath western Vermont. Distances are plotted relative to shot point 7. The Grenvillian crust is shown stippled, and the ramp structure is highlighted by the dotted line. See Figure 3 for key to phase identification.

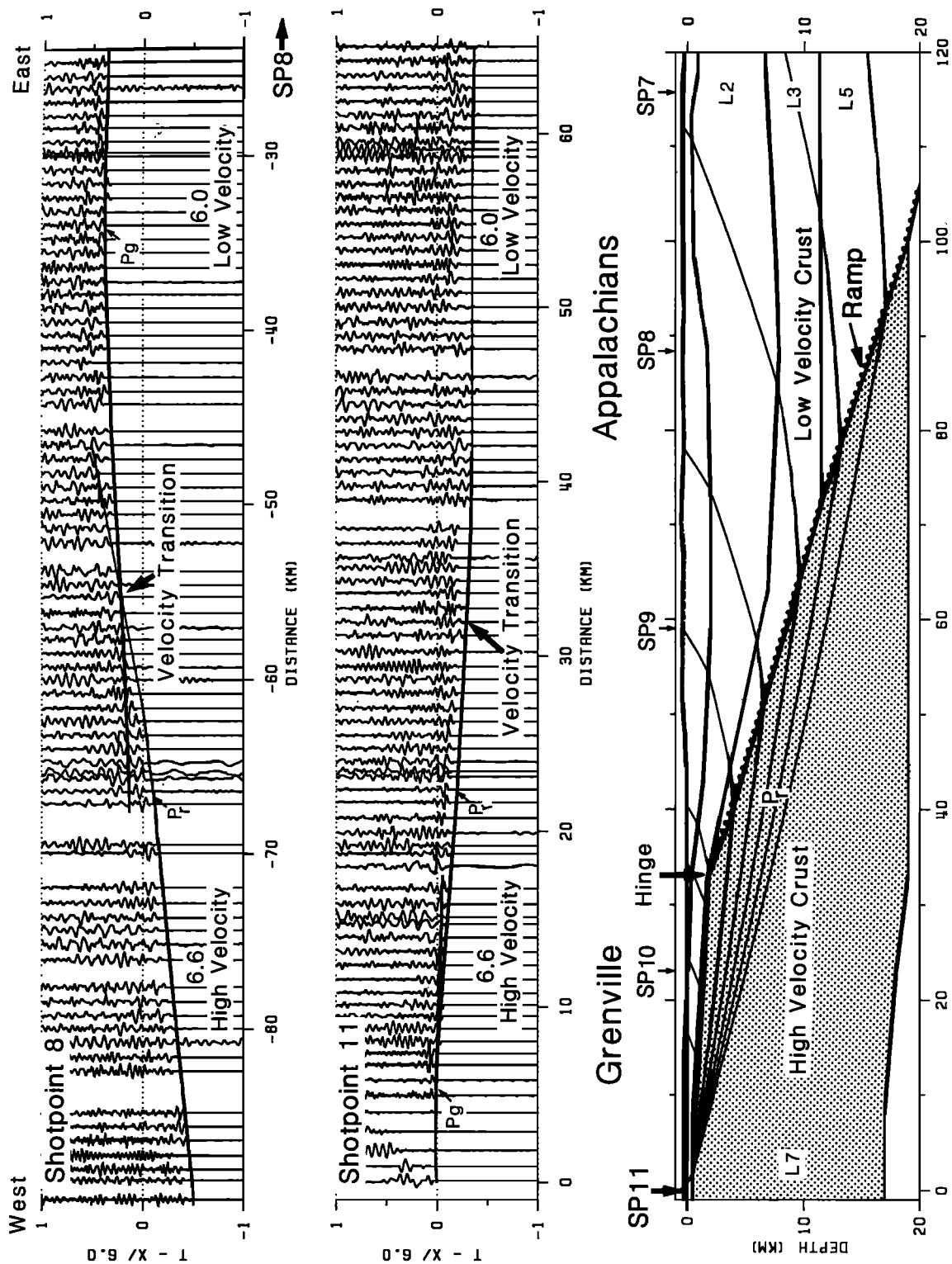

Fig. 11. The Appalachian-Grenville contact is characterized by a lateral velocity transition. This velocity transition is located at the same receiver position for all shot points traversing the boundary and is labeled "hinge". East of the hinge in the Adirondack upper crust, high velocities are observed, while west of the hinge, low Appalachian velocities are observed. The record section for shot point 8 (top) shows an increase in apparent velocity at offsets beyond the hinge. Shot point 11 (middle) shows a decrease in apparent velocity beyond the hinge. See Figure 3 for key to phase identification.

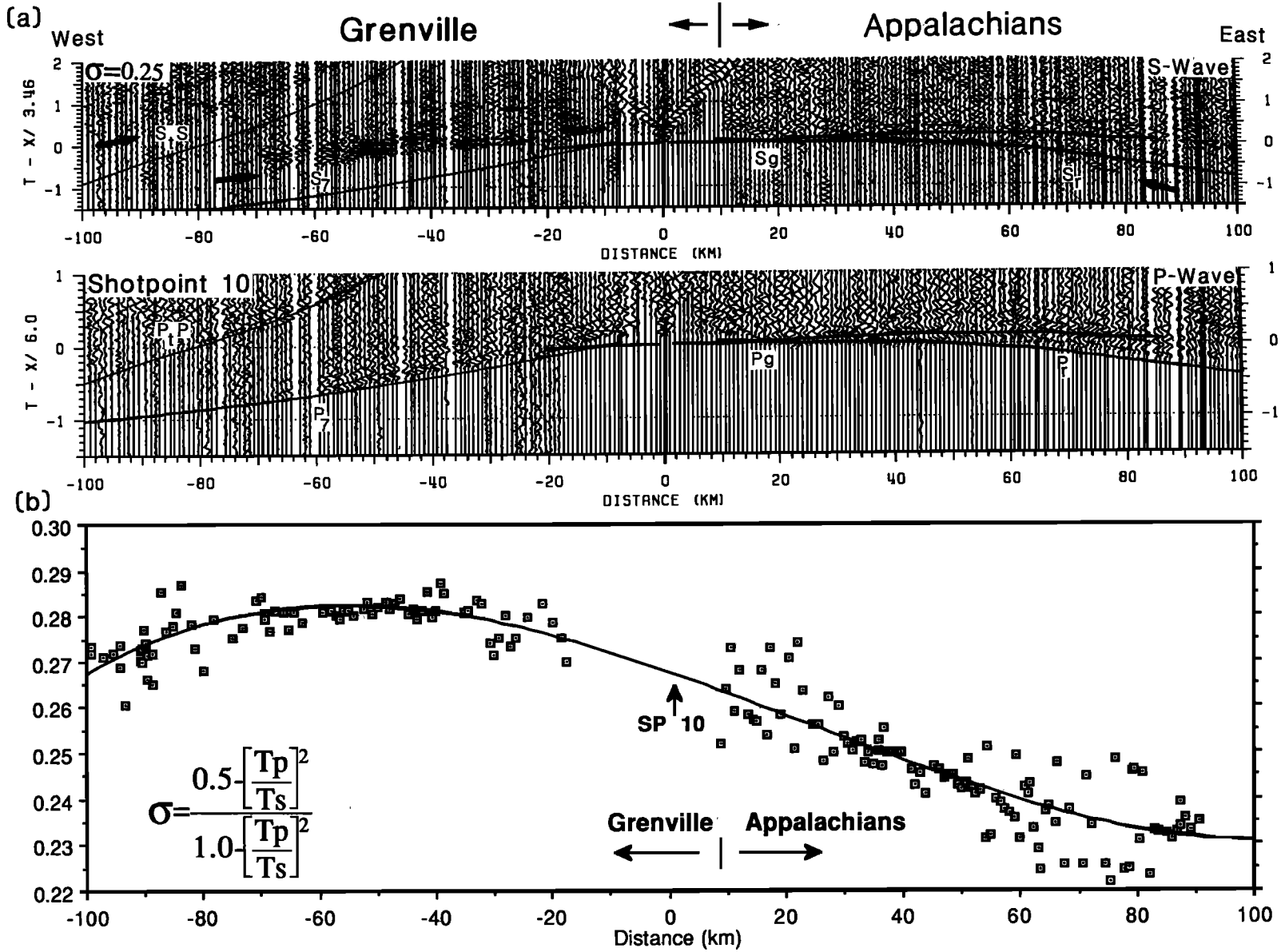

$$\sigma = \frac{0.5 - \left[\frac{Tp}{Ts}\right]^2}{1.0 - \left[\frac{Tp}{Ts}\right]^2}$$

Fig. 12. Variations in Poisson's ratio in upper crustal rocks near the edge of the Adirondack Mountains. (*a*) Record sections for shot point 10 show delayed *S* wave arrivals for ray paths through the Grenvillian crust and advanced *S* wave arrivals in the Appalachians. Predicted travel times (solid lines) for the model shown in Figure 2 are plotted on the *S* wave section, assuming a Poisson's ratio of 0.25. (*b*) Upper crustal P_g and S_g arrival times at each receiver station have been used to calculate Poisson's ratio from shot point 10. High Poisson's ratios observed in the Adirondack Highlands can be correlated with the Marcy Anorthosite, and normal Poisson's ratios observed for the upper crust in Vermont indicate the predominance of quartz-rich lithologies. See Figure 3 for key to phase identification.

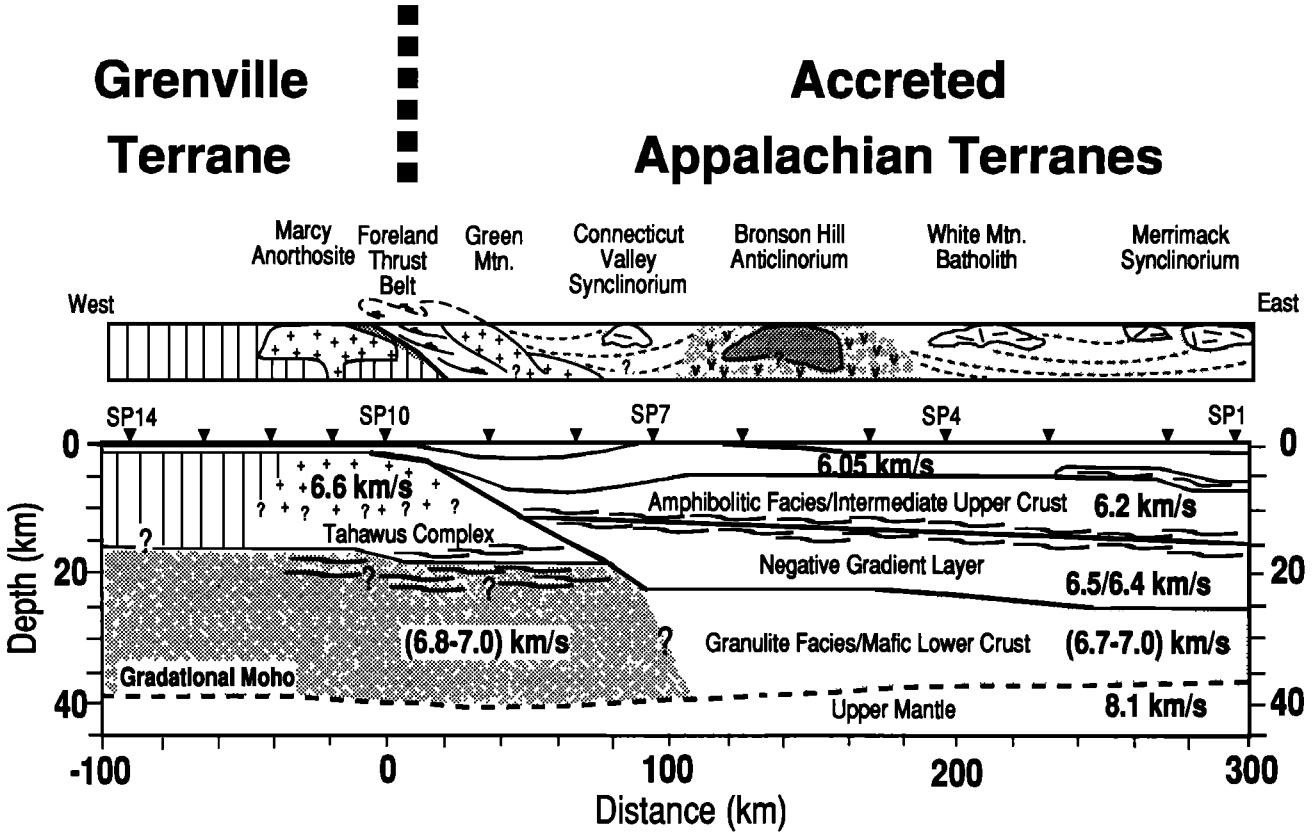

Fig. 13. Geologic interpretation of the first-order velocity model shown in Figure 2. A midcrustal penetrating ramp separates the Grenvillian crustal block from the accreted Appalachian terranes. A ramp structure divides the high-velocity Grenville terrane from the lower-velocity subhorizontally layered Appalachian crust. The lower crust is shown as a continuous layer, but it may be divided into discrete Appalachian/Grenville units. Solid lines indicate first-order velocity discontinuities; dashed lines indicate complex laminated gradational interfaces. Prominent midcrustal reflective interfaces are highlighted by the wavy lines.

Structure of the Grenvillian ramp: The Grenvillian ramp imaged by forward modeling of this seismic data set separates the autochthonous Grenville rocks and their "cover" sequence of the Adirondack region from the allochthonous Appalachian terranes. The relatively low resolution of the New England-New York seismic refraction profile means that only broad features of the seismic velocity structure of the crust are resolved. In short, we can trace a velocity interface that separates high seismic velocities characteristic of the Grenvillian upper crust from those of the lower-velocity rocks of the western Appalachians (Figure 13). The simplicity of this velocity interface belies the geological complexity of the basement-cover relationship of the Grenville crustal block. In the Champlain Valley, autochthonous platformal carbonates and quartzites lie in situ above the Grenvillian basement. These platformal rocks are imbricated with allochthonous slope rise lithologies of the Foreland Thrust Belt. Further east the Green Mountain Anticlinorium exposes obducted slices of Grenvillian basement interposed between the allochthonous "cover" sequence in the Taconic Orogeny. This imbricated wedge of allochthonous and autochthonous rocks is at its narrowest, and most structurally complex, at the point were the New England–New York seismic profile crosses into the Grenvillian crust. We interpret the Grenvillian ramp as the basal detachment of the allochthonous thrusted rocks of the Appalachians. The Grenville ramp is likely to be a highly complex thrust-imbricated and mylonitized remnant of the pre-Taconic (Ordovician) margin of proto–North America, upon which the accreted Bronson Hill island arc complex was obducted in Mid-Upper Ordovician times. Subsequent reactivation of the ramp in the Acadian Orogeny (Devonian) is strongly suggested by tectonic syntheses in the New England region [*Rowley and Kidd*, 1980; *Stanley and Ratcliffe*, 1985].

In the vicinity of our profile the transition from autochthonous Grenvillian lithologies to the accreted allochthons of the western Appalachians is delineated by the Champlain thrust (Logans Line). Comparison of results obtained from recent seismic experiments traversing the Appalachian-Grenville boundary may be usefully illustrated by aligning the models obtained from these experiments with respect to Logans Line (Figure 14). In northern Maine a major zone of reflections extends from shallow depths beneath the Foreland Thrust Belt to 25 km depth beneath the Chain Lakes Massif [*Stewart et al.*, 1986; *Spencer et al.*, 1987, 1989]. This reflection package has been interpreted as a "décollement" surface separating the allochthonous upper crustal units of the Appalachians from the autochthonous Grenvillian crust which underlies much of the western Appalachians (Figure 14*a*). Comparison of the Quebec-Maine "décollement" surface with the ramp model presented herein suggests that a remarkable degree of similarity exists along strike between these two models (Figure 14*b*). In the New England–New York seismic experiment the subcrop of the ramp structure

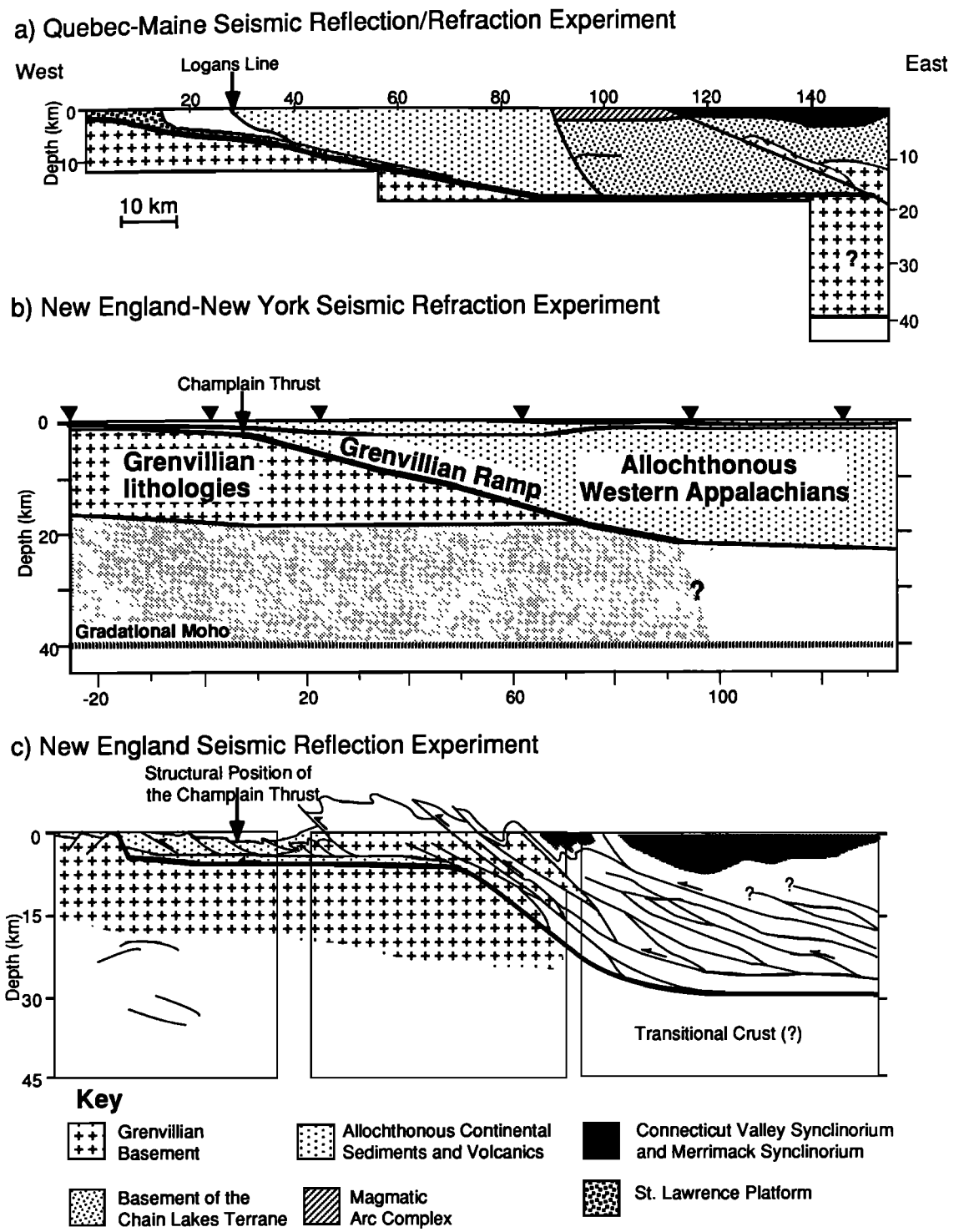

Fig. 14. Comparison of recent seismic experiments across the Appalachian-Grenville terrane boundary in New England. From north to south the results obtained from these seismic experiments are (*a*) the Quebec-Maine reflection/refraction experiment in southern Quebec [*Stewart et al.*, 1986; *Spencer et al.*, 1987, 1989], (*b*) the New England seismic refraction profile discussed herein, and (*c*) deep reflection profiling across the Taconic Allochthon in southern Vermont [*Brown et al.*, 1983; *Ando et al.*, 1984]. The boundary between the Grenvillian Province and the accreted Appalachians is characterized by noticeably similar planar ramp structures extending to midcrustal depths beneath the thrusted allochthons of the western Appalachians.

lies approximately at the position of the Champlain thrust. The resolution of the data does not allow us to definitively link these two features. Deep seismic reflection profiling in southern Vermont images a "thin skin" detachment beneath the Taconic allochthon which extends in the form of a steep "steplike" thrust imbricated structure beneath the Bronson Hill Anticlinorium to a depth of 30 km as shown in Figure 14*c* [*Brown et al.*, 1983; *Ando et al.*, 1984; *Phinney and*

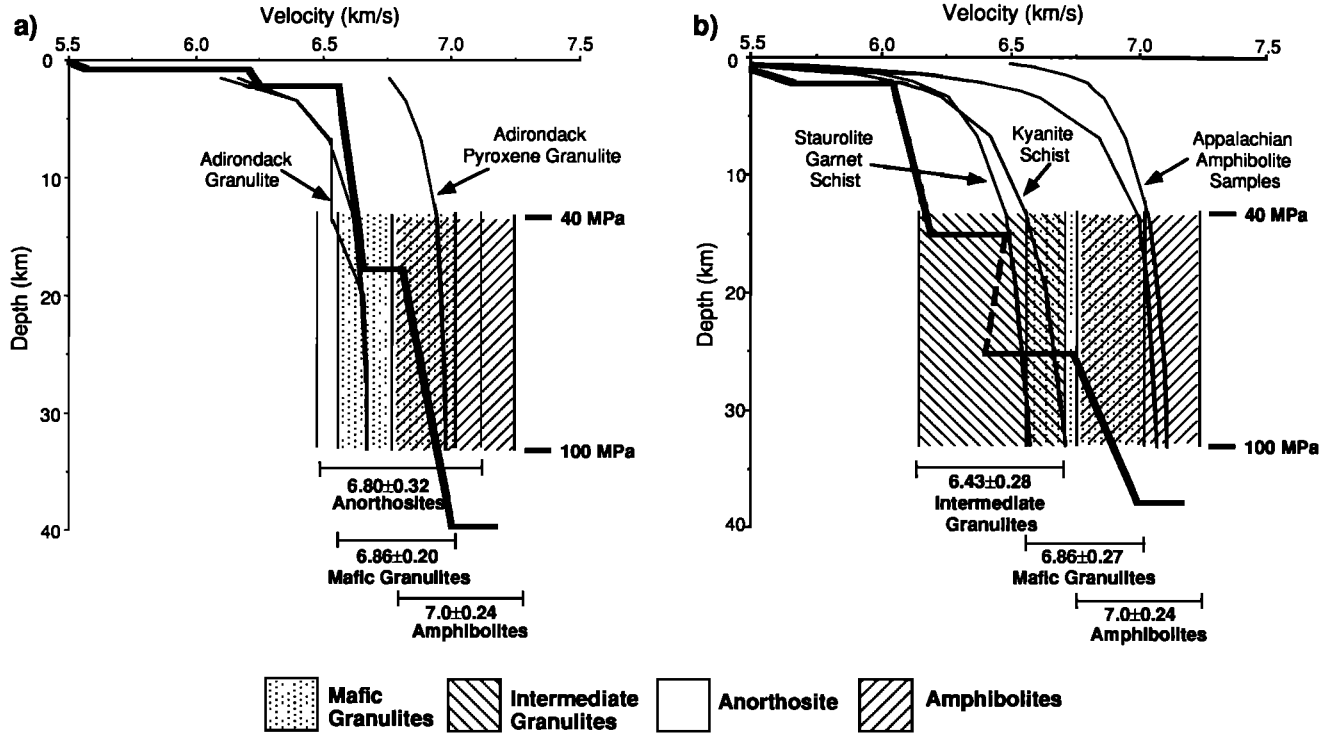

Fig. 15. Comparison of one-dimensional velocity functions (heavy line) for (*a*) the Appalachians (shot point 4) and (*b*) Adirondacks (shot point 11) with laboratory velocity measurements of samples at elevated pressures. Average seismic velocities are presented for possible constituents of the lower crust; ranges shown are one standard deviation [*Holbrook et al.*, 1991]. The lower crustal velocities beneath the central Appalachians are inferred to be best represented by mafic granulites (anhydrous feldspar, pyroxene, and garnet assemblages). Laboratory data have been corrected for temperature using a geotherm of 15°C/km [*Blackwell*, 1971] and an average thermal coefficient of 2.0×10^{-4} km/(s °C^{-1}) [*Christensen*, 1979; *Kern and Richter*, 1981]. Samples referenced are from *Christensen* [1965] and *Holbrook et al.* [1991].

Roy-Chowdhury, 1989]. Recent reprocessing of the southern Vermont profiles has resulted in a reinterpretation which suggests that the Appalachian/Grenville boundary is delineated by a series of steep planar imbricated fault zones extending into the lower crust [*Thigpen*, 1989]. Despite the relatively low resolution of seismic refraction profiling a consistent image of the buried edge of the Grenville Province emerges from comparison of the Quebec-Maine transect, the Vermont profiles, and the present study. The variations observed in the near-surface geometry of the ramp structure most likely owe their origin to lateral geologic discontinuities in the allochthonous Appalachian units. In the light of these results we tentatively suggest that the buried edge of the Grenville Province may be mapped extending beneath the Appalachians to a depth of around 25 km, at least as far as the eastern boundary of the Connecticut Valley Synclinorium.

Composition of the Grenvillian crust: In the present study the Grenvillian upper crust is characterized by high compressional wave velocities (6.6 km/s) and high Poisson's ratios (0.28 ± 0.01). Laboratory measurements of compressional wave velocities and Poisson's ratios for samples of Adirondack granulites and meta-anorthosites at elevated pressures are consistent with the derived velocity model shown in Figure 15*a* [*Birch*, 1960; *Christensen and Fountain*, 1975]. The Marcy Anorthosite is exposed at the western end of our profile as it crosses the metaigneous Adirondack massif. Gravity modeling of the Marcy Anorthosite indicates that it is tabular in shape and extends to a depth of 4 km, possibly with roots extending to 10–15 km [*Simmons*, 1964]. A suitable seismological analogue of the gravity model would be a 4-km-thick anorthosite layer with a velocity of 6.6 km/s, underlain by a layer composed of granulitic gneisses (exposed in the Adirondacks). Samples of granulitic gneisses in the high-pressure laboratory generally have upper crustal velocities less than those of anorthosite [*Birch*, 1960; *Christensen*, 1965; *Christensen and Fountain*, 1975]. Thus, if the Marcy Anorthosite were a shallow sheetlike intrusion as suggested by gravity modeling, a decrease in signal amplitude and a simultaneous delay in the arrival time branch from the lower-velocity gneissic crust would be observed. The absence of such features indicates that at the base of the Marcy Anorthosite, similar compressional wave velocities are observed for both the anorthosite and the underlying gneisses. At depths exceeding 10 km, meta-anorthosite and granulitic gneisses have similar compressional wave velocities and as such are seismically indistinguishable. The Marcy Anorthosite is likely to be around 10 km thick (Figure 13).

Composition of the Appalachian crust: The New England Appalachian upper crust is composed of upper greenschist to middle amphibolite facies sediments/volcanics and numerous intermediate to acidic metaigneous bodies. No identifiable reflections or travel time anomalies were observed from such major bodies as the Green Mountains, the Bronson Hill Anticlinorium, or the White Mountain Batholith. High-

amplitude upper crustal reflections observed beneath the easternmost extent of our profile may be explained by the presence of gneissic layering or by the subcrop of the New Hampshire Series granites exposed along the profile, and this would certainly fit with extrapolations of gravity models derived for the New Hampshire granites [*Nielson et al.*, 1976; *Hodge et al.*, 1982]. The modeled upper crustal velocities of around 6.1–6.2 km/s are consistent with laboratory measurements for a compositionally diverse set of gneisses, schists, metagabbros, and granodiorites [*Birch*, 1960; *Christensen*, 1965; *Christensen and Fountain*, 1975] (W. S. Holbrook et al., The seismic velocity structure of the deep continental crust, submitted to *Journal of Geophysical Research*, 1991).

The two-dimensional seismic velocity model for the New England Appalachian crust significantly lacks lateral velocity variations which might be correlated with terrane boundaries (Figure 13). This must, in part, be a consequence of the extensive obduction that formed the western Appalachians, where terrane boundaries are interpreted as highly imbricated structures [*Rowley and Kidd*, 1980; *Stanley and Ratcliffe*, 1985]. We envisage successive high-grade thermal "pulses" associated with at least three orogenic episodes resulting in regional amphibolite metamorphism, widespread plutonic intrusion, migmatization and, at deep levels, wholescale melting and mixing resulting in a largely homogenized Appalachian crustal block. Removal of the upper crust through successive periods of unroofing/isostatic uplift [*Eusden et al.*, 1987; *Chamberlain et al.*, 1985; *Harrison et al.*, 1989] reveals a window into highly deformed and altered midcrustal rocks which appear seismically homogeneous. The apparent seismic homogeneity of the New England upper crust is thus a possible indication of the overall mineralogical similarity of the constituents of the present-day upper crust. It is thus the case that although widely differing lithologies are observed at outcrop throughout the New England Appalachians, we are unable to resolve their seismological heterogeneity in the present study.

In this study, the midcrust (layer 5) is represented by a 10-km-thick layer which has been modeled with a negative seismic velocity gradient (Figure 13). This feature of the model may be related to compositional and thermal properties of the midcrust. Zones of velocity reversal can be produced by the anisotropic thermal expansion of the individual mineral constituents of the crust [*Christensen*, 1979; *Kern and Richter*, 1981]. In the eastern United States the geothermal gradient is ~15°C/km [*Blackwell*, 1971]. High thermal coefficients for likely constituents of the midcrust (amphibolitic granitic gneisses) mean that critical thermal gradients will be exceeded, and a velocity reversal will result [*Christensen*, 1979; *Kern and Richter*, 1981]. The magnitude of the velocity reversal produced by high temperatures is dependent on the the thermal gradient and the mineralogy of the crust, but it is unlikely to exceed 0.01 s^{-1} [*Christensen*, 1979]. At the top of the midcrust a planar reflecting horizon marks an abrupt increase in seismic velocity. The appearance of prominent midcrustal reflections over regional dimensions is a noticeable feature of this data set and of others collected in the vicinity [*Klemperer and Luetgert*, 1987; *Luetgert and Mann*, 1990; *Hennet et al.*, 1991]. Midcrustal reflectivity may be related to gneissic lamination, igneous "ponding", fluid rich zones in the midcrust, or bulk compositional changes. While all of the above may be considered as suitable proponents, the associated increase in seismic velocity observed in this study is most likely representative of bulk compositional change across the midcrustal interface. We consider that the midcrustal reflector delineates an increase in the mafic content of the crust.

Uncertainties in the derived velocity structure of the lower crust mean that lower crustal compositions cannot be unequivocally determined. In this study, shear wave velocity information is used to reduce the uncertainty in inferring the composition of the lower crust from compressional wave velocities alone, since shear wave velocities are sensitive to the felsic content of the crust. The incorporation of shear wave velocities into models of crustal composition enables the calculation of Poisson's ratio, a parameter which may be most usefully thought of as an indication of the relative quartz/feldspar content of the crust. Regions which exhibit low Poisson's ratios (low Vp/Vs) are typically quartz rich, since quartz has high shear wave velocities [*Christensen and Fountain*, 1975]. An estimate of Poisson's ratio for the lower crust may be obtained by removing the observed upper crustal Poisson's ratios from values obtained from phases traversing the whole crust. The delayed S_mS phase relative to a "normal" Vp/Vs ratio of 1.732 indicates an average crustal Poisson's ratio of 0.26 ± 0.01 (Figure 9*b*). Upper crustal rocks in New England have "normal" Poisson's ratios (0.24 ± 0.01). The travel time delay observed for phases traversing the entire crust must be restricted to the lower crust. Poisson's ratios for lower crustal rocks beneath the New England Appalachian are then likely to exceed 0.26.

A recent compilation of laboratory-measured rock velocities enables both compressional and shear wave velocities to be calculated for a particular rock type [*Holbrook et al.*, 1991]. Although the assignment of seismic velocity to rock type is highly dependent on the samples chosen to represent a particular compositional range, this data set provides a useful means of specifying end-members of a compositional series beyond which constraints imposed by in situ seismic velocities can not be satisfied. The high compressional wave velocities (6.7–7.0 km/s) and high Poisson's ratios (0.26–0.27) observed for rocks of the lower crust tend to favor an intermediate-mafic composition. Possible constituents of the lower crust include anorthosite, intermediate-mafic granulites, and amphibolitic assemblages. Laboratory determinations of Poisson's ratios for samples of anorthosites of around 0.29 [*Holbrook et al.*, 1991] suggest that anorthosite is an unlikely constituent of the lower crust in New England. Amphibolitic assemblages (metagabbro/hornblende, feldspar, pyroxene) at elevated pressures generally have compressional wave velocities exceeding those derived herein, while felsic granulites generally have compressional wave velocities much less than those observed beneath the New England Appalachians [*Birch*, 1960; *Christensen*, 1965; *Holbrook et al.*, 1991]. The most favorable composition for the lower crust is a mafic granulite facies assemblage containing feldspar, pyroxene, and garnet (Figure 15*b*).

Xenoliths provide direct evidence of lower crustal composition and can be used to reduce the nonuniqueness inherent in inferring composition from seismic velocities alone. Lamprophyre dike suites at Ayres Cliff, Quebec, and North Hartland, Vermont, contain granulite facies xenoliths [*Williams and McHone*, 1984; *Trzcienski and Marchildon*, 1989]. The xenoliths from Ayres Cliff are relatively unaltered and are commonly of two types: (1) metapelitic assemblages

originating from midcrustal depths, which are interpreted as Cambrian metasediments and (2) mafic assemblages and anorthosite fragments which are readily correlated to Grenville exposures in the Adirondacks. The North Hartland xenoliths are relatively unaltered lower crustal/upper mantle ultramafics and quartz-plagioclase granulites. These xenoliths support the existence of Grenville crust extending beneath the Appalachians at least as far as the western edge of the Connecticut Valley Synclinorium.

The obduction of the western Appalachians against the Grenvillian crustal block in the Taconic Orogeny has resulted in the juxtaposition of allochthonous lower Paleozoic continental sediments and volcanics against the Proterozoic protolith of North America. The seismic refraction date set obtained in this study allows us to characterize the seismic velocity structure of the accreted terranes in the New England Orogen. We can trace a steeply dipping ramp structure that divides the Grenvillian crust from the allochthonous Appalachian units emplaced during the Taconic Orogeny. The Grenvillian ramp extends to midcrustal depths at least as far as the western portion of the New England Appalachians. The Grenvillian lower crust appears seismically indistinguishable from the lower crust beneath the accreted Appalachian allochthons in spite of profound differences in the upper crustal structures and lithologies. This suggests that the lower crust may have been largely reformed, homogenized, and annealed during successive lower Paleozoic orogenic events and subsequent Mesozoic extension.

Acknowledgments. The data presented in this paper were collected by the U.S. Geological Survey, the Geological Survey of Canada, and the U.S. Air Force Geophysics Laboratory. We thank Walter Mooney (USGS), Jill McCarthy (USGS), and Bruce Beaudoin (Stanford University) for constructive reviews of earlier drafts of this manuscript. S.H. gratefully acknowledges financial support provided by the National Environmental Research Council, United Kingdom, (GT4/88/GS/64) and thanks his colleagues at the USGS, Menlo Park, California, for their assistance and encouragement. Reviews by Dave Stewart (USGS) and two anonymous reviewers greatly enhanced this manuscript.

REFERENCES

Ando, C. J., et al., Crustal profile of a mountain belt: COCORP deep seismic reflection profile in New England and implications for architecture of convergent mountain chains, *AAPG Bull.*, *68*, 819–837, 1984.

Birch, F., The velocity of compressional waves in rocks at 10 kbar, 1, *J. Geophys. Res.*, *65*, 1083–1102, 1960.

Blackwell, D. D., The thermal structure of the continental crust, in *The Structure and Physical Properties of the Earth's Crust*, *Geophys. Monogr. Ser.*, vol. 14, edited by J. G. Heacock, AGU, Washington, D. C., 1971.

Bradley, D. C., Tectonics of the Acadian Orogeny in New England and adjacent Canada, *J. Geol.*, *91*, 381–400, 1983.

Brown, L., C. Ando, S. Klemperer, J. Oliver, S. Kaufman, B. Czuchra, T. Walsh, and Y. W. Isachsen, Adirondack-Appalachian crustal structure: The COCORP northeast traverse, *Geol. Soc. Am. Bull.*, *94*, 1173–1184, 1983.

Cerveny, V., I. A. Molotkov, and I. Psencik, *Ray Method in Seismology*, 214 pp., Karolva University Press, Prague, 1977.

Chamberlain, C. P., and P. C. England, The Acadian thermal history of the Merrimack Synclinorium in New Hampshire, *J. Geol.*, *93*, 593–602, 1985.

Christensen, N. I., Compressional wave velocities in metamorphic rocks at pressures to 10 kbar, *J. Geophys. Res.*, *70*, 6147–6164, 1965.

Christensen, N. I., Compressional-wave velocities in rocks at high temperatures and pressures, critical thermal gradients, and crustal low velocity zones, *J. Geophys. Res.*, *84*, 6849–6857, 1979.

Christensen, N. I., and D. M. Fountain, Constitution of the lower continental crust based on experimental studies of seismic velocities in granulite, *Geol. Soc. Am. Bull.*, *86*, 227–236, 1975.

Costain, J. K., R. D. Hatcher, Jr., C. Coruh, T. J. Pratt, S. R. Taylor, J. J. Litehiser, and I. Zietz, Geophysical characteristics of the Appalachian crust, in *The Appalachian-Ouachita Orogen in the United States*, *The Geology of North America*, vol. F-2, edited by R. D. Hatcher, Jr., pp. 385–416, Geological Society of America, Boulder, Colo., 1990.

Eusden, J., W. A. Bothner, and A. M. Hussey, The Kearsarge-Central Maine synclinorium of southeast New Hampshire and southwestern Maine: Stratigraphic and structural relations of an inverted section, *Am. J. Sci.*, *287*, 246–264, 1987.

Harrison, M. T., F. S. Spear, and M. T. Heilzer, Geochronologic studies in central New England II: Post-Acadian hinged and differential uplift, *Geology*, *17*, 185–189, 1989.

Hatcher, R. D., Jr., P. H. Osberg, A. A. Drake, Jr., P. Robinson, and W. A. Thomas, Tectonic map of the U.S. Appalachians, in *The Appalachian-Ouachita Orogen in the United States*, *The Geology of North America*, vol. F-2, plate 1, edited by R. D. Hatcher, Jr., et al., Geological Society of America, Boulder, Colo., 1990.

Hennet, C. G., J. H. Luetgert, and R. A. Phinney, The crustal structure in central Maine from coherency processed refraction data, *J. Geophys. Res.*, *96*, 12,023–12,037, 1991.

Hodge, D. S., D. A. Abbey, M. A. Harbin, J. L. Patterson, M. J. Ring, and J. F. Sweeney, Gravity studies of subsurface mass distributions of granitic rocks in Maine and New Hampshire, *Am. J. Sci.*, *282*, 1289–1324, 1982.

Kern, H., and A. Richter, Temperature derivatives of compressional and shear wave velocities in crustal and mantle rocks at 6 Kbar confining pressure, *J. Geophys.*, *49*, 47–56, 1981.

Klemperer, S. L., and J. H. Luetgert, A comparison of reflection and refraction processing and interpretation methods applied to conventional refraction data from coastal Maine, *Bull. Seismol. Soc. Am.*, *77*, 614–630, 1987.

Klemperer, S. L., L. D. Brown, J. E. Oliver, C. J. Ando, B. L. Czuchra, and S. Kaufman, Some results of COCORP seismic reflection profiling in the Grenville-age Adirondack Mountains, New York State, *Can. J. Earth Sci.*, *22*, 141–153, 1985.

Luetgert, J. H., Users manual for RAY83/R83PLT: Interactive two-dimensional raytracing/synthetic seismogram package, *U.S. Geol. Surv. Open File Rep.*, *88-238*, 1988*a*.

Luetgert, J. H., Users manual for RSEC88: Interactive computer program for plotting seismic refraction record sections, *U.S. Geol. Surv. Open File Rep.*, *88-262*, 1988*b*.

Luetgert, J. H., Users manual for R1D84: Interactive modeling of one-dimensional velocity depth functions, *U.S. Geol. Surv. Open File Rep.*, *88-262*, 1988*c*.

Luetgert, J. H., and C. E. Mann, Avalon terrane in eastern coastal Maine: Seismic refraction-wide-angle reflection data, *Geology*, *18*, 878–881, 1990.

Luetgert, J. H., C. E. Mann, and S. L. Klemperer, Wide-angle crustal reflections in the northern Appalachians, *Geophys. J. R. Astron. Soc.*, *89*, 183–188, 1987.

Luetgert, J. H., S. Hughes, J. Cipar, S. Mangino, D. Forsyth, and I. Asudeh, Data report for O-NYNEX, the 1988 Grenville-Appalachian seismic refraction experiment in Ontario, New York and New England, *U.S. Geol. Surv. Open File Rep.*, *90-426*, 1990.

McHone, J. G., and J. R. Butler, Mesozoic igneous provinces of New England and the opening of the North Atlantic Ocean, *Geol. Soc. Am. Bull.*, *95*, 757–765, 1984.

McLelland, J. M., and Y. W. Isachsen, Synthesis of geology of the Adirondack Mountains, New York, and their tectonic setting within the southwestern Grenville Province, in The Grenville Province, edited by J. M. Moore, A. Davidson, and A. J. Baer, *Geol. Assoc. Can. Spec. Pap.*, *31*, 75–94, 1986.

Mooney, W. D., Seismic methods for determining earthquake source parameters and lithospheric structure, in Geophysical Framework of the Continental United States, edited by L. C. Pakiser and W. D. Mooney, *Mem. Geol. Soc. Am.*, *172*, 11–34, 1989.

Murphy, J. M., USGS FM cassette seismic-refraction recording system, *U.S. Geol. Surv. Open File Rep.*, *89-570*, 1989.

Nielson, D. L., R. G. Clark, J. B. Lyons, E. J. Englund, and D. J. Boris, Gravity models and mode of emplacement of the New Hampshire Plutonic Series, *Mem. Geol. Soc. Am., 146*, 301–318, 1976.

Osberg, P. H., Synthesis of the geology of the Northeastern Appalachians, U.S.A., in I.G.C.P. Project 27, Caledonian-Appalachian Orogen of the North Atlantic Region, edited by E. T. Tozer et al., *Pap. Geol. Surv. Can., 78-13*, 137–147, 1978.

Phinney, R. A., and K. Roy-Chowdhury, Reflection seismic studies in the eastern United States, in Geophysical Framework of the Continental United States, edited by L. C. Pakiser, and W. D. Mooney, *Mem. Geol. Soc. Am., 172*, 613–653, 1989.

Robinson, P., and L. M. Hall, Tectonic synthesis of southern New England, in *The Caledonides in the U.S.A., I.G.C.P. Project 27*, edited by D. R. Wones, pp. 73–81, Virginia Polytechnic Institute Press, Blacksburg, Va., 1979.

Rogers, J., *The Tectonics of the Appalachians, Reg. Geol. Ser.*, edited by L. U. De Sitter, pp. 91–115, Wiley-Interscience, New York, 1970.

Rowley, D. B., and W. S. F. Kidd, Stratigraphic relationships and detrital composition of the medial Ordovician flysch of western New England: Implications for the tectonic evolution of the Taconic Orogeny, *J. Geol., 89*, 199–218, 1980.

Selleck, B. W., Post orogenic history of the Adirondack region; a review, *Geol. Soc. Am. Bull., 91*, 120–124, 1980.

Simmons, G., Gravity survey and geological interpretation, northern New York, *Geol. Soc. Am. Bull., 75*, 81–98, 1964.

Spencer, C., A. Green, and J. H. Luetgert, More seismic evidence on the location of the Grenville basement beneath the Appalachians of Quebec-Maine, *Geophys. J. R. Astron. Soc., 89*, 177–182, 1987.

Spencer, C., A. Green, P. Morel-a-l'Huissier, B. Milkereit, J. H. Luetgert, D. B. Steward, J. D. Unger, and J. D. Phillips, Allochthonous units in the Northern Appalachians: Results from the Quebec-Maine seismic reflection and refraction surveys, *Tectonics, 8*, 667–696, 1989.

Stanley, R. S., and M. N. Ratcliffe, Tectonic synthesis of the Taconic Orogeny in western New England, *Geol. Soc. Am. Bull., 96*, 1227–1250, 1985.

Stewart, D. B., J. D. Unger, J. D. Phillips, R. Goldsmith, W. H. Poole, C. P. Spencer, A. G. Green, M. C. Loiselle, and P. St-Julien, The Quebec-Western Maine seismic reflection profile: Setting and first year results, in *Reflection Seismology: The Continental Crust, Geodyn. Ser.*, vol. 14, edited by M. Barazangi and L. Brown, pp. 189–199, AGU, Washington, D. C., 1986.

Stewart, D. B., B. E. Wright, J. D. Unger, J. D. Phillips, D. R. Hutchinson, J. H. Luetgert, W. A. Bothner, K. D. Klitgord, L. M. Liberty and C. Spencer, The Quebec-Maine-Gulf of Maine Transect, Southeastern Canada, Northeastern United States of America; Global Geoscience Transect 8, *U.S. Geol. Surv. Open File Rep., 91-353*, 1991.

Taylor, S. R., Geophysical framework of the Appalachians, in Geophysical Framework of the Continental United States, edited by L. C. Pakiser and W. D. Mooney, *Geol. Soc. Am. Mem., 172*, 317–348, 1989.

Taylor, S. R., and M. N. Töksoz, Crust and upper-mantle velocity structure in the Appalachian orogenic belt: Implications for tectonic evolution, *Geol. Soc. Am. Bull., 93*, 315–329, 1982.

Thigpen, J. T., Seismic reflection evidence for imbricate basement slices in central New England, Msc. thesis, 95 pp., Cornell Univ., Ithaca, N. Y., 1989.

Trzcienski, W. E., and N. Marchildon, Kyanite-garnet bearing Cambrian rocks and Grenville granulites from the Ayer's Cliff, Quebec, Canada, lamprophyre dike suite: Deep crustal fragments from the northern Appalachians, *Geology, 17*, 637–640, 1989.

Wiener, R. W., J. M. McLelland, W. I. Isachsen, and L. M. Hall, Stratigraphy and structural geology of the Adirondack Mountains, New York: Review and synthesis, in The Grenville Event in the Appalachians and Related Topics, edited by M. J. Bartholomew, *Spec. Pap. Geol. Soc. Am., 194*, 1–55, 1984.

Williams, H., Tectonic lithofacies map of the Appalachian Orogen, Map 1a, Canadian contribution, 5, I.G.C.P. project 27, the Appalachian-Caledonides Orogen, Memorial University of Newfoundland, 1978.

Williams, H., and R. D. Hatcher, Suspect terrains and the accretionary history of the Appalachian Orogen, *Geology, 10*, 530–536, 1982.

Williams, N. A., and J. G. McHone, Mantle and crustal xenoliths from the North Hartland dyke, Vermont, *Geol. Soc. Am. Abstr. Programs, 16*, 71, 1984.

Zen, E-an, Exotic terranes in the New England Appalachians-limits, candidates, and ages: A speculative essay, *Mem. Geol. Soc. Am., 158*, 55–81, 1983.

S. Hughes and J. H. Luetgert, U.S. Geological Survey, Branch of Seismology, MS 977, 345 Middlefield Road, Menlo Park, CA 94025.

(Received November 13, 1990;
revised April 10, 1991;
accepted May 29, 1991.)

JOURNAL OF GEOPHYSICAL RESEARCH, VOL. 96, NO. B10, PAGES 16,625–16,639, SEPTEMBER 10, 1991

The Relationship Between Plate Curvature and Elastic Plate Thickness: A Study of the Peru-Chile Trench

ANNE V. JUDGE[1] AND MARCIA K. MCNUTT

Department of Earth, Atmospheric, and Planetary Sciences, Massachusetts Institute of Technology, Cambridge, Massachusetts

The age of the Nazca plate where it enters the Peru and northern Chile trenches varies from 30 Ma in the north to 45 Ma in the south as its dip beneath the South American continent steepens from 13° to 30°. If the elastic thickness T_e of oceanic lithosphere depends only on its age, and therefore thermal state, we would expect that T_e determined from fitting the flexure of the lithosphere over the outer rise as revealed in the depth, geoid, and gravity anomalies would increase from the Peru Trench in the north to the northern Chile Trench further south. We find that the opposite is true: the lithosphere appears stiffer outboard of the Peru Trench than it does offshore Chile. To explain deflections of the lithosphere seaward of Peru, the isotherm controlling the elastic/ductile transition must be near 800°C, providing the thermal structure of the plate is that predicted by the standard thermal plate model. Because the decrease in plate stiffness to the south is correlated with an increase of plate curvature over the outer rise and outer trench wall, we interpret our result in terms of inelastic yielding of the oceanic lithosphere when bent to high strains. The magnitude of the reduction in strength, however, suggests that the standard oceanic yield strength envelope underestimates the amount of failure for lithosphere bent to high strains unless the stress field off northern Chile is characterized by 100-MPa-level tension. The more highly bent segment of subducting lithosphere at this trench also dips at a steeper angle at greater depth beneath the continent, but detailed analysis of plate geometry does not support a relationship between slab dip as determined by earthquake hypocenters and elastic behavior over the outer rise.

INTRODUCTION

It is generally agreed that oceanic lithosphere behaves as a thin elastic plate in response to applied stress over geologic time scales [*Walcott*, 1970; *Hanks*, 1971; *Watts and Cochran*, 1974; *Caldwell et al.*, 1976] and that the effective elastic thickness of the plate increases as the square root of age of the plate at the time of loading due to thermal control on the depth to the elastic-ductile transition [*Watts et al.*, 1980]. What is less certain is the magnitude of the reduction in the effective elastic thickness from the value predicted by lithospheric age due to inelastic processes within sharply bent plates at subduction zones, despite a number of attempts to explicitly include plastic deformation in flexural models [*Turcotte et al.*, 1978; *McAdoo et al.*, 1978; *Bodine and Watts*, 1979; *Carey and Dubois*, 1981] and the rheological arguments for its importance [*Goetze and Evans*, 1979; *McNutt and Menard*, 1982]. A better calibration of the yield strength of oceanic lithosphere is essential for understanding its rheology and state of stress.

The Peru-Chile Trench (Figure 1) provides a suitable natural laboratory for investigating lithospheric rheology, for as the age of the subducted Nazca plate increases from 30 Ma to 45 Ma to the south along the trench system [*Handschumacher*, 1976; *Hilde and Warsi*, 1984; *Herron*, 1972; *Scheidegger and Corliss*, 1981], the curvature of the plate on the outer rise and outer trench wall increases to accommodate a change from 13° to 30° in the dip of the downgoing slab beneath South America [*Barazangi and Isacks*, 1976, 1979]. Using observations of depth, geoid, and gravity anomalies, we will examine what constraints can be placed on the relative importance of temperature and bending stress in controlling effective elastic plate thickness. If failure of the plate at the higher stresses sustained in the south is unimportant, then the effective elastic plate thickness of that older lithosphere should be at least 5 km greater than that of the younger lithosphere to the north. If failure of the plate at high curvatures is more important than the 15 m.y. increase in age in controlling elastic plate thickness, then the effective elastic plate thickness to the south may actually be less than that of the younger lithosphere in the north.

THE MODEL

We begin by approximating the lithosphere as a one-dimensional thin elastic plate overlying a fluid mantle flexed by external forces and moments applied at the trench axis [*Caldwell et al.*, 1976; *Turcotte and Schubert*, 1982]. The elastic strength of such a plate is measured by its flexural rigidity D, which is related to the effective elastic plate thickness T_e via $D = E T_e^3/12(1-\nu^2)$, where E is Young's modulus and ν is Poisson's ratio. Its displacement w at a point x external to the loads is described by a solution to the thin plate equation

$$w(x) = A \exp\left(-\frac{x}{\alpha}\right) \sin\frac{x}{\alpha} \qquad (1)$$

where $\alpha^4 = (4D/\Delta\rho g)$, $\Delta\rho$ is the difference in density between the underlying mantle rock and the overlying water, g is the gravitational acceleration, A depends on the magnitude of all forces and moments applied landward of the trench axis, and x is measured from the first zero crossing seaward of the trench axis [*Turcotte et al.*, 1978; *Jones et al.*, 1978; *Turcotte and Schubert*, 1982]. This solution is only valid if the flexural rigidity is constant and there are no lateral forces applied to the plate.

The predicted bathymetry from elastic flexure is given directly by (1). The corresponding geoid and gravity anomalies can be generated using *Parker*'s [1972] method to calculate potential field anomalies from undulations of the surface and Moho as described by (1) seaward of the trench axis and by reflecting the profile about this point landward of the trench axis [*McAdoo and Martin*, 1984].

[1]Now at Geophysical Research, ELF Aquitaine, Pau, France.

Paper number 90JB01772.
0148-0227/90/90JB-01772$05.00

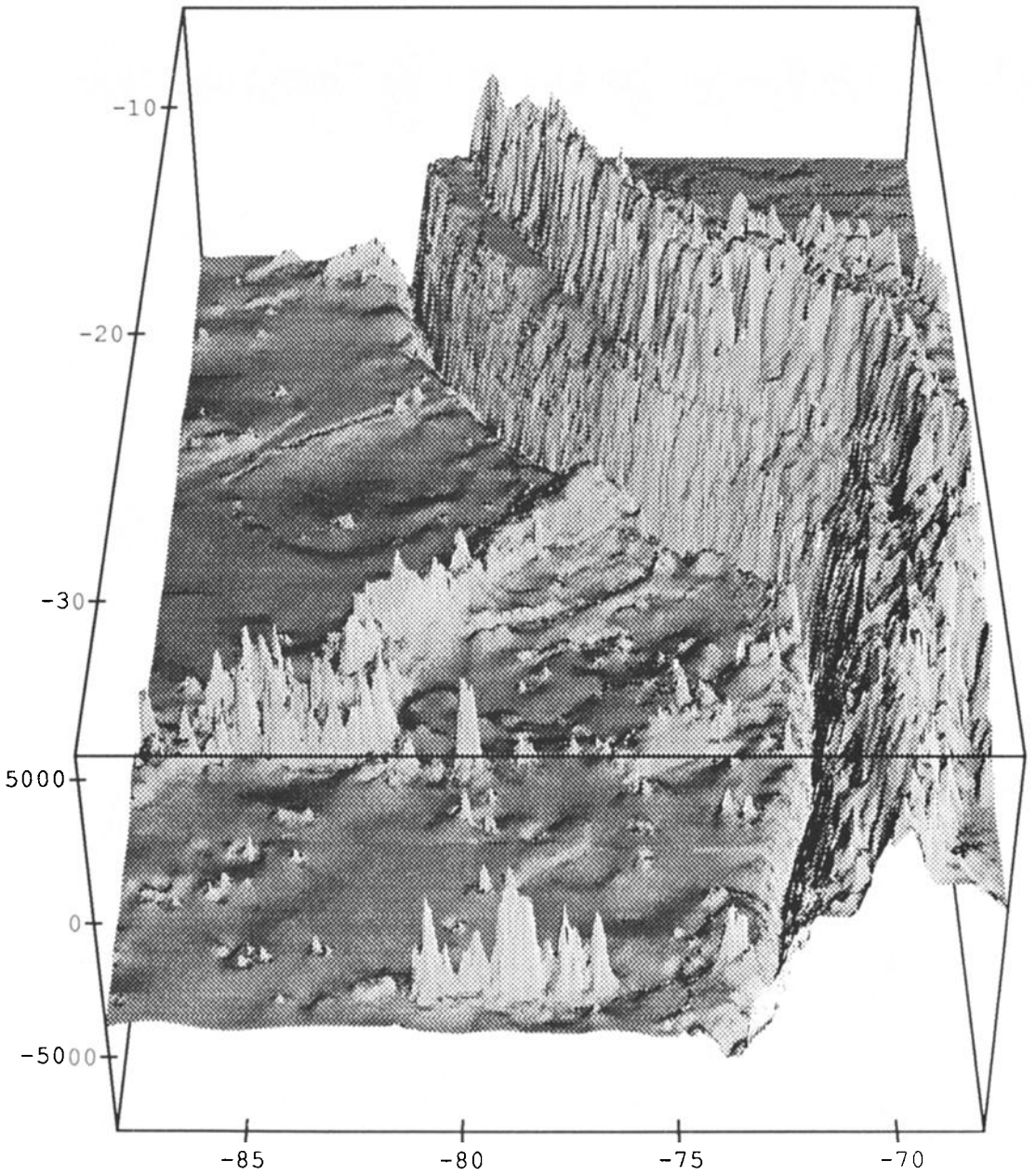

Fig. 1. Three-dimensional image of the topographic relief along the western coast of South America. The region referred to as the Peru province lies to the north of the northeast-trending Nazca Ridge, and the region referred to as the Northern Chile province lies to the south.

This approach gives similar results to a model in which the Moho deepens landward of the trench, and has the advantage of being easily reproducible, whereas an arbitrary choice of slope under the inner trench wall is not.

By varying both α and A, we can estimate the value of T_e which best explains the bathymetric, geoid, or gravity undulations seaward of the subduction zone. In most cases the portion of the bathymetric, geoid, or gravity profile to which the theoretical curve (1) was fit extended from the trench axis to a point 300 km seaward of the origin (second zero-crossing). In some cases a slightly shorter segment was used in order to avoid features, such as seamounts, which were obviously unrelated to the flexural response of the plate. These profiles included nearly undeflected seafloor as well as sharply bent lithosphere near the base of the trench. For each profile, a curve of minimum rms misfit versus elastic thickness was constructed by varying amplitude A until misfit was minimized for the value of α corresponding to each elastic thickness. The uncertainty assigned to each T_e-estimate is one-half the width of this curve where the misfit reached 1.5 times its minimum value, as shown in Figure 2. This measure was chosen because it is dependent on both the steepness of this curve and the minimum value the misfit obtains. A profile which is fit with small minimum misfit and a relatively wide, shallow curve (Figure 2*a*) and a profile fit with large misfit but a steep curve (Figure 2*b*) can both be considered to have a well-constrained elastic thickness and will both have a narrow half-width as determined by this method. In general, profiles for which the half-width was less than 10 km were considered to have a well-constrained value for T_e.

For profiles along which the flexural stresses are insufficient to exceed the strength of the lithosphere at depths shallower than the base of the elastic plate, T_e should correspond to the depth to some isotherm Θ_e that corresponds to the elastic/ductile transition and deepens as the square root of the age of the plate [*Watts et al.*, 1980]. Any yielding of the plate, such as via brittle failure near the

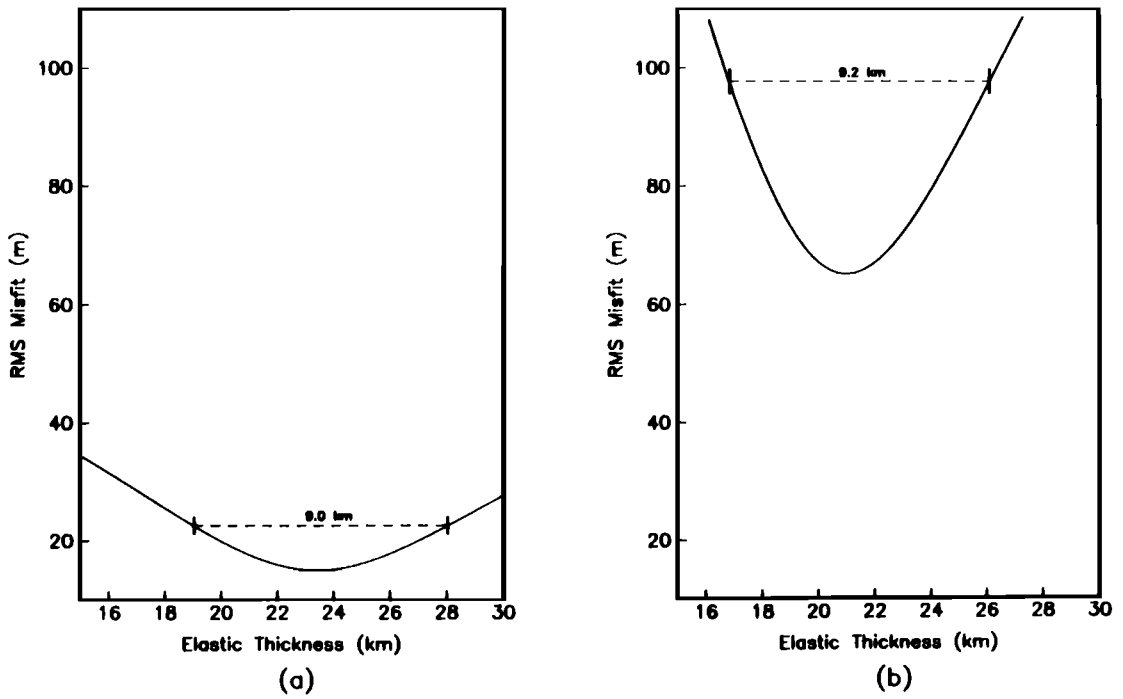

Fig. 2. (*a*) A plot of the minimum misfit at each value of elastic thickness for profile 3 in the northern region of the Peru province. The half-width is 4.5 km. (*b*) A similar plot for profile 5 in region 2 of the North Chile province. The half-width is 4.6 km.

upper surface or ductile creep near the base, in response to large elastic fiber stresses will cause T_e to underestimate the depth to the isotherm Θ_e. Thus given observations of changes in T_e with lithospheric age and curvature (the second derivative of the deflection w) along the Peru-Chile Trench, we can estimate the value of Θ_e and assess the magnitude of the reduction in the effective elastic plate thickness T_e caused by yielding of the lithosphere at high stresses [*Goetze and Evans*, 1979; *McNutt and Menard*, 1982].

THE DATA

In order to study flexure of the plate seaward of the Peru-Chile Trench, we extracted profiles perpendicular to the trench axis from global data sets of bathymetry [*Heirtzler and Edwards*, 1985], geoid [*Marsh et al.*, 1986], and gravity derived from geoid using the method of *Haxby* [1987]. We found that modeling three different types of data was useful for distinguishing which features of the profiles were unrelated to plate flexure. For example, seamounts and plateaus often led to a poor fit between the predictions of (1) and a bathymetric profile, but since those features are isostatically compensated, they were less apparent in the geoid profile. In addition, even though the geoid and gravity are only different representations of the same altimetric data set, the geoid proved to be sensitive, even at points far from the trench, to the exact configuration of mass assumed landward of the trench axis, whereas the gravity over the outer rise and even over most of the trench wall was insensitive to this geometry.

The gridded bathymetric data were originally interpolated from shipboard readings along tracks that provide generally good coverage of the area. The separation of ship tracks parallel to the trench is usually less than 30 km, whereas characteristic shapes of trench-related structures in that dimension in most cases can be traced over 80 km. We interpolated the bathymetric data onto profiles spaced at 10-km intervals perpendicular to a number of line segments fit to the trench axis. An attempt was made to subtract an age-depth curve from these profiles, but they had no apparent slope with age despite the young age of the crust.

Geoid and gravity data were obtained on a 15-min grid and interpolated onto profiles spaced 30 km apart, corresponding to every third bathymetric profile across the trench axis. A model GEM-T1 [*Marsh et al.*, 1988] reference field to degree and order 10 was removed from the geoid data. Removal of higher-order fields produced a geoid with no apparent relationship to the outer rise. After removal to degree and order 10, a long-wavelength variation was still apparent across the region of interest. Because this trend did not appear to relate to the topography of the outer rise and trench, and its slope was greater than that of the geoid-age relationship in young crust, it was simply removed by subtracting from each profile a line of constant slope.

RESULTS

We first present the results from modeling the depth, geoid, and gravity data from the Nazca plate seaward of the Peru and northern Chile trenches assuming two-dimensional flexure of a plate with constant rigidity and no applied in-plane stress. Enough profiles are adequately fit under these restrictive assumptions to estimate the elastic plate thickness and plate curvature in each area. However, at the end of this section we do discuss the effect of relaxing these assumptions to allow variable plate rigidity, three-dimensional bending, and horizontal thrusts.

Peru

The Peru trench can be approximated as a 300-km-long northern segment running from 6°S and 8.5°S and a 600-km-long southern segment continuing to 13.2°S, where the trench becomes shallower and less well-defined approaching the flanks of the Nazca Ridge (Figure 3). Some representative bathymetric profiles crossing the trench are shown in Figure 4, and the geoid profiles along the same tracks appear in Figure 5. The bathymetric profiles are numbered consecutively from north to south within each region.

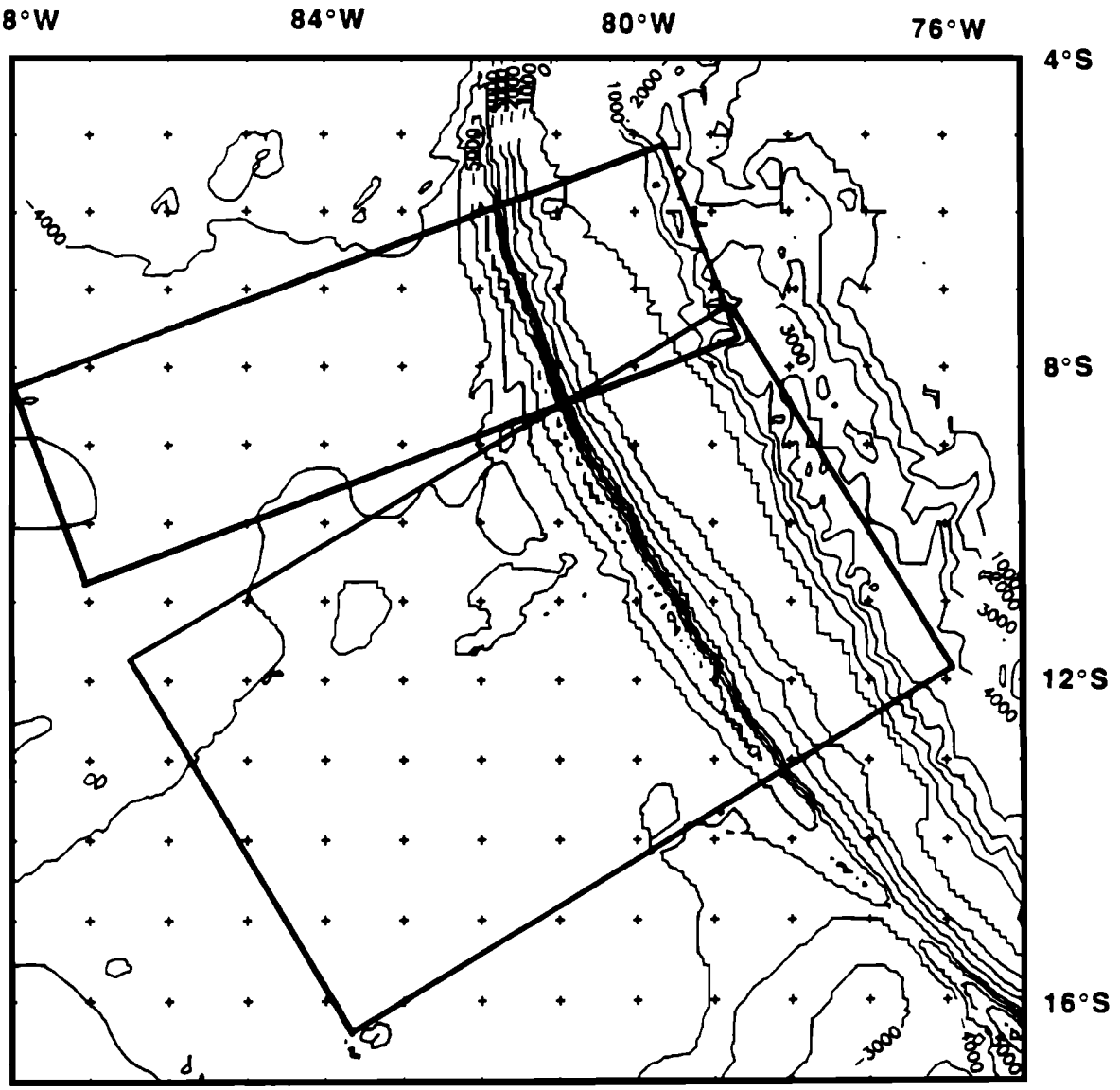

Fig. 3. Bathymetry of the region near the Peru Trench for which data were obtained, showing the location of the areas from which profiles were taken

Geoid height profiles are identified by the number of the corresponding bathymetric profile. Those profiles which could be fit by elastic theory are shown with the best fitting elastic curve superimposed, and the values for T_e are plotted in Figures 6*a* and 6*b*.

In general, there is fairly good agreement among the elastic plate thickness estimates derived from bathymetry, geoid, and gravity data for northern Peru, although there is a tendency for geoid data to indicate larger values of T_e and for bathymetry to indicate smaller values compared to those consistent with the gravity data (Figure 6*a*). Also, there is a monotonic decrease in elastic plate thickness determined from bathymetric data over the northernmost 100 km of the northern Peru Trench that is not indicated by the geoid or gravity data, which in general are more consistent across the area.

Only bathymetric profiles in the northernmost 250 km of the southern region (Figure 6*b*) could be fit by the elastic model, while nearly all of the geoid and gravity profiles displayed clear outer rises consistent with the shape predicted by (1). Even where the bathymetric profiles could be fit with an elastic model, the values for T_e are much smaller than those indicated by either geoid or gravity. Throughout the southern region, the outer rise in the bathymetry is small or nonexistent, and its disappearance cannot be explained by sediment thickness patterns [*Hussong et al.*, 1976; *Dang*, 1984]. The inconsistency between the small value for elastic thickness obtained from the bathymetry and the presence of distinct geoid and gravity highs indicates that the bathymetry does not reflect the behavior of the plate, and for this reason values derived from bathymetry were excluded in computing the average elastic thickness in the Peru province.

Near the northern edge of the southern region the Mendaño Fracture Zone intersects the trench, with an associated change in crustal age of 12 Ma. Averaging values of elastic thickness found for same-age crust results in a value of 32 ± 4 km for the 30-Ma lithosphere of the northern region and 39 ± 2 km for the 42-Ma lithosphere south of the fracture zone (Figure 7). In order to estimate the amount of yielding expected for each profile, we also computed the curvature of the plate at the first zero crossing seaward of the trench axis. At this location, the relationship between the bending moment supported by the plate and its curvature is independent of any applied in-plane stress [*McNutt and Menard*, 1982]. Average curvatures at the zero crossing K are $(2.4 \pm 0.6) \times 10^{-7}$ m^{-1} in the northern area and $(1.6 \pm 0.2) \times 10^{-7}$ m^{-1} in the south (Figure 7).

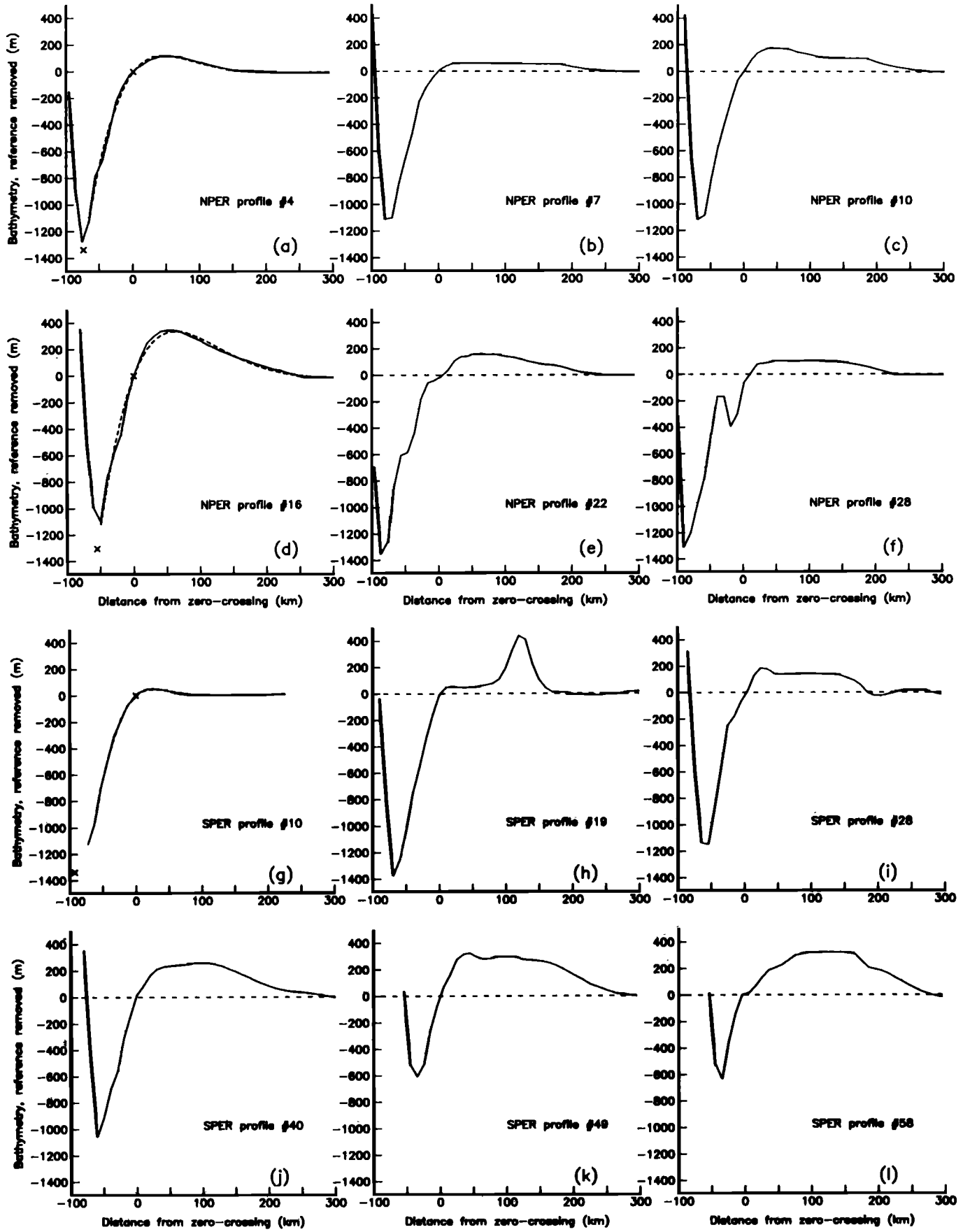

Fig. 4. A series of representative profiles across the Peru trench, extending 300 km to seaward and up to 70 km landward of the first zero crossing. NPER represents the northern region and SPER is the southern region. Those profiles which could be satisfactorily fit by the elastic model are shown with this model dashed in; those which could not are shown with a horizontal line at an estimated reference height.

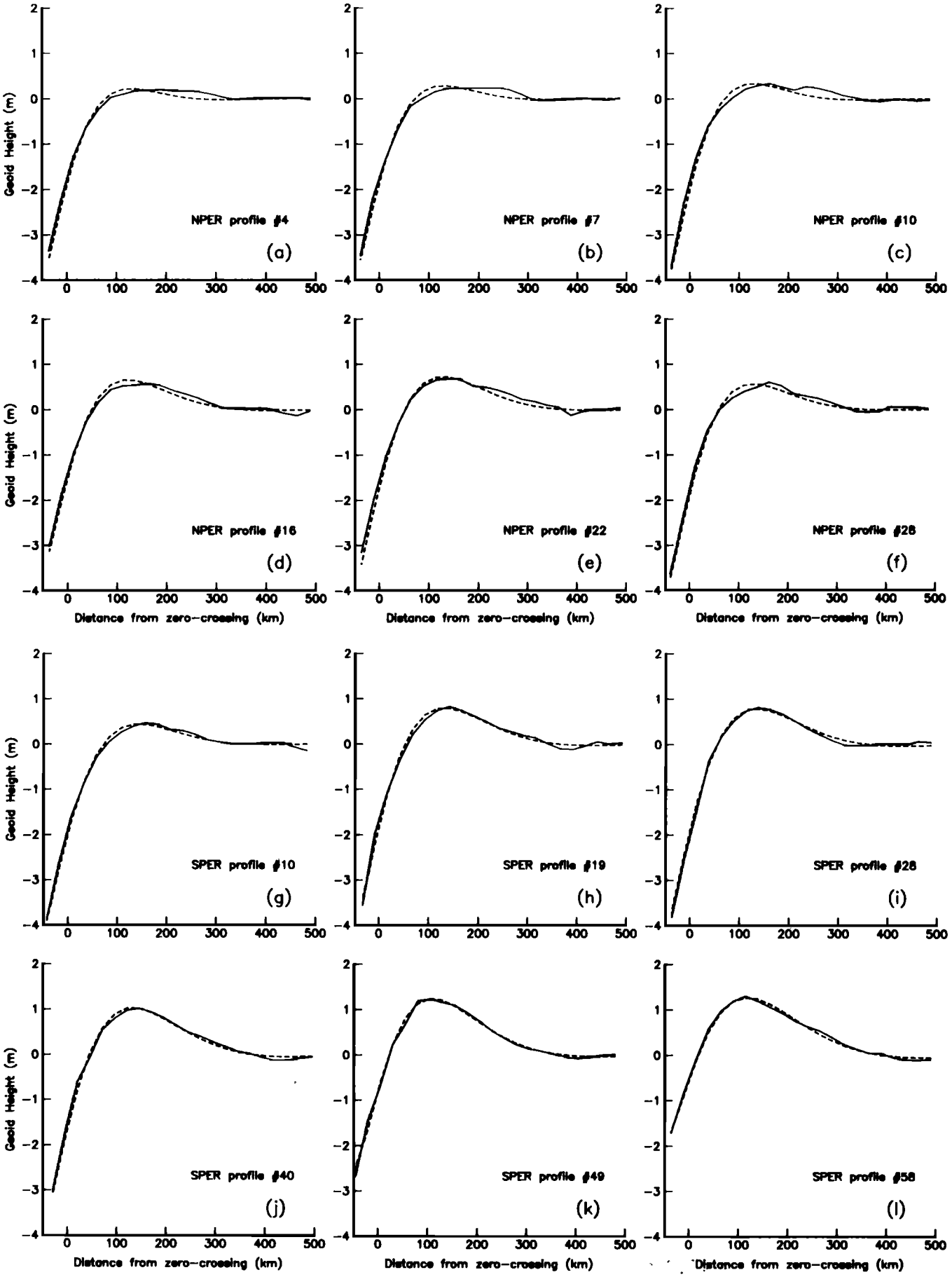

Fig. 5. The geoid along the same profiles for which bathymetry was shown in Figure 4. The solid line is the observed geoid, and the dashed line is the best fitting theoretical geoid which could be generated from an elastic curve.

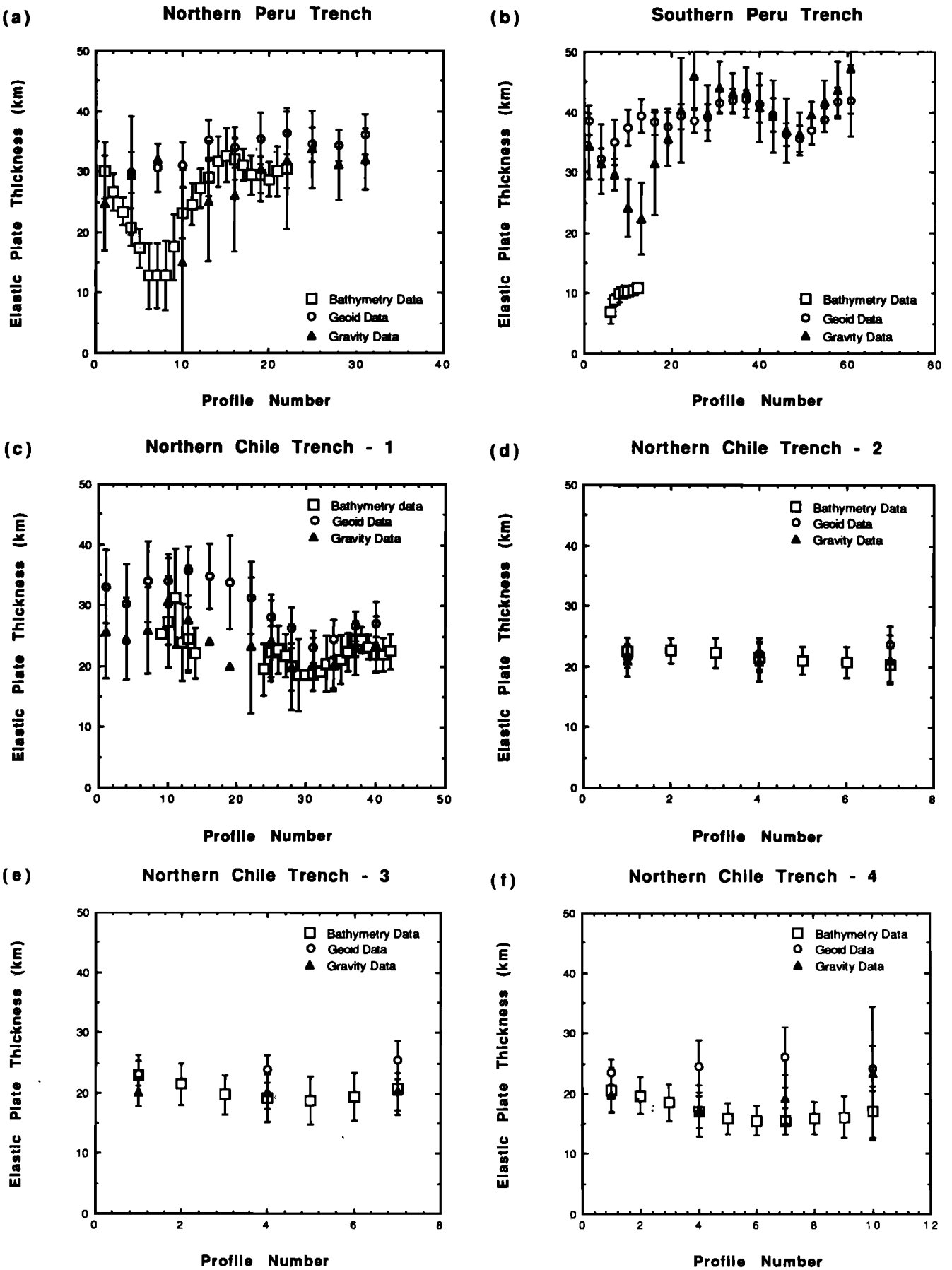

Fig. 6. Comparison of values of effective elastic thickness best fitting bathymetry, geoid, and gravity profiles within the two sections of the Peru Trench shown in Figure 3 and the five sections of the Chile Trench shown in Figure 8. Error bars give the uncertainty as determined from the half-width of the curve describing rms misfit as a function of T_e.

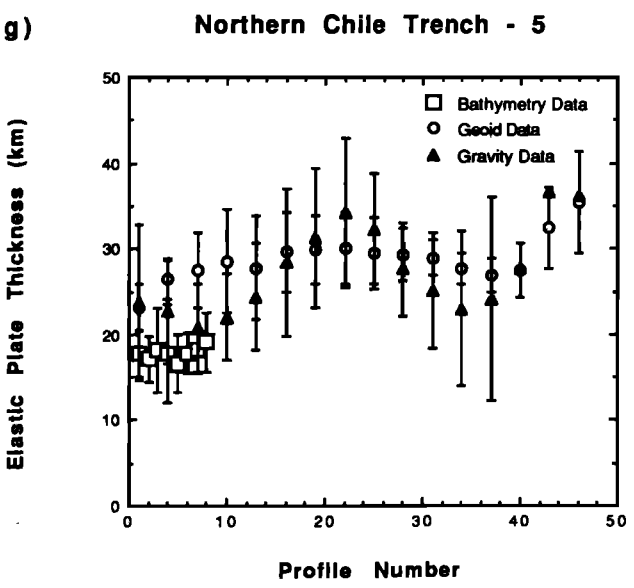

Fig. 6. (continued)

North Chile

The trench off northern Chile, from the Nazca ridge to 25°S, consists of two relatively straight segments separated by a short region with a radius of curvature of 310 km that we approximated as three short segments (Figure 8). The northernmost region 1 includes the northwest-southeast-trending 410-km-long portion of the trench lying immediately to the southeast of the Nazca ridge. The change in the dip of the slab occurs in the northwestern end of the region [*Barazangi and Isacks*, 1976, 1979]. In all of the profiles from the northern four of the five regions an outer bulge is apparent (Figures 9 and 10), and estimates of T_e computed from bathymetry, gravity, and geoid are fairly consistent (Figures 6*c* - 6*g*). Along the fifth segment of trench, except at its northern edge, the outer rise in the bathymetry is too rough to allow an estimate of T_e from bathymetry. The geoid and gravity signatures are less affected, and allow reasonable fits to plate flexure. Values for T_e derived from bathymetry, geoid, and gravity in Figures 6*c*–6*f* were used in computing the averages except along segment 5. We suspect that the digital bathymetric data base may not be as reliable as the satellite data in this southernmost region due to sparse ship tracks [*GEBCO*, 1980]. Average values for T_e and curvature of the plate in each segment are plotted in Figure 7.

Elastic Plates With Variable Rigidity

If inelastic processes caused by curvature-induced stresses produce failure in the plate, one would not expect the profiles to be completely described by an elastic profile with constant flexural rigidity. A look at those profiles best fit by elastic theory shows that this is the case. In both regions many of these profiles display a systematic deviation from the theoretical curves, with a more gradual slope to seaward of the bulge and a steeper slope landward of the peak than predicted by elastic theory. This often results in the observed position of the peak of the bulge being offset to landward of its predicted position.

The observed shape of these outer rises appears consistent with a model of a stiff plate which is weakened as it reaches the peak of the bulge. In order to model this effective thinning of an elastic plate brought on by failure, we used a finite difference algorithm that allows D to vary with position along the profile. The rigidity seaward of the peak of the outer rise was assumed constant and was derived from the flexural rigidity and curvature at the origin of the best fitting elastic curve by predicting the rigidity if no curvature and thus no thinning due to failure were present [*McNutt*, 1984], while the constant rigidity to landward and the exact position of the change in rigidity were chosen to best fit the observed profile. The results are shown for a profile off Peru in Figure 11*a* and for a profile off northern Chile in Figure 11*b*. In Peru the plate was best fit by an elastic thickness 5 km smaller landward of the bulge than to seaward, a decrease of 16%, whereas in northern Chile the plate was best fit by a model which thinned by more than a factor of 2. Allowing more than one rigidity change along a profile (Figure 11*c*) did not significantly improve the fit and sometimes led to physically unreasonable changes in rigidity, such as an increase in plate stiffness over the outer trench wall despite a corresponding increase in plate curvature.

The values of elastic thickness found earlier by considering each profile to be of constant rigidity can be considered weighted averages of the true elastic thickness along the length of the profile. These values, compared to the values found by modeling the profile with one change in flexural rigidity, are smaller than the elastic thickness on the seafloor, where no failure would be expected, but larger than that on the trench wall, near the zero-crossing. The values found when flexural rigidity is varied are similarly averages, but over smaller, arbitrarily chosen segments of the plate. At the Peru trench, profile 16 of the northern region is best fit by a constant 31.6-km-thick plate, or by a plate which changes in thickness from 32.8 and 27.6 km. Off northern Chile, profile 4 of region 2 is fit by a plate with a constant thickness of 21.5 km or by one which changes from 36.6 to 17.0 km. As the goal of this study is to understand the relationship between curvature-induced stresses and apparent elastic thickness, we wish to know if the curvature obtained by any elastic model is consistent with the plate thickness

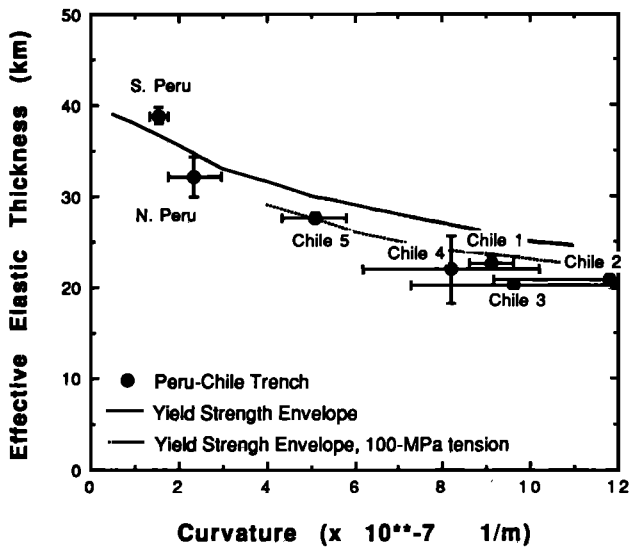

Fig. 7. Average values of elastic plate thickness within each of the seven sections of the Peru-Chile Trench plotted as a function of the curvature of the flexural profile at the first zero crossing seaward of the trench axis. The smooth line gives the predicted change in effective elastic thickness with increasing curvature for a more realistic rheology of the oceanic lithosphere that allows failure at high stress, as shown by the yield envelope in Figure 13 except with the elastic thickness of the plate extrapolated to zero curvature being 40 km. The dotted line gives the predicted reduction in elastic thickness if the lithosphere is subjected to 100 MPa of axial tension offshore northern Chile.

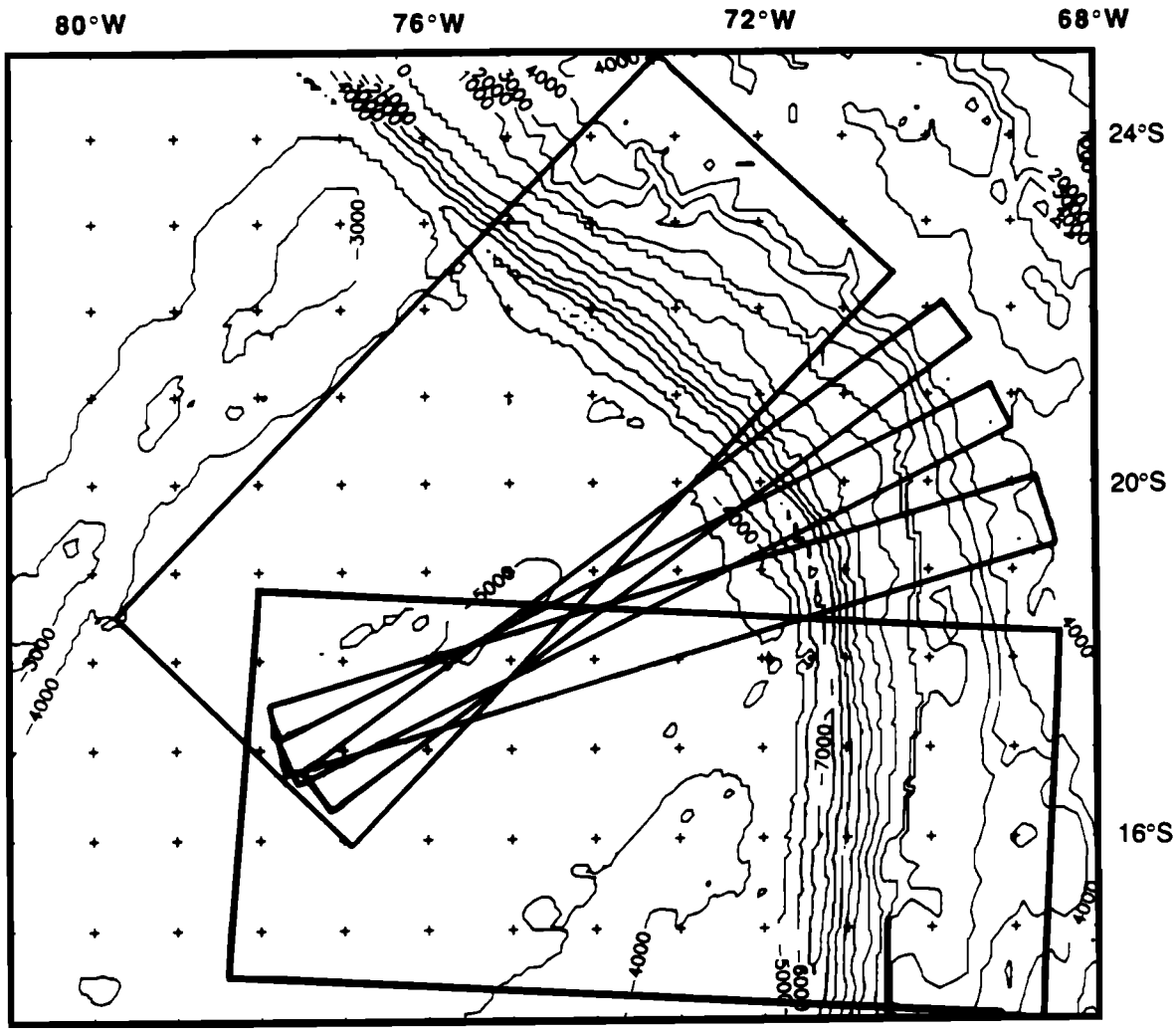

Fig. 8. Bathymetry of the region near the northern Chile Trench for which data were obtained, showing the location of the areas from which profiles were taken.

found according to that model at the point where curvature is measured. The curvatures of the profiles modeled here with variable rigidity were approximately 1.6 times their curvatures calculated assuming constant rigidity. This amount of change in curvature is consistent with the variation in elastic thickness at the zero-crossing as found by the two models [*McNutt*, 1984]. Therefore the values of elastic thickness found in this study should reflect the amount of thinning that the lithospheric plate is expected to undergo when it is bent to the calculated curvature.

Effect of In-Plane Stresses

In addition to a simple thinning of the plate with increasing curvature, horizontal compression or tension acting on the plate may influence the shape that it assumes. Lateral loads primarily affect the state of stress in the plate, though when large enough, it can affect the plate's shape. *McAdoo and Sandwell* [1985], in a study of the buckling of the lithosphere under the Indian Ocean, found that large compressive forces there have reduced the thickness of the elastic core of the plate to near one-tenth its full thickness. The effect of in-plane forces appears primarily in the measured thickness of the plate, not in the shape it assumes. Since the curvature of the bent plate is characterized by the remaining elastic core [*McAdoo and Sandwell*, 1985], we consider an elastic model a valid approximation of lithosphere entering a subduction zone, with horizontal loading serving to introduce another factor, in addition to plate curvature, which causes the effective elastic thickness of the plate to depart from its true mechanical thickness.

Three-Dimensional Effects

In the region of the Chile bight, where the strike of the trench changes over 45° within 175 km, the sharp turn in the trench may be affecting the shape and amplitude of the outer rise. The rise reaches peaks of over 1200 m, far larger than most outer rises, which are rarely larger than 600 m [*Caldwell et al.*, 1976; *Turcotte et al.*, 1978; *Jones et al.*, 1978; *Carey and Dubois*, 1981]. The bulge also has a gravity high of 80 mgal associated with it, which is larger than those observed over any other Pacific trench [*Schweller et al.*, 1981]. In the case of this much surface curvature in a trench, an approximation which treats it as a line load may not be valid. However, treating the trench as a cylindrical load of radius 350 km, using equations developed by *Brotchie* [1971], produced an elastic curve which best fit a profile off northern Chile that was nearly identical to the best fitting curve derived assuming a line load (Figure 12). The elastic parameters were slightly different in this case, with the elastic thickness which produced the best fitting cylindrical curve 1.5 km smaller, but this fell within the range of

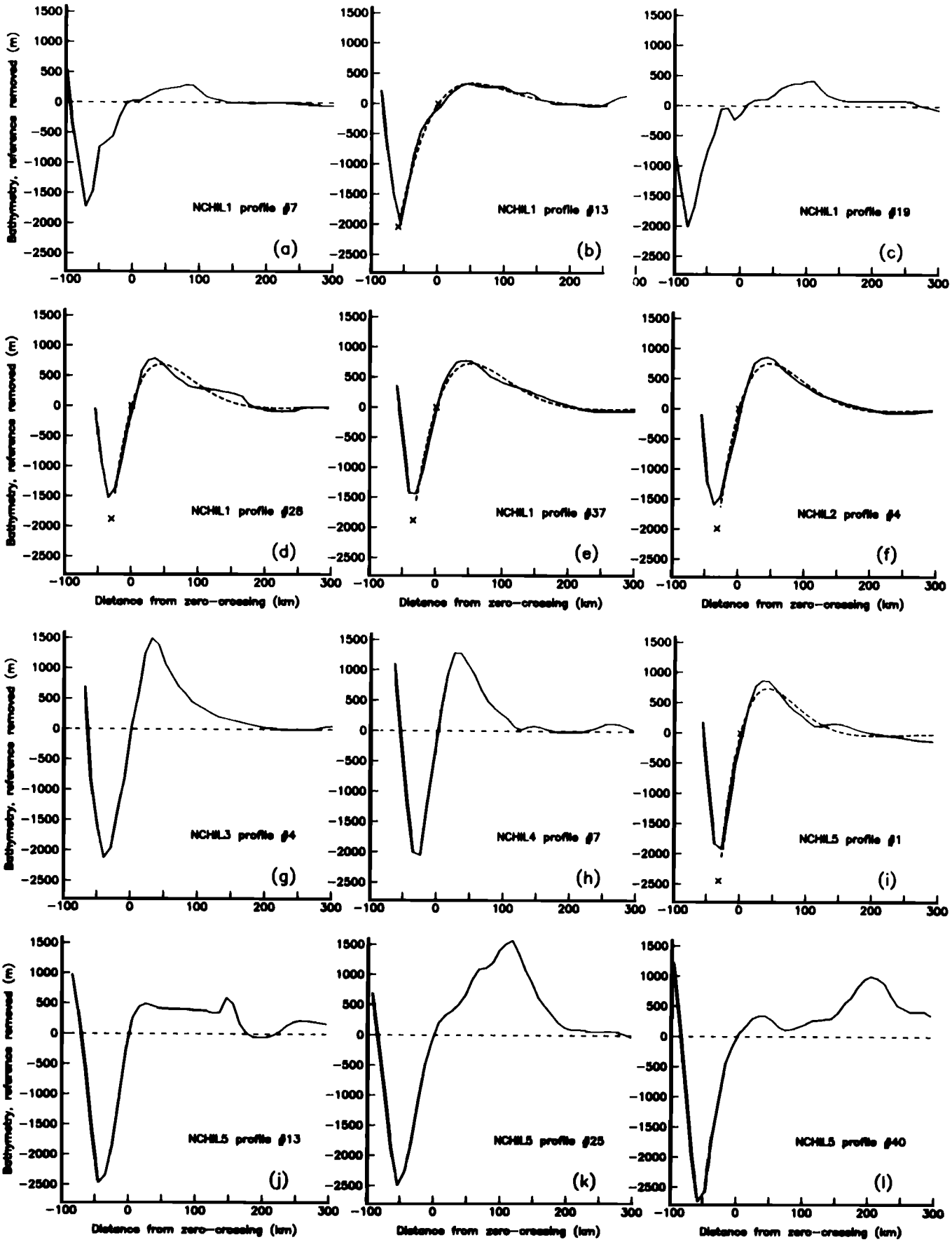

Fig. 9. A series of representative profiles across the northern part of the Chile trench, similar to those from the Peru Trench in Figure 4. NCHIL1 is region 1, NCHIL2 is region 2, and NCHIL3 is region 3. Those profiles which could be satisfactorily fit by the elastic model are shown with this model dashed in; those which could not are shown with a horizontal line at an estimated reference height.

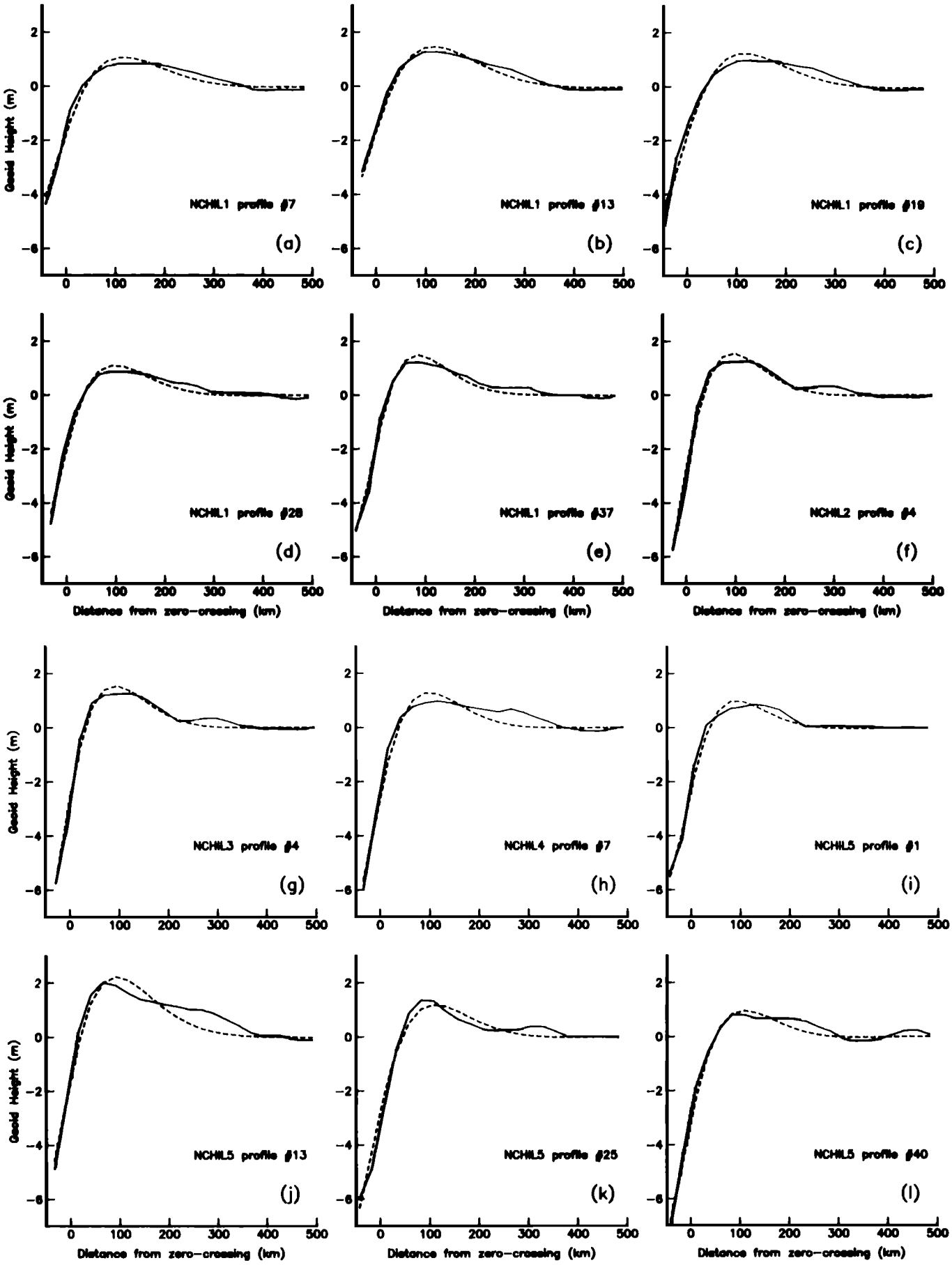

Fig. 10. The geoid along the same profiles for which bathymetry was shown in Figure 9. The solid line is the observed geoid, and the dashed line is the best fitting theoretical geoid generated from an elastic curve.

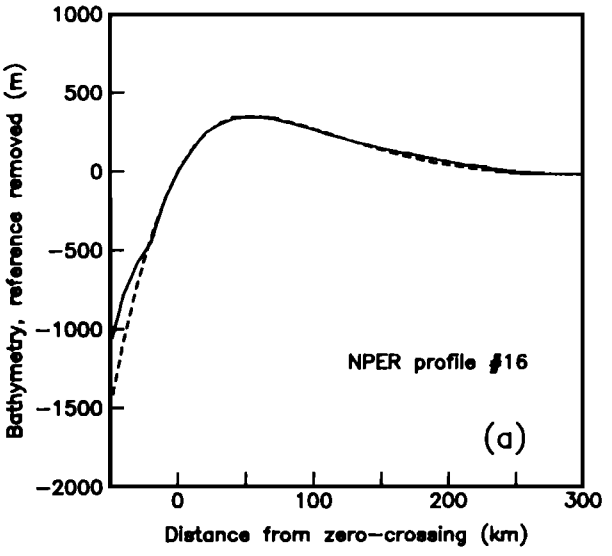

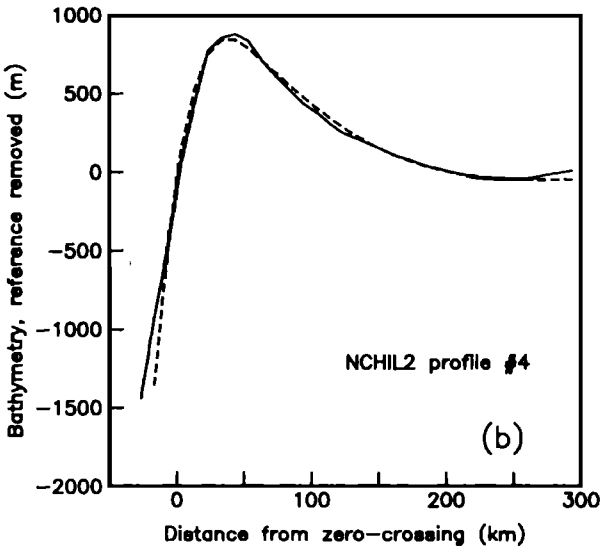

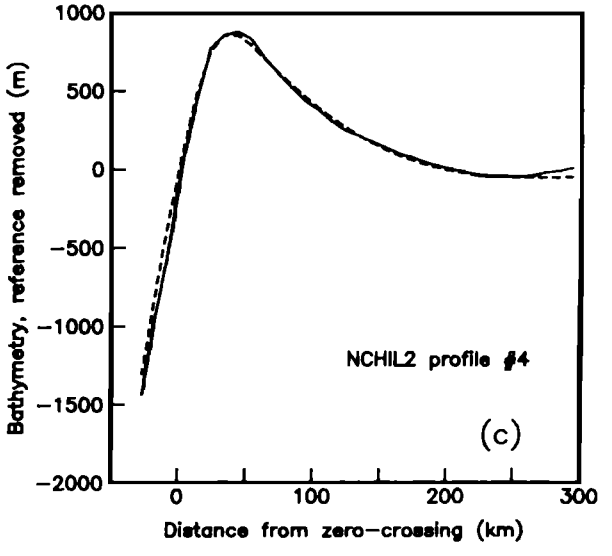

Fig. 11. Curves which result from modeling the bathymetry with an elastic plate of varying flexural rigidity. (*a*) The NPER profile 16 (solid line) shown with the curve which results when the flexural rigidity changes from 25 x 10^{22} Nm (T_e = 33 km) to 15 x 10^{22} Nm (T_e = 28 km) (dashed line). The change occurs 50 km seaward of the zero-crossing, with the larger rigidity occurring to seaward. The theoretical curve obtained assuming a constant rigidity is shown in Figure 4*d*. (*b*) The NCHIL2 profile 4 (solid line) shown with the curve which results when the flexural rigidity changes from 35 x 10^{22} Nm (T_e = 37 km) to 3.5 x 10^{22} Nm (T_e = 17 km) (dashed line). The change occurs 55 km seaward of the zero-crossing. The curve resulting from an elastic model with constant rigidity is shown in Figure 9*f*. (*c*) NCHIL2 profile 4 (solid line) shown with the curve which results when the flexural rigidity changes twice, from 35 x 10^{22} Nm (T_e = 37 km) greater than 70 km seaward of the zero-crossing, to 2.5 x 10^{22} Nm (T_e = 15 km) between 15 and 70 km seaward of the zero-crossing, to 15 x 10^{22} Nm (28 km) from x = 15 km to the trench (dashed line).

uncertainty in the elastic thickness determined earlier. It appears that if the sharp curvature of the trench has any effect on the shape of the plate, it cannot be modeled simply by changing the geometry of the load, and such complications can be safely ignored in favor of the model of a the two-dimensional line load.

Profiles Without Elastic Flexure

This discussion of means to better fit those profiles which could be explained by the elastic model neglects the many bathymetric profiles which could not be fit because of irregular seafloor in the region of the outer rise. *Erlandson et al.* [1981] have observed a region of rough basement along the entire area of the Peru-Chile Trench included in this study, extending 300 km seaward from the trench axis. The region shows evidence of faulting, upper crustal deformation, and volcanics, extending farther seaward than does the extensional faulting on the trench wall. They attribute these features to stresses encountered by the plate as it approaches the subduction zone. Regardless of the reason for this irregular bathymetry that masks the elastic behavior of the plate, the gravity and geoid data consistently indicate the presence of an outer rise along the Peru-Chile Trench.

DISCUSSION

Temperature at the Elastic-Ductile Transition

Along the Peru Trench, where the curvature of the plate is lower and therefore inelastic yielding should be less significant than further south, the average elastic thickness of the plate is 32 ± 2 km at 30 Ma and 39 ± 1 km at 42 Ma. If inelastic yielding can be completely ignored here and if the thermal structure of the Nazca plate in this region corresponds to the standard thermal plate model of *Parsons and Sclater* [1977], then these values of elastic plate thickness can be used to estimate the temperature Θ_e at the elastic-ductile transition. The *Parsons and Sclater* [1977] model predicts about 800 ± 50°C at the base of the elastic plate at these ages. Similar results were obtained by *McAdoo and Martin* [1984] and *McAdoo et al.* [1985], who modeled geoid data over nine trenches and found that Θ_e = 740°C. Studies of the focal depths of intraplate earthquakes [*Wiens and Stein*, 1983] also conclude that Θ_e = 800°C. If there is any inelastic yielding, then the actual depth to the elastic-ductile transition will be even greater, and the temperature even higher. This temperature agrees with that predicted for the elastic-ductile transition by simply extrapolating laboratory-derived flow laws to geologic strain rates [*Kirby*, 1980]. A temperature significantly lower than 700°C for the elastic-ductile transition would only be consistent with the data from the Peru Trench if the thermal structure of the Nazca plate is significantly colder than usual. The regional depth offshore Peru, however, is 4500 m,

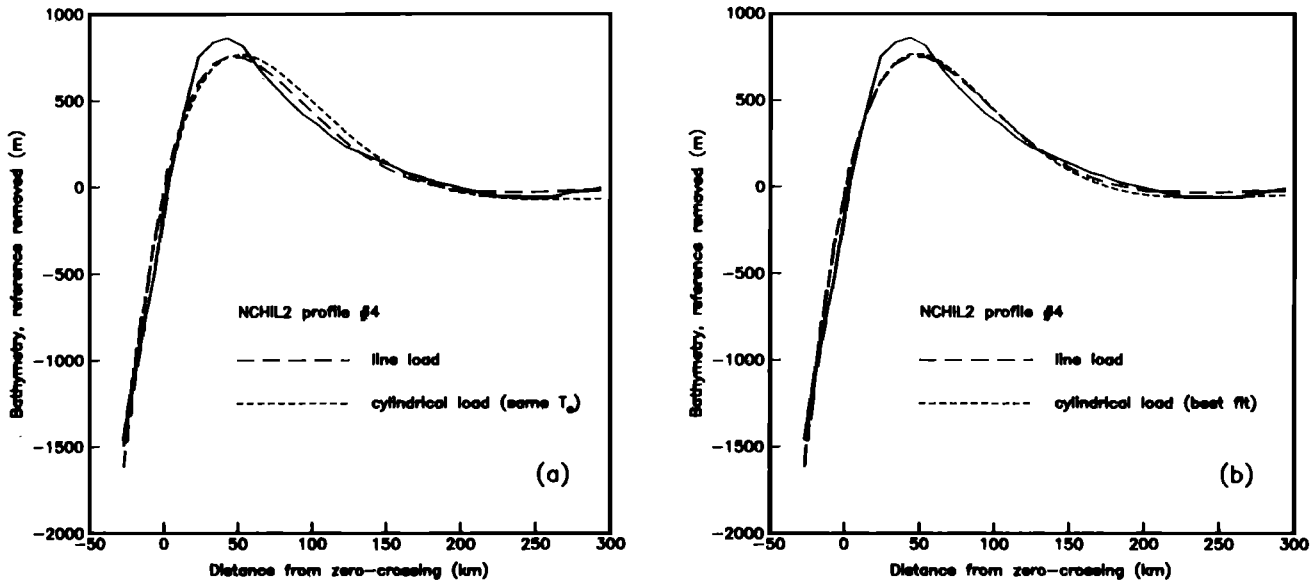

Fig. 12. Elastic curves resulting from a cylindrical load (short dashes) compared to that from a line load (long dashes) and the observed bathymetry (solid line) for NCHIL2 profile 4. The elastic curve produced by a line load uses the parameters which best fit the bathymetry (T_e = 21.4 km), and is that shown in Figure 9*f*. (*a*) The curve produced by a cylindrical load acting on a plate with the same elastic thickness as that acted on by the line load. (*b*) The curve produced by a cylindrical load which best fit the bathymetry, found using an elastic thickness of 19.8 km.

nearly the predicted value for normal 30-Ma lithosphere. Although there is no evidence at present that the thermal structure of the lithosphere is colder than average in this region, unusually hot thermal structure has been proposed as the explanation for the extremely small elastic plate thicknesses for French Polynesia just to the west of this study area [*McNutt and Fischer*, 1987]. We have proposed that a hot mantle upwelling is ultimately responsible for plate thinning [*McNutt and Judge*, 1990]. Perhaps the Nazca plate overlies the opposite limb of this convection cell, leading to colder lithosphere than usual. If further studies (using, for example, surface waves) determine that the thermal structure of the lithosphere is indeed normal in this region, then the fact that the effective elastic thickness of the lithosphere off Peru is so much greater than that found for lithosphere of similar age loaded by midplate volcanoes [*Watts et al.*, 1980] would imply that significant reheating of the lithosphere accompanies hot spot volcanism.

Inelastic Processes

The above discussion of T_e from the Peru Trench in terms of the depth to the isotherm at the elastic-ductile transition is predicated on the assumption that there is no inelastic yielding. However, the fact that the elastic plate thickness at North Chile is smaller (Figure 8) in spite of the greater lithospheric age suggests that inelastic yielding might be a factor, at least for North Chile if not for Peru. Apparently, at high plate curvature ($K > 5 \times 10^{-7}$ m^{-1}), the reduction in elastic plate thickness from such yielding can more than offset the expected increase in plate thickness over 15 m.y. of thermal cooling. Geologic evidence of faulting in and near the trench also supports the existence of yielding due to the curvature of the plate. Faulting on the outer trench wall is apparent in profiles taken along ship tracks across the Peru-Chile Trench [*Fisher and Raitt*, 1962; *Schweller et al.*, 1981]. These show numerous step faults and some graben structures. Step faults exist along the entire trench, with their average offset several hundred meters except in the North Chile region, where offsets of a kilometer exist [*Schweller et al.*, 1981]. Grabens appear primarily in the North Chile region. Evidence suggests that these features extend to depths of 4 to 7 km [*Schweller et al.*, 1981]. They reflect the failure that exists in the extensional, brittle upper zone of the plate. If this failure is the result of curvature-induced brittle failure, then it also suggests yielding at the base of the plate, although accomplished through different mechanisms (Figure 13).

In Figure 7 we compare the observed decrease in effective elastic thickness along the Peru-Chile Trench with that predicted from failure at high stresses of a lithosphere with finite yield strength as a function of depth given by a the yield envelope, such as that in Figure 13 [*McNutt*, 1984]. The impression from Figure 7 is that the lithosphere must be weaker than implied by the yield strength envelope in order to produce the observed amount of failure in the lithosphere when bent to high strains. Accounting for the expected increase of elastic plate thickness with increasing age would only increase the discrepancy in Figure 7 between the predicted and observed reduction in effective T_e. If, however, the stress field offshore northern Chile is characterized by tension normal to the trench axis at 16°S-27°S, but compression elsewhere, as has been proposed by *Wortel and Cloetingh* [1985] based on a finite element calculation incorporating plate-tectonic forces dependent on lithospheric age and kinematic parameters, additional weakening would be expected (Figure 7). Thus, although we are tempted to interpret our results as confirming the stress calculations of *Wortel and Cloetingh* [1985], we cannot rule out the possibility of thermal effects not predicted by lithospheric age. If, for example, the lithosphere is anomalously cold off Peru but normal off Chile, some of the reduction in T_e in Figure 7 may be controlled by temperature rather than state of stress.

Correlation Between Plate Dip and Elastic Thickness

Although a relationship between plate dip and the downward curvature of a plate is appealing, and the evidence from the Peru-Chile appears to support such a relationship, a further look at the region indicates that plate dip may not explain the variation in

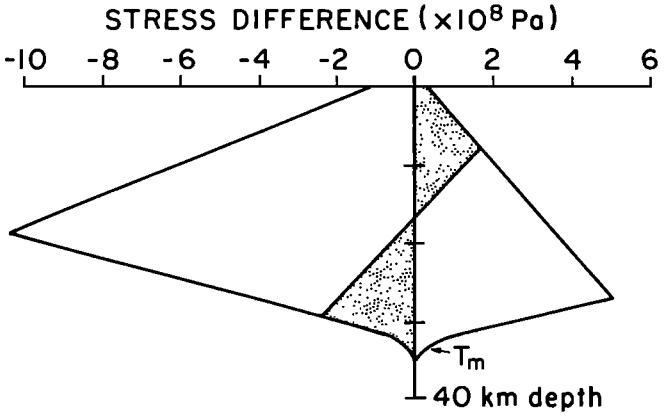

Fig. 13. An approximation of the yield envelope for a rheological model of the lithosphere which includes failure by frictional sliding at shallow depths and by ductile creep in the lower plate. T_m is the base of the mechanical lithosphere, assumed to correspond to the depth to an isotherm Θ_e. The inner line represents the stress difference due to flexure of such a plate that experiences yielding near the surface and base. The effective elastic thickness T_e of this plate computed by comparing its deformation to the predictions of the thin plate equation will always underestimate its true mechanical thickness T_m [from *McNutt*, 1984].

curvature, and therefore elastic thickness. The slope of the slab beneath Peru averages 15°, while beneath northern Chile it descends at approximately 33° [*Barazangi and Isacks*, 1976, 1979]. However, detailed analysis of the trends of the hypocentral surfaces indicates that in the upper 100 km the plate descends at the same slope in both regions, and then flattens under Peru while continuing to descend under northern Chile [*Bevis and Isacks*, 1984; *Chowdhury and Whiteman*, 1987]. Thus we find no support for a relationship between plate dip at depth and the elastic characteristics of that plate at the surface.

CONCLUSIONS

This investigation of the elastic thickness and curvature of the lithosphere entering the Peru-Chile Trench confirms the existence of a major change in many characteristics of the trench between the region lying off the coast of northern Peru from 6°S to 15°S and the region off the coast of northern Chile between 17°S and 20°S. The 30-m.y.-old plate off Peru appears to have an elastic thickness of 32 ± 2 km and a curvature of (2.4 ± 0.6) x 10^{-7} m^{-1}. It dips beneath the continent at 15°. The 45-m.y.-old plate off northern Chile has an elastic thickness of 23 ± 1 km, a curvature of (9.1 ± 0.5) x 10^{-7} m^{-1}, and dips at 33°. The older yet thinner plate of northern Chile indicates that the stresses induced by the curvature there are causing the plate to yield to a greater extent than occurs off Peru, where the smaller curvature induces correspondingly smaller stresses and less yielding. The presence of this failure in the plate is supported by the faulting observed on the outer trench wall, which is much more extensive in the sharply bent plate off Chile. However, it does not appear that the extreme downward curvature at the Chile Trench is related to the change in the dip of the plate at depth. Rather, it may be related to the intraplate stress field [*Wortel and Cloetingh*, 1985].

If the thermal structure of the lithosphere is normal for its age seaward of the Peru Trench, our results indicate that the isotherm defining the base of the mechanical lithosphere is 800° ± 50°C. This implies that the plate entering the North Chile Trench must be yielding to such an extent that the effective elastic thickness is approximately 50–65% of the plate's mechanical thickness, which is a larger amount of yielding than predicted by standard yield strength envelopes derived from laboratory experiments unless the intraplate stress field changes from offshore Peru to Chile [*Wortel and Cloetingh*, 1985]. In order to reconcile the relatively large elastic plate thickness for the Peru Trench with the results of lithospheric studies at midplate volcanoes, where stresses are lower and yielding should not occur, geotherms must be either significantly elevated beneath midplate swells [*McNutt*, 1984] or depressed offshore Peru.

Geoid heights and gravity anomalies show evidence of elastic flexure throughout the region studied, even in areas where the characteristic elastic profile is not evident in the bathymetry. In this respect it appears that geoid and gravity may be more reliable data sources for obtaining elastic plate thickness. However, where the bathymetry is well described by an elastic plate, values for elastic thickness obtained from the geoid are consistently larger than those obtained from bathymetry, an observation also made at numerous other subduction zones [*McAdoo and Martin*, 1984]. Such a systematic variation indicates that there may be characteristic subsurface density contrasts within a plate undergoing flexure which are reflected in the geoid but which are not apparent in the bathymetry, and that values of elastic thickness obtained from the two data sets should not be used interchangeably.

Acknowledgments. This paper benefitted from the constructive comments of four anonymous reviewers. This work was supported by National Science Foundation grant OCE-8710222.

REFERENCES

Barazangi, M., and B. L. Isacks, Spatial distribution of earthquakes and subduction of the Nazca plate beneath South America, *Geology*, *4*, 686–692, 1976.

Barazangi, M., and B. L. Isacks, Subduction of the Nazca plate beneath Peru: Evidence from spatial distribution of earthquakes, *Geophys. J. R. Astron. Soc.*, *57*, 537–555, 1979.

Bevis, M., and B. L. Isacks, Hypocentral trend surface analysis: Probing the geometry of Benioff zones, *J. Geophys. Res.*, *89*, 6153–6170, 1984.

Bodine, J. H., and A. B. Watts, On lithospheric flexure seaward of the Bonin and Mariana trenches, *Earth Planet. Sci. Lett.*, *43*, 132–148, 1979.

Brotchie, J. F., Flexure of a liquid-filled spherical shell in a radial gravity field, *Mod. Geol.*, *3*, 15–23, 1971.

Caldwell, J. G., W. F. Haxby, D. E. Karig, and D. L. Turcotte, On the applicability of a universal elastic trench profile, *Earth Planet. Sci. Lett.*, *31*, 239–246, 1976.

Carey, E., and J. Dubois, Behavior of the oceanic lithosphere at subduction zones: Plastic yield strength from a finite-element method, *Tectonophysics*, *74*, 99–110, 1981.

Chowdhury, D. K., and S. K. Whiteman, Structure of the Benioff zone under southern Peru to central Chile, *Tectonophysics*, *134*, 215–226, 1987.

Dang, S., Seismic refraction velocity structure, Sheet 9, in *Peru-Chile Trench Off Peru*, Ocean Margin Drilling Program, Regional Atlas Series, Atlas *9*, edited by D.M. Hussong, S.P. Dang, L.D. Kulm, R.W. Couch, and T.W.C. Hilde, Marine Science International, Woods Hole, Mass., 1984.

Erlandson, D. L., D. M. Hussong, and J. F. Campbell, Sediment and associated structure of the northern Nazca plate, Nazca Plate: Crustal Formation and Andean Convergence, *Mem. Geol. Soc. Am.*, *154*, 295–314, 1981.

Fisher, R. L., and R. W. Raitt, Topography and structure of the Peru-Chile trench, *Deep Sea Res.*, *9*, 423–443, 1962.

GEBCO, Bathymetric Chart of the Oceans, 1:10,000,000, 5th ed., Canadian Hydrographic Office, Ottawa, Canada, 1980.

Goetze, C., and B. Evans, Stress and temperature in the bending lithosphere as constrained by experimental rock mechanics, *Geophys. J. R. Astron. Soc.*, *59*, 463–478, 1979.

Handschumacher, D. W., Post-Eocene plate tectonics of the eastern

Pacific, in *The Geophysics of the Pacific Ocean Basin and its Margin, Geophys. Monogr. Ser.*, vol. 19, edited by G.H. Sutton, M.H. Manghnani, and R. Moberly, pp 177–202, AGU, Washington, D.C., 1976.

Hanks, T. C., The Kuril Trench-Hokkaido Rise system: Large shallow earthquakes and simple models of deformation, *Geophys. J. R. Astron. Soc.*, *23*, 173–189, 1971.

Haxby, W.F., *Gravity Field of the World's Oceans*, National Geophysical Data Center, NOAA, Boulder, Colo., 1987.

Heirtzler, J. R., and M. Edwards, Relief of the surface of the Earth, *Rep. MGG-2*, Nat. Geophys. Data Cent., Boulder, Colo., 1985.

Herron, E. M., Sea-floor spreading and the Cenozoic history of the East Central Pacific, *Geol. Soc. Am. Bull.*, *83*, 1671–1692, 1972.

Hilde, T. W. C., and W. E. K. Warsi, Magnetic anomaly profiles, Sheet 4, in *Peru-Chile Trench Off Peru*, Ocean Margin Drilling Program, Regional Atlas Series, Atlas *9*, edited by D.M. Hussong, S.P. Dang, L.D. Kulm, R.W. Couch, and T.W.C. Hilde, Marine Science International, Woods Hole, Mass., 1984.

Hussong, D. M., P. B. Edwards, S. H. Johnson, J. F. Campbell, and G. H. Sutton, Crustal structure of the Peru-Chile Trench: 8°–12° S latitude, in *The Geophysics of the Pacific Ocean Basin and its Margin, Geophys. Monogr. Ser.*, vol. 19, edited by G.H. Sutton, M.H. Manghnani, and R. Moberly, pp 71-85, AGU, Washington, D.C., 1976.

Jones, G. M., T. W. C. Hilde, G. F. Sharman, and D. C. Agnew, Fault patterns in outer trench walls and their tectonic significance, *J. Phys. Earth*, *26*, Suppl., S 85–S 101, 1978.

Kirby, S. H., Tectonic stresses in the lithosphere: Constraints provided by the experimental deformation of rocks, *J. Geophys. Res.*, *85*, 6353–6363, 1980.

Marsh, J. G., A. C. Brenner, B. D. Beckley, and T. V. Martin, Global mean sea surface based upon the Seasat altimeter data, *J. Geophys. Res.*, *91*, 3501–3506, 1986.

Marsh, J. G., F. J. Lerch, B. H. Putney, D. C. Christodoulidis, D. E. Smith, T. L. Felsentreger, B. V. Sanchez, S. M. Klosko, E. C. Pavlis, T. V. Martin, J. W. Robbins, R. G. Williamson, O. L. Colombo, D. D. Rowlands, W. F. Eddy, N. L. Chandler, K. E. Rachlin, G. B. Patel, S. Bhati, and D. S. Chinn, A new gravitational model for the Earth from satellite tracking data: GEM-T1, *J. Geophys. Res.*, *93*, 6169–6215, 1988.

McAdoo, D. C., and C. F. Martin, Seasat observations of lithospheric flexure seaward of trenches, *J. Geophys. Res.*, *89*, 3201–3210, 1984.

McAdoo, D. C., and D. T. Sandwell, Folding of oceanic lithosphere, *J. Geophys. Res.*, *90*, 8563–8569, 1985.

McAdoo, D. C., J. G. Caldwell, and D. L. Turcotte, On the elastic-perfectly plastic bending of the lithosphere under generalized loading with application to the Kuril Trench, *Geophys. J. R. Astron. Soc.*, *54*, 11–26, 1978.

McAdoo, D. C., C. F. Martin, and S. Poulose, Seasat observations of flexure: Evidence for a strong lithosphere, *Tectonophysics*, *116*, 209–222, 1985.

McNutt, M. K., Lithospheric flexure and thermal anomalies, *J. Geophys. Res.*, *89*, 11,180–11,194, 1984.

McNutt, M.K., and K.M. Fisher, The South Pacific superswell, in *Seamounts, Islands, and Atolls, Geophys. Monogr. 43*, edited by B. Keating, P. Fryer, R. Batiza, and G.W. Boehlert, AGU, Washington, D.C., 1987.

McNutt, M.K., and A.V. Judge, The superswell and mantle dynamics beneath the South Pacific, *Science*, *248*, 969–975, 1990.

McNutt, M. K., and H. W. Menard, Constraints on yield strength in the oceanic lithosphere derived from observations of flexure, *Geophys. J. R. Astron. Soc.*, *71*, 363–394, 1982.

Parker, R. L., The rapid calculation of potential anomalies, *Geophys. J. R. Astron. Soc.*, *31*, 447–455, 1972.

Parsons, B. E., and J. Sclater, An analysis of the variation of ocean floor bathymetry and heat flow with age, *J. Geophys. Res.*, *82*, 803–827, 1977.

Scheidegger, K. F., and J. B. Corliss, Petrogenesis and secondary alteration of upper layer 2 basalts of the Nazca plate, Nazca Plate: Crustal Formation and Andean Convergence, *Mem. Geol. Soc. Am.*, *154*, 77–107, 1981.

Schweller, W. J., L. D. Kulm, and R. A. Prince, Tectonics, structure, and sedimentary framework of the Peru-Chile Trench, Nazca Plate: Crustal Formation and Andean Convergence, *Mem. Geol. Soc. Am.*, *154*, 323–349, 1981.

Turcotte, D. L, and G. Schubert, *Geodynamics: Applications of Continuum Physics to Geological Problems*, John Wiley, New York, 1982.

Turcotte, D. L, D. C. McAdoo, and J. G. Caldwell, An elastic-perfectly plastic analysis of the bending of the lithosphere at a trench, *Tectonophysics*, *47*, 193–205, 1978.

Walcott, R. I., Flexure of the lithosphere at Hawaii, *Tectonophysics*, *9*, 435–446, 1970.

Watts, A. B., and J. R. Cochran, Gravity anomalies and flexure of the lithosphere along the Hawaiian–Emperor Seamount Chain, *Geophys. J. R. Astron. Soc.*, *38*, 119–141, 1974.

Watts, A. B., J. H. Bodine, and N. M. Ribe, Observations of flexure and the geological evolution of the Pacific Ocean basin, *Nature*, *283*, 532–537, 1980.

Wiens, D. A., and S. Stein, Age dependence of oceanic intraplate seismicity and implications for lithospheric evolution, *J. Geophys. Res.*, *88*, 6455–6468, 1983.

Wortel, M.J.R., and S.A.P.L. Cloetingh, Accretion and lateral variations in tectonic structure along the Peru-Chile trench, *Tectonophysics*, *112*, 443–462, 1985.

A.V. Judge, Geophysical Research, ELF Aquitaine, CSTCS avenue Larribou, 64018 Pau Cedex, FRANCE.

M.K. McNutt, 54-826 MIT, Cambridge, MA 02139

(Received July 19, 1988;
revised July 30, 1990;
accepted August 7, 1990.)

JOURNAL OF GEOPHYSICAL RESEARCH, VOL. 96, NO. B10, PAGES 16,585–16,595, SEPTEMBER 10, 1991

Rheological Nonlinearity and Flow Instability in the Deforming Bed Mechanism of Ice Stream Motion

BARCLAY KAMB

Division of Geological and Planetary Sciences, California Institute of Technology, Pasadena

Contrary to what has recently been assumed in modeling the proposed deforming bed mechanism for the rapid motion of Antarctic ice streams, the rheology of water saturated till is probably highly nonlinear, according to information from soil mechanics and preliminary experiments on till from the base of Ice Stream B. The equivalent flow law exponent n is probably as high as ~100, and the nonlinearities of the shear stress and effective pressure dependences are closely linked. The high nonlinearity has important consequences for the deforming bed mechanism. A flow system operating by this mechanism can be unstable as a result of feedback from the generation of basal water by shear heating of basal till. The short-term feedback effect is analyzed for a perturbation in a model ice stream in which the basal meltwater is transported through a distributed system of narrow gap-conduits at the ice-till interface. Although the analysis is approximate and some of the system parameters are poorly known, the results suggest that the deforming bed mechanism is unstable for $n>\sim 20$. The apparent lack of such an instability in the currently active ice streams implies that their motion is controlled not by the deforming bed mechanism but by some other as yet unidentified mechanism.

INTRODUCTION

The West Antarctic ice sheet is traversed by about a dozen ice streams ~50 km wide and ~500 km long, in which the ice is moving at speeds up to ~800 m yr^{-1}, in sharp contrast to the motions of ~10 m yr^{-1} in the general mass of the ice sheet outside the ice streams [*Bentley*, 1987]. There is interest in these rapid motions as a phenomenon of glacier mechanics [*Clarke*, 1987*a*] and as a process that may be important in a possible collapse of the ice sheet, with worldwide consequences [*Hughes*, 1977, p. 44; *Weertman and Birchfield*, 1982; *van der Veen*, 1987, p. 8; *Lingle and Brown*, 1987, p. 279; *Bindschadler*, 1990].

To explain the rapid ice stream motions there has been developed, on the basis of seismic reflection data [*Blankenship et al.*, 1987], a deforming bed model according to which the ice moves rapidly by deformation of a layer of soft, water-saturated till at its base [*Alley et al.*, 1987*a*, 1987*b*; 1989; *Alley*, 1989*a*, 1989*b*; *MacAyeal*, 1989]. From boreholes to the bottom of Ice Stream B, direct evidence of the basal till and of physical conditions suitable for its deformation has been obtained [*Engelhardt et al.*, 1990; *Kamb*, 1990]. Glacier and ice sheet movement by soft-bed deformation, instead of by the normally considered mechanisms of ice deformation and basal sliding, has been advocated as an important new paradigm of glaciology [*Boulton*, 1986] and as the flow mechanism for large parts of the ice age North American and Fennoscandian ice sheets [*Boulton and Jones*, 1979; *Boulton et al.*, 1985; *Brown et al.*, 1987].

Crucial to the deforming bed model are the mechanical properties of the basal till, which relate the shear deformation of the till to the shear stress at the base of the ice and specify how this relation is influenced by basal water pressure [*Alley et al.*, 1987*b*, p. 8937]. In the modeling of the deforming bed mechanism that has been done to date, a linear or nearly linear rheology has been assumed. The present paper undertakes to show that a highly nonlinear relation is much more likely and that such a relation has important consequences for the stability of ice stream motion if controlled by bed deformation.

Paper number 91JB00946.
0148-0227/91/91JB-00946$05.00

CONSTITUTIVE RELATION FOR TILL

Current View

In the modeling to date of ice stream motion by the deforming bed mechanism, the till flow law relating shear strain rate $\dot{\gamma}$ to shear stress τ and effective pressure $\hat{P}=P_I-P_W$ (where P_I is overburden pressure and P_W is pore pressure of water) has been assumed to have the form

$$\dot{\gamma} = C\,\tau^n/\hat{P}^m \qquad (1)$$

where C is a constant (the "softness parameter") and where $n=1$ [*Alley et al.*, 1987*b*; *Alley*, 1989*b*; *MacAyeal*, 1989] or $n=1.3$ [*Alley et al.*, 1989, Figures 3 and 4]. *Alley* [1989*b*] and *Alley et al.* [1989] worked with several values of m from 0 to 5, while *MacAyeal* [1989] did not include the effect of pore water pressure in his model. *Lingle and Brown* [1987, pp. 266 and 268] took $n=1$ and $m=1$ in a model that can be considered to be based on (1) if the assumed basal sliding law is interpreted as resulting from deformation of the postulated basal aquifer layer [*Lingle and Brown*, 1987, p. 251].

The assumed flow law was based on results of *Boulton and Hindmarsh* [1987] from field observation of the deformation of subglacial till near the terminus of an Icelandic glacier, Breidamerkurjokull. The data, seven triplets of values ($\dot{\gamma}$, τ, $\hat{P}$), fitted a law of the form (1) with $n=1.3$ and $m=1.8$, thus showing only slight rheological nonlinearity. *Boulton and Hindmarsh* [1987, p. 9063] also fitted to the data a flow law of the form

$$\dot{\gamma} = C\,(\tau-\tau_f)^n/(\hat{P})^m \qquad (\tau\geq\tau_f) \qquad (2)$$

where τ_f is yield strength, given by

$$\tau_f = c + \mu\hat{P} \qquad (3)$$

the constants c and μ being the cohesion and internal friction; for $\tau < \tau_f$, $\dot{\gamma}=0$. They obtained $n=0.6$, $m=1.2$, $\mu=0.6$, and $c=0.04$ bar, with no improvement in goodness of fit (correlation coefficient) over the law of form (1). Since the nonlinearity represented by nonzero τ_f in (2) tends to be compensated by the "sublinear" $n<1$, only a slight nonlinearity is again indicated by these results.

Clarke [1987*b*, p. 9027] postulated for saturated till a law of type (2)+(3) with $n=1$ (Bingham flow law), $m=0$, and c a somewhat complex function of $\hat{P}$. For application to landslides, *Iverson* [1985, p. 148] proposed a three dimensional generalization of (2)+(3), with $m=0$; fitting (2) to vertical profiles of flow velocity in four landslides gave $\tau_f \sim 0.4$ bar and n ranging from 0 to 5 [*Iverson*, 1985, Figure 4; 1986, Figures 4 and 5]. (The velocity profiles were rather irregular, which prevented a close fitting of the flow law.)

Evidence From Soil Mechanics

The constitutive relation for till, as a granular material with a high content of clay-size particles, should be consistent with what is known about such materials in soil mechanics. In the geotechnical literature on the creep of clay-rich soils, much of the creep data are fitted reasonably well by the Singh-Mitchell creep equation [*Singh and Mitchell*, 1968; Borja and Kavazanjian, 1985] based on rate process theory [*Mitchell et al.*, 1968; *Feda*, 1989]:

$$\dot{\gamma} = \dot{\gamma}_o (t_1/t)^s \exp(\alpha\tau/\tau_f) \qquad (4)$$

where t is time starting with $t=t_1$, at stress onset, and where t_1, $\dot{\gamma}_o$, s, and α are constants. The yield stress τ_f is given by (3), normally with $c=0$, and with μ dependent on the porosity of the soil. The relationship (4) is considered to apply for τ in the range $0.3\tau_f \le \tau \le 0.9\tau_f$ [*Singh and Mitchell*, 1968, p. 30], which is enough below the yield stress that the soil does not grossly fail and the strain does not increase to large values on the time scale of experimental tests. Thus typical values of s are in the range $0.75 \le s \le 1$, so that (4) describes transient, decelerating creep. The parameter α in (4) is typically in the range 3-7 for this type of creep [*Mitchell et al.*, 1968, Figures 11 and 12; *Singh and Mitchell*, 1968, Figures 17 and 21; *Borja and Kavazanjian*, 1985, p. 294; *Feda*, 1989, Figure 3].

The till flow law needed in order to model the deforming bed mechanism must describe steady state creep at large strains, with the till at failure ($\tau=\tau_f$), rather than decelerating transient creep at τ well below failure, as (4) does. The strength at large strains, called the residual strength, has been studied for a variety of clay-rich soils by laboratory testing with the ring-shear apparatus and by quantitative evaluation of landslides [*Bishop et al.*, 1971; *Bolton*, 1979, p. 255; *Skempton*, 1985; *Maksimovic*, 1989]. The flow law is, from the viewpoint of soil mechanics, the strain rate dependence of the residual strength. This has been investigated for clay-rich soils by *Skempton* [1985, p. 14], who finds that the residual strength τ_r increases with the shear rate, but only slightly. The dependence follows the form of (4), with τ replaced by τ_r, and with $s=0$ (steady state). Solved for τ_r, (4) gives the standard form for the strain rate dependence of the residual strength τ_r:

$$\tau_r = \tau_o \left(1 + \alpha^{-1} \ln(\dot{\gamma}/\dot{\gamma}_o)\right) \qquad (\dot{\gamma} \ge \dot{\gamma}_o) \qquad (5)$$

Here τ_o, which replaces τ_f in (4), is the residual strength at a reference strain rate $\dot{\gamma}_o$ below which τ_r becomes independent of $\dot{\gamma}$ and (5) no longer applies. (5) is given, in different symbols, by *Feda* [1989, equation (9)] and by *Prapaharan et al.* [1989, equation (10)]. The effective-pressure dependence of the creep strength in (5) is contained in the dependence of τ_o on $\hat{P}$ analogous to the dependence of τ_f on $\hat{P}$ in (3):

$$\tau_o = c_o + \mu_o \hat{P} \qquad (6)$$

normally with $c_o=0$ [*Feda*, 1989, p. 670].

In ring-shear tests reaching the residual state the sample usually develops a narrow internal shear zone, and it is therefore standard practice to replace the ratio $\dot{\gamma}/\dot{\gamma}_o$ in (5) with v/v_o where v is slip rate across the shear zone and v_o is a reference slip rate analogous to $\dot{\gamma}_o$.

The form (5) (with $\gamma/\dot{\gamma}_o \to v/v_o$), accompanied by (6), is used in the geophysical literature [*Tullis*, 1988; *Biegel et al.*, 1989; *Scholz*, 1990, Figures 2.18 and 2.22] to describe the shear rate dependence of the steady state frictional strength of fault gouge. Conventionally, a parameter $(a-b)/\mu_o$ is written in place of α^{-1} in (5). Gouge of course bears a relation to till in that both are granular materials produced at least in part by mechanical comminution.

Because of the form of (5), the dependence of residual strength on shear rate is commonly expressed in terms of the slope S of the curve of τ_r plotted against $\log_{10}\dot{\gamma}$; S is usually given as the percentage increase of τ_r per decade (or "log cycle") increase of $\dot{\gamma}$. Thus

$$S = 100\,\partial \ln \tau_r / \partial \log \dot{\gamma} \qquad (7)$$

Data given by *Skempton* [1985, p. 14] show $S=1.1$-3.1% per decade, and from residual-strength tests reported by *Bishop et al.* [1971, p. 302], $S=1.9\%$ per decade. From other tests on the strain rate dependence of soil strength not definitely at the residual limit, S is commonly reported in the range 7-13% per decade [*Borja and Kavazanjian*, 1985, Figure 8; *Nakase and Kamei*, 1986; *Prapaharan et al.*, 1989, p. 618; *O'Reilly et al.*, 1989, Figure 4].

A comparison of observed S values with what has been assumed in modeling the deforming bed mechanism is obtained by finding the equivalent value of n in (1), with $\tau \to \tau_r$; from (5) and (6),

$$n = \partial \ln \dot{\gamma} / \partial \ln \tau_r = (100 \ln 10)/S = \alpha \tau_r / \tau_o \approx \alpha \qquad (8)$$

(The last step follows because $\tau_r \approx \tau_o$ when the medium is deforming at failure.) Thus $S=13\%$ per decade corresponds to $n \approx 18$, and $S=2\%$ per decade corresponds to the prodigious value $n \approx 115$. The extreme nonlinearity represents mechanical behavior close to perfect plasticity, for which $S=0$ or $n \to \infty$. It contrasts with the relatively mild nonlinearity in the transient creep law (4), for which $\alpha \sim 3$-7 as noted earlier. The increase in sensitivity of strain rate to stress as $\tau \to \tau_f$ is a natural expectation [see *Mitchell et al.*, 1968, Figure 11].

The mechanical properties of the till under the ice streams are doubtless not exactly the same as those of the clay-rich soils tested by *Bishop* [1971] and *Skempton* [1985]. Because of the sand and pebble content of the till [*Engelhardt et al.*, 1990, Figure 4], its behavior will probably be closer to perfect treiboplastic failure than is the case with the clay-rich soils tested, so that the equivalent n value for the till flow law will probably be even higher than ~100.

In the relation (5) for the steady state strength of fault

gouge, from experiments to date α^{-1} is found to be a small quantity that increases gradually with the shear rate from about −0.007 at v=0.3 mm d^{-1} to about +0.013 at v=130 m d^{-1} [*Blanpied et al.*, 1987, Figure 3]. Negative α^{-1}, which is found for v<1.3 m d^{-1} and is called "velocity weakening," constitutes a more extreme rheological nonlinearity than is represented by small but positive α^{-1}. The extreme nonlinearity in the constitutive relation of gouge cannot be expected to apply directly to till, for one reason because the stress levels in the gouge experiments ($\tau \geq 50$ bar) are much higher than in the till under the ice streams ($\tau \leq 0.5$ bar). But the gouge behavior reinforces the view that the dependence of residual strength on shear rate is very slight (i.e., α is large) for such materials, and they can even show velocity weakening. This has its counterpart in the behavior of soils: *Lambe and Whitman* [1969, p. 314] have noted an ambivalence between slight strengthening and slight weakening in the effect of shear rate on soil strength.

Tests on Till From Ice Stream B

Freshly cored till from the base of Ice Stream B [*Engelhardt et al.*, 1990, p. 59] was tested by the direct-shear method [*Bolton*, 1979, p. 69] in a test cell of diameter 2.5 cm, operating in the creep mode (applied shear load held constant during the test; shear displacement recorded every 15 s). The material tested was packed into the test cell to a total depth of 3 cm, and rare coarse clasts encountered in the packing process were removed. The removed clasts, >~10 mm in size, constituted less than 2% of the sample volume. Tests were carried out in the open air and under a nominal normal stress of 0.017 bar. The pore pressure was not controlled, but because of the very low hydraulic conductivity of the till [*Engelhardt et al.*, 1990, p. 248] and the short test duration the tests were essentially undrained and therefore should reproduce the mechanical properties under in situ conditions, independent of the normal stress or external availability of pore water [*Bolton*, 1979, p. 94; *Lambe and Whitman*, 1969, p. 440].

The most informative results, from repeated tests on a single sample, are shown in Figure 1. Tests were done alternately at τ=0.018 bar and 0.022 bar. At the lower shear stress all tests resulted in decelerating creep; the open circles plotted are the initial shear displacement rates (averaged over the first 15 s of the test), and the arrows pointing downward indicate rates decreasing steadily to near unobservability in 1 or 2 min. At the higher stress all tests gave rapid shear displacement rates and accelerating creep leading quickly to "catastrophic" failure (arbitrarily large displacement, which was restrained by stops); the open circles plotted have the same meaning as before, and the small arrows pointing upward indicate accelerating slip rates leading to catastrophic failure. The large, open, arrows pointing upward are lower limit values for initial strain rates in tests in which the creep acceleration was so rapid that the moving part of the test cell hit the stops before the end of the first 15-s interval. In one experiment at τ=0.022 bar there was a short early stage of decelerating creep, followed by accelerating creep and failure, as arrows in Figure 1 indicate.

The results in Figure 1 show that in these tests the till behaved very much like a plastic material with yield stress of about 0.02 bar, reproducibly bracketed between the two stress levels tested. Decelerating creep was extensively observed at stresses below catastrophic yield, as in Figure 1; it corresponds

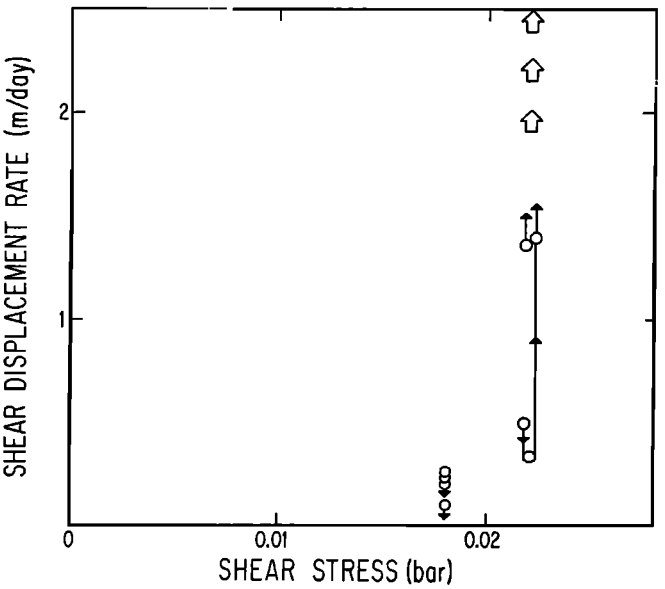

Fig. 1. Direct shear test data (shear displacement rate versus shear stress) for till from the base of Ice Stream B at Upstream B. Data are for a single specimen from a depth of 10 cm below the top of the till. The specimen was tested repeatedly, at shear stresses of 0.018 bar and 0.022 bar, alternately. Open circles are the average shear rate during the first 15 s after stress application, and small arrows indicate the direction of transient change of the shear rate. In the case where arrows point downward, the shear displacement rate decreased to <~1 mm d^{-1} in 2-3 min.; in case where arrows point upward, the rate increased to >~2 m d^{-1} in 15 s or less. Large, open arrows are lower limits for the shear rate in tests in which the initial shear rate was so high that the moving part of the shear box hit the stops before the end of the first 15 s.

qualitatively to the expectations of (4). Figure 1 cannot be used to fix an equivalent n value because steady state creep rates were not achieved, either in the decelerating creep below the yield stress or in the accelerating creep above; however, from the constraints that the data provide it is clear that n would have to be very large.

A second till sample was later tested in a larger direct-shear cell (diameter 6.35 cm) operating in the displacement-controlled mode (specimen sheared at a controlled slip rate, shear force recorded as a function of shear displacement). Figure 2 shows the results of 16 tests of this type, done at low, intermediate, and high shear rates as indicated in the figure caption. The range in shear displacement rates, from 0.09 m d^{-1} to 5.2 m d^{-1}, brackets the basal motion of Ice Stream B at Upstream B, 1.2 m d^{-1}. In all tests an approximately steady strength was reached toward the end. The strength varies by about ±6% from test to test. The strengths for slow, intermediate, and fast shear fall within the same scatter and are not clearly resolved from one another. The mean strength for the slow tests is 1.6±0.1 kPa and for the fast tests 1.7±0.1 kPa. The indicated value of S is 3±3% per decade. The equivalent n value from (8) is 75, but in relation to the standard deviation, S does not differ significantly from 0 (or n from ∞).

The observed strengths in the second series of tests are reasonably compatible with the 0.02 bar strength from the first series. (The second sample was tested 8 months later, having been stored at +1°C in packaging intended to minimize water loss by evaporation.) A later test was run on a sample from which all grains larger than 0.4 mm, 20% by volume of the

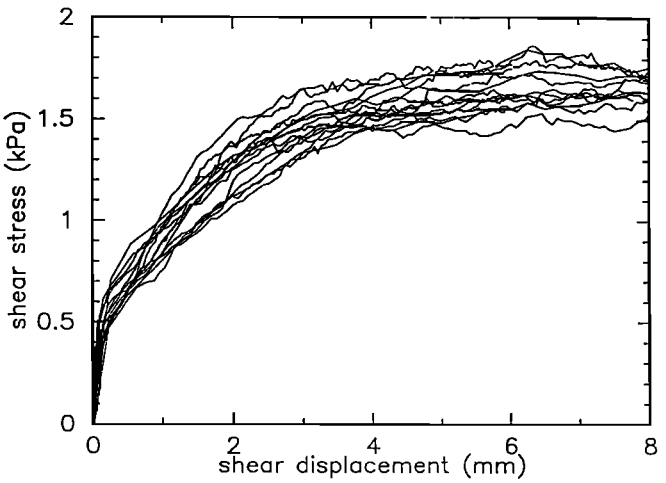

Fig. 2. Results of 16 controlled-strain direct shear tests on second till sample from the base of Ice Stream B, at three different shear rates. Shear stress is plotted against shear displacement in each test. Three tests were carried out at a shear displacement rate of 0.09 m d^{-1}, 10 tests at a rate of 0.86 m d^{-1}, and three at 5.2 m d^{-1}. Tests at the slowest rate give data curves of the most "jittery" character, and tests at the fastest rate give the least "jittery" curves, because the data sampling rate was the same for all tests. Data courtesy of H. Engelhardt.

original material, were removed; the strength was 0.018 bar, essentially unchanged from that of the original material. This makes it quite unlikely that removal of only the coarsest clasts (>~10 mm), constituting less than 2% by volume of the till as sampled, had more than a small effect on the strength. Drying the till and then reconstituting it back to the original water content (25% by weight) also had little effect on the strength. Since the till was probably undergoing shear deformation in situ, before sampling, and since it was necessarily deformed somewhat in the sampling process, the further disturbance involved in packing it into the test cell is unlikely to have altered its strength greatly. Disturbance of clay particle alignment that might be present in the residual state in situ would increase the strength over that in situ.

The tests cannot be considered to give a determination of S for the residual strength, because the total shear displacement was only 8 mm in the tests. On the basis of the earlier discussion, S is expected to be reduced in the residual state.

The features of mechanical behavior observed in the tests are qualitatively similar to those found in geotechnical testing of clay-rich soils at large strains, as described earlier. They are very different from what would be expected on the basis of flow law (1) with the parameters found by *Boulton and Hindmarsh* [1987].

Dependence on Effective Pressure

Whereas in flow law (1) the dependence of $\dot{\gamma}$ on τ is independent of the dependence on $\hat{P}$, so that the two can have very different nonlinearities, in (5)+(6) the two are coupled together. The $\hat{P}$ dependence in (5) can be compared with (1) by finding the equivalent value of m, from differentiation of (5) and (6):

$$m = -\left(\frac{\partial \ln \dot{\gamma}}{\partial \ln \hat{P}}\right)_{\tau_r} = \alpha \frac{\tau_r}{\tau_o} \cdot \frac{\mu_o \hat{P}}{c_o + \mu_o \hat{P}} \approx \alpha \frac{\tau_r}{\tau_o} \approx \alpha \quad (9)$$

The first approximate equality follows in case $c_o = 0$ or is small compared to $\mu_o \hat{P}$, as expected for an uncemented material [*Bolton*, 1979, p. 23]. Thus for flow law (5)+(6) the equivalent n from (8) is approximately the same as the equivalent m from (9). In view of the preceding discussion, suggesting $\alpha \sim 100$ for till or till-like soil, the current choices $m = 0$, 1, 2, or even 5 in modeling ice stream motion (as cited at the outset) give a greatly inadequate representation of the sensitivity of strain rate to effective pressure.

As long as the approximation $c_o \ll \mu_o P$ in (9) holds, the pressure sensitivity as measured by m does not depend, ostensibly, on the internal friction μ_o, which seems contrary to intuition. However, the viewpoint of gouge mechanics, which takes $\alpha = \mu_o/(a - b)$ as noted earlier and considers $(a - b)$ as a fundamental parameter, implies that α (and thus the equivalent m) does depend on the friction.

ICE STREAM FLOW STABILITY

If the till flow law is highly nonlinear, as the foregoing discussion suggests, there are important consequences for the deforming bed mechanism of ice stream motion. The highly nonlinear response to shear stress will lead to glacier flow behavior of types akin to those discussed by *Nye* [1951] for ice deforming as a perfectly plastic substance, but with the significant complication that the till yield stress is a function of the effective pressure. The highly nonlinear reciprocal dependence of flow on effective pressure, which according to (5)+(6) is directly linked to the nonlinear shear-stress dependence, will couple the flow sensitively to the basal water pressure. In particular, there is a basal-water-pressure feedback mechanism that for sufficiently nonlinear dependence results in instability of the flow system. This striking consequence of flow law nonlinearity is now considered. The instability is entirely separate from the marine ice sheet instability that has been much discussed in connection with the West Antarctic Ice Sheet [e.g., *Thomas et al.*, 1979; *van der Veen*, 1987].

Basal-Water-Pressure Feedback Mechanism

In a glacier or ice stream moving by the deforming bed mechanism, the deformability of the subglacial till is made possible by high pore water pressure [*Alley et al.*, 1987*a*; *Engelhardt et al.*, 1990]. For an Antarctic ice stream, in which the ice is below freezing except at its base, the source of the pore water is melting of basal ice, which is due to the frictional heat generated by till deformation, plus the geothermal heat flux, less the heat flux conducted upward within the subfreezing ice mass. The basal water pressure must adjust itself so that in a steady state the water produced by basal melting does not accumulate progressively but is conducted away, ultimately to the ocean at the grounding line, through some type of water conduit system. In such a flow system there can be a positive feedback mechanism for basal-water-pressure perturbations. If the water pressure increases, so that the till pore pressure increases, the till deformation rate will increase; this will increase the basal melting rate, which will result in a further increase in basal water pressure, unless the increased pressure causes the conduits to enlarge sufficiently. Depending on its physical parameters, the system can be either stable or unstable in relation to such water pressure perturbations.

This basic type of feedback effect and the resulting stability issue for the deforming bed mechanism has been noted but

not analyzed by *Alley et al.* [1987*b*, p. 8938]. It also arises for the basal sliding mechanism of ice stream or polar glacier motion, as has been discussed from various different points of view, mainly in relation to glacier or ice sheet surging, by *Weertman* [1969], *Budd* [1975], *Budd and McInnes* [1979], *Weertman and Birchfield* [1982], and *Oerlemans and van der Veen* [1984, pp. 107 and 189].

In this paper I investigate the immediate instability that can arise from the basal-water-pressure feedback mechanism in a simple ice stream flow model based on the deforming bed mechanism. By "immediate" I mean that which is an immediate consequence of the feedback, leaving out of consideration the effects of longer-term responses such as changes in ice thickness, till thickness, longitudinal stress gradient, or temperature distribution in the ice. These longer-term responses tend to provide ultimate damping effects on the immediate instability, as suggested by model calculations of *Oerlemans and van der Veen* [1984, p. 191].

Flow System with Feedback

Consider a laterally uniform, constant-width ice stream that can be treated as a one-dimensional flow system with longitudinal coordinate x, increasing downstream. The ice moves by shear of a basal till layer with flow law (5)+(6), whose basal-water-pressure dependence can for present purposes be written in differential form from (9) as

$$\partial v/\partial(P_I - P_W) = -nv/\hat{P} \qquad (10)$$

$v(x)$ is the basal ice velocity, equal to $\dot{\gamma}h$, where the (assumed uniformly shearing) till thickness is h, which drops out of (10) because of the logarithmic form of (9). $P_W(x)$ is the basal water pressure, assumed equal to the till pore pressure, $P_I(x)$ is the ice overburden pressure, and $\hat{P} = P_I - P_W$ is the effective pressure. In view of (8), n is written in place of α in (10), because α is so commonly used in the glaciological literature for ice surface slope. We consider a perturbation $\Delta P_W(x)$ in basal water pressure, which results, according to (10), in an ice velocity response

$$\Delta v = (nv/\hat{P})\,\Delta P_W \qquad (11)$$

This response is assumed for simplicity to be immediate, which neglects the time delay in equilibration of the till pore pressure to the perturbation in basal water pressure. In obtaining (11) from (10) it is assumed that over the time period considered, in the immediate response following the perturbation $\Delta P_W(x)$, there is insufficient time for appreciable readjustment of the ice thickness (hence P_I), till thickness h, or basal shear stress $\tau_B \approx \tau_r$, so that the velocity perturbation Δv is entirely the result of the pressure perturbation ΔP_W.

A change in v will result in a change in basal melting rate $\Delta\dot{M}$ given by

$$\Delta\dot{M} = \tau_B\,\Delta v/H \qquad (12)$$

where H is the latent heat of melting per unit volume of ice (H=0.31 G Pa).

The effect of $\Delta\dot{M}(x)$ on the pressure perturbation $\Delta P_W(x)$ depends on the nature of the conduit system through which the basal meltwater is conducted along the ice stream to the ungrounding line. Because little is known for a fact about this conduit system, it is necessary to make a heuristic assumption in order to proceed. Candidate model conduit systems that have been considered theoretically are the ice tunnel model [*Röthlisberger*, 1972; *Bindschadler*, 1983], the till channel or tunnel valley model [*Boulton and Hindmarsh*, 1987, p. 9077; *Alley*, 1989*a*, p. 112], the subglacial aquifer model [*Lingle and Brown*, 1987; *Shoemaker*, 1986], the water film model [*Weertman*, 1972; *Weertman and Birchfield*, 1982], and the linked cavity model [*Humphrey*, 1987; *Kamb*, 1987; *Lliboutry*, 1987]. Applied to Ice Stream B, the tunnel model appears to be ruled out because it gives at Upstream B an effective pressure $\hat{P}$=4 bars [*Bindschadler*, 1983, p. 10], which is much larger than the observed effective pressures of ~0.2 to 1.5 bar [*Engelhardt et al.*, 1990, p. 248; *Kamb*, 1990, p. 10]. Theoretical arguments against applicability of the ice tunnel model, the till channel model, and the subglacial aquifer model have been given by *Alley* [1989*a*], who favors a water film model with a nonuniform film of spatially varying thickness. Such a model seems to me fundamentally similar to a linked cavity model. I will here assume that the water conduit system under the model ice stream is of this general type, and I will represent it in a simplified form similar to that used by *Alley* [1989*a*, p. 115; 1989*b*, p. 119].

I thus make the heuristic assumption that there is a discontinuously present water layer of thickness d in a gap between the base of the ice and the top of the till, distributed in an interconnected manner over an areal fraction $\phi<1$ of the glacier sole. The interconnected water layer forms throughgoing conduits in which water can be transported along the base of the ice, at a local water pressure $P_W(x)$. The ice-till interface in places where the water-filled gap is absent supports a higher normal stress in the ice, so that the average overburden pressure $P_I > P_W$ is supported. Field evidence from two independent experiments at Upstream B suggests that d is about 1 mm (H. Engelhardt and B. Kamb, unpublished data, 1990), and a thickness of 4 mm at Upstream B was calculated theoretically by *Alley et al.* [1989, Figure 2]. The water layer conduit system provides water storage at the bed in the amount $W=\phi d$ per unit area of the bed. In both the water film and linked cavity models, both ϕ and d are decreasing functions of $\hat{P}$. For the former this is shown by *Alley* [1989*a*, equation (17)] and *Alley* [1989*b*, equation (3)], and for the latter by *Kamb* [1987, equations (4), (5), (8), (10), (17), (24), and Figures 7-10], if we equate d with the average gap width over the area of ice-bed separation (fractional area ϕ). I therefore make here the heuristic assumption that the water storage W varies with $\hat{P}$ as

$$W \sim c/\hat{P}^q \qquad (13)$$

which has the expected divergence as $\hat{P}\to 0$ and the ice stream goes afloat. The parameter q is a constant and c may vary with x. The differential response to a small perturbation is then

$$\Delta W \sim (qW/\hat{P})\,\Delta P_W = \mu\,\Delta P_W/\rho g \qquad (14)$$

The conduit response parameter $\mu = \rho g q W/\hat{P}$, where ρ is the density of water, is introduced for later convenience. The water storage adjustment to pressure change in (14) is for simplicity assumed to be instantaneous, although in reality some delay in the response must be involved.

To evaluate the effect of $\Delta\dot{M}$ on ΔP_W, we also need to be able to calculate the transport of water by the conduit system.

Because the water flow velocities and conduit dimensions are small (measured transport velocity is 7 mm s^{-1} at Upstream B: H. Engelhardt, unpublished data, 1990), it is reasonable to assume a linear relation between the water transport flux (per unit width of the ice stream) and the water pressure gradient:

$$\text{flux per unit width} = \kappa \partial P_W/\partial x \tag{15}$$

where κ is the effective hydraulic conductivity of the basal water system. In writing (15) it is assumed for simplicity that the bed is level, as it is under Ice Stream B to a reasonable approximation for 100 km upstream and downstream from Upstream B [*Shabtaie et al.*, 1987, Figure 3; *Shabtaie and Bentley*, 1988, Figure 2]. The results do not depend on this simplifying assumption, however. In the water layer conduit model the conductivity κ is given by

$$\kappa = \phi d^3/12\eta \tag{16}$$

where η is the viscosity of water [see, for example, *Alley's* [1989*a*] equation (25) with the correction $q \to q/f$ in his notation]. In (16) the appearance of ϕ as a simple factor represents a conduit system with minimal conduit constriction consistent with restriction of the conduit gap to an areal fraction ϕ of the ice-till interface. The differential variation of κ under a perturbation ΔW is thus

$$\Delta\kappa = (3\kappa/W)\Delta W \tag{17}$$

if for simplicity ϕ is assumed not to vary as the conduit thickness d adjusts. (Justification for this simplification as a reasonable approximation can be found in the logarithmic dependence of ϕ on d given in equation (3) of *Alley* [1989*b*]. The alternative simplification d=constant would lead to removal of the factor 3 in (17), and a full development would give a response intermediate between these two cases.)

The pressure adjustment ΔP_W to a change in basal melting rate $\Delta\dot{M}$ is determined by the water continuity condition, based on (15):

$$\frac{\partial \Delta W}{\partial t} = \Delta\dot{M} + \frac{\partial}{\partial x}\Delta\left(\kappa\frac{\partial P_W}{\partial x}\right) = \Delta\dot{M} + \frac{\partial P_W}{\partial x}\frac{\partial}{\partial x}\left(\frac{3\kappa}{W}\Delta W\right) + \frac{\partial \kappa}{\partial x}\frac{\partial \Delta P_W}{\delta x} + \kappa\frac{\partial^2 \Delta P_W}{\partial x^2} \tag{18}$$

in which the perturbation operation Δ is expanded for an infinitesimal perturbation, (17) is introduced, and the assumption $\partial^2 P_W/\partial x^2 = 0$ is made for a reason given below.

On the basis of (14) we can make the following expansion to evaluate the first term on the right side of (24):

$$\frac{\partial}{\partial x}\left(\frac{\kappa}{W}\Delta W\right) = \frac{\partial}{\partial x}\left(\frac{q\kappa}{\hat{P}}\Delta P_W\right) = \frac{q}{\hat{P}}\left(\frac{\partial \kappa}{\partial x} - \frac{\kappa}{\hat{P}}\frac{\partial \hat{P}}{\partial x}\right)\Delta P_W + \frac{q\kappa}{\hat{P}}\frac{\partial \Delta P_W}{\partial x} \tag{19}$$

The derivative $\partial\hat{P}/\partial x$ in (19) can be obtained from (10):

$$\partial\hat{P}/\partial x = -(\hat{P}/nv)\partial v/\partial x \tag{20}$$

The longitudinal strain rate $\partial v/\partial x$ could be taken from observation, but it seems more appropriate for the model treatment here to assume

$$\partial v/\partial x = v/L \tag{21}$$

The accuracy of (21) is not crucial, because the n in the denominator in (20) tends to suppress the contribution from this term.

The quantities W and κ and the derivatives $\partial\kappa/\partial x$ and $\partial P_W/\partial x$ that appear on the right side of (18) and (19) are to be evaluated for the datum state, from which the perturbations ΔP_W and ΔW depart. Because P_W is observed to be close to P_I in Ice Stream B [*Engelhardt et al.*, 1990, p. 248], we assume that in the datum state the hydraulic gradient is the same as the slope ß of the hydraulic grade line for ice flotation (0.9 times the surface slope if the bed is level):

$$\partial P_W/\partial x = -\rho g ß \tag{22}$$

For simplicity, ß is taken to be constant, so $\partial^2 P_W/\partial x^2 = 0$ as stated above. The effective conductivity κ is that which provides the required flow of basal meltwater in the datum state:

$$\kappa \rho g ß = \int_o^x \dot{M}(x)\,dx - \overline{v\tau}_B L/H \tag{23}$$

where $\overline{v\tau}_B$ is the average of the product $v\tau_B$ over the ice stream, of effective length L, above the point x. The conductivity in the datum state must increase downstream so as to accommodate the basal meltwater generated locally:

$$\rho g ß\,\partial\kappa/\partial x = \dot{M} \approx \tau_B v/H \tag{24}$$

In writing (23) and (24) we assume for simplicity that the geothermal heat flux is approximately in balance with the upward heat conduction in the basal ice, so that the basal melting is due to basal till deformation. Error in this assumption could be corrected by applying correction factors to the products $v\tau_B$ and $\overline{v\tau}_B$. In what follows we use $\psi = \overline{v\tau}_B/v\tau_B$ and can incorporate the correction factors in ψ.

When (19) is introduced into (18) and substitutions from (11), (12), (14), (20), (21), (22), (23), and (24) are made, the continuity equation (18) becomes

$$\frac{\partial \Delta P_W}{\partial t} = D\Delta P_W - E\frac{\partial \Delta P_W}{\partial x} + F\frac{\partial^2 \Delta P_W}{\partial x^2} \tag{25}$$

where

$$D = \frac{v\tau_B}{HW}\left(\frac{n}{q} - 1 - \frac{\psi}{n}\right) \tag{26}$$

$$E = \frac{v\tau_B}{H}\left(\frac{3L\psi}{W} - \frac{1}{ß\mu}\right) \tag{27}$$

$$F = \frac{v\tau_B L\psi}{Hß\mu} \tag{28}$$

An exact solution of (25) is available if the coefficients D, E, and F are constant. A solution of the form

$$\Delta P_W = \Re a \exp[(2\pi i x/\lambda) + \sigma t] \tag{29}$$

(where $\Re$ designates the real part) satisfies (25) if

$$\sigma = D - 2\pi i E/\lambda - 4\pi^2 F/\lambda^2 \tag{30}$$

It represents a spatially sinusoidal perturbation, as is commonly assumed in stability problems of this type. From (29) the time development of the perturbation is

$$\Delta P_W = a \exp \Re\sigma t \cos 2\pi (x - Et)/\lambda \quad (31)$$

If $\Re\sigma > 0$, the perturbation grows exponentially and the system is unstable. The instability condition is thus

$$\Re\sigma = D - \frac{4\pi^2}{\lambda^2} F = \frac{\nu \tau_B}{HW}\left(\frac{n-U}{q} - 1 - \frac{\psi}{n}\right) > 0 \quad (32)$$

where

$$U = \frac{4\pi^2 \psi L \hat{P}}{\lambda^2 \beta \rho g} \quad (33)$$

The above results are only approximate because D, E, and F in (25) vary (slowly) with x as a result of the longitudinal increase in basal water flux in the datum state. The effect of the x variation of the coefficients on the solutions of (25) is considered in the Appendix; although there is a definite effect, it does not alter the basic conclusions reached above on the basis of the solution for constant coefficients.

Evaluated for Ice Stream B at Upstream B, with parameter values $\beta \sim 0.1°$, $L \sim 100$ km, $\hat{P} \sim 1$ bar, $W \sim 1$ mm, $\tau_B \sim 0.2$ bar, $\nu \sim 400$ m yr^{-1}, $\psi \sim 0.5$, for a perturbation wavelength $\lambda \sim 30$ km, (33) gives $U \sim 13$, and from (32) we obtain

$$\Re\sigma = (14 \text{ days})^{-1}\left(\frac{n-13}{q} - 1\right) \quad (34)$$

The term $-\psi/n$ in (32) is neglected in (34) because we expect n to be large. Thus we conclude that if $n > 13 + q$, the system is unstable. The value of U (=13 in (34)) is inversely proportional to the square of the perturbation wavelength, λ^2, as (33) indicates; thus for λ longer than 30 km, the instability sets in for smaller flow nonlinearity n. For large λ, with $U \to 0$, the system is unstable for $n > q$.

There is no observational information on the value of the parameter q, but it can be derived theoretically. In the case of the linked-step-cavity model [*Kamb*, 1987], an analysis for laminar water flow, analogous to the derivation of equation (38*a*) of *Kamb* [1987] from equation (2) (for turbulent flow) in the same reference, yields $q = 1$. For the water film model of *Alley* [1989*a*, *b*], one can obtain from equation (17) of *Alley* [1989*a*] and equation (3) of *Alley* [1989*b*] the result $q = 1 + 10\phi \ln 10$ applicable to the differential relation (14) of the present paper; for $\phi \sim 0.5$, this gives $q \sim 12$. In empirical sliding laws of a form like (1), m appears mostly in the range 0-2 [*Bentley*, 1987, p. 8855], and one might be tempted, with a leap of imagination, to surmise on this remote basis that $q \sim m$. Within the wide foregoing range of constraints on q, a reasonably conservative conclusion is that the deforming bed system is unstable for $n > \sim 20$ for perturbations of 30 km wavelength or $n > \sim 5$ for 100 km wavelength.

From (31), the time scale of the instability (or of a stable response) is $|\Re\sigma|^{-1}$, which, from (32), is scaled by the time-dimensional factor $HW/\nu\tau_B$, equal to the time required to generate by basal melting enough water to replace the basal water storage in the datum state. For the parameter values assumed, $|\Re\sigma|^{-1}$ is 14 days divided by the absolute value of the quantity in the final parenthesis in (34). This time scale is extremely short in relation to typical glacier adjustment time scales of years, and the treatment of the instability as "immediate" in the sense discussed at the outset is thus justified. The time scale of days is of the same order as that of glacier minisurges, which occur by adjustments in the basal water system [*Kamb and Engelhardt*, 1987].

The perturbation (31) moves as a wave with speed E given by (27), which is 3 times the mean speed of water flow in the basal conduit system. For the parameters used (for which the second term on the right in (27) is negligible), $E/3$ is 4 cm s^{-1}; for $W = 2.4$ mm, $E/3$ is 1.8 cm s^{-1} and is equal to the transport speed implicit in (15)+(16)+(22), with $\phi = 0.5$. This speed is of the same order of magnitude as the water transport speed 0.7 cm s^{-1} measured by injection of salt-water in the basal water system of Ice Stream B (H. Engelhardt, unpublished data, 1990). E is the speed of kinematic waves in a conduit system of the type modeled. Such waves are an inherent feature of the conduit system, independent of the ice stream flow instability under examination in this paper.

DISCUSSION AND CONCLUSIONS

The results of the last section indicate that above a certain degree of nonlinearity in the till flow law the deforming bed mechanism of ice stream motion is unstable, because of feedback from the generation of basal meltwater by shear heating in the basal till. The instability is somewhat akin to creep instability by shear heating [*Clarke et al.*, 1977; *Oerlemans and van der Veen*, 1984, p. 96; *Hutter*, 1983, pp. 160-179], but the feedback mechanisms are quite different in the two instabilities.

The type of flow law nonlinearity that affects the deforming bed instability considered here is nonlinearity in the inverse dependence of shear strain rate or basal slip rate on effective pressure at fixed shear stress. This nonlinearity is linked by the form of the applicable flow law (5) to the nonlinearity in the dependence on shear stress; both have the same effective exponent n, as discussed earlier.

The deforming bed instability depends heavily on the relationship (13) that specifies the response sensitivity of the basal conduit system to changes in the basal water pressure. The assumed relation (13) is valid, with $q = 1$, for a linked cavity model of the basal water conduit system [*Kamb*, 1987], and is valid in its differential form (14) for a water film model [*Alley*, 1989*a*], with $q \sim 12$. The relationship gives only the final, steady state response of water storage to effective pressure, omitting the time-varying transient response by which the adjustment from the initial state to the final response proceeds once a perturbation has been imposed. To this extent, and also because of neglect of the transient delay in the equilibration of basal water pressure with till pore pressure, the time dependence of the perturbation given by (31) is incomplete. For an ice tunnel conduit model [*Röthlisberger*, 1972], the steady state relationship between W and $\hat{P}$ is like (13) but with negative q (for laminar water flow, $q = -3$), and there is the further complication that the steady state W decreases with the water pressure gradient as β^{-2}. Leaving aside the effect of the latter complication, the effect of negative q in the relation (32) is to make the system unstable against short wavelength perturbations in the case of small n, and stable for large n. However, it is not certain that the steady state would be reached, at least until after a period of oscillation, because the initial response of a tunnel to increased

water pressure or to increased ß is to enlarge, which is a response in the opposite direction from the steady state response. These complications are not encountered in the foregoing treatment because, for reasons given earlier, a water layer conduit model was assumed to be appropriate.

Although the treatment does not include the ice-dynamics-mediated adjustments in ice thickness, ice temperature distribution, and ice flow velocity that would follow the immediate perturbation response considered here and that might damp its further development, some insight into the effects of ice dynamics can be gained from the work of *Oerlemans and van der Veen* [1984, pp. 106 and 191], who include a feedback effect of basal melting on basal sliding in two of their numerical models of ice sheet behavior. For the effect of basal melting on ice velocity they assume $v=b_o+b_1W$, with constant b_o and b_1. It appears from their equation (6.4.1), by comparison with (18) above, that they implicitly assume $W=a_o+a_1P_W$ (constant a_o and a_1). Hence they in effect assume $v=c_o+c_1P_W$ (constant c_o and c_1), which for perturbations in P_W can approximately represent a nonlinear relation, as in (11) above. In one model they take $b_o=0$ and in the other $b_o\neq 0$, but since a_o is not necessarily 0, both models may be based in effect on nonlinear v versus P_W relations. Not enough information is given to deduce the effective n used in either type of model. The $b_o\neq 0$ model shows bounded instability associated with multiple steady states, and the $b_o=0$ model shows oscillatory behavior for large enough values of b_1, which seems to represent a more complex type of bounded instability. The models thus indicate that instability can arise from a sensitive enough dependence of ice flow on basal water pressure, even when the possibly stabilizing effects of ice dynamics are included in the analysis. However, the possible influence of nonlinearity of the v versus P_W relation on the stability-instability condition cannot be determined from the results, for the reason given above. Other differences between these models and the treatment here further limit the comparison: for example, the effective κ is either assumed constant or proportional to $\hat{P}$, and the water storage calculated in the models is 0.6 to 1.5 m, much greater than the $W\sim 1$ mm considered reasonable here. For parameters that seem appropriate to these models ($W\sim 1$ m, $\tau_B\sim 0.5$ bar, $v\sim 10$ m y^{-1}), the time constant $HW/v\tau_B$ in (32) is ~600 years; this makes it possible that the early, accelerating part of the oscillations calculated by *Oerlemans and van der Veen* [1984, Figure 11.13], which takes place on a comparable time scale, is a manifestation of the type of "immediate" instability treated here.

The critical value of n, above which the deforming bed flow mechanism is unstable for the water layer conduit model, cannot be closely fixed, partly because the physical model and mathematical treatment are only approximate, but primarily because our knowledge of system parameters for the ice streams is limited. Particularly uncertain is the parameter q. The theoretical q values of 1 and ~12 for two well-defined models of nonuniform water layer conduits leave a rather wide range of uncertainty as to what q value is appropriate to the real system, if (13) is applicable. The critical value of n depends strongly also on the wavelength of the perturbation that initiates the instability, according to (33), but we have no firm basis for choosing a value for this wavelength. Nevertheless, from the evaluation of the last section it appears that for reasonable choices of parameter values, the critical n is likely to lie in the range from about 5 to 20. This means that it makes a great difference for the functioning of the deforming bed mechanism whether basal till has flow properties like those assumed in current numerical modeling ($n\leq 1.3$) or instead like those that appear appropriate from the work in soil mechanics discussed in the first section ($n\sim$15-100). It seems reasonably certain that a deforming bed mechanism in which the till rheology controls the rate of glacier motion is unstable if the till behaves mechanically like clay-rich soil at residual strength, with $n>\sim 100$, and if (13) applies.

Unless a mechanism for preventing perturbations of wavelength longer than about 10 km were in operation, a flow system subject to the above instability could not persist in its unstable steady state over geologic time. Are the fast-moving ice streams as we see them today the result of past speed-ups promoted by this instability? The form of the instability criterion in (32) permits this, because the datum-state ice stream velocity v does not affect the condition of stability or instability (sign of $\Re\sigma$), although it does affect the time scale of its development. But by the same token, the present-day ice streams should still be unstable. Some type of instability in ice stream motion may be suggested by the recent stopping of Ice Stream C [*Whillans and Bolzan*, 1987], but no manifestation of instability in terms of rapid increase in ice stream velocities is currently observed.

From the seemingly stabilized motion of the currently active ice streams one is thus nudged to the conclusion that their motion is not now being controlled by till rheology, which, as the foregoing considerations indicate, would not provide stabilization. The implication is that some other mechanism limits the speed of motion.

An independent indication of the same conclusion is the low measured shear strength of the basal till, 0.02 bar from Figures 1 and 2, which makes the till an order of magnitude too weak to support the basal shear stress of 0.2 bar required mechanically as a regional average.

If an incipient ice stream (or an incipiently surging glacier) is subject to the deforming bed instability discussed above and begins to speed up rapidly because of it, the motion may become limited by some other resisting mechanism(s) at the bed before there is time for major adjustments in ice sheet configuration of the type modeled by *Oerlemans and van der Veen* [1984]. Such a course of events would be analogous to the theory of glacier surging by *Lliboutry* [1968, p. 51; 1969, p. 946], in which the sliding rate increases unstably because of basal cavitation over short-wavelength roughness elements, but the increase is ultimately stabilized by the sliding resistance of long-wavelength roughness elements. In the ice streams the stabilization could for example be achieved by the sliding resistance of scattered "sticky spots" of bedrock protruding through the basal till layer.

If the conclusion that some other mechanism controls the ice stream motions is correct, current attempts to model the ice stream motions on the assumption that they are controlled by the deforming bed mechanism are misdirected. Valid modeling of the ice stream motions can of course be done only when the mechanism that controls the motion has been securely identified and quantitatively formulated. The need for further effort in that direction is emphasized by the considerations here as to flow law nonlinearity in relation to stability/instability of the deforming bed mechanism.

APPENDIX

We consider here the effect of the x variation of the coefficients D, E, and F on the solutions of (25). A first approximation to the x variation is obtained by expanding the coefficients in power series in x, and keeping the constant and linear terms. To do this we expand the variations of (26), (27), and (28) differentially:

$$\frac{\delta D}{D} = \frac{\delta v}{v} - \frac{\delta W}{W} \tag{35}$$

$$\frac{\delta E}{E} = \frac{\delta D}{D} + \frac{\delta L}{L} \tag{36}$$

$$\frac{\delta F}{F} = \frac{\delta E}{E} + \frac{\delta \hat{P}}{\hat{P}} \tag{37}$$

The δ here designates differential changes from the values at an arbitrary point of interest (here taken at Upstream B), which will be designated $x=0$, so that $\delta L = \delta x = x$.

The longitudinal variation of v represents longitudinal strain rate e_{xx}:

$$\frac{\delta v}{v_o} = \frac{\dot{e}_{xx}}{v_o} x \sim \frac{v_o - v_u}{v_o} \frac{x}{L} \tag{38}$$

Here $v_u \sim 100$ m yr^{-1} is the flow velocity at a point distant $L \sim 100$ km upstream from the origin, where $v = v_o$; the last form of (38) assumes uniform longitudinal strain rate over this interval.

The variation of water storage δW in (35) is linked to the variation in conductivity $\delta\kappa$ by (17) and thence to x by (23) and (24):

$$\frac{\delta W}{W} = \frac{\delta \kappa}{3\kappa} = \frac{1}{3\psi} \frac{x}{L} \tag{39}$$

The variation of effective pressure $\Delta\hat{P}$ is linked to ΔW by (13) and thence to x via (39)

$$\frac{\delta \hat{P}}{\hat{P}} = -\frac{1}{q} \frac{\delta W}{W} = -\frac{1}{3\psi q} \frac{x}{L} \tag{40}$$

When (38)-(40) are combined in (35)-(37) and numerical values $\psi \sim 0.5$ and $q \sim 3$ introduced (as used in the evaluation in the main text), the variations become

$$\frac{\delta D}{D} \sim 0, \quad \frac{\delta E}{E} \sim \frac{x}{L}, \quad \frac{\delta F}{F} \sim \frac{x}{L} \tag{41}$$

In (41), the variations have been rounded for simplicity to the nearest integral multiple of x/L, but this is not essential in the treatment that follows.

On the basis of (41), the first approximation to the x variation is incorporated into (25) as follows:

$$\frac{\partial \Pi}{\partial t} = D\Pi - E(1+\epsilon x)\frac{\partial \Pi}{\partial x} + F(1+\epsilon x)\frac{\partial^2 \Pi}{\partial x^2} \tag{42}$$

where for compactness Π is written for ΔP_W, where $\epsilon = 1/L$, and where D, E, and F are now constants. To solve (42), a separation of variables is carried out in the usual way, with separation constant σ; the result is

$$\Pi(x,t) = e^{\sigma t}\Phi(x) \tag{43}$$

$$F(1+\epsilon x)\frac{d^2\Phi}{dx^2} - E(1+\epsilon x)\frac{d\Phi}{dx} + (D-\sigma)\Phi = 0 \tag{44}$$

A differential equation of type (44) can in principle be solved exactly with confluent hypergeometric functions [*Bateman Manuscript Project*, 1953, p. 249], but to obtain a practical solution I use instead a perturbation method, based on the small value of ϵx over an interval of adequate size around the point of interest. Let the solution of (44) be represented as

$$\Phi = \Re a e^{ikx}\left(1 + \epsilon f(x)\right) \tag{45}$$

in which $f(x)$ is an undetermined function and $k = 2\pi/\lambda$. Introduce (45) into (44), take σ as given in (30), and neglect terms in ϵ^2. The result is

$$\epsilon\left[Ff'' - (E - 2Fki)f' - (Fk^2 + Eki)x\right] = 0 \tag{46}$$

where primes denote differentiation. (46) is satisfied by

$$f = rx^2 + sx + p \tag{47}$$

when the constants r and s are

$$2r = -(Fk^2 + Eki)/(E - 2Fki) \tag{48}$$

$$s = 2rF/(E - 2Fki) \tag{49}$$

The constant p, which is a solution of the homogeneous equation associated with (46), can be chosen so as to minimize $f(x)$ in some sense, for example, so as to make $f(x)$ average to zero over an interval of interest $-l \le x \le l$:

$$f = rx^2 + sx - \tfrac{1}{3}rl^2 \tag{50}$$

In the spirit of seeking a perturbation solution that deviates little from the sinusoidal perturbation in (31), we do not prescribe rigid initial and boundary conditions; rather, we seek to minimize $f(x)$. A second solution of the homogeneous equation could be added to (47), but minimization of $f(x)$ is best achieved without it. Measures of the departure of $f(x)$ from 0 are $f(\pm l) = \tfrac{2}{3}rl^2 \pm sl$.

From the form of (43), (45), and (50) we see that the x variation of the coefficients D, E, and F in (25) affects the x dependence of the solution, through nonzero $f(x)$ in (45), while leaving unchanged the exponential t dependence in (31) and (43), with exponential coefficient σ given by (30). Thus an initial perturbation $\Delta P_W(x,o)$ of the form (45) with $f(x)$ given by (48)-(50) will decay or grow exponentially with time, depending on the sign of $\Re\sigma$ as in (31).

The perturbation, instead of a simple sinusoid, has the form of a sinusoid with amplitude and phase varying slowly with x. Measures of the departure of the amplitude from that of a simple sinusoid over the interval $-l \le x \le l$ are $|1 + \epsilon f(\pm l)| - 1$. Evaluated with $l = 10$ km and the parameters used in the main text, for which $r = 0.052 - 0.279i$ km^{-1}, $s = 0.094 - 0.148i$ (from (48) and (49) with parameter values via (26)-(28)), these measures are 0.033 and 0.011, thus

about 3% maximum. The assumption, for stability analysis, of a sinusoidal perturbation is of course an arbitrary choice adapted to the form of the solution (29). It is therefore equally reasonable to assume an initial perturbation of the form (45), especially when this perturbation differs only slightly (3% in amplitude, as shown above) from a sinusoidal perturbation over an x interval of length $2l \approx \lambda$. Thus the form of (43) justifies using the instability criterion (32) when D, E, and F are slowly varying functions of x.

Acknowledgments. The Antarctic field work upon which some of this paper is based was supported by the National Science Foundation (grant DPP-8519083). The experimental work giving the results in Figure 2 was done by Hermann Engelhardt. I thank Ronald F. Scott for access to the facilities of the Caltech Soil Mechanics Library. Charles Bentley made helpful comments on the manuscript. Caltech Division of Geological and Planetary Sciences, Contribution 4914.

REFERENCES

Alley, R.B., Water-pressure coupling of sliding and bed deformation: I. Water system, *J. Glaciol., 35*, 108-118, 1989*a*.

Alley, R.B., Water-pressure coupling of sliding and bed deformation: II. Velocity-depth profiles, *J. Glaciol., 35*, 119-129, 1989*b*.

Alley, R.B., D.D. Blankenship, C.R. Bentley, and S.T. Rooney, Till beneath Ice Stream B, 3, Till deformation: Evidence and implications, *J. Geophys. Res., 92*, 8921-8929, 1987*a*.

Alley, R.B., D.D. Blankenship, S.T. Rooney, and C.R. Bentley, Till beneath Ice Stream B, 4, A coupled ice-till flow model, *J. Geophys. Res., 92*, 8931-8940, 1987*b*.

Alley, R.B., D.D. Blankenship, S.T. Rooney, and C.R. Bentley, Water-pressure coupling of sliding and bed deformation. III. Application to Ice Stream B, *J. Glaciol., 35*, 131-139, 1989.

Bateman Manuscript Project, *Higher Transcendental Functions*, Vol. I, McGraw-Hill, New York, 1953.

Bentley, C.R., Antarctic ice streams: A review, *J. Geophys. Res., 92*, 8843-8858, 1987.

Biegel, R.L., C.G. Sammis, and J. Dieterich, Frictional properties of simulated gouge having a fractal particle size distribution, *J. Struct. Geol., 11*, 827-846, 1989.

Bindschadler, R., The importance of pressurized subglacial water in separation and sliding at the glacier bed, *J. Glaciol., 29*, 3-19, 1983.

Bindschadler, R.A., SeaRISE: a multidisciplinary research initiative to predict rapid changes in global sea level caused by collapse of marine ice sheets, NASA Conference Publication Preprint, Goddard Space Flight Center, Greenbelt, MD, 1990.

Bishop, A.W., G.E. Green, V.K. Garga, A. Andresen, and J.D. Brown, A new ring shear apparatus and its application to the measurement of residual strength, *Geotechnique, 21*, 273-328, 1971.

Blankenship, D.D., C.R. Bentley, S.T. Rooney, and R.B. Alley, Till beneath Ice Stream B, 1, Properties derived from seismic travel times, *J. Geophys. Res., 92*, 8903-8911, 1987.

Blanpied, M.L., T.E. Tullis, and J.D. Weeks, Frictional behavior of granite at low and high sliding velocity, *Geophys. Res. Lett., 14*, 554-557, 1987.

Bolton, M., *A Guide to Soil Mechanics*, John Wiley, New York, 1979.

Borja, R.I., and Kavazanjian, A constitutive model for the stress-strain-time behavior of "wet" clays, *Geotechnique, 35*, 283-298, 1985.

Boulton, G.S., A paradigm shift in glaciology?, *Nature, 322*, 18, 1986.

Boulton, G.S., and R.C.A. Hindmarsh, Sediment deformation beneath glaciers: Rheology and geological consequences, *J. Geophys. Res., 92*, 9059-9082, 1987.

Boulton, G.S., and A.S. Jones, Stability of temperate ice sheets resting on beds of deformable sediment, *J. Glaciol., 24*, 29-43, 1979.

Boulton, G.S., G.D. Smith, A.S. Jones, and J. Newsome, Glacial geology and glaciology of the last mid-latitude ice sheets, *Q. J. Geol. Soc. London, 142*, 447-474, 1985.

Brown, N.E., B. Hallet, and D.B. Booth, Rapid soft bed sliding of the Puget glacial lobe, *J. Geophys. Res., 92*, 8985-8997, 1987.

Budd, W.F., A first simple model for periodically self-surging glaciers, *J. Glaciol., 14*, 3-21, 1975.

Budd, W.F., and B.J. McInnes, Periodic surging of the Antarctic ice sheet – an assessment by modelling, *Hydrol. Sci. Bull., 24*, 95-104, 1979.

Clarke, G.K.C., Fast glacier flow: Ice streams, surging, and tidewater glaciers, *J. Geophys. Res., 92*, 8835-8841, 1987*a*.

Clarke, G.K.C., Subglacial till: A physical framework for its properties and processes, *J. Geophys. Res., 92*, 9023-9036, 1987*b*.

Clarke, G.K.C., V. Nitsen, and W.S.B. Paterson, Strain heating and creep instability in glaciers and ice sheets, *Rev. Geophys. Space Phys., 15*, 235-247, 1977.

Engelhardt, H., N. Humphrey, B. Kamb, and M. Fahnestock, Physical conditions at the base of a fast moving Antarctic ice stream, *Science, 248*, 57-59, 1990.

Feda, J., Interpretation of creep of soils by rate process theory, *Geotechnique, 39*, 667-677, 1989.

Hughes, T.J., West Antarctic ice streams, *Rev. Geophys. Space Phys., 15*, 1-46, 1977.

Humphrey, N.F., Coupling between water pressure and basal sliding in a linked cavity hydraulic system, *Publ. 170*, pp. 105-120, Int. Soc. Hydrol. Sci., Wallingford, United Kingdom, 1987.

Hutter, K., *Theoretical Glaciology*, D. Reidel, Norwell, MA, 1983.

Iverson, R.M., A constitutive equation for mass-movement behavior, *J. Geol., 93*, 143-160, 1985.

Iverson, R.M., Unsteady, nonuniform landslide motion: 1. Theoretical dynamics and the steady datum state, *J. Geol., 94*, 1-15, 1986.

Kamb, B., Glacier surge mechanism based on linked cavity configuration of the basal water conduit system, *J. Geophys. Res., 92*, 9083-9100, 1987.

Kamb, B., Is the Antarctic Ice Sheet disintegrating?, *Eng. Sci., 53*(3), 5-13, 1990.

Kamb, B., and H. Engelhardt, Waves of accelerated motion in a glacier approaching surge: the mini-surges of Variegated Glacier, Alaska, *J. Glaciol., 33*, 27-46, 1987.

Lambe, T.W., and R.V. Whitman, *Soil Mechanics*, John Wiley, New York, 1969.

Lingle, C.S., and T.J. Brown, A subglacial aquifer bed model and water pressure dependent basal sliding relationship for a West Antarctic ice stream, in *The Dynamics of the West Antarctic Ice Sheet*, edited by C.J. van der Veen and J. Oerlemans, pp. 249-285, D. Reidel, Norwell, MA, 1987.

Lliboutry, L., General Theory of subglacial cavitation and sliding of temperate glaciers, *J. Glaciol., 7*, 21-58, 1968.

Lliboutry, L., Contribution à la théorie des ondes glaciaires, *Can. J. Earth Sci., 6*, 943-954, 1969.

Lliboutry, L., Realistic, yet simple bottom boundary conditions for glaciers and ice sheets, *J. Geophys. Res., 92*, 9101-9109, 1987.

MacAyeal, D.R., Large-scale ice flow over a viscous basal sediment: Theory and application to Ice Stream B, Antarctica, *J. Geophys. Res., 94*, 4071-4087, 1989.

Maksimovic, M., On the residual shearing strength of clays, *Geotechnique, 39*, 347-351, 1989.

Mitchell, J.K., R.G. Campanella, and A. Singh, Soil creep as a rate process, *J. Soil Mech. Found. Div. Am. Soc. Civ. Eng., 94*(SM-1), 231-253, 1968.

Nakase, A., and T. Kamei, Influence of strain rate on undrained shear characteristics of K_o-consolidated cohesive soils, *Soils Found., 26*, 85-95, 1986.

Nye, J.F., The flow of glaciers and ice sheets as a problem in plasticity, *Proc. R. Soc. London, Ser. A, A207*, 554-572, 1951.

Oerlemans, J., and C.J. van der Veen, *Ice Sheets and Climate*, D. Reidel, Norwell, MA, 1984.

O'Reilly, M.P., S.F. Brown, and R.F. Overy, Viscous effects observed in tests on an anisotropically normally consolidated silty clay, *Geotechnique, 39*, 153-158, 1989.

Prapaharan, S., J.L. Chameau, and R.D. Holtz, Effect of strain rate on undrained strength derived from pressuremeter tests, *Geotechnique, 39*, 615-624, 1989.

Röthlisberger, H., Water pressure in intra- and subgalcial channels, *J. Glaciol., 11*, 177-203, 1972.

Scholz, C.H., *The Mechanics of Earthquakes and Faulting*, Cambridge University Press, New York, 1990.

Shabtaie, S., and C.R. Bentley, Ice-thickness map of the West Antarctic ice streams by radar sounding, *Ann. Glaciol., 11*, 126-136, 1988.

Shabtaie, S., I.M. Whillans, and C.R. Bentley, The morphology of Ice Streams A, B, and C, West Antarctica, and their environs, *J. Geophys. Res., 92*, 8865-8883, 1987.

Shoemaker, E.M., Subglacial hydrology for an ice sheet resting on a deformable aquifer, *J. Glaciol., 32*, 20-30, 1986.

Singh, A., and J.K. Mitchell, A general stress-strain-time function for soils, *J. Soil Mech. Found. Div. Am. Soc. Civ. Eng., 94*(SM-1), 21-46, 1968.

Skempton, A.W., Residual strength of clays in landslides, folded strata, and the laboratory, *Geotechnique, 35*, 3-18, 1985.

Thomas, R.H., Ice sheet margins and ice shelves, in *Climate Processes and Climate Sensitivity, Geophys. Monogr. Ser., Vol. 29*, edited by J.E. Hansen and T. Takahashi, 265-274, AGU, Washington, DC, 1984.

Thomas, R.H., T.J.O. Sanderson, and K.E. Rose, Effect of climatic warming on the West Antarctic ice sheet, *Nature, 277*, 355-358, 1979.

Tullis, T.E., Rock friction and constitutive behavior from laboratory experiments and its implications for an earthquake prediction program, *Pure Appl. Geophys., 126*, 555-585, 1988.

van der Veen, C.J., The West Antarctic Ice Sheet: the need to understand its dynamics, in *Dynamics of the West Antarctic Ice Sheet*, edited by C.J. Van der Veen, and J. Oerlemans, pp. 1-16, D. Riedel, Norwell, MA, 1987.

Weertman, J., Water lubrication mechanism of glacier surges, *Can. J. Earth Sci., 6*, 929-942, 1969.

Weertman, J., General theory of water flow at the base of a glacier or ice sheet, *Rev. Geophys. Space Phys., 10*, 287-333, 1972.

Weertman, J., and G.E. Birchfield, Subglacial water flow under ice streams and West-Antarctic ice-sheet stability, *Ann. Glaciol., 3*, 316-320, 1982.

Whillans, I.M., and J. Bolzan, Velocity of Ice Streams B and C, Antarctica, *J. Geophys. Res., 92*, 8895-8902, 1987.

(Received September 20, 1990;
revised March 4, 1991;
accepted March 25, 1991.)

JOURNAL OF GEOPHYSICAL RESEARCH, VOL. 96, NO. B10, PAGES 16,547–16,565, SEPTEMBER 10, 1991

Application of the Global Positioning System to Crustal Deformation Measurement 1. Precision and Accuracy

KRISTINE M. LARSON

Colorado Center for Astrodynamics Research, University of Colorado, Boulder

DUNCAN C. AGNEW

Institute of Geophysics and Planetary Physics, Scripps Institution of Oceanography, La Jolla, California

In this paper we assess the precision and accuracy of interstation vectors determined using the Global Positioning System (GPS) satellites. These vectors were between stations in California separated by 50-450 km. Using data from tracking the seven block I satellites in campaigns from 1986 through 1989, we examine the precision of GPS measurements over time scales of a several days and a few years. We characterize GPS precision by constant and length dependent terms. The north-south component of the interstation vectors has a short-term precision of 1.9 mm + 0.6 parts in 10^8; the east-west component shows a similar precision at the shortest distances, 2.1 mm, with a larger length dependence, 1.3 parts in 10^8. The vertical precision has a mean value of 17 mm, with no clear length dependence. For long-term precision, we examine interstation vectors measured over a period of 2.2 to 2.7 years. When we include the recent results of Davis et al. (1989) for distances less than 50 km, we can describe long-term GPS precision for baselines less than 450 km in length as 3.4 mm + 1.2 parts in 10^8, 5.2 mm + 2.8 parts in 10^8, 11.7 mm + 13 parts in 10^8 in the north- south, east-west, and vertical components. Accuracy has been determined by comparing GPS baseline estimates with those derived from very long baseline interferometry (VLBI). A comparison of eight interstation vectors shows differences ranging from 5 to 30 mm between the mean GPS and mean VLBI estimates in the horizontal components and less than 80 mm in the vertical. A large portion of the horizontal differences can be explained by local survey errors at two sites in California. A comparison which suffers less from such errors is between the rates of change of the baselines. The horizontal rates estimated from over 4 years of VLBI data agree with those determined with 1-2 years of GPS data to within one standard deviation. In the vertical, both GPS and VLBI find insignificant vertical motion.

INTRODUCTION

Many geodetic techniques have been used to measure crustal deformation across the North American/Pacific plate boundary in California. The oldest data come from triangulation measurements [e.g., *Hayford and Baldwin*, 1908]; more recently, precise electronic distance measurement (EDM) has provided many details about strain across faults of the plate boundary [e.g., *Savage*, 1983]. Both of these procedures measure through the atmosphere and require the measurement points to be intervisible; they are thus limited to distances up to a few tens of kilometers. Both require considerable skill and expensive equipment to pursue successfully.

In the past decade, measurements using extraterrestrial objects, such as satellite laser ranging (SLR) [*Christodoulidis et al.*, 1990; *Smith et al.*, 1990] and very long baseline interferometry (VLBI) [*Herring et al.*, 1986; *Clark et al.*, 1987], have made possible measurements between points hundreds to thousands of kilometers apart. This has enabled a direct determination of the total contemporary plate motion across the broad boundary in California. These observations are, however, even more expensive to make than the older, purely terrestrial, techniques.

The most recent advance in precise geodetic measurements has been the use of the Global Positioning System (GPS) satellites. The basic principles of this technique are similar to VLBI, with some important differences. The radio signals originate at satellites, rather than quasars, and GPS receivers make an instantaneous determination of the distance between the receiver and satellite, rather than requiring cross correlation of noise signals to determine the length between two sites. From enough measurements of signals arriving from different directions the complete vector baseline between two sites can be computed. Because the signal strength at the Earth is so much higher than for the quasar sources used in VLBI and because the signal has a known and well-controlled structure, GPS antennas (and all other equipment) weigh at most a few hundred pounds rather than the many tons needed for VLBI. A similar favorable ratio applies to the costs of the two techniques. For all these reasons, GPS is poised to become the method of choice for crustal deformation geodesy and in many areas has indeed already become so.

But since this is such a new technique, it is vital to establish just what its errors are. Judging from past experience with VLBI and SLR, constructing a formal error budget, while useful, is likely to give an incomplete picture because of the wide variety of semisystematic errors that are little understood (not to mention those that are overlooked). We feel that what is needed is an empirical investigation of the precision and accuracy of GPS measurements, judged from actual results: the precision being a measure of how exact the estimate is, and the accuracy a measure of how close the estimate is to the truth [*Bevington*, 1969]. Our measure of

Paper number 91JB01275.
0148–0227/91/91-JB-01275$05.00

precision is thus (as for others) the scatter of results about a mean value; our measure of accuracy is the agreement with some other technique (VLBI).

This paper is the first of three that describe results from nearly three years of measurements in central and southern California. This paper describes the precision and accuracy over baselines from 50-450 km. Though some earlier work [e.g., *Dong and Bock*, 1989] has demonstrated subcentimeter precision over these distances, this precision was only evaluated from data collected over a few days. Such estimates are likely to underestimate the long-term precision because a number of error sources probably do not change much over this span of time. The only paper that has looked at long-term precision and accuracy is that of *Davis et al.* [1989], but most of the data shown there were for baselines of 200 m to 50 km, not the longer regional scales we discuss here. This suite of measurements also allows us to discuss the role of orbit determination (fiducial) networks in establishing a consistent reference frame [*Larson et al.*, this issue] (hereafter referred to as paper 2), and the effect of different modeling procedures for the atmospheric delay (K.M. Larson and J.L. Davis, manuscript in preparation; hereinafter referred to as paper 3). In the next section of this paper, we describe how the GPS data were collected and the analysis techniques we used to determine the coordinates of the different stations. The following sections discuss precision and accuracy.

Experimental Procedure and Data Analysis

The data we use were collected during 11 "experiments" conducted between June 1986 and March 1989. The measurements in southern and central California were made by a four-university consortium, Scripps Institution of Oceanography, California Insitute of Technology, University of California, Los Angeles, and Massachusettes Institute of Technology, with substantial help from the U.S. Geological Survey (USGS) and the National Geodetic Survey (NGS). When possible, we also included data from the North American network of fixed GPS trackers that are part of the Cooperative International GPS NETwork (CIGNET) [*Chin*, 1988]. Table 1 lists 22 of the GPS sites observed. The stations located in California are shown in Figure 1. The remaining sites, all located in North America, were used for precise orbit determination, and are discussed in paper 2. While more sites than these were observed during the 11 experiments, only these 22 were measured at more than one epoch and thus can provide a useful estimate of long-term precision and accuracy. As noted above, the network formed by those of the stations in California yields baseline lengths from 50 to 450 km.

In each experiment the GPS satellites were tracked at each station using a TI-4100 dual-frequency receiver [*Henson et al.*, 1985], recording both carrier phase and pseudorange data at 30-s intervals. (Carrier phase is precise but ambiguous by an integer number of cycles; pseudorange is unambiguous but 2 orders of magnitude less precise.) The intention was to track for the 7-8 hours that several satellites were visible; for most of the experiments (all but those done in May, June, and September) this meant tracking almost entirely at night. For most experiments the plan was to record data for 4 or 5 consecutive days, a goal not always achieved in practice. Table 2 summarizes the data available from all the sites we have considered. The receiver antenna was centered over the geodetic monument at each site using an optical plummet, with a nominal accuracy of about 1 mm; the vertical offset between the antenna and the top of the monument was measured by a tape, with perhaps 2-

TABLE 1. GPS Stations

	Station	Location	Longitude, deg	Latitude, deg	Height, m	Stamping
1,	Algonquin	Ontario, Canada	-78.071	45.958	209	TELESCOPE REF A
2,	Blancas	Monterey	-121.284	35.666	50	none
3,	Blackhill	Morro Bay	-120.831	35.360	201	BLACKHILL 1881
4,	Brush	Catalina Isl.	-118.404	33.409	451	BRUSH 1976
5,	Buttonwillow	Bakersfield	-119.394	35.405	64	A364 1953
6,	Center	Santa Cruz Island	-119.753	33.996	394	CENTER 1934
7,	Churchill	Manitoba, Canada	-94.088	58.758	31	GEOS3
8,	Clembluf	San Clemente Island	-118.518	32.928	297	BLUFF 1933
9,	Fort Ord	Monterey	-121.773	36.671	39	FORT ORD NCMN 1981
10,	Lacumbre	Santa Barbara County	-119.713	34.496	1171	none
11,	Lospe	Vandenberg AFB	-120.605	34.896	505	none
12,	Madre	Miranda Pine Mountain	-120.067	35.077	914	MADRE ECC 1980
13,	Mojave	Goldstone	-116.888	35.333	904	CIGNET
14,	Niguel	Laguna Niguel	-117.730	33.516	238	NIGUEL A 1884 1981
15,	Nicholas	San Nicolas Island	-119.479	33.233	201	TWIN 1964
16,	OVRO	Owens Valley	-118.293	37.234	1195	MOBLAS 7114 1979
17,	Palos Verdes	Los Angeles	-118.403	33.745	73	PALOS VERDES ARIES 1976 1980
18,	Platteville	Colorado	-104.726	40.184	1530	PLATTEVILLE NCMN 1981
19,	Richmond	Florida	-80.384	25.615	23	CIGNET
20,	Soledad	La Jolla	-117.252	32.841	216	none
21,	Vandenberg	Vandenberg AFB	-120.616	34.558	24	VLBI STA 7223 RM1
22,	Westford	Haystack Obs., Mass.	-71.493	42.615	125	CIGNET

Geodetic coordinates of crustal deformation sites, referenced to NAD 83. The stamping is imprinted on the geodetic marker. CIGNET refers to the antenna phase center of the continuously monitoring GPS network [*Chin*, 1988]. Unless otherwise noted, all sites are in California.

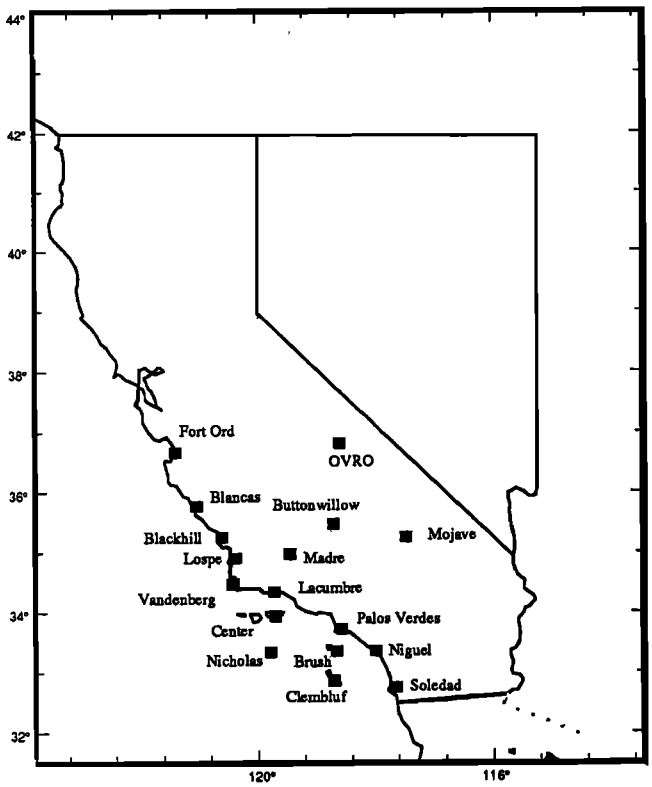

Fig. 1. GPS sites in southern and central California observed between 1986 and 1989 for crustal deformation studies. Table 1 gives the site names and coordinates, and Table 2 gives a breakdown of which sites were observed when. All but three (Mojave, Buttonwillow, and OVRO) lie west of the San Andreas fault.

mm error. While the observers at each site recorded local pressure, temperature, and humidity, we have not made use of these data (paper 3 discusses this in more detail).

The GPS data were analyzed with the GPS Inferred Positioning SYstem software (GIPSY) developed at the Jet Propulsion Laboratory [*Stephens*, 1986; *Lichten and Border*, 1987]. GPS carrier phase and pseudorange data at both frequencies were reformatted from the original data tapes, and the phase data were checked for cycle slips. This process was automated by using a computer program, Turboedit, described by *Blewitt* [1990]. In order to reduce the computer storage and CPU requirements, we subtracted a model of satellite and station positions from the observables, and a second order polynomial fit was used to compress the 30-s data to 6-min points. This technique is valid as long as the error sources over 6 min (satellite and receiver clocks and the ionosphere) can be modeled by a second-order polynomial. At this point, linear combinations were formed of the carrier phase and pseudorange data, which eliminated the highest-order effects of the ionosphere. Nominal satellite trajectories were determined by a module which integrates the equations of motion and the variational equations to obtain satellite coordinates and partial derivatives of these coordinates with respect to the satellite initial conditions and force parameters. Another module computed prefit residuals and partial derivatives from nominal station coordinates, nominal GPS orbits, and models for the Earth's rotation, tides, and atmospheric refraction [*Sovers and Border*, 1988]. Finally, a factorized Kalman filter was used to perform a least squares adjustment of station positions, satellite initial positions and velocities, tropospheric zenith delays, phase ambiguities, and satellite and receiver clocks.

The constraints we used for our standard estimation procedure are summarized in Table 3. We used the broadcast ephemeris to determine nominal values for initial position and velocity of each spacecraft. For each satellite, we estimated an initial position, initial velocity, and the behavior of the satellite clock. We fixed the positions of three "fiducial sites", whose coordinates were derived from VLBI measurements. If properly chosen, these fiducial sites, whose positions are known to better than 2 cm, provide sufficient strength to determine the satellite orbit to better than 2 m (see paper 2 for further detail on both the derivation of fiducial coordinates and their impact on orbit determination). If more than three "VLBI sites" were included in a GPS experiment, the nonfiducial VLBI sites were treated as "mobile sites" and estimated with a standard deviation of 2 km. In general, our starting (nominal) solution was within 1 m of the estimated position of all mobile stations.

We modeled the clock bias at each measurement point as white noise; in other words, each estimate was independent and uncorrelated with the clock bias at previous measurements. Some receivers we used were connected to hydrogen masers; the remainder used the quartz internal clock provided by the TI-4100. White noise clock modelling is essentially identical to the double differencing used in other softwares [*Beutler et al.*, 1990].

The optimal strategy for determining the atmospheric propagation delay is unclear at this time. *Tralli et al.* [1988] suggest time-varying estimation techniques are preferable, while *Davis et al.* [1989] achieve similar vertical component precision solving for a constant zenith delay parameter. Water vapor radiometers (WVR) were not in use during 10 of the 11 experiments, and therefore we have chosen to ignore what little WVR data were available. Paper 3 will address this issue in more detail. The strategy we have used in this paper was as follows: we first corrected for the dry troposphere delay using a crude relation between station elevation, pressure, and dry zenith delay. The pressures for hydrostatic zenith delay calculations were determined using the ellipsoidal height of the site and an assumed sea level pressure of 1013.24 mbar with an exponential profile with scale height 7 km. The temporal variation of the wet zenith path delay was modeled as a random walk, with an allowed variation of 49 mm over 7.5 hours.

Finally, a station-satellite parameter was estimated for each phase ambiguity. The nominal phase ambiguity solution was determined from the pseudorange data. Subsequently, ambiguity resolution was attempted. We used a 99% confidence criterion for "fixing" these ambiguities to their integer values, which is described by *Blewitt* [1989]. At this point, postfit residuals were visually inspected, primarily to determine if cycle slips had been incorrectly fixed. At this point the Cartesian station locations and their standard deviations can be retained for crustal deformation studies.

The reference frame we used was defined by the Goddard Space Flight Center Global Site Velocity model GLB223, which is based on over 4 years of VLBI data (C. Ma, personal communication, 1988). Further discussion of the reference frame is left to paper 2. Earth orientation values were taken from the monthly bulletins of the International Radio Interferometric Surveying (IRIS) Subcommission.

TABLE 2a. Data Summary

	Experiment										
	J86[a]	D86	J87	M87[b]	S87	M88a	M88b	J88	S88	M89a[c]	M89b
Month/year	June 1986	Dec. 1986	Jan. 1987	May 1987	Sept. 1987	March 1988	March 1988	June 1988	Sept. 1988	March 1989	March 1989
Dates	17-20	12/30-1/2	27-29	25, 27, 28	22,24,25	8,9,11	15-18	8-11	13-16	21-23	28-30
Total days of data	4	4	3	3	3	3	4	4	4	3	3
1, Algonquin	-	4	-	-	-	-	4	-	-	-	-
2, Blancas	-	2	-	-	-	-	4	-	-	-	3
3, Blackhill	-	4	-	3	3	-	4	-	-	-	3
4, Brush	-	-	3	-	-	3	-	-	-	3	-
5, Buttonwillow	-	4	-	-	-	-	4	-	-	-	3
6, Center	-	4	3	3	3	3	4	-	-	-	3
7, Churchill[d]	-	4F	-	-	-	3F	4	-	-	-	-
8, Clembluf	2	-	3	-	-	3	-	-	-	3	-
9, Fort Ord[e]	-	4F	-	-	3F	-	4F	-	4	-	-
10, Lacumbre	-	4	3f	-	-	-	4	-	-	-	2
11, Lospe	-	1.5	-	-	-	-	3.5	-	-	-	3
12, Madre	-	4	-	-	-	-	4	-	-	-	3
13, Mojave[f]	4F	1	3F	3	2.5	3F	2.5	3F	4F	3F	3F
14, Niguel	2	-	-	-	-	2	-	-	-	3	-
15, Nicholas	4	-	-	-	-	-	4	-	-	3	-
16, OVRO	-	1.5	-	3F	3	-	3.5	-	-	-	3f
17, Palos Verdes	4	-	3f	3	3	1	4	4	4	3f	3f
18, Platteville	-	4	-	-	3F	2	3	-	-	-	-
19, Richmond[g]	4F	-	-	-	-	1F	3F	3F	2F	0	0
20, Soledad	2	-	3	-	-	3	-	-	-	3	-
21, Vandenberg	3	4	-	3	3	3	3	4	3	3f	3f
22, Westford	4F	4	0	3F	3F	3F	4F	4F	2F	0	0

Site occupations are summarized for 11 experiments at 22 sites between June 1986 and March 1989. The total days of available data are listed. Individual station occupations are listed by experiment. F, the station position was not estimated, i.e. this is a fiducial site; f, the station position was estimated, with a standard deviation of 20 mm; Number of days of useful data. One day of data equals approximately 7 hours. If no f or F is listed, station position was estimated, with a standard deviation of 2 km. Dashes indicate the station was not scheduled to be observed during the experiment. Zero indicates the station was scheduled to be observed, but no useful data were collected.

[a] Experiment described in greater detail by *Blewitt* [1989]

[b] Austin, Texas used as third fiducial site. Coordinates provided by M. Murray (personal communication, 1990)

[c] Less than 10% of carrier phase ambiguities were resolved between sites in California.

[d] Fiducial coordinates for Churchill determined from data collected during experiment M88b

[e] Fort Ord was destroyed summer of 1988. Reference mark was occupied in S88

[f] Mojave refers to 3 "monuments". J86 = Mojave NCMN1; D86-J88 = CIGNET TI-4100 antenna; S88-M89b = CIGNET FRPA antenna. Mini-MAC data collected at Mojave for M89a and M89b were not used.

[g] CIGNET tracker at Richmond was unavailable until November 1988

TABLE 3. Parameter Estimation

Parameter	Estimation	Standard Deviation	Steady State Standard Deviation	Time Behavior
Satellite position, km	force model	100		
Satellite velocity, km/s	force model	1		
Satellite clock, s	stochastic	1	1	white noise
Station position (fiducial)	fixed (not estimated)			
Station position (mobile), km	constant	2		
Station clock, s	stochastic	1	1	white noise
Phase ambiguity, s	constant	10		
Zenith troposphere delay	stochastic	300 mm	3×10^{-7}km/$\sqrt{s}$	random walk
Data weights, mm	pseudorange	250		
	carrier phase	10		

PRECISION

Introduction

To characterize the precision of the vectors estimated by GPS, we use the scatter of independently estimated results. For short-term precision, we will use results from 18 stations observed during a single experiment in March 1988. Short-term precision will be defined by the weighted RMS scatter about the mean of daily estimates, each determined from a single-day orbit solution. If we have N independent values $y_1, y_2, \ldots y_N$ with (formal) standard errors $\sigma_1, \sigma_2, \ldots \sigma_N$, this scatter is S_{mean},

$$S_{mean} = \sqrt{\frac{\frac{N}{N-1}\sum_{i=1}^{N}\frac{(y_i - \langle y \rangle)^2}{\sigma_i^2}}{\sum_{i=1}^{N}\sigma_i^2}} \quad (1)$$

where $\langle y \rangle$ is the weighted mean of the y_i's. (This quantity has sometimes been termed the repeatability, a term we eschew because it leads to ambiguity: a high repeatability may be highly repeatable (good), or a large value (bad).) The reduced χ^2 statistic is defined for the weighted RMS about the mean as

$$\chi^2_{mean} = \frac{1}{N-1}\sum_{i=1}^{N}\frac{(y_i - \langle y \rangle)^2}{\sigma_i^2} \quad (2)$$

where y_i, σ_i, and $\langle y \rangle$ are defined as before. A reduced χ^2 of 1 indicates that the formal errors, σ_i, agree with the actual scatter in the measurements.

Since our measure of precision is weighted by our expected error, we need to describe how these formal errors were calculated. The measurement standard deviation is calculated by propagating standard deviations of the carrier phase and pseudorange data through the variance-covariance matrix. Our formal errors then are dependent on the data weights we assumed for the carrier phase and pseudorange data, 10 and 250 mm, respectively. These data weights were determined empirically in the following manner. For each station, we multiplied the RMS post-fit scatter by the quantity $\sqrt{N/(N-P)}$, where N is the number of data points and P is the number of parameters we have estimated. This data noise is then approximately what is required to make χ^2 one. In general, the RMS postfit scatter ranged from 4 to 6 mm, depending on the station, and the scaling quantity was approximately 1.5. This resulted in a data weight of 6-9 mm. In an effort to be conservative, we chose 10 mm and applied it uniformly to all stations. We determined the pseudorange data weight in the same manner. This data weight would have to be changed if we substantially increased the number of parameters we estimated, or we changed the data rate (i.e., from 6 to 3 min points). For the experiments listed in Table 2, we had fairly common data sets, in numbers of satellites, and we used consistent estimation procedures. Thus, while our formal errors may be incorrect, they were computed in an identical fashion for each experiment. Later in this section we will discuss whether our weighting scheme was appropriate.

We expect that short-term precision might underestimate the true precision, because over this time scale some errors change less than they would over longer times. Possible errors in this class are wet and dry tropospheric delays and set-up errors. To estimate long-term precison we use measurements spanning 1.2-2.7 years for 22 stations (including all those used for the short-term precision estimates). We could use equation (1) for long-term precision, but by neglecting actual plate motion we unnecessarily degrade the precision of the GPS estimate. Therefore, for long-term horizontal precision, we adopt a standard technique [*Ma et al.*, 1990] and calculate the weighted RMS about the best fitting line. (For long-term vertical precision, we assume no true vertical motion, and use equation (1) only.) The weighted RMS about the best fitting line, S_{line}, is defined

$$S_{line} = \sqrt{\frac{\frac{N}{N-2}\sum_{i=1}^{N}\frac{(y_i - (a + bt_i))^2}{\sigma_i^2}}{\sum_{i=1}^{N}\sigma_i^2}} \quad (3)$$

where a and b are the intercept and slope of the best fitting line and t_i is the time of the ith measurement. The reduced χ^2 statistic for S_{line} is

$$\chi^2_{line} = \frac{1}{N-2}\sum_{i=1}^{N}\frac{(y_i - (a + bt_i))^2}{\sigma_i^2} \quad (4)$$

These formulae are correct if we can assume that each es-

timate of an interstation vector is independent. In general, our data were collected several days in succession, separated by 6-12 months, and thus were not evenly distributed in time. Even though we have analyzed each day of GPS data independently, *Davis et al.* [1989] have pointed out that estimates only a few days apart will be correlated, due to common error sources. Therefore, Davis et al. attempted to separate short- and long-term error statistics. The short-term error was determined by the scatter about the mean for a single 3-5 day experiment, and the long-term error was computed from the RMS of these means about the best fitting line. The total error was then computed assuming the long- and short-term errors were independent. One problem with this formulation is that it ignores the formal errors, with all estimates being treated equally. When we used the Davis et al. technique, we found that measurements from the M89a and M89b experiments were the largest contributors to the long-term error. We know there were systematic errors in that particular experiment, caused by the fiducial network we were forced to use. Since this paper is a summary of a large quantity of data, we would like to leave discussion of known systematic errors to papers 2 and 3. If one adapts the method of Davis et al. to incorporate the formal errors, one is then computing nearly the same quantity as if equation (3) were used. We therefore use the simplest formulation we have for long-term precision, equation (3), although we recognize that we have not solved for the long- versus short-term error sources.

While much of the information about precision is best obtained from the plots of scatter, we also wish to summarize the results in a compact way. One way of summarizing errors of distance measurements is the expression [*Savage*, 1983]

$$\sigma^2 = A^2 + B^2 l^2 \tag{5}$$

where σ is the standard deviation and l is the baseline length. This equation derives from the nature of EDM measurements [*Rueger*, 1990], where the measuring instrument has a constant error A, a proportional error B being introduced by errors in the estimated atmospheric refraction. Equation (5) then follows from the usual law for the combination of independent errors.

The dependence of error on distance might be expected to be more complicated for GPS measurements. Over very short baselines (<100 m) the intrinsic precision and accuracy of the measurement are 2 mm or less [*Davis et al.*, 1989], though in many survey conditions we might expect the errors of locating the antenna relative to the geodetic monument to be several times this. Another source of error that is independent of length is the effect of antenna multipath: the signal received is the sum of the direct-arriving radio wave and waves that have been reflected off nearby objects (such as the ground). As the position in the sky of a satellite changes the relative contributions of these waves will vary, causing the apparent location of the antenna to wander about its true one. Because of the long duration of tracking during these measurements we expect this error to be small.

Over longer distances other error sources enter in. For distances of more than the troposphere scale height (a few kilometers), differences in wet and dry delay cease to cancel, at least relative to other error sources; at larger distances the same becomes true for the ionosphere. One well-understood error scales with baseline length: errors in the estimated orbits of the satellites. This contributes to an error in baseline

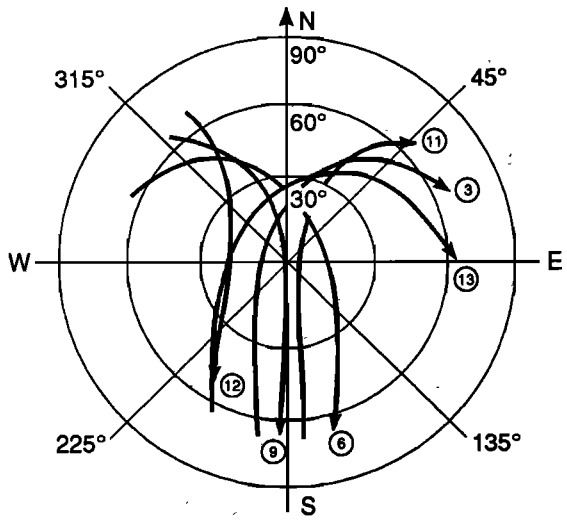

Fig. 2. GPS sky tracks over California for the six block I GPS satellites observed during the December 1986 campaign (modified from *Dong and Bock*[1989]). The anisotropy of these sky tracks gives measurements of north-south components greater inherent precision than those of east-west components.

length which is about $l\beta\sigma_{orb}/L$, where L is the distance from the GPS receiver to GPS satellites (about 20,000 km), σ_{orb} is the orbit error, and β is a constant that depends on network geometry; it is about 0.2 for continental scale networks [*Lichten*, 1990]. The GPS constellation observed during the experiments used here consisted of seven block I satellites. Figure 2 shows the sky paths of six of these satellites as seen from California; since the satellites cover a wider range of elevations along a north-south azimuth than to the east or west, we might expect the baseline error to be larger for east-west components than north-south ones. Similarly, because the data come only from satellites above the horizon, the vertical component precision can be expected to be much worse than either horizontal precision.

Because of the varied nature of errors in GPS baselines, there seems to be no good reason to adopt the form of equation (5) for the errors. However, some acknowledgment of the existence of proportional errors is appropriate; we have therefore adopted the simple law

$$\sigma = A + Bl \tag{6}$$

to summarize the change of precision with distance. We do not believe this relation truly reflects the underlying error structure of GPS; instead we use this relation as a means of summarizing the precision estimates we have made. Since our analysis is restricted to baselines from 50 to 450 km in length, we will incorporate the long-term precision results of *Davis et al.* [1989] for baselines less than 50 km in order to extend this assessment of GPS precision. Further studies will be required to determine the long-term precision of continental- and global-scale interstations vectors measured with GPS. At that time, it will be appropriate to investigate in a more systematic fashion whether equation (5), (6), or a more complicated expression adequately describes long-term precision.

Results

Short-term precision. The most successful experiment of the 11 listed in Table 2, in terms of high data yield, was the March 1988 central California campaign (designated M88b).

Four days of data were collected at 18 sites in North America, 13 in California. The short-term precision for the north-south, east-west, and vertical components for this experiment is plotted, as a function of baseline length, in Figures 3*a*-3*c* and is listed in Table 4.

The most prominent feature of these plots is the absence of significant baseline dependence for the north-south component. This has errors of 1.9+0.6 parts in 10^8. In the east-west component, the precision is described by 2.1 mm+1.3 parts in 10^8. The constant term for both components is in good agreement with the precision of 100-m baselines [*Davis et al.*, 1989]. The difference in baseline dependence for the two components is easily explained by the satellite geometry of the block I constellation discussed in the previous section. This is a similar network to the one studied by *Dong and Bock* [1989]. By fitting a line to their baseline scatter, Dong and Bock reported precision of 6 mm + 0.5 parts in 10^8 in the east-west component and 2.5 mm + 0.9 parts in 10^8 in the north- south component.

The vertical component is nearly an order of magnitude less precise than horizontal components. The scatter has a mean value of 17 mm, with no length dependence. Using data collected during the June 1986 southern California GPS experiment (see J86 in Table 2), *Blewitt* [1989] reported a mean RMS of 29 mm on baselines ranging from 50 to 650 km, which is in good agreement with formal errors from his analysis. Inspection of scatter plots in Blewitt's paper shows no baseline dependence. In contrast, *Dong and Bock* [1989] reported a slight dependence on baseline length for their vertical component precision, 12 mm + 6 parts in 10^8. The differences between our results and those of Dong and Bock may be due to the difference in fiducial networks we used. We leave this discussion to paper 2.

Discussion. Our primary objective is to use the scatter in the interstation vector estimates to determine GPS system precision. Another important question we address is the validity of the formal errors. It has long been recognized that formal errors underestimate the scatter in actual data. This is generally attributed to unmodeled systematic effects and to mismodeling of certain parameters. One technique commonly used to produce more reasonable errors is to scale formal errors so that the reduced χ^2 is 1 [*Clark et al.*, 1987]. In their study of GPS precision, *Davis et al.* [1989] discarded their formal errors and used an ad hoc technique, deriving a standard deviation from the actual scatter. While it is difficult to determine how the systematic errors impact on the precision, it is fairly simple to determine how representative the formal errors are of the actual scatter in the data. In other words, we compare the predicted standard deviation and the actual standard deviation.

Included with short-term precision in Figures 3*a*-3*c* are the formal error (the mean of the four single-day formal errors) as a function of baseline length. The north-south component indicates that the actual scatter is less than that predicted by the formal errors. The formal error predicts a scatter of 2.4 mm + 0.4 parts in 10^8, whereas the actual scatter is 1.9 mm + 0.6 parts in 10^8. For the east-west component, the formal error is 2.4 mm + 1.5 parts in 10^8, which is also close to the actual scatter of 2.1 mm + 1.3 parts in 10^8. For the vertical component, formal errors overpredict the scatter by a factor of 1.5. The vertical component formal errors are heavily dependent on the random walk parameterization we have chosen for the wet troposphere zenith delay. Thus, we leave discussion of vertical formal errors to

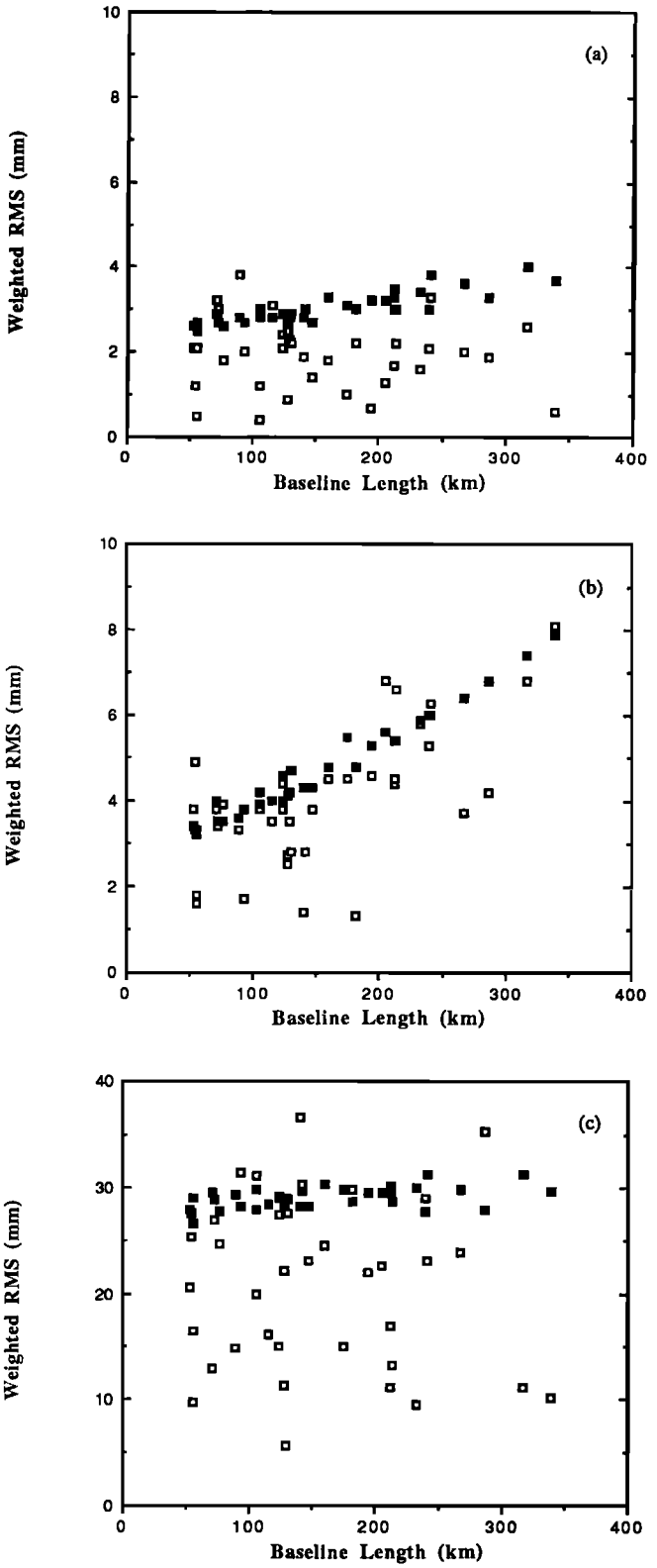

Fig. 3. The open squares are the short-term precision, defined by equation (1) as the weighted RMS about the mean, of different components of the baselines measured in March 1988, plotted as a function of line length. The solid squares are the mean of the formal 1-σ errors for the same quantities, as computed from the size of the residuals and the covariances of the least squares adjustment. Figure 3*a* is for the north-south component of the baseline; Figure 3*b* is for the east-west component, and Figure 3*c* for the vertical component. (The directions are those of a Cartesian coordinate system located at one end of the baseline, whose north is coincident with the local north, and vertical with the normal to the ellipsoid.)

TABLE 4. Short-Term Precision

Interstation Vector	Length, km	East, mm	χ^2	North, mm	χ^2	Vertical, mm	χ^2
Blackhill-Blancas	53	4.9	2.25	1.2	0.20	25.4	0.78
Lospe-Madre	53	3.8	1.29	2.1	0.68	20.6	0.52
Center-Lacumbre	55	1.6	0.22	2.1	0.64	16.4	0.33
Blackhill-Lospe	55	1.8	0.32	0.5	0.03	9.6	0.12
Buttonwillow-Madre	71	3.8	1.14	3.2	1.25	12.8	0.18
Madre-Lacumbre	72	3.4	0.96	3.0	1.13	27.0	0.82
Blackhill-Madre	76	3.9	1.25	1.8	0.46	24.7	0.73
Center-Nicholas	88	3.3	0.91	3.8	2.11	14.8	0.29
Lospe-Lacumbre	93	1.7	0.22	2.0	0.54	31.5	1.19
Buttonwillow-Lacumbre	105	4.2	1.13	0.4	0.02	31.2	1.06
Blancas-Lospe	105	3.8	1.01	1.2	0.18	19.9	0.48
Palos Verdes-Nicholas	115	3.5	0.80	3.1	1.30	16.0	0.34
Madre-Center	123	4.4	1.32	2.1	0.55	15.0	0.27
Lospe-Buttonwillow	123	3.8	0.80	2.4	0.74	27.4	0.89
Lospe-Center	127	2.7	0.52	2.5	0.86	22.2	0.64
Blancas-Madre	128	3.5	0.80	2.3	0.60	5.7	0.04
Palos Verdes-Center	128	2.5	0.43	0.9	0.11	11.3	0.18
Blackhill-Buttonwillow	131	2.8	0.45	2.2	0.60	27.6	0.88
Blackhill-Lacumbre	140	1.4	0.13	1.9	0.41	36.7	1.57
Nicholas-Lacumbre	142	2.8	0.48	3.0	1.00	30.4	1.07
Palos Verdes-Lacumbre	146	3.8	0.90	1.4	0.24	23.2	0.65
Buttonwillow-Center	160	4.5	0.98	1.8	0.31	24.6	0.70
Blancas-Buttonwillow	174	4.5	0.88	1.0	0.10	16.5	0.30
Blackhill-Center	180	1.3	0.08	2.2	0.50	29.9	1.14
Blancas-Lacumbre	193	4.6	0.95	0.7	0.05	22.0	0.52
Palos Verdes-Buttonwillow	204	6.8	2.00	1.3	0.16	22.7	0.60
Madre-Nicholas	211	4.4	0.80	3.0	0.74	11.1	0.14
Lospe-Nicholas	211	4.5	0.87	1.7	0.28	16.8	0.35
Palos Verdes-Madre	212	6.6	1.96	2.2	0.48	13.1	0.20
Blancas-Center	232	5.8	1.29	1.6	0.20	9.5	0.11
Palos Verdes-Lospe	239	5.3	1.11	2.1	0.45	29.0	1.09
Buttonwillow-Nicholas	240	6.3	1.29	3.3	0.77	23.1	0.58
Blackhill-Nicholas	267	3.7	0.44	2.0	0.31	23.9	0.67
Palos Verdes-Blackhill	286	4.2	0.55	1.9	0.32	35.3	1.53
Blancas-Nicholas	316	6.8	1.15	2.6	0.40	11.1	0.13
Palos Verdes-Blancas	339	8.1	1.60	0.6	0.02	10.2	0.12

paper 3. Comparably, plots of χ^2 as a function of baseline length, as shown in Figures 4*a*-4*c*, indicate that over the short term, the formal errors are comparable to the scatter. The outliers in the χ^2 plots, in both senses, those that are too small and those that are too large, are often for a single baseline. As an example, the interstation vector between Palos Verdes and Buttonwillow (204 km) has a χ^2 of 2.0 in the east-west component and a χ^2 of 0.16 in the north-south component. Noting the location of these stations in Figure 1, it is apparent that this baseline is aligned nearly north-south. The geometry of ground stations and satellites degrades the east-west component (and improves the north-south component), in a way that is not predicted by the formal errors.

The observed short-term precision is a function of our ability to remove error sources associated with satellite orbits, satellite and receiver clocks, and propagation delays; to precisely center the GPS antenna over the monument; and to measure the distance between the antenna base and monument. Precise orbits are not necessarily accurate orbits. Since the accuracy of GPS orbits will influence the accuracy of interstation vectors, we leave that discussion to the next section. Mismeasurement and miscentering of the GPS antenna over the monument are a significant limitation in geodetic measurements of crustal deformation. The constant terms for both horizontal components indicate that centering errors are no greater than 2 mm. It should be noted that over the course of these 11 experiments, no effort was made to send the same field crews and the same equipment to the same sites. Therefore long-term centering errors may be larger, since precise centering may not be accurate centering.

Long-term precision. Although our objective is to summarize long-term precision of interstation vectors from 50 to 450 km in length, it is appropriate to show a few, representative time series of estimates from these networks. We discuss results for two interstation vectors in detail and subsequently tabulate statistics using estimates from all 11 experiments. More time series of interstation vectors will be discussed in the accuracy section.

The baseline from Mojave to the Owens Valley Radio Observatory (OVRO) is frequently used for engineering tests [*Ware et al.*, 1986]. The baseline is approximately 240 km east of the San Andreas fault and is oriented N30°W. The north-south, east-west, and vertical components for this 245-km interstation vector are shown in Figure 5. Mojave-OVRO solutions from the March 1989 experiment are not displayed or used in this calculation of long-term precision because

both sites were tightly constrained to their VLBI values for that experiment. Ignoring this experiment limits the calculation of long-term precision to a temporal span of 14 months, with nine data points measured over four epochs. In the north-south component, the long-term precision is 2 mm. In the east-west component, it is significantly worse, 9 mm. There have been 62 VLBI observations of these sites between 1983 and 1988 [*Ma et al.*, 1990]. VLBI estimates the displacement rate between the sites to be 0.1±2.0 and -2.6±1.4 mm/yr in the north-south and east-west components, respectively. The very precise GPS north-south component is additional evidence that the VLBI measurement

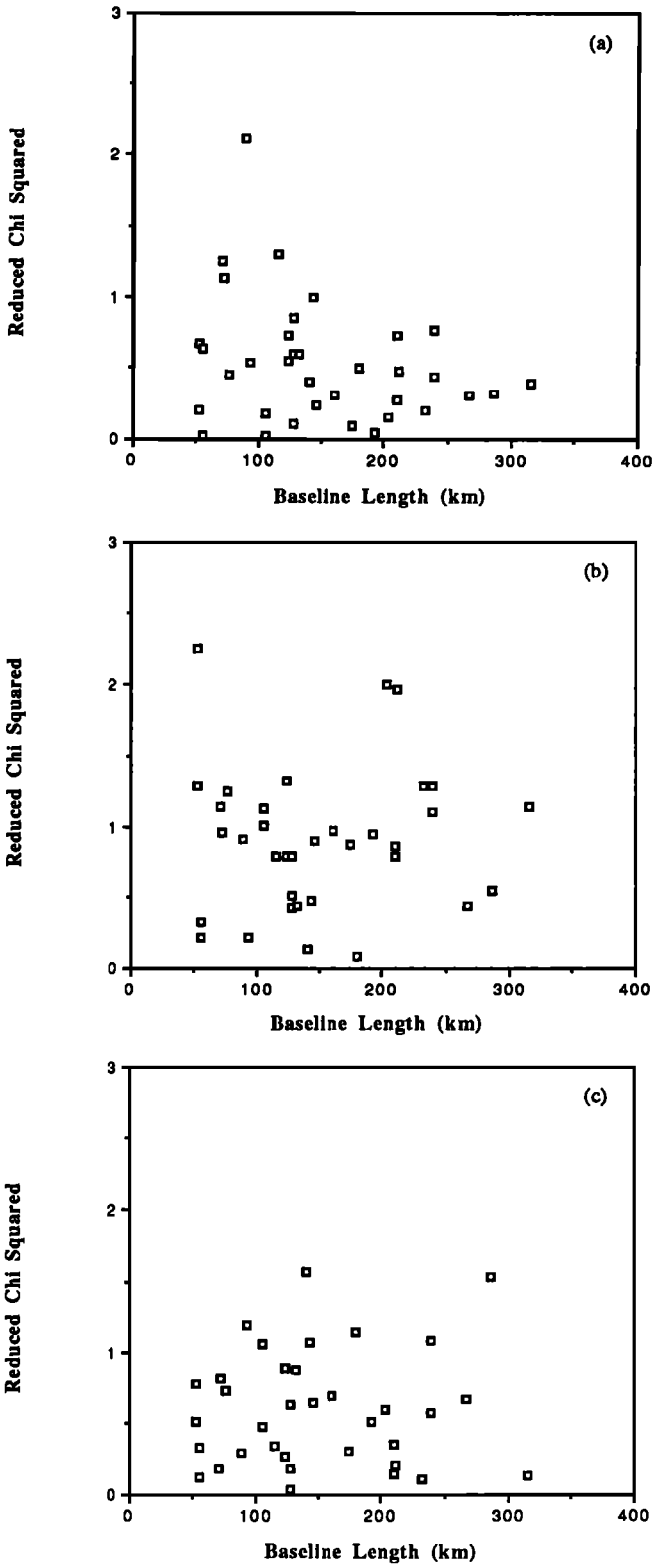

Fig. 4. χ^2 for the baselines shown in Figure 3.

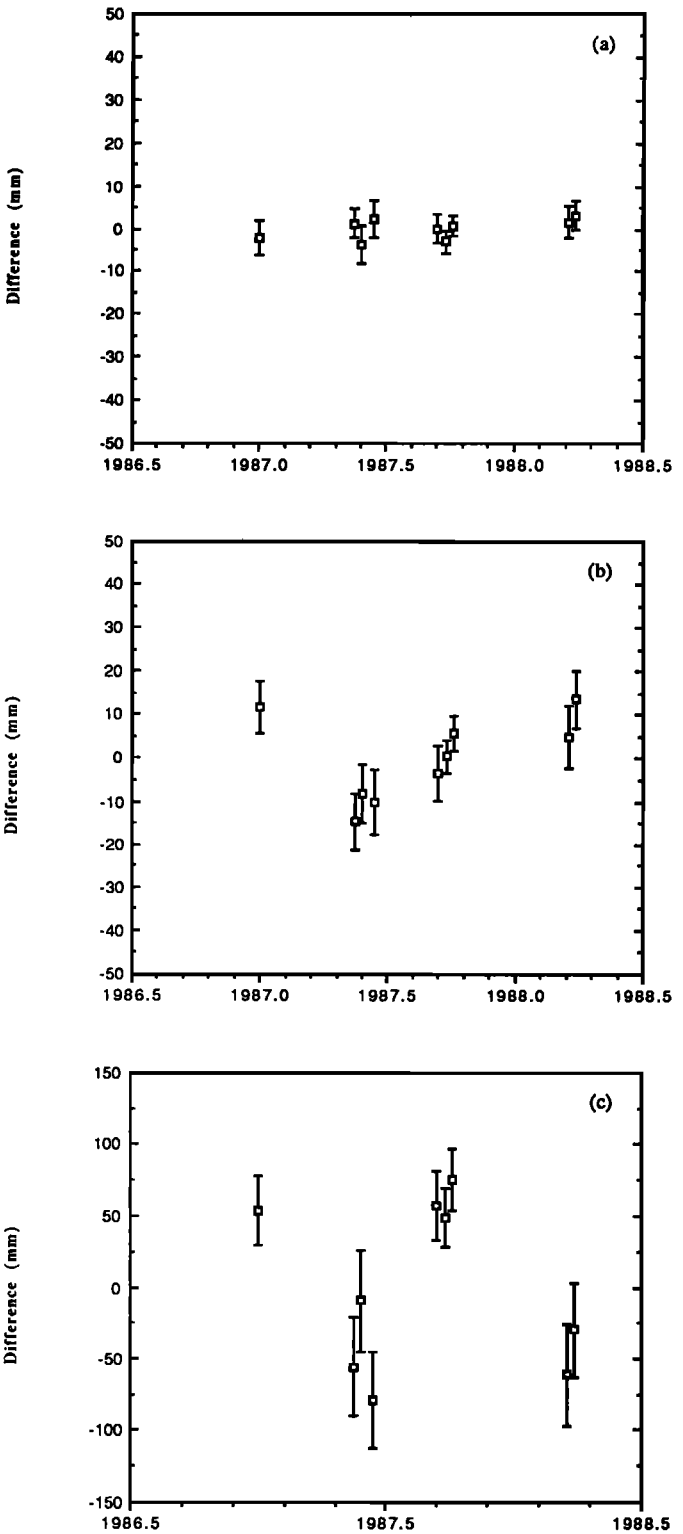

Fig. 5. Change of relative coordinates for the Mojave to OVRO baseline (245 km length), with zero being the mean value. The components shown are defined as in Figure 3, with the coordinate system being centered at the first station.

TABLE 5. Long-Term Precision

Interstation Vector	Length, km	East,[a] mm	χ^2	North,[a] mm	χ^2	Vertical,[b] mm	χ^2	Years	Number of Observations
Lospe-Vandenberg	37	4	2.2	4	2.4	16	0.3	2.2	8
Blancas-Blackhill	53	7	4.0	1	0.1	36	1.6	2.2	8
Clembluf-Brush	54	5	0.7	4	0.8	30	0.8	2.2	8
Lacumbre-Center	55	3	0.8	3	0.8	26	0.7	2.2	11
Madre-Buttonwillow	71	4	1.0	4	3.0	35	1.3	2.2	11
Vandenberg-Madre	76	4	0.9	4	2.0	22	0.6	2.2	10
Madre-Blackhill	76	4	1.0	2	0.4	27	0.8	2.2	11
Blackhill-Vandenberg	91	6	2.2	5	3.1	29	1.1	2.2	13
Palos Verdes-Clembluf	91	10	1.6	5	0.9	39	1.1	2.7	9
Vandenberg Center	101	5	1.4	4	2.5	25	0.8	2.2	16
Palos Verdes-Nicholas	115	8	1.9	4	1.1	29	0.9	2.7	10
Soledad-Clembluf	119	7	1.1	7	3.1	45	1.6	2.7	9
Madre-Center	123	4	1.0	2	0.4	30	1.0	2.2	11
Center-Palos Verdes	127	4	0.6	5	2.2	31	1.1	2.2	16
Buttonwillow-Blackhill	131	3	0.5	5	2.5	32	1.1	2.2	11
Buttonwillow-Blancas	173	6	1.2	5	2.0	42	1.7	2.2	9
Vandenberg-Nicholas	180	6	0.8	9	3.2	26	1.1	2.7	8
Blackhill-Center	181	6	1.5	3	0.6	39	1.5	2.2	16
Palos Verdes-Vandenberg	223	5	0.8	7	3.1	41	1.7	2.2	14
Mojave-Palos Verdes	224	9	1.4	6	1.4	38	1.2	2.2	18
Mojave-Ovro	245	9	1.9	2	0.4	57	4.3	1.2	9
Palos Verdes-Blackhill	286	7	0.9	4	1.0	41	1.6	2.2	12
Ovro-Blackhill	308	13	2.9	5	1.2	34	1.1	2.2	14
Mojave-Vandenberg	351	10	1.5	6	2.4	42	1.8	2.2	18
Mojave-Blackhill	358	6	0.9	4	1.3	46	2.0	2.2	12
Ovro-Vandenberg	363	14	3.0	5	1.2	33	0.9	1.2	11
Ovro-Center	382	14	2.6	5	0.9	47	2.0	2.2	15
				USGS Results[c]					
Mojave-NCMN1	1	2		2		5		2.0	4
10JDG-33JDG	7	6		3		12		3.0	27
10JDG-Joaquin	11	6		5		13		3.0	27
10JDG-Oquin	12	5		4		18		3.0	26
Loma Prieta-Eagle[d]	31	8		4		16		0.9	7
Loma Prieta-Allison[d]	43	8		4		21		0.9	8
Palos Verdes-Vandenberg	223	11		6		40		2.2	6

[a]Weighted RMS about best fitting line, as in equation (3).
[b]Weighted RMS about weighted mean, as in equation (1).
[c]USGS results are taken from *Davis et al.* [1989].
[d]J. Svarc (personal communication, 1990)

of no significant motion in this component is correct. The vertical precision of 57 mm is the worst listed in Table 5.

The long-term precision for the baseline from Vandenberg to Center (located on Santa Cruz Island) is shown in Figure 6. A 101-km baseline oriented NNW, it is considerably shorter than Mojave-OVRO but has been measured almost twice as often, with data spanning 2.2 years. The scatter about the best fit line is 5 and 4 mm for the east-west and north-south components, respectively. The vertical component scatter is 24 mm. All experiments were analyzed with continental-scale fiducial networks, with the exception of the March 1989 data.

The long-term precision statistics are listed in Table 5. For each interstation vector, we computed precision, as defined in the introduction of this section, and the reduced χ^2 statistic. Our criteria for selection of these interstation vectors were that they be estimated during three or more experiments, over at least 1.2 years, with eight or more independent estimates. The long-term precision results have been plotted as a function of baseline length in Figures 7*a*-7*c*. The long-term precision for the north-south component is 4 mm + 0.3 parts in 10^8. In the east-west component, the long-term precision is comparable to the short-term results with a slightly larger constant term, 3.4 mm + 2.0 parts in 10^8. As with our short-term precision results, the vertical component is less precise than either horizontal components and is described by 26 mm + 5 parts in 10^8 of the baseline length. A more careful inspection of Figure 7*c* indicates that long-term vertical precision ranges from 30 to 40 mm, for baselines longer than 50 km, and improves rapidly for smaller values. Thus, for baselines less than 50 km, vertical precision is far better than the constant term of our linear fit, 26 mm, would suggest.

Discussion. We have compiled the long-term precision statistics from *Davis et al.* [1989] and list them in Table 5 along with our interstation vectors. The USGS baselines range from 200 m to 223 km. *Davis et al.* defined precision as the RMS about the best fitting line for both horizontal and vertical components (we compute the RMS about the mean for the vertical component). By including the USGS results, we have a better estimate of GPS precision for baselines less than 450 km in length: 3.4 mm + 1.2 parts in 10^8,

5.2 mm + 2.8 parts in 10^8, 11.7 mm + 13 parts in 10^8 in the north-south, east-west, and vertical components. At 100 km, this would yield subcentimeter horizontal precision, 25 mm in the vertical. Our study overlaps with Davis et al. on one baseline, Palos Verdes to Vandenberg. Our long-term precision of 5, 7, and 41 mm in the north-south, east-west, and vertical only differs appreciably from that of Davis et al. (6, 11, and 40 mm) in the east-west component. We resolved ambiguities on nearly all estimates of this baseline, whereas Davis et al. did not attempt ambiguity resolution. Resolving ambiguities has been shown to improve short-term precision in the east-west component [*Dong and Bock*, 1989; *Blewitt*, 1989], and results from paper 3 indicate that am-

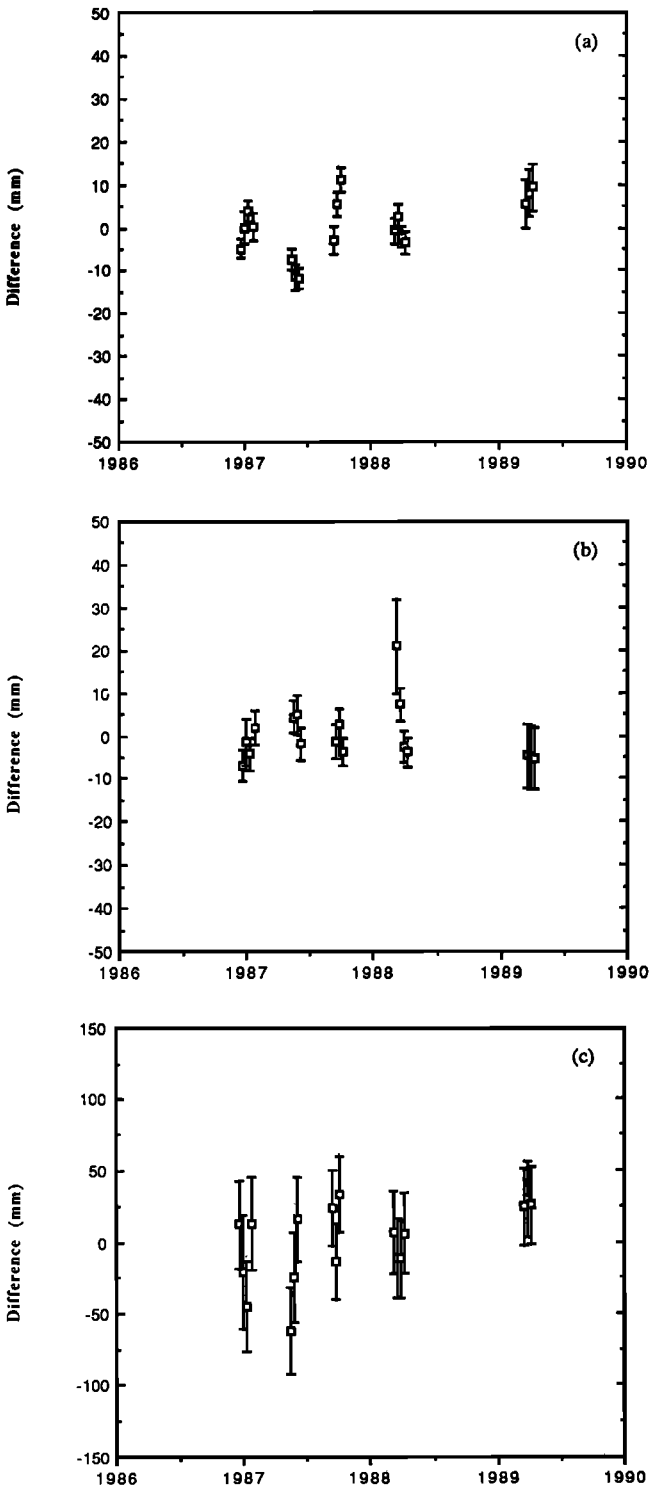

Fig. 6. Change of relative coordinates for the Center to Vandenberg vector (101 km), with zero being the mean value. The components shown are defined as in Figure 3.

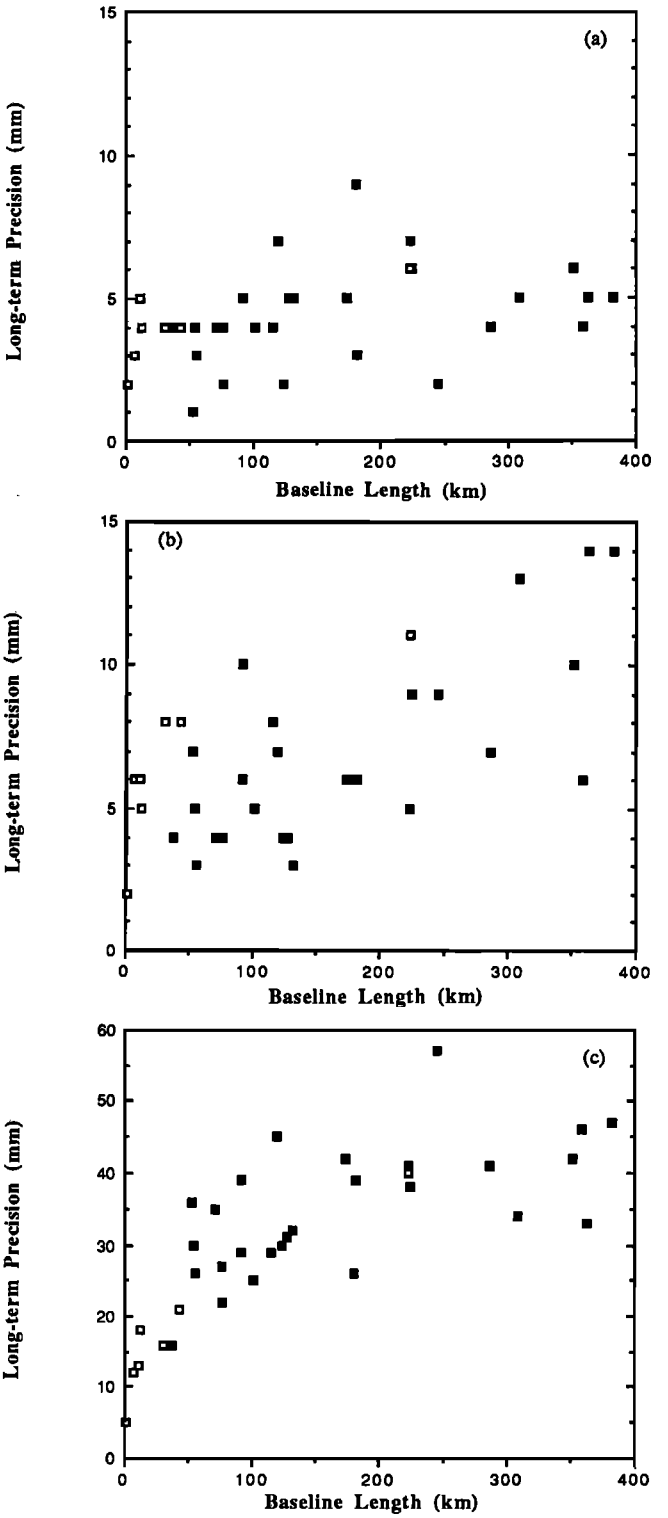

Fig. 7. The solid squares represent the long-term precision determined from experiments described in Table 2. For the horizontal components the precision is defined (equation (3)) as the weighted RMS about the best fitting straight line; for the vertical, by the weighted RMS about the mean (equation (1)). The components are defined as in Figure 3. Also shown are long-term precision determinations (open squares) from *Davis et al.* [1989] for baselines ranging from 200 m to 223 km in length.

biguity resolution improves precision in the long term as well. This may also explain the slightly less precise USGS east-west components for baselines less than 50 km.

Again, we address the question of the validity of our formal errors. In Figures 8*a*-8*c*, we plot χ^2 as a function of baseline length. For the north-south component, our formal errors underestimate the the actual scatter approximately half the time, although χ^2 does not increase with baseline length. For the east-west and vertical components, there is a slight increase of χ^2 with baseline length. Long-term error sources which we think have contributed to the degraded long-term precision are the accuracy of the GPS spacecraft orbit, the ability to resolve carrier phase ambiguities, adequate modeling of the ionosphere and atmosphere, and blunders. Since some of these errors (e.g., orbit accuracy and blunders) have not been accounted for in the formal error, we expect that this has inflated the long-term χ^2 statistic. We discuss each of these error sources in turn.

The orbit accuracy is primarily controlled by the accuracy of the fiducial coordinates, geometry of the fiducial network, and the number of hours of tracking data that were available. Experiments which suffered from failure or absence of continental fiducial sites were, in general, less precise. Additionally, mixing interstation vector estimates computed with different fiducial networks undoubtedly inflates the long-term precision statistic. For the 11 experiments in Table 2, 10 different fiducial networks were used (assuming the three monuments at Mojave to be independent.) Since the purpose of fiducial networks is to provide a consistent reference frame in which to determine crustal deformation rates, their stability is extremely important. The influence of the fiducial network on GPS precision and accuracy is discussed in paper 2. The consistency of our long-term precision with that of *Davis et al.* [1989] leads us to believe that high precision can be achieved with a "single-day" arc, where each day of data yields an independent estimate of satellite orbits and station positions. The precision of single-day arcs on these spatial scales may be dependent on the sophistication of the orbit determination software. For continental-scale (2000-3000 km) baselines, a "multiday" arc solution, as discussed by [*Lichten and Border*, 1987], may be required to achieve comparable precision.

The precision results that we and others (prominently *Dong and Bock* [1989] and *Blewitt* [1989]) have presented were for experiments where a high percentage of carrier phase ambiguities were resolved. The number of hours of tracking influences the confidence statistic used to decide whether the carrier phase ambiguity has been adequately resolved [*Blewitt*, 1989]. In general, we find that ambiguities can be easily resolved with more than an hour of data, with one additional criterion: the interstation spacing should be less than 100 km. In the S88 experiment, the closest spacing of two stations was 223 km. We were only able to resolve 4 of 32 ambiguities. In experiments with closer interstation spacing, e.g., M88b, we were able to resolve 83 of 85 ambiguities in California.

Experiments conducted over a few days do not provide an adequate sampling of tropospheric and ionospheric conditions. This may explain why long-term vertical precision is degraded relative to short-term precision. With the other error sources in these data, it is difficult to isolate the atmospheric and ionospheric contribution. Data that are collected continuously, with a stable fiducial network, will be required to discern the seasonal variations which may be present in these data. Continous GPS networks will also reduce the vertical scatter by eliminating the error associated with centering and measuring the height of the antenna over the monument. Some of the scatter in the vertical component may also be due to human error in translation of field notes into the site vector used in the analysis software.

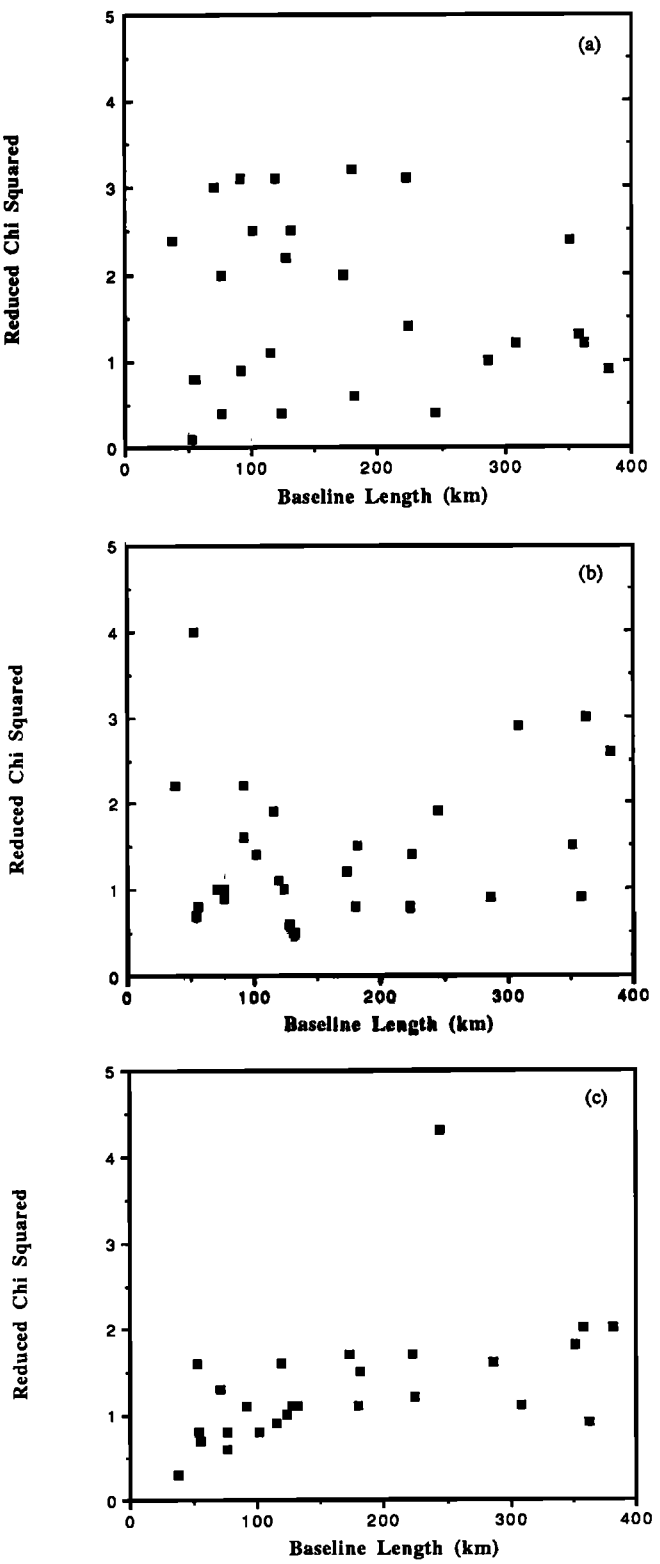

Fig. 8. χ^2 for the baselines shown in Figure 7.

ACCURACY

Introduction

High precision is necessary for, but not indicative of, accuracy. In order to assess accuracy, we must compare GPS vector estimates with vectors determined by an independent measurement system. Comparisons are also useful for identifying systematic errors in GPS, because different techniques presumably have different error sources. VLBI and SLR are two systems available to compare baselines longer than 50 km. No comparisons will be made between GPS and SLR measurements because there are few GPS occupations of SLR monuments in this data set. Unless otherwise noted, the VLBI results are from the 1989 Crustal Dynamics Project Annual Report [*Ma et al.*, 1990] and GLB223, the Goddard site velocity model that was used to determine the GPS fiducial coordinates.

Most estimates of GPS accuracy have been restricted to single epoch agreement with VLBI or SLR [*Dong and Bock*, 1989; *Blewitt*, 1989; *Bock et al.*, 1990], with the exception of work by *Davis et al.* [1989]. Using data from six experiments conducted in southern California, Davis et al. compared GPS and VLBI length estimates of the 223-km baseline between Palos Verdes and Vandenberg. Agreement was within the standard deviations of GPS and VLBI. They also compared line lengths from the Hebgen Lake (9-30 km) and Loma Prieta (30-50 km) networks with the Geodolite, a laser measurement system, with agreement of 1-2 mm at these lengths. At Parkfield, they compared the fault-parallel motion to creep meters and alignment arrays, where rates agreed to within 1-2 mm/yr. While we cannot compare our interstation vectors with as many different kinds of systems, we have concentrated our efforts on the accuracy of "regional" scale baselines. We assess the accuracy of GPS in two modes: agreement of interstation vectors and linear trends.

As with our precision study, we would like to know if accuracy degrades with baseline length. The literature has often referred to agreement with VLBI in terms of parts per baseline length. This is useful if there is a true deterioration of accuracy with baseline length but is inappropriate where errors are not necessarily dependent on baseline length. Certainly, orbit estimation may contribute a baseline dependent error for comparisons at the continental baseline scale, but for baselines shorter than 500 km, there is no evidence to date that the $|GPS - VLBI|$ discrepancy is length dependent.

Comparisons between new and standard measurement systems are essential for validation of the new measurement technique. The difficulty in comparison studies arises in determining the correct rotations which are required to compare vectors which were determined in different reference frames. Even simple comparisons of line lengths determined by EDM and GPS require that a scaling factor be introduced to account for the difference in the speed of light value used in the two data analysis systems. Since GPS vectors are referenced to a VLBI system of fiducial coordinates, GPS and VLBI comparisons are simplified somewhat. A more mundane element of vector comparisons is due to local site surveys. Different systems (VLBI, SLR, GPS) occupy different geodetic monuments at the same geographic location. Generally, these monuments are separated by only several hundred meters, and conventional surveys can be done with an accuracy of a millimeter at these distances. In practice, local surveys introduce uncertainty into the accuracy assessment.

Measurements between the different monuments at these sites (local surveys) are of several types and need to be treated differently. There are conventional surveys, differential GPS determinations, and simple measurements of height above a monument, which we discuss in turn. Conventional surveys have varying levels of redundancy and therefore accuracy. In many cases what are termed survey errors are actually errors in user understanding of the meaning of the coordinate differences coming from ground surveys or blunders in passing along information and not measurement error (W. Strange, personal communication, 1990). The precision of differential GPS surveys on these scales is several millimeters in the horizontals but is twice that in the vertical. *Davis et al.* [1989] reported long-term vertical precision of 5 mm for a 240-m baseline. This is considerably less precise than the best conventional surveys. On the other hand, the accuracy of differential GPS surveys is not well understood or documented. The accuracy of these surveys may be dependent on which GPS receivers were used and which software was used to analyze the measurements. Measurements of height above the geodetic monument are required for both GPS and VLBI. For the TI-4100 GPS receiver, it is assumed that the difference between the L_1 and L_2 phase centers and the antenna base is well known, although discrepancies have been reported (J. Svarc, personal communication, 1990). Likewise, errors in VLBI site vector measurements, for baselines with very few data, will map into a $|GPS - VLBI|$ discrepancy.

As an example of a typical situation in accuracy determinations, Figure 9 illustrates the number of vectors that must be added to compare VLBI and GPS baseline vectors between Mojave and Vandenberg. Terms which are underlined are GPS sites, or antenna phase centers. The numbers refer to the Crustal Dynamics Project site catalog. Two local surveys were required to recover the vector from the main

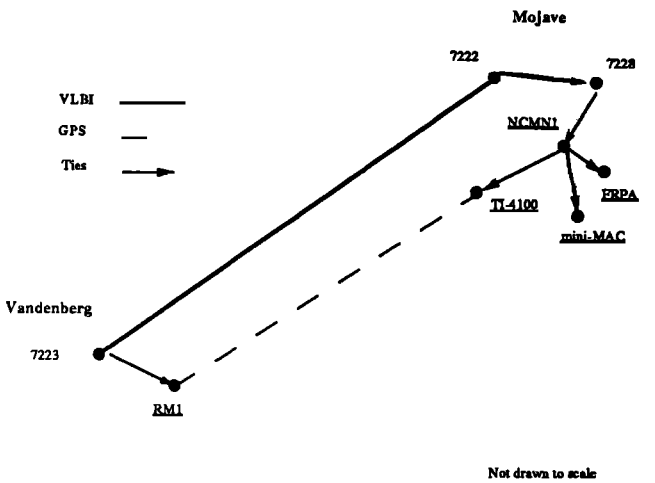

Fig. 9. Cartoon to show the vectors which must be measured to compare GPS and VLBI measurements on a typical baseline. The bold vector between VLBI monuments at Vandenberg and Mojave is 351 km long. The dashed line represents the vector between GPS monuments. GPS monuments/antennae are underlined. Each segment with an arrow represents a local survey which must be conducted to compare GPS and VLBI baseline solutions. This figure is not drawn to scale. Actual survey values are listed in Table 6.

VLBI mark at Mojave to the VLBI reference mark, NCMN1. These surveys were done conventionally. The measurements from NCMN1 to the three permanent antennae which were placed at Mojave between mid-1988 through early 1989 were made with GPS. For completeness, in Table 6 we have listed the relevant local survey information that we have used. In addition to crustal deformation measurement sites in California, we also list local surveys at fiducial sites.

Although it is important to compare interstation vectors at a single epoch (we compare a few vectors measured during the J86 experiment), long-term monitoring of the interstation vector will help to find probable local survey errors. We feel that comparison of rates is ultimately more useful for crustal deformation studies, because the fundamental measurement that we seek is the time rate of change of the vector between two sites. Rate determinations are not immune from local survey errors. If that station is used as a fiducial site in some estimates but not for others, this will influence the computed rate. We discuss only a few interstation vectors in detail.

Results

The data collected in Table 2 were directed toward measuring crustal deformation rates in California. Therefore, comparisons with VLBI are mostly limited to interstation vectors in California. Prominently featured in the available

TABLE 6. GPS-VLBI Local Survey Values

Station 1	Station 2	X, m	Y, m	Z, m	Survey Type	Agency	Reference
			Algonquin Park				
6381	Algonquin (GPS)	92.760	70.280	13.066	conventional	GSC	1
			Mojave				
7222	7288	-323.1130	148.2132	-43.9926	conventional		2
7288	NCMN1	69.6589	-5.9415	35.6147	conventional		2
NCMN1	CIGNET-TI4100	-209.804	120.407	1.836	GPS, NGS[a]	NGS	3
NCMN1	CIGNET-FRPA	-209.7820	120.4134	1.8247	GPS, Bernese[b]	USGS	3
			Owens Valley Radio Observatory				
7207	7853	-820.4891	549.1188	87.1157	conventional		3
7853	7114 (GPS)	-1.2227	-2.2611	-3.6171	conventional		3
			Richmond, Florida				
7219	TIMER 1962	59.722	35.2121	29.920	conventional		3
TIMER 1962	CIGNET-FRPA	0.5483	-3.2420	1.5754	conventional		3
			Westford Observatory				
7209	MICRO	111.191	84.088	43.334	conventional		3
MICRO	CIGNET-TI4100	-84.8933	-45.2645	-12.9246	GPS, NGS	NGS	3
			Vandenberg Air Force Base				
7223	RM1 (GPS)	23.105	-0.9629	17.253	conventional	NGS	1

Compilation of local survey information used, referenced to WGS84. Numbers are associated with the Crustal Dynamics Project VLBI marks. Full listings are given by *Noll* [1988]. For survey types, we distinguish between those done conventionally, and those done with GPS receivers. For GPS surveys, we indicate the software used. All GPS surveys were measured with TI-4100 GPS receivers. If known, the agency which conducted the survey and computed the survey values is listed. References: 1, M. Murray, (personal communication, 1990); 2, J. Ray, (personal communication, 1990); and 3, *Chin* [1988].

[a] *Mader* [1988].

[b] *Beutler et al.* [1987].

TABLE 7. GPS-VLBI Vector Differences

Interstation Vector		Length, km	East, mm	North, mm	Vertical, mm	GPS		VLBI	
						Years	Number of Observations	Years	Number of Observations
Yuma[a]	Monument Peak[a]	208	-10	5	-20	E	2	4.1	8
Mojave	Palos Verdes	224	-15	-12	-80	2.3	18	4.1	5
Mojave	Ovro	245	-8	10	-60	1.2	9	4.3	62
Fort Ord	Vandenberg	256	-10	-15	0	1.2	10	4.2	7
Fort Ord	Ovro	316	5	8	8	1.2	8	4.2	5
Mojave	Vandenberg	351	-15	-13	-50	2.3	18	4.3	89
Ovro	Vandenberg	364	-10	-30	-10	1.2	9	4.2	40
Monument Peak	Vandenberg	430	10	-16	7	E	2	4.0	18

E: single epoch measurement.

[a] See *Noll* [1988] for station description.

data are VLBI sites at Fort Ord, Mojave, OVRO, Vandenberg, and Palos Verdes. GPS and VLBI interstation vector changes will be displayed in a standard form, with the north-south, east-west, and vertical components. Zero is the mean value of the GPS estimates. The solid line in each figure is the VLBI baseline vector component which results from a simultaneous global estimate of site velocities (GLB223). Since this site velocity model was used to compute fiducial locations for the GPS experiments, this is the most appropriate measure of agreement with VLBI. The error bars for the GPS baseline components are one standard deviation. Based on our long-term precision study, these formal errors underestimate the actual uncertainty. The differences between GPS and VLBI for all baselines are listed in Table 7. The interstation vectors compared at more than one epoch which we discuss in greater detail are the vectors between Mojave and Vandenberg, Mojave and Palos Verdes, and OVRO and Fort Ord.

Mojave-Vandenberg-Palos Verdes. In June 1986, the USGS began an effort to regularly measure the interstation vectors between monuments at Mojave, Palos Verdes, and Vandenberg Air Force Base. Due to the commitment of both personnel and receiver time, these are now the most frequently occupied mobile GPS baselines in California longer than 200 km. For Vandenberg and Mojave, there were eight experiments over 33 months, spaced 4-6 months apart. Palos Verdes was occupied simultaneously with Mojave and Vandenberg in seven of those experiments.

Mojave to Vandenberg is the most frequently occupied VLBI baseline in California, with 89 observations between 1983 and 1988. This baseline is long enough to begin to show deterioration in the GPS east component due to poor orbit determination in several of the seven epochs shown, particularly J88 and S88, where we were unable to resolve a large number of the carrier phase ambiguities. Figure 10 displays the GPS vector components from 1986 through 1988. The offset between GPS and VLBI coordinates is 15 mm in the east and 13 mm in the north. The GPS rates derived for the north-south and east-west components of the Vandenberg-Mojave vector are -25.5 ± 2 and 28.9 ± 4 mm/yr, respectively. This agrees within one standard deviation of the VLBI estimates of -28.1 ± 2.0 and 27.6 ± 1.6 mm/yr. The GPS east-west component is significantly noisier than the north-south component, as evidenced by the weighted RMS about the best fitting line: 6 and 10 mm in the north-south and east-west components, respectively. In the vertical component, GPS has a RMS of 41 mm and disagrees with the VLBI mean by 50 mm. The VLBI vertical RMS about the best fitting line is 37 mm.

Palos Verdes was measured by VLBI only five times between 1983 and 1987. We have estimated 18 independent interstation vectors with the GPS data that were collected between 1986 and 1988, as shown in Figure 11. The VLBI and GPS monuments at Palos Verdes are identical. The rates from VLBI are -19 ± 3.7 and 20 ± 3.4 mm/yr in the north-south and east-west components respectively. The GPS rates are similar: -20 ± 2.5 and 28 ± 4 mm/yr. The horizontal components both exhibit an offset of approximately 15 mm. The weighted RMS about the best fitting line for GPS is 8 and 9 mm for the east-west and north-south components. In the vertical component, the precision is less than 50 mm for both VLBI and GPS, but their means disagree by 80 mm. This is the largest difference of eight baselines listed in Table 7.

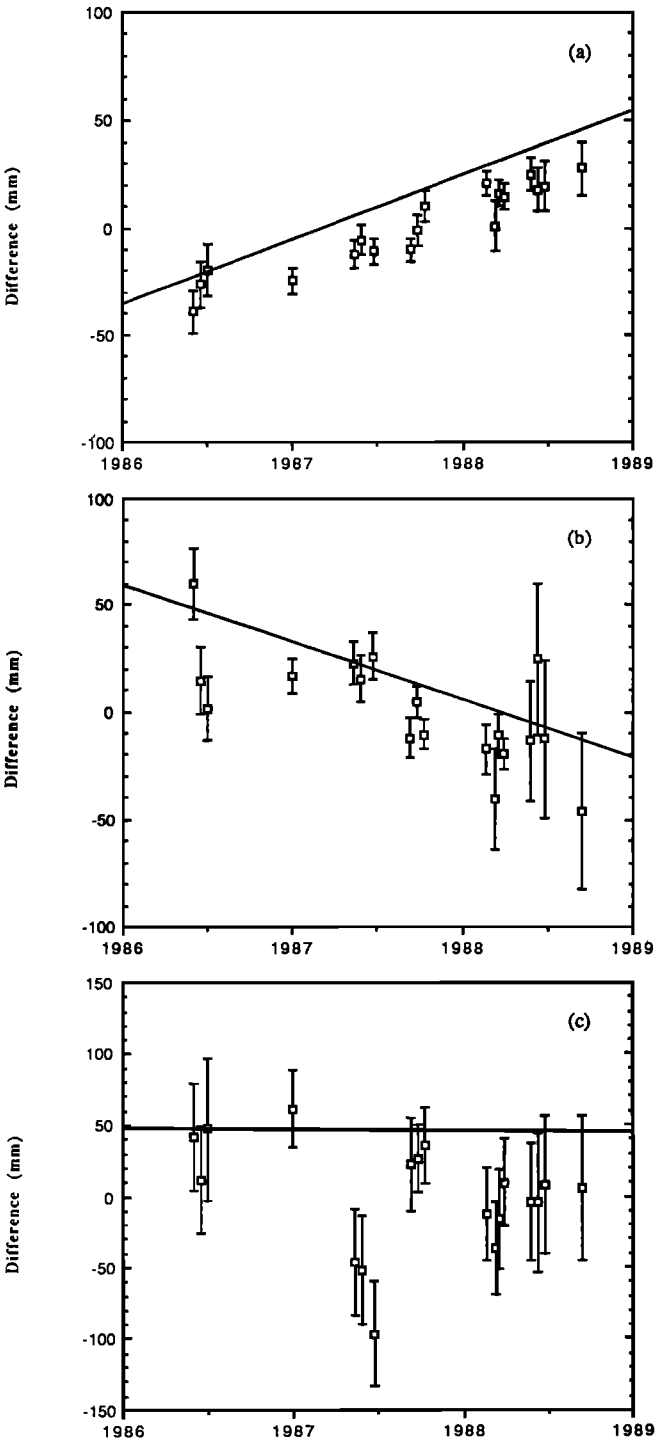

Fig. 10. The points with error bars are the GPS-derived relative coordinates for the Mojave to Vandenberg vector (351 km), taken relative to the mean. The solid line shows the coordinates given by a model fit (GLB223) to the VLBI data. While the agreement in rates is good, there is a persistent offset between the two types of measurement. Components are defined as in Figure 3.

OVRO-Fort Ord. The OVRO-Fort Ord baseline vector is 316 km long and oriented nearly east-west. OVRO requires a conventional survey, but the Fort Ord monument is used by both VLBI and GPS. There have only been three GPS experiments including Fort Ord, over the space of 1.2 years, whereas VLBI experiments span over 4 years. Agreement between GPS and VLBI is shown in Figure 12. Agreement of GPS to VLBI is 5 mm in the east and 10 mm in the

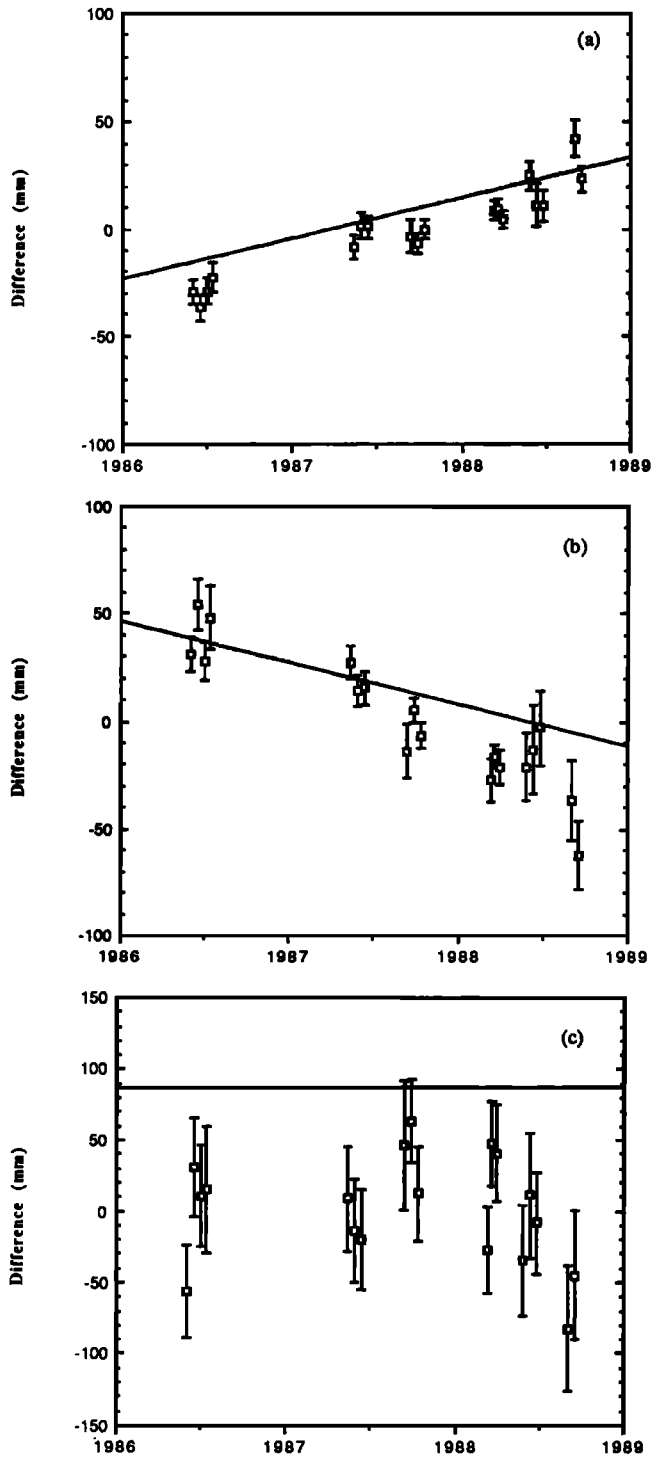

Fig. 11. Change of relative coordinates for the Mojave to Palos Verdes vector (224 km). See Figure 10 for details.

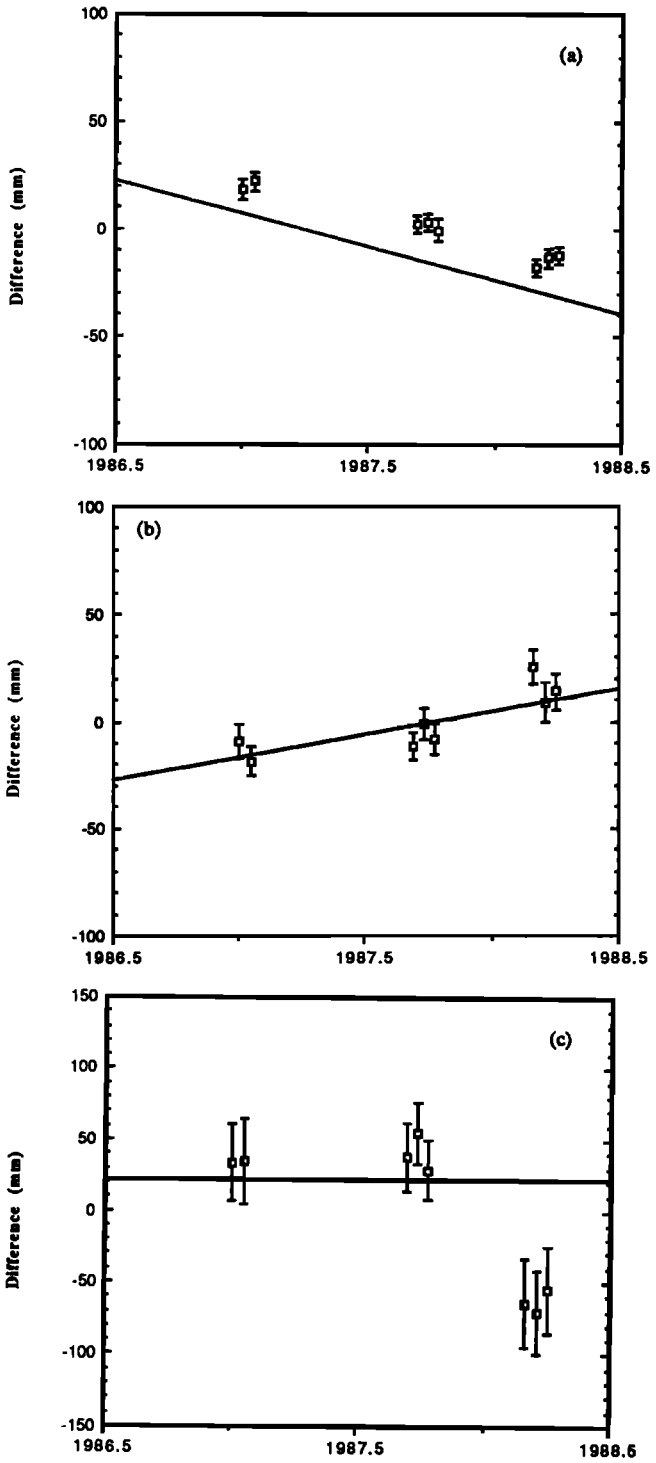

Fig. 12. Change of relative coordinates for the OVRO to Fort Ord vector (316 km). See Figure 10 for details.

north. The vertical agreement is within 20 mm for two experiments and 60 mm for the third. The computed rates for OVRO-Fort Ord agree with VLBI rates within one standard deviation, but the uncertainties on the GPS rate estimates are quite large, due to the short time-span of occupations.

Comparison of Vertical Components

The absolute value of the vertical component difference between GPS and VLBI is shown in Figure 13 as a function of baseline length. The error bar is determined from the weighted RMS about the best fitting line for VLBI and weighted RMS about the mean for GPS. The disagreement is less than 80 mm on baseline vectors ranging from 200 to 430 km. *Dong and Bock* [1989] compared single epoch vertical estimations for the Mojave-OVRO baseline and agreed within 22 mm of the VLBI solution. Results from *Blewitt* [1989] are more comparable to Figure 13, where at a single epoch, the agreement with VLBI was from 5 to 80 mm, measured on 15 baselines ranging from 100 to 1100 km.

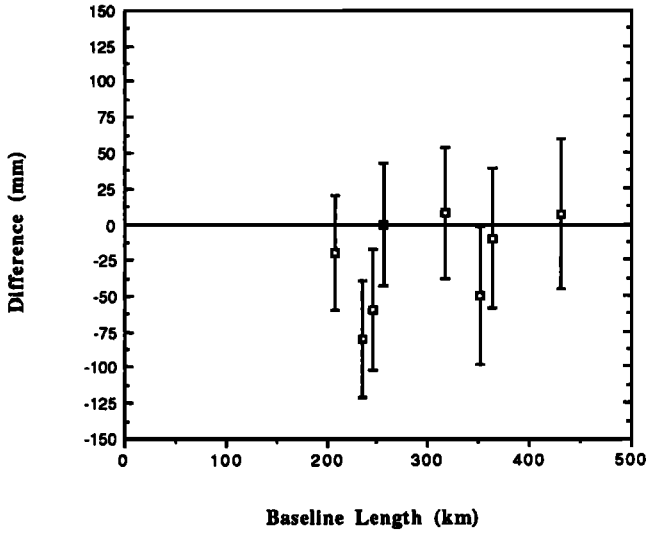

Fig. 13. The GPS-VLBI vertical component difference, plotted as a function of length. The error bar is determined from the weighted RMS about the best fitting line for VLBI [*Ma et al.*, 1990] and weighted RMS about the mean for GPS. More discussion can be found in the text and Table 7.

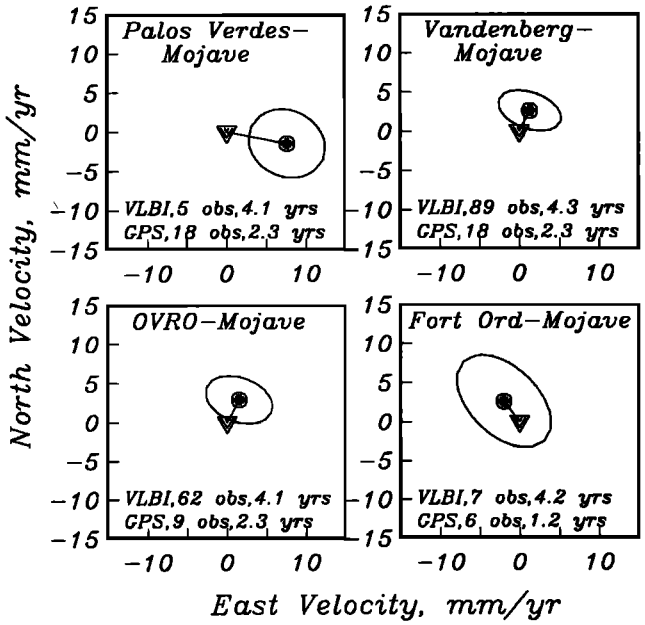

Fig. 14. Difference in vector rates for GPS and VLBI derived motion of Fort Ord, OVRO, Vandenberg, and Palos Verdes relative to Mojave. Zero, shown by the inverted triangle, is the VLBI horizontal rate, and the difference of the GPS rate is shown as a solid circle. Error ellipses are one standard deviation, including both GPS and VLBI. The number of observations and time span of measurements for each baseline are listed.

Comparison of Rates

Finally, we compare rates for four baseline vectors in southern and central California. Figure 14 shows the GPS-VLBI rate difference vector for interstation vectors between Mojave and OVRO, Vandenberg, Palos Verdes, and Fort Ord. The error ellipses were computed from the GPS and VLBI one standard deviations, and then projected onto the horizontal plane. The GPS standard deviations would yield ellipses oriented nearly along the north-south/east-west axes. The addition of the VLBI standard deviations rotates the ellipses slightly, although in general, the GPS standard deviations dominate the error ellipses. The GPS rates for Fort Ord and OVRO are determined from only 1.2 years; those at Palos Verdes and Vandenberg are determined from 2.3 years. The VLBI rates are determined from 4 or more years of data. The only significant difference between GPS and VLBI rates is for the east-west component of Palos Verdes. The vertical rates of deformation for both VLBI and GPS are less than their formal uncertainties.

Discussion

There are several possible reasons that VLBI and GPS vector components disagree, at this level. The differences on some of the interstation vectors listed in Table 7 are suggestive that a single "survey error" may, in fact, be responsible for a large portion of the GPS-VLBI horizontal discrepancy. In order to test this hypothesis, we have taken solutions from the four (D86, S87, M88a and M88b) experiments that include the VLBI sites OVRO, Fort Ord, Mojave, and Vandenberg. These experiments were all analyzed with continental-scale fiducial networks but not necessarily the same ones (as indicated in Table 2). Using the VLBI solutions for these sites at each epoch, we adjusted the GPS interstation vectors and solved for the best fitting "discrepancy" vector at OVRO, Vandenberg, and Mojave. We did not adjust Fort Ord, as the GPS and VLBI monuments are identical. The formal errors from the GPS estimates were used to weight the fit. The results of this calculation are shown in Table 8. The only offsets we consider to be significant are the discrepancies in the north-south and east-west components for Vandenberg, where the best fitting vector is -14 ± 8 and 13 ± 4, and the north-south component at OVRO, 13 ± 2. The

TABLE 8. Estimated Survey Discrepancy Vectors

Experiment	OVRO		Mojave		Vandenberg	
	North	East	North	East	North	East
D86	15±10	-9± 8	5±14	-9± 11	-12±11	-9±9
S87	14± 7	-21± 6	6± 8	-17± 7	-7± 7	-16±6
M88a,b	11 ±8	9± 6	-6± 8	13± 7	-21± 7	-11±7
Weighted mean	13±2	-7±16	1± 7	-3±17	-14±8	-13±4

All values are in millimeters.

latter is particularly surprising, given the energy which was expended to remeasure the line between Mojave and OVRO in the "MOTIES" experiment (J. Ray, personal communication, 1989). The result is consistent with the observed discrepancy between Mojave and OVRO of 10 mm. Likewise, the discrepancy at Vandenberg would explain the long-term discrepancy between Mojave and Vandenberg and would be sufficient to create the largest discrepancy on these regional baselines, between OVRO and Vandenberg

Another reason for horizontal component discrepancies is the robustness of the solution for the vector, either from GPS or VLBI. Both systems will reduce the uncertainty in the interstation vector with additional data. Some vectors (such as OVRO-Fort Ord) are measured by VLBI once per year, whereas the VLBI Mojave-Vandenberg vector is based on 89 measurements. Both Mojave and Vandenberg are fixed VLBI antennas, whereas Fort Ord is a mobile VLBI site. The interstation vectors between fixed antennas (which generally are measured more often) are more precisely known than those between mobile antennas.

The vertical component discrepancies, while troubling for some baseline vectors, are based on very few data points. We assumed that the GPS phase center, which varies with elevation angle to the GPS satellite, averaged to some mean value. This phase center variation may in fact introduce a systematic bias, which could introduce the offset we see between GPS and VLBI. GPS vertical components are particularly sensitive to poor fiducial networks (see paper 2). Another possible source of vertical discrepancies is differences due to the estimation technique used to determine propagation delays of the atmosphere. We discuss this further in paper 3.

The agreement between GPS and VLBI rates in all components is extremely encouraging, particularly considering the short time span of GPS data collection. We expect that the rate agreement will continue to improve as we collect more data and eliminate systematic errors.

CONCLUSIONS

We have analyzed nearly 3 years of GPS data collected in southern and central California between 1986 and 1989. On time scales of a few days, horizontal precision is 2 mm, with an additional length dependence of 0.6 and 1.3 parts in 10^8 for the north-south and east-west components, respectively. Short-term precision in the vertical is length independent, with a mean value of 17 mm. Horizontal precision determined over several years, where we have included recent precision estimates from the USGS [*Davis et al.*, 1989], has a constant bias of 5 mm, with a length dependence of 1 and 3 parts in 10^8 for the north-south and east-west components, respectively. These measurements were made when the GPS constellation was preferentially aligned north-south. Presumably, the precision of future GPS measurements will show less dependence on the direction of the interstation vector. Vertical measurements are much less precise than horizontal measurements, 11.7 mm + 13 parts in 10^8.

Accuracy (defined by agreement of horizontal components with those found from VLBI) is 5-30 mm for baselines from 200 to 430 km long. The pattern of these discrepancies is consistent with a survey discrepancy at two VLBI sites in California, Vandenberg and OVRO. For interstation vectors that do not include these sites, agreement of horizontal components is approximately 10 mm. The vertical discrepancies between VLBI and GPS are much larger, ranging from 0 to 80 mm. There does not seem to be a systematic bias between the two systems, which in any case is unlikely because VLBI defines the orientation and scale of the GPS reference system. For making crustal deformation measurements, the most important comparison may be between the vector rates determined by the two systems. The GPS-determined vector rates agree well with those determined from VLBI measurements.

These results confirm the study of *Davis et al.* [1989], which found that precision and accuracy (in rates) was subcentimeter on these spatial scales. In turn, this confirms that GPS geodetic measurements are appropriate for crustal deformation experiments, where signals range from several millimeters to hundreds of millimeters per year. This precision and accuracy may not, of course always be achieved, and there are reasons why the data set we have studied may be better than most. Although we cannot prove this assertion, we feel that one of the most important factors in repeating high-accuracy GPS measurements is keeping as many factors common to all experiments as possible. Although the tracking data for the different experiments have not been homogeneous, most other factors were: the same GPS receiver and data analysis software were used; the same type of GPS antenna was used at nearly all stations; and the same GPS satellites (which followed nearly the same apparent sky paths) were available. The challenge remains for the geodetic community to successfully mix different receivers, antennas, block I and block II GPS satellites, and analysis software and to retain the high precision and accuracy achieved with the block I GPS constellation.

Acknowledgments. Much of the GPS data used in this paper were collected as part of a collaborative project to measure crustal deformation in central and southern California by the Scripps Institution of Oceanography, California Insititute of Technology, University of California, Los Angeles, and Massachusetts Insitute of Technology. We are particularly indebted to dozens of graduate students who contributed their time to this effort. The principal investigators, Dave Jackson, Bob King, Tom Jordan, and Brad Hager, were instrumental in making these experiments possible. The scope of this study would not have been possible without the cooperation and participation of the NGS and USGS, which were conducting their own surveys in the region. We thank Bill Strange and Will Prescott for supervising the collection of high-quality GPS data in California. Tracking data were provided by CIGNET. We thank Jerry Mader, Miranda Chin, and Linda Nussear for helping us acquire these data. Additional data and receivers were provided by JPL, CIGNET, DMA, PMTC, and the Geodetic Squadron of Canada. Logistical (James Stowell) and archival (Judah Levine) support was provided by UNAVCO. One of the authors (K.M.L.) benefitted from numerous conversations with Jim Davis, Geoff Blewitt, Will Prescott, and Steve Lichten. K.M.L. would also like to thank Mark Murray, Frank Webb, Kurt Feigl, Jeff Freymueller, Jerry Svarc, and Shawn Larsen for helpful discussions on GPS data analysis techniques. Computing facilities and the GIPSY software were provided by the Jet Propulsion Laboratory. We particularly thank Tom Yunck and Tim Dixon and their groups for supporting this work. Written reviews by Jim Davis, Bill Strange, Steve Lichten, and George Born improved the quality and scope of this paper. The data collection was funded (at UCSD) by NSF EAR-8618165. This research was supported by a NASA Graduate Student Research Fellowship awarded to K.M.L. at Scripps Institution of Oceanography. The writing and publication were completed at the Colorado Center for Astrodynamics Research and supported by ONR N0001490J2010.

REFERENCES

Beutler, G., I. Bauersima, W. Gurtner, M. Rothacher, T. Schildknecht, G. L. Mader, and M.D. Abell, Evaluation of the 1984 Alaska Global Positioning System campaign with the Bernese GPS software, *J. Geophys. Res., 92,* 1295-1303, 1987.

Bevington, P., *Data Reduction and Error Analysis for the Physical Sciences*, McGraw-Hill, New York, 1969.

Blewitt, G., Carrier phase ambiguity resolution for the Global Positioning System applied to geodetic baselines up to 2000 km, *J. Geophys. Res., 94,* 10,187-10,203, 1989.

Blewitt, G., An automatic editing algorithm for GPS data, *Geophys. Res. Lett., 17,* 199-202, 1990.

Bock, Y., R., I. Abbot, C.C. Counselman III, and R.W. King, A demonstration of one to two parts in 10^7 accuracy using GPS, *Bull. Geod., 60,* 241-254, 1986.

Chin, M., CIGNET report, GPS bulletin, Global Positioning Subcommission of Comm. VIII, Int. Coord. of Space Technol. for Geod. and Geodyn., Natl. Geod. Surv., Rockville, Md., 1988.

Christodoulidis, D.C., D.E. Smith, R. Kolenkiewicz, S.M. Klosko, S.M. Torrence, and P.J. Dunn, Observing tectonic plate motions and deformations from satellite laser ranging, *J. Geophys. Res., 90,* 9249- 9263, 1985.

Clark, T.A., D. Gordon, W. E. Himwich, C. Ma, A. Mallama, and J. W. Ryan, Determination of relative site motions in the western United States using Mark III very long baseline interferometry, *J. Geophys. Res., 92,* 12,741-12,750, 1987.

Davis, J.L., W.H. Prescott, J. Svarc, and K. Wendt, Assessment of Global Positioning System measurements for studies of crustal deformation, *J. Geophys. Res., 94,* 13,635-13,650, 1989.

Dong, D., and Y. Bock, Global Positioning System network analysis with phase ambiguity resolution applied to crustal deformation studies in California, *J. Geophys. Res., 94,* 3949-3966, 1989.

Hayford, J. F., and A. L. Baldwin, Geodetic measurements of earth movements, in *The California Earthquake of April 18, 1906*, edited by A. L. Lawson, pp. 114-145, Carnegie Institution, Washington D.C., 1908.

Henson, D. J., E. A. Collier, and K. R. Schneider, Geodetic applications of the Texas Instruments TI 4100 GPS navigator, paper presented at the 1st International Symposium on Precise Positioning with the Global Positioning System, U.S. Dep. of Commer., Rockville, Md., April 15-19, 1985.

Herring, T. A., et al., Geodesy by radio interferometry: evidence for contemporary plate motion, *J. Geophys. Res., 91,* 8341-8347, 1986.

Larson, K. M., Precision, accuracy, and tectonics from the Global Positioning System, doctoral dissertation, Univ. of Calif., San Diego, 1990.

Larson, K. M., F.H. Webb, and D.C. Agnew, Application of the Global Positioning System to crustal deformation measurements. 2. The influence of orbit determination errors, *J. Geophys. Res.*, this issue.

Lichten, S.M., and J.S. Border, Strategies for high precision GPS orbit determination, *J. Geophys. Res., 92,* 12,751-12,762, 1987.

Lichten, S.M., High accuracy Global Positioning System orbit determination: Progress and prospects, in *Proceedings of the General Meeting of the I.A.G., August 3-12, 1989, Edinburgh, Scotland, GPS and Other Radio Tracking Systems*, edited by Y. Bock and N. Leppard, pp. 40-52, Springer-Verlag, New York, 1990.

Ma, C., J.W. Ryan, and D. Caprette, Crustal Dynamics Project data analysis-1988, *NASA Tech. Memo., TM-100723,* 1989.

Mader, G.L., GPS Data Processing Program Documentation, Geodetic Research and Development Lab, NGS Division, Rockville, MD, August, 1988.

Noll, C., Crustal Dynamics Project: Catalogue of site information, *NASA Ref. Publ., 1198,* 1988.

Rueger, J. M., *Electronic Distance Measurement: An Introduction*, Springer-Verlag, New York, 1990.

Savage, J. C., Strain accumulation in the western United States, *Ann. Rev. Earth Planet. Sci., 11,* 11-43, 1983.

Savage, J.C., and W.H. Prescott, Precision of Geodolite distance measurements for determining fault movements, *J. Geophys. Res., 78,* 6001-6007, 1973.

Smith, D.E., et al., Tectonic motion and deformation from satellite laser ranging to LAGEOS, *J. Geophys. Res., 95,* 22,013-22,042, 1990.

Sovers, O.J., and J. S. Border, Observation model and parameter partials for the JPL geodetic GPS modeling software GPSOMC, *JPL Publ., 87-21,* 1988.

Stephens, S., GIPSY frontend user's guide, *JPL Publ., D-3918,* 1986.

Tralli, D. M., T. H. Dixon, and S. Stephens, The effect of wet tropospheric path delays on estimation of geodetic baselines in the Gulf of California using the Global Positioning System, *J. Geophys. Res., 93,* 6545-6557, 1988.

Ware, R. H., C. Rocken, K. J. Hurst, and G. W. Rosborough, Determination of the OVRO-Mojave baseline during the spring 1985 GPS test, in *Proceedings of the Fourth International Geodetic Symposium on Satellite Positioning*, vol. 2, pp. 1089-1101, Natl. Geod. Surv., Rockville, Md., 1986.

D. C. Agnew, Institute of Geophysics and Planetary Physics, Scripps Institution of Oceanography, La Jolla, CA 92093.

K. M. Larson, Colorado Center for Astrodynamics Research, University of Colorado Boulder, CO 80309-0431.

(Received August 5, 1990;
revised May 6, 1991;
accepted May 6, 1991)

JOURNAL OF GEOPHYSICAL RESEARCH, VOL. 96, NO. B10, PAGES 16,567–16,584, SEPTEMBER 10, 1991

Application of the Global Positioning System to Crustal Deformation Measurement 2. The Influence of Errors in Orbit Determination Networks

KRISTINE M. LARSON

Colorado Center for Astrodynamics Research, Department of Aerospace Engineering, University of Colorado, Boulder

FRANK H. WEBB

Satellite Geodesy and Geodynamics Systems Group, Jet Propulsion Laboratory, California Institute of Technology, Pasadena

DUNCAN C. AGNEW

Institute of Geophysics and Planetary Physics, Scripps Institution of Oceanography, La Jolla, California

Global Positioning System (GPS) measurements of a geodetic network in southern and central California have been used to investigate the errors introduced by adopting different sets of stations as fixed. Such fixed points, called fiducial stations, are necessary to eliminate the errors of imprecise satellites orbits, which otherwise would dominate the error budget for distances greater than tens of kilometers. These fiducial stations also define the reference frame of the crustal deformation network. Establishing the magnitude of the effect of changing the fiducial network is essential for crustal deformation studies, so that these artifacts of the differences between fiducial networks used for the data analyses are not interpreted as geophysical signals. Solutions for a crustal deformation network spanning distances up to 350 km were computed with a variety of fiducial networks. We use fiducial coordinates determined from very long baseline interferometry (VLBI). We compare these solutions by computing the equivalent uniform strain and rotation that best maps one solution into another. If we use a continental-scale fiducial network with good geometry, the distortions between the solutions are about 10^{-8}, largely independent of the exact choice of stations. The one case of a large- scale fiducial network where the distortions are larger is when the three fiducial stations chosen all lie close to a great circle. Use of a fiducial network no larger than the crustal deformation network can produce apparent strains of up to 10^{-7}. Our work suggests that fiducial coordinates determined from GPS data analysis may be used, although they should be determined using a consistent reference frame, such as provided by VLBI and satellite laser ranging.

INTRODUCTION

The Global Positioning System (GPS) is revolutionizing the way in which high-accuracy crustal deformation experiments are being conducted. Previously, small-scale information on crustal deformation came from repeated electronic distance measurements (EDM), with precisions of 3 mm + 1 part in 10^7. This system measures only the length between stations with intervisibility and is limited to distances of approximately 50 km [*Savage and Prescott*, 1973]. On longer scales, over distances of thousands of kilometers, very long baseline interferometry (VLBI) and satellite laser ranging (SLR) have been used to measure contemporary relative plate motions [*Herring et al.*, 1986; *Clark et al.*, 1987; *Smith et al.*, 1990]. The strength of GPS over VLBI, SLR, and EDM is its ability to deliver three-dimensional vector positions easily and inexpensively between sites that are not intervisible.

Recent analyses of GPS measurements collected over a few days show that the scatter in the horizontal components of interstation vector estimates is a few millimeters for baselines out to distances of a few hundred kilometers, with a proportional error of perhaps 10^{-8} becoming apparent at greater distances [*Dong and Bock*, 1989; *Blewitt*, 1989; *Larson*, 1990a]. In these works, fiducial networks were used to compute precise satellite orbits. A fiducial network consists of ground stations which observe satellites that are also being observed by stations in the crustal deformation experiment. When the three-dimensional locations of these "fiducial" sites are known to better than several centimeters, the orbit of the GPS satellite can be estimated with great accuracy. In turn, improved knowledge of the satellite orbit improves the precision and accuracy with which interstation vectors within the crustal deformation network are known, relative to an Earth-fixed reference frame.

This is the second in a series of papers devoted to characterizing errors in GPS data and GPS modeling techniques. The first [*Larson and Agnew*, this issue] (hereinafter referred to as paper 1) calculated precision and accuracy from nearly 3 years of surveys in southern and central California. In order to provide a large sample of vector measurements, that work included analysis of data with a large variety of fiducial networks. The decision to use these fiducial networks was dictated by the scarcity of high-quality fiducial data. We wish to determine how much scatter in the data described in paper 1 is attributable to the a priori choice of fiducial network.

The choice of fiducial network is important for two reasons. First, fiducial networks affect the precision that can be achieved with a single GPS experiment, which in this

Paper number 91JB01276.
0148–0227/91/91JB-01276$05.00

period was generally conducted over 7 to 8 hours. Future crustal deformation experiments can benefit from this study, because it demonstrates that precision and accuracy can be optimized by choosing the correct fiducial stations. Secondy, crustal deformation studies, by definition, require the remeasurement of interstation vectors during several different experiments, usually over a several year period. Since there is no guarantee that each experiment will have useful data from the same network of fiducial stations, it is necessary to address the bias which is introduced by the choice of fiducial network. Specifically, if one is forced to use these different fiducial networks at different epochs over the course of the crustal deformation experiment, we want to be able to choose the fiducial networks for each experiment such that the fiducial network bias is minimized. Since fiducial networks define the scale and orientation of the reference frame, we expect that the effect of the fiducial network bias on the crustal deformation network would be equivalent to a network dilatation and rotation. That is, if the fiducial networks from each experiment are poorly matched, the bias of each fiducial network on the crustal deformation network may look like crustal strain. These effects may not be observed in the scatter, or short- term precision, calculated from several days of data. Establishing how the choice of fiducial network affects the interstation vector estimates within the crustal deformation network is essential, so that these biases are not interpreted as geophysical signals. We first present an overview of fiducial networks, how they work, and how we expect them to be affected by different sources of error. Subsequently, we describe our procedure for quantifying the effect of different fiducial networks on interstation vector estimates. Finally, we present results from our analysis of data and discuss how biases in fiducial networks can be taken into account in the final error analysis.

Fiducial Networks

The optimal size of a fiducial network ideally depends on the size of the crustal deformation network. However, the requirement of common satellite visibility between the fiducial stations and the crustal deformation stations places a practical limitation on the size and shape of the fiducial network. Generally, fiducial networks should be an order of magnitude larger than the geodetic network. This is because errors in the satellite's orbit are proportional to the scale of the fiducial network. These satellite orbit errors map proportionally into the baseline errors in the geodetic network. For the purposes of measuring crustal deformation in California [paper 1], where networks ranged in scale from 50 to 450 km, fiducial networks which span continental distances (2000-3000 km) are required. At these length scales, VLBI and Satellite Laser Ranging (SLR) provide the only sources of precise fiducial coordinates. Because the coordinates of the fiducial sites are fixed, the known measurement uncertainties in these coordinates are ignored. These uncertainties in fiducial coordinates, which are a combination of the uncertainty in the VLBI or SLR measurement history and errors in the local survey from the VLBI or SLR monument to the GPS monument, depend on which fiducial sites are chosen and the quality of the local surveys. Later in this paper we will address the issue of incorporating uncertainties of fiducial coordinates into the error budget.

Simple geometrical arguments can be used to describe the effect of fiducial networks on GPS baseline estimation. Letting f be the distance between two stations in a fiducial network and $|df|$ be the error in that baseline, then the upper bound on the magnitude of the error in a satellite's orbit, $|dr|$, is approximated by

$$\frac{|dr|}{r} \cong \frac{|df|}{f} \tag{1}$$

where r is the range to the satellite. Similarly, this error in the satellite orbit would be equal to the error, $|dx|$, on a baseline of length x in the geodetic network,

$$\frac{|dx|}{x} \cong \frac{|dr|}{r} \cong \frac{|df|}{f} \tag{2}$$

For example, if the fiducial network spans 3000 km on each side, equation (2) suggests that an error of 30 mm in the fiducial network coordinates will cause a 1 part in 10^8 error. The effect of the same absolute error on a fiducial network which spans 300 km on each side is an order of magnitude larger, 1 part in 10^7. On a 10-km baseline, a part in 10^7 yields an acceptable mm level error but results in a 10-mm error on a 100-km baseline. So, if one is using GPS to monitor short baselines, less than 10 km, the stations chosen for the fiducial network may not be important. At the simplest level, a fiducial network can be eliminated entirely by using broadcast ephemerides. This orbit information is determined by the Defense of Department (DOD) which operates the Global Positioning System. The precision and accuracy of these orbits can be intentionally degraded by the DOD at any time. Use of broadcast ephemerides places the interstation vector estimates in the reference frame of the DOD's tracking network. High-accuracy results at distances of 10-30 km using broadcast orbits have been described by *Prescott et al.* [1989]. But for measurements outside this spatial regime, the choice of fiducial network may significantly contribute to the fiducial bias of interstation vectors in the crustal deformation network.

The effect of fiducial networks on system precision and accuracy was studied on continental-scale baselines in North America by *Lichten et al.* [1989] with data collected during the November 1985 North American GPS experiment. Unlike a covariance analysis, studies using data take into account error sources associated with data gaps and ambiguity resolution. Lichten et al. used combinations of data from four GPS sites collocated with VLBI monuments (Westford, Massachusetts; Richmond, Florida; Fort Davis, Texas; and Hatcreek, California), fixing the position of three and estimating the position of the fourth. They then examined the differences between the interstation vector between the estimated site and the closest fiducial site and the VLBI-derived interstation vector. They found that the effect of changing the fiducial network (i.e., changing one site from fixed to estimated) was of the order of 1 part in 10^8 of the baseline length. The effect of altering fiducial networks on shorter, regional-scale interstation vectors has not been investigated elsewhere.

Until recently, there has been little opportunity to study the effect of changing the fiducial network on estimates of interstation vectors, because of the scarcity of more than three fiducial stations in any one experiment. An important objective of this paper is to investigate whether all fiducial networks determined from VLBI have the same effect on estimates of interstation vectors, particularly if the geometry

of fiducial sites is a contributing factor to the precision and accuracy of the fiducial network.

How to Compute Fiducial Coordinates

We derived our fiducial coordinates from a global VLBI velocity model, GLB223, provided by Goddard Space Flight Center (C. Ma, personal communication, 1988). In this solution, a least squares fit was made of the VLBI data, and initial positions and velocities of the VLBI sites, Earth orientation, and nutation were solved for. The azimuth from Westford to Fairbanks (Gilcreek) was held fixed. Westford's velocity was defined by AM-02 [*Minster and Jordan,* 1978], and the reference epoch of the initial positions was October

TABLE 1. VLBI Model GLB223

Site	CDP		Adjusted Value	Unscaled Error
Westford	X Component	7209	1492208554.00 mm	reference
Westford	Y Component	NOAM	-4458131329.00 mm	reference
Westford	Z Component		4296015877.00 mm	reference
Westford	X Velocity		-18.23 mm/yr	reference
Westford	Y Velocity		-2.85 mm/yr	reference
Westford	Z Velocity		3.38 mm/yr	reference
Algonquin	X Component	7282	918036730.70 mm	2.538 mm
Algonquin	Y Component	NOAM	-4346133033.33 mm	8.788 mm
Algonquin	Z Component		4561971539.22 mm	8.623 mm
Algonquin	X Velocity		-19.26 mm/yr	0.00 mm/yr
Algonquin	Y Velocity		-2.86 mm/yr	0.00 mm/yr
Algonquin	Z Velocity		1.16 mm/yr	0.00 mm/yr
Fort Ord	X Component	7266	-2697024787.76 mm	7.63 mm
Fort Ord	Y Component		-4354394350.65 mm	14.32 mm
Fort Ord	Z Component		3788078018.22 mm	15.92 mm
Fort Ord	X Velocity		-26.85 mm/yr	1.00 mm/yr
Fort Ord	Y Velocity		34.22 mm/yr	1.15 mm/yr
Fort Ord	Z Velocity		20.24 mm/yr	1.32 mm/yr
Mojave	X Component	7222	-2356169113.12 mm	2.97 mm
Mojave	Y Component	NOAM	-4646756751.66 mm	9.73 mm
Mojave	Z Component		3668471206.34 mm	11.96 mm
Mojave	X Velocity		-16.42 mm/yr	0.45 mm/yr
Mojave	Y Velocity		5.83 mm/yr	0.65 mm/yr
Mojave	Z Velocity		-3.22 mm/yr	0.72 mm/yr
Ovro	X Component	7207	-2409598847.92 mm	2.64 mm
Ovro	Y Component	NOAM	-4478350412.58 mm	9.55 mm
Ovro	Z Component		3838603810.08 mm	11.98 mm
Ovro	X Velocity		-18.61 mm/yr	0.41 mm/yr
Ovro	Y Velocity		7.15 mm/yr	0.68 mm/yr
Ovro	Z Velocity		-3.40 mm/yr	0.73 mm/yr
Platteville	X Component	7258	-1240706258.17 mm	7.51 mm
Platteville	Y Component	NOAM	-4720455192.09 mm	12.01 mm
Platteville	Z Component		4094482213.75 mm	13.3 mm
Platteville	X Velocity		-15.00 mm/yr	1.28 mm/yr
Platteville	Y Velocity		2.40 mm/yr	1.32 mm/yr
Platteville	Z Velocity		-1.81 mm/yr	1.52 mm/yr
Palos Verdes	X Component	7268	-2525450843.30 mm	15.10 mm
Palos Verdes	Y Component	PCFC	-4670036683.10 mm	21.20 mm
Palos Verdes	Z Component		3522887273.70 mm	20.40 mm
Palos Verdes	X Velocity		-28.30 mm/yr	1.70 mm/yr
Palos Verdes	Y Velocity		24.30 mm/yr	1.40 mm/yr
Palos Verdes	Z Velocity		12.00 mm/yr	1.90 mm/yr
Richmond	X Component	7219	961259853.99 mm	4.08 mm
Richmond	Y Component	NOAM	-5674090905.67 mm	6.24 mm
Richmond	Z Component		2740534229.84 mm	5.51 mm
Richmond	X Velocity		-14.40 mm/yr	0.71 mm/yr
Richmond	Y Velocity		-2.20 mm/yr	0.32 mm/yr
Richmond	Z Velocity		0.51 mm/yr	0.66 mm/yr
Vandenberg	X Component	7223	-2678092760.68 mm	4.00 mm
Vandenberg	Y Component	PCFC	-4525451894.49 mm	10.90 mm
Vandenberg	Z Component		3597410581.61 mm	13.20 mm
Vandenberg	X Velocity		-31.77 mm/yr	0.56 mm/yr
Vandenberg	Y Velocity		34.26 mm/yr	0.74 mm/yr
Vandenberg	Z Velocity		19.48 mm/yr	0.82 mm/yr

GLB223 global solution for fiducial stations used in paper 1 and this study. Westford's velocity is defined by AM0-2. The azimuth from Westford to Fairbanks is held fixed. The epoch of the initial positions is October 17, 1980. Solution provided by Goddard Space Flight Center (C. Ma, personal communication, 1988). CDP numbers are defined by *Noll* [1988]. PCFC stands for Pacific plate, NOAM for North American plate.

17, 1980. The initial position vectors $\mathbf{r}_{initial}$ and velocity vectors $\mathbf{v}$ are given in Table 1. For any epoch t, the coordinates of the VLBI monument are

$$\mathbf{r}_{vlbi}(t) = \mathbf{r}_{intial} + (t - t_{ref}) \cdot \mathbf{v} \quad (3)$$

VLBI is not sensitive to the geocenter, so we made a correction to all stations, using values derived from SLR measurements (M. Murray, personal communication, 1990). GPS fiducial coordinates were then calculated using the following equation:

$$\mathbf{r}_{gps}(t) = \mathbf{r}_{vlbi}(t) + \mathbf{r}_{gc} + \sum \mathbf{r}_{ls} \quad (4)$$

where $\sum \mathbf{r}_{ls}$ is the vector sum of all local survey vectors between GPS and VLBI reference monuments and $\mathbf{r}_{gc}$ is the offset of the VLBI reference frame from the geocenter. More recent Goddard Space Flight Center VLBI models now incorporate the geocenter offset (J. Ray, personal communication, 1991).

DATA ANALYSIS

These data were collected during the March 1988 central California experiment, which is described in paper 1 (there referred to as M88b). We define two kinds of sites: crustal deformation sites and fiducial sites. Fiducial sites are those which have been measured by VLBI and whose positions can be computed by equation (4). The positions of crustal deformation sites were estimated. Fiducial sites are shown in Figure 1. Crustal deformation sites (10 in all) are shown in paper 1. The interstation vectors which make up the crustal deformation network are listed in Table 4 of paper 1. Baselines range from 50 to 350 km in length. Although data retention in the crustal deformation network was nearly 100%, the fiducial sites were less reliable, with most losing at least 1 of 4 days available. The amount of data available at each fiducial site is listed in Table 2, in numbers of hours of station-satellite tracking. Thus, 4 hours viewing of seven satellites would yield 28 hours. The models we have used

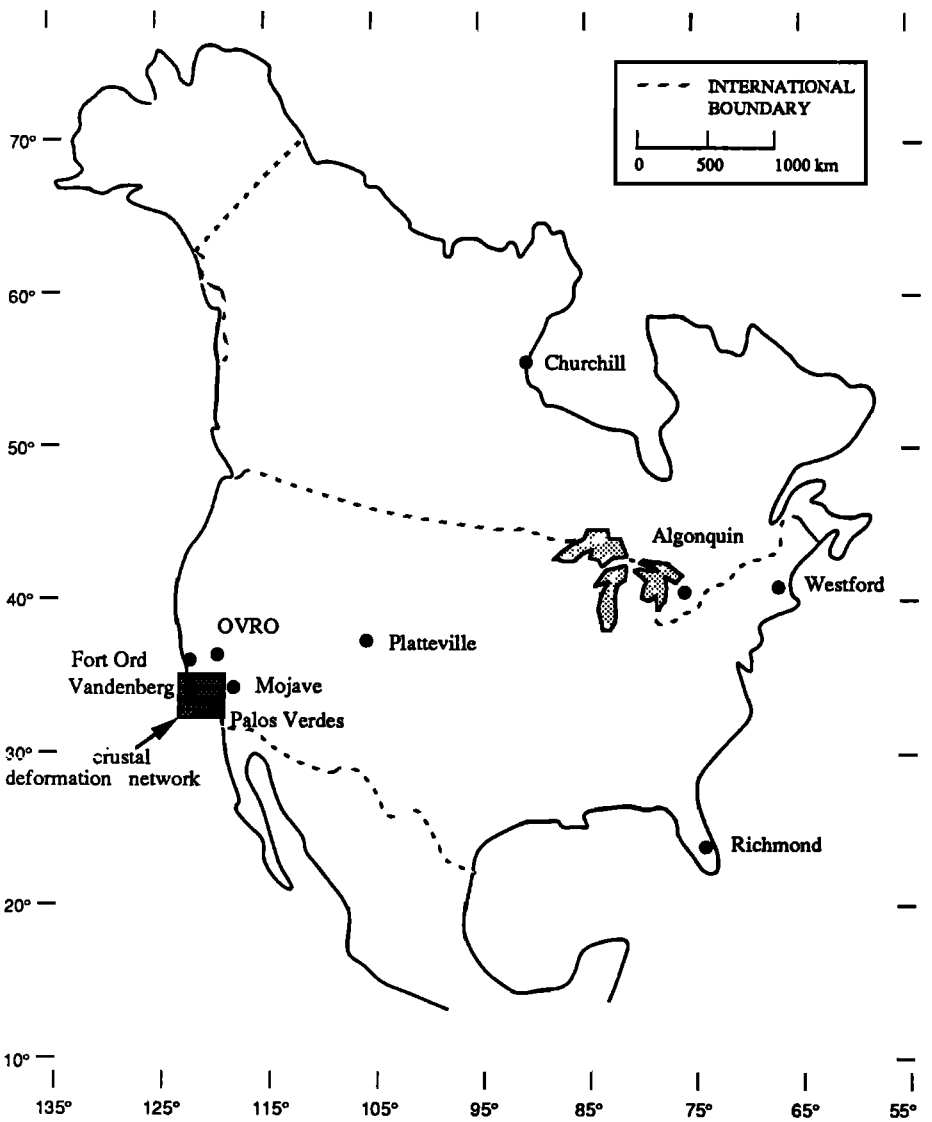

Fig. 1. North American fiducial sites. Westford, Richmond, and Mojave were continuously operating CIGNET sites [*Chin*, 1988]. Fort Ord, OVRO, Platteville, Algonquin, and Churchill were tracked with portable receivers. Coordinates of all sites (except for Churchill) were determined from VLBI measurements. Coordinates of Churchill were determined from GPS data discussed in this paper.

TABLE 2. Amount of Data Available at Each Fiducial Site

Station	Day of Year											
	75			76			77			78		
	Data, hours	ϕ_r, mm	P_r, mm	Data, hours	ϕ_r, mm	P_r, mm	Data, hours	ϕ_r, mm	P_r, mm	Data, hours	ϕ_r, mm	P_r, mm
Algonquin	27.7	3.9	900	27.6	4.2	993	27.2	4.3	1038	27.2	4.4	968
Churchill	23.7	4.0	836	16.4	-	-	24.1	4.1	878	25.0	4.3	889
Fort Ord	22.8	4.8	767	24.7	4.4	865	24.6	5.0	854	24.5	5.6	886
Mojave	0	-	-	20.5	7.3	1179	20.1	8.2	1267	28.4	7.5	1296
OVRO	21.8	5.2	829	25.5	4.9	812	13.7	-	-	19.2	5.0	777
Palos Verdes	24.8	5.5	1158	25.0	5.4	1247	24.6	5.8	1159	24.8	5.5	1127
Platteville	30.2	4.0	740	0	-	-	30.1	4.2	741	30.3	4.1	968
Richmond	27.8	5.1	1247	28.6	4.9	1048	10.1	-	-	28.8	5.7	1190
Vandenberg	0	-	-	25.0	3.6	718	21.5	3.7	763	24.5	3.5	783
Westford	26.6	4.6	1308	26.0	4.6	1368	26.8	4.6	1357	26.4	5.8	1330

ϕ_r carrier phase residual; P_r pseudorange residual.

to analyze these data were described in paper 1. We also list in Table 2 the computed postfit residual RMS for each fiducial station for each day of the experiment. We will use this information to support our arguments that certain combinations of fiducial sites produce less accurate orbits than others and that the amount and quality of data are not a contributing factor in this data set.

We test the effects of fiducial networks in a simple manner. We estimate all parameters identically and change which three fiducial sites we fix. We then examine the differences in the estimated coordinates of the crustal deformation network. We would like to be able to determine the precision and accuracy of the crustal deformation measurements. For precision, we compute the weighted RMS about the weighted mean of the daily estimates. Assessing the accuracy of different fiducial techniques from a single data set is difficult. So-called "single epoch" comparisons with VLBI are inadequate if there are survey errors between the GPS monument and VLBI reference monument (paper 1). VLBI comparisons also limit the scope of the study to a few baselines. Rather than accuracy, we will instead determine the local network stability given a particular fiducial configuration.

The relative effect of two different fiducial networks is quantified by estimating the effective mean local strain on the crustal deformation network resulting from the different fiducial networks used. The geodetic coordinates (longitude λ', latitude ϕ', and elevation h') of the ith crustal deformation site calculated with one fiducial network can be described with respect to the crustal deformation coordinates calculated using a reference fiducial network (λ, ϕ, h) in the following manner

$$\mathbf{u}_i' = \mathbf{u}_i + \mathbf{C}(\mathbf{u}_i - \mathbf{u}_r) \tag{5}$$

where $\mathbf{u}_i'$ and $\mathbf{u}_i$ are the vectors of the geodetic coordinates calculated using the two fiducial networks and $\mathbf{C}$ is the distortion in the station coordinates caused by the difference in fiducial networks. The subscript r refers to the coordinates of a reference station, which is defined here as Vandenberg. Explicitly, equation (5) has the form

$$\begin{vmatrix} \lambda' \\ \phi' \\ h' \end{vmatrix} = \begin{vmatrix} \lambda \\ \phi \\ h \end{vmatrix} + \begin{vmatrix} C_{\lambda\lambda} & C_{\lambda\phi} & 0 \\ C_{\phi\lambda} & C_{\phi\phi} & 0 \\ C_{h\lambda} & C_{h\phi} & 0 \end{vmatrix} \begin{vmatrix} \lambda - \lambda_r \\ \phi - \phi_r \\ h - h_r \end{vmatrix} \tag{6}$$

and follows the formulation of *Drew and Snay* [1989] for the analysis of crustal strain rates from geodetic data. Note that the elevation differences between the two sets of coordinates are strictly a function of the horizontal position of the station. That is, there is no vertical distortion, only horizontal distortions (strains) and network tilting.

$\mathbf{C}$ can then be decomposed into a horizontal displacement matrix, $\mathbf{L}$,

$$\mathbf{L} = \begin{vmatrix} \epsilon_{EE} & \epsilon_{EN} \\ \epsilon_{NE} & \epsilon_{NN} \end{vmatrix} = \begin{vmatrix} C_{\lambda\lambda} & \frac{C_{\lambda\phi} + R_p}{R_m} \\ \frac{C_{\phi\lambda} + R_m}{R_p} & C_{\phi\phi} \end{vmatrix} \tag{7}$$

and a network tilt vector $\mathbf{T}$:

$$\mathbf{T} = \begin{vmatrix} \tau_E \\ \tau_N \end{vmatrix} = \begin{vmatrix} \frac{-C_{h\lambda}}{R_p} \\ \frac{-C_{h\phi}}{R_m} \end{vmatrix} \tag{8}$$

In this representation, $\mathbf{L}$ and $\mathbf{T}$ refer to a planar coordinate system at the reference station, where the constants R_p and

R_m are given by

$$R_p = \frac{a}{W} cos\phi_r \tag{9}$$

$$R_m = \frac{a}{W^3}(1 - e^2) \tag{10}$$

$$W^2 = 1 - e^2 sin^2 \phi_r \tag{11}$$

The constants e and a are the eccentricity and length of the semimajor axis of the WGS84 reference ellipsoid, respectively.

In terms of evaluating the differences between fiducial networks, dilatation, rotation, and maximum tilt are useful parameters to compute from the horizontal and vertical strain components. The areal dilatation Δ is the sum of the strains in the east and north components:

$$\Delta = \epsilon_{EE} + \epsilon_{NN} \tag{12}$$

The clockwise rotation of the network is defined

$$\omega = \frac{\epsilon_{EN} - \epsilon_{NE}}{2} \tag{13}$$

Finally, the maximum tilt τ_{max} is defined

$$\tau_{max} = \sqrt{\tau_E^2 + \tau_N^2} \tag{14}$$

The areal dilatation Δ describes the expansion or contraction of the crustal deformation network, and the maximum tilt τ_{max} describes the vertical differences in the networks. Rotation ω is the rigid body motion of the crustal deformation network. For completeness, we also calculate the engineering strains γ_1 and γ_2:

$$\gamma_1 = \epsilon_{EE} - \epsilon_{NN} \tag{15}$$

$$\gamma_2 = \epsilon_{EN} + \epsilon_{NE} \tag{16}$$

To summarize network precision, we first calculate the precision of each baseline vector in the crustal deformation network, using the weighted RMS about the weighted mean, as defined in paper 1. We then use a simple linear relation to describe the variation of precision σ with baseline length l:

$$\sigma = A + Bl \tag{17}$$

Network precision and the results of our strain analysis are listed in Tables 3 and 4.

RESULTS

We first examine fiducial networks which span the North American continent, and are geometrically strong (i.e., networks that approximate an equal angle triangle). The interstation distances range from 3000 to 4000 km. Examples of geometrically robust fiducial networks can be seen in Figure 1, where Westford and Richmond are combined with a VLBI site in California, either Mojave, OVRO, or Fort Ord. Although this configuration produces orbits which are valid over the entire continent, the crustal deformation network, shown in grey, is only a small portion of the larger network. Vandenberg conceivably could be used with Westford and Richmond as well. Because we are interested in the motion of Vandenberg, we chose to estimate its position. In these three configurations, errors at Westford and Richmond would contribute equally, but errors at the three California sites are different. The Fort Ord GPS occupations have been at the VLBI monument. OVRO and Mojave have been more frequently measured with VLBI than Fort Ord (thus their coordinates are known with higher accuracy), but one must use local surveys to determine the coordinates of the fiducial sites at OVRO and Mojave. The OVRO GPS site is a VLBI reference mark, whereas the GPS site at Mojave is tied through a local ground survey to a VLBI reference mark, adding to the uncertainty in the station coordinates. Even so, the agreement of GPS and VLBI determined in-

TABLE 3. Interstation Vector Precision

Fiducial Network	East		North		Vertical		Length	
	A, mm	B, 10^8	A, mm	B, 10^8	A, mm	B, 10^8	A, mm	B, 10^8
Westford-Platteville-Fort Ord	1.6	1.4	0.9	1.7	12	11.3	1.1	1.1
Westford-Richmond-Fort Ord	2.1	1.3	1.9	0.6	17	0.1	1.5	1.0
Westford-Richmond-OVRO	1.6	1.8	1.7	0.2	17	0.1	1.6	1.0
Algonquin-Richmond-Fort Ord	3.0	0.4	1.8	0.2	17	−1.2	2.2	0.5
Westford-Richmond-Mojave	3.2	0.2	1.2	0.4	13	1.8	2.5	0.5
Mojave-OVRO-Palos Verdes Vandenberg-Fort Ord (20 mm)	3.8	1.4	1.0	0.3	21	2.3	2.8	1.1
Mojave-OVRO-Palos Verdes Vandenberg-Fort Ord (40 mm)	1.6	5.9	0.9	0.7	19	5.2	0.4	5.5

We compute the weighted RMS about the mean for the interstation vectors in the central California crustal deformation network. These short-term precision estimates σ are then summarized by a fit to $\sigma = A + B \cdot length$, as discussed in paper 1. The network consisting of Mojave-OVRO-Palos Verdes-Vandenberg-Fort Ord is shown for two cases, where fiducial sites were estimated with standard deviations of 20 or 40 mm. In both cases, Mojave was fixed.

TABLE 4. Effective Strain Components

	Dilatation Δ, 10^{-8} rad	Rotation ω, 10^{-8} rad	Maximum Tilt, 10^{-8} rad	γ_1, 10^{-8} rad	γ_2, 10^{-8} rad
Continental scale/good geometry 1, Westford-Richmond-Fort Ord 2, Westford-Richmond-OVRO	0.83	-0.15	2.20	0.72	0.15
Continental scale/one common station 1, Algonquin-Richmond-Fort Ord 2, Westford-Richmond-OVRO	0.68	-0.83	3.97	1.89	-1.06
Continental scale/poor geometry 1, Westford-Richmond-Fort Ord 2, Westford-Platteville-Fort Ord	7.87	-1.63	21.35	-2.46	-3.63
Local scale/five VLBI sites 1, Westford-Richmond-Fort Ord 2, Mojave-OVRO-Palos Verdes-Vandenberg-Fort Ord[a]	-8.36	-3.24	5.36	4.99	-1.84
Local scale/three VLBI sites 1, Westford-Richmond-Fort Ord 2, Mojave-Palos Verdes-Vandenberg[a]	-3.51	-5.25	18.10	22.46	-3.37

[a]Mojave fixed, other sites estimated with a standard deviation of 20 mm.

terstation vectors between OVRO, Fort Ord, and Mojave in paper 1 implies that the survey errors are no larger than 20 mm at each site.

The short-term precision for networks consisting of Westford, Richmond, and one of the three California VLBI sites, as listed in Table 3, are similar to each other, several millimeters plus 1 part in 10^8 of the baseline length for horizontal components. The dilatation between Westford-Richmond-OVRO and Westford-Richmond-Fort Ord is 0.8 parts in 10^{-8}, and the rotation is -0.15×10^{-8} rad. The maximum tilt between Westford-Richmond-OVRO and Westford-Richmond-Fort Ord is 2.2×10^{-8} rad. These statistics imply that the effect of substituting one fiducial network for another is at the 1 part in 10^8 level. Although the computed postfit residual RMS for Mojave is significantly higher than either Fort Ord or OVRO (Table 2), which may reflect site conditions at Mojave, it does not appear to affect the estimates of interstation vectors in the crustal deformation network, as indicated by the strain calculation between Westford-Richmond-Fort Ord and Westford-Richmond-Mojave.

Westford was frequently used as a fiducial site for GPS experiments conducted in North America between 1986 and 1988. It has well-determined VLBI coordinates and easily available data, since it is part of the continuously operating tracking network, CIGNET [*Chin*, 1988]. It might be necessary or desirable to occupy an alternative site. Algonquin Park, in Ontario, Canada, is geographically similar to Westford and has been measured with VLBI at two epochs, once in 1984 and again in 1985. A VLBI reference mark at Algonquin was occupied in March 1988, thus allowing us to compare solutions with and without Westford. Algonquin has been used as a fiducial site by others [*Dong and Bock*, 1989]. We have examined the network solutions for Algonquin-Richmond-Fort Ord and find that the short-term precision for horizontal components is comparable to that of Westford-Richmond-OVRO and Westford-Richmond-Fort Ord. The internal agreement between Alqonquin-Richmond-Mojave, Algonquin-Richmond-OVRO, and Algonquin-Richmond-Fort Ord is likewise similar to that when Westford was used instead of Algonquin.

The best test of whether the fiducial coordinates are internally consistent would be to compare fiducial networks which have no stations in common. There is not a sufficient distribution of VLBI stations in this data set, so instead we have compared fiducial networks Westford-Richmond-OVRO and Algonquin-Richmond-Fort Ord. The common stations in the networks have been reduced to one: Richmond. Both scale and rotation will then be independent, except of course for the common source of coordinates: VLBI. Figure 2 shows the length and north-south, east-west, and vertical component solutions, as a function of baseline length, for interstation vectors in the crustal deformation network. The Westford-Richmond-OVRO mean solution is plotted relative to the Algonquin-Richmond-Fort Ord mean solution. The agreement is within 2 mm for both horizontal components. The maximum vertical difference is 10 mm. The areal dilatation of the two networks is 0.7×10^{-8}, and the rotation is -0.8×10^{-8} rad. The maximum tilt is comparable to those when both Westford and Richmond were fiducial sites, and different sites in California were used, 3.9×10^{-8} rad. In addition to the evidence that different fiducial sites can be used without serious deterioration of precision, this result also confirms that the VLBI derived site velocity model, GLB223, is internally consistent and that local survey errors between VLBI and GPS monuments do not significantly degrade fiducial stability.

Having established that fixing three collocated VLBI sites is adequate for precise orbit determination and creates a stable reference frame, another aspect of "fiducial data quality" that needs to be considered is the geometry of the fiducial stations. Optimal fiducial networks were not always available during actual GPS field experiments conducted in California between 1986 and 1989 (see paper 1 for further details). Rather than discard measurements made with a poor fiducial network, it is important to at least have a qualitative estimate of the bias induced by using a suboptimal geometric network. Figure 1 includes three VLBI sites which suffer from "poor" network geometry: Westford, Platteville, and Fort Ord. By poor geometry, we mean stations that are nearly colinear. *Dong and Bock* [1989] used a similar fidu-

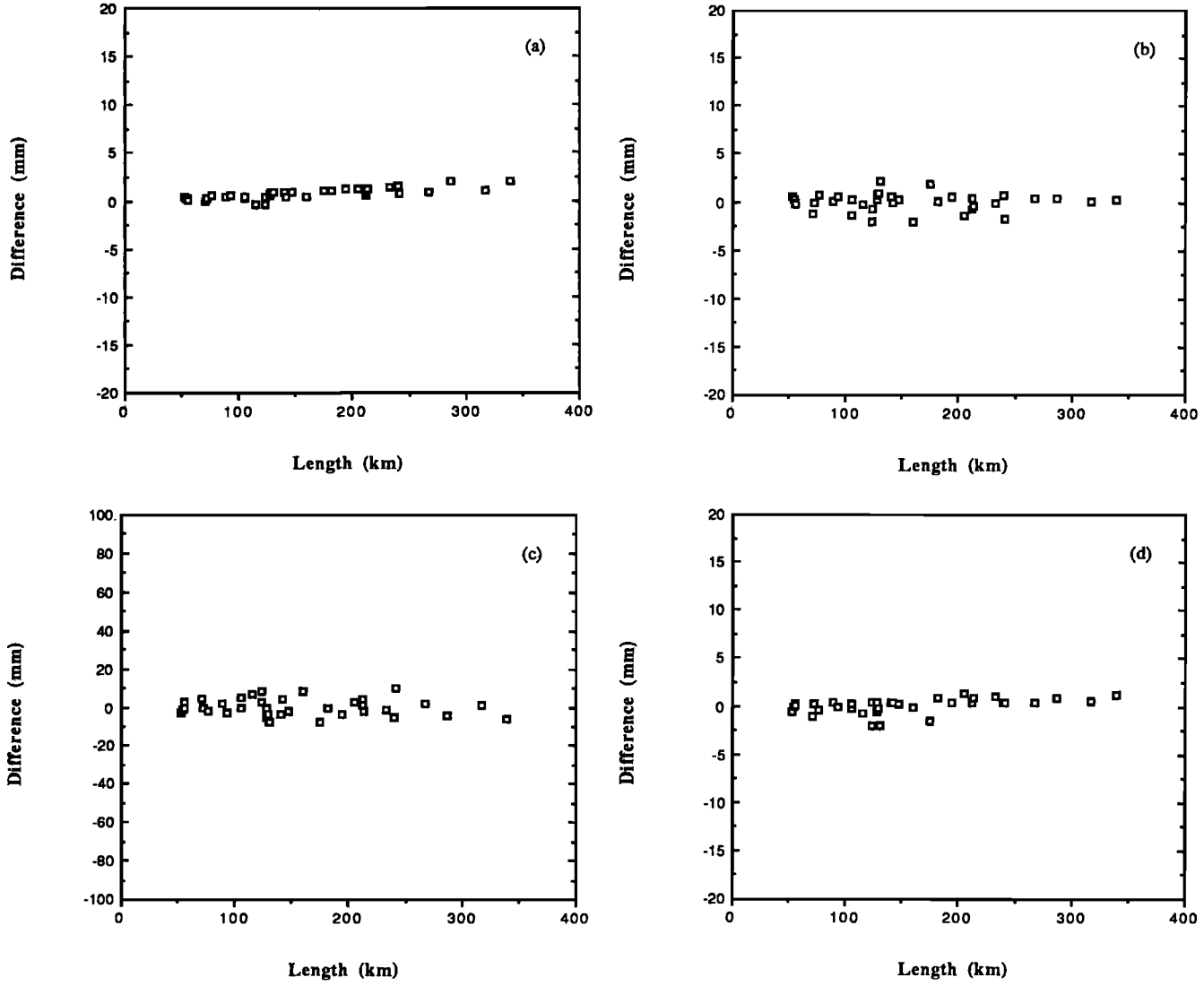

Fig. 2. Difference between interstation vectors in central California using two different fiducial networks: Westford-Richmond-OVRO and Algonquin-Richmond-Fort Ord. Zero is defined by the Westford- Richmond-OVRO mean solution, and the Algonquin-Richmond-Fort Ord is plotted relative to that. (*a*) north component. (*b*) east component. (*c*) vertical component. (*d*) length. Agreement between horizontal components is better than 2 mm. Vertical scatter is 110 mm. Dilation, as shown in Figure 2*d*, is small.

cial network for their analysis of data collected in southern and central California during January 1987: OVRO, Algonquin, and Platteville. They achieved very high precision. By fitting a line to their short-term precision estimate for interstation vectors, they report precision of 6 mm + 0.5 parts in 10^8 and 2.5 mm + 0.9 parts in 10^8 for the east-west and north-south components, respectively.

The short-term precision for this fiducial network is listed in Table 3 and shown in Figure 3, with the analogous precision for a geometrically strong network (Westford-Richmond-Fort Ord). By also showing Westford-Richmond-Fort Ord we see that the north-south precision for the Westford-Platteville-Fort Ord network is now length dependent, which contradicts the results for the "geometrically strong" fiducial networks. It is well known that block I GPS satellite tracks were preferentially aligned north-south over California (see Figure 2 in paper 1). For short-term precision, this resulted in better precision in the north-south component than the east-west component [*Blewitt*, 1989; paper 1]. Since the only factor we have changed for these data is the fiducial network we used (we cannot change the satellite geometry), it would appear that the geometry of the Westford-Platteville-Fort Ord fiducial network has influenced precision. Another indication that this is a suboptimal network is the vertical precision, which is substantially worse than that for Westford-Richmond-Fort Ord, and baseline dependent, as shown in Figure 3*c*. The vertical scatter reproduces another result of Dong and Bock: that vertical precision is dependent on baseline length using a fiducial network with poor geometry.

Although precision seems to be impacted by the geometry of the fiducial stations, the precision is still subcentimeter in the horizontal components of baselines less than 350 km in length. The more important question is whether the crustal deformation network has been rotated, sheared, dilated, or tilted relative to the solutions for a geometrically robust network. Figure 4 shows the Westford-Platteville-Fort Ord

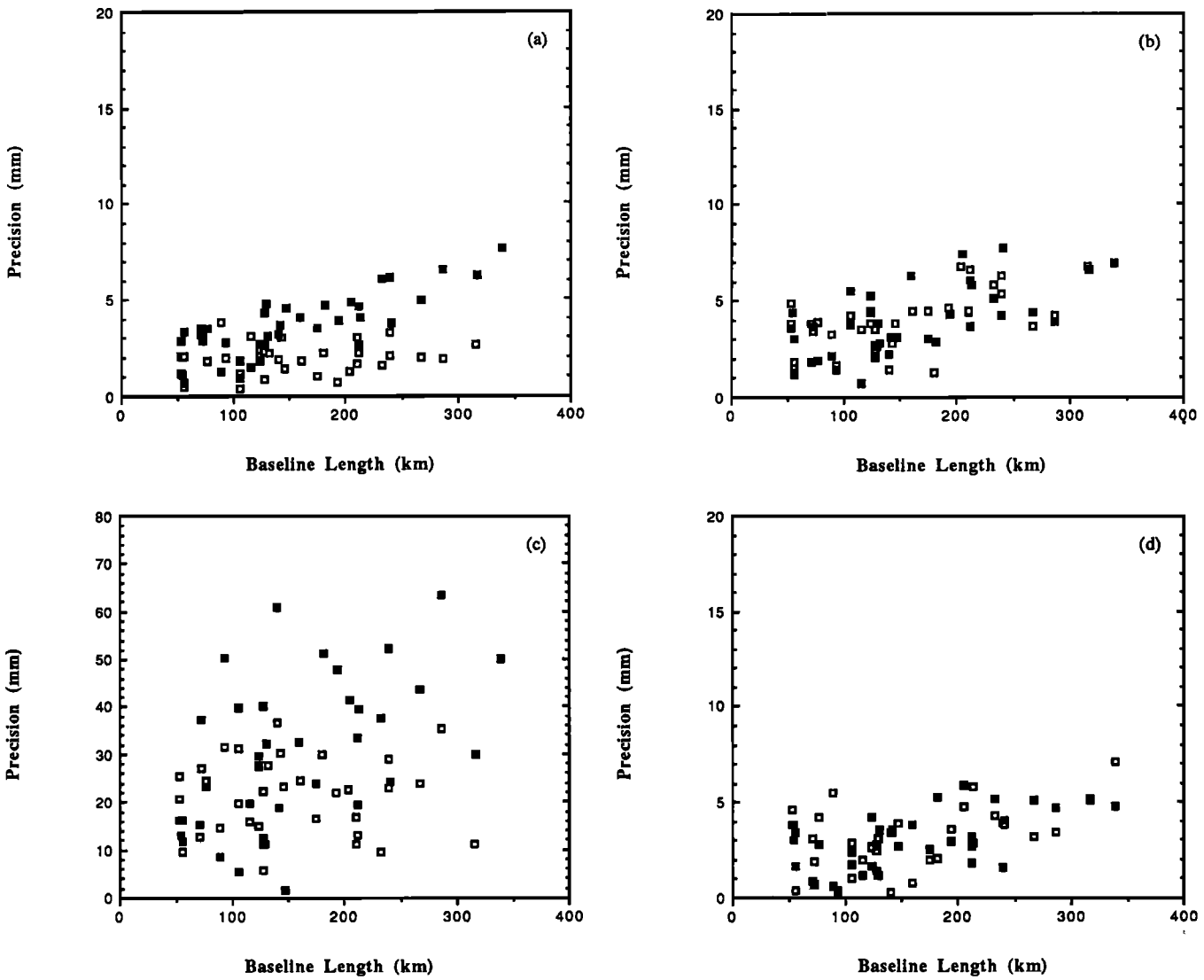

Fig. 3. Short-term precision, determined by the weighted RMS about the mean, for interstation vectors in the central California network for two fiducial networks: Westford-Richmond-Fort Ord, indicated by open squares and Westford-Platteville-Fort Ord, indicated by solid squares. The components are defined as in Figure 2. Note degraded precision of vertical for Westford-Platteville-Fort Ord fiducial network.

mean solution plotted relative to the Westford-Richmond-Fort Ord mean solution. The differences are an order of magnitude more than they were for the fiducial networks with "good" geometry. The pronounced difference in the length component is indicative of dilatation, which is also shown in the strain calculation. The dilatation for Westford-Platteville-Fort Ord network relative to the Westford-Richmond-Fort Ord network is 7.9×10^{-8}. The rotation is -1.6×10^{-8} rad. This rotation would produce an error of only 1.6 mm on a 100-km baseline but combined with the dilatation result, yields a 9.5-mm error on the same baseline vector. The maximum tilt is 2.1×10^{-7} rad, which is also an order of magnitude larger than maximum tilts for fiducial networks with good geometry. *Lichten et al.* [1989] found similar deterioration of accuracy for a baseline estimated with a geometrically deficient fiducial network of Hatcreek, Fort Davis, and Richmond. It might be argued that the data collected at Platteville were of poor quality. The post-fit residual RMS values for Platteville are equal to or better than several other fiducial sites. Also, more data were collected at Platteville than any other fiducial site. It might also be argued that the VLBI coordinates of Platteville are poorly known. This is not indicated by the formal errors in Table 1. These statistics indicate that geometry is the controlling factor, not quality or quantity of data collected at Platteville.

A large subset of the GPS data collected in southern and central California in paper 1 suffered from a more severe problem than poor fiducial geometry: simultaneous failure of a large percentage of tracking sites in North America. These data were analyzed with a fiducial network defined by VLBI sites in California. Therefore it is necessary to address the validity of fiducial networks which are defined on the same spatial scale as the crustal deformation network. Although one generally thinks of fiducial networks as merely a means to achieve some measure of orbit improvement, it is important to recall that these fiducial networks are also necessary for comparing repeated relative measure-

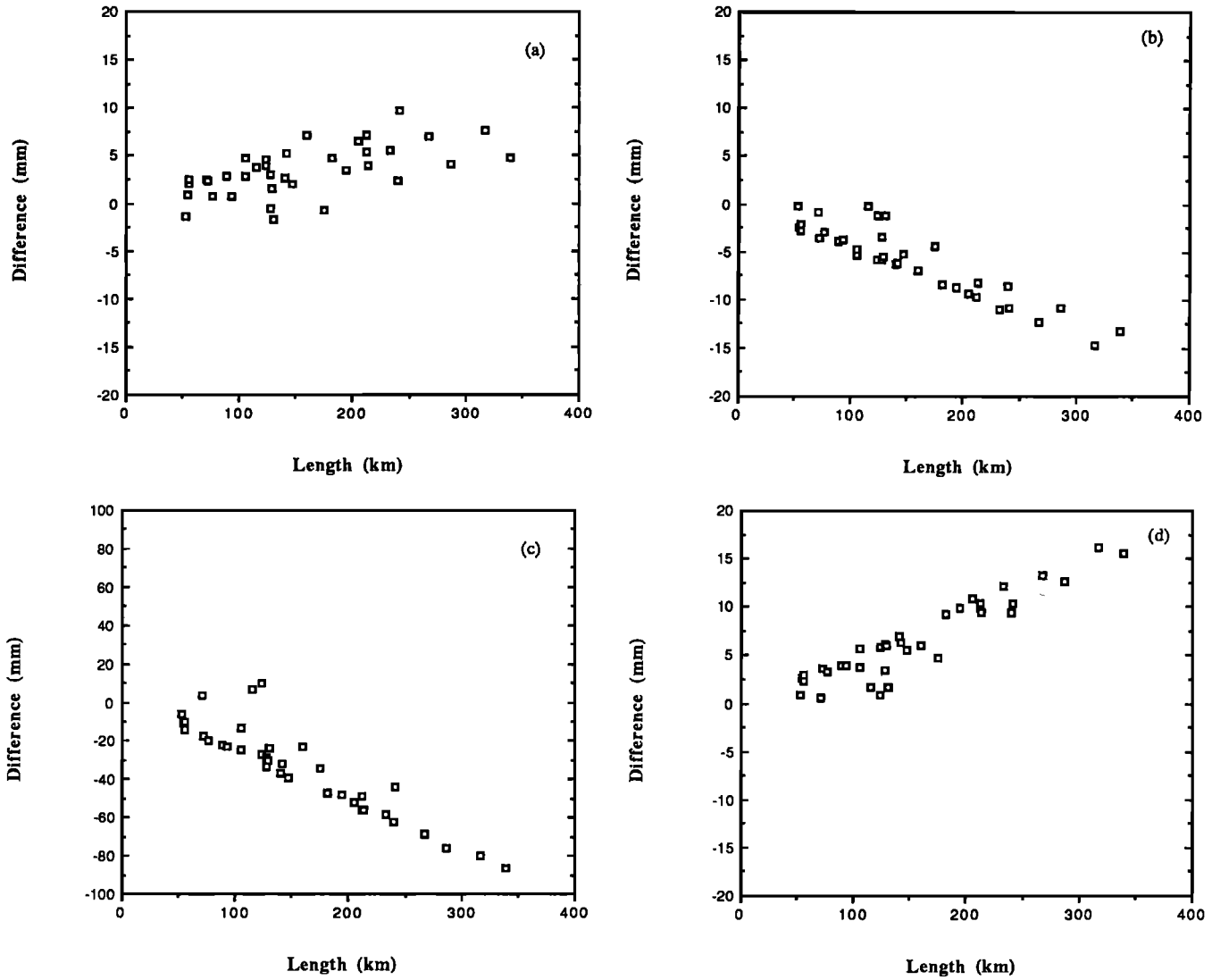

Fig. 4. Difference between interstation vectors in central California using two different fiducial networks: Westford-Platteville-Fort Ord and Westford-Richmond-Fort Ord. Zero is defined as the Westford- Richmond-Fort Ord mean solution, and the Westford-Platteville-Fort Ord mean solution is plotted relative to that. The components are defined as in Figure 2. Compared to Figure 2, where geometrically robust networks were compared, the horizontal component differences are nearly an order of magnitude greater. The vertical component differences are nearly 100 mm at 350 km. Note also the clear scale change for length (Figure 4*d*), which is indicative of areal dilatation.

ments. At best, the maximum length of fiducial baselines between California VLBI sites is 500 km. In addition to the rotation which might be caused by fixing sites on these spatial scales, inaccurate orbit solutions can adversely influence one's ability to resolve ambiguities (M. Murray, personal communication, 1989). So-called "local fiducial networks" are implicitly contained in the VLBI reference frame, as the self- consistent VLBI solution ties these sites in California to the continental solutions for Westford and Richmond. Yet, recalling the short discussion on the introduction of error or uncertainty in the position of a fiducial site, a several centimeter fiducial error on 500-km length scales would have an order of magnitude larger effect on interstation vector estimates than would a comparable error on a fiducial network defined over continental scales. If the locations of "local" fiducial sites should not be fixed, how tightly should local networks be constrained to their a priori locations? Do local networks achieve the same mm level precision and stability as Algonquin-Richmond-Fort Ord and Westford-Richmond-OVRO?

There were five VLBI sites occupied in California during the March 1988 experiment: Mojave, Fort Ord, OVRO, Vandenberg, and Palos Verdes. We tried three kinds of estimation strategies for this network. In each we fixed the position of Mojave. Then, we (1) estimated the positions of the other four sites with a 40-mm standard deviation in each coordinate, (2) estimated the positions of the other four sites with a 20-mm standard deviation in each coordinate, and (3) fixed all five fiducial sites. When the fiducial sites were estimated with a standard deviation of 40 mm, strategy 1, the baseline dependence of the scatter for the east-west component was 1.6 mm + 5.9 parts in 10^8, and 3.8 mm + 1.4 parts in 10^8 for a 20 mm standard deviation. Plots of precision for strategies 1 and 2 are shown in Figure 5. In the north-south component, 20 and 40 mm yield similar results, with a baseline dependence of less than 1 part in 10^8.

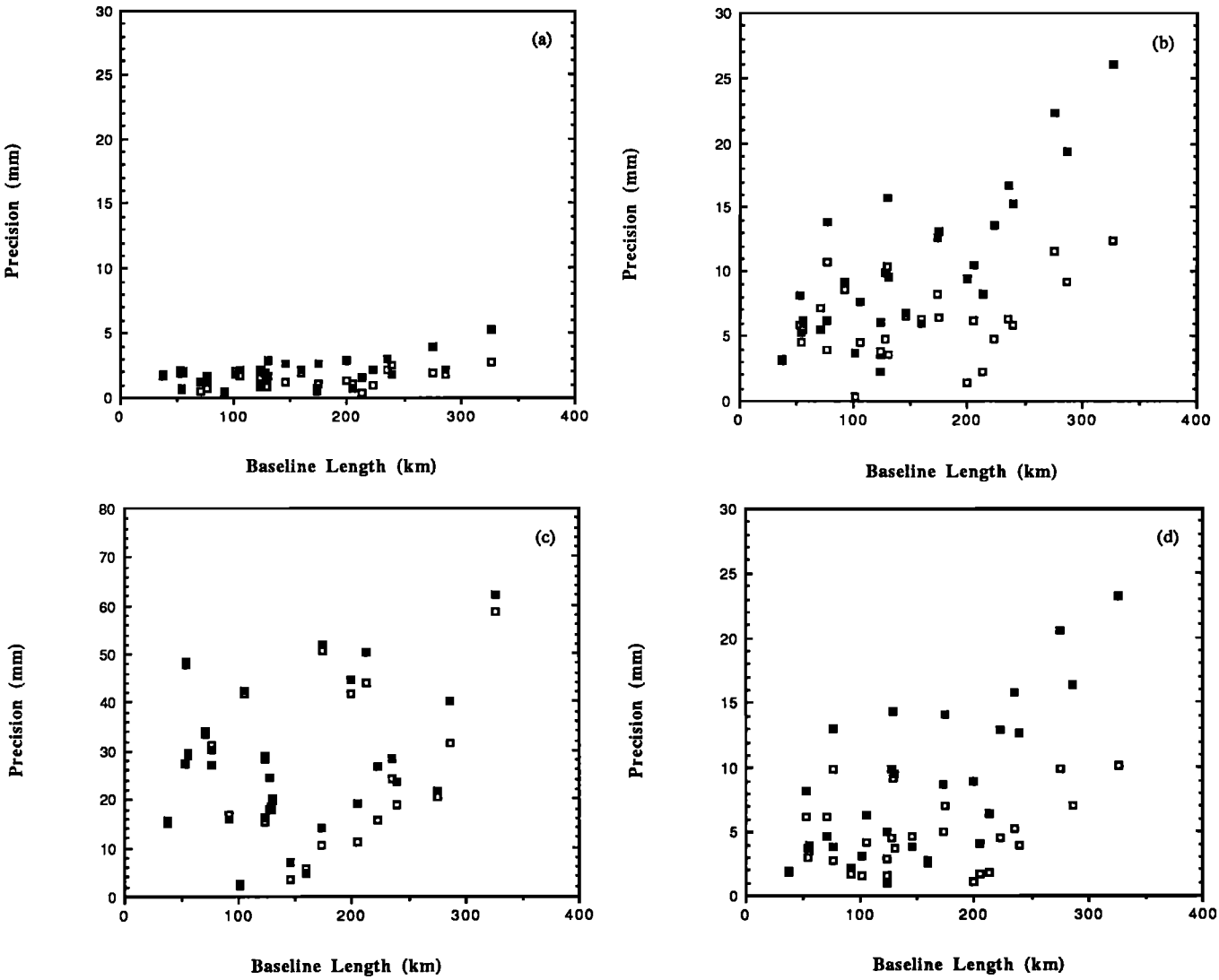

Fig. 5. Short-term precision, determined by the weighted RMS about the mean, for interstation vectors in the central California network for a fiducial network comprised of Mojave-OVRO-Palos Verdes- Vandenberg-Fort Ord. The open squares represent the case where fiducial sites were estimated with a standard deviation of 20 mm; the solid squares were estimated with a standard deviation of 40 mm. The components are defined as in Figure 2.

Given the satellite geometry over California, this result is not surprising. Vertical precision is markedly improved with a 20 mm standard deviation, as shown in Table 3. When we fixed all California VLBI sites, we found that the solution for the crustal deformation network differed only slightly from that computed with fiducial stations constrained to 20-mm, although the "all-fixed" solution was slightly less precise. Since a 20 mm standard deviation allowed us to compute meaningful formal errors for the interstation vectors in the crustal deformation network, we preferred this solution to the "all-fixed" solution, which we discuss later in this paper. As shown in Table 4, the strain analysis indicates that the Mojave-OVRO-Palos Verdes-Vandenberg-Fort Ord fiducial network dilates, shears, and rotates the crustal deformation network. Figure 6 shows the Mojave-OVRO-Palos Verdes-Vandenberg-Fort Ord mean solution plotted relative to the Westford-Richmond-Fort Ord mean solution. The dilatation for this network is -8.3×10^{-8}, the largest of all fiducial networks we studied. The rotation is -3.2×10^{-8} rad. Although Table 3 indicates that the north-south component is precise, Figure 6 indicates that the component has contracted, relative to the VLBI reference frame. The maximum tilt is significantly smaller than when we used the Westford-Platteville-Fort Ord fiducial network, only 5.3×10^{-8} rad. Presumably, constraining so many sites in California provides sufficient geometric strength to determine the vertical component.

We have also tested the effect of constraining only three VLBI sites in California: Mojave, Vandenberg, and Palos Verdes (this type of fiducial network was used in experiments J87 and M89a in paper 1). This network does not behave significantly differently than the five-station California fiducial network, although the rotation is slightly larger, which is consistent with a having fewer fiducial stations for geometric constraint, and a larger apparent shear. The dilatation of Mojave-Palos Verdes-Vandenberg is smaller than Mojave-OVRO-Palos Verdes-Vandenberg-Fort Ord, -3.5×10^{-8}, and the rotation is -5.3×10^{-8} rad. The maximum

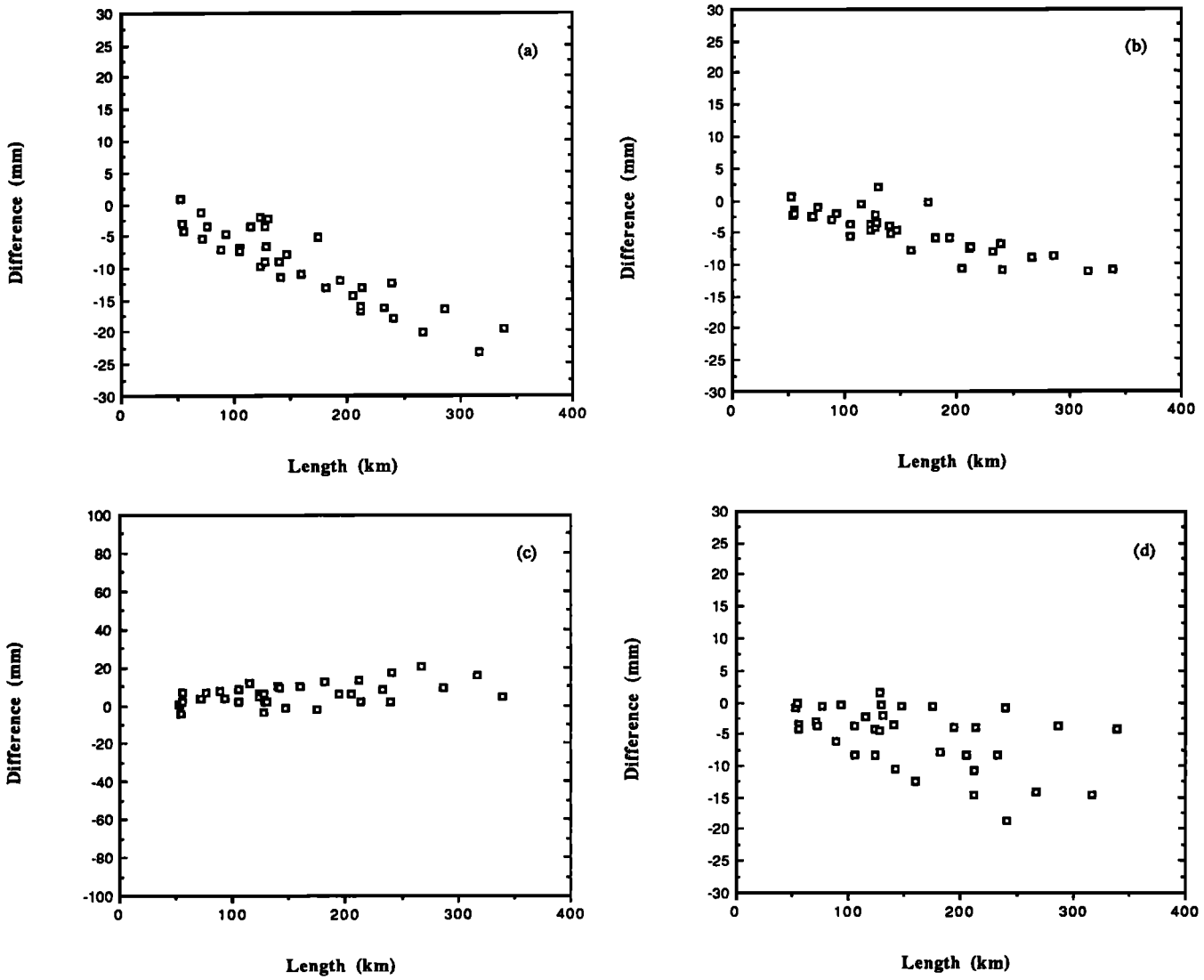

Fig. 6. Difference between interstation vectors in central California using two different fiducial networks: Mojave-OVRO-Palos Verdes- Vandenberg-Fort Ord and Westford-Richmond-Fort Ord. Zero is defined as the Westford-Richmond-Fort Ord mean solution, and the Mojave-OVRO-Palos Verdes-Vandenberg-Fort Ord mean solution is plotted relative to that. The components are defined as in Figure 2.

tilt, 1.8×10^{-7} rad, is twice as large as Mojave-OVRO-Palos Verdes-Vandenberg-Fort Ord, as might be expected given that there would be less of a vertical constraint from three fiducial sites than five.

DISCUSSION

We have shown that interstation vector estimates change considerably, depending on the fiducial network one uses. We think that these changes are consistent with the geometry and spatial scale of the fiducial stations. If "deficient" fiducial networks must be used, we need some way to represent this systematic error in our formal errors. One way to compensate for changes in fiducial network is by determining the sensitivity of interstation vectors in the crustal deformation network to uncertainties in fiducial coordinates. Such a sensitivity analysis, sometimes called a "consider" analysis, is dependent on the assumed uncertainties for the fiducial coordinates. Alternatively, one can estimate fiducial positions, with the appropriate weighted standard deviation. We briefly discuss these options, focusing on the results for the Westford-Platteville-Fort Ord and Mojave-OVRO-Palos Verdes-Vandenberg-Fort Ord fiducial networks, discuss concerns for the choice of fiducial sites, and present an example of the effect of fiducial bias on the determination of crustal deformation rates.

Sensitivity Analysis

Could we have predicted the effect that changing fiducial networks had on our crustal deformation network? The magnitude of any systematic error can be estimated by performing sensitivity analyses. By assigning plausible uncertainties to unadjusted parameters, one determines the sensitivity of estimated parameters, explicitly accounting for correlations through a full covariance analysis. Thus sensitivities are calculated from the measurement partials and geometry. This technique is used and described by *Lichten and Border* [1987]. We have computed the consider uncertainty for two fiducial networks, Westford-Richmond-Fort

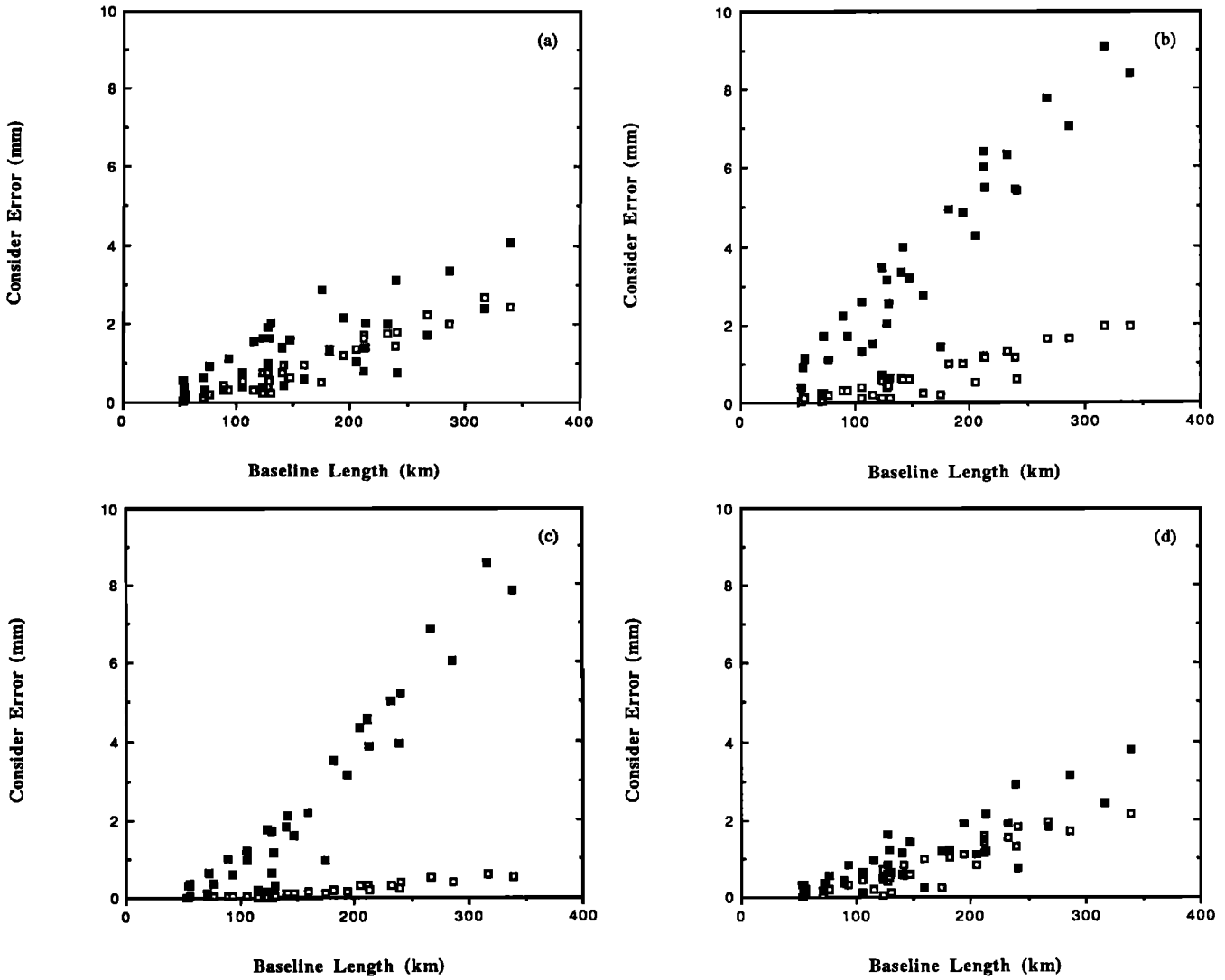

Fig. 7. Computed consider errors for the crustal deformation network, using fiducial networks: Westford-Platteville-Fort Ord (solid squares) and Westford-Richmond-Fort Ord (open squares). The components are defined as in Figure 2. Computation of consider errors described more fully in the text.

Ord and Westford-Platteville-Fort Ord. Each fiducial site was assigned an uncertainty of 20 mm in all three components. Although Lichten and Border [1987] have suggested more conservative errors for fiducial sites (up to 40 mm), we feel that the results of Lichten and Border and other accuracy analyses [*Blewitt*, 1989; paper 1], are more consistent with 20-mm fiducial uncertainty. There are certainly other systematic errors which have not been accounted for in the GPS error budget, but since we are only trying to determine the error contribution from fiducial coordinates, we prefer the smaller value. No correlations between the fiducial sites were used. The total error σ_{total} is then

$$\sigma^2_{total} = \sigma^2_{consider} + \sigma^2_{formal} \quad (18)$$

Our formal errors are described in paper 1. We first examine the fiducial (consider) contribution to the interstation vector estimate error, shown in Figure 7. We have plotted consider errors for both Westford-Richmond-Fort Ord and Westford-Platteville-Fort Ord, so that we can compare and contrast their effect on the crustal deformation network. For a geometrically "strong" network such as Westford-Richmond-Fort Ord, the horizontal consider error is small, less than 2 mm at 350 km, with little distinction between north- south and east-west components. The maximum vertical consider error using Westford-Richmond-Fort Ord is 1 mm. In contrast, the consider error for Westford-Platteville-Fort Ord is highly sensitive in the east-west and vertical components, with a baseline dependence of 3 parts in 10^8. The consider length error is not as pronounced as we saw with the actual data. The consider covariance analysis is consistent with a rotation between the east-west and vertical components but does not predict dilatation.

Are the consider errors sufficient to explain the differences we observed between Westford-Platteville-Fort Ord and strong geometry networks? In Figure 8, we plot the total error, as defined in equation (18), for the Westford-Platteville-Fort Ord solution, along with the offset of these estimates from the solutions computed with Westford-Richmond-Fort Ord (these offsets are also shown in Figure 4). In both north-south and east-west components, the modi-

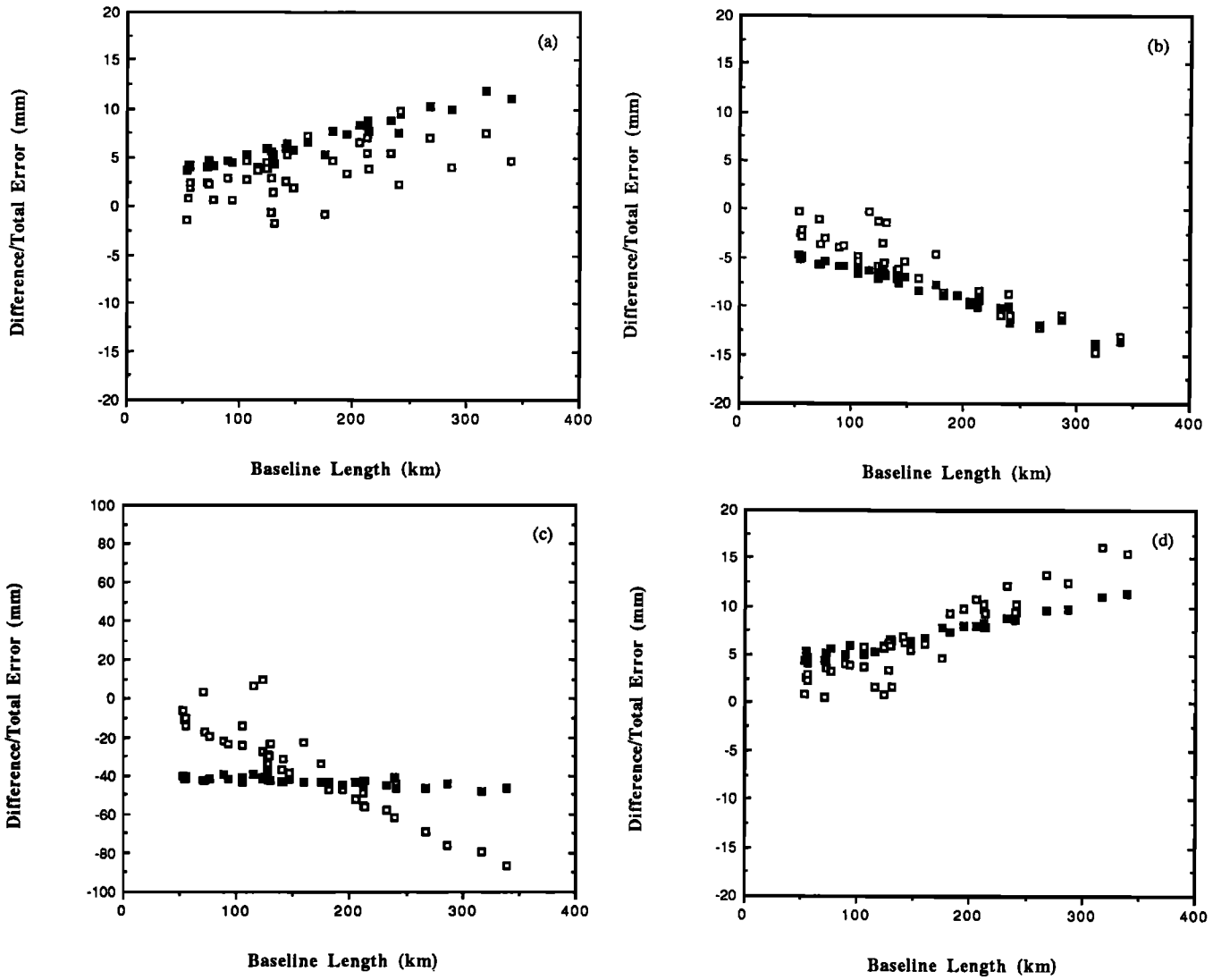

Fig. 8. Computed total errors for the crustal deformation network (solid squares) using fiducial network Westford-Platteville-Fort Ord. Also shown, offset of crustal deformation network interstation vectors from those computed using fiducial network Westford-Richmond-Fort Ord (open squares). These offsets were also shown in Figure 4. Whereas the offsets in the north-south and east-west components can be described by the formal errors, modified by fiducial consider errors, the vertical component and length are more highly degraded than expected. The components are defined as in Figure 2.

fied total errors are just large enough to describe the offset. In the vertical component, the total error does not have the pronounced baseline dependence we saw in the actual data. The length plot follows directly from the component results.

Estimation of Fiducial Coordinates

It is possible to estimate the positions of fiducial sites from GPS data. The standard deviations for the position uncertainties will then be reflected in the formal uncertainties of the interstation vectors. Unfortunately, by estimating fiducial locations, the reference frame will change, although only slightly, depending on the accuracy of the fiducial coordinates. Since we need to maintain a stable reference frame for comparing repeated measurements, we discourage estimating fiducial coordinates. In the one case we have estimated fiducial coordinates, the fiducial network Mojave-OVRO-Palos Verdes-Vandenberg-Fort Ord, the formal errors for the crustal deformation network interstation vectors were larger than for those estimated with Westford-Richmond-Fort Ord. Figure 9 displays the formal errors we have calculated for the interstation vectors in our crustal deformation network, using the fiducial networks Mojave- OVRO-Palos Verdes-Vandenberg-Fort Ord and Westford-Richmond- Fort Ord. While the vertical component formal error (Figure 9*c*) shows little dependence on which fiducial network we used, both horizontal components show a strong deterioration with baseline length when a "local" fiducial network was used, described by several mm + 4 parts in 10^8. The Westford-Richmond-Fort Ord network has formal errors in keeping with the short-term precision we calculated in paper 1, several millimeters + 0.5-1 parts in 10^8. The differences between interstation vectors computed from these two fiducial networks were shown in Figure 6. When we estimate the position of fiducial stations in a local network, the formal errors are large enough to explain the observed offsets from a stable fiducial network, such as Westford- Richmond-Fort Ord.

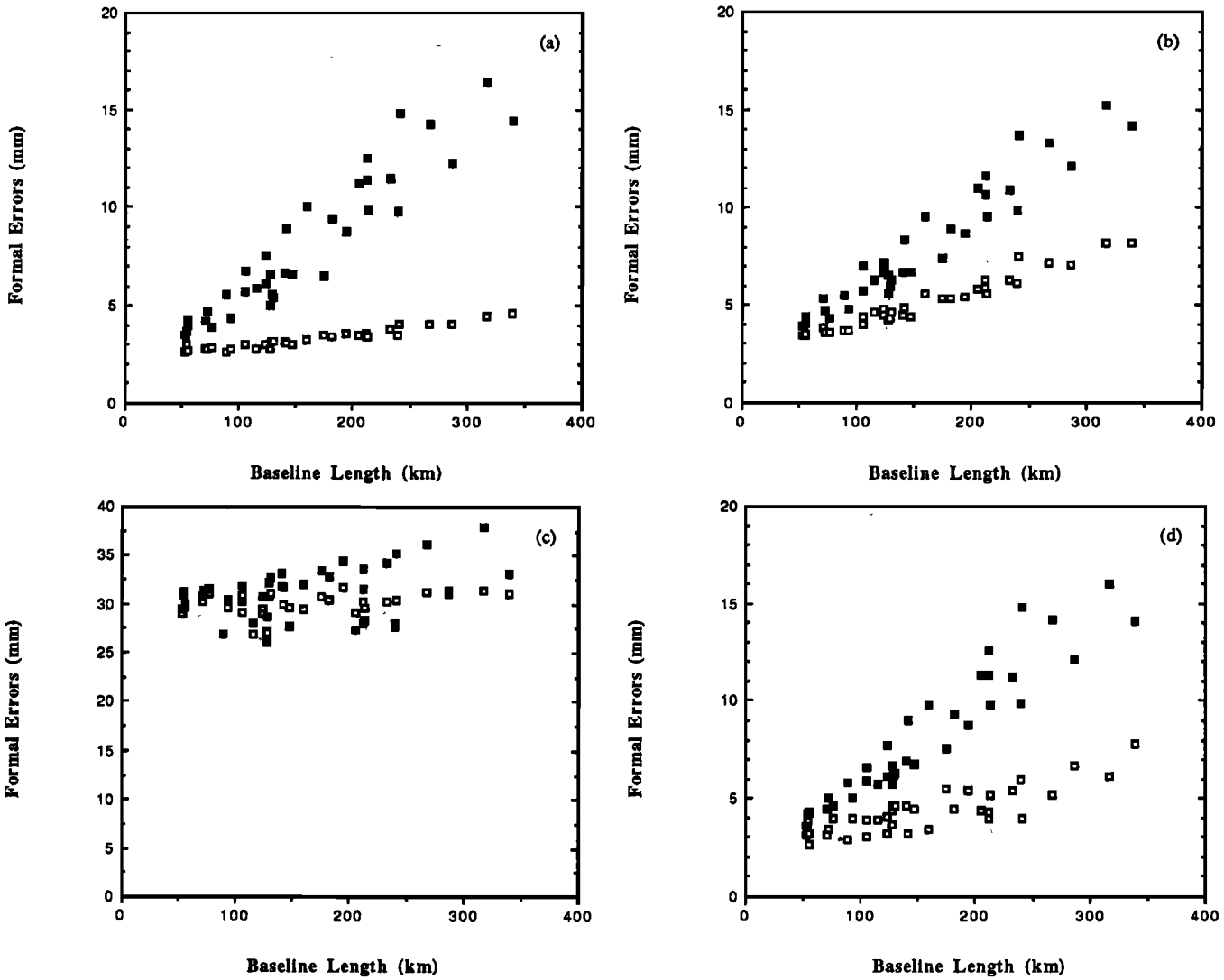

Fig. 9. Formal errors for interstation vectors in the crustal deformation network, using fiducial networks: Mojave-OVRO-Palos Verdes-Vandenberg-Fort Ord (solid squares) and Westford-Richmond-Fort Ord (open squares). Note the deterioration with baseline length for the north-south and east-west components using the Mojave-OVRO-Palos Verdes-Vandenberg-Fort Ord fiducial network. Vertical components (Figure 9c) are only slightly affected by these fiducial networks. The components are defined as in Figure 2.

Effect of Fiducial Biases on Crustal Deformation Rates

We are interested in applying GPS to crustal deformation measurements, and therefore, our underlying concern is that fiducial biases, such as we have described, will contaminate our determination of vector rates. The safest way to avoid bias of rate determinations is to use the same kind of fiducial network at each epoch of the measurement history, where the geometry of fiducial stations has been taken into account. If that kind of fiducial network is unavailable, it is possible that a fiducial bias, if common to all epochs, will not effect rates. An error in the geocenter correction is an example of such a fiducial bias, affecting interstation vectors equally at each epoch, and thus would be unimportant for rate determinations.

The effect of fiducial biases can be seen in some of the interstation vectors we estimated in paper 1. Because we have data spanning several years, we can also calculate the effect of a suspected fiducial bias on our crustal deformation rates. Figure 10 displays the north-south component of the interstation vector between OVRO and Blackhill, a baseline 308 km long. The first 13 measurements were made over four epochs, spaced approximately 5 months apart. The final three measurements were made 1 year later. The first four epochs were analyzed with continental-scale fiducial networks, with fairly good geometry (see Table 2 of paper 1 for details of these experiments). The final experiment (M89b) used a fiducial network of five VLBI sites in California. Recall that in our analysis of this type of fiducial network, there was an apparent strain and rotation of nearly 1 part in 10^7. The north-south component was particularly affected. The error bars for the M89b estimates are from 2 to 4 times larger than those computed with a continental scale fiducial network, because we have estimated the fiducial sites with a standard deviation of 20 mm (as described in the previous section). The three lines shown in Figure 10 are where we used data from all 5 epochs, weighted by the formal errors shown (solid line), only used the data from the first four epochs, weighted by the formal errors shown (dotted line), and used data from all five epochs, but the

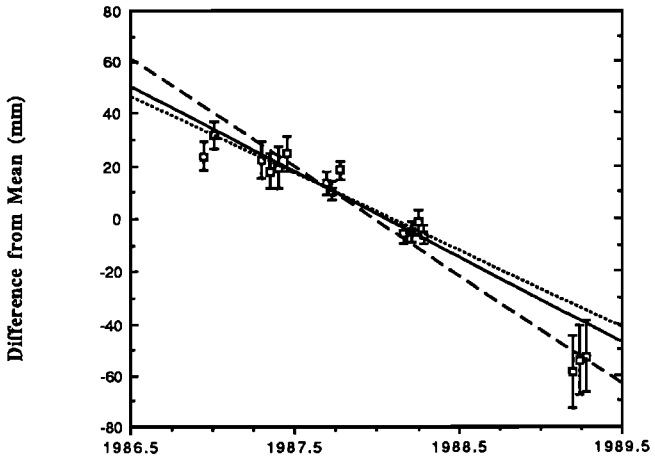

Fig. 10. Change of relative coordinates for the north-south component of the Blackhill to OVRO vector (308 km), with zero being the mean value. Also shown are three linear fits to the data. The solid line uses all data, weighted by the formal errors. The dotted line fit excludes the data from the last experiment (March 1989), and the dashed line uses all data, but the formal errors in the March 1989 estimates were not modified to take fiducial uncertainty into account. The estimates of slope vary from -33±3, -30±3, and -42±2 mm/yr using these three sets of data. More discussion in the text.

formal errors for the fifth experiment were not adjusted to take into account the poor geometry of the California-only fiducial network. Therefore the errors bars are based on data noise only; that is, the fiducial coordinates were held fixed in the estimation of interstation vectors, and no consider analysis was performed (dashed line). Linear fits to these three data sets result in slopes of -33±3, -30±3, and -42±2 mm/yr, with χ^2 of 1.1, 0.9, and 2.3, respectively (χ^2 defined in paper 1). Although the slopes for the first two data sets are slightly different, the agreement is far better than when one makes no consideration of fiducial bias, as in the last case. The difference between the linear fit excluding epoch 5 (dotted line) and the data from epoch 5 is 25 mm, which agrees with the expected difference for a 300-km baseline shown in Figure 6*a*. Thus fiducial biases can significantly affect GPS rate determinations.

How to Choose a Fiducial Network

Most GPS experiments are driven by cost considerations. Therefore it is most cost effective to use existing permanent, continuous networks, such as CIGNET. Although we have found that three fiducial sites are adequate for precise measurements, our work has been focused on California, where the block I GPS constellation was favorably oriented during our experiments. Others have suggested that four fiducial sites may be appropriate in North America [*King and Blewitt,* 1990]. For experiments which span continental distances, a tracking network which spans 10,000 km may be appropriate. Large tracking networks may also be necessary when the GPS constellation geometry is poor. During the CASA UNO experiment in South America, the block I constellation was visible for many hours, but the satellites were at low elevation angles, thus degrading accuracy and precision [*Freymueller and Gólombek,* 1986]. When *Kornreich-Wolf et al.* [1990] examined data from that experiment, they found that extending the tracking network to Europe and Australasia improved orbit estimation and thus baseline estimates in South America. Therefore the number and location of fiducial sites depend on the geometry of the crustal deformation experiment and the GPS constellation. Although the profusion of autonomous receivers makes it likely that global fiducial networks will be available to all GPS users, it is important to note that mixing of different types of GPS receivers has yet to be shown to be valid for centimeter level accuracies required for crustal deformation experiments.

We have used VLBI derived fiducial positions because they are accurate, easily available (i.e. CIGNET stations are located near VLBI sites) and self-consistent [*Clark et al.,* 1987]. This does not mean that VLBI (or SLR) measurements are the only source of fiducial stations. Accuracies of several centimeters have been reported from GPS over long continental-scale baselines [*Lichten and Border,* 1987], and since these GPS coordinates were derived in a VLBI reference frame, it should be possible to use GPS derived "fiducial" coordinates.

One indication we have that GPS can be used for fiducial coordinates comes from the experiment (M88b) used in this paper. Basically, if the estimated GPS coordinates agree with the a priori VLBI coordinates, within some acceptable limit, then we have sufficient accuracy that we can use the coordinates of the other GPS stations, which were not collocated with VLBI sites, as fiducial stations. Table 5 lists the offsets of three GPS stations, OVRO, Algonquin, and Mojave, from their expected VLBI coordinates. We used a fiducial network of Westford-Richmond-Fort Ord to compute these estimates and to report the weighted mean solution for 3 days of data. The uncertainties are one standard deviation. We did not compute consider uncertainties for these experiments. The GPS-VLBI offsets for Algonquin, Mojave, and OVRO range from 6 to 40 mm in magnitude in the three Cartesian components. Let us assume that the VLBI coordinates are perfect and that these offsets represent GPS error. Our consider covariance analysis can then be used to determine the effect of these GPS "errors" on the interstation vectors in the crustal deformation networks. We recomputed solutions for the crustal deformation network, using three separate fiducial networks: Algonquin-Richmond-Fort Ord, Westford-Richmond-Mojave, and Westford-OVRO-Richmond. The fiducial coordinates for all sites were derived using the VLBI model as before, but the consider uncertainties for Algonquin, Mojave, and OVRO were adopted from the uncertainties from Table 5. For consistency, we used a 20-mm consider error for the other two fiducial sites in each fiducial network. Table 6 lists the consider uncertainties we used, and the computed consider uncertainty in the crustal

TABLE 5. Offset of GPS Estimates From VLBI Coordinates

	X, mm	*Y*, mm	*Z*, mm
Algonquin	32±10	-6±22	-7±18
Mojave	-14±12	-17±21	-10±16
OVRO	36±20	40±23	-30±18

Solution computed with Fort Ord, Westford, and Richmond fixed. Uncertainties are unscaled standard deviations.

TABLE 6. Consider Analysis

Fiducial Network	Assumed Fiducial Uncertainty, mm			Computed Consider Uncertainty, 10^{-8}			
	X	Y	Z	East	North	Vertical	Length
Algonquin	32	6	7	0.7	0.9	0.8	0.8
Richmond	20	20	20				
Fort Ord	20	20	20				
Mojave	14	17	10	0.6	1.2	1.2	1.0
Westford	20	20	20				
Richmond	20	20	20				
OVRO	36	40	30	0.7	1.2	1.6	1.0
Westford	20	20	20				
Richmond	20	20	20				

Fiducial uncertainty of Algonquin, Mojave, and OVRO taken from Table 5. All other fiducial uncertainties set to 20 mm in each coordinate.

deformation network, as a function of baseline length. Even for OVRO, where offsets from VLBI are as large as 40 mm, the effect on the crustal deformation network is small, 1.2 parts in 10^8 in the north-south component, slightly larger in the vertical component, 1.6 parts in 10^8. These fiducial consider uncertainties are the same magnitude as we estimated from our strain calculations for different fiducial networks. Thus GPS-derived fiducial coordinates provide a comparable level of stability as VLBI. Single epoch estimates of GPS fiducial coordinates will not be as accurate as VLBI estimates which have been measured over many years, but they are an acceptable alternative.

We have also tested the use of GPS-determined fiducial coordinates. We estimated the fiducial coordinates of Churchill, Manitoba, using data from M88b. We cannot use our standard strain analysis technique to check a fiducial network consisting of, for example, Westford-Churchill-Fort Ord, since the coordinates of Churchill are consistent (in a least squares sense) with the fiducial coordinates and the data which were used to compute it. In order to validate the use of GPS-derived Churchill coordinates, we need to use the Churchill fiducial coordinates in an independent GPS survey. Paper 1 and *Larson* [1990*b*] used Churchill as a fiducial site during experiments D86, S87, M88a, adopting the coordinates determined from M88b. We observed no difference, larger than a part in 10^8, between those estimates which used Churchill as a fiducial, and those that did not. This is indirect evidence that GPS can be used to supplement the number of available fiducial stations. As an example of the agreement we are taking about, the first and third epochs shown in Figure 10 were determined using Churchill as a fiducial site. Note the agreement of the straight-line fit with the data from the second and fourth experiments, where Churchill was not used.

CONCLUSIONS

By comparing the interstation vector estimates for a crustal deformation network in central California, spanning approximately 350 km, where we have varied the fiducial networks, we have shown that three receivers collocated with VLBI sites provide a stable reference system at the several millimeter level in the horizontal and at 10 mm in the vertical components. This result implies that local survey errors between VLBI and GPS monuments at fiducial sites do not severely affect the estimation of interstation vectors. The geometry of the three fiducial sites must be taken into account if a stable reference frame is to be obtained. When the three fiducial stations all lie close to a great circle, strains and rotations as great as a part in 10^7 are produced. If there are not a sufficient number of VLBI sites in one's experiment, GPS-derived fiducial coordinates can be used. Of course, these coordinates should be determined in the same kind of reference frame, such as that defined by VLBI. Fiducial networks which span the same scale as the crustal deformation network dilate and rotate the crustal deformation network by a part in 10^7 and are not suitable for crustal deformation networks over 20 km in scale.

The bias that fiducial networks produce on crustal deformation networks can be mitigated somewhat by use of a consider covariance analysis. Although the adopted uncertainties for fiducial coordinates is somewhat arbitrary, this technique does allow the total error to reflect fiducial bias, in a way that reduces its affect on measurement of crustal deformation rates. Fiducial coordinates may be estimated, which would also increase the interstation vector standard deviations in the crustal deformation network, but this would also allow the reference frame to change, producing unwanted dilatation, rotation, and tilt.

The requirement for a fiducial network is most easily met if there is a preexisting, reliable, continuously operating network dedicated to precise orbit determination. If one's geodetic network includes baselines longer than 20 km, this strongly suggests that if such a tracking network does not exist or is not reliable, it is in one's best interest to create a fiducial network for the duration of the experiment. By sacrificing mobile sites in the crustal deformation network, those receivers and field operators can be sent to VLBI sites, thereby providing the data needed for precise orbit determination and a stable reference frame.

Acknowledgments. K.M.L. wishes to thank Stephen Lichten, Jim Davis, Peter Kroger, and Mark Murray for many valuable conservations on fiducial networks and fiducial coordinates. This manuscript was greatly improved by careful and helpful reviews

by Jim Davis and Bill Strange. We also thank the NGS for providing the DYNAP software. Computing facilities and the GIPSY software were provided by sections 335 and 326 of the Jet Propulsion Laboratory. This research was supported by a NASA Graduate Student Research Fellowship awarded to K.M.L. F.H.W. was partially supported by the Jet Propulsion Laboratory, under contract with the National Aeronautics and Space Administration. The writing and publication were completed at the Colorado Center for Astrodynamics Research and supported by ONR N0001490J2010. The data collection was funded (at Scripps) by NSF EAR-8618165.

REFERENCES

Blewitt, G., Carrier phase ambiguity resolution for the Global Positioning System applied to geodetic baselines up to 2000 km, *J. Geophys. Res., 94,* 10,187-10,203, 1989.

Chin, M., CIGNET report, GPS bulletin, Global Positioning Subcommission of Comm. VIII, Int. Coord. of Space Technol. for Geod. and Geodyn., Natl. Geod. Surv., Rockville., Md, 1988.

Clark, T.A., D. Gordon, W. E. Himwich, C. Ma, A. Mallama, and J. W. Ryan, Determination of relative site motions in the western United States using Mark III very long baseline interferometry, *J. Geophys. Res., 92,* 12,741-12,750, 1987.

Dixon, T.H., M. P. Golombek, and C. L. Thornton, Constraints on Pacific plate kinematics and dynamics with Global Positioning System measurements, *IEEE Trans. Geosci. Remote Sens., GE-23,* 491-501, 1985.

Dong, D., and Y. Bock, Global Positioning System network analysis with phase ambiguity resolution applied to crustal deformation studies in California, *J. Geophys. Res., 94,* 3949-3966, 1989.

Drew, A., and R. Snay, DYNAP: Software for estimating crustal deformation from geodetic data, *Tectonophysics, 162,* 331-343, 1989.

Freymueller, J., and M. Golombek, Geometry and treatment of fiducial networks: Effect on GPS baseline precision in South America, *Geophys. Res. Lett., 15,* 1467-1469, 1988.

Herring, T. A., et al., Geodesy by radio interferometry: Evidence for contemporary plate motion, *J. Geophys. Res., 91,* 8341-8347, 1986.

King, R.L., and G. Blewitt, Global Positioning System: An Overview, *Proceedings of the General Meeting of the I.A.G., August 3-12, 1989, Edinburgh, Scotland, GPS and Other Radio Tracking Systems,* edited by Y. Bock and N. Leppard, pp. 24-39, Springer-Verlag, New York, 1990.

Kornreich-Wolf, M. S., T. Dixon, and J. Freymueller, The effect of tracking network configuration on GPS baseline estimates for the CASA UNO experiment, *Geophys. Res. Lett., 17,* 647-650, 1990.

Larson, K., Precision, accuracy, and tectonics from the Global Positioning System, doctoral dissertation, Univ. of Calif., San Diego, 1990*a*.

Larson, K. M., Evaluation of GPS estimates of relative positions from central California, 1986-1988, *Geophys. Res. Lett., 17,* 2433- 2436, 1990*b*.

Larson, K.M., and D.C. Agnew, Application of the Global Positioning System to crustal deformation measurement 1. Precision and accuracy, *J. Geophys. Res.,* this issue.

Lichten, S. M., and J. S. Border, Strategies for high precision GPS orbit determination, *J. Geophys. Res., 92,* 12,751-12,762, 1987.

Lichten, S., W. Bertiger, and U. Lindqwister, The Effect of Fiducial network strategy on high-accuracy GPS orbit and baseline determination, in *Proceedings International Symposium on GPS Positioning,* pp. 516-525, Physical Science Lab., Las Cruces, N. M., 1989.

Minster, J.B., and T.H. Jordan, Present-day plate motions, *J. Geophys. Res., 83,* 5331-5354, 1978.

Noll, C., Crustal Dynamics Project: Catalogue of site information, *NASA Ref. Publ., 1198,* 1988.

Prescott, W.H., J. L. Davis, and J. Svarc, Global Positioning System measurements for crustal deformation: Precision and accuracy, *Science, 244,* 1337-1339, 1989.

Savage, J.C., and W.H. Prescott, Precision of Geodolite distance measurements for determining fault movements, *J. Geophys. Res., 78,* 6001-6007, 1973.

Smith, D.E., et al., Tectonic motion and deformation from satellite laser ranging to LAGEOS, *J. Geophys. Res., 95,* 22,013-22,042, 1990.

D. C. Agnew, Institute of Geophysics and Planetary Physics, La Jolla, CA 92093-0225

K. M. Larson, Colorado Center for Astrodynamics Research, University of Colorado, Boulder, Colorado 80309-0431

F. H. Webb, MS 238-624, Jet Propulsion Laboratory, Pasadena, CA 91109

(Received August 5, 1990;
revised May 6, 1991;
accepted May 6, 1991.)

JOURNAL OF GEOPHYSICAL RESEARCH, VOL. 96, NO. B10, PAGES 16,547–16,565, SEPTEMBER 10, 1991

Application of the Global Positioning System to Crustal Deformation Measurement 1. Precision and Accuracy

KRISTINE M. LARSON

Colorado Center for Astrodynamics Research, University of Colorado, Boulder

DUNCAN C. AGNEW

Institute of Geophysics and Planetary Physics, Scripps Institution of Oceanography, La Jolla, California

In this paper we assess the precision and accuracy of interstation vectors determined using the Global Positioning System (GPS) satellites. These vectors were between stations in California separated by 50-450 km. Using data from tracking the seven block I satellites in campaigns from 1986 through 1989, we examine the precision of GPS measurements over time scales of a several days and a few years. We characterize GPS precision by constant and length dependent terms. The north-south component of the interstation vectors has a short-term precision of 1.9 mm + 0.6 parts in 10^8; the east-west component shows a similar precision at the shortest distances, 2.1 mm, with a larger length dependence, 1.3 parts in 10^8. The vertical precision has a mean value of 17 mm, with no clear length dependence. For long-term precision, we examine interstation vectors measured over a period of 2.2 to 2.7 years. When we include the recent results of Davis et al. (1989) for distances less than 50 km, we can describe long-term GPS precision for baselines less than 450 km in length as 3.4 mm + 1.2 parts in 10^8, 5.2 mm + 2.8 parts in 10^8, 11.7 mm + 13 parts in 10^8 in the north- south, east-west, and vertical components. Accuracy has been determined by comparing GPS baseline estimates with those derived from very long baseline interferometry (VLBI). A comparison of eight interstation vectors shows differences ranging from 5 to 30 mm between the mean GPS and mean VLBI estimates in the horizontal components and less than 80 mm in the vertical. A large portion of the horizontal differences can be explained by local survey errors at two sites in California. A comparison which suffers less from such errors is between the rates of change of the baselines. The horizontal rates estimated from over 4 years of VLBI data agree with those determined with 1-2 years of GPS data to within one standard deviation. In the vertical, both GPS and VLBI find insignificant vertical motion.

INTRODUCTION

Many geodetic techniques have been used to measure crustal deformation across the North American/Pacific plate boundary in California. The oldest data come from triangulation measurements [e.g., *Hayford and Baldwin*, 1908]; more recently, precise electronic distance measurement (EDM) has provided many details about strain across faults of the plate boundary [e.g., *Savage*, 1983]. Both of these procedures measure through the atmosphere and require the measurement points to be intervisible; they are thus limited to distances up to a few tens of kilometers. Both require considerable skill and expensive equipment to pursue successfully.

In the past decade, measurements using extraterrestrial objects, such as satellite laser ranging (SLR) [*Christodoulidis et al.*, 1990; *Smith et al.*, 1990] and very long baseline interferometry (VLBI) [*Herring et al.*, 1986; *Clark et al.*, 1987], have made possible measurements between points hundreds to thousands of kilometers apart. This has enabled a direct determination of the total contemporary plate motion across the broad boundary in California. These observations are, however, even more expensive to make than the older, purely terrestrial, techniques.

The most recent advance in precise geodetic measurements has been the use of the Global Positioning System (GPS) satellites. The basic principles of this technique are similar to VLBI, with some important differences. The radio signals originate at satellites, rather than quasars, and GPS receivers make an instantaneous determination of the distance between the receiver and satellite, rather than requiring cross correlation of noise signals to determine the length between two sites. From enough measurements of signals arriving from different directions the complete vector baseline between two sites can be computed. Because the signal strength at the Earth is so much higher than for the quasar sources used in VLBI and because the signal has a known and well-controlled structure, GPS antennas (and all other equipment) weigh at most a few hundred pounds rather than the many tons needed for VLBI. A similar favorable ratio applies to the costs of the two techniques. For all these reasons, GPS is poised to become the method of choice for crustal deformation geodesy and in many areas has indeed already become so.

But since this is such a new technique, it is vital to establish just what its errors are. Judging from past experience with VLBI and SLR, constructing a formal error budget, while useful, is likely to give an incomplete picture because of the wide variety of semisystematic errors that are little understood (not to mention those that are overlooked). We feel that what is needed is an empirical investigation of the precision and accuracy of GPS measurements, judged from actual results: the precision being a measure of how exact the estimate is, and the accuracy a measure of how close the estimate is to the truth [*Bevington*, 1969]. Our measure of

Paper number 91JB01275.
0148–0227/91/91-JB-01275$05.00

precision is thus (as for others) the scatter of results about a mean value; our measure of accuracy is the agreement with some other technique (VLBI).

This paper is the first of three that describe results from nearly three years of measurements in central and southern California. This paper describes the precision and accuracy over baselines from 50-450 km. Though some earlier work [e.g., *Dong and Bock*, 1989] has demonstrated subcentimeter precision over these distances, this precision was only evaluated from data collected over a few days. Such estimates are likely to underestimate the long-term precision because a number of error sources probably do not change much over this span of time. The only paper that has looked at long-term precision and accuracy is that of *Davis et al.* [1989], but most of the data shown there were for baselines of 200 m to 50 km, not the longer regional scales we discuss here. This suite of measurements also allows us to discuss the role of orbit determination (fiducial) networks in establishing a consistent reference frame [*Larson et al.*, this issue] (hereafter referred to as paper 2), and the effect of different modeling procedures for the atmospheric delay (K.M. Larson and J.L. Davis, manuscript in preparation; hereinafter referred to as paper 3). In the next section of this paper, we describe how the GPS data were collected and the analysis techniques we used to determine the coordinates of the different stations. The following sections discuss precision and accuracy.

Experimental Procedure and Data Analysis

The data we use were collected during 11 "experiments" conducted between June 1986 and March 1989. The measurements in southern and central California were made by a four-university consortium, Scripps Institution of Oceanography, California Insitute of Technology, University of California, Los Angeles, and Massachusettes Institute of Technology, with substantial help from the U.S. Geological Survey (USGS) and the National Geodetic Survey (NGS). When possible, we also included data from the North American network of fixed GPS trackers that are part of the Cooperative International GPS NETwork (CIGNET) [*Chin*, 1988]. Table 1 lists 22 of the GPS sites observed. The stations located in California are shown in Figure 1. The remaining sites, all located in North America, were used for precise orbit determination, and are discussed in paper 2. While more sites than these were observed during the 11 experiments, only these 22 were measured at more than one epoch and thus can provide a useful estimate of long-term precision and accuracy. As noted above, the network formed by those of the stations in California yields baseline lengths from 50 to 450 km.

In each experiment the GPS satellites were tracked at each station using a TI-4100 dual-frequency receiver [*Henson et al.*, 1985], recording both carrier phase and pseudorange data at 30-s intervals. (Carrier phase is precise but ambiguous by an integer number of cycles; pseudorange is unambiguous but 2 orders of magnitude less precise.) The intention was to track for the 7-8 hours that several satellites were visible; for most of the experiments (all but those done in May, June, and September) this meant tracking almost entirely at night. For most experiments the plan was to record data for 4 or 5 consecutive days, a goal not always achieved in practice. Table 2 summarizes the data available from all the sites we have considered. The receiver antenna was centered over the geodetic monument at each site using an optical plummet, with a nominal accuracy of about 1 mm; the vertical offset between the antenna and the top of the monument was measured by a tape, with perhaps 2-

TABLE 1. GPS Stations

	Station	Location	Longitude, deg	Latitude, deg	Height, m	Stamping
1,	Algonquin	Ontario, Canada	-78.071	45.958	209	TELESCOPE REF A
2,	Blancas	Monterey	-121.284	35.666	50	none
3,	Blackhill	Morro Bay	-120.831	35.360	201	BLACKHILL 1881
4,	Brush	Catalina Isl.	-118.404	33.409	451	BRUSH 1976
5,	Buttonwillow	Bakersfield	-119.394	35.405	64	A364 1953
6,	Center	Santa Cruz Island	-119.753	33.996	394	CENTER 1934
7,	Churchill	Manitoba, Canada	-94.088	58.758	31	GEOS3
8,	Clembluf	San Clemente Island	-118.518	32.928	297	BLUFF 1933
9,	Fort Ord	Monterey	-121.773	36.671	39	FORT ORD NCMN 1981
10,	Lacumbre	Santa Barbara County	-119.713	34.496	1171	none
11,	Lospe	Vandenberg AFB	-120.605	34.896	505	none
12,	Madre	Miranda Pine Mountain	-120.067	35.077	914	MADRE ECC 1980
13,	Mojave	Goldstone	-116.888	35.333	904	CIGNET
14,	Niguel	Laguna Niguel	-117.730	33.516	238	NIGUEL A 1884 1981
15,	Nicholas	San Nicolas Island	-119.479	33.233	201	TWIN 1964
16,	OVRO	Owens Valley	-118.293	37.234	1195	MOBLAS 7114 1979
17,	Palos Verdes	Los Angeles	-118.403	33.745	73	PALOS VERDES ARIES 1976 1980
18,	Platteville	Colorado	-104.726	40.184	1530	PLATTEVILLE NCMN 1981
19,	Richmond	Florida	-80.384	25.615	23	CIGNET
20,	Soledad	La Jolla	-117.252	32.841	216	none
21,	Vandenberg	Vandenberg AFB	-120.616	34.558	24	VLBI STA 7223 RM1
22,	Westford	Haystack Obs., Mass.	-71.493	42.615	125	CIGNET

Geodetic coordinates of crustal deformation sites, referenced to NAD 83. The stamping is imprinted on the geodetic marker. CIGNET refers to the antenna phase center of the continuously monitoring GPS network [*Chin*, 1988]. Unless otherwise noted, all sites are in California.

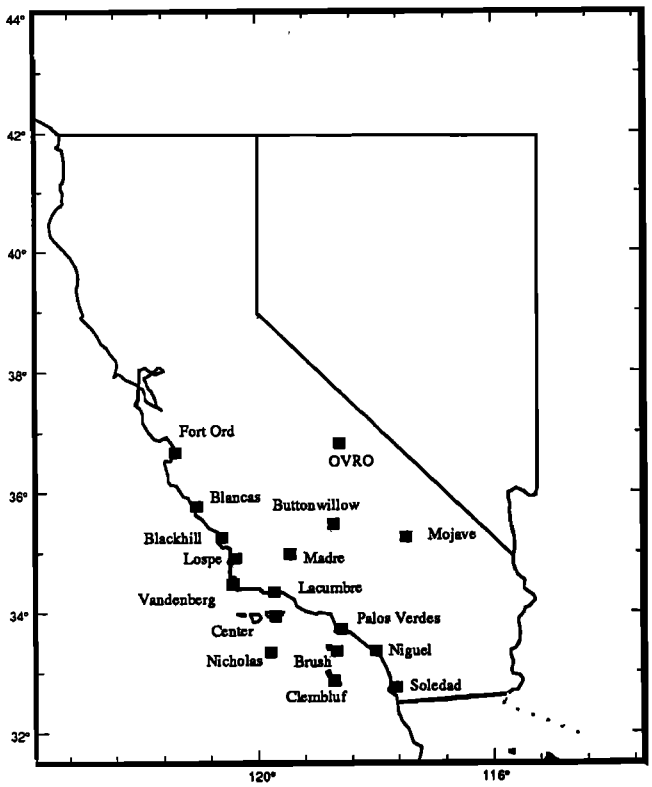

Fig. 1. GPS sites in southern and central California observed between 1986 and 1989 for crustal deformation studies. Table 1 gives the site names and coordinates, and Table 2 gives a breakdown of which sites were observed when. All but three (Mojave, Buttonwillow, and OVRO) lie west of the San Andreas fault.

mm error. While the observers at each site recorded local pressure, temperature, and humidity, we have not made use of these data (paper 3 discusses this in more detail).

The GPS data were analyzed with the GPS Inferred Positioning SYstem software (GIPSY) developed at the Jet Propulsion Laboratory [*Stephens*, 1986; *Lichten and Border*, 1987]. GPS carrier phase and pseudorange data at both frequencies were reformatted from the original data tapes, and the phase data were checked for cycle slips. This process was automated by using a computer program, Turboedit, described by *Blewitt* [1990]. In order to reduce the computer storage and CPU requirements, we subtracted a model of satellite and station positions from the observables, and a second order polynomial fit was used to compress the 30-s data to 6-min points. This technique is valid as long as the error sources over 6 min (satellite and receiver clocks and the ionosphere) can be modeled by a second-order polynomial. At this point, linear combinations were formed of the carrier phase and pseudorange data, which eliminated the highest-order effects of the ionosphere. Nominal satellite trajectories were determined by a module which integrates the equations of motion and the variational equations to obtain satellite coordinates and partial derivatives of these coordinates with respect to the satellite initial conditions and force parameters. Another module computed prefit residuals and partial derivatives from nominal station coordinates, nominal GPS orbits, and models for the Earth's rotation, tides, and atmospheric refraction [*Sovers and Border*, 1988]. Finally, a factorized Kalman filter was used to perform a least squares adjustment of station positions, satellite initial positions and velocities, tropospheric zenith delays, phase ambiguities, and satellite and receiver clocks.

The constraints we used for our standard estimation procedure are summarized in Table 3. We used the broadcast ephemeris to determine nominal values for initial position and velocity of each spacecraft. For each satellite, we estimated an initial position, initial velocity, and the behavior of the satellite clock. We fixed the positions of three "fiducial sites", whose coordinates were derived from VLBI measurements. If properly chosen, these fiducial sites, whose positions are known to better than 2 cm, provide sufficient strength to determine the satellite orbit to better than 2 m (see paper 2 for further detail on both the derivation of fiducial coordinates and their impact on orbit determination). If more than three "VLBI sites" were included in a GPS experiment, the nonfiducial VLBI sites were treated as "mobile sites" and estimated with a standard deviation of 2 km. In general, our starting (nominal) solution was within 1 m of the estimated position of all mobile stations.

We modeled the clock bias at each measurement point as white noise; in other words, each estimate was independent and uncorrelated with the clock bias at previous measurements. Some receivers we used were connected to hydrogen masers; the remainder used the quartz internal clock provided by the TI-4100. White noise clock modelling is essentially identical to the double differencing used in other softwares [*Beutler et al.*, 1990].

The optimal strategy for determining the atmospheric propagation delay is unclear at this time. *Tralli et al.* [1988] suggest time-varying estimation techniques are preferable, while *Davis et al.* [1989] achieve similar vertical component precision solving for a constant zenith delay parameter. Water vapor radiometers (WVR) were not in use during 10 of the 11 experiments, and therefore we have chosen to ignore what little WVR data were available. Paper 3 will address this issue in more detail. The strategy we have used in this paper was as follows: we first corrected for the dry troposphere delay using a crude relation between station elevation, pressure, and dry zenith delay. The pressures for hydrostatic zenith delay calculations were determined using the ellipsoidal height of the site and an assumed sea level pressure of 1013.24 mbar with an exponential profile with scale height 7 km. The temporal variation of the wet zenith path delay was modeled as a random walk, with an allowed variation of 49 mm over 7.5 hours.

Finally, a station-satellite parameter was estimated for each phase ambiguity. The nominal phase ambiguity solution was determined from the pseudorange data. Subsequently, ambiguity resolution was attempted. We used a 99% confidence criterion for "fixing" these ambiguities to their integer values, which is described by *Blewitt* [1989]. At this point, postfit residuals were visually inspected, primarily to determine if cycle slips had been incorrectly fixed. At this point the Cartesian station locations and their standard deviations can be retained for crustal deformation studies.

The reference frame we used was defined by the Goddard Space Flight Center Global Site Velocity model GLB223, which is based on over 4 years of VLBI data (C. Ma, personal communication, 1988). Further discussion of the reference frame is left to paper 2. Earth orientation values were taken from the monthly bulletins of the International Radio Interferometric Surveying (IRIS) Subcommission.

TABLE 2a. Data Summary

	Experiment										
	J86[a]	D86	J87	M87[b]	S87	M88a	M88b	J88	S88	M89a[c]	M89b
Month/year	June 1986	Dec. 1986	Jan. 1987	May 1987	Sept. 1987	March 1988	March 1988	June 1988	Sept. 1988	March 1989	March 1989
Dates	17-20	12/30-1/2	27-29	25, 27, 28	22,24,25	8,9,11	15-18	8-11	13-16	21-23	28-30
Total days of data	4	4	3	3	3	3	4	4	4	3	3
1, Algonquin	-	4	-	-	-	-	4	-	-	-	-
2, Blancas	-	2	-	-	-	-	4	-	-	-	3
3, Blackhill	-	4	-	3	3	-	4	-	-	-	3
4, Brush	-	-	3	-	-	3	-	-	-	3	-
5, Buttonwillow	-	4	-	-	-	-	4	-	-	-	3
6, Center	-	4	3	3	3	3	4	-	-	-	3
7, Churchill[d]	-	4F	-	-	-	3F	4	-	-	-	-
8, Clembluf	2	-	3	-	-	3	-	-	-	3	-
9, Fort Ord[e]	-	4F	-	-	3F	-	4F	-	4	-	-
10, Lacumbre	-	4	3f	-	-	-	4	-	-	-	2
11, Lospe	-	1.5	-	-	-	-	3.5	-	-	-	3
12, Madre	-	4	-	-	-	-	4	-	-	-	3
13, Mojave[f]	4F	1	3F	3	2.5	3F	2.5	3F	4F	3F	3F
14, Niguel	2	-	-	-	-	2	-	-	-	3	-
15, Nicholas	4	-	-	-	-	-	4	-	-	3	-
16, OVRO	-	1.5	-	3F	3	-	3.5	-	-	-	3f
17, Palos Verdes	4	-	3f	3	3	1	4	4	4	3f	3f
18, Platteville	-	4	-	-	3F	2	3	-	-	-	-
19, Richmond[g]	4F	-	-	-	-	1F	3F	3F	2F	0	0
20, Soledad	2	-	3	-	-	3	-	-	-	3	-
21, Vandenberg	3	4	-	3	3	3	3	4	3	3f	3f
22, Westford	4F	4	0	3F	3F	3F	4F	4F	2F	0	0

Site occupations are summarized for 11 experiments at 22 sites between June 1986 and March 1989. The total days of available data are listed. Individual station occupations are listed by experiment. F, the station position was not estimated, i.e. this is a fiducial site; f, the station position was estimated, with a standard deviation of 20 mm; Number of days of useful data. One day of data equals approximately 7 hours. If no f or F is listed, station position was estimated, with a standard deviation of 2 km. Dashes indicate the station was not scheduled to be observed during the experiment. Zero indicates the station was scheduled to be observed, but no useful data were collected.

[a] Experiment described in greater detail by *Blewitt* [1989]

[b] Austin, Texas used as third fiducial site. Coordinates provided by M. Murray (personal communication, 1990)

[c] Less than 10% of carrier phase ambiguities were resolved between sites in California.

[d] Fiducial coordinates for Churchill determined from data collected during experiment M88b

[e] Fort Ord was destroyed summer of 1988. Reference mark was occupied in S88

[f] Mojave refers to 3 "monuments". J86 = Mojave NCMN1; D86-J88 = CIGNET TI-4100 antenna; S88-M89b = CIGNET FRPA antenna. Mini-MAC data collected at Mojave for M89a and M89b were not used.

[g] CIGNET tracker at Richmond was unavailable until November 1988

TABLE 3. Parameter Estimation

Parameter	Estimation	Standard Deviation	Steady State Standard Deviation	Time Behavior
Satellite position, km	force model	100		
Satellite velocity, km/s	force model	1		
Satellite clock, s	stochastic	1	1	white noise
Station position (fiducial)	fixed (not estimated)			
Station position (mobile), km	constant	2		
Station clock, s	stochastic	1	1	white noise
Phase ambiguity, s	constant	10		
Zenith troposphere delay	stochastic	300 mm	3×10^{-7}km/$\sqrt{s}$	random walk
Data weights, mm	pseudorange	250		
	carrier phase	10		

PRECISION

Introduction

To characterize the precision of the vectors estimated by GPS, we use the scatter of independently estimated results. For short-term precision, we will use results from 18 stations observed during a single experiment in March 1988. Short-term precision will be defined by the weighted RMS scatter about the mean of daily estimates, each determined from a single-day orbit solution. If we have N independent values $y_1, y_2, \ldots y_N$ with (formal) standard errors $\sigma_1, \sigma_2, \ldots \sigma_N$, this scatter is S_{mean},

$$S_{mean} = \sqrt{\frac{\frac{N}{N-1}\sum_{i=1}^{N}\frac{(y_i - \langle y \rangle)^2}{\sigma_i^2}}{\sum_{i=1}^{N}\sigma_i^2}} \quad (1)$$

where $\langle y \rangle$ is the weighted mean of the y_i's. (This quantity has sometimes been termed the repeatability, a term we eschew because it leads to ambiguity: a high repeatability may be highly repeatable (good), or a large value (bad).) The reduced χ^2 statistic is defined for the weighted RMS about the mean as

$$\chi^2_{mean} = \frac{1}{N-1}\sum_{i=1}^{N}\frac{(y_i - \langle y \rangle)^2}{\sigma_i^2} \quad (2)$$

where y_i, σ_i, and $\langle y \rangle$ are defined as before. A reduced χ^2 of 1 indicates that the formal errors, σ_i, agree with the actual scatter in the measurements.

Since our measure of precision is weighted by our expected error, we need to describe how these formal errors were calculated. The measurement standard deviation is calculated by propagating standard deviations of the carrier phase and pseudorange data through the variance-covariance matrix. Our formal errors then are dependent on the data weights we assumed for the carrier phase and pseudorange data, 10 and 250 mm, respectively. These data weights were determined empirically in the following manner. For each station, we multiplied the RMS post-fit scatter by the quantity $\sqrt{N/(N-P)}$, where N is the number of data points and P is the number of parameters we have estimated. This data noise is then approximately what is required to make χ^2 one. In general, the RMS postfit scatter ranged from 4 to 6 mm, depending on the station, and the scaling quantity was approximately 1.5. This resulted in a data weight of 6-9 mm. In an effort to be conservative, we chose 10 mm and applied it uniformly to all stations. We determined the pseudorange data weight in the same manner. This data weight would have to be changed if we substantially increased the number of parameters we estimated, or we changed the data rate (i.e., from 6 to 3 min points). For the experiments listed in Table 2, we had fairly common data sets, in numbers of satellites, and we used consistent estimation procedures. Thus, while our formal errors may be incorrect, they were computed in an identical fashion for each experiment. Later in this section we will discuss whether our weighting scheme was appropriate.

We expect that short-term precision might underestimate the true precision, because over this time scale some errors change less than they would over longer times. Possible errors in this class are wet and dry tropospheric delays and set-up errors. To estimate long-term precison we use measurements spanning 1.2-2.7 years for 22 stations (including all those used for the short-term precision estimates). We could use equation (1) for long-term precision, but by neglecting actual plate motion we unnecessarily degrade the precision of the GPS estimate. Therefore, for long-term horizontal precision, we adopt a standard technique [*Ma et al.*, 1990] and calculate the weighted RMS about the best fitting line. (For long-term vertical precision, we assume no true vertical motion, and use equation (1) only.) The weighted RMS about the best fitting line, S_{line}, is defined

$$S_{line} = \sqrt{\frac{\frac{N}{N-2}\sum_{i=1}^{N}\frac{(y_i - (a + bt_i))^2}{\sigma_i^2}}{\sum_{i=1}^{N}\sigma_i^2}} \quad (3)$$

where a and b are the intercept and slope of the best fitting line and t_i is the time of the ith measurement. The reduced χ^2 statistic for S_{line} is

$$\chi^2_{line} = \frac{1}{N-2}\sum_{i=1}^{N}\frac{(y_i - (a + bt_i))^2}{\sigma_i^2} \quad (4)$$

These formulae are correct if we can assume that each es-

timate of an interstation vector is independent. In general, our data were collected several days in succession, separated by 6-12 months, and thus were not evenly distributed in time. Even though we have analyzed each day of GPS data independently, *Davis et al.* [1989] have pointed out that estimates only a few days apart will be correlated, due to common error sources. Therefore, Davis et al. attempted to separate short- and long-term error statistics. The short-term error was determined by the scatter about the mean for a single 3-5 day experiment, and the long-term error was computed from the RMS of these means about the best fitting line. The total error was then computed assuming the long- and short-term errors were independent. One problem with this formulation is that it ignores the formal errors, with all estimates being treated equally. When we used the Davis et al. technique, we found that measurements from the M89a and M89b experiments were the largest contributors to the long-term error. We know there were systematic errors in that particular experiment, caused by the fiducial network we were forced to use. Since this paper is a summary of a large quantity of data, we would like to leave discussion of known systematic errors to papers 2 and 3. If one adapts the method of Davis et al. to incorporate the formal errors, one is then computing nearly the same quantity as if equation (3) were used. We therefore use the simplest formulation we have for long-term precision, equation (3), although we recognize that we have not solved for the long- versus short-term error sources.

While much of the information about precision is best obtained from the plots of scatter, we also wish to summarize the results in a compact way. One way of summarizing errors of distance measurements is the expression [*Savage*, 1983]

$$\sigma^2 = A^2 + B^2 l^2 \tag{5}$$

where σ is the standard deviation and l is the baseline length. This equation derives from the nature of EDM measurements [*Rueger*, 1990], where the measuring instrument has a constant error A, a proportional error B being introduced by errors in the estimated atmospheric refraction. Equation (5) then follows from the usual law for the combination of independent errors.

The dependence of error on distance might be expected to be more complicated for GPS measurements. Over very short baselines (<100 m) the intrinsic precision and accuracy of the measurement are 2 mm or less [*Davis et al.*, 1989], though in many survey conditions we might expect the errors of locating the antenna relative to the geodetic monument to be several times this. Another source of error that is independent of length is the effect of antenna multipath: the signal received is the sum of the direct-arriving radio wave and waves that have been reflected off nearby objects (such as the ground). As the position in the sky of a satellite changes the relative contributions of these waves will vary, causing the apparent location of the antenna to wander about its true one. Because of the long duration of tracking during these measurements we expect this error to be small.

Over longer distances other error sources enter in. For distances of more than the troposphere scale height (a few kilometers), differences in wet and dry delay cease to cancel, at least relative to other error sources; at larger distances the same becomes true for the ionosphere. One well-understood error scales with baseline length: errors in the estimated orbits of the satellites. This contributes to an error in baseline

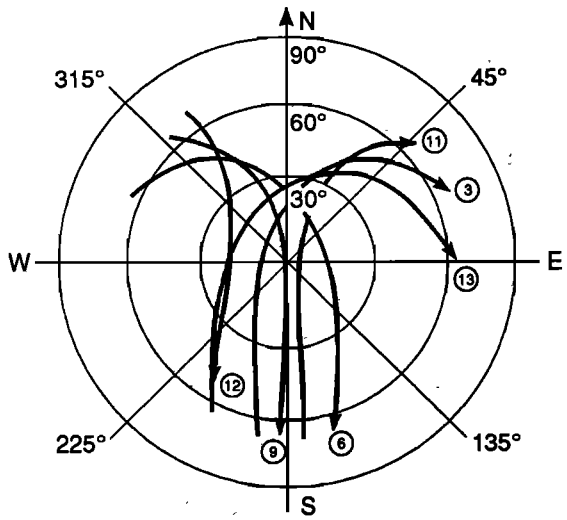

Fig. 2. GPS sky tracks over California for the six block I GPS satellites observed during the December 1986 campaign (modified from *Dong and Bock*[1989]). The anisotropy of these sky tracks gives measurements of north-south components greater inherent precision than those of east-west components.

length which is about $l\beta\sigma_{orb}/L$, where L is the distance from the GPS receiver to GPS satellites (about 20,000 km), σ_{orb} is the orbit error, and β is a constant that depends on network geometry; it is about 0.2 for continental scale networks [*Lichten*, 1990]. The GPS constellation observed during the experiments used here consisted of seven block I satellites. Figure 2 shows the sky paths of six of these satellites as seen from California; since the satellites cover a wider range of elevations along a north-south azimuth than to the east or west, we might expect the baseline error to be larger for east-west components than north-south ones. Similarly, because the data come only from satellites above the horizon, the vertical component precision can be expected to be much worse than either horizontal precision.

Because of the varied nature of errors in GPS baselines, there seems to be no good reason to adopt the form of equation (5) for the errors. However, some acknowledgment of the existence of proportional errors is appropriate; we have therefore adopted the simple law

$$\sigma = A + Bl \tag{6}$$

to summarize the change of precision with distance. We do not believe this relation truly reflects the underlying error structure of GPS; instead we use this relation as a means of summarizing the precision estimates we have made. Since our analysis is restricted to baselines from 50 to 450 km in length, we will incorporate the long-term precision results of *Davis et al.* [1989] for baselines less than 50 km in order to extend this assessment of GPS precision. Further studies will be required to determine the long-term precision of continental- and global-scale interstations vectors measured with GPS. At that time, it will be appropriate to investigate in a more systematic fashion whether equation (5), (6), or a more complicated expression adequately describes long-term precision.

Results

Short-term precision. The most successful experiment of the 11 listed in Table 2, in terms of high data yield, was the March 1988 central California campaign (designated M88b).

Four days of data were collected at 18 sites in North America, 13 in California. The short-term precision for the north-south, east-west, and vertical components for this experiment is plotted, as a function of baseline length, in Figures 3*a*-3*c* and is listed in Table 4.

The most prominent feature of these plots is the absence of significant baseline dependence for the north-south component. This has errors of 1.9+0.6 parts in 10^8. In the east-west component, the precision is described by 2.1 mm+1.3 parts in 10^8. The constant term for both components is in good agreement with the precision of 100-m baselines [*Davis et al.*, 1989]. The difference in baseline dependence for the two components is easily explained by the satellite geometry of the block I constellation discussed in the previous section. This is a similar network to the one studied by *Dong and Bock* [1989]. By fitting a line to their baseline scatter, Dong and Bock reported precision of 6 mm + 0.5 parts in 10^8 in the east-west component and 2.5 mm + 0.9 parts in 10^8 in the north- south component.

The vertical component is nearly an order of magnitude less precise than horizontal components. The scatter has a mean value of 17 mm, with no length dependence. Using data collected during the June 1986 southern California GPS experiment (see J86 in Table 2), *Blewitt* [1989] reported a mean RMS of 29 mm on baselines ranging from 50 to 650 km, which is in good agreement with formal errors from his analysis. Inspection of scatter plots in Blewitt's paper shows no baseline dependence. In contrast, *Dong and Bock* [1989] reported a slight dependence on baseline length for their vertical component precision, 12 mm + 6 parts in 10^8. The differences between our results and those of Dong and Bock may be due to the difference in fiducial networks we used. We leave this discussion to paper 2.

Discussion. Our primary objective is to use the scatter in the interstation vector estimates to determine GPS system precision. Another important question we address is the validity of the formal errors. It has long been recognized that formal errors underestimate the scatter in actual data. This is generally attributed to unmodeled systematic effects and to mismodeling of certain parameters. One technique commonly used to produce more reasonable errors is to scale formal errors so that the reduced χ^2 is 1 [*Clark et al.*, 1987]. In their study of GPS precision, *Davis et al.* [1989] discarded their formal errors and used an ad hoc technique, deriving a standard deviation from the actual scatter. While it is difficult to determine how the systematic errors impact on the precision, it is fairly simple to determine how representative the formal errors are of the actual scatter in the data. In other words, we compare the predicted standard deviation and the actual standard deviation.

Included with short-term precision in Figures 3*a*-3*c* are the formal error (the mean of the four single-day formal errors) as a function of baseline length. The north-south component indicates that the actual scatter is less than that predicted by the formal errors. The formal error predicts a scatter of 2.4 mm + 0.4 parts in 10^8, whereas the actual scatter is 1.9 mm + 0.6 parts in 10^8. For the east-west component, the formal error is 2.4 mm + 1.5 parts in 10^8, which is also close to the actual scatter of 2.1 mm + 1.3 parts in 10^8. For the vertical component, formal errors overpredict the scatter by a factor of 1.5. The vertical component formal errors are heavily dependent on the random walk parameterization we have chosen for the wet troposphere zenith delay. Thus, we leave discussion of vertical formal errors to

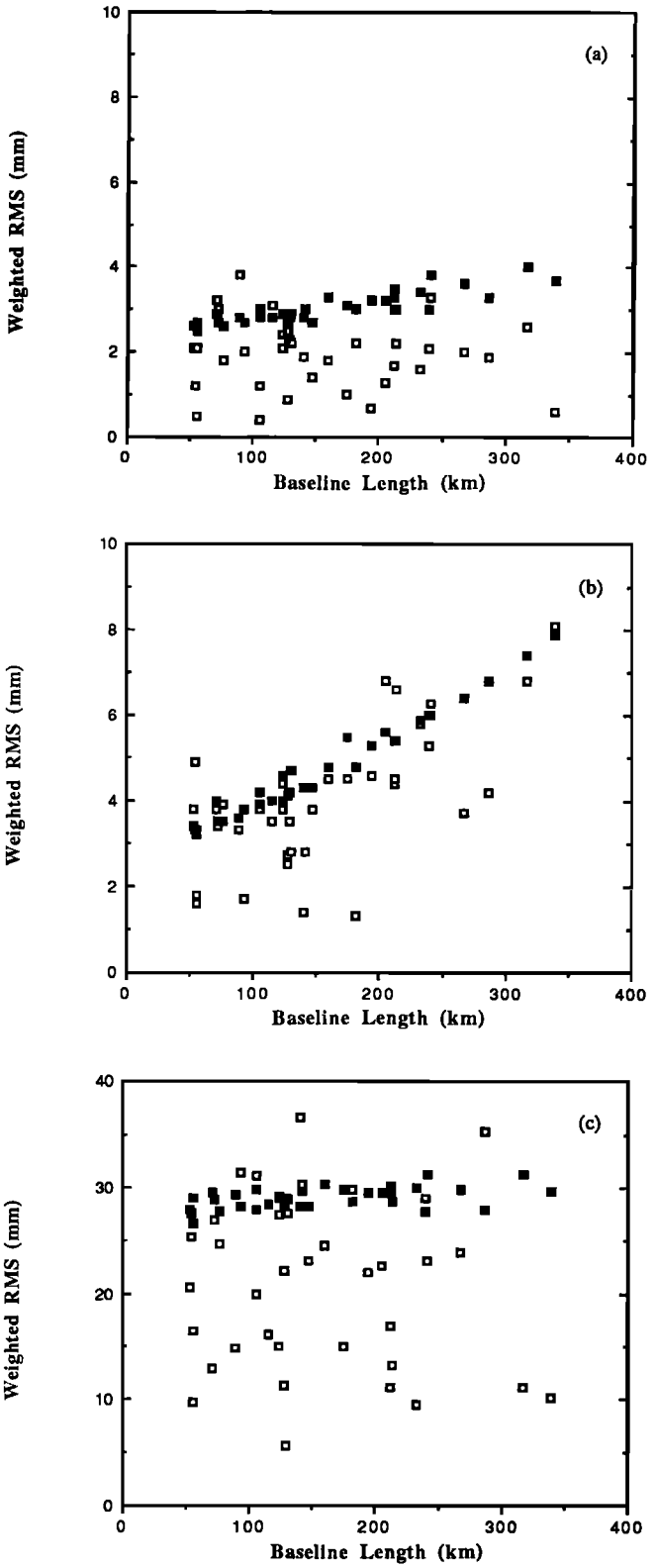

Fig. 3. The open squares are the short-term precision, defined by equation (1) as the weighted RMS about the mean, of different components of the baselines measured in March 1988, plotted as a function of line length. The solid squares are the mean of the formal 1-σ errors for the same quantities, as computed from the size of the residuals and the covariances of the least squares adjustment. Figure 3*a* is for the north-south component of the baseline; Figure 3*b* is for the east-west component, and Figure 3*c* for the vertical component. (The directions are those of a Cartesian coordinate system located at one end of the baseline, whose north is coincident with the local north, and vertical with the normal to the ellipsoid.)

TABLE 4. Short-Term Precision

Interstation Vector	Length, km	East, mm	χ^2	North, mm	χ^2	Vertical, mm	χ^2
Blackhill-Blancas	53	4.9	2.25	1.2	0.20	25.4	0.78
Lospe-Madre	53	3.8	1.29	2.1	0.68	20.6	0.52
Center-Lacumbre	55	1.6	0.22	2.1	0.64	16.4	0.33
Blackhill-Lospe	55	1.8	0.32	0.5	0.03	9.6	0.12
Buttonwillow-Madre	71	3.8	1.14	3.2	1.25	12.8	0.18
Madre-Lacumbre	72	3.4	0.96	3.0	1.13	27.0	0.82
Blackhill-Madre	76	3.9	1.25	1.8	0.46	24.7	0.73
Center-Nicholas	88	3.3	0.91	3.8	2.11	14.8	0.29
Lospe-Lacumbre	93	1.7	0.22	2.0	0.54	31.5	1.19
Buttonwillow-Lacumbre	105	4.2	1.13	0.4	0.02	31.2	1.06
Blancas-Lospe	105	3.8	1.01	1.2	0.18	19.9	0.48
Palos Verdes-Nicholas	115	3.5	0.80	3.1	1.30	16.0	0.34
Madre-Center	123	4.4	1.32	2.1	0.55	15.0	0.27
Lospe-Buttonwillow	123	3.8	0.80	2.4	0.74	27.4	0.89
Lospe-Center	127	2.7	0.52	2.5	0.86	22.2	0.64
Blancas-Madre	128	3.5	0.80	2.3	0.60	5.7	0.04
Palos Verdes-Center	128	2.5	0.43	0.9	0.11	11.3	0.18
Blackhill-Buttonwillow	131	2.8	0.45	2.2	0.60	27.6	0.88
Blackhill-Lacumbre	140	1.4	0.13	1.9	0.41	36.7	1.57
Nicholas-Lacumbre	142	2.8	0.48	3.0	1.00	30.4	1.07
Palos Verdes-Lacumbre	146	3.8	0.90	1.4	0.24	23.2	0.65
Buttonwillow-Center	160	4.5	0.98	1.8	0.31	24.6	0.70
Blancas-Buttonwillow	174	4.5	0.88	1.0	0.10	16.5	0.30
Blackhill-Center	180	1.3	0.08	2.2	0.50	29.9	1.14
Blancas-Lacumbre	193	4.6	0.95	0.7	0.05	22.0	0.52
Palos Verdes-Buttonwillow	204	6.8	2.00	1.3	0.16	22.7	0.60
Madre-Nicholas	211	4.4	0.80	3.0	0.74	11.1	0.14
Lospe-Nicholas	211	4.5	0.87	1.7	0.28	16.8	0.35
Palos Verdes-Madre	212	6.6	1.96	2.2	0.48	13.1	0.20
Blancas-Center	232	5.8	1.29	1.6	0.20	9.5	0.11
Palos Verdes-Lospe	239	5.3	1.11	2.1	0.45	29.0	1.09
Buttonwillow-Nicholas	240	6.3	1.29	3.3	0.77	23.1	0.58
Blackhill-Nicholas	267	3.7	0.44	2.0	0.31	23.9	0.67
Palos Verdes-Blackhill	286	4.2	0.55	1.9	0.32	35.3	1.53
Blancas-Nicholas	316	6.8	1.15	2.6	0.40	11.1	0.13
Palos Verdes-Blancas	339	8.1	1.60	0.6	0.02	10.2	0.12

paper 3. Comparably, plots of χ^2 as a function of baseline length, as shown in Figures 4*a*-4*c*, indicate that over the short term, the formal errors are comparable to the scatter. The outliers in the χ^2 plots, in both senses, those that are too small and those that are too large, are often for a single baseline. As an example, the interstation vector between Palos Verdes and Buttonwillow (204 km) has a χ^2 of 2.0 in the east-west component and a χ^2 of 0.16 in the north-south component. Noting the location of these stations in Figure 1, it is apparent that this baseline is aligned nearly north-south. The geometry of ground stations and satellites degrades the east-west component (and improves the north-south component), in a way that is not predicted by the formal errors.

The observed short-term precision is a function of our ability to remove error sources associated with satellite orbits, satellite and receiver clocks, and propagation delays; to precisely center the GPS antenna over the monument; and to measure the distance between the antenna base and monument. Precise orbits are not necessarily accurate orbits. Since the accuracy of GPS orbits will influence the accuracy of interstation vectors, we leave that discussion to the next section. Mismeasurement and miscentering of the GPS antenna over the monument are a significant limitation in geodetic measurements of crustal deformation. The constant terms for both horizontal components indicate that centering errors are no greater than 2 mm. It should be noted that over the course of these 11 experiments, no effort was made to send the same field crews and the same equipment to the same sites. Therefore long-term centering errors may be larger, since precise centering may not be accurate centering.

Long-term precision. Although our objective is to summarize long-term precision of interstation vectors from 50 to 450 km in length, it is appropriate to show a few, representative time series of estimates from these networks. We discuss results for two interstation vectors in detail and subsequently tabulate statistics using estimates from all 11 experiments. More time series of interstation vectors will be discussed in the accuracy section.

The baseline from Mojave to the Owens Valley Radio Observatory (OVRO) is frequently used for engineering tests [*Ware et al.*, 1986]. The baseline is approximately 240 km east of the San Andreas fault and is oriented N30°W. The north-south, east-west, and vertical components for this 245-km interstation vector are shown in Figure 5. Mojave-OVRO solutions from the March 1989 experiment are not displayed or used in this calculation of long-term precision because

both sites were tightly constrained to their VLBI values for that experiment. Ignoring this experiment limits the calculation of long-term precision to a temporal span of 14 months, with nine data points measured over four epochs. In the north-south component, the long-term precision is 2 mm. In the east-west component, it is significantly worse, 9 mm. There have been 62 VLBI observations of these sites between 1983 and 1988 [*Ma et al.*, 1990]. VLBI estimates the displacement rate between the sites to be 0.1±2.0 and -2.6±1.4 mm/yr in the north-south and east-west components, respectively. The very precise GPS north-south component is additional evidence that the VLBI measurement

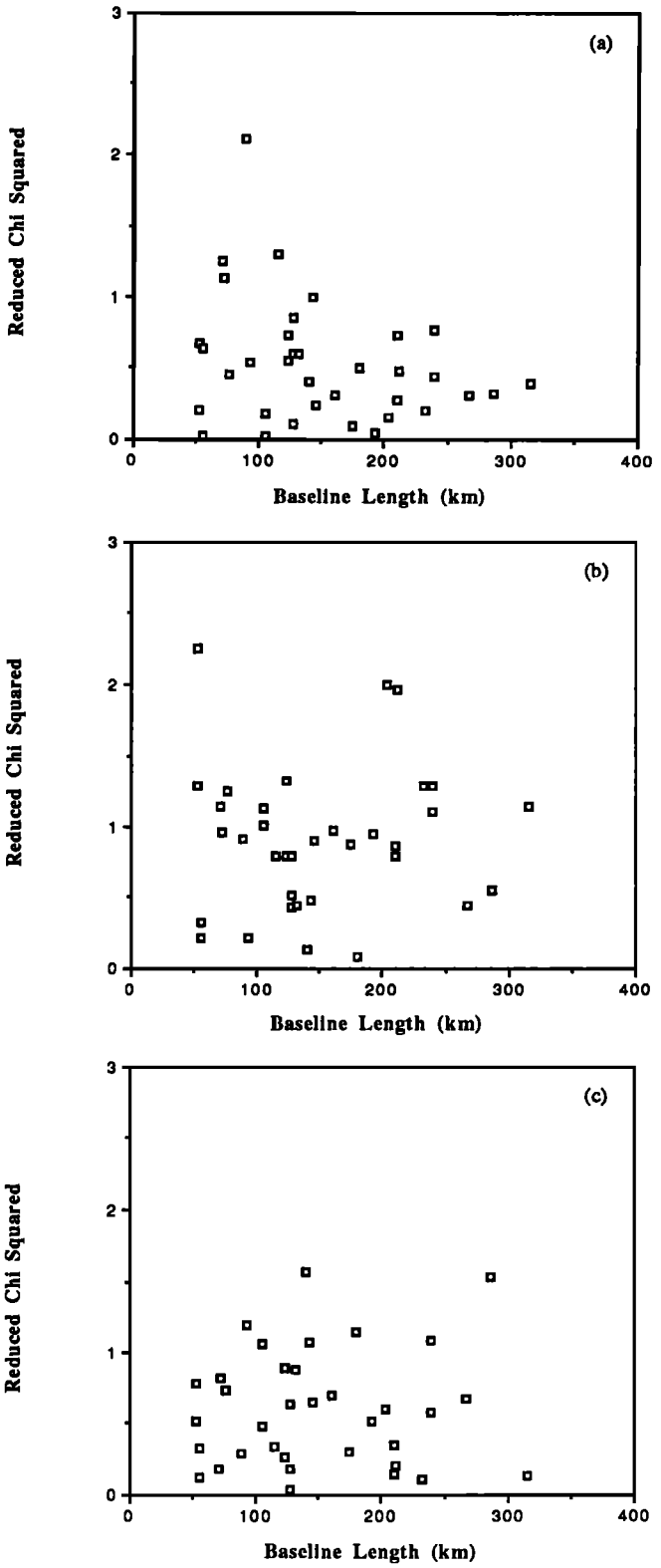

Fig. 4. χ^2 for the baselines shown in Figure 3.

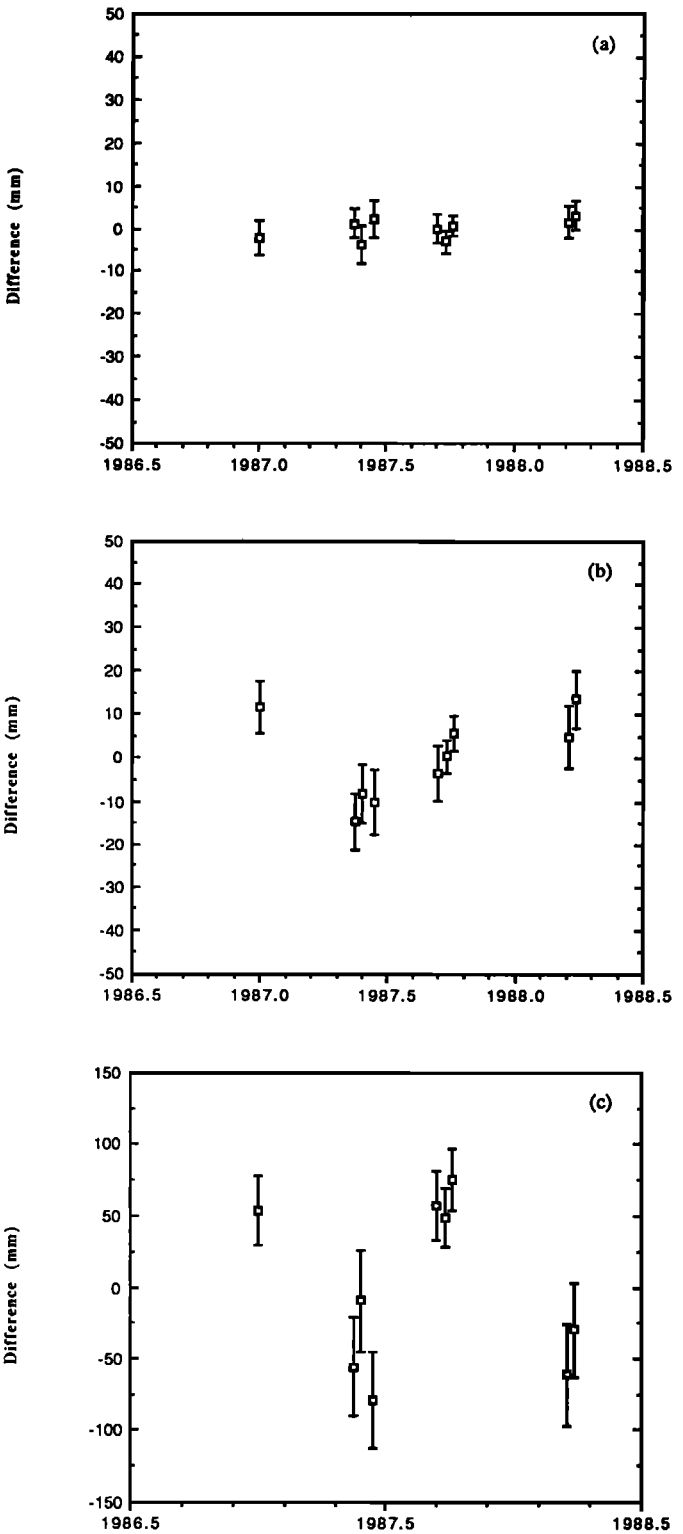

Fig. 5. Change of relative coordinates for the Mojave to OVRO baseline (245 km length), with zero being the mean value. The components shown are defined as in Figure 3, with the coordinate system being centered at the first station.

TABLE 5. Long-Term Precision

Interstation Vector	Length, km	East,[a] mm	χ^2	North,[a] mm	χ^2	Vertical,[b] mm	χ^2	Years	Number of Observations
Lospe-Vandenberg	37	4	2.2	4	2.4	16	0.3	2.2	8
Blancas-Blackhill	53	7	4.0	1	0.1	36	1.6	2.2	8
Clembluf-Brush	54	5	0.7	4	0.8	30	0.8	2.2	8
Lacumbre-Center	55	3	0.8	3	0.8	26	0.7	2.2	11
Madre-Buttonwillow	71	4	1.0	4	3.0	35	1.3	2.2	11
Vandenberg-Madre	76	4	0.9	4	2.0	22	0.6	2.2	10
Madre-Blackhill	76	4	1.0	2	0.4	27	0.8	2.2	11
Blackhill-Vandenberg	91	6	2.2	5	3.1	29	1.1	2.2	13
Palos Verdes-Clembluf	91	10	1.6	5	0.9	39	1.1	2.7	9
Vandenberg Center	101	5	1.4	4	2.5	25	0.8	2.2	16
Palos Verdes-Nicholas	115	8	1.9	4	1.1	29	0.9	2.7	10
Soledad-Clembluf	119	7	1.1	7	3.1	45	1.6	2.7	9
Madre-Center	123	4	1.0	2	0.4	30	1.0	2.2	11
Center-Palos Verdes	127	4	0.6	5	2.2	31	1.1	2.2	16
Buttonwillow-Blackhill	131	3	0.5	5	2.5	32	1.1	2.2	11
Buttonwillow-Blancas	173	6	1.2	5	2.0	42	1.7	2.2	9
Vandenberg-Nicholas	180	6	0.8	9	3.2	26	1.1	2.7	8
Blackhill-Center	181	6	1.5	3	0.6	39	1.5	2.2	16
Palos Verdes-Vandenberg	223	5	0.8	7	3.1	41	1.7	2.2	14
Mojave-Palos Verdes	224	9	1.4	6	1.4	38	1.2	2.2	18
Mojave-Ovro	245	9	1.9	2	0.4	57	4.3	1.2	9
Palos Verdes-Blackhill	286	7	0.9	4	1.0	41	1.6	2.2	12
Ovro-Blackhill	308	13	2.9	5	1.2	34	1.1	2.2	14
Mojave-Vandenberg	351	10	1.5	6	2.4	42	1.8	2.2	18
Mojave-Blackhill	358	6	0.9	4	1.3	46	2.0	2.2	12
Ovro-Vandenberg	363	14	3.0	5	1.2	33	0.9	1.2	11
Ovro-Center	382	14	2.6	5	0.9	47	2.0	2.2	15
				USGS Results[c]					
Mojave-NCMN1	1	2		2		5		2.0	4
10JDG-33JDG	7	6		3		12		3.0	27
10JDG-Joaquin	11	6		5		13		3.0	27
10JDG-Oquin	12	5		4		18		3.0	26
Loma Prieta-Eagle[d]	31	8		4		16		0.9	7
Loma Prieta-Allison[d]	43	8		4		21		0.9	8
Palos Verdes-Vandenberg	223	11		6		40		2.2	6

[a]Weighted RMS about best fitting line, as in equation (3).
[b]Weighted RMS about weighted mean, as in equation (1).
[c]USGS results are taken from *Davis et al.* [1989].
[d]J. Svarc (personal communication, 1990)

of no significant motion in this component is correct. The vertical precision of 57 mm is the worst listed in Table 5.

The long-term precision for the baseline from Vandenberg to Center (located on Santa Cruz Island) is shown in Figure 6. A 101-km baseline oriented NNW, it is considerably shorter than Mojave-OVRO but has been measured almost twice as often, with data spanning 2.2 years. The scatter about the best fit line is 5 and 4 mm for the east-west and north-south components, respectively. The vertical component scatter is 24 mm. All experiments were analyzed with continental-scale fiducial networks, with the exception of the March 1989 data.

The long-term precision statistics are listed in Table 5. For each interstation vector, we computed precision, as defined in the introduction of this section, and the reduced χ^2 statistic. Our criteria for selection of these interstation vectors were that they be estimated during three or more experiments, over at least 1.2 years, with eight or more independent estimates. The long-term precision results have been plotted as a function of baseline length in Figures 7*a*-7*c*. The long-term precision for the north-south component is 4 mm + 0.3 parts in 10^8. In the east-west component, the long-term precision is comparable to the short-term results with a slightly larger constant term, 3.4 mm + 2.0 parts in 10^8. As with our short-term precision results, the vertical component is less precise than either horizontal components and is described by 26 mm + 5 parts in 10^8 of the baseline length. A more careful inspection of Figure 7*c* indicates that long-term vertical precision ranges from 30 to 40 mm, for baselines longer than 50 km, and improves rapidly for smaller values. Thus, for baselines less than 50 km, vertical precision is far better than the constant term of our linear fit, 26 mm, would suggest.

Discussion. We have compiled the long-term precision statistics from *Davis et al.* [1989] and list them in Table 5 along with our interstation vectors. The USGS baselines range from 200 m to 223 km. *Davis et al.* defined precision as the RMS about the best fitting line for both horizontal and vertical components (we compute the RMS about the mean for the vertical component). By including the USGS results, we have a better estimate of GPS precision for baselines less than 450 km in length: 3.4 mm + 1.2 parts in 10^8,

5.2 mm + 2.8 parts in 10^8, 11.7 mm + 13 parts in 10^8 in the north-south, east-west, and vertical components. At 100 km, this would yield subcentimeter horizontal precision, 25 mm in the vertical. Our study overlaps with Davis et al. on one baseline, Palos Verdes to Vandenberg. Our long-term precision of 5, 7, and 41 mm in the north-south, east-west, and vertical only differs appreciably from that of Davis et al. (6, 11, and 40 mm) in the east-west component. We resolved ambiguities on nearly all estimates of this baseline, whereas Davis et al. did not attempt ambiguity resolution. Resolving ambiguities has been shown to improve short-term precision in the east-west component [*Dong and Bock*, 1989; *Blewitt*, 1989], and results from paper 3 indicate that am-

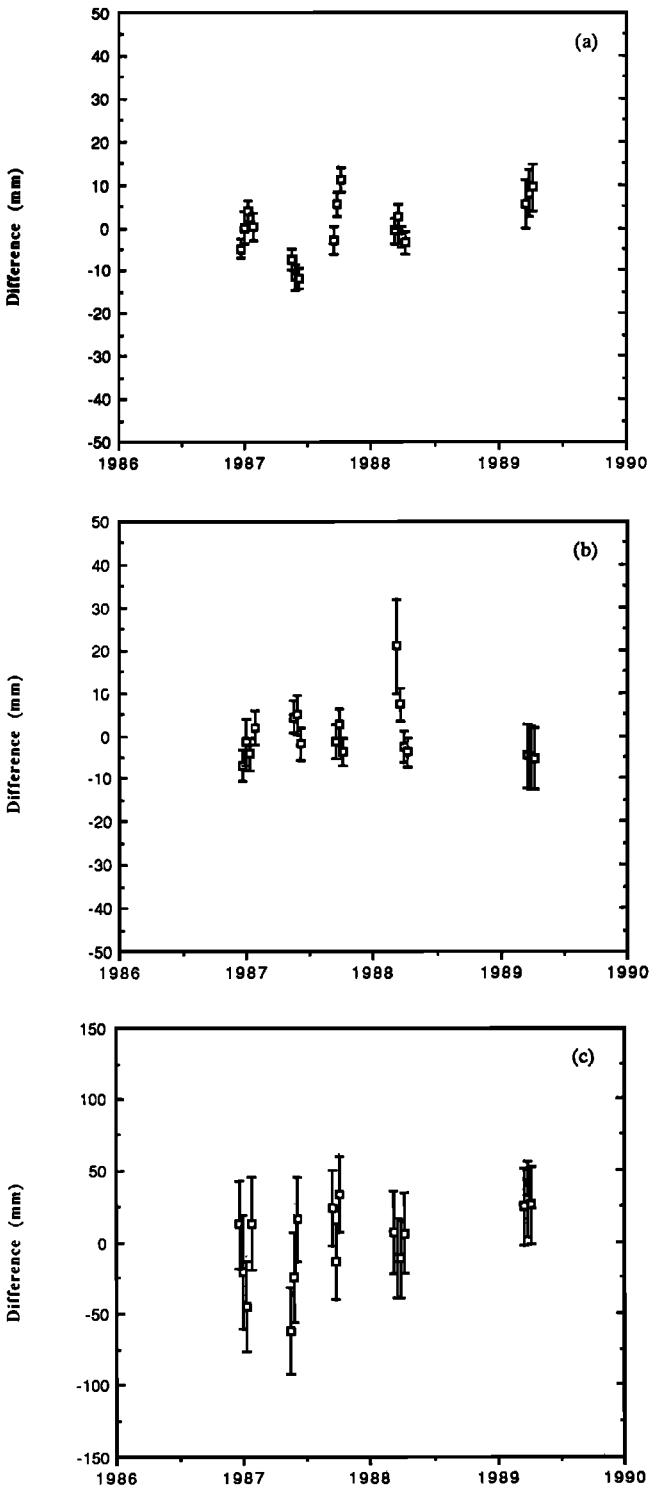

Fig. 6. Change of relative coordinates for the Center to Vandenberg vector (101 km), with zero being the mean value. The components shown are defined as in Figure 3.

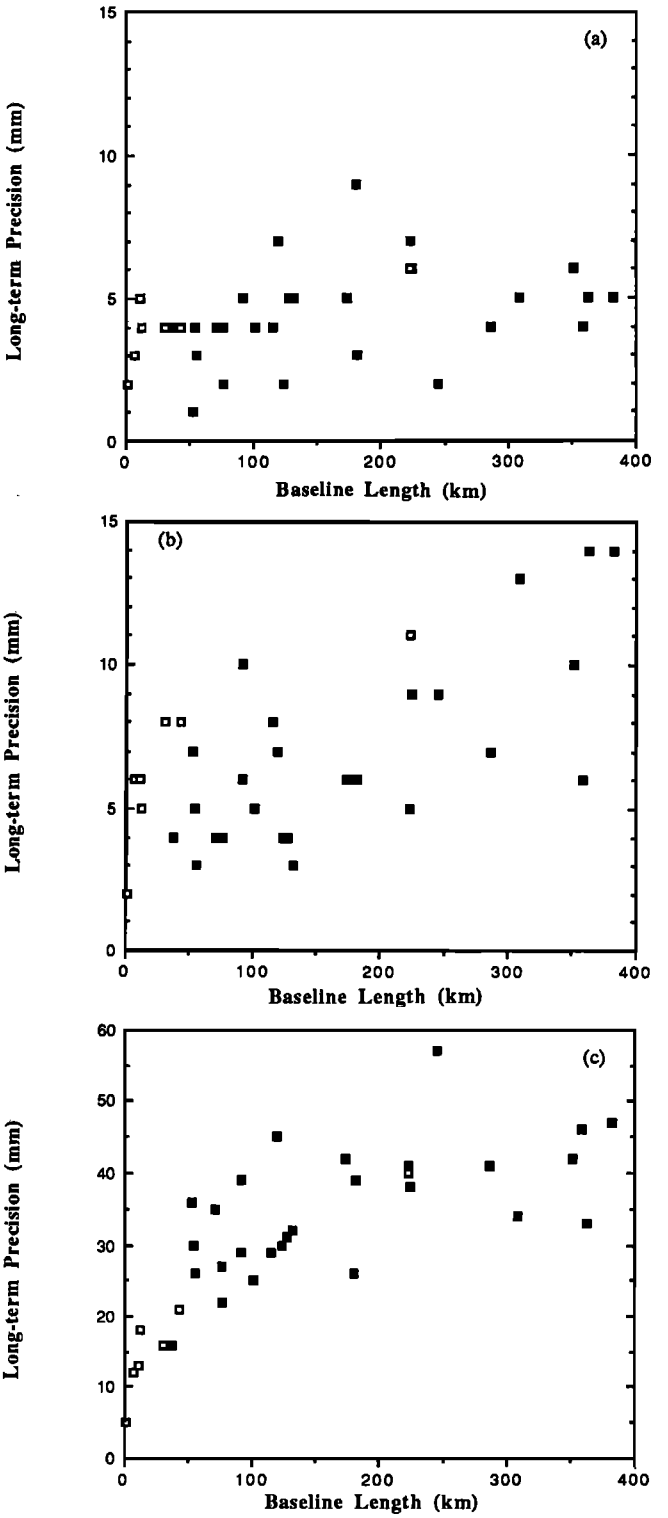

Fig. 7. The solid squares represent the long-term precision determined from experiments described in Table 2. For the horizontal components the precision is defined (equation (3)) as the weighted RMS about the best fitting straight line; for the vertical, by the weighted RMS about the mean (equation (1)). The components are defined as in Figure 3. Also shown are long-term precision determinations (open squares) from *Davis et al.* [1989] for baselines ranging from 200 m to 223 km in length.

biguity resolution improves precision in the long term as well. This may also explain the slightly less precise USGS east-west components for baselines less than 50 km.

Again, we address the question of the validity of our formal errors. In Figures 8*a*-8*c*, we plot χ^2 as a function of baseline length. For the north-south component, our formal errors underestimate the the actual scatter approximately half the time, although χ^2 does not increase with baseline length. For the east-west and vertical components, there is a slight increase of χ^2 with baseline length. Long-term error sources which we think have contributed to the degraded long-term precision are the accuracy of the GPS spacecraft orbit, the ability to resolve carrier phase ambiguities, adequate modeling of the ionosphere and atmosphere, and blunders. Since some of these errors (e.g., orbit accuracy and blunders) have not been accounted for in the formal error, we expect that this has inflated the long-term χ^2 statistic. We discuss each of these error sources in turn.

The orbit accuracy is primarily controlled by the accuracy of the fiducial coordinates, geometry of the fiducial network, and the number of hours of tracking data that were available. Experiments which suffered from failure or absence of continental fiducial sites were, in general, less precise. Additionally, mixing interstation vector estimates computed with different fiducial networks undoubtedly inflates the long-term precision statistic. For the 11 experiments in Table 2, 10 different fiducial networks were used (assuming the three monuments at Mojave to be independent.) Since the purpose of fiducial networks is to provide a consistent reference frame in which to determine crustal deformation rates, their stability is extremely important. The influence of the fiducial network on GPS precision and accuracy is discussed in paper 2. The consistency of our long-term precision with that of *Davis et al.* [1989] leads us to believe that high precision can be achieved with a "single-day" arc, where each day of data yields an independent estimate of satellite orbits and station positions. The precision of single-day arcs on these spatial scales may be dependent on the sophistication of the orbit determination software. For continental-scale (2000-3000 km) baselines, a "multiday" arc solution, as discussed by [*Lichten and Border*, 1987], may be required to achieve comparable precision.

The precision results that we and others (prominently *Dong and Bock* [1989] and *Blewitt* [1989]) have presented were for experiments where a high percentage of carrier phase ambiguities were resolved. The number of hours of tracking influences the confidence statistic used to decide whether the carrier phase ambiguity has been adequately resolved [*Blewitt*, 1989]. In general, we find that ambiguities can be easily resolved with more than an hour of data, with one additional criterion: the interstation spacing should be less than 100 km. In the S88 experiment, the closest spacing of two stations was 223 km. We were only able to resolve 4 of 32 ambiguities. In experiments with closer interstation spacing, e.g., M88b, we were able to resolve 83 of 85 ambiguities in California.

Experiments conducted over a few days do not provide an adequate sampling of tropospheric and ionospheric conditions. This may explain why long-term vertical precision is degraded relative to short-term precision. With the other error sources in these data, it is difficult to isolate the atmospheric and ionospheric contribution. Data that are collected continuously, with a stable fiducial network, will be required to discern the seasonal variations which may be present in these data. Continous GPS networks will also reduce the vertical scatter by eliminating the error associated with centering and measuring the height of the antenna over the monument. Some of the scatter in the vertical component may also be due to human error in translation of field notes into the site vector used in the analysis software.

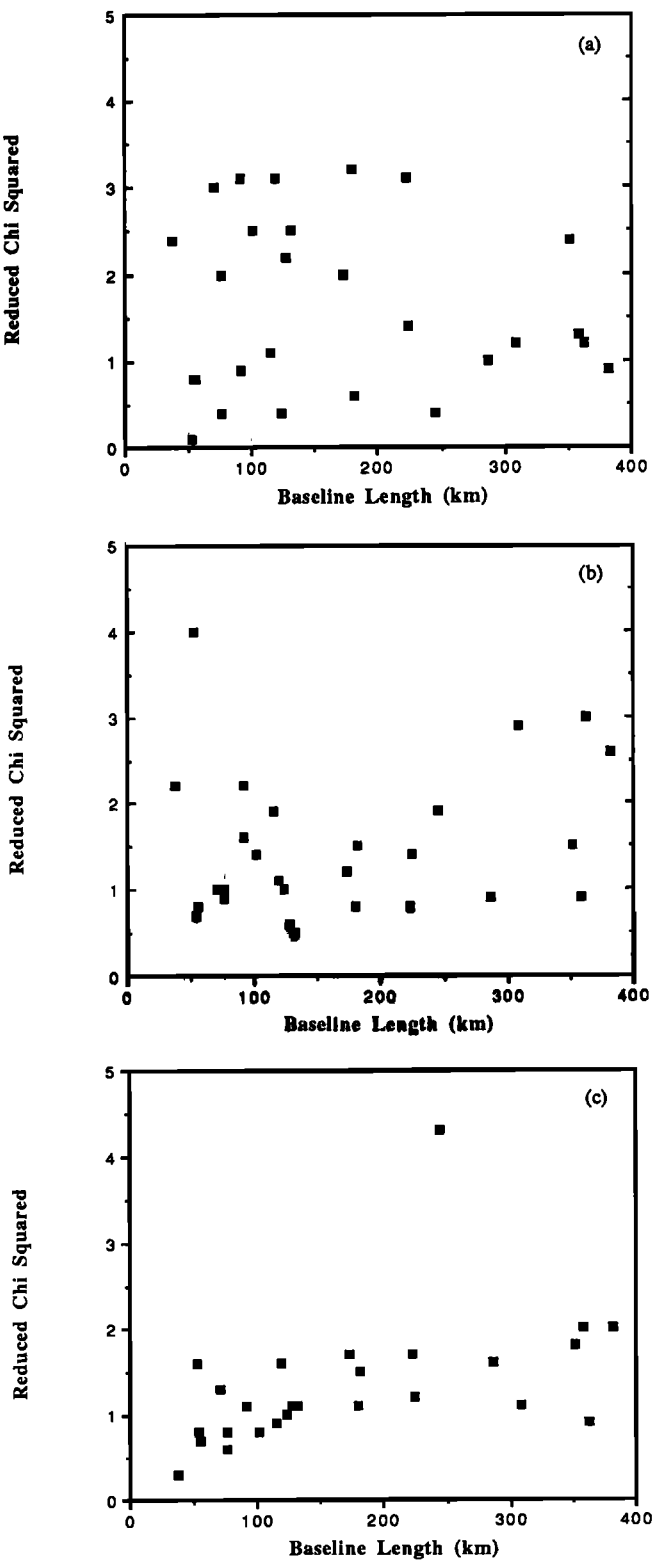

Fig. 8. χ^2 for the baselines shown in Figure 7.

ACCURACY

Introduction

High precision is necessary for, but not indicative of, accuracy. In order to assess accuracy, we must compare GPS vector estimates with vectors determined by an independent measurement system. Comparisons are also useful for identifying systematic errors in GPS, because different techniques presumably have different error sources. VLBI and SLR are two systems available to compare baselines longer than 50 km. No comparisons will be made between GPS and SLR measurements because there are few GPS occupations of SLR monuments in this data set. Unless otherwise noted, the VLBI results are from the 1989 Crustal Dynamics Project Annual Report [*Ma et al.*, 1990] and GLB223, the Goddard site velocity model that was used to determine the GPS fiducial coordinates.

Most estimates of GPS accuracy have been restricted to single epoch agreement with VLBI or SLR [*Dong and Bock*, 1989; *Blewitt*, 1989; *Bock et al.*, 1990], with the exception of work by *Davis et al.* [1989]. Using data from six experiments conducted in southern California, Davis et al. compared GPS and VLBI length estimates of the 223-km baseline between Palos Verdes and Vandenberg. Agreement was within the standard deviations of GPS and VLBI. They also compared line lengths from the Hebgen Lake (9-30 km) and Loma Prieta (30-50 km) networks with the Geodolite, a laser measurement system, with agreement of 1-2 mm at these lengths. At Parkfield, they compared the fault-parallel motion to creep meters and alignment arrays, where rates agreed to within 1-2 mm/yr. While we cannot compare our interstation vectors with as many different kinds of systems, we have concentrated our efforts on the accuracy of "regional" scale baselines. We assess the accuracy of GPS in two modes: agreement of interstation vectors and linear trends.

As with our precision study, we would like to know if accuracy degrades with baseline length. The literature has often referred to agreement with VLBI in terms of parts per baseline length. This is useful if there is a true deterioration of accuracy with baseline length but is inappropriate where errors are not necessarily dependent on baseline length. Certainly, orbit estimation may contribute a baseline dependent error for comparisons at the continental baseline scale, but for baselines shorter than 500 km, there is no evidence to date that the $|GPS - VLBI|$ discrepancy is length dependent.

Comparisons between new and standard measurement systems are essential for validation of the new measurement technique. The difficulty in comparison studies arises in determining the correct rotations which are required to compare vectors which were determined in different reference frames. Even simple comparisons of line lengths determined by EDM and GPS require that a scaling factor be introduced to account for the difference in the speed of light value used in the two data analysis systems. Since GPS vectors are referenced to a VLBI system of fiducial coordinates, GPS and VLBI comparisons are simplified somewhat. A more mundane element of vector comparisons is due to local site surveys. Different systems (VLBI, SLR, GPS) occupy different geodetic monuments at the same geographic location. Generally, these monuments are separated by only several hundred meters, and conventional surveys can be done with an accuracy of a millimeter at these distances. In practice, local surveys introduce uncertainty into the accuracy assessment.

Measurements between the different monuments at these sites (local surveys) are of several types and need to be treated differently. There are conventional surveys, differential GPS determinations, and simple measurements of height above a monument, which we discuss in turn. Conventional surveys have varying levels of redundancy and therefore accuracy. In many cases what are termed survey errors are actually errors in user understanding of the meaning of the coordinate differences coming from ground surveys or blunders in passing along information and not measurement error (W. Strange, personal communication, 1990). The precision of differential GPS surveys on these scales is several millimeters in the horizontals but is twice that in the vertical. *Davis et al.* [1989] reported long-term vertical precision of 5 mm for a 240-m baseline. This is considerably less precise than the best conventional surveys. On the other hand, the accuracy of differential GPS surveys is not well understood or documented. The accuracy of these surveys may be dependent on which GPS receivers were used and which software was used to analyze the measurements. Measurements of height above the geodetic monument are required for both GPS and VLBI. For the TI-4100 GPS receiver, it is assumed that the difference between the L_1 and L_2 phase centers and the antenna base is well known, although discrepancies have been reported (J. Svarc, personal communication, 1990). Likewise, errors in VLBI site vector measurements, for baselines with very few data, will map into a $|GPS - VLBI|$ discrepancy.

As an example of a typical situation in accuracy determinations, Figure 9 illustrates the number of vectors that must be added to compare VLBI and GPS baseline vectors between Mojave and Vandenberg. Terms which are underlined are GPS sites, or antenna phase centers. The numbers refer to the Crustal Dynamics Project site catalog. Two local surveys were required to recover the vector from the main

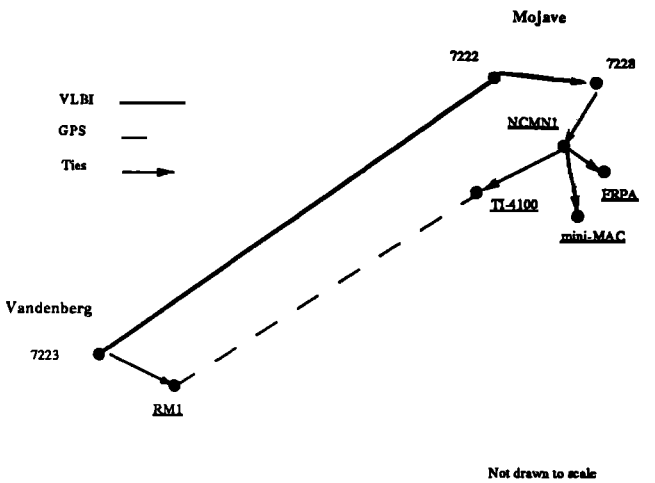

Fig. 9. Cartoon to show the vectors which must be measured to compare GPS and VLBI measurements on a typical baseline. The bold vector between VLBI monuments at Vandenberg and Mojave is 351 km long. The dashed line represents the vector between GPS monuments. GPS monuments/antennae are underlined. Each segment with an arrow represents a local survey which must be conducted to compare GPS and VLBI baseline solutions. This figure is not drawn to scale. Actual survey values are listed in Table 6.

VLBI mark at Mojave to the VLBI reference mark, NCMN1. These surveys were done conventionally. The measurements from NCMN1 to the three permanent antennae which were placed at Mojave between mid-1988 through early 1989 were made with GPS. For completeness, in Table 6 we have listed the relevant local survey information that we have used. In addition to crustal deformation measurement sites in California, we also list local surveys at fiducial sites.

Although it is important to compare interstation vectors at a single epoch (we compare a few vectors measured during the J86 experiment), long-term monitoring of the interstation vector will help to find probable local survey errors. We feel that comparison of rates is ultimately more useful for crustal deformation studies, because the fundamental measurement that we seek is the time rate of change of the vector between two sites. Rate determinations are not immune from local survey errors. If that station is used as a fiducial site in some estimates but not for others, this will influence the computed rate. We discuss only a few interstation vectors in detail.

Results

The data collected in Table 2 were directed toward measuring crustal deformation rates in California. Therefore, comparisons with VLBI are mostly limited to interstation vectors in California. Prominently featured in the available

TABLE 6. GPS-VLBI Local Survey Values

Station 1	Station 2	X, m	Y, m	Z, m	Survey Type	Agency	Reference
			Algonquin Park				
6381	Algonquin (GPS)	92.760	70.280	13.066	conventional	GSC	1
			Mojave				
7222	7288	-323.1130	148.2132	-43.9926	conventional		2
7288	NCMN1	69.6589	-5.9415	35.6147	conventional		2
NCMN1	CIGNET-TI4100	-209.804	120.407	1.836	GPS, NGS[a]	NGS	3
NCMN1	CIGNET-FRPA	-209.7820	120.4134	1.8247	GPS, Bernese[b]	USGS	3
			Owens Valley Radio Observatory				
7207	7853	-820.4891	549.1188	87.1157	conventional		3
7853	7114 (GPS)	-1.2227	-2.2611	-3.6171	conventional		3
			Richmond, Florida				
7219	TIMER 1962	59.722	35.2121	29.920	conventional		3
TIMER 1962	CIGNET-FRPA	0.5483	-3.2420	1.5754	conventional		3
			Westford Observatory				
7209	MICRO	111.191	84.088	43.334	conventional		3
MICRO	CIGNET-TI4100	-84.8933	-45.2645	-12.9246	GPS, NGS	NGS	3
			Vandenberg Air Force Base				
7223	RM1 (GPS)	23.105	-0.9629	17.253	conventional	NGS	1

Compilation of local survey information used, referenced to WGS84. Numbers are associated with the Crustal Dynamics Project VLBI marks. Full listings are given by *Noll* [1988]. For survey types, we distinguish between those done conventionally, and those done with GPS receivers. For GPS surveys, we indicate the software used. All GPS surveys were measured with TI-4100 GPS receivers. If known, the agency which conducted the survey and computed the survey values is listed. References: 1, M. Murray, (personal communication, 1990); 2, J. Ray, (personal communication, 1990); and 3, *Chin* [1988].

[a] *Mader* [1988].

[b] *Beutler et al.* [1987].

TABLE 7. GPS-VLBI Vector Differences

Interstation Vector		Length, km	East, mm	North, mm	Vertical, mm	GPS		VLBI	
						Years	Number of Observations	Years	Number of Observations
Yuma[a]	Monument Peak[a]	208	-10	5	-20	E	2	4.1	8
Mojave	Palos Verdes	224	-15	-12	-80	2.3	18	4.1	5
Mojave	Ovro	245	-8	10	-60	1.2	9	4.3	62
Fort Ord	Vandenberg	256	-10	-15	0	1.2	10	4.2	7
Fort Ord	Ovro	316	5	8	8	1.2	8	4.2	5
Mojave	Vandenberg	351	-15	-13	-50	2.3	18	4.3	89
Ovro	Vandenberg	364	-10	-30	-10	1.2	9	4.2	40
Monument Peak	Vandenberg	430	10	-16	7	E	2	4.0	18

E: single epoch measurement.

[a] See *Noll* [1988] for station description.

data are VLBI sites at Fort Ord, Mojave, OVRO, Vandenberg, and Palos Verdes. GPS and VLBI interstation vector changes will be displayed in a standard form, with the north-south, east-west, and vertical components. Zero is the mean value of the GPS estimates. The solid line in each figure is the VLBI baseline vector component which results from a simultaneous global estimate of site velocities (GLB223). Since this site velocity model was used to compute fiducial locations for the GPS experiments, this is the most appropriate measure of agreement with VLBI. The error bars for the GPS baseline components are one standard deviation. Based on our long-term precision study, these formal errors underestimate the actual uncertainty. The differences between GPS and VLBI for all baselines are listed in Table 7. The interstation vectors compared at more than one epoch which we discuss in greater detail are the vectors between Mojave and Vandenberg, Mojave and Palos Verdes, and OVRO and Fort Ord.

Mojave-Vandenberg-Palos Verdes. In June 1986, the USGS began an effort to regularly measure the interstation vectors between monuments at Mojave, Palos Verdes, and Vandenberg Air Force Base. Due to the commitment of both personnel and receiver time, these are now the most frequently occupied mobile GPS baselines in California longer than 200 km. For Vandenberg and Mojave, there were eight experiments over 33 months, spaced 4-6 months apart. Palos Verdes was occupied simultaneously with Mojave and Vandenberg in seven of those experiments.

Mojave to Vandenberg is the most frequently occupied VLBI baseline in California, with 89 observations between 1983 and 1988. This baseline is long enough to begin to show deterioration in the GPS east component due to poor orbit determination in several of the seven epochs shown, particularly J88 and S88, where we were unable to resolve a large number of the carrier phase ambiguities. Figure 10 displays the GPS vector components from 1986 through 1988. The offset between GPS and VLBI coordinates is 15 mm in the east and 13 mm in the north. The GPS rates derived for the north-south and east-west components of the Vandenberg-Mojave vector are -25.5 ± 2 and 28.9 ± 4 mm/yr, respectively. This agrees within one standard deviation of the VLBI estimates of -28.1 ± 2.0 and 27.6 ± 1.6 mm/yr. The GPS east-west component is significantly noisier than the north-south component, as evidenced by the weighted RMS about the best fitting line: 6 and 10 mm in the north-south and east-west components, respectively. In the vertical component, GPS has a RMS of 41 mm and disagrees with the VLBI mean by 50 mm. The VLBI vertical RMS about the best fitting line is 37 mm.

Palos Verdes was measured by VLBI only five times between 1983 and 1987. We have estimated 18 independent interstation vectors with the GPS data that were collected between 1986 and 1988, as shown in Figure 11. The VLBI and GPS monuments at Palos Verdes are identical. The rates from VLBI are -19 ± 3.7 and 20 ± 3.4 mm/yr in the north-south and east-west components respectively. The GPS rates are similar: -20 ± 2.5 and 28 ± 4 mm/yr. The horizontal components both exhibit an offset of approximately 15 mm. The weighted RMS about the best fitting line for GPS is 8 and 9 mm for the east-west and north-south components. In the vertical component, the precision is less than 50 mm for both VLBI and GPS, but their means disagree by 80 mm. This is the largest difference of eight baselines listed in Table 7.

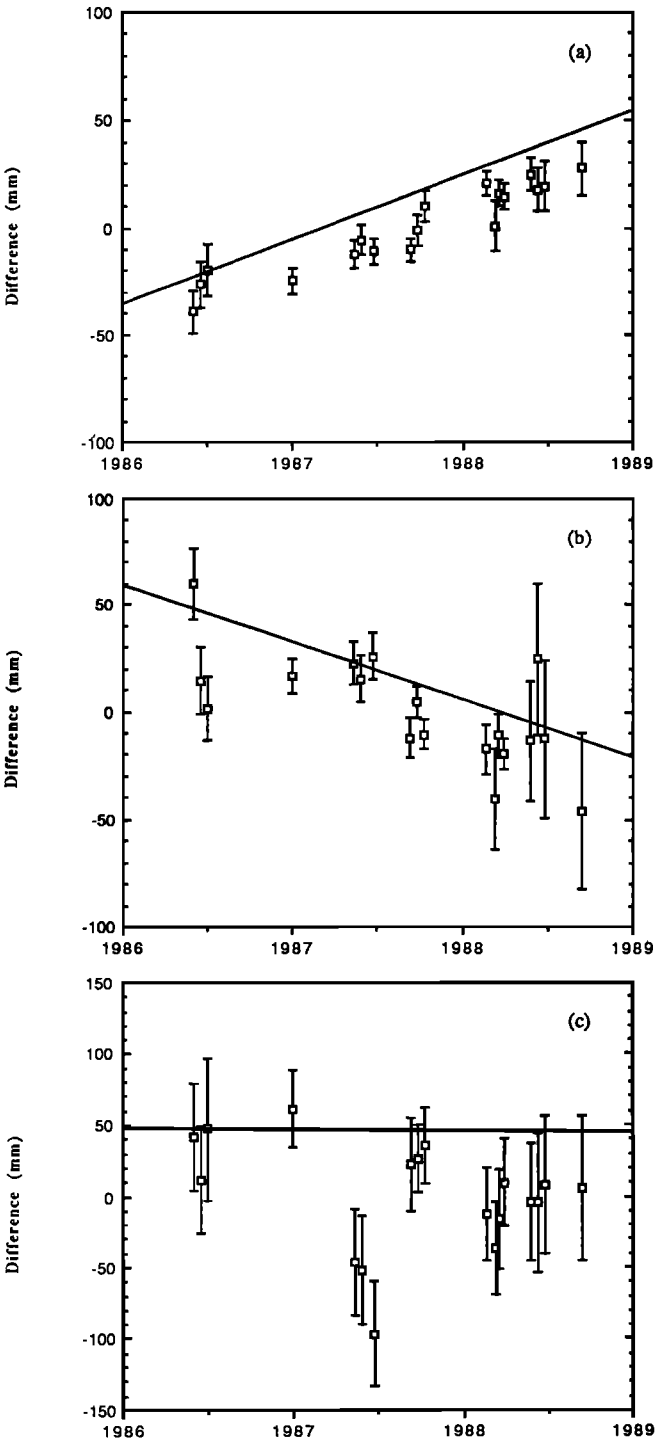

Fig. 10. The points with error bars are the GPS-derived relative coordinates for the Mojave to Vandenberg vector (351 km), taken relative to the mean. The solid line shows the coordinates given by a model fit (GLB223) to the VLBI data. While the agreement in rates is good, there is a persistent offset between the two types of measurement. Components are defined as in Figure 3.

OVRO-Fort Ord. The OVRO-Fort Ord baseline vector is 316 km long and oriented nearly east-west. OVRO requires a conventional survey, but the Fort Ord monument is used by both VLBI and GPS. There have only been three GPS experiments including Fort Ord, over the space of 1.2 years, whereas VLBI experiments span over 4 years. Agreement between GPS and VLBI is shown in Figure 12. Agreement of GPS to VLBI is 5 mm in the east and 10 mm in the

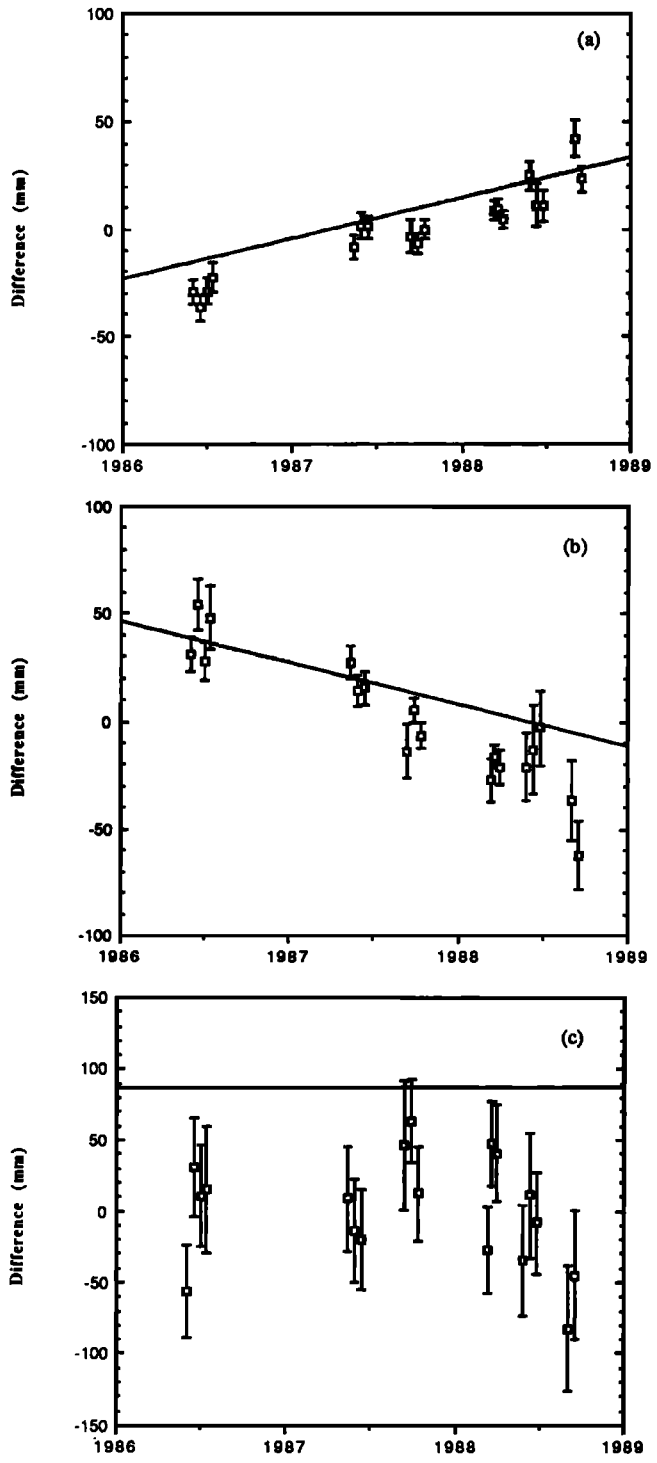

Fig. 11. Change of relative coordinates for the Mojave to Palos Verdes vector (224 km). See Figure 10 for details.

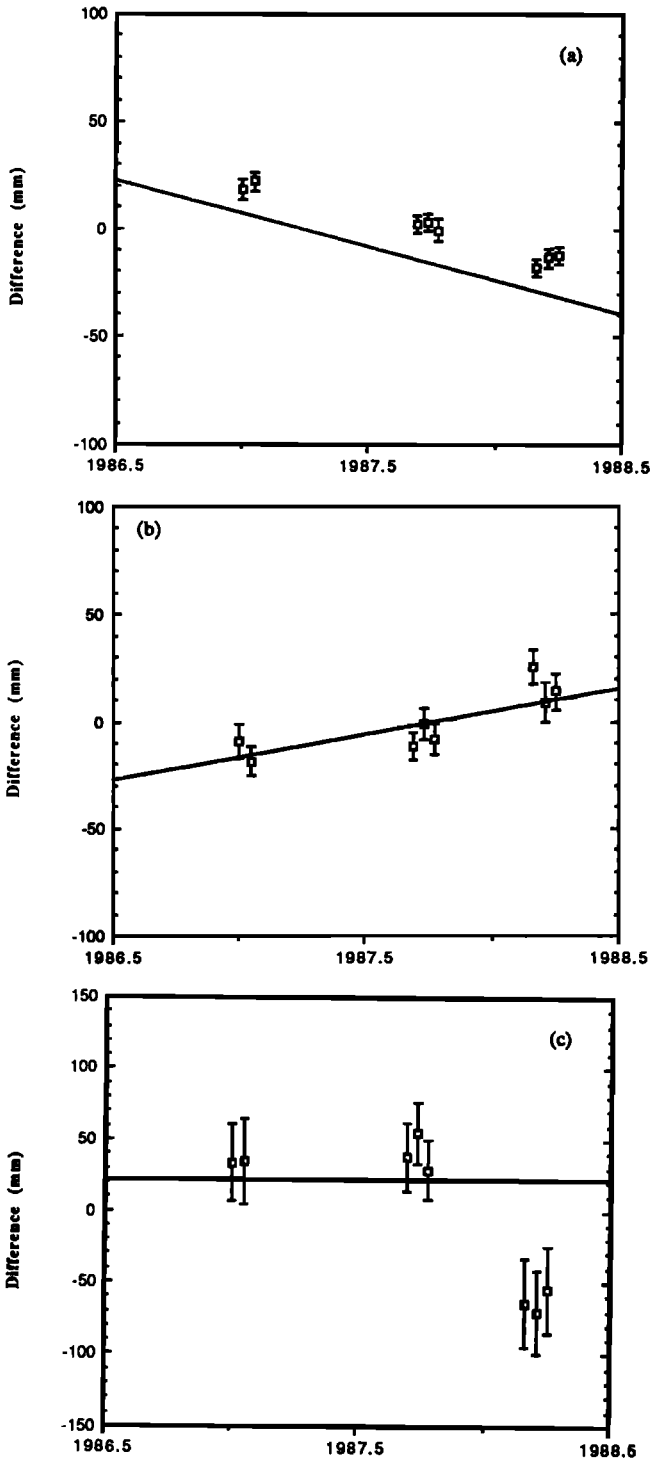

Fig. 12. Change of relative coordinates for the OVRO to Fort Ord vector (316 km). See Figure 10 for details.

north. The vertical agreement is within 20 mm for two experiments and 60 mm for the third. The computed rates for OVRO-Fort Ord agree with VLBI rates within one standard deviation, but the uncertainties on the GPS rate estimates are quite large, due to the short time-span of occupations.

Comparison of Vertical Components

The absolute value of the vertical component difference between GPS and VLBI is shown in Figure 13 as a function of baseline length. The error bar is determined from the weighted RMS about the best fitting line for VLBI and weighted RMS about the mean for GPS. The disagreement is less than 80 mm on baseline vectors ranging from 200 to 430 km. *Dong and Bock* [1989] compared single epoch vertical estimations for the Mojave-OVRO baseline and agreed within 22 mm of the VLBI solution. Results from *Blewitt* [1989] are more comparable to Figure 13, where at a single epoch, the agreement with VLBI was from 5 to 80 mm, measured on 15 baselines ranging from 100 to 1100 km.

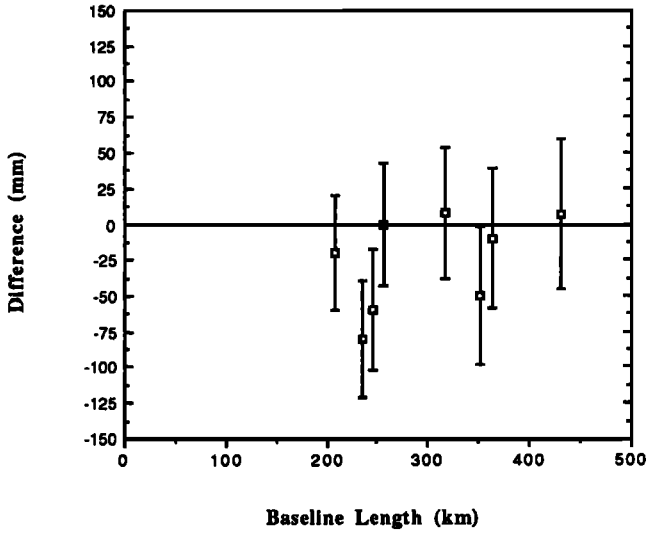

Fig. 13. The GPS-VLBI vertical component difference, plotted as a function of length. The error bar is determined from the weighted RMS about the best fitting line for VLBI [*Ma et al.*, 1990] and weighted RMS about the mean for GPS. More discussion can be found in the text and Table 7.

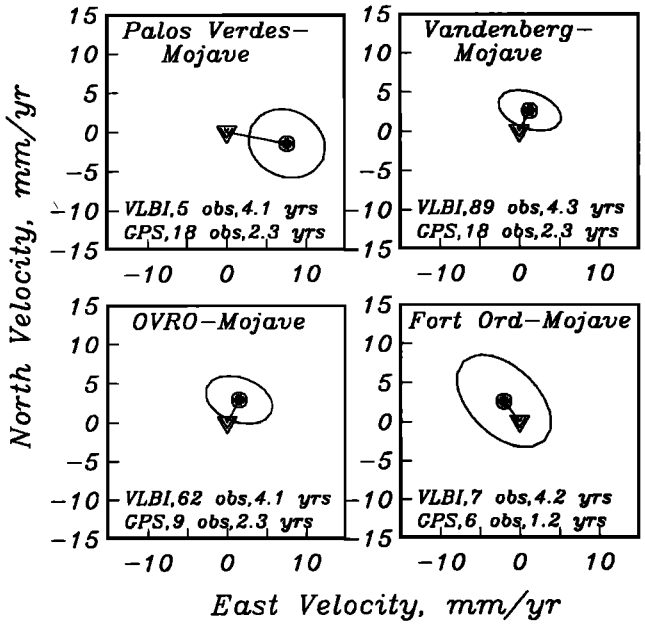

Fig. 14. Difference in vector rates for GPS and VLBI derived motion of Fort Ord, OVRO, Vandenberg, and Palos Verdes relative to Mojave. Zero, shown by the inverted triangle, is the VLBI horizontal rate, and the difference of the GPS rate is shown as a solid circle. Error ellipses are one standard deviation, including both GPS and VLBI. The number of observations and time span of measurements for each baseline are listed.

Comparison of Rates

Finally, we compare rates for four baseline vectors in southern and central California. Figure 14 shows the GPS-VLBI rate difference vector for interstation vectors between Mojave and OVRO, Vandenberg, Palos Verdes, and Fort Ord. The error ellipses were computed from the GPS and VLBI one standard deviations, and then projected onto the horizontal plane. The GPS standard deviations would yield ellipses oriented nearly along the north-south/east-west axes. The addition of the VLBI standard deviations rotates the ellipses slightly, although in general, the GPS standard deviations dominate the error ellipses. The GPS rates for Fort Ord and OVRO are determined from only 1.2 years; those at Palos Verdes and Vandenberg are determined from 2.3 years. The VLBI rates are determined from 4 or more years of data. The only significant difference between GPS and VLBI rates is for the east-west component of Palos Verdes. The vertical rates of deformation for both VLBI and GPS are less than their formal uncertainties.

Discussion

There are several possible reasons that VLBI and GPS vector components disagree, at this level. The differences on some of the interstation vectors listed in Table 7 are suggestive that a single "survey error" may, in fact, be responsible for a large portion of the GPS-VLBI horizontal discrepancy. In order to test this hypothesis, we have taken solutions from the four (D86, S87, M88a and M88b) experiments that include the VLBI sites OVRO, Fort Ord, Mojave, and Vandenberg. These experiments were all analyzed with continental-scale fiducial networks but not necessarily the same ones (as indicated in Table 2). Using the VLBI solutions for these sites at each epoch, we adjusted the GPS interstation vectors and solved for the best fitting "discrepancy" vector at OVRO, Vandenberg, and Mojave. We did not adjust Fort Ord, as the GPS and VLBI monuments are identical. The formal errors from the GPS estimates were used to weight the fit. The results of this calculation are shown in Table 8. The only offsets we consider to be significant are the discrepancies in the north-south and east-west components for Vandenberg, where the best fitting vector is -14 ± 8 and 13 ± 4, and the north-south component at OVRO, 13 ± 2. The

TABLE 8. Estimated Survey Discrepancy Vectors

Experiment	OVRO		Mojave		Vandenberg	
	North	East	North	East	North	East
D86	15±10	-9± 8	5±14	-9± 11	-12±11	-9±9
S87	14± 7	-21± 6	6± 8	-17± 7	-7± 7	-16±6
M88a,b	11 ±8	9± 6	-6± 8	13± 7	-21± 7	-11±7
Weighted mean	13±2	-7±16	1± 7	-3±17	-14±8	-13±4

All values are in millimeters.

latter is particularly surprising, given the energy which was expended to remeasure the line between Mojave and OVRO in the "MOTIES" experiment (J. Ray, personal communication, 1989). The result is consistent with the observed discrepancy between Mojave and OVRO of 10 mm. Likewise, the discrepancy at Vandenberg would explain the long-term discrepancy between Mojave and Vandenberg and would be sufficient to create the largest discrepancy on these regional baselines, between OVRO and Vandenberg

Another reason for horizontal component discrepancies is the robustness of the solution for the vector, either from GPS or VLBI. Both systems will reduce the uncertainty in the interstation vector with additional data. Some vectors (such as OVRO-Fort Ord) are measured by VLBI once per year, whereas the VLBI Mojave-Vandenberg vector is based on 89 measurements. Both Mojave and Vandenberg are fixed VLBI antennas, whereas Fort Ord is a mobile VLBI site. The interstation vectors between fixed antennas (which generally are measured more often) are more precisely known than those between mobile antennas.

The vertical component discrepancies, while troubling for some baseline vectors, are based on very few data points. We assumed that the GPS phase center, which varies with elevation angle to the GPS satellite, averaged to some mean value. This phase center variation may in fact introduce a systematic bias, which could introduce the offset we see between GPS and VLBI. GPS vertical components are particularly sensitive to poor fiducial networks (see paper 2). Another possible source of vertical discrepancies is differences due to the estimation technique used to determine propagation delays of the atmosphere. We discuss this further in paper 3.

The agreement between GPS and VLBI rates in all components is extremely encouraging, particularly considering the short time span of GPS data collection. We expect that the rate agreement will continue to improve as we collect more data and eliminate systematic errors.

CONCLUSIONS

We have analyzed nearly 3 years of GPS data collected in southern and central California between 1986 and 1989. On time scales of a few days, horizontal precision is 2 mm, with an additional length dependence of 0.6 and 1.3 parts in 10^8 for the north-south and east-west components, respectively. Short-term precision in the vertical is length independent, with a mean value of 17 mm. Horizontal precision determined over several years, where we have included recent precision estimates from the USGS [*Davis et al.*, 1989], has a constant bias of 5 mm, with a length dependence of 1 and 3 parts in 10^8 for the north-south and east-west components, respectively. These measurements were made when the GPS constellation was preferentially aligned north-south. Presumably, the precision of future GPS measurements will show less dependence on the direction of the interstation vector. Vertical measurements are much less precise than horizontal measurements, 11.7 mm + 13 parts in 10^8.

Accuracy (defined by agreement of horizontal components with those found from VLBI) is 5-30 mm for baselines from 200 to 430 km long. The pattern of these discrepancies is consistent with a survey discrepancy at two VLBI sites in California, Vandenberg and OVRO. For interstation vectors that do not include these sites, agreement of horizontal components is approximately 10 mm. The vertical discrepancies between VLBI and GPS are much larger, ranging from 0 to 80 mm. There does not seem to be a systematic bias between the two systems, which in any case is unlikely because VLBI defines the orientation and scale of the GPS reference system. For making crustal deformation measurements, the most important comparison may be between the vector rates determined by the two systems. The GPS-determined vector rates agree well with those determined from VLBI measurements.

These results confirm the study of *Davis et al.* [1989], which found that precision and accuracy (in rates) was subcentimeter on these spatial scales. In turn, this confirms that GPS geodetic measurements are appropriate for crustal deformation experiments, where signals range from several millimeters to hundreds of millimeters per year. This precision and accuracy may not, of course always be achieved, and there are reasons why the data set we have studied may be better than most. Although we cannot prove this assertion, we feel that one of the most important factors in repeating high-accuracy GPS measurements is keeping as many factors common to all experiments as possible. Although the tracking data for the different experiments have not been homogeneous, most other factors were: the same GPS receiver and data analysis software were used; the same type of GPS antenna was used at nearly all stations; and the same GPS satellites (which followed nearly the same apparent sky paths) were available. The challenge remains for the geodetic community to successfully mix different receivers, antennas, block I and block II GPS satellites, and analysis software and to retain the high precision and accuracy achieved with the block I GPS constellation.

Acknowledgments. Much of the GPS data used in this paper were collected as part of a collaborative project to measure crustal deformation in central and southern California by the Scripps Institution of Oceanography, California Insititute of Technology, University of California, Los Angeles, and Massachusetts Insitute of Technology. We are particularly indebted to dozens of graduate students who contributed their time to this effort. The principal investigators, Dave Jackson, Bob King, Tom Jordan, and Brad Hager, were instrumental in making these experiments possible. The scope of this study would not have been possible without the cooperation and participation of the NGS and USGS, which were conducting their own surveys in the region. We thank Bill Strange and Will Prescott for supervising the collection of high-quality GPS data in California. Tracking data were provided by CIGNET. We thank Jerry Mader, Miranda Chin, and Linda Nussear for helping us acquire these data. Additional data and receivers were provided by JPL, CIGNET, DMA, PMTC, and the Geodetic Squadron of Canada. Logistical (James Stowell) and archival (Judah Levine) support was provided by UNAVCO. One of the authors (K.M.L.) benefitted from numerous conversations with Jim Davis, Geoff Blewitt, Will Prescott, and Steve Lichten. K.M.L. would also like to thank Mark Murray, Frank Webb, Kurt Feigl, Jeff Freymueller, Jerry Svarc, and Shawn Larsen for helpful discussions on GPS data analysis techniques. Computing facilities and the GIPSY software were provided by the Jet Propulsion Laboratory. We particularly thank Tom Yunck and Tim Dixon and their groups for supporting this work. Written reviews by Jim Davis, Bill Strange, Steve Lichten, and George Born improved the quality and scope of this paper. The data collection was funded (at UCSD) by NSF EAR-8618165. This research was supported by a NASA Graduate Student Research Fellowship awarded to K.M.L. at Scripps Institution of Oceanography. The writing and publication were completed at the Colorado Center for Astrodynamics Research and supported by ONR N0001490J2010.

REFERENCES

Beutler, G., I. Bauersima, W. Gurtner, M. Rothacher, T. Schildknecht, G. L. Mader, and M.D. Abell, Evaluation of the 1984 Alaska Global Positioning System campaign with the Bernese GPS software, *J. Geophys. Res., 92,* 1295-1303, 1987.

Bevington, P., *Data Reduction and Error Analysis for the Physical Sciences*, McGraw-Hill, New York, 1969.

Blewitt, G., Carrier phase ambiguity resolution for the Global Positioning System applied to geodetic baselines up to 2000 km, *J. Geophys. Res., 94,* 10,187-10,203, 1989.

Blewitt, G., An automatic editing algorithm for GPS data, *Geophys. Res. Lett., 17,* 199-202, 1990.

Bock, Y., R., I. Abbot, C.C. Counselman III, and R.W. King, A demonstration of one to two parts in 10^7 accuracy using GPS, *Bull. Geod., 60,* 241-254, 1986.

Chin, M., CIGNET report, GPS bulletin, Global Positioning Subcommission of Comm. VIII, Int. Coord. of Space Technol. for Geod. and Geodyn., Natl. Geod. Surv., Rockville, Md., 1988.

Christodoulidis, D.C., D.E. Smith, R. Kolenkiewicz, S.M. Klosko, S.M. Torrence, and P.J. Dunn, Observing tectonic plate motions and deformations from satellite laser ranging, *J. Geophys. Res., 90,* 9249- 9263, 1985.

Clark, T.A., D. Gordon, W. E. Himwich, C. Ma, A. Mallama, and J. W. Ryan, Determination of relative site motions in the western United States using Mark III very long baseline interferometry, *J. Geophys. Res., 92,* 12,741-12,750, 1987.

Davis, J.L., W.H. Prescott, J. Svarc, and K. Wendt, Assessment of Global Positioning System measurements for studies of crustal deformation, *J. Geophys. Res., 94,* 13,635-13,650, 1989.

Dong, D., and Y. Bock, Global Positioning System network analysis with phase ambiguity resolution applied to crustal deformation studies in California, *J. Geophys. Res., 94,* 3949-3966, 1989.

Hayford, J. F., and A. L. Baldwin, Geodetic measurements of earth movements, in *The California Earthquake of April 18, 1906*, edited by A. L. Lawson, pp. 114-145, Carnegie Institution, Washington D.C., 1908.

Henson, D. J., E. A. Collier, and K. R. Schneider, Geodetic applications of the Texas Instruments TI 4100 GPS navigator, paper presented at the 1st International Symposium on Precise Positioning with the Global Positioning System, U.S. Dep. of Commer., Rockville, Md., April 15-19, 1985.

Herring, T. A., et al., Geodesy by radio interferometry: evidence for contemporary plate motion, *J. Geophys. Res., 91,* 8341-8347, 1986.

Larson, K. M., Precision, accuracy, and tectonics from the Global Positioning System, doctoral dissertation, Univ. of Calif., San Diego, 1990.

Larson, K. M., F.H. Webb, and D.C. Agnew, Application of the Global Positioning System to crustal deformation measurements. 2. The influence of orbit determination errors, *J. Geophys. Res.*, this issue.

Lichten, S.M., and J.S. Border, Strategies for high precision GPS orbit determination, *J. Geophys. Res., 92,* 12,751-12,762, 1987.

Lichten, S.M., High accuracy Global Positioning System orbit determination: Progress and prospects, in *Proceedings of the General Meeting of the I.A.G., August 3-12, 1989, Edinburgh, Scotland, GPS and Other Radio Tracking Systems*, edited by Y. Bock and N. Leppard, pp. 40-52, Springer-Verlag, New York, 1990.

Ma, C., J.W. Ryan, and D. Caprette, Crustal Dynamics Project data analysis-1988, *NASA Tech. Memo., TM-100723,* 1989.

Mader, G.L., GPS Data Processing Program Documentation, Geodetic Research and Development Lab, NGS Division, Rockville, MD, August, 1988.

Noll, C., Crustal Dynamics Project: Catalogue of site information, *NASA Ref. Publ., 1198,* 1988.

Rueger, J. M., *Electronic Distance Measurement: An Introduction*, Springer-Verlag, New York, 1990.

Savage, J. C., Strain accumulation in the western United States, *Ann. Rev. Earth Planet. Sci., 11,* 11-43, 1983.

Savage, J.C., and W.H. Prescott, Precision of Geodolite distance measurements for determining fault movements, *J. Geophys. Res., 78,* 6001-6007, 1973.

Smith, D.E., et al., Tectonic motion and deformation from satellite laser ranging to LAGEOS, *J. Geophys. Res., 95,* 22,013-22,042, 1990.

Sovers, O.J., and J. S. Border, Observation model and parameter partials for the JPL geodetic GPS modeling software GPSOMC, *JPL Publ., 87-21,* 1988.

Stephens, S., GIPSY frontend user's guide, *JPL Publ., D-3918,* 1986.

Tralli, D. M., T. H. Dixon, and S. Stephens, The effect of wet tropospheric path delays on estimation of geodetic baselines in the Gulf of California using the Global Positioning System, *J. Geophys. Res., 93,* 6545-6557, 1988.

Ware, R. H., C. Rocken, K. J. Hurst, and G. W. Rosborough, Determination of the OVRO-Mojave baseline during the spring 1985 GPS test, in *Proceedings of the Fourth International Geodetic Symposium on Satellite Positioning*, vol. 2, pp. 1089-1101, Natl. Geod. Surv., Rockville, Md., 1986.

D. C. Agnew, Institute of Geophysics and Planetary Physics, Scripps Institution of Oceanography, La Jolla, CA 92093.

K. M. Larson, Colorado Center for Astrodynamics Research, University of Colorado Boulder, CO 80309-0431.

(Received August 5, 1990;
revised May 6, 1991;
accepted May 6, 1991)

JOURNAL OF GEOPHYSICAL RESEARCH, VOL. 96, NO. B10, PAGES 16,495–16,508, SEPTEMBER 10, 1991

Observations Constraining Near-Source Ground Motion Estimated From Locally Recorded Seismograms

A. McGARR

U.S. Geological Survey, Menlo Park, California

To estimate the seismic hazard to underground facilities or operations in the environs of a mining-induced tremor or a natural earthquake, it is useful to be able to relate locally recorded seismic waveforms to peak ground velocity and slip at the causative fault. For this purpose, far-field S wave pulses are analyzed to define the faulting slip D and near-fault peak ground velocity $\dot{D}/2$ that give rise to the most significant ground motion. This most intense region of faulting, an assumed circular asperity, has radius r within a broader source zone of radius r_0, which is traditionally calculated from the corner frequency of the S wave spectrum. In developing relationships between peak far-field velocity $\mathbf{v}$ and peak acceleration $\mathbf{a}$, and the source processes of the asperity, D and $\dot{D}$, as well as its radius r, the key model assumption is that $r = k\beta/\omega$, where ω is the angular frequency of the sinusoidal velocity pulse of maximum amplitude, β is the shear wave speed, and k is a constant. Observations in deep-level gold mines of fault slip and slip velocity as well as laboratory observations of slip rate as a function of stress drop for stick-slip failure support a choice of about $k = 2.34$, the value commonly used for estimating r_0 using the Brune model. In particular, observations of fault slip up to 410 mm for mining-induced tremors in the moment magnitude range 4–5 are consistent with $D = 8.1\,R\mathbf{v}/\beta$, where R is hypocentral distance. Moreover, estimates based on underground damage of near-fault ground velocities ranging up to 3.5 m/s are in accord with $\dot{D}/2 = 1.28(\beta/\mu)\rho R\mathbf{a}$, where μ is the modulus of rigidity and ρ is the density. Alternatively, the average slip velocity $\langle\dot{D}\rangle$ can be expressed in terms of the stress drop $\Delta\sigma_a$ of the asperity as $\langle\dot{D}\rangle = 0.51\,\beta\,\Delta\sigma_a/\mu$, and the agreement of this relationship with measurements made during stick-slip failure in the laboratory is good. To the extent that seismic slip exterior to the asperity is a consequence of preevent suppression of slip due to the asperity, the broader-scale (r_0) slip can be related to that of the asperity. Just as the asperity radius r can be estimated from $r = 2.34\,\beta\mathbf{v}/\mathbf{a}$, an alternative estimate for r_0 is given by $r_0 = \rho R\mathbf{a}M_0/[75.8\rho\mu(R\mathbf{v})^2]$, the results of which are generally in good agreement with estimates based on the spectral corner frequency method.

INTRODUCTION

There are numerous situations for which seismic hazard is a consequence of ground motion within the actual source region of an earthquake at depth. Examples include deep mining operations, which often induce substantial seismicity, underground waste repositories, and many other types of underground installations, especially those situated in tectonically active regions. Because seismic data are nearly always recorded at hypocentral distances that are much greater than the source dimension, it is highly advantageous to be able to relate these far-field waveforms to the ground motion next to the causative fault.

Far-field observations of the ground motion associated with S waves [*McGarr et al.*, 1981] were the basis of the empirical relationship between peak velocity $\mathbf{v}$ recorded at hypocentral distance R to the local magnitude M_L of a mine tremor

$$\log R_{\mathbf{v}} = 0.57M_L - 0.05 \qquad (1)$$

where $R\mathbf{v}$ is in meters squared per second; (1), developed from underground recordings of events at depths of approximately 3 km, is appropriate for ground motion within a whole space. Multiplication by R takes the anticipated geometrical spreading of far-field body waves into account.

Although (1) has been utilized in the assessment of support requirements in deep gold mines [*Wagner*, 1984], it is in fact somewhat inadequate for this purpose inasmuch as most of the substantial damage due to mining-induced tremors appears to be in close proximity to the causative fault slip, that is, in the near-fault region where the far-field representation of the ground motion is inappropriate. The ground motion directly associated with the actual fault slip often seems to be the critical factor in cases of severe underground damage [e.g., *Wagner*, 1984; *Brummer and Rorke*, 1988; *van Aswegen*, 1990].

The Sudbury Neutrino Observatory [*Wolfenstein and Beier*, 1989] provides a current, though unusual, example of the need to be able to estimate the near-source ground motion from far-field seismic data [*Gibowicz and Young*, 1990; *McGarr*, 1990]. This facility is to be sited at a depth of 2 km in the Creighton Mine, near Sudbury, Ontario, unavoidably close to active mine production. In this case it is thought that the mining could induce a substantial tremor on a nearby fault, with a source dimension comparable to the distance between the source and the observatory chamber.

The point of departure for this report is an article by *McGarr and Bicknell* [1988], who described, somewhat tersely, a technique for estimating the peak ground motion in the near-field in terms of peak far-field ground velocity and acceleration recorded at typical hypocentral distances of 2–5 km. The primary purpose here is to provide observational justification for, as well as some elaboration of, the results of *McGarr and Bicknell* [1988]. Another purpose is to update and correct some of the analysis of *McGarr* [1981], who related ground motion parameters to inhomogeneous faulting.

The source processes of particular importance in the

Paper number 91JB01379.

context of underground damage are D, the maximum fault slip, $\dot{D}/2$, the peak ground velocity adjacent to the causative fault, and the extent of the fault surface over which maximum slip occurs. Here, this surface is idealized as a circle of radius r. $\dot{D}/2$ is perhaps the most important measure of underground damage, because the design requirements of underground support are often expressed in terms of peak velocity. If the causative fault intersects a shaft, tunnel, or stope, the magnitude of D can also be critical.

NEAR-FIELD INFERENCES FROM FAR-FIELD DATA

As reviewed by *Aki and Richards* [1980, equation 4.32] (see also *Brune* [1976]), the far-field contribution of the S wave to ground displacement at position $\mathbf{x}$ and time t in a whole space from a point double-couple source is

$$u(\mathbf{x}, t) = \frac{1}{4\pi\rho\beta^3} A^{FS} \frac{1}{R} \dot{M}_0(t - R/\beta) \qquad (2)$$

where ρ is density, β is the shear wave speed, A^{FS} is the radiation pattern for the far-field S wave, R is hypocentral distance, and $M_0(t)$ is the time history of the seismic moment M_0. Differentiating (1) and assigning a median value of 0.57 to A^{FS} [*Spottiswoode and McGarr*, 1975; *Boore and Boatwright*, 1984] gives

$$Rv(t) = \frac{0.57}{4\pi\rho\beta^3} \ddot{M}_0(t - R/\beta) \qquad (3)$$

where $v(t)$ is the ground velocity

$$\rho Ra(t) = \frac{0.57}{4\pi\beta^3} \ddot{M}_0(t - R/\beta) \qquad (4)$$

with $a(t)$ representing ground acceleration. In these expressions, as well as all others to follow that involve far-field ground motion, the only effect exterior to the source taken into account is geometrical spreading ($1/R$). Effects of scattering and anelastic attenuation, for example, are not included in this analysis, but the effect of recording at the surface is taken into account when appropriate.

In general terms then, (3) and (4) relate far-field S wave velocity and acceleration pulses to the source processes expressed as derivatives of the moment time history. To obtain results that allow one to relate far-field seismograms to near-fault ground motion, it is necessary to make a few assumptions about the moment time dependence $M_0(t)$ and its relationship to the finite seismic source. Thus we progress from the point source representations of (2), (3), and (4) by introducing the simplest possible source model of finite size; moreover, arbitrary assumptions are avoided by means of observational constraints.

The initial assumption here is that the ground velocity recorded in the far field (equation (3)) comprises one or more pulses each consisting of a single cycle of sine wave. That is, in (3)

$$\ddot{M}_0(t) = \sum_{1}^{N} \ddot{M}_{0_i}(t - t_i)$$

$$\ddot{M}_{0_i}(t) = a_i \sin \omega_i t \qquad 0 \le t \le 2\pi/\omega_i \qquad (5)$$

$$\ddot{M}_{0_i}(t) = 0 \qquad \text{otherwise}$$

where a_i is the amplitude of pulse i, ω_i its angular frequency, and t_i its beginning time. This representation was motivated by the observation that the pulses comprising the body wave train end as abruptly as they begin (e.g., Figure 1). Thus pulses involving exponential time dependence [e.g., *Brune*, 1970; *McGarr*, 1981] are, in retrospect, somewhat unrealistic observationally inasmuch as they have decay times that are longer than their rise times.

N in (5) represents the number of individual pulses that can be resolved within the body wave train. In practice, N is unlikely to exceed 4. Moreover, one of the pulses has a duration comparable to that of the body wave train, whereas the others are of significantly shorter duration.

The individual pulses in (5) are each assumed to be associated with the failure of some portion of the overall source region. The pulse of longest duration corresponds to failure distributed throughout the source region and consists of contributions from pulses that cannot be resolved individually, due partly to limited bandwidth recording. Often, only the pulse corresponding to the total source duration is resolvable. Such events appear to be simpler than those for which more than one pulse can be resolved, but this simplicity is probably just a consequence of limited bandwidth recording [e.g., *Frankel*, 1991].

To illustrate the observational motivation for (5), I now analyze the waveforms of event 203 0311 (Figure 1) in some detail. This event, located using an underground network [*van der Heever*, 1984] at a depth of 2.4 km, was recorded on the surface of the Klerksdorp mining district [*McGarr et al.*, 1989] using a general earthquake observation system (GEOS) digital event recorder [*Borcherdt et al.*, 1985]. The waveforms of event 203 0311 are typical of a large body of seismic data recorded at small hypocentral distances at sites on or within hard rock [e.g., *Spottiswoode and McGarr*, 1975; *McGarr et al.*, 1981; *Churcher*, 1988; *Bicknell and McGarr*, 1988; *Semadeni et al.*, 1988; *Young and Talebi*, 1988; *McGarr et al.*, 1990*a*]. Thus generalized results of analyzing event 203 0311 (Figure 1) will have at least moderately broad applicability.

The first step in analyzing event 203 0311, determining the moment tensor, was done by calculating synthetic seismograms for trial solutions [*McGarr and Bicknell*, 1990], using a program supplied by L. R. Johnson [*Johnson*, 1974], until the three components of observed displacement were fit as well as possible. The synthetic seismograms are for a point source in a homogeneous half-space, which is reasonably appropriate for this gold field inasmuch as high-velocity rock extends nearly to the surface [*Gay et al.*, 1984]. For each trial solution the moment rate tensor $\dot{M}_0(t)$ (equation (2)) has the form $1 - \cos 2\pi f_0 t$ [*McGarr and Bicknell*, 1990], consistent with a sine pulse for $\ddot{M}_0(t)$; only a single pulse was used for determining the moment tensor. The best fit to the displacement waveforms was achieved using $f_0 = 6$ Hz, corresponding to a displacement pulse duration of 0.167 s. The moment tensor involves mostly dip-slip normal faulting, and it turns out that the recording station is near a maximum in the S wave radiation pattern. After determining the best fitting moment tensor, with scalar moment M_0, I then considered the velocity and acceleration traces (Figure 1) for purposes of ascribing more detail to the source of event 203 0311. The east components received the most emphasis,

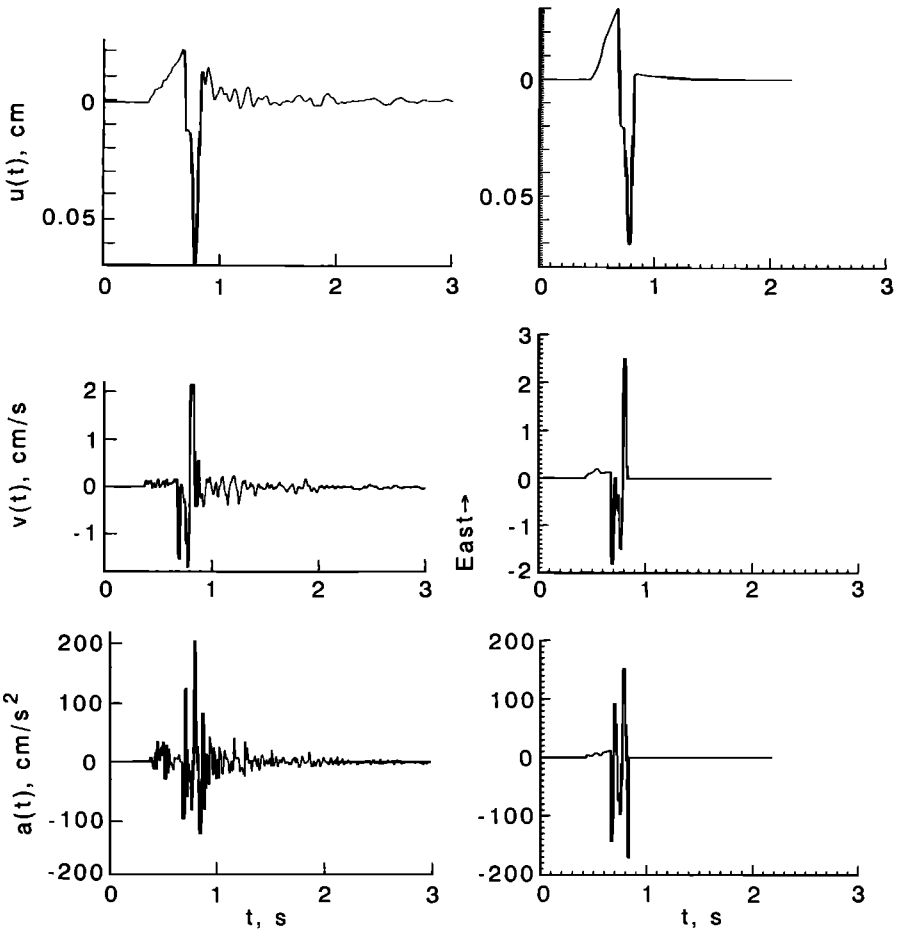

Fig. 1. East components of displacement, velocity and acceleration, from top to bottom, for event 203 0311. The observed traces are on the left, and the synthetics are on the right. Note that on the displacement records the near-field term dominates the seismogram between the P wave and S wave arrival times.

because this component has a substantially greater displacement amplitude than the other two. After some trial and error, I finally concluded that a good simulation to the observed ground motion can be obtained from the superposition of three subevents satisfying

$$M_0(t) = M_{0_1}(t - t_1) + M_{0_2}(t - t_2) + M_{0_3}(t - t_3) \qquad (6)$$

with $M_0(\infty) = M_0$, as determined above. Figure 2a shows the individual pulses for $\dot{M}_0(t)$ and $\ddot{M}_0(t)$, of form $1 - \cos 2\pi f_i(t - t_i)$ and $\sin 2\pi f_i(t - t_i)$, respectively. The frequencies f_i of the subevents are 6, 15.1, and 12.2 Hz, respectively, and their relative amplitudes are as indicated in Figure 2a. Subevents 1, 2, and 3 account for 0.63, 0.11, and 0.26, respectively, of the total seismic moment M_0.

As seen in Figure 1, the synthetic seismograms provide reasonably good replications of the displacement, velocity, and acceleration (calculated from $\ddot{M}_0(t)$) traces for event 203 0311. Considering that the synthetic seismograms were calculated for a homogeneous, elastic, half-space, the fit of calculated to observed seismograms is about as good as can be expected.

Thus in analyzing event 203 0311 I have resolved two individual pulses, corresponding to $M_{0_2}(t)$ and $M_{0_3}(t)$, within the wave train, and the remaining ground motion is associated with $M_{0_1}(t)$, which accounts for most of M_0. $M_{0_1}(t)$, easily resolvable as a whole (Figure 2a), may in fact

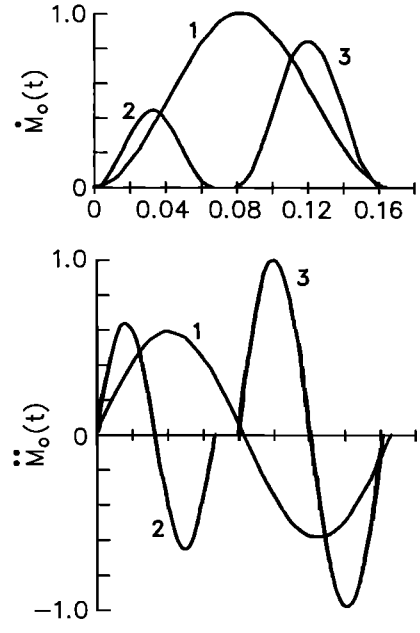

Fig. 2a. $\dot{M}_0(t)$ and $\ddot{M}_0(t)$ for each of the three subevents that were combined to produce the synthetic seismograms of Figure 1. In each case the vertical scale has been normalized to a peak amplitude of 1, but the relative amplitudes are as shown. Upward here corresponds to westward in Figure 1.

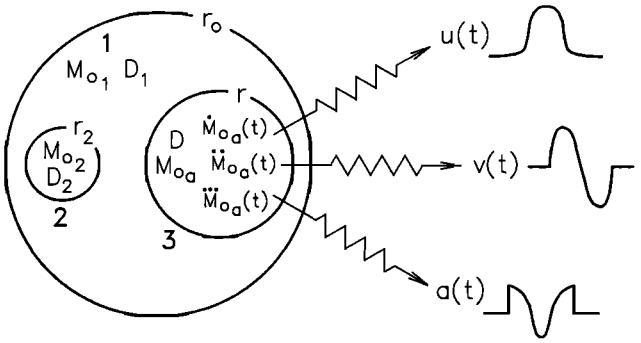

Fig. 2*b*. A schematic source model corresponding to the decomposition of event 203 0311 (Figure 1) into three subevents. Subevent 1, of duration 0.167 s, involves average slip D_1 within the circular area of radius r_0 excluding the portions occupied by subevents 2 and 3. Subevent 2, of duration 0.066 s, is associated with average slip D_2 within a circle of radius r_2. Similarly, subevent 3 is the result of slip D within radius r and of duration 0.082 s. The relationship between the source process of subevent 3, $M_{0_a}(t)$ (AKA $M_{0_3}(t)$), and the far field displacement, velocity, and acceleration pulses is also indicated.

consist of a superposition of many unresolvable subevents [e.g., *Frankel*, 1991]. The initial portion of the ground motion (Figure 1) involves interference between pulses 1 and 2, whereas the latter portion results from the superposition of pulses 1 and 3. Although $M_{0_1}(t)$ dominates in terms of contributing to both M_0 and the far-field displacement amplitude ($\dot{M}_0(t)$ in Figure 2*a*), the peak velocity and acceleration are a consequence of $M_{0_3}(t)$ (Figure 1).

Assuming that the duration of a particular pulse comprising the body wave train is proportional to the dimension of the fault surface over which causative slip occurs [e.g., *Brune*, 1970; *Savage*, 1972], then the rupture area corresponding to pulse 1 (Figure 2*a*) must be larger than those of pulses 2 and 3. If so, then one can analyze the seismic source in terms of models such as that of Figure 2*b* [e.g., *McGarr*, 1981], in which the portion of the fault that slips to produce the peak amplitude velocity and acceleration pulses is significantly smaller than the total fault surface of the earthquake [e.g., *Hartzell and Brune*, 1979]. As analyzed here, within a circular fault of radius r_0 [*Brune*, 1970] there are smaller circular rupture zones, often termed asperities, that are associated with the important velocity and acceleration pulses [*Boatwright*, 1988]. In the example of event 203 0311 (Figure 2) the circular asperities, denoted 2 and 3, rupture to produce pulses 2 and 3, whereas pulse 1 is presumably the result of slip somehow distributed over the area within the circle of radius r_0 not taken up by asperities 2 and 3 (Figure 2*b*).

In the following analysis we focus our attention on the asperity associated with the pulse of maximum ground velocity (for a description of the methodology see *McGarr* [1984]), pulse 3 in the example of Figure 2. Whereas the total source region, of radius r_0, experiences an average slip D_0 during the earthquake, there is an average slip of D over the smaller fault zone of radius r. It is convenient to define a small-scale seismic moment M_{0_a}, corresponding to the asperity failure, as

$$M_{0_a} = \mu \pi r^2 D \tag{7}$$

Accordingly, because subevent 3 in the example is associated with the peak velocity pulse (Figure 1), the symbol for its moment time history $M_{0_3}(t)$ (equation (6)) is changed (Figure 2*b*) to $M_{0_a}(t)$. M_{0_a} contributes of course to the total moment

$$M_0 = \mu \pi r_0^2 D_0 \tag{8}$$

Having shown by means of an example (Figures 1 and 2) that $\ddot{M}_0(t)$ is reasonably well represented by a time history formed from single cycles of sine waves, I now return to (3) to relate the pulse associated with the peak velocity to the corresponding source process $M_{0_a}(t)$. Writing $\ddot{M}_{0_a}(t') = A \sin \omega t'$ for this pulse, we integrate twice, first from 0 to t and then from 0 to $(2\pi)/\omega$, to find that

$$A = \frac{\omega^2}{2\pi} M_{0_a} = \frac{\omega^2}{2} \mu r^2 D \tag{9}$$

from (7).

To recapitulate, to this point I have assumed that there is an asperity of radius r within the overall earthquake fault of radius r_0 with a moment time history as indicated in Figure 2*b*. The observations just reviewed (Figures 1 and 2*a*) support the assertion that $\ddot{M}_{0_a}(t)$, corresponding to one far-field velocity pulse, can be represented as a single cycle of sine wave; the body wave train consists of one or more such pulses. Moreover, the duration of each pulse is presumably proportional to the size of the corresponding rupture zone (Figure 2*b*).

Accordingly, the final step before evaluating (3) is to make the assumption that for the asperity rupture,

$$\omega = (k\beta)/r \tag{10}$$

where, if one generalizes from *Brune* [1970, 1971], $k = 2.34$. Equation (10) represents a fundamental assumption, but one for which there is precedent. Moreover, assuming that (10) is accepted, there is still scope for debate regarding the value that k should take [e.g., *Savage*, 1972; *Madariaga*, 1976]. *Hanks and Wyss* [1972] provided some observational support for *Brune*'s [1970, 1971] choice of 2.34, although this was for purposes of evaluating r_0 (Figure 2*b*), not r. It turns out that $k = 2.34$ is close to optimal in terms of the observations emphasized here, as is shown below. For now, however, I leave k unspecified.

Combining (3), (7), (9), and (10) yields

$$\begin{aligned} Rv(t) &= 0.0227 \beta k^2 D \sin \omega t \qquad 0 < t < (2\pi)/\omega \\ Rv(t) &= 0 \qquad\qquad\qquad\qquad \text{otherwise} \end{aligned} \tag{11}$$

which has a peak value of

$$Rv = 0.0227 \beta k^2 D \tag{12}$$

where v is the peak value of $v(t)$. Although a sine pulse in isolation (Figure 2*b*) has two peaks of equal amplitude, the way in which this pulse interferes with the other components of the wave train (e.g., Figure 1) partly determines which of the peaks predominates; also, it should be emphasized that the sine pulse representation (equation (5)) is only an idealization.

Differentiating (11) yields for the peak acceleration pulse

$$\rho Ra(t) = 0.0227k^3\mu(D/r)\cos\omega t \quad 0 < t < (2\pi)/\omega$$
$$\rho Ra(t) = 0 \quad \text{otherwise} \tag{13}$$

which has a peak value of

$$\rho R\mathbf{a} = 0.0227k^3\mu D/r \tag{14}$$

with **a** representing the maximum value of $a(t)$.

The acceleration pulse of (13), in isolation, has three peaks of equal amplitude (Figure 2*b*), but the significance of those at the beginning and end of the pulse can almost certainly be discounted partly because such "step" waveforms could not propagate any distance through a realistic medium. Accordingly, one expects the peak in the middle of the pulse to predominate. Figure 1 illustrates this point quite nicely in that the portions of the synthetic accelerograms corresponding to pulses 2 and 3 (Figure 2*a*) show peak amplitudes at the beginning and end of these pulses, respectively; the high-amplitude westward swing at the beginning is due to constructive interference between the leading edges of pulses 1 and 2, and the even higher amplitude swing at the end is caused by trailing edge interference of pulses 1 and 3. These synthetic seismograms, of course, are for a nonattenuating medium. In contrast, the observed accelerogram shows eastward peak values (Figure 1) within the interiors of what I have identified as pulses 2 and 3; note in particular the eastward swing of peak amplitude greater than 200 cm/s^2 in the latter portion of the *S* wave train. For both pulses 2 and 3 then, the observed peak acceleration coincides with the center of the velocity pulse.

To relate the far-field ground motion to the near-fault ground velocity, it is necessary to consider the process of asperity failure. First, however, by assumption, $\dot{M}_{0_a}(t) = (A/\omega)(1 - \cos\omega t)$ (Figure 2*b*), which has a maximum value

$$\dot{M}_{0_a}(\max) = (2A)/\omega = \omega\mu r^2 D \tag{15}$$

from (9).

The circular asperity analyzed here (Figure 2*b*) is a region that, before the earthquake, has undergone no slip. In contrast, much of the fault surface surrounding the asperity has slipped due to previous seismic and aseismic failure [e.g., *McGarr*, 1981]. Previous seismic failure includes that due to previous earthquakes as well as seismic slip immediately preceding the asperity failure in the associated earthquake (e.g., subevent 3 of Figure 2). Before failure, the total stress loading the asperity consists of that due to the previous slip in its environs, as well as a contribution from the ambient regional stress field affecting the seismogenic zone.

As analyzed by *Das and Kostrov* [1983], the shear stress loading the asperity is highly concentrated near its periphery, and thus failure initiates at some point near the edge. The rupture front first encircles the asperity and then propagates inward from all directions. Failure of the asperity results in additional slip in the environs [*McGarr*, 1981; *Das and Kostrov*, 1983], as will be analyzed later. For now, however, the important point is that because the asperity fails from its boundary inward, the radius r of the rupture zone remains fixed. Thus if (7) is differentiated with respect to time, then to a good approximation $\dot{r} = 0$ and so

$$\dot{M}_{0_a}(t) = \mu\pi r^2\dot{D}(t) \tag{16}$$

where $D(t)$ is the time-dependent slip as averaged over the asperity. If $\dot{D}$ represents the maximum slip velocity, as averaged over the asperity, then from (15) and (16)

$$\dot{D} = \omega D/\pi = k\beta D/\pi r \tag{17}$$

from (10). Finally, substitution of (17) into (14) gives

$$\rho R\mathbf{a} = 0.143k^2(\mu/\beta)\dot{D}/2 \tag{18}$$

where $\dot{D}/2$ is the ground velocity adjacent to the circular fault of radius r.

From (14) it is straightforward to relate the peak acceleration parameter to the stress drop of the corresponding asperity. Equation (2) of *Das and Kostrov* [1983] can be integrated to find that the average stress drop within the asperity, due to slip D, is

$$\Delta\sigma_a = (16/7\pi)(\mu D/r) \tag{19}$$

Combining (19) with (14) then yields

$$\rho R\mathbf{a} = 0.0312k^3\Delta\sigma_a \tag{20}$$

Moreover, eliminating $\rho R\mathbf{a}$ between (18) and (20) provides a useful relationship between slip velocity and stress drop

$$\dot{D} = 0.44k\beta\Delta\sigma_a/\mu \tag{21}$$

Once k is assigned a value, then (12) and (18) provide quite an effective means of relating far-field *S* waves to the seismic source processes responsible for the most important ground motion. The peak velocity **v** is proportional to the maximum slip D, and the peak acceleration is linearly related to the peak near-fault ground velocity.

On the basis of the substantial precedent mentioned before [e.g., *Brune*, 1970, 1971; *Hanks and Wyss*, 1972; *McGarr*, 1981] I tentatively assign a value of 2.34 to k but reserve the option to change this value should observational constraints so dictate. For $k = 2.34$ then, from (12), (14), (18), (20), and (21) the results for the rupture of a single asperity are

$$R\mathbf{v} = 0.124\beta D \qquad D = 8.1R\mathbf{v}/\beta \tag{22}$$

$$\rho R\mathbf{a} = 0.291\mu D/r \tag{23}$$

$$\rho R\mathbf{a} = \frac{0.78\mu}{\beta}\dot{D}/2 \qquad \dot{D}/2 = 1.28(\beta/\mu)\rho R\mathbf{a} \tag{24}$$

$$\Delta\sigma_a = 2.50\rho R\mathbf{a} \tag{25}$$

$$\dot{D} = 1.03\beta\Delta\sigma_a/\mu \tag{26}$$

Moreover, combining (22) and (23) gives for r,

$$r = 2.34\beta\mathbf{v}/\mathbf{a} = 2.34\beta/\omega \tag{27}$$

inasmuch as $\mathbf{v}/\mathbf{a} = 1/\omega$ for the sinusoidal pulses assumed here. Additionally, in applying (22)–(27) to observations recorded in the South African gold fields, β is assigned a value of 3.8 km/s, and $\rho = 2.9 \times 10^3$ kg/m^3 [e.g., *McGarr et al.*, 1989].

For two reasons I digress here to note that (22) and (23) are similar to equations (17) and (18) of *McGarr* [1981]. First, for the record, there was a factor of 2 error introduced by *McGarr* [1981] between (12) and (13) that rendered (17) and (18) too high by the same factor. Taking this error into account yields revised coefficients of 0.10 and 0.30, respec-

tively, for (17) and (18) of *McGarr* [1981]. The second reason for this digression is to note that these coefficients are quite close to those of (22) and (23) of this report, 0.124 and 0.291, respectively. The agreement of the revised coefficients is significant in that the functional form assumed by *McGarr* [1981] for $\dot{M}_0(t)$ was $t^3 e^{-\omega t}$ instead of $1 - \cos \omega t$ used here. The fact that two quite different assumed functions led to very similar results suggests that (22) and (23) are at least moderately insensitive to the choice of functional form for $M_0(t)$.

Interestingly, (26) is remarkably similar to equation (19) of *Boatwright* [1980] (see also *Kostrov* [1964] and *Dahlen* [1974]) even though the seismic source model of Boatwright's analysis is quite distinct from the asperity model employed here. For the circular fault model of Boatwright, rupture initiates at the center and propagates outward. For typical rupture velocities, and taking account of the fact that the dynamic stress drop used by Boatwright is somewhat less than the static stress drop used here, equation (19) of *Boatwright* [1980] yields results that differ very little from those of (26).

To this point, the analysis has dealt only with the most intense failure within the seismic source that gives rise to the peak ground motion parameters. That is, within the overall source radius r_0 (Figure 2*b*), an asperity of radius r, slip D, and peak slip velocity $\dot{D}$ is of primary importance with regard to ground motion in both the near and far field.

Inhomogeneous Source

The intent here is to relate the small-scale failure on the scale of r to the larger-scale source of radius r_0 (Figure 2*b*). In particular, the analysis of *McGarr* [1981] is updated and corrected.

Consider a planar fault undergoing slip at some average long-term rate. On this fault surface, assume that there is a region of radius r that has not failed in such a long time that there is a slip deficit D within this region. That is, compared to the broader fault surface, the region within the asperity has undergone D less slip than the slip averaged over the entire fault. Additionally, there is a slip deficit surrounding the asperity $D - U(x)$ which can be estimated by modifying equation (A4) of *McGarr* [1981] to obtain

$$U(x) = (2/\pi)D \cos^{-1}(r/x) \qquad x \geq r \tag{28}$$

where x represents the radial distance from the center of the asperity. $U(x)$ represents the preseismic fault slip in the region surrounding the unfailed asperity of radius r with value 0 at $x = r$ and tending toward D the ambient, or average, fault slip as x becomes large; this ambient slip has, by assumption, occurred during the time period leading up to the failure of the asperity.

Failure of the asperity results in slip D for $x \leq r$ and slip $D - U(x)$ for $r < x \leq r_0$, where r_0 is the radius of the region over which slip occurs because of the asperity rupture; that is, for $x \geq r_0$ there is, by assumption, no slip as a consequence of the asperity failure. Note that for purposes of this analysis I have assumed that the center of the asperity coincides with the center of the overall source region of radius r_0. With these assumptions the seismic moment M_0 associated with the failure of the asperity is calculated by integrating the slip deficit over the entire source, $x \leq r_0$. Thus

$$M_0 = \mu\pi\left[r_0^2 D - \int_r^{r_0} U(x) 2x\, dx\right] \simeq 4\mu D r_0 r \tag{29}$$

to a good approximation; terms smaller by factors of $(r/r_0)^2$ or less have been neglected. Equation (29) includes of course the moment M_{0_a} due to failure within the asperity radius, given by (7).

Comparison of (29) to (7) indicates that $M_0/M_{0_a} > 2$ if $r_0/r > \pi/2$ or 1.57. The slip deficit, $D - U(x)$, indicates that r_0/r is likely to be in excess of 1.6 because, as seen in Figure 7, this deficit is still greater than 0.4 D at $x/r = \pi/2$. Specific examples to be discussed indicate that $\pi/2 < r_0/r < 10$ for nearly all events, and thus most of the seismic moment is due to failure exterior to the asperity, involving less slip but more area.

Traditionally, the source radius r_0 is estimated from the spectral corner frequency that is situated at the boundary between low- and high-frequency behavior. For displacement amplitude spectra of far-field S waves, for example, there is a plateau for frequencies out to the corner frequency beyond which spectral amplitudes decay, typically, as the second, or, occasionally, the third, power of inverse frequency. According to *Brune* [1970, 1971], the corner frequency f_0 is related to the source radius r_0 as

$$r_0 = (2.34\beta)/(2\pi f_0) \tag{30}$$

the relationship that of course motivated the choice of $k = 2.34$ in (10).

An alternative estimate of r_0 is obtained by combining (22), (23), (27), and (29) to obtain

$$r_0 = (\rho R \mathbf{a} M_0)/[75.8\rho\mu(R\mathbf{v})^2] \tag{31}$$

Among the advantages of (31), compared to (30), is that r_0 is estimated from quantities that are all straightforward to measure. Generally, less subjectivity is involved in determining peak ground motion, as well as M_0, than in fitting asymptotes to seismic spectra. To use (31), however, it is necessary that neither **a** nor **v** is affected by wave propagation in ways that cannot be taken into account. As will be seen, for events producing seismic data well suited to both estimates of r_0, (30) and (31) show moderately good agreement. Neither is appropriate for events with grossly nonequidimensional source areas.

Observations of Fault Slip and Peak Ground Motion

The peak velocity and peak acceleration data in Figures 3, 4, and 5 provide means of checking the validity of (22) and (24), at least in an approximate way, because in deep mines the fault slip causing mine-induced tremors is occasionally accessible [e.g., *McGarr*, 1971; *Gay and Ortlepp*, 1979; *McGarr et al.*, 1979] and estimates of near-source ground velocity have been made on the basis of damage [*Wagner*, 1984]. Observations of slip D for tremors of moment magnitude M [*Hanks and Kanamori*, 1979] between 3.6 and 5.1 fall in the range of 100 mm to 410 mm as documented in two reports. *Brummer and Rorke* [1988] summarized observations of slip for four tremors in two of the major gold mining districts of South Africa. According to them, the tremor of M 4.6 in April 1982 in the Welkom district involved fault slip as high as 500 mm. These observations were revised down-

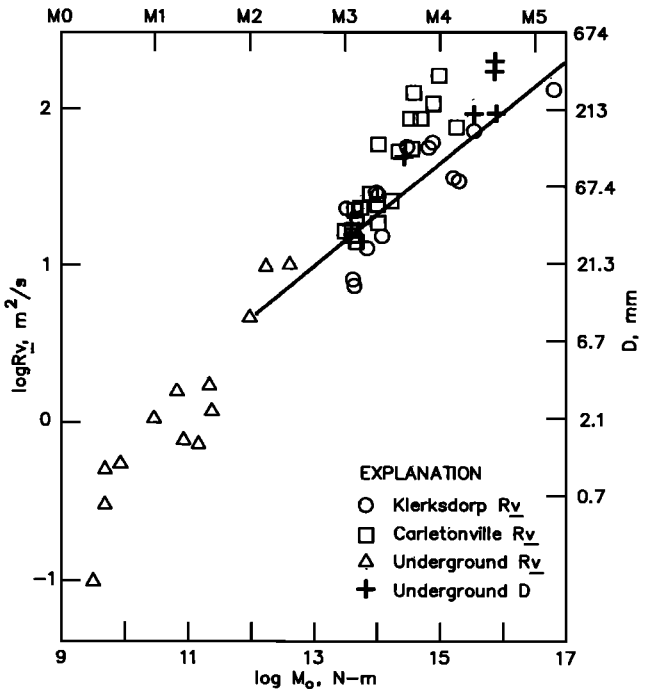

Fig. 3. Peak velocity parameter Rv and corresponding asperity slip D as functions of M_0 and M. The underground observations of slip D are from *Brummer and Rorke* [1988] and *van Aswegen* [1990]. The solid line of slope $\frac{1}{3}$ is from equation (16*a*) of *McGarr* [1984] and is for seismic events at a depth of 2 km.

ward to 410 mm, however, by *van Aswegen* [1990], who was a member of the group that actually made the underground observations of D following the 1982 tremor. Of the other three events considered by van Aswegen, slip estimates range from >150 mm up to 370 mm. From these reports then, as well as from a large body of undocumented observations including my own, it appears that $D \leq 410$ mm, at least to date, within the South African gold fields. For events in the magnitude range 4.4–5.0 it seems the D generally ranges from 200 to 400 mm. Most of these large events involve slip across preexisting throughgoing normal faults.

Figure 3 plots both Rv and D as functions of M_0 on the bottom scale or M at the top. The left- and right-hand vertical scales are related to each other according to (22). As seen in the figure, (22) appears to be ideal inasmuch as the underground observations of fault slip [*Brummer and Rorke*, 1988; *van Aswegen*, 1990] coincide very closely with Rv estimates at the same magnitude or moment.

One of the tremors represented in Figure 3, an event of $M = 4.4$ on April 14, 1987, (Table 1) near the Five shaft of Vaal Reefs Gold Mine, produced slip of 200 mm in a normal sense across a major preexisting fault [*Brummer and Rorke*, 1988; S. M. Spottiswoode, written communication, 1987]. From the ground velocity (Figure 4) measured at a hypocentral distance of 2.72 km the peak velocity parameter was found to be $Rv = 7.25 \times 10^2$ m^2/s, which from (22) corresponds to $D = 155$ mm. For this case then, (22) does quite well in relating the peak velocity of the far-field S pulse to the maximum fault slip, with the estimate from (22) being only 22% lower than the slip actually observed.

In Figure 5 the peak acceleration parameter $\rho R\mathbf{a}$ and estimates of near-fault particle velocity $\dot{D}/2$ are plotted as functions of M_0 or M, where (24) was used to relate the left- and right-hand vertical scales. Over the magnitude range 1–5, estimates of near-fault ground velocity from Table 1 of *Wagner* [1984] coincide very well with acceleration data presented by *McGarr and Bicknell* [1988]. Thus, for purposes of relating $\rho R\mathbf{a}$ to $\dot{D}/2$, (24) appears to be entirely satisfactory.

For $M > 2$, both $\dot{D}/2$ and $\rho R\mathbf{a}$ appear to be independent of

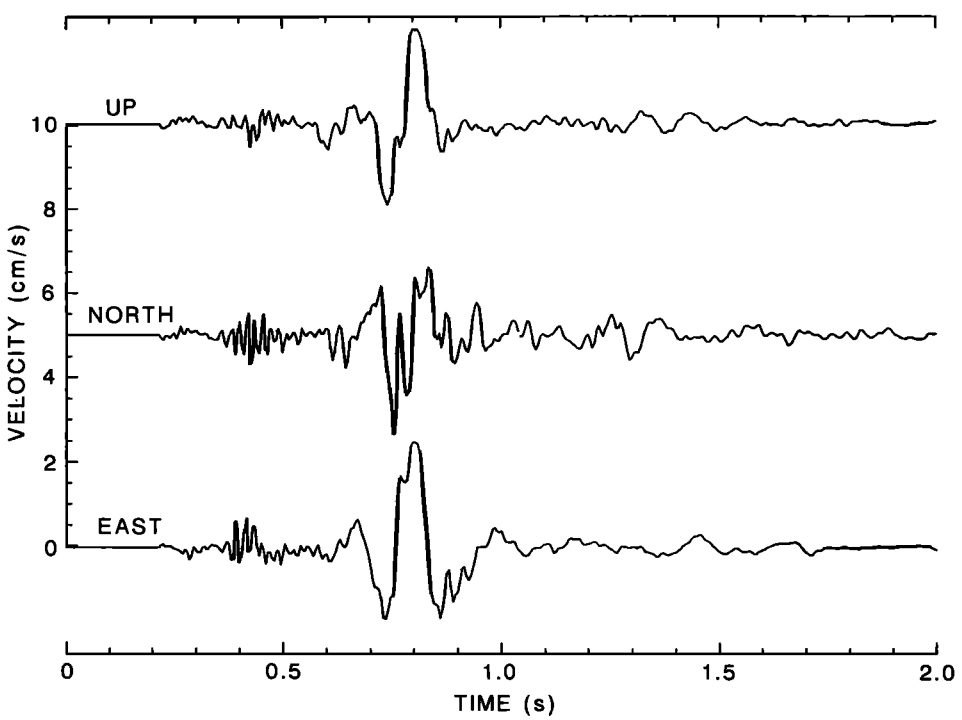

Fig. 4. Ground velocity for event 104 0939.

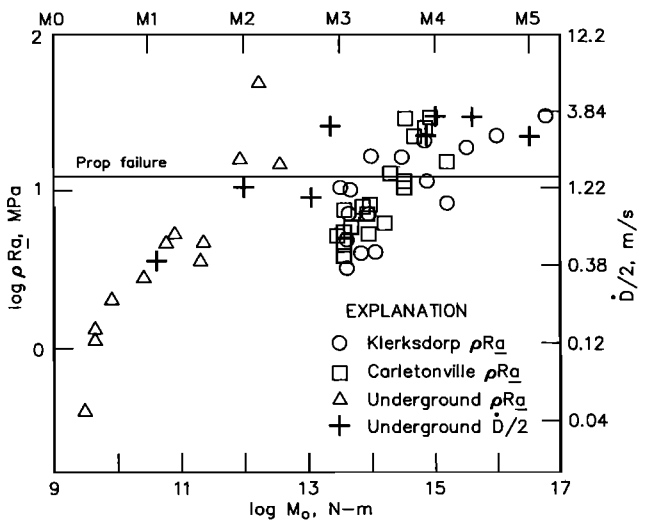

Fig. 5. Peak acceleration parameter ρRa and corresponding values of near-fault particle velocity $\dot{D}/2$ as functions of M_0 and M. The underground estimates of $\dot{D}/2$ are from *Wagner* [1984].

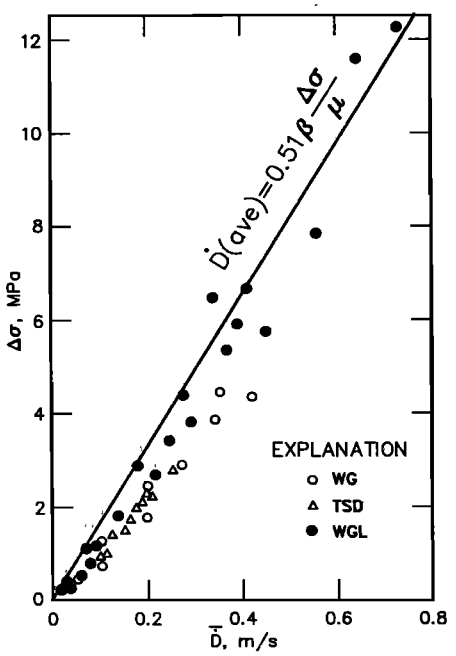

Fig. 6. Stress drop $\Delta\sigma$ as a function of slip rate $\dot{D}$ for stick-slip events occurring on Westerly granite sliding surfaces which are either clean (WG) or covered with Linde gouge (WGL). The third type of event involves Westerly granite sliding on Twin Sisters dunite (TSD). (Adapted from Figure 14 of *Johnson and Scholz* [1976].)

M_0 or M, although the surface observations of ρRa in the magnitude range 3–3.5 are presumably depressed as a consequence of several kilometers of propagation to the surface; the free surface, incidently, is taken into account here.

Additional evidence regarding peak levels of $\dot{D}/2$ comes from the performance of the rapid-yielding hydraulic props, the standard support system used at the faces of the mine stopes. According to *Wagner* [1984] (see also *Tyser and Wagner* [1977]), the props can accommodate ground velocities of at least 1 m/s but not as much as 2 m/s. A general observation is that the props nearly always perform as intended, but for those adjacent to the causative fault, prop failure sometimes occurs, indicating ground velocities in excess of 1.5 m/s typically. Accordingly, $\dot{D}/2 = 1.5$ m/s is indicated in Figure 5 as an additional demonstration that the near-fault velocities inferred using (24) are reasonable.

To recapitulate then, the available data, which are summarized in Figures 3 and 5, tend to confirm the validity of (22) and (24). Thus the choice of $k = 2.34$ (equations (12) and (18)) [*Brune*, 1970, 1971] seems to be as good as any. Certainly the data in Figures 3 and 5 are entirely compatible with this choice and almost certainly represent the most stringent test of this factor to date.

Laboratory Constraints

Measurements of "earthquakes" produced in laboratory experiments provide additional means of testing the methodology proposed here, including the choice of $k = 2.34$ in (10). Observations of the dependence of slip velocity on stress drop in stick-slip friction experiments, presented by *Johnson and Scholz* [1976] (Figure 6), are especially well suited to testing the validity of (26). Because Johnson and Scholz estimated slip velocity as an average over the slip event, it is necessary to alter (26), which involves the maximum slip velocity $\dot{D}$, into

$$\langle \dot{D} \rangle = \dot{D}/2 = 0.51\beta\Delta\sigma_a/\mu \qquad (32)$$

where $\langle \dot{D} \rangle$ is the average slip velocity during the asperity failure process.

According to *Johnson and Scholz* [1976], for the samples of Westerly granite used for most of the experiments represented in Figure 6, $\beta = 3.1$ km/s and $\rho = 2.65 \times 10^3$ kg/m^3, and so $\mu = 2.55 \times 10^4$ MPa. Equation (32), calculated on this basis, shows reasonably good agreement with the corresponding data (Figure 6), but several qualifications are in order.

The most important qualification involves the notion that an asperity failing seismically (Figure 2*b*) can be compared directly to a biaxial stick-slip friction experiment [*Brace and Byerlee*, 1966]. *Johnson and Scholz* [1976] noted that $\langle \dot{D} \rangle$ is related to the stress drop $\Delta\sigma$ by

$$\langle \dot{D} \rangle = (1/ST)\Delta\sigma \qquad (33)$$

where T is the sliding time and S is the stiffness of the loading system in terms of stress reduction per unit slip. The agreement between (32) and the data of *Johnson and Scholz* (Figure 6) is thus an indication that ST for the asperity model developed here is approximately the same as that for the biaxial apparatus of *Johnson and Scholz* [1976]. This agreement might be purely fortuitous although one could speculate that ST does not vary much from one system to another; both earthquakes and stick-slip friction experiments are considered as "systems" here. With regard to the asperity failure analyzed here, for example, for (19) and following *Walsh* [1971]

$$S = (16/7\pi))(\mu/r) \qquad (34)$$

and as $T = 2\pi/\omega = 2\pi r/2.34\ \beta$, from (27)

$$ST = 1.95\mu/\beta \qquad (35)$$

which is scale invariant and depends only on the bulk properties of the medium. The simplicity of (35) provides at least an encouraging indication that the factor ST may not vary much from one elastic loading system to another, whether for laboratory stick-slip experiments or for earthquakes.

Several other observations lend support to such conjecture. First, as reviewed by *Johnson and Scholz* [1976], *Abe* [1975] found that ST for five well-studied Japanese earthquakes is nearly the same as that determined for their stick-slip experiment (Figure 6). Second, particle velocities adjacent to faults in foam rubber models are reasonably compatible with (26) [*Brune*, 1973; *Archuleta and Brune*, 1975, Figure 8] as will be described in more detail. Thus the foam rubber experiments apparently also yield values of ST similar to that found by *Johnson and Scholz* [1976] inasmuch as they are compatible with (26). Accordingly, the conjecture that ST does not vary much from one earthquake loading system to another enjoys some very diverse observational support.

Second, the data in Figure 6 spanning the greatest range in slip rate and stress drop involve samples of Westerly granite sliding past one another along a precut fault containing Linde A polishing compound (WGL), which was meant to simulate fault gouge. The biaxial stick-slip data involving only Westerly granite (WG) in Figure 6 all have lower stress drops for a given sliding velocity than predicted using (32). From (21) we see that for the pure Westerly granite experiments with no gouge, increasing k above 2.34 would improve the fit of theory to data. It should also be noted, however, that the data of Figure 6 do not indicate a perfectly linear relationship between $\langle \dot{D} \rangle$ and $\Delta\sigma$. Instead, the slopes suggested by the data appear to steepen for $\langle \dot{D} \rangle$ greater than about 0.3 m/s.

In view of these qualifications, it is perhaps best not to overstate the significance of the agreement in Figure 6 between the observations and (32). If one accepts the agreement at face value, assuming that the assumptions leading to (32) apply also to the stick-slip experiments, then one concludes from Figure 6 that $k = 2.34$ is an acceptable choice; note that (21), the more general version of (32), involves a linear dependence on k.

SOME EXAMPLES

The various relationships developed here were applied to analyze source properties for mine tremors recorded both underground and on the surface as well as the largest aftershocks of both the 1975 Oroville, California sequence [*Fletcher et al.*, 1984] and the 1983 Coalinga, California, sequence [*McGarr et al.*, 1990*b*]. Table 1 lists the source and ground motion parameters described here for 27 events covering quite a broad range in M_0, from 4.6×10^9 to 4.5×10^{17} N m, a span of 8 orders of magnitude. For these events the moments, source radii (estimated using equation (30)), and ground motion parameters $R\mathbf{v}$ and $\rho R\mathbf{a}$ are from the studies referenced in the table. The remaining source quantities are estimated from the relations developed here and by *McGarr and Bicknell* [1988].

As seen in Table 1, D ranges from a few millimeters for the smallest events up to several meters for the largest. The only value of D listed here for which there is direct observational confirmation is that of Vaal Reefs event 104 0931 (April 14, 1987) as described before. $\dot{D}/2$ (Table 1) shows far less variation than D, which is no surprise inasmuch as $\rho R\mathbf{a}$, from which it is derived (equation (24)), is largely independent of M_0 [e.g., *McGarr*, 1984]. Some of the largest values of $\dot{D}/2$, the near-fault ground velocity, ranging from 5 to 10 m/s, are impressive in terms of levels of ground velocity necessary to damage structures or underground development (~1 m/s).

In all but a few cases, r, estimated from (27), is substantially less than r_0, indicating that a model of inhomogeneous faulting (Figure 2*b*) is probably appropriate. In the case of East Rand Proprietary Mines (ERPM) event 11, however, $r > r_0$, suggesting that the analysis is somehow misapplied. This exceptionally small event yielded a spectral corner frequency in the neighborhood of 200 Hz, implying a very small source radius of $r_0 = 8$ m [*McGarr et al.*, 1981, Figure 8]. If the asperity were one third as large as the overall source, then its radius would be less than 3 m, and the corresponding "corner frequency" for the associated ground motion pulse would be in excess of 500 Hz. This component of ground motion would have been poorly recorded as the records were low-pass filtered with the corner set at 400 Hz to avoid system resonances. In short, the system used to record event 11 lacked the capability to resolve the ground motion pulse presumably associated with an asperity.

As listed in Table 1 and seen in Figure 7, r_0 calculated from M_0 and the ground motion parameters shows reasonable agreement with r_0 estimated using the *Brune* [1970, 1971] spectral technique. All but four of the estimates are within a factor of 2 of each other, and if event 11 (Table 1) were eliminated for reasons just given, then for 26 events all but three show agreement for the two estimates of r_0 within a factor of 2. Considering the uncertainties generally associated with estimating r_0 [e.g., *Fletcher et al.*, 1984], the agreement illustrated in Figure 7 is as good as can be

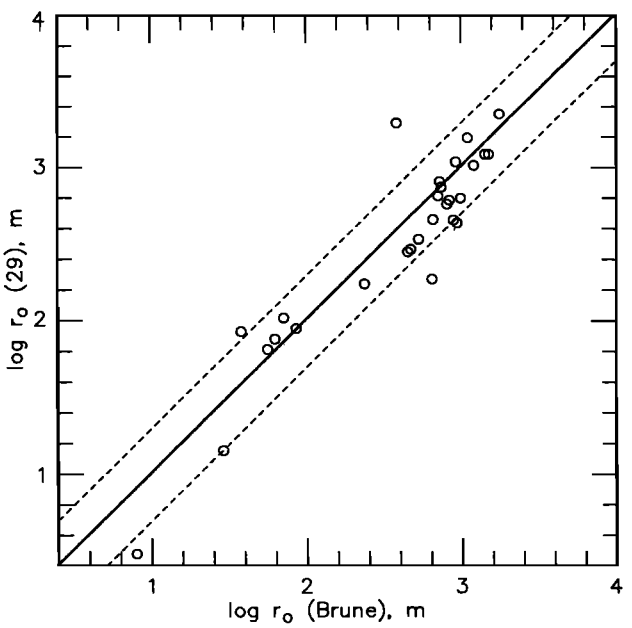

Fig. 7. Source radius r_0 calculated (29) against r_0 determined using the *Brune* [1970] spectral technique (Table 1). Solid line indicates agreement between the two estimates. Factor of 2 disagreement is shown by the dashed lines.

TABLE 1. Source and Ground Motion Parameters

Event	Depth, km	M_0, N m	r_0 (Brune), m	Rv, m^2/s	ρRa, MPa	D, m	$D/2$, m/s	r, m	r_0 (equation (28)), m	$\Delta\sigma_a$, MPa	r_0/r	M_{0a}, N m
ERPM Mine Tremors [McGarr et al., 1981; McGarr, 1984]												
3	~3	3.8×10^{12}	55	9.83	14.5	0.021	1.76	16.7	65	36.2	3.3	7.4×10^{11}
5	~3	6.3×10^{10}	29	1.50	4.5	0.003	0.55	8.2	14	11.2	3.5	2.5×10^{10}
6	~3	1.7×10^{12}	71	9.50	48.4	0.020	5.88	4.8	104	121.0	14.8	5.8×10^{10}
7	~3	2.3×10^{11}	86	1.15	4.5	0.002	0.55	6.3	89	11.2	13.6	1.0×10^{10}
8	~3	9.0×10^{11}	63	4.58	15.6	0.010	1.90	7.2	76	39.0	8.8	6.5×10^{10}
10	~3	8.1×10^{10}	38	0.74	5.1	0.002	0.62	3.6	86	12.8	10.6	3.3×10^{9}
11	~3	4.6×10^{9}	8	0.48	1.3	0.001	0.16	9.1	3	3.2	0.9	1.0×10^{10}
Vaal Reefs Mine Tremor, Oroville, California [McGarr et al., 1981; McGarr, 1984]												
1040939	1.8	4.7×10^{15}	393	72.5	18.7	0.16	2.27	100	1894	46.8	3.9	2.0×10^{14}
Vaal Reefs Mine Tremor, Oroville, California [Fletcher et al., 1984; McGarr, 1984]												
P	8.7	2.1×10^{15}	470	120	14.2	0.27	1.87	192	289	35.5	2.4	1.1×10^{15}
F	9.2	1.5×10^{16}	940	430	38.3	0.97	5.04	255	434	95.8	3.7	6.9×10^{15}
A	8.1	2.0×10^{16}	990	300	20.4	0.68	2.69	335	633	51.0	3.0	8.4×10^{15}
B	7.4	4.1×10^{15}	540	152	13.6	0.34	1.79	254	337	34.0	2.1	2.4×10^{15}
T	11.3	2.0×10^{15}	450	130	17.1	0.29	2.25	173	283	42.8	2.6	9.5×10^{14}
U	10.4	9.9×10^{15}	650	307	30.6	0.69	4.03	228	449	76.5	2.8	3.9×10^{15}
K	7.7	1.5×10^{16}	1400	180	18.7	0.40	2.46	219	1209	46.8	6.4	2.1×10^{15}
R	4.1	4.4×10^{16}	1400	215	9.1	0.48	1.20	538	1209	22.8	2.6	1.5×10^{16}
S	5.1	4.1×10^{15}	650	199	12.9	0.45	1.70	351	186	32.2	1.8	6.1×10^{15}
N	3.1	6.9×10^{15}	930	100	11.3	0.22	1.49	201	1088	28.2	4.6	9.8×10^{14}
Coalinga, California [McGarr et al., 1990]												
May 3; 1541*	7.9	3.97×10^{16}	897	690	36.5	1.60	4.96	417	451	91.2	2.2	2.9×10^{16}
May 4; 0728	13.0	2.5×10^{16}	814	396	24.7	0.92	3.35	354	583	61.8	2.3	1.2×10^{16}
May 9; 0249	12.0	4.2×10^{16}	842	619	36.8	1.43	5.00	371	597	92.0	2.3	2.0×10^{16}
May 9; 0326	12.4	2.12×10^{16}	1241	186	11.2	0.43	1.52	366	1016	28.0	3.4	6.0×10^{15}
May 24; 0902	8.9	2.12×10^{16}	740	256	15.7	0.59	2.13	360	752	39.2	2.1	7.9×10^{15}
July 9; 0740	9.0	6.32×10^{16}	1107	409	27.5	0.95	3.73	328	1538	68.8	3.4	1.1×10^{16}
July 22; 0239	7.4	4.5×10^{17}	1781	1480	74.3	3.42	10.09	439	2260	185.8	4.1	6.8×10^{16}
July 22; 0343	7.9	4.23×10^{16}	727	525	34.9	1.22	4.74	332	793	87.2	2.2	1.4×10^{16}
July 25; 2231	8.4	7.83×10^{16}	672	976	52.9	2.26	7.18	407	644	132.2	1.7	3.9×10^{16}

*Dates are in 1983; times are in UT.

expected. In particular, there does not seem to be any systematic departure of the data from a line of slope 1.

The localized stress drops $\Delta\sigma_a$, listed in Table 1 and calculated from (25), are quite high compared to the stress drops normally estimated for earthquakes that are usually in the range of 0.1 to 10 MPa [e.g., *Hanks*, 1977]. The values of $\Delta\sigma_a$, ranging up to nearly 200 MPa, are comparable to stress drops measured in laboratory samples in stress environments similar to those expected for the various events of Table 1 [e.g., *Byerlee and Brace*, 1968].

Finally, we note in Table 1 that r is usually significantly less than r_0, but in only two cases did the ratio r_0/r exceed 10, in agreement with expectations (Figure 8). Correspondingly, M_0, the moment due to failure within the asperity radius r (Figure 2*a*), is nearly always less than half of M_0, as was expected from the comparison of (29) to (7).

Updates and Corrections to the *McGarr* [1981] Model

As mentioned at the beginning, part of the intent here is to reanalyze the model of inhomogeneous faulting described by *McGarr* [1981] in a more realistic and correct fashion. Some of the expressions developed here and by *McGarr and Bicknell* [1988] differ somewhat from their counterparts in the 1981 report. The three important causes leading to these discrepancies are first, as noted before, there was a factor of 2 error introduced in *McGarr* [1981] between equations (12) and (13) of that paper; second, in 1981 the assumed time-dependent moment was such that the far-field velocity pulse ($\ddot{M}_0(t)$) begins much more abruptly than it ends, in contrast to pulses that are typically observed (Figure 1); third, the estimate of $\Delta\tau_i$ (corresponding to $\Delta\sigma_a$ here) using equation (4) of *McGarr* [1981] is appropriate for a crack but not for an asperity as outlined here in the development of (19). Fortunately, a few of these errors tended to cancel one another, so the discrepancies are less than they might have been. Results for events listed both in Table 1 of *McGarr* [1981] and Table 1 of this report are in fortuitously good agreement.

A fourth, less important, difference between the *McGarr* [1981] analysis and that reported here involves the inhomo-

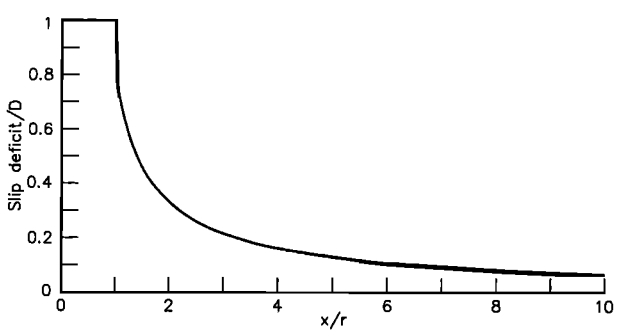

Fig. 8. Slip deficit for an asperity of radius r.

geneous source model. *McGarr* [1981] assumed an asperity within a penny-shaped crack. For the present analysis I first let the radius of the crack become exceedingly large compared to r of the asperity, in order to calculate the extent to which the asperity suppresses slip in its environs (equation (28)), and then simply integrated the resulting slip deficit out to a radius of r_0. This difference is of no consequence of course to any of the relationships between the ground motion parameters and the asperity failure.

Finally, I note that some results presented by *McGarr* [1982] also need to be corrected and updated, partly because this report used *McGarr* [1981] as a point of departure. A report in preparation will present these updates and corrections. Fortunately, the two key figures of *McGarr* [1982], Figures 1 and 2, change almost imperceptibly as a consequence of the corrections described here.

Some Remarks About Brune's Model and Scaling

The observations reviewed here (Figures 3, 5, and 6) provide support for the choice of $k = 2.34$ in (10). Thus the relationship between the duration of the S wave pulse and the dimension of the corresponding rupture surface agrees with that developed by *Brune* [1970, 1971]. This finding raises the obvious question "If Brune's model works this well, then why not use it, instead of (22) to (26), to analyze the data presented in Figures 3, 5, and 6?" As we shall see, it turns out that Brune's model yields results that are incompatible with these data.

To see why, consider the relationships deriving from Brune's model that correspond to (22)–(26). First, for the crack model used by *Brune* [1970] the homogeneous stress drop $\Delta\sigma$ is given by [*Keilis-Borok*, 1959]

$$\Delta\sigma = (7/16)(M_0/r_0^3) \tag{36}$$

Equation (4) of *Brune* [1970] relates this stress drop to the near-fault particle velocity according to

$$\dot{D}/2 = \Delta\sigma\beta/\mu \tag{37}$$

Note that (37) is identical to (26) except for a factor close to 2.

As developed by *McGarr et al.* [1981], the peak velocity in the far field consistent with *Brune*'s [1970, 1971] model is

$$(R\mathbf{v})^B = (0.57\beta\Delta\sigma r_0)/\mu \tag{38}$$

where, as before, a median radiation factor of 0.57 is assumed. Using (36), this peak velocity can also be expressed in terms of M_0 as

$$(R\mathbf{v})^B = 0.43(\beta/\mu)\Delta\sigma^{2/3}M_0^{1/3} \tag{39}$$

The expression of peak velocity in terms of fault slip is obtained by combining (8), (36), and (38), whereupon

$$(R\mathbf{v})^B = 0.783\beta D_0 = 0.522\beta D_m \tag{40}$$

where $D_m = 1.5\,D_0$ is the maximum slip at the center of the assumed penny-shaped crack; for the crack model, with homogeneous stress drop, the slip varies from zero at the edge to its maximum value D_m at the center [*Keilis-Borok*, 1959]. Equation (40) corresponds to (22) and differs by a factor of 6.3 or 4.2 depending on whether D_0 or D_m is taken as the representative fault slip.

Strictly speaking, the peak acceleration parameter from the *Brune* (1970) model has a value of infinity in that the peak acceleration pulse is a delta function. For limited-bandwidth accelerograms, however, *McGarr et al.* [1981] showed that for the far-field S wave and a median radiation factor of 0.57 the *Brune* [1970] model leads to

$$\rho R\mathbf{a}^B = (1.14\Delta\sigma r_0 f_s)/\beta \tag{41}$$

where f_s represents the bandwidth. Assuming that f_s is determined by factors external to the source, such as attenuation during wave propagation or band-limited recording, (41) corresponds to (25) but involves source scaling that differs by the factor r_0. This scaling can be expressed differently by combining (36) with (41) to obtain

$$\rho R\mathbf{a}^B = 0.865\Delta\sigma^{2/3}M_0^{1/3}f_s/\beta \tag{42}$$

Thus for both peak velocity (equations (38) and (39)) and peak acceleration (equations (41) and (42)) parameters the scaling is identical; if stress drop does not vary systematically with earthquake size, then each of these parameters scales as $M_0^{1/3}$.

We are now in a position to compare ground motion predictions stemming from *Brune*'s [1970, 1971] model with observations. To assess the veracity of (40), consider the data represented in Figure 3 and take the slip in (40) to be D_m, the maximum slip in the Brune model. For this case, if (40) had been used to construct Figure 3 instead of (22), the right-hand ordinate would be reduced by a factor of 4.2, which would, in effect, raise the underground observations of fault slip by the same factor. Four of the five slip data would move to positions above the top edge of the plot, and the fifth would shift upward to a point just below the upper margin. Thus, whereas in terms of (22) the observations of underground slip and the peak velocity parameters are quite compatible, (40) yields incompatibility by at least a factor of 4; that is, for a given value of $R\mathbf{v}$, (40) indicates maximum slip values that are unacceptably low in view of Figure 3.

The comparison of *Brune*'s [1970, 1971] model against the observations of Figure 5 requires both (37) and (42). Consider the surface observations of $\rho R\mathbf{a}$ (circles and squares, Figure 5) in the range $M \geq 3$. For this situation, *McGarr et al.* [1990*a*] showed that for S waves, several kilometers of upward wave propagation to the surface results in a bandwidth limitation f_s close to 40 Hz; the recording bandwidth at these sites extended to 100 Hz. Additionally, the Brune stress drops for these events [*Spottiswoode and McGarr*, 1975; *McGarr et al.*, 1981] are nearly all in the range 0.5–5 MPa, with 2 MPa being perhaps most typical. Accordingly, if (42) with $f_s = 40$ Hz and $\Delta\sigma = 2$ MPa is plotted in Figure 5, we see that agreement with the surface observations of $\rho R\mathbf{a}$ is good; for these parameter choices, (42) describes a line of slope $\frac{1}{3}$ in Figure 5 passing through the middle of the acceleration data. Note, also, that a choice of $\Delta\sigma = 2$ MPa works well if (39) is compared to the surface $R\mathbf{v}$ data of Figure 3; 5 and 0.5 MPa for $\Delta\sigma$ result in fits that are clearly too high or low, respectively, to be compatible with the data in Figure 3.

Having concluded that 2 MPa is a very solid choice for $\Delta\sigma$, on the basis of previous studies [e.g., *McGarr et al.*, 1981] as well as by comparing (39) and (42) to the ground motion data

of Figures 3 and 5, we can now ascertain the viability of Brune's model in terms of the estimates of $\dot{D}/2$ from underground observations. Equation (37) with $\Delta\sigma = 2$ MPa yields $\dot{D}/2 = 0.19$ m/s, a level of particle velocity that is situated more than an order of magnitude below most of the observations in Figure 5. A stress drop of at least 20 MPa would be required for compatibility, but then (39) and (42) would be totally out of accord with the corresponding ground motion data. Hence *Brune*'s [1970, 1971] model appears incapable of yielding compatibility between seismic observations of $\rho R\mathbf{a}$ and estimates of $\dot{D}/2$ from underground damage (Figure 5).

With regard to laboratory stick-slip friction experiments, although (37) and (26) differ by a factor of about 2, there is no straightforward way to relate (37) to the data of Figure 6 because of the difficulty of converting the peak particle velocity to an average value. This problem is related to the indefinite duration of the exponentially decaying Brune pulse. Both (26) and (37) can be compared, however, to the peak particle velocities measured in a foam rubber model by *Archuleta and Brune* [1975, Figure 8] (see also Figure 5.15 of *Brune* [1976]). From this experiment, 15 values of $\dot{D}/2$ were measured; these range from 0.19 $\Delta\sigma\beta/\mu$ to 1.3 $\Delta\sigma\beta/\mu$. The median value is 0.37 $\Delta\sigma\beta/\mu$. The prediction of (26), 0.51 $\Delta\sigma\beta/\mu$, exceeds the median observation by 38%, whereas (37), from *Brune* [1970], is higher than the median by 170% (1 versus 0.37). If (26) and (37) were plotted on Figure 8 of *Archuleta and Brune* [1975], (37) would be situated below one of the data but far above the other 14, whereas (26) would have five data above and 10 below. Thus although those foam rubber data show considerable scatter, they nonetheless provide support for (26) but not (37).

Turning now to the issue of peak acceleration scaling, the scaling associated with (25) can be defended on the basis of both fundamental principles and observations in contrast to (42), which cannot be so defended. With regard to scaling principles, as reviewed by *McGarr* [1984], according to *Dieterich* [1973] and Andrews [1975], a solution to the elastodynamic problem can be transformed to another solution using four independent scaling factors for length, displacement amplitude, elastic modulus, and density. Because the last two quantities do not change with earthquake size, the number of scaling factors is reduced to two, and for the assumption of constant stress drop there remains only one, as stress is proportional to the ratio of displacement amplitude to length. From these basic considerations it follows that $R\mathbf{v} \sim M_0^{1/3} \sim r$ and $\rho R\mathbf{a} \sim 1$ [e.g., *Andrews*, 1975; *McGarr*, 1984]. Thus, assuming that f_s is independent of the seismic source, (42), which derives from *Brune*'s [1970, 1971] model, is incompatible with fundamental scaling principles, in contrast to (25), for which the scaling is correct. (I note here that without taking band limitations into account, *Brune*'s [1970] model yields the proper peak acceleration scaling in that $\mathbf{a}$ is infinity, independent of earthquake size.)

The scaling associated with (25) also derives considerable support from observations covering a broad magnitude range. *Hanks and Johnson* [1976, p. 959] interpreted peak accelerations in the magnitude range $3.2 \leq M \leq 7.1$ as indicating that "physical processes in the source region responsible for generating these high-frequency acceleration amplitudes at $R \simeq 10$ km are independent of magnitude." Equation (3) of *Hanks and Johnson* [1976] is in fact identical in form to (25) of this report except that "dynamic shear stress difference" replaces the asperity stress drop used here.

Figure 2 of *McGarr* [1984], involving peak accelerations for events in the magnitude range $0.4 \leq M \leq 6.9$ illustrates the effects of focal depth and stress state on the parameter $\rho R\mathbf{a}$. Most interestingly, no magnitude dependence was suggested by these data, as explained in some detail [*McGarr*, 1984, pp. 6974–6975] (see also Figure 2 of *McGarr* [1982]).

In summary, the scaling of (25) is compatible with both the data in hand and fundamental scaling principles. That of (41) and (42), from *Brune*'s [1970, 1971] model, is not.

These are some of the reasons why I chose not to use Brune's model to interpret the observations reviewed here. Additional, but related, problems with Brune's model were described by *McGarr et al.* [1981, p. 314] and *Savage* [1972, p. 3793]. In short, the observational support presented here for $k = 2.34$ in (10) should not be construed as endorsement for the particular model used by *Brune* [1970, 1971].

Concluding Remarks

Equations (22), (24), (25), and (27) compose a useful technique for analyzing the portion of the earthquake source where rupture is the most intense. From the far-field S wave pulses one can infer the slip, slip velocity, stress drop, and dimension of the part of the seismic source that is of primary importance in terms of damaging ground motion, often termed an asperity. Observations underground, in deep-level gold mines (Figures 3 and 5), and in the laboratory (Figure 6) serve to confirm this technique.

An immediate practical application of (24) is the conclusion from the peak acceleration data (Figure 5) that underground support in the deep-level gold mines of South Africa should be capable of accommodating near-fault ground velocities ($\dot{D}/2$) of 3.5 m/s; this is similar to the recommendation of *Wagner* [1984] of at least 2 and preferably 3 m/s. More important, however, is that locally recorded S wave data are relatively easy to obtain compared to direct underground observations of near-fault ground velocity. Thus for any mining situation a seismic recording system could be used to provide the same sort of information, critical to support design requirements, as the data illustrated in Figure 5.

Equation (25) helps to resolve one of the long-standing problems in relating natural crustal earthquakes to their counterparts in the laboratory. That is, stick-slip stress drops increase with increasing normal stress across the fault [e.g., *Okubo and Dieterich*, 1984, Figure 6). In contrast, earthquake stress drops $\Delta\sigma$ do not seem to be related systematically to focal depth [e.g., *O'Neill*, 1984; *McGarr*, 1984, Figure 5]. (Presumably, the normal stress across a fault of a given orientation is proportional to depth.) As $\rho R\mathbf{a}$ tends to increase linearly with focal depth [*McGarr*, 1984], from (25), it is clear that $\Delta\sigma_a$, the stress drop of the asperity, should also increase linearly with depth and, correspondingly, with confining stress. Hence $\Delta\sigma_a$ from (25) is perhaps the appropriate earthquake stress drop for comparison with laboratory stick-slip failure [see *Hanks and Johnson*, 1976].

Gibowicz [1984] and *Gibowicz et al.* [1990] have argued that for mine tremors in Europe, $k = 1.32$, in the equation $r_0 = (k\beta)/(2\pi f_0)$, where f_0 is the spectral corner frequency [*Madariaga*, 1976], is more compatible with observed extents of underground damage than using $k = 2.34$ to estimate

r_0 [*Brune*, 1970, 1971]. From the various results presented here, I would propose that $k = 2.34$ is, in fact, a good choice for estimating both r and r_0 but that damage is related to r, the radius of high-slip-rate asperity failure, not r_0. For all but a few of the events listed in Table 1, r is less than half of r_0, suggesting that r_0, the overall source radius, is substantially larger than the expected extent of significant underground damage. Thus in terms of the inhomogeneous faulting model there seems to be no contradiction between a source radius r_0 estimated using *Brune*'s [1970, 1971] relation and a smaller extent of underground damage for a particular tremor.

Acknowledgments. I thank A. Frankel, J. Fletcher, J. N. Brune, J. Boatwright, and M. Blanpied for carefully reviewing this report. I am grateful to J. Bicknell for assistance in the preparation of Figure 1 and for numerous discussions during the course of this research. C. Sullivan provided valuable editorial assistance.

REFERENCES

Abe, K., Determination of static and dynamic fault parameters: The Saitame earthquake of July 1, 1968, *Tectonophysics*, *27*, 223–238, 1975.

Aki, K., and P. G. Richards, *Quantitative Seismology*: *Theory and Methods*, Freeman, Cooper, San Francisco, Calif., 1980.

Andrews, D. J., From antimoment to moment: Plane strain models of earthquakes that stop, *Bull. Seismol. Soc. Am.*, *65*, 163–182, 1975.

Archuleta, R. J., and J. N. Brune, Surface strong motion associated with a stick-slip event in a foam rubber model of earthquakes, *Bull. Seismol. Soc. Am.*, *65*, 1059–1071, 1975.

Bicknell, J., and A. McGarr, Underground recordings of mine tremors—Implications for earthquake source scaling, in *2nd International Symposium of Rockbursts and Seismicity in Mines*, edited by C. Fairhurst, University of Minnesota Press, Minneapolis, 1988.

Boatwright, J., A spectral theory for circular seismic sources; Simple estimates of source dimension, dynamic stress drop, and radiated seismic energy, *Bull. Seismol. Soc. Am.*, *70*, 1–27, 1980.

Boatwright, J., The seismic radiation from composite models of faulting, *Bull. Seismol. Soc. Am.*, *78*, 489–508, 1988.

Boore, D. M., and J. Boatwright, Average body-wave radiation coefficients, *Bull. Seismol. Soc. Am.*, *74*, 1615–1621, 1984.

Borcherdt, R. D., J. B. Fletcher, E. G. Jensen, G. L. Maxwell, J. R. Van Schaack, R. E. Warrick, E. Cranswick, M. J. S. Johnston, and R. McClearn, A general earthquake-observation system (GEOS), *Bull. Seismol. Soc. Am.*, *75*, 1783–1825, 1985.

Brace, W. F., and J. D. Byerlee, Stick slip as a mechanism for earthquakes, *Science*, *153*, 990–992, 1966.

Brummer, R. K., and A. J. Rorke, Case studies of large rockbursts in South African gold mines, in *2nd International Symposium of Rockbursts and Seismicity in Mines*, edited by C. Fairhurst, University of Minnesota Press, Minneapolis, 1988.

Brune, J. N., Tectonic stress and the spectra of seismic shear waves from earthquakes, *J. Geophys. Res.*, *75*, 4997–5009, 1970. (Correction, *J. Geophys. Res.*, *76*, 5002, 1971.)

Brune, J. N., Earthquake modeling by stick-slip along precut surfaces in stressed foam rubber, *Bull. Seismol. Soc. Am.*, *63*, 2105–2119, 1973.

Brune, J. N., The physics of earthquake strong motion, in *Seismic Risk and Engineering Decisions*, edited by C. Lomnitz and E. Rosenbluth, pp. 141–177, Elsevier, New York, 1976.

Byerlee, J. D., and W. F. Brace, Stick-slip, stable sliding and earthquakes—Effects of rock type, pressure, strain rate and stiffness, *J. Geophys. Res.*, *73*, 6031–6037, 1968.

Churcher, J. M., The effect of propagation path on the measurement of seismic parameters, in *2nd International Symposium of Rockbursts and Seismicity in Mines*, edited by C. Fairhurst, University of Minnesota Press, Minneapolis, 1988.

Dahlen, F. A., On the ratio of *P*-wave to *S*-wave corner frequencies for shallow earthquake sources, *Bull. Seismol. Soc. Am.*, *64*, 1159–1180, 1974.

Das, S., and B. V. Kostrov, Breaking of a single asperity: Rupture process and seismic radiation, *J. Geophys. Res.*, *88*, 4277–4288, 1983.

Dieterich, J. H., A deterministic near-field source model, Proceedings of the 5th World Conference on Earthquake Engineering, *Pap. 301*, 13 pp., World Conf. Earthquake Eng., Rome, 1973.

Fletcher, J. B., J. Boatwright, L. Haar, T. Hanks, and A. McGarr, Source parameters for aftershocks of the Oroville, California, earthquake, *Bull. Seismol. Soc. Am.*, *74*, 1101–1123, 1984.

Frankel, A., High-frequency spectral fall-off of earthquakes, fractal dimension of complex rupture, *b* value, and the scaling of strength on faults, *J. Geophys. Res.*, *96*, 6291–6302, 1991.

Gay, N. C., and W. D. Ortlepp, Anatomy of a mining induced fault zone, *Geol. Soc. Am. Bull.*, *90*, 47–58, 1979.

Gay, N. C., D. Spencer, J. J. van Wyk, and P. K. van der Heever, The control of geological and mining parameters on seismicity in the Klerksdorp mining district, in *Proceedings of the 1st International Congress on Rockbursts and Seismicity in Mines*, vol. 6, edited by N. C. Gay and E. H. Wainwright, pp. 107–120, South African Institute of Mining and Metallurgy, Johannesburg, 1984.

Gibowicz, S. J., The mechanism of large mining tremors in Poland, in *Proceedings of the 1st International Congress on Rockbursts and Seismicity in Mines*, *Symp. Ser.*, vol. 6, edited by N. C. Gay and E. H. Wainwright, pp. 17–28, South African Institute of Mining and Metallurgy, Johannesburg, 1984.

Gibowicz, S. J., and R. P. Young, Seismic Hazard Estimates for the Proposed Site of the Sudbury Neutrino Observatory at Creighton Mine, *Res. Rep. RP001SNO*, Dep. of Geol. Sci., Queen's Univ., Kingston, Ontario, Canada, Jan. 1990.

Gibowicz, S. J., H.-P. Harjes, and M. Schäfer, Source parameters of seismic events at Heinrich Robert Mine, Ruhr Basin, Federal Republic of Germany: Evidence for non-double-couple events, *Bull. Seismol. Soc. Am.*, *80*, 88–109, 1990.

Hanks, T. C., Earthquake stress drops, ambient tectonic stresses and stresses that drive plate motions, *Pure Appl. Geophys*, *115*, 441–458, 1977.

Hanks, T. C., and D. A. Johnson, Geophysical assessment of peak accelerations, *Bull. Seismol. Soc. Am.*, *66*, 959–968, 1976.

Hanks, T. C., and H. Kanamori, A moment magnitude scale, *J. Geophys. Res.*, *84*, 2348–2350, 1979.

Hanks, T. C., and M. Wyss, The use of body wave spectra in the determination of seismic source parameters, *Bull. Seismol. Soc. Am.*, *62*, 561–589, 1972.

Hartzell, S. H., and J. N. Brune, The Horse Canyon earthquake of August 2, 1975—Two stage stress-release process in a strike-slip earthquake, *Bull. Seismol. Soc. Am.*, *69*, 1161–1173, 1979.

Johnson, L. R., Green's function for Lamb's problem, *Geophys. J.*, *37*, 99–131, 1974.

Johnston, T. L., and C. H. Scholz, Dynamic properties of stick-slip friction of rock, *J. Geophys. Res.*, *81*, 881–888, 1976.

Keilis-Borok, V. I., On estimation of the displacement in an earthquake source and of source dimensions, *Ann. Geofis.*, *12*, 205–214, 1959.

Kostrov, B. V., Self-similar problems of propagation of shear cracks, *J. Appl. Math. Mech.*, Engl. Transl., *28*, 1077–1087, 1964.

Madariaga, R., Dynamics of an expanding circular fault, *Bull. Seismol. Soc. Am.*, *66*, 639–666, 1976.

McGarr, A., Violent deformation of rock near deep-level tabular excavations—Seismic events, *Bull. Seismol. Soc. Am.*, *61*, 1453–1466, 1971.

McGarr, A., Analysis of peak ground motion in terms of a model of inhomogeneous faulting, *J. Geophys. Res.*, *86*, 3901–3912, 1981.

McGarr, A., Upper bounds on near-source peak ground motion based on a model of inhomogeneous faulting, *Bull. Seismol. Soc. Am.*, *72*, 1825–1841, 1982.

McGarr, A., Scaling of ground motion parameters, state of stress, and focal depth, *J. Geophys. Res.*, *89*, 6969–6979, 1984.

McGarr, A., Report on seismic hazard estimate for the Sudbury Neutrino Observatory, 15 pp., Branch of Eng. Seismol. and Geol., U.S. Geol. Surv., Menlo Park, Calif., Feb. 1990.

McGarr, A., and J. Bicknell, Estimation of the near-fault ground motion of mining-induced tremors from locally recorded seismograms in South Africa, in *2nd International Symposium of Rockbursts and Seismicity in Mines*, edited by C. Fairhurst, University of Minnesota Press, Minneapolis, 1988.

McGarr, A., and J. Bicknell, Synthetic seismograms analysis of

locally-recorded mine tremors, in *Rock at Great Depth*, vol. 3, edited by V. Maury and D. Fourmaintraux, pp. 1407–1413, A. A. Balkeema, Rotterdam, 1990.

McGarr, A., S. M. Spottiswoode, N. C. Gay, and W. D. Ortlepp, Observations relevant to seismic driving stress, stress drop, and efficiency, *J. Geophys. Res.*, *84*, 2251–2261, 1979.

McGarr, A., R. W. Green, and S. M. Spottiswoode, Strong ground motion of mine tremors: some implications for near-source ground motion parameters, *Bull. Seismol. Soc. Am.*, *71*, 295–319, 1981.

McGarr, A., J. Bicknell, E. Sembera, and R. W. E. Green, Analysis of exceptionally large tremors in two gold mining districts of South Africa, *Pure Appl. Geophys.*, *129*, 295–307, 1989.

McGarr, A., J. Bicknell, J. Churcher, and S. Spottiswoode, Comparison of ground motion from tremors and explosions in deep gold mines, *J. Geophys. Res.*, *95*, 21,777–21,792, 1990*a*.

McGarr, A., C. Mueller, J. B. Fletcher, and M. Andrews, Ground motion and source parameters of the Coalinga earthquake sequence, in The Coalinga, California, Earthquake of May 2, 1983, edited by M. J. Rymer and W. L. Ellsworth, *U.S. Geol. Surv. Prof. Pap.*, *1487*, 215–234, 1990*b*.

Okubo, P. G., and J. H. Dieterich, Effects of physical fault properties on frictional instabilities produced on simulated faults, *J. Geophys. Res.*, *89*, 5817–5827, 1984.

O'Neill, M. E., Source dimensions and stress drops of small earthquakes near Parkfield, California, *Bull. Seismol. Soc. Am.*, *74*, 27–40, 1984.

Savage, J. C., Relation of corner frequency to fault dimensions, *J. Geophys. Res.*, *77*, 3788–3795, 1972.

Semadeni, T. J., P. Rochon, and J. Niewiadowski, Waveform analysis of mine-induced seismic events recorded at Rio Algom's Quirke Mine, in *2nd International Symposium of Rockbursts and Seismicity in Mines*, edited by C. Fairhurst, University of Minnesota Press, Minneapolis, 1988.

Spottiswoode, S. M., and A. McGarr, Source parameters of tremors in a deep-level gold mine, *Bull. Seismol. Soc. Am.*, *65*, 93–112, 1975.

Tyser, J. A., and H. Wagner, A review of six years of operations with the extended use of rapid-yielding hydraulic props at the East Rand Proprietary Mines, Limited, and experience gained throughout the industry, *Papers and Discussions*, *1976–1977*, pp. 321–341, Association of Mine Managers of South Africa, Johannesburg, 1977.

van Aswegen, G., Fault stability in SA gold mines, paper presented at the International Conference on the Mechanics of Jointed and Faulted Rock, Tech. Univ. of Vienna, Vienna, April 1990.

van der Heever, P. K., Some technical and research aspects of the Klerksdorp seismic network, in *Proceedings of the 1st International Congress on Rockbursts and Seismicity in Mines*, vol. 6, edited by N. C. Gay and E. H. Wainwright, pp. 349–350, South African Institute of Mining and Metallurgy, Johannesburg, 1984.

Wagner, H., Support requirements for rockburst conditions, in *Proceedings of the 1st International Congress on Rockbursts and Seismicity in Mines*, *Symp. Ser.*, vol. 6, edited by N. C. Gay and E. H. Wainwright, pp. 209–218, South African Institute of Mining and Metallurgy, Johannesburg, 1984.

Walsh, J. B., Stiffness in faulting and friction experiments, *J. Geophys. Res.*, *76*, 8597–8598, 1971.

Wolfenstein, L., and E. Beier, Neutrino oscillations and solar neutrinos, *Phys. Today*, *42*(7), 28–36, 1989.

Young, R. P., and S. Talebi, Microseismic monitoring and excavation damage assessment at Atomic Energy of Canada Limited's underground research laboratory, *Rep. RP001AECL*, Dep. of Geol. Sci., Queen's Univ., Kingston, Ontario, Canada, Sept. 1988.

A. McGarr, U.S. Geological Survey, Office of Earthquakes, Volcanoes and Engineering, 345 Middlepark Road, MS 977, Menlo Park, CA 94025.

(Received July 19, 1990;
revised May 13, 1991;
accepted May 7, 1991.)

JOURNAL OF GEOPHYSICAL RESEARCH, VOL. 96, NO. B10, PAGES 16,535–16,546, SEPTEMBER 10, 1991

A Tilt and Seismicity Episode in the New Hebrides (Vanuatu) Island Arc

R. MELLORS,[1,2] J.-L CHATELAIN,[3] B.L. ISACKS,[1] G. HADE,[1]
M. BEVIS,[4] AND R. PREVOT[3]

Tilt and seismicity have been monitored in the central New Hebrides island arc since 1978 using bench mark arrays, long tube water tiltmeters, borehole tiltmeters, and a local seismometer network. Releveling of the bench mark array on Efate island in late November 1986 revealed a 10 μrad tilt up to the NNW since the previous leveling in April 1986. The tilt event was preceded by a magnitude 5.9 thrust event that occurred on October 25, 1986, at a depth of 48 km and about 11 km NW of the tiltmeter instruments. Six days later, a shallow (<20 km) swarm of earthquakes occurred 12 km NNW of the tiltmeter instruments and 5 km north of the epicenter of the magnitude 5.9 earthquake. Closely coincident in time with the swarm, a 5 μrad tilt up to the NNW that occurred over a period of 5 days was recorded on both the 100 m baseline water tube tiltmeter and the borehole bubble level tiltmeter. A composite focal mechanism of 191 earthquakes selected from the swarm indicates a thrust mechanism with some component of strike-slip. Calculations show that the seismic slip associated with a swarm of this magnitude is apparently inadequate to cause the observed surface deformation. Two similar shallow swarms in November 1987 and July 1988 have occurred within 15 km of the 1986 swarm but with no apparent surface deformation. The most likely explanation, supported by simple modeling, is that the swarm and tilt are the result of a magmatic intrusion from island arc volcanism. An alternate hypothesis is that both the seismicity and the tilt are due to an episode of largely aseismic creep in the upper crust.

INTRODUCTION

Seismicity and crustal deformation have been monitored in the central New Hebrides island arc since the late 1970s in an effort to identify potential earthquake hazards. The seismicity has been recorded by a local seismic network installed in 1978 [*Isacks et al.*, 1981; *Chatelain et al.*, 1986] and the crustal deformation measured using geodetically levelled bench mark arrays [*Bevis and Isacks*, 1981], borehole bubble level tiltmeters [*Marthelot et al.*, 1980; *Isacks et al.*, 1978], and a two-component, long tube water tiltmeter. The monitoring is a cooperative project between Cornell University and the Institut Francais de Recherche Scientifique pour le Development en Cooperation (ORSTOM).

After 10 years of monitoring, the first clear tilt event was observed in October-November, 1986 when a large (at least 5 μrad) tilt was clearly recorded by all three instruments measuring crustal deformation on Efate island. This tilt event coincided in time and direction with a shallow (< 20 km) swarm of small ($M_L \leq 4.0$) earthquakes centered 12 km northwest of the tilt monitoring instruments. Six days prior to the swarm and the tilt event, an M_S 5.9 thrust earthquake occurred at a depth of 48 km just off the west coast of Efate island. The hypocenter of this preceding earthquake was 38 km below the center of the swarm.

The purpose of this paper is to document the spatial and temporal relationship of the initial thrust earthquake, the tilt event, and the shallow seismicity. This paper will also illustrate the use of a long tube water tiltmeter for crustal deformation measurements. Thus, we shall first briefly review the tectonics of the region, then describe the instrumentation and crustal deformation observations, and finally discuss the relationship of the tilt and seismicity.

TECTONICS, SEISMICITY AND GEOLOGY OF EFATE

The island of Efate lies in the central part of the New Hebrides island arc, which extends roughly from the Solomon trench at latitude 11°S to the Hunter Fracture Zone at latitude 22°S (Figure 1). This arc marks the subduction of the Australian-Indian plate under the North Fiji Basin at a convergence rate of approximately 11 cm/yr with a slip direction of N75°E [*Isacks et al.*, 1981; *Pascal et al.*, 1978; *Dubois et al.*, 1977]. The resulting Wadati-Benioff zone is steeply inclined with an average dip of 70° to the east and is continuous along the length of the arc. However, within the upper plate, the structure is anomalous in the central portion of the arc where the islands of Malekula and Santo occupy the expected position of the trench. The disruption of the upper plate is believed to be due to a combination of late Miocene rifting and Quaternary interaction with the subducting D'Entrecasteaux Fracture Zone (DFZ) [*Isacks et al.*, 1981; *Chung and Kanamori*, 1978]. Efate is located to the south of this disruption, near the northern end of the Southern New Hebrides Trench (Figure 2).

Seismicity along the central New Hebrides arc varies greatly but is especially distinctive in the Efate region. More specifically, in the 10 years of local network monitoring, the Efate segment has consistently shown the highest rate of seismic activity. This seismicity displays well-defined zones of repeated seismic activity and extensive clustering of earthquakes, with the highest amount of seismicity taking place between the island and the trench axis. This area has a high rate of background activity and is repeatedly activated by clusters of earthquakes, often associated with foreshock and aftershock sequences [*Chatelain et al.*, 1986]. Moderate events ($5.5 < M_S < 7.0$) are relatively frequent in the Efate segment, but few large events ($M_S > 7.0$) have occurred.

Most of the earthquakes in the Efate region occur along the intraplate boundary, and in the 8 years of monitoring before

[1] Institute for the Study of the Continents, Cornell University, Ithaca, New York.
[2] Now at Department of Geological Sciences, Indiana University, Bloomington.
[3] Institut Francais de Recherche Scientifique pour le Development en Cooperation, Noumea, New Caledonia (ORSTOM).
[4] Department of Marine, Earth and Atmospheric Sciences, North Carolina State University, Raleigh.

Paper number 91JB01181.
0148-0227/91/91JB-01181$05.00.

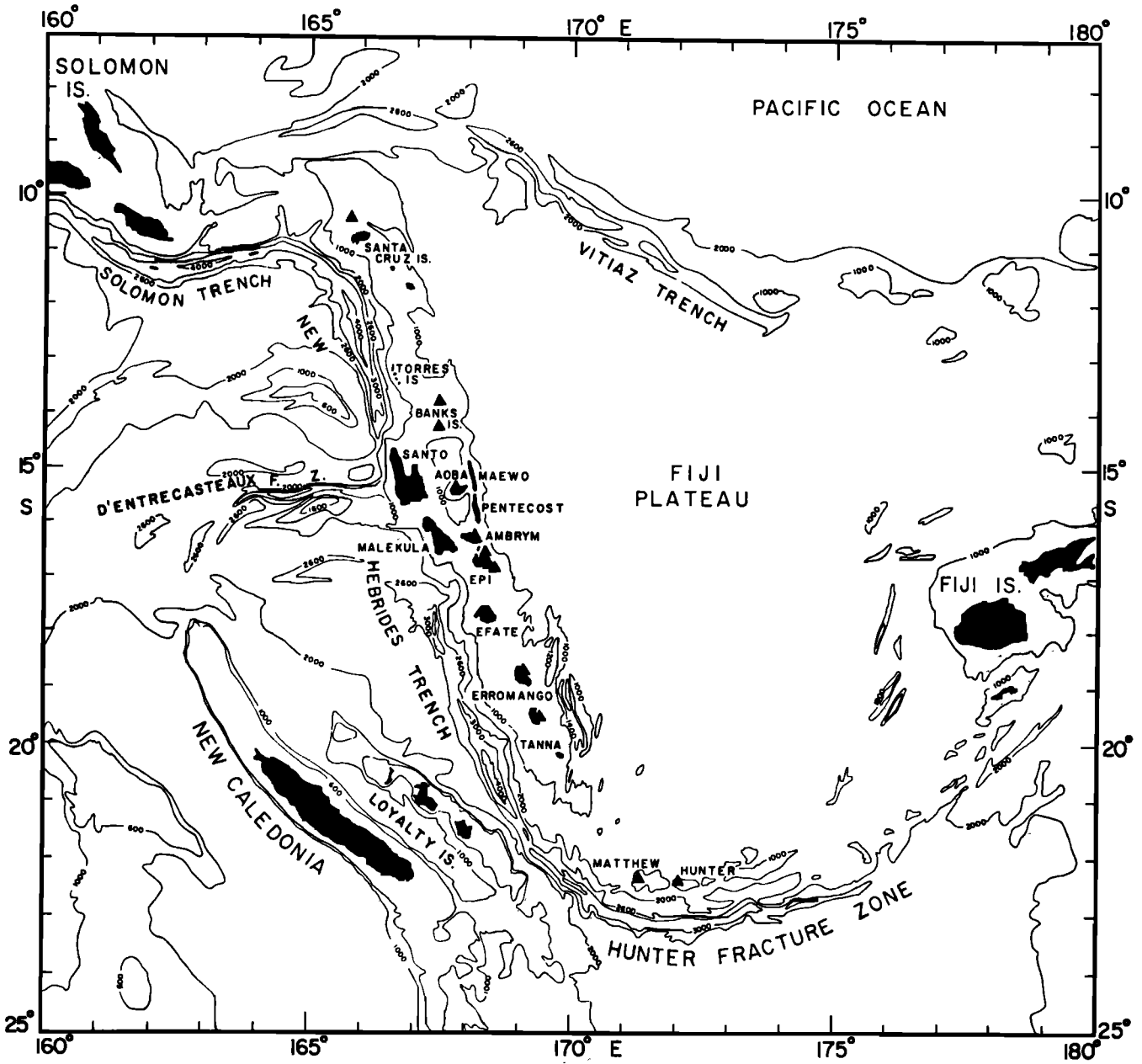

Fig. 1. Bathymetric map of the southwest Pacific region showing the New Hebrides island arc. Triangles represent Quaternary volcanic centers. The contours are in fathoms (1 fathom = 1. 829 m). Adapted from *Isacks et al.* [1981].

1986 only one small cluster had been located on Efate island itself. However, between 1986 and 1988, three unusual shallow swarms occurred on the island of Efate but were situated well above the interplate boundary. The largest swarm, in October and November 1986, was coincident in time with deformations recorded by tiltmeters on the island. Before 1986, in 8 years of monitoring, only one small group of shallow earthquakes had been located on Efate island.

The geology of Efate consists of a core of Plio-Pleistocene submarine volcanics partially covered by Holocene coral limestone (Figure 3). The volcanics consist of breccias and tuffs overlain by younger basalts [*Ash et al.*, 1978; *Carney et al.*, 1984]. The volcanism was centered in the north central part of the island but continued on the small nearby islands to the north after ceasing on the main island. Subaerial basalts found on the these small islands appear to range in age from the Late Pleistocene to Recent. These ages were inferred from an uppermost Late Pleistocene age for a superficial tuff found on Efate (from dated coral limestone) and by the state of preservation of the volcanic structures [*Ash et al.*, 1978].

The Holocene coral limestone on Efate is faulted and uplifted, often forming dramatic terraces created by the interaction of sea level variations with the uplift. Dating of the terraces using high-precision thorium 230 ages indicates an uplift rate of approximately 1 mm/yr for the last 200,000 years. [*Bloom et al.*, 1978; *Edwards et al.*, 1987, 1988]. The terraces are most obvious on the western side of Efate.

Currently, geothermal activity is present in at least four places on Efate. The largest area is located near the site of the most recent volcanism on the extreme north end of the island. This

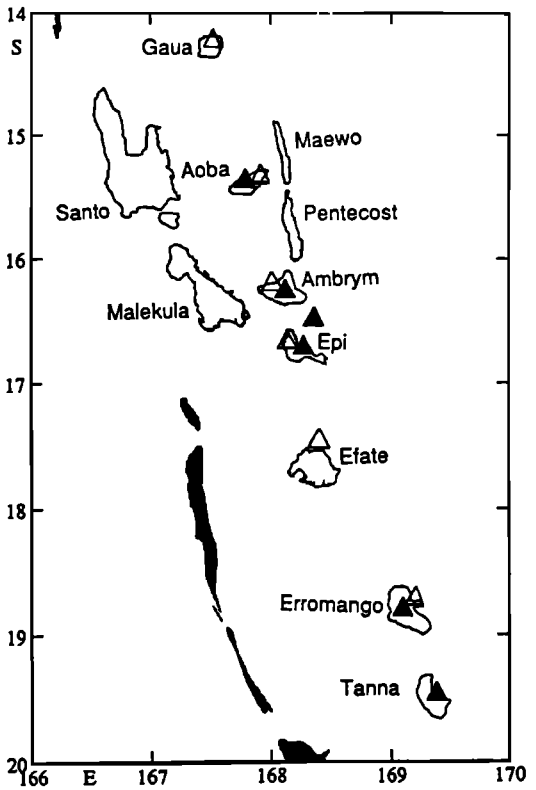

Fig. 2. Map of the central New Hebrides island arc. The solid triangles denote active volcanic centers, and the open triangles denote Quaternary volcanic centers. The shaded region denotes areas deeper than the 6000 m contour of the trench.

area is characterized by hot springs, fumaroles, and high ground temperatures. The other three areas of geothermal activity occur in the central and eastern parts of the island and are characterized by thermal springs with water temperatures up to 58°C [*Mallick*, 1972].

DESCRIPTION OF THE TILTMETER INSTRUMENTATION

Three separate systems for monitoring tilt are deployed on Efate island. Each recorded a tilt during October-November 1986. These systems consist of a periodically leveled bench mark array, a two-component long tube water tiltmeter, and two bubble level borehole tiltmeters (Figure 4). A full description of the bench mark array has been given by *Bevis and Isacks* [1981] and the borehole tiltmeters were discussed by *Marthelot et al.* [1980].

Bench mark array. The leveling array consists of 11 bench marks located within an area 1 km square that is releveled by professional surveyors using first-order procedures at intervals of 6 months to a year (Figure 5). During releveling, the difference in relative elevation is measured between pairs of benchmarks. The change in relative elevation from one survey to the next, divided by the distance between the bench marks, gives the tilt along the azimuth of the bench mark pair. A planar tilt is then determined for the independent pairs using an unweighted, least squares scheme and then expressed in terms of two vectors, a north-south component and an east-west component [*Bevis and Isacks*, 1981]. The resolution is about 1-2 μrad [*Isacks et al.*, 1978]. Apparent tilts can be caused by bench mark instability, measurement error, and loading due to ocean tides [*Bevis and Isacks*, 1981; *Beavan et al.*, 1984]. However, since the leveling procedure requires several observations along the same lines, loading due to tides tends to cancel out [*Bevis and Isacks*, 1981]. An estimate of the error is provided by the standard deviation of the fit of the planar tilt.

Long tube water tiltmeter. The second element in the tilt monitoring system is two orthogonal long tube water tiltmeters installed in 1978. One component is oriented parallel (N20°W) to the strike of the island chain, and the other is perpendicular (N70°E) to the strike. Each tiltmeter consists of a 100 m long, 10 cm diameter PVC pipe half filled with water and buried about 1 m in a trench cut into recrystallized coral bedrock. Detector end pots are anchored to concrete piers set in the underlying recrystalized coral. The water level at each end of the tube is measured using a probe fixed to a float that moves unimpeded in the bore of a fixed linear variable differential transformer (LVDT) body. The LVDT voltage is proportional to the float displacement and is recorded broadband time compressed on Rustrack recorders and band-pass filtered on clock-driven Esterline Angus strip chart recorders.

Because a tilt produces a change in water level that is in opposite direction at each end of the tube during a tilt, tilt signals can be effectively separated from changes caused by thermal and evaporation effects that cause identical changes at each end. This anticorrelation between the water level signals at each end distinguishes tilt from the long-term drift evident in the yearly record. This drift is believed to be caused primarily by evaporation, condensation, or secondary thermal effects. These effects have been decreased by conditioning the surface of the water with oil, but the ENE-WSW tube still exhibits considerable drift, recently shown to be caused by a minor leak in the system. A degree of redundancy is provided by performing first-order geodetic releveling on the piers of the long tube tiltmeter at the same time as the benchmark array. The accuracy of the long tube is very good for short-term events (less than a few days) but decreases with time as the long-term drift is difficult to identify and constrain. The tilt caused by tidal loading [*Marthelot et al.*, 1980; *Isacks et al.*, 1978] is clearly observed. The long tube is also surprisingly sensitive to apparent crustal loading due to tsunami signals near the resonant frequency of the underdamped half filled tube of water (about 6 min). Surface deformation due to rainfall and groundwater effects appears to be minimal, as no anomalous tilt has been observed in periods of extreme rainfall during hurricanes or after controlled pumping of local wells normally used for agricultural purposes.

Borehole tiltmeters. The third element of the tilt monitoring system consists of two Kinemetrics TM-B1 borehole bubble level biaxial tiltmeters installed in steel jacketed boreholes at 2 m depths and coupled to Rustrack recorders [*Isacks et al.*, 1978; *Marthelot et al.*, 1980]. The two borehole tiltmeters on Efate are located at Devil's Point near the long tube water tiltmeter and within the leveling array and at Tukutuku 5 km NW of Devil's Point. Again, the two components of measured tilt are N20°W and N70°E. The results from these instruments are fairly reliable for periods up to a few days but suffer from drift probably due to soil effects from thermal changes and root growth [*Isacks et al.*, 1978; *Wyatt and Berger*, 1980; *Wyatt et al.*, 1988].

Seismometers. The five seismic stations on Efate are part of the 19 station telemetry network operated by Cornell and ORSTOM since 1978. A sixth three-component intermediate

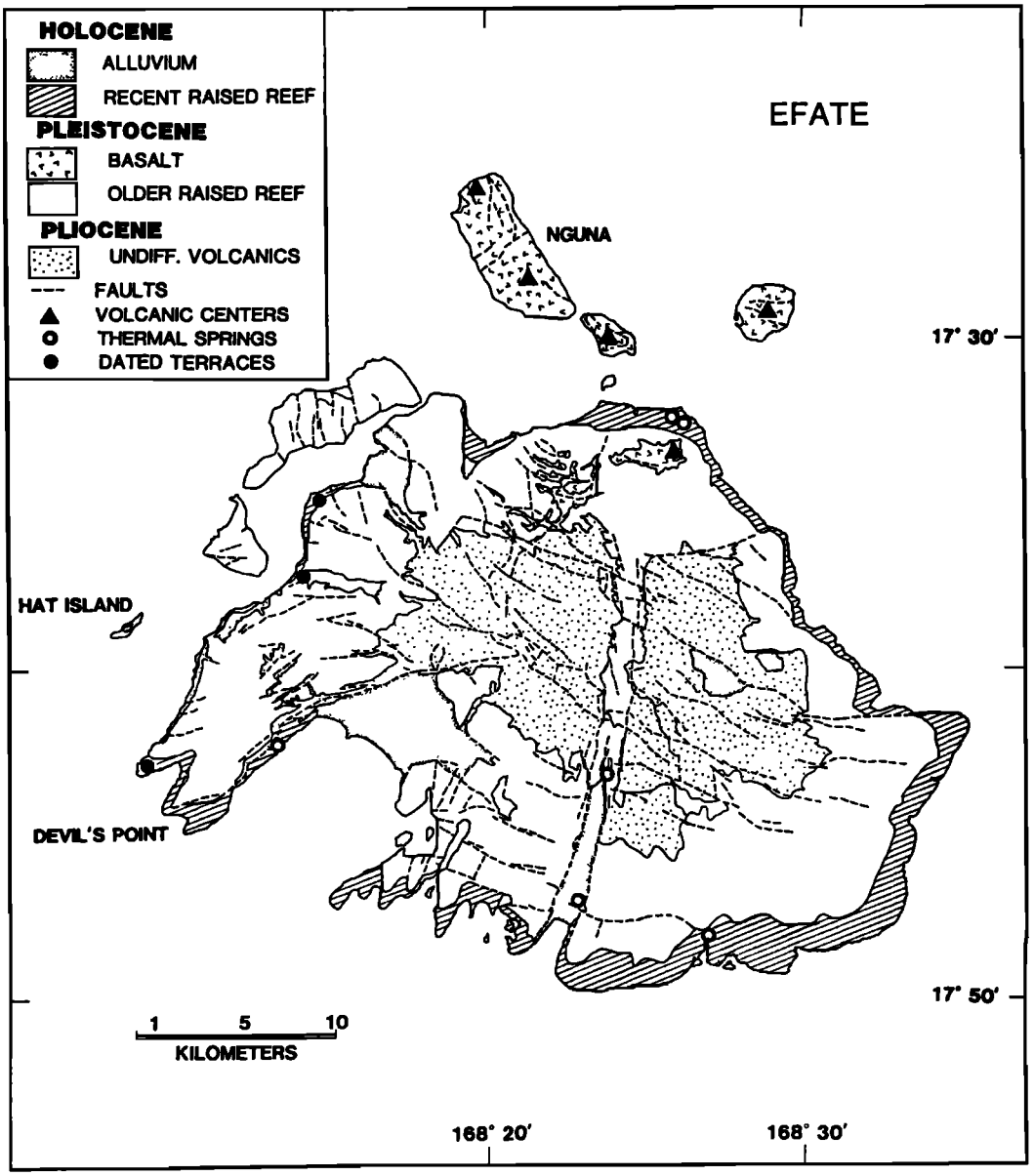

Fig. 3. Geologic map of Efate island. Adapted from *Ash et al.*, [1978] and from *Bevis and Isacks* [1981].

band station, PVC, is operated separately at Port Vila by ORSTOM. Three of the stations (NGA, RTV, MBV) record the vertical component only, while DVP and PVC each record a horizontal (E-W) and a vertical component. A low-gain station, CAV, operating at the base station at Port Vila, is added to the signals from the local network, and the signals are recorded there in both digital and analog form. Earthquake locations are derived using HYPOINVERSE [*Klein*, 1978] from manually picked phases. Magnitudes are determined from a local scale based on coda length and tied to the teleseismic m_b scale by *Chatelain et al.* [1986] from events reported in the Preliminary Determination of Epicenters (PDE) according to the method described by *Tsumura* [1967].

TILT AND SEISMICITY OBSERVATIONS

Prior to the October-November 1986 event, the only possible tectonic tilt recorded was a gradual 6 μrad tilt from 1976 to 1984 registered by the bench mark array at Devil's Point [*Bevis and Isacks*, 1981; *Chatelain et al.*, 1986]. This tilt was believed to be caused by a creep episode along the plate boundary, as no association with major earthquakes was apparent.

Tilt. In October and November 1986, however, a clear and unambiguous tilt episode was recorded by the instruments on Efate island. The first indications of this tilt event were observed upon analysis of the data from the November 26, 1986, leveling of the DVP array. An unprecedented amount of tilt had occurred between the April and November 1986 leveling. Upon the arrival and examination of the long tube tiltmeter and borehole tiltmeter data, it became clear that the deformation coincided with the unusual shallow seismicity recorded on Efate island from October 30 to November 5.

Analysis of the bench mark array data using a best fitting planar tilt calculated from the benchmark movement indicated a tilt of about 9-10 μrad up toward the north since the April 1986 leveling (Figure 6). It was initially suspected that the tilt was the

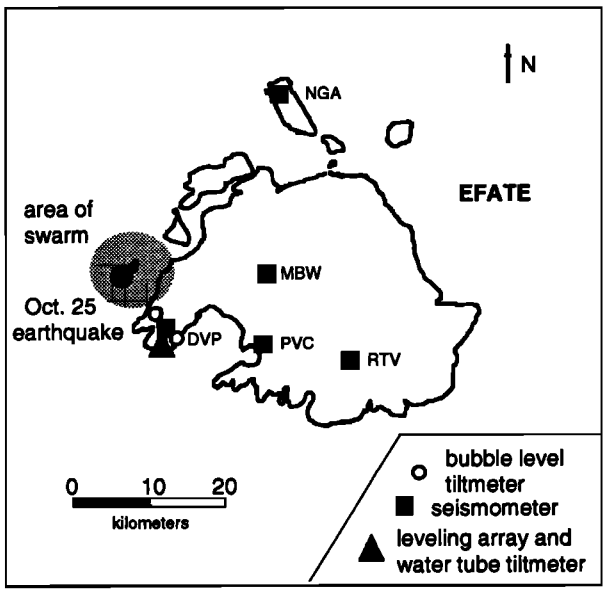

Fig. 4. Map of Efate showing the location of instrumentation and the location of the October-November 1986 shallow swarm. The solid circle is the epicenter of the October 25, 1986, magnitude 5.9 earthquake.

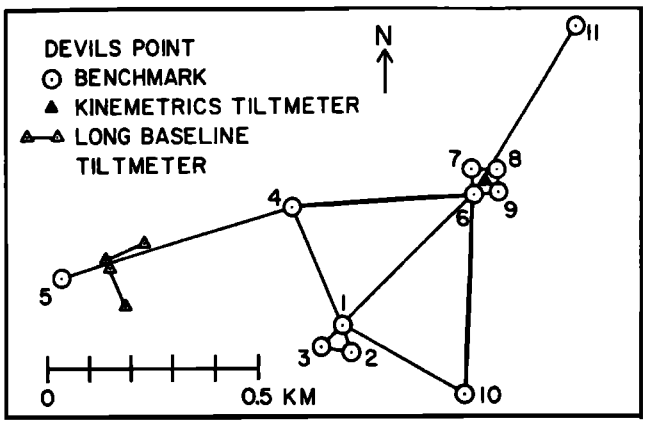

Fig. 5. Diagram of benchmark array. Taken from *Bevis and Isacks*, [1981].

result of bench mark instability, but further analysis of the leveling data showed that the tilt was relatively coherent over the array. The standard deviation of each bench mark observation was within previously recorded values, which argued against sudden bench mark instability. Subsequent relevelings in April and November 1987 appear to confirm the continued stability of the bench marks. Inspection of the data also revealed no misclosures or evidence of blunders in the surveying, implying that the tilt was real and extended over the width of the array. Also, no significant change in precipitation occurred during this period. Even if the maximum resolution error of 2 μrad is assumed on both April and November levelings, the resulting tilt is still at least 6 μrad.

Examination of the records from the long tube water tiltmeter confirm a clear 5 μrad tilt up to the NNW between November 1 and November 9 on the NNW-SSE component (Figure 7). The ENE-WSW component shows a slight amount of tilt (about 0.5 μrad) up to the west but instrumental recording problems and varying sensitivity in the west end of the ENE-WSW instrument prevented a clear estimation of tilt on this component. The long tube recordings also show evidence of a smaller tilt before the larger event. Close examination of the east end of the ENE-WSW long tube data appears to show a slight tilt down to the WSW on October 30 before the larger tilt on November 2 up to the NW, but the lack of a clear corresponding signal on the west end prevents verification.

Examination of the data from the long tube and the bench mark array illustrates two other observations. One is that the majority of the tilt occurs in a NNW-SSE direction. Very little tilt is observed on the ENE-WSW component. The amount of tidal loading on the long tube water tiltmeter is also greater on the NNW-SSE component. Examination of the instrument calibrations indicates that this is probably not instrumental bias

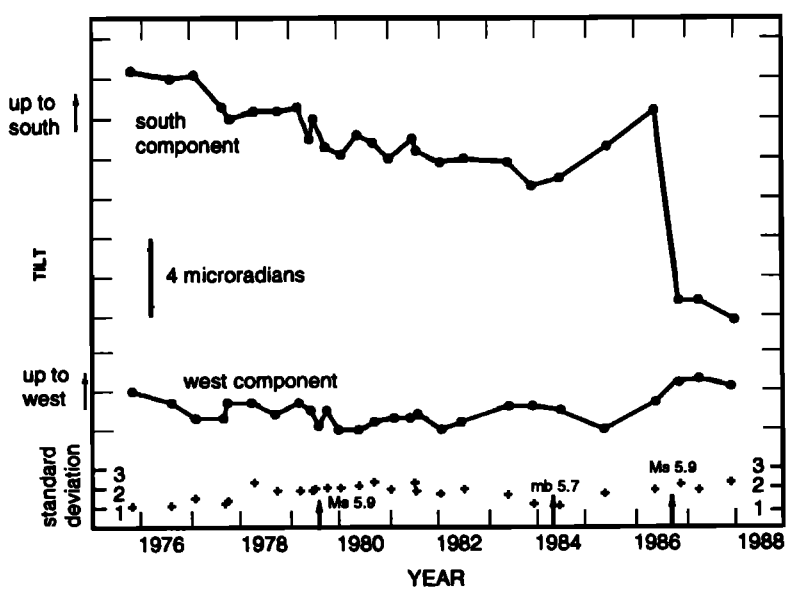

Fig. 6. North-south and east-west components of the planar tilt as calculated from the releveling of the bench mark array. The arrows mark the occurrence of larger earthquakes near Efate island. The small crosses mark the standard deviation of each set of data.

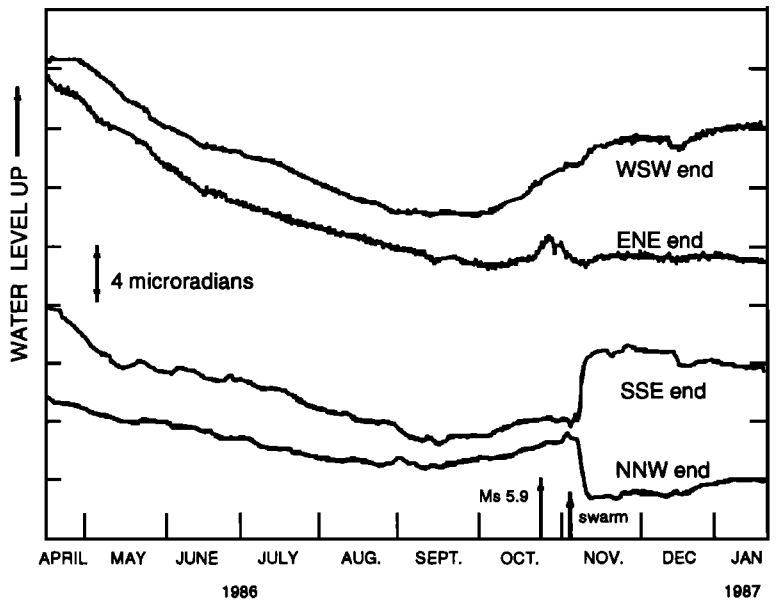

Fig. 7. Yearly record of the water level at each end of the two long tube tiltmeters. The calibration in microradians refers to the tilt as measured separately at each end. The SSE-NNW component has been filtered to remove the effects of tidal loading.

but appears to reflect actual tilt. The other observation is that the tilt as measured by the leveling array appears to follow a progressive tilt toward the north except for the two measurements immediately before the April-November 1986 event. This trend continues after the 1986 measurements. This may reflect a continuation of the tilt reported by *Bevis and Isacks* [1981].

Leveling observations are also made using the bench marks on the four water tube piers, but these measurements are not included in the calculation of tilt from the bench mark array. The measurements indicated a tilt of 5.5 μrad up to the north on the NNW-SSE tube piers and a tilt of 2.7 μrad up to the west on the ENE-WSW piers. Although the tilt measured by the NNW-SSE component agrees well with the calculated 5.5 μrad tilt up from the releveling of the N-S long tube piers, the range of error of these measurements is much greater than that of the bench mark array as the measurements are not redundant, have a short stability history, and have a short baseline.

The data from the borehole tiltmeter at Devil's Point confirms a tilt to the northwest (Figure 8), but an independent magnitude was difficult to determine due to a lack of adequate calibration and high noise levels. Unfortunately, the recorder associated with the borehole tiltmeter developed a problem on November 4 and the traces were truncated on that date. Nevertheless, a strong signal is observed on the NNW component that begins on November 1 and reaches a magnitude of roughly 4 μrad by

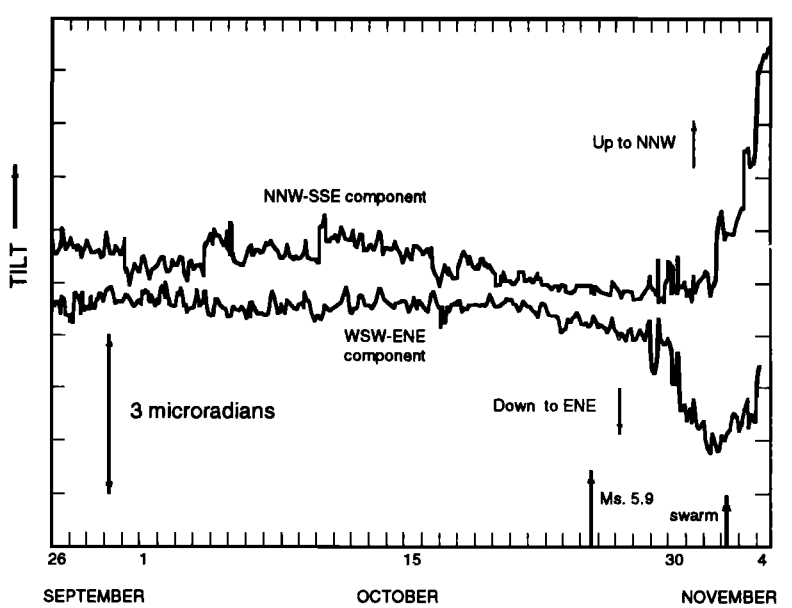

Figure 8. Relative tilt as measured by the borehole bubble level tiltmeter located in the leveling array at Devil's Point. The end of the data is due to instrumental problems.

November 4. This closely matches the signal recorded by the long tube tiltmeter. The ENE component of the borehole tiltmeter shows a 2 μrad excursion that begins on October 30 but largely reverses itself by the time the trace ends. This tilt transient on the ENE could be ground or instrument noise. We believe that the NNW trace reflects a real tilt excursion because of its magnitude and persistance but are not sure about the ENE component trace. The record from the other tiltmeter north of Devil's Point was badly contaminated by diurnal thermal drift, and it was impossible to detect any evidence of the episode.

Seismicity. Two separate seismic events occurred near the time and place of the measured crustal deformation. The first was an interplate thrust earthquake at a depth of 48 km 5 days before the start of the tilt. The second was the shallow swarm at a depth of about 12 km that occurred simultaneously with the tilt.

The initial earthquake, a M_S 5.9 thrust event (PDE, CMT solution) at 2047 UT, October 25, was located by the PDE at a depth of 31 km off the west coast of Efate almost directly below a small island (Hat Island) (Figure 4). The location calculated from the network data using HYPOINVERSE placed it farther south although this location was badly constrained (a large rms error) due to saturation of the *S* arrival and interference from another event. A re-location using both the local network *P* arrivals and the PDE teleseismic data with a teleseismic location program shifted the location just to the south of the island at a depth of 48 km. This depth is well constrained by the local *P* readings. This hypocenter is close to several apparent aftershocks which were well located by the network (as both *S* and *P* phases were clearly recorded). This depth places the earthquake hypocenter close to the presumed interplate boundary [*Chinn and Isacks*, 1983], which, along with the thrust-type focal mechanism, suggests strongly that it is an interplate event (Figure 9). This earthquake was followed by only a few aftershocks which is characteristic of events at that depth in the Efate area [*Chatelain et al.*, 1986].

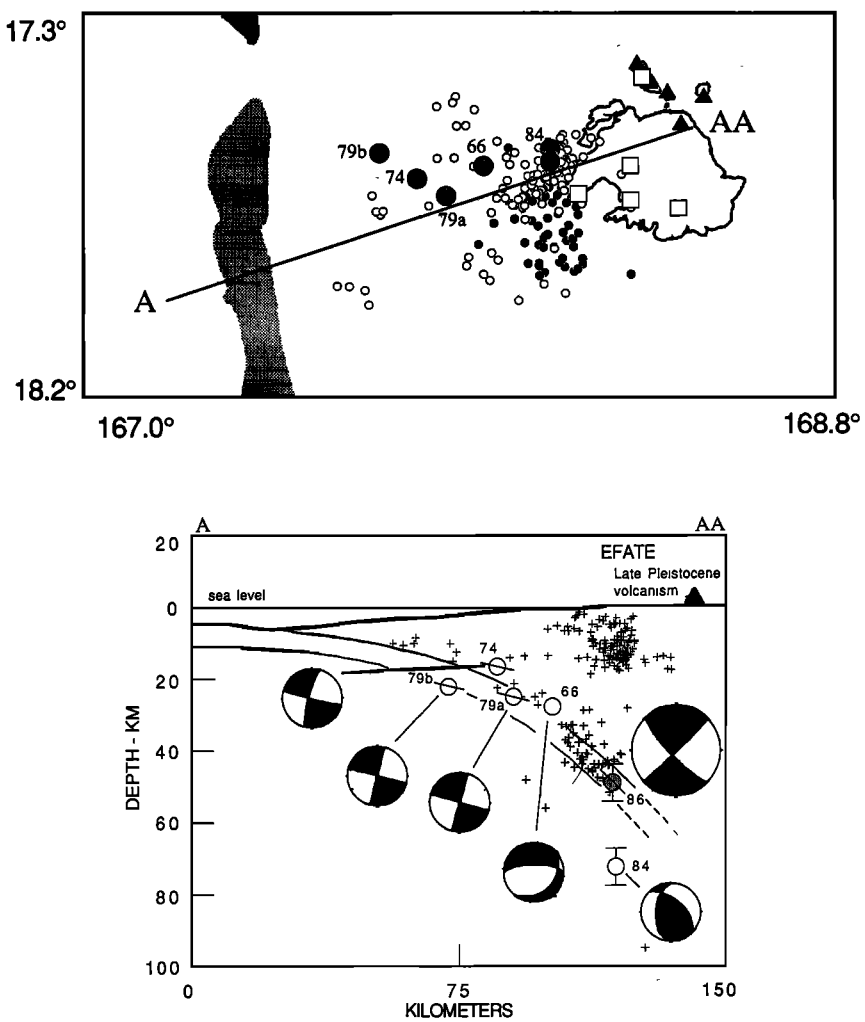

Fig. 9. Map of Efate island and cross-sectional view of the same region. The 6000 m contour is shaded. The squares are seismometers, and the solid triangles are Pleistocene volcanic centers. The small circles denote events in the seismic swarm with the hypocenters deeper than 30 km darkened. Larger circles are the epicenters of large, well-located earthquakes with the October 25, 1986, event shaded. In the cross section, only the well-located swarm events are shown (pluses). The short lines through events 79a, 79b, and 74 show the presumed fault plane orientation. The topography and inferred plate boundary are marked. Focal mechanisms are seen in cross section and the numbers correspond to the year in which they occurred. The 1966, 1974, and 1979 locations and mechanisms are from *Chinn and Isacks* [1983] and the 1986 and 1984 depths are from this study. The mechanisms for the 1986 and 1984 events are the Harvard centroid moment tensor solutions from the PDE. Error bars indicate the range of error on the depth of events 86 and 84.

The shallow seismic swarm consisted of 191 located earthquakes that occurred between October 30 and November 5, with a peak rate of 71 events per day on November 2. The center of the swarm was located beneath Hat Island, 5 km NW of the west coast of Efate and 12 km NNW of the tilt measuring instruments. No distinct main shock occurred during the swarm and the largest event was M_L 4.0. Total moment release was approximately 2.3 X 10^{23} dyn cm (calculated using log M_O = 1.5 M_L + 16.1 [*Hanks and Kanamori*, 1979]). Of the 14 earthquakes larger than magnitude 3.5, 12 were between 5 and 15 km deep. Eighty percent of the remaining earthquakes were less than 20 km deep with a median depth of 10 km, well above both the interplate boundary and the hypocenter of the October 25 earthquake. Consequently, this swarm does not appear to be a simple aftershock sequence to the October 25 earthquake, as it was delayed by 6 days and was located at a much shallower depth. The restricted azimuthal distribution of the four stations (and the rest of the network) prevented determination of a useful focal mechanism for any one earthquake, although a composite focal mechanism was generated (Figure 10). Only one focal plane is reasonably well constrained and defines a predominantly thrust solution with an unconstrained component of strike slip.

No reliable shape or trend to the swarm is apparent, although the range of error of the hypocenters would have obscured any fine structure. The well-located (vertical and horizontal errors <5 km, rms <0.2 s) events define a volume of about 250 km^3 located below Hat island.

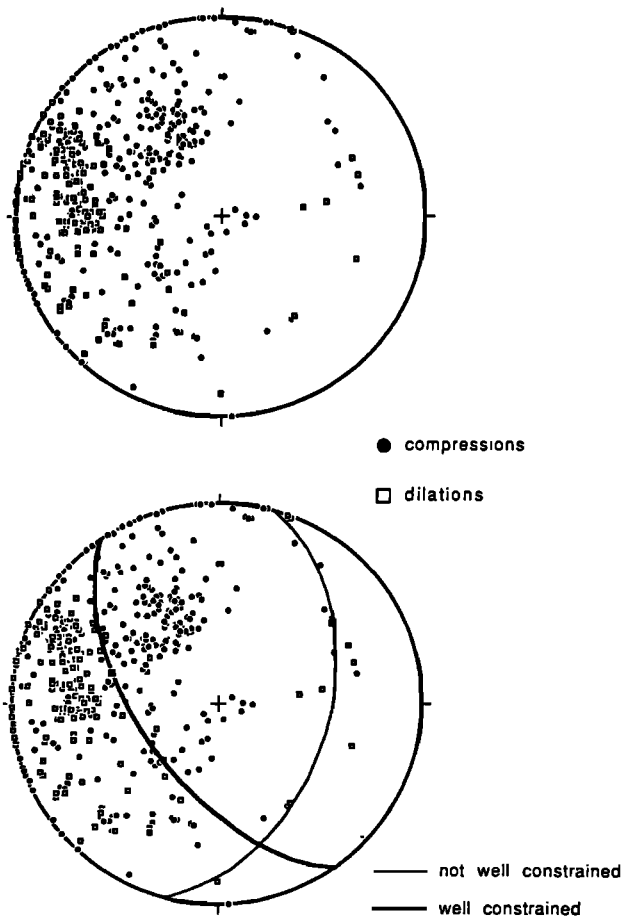

Fig. 10. Composite focal mechanism of the October-November 1986 swarm using the four stations on Efate and all earthquakes during the swarm with depth less than 30 km. The bottom figure shows a possible solution.

In the previous 10 years of recorded seismicity, no other shallow swarms similar to this one had been recorded on Efate. Only one small swarm, of much smaller magnitude, had been recorded on Efate itself, in December 1981. However, in the two years since the October-November 1986 swarm, two other swarms, in November 1987 and July 1988, have occurred. These were similar in character but smaller in size (<120 earthquakes). All lacked any definite main shock and were located at shallow depth in the upper plate. The November 1987 swarm is spatially more compact than the others, although this may be due to better constrained hypocenters as it is located almost directly below the DVP station. Due to the smaller size of the two other swarms and reductions in station coverage, composite focal mechanisms were much less well constrained, although the first motions as recorded at the station DVP were compressional for most events in both the October-November 1986 and the November 1987 swarms. None of the other swarms were associated with either tilt or larger earthquakes.

This swarm-type seismicity centered on Efate island appears to be distinct from previously recorded seismic activity in several ways. First, the majority of the earthquakes located prior to the Efate swarms were deeper and occurred close to the presumed interplate boundary. The interplate seismicity centered between Efate and the trench is characteristically at depths of 20-30 km. Second, many of the previous earthquake clusters were clearly either foreshock or aftershock sequences. The October-November 1986 swarm, although associated with a larger event, does not appear to be an aftershock sequence of the October 25 event as there is no evidence of a migration of events either spatially or temporally between the large event and the swarm.

A number of larger (M_S > 5.5) and well-located earthquakes have occurred in the immediate area, and four of these have occurred after the advent of the local network and the deformation monitoring program. None, except for the October 1986 event, are associated with any shallow seismicity or tilt.

DISCUSSION

Relationship of tilt and seismicity. The tilt and seismicity were very closely related in both direction and time (Figures 11 and 12). Figure 11 shows that the direction of the tilt vector as measured by the leveling array and the long tube tiltmeter agrees well with the direction of the seismicity. The reason for the difference in magnitude between the deformation measured by the two instruments is not as clear. One possibility is that a cumulative 10 μrad tilt did occur between April and November 1986 but was masked in the long tube data by the long-term drift. Since the discrepancy between the measured deformation is not much larger than the sum of the standard deviation of both instruments, it may also be explained in a large part by instrumental error.

The precise timing between the two events is shown by Figure 12. Interestingly, the deformation is not precisely contemporaneous with the swarm. The tilt and cumulative moment curves are quite similar in shape, but the tilt curve appears delayed by 2 or 3 days relative to the peak earthquake activity. The similarities in the time scale and waveform do suggest an intimate connection between the two phenomena.

The delay indicates that the tilt may not be due solely to seismic deformation. A rough, first-order calculation of the

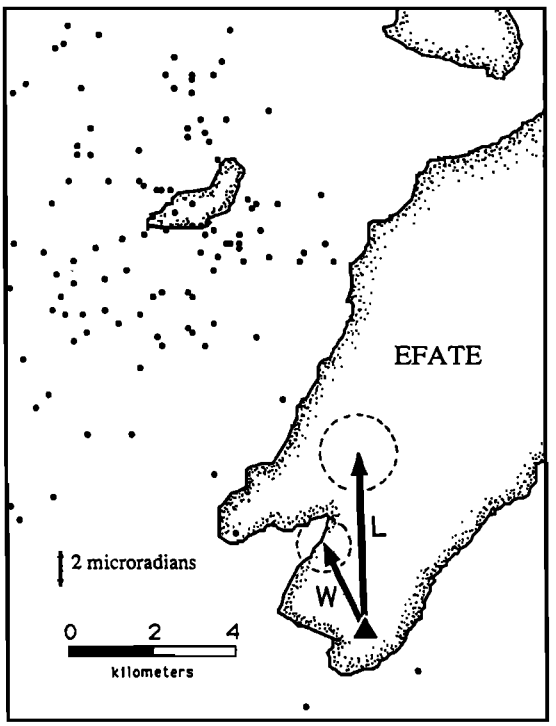

Fig. 11. Comparison of the tilt vectors showing direction of ground uplift as measured by the leveling array (L) from April to November 1986 and by the long tube water tiltmeter (W) from October 31 to November 5, 1986. Circles indicate the approximate range of the standard deviation of the measurements. The triangle marks the location of the tiltmeter instruments and earthquakes occurring between October 30 and November 5 are marked by small solid circles.

expected surface deformation from the swarm agrees with this observation. The total moment release of the swarm is about 1.32×10^{23} dyn cm, and if the rupture is modeled as occurring on a circular fault, the area of faulting can be calculated using the relationships

$$M_0 = \mu S D$$

and

$$\Delta s = \frac{7\pi\mu D}{16 a}$$

where M_0 is the moment, μ is the shear modulus, D is the average slip, a is the radius, and Δs is the stress drop [*Kanamori and Anderson*, 1975]. A shear modulus of 3×10^{11} dyn/cm^2 was used, and the calculations were made using stress drops of 10 and 100 bars. These parameters resulted in a fault varying in size from 2 km^2 with a slip of 18 cm (at 100 bars) to a fault 10 km^2 in size with 4 cm slip (at 10 bars). From these parameters, the surface deformation can be calculated by the method of *Savage and Hastie* [1966]. The faulting was modeled as a dislocation in an elastic half-space at a depth of 10 km. The depth was taken from the median depth of the larger earthquakes in the swarm. The dislocation was assumed to be centered in the swarm region, and the dip and fault dimensions were varied in order to maximize tilt at a point 12 km away (the distance from the center of the swarm to the instruments at Devil's Point). Using these parameters, the maximum modelled tilt was < 1 μrad and therefore insufficient to explain the observed 5 μrad tilt at Devil's Point. Nor were any of the larger earthquakes located significantly closer to Devil's Point than the swarm. Although these calculations are only a rough approximation, it appears that only a fraction of the deformation can be attributed directly to the seismic swarm.

Cause of tilt and seismicity. We believe that the most likely explanation appears to be a magmatic intrusion, possibly triggered by the October 25 interplate earthquake. An alternate explanation would be a largely aseismic creep event related to interplate slip following the earlier thrust event.

Several lines of evidence support a magmatic origin. First, the seismicity is typical of that associated with volcanic activity. Volcanic swarms usually lack a single definite main shock and often exhibit a symmetric temporal histogram [*Hill*, 1977; *Savage and Cockerham*, 1984]. This matches the characteristics

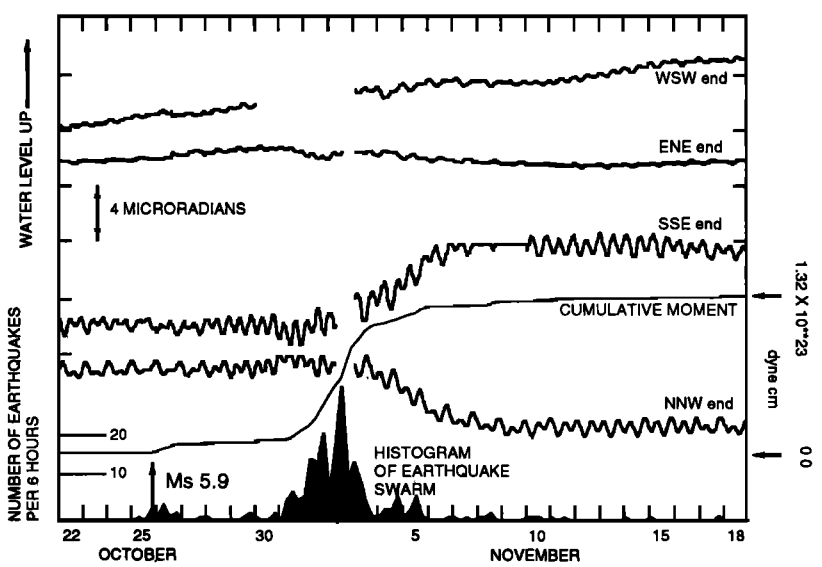

Fig. 12. Short-term record of long tube tiltmeter. Relative water level in both components of the long tube water tiltmeter over the time of the October 25 earthquake and the shallow swarm. The gaps in the data are due to the analog recorder running out of paper. No offset occurs during these periods. The shaded curve is a histogram of the number of earthquakes per 6 hours in the area of the swarm. The cumulative moment curve measures the summed moment of the swarm earthquakes but does not include the October 25 M_S 5.9 earthquake.

of the three Efate swarms, as none had any single larger shock and all displayed a sharp rise and decline in rate of seismicity over time. The pattern of repeated swarms in November 1986, November 1987, and July 1988 is also typical of seismicity in volcanic regions. Swarms and deformation have been observed in other clearly volcanic areas, notably at Long Valley Caldera [*Savage and Cockerham,* 1984], the Taupo volcanic zone in New Zealand [*Grindley and Hull*, 1986; *Otway*, 1986], and Campi Flegrei in Italy [*DeNatale et al.*, 1987]. The timing and duration of the swarm and tilt closely resemble those observed by *Shimada et al.* [1990] on the Izu peninsula in Japan near Teishi volcano. The lack of any observed harmonic tremor could possibly be explained by the distance of the stations and depth of the intrusion. The largely aseismic deformation following the peak of the seismicity has been noted in other volcanic areas and can be explained by dike inflation after the initial seismogenic crack propagation [*Rubin and Pollard*, 1988; *Jachens and Roberts,* 1985]. Although seismicity in volcanic regions is generally characterized by strike-slip or normal faulting, thrust focal mechanisms have been observed in other volcanic regions [*Savage and Cockerham,* 1984] so the thrust type focal mechanism does not necessarily refute a volcanic origin. Finally, a volcanic origin is consistent with the geology of the area. An extensive late Pleistocene-Recent volcanic complex is present on the the island of Nguna 40 km to the northeast of the swarm area. Fumaroles and hot springs occur on the coast of Efate opposite Nguna, and several hot springs are scattered over the rest of Efate.

A simple test of this idea was made using the approach of *Mogi* [1958], which assumes inflation of a spherical source in an elastic half-space. Although other geometries are clearly possible [*Dieterich and Decker*, 1975; *Larsen et al.*, 1986], the distribution of the seismicity tends to support a relatively compact source. Provided that the magma chamber has a radius that is small compared to its depth then the surface uplift and tilt fields are completely characterized by the depth of the chamber and the amplitude of surface uplift directly above the chamber. (This last quantity is simply related to the product of the chamber's volume and the hydrostatic pressure change responsible for its inflation). We find that if the chamber had a depth of 10 km and was located in the vicinity of the earthqauke swarm, then an inflation of 13 cm directly above the chamber would produce a 5 μrad tilt at Devils Point. Since maximum uplifts of this magnitude are believed to be fairly common just before and during volcanic eruptions (this uplift is more than an order of magnitude smaller than the better constrained uplifts seen in Hawaii, Rabaul, and Campi Flegrei), we conclude that a magmatic intrusion is a viable explanation of the observed tilt.

The relationship between a possible intrusion and the initial interplate earthquake is not as clear. The interplate boundary is about 50 km deep at the location of the swarm, which is unusually shallow. Normally, magmatism is at least about 100 km above the descending plate [*Gill,* 1981] but the steep dip of the subducting plate in the New Hebrides places the 100 km deep contour of the descending plate under the east side of the island. *Thatcher and Savage* [1982] suggested that several large interplate eathquakes were triggered by increased stress due to an inflating magma body on the Izu peninsula, and it may be possible that decreased stress after an earthquake may have triggered the intrusive activity. A number of other studies have attempted to relate deeper seismicity and volcanism, but few definite links between subduction zone seismicity and volcanic activity have been conclusively established [*Acharya,* 1987; *Carr*, 1983].

An alternative explanation of the tilt and seismicity is that they may be the result of processes related to subduction, possibly a creep episode at the interplate boundary associated with upper plate deformation following the October 25 earthquake. The close timing between the earthquake and the swarm supports this hypothesis, and the thrust-type focal mechanism of the swarm earthquake appears to be more consistent with this explanation. Both *Chatelain et al.* [1986] and *Taylor et al.* [1990] suggest that a portion of the interplate movement in the Central New Hebrides arc may be accommodated by aseismic slip. Modeling (using the method of *Savage and Hastie*, [1966] as before, with a stress drop of 20 bars) indicates that a large amount of interplate slip (at least equivalent to a magnitude 6.0 earthquake) in addition to the upper plate deformation attributed to the swarm would be necessary to produce the observed tilt. This amount of interplate slip seems large. Therefore, a significant amount of aseismic deformation would be required in the upper plate as well, simultaneous with the swarm. Significant coseismic deformation exceeding that calculated from the seismic moment (by about 25%) has been reported elsewhere [*Wyatt*, 1988], but a much greater difference would be required here. Therefore, an aseismic slip event seems unlikely, but possible.

Conclusion. A correlated tilt and seismicity episode was observed on Efate island in the central New Hebrides island arc in October and November 1986 six days after a magnitude 5.9 interplate earthquake. The swarm consisted of nearly 200 small earthquakes centered well within the upper plate. Simultaneous with the swarm a 5 μrad tilt was recorded 12 km away from the center of the swarm. The episode took place over a period of several days and was recorded by three different tiltmeters and the local network of seismometers. Since November 1986, two similar shallow swarms have occurred on Efate Island but with no observed tilt. The amount of measured deformation exceeds that generated seismically which indicates that much of the deformation was aseismic. The most likely cause of the tilt and seismicity is a magmatic intrusion, but it may have been caused by an episode of aseismic creep following the larger earthquake. Simple modeling supports the intrusion hypotheses.

APPENDIX: PROCESSING OF THE TILTMETER DATA

Long tube water tiltmeter data. The long tube water tiltmeter data is recorded on Efate on a Rustrak & Esterline Angus strip chart recorder. These charts record the change in water level over time as a continuous line along the charts. The position of the line relative to the center of the strip is directly proportional to the vertical movement of the water surface. Each chart usually consists of a approximately a month of data and has the local time marked on them at approximately two week intervals. The data is recorded in two ways, one as time compressed broad band (DC to 5 s) and the other as non-compressed band pass filtered (5 s to 1000 s). The broadband charts are then combined onto large 70 mm film spools which usually consist of three months of data. Because the data are in analog form, and the paper strips are several meters long, the data are processed to produce a digital and time compressed unity gain analog record to allow more manageable manipulation and analysis. In contrast to the usual digitizing procedure, where a pointer is moved along the data trace, this device scrolls the strip of paper past a pointer.

Two channels are recorded, one for the tilt signal and one for time marks and the nearby earthquake signals. Sampling is done at 15 hertz on the paper record, a rate which oversamples most tilts observable on the record but allows precise location of earthquake signals.

The digital records are then in a form suitable for further processing. The major task is to make the time base constant. The motors operating the recorders on Efate run off batteries which lose power gradually over time. This causes the recorders to operate at varying speeds. Since the batteries do not lose power equally, the amount of paper used by the different components varies considerably (up to 30%) which affects the actual real time between each digitized sample point of the tilt signal. The transformation to a set time base was performed by multiplying discrete segments (usually a few days) of the data by a constant. This constant was determined separately for each segment by using all available time data, including the time marks, earthquake signals, and tidal fluctuations. After converting to a fixed time base, the signals were calibrated to a constant vertical scale using the data from a calibration on September 18, 1986. The calibration involved adding a liter of water to each component and noting the amount of change measured by each instrument, an amount that varyed slightly due to differing instrument sensitivity. These calibration offsets were removed from the record, as were offsets due to re-centering of the instruments, in order to enhance the visibility of any tilt signal. A running average with a window of several hours was taken over the long term NNW-SSE component to remove the daily tidal fluctuations as they obscured the longer period changes.

Borehole bubble level tiltmeters. The data from the biaxial borehole bubble level tiltmeters is band pass filtered, amplified, and time compressed and then recorded with the time base enhanced on two Rustrak strip chart recorders. The compressed version of the Devils' Point record was digitized on a digitizing table and plotted versus time. Rainfall is also recorded on the strip of paper.

Acknowledgments. We thank C. Baldassari, F. Bondoux, R. Campillo, M. Chauvin, C. Douglas, R. Foy, L. Mollard, D. Nakedau, C. Reichenfeld, J.C. Willy and all others involved in the data collection and analysis operations in the New Hebrides. We would also like to thank M. Barazangi, W. Y. Chung, M. Hamburger, D. Karig, M. Regnier, and S. Wesnousky for useful and insightful discussions and R. Allmendinger for his steorenet program. J. Beavan and J. Savage deserve credit for thorough and helpful reviews. This work was performed under USGS contract 14-08-0001-G1160, in cooperation with ORSTOM. Cornell University Institute for the Study of the Continents contribution 148.

REFERENCES

Acharya, H., Spatial changes in volcanic and seismic activity prior to great earthquakes, *Pure Appl. Geophys., 125* (6), 1098-1117, 1987.

Ash, R. P., J. N. Carney, and A. Macfarlane, Geology of Efate and Offshore Islands, regional report, New Hebrides Geol. Surv.,Vila, 1978.

Beavan, J., R. Bilham, and K. Hurst, Coherent tilt signals observed in the Shumagin seismic gap: Detection of time-dependent subduction at depth?, *J. Geophys. Res., 89*, 4478-4492, 1984.

Bevis, M., and B. Isacks, Leveling arrays as multicomponent tiltmeters: Slow deformation in the New Hebrides Island arc, *J. Geophys. Res., 86*, 7808-7823, 1981.

Bloom, A.L., C. Jouannic, and F.W. Taylor, Appendix to Ash, R.P., J.N. Carney, A. Macfarlane, Geology of Efate and Offshore Islands, regional report, New Hebrides Geol. Surv. Vila, 1978.

Carney, J.N., A. Macfarlane, and D.I.J. Mallick, The Vanuatu island arc: an outline of the stratigraphy, structure, and petrology, in *The Ocean Basins and Margins*, vol. 7a, *The Pacific Ocean*, edited by A. E. M. Nairn, F. G. Swairns, and S. Uyeda, pp. 683-718, Plenum, New York, 1984.

Carr, M. J., Nests of intermediate depth (70-160 km) earthquakes adjacent to active volcanoes during 1963-1982, *J.Volcanol. Geotherm.Res., 19*, 349-365, 1983.

Chatelain, J. L., B. Isacks, R. K. Cardwell, R. Prevot, and M. Bevis, Patterns of seismicity associated with asperities in the Central New Hebrides Island arc, *J. Geophys. Res. , 91*, 12,497-12,519, 1986.

Chinn, D.S., and B.L. Isacks, Accurate source depths and focal mechanisms of shallow earthquakes in western South America and in the New Hebrides Island Arc, *Tectonics, 2*, (6),529-563, 1983.

Chung, W.-Y., and H. Kanamori, A mechanical model for plate deformation associated with aseismic ridge subduction in the New Hebrides arc, *Tectonophysics, 50*, 29-40, 1978.

DeNatale, G., G. Iannacone, M. Martin, and A Zollo, Seismic sources and attenuation properties at the Campi Flegrei Area, *Pure Appl. Geophys., 125*, (6), 883-917, 1987.

Dieterich, J. H., and R. W. Decker, Finite element modeling associated with volcanism, *J. Geophys. Res., 80*, 4094-4102, 1975.

Dubois, J., J. Launay, J. Recy, and J. Marshall, New Hebrides trench: Subduction rate from associated lithopheric bulge, *Can. J. Earth Sci., 14*, 250-255, 1977.

Edwards, R.L., J.H. Chen, T-L. Ku, and G.J. Wasserman, Precise timing of the last interglacial period from mass spectrometric determination of thorium-230 in corals, *Science, 236*, 1547-1351, 1987.

Edwards, R.L., F.W. Taylor and G.J. Wasserburg, Dating earthquakes with high precision thorium-230 ages of very young corals, *Earth Planet. Sci. Lett., 90*, 371-381, 1988.

Gill, J., *Orogenic Andesites and Plate Tectonics*, pp.14-15, Springer-Verlag, New York, 1981.

Grindley, G. W., and A.G. Hull, Historical Taupo earthquakes and earth deformation, in Recent Crustal Movements of the Pacific Region, Proceedings of the International Symposium on Recent Crustal Movements of the Pacific Region, Bull., edited by W.I. Reilly and B. E. Harford, *R. Soc. of N. Z.*, 24, 173-186, 1986.

Hanks, T., and H. Kanamori, A moment magnitude scale, *J. Geophys. Res., 84*, 2348-2350, 1979.

Hill, D. P., A model for earthquake swarms, *J. Geophys. Res.,82*, 1347-1351, 1977.

Isacks, B.L., G. Hade, R. Campillo, M. Bevis, D. Chinn, J. Dubois, J. Recy, and J. L. Saos, Measurements of tilt in the New Hebrides island arc, Proceedings of Conference VII, Stress and Strain Measurements Related to Earthquake Prediction,*U.S. Geol Surv. Open File Rep., 79-370*, 176-221, 1978.

Isacks, B.L., R. Cardwell, J.-L. Chatelain, M. Barazangi, J.-M. Marthelot, D. Chinn, and R. Louat, Seismicity and tectonics of the central New Hebrides island arc, in *Earthquake Prediction, An International Review, Maurice Ewing Ser.,* vol. 4, edited by D.W. Simpson and P.G. Richards, pp. 93-116, AGU, Washington, D.C., 1981.

Jachens, R.C., and C. W. Roberts, Temporal and areal gravity investigations at Long Valley Caldera, California, *J. Geophys. Res., 90*, 11,210-11,218, 1985.

Kanamori, H., and D.L. Anderson, Theoretical basis of some empirical relations in seismology, *Bull. Seismol. Soc Am., 65*, 1073-1095, 1975.

Klein, F.W., Hypocenter location program HYPOINVERSE, *U.S. Geol. Surv. Open File Rep., 78-694*, 113 pp., 1978.

Larsen, S., R. Reilinger, and L. Brown, Evidence of ongoing deformation related to magmatic activity near Socorro, New Mexico, *J. Geophys. Res., 91*, 6283-6292, 1986.

Mallick, D.I.J. , Annual Report of the Geological Survey for the year 1972, New Hebrides Condominium Geological Survey, Vila, 1972.

Marthelot, J. M., E. Coudert, and B. Isacks, Tidal tilt from localized ocean loading in the New Hebrides Island arc, *Bull. Seismol. Soc Am., 70*, 283-292, 1980.

Mogi, K., Relations between the eruptions of various volcanoes and the deformations of the ground surfaces around them, *Bull. Earthquake Res. Inst. Univ. Tokyo, 36*, 99-134, 1958.

Otway, P. M., Vertical deformation associated with the Taupo earthquake swarm, 1983, in Recent Crustal Movements of the Pacific Region, Proceedings of the International Symposium on Recent Crustal Movements of the Pacific Region, edited by W.I. Reilly and B. E. Harford, *R. Soc. of N. Z.*, 24, 173-186, 1986.

Pascal, G., B.L. Isacks, M. Barazangi, and J. Dubois, Precise relocations of earthquakes and seismitectonics of the New Hebrides island arc, *J. Geophys. Res., 83*, 4957-4973, 1978.

Rubin, A., and D. D. Pollard, Dike induced faulting in rift zones of Iceland and Afar, *Geology, 16*, 413-417, May,1988.

Savage, J.C. and R.S. Cockerham, Earthquake swarm in Long Valley Caldera, California, January 1983: Evidence for dike inflation?, *J. Geophys. Res. 89*, 8135-8324, 1984.

Savage, J.C., and L.M. Hastie, Surface deformation associated with dip-slip faulting, *J. Geophys. Res., 71*, 4897-4904, 1966.

Shimada, S., Y. Fujinawa, S. Sekiguchi, S. Ohmi, T. Eguchi., and Y. Okada, Detection of a volcanic fracture opening in Japan using Global Positioning System measurements, *Nature, 343*, 631-633, 1990.

Taylor, F.W., R.L. Edwards, G.J. Wasserburg, and Cliff Frohlich, Seismic recurrance intervals and timing of aseismic subduction inferred from emerged corals and reefs of the Central Vanuatu (New Hebrides) Frontal Arc, *J. Geophys. Res.,95*, 393-408, 1990.

Thatcher, W., and J. C. Savage, Triggering of large earthquakes by magma-chamber inflation, Izu Peninsula, Japan, *Geology, 10*, 637-640, 1982.

Tsumura K., Determination of earthquake magnitude from total duration of oscillation, *Bull. Earthquake Res. Inst. Univ. Tokyo, 15*, 7-18, 1967.

Wyatt, F., Measurements of coseismic deformation in southern California: 1972-1982, *J. Geophys. Res., 93*, 9197-9201, 1988.

Wyatt, F. and J. Berger, Investigations of tilt measurements using shallow borehole tiltmeters, *J. Geophys. Res., 85*, 4351-4362, 1980.

Wyatt, F., S. T. Morrisey, and D.C. Agnew, Shallow borehole tilt: A reprise, *J. Geophys. Res., 93*, 7923-7942, 1988.

M. Bevis, Department of Marine, Earth and Atmospheric Sciences, North Carolina State University, Raleigh, NC, 27695.

J-L. Chatelain, IRIGM-LGIT, BP 53X, 38041, Grenoble CEDEX, France.

G. Hade and B.L. Isacks, Institute for the Study of the Continents, Cornell University, Ithaca, NY, 14853.

R. Mellors, Department of Geological Sciences, Indiana University, Bloomington, IN 47405.

R. Prevot, Institut Francais de Recherche Scientifique pour le Development en Cooperation, Noumea, New Caledonia (ORSTOM).

(Received September 4, 1990;
revised April 8, 1991;
accepted April 22, 1991.)

JOURNAL OF GEOPHYSICAL RESEARCH, VOL. 96, NO. B10, PAGES 16,641–16,650, SEPTEMBER 10, 1991

Application of Cantor's Method for Fractal Analysis of Fractures in the Toyoha Mine, Hokkaido, Japan

THIERRY MERCERON

Laboratoire de Pétrologie des Altérations Hydrothermales, University of Poitiers, Poitiers, France

BRUCE VELDE

Geological Department, Ecole Normale Supérieure, Paris

Cantor's method has been used for fractal analysis of fractures in the Toyoha mine, Hokkaido, Japan. The analyses were performed on a two-dimensional area ranging from 30 cm^2 to 220 km^2. Cantor's analysis predicts the probability of fracture occurrence in rocks in a given distance. The probability of finding a fractured zone of length x is given by $P = x^{-D}$ where D is the fractal dimension. In the Toyoha mine the samples collected in Sugo and Izumo veins are characterized by D values of 0.25 and 0.10–0.24, respectively. The distribution of fractures in galleries (200 m long) is very similar ($D = 0.17$). At a kilometer scale the disposition of veins varies according to the directions of observation: $D = 0.20$ (E-W) and 0.25–0.28 (NW-SE). At a larger scale (Landsat map) the fault distribution appears very similar in all directions ($0.22 < D < 0.25$). In the vicinity of the Toyoha mine the fracture disposition is fractal at all scales of observation. Despite a scale factor that can vary by 10^6 the distribution of fractures remains fractal with similar fractal numbers (average $D = 0.25$). Moreover, D values gradually change according to the distance from the Toyoha mine, suggesting that the type of rupture and consequently the nature of stress are different far from the Toyoha mine.

INTRODUCTION

A constant preoccupation in geology is to interpret macroscopic events from observations made at microscopic scales. Fracturing occurs in rocks at all the scales from thin section (microcracks) to satellite (faults). The fractal geometry developed by *Mandelbrot* [1982] allows us to examine quantitatively complex patterns. The concept of self-similarity can be used to compare the fracture distributions at different scales and to check any relation to one another. The purpose of this study is to describe the type of ruptures in the Toyoha mine, Hokkaido, Japan, at various scales ranging from the thin section to the Landsat map by using Cantor's method. Recent investigations based on this original fractal analysis demonstrate that the fractal dimension of the fracture patterns may vary with the direction of measurement and is possibly related to the stress direction [*Velde et al.*, 1990]. However, these data were obtained from different examples of fracture fields in natural rocks selected in various geological occurrences. In this paper we present a complete investigation of the fracture distribution in a well-known mine deposit at different scales of observation in order to clarify the validity of the fractal concept for description of fracture distributions in nature.

CANTOR'S METHOD

In Cantor's method the expression of the probability of an event (P) is related to the unit length of measure (x) and the fractal dimension D according to the relation $P = x^{-D}$. Cantor's method has been used to describe linear or temporal phenomena such as earthquake precursors [*Smalley et al.*, 1987] or volcanic eruptions [*Dubois and Cheminée*, 1988].

The heterogeneity of the fracture distribution in rocks has been noted by geologists at all scales of observation. Bursts (high concentration of fractures) and gaps in the distribution can be understood by statistical analyses dependent on the scale and the direction of observation. Being a linear method, Cantor's analysis allows a description of fracture events according to azimuthal orientations (0°–180°) as shown by *Velde et al.* [1990] and hence reveals the fracture distribution anisotropy.

A detailed description of the specific analysis method used here is given by *Velde et al.* [1991]. A good description of Cantor's dust analysis is given by *Smalley et al.* [1987]. Briefly, the linear Cantor's analysis is executed in three steps (Figure 1):

1. The fracture pattern is recorded by photographic or mapping methods. Different observational scales (kilometric to centimetric) of recording are used in order to assess the scaling factor of the fracture events. The revealed fractures are emphasized by tracing them on paper.

2. A seven-line analysis grid is put on the fracture pattern, and the intersections of the fractures with seven parallel analyses grid lines are counted in the following way (Figures 1*a* and 1*b*). The grid lines are divided into intervals of a given length R. The probability of fracture occurrence (P) is obtained from the proportion of the measurement units which contain one or more fracture intersections compared to the total number of units in the grid. The length of the measurement interval is changed and the operation repeated for a given azimuthal direction and then for other directions (Figure 1*c*). The viable limit for these measurements is for values of P between 0 and 0.9 [*Smalley et al.*, 1987].

3. A linear relation on a plot of log R/log P indicates a power law relationship (Figure 1*d*). The slope of this relation gives the fractal dimension D as slope $= 1 - D$. High slopes

Paper number 91JB01419.
0148-0227/91/91JB-01419$05.00

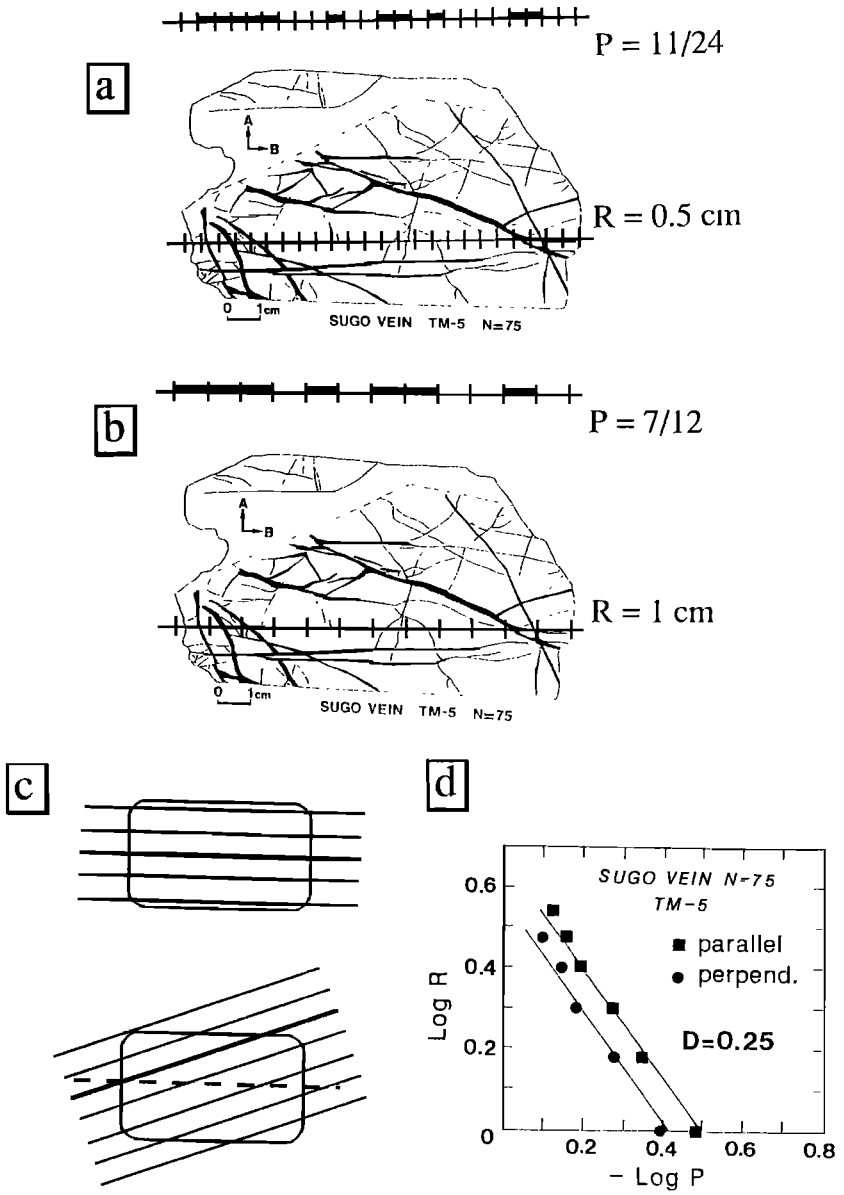

Fig. 1. (*a*) A typical data set (Sugo vein) is analyzed by using Cantor's method. The fracture occurrences along measurement grid lines are recorded according to the number of units of measure which contain one or more fracture intersections in the direction of analysis. The proportion of units containing a fracture (P) is defined as the number of fracture intersections divided by the total number of measurement units in the total length of the grid line. (*b*) The operation is repeated by changing the length R of the unit of measure. (*c*) The sequence of operations necessary to determine the log P/log R slope is repeated for different azimuthal orientations of the grid with respect to the initial fracture field. The rotations are made in steps of 10° over 180°, zero being the parallel direction in the figures of fracture patterns. (*d*) A plot is made of the values on log P–log R coordinates. The proportion of zones containing a fracture (P) is at most one and thus log P is always negative. The slope S = (log P)/(log R) of the logarithmic relation, when linear, varies from 1 (regular distribution of fractures) to near zero (irregular pattern). The fractal dimension D is related to the log P/log R slope S by the relation: $S = 1 - D$.

and low D indicate clustered events, and median slopes indicate more regular distributions (see *Velde et al.* [1991] for a graphical demonstration).

The linear method was chosen for its easy use. Because the method is in one dimension, the events need only to be counted. If one uses a higher dimension, a surface area (two dimensions) for example, the total length of the fracture intersections with the unit of analysis surface must be determined as shown by *Okubo and Aki* [1987] and *Aviles et al.* [1987]. In three dimensions the fracture surface within an analysis volume must be determined [*Brown and Scholz*, 1985]. The fractal dimension is a function of the geometric dimensions in which the analysis is projected. Volume analysis gives fractal dimensions of 2–3, surface analyses give dimensions of 1–2, a linear analysis gives values of 0–1. The fractality of the fracture patterns should be the same in any projection, i.e., 0.5 in one dimension, 1.5 in two dimensions, and 2.5 in three dimensions (see *Falconer* [1990, p. 93] for a mathematical demonstration). The graphical determination of the slope of a data set for one dimension is easier

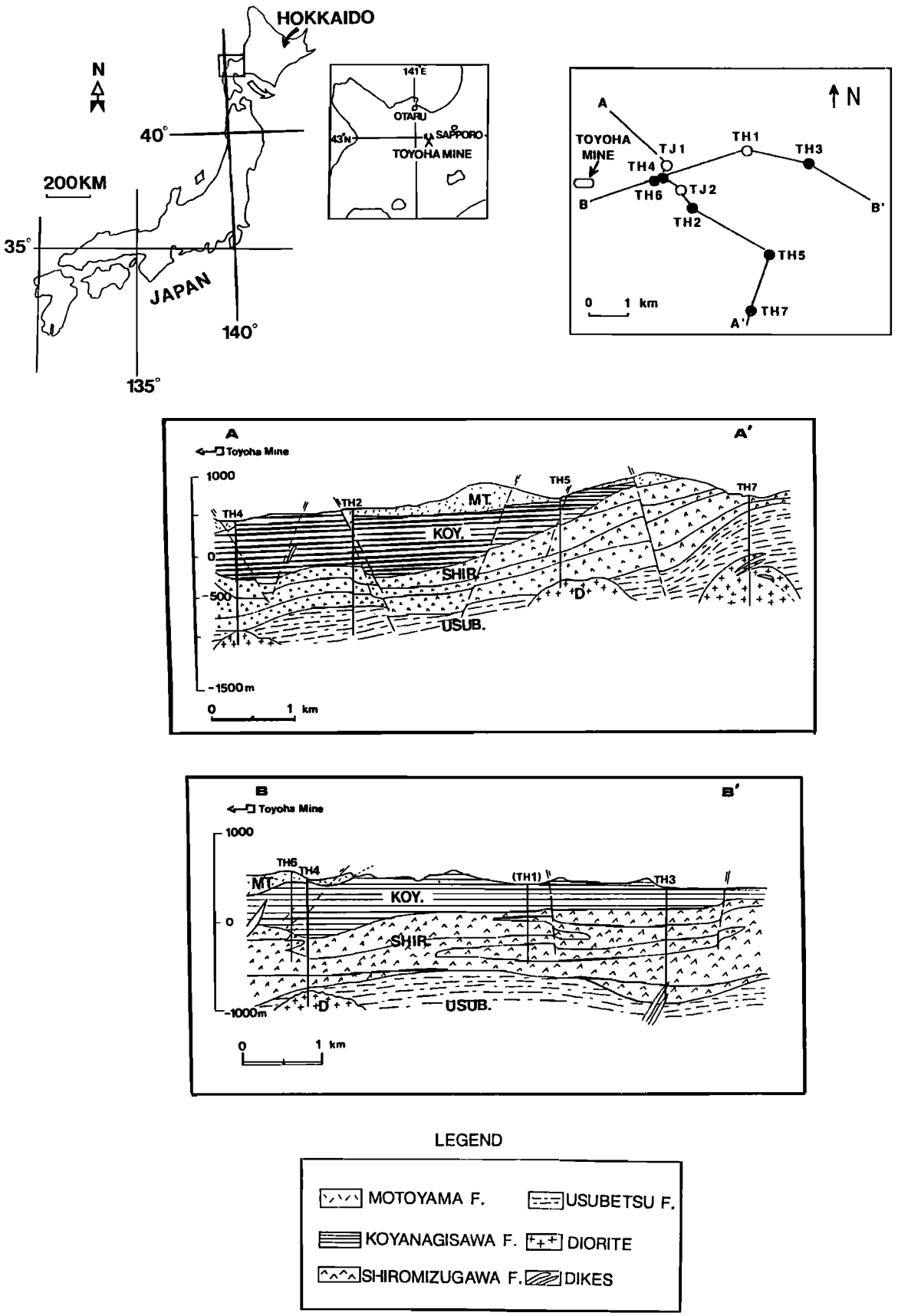

Fig. 2. Location of the Toyoha mine in Japan (upper part) and cross sections illustrating the geology and the position of the drill cores studied (lower part). Details concerning the lithology of the formations are given in the text.

TABLE 1. Drill Core Samples Studied

Sample	Cote, m	Rock Type and Formation	Distance From Toyoha Mine, km	Vein Filling			
				Calcite + Quartz	Chlorite	Epidote	Pyrite
TM-5	−150	Sugo vein	0.0				+++
TM-6	−150	Izumo vein	0.0				+++
TH-6	−747	propylite (Shiromizugawa)	1.8	+++			+
TH-4	−950	propylite (Shiromizugawa)	2.0	+++			+
TH-5	−194	tuff breccia (Koyanagisawa)	5.0	+++	+	trace	
TH-5	−372.5	propylite (Shiromizugawa)	5.0	++	+	+++	
TH-5	−838.5	tuff breccia (Shiromizugawa)	5.0		+++	trace	
TH-5	−867	tuff breccia (Shiromizugawa)	5.0	++	+++	trace	
TH-7	−172	tuff breccia (Shiromizugawa)	6.0	++	+++	trace	
TH-7	−557	propylite (Usubetsu)	6.0	++	+++	trace	
TH-7	−666	propylite (Usubetsu)	6.0	+++	+	trace	

The plus symbols indicate decreasing proportions of mineral filling in veins estimated from microscopic observations.

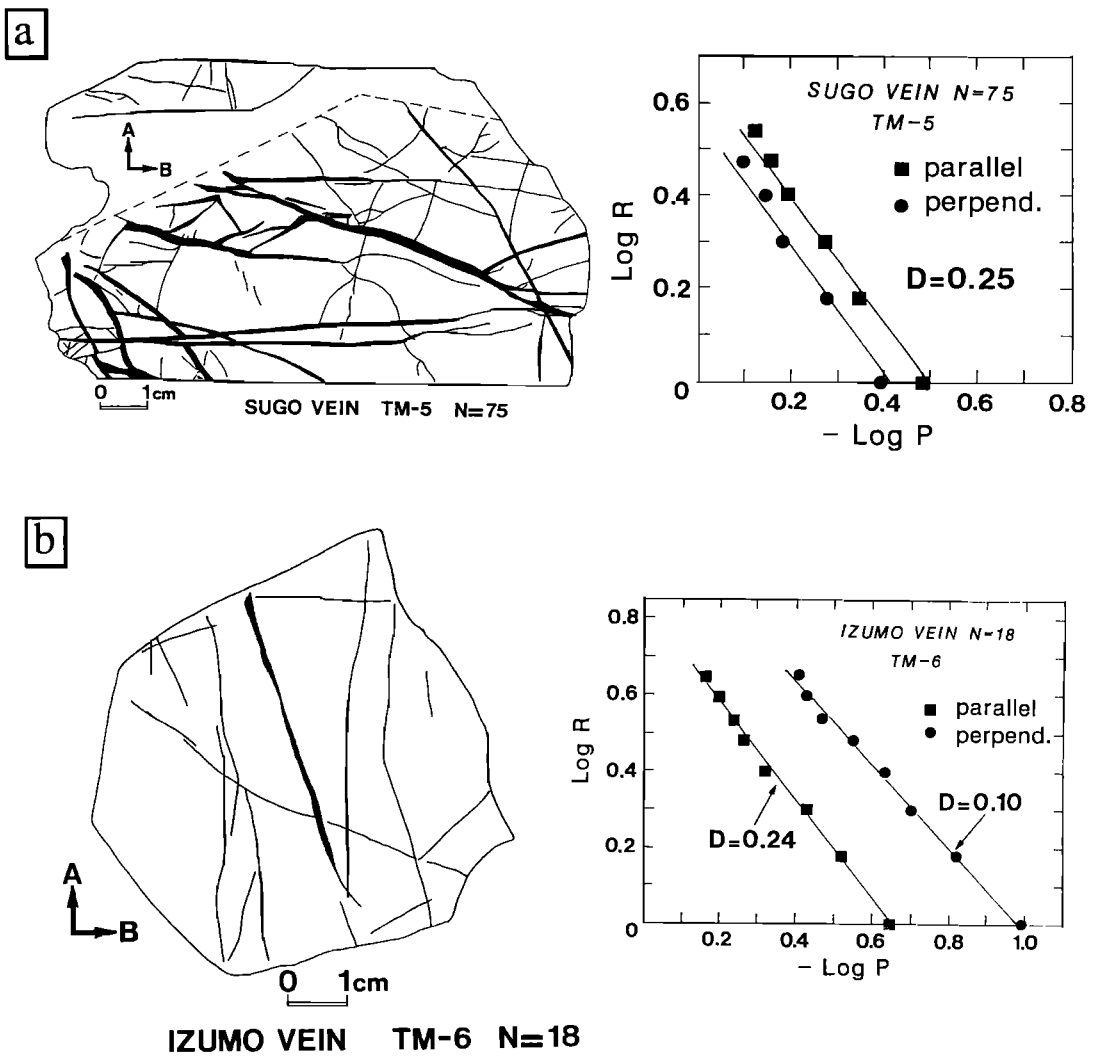

Fig. 3. (*a*) Fracture patterns for Sugo vein in the Toyoha mine. The veins are filled by pyrite crystals. Analyses are reported for two axis directions, perpendicular (A) and parallel (B). N indicates the total number of fractures. The spatial scale R used for normalization varies between 0.5 and 6.0 cm. The fractal dimension ($D = 0.25$) remains constant for all the directions of measurement. (*b*) On the contrary, for the Izumo vein the value of D ranges between 0.10 and 0.24 according to the direction of observation. Such a variation might be explained by the very small number of veins ($N = 18$) of this sample leading to a poor analysis. The spatial scale R used for normalization varies between 0.5 and 4.0 cm.

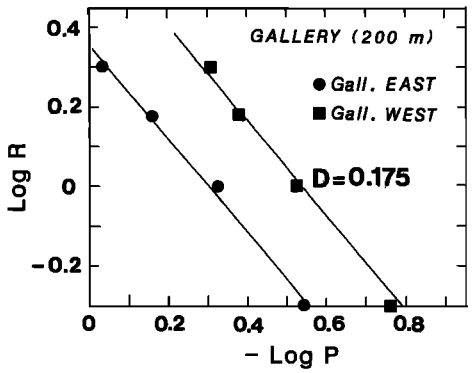

Fig. 4. Log P versus log R diagram illustrating the results of the fractal analysis for fracture distribution in galleries at 1.5 km of the Toyoha mine. The spatial scale R used for normalization varies between 3.5 and 7.5 m. The fractal dimension D is 0.175 for the two galleries analyzed.

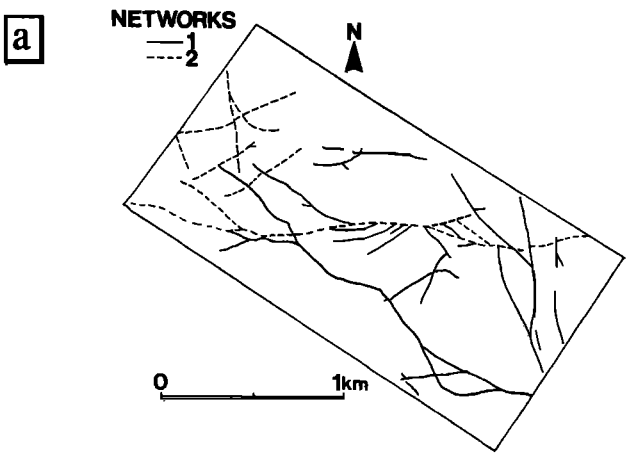

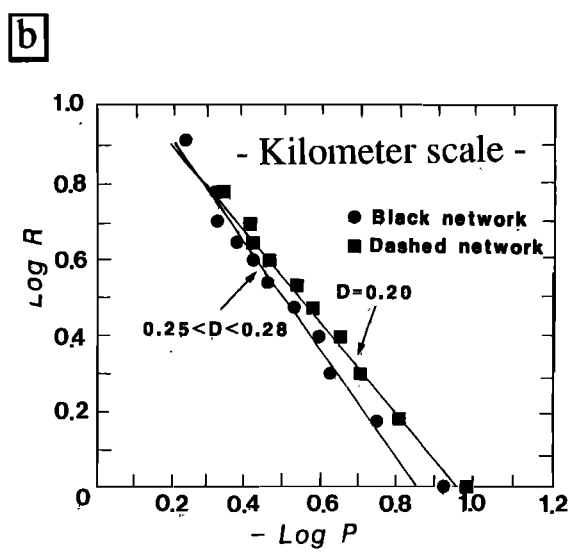

Fig. 5. (*a*) Representation of the fracture fields in the Toyoha mine (−150 m level). Two distinct fracture networks are distinguished: E-W (dashed lines) and NW-SE (black lines). (*b*) The results of the fractal analysis are reported in a log P–log R plot showing the values of the fractal dimension. The spatial scale R used for normalization varies between 100 and 800 m.

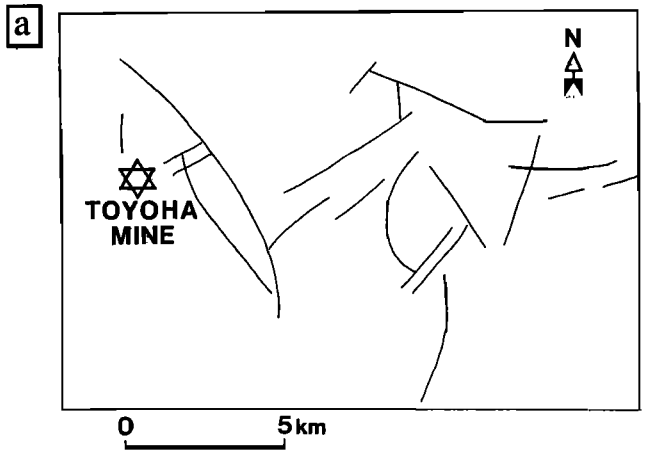

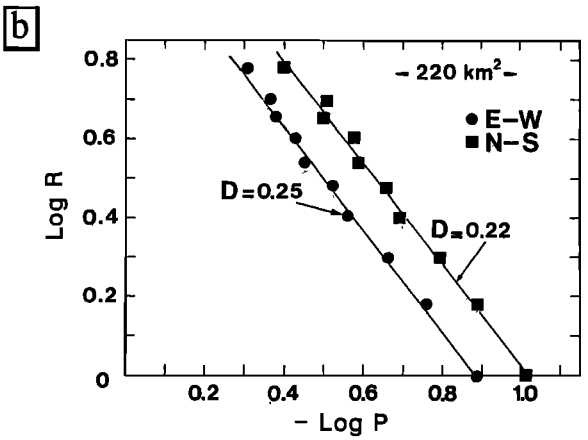

Fig. 6. (*a*) Representation of the fault in the Toyoha district (Landsat data). (*b*) The results of the fractal analysis are reported in a log P–log R diagram. The spatial scale R used for normalization varies between 0.90 and 5.4 km. D values are nearly the same along E-W and N-S directions of analysis.

than that for higher dimensions (i.e., it is easier to determine a slope between zero and 1 than a slope between 2 and 3). The information gained (the regularity of distribution of the fractures) is essentially the same in all cases; the only difference is the spatial projection.

In each fracture data set studied here the scale of variation of distances between the observed fracture events is about 1 order of magnitude or slightly more. In order to establish the fractal relation of self-similarity as a function of scale, the observations were made on greatly different scales. Thus each determination of fractality was made on a limited scale, but comparison is made for observations of fractures in the same rocks at different scales, i.e., satellite scale faults, fractures mapped in mines, and fractures in hand specimen samples. The argument is made that if the fractal dimension determined on the different scales of observation is the same, the self-similarity demonstration is made. *Barton and Larsen* [1985] have observed the fractality of fracture patterns mapped in two dimensions over several orders of magnitude on the same surfaces. *Velde et al.* [1991] have observed that maps at different scales of observation (up to a factor of 10^4 difference) of the same fractured rocks give the same fractal dimension values.

A very important factor to consider is the relative homogeneity of the rocks observed and the relative homogeneity

of the stress forces applied to them which provoke fractures. *Barton and Larsen* [1985] and *Velde et al.* [1991] indicate that the fractal relationship can be detected in fractured granites. The present study considers fractures in slightly more heterogeneous tuffaceous materials (see Figure 2).

Geological Setting and Samples Studied

The Toyoha mine is located in the northern part of the Green Tuff region in southwest Hokkaido, Japan. The Toyoha district is characterized by clastic sediments and pyroclastic rocks, lavas, dikes, and intrusive bodies of intermediate to acidic composition. They are lithologically correlated as being of Miocene age and have been subjected to various hydrothermal alterations.

Geological cross sections of the Toyoha district illustrating the position of the different drill cores studied are shown in Figure 2. Five geological formations are recognized. They are the Nagato, Motoyama, Koyanagisawa, Shiromizugawa, and Usubetsu formations in descending stratigraphic order. The Nagato formation, characterized by products of violent volcanic activity, occurs in the Toyoha mine. The Motoyama formation conformably overlies the Koyanagisawa formation and consists of alternating of basaltic andesite and pyroclastic rocks. The Koyanagisawa formation is composed of alternating of basaltic andesite and pyroclastic rocks. The Shiromizugawa consists of propylite, tuff breccia, mudstone, and sandstone. The Usubetsu formation is composed of alternating propylite and lava.

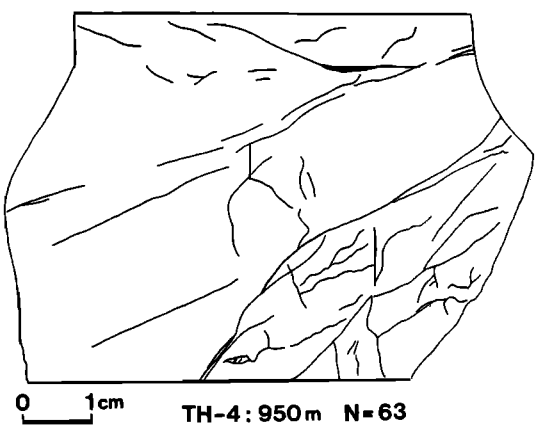

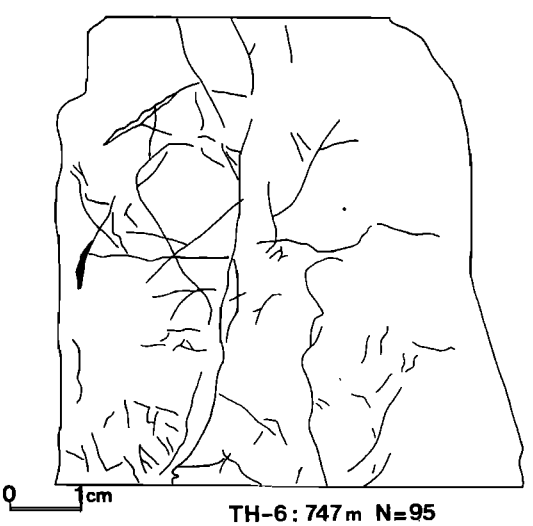

Fig. 7. Fracture patterns for the hand specimen samples (propylite) TH-6 (747 m) and TH-4 (950 m) located at 1.8 and 2.0 km, respectively, from the Toyoha mine.

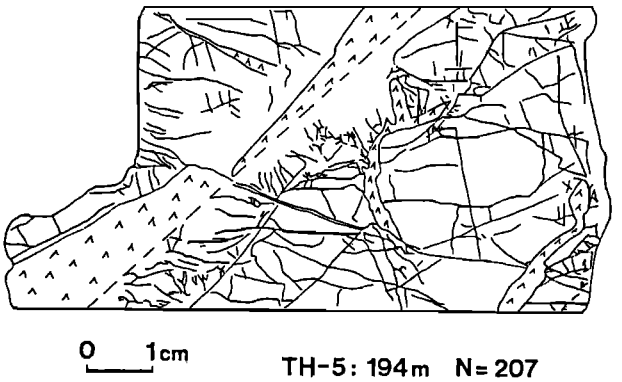

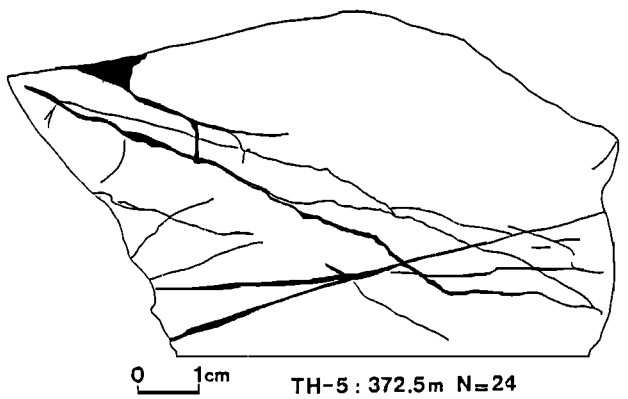

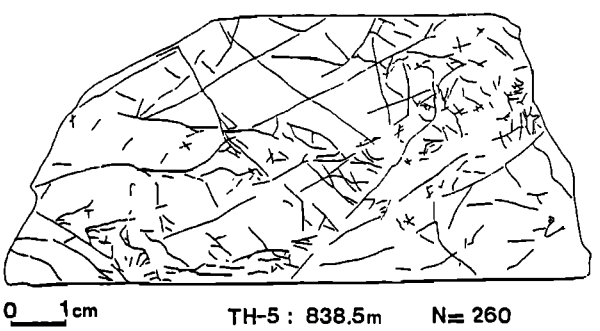

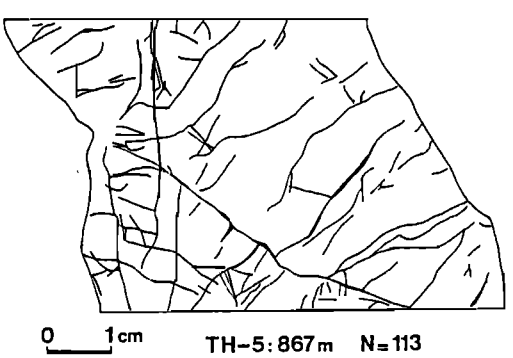

Fig. 8. Fracture patterns for the hand specimen samples of the core TH-5 (5 km from the Toyoha mine). The propylite sample TH-5 (372.5) m is characterized by small amount of fractures (N = 24) comparing to tuff breccia samples.

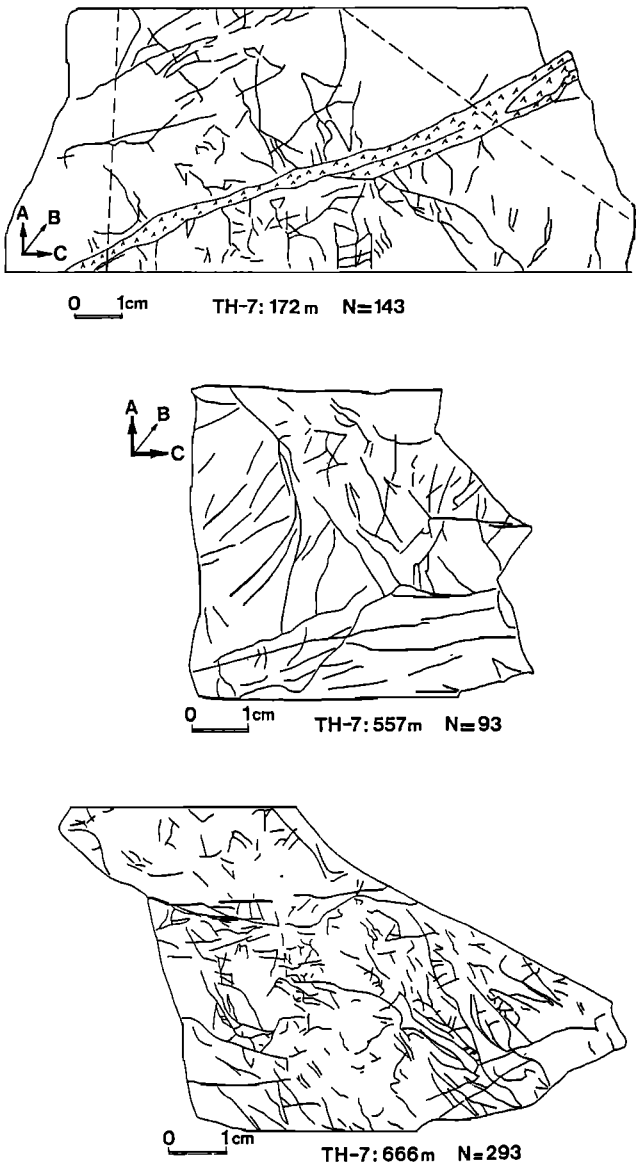

Fig. 9. Fracture patterns for the hand specimen samples of the core TH-7 (6 km from the Toyoha mine). The tuff breccia sample TH-7 (172 m) is crosscut by a quartz vein (vee pattern). The propylite samples TH-7 (557 and 666 m) are characterized by 93 and 293 fractures, respectively. However, their fractal dimensions are very similar with D = 0.43 and 0.475, respectively.

Propylite and tuff breccia occur in numerous bodies or lava flows. They contain most of the veins (Table 1). Detailed studies of the geology in the Toyoha region are reported by *Shikazono* [1975] and *Yajima and Ohta* [1979].

The 11 hand specimen samples studied are listed in Table 1 as a function of the distance from the Toyoha mine, the nature of the host rock, and the filling of the veins. Petrographic investigations indicate that the mineralization stage (pyrite veins) was associated with quartz, chlorite, sericite, and calcite stages as reported by *Sawai* [1986]. Moreover, microscopic observations suggest that a propylitization stage (chlorite-epidote assemblage) intensively affected the Toyoha region. This alteration is well developed in the drill cores TH-5 and TH-7 (Table 1). A later alteration event characterized by calcite veins affected these rocks. Calcite typically replaces chlorite and epidote minerals and occurs in the same vein network. This alteration, well developed in the cores TH-4 and TH-6, is locally associated with pyrite crystals.

At a larger scale the fracture distribution in two galleries located at about 1.5 km in the northwestern part of the Toyoha mine has been analyzed and compared with the general distribution of veins recorded by mining geologists at −150 m depth in the mine. The distribution of faults on a Landsat map of this region was also analyzed for comparison.

Fractal Analysis in the Toyoha Mine

The drawings of the fracture fields and the results of the fractal analysis of the samples collected in the Sugo and Izumo veins are illustrated in Figure 3. For the Sugo vein the fractal dimension (D = 0.25) remains constant for all the directions of measurement. On the contrary, the value of D for the Izumo fracture field ranges between 0.10 and 0.24 according to the direction of observation. Such a variation might be explained by the very small number of veins (N = 18) of this sample leading to a poor analysis.

Fractal analyses were performed on fracture fields in two galleries (200 m long) in the northwestern part of the mine. These galleries lie along E-W and NE-SW directions. About 270 veins (>0.5 cm in thickness) were taken into account for this study. Fractal analysis shows that the fractal dimension is 0.175 for both galleries, indicating a very high irregularity of the fracture distribution at this scale of observation (Figure 4).

TABLE 2. Main Characteristics of the Fracture Fields of the Drill Core Samples Studied

Sample	Cote, m	Total Number of Veins	Area, cm^2	Fracture Density	Total Length of Fracture, cm	Average Length, cm	Fractal Dimension D
TM-5	−150	75	59.78	1.25	123.8	1.65	0.25
TM-6	−150	18	42.10	0.42	49.37	2.74	0.10–0.24
TH-6	−747	95	35.85	2.65	65.0	0.68	0.25
TH-4	−950	63	37.72	1.67	64.6	1.02	0.27
TH-5	−194	207	37.70	5.49	117.1	0.56	0.52–0.55
TH-5	−372.5	24	40.68	0.59	56.35	2.35	0.20–0.40
TH-5	−838.5	260	46.76	5.56	136.5	0.52	0.38
TH-5	−867	113	28.97	3.90	82.3	0.72	0.22–0.28
TH-7	−172	143	37.63	3.80	133.3	0.86	0.43
TH-7	−557	93	28.97	3.21	84.0	0.90	0.43
TH-7	−666	293	32.77	8.94	139.23	0.47	0.475

Fracture density is measured per square centimeter.

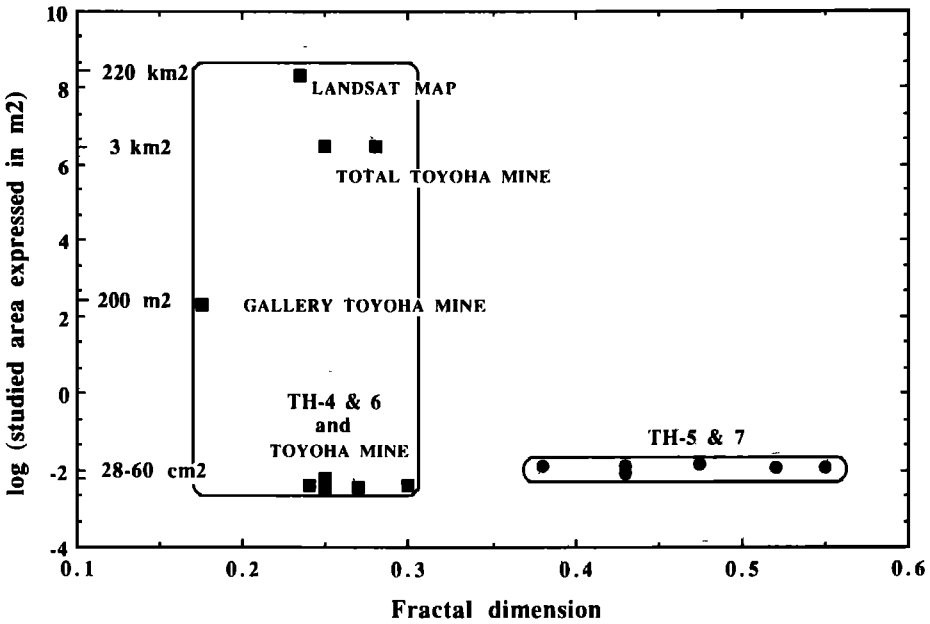

Fig. 10. Summary of the results of fractal analysis performed at different scales of observation in the Toyoha district. At the hand specimen scale (20 cm^3) the fractal dimensions are very similar to those determined at −150 m level in the Toyoha mine and at a regional scale (220 km^2). With a scale magnification factor over one million, the fracture distribution remains same (average $D = 0.25$). In the cores TH-5 (upper part) and TH-7 the style of rupture is different with D values ranging between 0.38 and 0.55.

At the kilometer scale, mining geologists have distinguished two distinct generations of fracture (E-W and NW-SE in directions) in the Toyoha mine (−150 m level) as illustrated in Figure 5 [*Yajima and Ohta*, 1979]. The fractal analysis indicates that the values of D are slightly different with 0.20 and 0.25–0.28 for E-W and NW-SE networks, respectively. The fractal dimension of the NW-SE network ($0.25 < D < 0.28$) is very similar to the D values described above for Sugo and Izumo fracture fields.

At the scale of many kilometers the fault distribution was analyzed from Landsat data (Figure 6). The analysis indicates that the fault distribution is very similar ($0.22 < D < 0.25$) to that at the kilometer scale ($0.20 < D < 0.28$). The D values vary slightly with direction of observation as observed at the hand specimen scale.

Fractal Analysis in the Drill Cores Around the Toyoha Mine

Fractal analysis was performed on nine highly fractured samples collected in four drill cores located at distances varying between 1.8 and 6.0 km from the Toyoha mine (Table 1). The main characteristics of the fracture field illustrated in Figures 7–9 are reported in Table 2. The spatial scale R used for normalization varies between 0.5 and 6.0 cm. It is apparent that in the samples studied the number of

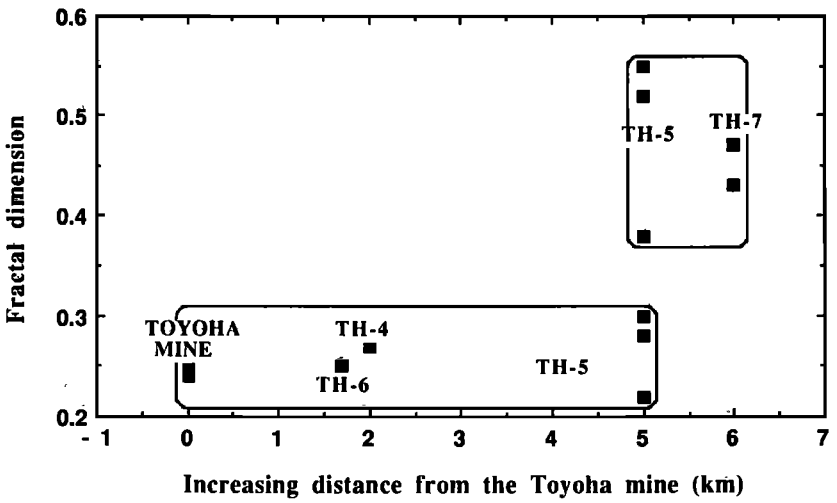

Fig. 11. Fractal dimensions versus increasing distance (in kilometers) from the Toyoha mine illustrating the results of the analysis performed on the hand specimen samples in the Toyoha district. Two groups are revealed for the fractal dimensions ($0.2 < D < 0.3$ and $0.4 < D < 0.55$).

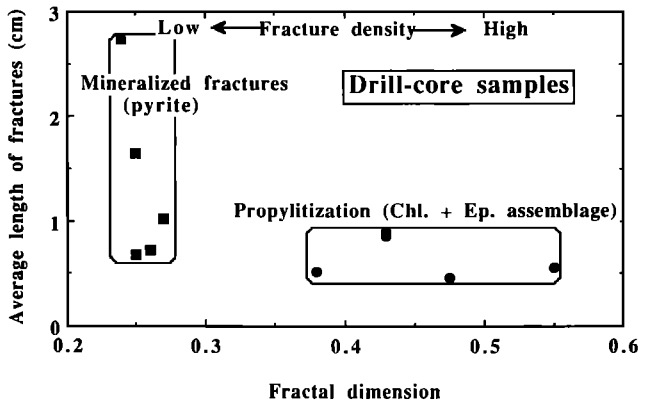

Fig. 12. Fractal dimension versus average length of fractures (in centimeters) illustrating the results of the fractal analysis performed on the hand specimen samples in the Toyoha district. As in Figure 11, two groups are revealed for the fractal dimensions ($0.2 < D < 0.3$ and $0.4 < D < 0.55$). These differences and the fracture density are related to the style of rupture: mineralized fractures (tectonic stress) and propylitized fractures (thermal cracking).

fractures (N) and their average length L can vary considerably ($24 < N < 293$; $0.47 < L < 2.35$ cm). Generally, the fracture density increases far from the Toyoha mine, while the average length decreases. The fractal dimension for the samples TH-6 and TH-4 located in the vicinity of the mine ranges between 0.25 and 0.27. In the drill core TH-5, the D values gradually decrease from 0.52–0.55 (194 m) to 0.22–0.28 (867 m). Moreover, the fracture field in the propylite (372.5 m) is quite distinct from the others. This is probably due to the small number of fractures ($N = 24$) as discussed above for the Izumo sample. In the core TH-7 the fractal dimension ($0.43 < D < 0.475$) is almost the same in the three samples studied, even though the lithology and depth of these samples differ.

CONCLUSIONS

The above analysis shows that the fracture distribution gives the same fractal dimension at all scales of observation in and around the Toyoha mine. The observational scale varies by 10^6. The average value is 0.25 in the mine and immediate vicinity (Figure 10). Therefore we assume that a scale-invariant relation pertains. In drill cores at varying distances from the mine, the fractal dimension changed, attaining a value of 0.55. Since the rock types are similar, this change is taken to indicate that the stresses and responses varied at depth away from the mine (Figures 10 and 11), cores TH-5 and TH-7).

This analysis suggests that the Toyoha district is characterized by at least two groups of fracture patterns (Figure 11). The first group ($0.20 < D < 0.30$) is related to the fracture patterns of the Toyoha mine and its close vicinity (1–5 km). It is characterized by long (0.5–2.8 cm in average length), mineralized, and generally interconnected fractures and also by low fracture density (Figure 12). The second group ($0.38 < D < 0.55$) presents a low fracture interconnection, a low average length (<1 cm), and a high fracture density.

It can be assumed that differences in the observed average lengths and fracture density are the result of differences in the mechanical processes creating the fractures. The fractures of the first group near the Toyoha mine are mineralized, and their formation was spatially controlled by the main regional directions of stress (E-W and NW-SE [*Yajima and Ohta*, 1979]). The propylitized fractures with shorter fracture lengths and higher density were probably characterized by a lower permeability than those with longer fracture lengths as well as by a lower density [*Long and Witherspoon*, 1985] and can be classified as thermally induced (thermal cracking) microfractures similar to those described in granite by *Wang et al.* [1989]. Locally, intermediate fractal values reflect mixtures of the two groups with different components of each fracture style as shown in the core TH-5.

Despite the simplicity of the approach used here, it is apparent that fractal analysis can be used to detect differences in fracture style and hence differences in the forces and events which caused them. The interest in the linear fractal measurement approach is that it can be used in drill holes which give a strictly linear dimension of detection of the three-dimensional fracture patterns. Justification for this statement can be found in the theoretical analysis of *Falconer* [1990]. As the projection of these fracture planes on a line maintains the geometry of the fracture field, the measurement in one dimension will give a faithful account of the fractal relations of the fracture field as a whole. Therefore variations of fractal dimensions detected in drill holes could be used to characterize the fracture field in three-dimensional space. This obviously represents an economy in detection methods.

Acknowledgments. This work was supported by Ministère des Affaires Etrangères of France. We thank S. R. Brown and J. F. Wang for their critical reviews. Special thanks to M. Utada of the University of Tokyo for the samples and financial support of the survey in the Toyoha mine. A. Inoue, J. T. Iiyama, and S. O'Hara of Chiba University and the geologists of the Toyoha mine are also acknowledged for technical assistance during this study.

REFERENCES

Aviles, C. A., C. H. Scholz, and J. Boatwright, Fractal analysis applied to characteristic segments of the San Andreas fault, *J. Geophys. Res.*, *92*, 331–344, 1987.

Barton, C. C., and E. Larsen, Fractal geometry of two dimensional networks at Yucca Mountain, Southwestern Nevada, in *Proceedings of the International Symposium on Fundamentals of Rock Joints*, edited by A. Stephannson, pp. 77–84, Bjorkliden, Norway, 1985.

Brown, S. R., and C. H. Scholz, Broad bandwidth study of the topography of natural rock surfaces, *J. Geophys. Res.*, *90*, 12,575–12,582, 1985.

Dubois, J., and J. L. Cheminée, Application d'une analyse fractale à l'étude des cycles éruptifs du Piton de La Fournaise (La Réunion): modèle d'une poussière de Cantor, *C. R. Acad. Sci. Paris*, *307*, 1723–1729, 1988.

Falconer, K., *Fractal Geometry*, 288 pp., John Wiley, New York, 1990.

Long, J. C. S., and P. A. Witherspoon, The relationship of the degree of interconnection to permeability in fracture networks, *J. Geophys. Res.*, *90*, 3087–3098, 1985.

Mandelbrot, B. B., *The Fractal Geometry of Nature*, 468 pp., W. H. Freeman, New York, 1982.

Okubo, P., and K. Aki, Fractal geometry in the San Andreas fault system, *J. Geophys. Res.*, *92*, 345–355, 1987.

Sawai, O., The distribution of alteration zones in the eastern part of the Toyoha mine, Hokkaido, Japan (in Japanese), *Min. Geol.*, *36*, 273–288, 1986.

Shikazono, N., Mineralization and chemical environment of the

Toyoha lead-zinc vein-type deposits, Hokkaido, Japan, *Econ. Geol.*, *70*, 694–705, 1975.

Smalley, R. F., L. L. Chatelain, D. L. Turcotte, and R. Prevot, A fractal approach of the clustering of earthquakes: Applications to the seismicity of the New Hébrides, *Bull. Seismol. Soc. Am.*, *77*, 1368–1381, 1987.

Velde, B., J. Dubois, A. Badri, and G. Touchard, Fractal analysis of fractures in rocks: The Cantor's dust method, *Tectonophysics*, *179*, 345–352, 1990.

Velde, B., J. Dubois, D. Moore, and G. Touchard, Fractal patterns of fractures in granites, *Earth Planet. Sci. Lett.*, *104*, 25–35, 1991.

Wang, H. F., B. P. Bonner, S. R. Carlson, B. J. Kowallis, and H. C. Heard, Thermal stress cracking in granite, *J. Geophys. Res.*, *94*, 1745–1758, 1989.

Yajima, J., and E. Ohta, Two-stage mineralization and formation process of the Toyoha deposits, Hokkaido, Japan, *Min. Geol.*, *29*, 291–306, 1979.

T. Merceron, Laboratoire de Pétrologie des Altérations Hydrothermales, University of Poitiers, 40 Avenue du Recteur Pineau, 86022 Poitiers Cédex, France.

B. Velde, Geological Department, Ecole Normale Supérieure, 24 Rue Lhomond, 75005 Paris Cédex, France.

(Received November 5, 1990;
revised April 24, 1991;
accepted May 20, 1991.)

JOURNAL OF GEOPHYSICAL RESEARCH, VOL. 96, NO. B10, PAGES 16,597–16,623, SEPTEMBER 10, 1991

A Rheologically Layered Three-Dimensional Model of the San Andreas Fault in Central and Southern California

CHARLES A. WILLIAMS[1] AND RANDALL M. RICHARDSON

Department of Geosciences, University of Arizona, Tucson

Three-dimensional kinematic finite element models of the San Andreas fault in central and southern California have been used to estimate the effects of rheological parameters and fault slip distribution on the horizontal and vertical deformation in the vicinity of the fault. The models include the effects of vertically layered power law viscoelastic rheology, and isostatic forces are considered in calculations of vertical uplift. Several different rheological layering schemes are used, using laboratory results on rock rheology to define the properties of the various layers. The depth to which the fault remains locked between earthquakes (D) is held constant at 20 km for the entire locked portion of the fault between Cholame and the Salton Sea. Between Hollister and Cholame the entire fault is assumed to slip at a rate consistent with a relative plate velocity of 35 mm/yr along a direction striking N41°W. Steady aseismic slip corresponding to plate velocity is imposed below the fault locking depth to a depth H on the locked section of the fault. The depth to which aseismic slip occurs (H) is assigned a value of either 20 km or 40 km, resulting in two versions of each rheological model. Variations in the model parameters are found to produce distinctive deformation patterns, providing a means for differentiating between models. Specifically, lower effective viscosities near the surface result in increased strain rates and uplift rates at all times during the earthquake cycle. Lower effective viscosities also produce subsidence near the creeping portion of the fault. Models that do not include aseismic slip below the fault locking depth (H = 20 km) display greater time dependence in both horizontal and vertical deformation than those including aseismic slip below the locking depth (H = 40 km). These differences are due, in part, to the time-invariant nature of the imposed slip condition. The differences are more pronounced as the effective viscosity close to the surface is increased. The vertical uplift rate is particularly sensitive to the depth of aseismic slip (H) at the two bends in the fault, especially for models with high effective viscosities below the surface. For models in which the effective viscosity near the surface is relatively low, measurements of total uplift at the two bends in the fault could provide sufficient resolution to distinguish between models with and without aseismic slip over time periods of 10 to 20 years or more with current abilities to measure vertical uplift. Among our San Andreas fault models, the one most consistent with current strain rate data includes aseismic slip between 20 and 40 km (H = 40 km) and uses assumed rheological properties from the surface to 100 km depth consistent with laboratory results for wet rock samples. The rheological parameters for this model are based on laboratory results for the following rock types wet granite in the upper crust (0 to 20 km), wet diabase in the lower crust (20 to 40 km), wet dunite in the upper mantle (40 to 100 km), and dry olivine below 100 km. These modeling results are preliminary, however, and several additional factors should be considered prior to constructing a comprehensive model. Furthermore, it should be emphasized that the present models represent a small subset of possible rheological models, and numerous other models may provide similar or better fits to the data. The field of possible models will continue to narrow with further knowledge of the variations in Earth composition and temperature with depth, with more information on rock rheology, and with further observations of the earthquake cycle.

INTRODUCTION

One of the primary goals of modern geophysical investigations is an understanding of the processes related to repeated earthquake occurrence at major plate boundaries. These studies are important not only in estimating earthquake hazard potential but also for the information they yield on plate movements, plate driving stresses, and the structure and composition of the Earth. The San Andreas fault in California represents an ideal location for this type of research. The proximity of the fault to major population and industrial centers and its easy accessibility have resulted in large quantities of high-quality deformation data, providing the necessary means for constraining physical models of strain accumulation and release on the San Andreas fault.

Numerous models of the earthquake cycle have been proposed for the San Andreas fault. Many of these are based on the model initially proposed by *Nur and Mavko* [1974], consisting of a displacement dislocation in an elastic layer overlying a linear viscoelastic (Maxwell) half-space. Models of this sort include those of *Savage and Prescott* [1978], *Spence and Turcotte* [1979], and *Rundle* [1986]. The model of *Savage and Prescott* [1978] was used by *Thatcher* [1983] to calculate shear strain rates, providing a reasonable fit to observations along the San Andreas fault. It has also been used by *Williams and Richardson* [1988] in an inverse analysis attempting to place some constraints on fault parameters with available shear strain rate observations. In addition to these kinematic models, several models have been proposed that consider the dynamic aspects of the problem, including those of *Li and Rice* [1987], *Li and Lim* [1988], and *Rundle* [1988*a*, *b*]. Most of these models consider the case of an infinitely long rectangular fault and are therefore essentially two-dimensional. The work of *Rundle* [1986, 1988*b*], however, has emphasized the importance of considering variations in fault geometry.

There are two primary points which have not yet been addressed by San Andreas fault models. First, only linear viscoelastic rheologies have been considered. In most cases, a simple elastic layer-over-viscoelastic-half-space model has been assumed. A large volume of work exists, however, indicating that actual Earth structure is considerably more complex [e.g., *Meissner and Strehlau*, 1982; *Chen and Molnar*, 1983; *Strehlau and Meissner*, 1987]. Furthermore, laboratory measurements show that actual rock rheology is better represented by a power law rather than a linear viscoelastic relationship [*Kirby*, 1983;

[1]Now at Department of Geological and Geophysical Sciences, Princeton University, Princeton, New Jersey.

Paper number 91JB01484.
0148-0227/91/91JB-01484$05.00

Kirby and Kronenberg, 1987*a*, *b*]. It is important to estimate the possible effects of laboratory-inferred power law rheology on model results. Second, current models calculate only the horizontal components of deformation, neglecting vertical uplift. With increased accuracy in leveling surveys, and the addition of other types of information such as that from the global positioning system (GPS), vertical uplift data represent an additional means of constraining San Andreas fault models.

This study attempts to address these points by producing fully three-dimensional finite element models of the San Andreas fault in central and southern California, using laboratory results on rock rheology [*Kirby*, 1983; *Kirby and Kronenberg*, 1987*a*, *b*] to define the properties of various layers in the Earth. Although a number of present models are consistent with current horizontal geodetic observations, it is quite possible that predicted vertical uplift may vary considerably among these models. In our study, both horizontal and vertical deformation patterns for several different models are calculated to determine whether the models predict distinctive patterns at various times in the earthquake cycle. In cases where distinctive patterns coincide with existing observations, these data may be used to evaluate the models. In many cases, the distinctive patterns occur in regions or times where no data are currently available. These regions thus represent potentially useful observation sites for the future.

The parameters of interest in this analysis are the depth to which the fault remains locked between earthquakes, the depth to which aseismic slip occurs below the locking depth, and the variation in the viscous properties of the Earth with depth. Recent models have produced a wide range of values for these parameters [*Thatcher*, 1983; *Thatcher and Rundle*, 1984; *Rundle*, 1986, 1988*b*; *Li and Rice*, 1987; *Li and Lim*, 1988]. Estimates of the fault locking depth range from 9 to 20 km, while the depth to which aseismic slip occurs (which corresponds to the base of the elastic layer for these models) has been assigned values ranging from 10 to 40 km. Estimates of viscosity for the Earth below the elastic layer have varied from 2×10^{18} to 1×10^{20} Pa s. It is likely that the use of layered power law viscoelastic models could significantly affect these parameter estimates. If, for example, the behavior of the upper crust were not purely elastic, it would be expected to strain more rapidly in response to imposed stress. If this fact is not considered, estimates of the model parameters will be in error. A more likely possibility is an alternating effective viscosity with depth, as discussed in the next section. In this case, relatively low effective viscosities would be expected throughout the lithosphere except near the tops of the upper crust, lower crust, and upper mantle. It is important to compare the results of this type of model with those obtained from models consisting of an elastic layer overlying a linearly viscoelastic half-space.

The models presented here are loosely based on the layer-over-a-half-space model of *Savage and Prescott* [1978], which is in turn derived from the model of *Nur and Mavko* [1974]. The layer-over-a-half-space model is the most common type of rheological model currently being used to study the San Andreas fault [e.g., *Rundle*, 1986, 1988*b*; *Li and Rice*, 1987; *Li and Lim*, 1988]. Figure 1 demonstrates the differences between the Savage and Prescott model and our model. The Savage and Prescott model, which is shown in cross section in Figure 1*a*, is characterized by a fault locking depth (D) and an elastic layer thickness (H). Aseismic slip is assumed to occur below D to the base of the elastic layer, on the dashed portion of the fault in Figure 1*a*. In our model (Figure 1*b*), there is no elastic layer as such, and the parameter H instead represents the depth to which aseismic slip occurs. There are therefore two primary differences between our model and that of Savage and Prescott. First of all, Earth structure is represented as a number of rheological layers, rather than a single elastic layer overlying a viscoelastic half-space. Secondly, the depth to which aseismic slip occurs is independent of the rheological layering scheme.

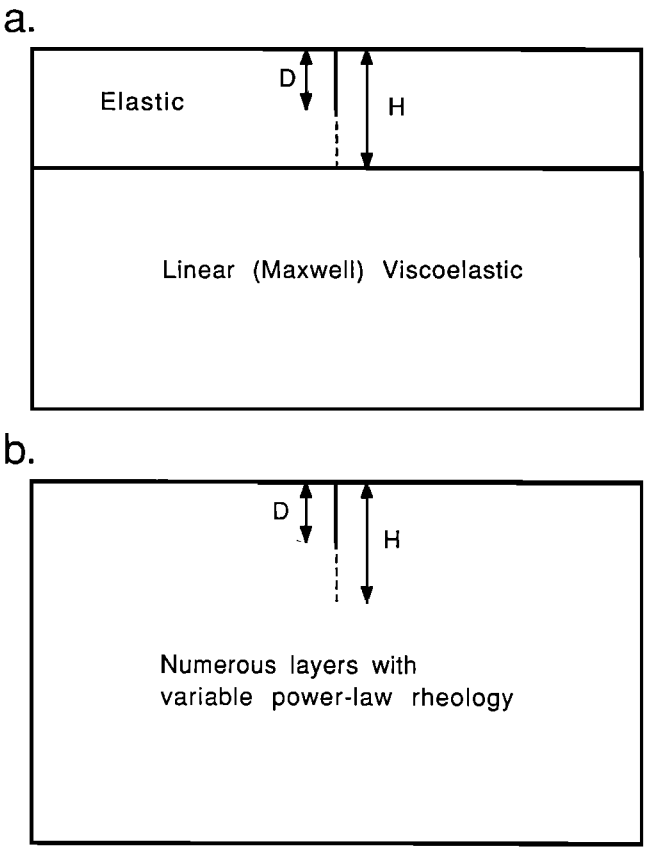

Fig. 1. Models used in the study. (*a*) *Savage and Prescott* [1978] model. (*b*) Nonlinear layered model.

Our models, like that of *Savage and Prescott* [1978], are purely kinematic, meaning that the slip on the fault is specified rather than being a result of the calculations. Several dynamic models have also been developed. One of these [*Li and Rice*, 1987; *Li and Lim*, 1988] is partially kinematic, as the amount of coseismic displacement and the earthquake recurrence interval are specified. Below the fault locking depth, however, we assume a constant resistive stress boundary condition rather than impose a constant slip rate. The assumption of aseismic slip below the locking depth is a common feature of current strike-slip fault models and is supported by the results of *Tse and Rice* [1986]. They found that steady state sliding is unstable above a certain depth within the Earth and is stable below this depth. Therefore stick-slip (seismic) behavior would be expected above this depth, with steady state sliding below. The results of *Tse and Rice* [1986] demonstrate that broadly distributed creep flow below the seismogenic zone is not the only possible mechanism of aseismic slip at depth. A final model is that of *Rundle* [1988*a*, *b*]. This is a three-dimensional model in which the fault displacements are completely determined as a result of the calculations.

Kinematic models are used in this study for the sake of simplicity. Our analysis focuses on the effects of rheological properties and the depth of aseismic slip on the observed deformation, and it does not consider other complexities of fault mechanics. In the Earth, it is likely that there is accelerated aseismic slip below the locking depth immediately following an earthquake, as in the model of *Savage* [1990]. The imposition of steady aseismic slip at depth in our models (for models with $H > D$) will probably result in an exaggerated difference between models including aseismic slip below the locking depth and those that do not. However, our results will serve to emphasize the differences between models in which slip at depth occurs on a discrete fault (aseismic slip at depth, i.e., $H > D$) and those in which slip at depth is accomplished by

viscous shear (no aseismic slip at depth, i.e., $H = D$). The exact values obtained from our models should be interpreted with some care, since the degree to which the results are influenced by imposed steady aseismic slip is not known.

Velocity boundary conditions corresponding to plate motion are applied along vertical planes at the extreme edges of the grid, far from the fault. An alternative method would be the application of these conditions along the base of the model. It is unlikely that our choice of boundary conditions will have a significant effect on the results, which are not calculated until steady flow has occurred at depth. Thus the entire "upper mantle" portion of the model is essentially moving at plate velocity at distances far from the fault. As described by *Li and Rice* [1987], the cyclically time-dependent displacement field of their solution depends only on the far-field plate velocity; it does not depend on the distance-varying velocity boundary conditions applied to the base of their model. Model results should therefore be insensitive to the method in which the time-independent velocity boundary conditions are applied.

Our boundary conditions are chosen to be consistent with geodetic determinations along the fault [*Minster and Jordan*, 1987; *DeMets et al.*, 1987] rather than with plate motion determinations, such as NUVEL1 [*DeMets et al.*, 1990]. One of the ramifications of this assumption is a reduction in the component of fault-normal stress, since NUVEL1 predicts a more northerly trending motion (N36°W as compared to N41°W) and a higher velocity (48 mm/yr as opposed to 35 mm/yr). Recent investigations have indicated that the primary stress component near the San Andreas fault is a compressive stress perpendicular to the fault [*Mount and Suppe*, 1987; *Zoback et al.*, 1987]. This can be explained if the San Andreas is a relatively weak fault, unable to support significant amounts of shear stress. This idea has strong observational support. The absence of a heat flow anomaly associated with the fault indicates that it cannot support shear stresses greater than about 10–20 MPa [*Brune et al.*, 1969; *Lachenbruch and Sass*, 1980]. More recently, *Jones* [1988] has used focal mechanisms for a number of small to intermediate earthquakes to determine the principal stress axes near the fault. These results show a nearly constant angle of about 65° between the maximum horizontal compressive stress and the local strike of the San Andreas, implying a weak fault.

Geodetic observations, on the other hand, are generally consistent with fault-parallel right-lateral shear [e.g., *Prescott and Savage*, 1976; *Prescott et al.*, 1979; *King and Savage*, 1983; *Savage*, 1983], such that the principal axes of strain rate are oriented at approximately 45° to the local strike of the fault. This observed discrepancy in direction between geodetic and stress determinations may be reconciled if the geodetic observations are considered to be the changes from a reference state induced by the earthquake cycle while the stress measurements represent the background value (J. Savage, personal communication, 1990). Thus our models more accurately reflect the short-term changes in deformation than the long-term stress state. For kinematic models, it is most reasonable to choose a framework defined by geodetic observations, particularly since these are the observations used to constrain the models. Since the effects of fault friction are effectively bypassed with kinematic models, the question of fault strength does not apply. Instead, slip on the fault is completely defined, regardless of the stresses acting on it.

POWER LAW VISCOELASTIC RHEOLOGY

The elastic rebound theory of *Reid* [1910, 1911] was based on the assumption that the Earth's behavior is perfectly elastic over extended periods of time. While elastic behavior is certainly a reasonable assumption over extremely short time periods, there is ample evidence of nonelastic behavior over longer periods. The first quantitative evidence of nonelastic behavior was the observed postglacial rebound in Scandinavia. This was explained by *Haskell* [1935, 1936] as the viscous response of the Earth's mantle to postglacial unloading. An analysis of viscosity variation with depth in the Earth's mantle was performed by *Gordon* [1965, 1967], who assumed that viscous deformation within the Earth occurred by Nabarro-Herring (diffusion) creep. This mechanism consists of the diffusion of lattice vacancies within crystal grains. A similar mechanism is grain boundary (Coble) creep, in which diffusion occurs along grain boundaries. Both of these mechanisms lead to a Newtonian fluid behavior, in which the steady state strain rate is linearly proportional to the applied stress.

An alternative mechanism, dislocation creep, was considered by *Weertman* [1970]. Dislocations contribute to creep primarily through dislocation climb or dislocation glide. Weertman's results indicated that dislocation creep should be the dominant mechanism except at very low stresses (less than 1000 Pa). A dislocation creep mechanism predicts that the steady state creep rate is proportional to a power of the stress. Dislocation creep deformation therefore leads to power law viscous behavior. Power law rheology has been examined by a number of authors, including *Weertman* [1970], *Melosh* [1980], *Turcotte and Schubert* [1982], *Kirby* [1983, 1985], and *Kirby and Kronenberg* [1987*a*, *b*].

Although more complicated formulations are possible (see, for example, *Kirby* [1985]), the creep law that represents dislocation processes may be described by the power law relationship

$$\dot{\varepsilon}_s = A\sigma^n \exp(-H^* / RT) \tag{1}$$

where $\dot{\varepsilon}_s$ is the steady state creep rate, $\sigma = (\sigma_1 - \sigma_3)$ is the differential stress, T is the absolute temperature, R is the ideal gas constant, A is a material constant, n is the power law exponent, and $H = E^* + PV^*$ is the activation enthalpy (E^* is the activation energy, V^* is the activation volume, and P is the mean normal stress). As discussed by *Strehlau and Meissner* [1987], the pressure factor PV^* is typically smaller than the uncertainties in E^* and is therefore neglected in this study.

A number of quantities may be defined in analogy to Newtonian (linear) viscosity [see *Melosh*, 1980]. Newtonian viscosity is defined in terms of the differential stress and the steady state creep rate as

$$\eta = \frac{\sigma}{2\dot{\varepsilon}_s} \tag{2}$$

An analogous quantity, the effective viscosity, may be defined for power-law behavior:

$$\eta_{eff} = \frac{\sigma}{2\dot{\varepsilon}_s} = \frac{\exp(H^*/RT)}{2A\sigma^{n-1}} \tag{3}$$

It can therefore be seen that the effective viscosity is dependent not only upon the type of rock under consideration but also upon the temperature and the applied differential stress. An increase in either the temperature or the differential stress results in a lower effective viscosity. The effective viscosity may also be described in terms of the strain rate, convenient for this study, where the emphasis is on deformation.

$$\eta_{eff} = \frac{1}{2}\dot{\varepsilon}_s^{\left(\frac{1-n}{n}\right)}\left[A\exp(-H^* / RT)\right]^{-\frac{1}{n}} \tag{4}$$

For all values of n greater than 1, the effective viscosity is inversely proportional to the strain rate. High strain rates may thus be expected to produce low effective viscosities. Since the stress and strain rate are generally not known beforehand, it is necessary to define a viscosity quantity that is independent of the applied stress or strain rate. A viscosity coefficient may be obtained from equation (3) by eliminating the stress term.

$$\eta_c = \frac{\exp(H^* / RT)}{2A} \tag{5}$$

The viscosity coefficient is the quantity used in the computa-

tions of this study and is incorporated into the finite element formulation [see *Melosh and Raefsky*, 1980].

Only viscous behavior has been considered to this point; however, the behavior of rocks in the Earth is more adequately described by viscoelastic behavior. The viscoelastic model used in this study is analogous to a Maxwell viscoelastic material. It may be represented by a linear elastic spring in series with a dashpot that has a power law viscous response. A useful measure of the time dependence of a viscoelastic material is the Maxwell time (τ_M), which is the amount of time necessary for the creep deformation to equal the elastic deformation. For a Maxwell viscoelastic material, in which the viscous behavior is Newtonian (linear), the Maxwell time is simply the viscosity of the material divided by its shear modulus. For a power law material, the effective viscosity may be substituted for the viscosity in the Maxwell model, yielding the following relationship:

$$\tau_M = \frac{\varepsilon_{elastic}}{\dot{\varepsilon}_s} = \frac{\eta_{eff}}{\mu} = \frac{\exp(H^*/RT)}{2\mu A \sigma^{(n-1)}} \quad (6)$$

The Maxwell time is a useful indicator of whether a material may be considered as an elastic solid or a viscous fluid over the time period of interest. The time period of interest in this study is of the order of 150 years (the earthquake recurrence interval). Any material with a Maxwell time considerably greater than this will thus behave elastically, while any material with a Maxwell time much less than this will behave as a viscous fluid.

A number of authors have addressed the problem of rheological layering within the Earth as it relates to laboratory results on power law flow [*Meissner and Strehlau*, 1982; *Chen and Molnar*, 1983; *Kusznir and Karner*, 1985; *Kusznir and Park*, 1986; *Ranalli and Murphy*, 1987; *Strehlau and Meissner*, 1987; *Bird*, 1989; *Melosh*, 1990]. One observation that has focused attention on this problem is the limited depth ranges over which earthquakes are observed [*Meissner and Strehlau*, 1982; *Chen and Molnar*, 1983]. *Chen and Molnar* [1983] found that in many areas, earthquakes were observed in the upper crust and upper mantle, but relatively few earthquakes were observed in the lower crust. This was attributed to a change in material types at the Moho combined with the increase of temperature with depth. As can be seen from (3) and (4), the effective viscosity decreases exponentially with increasing temperature and would thus decrease with depth. In the model of *Chen and Molnar* [1983], it was assumed that frictional failure (as described by *Byerlee* [1978]) was the dominant deformational mode in the upper crust. In the lower crust, deformation was assumed to be controlled by a quartz-diabase flow law, since the flow stress for geological strain rates (of the order of 10^{-15} s^{-1}) is less than the fracture stress at these depths. Mantle behavior was considered to be controlled by an olivine flow law. Since the flow stress for olivine is much greater than that for quartz or diabase at the same temperature and pressure, another region of high strength exists just below the Moho. The two regions of high yield stress (in the upper crust and upper mantle) are thus the only regions where seismic behavior is possible. By examining a large number of earthquakes and estimating the temperatures at the depths of the deepest events, *Chen and Molnar* [1983] found limiting temperatures of 250°–450°C for crustal materials and 600°–800°C for mantle materials. For the San Andreas fault, seismic behavior is generally absent below depths of 12 to 15 km, where the temperature is estimated to be about 350° ± 100°C [*Lachenbruch and Sass*, 1973, 1978]. A recent exception to this limit is the Loma Prieta earthquake of October 17, 1989, which occurred at a depth of approximately 18 km [*Ward and Page*, 1989].

Although much laboratory work has been done, caution must be used when applying laboratory results to actual geological situations. There is a fairly large uncertainty in the flow law parameters for any given rock type. As an example, the "best estimate" parameters given by *Kirby* [1983] for olivine in its natural state with no water added are: $\log_{10}A = 4.8 \pm 1.2$ (A in units of s^{-1} MPa^{-n}), $n = 3.5 \pm 0.6$, $E^* = 533 \pm 60$ kJ mol^{-1}, and $V^* = (17 \pm 4) \times 10^{-6}$ m^3 mol^{-1}. Additional uncertainties arise because of the effects of water and possible contributions of grain-size sensitive diffusional creep at fine grain sizes [*Kirby and Kronenberg*, 1987*a*]. A final problem is the exponential dependence of effective viscosity on temperature, as is seen in (3) and (4). As mentioned in the preceding paragraph, temperature estimates can vary by ±100°C. Later in this section it will be shown that if the assumed value of the surface heat flow varies by ±10 mW/m^2, the predicted effective viscosity can vary by 2 or more orders of magnitude. Despite the uncertainties in applying these laboratory results to the Earth, it is important to determine how incorporation of laboratory measurements into fault models influences the predicted deformation.

It is impossible to determine the composition and rheology of the Earth at every point in a fault model. A number of authors have found, however, that the creep rate within a polymineralic rock is controlled by the weakest phase if it composes at least 30% of the volume of the rock [*Carter et al.*, 1981; *Shelton and Tullis*, 1981]. The rheological behavior can then be estimated from the rheology of the principal constituents at the depth of interest. In the upper crust, the rheological properties are likely to be dominated by quartz. The lower crust, which probably has a lower quartz content, may be controlled by a feldspar or pyroxene rheology. Within the upper mantle, the flow rate is likely to be dominated by olivine.

For the finite element modeling, the materials chosen to represent the various rheological layers were granite, diabase, olivine, and dunite. The elastic and viscous properties of these materials are listed in Table 1. The viscosity parameters (power law exponent, A, and activation energy) were obtained from Table 1 of *Strehlau and Meissner* [1987]. The elastic parameters represent average values derived from several sources [*Birch*, 1966; *Turcotte and Schubert*, 1982], simplified for numerical

TABLE 1. Elastic and Viscoelastic Parameters Used in the Modeling for Various Material Types

Material Type	Young's Modulus, Pa	Poisson's Ratio	Shear Modulus, Pa	Density, kg/m^3	Power Law Exponent	$\log_{10}A$	Activation Energy, kJ/mol
"Elastic"	1.5×10^{11}	0.25	6.00×10^{10}	3000	1.0	–	–
"Viscoelastic"	1.5×10^{11}	0.25	6.00×10^{10}	*	1.0	–	–
Dry granite	5.0×10^{10}	0.25	2.00×10^{10}	3000	2.9	–0.2	106
Wet granite	5.0×10^{10}	0.25	2.00×10^{10}	3000	1.5	2.0	137
Dry diabase	8.0×10^{10}	0.25	3.20×10^{10}	3000	3.4	6.5	260
Wet diabase	8.0×10^{10}	0.25	3.20×10^{10}	3000	3.0	7.9	276
Dry olivine	1.6×10^{11}	0.28	6.25×10^{10}	3300	3.5	15.5	535
Wet dunite	1.6×10^{11}	0.28	6.25×10^{10}	3300	3.4	14.4	444

The logarithm base ten of A is given. The units of A are GPa^{-n} s^{-1}.

*Density is equal to 3000 kg/m^3 for all material above 40 km, and 3300 kg/m^3 for all material below 40 km.

convenience. This simplification seems justified due to the uncertainty in determining the actual composition of the region of interest. The densities were chosen to be 3000 kg/m^3 for all material above 40 km (the assumed Moho) and 3300 kg/m^3 for all material below this depth, to simplify the isostatic aspects of the problem. Also listed in Table 1 are materials labeled as "elastic" and "viscoelastic." These represent the properties used in a linear (Maxwell) viscoelastic model analogous to that of *Savage and Prescott* [1978], which is used for comparison to the nonlinear models.

Since effective viscosity decreases exponentially with increasing temperature (see equations (3) and (4)) it is necessary to construct a temperature profile for the region of interest. This is probably one of the major sources of uncertainty in the calculations. The rheological behavior is extremely sensitive to temperature, and the temperature at depth is difficult to determine accurately. A relatively simple profile was chosen for this study because of the difficulty in accurately determining the temperature and also because the temperature gradient represents an average over a large surface area (the grid covers an area approximately 700 km × 1300 km). The method chosen was that of *Chapman* [1986], which incorporates the mantle model of *Schatz and Simmons* [1972]. This method assumes steady state, one-dimensional conductive heat transfer, with observed heat flow as the principal constraint. Using this method, a geotherm consistent with a surface heat flow of 75 mW/m^2 was calculated. This value is consistent with the value of 78 mW/m^2 obtained by averaging the San Andreas heat flow values for regions 4, 5, 6, and 7 in Figure 8 and Table 2 of *Lachenbruch and Sass* [1980]. This profile is shown by the thin solid line in Figure 2. The discretization of the profile used in the finite element calculations is represented by the thick solid line in Figure 2. Also shown are the profiles that would be generated by assuming a heat flow of 65 mW/m^2 (thin dashed line) and 85 mW/m^2 (thin dotted line). The profiles for heat flows of 65 and 85 mW/m^2 are shown to demonstrate how uncertainties in the observed heat flow for the thermal model influence the predicted temperature. Further variations in the predicted temperature arise due to uncertainties in other model parameters (such as conductivity and heat generation) as well as the nature of the model itself. For the thermal models shown here, the slope changes dramatically at about 100 km depth, where the geotherm intercepts the mantle 1300°C adiabat. The assumed temperature below this depth is not particularly important, as the model results are relatively unaffected by viscosity changes below 100 km.

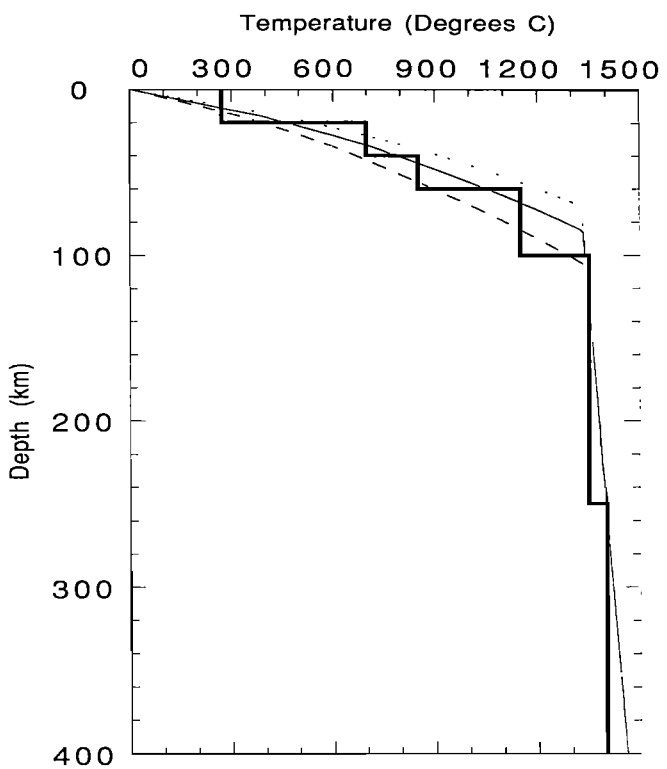

Fig. 2. Temperature profile used for the San Andreas modeling. The thin solid line represents the geotherm calculated for an assumed surface heat flow of 75 mW/m^2, and the thick solid line is the discretization of this profile used in the finite element calculations. The thin dashed line and the thin dotted line represent the geotherms calculated for assumed surface heat flows of 65 mW/m^2 and 85 mW/m^2, respectively.

The rheological properties of the various models are listed in Tables 2*a*–2*e*. The first model (Table 2*a*) is a linear (Maxwell) viscoelastic model that is used for comparison with the nonlinear models. The assumed temperature profile is not important in this case, as the model simply consists of an "elastic" layer overlying a "viscoelastic" layer. Since the grid extends to a depth of 400 km, a factor of 10 greater than the maximum depth of elastic behavior, the viscoelastic layer may be considered to be a half-space. For a Maxwell viscoelastic material, the viscosity coefficient (given by equation (5)) and the effective viscosity (given by equation (3)) are equivalent. For the nonlinear models, effective viscosity and Maxwell time were calculated for an assumed strain rate of 2×10^{-14} s^{-1}, a typical value for the strain rate close to the fault, as determined from the calculations. The Maxwell time may be calculated from (6). The properties of the linear model used in the finite element calculations are shown graphically in Figure 3, which shows the effective viscosity and Maxwell time as a function of depth. In Figure 3, and those that follow, effective viscosity will be shown with solid lines, and Maxwell time with dashed lines. There are two versions of the linear model in which aseismic slip occurs to different depths. The thick lines represent the model in which there is no aseismic slip below the locking depth (H = 20 km), while the thin lines represent a model that includes aseismic slip (H = 40 km). Throughout the rest of this paper, models that include aseismic slip at depth will be referred to as A models, while those that do not will be referred to as B models. The definitions of the fault locking depth (D) and elastic layer thickness (H) for the linear models are shown in Figure 1*a*. For the linear models, the A and B versions differ in both the depth of aseismic slip and in the thickness of the surface elastic layer. The viscosity chosen to simulate an elastic layer is sufficient to produce elastic behavior over any time period of geologic interest (1×10^{33} Pa s).

Although there are numerous possible rheological models, four were chosen for this study (in addition to the linear model described above). The viscoelastic properties are listed in Tables 2*b*–2*e*. The first of these models (Table 2*b*) is the simplest, but it is perhaps not geologically reasonable, as it assumes that the behavior of the entire crust is dominated by a granite rheology. Below the Moho, the rheological properties chosen are those for olivine. This is also true of models 2 and 3. In all models, the Moho depth is assumed to be 40 km. This is probably somewhat deep for southern California, but a shallower depth would have required elements with unacceptable aspect ratios near the surface. The effective viscosity and Maxwell time as a function of depth for model 1 are shown in Figure 4. Effective viscosity is shown with solid lines, and Maxwell time is shown with dashed lines. The thin lines represent the values determined from the temperature profile (75 mW/m^2) of Figure 2, while the thick lines represent the discrete values used in the finite element computations. Although this model contains only two different materials (granite and olivine), a number of layers occur in the finite element calculations due to the strong temperature dependence of rheological properties. Analysis of Figure 4 reveals that the upper crust and uppermost mantle would be expected to exhibit elastic behavior

TABLE 2*a*. Linear Model

Depth Range, km	Material Type	Temperature, °C	Viscosity Coefficient, Pa^n s	Effective Viscosity, Pa s	Maxwell Time, years
0-20	"elastic"	–	1×10^{33}	1×10^{33}	5.28×10^{14}
20-40*	"elastic"	–	1×10^{33}	1×10^{33}	5.28×10^{14}
20-40†	"viscoelastic"	–	2×10^{19}	2×10^{19}	10.6
40-400	"viscoelastic"	–	2×10^{19}	2×10^{19}	10.6

Tables 2*a*–2*e* list properties of the various models. Elastic and viscoelastic parameters used are listed in Table 1. Effective viscosity and Maxwell time were calculated assuming a strain rate of 2×10^{-14} s^{-1}.

*H = 40 km.

†H = 20 km.

TABLE 2*b*. Nonlinear Model 1

Depth Range, km	Material Type	Temperature, °C	Viscosity Coefficient, Pa^n s	Effective Viscosity, Pa s	Maxwell Time, years
0-20	dry granite	270	1.57×10^{36}	1.82×10^{21}	2880
20-40	dry granite	700	4.89×10^{31}	5.08×10^{19}	80.5
40-60	dry olivine	850	3.84×10^{40}	1.46×10^{21}	743
60-100	dry olivine	1150	2.18×10^{35}	4.64×10^{19}	23.5
100-250	dry olivine	1350	8.28×10^{32}	9.44×10^{18}	4.79
250-400	dry olivine	1400	2.53×10^{32}	6.73×10^{18}	3.42

TABLE 2*c*. Nonlinear Model 2

Depth Range, km	Material Type	Temperature, °C	Viscosity Coefficient, Pa^n s	Effective Viscosity, Pa s	Maxwell Time, years
0-20	dry granite	270	1.57×10^{36}	1.82×10^{21}	2880
20-40	dry diabase	700	5.72×10^{37}	3.65×10^{20}	362
40-60	dry olivine	850	3.84×10^{40}	1.46×10^{21}	743
60-100	dry olivine	1150	2.18×10^{35}	4.64×10^{19}	23.5
100-250	dry olivine	1350	8.28×10^{32}	9.44×10^{18}	4.79
250-400	dry olivine	1400	2.53×10^{32}	6.73×10^{18}	3.42

TABLE 2*d*. Nonlinear Model 3

Depth Range, km	Material Type	Temperature, °C	Viscosity Coefficient, Pa^n s	Effective Viscosity, Pa s	Maxwell Time, years
0-20	dry granite	270	1.57×10^{36}	1.82×10^{21}	2880
20-40	wet diabase	700	4.13×10^{33}	1.37×10^{20}	136
40-60	dry olivine	850	3.84×10^{40}	1.46×10^{21}	743
60-100	dry olivine	1150	2.18×10^{35}	4.64×10^{19}	23.5
100-250	dry olivine	1350	8.28×10^{32}	9.44×10^{18}	4.79
250-400	dry olivine	1400	2.53×10^{32}	6.73×10^{18}	3.42

TABLE 2*e*. Nonlinear Model 4

Depth Range, km	Material Type	Temperature, °C	Viscosity Coefficient, Pa^n s	Effective Viscosity, Pa s	Maxwell Time, years
0-20	wet granite	270	2.39×10^{24}	5.23×10^{20}	829
20-40	wet diabase	700	4.13×10^{33}	1.37×10^{20}	136
40-60	wet dunite	850	3.56×10^{36}	1.61×10^{20}	81.9
60-100	wet dunite	1150	1.58×10^{32}	8.46×10^{18}	4.29
100-250	dry olivine	1350	8.28×10^{32}	9.44×10^{18}	4.79
250-400	dry olivine	1400	2.53×10^{32}	6.73×10^{18}	3.42

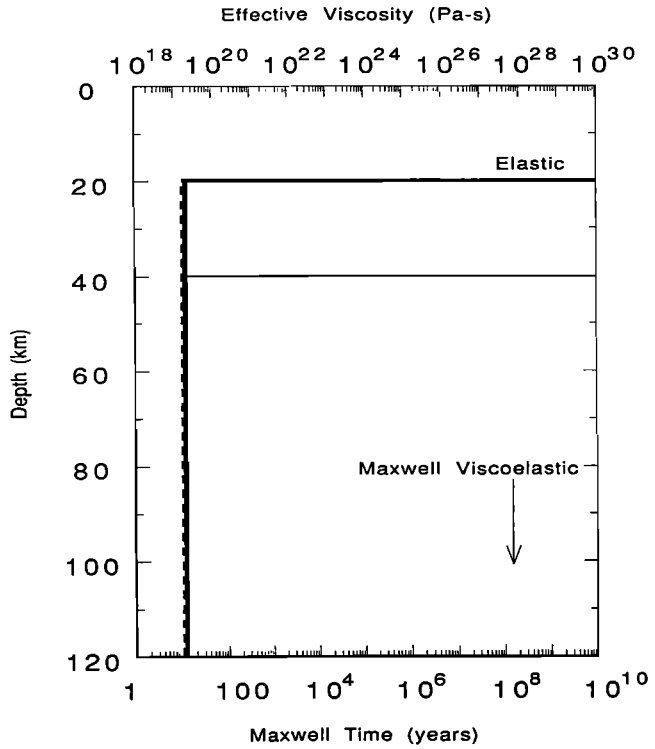

Fig. 3. Effective viscosity and Maxwell time for the linear models as a function of depth. Solid lines represent effective viscosities, and dashed lines represent Maxwell times. Thick lines are the profiles for models with H = 20 km (B models), and thin lines are the profiles for models with H = 40 km (A models).

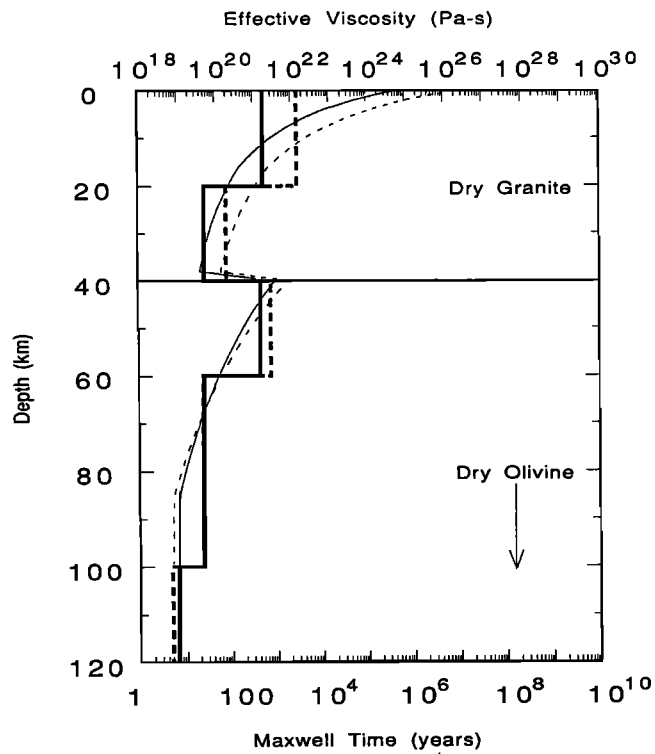

Fig. 4. Effective viscosity and Maxwell time for the nonlinear model 1 as a function of depth. Solid lines represent effective viscosities, and dashed lines represent Maxwell times. Thin lines represent the profiles calculated from the 75 mW/m^2 geotherm of Figure 2, and thick lines represent the discretized versions used in the finite element calculations.

over the time period of interest (150 years). The lower crust, on the other hand, has a Maxwell time of the order of the earthquake recurrence interval and would thus be expected to display some time-dependent behavior. Viscous behavior would also be expected from the mantle below 60 km depth.

The second nonlinear model (Table 2*c* and Figure 5) perhaps represents a more realistic view of actual Earth rheology. This model has rheological properties consistent with a granite upper crust and a diabase lower crust. The behavior of the mantle is consistent with laboratory results on dry olivine, as in model 1. The crustal layering results in two viscosity minima within the crust. Unfortunately, our finite element mesh is too coarse for this level of detail. For this model, time-dependent behavior would be restricted primarily to the mantle below 60 km (see Figure 5). Even ignoring the discretization effects, this model would display considerably less time dependence than model 1, since the Maxwell time at the base of the crust is considerably greater than model 1 (compare Figures 4 and 5).

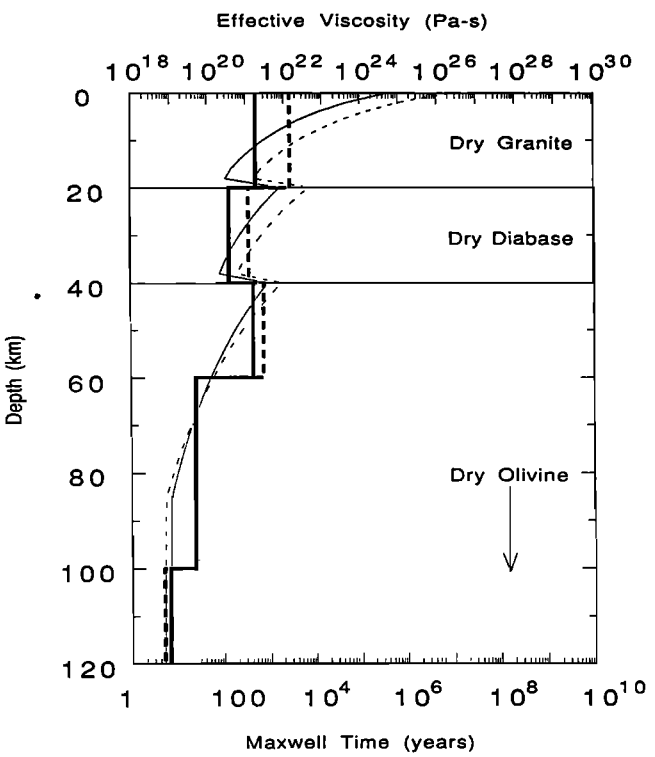

Fig. 5. Same results as Figure 4 for nonlinear model 2.

Models 1 and 2 describe completely dry rheologies; however, the presence of water can have a significant effect on viscous flow. This effect is included in model 3 (Table 2*d*), which includes laboratory results for wet diabase in the lower crust. The existence of water in the lower crust is somewhat debatable, but there is enough evidence for hydration at depth that it cannot be ruled out as a possibility (see *Strehlau and Meissner* [1987] for a summary). In this study, it is of interest to determine the effects of hydrated minerals on the model response. As may be seen from Figure 6, the presence of water has a significant effect on the rheological properties of diabase. The resulting profiles are similar to those of model 1, with a viscous layer in the lower crust sandwiched between the elastic layers in the upper crust and mantle. The time-dependent characteristics of models 1 and 3 should be similar.

The final model, model 4 (Table 2*e* and Figure 7), considers the entire crust and upper mantle to be hydrated to a depth of 100 km. The use of rheological properties for wet dunite in the

upper mantle results in a smaller difference between the behavior of the lower crust and upper mantle (compare Figure 7 with Figures 5 and 6). As a result, the discretized profile used in the finite element calculations does not include a low viscosity layer between the upper crust and lower mantle; instead it includes a fairly constant effective viscosity from 20 to 60 km depth. Below 100 km, the assumed rheology is that of dry olivine, as in the previous models. The relatively low effective viscosities down to 100 km depth should produce significant time-dependent effects. All of the models extend to a depth of 400 km, but only the first 120 km are shown in Figures 3–7. All of the models exhibit the same rheological behavior below 100 km depth, except for the linear models. Below 100 km, there is very little change in the effective viscosity because of the relatively shallow slope of the mantle adiabat (0.4°K/km) below this depth.

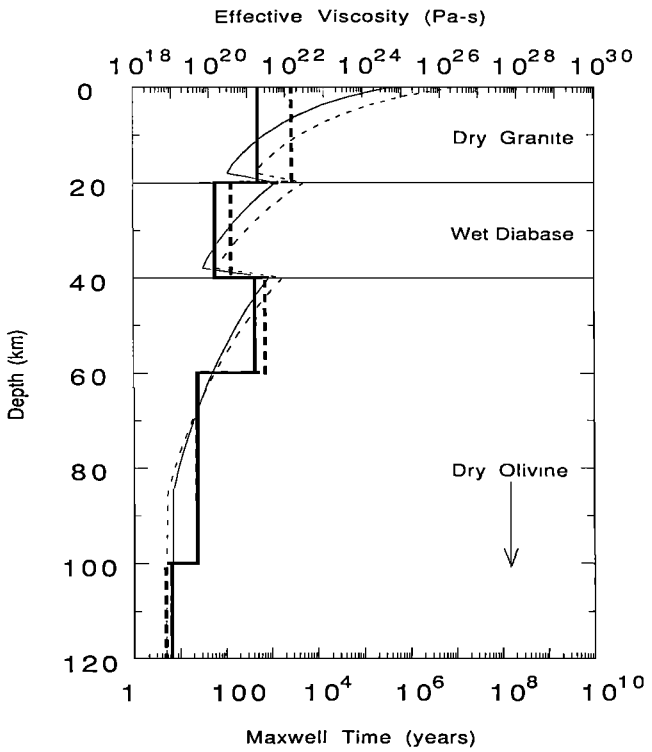

Fig. 6. Same results as Figure 4 for nonlinear model 3.

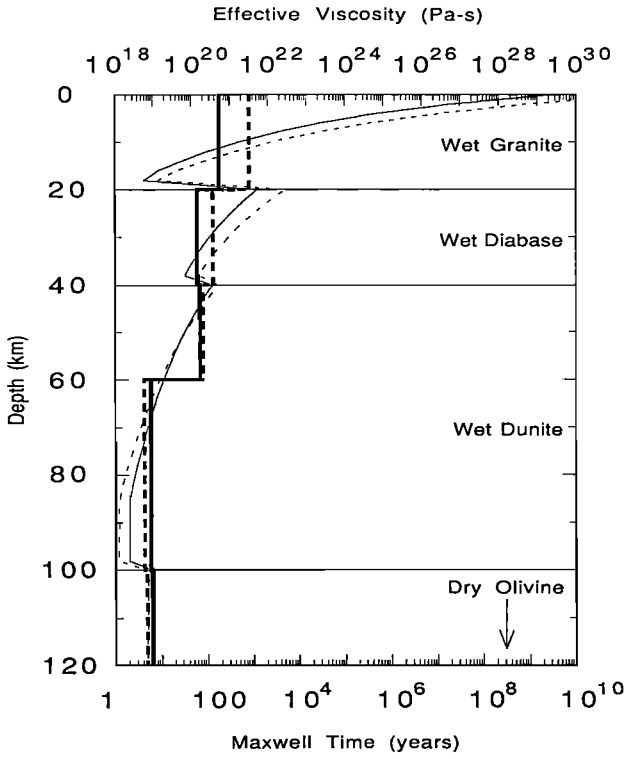

Fig. 7. Same results as Figure 4 for nonlinear model 4.

To evaluate the degree to which uncertainties in the temperature profile are propagated into the viscosity model, effective viscosities for model 4 were calculated for the two alternate temperature profiles shown in Figure 2. These results are shown in Figure 8. The results assuming a surface heat flow of 85 mW/m^2 (thin dotted line in Figure 2) are shown with a thin dotted line, and those for a surface heat flow of 65 mW/m^2 (thin dashed line in Figure 2) are shown with a thin dashed line. The viscosity profile representing the physical model upon which the finite element models are based (thin solid line) and the discrete representation of this profile used in the finite element models (thick solid line) are also shown. These results demonstrate that an uncertainty in the observed heat flow of 10 mW/m^2 can cause the effective viscosity to vary over almost 2 orders of magnitude for this particular model. This effect is most prominent near the base of the upper crust and gradually decreases with depth. Model results should therefore be interpreted very carefully, due to the large amount of uncertainty introduced by the strong temperature dependence of effective viscosity.

In all of the models, there are sharp boundaries between different material types, while in the Earth these boundaries are almost certainly gradational. This problem is always encountered when attempting to describe continuous phenomena in the real world with a discrete numerical technique. Our analysis should describe the first-order effects of a rheologically layered Earth. Higher-order effects may be evaluated by refining the finite element mesh used in the modeling.

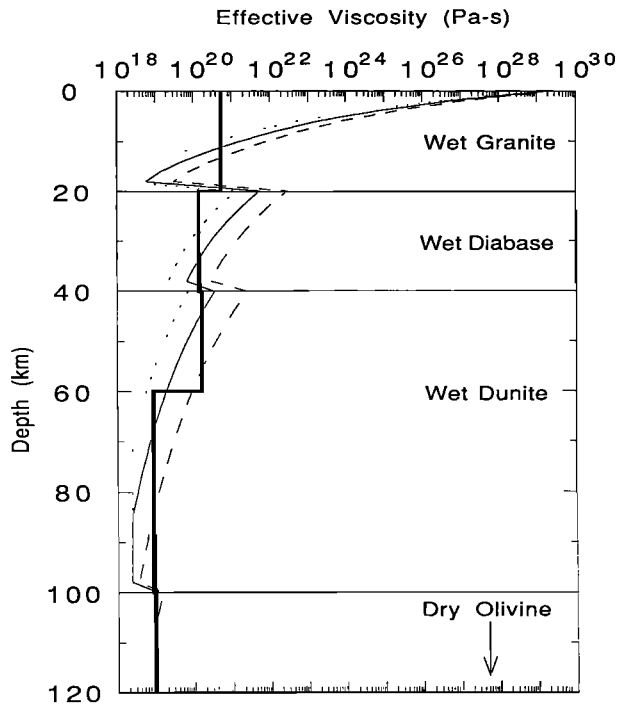

Fig. 8. Effective viscosity as a function of depth for nonlinear model 4 calculated for assumed surface heat flows of 65 mW/m^2 (thin dashed line), 75 mW/m^2 (thin solid line), and 85 mW/m^2 (thin dotted line). The thick solid line is the discretized profile used in the finite element calculations.

MODEL DESCRIPTION AND IMPLEMENTATION

Model Description

The models used in this study are derived from the infinite rectangular fault model described by *Savage and Prescott* [1978], as described previously and illustrated in Figure 1. The cross-sectional views shown in Figure 1 are understood to extend infinitely both into and out of the plane of the view. In practice, a half-space model may be adequately simulated by a numerical model with dimensions that are considerably greater than the thickness of the elastic layer. This procedure is followed in the present study, both in simulating the model of Figure 1*a* and in producing models of the type shown in Figure 1*b*. In both models, the fault is locked to a depth D between earthquakes. At time T (the earthquake recurrence time) coseismic displacement (U) occurs on the locked portion of the fault, with a magnitude determined by plate velocity. If plate motion is spatially uniform, occurring at a constant relative rate given by v_0 then $U = v_0T$. In the Savage and Prescott model, aseismic slip below the locking depth occurs to a depth H, which represents the thickness of the elastic layer. In the nonlinear models of this study, there is no elastic layer as such, and the parameter H instead represents the depth to which aseismic slip occurs. The aseismic slip rate between D and H is equal to the relative plate velocity.

The models in our study are completely three-dimensional, offering a number of advantages over two-dimensional models. First, our analysis is able to include the effects of both horizontally and vertically varying structures. In the present analysis, only horizontal variations (corresponding to changes in fault strike) are considered, as the variation of Earth structure with depth (i.e., changes in fault dip) is not well known. In any case, complex vertically varying geometries would not be warranted in this preliminary study. Another advantage of a three-dimensional analysis is the ability to calculate vertical as well as horizontal deformation. Although observations of vertical uplift along the San Andreas fault are presently restricted to a limited area and have large uncertainties, they could conceivably play an important role in resolving the differences between competing fault models (see *Stein* [1987], *Craymer and Vaníček* [1989], and *Stein et al.* [1989] for a discussion of the accuracy of vertical uplift measurements defining the "Palmdale uplift").

Calculation of Vertical Uplift

Although the calculation of vertical uplift with the finite element method is not difficult, it is important to consider a number of factors. Foremost among these are the effects of isostasy. Any uplift that occurs as a result of tectonic forces must be countered by isostatic forces proportional to the amount of uplift. If this were not true, tectonic uplift could continue indefinitely, resulting in infinite topography. Ordinarily, this would be the case in time-dependent finite element calculations, with or without the use of body forces. At each time step, uplift would proceed in a manner dictated by the present set of forces, regardless of the amount of uplift that had occurred in the previous time step. This is a result of the infinitesimal strain approximation used in most finite element calculations. All spatial quantities are referenced to the initial nodal positions, so that the entire grid geometry remains unchanged over the course of the calculations. Therefore, no matter how much vertical uplift has been induced by the applied boundary conditions, the system of body forces will be the same as it was initially.

A simple solution exists to remedy this problem that does not require major modifications to the finite element code. Isostasy in time-dependent problems may be simulated through the use of Winkler restoring forces (for an explanation, see Chapter 14 of *Desai* [1979]). This method has been incorporated into the finite element code by H. J. Melosh (unpublished computer program, 1988). These forces are essentially one-dimensional spring elements that are applied at the boundaries between density contrasts. The spring constant is chosen to be proportional to the magnitude of the density contrast. Therefore any vertical displacement increment away from the initial position results in a force in the opposite direction that is proportional to the density contrast and the amount of the displacement increment.

The situation is represented in Figure 9, which shows the case of a single layer with one-dimensional spring elements applied at the bottom and top of the layer. It is obvious that any vertical movement of the surface S_1 will be countered by a force increment k_1x, where k_1 is the spring constant for the upper set of springs and x is the vertical displacement increment. A similar situation exists for surface S_2. To simulate isostatic effects, it is only necessary to make the spring constants proportional to the corresponding density contrast. For the upper surface, this contrast would be $\Delta\rho_{10} = \rho_1 - \rho_0$. The contrast for the lower surface is $\Delta\rho_{21} = \rho_2 - \rho_1$. In the present finite element calculations, the surface S_1 represents the Earth's surface, and the surface S_2 represents the Moho; these are the two most prominent density contrasts in the lithosphere. For the sake of simplicity, these are the only density contrasts included in this analysis. The density contrast for surface S_1 would then be 3000 kg/m^3, while that for surface S_2 would be 300 kg/m^3 (see Table 1).

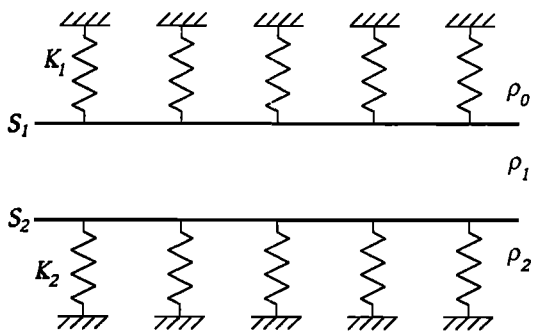

Fig. 9. Physical analogy of Winkler restoring forces. Springs with constants k_1 and k_2 are attached to surfaces S_1 and S_2.

In practice, the restoring forces are applied through a modification of the stiffness matrix. Assume, for the sake of simplicity, an element e with only two degrees of freedom. The local stiffness matrix for this simplified element is given by

$$K_{ij}^e = \begin{bmatrix} K_{11}^e & K_{12}^e \\ K_{21}^e & K_{22}^e \end{bmatrix} \tag{7}$$

Assume that K_{11}^e corresponds to the vertical degree of freedom for a node of element e that is contained in the surface S_1. Then the modified stiffness matrix including the restoring force is

$$K_{ij}^e = \begin{bmatrix} K_{11}^e + k_{11}^e & K_{12}^e \\ K_{21}^e & K_{22}^e \end{bmatrix} \tag{8}$$

The magnitude of k_{11}^e is given by

$$k_{11}^e = \frac{\Delta\rho_{10}\, g A_{S_1}^e}{n_{S_1}^e} \tag{9}$$

where $A_{S_1}^e$ is the area of element e contained in surface S_1, $n_{S_1}^e$ is the number of element nodal points in element e contained in S_1, and g is the gravitational acceleration (9.8 m/s^2). A similar situation exists for surface S_2.

The spring constant values are therefore added directly to the diagonal entries of the global stiffness matrix for the appropriate vertical degree of freedom. The sign of k^e_{11} is always positive, such that the restoring force acts in the direction opposite any displacement. Thus an upward displacement on surface S_1 (simulating the creation of new topographic highs) would result in a force directed downward, while a downward displacement of surface S_1 (resulting in a mass deficit) would produce an upward directed buoyancy force. For surface S_2 a downward displacement would simulate root formation, producing an upward directed buoyancy force, while an upward displacement would correspond to the production of a mass excess at depth, resulting in a downward directed force.

Body forces are not included in the calculations for several reasons. Foremost among these is the likelihood that the nontectonic (gravitationally induced) stresses in the crust and upper mantle approach a state of lithostatic stress [*McGarr*, 1988]. If this is true, the nontectonic deviatoric stress is zero everywhere in the Earth. Since the deformation is only affected by the deviatoric stress (recall that σ in (1)–(3) and (6) represents the differential stress), the gravitational body forces simply represent a depth-dependent pressure that can be removed from the calculations. Since this study is only concerned with deformation at the surface and not with stresses, body forces represent an unnecessary complication and are not included.

The present analysis does not include the effects of existing topography. The results are therefore valid for initially flat surfaces. In addition, the effects of erosion are not considered. Although both of these factors will influence the results, they were not included in the analysis for the sake of simplicity. Both of these effects may be included in more complex models.

Finite Element Modeling of the Problem

The finite element code used in this analysis is a three-dimensional adaptation of the two-dimensional code of *Melosh and Raefsky* [1980]. Fault slip is included by means of the split node technique [*Melosh and Raefsky*, 1981]. With this method, the fault displacement (or displacement increment) is specified. Using this technique, it is possible to apply either steady slip corresponding to plate velocity or abrupt slip at specified times. The split node method thus results in kinematic model behavior since the fault displacements are independent of the prevailing stress regime. A new method (the "slippery node" technique [*Melosh and Williams*, 1989]) allows fault slip to occur in response to stress and also allows fault friction to be specified. The use of this method would introduce an unnecessary degree of complexity to this preliminary investigation, however. At present, it is desirable to consider only rheological or geometrical parameters.

Two types of finite element calculations are performed. The first type of calculation assumes an infinitely long rectangular fault, analogous to the model of *Savage and Prescott* [1978]. This is done for two reasons. First, this allows a comparison of the numerical results with the analytical results of *Savage and Prescott* [1978] to test the accuracy of the numerical model. Second, this provides a simple means of examining the characteristics of the various models. The second type of calculation includes a more realistic representation of San Andreas fault geometry, with fault strike varying to match the observed strike of the fault. The grids used for the two types of calculations are similar, except for the assumed variation in fault strike. For the remainder of this paper, models that do not include variations in fault strike (infinitely long rectangular faults) will be referred to as "rectangular fault models," while those that include the effects of varying fault strike will be referred to as "San Andreas fault models."

The grid used for the rectangular fault models is shown in Figures 10*a* and 10*b*, and the grid incorporating San Andreas fault geometry is shown in Figures 11*a* and 11*b*. Figures 10*a* and 11*a* show map views of the grids and the imposed boundary conditions. The arrows represent velocity boundary conditions corresponding to the relative plate velocity and are applied to all nodes on the left- and right-hand sides of the grids

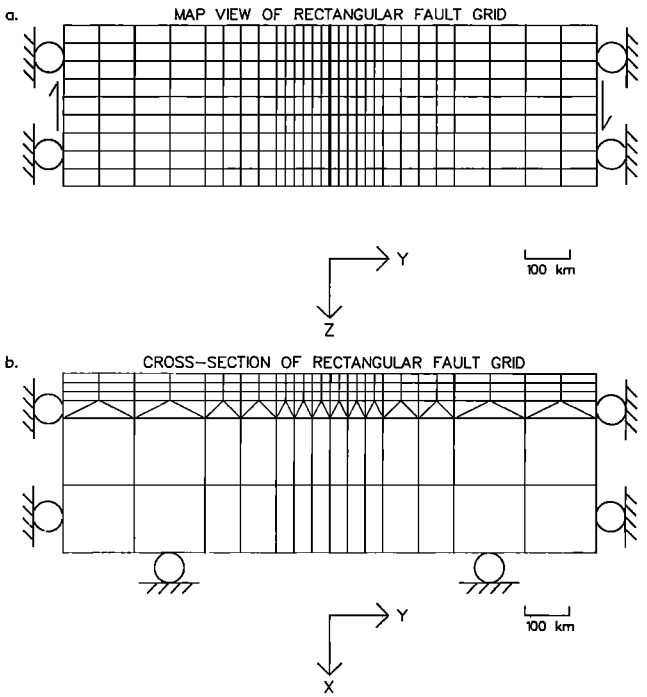

Fig. 10. Grid used in the rectangular fault modeling. The thick solid line represents the locked portion of the fault. (*a*) Map view. (*b*) Cross-sectional view.

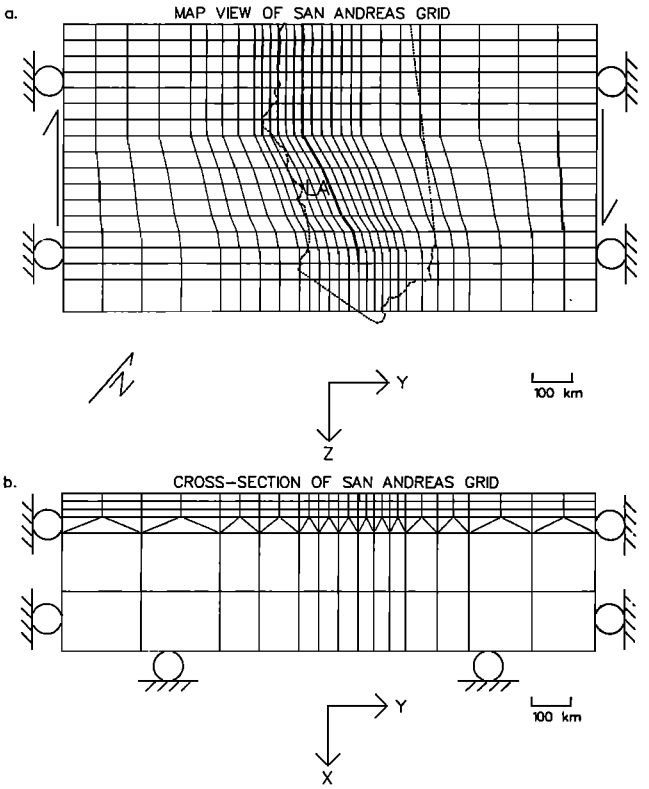

Fig. 11. Grid used in the models incorporating San Andreas fault geometry. The thick solid line represents the locked portion of the fault, and the dashed line represents the creeping section. (*a*) Map view. (*b*) Cross-sectional view of southern end of grid.

(corresponding to the minimum and maximum y values, respectively). The northern and southern boundaries of the grids (corresponding to the minimum and maximum z values, respectively) are left free. The thick, solid lines represent the portion of the fault that is locked between earthquakes. The dashed line on Figure 11*a* represents the creeping portion of the fault. Figures 10*b* and 11*b* are cross-sectional views of the grids. The thick, solid lines represent the locked portion of the fault. For B models, this line also represents the depth of aseismic slip, H (i.e., no aseismic slip). For A models, aseismic slip extends below this depth to the next layer of elements. The rheological properties are constant within each layer of elements (there are six layers). The San Andreas grid (Figure 11) is composed of 2618 three-dimensional elements containing 2898 nodal points. The x, y, and z dimensions are 400 km, 1350 km, and 720 km, respectively. The rectangular fault grid has x, y, and z dimensions of 400 km, 1200 km, and 360 km and contains 1386 elements and 1610 nodes. The smallest elements occur closest to the fault. These elements have dimensions of 20 km in the x and y directions and 40 km in the z direction.

The choice of element dimensions was dictated by three goals: keeping the elements as small as possible in the region of interest, making the elements as nearly equidimensional as possible, and using the minimum number of elements. The first goal arises from the desire to obtain maximum resolution in both the calculated deformation and the assigned material properties. The second goal is a result of the finite element formulation, in which the interpolations are performed for the idealized shape of a cube. The final goal reflects the limitations of the computer on which the calculations are performed. The present analysis was performed on a CONVEX C1, a vector processor with 32 megabytes of core memory. Although it was possible to use a finer mesh grid, the memory requirements of the resulting stiffness matrix exceeded the computer's capabilities. The memory swapping required to handle the stiffness matrix resulted in an excessively long calculation time. One solution to this problem is an alternate method of storing the stiffness matrix (sparse matrix techniques are presently being explored). The simplest method is to use a machine with a greater amount of core memory. The San Andreas fault models used in this study had run times of about 10 hours on a CONVEX C1.

The computer limitations place a number of constraints on the grid geometry. For instance, the maximum vertical resolution is 20 km, which occurs near the surface. For this reason, the fault locking depth (D) and the depth of aseismic slip (H) are constrained to values that are multiples of 20 km. In the calculations that follow, the locking depth will always be assumed to be equal to 20 km (except for the creeping portion of the fault, where $D = 0$), since earthquakes on the San Andreas are generally not observed below this depth. The depth of aseismic slip will be assumed to be either 20 km (no aseismic slip below the locking depth) or 40 km (aseismic slip between 20 and 40 km). On the creeping portion of the fault, aseismic slip occurs from the surface to the depth of aseismic slip, H. The changes in material properties are similarly constrained (see Tables 2*b*–2*e*). The horizontal resolution is also affected, which prevents the incorporation of adjacent faults into the present model. Although appreciable slip occurs on faults other than the San Andreas, it is presently not possible to include them in the analysis.

One assumption of this analysis is that the overall deformation field will be dominated by the largest magnitude earthquakes, with smaller earthquakes producing local perturbations in the overall pattern of deformation. For this reason, only the largest magnitude earthquakes which rupture a significant portion of the fault are included in the analysis. The last earthquake of such magnitude in southern California was the Fort Tejon earthquake of 1857, which had a magnitude greater than 8 and ruptured 360 to 400+ km of the fault [*Sieh*, 1978]. For simplicity, it is assumed that earthquakes with a relative coseismic displacement (U) of 5.25 m occur every 150 years, rupturing the entire fault from just south of Cholame to the southern end of the fault shown in Figure 11*a*, which is near the Salton Sea. This is the portion of the fault shown by the solid line in Figure 11*a*. The average recurrence time (T) of 150 years is consistent with the estimate of 132 years given by *Sieh et al.* [1989], determined by sediment analysis. The coseismic displacement in each earthquake is assumed to keep pace with the plate velocity. The assumed relative plate velocity ($v_0 = U/T$) is then 35 mm/year, which is applied parallel to the z axis (see Figures 9*a* and 10*a*). For the San Andreas calculations, the z axis is oriented N41°W, while for rectangular fault models the axis orientation has no particular meaning. These values are consistent with current geodetic and geologic determinations of motion on the San Andreas fault [*Minster and Jordan*, 1987; *DeMets et al.*, 1987]. Plate velocity is applied to a depth H below the locking depth on the fault, to simulate aseismic slip at depth. The results of *King et al.* [1987] indicate that shallow aseismic slip occurs near Cholame and increases with distance north of this location. To simulate this creeping portion of the fault, the locking depth is assumed to be zero for the fault segment between Hollister and Cholame (dashed section in Figure 11*a*). For this section, plate velocity is applied from the surface to a depth H.

Below the southern end of the San Andreas fault shown in Figure 11*a*, no slip is applied. The rectangular fault models, which use the grid shown in Figures 10*a* and 10*b*, do not include a creeping section or a permanently locked section. There are two extreme possibilities for the boundary conditions at the southern end of the San Andreas fault model: aseismic slip from the surface to a depth H, such that there is no accumulation of strain; or no slip at all, such that there is a secular buildup of strain. Although a number of arguments could be advanced for the first condition, we decided to apply the second condition to our models. The primary reason was the relative infrequency of large-magnitude earthquakes below the southern termination of the fault used in our model (Figure 11*a*). For example, *Wesnousky* [1986] indicates that no slip occurred along the Imperial fault for at least 700 years preceding the 1940 magnitude 6.9 earthquake. It is therefore clear that there is some strain accumulation in this region, although probably not as much as that used in our model. Over a sufficiently long time period, our boundary conditions would result in unreasonably large amounts of strain accumulation near the southern terminus of the fault; however, over the time period used in the modeling (1500 years), the strain accumulation is not excessive. When interpreting our model results, it should be recognized that the predicted strain magnitudes near the southern portion of the grid are probably greater than they should be. It is also important to realize that, because of the relatively coarse mesh of the finite element grid used for the calculations and because of the imposed slip boundary conditions, the deformation associated with the two bends in the fault is likely to be exaggerated as well. The coarse grid mesh results in relatively sharp fault bends. Thus, when slip is imposed, the sudden change in direction causes interference between material on either side of the fault. This effect would probably be reduced with a finer grid mesh and stress-dependent slip conditions.

In order to achieve steady state behavior, it is necessary to run the model through a number of earthquake cycles. After a sufficient number of cycles, the results for each cycle are identical. It was found that 10 earthquake cycles were generally sufficient to produce steady state model response. In the results that follow, all values are determined following the ninth earthquake in a sequence. For the nonlinear models, each earthquake cycle consists of 100 discrete time steps of 1.5 years each. For the linear models, it is possible to decrease the number of time steps without significantly affecting the accuracy of the results. Each earthquake cycle for these models is composed of 20 time steps. The size of the time steps ranges from 1.5 years near the beginning of the cycle (where the time dependence is greatest)

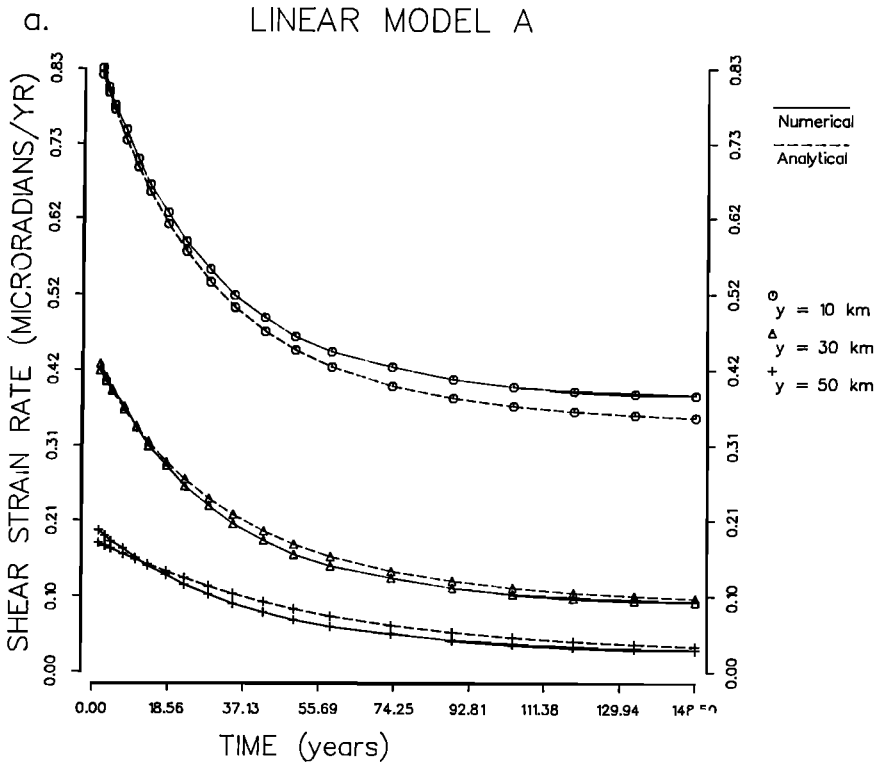

Fig. 12. Engineering shear strain rate as a function of time since the last earthquake for rectangular fault models at various distances from the fault. The finite element results are shown with solid lines, and the analytical solution is shown with dashed lines. The results are shown for (*a*) linear model A (H = 40 km) and (*b*) linear model B (H = 20 km).

to 15 years near the end of the cycle. It is not possible to substantially increase the size of the time steps for the nonlinear models because of numerical instabilities. This may be understood from an inspection of (1). Since the steady state strain rate is proportional to a power of the differential stress, a higher power law exponent means that the strain rate is more sensitive to the system of stresses. For materials with large power law exponents, it is therefore necessary to recalculate the stresses fairly frequently in order to accurately determine the strain rate. In other words, small time steps are necessary to successfully linearize a highly nonlinear problem.

RESULTS

Rectangular Fault Models

The quantities of interest for the rectangular fault models are values of horizontal shear strain rate parallel to the fault ($\dot{\gamma}_{yz}$ in Figure 10*a*). These values are calculated at various times since the last earthquake and various distances from the fault along a line perpendicular to the fault. Numerical results for a linear model are compared to an analytical solution to evaluate the accuracy of the finite element method. The analytical solution is obtained by taking spatial and time derivatives of the displacement equations given by *Savage and Prescott* [1978]. The results thus represent the out-of-plane strain rate for an infinitely long (into the plane) rectangular fault contained in an elastic layer overlying a Maxwell viscoelastic half-space. Figures 12*a* and 12*b* demonstrate how well the numerical results match the analytical solution. These are plots of shear strain rate ($\dot{\gamma}_{yz}$) versus time since the last earthquake at various distances from the fault. The units of shear strain rate in these plots are microradians per year, following the engineering convention. For the San Andreas results, all units will be in terms of microstrain per year, and shear strain rate ($\dot{\epsilon}_{yz}$) will thus be a tensor quantity (engineering shear strain rate, a scalar quantity, is twice the tensor shear strain rate). Both of these figures represent models with an elastic layer of thickness H containing a fault locked to a depth D = 20 km overlying a Maxwell viscoelastic half-space with a viscosity of 2×10^{19} Pa s. Figure 12*a* depicts the results for a model in which aseismic slip extends to a depth H = 40 km, while Figure 12*b* shows the results for a model in which there is no aseismic slip at depth (H = 20 km). Recall that for models of the type described by *Savage and Prescott* [1978] and *Thatcher* [1983], the parameter H, in addition to describing the depth to which aseismic slip occurs, also defines the thickness of the surface elastic layer. Thus the model described by Figure 12*a* (which will be referred to as linear model A) has an elastic layer with a thickness of 40 km, while that described by Figure 12*b* (linear model B) has an elastic layer thickness of 20 km.

The numerical results provide an excellent approximation to the analytical solution, as demonstrated by Figures 12*a* and 12*b*. The model with H = 40 km (Figure 12*a*) displays less time dependence close to the fault than does the model with H = 20 km (Figure 12*b*). This is consistent with the results of *Thatcher* [1983], who indicated that the influence of the viscoelastic half-space becomes greater as the thickness of the elastic layer is decreased.

To explore the effects of nonlinear rheologies on model results, four types of nonlinear models were used, with the rheological parameters given in Tables 2*b*–2*e* and Figures 4–7. There are two versions of each nonlinear model: those with H = 40 km (A models) and those with H = 20 km (B models). The engineering shear strain rate ($\dot{\gamma}_{yz}$) versus time since the last earthquake for model 1A (solid line) and model 1B (dashed line) is shown in Figure 13. These models, which assume a granite crust overlying an olivine mantle (see Figure 4), display less time dependence than the linear models. In addition, the effects of aseismic slip are much less noticeable than in the linear models, particularly close to the fault. Most available geodetic observations lie fairly close to the fault, and most of the

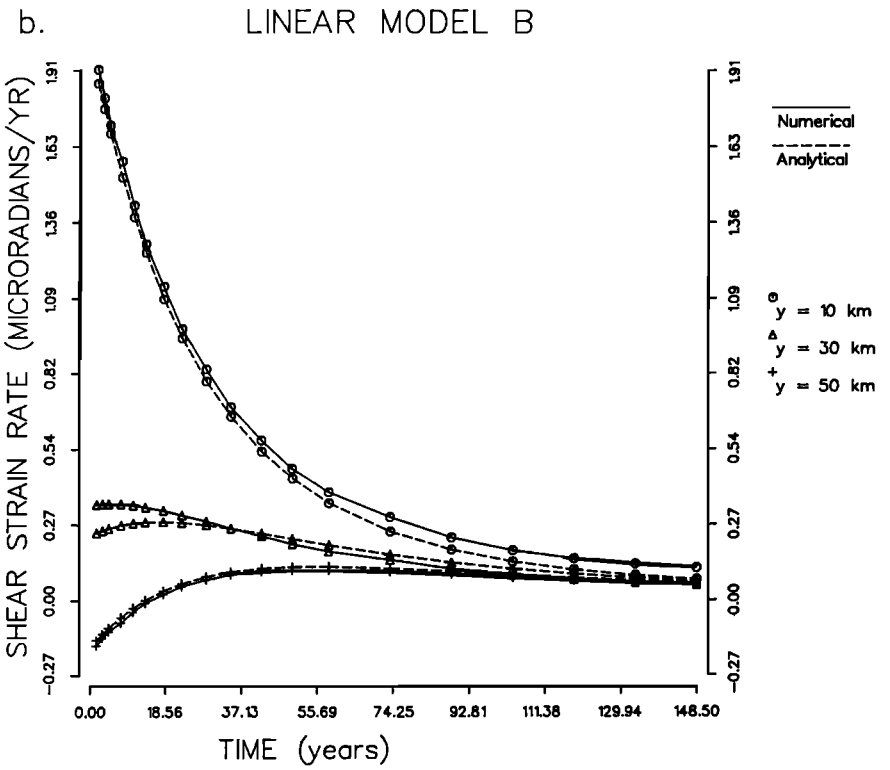

Fig. 12. (continued)

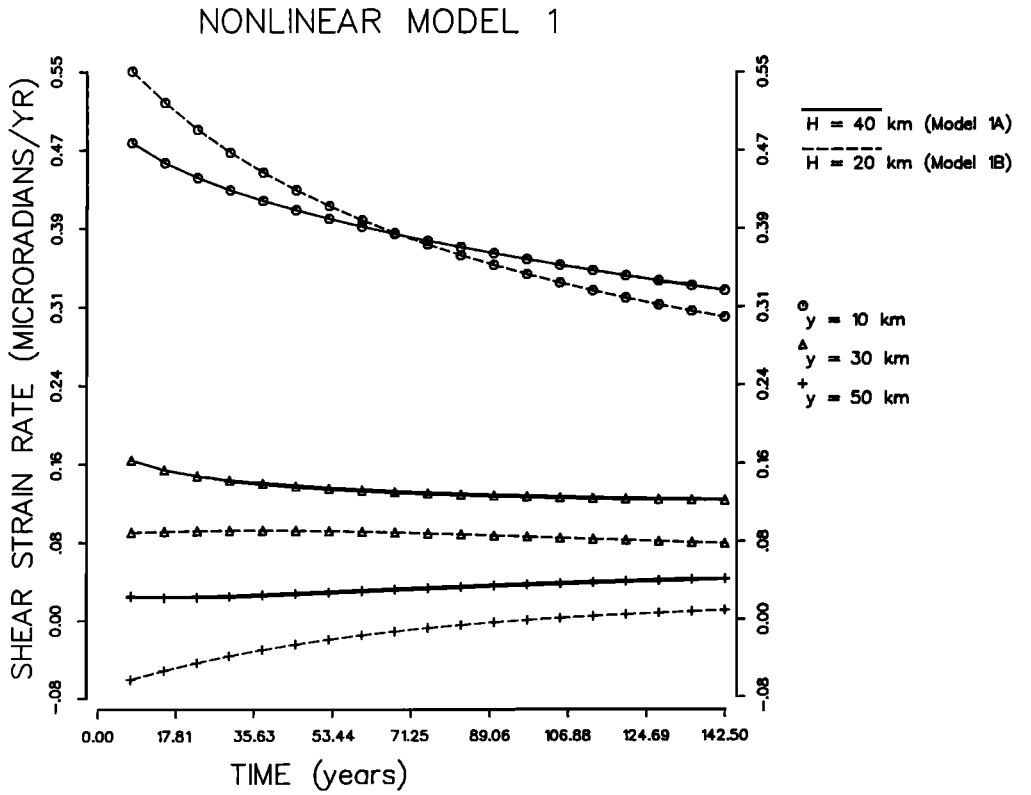

Fig. 13. Engineering shear strain rate as a function of time since the last earthquake for nonlinear model 1 (rectangular fault) at various distances from the fault. The solid lines represent the results for nonlinear model 1A (H = 40 km), and the dashed lines represent the results for nonlinear model 1B (H = 20 km).

accurate observations have been made relatively recently. If the 1857 earthquake is considered to be the time origin for this plot, then a time of 130 years would correspond to the year 1987, fairly close to the present. At a distance of 10 km from the fault and a time of about 130 years in Figure 13, there is very little difference in the predicted shear strain rate for models 1A and 1B. Therefore, although it might be possible to differentiate between these two models early in the earthquake cycle based

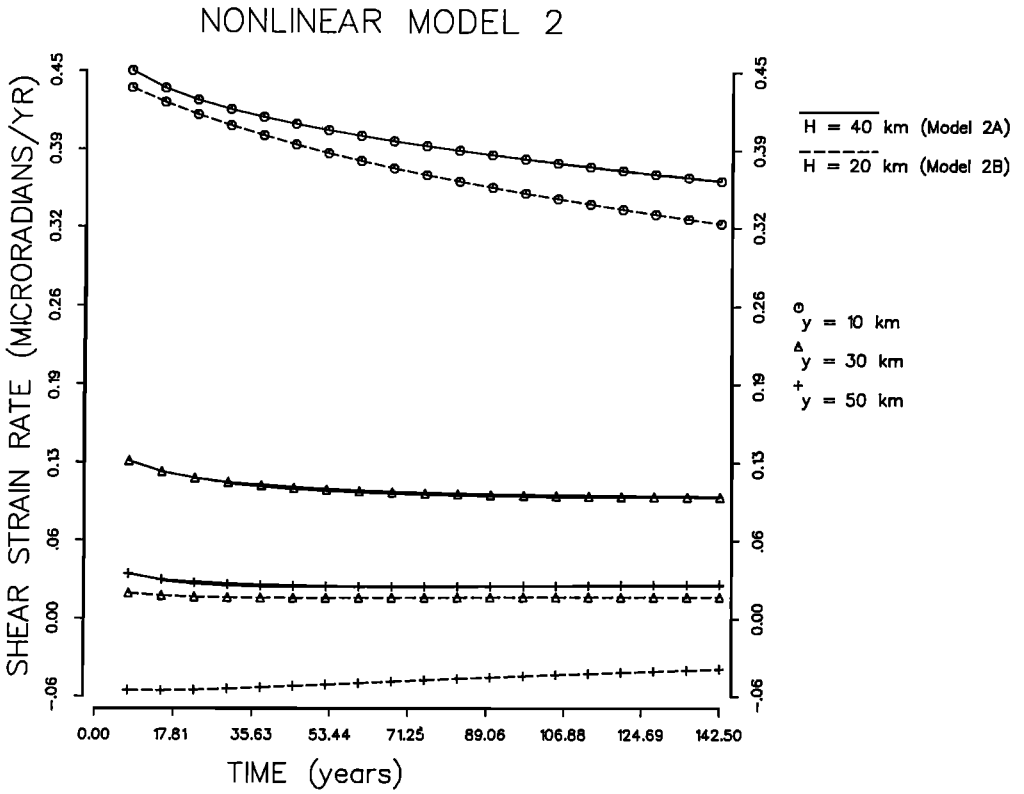

Fig. 14. Same results as Figure 13 for nonlinear model 2.

only on horizontal strain rate information, it would be difficult to do so at the present position within the earthquake cycle.

The characteristics of models 2A and 2B are demonstrated in Figure 14. As expected, these models display less time dependence than do models 1A and 1B (compare Figures 4 and 5). The presence of aseismic slip at depth (solid lines in Figure 14) appears to result in a higher shear strain rate, and this effect increases with distance from the fault. The same is generally true of models 1A and 1B (Figure 13), except for very close to the fault at times early in the earthquake cycle.

This same trend is observable for models 3A and 3B (Figure 15). In this case, aseismic slip at depth results in a higher shear strain rate at all times. Comparison of Figures 14 and 15 indicates that models 2A and 3A predict virtually identical shear strain rates at all times and distances from the fault. Model 1A (Figure 13) also predicts shear strain rates similar to models 2A and 3A, but the magnitude varies more with time. The corresponding models that do not include aseismic slip at depth (models 1B, 2B, and 3B) differ significantly, however. This seems to indicate that aseismic slip at depth may have a greater influence over the observed deformation than the rheological properties if the properties are not significantly different. The extent to which the results are influenced by aseismic slip at depth would probably be reduced if the slip were a calculated response rather than an imposed condition, however. These three model types are very similar in their viscoelastic properties, differing only in the lower crust.

Models 4A and 4B (Figure 16) provide ample evidence of the importance of rheological properties. The shear strain rate patterns predicted by these two models do not resemble those of any of the other models. In general, the predicted shear strain rates for models 4A and 4B are much higher than for the other models. Models 4A and 4B have significantly different properties in the upper crust and upper mantle than the other nonlinear models. Therefore, although the presence of aseismic slip at depth may control the observed deformation over a limited range of rheological properties, knowledge of the variation of rheological properties with depth is of primary importance in determining predicted deformation patterns.

The linear models (A and B) display a greater time dependence than do any of the nonlinear models. This is due to the fact that the linear models have a lower effective viscosity than the nonlinear models at depths less than 60 km (see Tables 2*a*–2*e*). Since time-dependent behavior is dominated by the viscosities at relatively shallow depths, the linear models are more affected by viscous behavior. The models that display the greatest time dependence (besides the linear models) are models 1A and 1B and models 4A and 4B. Models 1A and 1B have the shortest Maxwell time at depths from 20 to 40 km (see Figure 4 and Table 2*b*), while models 4A and 4B have the shortest Maxwell time from 0 to 20 km and 40 to 100 km depth (see Figure 7 and Table 2*e*). Results from other models (not shown here) indicate that changes in the Maxwell time below 100 km depth have no appreciable effect on the predicted deformation. With the temperature profile assumed for this analysis, the Maxwell time at depths greater than 100 km is less than 10 years, so the mantle below this depth should behave as a fluid over the time period of interest (150 years). The determination of the viscosity profile within 100 km of the Earth's surface is thus of primary importance in providing accurate models of the earthquake cycle on the San Andreas fault.

Through analysis of Figures 12–16, it should be possible to determine which models will be distinguishable on the basis of strain rate observations close to the fault at times close to the present. Linear model A and nonlinear models 1A, 1B, 2A, 2B, 3A, and 4B all predict similar strain rates at a distance of 10 km from the fault and a time of 130 years since the last earthquake in the area. Thus it is difficult to distinguish between these models based only on current strain rate observations that lie close to the fault. Linear model B and nonlinear model 3B predict significantly lower shear strain rates, while nonlinear model 4A predicts a higher shear strain rate. These models

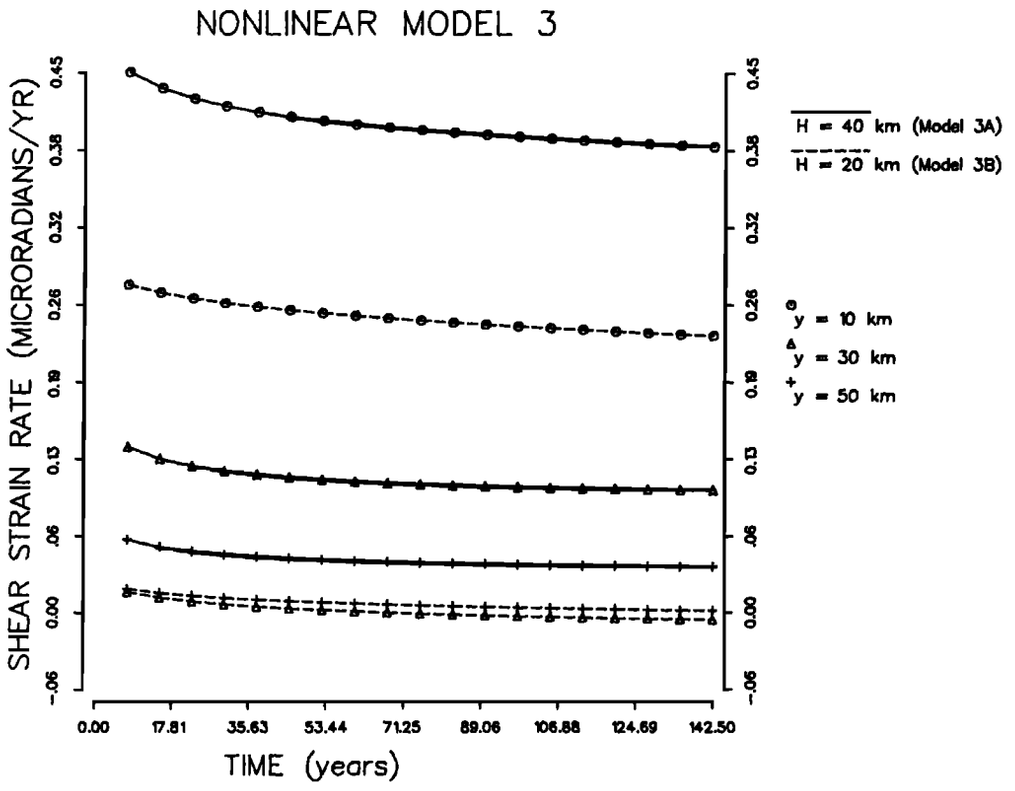

Fig. 15. Same results as Figure 13 for nonlinear model 3.

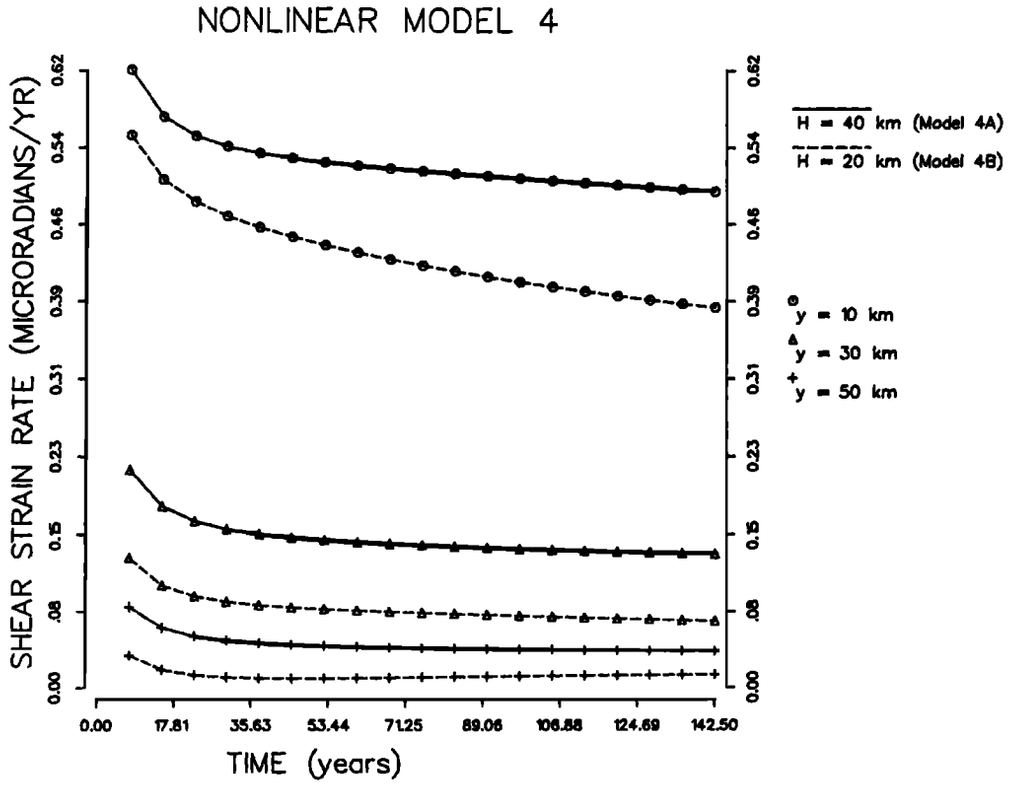

Fig. 16. Same results as Figure 13 for nonlinear model 4.

should thus be relatively simple to distinguish on the basis of strain rate observations. To test this hypothesis, it is useful to look at models which provide a better representation of actual San Andreas fault geometry.

Strain Rate Results for Models That Include Fault Geometry

For each of the models described in the previous section, results were calculated for a corresponding model that included

TABLE 3. Observed Values of Strain Rate Determined From Trilateration Results, and the Time Periods Over Which Measurements Were Taken

Network	$\dot{\varepsilon}_{11}$	$\dot{\varepsilon}_{22}$	$\dot{\varepsilon}_{12}$	Interval	Source
Salton	0.18 ± 0.01	−0.16 ± 0.01	−0.025 ± 0.005	1972–1984	*Savage et al.* [1986]
Anza	0.15 ± 0.01	−0.15 ± 0.01	0.005 ± 0.005	1973–1984	*Savage et al.* [1986]
Cajon	0.13 ± 0.03	−0.16 ± 0.02	0.095 ± 0.015	1974–1984	*Savage et al.* [1986]
Tehachapi	0.15 ± 0.01	−0.11 ± 0.01	0.060 ± 0.005	1973–1984	*Savage et al.* [1986]
Los Padres	0.12 ± 0.01	−0.14 ± 0.01	0.005 ± 0.005	1973–1984	*Savage et al.* [1986]
Carrizo	0.29 ± 0.06	−0.09 ± 0.06	−0.010 ± 0.030	1977–1981	*Savage* [1983]

The units of strain rate are in microstrain per year. The shear strain rate is thus a tensor quantity and does not follow engineering convention.

the variations in strike observed along the San Andreas fault. These computations were performed using the grid of Figures 11*a* and 11*b*, with the boundary conditions given in the section on finite element modeling of the problem. The observations of interest are determinations of horizontal strain rate. A number of such observations exist from a variety of sources. Most current observations are obtained from U.S. Geological Survey trilateration networks. These values are calculated by inverting a number of line-length changes within a network to obtain strain values. These calculations are performed at various times within an interval to provide an average strain rate for the interval. The methods used in determining strain rate are discussed by *Savage et al.* [1981, 1986]. The observations used in this study for comparison to predicted results are trilateration results determined from geodolite surveys of a number of networks [*Savage*, 1983; *Savage et al.*, 1986]. The values used in this analysis, the time period for which the results were obtained, and their corresponding standard deviations are listed in Table 3.

The results from six different networks are used in this analysis. The networks used are Salton, Anza, Cajon, Tehachapi, Los Padres, and Carrizo. In calculating the predicted values, it is necessary to take into account the area covered by each network. An approximate solution to this problem is as follows. First, the individual line locations for each network are obtained (those for this analysis were obtained from *Savage et al.* [1986] and W. Prescott (personal communication, 1990)). The strain rate is determined by averaging over the elements which contain any portion of a survey line. The weight assigned to each element is determined by the number of lines which pass through it. In addition, if a line passes through more than one element, the weight due to this line is divided equally between the elements through which it passes. This procedure provides a reasonable simulation of the method by which the strain rate observations are made; however, there will be some problems associated with the coarseness of the finite element grid. The strain rate magnitude falls off very quickly with distance from the fault, so any inaccuracies in the weighting of a particular element could have an appreciable effect on the predicted strain rate.

To determine how the predicted strain rate changes with time, it is necessary to observe the predicted values both early and late in the earthquake cycle. This is done in Figures 17–21. The first of each of these figures (Figures 17*a*, 18*a*, 19*a*, 20*a*, and 21*a*) represents the principal axes of strain rate at a time early in the earthquake cycle. For the linear models (Figure 17*a*), this time is 13.5 years since the last great earthquake in the area. Measuring from the 1857 earthquake, this corresponds to the year 1870.5. Figures 18*a*, 19*a*, 20*a*, and 21*a* depict the principal axes of strain rate at a time of 15 years since the last great earthquake (1872, as measured from the 1857 earthquake) for the nonlinear models. The lines with arrows on the end signify the principal axes of extension, while those with no arrows denote the principal axes of contraction. The axes with solid arrowheads (on the west side of the fault for each plot) represent models with no aseismic slip at depth (H = 20 km, or B models),

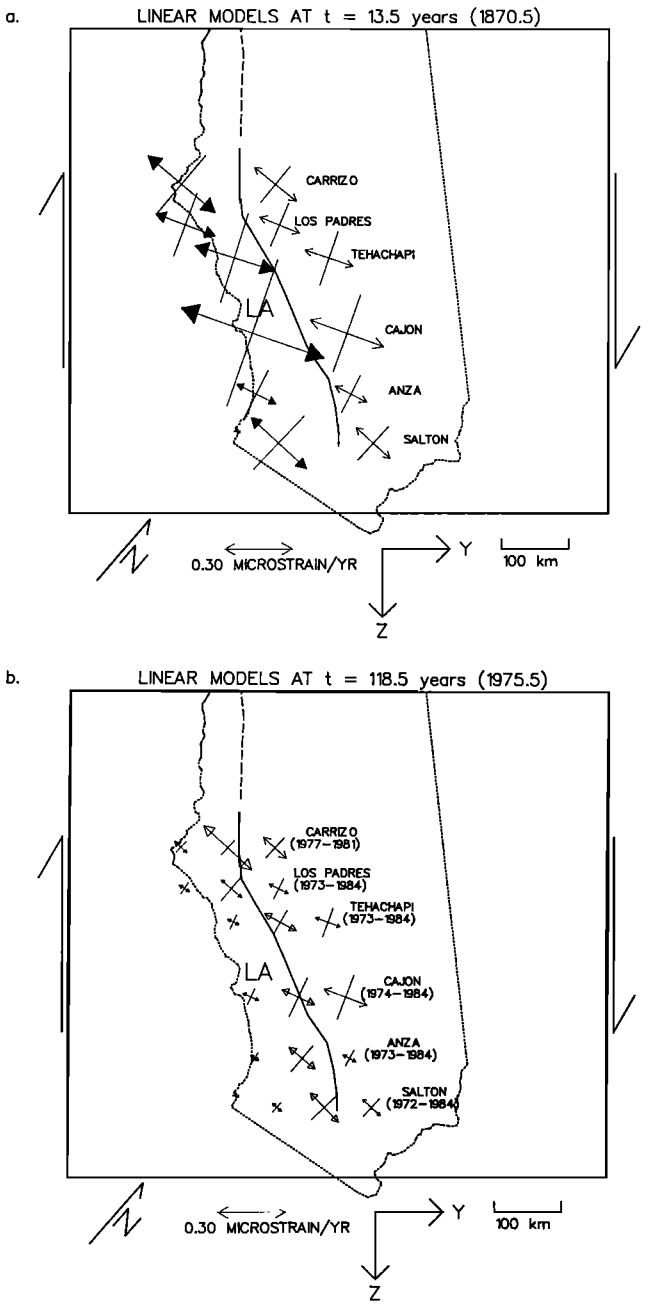

Fig. 17. Principal axes of strain rate for the linear models at (*a*) t = 13.5 years (1870.5) and (*b*) t = 118.5 years (1975.5). Arrows denote extension, and straight lines represent contraction. Axes with plain arrows (on the east side of the fault) are results for models with H = 40 km (A models). Axes with solid arrows (on the west side of the fault) are results for models with H = 20 km (B models). Axes with open arrows (in the center, shown only for t = 118.5 years) are trilateration results for the time periods listed in the legends to the right.

while those with plain arrowheads (on the east side of the fault) are the axes for models with $H = 40$ km (A models). To the right of the principal axes are the names of the corresponding trilateration networks.

The principal axes at a time close to the present are shown in Figures 17*b*, 18*b*, 19*b*, 20*b*, and 21*b*. For the linear models (Figure 17*b*), the axes are shown for a time of 118.5 years since the last great earthquake, corresponding to the year 1975.5. The results for the nonlinear models (Figures 18*b*, 19*b*, 20*b*, and 21*b*) show the principal axes at a time of 120 years since the last earthquake, which translates to the year 1977. Also shown in Figures 17*b*–21*b* are the observed values of strain rate determined from trilateration results (open arrowheads, between the two sets of predicted values). The locations of the principal axes denoting the observed values represent the approximate locations of the centroids of the networks. At the right are shown the network names and the time periods over which the observed values were calculated. It will be noted that the time periods for the observed and predicted results do not coincide exactly. This should not have a significant effect, however, since the strain rate does not change appreciably between adjacent time steps late in the earthquake cycle (see Figures 12–16).

Based on our previous analysis of the rectangular fault results shown in Figures 12–16, it should be possible to make some predictions about the model characteristics demonstrated in Figures 17–21. For example, the greatest time dependence should be displayed by the linear models and by nonlinear models 1 and 4. The linear models (Figures 17*a* and 17*b*) clearly display the greatest time dependence, with a dramatic decrease in the magnitude of the strain rate with time. This is particularly true for linear model B, which does not include aseismic slip at depth. This behavior could have been deduced from an analysis

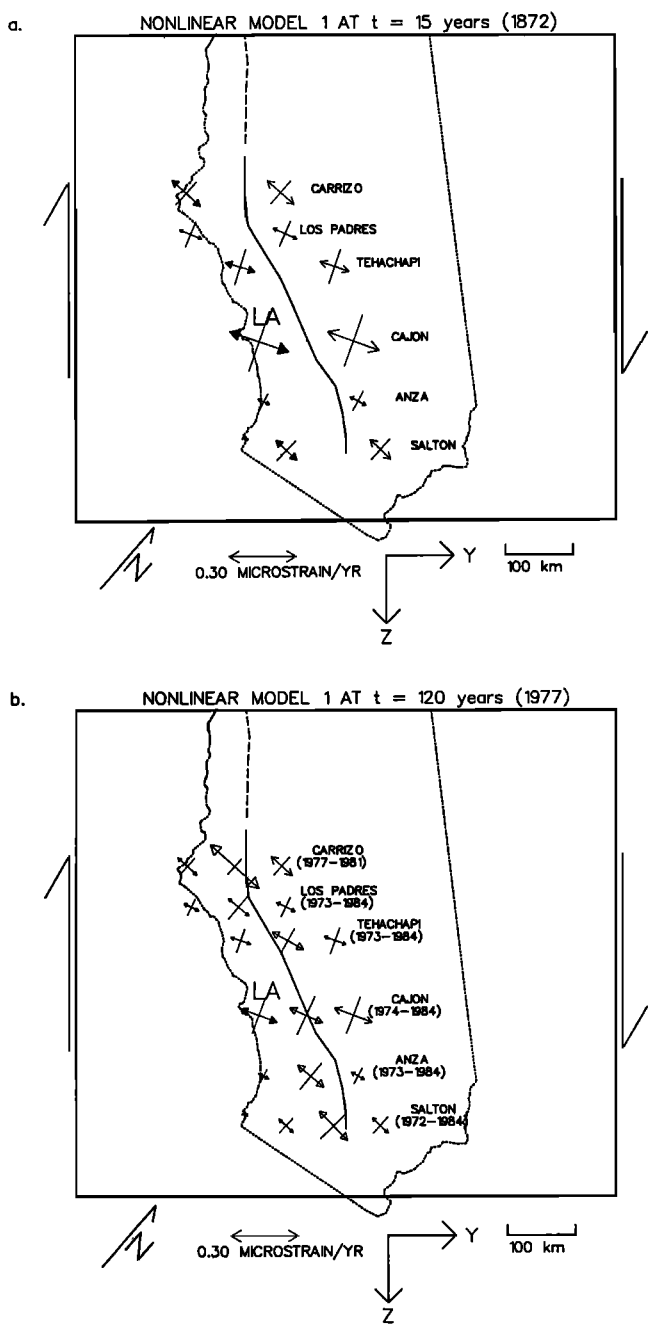

Fig. 18. Principal axes of strain rate for nonlinear model 1 at (*a*) $t = 15$ years (1872) and (*b*) $t = 120$ years (1977), using the same notation as Figure 17.

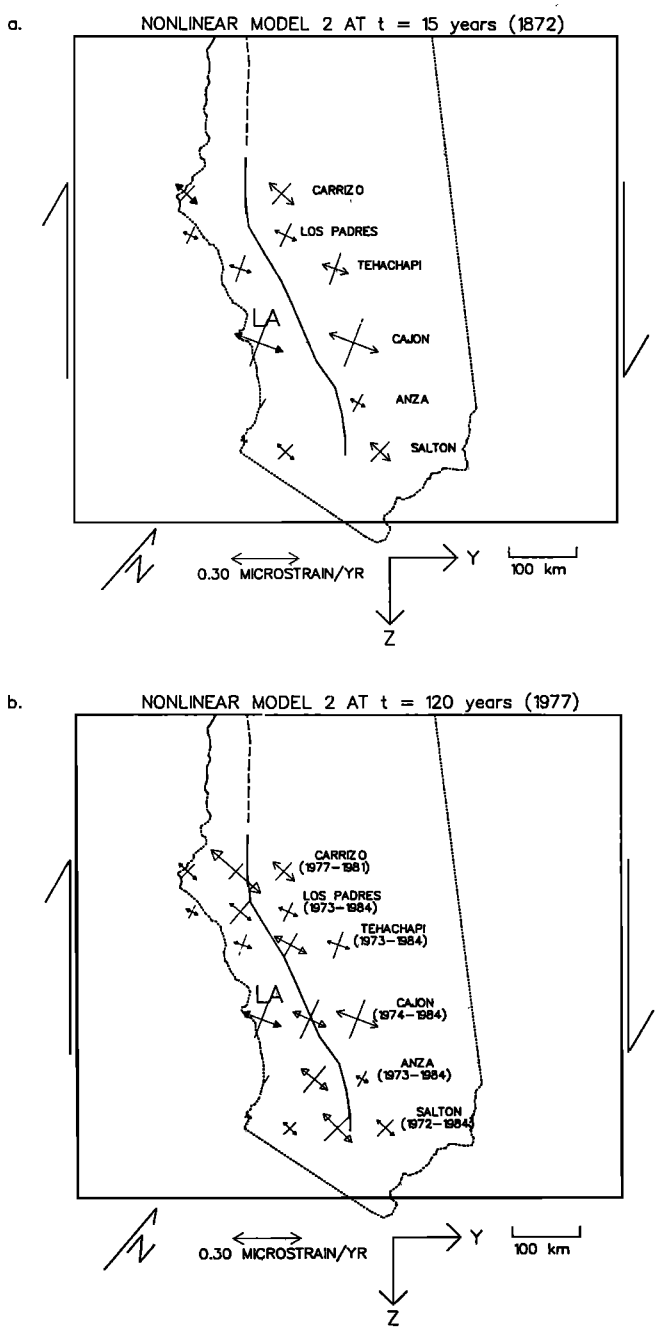

Fig. 19. Principal axes of strain rate for nonlinear model 2 at (*a*) $t = 15$ years (1872) and (*b*) $t = 120$ years (1977), using the same notation as Figure 17.

of Figures 12*a* and 12*b*. Inspection of Figures 18 and 21 reveals that nonlinear models 1 and 4 display a greater time dependence than the other nonlinear models, as anticipated from the analysis of rectangular fault models. Again, the effect is more pronounced for models which do not include aseismic slip at depth. Analysis of the rectangular fault models also indicates that nonlinear model 4 should produce strain rates that are greater in magnitude than the other models, which is again supported by the results of the San Andreas fault models (see Figures 16 and 21). The results of the rectangular fault models also suggested that linear model A and nonlinear models 1A, 1B, 2A, 2B, 3A, and 4B should all predict similar values for the strain rate at the present position within the earthquake cycle. This seems to be generally true, with the exception of model 2B, which predicts slightly smaller values than the other models. Linear model B and nonlinear model 3B produce lower strain rates, while nonlinear model 4A predicts a higher strain rate, in accordance with the rectangular fault models. All models are generally consistent with right-lateral shear, which results in a slight counterclockwise rotation (of the order of 15° to 20°) of the principal axes along the Big Bend portion of the fault.

Through an analysis of Figures 17–21 we can obtain a general impression of which models provide the closest fit to the data. For example, the predicted strain rates for linear model B and nonlinear model 3B are obviously much smaller than the observed values. However, it is difficult to truly evaluate the model results from this graphical representation. In order to quantify the differences in the model predictions, a more objective technique must be used. It should be emphasized that the uncertainties in the model parameters, and the possible range of

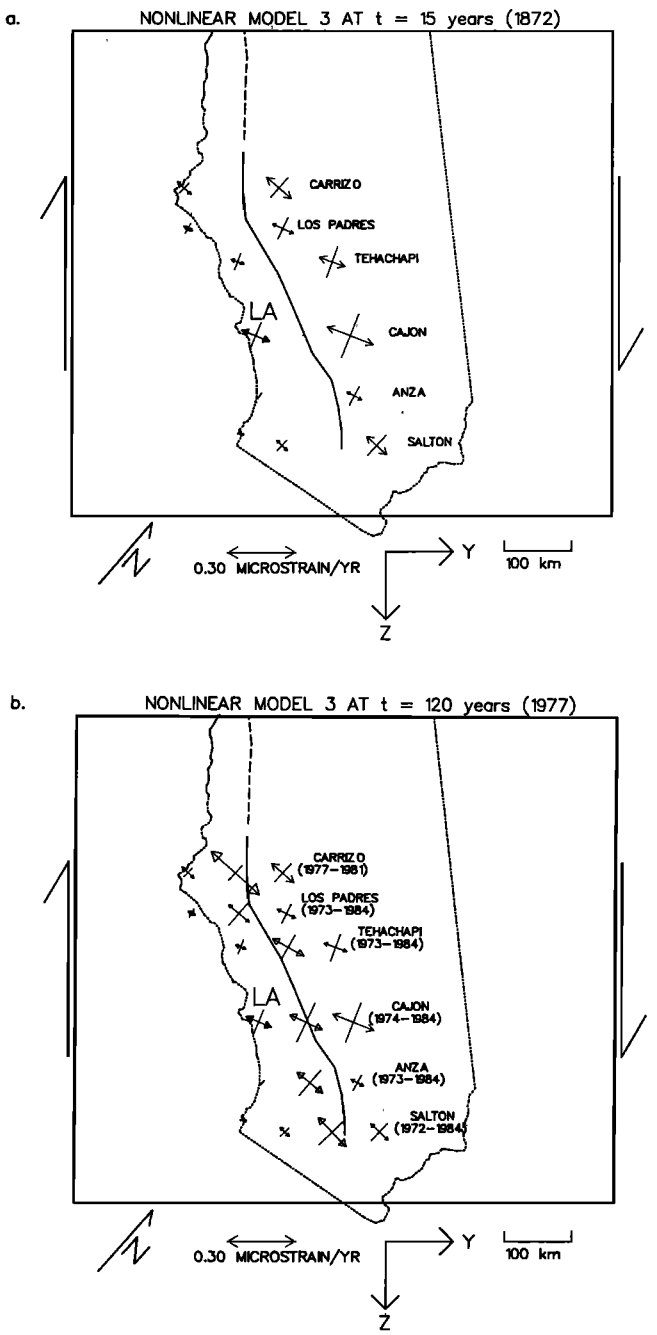

Fig. 20. Principal axes of strain rate for nonlinear model 3 at (*a*) $t = 15$ years (1872) and (*b*) $t = 120$ years (1977), using the same notation as Figure 17.

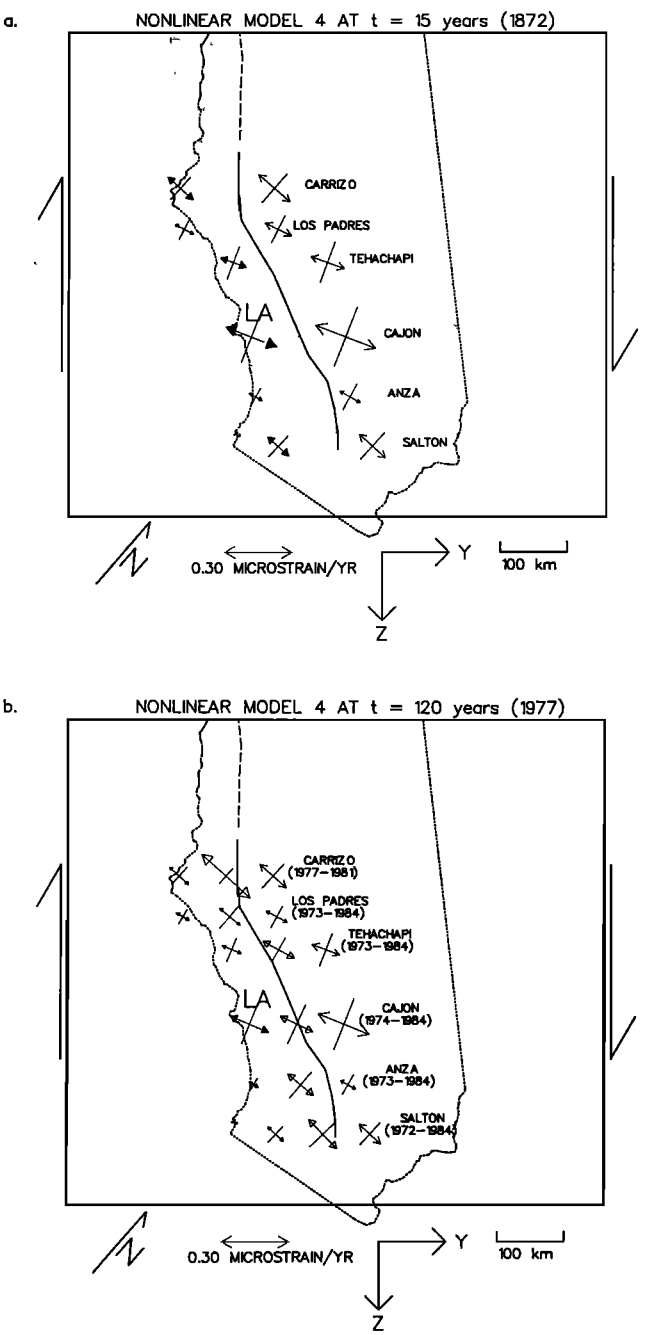

Fig. 21. Principal axes of strain rate for nonlinear model 4 at (*a*) $t = 15$ years (1872) and (*b*) $t = 120$ years (1977), using the same notation as Figure 17.

models, are much too large at this point to select one model over another on the basis of data misfit. The following analysis is simply a useful means of quantifying the differences between the models presented here. The method used follows that outlined by *Jackson* [1973]. First, all tensor components are rotated into a common coordinate system. The system chosen is that of *Savage et al.* [1986], in which the 1 axis is directed east and the 2 axis north. The data misfit for each network may then be determined. The data misfit may be defined as

$$b_i \equiv b_i^{obs} - b_i^{pre} \tag{10}$$

where the subscript i represents the particular observation under consideration and b_i^{obs} and b_i^{pre} denote observed and predicted values, respectively. The rms residual is then

$$r \equiv \sqrt{\frac{1}{n}\sum_{i=1}^{n} b_i^2} \tag{11}$$

where n represents the number of observations. For the present analysis, this would correspond to the number of tensor strain rate components under consideration.

Although the rms residual provides some idea of the fit to the data, it does not take into consideration the variations in the quality of the data. This may be accomplished by utilizing the data covariance matrix. For the case of statistically independent data errors, this reduces to a diagonal matrix of data variances. The weighted data misfit is then

$$\hat{b}_i \equiv \frac{b_i}{\sigma_i} \tag{12}$$

where σ_i is the standard deviation of the i^{th} observation. The weighted rms residual may be obtained by replacing b_i in (11) with the weighted data misfit from (12). This weighting scheme insures that misfits to observations that are not well known (i.e., those with large standard deviations) will contribute a smaller amount to the weighted rms residual than the misfits to well-known data. Note that the weighted rms residual is dimensionless, since the units of standard deviation are the same as those of the observation.

The predicted values for each model, along with the rms and weighted rms residuals, are given in Tables 4*a*–4*j*. The residuals are given for each network as well as for all six networks as a whole. Ideally, the total rms residual for a given model should be less than one. This would mean that, on average, the model is fitting the data to within the data uncertainties. This is not the case for the present models, however. The model that provides the closest fit to the data is model 4A (Table 4*i*), with a weighted rms residual of 4.53.

In almost all cases, the predicted values for $\dot{\varepsilon}_{11}$ and $\dot{\varepsilon}_{22}$ are substantially smaller than the observed values. This is true of all networks except Cajon, where the predicted values sometimes exceed the observed values. The small magnitudes for the normal components of strain rate represent, at least in part, a deficiency in the amount of fault-parallel shear strain rate. If $\dot{\varepsilon}_{11}$ were equal in magnitude to $\dot{\varepsilon}_{22}$, this would represent a case of pure right-lateral shear across a vertical plane striking N45°W, close to the average strike of the San Andreas fault. Although the observed values of $\dot{\varepsilon}_{11}$ and $\dot{\varepsilon}_{22}$ are generally not equal in magnitude, the predicted values could, in most cases, be increased (or decreased, in the case of $\dot{\varepsilon}_{22}$) by equal amounts to produce values closer to those of the data. The shear component $\dot{\varepsilon}_{12}$ represents right-lateral shear across a vertical plane striking N90°E, and the magnitudes should be expected to be relatively small. In general, the models which do not include aseismic slip at depth predict substantially smaller strain rate values. Therefore it seems reasonable that increasing the depth of aseismic slip should increase the magnitudes of the predicted strain rates and should thus provide a better fit to the data. Alternatively, the locking depth could be decreased. This should then result in an increase in the shear strain rate close to the fault and late in the earthquake cycle, in a manner similar to the results of *Thatcher* [1983]. A locking depth of 15 km is probably more appropriate than the value of 20 km assumed in this study, as earthquakes on the San Andreas fault are rarely observed below this depth [*Sibson*, 1982; *Jones*, 1988].

A better fit to the data could also be achieved by allowing the fault parameters to vary along the length of the fault. The simplest and most reasonable parameters to vary are, again, the fault locking depth and the depth of aseismic slip. The fault locking depth may be constrained by the maximum focal depths along different portions of the fault, and the depth of aseismic slip can then be adjusted to produce the proper amount of shear

TABLE 4*a*. Linear Model A

Network	$\dot{\varepsilon}_{11}$	$\dot{\varepsilon}_{22}$	$\dot{\varepsilon}_{12}$	RMS Residual	Weighted RMS Residual
Salton	0.109	−0.109	−0.00654	0.0517	5.49
Anza	0.0588	−0.0733	0.0304	0.0703	7.48
Cajon	0.156	−0.155	0.135	0.0275	1.61
Tehachapi	0.0844	−0.103	0.0860	0.0410	4.85
Los Padres	0.0799	−0.0858	0.0496	0.0467	6.45
Carrizo	0.138	−0.118	−0.00393	0.0893	1.49
Total	–	–	–	0.0580	5.10

Tables 4*a*–4*j* list predicted results and residuals (observed minus predicted values) for the various models. All values are in units of microstrain per year, except for the weighted rms residual, which is dimensionless.

TABLE 4*b*. Linear Model B

Network	$\dot{\varepsilon}_{11}$	$\dot{\varepsilon}_{22}$	$\dot{\varepsilon}_{12}$	RMS Residual	Weighted RMS Residual
Salton	0.0560	−0.0576	−0.000897	0.0939	9.69
Anza	0.0413	−0.0498	0.0163	0.0856	8.63
Cajon	0.0670	−0.0668	0.0433	0.0715	3.56
Tehachapi	0.0471	−0.0599	0.0353	0.0676	7.19
Los Padres	0.0533	−0.0569	0.0160	0.0618	6.28
Carrizo	0.0748	−0.0649	−0.00366	0.125	2.09
Total	–	–	–	0.0869	6.79

TABLE 4c. Nonlinear Model 1A

Network	$\dot{\varepsilon}_{11}$	$\dot{\varepsilon}_{22}$	$\dot{\varepsilon}_{12}$	RMS Residual	Weighted RMS Residual
Salton	0.0982	−0.0968	−0.00802	0.0605	6.28
Anza	0.0598	−0.0728	0.0299	0.0700	7.43
Cajon	0.138	−0.133	0.114	0.0197	1.08
Tehachapi	0.0741	−0.0923	0.0752	0.0458	4.83
Los Padres	0.0787	−0.0810	0.0477	0.0484	6.45
Carrizo	0.125	−0.105	−0.00342	0.0957	1.60
Total	–	–	–	0.0613	5.22

TABLE 4d. Nonlinear Model 1B

Network	$\dot{\varepsilon}_{11}$	$\dot{\varepsilon}_{22}$	$\dot{\varepsilon}_{12}$	RMS Residual	Weighted RMS Residual
Salton	0.0874	−0.0864	−0.00738	0.0691	7.13
Anza	0.0463	−0.0589	0.0243	0.0805	8.28
Cajon	0.129	−0.127	0.112	0.0216	1.17
Tehachapi	0.0659	−0.0811	0.0696	0.0516	5.25
Los Padres	0.0640	−0.0672	0.0390	0.0566	6.60
Carrizo	0.115	−0.0936	−0.00507	0.101	1.69
Total	–	–	–	0.0681	5.70

TABLE 4e. Nonlinear Model 2A

Network	$\dot{\varepsilon}_{11}$	$\dot{\varepsilon}_{22}$	$\dot{\varepsilon}_{12}$	RMS Residual	Weighted RMS Residual
Salton	0.102	−0.0996	−0.00812	0.0580	6.04
Anza	0.0548	−0.0693	0.0273	0.0732	7.65
Cajon	0.151	−0.142	0.120	0.0215	1.17
Tehachapi	0.0739	−0.0952	0.0761	0.0457	4.85
Los Padres	0.0774	−0.0797	0.0453	0.0486	6.31
Carrizo	0.127	−0.105	−0.00328	0.0947	1.58
Total	–	–	–	0.0614	5.20

TABLE 4f. Nonlinear Model 2B

Network	$\dot{\varepsilon}_{11}$	$\dot{\varepsilon}_{22}$	$\dot{\varepsilon}_{12}$	RMS Residual	Weighted RMS Residual
Salton	0.0794	−0.0756	−0.00906	0.0764	7.80
Anza	0.0255	−0.0363	0.0110	0.0974	9.76
Cajon	0.139	−0.132	0.115	0.0204	1.12
Tehachapi	0.0579	−0.0748	0.0603	0.0569	5.69
Los Padres	0.0514	−0.0555	0.0290	0.0643	6.87
Carrizo	0.107	−0.0842	−0.00844	0.106	1.77
Total	–	–	–	0.0756	6.32

TABLE 4g. Nonlinear Model 3A

Network	$\dot{\varepsilon}_{11}$	$\dot{\varepsilon}_{22}$	$\dot{\varepsilon}_{12}$	RMS Residual	Weighted RMS Residual
Salton	0.107	−0.106	−0.00776	0.0534	5.61
Anza	0.0563	−0.0724	0.0299	0.0717	7.59
Cajon	0.152	−0.144	0.121	0.0219	1.19
Tehachapi	0.0767	−0.0971	0.0788	0.0443	4.82
Los Padres	0.0783	−0.0799	0.0464	0.0485	6.38
Carrizo	0.132	−0.107	−0.00218	0.0920	1.54
Total	–	–	–	0.0595	5.11

TABLE 4*h*. Nonlinear Model 3B

Network	$\dot{\varepsilon}_{11}$	$\dot{\varepsilon}_{22}$	$\dot{\varepsilon}_{12}$	RMS Residual	Weighted RMS Residual
Salton	0.0574	−0.0534	−0.00722	0.0944	9.60
Anza	0.0155	−0.0230	0.00387	0.107	10.7
Cajon	0.0989	−0.0912	0.0718	0.0456	2.26
Tehachapi	0.0391	−0.0529	0.0372	0.0732	7.67
Los Padres	0.0342	−0.0387	0.0155	0.0769	7.56
Carrizo	0.0738	−0.0546	−0.00747	0.126	2.11
Total	–	–	–	0.0910	7.47

Table 4*i*. Nonlinear Model 4A.

Network	$\dot{\varepsilon}_{11}$	$\dot{\varepsilon}_{22}$	$\dot{\varepsilon}_{12}$	RMS Residual	Weighted RMS Residual
Salton	0.131	−0.134	−0.00684	0.0338	3.84
Anza	0.0714	−0.0951	0.0340	0.0578	6.47
Cajon	0.191	−0.188	0.152	0.0508	2.62
Tehachapi	0.0960	−0.124	0.0941	0.0377	5.08
Los Padres	0.0940	−0.0973	0.0473	0.0378	5.67
Carrizo	0.156	−0.143	−0.00448	0.0831	1.39
Total	–	–	–	0.0529	4.53

TABLE 4*j*. Nonlinear Model 4B

Network	$\dot{\varepsilon}_{11}$	$\dot{\varepsilon}_{22}$	$\dot{\varepsilon}_{12}$	RMS Residual	Weighted RMS Residual
Salton	0.0955	−0.0951	−0.00645	0.0624	6.51
Anza	0.0467	−0.0620	0.0187	0.0788	7.99
Cajon	0.148	−0.146	0.112	0.0166	0.85
Tehachapi	0.0709	−0.0921	0.0635	0.0469	4.70
Los Padres	0.0648	−0.0692	0.0251	0.0531	5.68
Carrizo	0.116	−0.105	−0.00455	0.101	1.68
Total	–	–	–	0.0653	5.23

strain rate. Other parameters that are likely to vary along the fault are earthquake recurrence time and coseismic displacement. As mentioned before, the kinematically imposed slip condition of our model is likely to exaggerate the effects of deep aseismic slip. Therefore, in order to achieve the same increase in shear strain rate for a dynamic model (in which deep aseismic slip is a calculated response), it would probably be necessary to extend the depth of aseismic slip by a greater amount than would be necessary in our model.

Among the models considered in this study, the best fit to the data is provided by linear model A and nonlinear models 1A, 2A, 3A, 4A, and 4B. The only models that seem to be completely ruled out on the basis of horizontal strain rate data are linear model B and nonlinear models 2B and 3B. In all cases, the models that include aseismic slip at depth (H = 40 km) provide a better fit to the data than the corresponding model which does not include aseismic slip (H = 20 km). Furthermore, the best fit is provided by models incorporating a wet rheology to a depth of 100 km. At present, however, it would be unwise to form a strong preference for any of these preliminary models based on the fit to horizontal strain rate data. Our models were not chosen to represent a detailed picture of earthquake occurrence on the San Andreas fault. They were selected to demonstrate the characteristics that should be expected from various fault models. Having investigated the horizontal deformation patterns produced by these models, it is instructive to consider the predicted vertical deformation.

Uplift Rate Results for Models That Include Fault Geometry

Comparison of model results to observed horizontal strain rate data provides useful constraints on the possible model types; however, stronger constraints may be imposed by also considering the vertical uplift predicted by the different models. Vertical uplift has historically been determined by leveling surveys, and the validity of these results is uncertain, particularly in relation to the so-called Palmdale uplift [*Stein*, 1987; *Craymer and Vaníček*, 1989; *Stein et al.*, 1989]. The basic debate stems from the question of whether the technique possesses sufficient resolution to determine an uplift of the stated magnitude. More recent procedures, however, have significantly increased the precision of leveling surveys (20 to 30 mm over a 100-km horizontal distance) (J. Savage, personal communication, 1990). Furthermore, with the advent of methods such as satellite laser ranging (SLR), very long baseline interferometry (VLBI), and GPS, the possibility of accurate vertical uplift measurements has become much more likely. For example, the U.S. Geological Survey has been using GPS measurements to survey several networks since 1986, with vertical resolutions of the order of 2 to 4 cm [*Davis et al.*, 1989]. It therefore appears that vertical uplift determinations may become an important consideration in constraining San Andreas fault models in the near future.

As mentioned in the previous section, all but three of the proposed models provide a similar fit to the horizontal strain

rate data. Among these models, however, many predict significantly different uplift rates at different points in the earthquake cycle. The predicted uplift rates for several models are contoured in Figures 22–26. Figures 22*a*, 23*a*, 24*a*, 25*a*, and 26*a* represent the predicted uplift rate at a time shortly after the last earthquake in the region. For linear model A (Figures 22*a* and 22*b*), this time is 13.5 years after the earthquake (corresponding to the year 1870.5), while for the nonlinear models (Figures 23–26) the results are shown for a time of 15 years after the last great earthquake in the region (corresponding to the year 1872). Figures 22*b*, 23*b*, 24*b*, 25*b*, and 26*b* show the predicted uplift rate at a time of 148.5 years (2005.5) for the linear model and 142.5 years (1999.5) for the nonlinear models. The values are given in millimeters per year, and the contour interval is 0.5 mm/yr. Uplift is indicated by solid contours, and subsidence is shown with dashed contours.

A common feature of these models is the relative absence of subsidence. Only in a few cases is a small region of negative uplift present along the creeping section of the fault. Subsidence is only prominent in the linear models (linear model A is shown in Figure 22). It is also present to a slight extent in nonlinear model 4A, shown in Figure 25. The regions of uplift associated with the two bends in the fault are prominent features. The maximum magnitude for this uplift occurs for nonlinear model 4A early in the earthquake cycle (Figure 25*a*), where it attains a value of 3.5 mm/yr at the northern bend.

Although there are some similarities between the uplift rates predicted by the various models, there are a number of important

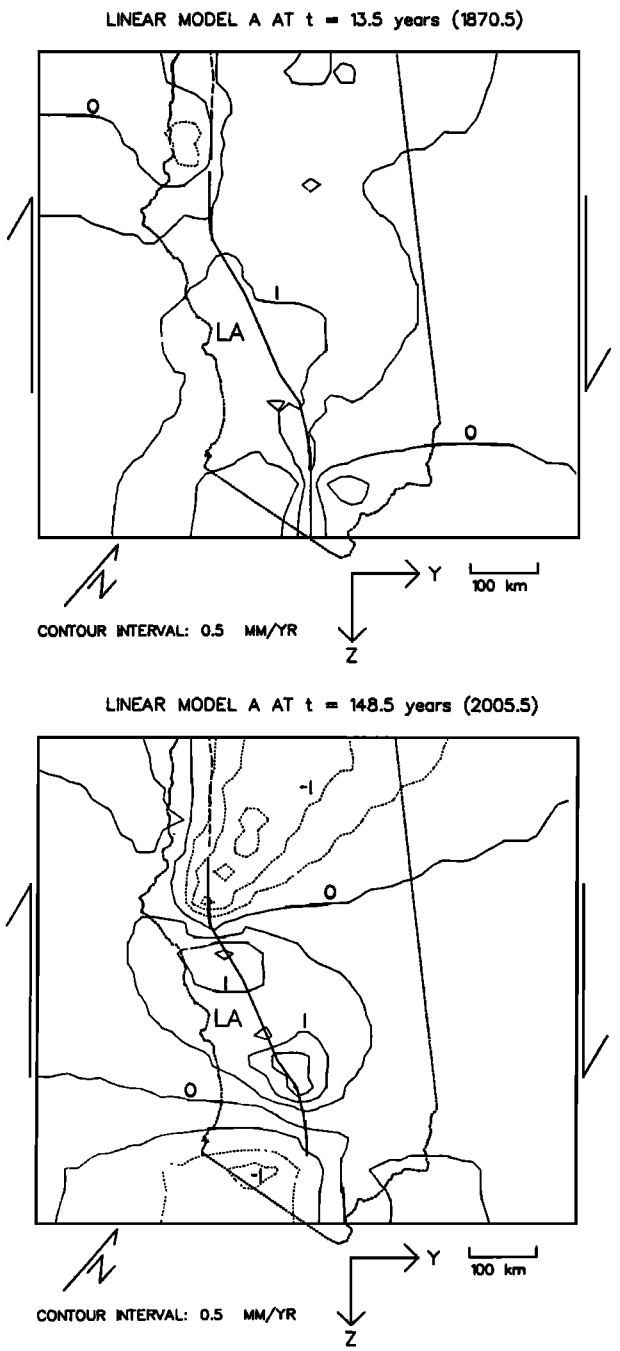

Fig. 22. Contours of uplift rate in millimeters per year for linear model A at (*a*) t = 13.5 years (1870.5) and (*b*) t = 148.5 years (2005.5). Solid contours represent uplift, and dashed lines represent subsidence.

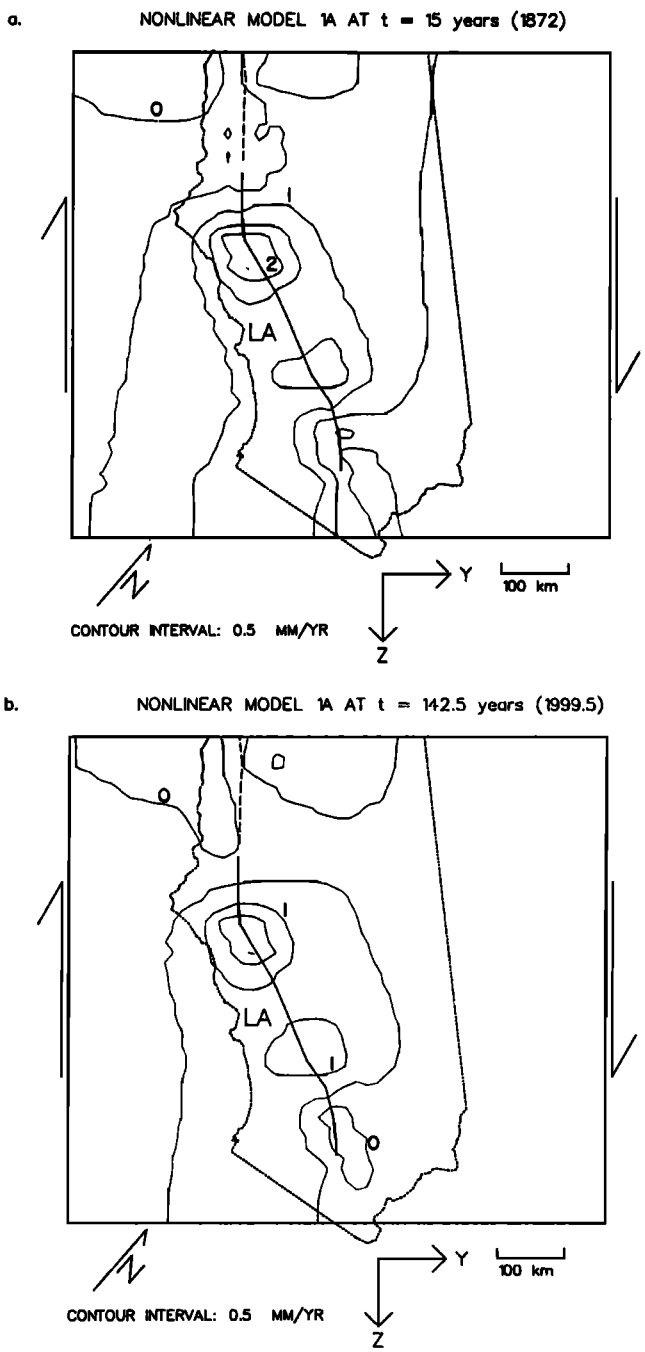

Fig. 23. Contours of uplift rate in millimeters per year for nonlinear model 1A at (*a*) t = 15 years (1872) and (*b*) t = 142.5 years (1999.5).

differences. The linear model (Figures 22*a* and 22*b*) displays a number of distinctive characteristics. For instance, the region of maximum uplift migrates with time, from near the southern termination of the fault to a position just north and east of the southern bend in the fault. In addition, the region of subsidence moves from the western to the eastern side of the creeping portion of the fault and increases in magnitude. The occurrence of subsidence appears to be correlated with a greater amount of time-dependent behavior, since models in which the effective viscosity near the surface is relatively high display virtually no subsidence at any point in the earthquake cycle.

Nonlinear model 1A (Figures 23*a* and 23*b*) predicts fairly constant uplift with time. The only perceptible change with time is a slight decrease in the magnitude of the uplift rate at times late in the earthquake cycle (compare Figures 23*a* and 23*b*). This provides a strong contrast to nonlinear model 1B (Figures 24*a* and 24*b*), which predicts essentially zero uplift at times late in the cycle. Initially, nonlinear models 1A and 1B (Figures 23*a* and 24*a*) predict fairly similar uplift patterns, although the predicted magnitudes are greater for model 1A. As time passes, however, the uplift rates for model 1A remain nearly constant, while those for model 1B decrease substantially. This is similar to the results for horizontal deformation. The presence of aseismic slip at depth tends to decrease the time dependence of the predicted deformation while increasing its magnitude. If current resolution of vertical uplift is of the order of 20 to 30 mm/yr, it should be possible to detect a difference in uplift rates of 2 mm/yr over a time period of 10–15 years, which

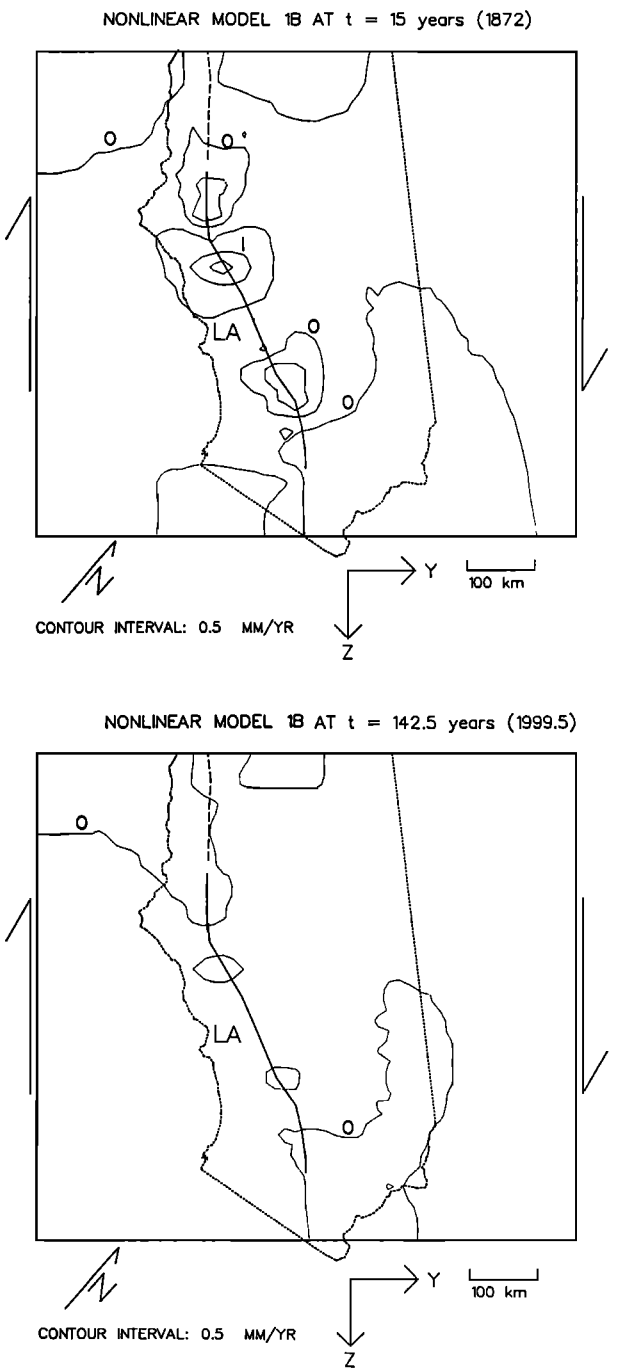

Fig. 24. Contours of uplift rate in millimeters per year for nonlinear model 1B at (*a*) t = 15 years (1872) and (*b*) t = 142.5 years (1999.5).

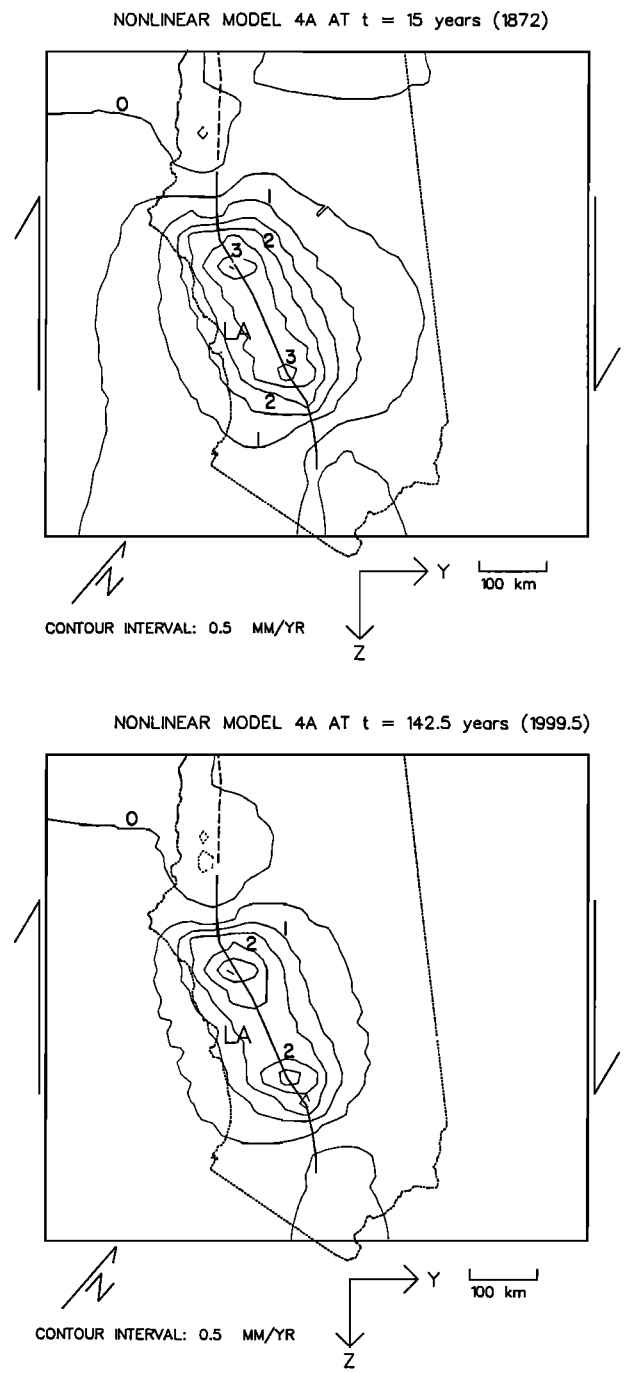

Fig. 25. Contours of uplift rate in millimeters per year for nonlinear model 4A at (*a*) t = 15 years (1872) and (*b*) t = 142.5 years (1999.5).

would be sufficient to differentiate between two models such as 1A and 1B.

Models 4A and 4B also display distinctive vertical uplift patterns. Model 4A (Figures 25*a* and 25*b*) predicts large uplift rates at all times during the cycle. The predicted uplift rates vary little with time, the primary differences being a decrease in the maximum magnitude (from 3.5 to 3.0 mm/yr) and a narrowing of the region of uplift around the Big Bend region at times late in the earthquake cycle. Model 4B (Figures 26*a* and 26*b*) again displays the reduction of uplift rate with time characteristic of models that do not include aseismic slip at depth, but the effect is not as dramatic as for the other models. In this case, the uplift rate decreases with time from a maximum of about 3.0 mm/yr to a value of 2.0 mm/yr, and the region of uplift narrows to include only the area immediately adjacent to the Big Bend.

It would be difficult to distinguish between models 4A and 4B based only on predicted vertical uplift rates, since the values differ by only about 1 mm/yr; however, the slight difference in predicted uplift rates could have a large effect on the cumulative uplift over an entire earthquake cycle, as demonstrated by Figures 27*a* and 27*b*. These show contours of total uplift since the last earthquake at a time of 142.5 years. Model 4A (Figure 27*a*) predicts a maximum uplift of 450 mm at the northern bend in the fault, while model 4B (Figure 27*b*) predicts an uplift of only 300 mm. Thus, although short-term measurements of uplift rate may not provide sufficient resolution to distinguish between models, determinations of vertical uplift over time scales of 10–20 years or more should provide useful constraints on possible fault models.

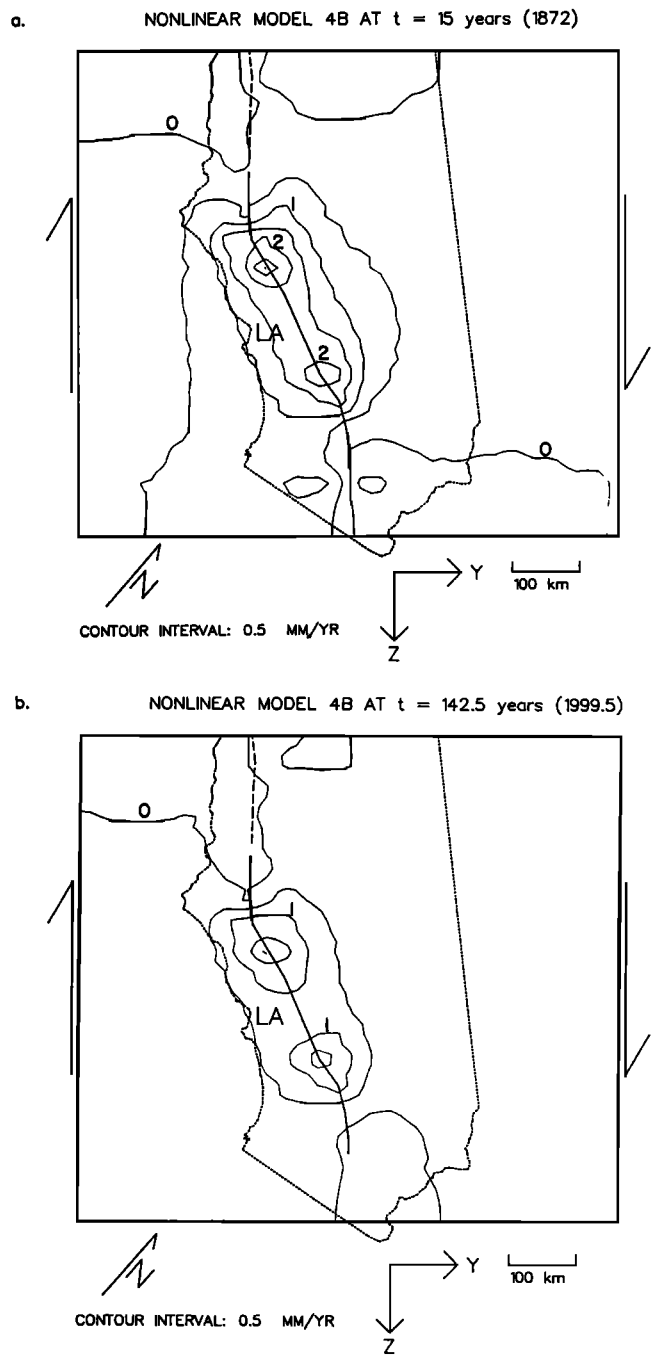

Fig. 26. Contours of uplift rate in millimeters per year for nonlinear model 4B at (*a*) t = 15 years (1872) and (*b*) t = 142.5 years (1999.5).

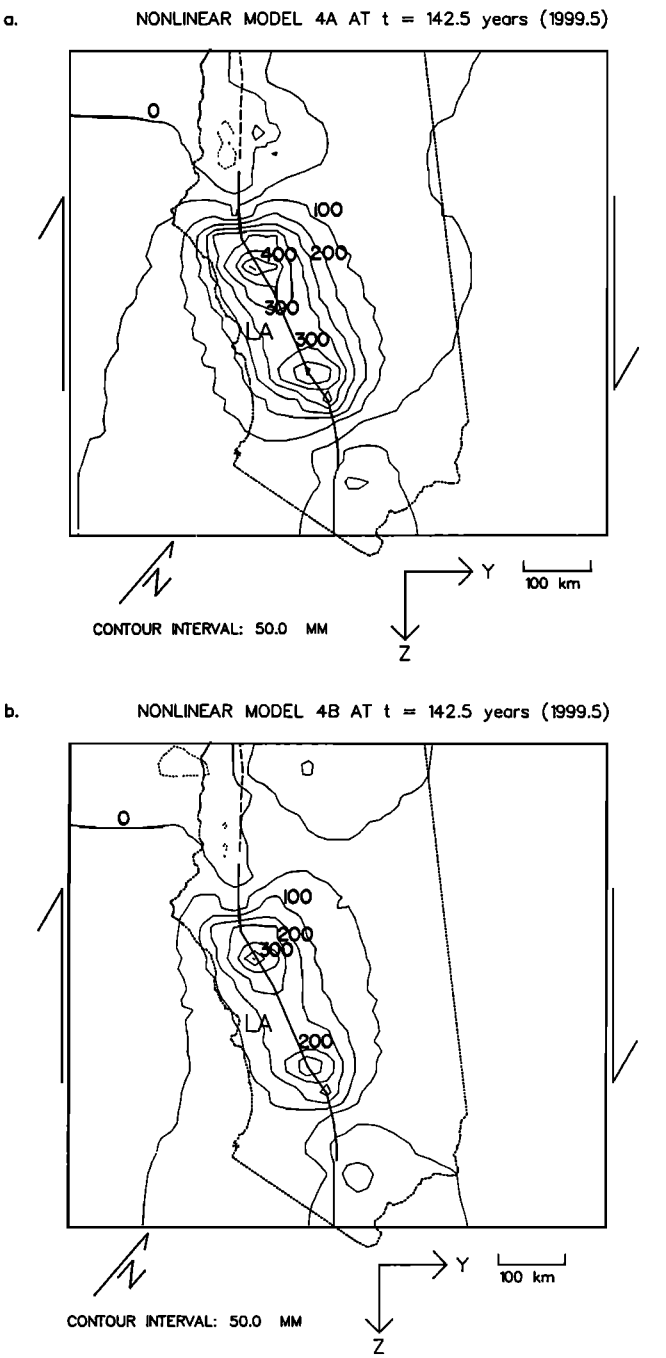

Fig. 27. Contours of total uplift in millimeters at t = 142.5 years (1999.5) for (*a*) nonlinear model 4A and (*b*) nonlinear model 4B.

DISCUSSION AND CONCLUSIONS

We have demonstrated that fault models with differing rheological stratification schemes and slip distributions predict distinctive deformation patterns, thus providing a means for distinguishing between various models. Models that do not include aseismic slip below the fault locking depth predict deformation patterns that are strongly dependent on time since the last earthquake. Both predicted strain rates and predicted uplift rates decrease dramatically in magnitude from the beginning to the end of the earthquake cycle. The results of *Thatcher* [1983] indicated that increasing the thickness of the elastic layer relative to the fault locking depth had the effect of damping the response of the underlying viscoelastic half-space, thus decreasing the time-dependent behavior of the model. The present results show that this effect could also be due, at least in part, to the depth to which aseismic slip occurs rather than simply the thickness of the surface elastic layer. All of the nonlinear models of this study have two versions: with and without aseismic slip below the fault locking depth. The rheological stratification for each model type was identical. For example, models 1A and 1B differed only in the depth to which aseismic slip occurred; they did not differ in their rheological properties. The only explanation for the enhanced time dependence of the B models is the absence of aseismic slip. Thus time-dependent behavior is influenced by the presence or absence of aseismic slip at depth as well as by the depth to which elastic behavior extends. The present models, as well as that of *Thatcher* [1983], specify steady aseismic slip at depth. If the aseismic slip instead occurred as a calculated response to stress conditions, it is likely that the differences between our A and B models would be substantially reduced.

The models incorporating aseismic slip below the locking depth display a lesser degree of time dependence. For the nonlinear models, the predicted strain rates near the beginning of the earthquake cycle are similar for models with and without aseismic slip; however, by the end of the cycle, the strain rates for models without slip have decreased substantially in magnitude relative to those with slip. The models without aseismic slip generally predict slightly smaller uplift rates at the beginning of the earthquake cycle and substantially smaller rates near the end of the cycle than do the corresponding models that include aseismic slip below the locking depth.

Modeling results indicate that the observed spatial and temporal pattern of surface deformation is controlled by the assumed rheological properties within 100 km of the Earth's surface. It is unlikely that changes in the properties below this depth would influence the results in any case, since the predicted rheology of olivine at this depth suggests a Maxwell time of the order of 10 years, which is considerably less than the earthquake recurrence interval of 150 years. The mantle below 100 km depth should behave essentially as an inviscid fluid on this time scale. The rheological properties above 100 km depth produce a number of observable characteristics. The first, and most obvious, is an enhanced time dependence of the predicted deformation for lower effective viscosities. For instance, the greatest time dependence among the nonlinear models is displayed by model 1, which has a relatively low effective viscosity from 20 to 40 km depth (dry granite rheology), and by model 4, which has relatively low viscosities from 0 to 20 km (wet granite rheology) and from 40 to 100 km depth (wet dunite rheology). The rheological properties of model 4 also result in higher overall values of strain rate and uplift rate. This is probably a result of the assumed wet granite rheology at the surface, which would be more readily deformed by applied stresses. Thus the commonly used assumption of a purely elastic layer at the surface may not be an accurate portrayal of actual Earth rheology, since viscoelastic effects may manifest themselves at depths as shallow as 10 km for a wet granite rheology (see Figure 7).

Among the present models, the best fit to the strain rate data is provided by nonlinear model 4A. This model assumes aseismic slip from 20 to 40 km depth and includes rheological properties corresponding to a wet granite upper crust, a wet diabase lower crust, and a wet dunite upper mantle from 40 to 100 km depth. This model fits the data best because it produces the largest fault-parallel shear strain rate. Even so, this model underestimates the magnitude of the strain rate for all networks except Cajon and Carrizo (compare Table 3 with Table 4*i*). The simplest method for achieving a better fit to the data would be to adjust the fault locking depth and the depth of aseismic slip along the length of the fault. For example, the depth of aseismic slip could be increased in regions where the strain rate is underestimated and decreased in areas where the strain rate is overestimated. Such a procedure, while it would result in a smaller rms residual, would not necessarily produce a realistic picture of San Andreas fault processes, since other parameters not yet considered may produce similar results.

From analysis of Figures 17–21 it is not obvious whether there are any particular regions where the horizontal strain rates would be more sensitive to changes in the locking depth, depth of aseismic slip, or rheological properties; however, the uplift rate (Figures 22–26) is very location specific. For example, the region adjacent to the creeping portion of the fault is sensitive to rheological changes. Models with relatively low effective viscosities near the surface predict subsidence in this area, while models with higher effective viscosities predict essentially zero uplift. Furthermore, some models, such as linear model A (Figure 22) and, to a much lesser extent, nonlinear model 4A (Figure 25), display a slight increase of subsidence in this area with time since the last earthquake. In the case of linear model A, the region of subsidence also moves with time.

The uplift rates at the two bends in the fault are sensitive to the depth of aseismic slip, particularly for models with relatively high effective viscosities at depth (compare nonlinear models 1A and 1B in Figures 23 and 24). In this case, models which do not include aseismic slip at depth show a dramatic decrease in uplift rates with time since the last earthquake. The total uplift over longer time scales in the Big Bend region may be a useful constraint for models with lower effective viscosities (see nonlinear models 4A and 4B in Figures 27*a* and 27*b*).

The observed strain rate data are best fit by model 4A, although the fit is not very good in a root mean square sense. There are a number of additional factors that could be included. One factor may be the discrepancy between the plate motions determined from plate models and those derived from geodetic observations along the fault, as discussed in the introduction. This may have some relation to the difference in orientations of the observed principal axes of stress and strain rate [*Mount and Suppe*, 1987; *Zoback et al.*, 1987]. To resolve problems of this nature it will be necessary to include adjacent faults in the model, since slip on these faults is likely to affect the stress regime of the San Andreas fault.

The two most important contributions of the present models are the incorporation of layered, power law viscoelastic rheologies and the calculation of vertical uplift. The use of power law viscoelastic behavior allows the direct application of laboratory results to actual Earth processes. The rheological properties of the present models are thus constrained not only by the fit of the model results to observed deformation data but also by current knowledge of variations in Earth composition and temperature with depth. Despite the uncertainties in laboratory measurements of rock rheology, it is obvious from our results that consideration of alternative rheologies can have a significant effect on predicted deformation patterns. The determination of vertical uplift provides another useful constraint on possible fault models. The present models show that the predicted uplift rate for different models can vary from essentially zero to as much as 3 mm/yr. The data necessary to resolve these small

values of uplift rate should be forthcoming in the near future. The addition of vertical uplift data to the existing horizontal deformation and stress orientation data sets should provide strong constraints on future San Andreas fault models.

Acknowledgments. We would like to thank William Prescott for providing us with a map of the Carrizo Geodolite network. This paper benefited greatly from reviews by J. C. Savage and an anonymous reviewer. This research was supported by NASA grant NAG-326.

REFERENCES

Birch, F., Compressibility; elastic constants, in Handbook of Physical Constants, edited by S. P. Clark, Jr., *Mem. Geol. Soc. Am.*, *97*, 97–173, 1966.

Bird, P., New finite element techniques for modeling deformation histories of continents with stratified temperature-dependent rheology, *J. Geophys. Res.*, *94*, 3967–3990, 1989.

Brune, J. N., T. L. Henyey, and R. F. Roy, Heat flow, stress, and rate of slip along the San Andreas fault, California, *J. Geophys. Res.*, *74*, 3821–3827, 1969.

Byerlee, J. D., Friction of rocks, *Pure Appl. Geophys.*, *116*, 615–626, 1978.

Carter, N. L., D. A. Anderson, F. D. Hansen, and R. L. Kranz, Creep and creep rupture of granitic rocks, in *Mechanical Behavior of Crustal Rocks, Geophys. Monogr. Ser.* , vol. 24, edited by N. L. Carter, M. Friedman, J. M. Logan, and D. W. Stearns, pp. 61–82, AGU, Washington, D. C., 1981.

Chapman, D. S., Thermal gradients in the continental crust, in The Nature of the Lower Continental Crust, edited by J. B. Dawson, D. A. Carswell, J. Hall, and K. H. Wedepohl, *Spec. Publ. Geol. Soc. Am.*, *24*, 63–70, 1986.

Chen, W.-P., and P. Molnar, Focal depths of intracontinental and intraplate earthquakes and their implications for the thermal and mechanical properties of the lithosphere, *J. Geophys. Res.*, *88*, 4183–4214, 1983.

Craymer, M. R., and P. Vaníček, Comment on "Saugus-Palmdale, California, field test for refraction error in historical leveling surveys" by R. S. Stein, C. T. Whalen, S. R. Holdahl, W. E. Strange, and W. Thatcher, and reply to "Comment on 'Further analysis of the 1981 southern California field test for levelling refraction by M. R. Craymer and P. Vaníček' by R. S. Stein, C. T. Whalen, S. R. Holdahl, W. E. Strange, and W. Thatcher," *J. Geophys. Res.*, *94*, 7667–7672, 1989.

Davis, J. L., W. H. Prescott, J. L. Svarc, and K. J. Wendt, Assessment of global positioning system measurements for studies of crustal deformation, *J. Geophys. Res.*, *94*, 13,635–13,650, 1989.

DeMets, C., R. G. Gordon, S. Stein, and D. F. Argus, A revised estimate of Pacific-North America motion and implications for western North America plate boundary zone tectonics, *Geophys. Res. Lett.*, *14*, 911–914, 1987.

DeMets, C., R. G. Gordon, D. F. Argus, and S. Stein, Current plate motions, *Geophys. J. Int.*, *101*, 425–478, 1990.

Desai, C. S., *Elementary Finite Element Method*, 434 pp., Prentice-Hall, Englewood Cliffs, N. J., 1979.

Gordon, R. B., Diffusion creep in the Earth's mantle, *J. Geophys. Res.*, *70*, 2413–2418, 1965.

Gordon, R. B., Thermally activated processes in the Earth: Creep and seismic attenuation, *Geophys. J.*, *14*, 33–43, 1967.

Haskell, N. A., The motion of a viscous fluid under a surface load, *Physics*, *6*, 265–269, 1935.

Haskell, N. A., The motion of a viscous fluid under a surface load, part II, *Physics*, *7*, 56–61, 1936.

Jackson, D. D., Marginal solutions to quasi-linear inverse problems in geophysics: the edgehog method, *Geophys. J. R. Astron. Soc.*, *35*, 121–136, 1973.

Jones, L. M., Focal mechanisms and the state of stress on the San Andreas fault in southern California, *J. Geophys. Res.*, *93*, 8869–8891, 1988.

King, N. E. and J. C. Savage, Strain-rate profile across the Elsinore, San Jacinto, and San Andreas faults near Palm Springs, California, 1973–81, *Geophys. Res. Lett.*, *10*, 55–57, 1983.

King, N. E., P. Segall, and W. Prescott, Geodetic measurements near Parkfield, California, 1959–1984, *J. Geophys. Res.*, *92*, 2747–2766, 1987.

Kirby, S. H., Rheology of the lithosphere, *Rev. Geophys. Space Phys.*, *21*, 1458–1487, 1983.

Kirby, S. H., Rock mechanics observations pertinent to the rheology of the continental lithosphere and the localization of strain along shear zones, *Tectonophysics*, *119*, 1–27, 1985.

Kirby, S. H., and A. K. Kronenberg, Rheology of the lithosphere: selected topics, *Rev. Geophys.*, *25*, 1219–1244, 1987*a*.

Kirby, S. H., and A. K. Kronenberg, Correction to "Rheology of the lithosphere: selected topics," *Rev. Geophys.*, *25*, 1680–1681, 1987*b*.

Kusznir, N. J., and G. Karner, Dependence of the flexural rigidity of the continental lithosphere on rheology and temperature, *Nature*, *316*, 138–142, 1985.

Kusznir, N. J., and R. G. Park, Continental lithosphere strength: the critical role of lower crustal deformation, in The Nature of the Lower Continental Crust, edited by J. B. Dawson, D. A. Carswell, J. Hall, and K. H. Wedepohl, *Spec. Pub. Geol. Soc. Am.*, *24*, 79–93, 1986.

Lachenbruch, A. H., and J. H. Sass, Thermo-mechanical aspects of the San Andreas fault system, in *Proceedings of the Conference on the Tectonic Problems of the San Andreas Fault System*, pp. 192–205, Stanford University Press, Palo Alto, Calif., 1973.

Lachenbruch, A. H., and J. H. Sass, Models of an extending lithosphere and heat flow in the Basin and Range province, *Mem. Geol. Soc. Am.*, *152*, 209–250, 1978.

Lachenbruch, A. H., and J. H. Sass, Heat flow and energetics of the San Andreas fault zone, *J. Geophys. Res.*, *85*, 6185–6222, 1980.

Li, V. C., and H. S. Lim, Modeling surface deformations at complex strike-slip plate boundaries, *J. Geophys. Res.*, *93*, 7943–7954, 1988.

Li, V. C., and J. R. Rice, Crustal deformation in great California earthquake cycles, *J. Geophys. Res.*, *92*, 11,533–11,551, 1987.

McGarr, A., On the state of lithospheric stress in the absence of applied tectonic forces, *J. Geophys. Res.*, *93*, 13,609–13,617, 1988.

Meissner, R., and J. Strehlau, Limits of stresses in continental crusts and their relation to the depth-frequency distribution of shallow earthquakes, *Tectonics*, *1*, 73–89, 1982.

Melosh, H. J., Rheology of the Earth: Theory and observation, in *Physics of the Earth's Interior*, edited by A. M. Dziewonski and E. Boschi, pp. 318–335, North-Holland, New York, 1980.

Melosh, H. J., Mechanical basis for low-angle normal faulting in the Basin and Range province, *Nature*, *343*, 331–335, 1990.

Melosh, H. J., and A. Raefsky, The dynamical origin of subduction zone topography, *Geophys. J. R. Astron. Soc.*, *60*, 333–354, 1980.

Melosh, H. J., and A. Raefsky, A simple and efficient method for introducing faults into finite element computations, *Bull. Seismol. Soc. Am.*, *71*, 1391–1400, 1981.

Melosh, H. J., and C. A. Williams, Mechanics of graben formation in crustal rocks: A finite element analysis, *J. Geophys. Res.*, *94*, 13,961–13,973, 1989.

Minster, J. B., and T. H. Jordan, Vector constraints on western U.S. deformation from space geodesy, neotectonics, and plate motions, *J. Geophys. Res.*, *92*, 4798–4804, 1987.

Mount, V. S., and J. Suppe, State of stress near the San Andreas fault: implications for wrench tectonics, *Geology*, *15*, 1143–1146, 1987.

Nur, A., and G. Mavko, Postseismic viscoelastic rebound, *Science*, *183*, 204–206, 1974.

Prescott, W. H., and J. C. Savage, Strain accumulation on the San Andreas fault near Palmdale, California, *J. Geophys. Res.*, *81*, 4901–4908, 1976.

Prescott, W. H., J. C. Savage, and W. T. Kinoshita, Strain accumulation rates in the western United States between 1970 and 1978, *J. Geophys. Res.*, *84*, 5423–5435, 1979.

Ranalli, G., and D. C. Murphy, Rheological stratification of the lithosphere, *Tectonophysics*, *132*, 281–295, 1987.

Reid, H. F., Permanent displacements of the ground, in *The California Earthquake of April 18, 1906, Report of the State Earthquake Investigation Commission, vol. 2*, pp. 16–28, Carnegie Institution of Washington, Washington, D. C., 1910.

Reid, H. F., The elastic-rebound theory of earthquakes, *Univ. Calif. Publ. Geol. Sci.*, *6*, 413–444, 1911.

Rundle, J. B., An approach to modeling present-day deformation in southern California, *J. Geophys. Res.*, *91*, 1947–1959, 1986.

Rundle, J. B., A physical model for earthquakes, 1, Fluctuations and interactions, *J. Geophys. Res.*, *93*, 6237–6254, 1988*a*.

Rundle, J. B., A physical model for earthquakes, 2, Application to southern California, *J. Geophys. Res.*, *93*, 6255–6274, 1988*b*.

Savage, J. C., Strain accumulation in the western United States, *Annu. Rev. Earth Planet. Sci.*, *11*, 11–43, 1983.

Savage, J. C., Equivalent strike-slip earthquake cycles in half-space and lithosphere-asthenosphere Earth models, *J. Geophys. Res.*, *95*, 4873–4879, 1990.

Savage, J. C., and W. H. Prescott, Asthenosphere readjustment and the earthquake cycle, *J. Geophys. Res.*, *83*, 3369–3376, 1978.

Savage, J. C., W. H. Prescott, M. Lisowski, and N. E. King, Strain accumulation in southern California, 1973-1980, *J. Geophys. Res.*, *86*, 6991–7001, 1981.

Savage, J. C., W. H. Prescott, and G. Gu, Strain accumulation in southern California, 1973–1984, *J. Geophys. Res.*, *91*, 7455–7473, 1986.

Schatz, J. F., and G. Simmons, Thermal conductivity of Earth materials at high temperatures, *J. Geophys. Res.*, *77*, 6966–6983, 1972.

Shelton, G. L., and J. Tullis, Experimental flow laws for crustal rocks (abstract), *Eos Trans. AGU*, *62*, 396, 1981.

Sibson, R. H., Fault zone models, heat flow, and the depth distribution of earthquakes in the continental crust of the United States, *Bull. Seismol. Soc. Am.*, *72*, 151–163, 1982.

Sieh, K. E., Slip along the San Andreas fault associated with the great 1857 earthquake, *Bull. Seismol. Soc. Am.*, *68*, 1421–1448, 1978.

Sieh, K., M. Stuiver, and D. Brillinger, A more precise chronology of earthquakes produced by the San Andreas fault in southern California, *J. Geophys. Res.*, *94*, 603–623, 1989.

Spence, D. A., and D. L. Turcotte, Viscoelastic relaxation of cyclic displacements on the San Andreas fault, *Proc. R. Soc. London Ser. A*, *365*, 121–149, 1979.

Stein, R. S., Contemporary plate motion and crustal deformation, *Rev. Geophys.*, *25*, 855–863, 1987.

Stein, R. S., C. T. Whalen, S. R. Holdahl, W. E. Strange, and W. Thatcher, Reply to "Comment on 'Saugus-Palmdale, California, field test for refraction error in historical leveling surveys' by R. S. Stein, C. T. Whalen, S. R. Holdahl, W. E. Strange, and W. Thatcher" by Michael R. Craymer and Peter Vaníček and comment on 'Further analysis of the 1981 southern California field test for levelling refraction' by M. R. Craymer and P. Vaníček," *J. Geophys. Res.*, *94*, 7673–7677, 1989.

Strehlau, J., and R. Meissner, Estimation of crustal viscosities and shear stresses from an extrapolation of experimental steady state flow data, in *Composition, Structure and Dynamics of the Lithosphere-Asthenosphere System, Geodyn. Ser.*, vol. 16, edited by K. Fuchs and C. Froidevaux, pp. 69–87, AGU, Washington, D. C., 1987.

Thatcher, W., Nonlinear strain buildup and the earthquake cycle on the San Andreas fault, *J. Geophys. Res.*, *88*, 5893–5902, 1983.

Thatcher, W., and J. B. Rundle, A viscoelastic coupling model for the cyclic deformation due to periodically repeated earthquakes at subduction zones, *J. Geophys. Res.*, *89*, 7631–7640, 1984.

Tse, S. T., and J. R. Rice, Crustal earthquake instability in relation to the depth variation of frictional slip properties, *J. Geophys. Res.*, *91*, 9452–9472, 1986.

Turcotte, D. L., and G. Schubert, *Geodynamics Applications of Continuum Physics to Geological Problems*, 450 pp., John Wiley, New York, 1982.

Ward, P. L., and R. A. Page, The Loma Prieta Earthquake of October 17, 1989, pamphlet, edited by L. D. Hodgen and J. A. Troll, 16 pp., U.S. Geol. Surv., Menlo Park, Calif., 1989.

Weertman, J., The creep strength of the Earth's mantle, *Rev. Geophys.*, *8*, 145–168, 1970.

Wesnousky, S. G., Earthquakes, Quaternary faults, and seismic hazard in California, *J. Geophys. Res.*, *91*, 12,587–12,631, 1986.

Williams, C. A., and R. M. Richardson, A nonlinear least-squares inverse analysis of strike-slip faulting with application to the San Andreas fault, *Geophys. Res. Lett.*, *15*, 1211–1214, 1988.

Zoback, M. D., M. L. Zoback, V. S. Mount, J. Suppe, J. P. Eaton, J. H. Healy, D. Oppenheimer, P. Reasenberg, L. Jones, C. B. Raleigh, I. G. Wong, O. Scotti, and C. Wentworth, New evidence on the state of stress of the San Andreas fault system, *Science*, *238*, 1105–1111, 1987.

R.M. Richardson, Department of Geosciences, University of Arizona, Tucson, AZ 85721.

C.A. Williams, Department of Geological and Geophysical Sciences, Princeton University, Princeton, NJ 08544.

(Received July 5, 1990;
revised April 10, 1991;
accepted May 28, 1991.)

JOURNAL OF GEOPHYSICAL RESEARCH, VOL. 96, NO. B10, PAGES 16,455–16,469, SEPTEMBER 10, 1991

Crustal Structure of the Active Margin, South Central Alaska: An Interpretation of Seismic Refraction Data From the Trans-Alaska Crustal Transect

LORRAINE W. WOLF

Phillips Laboratory, Earth Sciences Division, Hanscom Air Force Base, Massachusetts

DAVID B. STONE AND JOHN N. DAVIES

Geophysical Institute, University of Alaska, Fairbanks

Seismic refraction and wide-angle reflection data from the U.S. Geological Survey's Trans-Alaska Crustal Transect are used to investigate the upper crustal structure of southcentral Alaska and to develop a model using two-dimensional asymptotic ray theory. The data considered here are from the N-S 126-km Cordova Peak refraction profile, which was positioned to cross the Chugach and Prince William terranes. These two tectonostratigraphic terranes form part of a large accretionary complex related to the Alaska subduction zone. Interpretation of data from the Cordova Peak profile indicates systematically higher velocities in Chugach terrane rocks as compared with Prince William terrane rocks at comparable depths. Unconsolidated sediment and glacial ice overlie Chugach terrane rocks of unusually high compressional velocities (4.7–7.0 km/s) in the upper 10 km of crust. A northward thickening metasedimentary and metavolcanic flysch sequence, having an average velocity of 6.0 km/s, is underlain by metavolcanic mafic basement rocks having an average velocity of 6.6 km/s. The upper 10 km of the Prince William terrane have compressional velocities ranging from 3.7 to 6.2 km/s and are correlated with clastic sedimentary and volcanic rocks which are overlain by younger terrigenous sedimentary rocks and underlain by mafic to ultramafic Prince William terrane basement rocks. The upper crustal velocity structures of the Chugach and Prince William terranes are distinct to at least 10 km depth, which suggests that the Contact fault zone is a boundary which extends to at least 10 km. Midcrustal layers beneath the Chugach terrane contain two velocity reversals which may indicate the presence of off-scraped oceanic sediment, overpressurized zones, shear zones, or some combination of these possibilities. Data from energy sampling midcrustal layers beneath the Prince William terrane do not provide similar evidence for low-high velocity zones in that area.

INTRODUCTION

Southern Alaska is a geologically and tectonically complex area which offers a modern setting for the study of subduction environments and accretionary processes (Figure 1). It consists of a collection of tectonostratigraphic terranes which were accreted to North America along a convergent margin. A contribution to our understanding of the tectonic processes and geologic history of southern Alaska has come from the data collected as part of the Trans-Alaska Crustal Transect (TACT) project, an ongoing program of geological and crustal seismic investigations. The crustal model for south central Alaska presented here is based on an interpretation of the TACT Cordova Peak seismic refraction/wide-angle reflection profile. A model based on the intersecting Chugach profile was developed previously [*Wolf and Levander*, 1989] and is used to constrain the model developed in this paper.

The TACT corridor in southern Alaska is located in a transitional zone influenced by both convergent and transform tectonic margins (Figure 1). To the west, the Pacific plate is subducting beneath the North American plate, beginning along the Aleutian trench. To the east, transform motion is distributed along the Fairweather fault system. Relative motion between the Pacific and the North American plate was described by the RM1 model [*Minster et al.*, 1974] to be approximately NNW at a rate of 6 cm/yr, an estimate which is in agreement with more recent estimates for this region [*Engebretson et al.*, 1985; *Ma et al.*, 1989]. Estimates of convergence rates and paleolatitudes suggest that the terranes in southern Alaska contain accreted rocks originally formed south of their present latitudes [*Stone et al.*, 1982; *von Huene et al.*, 1985]. The Yakutat terrane, which is currently accreting to southern Alaska, appears to be moving with the Pacific plate, but at a slightly slower rate [*Perez and Jacob*, 1980; *Lahr and Plafker*, 1980; *Bruns*, 1983].

The 126-km Cordova Peak seismic refraction line is a N-S trending dip profile which crosses both the Chugach and Prince William terranes (Figure 2). At its midpoint, the Cordova Peak line intersects the Chugach line, a 135-km profile which parallels the regional E-W strike of the Chugach Mountains. The Chugach and Prince William terranes form an accretionary complex divided by the Contact Fault zone, a zone of steeply dipping faults along which rocks of the Prince William terrane have been thrust beneath older rocks of the Chugach terrane. In the western part of the Gulf of Alaska, the Aleutian trench forms the southern boundary of the Prince William terrane.

GEOLOGIC SETTING

The Chugach terrane consists of highly deformed, accreted and metamorphosed clastic sedimentary rock and oceanic crust [*Winkler et al.*, 1981]. It has been divided, from

Paper number 91JB01482.
0148-0227/91/91JB-01482$05.00

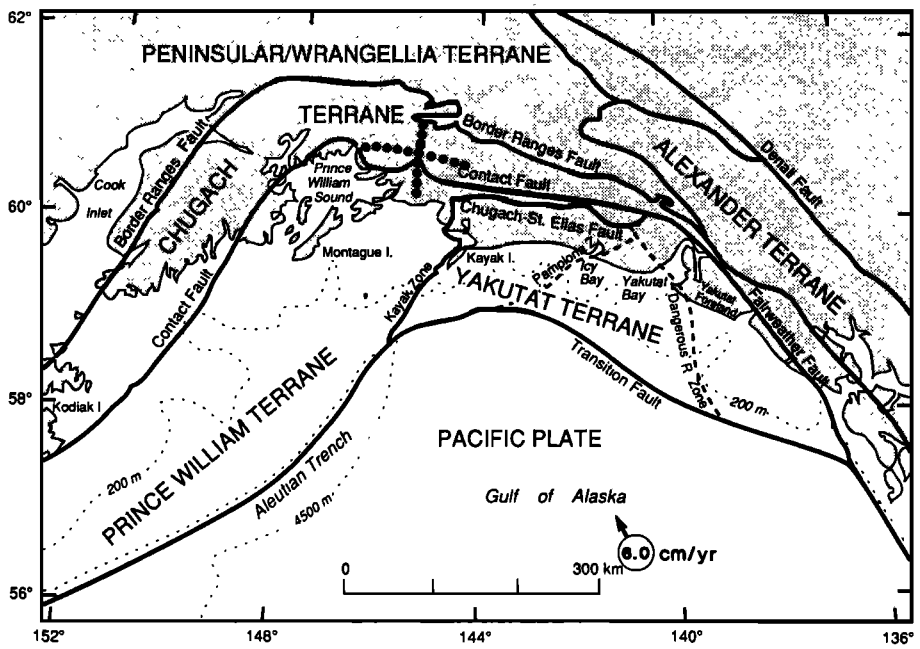

Fig. 1. Regional tectonic map of southern Alaska modified from *Jones et al.* [1981, 1987]. Arrow indicates relative motion between Pacific and North American plates [*Minster et al.*, 1974]. Small dots correspond to bathymetric contours. Large dots indicate location of TACT seismic refraction/wide-angle reflection lines discussed in this paper.

north to south, into three major fault-bounded sequences: the Upper Jurassic or older Liberty Creek schists, the Jurassic or older to Lower Cretaceous McHugh Complex, and the Upper Cretaceous Valdez Group [*Winkler et al.*, 1981; *Silberling and Jones*, 1984; *Plafker et al.*, 1989] (Figure 2).

The Valdez Group, which forms the bulk of the Chugach terrane, consists mainly of continentally derived sediments which were eroded from a magmatic arc and deposited in a deep-sea fan [*Winkler et al.*, 1981; *Plafker et al.*, 1989]. Beneath the deposited sedimentary rocks, mafic volcanic oceanic rocks form the terrane basement. The Chugach terrane moved northward to its present location, forming a thick accretionary prism which was later progressively metamorphosed in a low-pressure/high-temperature event beginning in latest Cretaceous and continuing in Paleogene time [*Hudson and Plafker*, 1982]. An observed metamorphic gradient in Valdez Group rocks increases from greenschist facies in the west to amphibolite facies east of the Copper River, in the Chugach Metamorphic Complex [*Hudson and Plafker*, 1982; *Sisson and Hollister*, 1988]. To the south, metavolcanic rocks exposed at the surface are juxtaposed with sedimentary rocks of the Prince William terrane along the Contact fault zone. The total stratigraphic thickness of the Chugach terrane is unknown.

The Prince William terrane contains accreted rocks of the Orca Group, a late Paleocene and early through middle Eocene deep-sea fan deposit interbedded with oceanic basalts, having an estimated thickness of 6–10 km [*Winkler and Plafker*, 1981; *Plafker*, 1987]. Overlying the Orca Group are late Eocene or older to Quaternary siliciclastic sedimentary rocks which were deposited in shelf or slope basins at their current locations. These younger sedimentary rocks constitute a relatively undeformed sequence estimated to be less than 4 km thick.

Similarity in lithology and depositional environment between the sandstones of the Chugach and Prince William terranes has raised some question as to whether the two terranes are geologically distinct entities [*Dumoulin*, 1988]. It has been argued that minor differences observed in rocks of the two terranes in central Prince William Sound may simply reflect a metamorphic gradient and that the Contact fault may be an out-of-sequence thrust fault, rather than a terrane boundary.

Felsic to intermediate Eocene hypabyssal and plutonic rocks were intruded into the Chugach and Prince William terranes at about 50 Ma, following the start of regional metamorphism [*Plafker et al.*, 1989]. The intrusions form dikes and dike swarms, as well as small stocks and sills, which crop out in the vicinity of the seismic transect. Crosscutting relationships indicate that the intrusions postdate deposition of Orca Group rocks and major motion along the Contact fault. Although rocks of the Yakutat terrane are not seen along the transect, subsurface boundaries of the terrane may well extend westward to the transect and beyond.

Data and Analysis

The N-S Cordova Peak profile extends from the Border Ranges fault zone to the Gulf of Alaska (Figure 2). It is a reversed profile consisting of five chemical explosions, rang-

Fig. 2. (Opposite) Generalized geologic map of southern Alaska showing location of TACT seismic refraction profiles (heavy lines). Other lines correspond to cross sections in Figure 12. Chugach refraction profile extends from SP 17 to SP 20; Cordova Peak profile extends from SP 11 to SP 37. SP 36 is the southern off-end shot for the Cordova Peak profile. Small dots indicate receiver positions. Crosses indicate shot points. Units Kvv, Kvg, and Kjm, metavolcanic rocks; Kvs, metamorphosed flysch; Kvg, rocks in Chugach Metamorphic Complex; Tg, igneous intrusive rocks; T0 and T1, sedimentary and volcanic rocks.

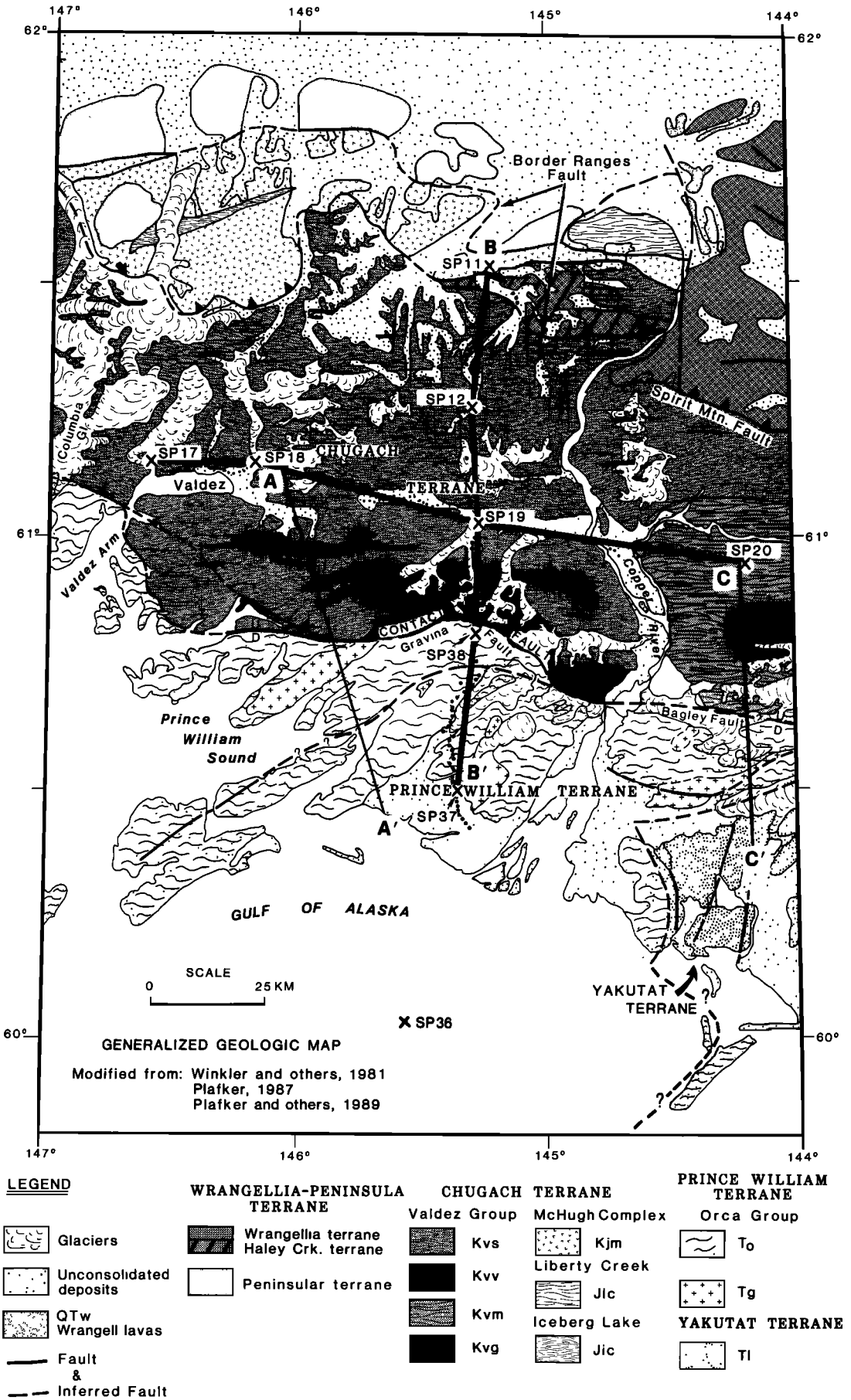

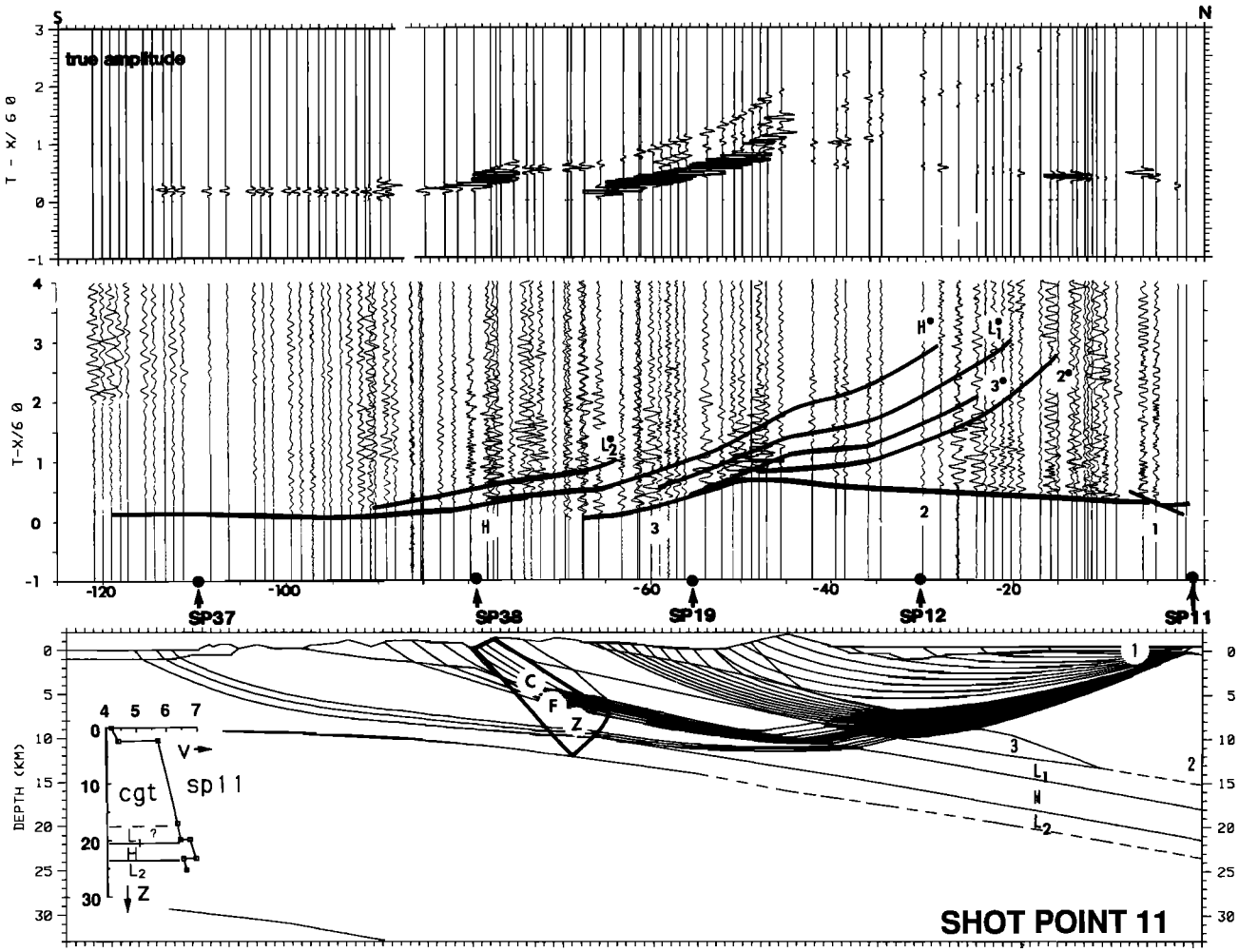

Fig. 3. Reduced-time true amplitude record section with calculated travel time curves, synthetic record section, and ray diagram for shot point 11 (SP 11). Calculated travel times from the same branch are connected and overlie observed data. Phases are correlated with layer numbers in the model (reflected branches marked with bullitts). Average velocities are shown in Figure 8. Ray diagram illustrates areas sampled by shot, but to avoid clutter, only some phases are shown. All phases are used to produce synthetic seismograms. Insert contains velocity-depth function for the model at the shot point. Dashed lines indicate no velocity discontinuity or lack of information. All subsequent data figures follow the same format (cgt, Chugach terrane; pwt, Prince William terrane; yak, Yakutat terrane; CFZ, Contact fault zone; L1, L2, H, low-/high-velocity zones).

ing in size from 926 to 1389 kg (2040–3060 lb) and spaced at approximately 40 km. Each shot was recorded by approximately 120 portable seismic cassette recorders spaced at 1-km intervals in a fixed array [*Wilson et al.*, 1987]. Shot points 11, 12, and 19 lie within the McHugh Complex and the Valdez Group rocks of the Chugach terrane. Shot points 38 and 37 lie south of the Contact fault zone, within rocks of the Prince William terrane. Shot point 19 marks the intersection of the Cordova Peak dip line with the Chugach strike line.

The five shots of the Cordova Peak profile have been interpreted using two-dimensional asymptotic ray methods [*Cerveny et al.*, 1977; *Luetgert*, 1987]. Field records indicate that the seismic data are of good quality except at long offsets, where signal to noise ratios make it difficult to pick first arrivals in some record sections. Calculated travel times were generally fit to within 0.10 s of observed arrivals. Synthetic seismograms produced using the program R86PLT [*Luetgert*, 1987] were used to analyze relative within-trace amplitudes and to refine the velocity structure within the model.

Results of the modeling are shown in Figures 3–7. Each figure contains a comparison of the field data from one shot point with the calculated travel times and synthetic seismograms from the preferred model. Record sections are plotted with a reduction velocity of 6 km/s and are trace normalized, except where indicated. Ray diagrams illustrate the subsurface areas sampled in different layers, but for simplification, only representative rays are shown. Simplified topography is drawn from local maxima and minima as determined from receiver elevations.

The starting model for the Cordova Peak interpretation was constructed from (1) a synthesis of one-dimensional models from each of the shot points, (2) a model based on surface geology and geologic cross sections, and (3) the previously derived model for the intersecting Chugach line [*Wolf and Levander*, 1989]. The starting model was then iteratively adjusted and revised. It was not possible to constrain rigorously the Cordova Peak dip model at shot point 19 (the intersecting point of the two lines) with the velocity-depth function from the Chugach model. Velocities

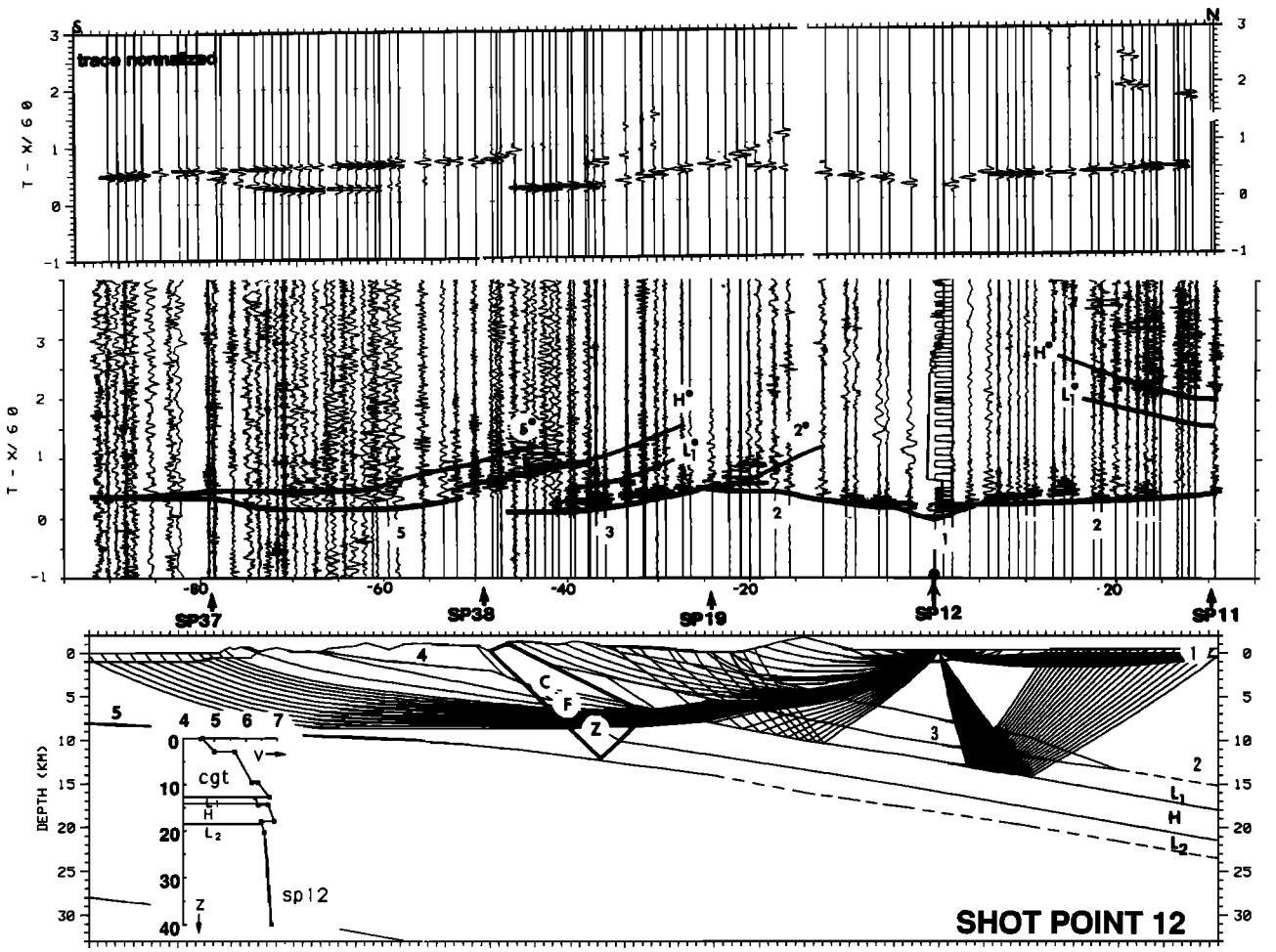

Fig. 4. Reduced-time record section with calculated travel times, synthetic record section, and simplified ray diagram for shot point 12 (SP 12). See Figure 3 caption for details.

of the strike line were systematically higher than those observed in the dip line. Possible explanations for velocity-depth function discrepancies between the strike and dip models in the upper crustal layers include out-of-plane reflections, nonuniqueness of solution, and anisotropy. The last possibility is discussed in more detail later.

Seismic Model

The seismic velocity model derived for the Cordova Peak profile is shown with a possible geologic model in Figure 8. Figure 8 displays average compressional velocities within each layer for specific areas of the model. Layers 1–3 represent rocks of the Chugach terrane, most of which have surface expression north of the Contact fault zone (Figure 2). Compressional velocities at the surface in the Chugach terrane range from a low of 4.0 km/s in sedimentary rocks to a high of 5.8 km/s in exposed bedrock. Clearly observed primary arrivals and prominent reflections generally provide good constraints on depths to interfaces of the first 3 layers (Figures 3–5). A comparison of primary arrivals at offsets within 20 km to the north and south in the record from shot point 19 shows slower apparent velocities to the north (Figure 5). To the north, no high-amplitude reflection occurs in the shot record until approximately 23 km offset and 0.75 s. To the south, wide-angle reflections from shallow dipping layers occur much closer to the shot point (18 km, 0.25 s). Similarly, the data from shot point 12 contain a strong high-amplitude phase to the south at 16 km offset and 1.0 s but lack a similar phase to the north (Figure 4). A true amplitude plot of the data from shot point 11 shows a decay of amplitudes with offset distance associated with the refracted phase within layer 2 and a lack of a strong, continuous reflected phase until about 45 km offset (Figure 3). The difference in observations of energy travelling northward from shot point 19 versus southward from shot point 11 is attributed to a northward thickening of the second layer related to the structural dip (Figure 8).

A strong refracted phase in the data from shot points 11, 12, and 19 provides justification for layer 3 in the model. Layer 3, exposed at the surface just north of the Contact fault zone, is 3–4 km thick and has a high average velocity (6.6 km/s). In the record from shot point 11, weak first-arriving energy at 30–45 km offset is followed at 47 km and 0.75 s by a strong phase, attributed to refracted energy within layer 3, having a high apparent velocity (Figure 3). In the record from shot point 12, a similar phase (labelled "3") occurs at 25 km offset to the south and 0.5 s but is absent in the data to the north, where offsets do not extend far enough to record refracted energy from this layer (Figure 4). Data from shot point 19 contain a strong arrival (labelled "3")

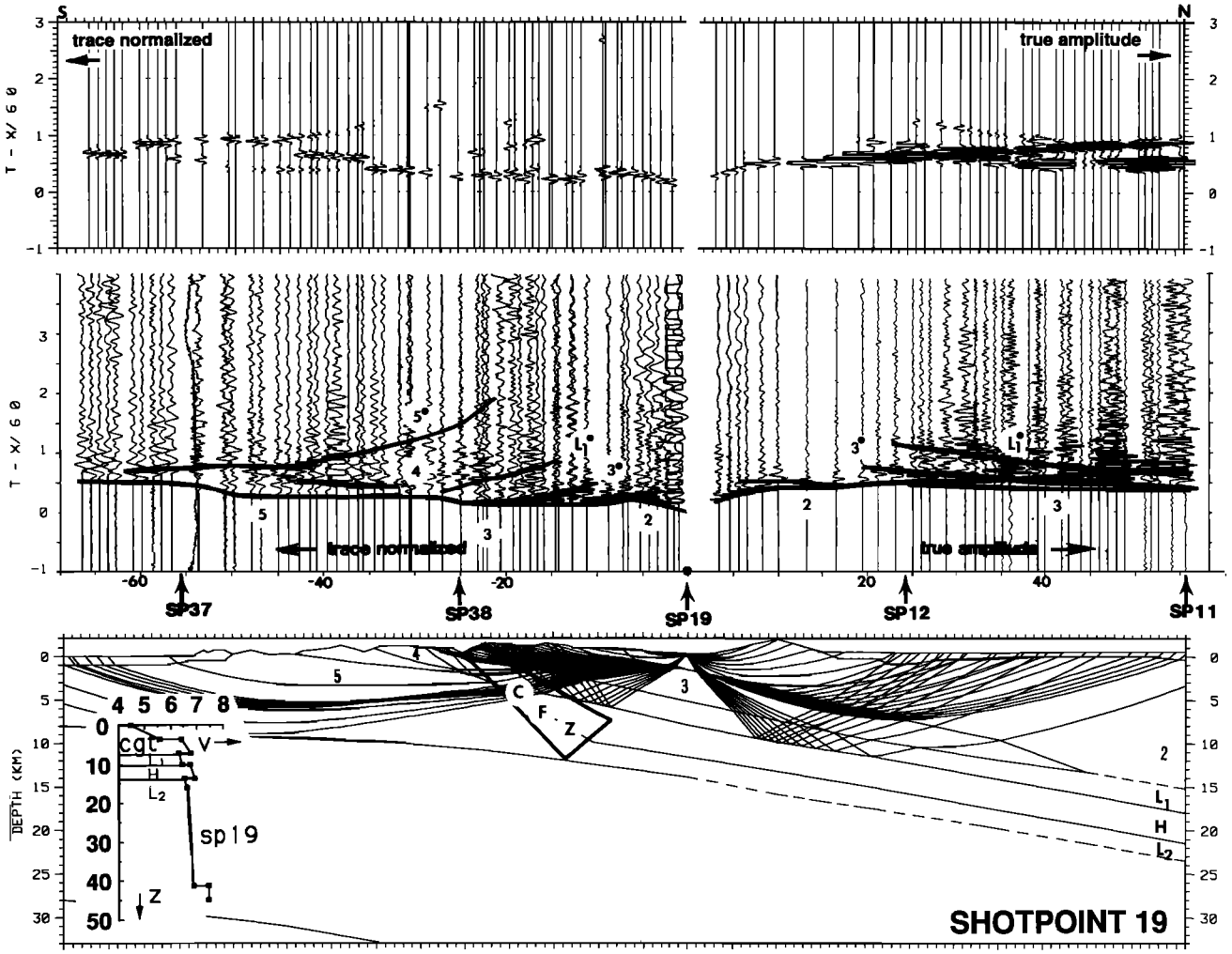

Fig. 5. Reduced-time record section with calculated travel times, synthetic record section, and simplied ray diagram for shot point 19 (SP 19). A true-amplitude plot is shown for data to the north, but data associated with energy travelling through the Contact fault zone are presented in trace-normalized format, since complexities of the structure here make amplitude modelling difficult. Shot point 19 marks the intersection of strike and dip profiles. See Figure 3 caption for details.

occurring within 10 km offset to the south; a counterpart is seen to the north at 26 km offset (Figure 5). The characteristic strength of this phase in the shot records and its association with faster apparent velocities to the south and slower apparent velocities to the north provide evidence for the northward dip of layer 3 in the model and a justification for its relatively steep vertical velocity gradient (6.4–6.75 km/s). Attempts to carry this layer northward over the entire length of the profile without invoking a substantial lateral velocity gradient resulted in travel times greater than 0.2 s faster than first arrivals observed in the record from shot point 11. As an alternative, layer 3 was modelled to pinch out and the thickness of layer 2 was increased to the north; this approach provided a more successful match to observed travel times in reversed shot records (Figures 3 and 5).

The velocity of surface rocks in the Prince William terrane range from a low of 3.7 km/s to a high of 5.6 km/s. The significantly lower velocities associated with Prince William terrane rocks as compared with those of the Chugach terrane at comparable depths are clearly evidenced in the shot records. Primary arrivals from shot point 38, which is located within the Contact fault zone, are fairly symmetric within 15 km of the shot point (Figure 6). Since the structure is assumed to be north dipping on the basis of geologic data, the similarity in apparent velocity of rocks to the north and south is attributed to the presence of higher velocity rocks north of the Contact fault zone. Beyond 15 km offset, slower apparent velocities are observed for energy arriving to the south than at similar offsets to the north, where rays penetrate the higher velocity Chugach terrane and midcrustal rocks. Reversed shots in the Prince William terrane indicate an average velocity of 6.1 km/s for rocks in the upper crust corresponding to layer 5 in the model (Figure 8). A high-amplitude secondary phase occurring in the record from shot point 37 at approximately 33 km offset to the north and 1.2 s is attributed to a reflection from the base of layer 5 in the model (Figure 7). In all shot records, travel time delays of approximately 0.17 s are observed in the vicinity of the Contact fault zone (Figures 3–7).

A group of midcrustal rocks containing low-/high-velocity pairs begins at approximately 6 km beneath shot point 19 in the model (Figure 8). The model contains two low-velocity

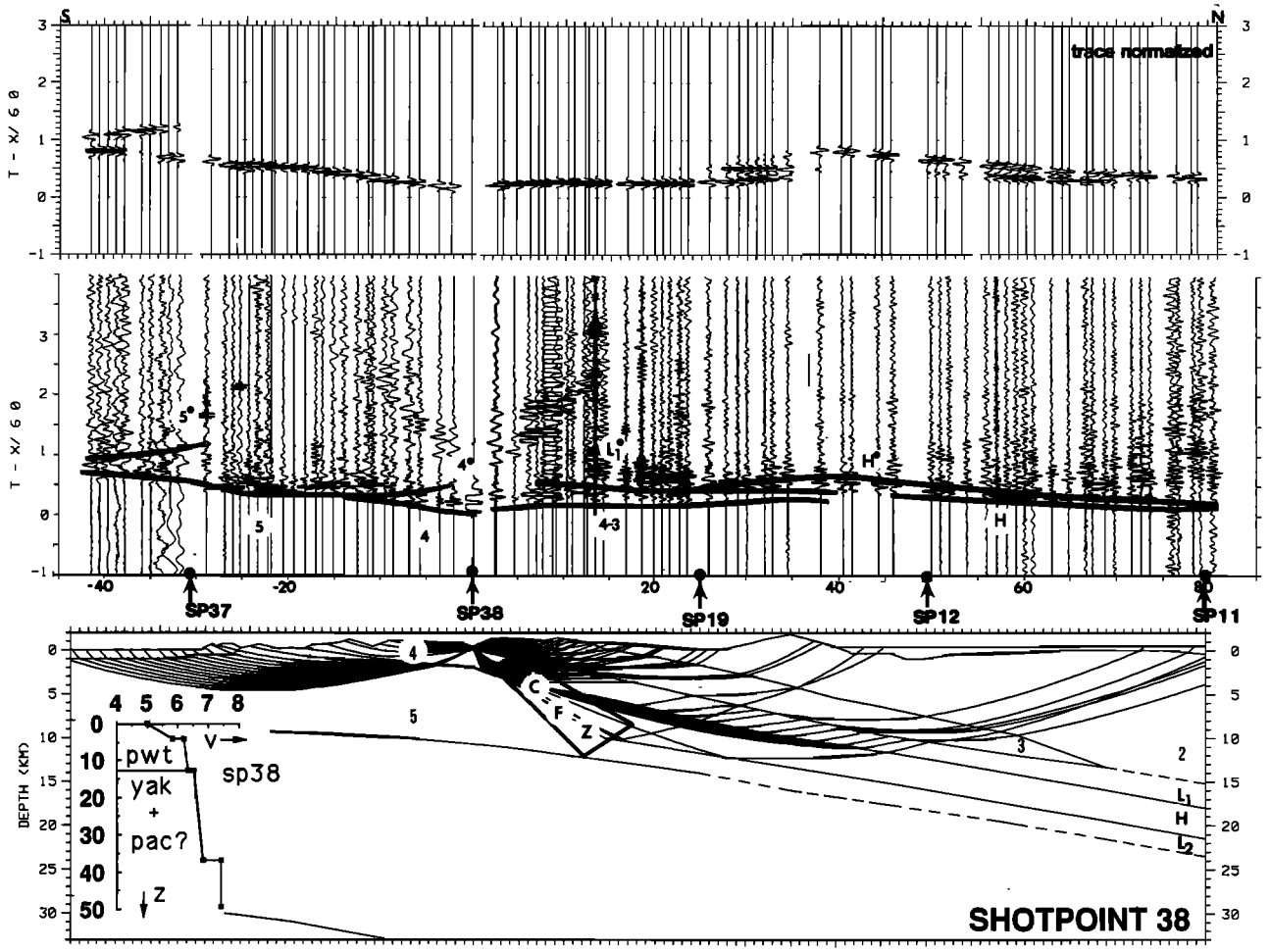

Fig. 6. Reduced-time record section with calculated travel times, synthetic record section, and simplied ray diagram for shot point 38 (SP 38). See Figure 3 caption for details.

zones: a 2.5-km-thick zone having an average velocity of 6.3 km/s (LVZ_1) and a 2- to 3-km-thick zone having an average velocity of 6.6 km/s (LVZ_2). Directly beneath the first velocity reversal is a sharp increase in average velocity to 6.8 km/s, corresponding to a high-velocity layer (HVZ). The low-velocity zones are indicated in the refraction data by (1) high-amplitude secondary arrivals (thought to result from energy reflecting from the base of the low-velocity layers), (2) complication in the record section associated with rays passing through midcrustal layers, and (3) delays or skips in the travel time curves. These travel time delays form en echelon arrivals that are best observed in the refraction data from the Chugach strike profile and are discussed in detail in that analysis [*Wolf and Levander*, 1989].

Preliminary models of the Chugach line used four low-/high-velocity pairs to match en echelon arrivals observed in the data [*Fuis and Ambos*, 1986; *Page et al.*, 1986]. This model resulted in primary arrivals from the higher-velocity layers occurring at distances not seen in the field data. A more successful approach used reflectivity methods to model en echelon arrivals in the data from the Chugach strike profile as multiple reflections within the second low-velocity zone [*Flueh et al.*, 1989]. Although the reflectivity method is more exact, it was not a suitable option for modelling the Cordova Peak line, where the crustal structure is complicated and interfaces are dipping. Offsets along the Cordova Peak dip profile are not adequate to constrain the depth or thickness of the second low-velocity zone, but it is included in the model based on interpretations of the Chugach line.

Evidence for the midcrustal low-velocity zones is best seen in the records from shot points 19 and 11. A secondary phase arriving at an offset of 25 km to the north and 1.2 s in the record from shot point 19 is correlated with energy reflecting off the base of LVZ_1 (Figure 5). A similar phase is observed to the south at 16 km offset and approximately 0.85 s. In the record from shot point 11, high-amplitude secondary arrivals as well as high apparent velocities at offsets of 45–85 km are attributed to rays passing through midcrustal areas containing the velocity reversals and high-velocity layer (Figure 3). An en echelon pattern, so predominant in data from the strike profile, is observed here.

Distinct horizons appearing in the Chugach seismic reflection data were used in the refraction model to provide some constraint on the depths to interfaces of these low-/high-velocity layers [*Fisher et al.*, 1989]. At least three bands of reflectors in the midcrust are imaged in the reflection data and are used here to provide information on the continuity of layers at the model's northern section, where reversed ray coverage is lacking. The absence of travel time delays and multiple high-amplitude secondary arrivals associated with

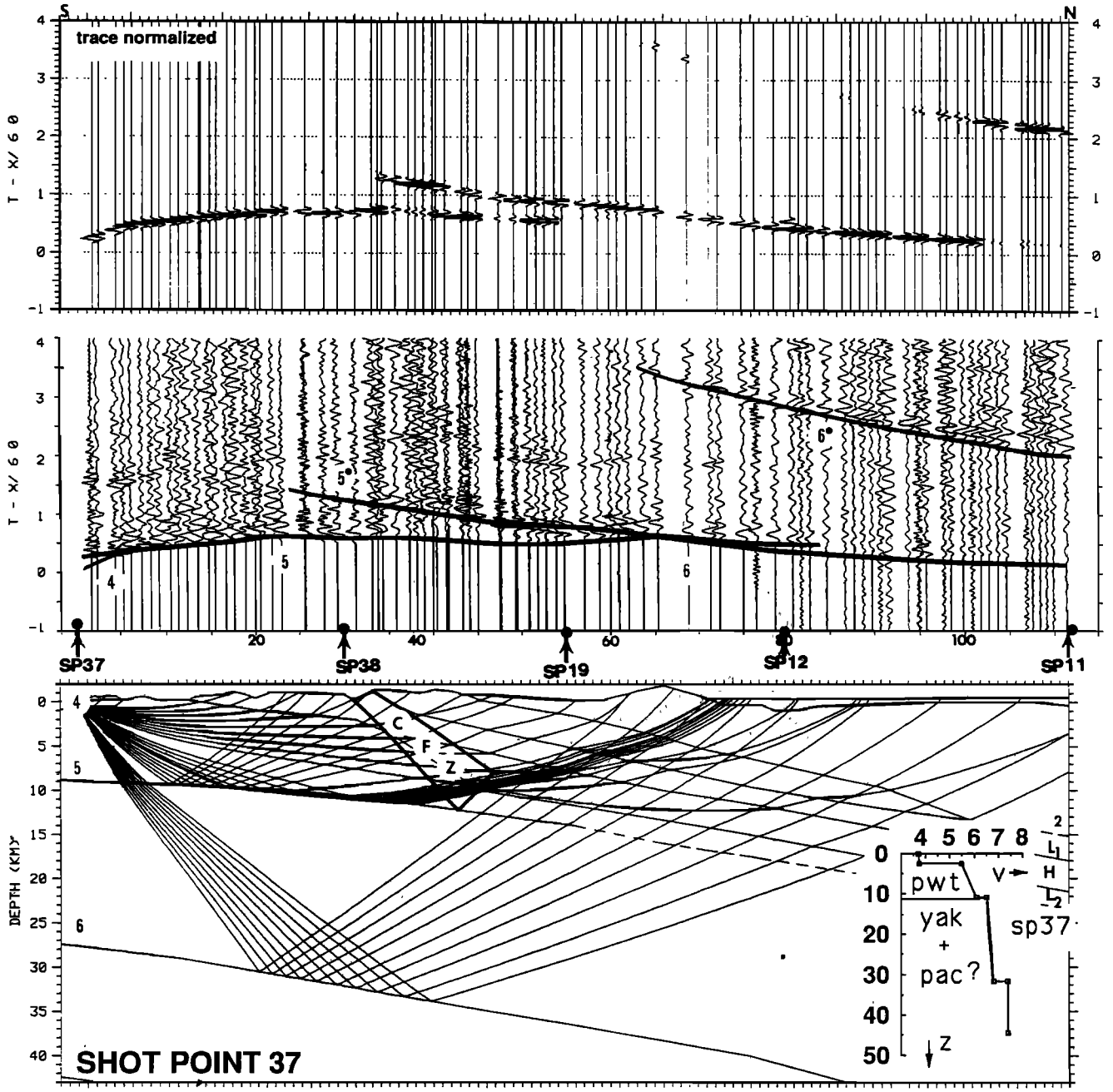

Fig. 7. Reduced-time record section with calculated travel times, synthetic record section, and simplied ray diagram for shot point 37 (SP 37). See Figure 3 caption for details.

energy sampling midcrustal regions beneath the Prince William terrane suggests that these low-/high-velocity zones are not present in that area. The midcrustal layers beneath the Chugach terrane are therefore not shown to extend southward beyond the Contact fault zone in the model.

The velocity structure of deeper layers beneath the Chugach and Prince William terranes is not well constrained by the Cordova Peak refraction data because offset coverage is insufficient. In the record from shot point 37, a late arriving phase is observed beginning at approximately 65 km offset and 3.5 s (Figure 7). This phase has an apparent velocity of 6.8 km/s and is modelled as a reflection from the lower crust (Figure 7). Without a refracted phase from the layer below, however, the depth and velocity of this layer are only weakly constrained. A late arriving phase also occurs in the record from shot point 11 at about 118 km offset and 2.1 s, but reliable identification of this phase or its apparent velocity is impossible without more data at longer offsets (Figure 3).

Earthquake hypocenters for events believed to be located within the subducting plate provide a lower limit for the overriding crust [*Davies*, 1975; *Lahr*, 1975; *Stephens et al.*, 1984; *Wolf and Levander*, 1989; *Page et al.*, 1989]. The upper limit of these hypocenters can be traced northward from the Aleutian trench to approximately a 22-km depth beneath shot point 19 (Figure 8). No corresponding high-

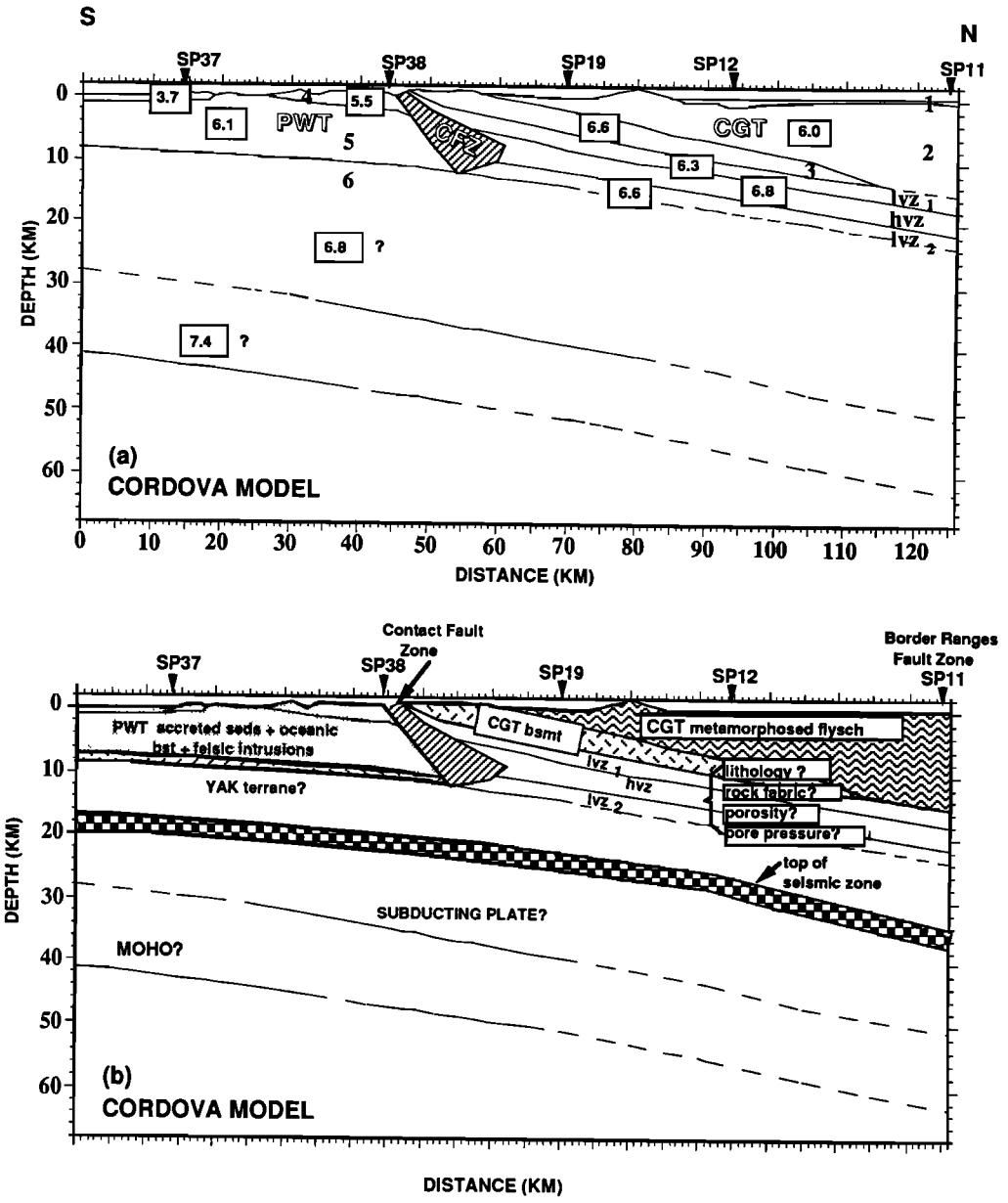

Fig. 8. Models showing average seismic velocities and possible geologic structure based on interpretation of U.S. Geological Survey Cordova Peak profile: (*a*) Seismic model showing average velocities (km/s) for model layers. Velocities and boundaries at model ends are not well constrained. (*b*) Possible geologic interpretation based on seismic model and cross section from *Plafker et al.* [1989]. Top of seismic zone constructed from *Page et al.* [1989].

amplitude phase is seen in the refraction data which can be correlated with a reflection from this depth, however. The lack of a prominent arrival could be the result of a low impedance contrast between the subducting and overriding plates or of high noise levels in the data at far offsets.

The data from shot point 36, an off-end shot to the south of the Cordova Peak profile, provide some information on deep structure. A high-amplitude late arriving phase is observed in the data beginning at approximately 80 km offset and 4 s, with an apparent velocity of 7.4 km/s (Figures 2 and 9). Since the subducting crust is presumed to be north dipping, the travel time of this phase indicates a reflector at greater depth (40–45 km) than that imaged in the data from shot points 37. It is postulated that the high-amplitude secondary phase observed in the off-end shot record is from energy sampling the crust/mantle boundary and that the phase beginning at 3.5 s in the data from shot point 37 indicates some intermediate reflector within the subducting crust.

Figure 10 is a composite rendition of information from earthquake and reflection data overlain on the seismic model proposed here. Figure 10 also contains a model based on refraction, reflection, and earthquake data acquired in the vicinity of Vancouver Island [*Hyndman et al.*, 1990]. Both diagrams are plotted at the same scale. Several similarities between the two areas are apparent. In both cases, a zone of prominent subhorizontal reflectors occurs in the midcrust, above earthquake hypocenters signifying the upper part of the subducting plate [*Page et al.*, 1989; *Hyndman et al.*, 1990]. *Clowes et al.* [1987] identified three bands of dipping reflectors which underlie a "lid" of accreted terranes (la-

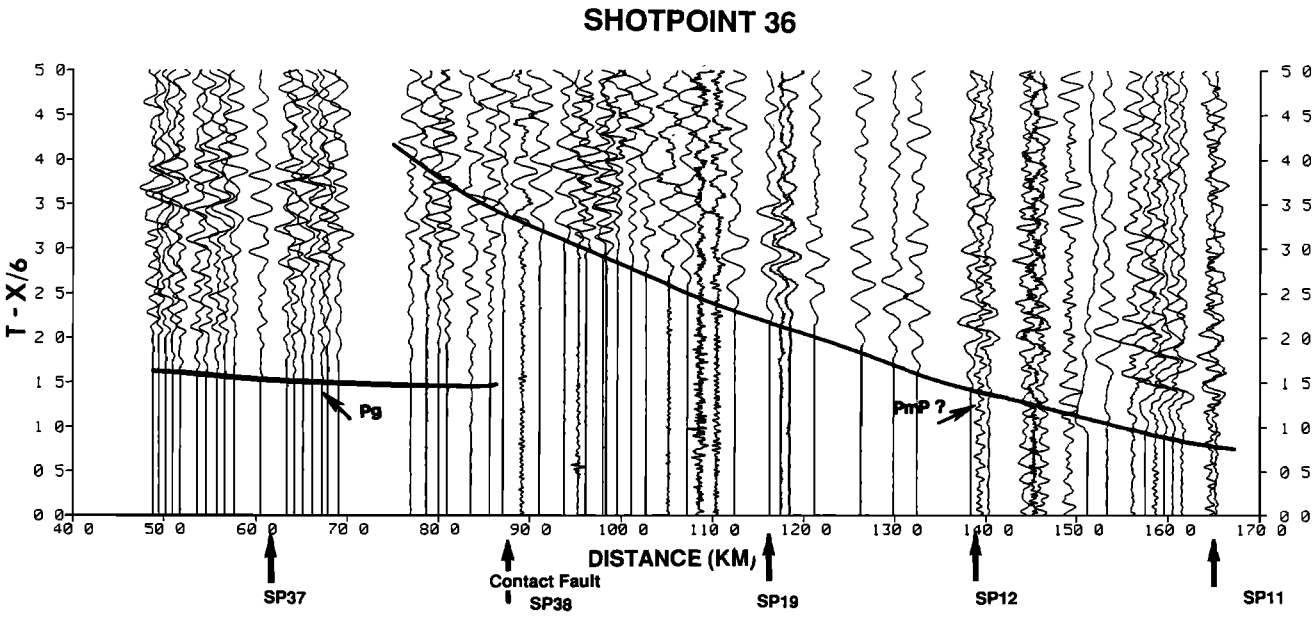

Fig. 9. Trace-normalized record section for shot point 36 (SP 36), an off-end shot for the Cordova Peak profile. The *Pg* phase dies out at approximately 90 km offset. A pronounced phase (*PmP*?) having an apparent velocity of 7.4 km/s appears at approximately 80 km and 4.0 s.

belled "C", "E" and "F" in Figure 10*a*). *Fisher et al.* [1989] imaged a similar set of reflecting zones beneath the accreted Chugach terrane (Figure 10*b*). In both cases, the midcrustal reflectors (forming a zone about 20 km thick) are approximately parallel to the inferred top of the subducting plate and occur at depths associated with velocity reversals in the refraction models. In both cases, the top of the seismic zone is nearly coincident with the deepest set of reflectors.

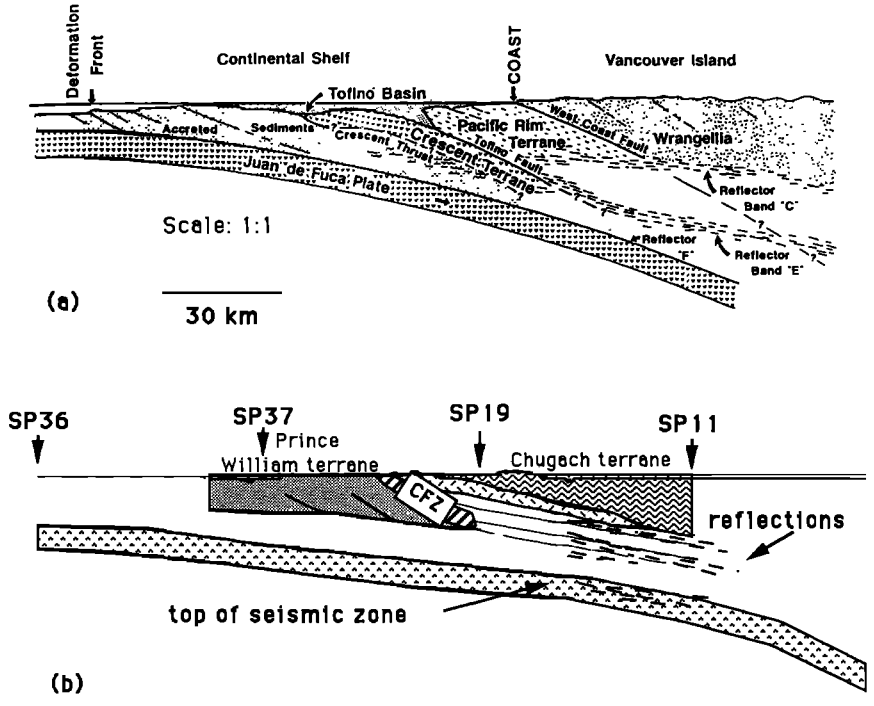

Fig. 10. Composite drawing showing similarities of crustal structure beneath southcentral Alaska and the Vancouver Island margin: (*a*) Interpretive crustal model from *Hyndman et al.* [1990, Figure 11] based on refraction, reflection and earthquake data [*Green et al.*, 1986; *Clowes et al.*, 1987; *Drew and Clowes*, 1990]. (*b*) Crustal model constructed from refraction interpretation (this paper), reflection data [*Fisher et al.*, 1989] and earthquake data [*Page et al.*, 1989]. In each case, a zone of prominent, subhorizontal midcrustal reflectors, about 20 km thick, occurs above the subducting plate and earthquake foci, where brittle failure is assumed. Reflections correlate well with positions of low-velocity zones in refraction interpretations from both areas.

GEOLOGIC INTERPRETATION

A possible geologic interpretation is shown with the detailed velocity model of the upper crustal structure along the Cordova Peak refraction profile in Figure 8. Layers 1–3 are correlated primarily with metamorphosed flysch and volcanic rocks of the Valdez Group. The northward thickening of layer 2 agrees with geologic models for the area and is in part due to thrust faulting and imbrication within the accretionary complex. Rocks of the McHugh Complex probably occur near the north end of the profile but are covered by surficial deposits. Complication in the record from shot point 11 close to the shot point may represent a subsurface contact between rocks of the Valdez Group and McHugh Complex or may be the result of diffracted or scattered energy from dikes which have intruded nearby areas of the transect. Although high-amplitude secondary arrivals are present in the record within 25 km offset from this shot point, they lack continuity between traces for any reasonable distance and do not form an identifiable phase (Figure 3). Another geologic feature which may contribute to the complicated arrival pattern and high near-surface velocities is the rootless Haley Creek terrane, a thin sliver of metasedimentary and metavolcanic rocks which has been thrust over Chugach terrane rocks in this area of the transect [*Wallace*, 1985; *Wolf and Wallace*, 1988; *Plafker et al.*, 1989; *Nokleberg et al.*, 1989] (Figure 2). Shot spacing and receiver density make detailed modelling of igneous intrusive rocks and the structural relationships between rocks of the Haley Creek terrane and those of the Chugach terrane difficult because the features are too small (<1–2 km).

Layer 3 of the model corresponds to an elongate outcrop belt of mafic volcanic rocks, just north of the Contact fault zone, which forms the oceanic basement of the terrane (Figures 2 and 8). High velocities associated with these rocks were also seen in the data from the Chugach seismic refraction profile [*Wolf and Levander*, 1989]. This volcanic unit makes a good marker for subsurface structure, because it produces prominent reflections and clear refracted arrivals in the seismic data. The change in the velocity-depth function between shot point 19 and shot points 11 and 12 indicates that layer 3, with its high velocities, probably pinches out to the north (Figure 8).

Layers 4 and 5 of the seismic model are correlated with Orca Group and overlying rocks of the Prince William terrane. Lateral variations in velocity within the upper 5 km of crust are associated with accreted sedimentary rocks which have been intruded by felsic igneous rocks, particularly near the fault zone, in the form of sills and plutons (Figure 2). Velocities in layer 5 (6.1 km/s) are consistent with those of sedimentary rocks which have been metamorphosed. A strong reflected phase from the base of layer 5 is attributed to a lithologic change at approximately 9 km depth. Mafic volcanic rocks, mainly oceanic basalts, have been observed in the Prince William terrane to the south of the transect and may project northward to occur at approximately this depth. These mafic rocks in contact with sedimentary rocks could provide an impedance contrast which would account for the high-amplitude secondary phase seen in the data (labelled 5* in Figure 7).

The seismic refraction data do not provide good constraints on the subsurface location of the Contact fault zone, which is better imaged by other geophysical techniques. The best fit model shown in Figure 8 is the result of iterative trials of over 15 different configurations of the Contact fault zone. Based on geologic investigations [*Winkler and Plafker*, 1981; *Plafker et al.*, 1986], potential field data (discussed below) and the best fit seismic model, the Contact fault system is shown as having moderate northward dips (approximately 45°). Layer 4 in the model appears to crosscut the fault zone and may represent a combination of intrusive igneous and sedimentary rocks. This crosscutting relationship has been observed at the surface (Figure 2). Although the precise geometry and location at depth of the boundary between the Prince William and Chugach terranes are not known, the seismic refraction data indicate very different velocity-depth functions for the two terranes to at least 10 km depth.

Midcrustal layers beneath the Chugach terrane are difficult to interpret because they are not seen in the mapped surface geology. Possible geologic interpretations have been discussed in the analysis of the Chugach strike profile [*Wolf and Levander*, 1989]. The dip profile through the Chugach terrane does not provide information which would clearly eliminate any of the possible models discussed in the earlier work. The preferred interpretation of the data is that there exist at least two low-velocity zones in the Chugach terrane: one which pinches out to the east in the strike direction [*Wolf and Levander*, 1989] and a deeper one which may be more laterally extensive (Figure 8). Low velocities could represent subducted oceanic or terrigenous clastic sediments in which variable porosity contributes to lateral and vertical velocity variations. High-velocity layers, which underlie the low-velocity zones, are thought to consist of mafic to ultramafic rocks, possibly comprising relict subducted oceanic crust. The low-/high-velocity zones could also indicate overpressurized areas or shear zones resulting from midcrustal decollements.

Geologic interpretation of the model with respect to deep structural relationships is speculative, since the area covered by rays from reversed shots is limited. Two reflecting horizons indicated by the refraction data appear to be located within the subducting Pacific plate (Figure 8). Only the phase velocities observed in the data from shot point 36, however, are high enough to be correlated with energy sampling the crust/mantle boundary within the subducting plate (Figure 9).

DISCUSSION OF OTHER GEOPHYSICAL DATA

Observed gravity and magnetic data provide restrictions on the crustal structure determined from seismic refraction data alone [*Andreason et al.*, 1964; *Barnes*, 1977; *U.S. Geological Survey*, 1979*a*, *b*; *Page et al.*, 1986]. Along the Cordova Peak line, complete Bouguer gravity values show a broad high located near shot point 19. Magnetic data along the transect show a relative high just to the north of the Contact fault zone which decreases gradually northward to the Border Ranges fault zone. Both high's correlate well with the high-velocity mafic oceanic basement rocks which crop out between the Contact fault zone and shot point 19 (Figures 2 and 8). Gravity values for the area near shot point 38 are interpreted to indicate an apparent dip of the Contact fault zone of approximately 45° to the north in the upper layers (D. Campbell, personal communication, 1988). Neither gravity nor seismic data, however, constrain the attitude of the fault in deeper layers. The decrease of gravity

and magnetic values northward in the dip direction corresponds to thickened sequences of flysch and steepened dip of the subducting plate beneath the Chugach terrane.

Rock samples collected along the transect for measurements of compressional velocities support the observation that Chugach terrane rocks are associated with unusually high velocities. Average velocities often attributed to mafic or ultramafic oceanic rocks (6.3–7.0 km/s at 300 MPa) are observed in metasedimentary rocks of the Valdez Group and average velocities at similar pressures for metavolcanic rocks, such as pillow basalts, are even higher (6.8–7.1 km/s) (N. Christensen, written communication, 1988). Although velocities observed in the seismic refraction data cannot be definitively correlated with rock type, the laboratory measurements provide guidelines for the geologic interpretation of the seismic model.

Studies of the Valdez Group rocks to determine anisotropy in the upper crust of the Chugach terrane show that energy travelling parallel to the foliation direction is significantly faster than that travelling perpendicular to foliation [*Brocher et al.*, 1989; *Brocher and Christensen*, 1990]. In addition, the studies show that the effects of anisotropy in the rocks can be seen to pressures of 600 MPa (6 kbar). A comparison of the velocity-depth functions and primary arrivals from shot point 19 in the Chugach profile with those from the Cordova Peak profile shows that velocities seen in data from the Cordova Peak line are slower than those observed at comparable depths along the Chugach line (Figure 11). Discrepancies between the strike and dip velocities in the Chugach terrane may be in part attributed to fracture or foliation orientations, out-of-plane reflections, changes in porosity and metamorphic grade, and the nonuniqueness of the model. This last factor is most pronounced for deeper layers.

Thermal studies of the Chugach terrane indicate that Valdez Group rocks have undergone high-temperature/low-pressure metamorphism not easily explained by mechanisms traditionally proposed for such regional events in subduction zone environments [*Hudson and Plafker*, 1982; *Sisson and Hollister*, 1988]. A regional event resulted in metamorphism of Chugach terrane rocks to greenschist facies. A second and more localized thermal event in early to middle Eocene time resulted in metamorphism to amphibolite facies in the core of the Chugach Metamorphic Complex. Studies of mineralogy and CO_2-rich fluid inclusions indicate that amphibolite facies metamorphism of the rocks occurred at approximately 10 km depth [*Sisson and Hollister*, 1988; *Sisson et al.*, 1989]. The significance of thermal history for the refraction interpretation is that it provides evidence that low-pressure/high-temperature metamorphosed rocks can occur at relatively shallow depths in subduction zone environments and that associated dewatering of underplated sediments can produce zones of high fluid pressures and high porosities at midcrustal depths. These, in turn, could account for low-velocity zones in midcrustal areas. In his interpretation of geophysical data from offshore British Columbia, *Hyndman* [1989] asserts that increased porosity in crustal layers can result in velocity reductions of up to 15%, a figure which would more than adequately account for the velocity reversals seen in the south central Alaska data.

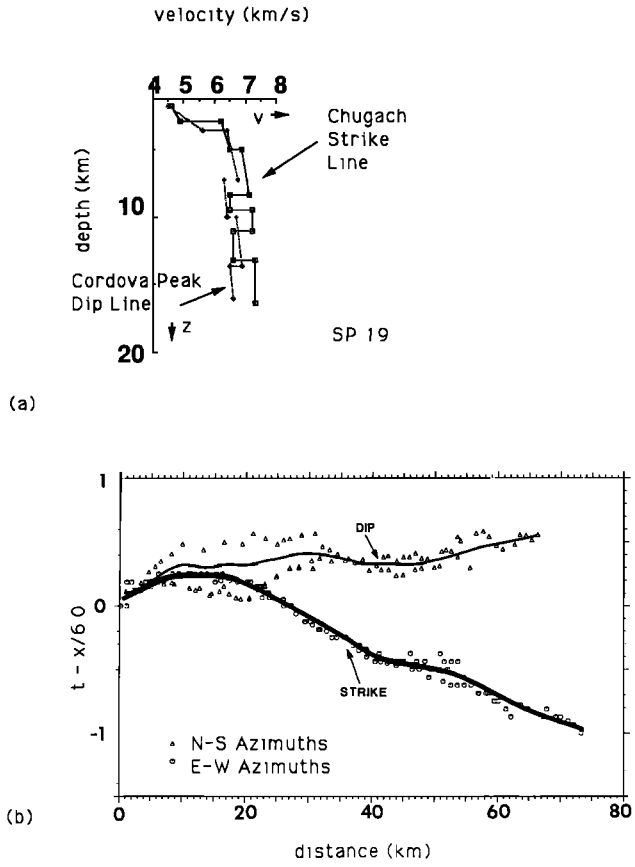

Fig. 11. A comparison of (*a*) velocity-depth functions at shot point 19 for the Cordova Peak and the Chugach seismic refraction profiles and (*b*) observed primary arrivals in records from shot point 19 for both profiles: triangles, Cordova Peak (N-S dip direction); circles, Chugach (E-W strike direction). Solid lines are averages between N-S directions (Cordova Peak line) and E-W directions (Chugach line), included to roughly account for the effect of dipping layers on travel times. Figures illustrate azimuthal variation of velocities and the corresponding discrepancies in seismic models for the Chugach and Cordova Peak profiles. Differences in velocities and interface locations for the upper crust can be explained in part by anisotropy, but differences for deeper layers probably reflect the nonuniqueness of the forward modelling method, limitations of the data due to receiver and shot spacing, and poor signal-to-noise ratios at long offsets.

Discussion and Summary

An attempt to tie the model for the Cordova Peak dip line with mapped surface geology and the previous interpretation of the Chugach strike line is illustrated by the fence diagram in Figure 12. This composite diagram shows the inferred structure beneath the Chugach profile as determined from the refraction data and projects it southward based on the mapped surface geology and refraction interpretation for the Cordova Peak line. The upper layers along each refraction line have been modelled to correspond with mapped contacts between surface rocks and to reflect observed structure as far as the ray-tracing algorithm would permit. Much lateral velocity variation exists within the upper 5 km of crust in both the Chugach and Prince William terranes. In both terranes, this variation is attributed to local areas of surficial deposits, to changes in metamorphic grade, and to laterally discontinuous igneous rocks which were intruded into country rock. Evidence for seismic anisotropy in the

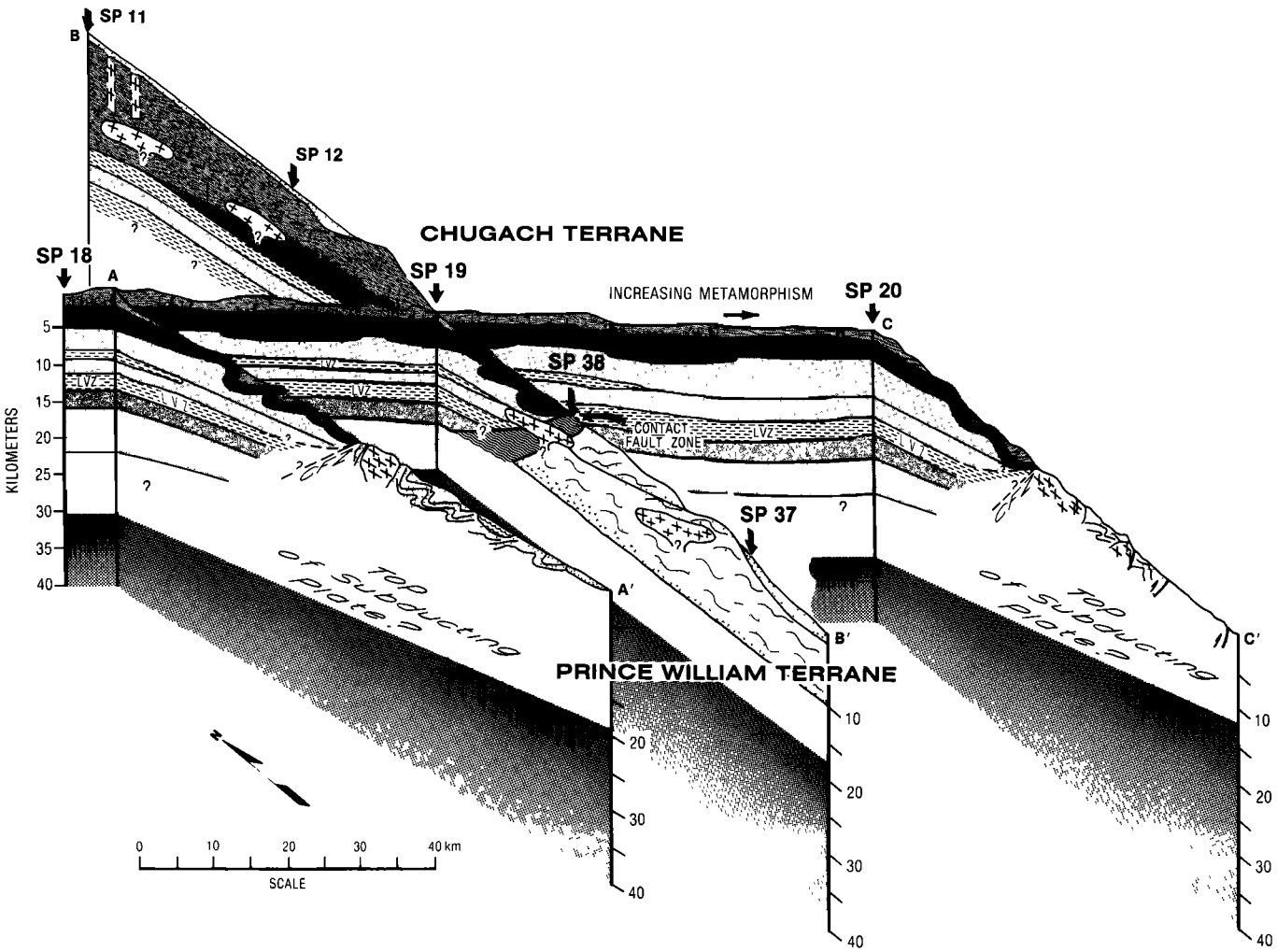

Fig. 12. Fence diagram illustrating possible geologic interpretation along lines shown in Figure 2. East-west cross section is based on interpretation of refraction data from the Chugach refraction profile [*Wolf and Levander*, 1989]. North-south cross section at SP 19 contains the model developed in this paper. Other cross sections are based on surface geology [*Winkler and Plafker*, 1981]. Both the Chugach and Prince William terranes are shown to extend to less than 10 km. The Chugach terrane is underlain by a region of midcrustal reflectors thought to contain two velocity reversals. A similar midcrustal package is not indicated by the data for the area beneath the Prince William terrane. Earthquake foci indicate approximate location of subducting plate and provide a lower limit to the overriding crustal package (western line from *Stephens et al.* [1984]; eastern line from *Wolf and Levander* [1986]). The Contact fault zone (CFZ) marks the boundary between the Chugach and Prince William terranes and is indicated by the data to extend to at least 10 km depth. Variation in shading pattern east of SP 19 marks the boundary of the Chugach Metamorphic Complex [*Hudson and Plafker*, 1982].

upper crust of the Chugach terrane from rock velocity studies is supported by the results of the refraction modelling presented here.

On the surface, the Contact fault zone appears to mark a major suture which separates two geologically different rock assemblages along the transect. The interpretation presented in Figures 8 and 12 is that rocks to the south have been accreted to and thrust under rocks of the Chugach terrane along the Contact fault zone. Although the Contact fault zone forms a boundary separating areas of the crust with differing velocity structures, it is uncertain from the seismic data whether the fault is a suture between geologically distinct assemblages or is simply an out-of-sequence thrust in an accretionary complex. A thrust of this sort could transport higher-velocity basement rocks closer to the surface, thus creating very different velocity-depth functions to either side of the fault plane.

Midcrustal layers beneath the Chugach terrane are assumed to be rocks which lack surface expression and do not extend southward beyond the Contact fault zone. These lower layers have velocities compatible with those of oceanic crust, and it is suggested that they comprise layered oceanic crust imbricated during large-scale subduction. Velocity reversals may represent subducted sedimentary rocks which have zones of high-porosity, overpressurized zones or shear zones associated with midcrustal decollements. Complication in the shot records, travel time delays, and high-amplitude secondary arrivals associated with energy passing through this region beneath the Chugach terrane are not observed in records of energy sampling midcrustal regions

beneath the Prince William terrane. The differences in velocity structure between northern and southern sections of the Cordova Peak profile indicate that the Contact fault zone is a boundary which extends to at least 10 km depth and either truncates or soles into midcrustal layers beneath the Chugach terrane. A coincident reflection survey along the profile through the Chugach terrane indicates strong midcrustal reflectors which approximately correspond to the positions of low-velocity zones in the refraction model. Similar midcrustal reflectors and associated low-velocity zones are imaged in seismic data from Vancouver Island.

Earthquake foci are believed to delineate the top of the subducting Pacific plate at approximately 22–30 km depth below the Chugach refraction profile and provide a lower limit for the upper crustal package (Figure 12). Although several models exist to describe the geometry of the Wadati-Benioff zone, the refraction data do not yield much information which would better define its shape. A lack of evidence in the refraction data for a sharp velocity contrast at the inferred location of the plate interface, however, suggests that the bottom of the overriding crust and the top of the subducting plate may have similar composition or physical properties. Although they are insufficient to determine uniquely the complex geometries and structural relationships of the accreted Chugach and Prince William terranes, particularly with respect to the lower crust, the refraction data from the Chugach and Cordova Peak profiles provide good constraints on upper crustal features which have dimensions of at least several kilometers.

Acknowledgments. The authors would like to thank the U.S. Geological Survey and Walter Mooney for providing the refraction data used in this study, J. Luetgert for gracious sharing of software, and B. Page for help with earthquake data. TACT workshops hosted by the USGS provided much valuable information and discussion. Reviews of the manuscript by G. Fuis, R. Clowes, and an anonymous reviewer greatly improved its quality. L.W. would also like to acknowledge support from the Air Force during manuscript preparation.

REFERENCES

Andreason, G. E., A. Grantz, I. Zietz, and D. F. Barnes, Geological interpretation of magnetic and gravity data in the Copper River Basin, Alaska, *U.S. Geol. Surv. Prof. Pap, 316-H*, 135–153, 1964.

Barnes, D. F., Bouguer gravity map of Alaska, scale 1:2,500,000, *U.S. Geol. Surv. Geophys. Invest. Map, GP-913*, 1977.

Brocher, T. M., and N. I. Christensen, Seismic anisotropy due to preferred mineral orientation in shallow crustal rocks in southern Alaska, *Geology*, *18*, 737–740, 1990.

Brocher, T. M., M. A. Fischer, E. L. Geist, and N. I. Christensen, High-resolution seismic reflection/refraction study of the Chugach-Peninsular terrane boundary, southern Alaska, *J. Geophys. Res.*, *94*, 4441–4455, 1989.

Bruns, T. R., Model for the origin of the Yakutat block, an accreting terrane in the northern Gulf of Alaska, *Geology*, *11*, 718–721, 1983.

Cerveny, V., A. Moltokov, and I. Psencik, *Ray Method in Seismology*, 214 pp., University of Karlova, Prague, Czechoslovakia, 1977.

Clowes, R. M., M. T. Brandon, A. G. Green, C. J. Yorath, A. Sutherland Brown, E. R. Kanasewich, and C. Spencer, LITHOPROBE—Southern Vancouver Island: Cenozoic subduction complex imaged by deep seismic reflections, *Can. J. Earth Sci.*, *24*, 31–51, 1987.

Davies, J. N., Seismological investigations of plate tectonics in south central Alaska, Ph.D. dissertation, 193 pp., Univ. of Alaska, Fairbanks, 1975.

Drew, J. J., and R. M. Clowes, A re-interpretation of the seismic structure across the active subduction of western Canada, in Studies of Laterally Heterogeneous Structures Using Seismic Refraction and Reflection Data, edited by A. G. Green, *Pap. Geol. Surv. Can.*, *89-13*, 115–132, 1990.

Dumoulin, J. A., Sandstone petrographic evidence and the Chugach-Prince William terrane boundary in southern Alaska, *Geology*, *16*, 456–460, 1988.

Engebretson, D., A. Cox, and R. G. Gordon, Relative motions between oceanic and continental plates in the Pacific Basin, *Spec. Pap. Geol. Soc. Am.*, *206*, 54 pp., 1985.

Fisher, M. A., T. M. Brocher, W. J. Nockleberg, G. Plafker, and G. L. Smith, Seismic reflection images of the crust of the northern part of the Chugach terrane, Alaska: Results of a survey for the Trans-Alaska Crustal Transect (TACT), *J. Geophys. Res.*, *94*, 4424–4440, 1989.

Flueh, E. R., W. D. Mooney, G. S. Fuis, and E. L. Ambos, Crustal structure of the Chugach Mountains, southern Alaska: A study of peg-leg multiples from a low-velocity zone, *J. Geophys. Res.*, *94*, 16,023–16,034, 1989.

Fuis, G. S., and E. L. Ambos, Deep structure of the Contact Fault and the Prince William terrane: Preliminary results of the 1985 TACT seismic-refraction survey, U.S. Geological Survey Accomplishments in Alaska, 1985, *U.S. Geol. Surv. Circ.*, *978*, 41–45, 1986.

Green, A. G., R. M. Clowes, C. J. Yorath, C. Spencer, E. R. Kanasewich, M. T. Brandon, and A. Sutherland Brown, Seismic reflection imaging of the subducting Juan de Fuca plate, *Nature*, *319*, 210–213, 1986.

Hudson, T., and G. Plafker, Paleogene metamorphism in an accretionary flysch terrane, eastern Gulf of Alaska, *Geol. Soc. Am. Bull.*, *92*, 1280–1290, 1982.

Hyndman, R. D., Dipping seismic reflectors, electrically conductive zones, and trapped water in the crust over a subducting plate, *J. Geophys. Res.*, *93*, 13,391–13,405, 1989.

Hyndman, R. D., C. J. Yorath, R. M. Clowes, and E. E. Davis, The northern Cascadia subduction zone at Vancouver Island: Seismic structure and tectonic history, *Can. J. Earth Sci.*, *27*, 313–329, 1990.

Jones, D. L., N. J. Silberling, H. C. Berg, and G. Plafker, Tectonostratigraphic terrane map of Alaska, *U.S. Geol. Surv. Open File Rep.*, *81-792*, 1981.

Jones, D. L., N. J. Silberling, P. J. Coney, and G. Plafker, Lithotectonic terrane map of Alaska (west of the 41st meridian), *U.S. Geol. Surv. Misc. Field Stud. Map, MF-1874-A*, 1987.

Lahr, J. C., Detailed seismic investigation of Pacific-North American plate interaction in southern Alaska, Ph.D. dissertation, 88 pp., Columbia Univ., New York, 1975.

Lahr, J. C., and G. Plafker, Holocene Pacific-North American plate interaction in southern Alaska: implications for the Yakataga seismic gap, *Geology*, *8*, 483–486, 1980.

Luetgert, J., Programs RAY86 and R86PLT: Interactive two-dimensional raytracing/synthetic seismogram package (VAX/VMS) version, *U.S. Geol. Surv.*, Menlo Park, Calif., 1987.

Ma, C., J. W. Ryan, and D. Caprette, Crustal dynamics project data analysis—1988, VLBI geodetic results 1979–87, *NASA Tech. Memo.*, *TM-100723*, 214 pp., 1989.

Minster, J. B., T. J. Jordan, P. Molnar, and E. Haines, Numerical modelling of instantaneous plate tectonics, *Geophys. J. R. Astron. Soc.*, *36*, 541–576, 1974.

Nokleberg, W. J., G. Plafker, J. S. Lull, W. K. Wallace, and G. R. Winkler, Structural analysis of the southern Peninsular, southern Wrangellia, and northern Chugach terranes along the Trans-Alaska Crustal Transect, northern Chugach Mountains, Alaska, *J. Geophys. Res.*, *94*, 4297–4320, 1989.

Page, R. A., G. Plafker, G. S. Fuis, W. J. Nokleberg, E. L. Ambos, W. E. Mooney, and D. L. Campbell, Accretion and subduction tectonics in the Chugach Mountains and Copper River Basin, Alaska: Initial results of the Trans-Alaska Crustal Transect, *Geology*, *14*, 501–505, 1986.

Page, R. A., C. D. Stephens, and J. C. Lahr, Seismicity of the Wrangell and Aleutian Wadati-Benioff zones and the North American plate along the Trans-Alaska Crustal Transect, Chugach Mountains and Copper River Basin, southern Alaska, *J. Geophys. Res.*, *94*, 16,059–16,082, 1989.

Perez, O. J., and K. H. Jacob, Tectonic model and seismic potential

of the eastern Gulf of Alaska and Yakataga seismic gap, *J. Geophys. Res.*, *85*, 7132–7150, 1980.

Plafker, G., Regional geology and petroleum potential of the northern Gulf of Alaska continental margin, in *Geology and Resource Potential of the Continental Margin of Western North America and Adjacent Ocean Basins, AAPG Circum-Pac. Earth Sci. Ser.*, vol. 6, edited by D. W. Scholl, A. Grantz, and J. G. Vedder, pp. 229–268, American Association of Petroleum Geologists, Houston, Tex., 1987.

Plafker, G., W. J. Nokleberg, J. S. Lull, S. M. Roeske, and G. R. Winkler, Nature and timing of deformation along the Contact Fault System in the Cordova, Bering Glacier and Valdez Quadrangle, U.S. Geological Survey Accomplishments in Alaska, 1985, *U.S. Geol. Surv. Circ.*, *978*, 74–77, 1986.

Plafker, G., W. J. Nokleberg, and J. S. Lull, Bedrock geology and tectonic evolution of the Wrangellia, Peninsular, and Chugach terranes along the Trans-Alaska Crustal Transect in the Chugach Mountains and southern Copper River Basin, *J. Geophys. Res.*, *94*, 4255–4295, 1989.

Silberling, N. J., and D. L. Jones, Lithotectonic terrane maps of the North American Cordillera, *U.S. Geol. Surv. Open File Rep.*, *84-523*, A1–A12, 1984.

Sisson, V. B., and L. S. Hollister, Low-pressure facies series metamorphism in an accretionary sedimentary prism, southern Alaska, *Geology*, *16*, 358–361, 1988.

Sisson, V. B., L. S. Hollister, and T. C. Onstott, Petrologic and age constraints on the origin of a low-pressure/high-temperature metamorphic complex, southern Alaska, *J. Geophys. Res.*, *94*, 4392–4410, 1989.

Stephens, C. D., K. A. Fogelman, J. C. Lahr, and R. A. Page, Wrangell Benioff zone, southern Alaska, *Geology*, *12*, 373–376, 1984.

Stone, D. B., B. C. Panuska, and D. R. Packer, Paleolatitudes versus time for southern Alaska, *J. Geophys. Res.*, *87*, 3697–3707, 1982.

U.S. Geological Survey, Aeromagnetic map of parts of the Cordova and Middleton Island 1 by 3 quadrangles, Alaska, scale 1:250,000, *U.S. Geol. Surv. Open File Rep.*, *79-223*, 1979*a*.

U.S. Geological Survey, Aeromagnetic map of part of the Valdez 1 by 3 quadrangle, Alaska, scale 1:250,000, *U.S. Geol. Surv. Open File Rep.*, *79-381*, 1979*b*.

von Huene, R., G. Keller, T. R. Bruns, and K. McDougall, Cenozoic migration of Alaskan terranes indicated by paleontologic study, in *Tectonostratigraphic Terranes of the Circum-Pacific Region, Earth Sci. Ser.*, vol. 1, edited by D. G. Howell, pp. 121–136, Circum-Pacific Council for Energy and Mineral Resources, Houston, Tex., 1985.

Wallace, W. K., Tectonic evolution of the Haley Creek terrane, a rootless thrust sheet in the Chugach Mountains, Alaska, *Geol. Soc. Am. Abstr. Programs*, *17*, 416, 1985.

Wilson, J. M., P. Meador, and G. Fuis, Data report for the 1985 TACT seismic refraction survey, south-central Alaska, *U.S. Geol. Surv. Open File Rep.*, *87-440*, 78 pp., 1987.

Winkler, G. R., and G. Plafker, Geologic map and cross sections of the Cordova and Middleton Island quadrangles, southern Alaska, scale 1:250,000, *U.S. Geol. Surv. Open File Rep.*, *81-1164*, 26 pp., 1 sheet, 1981.

Winkler, G. R., M. L. Silberman, A. Grantz, R. J. Miller, and E. M. MacKevett, Jr., Geologic map and summary geochronology of the Valdez quadrangle, southern Alaska, scale 1:250,000, *U.S. Geol. Surv. Open File Rep.*, *80-892A*, 2 sheets, 1981.

Wolf, L. W., and A. R. Levander, Upper crustal structure of the accreted Chugach terrane, Alaska, *J. Geophys. Res.*, *94*, 4457–4466, 1989.

Wolf, L. W., and W. K. Wallace, Upper crustal structure of the Chugach and Prince William terranes, Alaska, *Eos Trans. AGU*, *69*, 44, 1988.

J. N. Davies and D. B. Stone, Geophysical Institute, University of Alaska, Fairbanks, AK 99775.

L. W. Wolf, Air Force Geophysics Laboratory, LWH, Hanscom AFB, MA 01731-5000.

(Received July 17, 1989;
revised May 20, 1991;
accepted May 20, 1991.)

JOURNAL OF GEOPHYSICAL RESEARCH, VOL. 96, NO. B10, PAGES 16,509–16,524, SEPTEMBER 10, 1991

Surface Deformation and Energy Release Rates for Constant Stress Drop Slip Zones in an Elastic Half-Space

M. WU, J. W. RUDNICKI, C. H. KUO, AND L. M. KEER

Department of Civil Engineering, Northwestern University, Evanston, Illinois

Free surface displacements, stress intensity factors, and energy release rates are calculated for planar slip zones in an elastic half-space subjected to a prescribed shear stress drop. Although the method can treat arbitrarily shaped planar zones and distributed stress drops, for simplicity, results are presented only for circular and elliptic zones and uniform stress drops. Calculations of the stress intensity factors and energy release rates for various geometries indicate that solutions for the half-space differ by less than 10% from those in the full space if the distance from the slip zone center to the free surface is greater than the downdip width of the slip zone. In addition, the influence of the free surface is greater for decreasing dip angle. For slip zones that are near the free surface and, especially, those that break the surface there is a coupling between slip and normal relative displacement. That is, for a prescribed shear stress drop and zero normal stress change, slip induces relative normal displacement. As example applications, these solutions are used to reexamine the coseismic geodetic data from three earthquakes: 1966 Parkfield, 1983 Borah Peak, and 1987 Whittier Narrows. The geometries, moments, and stress drops are similar to those inferred in previous studies using dislocation methods. However, the stress drop inferred here may be more reliable because stress drop is one of the parameters adjusted to fit the observed surface deformations. In addition, the method makes it possible to estimate the critical energy release rate at the termination of rupture. Values for the Parkfield, Borah Peak, and Whittier Narrows earthquakes are 1.5×10^6 J/m^2, 1.2×10^6 J/m^2, and 2×10^8 J/m^2, respectively.

INTRODUCTION

Why do earthquake ruptures start and stop? In order to address this question we require a criterion for propagation. Although rupture criteria in the Earth's crust are not known with any certainty, a simple one that is widely used in fracture mechanics and is often adopted in faulting problems is that the energy released per unit area of slip advance is equal to a critical value [*Rudnicki*, 1980; *Rice*, 1980, 1983; *Li*, 1987]. This criterion is undoubtedly too simple to describe in detail the actual processes of rupture and slip propagation. Nevertheless, when these more complex processes occur in a zone near the fault rupture edge having a length scale much smaller than other relevant lengths, e.g., fault rupture length, distance to the free surface, etc., it is well known that the energy release criterion provides a good description of rupture [e.g., *Rudnicki*, 1980; Rice, 1980, 1983]. Furthermore, because the stress and displacement fields near the edge of a crack in a linear elastic body have a universal form characterized by the stress intensity factors (coefficients of the singular stresses), the energy release rate can be expressed in terms of these factors [*Rice*, 1968].

An impediment to the application of this criterion to slip in the Earth's crust has been the difficulty of calculating stress intensity factors for realistic geometries. Although many results are known for two-dimensional problems and for simple crack shapes in three-dimensional bodies [*Murakami*, 1987], there are few analytical results for cracks in an elastic half-space.

In this paper we present a numerical method for calculating the stresses and displacements in an elastic half-space due to embedded and surface-breaking zones of prescribed stress drop. For simplicity, we present results only for elliptical zones and constant stress drops, but the method is sufficiently general to treat arbitrary planar shapes and spatially varying stress drops. Because the method incorporates the exact asymptotic form of the slip near the edge of a crack in a linear elastic body, results for the stress intensity factors are accurate. Furthermore, the method is based upon integration of the exact form of the displacement due to a point force in a half-space and hence can treat accurately cases in which the slip zone intersects the surface of the half-space.

We present results for the effect of the free surface on the stress intensity factors, the moment, and the energy release rate. Two features are of particular interest: the distance from the free surface at which its effect is negligible and the effect of proximity of the free surface on the tendency of the rupture to propagate toward it.

As applications of this method, we reexamine the coseismic geodetic data for three earthquakes: 1966 Parkfield, 1983 Borah Peak, and 1987 Whittier Narrows. In this approach, the stress drop is a parameter of the model and hence is constrained by comparison of the calculated and observed surface displacements. Furthermore, if the slip zone is assumed to propagate according to the criterion that the energy release rate equals a critical value, then we are able to estimate the critical value at the termination of rupture.

The stress drop method which we use here can be contrasted with the more common dislocation approach. The dislocation approach models slip zones by approximating them as surfaces of prescribed displacement discontinuity. Comparison of the calculated surface deformations with observations is used to infer the geometry of the slip zones and the distribution of slip. An advantage of the dislocation approach is its simplicity: once the solution for an elemental point slip is determined, results for general distributions of slip and complex shapes can be obtained by quadrature. As a result, this approach has become a staple for inferring

Paper number 91JB01043.
0148-0227/91/91JB-01043$05.00

information about slip from surface deformation measurements.

A disadvantage of this dislocation approach is that it is purely kinematic: it relates surface deformation to slip at depth but does not directly yield information about the stresses that produced the slip. More specifically, when the distribution of slip is approximated by constant slip elements (as is usually the case), the average stress change is unbounded. Consequently, stress drop can be inferred only indirectly. For example, the typical method is to calculate the moment and infer the stress drop by using the relation between the moment and the stress drop for a circular crack in an infinite body. Thus the stress drop is determined from a slip distribution that is different from the one inferred from the observations and used to calculate the moment. Furthermore, because the stress near the edge of a zone modeled by constant slip elements is not only singular but nonintegrable, it is not possible to calculate an energy release rate. As a result, the information concerning rupture propagation obtained by this method is limited.

The next section of the paper briefly describes the formulation of the problem and the numerical method used. Succeeding sections present results for the effect of the free surface on slip zones of various geometries and depths and for application of the stress drop approach to reexamine the coseismic geodetic data for three earthquakes.

Method of Analysis

The goal is to obtain the stress and displacement fields in an elastic half-space caused by a prescribed stress drop on a planar surface of discontinuity S. To do this, we develop first an expression for the stress in the half-space due to a prescribed displacement discontinuity. When this expression is evaluated on the surface of discontinuity S, it becomes an integral equation for the unknown distribution of displacement discontinuities arising from the prescribed stress change on S. This equation is solved by using a numerical method that expresses it as a system of linear algebraic equations. Once the appropriate distribution of displacement discontinuities is determined, other quantities of interest, such as the free surface displacement and the stress intensity factors, can be determined.

Consider an elastic body in which the stresses σ_{ij} are related to the displacement gradients $u_{k,l}(=\partial u_k/\partial x_l)$ by

$$\sigma_{ij} = C_{ijkl}u_{k,l} \tag{1}$$

where C_{ijkl} is the tensor of elastic moduli. For the case of an isotropic material considered here C_{ijkl} has the following form:

$$C_{ijkl} = \frac{2\mu\nu}{(1-2\nu)}\,\delta_{ij}\delta_{kl} + \mu(\delta_{ik}\delta_{jl} + \delta_{il}\delta_{jk}) \tag{2}$$

where μ is the shear modulus, ν is Poisson's ratio, and δ_{ij} is the Kronecker delta. Let $B_1(\boldsymbol{\xi})$ be relative displacements

$$B_i(\boldsymbol{\xi}) = u_i^+ - u_i^- \tag{3}$$

on a planar surface of discontinuity S with a unit normal $\mathbf{n}$ directed from the (−) to the (+) side of S. The resulting displacements elsewhere in the body are given by [e.g., *Steketee*, 1958]

$$u_i(\mathbf{x}) = \int_S C_{klmn}n_m B_n(\boldsymbol{\xi})\,\frac{\partial G_{ik}}{\partial \xi_l}(\mathbf{x}, \boldsymbol{\xi})\,d\boldsymbol{\xi} \tag{4}$$

where $G_{ij}(\mathbf{x}, \boldsymbol{\xi})$ is the displacement in the ith direction at $\mathbf{x}$ due to a unit point force in the jth direction at $\boldsymbol{\xi}$. The corresponding stresses are obtained by substituting (4) into (1):

$$\sigma_{ij} = C_{ijkl}C_{pqmn}\int_S n_m B_n(\boldsymbol{\xi})\,\frac{\partial^2 G_{kp}}{\partial x_l\,\partial \xi_q}(\mathbf{x}, \boldsymbol{\xi})\,d\boldsymbol{\xi} \tag{5}$$

Although the displacement discontinuity is unknown, we require that it produce a prescribed stress (drop) p_j on S:

$$n_i\sigma_{ij} = -p_j \qquad \text{for } \mathbf{x} \text{ on } S \tag{6}$$

Substitution of (5) into (6) yields the following integral equation:

$$\int_S K_{mn}(\mathbf{x}, \boldsymbol{\xi})B_n(\boldsymbol{\xi})\,d\boldsymbol{\xi} = -p_m(\mathbf{x}) \qquad \text{for } \mathbf{x} \text{ on } S \tag{7}$$

where

$$K_{mn} = n_i C_{imkl}C_{pqrn}n_r\,\frac{\partial^2 G_{kp}}{\partial x_l\,\partial \xi_q} \tag{8}$$

Once the $B_n(\boldsymbol{\xi})$ are determined from (7), the displacements of any point in the half-space and, in particular, of the free surface can be obtained from (4).

In order to implement these results for elliptical slip zones in a half-space, we use the two coordinate systems shown in Figure 1. The origin of the y_1 system is at the center of the slip zone a distance h below the free surface. The y_1 and y_2 axes lie in the plane of the slip zone, and the y_3 axis is perpendicular to the slip surface. The y_1 axis is horizontal and points along one axis of the ellipse in the direction of the slip zone strike. The y_2 axis points along the other axis of the ellipse in the direction of slip zone dip and is inclined at an angle α from the vertical. Thus the slip zone dips at an angle $\pi/2 - \alpha$. The x_i system has its origin at the surface directly above the center of the slip zone. The x_1 axis is horizontal, parallel to the y_1 axis, and in the direction of slip zone strike. The x_2 axis is vertical and points down into the half-space. The x_3 axis is horizontal and in the same vertical plane as the x_2 axis.

The kernel (8) can be calculated from *Mindlin*'s [1936] solution for a point force in an elastic half-space (also see *Mindlin* [1955] and *Mindlin and Cheng* [1950]) or, alternatively, by specializing the results of *Lee and Keer* [1986] and of *Lee et al.* [1987] for a bimaterial interface. The appendix records expressions for these kernels in components relative to the slip zone coordinate system y_i. The kernels of the integral (4) are also listed there in components relative to the half-space coordinate system x_i.

The numerical solution of the integral equation (7) follows the method developed by *Lee and Keer* [1986] for a tensile crack near a bimaterial interface. A feature of the method is that the variation of the relative displacements near the edge of the slipping zone is constrained to have the form appropriate for a crack in an isotropic linear elastic body. More specifically, the relative displacements near the crack edge have the following asymptotic form [e.g., *Rice*, 1968]:

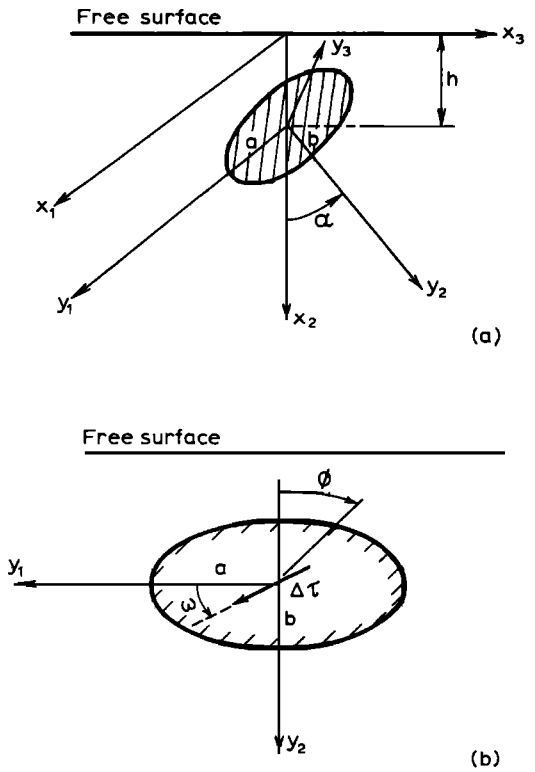

Fig. 1. (*a*) Geometry and coordinate systems for an inclined elliptical slip zone in the Earth's crust: The origin of the y_i system is at the center of the slip zone a distance h below the free surface. The y_1 and y_2 axes lie in the plane of the slip zone, and y_3 is perpendicular to the slip surface. The origin of the x_i system is on the half-space surface directly above the slip zone center. The x_1 axis is parallel to y_1 and in the direction of slip zone strike, and the x_2 axis is perpendicular to the half-space surface. The angle between the vertical (x_2 axis) and the y_2 axis is α. (*b*) View perpendicular to the plane of the slip zone (y_1y_2 plane). Polar angle ϕ is measured from the negative y_2 direction in the crack plane (y_1y_2). The orientation of the stress drop $\Delta\tau$ is defined by the angle ω measured from the y_1 (striking) direction.

$$(B_{\mathrm{I}}, B_{\mathrm{II}}, B_{\mathrm{III}}) = \frac{4(1-\nu)}{\mu}\left[\frac{\rho}{2\pi}\right]^{1/2}[K_{\mathrm{I}}, K_{\mathrm{II}}, K_{\mathrm{III}}/(1-\nu)] \tag{9}$$

as $\rho \rightarrow 0$, where ρ is distance from the crack edge, B_{I} is the relative opening (mode I), and B_{II} and B_{III} are relative displacements for shearing perpendicular to (mode II) and parallel to (mode III) the crack edge. The constants K_{I}, K_{II}, and K_{III} are the corresponding stress intensity factors. Because the relative displacements near the edge of any crack in a linear elastic isotropic body have this form (9), any differences in geometry or applied loading are reflected entirely in different values of the stress intensity factors. The result (9) is embedded in the numerical solution by choosing the $B_i(\xi)$ to have the following form:

$$B_i(\xi) = [2a\varepsilon - \varepsilon^2]^{1/2} f_i(\xi) \tag{10}$$

where ε is the shortest distance of the integration point ξ to the crack front, and a is the larger semiaxis of the elliptical slip zone [*Murakami and Nemat-Nasser*, 1983]. Hence resolving the B_i near the crack edge into components perpendicular and parallel to the edge and comparing with (9) yields results for the stress intensity factors. Once the stress intensity factors have been determined, the energy release rate, that is, the energy released per unit area of advance of the slip zone, is expressed in terms of these factors as follows:

$$\mathrm{G} = \frac{(1-\nu)}{2\mu}[K_{\mathrm{I}}^2 + K_{\mathrm{II}}^2 + K_{\mathrm{III}}^2/(1-\nu)] \tag{11}$$

The numerical solution of (7) proceeds by dividing the slip surface into triangular domains in which $f_i(\xi)$ are assumed to be constant over each triangle. Imposition of the stress drop values at the centers of the triangular elements reduces (7) to a set of algebraic equations. For all cases to be considered here, the loading and geometry are symmetric with respect to the y_2y_3 plane; hence only half of the crack surface is used in solving (7). More specifically, for the results to be presented, the half-crack is divided into 80 triangular elements. The regular portions of the integrals over the triangles are evaluated numerically, but a combination of exact and numerical integration is used to treat the singular part [*Lee and Keer*, 1986]. *Lee and Keer* [1986] have shown that for a circular crack subjected to uniform pressure in an infinite body the mode I stress intensity factor calculated by this method has 0.85% error in comparison with the exact solution.

Effect of the Free Surface

Although the solution for an elliptical shear crack in an infinite space can be obtained by specializing results of *Eshelby* [1957] and has been studied in detail by *Kostrov and Das* [1984], there exist no analytical results for shear cracks in an elastic half-space. In this section we present results for the energy release rate, stress intensity factors, and moment for slip zones in an elastic half-space. For simplicity, we consider only elliptical cracks and constant stress drops, but the solution method, as described in the previous section, can treat arbitrary planar configurations and distributed stress drops. In order to examine the effects of the free surface, we compare the results with those for a crack of the same geometry and stress drop in an infinite space.

As shown in Figure 1, the model contains six parameters: the depth of the slip center h; the lengths of the principal semiaxes (a and b); the inclination of the fault plane, defined by the angle α from the normal to half-space surface; the stress drop level $\Delta\tau$, and the stress drop direction, defined by the angle ω from the y_1 (striking) direction. The change in normal stress on the slip surface is specified to be zero. Two types of shear loading conditions are considered: the stress drop direction is parallel to the Earth's surface ($\omega = 0$), corresponding to strike-slip faulting; and the stress drop direction is along the dip direction of the fault ($\omega = +\pi/2$), corresponding to dip-slip (normal) faulting. For brevity, results for the stress intensity factors are presented only for an inclined ($\alpha = \pi/4$) circular slip zone with normal dip-slip loading ($\omega = \pi/2$). However, for the moment and energy release rates we consider both a circular crack and an elliptical crack with aspect ratio $a/b = 2$. For each crack shape we consider the following five possibilities: a deep vertical ($d/b = 3$; $\alpha = 0$), two moderately deep vertical ($d/b = 2$; $\alpha = 0$ and $d/b = 1$; $\alpha = 0$), a shallow vertical ($d/b = 0.1$; $\alpha = 0$), and a shallow inclined crack ($d/b = 0.1$; $\alpha = \pi/4$), where d is the depth of the crack top (See inset of

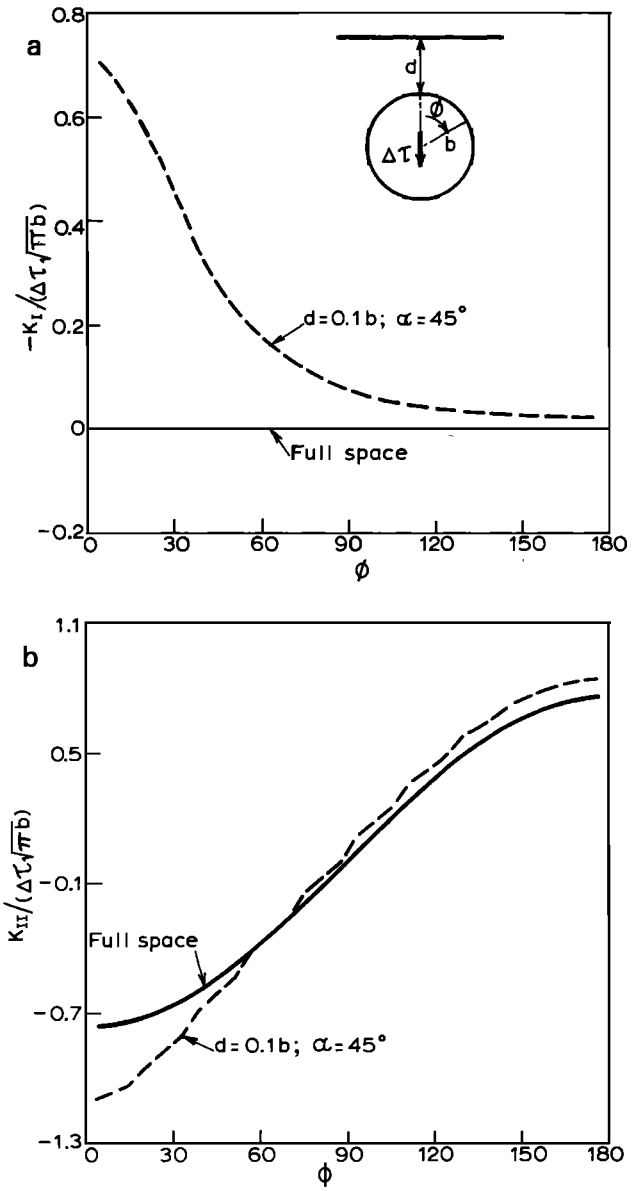

Fig. 2. Stress intensity factors (*a*) K_I, (*b*) K_{II}, and (*c*) K_{III}, divided by $\Delta\tau(\pi b)^{1/2}$, for a shallow inclined circular crack ($d = 0.1b$, $\alpha = 45°$; see inset in Figure 2*a*) against the polar angle ϕ. The solid line shows the result for a crack of the same geometry in a full space. (Because $K_I < 0$, the negative of the stress intensity factor is plotted in Figure 2*a*.)

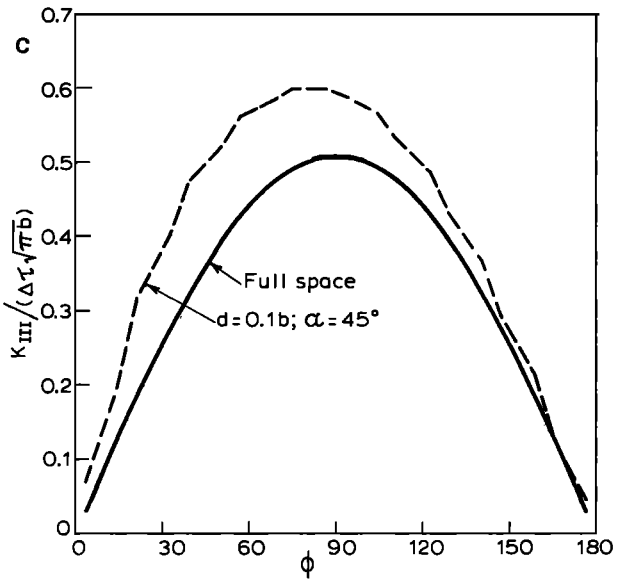

Fig. 2. (continued)

Figure 2*a*). In the calculations of the next two subsections, Poisson's ratio is taken to be 1/3, but $\nu = 1/4$ in the subsection on the moment.

Stress Intensity Factors

As an example of the effect of the free surface on the stress intensity factors K_I, K_{II}, and K_{III}, we examine the solution for an inclined circular crack ($d/b = 0.1$; $\alpha = \pi/4$) subjected to normal dip-slip ($\omega = \pi/2$) loading. The stress intensity factors, divided by $\Delta\tau(\pi b)^{1/2}$, are plotted against the polar angle ϕ (defined in Figure 1) and compared with the corresponding full space results in Figures 2*a*, 2*b*, and 2*c*. For a crack in an infinite isotropic elastic body there is no coupling between slip and normal relative displacement. Consequently, the mode I (opening) stress intensity factor K_I is identically zero, as shown in Figure 2*a*. However, the presence of the free surface causes a coupling between shear slip and normal relative displacement (in this case, interpenetration) and, as a result, K_I is nonzero. The corresponding effect in two-dimensional problems was noted by *Dmowska and Kostrov* [1973] and has been discussed by *Dmowska and Rice* [1986].

The magnitude of the effect diminishes with distance from the free surface and with the angle α. For vertical slip zones, symmetry rules out the possibility of relative normal displacement. However, for inclined slip zones near the free surface the effect can be substantial. For results shown in Figure 2 the magnitude of K_I at the shallowest point of the slip zone ($\phi = 0°$) is nearly 2/3 the maximum value of K_{II}, which also occurs at $\phi = 0°$.

In reality, interpenetration of the fault surfaces cannot occur and, except for slip zones very near the free surface, the ambient normal stress will presumably suppress any tendency for the slip to be accompanied by opening. The magnitude of normal stress changes can be estimated by solving (7) subject to the condition that $B_3 = 0$ (where B_3 is the relative displacement normal to the slip surface). Two of the equations (7) can then be solved for the slip components. Substituting these into the third yields the normal traction required to suppress any opening or interpenetration. In particular, for the crack shown in Figure 2 we found that the maximum compressive traction required to prevent interpenetration of the crack surfaces is about 87% of the applied shear stress drop. For this case, K_{II} and K_{III} differ from those shown in Figures 2*b* and 2*c* by less than 10% (K_I is zero).

As discussed by *Dmowska and Rice* [1986], the coupling of normal relative displacement and slip near the free surface means that the shear stress drop alone cannot be specified a priori; if slip is assumed to be governed by Coulomb friction, then only a linear combination of the changes in normal stress and the shear stress can be specified. Although, as noted above, this effect can be significant near the free surface, for simplicity, we do not consider it further here.

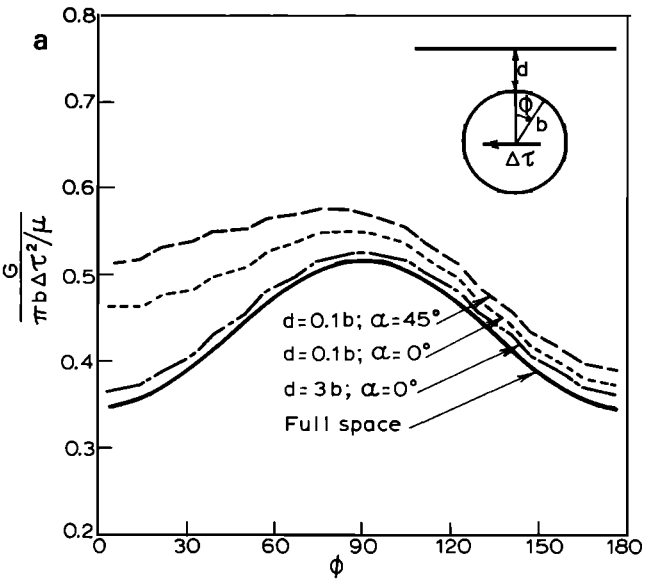

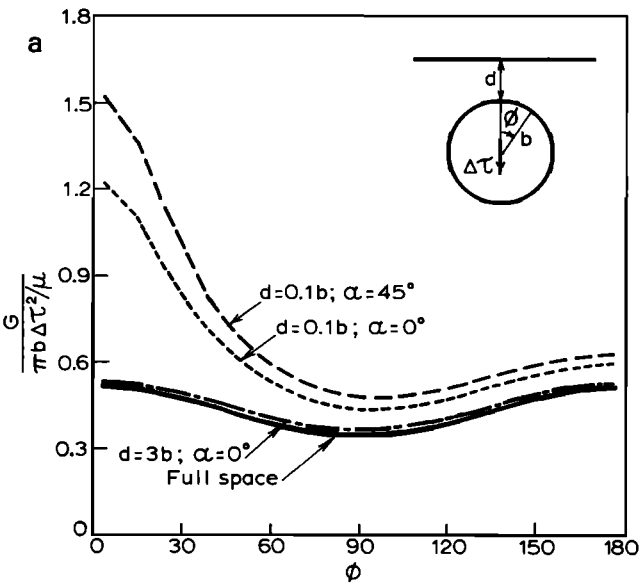

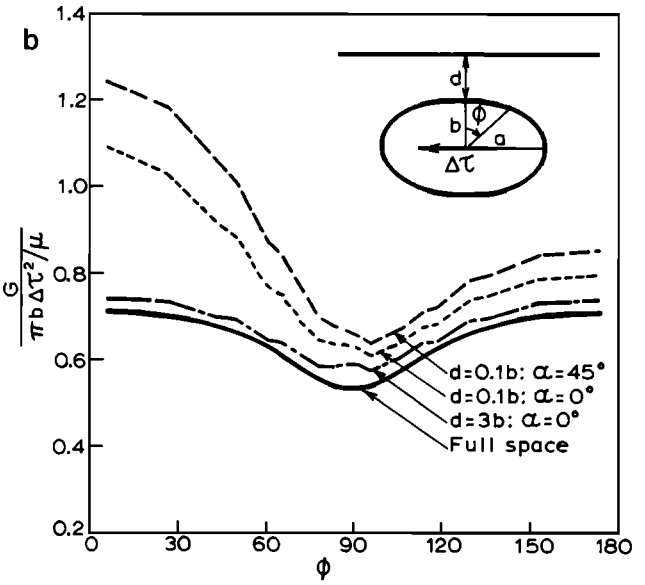

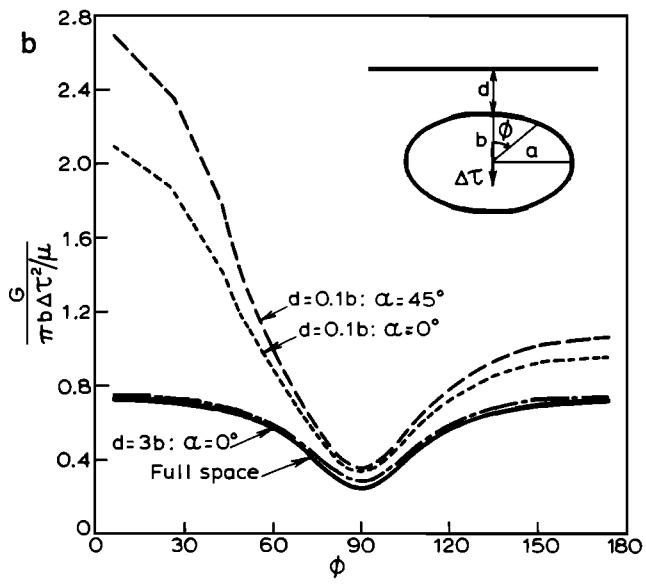

Fig. 3. Energy release rate G (11), divided by $\pi b\Delta\tau^2/\mu$, against ϕ for (*a*) circular and (*b*) elliptical (aspect ratio $a/b = 2$) slip zones subjected to strike-slip loading.

Fig. 4. Energy release rate G (11), divided by $\pi b\Delta\tau^2/\mu$, against ϕ for (*a*) circular and (*b*) elliptical (aspect ratio $a/b = 2$) slip zones subjected to dip-slip loading.

Energy Release Rate

Although it is instructive to consider the stress intensity factors individually, only the combination defined by (11) enters the expression for the energy release rate. Figures 3 and 4 plot the variation of the energy release rate G, divided by $\pi b\Delta\tau^2/\mu$, against the polar angle ϕ for different crack configurations for the cases of strike-slip and normal dip-slip motion. As indicated in these figures, the distributions of the normalized energy release rate for the deep slip zones ($d/b = 3$) are about the same as for the corresponding full-space sources, as expected. Only when the ratio $d/b = 1.0$ do the results differ by as much as 10% from those for the full space solutions. The energy release rates for the shallow slip zones, however, can differ significantly from the full space results, depending on the configuration and loading condition. Overall, the free-surface effect is greater for dip slip than for strike slip, given the same crack geometry.

For both the circular (Figure 3*a*) and the elliptical slip (Figure 3*b*) zones with strike-slip loading, the variation of the energy release rate with ϕ is similar to that for the same slip zone in an infinite body. For the circular zone the energy release rate is largest at the side ($\phi = 90°$) and decreases toward the top ($\phi = 0°$) and bottom ($\phi = 180°$). For the elliptical crack with aspect ratio $a/b = 2$, the energy release rate is greatest at the edge nearest the free surface and least at the side of the slip zone ($\phi = 90°$). The presence of the free surface causes G to increase for both the circular and elliptical zone with the greatest increase occurring nearest to the free surface. More specifically, for shallow dipping zones the energy release rate induced by the shallow vertical crack ($d/b = 0.1$; $\alpha = 0$) is greater than that for the full space source by about 33% near the top of the crack ($\phi \simeq 0$) and by less than 7% along the portion of the crack front away from the free surface of the Earth ($\phi > 90°$). When this shallow

source dips at 45° ($d/b = 0.1$; $\alpha = 45°$), the difference is increased about 15%. For the elliptical geometry (strike slip; $a/b = 2$), even larger differences (50% and 70%) occur for the shallow vertical ($d/b = 0.1$; $\alpha = 0$) and shallow inclined crack ($d/b = 0.1$; $\alpha = 45°$) (Figure 3*b*).

The difference in the variation of the energy release rates with ϕ for the circular and elliptic slip zones can be understood in terms of the behavior of the stress intensity factors for the full space solution [*Kostrov and Das*, 1984]. At $\phi = 0°$ (and 180°) the solution is pure mode III ($K_{II} = 0$), and at $\phi = 90°$ the solution is pure mode II ($K_{III} = 0$). As discussed in detail by *Kostrov and Das* [1984], the ratio of the mode II stress intensity factor at $\phi = 90°$ to the mode III stress intensity factor at $\phi = 0°$ (and 180°) is $(b/a)^{1/2}/(1 - \nu)$. Hence the corresponding ratio of the energy release rate at $\phi = 90°$ to that at $\phi = 0°$ is $(b/a)/(1 - \nu)$. Thus, for the circular slip zone, **G** at $\phi = 90°$ is 1.5 times that at $\phi = 0°$ (for $\nu = 1/3$). For the elliptical slip zone with aspect ratio $a/b = 2$, **G** at $\phi = 90°$ is 0.75 times that at $\phi = 0°$.

If the slip zone is assumed to spread in the direction of the greatest energy release rate, then the results of Figure 3*a* suggest that an initially circular zone propagates horizontally rather than toward the free surface. However, Figure 3*b* shows that an increase in the aspect ratio b/a increases the energy release rate both at the top and bottom of slip zone ($\phi = 0°$, 180°), but the increase is greater at the top near the free surface. Thus, for an initially circular slip zone, horizontal propagation would be followed by propagation toward the free surface before the aspect ratio reached $b/a = 2$. For an initially elliptical slip zone (with $b/a \geq 2$), propagation would occur first toward the free surface.

Figures 4*a* and 4*b* show the variation of the energy release rate with ϕ for dip-slip loading of circular (Figure 4*a*) and elliptical slip zones. As for the strike-slip loading, the variation is similar to that for the full space solutions. For both the circular and elliptical zones, **G** is least at $\phi = 90°$ and increases toward the top and bottom of the slip zone. For shallow zones the dip-slip loading causes a particularly large increase of **G** toward the free surface. Specifically, for a shallow ($d = 0.1b$) vertical ($\alpha = 0$), circular slip zone, the values exceed those for the full space solution by about 150% near the free surface and by 20% away from the free surface. For the inclined shallow circular crack ($d/b = 0.1$; $\alpha = 45°$) the difference is about 18% larger. Figure 4*b* shows that the energy release rates for the vertical ($\alpha = 0°$) elliptical crack at a depth of $d = 0.1$b exceed those for the full space by even larger amounts: 200% near the top of the crack and 38% near the bottom. For the inclined shallow elliptical crack ($d/b = 0.1$; $\alpha = 45°$) the difference can be as large as 250%. Because the maximum energy release rates all occur at the top of the slip zone for these two geometries, dip-slip rupture would tend to break to the surface rather than grow along strike.

Moment

The stress intensity factors and energy release rates arise naturally in considering crack models of slip zones. But a parameter more commonly used in interpreting observations is the seismic moment. Because the stress drop is specified in the approach used here, the slip distribution and hence the moment are calculated as part of the solution.

In this subsection we examine the effect of the free surface on the relation between the moment and the stress drop. In particular, consider the single component of the moment tensor given by

$$M = \mu \int_S B_\tau(\xi)\, d\xi \tag{12}$$

where B_τ is the relative slip in the direction of the applied stress drop (Figure 1). Hence M is the component M_{31} or M_{32} in the crack coordinate system (y_i), depending on whether the loading is strike slip or dip slip, respectively; similarly, B_τ is B_1 or B_2 depending on the loading. In general, the slip will also have a component orthogonal to the applied stress drop. For example, *Kostrov and Das* [1984] have shown that for an elliptical shear crack in an infinite body the slip is parallel to the applied shear stress only if the latter is applied in the direction of one of the principal axes of the ellipse. In the half-space problems considered here the slip will be in the direction of the applied shear stress only when the problem is symmetric with respect to the loading direction. The magnitude of the slip orthogonal to the applied stress is, however, much smaller than that in the direction of the shear stress. In addition, as noted previously, when the change in normal traction on the slip surface is taken as zero, there is a normal relative displacement, and hence M_{33} is nonzero. However, unless the slip surface is very near the free surface, this component is also small and, for simplicity, we ignore it.

For constant stress drop slip zones the moment M (equation (12)) is proportional to the stress drop $\Delta\tau$ and can be expressed as follows:

$$M = C\, \Delta\tau\, A^{3/2} \tag{13}$$

where A is the area of the slip surface and C is a nondimensional quantity that depends on Poisson's ratio and the geometry. For example, for a circular slip zone in an infinite space, C is

$$C = \frac{16(1 - \nu)}{3\pi^{3/2}(2 - \nu)} \tag{14}$$

For an elliptical slip zone in an infinite body with principal semiaxes a and $b < a$, C is given by

$$C = \frac{4}{3\pi^{1/2}}\, k_1^{1/2} k^2 [(k^2 - \nu)E(k) + \nu k_1^2 K(k)]^{-1} \tag{15}$$

if $\Delta\tau$ is applied parallel to the larger semiaxis, and by

$$C = \frac{4}{3\pi^{1/2}}\, k_1^{1/2} k^2 [(k^2 + \nu k_1^2)E(k) - \nu k_1^2 K(k)]^{-1} \tag{16}$$

if $\Delta\tau$ is applied parallel to the smaller semiaxis [*Dmowska and Rice*, 1986]. In (15) and (16), $k_1 = b/a$, $k = 1 - k_1^2$, and $E(k)$ and $K(k)$ are complete elliptic integrals of the first and second kinds, respectively.

The expression (13), with C given by (14), is often used to estimate the stress drop when the moment is determined by kinematic models. As noted earlier, for kinematic models using constant relative displacement elements, the actual average stress drop is unbounded. Furthermore, the value of C given by (14) is for an infinite space. Consequently, it is of interest to determine the effect of the free surface on the

TABLE 1. Values of $C = M/(\Delta\tau A^{3/2})$

	Strike Slip ($\omega = 0°$)		Dip Slip ($\omega = 90°$)	
	$a/b = 1$	$a/b = 2$	$a/b = 1$	$a/b = 2$
Full space	0.4105	0.4042	0.4105	0.3523
$d/b = 3$; $\alpha = 0°$	0.4169	0.4180	0.4177	0.3630
$d/b = 0.1$; $\alpha = 0°$	0.4327	0.4473	0.4823	0.4488
$d/b = 0.1$; $\alpha = 45°$	0.4481	0.4707	0.5117	0.4810

value of C and hence the effect on inference of the stress drop from the moment by (14).

Table 1 lists the values of C for the slip zones considered in Figures 3 and 4 and the corresponding values for a slip zone of the same geometry and loading in an infinite space. Poisson's ratio of $\nu = 0.25$ is used for these calculations. Values of C, using (12) and (13), for the deep cracks ($d/b = 3$) differ by less than 3% from those, using (14)–(16), for the full space cracks of the same geometries and stress drops. For the vertical shallow cracks, the half-space moments differ from the corresponding full space results by 6% for the circular and 11% for the elliptical crack for the case of strike slip and by 18% for the circular and 27% for the elliptical crack for the case of dip slip, respectively. For the inclined shallow cracks, additional differences up to 10% are observed. Because of the coupling between the shear slip and the normal relative displacement, the moment component M_{33} (along the normal direction of the crack surface) can be as large as about two thirds of the larger shear component.

INTERPRETATION OF COSEISMIC SURFACE DEFORMATIONS

As examples of the application of this method, we use it to reexamine the coseismic surface deformations of three earthquakes: 1987 Whittier Narrows, 1983 Borah Peak, and 1966 Parkfield. The coseismic deformations for these earthquakes have been studied previously using kinematic models. The present approach differs from those previous because the geometry and the stress drop, rather than the slip distribution, are inferred from the observations. The slip distribution is then calculated for the inferred stress drop and geometry.

For each earthquake a set of forward searches is performed to find the model parameters that give a best fit to the coseismic slip data subject to the constraint that the model geometry agrees roughly with the aftershock distribution. Then, by using the stress drop and crack geometry determined from a best model, the corresponding slip moment and energy release rate are calculated and compared, together with the model parameters, with those inferred from previous studies. The results are summarized in Table 2. For the calculations in this section, a Poisson's ratio $\nu = 0.25$ and a shear modulus $\mu = 3 \times 10^4$ MPa, an average value for the Earth's crust, are assumed.

1987 Whittier Narrows

The 1987 Whittier Narrows earthquake occurred within the Los Angeles basin in southern California. The geologic and tectonic setting have been described by *Davis et al.* [1989]. The coseismic surface elevation changes were detected by geodetic surveys [*Lin and Stein*, 1989]. A crosslike geodetic network, centered coincidentally on the epicenter, was surveyed 20 months before the earthquake and resurveyed immediately after. The surveys reveal that the ground surface was uplifted by 50 mm, but no surface rupture was observed. *Lin and Stein* [1989] used a model of an inclined rectangular dislocation of uniform dip slip in an elastic half-space [*Mansinha and Smylie*, 1971] to interpret the observed deformation as due to reverse dip slip of a deep thrust fault beneath the center of the network. Because the geodetic data alone cannot constrain the fault geometry and slip magnitude uniquely, *Lin and Stein* [1989] also considered the aftershocks which occupied a region extending from the depth of 12 km to 16 km. For their best model, the fault length along strike is 4.5 km, the downdip width is 6 km, the depth of the upper end of the fault plane is 12 km, the dip angle is 30°, and the coseismic slip is 1.1 m.

Here we employ an alternative approach to interpret coseismic deformation reported by *Lin and Stein* [1989]. Specifically, we model the event as reverse dip slip of an inclined elliptical slip zone in an elastic half-space and assume a stress drop along the negative dip direction (Figure 1: $\omega = -90°$). For the best model, which matches the deformation data well and is consistent with the aftershock locations, the slip zone is circular with a radius of 3.0 km, the depth of the fault center is 14.2 km, and the dip angle is 40°. The total rms misfit is 5.8 mm, slightly larger than the rms pure error, which is 4.9 mm. The surface projection of the fault plane of our preferred model is shown in Figure 5*a*; the

TABLE 2. Comparison Between Modeling Results

	Whittier Narrows ($M = 6.0$)		Parkfield ($M = 5.6$)		Borah Peak ($M = 6.9$)	
	Lin and Stein [1989]	This Study	*King et al.* [1987]	This Study	*Barrientos et al.* [1987]	This Study
Length (along strike), km	4.5	6.0	30	50	18 and 8	36
Width (downdip), km	6.0	6.0	5	14	18 and 8	18.5
Depth (to rupture top), km	12	12.3	3	1.75	0	0
Dip	30°N	40°N	90°	90°	49°SW	50°SW
Strike	N90°E	N90°E	···	N142°E	N152°E	N152°E
Slip, m	1.09	1.0/1.5 (ave/max)	0.91	0.5/0.76 (ave/max)	2.1 and 1.4	1.4/2.2 (ave/max)
Stress drop, MPa	17.5	16	···	1.43	3.0	1.8
Moment, dyn cm	1.0×10^{25}	0.96×10^{25}	4.5×10^{25}	7.2×10^{25}	2.9×10^{26}	2.4×10^{26}
G, J/m^2	···	2×10^8	···	1.5×10^6	···	1.2×10^6
rms/pure error	0.93	1.18	···	0.97	2.5	6

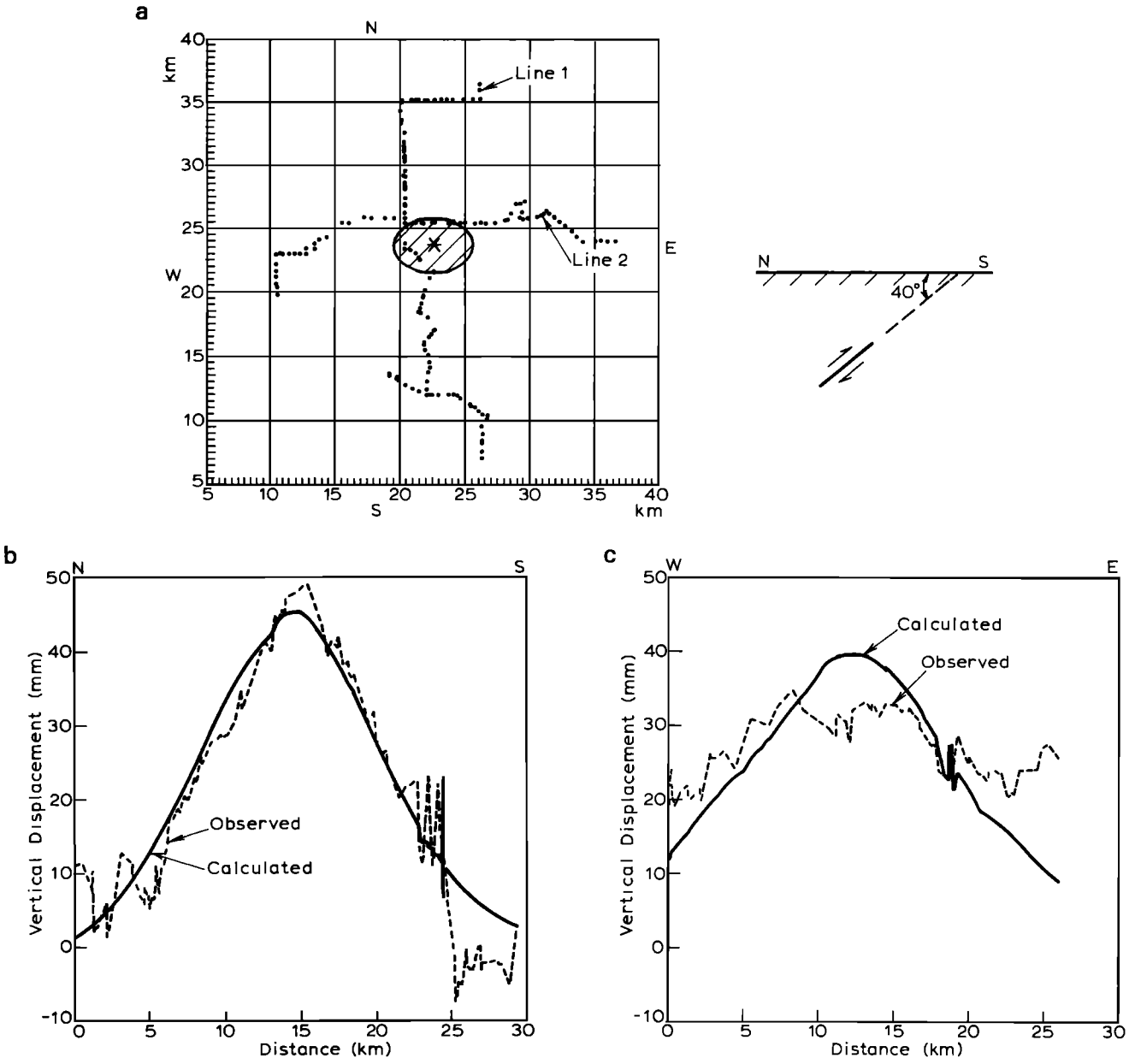

Fig. 5. Model fit to the coseismic surface deformation of the 1987 Whittier Narrows earthquake. (*a*) Leveling monuments and the surface projection of the model fault. Asterisk represents the epicenter of the earthquake. (*b*) Fit to data along leveling line 1. (*c*) Fit to data along leveling line 2.

model fits to data along two leveling routes, line 1 (N-S) and line 2 (E-W), are shown in Figures 5*b* and 5*c*, respectively.

As shown in Figure 5*b*, the predicted surface displacement agrees well with the observed data along line 1 except at the southern end. The fit to data is not as good along line 2 but is still satisfactory (Figure 5*c*). These results are similar to those of *Lin and Stein* [1989]. The stress drop and moment determined for the preferred model are 16 MPa and 0.96×10^{25} dyn cm, respectively, compared with the 17.5 MPa and the 1.0×10^{25} dyn cm determined by Lin and Stein. Because the ratio of the depth to slip zone radius is relatively large ($\simeq 4$), the energy release rate for this model is approximately constant along the fault front and is essentially identical to that for a slip zone of the same geometry and stress drop in an infinite body. The value is estimated to be about 2.0×10^8 J/m^2.

The dipping angle (40°) of our best model is about 10° larger than inferred by Lin and Stein using their dislocation method. If we use the same dip (30°) as theirs, the rms error is increased to 6.3 mm. The coseismic slip data are not critically sensitive to the radius of the slip region. More specifically, the area can be varied from moderately larger (radius 5 km) to much smaller (radius 1 km) than that defined by the aftershock distribution without affecting the rms error significantly. In addition, while keeping the width (along dip) of the fault to be 5 km, horizontal length of slip up to 16 km is permitted by the deformation data. Because the ratio of depth to slip region radius is large, the uplift data can be fit reasonably well by a point source. For the point dip-slip source having the same inclination, depth, and moment as the best crack model, the uplift data can be fitted with the

TABLE 3. Observed and Calculated Line Length Changes

Station-Station	Observed, mm	Calculated, mm	Residual, mm
Bench-Bonnie	−69 ± 24	−78.3	9.3
Bench-Cotton	42 ± 19	51.2	−9.2
Bench-Kenser	−137 ± 24	−163.4	26.4
Bench-Mason	30 ± 18	13.6	16.4
Bonnie-Cotton	27 ± 18	−16.3	43.3
Bonnie-Kenser	5 ± 16	−4.2	9.2
Bonnie-Mason	81 ± 24	85.5	−4.5
Castle-Shade	115 ± 38	88.8	26.2
Cotton-Kenser	−5 ± 24	−24.9	19.9
Cotton-Mason	167 ± 26	159.6	7.4
Kenser-Mason	−7 ± 20	−27.1	20.1
Mine Mountain-Shade	58 ± 18	65.4	−7.4
Park-Red Hill	−160 ± 24	−124.4	−35.6

Mean misfit (rms) = 21.4 mm.

rms error of 6.4 mm, only 10% larger than the crack model's misfit.

1966 Parkfield

Trilateration measurements made by several agencies since 1959 near Parkfield provide geodetic data that place constraints on the motion across the San Andreas fault [*King et al.*, 1987]. Line length changes observed shortly after the 1966 Parkfield earthquake in that area have been the focus of much effort. Several investigators modeled the 1966 shock as a vertical rectangular dislocation of uniform strike slip in an elastic half-space [e.g., *Chinnery*, 1961]. Distributed dislocation models were also considered by approximating the slip as uniform in small rectangular cells [*Stuart et al.*, 1985; *Segall and Harris*, 1987]. However, because there were only 13 lines near the 1966 rupture zone, the length, depth, and width of the slip region cannot be constrained strongly by the geodetic observations alone [*King et al.*, 1987; *Segall and Harris*, 1987].

Additional constraints come from the distribution of aftershocks, which were concentrated at depths of 2–4 and 8–10 km on a nearly vertical plane extending 30 km SE of the main shock epicenter [*Eaton et al.*, 1970]. The absence of surface offset immediately following the main shock [*Smith and Wyss*, 1968] indicates that the 1966 coseismic slip probably did not reach the Earth's surface. Therefore most coseismic slip models have used a rupture geometry that extends from a depth of 2–4 km to a depth of 8–10 km with the length ranging from 20 to 40 km [*Archuleta and Day*, 1980; *King et al.*, 1987; *Segall and Harris*, 1987].

We propose a model of a vertical elliptical crack embedded in an elastic half-space. The surface of the crack is subjected to a uniform shear stress drop along the strike direction (Figure 1; $\alpha = 0$ and $\omega = 0$). The fit of the preferred model to the line length changes [*King et al.*, 1987] is provided in Table 3. The trilateration net and the surface trace of the model slip zone are shown in Figure 6. The surface center of the model fault is located near the middle point of the line connecting Mason and Kenger stations, the strike direction is nearly parallel to that of the line of Mason and Bench stations, and the top, the bottom, and the horizontal length of the fault are 1.75, 15.75, and 50 km, respectively (Table 2 and Figure 6). Although the area of the model rupture plane is moderately larger than the region

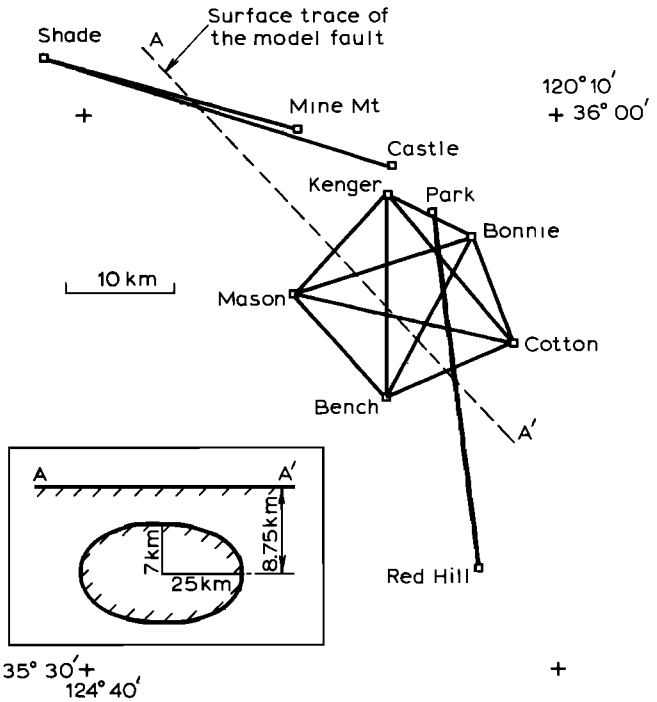

Fig. 6. Trilateration net and surface trace of the model slip zone inferred for the 1966 Parkfield earthquake.

defined by the aftershocks, the mean misfit to the data is significantly smaller (20% less) than models having slip areas much less than the aftershock region. The mean misfit of the preferred model to the data is 21.4 mm, lower that the average standard deviation of the data, which is 22.5 mm (Table 3). The only significant misfit occurs for the line connecting Bonnie and Cotton stations (Table 3). The observed line length change is 27 mm; the predicted value is −16 mm, close to the −10 mm predicted by *Segall and Harris* [1987] using a distributed dislocation model. The reason for this misfit is uncertain.

The stress drop and moment determined are about 1.43 MPa and 7.2×10^{25} dyn cm, respectively. Our estimated moment is larger than the 4.5×10^{25} dyn cm obtained by *King et al.* [1987] using the dislocation approach (Table 2) and the $(0.9–2.1) \times 10^{25}$ dyn cm inferred from surface waves by *Tsai and Aki* [1969] but falls within the range of $(3.7–8.1) \times 10^{25}$ dyn cm estimated by *Segall and Harris* [1987] using a distributed dislocation model. The maximum energy release rate occurs near the top of the slip zone and is estimated to be approximately 1.5×10^6 J/m^2. This value is consistent with the 0.8×10^6 J/m^2 estimated by *Aki* [1978] as corresponding to arrest of this earthquake but much greater than the estimate by *Husseini et al.* [1975] of 1.1×10^2 J/m^2.

If the area of the slip region is constrained so that its top, bottom, and horizontal length vary between 2–4, 8–10, and 20–40 km, where the aftershocks concentrated, then the model that fits the data best occupies the largest possible area. The mean misfit of this model to the data is 27 mm. Better fits are obtained when the rupture zone extends below the region of aftershocks to about 16 km depth. The coseismic line length changes permit slip extending even deeper than 16 km. The Park-Red Hill and Castle-Shade line length changes are much more sensitive to the horizontal length of

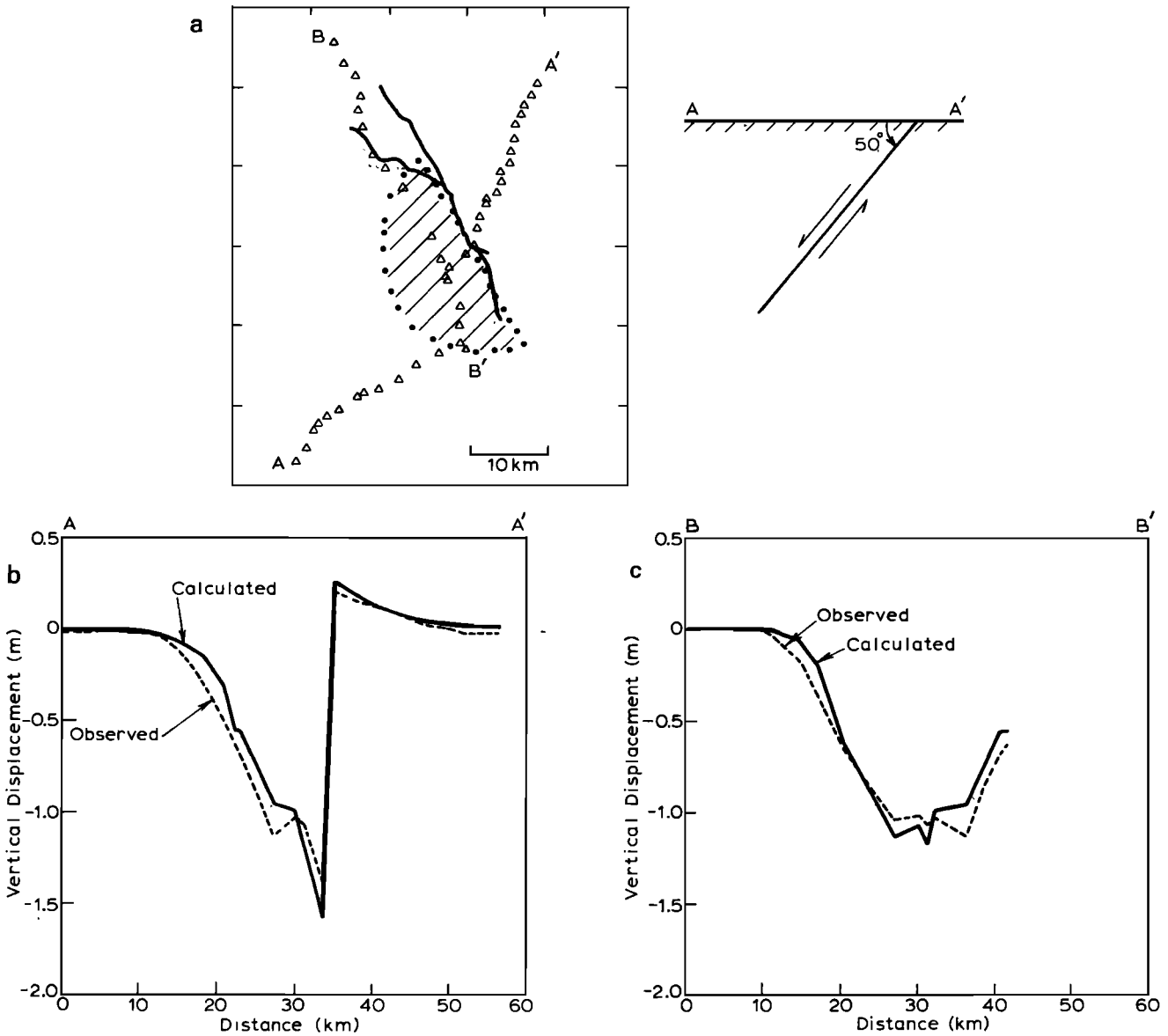

Fig. 7. Model fit to the coseismic surface deformation of the 1983 Borah Peak earthquake. (*a*) Leveling monuments and the surface projection of the model fault. (*b*) Fit to data along leveling line AA′ (pure error = 12 mm). (*c*) Fit to data along leveling line BB′ (pure error = 12 mm).

the slip region than other lines. Model fit can be degraded significantly for slip zones with horizontal lengths much shorter than 40 km, but longer length is permitted by the data. These results are in agreement with those of *King et al.* [1987].

1983 Borah Peak

The Borah Peak segment of the Lost River fault lies in the northern Basin and Range Province. The 1983 Borah Peak earthquake, a large normal-faulting event, presumably resulted from regional extension of the Basin and Range. The earthquake ruptured the central 35-km segment, the length of the surface rupture trace, of the 100-km-long Lost River fault [*Barrientos et al.*, 1987].

The surface deformation associated with this event was reported by *Stein and Barrientos* [1985]. Two leveling lines, with line AA′ nearly normal to the fault and line BB′ about parallel to the main fault trace, were surveyed in 1933 (Figure 7*a*). Line AA′ was surveyed again in 1948. Both lines were resurveyed in 1985. Thus the survey includes 20 months of deformation following the earthquake. *Stein and Barrientos* [1985] have shown that the 1983–1984 postseismic slip is about 2% of the coseismic slip. By using dislocation models, *Barrientos et al.* [1987] studied the 1933–1948 preseismic deformation and the 1985 postseismic data to invert for the subsurface fault geometry and slip magnitude at Borah Peak. In their inversion procedure the strike of rupture planes was fixed to be consistent with the fault trace. Their best model consists of two planes of the same dip and strike: an 18 × 18 km main plane with 2.1 m slip and an 8 × 8 km second plane with 1.4 m slip located along strike northwest of the main plane. The dip angle of the planes is 49°. The rms misfit is 30 mm, 2.5 times the data noise level. This geometry agrees well with the focal mechanism of the

main shock [*Doser and Smith*, 1985] and the aftershock distribution [*Richins et al.*, 1985].

We use a dip-slip crack model to reexamine the surface deformation associated with this 1983 earthquake. Because the fault ruptured to the surface in the Borah Peak event, the dip-slip zone is approximated by a semielliptical geometry. For the parameters shown in Figure 1 we take $\omega = 90°$ and $h = 0$. As shown in Table 2, the strike (150°) and dip (50°) of our best model are similar to those of *Barrientos et al.* [1987], but the surface center of the slip zone is 3 km SE of theirs. The horizontal length of 36 km and width along dip of 18.5 km for our model are larger than but close to those (26 km and 18 km) for their best model. Normal dip slip is required over the surface of the fault. Figure 7*a* shows the surface projection of the model fault plane; Figures 7*b* and 7*c* indicate the model fit to data along line AA′ and line BB′, respectively.

Overall, the predicted values roughly match the observations. However, the predicted displacement significantly overshoots the maximum elevation change and moderately underestimates the other large elevation changes for line AA′. For line BB′ the predicted displacement moderately overestimates about half of the data and underestimates the other half data. The rms error of the fit to data is large, about 70 mm, 6 times the rms pure error. The better fit obtained by *Barrientos et al.* [1987] using the distributed slip model and the pattern of the discrepancy between the predictions here and observations on line AA′ suggest that the constant stress drop assumption needs to be relaxed in order to improve the fit to the data: uniform stress drop constrains the slip to be distributed roughly elliptically, and therefore the slip is largest at the center and tapers to zero at the edge. However, because the purpose here is to illustrate the approach and to provide estimates for the slip-induced energy release rate rather than fit the data precisely, we have not pursued nonuniform stress drop models.

The stress drop and moment determined by our best model are 1.8 MPa and 2.4×10^{26} dyn cm, respectively, smaller than the 3.0 MPa and 2.9×10^{26} dyn cm inferred by Barrientos et al. using a single-plane model which is 18 km in width and 23 km in length (No stress drop and moment values were reported for their two-plane model). The maximum (calculated) energy release rate occurs at the ends of the surface trace of the rupture and is estimated to be 1.2×10^6 J/m^2.

Because this event breaks the surface, there is a strong coupling between slip and normal relative displacement. Because we have specified zero normal stress change on the slip surface in (6), the fault surfaces are predicted to interpenetrate. For the best fitting model the predicted interpenetration is about 1.6 m at the surface, 73% of the maximum relative displacement along dip, and decreases to zero at the deepest portion of the fault. Of course, in actuality, the fault will not interpenetrate because the normal stress will increase in compression. To estimate the magnitude of the normal stress change, we repeated the calculation but required that the normal relative displacement be zero. (This change has negligible effect on the fit of the leveling data.) The resulting normal traction is compressive (tending to open the crack) over most of the fault surface with a maximum value of about 110% of the applied shear stress drop occurring at the surface. Surprisingly, a small tensile stress (about 7% of the applied shear) is required on the deepest portions of the fault. Apparently, this occurs because preventing interpenetration of the crack faces near the surface tends to cause the deeper portions to open. A more complicated analysis that includes the effect of the change in normal stress on the resistance to slip is needed to determine more accurately the magnitude of the normal stress changes. However, these limiting cases suggest that the effect can be significant.

CONCLUDING DISCUSSION

In this paper we have described a numerical method for determining the displacements in an elastic half-space caused by slip on planar zones in response to a prescribed shear stress drop. Although, for simplicity, we have presented results only for uniform stress drops and elliptical slip zones, the method can be applied to arbitrarily shaped planar zones and distributed stress drops. By incorporating the appropriate asymptotic form of the displacement field near the edge of a crack in a linear elastic isotropic body, we are able to calculate accurately the stress intensity factors and hence the energy release rates. These quantities can be used in propagation criteria for determining the advance of the slip zone.

Because so few solutions exist for crack models of slip zones in a half-space, the magnitude and nature of the effect of the free surface have been uncertain. To examine this effect, we have presented results for the stress intensity factors and energy release rates for slip zones of various shapes, depths, and inclinations and compared them with solutions for slip zones of the same shape in an elastic full space. Although the details depend on the specific geometry, in general, when the distance of the slip zone center from the free surface (h) is greater than the downdip width of the slip zone ($2b$), the difference between the half-space and full space results is less than 10%. In addition, the influence of the free surface increases with decreasing dip angle.

We have also examined in detail the effect of the free surface on the relation between the seismic moment and the stress drop (see (13) and Table 1). The seismic moment is a relatively well-determined observational parameter, and the relation between the stress drop and the moment for a circular or elliptical crack in an infinite elastic body is often used to infer the stress drop. Again, the results indicate that the effect of the free surface is small (less than about 10%) unless the fault rupture is very near to the free surface (h less than the downdip width $2b$). The effect can, however, be significant for dipping faults that rupture to (or nearly to) the free surface.

Another effect of the free surface revealed by the calculations here is the coupling of slip with normal relative displacement which has been noted previously in two-dimensional problems by *Dmowska and Kostrov* [1973]. Because of this coupling, the shear resistance, which is proportional to the normal stress for a simple Coulomb condition, is coupled to the slip. Consequently, as remarked by *Dmowska and Rice* [1986], it is not possible to specify the shear stress drop a priori, and iteration is necessary to obtain the solution for a given shear stress drop. Although we have not pursued a full analysis of this coupling, some insight can be gained from consideration of the limiting cases in which either the normal stress change on the fault or the normal relative displacement is specified as zero.

When the change in normal stress is specified to be zero (as has been the case here, except where noted), the calculations indicate that the surfaces of reverse dip-slip faults tend to open and those of normal dip-slip faults tend to interpenetrate. (Actual interpenetration is prevented by an increase in normal compressive stress, and opening is opposed by the ambient compressive stress). Conversely, if the relative normal displacement is required to be zero, slip induces changes in normal stress. For reverse slip the change in normal stress is tensile (tending to prevent opening) over most of the rupture. For normal dip-slip motion the normal stress changes are compressive over most of the slip surface.

As example applications of the solutions, we have used them to reexamine surface deformation data from the 1987 Whittier Narrows, 1973 Borah Peak, and 1966 Parkfield earthquakes. In all three cases the geometries, stress drops, and moments inferred are similar to those obtained previously by others using kinematic models. The agreement lends additional confidence in the previous results, and the slight differences give an indication of the resolution. A significant difference between the approaches is the manner of determining the stress drop. In the solutions here the stress drop is one of the parameters adjusted to fit the observations. The slip distribution is then calculated for the inferred stress drop and geometry and used to determine the moment. In the kinematic models the slip magnitude and, possibly, distribution are chosen to fit the observations. The stress drop is then inferred from the moment, typically, by using the relation for a circular crack in an infinite body. As noted above, this relation is reasonably accurate, but significant loss in accuracy occurs if the slip zone is close to the free surface.

The additional information obtained by the present method is an estimate of the critical energy release rate (energy released per unit area advance of the slip zone). This estimate is obtained by assuming that the slip zone propagated according to the criterion that the energy release rate is equal to a critical value that reflects the resistance of the material. Although this criterion is simple, it is thought to be a good approximation when the actual inelastic processes associated with slip propagation occur in a zone near the slip zone edge that is small compared with other relevant length scales [*Rudnicki*, 1980; *Rice*, 1980, 1983; *Li*, 1987]. The slip zone stops advancing either because the available energy release decreases (perhaps due to a decrease in stress drop) or the slip zone has propagated into a region of higher critical energy release rate [*Husseini et al.*, 1975]. Thus the energy release rate inferred from the coseismic geodetic data is a lower bound on the critical energy release rate at the termination of rupture.

The critical energy release rates estimated for the three earthquakes considered here are 1.5×10^6 J/m^2 (Parkfield), 1.2×10^6 J/m^2 (Borah Peak), and 2×10^8 J/m^2 (Whittier Narrows). The value for Parkfield occurs at the top of the slip zone, and that for Borah Peak occurs at the ends of the surface trace of the slip zone. The Whittier Narrows event was deep enough that there was little variation around the edge. *Li* [1987] has tabulated values of the critical energy release rate inferred for crustal faulting (also see *Rudnicki* [1980]). These range from 10^0 to 10^8 J/m^2 with most of the values ranging from 10^5 to 10^8 J/m^2. The values inferred here are toward the upper end of this range, and that for the Whittier Narrows event is as large as any cited by *Li* [1987]. *Wong* [1982, 1986] has collected values of the critical energy release rate inferred from slip on sawcut laboratory specimens. These values are of the order of 10^4 J/m^2 and hence about 2 orders of magnitude less than typical for crustal faults. *Martel and Pollard* [1989] have estimated values of critical shear fracture energy release rates ranging from 5×10^2 to 2×10^4 J/m^2, of the order of laboratory values, from field observations of slip along small faults in granite rock.

As indicated by this short summary, currently available estimates of values of the critical energy release rate for crustal faulting are not numerous and exhibit considerable variation. Additional estimates and knowledge of their variation through the crust would contribute to a better understanding of the initiation and arrest of earthquake ruptures.

APPENDIX

The terms K_{mn} in (7) relative to the crack surface coordinate system y_i are given below:

$$K_{11} = \frac{\mu}{4\pi(\kappa+1)}\left\{\frac{2}{r_1^3}(\kappa-1) + \frac{3}{r_1^5}(3-\kappa)(y_1-\xi_1)^2 + \frac{2}{r_2^3}(\sin^2\alpha - \kappa + \kappa^2\cos^2\alpha) + \frac{3\bar{y}}{r_2^5}[-1 - 2\sin^2\alpha + \kappa(2\cos^2\alpha+1)] + \frac{12H}{r_2^5}(-5 + 7\cos^2\alpha + \kappa\sin^2\alpha) + \frac{120H}{r_2^7}[4H\sin^2\alpha + \bar{y}^2(3-4\cos^2\alpha)] - \frac{3360H^2\bar{y}^2\sin^2\alpha}{r_2^9} - 6\cos^2\alpha T_3\right\}$$

$$K_{12} = \frac{\mu}{4\pi(\kappa+1)}\left\{\frac{3}{r_1^5}(3-\kappa)(y_1-\xi_1)(y_2-\xi_2) + \frac{6\bar{y}\cos\alpha}{r_2^5}(h + y_2\cos\alpha) \cdot [-1 + 12\sin^2\alpha - \kappa(1+4\sin^2\alpha)] - \frac{3\bar{y}}{r_2^5}(y_2-\xi_2)[(1+4\sin^2\alpha - 2\sin^4\alpha) - \kappa(2\cos^2\alpha+1) - 2\kappa^2\sin^2\alpha\cos^2\alpha] + \frac{120H\bar{y}}{r_2^7}[2\cos\alpha(h + y_2\cos\alpha)(\kappa\sin^2\alpha + 7\cos\alpha - 6) + (y_2-\xi_2)(3-4\cos^2\alpha)] + \frac{3360H^2\sin^2\alpha\bar{y}}{r_2^9} \cdot [2\cos\alpha(h + y_2\cos\alpha) - (y_2-\xi_2)] - \frac{3}{2}\bar{y}\sin^2\alpha T_2\right\}$$

$$K_{13} = \frac{\mu\bar{y}\sin\alpha}{4\pi(\kappa+1)}\left\{\frac{24\cos^2\alpha}{r_2^5}(3-\kappa)(h+y_2\cos\alpha) - \frac{6\cos^3\alpha}{r_2^5}(1-\kappa^2)(y_2-\xi_2) + \frac{120H}{r_2^7}\cdot[(h+y_2\cos\alpha)(-1-7\cos 2\alpha+2\kappa\cos^2\alpha) - (y_2-\xi_2)(\kappa-1)\cos\alpha] - \frac{6720H^2\sin^2\alpha}{r_2^9}\cdot(h+y_2\cos\alpha) - 6\cos^3\alpha T_2\right\}$$

$$K_{22} = \frac{\mu}{4\pi(\kappa+1)}\left\{\frac{2}{r_1^3}(\kappa-1)+\frac{3}{r_1^5}(3-\kappa)(y_2-\xi_2)^2 + \frac{\cos 4\alpha}{r_2^3}(-7+\kappa)+\frac{48H}{r_2^5}(2+5\sin^2\alpha - 27\sin^2\alpha\cos^2\alpha+\kappa\sin^2\alpha\cos^2\alpha) + \frac{3\bar{y}^2}{r_2^5}[(3-22\sin^2\alpha\cos^2\alpha)-\kappa\cos 4\alpha - 2\kappa^2\sin^2\alpha\cos^2\alpha] + \frac{3\sin^2 2\alpha\sin^2\alpha}{2r_2^5}(\kappa^2-1)(y_2-\xi_2)^2 + \frac{60H}{r_2^7}[-8H\sin^2 2\alpha(9-16\cos^2\alpha) + \bar{y}^2(-2+7\sin^2 2\alpha-4\sin^2\alpha-\kappa\sin^2 2\alpha)] + \frac{3360H\sin^2\alpha}{r_2^9}(4H\sin^2\alpha-\bar{y}^2\cos 2\alpha) + \frac{3}{2}\sin^2 2\alpha T_1\right\}$$

$$K_{23} = \frac{\mu\sin\alpha}{4\pi(\kappa+1)}\left\{\frac{8\cos^3\alpha}{r_2^3}(4-\kappa) - \frac{24H\cos 2\alpha\cos\alpha}{r_2^5}(10-\kappa) + \frac{6\bar{y}^2\cos^3\alpha}{r_2^5}(-7+4\kappa-\kappa^2) + \frac{24\cos^2\alpha}{r_2^5}(y_2-\xi_2)[2h+(y_2+\xi_2)\cos\alpha] + \frac{3\sin^2 2\alpha\cos\alpha}{2r_2^5}(y_2-\xi_2)^2(\kappa^2-1) + \frac{120H\cos\alpha}{r_2^7}[-12H\sin^2\alpha+\bar{y}^2\cos 2\alpha(4-\kappa)] + \frac{1680H^2\bar{y}^2\sin 2\alpha\sin\alpha}{r_2^9} - \frac{120H}{r_2^7}\cdot(y_2-\xi_2)\left(3\cos 2\alpha+\frac{28H\sin^2\alpha}{r_2^7}\right)\cdot[2h+(y_2+\xi_2)\cos\alpha]+6\cos^3\alpha T_1\right\}$$

$$K_{33} = \frac{\mu}{4\pi(\kappa+1)}\left\{\frac{4}{r_1^3}-\frac{4}{r_2^3}(1-2\cos^4\alpha+2\kappa\cos^4\alpha) - \frac{12H}{r_2^5}[2(1+10\cos^2\alpha-14\cos^4\alpha)+\kappa\sin^2\alpha] + \frac{6\bar{y}^2\cos^4\alpha}{r_2^5}(-3+4\kappa-\kappa^2) + \frac{3\sin^2 2\alpha\cos^2\alpha}{2r_2^5}\cdot(\kappa^2-1)(y_2-\xi_2)^2 + \frac{240H\sin^2\alpha}{r_2^7}\cdot[4H(5\cos^2\alpha-2)+(\kappa-1)\bar{y}^2\cos^2\alpha] + \frac{13440H^3\sin^4\alpha}{r_2^9}+6\cos^4\alpha T_1\right\}$$

where

$$\kappa = 3-4\nu$$

$$T_1 = (\kappa^2-1)\left[\frac{1}{r_2r_4^2}-\frac{2\sin^2\alpha}{r_2^2r_4^2}\left(\frac{2}{r_4}+\frac{1}{r_2}\right)(y_2-\xi_2)^2 + \frac{\sin^4\alpha}{r_2^3r_4^2}\left(\frac{1}{r_2^2}+\frac{2}{r_2r_4}+\frac{2}{r_4^2}\right)(y_2-\xi_2)^4\right]$$

$$T_2 = (\kappa^2-1)(y_2-\xi_2)\left[\frac{1}{r_2^2r_4^2}\left(\frac{1}{r_2}+\frac{2}{r_4}\right) - \frac{\sin^2\alpha}{r_2^3r_4^2}\left(\frac{1}{r_2^2}+\frac{2}{r_2r_4}+\frac{2}{r_4^2}\right)(y_2-\xi_2)^2\right]$$

$$T_3 = (\kappa^2-1)\left[\frac{1}{r_2r_4^2}-\frac{\bar{y}^2\sin^2\alpha}{r_2^3r_4^2}\left(\frac{1}{r_2^2}+\frac{2}{r_2r_4}+\frac{2}{r_4^2}\right)(y_2-\xi_2)^2\right]$$

$$\bar{y} = y_1-\xi_1$$

$$r_1^2 = (y_1-\xi_1)^2+(y_2-\xi_2)^2$$

$$r_2^2 = \bar{y}^2+(y_2-\xi_2)^2+4H$$

$$r_4 = r_2+2h+(y_2+\xi_2)\cos\alpha$$

$$H = h^2+h(y_2+\xi_2)\cos\alpha+y_2\xi_2\cos^2\alpha$$

The reciprocal theorem requires that $K_{ij}(y, \xi) = K_{ji}(\xi, y)$, and this relation determines the remaining elements of K_{ij}.

The displacements in the elastic half-space are obtained by using (4), which can be written as follows:

$$u_i(\mathbf{x}) = \int_S \bar{K}_{in}(\mathbf{x}, \boldsymbol{\eta}) b_n(\boldsymbol{\eta})\, d\boldsymbol{\eta}$$

where

$$\bar{K}_{in}(\mathbf{x}, \boldsymbol{\eta}) = C_{jlmn} n_m \frac{\partial G_{ij}}{\partial \eta_l}(\mathbf{x}, \boldsymbol{\eta})$$

The terms $\bar{K}_{in}$ relative to the half-space coordinate system x_i are listed below:

$$\bar{K}_{i1}(\mathbf{x}, \boldsymbol{\eta}) = \mu\left[-\sin\alpha\left(\frac{\partial G_{i1}}{\partial \eta_2} + \frac{\partial G_{i2}}{\partial \eta_1}\right) + \cos\alpha\left(\frac{\partial G_{i1}}{\partial \eta_3} + \frac{\partial G_{i3}}{\partial \eta_1}\right)\right]$$

$$\bar{K}_{i2}(\mathbf{x}, \boldsymbol{\eta}) = \mu\left[-\sin 2\alpha\left(\frac{\partial G_{i2}}{\partial \eta_2} - \frac{\partial G_{i3}}{\partial \eta_3}\right) + \cos 2\alpha\left(\frac{\partial G_{i3}}{\partial \eta_2} + \frac{\partial G_{i2}}{\partial \eta_3}\right)\right]$$

$$\bar{K}_{i3}(\mathbf{x}, \boldsymbol{\eta}) = \lambda \frac{\partial G_{ij}}{\partial \eta_j} + 2\mu\left[\sin^2\alpha \frac{\partial G_{i2}}{\partial \eta_2} + \cos^2\alpha \frac{\partial G_{i3}}{\partial \eta_3} - \sin\alpha\cos\alpha\left(\frac{\partial G_{i2}}{\partial \eta_3} + \frac{\partial G_{i3}}{\partial \eta_2}\right)\right]$$

The derivatives of the Green's function are as follows:

$$\frac{\partial G_{ij}}{\partial \eta_n} = \frac{1}{16\pi\mu(1-\nu)}\left\{-(3-4\nu)\frac{\delta_{ij}}{R_1^2}\frac{\partial R_1}{\partial \eta_n} - \frac{\delta_{ij}}{R_2^2}\frac{\partial R_2}{\partial \eta_n} - \left[\frac{1}{R_1^3} + \frac{(3-4\nu)}{R_2^3}\right] \cdot [\delta_{in}(x_j - \eta_j) + \delta_{jn}(x_i - \eta_i)] - 3(x_i - \eta_i)(x_j - \eta_j)\left[\frac{1}{R_1^4}\frac{\partial R_1}{\partial \eta_n} + \frac{(3-4\nu)}{R_2^4}\frac{\partial R_2}{\partial \eta_n}\right] + \frac{2x_2\delta_{2n}\delta_{ij}}{R_2^3} - \frac{6x_2\eta_2\delta_{ij}}{R_2^4}\frac{\partial R_2}{\partial \eta_n} + \frac{6x_2}{R_2^5}[\delta_{in}\eta_2(x_j - \eta_j) + \delta_{jn}\eta_2(x_i - \eta_i) - \delta_{2n}(x_i - \eta_i)(x_j - \eta_j)] + \frac{30x_2\eta_2}{R_2^6}\frac{\partial R_2}{\partial \eta_n} \cdot (x_i - \eta_i)(x_j - \eta_j) - 4(1-\nu)(1-2\nu)\frac{\delta_{ij}}{\bar{R}_2^2}\frac{\partial \bar{R}_2}{\partial \eta_n} + \frac{4}{R_2\bar{R}_2^2}(1-\nu)(1-2\nu)[\delta_{in}(x_j - \eta_j) + \delta_{jn}(x_i - \eta_i)] + 4(1-\nu)(1-2\nu)(x_i - \eta_i)(x_j - \eta_j) \cdot \left[\frac{1}{R_2\bar{R}_2^2}\frac{\partial R_2}{\partial \eta_n} + \frac{1}{R_2\bar{R}_2^3}\frac{\partial \bar{R}_2}{\partial \eta_n}\right]\right\} \quad i, j = 1, 3$$

$$\frac{\partial G_{2j}}{\partial \eta_n} = \frac{1}{16\pi\mu(1-\nu)}\left\{-\left[\frac{1}{R_1^3} + \frac{(3-4\nu)}{R_2^3}\right] \cdot [\delta_{2n}(x_j - \eta_j) + \delta_{jn}(x_2 - \eta_2)] - \frac{3}{R_1^4}\frac{\partial R_1}{\partial \eta_n}(x_2 - \eta_2)(x_j - \eta_j) - \frac{3(3-4\nu)}{R_2^4}\frac{\partial R_2}{\partial \eta_n}(x_2 - \eta_2)(x_j - \eta_j) + \frac{6x_2}{R_2^5}[\delta_{jn}\eta_2(x_2 + \eta_2) - \delta_{2n}(x_j - \eta_j) \cdot (x_2 + \eta_2) - \delta_{2n}\eta_2(x_j - \eta_j)] + \frac{30x_2\eta_2}{R_2^6}\frac{\partial R_2}{\partial \eta_n}(x_2 + \eta_2)(x_j - \eta_j) - \frac{4\delta_{jn}}{R_2\bar{R}_2}(1-\nu)(1-2\nu) - 4(1-\nu) \cdot (1-2\nu)(x_j - \eta_j)\left(\frac{1}{R_2^2\bar{R}_2}\frac{\partial R_2}{\partial \eta_n} + \frac{1}{R_2\bar{R}_2^2}\frac{\partial \bar{R}_2}{\partial \eta_n}\right)\right\} \quad j = 1, 3$$

$$\frac{\partial G_{i2}}{\partial \eta_n} = \frac{1}{16\pi\mu(1-\nu)}\left\{-\left(\frac{1}{R_1^3} + \frac{(3-4\nu)}{R_2^3}\right) \cdot [\delta_{2n}(x_i - \eta_i) + \delta_{in}(x_2 - \eta_2)] - \frac{3}{R_1^4}\frac{\partial R_1}{\partial \eta_n}(x_2 - \eta_2)(x_i - \eta_i) - \frac{3(3-4\nu)}{R_2^4}\frac{\partial R_2}{\partial \eta_n}(x_2 - \eta_2)(x_i - \eta_i) + \frac{6x_2}{R_2^5}[\delta_{2n}(x_2 + \eta_2)(x_i - \eta_i) + \delta_{2n}\eta_2(x_i - \eta_i) - \delta_{in}\eta_2(x_2 + \eta_2)] - \frac{30x_2\eta_2}{R_2^6}\frac{\partial R_2}{\partial \eta_n}(x_2 + \eta_2)(x_i - \eta_i) + \frac{4\delta_{in}}{R_2\bar{R}_2}(1-\nu)(1-2\nu) + 4(1-\nu)(1-2\nu)(x_i - \eta_i) \cdot \left(\frac{1}{R_2^2\bar{R}_2}\frac{\partial R_2}{\partial \eta_n} + \frac{1}{R_2\bar{R}_2^2}\frac{\partial \bar{R}_2}{\partial \eta_n}\right)\right\} \quad i = 1, 3$$

$$\frac{\partial G_{22}}{\partial \eta_n} = \frac{1}{16\pi\mu(1-\nu)} \left\{ -\frac{(3-4\nu)}{R_1^2}\frac{\partial R_1}{\partial \eta_n} - \frac{2\delta_{2n}}{R_1^3}(x_2-\eta_2) - \frac{3}{R_1^4}\frac{\partial R_1}{\partial \eta_n}(x_2-\eta_2) - \frac{1}{R_2^2}\frac{\partial R_2}{\partial \eta_n}[8(1-\nu)^2-(3-4\nu)] + \frac{2\delta_{2n}}{R_2^3} \cdot [(3-4\nu)(x_2+\eta_2)-x_2] - \frac{3}{R_2^4}\frac{\partial R_2}{\partial \eta_n} \cdot [(3-4\nu)(x_2+\eta_2)^2 - 2x_2\eta_2] + \frac{6\delta_{2n}x_2}{R_2^5}(x_2+\eta_2)^2 + \frac{12\delta_{2n}x_2\eta_2}{R_2^5}(x_2+\eta_2) - \frac{30x_2\eta_2}{R_2^6}\frac{\partial R_2}{\partial \eta_n}(x_2+\eta_2)^2 \right\}$$

where

$$R_1 = [(x_1-\eta_1)^2 + (x_2-\eta_2)^2 + (x_3-\eta_3)^2]^{1/2}$$

$$R_2 = [(x_1-\eta_1)^2 + (x_2+\eta_2) + (x_3-\eta_3)^2]^{1/2}$$

$$\bar{R}_2 = R_2 + x_2 + \eta_2$$

Acknowledgments. This work has been supported jointly by the National Science Foundation and the U.S. Geological Survey through NSF grant EAR-8707392. Ross Stein provided the data for the Borah Peak and Whittier Narrows earthquakes. Paul Segall provided the data for the Parkfield earthquake. It is a pleasure to acknowledge their help. Thoughtful comments by reviewers Ruth Harris and Stephen Martel and by Associate Editor Jack Boatwright substantially improved the manuscript. In addition, we are grateful to Alan Rubin for pointing out an error in the sign of the normal relative displacement caused by slip.

REFERENCES

Aki, K., Origin of the seismic gap: What initiates and stops a rupture propagation along a plate boundary?, in Proceedings of Conference VI, Methodology for Identifying Seismic Gaps and Soon-to-Break Gaps, 1978, *U.S. Geol. Surv. Open File Rep., 78-943*, 3–46, 1978.

Archuleta, R. J., and S. M. Day, Dynamic rupture in a layered medium: The 1966 Parkfield earthquake, *Bull. Seismol. Soc. Am., 70*, 671–689, 1980.

Barrientos, S. E., R. S. Stein, and S. N. Ward, Comparison of the 1959 Hebgen Lake, Montana and the 1983 Borah Peak, Idaho, earthquakes from geodetic observations, *Bull. Seismol. Soc. Am., 77*, 784–808, 1987.

Chinnery, M. A., The deformation of the ground around surface faults, *Bull. Seismol. Soc. Am., 51*, 355–372, 1961.

Davis, T. L., J. Namson, and R. F. Yerkes, A cross section of Los Angeles basin: Seismically active fold and thrust belt, the Whittier Narrows earthquake and earthquake hazard along the northern edge of the Los Angeles basin, *J. Geophys. Res., 94*, 9644–9664, 1989.

Dmowska, R., and B. V. Kostrov, A shearing crack in a semi-space under plane strain conditions, *Arch. Mech., 25*, 421–440, 1973.

Dmowska, R., and J. R. Rice, Fracture theory and its seismological applications, in *Continuum Theories in Solid Earth Physics*, edited by R. Teisseyre, pp. 187–255, Polish Scientific, Warsaw, 1986.

Doser, D. I., and R. B. Smith, Source parameters of the October 28, 1983 Borah Peak, Idaho, earthquake from body wave analysis, *Bull. Seismol. Soc. Am., 75*, 1041–1051, 1985.

Eaton, J. P., M. E. O'Neill, and J. M. Murdock, Aftershocks of the 1966 Parkfield-Cholame, California earthquake: A detailed study, *Bull. Seismol. Soc. Am., 60*, 1151–1197, 1970.

Eshelby, J. D., The determination of the elastic field of an ellipsoidal inclusion, and related problems, *Proc. R. Soc. London, Ser. A, 241*, 276–396, 1957.

Husseini, M. I., D. B. Jovanovich, M. J. Randall, and L. B. Freund, The fracture energy of earthquakes, *Geophys. J. R. Astron. Soc., 43*, 367–385, 1975.

King, N. E., P. Segall, and W. Prescott, Geodetic measurements near Parkfield, California, 1959–1984, *J. Geophys. Res., 92*, 2474–2766, 1987.

Kostrov, B. V., and S. Das, Evaluation of stress and displacement fields due to an elliptical plane shear crack, *Geophys. J. R. Astron. Soc., 78*, 19–33, 1984.

Lee, J. C., and L. M. Keer, Study of a three-dimensional crack terminating at an interface, *J. Appl. Mech., 108*, 311–316, 1986.

Lee, J. C., T. N. Farris, and L. M. Keer, Stress intensity factors for cracks of arbitrary shape near an interfacial boundary, *Eng. Fract. Mech., 27*, 27–41, 1987.

Li, V., Mechanics of shear rupture applied to earthquake zones, in *Rock Fracture Mechanics and Geophysics*, edited by B. Atkinson, Academic, pp. 351–428, Academic, San Diego, Calif., 1987.

Lin, J., and R. S. Stein, Coseismic folding, earthquake recurrence, and the 1987 source mechanism at Whittier Narrows, Los Angeles basin, California, *J. Geophys. Res., 94*, 9614–9632, 1989.

Mansinha, L., and D. E. Smylie, The displacement fields on inclined faults, *Bull. Seismol. Soc. Am., 61*, 1433–1440, 1971.

Martel, S. J., and D. D. Pollard, Mechanics of slip and fracture along small faults and simple strike-slip fault zones in granite rock, *J. Geophys. Res., 94*, 9417–9428, 1989.

Mindlin, R. D., Force at a point in the interior of a semi-infinite solid, *Physics, 7*, 195–202, 1936.

Mindlin, R. D., Force at a point in the interior of a semi-infinite solid, *Proc. Midwest. Conf. Solid Mech., 1st*, 56–59, 1955.

Mindlin, R. D., and D. H. Cheng, Nuclei of strain in the semi-infinite solid, *J. Appl. Phys., 21*, 926–933, 1950.

Murakami, Y. (Ed.), *Stress Intensity Factors Handbook*, vol. 2, Pergamon, New York, 1987.

Murakami, Y., and S. Nemat-Nasser, Growth and stability of interacting surface flaws of arbitrary shape, *Eng. Fract. Mech., 17*, 193–210, 1983.

Rice, J. R., Mathematical analysis in the mechanics of fracture, in *Fracture: An Advanced Treatise*, vol. 2, edited by H. Liebowitz, pp. 191–311, Academic, San Diego, Calif., 1968.

Rice, J. R., The mechanics of earthquake rupture, in Physics of the Earth's Interior, edited by A. M. Dziewonski and E. Boschi, *Proc. Int. School Phys. Enrico Fermi, 78*, 555–649, 1980.

Rice, J. R., Constitutive relations for fault slip and earthquake instabilities, *Pure Appl. Geophys., 121*, 443–475, 1983.

Richins, W. D., R. B. Smith, C. J. Lanser, J. E. Zollweg, J. T. King, and J. C. Pechmann, The 1983 Borah Peak, Idaho, earthquake: Relationship of aftershocks to mainshock, surface faulting, and regional tectonics, in Workshop XXVIII on the Borah Peak Earthquake, *U.S. Geol. Surv., Open File Rep. 85-290*, 285–310, 1985.

Rudnicki, J. W., Fracture mechanics applied to the earth's crust, *Annu. Rev. Earth Planet. Sci., 8*, 489–525, 1980.

Segall, P., and R. Harris, Earthquake deformation cycle on the San Andreas fault near Parkfield, California, *J. Geophys. Res., 92*, 10,511–10,525, 1987.

Smith, S. W., and M. Wyss, Displacement on the San Andreas fault subsequent to the 1966 Parkfield earthquake, *Bull. Seismol. Soc. Am., 58*, 1955–1973, 1968.

Stein, R. S., and S. E. Barrientos, High-angle normal faulting in the intermountain seismic belt: Geodetic investigation of the 1983 Borah Peak, Idaho earthquakes, *J. Geophys. Res., 90*, 11,355–11,366, 1985.

Steketee, J. A., Some geophysical applications of the elasticity theory of dislocations, *Can. J. Phys., 36*, 1168–1198, 1958.

Stuart, W. D., R. J. Archuleta, and A. G. Lindh, Forecast model for moderate earthquakes near Parkfield, California, *J. Geophys. Res., 90*, 592–604, 1985.

Tsai, Y.-B., and K. Aki, Simultaneous determination of the seismic

moment and attenuation of seismic surface waves, *Bull. Seismol. Soc. Am.*, *59*, 275–287, 1969.
Wong, T.-F., Shear fracture energy of Westerly granite from post-failure behavior, *J. Geophys. Res.*, *87*, 990–1000, 1982.
Wong, T.-F., On the normal stress dependence of the shear fracture energy, in Earthquake Source Mechanics *Geophys. Monogr. Ser.*, vol. 37, edited by S. Das, J. Boatwright, and C. H. Scholz, pp. 1–11, AGU, Washington, D. C., 1986.

L. M. Keer, C. H. Kuo, J. W. Rudnicki, and M. Wu, Department of Civil Engineering, Northwestern University, Evanston, IL, 60208-3109.

(Received August 2, 1990;
revised February 27, 1991;
accepted April 8, 1991.)